

COMPREHENSIVE INORGANIC CHEMISTRY III

VOLUME 4



EDITORS IN CHIEF
JAN REEDIJK & KENNETH R. POEPELMEIER

SECTION EDITORS
PAT WOODWARD AND P. SHIV HALASYAMANI



COMPREHENSIVE INORGANIC CHEMISTRY III

COMPREHENSIVE INORGANIC CHEMISTRY III

EDITORS IN CHIEF

Jan Reedijk

Leiden Institute of Chemistry, Leiden University, Leiden, the Netherlands

Kenneth R. Poeppelmeier

Department of Chemistry, Northwestern University, Evanston, IL, United States

VOLUME 4

Solid State Inorganic Chemistry

VOLUME EDITORS

Pat Woodward

*Department of Chemistry and Biochemistry, Ohio State University,
Columbus, OH, United States*

P. Shiv Halasyamani

Department of Chemistry, University of Houston, Houston, TX, United States



Amsterdam • Boston • Heidelberg • London • New York • Oxford
Paris • San Diego • San Francisco • Singapore • Sydney • Tokyo

Elsevier
Radarweg 29, PO Box 211, 1000 AE Amsterdam, Netherlands
The Boulevard, Langford Lane, Kidlington, Oxford OX5 1GB, United Kingdom
50 Hampshire Street, 5th Floor, Cambridge MA 02139, United States

Copyright © 2023 Elsevier Ltd. All rights reserved

No part of this publication may be reproduced or transmitted in any form or by any means, electronic or mechanical, including photocopying, recording, or any information storage and retrieval system, without permission in writing from the publisher. Details on how to seek permission, further information about the Publisher's permissions policies and our arrangements with organizations such as the Copyright Clearance Center and the Copyright Licensing Agency, can be found at our website: www.elsevier.com/permissions.

This book and the individual contributions contained in it are protected under copyright by the Publisher (other than as may be noted herein).

Notices

Knowledge and best practice in this field are constantly changing. As new research and experience broaden our understanding, changes in research methods, professional practices, or medical treatment may become necessary.

Practitioners and researchers may always rely on their own experience and knowledge in evaluating and using any information, methods, compounds, or experiments described herein. In using such information or methods they should be mindful of their own safety and the safety of others, including parties for whom they have a professional responsibility.

To the fullest extent of the law, neither the Publisher nor the authors, contributors, or editors, assume any liability for any injury and/or damage to persons or property as a matter of products liability, negligence or otherwise, or from any use or operation of any methods, products, instructions, or ideas contained in the material herein.

Library of Congress Cataloging-in-Publication Data

A catalog record for this book is available from the Library of Congress

British Library Cataloguing-in-Publication Data

A catalogue record for this book is available from the British Library

ISBN 978-0-12-823144-9

For information on all publications visit our website at
<http://store.elsevier.com>



Publisher: Oliver Walter
Acquisitions Editors: Clodagh Holland-Borosh and Blerina Osmanaj
Content Project Manager: Pamela Sadhukhan
Associate Content Project Manager: Abraham Lincoln Samuel
Designer: Victoria Pearson Esser

CONTENTS OF VOLUME 4

<i>Editor Biographies</i>	<i>vii</i>
<i>Volume Editors</i>	<i>ix</i>
<i>Contributors to Volume 4</i>	<i>xv</i>
<i>Preface</i>	<i>xix</i>
4.01 Introduction: Solid state inorganic chemistry <i>P Shiv Halasyamani and Patrick M Woodward</i>	1
4.02 Inorganic nonlinear optical materials <i>Chunmei Huang, Fangfang Zhang, and Shilie Pan</i>	3
4.03 Thermoelectric materials <i>Philip Yox, Gayatri Viswanathan, Arka Sarkar, Jian Wang, and Kirill Kovnir</i>	45
4.04 Non-oxide p-block (semi-)metal chalcogenide cage compounds <i>Stefanie Dehnen and Niklas Rinn</i>	80
4.05 Piezoelectric and ferroelectric materials: Fundamentals, recent progress, and applications <i>Zenghui Liu, Hua Wu, Wei Ren, and Zuo-Guang Ye</i>	135
4.06 Intermetallic materials <i>Oliver Janka</i>	172
4.07 Critical charge transfer pairs in intermetallic superconductors <i>Ranuri S Dissanayaka Mudiyansele, Tomasz Klimczuk, and Weiwei Xie</i>	217
4.08 Magnetic materials <i>Michael Shatruk and Judith K Clark</i>	236
4.09 Luminescence in the solid state <i>Shruti Hariyani and Jakoah Brgoch</i>	262
4.10 Battery materials <i>Zachery WB Iton, Seong Shik Kim, Eshaan S Patheria, Michelle D Qian, Skyler D Ware, and Kimberly A See</i>	308
4.11 The chemistry of quantum materials <i>Tyrel M McQueen</i>	364
4.12 High pressure chemistry <i>Ulrich Schwarz, Kristina Spektor, and Ulrich Häussermann</i>	376

4.13	Mixed anion materials <i>Tong Zhu, Daichi Kato, Shenghan Gao, and Hiroshi Kageyama</i>	431
4.14	The zoology of two-dimensional van der waals materials <i>AJ Williams and JE Goldberger</i>	449
4.15	A practical guide to Three-dimensional halide perovskites: Structure, synthesis, and measurement <i>Kurt P Lindquist, Julian A Vigil, Alexander C Su, and Hemamala I Karunadasa</i>	499
4.16	Solid state inorganic color pigments: Ancient to modern <i>Jun Li, L Sandhya Kumari, and MA Subramanian</i>	560
4.17	Photoelectrochemical materials for solar energy conversion <i>Shaun O'Donnell, Jessica Chestnut, Magnus Pauly, and Paul A Maggard</i>	594
4.18	High temperature hydrothermal synthesis of inorganic compounds <i>Joseph W Kolis and Colin D McMillen</i>	628
4.19	Solid-state electrolytes for lithium-ion batteries <i>Sanoop Palakkathodi Kammampata, Mohammad Akbari Garakani, Zheyu Zhang, and Venkataraman Thangadurai</i>	658
4.20	High pressure studies of transition metal oxides <i>Masaki Azuma, Ikuya Yamada, Kazunari Yamaura, Alexei A Belik, Takafumi Yamamoto, and Masayuki Fukuda</i>	681

EDITOR BIOGRAPHIES

Editors in Chief

Jan Reedijk



Jan Reedijk (1943) studied chemistry at Leiden University where he completed his Ph.D. (1968). After a few years in a junior lecturer position at Leiden University, he accepted a readership at Delft University of Technology in 1972. In 1979 he accepted a call for Professor of Chemistry at Leiden University. After 30 years of service, he retired from teaching in 2009 and remained as an emeritus research professor at Leiden University. In Leiden he has acted as Chair of the Department of Chemistry, and in 1993 he became the Founding Director of the Leiden Institute of Chemistry.

His major research activities have been in Coordination Chemistry and Bioinorganic Chemistry, focusing on biomimetic catalysis, molecular materials, and medicinal inorganic chemistry. Jan Reedijk was elected member of the Royal Netherlands Academy of Sciences in 1996 and he was knighted by the Queen of the Netherlands to the order of the Dutch Lion (2008). He is also lifetime member of the Finnish Academy of Sciences and Letters and of Academia Europaea. He has held visiting professorships in Cambridge (UK), Strasbourg (France), Münster (Germany), Riyadh (Saudi Arabia), Louvain-la-Neuve (Belgium), Dunedin (New Zealand), and Torun (Poland). In 1990 he served as President of the Royal Netherlands Chemical Society.

He has acted as the Executive Secretary of the International Conferences of Coordination Chemistry (1988–2012) and served IUPAC in the Division of Inorganic Chemistry, first as a member and later as (vice/past) president between 2005 and 2018. After his university retirement he remained active as research consultant and in IUPAC activities, as well as in several editorial jobs. For Elsevier, he acted as Editor-in-Chief of the *Reference Collection in Chemistry* (2013–2019), and together with Kenneth R. Poeppelmeier for *Comprehensive Inorganic Chemistry II* (2008–2013) and *Comprehensive Inorganic Chemistry III* (2019–present). From 2018 to 2020, he co-chaired the worldwide celebrations of the International Year of the Periodic Table 2019.

Jan Reedijk has published over 1200 papers (1965–2022; cited over 58000 times; $h = 96$). He has supervised 90 Ph.D. students, over 100 postdocs, and over 250 MSc research students.

Kenneth R. Poeppelmeier



Kenneth R. Poeppelmeier (1949) completed his undergraduate studies in chemistry at the University of Missouri (1971) and then volunteered as an instructor at Samoa College—United States Peace Corps in Western Samoa (1971–1974). He completed his Ph.D. (1978) in Inorganic Chemistry with John Corbett at Iowa State University (1978).

He joined the catalysis research group headed by John Longo at Exxon Research and Engineering Company, Corporate Research–Science Laboratories (1978–1984), where he collaborated with the reforming science group and Exxon Chemicals to develop the first zeolite-based light naphtha reforming catalyst. In 1984 he joined the Chemistry Department at Northwestern University and the recently formed Center for Catalysis and Surface Science (CCSS). He is the Charles E. and Emma H. Morrison Professor of Chemistry at Northwestern University and a NAISE Fellow joint with Northwestern University and the Chemical Sciences and Engineering Division, Argonne National Laboratory. Leadership positions held include Director, CCSS, Northwestern University; Associate Division Director for Science, Chemical Sciences and Engineering Division, Argonne National Laboratory; President of the Chicago Area Catalysis Club; Associate Director, NSF Science and Technology Center for Superconductivity; and Chairman of the ACS Solid State Subdivision of the Division of Inorganic Chemistry.

His major research activities have been in Solid State and Inorganic Materials Chemistry focusing on heterogeneous catalysis, solid state chemistry, and materials chemistry. His awards include National Science Council of Taiwan Lecturer (1991); Dow Professor of Chemistry (1992–1994); AAAS Fellow, the American Association for the Advancement of Science (1993); JSPS Fellow, Japan Society for the Promotion of Science (1997); Natural Science Foundation of China Lecturer (1999); National Science Foundation Creativity Extension Award (2000)

and 2022); Institut Universitaire de France Professor (2003); Chemistry Week in China Lecturer (2004); Lecturer in Solid State Chemistry, China (2005); Visitantes Distinguidos, Universidad Complutense Madrid (2008); Visiting Professor, Chinese Academy of Sciences (2011); 20 years of Service and Dedication Award to Inorganic Chemistry (2013); Elected foreign member of Spanish National Academy: Real Academia de Ciencia, Exactas, Fisicas y Naturales (2017); Elected Honorary Member of the Royal Society of Chemistry of Spain (RSEQ) (2018); and the TianShan Award, Xinjiang Uygur Autonomous Region of China (2021).

He has organized and was Chairman of the Chicago Great Lakes Regional ACS Symposium on Synthesis and Processing of Advanced Solid State Materials (1987), the New Orleans National ACS Symposium on Solid State Chemistry of Heterogeneous Oxide Catalysis, Including New Microporous Solids (1987), the Gordon Conference on Solid State Chemistry (1994) and the First European Gordon Conference on Solid State Chemistry (1995), the Spring Materials Research Society Symposium on Environmental Chemistry (1995), the Advisory Committee of Intense Pulsed Neutron Source (IPNS) Program (1996–1998), the Spring Materials Research Society Symposium on Perovskite Materials (2003), the 4th International Conference on Inorganic Materials, University of Antwerp (2004), and the Philadelphia National ACS Symposium on Homogeneous and Heterogeneous Oxidation Catalysis (2004).

He has served on numerous Editorial Boards, including *Chemistry of Materials*, *Journal of Alloys and Compounds*, *Solid State Sciences*, *Solid State Chemistry*, and *Science China Materials*, and has been a co-Editor for *Structure and Bonding*, an Associate Editor for *Inorganic Chemistry*, and co-Editor-in-Chief with Jan Reedijk for *Comprehensive Inorganic Chemistry II* (published 2013) and *Comprehensive Inorganic Chemistry III* (to be published in 2023). In addition, he has served on various Scientific Advisory Boards including for the World Premier International Research Center Initiative and Institute for Integrated Cell-Material Sciences Kyoto University, the European Center SOPRANO on Functional Electronic Metal Oxides, the Kyoto University Mixed-Anion Project, and the Dresden Max Planck Institute for Chemistry and Physics.

Kenneth Poeppelmeier has published over 500 papers (1971–2022) and cited over 28000 times (h-index = 84). He has supervised over 200 undergraduates, Ph.D. students, postdocs, and visiting scholars in research.

VOLUME EDITORS

Risto S. Laitinen



Risto S. Laitinen is Professor Emeritus of Chemistry at the University of Oulu, Finland. He received the M.Sc and Ph.D. degrees from Helsinki University of Technology (currently Aalto University). His research interests are directed to synthetic, structural, and computational chemistry of chalcogen compounds focusing on selenium and tellurium. He has published 250 peer-reviewed articles and 15 book chapters and has edited 2 books: *Selenium and Tellurium Reagents: In Chemistry and Materials Science* with Raija Oilunkaniemi (Walther de Gruyter, 2019) and *Selenium and Tellurium Chemistry: From Small Molecules to Biomolecules and Materials* with Derek Woollins (Springer, 2011). He has also written 30 professional and popular articles in chemistry. He is the Secretary of the Division of Chemical Nomenclature and Structure Representation, International Union of Pure and Applied Chemistry, for the term 2016–2023. He served as Chair of the Board of Union of Finnish University Professors in 2007–2010. In 2017, Finnish Cultural Foundation (North Ostrobothnia regional fund) gave him an award for excellence in his activities for science and music. He has been a member of Finnish Academy of Science and Letters since 2003.

Vincent L. Pecoraro



Professor Vincent L. Pecoraro is a major contributor in the fields of inorganic, bioinorganic, and supramolecular chemistries. He has risen to the upper echelons of these disciplines with over 300 publications (an h-index of 92), 4 book editorships, and 5 patents. He has served the community in many ways including as an Associate Editor of *Inorganic Chemistry* for 20 years and now is President of the Society of Biological Inorganic Chemistry. Internationally, he has received a Le Studium Professorship, Blaise Pascal International Chair for Research, the Alexander von Humboldt Stiftung, and an Honorary PhD from Aix-Marseille University. His many US distinctions include the 2016 ACS Award for Distinguished Service in the Advancement of Inorganic Chemistry, the 2021 ACS/SCF FrancoAmerican Lectureship Prize, and being elected a Fellow of the ACS and AAAS. He also recently cofounded a Biomedical Imaging company, VIEWaves. In 2022, he was ranked as one of the world's top 1000 most influential chemists.

Zijian Guo



Professor Zijian Guo received his Ph.D. from the University of Padova and worked as a postdoctoral research fellow at Birkbeck College, the University of London. He also worked as a research associate at the University of Edinburgh. His research focuses on the chemical biology of metals and metallodrugs and has authored or co-authored more than 400 peer-reviewed articles on basic and applied research topics. He was awarded the First Prize in Natural Sciences from Ministry of Education of China in 2015, the Luigi Sacconi Medal from the Italian Chemical Society in 2016, and the Outstanding Achievement Award from the Society of the Asian Biological Inorganic Chemistry in 2020. He founded Chemistry and Biomedicine Innovation Center (ChemBIC) in Nanjing University in 2019, and is serving as the Director of ChemBIC since then. He was elected to the Fellow of the Chinese Academy of Sciences in 2017. He served as Associated Editor of *Coord. Chem. Rev* and an editorial board member of several other journals.

Daniel C. Fredrickson



Daniel C. Fredrickson is a Professor in the Department of Chemistry at the University of Wisconsin-Madison. He completed his BS in Biochemistry at the University of Washington in 2000, where he gained his first experiences with research and crystals in the laboratory of Prof. Bart Kahr. At Cornell University, he then pursued theoretical investigations of bonding in intermetallic compounds, the vast family of solid state compounds based on metallic elements, under the mentorship of Profs. Stephen Lee and Roald Hoffmann, earning his Ph.D. in 2005. Interested in the experimental and crystallographic aspects of complex intermetallics, he then carried out postdoctoral research from 2005 to 2008 with Prof. Sven Lidin at Stockholm University. Since starting at UW-Madison in 2009, his research group has created theory-driven approaches to the synthesis and discovery of new intermetallic phases and understanding the origins of their structural features. Some of his key research contributions are the development of the DFT-Chemical Pressure Method, the discovery of isolobal bonds for the generalization of the 18 electron rule to intermetallic phases, models for the emergence of incommensurate modulations in these compounds, and various design strategies for guiding complexity in solid state structures.

Patrick M. Woodward



Professor Patrick M. Woodward received BS degrees in Chemistry and General Engineering from Idaho State University in 1991, an MS in Materials Science, and a Ph.D. in Chemistry from Oregon State University (1996) under the supervision of Art Sleight. After a postdoctoral appointment in the Physics Department at Brookhaven National Laboratory (1996–1998), he joined the faculty at Ohio State University in 1998, where he holds the rank of Professor in the Department of Chemistry and Biochemistry. He is a Fellow of the American Chemical Society (2020) and a recipient of an Alfred P. Sloan Fellowship (2004) and an NSF Career Award (2001). He has co-authored two textbooks: *Solid State Materials Chemistry* and the popular general chemistry textbook, *Chemistry: The Central Science*. His research interests revolve around the discovery of new materials and understanding links between the composition, structure, and properties of extended inorganic and hybrid solids.

P. Shiv Halasyamani

Professor P. Shiv Halasyamani earned his BS in Chemistry from the University of Chicago (1992) and his Ph.D. in Chemistry under the supervision of Prof. Kenneth R. Poeppelmeier at Northwestern University (1996). He was a Postdoctoral Fellow and Junior Research Fellow at Christ Church College, Oxford University, from 1997 to 1999. He began his independent academic career in the Department of Chemistry at the University of Houston in 1999 and has been a Full Professor since 2010. He was elected as a Fellow of the American Association for the Advancement of Science (AAAS) in 2019 and is currently an Associate Editor of the ACS journals *Inorganic Chemistry* and *ACS Organic & Inorganic Au*. His research interests involve the design, synthesis, crystal growth, and characterization of new functional inorganic materials.

Ram Seshadri

Ram Seshadri received his Ph.D. in Solid State Chemistry from the Indian Institute of Science (IISc), Bangalore, working under the guidance of Professor C. N. R. Rao FRS. After some years as a Postdoctoral Fellow in Europe, he returned to IISc as an Assistant Professor in 1999. He moved to the Materials Department (College of Engineering) at UC Santa Barbara in 2002. He was recently promoted to the rank of Distinguished Professor in the Materials Department and the Department of Chemistry and Biochemistry in 2020. He is also the Fred and Linda R. Wudl Professor of Materials Science and Director of the Materials Research Laboratory: A National Science Foundation Materials Research Science and Engineering Center (NSF-MRSEC). His work broadly addresses the topic of structure–composition–property relations in crystalline inorganic and hybrid materials, with a focus on magnetic materials and materials for energy conversion and storage. He is Fellow of the Royal Society of Chemistry, the American Physical Society, and the American Association for the Advancement of Science. He serves as Associate Editor of the journals, *Annual Reviews of Materials Research* and *Chemistry of Materials*.

Serena Cussen

Serena Cussen née Corr studied chemistry at Trinity College Dublin, completing her doctoral work under Yuri Gun'ko. She then joined the University of California, Santa Barbara, working with Ram Seshadri as a postdoctoral researcher. She joined the University of Kent as a lecturer in 2009. She moved to the University of Glasgow in 2013 and was made Professor in 2018. She moved to the University of Sheffield as a Chair in Functional Materials and Professor in Chemical and Biological Engineering in 2018, where she now serves as Department Head. She works on next-generation battery materials and advanced characterization techniques for the structure and properties of nanomaterials. Serena is the recipient of several awards including the *Journal of Materials Chemistry* Lectureship of the Royal Society of Chemistry. She previously served as Associate Editor of Royal Society of Chemistry journal *Nanoscale* and currently serves as Associate Editor for the Institute of Physics journal *Progress in Energy*.

Rutger A. van Santen



Rutger A. van Santen received his Ph.D. in 1971 in Theoretical Chemistry from the University of Leiden, The Netherlands. In the period 1972–1988, he became involved with catalysis research when employed by Shell Research in Amsterdam and Shell Development Company in Houston. In 1988, he became Full Professor of Catalysis at the Technical University Eindhoven. From 2010 till now he is Emeritus Professor and Honorary Institute Professor at Technical University Eindhoven. He is a member of Royal Dutch Academy of Sciences and Arts and Foreign Associate of the United States National Academy of Engineering (NAE). He has received several prestigious awards: the 1981 golden medal of the Royal Dutch Chemical Society; in 1992, the F.G. Chiappetta award of the North American Catalysis Society; in 1997, the Spinoza Award from the Dutch Foundation for Pure and Applied Research; and in 2001, the Alwin Mittasch Medal Dechema, Germany, among others. His main research interests are computational heterogeneous catalysis and complex chemical systems theory. He has published over 700 papers, 16 books, and 22 patents.

Emiel J. M. Hensen



Emiel J. M. Hensen received his Ph.D. in Catalysis in 2000 from Eindhoven University of Technology, The Netherlands. Between 2000 and 2008, he worked at the University of Amsterdam, Shell Research in Amsterdam, and Eindhoven University of Technology on several topics in the field of heterogeneous catalysis. Since July 2009, he is Full Professor of Inorganic Materials and Catalysis at TU/e. He was a visiting professor at the Katholieke Universiteit Leuven (Belgium, 2001–2016) and at Hokkaido University (Japan, 2016). He is principal investigator and management team member of the gravitation program Multiscale Catalytic Energy Conversion, elected member of the Advanced Research Center Chemical Building Blocks Consortium, and chairman of the Netherlands Institute for Catalysis Research (NIOK). Hensen was Head of the Department of Chemical Engineering and Chemistry of Eindhoven University of Technology from 2016 to 2020. Hensen received Veni, Vidi, Vici, and Casmir grant awards from the Netherlands Organisation for Scientific Research. His main interests are in mechanism of heterogeneous catalysis combining experimental and computation studies. He has published over 600 papers, 20 book chapters, and 7 patents.

Artem M. Abakumov



Artem M. Abakumov graduated from the Department of Chemistry at Moscow State University in 1993, received his Ph.D. in Chemistry from the same University in 1997, and then continued working as a Researcher and Vice-Chair of Inorganic Chemistry Department. He spent about 3 years as a postdoctoral fellow and invited professor in the Electron Microscopy for Materials Research (EMAT) laboratory at the University of Antwerp and joined EMAT as a research leader in 2008. Since 2015 he holds a Full Professor position at Skolkovo Institute of Science and Technology (Skoltech) in Moscow, leading Skoltech Center for Energy Science and Technology as a Director. His research interests span over a wide range of subjects, from inorganic chemistry, solid state chemistry, and crystallography to battery materials and transmission electron microscopy. He has extended experience in characterization of metal-ion battery electrodes and electrocatalysts with advanced TEM techniques that has led to a better understanding of charge-discharge mechanisms, redox reactions, and associated structural transformations in various classes of cathode materials on different spatial scales. He has published over 350 papers, 5 book chapters, and 12 patents.

Keith J. Stevenson



Keith J. Stevenson received his Ph.D. in 1997 from the University of Utah under the supervision of Prof. Henry White. Subsequently, he held a postdoctoral appointment at Northwestern University (1997–2000) and a tenured faculty appointment (2000–2015) at the University of Texas at Austin. At present, he is leading the development of a new graduate level university (Skolkovo Institute for Science and Technology) in Moscow, Russia, where he is Provost and the former Director of the Center for Energy Science and Technology (CEST). To date he has published over 325 peer-reviewed publications, 14 patents, and 6 book chapters in this field. He is a recipient of Society of Electroanalytical Chemistry Charles N. Reilly Award (2021).

Evgeny V. Antipov



Evgeny V. Antipov graduated from the Department of Chemistry at Moscow State University in 1981, received his Ph.D. in Chemistry in 1986, DSc degree in Chemistry in 1998, and then continued working at the same University as a Researcher, Head of the Laboratory of Inorganic Crystal Chemistry, Professor, Head of Laboratory of fundamental research on aluminum production, and Head of the Department of Electrochemistry. Since 2018 he also holds a professor position at Skolkovo Institute of Science and Technology (Skoltech) in Moscow. Currently his research interests are mainly focused on inorganic materials for application in batteries and fuel cells. He has published more than 400 scientific articles and 14 patents.

Vivian W.W. Yam



Professor Vivian W.W. Yam is the Chair Professor of Chemistry and Philip Wong Wilson Wong Professor in Chemistry and Energy at The University of Hong Kong. She received both her B.Sc (Hons) and Ph.D. from The University of Hong Kong. She was elected to Member of Chinese Academy of Sciences, International Member (Foreign Associate) of US National Academy of Sciences, Foreign Member of Academia Europaea, Fellow of TWAS, and Founding Member of Hong Kong Academy of Sciences. She was Laureate of 2011 L'Oréal-UNESCO For Women in Science Award. Her research interests include inorganic and organometallic chemistry, supramolecular chemistry, photophysics and photochemistry, and metal-based molecular functional materials for sensing, organic optoelectronics, and energy research.

Also see: <https://chemistry.hku.hk/wwym>.

David L. Bryce



David L. Bryce (B.Sc (Hons), 1998, Queen's University; Ph.D., 2002, Dalhousie University; postdoctoral fellow, 2003–04, NIDDK/NIH) is Full Professor and University Research Chair in Nuclear Magnetic Resonance at the University of Ottawa in Canada. He is the past Chair of the Department of Chemistry and Biomolecular Sciences, a Fellow of the Royal Society of Chemistry, and an elected Fellow of the Royal Society of Canada. His research interests include solid-state NMR of low-frequency quadrupolar nuclei, NMR studies of materials, NMR crystallography, halogen bonding, mechanochemistry, and quantum chemical interpretation of NMR interaction tensors. He is the author of approximately 200 scientific publications and co-author of 1 book. He is the Editor-in-Chief of *Solid State Nuclear Magnetic Resonance* and Section Editor (Magnetic Resonance and Molecular Spectroscopy) for the *Canadian Journal of Chemistry*. He has served as the Chair of Canada's National Ultrahigh-Field NMR Facility for Solids and is a past co-chair of the International Society for Magnetic Resonance conference and of the Rocky Mountain Conference on Magnetic Resonance Solid-State NMR Symposium. His work has been recognized with the Canadian Society for Chemistry Keith Laidler Award and with the Gerhard Herzberg Award of the Canadian Association of Analytical Sciences and Spectroscopy.

Paul R. Raithby



Paul R. Raithby obtained his B.Sc (1973) and Ph.D. (1976) from Queen Mary College, University of London, working for his Ph.D. in structural inorganic chemistry. He moved to the University of Cambridge in 1976, initially as a postdoctoral researcher and then as a faculty member. In 2000, he moved to the University of Bath to take up the Chair of Inorganic Chemistry when he remains to the present day, having been awarded an Emeritus Professorship in 2022. His research interests have spanned the chemistry of transition metal cluster compounds, platinum acetylide complexes and oligomers, and lanthanide complexes, and he uses laboratory and synchrotron-based X-ray crystallographic techniques to determine the structures of the complexes and to study their dynamics using time-resolved photocrystallographic methods.

Angus P. Wilkinson



Angus P. Wilkinson completed his bachelors (1988) and doctoral (1992) degrees in chemistry at Oxford University in the United Kingdom. He spent a postdoctoral period in the Materials Research Laboratory, University of California, Santa Barbara, prior to joining the faculty at the Georgia Institute of Technology as an assistant professor in 1993. He is currently a Professor in both the Schools of Chemistry and Biochemistry, and Materials Science and Engineering, at the Georgia Institute of Technology. His research in the general area of inorganic materials chemistry makes use of synchrotron X-ray and neutron scattering to better understand materials synthesis and properties.

CONTRIBUTORS TO VOLUME 4

Masaki Azuma

Laboratory for Materials and Structures, Tokyo Institute of Technology, Yokohama, Japan

Alexei A Belik

International Center for Materials Nanoarchitectonics (WPI-MANA), National Institute for Materials Science, Tsukuba, Ibaraki, Japan

Jakoah Brgoch

Department of Chemistry and the Texas Center for Superconductivity, University of Houston, Houston, TX, United States

Jessica Chestnut

Department of Chemistry, North Carolina State University, Raleigh, NC, United States

Judith K Clark

Department of Chemistry and Biochemistry, Florida State University, Tallahassee, FL, United States

Stefanie Dehnen

Fachbereich Chemie and Wissenschaftliches Zentrum für Materialwissenschaften, Philipps Universität Marburg, Marburg, Germany

Ranuri S Dissanayaka Mudiyanse

Department of Chemistry and Chemical Biology, Rutgers University, Piscataway, NJ, United States

Masayuki Fukuda

International Center for Materials Nanoarchitectonics (WPI-MANA), National Institute for Materials Science, Tsukuba, Ibaraki, Japan

Shenghan Gao

Department of Energy and Hydrocarbon Chemistry, Graduate School of Engineering, Kyoto University, Nishikyo-ku, Kyoto, Japan

Mohammad Akbari Garakani

Department of Chemistry, University of Calgary, Calgary, AB, Canada

JE Goldberger

The Ohio State University, Columbus, OH, United States

P Shiv Halasyamani

Department of Chemistry, University of Houston, Houston, TX, United States

Shruti Hariyani

Department of Chemistry and the Texas Center for Superconductivity, University of Houston, Houston, TX, United States

Ulrich Häussermann

Department of Materials and Environmental Chemistry, Stockholm University, Stockholm, Sweden

Chunmei Huang

CAS Key Laboratory of Functional Materials and Devices for Special Environments, Xinjiang Technical Institute of Physics & Chemistry, CAS, Xinjiang Key Laboratory of Electronic Information Materials and Devices, Urumqi, China; and Center of Materials Science and Optoelectronics Engineering, University of Chinese Academy of Sciences, Beijing, China

Zachery WB Iton

Department of Applied Physics and Materials Science, California Institute of Technology, Pasadena, CA, United States

Oliver Janka

Universität des Saarlandes, Anorganische Festkörperchemie, Saarbrücken, Germany

Hiroshi Kageyama

Department of Energy and Hydrocarbon Chemistry, Graduate School of Engineering, Kyoto University, Nishikyo-ku, Kyoto, Japan

Sanoop Palakkathodi Kammampata

Department of Chemistry, University of Calgary, Calgary, AB, Canada

Hemamala I Karunadasa

Department of Chemistry, Stanford University, Stanford, CA, United States; and Stanford Institute for Materials and Energy Sciences, SLAC National Accelerator Laboratory, Menlo Park, CA, United States

Daichi Kato

Department of Energy and Hydrocarbon Chemistry, Graduate School of Engineering, Kyoto University, Nishikyo-ku, Kyoto, Japan

Seong Shik Kim

Division of Chemistry and Chemical Engineering, California Institute of Technology, Pasadena, CA, United States

Tomasz Klimczuk

Faculty of Applied Physics and Mathematics and Advanced Materials Center, Gdansk University of Technology, Gdansk, Poland

Joseph W Kolis

Department of Chemistry, Hunter Laboratories, Clemson University, Clemson, SC, United States

Kirill Kovnir

Department of Chemistry, Iowa State University, Ames, IA, United States; and US DOE Ames National Laboratory, Ames, IA, United States

Jun Li

Department of Chemistry, Oregon State University, Corvallis, OR, United States

Kurt P Lindquist

Department of Chemistry, Stanford University, Stanford, CA, United States

Zenghui Liu

Electronic Materials Research Laboratory, Key Laboratory of the Ministry of Education & International Center for Dielectric Research, School of Electronic Science and Engineering, Xi'an Jiaotong University, Xi'an, China

Paul A Maggard

Department of Chemistry, North Carolina State University, Raleigh, NC, United States

Colin D McMillen

Department of Chemistry, Hunter Laboratories, Clemson University, Clemson, SC, United States

Tyrel M McQueen

Department of Chemistry, Johns Hopkins University, Baltimore, MD, United States; Department of Materials Science and Engineering, Johns Hopkins University, Baltimore, MD, United States; and William H. Miller III Department of Physics and Astronomy, Johns Hopkins University, Baltimore, MD, United States

Shaun O'Donnell

Department of Chemistry, North Carolina State University, Raleigh, NC, United States

Shilie Pan

CAS Key Laboratory of Functional Materials and Devices for Special Environments, Xinjiang Technical Institute of Physics & Chemistry, CAS, Xinjiang Key Laboratory of Electronic Information Materials and Devices, Urumqi, China; and Center of Materials Science and Optoelectronics Engineering, University of Chinese Academy of Sciences, Beijing, China

Eshaan S Patheria

Division of Chemistry and Chemical Engineering, California Institute of Technology, Pasadena, CA, United States

Magnus Pauly

Department of Chemistry, North Carolina State University, Raleigh, NC, United States

Michelle D Qian

Division of Chemistry and Chemical Engineering, California Institute of Technology, Pasadena, CA, United States

Wei Ren

Electronic Materials Research Laboratory, Key Laboratory of the Ministry of Education & International Center for Dielectric Research, School of Electronic Science and Engineering, Xi'an Jiaotong University, Xi'an, China

Niklas Rinn

Fachbereich Chemie and Wissenschaftliches Zentrum für Materialwissenschaften, Philipps Universität Marburg, Marburg, Germany

L Sandhya Kumari

Department of Chemistry, Oregon State University, Corvallis, OR, United States

Arka Sarkar

Department of Chemistry, Iowa State University, Ames, IA, United States; and US DOE Ames National Laboratory, Ames, IA, United States

Ulrich Schwarz

Chemische Metallkunde, MPI-CPS, Dresden, Germany

Kimberly A See

Division of Chemistry and Chemical Engineering, California Institute of Technology, Pasadena, CA, United States

Michael Shatruk

Department of Chemistry and Biochemistry, Florida State University, Tallahassee, FL, United States

Kristina Spektor

Inorganic Chemistry, Faculty for Chemistry and Mineralogy, Leipzig University, Leipzig, Germany

Alexander C Su

Department of Chemistry, Stanford University, Stanford, CA, United States

MA Subramanian

Department of Chemistry, Oregon State University, Corvallis, OR, United States

Venkataraman Thangadurai

Department of Chemistry, University of Calgary, Calgary, AB, Canada

Julian A Vigil

Department of Chemistry, Stanford University, Stanford, CA, United States; and Department of Chemical Engineering, Stanford University, Stanford, CA, United States

Gayatri Viswanathan

Department of Chemistry, Iowa State University, Ames, IA, United States; and US DOE Ames National Laboratory, Ames, IA, United States

Jian Wang

Department of Chemistry, Wichita State University, Wichita, KS, United States

Skyler D Ware

Division of Chemistry and Chemical Engineering, California Institute of Technology, Pasadena, CA, United States

AJ Williams

The Ohio State University, Columbus, OH, United States

Patrick M Woodward

Department of Chemistry and Biochemistry, The Ohio State University, Columbus, OH, United States

Hua Wu

Department of Applied Physics, Donghua University, Shanghai, China

Weiwei Xie

Department of Chemistry and Chemical Biology, Rutgers University, Piscataway, NJ, United States

Ikuya Yamada

Department of Materials Science, Graduate School of Engineering, Osaka Metropolitan University, Sakai, Osaka, Japan

Takafumi Yamamoto

Laboratory for Materials and Structures, Tokyo Institute of Technology, Yokohama, Japan

Kazunari Yamaura

International Center for Materials Nanoarchitectonics (WPI-MANA), National Institute for Materials Science, Tsukuba, Ibaraki, Japan

Zuo-Guang Ye

Department of Chemistry and 4D LABS, Simon Fraser University, Burnaby, BC, Canada

Philip Yox

Department of Chemistry, Iowa State University, Ames, IA, United States; and US DOE Ames National Laboratory, Ames, IA, United States

Fangfang Zhang

CAS Key Laboratory of Functional Materials and Devices for Special Environments, Xinjiang Technical Institute of Physics & Chemistry, CAS, Xinjiang Key Laboratory of Electronic Information Materials and Devices, Urumqi, China; and Center of Materials Science and Optoelectronics Engineering, University of Chinese Academy of Sciences, Beijing, China

Zheyu Zhang

Department of Chemistry, University of Calgary, Calgary, AB, Canada

Tong Zhu

Department of Energy and Hydrocarbon Chemistry, Graduate School of Engineering, Kyoto University, Nishikyo-ku, Kyoto, Japan

PREFACE

Comprehensive Inorganic Chemistry III is a new multi-reference work covering the broad area of Inorganic Chemistry. The work is available both in print and in electronic format. The 10 Volumes review significant advances and examines topics of relevance to today's inorganic chemists with a focus on topics and results after 2012.

The work is focusing on new developments, including interdisciplinary and high-impact areas. Comprehensive Inorganic Chemistry III, specifically focuses on main group chemistry, biological inorganic chemistry, solid state and materials chemistry, catalysis and new developments in electrochemistry and photochemistry, as well as on NMR methods and diffractions methods to study inorganic compounds.

The work continues our 2013 work Comprehensive Inorganic Chemistry II, but at the same time adds new volumes on emerging research areas and techniques used to study inorganic compounds. The new work is also highly complementary to other recent Elsevier works in Coordination Chemistry and Organometallic Chemistry thereby forming a trio of works covering the whole of modern inorganic chemistry, most recently COMC-4 and CCC-3. The rapid pace of developments in recent years in all areas of chemistry, particularly inorganic chemistry, has again created many challenges to provide a contemporary up-to-date series.

As is typically the challenge for Multireference Works (MRWs), the chapters are designed to provide a valuable long-standing scientific resource for both advanced students new to an area as well as researchers who need further background or answers to a particular problem on the elements, their compounds, or applications. Chapters are written by teams of leading experts, under the guidance of the Volume Editors and the Editors-in-Chief. The articles are written at a level that allows undergraduate students to understand the material, while providing active researchers with a ready reference resource for information in the field. The chapters are not intended to provide basic data on the elements, which are available from many sources including the original CIC-I, over 50-years-old by now, but instead concentrate on applications of the elements and their compounds and on high-level techniques to study inorganic compounds.

Vol. 1: Synthesis, Structure, and Bonding in Inorganic Molecular Systems; Risto S. Laitinen

In this Volume the editor presents an historic overview of Inorganic Chemistry starting with the birth of inorganic chemistry after Berzelius, and a focus on the 20th century including an overview of "inorganic" Nobel Prizes and major discoveries, like inert gas compounds. The most important trends in the field are discussed in an historic context. The bulk of the Volume consists of 3 parts, i.e., (1) Structure, bonding, and reactivity in inorganic molecular systems; (2) Intermolecular interactions, and (3) Inorganic Chains, rings, and cages. The volume contains 23 chapters.

Part 1 contains chapters dealing with compounds in which the heavy p-block atom acts as a central atom. Some chapters deal with the rich synthetic and structural chemistry of noble gas compounds, low-coordinate p-block elements, biradicals, iron-only hydrogenase mimics, and macrocyclic selenoethers. Finally, the chemistry and application of weakly coordinating anions, the synthesis, structures, and reactivity of carbenes containing non-innocent ligands, frustrated Lewis pairs in metal-free catalysis are discussed. Part 2 discusses secondary bonding interactions that play an important role in the properties of bulk materials. It includes a chapter on the general theoretical considerations of secondary bonding interactions, including halogen and chalcogen bonding. This section is concluded by the update of the host-guest chemistry of the molecules of p-block elements and by a comprehensive review of closed-shell metallophilic interactions. The third part of the Volume is dedicated to chain, ring and cage (or cluster) compounds in molecular inorganic chemistry. Separate

chapters describe the recent chemistry of boron clusters, as well as the chain, ring, and cage compounds of Group 13 and 15, and 16 elements. Also, aromatic compounds bearing heavy Group 14 atoms, polyhalogenide anions and Zintl-clusters are presented.

Vol. 2: Bioinorganic Chemistry and Homogeneous Biomimetic Inorganic Catalysis; Vincent L. Pecoraro and Zijian Guo

In this Volume, the editors have brought together 26 chapters providing a broad coverage of many of the important areas involving metal compounds in biology and medicine. Readers interested in fundamental biochemistry that is assisted by metal ion catalysis, or in uncovering the latest developments in diagnostics or therapeutics using metal-based probes or agents, will find high-level contributions from top scientists. In the first part of the Volume topics dealing with metals interacting with proteins and nucleic acids are presented (e.g., siderophores, metallophores, homeostasis, biomineralization, metal-DNA and metal-RNA interactions, but also with zinc and cobalt enzymes). Topics dealing with iron-sulfur clusters and heme-containing proteins, enzymes dealing with dinitrogen fixation, dihydrogen and dioxygen production by photosynthesis will also be discussed, including bioinspired model systems.

In the second part of the Volume the focus is on applications of inorganic chemistry in the field of medicine: e.g., clinical diagnosis, curing diseases and drug targeting. Platinum, gold and other metal compounds and their mechanism of action will be discussed in several chapters. Supramolecular coordination compounds, metal organic frameworks and targeted modifications of higher molecular weight will also be shown to be important for current and future therapy and diagnosis.

Vol. 3: Theory and Bonding of Inorganic Non-molecular Systems; Daniel C. Fredrickson

This volume consists of 15 chapters that build on symmetry-based expressions for the wavefunctions of extended structures toward models for bonding in solid state materials and their surfaces, algorithms for the prediction of crystal structures, tools for the analysis of bonding, and theories for the unique properties and phenomena that arise in these systems. The volume is divided into four parts along these lines, based on major themes in each of the chapters. These are: Part 1: Models for extended inorganic structures, Part 2: Tools for electronic structure analysis, Part 3: Predictive exploration of new structures, and Part 4: Properties and phenomena.

Vol. 4: Solid State Inorganic Chemistry; P. Shiv Halasyamani and Patrick M. Woodward

In a broad sense the field of inorganic chemistry can be broken down into substances that are based on molecules and those that are based on extended arrays linked by metallic, covalent, polar covalent, or ionic bonds (i.e., extended solids). The field of solid-state inorganic chemistry is largely concerned with elements and compounds that fall into the latter group. This volume contains nineteen chapters covering a wide variety of solid-state inorganic materials. These chapters largely focus on materials with properties that underpin modern technology. Smart phones, solid state lighting, batteries, computers, and many other devices that we take for granted would not be possible without these materials. Improvements in the performance of these and many other technologies are closely tied to the discovery of new materials or advances in our ability to synthesize high quality samples. The organization of most chapters is purposefully designed to emphasize how the exceptional physical properties of modern materials arise from the interplay of composition, structure, and bonding. Not surprisingly this volume has considerable overlap with both Volume 3 (Theory and Bonding of Inorganic Non-molecular Systems) and Volume 5 (Inorganic Materials Chemistry). We anticipate that readers who are interested in this volume will find much of interest in those volumes and vice versa

Vol. 5: Inorganic Materials Chemistry; Ram Seshadri and Serena Cussen

This volume has adopted the broad title of Inorganic Materials Chemistry, but as readers would note, the title could readily befit articles in other volumes as well. In order to distinguish contributions in this volume from

those in other volumes, the editors have chosen to use as the organizing principle, the role of synthesis in developing materials, reflected by several of the contributions carrying the terms “synthesis” or “preparation” in the title. It should also be noted that the subset of inorganic materials that are the focus of this volume are what are generally referred to as functional materials, i.e., materials that carry out a function usually through the way they respond to an external stimulus such as light, or thermal gradients, or a magnetic field.

Vol. 6: Heterogeneous Inorganic Catalysis; Rutger A. van Santen and Emiel J. M. Hensen

This Volume starts with an introductory chapter providing an excellent discussion of single sites in metal catalysis. This chapter is followed by 18 chapters covering a large part of the field. These chapters have been written with a focus on the synthesis and characterization of catalytic complexity and its relationship with the molecular chemistry of the catalytic reaction. In the 1950s with the growth of molecular inorganic chemistry, coordination chemistry and organometallic chemistry started to influence the development of heterogeneous catalysis. A host of new reactions and processes originate from that time. In this Volume chapters on major topics, like promoted Fischer-Tropsch catalysts, structure sensitivity of well-defined alloy surfaces in the context of oxidation catalysis and electrocatalytic reactions, illustrate the broadness of the field. Molecular heterogeneous catalysts rapidly grew after high-surface synthetic of zeolites were introduced; so, synthesis, structure and nanopore chemistry in zeolites is presented in a number of chapters. Also, topics like nanocluster activation of zeolites and supported zeolites are discussed. Mechanistically important chapters deal with imaging of single atom catalysts. An important development is the use of reducible supports, such as CeO_2 or Fe_2O_3 where the interaction between the metal and support is playing a crucial role.

Vol. 7: Inorganic Electrochemistry; Keith J. Stevenson, Evgeny V. Antipov and Artem M. Abakumov

This volume bridges several fields across chemistry, physics and material science. Perhaps this topic is best associated with the book “Inorganic Electrochemistry: Theory, Practice and Applications” by Piero Zanello that was intended to introduce inorganic chemists to electrochemical methods for study of primarily molecular systems, including metallocenes, organometallic and coordination complexes, metal complexes of redox active ligands, metal-carbonyl clusters, and proteins. The emphasis in this Volume of CIC III is on the impact of inorganic chemistry on the field of material science, which has opened the gateway for inorganic chemists to use more applied methods to the broad areas of electrochemical energy storage and conversion, electrocatalysis, electroanalysis, and electrosynthesis. In recognition of this decisive impact, the Nobel Prize in Chemistry of 2019 was awarded to John B. Goodenough, M. Stanley Whittingham, and Akira Yoshino for the development of the lithium-ion battery.

Vol. 8: Inorganic Photochemistry; Vivian W. W. Yam

In this Volume the editor has compiled 19 chapters discussing recent developments in a variety of developments in the field. The introductory chapter overviews the several topics, including photoactivation and imaging reagents. The first chapters include a discussion of using luminescent coordination and organometallic compounds for organic light-emitting diodes (OLEDs) and applications to highlight the importance of developing future highly efficient luminescent transition metal compounds. The use of metal compounds in photo-induced bond activation and catalysis is highlighted by non-sacrificial photocatalysis and redox photocatalysis, which is another fundamental area of immense research interest and development. This work facilitates applications like biological probes, drug delivery and imaging reagents. Photochemical CO_2 reduction and water oxidation catalysis has been addressed in several chapters. Use of such inorganic compounds in solar fuels and photocatalysis remains crucial for a sustainable environment. Finally, the photophysics and photochemistry of lanthanoid compounds is discussed, with their potential use of doped lanthanoids in luminescence imaging reagents.

Vol. 9: NMR of Inorganic Nuclei; David L. Bryce

Nuclear magnetic resonance (NMR) spectroscopy has long been established as one of the most important analytical tools at the disposal of the experimental chemist. The isotope-specific nature of the technique can provide unparalleled insights into local structure and dynamics. As seen in the various contributions to this Volume, applications of NMR spectroscopy to inorganic systems span the gas phase, liquid phase, and solid state. The nature of the systems discussed covers a very wide range, including glasses, single-molecule magnets, energy storage materials, bioinorganic systems, nanoparticles, catalysts, and more. The focus is largely on isotopes other than ^1H and ^{13}C , although there are clearly many applications of NMR of these nuclides to the study of inorganic compounds and materials. The value of solid-state NMR in studying the large percentage of nuclides which are quadrupolar (spin $I > \frac{1}{2}$) is apparent in the various contributions. This is perhaps to be expected given that rapid quadrupolar relaxation can often obfuscate the observation of these resonances in solution.

Vol. 10: X-ray, Neutron and Electron Scattering Methods in Inorganic Chemistry; Angus P. Wilkinson and Paul R. Raithby

In this Volume the editors start with an introduction on the recent history and improvements of the instrumentation, source technology and user accessibility of synchrotron and neutron facilities worldwide, and they explain how these techniques work. The modern facilities now allow inorganic chemists to carry out a wide variety of complex experiments, almost on a day-to-day basis, that were not possible in the recent past. Past editions of Comprehensive Inorganic Chemistry have included many examples of successful synchrotron or neutron studies, but the increased importance of such experiments to inorganic chemists motivated us to produce a separate volume in CIC III dedicated to the methodology developed and the results obtained.

The introduction chapter is followed by 15 chapters describing the developments in the field. Several chapters are presented covering recent examples of state-of-the-art experiments and refer to some of the pioneering work leading to the current state of the science in this exciting area. The editors have recognized the importance of complementary techniques by including chapters on electron crystallography and synchrotron radiation sources. Chapters are present on applications of the techniques in e.g., spin-crossover materials and catalytic materials, and in the use of time-resolved studies on molecular materials. A chapter on the worldwide frequently used structure visualization of crystal structures, using PLATON/PLUTON, is also included. Finally, some more specialized studies, like Panoramic (in beam) studies of materials synthesis and high-pressure synthesis are present. Direct observation of transient species and chemical reactions in a pore observed by synchrotron radiation and X-ray transient absorption spectroscopies in the study of excited state structures, and ab initio structure solution using synchrotron powder diffraction, as well as local structure determination using total scattering data, are impossible and unthinkable without these modern diffraction techniques.

Jan Reedijk, *Leiden, The Netherlands*
Kenneth R. Poeppelmeier, *Illinois, United States*
March 2023

4.01 Introduction: Solid state inorganic chemistry

P. Shiv Halasyamani^a and Patrick M. Woodward^b, ^a Department of Chemistry, University of Houston, Houston, TX, United States; and ^b Department of Chemistry and Biochemistry, The Ohio State University, Columbus, OH, United States

© 2023 Elsevier Ltd. All rights reserved.

Abstract

In a broad sense the field of inorganic chemistry can be broken down into substances based on molecules and those that are based on extended arrays linked by metallic, covalent, polar covalent, or ionic bonds. The field of solid state inorganic chemistry is largely concerned with elements and compounds that fall into the latter group. As a general rule, the electrical, optical, magnetic and structural properties of extended solids differ in important aspects from those of molecular solids. The extended nature of the bonding is much more amenable to achieving electronic properties such as metallic conductivity or superconductivity that are essential for many modern and not so modern applications. Long range magnetic ordering can be sustained to temperatures that enable practical applications. The direction and orientation of electric dipole moments can be organized so as to enable technologically important properties like piezoelectricity and ferroelectricity. That's not to say that examples of superconductivity, magnetism, or ferroelectricity cannot be achieved in molecular solids, but it is fair to say that it to do so is to take the hard road. This volume contains 19 chapters that provide an in depth look at the synthesis, crystal structures, properties and applications of a wide variety of solid state inorganic materials.

In a broad sense the field of inorganic chemistry can be broken down into substances based on molecules and those that are based on extended arrays linked by metallic, covalent, polar covalent, or ionic bonds. The field of solid state inorganic chemistry is largely concerned with elements and compounds that fall into the latter group. As a general rule, the electrical, optical, magnetic and structural properties of extended solids differ in important aspects from those of molecular solids. The extended nature of the bonding is much more amenable to achieving electronic properties such as metallic conductivity or superconductivity that are essential for many modern and not so modern applications. Long range magnetic ordering can be sustained to temperatures that enable practical applications. The direction and orientation of electric dipole moments can be organized so as to enable technologically important properties like piezoelectricity and ferroelectricity. That's not to say that examples of superconductivity, magnetism, or ferroelectricity cannot be achieved in molecular solids, but it is fair to say that it to do so is to take the hard road.

This volume contains 19 chapters on wide variety of solid state inorganic materials. The list of chapters was largely chosen to focus on the properties that underpin modern technology. Smart phones, solid state lighting, batteries, computers, and many other modern conveniences that we take for granted would not be possible without these materials. Improvements in the performance of these and many other technologies are closely tied to the discovery of new materials or advances in our ability to synthesize higher quality samples. The organization of most chapters is purposefully designed to emphasize how the exceptional physical properties of modern materials arise from the interplay of composition, structure, and bonding. Not surprisingly this volume has considerable overlap with both Volume 3 (Theory and Bonding of Inorganic Non-Molecular Systems) and Volume 5 (Inorganic Materials Chemistry). We anticipate that readers who are interested in this volume will find much of interest in those volumes and vice versa.

The search for new materials that can facilitate more efficient ways to generate, convert, and store energy is a critical component of the broader scientific effort to meet the societal challenges associated with climate change. Recognizing the importance of this effort this volume contains four chapters devoted to energy materials. See and co-workers provide a comprehensive overview of battery materials. Their [Chapter 4.10](#) describes battery types that range from lead-acid batteries, to lithium-ion batteries, to conversion batteries based on oxygen or sulfur. In each section, the historical development, crystal structure, and electrochemical properties of important materials are discussed. The [Chapter 4.10](#) concludes with a discussion of batteries based on cations other than lithium, including Na⁺, K⁺, Mg²⁺, Zn²⁺ and Ca²⁺. Continuing the exploration of battery materials, the [Chapter 4.19](#) by Thangadurai and co-workers provides a systematic overview of solid-state electrolytes for all-solid-state Li-ion batteries. This [Chapter 4.19](#) contains a detailed look at promising Li-ion conductors as well as a critical look at lab-based examples of all-solid-state Li-ion batteries. Thermoelectric materials are covered in a [Chapter 4.03](#) by Kovnir and co-workers. Following an introduction to thermoelectric devices and applications this [Chapter 4.03](#) examines strategies to optimize the thermal and optical properties of such materials. The latter half of the [Chapter 4.03](#) provides an in-depth look at important classes of thermoelectric materials. The final [Chapter 4.17](#) on energy materials, a contribution by Maggard and co-workers, turns a spotlight on photocatalysts – materials that directly convert solar energy into chemical fuels. The [Chapter 4.17](#) focuses on foundational structure-property relationships of selected oxide and nitride semiconductors and their photoelectrochemical performance.

Electronic, magnetic, and quantum materials are discussed in the contributions from Zou, Xie, Shatruck, and McQueen. Zou and co-workers (*see* [Chapter 4.05](#)) describe piezoelectric and ferroelectric materials. Starting with the history of both phenomena, they quickly move to the characteristic properties, basic theory, and classification. From there, specific classes of materials are discussed including lead and non-lead based compounds, in both ceramic and single crystal form. A summary and perspective are given at the end of the chapter. Another technologically important property, superconductivity, is discussed by Xie and co-workers. They describe a subset of superconducting materials, the intermetallic superconductors. Their [Chapter 4.07](#) focuses on families of

superconductors and provides correlations between their crystal structures and chemical bonding. Empirical chemical-based approaches to new superconducting materials are described through structural connections and electron counting rules. The [Chapter 4.07](#) finishes with strategies for discovery of new superconducting materials. Shatruk and co-worker (*see* [Chapter 4.08](#)) discuss the magnetism of solids, including various types of magnetic materials (non-molecular). They focus on principles and equations that are most relevant to everyday research carried out by solid-state materials chemists. Their treatment includes both conventional and unconventional types of magnetic materials, as well as an overview of current and emerging applications of magnetic materials. The last [Chapter 4.11](#) in this grouping is an overview of quantum materials from a chemist's perspective. In this [Chapter 4.11](#), McQueen describes the history of the field and makes connections between chemistry and quantum materials. The convergence of synthesis, characterization, and theory with data science and quantum information makes for an interesting read. The treatment is aimed at a broad audience interested in chemical aspects of quantum materials.

Optical materials are described in three excellent chapters by professors Pan, Brgoch, and Subramanian. Pan and co-workers describe inorganic nonlinear optical (NLO) materials that generate coherent radiation ranging from the infrared to the deep-ultraviolet. Topics that are addressed include crystal structures, linear and nonlinear optical properties, single crystal growth, and applications. The [Chapter 4.02](#) finishes with a look at the criteria required for discovery and development of the next generation of NLO materials. Brgoch and co-worker discuss luminescence in the solid-state. Their [Chapter 4.09](#) describes the origin of luminescence in the solid state, as well as essential materials for phosphors, scintillators, semiconductors, and quantum dots. Finally, combinatorial, computational, and data-driven chemistry for discovering new luminescent materials are discussed. Subramanian and co-workers discuss solid state inorganic color pigments in their [Chapter 4.16](#). The historical importance of inorganic pigments, as well as the origin of color in solids are described. Finally, structure-property relationships are developed to better understand pigments in inorganic materials.

Several chapters are organized around various classes of materials – chalcogenide clusters, intermetallics, mixed-anion, and two-dimensional materials. In each case the properties can vary considerably, and a variety of applications are possible. Dehnen and co-worker describe non-oxide (semi)metallic chalcogenide clusters, i.e. those containing S, Se, or Te. In addition to a summary of different cage and cluster architectures, they discuss a variety of chemical and physical properties (*see* [Chapter 4.04](#)). Janka describes intermetallic materials. This [Chapter 4.06](#) covers a selection of intermetallic materials and focuses on their different structures and compositions. Selected examples that find widespread application in daily life are explored in more detail. Kageyama and co-workers describe ionic and polar-covalent solids that contain multiple anions, so-called mixed-anion materials. They begin by outlining how the combination of different anions provides the possibility for improved properties, as well as new functionalities. The [Chapter 4.13](#) covers the synthesis, crystal structures and properties of oxynitrides, oxyhydrides, oxyfluorides, oxychalcogenides, and oxypnictides. The [Chapter 4.13](#) serves as an entry point into a class of materials that is relatively underexplored. Finally, Goldberger and co-worker discuss two-dimensional (2D) van der Waals materials. Their [Chapter 4.14](#) surveys the range of 2D van der Waals materials. Synthetic methods are discussed, as are structure, properties, and applications. The [Chapter 4.14](#) concludes by describing emerging families of 2D van der Waals materials.

The development of novel synthetic methods is essential to the continued growth of solid state materials chemistry. Specialized approaches to synthesis are described in the chapters by Häussermann, Kolis, and Azuma. Häussermann and co-workers discuss high pressure chemistry (*see* [Chapter 4.12](#)). Devices for high pressure chemistry are described, along with inorganic materials that may be synthesized through high pressure routes. Materials that are discussed include intermetallics, hydrides, carbides, nitrides, oxides, mixed-anion systems, and open framework compounds. Kolis and co-workers also describe high pressure synthesis but from a high temperature hydrothermal perspective. Here reactions are performed above the supercritical temperature of water (between 400 °C–750 °C). The final crystalline product is emphasized, as intermediates and reaction mechanisms are generally unknown. Both oxides and non-oxides are discussed, and the [Chapter 4.18](#) concludes with a description of opportunities for future work. The [Chapter 4.20](#) by Azuma and co-workers also covers high pressure chemistry, but with a focus on transition metal oxides. Given the dense packing of ions, materials with the perovskite structure feature prominently in their treatment. A comprehensive discussion of synthetic methods, crystal structures, and physical properties allows them to highlight important structure-property relationships.

4.02 Inorganic nonlinear optical materials

Chunmei Huang^{a,b}, Fangfang Zhang^{a,b}, and Shilie Pan^{a,b}, ^aCAS Key Laboratory of Functional Materials and Devices for Special Environments, Xinjiang Technical Institute of Physics & Chemistry, CAS, Xinjiang Key Laboratory of Electronic Information Materials and Devices, Urumqi, China; and ^bCenter of Materials Science and Optoelectronics Engineering, University of Chinese Academy of Sciences, Beijing, China

© 2023 Elsevier Ltd. All rights reserved.

4.02.1	Introduction	4
4.02.2	Mid- and far-infrared nonlinear optical materials	5
4.02.2.1	Main mid- and far-infrared nonlinear optical materials	6
4.02.2.1.1	Silver thiogallate AgGaS ₂ (AGS)	6
4.02.2.1.2	Silver gallium selenide AgGaSe ₂ (AGSe)	6
4.02.2.1.3	ZnGeP ₂ , zinc germanium phosphide (ZGP)	7
4.02.2.2	Newly developed mid- and far-infrared nonlinear optical materials	8
4.02.2.2.1	Pnictides	8
4.02.2.2.2	Chalcogenides	10
4.02.2.2.3	Quasi-phase-matched (QPM) semiconductors	11
4.02.3	Near-infrared and visible nonlinear optical materials	12
4.02.3.1	Representative near-infrared and visible nonlinear optical materials	12
4.02.3.1.1	Potassium dihydrogen phosphate KH ₂ PO ₄ (KDP)	12
4.02.3.1.2	Potassium titanyl phosphate KTiOPO ₄ (KTP)	13
4.02.3.1.3	Lithium niobate LiNbO ₃ (LN)	14
4.02.3.1.4	Potassium niobate KNbO ₃ (KN)	15
4.02.3.1.5	Lithium iodate α-LiIO ₃	16
4.02.3.2	Newly developed near-infrared and visible nonlinear optical materials	16
4.02.3.2.1	Phosphates	16
4.02.3.2.2	Iodates	17
4.02.3.2.3	Borates	18
4.02.4	Ultraviolet nonlinear optical materials	19
4.02.4.1	Representative ultraviolet nonlinear optical materials	19
4.02.4.1.1	β-barium borate β-BaB ₂ O ₄ (β-BBO)	19
4.02.4.1.2	Lithium triborate LiB ₃ O ₅ (LBO)	21
4.02.4.1.3	Cesium triborate CsB ₃ O ₅ (CBO)	22
4.02.4.1.4	Cesium lithium borate CsLiB ₆ O ₁₀ (CLBO)	22
4.02.4.2	Newly developed ultraviolet nonlinear optical materials	24
4.02.4.2.1	SBBO family	24
4.02.4.2.2	Other materials	26
4.02.5	Deep-ultraviolet nonlinear optical materials	27
4.02.5.1	Representative deep-ultraviolet nonlinear optical materials	28
4.02.5.1.1	Potassium aluminum borate KBe ₂ BO ₃ F ₂ (KBBF)	28
4.02.5.2	Newly developed deep-ultraviolet nonlinear optical materials	29
4.02.5.2.1	KBBF family	29
4.02.5.2.2	Fluorooxoborates	31
4.02.5.2.3	Other materials	33
4.02.6	Conclusion	35
Acknowledgments		35
References		36

Abbreviations

BPM	Birefringent-phase-matching
CW	Continuous wave
DFG	Difference-frequency generation
DFT	Density functional theory
DUV	Deep-ultraviolet
FHG	Fourth-harmonic generation

HPVT High pressure vapor transport
 IR Infrared
 Nd: YLF Nd-doped yttrium orthoaluminate
 Nd:YAG Nd-doped yttrium aluminum garnet
 NLO Nonlinear optical
 OPG Optical parametric generation
 OPO Optical parametric oscillation
 OR Optical rectification
 PP Periodically poled
 QPM Quasi-phase-matching
 SFG Sum-frequency generation
 SHG Second-harmonic generation
 THG Third-harmonic generation
 TSSG Top-seeded solution growth
 UV Ultraviolet

Abstract

Inorganic nonlinear optical material is one of the key branches of materials science which has attracted much attention as important nonlinear media. In this chapter, the most widely used and newly developed inorganic nonlinear optical materials in infrared, near-infrared to visible, ultraviolet and deep-ultraviolet spectral ranges are described, including their structures, linear and nonlinear optical properties, single-crystal growth and applications in the laser systems according to their development history. This chapter provides a comprehensive perspective on the present development and necessary improvement in the future of inorganic nonlinear optical materials.

4.02.1 Introduction

The laser is often grouped with the nuclear energy, transistor and the computer as four landmark inventions of the 20th century.¹⁻³ Laser has promoted the rapid development of modern science and technology due to its excellent properties such as highly directional luminescence, high brightness and high energy density, etc. Remarkably, the frequency of laser can be converted to new coherent and tunable laser sources by nonlinear optical (NLO) materials, which significantly extend the wavelength range and rapidly promote the application of laser in more fields.⁴⁻⁶

The beginning of the field of nonlinear optics is often taken to be the discovery of second-harmonic generation (SHG) in quartz crystal by Franken et al. (1961),⁷ shortly after the demonstration of the first working laser by Maiman in 1960.^{8,9} While 10^{-8} photon conversion efficiency was achieved in this first SHG experiment (1961), which corresponds to $3 \times 10^{-10} \% \cdot W^{-1}$, at present the improvement using engineered nonlinear devices is by more than 12 orders of magnitude. In 1962, Giordmaine and Maker et al. proposed an ingenious method of birefringent-phase-matching (BPM) between fundamental and SHG wave, which greatly improved the efficiency of laser frequency conversion and was widely used in applied NLO territory during next decades.^{10,11} In the same year, Armstrong et al. proposed another method of phase-matching, so-called quasi-phase-matching (QPM).¹² Three decades later, the emergence of an electric-field poling technique allowed the periodical reversing of ferroelectric domain polarity, which led to the practical implementation of the QPM approach.¹³⁻¹⁵ At present, the periodically poled crystals PP-BaTiO₃, PP-LiTaO₃, PP-KTiOPO₄, and PP-GaAs are used widely.¹⁶⁻¹⁹ Therefore, NLO materials have attracted much attention and developed into one of the key branches of materials science.

When a single beam of strong monochromatic light impinges on an appropriate NLO material, its frequency, phase, polarization, etc., change, which cause changes in refractive index, light absorption, light scattering and other states of incident light.^{20,21} Accordingly, NLO materials can be used for frequency conversion and signal processing, such as, using the frequency-mixing process to amplify the weak light signal and using the nonlinear response to achieve optical recording and computing functions. Obviously, NLO materials have important application value in the fields of laser, communication, electronic instruments and medical equipment, etc.²²⁻²⁵

Soon afterwards the theory of the general optical parametric interactions was developed,^{26,27} and experiments of many frequency-mixing processes were carried out,²⁸⁻³³ such as, sum-frequency generation (SFG), difference-frequency generation (DFG), and especially optical parametric oscillation (OPO) which is the nonlinear effect that allows us to obtain continuously tunable coherent light source and was first demonstrated in 1965 by Giordmaine et al. at Bell Telephone Laboratories OPO based

on LiNbO₃ (LN).³⁴ Here, only three-photon nonlinear process is considered, i.e., second-order nonlinear, which is the most effective method applied to frequency conversion technology so far.

Second-order nonlinear optical effects²⁰:

- 1) sum-frequency generation (SFG)
- 2) second-harmonic generation (SHG)
- 3) difference-frequency generation (DFG)
- 4) optical parametric amplification (OPA)
- 5) optical parametric oscillation (OPO)
- 6) optical parametric generation (OPG)
- 7) high-harmonic generation (including third-, fourth-, fifth-, sixth-harmonic generation, etc.)
- 8) linear electro-optical effect
- 9) optical rectification (OR)

With SHG technique, the 1064 nm output from Nd:YAG lasers or the 800 nm output from Ti:sapphire lasers can be converted to visible light, with wavelengths of 532 nm (green) or 400 nm (violet), respectively. Practically, frequency doubling is carried out by placing a nonlinear medium in a laser beam. While there are many types of nonlinear media, one of the most common media are inorganic crystal materials. At present, commonly used NLO crystals are β -barium borate (β -BaB₂O₄), lithium triborate (LiB₃O₅), potassium dihydrogen phosphate (KH₂PO₄), potassium titanyl phosphate (KTiOPO₄), and lithium niobate (LiNbO₃), silver thiogallate (AgGaS₂), silver gallium selenide (AgGaSe₂) and zinc germanium phosphide (ZnGeP₂). These crystals have the necessary properties of being suitable birefringence (necessary to obtain phase-matching, see below), having a specific crystal symmetry, being transparent for both impinging laser light and the frequency-doubled wavelength, and having high damage thresholds, which makes them resistant against the high-intensity laser light.

This chapter contains information on the most widely used and newly developed inorganic NLO crystals with promising applications, which is classified and discussed according to the optical transparency windows (Fig. 1). And we will start with the IR NLO crystals materials.

4.02.2 Mid- and far-infrared nonlinear optical materials

There is no unique definition of mid- and far-IR spectral range. In this chapter, we divide it begin from 0.8 μ m. The applications of coherent mid- and far-IR light sources include detection and quantification of molecular trace gases, military applications, medical applications, evaporation and thin-film deposition of polymers, spectroscopy and other scientific applications like high resolution and time resolved.^{35–37}

Based on different laser generation mechanisms, a variety of mid-IR light sources have appeared, such as ion-doped solid laser, CO₂ gas laser, semiconductor quantum cascade laser, free-electron laser, chemical laser, etc. Attractively, NLO frequency conversion devices using BPM techniques or periodic structure of QPM optical technology of IR NLO crystal materials can realize optical frequency transformation, which has unique advantages in producing mid-IR laser with wide tunable range and can cover inaccessible wavelength ranges. Especially, it can promote the development of all-solid miniature lasers, and can achieve high power, narrow linewidth IR laser output.^{35,38} The main progresses of the mid- and far-IR solid-state lasers technology in the last two decades did follow the advancement of the NLO materials.

IR NLO materials are the key components of NLO frequency conversion devices, which mainly use parametric down-conversion processes (such as DFG, OPG, OPA, OPO, etc.) to generate mid-IR laser radiation.³⁵ In terms of physical properties, the IR NLO crystal is required to have large second-order NLO coefficients, wide transparency spectral range, low residual losses, high thermal conductivity, high laser threshold, relatively wide bandgap, good machining performance, and the possibility for realizing PM. Since the performance of oxide-based crystals is affected by multi-phonon absorption starting from about 4 μ m, they are partially transparent in the mid-IR. Thus, non-oxide materials have been commonly used, such as pnictide, chalcogenides, halides, etc. Some of these inorganic crystals transmit up to 20–30 μ m before multi-phonon absorption occurs as an intrinsic limit. The large size single non-oxide single crystals can only be grown by the complex Bridgman Stockbarger growth technique in sealed (high atmosphere) ampoules due to the volatile and chemically reactive starting components, which hampered their development. All the special post-growth treatments are needed to restore stoichiometry and improve their optical quality. We will start with the

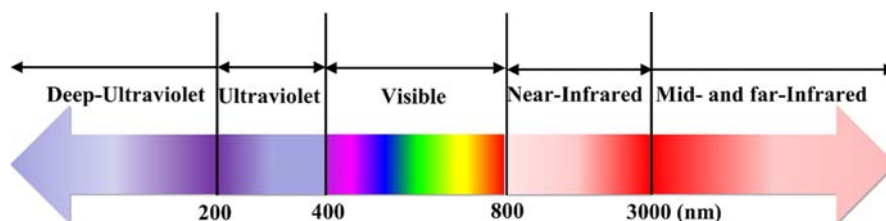


Fig. 1 Spectral range divided in this chapter.

most commonly used commercial mid-IR materials, and the crystal structures, optical properties, and crystal growth are briefly introduced.

4.02.2.1 Main mid- and far-infrared nonlinear optical materials

4.02.2.1.1 Silver thiogallate AgGaS_2 (AGS)

AGS crystal belongs to the $\bar{4}2m$ point group with unit cell parameters of $a = 5.75722 \text{ \AA}$, $c = 10.3036 \text{ \AA}$ and $Z = 4$.³⁹ In its structure, both Ag and Ga atoms are coordinated with four S atoms forming the tetrahedral AgS_4 and GaS_4 building units, respectively, which are further linked via corner-sharing to form the final chalcopyrite-type framework (Fig. 2). AGS is a representative member of $A^I B^{III} C^{VI}_2$ family in the field of NLO material since it has a high NLO coefficient ($d_{36} = 13.7 \text{ pm} \cdot \text{V}^{-1}$ at 2.53 \mu m), and the relatively large birefringence enables it to achieve phase matching within most of its transparency regions ($\sim 0.5\text{--}12.9 \text{ \mu m}$).^{40–43} Besides, AGS has low-absorption and scattering, high-coupling coefficient, and good mechanical properties, which provide the basis for visible, and near-IR pumped OPO and SFG/DFG for producing tunable laser radiation from approximately $0.5\text{--}12 \text{ \mu m}$.^{44–47} The tunable lasers have wavelengths particularly well-suited for use with AGS. Potential applications fields of AGS include spectroscopy, medicine, materials processing, nonlinear optics, sodium guide star generation, and remote sensing, etc. Notably, the low laser damage threshold of AGS crystal shortens the lifetime of devices and limits its applications in high-power lasers.

The development of devices requires suitable high quality crystals. Moving the promising NLO materials into production will be a long and storied process that could last for decades. This slow progress reflects the inherent difficulties of single-crystal growth, especially those involving multicomponent systems. Up to now, a great deal of research work has been devoted to the growth of large and crack-free bulk AGS crystals with high optical quality for device application.^{44,48–51} And the growth of AGS crystal is mainly by Bridgman-Stockbarger method. Recently, the AGS crystal with size of $\Phi 8 \text{ mm} \times 45 \text{ mm}$ was grown by Karunakaran et al., which has the following distinct steps⁵¹:

The single-phase polycrystalline AGS was synthesized by mixing elements Ag, Ga and S in the molar ratio of 1:1:2 and an excess of 5% S into a quartz ampoule. Quartz ampoule can be continuously rotated with suitable mechanical arrangement in horizontal furnace, which combined with a temperature oscillation allow the materials to react adequately. Then, using the synthesized single-phase polycrystalline AGS to grow the single crystal in a well-designed two-region Bridgman furnace. TG-DSC analysis shows that the melting temperature of the AGS polycrystalline material was about $1010 \text{ }^\circ\text{C}$. Therefore, the temperature at the upper zone was set to above $1010 \text{ }^\circ\text{C}$, and the temperature at the lower zone was below $900 \text{ }^\circ\text{C}$. By constantly adjusting the temperature in the upper/lower zones, the temperature gradient between melting and solidification in the ampoule is suitable for the growth of single crystals with high optical quality. Notably, the declining rate of the annealing is also the key factor for single crystal growth.

4.02.2.1.2 Silver gallium selenide AgGaSe_2 (AGSe)

Single crystal AGSe is known as one of the widest spread materials for nonlinear converters of coherent radiation operating in the mid-IR. AGSe crystal is isostructural with AGS and also possesses the chalcopyrite-type structure. (Fig. 3). AGSe crystallizes in the tetragonal space group $I\bar{4}2d$ (No. 122) with unit cell parameters of $a = 5.9220 \text{ \AA}$, $c = 10.8803 \text{ \AA}$ and $Z = 4$, which is a negative uniaxial crystal with $n_o > n_e$ and appears dark gray at room temperature.⁵² Owing to wide range of transparency ($0.7\text{--}19 \text{ \mu m}$) and large second order NLO coefficient ($d_{36} = 41.4 \pm 2 \text{ pm} \cdot \text{V}^{-1}$ at 9.27 \mu m) of AGSe, it is possible to generate continuously tunable mid-IR coherent radiation from 2.5 \mu m to 18 \mu m with frequency-mixing processes or OPO technology.^{53–56} In addition, being a semiconductor with a band gap of about 1.8 eV , AGSe has also a fair potential for some other applications: such as a single crystal in detectors of photons or ionizing particles, as well as a thin film in solar cells.^{57–59}

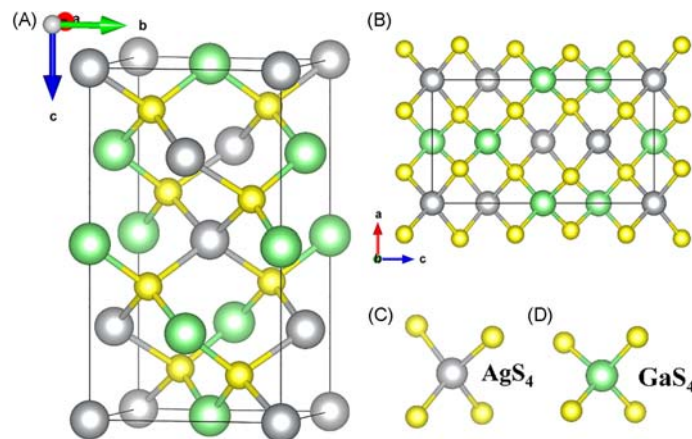


Fig. 2 The unit cell structure of AGS (A), the structural arrangement in ac plane (B), the AgS_4 tetrahedron (C) and GaS_4 tetrahedron (D).

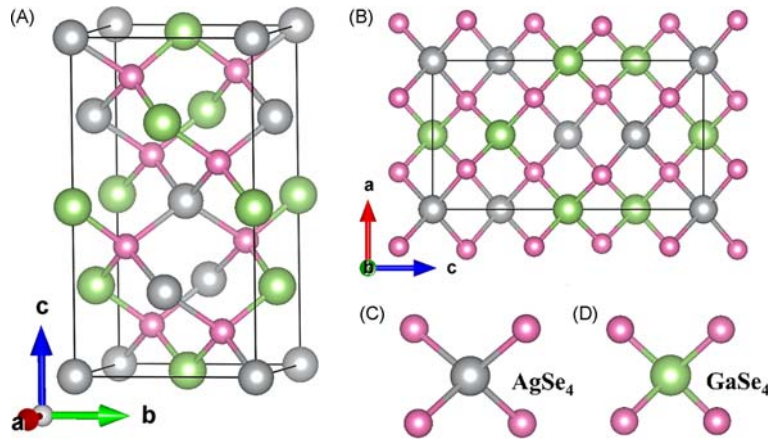


Fig. 3 The unit cell structure of AGSe (A) and the structural arrangement in ac plane (B), the AgSe_4 tetrahedron (C) and GaSe_4 tetrahedron (D).

The melting point (860°C) of AGSe is low enough to permit convenient growth from the melt by the vertical Bridgman method in fused-silica ampoules.^{60–62} However, since the thermal expansion coefficient of AGSe parallel to the c -axis is found to be negative, the single crystals usually become cracked during cooling. Coupled with the fact that Se is volatile, it is easy to cause the chemical ratio deviation of the crystal during raw material synthesis and crystal growth, so it is extremely difficult to obtain a crack-free single crystal with high optical mass.⁶⁰ The polycrystalline ingots crack, originating from grain boundaries, because of differences between the thermal expansion coefficients in different crystallographic directions. These differences occur because AGSe has the tetragonal chalcopyrite structure, which is derived from the cubic zincblende structure by the ordered distribution of Ag and Ga atoms among the cation sites to produce a doubling of the c -axis.

Since the 1990s, great progress has been made in the growth of single crystal AGSe, mainly due to overcoming the cracking during cooling and the thermal annealing technology to eliminate the low-temperature phase precipitation. However, in order to grow high quality and large size single crystal industrially, it is necessary to further improve the synthetic purity of AGSe polycrystalline samples and optimize crystal growth methods.

At present, it is more convenient and widely used to directly synthesize the AGSe polycrystalline samples with high-purity elements as raw material. However, owing to the low melting point of Ga, high vapor pressure of Se and high mobility of Ag, it is difficult to control the chemical ratio of compounds during melt growth. Therefore, a new method was developed with binary compounds Ag_2Se and Ga_2Se_3 as raw materials for synthesizing more uniform polycrystalline samples. For the crystal growth, reproducible growth of large, crack-free single crystals can be achieved by seeded vertical Bridgman method with the seeds oriented parallel to the c -axis. Besides, the traditional Bridgman method is improved in the process of exploring the growth of perfect crystal. The reaction ampoule of special conic shape is coated with a layer of pyrolytic carbon by cracking acetone gas at 1100°C , and the carbon plating ampoule is baked by oxyhydrogen flame in the air for eliminating the carbon particles attached to the carbon film and making the carbon film uniform and smooth.

4.02.2.1.3 ZnGeP_2 , zinc germanium phosphide (ZGP)

The ternary compound ZGP is a representative member of $\text{A}^{\text{II}}\text{B}^{\text{IV}}\text{C}^{\text{V}}_2$ family in the field of NLO material in the IR region.⁶³ ZGP belongs to the $\bar{4}2m$ point group symmetry with unit cell parameters of $a = 5.46 \text{ \AA}$, $c = 10.71 \text{ \AA}$ and $Z = 4$, and is a semiconducting material with the chalcopyrite structure (Fig. 4).⁶⁴ It has a wide transparency range ($\sim 0.7\text{--}12 \mu\text{m}$), large nonlinear coefficient

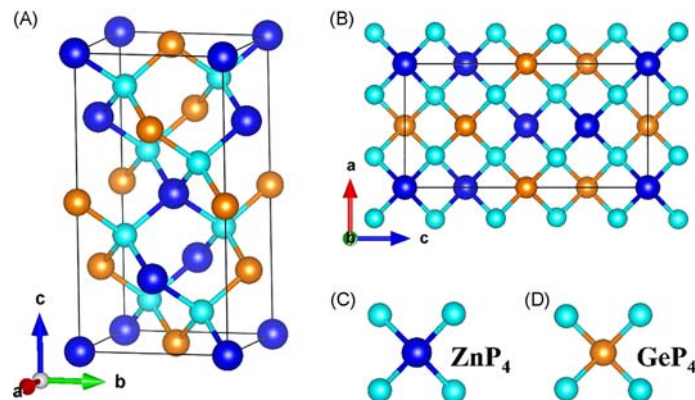


Fig. 4 The unit cell structure of ZGP (A) and the structural arrangement in ac plane (B), the ZnP_4 tetrahedron (C) and GeP_4 tetrahedron (D).

($d_{36} = 75 \pm 8 \text{ pm} \cdot \text{V}^{-1}$, $9.6 \mu\text{m}$), high laser damage threshold ($0.003 \text{ GW} \cdot \text{cm}^{-2}$ at $1.064 \mu\text{m}$, $\tau_p = 10 \text{ ns}$), high thermal conductivity ($0.35 \text{ W} \cdot (\text{cm} \cdot \text{K})^{-1}$ at 293 K) and suitable birefringence ($0.040\text{--}0.042$).^{63,65–69} ZGP-OPOs can generate tunable mid-IR coherent light from $2.5 \mu\text{m}$ to $10 \mu\text{m}$. At the same time, the ZGP crystal has good chemical stability, good mechanical properties and is not easy to be deliquesced.⁷⁰ It has the highest conversion efficiency and output power in $3\text{--}5 \mu\text{m}$, which is of great importance for many applications, such as IR countermeasure, spectra, chemical monitoring, medical apparatus, and remote sensing.^{71–73} However, ZGP crystals can only be pumped with $2 \mu\text{m}$ or longer wavelengths due to the serious optical absorption of ZGP crystals in the range less than $2 \mu\text{m}$. Besides, since the volatilization of phosphorus and the strong thermal expansion anisotropy of ZGP crystal, it is difficult to grow large size and high quality single crystals.^{74–76} Thus, many crystal growth methods have been studied, such as Bridgman method, vertical gradient freezing method, horizontal gradient freezing method, a liquid encapsulated Czochralski method and high pressure vapor transport (HPVT) method.^{75,77–81}

The crystals growth takes place in two steps, including synthesis of the single-phase polycrystalline ZGP and single-crystal growth^{81,82}: High purity and single-phase ZGP polycrystalline materials can be synthesized by a two-temperature zone method. According to the stoichiometry of ZGP with excess of $0.1\text{--}0.5\%$ phosphorus, zinc and germanium were loaded into hot zone and red phosphorus was placed in cold zone of horizontal furnace, respectively (Fig. 5). During the process of reaction, red phosphorus was vaporized and transported into the hot zone, in which ZGP polycrystalline material was synthesized. Then, ZGP single crystals were grown by vertical Bridgman technique by using the ZGP polycrystalline charge (Fig. 6). Notably, excess red phosphorus was added for the maintenance of the dissociation pressure above the ZGP melt to avoid the deviation from stoichiometry during crystal growth.

4.02.2.2 Newly developed mid- and far-infrared nonlinear optical materials

In recent years, with the rapid development of NLO frequency transformation technology, more and more mid- and far-IR NLO materials have been studied and reported. At present, mid- and far-IR NLO materials widely studied and applied are mainly phosphides, chalcogenides, as well as QPM crystals in the non-oxygen system. According to the above classifications, a series of new infrared materials developed in recent years are introduced.

4.02.2.2.1 Prictides

The NLO crystal CdSiP_2 (CSP) belongs to the tetragonal point group $\bar{4}2m$, with lattice constants $a = 5.68 \text{ \AA}$, $c = 10.431 \text{ \AA}$, and $Z = 4$ (Fig. 7).⁸³ CSP is optically negative uniaxial chalcopyrite so the non-critical type-I (o + o-e) phase-matching is possible in contrast to the positive ZGP which is the only commercially available II-IV-V₂ type chalcopyrite.⁸⁴ The birefringence of ~ 0.05 is large enough for phase matching within its transparency range yet small enough to prevent significant walk-off.^{85,86} Its high thermal conductivity ($13.6 \text{ W} \cdot \text{mK}^{-1}$), along with a relatively high hardness ($930 \text{ kg} \cdot \text{mm}^{-3}$) and melting point ($1133 \text{ }^\circ\text{C}$) make it attractive for high average power applications and facilitates cutting, polishing, and coating of optical components.^{84,87} However, it was grown in the past in small sizes that did not allow measurement of essential physical properties due to some significant crystal growth challenges compared to the more widely used II-IV-V₂ chalcopyrite analog ZGP. In 2008, high optical quality crystals of CSP with sizes reaching $70 \times 25 \times 8 \text{ mm}^3$ were grown successfully by Schunemann et al. from the melt using high purity starting materials via the horizontal gradient freeze technique (Fig. 8).⁸⁸ Besides, other efforts are continuous to grow larger crystals with better optical quality to meet market demand.^{89–93}

CdGeAs_2 (CGA) is optically positive uniaxial chalcopyrite belonging to tetragonal point group $\bar{4}2m$, with lattice constants $a = 5.9432 \text{ \AA}$, $c = 11.2163 \text{ \AA}$, and $Z = 4$ (Fig. 9).⁹⁴ CGA has attracted researchers' interests for many years with its enormous nonlinear coefficient ($d_{36} = 236 \text{ pm} \cdot \text{V}^{-1}$ at $10.6 \mu\text{m}$), broad transparency regions ($2.4\text{--}18 \mu\text{m}$), as well as moderate birefringence (~ 0.09 at $10 \mu\text{m}$) to realize BQM, but severe cracking due to anisotropic thermal expansion precluded the growth of device-quality crystals.^{95–97} Seeded crystal growth in low-gradient, horizontal transparent furnaces made possible reproducible growth of

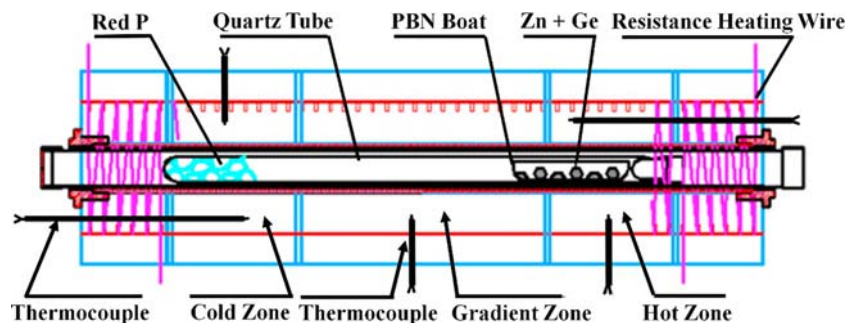


Fig. 5 Schematic of furnace for ZGP synthesis and temperature profiles.

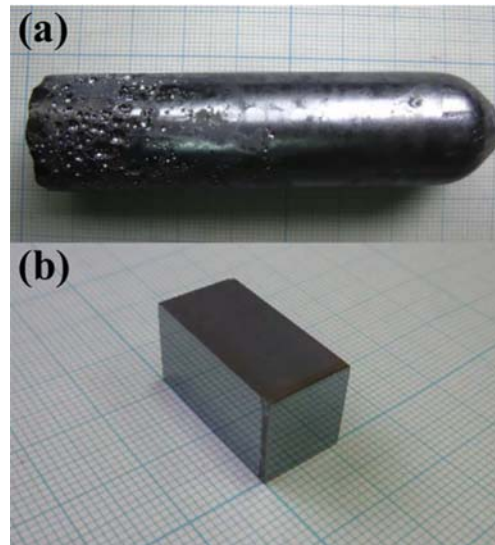


Fig. 6 Photograph of ZGP crystal grown in PBN crucible in a six-section furnace (A) and a ZGP-OPO sample.

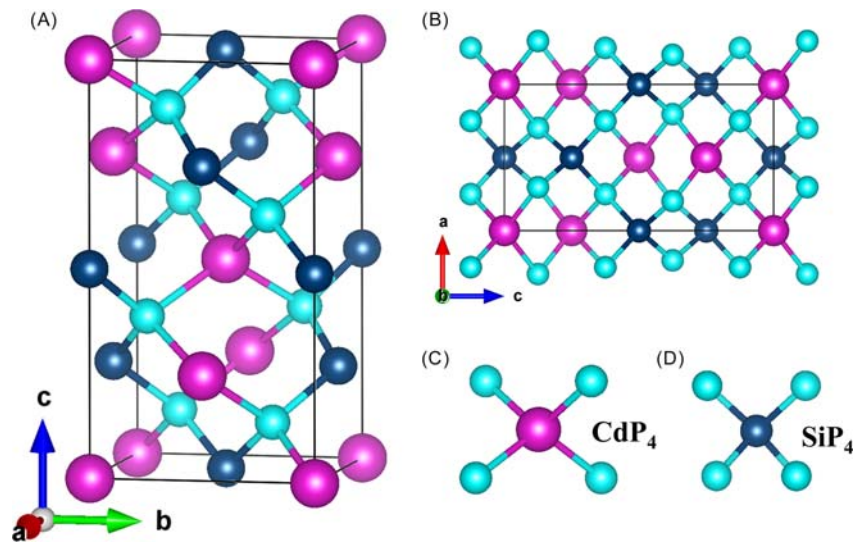


Fig. 7 The unit cell structure of CSP (A) and the structural arrangement in ac plane (B), the CdP_4 tetrahedron (C) and SiP_4 tetrahedron (D).



Fig. 8 Photograph of oriented, polished CSP single crystal samples grown by horizontal gradient freeze technique.

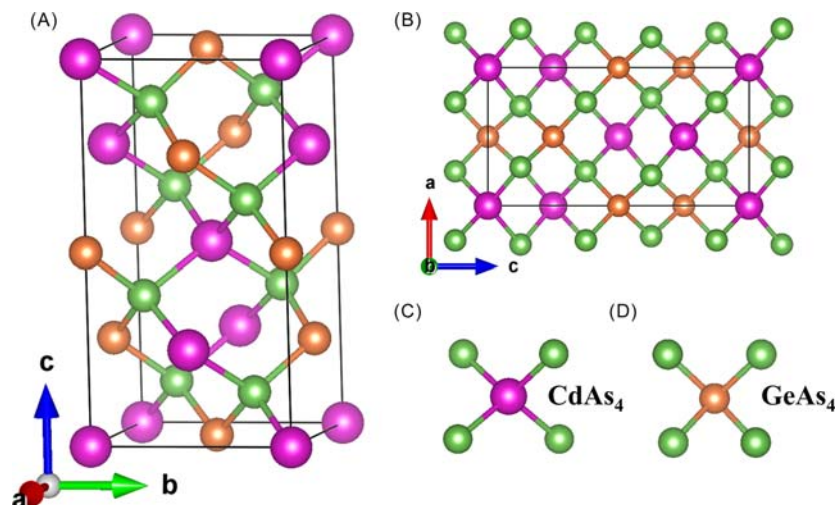


Fig. 9 The unit cell structure of CGA (A) and the structural arrangement in *ac* plane (B), the CdAs_4 tetrahedron (C) and GeAs_4 tetrahedron (D).

crack-free single crystals, which can reduce mid-IR absorption losses.^{95,98,99} For long-wavelength (8–12 μm) OPO applications, however, the short-wavelength cutoff edge of CGA ($\sim 2.4 \mu\text{m}$) makes it incompatible with most practical solid state pump lasers.¹⁰⁰

4.02.2.2.2 Chalcogenides

LiInS_2 (LIS), LiInSe_2 (LISE), LiGaS_2 (LGS) and LiGaSe_2 (LGSE) crystallize in the orthorhombic point group $mm2$ with wurtzite type structures. Fig. 10 shows the structure of LIS and crystal samples of LIS, LISe, LGS and LGSe. Generally speaking, Li-compounds exhibit improved properties than their Ag-analogs (AGS, AGSe, etc.), such as wider band-gap and better thermo-mechanical, which are beneficial for damage resistances.^{38,101–107} However, the NLO coefficient of the Li-compounds is lower than those of their Ag-analogs, comparable to some oxide NLO materials. Nevertheless, LGS, LIS, and LGSe are the rare known non-oxide materials that can be pumped by femtosecond Ti:sapphire laser systems operating near 800 nm without two-photon absorption. Recently, their growth technology was improved to such an extent that it was possible to perform extensive characterization and even realized some application, especially exhibiting the great potential serving as NLO materials in the range of 8–12 μm .³⁵

BaGa_4S_7 and BaGa_4Se_7 were first reported as NLO materials by Lin et al.¹⁰⁸ and Yao et al.,¹⁰⁹ and then Badikov et al. tracked the growth and properties of the two crystals.^{110,111} They crystallize in the orthorhombic and monoclinic space groups, i.e., $Pmn2_1$ (No. 31) and Pc (No. 7) for BaGa_4S_7 and BaGa_4Se_7 , respectively. They feature the different 3D frameworks which are mainly attributed by the different coordination number of Ba, i.e., eight-coordinated with S atoms and six-coordinated with Se atoms, respectively (Fig. 11). BaGa_4S_7 and BaGa_4Se_7 can be both grown via the Bridgman-Stockbarger method.^{112,113} They have high laser damage threshold ($235 \text{ MW} \cdot \text{cm}^{-2}$ at 1 e^{-2} beam diameter and 9.58 nm for BaGa_4S_7 , $557 \text{ MW} \cdot \text{cm}^{-2}$ at 1.064 μm , 5 ns, 1 Hz for BaGa_4Se_7), wide transparency range (~ 0.35 –13.7 for BaGa_4S_7 , ~ 0.45 –20 μm for BaGa_4Se_7) and large nonlinear coefficient ($d_{32} = 5.7 \text{ pm} \cdot \text{V}^{-1}$ at 2.3 μm for BaGa_4S_7 , $d_{11} = 24.3 \text{ pm} \cdot \text{V}^{-1}$ and $d_{13} = 20.4 \text{ pm} \cdot \text{V}^{-1}$ at 1.064 μm for BaGa_4Se_7), they can theoretically achieve the wide tuning range from medium-wavelength to long-wavelength IR.^{109,112–115} Owing to their good optical transparency and phase matching conditions at 1 μm , both BaGa_4S_7 and BaGa_4Se_7 can be used in 1 or 2 μm -pumped laser systems. At present, one of the most urgent task is to grow large-size single crystal with good optical quality to promote their practical application.

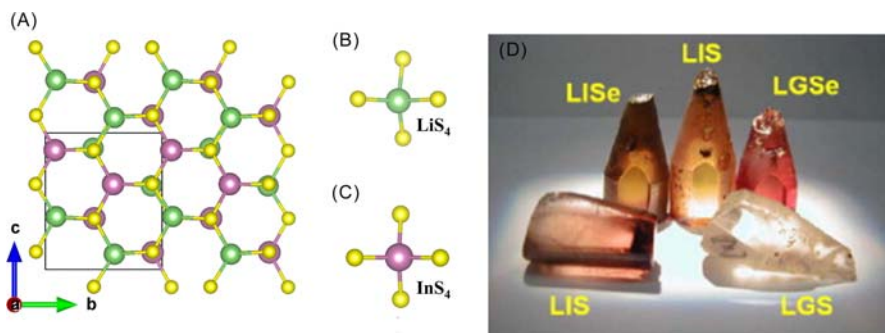


Fig. 10 The structure of LIS viewed along the *a*-axis (A), the LiS_4 tetrahedron (B) and InS_4 tetrahedron (C), the crystal samples of LIS, LISe, LGS and LGSe (D).

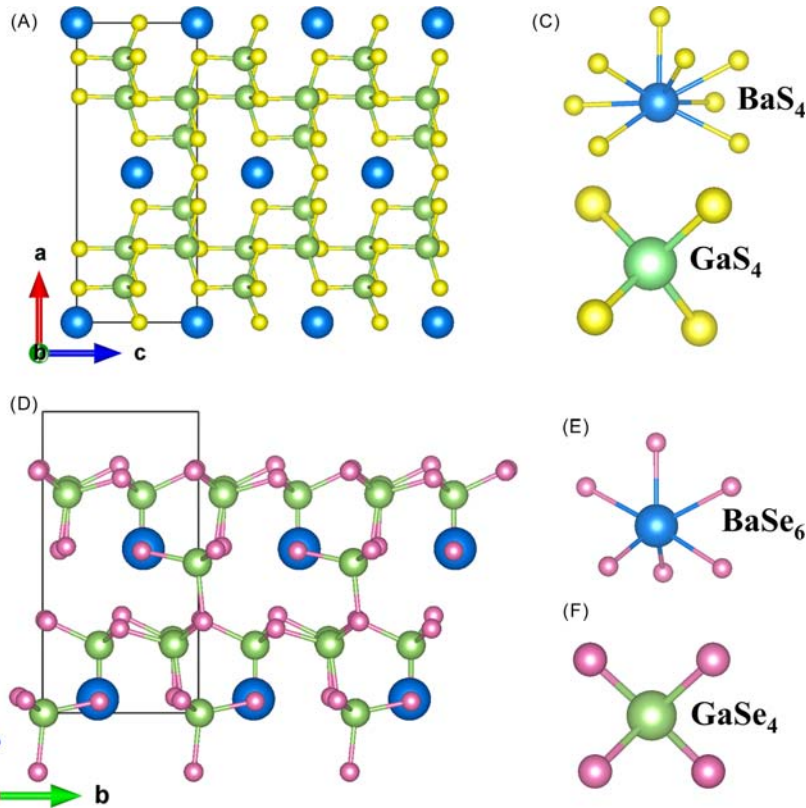


Fig. 11 The structure of BaGa_4S_7 viewed along the b -axis (A), the coordination environment of Ba atom (B) and GaS_4 tetrahedron (C); The structure of BaGa_4S_7 viewed along the a -axis (D), the coordination environment of Ba atom (E) and GaSe_4 tetrahedron (F).

CdSe: It is a kind of II-VI semiconductor material with excellent performance of straight backward transition. CdSe crystals exhibit two structure types, namely wurtzite and sphalerite structure types. Herein, wurtzite-type CdSe crystal ($P6_3mc$, No. 186) has excellent photoelectric properties and great potential in the application of mid and far-IR laser due to the wide transparency range of 0.7–24.0 μm , low optical absorption ($<0.01 \text{ cm}^{-1}$, 1–10 μm), without two-photon absorption in the range of 8–15 μm , as well as good mechanical properties, etc.^{116–121} At present, the crystal growth methods for wurtzite-type CdSe include: high-pressure vertical Bridgman, high-pressure vertical zone melting, physical vapor transport, etc. However, owing to the high melting point ($\sim 1264 \text{ }^\circ\text{C}$) and vapor pressure ($>1 \text{ MPa}$), it is still a challenge to grow large-size and high-quality CdSe single crystal, which greatly restricts its application.

GaSe: It crystallizes in the hexagonal system with space group of $P\bar{6}m2$ (No. 189). GaSe crystal possesses excellent NLO properties, including large NLO coefficient ($d_{22} = 54 \text{ pm} \cdot \text{V}^{-1}$), wide transparency range (0.6–20 μm) and high thermal conductivity ($16.2 \text{ W} \cdot (\text{m k})^{-1}$), etc.^{122–128} However, the layer structure of the GaSe crystal (Fig. 12) has poor mechanical property and it cannot be processed in accordance with the designed phase-matching angles, which severely limits it to apply in nonlinear frequency conversion devices. Interestingly, researchers have found that doping elements into the crystal, including S, In, Te and other elements with the same valence state, can effectively improve its physical properties.^{129,130} At present, S-doping GaSe crystal exhibits the best effect owing to the high ratio of doping (0.413) and the small temperature dispersion coefficient, which can be used in high-power and high-energy laser frequency conversion device. However, there are few studies on the performance of doped GaSe crystals, mainly because the growth technology is not mature, and large-size single crystals with stable performance and high quality cannot be obtained.

In addition to element doping, the formation of new crystals by compound blending is one of the development trends for NLO crystal materials. The new ternary or quaternary compound crystals formed by the mixing of two parent phases can change the crystal structure of the parent phase, which further change the bandgap, birefringence or mechanical properties of the parent phase. AgGaGeS_4 , $\text{AgGaGe}_3\text{S}_8$ and $\text{AgGaGe}_5\text{Se}_{12}$ are representatives of the mixed-crystals.^{131–135} Compared with AGS and AGSe, their anisotropy of thermal expansion is significantly reduced and the laser damage resistance is greatly increased. Moreover, $\text{AgGaGe}_5\text{Se}_{12}$ has a larger bandgap and birefringence than AGSe that can achieve phase matching at 1064 nm.

4.02.2.2.3 Quasi-phase-matched (QPM) semiconductors

The advent of the first practical QPM material—periodically poled lithium niobate (PPLN)—represented a new paradigm in NLO materials development.^{35,38,136} Comparing with birefringence phase matching, using QPM technology to realize laser frequency

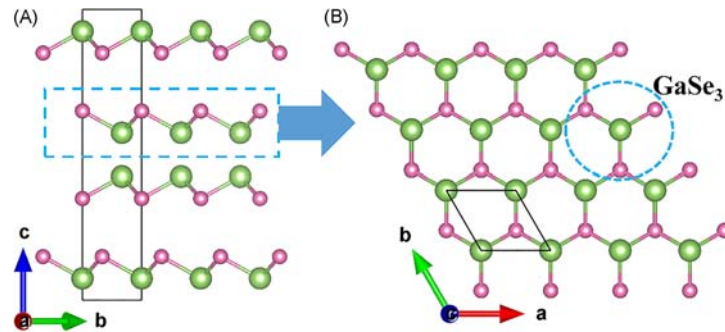


Fig. 12 The layer structure of GaSe viewed along the a -axis (A) and the single layer stretching in ab plane (B).

conversion has the following advantages: (1) The fundamental and the harmonic waves are in the same polarization state so that the maximum second-order nonlinear coefficient of the crystal can be used; (2) Long interaction length can be realized without walk-off effect; (3) It is the most important that QPM method has a large degree of freedom in design. Through the design of the structure, it can realize the phase-matching in any wavelength within the transparency range of crystal.

Orientation-patterned GaAs (OP-GaAs) was the first realization of a practical and efficient QPM semiconductor.^{137,138} GaAs is a cubic zinc blende semiconductor crystal possessing a very large second-order nonlinear susceptibility ($d_{14} = 104 \text{ pm} \cdot \text{V}^{-1}$), high thermal conductivity ($0.46 \text{ W} \cdot (\text{cm K})^{-1}$), and low absorption losses over most of its transparency range ($0.9\text{--}18 \mu\text{m}$).⁹⁸ OP-GaAs can be grown by hydride vapor phase epitaxy, and has been commercialized. The all-epitaxial processing has harvested bulk OP-GaAs devices both for internal use and external sale by BAE Systems.^{98,139,140}

OP-GaP exhibits the excellent properties including large second-order nonlinear susceptibility ($d_{14} = 70.6 \text{ pm} \cdot \text{V}^{-1}$) and high thermal conductivity ($110 \text{ W} \cdot (\text{cm K})^{-1}$). Besides, it has been successfully applied in $1 \mu\text{m}$ -pumped laser systems, owing to the lower two-photon absorption than OP-GaAs.^{141–143}

4.02.3 Near-infrared and visible nonlinear optical materials

The solid-state near-IR and visible lasers have stable performance, compact structure and integrability, which makes them have a good application prospect in optical storage, optical communication and laser medical instrument, etc.^{144–148} At present, the output of laser radiations in the spectra range of $400\text{--}3500 \text{ nm}$ needs the help of frequency conversion of NLO crystal materials. From visible to near-infrared spectral range, many NLO crystals have been studied, and now there are quite a few inorganic NLO candidates, including phosphate, iodate and niobate, etc., which exhibit excellent properties and can almost meet the current market demands.

4.02.3.1 Representative near-infrared and visible nonlinear optical materials

4.02.3.1.1 Potassium dihydrogen phosphate KH_2PO_4 (KDP)

KDP crystallizes in tetragonal system with non-centrosymmetric space group $I2d$, and its unit cell dimensions is $a = 7.453 \text{ \AA}$, $c = 6.973 \text{ \AA}$, $Z = 4$.¹⁴⁹ The crystal structure along the a -axis is mainly constructed by the H_2PO_4 groups through the strong hydrogen bonds (Fig. 13). The constituent K atoms locate at the interspaces of the anionic groups and interconnect the adjacent anionic networks via K–O bonds. In the structure, the K atom is eight-coordinated with O atoms to form the KO_8 polyhedron, and

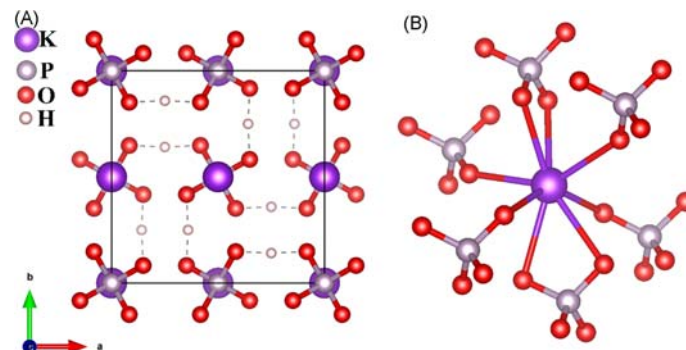


Fig. 13 The structure of KDP viewed along the c -axis (A) and the coordinated environment of K atom (B).

each KO_8 polyhedron is linked with six PO_4 groups. KDP crystal is a very classical NLO material and commonly used as optical frequency converters owing to the applicable NLO coefficient ($d_{36} = 0.39 \text{ pm} \cdot \text{V}^{-1}$ at 1064 nm), high laser damage threshold (7 J cm^{-2} , 5.5 nm pulse width at 355 nm base on 1-on-1 test mode), high transmittance from near-IR to UV, as well as easy to grow.^{150–153}

KDP crystals have been widely applied since the first experiments made in the 1960s in fields of SHG, OPO, Q-switch, and electro-optic modulators.^{154–156} Especially, with the development of high-power laser technology and inertial-confinement fusion, damage-resistant and wide-aperture SHG and THG crystals are needed.^{157,158} For these purposes, the rapid crystals growth of KDP with larger-size and higher optical-quality are needed.

KDP crystal is usually grown from saturated aqueous solution in which the driving force of growth is the supersaturation of the solution.^{159–162} The most obvious advantage of this method is that it is easy to grow large size of single crystal with high optical quality. It is important that the solution in contact with the crystal growth surface should be strictly controlled to be stable and retain a suitable supersaturation.

KDP crystals are primarily grown using conventional methods or rapid techniques. The disadvantages of conventional method are slow rate of growth ($1\text{--}2 \text{ mm d}^{-1}$) and long periods (months or more than 1 year). Therefore, rapid growth techniques with shorter periods (~ 3 months) have been drawn considerable attention. Comparing with the conventional method, the rapid growth of KDP crystals has a higher growth rate but the quality and uniformity are reduced. Therefore, in order to rapidly grow large-size KDP crystals with high-quality, it is necessary to study the relationship between status, properties and stability of the solution and growth rate, and to strengthen the fluid effect of the solution and increase the supersaturation of the solution while keeping the solution stable.^{163,164}

4.02.3.1.2 Potassium titanyl phosphate KTiOPO_4 (KTP)

KTP crystallize in tetragonal system with the space group of $Pna2_1$ (33) and the unit cell dimensions of $a = 12.814 \text{ \AA}$, $b = 10.616 \text{ \AA}$, $c = 6.404 \text{ \AA}$, and $Z = 8$.¹⁶⁵ KTP exhibits a $3\text{D}^3[\text{TiOPO}_4]_\infty$ anionic framework built by alternating bridged PO_4 tetrahedra and $[\text{TiO}_6]_\infty$ chains, and the K atoms are located in cavities (Fig. 14). The open nature of this framework allows atoms to diffuse easily along the c direction, which allows ion exchange to take place. Alternating long and short Ti–O bonds occurs along the $[\text{TiO}_6]_\infty$ chains with Ti–O bond distance varied by as much as 0.38 \AA and results in a net c -directed polarization, which makes the major contribution to the large NLO coefficient ($d_{31} = 6.5$, $d_{32} = 5.0$, $d_{33} = 13.7$, $d_{24} = 7.6$ and $d_{15} = 6.1 \text{ pm} \cdot \text{V}^{-1}$ near $1 \mu\text{m}$).¹⁶⁵

In addition, owing to its wide transparency range from $0.35 \mu\text{m}$ to $4.5 \mu\text{m}$,^{166,167} high optical damage threshold ($> 2\text{--}3 \text{ GW cm}^{-2}$, 10 ns, 10 Hz, 1064 nm),¹⁶⁸ good thermal stability and PM properties, KTP crystal is widely used as NLO materials. Typical application domains include SHG of Nd-doped laser systems for green or red light output, parametric sources (OPG, OPA and OPO) for 600–4500 nm tunable output, E-O modulators, optical switches, directional couplers, optical waveguides for integrated NLO and E-O devices, etc.^{169–172} One disadvantage of KTP is its susceptibility to photochromic damage, known as gray- or gray-tracking, which occurs under green pulsed or CW laser irradiation most commonly presented at 532 or 514.5 nm irradiation.¹⁷³ In addition to the photochromic effect, photorefractive damage also presents in KTP.¹⁷⁴

In 1971, Masse and Grenier firstly grew the KTP crystals from flux,¹⁷⁵ which often introduced impurities (such as Fe and other transition metals) into the crystal during the growth process so that leading to a lower laser damage threshold and lower ability to anti-gray track.^{176,177} Later, more methods were explored to grow the KTP crystals including hydrothermal method and high temperature solution method. KTP decomposes at $\sim 1150 \text{ }^\circ\text{C}$, and the process of crystal growth by high temperature solution method is KTP crystallizing out of a molten KTP and flux composition when cooled.¹⁶⁵ Generally, phosphate system is chosen as the flux,^{178,179} which has the advantage of strong solubility to KTP and KTP is the only stable phase in the range of $760\text{--}1000 \text{ }^\circ\text{C}$ that avoids the introduction of impurities. Besides, the melting point of phosphate system is low and the decomposition

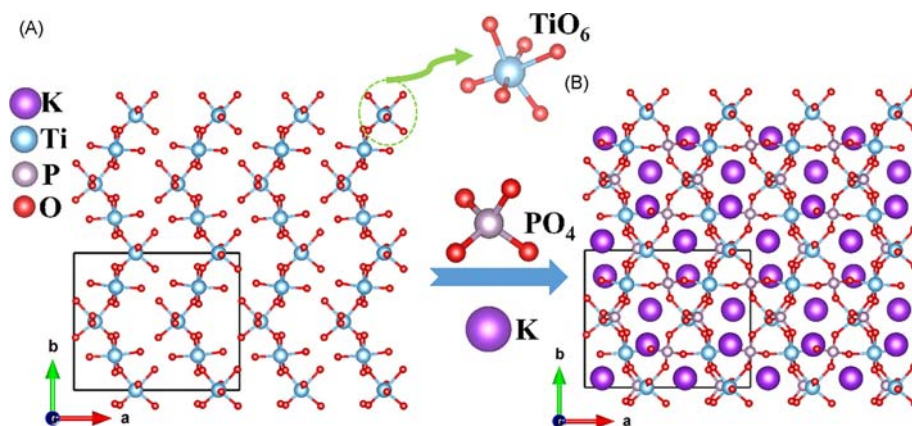


Fig. 14 The $[\text{TiO}_6]_\infty$ chains arranged in the ab plane (A) and the structure of KTP viewed along the c -axis (B).

temperature is high. However, its disadvantage is that the viscosity increases of the solution, which increases the difficulty of crystal growth. Up to now, TSSG and spontaneous nucleation technique is widely used to grow KTP crystals from flux.

For the hydrothermal method, the bulk KTP crystals free of macroscopic defects (the inset of Fig. 15) can be grown using crushed flux KTP crystals as nutrients in solution composed of $2.0 \text{ mol L}^{-1} \text{ K}_2\text{HPO}_4 + 0.1 \text{ mol L}^{-1} \text{ K}_2\text{HPO}_4 + 1 \text{ wt\% H}_2\text{O}_2$. There is an obvious disadvantage in the KTP crystal grown by the hydrothermal method, that is an absorption peak near 2750 nm wavelength, which is caused by the vibration of OH^- (Fig. 15), while there is no that absorption peak of KTP crystal grown by the high temperature solution method.¹⁸⁰ Therefore, the single crystals of KTP are mostly grown by the high temperature solution method and this is the most popular method.^{181–183}

4.02.3.1.3 Lithium niobate LiNbO_3 (LN)

LN crystallizes in an asymmetric space group $R3c$ (No. 161) with unit cell parameters of $a = 5.14829 \text{ \AA}$, $c = 13.8631 \text{ \AA}$, and $Z = 6$.¹⁸⁴ LN crystal exhibits perovskite-type structure, which is built by LiO_6 and NbO_6 octahedra. A LiO_6 (NbO_6) octahedron can link with six surrounding LiO_6 (NbO_6) octahedra via corner-sharing O atoms forming the 3D-networks $[\text{LiO}_3]_\infty$ ($[\text{NbO}_3]_\infty$). Then, the $[\text{LiO}_3]_\infty$ and $[\text{NbO}_3]_\infty$ networks are joint together to form the whole structure (Fig. 16).

LN crystal possesses large NLO coefficient ($d_{22} = 2.46$, $d_{22} = -4.64$, $d_{33} = -41.7 \text{ pm V}^{-1}$ at 1058 nm),¹⁸⁵ moderate birefringence (0.08 at 633 nm),¹⁸⁶ wide transparency range from UV to mid-IR spectra (0.45–5.5 μm),¹⁸⁶ stabilized physical and chemical properties, and easy to grow large-size optical crystals, etc.¹⁸⁷ In addition, owing to the lattice structure and rich defect structures in the LN crystal whose properties are highly adjustable, many optical properties of LN can be substantially adjusted by crystal components adjusting, element doping, valence control and so on. Moreover, LN crystal has excellent photoelectric effects including piezoelectric effect, electro-optic effect, NLO effect, photorefractive effect, photovoltaic effect, photoelastic effect, acousto-optic effect and so on. Therefore, LN crystal is one of the most frequently used insulator crystals that can be processed into surface acoustic filters, optical modulators, phase modulators, optical isolators, electro-optic Q switches and other photoelectric devices, which are widely applied in the fields of electronic technology, optical communication technology, laser technology and so on.^{188–193} Recently, with the breakthrough of the 5th generation wireless communication (5G), micro-nano photonics, integrated photonics and quantum optics and other application fields, LN crystal has once again attracted extensive attention.¹⁹⁴

According to the phase diagram of the $\text{Li}_2\text{O-Nb}_2\text{O}_5$ binary system, stoichiometric LN crystal melts incongruently, while it melts congruently in a non-stoichiometric composition of 48.6 mol% Li_2O and 51.4 mol% Nb_2O_5 .^{195–199} Up to now, the non-stoichiometric high-quality single crystals of LN are easier to be grown from the melt by the Czochralski method.^{200,201} Thus the non-stoichiometric congruent LN (CLN) crystal has been widely applied. However, owing to the Li^+ cations deficiency in the CLN crystal, a large number of lattice defects have been generated, which on the one hand affect the optical properties (e.g., the values of NLO coefficient and linear electro-optic coefficient are low and coercive field is high in defect CLN crystal) of the crystal, on the other hand that the lattice defects provide vacancies for ions doping.^{202–206} Fig. 17 shows the CLN and Mg-doped crystals grown through Czochralski method by Riscob et al.^{187,201}

Near-stoichiometric LN (NSLN) crystal also shows many excellent photoelectric properties (i.e., short UV cutoff edge, the narrowing of several spectral lines, and easier to produce periodically polarized structures for QPM), which are expected to show

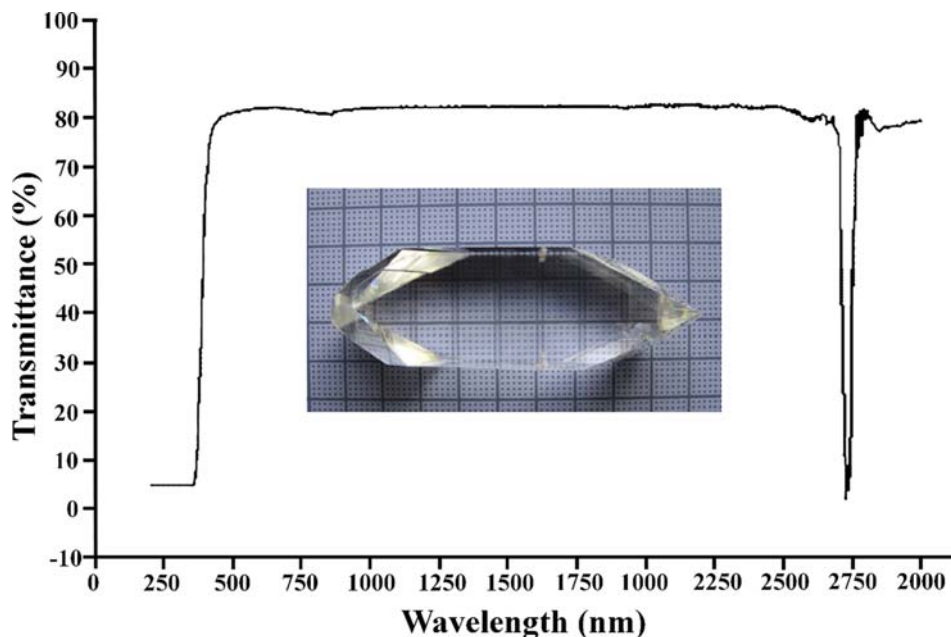


Fig. 15 Transparency curve of KTP crystal grown by the hydrothermal method, Inset: KTP crystal grown by the hydrothermal method.

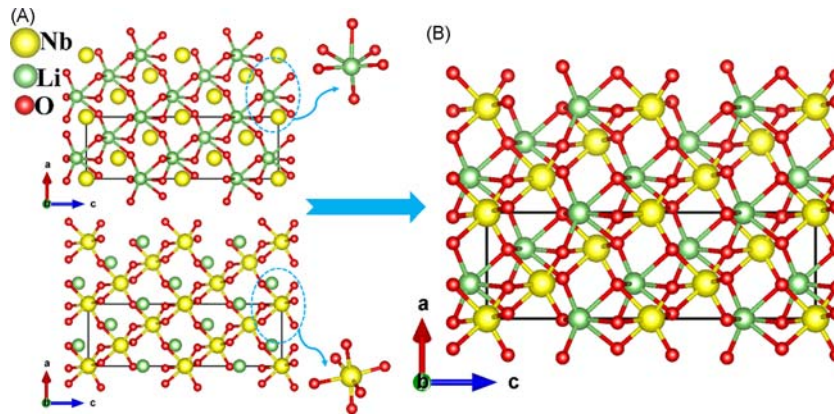


Fig. 16 The $[\text{LiO}_3]_\infty$ (top) and $[\text{NbO}_3]_\infty$ (bottom) networks extending in the ac plane (A) and the structure of LN in the ac plane (B).

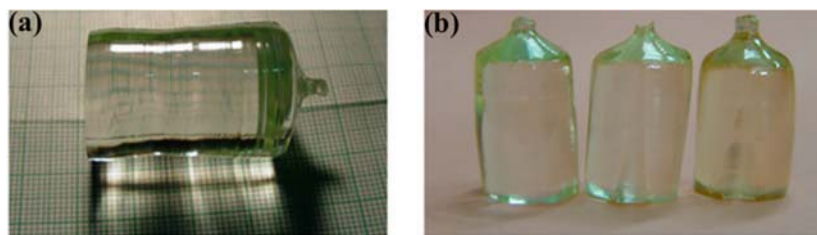


Fig. 17 Photographs of undoped CLN (A) and Mg (2, 4 and 6 mol% from left to right) doped CLN crystal (B).

improved performance for some applications.^{207–209} During the last two decades significant innovations in growth techniques have directed the research and development towards the growth of NSLN crystals. The main growth methods contain the high temperature solution method, vapor transport equilibration method in a Li-rich ambience, as well as lithium-rich melting method.^{209–212}

4.02.3.1.4 Potassium niobate KNbO_3 (KN)

KN crystal belongs to $mm2$ point group with the unit cell parameters of $a = 5.6896 \text{ \AA}$, $b = 3.9692 \text{ \AA}$, $c = 5.7256 \text{ \AA}$, and $Z = 2$.²¹³ It features a CaTiO_3 -type perovskite structure which is built by distorted NbO_6 octahedra and K atoms. Each distorted NbO_6 octahedron links with the surrounding six ones via corner-sharing to form the $3\text{D } ^3[\text{NbO}_3]_\infty$ framework which exhibits quadrilateral holes stacked in the ab plane in which the K atoms located in the holes (Fig. 18). With decreasing from high temperature to 425, 225 and -10°C , KN undergoes a series of structural phase transitions, which hangs from the cubic (centrosymmetric $Pm\bar{3}m$) to tetragonal (non-centrosymmetric $P4mm$), orthorhombic (non-centrosymmetric $Amm2$), and rhombohedral (non-centrosymmetric $R3m$) phases, respectively.²¹⁴

KN possesses large nonlinear optical coefficients ($d_{31} = 11.9$, $d_{32} = 13.7$, $d_{33} = 20.6 \text{ pm V}^{-1}$ at 1064 nm), wide transparency range (0.4–5 μm) and favorable electro-optic quality factor, photorefractive quality factor, piezoelectric property, as well as good chemical stability and fast crystal growth rate.^{215–219} As an NLO material, KN crystal is mainly used for low power, especially the milli-watt frequency conversion based on the semiconductor laser, in which, it has the highest conversion efficiency compared with other commonly used NLO materials, such as KTP and LN crystal, etc. KN can be used for OPO when pumped by Nd:YAG lasers at either the fundamental or the SHG wavelength, producing tunable radiation in the near-IR spectral region between

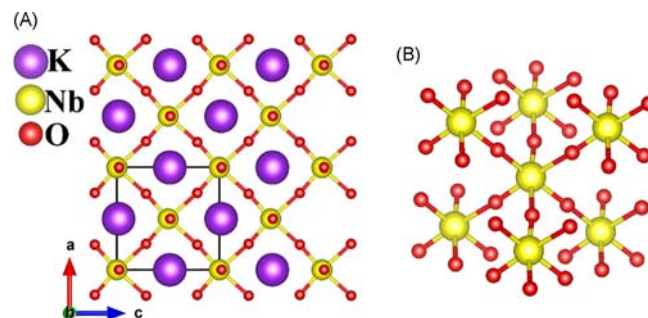


Fig. 18 The structure of KN viewed along the b -axis (A) and the NbO_6 octahedron linked with the surrounding six via corner-sharing O atoms (B).

0.7 μm and 3 μm .^{220–222} Besides, KN crystals have been developed as a bulk acoustic wave and surface acoustic wave devices with a high coupling and zero-temperature coefficient of delay.²²³ However, there are also some disadvantages: The refractive index of KN crystal changes largely with temperature, which make its phase matching change and results in unstable laser output.²²⁴ Low laser damage threshold of KN crystal limits the application in high-power laser system.^{225,226} In addition, two structural phase transitions have been happened in the process of KN crystal growth, which results in multi-domain crystal, and in which the complex domain-wall stress causes the crystal easy to crack that makes it difficult to obtain large-size single-domain crystal with complete structure.²²⁷

According to the phase equilibrium diagram of the $\text{K}_2\text{O-Nb}_2\text{O}_5$ binary system, a stoichiometric KN could not be grown from the melt by the Czochralski method.^{227–229} While, KN single crystal can be successfully grown from a solution with potassium enriched under the condition of shallow temperature gradient using the Kyropoulos or TSSG techniques. However, the crystal obtained usually contained many cracks presumably due to the thermal stress generated in the process of the phase transition. After many years of systematic research, it shows that those cracking can be prevented by controlling a low temperature gradient in solid-liquid contact surface during the crystal growth, and going through a long time cooling. In addition, poling treatment is also an effective way.

4.02.3.1.5 Lithium iodate $\alpha\text{-LiIO}_3$

$\alpha\text{-LiIO}_3$ crystallizes in an asymmetric space group $P6_3$ (No. 173) with unit cell parameters of $a = 5.4815 \text{ \AA}$, $c = 5.1709 \text{ \AA}$, and $Z = 2$.²³⁰ In the structure, each I atom is coordinated with three O atoms forming the isolated umbrella-type IO_3 unit, which is parallel to each other, and the Li atoms can link with the surrounding six IO_3 unit via Li–O bonds (Fig. 19). Its SHG coefficient ($d_{15} = -5.53 \text{ pm V}^{-1}$ at 1064 nm) is one order of magnitude larger than that of KDP, and its crystal has good optical uniformity and wide transparency range (0.28–6.0 μm), and it is easy to grow large-size single crystal with high optical quality from aqueous solution, which shows that it is a kind of practical crystal.^{231–236} However, the application of $\alpha\text{-LiIO}_3$ crystal as NLO materials is seriously limited due to its hygroscopic, low laser damage threshold, as well as low conversion efficiency since it cannot achieve the optimal phase matching.²³⁷ In addition to the NLO effects, $\alpha\text{-LiIO}_3$ has optical rotation, pyroelectric and electro-optical effects, while does not have ferroelectric effects.^{238–241}

4.02.3.2 Newly developed near-infrared and visible nonlinear optical materials

4.02.3.2.1 Phosphates

KDP family: Ammonium dihydrogen phosphate $\text{NH}_4\text{H}_2\text{PO}_4$ (ADP) is an important member of the KDP family, which shows the similar structure with KDP (Fig. 20). In 1938, Bush et al. studied the crystal growth habits of ADP. In the 1940s, they found that ADP had piezoelectric properties, and subsequently, ADP was used in sonar equipment that was devoted to the war. In the 1960s, after the advent of the laser technology, it was found that ADP crystal has good NLO properties and can realize the SHG, THG and FHG based on 1064 nm pumped laser.^{242,243} At $T_C = 122.7 \text{ K}$, KDP becomes ferroelectric while ADP becomes antiferroelectric at $T_N = 148.2 \text{ K}$. The transparency spectral range (50% transmission level for 0.2-cm-long crystal) of ADP crystal is from 184 nm to more than 1500 nm, and it has a considerable SHG coefficient ($d_{36} = 0.47 \text{ pm} \cdot \text{V}^{-1}$), thus it is widely employed as electro-optic devices.^{244,245} The ADP crystal is usually grown from saturated aqueous solution by slowly cooling.²⁴⁶

Deuterated potassium dihydrogen phosphate KD_2PO_4 (DKDP) is isotopic crystal of KDP, and it has two phases, tetragonal and monoclinic,^{247,248} in which, the phase DKDP crystallized in the tetragonal system is widely used as an NLO material. DKDP crystal has higher transmittance in the IR range and comparable SHG responses to KDP, which is currently used as the SHG material of the high-energy loaded in high-power laser fusion devices.^{249–252} The DKDP crystals can be grown by the slow evaporation method.

KTP family: ATiOAsO_4 ($A = \text{NH}_4, \text{K}, \text{Rb}, \text{Tl}$) and ATiOPO_4 ($A = \text{NH}_4, \text{Tl}$) have been obtained through the monovalent substitution of A cations in ATiOAsO_4 and ATiOPO_4 . They are isostructural with KTP and crystallize in the space group of $Pna2_1$ (No. 33), which preserve the structure features and excellent properties of KTP. ATiOAsO_4 ($A = \text{NH}_4, \text{K}, \text{Rb}, \text{Tl}$) and ATiOPO_4 ($A = \text{NH}_4, \text{Tl}$) exhibit the 3D $^3[\text{TiOAsO}_4]_\infty$ and $^3[\text{TiOPO}_4]_\infty$ anionic frameworks, respectively, and the A cations are located in cavities (Fig. 21).^{253–258} They exhibit large SHG efficient and wide transparency ranges, which are comparable or slightly superior to KTP crystal. They can be grown from high temperature flux.

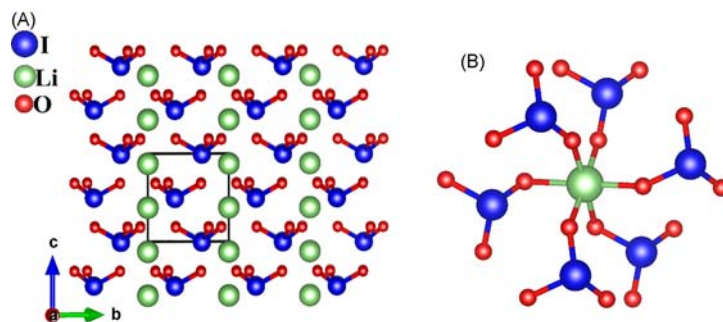


Fig. 19 The isolated umbrella-type IO_3 units and Li atoms arranged in the bc plane (A) and the coordinated environment of Li atom (B).

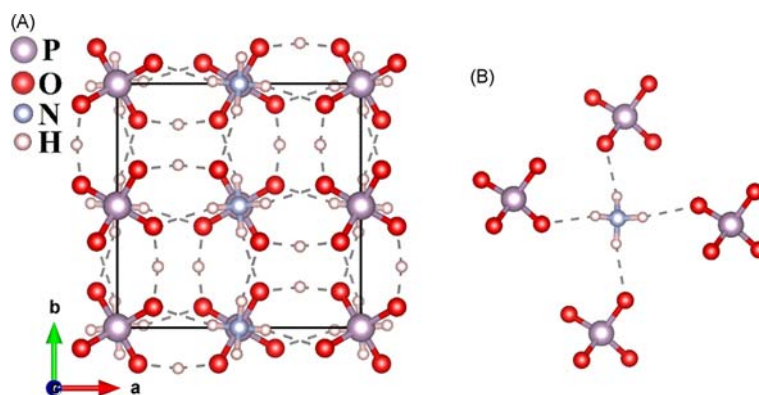


Fig. 20 The structure of ADP viewed along the c -axis (A) and the coordinated environment of the NH_4 group (B).

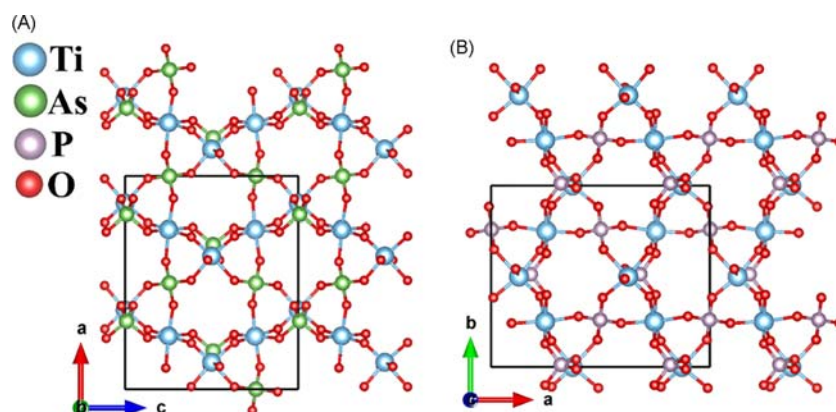


Fig. 21 The 3D $^3[\text{TiOAsO}_4]_\infty$ anionic framework in KTiOAsO_4 (A) and $^3[\text{TiOPO}_4]_\infty$ anionic framework in TlTiOPO_4 (B).

4.02.3.2.2 Iodates

$\text{BiO}(\text{IO}_3)$: $\text{BiO}(\text{IO}_3)$ was obtained using a hydrothermal method by Halasyamani et al. in 2011. It crystallizes in the orthorhombic system ($Pca2_1$, No. 29)²⁵⁹ and structurally features a $^1[\text{Bi}_2\text{O}_2]_\infty$ chain along the b -axis with the iodate groups hanging on both sides of the chains (Fig. 22). The local dipole moment of the IO_3 polyhedra is additive and results in a macroscopic polarization along the c -axis. $\text{BiO}(\text{IO}_3)$ exhibits strong SHG response of about $12.5 \times \text{KDP}$ based on the 1064 nm radiation and its measured band gap is about 3.3 eV.^{260,261}

$\text{BaNbO}(\text{IO}_3)_5$: $\text{BaNbO}(\text{IO}_3)_5$ was synthesized by the hydrothermal reaction by Mao group in 2009.²⁶² It crystallizes in the acentric space group Cc (No. 9), and its structure features isolated $\text{NbO}(\text{IO}_3)_4(\text{IO}_4)$ group which is built up of a Nb atom and surrounding four IO_3 units, a IO_4 unit and a terminal O atom. The $\text{NbO}(\text{IO}_3)_4(\text{IO}_4)$ groups are further linked via Ba–O bonds forming the whole 3D structure framework (Fig. 23). By the combination of the Nb^{5+} cation which has a d^0 electronic configuration and the lone-pair-containing iodate anion, $\text{BaNbO}(\text{IO}_3)_5$ exhibits a large SHG response ($\sim 14 \times \text{KDP}$ based on the powder SHG

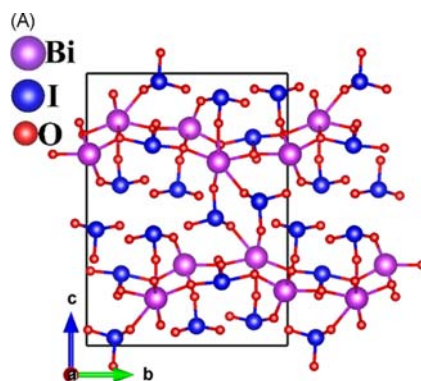


Fig. 22 The structure of $\text{BiO}(\text{IO}_3)$.

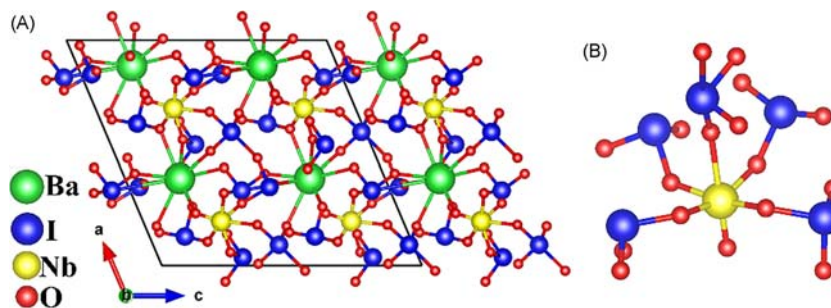


Fig. 23 The structure of $\text{BaNbO}(\text{IO}_3)_5$ (A) and the $\text{NbO}(\text{IO}_3)_4(\text{IO}_4)$ group (B).

measurement). The optical diffuse reflectance spectrum indicates an optical band gap of 3.64 eV. More optical properties are waiting for evaluation based on large-size crystals.

4.02.3.2.3 Borates

α - and δ - BiB_3O_6 : α - BiB_3O_6 and δ - BiB_3O_6 were discovered first in 1962 by Levin et al. and in 2006 by Huppertz et al., respectively.^{263,264} They crystallize in the space group of $C2$ (No. 5) and $Pca2_1$ (No. 29), respectively. α - BiB_3O_6 features the 2D $^2[\text{B}_3\text{O}_6]_\infty$ layers that are made up by B_3O_8 FBBs (Fig. 24A and B). In 1998, Hellwig et al. reported that α - BiB_3O_6 crystal can be considered as an NLO material owing to large SHG coefficient ($d_{\text{eff}} = 3.2 \text{ pm} \cdot \text{V}^{-1}$), wide transparency ranges covering the visible and near-infrared regions and high transmittance ($\sim 80\%$).^{265,266} Moreover, it possesses large birefringence and has realized SHG output within the type-I BPM technology under continuous and pulsed wave pump at 1064 nm. Besides, the SHG of the signal wave of a quasi-continuous OPO (777–1036 nm, 10 kHz, 50 ns) was performed in α - BiB_3O_6 ; as a result, the tuning in the UV range from 450 nm to 494 nm was achieved with maximum blue output of 1.3 W at 470 nm. α - BiB_3O_6 melts congruently with the melting point of 826 °C, which was conventionally grown by TSSG technique. For the δ - BiB_3O_6 crystal, its structure is exclusively built up of BO_4 tetrahedra which share common oxygen to form 3D $^3[\text{B}_3\text{O}_6]_\infty$ framework, and Bi atoms are located in voids (Fig. 24C). The large NLO coefficient ($d_{\text{eff}} = 1.2 \text{ pm} \cdot \text{V}^{-1}$), moderate birefringence (0.0756 at 1014 nm), and wide the transmission range (from 315 nm to more than 3500 nm, 50% transmission level) indicate that δ - BiB_3O_6 crystal is suitable for doubling the laser with a wavelength 1.32 μm , especially as the concentrated SFD laser crystal for this wavelength.²⁶⁷

$\text{Pb}_2\text{BO}_3\text{X}$ (X=Cl, Br, I): $\text{Pb}_2\text{BO}_3\text{Cl}$ was reported earliest by Ok et al. in 2016.²⁶⁸ Subsequently, $\text{Pb}_2\text{BO}_3\text{Br}$ and $\text{Pb}_2\text{BO}_3\text{I}$ were reported by Ye et al. and Halasyamani et al. in 2018, respectively.^{269,270} They crystallize in the trigonal space group of $P321$

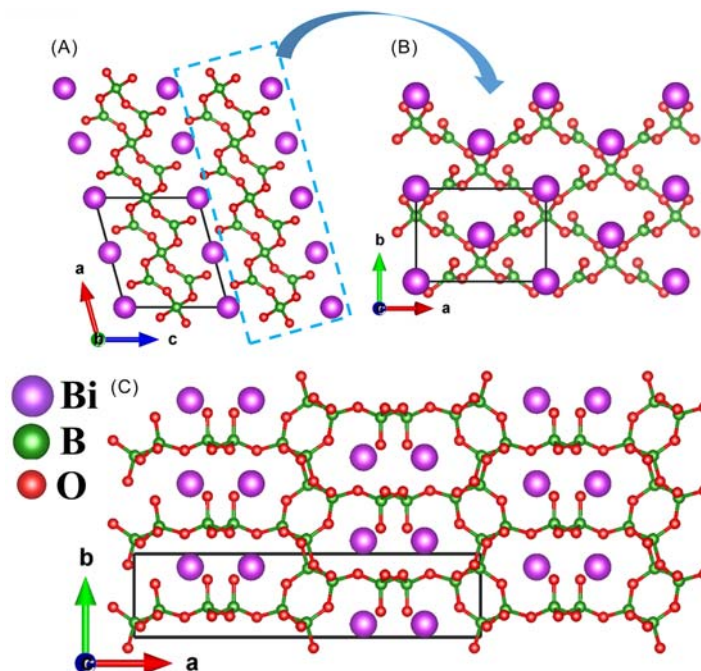


Fig. 24 The structure of α - BiB_3O_6 viewed along the *c*-axis (A), a 2D $^2[\text{B}_3\text{O}_6]_\infty$ layers of α - BiB_3O_6 stretching in the *ab* plane (B), and the structure of δ - BiB_3O_6 viewed along the *c*-axis (C).

(No. 150) and their structures feature the ${}^2[\text{Pb}_2\text{BO}_3]_\infty$ layers which are linked by Pb-X (X=Cl, Br, I) bonds to form the final 3D frameworks (Fig. 25). The uniform arrangement of the isolated BO_3 units and PbO_3 trigonal pyramids in the structure leads to the maximum superposition of SHG effect (~ 9 , 9.5 and $10 \times \text{KDP}$ for Cl, Br and I analogs based on the powder SHG measurements). In addition, they have wide transparency windows from the UV to the mid-IR region,^{268,270,425} thus the $\text{Pb}_2\text{BO}_3\text{X}$ (X=Cl, Br, I) family is considered as NLO materials candidates.

4.02.4 Ultraviolet nonlinear optical materials

UV NLO crystal materials are the key components for multi-stage frequency conversion of UV lasers, especially solid-state laser, which mainly use parametric up-conversion processes (such as SHG, SFG, THG, etc.) and OPO technology to generate UV laser radiation.^{271–273} Obviously, the primary requirement for the optical properties of UV NLO materials is that they have high transparency in the UV spectral rang. Besides, it is also necessary to possess a large second-order NLO coefficient ($d_{ij} > 0.39 \text{ pm} \cdot \text{V}^{-1}$), a suitable birefringence (0.05–0.10 at 1064 nm) to achieve the phase-matching conditions in the UV spectral range, a large laser damage threshold, favorable chemical stability, easy growth of large-sized single crystals, as well as other good physical and chemical properties.^{82,274} Over the past several decades, many efforts have been devoted to search UV NLO materials with excellent comprehensive properties. A series of UV NLO materials have been reported, such as β -BBO, LBO, and CBO, etc., which have been widely used.^{82,275–278} Remarkably, inorganic borates have the shortest wavelength boundary of the natural absorption of radiation (150–200 nm), which is a significant advantage over other inorganic materials (niobates, titanates, iodates) used in UV lasers.^{279,280} Besides, most nitrates dissolve easily in water and would not be suitable for industrial applications. And for the carbonates, it is difficult to grow due to the decomposition easily of the carbonates at high temperature. Therefore, borate is the most research inorganic NLO material system in UV and DUV spectra.

4.02.4.1 Representative ultraviolet nonlinear optical materials

4.02.4.1.1 β -barium borate $\beta\text{-BaB}_2\text{O}_4$ ($\beta\text{-BBO}$)

β -BBO was discovered in 1985 by Chen et al., and it quickly became the most popular crystal for visible and UV spectra applications owing to its excellent overall performance.²⁷⁶ In the last few decades, the crystal structure, phase transition behavior, crystal growth, comprehensive optical properties and microscopic mechanism of β -BBO were systematically studied.

β -BBO crystallizes in an asymmetric space group R3 (No. 146) with $a = 12.532 \text{ \AA}$, $c = 12.717 \text{ \AA}$ and $Z = 6$. In the structure, three BO_3 units connect with each other by corner-sharing O atoms to form the isolated six-membered B_3O_6 ring, which stacks along the c -axis, and the Ba^{2+} cations balance the charge in the cavity (Fig. 26). The structure-performance analysis shows that the approximately parallel B_3O_6 groups are beneficial for large birefringence (0.11 at 1064 nm) and SHG coefficient ($d_{\text{eff}} = 6 \times \text{KDP}$).²⁷⁶ The alkaline-earth metal Ba atoms without d-d and f-f electron transition are beneficial for the β -BBO crystal to display a wide transparency range (0.189–3.5 μm). It is a negative uniaxial crystal with the shortest phase-matching wavelength of 205 nm, the high laser damage threshold (23 GW cm^{-2} for 14 ns pulses at 1064 nm), favorable mechanical properties and good chemical stability. These excellent properties make it virtually irreplaceable in certain applications.^{281–284} At present, β -BBO crystals are widely used in the processes of the SHG, THG, FHG of Nd: YAG and Nd: YLF leaser. Also, β -BBO crystal has been extensively applied in the other lasers with SHG, SFG, OPO, OPA technologies.^{285–289}

β -BBO has a melting point of 1095 $^\circ\text{C}$ and a transition temperature of around 925 $^\circ\text{C}$.²⁷⁶ Therefore, β -BBO crystals are generally grown by high temperature solution method with TSSG, in which, a variety of oxides or fluorides including, B_2O_3 , Na_2O , K_2O , NaF, LiF, LiF-Li₂O, $\text{Na}_2\text{O-B}_2\text{O}_3$, $\text{Na}_2\text{O-BaO}$, etc., as well as $\text{K}_2\text{B}_2\text{O}_4$, $\text{Na}_2\text{B}_2\text{O}_4$ can be selected as the fluxes.^{291–295} Herein, three typical phase diagrams are briefly summarized.

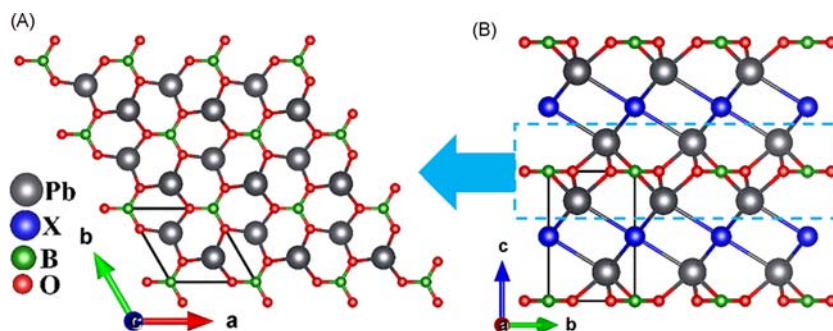


Fig. 25 The ${}^2[\text{Pb}_2\text{BO}_3]_\infty$ layer stretching in the ab plane (A) and the structure of $\text{Pb}_2\text{BO}_3\text{X}$ (X=Cl, Br, I) viewed along the a -axis (B).

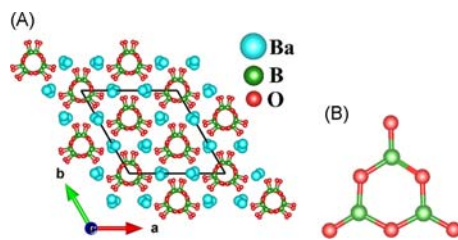


Fig. 26 The structure of β -BBO (A) and isolated six-membered B_3O_6 ring (B).

- 1) The binary BBO- Na_2O system: The phase equilibrium relation of BBO- Na_2O is shown in Fig. 27, which was determined by Huang and Liang.²⁹⁰ It is clearly seen that the crystallization temperature of β -BBO crystal can be extended from ~ 920 to ~ 755 °C when the solvent concentration is from 22% to 30% in molar ratio.
- 2) The binary BBO-NaF system: The BBO-NaF pseudo-binary diagram was investigated first by Roth and Perlov and later refined by Bekker et al. (Fig. 28).^{295,296} The ternary BaO- B_2O_3 -NaF system was found to be suitable for growing β -BBO crystal due to the reduced viscosity and wide temperature range of crystallization. The diagram of phase equilibrium shows that β -BBO can be crystallized in the range of 925–805 °C and the quantity of NaF varies in the range of 31–47% in molar ratio.
- 3) Phase equilibrium in β -BBO-LiF system: The BaO- B_2O_3 -LiF system was studied by Bykov et al., in 1994 which noted the narrow growth temperature range.²⁹⁷ In 2015, the phase equilibrium in β -BBO-LiF system was analyzed by Simonova et al.²⁹⁸ The concentration changes from 67.5% to 60% β -BBO corresponding to the primary crystallization regions of β -BBO, and the liquidus curve bends at the point defined by the concentration of 50% β -BBO corresponding to a temperature of 860 °C. The study reveals that the β -BBO-LiF system can be considered applicable for growing β -BBO crystals owing to the decreased viscosity of solution and the high yield.

According to the phase diagram, the ratio of raw materials and the temperature range of growth can be roughly determined. Two methods can be used for the preparation of crystallization of raw materials, one is to mix the components (Ba-contained

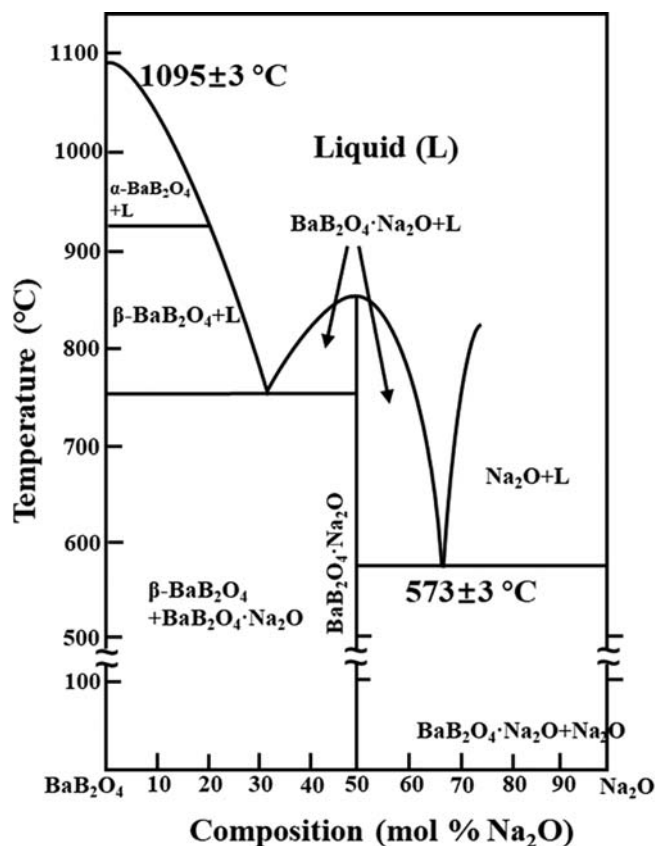


Fig. 27 The BBO- Na_2O pseudo-binary diagram determined by Huang and Liang.²⁹⁰

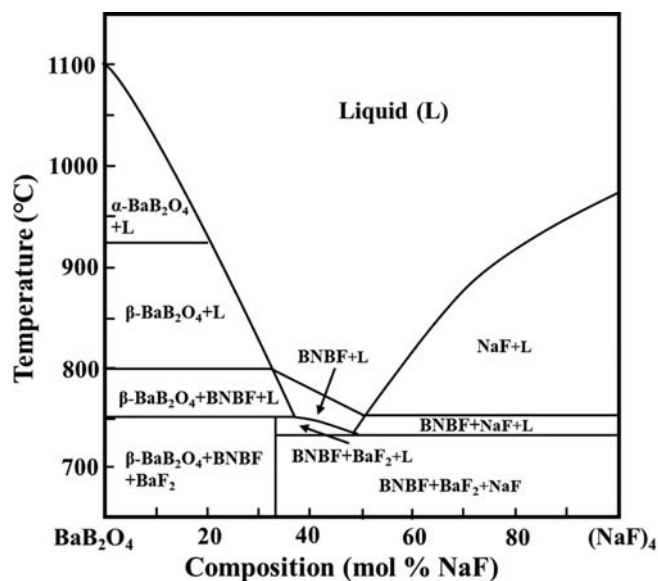


Fig. 28 The BBO-NaF pseudo-binary diagram. Adapted with permission from Ref. Bekker, T. B.; Fedorov, P. P.; Kokh, A. E. The Ternary Reciprocal System Na, Ba/BO₂, F. *Cryst. Growth Des.* **2012**, *12*(1), 129–134. Copyright © 2012, American Chemical Society.

compound, B₂O₃/H₃BO₃, and solvents) directly, the other is to synthesize polycrystalline single-phase samples of β-BBO as raw materials, and then add the solvent according to the ratio.^{299,300}

4.02.4.1.2 Lithium triborate LiB3O5 (LBO)

The LBO crystal is another NLO material discovered by Chen and coworkers with excellent NLO properties in the UV spectral range.²⁷⁷ It crystallizes in the orthorhombic space group *Pna*2₁ (No. 33) with unit cell $a = 8.46 \text{ \AA}$, $b = 7.38 \text{ \AA}$, $c = 5.13 \text{ \AA}$, $Z = 4$.³⁰¹ The crystal structure is built up of the fundamental building unit B₃O₇ groups consisting of two BO₃ triangles and one BO₄ tetrahedron. Each B₃O₇ group is connected to the surrounding four groups mutually via corner-sharing O atoms to form the final 3D framework with channels, where the Li atoms are located (Fig. 29).

According to the study of the relationship between the microstructure and properties by Chen et al.,²⁸⁰ the B₃O₇ group is the main contributor to the large SHG coefficient ($d_{31} = 0.67$, $d_{32} = 0.85$, $d_{33} = 0.04 \text{ pm} \cdot \text{V}^{-1}$) of LBO.³⁰² Besides, since the *exo*-ring O atoms are shared by two B₃O₇ groups, the dangling bonds of the group are removed which results in a short UV cutoff edge (155 nm). Besides, the high laser damage threshold (18.9 GW cm⁻² for 1.3 ns pulses at 1053 nm), wide receiving angle and discrete angle, large effective SHG coefficient ($\sim 3 \times \text{KDP}$), as well as good physical and chemical properties make it be widely used in frequency conversion which concentrates around SHG and THG of high-power lasers.^{303–307} However, its major shortcoming as a UV NLO crystal is that the unfavorable birefringence (0.043 at 532 nm) limits the PM wavelength ($\lambda_{\text{shortest, BPM}} = 277 \text{ nm}$).³⁰⁸

LBO was first considered a congruent compound by Mazzetti and Carli,³⁰⁹ but was proved to melt incongruently by Rollet and Bouaziz in 1955.³¹⁰ After these, Sastry and Hummel studied the relationships of Li₂O-B₂O₃ system by the quenching method using 20 compositions giving a pseudo-binary phase diagram in 1958.³¹¹ It indicates that LBO crystal can be grown at the B-rich region. However, the high viscosity and the difficulty of the mass transportation of the solution made the growth rate of LBO crystal too

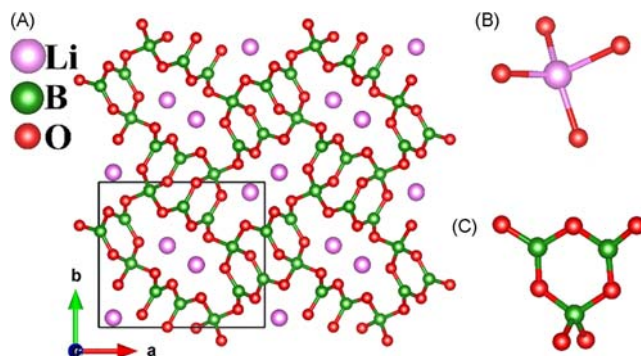


Fig. 29 The structure of LBO viewed along the *c*-axis (A), the coordination environment of the Li atom (B) and the B₃O₇ group (C).

low, and the solution tended to super cool. Many efforts were made to find suitable flux to reduce the solution viscosity.^{312–314} Parfeniuk et al. found that introducing MoO₃ into the solution can reduce the viscosity of the solution, which was suitable for growing LBO crystal. After, the Li₂O-B₂O₃-MoO₃ system was investigated in detail and new growth techniques for LBO crystals were also developed.³¹⁵ In 2010, on the basis of combining the accelerated crucible rotation technique and TSSG methods, Hu's group successfully grew LBO crystals along the near-phase-matching angle direction in the LBO-MoO₃ solutions, with the LBO crystal weight of 1.988 kg (Fig. 30).³¹⁶ In 2014, high-quality single crystal without visible inclusions were grown by Martirosyan et al. in the Li₂O-B₂O₃-MoO₃ system.^{273,317} In their report, crystals were grown by the Kyropoulos method in a two-zone heating furnace with vertically positioned heating elements around the muffle. Highly pure Li₂O, B₂O₃, and MoO₃ compounds and synthesized LBO powder were used as initial agents, and a concentration of 30 wt% was used to grow LBO crystals.

4.02.4.1.3 Cesium triborate CsB₃O₅ (CBO)

In 1958, cesium triborate (CBO) was first reported by Krogh-Moe,³¹⁸ and then the crystal structure of CBO was refined in 1974. It belongs to 222 point group and crystallizes in the orthorhombic space group $P2_12_12_1$ (No. 18) with cell dimensions $a = 6.213$, $b = 8.521$, $c = 9.170$ Å, $Z = 4$.³¹⁹ The unit cell of CBO is shown in Fig. 31. The structure of CBO is very similar to that of LBO which can be described as an infinite 3D network with spiral chains formed by B₃O₇ groups. Each of the four *exo*-ring oxygen atoms is shared by the surrounding four B₃O₇ groups with Cs atoms located in the interstices.

In 1989, Chen et al. estimated the SHG coefficients of CBO crystal by the DFT calculation.²⁷⁸ In 1993, Wu et al. grew the centimeter-scale CBO crystals from the melt and evaluated the SHG coefficients. Meanwhile, the linear and NLO properties of CBO crystal were also studied.³²⁰ The CBO crystals possess high SHG coefficients ($d_{14} = 1.08$ pm · V⁻¹, $\lambda = 1064$ nm), moderate birefringence (0.0597 at 1064 nm), wide transparency range (0.17–3.0 μm), large laser-induced damage threshold (26 GW cm⁻² for 1 ns pulses at 1053 nm) etc. excellent optical properties, which indicate that CBO is a promising NLO crystal for NLO frequency conversion in the UV spectral region.^{278,321–326} However, the severe deliquescence limits its application to some extent.

Phase equilibrium in the Cs₂O-B₂O₃ system was first reported by Krogh-Moe in 1958,³¹⁸ then Penin et al. presented a Cs₂O-B₂O₃ phase diagram in 2003.³²⁷ In the view of the phase diagram (Fig. 32), CBO is a congruent compound with the melt point of 835 °C, and has a broad crystallization composition ranging from 67 to 81 mol% B₂O₃, which indicates that many growth techniques (such as Kyropoulos, Czochralski and TSSG method) could be used to grow CBO single crystals. For example, Kyropoulos technique using a two-zone resistance-heated furnace was employed to grow the CBO crystal.^{323,328–330} Platinum crucible with polycrystalline powder samples of CBO was heated to ~900 °C to make the solid completely melt, and then cooled to 837 °C and the seed was introduced to start crystal growth. CBO crystals grown in different seed orientation (*a*- or *c*-axis) exhibit similar morphology. When CBO crystal was grown by Czochralski or TSSG method, appropriate excessive of Cs₂O components can not only reduce the solution viscosity but also make up the volatilization of Cs₂O at high temperature.^{331,332} The grown CBO crystals often contain a high density of optical scattering centers, which are responsible for the optical loss and reduction in the harmonic generation efficiency.³³³ Thus, many efforts are needed for obtaining high-quality CBO crystal. Recently, single crystals without scattering centers have been successfully grown from the Cs₂O-B₂O₃-MoO₃ ternary system by the TSSG method by Liu et al. (Fig. 33).³³⁴

4.02.4.1.4 Cesium lithium borate CsLiB₆O₁₀ (CLBO)

CLBO was reported first as NLO materials by More et al. in 1995.³³⁵ It crystallizes in a tetragonal space group of $I\bar{4}2d$ (No. 122) with $a = 10.494$ Å, $c = 8.939$ Å, and $Z = 4$.³³⁵ In the structure, two kinds of crystallographically independent B atoms are surrounded by three and four O atoms forming the BO₃ triangle and BO₄ tetrahedra, respectively, which further connect via corner-sharing O atoms to form the fundamental building block B₃O₇. Furthermore, B₃O₇ groups are linked with each other to form the final

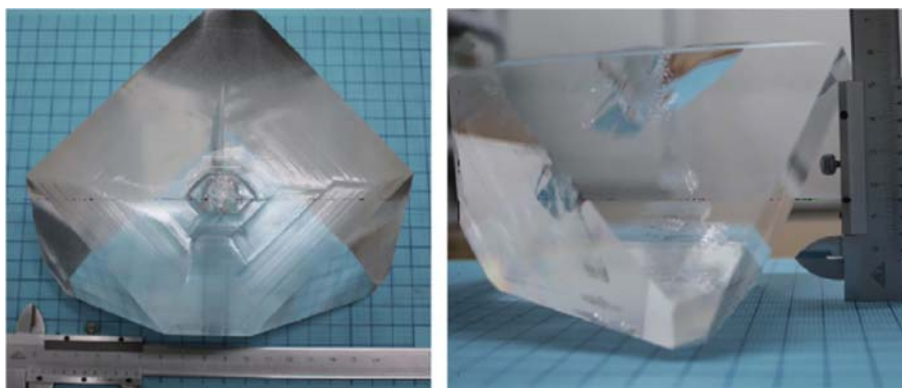


Fig. 30 LBO crystals grown by Hu's group with the size of $160 \times 150 \times 77$ mm³ and weight of 1988 g.

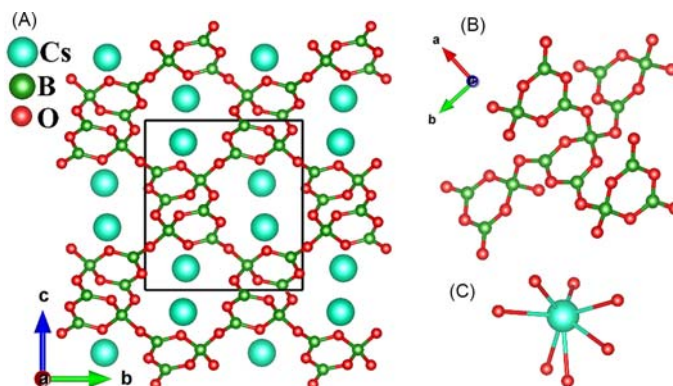


Fig. 31 The structure of CBO viewed along the *a*-axis (A), the B₃O₇ groups linked with neighboring four (B) and the coordinated environment of Cs atom (C).

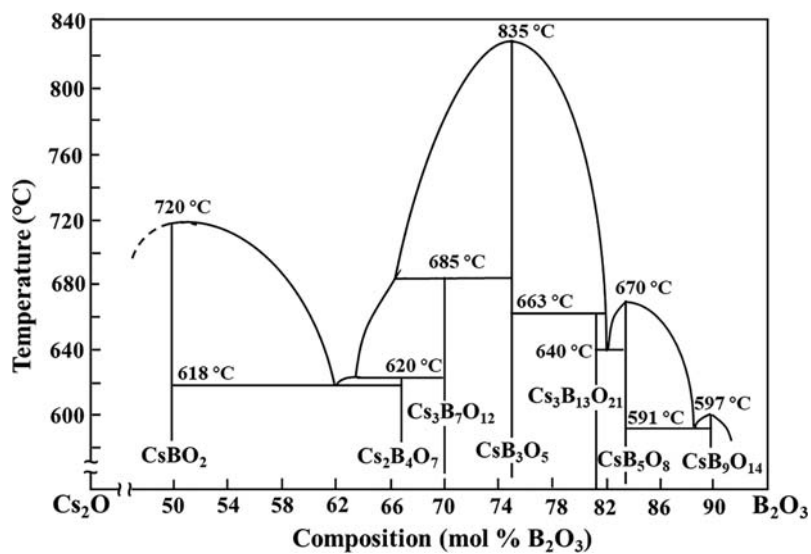


Fig. 32 The Cs₂O-B₂O₃ phase diagram.

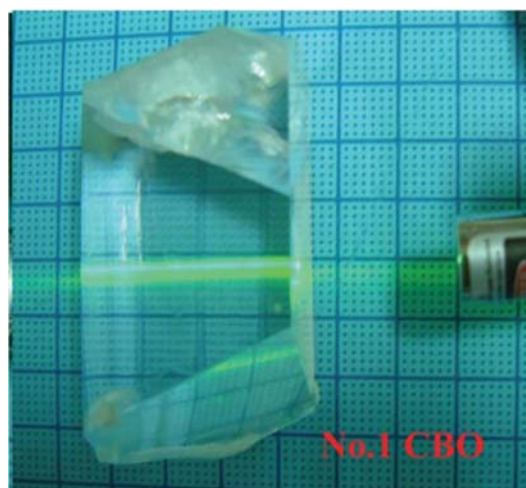


Fig. 33 CBO crystal grown from solution by the seed-submerged growth method. Adapted from Ref. Liu, S.; Zhang, G.; Li, X.; Yang, F.; Bo, Y.; Fu, P.; Wu, Y. Growth and Characterization of CsB₃O₅ Crystals Without Scattering Centers. *CrystEngComm* **2012**, *14*(14), 4738–4744, with permission from The Royal Society of Chemistry.

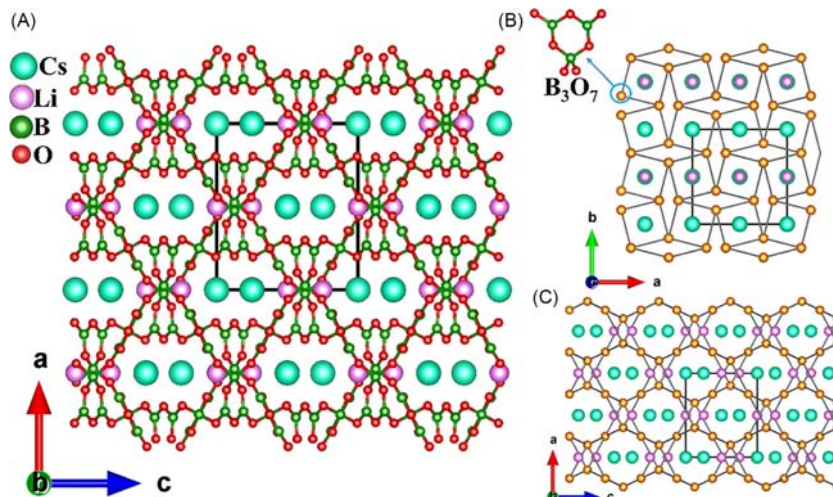


Fig. 34 The structure of CLBO viewed along the b -axis (A), the topological structure viewed along the c -axis (B) and viewed along the b -axis (C). The B_3O_7 groups considered as 4-connected nodes.

reticular framework (Fig. 34). The Li and Cs atoms are four and eight-coordinated with O atoms in the CLBO crystal, respectively, which make them strongly bound in vacant space. Topologically, when the B_3O_7 groups are considered as 4-connected nodes, a simplified anionic framework can be described as a point Schläfli symbol of $\{4^2.8^4\}$ (Fig. 34).

CLBO is a negative uniaxial crystal exhibiting outstanding NLO properties as a frequency converter including short UV cutoff edge (180 nm), relatively large SHG coefficient ($d_{36} = 0.95 \text{ pm V}^{-1}$ at 1064 nm), large angular and temperature bandwidths, small walk-off angles, large laser-induced surface damage threshold ($24\text{--}26 \text{ GW cm}^{-2}$ for 1.1 ns pulses at 1064 nm), etc.^{336–339} CLBO crystal has been used for second-, third-, fourth-, and even fifth-harmonic generations of the laser frequency conversion.^{340–344} Unfortunately, CLBO crystals are extremely hygroscopic to make it have a tendency to crack in air at room temperature, which has greatly limited their application of devices.^{345,346} During the last few years, some techniques have been put out to promote the progress in the practical application of CLBO.^{347,348} For example, the earlier studies show that water impurity of CLBO crystal can be effectively eliminated by long time heat treatment at $150\text{--}160^\circ\text{C}$ and subsequently in dry atmosphere. Recent studies reveal that surface degradation due to the invasion of water can be significantly suppressed by Al-doped (Fig. 35).^{349,350} However, it is difficult to grow Al-doped CLBO crystals with high-quality.

CLBO is a congruent melting compound with the melting point of 848°C and the TSSG method has been commonly used to grow CLBO crystals.^{350–352} Traditional TSSG is to stir the solution by rotating a seed crystal. However, Sasaki et al. developed an effective solution stirring technique that add crucible rotation equipment to stir the solution with the high viscosity.^{353,354} The improved TSSG technology, defined as solution-stirring TSSG, increases the convection of solution and keeps the solution fully uniform. In addition, Nishioka et al. found that high quality starting materials could be efficiently prepared from a mixture of raw materials (Cs_2CO_3 (99.99%), Li_2CO_3 (99.99%) and B_2O_3 (99.999%) in a ratio of 1:1:5.5) and aqueous solution.^{355,356} The crystals grown by using this starting material possess an approximately twofold higher LIDT than those grown by the conventional method.

4.02.4.2 Newly developed ultraviolet nonlinear optical materials

4.02.4.2.1 SBBO family

$\text{Sr}_2\text{Be}_2\text{B}_2\text{O}_7$ (SBBO): SBBO was the earliest attempt to overcome the layering tendency of KBBF crystals (described in next section). Structurally, SBBO belongs to the space group of $P6_2c$ (No. 190) and features $^2[\text{Be}_2\text{B}_2\text{O}_7]_\infty$ double layers, in which all the BO_3 units are NLO-active and aligned optimally; the BeO_4 units eliminate the dangling bonds of the BO_3 units (Fig. 36). SBBO crystal was considered as an NLO material owing to the large SHG response (about $3.8 \times \text{KDP}$ at 1064 nm), short DUV cutoff edge (155 nm), a moderate birefringence (about 0.062 at 589 nm based on the DFT calculation), as well as a short phase matching wavelength (about 200 nm).³⁵⁷ Unfortunately, the cohesion forces between the $^2[\text{Be}_2\text{B}_2\text{O}_7]_\infty$ layers make the structure of SBBO unstable and limit its further application.³⁵⁸

$\text{K}_2\text{Al}_2\text{B}_2\text{O}_7$ (KABO): In 1998, KABO was reported by Chinese and Japanese scientists as a new NLO material.^{359,360} It crystallizes in the trigonal space group $P321$ (No. 150) with $a = 8.5657(9) \text{ \AA}$, $c = 8.463(2) \text{ \AA}$, and $Z = 3$.³⁶¹ The structure of KABO contains K atoms, BO_3 groups, and AlO_4 groups. All the BO_3 groups are approximately parallel to the c -axis which connect with AlO_4 tetrahedra via corner-sharing O atoms to form $[\text{Al}_2(\text{B}_2\text{O}_7)_2\text{O}]_\infty$ sheets in the ab plane. The $[\text{Al}_2(\text{B}_2\text{O}_7)_2\text{O}]_\infty$ sheets are bonded to each other through O atoms in the AlO_4 tetrahedra forming a 3D $^3[\text{Al}_2(\text{B}_2\text{O}_7)_2\text{O}]_\infty$ framework which exhibits large 11-membered rings along the c -axis where the K atoms are located (Fig. 37).

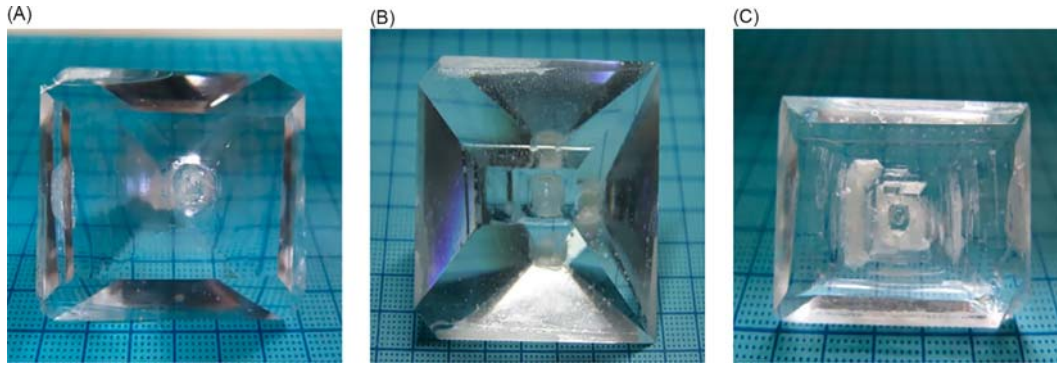


Fig. 35 Photograph of as-grown crystals in the $\text{Cs}_2\text{O-Li}_2\text{O-B}_2\text{O}_3\text{-MoO}_3$ system: (A) undoped CLBO; (B) 2.5% Al-doped CLBO; (C) 5% Al-doped CLBO.

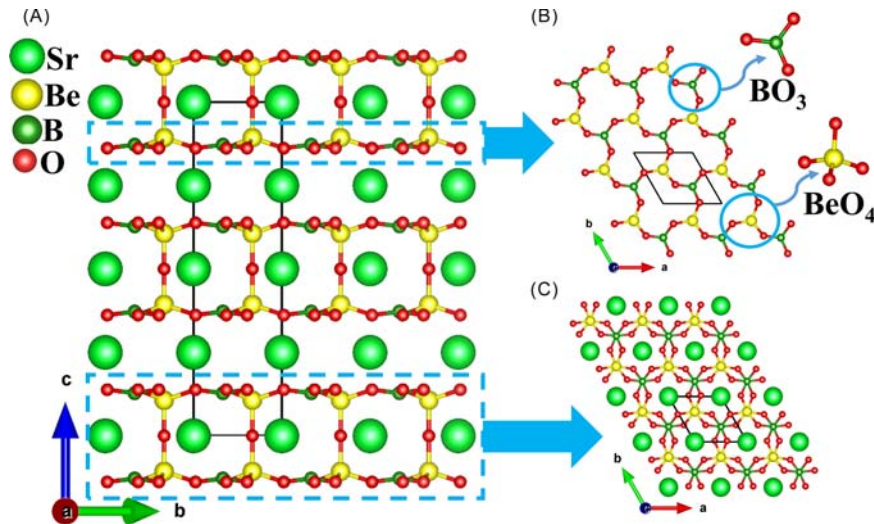


Fig. 36 The structure of SBBO viewed along the a -axis (A), the single-layer ${}^2[\text{BeBO}_4]_\infty$ (B) and the double-layer ${}^2[\text{Be}_2\text{B}_2\text{O}_7]_\infty$ stretching in the ab plane with the Sr atoms located in the voids (C).

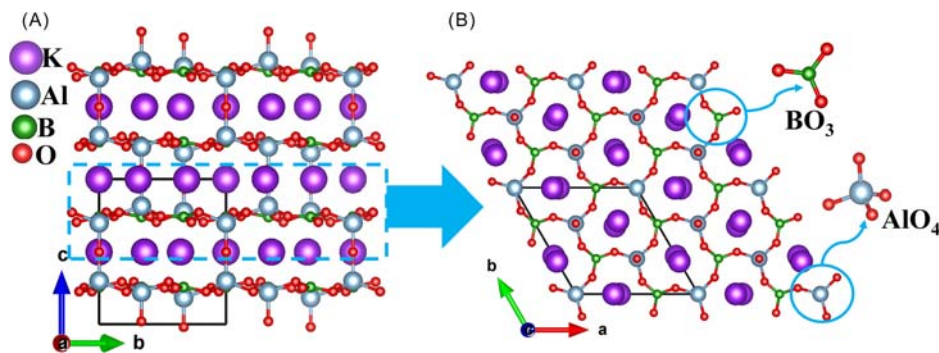


Fig. 37 The structure of KABO viewed along the a -axis (A), the $[\text{Al}_2(\text{B}_2\text{O}_7)_2\text{O}]_\infty$ sheets in the ab plane with the K atoms located in the voids (B).

The KABO crystal is transparent far into the DUV region (180–3600 nm). It has a moderate birefringence (0.070 at 1064 nm) which makes it be phase-matching to 232.5 nm.³⁶² The values of NLO coefficient and laser damage threshold are measured to be $d_{11} = 0.45 \text{ pm V}^{-1}$ and 15 GW cm^{-2} under 10 ns pulses at 1064 nm, respectively.³⁶² Besides, KABO has the merits of easy growth and good radiation resistance to UV light. Single crystal has been grown by the TSSG method with NaF as a flux.³⁶³ KABO crystal can be used for the generation of 266 nm laser by FHG and 193 nm laser by SFG of Nd-based laser systems.³⁶⁴ For a long time, KABO crystal is shown to exhibit abnormal UV absorption around 230 nm, which is proved to be caused by Fe impurities and thus reduce the conversion efficiency from 532 nm to 266 nm. Faced with this, large and high optical quality KABO crystals were grown in

a non-oxygen atmosphere by Chen et al. in 2011 for the first time, which effectively eliminated the abnormal absorption in the UV region.³⁶⁵ A 280 mW average output power was obtained by using a 8.85-mm-thick KABO crystal through fourth-harmonic generation of Nd: YAG laser with 10 kHz, 10 ns pulse.

$K_3Ba_3Li_2Al_4B_6O_{20}F$, $K_3Sr_3Li_2Al_4B_6O_{20}F$ and $Rb_3Ba_3Li_2Al_4B_6O_{20}F$: In 2016, Luo et al. reported $K_3Ba_3Li_2Al_4B_6O_{20}F$ with a framework structure that exhibits the structural merits of SBBO double-layer configuration.³⁶⁶ It crystallizes in the hexagonal $P6_2c$ (No. 190) space group with 0D isolated BO_3 units. The BO_3 units are linked by the AlO_4 and LiO_3F tetrahedra forming ${}^2[LiAl_2B_3O_{10}F]_{\infty}$ sheets stretching in the ab plane, which are further linked along the c -axis by Al–O and Li–F bonds to form the ${}^2[Li_2Al_4B_6O_{20}F]_{\infty}$ double layers. The ${}^2[Li_2Al_4B_6O_{20}F]_{\infty}$ double layers are linked by the Ba cations, while the K cations are located in the interlayers (Fig. 38). The $K_3Ba_3Li_2Al_4B_6O_{20}F$ crystal preserves the excellent NLO properties, including a DUV absorption edge of 190 nm, a sufficiently large SHG response of $1.5 \times$ KDP and a suitable birefringence (~ 0.068 at 852.1 nm), which make it have the potential to generate the 266 nm coherent light by a direct SHG process.³⁶⁷ In 2018, Luo et al. reported that the single crystal with sizes up to $18 \times 13 \times 8$ mm³ has been grown by the TSSG method.³⁶⁷

In 2017, two more new members in this family, $K_3Sr_3Li_2Al_4B_6O_{20}F$ and $Rb_3Ba_3Li_2Al_4B_6O_{20}F$, were reported nearly simultaneously by Luo et al.³⁶⁸ and Halasyamani et al.^{369,370} Their structures both feature the similar $[Li_2Al_4B_6O_{20}F]_{\infty}$ double layers with $K_3Ba_3Li_2Al_4B_6O_{20}F$, while they crystallize in different space groups of $P6_2c$ (No. 190) and $R32$ (No. 155), respectively. Both crystals exhibit absorption edges below 200 nm, satisfactory SHG responses (1.7 and $1.5 \times$ KDP), moderate birefringence (0.0637 and 0.057 at 1064 nm for $K_3Sr_3Li_2Al_4B_6O_{20}F$ and $Rb_3Ba_3Li_2Al_4B_6O_{20}F$), and shortest type I SHG wavelengths below 266 nm (224 and 243 nm).^{368–371} Thus, together with $K_3Ba_3Li_2Al_4B_6O_{20}F$ analog, they are all potential candidates to generate 266 nm radiation by direct SHG method. The centimeter-size $K_3Sr_3Li_2Al_4B_6O_{20}F$ and $Rb_3Ba_3Li_2Al_4B_6O_{20}F$ crystals can be grown by the TSSG with a Li_2O - SrF_2 / BaF_2 - B_2O_3 flux.^{369–371}

4.02.4.2.2 Other materials

$Li_4Sr(BO_3)_2$: The $Li_4Sr(BO_3)_2$ crystal was obtained first by Luo et al. in 2014 with the low symmetry of Cc (No. 9).³⁷² The structure is built up of isolated BO_3 units and Li and Sr cations (Fig. 39). $Li_4Sr(BO_3)_2$ crystals without layering tendency were initially grown by the TSSG method from the self-flux system.³⁷² It shows a UV absorption cutoff edge of 186 nm measured based on powders. Owing to the optically aligned NLO-active anionic groups in the structure of $Li_4Sr(BO_3)_2$, the powder SHG responses of $Li_4Sr(BO_3)_2$ are detected to be $\sim 2 \times$ KDP under incident laser at 1064 nm.³⁷² The theoretical birefringence of 0.056 at 532 nm for $Li_4Sr(BO_3)_2$ is sufficient for the phase-matching in the SHG process of 1064 and 532 nm incident lasers. However, attributable to the lack of large single crystals, the SHG coefficients, laser damage threshold and birefringence have not yet been experimentally measured.

$Ba_3(ZnB_5O_{10})PO_4$ (BZBP): BZBP was synthesized by Halasyamani et al. in 2015.³⁷³ The BZBP crystals with sizes up to $9 \times 7 \times 3$ mm³ were grown from H_3BO_3 -ZnO flux by TSSG method. BZBP crystallizes in the noncentrosymmetric orthorhombic polar space group Pmn_21 (No. 31). In the structure, BO_3 and BO_4 units are linked by corner-sharing O atoms to form the ${}^2[B_5O_{10}]_{\infty}$ layers stretching in the ac plane with the large channels, where the isolated PO_4 units are located. The ${}^2[B_5O_{10}]_{\infty}$ layers connect with ZnO_4 tetrahedra to create a ${}^3[ZnB_5O_{10}]_{\infty}$ framework, and the Ba atoms and isolated PO_4 tetrahedra are located in the voids (Fig. 40). BZBP crystal exhibits a DUV absorption edge (180 nm), large SHG responses ($\sim 4 \times$ KDP based on the powder SHG measurement at 1064 nm), while it has a small birefringence (~ 0.04 at 532 nm).^{373,374} Besides, the crystal is stable in both air and water and melts congruently, enabling the facile growth of large single crystals.

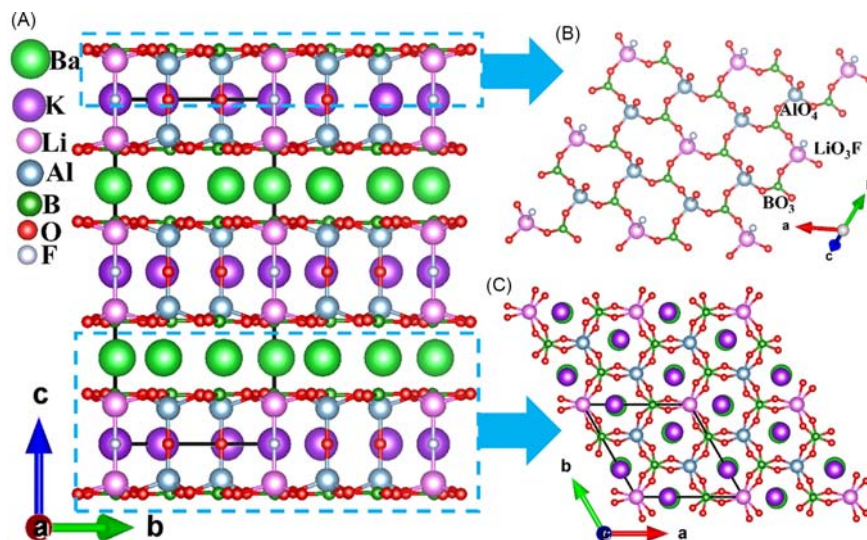


Fig. 38 The structure of $K_3Ba_3Li_2Al_4B_6O_{20}F$ viewed along the a -axis (A), the ${}^2[LiAl_2B_3O_{10}F]_{\infty}$ sheets (B), and the ${}^2[Li_2Al_4B_6O_{20}F]_{\infty}$ double layers stretching in the ab plane.

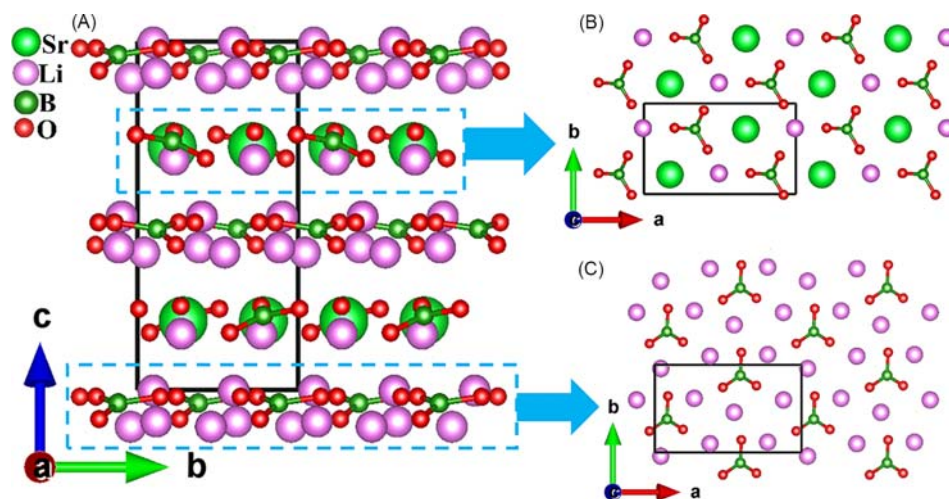


Fig. 39 The structure of $\text{Li}_4\text{Sr}(\text{BO}_3)_2$ viewed along the a -axis (A), the pseudolayer viewed along the c -axis built by isolated BO_3 units and Li and Sr atoms (B) and the pseudolayer viewed along the c -axis built by isolated BO_3 units and Li atoms (C).

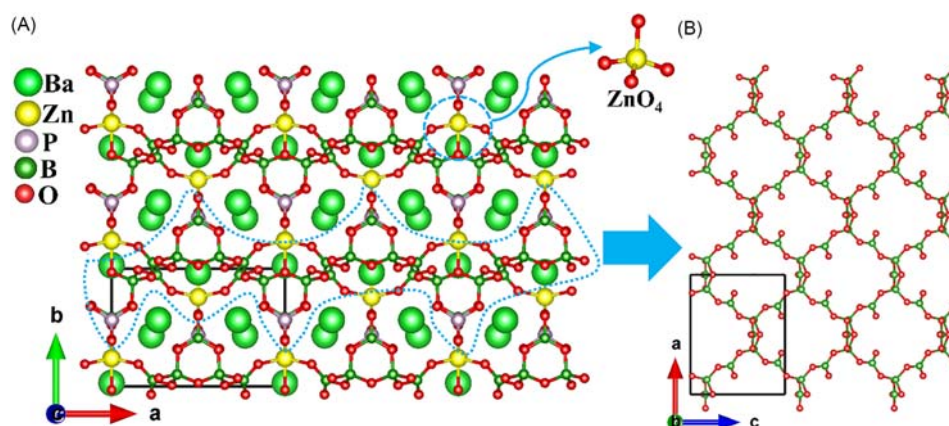


Fig. 40 The structure of BZBP viewed along the c -axis (A) and the ${}^2[\text{B}_5\text{O}_{10}]_\infty$ layers stretching in the ac plane (B).

$\text{M}_2(\text{OH})_3\text{NO}_3$ ($\text{M}=\text{Ba}, \text{Sr}$): $\text{M}_2(\text{OH})_3\text{NO}_3$ ($\text{M}=\text{Ba}, \text{Sr}$) were synthesized first by Simone et al. in 2007,³⁷⁵ and Huang and Dong et al.³⁷⁶ reported their NLO properties in 2015 and 2018, respectively. $\text{Sr}_2(\text{OH})_3\text{NO}_3$ and $\text{Ba}_2(\text{OH})_3\text{NO}_3$ crystal are isostructural and belong to the hexagonal space group $P\bar{6}2m$ (No. 189). Their structures are built by M cations, OH and plane NO_3 units (Fig. 41). They exhibit large NLO effects (3.6 and $4 \times \text{KDP}$ for $\text{Sr}_2(\text{OH})_3\text{NO}_3$ and $\text{Ba}_2(\text{OH})_3\text{NO}_3$) and moderate birefringence of 0.08 at 589.6 nm for $\text{Ba}_2(\text{OH})_3\text{NO}_3$ owing to the alignment of the NO_3 units (the birefringence for $\text{Sr}_2(\text{OH})_3\text{NO}_3$ has not been reported due to the lack of suitable crystal). Moreover, thermal studies have shown that $\text{Sr}_2(\text{OH})_3\text{NO}_3$ and $\text{Ba}_2(\text{OH})_3\text{NO}_3$ can be stable up to $450 \text{ }^\circ\text{C}$ and $320 \text{ }^\circ\text{C}$, respectively. Both of them have UV absorption edges shorter than 200 nm , and $\text{Ba}_2(\text{OH})_3\text{NO}_3$ crystal exhibits good physicochemical stabilities.

4.02.5 Deep-ultraviolet nonlinear optical materials

Deep-Ultraviolet (DUV) light sources with wavelength ranges shorter than 200 nm play an important role in photoemission spectroscopy, laser processing, precise micromachining, chemical reaction dynamics, surface physics, semiconductor materials and other scientific and industrial frontier fields.^{377–379} Several approaches, including synchrotron radiation, gas discharge lamps (He and Xe), excimer lasers (193 nm ArF and 157 nm F_2 pulsed lasers), free electron lasers, and nonlinear frequency conversion can generate the DUV light.^{380–383} Remarkably, nonlinear frequency conversion has a great application prospecting producing DUV coherent light based on cascaded SHG with a diode-pumped solid-state laser as the fundamental pump.^{378,379,384–387} So far, SHG with a $\text{KBa}_2\text{BO}_3\text{F}_2$ (KBBF) NLO crystal is the best way, which is both precise and practical.^{388,389} However, the layering growth habit in the KBBF crystal brings significant challenge of single-crystal growth. In last decades, in addition to improve the growth techniques of KBBF, some crystals with potential application as DUV NLO materials have been explored which are introduced in this chapter.

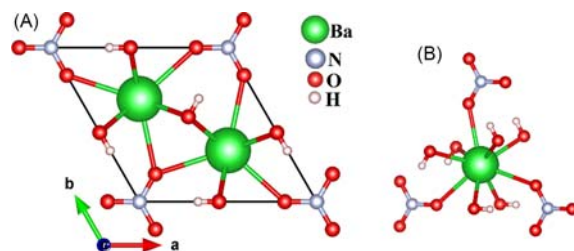


Fig. 41 The structure of $\text{Ba}_2(\text{OH})_3\text{NO}_3$ viewed along the c -axis (A) and the coordinated environment of Ba cations (B).

4.02.5.1 Representative deep-ultraviolet nonlinear optical materials

4.02.5.1.1 Potassium aluminum borate $\text{KBe}_2\text{BO}_3\text{F}_2$ (KBBF)

KBBF compound was first synthesized in the KBF_4 -BeO system by former Soviet Union scientists in 1968.³⁹⁰ In 1990s, Chen's group successfully grew KBBF single crystal with the size of about $10 \times 10 \times 0.3 \text{ mm}^3$ by using the top-seeded high temperature flux method and they reported that KBBF was a promising DUV NLO material and might achieve sixth-harmonic generation of Nd-based lasers.^{391,392}

KBBF crystal was finally determined to crystallize in the trigonal system with the space group of $R\bar{3}2$ (No. 155). Its unit cell dimensions are $a = 4.427 \text{ \AA}$, $c = 18.774 \text{ \AA}$, and $Z = 3$. In the structure of KBBF, the BO_3 and BeO_3F units are linked by corner-sharing O atoms forming the 2D infinite planar ${}^2[\text{Be}_2\text{BO}_3\text{F}_2]_\infty$ layer optimally aligned in the ab -plane (Fig. 42). The ${}^2[\text{Be}_2\text{BO}_3\text{F}_2]_\infty$ layers are connected by the K-F ionic bond. Thus, the weak interactions between the layers make it difficult to grow along the direction of $[001]$.

KBBF has excellent optical properties and is the sole NLO material that can successfully applied in DUV laser through the SHG method. The UV cutoff edge of KBBF is 147 nm which blueshifts 42 nm compared to that of the BBO crystal. According to the anion group theory reported by Chen et al. terminal O atoms of the BO_3 units are linked with BeO_3F units in KBBF crystal to eliminate the dangling bonds, which are beneficial to increase the band gap.³⁹³⁻³⁹⁵ And the moderate birefringence (0.77 at 1064 nm) makes it have wide phase-matching wavelength range (shortest phase-matching wavelength $< 200 \text{ nm}$).^{396,397} Maker fringes measurement shows that the d_{11} coefficient of KBBF is 0.47 pm V^{-1} which matches well with the calculated value of 0.351 pm V^{-1} .³⁹⁸ Preliminary measurements show that the damage threshold of KBBF is as high as 900 GW cm^{-2} and 72 J cm^{-2} to the following laser parameters of 1064 nm, 80 ps, 1 Hz, and 60 GW cm^{-2} at 390 nm with a 200 fs pulse width and 1 kHz repetition rate laser.³⁹⁹ With the optically contacted KBBF-prism-coupled device, the sixth harmonic of Nd-based lasers and fourth harmonic of Ti:sapphire lasers have been successfully generated.^{378,400,401} In 2016, the shortest solid-state laser wavelength generated is 164.9 nm which was demonstrated by the eighth harmonic generation based on a 1319 nm Nd:YAG laser.⁴⁰²

KBBF crystals can be grown by the flux method and the hydrothermal method.^{397,403,404} Unfortunately, it is found that KBBF crystals grown by the hydrothermal method have intrinsic structural problems, which results in the very weak SHG responses, and the conversion efficiency is 1-2 orders of magnitude lower than that of flux-grown crystals, which makes it difficult to be used practically.^{405,406} So far, the practically used crystals have been grown by the flux method. Polycrystalline KBBF prepared by a traditional solid reaction with the stoichiometric amounts of BeO, KBF_4 , and B_2O_3 were put into platinum crucible and sealed. The crucible was heated above to $700 \text{ }^\circ\text{C}$ and hold at this temperature for about 50 h. Notably, all the operations must be performed in a ventilated system to protect the operators from BeO toxicity. Using the flux method, the crystal is grown in a high-temperature solution growth process, in which KBBF crystallizes out of a molten KBBF and self-flux composition ($\text{KF} + \text{B}_2\text{O}_3$). Up to now, many attempts to grow KBBF crystal by seeded technique were unsuccessful, so its crystal growth was performed by spontaneous nucleation.⁴⁰⁷ The crystal can be obtained after the residues in the crucible are dissolved by dilute acid.

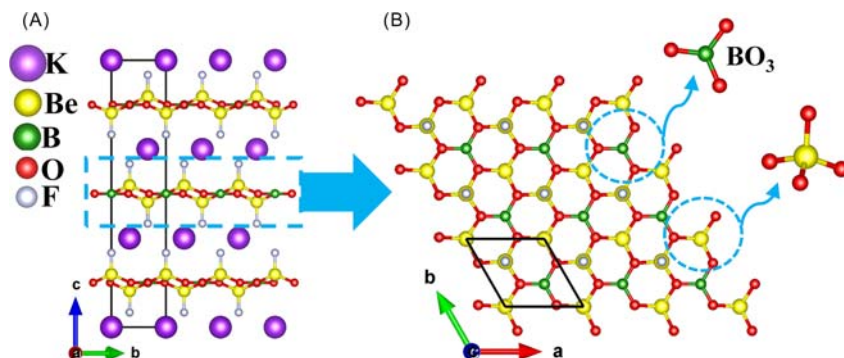


Fig. 42 The whole structure of KBBF viewed along the a -axis (A) and the planar ${}^2[\text{Be}_2\text{BO}_3\text{F}_2]_\infty$ layer optimally aligned in the ab plane (B).

Different from seeded growth technique, the spontaneous nucleation growth technique always forms many small crystals. Chen et al. developed the “localized spontaneous nucleation technique”, which can control or restrict nucleation over one spot or a narrow region where the crystal starts to grow, and which can combine with the temperature oscillation in the early stages of growth to further select relatively one single nucleus for growth. Fig. 43 shows the temperature-oscillation process and the as-grown KBBF crystal grown by Chen et al.⁴⁰⁷

4.02.5.2 Newly developed deep-ultraviolet nonlinear optical materials

4.02.5.2.1 KBBF family

RbBe₂BO₃F₂ (RBBF): RBBF crystal was synthesized first by former Soviet Union scientists in 1975, which determined that its structure belongs to the monoclinic system with the space group C2 (No. 5).⁴⁰⁸ Later, Chen et al. collected and integrated the single-crystal X-ray diffraction data based on the grown single crystal and refined the structure and proved that it belongs to the uniaxial and hexagonal system R32 (No. 155) with unit cell dimensions $a = 4.434 \text{ \AA}$, $c = 19.758 \text{ \AA}$, and $Z = 3$.⁴⁰⁹ The crystal structure of RBBF is similar to that of KBBF. Its structure is made up of an infinite lattice network of ${}^2[\text{Be}_2\text{BO}_3\text{F}_2]_\infty$ extended in the ab -plane with the Rb atoms located between the layers (Fig. 44). The distance between neighboring layer is about 6.3 \AA and the weak Rb–F interactions connect the layers to grow thicker crystals difficultly, like KBBF.

RBBF and KBBF have similar crystal growth habit and similar optical properties. Its NLO effect values of $1.15 \times \text{KDP}$ at 1064 nm , and it possesses moderate birefringence (0.073 at 1064 nm) and a short phase-matching cutoff edge (170 nm) that can be used to direct SHG method to generate DUV laser. At present, RBBF has been experimentally shown to produce DUV coherent laser through direct SHG.⁴¹⁰ However, compared with KBBF, the layered behavior of RBBF is not improved, which still limits the device application.

NH₄Be₂BO₃F₂: In 2015, Ye and Lin et al. predicted NH₄Be₂BO₃F₂ (ABBF) first by optimizing the KBBF structure by replacing monovalent K⁺ with NH₄⁺.⁴¹¹ Subsequently, centimeter-level ABBF was successfully synthesized by the hydrothermal method in 2018.⁴¹² ABBF exhibits a similar structure with KBBF. It crystallizes in R32 (No. 155) space group with the unit cell parameters $a = 4.441$, $c = 19.909 \text{ \AA}$, $Z = 3$. The NH₄⁺ groups occupy the sites of K⁺ cations and are located between the ${}^2[\text{Be}_2\text{BO}_3\text{F}_2]_\infty$ layers in which the N–H⋯F hydrogen bonding interactions form the final architecture (Fig. 45). The distance of the H–F bond (1.993 \AA) in ABBF is shorter than that of K–F (2.765 \AA) in KBBF, indicating the stronger interlayer binding force in ABBF, which effectively improve the layered behavior. In addition, ABBF also preserves the NLO-favorable features, such as a suitable SHG response ($1.2 \times \text{KDP}$ at 1064 nm), moderate calculated birefringence (0.057 at 400 nm), and wide transparency range ($153\text{--}2000 \text{ nm}$), but the more physicochemical properties need further evaluation by growing larger-size single crystals.

NaBe₂BO₃F₂ (NBBF): The NBBF compound was first reported by Batdtna, and it was first considered to be promising DUV NLO material by Mei et al. in 1993.⁴¹³ NBBF crystal is the member of KBBF family, but in contrast with other crystal of KBBF-family, including KBBF, it crystallizes in the monoclinic system with the unit cell parameters $a = 12.643 \text{ \AA}$, $b = 8.729 \text{ \AA}$, $c = 7.591 \text{ \AA}$,

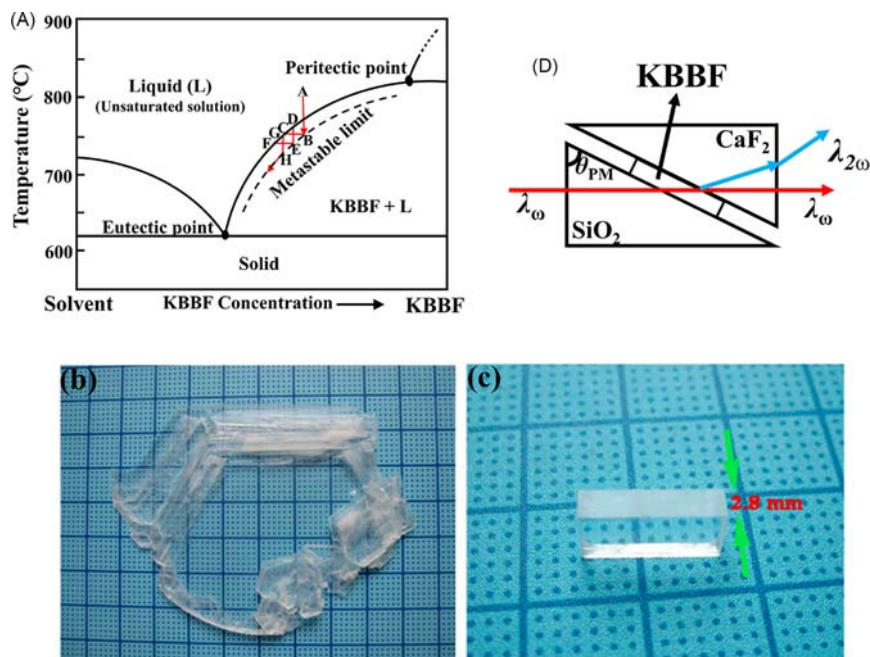


Fig. 43 The temperature-oscillation illustration in the phase diagram (A), as-grown crystal (B) and device of KBBF (C), scheme of a special prism-coupling equipment with KBBF crystal (D).

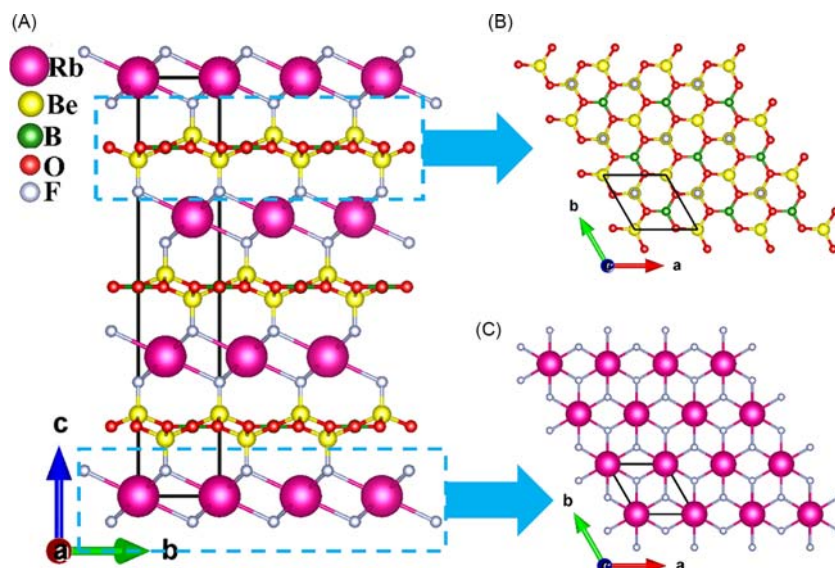


Fig. 44 The whole structure of RBBF viewed along the a -axis (A), the ${}^2[\text{Be}_2\text{BO}_3\text{F}_2]_\infty$ extended in the ab plane (B) and the ${}^2[\text{RbF}]_\infty$ layer (C).

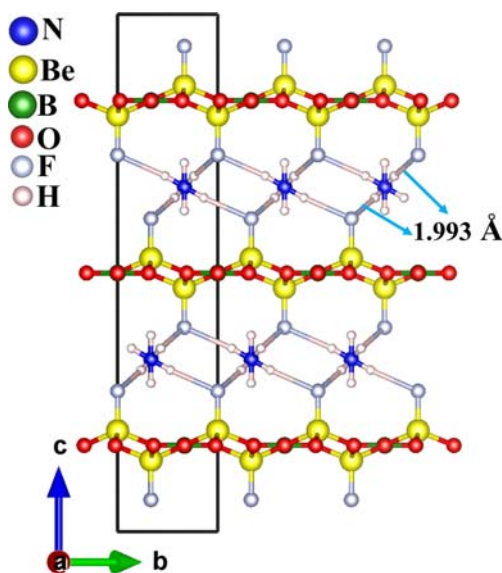


Fig. 45 The structure of ABBF viewed along the a -axis.

$\beta = 113.6^\circ$. Its structure is built by the 2D ${}^2[\text{Be}_2\text{BO}_3\text{F}_2]_\infty$ layers and 1D ${}^1[\text{NaF}]_\infty$ chains, and they are connected by Na–F ionic bonding (Fig. 46). The unequal Na–F bonds form distorted polyhedron breaking the threefold rotation symmetry in $R32$ (No. 155) and therefore, the crystal adopts the lower space group $C2$ (No. 5). However, NBBF retains the excellent optical properties confirmed by some experimental results: short-wavelength absorption edge ($\lambda_{\text{cutoff}} = 155 \text{ nm}$), a comparative SHG coefficient ($1.1 \times \text{KBBF}$) and a moderate birefringence (0.091 at 200 nm).⁴¹⁴ Recently, the NBBF crystal with dimensions of $20 \times 20 \times 1.5 \text{ mm}^3$ has been grown from the $\text{NaBF}_4\text{-NaF-B}_2\text{O}_3$ flux system.⁴¹⁴

$\gamma\text{-Be}_2\text{BO}_3\text{F}$ ($\gamma\text{-BBF}$): $\gamma\text{-BBF}$ was synthesized through high-pressure solid state reaction in a sealed platinum tube by Lin et al.⁴¹² It crystallizes in $R32$ (No. 155) space group with the cell dimensions of $a = 4.4398 \text{ \AA}$, $c = 12.4697 \text{ \AA}$, $Z = 3$. $\gamma\text{-BBF}$ exhibits a similar structure with KBBF and also preserves the NLO-favorable properties. Notably, The Be–F ionic bond (1.568 \AA) in $\gamma\text{-BBF}$ exhibits super strong bond ability between the adjacent ${}^2[\text{Be}_2\text{BO}_3\text{F}_2]_\infty$ layers (Fig. 47), and the inter-layer spacing has been greatly shortened to 4.157 \AA , which is much shorter than that in KBBF (6.25 \AA). However, there are still no large enough crystals for further physical and chemical properties evaluation, thus, more efforts on crystal growth are needed.

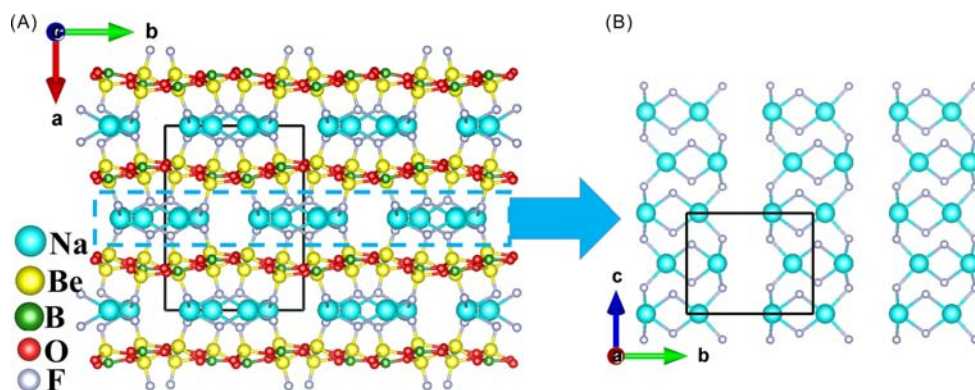


Fig. 46 The structure of NBBF viewed along the c -axis (A) and 1D $[\text{NaF}]_{\infty}$ chains viewed along the a -axis (B).

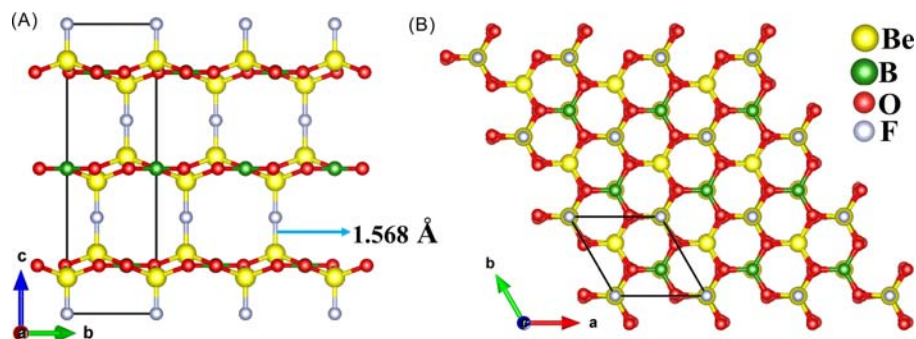


Fig. 47 The structure of BBF viewed along the a -axis (A) and viewed along the c -axis (B).

4.02.5.2.2 Fluorooxoborates

In recent years, fluorooxoborates containing both B–O and B–F covalent bonds are widely researched due to its exciting optical properties, especially in the DUV spectral range. It has been recognized that the partial O/F substitutions in the BO_4 tetrahedra forming the $\text{BO}_x\text{F}_{4-x}$ units reduce the symmetry, which is beneficial to obtain the non-centrosymmetric structures. The non-bridge O atoms are replaced by F atoms in the borate can eliminate the dangling bonds and lead to a wide UV transmission region; Compared to BO_4 in borates, the $\text{BO}_x\text{F}_{4-x}$ units in fluorooxoborates possess comparable or even superior properties in terms of polarizability anisotropy, hyperpolarizability, and band gap.^{415–417} Therefore, a series of fluorooxoborates with excellent optical properties and potential applications of DUV NLO materials have been synthesized and reported, such as $\text{Li}_2\text{B}_6\text{O}_9\text{F}_2$, $\text{NH}_4\text{B}_4\text{O}_6\text{F}$ (ABF), $\text{CsB}_4\text{O}_6\text{F}$ (CBF), $\text{CaB}_5\text{O}_7\text{F}_3$, and $\text{SrB}_5\text{O}_7\text{F}_3$, etc.

4.02.5.2.2.1 ABF family

$\text{NH}_4\text{B}_4\text{O}_6\text{F}$ (ABF): ABF crystallizes in an orthorhombic crystal system and polar space group $Pna2_1$ (No. 33) with the cell dimensions of $a = 7.5457$ (14) Å, $b = 11.177$ (2) Å, $c = 6.5805$ (13) Å, $Z = 3$, which was refined based on the X-ray diffraction data at 140 K.⁴¹⁸ Its structure features ${}^2[\text{B}_4\text{O}_6\text{F}]_{\infty}$ layered configurations with NH_4^+ cations located between the individual layers, and the hydrogen bonds connect the layers to construct the final 3D framework. As shown in Fig. 48A, the structure of ABF exhibits similar structural features of KBBF. The BO_3 units align almost in the same direction and the dangling bonds of terminal O atoms are eliminated by the BO_3F groups, which are beneficial for a short UV cutoff edge. The layer spacing in ABF is reduced from 6.25 Å in KBBF to ~ 3.8 Å, resulting in improved interlayer interactions. In addition, the wide transparency range, large SHG effect (~ 2.3 KBBF), short PM SHG wavelength (down to 158 nm) indicate that ABF crystal is a promising DUV NLO candidate material.⁴¹⁸

Subsequently, a series of new fluorooxoborates, $\text{CsB}_4\text{O}_6\text{F}$ (CBF), $\text{NaB}_4\text{O}_6\text{F}$ (NBF), $\text{RbB}_4\text{O}_6\text{F}$ (RBF), $\text{CsKB}_8\text{O}_{12}\text{F}_2$ (CKBF) and $\text{CsRbB}_8\text{O}_{12}\text{F}_2$ (CRBF), etc., were synthesized.^{419–421} Although their structure exhibits similar 2D ${}^2[\text{B}_4\text{O}_6\text{F}]_{\infty}$ layered features of ABF, the FBBs of BO_3 and BO_3F have different connection style (Fig. 48). The FBBs of NBF and RBF are composed of near-planar rings B_3O_6 and tetrahedral BO_3F units, while others are made up of non-planar rings $\text{B}_3\text{O}_6\text{F}$ and trigonal BO_3 units (Fig. 48). According to the experimental and theoretical results, they exhibit sufficiently large powder SHG efficiencies (0.9 – $1.9 \times \text{KDP}$ at 1064 nm), short DUV absorption edges (all lower than 180 nm), as well as the short DUV SHG phase-matching wavelengths (experimental values of CBF is 172 nm, calculated values of other four crystals are from 166 nm to 171 nm). These results suggest that they have great potential to generate DUV light once they are grown to sizable crystals.

$\text{CsAlB}_3\text{O}_6\text{F}$ (CABF): CABF crystallizes in the orthorhombic polar space group $Pna2_1$ (No. 33).⁴²² The crystal structure shows some similarities to that of CBF (Fig. 48G), in which the BO_3F unit is replaced by AlO_3F tetrahedron to build the 2D ${}^2[\text{AlB}_3\text{O}_6\text{F}]_{\infty}$

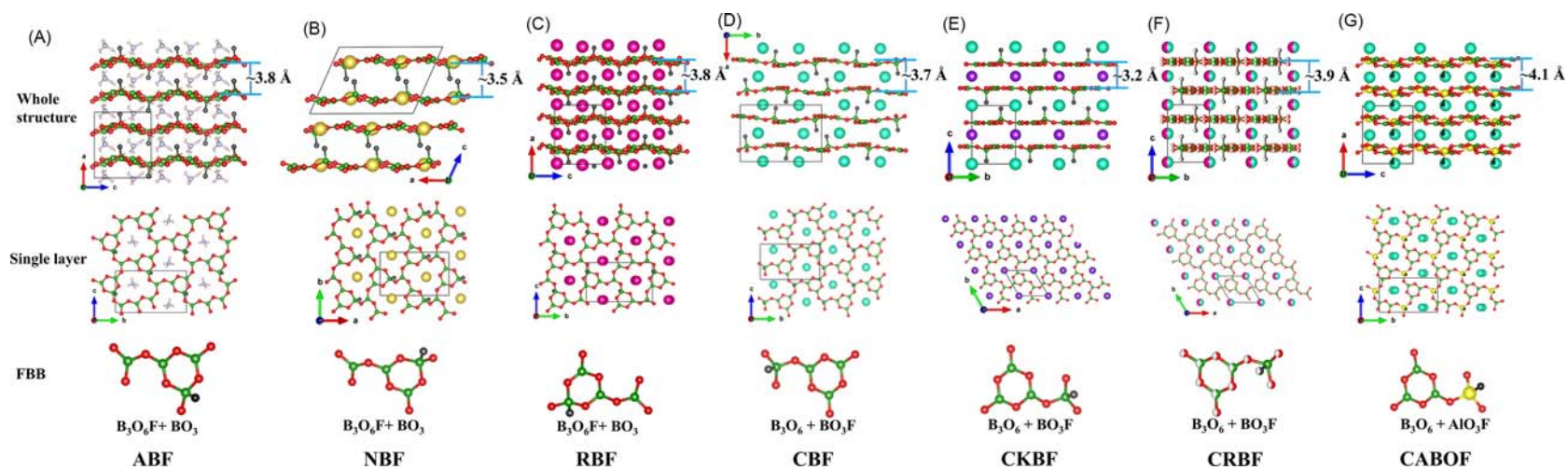


Fig. 48 The structure of ABF (A), NBF (B), RBF (C), CBF (D), CKBF (E), CRBF (F) and CABF (G).

layers and the Cs^+ cations reside in the interlayer space. CABF exhibits a high optical transmittance with absorption edge shorter than 190 nm, large powder SHG intensities ($2.0 \times \text{KDP}$), and suitable birefringence (calculated value of 0.091 at 1064 nm) for phase-matching under 200 nm, so that CABF crystal is considered as the candidate for DUV NLO materials. However, the large-size crystals need to be grown for further evaluation.

4.02.5.2.2.2 Other fluorooxoborates

$\text{Li}_2\text{B}_6\text{O}_9\text{F}_2$ and $\text{MB}_5\text{O}_7\text{F}_3$ ($\text{M}=\text{Ca}$ or Sr): They are studied as DUV NLO materials.^{415,423–426} A branched 3D framework is built by $\text{B}_6\text{O}_{11}\text{F}_2$ FBBs in the structures of $\text{Li}_2\text{B}_6\text{O}_9\text{F}_2$ (Fig. 49). And the 2D zigzag $^2[\text{B}_5\text{O}_7\text{F}_3]_\infty$ single layers composed of $\text{B}_5\text{O}_9\text{F}_3$ FBBs in the structures of $\text{MB}_5\text{O}_7\text{F}_3$ ($\text{M}=\text{Ca}$ or Sr) are shown in Fig. 50. Both $\text{Li}_2\text{B}_6\text{O}_9\text{F}_2$ and $\text{MB}_5\text{O}_7\text{F}_3$ ($\text{M}=\text{Ca}$ or Sr) have short UV absorption wavelength (< 190 nm), moderate birefringence (~ 0.07 at 1064 nm), suitable powder SHG efficiencies ($0.9\text{--}2.3 \times \text{KDP}$ at 1064 nm), as well as short deep-UV SHG phase-matching wavelengths (calculated values from 171 nm to 192 nm). Notably, the experimental evaluation for these fluorooxoborates phase-matching in the DUV spectra range is lacked, which determines whether they can be practically applied as DUV NLO crystals.

4.02.5.2.3 Other materials

Fluorophosphates: $\text{NaNH}_4\text{PO}_3\text{F} \cdot \text{H}_2\text{O}$ is the first example among all the available phosphates and fluorophosphates that could be phase-matchable in the DUV spectral region. Its structure features unique $^2[\text{NaPO}_3\text{F} \cdot \text{H}_2\text{O}]_\infty$ layer bonded by the $\text{N}\text{--}\text{H} \cdots \text{O}$ bonds (Fig. 51). The polar $\text{P}\text{--}\text{F}$ bonds of the PO_3F units lead to the strong anisotropy of unoccupied states around the P atom, which results in the larger birefringence (0.046 and at 1064 nm) than most of other phosphates and moderate powder SHG responds ($1.1 \times \text{KDP}$). Owing to such a large birefringence, the shortest PM wavelength of $\text{NaNH}_4\text{PO}_3\text{F} \cdot \text{H}_2\text{O}$ is blue-shifted to 194 nm, which is much shorter than that of KDP (258 nm).⁴²⁷ The laser induced damage threshold is measured to be 118.1 MW cm^{-2} . The SHG processes from 800, 670, and 630 to their second harmonic 400, 335, and 315 nm were obtained based on the [010] wafers of $\text{NaNH}_4\text{PO}_3\text{F} \cdot \text{H}_2\text{O}$. Besides, it had been grown to the size of $14 \times 9 \times 2.3 \text{ mm}^3$ by dissolving the starting materials in water and precipitating the product using acetone, which shows feasible growth of large crystals. Thus, in contrast to known phosphates, fluorophosphates with improved optical properties might also be suitable for DUV applications.

$\text{AEB}_8\text{O}_{15}\text{H}_4$ ($\text{AE}=\text{Sr}, \text{Ca}$): Recently, Lin group screened from the inorganic structure database and found that two hydroxyborates $\text{AEB}_8\text{O}_{15}\text{H}_4$ ($\text{AE}=\text{Ca}, \text{Sr}$, abbreviated CBOH and SBOH) exhibited excellent NLO properties.⁴²⁸ They crystallize in the space group of $P2_1$ (No. 4), and the BO_3 , $\text{BO}_2(\text{OH})$ and BO_4 basic units connect via corner-sharing O atoms to form the $\text{B}_8\text{O}_{17}\text{H}_4$ FBBs. The $\text{B}_8\text{O}_{17}\text{H}_4$ FBBs are further linked to form the branched $^2[\text{B}_8\text{O}_{15}\text{H}_4]_\infty$ layer stacking along the a -axis, and each adjacent layers are bonded mainly by the $\text{Sr}\text{--}\text{O}$ bonds (Fig. 52). Theoretical and experimental results demonstrate that they can realize large bandgaps ($E_g = 7.43$ and 7.02 eV), strong SHG effects ($2 \times \text{KDP}$ and $1.8 \times \text{KDP}$) and sufficient birefringence (~ 0.093 and 0.087), respectively. First-principles analyses show that the balanced properties are closely related to the introduction of H. In addition, CBOH and SBOH have the shortest phase-matching wavelength reaching to 174 and 185 nm, respectively, according to the first-principles calculations, which indicate that they have potential applications in the DUV region. At present, the single crystals of submillimeter-level CBOH and polycrystalline powders of SBOH can be synthesized by the hydrothermal method. However, the large-size crystals should be grown for more performance evaluations in DUV lasers applications.

Carbonates: The carbonate fluorides ABCO_3F ($\text{A}=\text{K}, \text{Rb}, \text{Cs}$; $\text{B}=\text{Ca}, \text{Sr}$) (abbreviated as ABCO_3F family) were synthesized by spontaneous crystallization with molten fluxes by Zou and Ye et al.⁴²⁹ ASrCO_3F ($\text{A}=\text{K}, \text{Rb}$) and KCaCO_3F are isostructural and crystallize into a hexagonal crystal system with an acentric space group of $Pm2$ (No. 187), and RbCaCO_3F and CsCaCO_3F are isostructural and also crystallize in the space group of $Pm2$. In their crystal structure, the CO_3 basic units have a coplanar arrangement

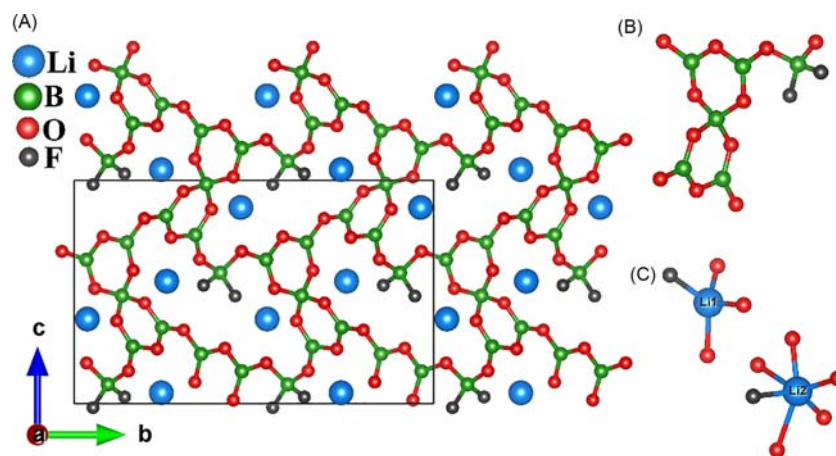


Fig. 49 The structure of $\text{Li}_2\text{B}_6\text{O}_9\text{F}_2$ viewed along the a -axis (A), the $\text{B}_6\text{O}_{11}\text{F}_2$ FBB (B) and the coordination environment of Li atoms (C).

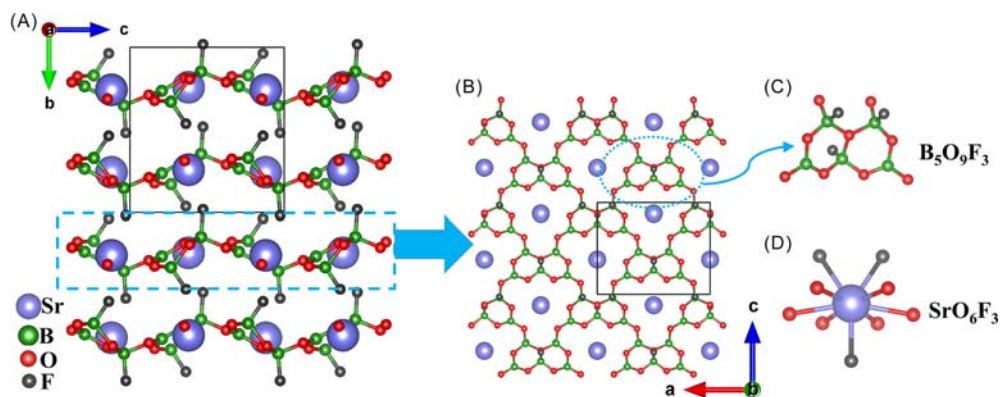


Fig. 50 The structure of $\text{SrB}_5\text{O}_7\text{F}_3$ viewed along the a -axis (A), the single layer with large channels stretching in ac plane (B), the $\text{B}_5\text{O}_9\text{F}_3$ FBB (C) and the coordination environment of Sr atom (D).

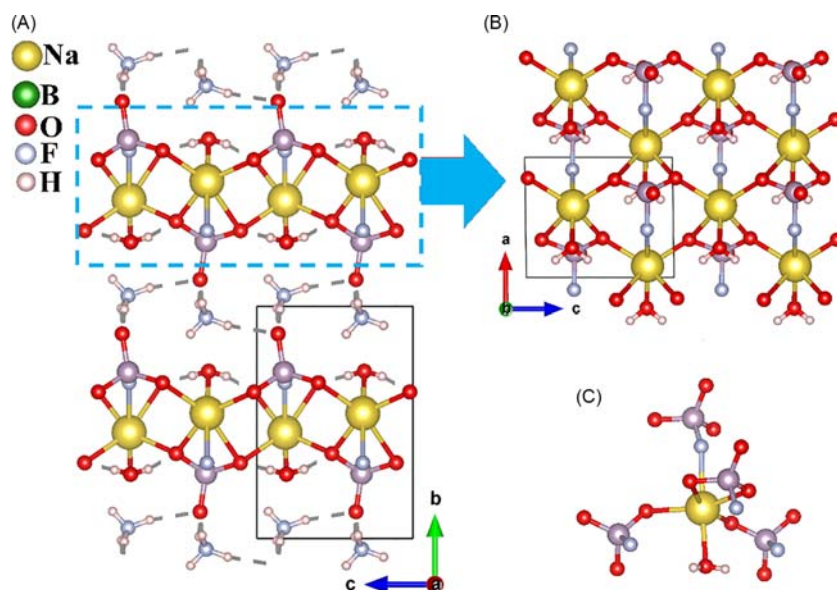


Fig. 51 The structure of $\text{NaNH}_4\text{PO}_3\text{F}\cdot\text{H}_2\text{O}$ viewed along the a -axis (A), the $[\text{NaPO}_3\text{F}\cdot\text{H}_2\text{O}]$ layer viewed along the b -axis (B) and the coordinated environment of Na atom (C).

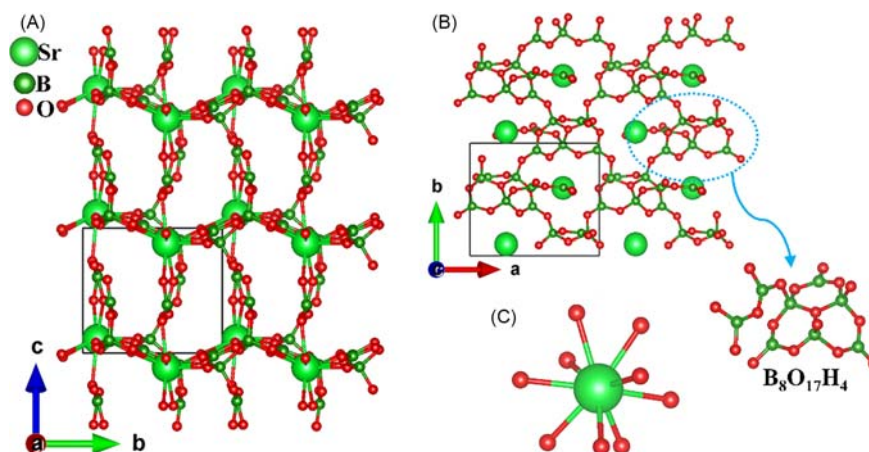


Fig. 52 The structure of $\text{SrB}_8\text{O}_{15}\text{H}_4$ viewed along the a -axis (A), a branched ${}^2[\text{B}_8\text{O}_{15}\text{H}_4]_\infty$ layer stretching in the ab plane (B) and the coordination environment of Sr atom (C).

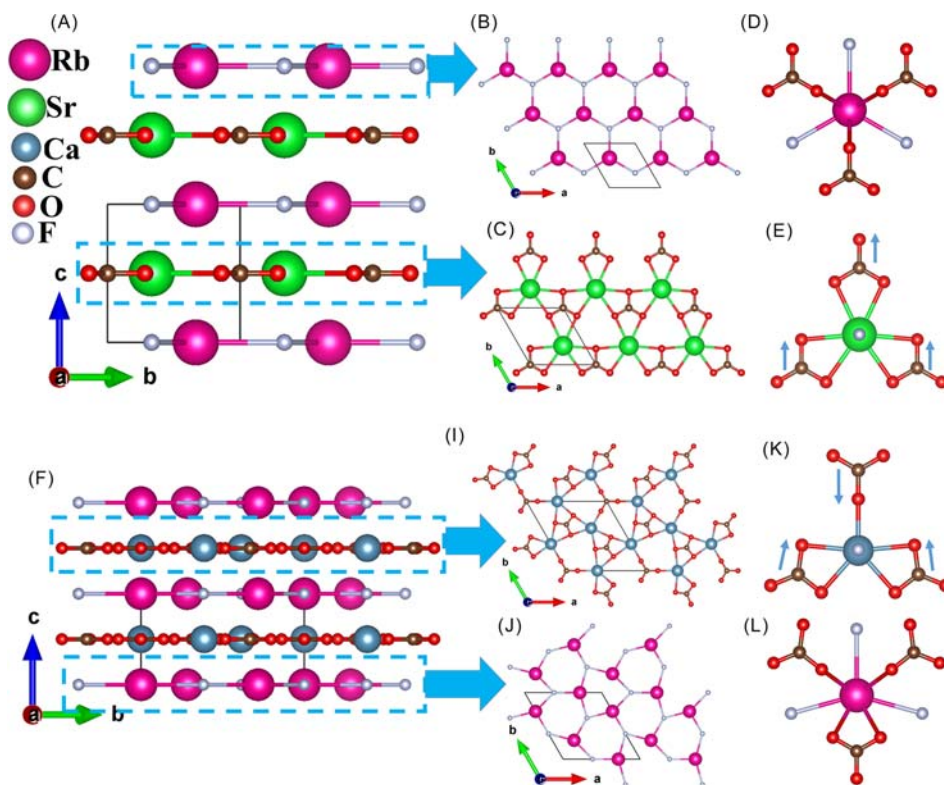


Fig. 53 The whole structure of RbSrCO_3F viewed along the a -axis (A), the ${}^2[\text{RbF}]_\infty$ layer (B) and the ${}^2[\text{SrCO}_3]_\infty$ layer (C) stretching in the bc plane, the coordination environment of Rb (D) and Sr (E) atoms; The whole structure of RbCaCO_3F viewed along the a -axis (F), the ${}^2[\text{RbF}]_\infty$ layer (I) and the ${}^2[\text{CaCO}_3]_\infty$ layer (J) stretching in the bc plane, the coordination environment of Rb (K) and Ca (L) atoms.

in the ab plane, giving the contribution to a large birefringence and macroscopic SHG effect. However, the different orientations of CO_3 units in ABCO_3F family directed mainly by the different coordination behaviors of the B-site cations result in a different nonlinearity for these carbonates. For ASrCO_3F ($A=\text{K}, \text{Rb}$) and KCaCO_3F , the B-site cations are in eight-coordinate $[\text{BO}_6\text{F}_2]$ hexagonal bipyramids (Fig. 53), which makes all the CO_3 units align parallelly in the ab plane and give the maximum contribution to the large macroscopic SHG effects ($3.33\text{--}3.61 \times \text{KDP}$ at 1064 nm). While in the structure of RbCaCO_3F and CsCaCO_3F crystal, the B-site cations are in seven-coordinate pentagonal bipyramids $[\text{BO}_5\text{F}_2]$, which make one-third of the CO_3 units align antiparallely to the others, weakening the SHG coefficients to $1.11 \times \text{KDP}$ at 1064 nm. And they have been evaluated and shown the potential applications as DUV crystals due to the short-wavelength absorption edges (< 200 nm) resulted from the UV-vis diffuse reflectance spectroscopy studies) and the sufficient birefringences (calculated values from 0.102–0.116 at 1064 nm by Lin group) enable phase-matching to the DUV spectra.⁴³⁰

4.02.6 Conclusion

This chapter briefly summarized the developments of primary inorganic nonlinear optical materials, including their structures, linear and nonlinear optical properties, single-crystal growth and applications in the laser system. Through the analysis of the relationship between the structures and the properties, some ideas of material design were put forward which have served as a guide to create excellent and exciting nonlinear optical materials. Since the laser was invented, the better part of the past six decades has witnessed the thriving of inorganic nonlinear optical materials. However, commercial inorganic nonlinear materials are still few and cannot meet social needs. The growth of single crystal with large size and high optical quality is one of the problems that need to be solved urgently at present.

Acknowledgments

This work was financially supported by the National Natural Science Foundation of China (61922084), the Science and Technology Service Network Initiative of CAS (KJFJ-STIS-QYZD-130) and the Key Research Project of Frontier Science of CAS (QYZDB-SSW-JSC049).

References

1. Hecht, J. Short History of Laser Development. *Appl. Optics* **2010**, *49* (25), 99–122.
2. Coupric, M. E. New Generation of Light Sources: Present and Future. *J. Electron Spectros.* **2014**, *196*, 3–13.
3. Suckewer, S.; Jaeglé, P. X-Ray Laser: Past, Present, and Future. *Laser Phys. Lett.* **2009**, *6* (6), 411–436.
4. Gu, M.; Li, X.; Cao, Y. Optical Storage Arrays: A Perspective for Future Big Data Storage. *Light-Sci. Appl.* **2014**, *3* (5), 177.
5. Duarte, F. J., Ed.; *Tunable Laser Applications*, 2nd ed.; CRC Press: Boca Raton, 2009; pp 245–280. ch. 9.
6. Petrov, V. Parametric Down-Conversion Devices: The Coverage of the Mid-Infrared Spectral Range by Solid-State Laser Sources. *Opt. Mater.* **2012**, *34* (3), 536–554.
7. Franken, P. A.; Hill, A. E.; Peters, C. W.; Weinreich, G. Generation of Optical Harmonics. *Phys. Rev. Lett.* **1961**, *7* (4), 118–119.
8. Maiman, T. H. Optical and Microwave-Optical Experiments in Ruby. *Phys. Rev. Lett.* **1960**, *4* (11), 564–566.
9. Maiman, T. H. Stimulated Optical Radiation in Ruby. *Nature* **1960**, *187* (4736), 493–494.
10. Giordmaine, J. A. Mixing of Light Beams in Crystals. *Phys. Rev. Lett.* **1962**, *8* (1), 19–20.
11. Maker, P. D.; Terhune, R. W.; Nicenoff, M.; Savege, M. C. Effects of Dispersion and Focusing on the Production of Optical Harmonics. *Phys. Rev. Lett.* **1962**, *8* (1), 21–22.
12. Armstrong, J. A.; Bloembergen, N.; Ducuing, J.; Pershan, P. S. Interactions Between Light Waves in a Nonlinear Dielectric. *Phys. Ther. Rev.* **1962**, *127* (6), 1918–1939.
13. Fejer, M. M.; Magel, G. A.; Jundt, D. H.; Byer, R. L. Quasi-Phase-Matched Second Harmonic Generation: Tuning and Tolerances. *IEEE. J. Quant. Electr.* **1992**, *28* (11), 2631–2654.
14. Myers, L. E.; Eckardt, R. C.; Fejer, M. M.; Byer, R. L.; Bosenberg, W. R.; Pierce, J. W. Quasi-Phase-Matched Optical Parametric Oscillators in Bulk Periodically Poled LiNbO₃. *J. Opt. Soc. Am. B* **1995**, *12* (11), 2102–2116.
15. Myers, L. E.; Bosenberg, W. R. Periodically Poled Lithium Niobate and Quasi-Phase-Matched Optical Parametric Oscillators. *IEEE. J. Quant. Electr.* **1997**, *33* (10), 1663–1672.
16. Setzler, S. D.; Schunemann, P. G.; Pollak, T. M.; Pomeranz, L. A.; Missey, M. J.; Zelmon, D. E. Periodically poled barium titanate as a new nonlinear optical material. In *Advanced Solid State Lasers, OSA Trends in Optics and Photonics Series*; Fejer, M. M., Injeyan, H., Keller, U., Eds.; vol. 26; OSA: Washington DC, 1999; pp 676–680.
17. Liu, Z. W.; Zhu, S. N.; Zhu, Y. Y.; Qin, Y. Q.; He, J. L.; Zhang, C.; Wang, H. T.; Ming, N. B.; Liang, X. Y.; Xu, Z. Y. Quasi-CW Ultraviolet Generation in a Dual-Periodic LiTaO₃ Superlattice by Frequency Tripling. *Jpn. J. Appl. Phys.* **2001**, *40* (12), 6841–6844.
18. Arie, A.; Rosenman, G.; Mahal, V.; Skliar, A.; Oron, M.; Katz, M.; Eger, D. Green and Ultraviolet Quasi-Phase-Matched Second Harmonic Generation in Bulk Periodically-Poled KTiOPO₄. *Opt. Commun.* **1997**, *142* (4-6), 265–268.
19. Lallier, E.; Brevignon, M.; Lehoux, J. Efficient Second-Harmonic Generation of a CO₂ Laser With Quasi-Phase-Matched GaAs Crystal. *Opt. Lett.* **1998**, *23* (19), 1511–1513.
20. Boyd, R. W. *Nonlinear Optics*, 3rd ed.; Academic Press, 2008; pp 1–13.
21. Shen, Y. R. *The Principles of Nonlinear Optics*, Wiley-Interscience, 2002; p 576.
22. Sparkes, M.; Gross, M.; Celotto, S.; Zhang, T.; O'Neil, W. Practical and Theoretical Investigations Into Inert Gas Cutting of 304 Stainless Steel Using a High Brightness Fiber Laser. *J. Laser Appl.* **2008**, *20* (1), 59–67.
23. Xu, Z. Y.; Zhang, S. J.; Zhou, X. J.; Zhang, F. F.; Yang, F.; Wang, Z. M.; Zong, N.; Liu, G. D.; Zhao, L.; Yu, L.; Chen, C. T.; Wang, X. Y.; Peng, Q. J. Advances in Deep Ultraviolet Laser Based High-Resolution Photoemission Spectroscopy. *Front. Inform. Technol. Elect. Eng.* **2019**, *20* (7), 885–913.
24. Müncheberg, S.; Gal, C.; Horwath, J.; Kinter, H.; Martin Navajas, L.; Soutullo, M. Development Status and Breadboard Results of a Laser Communication Terminal for Large LEO Constellations. *SPIE* **2019**, *11180*, 1118034.
25. Espina, V.; Heiby, M.; Pierobon, M.; Liotta, L. A. Laser capture Microdissection Technology. *Expert Rev. Mol. Diagn.* **2007**, *7* (5), 647–657.
26. Bloembergen, N. *Wave Propagation in Nonlinear Electromagnetic Media*, vol. 51; IEEE, 1963; pp 124–131.
27. Akhmanov, S. A.; Khokhlov, R. V. *Problems of Nonlinear Optics*, VINITI: Moscow, In Russian, 1964.
28. Bokut, B. V. Optical Mixing in Biaxial Crystals. *Zh. Prikl. Spektrosk.* **1967**, *7* (4), 621–624.
29. Kurtz, S. K.; Perry, T. T.; Bergman, J. G. Alpha-Iodic Acid: A Solution-Grown Crystal for Nonlinear Optical Studies and Applications. *Appl. Phys. Lett.* **1967**, *12* (5), 186–188.
30. Bjorkholm, J. E. Relative Measurement of the Optical Nonlinearities of KDP, ADP, LiNbO₃, and α -HIO₃. *IEEE. J. Quant. Electr.* **1968**, *4* (11), 970–972.
31. Midwinter, J. E.; Warner, J. The Effects of Phase Matching Method and of Uniaxial Crystal Symmetry on the Polar Distribution of Second-Order Non-Linear Optical Polarization. *Br. J. Appl. Phys.* **1965**, *16* (8), 1135–1142.
32. Suvorov, V. S.; Sonin, A. S.; Rez, I. S. Some Nonlinear Optical Properties of Crystals of the KDP Group. *Zh. Eksp. Teor. Fiz.* **1967**, *53* (1), 49–55.
33. Geusic, J. E.; Levinstein, H. J.; Singh, S.; Smith, R. G.; van Uitert, L. G. Continuous 0.532 μ m Solid-State Source Using Ba₂Nb₅O₁₅. *Appl. Phys. Lett.* **1968**, *12* (9), 306–308.
34. Giordmaine, J. A.; Miller, R. C. Tunable Coherent Parametric Oscillation in LiNbO₃ at Optical Frequencies. *Phys. Rev. Lett.* **1965**, *14* (24), 973–976.
35. Petrov, V. Parametric Down-Conversion Devices: The Coverage of the Mid-Infrared Spectral Range by Solid-State Laser Sources. *Opt. Mater.* **2012**, *34* (3), 536–554.
36. Agroskin, V. Y.; Bravy, B. G.; Chernyshev, Y. A.; Kashtanov, S. A.; Kirianov, V. I.; Makarov, E. F.; Papin, V. G.; Sotnichenko, S. A.; Vasiliev, G. K. Aerosol Sounding With A Lidar System Based on a DF Laser. *Appl. Phys. B* **2005**, *81* (8), 1149–1154.
37. Karaganov, V.; Law, M.; Kaesler, M.; Lancaster, D.; Taylor, M. Engineering Development of a Directed IR Countermeasure Laser. *SPIE* **2004**, *5615*, 48–53.
38. Schunemann, P. G.; Zawilski, K. T.; Pomeranz, L. A.; Creeden, D. J.; Budni, P. A. Advances in Nonlinear Optical Crystals for Mid-Infrared Coherent Sources. *J. Opt. Soc. Am. B* **2016**, *33* (11), D36–D43.
39. Abrahams, S. C.; Bernstein, J. L. Crystal Structure of Piezoelectric Nonlinear-Optic AgGaS₂. *J. Chem. Phys.* **1973**, *59* (4), 1625–1629.
40. Zondy, J. J.; Touahri, D.; Acef, O. Absolute Value of the d₃₆ Nonlinear Coefficient of AgGaS₂: Prospect for a Low-Threshold Doubly Resonant Oscillator-Based 3:1 Frequency Divider. *J. Opt. Soc. Am. B* **1997**, *14* (10), 2481–2497.
41. Fan, Y. X.; Eckardt, R. C.; Byer, R. L.; Route, R. K.; Feigelson, R. S. AgGaS₂ Infrared Parametric Oscillator. *Appl. Phys. Lett.* **1984**, *45* (4), 313–315.
42. Hanna, D.; Rampal, V.; Smith, R. Tunable Medium Infrared Generation in Silver Thiogallate (AgGaS₂) by Down-Conversion of Flash-Pumped Dye-Laser Radiation. *IEEE J. Quant. Electr.* **1974**, *10* (4), 461–462.
43. Kato, K.; Shirahata, H. Nonlinear IR Generation in AgGaS₂. *Jpn. J. Appl. Phys.* **1996**, *35* (9R), 4645–4648.
44. Catella, G. C.; Burlage, D. Crystal Growth and Optical Properties of AgGaS₂ and AgGaSe₂. *MRS Bulletin* **1998**, *23* (7), 28–36.
45. Badikov, V. V.; Matveev, I. N.; Shenichnikov, S. M.; Skrebneva, O. V.; Trotsenko, N. K.; Ustinov, N. D. Dispersion of Birefringence and the Optical Activity of AgGa(S_{1-x}Se_x)₂ Crystals. *Kristallogr.* **1991**, *26* (3), 537–539.
46. Krause, H. J.; Daum, W. High-Power Source of Coherent Picosecond Light Pulses Tunable From 0.41 to 12.9 μ m. *Appl. Phys. B* **1993**, *56* (1), 8–13.
47. Saito, N.; Akagawa, K.; Wada, S.; Tashiro, H. Difference-Frequency Generation by Mixing Dual-Wavelength Pulses Emitting From An Electronically Tuned Ti:Sapphire Laser. *Appl. Phys. B* **1999**, *69* (2), 93–97.
48. Korczak, P.; Staff, C. B. Liquid Encapsulated Czochralski Growth of Silver Thiogallate. *J. Cryst. Growth* **1974**, *24–25*, 386–389.
49. Feigelson, R.; Route, R. Recent Developments in the Growth Of Chalcopyrite Crystals for Nonlinear Infrared Applications. *Optim. Eng.* **1987**, *26* (2), 113–119.
50. Chen, B.; Zhu, S.; Zhao, B.; Zhang, J.; Huang, Y.; Li, M.; Liu, J.; Tan, B.; Wang, R.; He, Z. Growth of AgGaS₂ Single Crystals by Modified Furnace. *J. Cryst. Growth* **2006**, *292* (2), 490–493.
51. Karunakaran, N.; Ramasamy, P. Synthesis, Growth and Physical Properties of Silver Gallium Sulfide Single Crystals. *Mater. Sci. Semicond. Process.* **2016**, *41*, 54–58.
52. Boyd, G. D.; Kasper, H. M.; McFee, J. H.; Storz, F. G. Linear and Nonlinear Optical Properties of Some Ternary Selenides. *IEEE. J. Quant. Electr.* **1972**, *8* (12), 900–908.

53. Whittaker, M. T.; Stenger, T. E.; Krause, D. G.; Matthiesen, D. H. Infrared Absorption and Electrical Properties of AgGaSe₂. *J. Cryst. Growth* **2008**, *310* (7), 1904–1909.
54. Byer, R. L.; Choy, M. M.; Herbst, R. L.; Chelma, D. S.; Feigelson, R. S. Second Harmonic Generation and Infrared Mixing in AgGaSe₂. *Appl. Phys. Lett.* **1974**, *24* (2), 65–68.
55. Harasaki, A.; Kato, K. New Data On the Nonlinear Optical Constant, Phase-Matching, and Optical Damage of AgGaSe₂. *Jpn. J. Appl. Phys.* **1997**, *36* (2), 700–703.
56. Fraser, J. M.; Wang, D.; Hache, A.; Allan, G. R.; Driel, H. M. Generation of Highrepetition-Rate Femtosecond Pulses From 8 to 18 μm. *Appl. Optics* **1997**, *36* (21), 5044–5047.
57. Roy, U. N.; Cui, Y.; Hawrami, R.; Burger, A.; Orona, L.; Goldstein, J. T. AgGaSe₂: A Highly Photoconductive Material. *Solid State Commun.* **2006**, *139* (10), 527–530.
58. Roy, U.; Groza, M.; Cui, Y.; Burger, A.; Bell, Z.; Carpenter, D. Crystal Growth, Characterization, and Fabrication of AgGaSe₂ Crystals As Novel Material for Room-Temperature Radiation Detectors. *SPIE* **2004**, *5540*, 177–185.
59. Murthy, Y. S.; Hussain, O. M.; Naidu, B. S.; Reddy, P. J. Characterization of p-AgGaSe₂/n-CdS Thin Film Heterojunction. *Mater. Lett.* **1991**, *10* (11), 504–508.
60. Babu, G. A.; Raja, R. S.; Karunagaran, N.; Ramasamy, R. P.; Ramasamy, P.; Ganesamoorthy, S.; Gupta, P. K. Growth Improvement of AgGaSe₂ Single Crystal Using the Vertical Bridgman Technique With Steady Ampoule Rotation and Its Characterization. *J. Cryst. Growth* **2012**, *338* (1), 42–46.
61. Iseler, G. W. Thermal Expansion and Seeded Bridgman Growth of AgGaSe₂. *J. Cryst. Growth* **1977**, *41* (1), 146–150.
62. Yeliseyev, A.; Krinitsin, P.; Isaenko, L. Spectroscopic Features of Nonlinear AgGaSe₂ Crystals. *J. Cryst. Growth* **2014**, *387*, 41–47.
63. Boyd, G. D.; Buehler, E.; Storz, F. G. Linear and Nonlinear Optical Properties of ZnGeP₂ and CdSe. *Appl. Phys. Lett.* **1971**, *18* (7), 301–304.
64. Lind, M. D.; Grant, R. W. Structural Dependence of Birefringence in the Chalcopyrite Structure. Refinement of the Structural Parameters of ZnGeP₂ and ZnSiAs₂. *J. Chem. Phys.* **1973**, *58* (1), 357–362.
65. Nikogosyan, D. N. *Nonlinear Optical Crystals: A Complete Survey*, Springer Science & Business Media, 2006; pp 96–103.
66. Vodopyanov, K. L. Parametric Generation of Tunable Infrared Radiation in ZnGeP₂ and GaSe Pumped at 3 μm. *J. Opt. Soc. Am. B* **1993**, *10* (9), 1723–1729.
67. Mason, P. D.; Jackson, D. J.; Gorton, E. K. CO₂ Laser Frequency Doubling in ZnGeP₂. *Opt. Commun.* **1994**, *110* (1–2), 163–166.
68. Beasley, J. D. Thermal Conductivities of Some Novel Nonlinear Optical Materials. *Appl. Optics* **1994**, *33* (6), 1000–1003.
69. Zakharov, S. V.; Negin, A. E.; Filippov, P. G.; Zhilis, E. F. Sellmeier Equation and Conversion of the Radiation of a Repetitively Pulsed Tunable TEA CO₂ Laser Into the Second Harmonic in a ZnGeP₂ Crystal. *Quant. Electr.* **1999**, *29* (9), 806–810.
70. Vodopyanov, K. L.; Ganikhanov, F.; Maffetone, J. P.; Zwieback, I.; Ruderman, W. ZnGeP₂ Optical Parametric Oscillator With 3.8–12.4 μm Tunability. *Opt. Lett.* **2000**, *25* (11), 841–843.
71. Haakestad, M. W.; Fonnum, H.; Lippert, E. Mid-Infrared Source With 0.2 J Pulse Energy Based on Nonlinear Conversion of Q-Switched Pulses in ZnGeP₂. *Opt. Express* **2014**, *22* (7), 8556–8564.
72. Dergachev, A.; Armstrong, D.; Smith, A.; Drake, T.; Dubois, M. 3.4 μm ZGP RISTRA Nanosecond Optical Parametric Oscillator Pumped by a 2.05 μm Ho:YLF MOPA System. *Opt. Express* **2007**, *15* (22), 14404–14413.
73. Petrov, V.; Rotermund, F.; Noack, F.; Schunemann, P. Femtosecond Parametric Generation in ZnGeP₂. *Opt. Lett.* **1999**, *24* (6), 414–416.
74. Yang, D. H.; Zhao, B. J.; Chen, B. J.; Zhu, S. F.; He, Z. Y.; Zhao, Z. R.; Liu, M. D. Growth of ZnGeP₂ Single Crystals by Modified Vertical Bridgman Method for Nonlinear Optical Devices. *Mater. Sci. Semicond. Process.* **2017**, *67*, 147–151.
75. Cheng, J.; Zhu, S.; Zhao, B.; Chen, B.; He, Z.; Fan, Q.; Xu, T. Synthesis and Growth of ZnGeP₂ Crystals: Prevention of Non-Stoichiometry. *J. Cryst. Growth* **2013**, *362*, 125–129.
76. Verozubova, G. A.; Gribenyukov, A. I.; Korotkova, V. V.; Ruzaikin, M. P. ZnGeP₂ Synthesis and Growth From Melt. *Mater. Sci. Eng. B* **1997**, *48* (3), 191–197.
77. Verozubova, G. A.; Gribenyukov, A. I.; Korotkova, V. V.; Vere, A. W.; Flynn, C. J. ZnGeP₂ Growth: Melt Non-Stoichiometry and Defect Substructure. *J. Cryst. Growth* **2002**, *237–239*, 2000–2004.
78. Shimony, Y.; Kimmel, G.; Raz, O.; Dariel, M. P. X-Ray Diffraction Analysis of Melt-Grown ZnGeP₂ (ZGP). *J. Cryst. Growth* **1999**, *198–199*, 583–587.
79. Hobgood, H. M.; Henningsen, T.; Thomas, R. N.; Hopkins, R. H.; Ohmer, M. C.; Mitchel, W. C.; Fischer, D. W.; Hegde, S. M.; Hopkins, F. K. ZnGeP₂ Grown by the Liquid Encapsulated Czochralski Method. *J. Appl. Phys.* **1993**, *73* (8), 4030–4037.
80. Xing, G. C.; Bachmann, K. J.; Posthill, J. B. High-Pressure Vapor Transport of ZnGeP₂. *Appl. Phys. Lett.* **1990**, *56* (3), 271–273.
81. Lei, Z.; Zhu, C.; Xu, C.; Yao, B.; Yang, C. Growth of Crack-Free ZnGeP₂ Large Single Crystals for High-Power Mid-Infrared OPO Applications. *J. Cryst. Growth* **2014**, *389*, 23–29.
82. Yang, Y.; Jiang, X.; Lin, Z.; Wu, Y. Borate-Based Ultraviolet and Deep-Ultraviolet Nonlinear Optical Crystals. *Crystals* **2017**, *7* (4), 95.
83. Abrahams, S. G.; Bernstein, J. L. Luminescent Piezoelectric CdSiP₂: Normal Probability Plot Analysis, Crystal Structure, and Generalized Structure of the A^bB^cV₂ Family. *J. Chem. Phys.* **1971**, *55* (2), 796–803.
84. Kemlin, V.; et al. Nonlinear, Dispersive, and Phase-Matching Properties of the New Chalcopyrite CdSiP₂. *Opt. Mater. Express* **2011**, *1* (7), 1292–1300.
85. Lambrecht, W. R. L.; Jiang, X. Noncritically Phase-Matched Second-Harmonic-Generation Chalcopyrites Based on CdSiAs₂ and CdSiP₂. *Phys. Rev. B* **2004**, *70* (4), 045204.
86. Kemlin, V.; Brand, P.; Boulanger, B.; Segonds, P.; Schunemann, P. G.; Zawilski, K. T.; Ménaert, B.; Debray, J. Phase-Matching Properties and Refined Sellmeier Equations of the New Nonlinear Infrared Crystal CdSiP₂. *Opt. Lett.* **2011**, *36* (10), 1800–1802.
87. Schunemann, P. G.; Zawilski, K. T.; Pollak, T. M.; Zelmon, D. E.; Fernelius, N. C.; Kenneth Hopkins, F. *New Nonlinear Optical Crystal for Mid-IR OPOs: CdSiP₂*, Advanced Solid-State Photonics OSA: Nara, Japan, 2008. MG6.
88. Zawilski, K. T.; Schunemann, P. G.; Pollak, T. C.; Zelmon, D. E.; Fernelius, N. C.; Kenneth Hopkins, F. Growth and Characterization of Large CdSiP₂ Single Crystals. *J. Cryst. Growth* **2010**, *312* (8), 1127–1132.
89. Verozubova, G. A.; Okunev, A. O.; Gribenyukov, A. I.; Trofimov, A. Y.; Trukhanov, E. M.; Kolesnikov, A. V. Growth and Defect Structure of ZnGeP₂ Crystals. *J. Cryst. Growth* **2010**, *312* (8), 1122–1126.
90. Zawilski, K. T.; Schunemann, P. G.; Setzler, S. D.; Pollak, T. M. Large Aperture Single Crystal ZnGeP₂ for High-Energy Applications. *J. Cryst. Growth* **2008**, *310* (7), 1891–1896.
91. Zhao, X.; Zhu, S.; Zhao, B.; Chen, B.; He, Z.; Wang, R.; Yang, H.; Sun, Y.; Cheng, J. Growth and Characterization of ZnGeP₂ Single Crystals by the Modified Bridgman Method. *J. Cryst. Growth* **2008**, *311* (1), 190–193.
92. Zhang, G.; Tao, X.; Ruan, H.; Wang, S.; Shi, Q. Growth of CdSiP₂ Single Crystals by Self-Seeding Vertical Bridgman Method. *J. Cryst. Growth* **2012**, *340* (1), 197–201.
93. Fan, L.; Zhu, S.; Zhao, B.; Chen, B.; He, Z.; Yang, H.; Liu, G. Synthesis of High-Quality CdSiP₂ Polycrystalline Materials Directly From the Constituent Elements. *J. Cryst. Growth* **2012**, *338* (1), 228–231.
94. Abrahams, S. C.; Bernstein, J. L. Piezoelectric Nonlinear Optic CuGaSe₂ and CdGeAs₂: Crystal Structure, Chalcopyrite Microhardness, and Sublattice Distortion. *J. Chem. Phys.* **1974**, *61* (3), 1140–1146.
95. Schunemann, P. G.; Pollak, T. M. Single Crystal Growth of Large, Crack-Free CdGeAs₂. *J. Cryst. Growth* **1997**, *174* (1), 272–277.
96. Schunemann, P.; Pollak, T. Ultralow Gradient HGF-Grown ZnGeP₂ and CdGeAs₂ and Their Optical Properties. *MRS Bulletin* **1998**, *23* (7), 23–27.
97. Iseler, G. W.; Kildal, H.; Menyuk, N. Optical and Electrical Properties of CdGeAs₂. *J. Electr. Mater.* **1978**, *7* (6), 737–755.
98. Schunemann, P. Improved NLO Crystals for Mid-IR Laser Applications. *SPIE* **2007**, *6455*, 64550R.
99. Schunemann, P. G.; Setzler, S. D.; Pollak, T. M.; Ptak, A. J.; Myers, T. H. Defect Segregation in CdGeAs₂. *J. Cryst. Growth* **2001**, *225* (2), 440–444.
100. Harrison, R. G.; Gupta, P. K.; Taghizadeh, M. R.; Kar, A. K. Efficient Multikilowatt Mid Infrared Difference Frequency Generation in CdGeAs₂. *IEEE J. Quant. Electr.* **1982**, *18* (8), 1239–1242.
101. Isaenko, L. I.; Yeliseyev, A. P. Recent Studies of Nonlinear Chalcogenide Crystals for the Mid-IR. *Semicond. Sci. Tech.* **2016**, *31* (12), 123001.

102. Fossier, S.; Salaün, S.; Mangin, J.; Bidault, O.; Thenot, I.; Zondy, J. J.; Chen, W.; Rotermund, F.; Petrov, V.; Petrov, P.; Henningsen, J.; Yelisseyev, A.; Isaenko, L.; Lobanov, S.; Balachninaite, O.; Slekys, G.; Sirutkaitis, V. Optical, Vibrational, Thermal, Electrical, Damage and Phase-Matching Properties of Lithium Thioindate. *J. Opt. Soc. Am. B* **2004**, *21* (11), 1981–2007.
103. Eifler, A.; Riede, V.; Brückner, J.; Weise, S.; Krämer, V.; Lippold, G.; Schmitz, W.; Bente, K.; Grill, W. Band Gap Energies and Lattice Vibrations of the Lithium Ternary Compounds LiInSe_2 , LiInS_2 , LiGaSe_2 and LiGaS_2 . *Jpn. J. Appl. Phys.* **2000**, *39* (S1), 279–281.
104. Isaenko, L.; Yelisseyev, A.; Lobanov, S.; Petrov, V.; Rotermund, F.; Slekys, G.; Zondy, J. J. LiInSe_2 : A Biaxial Ternary Chalcogenide Crystal for Nonlinear Optical Applications in the Midinfrared. *J. Appl. Phys.* **2002**, *91* (12), 9475–9480.
105. Dmitriev, V. G.; Nikogosyan, D. N. Effective Nonlinearity Coefficients for Three-Wave Interactions in Biaxial Crystal of mm^2 Point Group Symmetry. *Opt. Commun.* **1993**, *95* (1), 173–182.
106. Wang, S.; Zhang, X.; Zhang, X.; Li, C.; Gao, Z.; Lu, Q.; Tao, X. Modified Bridgman Growth and Properties of Mid-Infrared LiInSe_2 Crystal. *J. Cryst. Growth* **2014**, *401*, 150–155.
107. Kuriyama, K.; Nozaki, T. Single-Crystal Growth and Characterization of LiGaSe_2 . *J. Appl. Phys.* **1981**, *52* (10), 6441–6443.
108. Lin, X.; Zhang, G.; Ye, N. Growth and Characterization of BaGa_4S_7 : A New Crystal for Mid-IR Nonlinear Optics. *Cryst. Growth Des.* **2009**, *9* (2), 1186–1189.
109. Yao, J.; Mei, D.; Bai, L.; Lin, Z.; Yin, W.; Fu, P.; Wu, Y. BaGa_4Se_7 : A New Congruent-Melting IR Nonlinear Optical Material. *Inorg. Chem.* **2010**, *49* (20), 9212–9216.
110. Badikov, V.; Badikov, D.; Shevrydyeva, G.; Tyazhev, A.; Marchev, G.; Panyutin, V.; Petrov, V.; Kwasiński, A. BaGa_4S_7 : Wide-Bandgap Phase-Matchable Nonlinear Crystal for the Mid-Infrared. *Opt. Mater. Express* **2011**, *1* (3), 316–320.
111. Badikov, V.; Badikov, D.; Shevrydyeva, G.; Tyazhev, A.; Marchev, G.; Panyutin, V.; Petrov, V.; A. Phase-Matching Properties of BaGa_4S_7 and BaGa_4Se_7 : Wide-Bandgap Nonlinear Crystals for the Mid-Infrared. *Phys. Status Solidi RRL* **2011**, *5* (1), 31–33.
112. Guo, Y.; Zhou, Y.; Lin, X.; Chen, W.; Ye, N. Growth and Characterizations of BaGa_4S_7 Crystal. *Opt. Mater.* **2014**, *36* (12), 2007–2011.
113. Yelisseyev, A. P.; Lobanov, S. I.; Krinitsin, P. G.; Isaenko, L. I. The Optical Properties of the Nonlinear Crystal BaGa_4Se_7 . *Opt. Mater.* **2020**, *99*, 109564.
114. Zhang, X.; Yao, J.; Yin, W.; Zhu, Y.; Wu, Y.; Chen, C. Determination of the Nonlinear Optical Coefficients of the BaGa_4Se_7 Crystal. *Opt. Express* **2015**, *23* (1), 552–556.
115. Zhao, B.; Chen, Y.; Yao, B.; Yao, J.; Guo, Y.; Wang, R.; Dai, T.; Duan, X. High-Efficiency, Tunable 8–9 μm BaGa_4Se_7 Optical Parametric Oscillator Pumped at 2.1 μm . *Opt. Mater. Express* **2018**, *8* (11), 3332–3337.
116. Voronkova, E. M.; Grechushnikov, B. N.; Distler, G. I.; Petrov, I. P. *Optical Materials for Infrared Technique Nauka, Moscow, In Russian*, 1965.
117. Zhang, K. C.; Wang, X. M. *Nonlinear Optics Crystal Materials Science*, Science Press, 2006; pp 325–329.
118. Chai, B. H. T. Optical Crystals. In *CRC Handbook of Laser Science and Technology, Supplement 2: Optical Materials*; Weber, M. J., Ed., CRC Press: Boca Raton, 1995; pp 3–65.
119. Zotova, I. B.; Ding, Y. J. Spectral Measurements of Two-Photon Absorption Coefficients for CdSe and GaSe Crystals. *Appl. Optics* **2001**, *40* (36), 6654–6658.
120. Yoshioka, K.; Igarashi, I.; Yoshida, S.; Arashida, Y.; Katayama, I.; Takeda, J.; Shigekawa, H. Subcycle Mid-Infrared Coherent Transients at 4 MHz Repetition Rate Applicable to Light-Wave-Driven Scanning Tunneling Microscopy. *Opt. Lett.* **2019**, *44* (21), 5350–5353.
121. Yuan, J.; Chen, Y.; Duan, X.; Yao, B.; Dai, T.; Ju, Y. CdSe Optical Parametric Oscillator Operating at 12.07 μm With 170 mW Output. *Opt. Laser Technol.* **2017**, *92*, 1–4.
122. Grigoriev, I. S.; Meilikhov, E. Z. *Physical Quantities. Handbook, Energoatomizdat, Moscow; In Russian*, 1991.
123. Roberts, D. A. Simplified Characterization of Uniaxial and Biaxial Nonlinear Optical Crystals: A Plea for Standardization of Nomenclature and Conventions. *IEEE J. Quant. Electr.* **1992**, *28* (10), 2057–2074.
124. Vodopyanov, K. L.; Kulevskii, L. A.; Voevodin, V. G.; Gribenyukov, A. I.; Allakhverdiev, K. R.; Kerimov, T. A. High Efficiency Middle IR Parametric Superradiance in ZnGeP_2 and GaSe Crystals Pumped by An Erbium Laser. *Opt. Commun.* **1991**, *83* (5), 322–326.
125. Vodopyanov, K. L.; Chazapis, V. Extra-Wide Tuning Range Optical Parametric Oscillator. *Opt. Commun.* **1997**, *135* (13), 98–102.
126. Kaindl, R. A.; Smith, D. C.; Joschko, M. M.; Hasselbeck, P.; Woerner, M.; Elsaesser, T. Femtosecond Infrared Pulses Tunable From 9 to 18 μm at an 88-MHz Repetition Rate. *Opt. Lett.* **1998**, *23* (11), 861–863.
127. Gaida, C.; Gebhardt, M.; Heuermann, T.; Stutzki, F.; Jauregui, C.; Antonio-Lopez, J.; Schülzgen, A.; Amezcua-Correa, R.; Tünnermann, A.; Pupeza, I.; Limpert, J. Watt-Scale Super-Octave Mid-Infrared Intracavity Difference Frequency Generation. *Light: Science & Appl.* **2018**, *7* (1), 94.
128. Liu, K.; Liang, H.; Wang, L.; Qu, S.; Lang, T.; Li, H.; Wang, Q.; Zhang, Y. Multimicrojoule GaSe-Based Midinfrared Optical Parametric Amplifier With An Ultrabroad Idler Spectrum Covering 4.2–16 μm . *Opt. Lett.* **2019**, *44* (4), 1003–1006.
129. Petrov, V.; Panyutin, V. L.; Tyazhev, A.; Marchev, G.; Zagumennyi, A. I.; Rotermund, F.; Noack, F.; Miyata, K.; Iskhakova, L. D.; Zerrouk, A. F. $\text{GaS}_{0.4}\text{Se}_{0.6}$: Relevant Properties and Potential for 1064 nm Pumped Mid-IR OPOs and OPGs Operating Above 5 μm . *Laser Phys.* **2011**, *21* (4), 774–781.
130. Panyutin, V. L.; Zagumennyi, A. I.; Zerrouk, A. F.; Noack, F.; Petrov, V. *GaS_xSe_{1-x} Compounds for Nonlinear Optics*, CLEO/OEA, 2009; p CWJ1.
131. Badikov, V.; Tyulyupa, A. G.; Shevrydyeva, G. S.; Sheina, S. Solid Solutions in the AgGaS_2 - GeS_2 and AgGaSe_2 - GeSe_2 Systems. *Inorg. Mater.* **1991**, *27*, 177–180.
132. Petrov, V.; Badikov, V.; Shevrydyeva, G.; Panyutin, V.; Chizhikov, V. Phase-Matching Properties and Optical Parametric Amplification in Single Crystals of AgGaGeS_4 . *Opt. Mater.* **2004**, *26* (3), 217–222.
133. Oleksyuk, I. D.; Gulyak, A. V.; Sysa, L. V.; Gorgut, G. P.; Lomzin, A. F. Crystal Chemical Properties and Preparation of Single Crystals of $\text{AgGaSe}_2\text{GeSe}_2$ γ -Solid Solutions. *J. Alloys Compd.* **1996**, *241* (1), 187–190.
134. Petrov, V.; Noack, F.; Badikov, V.; Shevrydyeva, G.; Panyutin, V.; Chizhikov, V. Phase-Matching and Femtosecond Difference-Frequency Generation in the Quaternary Semiconductor $\text{AgGaGe}_2\text{Se}_{12}$. *Appl. Optics* **2004**, *43* (23), 4590–4597.
135. Huang, W.; He, Z.; Zhao, B.; Zhu, S.; Chen, B. Crystal Growth, Structure, and Optical Properties of New Quaternary Chalcogenide Nonlinear Optical Crystal AgGaGeS_4 . *J. Alloys Compd.* **2019**, *796*, 138–145.
136. Giordmaine, J. A.; Miller, R. C. Tunable Coherent Parametric Oscillation in LiNbO_3 at Optical Frequencies. *Phys. Rev. Lett.* **1965**, *14* (24), 973–976.
137. Szilagyi, A.; Hordvik, A.; Schlossberg, H. A Quasi-Phase-Matching Technique for Efficient Optical Mixing and Frequency Doubling. *J. Appl. Phys.* **1976**, *47* (5), 2025–2032.
138. Thompson, D. E.; McMullen, J. D.; Anderson, D. B. Second-Harmonic Generation in GaAs “stack of plates” Using High-Power CO_2 Laser Radiation. *Appl. Phys. Lett.* **1976**, *29* (2), 113–115.
139. Eyres, L. A.; Tourreau, P. J.; Pinguet, T. J.; Ebert, C. B.; Lallier, E.; Harris, J. S.; Fejer, M. M.; Gerard, B. Quasi-Phase-matched Frequency Conversion in Thick All-Epitaxial, Orientation-Patterned GaAs Films, in Advanced Solid State Lasers, Trends in Optics and Photonics. *OSA Technical Digest Series* **2000**, 258–261.
140. Lynch, C.; Bliss, D. F.; Zens, T.; Lin, A.; Harris, J. S.; Kuo, P. S.; Fejer, M. M. Growth of mm-Thick Orientation-Patterned GaAs for IR and THz Generation. *J. Cryst. Growth* **2008**, *310* (24), 5241–5247.
141. Parsons, D. F.; Coleman, P. D. Far Infrared Optical Constants of Gallium Phosphide. *Appl. Optics* **1971**, *10* (7), 1683–1685.
142. Pomeranz, L. A.; Schunemann, P. G.; Magarrell, D. J.; McCarthy, J. C.; Zawilski, K.; Zelmon, D. E. *1064-nm-Pumped Mid-Infrared Optical Parametric Oscillator Based on Orientation-Patterned Gallium Phosphide (OP-GaP)*, CLEO, 2015. SW30.4.
143. Lee, K. F.; Hensley, C. J.; Schunemann, P. G.; Fermann, M. E. Broadly Tunable Difference Frequency Generation in Orientation Patterned Gallium Phosphide. In *High-Brightness Sources and Light-Driven Interactions*, OSA Technical Digest, 2016; p JT3A.4.
144. Gu, M.; Li, X.; Cao, Y. Optical Storage Arrays: A Perspective for Future Big Data Storage. *Light Sci. Appl.* **2014**, *3* (5), 177.
145. Tang, D. Y.; Zhang, H.; Zhao, L. M.; Wu, X. Observation of High-Order Polarization-Locked Vector Solitons in a Fiber Laser. *Phys. Rev. Lett.* **2008**, *101* (15), 153904.
146. Hamza, M.; El-Ahl, M.; Hamza, A. Blue-Green Diode-Pumped Solid State Laser System for Transcutaneous Bilirubinometry in Neonatal Jaundice. *SPIE* **2001**, *4158*, 75–80.
147. Kokavec, J.; Wu, Z.; Sherwin, J. C.; Ang, A. J. S.; Ang, G. S. Nd:YAG Laser Vitreolysis Versus Pars Plana Vitrectomy for Vitreous Floaters. *Cochrane Database Syst. Rev.* **2017**, *6* (6), 1465–1858.

148. Stevenson, D. J.; Lake, T. K.; Agate, B.; Gárcés-Chávez, V.; Dholakia, K.; Gunn-Moore, F. Optically Guided Neuronal Growth at Near Infrared Wavelengths. *Opt. Express* **2006**, *14* (21), 9786–9793.
149. Tibballs, J. E.; Nelmes, R. J.; McIntyre, G. J. The Crystal Structure of Tetragonal KH_2PO_4 and KD_2PO_4 as a Function of Temperature and Pressure. *J. Phys. C: Solid State Phys.* **1982**, *15* (1), 37–58.
150. Shoji, I.; Kondo, T.; Kitamoto, A.; Shirane, M.; Ito, R. Absolute Scale of Second-Order Nonlinear-Optical Coefficients. *J. Opt. Soc. Am. B* **1997**, *14* (9), 2268–2294.
151. Xu, L.; Lu, C.; Wang, S.; Huang, P.; Liu, H.; Zhang, L.; Li, X.; Wang, B.; Wang, D. A Study On Nonlinear Absorption Uniformity in a KDP Crystal at 532 nm. *CrystEngComm* **2020**, *22* (32), 5338–5344.
152. Vekilov, P. G. What Determines the Rate of Growth of Crystals From Solution? *Cryst. Growth Des.* **2007**, *7* (12), 2796–2810.
153. Chen, D.; Wang, B.; Wang, H.; Zheng, L.; Zhang, H.; Qi, H.; Shao, J. Rapid Growth of a Cuboid DKDP ($\text{KD}_x\text{H}_{2-x}\text{PO}_4$) Crystal. *Cryst. Growth Des.* **2019**, *19* (5), 2746–2750.
154. Jona, F.; Shirane, G. *Ferroelectric Crystals*, Pergamon Press: Oxford, 1962; p 512.
155. De Yoreo, J. J.; Burnham, A.; Whitman, P. K. Developing KH_2PO_4 and KD_2PO_4 Crystals for the World' S Most Powerful Laser. *Int. Mater. Rev.* **2002**, *47* (3), 113–152.
156. Jones, M.; Massey, G. Milliwatt-Level 213 nm Source Based on a Repetitively Q-Switched, CW-Pumped Nd:YAG Laser. *IEEE J. Quant. Electr.* **1979**, *15* (4), 204–206.
157. Bareika, B. F.; Begishev, I. A.; Burdulis, S. A.; Gulamov, A. A.; Erofeev, E. A.; Piskarskas, A. S.; Sirutkaitis, V. A.; Usmanov, T. Highly Efficient Parametric Generation During Pumping With High-Power Subnanosecond Pulses. *Pisma Zh. Tekh. Phys.* **1986**, *12* (2), 186–189.
158. Seka, W.; Jacobs, S. D.; Rizzo, J. E.; Boni, R.; Craxton, R. S. Demonstration of High Efficiency Third Harmonic Conversion of High Power Nd-Glass Laser Radiation. *Opt. Commun.* **1980**, *34* (3), 469–473.
159. Zaitseva, N. P.; De Yoreo, J. J.; Dehaven, M. R.; Vital, R. L.; Montgomery, K. E.; Richardson, M.; Atherton, L. J. Rapid Growth of Large-Scale (40–55 cm) KH_2PO_4 Crystals. *J. Cryst. Growth* **1997**, *180* (2), 255–262.
160. Wilcox, W. R. Influence of Convection on the Growth of Crystals From Solution. *J. Cryst. Growth* **1983**, *65* (1–3), 133–142.
161. Robey, H. F.; Potapenko, S. Y.; Summerhays, K. D. "Bending" of Steps on Rapidly Grown KH_2PO_4 Crystals Due to an Inhomogeneous Surface Supersaturation Field. *J. Cryst. Growth* **2000**, *213* (3–4), 340–354.
162. Zhu, Y.; Li, M.; Yin, H.; Wang, P.; Huang, J.; Liu, H. Growth and Characterization of KDP Crystals Grown by the 2D-Translation Method Equipped With Continuous Filtration. *Cryst. Growth Des.* **2020**, *20* (6), 3772–3779.
163. Booth, N. A.; Chernov, A. A.; Vekilov, P. G. Characteristic Length Scales of Step Bunching in KDP Crystal Growth: In Situ Differential Phase-Shifting Interferometry Study. *J. Cryst. Growth* **2002**, *237–239*, 1818–1824.
164. Robey, H. F.; Potapenko, S. Y. Ex Situ Microscopic Observation of the Lateral Instability of Macrosteps on the Surfaces of Rapidly Grown KH_2PO_4 Crystals. *J. Cryst. Growth* **2000**, *213* (3–4), 355–367.
165. Bierlein, J. D.; Vanherzeele, H. Potassium Titanyl Phosphate: Properties and New Applications. *J. Opt. Soc. Am. B* **1989**, *6* (4), 622–633.
166. Kato, K. Parametric Oscillation at 3.2 μm in KTP Pumped at 1.064 μm . *IEEE J. Quant. Electr.* **1991**, *27* (5), 1137–1140.
167. Hansson, G.; Karlsson, H.; Wang, S.; Laurell, F. Transmission Measurements in KTP and Isomorphous Compounds. *Appl. Optics* **2000**, *39* (27), 5058–5069.
168. Ahmed, F. Laser Damage Threshold of KTiOPO_4 . *Appl. Optics* **1989**, *28* (1), 119–122.
169. Garrec, B. J. L.; Raze, G. J.; Thro, P. Y.; Gilbert, M. High-Average-Power Diode-Array Pumped Frequency-Doubled YAG Laser. *Opt. Lett.* **1996**, *21* (24), 1990–1992.
170. Pierre, R. J. S.; Mordaunt, D. W.; Injeyan, H.; Berg, J. G.; Hilyard, R. C.; Weber, M. E.; Wickham, M. G.; Harpole, G. M.; Senn, R. Diode Array Pumped Kilowatt Laser. *IEEE J. Sel. Topics Quant. Electr.* **1997**, *3* (1), 53–58.
171. Honea, E. C.; Ebbers, C. A.; Beach, R. J.; Speth, J. A.; Skidmore, J. A.; Emmanuel, M. A.; Payne, S. A. Analysis of an Intracavity-Doubled Diode-Pumped Q-Switched Nd:YAG Laser Producing More Than 100 W of Power at 0.532 μm . *Opt. Lett.* **1998**, *23* (15), 1203–1205.
172. Arie, A.; Rosenman, G.; Mahal, V.; Skliar, A.; Oron, M.; Katz, M.; Eger, D. Green and Ultraviolet Quasi-Phase-Matched Second-Harmonic Generation in Bulk Periodically-Poled KTiOPO_4 . *Opt. Commun.* **1997**, *142* (4–6), 265–268.
173. Boulanger, B.; Rousseau, I.; Feve, J. P.; Maglione, M.; Menaert, M.; Mamier, G. Optical Studies of Laser-Induced Gray-Tracking in KTP. *IEEE J. Quant. Electr.* **1999**, *35* (3), 281–286.
174. Tyminski, J. K. Photorefractive Damage in KTP Used as Second-Harmonic Generator. *J. Appl. Phys.* **1991**, *70* (10), 5570–5576.
175. Mass, R.; Grenier, J. C. Process for Crystal Growth of KTiOPO_4 From High Temperature Solution. *Bull. Soc. Frand Mineral Crystallogr.* **1971**, *94*, 437–439.
176. Scripsick, M. P.; Lofacono, D. N.; Rottenberg, J. Defects Responsible for Gray Tracks in Flux-Grown KTiOPO_4 . *Appl. Phys. Lett.* **1995**, *66* (25), 3428–3430.
177. Wang, J. Y.; Wei, J. Q.; Liu, Y. G.; Yin, X.; Hu, X. B.; Shao, Z. G.; Jiang, M. H. A Survey of Research on KTP and Its Analogue Crystals. *Prog. Cryst. Growth Charact. Mater.* **2000**, *40* (1–4), 3–15.
178. Gharibshahiana, E.; Tafreshia, M. J.; Fazli, M. Growth of KTiOPO_4 Crystals by Flux Technique and Their Characterization. *Indian J. Pure Appl. Phys.* **2009**, *47*, 356–361.
179. Zhang, Y.; Li, J.; Cao, X.; Yang, J.; Wang, J.; Jiang, H. A Study of Vacancy Defects Related to Gray Tracks in KTiOPO_4 (KTP) Using Positron Annihilation. *AIP Advances*. **2014**, *4* (12), 127103.
180. Zhang, C. L.; Hu, Z. G.; Huang, L. X.; Zhou, W. N.; Lv, Z.; Zhang, G.; Liu, Y. C.; Zou, Y. B.; Lu, F. H.; Hou, H. D.; Qin, S. J.; Zhang, H. X.; Bai, L. Growth and Optical Properties of Bulk KTP Crystals by Hydrothermal Method. *J. Cryst. Growth* **2008**, *310* (7), 2010–2014.
181. Lu, T.; Hu, Z.; Li, X.; Yue, Y.; Yu, X.; Wu, Z. KTP Crystal Growth From the Starting Materials Reacted in Solution. *Cryst. Res. Technol.* **2012**, *47* (8), 882–887.
182. Shumov, D. P.; Nikolov, V. S.; Iliev, K. N.; Aleksandrovskii, A. L. KTiOPO_4 (KTP) Crystal Growth From High-Temperature Solutions Containing WO_3 . *Cryst. Res. Technol.* **1990**, *25* (11), 1245–1250.
183. Kannan, C. V.; Ganesamoorthy, S.; Kumaragurubaran, S.; Subramanian, C.; Sundar, R.; Ramasamy, P. Growth of Inclusion Free KTP Crystals by Top Seeded Solution Growth and Their Characterization. *Cryst. Res. Technol.* **2002**, *37* (10), 1049–1057.
184. Abrahams, S. C.; Levinstein, H. J.; Reddy, J. M. Ferroelectric Lithium Niobate. 5. Polycrystal X-ray Diffraction Study Between 24 and 1200 °C. *J. Phys. Chem. Solid* **1966**, *27* (6), 1019–1026.
185. Roberts, D. A. Simplified Characterization of Uniaxial and Biaxial Nonlinear Optical Crystals: A Plea for Standardization of Nomenclature and Conventions. *IEEE J. Quant. Electr.* **1992**, *28* (10), 2057–2074.
186. Boyd, G. D.; Miller, R. C.; Nassau, K.; Bond, W. L.; Savage, A. LiNbO_3 : An Efficient Phase Matchable Nonlinear Optical Material. *Appl. Phys. Lett.* **1964**, *5* (11), 234–236.
187. Bhatt, R.; Bhaumik, I.; Ganesamoorthy, S.; Bright, R.; Soharab, M.; Karnal, A. K.; Gupta, P. K. Control of Intrinsic Defects in Lithium Niobate Single Crystal for Optoelectronic Applications. *Crystals* **2017**, *7* (2), 23.
188. Armstrong, J. A.; Bloembergen, N.; Ducuing, J.; Pershan, P. S. Interactions Between Light Waves in a Nonlinear Dielectric. *Phys. Ther. Rev.* **1962**, *127* (6), 1918–1939.
189. Hesselink, L.; Orlov, S. S.; Liu, A.; Akella, A.; Lande, D.; Neurgaonkar, R. R. Photorefractive Materials for Nonvolatile Volume Holographic Data Storage. *Science* **1998**, *282* (5391), 1089–1094.
190. Canalias, C.; Pasiskevicius, V. Mirror-Less Optical Parametric Oscillator. *Nat. Photonics* **2007**, *1*, 459.
191. Buse, K.; Adibi, A.; Psaltis, D. Non-Volatile Holographic Storage in Doubly Doped Lithium Niobate Crystals. *Nature* **1998**, *393* (6686), 665–668.
192. Lim, H. H.; Prakash, O.; Kim, B. J.; Pandiyan, K.; Rhee, B. K. Ultra-Broadband Optical Parametric Generation and Simultaneous RGB Generation in Periodically Poled Lithium Niobate. *Opt. Express* **2007**, *15* (26), 18294–18299.
193. Meyn, J. P.; Fejer, M. M. Tunable Ultraviolet Radiation by Second-Harmonic Generation in Periodically Poled Lithium Tantalate. *Opt. Lett.* **1997**, *22* (16), 1214–1216.
194. Burrows L. (n.d.) Now Entering, Lithium Niobate Valley [EB/OL]. <https://www.Seas.harvard.edu/news/2017/12/now-entering-lithium-niobate-valley>.
195. Safaryan, F. P.; Feigelson, R. S.; Petrosyan, A. M. An Approach to the Defect Structure Analysis of Lithium Niobate Single Crystals. *J. Appl. Phys.* **1999**, *85* (12), 8079–8082.
196. Lerner, P.; Legras, C.; Dumas, J. P. Stoechiométrie des monocristaux de métaniobate de lithium. *J. Cryst. Growth* **1968**, *3–4*, 231–235.

197. Feigelson, R. Physics and Chemistry of Crystalline Lithium Niobate. *Science* **1991**, *251*, 1510.
198. Schirmer, O. F.; Thiemann, O.; Wöhlecke, M. Defects in LiNbO₃-I. Experimental Aspects. *J. Phys. Chem. Solid* **1991**, *52* (1), 185–200.
199. Svassand, L. O.; Eriksrud, M.; Nakken, G.; Grande, A. P. Solid-Solution Range of LiNbO₃. *J. Cryst. Growth* **1974**, *22* (3), 230–232.
200. Ballman, A. A. Growth of Piezoelectric and Ferroelectric Materials by the Czochralski Technique. *J. Am. Ceram. Soc.* **1965**, *48* (2), 112–113.
201. Riscob, B.; Bhaumik, I.; Ganesamoorthy, S.; Bhatt, R.; Vijayan, N.; Karnal, A. K.; Wahab, M. A.; Bhagavannarayana, G. Effect of Mg Doping on the Growth Aspects, Crystalline Perfection, and Optical and Thermal Properties of Congruent LiNbO₃ Single Crystals. *J. Appl. Cryst.* **2013**, *46* (6), 1854–1862.
202. Kovács, L.; Ruschhaupt, G.; Polgár, K.; Corradi, G.; Wöhlecke, M. Composition Dependence of the Ultraviolet Absorption Edge in Lithium Niobate. *Appl. Phys. Lett.* **1997**, *70* (21), 2801–2803.
203. Kovács, L.; Szalay, V.; Capelletti, R. Stoichiometry Dependence of the OH⁻ Absorption Band in LiNbO₃ Crystals. *Solid State Commun.* **1984**, *52* (12), 1029–1031.
204. Lengyel, K.; Péter, Á.; Kovács, L.; Corradi, G.; Pálfalvi, L.; Hebling, J.; Unferdorben, M.; Dravec, G.; Hajdara, I.; Szaller, Z.; Polgár, K. Growth, Defect Structure, and THz Application of Stoichiometric Lithium Niobate. *Appl. Phys. Rev.* **2015**, *360* (4), 158–161.
205. Kong, Y.; Li, B.; Chen, Y.; Huang, Z.; Chen, S.; Zhang, L.; Liu, S.; Xu, J.; Liu, H.; Wang, Y.; Yan, W.; Xie, X.; Li, X.; Shi, L.; Zhang, W.; Zhang, G. *In the Highly Optical Damage Resistance of Lithium Niobate Crystals Doping With Mg Near Its Second Threshold, Photorefractive Effects, Materials, and Devices*; vol. 87; OSA/TOPS, 2003; p 53.
206. Fischer, C.; Wöhlecke, M.; Volk, T.; Rubinina, N. Influence of the Damage Resistant Impurities Zn and Mg on the UV-Excited Luminescence in LiNbO₃. *Phys. Status Solidi A* **1993**, *137* (1), 247–255.
207. Gopalan, V.; Mitchell, T. E.; Furukawa, Y.; Kitamura, K. The Role of Nonstoichiometry in 180° Domain Switching of LiNbO₃ Crystals. *Appl. Phys. Lett.* **1998**, *72* (16), 1981–1983.
208. Liu, X.; Terabe, K.; Kitamura, K. Ferroelectric Nanodomain Properties in Near-Stoichiometric and Congruent LiNbO₃ Crystals Investigated by Scanning Force Microscopy. *Jpn. J. Appl. Phys.* **2005**, *44* (9), 7012–7014.
209. Polgár, K.; Péter, Á.; Földvári, I. Crystal Growth and Stoichiometry of LiNbO₃ Prepared by the Flux Method. *Opt. Mater.* **2002**, *19* (1), 7–11.
210. Bordui, P. F.; Norwood, R. G.; Jundt, D. H.; Fejer, M. M. Preparation and Characterization of Off-Congruent Lithium Niobate Crystals. *J. Appl. Phys.* **1992**, *71* (2), 875–879.
211. Sun, J.; Kong, Y.; Zhang, L.; Yan, W.; Wang, X.; Xu, J.; Zhang, G. Growth of Large-Diameter Nearly Stoichiometric Lithium Niobate Crystals by Continuous Melt Supplying System. *J. Cryst. Growth* **2006**, *292* (2), 351–354.
212. Lengyel, K.; Péter, Á.; Kovács, L.; Corradi, G.; Pálfalvi, L.; Hebling, J.; Unferdorben, M.; Dravec, G.; Hajdara, I.; Szaller, Z.; Polgár, K. Growth, Defect Structure, and THz Application of Stoichiometric Lithium Niobate. *Appl. Phys. Rev.* **2015**, *2* (4), 040601.
213. Zysset, B.; Biaggio, I.; Günter, P. Refractive Indices of Orthorhombic KNbO₃. I. Dispersion and Temperature Dependence. *J. Opt. Soc. Am. B* **1992**, *9* (3), 380–386.
214. Shirane, G.; Newnham, R.; Pepinsky, R. Dielectric Properties and Phase Transitions of NaNbO₃ and (Na,K)NbO₃. *Phys. Ther. Rev.* **1954**, *96* (3), 581–588.
215. Baumert, J. C.; Hoffnagle, J.; Günter, P. High-Efficiency Intracavity Frequency Doubling of a Styryl-9 Dye Laser With KNbO₃ Crystals. *Appl. Optics* **1985**, *24* (9), 1299–1301.
216. Sheik-Bahae, M.; Ebrahimzadeh, M. Measurements of Nonlinear Refraction in the Secondorder $\chi^{(2)}$ Materials KTiOPO₄, KNbO₃, β -BaB₂O₄, and LiB₃O₅. *Opt. Commun.* **1997**, *142* (4–6), 294–298.
217. Bosenberg, W. R.; Jarman, R. H. Type-II Phase-Matched KNbO₃ Optical Parametric Oscillator. *Opt. Lett.* **1993**, *18* (16), 1323–1325.
218. Umemura, N.; Yoshida, K.; Kato, K. Phase-matching properties of KNbO₃ in the mid-infrared. *Appl. Optics* **1999**, *38* (6), 991–994.
219. Uematsu, Y.; Fukuda, T. Nonlinear Optical Properties of KNbO₃ Single Crystals. *Jpn. J. Appl. Phys.* **1971**, *10* (4), 507.
220. Umemura, N.; Yoshida, K.; Kato, K. Thermo-Optic Dispersion Formula of KNbO₃ for Mid-Infrared OPO. *SPIE* **2000**, *3889*, 472–480.
221. Risk, W. P.; Pon, R.; Lenth, W. Diode Laser Pumped Blue-Light Source at 473 nm Using Intracavity Frequency Doubling of a 946 nm Nd:YAG Laser. *Appl. Phys. Lett.* **1989**, *54* (17), 1625–1627.
222. Ewbank, M. D.; Rosker, M. J.; Bennett, G. L. Frequency Tuning a Mid-Infrared Optical Parametric Oscillator by the Electro-Optic Effect. *J. Opt. Soc. Am. B* **1997**, *14* (3), 666–671.
223. Yamanouchi, K.; Odagawa, H.; Kojima, T.; Matsumura, T. Theoretical and Experimental Study of Super-High Electromechanical Coupling Surface Acoustic Wave Propagation in KNbO₃ Single Crystal. *Electron. Lett.* **1997**, *33* (3), 193–194.
224. Jundt, D. H.; Günter, P.; Zysset, B. A Temperature-Dependent Dispersion Equation for KNbO₃. *Nonlinear Opt.* **1993**, *4* (4), 341–345.
225. Fluck, D.; Pliska, T.; Günter, P. Compact 10 mW All-Solid-State 491 nm Laser Based on Frequency Doubling a Master Oscillator Power Amplifier Laser Diode. *Opt. Commun.* **1996**, *123* (4–6), 624–628.
226. Ellenberger, U.; Weber, R.; Balmer, J. E.; Zysset, B.; Elgehausen, D.; Mizell, G. J. Pulsed Optical Damage Threshold of Potassium Niobate. *Appl. Optics* **1992**, *31* (36), 7563–7569.
227. Adachi, M.; Fujita, N.; Norimatsu, Y.; Karaki, T. Growth of Potassium Niobate (KNbO₃) Single Crystals for Piezoelectric Applications. *Ferroelectrics* **2006**, *334* (1), 91–96.
228. Kakimoto, K. I.; Hibino, T.; Masuda, I.; Ohsato, H. Development of Transparent Single-Crystalline KNbO₃ Thin Film by LPE Technique. *Sci. Technol. Adv. Mater.* **2005**, *6* (1), 61–65.
229. Wada, S.; Seike, A.; Kakimoto, H.; Tsurumi, T. Piezoelectric Properties of KNbO₃ Single Crystals With Various Crystallographic Orientations. *Ferroelectrics* **2002**, *273* (1), 339–344.
230. Rosenzweig, A.; Morosin, B. A Reinvestigation of the Crystal Structure of LiIO₃. *Acta Crystallogr.* **1966**, *20*, 758–761.
231. Nath, G.; Mehmanesh, H.; Gsänger, M. Efficient Conversion of a Ruby Laser Radiation to 0.347 μ m in Low-Loss Lithium Iodate. *Appl. Phys. Lett.* **1970**, *17* (7), 286–288.
232. Andreev, R. B.; Volosov, V. D.; Kalintsev, A. G. Spectral, Angular, and Temperature Characteristics of HIO₃, LiIO₃, CDA, DKDP, KDP and ADP Non-Linear Crystals in Second- and Fourth-Harmonic Generation. *Opt. Spektrosk.* **1974**, *37* (2), 294–299.
233. Midwinter, J. E.; Warner, J. The Effects of Phase Matching Method and of Uniaxial Crystal Symmetry on the Polar Distribution of Second-Order Non-Linear Optical Polarization. *Br. J. Appl. Phys.* **1965**, *16* (11), 1135–1142.
234. Gehr, R. J.; Smith, A. V. Separated-Beam Nonphase-Matched Second-Harmonic Method of Characterizing Nonlinear Optical Coefficients. *J. Opt. Soc. Am. B* **1998**, *15* (8), 2298–2307.
235. Okada, M.; Ieiri, S. Kleinman's Symmetry Relation in Nonlinear Optical Coefficient of LiIO₃. *Phys. Lett. A* **1971**, *34* (1), 63–64.
236. Chesler, R. B.; Karr, M. A.; Geusic, J. E. Repetitively Q-Switched Nd:YAG LiIO₃ 0.53 μ m Harmonic Source. *J. Appl. Phys.* **1970**, *41* (10), 4125–4127.
237. Armstrong, L.; Neister, S. E.; Adhav, R. Measuring CFP Dye Laser Damage Thresholds on UV Doubling Crystals. *Laser Focus* **1982**, *18* (12), 49–53.
238. Nash, F. R.; Bergman, J. G.; Boyd, G. D.; Turner, E. H. Optical Nonlinearities in LiIO₃. *J. Appl. Phys.* **1969**, *40* (13), 5201–5206.
239. Gettemy, D. J.; Harker, W. C.; Lindholm, G.; Barnes, N. P. Some Optical Properties of KTP, LiIO₃, and LiNbO₃. *IEEE J. Quant. Electr.* **1988**, *24* (11), 2231–2237.
240. Crettez, J. M.; Comte, J.; Coquet, E. Optical Properties of α - and β -Lithium Iodate in the Visible Range. *Opt. Commun.* **1972**, *6* (1), 26–29.
241. Jerphagnon, J. Optical Nonlinear Susceptibilities of Lithium Iodate. *Appl. Phys. Lett.* **1970**, *16* (8), 298–299.
242. Massey, G.; Johnson, J. Wavelength-Tunable Optical Mixing Experiments Between 208 nm and 259 nm. *IEEE J. Quantum Elect.* **1976**, *12* (11), 721–727.
243. Suvorov, V. S.; Sonin, A. S. Nonlinear Optical Materials. *Kristallogr.* **1966**, *11* (5), 832–848.
244. Hagimoto, K.; Mito, A. Determination of the Second-Order Susceptibility of Ammonium Dihydrogen Phosphate and α -Quartz at 633 and 1064 nm. *Appl. Optics* **1995**, *34* (36), 8276–8282.
245. Huth, B. G.; Kiang, Y. C. 90° Phase Matching for Second-Harmonic Conversion to the Ultraviolet. *J. Appl. Phys.* **1969**, *40* (12), 4976–4977.
246. Ren, X.; Xu, D.; Xue, D. Crystal Growth of KDP, ADP, and KADP. *J. Cryst. Growth* **2008**, *310* (7), 2005–2009.
247. Cook, W. R. Thermal Expansion of Crystals With KH₂PO₄ Structure. *J. Appl. Phys.* **1967**, *38* (4), 1637–1642.

248. Kim, S. A.; Kang, S. K.; Lee, E. K.; Shim, H.-S.; Lee, C.-H. Refinement of the Crystal Structure of Potassium Dideuterium Phosphate, KD_2PO_4 . *Z. Kristallogr. NCS* **2001**, *276* (1–4), 203–204.
249. Sliker, R.; Burlage, S. R. Some Dielectric and Optical Properties of KD_2PO_4 . *J. Appl. Phys.* **1963**, *34* (7), 1837–1840.
250. Eimerl, D. High Average Power Harmonic Generation. *IEEE J. Quant. Electr.* **1987**, *23* (5), 575–592.
251. Fill, E. E. Generation of Higher Harmonics of Iodine Laser Radiation. *Opt. Commun.* **1980**, *33* (3), 321–322.
252. Adhav, R. S. Materials for Optical Harmonic Generation. *Laser Focus* **1983**, *19* (6), 73–78.
253. Yang, F.; Wang, L.; Huang, L.; Zou, G. The Study of Structure Evolution of KTiOPO_4 Family and Their Nonlinear Optical Properties. *Coord. Chem. Rev.* **2020**, *423*, 213491.
254. Eddy, M. M.; Gier, T. E.; Keder, N. L.; Stucky, G. D.; Cox, D. E.; Bierlein, J. D.; Jones, G. Inclusion Tuning of Nonlinear Optical Materials: Sorbates on the KTP Structure. *Inorg. Chem.* **1988**, *27* (11), 1856–1858.
255. Thomas, P. A.; Mayo, S. C.; Watts, B. E. Crystal Structures of RbTiOAsO_4 , $\text{KTiO}(\text{P}_{0.58}\text{As}_{0.42})\text{O}_4$, RbTiOPO_4 and $(\text{Rb}_{0.465}\text{K}_{0.535})\text{TiOPO}_4$, and Analysis of Pseudosymmetry in Crystals of the KTiOPO_4 Family. *Acta Crystallogr. B* **1992**, *48* (4), 401–407.
256. Bierlein, J. D.; Vanherzeele, H.; Ballman, A. A. Linear and Nonlinear Optical Properties of Flux-Grown KTiOAsO_4 . *Appl. Phys. Lett.* **1989**, *54* (9), 783–785.
257. Harrison, W. T.; Gier, T. E.; Stucky, G. D.; Schultz, A. J. Structural Study of the Ferroelectric to Paraelectric Phase Transition in TlTiOPO_4 . *Mater. Res. Bull.* **1995**, *30* (11), 1341–1349.
258. Kunz, M.; Dinnebier, R.; Cheng, L. K.; McCarron, E. M.; Cox, D. E.; Parise, J. B.; Gehrke, M.; Calabrese, J.; Stephens, P. W.; Vogt, T.; Papoular, R. $\text{Cs}(\text{TlAs})\text{O}_5$ and $\text{Cs}(\text{TiP})\text{O}_5$: A Disordered Parent Structure of ABOCo_4 Compounds. *J. Solid State Chem.* **1995**, *120* (2), 299–310.
259. Nguyen, S. D.; Yeon, J.; Kim, S. H.; Halasyamani, P. S. $\text{BiO}(\text{IO}_3)$: A New Polar Iodate That Exhibits An Aurivillius-Type $(\text{Bi}_2\text{O}_2)^{2+}$ Layer and a Large SHG Response. *J. Am. Chem. Soc.* **2011**, *133* (32), 12422–12425.
260. Huang, H.; Xiao, K.; Liu, K.; Yu, S.; Zhang, Y. In Situ Composition-Transforming Fabrication of $\text{BiO}/\text{BiOIO}_3$ Heterostructure: Semiconductor p–n Junction and Dominantly Exposed Reactive Facets. *Cryst. Growth Des.* **2016**, *16* (1), 221–228.
261. Zhang, J.; Du, X.; Ke, S. H.; Xu, B.; Zheng, G.; Rowlands, D. A.; Yao, K. Dielectric, Piezoelectric and Nonlinear Optical Properties of Polar Iodate $\text{BiO}(\text{IO}_3)$ From First-Principles Studies. *J. Solid State Chem.* **2020**, *281*, 121057.
262. Sun, C. F.; Hu, C. L.; Xu, X.; Ling, J. B.; Hu, T.; Kong, F.; Long, X. F.; Mao, J. G. $\text{BaNbO}(\text{IO}_3)_5$: A New Polar Material With A Very Large SHG Response. *J. Am. Chem. Soc.* **2009**, *131* (27), 9486–9487.
263. Levin, E. M.; Mcdaniel, C. L. The System Bi_2O_3 - B_2O_3 . *J. Am. Ceram. Soc.* **1962**, *45* (8), 355–360.
264. Knyrim, J. S.; Becker, P.; Johrendt, D.; Huppertz, H. A New Non-Centrosymmetric Modification of BiB_3O_6 . *Angew. Chem. Int. Ed.* **2006**, *45* (48), 8239–8241.
265. Hellwig, H.; Liebertz, J.; Bohaty, L. Linear Optical Properties of the Monoclinic Bismuth Borate BiB_3O_6 . *J. Appl. Phys.* **2000**, *88* (1), 240–244.
266. Ishii, N.; Kitano, K.; Kanai, T.; Watanabe, S.; Itatani, J. Carrier-Envelope-Phase-Preserving, Octave-Spanning Optical Para-Metric Amplification in the Infrared Based on BiB_3O_6 Pumped by 800 nm Femtosecond Laser Pulses. *Appl. Phys. Express* **2011**, *4*, 022701.
267. Cherepakhin, A. V.; Zaitsev, A. I.; Aleksandrovsky, A. S.; Zamkov, A. V. Optical and Nonlinear Optical Properties of Orthorhombic BiB_3O_6 . *Opt. Mater.* **2012**, *34* (5), 790–792.
268. Zou, G. H.; Lin, C.; Jo, H.; Nam, G.; You, T. S.; Ok, K. M. $\text{Pb}_2\text{BO}_3\text{Cl}$: A Tailor-Made Polar Lead Borate Chloride With Very Strong Second Harmonic Generation. *Angew. Chem. Int. Ed.* **2016**, *55* (39), 12078–12082.
269. Luo, M.; Song, Y. X.; Liang, F.; Ye, N.; Lin, Z. S. $\text{Pb}_2\text{BO}_3\text{Br}$: A Novel Nonlinear Optical Lead Borate Bromine With a KBBF-Type Structure Exhibiting Strong Nonlinear Optical Response. *Inorg. Chem. Front.* **2018**, *5* (4), 916–921.
270. Yu, H. W.; Koocher, N. Z.; Rondinelli, J. M.; Halasyamani, P. S. Pb_2BO_3 : a Borate Iodide With The Largest Second-Harmonic Generation (SHG) Response in the $\text{KB}_2\text{BO}_3\text{F}_2$ (KBBF) Family of Nonlinear Optical (NLO) Materials. *Angew. Chem. Int. Ed.* **2018**, *57* (21), 6100–6103.
271. Franken, P. A.; Hill, A. E.; Peters, C. W.; Weinreich, G. Generation of Optical Harmonics. *Phys. Rev. Lett.* **1961**, *7*, 118–119.
272. Taylor, N. *Laser: The Inventor, the Nobel Laureate, and the Thirty-Year Patent War*, Simon Schuster: New York, 2007.
273. Bordui, P. F.; Fejer, M. M. Inorganic Crystals for Nonlinear Optical Frequency Conversion. *Annu. Rev. Mater. Sci.* **1993**, *23*, 321–379.
274. Halasyamani, P. S.; Moepplmeier, K. R. Noncentrosymmetric Oxides. *Chem. Mater.* **1998**, *10* (10), 2753–2769.
275. Sasaki, T.; Mori, Y.; Yoshimura, M.; Yap, Y. K.; Kamimura, T. Recent Development of Nonlinear Optical Borate Crystals: Key Materials for Generation of Visible and UV Light. *Mater. Sci. Eng. Rep.* **2000**, *30* (1), 1–54.
276. Chen, C. T.; Wu, B. C.; Jiang, A. D.; You, G. M. A New-Type Ultraviolet SHG Crystal β - BaB_2O_4 . *Sci. Sin. B* **1985**, *28* (3), 235–243.
277. Chen, C. T.; Wu, Y. C.; Jiang, A. D.; Wu, B. C.; You, G. M.; Li, R. K.; Lin, S. J. New Nonlinear-Optical Crystal: LiB_3O_5 . *J. Opt. Soc. Am. B* **1989**, *6* (4), 616–621.
278. Wu, Y. C.; Sasaki, T.; Nakai, N.; Yokotani, A.; Tang, H. G.; Chen, C. T. CsB_3O_5 : A New Nonlinear Optical Crystal. *Appl. Phys. Lett.* **1993**, *62*, 2614–2615.
279. Chen, C.; Lin, Z.; Wang, Z. The Development of New Borate-Based UV Nonlinear Optical Crystals. *Appl. Phys. B* **2005**, *80* (1), 1–25.
280. Chen, C.; Wu, Y.; Li, R. The Anionic Group Theory of the Non-Linear Optical Effect and Its Applications in the Development of New High-Quality NLO Crystals in the Borate Series. *Int. Rev. Phys. Chem.* **1989**, *8* (1), 65–91.
281. Adhav, R. S.; Adhav, S. R.; Pelaprat, J. M. BBO 's Nonlinear Optical Phase-Matching Properties. *Laser Focus* **1987**, *23* (9), 88–100.
282. Kouta, H. Wavelength Dependence of Repetitive-Pulse Laser-Induced Damage Threshold in β - BaB_2O_4 . *Appl. Optics* **1999**, *38* (3), 545–547.
283. Eimerl, D.; Davis, L.; Velsko, S.; Graham, E. K.; Zalkin, A. Optical, Mechanical, and Thermal Properties of Barium Borate. *J. Appl. Phys.* **1987**, *62* (5), 1968–1983.
284. Guo, R.; Bhalla, A. S. Pyroelectric, Piezoelectric, and Dielectric Properties of β - BaB_2O_4 Single Crystal. *J. Appl. Phys.* **1989**, *66* (12), 6186–6188.
285. Rehse, S. J.; Lee, S. A. Generation of 125 mW Frequency Stabilized Continuous-Wave Tunable Laser Light at 295 nm by Frequency Doubling in a BBO Crystal. *Opt. Commun.* **2002**, *213* (46), 347–350.
286. Bromley, L. J.; Guy, A.; Hanna, D. C. Synchronously Pumped Optical Parametric Oscillation in Beta Barium Borate. *Opt. Commun.* **1988**, *67* (4), 316–320.
287. Kouta, H.; Kuwano, Y. Attaining 186-nm Light Generation in Cooled β - BaB_2O_4 Crystal. *Opt. Lett.* **1999**, *24* (13), 1230–1232.
288. Huot, N.; Jonin, C.; Sanner, N.; Baubeau, E.; Audouard, E.; Laporte, P. High UV Average Power at 15kHz by Frequency Doubling of a Copper HyBrD Vapor Laser in β -Barium Borate. *Opt. Commun.* **2002**, *211* (1–6), 277–282.
289. Liu, Q.; Yan, X. P.; Fu, X.; Gong, M.; Wang, D. S. High Power All-Solid-State Fourth Harmonic Generation of 266 nm At the Pulse Repetition Rate of 100kHz. *Laser Phys. Lett.* **2009**, *6* (3), 203–206.
290. Huang, Q. Z.; Liang, J. G. The Crystal Growth of BaB_2O_4 Low Temperature Phase and the Study of Phase Diagrams of Related Systems. *Acta Phys. Sin.* **1981**, *30* (4), 559–564.
291. Tang, D. Y.; Zeng, W. R.; Zhao, Q. L. A Study on Growth of β - BaB_2O_4 Crystals. *J. Cryst. Growth* **1992**, *123* (3), 445–450.
292. Feigelson, R. S.; Raymakers, R. J.; Route, R. K. Solution Growth of Barium Metaborate Crystals by Top Seeding. *J. Cryst. Growth* **1989**, *97* (2), 352–366.
293. Kokh, A. E.; Kononova, P. P.; Fedorov, N. G.; Bekker, T. B.; Kuznetsov, S. V. Growth of Bulk β - BaB_2O_4 Crystals of High Optical Quality in the BaB_2O_4 - NaBaBO_3 System. *Inorg. Mater.* **2005**, *41* (1), 60–64.
294. Simonova, E. A.; Kokh, A. E.; Kononova, N. G.; Shevchenko, V. S.; Fedorov, P. P. Chemical Reactions and Phase Equilibria in BaB_2O_4 -MF (M = Li, Na, or K) Systems. *Russ. J. Inorg. Chem.* **2015**, *60* (3), 318–323.
295. Roth, M.; Perlov, D. Growth of Barium Borate Crystals From Sodium Fluoride Solutions. *J. Cryst. Growth* **1996**, *169* (4), 734–740.
296. Bekker, T. B.; Fedorov, P. P.; Kokh, A. E. The Ternary Reciprocal System Na, Ba/ BO_2 , F. *Cryst. Growth Des.* **2012**, *12* (1), 129–134.
297. Bykov, A. B.; Dozmarov, V. V.; Mel'nikov, O. K. Growing β - BaB_2O_4 Single Crystals From Fluorine-Containing Fluxes. *Crystallogr. Rep.* **1994**, *39* (4), 651–655.
298. Simonova, E. A.; Kokh, A. E.; Kononova, N. G.; Shevchenko, V. S.; Kokh, D. A. Phase Equilibria in BaB_2O_4 -LiF System and β - BaB_2O_4 Bulk Crystals Growth. *Cryst. Res. Technol.* **2015**, *50* (8), 654–657.

299. Bekker, T. B.; Kokh, A. E.; Kononova, N. G.; Fedorov, P. P.; Kuznetsov, S. V. Crystal Growth and Phase Equilibria in the BaB_2O_4 – NaF System. *Cryst. Growth Des.* **2009**, *9* (9), 4060–4063.
300. Perlov, D.; Livneh, S.; Czechowicz, P.; Goldgirsh, A.; Loiacono, D. Progress in Growth of Large β - BaB_2O_4 Single Crystals. *Cryst. Res. Technol.* **2011**, *46* (7), 651–654.
301. Xu, Y. N.; Ching, W. Y. Electronic Structure and Optical Properties of LiB_3O_5 . *Phys. Rev. B* **1990**, *41* (8), 5471–5474.
302. Roberts, D. A. Simplified Characterization of Uniaxial and Biaxial Nonlinear Optical Crystals: A Plea for Standardization of Nomenclature and Conventions. *IEEE J. Quant. Electr.* **1992**, *28* (10), 2057–2074.
303. Pavel, N.; Saikawa, J.; Taira, T. Diode End-Pumped Passively Q-Switched Nd:YAG Laser Intra-Cavity Frequency Doubled by LBO Crystal. *Opt. Commun.* **2001**, *195* (1–4), 233–240.
304. Lin, S. J.; Sun, Z. Y.; Wu, B. C.; Chen, C. T. The Nonlinear Optical Characteristics of a LiB_3O_5 Crystal. *J. Appl. Phys.* **1990**, *67* (2), 634–638.
305. Li, D. H.; Li, P. X.; Zhang, Z. G.; Zhang, S. W. Compact High-Power Blue Light From a Diode-Pumped Intracavity-Doubled Nd:YAG Laser. *Chin. Phys. Lett.* **2002**, *19* (11), 1632–1634.
306. Yamamoto, H.; Toyoda, K.; Matsubara, K.; Watanabe, M.; Urabe, S. Development of a Tunable 209 nm Continuous-Wave Light Source Using Two-Stage Frequency Doubling of a Ti:Sapphire Laser. *Jpn. J. Appl. Phys.* **2002**, *41* (6A), 3710–3713.
307. Wang, Y.; Xu, Z.; Deng, D.; Zheng, W.; Wu, B.; Chen, C. Visible Optical Parametric Oscillation in LiB_3O_5 . *Appl. Phys. Lett.* **1991**, *59* (5), 531–533.
308. Velsko, S. P.; Webb, M.; Davis, L.; Huang, C. Phase-Matched Harmonic Generation in Lithium Triborate (LBO). *IEEE J. Quant. Electr.* **1991**, *27* (9), 2182–2192.
309. Mazzetti, C.; Carli, F. D. Borates of Lithium, Cadmium, Lead, and Manganese. *Gazz. Chim. Ital.* **1926**, *56*, 19–28.
310. Rollet, A. P.; Bouaziz, R. The Binary System Lithium Oxide-Boric Anhydride. *Comp. Rend.* **1955**, *240*, 2417–2419.
311. Sastry, B. S. R.; Hummel, F. A. Studies in Lithium Oxide Systems: I, $\text{Li}_2\text{O}-\text{B}_2\text{O}_3-\text{B}_2\text{O}_3$. *J. Am. Ceram. Soc.* **1958**, *41* (1), 7–17.
312. Wu, Y. C.; Jiang, A. D.; Lu, S. F.; Chen, C. T.; Shen, Y. S. Crystal Growth and Structure of $\text{Li}_2\text{O}-3\text{B}_2\text{O}_3$. *J. Synth. Cryst.* **1990**, *19* (1), 33–38.
313. Ukachi, T.; Lane, R. J.; Bosenberg, W. R.; Tang, C. L. Phase-Matched Second-Harmonic Generation and Growth of a LiB_3O_5 Crystal. *J. Opt. Soc. Am. B* **1992**, *9* (7), 1128–1133.
314. Zhong, W. Z.; Tang, D. Y. Growth Units and Morphology of Lithium Triborate (LBO) Crystals. *J. Cryst. Growth* **1996**, *166* (1–4), 91–98.
315. Parfeniuk, C.; Samarasekera, I. V.; Weinberg, F. Growth of Lithium Triborate Crystals I. Mathematical Model. *J. Cryst. Growth* **1996**, *158* (4), 514–522.
316. Hu, Z.; Zhao, Y.; Yue, Y.; Yu, X. Large LBO Crystal Growth at 2kg-Level. *J. Cryst. Growth* **2011**, *335* (1), 133–137.
317. Martirosyan, N. S.; Kononova, N. G.; Kokh, A. E. Growth of Lithium Triborate (LiB_3O_5) Single Crystals in the $\text{Li}_2\text{O}-\text{B}_2\text{O}_3-\text{MoO}_3$ System. *Crystallogr. Rep.* **2014**, *59* (5), 772–777.
318. Krogh-Moe, J. Some New Compounds in the System Cesium Oxide-Boron Oxide. *Arkiv. Kemi.* **1958**, *12* (26), 247–249.
319. Krogh-Moe, J. Refinement of the Crystal Structure of Cesium Triborate, $\text{Cs}_2\text{O}_3\cdot\text{B}_2\text{O}_3$. *Acta Crystallogr. B* **1974**, *30*, 1178–1180.
320. Wu, Y.; Sasaki, T.; Nakai, S.; Yokotani, A.; Tang, H.; Chen, C. CsB_3O_5 : A New Nonlinear Optical Crystal. *Appl. Phys. Lett.* **1993**, *62* (21), 2614–2615.
321. Bokut, B. V. Optical Mixing in Biaxial Crystals. *Zh. Prikl. Spektrosk.* **1967**, *7* (4), 621–624.
322. Kato, K. Tunable UV Generation to 0.185 μm in CsB_3O_5 . *IEEE J. Quant. Electr.* **1995**, *31* (1), 169–171.
323. Wu, Y. C. Crystal Growth and Nonlinear Optical Properties of Cesium Triborate. In Sasaki, T., Ed. Proceedings of International Symposium on Laser and Nonlinear Optical Materials; 1997; pp 120–125.
324. Kitano, H.; Matsui, T.; Sato, K.; Ushiyama, N.; Yoshimura, M.; Mori, Y.; Sasaki, T. Efficient 355-nm Generation in CsB_3O_5 Crystal. *Opt. Lett.* **2003**, *28* (4), 263–265.
325. Wu, Y. C.; Fu, P. Z.; Wang, J. X.; Xu, Z. Y.; Zhang, L.; Kong, Y. F.; Chen, C. T. Characterization of CsB_3O_5 Crystal for Ultraviolet Generation. *Opt. Lett.* **1997**, *22* (24), 1840–1842.
326. Rajesh, D.; Yoshimura, M.; Eiro, T.; Mori, Y.; Sasaki, T.; Jayavel, R.; Kamimura, T.; Katsura, T.; Kojima, T.; Nishima, J.; Yasui, K. UV Laser Induced Damage Tolerance Measurements of CsB_3O_5 Crystals and Its Application for UV Light Generation. *Opt. Mater.* **2008**, *31* (2), 461–463.
327. Penin, N.; Touboul, M.; Nowogrocki, G. New Form of the $\text{Cs}_2\text{O}-\text{B}_2\text{O}_3$ Phase Diagram. *J. Cryst. Growth* **2003**, *256* (3–4), 334–340.
328. Kouta, H.; Kuwano, Y. β - BaB_2O_4 Single Crystal Growth by Czochralski Method. II. *J. Cryst. Growth* **1991**, *114* (4), 676–682.
329. Fu, P. Z.; Wang, J. X.; Hu, Z. G.; Wu, Y. C.; Yin, S. T.; Xu, Z. Y. Growth and Properties of Ultraviolet Nonlinear Optical Cesium Triborate. *J. Synth. Cryst.* **1999**, *28* (3), 215–218.
330. Kagebayashi, Y.; Mori, Y.; Sasaki, T. Crystal Growth of Cesium Triborate, CsB_3O_5 by Kyropoulos Technique. *Bull. Mater. Sci.* **1999**, *22* (6), 971–973.
331. Chang, F.; Fu, P.; Wu, Y.; Chen, G.; Xu, Z.; Chen, C. Growth of Large CsB_3O_5 Crystals. *J. Cryst. Growth* **2005**, *277* (1), 298–302.
332. Saji, T.; Hisaminato, N.; Nishioka, M.; Yoshimura, M.; Mori, Y.; Sasaki, T. Growth of Nonlinear Optical Crystal CsB_3O_5 From Self-Flux Solution. *J. Cryst. Growth* **2005**, *274* (1–2), 183–190.
333. Rajesh, D.; Yoshimura, M.; Shimatani, H.; Mori, Y.; Jayavel, R.; Sasaki, T. Investigations on Scattering Centers in CsB_3O_5 Crystals. *Cryst. Growth Des.* **2008**, *8* (10), 3713–3716.
334. Liu, S.; Zhang, G.; Li, X.; Yang, F.; Bo, Y.; Fu, P.; Wu, Y. Growth and Characterization of CsB_3O_5 Crystals Without Scattering Centers. *CrystEngComm* **2012**, *14* (14), 4738–4744.
335. Sasaki, T.; Mori, Y.; Kuroda, I.; Nakajima, S.; Yamaguchi, K.; Watanabe, S.; Nakai, S. Caesium Lithium Borate: A New Nonlinear Optical Crystal. *Acta Crystallogr. C* **1995**, *51* (11), 2222–2224.
336. Mori, Y.; Kuroda, I.; Nakajima, S.; Sasaki, T.; Nakai, S. Nonlinear Optical Properties of Cesium Lithium Borate. *Jpn. J. Appl. Phys.* **1995**, *34*, L296–L298.
337. Umemura, N.; Yoshida, K.; Kamimura, T.; Mori, Y.; Sasaki, T.; Kato, K. *New Data of Phasematching Properties of $\text{CsLiB}_6\text{O}_{10}$* . OSA. TOPS; vol. 26; Advanced Solid-State Lasers, 1999; pp 715–719.
338. Shoji, I.; Nakamura, H.; Ito, R.; Kondo, T.; Yoshimura, M.; Mori, Y.; Sasaki, T. Absolute Measurement of Second-Harmonic Nonlinear-Optical Coefficients of $\text{CsLiB}_6\text{O}_{10}$ for Visible-Toultraviolet Second-Harmonic Wavelengths. *J. Opt. Soc. Am. B* **2001**, *18* (3), 302–307.
339. Brown, D. J. W.; Withford, M. J. High-Average-Power (15-W) 255 nm Source Based on Second-Harmonic Generation of a Copper Laser Master Oscillator Power Amplifier System in Cesium Lithium Borate. *Opt. Lett.* **2001**, *26* (23), 1885–1887.
340. Mori, Y.; Nakajima, S.; Miyamoto, A.; Inagaki, M.; Sasaki, T.; Yoshida, H.; Nakai, S. Generation of Ultraviolet Light by Using New Nonlinear Optical Crystal $\text{CsLiB}_6\text{O}_{10}$. *SPIE* **1995**, *2633*, 299–307.
341. Petrov, V.; Noack, F.; Rotermund, F.; Tanaka, M.; Okada, Y. Sum-Frequency Generation of Femtosecond Pulses in $\text{CsLiB}_6\text{O}_{10}$ Down to 175 nm. *Appl. Optics* **2000**, *39* (27), 5076–5079.
342. Yap, Y. K.; Inagaki, M.; Nakajima, S.; Mori, Y.; Sasaki, T. Highpower Fourth- and Fifth-Harmonic Generation of a Nd:YAG Laser by Means of a $\text{CsLiB}_6\text{O}_{10}$. *Opt. Lett.* **1996**, *21* (17), 1348–1350.
343. Kaneda, Y.; Yarborough, J. M.; Li, L.; Peyghambarian, N.; Fan, L.; Hennesen, C.; Fallahi, M.; Hader, J.; Moloney, J. V.; Honda, Y.; Nishioka, M.; Shimizu, Y.; Miyazono, K.; Shimatani, H.; Yoshimura, M.; Mori, Y.; Kitaoka, Y.; Sasaki, T. Continuous-Wave All-Solid-State 244nm Deep-Ultraviolet Laser Source by Fourth-Harmonic Generation of an Optically Pumped Semiconductor Laser Using $\text{CsLiB}_6\text{O}_{10}$ in an External Resonator. *Opt. Lett.* **2008**, *33* (15), 1705–1707.
344. Kamimura, T.; Ono, R.; Yap, Y. K.; Yoshimura, M.; Mori, Y.; Sasaki, T. Influence of Crystallinity on the Bulk Laser-Induced Damage Threshold and Absorption of Laser Light in $\text{CsLiB}_6\text{O}_{10}$ Crystals. *Jpn. J. Appl. Phys.* **2001**, *40* (2A), 111–113.
345. Sennova, N. A.; Cordier, G.; Albert, B.; Filatov, S. K.; Bubnova, R. S.; Isaenko, L. I.; Gubenko, L. I.; Klöckner, J. P.; Prosenk, M. H. Temperature- and Moisture-Dependency of $\text{CsLiB}_6\text{O}_{10}$. A New Phase, β - $\text{CsLiB}_6\text{O}_{10}$. *Z. Kristallogr.-Cryst. Mater.* **2014**, *229* (11), 741–751.
346. Pan, F.; Wang, X. Q.; Shen, G. Q.; Shen, D. Z. Cracking Mechanism in CLBO Crystals at Room Temperature. *J. Cryst. Growth* **2002**, *241* (1–2), 129–134.

347. Taguchi, A.; Miyamoto, A.; Mori, Y.; Haramura, S.; Inoue, T.; Nishijima, K.; Kagebayashi, Y.; Sakai, H.; Yap, Y. K.; Sasaki, T. *Effect of the Moisture on CLBO. OSA. TOPS*, vol. 10; Advanced Solid-State Lasers, 1997; pp 19–23.
348. Yap, Y. K.; Inoue, T.; Sakai, H.; Kagebayashi, Y.; Mori, Y.; Sasaki, T.; Deki, K.; Horiguchi, M. Long-Term Operation of CsLiB₆O₁₀ at Elevated Crystal Temperature. *Opt. Lett.* **1998**, *23* (1), 34–36.
349. Takei, H.; Suzuki, T.; Mamiya, M.; Sakai, F.; Koike, M.; Mori, Y.; Sasaki, T. Thermal Expansions of Pure and Al-doped CsLiB₆O₁₀ Crystals for Nonlinear Optical Applications. *Jpn. J. Appl. Phys.* **1997**, *36*, 126–128.
350. Zhu, X.; Tu, H.; Zhao, Y.; Hu, Z. Growth of High Quality Al-Doped CsLiB₆O₁₀ Crystals Using Cs₂O-Li₂O-MoO₃ Fluxes. *Crystals* **2017**, *7* (3), 83.
351. Yuan, X.; Shen, G. Q.; Wang, X. Q.; Shen, D. Z.; Wang, G. L.; Xu, Z. Y. Growth and Characterization of Large CLBO Crystals. *J. Cryst. Growth* **2006**, *293* (1), 97–101.
352. Ryu, G.; Yoon, C. S.; Han, T. P. J.; Gallagher, H. G. Growth and Characterisation of CsLiB₆O₁₀ (CLBO) Crystals. *J. Cryst. Growth* **1998**, *191* (3), 492–500.
353. Nishioka, M.; Kawamura, F.; Yoshimura, M.; Mori, Y.; Sasaki, T. Growth of High-Quality CsLiB₆O₁₀ Crystals From Materials Mixed in Aqueous Solution. *Jpn. J. Appl. Phys.* **2004**, *43*, 1073–1075.
354. Sasaki, T.; Mori, Y.; Yoshimura, M. Progress in the Growth of a CsLiB₆O₁₀ Crystal and Its Application to Ultraviolet Light Generation. *Opt. Mater.* **2003**, *23*, 343–351.
355. Nishioka, M.; Kanoh, A.; Yoshimura, M.; Mori, Y.; Sasaki, T. Growth of CsLiB₆O₁₀ Crystals With High Laserdamage Tolerance. *J. Cryst. Growth* **2005**, *279* (1-2), 76–81.
356. Nishioka, M.; Kanoh, A.; Yoshimura, M.; Mori, Y.; Sasaki, T.; Katsura, T.; Kojima, T.; Nishimae, J. Improvement in UV Optical Properties of CsLiB₆O₁₀ by Reducing Water Molecules in the Crystal. *Jpn. J. Appl. Phys.* **2005**, *44*, 699–700.
357. Chen, C.; Wang, Y.; Wu, B.; Wu, K.; Zeng, W.; Yu, L. Design and Synthesis of An Ultraviolet-Transparent Nonlinear Optical Crystal Sr₂Be₂B₂O₇. *Nature* **1995**, *373* (6512), 322–324.
358. Meng, X. Y.; Wen, X. H.; Liu, G. L. Structure and Stacking Faults in Sr₂Be₂B₂O₇ Crystal. *JKPS*. **2008**, *52* (4), 1277–1280.
359. Ye, N.; Zeng, W.; Wu, B.; Chen, C. Two New Nonlinear Optical Crystals: BaAl₂B₂O₇ and K₂Al₂B₂O₇. *SPIE*. **1998**, *3556*, 21–23.
360. Hu, Z. G.; Mori, Y.; Higashiyama, T.; Yap, Y. K.; Kagebayashi, Y.; Sasaki, T. K₂Al₂B₂O₇: A New Nonlinear Optical Crystal. *SPIE* **1998**, *3556*, 156–161.
361. Hu, Z.; Higashiyama, T.; Yoshimura, M.; Yap, Y. K.; Mori, Y.; Sasaki, T. A New Nonlinear Optical Borate Crystal K₂Al₂B₂O₇ (KAB). *Jpn. J. Appl. Phys.* **1998**, *37* (10A), L1093–L1094.
362. Ye, N.; Zeng, W. R.; Jiang, J.; Wu, B. C.; Chen, C. T.; Feng, B.; Zhang, X. New Nonlinear Optical Crystal K₂Al₂B₂O₇. *J. Opt. Soc. Am. B* **2000**, *17* (5), 764–768.
363. Zhang, C.; Wang, J.; Chen, X. F.; Hu, X. B.; Jiang, H. D.; Liu, Y. G.; Chen, C. T. Growth and Properties of K₂Al₂B₂O₇ Crystal. *Opt. Mater.* **2003**, *23* (1-2), 357–362.
364. Umemura, N.; Ando, M.; Suzuki, K.; Takaoka, E.; Kato, K.; Hu, Z. G.; Yoshimura, M.; Mori, Y.; Sasaki, T. 200-MW-Average Power Ultraviolet Generation at 0.193 mm in K₂Al₂B₂O₇. *Appl. Optics* **2003**, *42* (15), 2716–2719.
365. Liu, C. L.; Liu, L. J.; Zhang, X.; Wang, L. R.; Wang, G. L.; Chen, C. T. Crystal Growth and Optical Properties of Non-UV Absorption K₂Al₂B₂O₇ Crystals. *J. Cryst. Growth* **2011**, *318* (1), 618–620.
366. Zhao, S. G.; Kang, L.; Shen, Y. G.; Wang, X. D.; Asghar, M. A.; Lin, Z. S.; Xu, Y. Y.; Zeng, S. Y.; Hong, M. C.; Luo, J. H. Designing a Beryllium-Free Deep-Ultraviolet Nonlinear Optical Material Without a Structural Instability Problem. *J. Am. Chem. Soc.* **2016**, *138* (9), 2961–2964.
367. Zhao, B. Q.; Bai, L.; Li, B. X.; Zhao, S. G.; Shen, Y. G.; Li, X. F.; Ding, Q. R.; Ji, C. M.; Lin, Z. S.; Luo, J. H. Crystal Growth and Optical Properties of Beryllium-Free Nonlinear Optical Crystal K₃Ba₃Li₂Al₄B₆O₂₀F. *Cryst. Growth Des.* **2018**, *18* (2), 1168–1172.
368. Shen, Y. G.; Zhao, S. G.; Yang, Y.; Cao, L. L.; Wang, Z. J.; Zhao, B. Q.; Sun, Z. H.; Lin, Z. S.; Luo, J. H. A New KBBF-Family Nonlinear Optical Material With Strong Interlayer Bonding. *Cryst. Growth Des.* **2017**, *17* (8), 4422–4427.
369. Wu, H. W.; Yu, H. P.; Pan, S. L.; Halasyamani, P. S. Deep-Ultraviolet Nonlinear-Optical Material K₃Sr₃Li₂Al₄B₆O₂₀F: Addressing the Structural Instability Problem in KB₂BO₃F₂. *Inorg. Chem.* **2017**, *56* (15), 8755–8758.
370. Yu, H. W.; Young, J.; Wu, H. P.; Zhang, W. G.; Rondinelli, J. M.; Halasyamani, P. S. The Next-Generation of Nonlinear Optical Materials: Rb₃Ba₃Li₂Al₄B₆O₂₀F-Synthesis, Characterization, and Crystal Growth. *Adv. Opt. Mater.* **2017**, *5* (23), 1700840.
371. Meng, X. H.; Liang, F.; Xia, M. J.; Lin, Z. S. Beryllium-Free Nonlinear-Optical Crystals A₃Ba₃Li₂Ga₄B₆O₂₀F (A = K and Rb): Members of the Sr₂Be₂(BO₃)₂O Family With a Strong Covalent Connection Between the ²[Li₂Ga₄B₆O₂₀F]₉ Double Layers. *Inorg. Chem.* **2018**, *57* (9), 5669–5676.
372. Zhao, S. G.; Gong, P. F.; Bai, L.; Xu, X.; Zhang, S. Q.; Sun, Z. H.; Lin, Z. S.; Hong, M. C.; Chen, C. T.; Luo, J. H. Beryllium-Free Li₄Sr(BO₃)₂ for Deep-Ultraviolet Nonlinear Optical Applications. *Nat. Commun.* **2014**, *5* (1), 4019.
373. Yu, H.; Zhang, W.; Young, J.; Rondinelli, J. M.; Halasyamani, P. S. Design and Synthesis of the Beryllium-Free Deep-Ultraviolet Nonlinear Optical Material Ba₃(ZnB₅O₁₀)PO₄. *Adv. Mater.* **2015**, *27* (45), 7380–7385.
374. Yu, H.; Cantwell, J.; Wu, H.; Zhang, W.; Poeppelmeier, K. R.; Halasyamani, P. S. Top-Seeded Solution Crystal Growth, Morphology, Optical and Thermal Properties of Ba₃(ZnB₅O₁₀)PO₄. *Cryst. Growth Des.* **2016**, *16* (7), 3976–3982.
375. Huang, L.; Zou, G.; Cai, H.; Wang, S.; Lin, C.; Ye, N. Sr₂(OH)₃NO₃: The First Nitrate as a Deep UV Nonlinear Optical Material With Large SHG Responses. *J. Mater. Chem. C* **2015**, *3* (20), 5268–5274.
376. Gong, P.; Liu, X.; Kang, L.; Lin, Z. Inorganic Planar π -Conjugated Groups in Nonlinear Optical Crystals: Review and Outlook. *Inorg. Chem. Front.* **2020**, *7* (4), 839–852.
377. Couprie, M. E. New Generation of Light Sources: Present and Future. *J. Electron Spectrosc.* **2014**, *196*, 3–13.
378. Xu, Z. Y.; Zhang, S. J.; Zhou, X. J.; Zhang, F. F.; Yang, F.; Wang, Z. M.; Zong, N.; Liu, G. D.; Zhao, L.; Yu, L.; Chen, C. T.; Wang, X. Y.; Peng, Q. J. Advances in Deep Ultraviolet Laser Based High-Resolution Photoemission Spectroscopy. *Front. Inform. Technol. Elect. Eng.* **2019**, *20* (7), 885–913.
379. Peng, Q.; Zong, N.; Zhang, S.; Wang, Z.; Yang, F.; Zhang, F.; Xu, Z.; Zhou, X. DUV/VUV All-Solid-State Lasers: Twenty Years of Progress and the Future. *IEEE J. Sel. Top. Quant. Electr.* **2018**, *24* (5), 1–12.
380. Greber, T.; Raetz, O.; Kreutz, T. J.; Schwaller, P.; Deichmann, W.; Wetli, E.; Osterwalder, J. A Photoelectron Spectrometer for k-Space Mapping Above the Fermi Level. *Rev. Sci. Instrum.* **1997**, *68* (12), 4549–4554.
381. Kurosu, A.; Nakano, M.; Yashiro, M.; Yoshino, M.; Tsushima, H.; Masuda, H.; Kumazaki, T.; Matsumoto, S.; Kakizaki, K.; Matsunaga, T.; Okazaki, S.; Fujimoto, J.; Mizoguchi, H. A Reliable Higher Power ArF Laser With Advanced Functionality for Immersion Lithography. *SPIE*. **2012**, *8326*.
382. Grüner, F.; Becker, S.; Schramm, U.; Eichner, T.; Fuchs, M.; Weingartner, R.; Habs, D.; Meyer-ter-Vehn, J.; Geissler, M.; Ferrario, M.; Serafini, L.; van der Geer, B.; Backe, H.; Lauth, W.; Reiche, S. Design Considerations for Table-Top, Laser-Based VUV and X-Ray Free Electron Lasers. *Appl. Phys. B* **2007**, *86*, 431–435.
383. Petrov, V.; Rotermond, F.; Noack, F. Generation of Tunable Femtosecond Pulses to As Low As 172.7 nm by Sum-Frequency Mixing in Lithium Triborate. *Opt. Lett.* **1994**, *19* (19), 1538–1540.
384. Mutalipju, M.; Zhang, M.; Yang, Z.; Pan, S. Targeting the Next Generation of Deep-Ultraviolet Nonlinear Optical Materials: Expanding From Borates to Borate Fluorides to Fluorooborates. *Acc. Chem. Res.* **2019**, *52* (3), 791–801.
385. Ciapponi, A.; Riede, W.; Tzeremes, G.; Schröder, H.; Mahnke, P. Non-Linear Optical Frequency Conversion Crystals for Space Applications. *SPIE* **2011**, *7912*, 791205.
386. Zhang, S.; Cui, D.; Zhang, F.; Xu, Z.; Wang, Z.; Yang, F.; Zong, N.; Tu, W.; Chen, Y.; Xu, H.; Xu, F.; Peng, Q.; Wang, X.; Chen, C.; Xu, Z. High Power All Solid State VUV Lasers. *J. Electron Spectrosc.* **2014**, *196*, 20–23.
387. Teruto, K.; Takeshi, K.; Taro, S.; Shuntaro, W.; Tadashi, T.; Chen, C.; Zhang, C.; Xu, Z.; Wang, J. Generation of Vacuum-Ultraviolet Light Below 160 nm in a KBBF Crystal by the Fifth Harmonic of a Single-Mode Ti:Sapphire Laser. *J. Opt. Soc. Am. B* **2004**, *21* (2), 370–375.
388. Chen, C. T. Recent Advances in Deep and Vacuum-UV Harmonic Generation With KBBF Crystal. *Opt. Mater.* **2004**, *26*, 425–429.
389. Cyranoski, D. Materials Science: China's Crystal Cache. *Nature* **2009**, *457* (7232), 953–955.
390. Batsanova, L. R.; Egorov, V. A.; Nikolaev, A. V. Fluoroborate of Beryllium. *Dokl. A. N. SSSR*. **1968**, *178*, 1317–1319.

391. Chen, C.; Wang, Y.; Xia, Y.; Wu, B.; Tang, D.; Wu, K.; Wenrong, Z.; Yu, L.; Mei, L. New Development of Nonlinear Optical Crystals for the Ultraviolet Region With Molecular Engineering Approach. *J. Appl. Phys.* **1995**, *77* (6), 2268–2272.
392. Xia, Y. N.; Chen, C. T.; Wu, B. C.; Tang, D. Y. New Nonlinear Optical Crystals for UV and VUV Harmonic Generation. *Adv. Mater.* **1995**, *7* (1), 79–81.
393. Chen, C.; Wu, Y.; Li, R. The Anionic Group Theory of the Non-Linear Optical Effect and Its Applications in the Development of New High-Quality NLO Crystals in the Borate Series. *Int. Rev. Phys. Chem.* **1989**, *8* (1), 65–91.
394. Chen, C. T.; Liu, G. Z. Recent Advances in Nonlinear Optical and Electro-Optical Materials. *Annu. Rev. Mat. Res.* **1986**, *16* (1), 203–243.
395. Chen, C.; Lin, Z.; Wang, Z. The Development of New Borate-Based UV Nonlinear Optical Crystals. *Appl. Phys. B* **2005**, *80* (1), 1–25.
396. Chen, C. T.; Xu, Z. Y.; Deng, D. Q.; Zhang, J.; Wong, G. K. L.; Wu, B. C.; Ye, N.; Tang, D. Y. The Vacuum Ultraviolet Phase-Matching Characteristics of Nonlinear Optical $\text{KBe}_2\text{BO}_3\text{F}$ Crystal. *Appl. Phys. Lett.* **1996**, *68* (21), 2930–2932.
397. Chen, C. T.; Wang, G. L.; Wang, X. Y.; Xu, Z. Y. Deep-UV Nonlinear Optical Crystal $\text{KBe}_2\text{BO}_3\text{F}_2$ —Discovery, Growth, Optical Properties and Applications. *Appl. Phys. B* **2009**, *97* (1), 9–25.
398. Lin, Z. S.; Wang, Z. Z.; Chen, C. T.; Chen, S. K.; Lee, M. H. Mechanism for Linear and Nonlinear Optical Effects in $\text{KBe}_2\text{BO}_3\text{F}_2$ (KBBF) Crystal. *Chem. Phys. Lett.* **2003**, *367* (56), 523.
399. Chen, C.; Sasaki, T.; Li, R.; Wu, Y.; Lin, Z.; Mori, Y.; Hu, Z.; Wang, J.; Uda, S.; Yoshimura, M.; Kaneda, Y. Borate Nonlinear Optical Crystals for Frequency Conversion. In *Nonlinear Optical Borate Crystals*, Wiley, 2012; pp 117–260.
400. Chen, C.; Xu, Z.; Lu, J.; Wang, G. *Prism-Nonlinear Optical Crystal Coupler for Laser Frequency Conversion*. U.S. Patent No. 6,859,305, 2005.
401. Xu, Z. Y.; Lü, J. H.; Wang, G. L.; Chen, C. *Nonlinear Optical Crystal Laser Frequency Variable Grating Coupler*. Chinese Patent No. CN01123553A, 2001.
402. Dai, S. B.; Chen, M.; Zhang, S. J.; Wang, Z. M.; Zhang, F. F.; Yang, F.; Wang, Z. C.; Zong, N.; Liu, L. J.; Wang, X. Y.; Zhang, J. Y.; Bo, Y.; Cui, D. F.; Peng, Q. J.; Li, R. K.; Chen, C. T.; Xu, Z. Y. 2.14 MW Deep-Ultraviolet Laser at 165 nm by Eighth-Harmonic Generation of a 1319 nm Nd:YAG Laser in KBBF. *Laser Phys. Lett.* **2016**, *13* (3), 035401.
403. Ye, N.; Tang, D. Hydrothermal Growth of $\text{KBe}_2\text{BO}_3\text{F}_2$ Crystals. *J. Cryst. Growth* **2006**, *293* (2), 233–235.
404. Wang, X. Y.; Liu, L. J.; Li, R. K. Recent Research Progress on KBBF Deep-UV Nonlinear Optical Crystal. *J. Syn. Cryst.* **2019**, *48* (10), 1790–1798.
405. Yu, J.; Liu, L.; Jin, S.; Zhou, H.; He, X.; Zhang, C.; Zhou, W.; Wang, X.; Chen, X.; Chen, C. Superstructure and Stacking Faults in Hydrothermal-Grown $\text{KBe}_2\text{BO}_3\text{F}_2$ Crystals. *J. Solid State Chem.* **2011**, *184* (10), 2790–2793.
406. Yu, J. Q.; Liu, L. J.; Wang, X. Y.; Zhou, H.; He, X.; Zhang, C.; Zhou, W.; Chen, C. Study on Defects in Hydrothermal-Grown $\text{KBe}_2\text{BO}_3\text{F}_2$ Crystals. *J. Cryst. Growth* **2011**, *318* (1), 621–624.
407. Wang, X.; Yan, X.; Luo, S.; Chen, C. Flux Growth of Large KBBF Crystals by Localized Spontaneous Nucleation. *J. Cryst. Growth* **2011**, *318* (1), 610–612.
408. Baydina, I. A.; Bakakin, V. V.; Bacanova, L. P.; Palchik, N. A. X-Ray Structural Study of Boratofluoroberyllates With the Composition $\text{MBe}_2(\text{BO}_3)\text{F}_2$ (M Na, K, Rb, Cs). *Z. Strukt. Khimi.* **1975**, *16* (6), 963–965.
409. Chen, C. T.; Luo, S. Y.; Wang, X. Y.; Wang, G. L.; Wen, X. H.; Wu, H. X.; Zhang, X.; Xu, Z. Y. A Novel Deep-UV Nonlinear Optical Crystal: $\text{RbBe}_2(\text{BO}_3)\text{F}_2$. *J. Opt. Soc. Am. B* **2009**, *26* (8), 1519–1525.
410. Chen, C. T.; Lu, J. H.; Wang, G. L.; Xu, Z. Y.; Wang, J. Y.; Zhang, C. Q.; Liu, Y. G. Deep Ultraviolet Harmonic Generation With $\text{KBe}_2\text{BO}_3\text{F}_2$. *Chin. Phys. Lett.* **2001**, *18* (8), 1081.
411. Kang, L.; Luo, S.; Peng, G.; Ye, N.; Wu, Y.; Chen, C.; Lin, Z. First-Principles Design of a Deep-Ultraviolet Nonlinear-Optical Crystal From $\text{KBe}_2\text{BO}_3\text{F}_2$ to $\text{NH}_4\text{Be}_2\text{BO}_3\text{F}_2$. *Inorg. Chem.* **2015**, *54* (22), 10533–10535.
412. Peng, G.; Ye, N.; Lin, Z.; Kang, L.; Pan, S.; Zhang, M.; Lin, C.; Long, X.; Luo, M.; Chen, Y.; Tang, Y. H.; Xu, F.; Yan, T. $\text{NH}_4\text{Be}_2\text{BO}_3\text{F}_2$ and $\gamma\text{-Be}_2\text{BO}_3\text{F}$: Overcoming The Layering Habit in $\text{KBe}_2\text{BO}_3\text{F}_2$ for the Next-Generation Deep-Ultraviolet Nonlinear Optical Materials. *Angew. Chem. Int. Ed.* **2018**, *57* (29), 8968–8972.
413. Mei, L.; Wang, Y.; Chen, C.; Wu, B. Nonlinear Optical Materials Based on $\text{MBe}_2\text{BO}_3\text{F}_2$ (M = Na, K). *J. Appl. Phys.* **1993**, *74* (11), 7014–7015.
414. Guo, S.; Kang, L.; Liu, L.; Xia, M.; Lin, Z.; Huang, Q.; Hou, Z.; Tang, C.; Wang, X.; Chen, C. Deep-Ultraviolet Nonlinear Optical Crystal $\text{NaBe}_2\text{BO}_3\text{F}_2$ —Structure, Growth and Optical Properties. *J. Cryst. Growth* **2019**, *518*, 45–50.
415. Zhang, B.; Shi, G.; Yang, Z.; Zhang, F.; Pan, S. Fluorooxoborates: Beryllium-Free Deep-Ultraviolet Nonlinear Optical Materials Without Layered Growth. *Angew. Chem. Int. Ed.* **2017**, *56* (14), 3916–3919.
416. Han, G.; Wang, Y.; Zhang, B.; Pan, S. Fluorooxoborates: Ushering in a New Era of Deep Ultraviolet Nonlinear Optical Materials. *Chem.-Eur. J.* **2018**, *24* (67), 17638–17650.
417. Mutailipu, M.; Pan, S. Emergent Deep-Ultraviolet Nonlinear Optical Candidates. *Angew. Chem. Int. Ed.* **2020**, *59* (46), 20302–20317.
418. Shi, G.; Wang, Y.; Zhang, F.; Zhang, B.; Yang, Z.; Hou, X.; Pan, S.; Poepplmeier, K. R. Finding the Next Deep-Ultraviolet Nonlinear Optical Material: $\text{NH}_4\text{B}_4\text{O}_6\text{F}$. *J. Am. Chem. Soc.* **2017**, *139* (31), 10645–10648.
419. Wang, X.; Wang, Y.; Zhang, B.; Zhang, F.; Yang, Z.; Pan, S. $\text{CsB}_4\text{O}_6\text{F}$: A Congruent-Melting Deep-Ultraviolet Nonlinear Optical Material by Combining Superior Functional Units. *Angew. Chem. Int. Ed.* **2017**, *56*, 14119–14123.
420. Zhang, Z.; Wang, Y.; Zhang, B.; Yang, Z.; Pan, S. Polar Fluorooxoborate $\text{NaB}_4\text{O}_6\text{F}$: A Promising Material for Ionic Conduction and Nonlinear Optics. *Angew. Chem. Int. Ed.* **2018**, *57*, 6577–6581.
421. Wang, Y.; Zhang, B.; Yang, Z.; Pan, S. Cation-Tuned Synthesis of Fluorooxoborates: Towards Optimal Deep-Ultraviolet Nonlinear Optical Materials. *Angew. Chem. Int. Ed.* **2018**, *57*, 2150–2154.
422. Liu, H.; Wang, Y.; Zhang, B.; Yang, Z.; Pan, S. $\text{CsAlB}_3\text{O}_6\text{F}$: A Beryllium-Free Deep-Ultraviolet Nonlinear Optical Material With Enhanced Thermal Stability. *Chem. Sci.* **2020**, *11* (3), 694–698.
423. Pilz, T.; Jansen, M. $\text{Li}_2\text{B}_6\text{O}_9\text{F}_2$, A New Acentric Fluorooxoborate. *Z. Anorg. Allg. Chem.* **2011**, *637*, 2148–2152.
424. Mutailipu, M.; Zhang, M.; Zhang, B.; Wang, L.; Yang, Z.; Zhou, X.; Pan, S. $\text{SrB}_5\text{O}_7\text{F}_3$ Functionalized With $[\text{B}_5\text{O}_9\text{F}_3]^{6-}$ Chromophores: Accelerating The Rational Design of Deep-Ultraviolet Nonlinear Optical Materials. *Angew. Chem. Int. Ed.* **2018**, *57*, 6095–6099.
425. Luo, M.; Liang, F.; Song, Y.; Zhao, D.; Xu, F.; Ye, N.; Lin, Z. $\text{M}_2\text{B}_{10}\text{O}_{14}\text{F}_6$ (M = Ca, Sr): Two Noncentrosymmetric Alkaline Earth Fluorooxoborates As Promising Next-Generation Deep Ultraviolet Nonlinear Optical Materials. *J. Am. Chem. Soc.* **2018**, *140*, 3884–3887.
426. Zhang, Z.; Wang, Y.; Zhang, B.; Yang, Z.; Pan, S. $\text{CaB}_5\text{O}_7\text{F}_3$: A Beryllium-Free Alkaline-Earth Fluorooxoborate Exhibits Excellent Nonlinear Optical Performances. *Inorg. Chem.* **2018**, *57* (4820), 4823.
427. Xiong, L.; Chen, J.; Lu, J.; Pan, C. Y.; Wu, L. M. Monofluorophosphates: A New Source of Deep-Ultraviolet Nonlinear Optical Materials. *Chem. Mater.* **2018**, *30* (21), 7823–7830.
428. Gong, P.; Kang, L.; Lin, Z. Realizing Deep-Ultraviolet Second Harmonic Generation by First-Principles-Guided Materials Exploration in Hydroxyborates. *J. Am. Chem. Soc.* **2020**, *142* (35), 15157–15163.
429. Zou, G.; Ye, N.; Huang, L.; Lin, X. Alkaline-Alkaline Earth Fluoride Carbonate Crystals ABCO_3F (A = K, Rb, Cs; B = Ca, Sr, Ba) as Nonlinear Optical Materials. *J. Am. Chem. Soc.* **2011**, *133* (49), 20001–20007.
430. Zhang, W.; Halasyamani, P. S. Crystal Growth and Optical Properties of a UV Nonlinear Optical Material $\text{K SrCO}_3\text{F}$. *CrystEngComm* **2017**, *19* (32), 4742–4748.

4.03 Thermoelectric materials

Philip Yox^{a,b,*}, Gayatri Viswanathan^{a,b,*}, Arka Sarkar^{a,b,*}, Jian Wang^{c,*}, and Kirill Kovnir^{a,b,*}, ^a Department of Chemistry, Iowa State University, Ames, IA, United States; ^b US DOE Ames National Laboratory, Ames, IA, United States; and ^c Department of Chemistry, Wichita State University, Wichita, KS, United States

© 2023 Elsevier Ltd. All rights reserved.

4.03.1	Introduction to thermoelectrics	46
4.03.1.1	Basic thermoelectric parameters related to efficiency	48
4.03.2	Common approaches to thermoelectric materials development and optimization	50
4.03.3	Classic thermoelectric materials	53
4.03.3.1	Bi ₂ Te ₃	54
4.03.3.2	SiGe	56
4.03.4	Equimolar tetrel chalcogenides	57
4.03.4.1	PbTe	60
4.03.4.2	PbSe	60
4.03.4.3	GeTe	60
4.03.4.4	SnSe	61
4.03.4.5	SnTe	62
4.03.4.6	GeSe	62
4.03.4.7	Complex tetrel chalcogenide thermoelectric materials	62
4.03.5	Mg-containing thermoelectric materials	64
4.03.5.1	Mg ₂ Si	64
4.03.5.2	Mg ₃ Sb ₂	66
4.03.5.3	MgAgSb	66
4.03.5.4	Yb ₁₄ MgSb ₁₁	67
4.03.6	Complex crystal structures for thermoelectric materials	68
4.03.6.1	Crystal structure—Phonon structure—Thermal conductivity relationship	68
4.03.6.2	Large unit cells in 14-1-11 compounds	69
4.03.6.3	Atomic disorder in zinc antimonides	70
4.03.6.4	Skutterudites and clathrates: Rattling atoms and superstructures	70
4.03.6.5	Complex Intermetallics of the R ₁₁₇ Fe ₅₂ Ge ₁₁₂ structure-type	71
4.03.7	Outlook	72
4.03.8	Appendix A: Summary of zT values for materials discussed in this chapter.	72
Acknowledgments		73
References		74

Abstract

In this chapter, the chemistry of the thermoelectric materials is discussed. First a basic introduction to the thermoelectrics phenomena, fundamental materials parameters, and potential device applications is provided. Then, basic approaches to optimize thermoelectric properties are discussed by relating phonon and electronic structure to heat and charge transport properties, respectively, in both single-phase materials and multi-phase composites. The next four sections cover selected examples from different families of materials to emphasize the chemical and structural diversity of thermoelectrics, to provide examples of state-of-the-art thermoelectric materials, and to illustrate the aforementioned optimization strategies. The described materials include: classic thermoelectric materials, such as Bi₂Te₃ and Si-Ge alloys; tetrel monochalcogenides with record-high thermoelectric performance at elevated temperatures; earth-abundant, inexpensive, and environmentally-benign Mg-containing thermoelectrics; as well as compounds with complex crystal structures that exhibit atomic disorder and rattling species that aid in decoupling electron-phonon interactions.

*All authors equally contributed to this work.

4.03.1 Introduction to thermoelectrics

Modern society is highly reliant on energy. Besides all the issues associated with energy generation, the utilization of energy is a process where significant losses occur. Lawrence Livermore National Laboratory monitors the annual generation and consumption of energy in the US (Fig. 1).¹ This flowchart shows that more than 2/3 of the energy generated in 2020 was wasted. Converting even 2% of the rejected energy into a useful form would be comparable to all the energy generated by photovoltaics. When reading this chapter, you are emitting $\sim 100 \text{ W (J}\cdot\text{s)}$ which is comparable to the emission of incandescent light bulb. A gasoline combustion car's efficiency is 30–35% and majority of the wasted energy is in the form of heat. The majority of industrial processes, such as fossil fuel power plants or steelmaking, involve heating and the emission of heat. In this chapter, we discuss thermoelectric (TE) materials which are used in solid state devices and capable of direct conversion of heat into electrical energy, and vice versa, to aid in waste heat reduction and recovery.

An attractive idea of utilizing a thermal gradient to generate useful energy was recognized a while ago and popularized in science fiction. Back in 1870, thermoelectric power generation was proposed in the classic novel "Twenty Thousand Leagues under the Sea" by Jules Verne. He proposed that the submarine of the main hero, Captain Nemo, was powered by a thermoelectric generator: "...by establishing a circuit between two wires immersed to different depths, I'd be able to obtain electricity through the diverging temperatures they experience."² Another attractive idea originating in science fiction is using nuclear fuel to replace fossil fuels, such as for driving a car or navigating a ship. For a large ship or submarine, it is feasible to have the complex assembly of a nuclear reactor on board with all the associated safety concerns. For small cars, the only promise for this technology is to convert heat from radioisotope decay directly into electrical energy using a thermoelectric device. This concept has long been realized in practice by the National Aeronautics and Space Administration (NASA) who pioneered the use of TE power generators. Missions to explore deep space, outer planets, or extraterrestrial surfaces cannot rely on solar energy and must have an autonomous, reliable, and long-lasting power source. For example, Voyager 1, the farthest human-made object from Earth in February 2022, is powered by a thermoelectric radioisotope power generator (RTG). In RTGs, the radioactive decay of a ^{238}Pu source produces heat which is converted to electrical power by a thermoelectric generator. As of January 2022, 44 years since its launch, the RTG in Voyager 1 still provides power for

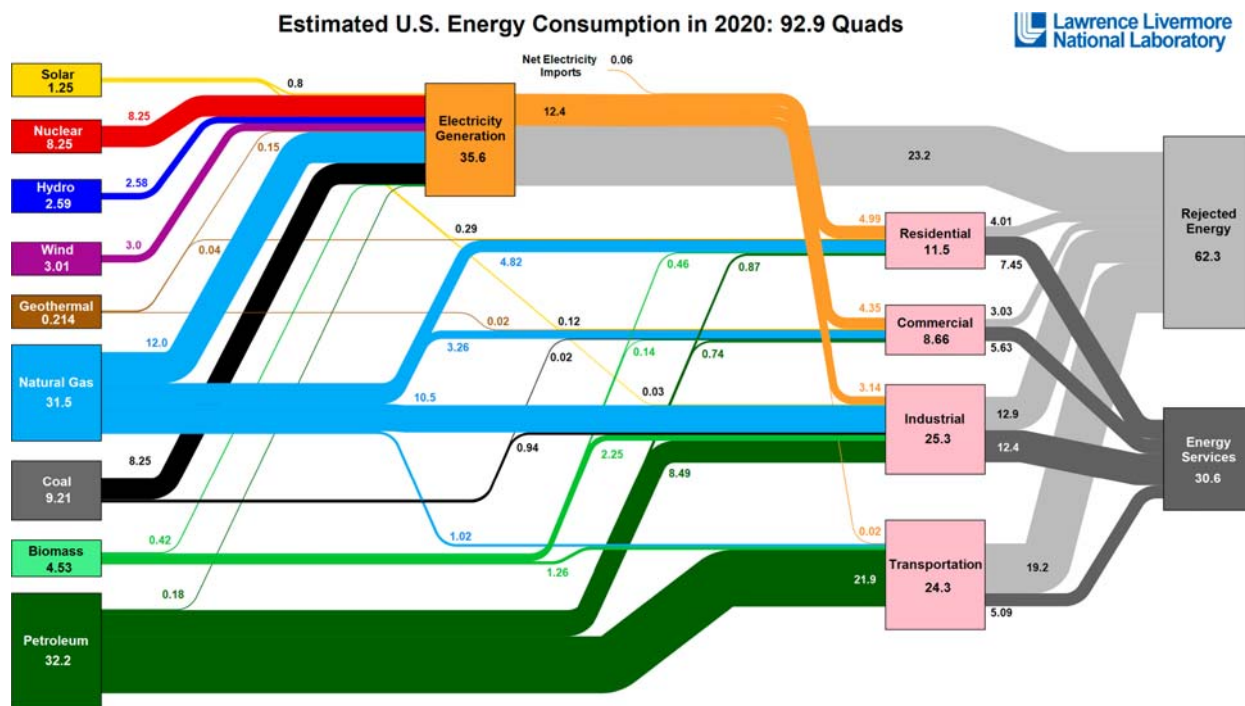


Fig. 1 The Estimated US energy consumption in 2020 created by Lawrence Livermore National Laboratory under auspices of the US Department of Energy. A quad is a unit of energy equal to 10^{15} BTU, or 1.055×10^{18} J. The British thermal unit (BTU) is the amount of heat required to raise the temperature of one pound of water by one degree Fahrenheit. $1 \text{ BTU} = 1055 \text{ J}$. Source: LLNL March, 2021. Data is based on DOE/EIA HER (2020). If this information or a reproduction of it is used, credit must be given to the Lawrence Livermore National Laboratory and the Department of Energy, under whose auspices the work was performed. Distributed electricity represents only retail electricity sales and does not include self-generation. EIA reports consumption of renewable resources (i.e., hydro, wind, geothermal and solar) for electricity in BTU-equivalent values by assuming a typical fossil fuel plant heat rate. The efficiency of electricity production is calculated as the total retail electricity delivered divided by the primary energy input into electricity generation. End use efficiency is estimated as 65% for the residential sector, 65% for the commercial sector, 21% for the transportation sector and 49% for the industrial sector, which was updated in 2017 to reflect DOE's analysis of manufacturing. Totals may not equal sum of components due to independent rounding. LLNL-MI-410527.

the mission.³ In addition to other NASA missions for deep space exploration (New Horizons, Cassini-Huygens, etc.), two recent Mars exploration rovers are also powered by RTGs: Curiosity and Perseverance (Fig. 2).⁴

The thermoelectric phenomena were discovered in the beginning of the 19th century. The Seebeck effect is named after the discoverer, *Thomas Seebeck*. He observed that heating one of two junctions of wires of two different metals deflected a compass magnet; moreover, the deviation of the compass increased with increasing temperature difference of the two junctions.⁵ In the current interpretation, placing a material in a temperature gradient creates a potential because charge carriers excited by the temperature gradient diffuse toward the colder, lower energy boundary. When two materials with opposite charge carrier types—i.e., a *p*-type semiconductor (holes are the majority carriers) and an *n*-type semiconductor (electrons are the majority carriers)—are connected in series and placed in a temperature gradient, an electrical current is generated (Fig. 3A). This is the basis for a thermoelectric generator. The opposite effect, known as the Peltier effect, was discovered several years later by *Jean Charles Athanase Peltier* during an experiment where he passed an electric current through a circuit composed of two wires of different metals. *Peltier* was able to obtain either heating or cooling of the junction depending on the direction of the current.⁶ In the Peltier process, the application of a voltage bias causes cooling of the working junction due to the removal of charge carriers. Considering a TE device composed of two materials, the application of a current induces a temperature gradient, as in the Seebeck effect (Fig. 3B). The term, *thermoelectric*, was introduced by *Hans Christian Ørsted* upon realization of the first thermoelectric device.⁷ A more detailed history of the thermoelectric effect discovery is provided in *Beretta et al.*⁸

The basic advantages of thermoelectrics are due to the solid-state nature of the devices—they are small in size, have no moving parts, no vibrations, and thus have very long lifetimes. The Voyager RTG, which was manufactured using 1970s technology, is still operational today after 44 years. After the discovery and misinterpretation of the basic physics behind the Peltier and Seebeck effects, thermoelectrics found no application for almost a century. However, in the mid-20th century, research studying semiconductors as thermoelectrics was performed by *Abram Fedorovich Ioffe* and inspired a burgeoning interest in thermoelectric applications.⁹ Several traditional thermoelectric materials used today are based on Bi₂Te₃, PbTe, and SiGe.^{10–12}

Nowadays, TE materials are used for both cooling and waste heat conversion purposes. Peltier coolers are implemented in applications where reliability and precise temperature control are required, such as in CCD (charge-coupled device) detectors or in the heat sinks of microprocessors. Passenger-selective TE cooling in automobiles is an attractive, energy efficient, and actively-developing replacement to convection air-conditioning. The absence of vibrations is crucial for wine coolers which therefore often rely on thermoelectric-based cooling. However, the lower conversion efficacy of TE coolers prevents them from being competitive with modern compressor-based refrigerators. Heat conversion applications range from converting different sources of heat from the human body to power portable electronics and medical sensors, to modules in the exhaust pipe of the combustion engine vehicles. However, for these technologies to come to commercial fruition, the energy conversion efficiencies of these generators must be enhanced.¹³

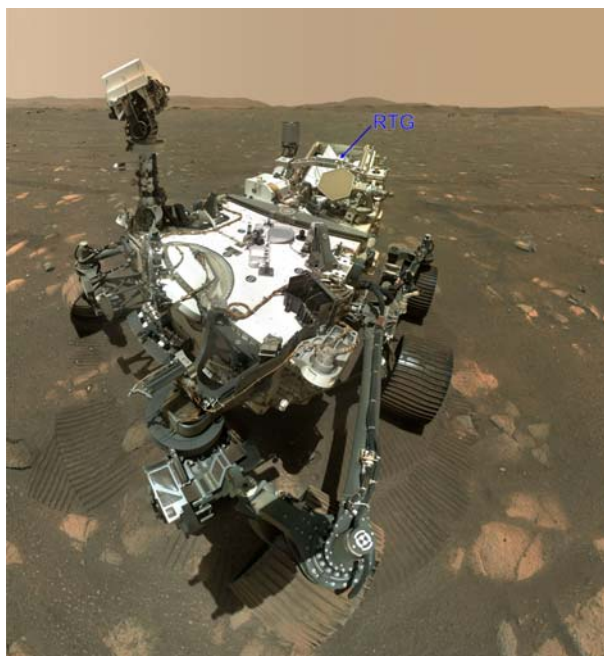


Fig. 2 NASA's Perseverance Mars rover took a selfie. This image was taken by the WASTON camera on the rover's robotic arm on April 6, 2021, the 46th Martian day, or sol, of the mission. Credits: NASA/JPL-Caltech/MSSS. RTG radiator is pointed out in the back.

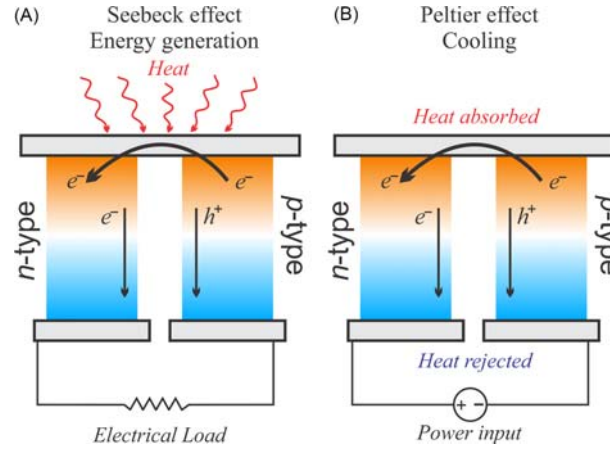


Fig. 3 Schematics of (A) a Seebeck power generation TE device and (B) a Peltier cooler.

4.03.1.1 Basic thermoelectric parameters related to efficiency

The efficiency of the thermoelectric generator describes its ability to convert thermal energy into useful electrical energy. For TE coolers it is opposite—the ability to convert applied electrical energy into cooling power. Formally, a thermoelectric generator's efficiency, η , is defined as the ratio of the energy provided at the electrical load to the heat energy absorbed at the hot junction. According to the basic principles of thermodynamics, the Carnot theorem postulates that for any heat engine operating between a cold temperature, T_C , and a hot temperature, T_H , the maximum efficiency is $\eta_{Carnot} = \frac{T_H - T_C}{T_H}$. This idealized efficiency cannot be practically obtained, and any engine will have lower than Carnot efficiency. For the thermoelectric generator, efficiency η_{TM} depends on the intrinsic properties of the specific materials used:

$$\eta_{TM} = \frac{T_H - T_C}{T_H} \times \frac{\sqrt{1 + Z\bar{T}} - 1}{\sqrt{1 + Z\bar{T}} + \frac{T_C}{T_H}} \quad (1)$$

where $\bar{T} = \frac{T_H + T_C}{2}$.¹⁴ Individual *p*- and *n*-type materials can be described by the parameter z which summarizes a material's intrinsic transport properties. The thermoelectric figure-of-merit, zT , is a product of z and temperature; this value is preferred to describe a material's thermoelectric efficiency because zT is dimensionless.

$$zT = \frac{S^2 \sigma}{\kappa} T \quad (2)$$

In Eq. (2), S is the thermopower (μVK^{-1}), also called Seebeck coefficient; T is the absolute temperature (K); σ is the electrical conductivity ($\Omega^{-1} \text{m}^{-1}$); and κ is the thermal conductivity ($\text{Wm}^{-1} \text{K}^{-1}$).¹⁴ A positive value for thermopower indicates that holes are the primary charge carrier (*p*-type), while negative Seebeck corresponds to electrons as the main carrier (*n*-type).

For a material to be an efficient thermoelectric, it should conduct electricity well (high σ) to pass current through and conduct heat poorly (low κ) to maintain the thermal gradient. In addition, a high induced voltage response to the temperature gradient (high S) is required. The optimization of TE properties is challenging because of the interdependent nature of intrinsic transport properties (Eq. 3 and 4). Electrical conductivity is proportional to charge carrier concentration (n), mobility (μ), and charge of the carrier (e). Thermopower is proportional to effective mass (m^*) and inversely related to carrier concentration, indicating that a simple adjustment of charge carrier concentration might not be sufficient to optimize materials' thermoelectric performance.

$$\sigma = ne\mu \quad (3)$$

$$S = \frac{8\pi^2 k_B^2}{3eh^2} m^* T \left(\frac{\pi}{3n} \right)^{2/3} \quad (4)$$

In fact, materials with high carrier concentration (metals) exhibit high electrical conductivities but low thermopowers, while insulators suffer from low electrical conductivities despite having high thermopowers (Fig. 4).

Total thermal conductivity is also dependent on a material's carrier concentration. It can be represented as a sum of the electronic and lattice contributions, $\kappa_{\text{electronic}}$ and κ_{lattice} , respectively. The lattice contribution comes from phonon interactions in a solid and is independent of the charge carrier concentration (Fig. 5A). κ_{lattice} is determined by the crystal structure and type and strength of chemical bonds in the compound. The electronic contribution, $\kappa_{\text{electronic}}$, can be approximated by the Wiedemann-Franz law, where L is the Lorenz number (Fig. 5A).^{14,15}

$$\kappa_{\text{electronic}} = LT\sigma = LTne\mu \quad (5)$$

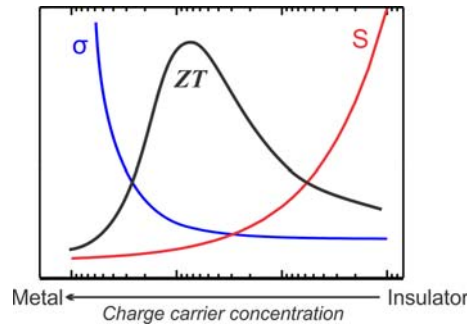


Fig. 4 Schematic of the dependencies of Seebeck coefficient, S (red), electrical conductivity σ (blue), and thermoelectric figure-of-merit zT (black) as a function of charge carrier concentration.

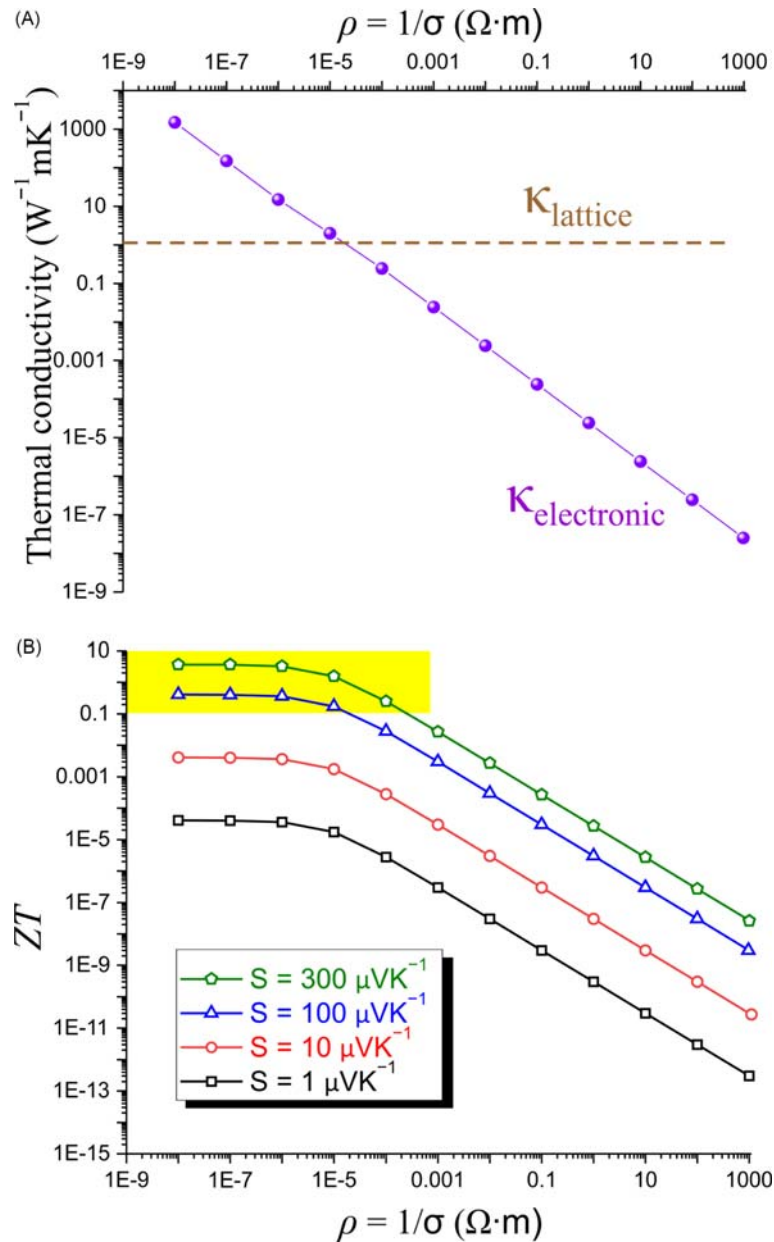


Fig. 5 (A) Schematic of the dependence of the lattice and electronic contributions to total thermal conductivity on the material's resistivity; (B) Dependence of zT on resistivity for selected values of the thermopower. In all cases, the lattice thermal conductivity is assumed to be $1 \text{ Wm}^{-1} \text{ K}^{-1}$ and temperature $T = 300 \text{ K}$. Not all shown combinations of S and ρ can be realized practically due to their interdependence. The yellow area highlights practically relevant values of zT . Note the double-log scale in both graphs.

As seen from Fig. 4, the materials best suited for TE applications are heavily doped semiconductors with a charge carrier concentration ranging from 10^{19} to 10^{21} cm^{-3} , depending on the particular system, i.e., the mobility and effective mass of the carrier. When measurable thermoelectric properties are considered, practically relevant values of zT may be achieved only for specific combinations of transport properties (yellow area in Fig. 5B). For example, if the material's thermopower is $10 \mu\text{VK}^{-1}$ (red curve in Fig. 5B), the material cannot achieve practically relevant values of $zT > 0.1$ for any combination of other properties. Similarly, if a material's electrical resistivity is higher than $0.001 \Omega \text{ m}$, high values of zT are not attainable for any practical values of the thermopower. Fig. 5A also illustrates that the optimum resistivity for a thermoelectric material is around $10^{-5} \Omega \text{ m}$ ($\sim 1 \text{ m}\Omega \text{ cm}$). A further decrease in resistivity results in a substantial electronic contribution to thermal conductivity, which causes a plateau of zT values in the left part of the Fig. 5B. Given that resistivity and Seebeck coefficient are related, high Seebeck coefficients are impossible for good metals with resistivities of 10^{-8} – $10^{-7} \Omega \text{ m}$; however, in heavily doped semiconductors with resistivities of 10^{-4} – $10^{-6} \Omega \text{ m}$, reasonably high values of the thermopower can be obtained.

In addition to the interrelation of the transport properties for a material at a fixed temperature, all thermoelectric parameters vary with temperature (Fig. 6). Generally, at higher temperatures zT is higher for an obvious reason— zT has a multiplier of temperature—as well as the following reasons. First, the electrical resistivity of a semiconductor decreases with temperature due to activation of the charge carriers over the bandgap into the conduction band. Thermal conductivity first increases with temperature due to the population of additional phonon levels but eventually, at quite low temperatures of $\sim 100 \text{ K}$, lattice thermal conductivity starts to decrease with temperature due to Umklapp phonon-phonon scattering. The absolute value of the Seebeck coefficient increases with temperature up to a maximum value. At this temperature the activation of the minority charge carriers over the bandgap occurs, resulting in the decrease of magnitude of the thermopower. The latter process is one of the factors which limits the maximum application temperature for a given thermoelectric material. Another more important reason for this limitation is the stability of the compound. Obviously, melting or decomposition temperature is a limiting factor. Even at temperatures lower than the melting/decomposition point, a thermoelectric material may develop substantial vapor pressure of the constituent elements, such as S, Se, Te, P, As, Sb, Bi, or react with the metallic leads; both processes will deteriorate the device.

In research papers, zT is reported at specified temperatures and, sometimes, the main achievement is perceived as producing as high zT as possible. Currently, values of $zT \sim 3$ have been experimentally reported for bulk materials at elevated temperatures. However, from the point of view of practical application, the maximum zT is less crucial and the real property which defines the energy efficacy of TE generator or cooler is the average zT over the desired operating temperature range.¹⁶

4.03.2 Common approaches to thermoelectric materials development and optimization

The ideal thermoelectric material will have high electrical conductivity, poor thermal conductivity, and high voltage response across a temperature gradient. It should also be thermally and chemically stable for the desired application temperature, composed of earth-abundant elements, and inexpensive so the material can be practical for commercial applications. So far, no such perfect material exists. *So how do we approach developing promising thermoelectrics?* The discovery of novel thermoelectrics with outstanding properties is still serendipitous; examples of ab initio prediction of novel types of thermoelectrics are extremely rare. On the other hand, there are several guiding principles and pathways to designing a new material or improving the performance of a specific material or composite for thermoelectric applications. Depending on the transport properties of the prototype material, modifications target either charge or heat transport (Fig. 7).

Knowledge of composition-structure-property relationships are crucial to developing functional thermoelectrics. From a composition perspective, heavy elements such as Pb, Bi, and Te have been used to promote low thermal conductivity and good electronic properties in materials. However, the common use of these materials is inhibited by the scarcity of these heavy elements and the potential health and environmental issues associated with them. Several good thermoelectric materials are known with light

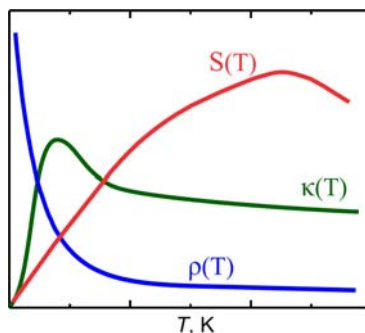


Fig. 6 Temperature dependence of electrical resistivity, ρ , (blue), total thermal conductivity, κ , (green), and thermopower, S , (red) for a semiconductor.

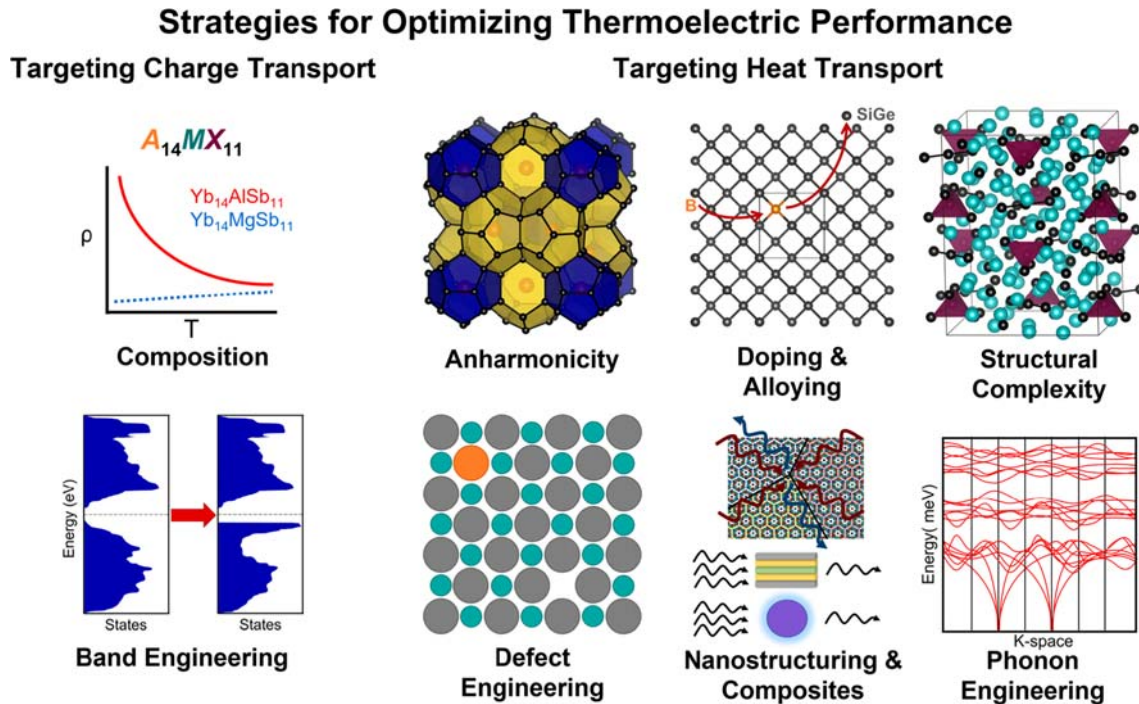


Fig. 7 Strategies for optimizing thermoelectric performance are graphically illustrated showing two major categories: optimization of charge transport (left), and optimization of heat transport (right).

elements like Mg or Si. These elements are cheaper and more mechanically robust, making them good candidates for practical use. An ongoing challenge is addressing the high thermal conductivity in materials containing such elements.

Complexity, both in a material's composition and crystal structure, is another way of modifying thermoelectric properties. It can be introduced by increasing the number of components (i.e., elements or phases) in a material, forming large unit cells, introducing crystallographic disorder, and combining various types of bonding. As a result, complex materials often exhibit inherently low thermal conductivities. Zintl phases are a popular choice for exploration of thermoelectrics because they offer a good balance of electrical conductivity and Seebeck coefficient.¹⁷ These complex intermetallics exhibit crystal structures that combine ionic, covalent, and metal-metal bonding. The Zintl-Klemm approach is applied for counting valence electrons to determine whether a material is charge-balanced (semiconducting or semimetallic in nature) or imbalanced (metallic). This concept of electron-counting can be quite powerful in designing materials for thermoelectrics by (i) tuning an imbalanced (electron-poor or electron-rich) composition toward a charge-balanced one, or (ii) taking an existing electron-balanced composition and substituting elements of different valence to carefully modify carrier concentration (Fig. 8). Additional examples of complex structures will be described later in this chapter.

Anisotropic crystal structures offer avenues for exploration of direction-dependent charge and heat transport. In layered materials, covalent bonding within the layers allows for efficient charge carrier conduction and good transfer of phonons. Meanwhile, the van der Waals gaps between layers inhibit the conduction of heat and charge. In materials with high thermopower, promising thermoelectric properties can be achieved in certain orientations. Incorporating structural complexity into these materials can reduce lattice thermal conductivity further to enhance the thermoelectric figure-of-merit. Aliovalent substitution, or aliovalent doping, is another technique that can be used to tune thermal and electronic character to maximize thermoelectric performance. Doping aims at optimizing charge carrier concentration, mobility, and effective mass as well as altering the electronic density of states (DOS) curvature near the Fermi level (E_F) to enhance thermopower. Such approaches include convergence of electronic band valleys, hybridization gaps, Kondo levels, or resonant levels in DOS.^{18–21} Alloying can have similar effects on the electronic structure as well as reducing the lattice thermal conductivity. For example, pristine Bi_2Te_3 has low thermal conductivity as well as a substantial thermoelectric quality factor, a parameter which describes the maximum feasible zT in doped semiconductor alloys.²² This factor is dependent on a material's crystal and electronic structure and rationalizes how a material's power factor ($S^2\sigma$) can be tuned by doping and alloying. The superior quality factor for Bi_2Te_3 has been one motivating factor in studying its alloys and conducting related properties optimization over the last few decades.

While the electronic contribution to thermal conductivity is defined by charge transport, lattice thermal conductivity can be significantly reduced either within a single material or by making composites. Anharmonicity in thermal conductivity can be realized in a single crystal by size mismatches of neighboring atoms, the presence of heavy atoms with anharmonic vibrations, or the mixing of different types of bonding i.e., ionic vs. covalent vs. van der Waals. When combined with overall complexity of the crystal structure, this can yield a complex phonon structure with multiple crossings of acoustic and optical phonon branches. Defect

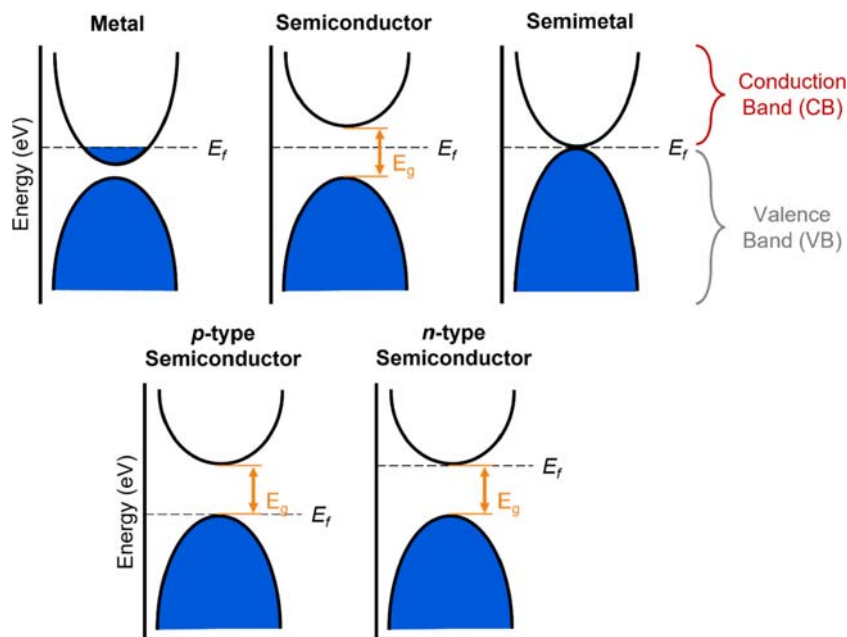


Fig. 8 Comparison of the band structure of a metal, semiconductor, and semimetal. The blue region represents bands occupied by electrons while the white region is composed of empty bands. The Fermi level is given by the dashed line labeled E_f . In metals, the Fermi level is found inside one or more bands leading to partial filling of the conduction (CB) or valence (VB) band. However, in semiconductors the VB is filled, and a bandgap (E_g) separates the VB and CB; the Fermi level may fall at the top of the VB (p-type), bottom of the CB (n-type), or in between the two bands (intrinsic). In semimetals, one or more bands touch or cross at the Fermi level leading to small overlap between the bottom of the CB and top of the VB; there is no bandgap and a negligible number of states at the Fermi level.

engineering manipulates electron-phonon interactions in solids through controlling the number, size, and distribution of crystallographic defects (vacancies, interstitial sites, atomic mixing), intrinsic strain, Kondo interactions, spin-state transitions, etc.²³ In bulk polycrystalline materials, the shortening of the mean free path for phonons can be achieved by increasing the number of grain boundaries and structural defects. Point defects in solid solutions and the rattling of guest atoms in some materials can also affect the mean free path of phonons with minimal influence on electrical properties. Nanostructuring is another promising method to enhance thermoelectric performance by drastic reduction in lattice thermal conductivity.^{24,25} Nano-inclusions scatter phonons more effectively by shortening their mean free path. In the case of composite materials, the formation of point defects or nano- or

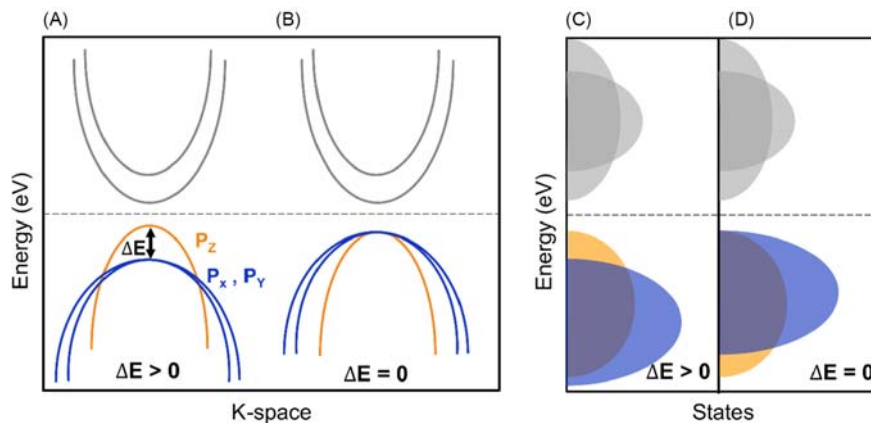


Fig. 9 Band structure (left) and density-of-states (right) for a hypothetical semiconductor. Grey bands and shaded regions correspond to conduction band orbitals, while colored ones correspond to P_z (orange) or P_x, P_y orbitals (blue), respectively. The Fermi level is given by the dashed line. (A) Bands corresponding to p -orbitals in the valence band are diverged with energy difference, ΔE , between the maxima of the P_z and degenerate P_x, P_y orbitals. (B) With band engineering, the positions of bands can be tuned such that $\Delta E = 0$ due to convergence of all three p -orbital bands. (C and D) The corresponding density-of-states (DOS) shows that this modification of the band structure leads to a higher number of total states just below the Fermi level, which can lead to improvement in a material's electronic properties.

mesoscale precipitates will also affect the phonon mean free path. In nanocomposites of SiGe, the random distribution of nanostructures promotes a significant reduction in thermal conductivity and can even enhance the power factor.²⁶

Computational methods allow for prediction of electron-phonon interactions and transport in materials.^{21,27–29} Band engineering allows for tuning of the band structure by modification of composition, such as alloying or doping. By inducing band convergence and increasing the degeneracy of states at the top of the valence band or bottom of the conduction band, power factor can be enhanced (Fig. 9). As mentioned previously, shortening the mean free path of phonons can reduce thermal conductivity in materials. Calculating accurate phonon band structures and exploring the effects of defects on the acoustic and phonon branches is an active area of current research. Apart from calculating the electronic and phonon structures of single materials, high-throughput studies across various chemical and structural phase spaces can arouse interest in new classes of thermoelectrics. Further tailoring of the composition and crystal structure of these predicted compounds allows for the rational design of materials with desired transport properties.

The popularization of ‘predictive power’ has prompted the use of chemical heuristics, data mining, and machine learning to aid in materials discovery. Extrapolation of chemical trends from the classification of known thermoelectric materials can provide predictions of novel or unexplored high-performance materials for future investigation.^{30–32} Visualizing thousands of data points from experimental studies provides insight to phase spaces for continued exploration of thermoelectric materials with favorable transport properties, while also considered scarcity and supply rick for commercialization purposes.³³ Combining machine learning with high-throughput calculations can guide synthetic efforts to discover new members in known classes of materials such as full-Heuslers, which are attractive for thermoelectric applications.³⁴ While the goal of these predictive methods is to minimize the time and cost of materials discovery, the success of this method is dependent on obtaining large amounts of high-quality experimental data that can be used as training sets for predictions. The subsequent need for experimental validation creates a crucial feedback loop between experimental and data-driven efforts, further emphasizing the importance of collaboration within the field of thermoelectrics.

The remainder of this chapter is divided into four sections corresponding to different classes of thermoelectric materials. The first section addresses “classic” thermoelectrics that were discovered nearly 200 years ago, but still dominate thermoelectric applications today. The following section describes chalcogenide materials that exhibit unique changes in their structure and properties at low vs. high temperature. The third section discusses the dual role of Mg in thermoelectric materials and highlights some promising compounds for continued research. The final class of materials discussed in this chapter exhibit varying degrees of structural complexity which drastically lowers the materials’ lattice thermal conductivities. While there are several other interesting compositional and structural phase spaces to discuss in the field of thermoelectrics, the selected materials provide an idea of the history and current stage of research for well-known compounds in the community. The reader is referred to additional sources to get deeper understanding of fundamental concepts and recent advances in thermoelectrics.^{8,28,29,35–38}

4.03.3 Classic thermoelectric materials

Like other functional materials, studies of thermoelectrics can be perceived as falling into three general stages: (i) materials discovery, (ii) characterization, and (iii) properties optimization. Given the long history of thermoelectrics, one may conceive that most modern research efforts are concentrated on the last stage. However, even today, novel materials are synthesized and identified as potential candidates for clean energy conversion. Studying structure-property relationships among known materials provides chemists with guidelines for what characteristics are desired or should be avoided in potential thermoelectrics. Often many of the developed optimization techniques are first tested on so-called “classic” thermoelectric materials which were initially investigated over 200 years ago.

Early studies of thermoelectric properties were qualitative and limited to elements, alloys, or simple compounds observed in naturally occurring minerals. In the early 1800s, *Johann Seebeck* studied materials such as Bi, PbS (galena), and CoAs₃ (skutterudite), then developed a qualitative ordering of their relative Seebeck values.³⁹ Investigations in the following century adopted a quantitative approach to compare materials’ Seebeck coefficients and electrical conductivities, while simultaneously moving into more complex materials such as metal alloys, zinc antimonides, and tetradymites.⁴⁰ High Seebeck coefficients and overall promising thermoelectric properties were observed in variety of materials, notably binary tellurides and silicon-containing materials.

In the mid-20th century, *Abram Fedorovich Ioffe’s* investigations into the thermoelectric properties of semiconducting materials revealed that heavily doped semiconductors composed of tellurium (such as Bi₂Te₃, PbTe, and Sb₂Te₃) were the most promising candidates for thermoelectric conversion.⁹ With minimal optimization, these heavy metal-containing materials already exhibited favorable properties and came to the forefront as prime candidates for implementation into thermoelectric devices. These “classic” thermoelectric materials have relatively simple crystal structures and have served as a platform for studying the modification of carrier concentration through doping or the reduction of thermal conductivity by alloying.

The following section discusses the merits of two well-studied thermoelectric materials: Bi₂Te₃ and SiGe. For over half a century, Bi₂Te₃ and its alloys have dominated the low temperature regime for thermoelectric cooling (with $T_H = 300$ K) with peak efficiency near room temperature. On the other hand, SiGe alloys have long been studied for their thermal stability and promising properties at high temperatures for waste heat conversion. Both materials have been adopted into modern technologies such as refrigerators and RTGs, respectively, to aid in thermoelectric conversion. But, even today, a significant portion of research in thermoelectrics is

dedicated to understanding the origin of superior properties in these classic thermoelectrics and exploring pathways to further improve the efficiency of these materials.

4.03.3.1 Bi₂Te₃

Bismuth chalcogenides in naturally occurring minerals such as such as pilsenite (Bi₄Te₃) and bismuth glance (Bi₂S₃) were originally investigated by *Johann Seebeck* in the early 1800s. Investigations into the Bi-Te phase space led to the discovery of tellurobismuthite, the mineral form of Bi₂Te₃, in 1815. Initial characterization studies conducted by *Werner Haken* revealed that Bi₂Te₃ possessed a large Seebeck coefficient and could be prepared as a *p*-type or *n*-type material depending on whether the composition was Bi or Te-rich, respectively.⁴⁰ Today, bismuth telluride is considered a state-of-the-art thermoelectric material for low temperature applications, such as refrigerators or CCD coolers.⁴¹ Commercial Peltier coolers with bismuth telluride exhibit maximum temperature differences of 65–75 K with the hot end maintained at 300 K.⁴²

The large *zT* of bismuth telluride and its alloys is ultimately a result of the materials' crystal and electronic structures. Bi₂Te₃ crystallizes in the tetradymite structure type in the rhombohedral space group *R* $\bar{3}m$ (No.166). The structure can be considered a derivative of the NaCl rock-salt structure with tilted Bi@Te₆ octahedra (Fig. 10). However, every third Bi layer is absent allowing for charge balance between the Bi³⁺ and Te²⁻ ions. The resulting layered crystal structure has 2 inequivalent crystallographic sites for tellurium: Te(1) and Te(2). 2D Slabs of Bi₂Te₃ stack along the *c*-axis with a [Te(1)-Bi-Te(2)-Bi-Te(1)] ordering where each Bi atom is connected to 3 Te(1) and 3 Te(2) atoms in a facial coordination. The interlayer distance between the Te(1) planes is ~ 2.6 Å. It is uncertain whether the Te(1)-Te(1) interactions between layers are exclusively van der Waals bonding or if there is a degree of weak covalent bonding.⁴³ The combination of weak interlayer interactions and heavy element atoms in Bi₂Te₃ manifests as low lattice thermal conductivity on the order of 1.5 Wm⁻¹ K⁻¹.¹⁰ The anisotropic structure of Bi₂Te₃ makes it an excellent candidate for studying directional thermoelectric properties, i.e., within the plane of Bi₂Te₃ slabs or across the interlayer spacing. From oriented single crystals, it was found that the *zT* of Bi₂Te₃ is nearly doubled in the *ab*-plane in comparison to along the *c*-stacking axis.⁴⁴ This difference in *zT* originates from differences in thermal conductivity (lower when measured perpendicular to the plane of the layers) and electrical conductivity (higher when measured parallel to the plane of the layers).

Bi₂Te₃ exhibits great thermoelectric efficiency due to its electronic structure. Pristine Bi₂Te₃ is a narrow bandgap semiconductor with ~ 0.15 eV bandgap. Depending on the synthetic technique employed, Bi₂Te₃ can be made *p*-type (Bi-rich composition) or *n*-type (Te-rich composition). Both *p*- and *n*-type Bi₂Te₃ exhibit similar magnitudes of Seebeck coefficient because the isotropic nature of the density-of-states.²² As a result, both types of Bi₂Te₃ can be used as platforms for the optimization of thermoelectric properties. Bi₂Te₃ has high band degeneracy, low effective mass, and high carrier mobility. Combined with low thermal conductivity, this gives bismuth telluride a substantial thermoelectric quality factor, meaning the electronic and thermal properties of Bi₂Te₃ can be tuned effectively through the doping of its alloys.²²

Changes in carrier type can be induced in Bi₂Te₃ by alloying with other tetradymites such as Sb₂Te₃ and Bi₂Se₃ or tellurides like PbTe. The large band degeneracy at the Fermi level in the density-of-states can be increased with minor alloying to improve the Seebeck coefficient.²⁸ Alloying with isostructural Sb₂Te₃ or Bi₂Se₃ further increases the bandgap and improves the thermoelectric performance of these materials above room temperature. The resultant band convergence reduces lattice thermal conductivity to

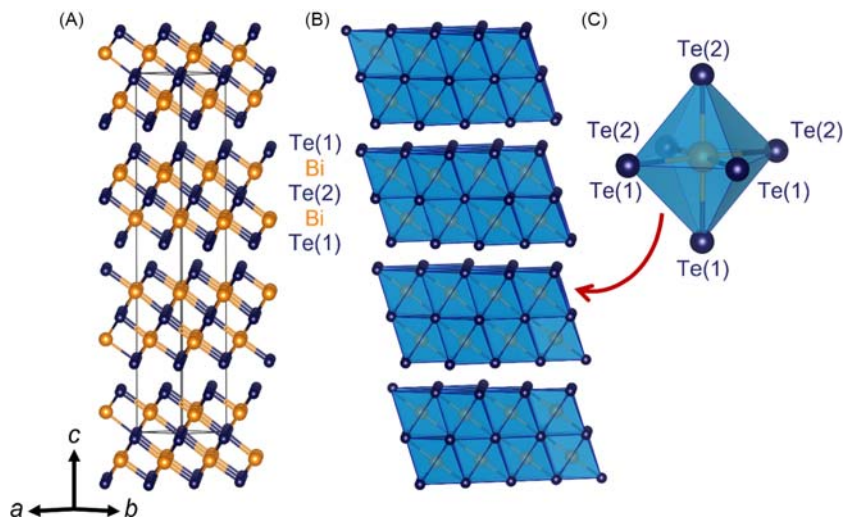


Fig. 10 (A) Layered crystal structure of Bi₂Te₃ highlighting the connectivity of Bi and Te atoms. The absence of every third Bi atom results in two inequivalent chalcogen sites: Te(1) and Te(2). (B) Polyhedral view of Bi₂Te₃ emphasizing the stacking of [Bi₂Te₃] slabs along the *c*-axis. (C) Facial coordination of Te(1) and Te(2) atoms around Bi in tilted Bi@Te₆ octahedra.

enhance thermoelectric efficiency as well. Today, commercial thermoelectric cooling relies on alloys of Bi_2Te_3 with p -type $\text{Bi}_{2-x}\text{Sb}_x\text{Te}_3$ boasting a zT of ~ 1 at 300 K, while n -type $\text{Bi}_2\text{Te}_{3-x}\text{Se}_x$ has a slightly lower efficiency of $zT = 0.8$ at 300 K.⁴⁵

Band engineering, defect engineering, and nanostructuring are growing research areas that strive to enhance the thermoelectric performance of materials.^{28,29} The desire to study bismuth telluride as a topological insulator (TI) has led to more accurate predictions of the bulk band structure which have also been useful to those studying the material for thermoelectrics.^{22,46,47} Band engineering studies can help enhance the power factor of a material by increasing the band degeneracy. Grain boundary engineering has been shown to be an effective method to dissipate phonons and reduce thermal conductivity in Bi_2Te_3 . Nanostructuring is an alternate approach that can be applied as the difference in the mean free paths between electrons and phonons allows for effective scattering of phonons with limited detriment to the electrical conductivity.⁴¹ Further control of microstructure and defects can be achieved through various synthetic techniques and offer an alternate method to enhance the thermoelectric efficiency of Bi_2Te_3 .³⁶

From its discovery nearly two centuries ago, Bi_2Te_3 has a long history within the thermoelectrics community and is still employed in cooling devices. Studies have spanned the previously discussed three stages of materials research with optimization efforts ranging from simple doping/alloying via crystal structure engineering to more recent works on employing band, defect, and nanostructure engineering to enhance performance (Fig. 11). Research on Bi_2Te_3 is still a hot topic today and continues to advance our understanding on key factors when designing novel materials for thermoelectric applications. One important consideration for the future of Bi_2Te_3 will be accounting for the cost-effectiveness and toxicity of tellurium, which was featured on the 2022 United States Geological Survey list of critical minerals.⁵³ With the push for implementation of predictive tools such as machine learning, future studies on Bi_2Te_3 may focus on compiling the numerous experimental data points reported in literature over the last few decades to obtain valuable trends and insights. Combining this research with advancing computational methods could provide guidance for experimentalists to prepare more efficient materials for implementation in thermoelectric devices.

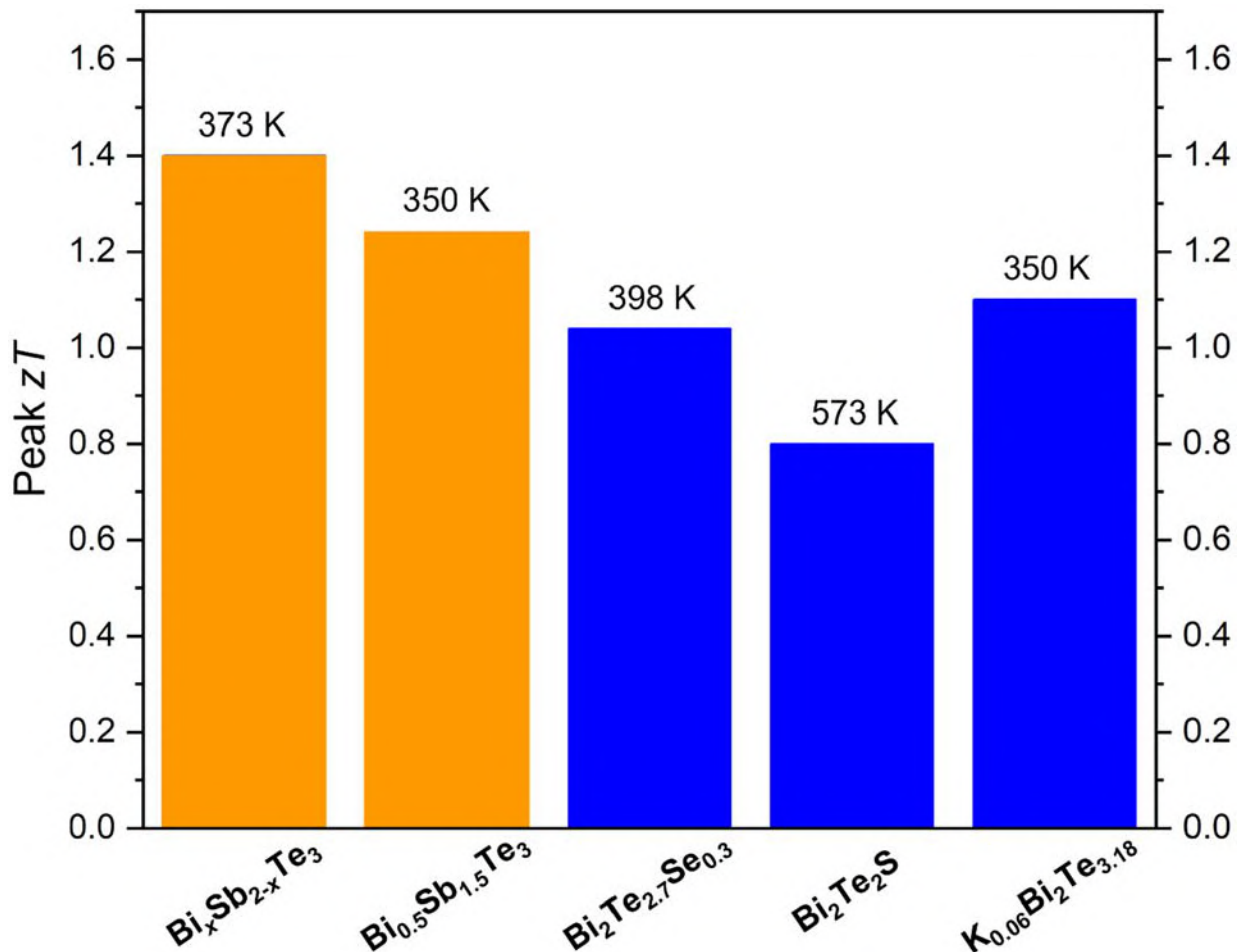


Fig. 11 Summary of peak zT values for selected Bi_2Te_3 alloys. The orange bars indicate p -type materials, while blue bars correspond to n -type materials. The peak zT temperature is given above each bar.^{48–52}

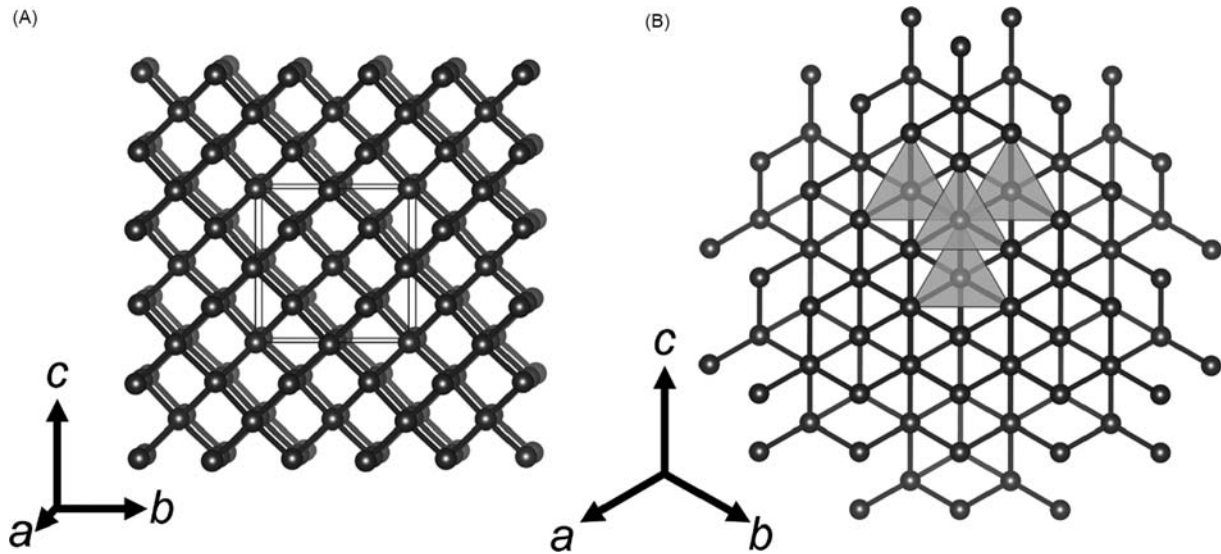


Fig. 12 (A) Diamond-type crystal structure of Si, Ge, and $\text{Si}_{1-x}\text{Ge}_x$ alloys. (B) Body-diagonal perspective of alloy emphasizing tetrahedral coordination about tetrel atoms. Tetrahedra share corners resulting in a 3D crystal structure.

4.03.3.2 SiGe

Amorphous silicon was discovered in the early 19th century by *Jöns Jacob Berzelius* and later prepared in its crystalline form by *Henri Sainte-Claire Deville*.^{54,55} Si crystallizes in the $Fd\bar{3}m$ space group (No. 227) in the diamond structure. In the crystal structure, Si atoms are tetrahedrally-coordinated resulting in $\text{Si}@\text{Si}_4$ tetrahedra that share corners to generate a three-dimensional structure (Fig. 12). An alternative description is a cubic close packing of Si atoms with $\frac{1}{2}$ of all the tetrahedral holes filled with Si atoms. Silicon has been well-studied for its uses in the semiconductor industry for optoelectronics and circuitry, as well as for high temperature thermoelectric applications. Compared to other classic thermoelectric materials like Bi_2Te_3 , silicon is thermally stable at much higher temperatures (melting point > 1400 °C) and has a larger bandgap (~ 1.1 eV) making it a great potential high-temperature thermoelectric. As the second most abundant element in the earth's crust (primarily found in mineral silicates), Si is significantly easier to obtain and cheaper for commercialization than other elements associated with classic thermoelectrics. High mechanical strength and non-toxicity are additional benefits posed by silicon-based thermoelectrics as opposed to their tellurium counterparts.

Despite the numerous merits of silicon, it has one significant drawback when considered for thermoelectric applications—its thermal conductivity. Crystalline silicon is an excellent conductor of heat with lattice thermal conductivity of $\sim 150 \text{ W m}^{-1} \text{ K}^{-1}$ at 300 K which inhibits its thermoelectric efficiency ($zT \sim 0.01$ at 300 K).^{8,56} In the mid-20th century, $\text{Si}_{1-x}\text{Ge}_x$ alloys were studied as an alternative to elemental Si. Germanium is isostructural to silicon and has a narrower bandgap of ~ 0.7 eV. On its own, Ge exhibits thermal conductivity of $\sim 60 \text{ W m}^{-1} \text{ K}^{-1}$ but alloying with Si reduces this value significantly. Nanostructured SiGe alloys can exhibit thermal conductivities of $2\text{--}5 \text{ W m}^{-1} \text{ K}^{-1}$ with zT values exceeding 1 at elevated temperatures.⁵⁷

The ability to form the full solid solution of $\text{Si}_{1-x}\text{Ge}_x$ allowed for methodical studies of the thermoelectric properties of SiGe. In general, SiGe alloys have high electrical conductivity which leads to an enhanced power factor.⁵⁸ The best balance of properties is observed for Si-rich alloys with $\text{Si}_{0.8}\text{Ge}_{0.2}$ and $\text{Si}_{0.7}\text{Ge}_{0.3}$ compositions. These compositions have been the focus of subsequent studies including large crystal growth and properties optimization. While Ge is miscible in Si for the full range of the solid solution, it is challenging to pull large homogenous crystals of alloys due to segregation of the solidus and liquidus curves in the Si-Ge phase diagram.⁵⁹ Despite these challenges, even initial studies of SiGe alloys showed promising efficiency. *Dismukes* et al. first reported the thermoelectric properties of $\text{Si}_{0.7}\text{Ge}_{0.3}$ alloys doped with triels (such as B) or pnictogens (such as P or As). At ~ 1100 K, these materials had zT values of ~ 0.7 and ~ 1.0 for *p*- and *n*-type, respectively.¹²

$\text{Si}_{1-x}\text{Ge}_x$ alloys have been applied for high temperature thermoelectric applications with a maximum operating temperature of 1200–1300 K. Both *p*- and *n*-type materials have been implemented into GPHS (general purpose heat source) RTGs for deep space exploration since the 1970s for missions such as *Voyagers 1* and *2* as well as *New Horizons*. In the late 1990s, PbTe and related materials came into the limelight for use in MM (multi-mission) RTGs and have dominated the application for the first part of the 21st century. However, today, NASA is once again considering SiGe uncouples for implementation in the Next-Generation RTG.⁶⁰ Compared to other candidate materials for RTGs, SiGe alloys have longer lifetimes, are less sensitive to radiation damage, and are more attractive for multi-year deep space exploration missions. By combining modern fabrication methods with decades-old knowledge of SiGe alloys, current researchers aim to design a long-term high performance RTG that could be used on future missions such as the *Interstellar Probe*.⁶⁰

Most studies on bulk samples of SiGe were conducted in the late 1990s. This was followed by several decades of stalemate in terms of enhancement of the thermoelectric performance of these alloys. With emerging technologies in thin films and

nanostructures, significant advances in the research of SiGe alloys have been made. The thermal conductivity of Si is substantially reduced by alloying with Ge such that room temperature κ is $\sim 9 \text{ Wm}^{-1} \text{ K}^{-1}$ for $\text{Si}_{0.8}\text{Ge}_{0.2}$; this value, however, is still quite high for thermoelectrics.⁶¹ Thermal conductivity can be lowered further via nanostructuring and nanoinclusions. Compared to the bulk SiGe alloy found in RTGs, hot-pressed mechanically alloyed SiGe nanopowders showed much improved zT . The presence of randomly oriented polycrystals of varying sizes allowed for increased dissipation of phonons at the grain boundaries while retaining the pristine alloy's notoriously strong electrical conductivity and high power factor at elevated temperatures.⁶² n -type phosphorus-doped $\text{Si}_{0.8}\text{Ge}_{0.2}$ with SiC nanoinclusions was found to exhibit a high $zT \sim 1.7$ at 1173 K, a significant improvement over the SiGe alloys previously employed in space exploration (Fig. 13).⁶³ Future research in SiGe alloys will likely be approached by a combination of multi-element doping, formation of composite materials, and microstructure manipulation.

Classic thermoelectric materials have clearly spanned the three general stages of research—materials discovery, characterization, and properties optimization. For several decades, Bi_2Te_3 and SiGe have dominated low and high-temperature thermoelectric applications, respectively. These compounds exhibit simple crystal structures, are relatively easy to synthesize, and can be manipulated in their bulk, micro-, and nanostructure forms. While they are “well-studied” by the thermoelectrics community, interest in these classic materials is still strong and attempts to enhance their performance are continuously explored. Our understanding of the fundamental relationships between composition, crystal structure, electron and phonon structure, defects, microstructure, and chemical bonding in these well-known materials can guide the exploration of novel thermoelectrics and allude to new optimization strategies.

4.03.4 Equimolar tetrel chalcogenides

Equimolar tetrel chalcogenides, TQ (T : tetrel elements Si, Ge, Sn, or Pb; Q : chalcogen elements S, Se, or Te) are one of the most widely studied materials in the field of thermoelectricity. The fascinating and complex chemistry is the reason for the high thermoelectric performance observed in these materials. They crystallize in different crystal structures which are dictated by the stereochemistry of the electron lone pair and electronegativity of the chalcogen. Rock-salt structures with octahedral $T@Q_6$ building blocks are formed when more electropositive chalcogens are combined with lead or tin with suppressed stereoactivity of the electron lone pair

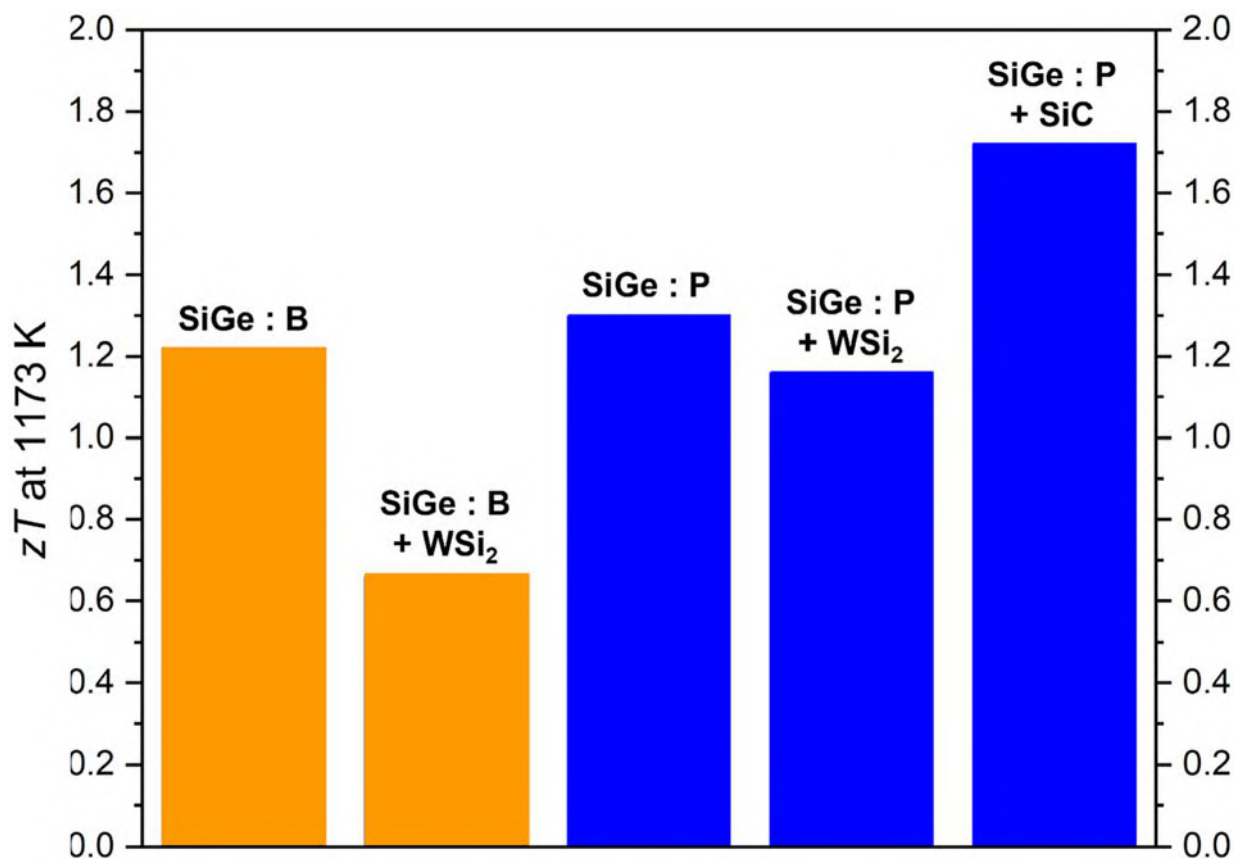


Fig. 13 Summary of zT values for selected SiGe alloys at 1173 K. The orange bars indicate p -type materials, while blue bars correspond to n -type materials. The general notation “SiGe: $X + Y$ ” conveys that the SiGe alloy is doped with X and has nanoinclusions of Y .^{63–66}

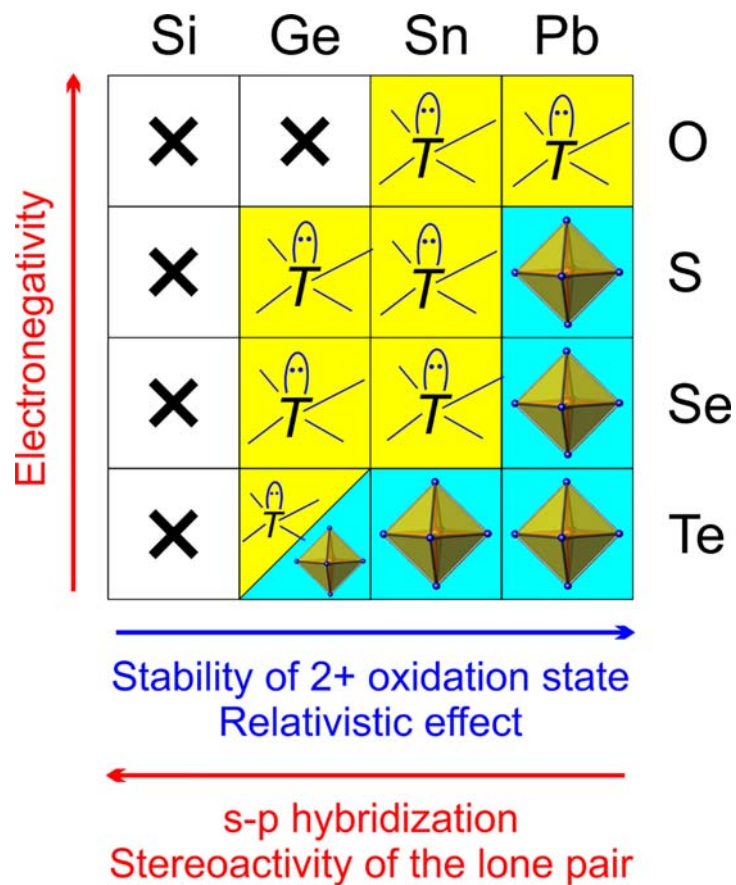


Fig. 14 An overview of the tetrel-centered building blocks in the crystal structures of tetrel monochalcogenides. Regular octahedral environment is achieved only in the cases of the suppressed stereoactivity of the electron lone pair, while distorted local coordination environments are observed for other compositions. Note that, GeO and SiQ monochalcogenides have not been reported, unlike compounds with 4+ oxidation states, such as GeO_2 or SiSe_2 .

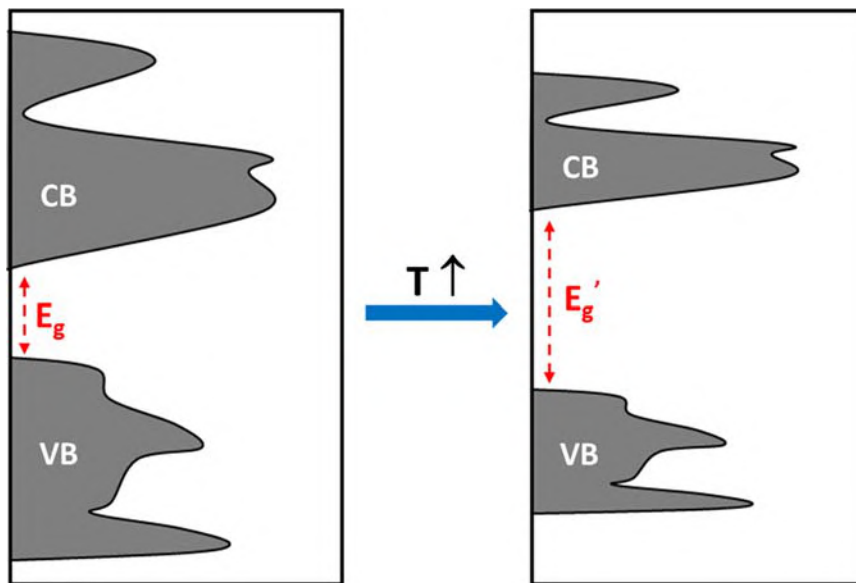


Fig. 15 An increase in the band gap between the valence band and the conduction band is observed with increasing temperature due to the decrease in band dispersion.

due to the relativistic effects and the poor shielding by $4f/5d$ (Pb) or $4d$ (Sn) electrons. When the electronegativity of chalcogen increases, different structures can form with reduced coordination number for the tetrel (Fig. 14).

Unlike most semiconductors, tetrel chalcogenides demonstrate an increase in their bandgap and decrease in their symmetry with increasing temperature. From the perspective of high-temperature thermoelectric applications, lower symmetry decreases band dispersion in these materials which leads to an increased gap between the valence and conduction bands (Fig. 15). This phenomenon can be explained by the existence of the 'inert lone pair' because of relativistic effects and the ineffective shielding by core d/f electrons for heavy elements such as Pb and Sn.⁶⁷ Two types of environments are possible in octahedral TQ_6 coordination: (i) the lone pair being 'quenched', resulting in a perfect octahedral environment, or (ii) the lone pair being stereo-active and expressed, violating the overall octahedral symmetry and sometimes leading to much lower coordination numbers (Fig. 16). Valence s orbitals of the tetrel contribute near the Fermi level, and changing the coordination environment in the structure can have significant impacts on the bandgap.

The thermoelectric performance of equimolar tetrel chalcogenides is enhanced with temperature in several ways. As band gap increases with increasing temperature, bipolar conduction reduces and band convergence takes place which enhances the Seebeck coefficient. For cubic NaCl-type structures, states originating from the suppressed valence s^2 -lone pair shift the valence band to the L point in the Brillouin zone, with predominantly s -like characteristics. The resulting direct band gap at the L-point, which has high valley degeneracy (N_v), improves the thermoelectric quality factor, and the Seebeck coefficient. Lead chalcogenides (PbQ) exhibit high N_v in the valence band, which can drastically improve the properties for doped p -type materials. Band convergence with increasing temperatures can further increase the effective N_v resulting in an enhanced zT . Doping with more ionic elements can increase the band gap and band convergence, such as in Sr- or Mg-doped PbTe.^{28,36,68-71} Besides the above-mentioned factors, thermal conductivity also has a significant contribution to the overall thermoelectric performance of these TQ materials. Heavier elements and the structural distortion due to the s^2 -lone pair result in substantial reduction of lattice thermal conductivity.²⁸

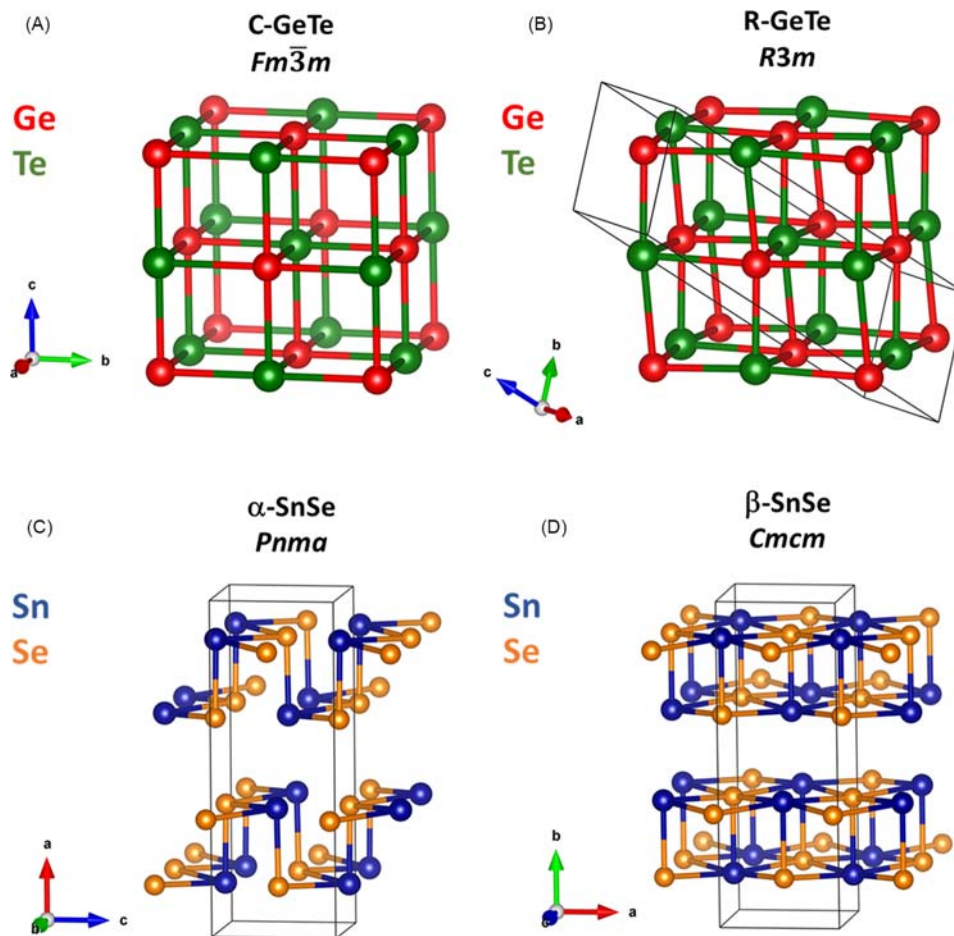


Fig. 16 A few common crystal structure types of equimolar tetrel chalcogenides (A) cubic $Fm\bar{3}m$ rock-salt type which is the most common structure type for TQ materials; (B) rhombohedral $R3m$ structure type, on the example of GeTe; (C) room temperature orthorhombic $Pnma$ structure of α -SnSe; (D) high temperature orthorhombic $Cmcm$ structure of β -SnSe.

For the sake of simplicity, the following discussion will begin with the tetrel chalcogenides with the simplest structures and build to more complex ones.

4.03.4.1 PbTe

PbTe is the top performing thermoelectric material for this class of compounds in the elevated temperature range of 500–900 K. It crystallizes in NaCl structure-type, in cubic $Fm\bar{3}m$ space group and is an n -type semiconductor. As discussed above, the presence of the heavy ligand Te and the strong relativistic effect of Pb help quench the $6s^2$ -lone pair, making the structure highly symmetric with each atom coordinated in a regular octahedral manner. As a result of band convergence at elevated temperatures, the thermoelectric performance of PbTe-based materials improves at higher temperatures. For example, the energy difference between the two VB's at L- and Σ -points are in the range of 0.15–0.20 eV at 300 K. Due to such close lying VB's, band engineering via doping has been explored to enhance the degeneracy. In $\text{PbTe}_{1-x}\text{Se}_x$ alloys, doping leads to the convergence of at least 12 valleys and results in a high zT of 1.8 at 850 K.²⁰

Complex nanostructuring in PbTe has led to both band convergence and the introduction of point defects which can simultaneously increase thermopower and decrease lattice thermal conductivity, respectively. Co-doping of PbTe with SrTe and Na introduces nanostructural inclusions (SrTe) and point defects (Na). The material PbTe -(4 mol% SrTe)-(2 mol% Na) exhibits low κ_{lattice} of $0.5 \text{ Wm}^{-1} \text{ K}^{-1}$ at 850 K and an ultra-high zT of 2.2 at 913 K. Although the thermodynamic solubility limit of SrTe in PbTe is < 1 mol%, non-equilibrium processes were explored to help extend SrTe solubility. As a result, hole-doped PbTe -(8% SrTe) demonstrated a widened band gap and band convergence, resulting in an improved power factor ($S^2\sigma$) of $30 \mu\text{Wcm}^{-1} \text{ K}^{-2}$ at 500 K. Endotaxial SrTe nanostructures helped lower κ_{lattice} to $0.5 \text{ Wm}^{-1} \text{ K}^{-1}$ at 950 K. A maximum zT of 2.5 at 923 K was observed for hole-doped PbTe -8% SrTe.⁷² Another example of a co-doped PbTe-based material is $\text{Na}_{0.03}\text{Eu}_{0.03}\text{Sn}_{0.02}\text{Pb}_{0.92}\text{Te}$ in which a significant reduction of κ_{lattice} was observed without any reduction in carrier mobility. The introduction of stable lattice dislocations led to a low κ_{lattice} of $0.5 \text{ Wm}^{-1} \text{ K}^{-1}$ at 850 K and a high zT of 2.57 at 850 K.⁷³

4.03.4.2 PbSe

PbSe is a less popular candidate for thermoelectric studies in this group of materials, generally due to its low valley degeneracy. PbSe crystallizes in cubic $Fm\bar{3}m$ space group and is a low-cost n -type material to synthesize. Resonant level engineering has been reported for Al-doped PbSe, where an ultra-high power factor of $2030 \mu\text{Wcm}^{-1} \text{ K}^{-2}$ was reported with 2% Al-doping and a high zT of 1.3 at 850 K was reported with 1% Al-doping.⁷⁴ Increased band effective mass was obtained in 1% Mo-doped PbSe, with a peak power factor of $3300 \mu\text{Wcm}^{-1} \text{ K}^{-2}$ and a peak zT of 0.5 at 673 K.⁷⁵ In the composite PbSe-SiO_2 , boundary scattering resulted in a low κ_{lattice} of $0.6 \text{ Wm}^{-1} \text{ K}^{-1}$ at 600 K.⁷⁶ One of the most interesting examples of PbSe-based materials with ultra-low κ_{lattice} is $\text{Pb}_{0.95}(\text{Sb}_{0.033}\square_{0.017})\text{Se}_{1-y}\text{Te}_y$, where a combination of vacancy-driven dense dislocations, point defects, nanoprecipitates of different sizes, and mass fluctuations are considered to be the reasons for the ultra-low lattice thermal conductivity of $0.4 \text{ Wm}^{-1} \text{ K}^{-1}$.⁷⁷

4.03.4.3 GeTe

At low temperatures, pristine GeTe crystallizes in a rhombohedral $R\bar{3}m$ space group with a distorted rock-salt structure (Fig. 16). Rhombohedral GeTe converts to the more symmetric cubic rock-salt structure at ~ 700 K. Cubic GeTe (c -GeTe) exhibits better thermoelectric behavior than its rhombohedral (r -GeTe) counterpart.

GeTe as a p -type material usually has a very high carrier concentration $\sim 10^{21} \text{ cm}^{-3}$ which inhibits achieving superior thermoelectric properties. But high band degeneracy and strong band anisotropy result in a high hole effective mass which helps achieve a high power factor. c -GeTe has a higher band degeneracy than r -GeTe due to the lower energy gap, ΔE , between multiple valence band maxima in the cubic phase. The cubic phase is a direct gap semiconductor while the rhombohedral phase is an indirect gap semiconductor. The large bandgap in the cubic phase reduces the bipolar conduction which adversely affects thermopower at high temperatures. On the other hand, strong anharmonicity and large acoustic-optical phonon scattering lend to low lattice thermal conductivity in GeTe, especially for the cubic phase.

Despite the above-mentioned properties, pristine GeTe has a peak thermoelectric figure of merit of less than 1. To achieve a higher zT in robust, stable GeTe-based materials, recent research has focused on bringing the structural transition temperature down, reducing carrier concentration, introducing phonon scattering, and increasing band degeneracy by means of doping and alloying.⁷⁸ Doping of GeTe can result in significant improvements in the properties compared to the pristine material. Doping with elements that lack an s^2 -lone pair at the cationic site can decrease the energy difference between multiple VB maxima. However, a group 15 dopant (pnictogens) on the cationic site can decrease the carrier concentration as well. Two such materials, $\text{Ge}_{1-x}\text{Sb}_{2x/3}\text{Te}$ and $\text{Ge}_{1-x}y\text{Bi}_x\text{Cu}_y\text{Te}$, have been found so far with significantly reduced carrier concentrations; the latter having the lowest observed carrier concentration ($5.8 \times 10^{19} \text{ cm}^{-3}$) reported so far for any GeTe-based material.^{79,80}

Band engineering has been attempted on GeTe in various ways. Doping with Zn or Cd improves the thermopower due to band convergence. As stated before, ΔE decreases with using dopants that are devoid of valence s^2 -lone pair. Some examples of such materials are $\text{Ge}_{1-x}\text{Cd}_x\text{Te}$, $\text{Ge}_{1-x}y\text{Sb}_x\text{Zn}_y\text{Te}$, and $\text{Ge}_{1-x}y\text{Cd}_x\text{Bi}_y\text{Te}$. DOS distortion has been reported by resonant level doping, such as in

$\text{Ge}_{63}\text{InTe}_{64}$ and $\text{Ge}_{1-x}\text{Sb}_x\text{In}_y\text{Te}$, which improves the overall thermopower. Reduction of symmetry can also induce a higher band degeneracy.⁸¹

In addition to the above-mentioned techniques, the common practice of enhancing phonon scattering has been studied in GeTe materials. Alloying GeTe with Sb can reduce phonon group velocity and lower lattice thermal conductivity. GeTe can also have vacancies that enhance phonon scattering. Introducing planar vacancies can scatter mid-frequency phonons while Ge-vacancies and alloy scattering can perturb high-frequency phonons. $\text{Ge}_{0.9}\text{Sb}_{0.1}\text{Te}_{0.86}\text{Se}_{0.14}$ has a low κ_{lattice} of $0.5 \text{ Wm}^{-1} \text{ K}^{-1}$ because of point defect scattering induced by Sb and Se-alloying.⁸² Formation of sub-microfeatures and interfaces in $\text{Ge}_{0.87}\text{Pb}_{0.13}\text{Te}$ cause yields a low lattice contribution to thermal conductivity of $0.4 \text{ Wm}^{-1} \text{ K}^{-1}$ at 423 K, while the emergence of dense planar vacancies in $\text{GeCd}_{0.05}\text{Bi}_{0.05}\text{Te}$ can lead to a κ_{lattice} of $0.4 \text{ Wm}^{-1} \text{ K}^{-1}$ at 650 K.^{83,84} The lowest recorded κ_{lattice} for any GeTe-based material is $0.2 \text{ Wm}^{-1} \text{ K}^{-1}$ at 800 K for $\text{Ge}_{0.86}\text{Mn}_{0.1}\text{Sb}_{0.04}\text{Te}$.⁸⁵ A combination of regular and twin grain boundaries, point defects created by Ge-vacancies and Sb/Mn-doping, low phonon group velocity, and the emergence of dislocations is believed to be the reason for the ultra-low thermal conductivity. Scanning electron microscopy (SEM) can be used to detect further reasons for phonon scattering. The appearance of nanoprecipitates, multigrain features and high-density stripes were detected on $\text{Ge}_{0.89}\text{Sb}_{0.1}\text{In}_{0.01}\text{Te}$ pellets, causing a reduction in κ_{lattice} . Transmission electron microscopy (TEM) studies carried out on $\text{Ge}_{1-x}\text{Cd}_x\text{Bi}_y\text{Te}$ pellets have also established the presence of an array of planar vacancies.⁸⁴

Besides having a high average zT , thermoelectric materials must be stable and robust for practical applications, like GeTe. Some GeTe-based materials have been reported to achieve promising efficiencies for potential practical usage. Thermoelectric generators with $\text{Ge}_{0.87}\text{Pb}_{0.13}\text{Te}$ as a p -type material exhibited a 14% conversion at 723 K. p -type $\text{Ge}_{0.9}\text{Sb}_{0.1}\text{Te}$ and n -type $(\text{Pb}_{0.95}\text{Sn}_{0.05}\text{Te})_{0.92}(\text{PbS})_{0.08}$ can be coupled and reach 12% conversion at 700 K. p -type $\text{Ge}_{0.87}\text{Pb}_{0.13}\text{Te}$ can be coupled with PbTe-based n -type sides to reach an efficiency of 11.5% at 773 K.⁷⁸

4.03.4.4 SnSe

In SnSe the stereoactivity of the $5s^2$ electron lone pair is present. Unique structural transitions have been noted for SnSe. At low temperatures, it crystallizes in the orthorhombic $Pnma$ space group where Sn is essentially three coordinated (Fig. 16C). This form, termed as α -SnSe, converts to orthorhombic $Cmcm$ β -SnSe around 600 K. In the latter structure, Se atoms form square pyramid around Sn atoms (Fig. 16D). This phase transition has been confirmed by diffraction and electron microscopy studies for both single crystalline and polycrystalline doped and undoped SnSe samples. For polycrystalline $\text{Sn}_{0.98}\text{Se}$ samples, the phase transition is continuous from 573 K to 843 K, with a peak zT of 1.4 being observed at 823 K. α -SnSe (0.92 eV) has a larger band gap than β -SnSe (0.28 eV). The enhanced power factor in SnSe materials can be attributed to the presence of multi-valley valence bands. As a result, a peak zT of 1.37 for pristine polycrystalline SnSe was recorded at 823 K. Thus, recent thermoelectric research has focused on employing band convergence in SnSe to increase carrier mobility while retaining high thermopower.⁶⁸

Another unique intrinsic feature of the SnSe structure is the presence of strong anharmonic bonding which leads to unbalanced phonon transmission and increased phonon-phonon scattering which contributes to the ultra-low lattice thermal conductivity. This intrinsically low lattice thermal conductivity has led to exceptional zT values in single crystalline SnSe. Direction-dependent transport properties on single crystals reveal outstanding zT values of 2.6 ± 0.3 along the b -axis and 2.3 ± 0.3 along the c -axis, while only a moderate zT of 0.8 ± 0.2 was obtained along the a -axis.⁸⁶

Further studies were focused on the polycrystalline samples. Lower formation energy of tin vacancies (V_{Sn}) than that of selenium vacancies (V_{Se}) explains the p -type behavior in SnSe. Since vacancies can influence the band gap of a material, zT can be engineered by manipulating the carrier concentration which can consequently change the formation energies of Sn and Se vacancies. In $\text{Sn}_{0.948}\text{Cd}_{0.023}\text{Se}$, Cd-doping results in 2.9% cation vacancies; this reduces the formation energy of V_{Sn} enabling a peak zT of 1.7 with a hole concentration of $2.6 \times 10^{19} \text{ cm}^{-3}$. On the other hand, the high V_{Se} of 2.0% in $\text{SnSe}_{0.96}\text{Sb}_{0.02}$ leads to a carrier concentration of $3.9 \times 10^{19} \text{ cm}^{-3}$ and a peak zT of 1.1 at 773 K. In $\text{Sn}_{0.95}\text{Se}$ (with 5% V_{Sn}), a combination of higher hole carriers, enhanced power factor, and reduced lattice thermal conductivity by lattice distortions leads to a zT of 2.1 at 873 K. Doping with heteroatoms such as Na can move the Fermi level closer to the valence band, turning SnSe into a p -type degenerate semiconductor. This also flattens the VB maximum and thus provides extra holes which increases electrical conductivity. In $\text{Sn}_{0.985}\text{Na}_{0.015}\text{Se}$, interstitial atoms help scatter phonons which, combined with a high power factor of $15 \mu\text{W cm}^{-1} \text{ K}^{-2}$, can lead to a zT of 2.0 at 773 K. Lattice distortions due to the presence of heteroatoms such as 2% Te-alloying in $\text{Sn}_{0.98}\text{Na}_{0.02}\text{Se}$ leads to a high $zT > 2$ at 723 K, due to enhanced $S^2\sigma$ and reduced κ_{lattice} .^{87–89}

In $\text{SnSe}_{0.9}\text{Br}_{0.1}$, the introduction of edge-dislocations reduces κ_{lattice} and helps achieve a zT of 1.3 at 773 K.⁹⁰ The introduction of heterojunctions as phase boundaries at the interfaces of dominant and secondary phases can scatter phonons and lower lattice thermal conductivity. This has been observed in the $\text{SnSe-Ag}_8\text{SnSe}_6$ alloy with high-resolution TEM in which the presence of distortions, dislocations, and stacking faults lowered κ_{lattice} and helped increase zT to 1.33 at 773 K.⁹¹ Nano-inclusions in the form of nano-precipitates and nano-pores can reduce κ_{lattice} to enhance zT . For example, the introduction of SnSe_2 microdomains in SnSe nanoparticles lowered the total thermal conductivity to $0.54 \text{ Wm}^{-1} \text{ K}^{-1}$ and yielded an ultra-high zT of 2.2 at 773 K.⁹² The introduction of nanopores can work in a similar way although it may hamper the power factor such as in bulk polycrystalline SnSe-1.0 wt% LaCl_3 , where κ is reduced to $0.3 \text{ Wm}^{-1} \text{ K}^{-1}$ and the highest zT achieved is 0.55 at 750 K.⁹³

The synthesis of nanocrystals of SnSe in solution has been explored heavily in recent years, where quantum confinement can lead to an enlargement of the band gap (up to ~ 2.8 eV) and nanostructures can lead to more grain boundaries than in bulk SnSe, which helps lower lattice thermal conductivity. Heavily Cu-doped nanobelts of SnSe achieved a high $S^2\sigma$ of $5.57 \mu\text{Wcm}^{-1} \text{ K}^{-2}$, low κ of

$0.32 \text{ Wm}^{-1} \text{ K}^{-1}$, and zT of 1.41 at 823 K.⁹⁴ Nanosheets are also suitable for fabrication of 2D flexible thermoelectric materials. SnSe nanosheets/PEDOT:PSS hybrid films incorporating 20% SnSe can reach a peak zT of 0.32 at room temperature.⁹⁵

One of the biggest drawbacks in polycrystalline SnSe is the occurrence of fast surface oxidation, resulting in moderate zT values, in contrast to the single crystals of SnSe discussed before. Surface oxidation leads to both higher resistivity and thermal conductivity. Recently, hole-doped polycrystalline SnSe reduced under a hydrogen atmosphere exhibited an extraordinary peak zT of 3.1 at 783 K, overtaking the previous record held by single crystalline SnSe.⁹⁶

While tin monoselenide (SnSe) is popular material in current thermoelectrics research, it is also important to mention layered SnSe₂, which can be synthesized in the solution phase, and is also a decent thermoelectric material. An in-plane zT of 0.63 at 673 K can be achieved in pellets of 1.5% Cu-doped SnSe_{1.95} nanoplates.⁹⁷ Overall, SnSe materials are one of the most promising materials in the field of thermoelectrics and have been subject to numerous optimizations in recent years.

4.03.4.5 SnTe

Like SnSe, SnTe is also a promising material in the field of thermoelectrics and has been explored a lot in recent years. SnTe has three different polymorphs: (i) rhombohedral $R3m$ α -SnTe which is a very low-temperature phase that exists below 100 K, (ii) cubic $Fm\bar{3}m$ β -SnTe which is the most stable form and exists above 100 K, and (iii) orthorhombic $Pnma$ γ -SnTe which is formed by applying > 18 kbar pressure to β -SnTe. As β -SnTe is the most stable form under ambient pressure and in a wide temperature range, it is the most studied phase for thermoelectric properties. β -SnTe is a direct gap semiconductor with a band gap of 0.18 eV at the L-point in the Brillouin zone.⁷⁰

Like SnSe, the abundance of V_{Sn} makes pristine SnTe a p -type material with a high carrier concentration of 10^{20} – 10^{21} cm^{-3} which leads to high σ but low S at room temperature. Thus, one of the main focuses in SnTe research has been optimizing its carrier concentration. In iodine doped SnTe_{0.985}I_{0.015}, a peak zT of 0.6 (twice that of pristine SnTe) was obtained due to the lower carrier concentration of $4 \times 10^{19} \text{ cm}^{-3}$.⁹⁸

Several attempts at band engineering have been carried out on SnTe to enhance electronic behavior. Mg-doping in Sn_{0.95}Mg_{0.08}Te increases the carrier effective mass and increased thermopower to $200 \mu\text{VK}^{-1}$, compared to $10 \mu\text{VK}^{-1}$ for Sn_{1.03}Te at 856 K.⁹⁹ Valence band convergence and increasing the carrier effective mass were carried out by doping SnTe with Mn to form Sn_{0.93}Mn_{0.04}Te; the Seebeck in this material reaches $270 \mu\text{VK}^{-1}$ at 873 K. The energy difference between VB maxima drops to as low as 0.13 eV due to Mn-doping.¹⁰⁰ Resonance energy level engineering was reported in In_{0.0025}Sn_{0.9975}Te where In-doping resulted in an increase in DOS near the Fermi level. This enabled a peak $S^2\sigma$ of $20.3 \mu\text{Wcm}^{-1} \text{ K}^{-2}$ and peak zT of 1.1 at 873 K. The synergistic effect combines resonance energy level doping and VB maxima convergence. Applying this to In/Cd co-doped SnTe yielded a peak S of $200 \mu\text{VK}^{-1}$ and a peak zT of 1.4 at 823 K. In/Mg co-doping have a similar effect achieving a peak power factor of $42 \mu\text{Wcm}^{-1} \text{ K}^{-2}$ and a peak zT of 1.5 at 840 K.^{100,101}

Reduction of lattice thermal conductivity by various means have also been reported for SnTe. Point defect scattering has been observed in SnTe-Cu₂Te alloys; an ultra-low κ_{lattice} of $0.5 \text{ Wm}^{-1} \text{ K}^{-1}$ and maximum zT of > 1 at 850 K were found in Sn_{0.94}Cu_{0.12}Te. Formation of nanoprecipitates of 5% SrTe in Sn_{0.97}Bi_{0.03}Te can help achieve low κ_{lattice} values of $0.7 \text{ Wm}^{-1} \text{ K}^{-1}$ at 823 K, while 3% SrTe nanoprecipitates in Sn_{0.97}Bi_{0.03}Te improve the zT to 1.2 at 823 K.^{102,103}

In conclusion, SnTe has been a moderately popular candidate among tetrel chalcogenides for thermoelectric applications. One of the best SnTe-based candidates is Ca/In co-doped SnTe with 5% Cu₂Te alloying that has been reported to have a high zT of 1.85 at 823 K. This high performance is achieved as a result of the presence of grain boundaries, dense dislocations, and the synergistic effect.¹⁰⁴

4.03.4.6 GeSe

Like PbSe, GeSe has been explored to a lesser extent due to its moderate thermoelectric performance. Under ambient conditions, GeSe crystallizes in orthorhombic $Pnma$ which is isostructural to α -SnSe. However, owing to a large band gap and strong covalent bonding, pristine GeSe has a low zT of 0.2.¹⁰⁵ GeSe can also exist in the rhombohedral $R3m$ space group. With the application of temperature and pressure, the rhombohedral phase can be transformed into the cubic $Fm\bar{3}m$ polymorph. The different polymorphs of GeSe exhibit drastically different solubility of the dopants. The rhombohedral phase is more intriguing in terms of thermoelectric properties due to much smaller band gap. The best performing GeSe-based thermoelectric material is p -type (GeSe)_{0.9}(AgBiTe₂)_{0.1} with a reported zT of 1.35 at 627 K. Band convergence in this material results in an elevated power factor of $12.8 \mu\text{Wcm}^{-1} \text{ K}^{-2}$. The presence of soft optical phonons results in an ultra-low κ_{lattice} of $0.38 \text{ Wm}^{-1} \text{ K}^{-1}$ at 578 K.¹⁰⁶

4.03.4.7 Complex tetrel chalcogenide thermoelectric materials

In addition to having a high thermoelectric figure-of-merit, a material needs to have long durability, high elastic modulus, and low toxicity for practical applications. Most high-performing thermoelectric materials are restricted by the drawbacks arising from one or more of these parameters. Thus, it has been extremely important in this research area to select prospective candidates for commercial applications based on practicality as well as thermoelectric performance.

One of the most widely used thermoelectric materials has been the $(\text{GeTe})_x(\text{AgSbTe}_2)_{100-x}$ solid solution, which is commonly referred to as TAGS- x (abbreviating Tellurium—Antimony—Germanium—Silver with x being the percentage of GeTe in the alloy). TAGS- x is used as the p -type leg in MMRTGs for deep space missions.¹⁰⁷ In these alloys, the band structure of GeTe is manipulated by doping with AgSbTe₂, where the concentration of AgSbTe₂ results in varying degrees of band engineering, while simultaneously introducing a microstructure that reduces lattice thermal conductivity to realize high thermopower and zT . AgSbTe₂ exhibits the rock-salt type $Fm\bar{3}m$ structure at room temperature, while GeTe exhibits the rhombohedral $R\bar{3}m$ structure and undergoes a phase transition to cubic $Fm\bar{3}m$ above 700 K, as mentioned in Section 4.03.4.3. TAGS alloys retain the rhombohedral structure of GeTe at room temperature and TAGS- x alloys with $x \geq 80$ show phase transition behavior like GeTe at high temperatures. The cubic and rhombohedral phases of TAGS alloys are isostructural to the ones depicted in Fig. 16A and B.

One of the most explored TAGS alloys is TAGS-85 which has been reported to show a peak zT of 1.5 at 720 K.¹⁰⁸ Self-doping by optimizing the Ag:Sb ratio in TAGS-80 can optimize the carrier concentration. A peak zT of 1.8 at 700 K has been reported for $(\text{Ge}_{0.97}\text{Sb}_{0.03}\text{Te})_{0.8}[(\text{Ag}_2\text{Te})_{0.4}(\text{Sb}_2\text{Te}_3)_{0.6}]_{0.2}$ where the Ag:Sb ratio was modified to 2:3.¹⁰⁷ The introduction of rare-earth elements with localized magnetic moments site can introduce resonant states around Fermi level. Such an example is 1% Yb doped TAGS-85 where an increase in Seebeck coefficient raises the peak zT up to 1.8 at 730 K.¹⁰⁹ Thermoelectric devices with PbTe as the n -type leg and TAGS as the p -type leg have been used in MMRTGs for power generation on the Mars Perseverance Rover by NASA in 2020 (Fig. 2). While this PbTe/TAGS thermoelectric couple has been reliably employed in MMRTGs for several NASA missions, at the same time a continuous search for higher performance materials is underway.

Tetrel chalcogenides have been one of the most promising groups of materials in thermoelectric research, possessing high figure-of-merits at elevated temperatures. The widespread focus on band engineering, phonon scattering, doping, optimization of carrier concentration, and tuning effective mass has led to ever-improving zT values for materials based on this class of compounds. Fig. 17 shows the peak zT values of selected materials based on PbTe, GeTe, SnSe, and SnTe in recent years. Due to simplicity of equimolar tetrel chalcogenide crystal structures and the presence of only two elements in the parent phase, the effects of dopants on the electronic structure can be relatively well-estimated using a combination of experimental and computational methods. The differing chemical nature of the dopants (such as Na, Sr, Sb, Cu, and Ag) as compared to the tetrel or chalcogen is expected to alter the local bonding in the crystal structure or lead to phase segregation and the formation of nanoprecipitates. While the latter case can be probed with electron microscopy, small perturbations of the local structure are often ignored, and optimal dopants are found serendipitously. Local probes, such as HRTEM, extended X-ray absorption fine structure (EXAFS) spectroscopy, and total scattering

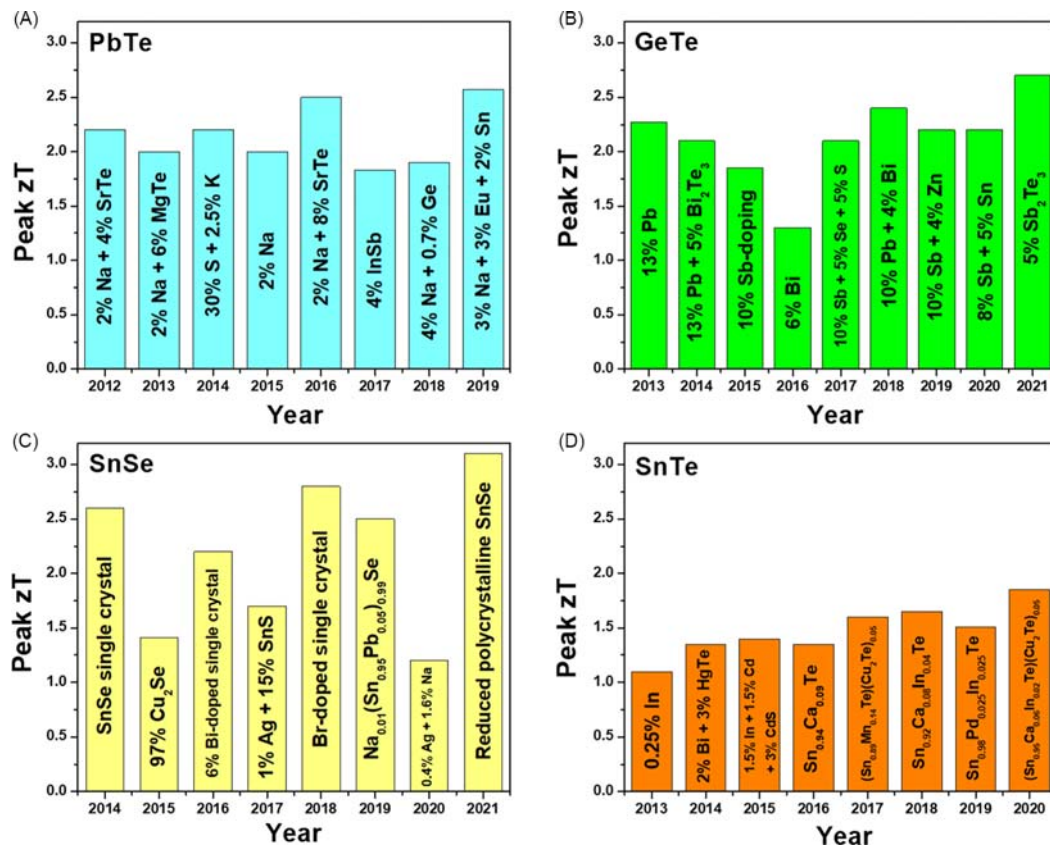


Fig. 17 Peak zT values for TQ thermoelectric materials based on (A) PbTe, (B) GeTe, (C) SnSe, and (D) SnTe.

	1	2	3	4	5	6	7	8	9	10	11	12	13	14	15	16	17	18
1	H																	He
2	Li	Be											B	C	N	O	F	Ne
3	Na	Mg											Al	Si	P	S	Cl	Ar
4	K	Ca	Sc	Ti	V	Cr	Mn	Fe	Co	Ni	Cu	Zn	Ga	Ge	As	Se	Br	Kr
5	Rb	Sr	Y	Zr	Nb	Mo	Tc	Ru	Rh	Pd	Ag	Cd	In	Sn	Sb	Te	I	Xe
6	Cs	Ba	57-71	Hf	Ta	W	Re	Os	Ir	Pt	Au	Hg	Tl	Pb	Bi	Po	At	Rn
7	Fr	Ra	89-103	Rf	Db	Sg	Bh	Hs	Mt	Ds	Rg	Cn	Nh	Fl	Mc	Lv	Ts	Og
			6	La	Ce	Pr	Nd	Pm	Sm	Eu	Gd	Tb	Dy	Ho	Er	Tm	Yb	Lu
			7	Ac	Th	Pa	U	Np	Pu	Am	Cm	Bk	Cf	Es	Fm	Md	No	Lr

Fig. 18 A summary of commonly used elements in the thermoelectric community, excluding dopant elements which are present in thermoelectrics in small quantities. The orange color indicates the cationic role of the element, while the blue color indicates the anionic role of the element. Mg is the only element located on the left side of the periodic table which plays a dual role.

methods are crucial to understand the local structure around dopant elements and perform composition optimization in the more rational way.

4.03.5 Mg-containing thermoelectric materials

The first question encountered upon designing new thermoelectric materials is “which elements should I start with?” The elements commonly used in the thermoelectric community are presented in Fig. 18.

Thermoelectric materials should simultaneously demonstrate low thermal conductivity and high electrical conductivity. To suppress thermal conductivity, heavy elements located in the right bottom corner of the periodic table are preferred, such as tellurium, antimony, lead, bismuth, etc. Low thermal conductivity is not enough, as a “simple and tunable electronic structure” is another criterion that must meet. This requirement is crucial since most thermoelectric materials require various strategies to achieve a good balance between thermal and charge transport properties.^{14,29,35,38,110} Translating these criteria into chemistry language would mean selecting an element or a combination of elements. Magnesium is a dual-role element able to serve as cation or as covalent metal which forms directed bonds with extremely flexible coordination environments.¹¹¹ Such Janus-like properties makes Mg a good choice for designing thermoelectric materials from the point-of-view of the “simple and tunable electronic structure” requirement. In this part, selected Mg-containing thermoelectric materials are discussed, including Mg₂Si, Mg₃Sb₂, α -MgAgSb, and Yb₁₄MgSb₁₁. The thermoelectric properties of these Mg-containing thermoelectrics and their structure-property relationships are summarized. The highest reported zT of Mg-containing thermoelectric materials are summarized in Fig. 19.

4.03.5.1 Mg₂Si

Mg₂Si was selected as the first example due to its simple crystal structure (Fig. 20A). Mg₂Si crystallizes in the anti-CaF₂-structure, where Si atoms construct a FCC (face-centered cubic) lattice with all tetrahedral voids filled by Mg atoms. Mg and Si atoms occupy $8c$ ($\frac{1}{4};\frac{1}{4};\frac{1}{4}$) and $4a$ (0;0;0) sites, respectively, with 100% occupancy. Each Si is surrounded by cube made of eight Mg atoms. The coordination number of fully occupied Mg is four, which constructs a tetrahedron. There is an additional interstitial site $4b$ ($\frac{1}{2};\frac{1}{2};\frac{1}{2}$) which is partially occupied by Mg atoms with an occupancy of $\sim 10\%$, as shown in Fig. 20B. The interstitial Mg atoms are in the center of a Si₆ octahedron. These interstitial Mg atoms play a dominant role in controlling the major carrier type in Mg₂Si and affects the thermoelectric properties.¹¹⁸

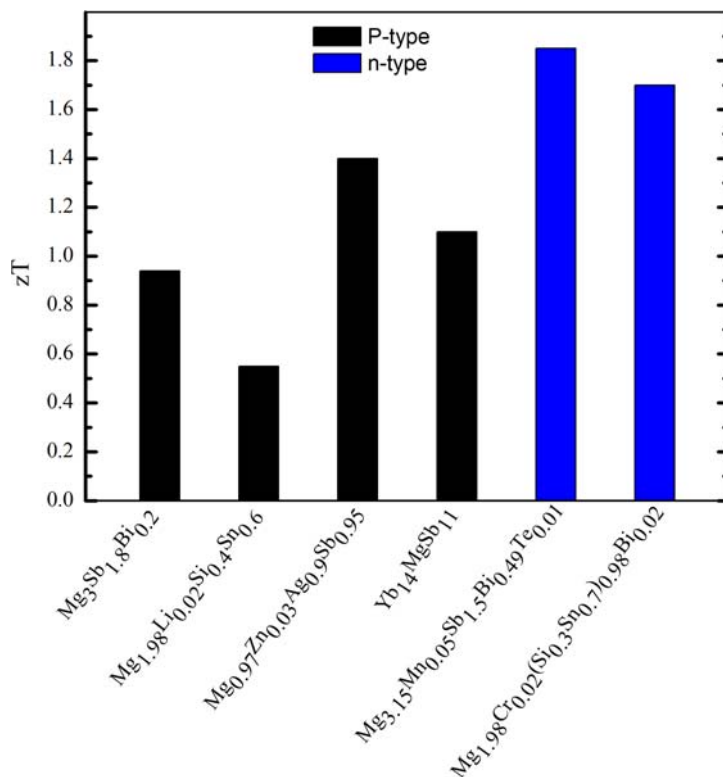


Fig. 19 The highest reported zT values of selected Mg-containing thermoelectric materials. $\text{Mg}_3\text{Sb}_{1.8}\text{Bi}_{0.2}$,¹¹² $\text{Mg}_{3.15}\text{Mn}_{0.05}\text{Sb}_{1.5}\text{Bi}_{0.49}\text{Te}_{0.01}$,¹¹³ $\text{Mg}_{1.98}\text{Cr}_{0.02}(\text{Si}_{0.3}\text{Sn}_{0.7})_{0.98}\text{Bi}_{0.02}$,¹¹⁴ $\text{Mg}_{1.98}\text{Li}_{0.02}\text{Si}_{0.4}\text{Sn}_{0.6}$,¹¹⁵ $\text{Mg}_{0.97}\text{Zn}_{0.03}\text{Ag}_{0.9}\text{Sb}_{0.95}$,¹¹⁶ $\text{Yb}_{14}\text{MgSb}_{11}$.¹¹⁷

One reason that Mg_2Si attracts the attention of the thermoelectric community is its cost-effectiveness and non-toxic constituent elements. When abundant terrestrial applications are considered, the cost of the constituent elements and processing becomes a dominant factor for industry to decide on the type of thermoelectric material to use. Moreover, Mg_2Si exhibits excellent transport properties which combine a high Seebeck coefficient and good electrical conductivity. A disadvantage comes from the high thermal conductivity, which is expected for a simple crystal structure composed of the light elements, Mg and Si. Hence many efforts have been focused on substituting Si with heavier Ge or Sn to reduce thermal conductivity.^{119–121} Due to the presence of interstitial Mg atoms, Mg_2Si can be tuned to be an n -type material. As shown in Fig. 19, the zT of n -type Cr- and Bi-doped and Sn-substituted Mg_2Si [$\text{Mg}_{1.98}\text{Cr}_{0.02}(\text{Si}_{0.3}\text{Sn}_{0.7})_{0.98}\text{Bi}_{0.02}$] is 1.7 at 680 K.¹¹⁴ This is about two times higher than the highest values achieved for p -type Mg_2Si ($\text{Mg}_{1.98}\text{Li}_{0.02}\text{Si}_{0.4}\text{Sn}_{0.6}$, $zT = 0.7$ at 780 K).¹¹⁵ Other effective dopants are heavier Sb and Bi, which would play a dual-role of reducing lattice thermal conductivity and enhancing the electron concentration given the additional valence electron compared to that of Si.^{122,123} A few examples such as $\text{Mg}_{2.08}\text{Si}_{0.364}\text{Sn}_{0.6}\text{Sb}_{0.036}$ ¹²⁰ and $\text{Mg}_{2.08}\text{Si}_{0.37}\text{Sn}_{0.6}\text{Bi}_{0.03}$,¹¹⁹ have demonstrated zT values of 1.55 at 773 K and 1.5 at 716 K, respectively. For n -type Mg_2Si , the substitution of Mg by other elements is not as common as the

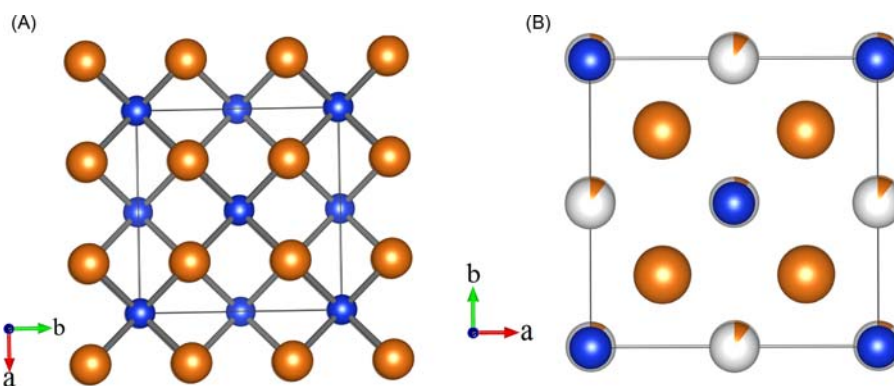


Fig. 20 (A) Idealized crystal structure of Mg_2Si without interstitial Mg atoms viewed along $[001]$ direction. (B) Crystal structure of Mg_2Si viewed along $[001]$ direction with the interstitial Mg atoms shown. Mg: orange, Sb: blue.

replacement of Si atoms. *p*-type Mg_2Si -based thermoelectric materials are heavily underdeveloped. To shift the major carrier type of Mg_2Si from electrons to holes, monovalent metals should be selected to substitute divalent Mg. The ionic size of Mg^{2+} is 0.72 Å, which is comparable to Li^+ of 0.76 Å.^{124,125} A few Li-doped compounds including $\text{Mg}_{1.98}\text{Li}_{0.02}\text{Si}_{0.4}\text{Sn}_{0.6}$ ¹²⁶ and $\text{Mg}_2\text{Li}_{0.025}\text{Si}_{0.4}\text{Sn}_{0.6}$ ¹¹⁵ have been reported so far. The former compound exhibits promising performance with $zT = 0.55$ at 700 K. Future research on Mg_2Si will mainly focus on the enhancement of properties of *p*-type Mg_2Si and improving the stability and mechanical properties of these materials.

4.03.5.2 Mg_3Sb_2

Mg_3Sb_2 is another system composed of non-toxic and cheap constituent elements. Both, *n*-type and *p*-type materials based on Mg_3Sb_2 can be produced, making it attractive for practical applications.^{112,127} The same material used for both legs of a thermoelectric device eliminates issues associated with the different thermal expansion coefficients of the *p*- and *n*-type legs. Mg_3Sb_2 belongs to the AM_2X_2 family, where Mg atoms occupy both the A and M atomic positions (Fig. 21). Hence, the chemical formula of Mg_3Sb_2 can be presented as $\text{Mg}^{\text{I}}\text{Mg}^{\text{II}}_2\text{Sb}_2$. Mg_3Sb_2 crystallizes in the hexagonal system in the space group $P\bar{3}m1$ in the La_2O_3 crystal structure type.¹¹¹ There are three distinct atomic sites, Mg^{I} (0;0;0), Mg^{II} ($1/3; 2/3; 0.6339$), and $\text{Sb}1$ ($1/3; 2/3; 0.2283$) in the asymmetric unit cell. Mg_3Sb_2 features anionic $[\text{Mg}_2\text{Sb}_2]$ slabs which are built by $[\text{Mg}^{\text{II}}\text{Sb}_4]$ tetrahedra sharing edges with $\text{Mg}^{\text{II}}\text{—Sb}$ bond distances of 2.82–2.86 Å. The anionic $[\text{Mg}_2\text{Sb}_2]$ slabs are sandwiched by layers of Mg^{I} atoms, where Mg^{I} are surrounded by six Sb atoms in a regular octahedron with $\text{Mg}^{\text{I}}\text{—Sb}$ distances of 3.12 Å. Analysis of the chemical bonding in Mg_3Sb_2 shows that a significant degree of covalent interactions are still present in $[\text{Mg}^{\text{I}}\text{Sb}_6]$ octahedra.^{111,128,129}

Similar to magnesium silicide, *n*-type Mg_3Sb_2 shows much better performance than *p*-type Mg_3Sb_2 (Fig. 19). *n*-type Mg_3Sb_2 can be realized via incorporating excess amounts of Mg atoms, which makes the chemical formula of $\text{Mg}_{3+x}\text{Sb}_2$ ($x > 0$). The small percentage of additional Mg atoms reside at the interstitial atomic positions within Mg_3Sb_2 . Mg atoms play an important role in contributing to the electrical properties by forming a highly degenerate conduction band structure.^{111,128,129} The six-coordinated Mg^{I} has a major contribution to the bottom of the conduction band coupled with a significant contributions from four-coordinated Mg^{II} and Sb atoms. In contrast to conventional Zintl compounds, which exhibit coexistence of ionic and covalent bonds within one crystal structure, all Mg–Sb interactions in Mg_3Sb_2 exhibit strong covalent character.^{111,128,129} The complex bonding picture of Mg_3Sb_2 may account for its promising electrical properties and low thermal conductivity. In addition to the interstitial Mg atoms, aliovalent substitutions, such as trivalent metals to replace divalent Mg atoms, were proved to be an efficient way to control the carrier concentration.^{130,131} For Mg_3Sb_2 , most doping activities happen at Sb atomic sites. Replacement of the Sb with the heavier Bi atoms suppresses the lattice thermal conductivity.^{132–138} Aliovalent Sb/Te substitution is another efficient way to tune the carrier concentration as well as lowering the thermal conductivity.^{132,134,137} Future research efforts will be mainly focused on enhancing the properties of *p*-type Mg_3Sb_2 , perhaps with Li as potential dopant, as in the case of Mg_2Si . Another applicable optimization method would be microstructure management, which can further suppress thermal conductivity and improve thermoelectric performance.

4.03.5.3 MgAgSb

α - MgAgSb has sparked growing research interests with promising thermoelectric performance around room temperature. A recent study demonstrated that an $\text{Mg}_3\text{Sb}_2/\text{MgAgSb}$ module can achieve $\sim 7.3\%$ thermoelectric efficiency for low-temperature energy harvesting.¹³⁹ α - MgAgSb crystallizes in the non-centrosymmetric tetragonal space group $I4c2$. The structure of α - MgAgSb is built by

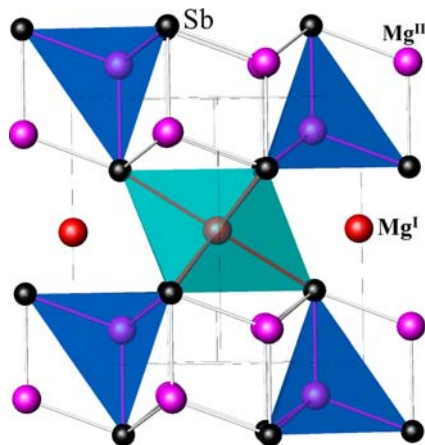


Fig. 21 The crystal structure of Mg_3Sb_2 viewed along the [110] direction. Mg^{I} : red, Mg^{II} : pink, Sb: black. $[\text{Mg}^{\text{I}}\text{Sb}_6]$ octahedra and $[\text{Mg}^{\text{II}}\text{Sb}_4]$ tetrahedra are presented in cyan and blue colors, respectively.

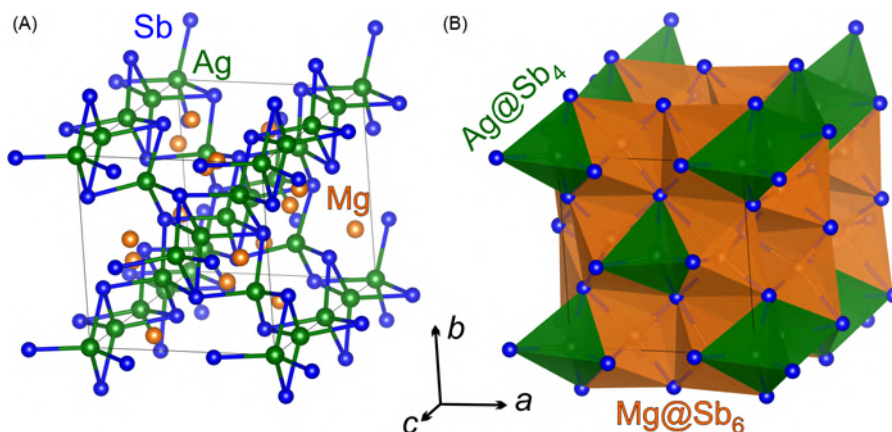


Fig. 22 (A) Ball-and-stick and (B) polyhedral representations of the crystal structure of α -MgAgSb viewed along [001] direction. Mg: orange, Ag: green, Sb; blue.

interconnected edge-sharing $[\text{AgSb}_4]$ tetrahedra forming a three-dimensional framework (Fig. 22A) in which voids are filled with highly distorted $[\text{MgSb}_6]$ octahedra (Fig. 22B). In the asymmetric unit of α -MgAgSb, there are five fully occupied independent atomic positions, one for Mg, one for Sb, and three for Ag atoms. Despite the simple equimolar formula, the crystal structure of α -MgAgSb is complex and contains 24 atoms within a unit cell.

The complex crystal structure of α -MgAgSb accounts for its low thermal conductivity. Two structural features can be considered the origin of low thermal conductivity of α -MgAgSb. One is the unique three-centered Mg–Ag–Sb bonds.¹⁴⁰ Another is the rattling-like behavior of Ag atoms in $\text{Ag}@\text{Sb}_4$ tetrahedra.^{141–145} Ag defects play a dominant role in controlling the thermoelectric properties of α -MgAgSb. There are three crystallographic Ag positions. Both theoretical and experimental findings verify the presence of intrinsic Ag defects in α -MgAgSb, which may explain why the major carriers are holes. Intrinsic Ag imperfections were applied to suppress the lattice thermal conductivity and tune the electrical properties of α -MgAgSb simultaneously.^{142,146} Various dopants, such as Li, Ca, and Yb replacing Mg atoms or As, Sn, Bi, and Pb substituting Sb atoms, have been incorporated to enhance the thermoelectric properties of α -MgAgSb.^{142,146} Like Mg_2Si , the major theme of the future research on α -MgAgSb will be pursuing high-purity samples free from secondary admixtures and investigating proper dopants.

4.03.5.4 $\text{Yb}_{14}\text{MgSb}_{11}$

As discussed in the Sections 4.03.2 and 4.03.6, Zintl phases with complex crystal structures are promising thermoelectrics due to their intrinsically low thermal conductivity. $\text{Yb}_{14}\text{MnSb}_{11}$, the first example of a high-temperature thermoelectric material in the $A_{14}MX_{11}$ family, was reported in 2006.¹⁴⁷ The “14-1-11” structure type demonstrates amazing flexibility and many compounds have been synthesized with overall composition of $A_{14}MX_{11}$ ($A = \text{Ca}, \text{Sr}, \text{Ba}, \text{Yb}, \text{Eu}$; $M = \text{Al}, \text{Zn}, \text{Cd}, \text{Mn}, \text{Mg}$; $X = \text{As}, \text{Sb}, \text{Bi}$).^{148,149} 9 years later Mn was replaced with isovalent Mg, resulting in the formation of $\text{Yb}_{14}\text{MgSb}_{11}$.¹¹⁷ The crystal structure of $\text{Yb}_{14}\text{MgSb}_{11}$ can be represented as a combination of an anionic sublattice of $[\text{MgSb}_4]^{9-}$ tetrahedra, linear $[\text{Sb}_3]^{7-}$ trimers, and isolated Sb^{3-} anions surrounded by the Yb^{2+} cations (Fig. 23A), or as a three-dimensional network of Sb-centered $[\text{Yb}_7]$ or $[\text{Yb}_6\text{Mg}]$ polyhedra, hosting $[\text{Sb}_3]$ trimers (Fig. 23B).

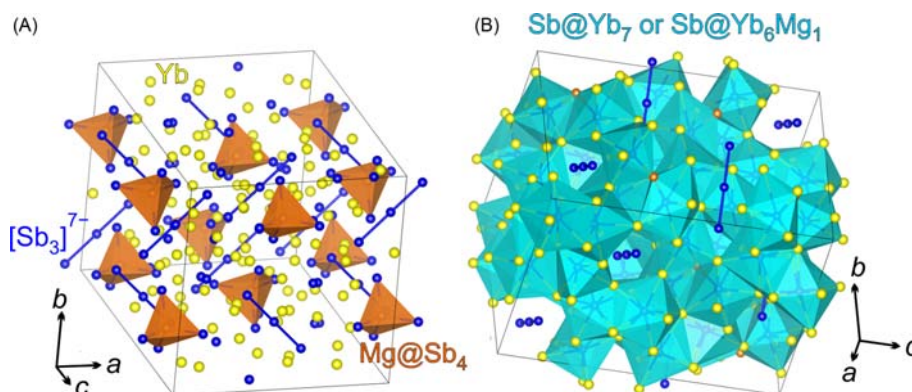


Fig. 23 The crystal structure of $\text{Yb}_{14}\text{MgSb}_{11}$. (A) A view emphasizing MgSb_4 tetrahedra and Sb_3 trimers. (B) An alternative view showing polyhedra around isolated Sb atoms—either $\text{Sb}@Yb_7$ or $\text{Sb}@Yb_6\text{Mg}_1$. Yb: yellow, Mg: orange, Sb: blue.

In $A_{14}MX_{11}$, different di- and trivalent cations M may be realized: $M = \text{Al, Zn, Cd, Mn, and Mg}$. The latter three elements all exhibit formal +2 oxidation state with identical valence electron counts. Nevertheless, $\text{Yb}_{14}\text{MgSb}_{11}$ is the record holder of zT within the $A_{14}MX_{11}$ family when stoichiometric, unsubstituted, or undoped compositions are considered. Chemical bonding analysis verified the covalent nature of Mg–Sb interactions. A recent study revealed the complex crystal structure nature of $\text{Yb}_{14}\text{MgSb}_{11}$ with Mg atoms partially occupying the Yb positions.¹⁵⁰ The coexistence of covalent and ionic bonding types in one compound are important for both charge and heat transport properties. With high performance of the unoptimized material, there are multiple ways to improve the thermoelectric performance of $\text{Yb}_{14}\text{MgSb}_{11}$ such as carefully controlling the hole concentration, alloy engineering to further reduce lattice thermal conductivity, and microstructure management.

In summary, the element magnesium—which is cheap, abundant, and nontoxic—plays an important role in the field of thermoelectrics. The flexible chemical characteristics such as the ability to form ionic or covalent bonds (sometimes within the same compound) and variable coordination environments enable high zT values by forming complex crystal structures and contributing to the electronic structure. During synthesis, a precise control of the stoichiometry of Mg is challenging due to the high vapor pressure of Mg, which needs careful attention. Isovalent replacement of Mg by Mn, Zn, or Cd is possible due to their comparable ionic sizes.^{124,125} Aliovalent substitution of Mg is more difficult due to the small ionic size of Mg^{2+} (0.72 Å), leaving Li^+ (0.76 Å) and Y^{3+} (1.01 Å) as potential candidates. For practical applications, the mechanical properties (brittleness) of Mg-containing materials also need to be improved.

4.03.6 Complex crystal structures for thermoelectric materials

4.03.6.1 Crystal structure—Phonon structure—Thermal conductivity relationship

As discussed previously, optimization of the thermoelectric figure-of-merit depends on many interdependent material properties. For many traditional thermoelectric materials discussed in the previous sections, the electrical resistivity and Seebeck effect are preeminent while the thermal conductivity leaves something to be desired. Many attempts to lower the thermal conductivity result in negative impacts on the resistivity and Seebeck. While the charge carrier contribution to electronic thermal conductivity cannot be avoided, lattice thermal conductivity can be reduced somewhat independently. Therefore, the disentanglement of the thermal conductivity and electronic properties is highly attractive. From the point-of-view of the phonon structure, acoustic phonons transfer heat while optical phonons, upon crossing with the acoustic ones, are responsible for the heat dissipation. In materials with simple cubic structures, like diamond or boron arsenide, there is an optical gap between acoustic and thermal phonons which leads to extremely high lattice thermal conductivities of $> 1000 \text{ Wm}^{-1} \text{ K}^{-1}$ (Fig. 24A).^{151–154} For complex crystal structures with many atoms in the unit cell, multiple crossings of the optical and acoustic phonons lead to an overall decrease in the thermal conductivity (Fig. 24B). An even higher degree of the disentanglement can be achieved if the structure has weakly-bound atoms, or “rattlers.” This was first proposed by G.A. Slack who coined the “phonon-glass-electron-crystal” concept.¹⁴ In the proposed hypothetical material, phonons are efficiently scattered just as they are in a glass-like compound which lacks any long-range order. Meanwhile, the charges (electrons or holes) move as they do in a crystalline lattice. The presence of rattling atoms introduces low-energy flat optical modes which suppress the acoustic phonon branches (Fig. 24C).

A complex crystal structure with many atoms and some weakly-bound atoms is preferable for low lattice thermal conductivity. *But what does it mean for a crystal structure to be complex?* Several factors can contribute to the complexity of a given crystal structure such as unit cell volume, atomic disorder, vacancies, mixed occupied sites, and the presence of different types of bonding (covalent, ionic, etc.). Increasing structural complexity generally decreases lattice thermal conductivity making complex crystal structures an

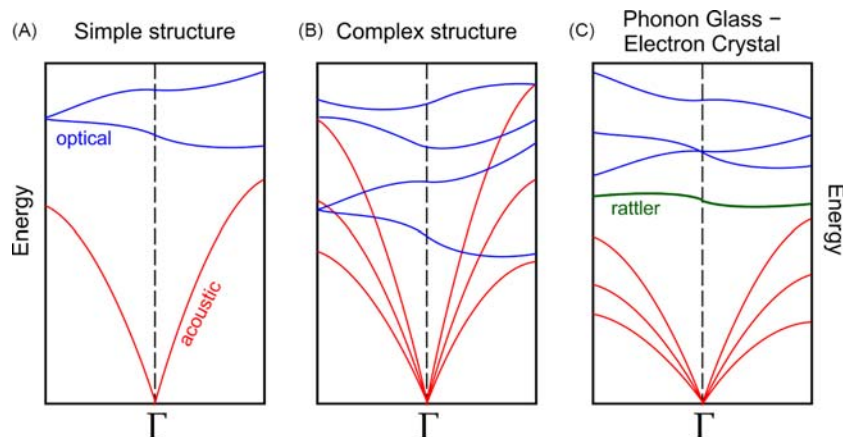


Fig. 24 Schematic representation of the phonon structure of different hypothetical materials. (A) A simple crystal structure with an optical gap between the acoustic and optical phonons. (B) A complex crystal structure with multiple acoustic-optical phonons overlapping. (C) A structure with rattling atoms and corresponding flat optical modes which suppress the acoustic phonon branches.

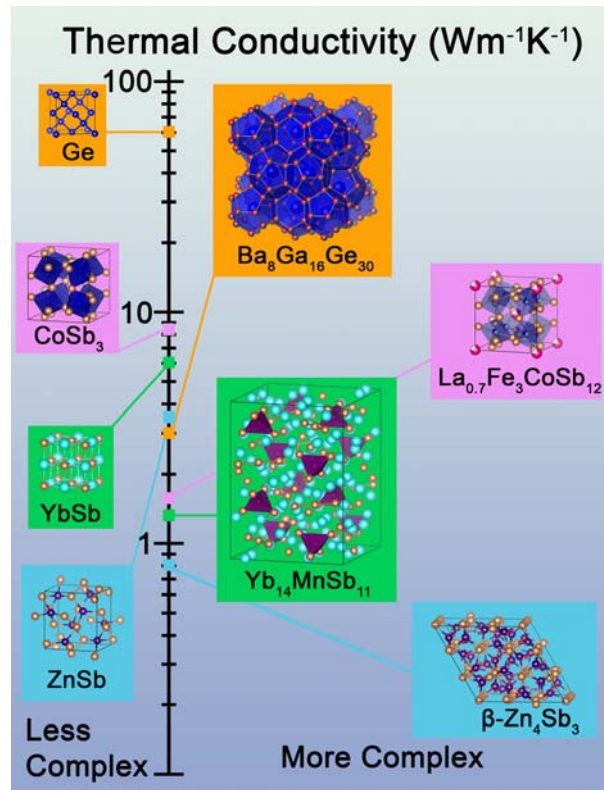


Fig. 25 A comparison of the room temperature thermal conductivities of relatively simple (left) and complex (right) structures composed of similar elements.

enticing characteristic for developing highly efficient thermoelectric materials. To better explain the intricacy of complex crystal structures, contrasting a simple crystal structure is helpful. Silicon has a very simple face-centered cubic crystal structure with a unit cell volume of only 160 \AA^3 . The crystal structure contains no vacancies or partially occupied sites, and only one type of bonds can be found (i.e., Si–Si covalent bonds). As a result of its simple structure, the thermal conductivity of elemental silicon is above $100 \text{ Wm}^{-1} \text{ K}^{-1}$ at 300 K. Increasing the complexity of the crystal structure can lead to a significant decrease in thermal conductivity, as seen in SiGe alloys (Section 4.03.3.2), and crystalline materials with very complex structures are known to have thermal conductivities below $1 \text{ Wm}^{-1} \text{ K}^{-1}$ at 300 K (Fig. 25). Of course, the need for favorable electronic conduction and high Seebeck coefficient further limits the selection of promising materials for thermoelectric applications. In this section, several promising thermoelectric materials will be discussed—all of which possess low lattice thermal conductivities due to their complex crystal structures.

4.03.6.2 Large unit cells in 14-11 compounds

One example of materials with very large unit cell volumes are the $A_{14}BX_{11}$ compounds briefly discussed in Section 4.03.5.4. The unit cell of $\text{Yb}_{14}\text{MgSb}_{11}$ does not contain substantial atomic disorder or significant vacancies, but the unit cell volume is over 6100 \AA^3 and the structure contains a variety of bonding types. The Mg–Sb bonds can be considered covalent as well as the Sb–Sb bonds in Sb_3 trimer, while the interactions between Yb and isolated Sb atoms are ionic. The Mg atoms are tetrahedrally coordinated by 4 Sb atoms making the $[\text{MgSb}_4]^{10-}$ unit. Another structural unit is the Sb trimer $[\text{Sb}_3]^{7-}$. These trimers feature linear bonding due to the hypervalent nature of the central Sb atom. These tetrahedral and trimer motifs combine with 12 Yb^{2+} cations and 4 Sb^{3-} anions to make up the $\text{Yb}_{14}\text{MgSb}_{11}$ crystal structure. The multiple types of bonding and large unit cell constitute a complex crystal structure with a thermal conductivity of $\sim 0.8 \text{ Wm}^{-1} \text{ K}^{-1}$ at 300 K.¹¹⁷

This structure type has been thoroughly studied and it has been found that the electronic properties of these materials can be adjusted while maintaining or even further lowering the thermal conductivity. $\text{Yb}_{14}\text{MnSb}_{11}$ and $\text{Yb}_{14}\text{MgSb}_{11}$ have high zT values of ~ 1 approaching 1000 K, making them a very attractive platform for high-temperature thermoelectric applications.^{117,147} Many approaches have been taken to further increase the efficiency of these materials. The Mn site can be fully alloyed with Mg, Zn, and Al. The Sb site can be replaced with Bi or partially replaced with Sn. Yb can be partially replaced with La or fully replaced with Ca, Sr, and Eu. This resulting vast phase space generates an enormous number of possibilities to tune the electronic and thermal transport in this family of materials.

An interesting aspect of complex crystal structures is that they are complex because of the elements that have been combined and, therefore, a structure with similar composition has a potential to exhibit similar complexity. Such is the case for $\text{Yb}_{21}\text{Mn}_4\text{Sb}_{18}$.¹⁵⁵

$\text{Yb}_{21}\text{Mn}_4\text{Sb}_{18}$ combines large unit cell volume with another form of structural complexity: positional atomic disorder. The increase in the concentration of Mn compared to $\text{Yb}_{14}\text{MnSb}_{11}$ is realized through the condensation of the $[\text{MnSb}_4]^{9-}$ unit into the tetramer $[\text{Mn}_4\text{Sb}_{10}]^{22-}$. However, within the voids filled by Yb^{2+} , one of the Yb sites becomes disordered, presumably as the void becomes larger, and the Yb atom's electron density is partially distributed over two crystallographic sites. Often atomic disorder creates a cascade of partially distributed sites; accordingly, the crystal structure of $\text{Yb}_{21}\text{Mn}_4\text{Sb}_{18}$ has Yb, Sb, and Mn positional disorder. The complexity of the unit cell again manifests as ultra-low thermal conductivity of $0.4 \text{ Wm}^{-1} \text{ K}^{-1}$ at 300 K.

4.03.6.3 Atomic disorder in zinc antimonides

As mentioned previously, atomic disorder is another way of introducing structural complexity and lowering the thermal conductivity. Vacancies or partially occupied sites are a type of atomic disorder in which the presence of an atom in the unit cell is statistical. For example, if a particular atom site has a 20% occupancy, then one in five unit cells in the material will contain that atom in that crystallographic site.

$\beta\text{-Zn}_4\text{Sb}_3$ is an example of a good thermoelectric material with $zT > 1$ that exhibits atomic disorder.¹⁵⁶ $\beta\text{-Zn}_4\text{Sb}_3$ crystallizes in the $R\bar{3}c$ space group and has a unit cell volume of $\sim 1600 \text{ \AA}^3$. The antimony atoms form both isolated Sb^{3-} ions as well as $[\text{Sb}_2]^{4-}$ dimers. The Zn 3*df* site is partially occupied at $\sim 90\%$ resulting in an actual composition of $\text{Zn}_{13}\text{Sb}_{10}$. This means that the Zn atom is missing in one out of 10 unit cells. This description of the unit cell has not been depicted consistently in the literature. Originally Mayer et al. reported that Zn partially occupied an Sb site so that the stoichiometry was in agreement with the nominal composition.¹⁵⁷ Later, reinvestigation found that the composition was Zn deficient and there were several very closely related phases with varying Zn content.¹⁵⁸ Even more detailed structural studies were performed with synchrotron radiation and revealed that additional partially occupied Zn sites were present in the crystal structure.^{159,160} These interstitial Zn atoms effectively lower thermal conductivity by introducing disorder into the lattice.

ZnSb is another binary of Zn and Sb with room temperature thermal conductivity of $\sim 3.5 \text{ Wm}^{-1} \text{ K}^{-1}$, while $\beta\text{-Zn}_4\text{Sb}_3$ has a thermal conductivity of $0.8 \text{ Wm}^{-1} \text{ K}^{-1}$.^{159,161} From electronic structure calculations, the modulation of interstitial Zn atoms should have a large effect on electronic properties. This is consistent with the variability of thermoelectric property data for this phase. In a systematic manipulation of the Zn content for single phase $\beta\text{-Zn}_4\text{Sb}_3$, the Seebeck coefficient changed by as much as 20%.¹⁵⁹ Other binary Zn antimonides have been reported to have similar disorder of Zn sites and low lattice thermal conductivities, such as $\beta\text{-Zn}_8\text{Sb}_7$ and Zn_9Sb_7 .^{162,163}

4.03.6.4 Skutterudites and clathrates: Rattling atoms and superstructures

Skutterudites are compounds with the CoAs_3 -type structure, crystallizing in the cubic $Im\bar{3}$ space group. The structure contains 8 corner-sharing tilted Co@As_6 octahedral units per unit cell. The octahedral units are connected in such a way that there is a large icosahedral void in the crystal structure (Fig. 26). While skutterudites can be composed of metals Co, Rh, and Ir and pnictogens (P, As, and Sb), the Sb-based materials are of interest for thermoelectrics due to their favorable electrical resistivities and Seebeck coefficients. CoSb_3 has a reasonable power factor of $30 \mu\text{Wcm}^{-1} \text{ K}^{-2}$; however, the thermal conductivity is too high at $8.9 \text{ Wm}^{-1} \text{ K}^{-1}$.¹⁶⁴ Lowering the thermal conductivity is an active challenge for this class of materials and adding complexity to the crystal structure is a potential solution. An effective way to achieve this is by introducing a rattling atom in the void of the crystal structure.

Upon occupation of the interstitial space—that is the two icosahedral voids in the structure—with a rattling atom, (Fig. 26), the compound is referred to as a filled skutterudite with composition $\text{A}_{1-\delta}\text{T}_4\text{Z}_{12}$. These are some of the most promising thermoelectric materials in the skutterudite family. Many elements have been incorporated into the Co (*T*) and As (*Z*) sites of the filled skutterudite ($T = \text{Fe, Co, Ni, Ru, Rh, Os, Ir, Pt, Au}$; $Z = \text{Si, P, Ge, As, Sn, Sb}$).¹⁶⁵ Cations *A* such as alkali (Li, Na, K, Rb) and alkaline-earth metals (Ca, Sr, Ba), triels (In, Tl), early transition metals (Y, Hf), lanthanides (La, Ce, Pr, Nd, Sm, Eu, Yb), and actinides (Th, U, Np) can be partially or fully inserted into the large void between the tilted octahedra. Even the smallest inclusion of cations into the void can moderately lower the thermal conductivity such as in $\text{K}_{0.22}\text{Co}_4\text{Sb}_{12}$ with κ_{lattice} of $6.7 \text{ Wm}^{-1} \text{ K}^{-1}$ at 300 K.³⁶ However, the

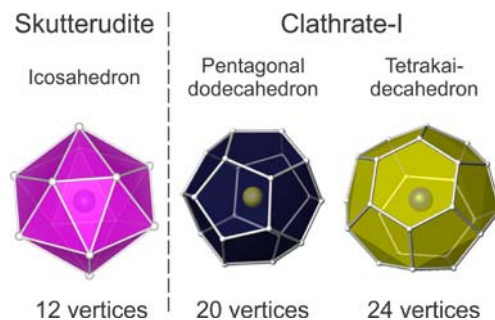


Fig. 26 Polyhedral view of cages with rattling cations inside shown for the skutterudite (left) and clathrate-I (right) structure types.

interstitial atom also affects the charge carrier concentration which effectively modulates the electrical resistivity and Seebeck coefficient. Adding interstitial atoms reduces thermal conductivity which improves overall zT , but it also adds additional electrons making all subsequent materials n -type. For the $\text{Co}_4\text{Sb}_{12}$ framework, there is a limit to incorporating interstitial atoms before the excess electrons destabilize the structure. However, higher occupancies of the interstitial site can be accommodated when the Co site is alloyed with Fe. In $\text{La}_{0.7}\text{Fe}_3\text{CoSb}_{12}$, the thermal conductivity was reduced to $1.6 \text{ W m}^{-1} \text{ K}^{-1}$. This low thermal conductivity combined with the electrical transport properties brought the overall zT to approach 1 at 800 K.¹⁶⁶

Clathrates are a large family of cage-like compounds. (Figs. 25 and 26). The cages in clathrates are formed by tetrahedrally-coordinated “framework atoms” and the atoms that occupy the space in these cages are referred to as “guest atoms”. Guest atoms may have either positive charge (serving a cationic role, the more common case), or negative charge (anions, which are present in so-called inverted clathrates).^{167,168} Similar to skutterudites, these guest atoms are rattlers and play a role in lowering the thermal conductivity of these materials. Out of the 11 structure-types of clathrates reported, type I clathrates are the most common with over 200 compounds reported.¹⁶⁹ Type I clathrates crystallize in the space group $Pm\bar{3}n$ and have the composition of A_8X_{46} where A represents the guest atoms and X denotes the framework atoms. The unit cell consists of 2 pentagonal dodecahedra and 6 tetra-kaidecahedra (Fig. 26).

Because all the framework atoms are tetrahedral in coordination, tetrel elements (Si, Ge, and Sn) compose many of the reported clathrate frameworks. As discussed earlier, unit cell volume has a great influence on the thermal conductivity, and type I clathrates have a unit cell volume on the order of $\sim 1000 \text{ \AA}^3$. This sufficiently large unit cell is only one of the factors that reduces thermal conductivity. The guest atoms in the clathrates also reduce lattice thermal conductivity as they are loosely bound to the cages and often have large anisotropic atomic displacement parameters. Sometimes, the guest atoms are even best described as being positionally disordered in the large cages. Calculation of phonon modes help us understand the addition of certain complexity. Just like Si, α -Ge has high thermal conductivity (Fig. 25) due to its small unit cell and lack of complexity. A study comparing the phonon modes of crystalline α -Ge, Ge_{46} (clathrate-I structure without guest atoms), and $\text{Sr}_6\text{Ge}_{46}$ (clathrate-I with Sr guest atoms) found that the larger unit cell of Ge_{46} , even without occupancy of the guest atom positions, exhibited much lower thermal conductivity than α -Ge.¹⁷⁰ Upon addition of Sr guest atoms, additional phonon modes were observed that dramatically impact the scattering of heat-carrying phonons which lowers the thermal conductivity even further. Just like the other structures discussed in this section, the low thermal conductivity of clathrates provides a suitable starting point for potential thermoelectric materials. Exceptionally low thermal conductivities for $\text{Ba}_8\text{Au}_{16}\text{P}_{30}$ ($0.6 \text{ W m}^{-1} \text{ K}^{-1}$ at 300 K) and $\text{Ba}_8\text{Ga}_{15.9}\text{Sn}_{30.1}$ ($0.71 \text{ W m}^{-1} \text{ K}^{-1}$ at 300 K) have been reported. However, optimal efficiency can only be reached if the clathrate’s electrical properties are exceptional. Optimization of the electrical properties in clathrates can be achieved by substitution of the framework atoms. A few clathrates have surpassed a peak zT of >1 including $\text{Ba}_8\text{Sb}_2\text{Ga}_{14}\text{Ge}_{30}$, $\text{Ba}_8\text{Ga}_{5.23}\text{Al}_{10.52}\text{Sn}_{30.26}$, and $\text{Ba}_8\text{Ga}_{15.8}\text{Cu}_{0.033}\text{Sn}_{30.17}$.¹⁶⁹

Type-I clathrates can exhibit a range of electrical properties from metallic to semiconducting with a straightforward design principle guided by electron counting. For a semiconducting type-I clathrate, the 46 framework atoms need 4 valence electrons per atom (184 total). The guest atoms donate their valence electrons (v.e.) to the framework in accordance with the Zintl concept. One of the best performing clathrates, $\text{Ba}_8\text{Ga}_{16}\text{Ge}_{30}$, satisfies this criteria with 8×2 v.e. from Ba, 16×3 v.e. from Ga, and 30×4 v.e. from Ge. In total this yields 184 v.e. and $\text{Ba}_8\text{Ga}_{16}\text{Ge}_{30}$ exhibits intrinsic semiconducting behavior. Advantageously, the 184-electron rule is not a rigid rule and there is some tolerance—although the extent of this boundary is not necessarily well-defined. For instance, $\text{Na}_8\text{Si}_{46}$ has an electron count of 192 v.e. and accordingly shows n -type metallic behavior.¹⁷¹ This clathrate framework made from Si can accept 8 excess electrons, but the Ge framework is less accepting. $\text{Ba}_8\text{Ge}_{46}$ does not exist presumably because the total electron count would be too high at 200 v.e. Instead of inducing vacancy formation in the guest atom sites, the clathrate framework starts to form vacancies. $\text{Ba}_8\text{Ge}_{43}$ forms a clathrate-I type structure with three framework vacancies per formula unit to bring the v.e. count to 188.

Another interesting discovery in $\text{Ba}_8\text{Ge}_{43}$ is the formation of a superstructure.¹⁷² A superstructure is formed when there is a change in the crystal structure (like vacancies or mixed occupancies in one site). To accommodate this change in the ordered structure, there is a need to break original translational symmetry via either decreasing the symmetry or increasing the volume of the primitive part of the unit cell or both. In $\text{Ba}_8\text{Ge}_{43}$, the translation of the primitive unit cell is broken when the framework vacancies become ordered. Because it is still a crystalline material, a unit cell is larger, or less symmetric, or both. In $\text{Ba}_8\text{Ge}_{43}$, the new unit cell is defined as $2 \times 2 \times 2$ superstructure of the archetypal clathrate-I cell.

Type I clathrate frameworks are typically composed of tetrel elements, but the discovery of $\text{Ba}_8\text{Cu}_{16}\text{P}_{30}$ realized clathrate frameworks devoid of Si, Ge, or Sn.¹⁷³ This growing subset of clathrates, termed “unconventional clathrates,”¹⁷⁴ is especially prone to forming superstructures. Because Cu and P have different bonding preferences and electronegativity values, they segregate over different Wyckoff sites and create a superstructure. As a result, $\text{Ba}_8\text{Cu}_{16}\text{P}_{30}$ crystallizes in $Pbcn$ with a unit cell four times the size of the primitive cubic clathrate. Enlargement of the unit cell helps reduce the thermal conductivity thus making superstructure formation an important mechanism to understand so that it may be used as a strategy for thermoelectric optimization.^{174–178}

4.03.6.5 Complex Intermetallics of the $\text{R}_{17}\text{Fe}_5\text{Ge}_{112}$ structure-type

An extreme case of structure complexity can be achieved in intermetallic compounds with giant unit cells. Simple compositions, like Mg_2Al_3 or NaCd_2 , may correspond to a complex unit cell with volumes over $22,000 \text{ \AA}^3$.^{179–181} Ternary structures exhibit even more complicated structures such as in Al–Cu–Ta intermetallics with unit cell volumes of $93,000\text{--}365,000 \text{ \AA}^3$.^{182,183} As stated above,

ternary systems with a combination of ionic and covalent bonding are preferred for thermoelectric applications, such as materials with the $R_{117}Fe_{52}Ge_{112}$ (R = rare earth) structure type. This complex structure type is an intergrowth of various nested polyhedra with the Ge-containing compounds having unit cell volumes of 23,000–24,000 Å³, while the Sn-based analogues have larger volumes of 27,000–29,000 Å³.^{184,185} Lattice thermal conductivity of these compounds is, as expected, very low owing to the structural complexity of these compounds. A κ_{lattice} value of 0.28 Wm⁻¹ K⁻¹ was reported for Gd₁₁₇Co₅₆Sn₁₁₂.¹⁸⁶ The main drawback of such complex intermetallics is the low Seebeck coefficient which prevents their utilization as effective thermoelectric materials. However, recent developments in the method of analysis of chemical bonding in complex intermetallic structures¹⁸⁷ and the discovery of semiconducting intermetallics such as TaIrGe^{188–190} leave hope for complex intermetallics to find future applications in the thermoelectrics field.

Complex unit cells are one way of ensuring low thermal conductivity for a given material. However, certain challenges in the characterization and understanding of the materials arise from this complexity. For instance, β -Zn₄Sb₃ is a misnomer because its composition is much closer to Zn_{3.9}Sb₃ = Zn₁₃Sb₁₀. This mistake originates from the difficulty in determining the partial site occupancy of the disordered Zn atom. Originally the structure was also thought to have Zn/Sb site mixing, and this was later shown to be an incorrect interpretation of X-ray diffraction data. The incorrect composition and/or crystal structure description can distort the fundamental understanding of the experimental properties and prevent rational ‘materials’ optimization. Another challenge in studying mixed or partially occupied crystallographic sites is the difficulty in performing computations on these materials. Calculating accurate band structures and predicting optimal carrier concentrations for a given material provides an invaluable feedback loop for experimentalists that can greatly reduce laboratory efforts when designing efficient thermoelectric materials. The efficiency of such approach was demonstrated for tetrel monochalcogenides as discussed in Section 4.03.4. However, large unit cells of complex thermoelectrics increase computational costs and disorder or mixed occupied sites cannot be easily accounted for in computations. As computational efficiency is improving, and high-quality instrumentation is becoming more available, complex materials are becoming more routine to fully characterize. This sector of thermoelectrics remains an active and exciting research area for both experimental and theoretical chemists.

4.03.7 Outlook

Thermoelectric materials are important for the solid-state interconversion of heat and electrical energy. There are multiple potential applications for thermoelectrics in both refrigeration (food, vehicle air-conditioning, CCD matrices, microelectronics, and light sources) and energy generation (wearable technology for body heat conversion, waste heat from combustion engine operations and manufacturing, and RTGs for space exploration). These applications dictate the operating temperature regimes and basic requirements for performance, cost, toxicity, and compatibility of the component materials. Development of novel thermoelectric materials with improved performance is a dynamic field located on the intersection of solid-state chemistry, condensed matter physics, and materials science. Optimization of the charge and heat transport in thermoelectric materials requires an understanding of the relationship between composition, real long-range and short-range crystal structures, interstitial and substitutional defects, microstructure and phase boundaries, electronic and phonon structures, and chemical bonding. In this chapter, several examples of different families of thermoelectric materials were discussed to illustrate the diversity of these chemical systems and various optimization approaches. Clearly, there is no single recipe for how to produce a superior thermoelectric material, and new exciting discoveries from both well-studied “classic” and completely new systems are yet to come.

4.03.8 Appendix A: Summary of zT values for materials discussed in this chapter.

For more extensive lists of the thermoelectric properties in inorganic materials, the reader is referred to the recent topical review by Freer et al.³⁶

Composition	Temperature (K)	zT
Bi _{2-x} Sb _x Te ₃	300	1
Bi ₂ Te _{3-x} Se _x	300	0.8
Bi _x Sb _{2-x} Te ₃	373	1.4
Bi _{0.5} Sb _{1.5} Te ₃	350	1.24
Bi ₂ Te _{2.7} Se _{0.3}	398	1.04
Bi ₂ Te ₂ S	573	0.8
K _{0.06} Bi ₂ Te _{3.18}	350	1.1
Si	300	0.01
Si _{0.7} Ge _{0.3} : B	1100	0.7
Si _{0.7} Ge _{0.3} : P	1100	1
Si _{0.8} Ge _{0.2} : B	1173	1.22
Si _{0.8} Ge _{0.2} : B + WSi ₂	1173	0.66

(Continued)

Composition	Temperature (K)	zT
Si _{0.8} Ge _{0.2} : P	1173	1.3
Si _{0.8} Ge _{0.2} : P + WSi ₂	1173	1.16
Si _{0.8} Ge _{0.2} : P + SiC	1173	1.72
PbTe _{1-x} Se _x	850	1.8
PbTe—(4 mol% SrTe)—(2 mol% Na)	913	2.2
PbTe—8% SrTe	923	2.5
Na _{0.03} Eu _{0.03} Sn _{0.02} Pb _{0.92} Te	850	2.57
PbSe—1% Al	850	1.3
PbSe—1% Mo	673	0.5
Sn _{0.98} Se	823	1.4
SnSe	823	1.37
SnSe (single crystal; along <i>b</i> -axis)	923	2.6
SnSe (single crystal; along <i>a</i> -axis)	923	0.8
Sn _{0.948} Cd _{0.023} Se	823	1.7
SnSe _{0.96} Sb _{0.02}	773	1.1
Sn _{0.95} Se	873	2.1
Sn _{0.985} Na _{0.015} Se	773	2.0
Sn _{0.98} Na _{0.02} Se—2% Te	723	>2
SnSe _{0.9} Br _{0.1}	773	1.3
SnSe—Ag ₈ SnSe ₆	773	1.33
(SnSe) _{1-x} (SnSe ₂) _x	773	2.2
SnSe—1.0 wt% LaCl ₃	750	0.55
SnSe: Cu	823	1.41
SnSe nanosheets/PEDOT:PSS hybrid films incorporating 20% SnSe	300	0.32
Reduced hole-doped polycrystalline SnSe	783	3.1
SnSe _{1.95} —1.5% Cu	673	0.63
SnTe _{0.985} l _{0.015}	700	0.6
In _{0.0025} Sn _{0.9975} Te	873	1.1
SnTe: In/Cd	823	1.4
SnTe: In/Mg	840	1.5
Sn _{0.94} Cu _{0.12} Te	850	>1
Sn _{0.97} Bi _{0.03} Te + SrTe	823	1.2
SnTe: Ca/In +5% Cu ₂ Te	823	1.85
Ge _{0.79} Ag _{0.01} Sn _{0.2} Se	700	0.2
(GeSe) _{0.9} (AgBiTe ₂) _{0.1}	627	1.35
(GeTe) _{0.85} (AgSbTe ₂) _{0.15}	720	1.5
(Ge _{0.97} Sb _{0.03} Te) _{0.8} [(Ag ₂ Te) _{0.4} (Sb ₂ Te ₃) _{0.6}] _{0.2}	700	1.8
(GeTe) _{0.85} (AgSbTe ₂) _{0.15} —1% Yb	730	1.8
Mg _{1.98} Cr _{0.02} (Si _{0.3} Sn _{0.7}) _{0.98} Bi _{0.02}	680	1.7
Mg _{1.98} Li _{0.02} Si _{0.4} Sn _{0.6}	780	0.7
Mg _{2.08} Si _{0.364} Sn _{0.6} Sb _{0.036}	773	1.55
Mg _{2.08} Si _{0.37} Sn _{0.6} Bi _{0.03}	716	1.5
Mg ₃ Sb _{1.8} Bi _{0.2}	773	0.94
Mg _{3.15} Mn _{0.05} Sb _{1.5} Bi _{0.49} Te _{0.01}	720	1.85
Mg _{0.97} Zn _{0.03} Ag _{0.9} Sb _{0.95}	423	1.4
Yb ₁₄ MgSb ₁₁	1075	1.02
Yb ₁₄ MnSb ₁₁	1223	1
β-Zn ₄ Sb ₃	550	0.8
La _{0.7} Fe ₃ CoSb ₁₂	800	1
Ba ₈ Sb ₂ Ga ₁₄ Ge ₃₀	980	1.1
Ba ₈ Ga _{5.23} Al _{10.52} Sn _{30.26}	480	1.2
Ba ₈ Ga _{15.8} Cu _{0.033} Sn _{30.17}	550	1.38

Acknowledgments

Authors acknowledge the financial support from U.S. Department of Energy, Office of Basic Energy Sciences, Division of Materials Science and Engineering, grant DE-SC0022288.

References

- Lawrence Livermore National Laboratory (LLNL). *Energy Flow Chart Page. Chart detailing energy production and percentage that is wasted.* <https://flowcharts.llnl.gov/> (Accessed 09-03-2022).
- Verne, J. *Twenty Thousand Leagues Under the Sea*, Oxford University Press: Oxford, UK, 1998.
- The NASA. *Jet Propulsion Laboratory (JPL) page for the Voyager Interstellar Mission.* <https://voyager.jpl.nasa.gov/> (accessed 09-03-2022).
- The NASA. *Radioisotope Power Systems (RPS) Program.* <https://rps.nasa.gov/missions> (accessed 09-03-2022).
- Seebeck, T. J. Ueber Die Magnetische Polarisation Der Metalle Und Erze Durch Temperatur-Differenz. *Ann. Phys.* **1826**, 82 (1), 1–20. <https://doi.org/10.1002/andp.18260820102>.
- Peltier, C. A. Nouvelles Experiences sur la Caloricitedes Courants Electriques. *Ann. Chim. Phys.* **1834**, 56, 371–386.
- Roget, P. M. *Treatises on Electricity, Galvanism, Magnetism, and Electro-Magnetism*, Baldwin and Cradock of Paternoster-Row: London, UK, 1832.
- Beretta, D.; Neophytou, N.; Hodges, J. M.; Kanatzidis, M. G.; Narducci, D.; Martin- Gonzalez, M.; Beekman, M.; Balke, B.; Cerretti, G.; Tremel, W.; Zevalkin, A.; Hofmann, A. I.; Müller, C.; Döring, B.; Campoy-Quiles, M.; Caironi, M. Thermoelectrics: From History, a Window to the Future. *Mater. Sci. Eng. R* **2019**, 138, 100501. <https://doi.org/10.1016/j.mser.2018.09.001>.
- Ioffe, A. F. *Semiconductor Thermoelectrics and Thermoelectric Cooling*, Infosearch Limited: London, UK, 1957.
- Satterthwaite, C. B.; Ure, R. W. Electrical and Thermal Properties of Bi₂Te₃. *Phys. Ther. Rev.* **1957**, 108 (5), 1164–1170. <https://doi.org/10.1103/PhysRev.108.1164>.
- Goldsmid, H. J. X. V. I. I. Thermoelectric Applications of Semiconductors. *Int. J. Electron.* **1955**, 1 (2), 218–222. <https://doi.org/10.1080/00207215508961410>.
- Dismukes, J. P.; Ekstrom, L.; Steigmeier, E. F.; Kudman, I.; Beers, D. S. Thermal and Electrical Properties of Heavily Doped Ge-Si Alloys up to 1300°K. *J. Appl. Phys.* **1964**, 35 (10), 2899–2907. <https://doi.org/10.1063/1.1713126>.
- Fluerial, J.-P. Thermoelectric Power Generation Materials: Technology and Application Opportunities. *JOM* **2009**, 61 (4), 79–85. <https://doi.org/10.1007/s11837-009-0057-z>.
- Slack, G. A.; Rowe, D. *CRC Handbook of Thermoelectrics*, CRC Press: Boca Raton, FL, 1995.
- Kim, H. S.; Gibbs, Z. M.; Tang, Y.; Wang, H.; Snyder, G. J. Characterization of Lorenz Number With Seebeck Coefficient Measurement. *APL Mater.* **2015**, 3 (4), 1–6. <https://doi.org/10.1063/1.4908244>.
- Kim, H. S.; Liu, W.; Chen, G.; Chu, C.-W.; Ren, Z. Relationship Between Thermoelectric Figure of Merit and Energy Conversion Efficiency. *Proc. Natl. Acad. Sci.* **2015**, 112 (27), 8205–8210. <https://doi.org/10.1073/pnas.1510231112>.
- Toberer, E. S.; May, A. F.; Snyder, G. J. Zintl Chemistry for Designing High Efficiency Thermoelectric Materials. *Chem. Mater.* **2010**, 22 (3), 624–634. <https://doi.org/10.1021/cm901956v>.
- Heremans, J. P.; Jovovic, V.; Toberer, E. S.; Saramat, A.; Kurosaki, K.; Charoenphakdee, A.; Yamanaka, S.; Snyder, G. J. Enhancement of Thermoelectric Efficiency in PbTe by Distortion of the Electronic Density of States. *Science* **2008**, 321 (5888), 554–557. <https://doi.org/10.1126/science.1159725>.
- Heremans, J. P.; Wiodlocha, B.; Chamoire, A. M. Resonant Levels in Bulk Thermoelectric Semiconductors. *Energ. Environ. Sci.* **2012**, 5 (2), 5510–5530. <https://doi.org/10.1039/C1EE02612G>.
- Pei, Y.; Shi, X.; LaLonde, A.; Wang, H.; Chen, L.; Snyder, G. J. Convergence of Electronic Bands for High Performance Bulk Thermoelectrics. *Nature* **2011**, 473 (7345), 66–69. <https://doi.org/10.1038/nature09996>.
- Pei, Y.; Wang, H.; Snyder, G. J. Band Engineering of Thermoelectric Materials. *Adv. Mater.* **2012**, 24 (46), 6125–6135. <https://doi.org/10.1002/adma.201202919>.
- Witting, I. T.; Chasapis, T. C.; Ricci, F.; Peters, M.; Heinz, N. A.; Hautier, G.; Snyder, G. J. The Thermoelectric Properties of Bismuth Telluride. *Adv. Electron. Mater.* **2019**, 5 (6), 1800904. <https://doi.org/10.1002/aem.201800904>.
- Li, Z.; Xiao, C.; Zhu, H.; Xie, Y. Defect Chemistry for Thermoelectric Materials. *J. Am. Chem. Soc.* **2016**, 138 (45), 14810–14819. <https://doi.org/10.1021/jacs.6b08748>.
- Kanatzidis, M. G. Nanostructured Thermoelectrics: The New Paradigm? *Chem. Mater.* **2010**, 22, 648–659. <https://doi.org/10.1021/cm902195j>.
- Liu, W.; Yan, X.; Chen, G.; Ren, Z. Recent Advances in Thermoelectric Nanocomposites. *Nano Energy* **2012**, 1 (1), 42–56. <https://doi.org/10.1016/j.nanoen.2011.10.001>.
- Dresselhaus, M. S.; Chen, G.; Tang, M. Y.; Yang, R. G.; Lee, H.; Wang, D. Z.; Ren, Z. F.; Fluerial, J.-P.; Gogna, P. New Directions for Low-Dimensional Thermoelectric Materials. *Adv. Mater.* **2007**, 19 (8), 1043–1053. <https://doi.org/10.1002/adma.200600527>.
- Gorai, P.; Stevanović, V.; Toberer, E. S. Computationally Guided Discovery of Thermoelectric Materials. *Nat. Rev. Mater.* **2017**, 2 (9), 1–16. <https://doi.org/10.1038/natrevmats.2017.53>.
- Zeier, W. G.; Zevalkin, A.; Gibbs, Z. M.; Hautier, G.; Kanatzidis, M. G.; Snyder, G. J. Thinking Like a Chemist: Intuition in Thermoelectric Materials. *Angew. Chem. Int. Ed.* **2016**. <https://doi.org/10.1002/anie.201508381>.
- Tan, G.; Zhao, L.-D.; Kanatzidis, M. G. Rationally Designing High-Performance Bulk Thermoelectric Materials. *Chem. Rev.* **2016**, 116 (19), 12123–12149. <https://doi.org/10.1021/acs.chemrev.6b00255>.
- Ohkubo, I.; Mori, T. Rational Design of 3d Transition-Metal Compounds for Thermoelectric Properties by Using Periodic Trends in Electron-Correlation Modulation. *J. Am. Chem. Soc.* **2022**, 144 (8), 3590–3602. <https://doi.org/10.1021/jacs.1c12520>.
- Sparks, T. D.; Gaultois, M. W.; Oliynyk, A.; Brgoch, J.; Meredig, B. Data Mining Our Way to the next Generation of Thermoelectrics. *Scr. Mater.* **2016**, 111, 10–15. <https://doi.org/10.1016/j.scriptamat.2015.04.026>.
- Wan, X.; Feng, W.; Wang, Y.; Wang, H.; Zhang, X.; Deng, C.; Yang, N. Materials Discovery and Properties Prediction in Thermal Transport via Materials Informatics: A Mini Review. *Nano Lett.* **2019**, 19 (6), 3387–3395. <https://doi.org/10.1021/acs.nanolett.8b05196>.
- Gaultois, M. W.; Sparks, T. D.; Borg, C. K. H.; Seshadri, R.; Bonificio, W. D.; Clarke, D. R. Data-Driven Review of Thermoelectric Materials: Performance and Resource Considerations. *Chem. Mater.* **2013**, 25 (15), 2911–2920. <https://doi.org/10.1021/cm400893e>.
- Oliynyk, A. O.; Antono, E.; Sparks, T. D.; Ghadbeigi, L.; Gaultois, M. W.; Meredig, B.; Mar, A. High-Throughput Machine-Learning-Driven Synthesis of Full-Heusler Compounds. *Chem. Mater.* **2016**, 28 (20), 7324–7331. <https://doi.org/10.1021/acs.chemmater.6b02724>.
- Owens-Baird, B.; Heinrich, S.; Kovnir, K. Thermoelectric Materials. In *Encyclopedia of Inorganic and Bioinorganic Chemistry*, John Wiley & Sons, Ltd: Chichester, UK, 2017; pp 1–35. <https://doi.org/10.1002/9781119951438.eibc2497>.
- Freer, R.; Ekren, D.; Ghosh, T.; Biswas, K.; Qiu, P.; Wan, S.; Chen, L. D.; Han, S.; Fu, C.; Zhu, T.-J.; Ashiquzzaman Shawon, A. K. M.; Zevalkin, A.; Imasato, K.; Snyder, G. J.; Ozen, M.; Saglik, K.; Aydemir, U.; Cardoso-Gil, R.; Svanidze, E.; Funahashi, R.; Powell, A. V.; Mukherjee, S.; Tippireddy, S.; Vaquero, P.; Gascoin, F.; Kyratsi, T.; Sauerstich, P.; Mori, T. Key Properties of Inorganic Thermoelectric Materials—Tables (Version 1). *J. Phys. Energy* **2022**. <https://doi.org/10.1088/2515-7655/ac49dc>.
- Zhou, X.; Yan, Y.; Lu, X.; Zhu, H.; Han, X.; Chen, G.; Ren, Z. Routes for High-Performance Thermoelectric Materials. *Mater. Today* **2018**, 21 (9), 974–988. <https://doi.org/10.1016/j.mattod.2018.03.039>.
- Zevalkin, A.; Smiadak, D. M.; Blackburn, J. L.; Ferguson, A. J.; Chabiny, M. L.; Delaire, O.; Wang, J.; Kovnir, K.; Martin, J.; Schelhas, L. T.; Sparks, T. D.; Kang, S. D.; Dylla, M. T.; Snyder, G. J.; Ortiz, B. R.; Toberer, E. S. A Practical Field Guide to Thermoelectrics: Fundamentals, Synthesis, and Characterization. *Appl. Phys. Rev.* **2018**, 5 (2), 021303. <https://doi.org/10.1063/1.5021094>.
- Seebeck, T. J. *Magnetische Polarisation Der Metalle Und Erze Durch Temperatur-Differenz*. Abh. Dtsch. Akad. Wiss. Berlin, 1822.
- Haken, W. Beitrag Zur Kenntnis Der Thermoelektrischen Eigenschaften Der Metalllegierungen. *Ann. Phys.* **1910**, 337 (7), 291–336. <https://doi.org/10.1002/andp.19103370704>.
- Mao, J.; Chen, G.; Ren, Z. Thermoelectric Cooling Materials. *Nat. Mater.* **2021**, 20 (4), 454–461. <https://doi.org/10.1038/s41563-020-00852-w>.

42. Zhao, D.; Tan, G. A Review of Thermoelectric Cooling: Materials, Modeling and Applications. *Appl. Therm. Eng.* **2014**, *66* (1), 15–24. <https://doi.org/10.1016/j.applthermaleng.2014.01.074>.
43. Kullmann, W.; Geurts, J.; Richter, W.; Lehner, N.; Rauh, H.; Steigenberger, U.; Eichhorn, G.; Geick, R. Effect of Hydrostatic and Uniaxial Pressure on Structural Properties and Raman Active Lattice Vibrations in Bi_2Te_3 . *Phys. Status Solidi* **1984**, *125* (1), 131–138. <https://doi.org/10.1002/pssb.2221250114>.
44. Goldsmid, H. J. The Improvement of a Specific Material—Bismuth Telluride. In *Introduction to Thermoelectricity*; Goldsmid, H. J., Ed.; Springer Series in Materials Science, Springer: Berlin, Heidelberg, 2016; pp 85–107. https://doi.org/10.1007/978-3-662-49256-7_6.
45. Mao, J.; Zhu, H.; Ding, Z.; Liu, Z.; Gamage, G. A.; Chen, G.; Ren, Z. High Thermoelectric Cooling Performance of N-Type Mg_3Bi_2 -Based Materials. *Science* **2019**, *365* (6452), 495–498. <https://doi.org/10.1126/science.aax7792>.
46. Chen, Y. L.; Analytis, J. G.; Chu, J.-H.; Liu, Z. K.; Mo, S.-K.; Qi, X. L.; Zhang, H. J.; Lu, D. H.; Dai, X.; Fang, Z.; Zhang, S. C.; Fisher, I. R.; Hussain, Z.; Shen, Z.-X. Experimental Realization of a Three-Dimensional Topological Insulator, Bi_2Te_3 . *Science* **2009**, *325* (5937), 178–181. <https://doi.org/10.1126/science.1173034>.
47. Heremans, J. P.; Cava, R. J.; Samarth, N. Tetradymites as Thermoelectrics and Topological Insulators. *Nat. Rev. Mater.* **2017**, *2* (10), 1–21. <https://doi.org/10.1038/natrevmats.2017.49>.
48. Poudel, B.; Hao, Q.; Ma, Y.; Lan, Y.; Minnich, A.; Yu, B.; Yan, X.; Wang, D.; Muto, A.; Vashaee, D.; Chen, X.; Liu, J.; Dresselhaus, M. S.; Chen, G.; Ren, Z. High-Thermoelectric Performance of Nanostructured Bismuth Antimony Telluride Bulk Alloys. *Science* **2008**, *320* (5876), 634–638. <https://doi.org/10.1126/science.1156446>.
49. Deng, R.; Su, X.; Zheng, Z.; Liu, W.; Yan, Y.; Zhang, Q.; Dravid, V. P.; Uher, C.; Kanatzidis, M. G.; Tang, X. Thermal Conductivity in $\text{Bi}_{0.5}\text{Sb}_{1.5}\text{Te}_{3+x}$ and the Role of Dense Dislocation Arrays at Grain Boundaries. *Sci. Adv.* **2018**, *4* (6), eaar5606. <https://doi.org/10.1126/sciadv.aar5606>.
50. Yan, X.; Poudel, B.; Ma, Y.; Liu, W. S.; Joshi, G.; Wang, H.; Lan, Y.; Wang, D.; Chen, G.; Ren, Z. F. Experimental Studies on Anisotropic Thermoelectric Properties and Structures of N-Type $\text{Bi}_2\text{Te}_{2.7}\text{Se}_{0.3}$. *Nano Lett.* **2010**, *10* (9), 3373–3378. <https://doi.org/10.1021/nl101156v>.
51. Liu, W.; Lukas, K. C.; McEnaney, K.; Lee, S.; Zhang, Q.; Opeil, C. P.; Chen, G.; Ren, Z. Studies on the Bi_2Te_3 - Bi_2Se_3 - Bi_2S_3 System for Mid-Temperature Thermoelectric Energy Conversion. *Energ. Environ. Sci.* **2013**, *6* (2), 552–560. <https://doi.org/10.1039/C2EE23549H>.
52. Park, K.; Ahn, K.; Cha, J.; Lee, S.; Chae, S. I.; Cho, S.-P.; Ryee, S.; Im, J.; Lee, J.; Park, S.-D.; Han, M. J.; Chung, I.; Hyeon, T. Extraordinary Off-Stoichiometric Bismuth Telluride for Enhanced n-Type Thermoelectric Power Factor. *J. Am. Chem. Soc.* **2016**, *138* (43), 14458–14468. <https://doi.org/10.1021/jacs.6b09222>.
53. Jason Burton. *U.S. Geological Survey Releases 2022 List of Critical Minerals*. <https://www.usgs.gov/news/national-news-release/us-geological-survey-releases-2022-list-critical-minerals> (accessed 09-03-2022).
54. Berzelius, J. J. Untersuchungen Über Die Flussspathsäure Und Deren Merkwürdigsten Verbindungen. *Ann. Phys.* **1824**, *77* (6), 169–230. <https://doi.org/10.1002/andp.18240770603>.
55. Deville, H. S. C. Mémoire sur le Silicium. *Ann. Chim. Phys.* **1857**, *49* (3), 62–79.
56. Basu, R.; Singh, A. High Temperature Si–Ge Alloy towards Thermoelectric Applications: A Comprehensive Review. *Mater. Today Phys* **2021**, *21*, 100468. <https://doi.org/10.1016/j.mtphys.2021.100468>.
57. Gayner, C.; Kar, K. K. Recent Advances in Thermoelectric Materials. *Prog. Mater. Sci.* **2016**, *83*, 330–382. <https://doi.org/10.1016/j.pmatsci.2016.07.002>.
58. Wolf, M.; Hinterding, R.; Feldhoff, A. High Power Factor vs. High ZT—A Review of Thermoelectric Materials for High-Temperature Application. *Entropy* **2019**, *21* (11), 1058. <https://doi.org/10.3390/e21111058>.
59. Stöhr, H.; Klemm, W. Über Zweistoffsysteme mit Germanium. I. Germanium/Aluminium, Germanium/Zinn und Germanium/Silicium. *Z. Anorg. Allg. Chem.* **1939**, *241* (4), 305–323. <https://doi.org/10.1002/zaac.19392410401>.
60. Jeremy Rehm. *Reviving a Legacy Technology for Spacecraft Exploration*. <https://www.jhuapl.edu/FeatureStory/211025-apl-scientists-help-resurrect-legacy-tech-with-new-twist-nasa-rtg/> (accessed 09-03-2022).
61. Perez-Taborda, J. A.; Muñoz Rojo, M.; Maiz, J.; Neophytou, N.; Martin-Gonzalez, M. Ultra-Low Thermal Conductivities in Large-Area Si-Ge Nanomeshes for Thermoelectric Applications. *Sci. Rep.* **2016**, *6* (1), 32778. <https://doi.org/10.1038/srep32778>.
62. Joshi, G.; Lee, H.; Lan, Y.; Wang, X.; Zhu, G.; Wang, D.; Gould, R. W.; Cuff, D. C.; Tang, M. Y.; Dresselhaus, M. S.; Chen, G.; Ren, Z. Enhanced Thermoelectric Figure-of-Merit in Nanostructured p-Type Silicon Germanium Bulk Alloys. *Nano Lett.* **2008**, *8* (12), 4670–4674. <https://doi.org/10.1021/nl8026795>.
63. Bathula, S.; Jayasimhadri, M.; Gahtori, B.; Kumar, A.; Srivastava, A. K.; Dhar, A. Enhancement in Thermoelectric Performance of SiGe Nanoalloys Dispersed with SiC Nanoparticles. *Phys. Chem. Chem. Phys.* **2017**, *19* (36), 25180–25185. <https://doi.org/10.1039/C7CP04240J>.
64. Bathula, S.; Jayasimhadri, M.; Gahtori, B.; Singh, N. K.; Tyagi, K.; Srivastava, A. K.; Dhar, A. The Role of Nanoscale Defect Features in Enhancing the Thermoelectric Performance of P-Type Nanostructured SiGe Alloys. *Nanoscale* **2015**, *7* (29), 12474–12483. <https://doi.org/10.1039/C5NR01786F>.
65. Mackey, J.; Dynys, F.; Sehirlioglu, A. Si/Ge–W/Si₂ Composites: Processing and Thermoelectric Properties. *Acta Mater.* **2015**, *98*, 263–274. <https://doi.org/10.1016/j.actamat.2015.07.025>.
66. Wang, X. W.; Lee, H.; Lan, Y. C.; Zhu, G. H.; Joshi, G.; Wang, D. Z.; Yang, J.; Muto, A. J.; Tang, M. Y.; Klatsky, J.; Song, S.; Dresselhaus, M. S.; Chen, G.; Ren, Z. F. Enhanced Thermoelectric Figure of Merit in Nanostructured N-Type Silicon Germanium Bulk Alloy. *Appl. Phys. Lett.* **2008**, *93* (19), 193121. <https://doi.org/10.1063/1.3027060>.
67. Laurita, G.; Seshadri, R. Chemistry, Structure, and Function of Lone Pairs in Extended Solids. *Acc. Chem. Res.* **2022**, *55* (7), 1004–1014. <https://doi.org/10.1021/acs.accounts.1c00741>.
68. Shi, X.-L.; Chen, W.-Y.; Tao, X.; Zou, J.; Chen, Z.-G. Rational Structural Design and Manipulation Advance SnSe Thermoelectrics. *Mater. Horiz.* **2020**, *7* (12), 3065–3096. <https://doi.org/10.1039/D0MH00954G>.
69. Jia, B. H.; Jiang, B. B.; He, J. Q. Recent Advances of N-Type Low-Cost PbSe-Based Thermoelectric Materials. *Dent. Mater.* **2019**, *4* (100029), 1–12.
70. Moshwan, R.; Yang, L.; Zou, J.; Chen, Z.-G. Eco-Friendly SnTe Thermoelectric Materials: Progress and Future Challenges. *Adv. Funct. Mater.* **2017**, *27* (43), 1703278. <https://doi.org/10.1002/adfm.201703278>.
71. Peng, P.-P.; Wang, C.; Li, L.-W.; Li, S.-Y.; Chen, Y.-Q. Research Status and Performance Optimization of Medium-Temperature Thermoelectric Material SnTe. *Chinese Phys. B* **2021**. <https://doi.org/10.1088/1674-1056/ac20c9>.
72. Tan, G.; Shi, F.; Hao, S.; Zhao, L.-D.; Chi, H.; Zhang, X.; Uher, C.; Wolverton, C.; Dravid, V. P.; Kanatzidis, M. G. Non-Equilibrium Processing Leads to Record High Thermoelectric Figure of Merit in PbTe–SrTe. *Nat. Commun.* **2016**, *7* (1), 12167. <https://doi.org/10.1038/ncomms12167>.
73. Wu, Y.; Chen, Z.; Nan, P.; Xiong, F.; Lin, S.; Zhang, X.; Chen, Y.; Chen, L.; Ge, B.; Pei, Y. Lattice Strain Advances Thermoelectrics. *Joule* **2019**, *3* (5), 1276–1288. <https://doi.org/10.1016/j.joule.2019.02.008>.
74. Zhang, Q.; Wang, H.; Liu, W.; Wang, H.; Yu, B.; Zhang, Q.; Tian, Z.; Ni, G.; Lee, S.; Esfarjani, K.; Chen, G.; Ren, Z. Enhancement of Thermoelectric Figure-of-Merit by Resonant States of Aluminium Doping in Lead Selenide. *Energ. Environ. Sci.* **2012**, *5* (1), 5246–5251. <https://doi.org/10.1039/C1EE02465E>.
75. Zhang, Q.; Chere, E. K.; McEnaney, K.; Yao, M.; Cao, F.; Ni, Y.; Chen, S.; Opeil, C.; Chen, G.; Ren, Z. Enhancement of Thermoelectric Performance of N-Type PbSe by Cr Doping with Optimized Carrier Concentration. *Adv. Energy Mater.* **2015**, *5* (8), 1401977. <https://doi.org/10.1002/aenm.201401977>.
76. Wu, C.-F.; Wei, T.-R.; Sun, F.-H.; Li, J.-F. Nanoporous PbSe–SiO₂ Thermoelectric Composites. *Adv. Sci.* **2017**, *4* (11), 1700199. <https://doi.org/10.1002/advs.201700199>.
77. Zhou, C.; Lee, Y. K.; Cha, J.; Yoo, B.; Cho, S.-P.; Hyeon, T.; Chung, I. Defect Engineering for High-Performance n-Type PbSe Thermoelectrics. *J. Am. Chem. Soc.* **2018**, *140* (29), 9282–9290. <https://doi.org/10.1021/jacs.8b05741>.
78. Hong, M.; Zou, J.; Chen, Z.-G. Thermoelectric GeTe with Diverse Degrees of Freedom Having Secured Superhigh Performance. *Adv. Mater.* **2019**, *31* (14), 1807071. <https://doi.org/10.1002/adma.201807071>.
79. Zhang, X.; Li, J.; Wang, X.; Chen, Z.; Mao, J.; Chen, Y.; Pei, Y. Vacancy Manipulation for Thermoelectric Enhancements in GeTe Alloys. *J. Am. Chem. Soc.* **2018**, *140* (46), 15883–15888. <https://doi.org/10.1021/jacs.8b09375>.

80. Shimano, S.; Tokura, Y.; Taguchi, Y. Carrier Density Control and Enhanced Thermoelectric Performance of Bi and Cu Co-Doped GeTe. *APL Mater.* **2017**, *5* (5), 056103. <https://doi.org/10.1063/1.4983404>.
81. Roychowdhury, S.; Biswas, K. Slight Symmetry Reduction in Thermoelectrics. *Chem* **2018**, *4* (5), 939–942. <https://doi.org/10.1016/j.chempr.2018.04.013>.
82. Li, J.; Zhang, X.; Lin, S.; Chen, Z.; Pei, Y. Realizing the High Thermoelectric Performance of GeTe by Sb-Doping and Se-Alloying. *Chem. Mater.* **2017**, *29* (2), 605–611. <https://doi.org/10.1021/acs.chemmater.6b04066>.
83. Gelbstein, Y.; Davidov, J.; Girard, S. N.; Chung, D. Y.; Kanatzidis, M. Controlling Metallurgical Phase Separation Reactions of the $\text{Ge}_{0.87}\text{Pb}_{0.13}\text{Te}$ Alloy for High Thermoelectric Performance. *Adv. Energy Mater.* **2013**, *3* (6), 815–820. <https://doi.org/10.1002/aenm.201200970>.
84. Hong, M.; Wang, Y.; Liu, W.; Matsumura, S.; Wang, H.; Zou, J.; Chen, Z.-G. Arrays of Planar Vacancies in Superior Thermoelectric $\text{Ge}_{1-x-y}\text{Cd}_x\text{Bi}_y\text{Te}$ with Band Convergence. *Adv. Energy Mater.* **2018**, *8* (30), 1801837. <https://doi.org/10.1002/aenm.201801837>.
85. Zheng, Z.; Su, X.; Deng, R.; Stoumpos, C.; Xie, H.; Liu, W.; Yan, Y.; Hao, S.; Uher, C.; Wolverton, C.; Kanatzidis, M. G.; Tang, X. Rhombohedral to Cubic Conversion of GeTe via MnTe Alloying Leads to Ultralow Thermal Conductivity, Electronic Band Convergence, and High Thermoelectric Performance. *J. Am. Chem. Soc.* **2018**, *140* (7), 2673–2686. <https://doi.org/10.1021/jacs.7b13611>.
86. Zhao, L. D.; Lo, S. H.; Zhang, Y.; Sun, H.; Tan, G.; Uher, C.; Wolverton, C.; Dravid, V. P.; Kanatzidis, M. G. Ultralow Thermal Conductivity and High Thermoelectric Figure of Merit in SnSe Crystals. *Nature* **2014**, *508* (7496), 373–377. <https://doi.org/10.1038/nature13184>.
87. Shi, X.; Wu, A.; Feng, T.; Zheng, K.; Liu, W.; Sun, Q.; Hong, M.; Pantelides, S. T.; Chen, Z.-G.; Zou, J. High Thermoelectric Performance in P-Type Polycrystalline Cd-Doped SnSe Achieved by a Combination of Cation Vacancies and Localized Lattice Engineering. *Adv. Energy Mater.* **2019**, *9* (11), 1803242. <https://doi.org/10.1002/aenm.201803242>.
88. Shi, X.-L.; Zheng, K.; Liu, W.-D.; Wang, Y.; Yang, Y.-Z.; Chen, Z.-G.; Zou, J. Realizing High Thermoelectric Performance in N-Type Highly Distorted Sb-Doped SnSe Microplates via Tuning High Electron Concentration and Inducing Intensive Crystal Defects. *Adv. Energy Mater.* **2018**, *8* (21), 1800775. <https://doi.org/10.1002/aenm.201800775>.
89. Wei, W.; Chang, C.; Yang, T.; Liu, J.; Tang, H.; Zhang, J.; Li, Y.; Xu, F.; Zhang, Z.; Li, J.-F.; Tang, G. Achieving High Thermoelectric Figure of Merit in Polycrystalline SnSe via Introducing Sn Vacancies. *J. Am. Chem. Soc.* **2018**, *140* (1), 499–505. <https://doi.org/10.1021/jacs.7b11875>.
90. Li, S.; Wang, Y.; Chen, C.; Li, X.; Xue, W.; Wang, X.; Zhang, Z.; Cao, F.; Sui, J.; Liu, X.; Zhang, Q. Heavy Doping by Bromine to Improve the Thermoelectric Properties of N-Type Polycrystalline SnSe. *Adv. Sci.* **2018**, *5* (9), 1800598. <https://doi.org/10.1002/adv.201800598>.
91. Luo, Y.; Cai, S.; Hua, X.; Chen, H.; Liang, Q.; Du, C.; Zheng, Y.; Shen, J.; Xu, J.; Wolverton, C.; Dravid, V. P.; Yan, Q.; Kanatzidis, M. G. High Thermoelectric Performance in Polycrystalline SnSe Via Dual-Doping with Ag/Na and Nanostructuring With Ag₈SnSe₆. *Adv. Energy Mater.* **2019**, *9* (2), 1803072. <https://doi.org/10.1002/aenm.201803072>.
92. Qin, B.; Zhang, Y.; Wang, D.; Zhao, Q.; Gu, B.; Wu, H.; Zhang, H.; Ye, B.; Pennycook, S. J.; Zhao, L.-D. Ultrahigh Average ZT Realized in P-Type SnSe Crystalline Thermoelectrics through Producing Extrinsic Vacancies. *J. Am. Chem. Soc.* **2020**, *142* (12), 5901–5909. <https://doi.org/10.1021/jacs.0c01726>.
93. Li, F.; Wang, W.; Ge, Z.-H.; Zheng, Z.; Luo, J.; Fan, P.; Li, B. Enhanced Thermoelectric Properties of Polycrystalline SnSe via LaCl₃ Doping. *Dent. Mater.* **2018**, *11* (2), 203. <https://doi.org/10.3390/ma11020203>.
94. Shi, X.; Zheng, K.; Hong, M.; Liu, W.; Moshwan, R.; Wang, Y.; Qu, X.; Chen, Z.-G.; Zou, J. Boosting the Thermoelectric Performance of P-Type Heavily Cu-Doped Polycrystalline SnSe via Inducing Intensive Crystal Imperfections and Defect Phonon Scattering. *Chem. Sci.* **2018**, *9* (37), 7376–7389. <https://doi.org/10.1039/C8SC02397B>.
95. Ju, H.; Kim, J. Chemically Exfoliated SnSe Nanosheets and Their SnSe/Poly(3,4-Ethylenedioxythiophene):Poly(styrenesulfonate) Composite Films for Polymer Based Thermoelectric Applications. *ACS Nano* **2016**, *10* (6), 5730–5739. <https://doi.org/10.1021/acsnano.5b07355>.
96. Zhou, C.; Lee, Y. K.; Yu, Y.; Byun, S.; Luo, Z.-Z.; Lee, H.; Ge, B.; Lee, Y.-L.; Chen, X.; Lee, J. Y.; Cojocaru-Mirédin, O.; Chang, H.; Im, J.; Cho, S.-P.; Wuttig, M.; Dravid, V. P.; Kanatzidis, M. G.; Chung, I. Polycrystalline SnSe with a Thermoelectric Figure of Merit Greater than the Single Crystal. *Nat. Mater.* **2021**, *20* (10), 1378–1384. <https://doi.org/10.1038/s41563-021-01064-6>.
97. Luo, Y.; Zheng, Y.; Luo, Z.; Hao, S.; Du, C.; Liang, Q.; Li, Z.; Khor, K. A.; Hippalgaonkar, K.; Xu, J.; Yan, Q.; Wolverton, C.; Kanatzidis, M. G. N-Type SnSe₂ Oriented-Nanoplate-Based Pellets for High Thermoelectric Performance. *Adv. Energy Mater.* **2017**, *8* (8), 1702167. <https://doi.org/10.1002/aenm.201702167>.
98. Zhou, M.; Gibbs, Z. M.; Wang, H.; Han, Y.; Xin, C.; Li, L.; Snyder, G. J. Optimization of Thermoelectric Efficiency in SnTe: The Case for the Light Band. *Phys. Chem. Chem. Phys.* **2014**, *16* (38), 20741–20748. <https://doi.org/10.1039/C4CP02091J>.
99. Banik, A.; Shenoy, U. S.; Anand, S.; Waghmare, U. V.; Biswas, K. Mg Alloying in SnTe Facilitates Valence Band Convergence and Optimizes Thermoelectric Properties. *Chem. Mater.* **2015**, *27* (2), 581–587. <https://doi.org/10.1021/cm504112m>.
100. He, J.; Tan, X.; Xu, J.; Liu, G.-Q.; Shao, H.; Fu, Y.; Wang, X.; Liu, Z.; Xu, J.; Jiang, H.; Jiang, J. Valence Band Engineering and Thermoelectric Performance Optimization in SnTe by Mn-Alloying via a Zone-Melting Method. *J. Mater. Chem. A* **2015**, *3* (39), 19974–19979. <https://doi.org/10.1039/C5TA05535K>.
101. Zhang, Q.; Liao, B.; Lan, Y.; Lukas, K.; Liu, W.; Esfarjani, K.; Opeil, C.; Broido, D.; Chen, G.; Ren, Z. High Thermoelectric Performance by Resonant Dopant Indium in Nanostructured SnTe. *PNAS* **2013**, *110* (33), 13261–13266. <https://doi.org/10.1073/pnas.1305735110>.
102. Pei, Y.; Zheng, L.; Li, W.; Lin, S.; Chen, Z.; Wang, Y.; Xu, X.; Yu, H.; Chen, Y.; Ge, B. Interstitial Point Defect Scattering Contributing to High Thermoelectric Performance in SnTe. *Adv. Electron. Mater.* **2016**, *2* (6), 1600019. <https://doi.org/10.1002/aem.201600019>.
103. Zhao, L.-D.; Zhang, X.; Wu, H.; Tan, G.; Pei, Y.; Xiao, Y.; Chang, C.; Wu, D.; Chi, H.; Zheng, L.; Gong, S.; Uher, C.; He, J.; Kanatzidis, M. G. Enhanced Thermoelectric Properties in the Counter-Doped SnTe System with Strained Endotaxial SrTe. *J. Am. Chem. Soc.* **2016**, *138* (7), 2366–2373. <https://doi.org/10.1021/jacs.5b13276>.
104. Hussain, T.; Li, X.; Danish, M. H.; Rehman, M. U.; Zhang, J.; Li, D.; Chen, G.; Tang, G. Realizing High Thermoelectric Performance in Eco-Friendly SnTe via Synergistic Resonance Levels, Band Convergence and Endotaxial Nanostructuring with Cu₂Te. *Nano Energy* **2020**, *73*, 104832. <https://doi.org/10.1016/j.nanoen.2020.104832>.
105. Zhang, X.; Shen, J.; Lin, S.; Li, J.; Chen, Z.; Li, W.; Pei, Y. Thermoelectric Properties of GeSe. *J. Materiomics* **2016**, *2*, 331–337. <https://doi.org/10.1016/j.jmat.2016.09.001>.
106. Sarkar, D.; Roychowdhury, S.; Arora, R.; Ghosh, T.; Vasdev, A.; Joseph, B.; Sheet, G.; Waghmare, U. V.; Biswas, K. Metavalent Bonding in GeSe Leads to High Thermoelectric Performance. *Angew. Chem. Int. Ed.* **2021**, *60* (18), 10350–10358. <https://doi.org/10.1002/anie.202101283>.
107. Liu, H.; Zhang, X.; Li, W.; Pei, Y. Advances in Thermoelectric (GeTe) x (AgSbTe₂)_{100-x}. *Chinese Phys. B* **2021**. <https://doi.org/10.1088/1674-1056/ac3cae>.
108. Yang, S. H.; Zhu, T. J.; Sun, T.; He, J.; Zhang, S. N.; Zhao, X. B. Nanostructures in High-Performance (GeTe)(AgSbTe₂)_{100-x} Thermoelectric Materials. *Nanotechnology* **2008**, *19* (24), 245707. <https://doi.org/10.1088/0957-4484/19/24/245707>.
109. Cook, B. A.; Harringa, J. L.; Besser, M.; Venkatasubramanian, R. Improvement in the Thermoelectric Figure-of-Merit of TAGS-85 by Rare Earth Additions. *MRS OPL* **2011**, *1325* (1), 703. <https://doi.org/10.1557/opl.2011.1258>.
110. Wang, J.; Lebedev, O. I.; Lee, K.; Dolyuniuk, J.-A.; Klavins, P.; Bux, S.; Kovnir, K. High-Efficiency Thermoelectric Ba₈Cu₁₄Ge₆P₂₆: Bridging the Gap between Tetrel-Based and Tetrel-Free Clathrates. *Chem. Sci.* **2017**, *8* (12), 8030–8038. <https://doi.org/10.1039/C7SC03482B>.
111. Wang, J.; Mark, J.; Woo, K. E.; Voyles, J.; Kovnir, K. Chemical Flexibility of Mg in Pnictide Materials: Structure and Properties Diversity. *Chem. Mater.* **2019**, *31* (20), 8286–8300. <https://doi.org/10.1021/acs.chemmater.9b03740>.
112. Bhardwaj, A.; Chauhan, N. S.; Misra, D. K. Significantly Enhanced Thermoelectric Figure of Merit of P-Type Mg₃Sb₂-Based Zintl Phase Compounds via Nanostructuring and Employing High Energy Mechanical Milling Coupled with Spark Plasma Sintering. *J. Mater. Chem. A* **2015**, *3* (20), 10777–10786. <https://doi.org/10.1039/C5TA02155C>.
113. Chen, X.; Wu, H.; Cui, J.; Xiao, Y.; Zhang, Y.; He, J.; Chen, Y.; Cao, J.; Cai, W.; Pennycook, S. J.; Liu, Z.; Zhao, L.-D.; Sui, J. Extraordinary Thermoelectric Performance in N-Type Manganese Doped Mg₃Sb₂ Zintl: High Band Degeneracy, Tuned Carrier Scattering Mechanism and Hierarchical Microstructure. *Nano Energy* **2018**, *52*, 246–255. <https://doi.org/10.1016/j.nanoen.2018.07.059>.
114. Goyal, G. K.; Mukherjee, S.; Mallik, R. C.; Vitta, S.; Samajdar, I.; Dasgupta, T. High Thermoelectric Performance in Mg₂(Si_{0.3}Sn_{0.7}) by Enhanced Phonon Scattering. *ACS Appl. Energy Mater.* **2019**, *2* (3), 2129–2137. <https://doi.org/10.1021/acsaem.8b02148>.

115. de Boor, J.; Saparamadu, U.; Mao, J.; Dahal, K.; Müller, E.; Ren, Z. Thermoelectric Performance of Li Doped, p-Type $\text{Mg}_2(\text{Ge},\text{Sn})$ and Comparison With $\text{Mg}_2(\text{Si},\text{Sn})$. *Acta Mater.* **2016**, *120*, 273–280. <https://doi.org/10.1016/j.actamat.2016.08.057>.
116. Zheng, Y.; Liu, C.; Miao, L.; Li, C.; Huang, R.; Gao, J.; Wang, X.; Chen, J.; Zhou, Y.; Nishibori, E. Extraordinary Thermoelectric Performance in MgAgSb Alloy With Ultralow Thermal Conductivity. *Nano Energy* **2019**, *59*, 311–320. <https://doi.org/10.1016/j.nanoen.2019.02.045>.
117. Hu, Y.; Wang, J.; Kawamura, A.; Kovnir, K.; Kauzlarich, S. M. $\text{Yb}_{14}\text{MgSb}_{11}$ and $\text{Ca}_{14}\text{MgSb}_{11}$ —New Mg-Containing Zintl Compounds and Their Structures, Bonding, and Thermoelectric Properties. *Chem. Mater.* **2015**, *27* (1), 343–351. <https://doi.org/10.1021/cm504059t>.
118. Hayashi, K.; Saito, W.; Sugimoto, K.; Ohoyama, K.; Hayashi, K.; Happo, N.; Harada, M.; Oikawa, K.; Inamura, Y.; Miyazaki, Y. Preparation, Thermoelectric Properties, and Crystal Structure of Boron-Doped Mg_2Si Single Crystals. *AIP Adv.* **2020**, *10* (3), 035115. <https://doi.org/10.1063/1.5143839>.
119. Gao, P.; Davis, J. D.; Poltavets, V. V.; Hogan, T. P. The P-Type $\text{Mg}_2\text{Li}_x\text{Si}_{0.4}\text{Sn}_{0.6}$ Thermoelectric Materials Synthesized by a B_2O_3 Encapsulation Method Using Li_2CO_3 as the Doping Agent. *J. Mater. Chem. C* **2016**, *4* (5), 929–934. <https://doi.org/10.1039/C5TC03692E>.
120. Gao, P.; Berkun, I.; Schmidt, R. D.; Luzenski, M. F.; Lu, X.; Bordon Sarac, P.; Case, E. D.; Hogan, T. P. Transport and Mechanical Properties of High-ZT $\text{Mg}_{2.06}\text{Si}_{0.4-x}\text{Sn}_{0.6}\text{Sb}_x$ Thermoelectric Materials. *J. Electron. Mater.* **2014**, *43* (6), 1790–1803. <https://doi.org/10.1007/s11664-013-2865-8>.
121. Yin, K.; Su, X.; Yan, Y.; You, Y.; Zhang, Q.; Uher, C.; Kanatzidis, M. G.; Tang, X. Optimization of the Electronic Band Structure and the Lattice Thermal Conductivity of Solid Solutions According to Simple Calculations: A Canonical Example of the $\text{Mg}_2\text{Si}_{1-x}\text{YGeSn}_x$ Ternary Solid Solution. *Chem. Mater.* **2016**, *28* (15), 5538–5548. <https://doi.org/10.1021/acs.chemmater.6b02308>.
122. Khan, A. U.; Vlachos, P.; Kyratsi, T. High Thermoelectric Figure of Merit of $\text{Mg}_2\text{Si}_{0.55}\text{Sn}_{0.4}\text{Ge}_{0.05}$ Materials Doped With Bi and Sb. *Scr. Mater.* **2013**, *69* (8), 606–609. <https://doi.org/10.1016/j.scriptamat.2013.07.008>.
123. Liu, W.; Zhang, Q.; Yin, K.; Chi, H.; Zhou, X.; Tang, X.; Uher, C. High Figure of Merit and Thermoelectric Properties of Bi-Doped $\text{Mg}_2\text{Si}_{0.4}\text{Sn}_{0.6}$ Solid Solutions. *J. Solid State Chem.* **2013**, *203*, 333–339. <https://doi.org/10.1016/j.jssc.2013.04.041>.
124. Cordero, B.; Gómez, V.; Platero-Prats, A. E.; Revés, M.; Echeverría, J.; Cremades, E.; Barragán, F.; Alvarez, S. Covalent Radii Revisited. *Dalton Trans.* **2008**, *21*, 2832–2838. <https://doi.org/10.1039/B801115J>.
125. Shannon, R. D. Revised Effective Ionic Radii and Systematic Studies of Interatomic Distances in Halides and Chalcogenides. *Acta Cryst A* **1976**, *32* (5), 751–767. <https://doi.org/10.1107/S0567739476001551>.
126. Kamila, H.; Sahu, P.; Sankhla, A.; Yasser, M.; Pham, H.-N.; Dasgupta, T.; Mueller, E.; de Boor, J. Analyzing Transport Properties of P-Type Mg_2Si – Mg_2Sn Solid Solutions: Optimization of Thermoelectric Performance and Insight into the Electronic Band Structure. *J. Mater. Chem. A* **2019**, *7* (3), 1045–1054. <https://doi.org/10.1039/C8TA08920E>.
127. Li, A.; Fu, C.; Zhao, X.; Zhu, T. High-Performance $\text{Mg}_3\text{Sb}_{2-x}\text{Bi}_x$ Thermoelectrics: Progress and Perspective. *Research* **2020**, *2020*. <https://doi.org/10.34133/2020/1934848>.
128. Zhang, J.; Song, L.; Iversen, B. B. Insights into the Design of Thermoelectric Mg_3Sb_2 and Its Analogs by Combining Theory and Experiment. *NPJ Comput Mater* **2019**, *5* (1), 1–17. <https://doi.org/10.1038/s41524-019-0215-y>.
129. Peng, W.; Petretto, G.; Rignanes, G.-M.; Hautier, G.; Zevkink, A. An Unlikely Route to Low Lattice Thermal Conductivity: Small Atoms in a Simple Layered Structure. *Joule* **2018**, *2* (9), 1879–1893. <https://doi.org/10.1016/j.joule.2018.06.014>.
130. Imasato, K.; Wood, M.; Kuo, J. J.; Snyder, G. J. Improved Stability and High Thermoelectric Performance through Cation Site Doping in N-Type La-Doped $\text{Mg}_3\text{Sb}_{1.5}\text{Bi}_{0.5}$. *J. Mater. Chem. A* **2018**, *6* (41), 19941–19946. <https://doi.org/10.1039/C8TA08975B>.
131. Chen, X.; Zhu, J.; Qin, D.; Qu, N.; Xue, W.; Wang, Y.; Zhang, Q.; Cai, W.; Guo, F.; Sui, J. Excellent Thermoelectric Performance of Boron-Doped n-Type Mg_3Sb_2 -Based Materials via the Manipulation of Grain Boundary Scattering and Control of Mg Content. *Sci. China Mater.* **2021**, *64* (7), 1761–1769. <https://doi.org/10.1007/s40843-020-1559-4>.
132. Mao, J.; Wu, Y.; Song, S.; Zhu, Q.; Shuai, J.; Liu, Z.; Pei, Y.; Ren, Z. Defect Engineering for Realizing High Thermoelectric Performance in N-Type Mg_3Sb_2 -Based Materials. *ACS Energy Lett.* **2017**, *2* (10), 2245–2250. <https://doi.org/10.1021/acsenergylett.7b00742>.
133. Imasato, K.; Kang, S. D.; Snyder, G. J. Exceptional Thermoelectric Performance in $\text{Mg}_3\text{Sb}_{0.6}\text{Bi}_{1.4}$ for Low-Grade Waste Heat Recovery. *Energ. Environ. Sci.* **2019**, *12* (3), 965–971. <https://doi.org/10.1039/C8EE03374A>.
134. Tamaki, H.; Sato, H. K.; Kanno, T. Isotropic Conduction Network and Defect Chemistry in $\text{Mg}_{3+x}\text{Sb}_2$ -Based Layered Zintl Compounds with High Thermoelectric Performance. *Adv. Mater.* **2016**, *28* (46), 10182–10187. <https://doi.org/10.1002/adma.201603955>.
135. Shi, X.; Sun, C.; Bu, Z.; Zhang, X.; Wu, Y.; Lin, S.; Li, W.; Faghaninia, A.; Jain, A.; Pei, Y. Revelation of Inherently High Mobility Enables Mg_3Sb_2 as a Sustainable Alternative to $\text{N-Bi}_2\text{Te}_3$ Thermoelectrics. *Adv. Sci.* **2019**, *6* (16), 1802286. <https://doi.org/10.1002/advs.201802286>.
136. Imasato, K.; Anand, S.; Gurunathan, R.; Snyder, G. J. The Effect of Mg_3As_2 Alloying on the Thermoelectric Properties of N-Type $\text{Mg}_3(\text{Sb}, \text{Bi})_2$. *Dalton Trans.* **2021**, *50* (27), 9376–9382. <https://doi.org/10.1039/D1DT01600H>.
137. Kanno, T.; Tamaki, H.; Sato, H. K.; Kang, S. D.; Ohno, S.; Imasato, K.; Kuo, J. J.; Snyder, G. J.; Miyazaki, Y. Enhancement of Average Thermoelectric Figure of Merit by Increasing the Grain-Size of $\text{Mg}_{3-x}\text{Sb}_{1.5}\text{Bi}_{0.49}\text{Te}_{0.01}$. *Appl. Phys. Lett.* **2018**, *112* (3), 033903. <https://doi.org/10.1063/1.5016488>.
138. Pan, Y.; Yao, M.; Hong, X.; Zhu, Y.; Fan, F.; Imasato, K.; He, Y.; Hess, C.; Fink, J.; Yang, J.; Büchner, B.; Fu, C.; Snyder, G. J.; Felser, C. $\text{Mg}_3(\text{Bi},\text{Sb})_2$ Single Crystals towards High Thermoelectric Performance. *Energ. Environ. Sci.* **2020**, *13* (6), 1717–1724. <https://doi.org/10.1039/D0EE00838A>.
139. Liu, Z.; Sato, N.; Gao, W.; Yubuta, K.; Kawamoto, N.; Mitome, M.; Kurashima, K.; Owada, Y.; Nagase, K.; Lee, C.-H.; Yi, J.; Tsuchiya, K.; Mori, T. Demonstration of Ultrahigh Thermoelectric Efficiency of $\sim 7.3\%$ in $\text{Mg}_3\text{Sb}_2/\text{MgAgSb}$ Module for Low-Temperature Energy Harvesting. *Joule* **2021**, *5* (5), 1196–1208. <https://doi.org/10.1016/j.joule.2021.03.017>.
140. Ying, P.; Li, X.; Wang, Y.; Yang, J.; Fu, C.; Zhang, W.; Zhao, X.; Zhu, T. Hierarchical Chemical Bonds Contributing to the Intrinsically Low Thermal Conductivity in α - MgAgSb Thermoelectric Materials. *Adv. Funct. Mater.* **2017**, *27* (1), 1604145. <https://doi.org/10.1002/adfm.201604145>.
141. Li, X.; Liu, P.-F.; Zhao, E.; Zhang, Z.; Guidi, T.; Le, M. D.; Avdeev, M.; Ikeda, K.; Otomo, T.; Kofu, M.; Nakajima, K.; Chen, J.; He, L.; Ren, Y.; Wang, X.-L.; Wang, B.-T.; Ren, Z.; Zhao, H.; Wang, F. Ultralow Thermal Conductivity from Transverse Acoustic Phonon Suppression in Distorted Crystalline α - MgAgSb . *Nat. Commun.* **2020**, *11* (1), 942. <https://doi.org/10.1038/s41467-020-14772-5>.
142. Liu, Z.; Mao, J.; Sui, J.; Ren, Z. High Thermoelectric Performance of α - MgAgSb for Power Generation. *Energ. Environ. Sci.* **2018**, *11* (1), 23–44. <https://doi.org/10.1039/C7EE02504A>.
143. Ying, P.; Liu, X.; Fu, C.; Yue, X.; Xie, H.; Zhao, X.; Zhang, W.; Zhu, T. High Performance α - MgAgSb Thermoelectric Materials for Low Temperature Power Generation. *Chem. Mater.* **2015**, *27* (3), 909–913. <https://doi.org/10.1021/cm5041826>.
144. Mi, J.-L.; Ying, P.-J.; Sist, M.; Reardon, H.; Zhang, P.; Zhu, T.-J.; Zhao, X.-B.; Iversen, B. B. Elaborating the Crystal Structures of MgAgSb Thermoelectric Compound: Polymorphs and Atomic Disorders. *Chem. Mater.* **2017**, *29* (15), 6378–6388. <https://doi.org/10.1021/acs.chemmater.7b01768>.
145. Yang, J.-Y.; Zhang, W.; Hu, M. Decoupling Thermal and Electrical Transport in α - MgAgSb with Synergic Pressure and Doping Strategy. *J. Appl. Phys.* **2019**, *125* (20), 205105. <https://doi.org/10.1063/1.5090456>.
146. Zhao, H.; Sui, J.; Tang, Z.; Lan, Y.; Jie, Q.; Kraemer, D.; McEnaney, K.; Guloy, A.; Chen, G.; Ren, Z. High Thermoelectric Performance of MgAgSb -Based Materials. *Nano Energy* **2014**, *7*, 97–103. <https://doi.org/10.1016/j.nanoen.2014.04.012>.
147. Brown, S. R.; Kauzlarich, S. M.; Gascoin, F.; Snyder, G. J. $\text{Yb}_{14}\text{MnSb}_{11}$: New High Efficiency Thermoelectric Material for Power Generation. *Chem. Mater.* **2006**, *18* (7), 1873–1877. <https://doi.org/10.1021/cm060261t>.
148. Cordier, G.; Schäfer, H.; Stelter, M. Darstellung und Struktur der Verbindung $\text{Ca}_{14}\text{AlSb}_{11}$. *Z. Anorg. Allg. Chem.* **1984**, *519* (12), 183–188. <https://doi.org/10.1002/zaac.19845191219>.

149. Hu, Y.; Cerretti, G.; Kunz Wille, E. L.; Bux, S. K.; Kauzlarich, S. M. The Remarkable Crystal Chemistry of the $\text{Ca}_{14}\text{AlSb}_{11}$ Structure Type, Magnetic and Thermoelectric Properties. *J. Solid State Chem.* **2019**, *271*, 88–102. <https://doi.org/10.1016/j.jssc.2018.12.037>.
150. Wille, E. L. K.; Jo, N. H.; Fettingler, J. C.; Canfield, P. C.; Kauzlarich, S. M. Single Crystal Growth and Magnetic Properties of the Mixed Valent Yb Containing Zintl Phase, $\text{Yb}_{14}\text{MgSb}_{11}$. *Chem. Commun.* **2018**, *54* (92), 12946–12949. <https://doi.org/10.1039/C8CC05471A>.
151. Lindsay, L.; Broido, D. A.; Reinecke, T. L. First-Principles Determination of Ultrahigh Thermal Conductivity of Boron Arsenide: A Competitor for Diamond? *Phys. Rev. Lett.* **2013**, *111* (2), 025901 <https://doi.org/10.1103/PhysRevLett.111.025901>.
152. Kang, J. S.; Li, M.; Wu, H.; Nguyen, H.; Hu, Y. Experimental Observation of High Thermal Conductivity in Boron Arsenide. *Science* **2018**, *361* (6402), 575–578. <https://doi.org/10.1126/science.aat5522>.
153. Li, S.; Zheng, Q.; Lv, Y.; Liu, X.; Wang, X.; Huang, P. Y.; Cahill, D. G.; Lv, B. High Thermal Conductivity in Cubic Boron Arsenide Crystals. *Science* **2018**, *361* (6402), 579–581. <https://doi.org/10.1126/science.aat8982>.
154. Tian, F.; Song, B.; Chen, X.; Ravichandran, N. K.; Lv, Y.; Chen, K.; Sullivan, S.; Kim, J.; Zhou, Y.; Liu, T.-H.; Goni, M.; Ding, Z.; Sun, J.; Udalamatta Gamage, G. A. G.; Sun, H.; Ziyadeh, H.; Huyan, S.; Deng, L.; Zhou, J.; Schmidt, A. J.; Chen, S.; Chu, C.-W.; Huang, P. Y.; Broido, D.; Shi, L.; Chen, G.; Ren, Z. Unusual High Thermal Conductivity in Boron Arsenide Bulk Crystals. *Science* **2018**, *361* (6402), 582–585. <https://doi.org/10.1126/science.aat7932>.
155. He, A.; Bux, S. K.; Hu, Y.; Uhl, D.; Li, L.; Donadio, D.; Kauzlarich, S. M. Structural Complexity and High Thermoelectric Performance of the Zintl Phase: $\text{Yb}_{21}\text{Mn}_4\text{Sb}_{18}$. *Chem. Mater.* **2019**, *31* (19), 8076–8086. <https://doi.org/10.1021/acs.chemmater.9b02671>.
156. Caillat, T.; Fleurial, J.-P.; Borschchovsky, A. Preparation and Thermoelectric Properties of Semiconducting Zn_4Sb_3 . *J. Phys. Chem. Solid* **1997**, *58* (7), 1119–1125. [https://doi.org/10.1016/S0022-3697\(96\)00228-4](https://doi.org/10.1016/S0022-3697(96)00228-4).
157. Mayer, H. W.; Mikhail, I.; Schubert, K. Über einige phasen der Mischungen ZnSb und CdSb . *J. Less-Common Met.* **1978**, *59* (1), 43–52. [https://doi.org/10.1016/0022-5088\(78\)90109-1](https://doi.org/10.1016/0022-5088(78)90109-1).
158. Mozharivskiy, Y.; Pecharsky, A. O.; Bud'ko, S.; Miller, G. J. A Promising Thermoelectric Material: Zn_4Sb_3 or $\text{Zn}_{6-\Delta}\text{Sb}_5$. Its Composition, Structure, Stability, and Polymorphs. Structure and Stability of $\text{Zn}_{1-\Delta}\text{Sb}$. *Chem. Mater.* **2004**, *16* (8), 1580–1589. <https://doi.org/10.1021/cm035274a>.
159. Toberer, E. S.; Rauwel, P.; Gariel, S.; Taftø, J.; Snyder, G. J. Composition and the Thermoelectric Performance of $\beta\text{-Zn}_4\text{Sb}_3$. *J. Mater. Chem.* **2010**, *20* (44), 9877–9885. <https://doi.org/10.1039/C0JM02011G>.
160. Snyder, G. J.; Christensen, M.; Nishibori, E.; Caillat, T.; Iversen, B. B. Disordered Zinc in Zn_4Sb_3 with Phonon-Glass and Electron-Crystal Thermoelectric Properties. *Nat. Mater.* **2004**, *3* (7), 458–463. <https://doi.org/10.1038/nmat1154>.
161. Shaver, P. J.; Blair, J. Thermal and Electronic Transport Properties of $\beta\text{-ZnSb}$. *Phys. Ther. Rev.* **1966**, *141* (2), 649–663. <https://doi.org/10.1103/PhysRev.141.649>.
162. Wang, J.; Kovnir, K. Elusive $\beta\text{-Zn}_4\text{Sb}_3$: A New Zinc Antimonide Thermoelectric. *J. Am. Chem. Soc.* **2015**, *137* (39), 12474–12477. <https://doi.org/10.1021/jacs.5b08214>.
163. He, A.; Svitylyk, V.; Chernyshov, D.; Mozharivskiy, Y. Identification, Structural Characterization and Transformations of the High-Temperature $\text{Zn}_{9-\delta}\text{Sb}_7$ Phase in the Zn–Sb System. *Dalton Trans.* **2015**, *44* (48), 20983–20990. <https://doi.org/10.1039/C5DT03509K>.
164. Rull-Bravo, M.; Moure, A.; Fernández, J. F.; Martín-González, M. Skutterudites as Thermoelectric Materials: Revisited. *RSC Adv.* **2015**, *5* (52), 41653–41667. <https://doi.org/10.1039/C5RA03942H>.
165. Luo, H.; Krizan, J. W.; Muechler, L.; Haldolaarachchige, N.; Klimczuk, T.; Xie, W.; Fuccillo, M. K.; Felser, C.; Cava, R. J. A Large Family of Filled Skutterudites Stabilized by Electron Count. *Nat. Commun.* **2015**, *6* (1), 6489. <https://doi.org/10.1038/ncomms7489>.
166. Sales, B. C.; Mandrus, D.; Williams, R. K. Filled Skutterudite Antimonides: A New Class of Thermoelectric Materials. *Science* **1996**, *272* (5266), 1325–1328. <https://doi.org/10.1126/science.272.5266.1325>.
167. Nolas, G. S., Ed.; The Physics and Chemistry of Inorganic Clathrates; *Springer Series in Materials Science* vol. 199; Springer Netherlands: Dordrecht, 2014. <https://doi.org/10.1007/978-94-017-9127-4>.
168. Shevelkov, A.; Kovnir, K. Zintl Clathrates. In *Zintl Phases: Principles and Recent Developments*; Fässler, T. F., Ed.; *Structure and Bonding*, Springer, 2011; pp 97–142.
169. Dolyaniuk, J. A.; Owens-Baird, B.; Wang, J.; Zaikina, J. V.; Kovnir, K. Clathrate Thermoelectrics. *Mater. Sci. Eng. R* **2016**, *108*, 1–46. <https://doi.org/10.1016/j.mser.2016.08.001>.
170. Dong, J.; Sankey, O. F.; Myles, C. W. Theoretical Study of the Lattice Thermal Conductivity in Ge Framework Semiconductors. *Phys. Rev. Lett.* **2001**, *86* (11), 2361–2364. <https://doi.org/10.1103/PhysRevLett.86.2361>.
171. Stefanoski, S.; Martin, J.; Nolas, G. S. Low Temperature Transport Properties and Heat Capacity of Single-Crystal $\text{Na}_3\text{Si}_4\text{Ge}_4$. *J. Phys. Condens. Matter* **2010**, *22* (48), 485404. <https://doi.org/10.1088/0953-8984/22/48/485404>.
172. Carrillo-Cabrera, W.; Budnyk, S.; Prots, Y.; Grin, Y.; Ba₈Ge₄₃ Revisited: A $2a \times 2a \times 2a$ Superstructure of the Clathrate-I Type with Full Vacancy Ordering. *Z. Anorg. Allg. Chem.* **2004**, *630* (13–14), 2267–2276. <https://doi.org/10.1002/zaac.200400268>.
173. Dünner, J.; Mewis, A. Ba₈Cu₁₆P₃₀—Eine Neue Ternäre Variante Des Clathrat I-Strukturtyps. *Z. Anorg. Allg. Chem.* **1995**, *621* (2), 191–196. <https://doi.org/10.1002/zaac.19956210205>.
174. Wang, J.; Dolyaniuk, J.-A.; Kovnir, K. Unconventional Clathrates With Transition Metal–Phosphorus Frameworks. *Acc. Chem. Res.* **2018**, *51* (1), 31–39. <https://doi.org/10.1021/acs.accounts.7b00469>.
175. Fulmer, J.; Lebedev, O. I.; Roddatis, V. V.; Kaseman, D. C.; Sen, S.; Dolyaniuk, J. A.; Lee, K.; Olenev, A. V.; Kovnir, K. Clathrate Ba₈Au₁₆P₃₀: The “Gold Standard” for Lattice Thermal Conductivity. *J. Am. Chem. Soc.* **2013**, *135* (33), 12313–12323. <https://doi.org/10.1021/ja4052679>.
176. Yox, P.; Lebedev, O. I.; Donadio, D.; Kovnir, K. Unprecedented Superstructure in the Type I Family of Clathrates. *Chem. Commun.* **2021**, *57*, 13780–13783. <https://doi.org/10.1039/D1CC05167A>.
177. Owens-Baird, B.; Wang, J.; Wang, S. G.; Chen, Y. S.; Lee, S.; Donadio, D.; Kovnir, K. III-V Clathrate Semiconductors with Outstanding Hole Mobility: Cs₈In₂₇Sb₁₉ and A₈Ga₂₇Sb₁₉ (A = Cs, Rb). *J. Am. Chem. Soc.* **2020**, *142* (4), 2031–2041. <https://doi.org/10.1021/jacs.9b12351>.
178. Owens-Baird, B.; Yox, P.; Lee, S.; Carroll, X. B.; Grass Wang, S.; Chen, Y.-S.; Lebedev, O. I.; Kovnir, K. Chemically Driven Superstructural Ordering Leading to Giant Unit Cells in Unconventional Clathrates Cs₈Zn₁₈Sb₂₈ and Cs₈Cd₁₈Sb₂₈. *Chem. Sci.* **2020**, *11* (37), 10255–10264. <https://doi.org/10.1039/D0SC03846F>.
179. Samson, S. Crystal Structure of NaCd₂. *Nature* **1962**, *195* (4838), 259–262. <https://doi.org/10.1038/195259a0>.
180. Yang, Q.-B.; Andersson, S.; Stenberg, L. An Alternative Description of the Structure of NaCd₂. *Acta Crystallogr. B* **1987**, *43* (1), 14–16. <https://doi.org/10.1107/S0108768187098379>.
181. Samson, S. The Crystal Structure of the Phase $\beta\text{Mg}_2\text{Al}_3$. *Acta Crystallogr.* **1965**, *19* (3), 401–413. <https://doi.org/10.1107/S0365110X65005133>.
182. Weber, T.; Dshemuchadse, J.; Kobas, M.; Conrad, M.; Harbrecht, B.; Steurer, W.; Large, L. Largest—A Family of Cluster-Based Tantalum Copper Aluminides with Giant Unit Cells. I. Structure Solution and Refinement. *Acta Crystallogr. B* **2009**, *65* (3), 308–317. <https://doi.org/10.1107/S0108768109014001>.
183. Conrad, M.; Harbrecht, B.; Weber, T.; Jung, D. Y.; Steurer, W.; Large, L. Largest—A Family of Cluster-Based Tantalum Copper Aluminides with Giant Unit Cells. II. The Cluster Structure. *Acta Crystallogr. B* **2009**, *65* (3), 318–325. <https://doi.org/10.1107/S0108768109014013>.
184. Kovnir, K.; Shatruk, M. Magnetism in Giant Unit Cells—Crystal Structure and Magnetic Properties of $\text{R}_{17}\text{Co}_{52+\delta}\text{Sn}_{12+\gamma}$ (R = Sm, Tb, Dy). *Euro. J. Inorg. Chem* **2011**, *2011* (26), 3955–3962. <https://doi.org/10.1002/ejic.201100200>.
185. Pecharsky, V. K.; Bodak, O. I.; Bel'skii, V. K.; Starodub, P. K.; Mokra, I. R.; Gladyshevskii, E. I. Crystal Structure of $\text{Tb}_{17}\text{Fe}_{52}\text{Ge}_{12}$. *Kristallografiya* **1987**, *32*, 334–338.
186. Schmitt, D. C.; Haldolaarachchige, N.; Xiong, Y.; Young, D. P.; Jin, R.; Chan, J. Y. Probing the Lower Limit of Lattice Thermal Conductivity in an Ordered Extended Solid: $\text{Gd}_{17}\text{Co}_{56}\text{Sn}_{112}$, a Phonon Glass–Electron Crystal System. *J. Am. Chem. Soc.* **2012**, *134* (13), 5965–5973. <https://doi.org/10.1021/ja300240g>.

187. Fredrickson, D. C. Parallels in Structural Chemistry between the Molecular and Metallic Realms Revealed by Complex Intermetallic Phases. *Acc. Chem. Res.* **2018**, *51* (2), 248–257. <https://doi.org/10.1021/acs.accounts.7b00625>.
188. Gautier, R.; Zhang, X.; Hu, L.; Yu, L.; Lin, Y.; Sunde, T. O. L.; Chon, D.; Poeppelmeier, K. R.; Zunger, A. Prediction and Accelerated Laboratory Discovery of Previously Unknown 18-Electron ABX Compounds. *Nat. Chem.* **2015**, *7* (4), 308–316. <https://doi.org/10.1038/nchem.2207>.
189. Antonyshyn, I.; Wagner, F. R.; Bobnar, M.; Sichevych, O.; Burkhardt, U.; Schmidt, M.; König, M.; Poeppelmeier, K.; Mackenzie, A. P.; Svanidze, E.; Grin, Y. Micro-Scale Device—An Alternative Route for Studying the Intrinsic Properties of Solid-State Materials: The Case of Semiconducting TaGe. *Angew. Chem. Int. Ed.* **2020**, *59* (27), 11136–11141. <https://doi.org/10.1002/anie.202002693>.
190. Wei, J.; Wang, G. Properties of Half-Heusler Compounds TaIrGe by Using First-Principles Calculations. *Appl. Phys. A* **2017**, *123* (5), 375. <https://doi.org/10.1007/s00339-017-0990-6>.

4.04 Non-oxide p-block (semi-)metal chalcogenide cage compounds

Stefanie Dehnen and Niklas Rinn, Fachbereich Chemie and Wissenschaftliches Zentrum für Materialwissenschaften, Philipps Universität Marburg, Marburg, Germany

© 2023 Elsevier Ltd. All rights reserved.

4.04.1	Introduction	80
4.04.2	Group 13 chalcogenide clusters	81
4.04.2.1	Heterocubane-type and related cluster cores	81
4.04.2.1.1	General synthesis methods of group 13 chalcogenide clusters	81
4.04.2.1.2	Reactivity and application	82
4.04.2.2	Supertetrahedral clusters	85
4.04.2.3	Clusters based on other architectures	88
4.04.3	Group 14 chalcogenide clusters	91
4.04.3.1	Compounds based on purely inorganic $[T_4E_{10}]^{4-}$ supertetrahedra	92
4.04.3.2	Organotetrel chalcogenide clusters based on adamantane-type $\{T_4E_6\}$ or semicubane-type $\{T_3E_4\}$ cores	98
4.04.3.2.1	Structural motifs of the inorganic cores of organotetrel chalcogenide clusters, and their general synthetic approach	98
4.04.3.2.2	Synthesis and structures of organotetrel chalcogenide clusters	100
4.04.3.3	Tetrel chalcogenide clusters with or without organic ligands based on other architectures	121
4.04.4	Group 15 chalcogenide clusters	128
4.04.5	Clusters with p-block (semi)metals from different groups	130
4.04.6	Conclusion	131
References		132

Abstract

Non-oxide (semi)metal chalcogenide clusters bear a large variety of structural motifs, mainly due to the large atomic size of the S, Se, and Te atoms, as compared to an O atom, connecting the (semi)metal atoms. This way, not only the bridging modes are more flexible, easily reaching a μ^4 - or μ^5 -type situations, but also a larger distance of the positively charged (semi)metal atoms that are connected by larger atoms enable an increase of the variety of possible connection patterns. In this survey, we present the variety of non-oxide chalcogenide clusters of p-block (semi)metals. Besides a summary of the broad spectrum of different cage and cluster architectures, we also refer to other chemical or physical properties of such compounds, which point towards their meaningfulness beyond purely fundamental synthetic or analytic work. However, we would like to emphasize that the basic research that allowed for to the discovery of this multitude of cluster types was key to all subsequent findings.

4.04.1 Introduction

(Semi)metal chalcogenide clusters have been in the focus of many research groups over the past decades, as they exhibit a large variety of interesting structural, chemical, and physical properties as a consequence of different synthetic approaches as well as difference elemental combinations.^{1–4} While the structures inform about possible formation processes and trends as well as restrictions during the generation of such species, the elemental combinations enable to fine-tune not only the structures but also the opto-electronic properties; the latter affects both the physical properties of the cluster compounds and their reactivity in homogeneous and heterogeneous environments.^{5–7}

In this review chapter, we summarize known cage and cluster compounds, in which p-block (semi)metal atoms of group 13 (triels, Tr; Al, Ga, In, Tl), group 14 (tetrels, Tt; Si, Ge, Sn, Pb), or group 15 (pnictogens, Pn; Sb, Bi) are combined with group 16 atoms (chalcogens, E; S, Se, Te) as ligands. We exclude oxide clusters, which would probably double the contents, and concentrate the collection on heavier homologues, mostly because these allow for narrower band gaps and an even broader structural variety. The latter can be put down to the general possibility to expand the bridging mode of the chalcogenide ligand, and to allow for virtually all possible modes of connections of subunits given the larger atomic sizes. We intend to introduce all kinds of structural motifs and the compounds based on them, and shed light on additional physical and chemical properties of the compounds.

In the sections to follow, we will present molecular compounds of group 13, 14, or 15 atoms, ordered by S, Se, or Te atoms as bridging ligands. We will use common cluster structures with increasing size as another classification criterion. We explicitly exclude all kinds of extended structures in this overview.

4.04.2 Group 13 chalcogenide clusters

Chalcogenide clusters of group 13 (semi)metals are often discussed with respect to the semiconducting properties of the underlying binary phases, as the molecules may be used as precursors for controlled single-source phase-formation, and for the preparation of corresponding quantum dots or other model systems. Dominating cluster archetypes found for the corresponding elemental combinations are heterocubane-type cages and different types of supertetrahedral architectures. Both will be detailed below.

4.04.2.1 Heterocubane-type and related cluster cores

The most common structural archetype in group 13 chalcogenide cluster chemistry is the ligand-stabilized heterocubane $[\text{RTrE}]_4$ ($\text{Tr} = \text{Al}, \text{Ga}, \text{In}$; $\text{E} = \text{S}, \text{Se}, \text{Te}$). In the following paragraphs, we will summarize general synthesis methods, besides reactivity and applications of such compounds.

4.04.2.1.1 General synthesis methods of group 13 chalcogenide clusters

The first successful synthesis and structural characterizations were carried out in 1991, simultaneously by two groups. In one of the reports, this cluster family was observed during an investigation of the reactivity of ${}^t\text{Bu}_3\text{Ga}$ towards an excess of H_2S .⁸ The resulting dimeric complex $[\text{}^t\text{Bu}_2\text{Ga}(\mu\text{-SH})]_2$ eliminates ${}^t\text{Bu}$ units above $45\text{ }^\circ\text{C}$ to form the air-insensitive and temperature-stable $[\text{}^t\text{BuGaS}]_4$ (**1**, Fig. 1), which is based on a heterocubane-type cage. The other author team obtained the same compound and its heavier congeners by using elemental chalcogenides instead of H_2E ,⁹ a synthesis method which was also explored in a follow up paper.¹⁰ $[\text{}^t\text{BuGaS}]_4$ (**1**) can be obtained via the usage of S_8 at higher temperatures, while an analogue reaction using red Se can already transform ${}^t\text{Bu}_3\text{Ga}$ to $[\text{}^t\text{BuGaSe}]_4$ (**2**) at room temperature. Gray selenium as well as tellurium only yield the chalcogenolate-bridged dimers $[(\text{}^t\text{Bu})_2\text{Ga}(\mu\text{-Et,Bu})]_2$ ($\text{E} = \text{Se}, \text{Te}$). To generate the desired heterocubane-type clusters-type clusters **2** or $[\text{}^t\text{BuGaTe}]_4$ (**3**), either those chalcogenolate dimers or ${}^t\text{Bu}_3\text{Ga}$ need to be treated with an excess of the corresponding chalcogen at higher temperatures. The work reported in ref. 9 additionally covered analogous reactions of ${}^t\text{Bu}_3\text{Al}$ to form $[\text{}^t\text{BuAlE}]_4$ ($\text{E} = \text{S}$: **4**; $\text{E} = \text{Se}$: **5**; $\text{E} = \text{Te}$: **6**), which mirror those of their Ga homologues.⁹

Another synthesis method for obtaining Al-containing heterocubane-type chalcogenide clusters is the treatment of the tetrahedral Al(I) compound $[\text{Cp}^*\text{Al}]_4$ ($\text{Cp}^* = \eta^5\text{-C}_5\text{Me}_5$) with elemental Se or Te at room temperature to quantitatively form the compounds $[\text{Cp}^*\text{AlE}]_4$ ($\text{E} = \text{Se}$: **7**; $\text{E} = \text{Te}$: **8**, Fig. 1).¹¹ The reactivity in this case can be attributed to the formation of a (favored) Al(III) product. The utilization of H_2E ($\text{E} = \text{S}, \text{Se}$) as a chalcogenide source in reactions with $(\text{Me}_2\text{EtC})_3\text{Al}$ can lead to $[\text{Me}_2\text{EtCAIE}]_4$ ($\text{E} = \text{S}$: **9**; $\text{E} = \text{Se}$: **10**), similarly to reactions with Ga congeners described above, while the heaviest homologue, $[\text{Me}_2\text{EtCAITe}]_4$ (**11**), remains accessible through the use of elemental Te only.¹²

Similar to one of the Al-based examples described above, the first In congeners stabilized by organic ligands could be obtained by reacting tetrahedral $[\text{RIn}]_4$ compounds with elemental chalcogens, although elevated temperatures are needed for the reactions to take place. This way, the cages $[\{(\text{SiMe}_3)_3\text{C}\}\text{InE}]_4$ ($\text{E} = \text{S}$: **12**, $\text{E} = \text{Se}$: **13**, $\text{E} = \text{Te}$: **14**, Fig. 1) can be isolated from $[\text{In}\{(\text{SiMe}_3)_3\text{C}\}]_4$.^{13,14} It was shown later that R_3In can also be used as In source to form compounds like $[(\text{Me}_2\text{EtC})\text{InSe}]_4$ (**15**) or $[(\text{Me}_2\text{EtC})\text{InTe}]_4$ (**16**).^{15,16}

Apart from elemental and hydrogenated chalcogen sources, a third valuable alternative are silylated compounds $\text{E}(\text{SiMe}_3)_2$, which can be used to generate heterocubane-type clusters upon addition to RTrCl_2 . This was shown first for a reaction of Cp^*GaCl_3 with $\text{Te}(\text{SiMe}_3)_2$ resulting in the synthesis of $[\text{Cp}^*\text{GaTe}]_4$ (**17**).¹⁷

While other routes starting out from dimeric intermediates exist, similar to the first ones described for Ga compounds, these can most often be skipped by using an excess of the chalcogen source and/or higher temperatures. Thus, the three predominant synthesis methods for heterocubane-type cages can be summarized in Scheme 1.

There are a few different and more exotic methods of cluster preparation. It was reported, for instance, that tmp_2GaCl ($\text{tmp} = 2,2,6,6\text{-tetramethylpiperidin}$) forms $[\text{tmpGaS}]_4$ (**18**) upon treatment with KSCN as the sulfide source and a K^+ -sequestering reagent (18-crown-6).¹⁸

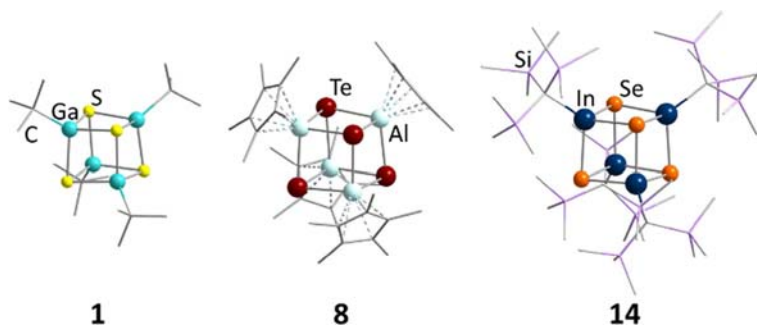
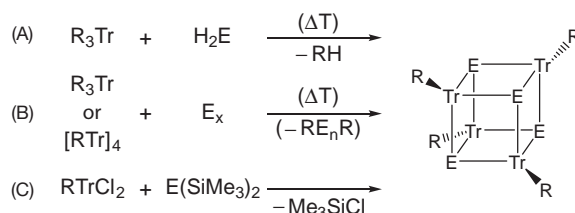


Fig. 1 Three examples of simple group 13/16 heterocubane-type clusters with different elemental compositions and ligands. $[\text{}^t\text{BuGaS}]_4$ (**1**), $[\text{Cp}^*\text{AlTe}]_4$ (**8**), and $[\{(\text{SiMe}_3)_3\text{C}\}\text{InSe}]_4$ (**14**).



Scheme 1 Three possible synthesis routes towards heterocubane-type clusters: (A) using H_2E and R_3Tr , (B) starting from an elemental chalcogen and R_3Tr or $[\text{RTr}]_4$ and (C) utilizing a condensation reaction of $\text{E}(\text{SiMe}_3)_2$ with RTrCl_2 .

In a variation to method C, the addition of H_2S to $(\text{Me}_3\text{Si})_3\text{CALMe}_2$ resulted in a dimeric solvent-coordinated intermediate, $[(\text{thf})\{\text{Me}_3\text{Si}\}_3\text{CAl}(\mu\text{-SH})_2]$ which upon heating yields a mixture of $[(\text{Me}_3\text{Si})_3\text{CALSi}]_4$ (19) and the unsymmetrically substituted cluster $[\{(\text{Me}_3\text{Si})_3\text{CAL}\}_3\text{MeAlSi}_4]$ (20), in which one organic ligand is replaced by a Me group stemming from the decomposition of the $(\text{Me}_3\text{Si})_3\text{C}$ ligand (Fig. 2).¹⁹

Although in this survey, we intend to concentrate on cages that do not contain transition metal atoms, it needs to be noted that In and Ga heterocubane-type clusters that are prepared via route C can also be stabilized by $\{(\text{Cp})(\text{CO}_2)_2\text{M}\}$ moieties ($\text{M} = \text{Fe}, \text{Mo}$) instead of an organic ligand. In this way, $[\{(\text{Cp})(\text{CO}_2)_2\text{Fe}\}\text{InE}]_4$ ($\text{E} = \text{S}$: 21; $\text{E} = \text{Se}$: 22), $[\{(\text{Cp})(\text{CO}_2)_2\text{Mo}\}\text{InE}]_4$ ($\text{E} = \text{S}$: 23; $\text{E} = \text{Te}$: 24), and $[\{(\text{Cp})(\text{CO}_2)_2\text{Fe}\}\text{InE}]_4$ ($\text{E} = \text{S}$: 25; $\text{E} = \text{Se}$: 26; $\text{E} = \text{Te}$: 27) were obtained.^{20,21}

The solvothermal reaction of InCl_3 with the tridentate chelating ligand 1,10-phenanthroline (phen) and elemental S or Se in aqueous solution leads to the formation of heterocubane-type clusters $[\text{phenInClE}]_4$ (28: $\text{E} = \text{S}$; 29: $\text{E} = \text{Se}$, Fig. 3), stabilized by the coordinative attachment of a neutral ligand.²² To compensate for the resulting positive charges, each In atom additionally carries a Cl ligand, thereby expanding the coordination sphere to an octahedron. The experiments could also be reproduced using 2,2'-bipyridine (bipy) instead of phen, leading to the isostructural molecules $[2,2'\text{-bipyInClE}]_4$ ($\text{E} = \text{S}$: 30; $\text{E} = \text{Se}$: 31).²³ The absorption behavior of these compounds is of interest, owing to the cluster-ligand charge transfer, which affects the electronic properties of the compounds.

Going one step further, a cationic cage with exclusively neutral ligands, $[(\text{dmtf})_3\text{InS}_4(\text{ClO}_4)_4]$ (32, Fig. 3), was realized in 2011 by reaction of indium perchlorate with *N,N*-dimethylthioformamid (DMTF). The cluster exhibits an octahedral coordination sphere at the In atoms.²⁴

Notably, a stable Tl congener could not be obtained yet. When using an unconventional synthesis method by reacting the ditriels $[\text{R}_2\text{Tr}]_2$ ($\text{R} = \text{Si}^t\text{Bu}_3$) with elemental selenium the presence of $[(\text{Si}^t\text{Bu}_3)\text{TlSe}]_4$ (33) is suggested by ⁷⁷Se NMR, while the Al and In congeners could be isolated using this approach.²⁵

4.04.2.1.2 Reactivity and application

While most heterocubane-type clusters can be sublimated without decomposition, repeated vaporization and recrystallization of $[\text{BuGaS}]_4$ (1) at atmospheric pressure leads to the formation of an octameric cluster $[\text{BuGaS}]_8$ (34). Most likely, it consists of two $\{\text{Ga}_4\text{S}_4\}$ eight-membered rings that are arranged in an octagonal-prismatic fashion.¹⁰ This rearrangement was expanded in a subsequent study, where it was shown that prolonged refluxing in *n*-hexane or a solid state thermolysis caused the formation of a heptamer, $[\text{BuGaS}]_7$ (35), the crystal structure of which could be determined. According to it, a condensation of two defect-heterocubane subunits, $[(\text{BuGa})_4\text{S}_3]$ and $[(\text{BuGa})_3\text{S}_4]$, obviously took place at their deficient position. Dissolving 1, or any of the aforementioned oligomers, in pyridine yields compounds based on a trimeric unit, $[\text{BuGa}(\text{py})\text{S}]_3$, that can be further pyrolysed to form hexagonal crystals of the hexagonal prismatic hexamer $[\text{BuGaS}]_6$ (36, Fig. 4). Here, two parallel, six-membered rings are

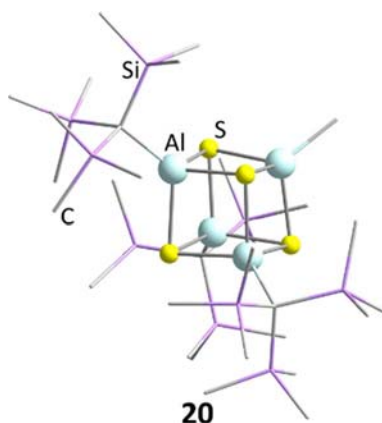


Fig. 2 Compound $[\{(\text{Me}_3\text{Si})_3\text{CAL}\}_3\text{MeAlSi}_4]$ (20) with an unsymmetrical substitution pattern.

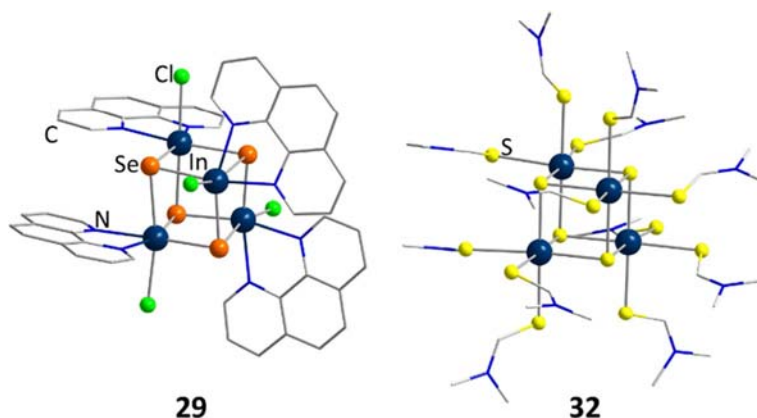


Fig. 3 Cluster compounds with neutral organic ligands [*phen*InClSe]₄ (**29**, phen = 1,10-phenanthroline) and [(*dmtf*)₃InS]₄(ClO₄)₄ (**32**, *dmtf* = *N,N*-dimethylthioformamid).

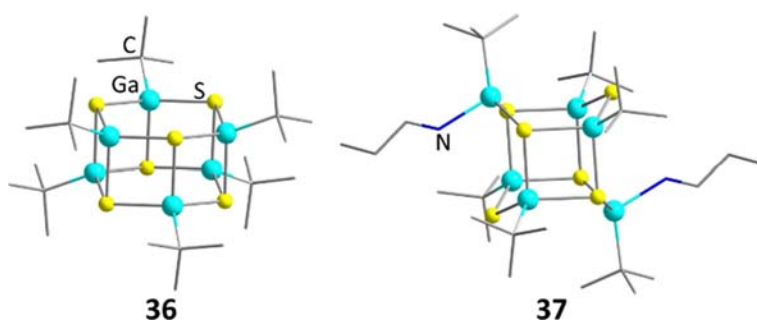
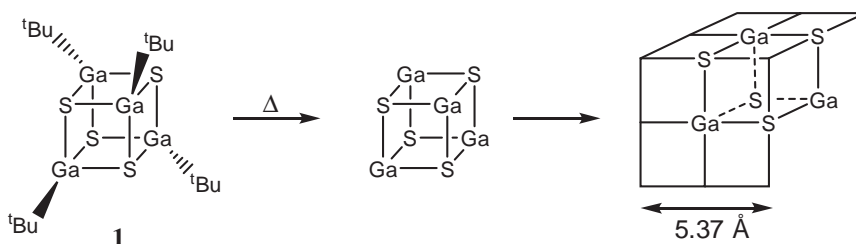


Fig. 4 Hexameric clusters [^{*t*}BuGaS]₄ (**36**) and [(^{*t*}BuGa)₆(μ₃-S)₄(μ-S)₂(^{*n*}PrNH₂)₂] (**37**) formed from [^{*t*}BuGaS]₄ (**1**).

slightly distorted towards a chair conformation.²⁶ A hexameric unit with a different structural motif, [(^{*t*}BuGa)₆(μ₃-S)₄(μ-S)₂(^{*n*}PrNH₂)₂] (**37**, Fig. 4) is obtained by the addition of ^{*n*}PrNH₂ to **1** and subsequent heating in toluene.²⁷ The inorganic core comprises two Ga₃S₃ six-membered rings adopting a boat conformation. These are connected via four in-plane Ga and S atom by four Ga–S bonds between the rings to result in a heterocubane-type motif. Each of the Ga atoms carries a ^{*t*}Bu ligand, with the two out-of-plane Ga atoms being additionally coordinated by an ^{*n*}PrNH₂ unit each. This ligand interacts with the out-of-plane μ-S ligand of an adjacent cluster via hydrogen bridging. Heating at 110 °C in vacuum leads to the elimination of ^{*n*}PrNH₂ and subsequent formation of **36** by returning the out-of-plane Ga and S atoms to an in-plane position.

For compounds with sterically highly demanding ligands, like [(SiMe₃)₃C]GaS]₄ (**38**), the dissociation of the heterocubane into two dimeric molecules [(SiMe₃)₃C]GaS]₂ was shown in benzene, with the coordinatively unsaturated product being stabilized by its shielding ligands. This effect does not occur in the Se and Te congeners, which is attributed to the higher strain on the cage in **38**.²⁸

The stability and relative ease of sublimation of the heterocubane-type clusters, which was observed in studies on their formation, and later more deeply explored in a study about the volatility of [RGaE]₄ (R = Me_xEt_{3-x}C; E = S, Se, Te),²⁹ render them interesting single source precursors for the generation of TrE semiconductor layers or nanoparticles by metal organic chemical vapor deposition (MOCVD). [^{*t*}BuGaS]₄ (**1**) can be evaporated at 225 °C and deposited on various substrates at 400 °C to form a previously unknown metastable cubic modification of GaS with a NaCl-type crystal structure (Scheme 2 and Fig. 5).³⁰



Scheme 2 Vapor-phase deposition leading to a cubic GaS phase under retention of structural features of [^{*t*}BuGaS]₄ (**1**).

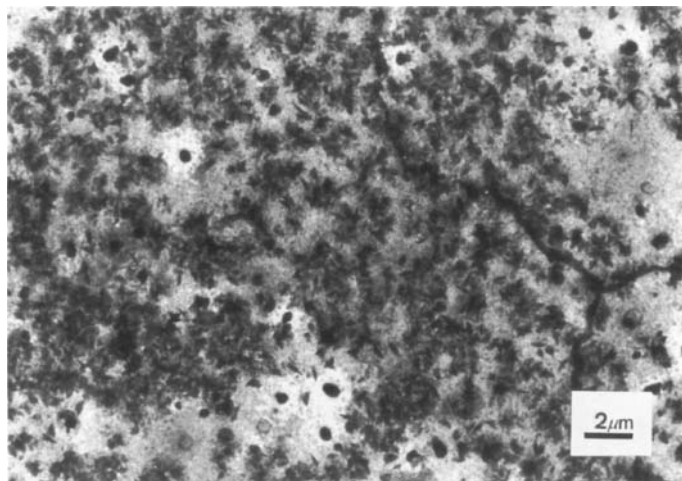


Fig. 5 Bright-field image of polycrystalline cubic GaS generated by gas-phase deposition of $[\text{}^t\text{BuGaS}]_4$ (**1**).³⁰

Below a temperature of 380 °C, or above 400 °C, a deposition leads to amorphous layers instead, with the high temperature deposition showing an additional sulfur-rich polycrystalline, yet unidentified, phase down-flow of a sulfur deficient amorphous phase.³¹ As neither the heptameric $[\text{}^t\text{BuGaS}]_7$ (**35**) nor a dimeric compound $[(\text{}^t\text{Bu})_2\text{GaS}]_2$ can be used to deposit the novel cubic GaS-phase, it was concluded that the arrangement of the inorganic cores plays a major role during MOCVD; presumably, the retention of the cubic structure in **1** can lead to a crystal packing, while the topology of **35** does not allow for it, hence logically yielding amorphous materials. Similarly, if the cluster core were to decompose before deposition, as was shown through photolysis during photo-assisted CVD, the thermodynamically stable hexagonal GaS would be favored.³²

In order to create a liquid alternative to **1** that does not rearrange to a heptamer, and at the same time can be synthesized more easily in large scale, two derivatives with asymmetric ligands were synthesized, $[(\text{Me}_2\text{EtC})\text{GaS}]_4$ (**39**) and $[(\text{MeEt}_2\text{C})\text{GaS}]_4$ (**40**).³³ Both compounds show an excellent stability in the solid state as well as in the gas phase and, while vaporizing at higher temperatures when compared to **1**, melt before doing so. In addition, they do not exhibit any rearrangement of the cluster core under thermal treatment. Compound **39**, vaporizing at lower temperatures (221 °C) was also shown to produce the same cubic GaS layer as was observed for **1**.

To investigate the deposition of heterocubanes-type compounds with a different elemental buildup, $[\text{}^t\text{BuGaSe}]_4$ (**2**) and $[(\text{Me}_2\text{EtC})\text{InSe}]_4$ (**15**) were vaporized (which required vacuum conditions for **15**) and deposited, and the resulting films were analyzed.¹⁵ These were shown to consist of nanoparticulate spheres of hexagonal GaSe and InSe (Fig. 6). The fact that no cubic

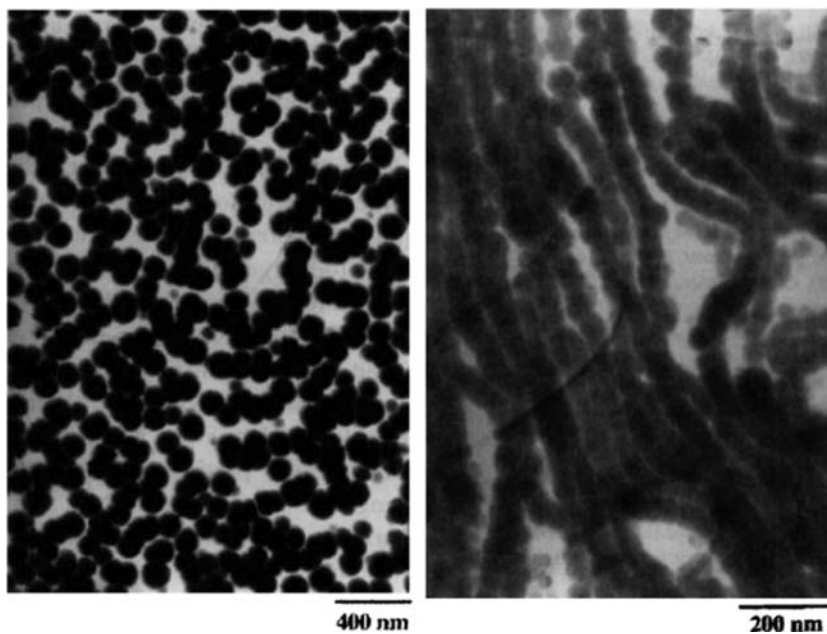


Fig. 6 TEM images of polycrystalline spheres of InS (left) obtained from $[(\text{Me}_2\text{EtC})\text{InS}]_4$ (**15**), and strings of beads of GaSe (right) obtained from $[\text{}^t\text{BuGaSe}]_4$ (**2**).¹⁵

structure related to the cluster cores was found was put down to the weaker bonds in the (semi)metal selenide cluster cores; their much quicker decomposition thus leads to similar results as in the photo-assisted CVD studies discussed before.

The telluride compound $[\text{BuGaTe}]_4$ (3) as well as its derivatives $[(\text{Me}_2\text{EtC})\text{GaTe}]_4$ (41) and $[(\text{MeEt}_2\text{C})\text{Te}]_4$ (42) could only be successfully volatilized in vacuum.³⁴ The layers resulting from MOCVD consist of a hexagonal GaTe modification analogous to that obtained from GaSe heterocubane-type clusters, albeit metastable in this case. This also sheds light on the decomposition mechanism of the heterocubane-type clusters in the gas phase. An indiscriminate decomposition would lead to the thermodynamically most stable modifications, or an amorphous layer being formed, but the consistent formation of hexagonal phases suggests a more controlled deconstruction of the cluster compounds to $[\text{RTrE}]_3$ ($\text{E} = \text{Se}, \text{Te}$) trimers, which can also be found in mass spectra of such compounds.

The notable influence of the organic ligand on the buildup of deposited layers was made obvious in a study about CVD experiments using $[\text{Cp}^*\text{GaS}]_4$ (43) and $[\text{Cp}^*\text{GaSe}]_4$ (44).³⁵ While these compounds can be sublimed without decomposition at 185 °C and 205 °C, respectively, depositions on substrates at a temperature of 310 °C and 290 °C does lead to Ga-deficient uniform and amorphous layers with an elemental composition of Ga_2E_3 ($\text{E} = \text{S}, \text{Se}$). Thus, unlike for the previously discussed Se and Te compounds, these cluster cores seem to decompose more heavily, or in a more uncontrolled fashion. This effect was also reported for $[\text{BuInSe}]_4$ (45), a compound more similar to the previously discussed $[(\text{Me}_2\text{EtC})\text{InSe}]_4$ (46). MOCVD of 45 leads to smooth In metal layers, while hexagonal crystalline material could not be observed at any temperature or substrate such as for 15.³⁶

One study on the reactivity of a heterocubane-type cluster with a transition metal complex has been reported.³⁷ Addition of $[\text{Cp}_2\text{ZrMe}_2]$ to $[\text{BuAlS}]_4$ (4) in a 1:1 ratio leads to the fragmentation of the initial cluster under formation of the intermediate products $[\text{Cp}_2\text{Zr}(\mu\text{-S})(\mu\text{-Me})\text{Al}(\text{Bu})\text{Me}]$ and $[\text{Cp}_2\text{Zr}(\mu_3\text{-S})_3\text{Al}_3(\text{Bu})_3\text{Me}_2]$, both of which decompose over time to form the dimeric compound $[\text{Cp}_2\text{Zr}(\mu\text{-S})_2]$. The same reaction, yet starting from $[\text{BuGaS}]_4$ (1), only yielded the analogous cage compound $[\text{Cp}_2\text{Zr}(\mu_3\text{-S})_3\text{Ga}_3(\text{Bu})_3\text{Me}_2]$. Those cages can be understood as a $[\text{BuTrS}]_3$ trimer with a Dewar benzene like buildup complemented by Cp_2Zr . When changing the reactant ratio of 1 versus Cp_2ZrMe_2 to 4:1, only the dimeric complex $[\text{Cp}_2\text{Zr}\{\mu\text{-SGa}(\text{Me}_2)\text{Bu}\}]$ is obtained.

4.04.2.2 Supertetrahedral clusters

Another prominent structural motif for many chalcogenide clusters across the periodic table is the supertetrahedron in its diverse modes of appearance. The construction of larger tetrahedral molecules by (formally) condensing tetrahedral $\{\text{TrE}_4\}$ units via corner-sharing is summarized in the Tn nomenclature. This is based upon the number of $\{\text{TrE}_4\}$ units along one edge of the large tetrahedron (see Fig. 7). A T1 cluster thus denominates a simple $\{\text{TrE}_4\}$ unit, while an adamantane-like topology corresponds to a T2 cluster, and so on. Another series of supertetrahedra are constructed by additionally considering inverted tetrahedral units, $\{\text{EM}_4\}$ (with M being a (semi) metal in general), thus leading to another construction principle and the so-called pentatetrahedral Pn family. There exist also defect-variants of the respective clusters or mixed forms, which are not detailed herein. As there are many different synthetic approaches, we mention them in the context of the respective compounds.

In this chapter, all known compounds of such clusters will be discussed, starting from adamantane-type units and proceeding to the larger T3-type compounds.

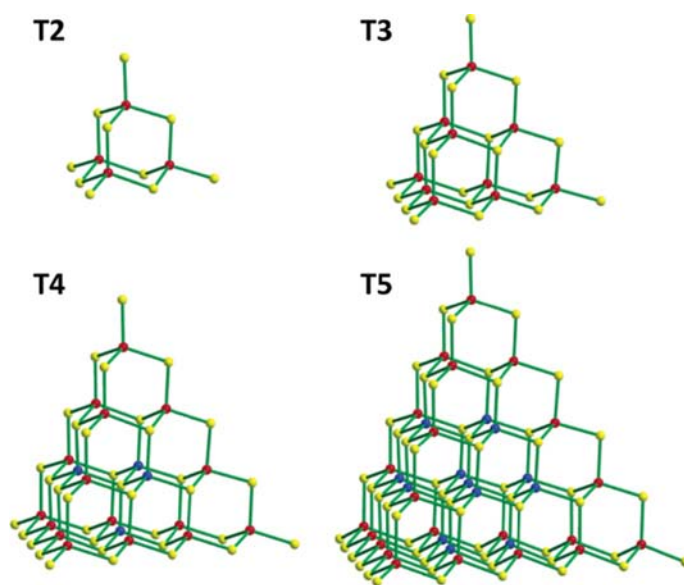


Fig. 7 Examples for the first four family members of Tn-type supertetrahedral clusters beyond the simple tetrahedron T1.³

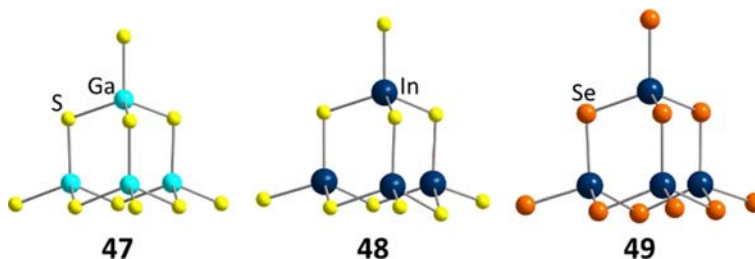


Fig. 8 Anionic adamantane-type clusters $[\text{Ga}_4\text{S}_{10}]^{8-}$ (47), $[\text{In}_4\text{S}_{10}]^{8-}$ (48) and $[\text{In}_4\text{S}_{10}]^{8-}$ (49) as simple examples for T2 clusters.

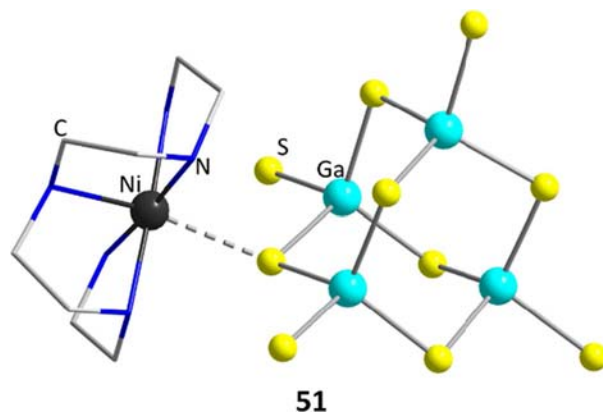


Fig. 9 Anionic adamantane-type cluster $[\text{Ga}_4\text{S}_6(\text{SH})_4]^{4-}$ and its coordination to a $[\text{Ni}(\text{tepa})]^{2+}$ (tepa = tetraethylenepentamine) complex fragment in compound 51.

The first examples of adamantane-type group 13 chalcogenide compounds were obtained by reactions of Ga_2S_3 or In_2S_3 with K_2S , or In_2Se_3 with K_2Se . In all cases, the products were reacted in aqueous solutions at 90°C to yield air-sensitive potassium salts of the anions $[\text{Tr}_4\text{E}_{10}]^{8-}$ (Tr = Ga, E = S: 47; Tr = In, E = S: 48; Tr = In, E = Se: 49; Fig. 8).³⁸

The charge of the anion in $\{(\text{C}_3\text{H}_7)_2\text{N}\}_4[\text{In}_4\text{S}_6(\text{SH})_4]$ (50) was reduced by protonation of the terminal sulfide ligands.³⁹ It was obtained as a side product during the formation of a salt with a layered anionic substructure of the sum formula $\{[\text{In}_6\text{S}_{11}\text{H}]^{3-}\}_\infty$ in a reaction of the elements and dipropylamine. 50 was found to crystallize only after the layered compound crystallized from the mother liquor.

The only other example of a $[\text{Tr}_4\text{E}_{10}]$ T2-type compound was observed much later in reactions of elemental Ga and S with NiS and the reagent tetraethylenepentamine (tepa) under solvothermal conditions. The resulting compound, $\{[\text{Ni}(\text{tepa})]_2\text{SO}_4\}[\text{Ni}(\text{tepa})(\text{Ga}_4\text{S}_6(\text{SH})_4)]$ (51, Fig. 9), comprises $[\text{Ga}_4\text{S}_6(\text{SH})_6]^{4-}$ units, which coordinate to one $[\text{Ni}(\text{tepa})]^{2+}$ fragment via one of their $\mu\text{-S}^{2-}$ ligands to form the $[\text{Ni}(\text{tepa})(\text{Ga}_4\text{S}_6(\text{SH})_4)]^{2-}$ anion.⁴⁰

In neutral adamantane-like compounds of groups 13 and 14, the terminal chalcogenide ligands are exchanged with lower-charge alternatives, and/or the $\mu\text{-E}$ atoms are replaced with chalcogenolate groups. For Ga and Al, this is achieved by reacting Me_2S_2 and Ga_2I_4 (for the Ga species) or AlGaI_4 (for the Al species) in boiling Me_2S_2 . Crystals of $[(\text{Tr})_4(\mu\text{-S})_2(\text{SMe})_4]$ (Tr = Al: 52; Tr = Ga: 53; Fig. 10) form at cooling, all with significant distortion in their adamantane-type buildup.^{41,42}

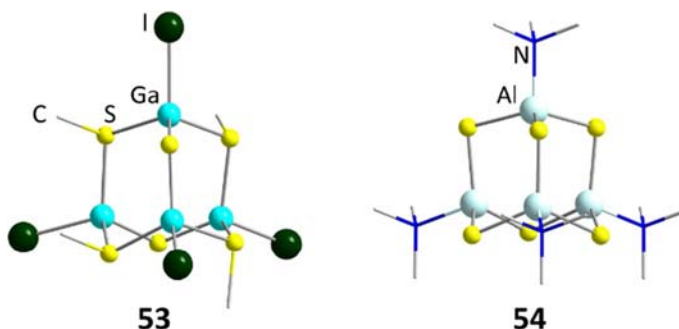


Fig. 10 Neutral adamantane-type clusters $[(\text{IGa})_4(\mu\text{-S})_2(\text{SMe})_4]$ (53) and $[(\text{Me}_3\text{NAl})_4\text{S}_6]$ (54).

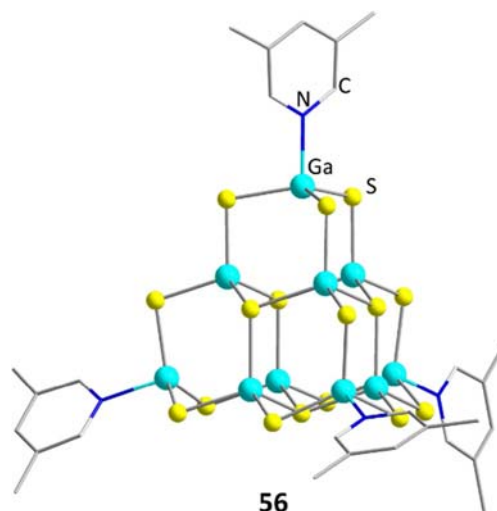


Fig. 11 Anion with a ligand-substituted T3 buildup in $(\text{H}3,5\text{-dmep})_2[\text{Ga}_{10}\text{S}_{16}(3,5\text{-dmep})_4]$ (**53**, dmep = dimethylpyridine).

Another example of the exchange of the terminal chalcogenide ligand is given by $[(\text{Me}_3\text{NAl})_4\text{S}_6]$ (**54**, Fig. 10), in which a neutral ligand causes a neutral cluster to form. **54** is obtained by a stoichiometric reaction of 4 equivalents of $[\text{Me}_3\text{NAlH}_3]$ with 6 equivalents of $\text{S}(\text{SiMe}_3)_2$.⁴³ In a similar reaction, (dmep)dichlorogallane (dmep = 4-dimethylamino-pyridine) is treated with $\text{S}(\text{SiMe}_3)_2$ to yield an unknown intermediate product, which is converted by an excess of dmep in a second step to yield the desired adamantane-like cluster $[\{(dmep)\text{Ga}\}_4\text{S}_6]$ (**55**).⁴⁴

Clusters based on the larger T3-type core are the biggest representatives of group 13 chalcogenide supertetrahedra, as a further increase in size would lead to an overabundance of bond valence at the core sulfur sites.³ Due to the high formal charge of $[\text{Tr}_{10}\text{E}_{20}]^{10-}$, these clusters tend to form networks unless stabilized by ligands to remain molecular (and exhibit lower charges). This was first achieved by a solvothermal reaction of Ga and S in 3,5-3,5'-dimethylpyridine (3,5-dmep) for 16 days.⁴⁵ The cluster formed in this reaction was obtained in an ionic compound $(\text{H}3,5\text{-dmep})_2[\text{Ga}_{10}\text{S}_{16}(3,5\text{-dmep})_4]$ (**56**, Fig. 11); the four terminal sulfur atoms were replaced by pyridine ligands, as compared to the naked T3-type cluster. This followed the same principle described for some ligands in T2-based compounds above.

Upon addition of bidentate ligands to the reaction mixture, crystals comprising linked T3-type cluster anions are obtained.⁴⁶ By using 1,2-di-4-pyridylethylene (dpe), crystals of $(\text{H}3,5\text{-dmep})_6[(\text{Ga}_{10}\text{S}_{16}(3,5\text{-dmep})_2\text{SH})_2\text{dpe}]$ (**57**, Fig. 12) form, in which two T3 clusters with one terminal SH and two terminal 3,5-dmep moieties each are linked by a DPE spacer at their remaining terminal position. A similar result was obtained by using 4,4'-bipyridine instead. However, in the crystals of the resulting compound $(\text{H}3,5\text{-dmep})_6[(\text{Ga}_{10}\text{S}_{16}(3,5\text{-dmep})(4,4'\text{-bipy})_3)][(\text{Ga}_{10}\text{S}_{16}(4\text{-mep})_2\text{NH}_3)_2(4,4'\text{-bipy})]$ (**58**, mep = methylpyridin, Fig. 12), not only SH groups are replaced by NH_3 , as compared to **57**: in addition, a monomeric T3-type cluster forms, $[(\text{Ga}_{10}\text{S}_{16}(3,5\text{-dmep})(4,4'\text{-bipy})_3)]^{2-}$, being terminated by three non-bridging 4,4'-bipy molecules and one 3,5-dmp ligand.

Inspired by the successful utilization of pyridine derivatives, more strongly coordinating organic superbases were used to better stabilize highly charged molecules and obtain larger supertetrahedra.⁴⁷ This approach was successful in creating discrete T4-type and T5-type anions, yet only with transition metal ions included in the cluster cores. Nevertheless, when screening reactivities of different organic ligands, two new Ga chalcogenide T3-type cluster and one corresponding In compound were synthesized, $(\text{H}3,5\text{-dmp})_3[\text{Ga}_{10}\text{S}_{16}(3,5\text{-dmp})_3\text{SH}]$ (**59**) $[\text{Ga}_{10}\text{S}_{16}(3,4\text{-dmp})_3\text{SH}]^{3-}$ (**60**, cations could not be determined) and $(\text{Hdbn})_2[\text{In}_{10}\text{S}_{16}(\text{dbn})_4] \cdot \text{MeCN} \cdot 2.5(2\text{-amino-1-butanol}) \cdot \text{H}_2\text{O}$ (**61**, dpn = 1,5-diazabicyclo[4.3.0]non-5-ene).

The synthesis of a series of indium sulfide cluster anions of the formula $[\text{In}_{10}\text{S}_{20}\text{H}_n]^{(10-n)-}$ provided virtually "naked" indium sulfide T3-type anions.⁴⁸ Although the hydrogen atoms in those anions could not be observed directly from the crystallographic data, a combination of elemental analysis, IR, In–S bond lengths analysis, and charge balance considerations resulted in sum formulas $(\text{Hdma})_2[\text{Ni}(\text{phen})_3]_3[\text{In}_{10}\text{S}_{20}\text{H}_2] \cdot 7\text{H}_2\text{O}$ (**62**, dma = dimethylamine, Fig. 13) and $[\text{Ni}(\text{phen})_3]_3[\text{In}_{10}\text{S}_{20}\text{H}_4] \cdot 14.5\text{H}_2\text{O}$ (**63**), with dma stemming from the decomposition of the solvent DMF. Again, the clusters were generated by solvothermal reactions from the elemental metals and the phen ligand over multiple days, with the sulfur sources being L-cystine for **62** and Na_2S for **63**. The phen complex in **62** and **63** is needed for two reasons: First, it stabilizes the anions by steric hindrance as well as providing an aromatic system in close contact to it, as can be concluded from the strong C–S interactions. Second, it leads to an intense charge transfer between the anion and cation in the absorption spectra.

A compound with the same anion as in **60** was obtained later on with a different Ni complex ligand, $[\text{Ni}(2,2'\text{-bipy})_3]_3[\text{In}_{10}\text{S}_{20}\text{H}_4] \cdot 2,2'\text{-bipy} \cdot 2\text{EG} \cdot 6\text{H}_2\text{O}$ (**64**; EG = ethylene glycol). It formed from a solvothermal reaction with elemental sulfur in an aqueous EG solution.⁴⁹

Finally, reactions in ionic liquids can substitute traditional solvothermal approaches for synthesizing supertetrahedral cluster compounds. However, for the 13/16 elemental compositions, only one publication exists to date.⁵⁰ During the reactions of indium

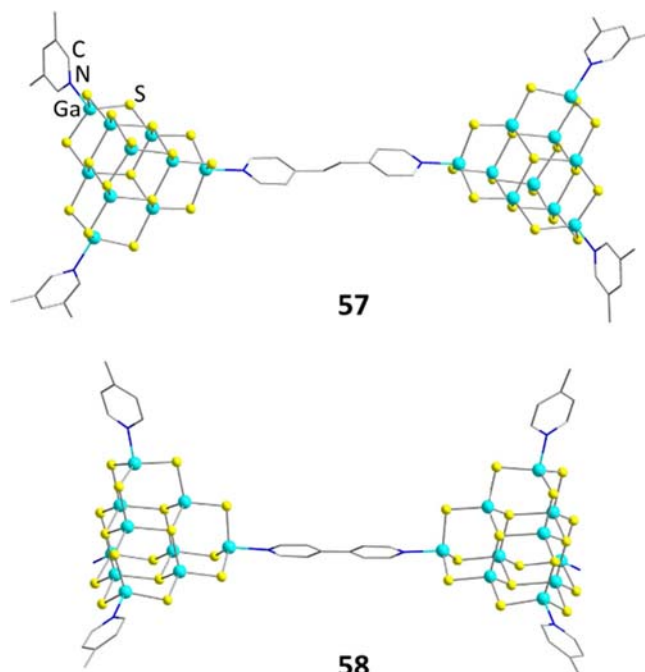


Fig. 12 Linked T3-type clusters in $(\text{H}3,5\text{-dmp})_6[\text{Ga}_{10}\text{S}_{16}(3,5\text{-dmp})_2\text{SH}]_2\text{dpe}$ (**57**; dmp = dimethylpyridine; dpe = 1,2-di-4-pyridylethylene, top) and $(\text{H}3,5\text{-dmp})_6[\text{Ga}_{10}\text{S}_{16}(3,5\text{-dmp})(4,4'\text{-bipy})_3][\text{Ga}_{10}\text{S}_{16}(3,5\text{-dmp})_2\text{NH}_3]_24,4'\text{-bipy}$ (**58**; bipy = bipyridine, bottom).

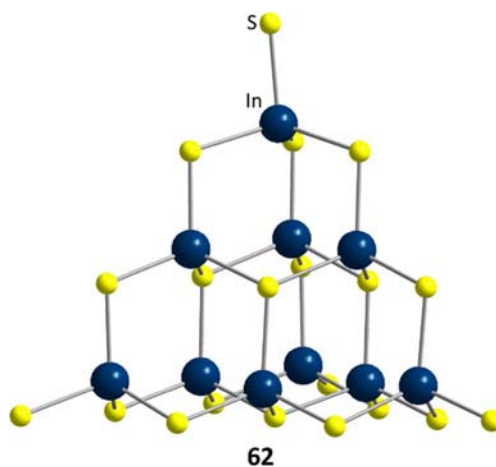


Fig. 13 T3-type anion $[\text{In}_{10}\text{S}_{20}\text{H}_2]^{8-}$ in **62** (without H atoms).

with elemental chalcogens in 1-butyl-2,3-dimethylimidazolium chloride, $(\text{C}_4\text{C}_1\text{C}_1\text{Im})\text{Cl}$, in the presence of an aqueous solution of methylamine as a viscosity-lowering auxiliary solvent, the ionic liquid partially decomposes to form 1-butyl-2-methylimidazole (bim), which then coordinates the products $(\text{C}_4\text{C}_1\text{C}_1\text{Im})_5[\text{In}_{10}\text{E}_{16}\text{Cl}_3\text{bim}]$ ($\text{E}_{16} = \text{S}$: **65**; $\text{E}_{16} = \text{S}_{7.12}\text{Se}_{8.88}$: **66**; $\text{E}_{16} = \text{Se}_{16}$: **67**; $\text{E}_{16} = \text{Se}_{13.80}\text{Te}_{2.20}$: **68**, Fig. 14). Even though the chalcogens were used in a near 1:1 ratio at the formation of both **66** and **68**, Te was barely incorporated into the anion in **68**, as was determined by EDX analysis and from crystal structure refinement.

4.04.2.3 Clusters based on other architectures

While a reaction using stoichiometric amounts of the reactants $[\text{Me}_3\text{NAlH}_3]$ and $(\text{SiMe}_3)_2\text{S}$ leads to the formation of compound **54**, a change of the ratio from 4:6 to 4:5 yields a different cluster compound, $[(\text{Me}_3\text{N})_4\text{H}_2\text{Al}_4\text{S}_5]$ (**69**, Fig. 15) with a borax-like buildup.⁴³ Two six-membered Al_3S_3 rings in boat conformation are condensed together, creating two different Al positions. The two bridgehead Al atoms are bonded to three sulfur atoms and one Me_3N ligands, while the metal atoms at the other position are bonded to two sulfur atoms, one Me_3N ligand, and a hydrogen. The transformation of **69** to **54** by addition of $(\text{SiMe}_3)_2\text{S}$ has only been successful in low yields, as an unidentified side product occurs when trying to re-dissolve compound **69**. The

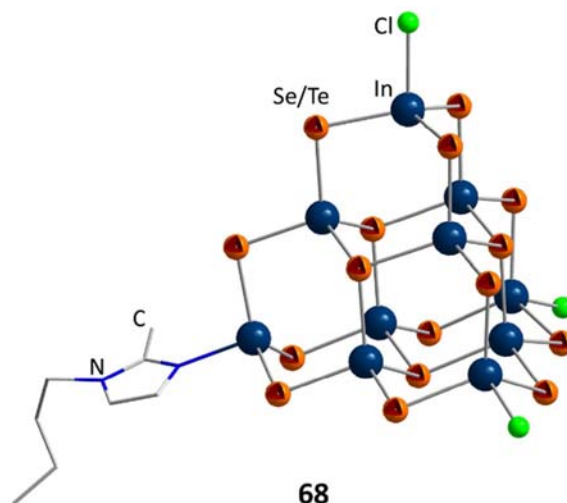


Fig. 14 T3-type cluster with mixed chalcogenide sites in $(\text{Bmmim})_5[\text{In}_{10}\text{Se}_{13.80}\text{Te}_{2.20}\text{Cl}_3\text{bim}]$ (**68**, $\text{C}_4\text{C}_1\text{C}_1\text{Im}$ = 1-butyl-2,3-dimethylimidazolium, bim = 1-butyl-2-methylimidazolium), obtained from an ionothermal reaction.

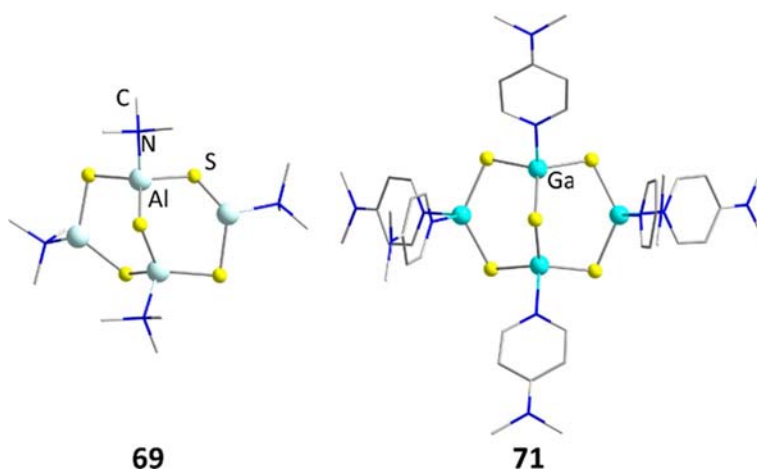


Fig. 15 Neutral $[(\text{Me}_3\text{N})_4\text{H}_2\text{Al}_4\text{S}_5]$ (**69**) and cationic cluster in $[(\text{dmap})_6\text{Ga}_4\text{S}_5]\text{Br}_2$ (**71**, dmap = 4-dimethylamino-pyridine).

selenium congener was generated by a different reaction in a simultaneous study involving the dimer $[(\text{Me}_3\text{N})\text{HAlSe}]_2$. Addition of $\text{N}\cdot\text{N}\cdot\text{N}'\cdot\text{N}''\cdot\text{N}'''$ -pentamethyldiethylenetriamine in toluene in a 1:1 ratio initiated the rearrangement towards $[(\text{Me}_3\text{N})_4\text{H}_2\text{Al}_4\text{S}_5]$ (**70**).⁵¹

The same structural motif is present in the ionic compound $[(\text{dmap})_6\text{Ga}_4\text{S}_5]\text{Br}_2$ (**71**, Fig. 15).⁵² The target compound is obtained by reacting $[\text{GaSBr}]_n$ with dmap in MeCN under reflux conditions. Reactions at room temperature yield an intermediate based on a six-membered $\{\text{Ga}_3\text{S}_3\}$ ring, $[(4\text{-Me}_2\text{NC}_5\text{H}_4\text{N})\text{GaSBr}]_3$, which can be further reacted to yield **71** by heating and addition of more ligand.

Another small cluster family comprises $[\text{In}_{18}\text{Te}_{30}]^{6-}$ nanowheels. The first example was stabilized by addition of 1,2-diaminocyclohexane (dach) ligands, as well as by $(\text{Hdach})^+$ and $[\text{Mn}(\text{dach})_3]^{2+}$ counteranions. Upon solvothermal treatment of InCl with Mn and Te powder in an aqueous dach solution, the compound was isolated as $[\text{Mn}(\text{dach})_3]_2[\text{In}_{18}\text{Te}_{30}(\text{dach})_6]\cdot 2\text{Hdach}\cdot\text{H}_2\text{O}$ (**72**, Fig. 16).⁵³ The anion comprises six $\{\text{In}_2\text{Te}_6\}$ units constructed from condensed $\{\text{InTe}_4\}$ tetrahedra and six $\{\text{InTe}_3(\text{dach})\}$ subunits with bipyramidally-coordinated In sites. This creates wheels with average outer diameters of 15.54 \AA centered around an Hdach -coordinated water molecule, which is ascribed a templating function. Two further rings of this type are obtained by varying the ligands and the transition metal ions.

Addition of phen to a solvothermal reaction of elemental Te , In , and M ($\text{M} = \text{Fe}, \text{Ni}$) in 1,3-diaminepropane (dapn) results in the formation of crystals of the two derivatives $[\text{Fe}(\text{phen})_3]_2[\text{In}_{18}\text{Te}_{30}(\text{dapn})_6]\cdot 2\text{Hdapn}\cdot\text{dapn}$ (**73**) and $[\text{Ni}(\text{phen})_3]_2[\text{In}_{18}\text{Te}_{30}(\text{dapn})_6]\cdot 2\text{Hdapn}\cdot\text{dapn}$ (**74**).⁵⁴ Both compounds do not differ significantly in their anionic sub-structures though. Due to the monodentate coordination of dapn , however, the In atom in the $\{\text{InTe}_3(\text{dapn})\}$ subunits of the nanoclusters adopt a tetrahedral coordination sphere. As discussed before, the presence of $[\text{M}(\text{phen})_x]^{n+}$ complexes leads to strong cation-anion interaction in the clusters' optical spectra.

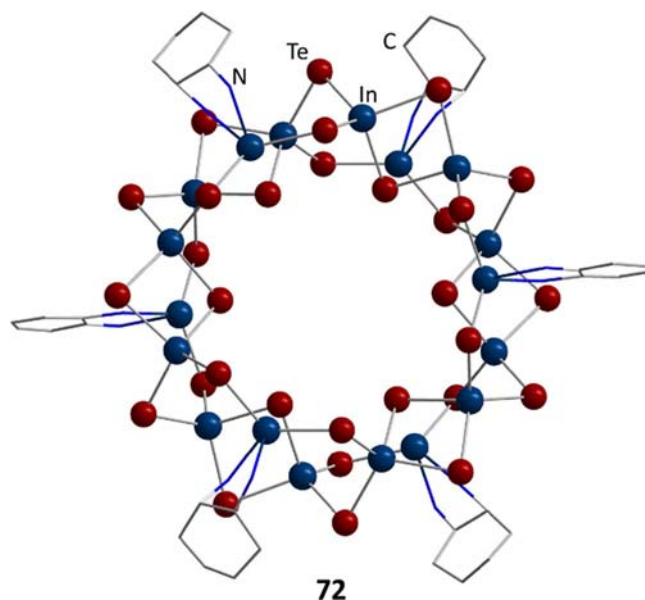


Fig. 16 Wheel-shaped cluster anion in $[\text{Mn}(\text{dach})_3]_2[\text{In}_{18}\text{Te}_{30}(\text{dach})_6] \cdot 2\text{Hdach} \cdot \text{H}_2\text{O}$ (**69**, $\text{dach} = 1,2$ -diaminocyclohexane).

Another type of an In/Te nanocluster, $[\text{In}_8\text{Te}_{12}(\text{trien})_4]$ (**75**, $\text{trien} = \text{triethylenetetramine}$, **Fig. 17**), consists of four corner-sharing $\{\text{InTe}_4\}$ tetrahedra that are further connected to four $\{\text{In}(\text{trien})\}$ units.⁵⁵ This resembles a cutout of the α - In_2Te_3 phase at a diameter of about 1 nm. The nanoclusters can be dispersed in ethanol and deposited on surfaces, where they form particles of 8–10 nm. Owing to the nano-structuring and the shielding by organic ligands, the optical gap of these clusters is heavily blue-shifted relative to the gap of α - In_2Te_3 bulk (2.7 eV as compared to 0.6 eV).

A compound that is structurally more closely related to a cubane-type cage is $[(\text{NEt}_4)]_5[\text{In}_3\text{Te}_7] \cdot 0.5\text{Et}_2\text{O}$ (**76**, **Fig. 18**). Its inorganic cluster can be derived from a heterocubane-like architecture, in which one In corner is missing. In addition, the three remaining In moieties carry another Te ligand each, instead of an organic rest. This defect-heterocubane-type structural motif is much more often encountered in group 14 chalcogenides.⁵⁶ To obtain **76**, potassium was dissolved together with the sequestering reagent 4,7,13,16,21,24-hexaoxa-1,10-diazabicyclo[8.8.8]hexacosane (crypt-222) in liquid ammonia and reacted with In_2Te_3 powder for 2 days. After evaporation of the solvent, the mixture was extracted with acetonitrile and treated with NEt_4Br . Crystals could be grown by layering with Et_2O .

While no crystals of Tl congeners of the more common structural motifs have been reported in the literature, some examples exist with varying structural motifs. The mixed-valence compound $[\text{K}(\text{crypt-222})_3[\text{Tl}_5\text{Se}_5]]$ (**77**, **Fig. 19**) comprises an inorganic cage that can be described as a $\{\text{Tl}^{\text{III}}_4\text{Se}_4\}$ heterocubane, which is further extended by an $\{\text{SeTl}^{\text{I}}\}$ unit above one of its planes.⁵⁷ It is obtained by extracting KTlSe with ethylenediamine (*en*) in the presence of crypt-222. Two further compounds, which reversibly transform into one another in a 1:1 equilibrium, can be extracted from the same precursor in liquid ammonia. While the latter do not form crystals, NMR experiments lead to the sum formulas $[\text{Tl}_4\text{Se}_5]^{4-}$ and $[\text{Tl}_4\text{Se}_6]^{4-}$ for their inorganic cores. Both, like **77**, are

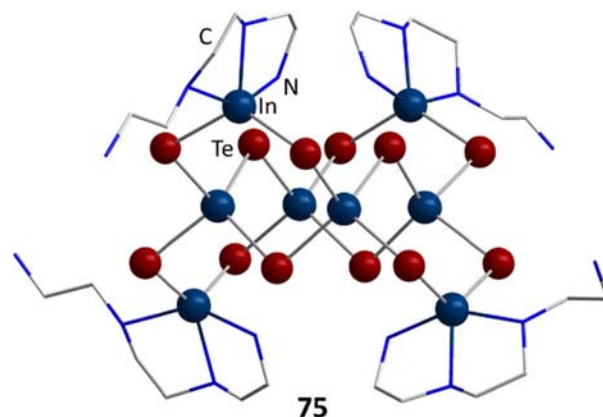


Fig. 17 $[\text{In}_8\text{Te}_{12}(\text{trien})_4]$ (**75**, $\text{trien} = \text{triethylenetetramine}$), based on a cutout of the α - In_2Te_3 phase.

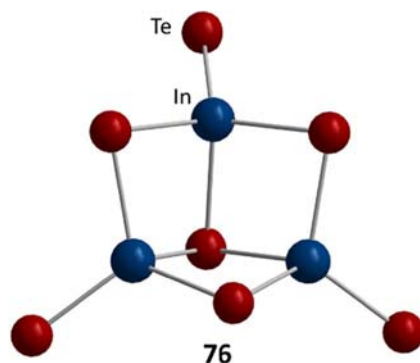


Fig. 18 Anion in $(\text{NEt})_4[\text{In}_3\text{Te}_7] \cdot 0.5\text{Et}_2\text{O}$ (**76**) exhibiting a defect-heterocubane-type structure.

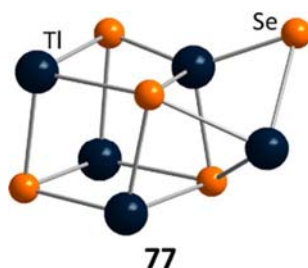


Fig. 19 Anion in $(\text{NEt})_4[\text{Tl}_5\text{Se}_5] \cdot 0.5\text{Et}_2\text{O}$ (**77**) with a defect-heterocubane-type structure.

assumed to possess a $\{\text{Tl}_4\text{Se}_4\}$ heterocubane-like structure with one or two Tl atoms, respectively, being coordinated by an additional Se atom.

By reactions of thiolates with Tl(I) salts, the neutral compound $[\text{Tl}_8(\text{S}^t\text{Bu})_8]$ (**78**, Fig. 20) was isolated.⁵⁸ It can be regarded as two $\{\text{Tl}_3\text{S}_4\}$ defect-heterocubane-type cages that are connected at their missing corner via two Tl atoms.

4.04.3 Group 14 chalcogenide clusters

Chalcogenido metalates of Group 14 elements have been shown to form extended networks, most prominently based on super-tetrahedral or $\{\text{T}_3\text{E}_4\}$ defect-heterocubane-type subunits. However, these and other chalcogenido metalate units can also be obtained in a molecular form, either as $[\text{T}_4\text{E}_{10}]^{4-}$ anions, which will be presented first hereupon, or as neutral clusters with organic ligands that saturate the T atoms, which are outlined thereafter. Especially the organometallic clusters show a variety of structural motifs, that can be converted into one another or coexist in corresponding equilibria. We will thus illustrate the basic structural motifs and the relationship between the cluster topologies in a chapter to follow.

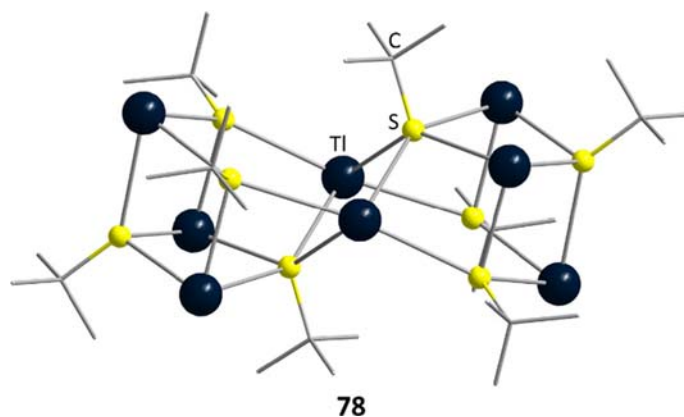


Fig. 20 The thiolate cluster $[\text{Tl}_8(\text{S}^t\text{Bu})_8]$ (**78**) with two Tl-bridged defect-heterocubane-type units.

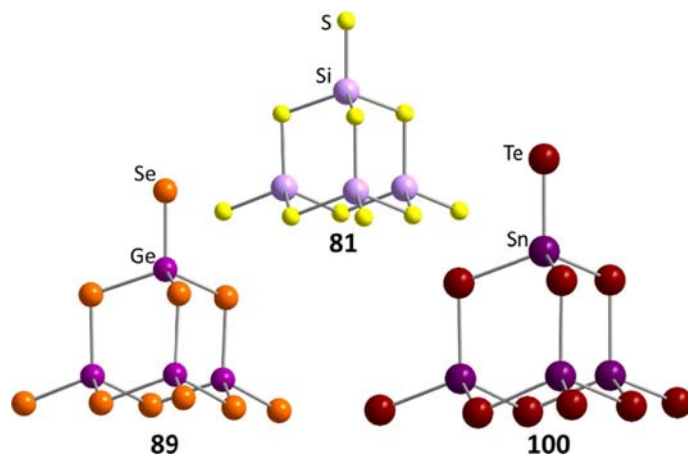


Fig. 21 Adamantane-type clusters with different elemental combinations in $\text{Na}_4[\text{Si}_4\text{S}_{10}]$ (**78**, top), $\text{Rb}_4[\text{Ge}_4\text{Se}_{10}]$ (**89**, left) and $[\text{K}(18\text{-crown-6})]_4[\text{Sn}_4\text{Te}_{10}]$ (**100**, right).

4.04.3.1 Compounds based on purely inorganic $[\text{T}_4\text{E}_{10}]^{4-}$ supertetrahedra

A plethora of salts comprising $[\text{T}_4\text{E}_{10}]^{4-}$ anions and a variety of cations have been known. Their simplest examples, which comprise metal or ammonium cations, were reported mainly regarding their syntheses and structures. Most of these compounds were obtained by high-temperature solid-state or solvothermal synthesis from the elements or from simple binary salts. Eventually, the research focused on more complex compounds and their specific chemical and physical properties.

The first structural elucidation of a monomeric adamantane-type anion was carried out in 1971 on crystals obtained from a saturated solution of GeS_2 and Cs_2S . The resulting compound, $\text{Cs}_4[\text{Ge}_4\text{S}_{10}]$ (**79**), contains adamantane-like anions with only slight deviations from an ideal T_d symmetry.⁵⁹ Its high stability in solutions over a broad pH range, as compared to other thiogermanates, was attributed to its rigid structure, which sterically hinders Ge–S bond cleavage needed for further reaction to GeS_2 .⁶⁰

A solid-state synthesis at high temperatures can also be used to form discrete $[\text{T}_4\text{S}_{10}]^{4-}$ anions. GeS_2 or SiS_2 react with Na_2S to generate crystals of the sodium salts $\text{Na}_4[\text{Ge}_4\text{S}_{10}]$ (**80**) and $\text{Na}_4[\text{Si}_4\text{S}_{10}]$ (**81**, Fig. 21), respectively, albeit the crystals of **81** could not yet be grown in a sufficiently high quality for exact structural elucidation.^{61,62} Also Tl(I) cations play a role in this context; $\text{Tl}_4[\text{Ge}_4\text{S}_{10}]$ (**82**) was obtained from a similar reaction of Tl_2S and GeS_2 .⁶³ Through the combination of GeS_2 and BaS at 1250 °C, dications could also be introduced, thereby forming crystalline $\text{Ba}_2[\text{Ge}_4\text{S}_{10}]$ (**83**).⁶¹

The first selenium analogue, $\text{Tl}_4[\text{Ge}_4\text{Se}_{10}]$ (**84**), was synthesized via the route applied to generate **82**.⁶⁴ The Se compounds were found to quickly hydrolyze and form H_2Se when exposed to traces of water. Simple stoichiometric reactions from the elements, leading to $\text{Na}_4[\text{Si}_4\text{Se}_{10}]$ (**85**) at first, could also be realized.⁶⁵ The heavier congeners, $\text{Na}_4[\text{Ge}_4\text{Se}_{10}]$ (**86**) and $\text{K}_4[\text{Ge}_4\text{Se}_{10}]$ (**87**), were isolated from analogous reactions.^{66,67} The Cs and Rb compounds $\text{Cs}_4[\text{Ge}_4\text{Se}_{10}] \cdot 2\text{MeOH}$ (**88**) and $\text{Rb}_4[\text{Ge}_4\text{Se}_{10}] \cdot \text{MeOH}$ (**89**, Fig. 21) emerge from solvothermal reactions of M_2CO_3 ($\text{M} = \text{Rb}$ or Cs), Se, and Ge in methanol at 190 °C beside crystals of $\text{Cs}_4[\text{Ge}_2\text{Se}_8]$ or $\text{Rb}_2[\text{GeSe}_4]$, respectively.^{68,69}

First Sn analogs of these adamantane-type anions were obtained much later and via a different route: By fusion of the elements, an alloy of the nominal composition $\text{KSn}_{0.67}\text{Se}_{1.93}$ was created and extracted in *en* and liquid ammonia in the presence of the sequestering reagent crypt-222 or 1,4,7,10,13,16-hexaoxacyclooctadecan (18-crown-6), resulting in crystals of $[\text{K}(\text{crypt-222})]_4[\text{Sn}_4\text{Se}_{10}]$ (**90**) or $[\text{K}(18\text{-crown-6})]_4[\text{Sn}_4\text{Se}_{10}]$ (**91**), respectively, upon addition of THF.^{70,71} The elemental combination allowed for thorough investigation by NMR spectroscopy, confirming the adamantane-type structure in solution. For another example, an Sn_2Se_3 cathode was used in an electrochemical reaction in an NEt_4Br electrolyte solution in *en*, resulting in the formation of $[\text{NEt}_4]_4[\text{Sn}_4\text{Se}_{10}]$ (**92**).⁷² In the framework of a comprehensive study on a series of compounds $[\text{NR}_4]_4[\text{Sn}_4\text{E}_{10}]$ ($\text{R} = \text{Me}$; $\text{E} = \text{S}, \text{Se}, \text{Te}$ **93, 94, 95; $\text{R} = \text{Et}$: $\text{E} = \text{S}, \text{Se}, \text{Te}$ **96, 92, 97**), the first sulfur and tellurium congeners were fully described, which were isolated after extracting the corresponding, stoichiometric, alloys with NR_4Br in *en*.⁷³**

As already mentioned for group 13 chalcogenide clusters, compounds containing telluride ligands are much rarer and more sensitive than their lighter congeners. To obtain the first adamantane-type cluster with Te atoms, $\text{K}_4[\text{Si}_4\text{Te}_{10}]$ (**98**), a solid state reaction was carried out starting from the elements.⁷⁴ The Ge congener was obtained by extraction of a solid with the nominal composition $\text{K}_4\text{Ge}_4\text{Te}_{10}$, formed by fusion of K_2Te , Ge, and Te at high temperature, with *en* and subsequent layering with a solution of NEt_4Br . The resulting black crystals were determined to be $(\text{NEt}_4)_4[\text{Ge}_4\text{Te}_{10}]$ (**99**).⁷⁵ Analogous to the synthesis of **91**, extraction of $\text{K}_4\text{Sn}_4\text{Te}_{10}$ yielded $[\text{K}(18\text{-crown-6})]_4[\text{Sn}_4\text{Te}_{10}]$ (**100**, Fig. 21). The homologous series was completed with **95** and **96**, which were synthesized later in time.⁷¹

The air-stable ammonium salt $(\text{NMe}_4)_4[\text{Ge}_4\text{S}_{10}]$ (**101**), which served as starting material for many follow-up syntheses, was formed by a solvothermal reaction between GeS_2 and Me_4NHS in an aqueous solution of H_2S .⁷⁶ Nearly simultaneously, an alternate synthesis route was developed independently, in which GeS_2 was reacted with Me_4NCl without an additional sulfur source.⁷⁷ The salt was subsequently used as a monomeric building block for the formation of three-dimensional open-framework

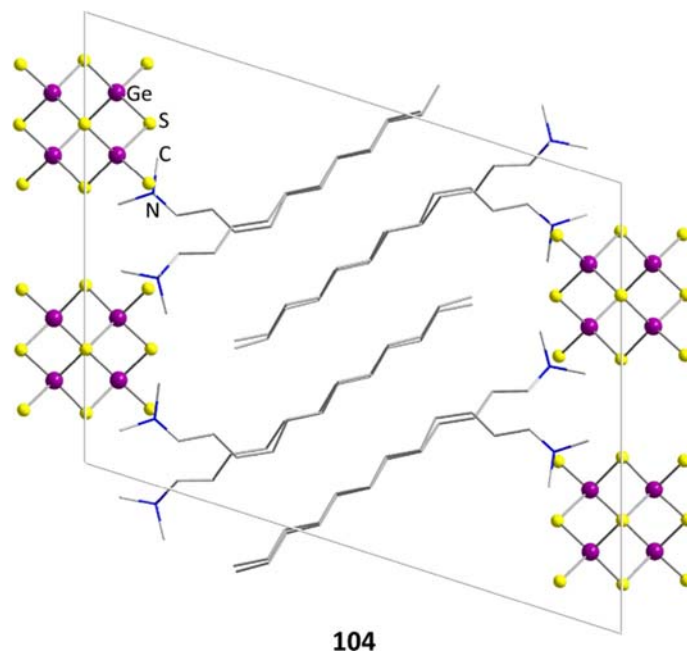


Fig. 22 Lamellar buildup of $(n\text{-C}_{12}\text{C}_{25}\text{NMe}_3)_4[\text{Ge}_4\text{S}_{10}]$ (**104**), shown in a cutout of the crystal structure.

compounds of the type $(\text{NMe}_4)_{2n}[\text{MGe}_4\text{S}_{10}]_n$ by addition of M^{2+} ions ($\text{M} = \text{Mn}, \text{Fe}, \text{Co}, \text{Zn}$). These demonstrate the possibility for the formation of porous materials with diamond-type topology from adamantane-type anions.^{78–80} The experiments could additionally be expanded to the Se congener, $(\text{NMe}_4)_4[\text{Ge}_4\text{Se}_{10}]$ (**102**), and respective networks,⁸¹ as well as to the corresponding Sn compounds **93–97**.⁷³ Especially the latter were systematically characterized for their physical properties as well as their electronic situation.

In a very similar reaction, the mixed-ammonium compound $(\text{EtNH}_3)_3(\text{MeNH}_3)[\text{Ge}_4\text{S}_{10}]$ (**103**), generated by heating of $[\text{MeNH}_3]\text{Ge}_2\text{S}_6$ in an ethanolic solution of ethylamine, forms linear chains of the composition $(\text{NEt}_4)_4[\text{MGe}_4\text{S}_{10}]$ ($\text{M} = \text{Cu}, \text{Ag}$), when CuCl or AgOAc are added together with tetraethylammonium bromide and methylurea.⁸² In either case, neighboring adamantane subunits are linked via metal coordination of terminal sulfur atoms to metal ions in between.

A different order of cations and adamantane-type anions was realized in the lamellar structures of $(n\text{-C}_n\text{H}_{2n+1}\text{NMe}_3)_4[\text{Ge}_4\text{S}_{10}]$ ($n = 12, 14, 16$ and 18 ; **104–107**, Fig. 22), in which layers of anions are separated by layers of alkyltrimethyl surfactant molecules

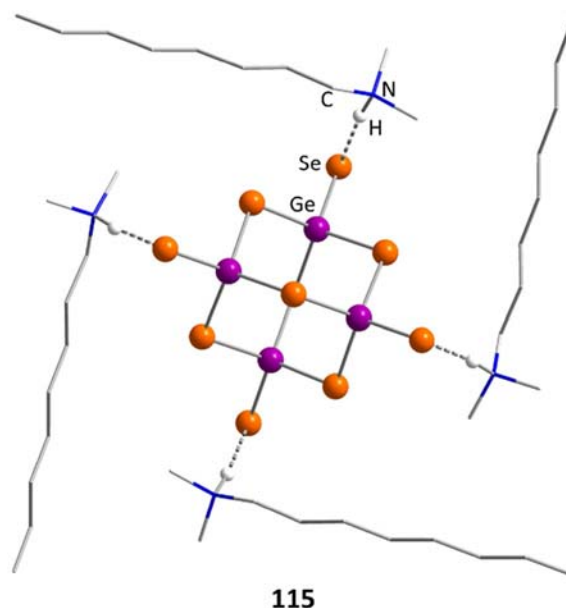


Fig. 23 Non-lamellar arrangement of the cations around the anion in $(n\text{-C}_8\text{C}_{17}\text{NMe}_2\text{H})_4[\text{Ge}_4\text{Se}_{10}]$ (**115**).

that interact with each other through van der Waals interactions.⁸³ The thickness of the organic layers is strictly dependent on n , which provides adjustability at the mesoscopic scale. A thicker layer also correlates with a decrease of the temperature for a solid-to-solid phase transition. It is possible for all these compounds to reversibly absorb linear alcohols. The speed of both the absorption and the desorption process depends on the size of the alcohol molecules. Those results prompted the extensive studies of similar selenium anions separated by layers of alkyl trimethylammonium cations $(n\text{-C}_n\text{H}_{2n+1}\text{NMe}_3)_4[\text{Ge}_4\text{Se}_{10}]$ ($n = 8, 9, 10, 12, 14, 16, 18$; **108–114**), and the respective hydrogen substitute $(n\text{-C}_8\text{H}_{17}\text{NMe}_2\text{H})_4[\text{Ge}_4\text{Se}_{10}]$ (**115**).⁸⁴ These compounds were obtained by metathesis reaction of $\text{K}_4[\text{Ge}_4\text{Se}_{10}]$ (**87**) and the corresponding ammonium halide in solution, which takes place readily for smaller side chains, but requires elevated temperatures for ammonium salts with larger spatial demand. Single crystals suitable for X-ray diffraction (XRD) of **108**, **109** and **115** were observed after about a day, whereas compounds **110–114** remain microcrystalline. The structures of **108** and **109** mirror the lamellar buildup observed for **104–107**, with **110–114** most likely following suit according to powder X-ray diffraction (PXRD) data. Due to strong secondary $\text{N}\cdots\text{H}\cdots\text{Se}$ (2.38 Å) interactions in **115**, the anionic adamantane-type clusters do not form layers, but arrange in loose columns, with a large non-bonding distance of >7.27 Å between them. This enables a close coordination of 4 ammonium cations by each adamantane-type anion (Fig. 23).

A similar arrangement was found in the compound $\{(n\text{-C}_4\text{H}_9)_3\text{NH}\}_4[\text{Ge}_4\text{Se}_{10}]$ (**116**), obtained from **87** through treatment with tributylamine under acidic conditions. Again, reversible absorption of alcohols was observed for **108–114**, but not for **115**; this suggests that the alcohols normally intercalate between the organic surfactants and the clusters, which seem to be too strongly bonded in **115**. All materials, **104–116**, were shown to be isolators or semiconductors by UV-vis spectroscopy, with the Se compounds exhibiting smaller band gaps in general, and **115** showing the smallest value of 2.14 eV. Another study explored more heavily protonated samples $(n\text{-C}_n\text{H}_{2n+1}\text{NH}_3)_4[\text{Ge}_4\text{S}_{10}]$ ($n = 12, 14, 16, 18$; **117–120**) obtained from **80** and the corresponding ammonium chloride in water.⁸⁵ These compounds seem to exhibit an orderly lamellar structure, with the thickness of the organic layers being purely dependent on the chain length of the ammonium cations, as was corroborated by PXRD and XRD in the case of **117** and **118**. The organic and inorganic layers are connected by short $\text{N}\cdots\text{H}\cdots\text{S}$ hydrogen bonds (average $\text{N}\cdots\text{S}$ distance of 2.6 Å). A similar solid-state phase transition as was observed for **104–107** was detected here, too, again reinforcing the related buildup. In contrast to the quoted materials, however, no alcohol intercalation can be observed here due to the strong adhesion between the layers.

A crystal structure akin to that of **115** and **116** can also be observed in the Sn compound $\{(\text{C}_3\text{H}_7)_2\text{NH}_2\}_4[\text{Sn}_4\text{Se}_{10}]\cdot 4\text{H}_2\text{O}$ (**121**), in which a much larger $\text{N}\cdots\text{H}\cdots\text{Se}$ (3.44 Å) distance was detected, and in which the second proton forms hydrogen bonds to a water molecule present in the crystal structure.⁸⁶ This compound was unexpectedly observed during investigations of $\{[\text{Sn}_3\text{Se}_7]^{2-}\}_n$ networks emerging from hydrothermal treatment of the elements in an amine solution. The band gap of **121**, 2.41 eV is larger than that of **115**. The related compound $\{(\text{sec-C}_4\text{H}_9)_2\text{NH}_2\}_4[\text{Sn}_4\text{Se}_{10}]\cdot 2\text{H}_2\text{O}$ (**122**), again obtained by hydrothermal reaction of the elements in the corresponding amine, arranges in a different fashion, with discrete anions coordinating to three cations only (average $\text{N}\cdots\text{H}\cdots\text{Se} = 3.42$ Å).⁸⁷ Two of the cations interact with the same Se atom, while the fourth ammonium ion is coordinated by two water molecules, thereby forming channels in the crystal. At higher temperatures, water and some of the ammonium ions are released, and a layered structure is formed according to PXRD data. From 188 °C onwards, a decomposition to SnSe_2 , and at 536 °C further to SnSe , is observed.

In the presence of 4,4'-bipyH₂ bication, another type of inorganic-organic hybrid network is formed. In $(4,4'\text{-bipyH}_2)_2[\text{Ge}_4\text{S}_{10}]\cdot 4,4'\text{-bipy}\cdot 7\text{H}_2\text{O}$ (**123**, Fig. 24), alternating inorganic and organic layers, comprising the adamantane-type anions

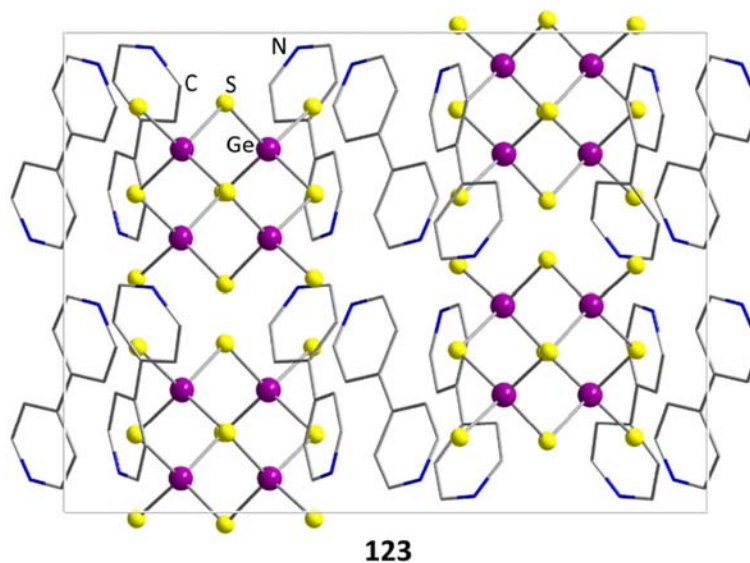
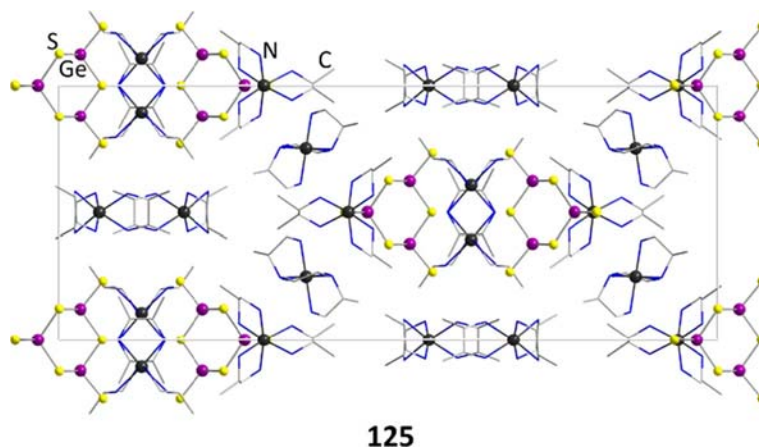


Fig. 24 Cutout of the layered structure in $(4,4'\text{-bipyH}_2)_2[\text{Ge}_4\text{S}_{10}]\cdot 4,4'\text{-bipy}\cdot 7\text{H}_2\text{O}$ (**123**). Water molecules are omitted for clarity.



125

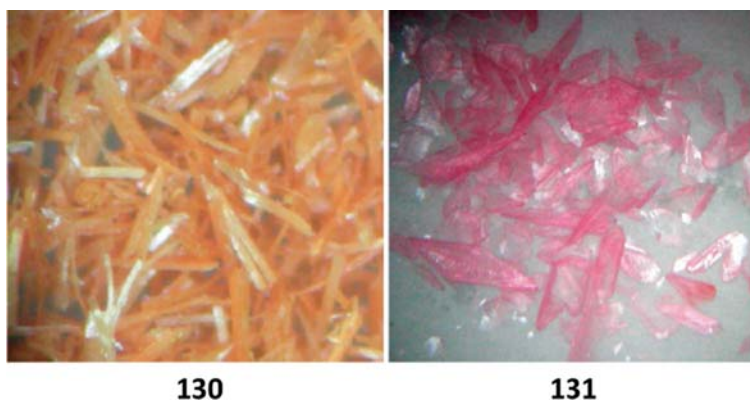
Fig. 25 Cutout of the structure of $[\text{Ni}(\text{dap})_3]_2[\text{Ge}_4\text{S}_{10}]\text{Cl}_4$ (**125**). Cl^- anions are omitted for clarity.

as well as coordinating water molecules and hydrogen-bonded $[4,4'\text{-bipyH}_2 \cdots 4,4'\text{-bipy} \cdots 4,4'\text{-bipyH}_2]$ trimers with π -stacking interaction between them form the crystal structure.⁸⁸ **123** was synthesized from **101** hydrothermally with 4,4'-bipy and $\text{Cu}(\text{NO}_3)_2$.

Apart from purely organic templates, organometallic complexes have been used to create different crystal structures with adamantane-type anions. The isostructural compounds $[\text{M}(\text{dap})_3]_2[\text{Ge}_4\text{S}_{10}]\text{Cl}_4$ (dap = 1,2-propanediamine, M = Co: **124**, M = Ni: **125**, **Fig. 25**) are prepared by a solvothermal reaction of GeO_2 , sulfur, antimony, and $\text{MCl}_2 \cdot 6\text{H}_2\text{O}$ in dap. They occur as zig-zig chains formed by the metal complexes and chloride anions, in between which the adamantane-type molecules undergo $\text{S} \cdots \text{H}$ interactions with the $-\text{NH}_2$ groups of the dap molecules.⁸⁹ Curiously enough, Sb atoms are not observed in the product, but seem to be necessary for crystal formation.

Two further examples contain Ni complexes of triethylenetetramine (teta), which are also obtained by a solvothermal reaction from GeO_2 , $\text{NiCl}_2 \cdot 6\text{H}_2\text{O}$, and the elemental chalcogen in teta, heated at 170°C for 12 days.⁹⁰ In $[\text{Ni}_2(\mu\text{-teta})(\text{teta})_2][\text{Ge}_4\text{S}_{10}] \cdot \text{H}_2\text{O}$ (**126**), two Ni atoms coordinated by all four amine sites of one teta molecule each are bridged by an additional teta moiety, which coordinates to each of the Ni centers with two of its nitrogen atoms. When repeating the reaction with Se and heating for 16 days, crystals of $[\text{Ni}_2(\text{teta})_2][\text{Ge}_4\text{Se}_{10}] \cdot 0.5\text{H}_2\text{O}$ (**127**) are formed; here, the cations contains one η^4 -teta ligand and one η^2 -teta ligand. When using the reaction parameters of **126**, but carrying out the reaction at 160°C for 5 days instead, water free $[\text{Ni}_2(\text{teta})_2][\text{Ge}_4\text{S}_{10}]$ (**128**) is obtained, featuring the same cationic substructure as in **126**.⁹¹ Changing the reaction temperature to 200°C leads to an isomer (**129**) of **126** with a chiral, helical structure in 6 days reaction time.⁹² In **129**, the dimeric cation, the adamantane-type anions, and the water molecules contained in the crystal form helices through extended hydrogen bonding between all subunits. Enantiopure crystals of both configurations were isolated in small yields.

The solvent molecules in $[\text{Ni}_2(\text{phen})_3]_2[\text{Ge}_4\text{S}_{10}] \cdot \text{solv}$ (4MeOH \cdot 12H₂O: **130**; 24H₂O: **131**) play an important role in the optical properties of these substances, as solvochromism leads to a rapid color change from yellow (**130**) to pink (**131**) when immersing crystals in water or methanol, respectively (**Fig. 26**).⁹³ This is explained through fast re-crystallization taking place when exposed to these liquids, as was proven through XRD experiments. Other alcohols can also induce a color change of **131**, although at a much slower pace, and without the growth of crystals usable for XRD. However, the selective access of both compounds from compound **101** required specific steps. While **131** can be easily obtained by reacting **101** with $[\text{Ni}(\text{phen})_3\text{Cl}_2]$ in a DMF/water mixture,



130

131

Fig. 26 Photographs of crystals of solvates of $[\text{Ni}(\text{phen})_3]_2[\text{Ge}_4\text{S}_{10}] \cdot \text{solv}$ (phen = 1,10-phenanthroline) exhibiting solvochromism. (Left) solv = 4 MeOH \cdot 12 H₂O (**130**), (right) solv = 24 H₂O (**131**).⁹³

a methanolic solution of $[\text{Ni}(\text{phen})_3\text{Cl}_2]$ needs to be layered over an aqueous solution of **101**, being allowed to slowly diffuse into it, in order to isolate compound **130**.

$[\text{Ho}_2(\text{tepa})_2(\mu\text{-OH})_2\text{Cl}_2]_2[\text{Sn}_4\text{Se}_{10}] \cdot 4\text{H}_2\text{O}$ (tepa = tetraethylenepentamin, **132**), prepared from $\text{SnCl}_4 \cdot 5\text{H}_2\text{O}$, HoCl_3 and Se powder in a solvothermal reaction in tepa, represents an example for a lanthanide complex acting as a structural template.⁹⁴ In the crystal, the adamantane-type anions are arranged in a halite-like manner; the dimeric Ho complexes are situated in between them, thus also forming a substructure of the NaCl-type. Still, the specific shape of the ions allows channels in the [001] directions to form, which are filled with water molecules. All parts of this network are connected via hydrogen bridges. The band gap, found at 2.49 eV, is dominated by excitation events within the anion, as is often found for cluster compounds based on adamantane-type units. By measurement of the magnetic properties, the $\chi_{\text{M}}T$ value at 300 K was determined to be close to the one for two uncoupled Ho^{3+} ions. The $\chi_{\text{M}}T$ product decreases with decreasing temperature, and the inverse susceptibility can be fitted to the Curie-Weiss law with $C = 32.3 \text{ cm}^3 \text{ K mol}^{-1}$ and $\Theta = -11.5 \text{ K}$. In a follow-up study, a series of isostructural compounds similar to **132**, $[\text{M}_2(\text{tepa})_2(\mu\text{-OH})_2\text{Cl}_2]_2[\text{Sn}_4\text{Se}_{10}] \cdot 4\text{H}_2\text{O}$ ($\text{M} = \text{Y, Dy, Er, Tm}$; **133–136**) was found to co-crystallize with the corresponding $[\text{M}_2(\text{tepa})_2(\mu\text{-OH})_2\text{Sn}_2\text{Se}_6]$ compounds with one-dimensionally extended substructures as the minority product.⁹⁵ The synthesis conditions are similar to those of **131**, when substituting Ho with M, but the addition of Ag powder to the reaction mixture appeared to be vital to obtain crystalline material.

In another synthetic approach using two liquid phases, **101** was dissolved in water and added to a solution of a transition metal complex in acetonitrile.⁹⁶ The products of this type of reactions are $[\text{Ni}(\text{cyclam})]_3[\text{Ni}(\text{cyclam})(\text{H}_2\text{O})_2][\text{Ge}_4\text{S}_{10}] \cdot 21\text{H}_2\text{O}$ (**137**, cyclam = 1,4,8,11-tetraazacyclotetradecane), $[\text{Mn}(2,2'\text{-bipy})_2\text{H}_2\text{O}]_2[\text{Ge}_4\text{S}_{10}] \cdot 3\text{H}_2\text{O}$ (**138**), and $[\text{Fe}(2,2'\text{-bipy})_3]_2[\text{Ge}_4\text{S}_{10}] \cdot 10\text{H}_2\text{O}$ (**139**). The structure of **137** is composed of alternating layers. Layer 1 contains anions and $[\text{Ni}(\text{cyclam})]^{+}$ in a 1:2 fashion, being connected by some water molecules, while in layer 2, $[\text{Ni}(\text{cyclam})]^{+}$ and $[\text{Ni}(\text{cyclam})(\text{H}_2\text{O})_2]^{+}$ are surrounded by water clusters. **138** can be viewed as two Mn complexes that are covalently bonded to an adamantane-type anion via bridging sulfur moieties. Lastly, the iron complexes in **139** form rods by π -interactions, leaving channels accommodating the adamantane-type units. A solvothermal reaction of Sn, Se, and $\text{NiAc}_2 \cdot 4\text{H}_2\text{O}$ in a mixture of tetra and N-(2-hydroxyethyl)-ethylenediamine (hda) afforded $[\text{Ni}(\text{teta})(\text{en})][[\text{Ni}(\text{teta})(\text{hda})][[\text{Sn}_4\text{Se}_{10}]]$ (**140**); the en molecules stem from in-situ decomposition of hda.⁹⁷ Based on investigations of the optical properties, including its photocurrent response, **141** exhibits moderate photoelectric conversion properties as compared to other chalcogenido stannates.

Another type of templating ligands for the formation of inorganic-organic hybrid materials in this chemistry are purely organic polyaromatic substances. Two products, $[\text{DMBPE}]_2[\text{Ge}_4\text{S}_{10}] \cdot 8\text{H}_2\text{O}$ (**141**, DMBPE = *N,N'*-dimethyl-1,2-bis(4-pyridinium)-ethylene) and $[\text{DMBPE}]_2[\text{Ge}_4\text{S}_{10}] \cdot 5\text{H}_2\text{O}$ (**142**), can be obtained from the same simple reaction of **101** and DMBPEI_2 in water.⁹⁸ In both cases, anions and cations are connected by $\text{N} \cdots \text{S}$ and $\text{C} \cdots \text{H} \cdots \text{S}$ interactions. In **141**, all cations are arranged in a parallel fashion and show π -stacking (Fig. 27), whereas one out of three cations in **142** adopts an orthogonal position relative to the two other ones, and is therefore not available for such interactions. The measured band gap in the solid state is 2.15 eV, which is significantly lower than that of **101** (3.60 eV) or other comparable compounds, like **128** (2.31 eV). This is attributed to ion-pair charge transfer (IPCT) processes between the organic and inorganic subunits.

The *N,N'*-dimethyl-4,4'-bipyridinium cation, also known as methylviologen dication (MV^{2+}), is an electron acceptor, and as such also serves to form IPCT compounds based on adamantane-type anions. **101** and MVI_2 react in a mixture of water, DMF, and methanol to form $[\text{MV}]_2[\text{Ge}_4\text{S}_{10}] \cdot 6\text{H}_2\text{O}$ (**143**), which crystallizes in a green (**143a**) and an orange (**143b**) polymorph (Fig. 28).⁹⁹ **143a** crystallizes in the highly symmetric tetragonal space group $I4_1/a$. All terminal sulfide ligands of the anions connect to a neighboring anion's sulfide ligands through a $\mu\text{-(OH}_2)$ molecule, thus forming an extended three-dimensional network. In addition, each anion undergoes two $\text{S} \cdots \text{C}$ contacts to MV^{2+} cations at opposite $\mu\text{-S}$ positions, as well as several $\text{S} \cdots \text{H} \cdots \text{C}$ interactions. In **143b** (monoclinic space group $C2/c$), the cations form pairs through π -stacking and connect to the anions via their terminal S atoms. The water and adamantane-type anions form zig-zag chains along the *c*-axis. When layering an aqueous solution of **101** with MVI_2 dissolved in methanol, red needles of $[\text{MV}]_2[\text{Ge}_4\text{S}_{10}] \cdot \text{MeOH}$ (**144**) crystallize instead (Fig. 28), in which the anions and solvent molecule form extended networks through hydrogen bridges. The anion \cdots cation contacts are closer than those in the polymorphs of **143**, leading to a lower-energy charge-transfer transition between the ion pairs as compared to compounds (**143a**: 2.21 eV, **143b**: 2.08 eV and **144**: 1.65 eV; Fig. 28). **143** turns a red color when exposed to MeOH, which causes reflexes of **144** to appear in the PXRD. The process can be reversed by exposure to water. **143** exhibits a photocurrent response with fast separation and transfer rates when irradiated by xenon light during its use for coating indium tin oxide working electrodes in three-electrode photochemical cells.

In a subsequent study, the methyl substituent in MV^{2+} was exchanged with different simple organic groups to generate the ethyl (EV^{2+}), *n*-butyl ($n\text{-BV}^{2+}$), *n*-pentyl (PV^{2+}), and benzyl (BV^{2+}) derivatives, and their corresponding compounds with $[\text{Ge}_4\text{S}_{10}]^{4-}$ (**145–148**).¹⁰⁰ Additionally, the solvate $[\text{MV}]_2[\text{Ge}_4\text{S}_{10}] \cdot 5\text{H}_2\text{O}$ (**149**) was generated in a buildup, which is very close to that of **143b**. The $\text{N} \cdots \text{S}$ cation anion contacts in **145**, involving both the terminal as well as the bridging sulfur atoms, vary in a broad range, from 3.345 Å to 3.994 Å due to the very unsymmetrical coordination of the adamantane-type clusters in the crystal. According to their higher symmetry, the tetragonal compounds **146–148** exhibit four equal $\text{N} \cdots \text{S}$ distances each, between the terminal S positions and *n*- BV^{2+} (3.454 Å), PV^{2+} (3.493 Å), or BV^{2+} (3.773) cations. This results in charge transfer bands between 2.50 and 1.75 eV, with shrinking bandgaps in the order **143** > **148** > **145** > **147**. While the compounds with aliphatic substituents, **143** and **145–147**, show a decrease of the photocurrent response after 30 cycles of irradiation due to photodegradation, the benzyl derivative **148** remains stable over multiple cycles, which is attributed to the steric hindrance of the ligand.

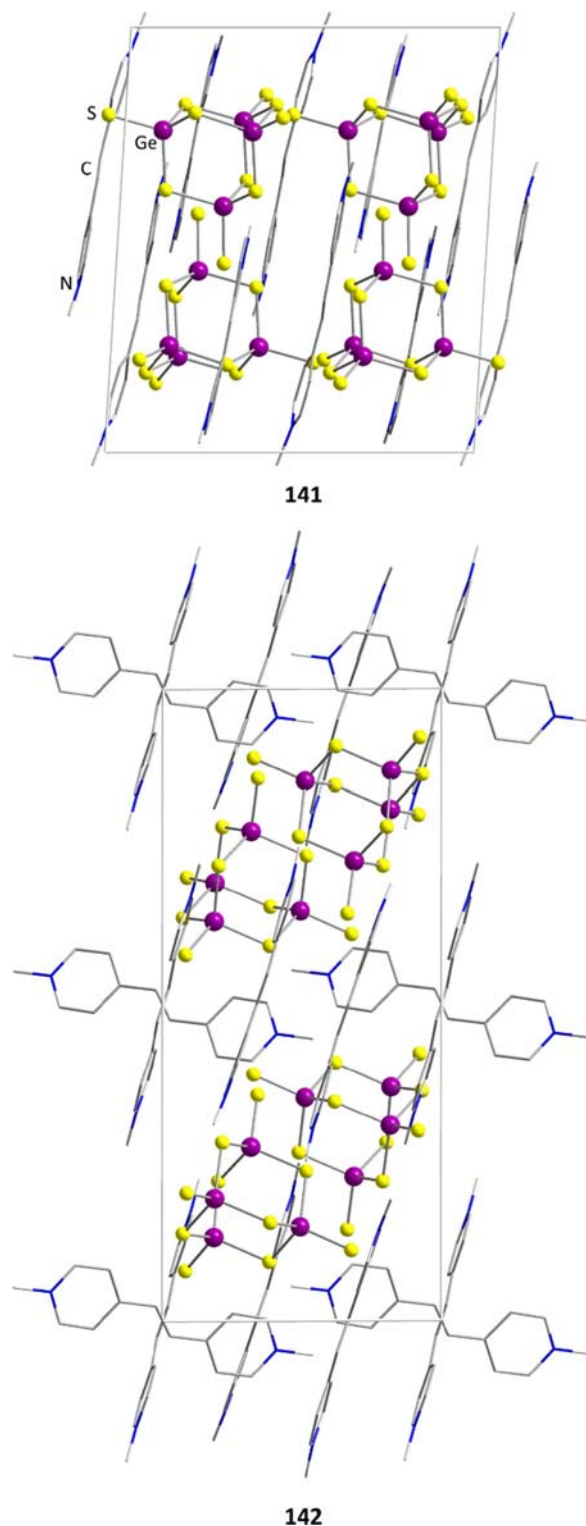


Fig. 27 Cutout of the structures of $[\text{DMBPE}]_2[\text{Ge}_4\text{S}_{10}] \cdot 8\text{H}_2\text{O}$ (**141**, DMBPE = *N,N*-dimethyl-1,2-bis(4-pyridinium)-ethylene, top) with parallel cations only, and $[\text{DMBPE}]_2[\text{Ge}_4\text{S}_{10}] \cdot 5\text{H}_2\text{O}$ (**142**, bottom) comprising parallel and orthogonal DMBPE molecules. Water molecules are omitted for clarity.

The macrocycle 5,10,15,20-tetrakis-(*N*-methyl-4-pyridyl)-porphyrin (TMPyP) can also be used to form IPCT complexes in a solvothermal reaction of TMPyP-(PF₆)₄ with **101** at moderate temperatures.¹⁰¹ The resulting compound, $\text{TMPyP}[\text{Ge}_4\text{S}_{10}] \cdot 5\text{H}_2\text{O}$ (**149**, Fig. 29), forms dark green crystals, in which the anions interact with a porphyrin unit each (short contacts S⋯N = 3.223 Å and S⋯H–C = 3.484 Å). Additionally, each porphyrin comes close to four additional adamantane units via their pyrrole rings, with

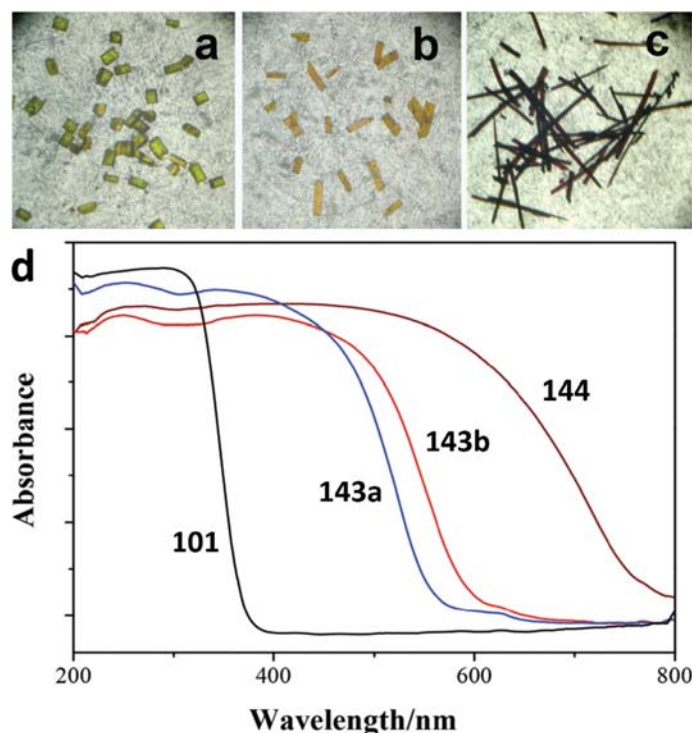


Fig. 28 (A–C) Photographs of crystals of the polymorphs $[MV]_2[Ge_4S_{10}] \cdot 6H_2O$ (**143a**, **a**; **143b**, **b**, $MV = N,N$ -dimethyl-4,4'-bipyridinium), as well as the methanol solvate $[MV]_2[Ge_4S_{10}] \cdot MeOH$ (**144**, **c**).⁹⁹ (D) Optical absorption spectra of compounds **101**, **143a**, **143b**, and **144**.

$S \cdots C = 3.238 \text{ \AA}$ and 3.362 \AA , thus providing pathways for the charge transfer in this compound. By addition of $MnCl \cdot 5H_2O$ during the reaction that yielded **149**, the porphyrin unit acts as a macrocyclic ligand for the transition metal cation. $[MnTMPyP][Ge_4S_{10}] \cdot 13H_2O$ (**150**, Fig. 29) is thus obtained, in which a Mn atom resides slightly off-plane in the center of the cationic porphyrin moiety; in addition, the transition metal cation is coordinated by a terminal sulfide ligand of one adamantane anion. Moreover, these ion pairs form dimers via weak $C \cdots Mn$ interactions between their cations. **149** shows a stronger charge transfer when compared to **150**, which also causes a stronger photocurrent to occur in **149**, as well as a more efficient quenching of the fluorescence that is observed in simple TMPyP compounds.

4.04.3.2 Organotetrel chalcogenide clusters based on adamantane-type $\{T_4E_6\}$ or semicubane-type $\{T_3E_4\}$ cores

When (formally) exchanging the terminal chalcogenide ligands in the previously discussed adamantane-type clusters by organic ligands, a mostly neutral family of cluster compounds is obtained. However, the molecular structures of such organotetrel chalcogenide clusters are not limited to an adamantane-like buildup, but is dependent on factors like the sterical demand or the Lewis basicity of the ligand, the chosen synthetic approach, or the elements present in the inorganic core. In some cases, equilibria between isomeric structures are found, which can be influenced by parameters like temperature or reactant ratios. For these reasons, the most prominent archetypes will be introduced here to give an overview of the cluster family before discussing individual compounds in more detail.

4.04.3.2.1 Structural motifs of the inorganic cores of organotetrel chalcogenide clusters, and their general synthetic approach

Two isomeric sesquichalcogenide structures of the composition $[(RT)_4E_6]$, one being the above mentioned adamantane (AD), and one the so-called double-decker (DD) type, are the most prominent archetypes. The double-decker-type can be understood as two coplanar $\{T_2E_2\}$ four-membered rings, the T position of which are connected by two further μ -E atoms. For a few elemental compositions and synthetic routes, a noradamantane (NA) type buildup $[(RT)_4E_5]$ is preferred, in which one chalcogenide ligand from the AD-type structure is eliminated in favor of a direct T–T bond. Especially in the presence of back-coordinating ligands, defect-heterocubane (DHC) type molecules $[(RT)_3E_4X]$ are often found to form, in which X is a monoanion that can either be bonded directly to a T position in an overall neutral cluster, or be comprised in a counterion that shows weaker interactions to an overall cationic cluster molecule. Especially for more sterically demanding organic ligands, an aggregation into a bis-defect-heterocubane (BDHC) type cluster structure of the composition $[(RT)_4T_2E_{10}]$ was observed, in which two DHC units are bridge via a central $\{T_2E_2\}$ four-membered ring, while the third organic group per DHC unit was released in a concomitant redox step. The mentioned structural archetypes are shown in Scheme 3.

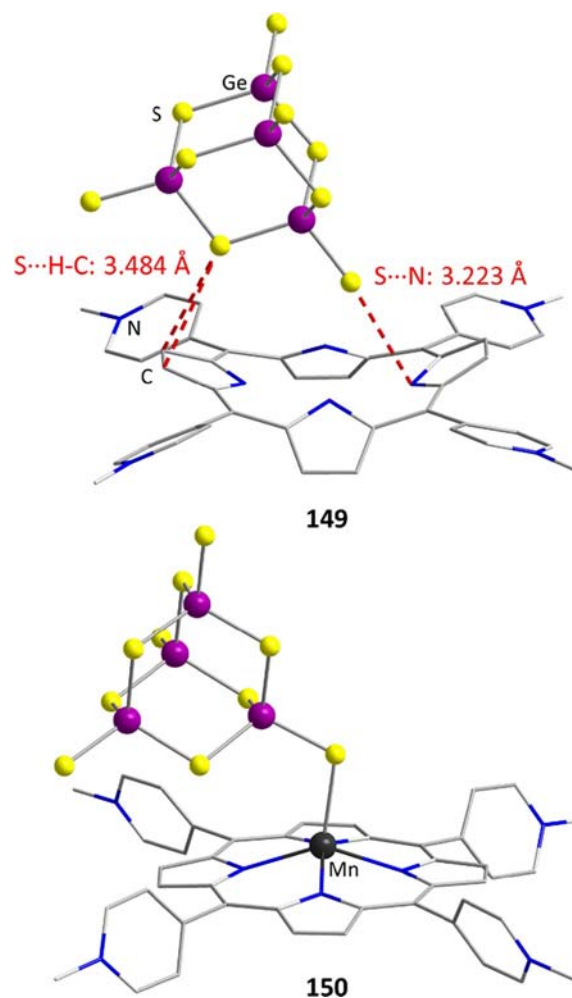
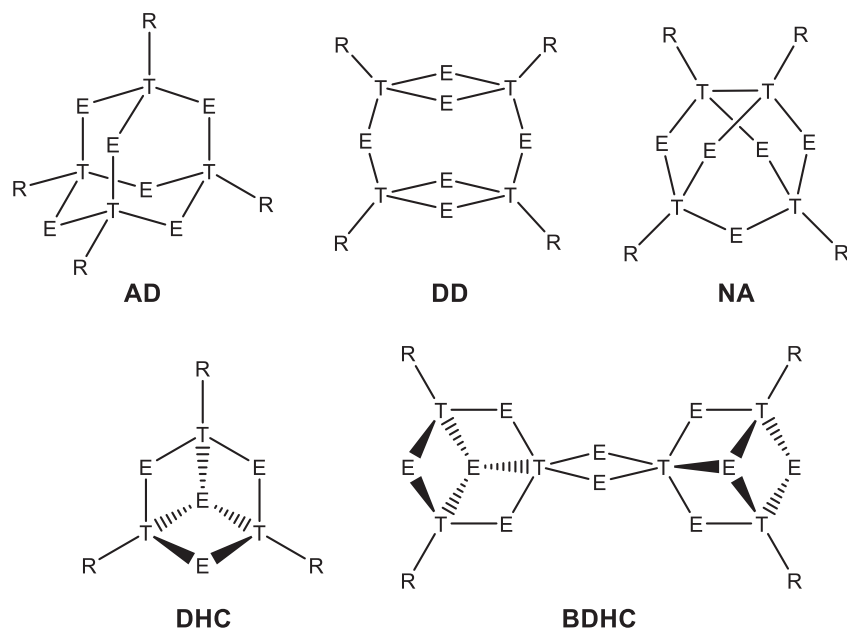


Fig. 29 Ion pairs in TMPyP[Ge₄S₁₀]·5H₂O (**149**, top) and [MnTMPyP][Ge₄S₁₀]·13H₂O (**150**, bottom). TMPyP = 5,10,15,20-tetrakis-(*N*-methyl-4-pyridyl)porphyrin.



Scheme 3 Predominant archetypes in organotetrel chalcogenide clusters along with their common abbreviations: adamantane (AD), double-decker (DD), noradamantane (AD), defect-heterocubane (DHC) and bis-defect-heterocubane (BDHC).

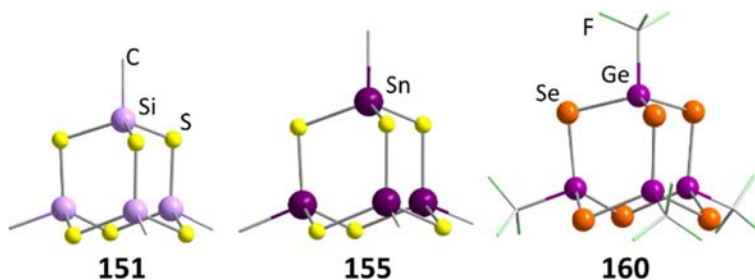


Fig. 30 Examples of different organotetrel chalcogenide hetero adamantane-type clusters [(MeSi)₄S₆] (**151**), [(MeSn)₄S₆] (**155**) and [(CF₃Ge)₄Se₆] (**160**).

The most prevalent syntheses for the named types of compounds is achieved via condensation reaction of an organotetrel trihalide, in most cases RTCl₃ (R = organic rest, T = Si, Ge, Sn) with a chalcogenide source A₂E (A = hydrogen, alkali metal, SiMe₃; E = S, Se, Te) under elimination of ACl in common solvents. When no synthesis route is given in the text, this general route was applied.

4.04.3.2.2 Synthesis and structures of organotetrel chalcogenide clusters

The synthesis and structure of so-called “sesquichalcogenides” of the general formula “(RT)₂E₃” has been discussed in dated literature since 1903, when first investigation on the reactivity of methyl tin compounds with H₂S were reported.¹⁰² The correct AD structure, with double the formula unit, was first experimentally implicated by interpretation of mass spectra, as well as infrared and NMR spectra 60 years later for the compounds [(MeSi)₄E₆] (E = S: **151**, Fig. 30; E = Se: **152**), and [(Et₂Si)₄E₆] (E = S: **153**, E = Se: **154**), which were obtained from RSiH₃ and H₂E at elevated temperatures.¹⁰³ A similar suggestion was made for the organotin sulfide congeners [(RSn)₄S₆] (R = Me: **155**; R = *n*-propyl: **156**, R = *n*-butyl: **157**), produced from the corresponding alkytin oxide and Na₂S in an acidic environment.¹⁰⁴ The first successful XRD experiment was conducted on compound **155** (Fig. 30), which confirmed the suggested AD topology and excluded the DD-type alternative.¹⁰⁵ Structural investigations on the Ge congener of **155** [(MeGe)₄S₆] (**158**) has come to the same conclusion 1 year later,¹⁰⁶ and a publication on XRD measurements of **151** followed (Fig. 30).¹⁰⁷ The structure of Se homologues, which show a higher sensitivity to hydrolysis than the corresponding sulfides, was subsequently elucidated for [(MeSn)₄Se₆] (**159**),¹⁰⁸ [(CF₃Ge)₄Se₆] (**160**, Fig. 30),¹⁰⁹ and [(ThexSi)₄Se₆] (**161**; Thex = 1,1,2-trimethyl propyl). AD-type clusters with a variety of different organic ligands were rapidly realized and spectroscopically analyzed by the routes given above, most of them containing simple aliphatic or other non-polar organic groups. Examples are: [(CF₃Ge)₄S₆] (**161**), [(EtGe)₄S₆] (**162**),¹⁰⁹ [(RSn)₄S₆] (R = mesityl: **163**; R = 1-naphthyl: **164**; R = 4-methylphenyl: **165**; R = 4-methoxyphenyl: **166**; R = 4-fluorophenyl: **167**; R = 3-fluorophenyl: **168**; R = C₆F₅: **169**; R = C₆H₅: **170**),¹¹⁰ [(trisSn)₄E₆] (tris = C(SiMe₃)₃; E = S: **171**, E = Se: **172**), [(*n*-BuSn)₄E₆] (E = S: **173**, E = Se: **174**).¹¹¹

In other cases, the organic ligands could be replaced by transition metal complexes, as in the case of [{FeCp(CO)₂Sn}₄Se₆] (**175**, Fig. 31)¹¹² and [{MoCp(CO)₃Sn}₄Te₆] (**176**, Fig. 31),¹¹³ both obtained by reactions of [{MCp(CO)_x}SnCl₃] and the corresponding sulfide E(SiMe₃)₂. **176** remains one of the few examples of organotetrel telluride clusters exhibiting the AD-type topology to this day.

In a later study, the sulfur congener [{FeCp(CO)₂Sn}₄S₆] (**177**) was isolated in higher yields upon using (Bu₃Sn)₂S as sulfide source.¹¹⁴ Attempts to obtain the exact sulfide analog of **175** by reacting S(SiMe₃)₂ with [{FeCp(CO)₂Sn]₂SnCl₂] yielded a dimeric intermediate first, [{FeCp(CO)₂Sn]₄Sn₂Se₂], and crystals of [{Fe₄Cp₄(CO)₇Sn₃S₄] (**178**, Fig. 32) a few days later. **178** was the first

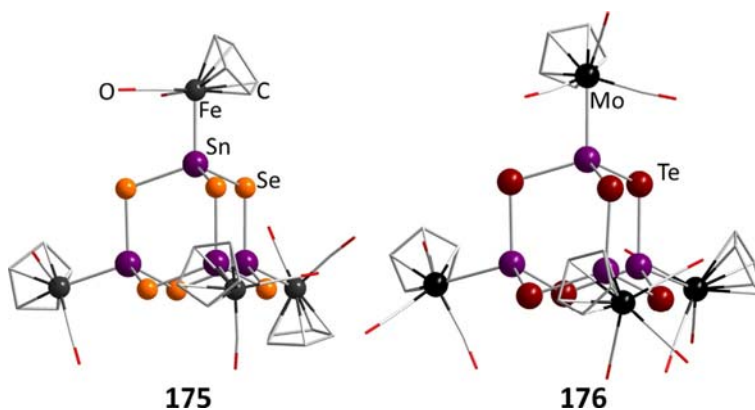


Fig. 31 AD-type clusters with transition metal complex ligands instead of organic ligands, [{FeCp(CO)₂Sn}₄Se₆] (**175**) and [{MoCp(CO)₃Sn]₄Te₆] (**176**).

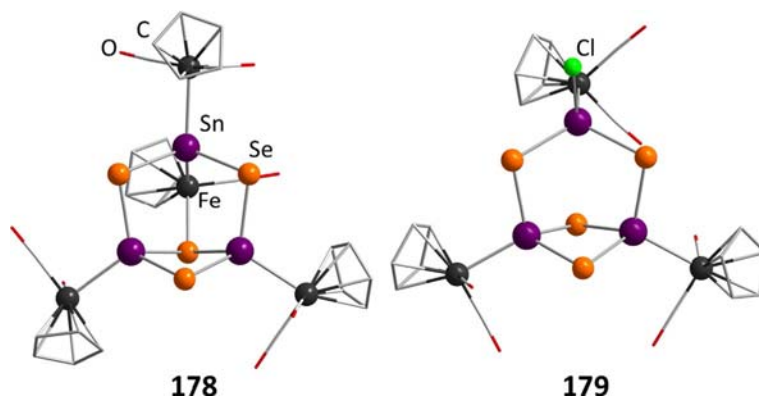


Fig. 32 DHC-type clusters with transition metal complex ligands instead of organic ligands, $[\text{Fe}_4\text{Cp}_4(\text{CO})_7\text{Sn}_3\text{Se}_4]$ (**175**) and $[\{\text{FeCp}(\text{CO})_2\text{Sn}\}_3\text{Se}_4\text{Cl}]$ (**176**).

example to crystallize in a DHC-like architecture (more about this below), yet with one peculiarity: one of its Sn atoms is bonded to two metalloligands, in one of which a CO group was replaced by a unique additional μ_3 -S bridge.¹¹²

$[\{\text{FeCp}(\text{CO})_2\text{Sn}\}_3\text{Se}_4\text{Cl}]$ (**179**, Fig. 32), with a more typical DHC-type buildup, was obtained in a similar reaction as the one affording **175**, but by using Na_2Se as a selenide source instead of $\text{Se}(\text{SiMe}_3)_2$.¹¹⁵

A different way of utilizing organometallic complexes as ligands for adamantane-type clusters is the use of a ferrocenyl (Fc) precursor FcSnCl_3 , which leads to the formation of $[(\text{FcSn})_4\text{S}_6]$ (**180**) or $[(\text{FcSn})_4\text{Se}_6]$ (**181**, Fig. 33), depending on the chalcogenide source used.^{116,117} The UV-visible absorption edge is red-shifted in both cases, as compared to ferrocene alone, but more so for **181**. Their electrochemical properties were investigated by cyclic and differential-pulse voltammetry, with both compounds showing

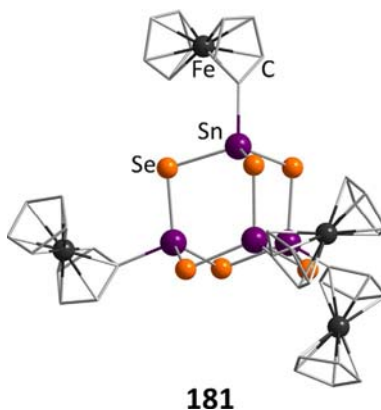


Fig. 33 AD-type organotin selenide cluster decorated with ferrocenyl (Fc) ligands, $[(\text{FcSn})_4\text{Se}_6]$ (**181**).

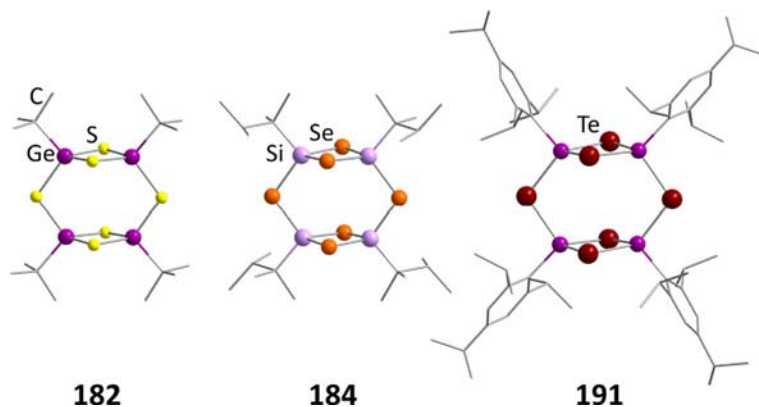


Fig. 34 Molecules with a DD-type structure $[(^t\text{BuGe})_4\text{S}_6]$ (**182**), $[(\text{TheXSi})_4\text{Se}_6]$ (**184**; TheX = 1,1,2-trimethyl propyl) and $[(2,4,6\text{-}i\text{Pr}_3\text{C}_6\text{H}_2\text{Ge})_4\text{Te}_6]$ (**191**).

a reversible single-step oxidation, although the broad peak shape especially in the spectra of **181** hints at a communication between the redox sites.

Eventually, the first DD-type cluster [${}^t\text{BuGe}_4\text{S}_6$] (**182**, Fig. 34) was obtained by a reaction of ${}^t\text{BuGeCl}_3$ with ammonium pentasulfide at room temperature.¹¹⁸ When reacting the precursor with H_2S at elevated temperatures instead, the AD-type isomer [${}^t\text{BuGe}_4\text{S}_6$] (**183**) was isolated. As **182** can be transformed to **183** by heating, the DD-type structure seems to be a kinetic product in this case and rearranges to form the thermodynamically more stable AD-type topology upon tempering.

This rearrangement has been studied more systematically for the family of compounds [$(\text{ThexT})_4\text{E}_6$], with T = Si, E = S: **184** (DD, Fig. 34), **162** (AD), E = Se: **185** (DD), **186** (AD); T = Ge, E = S: **187** (DD), **188** (AD), E = Se: **189** (DD), **190** (AD).¹¹⁹ Again, the steric demand of the Thex ligands leads the reaction towards the DD-type structure upon reaction of ThexTCl_3 and Li_2E . When heating the sample in decalin, the sulfide clusters **184** and **187** were observed to rearrange at 195°C , while the Ge/Se compound **189** changed its structure to form **190** at a significantly lower temperature, 80°C . The authors expanded on their findings in a further study, where they could also discover the rearrangement of **187** to **188**.¹²⁰ Additionally, they discovered that a reverse reaction of some of the named compounds was also possible, and that the reactions between the DD and the AD type can thus be viewed as being a temperature-dependent equilibrium. An exception seems to be compound **188**, which could not be transformed to **187** under any tested conditions. The kinetics of these rearrangements have been studied in great detail in the context of this comprehensive study.

Another DD-type compound [$(2,4,6\text{-iPr}_3\text{C}_6\text{H}_2\text{Ge})_4\text{Te}_6$] (**191**, Fig. 34) was isolated as the minor product in a reaction of hexakis(2,4,6-triisopropylphenyl)tetragermabuta-1,3-diene with Et_3PTe , for which the major products were based on six-membered and three-membered rings of Te and RGe.¹²¹

Another reoccurring structural motif containing direct T–T bonds, is the NA type, which is formally generated by removal of a chalcogenide ligand from the AD-type structure. It was first observed in [$(\text{MesGe})_4\text{S}_5$] (**192**; Mes = mesityl), which forms besides [$(\text{MesGe})_4\text{S}_6$] (**193**) when reacting MesGeCl_3 with $\text{S}(\text{SiM}_3)_2$ in benzene at 80°C ; notably, **192** was not observed when using other sulfur reagents.¹²² When choosing a dimeric precursor that already contained T–T bonds, $({}^t\text{BuSi})_2\text{Cl}_4$, and reacting it with Li_2E , the NA-type clusters [$({}^t\text{BuSi})_4\text{E}_5$] (E = S: **194**; E = Se: **195**) are obtained selectively. The Ge analogue $({}^t\text{BuGe})_2\text{Cl}_4$ only generates [$({}^t\text{BuGe})_4\text{S}_5$] (**196**) selectively in reactions with H_2S . Other reagents and conditions lead to mixtures with **183** and/or [$({}^t\text{BuGe})_4\text{S}_4$] (**197**), in a rare bisnoradamantane-type architecture, in which a second bridging chalcogenide ligand in **196** (the one opposing the already existing Ge–Ge bond) was formally removed in favor of a second Ge–Ge contact. The reaction leading to **194** and **195** can also be carried out with the corresponding methyl precursor to yield [$(\text{MeSi})_4\text{E}_5$] (E = S: **198**, Fig. 35; E = Se: **199**), even though 1 equivalent of MeSiCl_3 and NEt_3 needed to be added to the mixture in order to obtain **198**.¹²³ This proves that sterically demanding ligands are not urgently required to stabilize NA-type structures.

Reactions using a monomeric and a dimeric tetrel source, like that leading to **198**, open up the possibility to generate mixed-tetrel chalcogenide clusters. Indeed, the simultaneous reaction of $(\text{MeSi})_2\text{Cl}_4$ and MeGeCl_3 with H_2S and NEt_3 affords [$(\text{MeSi})_2(\text{MeGe})_2\text{S}_5$] (**200**, Fig. 35), and [$(\text{MeSi})_2(\text{PhSn})_2\text{Se}_5$] (**201**) can be obtained from $(\text{MeSi})_2\text{Cl}_4$, PhSnCl_3 , and Li_2Se .¹²⁴ Both compounds contain Si–Si bonds over Sn–Sn bonds exclusively in accordance with the nature of their precursors.

A very efficient way to influence the formation of either AD-type or DD-type organotetrel chalcogenide cluster is the utilization of ligands that contain donor atoms at a position that enable back-coordinating to the tetrel atoms. This was first demonstrated for [$(\text{DEAPSn})_4\text{S}_6$]· CHCl_3 (**202** DEAP = 2-(dimethylaminoethyl)phenyl), in which the lone pairs of the amino groups coordinate in an intramolecular fashion to the Sn atoms under formation of five-membered rings.¹²⁵ At the same time, the coordination number of the Sn atoms is increased from 4 to 5, which results in a trigonal bipyramidal coordination sphere at the tetrel atom. This seems to be sterically unfavorable for an AD-type cluster structure, which explains the preference of the DD-type for such ligands. In compound **202**, this comes along with twisting of the two four-membered rings against each other in the DD-type cluster core (Fig. 36). The phenomenon was thoroughly investigated experimentally and by means of complementary quantum chemical studies on the example of the back-coordinating ligands $\text{R}^1 = \text{CMe}_2\text{CH}_2\text{C}(\text{O})\text{Me}$ and $\text{R}^2 = \text{C}_2\text{H}_4\text{COO}^-$ with keto and carboxyl

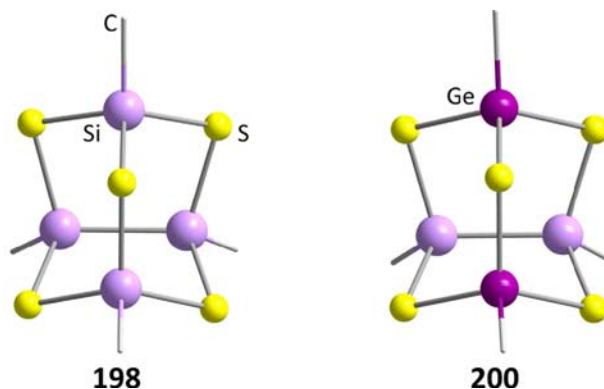


Fig. 35 Molecules with a NA-type structure, silicon based [$(\text{MeSi})_4\text{S}_5$] (**198**) and mixed Si/Ge [$(\text{MeSi})_2(\text{MeGe})_2\text{S}_5$] (**200**).

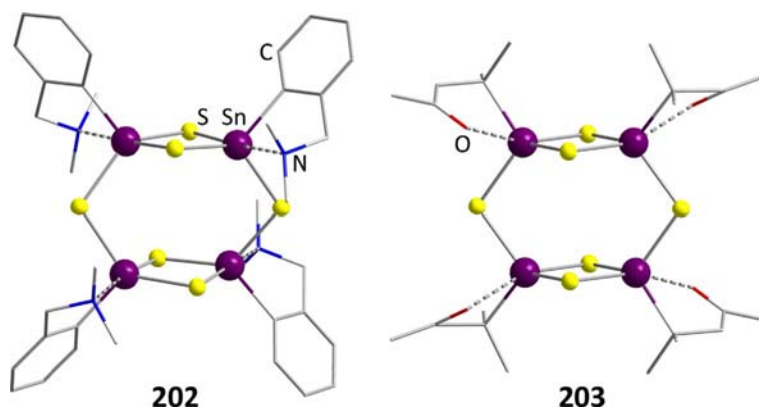


Fig. 36 DD-type clusters with back-coordinating ligands in $[(\text{DEAPSn})_4\text{S}_6] \cdot \text{CHCl}_3$ (**202**, DEAP = 2-(dimethylaminoethyl)phenyl) and $[(\text{R}^1\text{Sn})_4\text{S}_6]$ (**203**, $\text{R}^1 = \text{CMe}_2\text{CH}_2\text{C}(\text{O})\text{Me}$).

functionalities, respectively. Like discussed for **202**, also $[(\text{R}^1\text{Sn})_4\text{S}_6]$ (**203**, Fig. 36) exhibits such five-ring formation, and thus occurs in the DD-type isomer only.¹²⁶ However, as for most of these compounds, no twisting of the ideal structure was detected, in contrast to the observations reported for **202**.

For $[(\text{R}^1\text{Ge})_4\text{S}_6] \cdot \text{CHCl}_3$ (**204**, Fig. 37) and $[(\text{HR}^2\text{Ge})_4\text{S}_6]$ (**205**), however, no such back-coordination was observed, and the AD topology was found to form instead. It was thus assumed that a reduction of the steric strain of the five-coordinate tetrel atom in the DD structure applies only to Sn atoms (at least for S as bridging atoms), so the Ge/S elemental combination prefers to remain in a four-coordinate version and form the AD-type cluster. Indeed, density functional theory (DFT) calculation indicate a much smaller energetic preference of a DD-type structure over an AD-type isomer, which can easily be overcompensated by additional effects in the crystal.

In a study addressing reactions of RGeCl_3 with alkali metal tellurides, the product was observed to form a DD-type structure, $[(\text{R}^1\text{Ge})_4\text{Te}_6]$ (**206**, Fig. 37), and to exhibit ligand back-coordination in contrast to **204**.¹²⁷ Calculations revealed the DD-type topology to be nearly isoenergetic with the AD-type buildup in this case, so the observed structure could not be clearly predicted.

For organogermanium telluride compounds, ligands that are terminated by an acid functionality lead to the formation of crystals comprising clusters of an NA-type topology, $[(\text{RGe})_4\text{Te}_5]$ ($\text{R} = \text{HR}^2$: **207**, Fig. 38; $\text{R} = \text{CH}(\text{CH}_2\text{COOH})_2$: **208**). Here, the organic

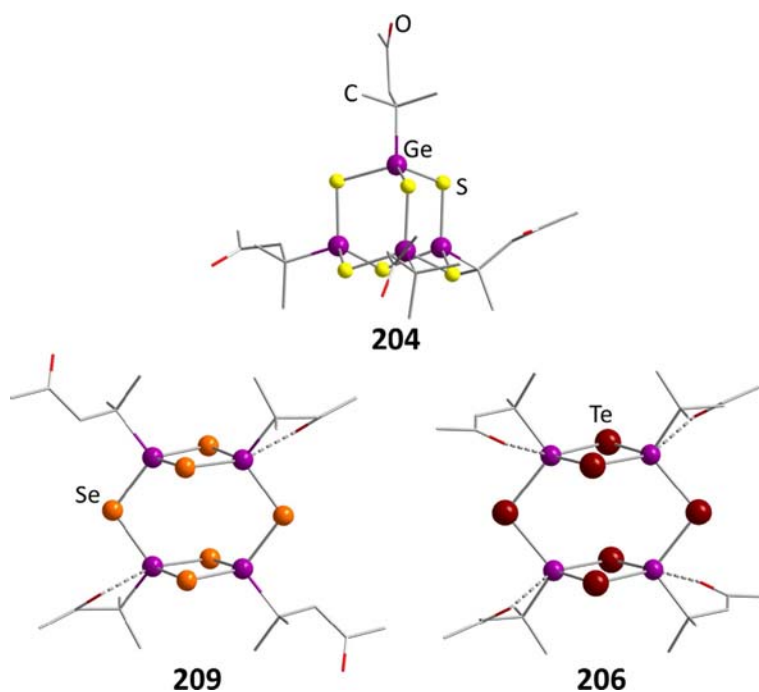


Fig. 37 Influence of the elemental composition on the back-coordination of the ligand and thus the resulting structure type, illustrated with clusters with ligands R^1 ($\text{R}^1 = \text{CMe}_2\text{CH}_2\text{C}(\text{O})\text{Me}$). The examples exhibit no ($[(\text{R}^1\text{Ge})_4\text{S}_6] \cdot \text{CHCl}_3$; **204**), two ($[(\text{R}^1\text{Ge})_4\text{Se}_6]$; **209**), or four ($[(\text{R}^1\text{Ge})_4\text{Te}_6]$; **206**) ligands in an intramolecular back-coordination mode.

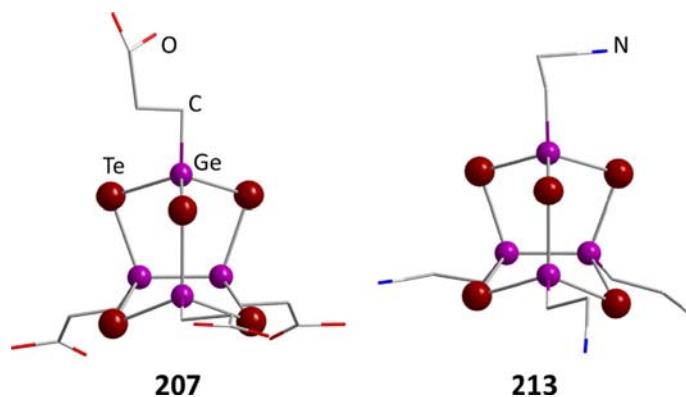


Fig. 38 Organogermanium telluride clusters with NA-buildup, $[(HR^2Ge)_4S_5]$ (**207**, $R^2 = C_2H_4COO^-$) and $[(NCC_2H_4Ge)_4S_5]$ (**213**).

ligands do not undergo $Ge \cdots O$ interactions—presumably owing to steric restrictions at the small Ge atoms again. The Ge–Ge bond formation, coupled with a reduction of the corresponding Ge atoms, is possible due to the reductive power of Te^{2-} . The results prompted the authors to investigate the isomerization energies and the reaction energies for cluster rearrangements between the DD-, AD-, and NA-type for all elemental combinations of $T = Ge, Sn$ and $E = S, Se, Te$ with the ligands R^1 (Table 1) and R^2 by means of comprehensive quantum chemical calculations. As observed in previous studies, DD-type clusters are preferred for Sn compounds with R^1 , while Ge congeners rather adopt an AD-type structure. The presence of R^2 , in contrast, leads to a preference of AD-type clusters in all cases (with the DD-type architecture being only slightly unfavorable for Sn homologues), except for the Ge/Te combination described here. Only this elemental combination offers a favorable T–T over T–E bond formation, while potential $Ge \cdots O$ interactions, which would stabilize the DD-type buildup, are sufficiently weak to be overcompensated. After all, the theoretical work suggested the findings to be widely in agreement with the experimental findings and thus comprehensible. It demonstrated the subtle interplay of R, T, and E in the formation and stabilization of such related organotetrel chalcogenide cluster cores.

The subtletness of these parameters became even more obvious with the finding that, unexpectedly, crystals of the Se congener $[(R^1Ge)_4Se_6]$ (**209**, Fig. 37) revealed a DD-type structure. At first glance, this seemed to contradict the previously published calculations, but a closer look at the structure revealed that only two of the four ligands exhibited a back-coordination to Ge. This change in conformation causes this structure to be isoenergetic with an AD-type alternative within the errors of the method (see Table 1). Hence, the nature of the mentioned components, as well as the back-coordination pattern need to be considered for getting a comprehensive picture.

It was further shown that UV radiation can prompt a rearrangement of **207** to an ionic variant of the NA-type compound $[Na(thf)_2][(R^1Ge^{IV})_2(Ge^{III}Se)(R^1Ge^{III})Se_5]$ (**210**, Fig. 39) under elimination of a chlorinated R^1 ligand. The energy difference calculated between a DD-type and an NA-type cluster is in good agreement with the finding of radiation leading to this transformation.

The preference for Te compounds to adopt the NA-type structure was also observed for nitrile-decorated compounds synthesized from $NC(CH_2)_2GeCl_3$ and the corresponding Na_2E salts. While the lighter homologues form the AD-type complexes $[(NCC_2H_4Ge)_4E_6]$ ($E = S$: **211**; $E = Se$: **212**), the NA-type compound $[(NCC_2H_4Ge)_4Te_5]$ (**213**, Fig. 38) was formed with telluride ligands.¹²⁸

Table 1 Energetics of hypothetical reactions between clusters of the composition $[(R^1T)_4E_6]$ in DD-type or AD-type topology or $[(R^1T)_4E_5]$ in NA-type topology: Energies of the isomerization reaction between AD and DD, ΔE_{DD-AD} , and reaction energies for transformations between DD and NA + E, ΔE_{NA-DD} , and AD and NA + E, ΔE_{NA-AD} , corrected by the atomization energy of the released equivalent of chalcogen E ($R^1 = CMe_2CH_2C(O)Me$; energies given in kJ mol^{-1}).

T/E	ΔE_{DD-AD}	ΔE_{NA-DD}	ΔE_{NA-AD}
Ge/S	19.42	70.01	89.43
Ge/Se	11.35	47.41	58.76
Ge/Te	1.71	19.52	21.23
Sn/S	−23.71	104.76	81.06
Sn/Se	−27.77	85.91	58.14
Sn/Te	−29.04	55.96	26.92



Fig. 39 NA-type cluster anion and its coordination to a nearby $[\text{Na}(\text{thf})_2]^+$ complex in $[\text{Na}(\text{thf})_2][(\text{R}^1\text{Ge})_2(\text{Ge}^{\text{III}}\text{Se})(\text{R}^1\text{Ge}^{\text{III}})\text{Se}_5]$ (**210**, $\text{R}^1 = \text{CMe}_2\text{CH}_2\text{C}(\text{O})\text{Me}$).

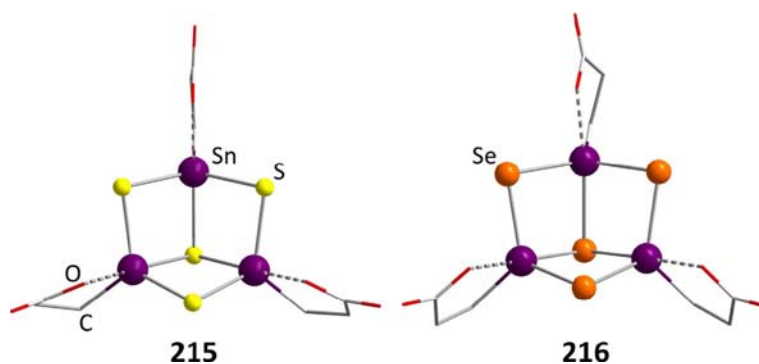


Fig. 40 DHC-Type cations in $[\text{Na}_2(\text{MeOH})_{1.66}(\text{H}_2\text{O})][(\text{R}^2\text{Sn})_3\text{S}_4]$ (**215**, $\text{R}^2 = \text{C}_2\text{H}_4\text{COO}^-$) and $[\text{Na}_2(\text{MeOH})_2][(\text{R}^2\text{Sn})(\text{HR}^2\text{Sn})_2\text{Se}_4]$ $[(\text{HR}^2\text{Sn})(\text{R}^2\text{Sn})_2\text{Se}_4] \cdot 3\text{H}_2\text{O}$ (**216**).

By utilization of potentially back-coordinating ligands, compounds could also be isolated in a DHC-type arrangement for a variety of elemental combinations. The first example was $[\text{Na}_2(\text{EtOH})_3][(\text{R}^2\text{Sn})_3\text{S}_4] \cdot 0.5\text{EtOH}$ (**214**), synthesized from R^2SnCl_3 , Na, and S_8 in liquid ammonia.¹²⁶ In **214**, the carboxyl groups coordinate back to all three Sn atoms and furthermore act as ligands of the sodium atoms in the crystal lattice, which leads to the formation of a loosely-connected three-dimensional network. Repeating the reaction with Na_2S in a water/acetone mixture yields a different solvate, $[\text{Na}_2(\text{MeOH})_{1.66}(\text{H}_2\text{O})][(\text{R}^2\text{Sn})_3\text{S}_4]$ (**215**, Fig. 40), after extraction with MeOH and layering with Et_2O . In **215**, the counterions and solvent molecules form layers between the cluster through coordination interactions with each other and the latter.¹²⁹ The analogous reaction with Na_2Se cannot be carried out in water owing to the water-sensitivity of the latter; it was thus carried out in liquid ammonia, affording the partially protonated $[\text{Na}_2(\text{MeOH})_2][(\text{R}^2\text{Sn})(\text{HR}^2\text{Sn})_2\text{Se}_4][(\text{HR}^2\text{Sn})(\text{R}^2\text{Sn})_2\text{Se}_4] \cdot 3\text{H}_2\text{O}$ (**216**, Fig. 40), in which monoprotonated and diprotonated clusters form one-dimensional chains through coordination to Na^+ cations. This study indicated the importance of the applied solvent for selectively obtaining the DHC-type or DD-type structures with ligands capable of back-coordination. This was corroborated by many follow-up studies.

In a subsequent work, further neutral and ionic species of the DHC-type architecture were obtained.¹³⁰ $[(\text{R}^1\text{Sn})_3\text{S}_4\text{Cl}]$ (**217**, Fig. 41) was isolated either by reacting stoichiometric amounts of R^1SnCl_3 and $\text{S}(\text{SiMe}_3)_2$ in dichloromethane, or by using an excess of $\text{S}(\text{SiMe}_3)_2$ and filtering off the precipitating product in toluene. Through the additional Cl^- ligand at one of the Sn atoms, the

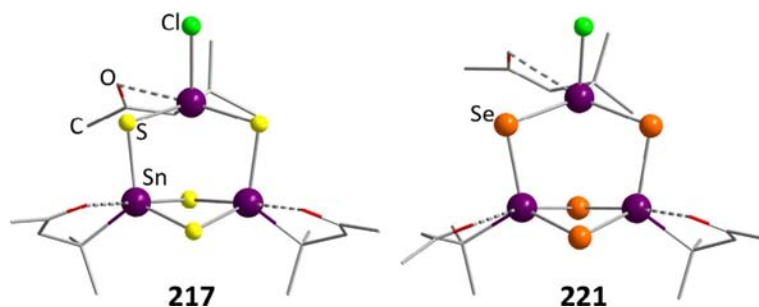
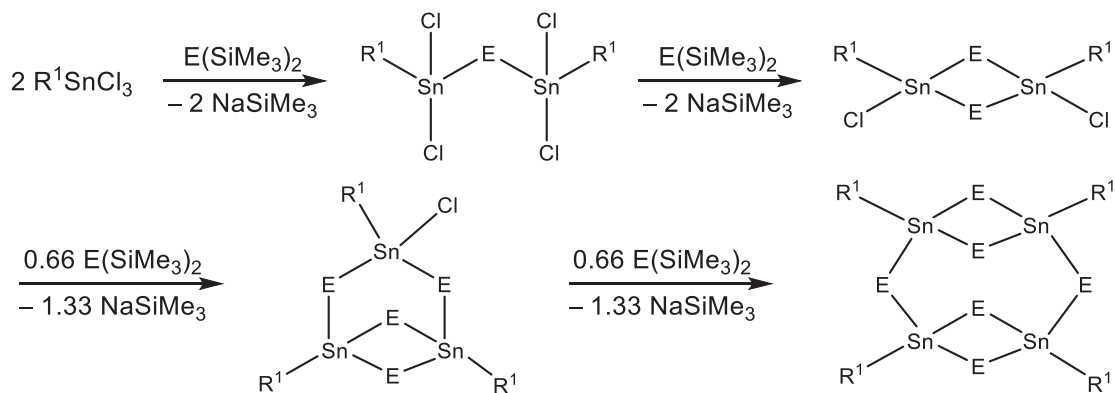


Fig. 41 Neutral DHC-type clusters $[(\text{R}^1\text{Sn})_3\text{S}_4\text{Cl}]$ (**217**, $\text{R}^1 = \text{CMe}_2\text{CH}_2\text{C}(\text{O})\text{Me}$) and $[(\text{R}^1\text{Sn})_3\text{Se}_4\text{Cl}]$ (**221**).



Scheme 4 Stepwise reaction cascade from R^1SnCl_3 towards DD-type clusters via addition of $E(SiMe_3)_2$.

coordination sphere is expanded to a significantly distorted octahedral environment, with the $\mu_3-S \cdots Sn$ contact (not indicated in Fig. 41) being significantly widened.

It could also be shown by a combined experimental and theoretical study, that the DHC-type clusters represent an intermediate structure in a condensation reaction cascade from R^1SnCl_3 towards the DD-type cluster upon stepwise addition of $S(SiMe_3)_2$ (Scheme 4). Besides detection of the intermediates in corresponding stoichiometric reactions by NMR spectroscopy, and corroboration of the findings by quantum chemical calculation of the NMR shifts, the species $[(R^1SnCl_2)_2S]$ and $[(R^1SnCl)_2S_2]$ were isolated in crystalline form. The assumed driving force of these condensation reactions is the formation of $SiMe_3Cl$ in all cases.

The analogue reaction with $Se(SiMe_3)_2$ yielded a white precipitate, which could be re-dissolved. Layering of the solution afforded $[(R^1Sn)_3Se_4][SnCl_3] \cdot CH_2Cl_2$ (218), hinting at slight decomposition of the material and reduction of the tetrel atom under release of RCl as was already shown for 210. Repeating the reaction with HR^2SnCl_3 and Li_2Se in THF instead yielded a mixture of the ionic chloride compounds $[Li(thf)][R^2Sn(HR^2Sn)_2Se_4Cl]$ (219) and $[Li(thf)_2][R^2Sn(HR^2Sn)_2Se_4Cl]_2 \cdot 4THF$ (220). 219 forms one dimensional chains through coordination between the cations and anions, while 220 is buildup of dimers, with O_2Li_2 four membered rings formed by the clusters ligands and the cations. Again, the additional Cl ligand leads to the elongation of a $Sn \cdots Se$ bond. An even more systematic study of organotin selenium clusters revealed an analogue reaction cascade induced by addition of $Se(SiMe_3)_2$ to R^1SnCl_3 . It leads through $[(R^1SnCl_2)_2Se]$, $[(R^1SnCl)_2Se_2]$, and $[(R^1Sn)_3Se_4Cl]$ (221, Fig. 41) to finally form the DD-type cluster $[(R^1Sn)_4Se_6]$ (222).¹³¹ The neutral species 221 was obtained here by layering the reactive solution to inhibit further progress of the reaction.

The same cascade was also investigated for the homologous Te compounds, in which the dimeric intermediates and the final product $[(R^1Sn)_4Te_6]$ (223) with DD-type architecture could be crystallized and isolated, too, yet not the DHC-type cluster.¹³²

In addition to the back-coordination provided by R^1 , this ligand type also enables a chemical post-functionalization by condensation reactions with hydrazine and hydrazone derivatives. The practically instantaneous reactions were used to introduce a multitude of ligand extensions and functionalities to the cluster compounds. The most simple version is the reaction with hydrazine itself, in the form of hydrazine hydrate or its THF adduct for safety reasons, both of which transform R^1 into the equally back-coordinating ligands $R^3 = CMe_2CH_2C(NNH_2)Me$. This transformation was possible for the following starting compounds to form their respective derivatives: 203 to $[(R^3Sn)_4S_6]$ (224),¹²⁶ 217 to $[(R^3Sn)_3S_4Cl] \cdot 3CH_2Cl_2$ (225), 218 to $[(R^3Sn)_3Se_4][SnCl_3]$ (226),¹³⁰ 221 to $[(R^3Sn)_3Se_4Cl] \cdot 3CH_2Cl_2$ (227, Fig. 42), 222 to $[(R^3Sn)_4Se_6]$ (228),¹³¹ and 223 to $[(R^3Sn)_4Te_6]$ (229, Fig. 42).¹³² In all of these

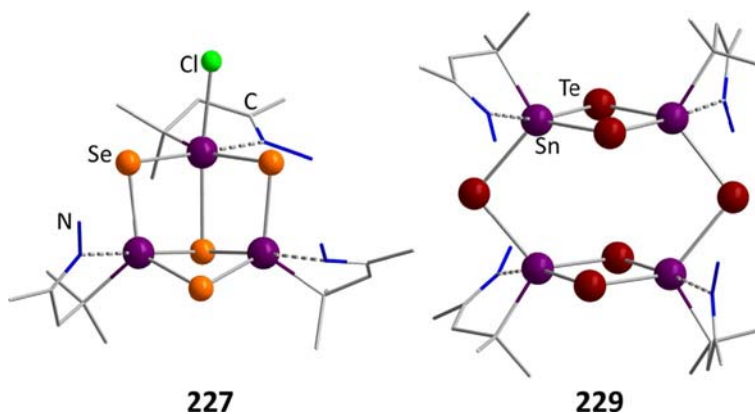


Fig. 42 $[(R^3Sn)_3Se_4Cl]$ (227, $R^3 = CMe_2CH_2C(NNH_2)Me$) and $[(R^3Sn)_4Te_6]$ (229), formed by post-functionalization of clusters terminated with R^1 ligands in reactions with hydrazine.

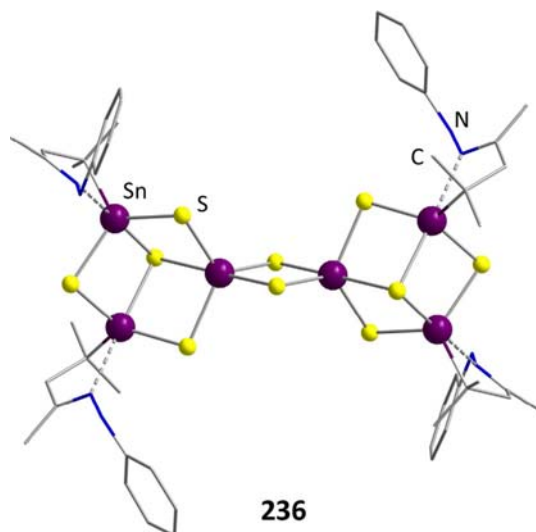


Fig. 43 BDHC-type cluster buildup in $[(R^4Sn)_4Sn_2S_{10}]$ (**236**, $R^4 = CMe_2CH_2C(NNHPH)Me$).

cases, the inorganic core does not significantly change, with the exception of **227**, in which the μ_3 -Se is nearly equidistant to all Sn atoms in spite of the Cl ligand on one of them (see the solid line drawn in **Fig. 42**), and **229**, which experiences a minor twist similar to that observed for **202** (**Fig. 42**). Through a corresponding reaction with the dimeric intermediate $[(R^1SnCl)_2Te_2]$, the DHC-type telluride cluster compound $[(R^3Sn)_3Te_4][SnCl_3]$ (**230**) could finally be realized, too.¹³²

By choosing hydrazine derivatives H_2NNHR as a reagent, it was possible to introduce new organic groups R into clusters with the R^1 ligand. As a prove of principle, phenylhydrazine was reacted with clusters terminated by R^1 to generate a new ligand $R^4 = CMe_2CH_2C(NNHPH)Me$ in several reactions: **203** to $[(R^4Ge)_4S_6]$ (**231**),¹²⁶ **222** to $[(R^4Sn)_4Se_6]$ (**232**),¹³¹ and **223** to $[(R^4Sn)_4Te_6]$ (**233**).¹³² Again, the organotin telluride DHC-type cluster $[(R^4Sn)_3Te_4][SnCl_3] \cdot C_6H_{14}$ (**234**) was obtained from the dimeric intermediate. **221** was reacted with phenylhydrazine under partial decomposition to form the known motif in $[(R^4Sn)_3Se_4][SnCl_3] \cdot toluene$ (**235**), being thus homologous to **234**.¹³¹

In reactions of **203** with phenylhydrazine, a rearrangement of the cluster core was observed to form the BDHC-type topology in $[(R^4Sn)_4Sn_2S_{10}]$ (**236**, **Fig. 43**). This was explained by the steric demand of the R^4 group in its back-coordinating conformation.¹²⁶ However, when changing the solvent for the reaction that in dichloromethane would yield **224** to THF, a corresponding transformation is observed with R^3 , thus yielding $[(R^3Sn)_4Sn_2S_{10}]$ (**237**) in spite of a lower steric demand of the involved organic ligand.¹³⁰ This, and the fact that no BDHC-type compounds with R^1 were observed to date, suggest that the presence of a hydrazine/hydrazone moiety is vital, most likely due to its redox properties that are needed to release ligands from the Sn atoms of the $\{Sn_4S_4\}$ ring in the center of the BDHC-type cluster core.

To obtain the Se congeners in the BDHC-type topology, $Se(SiMe_3)_2$ needs to be added to **222** in addition to the corresponding hydrazine derivative. In this way, compounds of the type $[(RSn)_4Sn_2Se_{10}]$ ($R = R^3$: **238**; $R = R^4$: **239**) were synthesized and isolated in single-crystalline form.¹³³

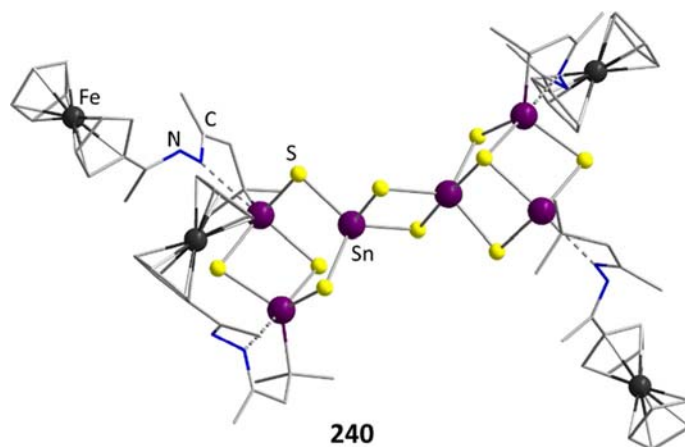


Fig. 44 Ferrocenyl (Fc) decorated BDHC-type compound $[(CMe_2CH_2CMeNNCMeFc)Sn]_4Sn_2Se_{10}$ (**240**).

In further studies, organic rests with a multitude of structures and functionalities were added to basic organotin chalcogenide clusters. A ferrocenyl-terminated hydrazine group, $\text{H}_2\text{NNCMeFc}$, induced rearrangement of **203** to form $[\{(\text{CMe}_2\text{CH}_2\text{CMeNNCMeFc})\text{Sn}\}_4\text{Sn}_2\text{S}_{10}]$ (**240**, Fig. 44) in the BDHC-type structure.¹³⁴ For both compounds, a simple cation $[(\text{RSn})_3\text{S}_4]^+$ with a presumed DHC-type buildup seems to be present in solution, which could not be isolated in any way. Both cyclic and differential pulse voltammetry reveal a reversible two step oxidation of **240** in solution, which clearly indicates electronic communication between the vicinal Fc units. In the presence of HCl, a degradation to $[(\text{RSnCl}_2)_2\text{S}]$ or HRSnCl_4 can be observed, depending on the concentration of the acid.

A similar structure was obtained when adding the analogous ruthenocenyl (Rc) terminated hydrazone, $\text{H}_2\text{NNCMeRc}$.¹³⁵ However, $[\{(\text{CMe}_2\text{CH}_2\text{CMeNNCMeRc})\text{Sn}\}_4\text{Sn}_2\text{S}_{10}]$ (**241**) showed a vastly different cyclic voltammogram, even though the partial decomposition of the material upon addition of a ferrocene internal reference does not allow for more than a qualitative statement. Two irreversible oxidation peaks could be recorded in the first cycle at 1.13 and 2.02 V. In further cycles, the first peak was shifted to 1.18, while the second only greatly diminished in intensity and was reduced to a shoulder in the voltammogram, all of which hints at the decomposition of the material. The reason of the different behavior in comparison with **240** was attributed to the presence of the ruthenocenium moieties, which exhibit a high reactivity in order to obtain the desired 18-electron shell. The photoluminescence behavior upon laser irradiation showed a (slow) photodegradation of the compound to take place.

Both 1-adamantylmethylhydrazone and adamantane-1-carbohydrazide were added to **203** to form BDHC-type compounds $[(\text{RSn})_4\text{Sn}_2\text{S}_{10}]$ ($\text{R} = \text{CMe}_2\text{CH}_2\text{CMeNNCMeAd}$: **242**, $\text{Ad} = \text{adamantyl}$; $\text{R} = \text{CMe}_2\text{CH}_2\text{CMeNNHCOAd}$: **243**),¹³⁶ which indicated that these bulky ligands have similar effects as the aforementioned phenyl groups at these positions.

More extended (hetero)aromatic ligands were introduced through the same method, with the final goal to incorporate additional metal ions to these moieties, or to enable interactions with metal surfaces. A hydrazine derivative with terminal bispyridyl units, $\text{H}_2\text{NNC}(2\text{-pyridyl})_2$, was reacted with **203**, resulting in compounds with DHC-type and BDHC-type structures.¹³⁷ While the simple DHC-cation $[(\text{CMe}_2\text{CH}_2\text{C}(\text{Me})\text{NNC}(2\text{-pyridyl})_2\text{Sn})_3\text{S}_4]^+$ was detected in the reactive solution by mass spectrometry only, the BDHC-based compound $[\{(\text{CMe}_2\text{CH}_2\text{C}(\text{Me})\text{NNC}(2\text{-pyridyl})_2\text{Sn})_4\text{Sn}_2\text{S}_{10}\}]$ (**244**, Fig. 45) was isolated from such solutions in crystalline form. During crystallization, **244** was observed to be the main product with a minor species occurring in DHC-type topology, $[(\text{CMe}_2\text{CH}_2\text{C}(\text{Me})\text{NNC}(2\text{-pyridyl})_2\text{Sn})_2(\text{CMe}_2\text{CH}_2\text{C}(\text{Me})\text{NHNC}(2\text{-pyridyl})_2\text{SnS})\text{S}_4]$ (**245**). Different from the situation observed most often for DHC-type clusters, there is no additional Cl atom bound to one of the Sn atoms, but one of the ligands is protonated, and an additional sulfide atom forms a bridge to the organic ligand. **245** can be understood as an intermediate between the “normal” DHC-type cation and the finally observed cluster in BDHC-type architecture, **244**. An equilibrium between DHC and BDHC in solution, or decomposition of the latter into the first, are probable scenarios for (mutual) transformation of such compounds.

Experiments to use the bispyridyl ligands for a mere coordination of Zn^{2+} ions failed, as the transition metal ion was (also) incorporated into the inorganic cluster core instead, thereby forming a ternary cluster core with a unique architecture.

In subsequent works, a library of cluster compounds with different (hetero)aromatic ligands was obtained by a systematic study of the addition of different hydrazine derivatives to **203**. For all of the resulting compounds, $[(\text{CMe}_2\text{CH}_2\text{CMeNNR})_4\text{Sn}_2\text{S}_{10}]$ ($\text{R} = \text{CHPh}$: **245**; $\text{R} = \text{CMe}(1\text{-naphthyl})$: **246**; $\text{R} = \text{CMe}(2\text{-naphthyl})$: **247**; $\text{R} = \text{CH}(3\text{-quinoliny})$: **248**; $\text{R} = \text{CH}(6\text{-quinoliny})$: **249**; $\text{R} = \text{CMe}(3\text{-quinoliny})$: **250**; $\text{R} = \text{CMe}(4\text{-isoquinoliny})$: **251**; $\text{R} = \text{CMe}(2\text{-anthraceny})$: **252**; $\text{R} = \text{CMe}(2\text{-phenanthreny})$: **253**) the presence of DHC-type units in solution was confirmed by mass spectrometry.¹³⁸ A BDHC-type cluster buildup to exist in the solid state, most probably resulting from a corresponding shift of the mentioned DHC-BDCH equilibrium at crystallization,

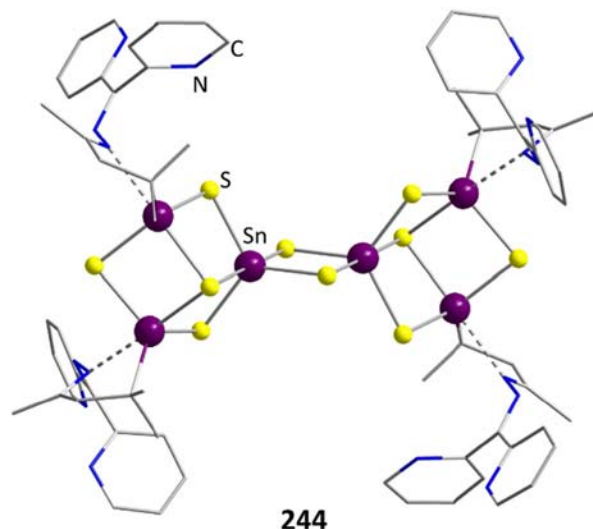


Fig. 45 Chelating ligands attached to a BDHC-type cluster in $[\{(\text{CMe}_2\text{CH}_2\text{CMeNNC}(2\text{-pyridyl})_2\text{Sn})_4\text{Sn}_2\text{S}_{10}\}]$ (**244**).

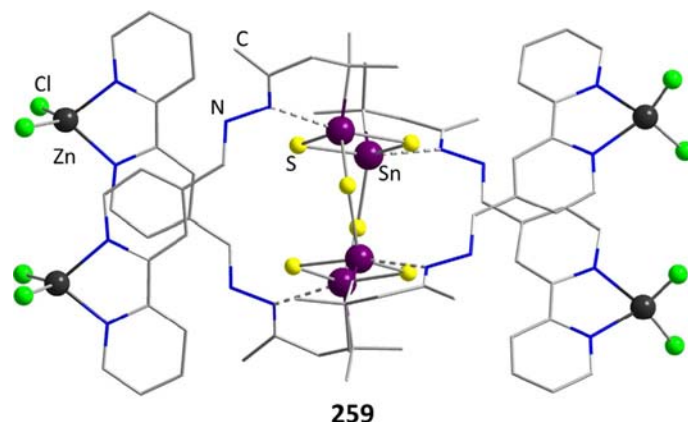


Fig. 46 $[(\text{CMe}_2\text{CH}_2\text{CMeNNCH}(2,2'\text{-bipy-4-yl})\text{ZnCl}_2)_4\text{Sn}_6]$ (**259**, bipy = bipyridine) with DD-type buildup, resulting from the capturing of ZnCl_2 units by **258**.

was verified for 245–247 and 249 by XRD. It is likely that a larger number of aromatic rings inhibited crystallization of the other compounds.

Crystals of a cluster terminated with other potentially chelating ligands, $[\{\text{CMe}_2\text{CH}_2\text{CMeNNCMe}(2,2'\text{-bipy})\text{Sn}\}_4\text{Sn}_2\text{S}_{10}]$ (**254**) were also prepared, and the complexation behavior of the ligands was tested by addition of an Ir complex to a solution of such crystals.¹³⁹ However, similar as observed for **244**, the transition metal atoms were integrated into the cluster core instead of being trapped by the ligands.

Two further aromatic rests were attached to the cluster ligands to yield $[\{\text{CMe}_2\text{CH}_2\text{CMeNN}(2\text{-benzothiazole})\text{Sn}\}_4\text{Sn}_2\text{S}_{10}]$ (**255**), obtained from **203** by the previously discussed method, and $[\{\text{CMe}_2\text{CH}_2\text{CMeNNCH}(1\text{-furanyl})\text{Sn}\}_4\text{Sn}_2\text{S}_{10}]$ (**256**), by an inverse reaction of the hydrazine-decorated compound **224** with furaldehyde diethyl acetate.¹⁴⁰ Time-resolved photoluminescence measurements on single crystals were carried out, and the spectra were compared to the ruthenoceny decorated compound **241**. **255** shares an emission maximum with **241**, but exhibits a much broader spectrum. The spectrum for **256** is additionally blue shifted, which is partially attributed to the intermolecular and intramolecular interaction of the aromatic ligands in this compound. Another reason could be unraveled through DFT calculations, which revealed the HOMO to be localized mainly at the cluster core and the LUMO mainly at the ligands for **256**, which differs from the situation in **241**. The broadening of the spectrum was attributed to the less bulky and electronically less extended terminal ligands in **255** and **256**. Higher mobility of the electrons in those two compounds also seemed to influence both the intensity of the photoluminescence and the decay of the signal over time.

Heteroaromatic ligands were also attached to the organic ligand sphere of DD-type clusters. Reacting **224** with the corresponding aldehydes yields $[(\text{CMe}_2\text{CH}_2\text{CMeNNCHR}\text{Sn})_4\text{S}_6]$ ($R = 1,10\text{-phenanthrol-5-yl}$: **257**, $R = 2,2'\text{-bipy-4-yl}$: **258**).¹⁴¹ **258** was able to form complexes with ZnCl_2 under retention of its inorganic core, leading to crystals of $[(\{\text{CMe}_2\text{CH}_2\text{CMeNNCH}(2,2'\text{-bipy-4-yl})\text{ZnCl}_2\}_4\text{Sn}_6)]$ (**259**, Fig. 46). Addition of ZnCl_2 units to the cluster leads to a blue shift of the UV-vis spectrum in comparison with the parent cluster compound. In turn, the influence of the inorganic core on the photoluminescence of a separate $[\text{Zn}(2,2'\text{-bipy})\text{Cl}_2]$ complex was determined to be limited to a decrease of the intensity of the signals. Thus, the energy of the photoluminescence process is mainly defined by Zn-bipy interactions, while the Sn/S cluster core plays a role in the transition statistics.

The largest heteroaromatic system grafted onto organotin chalcogenide clusters to date, is a pyrene unit. **224** was converted to $[(\text{R}^{\text{py}}\text{Sn})_4\text{S}_6] \cdot 2\text{CH}_2\text{Cl}_2$ (**260**, $\text{R}^{\text{py}} = \text{CMe}_2\text{CH}_2\text{CMeNNCH}(\text{C}_{16}\text{H}_9)$) under retention of its DD-type buildup. When not layering the reactive solution after 1 day reaction time, but waiting for 5 more days, crystals of the rearranged cluster $[(\text{R}^{\text{py}}\text{Sn})_4\text{Sn}_2\text{S}_{10}] \cdot 4\text{CH}_2\text{Cl}_2$ (**261**) with BDHC-type structure were obtained. In both compounds, the π -systems within the ligands of one cluster and between neighboring molecules interact in the crystal structure, which is much more pronounced in **261**. In addition, X-ray photoelectron spectroscopy (XPS) and single-tunneling microscopy (STM) proved successful deposition of **261** on Au(111) surfaces through neutral-spray vacuum deposition.

Similar to organic adamantane-type clusters, organotin chalcogenide clusters were calculated to have the right size to fit to specific biomolecules, making them potential inhibitors for protein kinases. To that end, first experiment towards the installation of biomolecules on the cluster surfaces were made. When treating **203** with a simple amino acid hydrazide, like phenylalanine hydrazide, the organic ligand was observed to undergo an undesired intramolecular condensation reaction, thereby forming intramolecular bridges.¹⁴² The hydrazide and the amino functionalities both reacted with the ketone ligand R^1 , which also caused the inorganic core to rearrange into two condensed six-membered rings, resulting in the cluster compound $[(\text{CMe}_2\text{CH}_2\text{CMeNNC}(\text{O})\text{CH}(\text{CH}_2\text{Ph})\text{NC}(\text{Me})\text{CH}_2\text{CMe}_2)_2\text{Sn}_4\text{S}_5]$ (**262**, Fig. 47) featuring a (distorted) borax-like structure, similar as discussed above for organo-group 13 chalcogenide clusters.

As the original idea was to be able to grow longer peptide chains on the cluster surface, the amino acids thus had to be protected to retain their reactivity, which would be recovered in a subsequent de-protection step. This was proven possible by the generation of two different Boc-protected dipeptide-functionalized clusters, $[(\text{CMe}_2\text{CH}_2\text{CMeNNHpepSn})_3\text{S}_4]^+$ (pep = L-Ala-L-Ala-Boc: **263**;

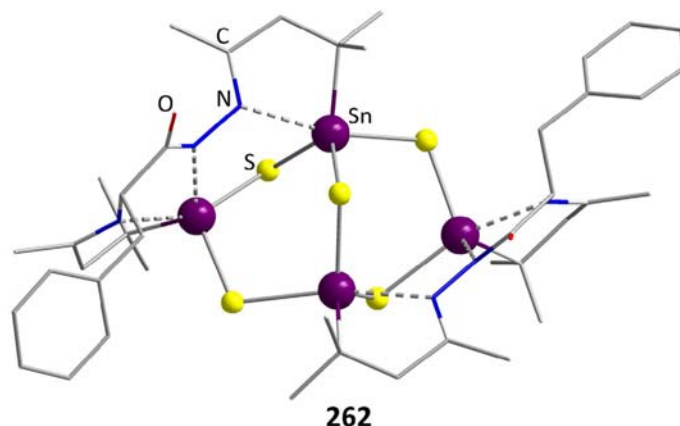


Fig. 47 Amino acid-decorated cluster $[(\text{CMe}_2\text{CH}_2\text{CMeNNC}(O)\text{CH}(\text{CH}_2\text{Ph})\text{NC}(\text{Me})\text{CH}_2\text{CMe}_2)_2\text{Sn}_4\text{S}_5]$ (**262**), with a borax-like cluster core.

pep = L-Phe-L-Val-Boc; Boc = *tert*-butyloxycarbonyl). The DHC-type clusters were obtained by reacting organotin sulfide clusters bearing R^1 ligands with the corresponding dipeptide hydrazides. It did not matter in these cases, whether **203** with DD-type structure or the corresponding DHC-type compound **217** was used in the synthesis.

With the view towards the behavior of corresponding clusters in biological environments, and thus, to prevent undesirable reactions with other biological materials, a coupling mechanism beyond a carbonyl hydrazine reaction was developed. For this, a terminal azide group was introduced into the ligand sphere of **214** by reacting its R^1SnCl_3 precursor with an azide-functionalized organic adamantane carboxylic acid hydrazide, and subsequently forming the cluster through addition of $\text{S}(\text{SiMe}_3)_2$.¹⁴³ The resulting compound, $[\{\text{CMe}_2\text{CH}_2\text{CMeNNHC}(O)\text{AdN}_3\text{Sn}\}_3\text{S}_4\text{Cl}]$ (**265**; Ad = adamantyl; Fig. 48), displayed a distorted neutral DHC-type buildup, in which the Sn atom carrying the additional Cl^- ligand deviates more than usual from the cubane-like position, as it is positioned farther away from the $\mu_3\text{-S}$ atom in favor of forming intramolecular $\text{Cl}\cdots\text{H}$ interactions with the organic groups.

265 could be reacted with oligopeptides as planned, via a strain promoted azide-alkyne cycloaddition (SPAAC) with a cyclic alkyne ligated to an oligopeptide. The obtained cluster, $[\{\text{CMe}_2\text{CH}_2\text{CMeNNHC}(O)\text{Ad}(\text{C}_{39}\text{H}_{53}\text{N}_3\text{O}_6)\text{Sn}\}_3\text{S}_4\text{Cl}]$ (**266**), features the terminal oligopeptide Ala-Val-Phe-OMe (Scheme 5); it was characterized by NMR and mass spectrometry, as the highly flexible peptide environment did not allow for crystallization of the compound to this day.

A less symmetrical alkyne, azadibenzocyclooctyne-amine, was also reacted with **265**. To interpret the mass spectrum obtained from the product in solution, it was assumed that R^1 was restored through intermediate formation of an intramolecular ligand and cleavage of it by hydrolysis, and subsequent reaction of R^1 with the amine functionality of another ligand.¹⁴⁴ The proposed structure

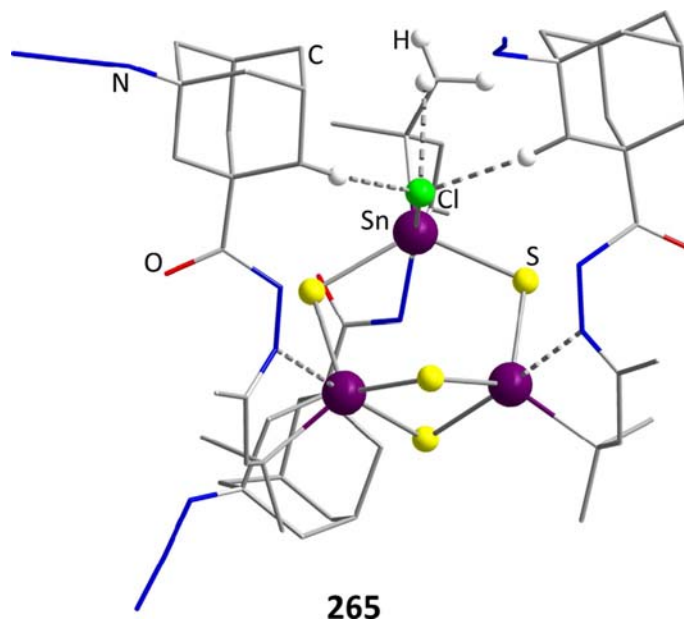
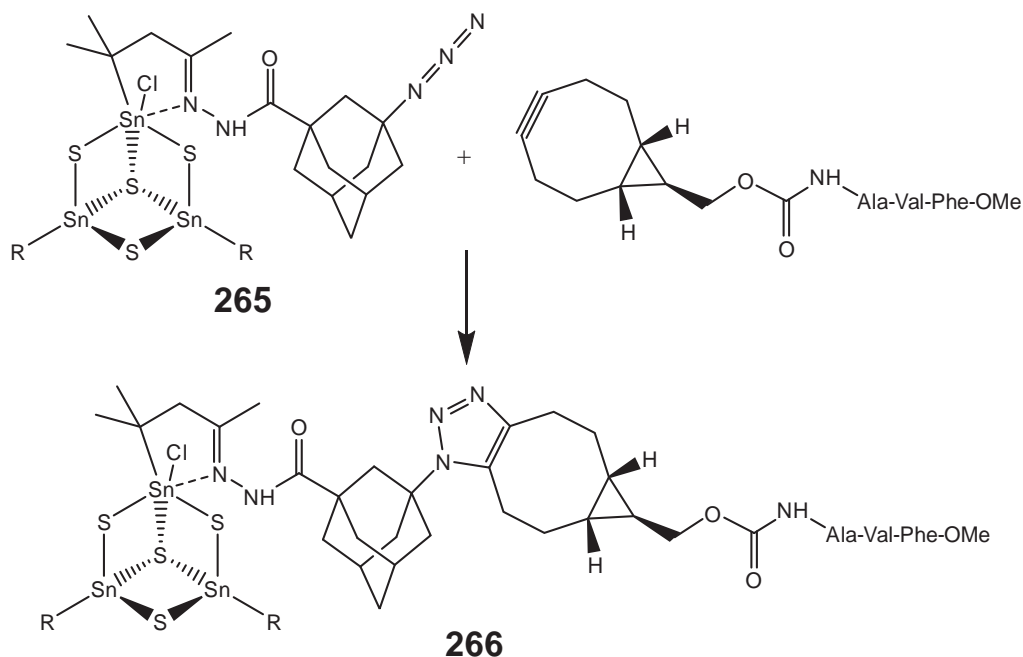


Fig. 48 Azide-functionalized DHC-type cluster $[(\text{CMe}_2\text{CH}_2\text{CMeNNC}(O)\text{AdN}_3\text{Sn})_3\text{S}_4\text{Cl}]$ (**265**, ad = adamantyl).



Scheme 5 Reaction of the DCH-cluster $[\{CMe_2CH_2CMeN-NHC(O)adN_3Sn_3S_4Cl\}]$ (**265**, ad = adamantly) to the proposed DCH-type compound $[\{CMe_2CH_2CMeNNHC(O)ad-(C_{39}H_{53}N_3O_6)Sn_3S_4Cl\}]$ (**266**) as indicated by mass spectra and NMR experiments.

model of $[\{CMe_2CH_2CMeNNHC(O)Ad(C_{18}H_{16}O_1N_5)SnCl\} \{CMe_2CH_2CMeNNHC(O)Ad(C_{18}H_{14}O_1N_5)CMeCH_2CMe_2Sn\}_2S_4]$ (**267**), with a DHC-type inorganic core, was obtained by geometry optimization employing DFT methods, see Fig. 49.

Condensation of the alkyne precursor with a Boc-protected oligopeptide, HO-L-Ala-L-Phe-L-Val-Boc, via its amine functionality enables the attachment of an oligopeptide to **265**. The resulting mass spectrum shows signals for the successful condensation to have occurred at three, two, one and zero organic ligands. While it is difficult to tell whether this observation is due to fragmentation under MS conditions, or due to the compound's (limited) reactivity, the ^{119}Sn NMR spectrum shows only two signals. This is consistent with a single DHC-type cluster to be present in solution, indicating the successful formation of the targeted compound $[\{CMe_2CH_2CMeNNHC(O)Ad(C_{18}H_{15}O_1N_5)l-Ala-L-Phe-L-Val-Boc\}Sn_3S_4Cl]$ (**268**) with threefold substitution.

Another, more straight-forward approach to peptide-functionalized clusters is realized by condensation of Boc-protected amino acids to the cluster precursor R^1 and subsequent reaction of the resulting compounds with $S(SiMe_3)_2$. This reaction was successfully carried out for eight different amino acids, thereby accessing clusters of the general type $[(R^{Ac}Sn)_xS_yCl_z]$, with the amino acids in R^{Ac} being BocVal (**269**), BocAla (**270**), BocLeu (**271**), BocPhe (**272**), BocMet (**273**), BocSer (**274**), BocTyr (**275**), BocHis (**276**).¹⁴⁵ The products were analyzed via mass spectrometry and NMR spectroscopy, which revealed that, for **274** and **275**, the $-OH$ groups in the side chains exchanged their proton for a $-SiMe_3$ group from $S(SiMe_3)_2$. NMR studies revealed that the compounds **274–276** most likely possess a DD-type buildup, which seemingly clashes with the DHC-like sum formulas found for all compounds in mass spectrometry. However, a rearrangement of DD-type clusters to DHC-type complexes has been known to occur under ESI-mass conditions from previous work.¹³⁷

The deprotection and stability of such compounds was investigated on the example of compounds **271** and **272**, which were systematically exposed to a variety of acids.¹⁴⁶ To explore the stability of this class of compounds more generally, the same was also done with **214**. Using 4–6 equivalents of trifluoroacetic acid in DCM leads to a partial deprotection only, whereas a higher excess results in full decomposition of the clusters. Treating **214** with HCl or HBr leads to the formation of H_2S and the formation of corresponding organotin halides R^1SnX_3 ($X = Cl, Br$). Monitoring of the reaction with HCl via NMR spectroscopy revealed an intermediate $S(R^1SnCl_2)$ to form, which is also found in the formation reaction cascade described in Scheme 4. Thus, HCl or HBr seem to reverse the cluster formation process. Similar results were observed for **272**. Addition of H_2SO_4 leads to full degradation and formation of SnO_2 in all cases. Weaker acids, like acetic acid or NH_4Cl , do not react with either compounds, while an excess of water will degrade **214** and, to a lesser extent, also **271** and **272**.

Apart from the serendipitous access to **262**, more controlled experiments towards linking two R^1 ligands either in an intramolecular or an intermolecular way have been carried out. Simple bifunctional hydrazine derivatives, like carbonyldihydrazide, $H_2NNH(CO)HNH_2$, were used for an intramolecular linkage of the organic ligands in **203**, thereby forming $[\{CMe_2CH_2CMeN-NH\}_2CO\}Sn_2)_2S_6] \cdot MeOH \cdot 2H_2O$ (**277**, Fig. 50) with both ligands arranged on the same side of the cluster compound in a *syn*-parallel fashion.¹⁴⁷ This, coupled with the small spacer length ($N_{coord} \cdots N_{coord}$ 380 nm), leads to tilting of the two $\{Sn_2S_2\}$ four-membered rings in the DD-type structure motif towards each other.

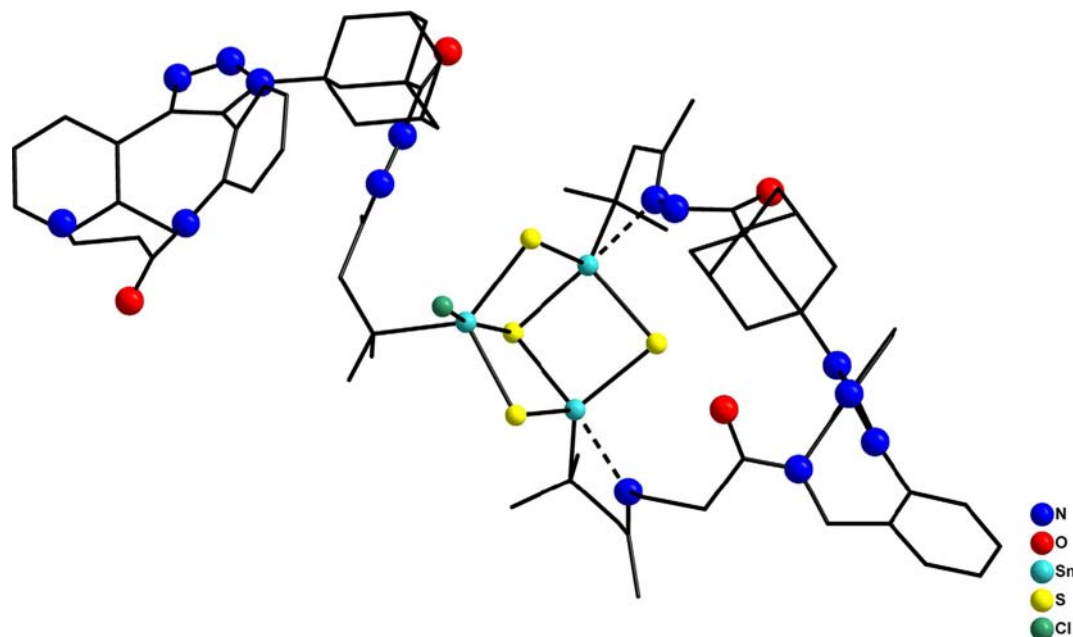


Fig. 49 Calculated (DFT) model of $[(\text{CMe}_2\text{CH}_2\text{CMeNNHC}(\text{O})\text{Ad}(\text{C}_{18}\text{H}_{16}\text{O}_1\text{N}_5)\text{SnCl})-(\text{CMe}_2\text{CH}_2\text{CMeNNHC}(\text{O})\text{Ad}(\text{C}_{18}\text{H}_{14}\text{O}_1\text{N}_5)\text{CMeCH}_2\text{CMe}_2\text{Sn}_2\text{S}_4)]$ (**267**, Ad = adamantyl).

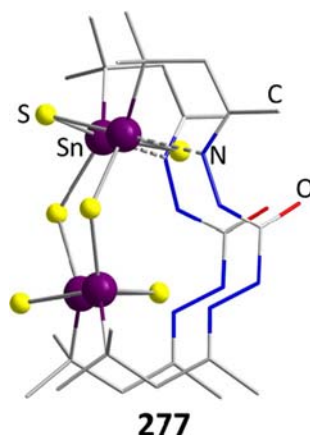


Fig. 50 The DD-type cluster compound $[((\text{CMe}_2\text{CH}_2\text{CMeNNH})_2\text{CO})\text{Sn}_2\text{S}_6]$ (**277**) with a *syn*-parallel arrangement of the organic ligands that act as intramolecular bridges in a back-back- like fashion.

Repeating the experiment with a larger (850 pm) and more rigid spacer including a naphthyl (Np) group affords $\{[(\text{CMe}_2\text{CH}_2\text{CMeNNH})_2\text{Np}]_4\text{Sn}_{12}\text{S}_{20}\} \cdot 4\text{DMF} \cdot 3\text{CHCl}_3 \cdot \text{H}_2\text{O}$ (**278**, Fig. 51), in which two BDHC-type clusters that result from the typical rearrangement are linked to each other by four organic bridges.¹⁴⁸ A cavity within the macrocyclic structure (~ 402 Å) accommodates solvent molecules in the crystal. By addition of HSnCl_3 or HClO_4 to **278**, another rearrangement of the BDHC-type to DHC-type cores is observed, yielding a capsule-like ionic cluster in $\{[(\text{CMe}_2\text{CH}_2\text{CMeNNH})_2\text{Np}]_3\text{Sn}_6\text{S}_8\} [\text{SnCl}_3]_2 \cdot 3\text{DMF} \cdot 1.5\text{H}_2\text{O}$ with three ligand bridges (**279**, Fig. 51), again encapsulating solvent molecules in the cavity (~ 134 Å).

To better understand cluster molecules that feature intramolecular bridging, a systematic study was carried out to correlate the structural findings with the spacer length. *Ortho*-phthalaldehyde was used, because its $\text{N} \cdots \text{N}$ distance (670 pm) was assumed not to induce any structural change of the DD-type motif.¹⁴⁹ This proved to be true for $\{[(\text{CMe}_2\text{CH}_2\text{CMeNNCH})_2\text{C}_6\text{H}_4]\text{Sn}_2\text{S}_6\} \cdot 2\text{DMF} \cdot \text{MeOH} \cdot \text{H}_2\text{O}$ (**280**, Fig. 52), where the bridging ligands connect two tin atoms on each side of the DD-type cluster in a diagonal fashion. This criss-cross bridging mode results in twisting and slight tilting of the two $\{\text{Sn}_2\text{S}_2\}$ four-membered rings against each other, as was observed in compounds like **202** and **229** before.

The same reaction carried out at lower temperatures led to the observation of a slightly different bridging mode, due to a change in conformation of the bridging ligand from *s-trans*, *s-trans* to *s-cis*, *s-trans*. This caused the spacer length to decrease notably, to 512 pm, hence enforcing the linkage between two neighboring, μ -S-connected Sn atoms in the resulting conformer **281**. As a result,

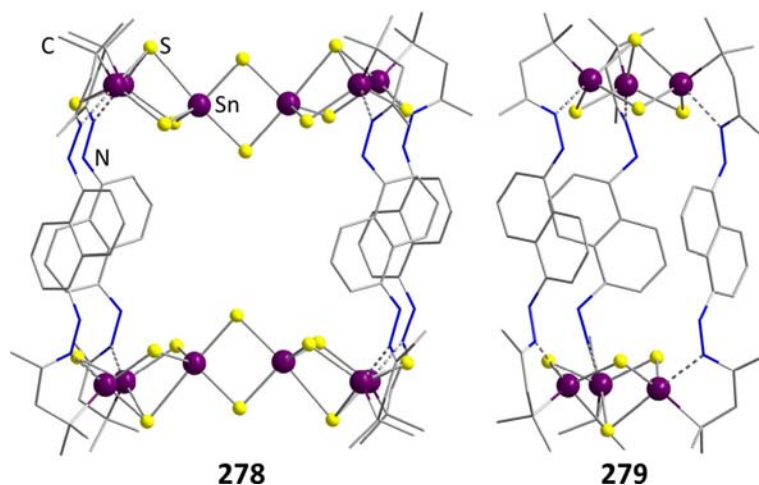


Fig. 51 Macrocyclic $[\{(CMe_2CH_2CMeNNH)_2Np\}_4Sn_{12}S_{20}] \cdot 4DMF \cdot 3CHCl_2 \cdot H_2O$ (**278**) based on two BDHC-type units and the cationic cavitaad in $[\{(CMe_2CH_2CMeNNH)_2Np\}_3Sn_6S_8][SnCl_3]_2 \cdot 3DMF \cdot 1.5H_2O$ (**279**) based on two DHC-type moieties, linked by their respective organic bridging ligands.

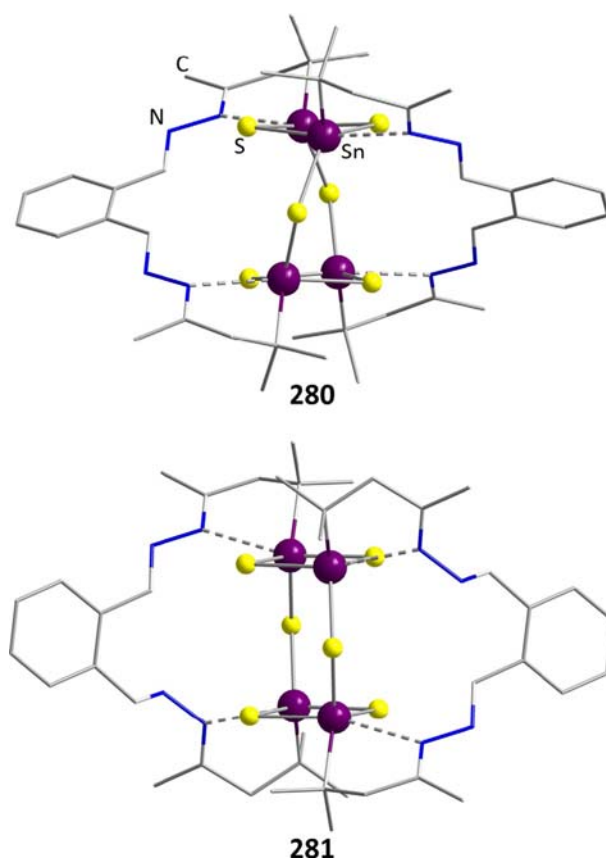


Fig. 52 Two conformers of $[\{(CMe_2CH_2CMeNNCH)_2C_6H_4\}Sn_2]_2S_6$, with criss-cross (**280**) and anti-parallel arrangement (**281**).

the ligands are situated in an anti-parallel fashion (Fig. 52), as opposed to 277. The DD-type core remains undistorted in this case, with no significant deviation from the simple hydrazine-functionalized cluster 224. The same conformation is also found in the derivatives $[\{(CMe_2CH_2CMeNNH)_2C_6H_4\}Sn_2]_2S_6 \cdot 2DMF \cdot 2CHCl_3$ (**282**) and $[\{(CMe_2CH_2CMeNN)_2C_2H_2\}Sn_2]_2S_6$ (**283**) with spacer lengths of 502 pm and 463 pm, respectively. Like for 278, 1,4-bis(diazomethyl)benzene with a larger spacer length of 988 pm caused the formation of a macrocycle based on two BDHC-type units, $[\{(CMe_2CH_2CMeNNCH)_2C_6H_4\}_4Sn_6S_{10}] \cdot 1.5MeOH$ (**284**), with a cavity size of $\sim 108 \text{ \AA}^3$. Spacers with N...N distances between 700 and 880 pm could not successfully be integrated into such clusters; solutions comprising corresponding bishydrazine derivatives and 203 decomposed under the

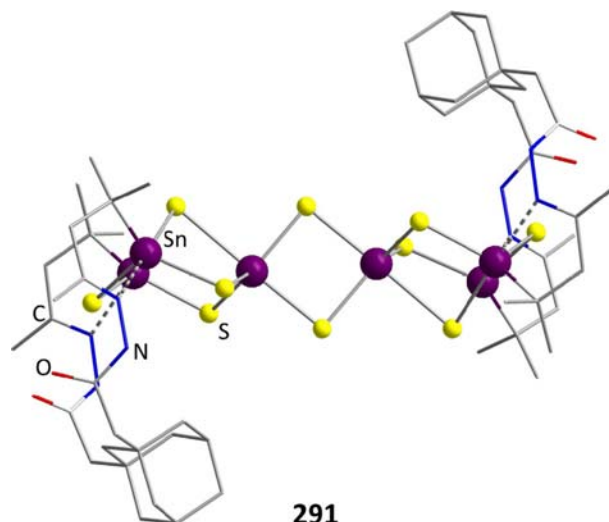


Fig. 53 BDHC-type cluster $[\{(\text{CMe}_2\text{CH}_2\text{CMeNNHC}(\text{O})\text{CH}_2)_2\text{Ad}\}\text{Sn}_2\}_2\text{Sn}_2\text{S}_6]$ (**291**) with intramolecular ligand bridges based on adamantyl moieties.

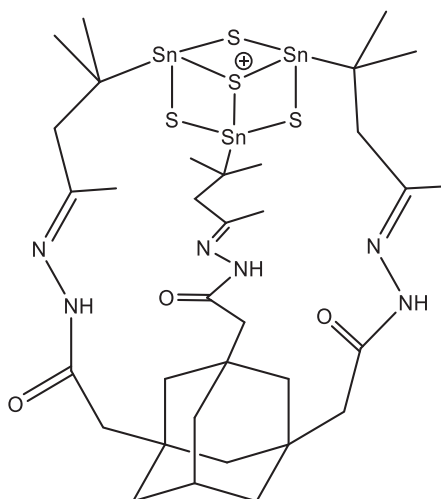
formation of H_2S and SnS_2 instead. DFT calculations on hypothetical compounds made from 2,6-pyridinedecarbaldehyde and **224** find this ligand to be too long and at the same time too rigid for intramolecular bridging, but on the other hand too short as to prevent a steric clash between the inorganic cluster cores in cavitand-like molecules. This was in line with the experimental findings.

A transfer of these results to the Se congeners was possible. In an analogous reaction of the one leading to compound **277**, but starting out from the DD-type selenide cluster **228**, crystals of $[\{(\text{CMe}_2\text{CH}_2\text{CMeNNCH})_2\text{C}_6\text{H}_4\}\text{Sn}_2\}_2\text{Se}_6] \cdot 2\text{CH}_2\text{Cl}_2$ (**285**) were grown, which exhibit the same cluster conformation as described for **228**.¹³³ Employment of reactants for bridging ligands with larger $\text{N}\cdots\text{N}$ distances in combination with the DHC cluster **221** led to the formation of cavitands sharing their buildup with compound **279**. From adipinic acid dihydrazide, two different co-crystallizing compounds were obtained, $[\{(\text{CMe}_2\text{CH}_2\text{CMeN-NHCO})_2(\text{C}_2\text{H}_4)_2\}_3\text{Sn}_6\text{Se}_8][\text{SnCl}_3]_2 \cdot 4\text{CH}_2\text{Cl}$ (**286**) and $[\{(\text{CMe}_2\text{CH}_2\text{CMeN-NHCO})_2(\text{C}_2\text{H}_4)_2\}_3\text{Sn}_6\text{Se}_8]\text{Cl}_2 \cdot 3\text{H}_2\text{O} \cdot 4\text{CH}_2\text{Cl}$ (**287**). **287** contains one molecule of disordered SnCl_3 in its center, while in **287** the cavity is filled with the two chloride counter anions and three water molecules. In all cases, the molecules are connected by hydrogen bridges in the crystal. Involvement of an Np linker, such as used in **279**, leads to the direct congener of the latter, $[\{(\text{CMe}_2\text{CH}_2\text{CMeN-NH})_2\text{Np}\}_3\text{Sn}_6\text{Se}_8][\text{SnCl}_3]_2 \cdot 3\text{CH}_2\text{Cl}$ (**288**), yet with a DCM molecules situated within the cavity.

Bisfunctionalized ferrocene derivatives can also bridge DD-type clusters. A reaction of **203** with ferrocene-1,1'-dicarboxylic acid hydrazide, or of **223** with 1,1'-diformylferrocene yielded $[\{(\text{CMe}_2\text{CH}_2\text{CMeN})_2\text{R}\}\text{Sn}_2\}_2\text{S}_6] \cdot \text{MeOH} \cdot 2\text{H}_2\text{O}$ ($\text{R} = (\text{N-HCO})_2\text{Fc}$: **289**; $\text{R} = (\text{NCH})_2\text{Fc}$: **290**), both of which share their criss-cross-type intramolecular ligand conformation with **280**, with **289** showing an additional tilt and distortion of the four membered rings.¹⁵⁰ The $\text{N}\cdots\text{N}$ distances defining the spacer length of the ligands is 629–755 pm for **289** and 731–737 pm for **290**, thus falling into the range that was unsuccessful in the previous study. The formation of these compounds in spite of this can be attributed to the higher conformational flexibility of the ferrocenyl-based ligands. Cyclic and differential pulse voltammetry revealed no electronic communication between the Fe ions and a simple reversible single-step oxidation in **290** at 466 mV, but a second irreversible process for **289**. Here, a first anodic oxidation step at 706 mV can be attributed to the Fc moieties, while a second with half the intensity at 836 mV seems to be connected with a decomposition process.

In the case of organic adamantyl spacers, difunctional diamondoids also lead to intramolecular bridging of corresponding clusters, with the observed structural details again depending on the spacer length. Ligands derived from $\text{Ad}(\text{CON}_2\text{H}_3)_2$ and $\text{Ad}(\text{CON}_2\text{H}_3)(\text{CH}_2\text{CON}_2\text{H}_3)$ exhibit relatively low reactivity with **203**, and produce low yields of a proposed bridged DD-type cluster in the mass spectra of the reactive solutions.¹³⁶ This can be explained by the medium-size spacer length that was already found to be unfavorable in previously described studies. However, the larger, and thus more flexible, spacer derived from $\text{Ad}(\text{CH}_2\text{CON}_2\text{H}_3)_2$ applied in a corresponding reaction afforded crystals of the BDHC-type compounds $[\{(\text{CMe}_2\text{CH}_2\text{CMeN-NHC}(\text{O})\text{CH}_2)_2\text{Ad}\}\text{Sn}_2\}_2\text{Sn}_2\text{S}_{10}] \cdot \text{solv}$ ($\text{solv} = 2(1,4\text{-dioxane}) \cdot 4\text{CHCl}_3$: **291**, Fig. 53; $\text{solv} = m\text{-xylene}$: **292**). With spacer lengths of 653 and 656 nm, respectively, it was assumed that the products would retain their DD-type cluster cores with a criss-cross bridging pattern; in contrast to the expectations, however, the clusters rearrange to form BDHC-type cluster cores, as was already seen for compounds with monofunctional Ad ligands. This indicates that the rigidity of the adamantyl group plays a structure-directing role, too.

A larger spacer comprising a diamantyl (Dia) group, $\text{Dia}(\text{CH}_2\text{CON}_2\text{H}_3)_3$, was used to generate compound **293**, which according to NMR spectroscopy and mass spectrometry contains $[\{(\text{CMe}_2\text{CH}_2\text{CMeNNHCOCH}_2)_2\text{Dia}\}_3\text{Sn}_6\text{S}_8]^{2+}$ cations with a cavitand-like buildup. Finally, the use of a threefold hydrazide-functionalized adamantane caused a rearrangement of **203** into the DHC-like cluster cation $[\{(\text{CMe}_2\text{CH}_2\text{CMeN-NHCOCH}_2)_3\text{AdSn}_3\text{S}_4\}]^+$ (in **294**, Scheme 6) in which all tin atoms are connected with each other by this kind of a tripod ligand. Again, **294** could only be analyzed by NMR and mass spectrometry, as it was not possible to obtain the compound in single-crystalline form.



Scheme 6 Proposed structure of the cation $[(\text{CMe}_2\text{CH}_2\text{CMeN-NHC}(\text{O})\text{CH}_2)_3\text{Ad})\text{Sn}_3\text{S}_4]^+$ (in **294**).

Before talking about some more properties and reactivities of organotetrel chalcogenide clusters, a few unique examples should be mentioned. In an unorthodox reaction starting from the Sn^{II} precursor $\{\text{N}(\text{SiMe}_3)\text{Dipp}\}\text{SnCl}$ (Dipp = 2,6-*i*Pr₂C₆H₃) with elemental sulfur or selenium, the AD-type clusters $[\{\{\text{N}(\text{SiMe}_3)\text{Dipp}\}\text{Sn}\}_4\text{E}_6]$ (E = S: **295**; E = Se: **296**) were formed along with the side product $\{\text{N}(\text{SiMe}_3)\text{Dipp}\}\text{SnCl}_3$. Both compounds have been shown to show good solubility in organic solvents as well as a high activity in the initiation of the ring opening polymerization of ϵ -caprolactone.¹⁵¹

Another precursor material utilizing this ligand is $[\text{Si}_4\{\text{N}(\text{SiMe}_3)\text{Dipp}\}_4]$, which similarly reacts with elemental chalcogens.¹⁵² In a reaction with S_8 at 110 °C in toluene, $[\{\{\text{N}(\text{SiMe}_3)\text{Dipp}\}\text{Si}\}_4\text{S}_3]\cdot\text{solv}$ (solv = 3THF: **297**; solv = toluene: **298**; Fig. 54) can be isolated after workup. In **297**, a minor species with an abundance of ca. 8% and a buildup similar to P_4S_4 was identified to be $[\{\{\text{N}(\text{SiMe}_3)\text{Dipp}\}\text{Si}\}_4\text{S}_4]$, thus rendering the actual formula of the crystalline compound to be $[\{\{\text{N}(\text{SiMe}_3)\text{Dipp}\}\text{Si}\}_4\text{S}_{3.08}]\cdot 3\text{THF}$. The cluster core of the main species, $\{\text{Si}_4\text{S}_3\}$, consists of two distorted $\{\text{Si}_3\text{S}\}$ rings and two five-membered $\{\text{Si}_3\text{S}_2\}$ cycles. The analogue reaction with gray selenium leads to the homologous cluster $[\{\{\text{N}(\text{SiMe}_3)\text{Dipp}\}\text{Si}\}_4\text{Se}_3]\cdot 2.25\text{THF}$ (**299**, Fig. 54), with a few crystals of an isomeric minority compound $[\{\{\text{N}(\text{SiMe}_3)\text{Dipp}\}\text{Si}\}_4\text{Se}_3]\cdot 1.5\text{toluene}$ (**300**, Fig. 54) adopting a nortricyclane-type cage structure.¹⁵³ Repeating the reaction at lower temperatures with red selenium yields exclusively **300**, which hints at the possibility of a thermal conversion of **300** to **299**. However, heating of any of these two isomers leads to yet another rearrangement to form $[\{\{\text{N}(\text{SiMe}_3)\text{Dipp}\}\text{Si}\}_4\text{Se}_3]$ (**301**, Fig. 54) with a structure reminiscent of the DHC-type buildup, where the μ_3 -S atom is substituted with an $[\text{Si}\{\text{N}(\text{SiMe}_3)\text{Dipp}\}]$ group. In reactions with elemental tellurium in contrast, no product could be isolated. Depending on the position of the Si atoms in these three clusters, the oxidation state ranges from I to IV. By using $\text{TeP}(n\text{-Bu})_3$ as the chalcogenide source, however, the corresponding homologue of **295** and **296** was finally obtained, $[\{\{\text{N}(\text{SiMe}_3)\text{Dipp}\}\text{Si}\}_4\text{Te}_6]$ (**302**).

As was shown for **301**, chalcogen atoms within the clusters can be (partially) replaced by isolobal fragments. In a systematic synthetic approach for this, $\text{CR}_2(\text{SnR}'\text{Cl}_2)_2$ is reacted with a chalcogenide source to form $[(\text{R}'\text{Sn})_4\text{E}_4(\text{CR}_2)_2]$ (E = S, R' = Ph, R = H: **303**, Fig. 55; E = S, R' = CH_2SiMe_3 , R = H: **304**, E = Se, R' = Ph, R = H: **305**; E = Se, R' = Me, R = Me: **306**; E = Te, R' = Ph, R = H: **307**).¹⁵⁴ Here, AD-type structures are formed, in which two E atoms on opposing Sn...Sn edges are formally replaced by CH_2 moieties. Upon mixing **303** and **304**, the terminal ligands are exchanged in an equilibrium to form $[(\text{PhSn})_2(\text{Me}_3\text{SiCH}_2\text{Sn})_2\text{S}_4(\text{CH}_2)_2]$ (**308**) within 48 h. The addition of Bu_4NCl triggers the compounds to equilibrate instantaneously, which hints at a catalytic role of the Cl^- ions. Similarly, **303** and **305** will exchange chalcogen atoms to form four new species $[(\text{PhSn})_4\text{Se}_x\text{S}_{4-x}(\text{CH}_2)_2]$ ($x = 1$: **309**; $x = 2$, Se atoms opposing each other: **310**, $x = 2$: **311**, Se atoms neighboring $x = 3$: **312**), which are observable by NMR.

Corresponding Si compounds were isolated from reactions of $\text{CH}_2(\text{SiMeCl}_2)_2$ with $\text{H}_2\text{S}/\text{NEt}_3$ or of Li_2Se or Li_2Te with $[(\text{MeSi})_4\text{E}_4(\text{CH}_2)_2]\cdot\text{solv}$ (E = S, no solv: **313**; E = Se, no solv: **314**, Fig. 55; E = Te, solv = CDCl_3 : **315**). Again, CH_2 groups are observed on two opposing sides of the cluster cores.¹²³

Addition of the disilane $(\text{MeSiCl}_2)_2$ to the reaction yielding **313** and **314** affords NA-type compounds $[(\text{MeSi})_4\text{E}_4(\text{CH}_2)]$ (E = S: **316**, Fig. 56; E = Se: **317**) instead, with the CH_2 moiety opposing the Si–Si bond.

The research was expanded to reactions with the trisilane $\text{Me}_2\text{Si}(\text{MeSiCl}_2)_2$. Corresponding reactions with Li_2S and Li_2Se yielded the AD-type clusters $[(\text{MeSi})_4(\text{SiMe}_2)_2\text{E}_4]$ (E = S: **318**; E = Se: **319**), in which two opposing chalcogenides were formally replaced by SiMe_2 units in analogy to the situation described for **313**–**315**.¹⁵⁵ It is also possible to react the trisilane with the previously discussed disilane and H_2S to obtain an NA-type compound, $[(\text{MeSi})_4\text{S}_4(\text{SiMe}_2)]$ (**320**, Fig. 56), in analogy to **316**.

Apart from the AD-type, BDHC-type, and DHC-type compounds, **203** is also known to rearrange to an additional topology, in which two tin atom, bridged by three $\{\text{R}^1\text{Sn}\}_2\text{S}_4\}$ subunits, form a direct Sn–Sn bond and are therefore reduced to Sn^{III} . This

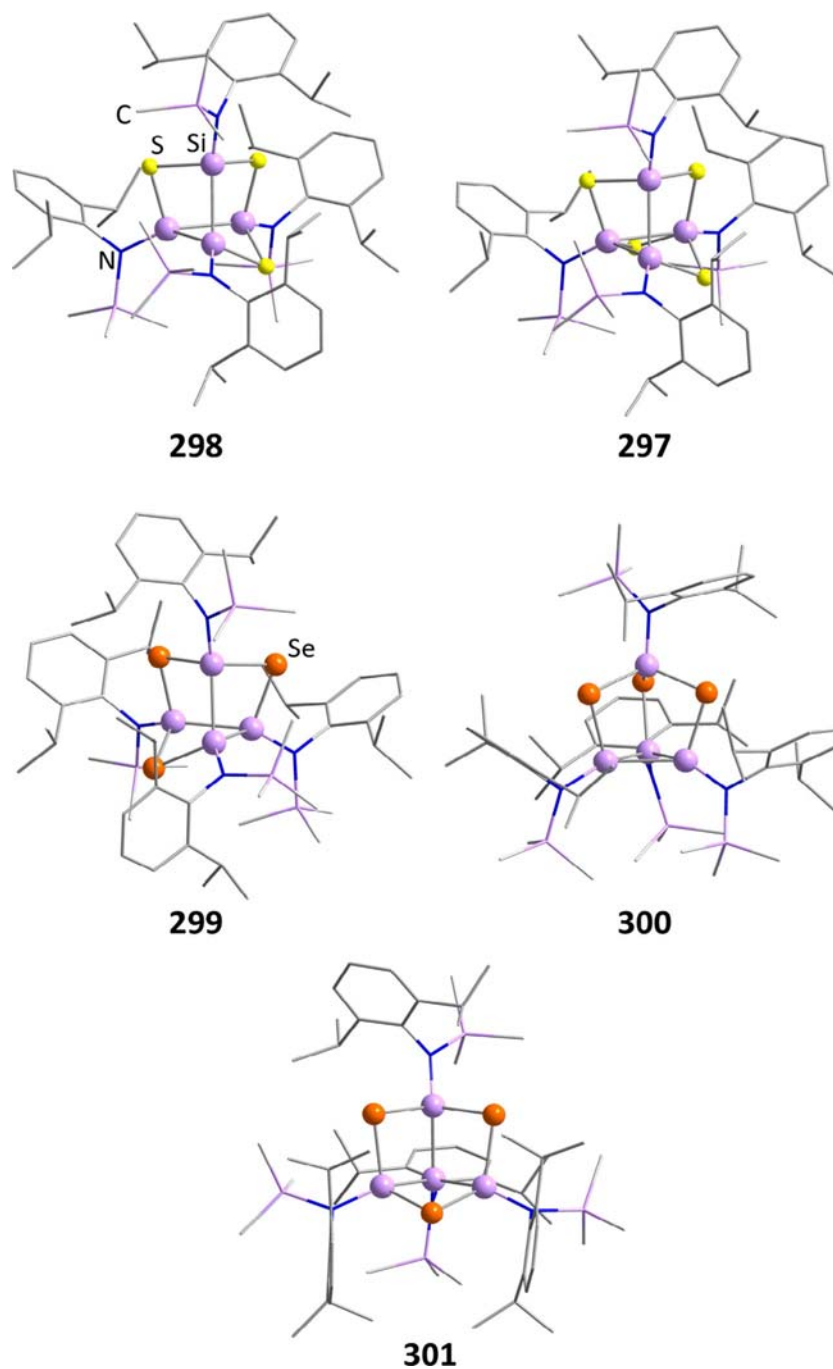


Fig. 54 The cluster family $[(R\text{Si})_4E_x]$ ($E = \text{S, Se}; x = 3 \dots 4$) with R representing the $\{\text{N}(\text{SiMe}_3)\text{Dipp}\}$ ligand ($\text{Dipp} = 2,6\text{-iPr}_2\text{C}_6\text{H}_3$): $[\{(\text{N}(\text{SiMe}_3)\text{Dipp})\text{Si}\}_4\text{S}_3] \cdot \text{toluene}$ (**298**, top left), also representing the majority component in $[\{(\text{N}(\text{SiMe}_3)\text{Dipp})\text{Si}\}_4\text{S}_{3.08}] \cdot 3\text{THF}$ (**297**). Minority component $[\{(\text{N}(\text{SiMe}_3)\text{Dipp})\text{Si}\}_4\text{S}_4]$ in **297** (top right). Three isomeric selenide clusters $[\{(\text{N}(\text{SiMe}_3)\text{Dipp})\text{Si}\}_4\text{Se}_3] \cdot 2.25\text{THF}$ (**299**, center left) isostructural to **298**, $[\{(\text{N}(\text{SiMe}_3)\text{Dipp})\text{Si}\}_4\text{Se}_3] \cdot 1.5\text{toluene}$ (**300**, center right) with nortricyclane-type structure, and $[\{(\text{N}(\text{SiMe}_3)\text{Dipp})\text{Si}\}_4\text{Se}_3] \cdot$ (**301**, bottom), in a DHC-like structure. Solvent molecules are not drawn.

change can be induced by UV irradiation, resulting in crystals of $[\{(R^1\text{Sn}^{\text{IV}})_2\text{S}_4\}_3\text{Sn}^{\text{III}}_2] \cdot 0.93\text{CH}_2\text{Cl}_2 \cdot 1.08\text{H}_2\text{S}$ (**321**, Fig. 57), in which the two Sn^{III} atoms occur in a trigonal-pyramidal coordination, with three S atoms at the basal position and the Sn neighbor at the apex.¹⁵⁶ The reduction of the Sn atoms was confirmed by Mößbauer spectroscopy. This rearrangement can also be induced by freshly-distilled CS_2 , as was discovered in a second study.¹⁵⁷

In recent years, the optical properties of AD-type compounds have come into focus, as a directed white-light generation (WLG) was detected upon irradiation of the amorphous powder of $[\{(\text{StySn})_4\text{S}_6\}]$ (**322**, Sty = styryl) with a low-cost continuous wave

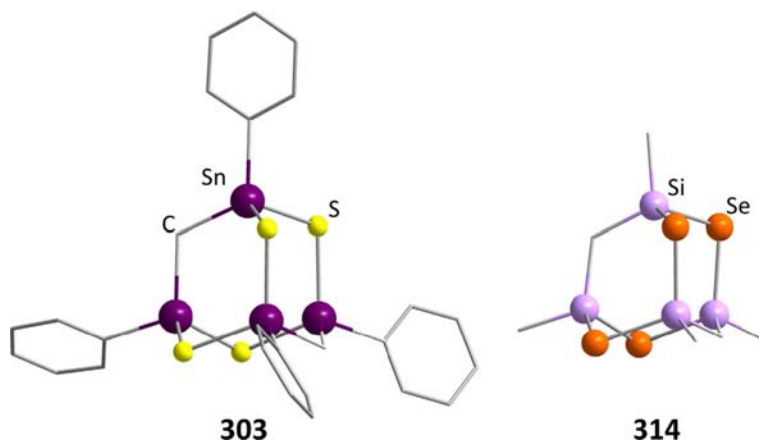


Fig. 55 AD-type clusters upon isolobal replacement of a chalcogen atom with a CH₂ group in [(PhSn)₄(CH₂)₂S₄] (**303**) and [(MeSi)₄(CH₂)₂Se₄] (**314**).

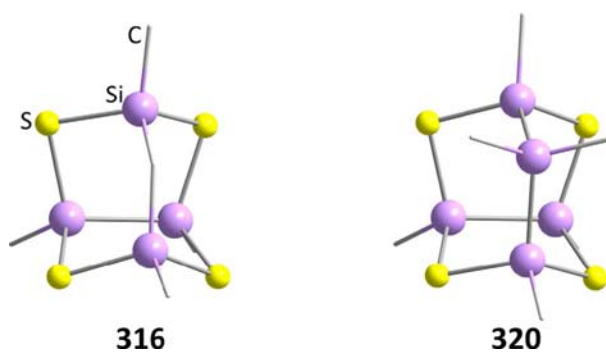


Fig. 56 NA-type clusters upon isolobal replacement of an S atom with a CH₂ group in [(MeSi)₄(CH₂)₂S₄] (**316**) and [(MeSi)₄(SiMe₂)₂S₄] (**320**).

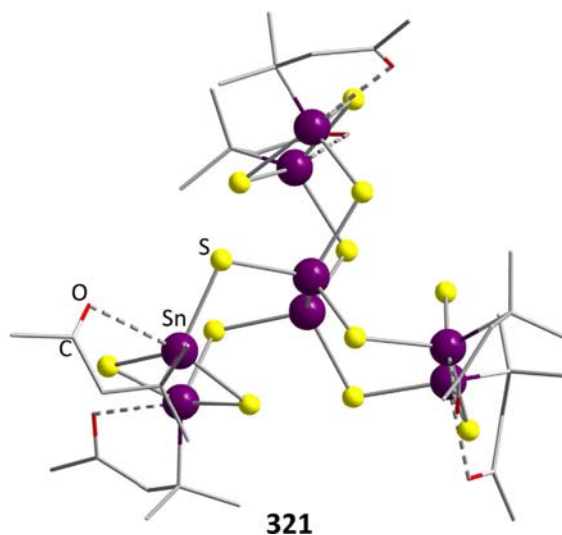


Fig. 57 Mixed-valence cluster in [(R^ISn^{IV})₂S₄Sn^{III}]₂ · 0.93CH₂Cl₂ · 1.08H₂S (**321**).

infrared laser.¹⁵⁸ The white-light output power showed an extremely nonlinear dependency on the pump-power density, as is to be expected for nonlinear optical effects of higher order (Fig. 58). Additionally, due to the styryl group terminating the cluster molecules, it could be deposited onto GaAs (001) or Si (001) surfaces.

To study this effect in greater detail, several variations of AD-based molecules were investigated. The effect of white-light generation (WLG) could be observed for the amorphous compound [(PhSn)₄S₆] (**323**) and its Ge congener [(PhGe)₄S₆] (**324**), albeit

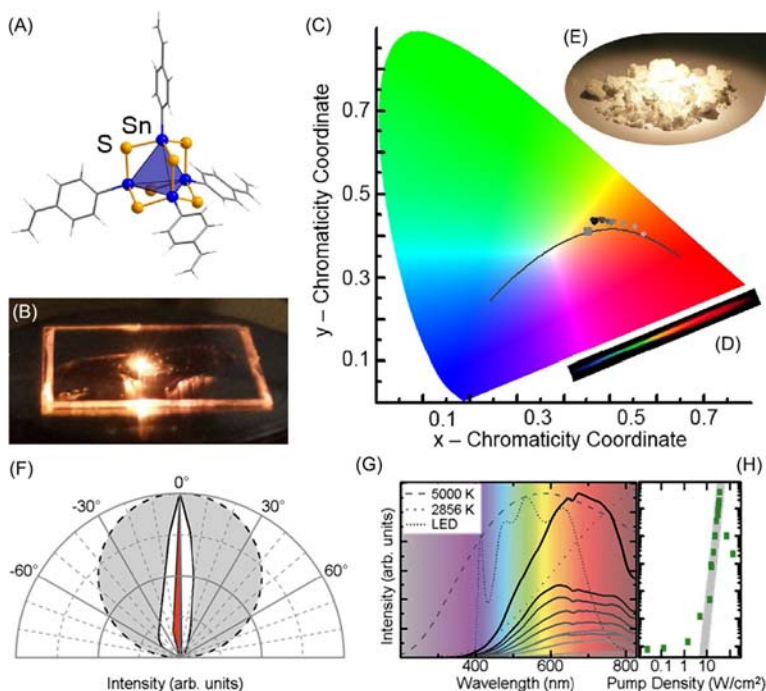


Fig. 58 (A) Molecular model of $[(\text{StySn})_4\text{S}_6]$ (**322**). (B) Photograph of **322** in a polymer film sandwiched between two glass slips excited by a 800 nm laser. (C) Color impression of the white-light emission of **322** for different excitation fluencies, indicated by the data points given as gray-scale spheres, next to the ideal black-body emission at varying temperatures (gray line) and the color impression of a standard emitter at 2856 K (gray square). (D) Photograph of the rainbow spectrum of the white light obtained from **322**. (E) Photograph of the as-prepared, air-stable, powdery sample of **322**. (F) Highly directional spatial emission pattern of the white-light spectrum emitted by **322** (white) and the CW excitation laser at 980 nm (red) compared to a perfect Lambertian emitter (gray sphere). (G) Spectra of the white light emission of **322** upon excitation with a 980 nm laser at varying pump powers from 6 mW (light gray solid line) to 18 mW (black solid line). For comparison the normalized spectra of a black body emitter at 2856 K (spaced dots) and 5000 K (dashed line) as well as the white-light of a commercial GaN-based LED (narrow dots) are given. (H) Double-logarithmic plot of the white-light input-output characteristics.

with a small blue shift of the maximum emission wavelength in the latter case.¹⁵⁹ Changing the ligand to an aliphatic rest, as in **155** or **157**, caused strong second harmonic generation (SHG) instead, as a consequence of phase matching (Fig. 59). The same is true when investigating crystalline material like $[(\text{PhSi})_4\text{S}_6]$ (**325**); it should be noted that the crystals are not non-centrosymmetric, hence the non-linear optical effects are most likely due to crystal defects or symmetry-breaking at the surfaces, especially for small crystals or pulverized samples. In summary, it was proposed that an amorphous habitus of the material and the presence of a non-aliphatic ligand is necessary to produce WLG. Surprisingly, the apparently amorphous compound $[(\text{NpSn})_4\text{S}_6]$ (**326**) also exhibited SHG instead, which was attributed to intense π -stacking interactions of the more extended aromatic system, which leads to a certain degree of order in the material.

The influence of the nature of the chalcogenide ligands as well as the impact of an even larger diversity of organic ligands were the topic of a further study. Different organotin sulfide clusters of the AD-type, $[(\text{RSn})_4\text{S}_6]$ (R = benzyl: **327**; R = $\text{CH}_2\text{CH}_2(\text{C}_6\text{H}_4)\text{COO}_2\text{Et}$: **328**; R = $\eta^1\text{-Cp}$: **329**; R = cyclohexyl: **330**), and their selenide counterparts, $[(\text{RSn})_4\text{Se}_6]$ (R = phenyl: **331**; R = benzyl: **332**; R = $\text{CH}_2\text{CH}_2(\text{C}_6\text{H}_4)\text{COO}_2\text{Et}$: **333**; R = $\eta^1\text{-Cp}$: **334**; R = cyclohexyl: **335**), were prepared, with only the benzyl-functionalized compounds **327** and **332** showing a tendency to crystallize.¹⁶⁰ **327** exhibited SHG as expected, while **332** emitted white light. The latter was assumed to be due to the material melting under the laser irradiation and thus losing its structural ordering, which was additionally confirmed by TGA and DSC measurements of the compounds. In all other compounds, WLG was observed with only minor shifts in the spectra when going from S to Se. Most notably, these results indicated that a π -electron system is not urgently needed to generate the WLG effect, but an electron rich ring system, such as found in the cyclohexyl substituent, seems to be both necessary and sufficient. It stands to reason from calculations of the HOMO-LUMO gap of all measured substances that for generating the WLG effect, electrons near the Fermi levels need to be excited to short-lived virtual states in the band gap.

Very obviously, the intermolecular order of the AD-type cluster, and their resulting nature of being an amorphous powder, seems to play an important role. Efforts have thus been made to elucidate the structure of the material by X-ray scattering experiments coupled with Reverse Monte Carlo (RMC) modeling. By this method, inter-molecular correlations in **323** were investigated and favored molecule orientations could be identified. Although the data were not perfect, it could be clearly shown that the amorphous powder consists of AD-type clusters as expected (Fig. 60).^{161,162}

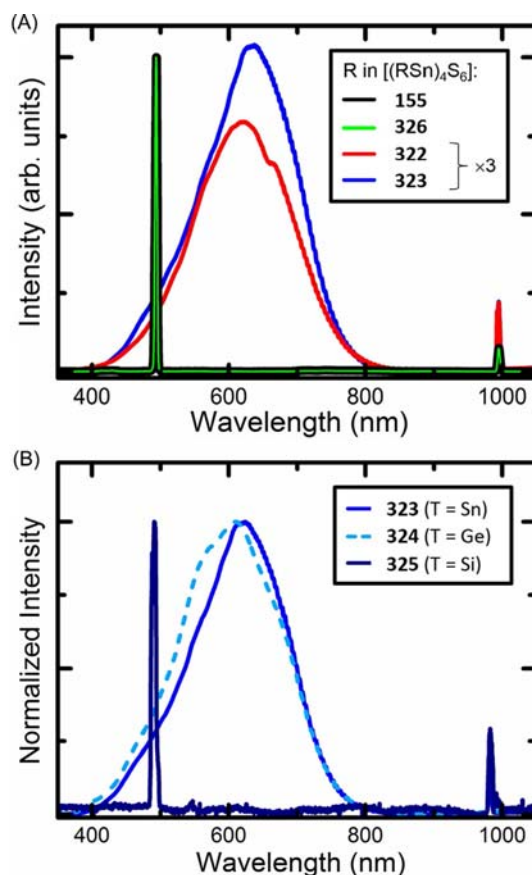


Fig. 59 Spectra illustrating second harmonic generation (SHG) of (A) organotin sulfide clusters [(MeSn)₄S₆] (**155**) or [(NpSn)₄S₆] (**326**, Np = naphthyl) or broad white-light emission for [(StySn)₄S₆] (**322**, Sty = styryl), and [(PhSn)₄S₆] (**323**), as well as corresponding effects of (B) Ph-substituted clusters [(PhT)₄S₆] (T = Sn: **323**; T = Ge: **324**; T = Si: **325**), upon irradiation with a CW infrared laser.

The most recent study published in this field reported the synthesis and non-linear optical properties of the crystalline material [(NpSi)₄S₆] (**336**), which shows SHG, and the synthesis of [(StySi)₄S₆] (**337**), which slowly auto-polymerized over time as opposed to **322**.¹⁶³ A comprehensive theoretical study was undertaken in order to understand the reasons for different ordering—and thus, crystallization—tendencies of organosilicon versus organotin clusters with Ph and Np ligands: while the Si congeners preferably crystallize, the corresponding Sn compounds stay notoriously amorphous, which influences the non-linear optical behavior, as explained above. To get an idea of intrinsic differences that lead to this observation, binding energies were calculated for cluster dimers of molecules **323**, **325**, **326**, and **336**. Surprisingly, not only different ligand-ligand interactions play a role here, but the strength of the ligand-ligand interaction in relation to the core-core interaction seem to be important. As illustrated in Fig. 61, the latter are much more pronounced for the Sn compounds than for the Si compounds, hence, the (rather directional) ligand effects are much stronger for organosilicon sulfide cluster, while the (rather isotropic) core-core interactions seem to outplay such effects for the Sn congeners. In other words, the higher (relative) degree of directional interaction in Si compounds was supposed to be the main reason of their tendency for crystallization, while the larger isotropic interactions in tin congeners explains their preference for an unordered nature. This explains the importance of the nature of all components, R, T, and E, for the habitus and thus non-linear optical response of organotetrel chalcogenide cluster materials.

It is possible to replace a single phenyl group in **323** with a metal complex by adding 1 equivalent of a group 11 phosphine complex to its solution. The resulting clusters [(MPR₃Sn)(PhSn)₃S₆] (MPR₃ = AuPMe₃: **338**; MPR = AgPEt₃: **339**; MPR = CuPMe₃: **340**, Fig. 62) retained their AD-type cluster core according to single-crystal X-ray diffraction. The optical properties of the crystalline material were investigated.¹⁶⁴ In spite of their crystallinity, **338** and **339** exhibited WLG. However, when examining the material after laser irradiation, it was found that both compounds lost their crystallinity during the experiment, which rationalized the findings. **340** neither showed SHG nor WLG, as reabsorption processes hindered the effects. A curious product was observed, when increasing the ratio of the gold phosphine complex to 4 equivalents: besides precipitation of elemental gold, crystals of [Au(PMe₃)₄][Au(PMe₃)₂][(PhSnCl)₃S₄] (**341**) were obtained, comprising two different gold phosphine complexes and an unprecedented DHC-type dianion.

In addition to the properties of organotetrel chalcogenide clusters that were described and discussed in the sections above, such species have been known for their tendency to incorporate transition metal ions for extending their inorganic cluster cores. This was

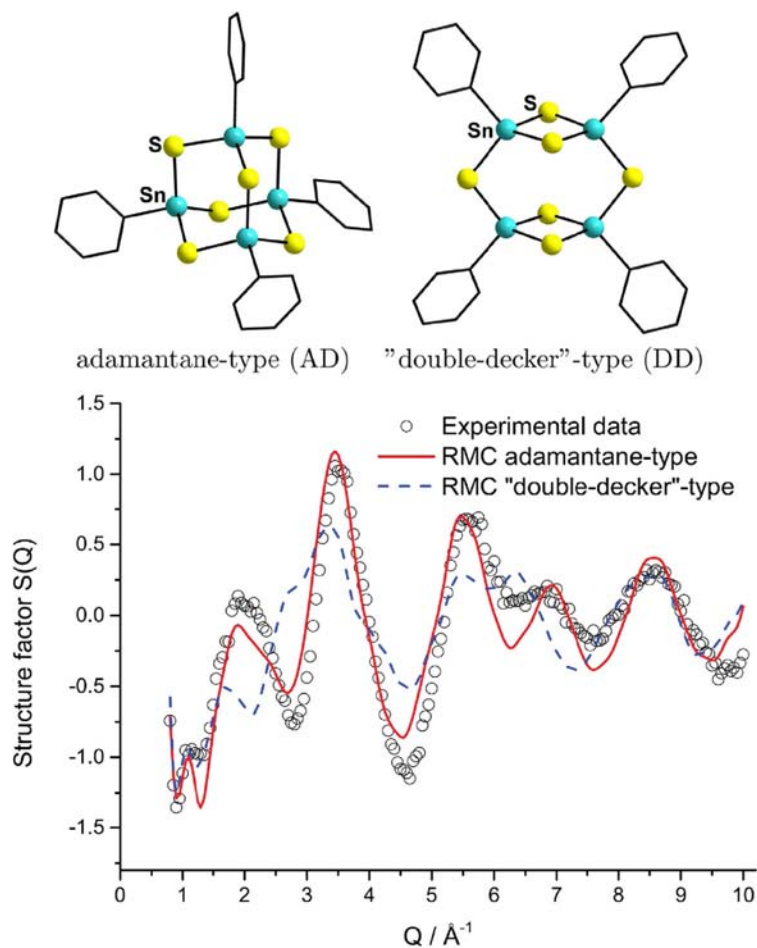


Fig. 60 Fitting of experimental X-ray scattering data at low angles by Reverse Monte Carlo (RMC) simulations suggests an AD-type buildup in $[(\text{PhSn})_4\text{S}_6]$ (**323**) over a DD alternative.

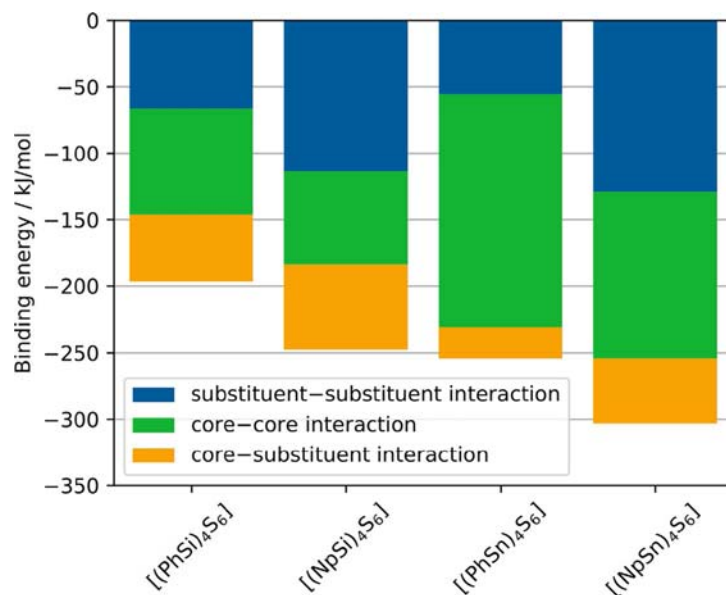


Fig. 61 Interactions between different cluster parts and their binding energies between cluster dimers in **323**, **325**, **326** and **336**.

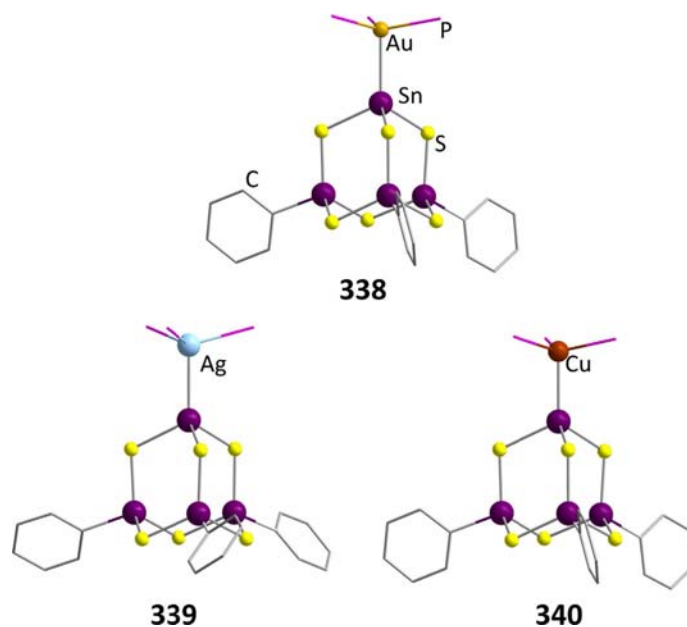


Fig. 62 AD-type clusters with metal-complexes replacing one Ph group, $[(\text{MPR}_3\text{Sn})(\text{PhSn})_3\text{S}_6]$ ($\text{MPR} = \text{AuPMe}_3$: **338**; $\text{MPR} = \text{AgPEt}_3$: **339**; $\text{MPR} = \text{CuPMe}_3$: **340**). Organic ligands on the phosphine moieties are omitted for clarity.

reported for compounds comprising AD, DD, DHC or BDHC-type structures, as was already alluded to in previous paragraphs. Especially group 11 and group 10 metals have been the subject of many studies,^{117,126,131,147,163,165–173} but other transition metal ions have also been successfully incorporated into such clusters, leading to a large variety of ternary or even multinary metal chalcogenide cluster architectures.^{139,174} However, their more detailed description does not match the scope of this work, in which we intend to focus on p-block (semi)metal chalcogenide clusters; we thus refer to the cited literature at this place.

4.04.3.3 Tetrel chalcogenide clusters with or without organic ligands based on other architectures

Through variation of the applied reaction conditions, cluster compounds were observed with unique structural features that are not connected to the compound families presented above. As was already the case for group 13 elements and **262**, compounds with a borax-like buildup could be isolated, with some more examples given here. $[(^t\text{BuGe})_2(^t\text{BuGeCl})_2\text{E}_5]$ ($\text{E} = \text{S}$: **341**; $\text{E} = \text{Se}$: **342**) were obtained from refluxing $^t\text{BuGeCl}_3$ with the corresponding Na_2E in toluene.¹⁷⁵ A complex with the same architecture, in which the Cl ligands are replaced by SH moieties, $[(^t\text{BuGe})_2(^t\text{BuGeSH})_2\text{S}_5]$ (**343**), resulted from a reaction of $^t\text{BuGeCl}_3$ with H_2S in pyridine at room temperature.¹¹⁸ Heating causes the product to eliminate H_2S and form **183**, while changing the sulfur source to ammonium pentasulfide generates **182**, as described above.

Cages containing Pb atoms are incredibly rare due to the element's tendency to adopt smaller coordination numbers and lower oxidation states. Instead, $\text{Pb}(\text{NO}_3)_2$ reacts with the thiol 2- $\text{HSC}_5\text{H}_3\text{N}$ -3- SiMe_3 to form the trinuclear complex $[\text{Pb}_3(2\text{-SC}_5\text{H}_3\text{N}-3\text{-SiMe}_3)_6]$ (**344**).¹⁷⁶ A central Pb atom is connected by a total of six sulfur atoms from the three thiolate ligands which serve as bridges to the other two Pb atoms. In summary, this coordination mode creates two trigonal bipyramids. The Pb–S bond lengths to the central Pb atom is unequal, with one short (2.934 Å) and two longer (3.158 and 3.319 Å) contacts. Each Pb atom is further coordinated by two nitrogen moieties from the chelating ligand, which leads to a total coordination number of eight for the central Pb, and five for the two outer Pb sites.

The same structural motif was found in the hexacation in $[\text{Pb}_3(4\text{-Me}_3\text{NC}_6\text{H}_4\text{S})_6][\text{PF}_6]_6$ (**345**, Fig. 63). Yet, different from the structure of **344**, the zwitterionic ammonium thiolates do not act as chelating ligands here, and the condensed trigonal bipyramids are much more regular in shape.¹⁷⁷ Compound **345** was obtained in a reaction of $\text{Pb}(\text{OOCCH}_3)_2$ with $[4\text{-Me}_3\text{NC}_6\text{H}_4\text{SH}][\text{PF}_6]$.

Four other Pb thiolate clusters were observed to yield from a reaction of $\text{Pb}(\text{OOCCH}_3)_2 \cdot 3\text{H}_2\text{O}$ with 2,6- $\text{Me}_2\text{C}_6\text{H}_3\text{SH}$ at 60 °C in a mixture of ethanol and water, which was originally performed with the intention of obtaining $[\text{Pb}(\text{S}-2,6\text{-Me}_2\text{C}_6\text{H}_3)_2]$. The resulting crude and unidentified orange powder gave rise to four new cluster compounds, depending on the crystallization process applied.¹⁷⁸

Dissolving 0.49 g of it in 10 mL of THF and layering the solution with pentane resulted in the formation of three different crystalline species: $[\text{Pb}_{10}(\text{S}-2,6\text{-Me}_2\text{C}_6\text{H}_3)_{20}]$ (**346**, Fig. 64), $[\text{Pb}_6\text{S}(\text{S}-2,6\text{-Me}_2\text{C}_6\text{H}_3)_{10}(\text{thf})_4]$ (**347**, Fig. 65), and $[\text{Pb}_8\text{O}_2(\text{S}-2,6\text{-Me}_2\text{C}_6\text{H}_3)_{12}]$ (**348**, Fig. 66). Compound **349** features four DHC-type subunits that are condensed in different ways and form a complex molecule with crystallographic mirror symmetry. It can be understood as a central BDHC-like $\{\text{Pb}_6\text{S}_{10}\}$ subunit, to which two further DHC-type moieties are fused by Pb–corner-sharing. One of the Pb atoms of these additional DHC-type additions each bind to an additional terminal thiolate group. **347** features a different, more spherical molecular structure: a central sulfur atom

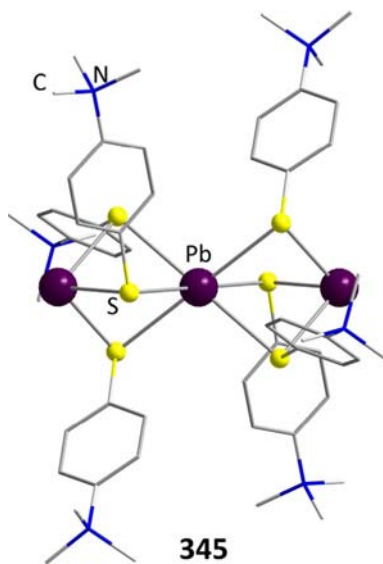


Fig. 63 The trinuclear Pb thiolate complex in $[\text{Pb}_3(4\text{-Me}_3\text{NC}_6\text{H}_4\text{S})_6][\text{PF}_6]_6$ (**345**).

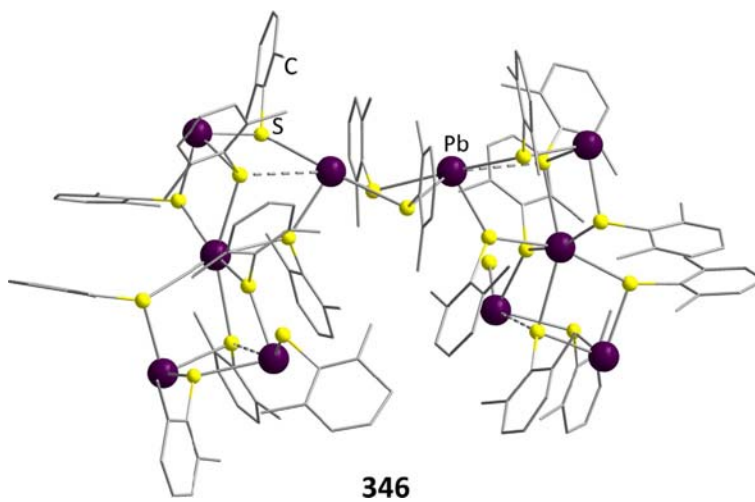


Fig. 64 The Pb thiolate cluster $[\text{Pb}_{10}(\text{S-2,6-Me}_2\text{C}_6\text{H}_3)_{20}]$ (**346**).

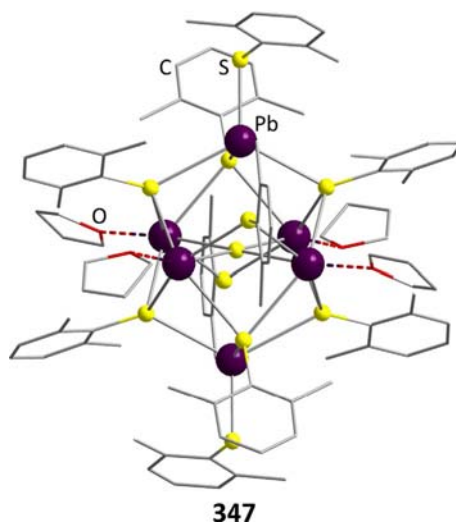


Fig. 65 The Pb thiolate cluster $[\text{Pb}_6\text{S}(\text{S-2,6-Me}_2\text{C}_6\text{H}_3)_{10}(\text{thf})_4]$ (**347**).

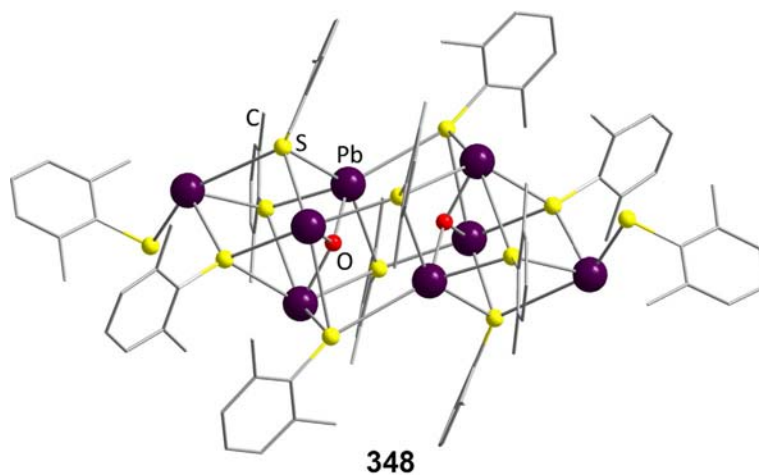


Fig. 66 The Pb thiolate cluster $[\text{Pb}_8\text{O}_2(\text{S}-2,6\text{-Me}_2\text{C}_6\text{H}_3)_{12}]$ (**348**).

coordinates four THF-coordinated Pb atoms in a square planar arrangement. Two further lead atoms are situated above and below this plane, and carry a terminal thiolate ligand each, thus completing an elongated (non-bonded) octahedron of Pb atoms. A total of eight μ_3 -thiolate ligands above and below the central plane interconnect the Pb sites, while the two apical Pb atoms are coordinated by another terminal thiolate ligand each instead of a THF molecule. The third cluster of this series, **348**, features two $\{\text{Pb}_3\text{O}\}$ subunits that connect to an additional Pb moiety with a terminal thiolate each via three μ_3 -thiolates. These two subunits are interconnected by four further bridging thiolate ligands. Altogether, this cluster structure can be understood as being based on two distorted and connected $\{\text{Pb}_4\text{S}_4\}$ heterocubane units.

Repeating the layering with a more diluted solution (0.49 g of the orange powder in 50 mL of THF) leads to the formation of yet another compound, $[\text{Pb}_{14}\text{O}_6(\text{S}-2,6\text{-Me}_2\text{C}_6\text{H}_3)_{16}]$ (**349**, Fig. 67). It contains a central corrugated sheet-like moiety $\{\text{Pb}_{12}\text{O}_6\}$, which resembles a cutout from the crystal structure of PbO. The edges of this layer are coordinatively saturated by 10 thiolate ligands and connected to two $\{\text{Pb}(\text{S}-2,6\text{-Me}_2\text{C}_6\text{H}_3)_3\}$ moieties. An elemental analysis of the orange powder indicated the presence of oxygen atoms, which were recovered in the structures of **348** and **349**. Pure crystals of **347** were additionally obtained by removing the solvent of the supernatant solution during the crystallization of **349**, redissolving the resulting yellow powder in 10 mL of THF

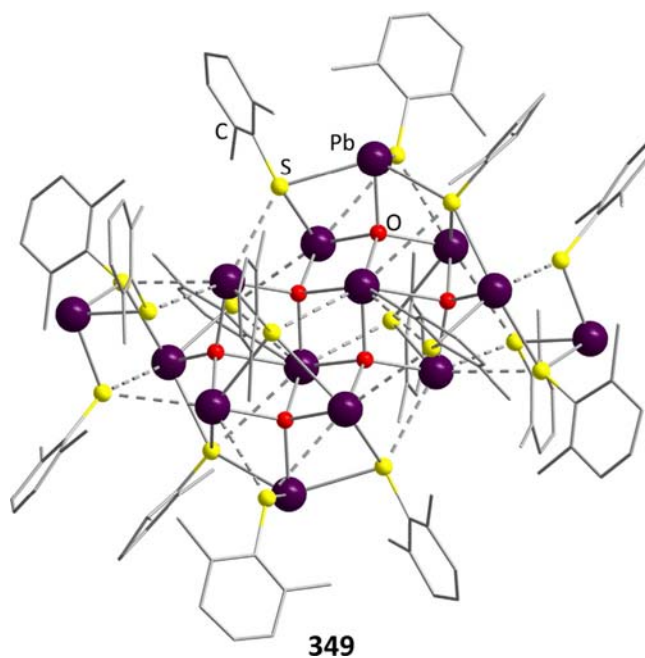


Fig. 67 The Pb thiolate cluster $[\text{Pb}_{14}\text{O}_6(\text{S}-2,6\text{-Me}_2\text{C}_6\text{H}_3)_{16}]$ (**349**) with a core buildup based on a $\{\text{Pb}_{10}\text{O}_6\}$ unit similar to a structural fragment of PbO.

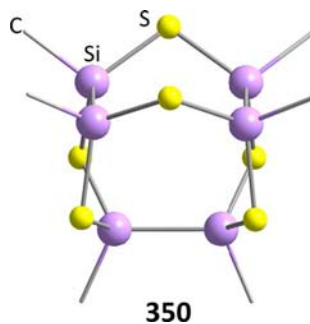


Fig. 68 Cluster molecule $[(\text{Me}_2\text{Si}_2)_3\text{S}_6]$ (**350**) with three bridged Si-Si units.

and slowly layering with 6 mL of pentane; layering with additional pentane leads to pure needles of **346**—all hinting towards a close relationship of these compounds and equilibria between them to exist in the reaction mixtures.

An extensive study about polycyclic silithianes resulted in the formation of several cage compounds. The disilane $(\text{MeSiCl}_2)_2$, already discussed for its role in the formation of NA-type compounds, was treated with H_2S and NEt_3 to generate a trimeric species with the sum formula $[(\text{Me}_2\text{Si}_2)_3\text{S}_6]$ (**350**, Fig. 68), in which two parallel and one orthogonal Si-Si units are connected by μ -S atoms.¹⁷⁹

The asymmetric disilane $\text{Cl}_2\text{MeSiSiMe}_2\text{Cl}$ can be converted by H_2S and NEt_3 into another cage compound, $[(\text{MeSi})_2(\text{Me}_2\text{Si})_2\text{S}_3]$ (**351**). The latter can be described as a $\{\text{Si}_2\text{SSi}_2\text{S}\}$ six-membered ring that is capped by a bridging sulfur atom, similar to the norbornane topology. The use of a 1:1 mixture of the trisilane $\text{MeSiCl}(\text{Me}_2\text{SiCl})_2$ and MeSiCl_3 , in contrast, yielded an isomeric version of $[(\text{MeSi})_2(\text{Me}_2\text{Si})_2\text{S}_3]$ (**352**), which differs from **351** by a trisilane unit being integrated in its six-membered ring with a corresponding composition of $\{\text{Si}_3\text{SSiS}\}$. Mixing the disilane and the trisilane in a 1:1 fashion leads to an increase of the size of the underlying ring in $[(\text{MeSi})_2(\text{Me}_2\text{Si})_3\text{S}_3]$ (**353**) to seven, with an $\{\text{Si}_3\text{SSi}_2\text{S}\}$ order of atoms. Finally, the trisilane alone was employed to form $[(\text{MeSi})_2(\text{Me}_2\text{Si})_4\text{S}_3]$ (**354**) with an eight-membered ring being capped by an S atom.

A branched precursor of the type $\text{MeSi}(\text{Me}_2\text{SiCl})_3$ was reacted in a similar way with MeSiCl_3 and $\text{H}_2\text{S}/\text{NEt}_3$, which allowed the isolation of $[(\text{MeSi})_2(\text{Me}_2\text{Si})_2\text{S}_3]$ (**355**). Here, a six-membered ring $\{\text{Si}_3\text{SSiS}\}$, like in **352**, is bridged by an S-Si units, so the cage comprises three condensed six-membered rings.

The synthesis of the Se congener of **351**, $[(\text{MeSi})_2(\text{Me}_2\text{Si})_2\text{Se}_3]$ (**356**), was achieved in a subsequent study by reacting $\text{Cl}_2\text{MeSiSiMe}_2\text{Cl}$ with Li_2Se .¹⁸⁰ As both **351** and **356** are liquids, access to a crystalline material suitable for XRD was sought to be realized by using a starting material with a larger organic ligands. For this, $\text{Cl}_2\text{MeSiSiMePhCl}$ was utilized to generate $[(\text{MeSi})_2(\text{MePhSi})_2\text{E}_3]$ (E = S: **357**; E = Se: **358**; E = Te: **359**) in reactions with $\text{H}_2\text{S}/\text{NEt}_3$, Li_2Se , or Li_2Te , respectively. All three compounds were obtained in three distinct isomeric forms, with the two phenyl rings being situated in axial positions relative to the six-membered ring, or in equatorial positions, or with both Ph groups adopting different positions. Theoretical studies, as well as the ratios found for the isomers, point to the equatorial positions to be favored though. This preference was additionally confirmed by structure analysis of **357**, which was the only compound in this series to properly crystallize (Fig. 69).

Another cluster was isolated from the reaction of the disilane $\{\text{Si}(\text{NH}_2)_2(\text{CH}(\text{SiMe}_3)_2)\}_2$ with liquid H_2S in toluene at low temperatures. $[\{\text{CH}(\text{SiMe}_3)_2\text{Si}\}_4\text{S}_4]$ (**360**, Fig. 70) shares its molecular buildup with that of realgar, with two RSiSiR dimers being oriented orthogonal to each other and being connected by four μ -S bridges.¹⁸¹

With the sterically demanding 2,6-dimesitylphenyl (dmph) ligand, a series of organogermanium clusters are obtained with a strong relationship to the DHC-type structure.¹⁸² Here, dmphGeH_3 transforms to a mixture of $[(\text{dmphGe})_3\text{S}_4\text{SH}]$ (**361**) and $[(\text{dmphGe})_2\text{S}_{2+x}]$ ($x = 3$: **362**; $4 = 2$: **363**; $5 = 3$: **364**) upon reaction with S_8 at 200°C (Fig. 71). The structure of **361** resembles

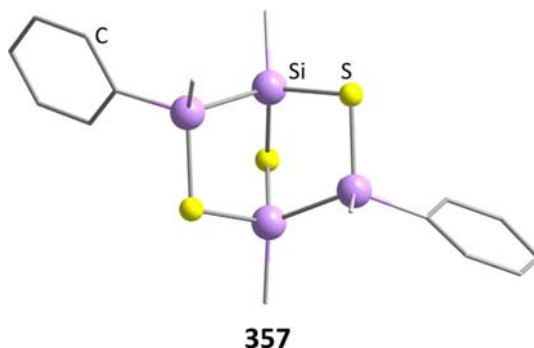


Fig. 69 Norbornane-like molecule $[(\text{MeSi})_2(\text{MePhSi})_2\text{S}_3]$ (**357**) with the Ph groups being situated in equatorial positions relative to the corrugated six-membered ring in chair conformation.

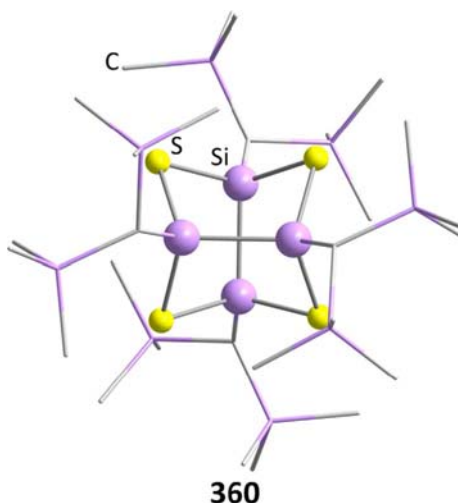


Fig. 70 Realgar-like buildup in $[(\text{CH}(\text{SiMe}_3)_2\text{Si})_4\text{S}_4]$ (**360**).

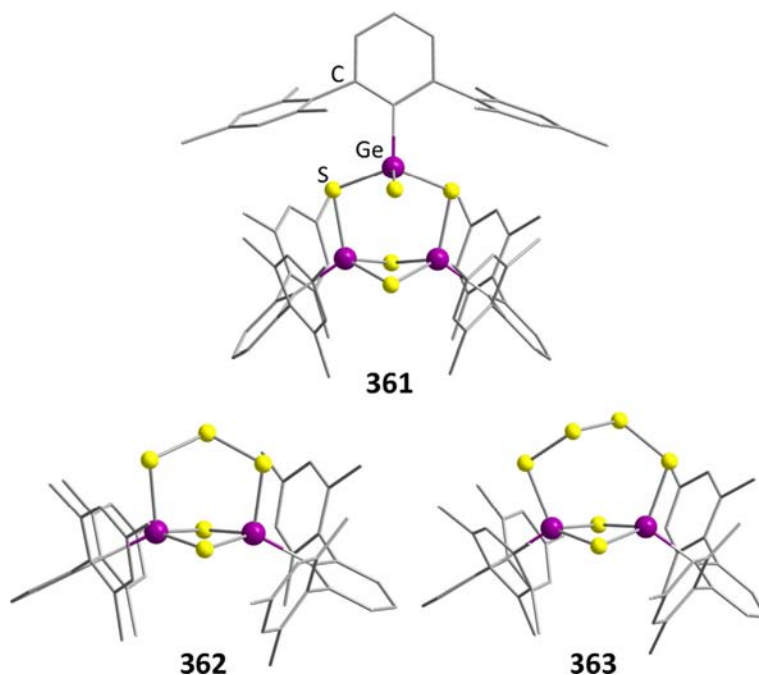


Fig. 71 Cluster compounds $[(\text{dmphGe})_3\text{S}_4\text{SH}]$ (**361**), $[(\text{dmphGe})_2\text{S}_3]$ (**362**) and $[(\text{dmphGe})_2\text{S}_4]$ (**363**) from the same reactive mixture.

a DHC-type cage, in which one Ge atom carrying an additional SH group is bent away from the $\{\text{Ge}_2\text{S}_2\}$ four-membered ring. In **362**, **363** and **364**, this RGeSH unit is replaced by a single S atom, an S_2 unit, or an S_3 chain, respectively.

From SnBr_4 and Na_2Se , an orange solution was obtained at -40°C , which was then reacted with $(\text{Et}_4\text{N})\text{PF}_6$ to yield crystals of $(\text{NEt}_4)_2[\text{Sn}_6\text{Se}_{10}\text{Br}_6]$ (**365**, Fig. 72) upon layering.¹⁸³ The anionic cluster in **365** features a central Se atom coordinated by six Sn atoms in a trigonal-prismatic fashion. Each Sn atom binds to a terminal bromide ligand, and it is furthermore connected to its neighboring Sn atoms by one μ -Se bridge each. Three additional μ -Se bridges connect the atoms within the Sn_3 triangles above and below the central Se atom.

The largest clusters described in this publication are the anions in the compounds $(\text{C}_4\text{C}_1\text{C}_1\text{Im})_{24}[\text{Sn}_{36}\text{Ge}_{24}\text{Se}_{132}]$ (**366**, Fig. 73) and $(\text{C}_4\text{C}_1\text{Im})_{24}[\text{Sn}_{32.5}\text{Ge}_{27.5}\text{Se}_{132}]$ (**367**, $\text{C}_4\text{C}_1\text{Im}$ = 1-butyl-3-methylimidazolium). Both were generated from ionothermal synthesis of $[\text{K}_4(\text{H}_2\text{O})_3][\text{Ge}_4\text{Se}_{10}]$ and $\text{SnCl}_4 \cdot 5\text{H}_2\text{O}$ in the corresponding ionic liquids $(\text{C}_4\text{C}_1\text{C}_1\text{Im})[\text{BF}_4]$ or $(\text{C}_4\text{C}_1\text{Im})[\text{BF}_4]$ (in the absence or presence of a small amount of 2,6-dimethylmorpholine).^{184,185} The so-called "Zeoball anion" $[\text{Sn}_{36}\text{Ge}_{24}\text{Se}_{132}]^{24-}$ in **366** consists of a spherical arrangement of two subunits, $\{\text{Ge}_3\text{Se}_9\}$ and $\{\text{Sn}_6\text{Se}_{18}\}$, which are condensed by sharing their terminal Se atoms. $\{\text{Ge}_3\text{Se}_9\}$ is formally obtained by removing one $\{\text{GeSe}\}$ unit from a $[\text{Ge}_4\text{Se}_{10}]^{4-}$ AD-type cluster, while $\{\text{Sn}_6\text{Se}_{18}\}$ is based on an $\{\text{Sn}_6\text{Se}_{10}\}$ BDHC-type moiety, with the four outer Sn atoms additionally carrying two terminal selenide ligands

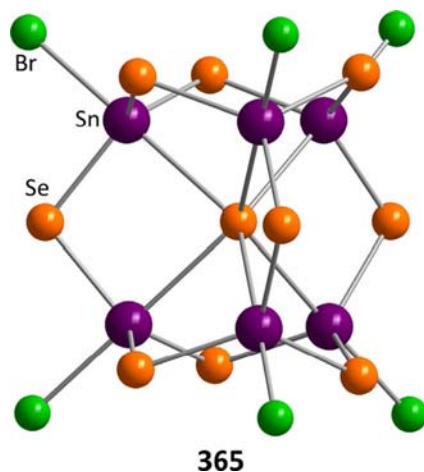


Fig. 72 Anion in $(\text{NEt}_3)_2[\text{Sn}_6\text{Se}_{10}\text{Br}_6]$ (**365**).

each. The barycenters of the $\{\text{Ge}_3\text{Se}_9\}$ subunits form a cube, in which an imagined octahedron is inscribed with the $\{\text{Sn}_6\text{Se}_{18}\}$ subunits arranged on its corners; vice-versa, each of the $\{\text{Ge}_3\text{Se}_9\}$ moieties is positioned above the imagined faces of said octahedron. This leads to a spherical molecule with 192 atoms, an outer diameter of about 2.83 nm, an inner spherical cavity of about 11.6 Å (considering the van der Waals radii of the involved atoms), and 12 windows, above which some of the counterions are situated.

In **367**, a partial disorder of the Sn and Ge position leads to a slightly deviating sum formula, but the anionic structure remains the same. The counterions are not covalently bound to the anion and some of them are partially disordered, which hints at a high mobility of the organic molecules. Thus, trapping experiments with I_2 have been carried out. Either through I_2 vapor or through contact with dissolved I_2 , the Zeoball was shown to reversibly incorporate I_2 and heterolytically cleave the I–I bond without showing decomposition itself.

In the meantime, many further salts of this extraordinarily stable anion were obtained with a variety of different ionic liquid counterions in studies of the impact of the ionic liquid and its purity as well as different additives on the zeoball formation.¹⁸⁶ A noticeable decrease in yield was observed when repeating the reactions described above, which was found out to stem from an absence of chloride ion impurities in the ionic liquids, as their commercial production has been improved to yield purer products since the last study. Intentional addition of chlorides to the reactive mixtures thus led to a recovery and even improvement of the yields, and to the observation of new crystal structure of $(\text{C}_4\text{C}_1\text{C}_1\text{Im})_{24}[\text{Sn}_{36}\text{Ge}_{24}\text{Se}_{132}]$ (**368**) and $(\text{C}_4\text{C}_1\text{Im})_{24}[\text{Sn}_{36}\text{Ge}_{24}\text{Se}_{132}]$ (**369**) for both previously investigated ionic liquids. The addition of NMe_4Br or 18-crown-6 to the reaction mixture of **366** leads to an incorporation of those new cations in the crystals of **370** and **371**. However, due to the high tendency of disorder, the exact amount of counterions could not be determined crystallographically for all of these structures. Also, an extension of the side chains of the ionic liquid from butyl in $(\text{C}_4\text{C}_1\text{Im})[\text{BH}_4]$ to hexyl in $(\text{C}_6\text{C}_1\text{Im})[\text{BH}_4]$ or heptyl in $(\text{C}_7\text{C}_1\text{Im})[\text{BH}_4]$ enabled the isolation of two crystalline compounds $(\text{C}_6\text{C}_1\text{Im})_{24}[\text{Sn}_{36}\text{Ge}_{24}\text{Se}_{132}]$ (**372** and **373**) or $(\text{C}_7\text{C}_1\text{Im})_{24}[\text{Sn}_{36}\text{Ge}_{24}\text{Se}_{132}]$ (**374**), respectively.

It should be mentioned that many attempts to obtain variations of this unique cluster, be it with varied structural units or sizes of the ball or with other elemental combinations, failed. Obviously, this elemental combination and the exact cluster structure warrants an extremely favorable architecture.

The compound $[(\text{PPh}_2\text{NSiMe}_3)(\text{PPh}_2\text{S})\text{CSn}]$, formally comprising a ligand-stabilized $\{\text{Sn}=\text{S}\}$ unit, was treated with S_8 to form an $\{\text{Sn}_3\text{S}_3\}$ six-membered ring capped by such this unit that became part of an $\{\text{S}\cdots\text{Sn}^{\text{II}}\text{S}_3\}$ moiety in $[\{(\mu\text{-S})\text{Sn}^{\text{IV}}\text{C}(\text{PPh}_2\text{NSiMe}_3)(\text{PPh}_2\text{S})\}_3\text{Sn}^{\text{II}}(\mu_3\text{-S})]\cdot 4\text{C}_6\text{D}_6$ (**375**, Fig. 74); the compound was obtained beside $[\text{CH}_2(\text{PPh}_2\text{NSiMe}_3)(\text{PPh}_2\text{S})]$ and some other unidentified minor products.¹⁸⁷

The six-membered ring in chair conformation is capped at its Sn^{IV} sites by the sulfur atom of the $\{\text{Sn}^{\text{II}}\text{-S}\}$ fragment, while the Sn^{II} atom interacts with the sulfur atoms of the $\{\text{SPPH}_2\}$ groups of the ligand, leading to a *pseudo*- C_3 symmetry of the resulting molecule. The $\text{Sn}^{\text{II}}\text{-SPPH}_2$ distances in said $\{\text{S}\cdots\text{Sn}^{\text{II}}\text{S}_3\}$ moiety are not equal however, with 2.686, 2.813, and 2.920 Å, indicating a smooth transition from regular covalent bonds to weaker secondary interactions with the Sn^{II} site. The different oxidation states at the Sn atoms were rationalized by means of Mössbauer spectroscopy.

The structure of another cluster comprising Sn^{II} sites, $[\{(\text{Me}_3\text{Si})_3\text{SiTe}\}_4\text{Te}_2\text{Sn}_4]$ (**376**, Fig. 75) can be understood as two DHC-type subunits that share one of their (idealized) square faces; the silyl ligands are attached to four of the six Te atoms.¹⁸⁸ The compound was obtained from the unsymmetrically substituted silyl telluride $(\text{SiMe}_3)_3\text{SiTeSiMe}_3$ and SnCl_2 .

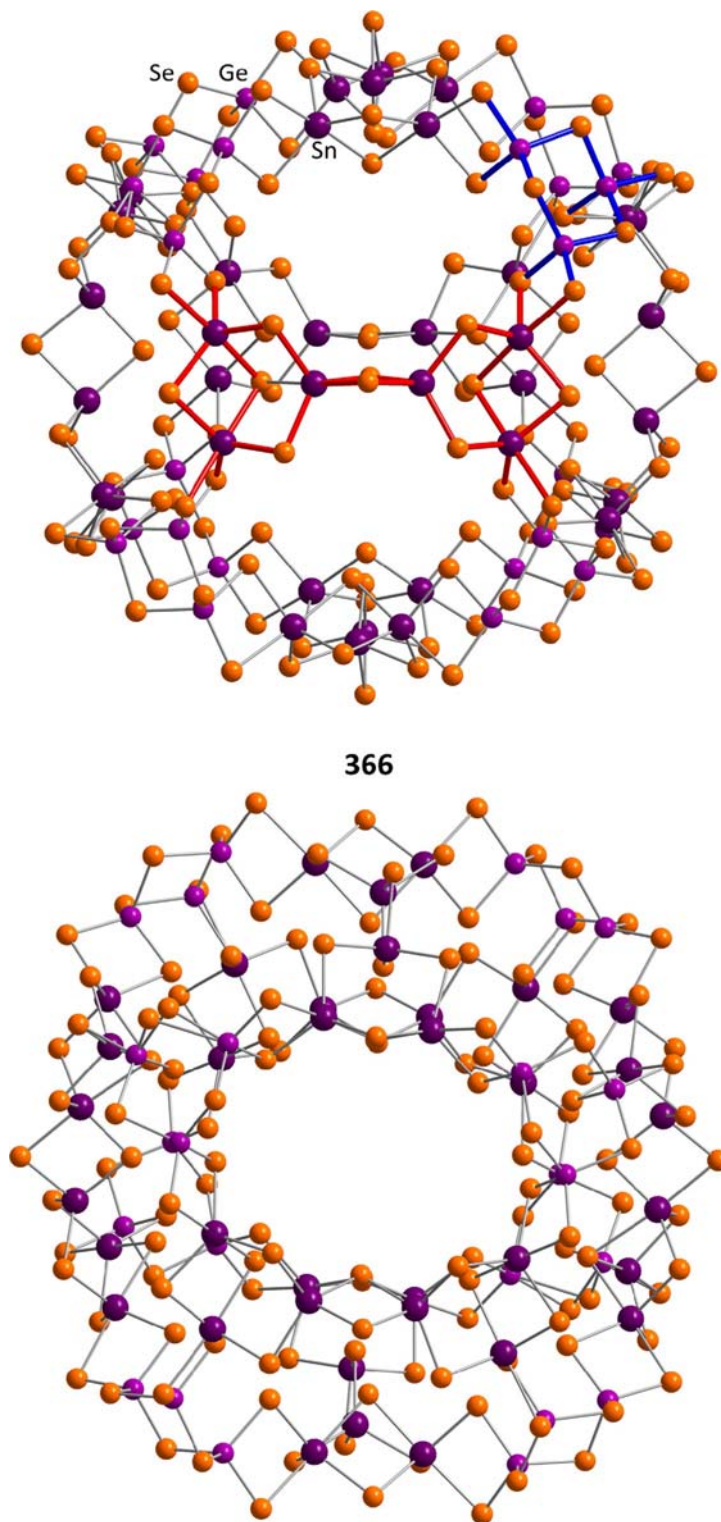


Fig. 73 Zeoball cluster anion in $(C_4C_1Im)_{24}[Sn_{36}Ge_{24}Se_{132}]$ (**366**, $C_4C_1Im = 1\text{-butyl-3-methylimidazolium}$) in two different views. In the top view, a subunit each is highlighted, $\{Sn_6S_{18}\}$ in red and $\{Sn_3S_9\}$ in blue, while the bottom view shows the large windows into the cluster core.

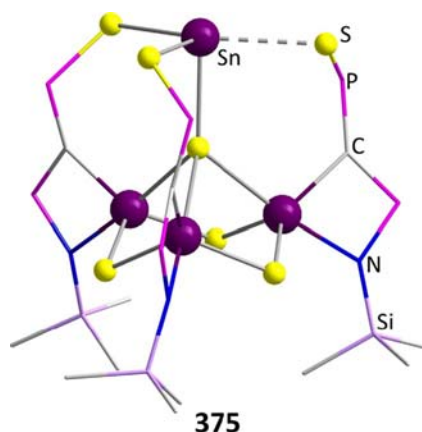


Fig. 74 Extended DHC-type-type cluster in $[\{(\mu\text{-S})\text{Sn}^{\text{IV}}\text{C}(\text{PPh}_2\text{NSiMe}_3)(\text{PPh}_2\text{S})_3\text{Sn}^{\text{II}}(\mu_3\text{-S})\}] \cdot 4\text{C}_6\text{D}_6$ (**375**). H atoms and Ph groups are omitted for clarity.

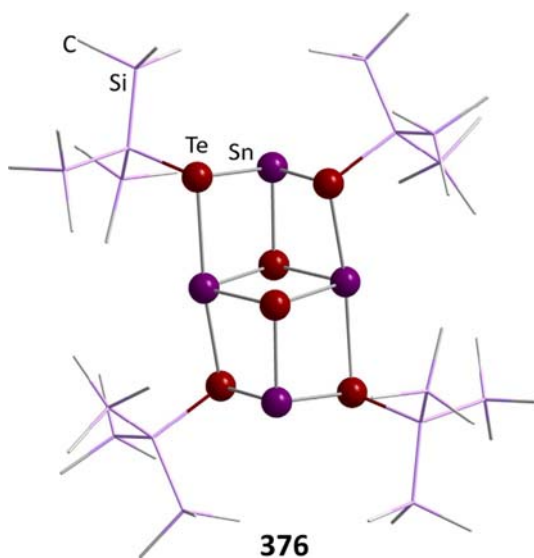


Fig. 75 Condensed DHC-type units in $[\{(\text{Me}_3\text{Si})_3\text{SiTe}_4\text{Te}_2\text{Sn}_4\}]$ (**376**).

4.04.4 Group 15 chalcogenide clusters

In contrast to the large number and great variety of compounds comprising group 13 or group 14 chalcogenide clusters, metal chalcogenide clusters of group 15 (semi)metals are very rare. This applies in particular when excluding compounds exhibiting P and As atoms as their central sites, which was done in this report, as we intended to limit it to clusters of the more metallic elements Sb and Bi. So we are going to discuss four compounds here only.

The compound $[\text{PPh}_4]_4[\text{Sb}_{12}\text{Se}_{20}] \cdot 2\text{DMF}$ (**377**, Fig. 76), was obtained through reduction of Sb_4Se_4 with K in DMF. It was the first cluster that was reported for a heavy group 15 chalcogenide combination.¹⁸⁹ In its structure, two DHC-type $\{\text{Sb}_3\text{Se}_4\}$ units situated at opposite sides of a rugby-ball-shaped molecule. The Sb atoms of these units are connected via $\mu\text{-Se}$ ligands to a central, crown-shaped 12-membered $\{\text{Sb}_6\text{Se}_6\}$ ring, thereby forming a polycyclic cluster molecule altogether.

$(\text{NEt}_4)_4[\text{Sb}_6\text{Te}_9] \cdot 0.5\text{en}$ (**378**, Fig. 77) is a borderline case for categorization as a cage compound. It is the minor product to form from an electrochemical reaction of an Sb_2Te_3 cathode besides $(\text{NEt}_4)_4[\text{Sb}_2\text{Te}_5]$.¹⁹⁰ The essentially tricyclic anion comprises a central $\{(\text{Sb}_2)_2\text{Te}_2\}$ ring in boat conformation, to which two $\{\text{SbTe}_3\}$ units are attached to form an envelope-shaped five-membered ring with an additional terminal Te atom each. The central ring additionally is capped by a weakly-bound Te atom, with $\text{Te} \cdots \text{Sb}$ distances between 3.133 and 3.229 Å.

In a reaction of BiBr_3 with PhSeSiMe_3 , under addition of $\text{P}^{\text{III}}\text{Pr}$ to stabilize intermediates, a cyclic compound was obtained that comprises an oligomeric bismuth selenolate “ $\{\text{Bi}(\text{SPh})_3\}_4$ ”.¹⁹¹ $[\text{HP}^{\text{III}}\text{Pr}_3][\text{Bi}_4(\text{PhSe})_{13}] \cdot 0.5\text{THF}$ (**379**, Fig. 78) features an eight-membered $\{\text{Bi}_4\text{Se}_4\}$ ring, with Ph substituents at the Se atoms, and two additional SePh ligands at each of the Bi atoms. This macrocycle embeds the Se atom of a 13th SePh unit at a slightly off-center position. The distances between the four Bi atoms and this

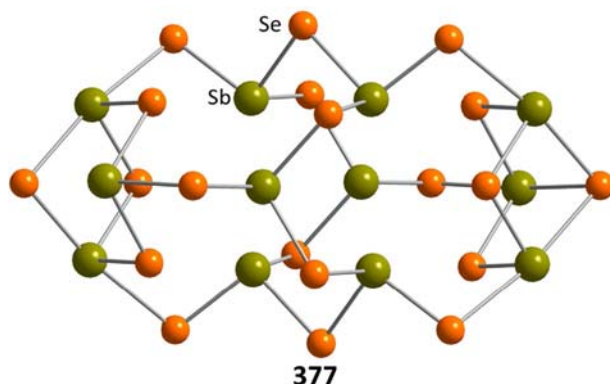


Fig. 76 Polycyclic binary anion in $[\text{PPh}_4]_4[\text{Sb}_{12}\text{Se}_{20}] \cdot 2\text{DMF}$ (**377**).

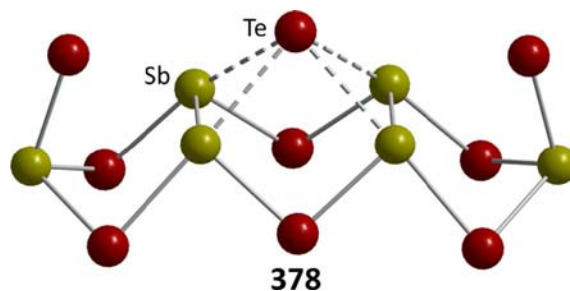


Fig. 77 Tricyclic binary anion with additional Te ligands in $(\text{NEt}_4)_4[\text{Sb}_6\text{Te}_9] \cdot 0.5\text{en}$ (**378**).

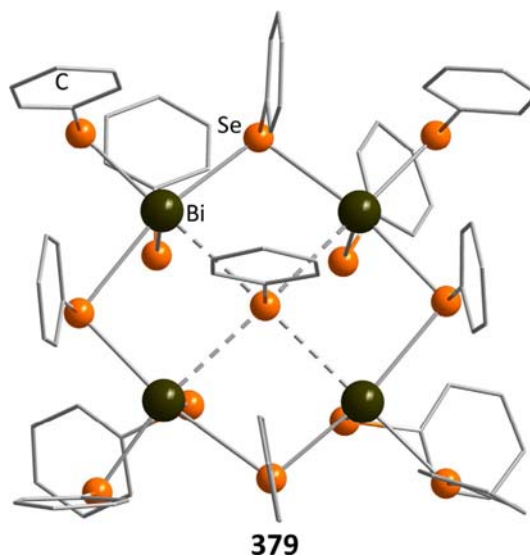


Fig. 78 Complex bismuth selenolate anion in $[\text{HP}^n\text{Pr}_3][\text{Bi}_4(\text{PhSe})_{13}] \cdot 0.5\text{THF}$ (**379**).

central atom (3.248(3)–3.337(3) Å) are larger than the sum of the covalent radii (2.69 Å), thus indicating mostly ionic interactions between the cyclic host and the anionic guest. The total charge of this assembly is compensated by the $[\text{HP}^n\text{Pr}_3]^+$ phosphonium cation.

A pentanuclear complex with zwitterionic ammonium thiolate units was synthesized from $\text{Bi}(\text{NO}_3)_3$ and TabHPPF_6 (Tab = 4-(trimethylammonio)benzenethiolato) in the presence of NEt_3 .¹⁹² The molecular structure of the cation in $[\text{Bi}_5(\text{Tab})_{18}](\text{PF}_6)_7(\text{NO}_3)_8 \cdot 6\text{MeCN}$ (**380**, Fig. 79) is reminiscent of the one observed in compounds **344** and **345**, as it is formally generated by the condensation of trigonal-bipyramidal units $\{\text{Bi}_2(\text{SR})_3\}$ by their Bi corners, with the difference being the longer chain of four such polyheders. The Bi atoms at both ends carry three terminal thiolates, which leads to a coordination number of six for all metal atoms. Organic ligands of the thiolates are monodentate and serve to shield the inorganic core of this polynuclear complex. Even so, the compound remains moisture and oxygen sensitive, however.

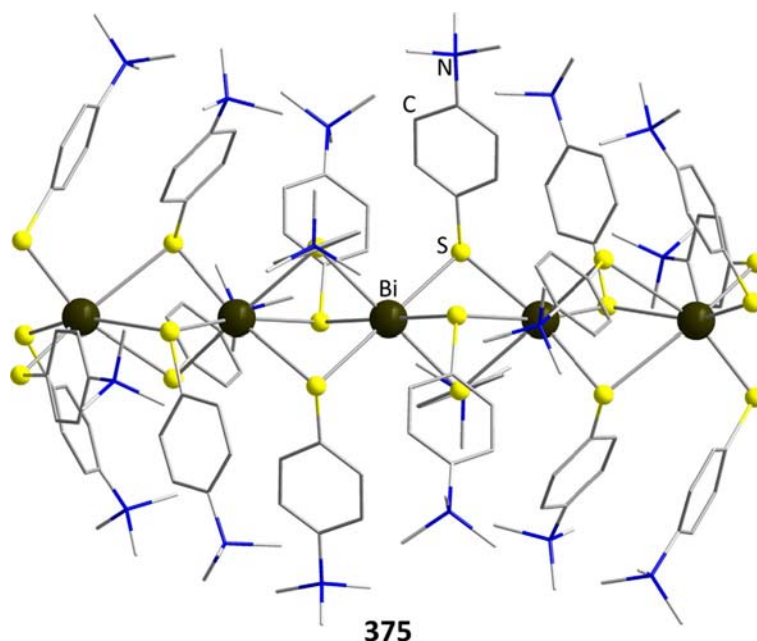


Fig. 79 Pentanuclear cation comprising zwitterionic ammonium thiolate ligands in $[\text{Bi}_5(\text{Tab})_{18}](\text{PF}_6)_7(\text{NO}_3)_8 \cdot 6\text{MeCN}$ (**380**, $\text{Tab} = 4$ -trimethylammonio)benzenethiolate).

4.04.5 Clusters with p-block (semi)metals from different groups

In addition to the compounds presented and discussed in the preceding sections, there exist a few compounds that comprise chalcogenide clusters with (semi)metal atoms from different groups of the p-block groups 13–15. These will be given below.

$[\text{LAl}\{\text{SLi}\}_2(\text{thf})_2]_2$ ($\text{L} = \text{HC}\{\text{CMeN}(2,6\text{-}i\text{Pr}_2\text{C}_6\text{H})\}_2$) was reacted with $\text{GeCl}_2 \cdot \text{dioxane}$ in a 7:16 ratio at low temperatures, resulting in the formation of $[\{\text{LAl}(\mu\text{-S})_2\text{Ge}_2\}_2(\mu\text{-S})_3\text{Li}_2(\text{thf})_2]$ (**381**, **Fig. 80**) featuring $\text{Ge}^{\text{II}}\text{-Ge}^{\text{II}}$ bonds.¹⁹³ One half of the cluster core is built from two LAl units that are bridged via two S atoms to a $\{\text{Ge-Ge}\}$ subunit. The two halves are then connected by three sulfur bridges between the Ge atoms, and an additional coordination of two $\{\text{Li}(\text{thf})\}$ units via the sulfide ligands. This way, the two different Ge sites in each of the cluster halves are coordinated by two or three sulfur neighbors (besides the Ge–Ge bond), respectively, with the four-coordinate Ge^{II} site ones acting as electron donors towards the three-coordinate Ge^{II} atom.

A solvothermal reaction of GeO_2 , elemental Sb, and S_8 in DMF, afforded a compound with two cluster anions, $[\text{Me}_2\text{NH}_2]_6[\text{Ge}_2\text{Sb}_2\text{S}_7][\text{Ge}_4\text{S}_{10}]$ (**382**, **Fig. 81**).¹⁹⁴ One anion is the binary AD-type $[\text{Ge}_4\text{S}_{10}]^{4-}$ discussed above, the other cluster is ternary in nature, $[\text{Ge}_2\text{Sb}_2\text{S}_7]^{2-}$. Its structure can be derived from an NA-type core, with an Sb–Sb bond and terminal sulfide ligands at the Ge atoms. $[\text{Ge}_4\text{S}_{10}]^{4-}$ uses its terminal S atoms to coordinate to the Sb atoms of $[\text{Ge}_2\text{Sb}_2\text{S}_7]^{2-}$, forming zig-zag chains in the crystal.

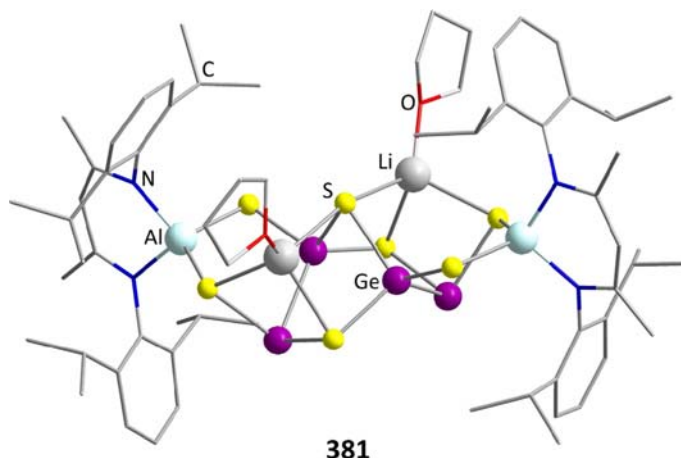


Fig. 80 Ternary group 13/14/16 cluster $[\{\text{LAl}(\mu\text{-S})_2\text{Ge}_2\}_2(\mu\text{-S})_3\text{Li}_2(\text{thf})_2]$ (**381**, $\text{L} = \text{HC}\{\text{CMeN}(2,6\text{-}i\text{Pr}_2\text{C}_6\text{H})\}_2$).

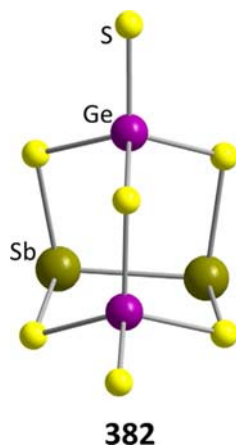


Fig. 81 Ternary group 14/15/16 NA-type cluster anion in $[\text{Me}_2\text{NH}_2]_6[\text{Ge}_2\text{Sb}_2\text{S}_7][\text{Ge}_4\text{S}_{10}]$ (**382**).

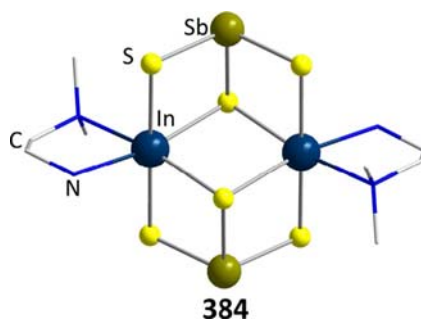


Fig. 82 Ternary group 13/14/16 cluster $[\text{In}_2(\text{N},\text{N-dmen})_2\text{Sb}_2\text{S}_6]$ (**384**, dmen = dimethylethylenediamine).

The same ternary cluster anion was also obtained from a reaction of $\text{K}[\text{Ge}_4\text{S}_{10}]$ with SbCl_3 upon application of ionothermal synthesis conditions in $\text{C}_4\text{C}_1\text{C}_1\text{Im}[\text{BF}_4]$ and en. In this case, however, the NA-like anion co-crystallized with the T1 anion $[\text{GeS}_4]^{4-}$ in the double-salt $[\text{C}_4\text{C}_1\text{C}_1\text{Im}]_{16}[\text{Ge}_2\text{Sb}_2\text{S}_7]_6[\text{GeS}_4]$ (**383**).¹⁹⁵ The two different anions form spherical assemblies of $\{[\text{Ge}_2\text{Sb}_2\text{S}_7]_6[\text{GeS}_4]\}$, albeit lacking significant interactions between the anions, which are packed in a diamond-like superstructure in the crystal, separated by the organic counterions. The addition of Sb atoms into the compound served to lower its bandgap (2.62 eV), even below the value known for to bulk GeS_2 (3.43 eV).

Finally, the combination of $\text{In}(\text{NO}_3)_3 \cdot 5\text{H}_2\text{O}$, SbCl_3 , thiourea and *N,N*-dimethylethylenediamine (*N,N*-dmen) in a solvothermal reaction yielded compound $[\text{In}_2(\text{N},\text{N-dmen})_2\text{Sb}_2\text{S}_6]$ (**384**, Fig. 82), in which two trigonal-pyramidal $\{\text{SbS}_3\}$ units coordinate two $\text{In}(\text{N}\cdot\text{N-dmen})$ moieties. This leads to the same buildup of condensed DHC-units as was observed in the otherwise unrelated cluster compound **376**, indicating the relationship between group 13/15/16 and group 14/16 elemental combinations.

4.04.6 Conclusion

In this chapter we provided a comprehensive survey of the large structural variety of molecular p-block (semi)metal chalcogenide cage and cluster compounds. All (semi)metals of groups 13 through 15 have been observed in such structures, with a clear predominance of group 14 elements in corresponding elemental combinations.

In spite of a broad spectrum of cluster architectures, many of the molecules summarized herein can be assigned to general underlying structural types, which seem to be favorable in terms of their thermodynamic stability. Essentially all elemental combinations—including some examples of ternary cluster cores—have been found in purely inorganic clusters or in molecules exhibiting organic, bioorganic, or organometallic ligand environments, which—in addition to their effects on the physical properties of the compounds—enable kinetic shielding and may allow for further reactivity.

Of course, the underlying elemental combinations of all clusters discussed herein, all of which refer to semiconductor materials when being extended into solids, have an intrinsic impact on the properties of the compounds. These range from different colors and stabilities to uncommon opto-electronic properties including extreme non-linear optical responses. The recent past has shown that many surprises are still buried in this field, waiting to be discovered. Hence the activity in the synthesis and detailed exploration of this fascinating family of molecular materials continuous to increase.

References

1. Fuhr, O.; Dehnen, S.; Fenske, D. *Chem. Soc. Rev.* **2013**, *42*, 1871–1906.
2. Dornsiepen, E.; Geringer, E.; Rinn, N.; Dehnen, S. *Coord. Chem. Rev.* **2019**, *380*, 136–169.
3. Feng, P.; Bu, X.; Zheng, N. *Acc. Chem. Res.* **2005**, *38*, 293–303.
4. Dance, I.; Fisher, K. *Prog. Inorg. Chem.* **2007**, *41*, 637–803.
5. Crespo, O.; Gimeno, M. C.; Laguna, A.; Larraz, C.; Villacampa, M. D. *Chem. A Eur. J.* **2007**, *13*, 235–246.
6. Gray, T. G.; Rudzinski, C. M.; Meyer, E. E.; Holm, R. H.; Nocera, D. G. *J. Am. Chem. Soc.* **2003**, *125*, 4755–4770.
7. Nguyen, K. A.; Pachter, R.; Day, P. N.; Su, H. *J. Chem. Phys.* **2015**, *142*, 234305.
8. Power, M. B.; Barron, A. R. *J. Chem. Soc. Chem. Commun.* **1991**, 1315–1317.
9. Cowley, A. H.; Jones, R. A.; Harris, P. R.; Atwood, D. A.; Contreras, L.; Burek, C. J. *Angew. Chem. Int. Ed.* **1991**, *30*, 1143–1145.
10. Power, M. B.; Ziller, J. W.; Tyler, A. N.; Barron, A. R. *Organometallics* **1992**, *11*, 1055–1063.
11. Schulz, S.; Roesky, H. W.; Koch, H. J.; Sheldrick, G. M.; Stalke, D.; Kuhn, A. *Angew. Chem. Int. Ed.* **1993**, *32*, 1729–1731.
12. Harlan, C. J.; Gillan, E. G.; Bott, S. G.; Barron, A. R. *Organometallics* **1996**, *15*, 5479–5488.
13. Uhl, W.; Graupner, R.; Layh, M.; Schütz, U. *J. Organomet. Chem.* **1995**, *493*, C1–C5.
14. Uhl, W.; Graupner, R.; Pohlmann, M.; Pohl, S.; Saak, W. *Chem. Ber.* **1996**, *129*, 143–146.
15. Stoll, S. L.; Gillan, E. G.; Barron, A. R. *Chem. Vap. Depos.* **1996**, *2*, 182–184.
16. Stoll, S. L.; Bott, S. G.; Barron, A. R. *J. Chem. Soc. Dalton Trans.* **1997**, 1315–1321.
17. Schulz, S.; Andruh, M.; Pape, T.; Heinze, T.; Roesky, H. W.; Häning, L.; Kuhn, A.; Herbst-Irmer, R. *Organometallics* **1994**, *13*, 4004–4007.
18. Linti, G.; Bühler, M.; Urban, H. Z. *Anorg. Allg. Chem.* **1998**, *624*, 517–520.
19. Schnitter, C.; Klemp, A.; Roesky, H. W.; Schmidt, H.; Röpken, C.; Herbst-Irmer, R.; Noltemeyer, M. *Eur. J. Inorg. Chem.* **1998**, 2033–2039.
20. Merzweiler, K.; Rudolph, F.; Brands, L. *Z. Naturforsch. B* **1992**, *47b*, 978–982.
21. App, U.; Merzweiler, K. *Z. Anorg. Allg. Chem.* **1997**, *623*, 478–482.
22. Lei, Z. X.; Zhu, Q. Y.; Zhang, M. H.; Jiang, J. B.; Zhang, Y. P.; Dai, J. *Inorg. Chem.* **2010**, *49*, 353–355.
23. Zhang, Y.; Lei, Z.; Jiang, J.; Zhu, Q.; Zhang, X.; Bian, G.; Dai, J. *Inorg. Chim. Acta* **2011**, *376*, 645–650.
24. Topel, Ö.; Persson, I.; Lundberg, D.; Ullström, A. S. *Inorg. Chim. Acta* **2011**, *365*, 220–224.
25. Wiberg, N.; Blank, T.; Amelunxen, K.; Nöth, H.; Schnöckel, H.; Baum, E.; Purath, A.; Fenske, D. *Eur. J. Inorg. Chem.* **2002**, 341–350.
26. Power, M. B.; Ziller, J. W.; Barron, A. R. *Organometallics* **1992**, *11*, 2783–2790.
27. Barbarich, T. J.; Bott, S. G.; Barren, A. R. *J. Chem. Soc. Dalton Trans.* **2000**, 6, 1679–1680.
28. Uhl, W.; Benter, M.; Saak, W.; Jones, P. G. *Z. Anorg. Allg. Chem.* **1998**, *624*, 1622–1628.
29. Gillan, E. G.; Bott, S. G.; Barron, A. R. *Chem. Mater.* **1997**, *9*, 796–806.
30. MacInnes, A. N.; Power, M. B.; Barron, A. R. *Chem. Mater.* **1992**, *4*, 11–14.
31. MacInnes, A. N.; Power, M. B.; Barron, A. R. *Chem. Mater.* **1993**, *5*, 1344–1351.
32. Pernet, P. J.; Barron, A. R. *Chem. Vap. Depos.* **1995**, *1*, 75–78.
33. Power, M. B.; Barron, A. R.; Hnyk, D.; Robertson, H. E.; Rankin, D. W. H. *Adv. Mater. Opt. Electron.* **1995**, *5*, 177–185.
34. Gillan, E. G.; Barron, A. R. *Chem. Mater.* **1997**, *9*, 3037–3048.
35. Schulz, S.; Gillan, E. G.; Ross, J. L.; Rogers, L. M.; Rogers, R. D.; Barron, A. R. *Organometallics* **1996**, *15*, 4880–4883.
36. Stoll, S. L.; Barron, A. R. *Chem. Mater.* **1998**, *10*, 650–657.
37. Jeff Harlan, C. *J. Clust. Sci.* **1996**, *7*, 455–467.
38. Krebs, B.; Voelker, D.; Stiller, K.-O. *Inorg. Chim. Acta* **1982**, *65*, L101–L102.
39. Cahill, C. L.; Parise, J. B. *J. Chem. Soc. Dalton Trans.* **2000**, 1475–1482.
40. Zhou, J.; Zhang, Y.; Bian, G. Q.; Li, C. Y.; Chen, X. X.; Dai, J. *Cryst. Growth Des.* **2008**, *8*, 2235–2240.
41. Boardman, A.; Jeffs, S. E.; Small, R. W. H.; Worrall, I. J. *Inorg. Chim. Acta* **1984**, *83*, L39–L40.
42. Boardman, A.; Small, R. W. H.; Worrall, I. J. *Inorg. Chim. Acta* **1986**, *120*, L23–L24.
43. Wehmschulte, R. J.; Power, P. P. *J. Am. Chem. Soc.* **1997**, *119*, 9566–9567.
44. Schmidbaur, H.; Nogai, S. D. *Z. Anorg. Allg. Chem.* **2004**, *630*, 2218–2225.
45. Vaqueiro, P.; Romero, M. L. *Chem. Commun.* **2007**, *16*, 3282–3284.
46. Vaqueiro, P.; Lucia Romero, M. *Inorg. Chem.* **2009**, *48*, 810–812.
47. Wu, T.; Bu, X.; Liao, P.; Wang, L.; Zheng, S. T.; Ma, R.; Feng, P. *J. Am. Chem. Soc.* **2012**, *134*, 3619–3622.
48. Lei, Z. X.; Zhu, Q. Y.; Zhang, X.; Luo, W.; Mu, W. Q.; Dai, J. *Inorg. Chem.* **2010**, *49*, 4385–4387.
49. Zhang, Y. P.; Zhang, X.; Mu, W. Q.; Luo, W.; Bian, G. Q.; Zhu, Q. Y.; Dai, J. *Dalton Trans.* **2011**, *40*, 9746–9751.
50. Shen, N. N.; Hu, B.; Cheng, C. C.; Zou, G. D.; Hu, Q. Q.; Du, C. F.; Li, J. R.; Huang, X. Y. *Cryst. Growth Des.* **2018**, *18*, 962–968.
51. Godfrey, P. D.; Raston, C. L.; Skelton, B. W.; Tolhurst, V. A.; White, A. H. *Chem. Commun.* **1997**, *5*, 2235–2236.
52. Nogai, S. D.; Schmidbaur, H. *Dalton Trans.* **2003**, 2488–2495.
53. Wang, Y. H.; Luo, W.; Jiang, J. B.; Bian, G. Q.; Zhu, Q. Y.; Dai, J. *Inorg. Chem.* **2012**, *51*, 1219–1221.
54. Zhang, X.; Pu, Y. Y.; You, L. S.; Bian, G. Q.; Zhu, Q. Y.; Dai, J. *Polyhedron* **2013**, *52*, 645–649.
55. Zhang, R.; Emge, T. J.; Zheng, C.; Li, J. *J. Mater. Chem. A* **2013**, *1*, 199–202.
56. Park, C.; Salm, R. J.; Ibers, J. A. *Angew. Chem. Int. Ed.* **1995**, *34*, 1879–1880.
57. Campbell, J.; Mercier, H. P. A.; Santry, D. P.; Suontamo, R. J.; Borrmann, H.; Schrobilgen, G. J. *Inorg. Chem.* **2001**, *40*, 233–254.
58. Krebs, B.; Brömmelhaus, A. *Angew. Chem. Int. Ed.* **1989**, *28*, 1682–1683.
59. Krebs, B.; Pohl, S. *Z. Naturforsch.* **1971**, *26b*, 853–854.
60. Krebs, B.; Pohl, S. *Z. Anorg. Allg. Chem.* **1976**, *424*, 265–272.
61. Ribes, M.; Olivier-Fourcade, J.; Philippot, E.; Maurin, M. *J. Solid State Chem.* **1973**, *8*, 195–205.
62. Philippot, E.; Ribes, M.; Lindquist, O. *Rev. Chim. Mineral.* **1971**, *8*, 477–489.
63. Eulenberger, G. *Acta Crystallogr.* **1974**, *B32*, 3059–3063.
64. Eulenberger, G. *Z. Naturforsch.* **1981**, *36b*, 521–523.
65. Eisenmann, B.; Hansa, J.; Schäfer, H. *Z. Naturforsch.* **1985**, *40b*, 450–457.
66. Eisenmann, B.; Hansa, J. *Z. Krist.* **1993**, *206*, 101–102.
67. Eisenmann, B.; Hansa, J. *Z. Krist.* **1993**, *205*, 325–326.
68. Sheldrick, W. S.; Schaaf, B. *Z. Naturforsch.* **1994**, *49b*, 655–659.
69. Sheldrick, W. S.; Schaaf, B. *Z. Naturforsch.* **1995**, *50b*, 1469–1475.
70. Campbell, J.; DiCiommo, D. P.; Mercier, H. P. A.; Pirani, A. M.; Schrobilgen, G. J.; Willuhn, M. *Inorg. Chem.* **1995**, *34*, 6265–6272.

71. Pirani, A. M.; Mercier, H. P. A.; Dixon, D. A.; Borrmann, H.; Schrobilgen, G. J. *Inorg. Chem.* **2001**, *40*, 4823–4829.
72. Park, C.-W.; Pell, M. A.; Ibers, J. A. *Inorg. Chem.* **1996**, *35*, 4555–4558.
73. Tsamourtzis, K.; Song, J.-H.; Bakas, T.; Freeman, A. J.; Trikalitis, P. N.; Kanatzidis, M. G. *Inorg. Chem.* **2008**, *47*, 11920–11929.
74. Eisenmann, B.; Schäfer, H. Z. *Anorg. Allg. Chem.* **1982**, *491*, 67–72.
75. Dhingra, S. S.; Haushalter, R. C. *Polyhedron* **1994**, *13*, 2775–2779.
76. Yaghi, O. M.; Sun, Z.; Richardson, D. A.; Groy, T. L. *J. Am. Chem. Soc.* **1994**, *116*, 807–808.
77. Pivan, J. Y.; Achak, O.; Louër, M.; Louër, D. *Chem. Mater.* **1994**, *6*, 827–830.
78. Achak, O.; Maunaye, M.; Louer, M.; Louer, D. *J. Alloys Compd.* **1995**, *219*, 111–115.
79. Yaghi, O. M.; Richardson, D. A.; Li, G.; Davis, C. E.; Groy, T. L. *Mater. Res. Soc. Symp. Proc.* **1995**, *371*, 15–19.
80. Bowes, C. L.; Lough, A. J.; Malek, A.; Ozin, G. A.; Petrov, S.; Young, D. *Chem. Ber.* **1996**, *129*, 283–287.
81. Ahari, H.; Garcia, A.; Kirby, S.; Ozin, G. A.; Young, D.; Lough, A. J. *J. Chem. Soc. Dalton Trans.* **1998**, 2023–2027.
82. Wang, K. Y.; Zhang, S.; Liu, H. W.; Cheng, L.; Wang, C. *Inorg. Chem.* **2019**, *58*, 12832–12842.
83. Bonhomme, F.; Kanatzidis, M. G. *Chem. Mater.* **1998**, *10*, 1153–1159.
84. Wachhold, M.; Kanatzidis, M. G. *Chem. Mater.* **2000**, *12*, 2914–2923.
85. Rangan, K. K.; Kanatzidis, M. G. *Inorg. Chim. Acta* **2004**, *357*, 4036–4044.
86. Fehlker, A.; Blachnik, R. Z. *Anorg. Allg. Chem.* **2001**, *627*, 1128–1134.
87. Fehlker, A.; Blachnik, R. Z. *Anorg. Allg. Chem.* **2001**, *627*, 411–418.
88. Wang, M.; Chen, W.; Cai, L.; Zhou, G.; Guo, G.; Huang, J. *J. Clust. Sci.* **2003**, *14*, 495–504.
89. Zhang, F.; Liu, X.; Zhou, J.; Yin, X. H.; He, J. *Monatsh. Chem.* **2011**, *142*, 763–768.
90. Zhang, F.; Yin, X. H.; Liu, X.; Zhou, J. Z. *Anorg. Allg. Chem.* **2011**, *637*, 1388–1393.
91. Liang, J. J.; Zhao, J.; Tang, W. W.; Zhang, Y.; Jia, D. X. *Inorg. Chem. Commun.* **2011**, *14*, 1023–1026.
92. Liu, G. N.; Di Lin, J.; Xu, Z. N.; Liu, Z. F.; Guo, G. C.; Huang, J. S. *Cryst. Growth Des.* **2011**, *11*, 3318–3322.
93. Mu, W. Q.; Zhu, Q. Y.; You, L. S.; Zhang, X.; Luo, W.; Bian, G. Q.; Dai, J. *Inorg. Chem.* **2012**, *51*, 1330–1335.
94. Xiao, H. P.; Zhou, J.; Wang, X. L.; Zou, H. H.; Zhao, R. Q. *Dalton Trans.* **2014**, *43*, 12306–12312.
95. Zhou, J.; Xiao, H.; Xiao, H. P.; Yang, T.; Zou, H. H.; Liu, X.; Zhao, R. Q.; Tang, Q. *Dalton Trans.* **2014**, *44*, 1350–1357.
96. Danker, F.; Näther, C.; Pielhofer, F.; Bensch, W. *Eur. J. Inorg. Chem.* **2017**, *2017*, 4317–4323.
97. Luo, H. Y.; Zhou, J. *Dalton Trans.* **2018**, *47*, 14751–14759.
98. Sun, X. L.; Zhu, Q. Y.; Qian, L. W.; Yu, L.; Ren, Z. G.; Bian, G. Q.; Dai, J. *Inorg. Chem. Commun.* **2014**, *46*, 130–133.
99. Sun, X. L.; Zhu, Q. Y.; Mu, W. Q.; Qian, L. W.; Yu, L.; Wu, J.; Bian, G. Q.; Dai, J. *Dalton Trans.* **2014**, *43*, 12582–12589.
100. Lin, J.; Fu, Z.; Zhang, J.; Zhu, Y.; Hu, D.; Li, D.; Wu, T. *Inorg. Chem.* **2017**, *56*, 3119–3122.
101. Xu, J.; Xue, L. J.; Le Hou, J.; Yin, Z. N.; Zhang, X.; Zhu, Q. Y.; Dai, J. *Inorg. Chem.* **2017**, *56*, 8036–8044.
102. Pfeiffer, P.; Lehnardt, R. *Ber. Dtsch. Chem. Ges.* **1903**, *36*, 3027–3030.
103. Forstner, A.; Muetterties, E. L. *Inorg. Chem.* **1965**, *5*, 552–554.
104. Komura, M.; Okawara, R. *Inorg. Nucl. Chem. Lett.* **1966**, *2*, 93–95.
105. Kobelt, D.; Paulus, E. F.; Scherer, H. *Acta Crystallogr. B* **1972**, *28*, 2323–2326.
106. Benno, R. H.; Fritchie, C. J. *J. Chem. Soc. Dalton Trans.* **1973**, *422*, 543–546.
107. Bart, J. C. J.; Daly, J. J. *J. Chem. Soc. Dalton Trans.* **1975**, *0*, 2063–2067.
108. Blecher, A.; Dräger, M.; Mathiasch, B. *Z. Naturforsch. B* **1981**, *36*, 1361–1367.
109. Haas, A.; Kutsch, H. J.; Krüger, C. *Chem. Ber.* **1987**, *120*, 1045–1048.
110. Berwe, H.; Haas, A. *Chem. Ber.* **1987**, *120*, 1175–1182.
111. Wraage, K.; Pape, T.; Herbst-Irmer, R.; Noltemeyer, M.; Schmidt, H. G.; Roesky, H. W. *Eur. J. Inorg. Chem.* **1999**, *1496*, 869–872.
112. Merzweiler, K.; Weisse, L. *Z. Naturforsch. B* **1990**, *45b*, 971–978.
113. Merzweiler, K.; Kraus, H. Z. *Naturforsch. B* **1994**, *49b*, 621–626.
114. Harker, R. M.; Mahon, M. F.; Molloy, K. C. *Main Group Met. Chem.* **1996**, *270*, 29–38.
115. Kraus, H.; Merzweiler, K. Z. *Naturforsch. B* **1993**, *48b*, 1009–1012.
116. Pöhlker, C.; Schellenberg, I.; Pöttgen, R.; Dehnen, S. *Chem. Commun.* **2010**, *46*, 2605–2607.
117. You, Z.; Bergunde, J.; Gerke, B.; Poettgen, R.; Dehnen, S. *Inorg. Chem.* **2014**, *53*, 12512–12518.
118. Ando, W.; Kadowaki, T.; Kabe, Y. *Angew. Chem. Int. Ed.* **1992**, *31*, 59–61.
119. Unno, M.; Kawai, Y.; Shioyama, H.; Matsumoto, H. *Organometallics* **1997**, *16*, 4428–4434.
120. Unno, M.; Ishii, D.; Matsumoto, H. *Bull. Chem. Soc. Jpn.* **1999**, *72*, 2469–2473.
121. Ramaker, G.; Saak, W.; Haase, D.; Weidenbruch, M. *Organometallics* **2003**, *22*, 5212–5216.
122. Ando, W.; Kadowaki, T.; Watanabe, A.; Choi, N.; Kabe, Y.; Erata, T.; Ishii, M. *Nippon Kagaku Kaishi* **1994**, *3*, 214–223.
123. Herzog, U.; Rheinwald, G. *J. Organomet. Chem.* **2001**, *628*, 133–143.
124. Herzog, U.; Borrmann, H. *J. Organomet. Chem.* **2003**, *675*, 42–47.
125. Varga, R. A.; Silvestru, C. *Acta Crystallogr., Sect. E: Struct. Rep. Online* **2007**, *63*, 2789.
126. Hassanzadeh Fard, Z.; Xiong, L.; Müller, C.; Holyriska, M.; Dehnen, S. *Chem. A Eur. J.* **2009**, *15*, 6595–6604.
127. Heimann, S.; Holyriska, M.; Dehnen, S. *Chem. Commun.* **2011**, *47*, 1881–1883.
128. Heimann, S.; Thiele, G.; Dehnen, S. *J. Organomet. Chem.* **2016**, *813*, 36–40.
129. Hassanzadeh Fard, Z.; Holyriska, M.; Dehnen, S. *Inorg. Chem.* **2010**, *49*, 5748–5752.
130. Eußner, J. P.; Barth, B. E. K.; Leusmann, E.; You, Z.; Rinn, N.; Dehnen, S. *Chem. A Eur. J.* **2013**, *19*, 13792–13802.
131. Rinn, N.; Eußner, J. P.; Kaschuba, W.; Xie, X.; Dehnen, S. *Chem. A Eur. J.* **2016**, *22*, 3094–3104.
132. Eußner, J. P.; Kusche, R. O.; Dehnen, S. *Chem. Eur. J.* **2015**, *21*, 12376–12388.
133. Hanau, K.; Rinn, N.; Argentari, M.; Dehnen, S. *Chem. A Eur. J.* **2018**, *24*, 11711–11716.
134. You, Z.; Dehnen, S. *Inorg. Chem.* **2013**, *52*, 12332–12334.
135. Leusmann, E.; Wagner, M.; Rosemann, N. W.; Chatterjee, S.; Dehnen, S. *Inorg. Chem.* **2014**, *53*, 4228–4233.
136. Barth, B. E. K.; Tkachenko, B. A.; Eußner, J. P.; Schreiner, P. R.; Dehnen, S. *Organometallics* **2014**, *33*, 1678–1688.
137. Barth, B. E. K.; Leusmann, E.; Harms, K.; Dehnen, S. *Chem. Commun.* **2013**, *49*, 6590–6592.
138. Leusmann, E.; Schneck, F.; Dehnen, S. *Organometallics* **2015**, *34*, 3264–3271.
139. Leusmann, E.; Geringer, E.; Weinert, B.; Dehnen, S. *Dalton Trans.* **2016**, *45*, 15298–15302.
140. Leusmann, E.; Rosemann, N. W.; Weinert, B.; Chatterjee, S.; Dehnen, S. *Eur. J. Inorg. Chem.* **2016**, *2016*, 5300–5304.
141. Geringer, E.; Leusmann, E.; Tambornino, F.; Gerhard, M.; Koch, M.; Dehnen, S. *Chem. Commun.* **2020**, *56*, 4769–4772.
142. Rinn, N.; Berndt, J.; Kreher, A.; Hrdina, R.; Reinmuth, M.; Schreiner, P. R.; Dehnen, S. *Organometallics* **2016**, *35*, 3215–3220.
143. Berndt, J.; Engel, A.; Hrdina, R.; Dehnen, S.; Schreiner, P. *Organometallics* **2019**, *38*, 320–335.

144. Engel, A.; Dornsiepen, E.; Dehnen, S. *Inorg. Chem. Front.* **2019**, *6*, 1973–1976.
145. Engel, A.; Dehnen, S. *Eur. J. Inorg. Chem.* **2019**, 4313–4320.
146. Engel, A.; Dewald, H.; Reuter, A.; Klippstein, J.; Dehnen, S. *Eur. J. Inorg. Chem.* **2020**, 2809–2815.
147. Halvagiar, M. R.; Hassanzadeh Fard, Z.; Dehnen, S. *Chem. Commun.* **2010**, *46*, 4716–4718.
148. Hassanzadeh Fard, Z.; Halvagiar, M. R.; Dehnen, S. *J. Am. Chem. Soc.* **2010**, *132*, 2848–2849.
149. Halvagiar, M. R.; Hassanzadeh Fard, Z.; Dehnen, S. *Chem. A Eur. J.* **2011**, *17*, 4371–4374.
150. You, Z.; Fenske, D.; Dehnen, S. *Dalton Trans.* **2013**, *42*, 8179–8182.
151. Zhong, M.; Yang, Z.; Yi, Y.; Zhang, D.; Sun, K.; Roesky, H. W.; Yang, Y. *Dalton Trans.* **2015**, *44*, 19800–19804.
152. Keuter, J.; Schwedtmann, K.; Hepp, A.; Bergander, K.; Janka, O.; Doerenkamp, C.; Eckert, H.; Mück-Lichtenfeld, C.; Lips, F. *Angew. Chem. Int. Ed.* **2017**, *56*, 13866–13871.
153. Schwedtmann, K.; Hepp, A.; Schwedtmann, K.; Weigand, J. J.; Lips, F. *Eur. J. Inorg. Chem.* **2019**, *2*, 4719–4726.
154. Dakternieks, D.; Jurkschat, K.; Wu, H.; Tiekink, E. R. T. *Organometallics* **1993**, *12*, 2788–2793.
155. Herzog, U.; Borrmann, H. *J. Organomet. Chem.* **2003**, *681*, 5–11.
156. Hassanzadeh Fard, Z.; Müller, C.; Harmening, T.; Pöttgen, R.; Dehnen, S. *Angew. Chem. Int. Ed.* **2009**, *48*, 4441–4444.
157. Eußner, J. P.; Barth, B. E. K.; Justus, U.; Rosemann, N. W.; Chatterjee, S.; Dehnen, S. *Inorg. Chem.* **2015**, *54*, 22–24.
158. Rosemann, N. W.; Eußner, J. P.; Beyer, A.; Koch, S. W.; Volz, K.; Dehnen, S.; Chatterjee, S. *Science* **2016**, *352*, 1301–1305.
159. Rosemann, N. W.; Eußner, J. P.; Dornsiepen, E.; Chatterjee, S.; Dehnen, S. *J. Am. Chem. Soc.* **2016**, *138*, 16224–16227.
160. Dornsiepen, E.; Dobener, F.; Chatterjee, S.; Dehnen, S. *Angew. Chem. Int. Ed.* **2019**, *58*, 17041–17046.
161. Klee, B. D.; Dornsiepen, E.; Stellhorn, J. R.; Paulus, B.; Hosokawa, S.; Dehnen, S.; Pilgrim, W. C. *Phys. Status Solidi B* **2018**, *255*, 1800083.
162. Klee, B. D.; Paulus, B.; Hosokawa, S.; Wharmby, M. T.; Dornsiepen, E.; Dehnen, S.; Pilgrim, W. C. *J. Phys. Commun.* **2020**, *4*, 035004.
163. Hanau, K.; Schwan, S.; Schäfer, M. R.; Müller, M. J.; Dues, C.; Rinn, N.; Sanna, S.; Chatterjee, S.; Mollenhauer, D.; Dehnen, S. *Angew. Chem.* **2021**, *133*, 1196–1206.
164. Dornsiepen, E.; Dobener, F.; Mengel, N.; Lenchuk, O.; Dues, C.; Sanna, S.; Mollenhauer, D.; Chatterjee, S.; Dehnen, S. *Adv. Opt. Mater.* **2019**, *7*, 1801793.
165. Eußner, J. P.; Dehnen, S. *Chem. Commun.* **2014**, *50*, 11385–11388.
166. Dornsiepen, E.; Eußner, J. P.; Rosemann, N. W.; Chatterjee, S.; Dehnen, S. *Inorg. Chem.* **2017**, *56*, 11326–11335.
167. Halvagiar, M. R.; Hassanzadeh Fard, Z.; Xiong, L.; Dehnen, S. *Inorg. Chem.* **2009**, *48*, 7373–7377.
168. Dornsiepen, E.; Weigand, F.; Dehnen, S. *Chem. A Eur. J.* **2019**, *25*, 2486–2490.
169. Hauser, R.; Merzweiler, K. *Z. Anorg. Allg. Chem.* **2007**, *628*, 905–906.
170. Rinn, N.; Hanau, K.; Guggolz, L.; Rinn, A.; Chatterjee, S. *Z. Anorg. Allg. Chem.* **2017**, *643*, 1508–1512.
171. Rinn, N.; Guggolz, L.; Lange, J.; Chatterjee, S.; Block, T. *Chem. A Eur. J.* **2018**, *24*, 5840–5848.
172. Rinn, N.; Guggolz, L.; Gries, K.; Volz, K.; Senker, J.; Dehnen, S. *Chem. A Eur. J.* **2017**, *23*, 15607–15611.
173. Hanau, K.; Rinn, N.; Dehnen, S. *Inorg. Chem.* **2020**, *59*, 198–202.
174. Hassanzadeh Fard, Z.; Clérac, R.; Dehnen, S. *Chem. A Eur. J.* **2010**, *16*, 2050–2053.
175. Puff, H.; Braun, K.; Franken, S.; Kök, T. R.; Schuh, W. *J. Organomet. Chem.* **1987**, *335*, 167–178.
176. Block, E.; Ofori-Okai, G. *Inorg. Chim. Acta* **1991**, *190*, 5–6.
177. Briand, G. G.; Decken, A.; Finniss, M. C.; Gordon, A. D.; Hughes, N. E.; Scott, L. M. *Polyhedron* **2012**, *33*, 171–178.
178. Eichhöfer, A. *Eur. J. Inorg. Chem.* **2005**, *4*, 1683–1688.
179. Herzog, U.; Böhme, U.; Roewer, G.; Rheinwald, G.; Lang, H. *J. Organomet. Chem.* **2000**, *602*, 193–207.
180. Herzog, U.; Böhme, U.; Rheinwald, G. *J. Organomet. Chem.* **2001**, *627*, 144–152.
181. Ackerhans, C.; Roesky, H. W.; Noltemeyer, M. *Organometallics* **2001**, *20*, 1282–1284.
182. Matsumoto, T.; Matsui, Y.; Ito, M.; Tatsumi, K. *Chem. Asian J.* **2008**, *3*, 607–613.
183. Schmidtke, M.; Krautscheid, H. *Z. Anorg. Allg. Chem.* **2006**, *632*, 1399–1401.
184. Lin, Y.; Massa, W.; Dehnen, S. *J. Am. Chem. Soc.* **2012**, *134*, 4497–4500.
185. Lin, Y.; Massa, W.; Dehnen, S. *Chem. A Eur. J.* **2012**, *18*, 13427–13434.
186. Santner, S.; Yogendra, S.; Weigand, J. J.; Dehnen, S. *Chem. A Eur. J.* **2017**, *23*, 1999–2004.
187. Guo, J. Y.; Xi, H. W.; Nowik, I.; Herber, R. H.; Li, Y.; Lim, K. H.; So, C. W. *Inorg. Chem.* **2012**, *51*, 3996–4001.
188. Traut, S.; von Hänisch, C.; Hähnel, A. P.; Stahl, S. *Chem. Commun.* **2012**, *48*, 6984–6986.
189. Martin, T. M.; Wood, P. T.; Kolis, J. W. *Inorg. Chem.* **1994**, *33*, 1587–1588.
190. Warren, C. J.; Dhingra, S. S.; Ho, D.; Haushalter, R. C.; Bocarsly, A. B. *Inorg. Chem.* **1994**, *33*, 2709–2710.
191. DeGroot, M. W.; Corrigan, J. F. *J. Chem. Soc. Dalton Trans.* **2000**, *666*, 1235–1236.
192. Chen, J. X.; Tang, X. Y.; Ren, Z. G.; Zhang, Y.; Lang, J. P. *Eur. J. Inorg. Chem.* **2009**, *5*, 38–41.
193. Yang, Z.; Ma, X.; Oswald, R. B.; Roesky, H. W.; Cui, C.; Schmidt, H. G.; Noltemeyer, M. *Angew. Chem. Int. Ed.* **2006**, *45*, 2277–2280.
194. Feng, M. L.; Xiong, W. W.; Ye, D.; Li, J. R.; Huang, X. Y. *Chem. Asian J.* **2010**, *5*, 1817–1823.
195. Peters, B.; Krampe, C.; Klärner, J.; Dehnen, S. *Chem. A Eur. J.* **2020**, *26*, 16683–16689.

4.05 Piezoelectric and ferroelectric materials: Fundamentals, recent progress, and applications

Zenghui Liu^a, Hua Wu^b, Wei Ren^a, and Zuo-Guang Ye^c, ^aElectronic Materials Research Laboratory, Key Laboratory of the Ministry of Education & International Center for Dielectric Research, School of Electronic Science and Engineering, Xi'an Jiaotong University, Xi'an, China; ^bDepartment of Applied Physics, Donghua University, Shanghai, China; and ^cDepartment of Chemistry and 4D LABS, Simon Fraser University, Burnaby, BC, Canada

© 2023 Elsevier Ltd. All rights reserved.

4.05.1	Introduction	136
4.05.1.1	General introduction to piezoelectricity and ferroelectricity	136
4.05.1.1.1	Piezoelectric materials	136
4.05.1.1.2	Ferroelectric materials	137
4.05.1.2	Characteristic properties and basic equations	137
4.05.1.2.1	Piezoelectric equations	137
4.05.1.2.2	Curie temperature and Curie-Weiss law	138
4.05.1.2.3	Dielectric hysteresis loop and ferroelectric domain	138
4.05.1.2.4	Effects of crystal symmetry	139
4.05.1.3	Basic theories of ferroelectrics	140
4.05.1.3.1	Phenomenological theory	140
4.05.1.3.2	Soft-mode theory	142
4.05.1.4	Classification of ferroelectric and piezoelectric materials	143
4.05.2	Lead zirconate-titanate (PZT) ceramics	143
4.05.2.1	The perovskite structure	143
4.05.2.2	Phase diagram of PZT and the morphotropic phase boundary	143
4.05.2.3	Origin of the high piezoelectric response in PZT near the MPB region	145
4.05.2.3.1	Conventional pictures of MPB	145
4.05.2.3.2	Monoclinic phase and high piezoelectricity	145
4.05.2.3.3	Meso- to nanoscale description of the MPB	145
4.05.2.4	Effect of chemical modifications	146
4.05.2.4.1	Donor doping	146
4.05.2.4.2	Acceptor doping	146
4.05.2.4.3	Isovalent substitutions	147
4.05.2.4.4	Complex doping	147
4.05.3	Relaxor-based piezoelectric single crystals	147
4.05.3.1	Relaxor ferroelectrics: An introduction	147
4.05.3.2	Solid solutions between relaxors and ferroelectric PbTiO ₃	148
4.05.3.3	Relaxor-PT piezoelectric single crystals: A new era of piezoelectric materials	148
4.05.3.4	Growth of relaxor-based piezoelectric single crystals	148
4.05.3.4.1	The flux method	149
4.05.3.4.2	Top-seeded solution growth method	149
4.05.3.4.3	The solid-state crystal growth method	150
4.05.3.4.4	The modified Bridgman method	150
4.05.3.5	Tailoring the properties of relaxor-based piezoelectric single crystals	150
4.05.3.6	Property anisotropy and domain engineering	151
4.05.3.7	Origin of the ultrahigh piezoelectric response in relaxor-based piezoelectric single crystals	151
4.05.3.7.1	Macroscopic explanation: MPB facilitating polarization rotation	151
4.05.3.7.2	Meso- to nanoscopic understanding: Roles of local polar regions	153
4.05.3.8	Perspectives and challenges for relaxor-based piezoelectric single crystals	153
4.05.4	Lead-free perovskite piezoelectric materials	154
4.05.4.1	Restriction of lead components in applications	154
4.05.4.2	Lead-free piezoelectric materials: A historical overview	154
4.05.4.3	Approaches to obtain lead-free piezoelectric materials with better performance	154
4.05.4.3.1	Chemical modification and phase boundary engineering	154
4.05.4.3.2	Microstructure engineering	155
4.05.4.3.3	Growth of single crystals and preparation of textured ceramics	155
4.05.4.4	Progress in main lead-free piezoelectric material systems	155
4.05.4.4.1	BaTiO ₃ -based systems	155
4.05.4.4.2	(Bi _{1/2} Na _{1/2})TiO ₃ -based systems	156

4.05.4.4.3	(K,Na)NbO ₃ -based systems	157
4.05.4.4.4	BiFeO ₃ -based systems	158
4.05.4.5	Perspectives and challenges of lead-free perovskite piezoelectric materials	158
4.05.5	High-temperature piezoelectric materials	159
4.05.5.1	Need for high-temperature piezoelectric materials	159
4.05.5.2	High-temperature piezoelectric single crystals	159
4.05.5.2.1	Quartz (SiO ₂)	159
4.05.5.2.2	Tourmaline	159
4.05.5.2.3	LiNbO ₃ and LiTaO ₃	160
4.05.5.2.4	Lithium tetraborate (Li ₂ B ₄ O ₇)	160
4.05.5.2.5	AlN	160
4.05.5.2.6	Langasite family	160
4.05.5.2.7	Quartz analogs	160
4.05.5.2.8	Rare earth-calcium oxyborate	160
4.05.5.3	High-temperature polycrystalline piezoelectric materials	161
4.05.5.3.1	Perovskite system	161
4.05.5.3.2	Tungsten bronze system	161
4.05.5.3.3	Bismuth-based layered structure	161
4.05.5.3.4	Layered perovskite structure	161
4.05.5.4	Perspectives and challenges of high-temperature piezoelectric materials	161
4.05.6	Textured piezoelectric ceramics	163
4.05.6.1	Motivation for developing textured ceramics	163
4.05.6.2	Progress in textured ceramics	163
4.05.6.2.1	Development of textured ceramics—A brief overview	163
4.05.6.2.2	Texturing techniques by TGG and RTGG	164
4.05.6.2.3	Mechanism of templated grain growth	165
4.05.6.2.4	Selection of templates	166
4.05.6.2.5	Piezoelectric properties of textured ceramics	166
4.05.6.3	Summary and perspectives	166
4.05.7	Applications of piezo-/ferroelectric materials: Present and future	167
4.05.7.1	General introduction to piezoelectric devices and application	167
4.05.7.2	Medical and health care	167
4.05.7.3	Industrial manufacturing, processing and detection	168
4.05.7.4	Automotive	168
4.05.7.5	Consumer electronics	168
4.05.7.6	Internet of Things	168
Acknowledgments		168
References		169

Abstract

Piezo-/ferroelectric materials form an important class of functional materials that convert energies between electrical and mechanical energies, thus are critical for numerous applications. This chapter starts with an introduction of the piezo-/ferroelectric materials, followed by a detailed discussion on the recent progress on lead zirconate titanate (PZT)-based ceramics, relaxor-based piezoelectric single crystals, lead-free perovskite piezoelectric materials, high-temperature piezoelectric materials and textured piezoelectric ceramics. At last, the current and potential applications of piezo-/ferroelectric materials are presented.

4.05.1 Introduction

4.05.1.1 General introduction to piezoelectricity and ferroelectricity

4.05.1.1.1 Piezoelectric materials

Electric charges develop on the surface of a dielectric crystal when an electric field is applied to it. In some dielectrics, charges can also be induced under mechanical pressure. Materials with such a property are called piezoelectrics and this phenomenon is known as direct piezoelectric effect (Fig. 1A), which was first discovered by French physicists Pierre Curie and Jacques Curie (the Curie brothers) in 1880. They found that certain materials, such as quartz crystal, can generate electrical charges upon pressure with its

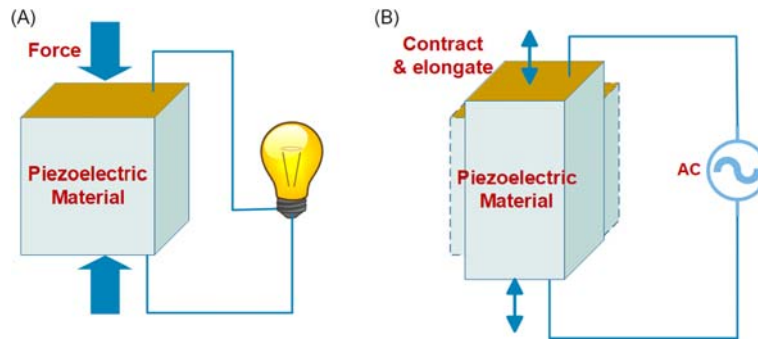


Fig. 1 Diagrams illustrating (A) direct piezoelectric effect and (B) converse piezoelectric effect.

density being proportional to the external mechanical forces. The piezoelectric materials can also be elongated or contracted elastically by an external electric field, which is called converse piezoelectric effect (discovered by Gabriel Lippmann in 1881), and the deformation is proportional to the intensity of the external electric field (Fig. 1B). Therefore, piezoelectric materials are functional materials capable of converting mechanical energy into electrical energy and vice versa.^{1,2}

It was not until World War I that piezoelectric materials came into practical use. Taking advantage of the piezoelectric effect, Paul Langevin and coworkers designed the first ultrasonic submarine detector (known as the Langevin sonar) in 1917, using a quartz crystal to transmit ultrasonic pulses for underwater detecting. The Langevin sonar played a very important role in the Atlantic campaign during World War II, and also became the most important demonstrations in the development of piezoelectric materials. It is the successful application of the Langevin sonar system that unraveled the curtain of modern exploration of high-performance piezoelectric materials.³

4.05.1.1.2 Ferroelectric materials

Piezoelectric materials have entered a new era following the discovery of ferroelectricity and ferroelectric materials. A ferroelectric material has a built-in spontaneous electric polarization that can be reoriented by applying an external electric field to it. This concept was firstly conjectured by Schrödinger in the early 1910s as an analogy to the earlier-known ferromagnetism. The discovery of the first ferroelectric material can be traced back to 1655 when Rochelle salt (sodium potassium tartrate tetrahydrate, $\text{KNaC}_4\text{H}_4\text{O}_6 \cdot 4\text{H}_2\text{O}$) was first prepared by pharmacist Elie Seignette in La Rochelle, France, for medicinal purposes. Late in the 19th century, the physical properties of Rochelle salt began to attract more interest. The pyroelectricity (property of generating electric charges with change of temperature) of Rochelle salt was firstly noticed by Brewster in 1824, and the first systematic studies of its piezoelectricity were reported by the Curie brothers in the 1880s. It was not until 1921 that ferroelectricity was first discovered in Rochelle salt by Joseph Valasek who found a hysteretic relation when he measured the polarization as a function of an applied AC electric field. Rochelle salt is fragile and water-soluble, which makes it unsuitable for practical applications as a functional material.³

During World War II, new piezoelectric materials were found and investigated to improve the sensitivity of submarine detection sonar. It was at that time that polycrystalline barium titanate (BaTiO_3 , BT) was developed independently in the United States, the USSR, and Japan, which became the first man-made perovskite ferroelectric material. BT ceramics exhibit robust ferroelectricity and much better piezoelectricity ($\sim 191 \text{ pC} \cdot \text{N}^{-1}$) than that of the quartz crystal ($\sim 2 \text{ pC} \cdot \text{N}^{-1}$). The successful development of BT has led to a wide range of industrial and commercial applications of ferroelectric piezoelectric materials.^{1,4} The development of BT and other lead-free piezo-/ferroelectric materials will be discussed in detail in Section 4.05.4.

The demonstration of ferroelectricity in BT has stimulated the study of other oxide perovskites. One of the most important discoveries was lead zirconate titanate ($\text{Pb}(\text{Zr}_{1-x}\text{Ti}_x)\text{O}_3$, abbreviated as PZT) solid solution by Jaffe and coworkers in 1954.⁵ PZT ceramics exhibit an attractive electromechanical performance ($\sim 220 \text{ pC} \cdot \text{N}^{-1}$) and a relatively high Curie temperature ($\sim 380^\circ\text{C}$) with compositions near the morphotropic phase boundary (MPB) region ($x \approx 0.46\text{--}0.51$).^{1,6} Commercially, PZT ceramics are usually doped with different dopants to modify its properties depending on the requirements of applications.^{1,4} After about 70 years of research and development, PZT-based ceramics have become the most widely used and best understood piezoelectric materials, and are still subject of intensive research. The developments of PZT-based ceramics will be described in Section 4.05.2.

Another milestone in the development of piezoelectric materials is the discovery of relaxor-based piezoelectric single crystals of the complex perovskite structure. A good example is the $\text{Pb}(\text{Mg}_{1/3}\text{Nb}_{2/3})\text{O}_3\text{-PbTiO}_3$ (PMN-PT) and $\text{Pb}(\text{Zn}_{1/3}\text{Nb}_{2/3})\text{O}_3\text{-PbTiO}_3$ (PZN-PT) solid solutions with compositions near the MPB region, which show remarkably high piezoelectric coefficients ($d_{33} > 2000 \text{ pC} \cdot \text{N}^{-1}$) and large electromechanical coupling factors ($k_{33} > 90\%$).⁷⁻¹⁰ By chemical modification, the piezoelectric coefficients and other physical properties of relaxor-based piezoelectric single crystals could be further improved.^{9,11-16} The recent developments of relaxor-based piezoelectric single crystals will be discussed in Section 4.05.3.

4.05.1.2 Characteristic properties and basic equations

4.05.1.2.1 Piezoelectric equations

Piezoelectricity is quantified by the piezoelectric equations, which describe the linear relations between the electrical and mechanical parameters including electric displacement (D), electric field (E), strain (S) and stress (T). Four forms of piezoelectric equations

can be written by considering any of the two above-mentioned parameters as independent variables. Eq. (1) shows the most common representation as:

$$\mathbf{D} = \mathbf{d}\mathbf{T} + \boldsymbol{\epsilon}^T \mathbf{E}, \quad (1a)$$

$$\mathbf{S} = \mathbf{s}^E \mathbf{T} + \mathbf{d}\mathbf{E}, \quad (1b)$$

where \mathbf{d} is the piezoelectric coefficient, $\boldsymbol{\epsilon}^T$ represents the dielectric permittivity measured at constant (or zero) stress, and \mathbf{s}^E represents the elastic compliance coefficient measured at a constant (or zero) electric field. Here \mathbf{S} , \mathbf{T} and \mathbf{E} are second-rank tensors, and \mathbf{D} and \mathbf{E} are vectors (first-rank tensors). So, \mathbf{d} is a third-rank tensor, and \mathbf{s}^E is a fourth-rank tensor.

We consider the simplest case that the electric displacement in piezoelectric materials is only induced under stress (see Fig. 1A), and then the direct piezoelectric effect can be expressed as,

$$D_i = d_{ijk} T_{jk}, \quad (2a)$$

where subscripts i, j, k take the values 1, 2, 3, and define the three spatial dimensions of a crystal. For the converse piezoelectric effect (see Fig. 1B), the material is strained under an applied electric field, and Eq. (1b) can be written as:

$$S_{ij} = d_{kij} E_k. \quad (2b)$$

The two piezoelectric coefficient d for the direct and converse piezoelectric effects are thermodynamically equivalent (i.e., $d_{ijk} = d_{kij}$), and are generally represented in the units of $\text{pC} \cdot \text{N}^{-1}$ and $\text{pm} \cdot \text{V}^{-1}$, respectively.

Due to the symmetry relation, the piezoelectric tensors are more commonly written by replacing the subscripts $11 \rightarrow 1$, $22 \rightarrow 2$, $33 \rightarrow 3$, $23/32 \rightarrow 4$, $13/31 \rightarrow 5$, $12/21 \rightarrow 6$, as:

$$D_i = d_{im} T_m, \quad (2c)$$

$$S_m = d_{im} E_i, \quad (2d)$$

where subscripts i takes the values 1, 2, 3, and m takes the values 1, 2, ..., 6. This notation is known as Voigt notation, which reduces the order of higher rank tensors to a lower order matrix form. Here, $m = 1, 2, 3$, and $m = 4, 5, 6$ represent linear and shear components of the strain, respectively. For practical applications, a high piezoelectric coefficient is desired.

In addition to the piezoelectric coefficient, the electromechanical coupling factor is another important parameter describing the conversion efficiency between the electrical and the mechanical energies, as:

$$k^2 = \frac{\text{electrical energy converted to mechanical energy}}{\text{input electrical energy}} \quad (3)$$

$$k^2 = \frac{\text{mechanical energy converted to electrical energy}}{\text{input mechanical energy}}.$$

It should be noted that all dielectric materials can deform under an electric field due to electrostrictive effect. The differences between piezoelectric and electrostrictive effects are as follows: (i) the strain induced by the electrostrictive effect is proportional to the second power of the applied electric field, while the piezoelectric effect is a linear effect; and (ii) dielectric materials with only electrostrictive effect but without piezoelectric effect cannot produce polarization and charges under stress.

4.05.1.2.2 Curie temperature and Curie-Weiss law

The Curie temperature (T_C) of a ferroelectric material is the temperature at which the material undergoes the phase transition from a low-temperature ferroelectric phase to a high-temperature paraelectric phase upon heating. Ferroelectricity and piezoelectricity disappear at T_C . Therefore, a higher T_C is desired to achieve better temperature stability and a wider temperature range for applications. T_C can be determined by measuring the temperature-dependent dielectric constant, which typically exhibits a very sharp maximum at T_C . Above T_C , the dielectric constant of a ferroelectric usually follows the Curie-Weiss law,

$$\epsilon = \frac{C}{T - T_0}, \quad (4)$$

where C and T_0 are the Curie-Weiss constant and Curie-Weiss temperature, respectively.

4.05.1.2.3 Dielectric hysteresis loop and ferroelectric domain

When a sufficiently high electric field is applied to a ferroelectric crystal, the polarization P vs electric field E (P - E) hysteresis loop can be displayed, as shown in Fig. 2. The P - E loop gives the most direct evidence of ferroelectricity. It reflects the switching process of the polarization and provides information on ferroelectric property. Before applying an electric field, a ferroelectric crystal exhibits nearly zero net polarization as differently oriented dipoles typically cancel out. When the electric field increases positively, the polarization increases as the dipoles are aligned along the field direction, and reaches saturation at a sufficiently large field. When the applied electric field is reduced to zero, a non-zero polarization is retained, represented by the length of OA, which is defined as the remanent polarization P_r . The spontaneous polarization P_s can be obtained by extrapolation from the saturated polarization.

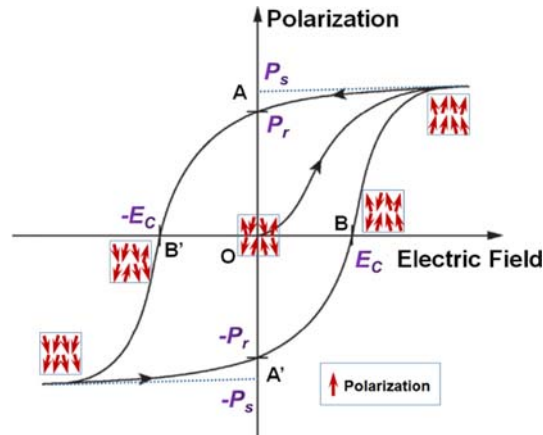


Fig. 2 Polarization P vs electric field E (P - E) hysteresis loop displayed in ferroelectric materials.

Another important parameter given by the P - E loop is the coercive field E_c , shown by the length of OB , which determines the minimum field needed to reverse the polarization.

Domains, which are defined as the regions with the same spontaneous polarization direction, form when a ferroelectric crystal is cooled below T_C with the spontaneous polarizations aligning along the symmetry-allowed directions. Generally, a multidomain structure is favored to a single domain state so as to minimize the free energy of the system, which includes electrostatic and elastic energies. Due to the multidomain structure and domain clamping effect, P_r is usually smaller than P_s , and this phenomenon becomes more significant in polycrystalline materials. The piezoelectric properties are also closely related to the domain structures and their configurations. Detailed explanations will be given in [Sections 4.05.2.3, 4.05.3.6, and 4.05.3.7](#).

4.05.1.2.4 Effects of crystal symmetry

The piezoelectric and ferroelectric properties of a material are determined by its crystal symmetry. For instance, piezoelectric effect can only be found in crystals of non-centrosymmetric structures, and ferroelectricity is only permitted in materials of non-centrosymmetric and polar structures. [Table 1](#) shows the classification of crystallographic point groups in terms of symmetry, polarity and properties. According to the principle of crystallographic symmetry, there are 32 point groups for all crystals, and only 21 of them are non-centrosymmetric, which have one or more polar axis (axes). Among them, except for the cubic 432 point group, the remaining 20 classes are piezoelectric points groups. Of the 20 piezoelectric groups, 10 groups have a unique polar axis, which allow a spontaneous polarization, and those crystals belong to the pyroelectric family. Ferroelectric crystals are a subclass of the pyroelectric family, with switchable spontaneous polarization under an electric field. [Fig. 3](#) summarizes the relation of different kinds of materials.

As for a ferroelectric ceramic, it has a zero net polarization due to the random orientation of the grains (and multidomains) in its original state (see [Fig. 4A](#)). By poling (applying a strong temporary electric field to align the polarization in each grain), domains align parallel to the field as much as possible. Once the field is removed, some of them will relax back while most of the domains remain locked into a configuration of near alignment, leading to a non-zero remanent polarization. A simple diagram of this poling

Table 1 Classification of crystallographic point groups in terms of symmetry and polarity.

Crystal systems	Crystal symmetry classes							
	Centrosymmetric classes		Non-centrosymmetric classes					
			Non-piezoelectric classes		Piezoelectric classes			
					Non-polar classes		Polar classes (Pyroelectric or ferroelectric)	
Cubic	$m\bar{3}m$	$m\bar{3}$	432	$\bar{4}3m$	23			
Hexagonal	$6/mmm$	$6/m$		622	$\bar{6}$	$\bar{6}m2$	6	$6mm$
Tetragonal	$4/mmm$	$4/m$		422	$\bar{4}$	$\bar{4}2m$	4	$4mm$
Trigonal	$3m$	$\bar{3}$		32			3	$3m$
Orthorhombic	mmm			222			$mm2$	
Monoclinic	$2/m$						2	m
Triclinic	$\bar{1}$						1	

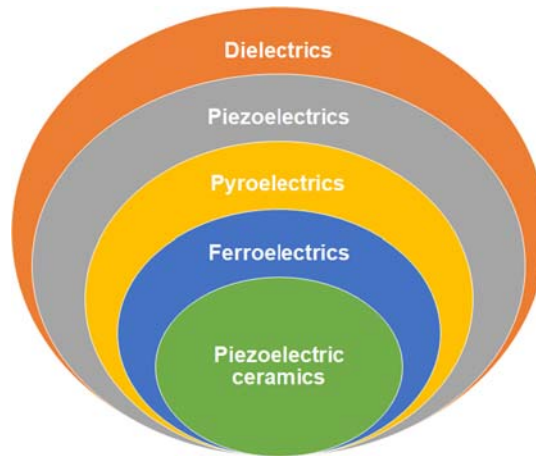


Fig. 3 Hierarchical relationship among the various subgroups of dielectric materials.

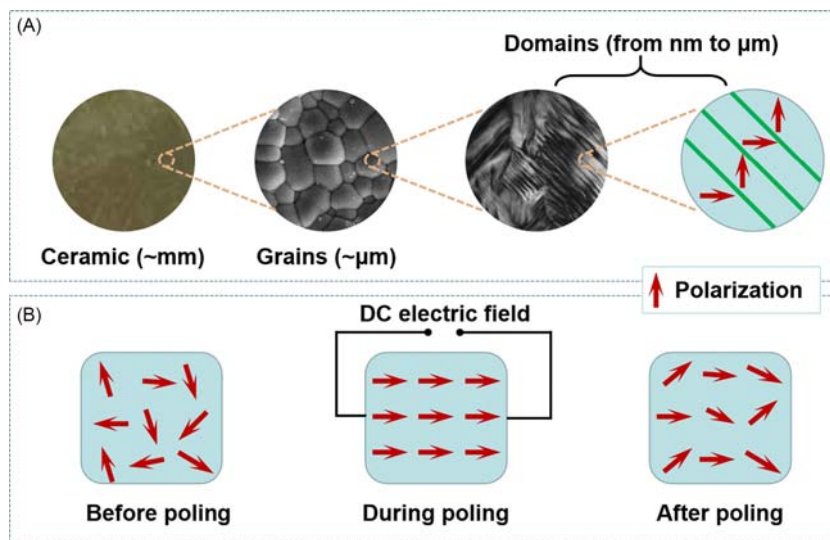


Fig. 4 Ferroelectric domains: (A) grains and domains in piezoelectric ceramics, and (B) domain reorientation by poling.

process is shown in Fig. 4B. By analogy to the class $6mm$, poled ferroelectric ceramics become piezoelectric with symmetry of ∞mm (cylindrical polar symmetry). For the dielectric, piezoelectric, and elastic constants, a six-fold symmetry axis is equivalent to the infinite-fold axis.

4.05.1.3 Basic theories of ferroelectrics

4.05.1.3.1 Phenomenological theory

The physical properties of ferroelectrics can be well described by the Landau-Devonshire phenomenological theory.^{17–19} This theory gives the general thermodynamic descriptions of ferroelectrics. Though it does not involve any microscopic mechanism, it provides a basic mathematical framework to describe the critical phenomena in ferroelectrics and can lead to very reasonable general conclusions.

According to this theory, if the polarization P is selected as the order parameter, the Landau expansion of the free energy density in powers of P can be written as:

$$G(TP) = G_0(T) + \frac{1}{2}a'(T)P^2 + \frac{1}{4}b'(T)P^4 + \frac{1}{6}c'(T)P^6 + \dots, \quad (5)$$

where a' , b' , c' ... are the temperature-dependent power series coefficients of the free energy density. In this expression, only the even terms appear, since G is invariant with the direction of the polarization. By determining each coefficient, the spontaneous polarization in the equilibrium state can be calculated and the phase transition of ferroelectrics can be well described. With this expression, the spontaneous polarization at a certain temperature can be obtained at the free energy minimum,

$$\left(\frac{\partial G(TP)}{\partial P}\right)_{P_s} = 0, \quad (6)$$

i.e.,

$$P_s [a'(T) + b'(T)P_s^2 + c'(T)P_s^4] = 0. \quad (7)$$

One of the solutions $P_s = 0$ corresponds to the paraelectric phase and other solutions $P_s \neq 0$ correspond to the ferroelectric phases.

In the paraelectric phase ($P_s = 0$), the inverse dielectric susceptibility can be calculated by

$$1/\chi = \frac{\partial^2 G}{\partial^2 P}. \quad (8)$$

From there, we get

$$\chi = \frac{1}{a'(T)} > 0. \quad (9)$$

Therefore, the coefficient $a'(T)$ is positive in the paraelectric state. The stability limit of the paraelectric phase at the critical temperature T_0 (the temperature at which the crystal transforms from the paraelectric phase to an embryonic ferroelectric state) is given by $a'(T_0) = 0$. In the vicinity of T_0 , the coefficient $a'(T)$ can be expanded as a Taylor series in terms of $(T - T_0)$. Taking into account the first-order term only, we obtain the Curie-Weiss law,

$$\varepsilon \approx \chi = \frac{1}{a'_0(T - T_0)}, T > T_0, \quad (10)$$

where a'_0 is a positive constant.

We can further assume that the coefficients b' and c' are temperature independent as they generally have a very weak dependence on temperature. In the case of $P_s \neq 0$ (ferroelectric phase), we can find different variations (continuous or discontinuous) of the polarization through the transition point depending on the sign of b' .

If $b' > 0$, we can neglect c' without loss of significance. In this case, one of the solutions of Eq. (7) is $P_s = 0$, which corresponds to the minimum free energy when $T > T_0$. When $T < T_0$, other solutions of Eq. (7) can be calculated as

$$P_s = \pm \sqrt{a'_0(T_0 - T)/b'}. \quad (11)$$

The dielectric susceptibility at $T < T_0$ can be obtained as

$$\chi = \frac{1}{2a'_0(T_0 - T)}. \quad (12)$$

Therefore, the Curie-Weiss constant above T_0 is two times higher than that below T_0 . Eqs. (11) and (12) also indicate that the spontaneous polarization varies continuously through the transition temperature and the dielectric susceptibility becomes infinite at the transition temperature $T_C = T_0$. This kind of phase transition is called the second-order phase transition (Fig. 5A and B).

If $b' < 0$ and $c' > 0$, the solutions of Eq. (7) become

$$P_s = \pm \sqrt{\frac{-b' + \sqrt{b'^2 - 4a'_0c'(T - T_0)}}{2c'}}. \quad (13)$$

The dielectric susceptibility of the ferroelectric phase can be calculated to be

$$\chi = 1/\left[\left(\frac{b'^2}{c'}\right)\sqrt{\left(1 - \frac{4a'_0c'}{b'^2}\right)(T - T_0)} \cdot \left(1 + \sqrt{\left(1 - \frac{4a'_0c'}{b'^2}\right)(T - T_0)}\right)\right] \quad (14)$$

The upper limit (onset) temperature of the ferroelectric phase obtained from $1/\chi = 0$ is

$$T_1 = T_0 + \frac{b'^2}{4a'_0c'}. \quad (15)$$

Therefore, the temperatures of the lower limit for the paraelectric phase and of the upper limit for the ferroelectric phases are different. This kind of phase transition is called the first-order phase transition.

Fig. 5C shows the free energy curves of the first-order phase transition. Below T_0 , the free energy has two minima ($\pm P_s$). Upon heating at $T_0 < T < T_C$, an additional local minimum appears at $P_s = 0$, where the ferroelectric phase remains stable while at the same time the paraelectric phase starts to emerge. At $T = T_C$, the free energies of the ferroelectric and paraelectric phases are equal ($G = 0$), and the transition temperature can be calculated to be

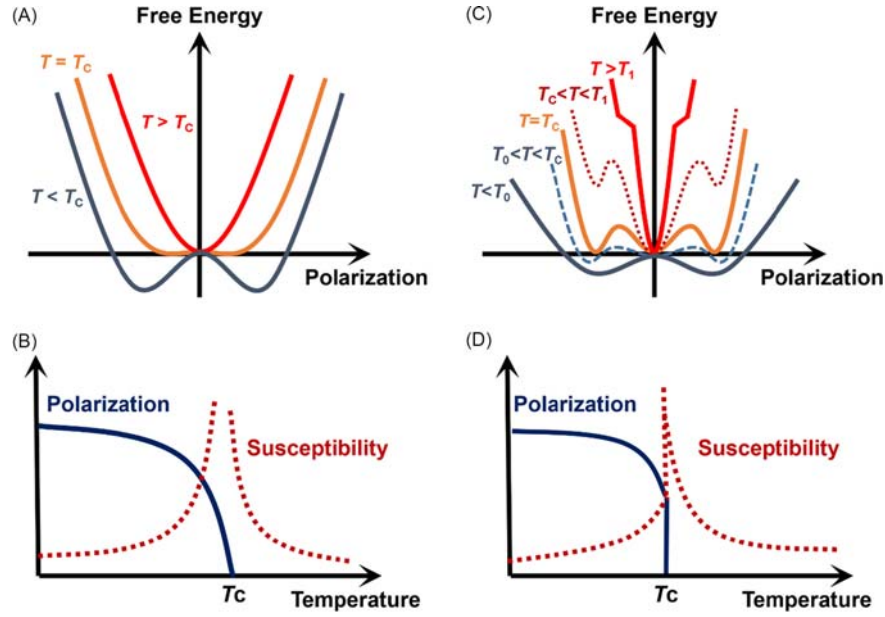


Fig. 5 Free energy curves (A and C) and temperature-dependent polarization and dielectric susceptibility (B and D) for the second-order (A and B) and the first-order (C and D) phase transitions.

$$T_C = T_0 + \frac{3b'^2}{16a'_0c'} \quad (16)$$

Just before reaching T_C , the spontaneous polarization P_s has a finite value, and at the transition temperature $T = T_C$ it drops to zero discontinuously (Fig. 5D). At $T_C < T < T_1$, the free energy at $P_s = 0$ is smaller than that at $\pm P_s$, indicating that the paraelectric phase is stable and the ferroelectric phase becomes metastable. Above T_1 , only one minimum exists and the system contains the paraelectric phase alone.

4.05.1.3.2 Soft-mode theory

Different from the phenomenological theory which gives a macroscopic picture of the properties in ferroelectrics, the soft-mode theory provides explanations from a microscopic aspect.

In a crystal, atoms or ions are not static and they always vibrate around their equilibrium positions. From the lattice dynamics point of view, the lattice must be stable in three different types of deformation: (i) long wavelength homogenous deformation (zone-center acoustic modes), (ii) long wavelength inhomogeneous deformation (zone-center optic mode), and (iii) short wavelength deformation (such as zone-boundary modes).²⁰ Therefore, the general condition for lattice stability is that all normal vibration modes (phonon) have real and finite frequencies. The crystal becomes unstable when the frequency of the phonon (the “soft mode”) decreases and approaches zero. Here, the word “soft” means the vibrational frequency becomes lower just like in a softer spring oscillator (with a lower stiffness coefficient) that has a lower frequency under simple harmonic vibration. If that happens, once the atoms are displaced in a specific vibration process, there is no restoring force to make them return to the original equilibrium position. Therefore, a structural phase transition occurs.

Historically speaking, Raman and Nedungadi were the first to observe a soft mode in a structural phase transition in 1940.²¹ However, it was not until 1960 that the soft mode theory attracted wide interest when Cochran and other researchers applied it to the ferroelectric phase transition.^{22–24} The basic concept of the soft mode theory in ferroelectrics is that the appearance of the spontaneous polarization (ferroelectric phase transition) is directly related to the softening of the transverse optic (TO) phonon mode at the center of the Brillouin zone.

Consider a ferroelectric crystal upon cooling from the high temperature paraelectric phase to a low temperature ferroelectric phase. It has been found that the temperature dependence of the frequency for the soft phonon ω_s follows the Curie-Weiss law above T_C , i.e.,

$$\omega_s^2(q_s j) = A(T - T_C), \quad (17)$$

where A is a constant related to the properties of the crystal, q_s represents the wavevector of the soft mode, and j is the branch index. Fig. 6 schematically illustrates the temperature dependences of the soft mode frequency for the first-order and second-order phase transitions. The frequency of the softening phonon gradually decreases to zero and the new phonon hardens when the temperature approaches T_C (for the second-order phase transition). In other words, the vibration (or the atomic positions) becomes “frozen” at T_C , and the atom presents a new equilibrium position determined by the symmetry of the mode. For the first-order phase transition,

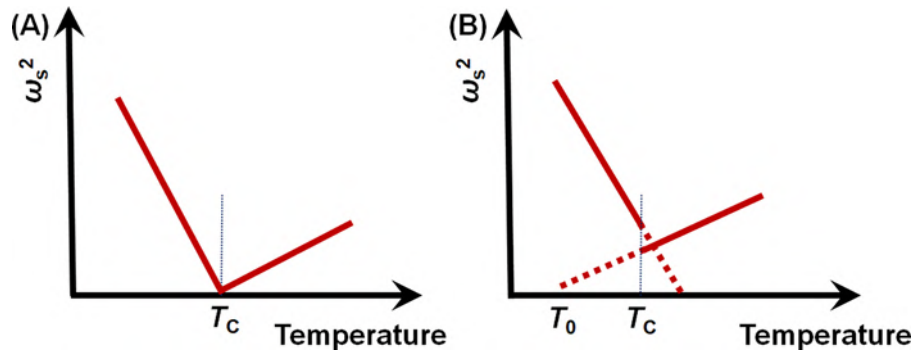


Fig. 6 Temperature dependence of the soft mode frequency for (A) the second-order phase transition, and (B) the first-order phase transition.

the frequency of the softening phonon does not become zero at T_C . Then the old mode disappears and the new phonon hardens. In this way, the structure of a lower symmetry with a finite dipole moment is induced. The decrease to zero of the soft-mode frequency as the transition is approached is due to the counteraction between the short-range repulsive force and the long-range Coulomb force in ferroelectrics.

The soft mode theory was initially used to explain the mechanism of displacive ferroelectric phase transitions (such as in BaTiO_3 (Recent investigations indicate that BaTiO_3 is not a pure displacive-type ferroelectric crystal, but shows some order-disorder characters. See refs. 25,26.)). Later the soft mode theory was extended to the order-disorder transitions (such as in KH_2PO_4), in which the pseudospin wave (instead of phonon) is softened. With these developments, the soft mode theory has become one of the most successful and important theories for ferroelectricity.

4.05.1.4 Classification of ferroelectric and piezoelectric materials

There are different ways of classification. According to their chemical compositions, piezoelectrics and ferroelectrics can be divided into inorganic, organic, and composite materials. In this chapter, we focus on inorganic piezo-/ferroelectric materials. According to their physical properties, piezoelectric materials can be divided into ferroelectric and non-ferroelectric piezoelectric materials. Among all the piezoelectrics, ferroelectric materials generally have better piezoelectricity due to the existence of spontaneous polarization (intrinsic effect) and domains and domain walls (extrinsic effect). Therefore, in this chapter, special attention is paid to ferroelectric-type piezoelectric materials. According to their crystal structures, piezoelectric and ferroelectric materials can be classified into the perovskite structure, the tungsten bronze structure, the layered perovskite structure, the bismuth-based layer structure, the LiNbO_3 -type structure, etc. Generally, the perovskite family shows better piezoelectricity at room temperature, while other families may exhibit good piezoelectric effect at high temperatures. A detailed discussion on this topic will be given in Section 4.05.5.

In the following sections, we will describe the recent progress in different piezo-/ferroelectric materials, including PZT ceramics, relaxor-based single crystals, lead-free perovskites, high temperature piezoelectrics, and textured piezoelectric ceramics. At last, the current and potential applications of piezo-/ferroelectric materials are presented.

4.05.2 Lead zirconate-titanate (PZT) ceramics

4.05.2.1 The perovskite structure

The perovskite is one of the most important crystal structures in which many piezo-/ferroelectric materials crystallize, which show excellent performance, as represented by the lead zirconate-titanate solid solution (PZT). The perovskite structure was named after the calcium titanate (CaTiO_3) mineral. The oxide perovskites have the general chemical formula of ABO_3 , where O is oxygen, A represents a large cation with a coordination number of 12, and a valence from +1 to +3 (e.g., K^+ , Pb^{2+} and Bi^{3+}), and B is a smaller cation with a valence from +3 to +5 (e.g., Fe^{3+} , Ti^{4+} and Nb^{5+}). The ideal cubic perovskite structure has the $Pm\bar{3}m$ space group. Fig. 7 shows a cubic perovskite unit cell, in which A-cation occupies the eight corners of the unit cell, O occupies the face centers of the unit cell and forms an oxygen octahedron, and B-cation sits at the center of the oxygen octahedron.¹ In reality, the ideal cubic perovskite is not very common due to the fact that perovskite structure tends to undergo various structural distortions, resulting in phases of lower symmetry with spontaneous polarization, which gives rise to many interesting properties like piezoelectricity, pyroelectricity and ferroelectricity, useful for numerous technological applications.^{1,12}

4.05.2.2 Phase diagram of PZT and the morphotropic phase boundary

Lead zirconate and lead titanate form a continuous solid solution, $\text{Pb}(\text{Zr}_{1-x}\text{Ti}_x)\text{O}_3$ (PZT), with Ti^{4+} and Zr^{4+} ions occupying the perovskite B site randomly. The composition of PZT can be tailored by varying the Zr:Ti ratio, leading to different crystal structures and physical properties. The most important compositions of PZT are around the morphotropic phase boundary (MPB)

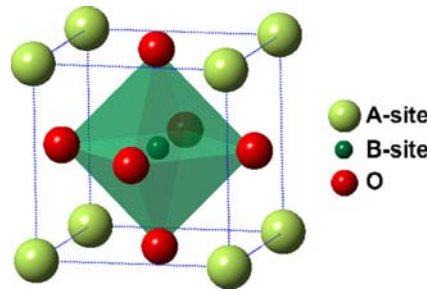


Fig. 7 The ideal oxide perovskite structure, ABO_3 .

($x \approx 0.46$ – 0.51), which is a nearly temperature-independent line (or region) in the temperature—composition phase diagram, as shown in **Fig. 8A**.^{1,6} The MPB separates the ferroelectric rhombohedral (on the Zr-rich side) and tetragonal (on the Ti-rich side) phases. The MPB was initially presented as a line in the phase diagram by Jaffe et al.¹, and it was later observed that the rhombohedral and tetragonal phases can coexist in a finite range of compositions, which may vary with different processing methods and conditions, etc.²⁷ More recently, it was found that the MPB in fact represents a composition region in which a monoclinic phase (M_A -type, space group Cm) exists (**Fig. 8B**).⁶ This will be discussed in more detail in **Section 4.05.2.3.2**.

In the MPB region, the crystal structure of PZT changes in a complex way, and most importantly, the dielectric, piezoelectric and electromechanical properties peak (**Fig. 8C**).^{1,5} These interesting phenomena have raised extensive interest in understanding the origin of the high performance in the MPB compositions.

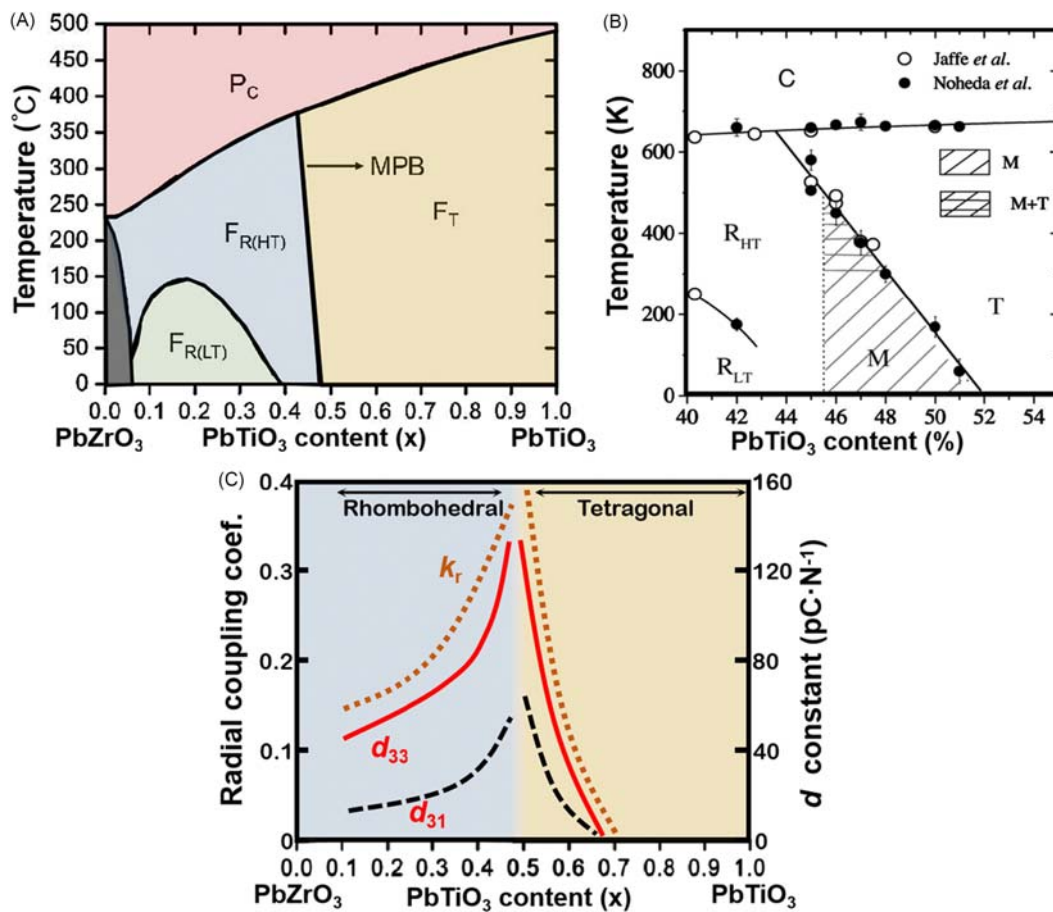


Fig. 8 (A) Original temperature—composition phase diagram of the $Pb(Zr_{1-x}Ti_x)O_3$ (PZT) solid solution. (B) Updated PZT phase diagram around the MPB indicating the existence of the monoclinic (M) phase (shaded with diagonal lines). (C) Composition dependence of electromechanical properties of PZT ceramics. Adapted with permission from Jaffe, B.; William, C.; Jaffe, H., *Piezoelectric Ceramics*. London: Academic Press, 1971, Jaffe, B.; Roth, R. S.; Marzullo, S., *J. Appl. Phys.* **1954**, 25 (6), 809–810, Noheda, B.; Cox, D.; Shirane, G.; Guo, R.; Jones, B.; Cross, L., *Phys. Rev. B* **2000**, 63 (1), 014103.

4.05.2.3 Origin of the high piezoelectric response in PZT near the MPB region

The piezoelectric response consists of intrinsic and extrinsic contributions. The intrinsic contribution originates from the unit cell deformation, which is determined by the crystal structure. The extrinsic contributions are produced by the domain switching and domain-wall motions, which are determined by the domain structure, such as the domain sizes and orientations, domain wall density, polarization and flexibility of the domain walls.^{28–30} In order to clarify the origin of the high piezoelectric response in the MPB, different mechanisms have been proposed.

4.05.2.3.1 Conventional pictures of MPB

For a long time, the MPB was regarded as an intermediate composition line (or region), where the rhombohedral and tetragonal phases coexist. The coexistence of the two phases in PZT ceramics allows more permissible ferroelectric domain variants (eight in the rhombohedral and six in the tetragonal phase), as shown in Fig. 9, making them easier to be reoriented during poling and to align their polar vectors along the poling direction, in other words, more electrically active.¹

Another interpretation is that in the MPB region, the rhombohedral and tetragonal phases have nearly equal Gibbs free energies. Therefore, a weak external stimulus is possible to induce phase transitions and domain switching in between.²⁷ As a result, the coexistence of the two phases could augment the polarizability by coupling between two thermodynamically equivalent energy states, leading to enhanced dielectric and piezoelectric properties in the vicinity of MPB.

4.05.2.3.2 Monoclinic phase and high piezoelectricity

In 1999, a monoclinic phase (M_A -type, space group Cm) was discovered in the MPB region of PZT by Noheda and coworkers, which is stable in the composition range $0.46 \leq x \leq 0.51$.^{6,31} The unit cell of the monoclinic M_A phase is doubled in volume with respect to the tetragonal one, with a_M and b_M lying along the pseudocubic $[\bar{1}\bar{1}0]_c$ and $[1\bar{1}0]_c$ directions, respectively, and c_M deviating slightly from the $[001]_c$ direction, such that the angle β between a_M and c_M is slightly larger than 90° . This finding represents one of the major advances in the studies of PZT since the initial reports of the MPB phase diagram and related phenomena, and provides new insights into the understanding of the high piezoelectricity of PZT in the MPB. The existence of the monoclinic phase provides more possible directions for the polarization and acts as a structural bridge since the apparent direct phase transition from the rhombohedral to tetragonal phase across the MPB region is not symmetrically allowed by group-subgroup relations. The symmetry element in the Cm phase is the single $\{110\}_c$ mirror plane, and the monoclinic plane contains the polar axes of both rhombohedral and tetragonal phases.³² This series of work has revealed a new and complex picture of the MPB phases and originally attributed the origin of the unusually high piezoelectric response of PZT to the monoclinic distortion.³³

4.05.2.3.3 Meso- to nanoscale description of the MPB

From microscopic point of view, the MPB can be described by the “adaptive ferroelectric phase” model.^{34,35} According to this model, the MPB is considered as a kind of adaptive phase, which has a very low domain wall energy and consists of finely twinned rhombohedral or tetragonal phase. As such, the monoclinic phase in the MPB region could be considered as a result of the coherent effects of rhombohedral (or tetragonal) nanodomains. Experimentally, the nanodomain structures were clearly observed in PZT near the MPB by transmission electron microscopy (TEM), as shown in Fig. 10. The nanodomains suggest high domain-wall mobility, which was believed to be beneficial to the high piezoelectricity (extrinsic contributions).^{36,37}

Another approach to describe the MPB is the consideration of short-range and long-range monoclinic phases. For a complex perovskite solid solution with cation disorder, such as in PZT, the local structure at the unit cell level can differ from the average macroscopic symmetry.^{38,39} According to this approach, from the local scale (down to several unit cells) point of view, monoclinic phases exist in all the compositions of PZT. Therefore, strictly speaking, there is no clear boundary for the MPB locally, and instead, the rhombohedral and tetragonal phases are an average effect of the local monoclinic phase due to different degrees of structural disorder, and the monoclinic phase found in the well-accepted MPB region is a result of long-range ordering of local monoclinic phase.^{40,41}

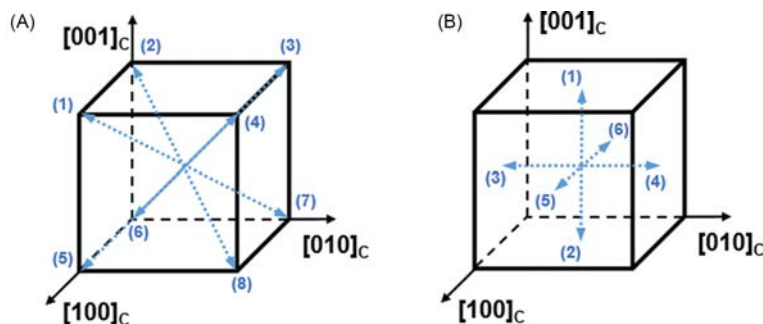


Fig. 9 Possible ferroelectric domain variants in (A) a rhombohedral and (B) a tetragonal crystal.

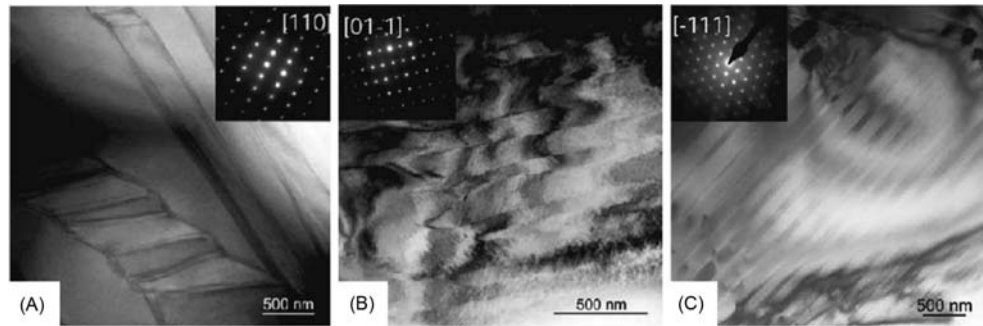


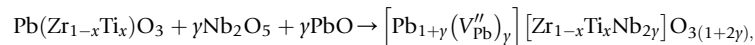
Fig. 10 Domain structures of PZT with different compositions: (A) PZT54/46 (rhombohedral), (B) PZT55/45 (near the MPB) and (C) PZT45/55 (tetragonal). Reprinted with permission from Schönau, K. A.; Schmitt, L. A.; Knapp, M.; Fuess, H.; Eichel, R.-A.; Kungl, H.; Hoffmann, M. J., *Phys. Rev. B* **2007**, 75 (18), 184117.

4.05.2.4 Effect of chemical modifications

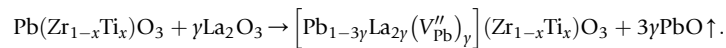
In most practical uses, PZT ceramics are doped for specific applications. After over half a century of investigations, different modification strategies (including donor doping, acceptor doping, isovalent substitutions, and complex doping) have been developed by controlling the extrinsic contributions via defect chemistry. With these modifications, PZT-based ceramics have become a model piezo-/ferroelectric material, and have been widely used in electromechanical applications.^{1,42}

4.05.2.4.1 Donor doping

Donor doping is realized by substitution with cations of higher valence, such as La^{3+} for Pb^{2+} on the A site, or Nb^{5+} for $\text{Zr}^{4+}/\text{Ti}^{4+}$ on the B site. This kind of doping creates lead vacancies to maintain electroneutrality. For example, in La^{3+} -doped and Nb^{5+} -doped PZT ceramics prepared by traditional processing, the respective chemical reactions can be written as:



and



It should be noted that the amount of lead in PZT ceramics can be self-regulated, as PbO can be lost by volatilization from the samples or can be obtained from the surrounding protective atmosphere at high temperatures.

In a lattice with lead vacancies, the transfer of atoms becomes easier than in a perfect lattice, and thereby the domain motion is facilitated. Generally, donor doping leads to electrically “soft” PZT ceramics with lower T_C , coercive field and mechanical quality factor (Q_m), but higher dielectric permittivity, dielectric loss, piezoelectric charge coefficients and coupling factors (Table 2), making them suitable for sensors, actuators, low-power motor-type transducers, receivers, and low power generators. Typical soft PZT for industrial applications includes PZT-5A, PZT-5H, etc.^{1,42}

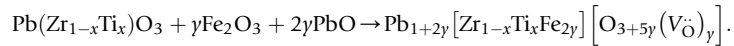
4.05.2.4.2 Acceptor doping

Acceptor doping refers to doping with cations of lower valence, such as K^+/Na^+ for Pb^{2+} or $\text{Fe}^{3+}/\text{Mn}^{2+}$ for $\text{Zr}^{4+}/\text{Ti}^{4+}$, which creates oxygen vacancies to balance the charge. Taking Fe^{3+} -doped PZT as an example, the equation can be written as:

Table 2 Typical properties of commercial soft and hard PZT ceramics.

Material properties	Soft PZT		Hard PZT	
	PZT-5A	PZT-5H	PZT-4	PZT-8
Permittivity, ϵ' (at 1 kHz)	1800	3450	1300	1000
Dielectric loss, $\tan \delta$ (at 1 kHz)	0.02	0.02	0.005	0.004
Curie temperature, T_C (°C)	350	242	325	325
Mechanical quality factor, Q_m	80	50	500	1000
Coercive field, E_c ($\text{kV}\cdot\text{cm}^{-1}$)	14.9	8.8	/	/
Planar electromechanical coupling factor, k_p	0.63	0.74	0.55	0.51
Piezoelectric coefficient, d_{33} ($\text{pC}\cdot\text{N}^{-1}$)	350	600	280	230

Data are from CTS Corporation. (<https://www.ctscorp.com/products/piezoelectric-products/>).



Acceptor doping facilitates the alignment of re-orientable dipoles in the direction of the polarization vector within domains, creating internal fields that stabilize the domain configuration and inhibit the domain wall motion. Such a “hardening” effect usually leads to a reduction in dielectric permittivity, dielectric loss and piezoelectric activity, but an enhancement of the coercive field and mechanical quality factor (Table 2). Therefore, hard PZT ceramics can endure high electrical and mechanical stresses with only minor changes in their physical properties, and also avoid the heating problem during usage. These characters make hard PZT suitable for high-voltage or high-power generators and transducers, ultrasonic cleaning, ultrasonic processors, etc. Typical hard PZT for industrial applications includes PZT-4, PZT-8, etc.^{1,42}

4.05.2.4.3 Isovalent substitutions

Isovalent substitutions are also performed to tailor the structure and properties of PZT-based perovskite materials, such as the substitution of $\text{Ba}^{2+}/\text{Sr}^{2+}$ for Pb^{2+} , and Sn^{4+} for $\text{Zr}^{4+}/\text{Ti}^{4+}$. Such chemical modifications usually shift the T_C downward, intrinsically enhancing the dielectric and piezoelectric properties.^{43,44}

4.05.2.4.4 Complex doping

Complex doping refers to the doping process in which two or more elements are introduced (i.e., doping with both the soft and hard dopants). This method is intended to combine the properties of donor- and/or acceptor-doped PZT, in order to achieve better stability and improved piezoelectric properties than the single element-doped PZT.

Many perovskite compounds have been introduced to PZT to form complex perovskite solid solutions, which can be regarded as a kind of complex doping. The formation of complex solid solutions typically modifies the MPB region of the materials, which can further optimize the piezoelectric properties of PZT.^{45,46}

4.05.3 Relaxor-based piezoelectric single crystals

4.05.3.1 Relaxor ferroelectrics: An introduction

Relaxor ferroelectrics (or briefly relaxors) were firstly discovered by Smolenskii and Isupov in the 1950s, when they developed a new class of perovskite compounds with the general formula of $A(\text{B}'_{1/3}\text{B}''_{2/3})\text{O}_3$, such as $\text{Pb}(\text{Mg}_{1/3}\text{Nb}_{2/3})\text{O}_3$ (PMN).⁴⁷ Since its discovery, relaxors have attracted considerable attention from the scientific community due to their unique properties. The term relaxor ferroelectric originated from the fact that these materials show some characters of ferroelectricity under certain conditions, and most notably, exhibit strong frequency dispersion in the temperature dependence of dielectric permittivity (Fig. 11), which is different from normal ferroelectrics (such as BaTiO_3). Some general characters that distinguish canonical relaxor ferroelectrics like PMN from normal ferroelectrics are summarized in Table 3.^{8,48,49}

Several models have been proposed to explain the possible mechanisms of the unique dielectric relaxation and the polarization behavior in relaxors, including compositional fluctuation model, superparaelectric model, dipolar glass model, random field model, etc.^{8,48,50–58} However, none of them could comprehensively explain the physical properties of relaxors. Though the mechanisms of relaxor behaviors remains controversial, it is generally accepted that these properties are related to the dynamics of the polar nanoregions (PNRs) formed from the unique order-disordered nanostructure in relaxors. PNRs are lower-symmetry structural regions embedded in an average cubic matrix. PNRs appear at a certain high temperature (called the Burns temperature) and their

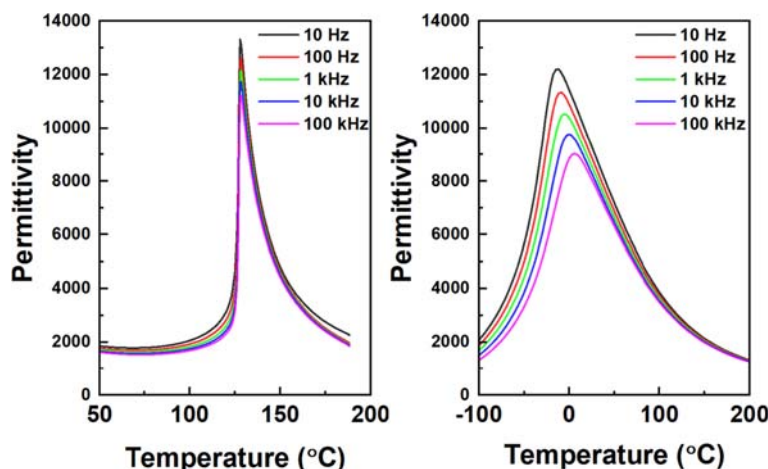


Fig. 11 Temperature dependences of the dielectric permittivity of (A) BaTiO_3 ceramic (normal ferroelectric) and (B) $\text{Pb}(\text{Mg}_{1/3}\text{Nb}_{2/3})\text{O}_3$ ceramic (relaxor).

Table 3 Comparison of relaxor and normal ferroelectric materials.

Structure and property	Normal ferroelectrics	Relaxor
Crystal structure	<ul style="list-style-type: none"> • Non-cubic and polar symmetry 	<ul style="list-style-type: none"> • Cubic structure on average
Temperature and frequency dependence of dielectric permittivity	<ul style="list-style-type: none"> • Sharp peak with little frequency dispersion ($<10^{12}$ Hz) • Dielectric permittivity follows the Curie-Weiss law above T_C 	<ul style="list-style-type: none"> • The temperature of the dielectric permittivity maximum (T_m) increasing and its magnitude decreasing with increasing frequency • Broad peak with strong frequency dispersion • Dielectric permittivity around T_m deviates the Curie-Weiss law
Phase transition	<ul style="list-style-type: none"> • Paraelectric to ferroelectric phase transition at T_C 	<ul style="list-style-type: none"> • No macroscopic phase transition around T_m
Domains and polarization	<ul style="list-style-type: none"> • Macro-size ferroelectric domain • No polar domain above T_C • Strong remanent polarization 	<ul style="list-style-type: none"> • Nano-size domains persist well above T_m • No macro polarization can develop without the application of an electric field • Non-linear P-E relation with weak or no remanent polarization

size grows and interaction increases slightly upon cooling, but they do not form a long-range ferroelectric order. It is commonly believed that it is the quenched compositional disorder on the B-site ionic arrangement (such as Mg^{2+} and Nb^{5+} for PMN) that prevents the long-range ferroelectric order from occurring and consequently leads to the development of the relaxor state. The characteristic frequency dispersion results from the dipole relaxation in PNRs, with the dipole dynamics slowing down upon cooling. Since the PNRs are arranged randomly and their correlations are limited to nanoscale, the associated structural distortions remain local, and thereby canonical relaxors typically show a pseudo-cubic symmetry on average across the temperature of permittivity maximum, as determined by conventional X-ray and neutron diffraction techniques.^{49,59–61}

4.05.3.2 Solid solutions between relaxors and ferroelectric $PbTiO_3$

By introducing ferroelectric $PbTiO_3$ (PT) into a relaxor to form a binary solid solution, a long-range ferroelectric phase can develop accompanied with a structural change from the cubic to a non-cubic polar phase (of rhombohedral symmetry in most cases). Similar to PZT, an MPB exists between the rhombohedral phase of relaxor-side and the tetragonal phase of PT-side. Solid solutions of $(1-x)Pb(Mg_{1/3}Nb_{2/3})O_3-xPbTiO_3$ ((1-x)PMN-xPT) and $(1-x)Pb(Zn_{1/3}Nb_{2/3})O_3-xPbTiO_3$ ((1-x)PZN-xPT) are the most representative relaxor-PT systems, which exhibit excellent dielectric and electromechanical properties for compositions near the MPB.

Fig. 12 shows the phase diagrams of the (1-x)PMN-xPT and (1-x)PZN-xPT systems around the MPB. Similar to PZT, an intermediate phase(s) of lower symmetry has been found in the MPB region, which is believed to act as a structural bridge between the rhombohedral and tetragonal phases. But different from PZT in which the monoclinic phase is of M_A -type ($x \approx 0.46$ – 0.51), the lower symmetry phase is of monoclinic M_C -type in PMN-PT ($x \approx 0.30$ – 0.37), and orthorhombic in PZN-PT ($x \approx 0.09$ – 0.10), respectively. In the M_C phase, the monoclinic b_M axis lies along a $[010]_c$ direction, and notably, this phase is orthorhombic to its limit when $a_M = c_M$.^{6,62,63}

4.05.3.3 Relaxor-PT piezoelectric single crystals: A new era of piezoelectric materials

The interesting properties of relaxor-PT single crystals were first reported by Nomura and coworkers in the PZN-PT single crystals in 1982.⁶⁴ In the late 1990s, Shrout and co-workers systematically investigated the piezoelectric properties of PMN-PT and PZN-PT single crystals and found that they exhibit a piezoelectric coefficient d_{33} larger than $2000 \text{ pC} \cdot \text{N}^{-1}$, an electromechanical coupling factor over 90%, and a strain level exceeding 1%.⁷ This outstanding performance far outperforms the state-of-art PZT-based ceramics. In the past two decades, several relaxor-based binary, ternary and chemically modified single crystals have been developed and the physical properties of the crystals have been further improved (see Fig. 13). Their outstanding piezoelectric performance has made the relaxor-PT solid solution crystals a new generation of piezoelectric materials for advanced electromechanical transducer applications.^{9,11,13,14}

4.05.3.4 Growth of relaxor-based piezoelectric single crystals

In order to explore their excellent piezoelectric properties, several techniques have been developed to grow the relaxor-based single crystals, including the flux growth method, the top-seeded solution growth, the solid-state crystal growth, and the modified Bridgman growth.

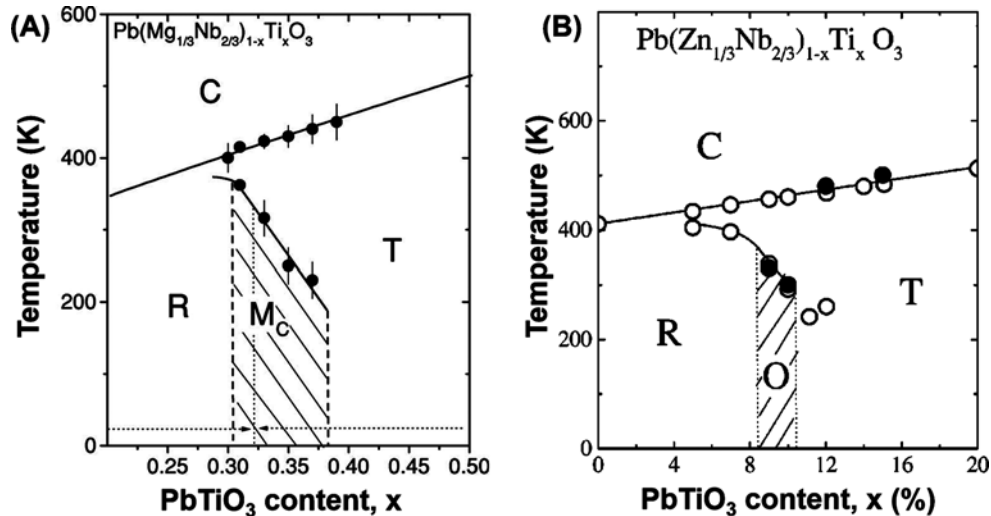


Fig. 12 Phase diagram of the $(1-x)$ PMN- x PT and $(1-x)$ PZN- x PT solid solutions around the MPB. Adapted with permission from Noheda, B.; Cox, D.; Shirane, G.; Gao, J.; Ye, Z.-G., *Phys. Rev. B* **2002**, *66* (5), 054104, La-Orauttapong, D.; Noheda, B.; Ye, Z.-G.; Gehring, P. M.; Toulouse, J.; Cox, D. E.; Shirane, G., *Phys. Rev. B* **2002**, *65* (14), 144101.

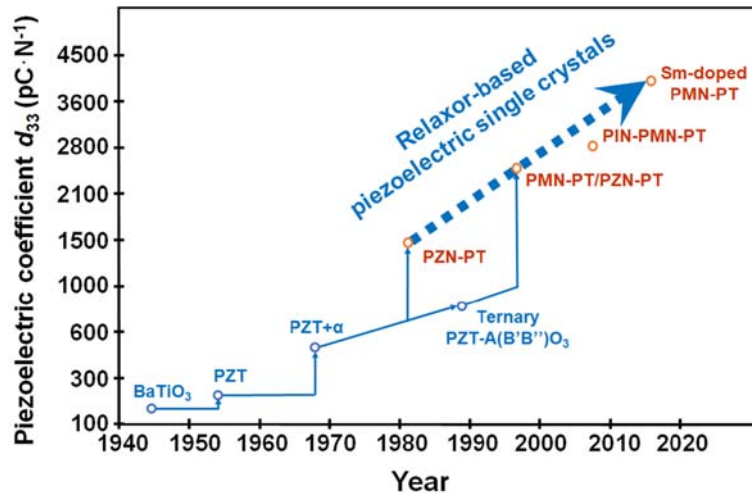


Fig. 13 Historical development of perovskite-based piezoelectric materials in terms of piezoelectric coefficient d_{33} . Adapted from Ye, Z.-G., *MRS Bull.* **2009**, *34* (4), 277–283.

4.05.3.4.1 The flux method

The flux method, or the high-temperature solution method, has been widely used to grow piezoelectric single crystals with complex compositions. This method is suitable to grow strain-free single crystals with well-developed pseudocubic morphology.⁶⁵ The basic principle of the flux method is based on the spontaneous nucleation that occurs when supersaturation is reached upon slow cooling of the high-temperature solution. One of the advantages of this method is that it is a relatively simple process, but the drawback is that it is difficult to control the nucleation and as a result, a large number of crystals can form and the as-grown crystals are generally small in size (from millimeters to a couple of centimeters). The key parameters to be mastered in the flux growth so as to enlarge the crystal size and improve the crystal quality include the optimization of the chemical (flux composition and flux-charge ratio) and thermodynamic (soaking temperature and heating/cooling rates) parameters. Generally, PbO (with additives such as B₂O₃) is selected as flux as it has a good solubility for other metal oxides and it is a component of the relaxor-based crystals to be grown. A typical thermal profile include heating up to the soaking temperatures of 1100–1200 °C, followed by a slow cooling at the rate of 0.5–5 °C/h.⁶⁶

4.05.3.4.2 Top-seeded solution growth method

The top-seeded solution growth (TSSG) method has been developed to control nucleation by introducing a seed crystal on the top of the high-temperature solution to make the crystal grow epitaxially around it. TSSG has been proved to be effective to grow

relaxor-based piezoelectric single crystals with larger size and better quality compared with those grown by the flux method. TSSG could also enhance the transport of solute and thereby leads to a more homogenous crystal composition. Additionally, the as-grown relaxor-based piezoelectric single crystals by the TSSG method generally exhibit naturally developed $\{001\}_c$ faces, which facilitate subsequent cutting and orientation of the crystals.^{67–69}

4.05.3.4.3 The solid-state crystal growth method

The solid-state crystal growth (SSCG) was developed as a cost-effective approach to grow large-sized relaxor-based piezoelectric single crystals. This method allows the ceramics of desired composition to convert to single crystals based on abnormal grain growth. In this technique, a seed crystal is buried in the polycrystalline body with high density and annealed for a certain time (from a dozen hours to hundreds of hours) at temperatures 100–200 °C below their respective melting points. SSCG can grow single crystals at relatively low temperatures and it is a time-saving method. However, a main drawback of SSCG is the porosity in the grown crystals, which is difficult to be completely eliminated, and may deteriorate the physical properties of the crystals.^{70–72}

4.05.3.4.4 The modified Bridgman method

The modified Bridgman method was developed for mass production of relaxor-based piezoelectric single crystals with large size and high quality to meet the increasing demand for various applications. The principle of the Bridgman growth is to realize a directional solidification by moving the melt through the cooler zone of the furnace so that a crystal grows (from a seed crystal) from the bottom of the crucible. Due to the nearly congruent melting nature of PMN-PT, the crystals can be grown directly from a stoichiometric charge in a sealed Pt crucible. To grow the PZN-PT single crystals, an excess amount of PbO is needed to stabilize the perovskite structure. The major issues of the modified Bridgman method are to control the crystal growth direction (along $\{001\}_c$) and to improve the composition uniformity.⁷³ So far, the modified Bridgman method has become the most viable technique for the commercial growth of relaxor-based piezoelectric single crystals of large size (up to 5 in. in diameter) and high quality.^{9,14,74} Fig. 14 demonstrates various relaxor-based binary and ternary piezocrystals grown by the modified Bridgman technique.

4.05.3.5 Tailoring the properties of relaxor-based piezoelectric single crystals

Although the PMN-PT and PZN-PT crystals exhibit excellent piezoelectric properties, they suffer from some drawbacks, including low T_C , low phase transition temperatures (namely the rhombohedral to tetragonal phase transition temperature (T_{R-T}) or the phase transition temperature at MPB (T_{MPB})), low coercive field E_c and low mechanical quality factor Q_m . The low T_C and low T_{R-T}/T_{MPB}

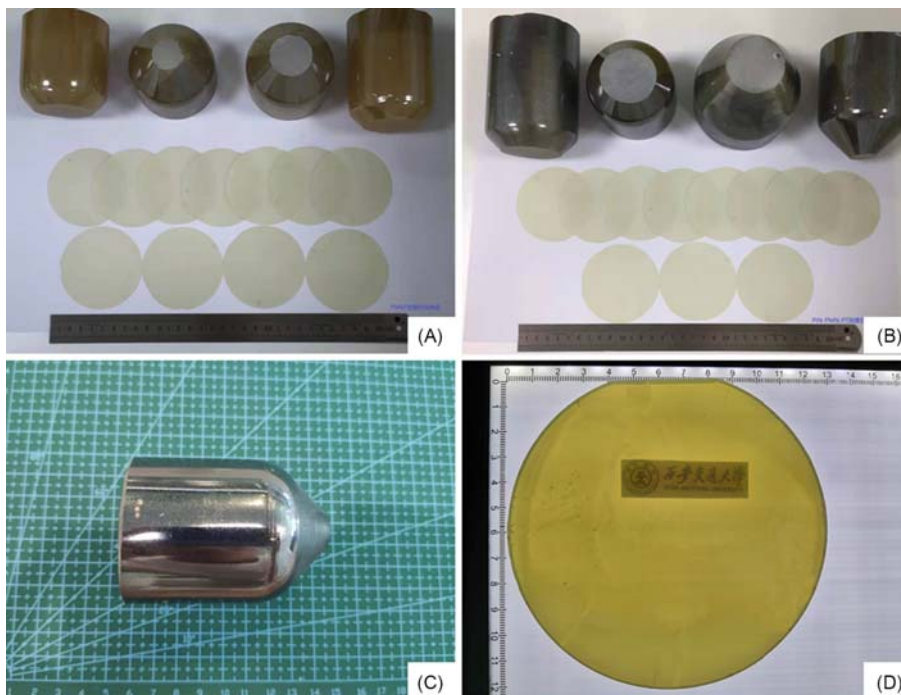


Fig. 14 As-grown relaxor-based piezoelectric single crystals grown by the modified Bridgman method and the resulting crystal wafers: (A) PMN-PT single crystals, (B) $\text{Pb}(\text{In}_{1/2}\text{Nb}_{1/2})\text{O}_3\text{-Pb}(\text{Mg}_{1/3}\text{Nb}_{1/3})\text{O}_3\text{-PbTiO}_3$ (PIN-PMN-PT) single crystals, (C) Mn-doped PIN-PMN-PT single crystal, and (D) 5-inch-diameter PIN-PMN-PT single crystal wafer. (A, B and C) Courtesy of Dr. Haosu Luo, Shanghai Institute of Ceramics, Chinese Academy of Sciences, (D) courtesy of Dr. Zhuo Xu, Xi'an Jiaotong University.

make the crystals easily depole under moderate temperatures, which limits their working temperature range. The low E_c leads to poor polarization stability under high driving field conditions. As a result, an additional DC bias electric field is needed to maintain the polarization and the performance of the devices, which adds extra complexity and cost. The low E_c and low Q_m prevent these crystals from being used for high-power transducers and resonance-based acoustic devices. Therefore, it is necessary to develop novel piezoelectric single crystals with improved thermal range and polarization stability.

Over the past decades, extensive efforts have been made to develop new relaxor-based piezoelectric single crystals, leading to three generations of materials (Table 4). The first-generation (Gen. I) piezocrystals, represented by PMN-PT and PZN-PT, exhibit high electromechanical coupling factors and large piezoelectric coefficients. The electromechanical transducers using the first-generation piezoelectric single crystals have a larger bandwidth (by 2–3 times) and higher sensitivity (+10 dB) compared with those using PZT ceramics, and they have been commercially available for high-end medical ultrasound imaging and diagnosis. The second-generation (Gen. II) crystals, represented by the ternary solid solution of $\text{Pb}(\text{In}_{1/2}\text{Nb}_{1/2})\text{O}_3\text{-Pb}(\text{Mg}_{1/3}\text{Nb}_{1/3})\text{O}_3\text{-PbTiO}_3$ (PIN-PMN-PT), show similar electromechanical properties but with higher T_C and larger E_c than the first-generation crystals, which reduce the need for additional thermally conductive components (e.g., heat shunts) and the application of DC fields. The third-generation (Gen. III) piezoelectric single crystals refer to doped crystals with a higher Q_m to meet specific device requirements. Typical materials include Mn-doped PIN-PMN-PT and Mn-doped $\text{Pb}(\text{Mg}_{1/3}\text{Nb}_{1/3})\text{O}_3\text{-PbZrO}_3\text{-PbTiO}_3$ (Mn-PMN-PZT). A high Q_m is beneficial to high-power ultrasonic transducers and other resonance-based devices.^{9,16,75}

4.05.3.6 Property anisotropy and domain engineering

Different from polycrystalline materials, such as PZT ceramics, relaxor-based piezoelectric single crystals show strong anisotropic characteristics, namely, the piezoelectric properties are strongly related to the crystallographic direction, poling direction, and vibration modes.

An important feature in relaxor-based piezoelectric single crystals is that the largest piezoelectric coefficients and dielectric constants are generally found along some directions away from the polar axis. For example, the piezoelectric coefficient d_{33} of $\langle 001 \rangle$ -oriented and -poled rhombohedral PMN-PT crystals is 3–5 times larger than that in $\langle 111 \rangle$ -oriented crystals.^{64,76} Such behavior is associated with the “engineered domain states” formed in the crystals.

A domain-engineered crystal poled along one of the possible polar axes other than its zero-field polar axis creates a set of equivalent domains, so that their angles to the poling direction are minimized. This approach was successfully used to obtain better piezoelectric properties in relaxor-based piezoelectric single crystals.⁹ Taking the rhombohedral PMN-PT crystals as an example, as shown in Fig. 15, 4, 2 and 1 polarization states (named as 4R, 2R and 1R domain configurations, respectively) with a macroscopic symmetry of $4mm$, $mm2$ and $3m$, respectively, could be artificially created when poled along the crystallographic $[001]_c$, $[011]_c$ and $[111]_c$ directions, respectively. The $[001]_c$ -poled crystal (with 4R domain configuration) has the largest longitudinal piezoelectric coefficient d_{33} , while the $[111]_c$ -poled crystal (with 1R domain configuration) has the largest thickness shear piezoelectric coefficient d_{15} (see Table 5 for more details).^{9,77} The formation of engineered domain configurations has proved to be very useful for achieving better piezoelectricity in relaxor-based piezoelectric single crystals.

4.05.3.7 Origin of the ultrahigh piezoelectric response in relaxor-based piezoelectric single crystals

In this section, current understanding of the origin of the ultrahigh piezoelectric response in relaxor-based piezoelectric single crystals is discussed.

4.05.3.7.1 Macroscopic explanation: MPB facilitating polarization rotation

Similar to PZT ceramics, the best electromechanical properties in relaxor-based piezoelectric single crystals are achieved in the compositions near the MPB region where lower symmetry phases, including orthorhombic and different monoclinic phases (M_A , M_B and M_C), are found to be present, and may coexist along with the rhombohedral and/or tetragonal phases.^{78–82} These

Table 4 Physical properties of the three generations of relaxor-PT piezoelectric single crystals. Data of commercial PZT ceramics are also listed for comparison.

Materials	T_C ($^{\circ}\text{C}$)	T_{R-T}/T_{MPB} ($^{\circ}\text{C}$)	E_c ($\text{kV}\cdot\text{cm}^{-1}$)	d_{33} ($\text{pC}\cdot\text{N}^{-1}$)	k_{33}	ϵ_{33}	Q_m
PMN-PT (Gen. I)	155	65	2.8	2800	0.95	8200	100
PIN-PMN-PT (Gen. II)	197	96	5.5	2700	0.95	7200	120
Mn-PIN-PMN-PT (Gen. III)	193	119	6.0	1100	0.90	3700	800
Mn-PMN-PZT (Gen. III)	203	141	6.3	1100	0.92	3400	1050
PZT-5H	242	/	14.9	600	0.78	3450	50
PZT-8	325	/	/	230	0.62	1000	1000

Data are from Zhang, S.; Li, F.; Jiang, X.; Kim, J.; Luo, J.; Geng, X., *Prog. Mater. Sci.* **2015**, *68*, 1–66, and CTS Corporation. (<https://www.ctscorp.com/products/piezoelectric-products/>).

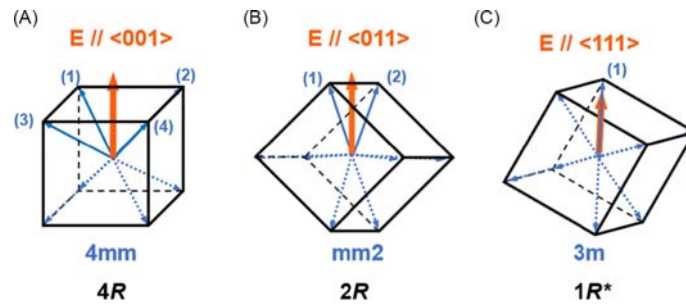


Fig. 15 Engineered domain configurations in rhombohedral crystal. Note that the $1R$ configuration is not stable due to the high electrical and mechanical energies.

Table 5 Piezoelectric anisotropy in the rhombohedral PMN-PT crystals with different domain configurations. The PMN-PT ceramic counterpart is shown for comparison.

Materials	Domain configuration	d_{33} ($\text{pC}\cdot\text{N}^{-1}$)	d_{31} ($\text{pC}\cdot\text{N}^{-1}$)	d_{15} ($\text{pC}\cdot\text{N}^{-1}$)
$\langle 001 \rangle$ -poled crystal	$4R$	1180	-570	122
$\langle 011 \rangle$ -poled crystal	$2R$	860	450	2160
$\langle 111 \rangle$ -poled crystal	$1R$	97	-43	2380
PMN-PT ceramic	/	800	-395	1090

Data are from Zhang, S.; Li, F.; Jiang, X.; Kim, J.; Luo, J.; Geng, X., *Prog. Mater. Sci.* **2015**, *68*, 1–66.

findings suggest that MPB constitutes an important factor responsible for the excellent piezoelectric performance in relaxor-based piezoelectric single crystals.

In 1997, Park and Shrout proposed a polarization rotation model to explain the high field-induced strain and piezoelectric performance of $\langle 001 \rangle$ -oriented relaxor-PT single crystals. They suggested that the polarization vector of the rhombohedral phase could rotate from the $\langle 111 \rangle$ direction towards the $\langle 001 \rangle$ axis in which the electric field is applied, which could result in the observed large piezoelectricity.⁷ This conjecture was later developed by Fu and Cohen into the “polarization rotation mechanism” by means of the first principles calculations based on simple ferroelectric perovskite BaTiO_3 .⁷⁹ Fig. 16 shows the polarization rotation from the $\langle 001 \rangle$ to $\langle 111 \rangle$ direction along the a-b-c-d-e and a-f-g-e paths, respectively, and the corresponding calculated free energies. It is clearly more favorable for the polarization to rotate via the a-f-g-e path, i.e., within the $\{110\}$ symmetry plane of the monoclinic phase, due to the flatter energy profile. The result not only supports the polarization rotation mechanism, but also reveals the crucial role of the monoclinic phase in facilitating such a rotation.

As shown in Fig. 17, the polar axes of the monoclinic phases in the MPB are free to rotate within their mirror planes between the limiting directions of the rhombohedral (R), orthorhombic (O) and tetragonal (T) phases. Since the presence of a monoclinic (or orthorhombic) phase(s) is a common structural feature for the relaxor-PT crystals of MPB compositions, it is sensible to state that the excellent piezoelectric performance in relaxor-based single crystals can generally be attributed to the energetically favorable polarization rotation facilitated by the monoclinic phase(s) within the MPB.

The polarization rotation mechanism is also successful in explaining the high shear piezoelectric response (e.g., d_{15}) found in relaxor-based piezoelectric single crystals. As shown in Fig. 18, by applying an electric field perpendicular to the polar axis of a tetragonal piezo crystal, a shear deformation of the lattice is induced. At the same time, the polarization rotates in order to minimize the

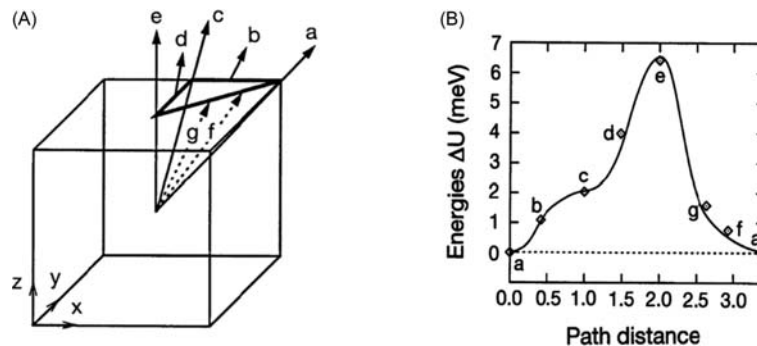


Fig. 16 Polarization rotation paths (A) and related free energies (B) obtained from the first principles calculations based on BaTiO_3 . Reprinted with permission from Fu H.; Cohen, R. E., *Nature* **2000**, *403* (6767), 281–283.

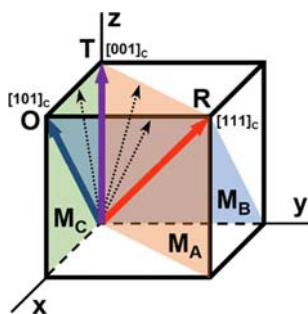


Fig. 17 Possible monoclinic phases found in relaxor-based piezoelectric single crystals. The polarization vectors are constrained to lie in the mirror plane of each phase.

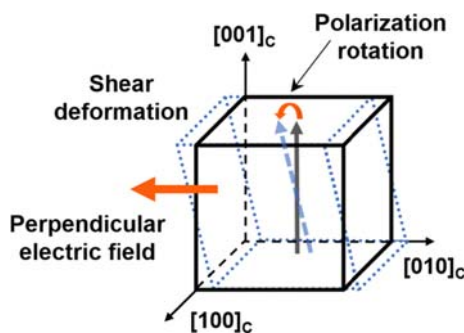


Fig. 18 Shear piezoelectric deformation and polarization rotation under an electric field perpendicular to the polar axis in a tetragonal single crystal.

free energy.^{9,77} Thus, the high piezoelectricity results from the ease of polarization rotation under an electric field.⁸³ Thermodynamics analysis has indicated that the shear piezoelectric coefficient peaks in the MPB region,⁸⁴ which further confirms that the polarization rotation is notably facilitated in the MPB region, thereby leading to enhanced piezoelectric properties.

4.05.3.7.2 Meso- to nanoscopic understanding: Roles of local polar regions

The above-mentioned mechanisms give a general explanation of the excellent piezoelectric performances near the MPB. However, they could not explain why relaxor-based piezoelectric single crystals exhibit much higher piezoelectric activity than other ferroelectric solid solutions with MPB. Therefore, it is necessary to examine the uniqueness of relaxor-based piezoelectric single crystals from a more microscopic perspective.

In contrast to normal ferroelectrics, the most prominent microstructural feature of relaxor-based piezoelectric single crystals is the presence of the polar nanoregions which originate from the relaxor end member, such as PMN, as mentioned in [Section 4.05.3.1](#). Such a special nanostructure is believed to be responsible for enhanced piezoelectric properties in relaxor-based piezoelectric single crystals.

A general model to express the nanoscale structure of relaxor-based piezoelectric single crystals is the coexistence of PNRs and the long-range ferroelectric domains near the MPB region. Xu et al. indicated that PNRs are associated with the phonon softening and phase instability in the PZN-PT single crystals, which may account for the ultrahigh piezoelectricity in relaxor-based single crystals.⁸⁵ Manley et al. proposed that there is a hybridization of PNRs with transverse acoustic (TA) phonons, and the aligned PNRs under an external electric field can enhance the phonon softening, further promoting the piezoelectric properties of relaxor-based piezo-/ferroelectrics.⁸⁶ Recent investigations by Li et al. suggest that the PNRs can behave as seeds to facilitate macroscopic polarization rotation and contribute to 50–80% of the room temperature dielectric/piezoelectric properties.^{15,87} Although controversy remains, most investigations point to a strong correlation between PNRs and the high piezoelectricity in relaxor-based piezoelectric single crystals.

4.05.3.8 Perspectives and challenges for relaxor-based piezoelectric single crystals

Relaxor-based single crystals show excellent piezoelectric performance, and they have already demonstrated significant advantages in a series of electromechanical transducers with higher sensitivity, wider bandwidth and better resolution. However, to meet the ever-increasing demands in more advanced applications, some important issues need to be solved. The first issue is how to further enhance the temperature stability and optimize the piezoelectric properties for a broader working temperature range. Requirements such as high T_C , high T_{R-T}/T_{MPB} , high electromechanical coupling factor, high Q_m , and low loss should be satisfied. To achieve this goal, careful chemical modifications need to be performed. Another challenge is to gain a deeper insight into the structure-property

relations so as to understand the complex nanostructures and the origin of the ultrahigh piezoelectric response in relaxor-based piezoelectric single crystals.

4.05.4 Lead-free perovskite piezoelectric materials

4.05.4.1 Restriction of lead components in applications

As discussed in Sections 4.05.2 and 4.05.3, a majority of materials with excellent piezoelectric performances in the market contain lead. In PZT ceramics and relaxor-based single crystals, the content of lead oxide (PbO) exceeds 60 wt%, which might cause environmental and health concerns during the preparation, usage, and even disposal and recycling of such materials. As a result, a series of laws and regulations have been introduced to restrict or prohibit the use of lead in the electrical and electronic industries. For example, the European Union passed the “Restriction of Hazardous Substances (RoHS)” law in 2003 and the “Waste Electrical and Electronic Equipment (WEEE)” law in 2012. Japan passed the “Household Electronic Products Recycling Law” and China established the “Electronic Information Product Pollution Control Management Regulation” in 2006.^{88–91} Therefore, it is essential and urgent to develop lead-free piezoelectric materials with high performance for more environmentally friendly applications.

4.05.4.2 Lead-free piezoelectric materials: A historical overview

Lead-free (perovskite) piezoelectric materials were in fact the first oxide piezo-/ferroelectrics developed following the discovery of barium titanate (BaTiO₃) ceramic in the 1940s, but the major interest shifted quickly to lead-based piezoelectrics after the discovery of PZT ceramics with much better properties. For a long time, the piezoelectric performance of lead-free materials had been thought to be much inferior to that of lead-based materials. Nevertheless, attempts to replace lead have never stopped and several lead-free piezoelectric material systems have been developed, such as (Bi_{1/2}Na_{1/2})TiO₃ (BNT), (K,Na)NbO₃ (KNN), BiFeO₃ (BF) and their derivatives.^{47,89,90,92–96} A breakthrough was achieved in 2004 when Saito et al. reported a remarkably high piezoelectric coefficient d_{33} up to 416 pC·N⁻¹ in KNN-based textured ceramics.⁹⁷ This discovery has fueled a world-wide campaign for research and development of novel lead-free piezoelectric materials. During the past nearly two decades, driven by the increasing concerns about lead toxicity, stimulated by policy and regulations and inspired by the breakthrough, extensive efforts have been made, and remarkable progress has been achieved, in the research and development of lead-free perovskite piezoelectrics, including the BaTiO₃-based, (Bi_{1/2}Na_{1/2})TiO₃-based, (K,Na)NbO₃-based, and BiFeO₃-based material systems, as illustrated by the statistics shown in Fig. 19. A more detailed discussion on these progresses will be given in the subsequent sections.

4.05.4.3 Approaches to obtain lead-free piezoelectric materials with better performance

The main strategies used to design and synthesize lead-free perovskite piezoelectric materials with better performance are briefly summarized below, followed by a more detailed discussion on each of the representative material systems in Section 4.05.4.4.

4.05.4.3.1 Chemical modification and phase boundary engineering

The concept of MPB discovered in PZT has become a great success in developing piezoelectrics with high performance. In the temperature-composition phase diagram of PZT, the MPB is a nearly vertical line (or region), dependent on composition but almost independent of temperature, which distinguishes it from other phase boundaries. Different from PZT, the phase boundaries in most

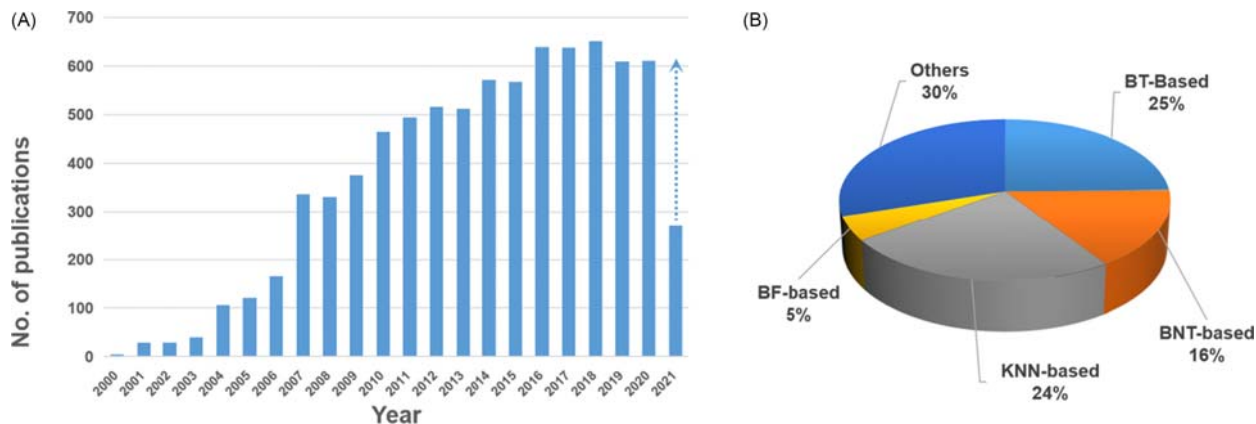


Fig. 19 (A) Annual publications on lead-free piezoelectric materials from 2000 up to date obtained from ISI Web of Science using the keywords “lead-free” and “piezoelectric.” (B) Distribution of the publications according to different lead-free material systems.

lead-free piezoelectric materials are dependent both on composition and temperature, and thus considered to be a polymorphic phase boundary (PPB) (Fig. 20).^{1,88,90,91}

By chemical modifications (e.g., ion substitutions, doping, forming binary or ternary solid solutions, etc.), different phase boundaries can be introduced in lead-free piezoelectric materials. In the vicinity of the phase boundary, different phases generally coexist with a very low energy barrier between them, which makes the polarization rotation among different symmetries possible, leading to enhanced piezoelectric performance near the phase boundary.

Detailed examples of phase boundary engineering will be presented in Section 4.05.4.4.

4.05.4.3.2 Microstructure engineering

Microstructure engineering is an effective strategy to enhance piezoelectric properties. The microstructure here is referred to the grain size and arrangement and domain structure. The grain size can be tailored by preparation conditions, which also determine the domain structure. Generally, the domain size and grain size change by the same trend in polycrystalline materials. Although the basic configuration of the ferroelectric/ferroelastic domains is governed by the symmetry of the crystal, the actual domain structure is also determined by the mechanical and electrical compatibility principles.

A useful way to improve the electromechanical properties in lead-free piezoelectric materials is to regulate the domains with sub-micrometer or even nanometers in size. Domains of relatively small size are highly active to the stimuli and can facilitate domain wall motion due to low energy barrier. Under an electric field, the domain structure in some lead-free piezoelectric materials can transform, accompanied by a field-induced phase transformation, leading to a significant enhancement of piezoelectricity.

4.05.4.3.3 Growth of single crystals and preparation of textured ceramics

Compared with polycrystalline materials, single crystals generally exhibit improved piezoelectricity with less defects and better-aligned polarizations. Therefore, the growth of single crystals has also proved to be an effective way to achieve better piezoelectric performance in lead-free perovskite materials. However, growing single crystals is costly, time-consuming and sometime very difficult. To overcome these drawbacks, textured ceramics can be a viable alternative to single crystals as they exhibit piezoelectric properties close to single crystals and are more cost-effective. A thorough discussion on textured ceramics will be given in Section 4.05.6.

4.05.4.4 Progress in main lead-free piezoelectric material systems

The above-mentioned methods and principles provide a general guide to optimize the performance of lead-free piezoelectric materials. In this section, recent progress in some key lead-free perovskite piezoelectric systems is overviewed.

4.05.4.4.1 BaTiO₃-based systems

Barium titanate (BaTiO₃) was initially reported to show a very high dielectric permittivity of ~ 2000 and a moderate piezoelectric coefficient of $d_{33} \approx 191 \text{ pC}\cdot\text{N}^{-1}$ in the form of ceramics at room temperature.¹ By optimizing the microstructure (including grain and domain structures), the piezoelectric properties of BT ceramics can be improved with $d_{33} > 400 \text{ pC}\cdot\text{N}^{-1}$,^{98,99} and the best piezoelectric and dielectric performance is found in BT ceramics with a grain size $\sim 1 \mu\text{m}$, as shown in Fig. 21.¹⁰⁰

BT has three phase transitions, from rhombohedral to orthorhombic, orthorhombic to tetragonal, and tetragonal to cubic at around -90°C (T_{R-O}), 0°C (T_{O-T}) and 120°C (T_C), respectively.¹ The phase boundaries can be adjusted by chemical modifications to enhance the piezoelectricity of BT-based ceramics. An effective way is to shift T_{R-O} and T_{O-T} so that the R-T and O-T phase boundaries could merge around room temperature. In this way, a large d_{33} of $620 \text{ pC}\cdot\text{N}^{-1}$ was obtained in the $0.5\text{Ba}(\text{Ti}_{0.8}\text{Zr}_{0.2})\text{O}_3-0.5(\text{Ba}_{0.7}\text{Ca}_{0.3})\text{TiO}_3$ (BZT-BCT) ceramics with a rhombohedral-tetragonal-cubic “tricritical” point near room temperature.¹⁰¹ The high piezoelectricity can be attributed to the “tricritical” point which leads to a low energy barrier for structural change and polarization rotation between the R and T phases (Fig. 22).^{101,102} The piezoelectric performance of BZT-BCT was further improved ($d_{33} = 755 \text{ pC}\cdot\text{N}^{-1}$ and $d_{33}^* = 2027 \text{ pm}\cdot\text{V}^{-1}$) by developing highly textured ceramics.¹⁰³

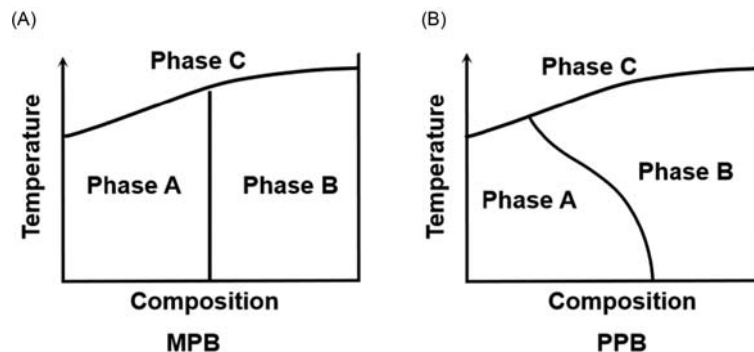


Fig. 20 Schematic phase diagrams showing the difference between (A) morphotropic phase boundary (MPB) and (B) polymorphic phase boundary (PPB).

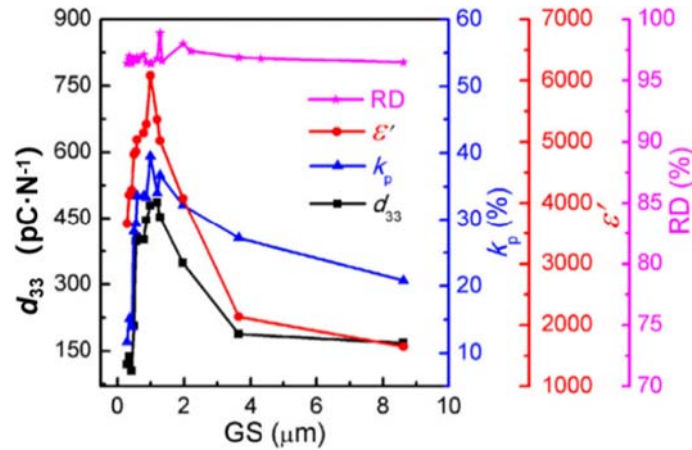


Fig. 21 Dependences of the dielectric permittivity (ϵ'), piezoelectric coefficient (d_{33}), planar electromechanical coupling factor (k_p), and relative density (RD) on the grain size (GS) of the BT ceramics. Reprinted with permission from Huan, Y.; Wang, X.; Fang, J.; Li, L., *J. Eur. Ceram. Soc.* **2014**, *34* (5), 1445–1448.

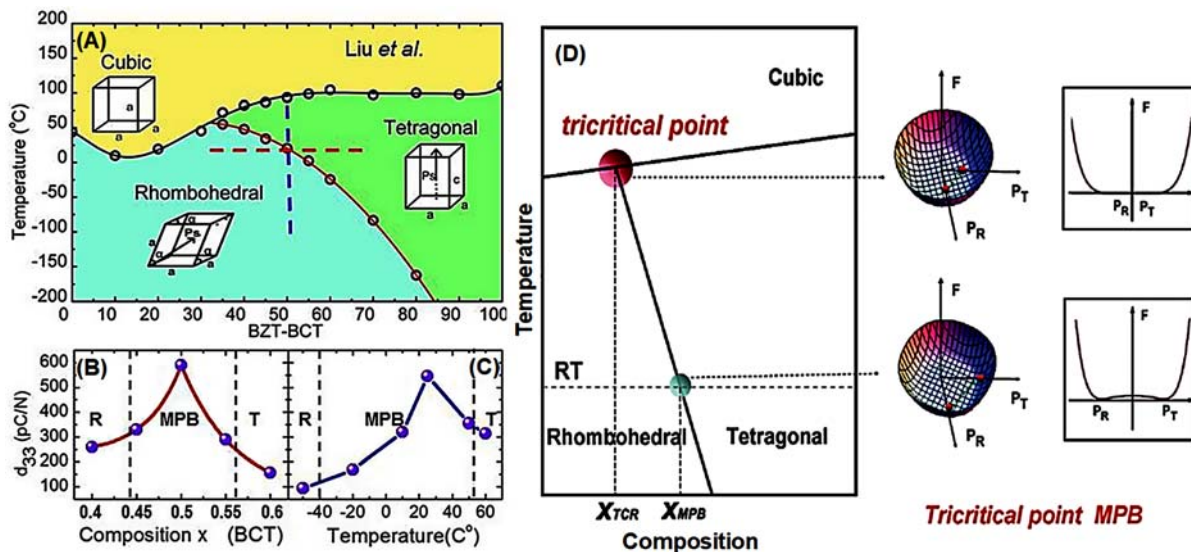


Fig. 22 (A) Temperature—composition phase diagram of $(1-x)\text{Ba}(\text{Zr}_{0.2}\text{Ti}_{0.8})\text{O}_3-x(\text{Ba}_{0.7}\text{Ca}_{0.3})\text{TiO}_3$. (B) Composition dependence of d_{33} across the composition-induced R-MPB-T transition along the horizontal line (red) in (A). (C) Temperature-dependence of d_{33} across the temperature-induced R-MPB-T transition along the vertical line (blue) in (A). (D) Free energy profiles of compositions near the “tricritical” point. Reprinted with permission from Liu, W.; Ren, X., *Phys. Rev. Lett.* **2009**, *103* (25), 257602. Gao, J.; Xue, D.; Wang, Y.; Wang, D.; Zhang, L.; Wu, H.; Guo, S.; Bao, H.; Zhou, C.; Liu, W.; Hou, S.; Xiao, G.; Ren, X., *Appl. Phys. Lett.* **2011**, *99* (9), 092901.

Although high piezoelectric performance has been achieved in BT-based ceramics, a major drawback is their low T_C and significant temperature-dependent physical properties. Therefore, BT-based ceramics have very limited applications.

4.05.4.4.2 $(\text{Bi}_{1/2}\text{Na}_{1/2})\text{TiO}_3$ -based systems

Bismuth sodium titanate ($(\text{Bi}_{1/2}\text{Na}_{1/2})\text{TiO}_3$, BNT) is another well-studied lead-free piezoelectric material which was first discovered by Smolenskii et al. in 1961.⁴⁷ The crystal structure at room temperature was originally determined to be rhombohedral ($R3c$ space group) on average, while recent investigation indicated that the structure is more likely to be monoclinic (Cc).^{104,105} BNT ceramics exhibit a large remanent polarization P_r of $38 \mu\text{C}\cdot\text{cm}^{-2}$, a high coercive field E_c of $73 \text{ kV}\cdot\text{cm}^{-1}$ and a relatively low piezoelectric coefficient d_{33} of $\sim 70 \text{ pC}\cdot\text{N}^{-1}$. However, BNT ceramics suffer from high conductivity and low density which make it difficult to pole them properly.^{106,107} Therefore, pure BNT ceramics can hardly be used in piezoelectric devices.

To improve the piezoelectric performance, chemical modifications have been carried out on BNT to engineer phase boundaries. Generally, two types of phase boundaries are established, which are named as PB1 and PB2, respectively. PB1 delimits the ferroelectric rhombohedral and tetragonal phases at room temperature, at which improved piezoelectric coefficients can be obtained, such as in the $(\text{Bi}_{1/2}\text{Na}_{1/2})\text{TiO}_3\text{-BaTiO}_3$ (BNT-BT) ceramics with $d_{33} \approx 200 \text{ pC}\cdot\text{N}^{-1}$.⁹² In addition to the beneficial effects of the

phase boundary, the enhancement of the piezoelectricity in BNT-BT ceramics could be attributed to the unique domain structures at the phase boundary where the ferroelectric state (with domains size of hundreds of nanometers to several micrometers) and the relaxor state (with polar nanodomains) coexist, as revealed by piezoresponse force microscopy (PFM) (Fig. 23).¹⁰⁸

The piezoelectric coefficient of BNT-based solid solutions can be further improved by growing single crystals. For example, a high d_{33} of $483 \text{ pC}\cdot\text{N}^{-1}$ has been obtained in BNT-BT single crystals.¹⁰⁹

PB2 refers to the phase boundary between the relaxor (nonpolar) and the ferroelectric (polar) phases. Such type of phase boundary generally leads to giant electric-field-induced strain. Fig. 24 shows an example of the field-induced strain in the $(0.94-x)(\text{Bi}_{1/2}\text{Na}_{1/2})\text{TiO}_3-0.06\text{BaTiO}_3-x(\text{K}_{1/2}\text{Na}_{1/2})\text{NbO}_3$ ceramics, which is much larger than that in soft PZT.¹¹⁰ A higher strain of $\sim 0.9\%$ with a higher d_{33} of $840 \text{ pC}\cdot\text{N}^{-1}$ was further achieved in the single-crystal counterpart.¹¹¹ The giant strains in BNT-based materials were believed to arise from the electric-field-induced relaxor to ferroelectric phase transition and the related domain switching.¹¹²

However, a major shortcoming of BNT-based materials is the large strain hysteresis caused by domain-wall motion, which is undesirable for actuator applications. Additionally, the induced strain in BNT-based materials is accompanied by a decrease in the ferroelectric-to-relaxor transition temperature T_{F-R} (or depoling temperature T_d).^{88,91} Although the best strain performance can be achieved in materials with T_{F-R} or T_d around room temperature, it exhibits poor temperature stability. Therefore, to make the BNT-based materials viable for applications, further efforts should be made to decrease the strain hysteresis and to improve the temperature stability.

4.05.4.4.3 (K,Na)NbO₃-based systems

Potassium sodium niobate ((K,Na)NbO₃, KNN) was firstly reported by Shirane et al. in 1954, which showed a high T_C of $\sim 410^\circ\text{C}$, a large remanent polarization P_r of $\sim 33 \mu\text{C}\cdot\text{cm}^{-2}$ and a moderate piezoelectric coefficient of $\sim 80 \text{ pC}\cdot\text{N}^{-1}$ (for $(\text{K}_{1/2}\text{Na}_{1/2})\text{NbO}_3$).^{1,93} During the last two decades, extensive investigations have been conducted on KNN-based piezoelectrics, and the piezoelectricity has been substantially improved.⁹⁰

KNN exhibits complex phase transitions with the changes of composition and temperature, resulting in various phase boundaries in KNN-based materials. For example, $(\text{K}_{1/2}\text{Na}_{1/2})\text{NbO}_3$ undergoes the rhombohedral \rightarrow orthorhombic \rightarrow tetragonal \rightarrow cubic phase transitions at around -160°C (T_{R-O}), 200°C (T_{O-T}), and 410°C (T_C), respectively. Generally, three kinds of phase

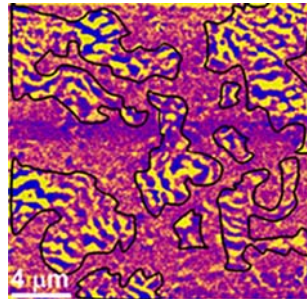


Fig. 23 Out of plane phase images of BNT-BT ceramics measured by piezoresponse force microscopy (PFM). Areas encircled by dark lines indicate ferroelectric domains, and the remaining indicates polar nanodomains. Reprinted with permission from Zhao, J.; Zhang, N.; Ren, W.; Niu, G.; Walker, D.; Thomas, Pamela A.; Wang, L.; Ye, Z.-G., *J. Am. Ceram. Soc.* **2019**, *102* (1), 437–447.

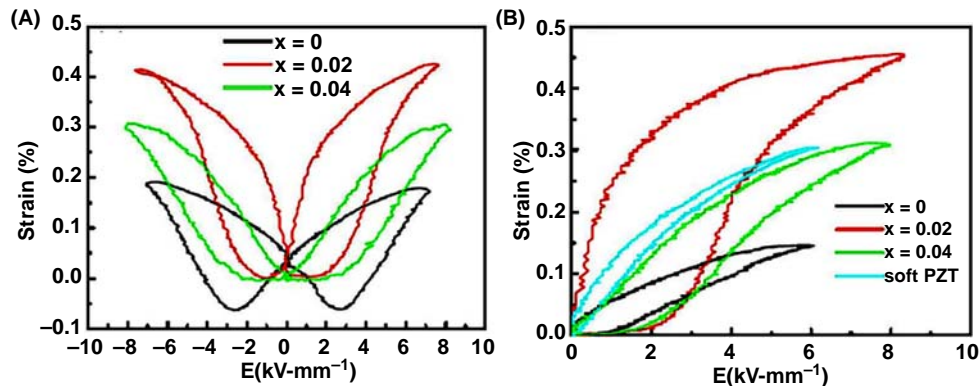


Fig. 24 Electric field-induced (A) bipolar and (B) unipolar strains in the $(0.94-x)(\text{Bi}_{1/2}\text{Na}_{1/2})\text{TiO}_3-0.06\text{BaTiO}_3-x(\text{K}_{1/2}\text{Na}_{1/2})\text{NbO}_3$ ceramics. Data of soft PZT are also given for comparison. Reproduced with permission from Zhang, S.-T.; Kounga, A. B.; Aulbach, E.; Ehrenberg, H.; Rödel, J., *Appl. Phys. Lett.* **2007**, *91* (11), 112906.

boundaries are used to design KNN-based materials with better piezoelectricity, i.e., the rhombohedral-orthorhombic (R-O), orthorhombic-tetragonal (O-T), and rhombohedral-tetragonal (R-T) phase boundaries (Fig. 25). By appropriate chemical modifications, these phase boundaries can be shifted to room temperature, leading to enhanced piezoelectricity. An example of this approach is the downward displacement of the O-T phase boundary by doping KNN with the Li^+ and Ag^+ ions, which results in good piezoelectricity with $d_{33} > 300 \text{ pC}\cdot\text{N}^{-1}$.¹¹³ Alternatively, the R-O phase boundary can also be moved upward to room temperature by the Sb^{5+} and Ta^{5+} doping, however, the piezoelectricity ($d_{33} \approx 200 \text{ pC}\cdot\text{N}^{-1}$) is lower than the former.¹¹⁴ It is also possible to suppress the orthorhombic phase by chemical modifications, and the resulting R-T phase boundary has proved to be beneficial to obtaining better piezoelectricity ($d_{33} > 400 \text{ pC}\cdot\text{N}^{-1}$), as demonstrated in materials like $0.96(\text{K}_{0.5}\text{Na}_{0.5})_{0.95}\text{Li}_{0.05}\text{Nb}_{0.93}\text{Sb}_{0.07}\text{O}_3\text{-}0.04\text{BaZrO}_3$.^{115–117}

In addition to the phase boundary engineering, formation of textured microstructure is also an effective way to enhance the piezoelectric properties of KNN-based materials. For example, an ultrahigh piezoelectric coefficient of $d_{33} \approx 700 \text{ pC}\cdot\text{N}^{-1}$ and a high planar electromechanical coupling factor ($k_p \approx 0.76$) have been found in textured KNN-based ceramics.¹¹⁸

Although the KNN-based piezoelectric materials exhibit decent piezoelectricity, they possess a common disadvantage. Namely, their properties are highly temperature-sensitive due to the polymorphic phase transition(s). Therefore, additional efforts are being made to improve the temperature stability of this class of materials.^{90,119}

4.05.4.4 BiFeO₃-based systems

Bismuth ferrite (BiFeO_3 , BF) has received a great deal of attention due to its multiferroicity with the coexistence of magnetic and ferroelectric orders at room temperature. Besides, BF is also a promising lead-free piezoelectric material with a giant polarization ($P_s > 60 \mu\text{C}\cdot\text{cm}^{-2}$) and an ultrahigh Curie temperature ($T_C = 830 \text{ }^\circ\text{C}$).^{120,121} BF has a rhombohedral symmetry ($R3c$ space group) at room temperature and no other structural phase transition occurs before transforming to the paraelectric phase at T_C . However, the preparation of pure BF is problematic due to its unstable perovskite phase. Moreover, it suffers from a large leakage current arising from the existence of mixed valences of $\text{Fe}^{3+}/\text{Fe}^{2+}$ and oxygen vacancies, which makes it difficult to achieve the expected piezoelectric performances.¹²² As a consequence, chemical modifications, such as forming solid solutions, have been used to stabilize the perovskite phase and to improve the electric properties. In BF-BT-based materials, one of the most promising lead-free systems, MPBs between the rhombohedral and tetragonal phases were established, similar to PZT. A breakthrough was made in the Ga-modified BF-BT ceramics, which exhibits a high T_C up to $454 \text{ }^\circ\text{C}$ along with excellent piezoelectric performance ($d_{33} = 454 \text{ pC}\cdot\text{N}^{-1}$).^{123,124} It is worth noting that the piezoelectric properties in BF-based materials are very sensitive to the processing parameters (e.g., annealing and quenching) which influence their crystal symmetry and microstructure and thereby the properties.^{124–126}

4.05.4.5 Perspectives and challenges of lead-free perovskite piezoelectric materials

During the last two decades, extensive studies have been carried out on lead-free perovskite piezoelectric materials. Especially, significant progress has been made on such material families as BT-based, BNT-based, KNN-based and BF-based piezoelectrics by chemical modifications, microstructure engineering and other techniques. Up to now, the piezoelectric performance of lead-free piezoelectric materials of perovskite structure has been improved remarkably, with the best performance being comparable to that of the lead-based piezoelectric materials. However, the following issues still need to be addressed before large-scale applications of those materials become viable.

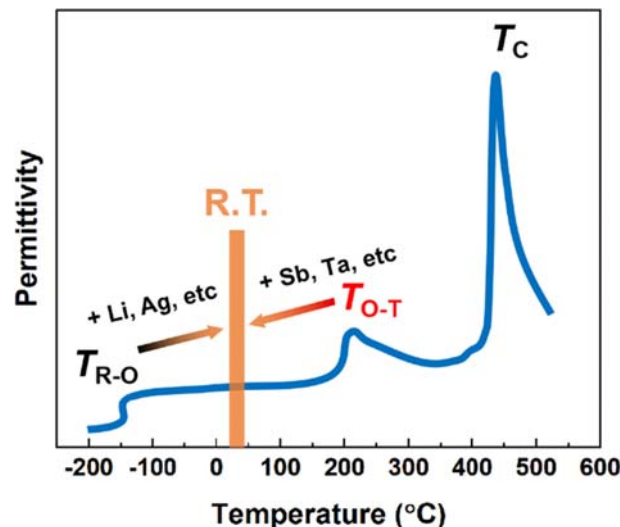


Fig. 25 Phase boundary engineering strategy in KNN-based materials. R.T. represents room temperature.

- (I) Improving the temperature stability. Owing to the nature of polymorphic phase transition(s) around room temperature in most of the lead-free perovskite piezoelectric materials, a common shortcoming is their strong temperature-dependent properties. For example, BT-based materials show high piezoelectricity but very low T_C . BNT-based materials suffer from low depoling temperature below T_C . Similarly, KNN-based materials exhibit a large d_{33} which is strongly temperature dependent. This shortcoming has been a major obstacle preventing lead-free piezoelectric materials from being used in applications. To solve this problem, further chemical modifications are necessary to form phase boundaries with MPB characteristics rather than PPT.
- (II) Enhancing the strain and reducing its hysteresis. BNT-based piezoelectric materials show an improved electric-field induced strain compared to that in lead-based and other lead-free piezoelectric materials. However, they suffer from a large strain hysteresis, which has hindered their application for actuators. The strain level of other lead-free piezoelectric materials is still inferior to that of most PZT-based materials. Therefore, extra efforts are needed to improve the strain in lead-free piezoelectric materials.
- (III) Optimizing the microstructure and reducing the leakage current. BF-based materials exhibit high piezoelectricity and good temperature stability, which are comparable to lead-based piezoelectric materials. However, further efforts should be devoted to optimize the microstructure and to reduce the leakage current.

With continuous efforts and steady progress, it is highly expected that the lead-free piezoelectric materials could partially replace the lead-based piezoelectric materials in a wide range of practical applications in the near future.

4.05.5 High-temperature piezoelectric materials

4.05.5.1 Need for high-temperature piezoelectric materials

In many technological applications, piezoelectric materials that can work in a broad temperature range are needed. For example, in the downhole oil industry, piezoelectrics for temperature, pressure, and flow rate sensing, and ultrasonic imaging, are all required to work at temperatures over 200 °C for deep drilling. In automobile electronics, high-temperature devices are needed for signal conditioning and activity control, some of which are required to be functional at temperatures up to 300 °C. In aerospace, engine vibration monitoring requires piezoelectric devices to work stably for tens of thousands of hours at high temperatures. Those harsh working environments pose severe challenges to piezoelectric materials in terms of temperature range and stability.^{127,128}

Some basic requirements must be satisfied for piezoelectric materials to be useful at high temperatures, including high-temperature stability (high depoling temperature), good piezoelectric performances (high piezoelectric coefficients, electromechanical coupling factor, and mechanical quality factor), high resistivity (low dielectric loss), high mechanical strength, small thermal expansion, etc.^{129,130} For example, currently, the commercially available piezoelectric materials are mainly PZT-based ceramics, but they suffer from thermal depolarization at around 150 °C, making them unsuitable for high-temperature piezoelectric devices. Therefore, it is crucial to develop piezoelectric materials with high piezoelectric performance and thermal stability.

Given the strict requirements, only a limited number of piezoelectric materials are available for high-temperature applications, and they can be primarily classified into two groups, i.e., single crystals and polycrystalline materials. Some representative high-temperature piezoelectric materials from each group are discussed below.

4.05.5.2 High-temperature piezoelectric single crystals

Piezoelectric single crystals constitute the major part of high-temperature piezoelectric materials. Since the discovery of quartz, several piezoelectric single crystals have been developed, including tourmaline, LiNbO₃, lithium tetraborate, AlN, langasite, quartz analogs, rare earth-calcium oxyborate, etc.

4.05.5.2.1 Quartz (SiO₂)

Quartz (silicon dioxide SiO₂) is the first discovered, and still the most widely used, piezoelectric crystal. At room temperature, it crystallizes in the trigonal system with 32 point group (α phase), and upon heating, it transforms to the hexagonal system (β phase) at 573 °C. At first, natural quartz was mainly used, but now it has been widely replaced by synthetic quartz grown by the hydrothermal method. Quartz possesses such properties as excellent electrical resistivity ($> 10^{17}$ Ω cm at room temperature), ultralow mechanical loss, and narrow bandwidth, which are nearly temperature independent. Therefore, quartz crystals have been widely used in oscillators, resonators, and filters. However, the drawbacks of quartz crystal include low dielectric constant ($\epsilon_r = 5$), weak piezoelectric coefficient ($d_{11} = 2.31$ pC·N⁻¹), low α - β phase transition temperature and low mechanical twinning temperature (~ 300 °C), which limit their further applications at high temperatures.^{129,131–133}

4.05.5.2.2 Tourmaline

Tourmaline represents the family of aluminum borosilicate minerals with complex compositions of (Na,Ca)(Mg,Fe)₃B₃Al₆Si₆(O,OH,F)₃₁ (sometimes containing Li, Mn, Ti, Fe or Cr). It belongs to the trigonal crystal system with the $3m$ point group, and poses a variety of colors and a wide range of resistivity depending on the composition. The piezoelectric coefficient d_{33} and dielectric permittivity were reported to be 1.8 pC·N⁻¹ and 6–8, respectively. No phase transition occurs in the tourmaline before

its melting point (around 1100 °C). However, the usage temperature is limited to <900 °C due to its high pyroelectric coefficient ($\sim 4 \times 10^{-6} \text{ C} \cdot \text{m}^{-2} \cdot \text{K}^{-1}$) which may interfere with the signals generated from the piezoelectric effect and thus lower the sensitivity of the devices.^{129,131} Attempts were made to grow tourmaline crystals by the hydrothermal method, however, the size is too small for practical applications.^{134,135}

4.05.5.2.3 LiNbO₃ and LiTaO₃

Both lithium niobate (LiNbO₃, LN) and lithium tantalate (LiTaO₃, LT) crystals are ferroelectric. They are isostructural and belong to the trigonal crystal system with the $3m$ point group at room temperature. LN and LT have high T_{C} s of ~ 1150 °C and ~ 720 °C, respectively, reducing the likelihood of depoling at elevated temperatures. The piezoelectric coefficients are $d_{33} = 6 \text{ pC} \cdot \text{N}^{-1}$ and $d_{15} = 68 \text{ pC} \cdot \text{N}^{-1}$ for LN, and $d_{33} = 9 \text{ pC} \cdot \text{N}^{-1}$ and $d_{15} = 26 \text{ pC} \cdot \text{N}^{-1}$ for LT. In addition, LN and LT crystals exhibit excellent optical, electro-optical and pyroelectric properties. Therefore, they have been widely used for piezoelectric sensors, infrared detectors, frequency doublers, electro-optical devices and surface acoustic wave (SAW) devices. Due to their low resistivity at high temperatures, the usage temperature of LN crystal is limited to <600 °C. Nowadays, LN and LT crystals are mainly grown by the Czochralski method with control of stoichiometry, and are widely commercially available.^{129,136,137}

4.05.5.2.4 Lithium tetraborate (Li₂B₄O₇)

Lithium tetraborate (Li₂B₄O₇, LTB) crystals were claimed to be ferroelectric with tetragonal $4mm$ point group.¹³⁸ The piezoelectric coefficient d_{33} and dielectric permittivity ϵ_r' were reported to be $19.5 \text{ pC} \cdot \text{N}^{-1}$ and 10.1, respectively. Though no phase transition occurs below its melting point (917 °C), the high ionic conductivity makes LTB crystals unsuitable for high-temperature applications at low frequencies.¹²⁹

4.05.5.2.5 AlN

AlN has the wurtzite structure with point group $6mm$. The piezoelectric properties of AlN were reported to be $d_{33} = 5.6 \text{ pC} \cdot \text{N}^{-1}$ and $d_{14} = 9.7 \text{ pC} \cdot \text{N}^{-1}$. Bulk AlN single crystals with high quality are difficult to grow and most AlN crystals are grown in the form of thin films by various methods such as molecular beam epitaxy (MBE), metal-organic chemical vapor deposition (MOCVD) and physical vapor transport (PVT). AlN crystal has a high melting point of >2000 °C with no solid-solid phase transitions. The usage temperature of AlN is generally limited to <700 °C due to surface oxidation.^{129,139,140}

4.05.5.2.6 Langasite family

Langasite (La₃Ga₅SiO₁₄, LGS) was initially developed as a laser crystal in the USSR in the 1980s.¹⁴¹ After that, a series of materials with a similar structure to LGS was developed as the langasite family. Langasite family crystals have a general formula of A₃BC₃D₂O₁₄, where A and B represent the cations on decahedral sites coordinated by eight oxygens and an octahedral site coordinated by six oxygens, respectively, and C and D cations occupy the large and small tetrahedral sites, respectively, with the coordination number of four. In LGS, the large La³⁺ occupies the A sites, Ga³⁺ occupies the B site, C sites and part of the D sites, while Si⁴⁺ occupies the remaining D sites. LGS belongs to the trigonal system with 32 point group, and it exhibits piezoelectricity up to its melting (around 1500 °C). Due to the attractive electric performance at high temperatures, such as relatively high piezoelectricity ($d_{11} = 6.2 \text{ pC} \cdot \text{N}^{-1}$), large electromechanical coupling factors ($k_{12} = 0.16$), high resistivity ($9 \times 10^6 \Omega \text{ cm}$ at 500 °C), good temperature stability and low acoustic loss, LGS has been widely used for the fabrication of SAW devices and bulk acoustic wave (BAW) devices.¹⁴² By doping and substitution (e.g., with Al³⁺ and Nb⁵⁺), the dielectric and piezoelectric properties of the langasite family crystals can be further improved. Generally, their usage temperature range is limited to <800 °C due to the reduced resistivity. The langasite family crystals with a large size and high quality can be grown by the Czochralski method and the Bridgman method, making them the most viable materials for broad applications at high temperatures.^{129,131,143}

4.05.5.2.7 Quartz analogs

A number of crystals including GaPO₄, AlPO₄ and GaAsO₄ crystallize in the structure similar to quartz (32 point group), and they constitute the family of quartz analogs that are promising high-temperature piezoelectric materials. For example, GaPO₄ retains the advantages of quartz, with high electric resistivity and mechanical quality factor, while exhibiting higher electromechanical coupling factor and better piezoelectricity ($d_{11} = 4.5 \text{ pC} \cdot \text{N}^{-1}$) at temperatures up to 970 °C, where an α - β phase transition occurs. GaPO₄ crystals can be grown by the hydrothermal growth method.^{129,144}

4.05.5.2.8 Rare earth-calcium oxyborate

Rare earth-calcium oxyborate (ReCOB) crystals have a monoclinic m symmetry with a general formula of ReCa₄O(BO₃)₃, where Re represents a rare earth ion, such as La³⁺, Nd³⁺ or Pr³⁺. ReCOB crystals exhibit superior piezoelectric properties among the high-temperature piezoelectric crystals. For example, the piezoelectric coefficient d_{26} of PrCOB reaches $15.8 \text{ pC} \cdot \text{N}^{-1}$ with an electromechanical coupling factor $k_{24} = 0.315$. Similar to langasite crystals, ReCOB has no phase transition up to its melting temperature (~ 1500 °C), and can be grown by the Czochralski method and the Bridgman method. The usage temperature range of ReCOB is limited by its electrical resistivity, generally up to ~ 1000 °C.^{129,145}

Table 6 lists the structure and physical properties of some representative piezoelectric single crystals, which show great potential for high-temperature electromechanical applications.

Table 6 Summary of the high-temperature piezoelectric single crystals.

Crystals	Symmetry	Piezoelectric coefficient ($\text{pC} \cdot \text{N}^{-1}$)	Transition temperature ($^{\circ}\text{C}$)	Permittivity	Crystal growth method	References
α -Quartz	32	$d_{11} = 2.31$ $d_{14} = 0.73$	573	5	Hydrothermal growth	129,131–133
Tourmaline	3m	$d_{11} = 2.31$	~ 1100	6–8	Hydrothermal growth	129,131
LiNbO ₃	3m	$d_{33} = 9$ $d_{15} = 26$	1150	25	Czochralski method	129,136,137
Lithium tetraborate	4mm	$d_{33} = 19.5$	917	10.1	Czochralski and Bridgman methods	129
AlN	6mm	$d_{33} = 5.6$ $d_{14} = 9.7$	> 2000	~ 9	MBE, MOCVD and PVT	129,139,140
La ₃ Ga ₅ SiO ₁₄	32	$d_{11} = 6.2$	~ 1500	18	Czochralski and Bridgman methods	129,131,142
GaPO ₄	32	$d_{11} = 4.5$	970	~ 6	Hydrothermal growth	129,144
PrCa ₄ O(BO ₃) ₃	m	$d_{26} = 15.8$	~ 1500	15.3	Czochralski and Bridgman methods	129,145

4.05.5.3 High-temperature polycrystalline piezoelectric materials

In addition to the piezoelectric single crystals, some ferroelectric polycrystalline materials are also suitable for high-temperature piezoelectric applications. They are grouped here according to their crystal structures.

4.05.5.3.1 Perovskite system

While most ferroelectric materials with perovskite structure show a relatively low T_C , making them unsuitable for high-temperature applications, the ceramics of bismuth-based perovskite solid solution BiScO₃-PbTiO₃ (BS-PT) were recently found to show both high T_C (450 $^{\circ}\text{C}$) and large piezoelectricity ($d_{33} = 460 \text{ pC} \cdot \text{N}^{-1}$) in the MPB region, which outperform the hard PZT ceramics. Thus, they are promising materials for electromechanical transduction applications at high temperatures.^{146,147} Generally, the usage temperature of these materials is limited to the half of T_C due to the phase transition at MPB.

4.05.5.3.2 Tungsten bronze system

Materials with tungsten bronze structure represent the second largest family of ferroelectrics, with a general formula of $((A1)_2(A2)_4C_4)((B1)_2(B2)_8)O_{30}$. The tungsten bronze structure consists of a complex array of distorted BO₆ octahedra sharing corners, forming two tetra-atomic rings (A1), four five-membered rings (A2), and four triatomic rings (C), as shown in Fig. 26. A representative material of this family is PbNb₂O₆ (lead metaniobate), which possesses a high T_C (570 $^{\circ}\text{C}$), a high degree of piezoelectric anisotropy ($d_{33} = 85 \text{ pC} \cdot \text{N}^{-1}$ and $d_{31} = -9 \text{ pC} \cdot \text{N}^{-1}$) and low mechanical quality factors (~ 20). As a result, PbNb₂O₆ is suitable for non-destructive evaluation type transducers above room temperature.¹

4.05.5.3.3 Bismuth-based layered structure

Bismuth layer structured ferroelectrics (BLSFs) have a general formula of $(\text{Bi}_2\text{O}_2)^{2+}(\text{A}_{m-1}\text{B}_m\text{O}_{3m+1})^{2-}$, where the perovskite slabs $(\text{A}_{m-1}\text{B}_m\text{O}_{3m+1})^{2-}$ are interleaved with the bismuth oxide layers $(\text{Bi}_2\text{O}_2)^{2+}$ along the c -axis (Fig. 27). In this formula, A is a mono-, di-, tri- valent ion or combination of them allowing dodecahedral coordination, B is a combination of cations well suited for octahedral coordination, and m is the number of octahedral layers in the perovskite slab. The number of layers (m) generally varies from 1 to 6, leading to various materials, such as Bi₃TiNbO₉ ($m = 2$), Bi₄Ti₃O₁₂ ($m = 3$), SrBi₄Ti₄O₁₅ ($m = 4$). BLSFs show high T_C s (530–940 $^{\circ}\text{C}$), high mechanical quality factors, good piezoelectricity ($d_{33} = 5\text{--}45 \text{ pC} \cdot \text{N}^{-1}$), low dielectric permittivity, strong anisotropic electromechanical properties and low aging rates. Therefore, they are promising candidates for high-temperature sensor applications. However, drawbacks of BLSFs include high coercive fields, thermal aging, and large dielectric losses at high temperatures. Generally, the usage temperature range of BLSFs is limited to $< 600 \text{ }^{\circ}\text{C}$.^{148,149}

4.05.5.3.4 Layered perovskite structure

Ferroelectric materials with a general formula of $\text{A}_n\text{B}_n\text{O}_{3n+2}$ belong to the layered perovskite structure family. This structure is characterized by corner-sharing BO₆ octahedra and 12-coordinated A cations within the perovskite-like layers, which are linked by A cations at their boundaries (see Fig. 28). Typical materials include Sr₂Nb₂O₇, La₂Ti₂O₇ and Pr₂Ti₂O₇, which exhibit extremely high T_C s of 1342 $^{\circ}\text{C}$, 1482 $^{\circ}\text{C}$ and 1550 $^{\circ}\text{C}$, respectively. The piezoelectric coefficients d_{33} of layered perovskite-structured crystals are on the range of 0.5–2.6 $\text{pC} \cdot \text{N}^{-1}$ with a relatively high resistivity at high temperatures. The usage temperature range of the crystals is estimated to be $< 900 \text{ }^{\circ}\text{C}$.^{150–152}

4.05.5.4 Perspectives and challenges of high-temperature piezoelectric materials

High-temperature piezoelectric materials are of great importance for a wide range of applications. The various materials developed for the purpose follow a general trend that a higher usage temperature corresponds to lower piezoelectricity, as shown in Fig. 29.

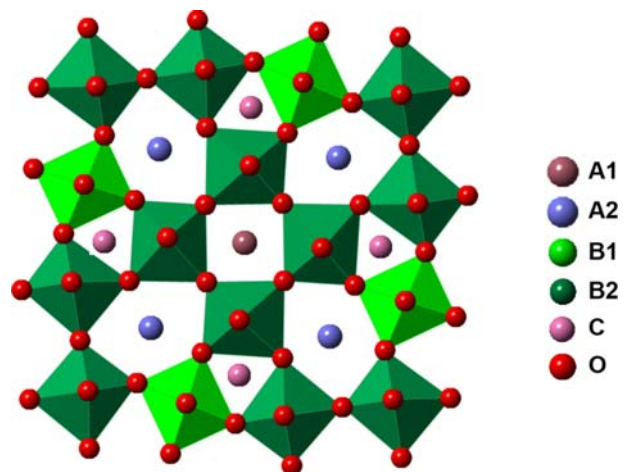


Fig. 26 Tungsten bronze structure.

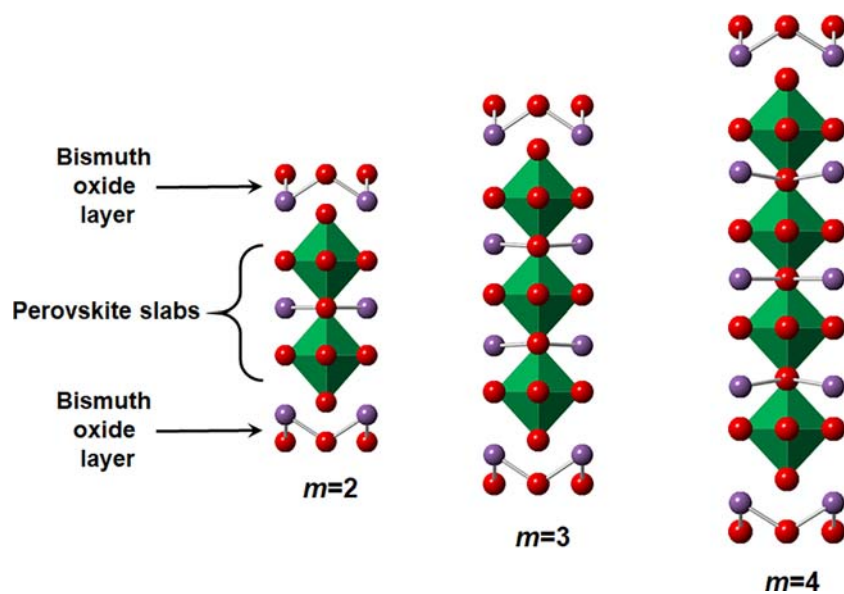


Fig. 27 Bismuth-based layered perovskite structures.

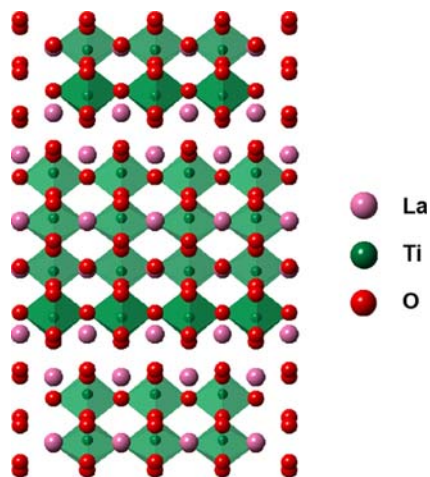


Fig. 28 Crystal structure of $\text{La}_2\text{Ti}_2\text{O}_7$.

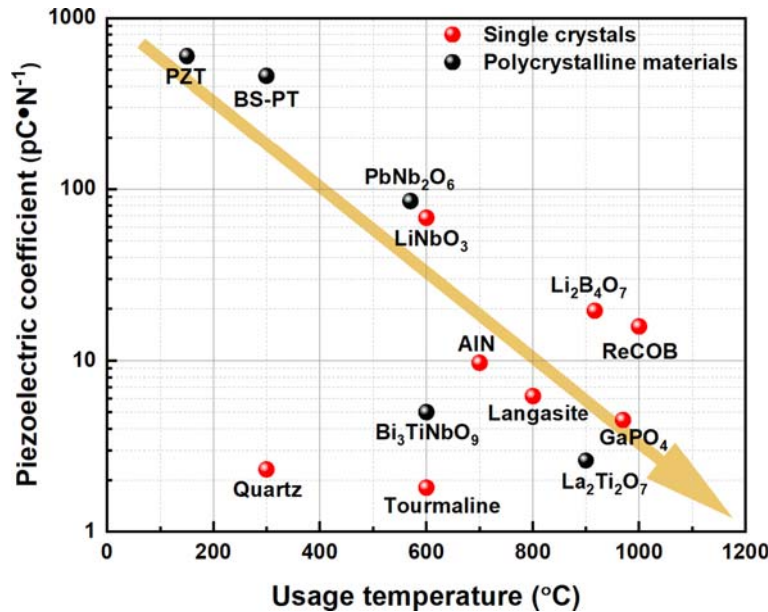


Fig. 29 Piezoelectric coefficient as a function of usage temperature for various high-temperature piezoelectric materials.

Therefore, developing piezoelectric materials with both high piezoelectricity and a broad usage temperature range is still a challenging task which could be fulfilled from the following aspects.

- (I) Enhancing the piezoelectricity of non-perovskite piezoelectric single crystals and piezo-/ferroelectric polycrystalline materials, by appropriate compositional design, optimized preparation conditions and engineered microstructure.
- (II) Increasing the Curie temperature and improving high-temperature piezoelectric performance of perovskite materials by forming solid solutions with a high-temperature MPB.
- (III) Systematically optimizing the key parameters required for high-temperature piezoelectric materials, for example, high resistivity at high temperatures, by rationalized chemical modifications.

4.05.6 Textured piezoelectric ceramics

4.05.6.1 Motivation for developing textured ceramics

Piezoelectric single crystals (with specific orientation) exhibit superior piezoelectric and dielectric performance when compared to their polycrystalline counterparts due to the absence of grain boundaries and the associated defects and the presence of inherent anisotropy in material properties (see Section 4.05.2). However, the growth of single crystals is costly (platinum crucibles are needed) and time-consuming (it usually takes several weeks). In addition, compositional segregation and volatilization usually occur during the crystal growth process, making it very difficult to grow single crystals with desirable compositions.^{73,153}

In this context, textured piezoelectric ceramics can be a good alternative to single crystals. Textured ceramics or grain-oriented ceramics refer to the ceramics in which a particular crystallographic axis is intentionally aligned. Generally, the piezo-/dielectric performances of textured ceramics can be enhanced significantly by increasing the texturing degree, approaching those of single crystals along a particular direction, as schematically presented in Fig. 30. In addition, the preparation of textured ceramics is relatively simpler and more cost-effective than the growth of single crystals (see Section 4.05.6.2.1 for details). Moreover, textured ceramics generally have stronger mechanical strength than their single-crystal counterparts. These features make textured ceramics favorable for use in a wide range of engineering applications.^{153–155}

4.05.6.2 Progress in textured ceramics

4.05.6.2.1 Development of textured ceramics—A brief overview

Textured piezoelectric ceramics were firstly developed with SbSI in Japan in the 1960s.¹⁵⁶ Since then, some efforts have been devoted to ferroelectrics with bismuth layer and tungsten bronze structures which show strong anisotropy (see Section 4.05.5). Originally, hot-pressing and hot-forging processes were utilized to develop texture in those ceramics. Later, these methods were replaced by a simpler technique based on molten salt synthesis and tape casting (the rudiment of templated grain growth which will be discussed later on).^{157,158} By means of these methods, a remarkable improvement of piezoelectricity has been realized

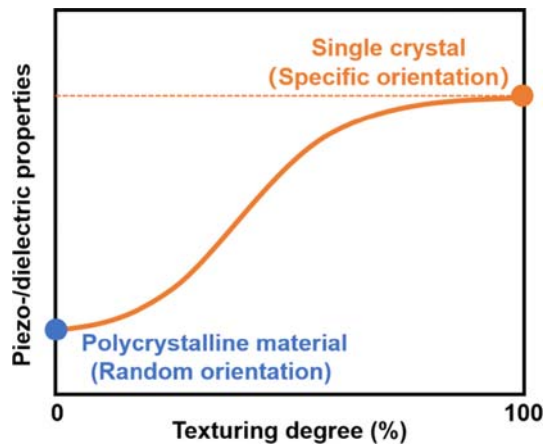


Fig. 30 Schematic diagram of the piezo-/dielectric properties as a function of texturing degree.

Table 7 Physical properties of textured ceramics with different crystal structures.

Materials	Method	Template	Texture degree	d_{33} ($\mu\text{C} \cdot \text{N}^{-1}$)	Enhancement (%) ^a	References
<i>Bismuth layer structure</i>						
$\text{Bi}_4\text{Ti}_3\text{O}_{12}$	TGG	$\text{Bi}_4\text{Ti}_3\text{O}_{12}$	>95%	10	~100	157
$\text{CaBi}_4\text{Ti}_4\text{O}_{15}$	RTGG	$\text{Bi}_4\text{Ti}_3\text{O}_{12}$	~100%	45	~200	159
<i>Tungsten bronze structure</i>						
PbNb_2O_6	TGG	$\text{Bi}_4\text{Ti}_3\text{O}_{12}$	/	145	~70	1,158
$\text{Sr}_{0.53}\text{Ba}_{0.47}\text{Nb}_2\text{O}_6$	TGG	$\text{KSr}_2\text{Nb}_5\text{O}_{15}$	>90	78	~100	160
<i>Perovskite structure</i>						
PMN-PIN-PT	TGG	BT	94%	1620	~100	161
$(\text{Ba}_{0.94}\text{Ca}_{0.06})(\text{Ti}_{0.95}\text{Zr}_{0.05})\text{O}_3$	TGG	BT	98.6%	755	~100	103
0.93BNT-0.07BT	TGG	BNT	92%	322	~100	162
$0.96(\text{K}_{0.5}\text{Na}_{0.5})(\text{Nb}_{0.965}\text{Sb}_{0.035})\text{O}_3-0.01\text{CaZrO}_3-0.03(\text{Bi}_{0.5}\text{K}_{0.5})\text{HfO}_3$	TGG	NaNbO_3	98%	~700	~150	118

^aEnhancement is defined as the percentage increase vs randomly oriented ceramics.

(see Table 7 for some examples). Nevertheless, the piezoelectric performance of the textured ceramics with bismuth layer and tungsten bronze structures are still mediocre, as the development of those textured ceramics has been relatively slow.

Since the 2000s, the development of textured ceramics has been accelerated due to the realization of texture in ferroelectric perovskites by tape casting together with the templated grain growth (TGG)/reactive templated grain growth (RTGG) method.^{97,163} Nowadays, these techniques have been widely adopted to develop high-performance textured piezoelectric ceramics.

4.05.6.2.2 Texturing techniques by TGG and RTGG

Currently, TGG and RTGG are the most commonly used techniques to fabricate textured ceramics. The processing flows of TGG and RTGG are basically the same, as illustrated in Fig. 31. The main procedures can be described as follows: (i) mix the powder, binder and organic solvent by ball milling to prepare a slurry; (ii) add the appropriate pre-synthesized template to the slurry and stir to mix them uniformly; (iii) prepare films by tap casting; (iv) the films are dried, sliced, laminated and pressed to make a green body; (v) the green body is thermal-treated at appropriate temperatures to burn out the organic materials and to allow an oriented growth. Among these procedures, the tape casting process is a crucial step which results in the alignment of the large anisotropic templates in the ceramic film via doctor blading, leading to the fabrication of textured ceramics with a desirable orientation by TGG or RTGG.¹⁵³

The main difference between TGG and RTGG lies in the growth mode of the template grains (Fig. 32). In RTGG, reactive templates are utilized with a crystal structure (at least partially) similar to the target material to be textured. During the subsequent heat treatment, solid-state reactions occur between the templates and complementary reactants in the matrix to form the oriented textured ceramics of desired phase. In other words, the reactions and the directional growth of grains take place simultaneously during sintering, which leads to a large volume shrinkage of the ceramics. In comparison, TGG directly converts the pre-synthesized material to textured ceramics during sintering via epitaxial growth around the templates, that is, no chemical reaction occurs during the thermal treatments.^{164,165}

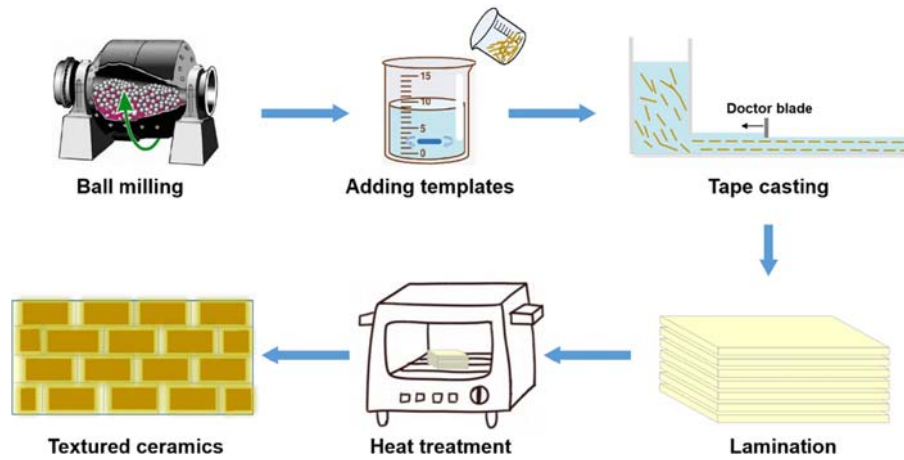


Fig. 31 Processing flow diagram for the preparation of textured ceramics by TGG or RTGG.

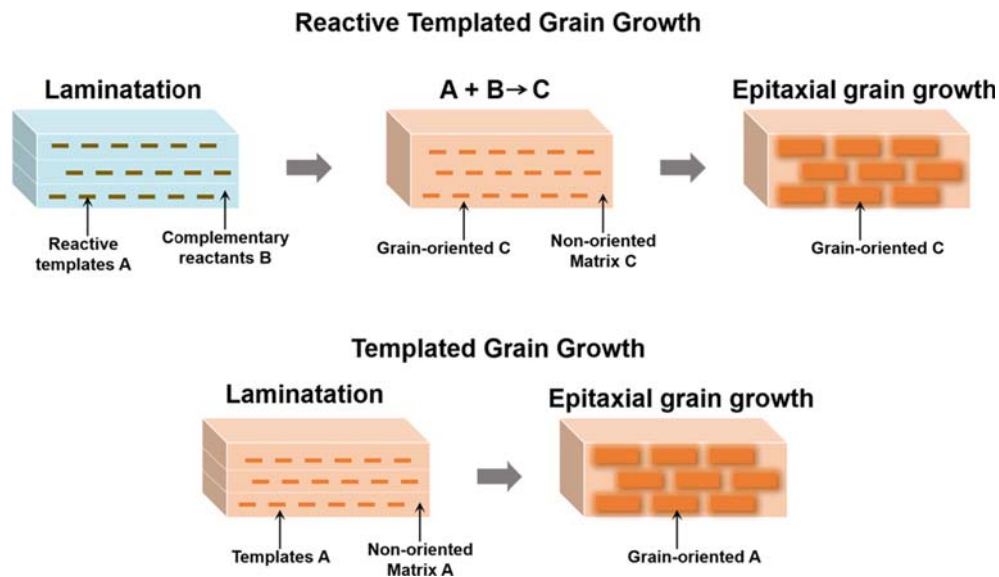


Fig. 32 Schematic diagrams indicating the difference between RTGG and TGG.

4.05.6.2.3 Mechanism of templated grain growth

The templated grain growth is a key process in the fabrication of textured ceramics. In this section, the mechanism of oriented grain growth is introduced.

When the template seeds and ceramic matrix particles have the same chemical composition and crystal structure, but different surface characters, the grains grow epitaxially on the surfaces of the templates. Such a process is called TGG. It is based on the well-known Ostwald ripening phenomenon, that is, the large template grains grow in the way of swallowing the small particles.¹⁶⁶ On the other hand, when the templates and the matrix particles have similar crystal structure and lattice parameters, but different chemical compositions, the morphology of the grains will gradually become the same as that of the templates during the heat treatment. This process is called Hetero-TGG. Since in the TGG process, it is not easy to obtain the templates with desirable morphology and composition,¹⁵³ in most circumstances, Hetero-TGG is used to fabricate textured ceramics. Thus, in this section, we simply use the term TGG which includes Hetero-TGG.

The texturing mechanism by TGG includes three major stages: (i) nucleation on the templates, (ii) rapid growth of textured grains, and (iii) slow growth of textured grains after impingement. In the first stage, sintering provides enough activation energy, leading to a gradually enlarged contact area between the templates and the matrix powder. Driven by the difference in surface energies, nucleation occurs on the surfaces of the templates with the lowest energy. At this time, the crystallization interfaces migrate from the template boundaries into the polycrystalline matrix, accompanied by the formation of textured grains. After nucleation, the grains grow rapidly in a homoepitaxial way. In this case, the process is simply the Ostwald ripening. With the extension of heating time, the large texture grains begin to collide with each other when they reach the critical growth distance, and the texture

development enters the final stage. At this stage, the growth rate of the textured grains decreases remarkably due to the lowering driving force at the boundaries between the impinging grains.^{154,161}

As for RTGG, the mechanism could be more complex, as additional chemical reactions occur during the sintering process. In a way, TGG could be a part of RTGG. Although some preliminary mechanisms have been proposed, such as in situ topochemical conversion and oriented seeding of a phase transformation,^{165,167} more detailed investigations are still needed to better understand the mechanism of RTGG.

4.05.6.2.4 Selection of templates

The texture degree is strongly dependent on the type of templates selected, which should ideally satisfy the following three requirements: (i) the crystal structure of the templates should be similar to the final ceramic system with a lattice mismatch of less than 15%. (ii) The templates must have larger anisotropic dimensions (or higher aspect ratios) (i.e., strip, whisker or sheet) compared to those of the particles in the ceramic matrix (see Fig. 33 for examples), so that they can be easily aligned by the tape casting process. (iii) The templates should be thermodynamically stable.^{153,154,165}

To meet these requirements, several methods have been developed to prepare templates, including the hydrothermal method, molten salt method and sol-gel method. With these techniques, many compounds, such as BT, SrTiO₃, NaNbO₃, BNT, and Bi₄Ti₃O₁₂ have been successfully synthesized as templates and widely used to fabricate textured ceramics of different structures.¹⁶¹

4.05.6.2.5 Piezoelectric properties of textured ceramics

The fabrication techniques developed so far have promoted a rapid development of textured ceramics in recent years, especially, with the perovskite materials. Table 7 compares the piezoelectric performances of the randomly-oriented and textured ceramics with different crystal structures, demonstrating clearly the enhancement of piezoelectricity by forming texture. Compared to other structures, materials belonging to the perovskite family show much higher piezoelectricity. For example, using BT as templates, ultrahigh piezoelectricity was achieved in PIN-PMN-PT textured ceramics, making them a suitable replacement for piezoelectric single crystals in some electromechanical applications.¹⁶¹ It is worth noting that the enhancement of piezoelectric properties is particularly significant in textured lead-free materials. In fact, in recent years, remarkable progress has been made on various lead-free perovskite systems, including KNN-based, BT-based and BNT-based textured ceramics. These materials show superior piezoelectric performance (with d_{33} in the range of 322–755 pC·N⁻¹), comparable to that of PZT-based piezoelectric ceramics.^{97,103,118,162,168} Therefore, developing textured ceramics has proved to be an effective way to augment the piezoelectric properties.

4.05.6.3 Summary and perspectives

Textured ceramics fall between single crystals and randomly oriented polycrystalline ceramics, whose piezoelectric performance can be tuned to be close to that of single crystals. They have the advantages of a relatively simple preparation process, lower cost and a wide range of applicability compared with piezoelectric single crystals. Therefore, textured piezoelectric ceramics have a very promising future for large-scale engineering applications.

To develop textured ceramics with better and well-controlled performances, several issues should be addressed, including (i) investigating the fabrication parameters in a more systematic way by optimizing the slurry composition, casting procedure and heat treatment profile, etc., (ii) developing various methods to fabricate templates with desirable morphology and optimizing the selection of templates, and (iii) clarifying the mechanism of the grain growth, especially in RTGG, to achieve a highest possible degree of texture. Once all these issues have been resolved, textured ceramics will become a truly viable resource of piezoelectric materials for a broad range of applications.

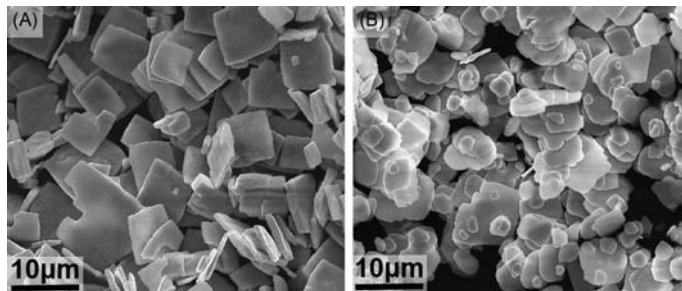


Fig. 33 Morphology of (A) BaTiO₃ and (B) Bi₄Ti₃O₁₂ templates commonly used for preparing textured piezoelectric ceramics.

4.05.7 Applications of piezo-/ferroelectric materials: Present and future

4.05.7.1 General introduction to piezoelectric devices and application

Piezoelectric materials have the unique capability of converting mechanical energy into electric energy, and vice versa, based on the direct and converse piezoelectric effects, respectively, which makes them most versatile for a wide range of industrial, commercial and technological applications. Recent developments of piezo-/ferroelectric materials as presented in the previous sections have accelerated the design, fabrication and commercialization of piezoelectric devices across various sectors. The global market for piezoelectric devices is valued to be \$35.4 billion by 2026, with an expected annual growth rate of 4.3% from the estimated \$28.7 billion in 2021.¹⁶⁹

According to the type of products and their working principles, piezoelectric devices can be divided into four categories: sensors, generators, actuators and transducers (Table 8).

Piezoelectric sensors utilize the direct piezoelectric effect, which can detect changes in force and other related physical quantities such as acceleration, strain, pressure, acoustic wave, vibration, etc., by producing electrical charges. Compared with other types of sensors, piezoelectric sensors have the advantages of high sensitivity, fast response, small size and simple structure, and therefore, they have been widely used for flexible motion, touch, vibration and shock measurements, among many others.^{170–172}

Piezoelectric generators convert mechanical energy into electrical energy. They have the advantages of smaller size and better versatility compared to traditional generators in which electromagnetic coils are used. Piezoelectric generators have been used to harvest electricity from vibrational energy, tidal energy, etc., to power electronic devices like cell phones, and to produce impulse electricity.^{172–174}

Piezoelectric actuators operate based on the converse piezoelectric effect by which mechanical displacement or vibration can be realized under the application of an electric field. Piezoelectric actuators offer a number of benefits such as extremely high resolution (within the nanometer range), very short response time (under 1 ms), high actuation forces, long lifetime, low power consumption and good usability. Therefore, they have been widely used for high-precision positioning, acoustic projection/transmission, ultrasonic welding and active control of vibrations/noises.^{172,175,176}

Piezoelectric transducers use piezoelectric materials to realize conversion between electrical and mechanical energies. Generally, they consist of ultrasound generating parts (transmitters) and echo detecting parts (receivers). Piezoelectric transducers have been used for underwater acoustic applications, non-destructive testing/evaluation, ultrasonic imaging, medical diagnosis, etc.^{9,172,177}

In the subsequent sections, the most important applications at present and some forward-looking technologies of piezoelectric devices are discussed, with focus on the following areas: medical and health care, industrial manufacturing, processing and detection, automotive, consumer electronics and Internet of Things.

4.05.7.2 Medical and health care

Ultrasound imaging has become one of the main medical imaging and diagnosis tools. It uses a transducer to transmit high-frequency acoustic waves, and detect the sound reflected back from the organisms of a human or animal body. After signal treatments, detailed 3D images of the organs/tissues can be reconstructed and displayed at high resolution. This technique helps the doctors to perform physician evaluation and diagnose in a more efficient and accurate way.^{9,119}

Ultrasound has also been used for therapy, in which ultrasonic sound energy is deposited in the tissue to induce various biological effects. Up to now, many applications have been proposed and some of them have been in clinical use for cancer treatment, tissue regeneration, lithotripsy, neurotrauma and neurodegenerative treatment, implant removing, and antifouling treatment.¹⁷⁸

Other medical and health applications of piezoelectric materials and devices include ultrasonic atomizing, hearing aids, dental scaling, precision dosing, and various sensors for physical health monitoring.

With continuous progress in basic research and clinical trials, more and more advanced diagnostic and therapeutic techniques are expected to be developed based on high-performance piezoelectric materials.

Table 8 Categories of piezoelectric devices.

Type of devices	Piezoelectric effect	Working principle	Examples
Sensors	Direct	Convert physical quantity into electrical signal	Accelerometer, pressure sensor, flaw detector, microphone, etc.
Generators	Direct	Generate power under mechanical stimuli	Spark igniter, energy harvesting, etc.
Actuators	Converse	Convert electrical signal into mechanical displacement/vibration	Ultrasonic motor, ultrasonic welding, speakers, etc.
Transducers	Both	Convert between electrical and mechanical energy	Sonar, non-destructive testing, medical ultrasonic imaging, etc.

4.05.7.3 Industrial manufacturing, processing and detection

Piezoelectric materials can be found in a large number of applications in advanced industrial manufacturing and processing. For example, different kinds of piezoelectric actuators are used in machining, semiconductor-related testing, assembling and manufacturing, etc., which enable the control and positioning of the equipment with a much higher precision than the traditional electromagnetic actuators.²

In addition, piezoelectric transducers and shock wave generation devices have been utilized for ultrasonic cleaning, ultrasonic welding and mixing, etc. In recent years, the ultrasonic welding technique has been widely utilized for the manufacture of masks and other products. Generally, piezoelectric devices used in these applications need to be of high power to ensure efficiency.

Acoustic detection is also an important application branch. The sonar system has been the most effective technique for underwater imaging, navigation and communication since World War II. Nowadays, the detection/measurement based on acoustic wave echo has become a mainstream technique for underwater exploration. For example, the sonic well logging technique is developed to obtain high resolution 3D models of oil and gas wells.^{2,179}

In the near future, novel piezoelectric materials with better performances will further enhance the accuracy, reliability and efficiency of these devices, and expand the range of applications.

4.05.7.4 Automotive

In the automotive industry, many piezoelectric devices have been developed and used to achieve a variety of functions. For example, engine knock sensors, tire pressure sensors, dynamic pressure sensors, airbag and seatbelt sensors, etc., can be found in most of the new vehicles these days. Piezoelectric actuators made by high-temperature piezoelectric materials are used as fuel injectors to control the spray of fuel to improve the fuel economy and to reduce emissions. Piezoelectric transducers have been designed and used for objects detection and auto parking.^{176,180,181}

More advanced and newly-developed piezoelectric sensors, actuators and transducers will be key components in future self-driving vehicles with better safety and reliability.

4.05.7.5 Consumer electronics

Consumer electronics represent a large market share of piezoelectric devices. A popular category of devices is piezoelectric speakers (such as in cellphone, earbuds and some musical greeting cards), which have the advantages of smaller size, impervious to magnetic field and low-power input compared to conventional speakers. Conversely, piezoelectric transducers can achieve active noise control and reduction, by monitoring the environmental noise, and then, through feedback, producing an "opposite" sound wave with an inverted phase to cancel the noise. Based on this principle, some noise reduction/cancellation headphones have been designed and fabricated. However, their application is still limited because of the complications involving the integration of the sensors, actuators, power supply and related control.¹⁸²

In addition to the sound-related applications, piezoelectric devices are essential for some high-precision control and actuation in many electronic products. An example is the piezoelectric motors which are used as auto-focusing drive in cameras with such advantages as precision, silence and low power consumption compared with electromagnetic motors. Another example is the inkjet printer, where piezoelectric actuators in the printer head act on small diaphragms or change the geometry of the inkwell to extrude the ink droplets from the orifice onto the paper.¹⁷⁵ Similar kind of devices has been used in 3D printers where piezoelectric actuators are used to control the nozzle that can deliver a precise amount of powder or liquid with high speed.¹⁸³

Another type of up-to-date devices is piezoelectric gyroscopes which have been used in navigation, aviation, space exploration and many consumer electronic products such as smart phones. The piezoelectric gyroscopes can track complex motion accurately without being affected by magnetic fields. The utilization of piezoelectric gyroscopes offers multi-functional versatility, e.g., leading to smarter applications of cell phones.^{184,185}

4.05.7.6 Internet of Things

As an emerging technology, the Internet of Things (IoT) relies on the construction of large-scale sensor networks and systems to perceive the world and to act accordingly. As one of the key components, piezoelectric sensors and actuators have the potential to be used in almost every system that is connected to the IoT.^{186,187}

One of the major challenges that the IoT is facing is the availability of power. To solve this problem, piezoelectric generators could be an excellent solution by harvesting energy from vibrations, shocks and movements to power the devices. It is expected that, with the development of new high-performance piezoelectric materials and the improvement of efficiency of the piezoelectric generators, the integration of piezoelectric sensors, actuators and generators into the IoT will be achieved in the near future.^{173,188}

Acknowledgments

This work was supported by the Natural Science Foundation of China (Grant No. 51902244), the China Postdoctoral Science Foundation (Grant No. 2018M643632), the Natural Science Foundation of Shaanxi Province of China (Grant No. 2019JQ-389), the Fundamental Research Funds for the Central Universities of China (Grant No. zxy012021025), the "111 Project" of China (Grant No. B14040), the U. S. Office of Naval Research (Grants

No. N00014-16-1-3106 and N00014-21-1-2085), and the Natural Sciences and Engineering Research Council of Canada (NSERC, Grant No. RGPIN-2017-06915).

References

- Jaffe, B.; William, C.; Jaffe, H. *Piezoelectric Ceramics*, Academic Press: London, 1971.
- Safari, A., Akdogan, E. K., Eds.; *Piezoelectric and Acoustic Materials for Transducer Applications*, Springer: Boston, MA, 2008.
- Uchino, K., Ed.; *Advanced Piezoelectric Materials: Science and Technology*, Woodhead Publishing: Cambridge, UK, 2010.
- Xu, Y. *Ferroelectric Materials and Their Applications*, North-Holland: New York, 1991.
- Jaffe, B.; Roth, R. S.; Marzullo, S. *J. Appl. Phys.* **1954**, *25* (6), 809–810.
- Noheda, B.; Cox, D.; Shirane, G.; Guo, R.; Jones, B.; Cross, L. *Phys. Rev. B* **2000**, *63* (1), 014103.
- Park, S.-E.; Shrout, T. R. *J. Appl. Phys.* **1997**, *82* (4), 1804–1811.
- Ye, Z.-G. *Key Eng. Mater.* **1998**, *155*, 81–122.
- Zhang, S.; Li, F.; Jiang, X.; Kim, J.; Luo, J.; Geng, X. *Prog. Mater. Sci.* **2015**, *68*, 1–66.
- Bowen, C. R.; Topolov, V. Y.; Isaeva, A. N.; Bisegna, P. *CrstEngComm* **2016**, *18* (32), 5986–6001.
- Li, F.; Cabral, M. J.; Xu, B.; Cheng, Z.; Dickey, E. C.; LeBeau, J. M.; Wang, J.; Luo, J.; Taylor, S.; Hackenberger, W.; Bellaiche, L.; Xu, Z.; Chen, L.-Q.; Shrout, T. R.; Zhang, S. *Science* **2019**, *364* (6437), 264–268.
- Ye, Z.-G., Ed.; *Handbook of Advanced Dielectric, Piezoelectric and Ferroelectric Materials: Synthesis, Properties and Applications*, Woodhead Publishing: Cambridge, UK, 2008.
- Ye, Z.-G. *MRS Bull.* **2009**, *34* (4), 277–283.
- Sun, E.; Cao, W. *Prog. Mater. Sci.* **2014**, *65*, 124–210.
- Li, F.; Zhang, S.; Damjanovic, D.; Chen, L.-Q.; Shrout, T. R. *Adv. Funct. Mater.* **2018**, *28* (37), 1801504.
- Zhang, S.; Li, F.; Yu, F.; Jiang, X.; Lee, H.-Y.; Luo, J.; Shrout, T. R. *J. Korean Ceram. Soc.* **2018**, *55* (5), 419–439.
- Landau, L. D. *Zh. Eksp. Teor. Fiz.* **1937**, *11*, 19.
- Devonshire, A. F. *The London, Edinb., and Dublin Philos. Mag. and J. Sci.* **1949**, *40* (309), 1040–1063.
- Devonshire, A. F. *The London, Edinb., and Dublin Philos. Mag. and J. Sci.* **1951**, *42* (333), 1065–1079.
- Samara, G. A. *Solid State Phys.* **2001**, *56*, 239–458.
- Raman, C. V.; Nedungadi, T. M. K. *Nature* **1940**, *145* (3665), 147.
- Cochran, W. *Adv. Phys.* **1960**, *9* (36), 387–423.
- Venkataraman, G. *Bull. Mater. Sci.* **1979**, *1* (3), 129–170.
- Bilinc, R. *Ferroelectrics* **1987**, *74* (1), 301–303.
- Stern, E. A. *Phys. Rev. Lett.* **2004**, *93* (3), 037601.
- Tsuda, K.; Sano, R.; Tanaka, M. *Phys. Rev. B* **2012**, *86* (21), 214106.
- Cao, W.; Cross, L. E. *Phys. Rev. B* **1993**, *47* (9), 4825.
- Randall, C. A.; Kim, N.; Kucera, J.-P.; Cao, W.; Shrout, T. R. *J. Am. Ceram. Soc.* **1998**, *81* (3), 677–688.
- Zhang, N.; Gorfman, S.; Choe, H.; Vergentev, T.; Dyadkin, V.; Yokota, H.; Chernyshov, D.; Wang, B.; Glazer, A. M.; Ren, W.; Ye, Z.-G. *J. Appl. Cryst.* **2018**, *51* (5), 1396–1403.
- Zhao, C.; Hou, D.; Chung, C.-C.; Zhou, H.; Kynast, A.; Hennig, E.; Liu, W.; Li, S.; Jones, J. L. *Acta Mater.* **2018**, *158*, 369–380.
- Noheda, B.; Cox, D. E.; Shirane, G.; Gonzalo, J. A.; Cross, L. E.; Park, S.-E. *Appl. Phys. Lett.* **1999**, *74* (14), 2059–2061.
- Noheda, B.; Gonzalo, J. A.; Cross, L. E.; Guo, R.; Park, S. E.; Cox, D. E.; Shirane, G. *Phys. Rev. B* **2000**, *61* (13), 8687–8695.
- Guo, R.; Cross, L.; Park, S.; Noheda, B.; Cox, D.; Shirane, G. *Phys. Rev. Lett.* **2000**, *84* (23), 5423.
- Jin, Y. M.; Wang, Y. U.; Khachatryan, A. G.; Li, J. F.; Viehland, D. *Phys. Rev. Lett.* **2003**, *91* (19), 197601.
- Jin, Y. M.; Wang, Y. U.; Khachatryan, A. G.; Li, J. F.; Viehland, D. *J. Appl. Phys.* **2003**, *94* (5), 3629–3640.
- Schönau, K. A.; Schmitt, L. A.; Knapp, M.; Fuess, H.; Eichel, R.-A.; Kungl, H.; Hoffmann, M. J. *Phys. Rev. B* **2007**, *75* (18), 184117.
- Theissmann, R.; Schmitt, L. A.; Kling, J.; Schierholz, R.; Schönau, K. A.; Fuess, H.; Knapp, M.; Kungl, H.; Hoffmann, M. J. *J. Appl. Phys.* **2007**, *102* (2), 024111.
- Glazer, A. M.; Thomas, P. A.; Baba-Kishi, K. Z.; Pang, G. K. H.; Tai, C. W. *Phys. Rev. B* **2004**, *70* (18), 3352–3359.
- Yokota, H.; Zhang, N.; Taylor, A. E.; Thomas, P. A.; Glazer, A. M. *Phys. Rev. B* **2009**, *80* (10), 754–758.
- Zhang, N.; Yokota, H.; Glazer, A.; Ren, Z.; Keen, D.; Keeble, D.; Thomas, P.; Ye, Z.-G. *Nat. Commun.* **2014**, *5*, 5231.
- Zhang, N.; Yokota, H.; Glazer, A. M.; Keen, D. A.; Gorfman, S.; Thomas, P. A.; Ren, W.; Ye, Z.-G. *IUCrJ* **2018**, *5*, 73–81.
- Haertling, G. H. *J. Am. Ceram. Soc.* **1999**, *82* (4), 796–818.
- Panda, P.; Sahoo, B. *Ferroelectrics* **2015**, *474* (1), 128–143.
- Damjanovic, D.; Newnham, R. E. *J. Intell. Mater. Syst. Struct.* **1992**, *3* (2), 190–208.
- Alemany, C.; Briančin, J.; Bruncková, H.; Saksl, K. *J. Eur. Ceram. Soc.* **2003**, *23* (7), 1157–1166.
- Vittayakorn, N.; Rujijanagul, G.; Tan, X.; Marquardt, M. A.; Cann, D. P. *J. Appl. Phys.* **2004**, *96* (9), 5103–5109.
- Smolenskii, G.; Isupov, V.; Agranovskaya, A.; Krainik, N. *Sov. Phys. Solid State* **1961**, *2* (11), 2651–2654.
- Cross, L. E. *Ferroelectrics* **1994**, *151* (1), 305–320.
- Bokov, A. A.; Ye, Z.-G. *J. Mater. Sci.* **2006**, *41* (1), 31–52.
- Smolenskii, G. A. *J. Physical Soc. Japan* **1970**, *28* (1), 26–37.
- Smolensky, G. *Ferroelectrics* **1984**, *53* (1), 129–135.
- Bell, A.; Phys, J. *Condens. Matter* **1993**, *5* (46), 8773.
- Glinchuk, M.; Farhi, R. *J. Phys. Condens. Matter* **1996**, *8* (37), 6985.
- Kleemann, W. *J. Adv. Dielectr.* **2012**, *2* (02), 1241001.
- Viehland, D.; Wuttig, M.; Cross, L. *Ferroelectrics* **1991**, *120* (1), 71–77.
- Viehland, D.; Li, J. F.; Jang, S. J.; Cross, L. E.; Wuttig, M. *Phys. Rev. B* **1992**, *46* (13), 8013.
- Setter, N.; Cross, L. *J. Mater. Sci.* **1980**, *15* (10), 2478–2482.
- Xi, Y.; Zhili, C.; Cross, L. E. *Ferroelectrics* **1984**, *54* (1), 3399–3403.
- Bokov, A. A.; Ye, Z.-G. *J. Adv. Dielectr.* **2012**, *02* (02), 1241010.
- Wirunichit, S.; Laoratanakul, P.; Vittayakorn, N. *J. Phys. D Appl. Phys.* **2008**, *41* (12), 125406.
- Ye, Z.-G.; Bing, Y.; Gao, J.; Bokov, A. A.; Stephens, P.; Noheda, B.; Shirane, G. *Phys. Rev. B* **2003**, *67* (10), 104104.
- Noheda, B.; Cox, D.; Shirane, G.; Gao, J.; Ye, Z.-G. *Phys. Rev. B* **2002**, *66* (5), 054104.
- La-Orauttapong, D.; Noheda, B.; Ye, Z.-G.; Gehring, P. M.; Toulouse, J.; Cox, D. E.; Shirane, G. *Phys. Rev. B* **2002**, *65* (14), 144101.

64. Kuwata, J.; Uchino, K.; Nomura, S. *Jpn. J. Appl. Phys.* **1982**, *21* (9R), 1298.
65. Bugaris, D. E.; zur Loye, H.-C. *Angew. Chem. Int. Ed.* **2012**, *51* (16), 3780–3811.
66. Dong, M.; Ye, Z.-G. *J. Cryst. Growth* **2000**, *209* (1), 81–90.
67. Long, X.; Ye, Z.-G. *Acta Mater.* **2007**, *55* (19), 6507–6512.
68. Long, X.; Ling, J.; Li, X.; Wang, Z.; Ye, Z.-G. *Cryst. Growth Des.* **2008**, *9* (2), 657–659.
69. He, C.; Li, X.; Wang, Z.; Long, X.; Mao, S.; Ye, Z.-G. *Chem. Mater.* **2010**, *22* (19), 5588–5592.
70. Li, T.; Scotch, A. M.; Chan, H. M.; Harmer, M. P.; Park, S. E.; Shrout, T. R.; Michael, J. R. *J. Am. Ceram. Soc.* **1998**, *81* (1), 244–248.
71. Kang, S. J. L.; Park, J. H.; Ko, S. Y.; Lee, H. Y. *J. Am. Ceram. Soc.* **2015**, *98* (2), 347–360.
72. Millisavljevic, I.; Wu, Y. *BMC Mater.* **2020**, *2* (1), 2.
73. Zhang, Y.; Li, X.; Liu, D. A.; Zhang, Q.; Wang, W.; Ren, B.; Lin, D.; Zhao, X.; Luo, H. *J. Cryst. Growth* **2011**, *318* (1), 890–894.
74. Song, K.; Li, Q.; Guo, H.; Hu, Q.; Li, Z.; Li, F.; Fan, S.; Xu, Z. *J. Alloys Compd.* **2021**, *851*, 156145.
75. Trolrier-McKinstry, S.; Zhang, S.; Bell, A. J.; Tan, X. *Annu. Rev. Mater. Res.* **2018**, *48* (1), 191–217.
76. Shrout, T. R.; Chang, Z. P.; Kim, N.; Markgraf, S. *Ferroelectr. Lett.* **1990**, *12* (3), 63–69.
77. Han, P. D.; Yan, W. L.; Tian, J.; Huang, X. L.; Pan, H. X. *Appl. Phys. Lett.* **2005**, *86* (5), 052902.
78. Davis, M. J. *Electroceram.* **2007**, *19* (1), 25–47.
79. Fu, H.; Cohen, R. E. *Nature* **2000**, *403* (6767), 281–283.
80. Noheda, B.; Cox, D. E.; Shirane, G.; Park, S. E.; Cross, L. E.; Zhong, Z. *Phys. Rev. Lett.* **2001**, *86* (17), 3891–3894.
81. Ye, Z.-G.; Noheda, B.; Dong, M.; Cox, D.; Shirane, G. *Phys. Rev. B* **2001**, *64* (18), 184114.
82. Noheda, B. *Curr. Opin. Solid State Mater. Sci.* **2002**, *6* (1), 27–34.
83. Li, F.; Zhang, S.; Xu, Z.; Wei, X.; Shrout, T. R. *Adv. Funct. Mater.* **2011**, *21* (11), 2118–2128.
84. Davis, M.; Budimir, M.; Damjanovic, D.; Setter, N. *J. Appl. Phys.* **2007**, *101* (5), 054112.
85. Xu, G. Y.; Wen, J. S.; Stock, C.; Gehring, P. M. *Nat. Mater.* **2008**, *7* (7), 562–566.
86. Manley, M. E.; Abernathy, D. L.; Sahul, R.; Parshall, D. E.; Lynn, J. W.; Christianson, A. D.; Stonaha, P. J.; Specht, E. D.; Budai, J. D. *Sci. Adv.* **2016**, *2* (9), e1501814.
87. Li, F.; Zhang, S.; Yang, T.; Xu, Z.; Zhang, N.; Liu, G.; Wang, J.; Cheng, Z.; Ye, Z.-G. *Nat. Commun.* **2016**, *7*, 13807.
88. Rödel, J.; Jo, W.; Seifert, K. T.; Anton, E. M.; Granzow, T.; Damjanovic, D. *J. Am. Ceram. Soc.* **2009**, *92* (6), 1153–1177.
89. Rödel, J.; Webber, K. G.; Dittmer, R.; Jo, W.; Kimura, M.; Damjanovic, D. *J. Eur. Ceram. Soc.* **2015**, *35* (6), 1659–1681.
90. Wu, J.; Xiao, D.; Zhu, J. *Chem. Rev.* **2015**, *115* (7), 2559–2595.
91. Zheng, T.; Wu, J.; Xiao, D.; Zhu, J. *Prog. Mater. Sci.* **2018**, *98*, 552–624.
92. Takenaka, T.; Maruyama, K.-I.; Sakata, K. *Jpn. J. Appl. Phys.* **1991**, *30* (9S), 2236.
93. Shirane, G.; Newnham, R.; Pepinsky, R. *Phys. Rev.* **1954**, *96* (3), 581–588.
94. Sasaki, A.; Chiba, T.; Mamiya, Y.; Otsuki, E. *Jpn. J. Appl. Phys.* **1999**, *38* (9S), 5564.
95. Shrout, T. R.; Zhang, S. J. *J. Electroceram.* **2007**, *19* (1), 113–126.
96. Li, J. F.; Wang, K.; Zhu, F. Y.; Cheng, L. Q.; Yao, F. Z. *J. Am. Ceram. Soc.* **2013**, *96* (12), 3677–3696.
97. Saito, Y.; Takao, H.; Tani, T.; Nonoyama, T.; Takatori, K.; Homma, T.; Nagaya, T.; Nakamura, M. *Nature* **2004**, *432* (7013), 84–87.
98. Shen, Z.-Y.; Li, J.-F. *J. Ceram. Soc. Jpn.* **2010**, *118* (1382), 940–943.
99. Zhang, J.; Ji, P.; Wu, Y.; Zhao, X.; Tan, Y.; Wang, C. *Appl. Phys. Lett.* **2014**, *104* (22), 222909.
100. Huan, Y.; Wang, X.; Fang, J.; Li, L. *J. Eur. Ceram. Soc.* **2014**, *34* (5), 1445–1448.
101. Liu, W.; Ren, X. *Phys. Rev. Lett.* **2009**, *103* (25), 257602.
102. Gao, J.; Xue, D.; Wang, Y.; Wang, D.; Zhang, L.; Wu, H.; Guo, S.; Bao, H.; Zhou, C.; Liu, W.; Hou, S.; Xiao, G.; Ren, X. *Appl. Phys. Lett.* **2011**, *99* (9), 092901.
103. Liu, Y.; Chang, Y.; Li, F.; Yang, B.; Sun, Y.; Wu, J.; Zhang, S.; Wang, R.; Cao, W. *ACS Appl. Mater. Interfaces* **2017**, *9* (35), 29863–29871.
104. Zvirgzds, J.; Kapostin, P.; Zvirgzde, J.; Kruzina, T. *Ferroelectrics* **1982**, *40* (1), 75–77.
105. Levin, I.; Reaney, I. M. *Adv. Funct. Mater.* **2012**, *22* (16), 3445–3452.
106. Hiruma, Y.; Nagata, H.; Takenaka, T. *J. Appl. Phys.* **2009**, *105* (8), 084112.
107. Sung, Y.; Kim, J.; Cho, J.; Song, T.; Kim, M.; Park, T. *Appl. Phys. Lett.* **2011**, *98* (1), 012902.
108. Zhao, J.; Zhang, N.; Ren, W.; Niu, G.; Walker, D.; Thomas, P. A.; Wang, L.; Ye, Z.-G. *J. Am. Ceram. Soc.* **2019**, *102* (1), 437–447.
109. Zhang, Q.; Zhang, Y.; Wang, F.; Wang, Y.; Lin, D.; Zhao, X.; Luo, H.; Ge, W.; Viehland, D. *Appl. Phys. Lett.* **2009**, *95* (10), 102904.
110. Zhang, S.-T.; Kounga, A. B.; Aulbach, E.; Ehrenberg, H.; Rödel, J. *Appl. Phys. Lett.* **2007**, *91* (11), 112906.
111. Wang, Y.; Luo, C.; Wang, S.; Chen, C.; Yuan, G.; Luo, H.; Viehland, D. *Adv. Electron. Mater.* **2020**, *6* (1), 1900949.
112. Liu, X.; Tan, X. *Adv. Mater.* **2016**, *28* (3), 574–578.
113. Zhao, P.; Zhang, B.-P.; Li, J.-F. *Appl. Phys. Lett.* **2007**, *90* (24), 242909.
114. Zuo, R.; Fu, J.; Lv, D.; Liu, Y. *J. Am. Ceram. Soc.* **2010**, *93* (9), 2783–2787.
115. Zhang, B.; Wu, J.; Cheng, X.; Wang, X.; Xiao, D.; Zhu, J.; Wang, X.; Lou, X. *ACS Appl. Mater. Interfaces* **2013**, *5* (16), 7718–7725.
116. Wu, B.; Wu, H.; Wu, J.; Xiao, D.; Zhu, J.; Pennycook, S. J. *J. Am. Ceram. Soc.* **2016**, *138* (47), 15459–15464.
117. Xu, K.; Li, J.; Lv, X.; Wu, J.; Zhang, X.; Xiao, D.; Zhu, J. *Adv. Mater.* **2016**, *28* (38), 8519–8523.
118. Li, P.; Zhai, J.; Shen, B.; Zhang, S.; Li, X.; Zhu, F.; Zhang, X. *Adv. Mater.* **2018**, *30*, 1705171.
119. Quan, Y.; Fei, C.; Ren, W.; Wang, L.; Niu, G.; Zhao, J.; Zhuang, J.; Zhang, J.; Zheng, K.; Lin, P.; Sun, X.; Chen, Q.; Ye, Z. G.; Karaki, T. *IEEE Trans. Ultrason. Ferroelectr. Freq. Control* **2021**, *68* (5), 1979–1987.
120. Wu, J. G.; Fan, Z.; Xiao, D. Q.; Zhu, J. G.; Wang, J. *Prog. Mater. Sci.* **2016**, *84*, 335–402.
121. Rojac, T.; Makarovic, M.; Walker, J.; Ursic, H.; Damjanovic, D.; Kos, T. *Appl. Phys. Lett.* **2016**, *109* (4), 042904.
122. Rojac, T.; Bencan, A.; Malic, B.; Tutuncu, G.; Jones, J. L.; Daniels, J. E.; Damjanovic, D. *J. Am. Ceram. Soc.* **2014**, *97* (7), 1993–2011.
123. Lee, M. H.; Kim, D. J.; Park, J. S.; Kim, S. W.; Song, T. K.; Kim, M. H.; Kim, W. J.; Do, D.; Jeong, I. K. *Adv. Mater.* **2015**, *27* (43), 6976–6982.
124. Lee, M. H.; Kim, D. J.; Choi, H. I.; Kim, M.-H.; Song, T. K.; Kim, W.-J.; Do, D. *ACS Appl. Electron. Mater.* **2019**, *1* (9), 1772–1780.
125. Wang, D.; Wang, G.; Murakami, S.; Fan, Z.; Feteira, A.; Zhou, D.; Sun, S.; Zhao, Q.; Reaney, I. M. *J. Adv. Dielectr.* **2018**, *08* (06), 1830004.
126. Calisir, I.; Kleppe, A. K.; Feteira, A.; Hall, D. A. *J. Mater. Chem. C* **2019**, *7* (33), 10218–10230.
127. Watson, J.; Castro, C. *Analog Dialogue* **2012**, *46* (4), 3–9.
128. Goujon, N.; Hori, H.; Liang, K. K.; Sinha, B. K. *IEEE Trans. Ultrason. Ferroelectr. Freq. Control* **2012**, *59* (9), 2042–2050.
129. Zhang, S.; Yu, F. *J. Am. Ceram. Soc.* **2011**, *94* (10), 3153–3170.
130. Bar-Cohen, Y., Ed.; *High Temperature Materials and Mechanisms*, CRC Press, Taylor & Francis Group: New York, 2014.
131. Damjanovic, D. *Curr. Opin. Solid State Mater. Sci.* **1998**, *3* (5), 469–473.
132. Bechmann, R. *Phys. Rev.* **1958**, *110* (5), 1060–1061.
133. Cook, R. K.; Weissler, P. G. *Phys. Rev.* **1950**, *80* (4), 712.
134. London, D. *Can. Mineral.* **2011**, *49* (1), 117–136.
135. Setkova, T.; Shapovalov, Y.; Balitsky, V. *J. Cryst. Growth* **2011**, *318* (1), 904–907.

136. Weis, R.; Gaylord, T. *Appl. Phys. A Mater. Sci. Process.* **1985**, *37* (4), 191–203.
137. Smith, R.; Welsh, F. *J. Appl. Phys.* **1971**, *42* (6), 2219–2230.
138. Cha, J. W.; Kim, J. N. *Ferroelectrics* **1997**, *197* (1), 93–96.
139. Muensit, S.; Goldys, E. M.; Guy, I. L. *Appl. Phys. Lett.* **1999**, *75* (25), 3965–3967.
140. Sotnikov, A. V.; Schmidt, H.; Weihnacht, M.; Smirnova, E. P.; Chemekova, T. Y.; Makarov, Y. N. *IEEE Trans. Ultrason. Ferroelectr. Freq. Control* **2010**, *57* (4), 808–811.
141. Kaminskii, A. A.; Mill, B. V.; Khodzhabagyan, G. G.; Konstantinova, A. F.; Okorchkov, A. I.; Silvestrova, I. M. *Phys. Status Solidi A* **1983**, *80* (1), 387–398.
142. Zhang, S.; Zheng, Y.; Kong, H.; Xin, J.; Frantz, E.; Shrout, T. R. *J. Appl. Phys.* **2009**, *105* (11), 114107.
143. Uda, S.; Inaba, H.; Harada, J.; Hoshikawa, K. *J. Cryst. Growth* **2004**, *271* (1), 229–237.
144. Krempel, P. In *Quartz Homeotypic Gallium-Orthophosphate-A New High Tech Piezoelectric Material*. 1994 Proceedings of IEEE Ultrasonics Symposium, IEEE; 1994; pp 949–954.
145. Zhang, S. J.; Yu, F. P.; Xia, R.; Fei, Y. T.; Frantz, E.; Zhao, X.; Yuan, D. R.; Chai, B. H. T.; Snyder, D.; Shrout, T. R. *J. Cryst. Growth* **2011**, *318* (1), 884–889.
146. Richard, E. E.; Clive, A. R.; Thomas, R. S.; Paul, W. R.; Wes, H.; Seung-Eek, P. *Jpn. J. Appl. Phys.* **2001**, *40* (10R), 5999.
147. Zhang, S.; Randall, C. A.; Shrout, T. R. *Appl. Phys. Lett.* **2003**, *83* (15), 3150–3152.
148. Jardiel, T.; Caballero, A.; Villegas, M. *J. Ceram. Soc. Jpn.* **2008**, *116* (1352), 511–518.
149. Subbarao, E. *J. Phys. Chem. Solid* **1962**, *23* (6), 665–676.
150. Gao, Z.; Yan, H.; Ning, H.; Reece, M. *Adv. Appl. Ceram.* **2013**, *112* (2), 69–74.
151. Yan, H.; Ning, H.; Kan, Y.; Wang, P.; Reece, M. *J. Am. Ceram. Soc.* **2009**, *92* (10), 2270–2275.
152. Nanamatsu, S.; Kimura, M.; Doi, K.; Matsushita, S.; Yamada, N. *Ferroelectrics* **1974**, *8* (1), 511–513.
153. Moriana, A. D.; Zhang, S. *J. Mater.* **2018**, *4*, 277–303.
154. Messing, G. L.; Trolrier-McKinstry, S.; Sabolsky, E.; Duran, C.; Kwon, S.; Brahmarrout, B.; Park, P.; Yilmaz, H.; Rehrig, P.; Eitel, K. *Crit. Rev. Solid State Mater. Sci.* **2004**, *29* (2), 45–96.
155. Kimuar, T. *J. Ceram. Soc. Jpn.* **2006**, *114* (1325), 15–25.
156. Okazaki, K.; Narushima, S. *J. Ceram. Soc. Jpn.* **1968**, *76*, 21–27.
157. Swartz, S.; Schulze, W. A.; Biggers, J. V. *Ferroelectrics* **1981**, *38* (1), 765–768.
158. Granahan, M.; Holmes, M.; Schulze, W. A.; Newnham, R. E. *J. Am. Ceram. Soc.* **1981**, *64* (4), c-68–c-69.
159. Takeuchi, T.; Tani, T.; Saito, Y. *Jpn. J. Appl. Phys.* **1999**, *38* (9S), 5553.
160. Duran, C.; Trolrier-McKinstry, S.; Messing, G. L. *J. Am. Ceram. Soc.* **2000**, *83* (9), 2203–2213.
161. Chang, Y.; Sun, Y.; Wu, J.; Wang, X.; Zhang, S.; Yang, B.; Messing, G. L.; Cao, W. *J. Eur. Ceram. Soc.* **2016**, *36* (8), 1973–1981.
162. Maurya, D.; Zhou, Y.; Yan, Y.; Priya, S. *J. Mater. Chem. C* **2013**, *1* (11), 2102–2111.
163. Tani, T. *J. Korean Phys. Soc.* **1998**, *32* (9), 1217.
164. Tani, T.; Kimura, T. *Adv. Appl. Ceram.* **2006**, *105* (1), 55–63.
165. Tani, T. *J. Ceram. Soc. Jpn.* **2006**, *114* (1329), 363–370.
166. Baldan, A. *J. Mater. Sci.* **2002**, *37* (11), 2171–2202.
167. Yilmaz, H.; Messing, G. L.; Trolrier-McKinstry, S. *J. Electroceram.* **2003**, *11* (3), 207–215.
168. Quan, Y.; Ren, W.; Niu, G.; Wang, L.; Zhao, J.; Zhang, N.; Liu, M.; Ye, Z.-G.; Liu, L.; Karaki, T. *ACS Appl. Mater. Interfaces* **2018**, *10* (12), 10220–10226.
169. Markets and Markets™. *Piezoelectric Devices Market With COVID-19 Impact Analysis by Material (Piezoelectric Ceramics, Polymers), Product (Piezoelectric Actuators, Transducers, Motors), Application (Aerospace & Defense, Industrial, Consumer), and Region - Global Forecast to 2026*, 2021.
170. Tressler, J. F.; Alkoy, S.; Newnham, R. E. *J. Electroceram.* **1998**, *2* (4), 257–272.
171. Steinem, C.; Janshoff, A., Eds.; *Piezoelectric Sensors*; vol. 5; Springer Science & Business Media, 2007.
172. Uchino, K. *Ferroelectric Devices*, 2nd ed.; Marcel Dekker, Inc.: New York, 2000.
173. Liu, H. C.; Zhong, J. W.; Lee, C.; Lee, S. W.; Lin, L. W. *Appl. Phys. Rev.* **2018**, *5* (4), 041306.
174. Yang, Z.; Zhou, S.; Zu, J.; Inman, D.; Rosseinsky, M. *J. Joule* **2018**, *2* (4), 642–697.
175. Gao, X.; Yang, J.; Wu, J.; Xin, X.; Li, Z.; Yuan, X.; Shen, X.; Dong, S. *Adv. Mater. Technol.* **2019**, *5* (1), 1900716.
176. Randall, C.; Kelnberger, A.; Yang, G.; Eitel, R.; Shrout, T. *J. Electroceram.* **2005**, *14* (3), 177–191.
177. Arnau, A., Ed.; *Piezoelectric Transducers and Applications*. Springer-Verlag: Berlin, Heidelberg, 2004.
178. Xu, Q.; Gao, X.; Zhao, S.; Liu, Y. N.; Zhang, D.; Zhou, K.; Khanbareh, H.; Chen, W.; Zhang, Y.; Bowen, C. *Adv. Mater.* **2021**, *33* (27), e2008452.
179. Mondol, N. H. Well Logging: Principles, Applications and Uncertainties. In *Petroleum Geoscience: From Sedimentary Environments to Rock Physics*; Bjørlykke, K., Ed.; Springer Berlin Heidelberg: Berlin, Heidelberg, 2015; pp 385–425.
180. Levinson, J.; Askeland, J.; Becker, J.; Dolson, J.; Held, D.; Kammel, S.; Kolter, J. Z.; Langer, D.; Pink, O.; Pratt, V.; Sokolsky, M.; Stanek, G.; Stavens, D.; Teichman, A.; Werling, M.; Thrun, S. Towards fully autonomous driving: Systems and algorithms. 2011 IEEE Intelligent Vehicles Symposium; 2011; pp 163–168.
181. Gonzalez, D.; Perez, J.; Milanes, V.; Nashashibi, F. *IEEE Trans. Intell. Transp. Syst.* **2016**, *17* (4), 1135–1145.
182. Manjón-Sanz, A. M.; Dolgos, M. R. *Chem. Mater.* **2018**, *30* (24), 8718–8726.
183. Saunders, R. E.; Derby, B. *Int. Mater. Rev.* **2014**, *59* (8), 430–448.
184. Tadigadapa, S.; Mateti, K. *Meas. Sci. Technol.* **2009**, *20* (9), 092001.
185. Xia, D.; Yu, C.; Kong, L. *Sensors* **2014**, *14* (1), 1394–1473.
186. Atzori, L.; Iera, A.; Morabito, G. *Comput. Netw.* **2010**, *54* (15), 2787–2805.
187. Zanella, A.; Bui, N.; Castellani, A.; Vangelista, L.; Zorzi, M. *IEEE Internet Things J.* **2014**, *1* (1), 22–32.
188. Kamalinejad, P.; Mahapatra, C.; Sheng, Z.; Mirabbasi, S.; Leung, V. C. M.; Guan, Y. L. *IEEE Commun. Mag.* **2015**, *53* (6), 102–108.

4.06 Intermetallic materials

Oliver Janka, Universität des Saarlandes, Anorganische Festkörperchemie, Saarbrücken, Germany

© 2023 Elsevier Ltd. All rights reserved.

4.06.1	Introduction	172
4.06.2	Definition, terminology and classification	173
4.06.2.1	Definition	173
4.06.2.2	Terminology	173
4.06.2.3	Classification	173
4.06.3	Synthesis	174
4.06.3.1	Starting materials	174
4.06.3.2	Container materials	174
4.06.3.3	Heating	175
4.06.3.4	Flux assisted synthesis	175
4.06.3.5	Electrochemistry	176
4.06.4	Structures	176
4.06.4.1	Elements & derivatives of closed packed structures	176
4.06.4.2	Laves-phases	178
4.06.4.3	Hume-Rothery phases	179
4.06.4.4	Zintl-phases	180
4.06.4.5	Selected binary and ternary phases	183
4.06.4.5.1	Group 2/12	183
4.06.4.5.2	Group 13	191
4.06.4.5.3	Group 14	198
References		204

Abstract

Intermetallic compounds are a vast and diverse class of materials, originating from the fact, that over 80 elements of the periodic table are metals. The sheer combinatory possibilities, set aside their respective potential physical properties, already give a good impression why this class of compounds interests scientist all around the world. A huge number of these elements can form specific compounds with a unique crystal structure, separating these from classical alloys. This chapter covers a selection of intermetallic materials focusing on their different structures and compositions as well as for some selected examples on their properties and their appearances in every-day life.

4.06.1 Introduction

The latest release of the periodic table contains, as of December 2018, contains 118 named elements.¹ Of these, 80+ elements are metallic, adopting in many cases closest packed structures. However, even among the elements, peculiarities in their structures and respective bonding situations arise. Manganese (α -Mn),² for example, adopts one of the most complex elemental structures with four independent crystallographic sites and 58 atoms per unit cell. All of these metallic elements with their plethora of structures and (physical) properties are potential candidates for the formation of so-called intermetallic compounds.

Even before systematic investigations, intermetallic compounds were used, as they occur in long known materials such as steel, bronze or brasses. But also, over the last decades, this class of materials has gained dramatically in importance. Without the knowledge regarding intermetallic materials, probably no light-weight aluminum- or magnesium-based alloys would exist for the application in the transportation or aviation sector or as e.g., material for casings of modern-day handheld devices such as phones, tablets or notebooks. Different titanium- or nickel-based based “super alloys” are used as coating for jet turbine blades, or silicon based intermetallics occur in microelectronics. Dental amalgams also contain various intermetallics and superconducting intermetallics are used for medical purposes in MRT devices while hard-magnetic $\text{Nd}_2\text{Fe}_{14}\text{B}$ is used in wind turbines, in the motors of electric vehicles or in miniaturized form in speakers. And these are probably just the most prominent examples.

It should be mentioned, that the topic *intermetallics* has been addressed in a series of text books suitable for master and PhD students,^{3,4} as well as some for advanced readers,^{5,6} also targeting the growth of these compounds.⁷ A more materials based point of view has also been employed.^{8–10} The structures and properties of rare-earth containing intermetallics have also been summarized and extended over the last decades.¹¹ The “Handbook on the Physics and Chemistry of Rare Earths” contains numerous articles addressing the structures as well as physical and spectroscopic properties of intermetallics, exemplarily the first and the most recent volume are given.^{12,13}

Finally, a selected number of reviews published within the last years addressing synthesis, structures and bonding,^{14–20} nanoparticles,^{21–23} electrochemistry and catalysis,^{24,25} and physical and spectroscopic properties^{26–32} should be mentioned.

4.06.2 Definition, terminology and classification

4.06.2.1 Definition

Intermetallic compounds consist of two or more metals or of a combination between metals and metalloids and exhibit, in contrast to alloys, a distinct chemical composition and a different structure than the respective starting materials. This is one of the sentences that can be found in a similar phrasing in many textbooks about general chemistry. And it already summarizes most of the aspects quite accurately. From a historical point of view, intermetallic materials were already used in everyday life before scientists started to think about their structures and bonding. Especially the latter point posed a problem for many chemists as these compounds do not follow the usual valence rules. Therefore, these substances were not really considered as inorganic compounds for a longer time and thus not distinguished from alloys.

4.06.2.2 Terminology

Alloys, intermetallics, solid solutions—these are terms that are often used in the literature, however, also quite often incorrectly. As already stated above, an intermetallic compound exhibits its own crystal structure, with respect to the starting materials. NiAl should serve as an example here. Both Ni and Al crystallize in the cubic fcc type structure (Cu type, $Fm\bar{3}m$),³³ however, when mixed in a one to one ratio and heated above their melting points, upon cooling and solidification a new structure forms, the cubic CsCl type ($Pm\bar{3}m$) structure. The structure and also the bonding situation in this new compound is different to the starting materials, hence this has to be considered as an intermetallic material. When, for example, Cu and Au are heated in a 1:1 ratio and the melt is quenched at high temperatures, the diffraction pattern shows the characteristic reflections of the Cu type structure (Fig. 1, black lines), therefore this material has to be described as an alloy according to $\text{Cu}_{0.5}\text{Au}_{0.5}$. Upon annealing, the diffraction pattern changes drastically, additional reflections arise, originating from the rearrangement of the atoms and the formation of the tetragonal intermetallic phase CuAu (CuAu type, $P4/mmm$, Fig. 1, red lines).

Finally, the term solid solution should be explained. A solid solution describes a series of compounds, which exhibit a range of different compositions, while at the same time forming all a sole crystal structure. Solid solution can be formed by accident due to a certain homogeneity range or on purpose, e.g., to modify the physical properties of the system. Substitutions can, in principle, occur for every element in the structure and on every crystallographic site. In the case of rare earth (RE) element containing intermetallics, solid solutions can be used to investigate and modify the magnetic ground state of the RE atoms. The solid solution $\text{CePt}_{1-x}\text{Pd}_x\text{Al}$ ($x = 0.1–0.8$) for example crystallizes in the TiNiSi type structure (Fig. 25D) and orders ferromagnetically for $x = 0$ and 0.1. For larger values of x (>0.1), the ferromagnetic ground state gets destroyed and antiferromagnetic ordering is observed.³⁴ While in this example a formally isovalent substitution takes place, in the solid solutions $\text{CeRu}_{1-x}\text{Ni}_x\text{Al}$ ($x = 0.1–0.85$, LaNiAl type structure)³⁵ and $\text{CeRu}_{1-x}\text{Pd}_x\text{Al}$ ($x = 0.1–0.9$)³⁶ a change in the valence electron concentration (VEC) occurs, shifting the cerium valence from an intermediate valence state towards a pure trivalent one. In the $\text{Eu}_{1-x}\text{Sr}_x\text{PtIn}_2$ ($x = 0–1$)³⁷ and $\text{Tb}_{1-x}\text{Lu}_x\text{PdAl}_2$ ($x = 0–1$) series in contrast, the change in magnetic properties was investigated with respect to a dilution of the magnetic spins of Eu or Tb by diamagnetic Sr or Lu atoms, respectively.

4.06.2.3 Classification

Within the vast number of binary (and ternary) intermetallics, one can think about ways to classify these compounds. One possibility is to systematize their structures with respect to their structural hierarchy, e.g., using group-subgroup relations. These relations can be described using the tools given in the International Tables for Crystallography A1³⁸ and the guidelines presented by Bärnighausen³⁹ and Müller.^{40–42} Numerous examples have been published for individual intermetallic compounds or larger families, e.g.,

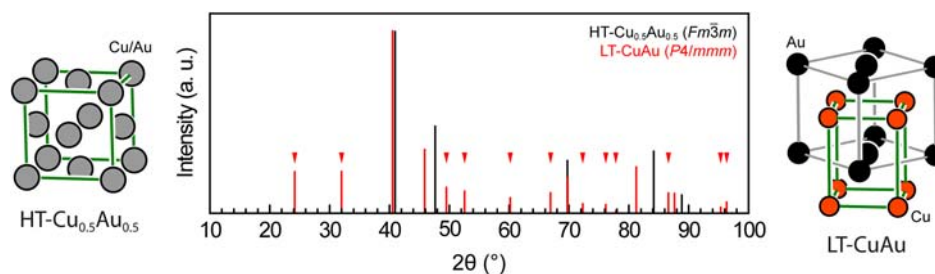


Fig. 1 Calculated powder diffraction patterns for HT- $\text{Cu}_{0.5}\text{Au}_{0.5}$ (black) and LT-CuAu (red). The super structure reflections are marked with a triangle, the structures of both compounds are given.

the AlB_2 ⁴³ or the Fe_2P^{44} related structures. The coloring variants, structural distortions, and puckering effects in selected intermetallic structures have been discussed by Pöttgen in a review article.⁴⁵

Another possibility is to sort intermetallic compounds by specific structural or electronic characteristics. For the following sections (4.06.4.2–4.06.4.4) addressing the Laves-, Hume-Rothery- and Zintl-phases, this is a rather easy task. While the formation of the different Laves-phases mainly depends on the size ratios of the respective elements and can therefore be considered topologically close-packed structures, for Hume-Rothery- and Zintl-phases a dependency on the respective valence electron concentration (VEC) can be established. Sometimes, intermetallic phases located in between the two electronic situations are referred to as “polar intermetallics.”

Finally, the structures can be grouped with respect to their constituent elements. This sorting has been conducted in section 4.06.4, after addressing Laves-, Hume-Rothery- and Zintl-phases. Here the compounds are sorted after one of the contained elements. This is done for elements from groups 2/12 (section 4.06.4.5.1) to 14 (section 4.06.4.5.3), which in many of the given binary and ternary examples are participating in an extended polyanion. And although the respective prototypes might contain a different main group metal forming the polyanion, the important prototypes will be listed according to their appearances within the context.

4.06.3 Synthesis

4.06.3.1 Starting materials

Intermetallic compounds are typically synthesized from the elements via the various techniques discussed below. A very important prerequisite for synthesizing “pure” samples, e.g., for the characterization of properties, is the use of highly pure starting materials. And although high purity metals are readily available at numerous suppliers, the quality is usually only given based on trace metal base. These quality criteria, however, exclude e.g., oxidic, hydroxidic or carbonate impurities quite frequently found on the surface of metals. Such surface impurities are especially important to consider when using metal powders due to the enhanced surface area. Therefore, one should consider, where possible, to use larger pieces to minimize the surface area.

In a number of cases these surface impurities can be chemically removed. Cobalt powder for example can be purified by removing the oxidic layer in hydrochloric acid. To prevent reoxidation, the powder is washed with ethanol and cyclohexane and subsequently stored in Schlenk tubes under argon atmosphere. Lead can be purified by segregation. Since lead oxides are lighter compared to the elemental metal, they float on top of the melt. After cooling, the top part can be mechanically removed. The oxidic impurities on electrolytic manganese chips for example can be removed by diluted nitric acid. Alternatively, the chips can be sealed in silica ampoules along with some silica shards. The ampoule is quickly heated to 1473 K and dwelled for 6 h. By this heat treatment, the manganese oxides react with the glass shards leading to surface cleaned Mn chips. Elements like magnesium or aluminum form passivating transparent oxide or hydroxide layers. These should, if possible, be removed before using these elements. Europium for example readily forms EuO when exposed to air, which is ferromagnetic below $T_C = 70$ K, affecting magnetic measurements quite drastically. Finally, lithium not only readily forms oxidic and hydroxidic surface impurities but also reacts with elemental nitrogen to Li_3N . The nitride itself is susceptible to hydrolysis leading to a plethora of decomposition products.

Since some elements are industrially prepared via hydrogen reduction, hydrides or interstitial hydrogen can remain in the product. This can not only lead to the formation of undesired side products, in the cases of $\text{Sr}_5\text{Sb}_3\text{H}^{46}$ and $\text{Ba}_5\text{Ga}_6\text{H}_2$,⁴⁷ these compounds were initially reported to be binaries. Therefore, alkaline earth metals, along with Eu and Yb should be purified by vacuum distillation or sublimation before use.

Finally, it should be mentioned that many of the starting materials and also some of the products readily react with oxygen, nitrogen or moisture, especially at elevated temperatures. Handling and heating of these elements should therefore be carried out under a protective gas atmosphere. This can be done in glove boxes that are commercially available or using Schlenk techniques. For both ways, it has to be assured that pure protective gas, e.g., argon is used. While glove box systems usually contain automated gas purification systems, for Schlenk lines the argon needs an additional purification step. Oxygen is usually removed via a BTX catalyst, while moisture can be removed by molecular sieve or chemically e.g., via P_2O_5 . Alternatively, getter materials can be used in the gas supply stream, here typically heated Ti sponge is employed.

4.06.3.2 Container materials

The formation and annealing of intermetallics usually takes place at elevated temperatures, therefore, suitable container materials are required.⁴⁸ Post synthetic annealing steps to e.g. increase the crystallinity of the target compound are usually carried out below the melting point but still temperatures of 1273 K are frequently used. Since a lot of the intermetallics get oxidized at elevated temperatures, they must be protected from atmospheric components. This can be achieved by encapsulating them in evacuated silica ampoules. Silica has, in comparison to e.g., borosilicate glasses, the advantage of a much higher softening point of about 1800 K. In turn, this leads to the necessity of using a hydrogen/oxygen burner to achieve the required temperatures. Since silica tubes contain absorbed moisture at their surfaces, they have to be flame-dried prior to use.

However, there are cases where the materials react with the silica ampoule leading to the formation of metal oxides or even silicides. This can be avoided by either using crucible materials (see below) or by wrapping the sample in metallic foils. Typically, thin molybdenum, niobium and tantalum foils are used that prevent the contact of the sample with the wall of the ampoule. Direct

reactions or melt assisted syntheses can also be carried out in silica ampoules if the materials do not react with the glass. Alternatively, crucibles or graphitized ampoules can be used.

Crucibles, both for synthesis and annealing, can be obtained in a wide range of materials. Typically, ceramic or metallic materials are utilized. The most commonly used ceramic materials are corundum (Al_2O_3), magnesia (MgO), and zirconia (ZrO_2). Crucibles made of these materials are readily available in different sizes and volumes. They are usually inert to most metallic materials used, however, one should not forget that these oxides have high melting points. So, in order to sinter powders to form crucibles, often sintering aids are added. This can be observed, since these crucibles often are slightly yellowish instead of the expected plain white. Therefore, one has to keep potential side reactions with the sintering aids in mind.

Metallic container materials, both for crucibles and ampoules have to exhibit high melting temperatures along with a good chemical inertness. This is usually achieved by using refractory metals such as Nb, Ta, Mo or even W. When used as ampoule materials, one of two ways is typically employed. The tubes can be squeezed at both ends or cylindrical ampoules can be built from a tube and two lids. The lids are typically obtained from sheet material via a stencil to obtain circular pieces followed by reforming them into lids. In both cases, the seams of the ampoules are sealed by arc-welding under protective gas atmosphere. It is important to note that, although refractory metals can sustain high temperatures, they are easily oxidized. Therefore, metal crucibles or ampoules have to be heat treated either under a protective gas atmosphere or by sealing them in evacuated silica containers. These crucible materials are especially suitable for the use of elements with low boiling points such as alkali and alkaline earth metals, Zn and Cd or Eu and Yb.

Finally, crucibles made from e.g., hexagonal BN (*h*-BN), graphite or glassy carbon should be mentioned. All of these materials should be heated under inert conditions to avoid reaction with the atmospheric components. While graphite and *h*-BN crucibles are rather cheap and can easily be fabricated from rod material on a lathe, glassy carbon is an expensive crucible material. In contrast to the two materials mentioned before, it is rather hard, chemically more inert and shows a poor wettability for molten metals, making it an interesting crucible material.

4.06.3.3 Heating

Heating can be conducted via classical resistance furnaces that are available in different sizes and shapes. Box, muffle or tube furnaces are commercially readily available from different companies. These furnaces can be programmed, so that ramping for both heating and cooling is possible. In many cases they can be equipped with a vacuum or inert gas system, enabling a manifold of chemical reactions. Considerably cheap tube furnaces can be constructed using ceramic tubes, heating tape and insulation, as described in a recent text book.⁴

In the case of metallic ampoules, metallic crucibles, graphite or glassy carbon, induction furnaces can be used to heat the respective container material. This technique is only applicable to electrically conductive materials (see before), since it is based on the generation of an eddy current within the material. In order to achieve this, the material has to be centered in an induction coil. By applying a high-frequency alternating current (5–15 kW, 50–1500 kHz), a fast oscillation of the charge carriers takes place, which in turn leads to Joule heating due to the resistance of the crucible material. Induction furnaces are quite frequently used in industrial applications when metals have to be heated. This ranges from induction-based welding to melting metals for casting or purification. For laboratory purposes, the ampoules, crucibles or even arc-melted buttons⁴⁹ get centered in specific water-cooled chambers within the induction coil. By increasing the power output, they can be heated to the desired temperature. Pyrometers can be utilized to measure or at least estimate the temperature of the heated specimen.

4.06.3.4 Flux assisted synthesis

Flux assisted syntheses can be carried out for several reasons. Besides the ability to often use lower reaction temperatures due to the dissolution of the reactants in the fluxing agent, also larger single crystals can usually be grown from flux aided syntheses. One has to differ between reactive and inert fluxes as well as between metallic and salt fluxes. The potential, the execution and possible applications have been summarized in two review articles addressing metal flux⁵⁰ and salt flux⁵¹ syntheses. Therefore, only the most important details will be given in the next paragraph.

Kanatidis, Pöttgen and Jeitschko⁵⁰ name the following characteristics for metals to be suitable fluxing agents: (1) the melting point of the metal should be reasonably low that normal heating equipment can be used, (2) the metal should exhibit a large liquidus range (large ΔT between m.p. and b.p.), (3) it should be possible to separate the flux from the respective product by chemical dissolution, filtration in the liquid state or by mechanical removal and (4) in the case of inert fluxes, the metal should not form stable products with the other reactants. Typical metals that are used as both inert and reactive fluxes are Sn (m.p. 505 K), e.g., for the synthesis of binary and ternary phosphides (IrP_2 ,⁵² PtP_2 ,⁵³ ANi_2P_2 with $A = \text{Ca, La-Yb}$ ⁵⁴) or Pb (m.p. 600 K), also used for the synthesis of phosphides (e.g., AEIr_2P_2 with $\text{AE} = \text{Ca-Ba}$ ⁵⁵) or silicides (REMn_2Si_2 with $\text{RE} = \text{Y, Tb-Lu}$ ^{56,57}). But also, Al (m.p. 934 K), Ga (m.p. 303 K), In (m.p. 430 K) or alkali metals (Li: m.p. 454 K) have been used as metallic fluxes.⁵⁰

Bugaris and zur Loye⁵¹ name similar criteria for salt fluxes. The fluxing agent should be able to (1) dissolve a substantial quantity of the reagents, it should possess a (2) low melting point, (3) a significant change of the solubility with temperature, (4) a low volatility, it should be (5) unreactive towards the container that contains the melt, (6) easily removable after crystal growth, (7) commercially available at low cost, and finally (8) exhibit a low toxicity. Since their review article focusses on the synthesis of oxides from salt fluxes, it should be additionally referred to a textbook addressing the synthesis of intermetallic materials from molten salts.^{3,4} As examples,

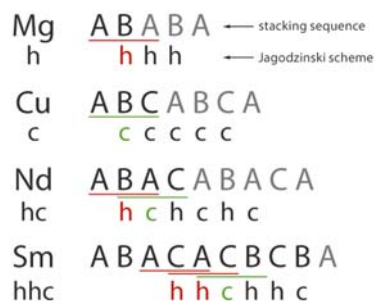


Fig. 3 Stacking sequences for the Mg, Cu, Nd and Sm type structures along with the respective Jagodzinski nomenclature.

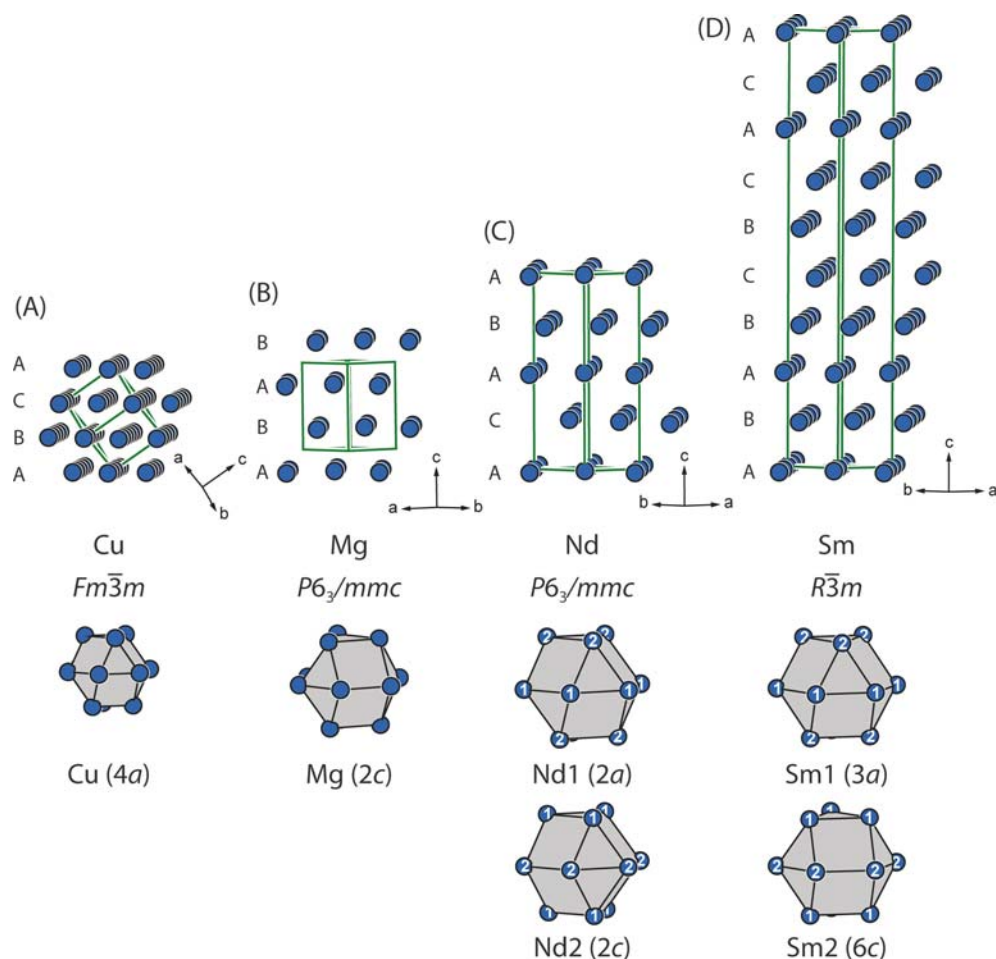


Fig. 4 Comparison of the (A) Cu, (B) Mg, (C) Nd and (D) Sm type structures along with the respective coordination polyhedra. The stacking sequences are given.

With three orientation that are possible with these hexagonal close packed layers, one might imagine, that in principle even more stacking sequences could be possible. This is realized e. g. among the structures of the lanthanides. Nd⁶⁹ ($P6_3/mmc$, $a = 366$, $c = 1180$ pm, $c/a = 3.226$) and Sm⁷⁰ ($R\bar{3}m$, $a = 363$, $c = 2620$ pm, $c/a = 7.220$) form two additional structure types that can be described as stacking variant of the cubic and hexagonal closest packing sequences. In order to describe these stacking sequences in a lucid way, the nomenclature proposed by Jagodzinski⁷¹ can be used. He introduced abbreviations for the specific stacking sequences, labeling the ABA sequence with h , as this is the arrangement found in the hexagonal closest packing, while the ABC sequence is labeled c due it being a cutout of the cubic closest packed structure. Subsequently, other stacking sequences can be abbreviated as shown in Fig. 3. For the Nd type structure (Figs. 3 and 4C), the ABAC stacking sequence leads to a the Jagodzinski symbol hc , while the more complex ABACACBCB stacking, realized in elemental Sm (Figs. 3 and 4D), can be abbreviated as hhc . All of these structure types exhibit a space filling of 74% as they are derived from closest packings.

While the Cu type structure only has one variable, being the lattice parameter a ($a = 360$ pm with Cu on $4a$ with $0, 0, 0$), the Mg and Nd type structures have the c lattice parameter as an additional degree of freedom ($a = 322$, $c = 523$ pm with Mg on $2c$, $1/3$, $2/3$, $1/4$; $a = 366$, $c = 1180$ pm with Nd1 on $2a$, $0, 0, 0$ and Nd2 on $2c$, $1/3$, $2/3$, $1/4$). The ideal c/a ratio for the *hcp* is 1.633 with several metals (Co⁷² $c/a = 1.631$; Ni⁷³ $c/a = 1.633$) exhibiting ratios very close or even exactly this ideal value. Some elements e.g., Be⁷⁴ ($c/a = 1.586$) or Ru⁷⁵ ($c/a = 1.590$) exhibit smaller c/a ratios, while in Zn⁷⁶ or Cd⁷⁶ significantly larger ratios of even $c/a = 1.860$ and $c/a = 1.890$ can be observed. These differing ratios can be attributed to a different extent of mixing of the s and p orbitals along with an electronic contribution originating from the interplay between the band energy and the electrostatic (Madelung) energy.⁷⁷ In the rhombohedral Sm type structure finally another degree of freedom is introduced. Besides the c/a ratio now also the Sm2 position gains a free positional z parameter (Sm1 on $3a$ with $0, 0, 0$; Sm2 on $6c$ with $0, 0, 0.222(3)$). This allows for another possibility to stabilize this structure.

Another important structure type found for e.g., the alkali metals and some early transition metals is the body centered cubic W type (Fig. 5C, $Im\bar{3}m$, $a = 318$ pm).⁷⁸ In contrast to the Cu and Mg type structure, a reduced space filling of 68% is observed. The respective atoms exhibit a coordination number of 8 and are surrounded in the shape of a cube.

Finally, quite a number of unique structure types can be observed. Probably one of the most known and at the same time least complex structure is the one of cubic α -Po. It exhibits a cubic primitive unit cell (Fig. 5A, $Pm\bar{3}m$, $a = 334$ pm) in which the atoms only occupy the corners, leading to a space filling of 52%.⁷⁹ Above 309 K, rhombohedral β -Po becomes stable. The rhombohedral structure (Fig. 5B, $R\bar{3}m$, $a = 508$, $c = 493$ pm)⁷⁹ can be derived from the cubic one via an elongation along the space diagonal. In both cases, octahedral coordination environments are found.

Indium for example crystallizes in an elongated tetragonal unit cell (Fig. 5D, $I4/mmm$, $a = 324$, $c = 486$ pm)⁷⁵ that can be derived from the Cu type structure (*fcc*). The coordination number remains 12, however due to the distortion, 4 shorter and 8 longer distances can be observed. Ga exhibits an orthorhombic structure ($Cmce$, $a = 451$, $b = 764$, $c = 452$ pm)⁸⁰ which can be described based on the Ga₂ dumbbells (Ga–Ga = 248 pm) found in the structure. Each atom is furthermore surrounded by 6 additional atoms, forming corrugated layers within the ac plane that get connected along $[010]$. In both cases, the distortions can be explained by electronic instabilities in a typical metal structure that get countered by the respective distortion.^{81,82} This in turn leads to significantly different properties compared to other metals, like low melting points (m.p.(Ga) = 303 K; m.p.(In) = 430 K).⁸³

The last elemental structure that should be mentioned is at the same time probably the most complex elemental modification. In the cubic unit cell of α -Mn² ($I\bar{4}3m$, $a = 891$ pm) 58 atoms can be found, originating from four crystallographic sites. All sites have large coordination numbers of CN = 12–16 that belong to the Frank-Kasper type polyhedra.^{84,85} Between 1000 and 1370 K, the β -modification of elemental Mn is observed.⁸⁶ This high-temperature variant crystallizes in the cubic primitive crystal system ($P4_132$, $a = 632$ pm) and exhibits only two crystallographic independent Mn sites, again with large coordination numbers of 12 and 14.

4.06.4.2 Laves-phases

The Laves-phases, named after the German mineralogist Fritz Laves,^{87,88} exhibit the general composition AB_2 , for which three prototypes are known (MgCu₂,⁸⁹ MgZn₂⁹⁰ and MgNi₂⁹¹).⁹² The *Pearson Crystal Data Base*⁶⁷ lists thousands of entries for these structure types, along with a plethora of related structures. In 2006, a special issue was published on the occasion of Laves' 100th birthday (*Z. Kristallogr.* 2006, 221, issues 5-7) summarizing the work on Laves phases.

Laves-phases are close-packed structures with the general composition AB_2 , where the smaller B atoms form a network of empty B_4 tetrahedra, while the larger A atoms reside within cavities. Both atomic positions exhibit large coordination numbers of $CN(A) = 16$ ($4A + 12B$) and $CN(B) = 12$ ($6A + 6B$), in the shape of a 16-vertex Frank-Kasper polyhedron and icosahedra, respectively. For

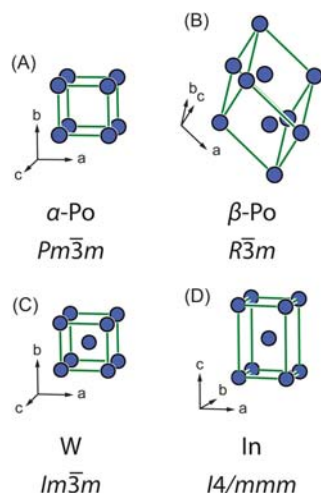


Fig. 5 Comparison of the (A) α -Po, (B) β -Po, (C) W and (D) In type structures.

closest-packed structures, the ideal atomic radii ratio is $r_A/r_B = (3/2)^{1/2} \approx 1.225$, which is realized for quite a number of compounds. However, also Laves-phases with deviating ratios ranging from ~ 1.1 to ~ 1.7 have been observed. The fact that these phases are rather driven by packing effects can be illustrated by the fact, that NeHe_2 crystallizes in the MgZn_2 type structure at high pressures.⁹³

The unit cells of the cubic MgCu_2 ($Fd\bar{3}m$, C15; Mg on 8b; Cu on 16c) and the hexagonal MgZn_2 ($P6_3/mmc$, C14; Mg on 4f; Zn1 on 6h; Zn2 on 2a) and MgNi_2 ($P6_3/mmc$, C36; Mg1 on 4f; Mg2 on 4e; Ni1 on 6h; Ni2 on 6g; Ni3 on 4f) type structures are shown in Fig. 6. While in the cubic MgCu_2 type structure, the B_4 tetrahedra are connected via all corners to four other tetrahedra, in the hexagonal MgZn_2 phase, two tetrahedra are connected by a common face, forming a trigonal bipyramid. This entity is connected to five other entities over all corners. Finally, in the MgNi_2 type structure both connection modes are observed. The Mg atoms are located in cavities of the B_4 tetrahedra network and exhibit atomic arrangements, when focused only on the Mg substructure, that are comparable to the ones in cubic (MgCu_2) or hexagonal (MgZn_2 , MgNi_2) diamond.

Despite the geometric influences, that seem to be a dominating factor, the influence of electronic contributions has been addressed and studied numerous times.^{94–100} Laves already discussed the influence of the VEC on the formation of these compounds in one of his early works.⁹²

Due to the large number of known compounds, especially the rare-earth containing Laves phases have received great interest,¹⁰¹ due to their intriguing physical properties,^{102–107} which e.g., sometimes even cause structural distortions below the magnetic transition temperature.¹⁰⁸

While in the MgCu_2 type structure, only two crystallographic positions for Mg and Cu are observed, in the MgZn_2 type structure one Mg and two Zn sites with a respective ratio of 1:3 are found. Therefore, one could think about substitution of one of the Zn sites by other elements, forming ordered ternary Laves phase derivatives. The first compound reported to crystallize with this coloring variant is $\text{Mg}_2\text{Cu}_3\text{Si}$.¹⁰⁹ Here the Cu atoms are found on the Zn1 site (6h) while the Si atoms occupy the Zn2 site (2a). Besides the already mentioned silicide, quite a number of compounds have been reported to crystallize with this structure type, including other silicides like $\text{Sc}_2\text{T}_3\text{Si}$ ($T = \text{Fe, Co Ni}$)¹¹⁰ or $\text{Ti}_2\text{Ni}_3\text{Si}$,¹¹¹ but also germanides ($\text{U}_2\text{Mn}_3\text{Ge}$,¹¹² $\text{U}_2\text{Co}_3\text{Ge}$,¹¹³ $\text{Mn}_2\text{Co}_3\text{Ge}$,¹¹⁴ $\text{Mn}_2\text{Cu}_3\text{Ge}$ ¹¹⁵) or the sole aluminum ($\text{U}_2\text{Cu}_3\text{Al}$ ¹¹⁶) or gallium ($\text{U}_2\text{Fe}_3\text{Ga}$ ¹¹⁷) compounds have been reported. In all these cases, the main group element is located on the 2a site. For the inverse variant, far less compounds (e.g., Eu_2IrGa_3 ,¹¹⁸ Li_2IrSi_3 ,¹¹⁹ Ce_2RuAl_3 ¹²⁰) are reported. Besides these rather straight forward substitutional variants, also more complex superstructures of MgZn_2 can be observed, e.g., $\text{Yb}_6\text{Ir}_5\text{Ga}_7$ ¹²¹ and the isotypic $\text{RE}_6\text{Ir}_5\text{Ga}_7$ ($\text{RE} = \text{Sc, Y, Nd, Sm, Gd-Tm, Lu}$)¹²² and $\text{RE}_6\text{Ir}_5\text{Al}_7$ ($\text{RE} = \text{Sc, Y, Ce-Nd, Sm, Gd-Lu, T} = \text{Ru, Ir}$)¹²³ series.

A ternary substitutional or coloring variant of the MgCu_2 type structure in contrast is not possible since only one Mg and one Cu position exist in the prototype. However, both the $\text{Mg}_2\text{Ni}_3\text{Si}$ ¹²⁴ and the MgCu_4Sn ^{125,126} structure types can be derived from the cubic Laves phase via symmetry reductions. The crystallographic relationships have been shown, based on group-subgroup schemes, for $\text{Ce}_2\text{Rh}_3\text{Ga}$.¹²⁷ For both structure types, several dozens of compounds have been reported, therefore it is referred to a structural database.⁶⁷

4.06.4.3 Hume-Rothery phases

In contrast to the Laves phases, which can be explained by the atomic radii ratio of the constituent elements, Hume-Rothery phases, named after the British metallurgist *William Hume-Rothery*, are strictly dependent on the valence electron concentration VEC. He discovered, that in different binary phase diagrams the same structures can be observed with increasing electron count or VEC. The first phase observed at lowest VEC is the so called α -phase that forms the fcc/Cu type structure ($Fm\bar{3}m$). Subsequently, the

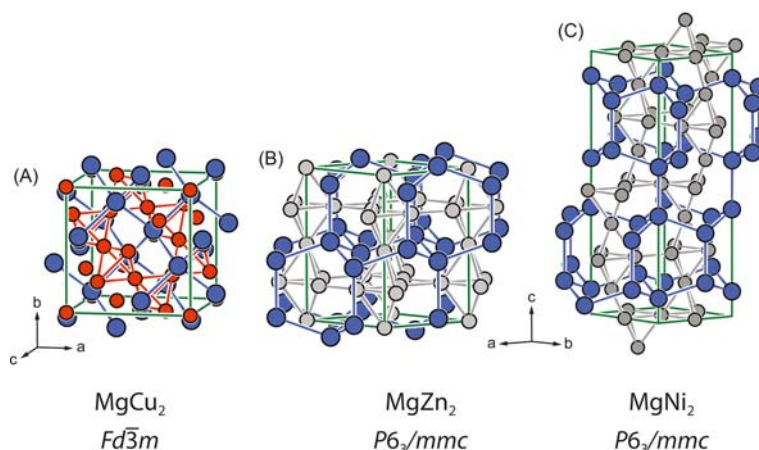


Fig. 6 Comparison of the (A) MgCu_2 , (B) MgZn_2 , and (C) MgNi_2 type structures. Mg atoms are depicted in blue, Cu atoms in orange, Zn and Ni in gray. The connectivity of the tetrahedral Cu/Zn/Ni networks as well as the respective Mg frameworks are highlighted.

β -phase forms, however, between two distinct phases always a two-phase region is observed. The β -phase crystallizes in the *bcc/W* type structure (*Im* $\bar{3}m$) and exhibits a VEC of $3/2 = 1.5$, while the γ -phase exhibits a VEC of $21/13 = 1.615$. It crystallizes in a large cubic unit cell with 52 atoms (*I* $\bar{4}3m$). The δ - and ζ -phases are usually only observed at higher temperatures with the latter being quite rare. Next in line is the ε -phase with a VEC of $21/12 = 1.75$ adopting the Mg type structure (*hcp*, *P6* $\bar{3}/mmc$). As in the α -phase, the single crystallographic position is mixed occupied by the two respective elements. The η -phase, adopting the β -Mn type structure (*P4* $\bar{1}32$), is followed by another two-phase region before the last phase crystallizing in the hexagonal close packing is observed. Zn exhibits only a minor solubility for Cu, therefore this region is small. The VEC, in general, is calculated as sum of the electrons supplied by the constituent atoms divided by the number of atoms in the formula unit. A good example to illustrate the influence of the VEC are the brass phases. They consist of different ratios of Cu to Zn, where Cu supplies $1 e^-$ while Zn supplies $2 e^-$. The β -phase has a VEC of 3:2 which is achieved with a one-to-one ratio of Cu and Zn: $VEC(\text{CuZn}) = (1 \times 1 + 1 \times 2)/2 = 3/2 = 21/14$. The γ -phase can be found for Cu_5Zn_8 with $VEC(\text{Cu}_5\text{Zn}_8) = (5 \times 1 + 8 \times 2)/(5 + 8) = 21/13$ while finally the ε -phase is CuZn_3 with $VEC(\text{CuZn}_3) = (1 \times 1 + 3 \times 2)/(1 + 3) = 7/4 = 21/12$. Fig. 7 illustrates the different phase in the copper-zinc phase diagram. What makes this concept so useful is that it also applies to other phase diagrams. So for the Cu-Al system, the β -phase is Cu_3Al ($VEC(\text{Cu}_3\text{Al}) = (3 \times 1 + 1 \times 3)/(3 + 1) = 6/4$), Cu_9Al_4 adopts the γ -phase ($VEC(\text{Cu}_9\text{Al}_4) = (9 \times 1 + 4 \times 3)/(9 + 4) = 21/13$) and finally Cu_5Al_3 the ε -phase ($VEC(\text{Cu}_5\text{Al}_3) = (5 \times 1 + 3 \times 3)/(5 + 3) = 14/8 = 21/12$).

4.06.4.4 Zintl-phases

Zintl compounds or Zintl phases, named after the German chemist *Eduard Zintl*, are compounds that can be positioned between the class of intermetallic compounds and insulating valence compounds.¹²⁸ It was *Fritz Laves* (see Laves phases, section 4.06.4.2) who suggested to name all intermetallic compounds obeying the $(8 - N)$ rule as Zintl compounds.¹²⁹ In the classical sense, these compounds are formed by elements with low electronegativity (*A*, groups 1, 2) that donate their valence electrons to more electronegative elements (*B*, groups 13–15). These electrons are often used to form covalent bonds between themselves, so that each atom can achieve a noble gas electron configuration. Between the two sorts of atoms, ionic interactions take place. If sufficient electrons are transferred onto the *B* atoms, isolated anions are formed, if not, polyanions with two-center-two-electron *B–B* bonds will be observed. These polyanions often adopt structural fragments that are also observed in elemental modifications with equal electron count (*vide infra*). The ionic interactions, however, make them (partially) soluble in polar solvents, enabling the isolation of the cluster anions of the heavier main group elements that are also called Zintl anions.^{130–132} Due to this unique bonding situation, most of the compounds obeying these rules are semiconductors. The versatility of their physical properties makes them excellent candidates for various applications such as thermoelectrics,^{133,134} hydrogenation catalyst¹³⁵ or battery materials.¹³⁶ Since this field of research is very active, some recent reviews targeting the different aspects should be mentioned.^{137–142}

Probably the easiest to understand Zintl compounds are the ones where the electronegative element exhibits a filled valence shell and is therefore isoelectronic with a noble gas. For the group 14 elements (tetrels, *Tt*) these are Tt^{4-} (e.g., Si^{4-}) for the group 15 elements (pnictogens, *Pn*) Pn^{3-} (e.g., P^{3-}) anions. In combination with an alkaline earth element *AE*, the composition AE_2Tt can be observed for all combinations of (Mg–Ba) with (Si–Pb). The Mg compounds adopt the *anti*- CaF_2 or Mg_2Si type structure (*Fm* $\bar{3}m$, Fig. 8A),^{143,144} while the other combinations crystallize in the *anti*- PbCl_2 or $\beta\text{-Co}_2\text{Si}$ type structure (*Pnma*, Fig. 8B).^{145–152} With the group 15 elements, the alkali metals form the A_3Pn composition (*A* = Li–Cs, *Pn* = P–Bi) adopting either the cubic BiF_3 (*Fm* $\bar{3}m$, Fig. 8C) or the hexagonal Na_3As type structure (*P6* $\bar{3}/mmc$, Fig. 8D),^{153,154} while for the alkaline earth elements the AE_3Pn_2 (*AE* = Be–Ba, *Pn* = P–Bi) compounds with either the *anti*- Mn_2O_3 (*la* $\bar{3}$, Fig. 8E) or the *anti*- La_2O_3 type structure (*P* $\bar{3}m1$, Fig. 8F) are formed.^{143,155–158}

If the electron transfer does not lead to a noble gas electron configuration, polyatomic anions are formed. In the following paragraph, just a few examples, to explain the general concept, are given. As mentioned before, the polyanions often adopt structural fragments that are related to structural features found in elemental modifications. The prototypic Zintl compounds are probably those crystallizing with the NaTl structure type (*Fd* $\bar{3}m$, Fig. 9A).¹⁵⁹ The compound can be divided into ions according to Na^+Tl^- ,

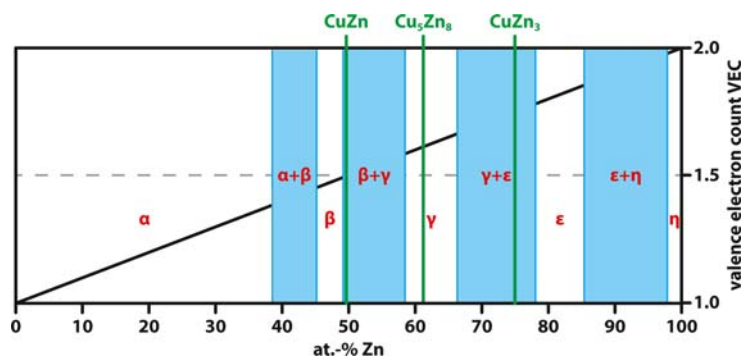


Fig. 7 Hume-Rothery phases (green lines) in the Cu-Zn phase diagram. The respective phases are labeled; the two-phase ranges are highlighted in blue.

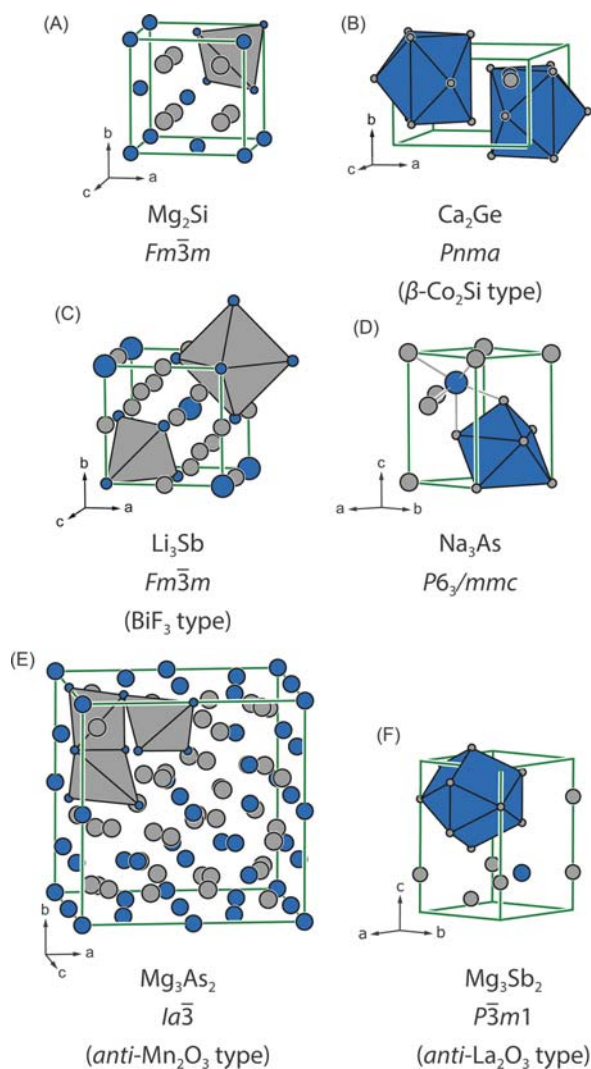


Fig. 8 Comparison of different binary Zintl phases. (A) Mg_2Si , (B) $\beta\text{-Co}_2\text{Si}$, (C) Li_3Sb , (D) Na_3Sb , (E) Mg_3As_2 and (F) Mg_3Sb_2 . The A or AE atoms are depicted in gray, the respective other atoms in blue.

with the Tl^- being isoelectronic to group 14. According to the $(8 - N)$ rule, the Tl atoms therefore form 4 bonds and adopt the cubic diamond type structure, the sodium cations can be found in the cavities of the polyanion. Beside the elements of the prototype it is also formed by $A = \text{Li}, \text{Na}$ with $\text{Tr} = \text{Al-Tl}$,¹⁵⁹⁻¹⁶¹ and *hp*-KTI.¹⁶² The alkali tetrelides ATl ($=\text{A}_4\text{Tl}_4$) can be formally described as A^+Tl^- , with Tl^- being isoelectronic to group 15. Each atom exhibits 3 bonds to neighboring Tl atoms and one lone pair, leading to white phosphorus analog Tl_4^{4-} anions. For the different combinations of A and Tl atoms, three different structure types can be found: the monoclinic Na_4Si_4 ($C2/c$, Fig. 9B)¹⁶³ with its own structure type being the sole representative, the cubic K_4Ge_4 type ($P\bar{4}3n$)¹⁶⁴ also found for K_4Si_4 ,¹⁶⁴ Rb_4Si_4 ,¹⁶⁴ Cs_4Si_4 ,¹⁶⁴ Rb_4Ge_4 ,¹⁶⁴ Cs_4Ge_4 ¹⁶⁴ and $\beta\text{-Cs}_4\text{Sn}_4$ ¹⁶⁵ and finally, the tetragonal Na_4Pb_4 type ($I4_1/acd$)¹⁶⁶ with Na_4Sn_4 ,¹⁶⁷ K_4Sn_4 ,¹⁶⁸ Rb_4Sn_4 ,¹⁶⁸ $\alpha\text{-Cs}_4\text{Sn}_4$,¹⁶⁸ K_4Pb_4 ¹⁶⁸ and Rb_4Sn_4 .¹⁶⁸ Besides the alkali metal compounds, monovalent tetrelide anions can also be observed in alkaline earth compounds with the general composition AETl_2 ($=\text{AE}^{2+}(\text{Tl}^-)_2$). While in the CaSi_2 type structure ($R\bar{3}m$, Fig. 9C) corrugated layers, isostructural with gray As, are observed, the SrSi_2 type structure ($P4_132$, Fig. 9D) exhibits a network formed by 3-bonded Si atoms and finally in the BaSi_2 type structure ($Pnma$, Fig. 9E) again Si_4^{4-} tetrahedra are observed. When transferring 2 electrons onto the electronegative element, planar zigzag chains can be observed in the AETl ($=\text{AE}^{2+}\text{Tl}^{2-}$) representatives crystallizing in the CaSi/CrB type structure ($Cmcm$, Fig. 9F), while spiraled chains, comparable to the ones in elemental selenium can be observed in the LiAs type structure ($P2_1/c$, Fig. 9G),¹⁶⁹ also reported for LiP,¹⁷⁰ NaSb¹⁷¹ or KSb.¹⁷⁰

With respect to ternary compounds, a plethora of elemental combinations arise, since, besides the electron donating and the electron accepting elements, also main group or transition metals can be included. Describing all of these possible structures is by far unrealistic, therefore a few selected examples are given. When keeping the idea of structurally related compounds in

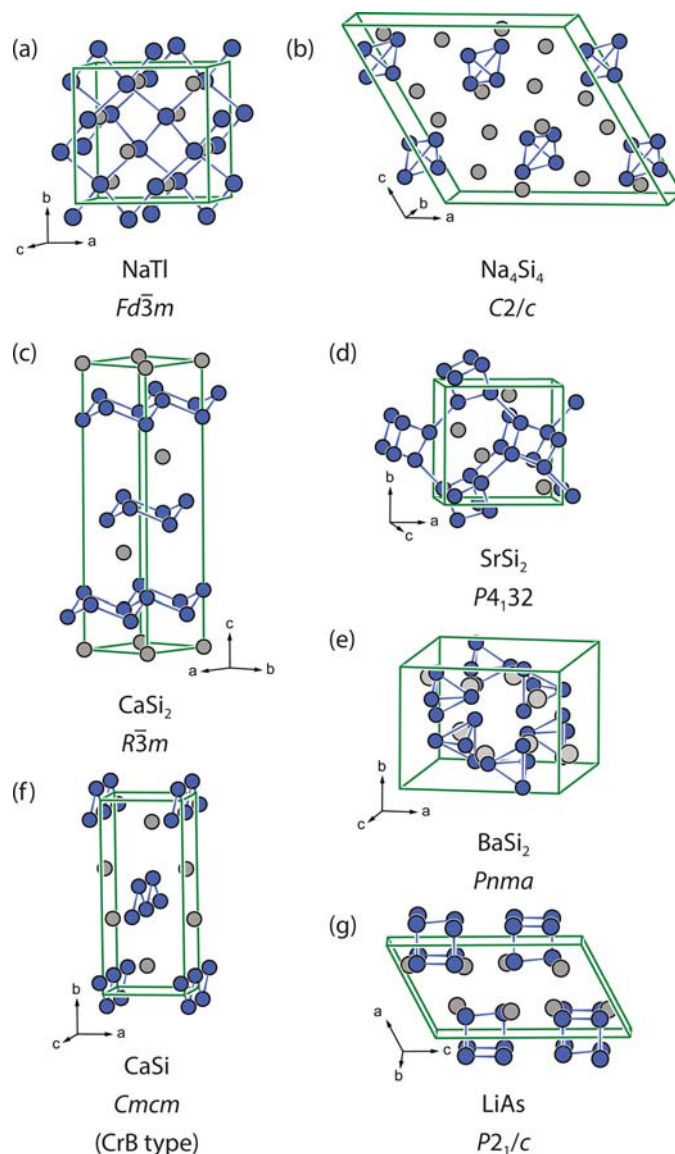


Fig. 9 Comparison of different binary Zintl phases. (A) NaTl, (B) Na_4Si_4 , (C) CaSi_2 , (D) SrSi_2 , (E) BaSi_2 , (F) CaSi and (G) LiAs. The A or AE atoms are depicted in gray, the respective other atoms in blue.

mind, one can draw a comparison of Zintl anions to complex oxoanions like the sulfate $[\text{SO}_4]^{2-}$, the phosphate $[\text{PO}_4]^{3-}$ or the orthosilicate $[\text{SiO}_4]^{4-}$. The combination of an element of group 13 or 14, surrounded by 4 group 15 atoms can lead to structurally related tetrahedral entities like the isolated orthoarsenidosilicate anions $[\text{SiAs}_4]^{8-}$ in the Ba_4SiAs_4 type structure ($P\bar{4}3n$; AE_4TtPn_4 with $AE = \text{Ca-Ba}$; $Tt = \text{Si, Ge}$; $Pn = \text{P, As}$, Fig. 10A)^{172–174} and isostructural compounds. But also edge-sharing tetrahedra can be observed, e.g., in the A_2TtPn_2 ($K_2\text{MnS}_2$ type, *Ibam*, Fig. 10B) compounds with $A = \text{K, Rb, Cs}$; $Tt = \text{Si, Ge, Sn}$; $Pn = \text{P, As}$.^{175–178} Double tetrahedra can form e.g., in the AE_3TrPn_3 compounds ($AE = \text{Ca-Ba}$; $Tr = \text{Al-In}$; $Pn = \text{P-Sb}$) with either Ca_3AlAs_3 type (*Pnma*, Fig. 10C), Ba_3AlSb_3 type (*Cmce*, Fig. 10D) or Ba_3GaSb_3 (*Pnma*, Fig. 10E) type structures.^{179–184} More complex (branched) chains for example can be found in the $AE_5Tr_2Pn_6$ compounds ($AE = \text{Ca-Ba}$; $Tr = \text{Al-In}$; $Pn = \text{As-Bi}$), which can adopt the $\text{Ca}_5\text{Al}_2\text{Bi}_6$ (*Pbam*, Fig. 10F), $\text{Ca}_5\text{Ga}_2\text{As}_6$ (*Pbam*, Fig. 10G) or the $\text{Sr}_5\text{Al}_2\text{Sb}_6$ (*Pbam*, Fig. 10H) type structures.^{179,182,185–192} In many cases, also the respective rare earth compounds with Yb^{2+} ($\text{Yb}_5\text{Tr}_2\text{Pn}_6$; $Tr = \text{Al-In}$; $Pn = \text{As-Bi}$)^{193–195} being approximately the same size as Ca^{2+} and Eu^{2+} ($\text{Eu}_5\text{Tr}_2\text{Pn}_6$; $Tr = \text{Al-In}$; $Pn = \text{As-Bi}$)^{196–202} being comparable to Sr^{2+} have been synthesized and characterized with respect to their magnetic, ^{121}Sb and ^{151}Eu Mössbauer spectroscopic and thermoelectric properties. With respect to thermoelectric properties, probably the $M_{14}TPn_{11}$ compounds are the most popular ones. $\text{Ca}_{14}\text{AlSb}_{11}$ is the respective prototype ($I4_1/acd$)²⁰³ which has been observed for a wide range of elemental combinations with $M = \text{Ca-Ba, Eu, Yb}$, $T = \text{Mn, Zn, Al-In}$ and $Pn = \text{P-Bi}$ and investigated by numerous methods.^{203–241}

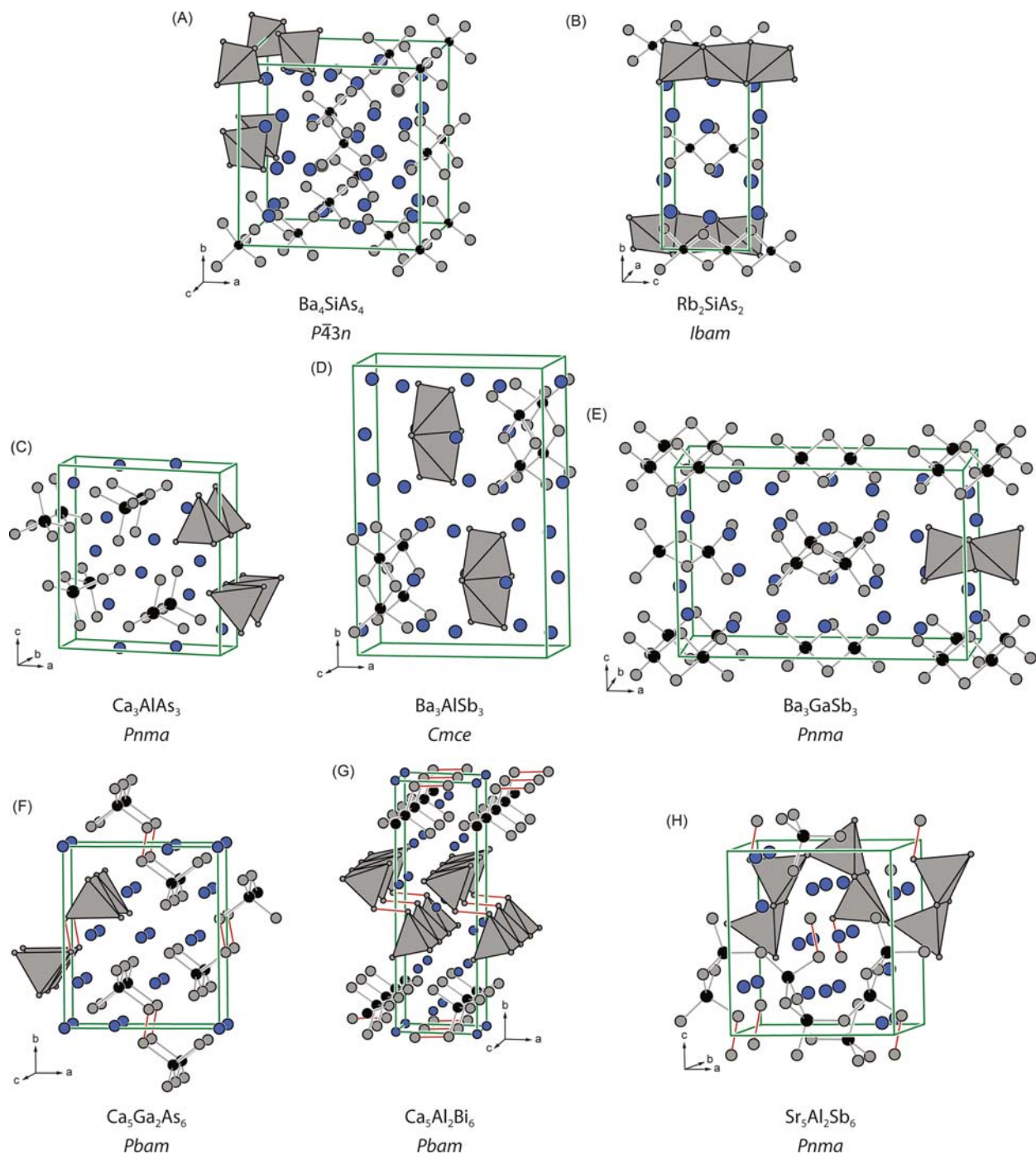


Fig. 10 Comparison of different ternary Zintl phases. (A) Ba_4SiAs_4 , (B) Rb_2SiAs_2 , (C) Ca_3AlAs_3 , (D) Ba_3AlSb_3 , (E) Ba_3GaSb_3 , (F) $\text{Ca}_5\text{Ga}_2\text{As}_6$, (G) $\text{Ca}_5\text{Al}_2\text{Bi}_6$, and (H) $\text{Sr}_5\text{Al}_2\text{Sb}_6$. The A or AE atoms are depicted in blue, group 13 or 14 atoms in black and the Pn atoms in gray.

4.06.4.5 Selected binary and ternary phases

4.06.4.5.1 Group 2/12

4.06.4.5.1.1 Beryllium

Although the Pearson data base⁶⁷ contains >450 entries for binary and ternary compounds containing Be (excluding chalcogens, halogens and hydrogen in the search), the overall information about these compounds is rather scarce. To quote the authors of a recent review article: "Although beryllium is widely used as alloying component in diverse light-weight alloys, the crystal chemistry of beryllium containing Zintl phases and intermetallic compounds is only scarcely developed and only few phase diagrams, mostly the industrially relevant ones, have been studied in detail."²⁴²

As for most of the other classes of compounds described in the following chapters, Laves phases, both of the MgCu_2 (Fig. 6A) and MgZn_2 (Fig. 6B) type structure have also been reported for Be intermetallics. Besides them, also a large number of Be-rich intermetallics have been reported with the NaZn_{13} and ThMn_{12} type representatives being the most prominent ones. Due to the high Be-content of >90 at.%, the transition metals atoms are solely surrounded by Be atoms forming highly symmetric polyhedra. In the NaZn_{13} type structure, e.g., formed by $M\text{Be}_{13}$ ($M = \text{Mg-Ba}^{243,244}$), $T\text{Be}_{13}$ ($T = \text{Zr, Hf}^{245,246}$), $RE\text{Be}_{13}$ ($RE = \text{Sc, Y, La-Nd, Sm-Lu}^{245,247,248}$), a 24-vertex pseudo Frank-Kasper polyhedron is observed (Fig. 11A), in the ThMn_{12} type structure, a 20-vertex pseudo Frank-Kasper polyhedron is found (Fig. 11B). While the alkaline earth, rare-earth and only a few transition metals form the NaZn_{13} type, the $T\text{Be}_{12}$ compounds (ThMn_{12} type structure) in contrast are reported for numerous transition metals, e.g., $T = \text{Ti, V, Nb, Ta, Cr, Mo, W, Mn, Fe, Co, Pd, Pt, Ag and Au}^{249-255}$.

It is interesting to note, that although the combinatory manifold for ternary compounds is way larger compared to binaries, only ~ 150 entries are listed for ternary Be compounds versus >300 binary ones.⁶⁷ Here, for the ZrBeSi ($P6_3/mmc$) and the $\text{Ta}_6\text{Cu}_8\text{Be}_{15}$ ($Fm\bar{3}m$) type structures the most compounds are reported. While the latter can be derived from the $\text{Th}_6\text{Mn}_{23}$ type structure, ZrBeSi (Fig. 12A) can be described based on AlB_2 by a doubling of the c axis (*klassengleiche* transition of index 2). The hexagonal unit cell ($P6_3/mmc$) contains two honey-comb $[\text{BeSi}]^{\delta-}$ layers that are stacked with the same orientation, however, the Si atoms of one layer are situated above and below Be atoms, the same is true for the Be atoms. The Zr atoms are located in the center above and below each hexagon. The $\text{Ta}_6\text{Cu}_8\text{Be}_{15}$ type structure (Fig. 12B) can be divided into three subsections. On the corners and faces, Cu centered Be cubes (Cu@Be_8) are observed, while on the edges empty Ta_6 octahedra can be found. In between, a complex Be network is located, the respective polyhedra can be found in large cavities within this network.

4.06.4.5.1.2 Magnesium

Magnesium intermetallics, especially the ternary ones, play an important role in the field of light-weight alloys. The most prominent structure types, according to the Pearson data base,⁶⁷ will be discussed in the following paragraph. Also a review article from 2007, summarizing the field of magnesium-containing rare-earth transition metal intermetallics should be mentioned.²⁵⁶

As already seen from the chemical composition, the Laves phases MgCu_2 , MgNi_2 and MgZn_2 along with all isotypic representatives are important Mg-containing intermetallics. With copper, the cubic Laves phase forms as MgCu_2 (Fig. 6A), all other Mg representatives, however, exhibit an "inverse" composition according to MMg_2 . In these compounds the Mg atoms are located on the Cu position forming the tetrahedral network, while the M atoms ($M = \text{La-Nd, Sm, Gd, Th}^{257-259}$) occupy the Mg positions of the prototype. The late rare earth metals also form REMg_2 compounds ($RE = \text{Y, Eu, Tb-Lu}^{260-263}$) now crystallizing in the hexagonal MgZn_2 type structure (Fig. 6B). Besides the REMg_2 representatives also the alkaline-earth AEMg_2 ($AE = \text{Ca-Ba}^{264,265}$) have been reported to adopt this structure type. The only other transition metal compounds, besides the prototype, forming the MgZn_2 type structure are MgCo_2^{266} and MgIr_2^{267} . Finally, for the MgNi_2 type structure (Fig. 6C), only ThMg_2^{258} (which was also reported to adopt the MgCu_2 type structure) and metastable $\text{Mg}_{1.2}\text{Al}_{1.8}^{268}$ have been found so far.

The most representatives for a binary structure type are reported for MMg adopting the cubic CsCl type structure (Fig. 13A). As second constituent metal, a large variety of elements have reported, namely $M = \text{Sr, Sc, Y, La-Nd, Sm-Lu, Rh, Pd, Ag, Au, Hg and Tl}^{67}$. Besides the 1:1 and the 1:2 compounds, also larger series with the compositions REMg_3 ($RE = \text{La-Nd, Sm, Gd-Dy}^{257,259,269}$), BiF_3 type, $Fm\bar{3}m$, Fig. 13C), TMg_3 ($T = \text{Rh, Pd, Ag, Ir, Pt, Au}^{270-273}$), Cu_3P type, $P6_3cm$, Fig. 13D) as well as $T'_3\text{Mg}$ ($T' = \text{Ni, Pd, Ag, In, Pt}^{274-278}$), Cu_3Au type, $Pm\bar{3}m$, Fig. 13B) have been reported. It should be noted, that the TMg_3 compounds were previously reported to crystallize in the Na_3As type structure. Reinvestigations revealed that the Cu_3P type structure is the correct one, which can be derived from the Na_3As type structure¹⁵⁴ by an $\sqrt{2} \times \sqrt{2} \times 2$ enlargement of the original cell. This has been demonstrated by a group-subgroup relation for RhMg_3^{272} .

For the Mg intermetallics, a significantly larger number of ternary compounds (compared to the Be ones) have been reported. As for several other ternary systems (*vide infra*), the largest manifold of compounds is reported for the ZrNiAl type structure ($P\bar{6}2m$). This structure type is probably one of the most important ones (besides the TiNiSi type structure) as it is formed by a plethora of

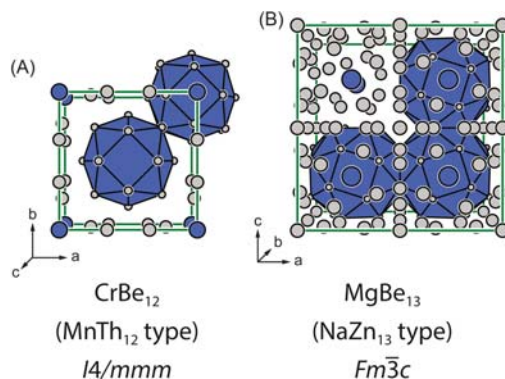


Fig. 11 Comparison of the (A) $T\text{Be}_{12}$ (MnTh_{12} type) and (B) $M\text{Be}_{13}$ (NaZn_{13} type) structures formed by numerous binary Be-intermetallics (see text). The Be atoms are depicted in gray, the respective other atoms in blue.

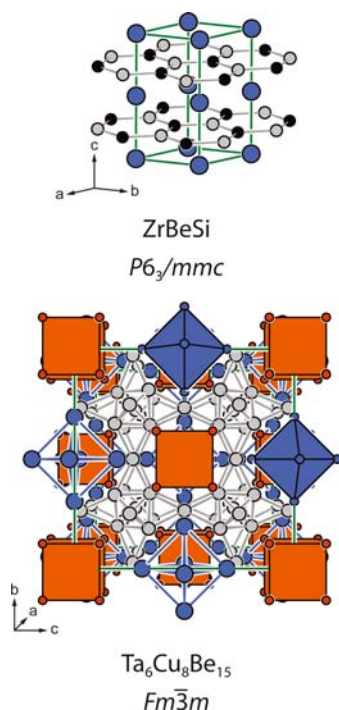


Fig. 12 Comparison of the (A) ZrBeSi and (B) Ta₆Cu₈Be₁₅ type structures as examples for ternary Be-intermetallics (see text). The Be atoms are depicted in gray, the Zr/Ta atoms in blue, the Si atoms in black and the Cu atoms in orange.

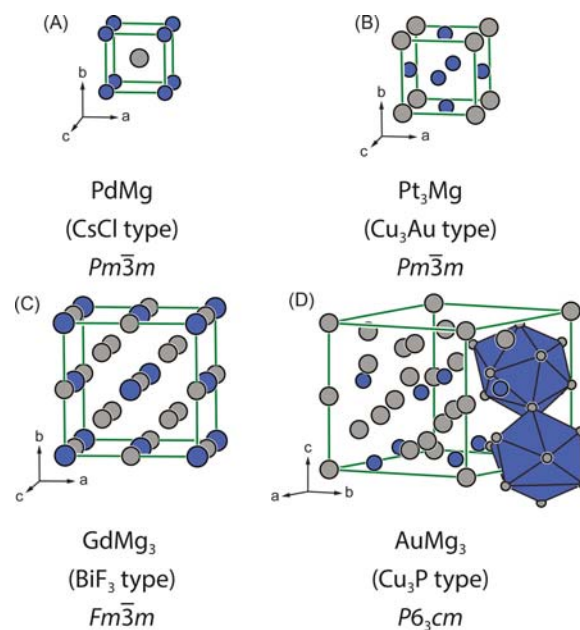


Fig. 13 Comparison of the (A) *MMg* (CsCl type), (B) *T*₃Mg (Cu₃Au type), (C) *MMg*₃ (BiF₃ type) and (D) *T*₃Mg (Cu₃P type) structures as examples for binary Mg-intermetallics (see text). The Mg atoms are depicted in gray, respective *M* or *T* atoms in blue.

equiatomic compounds. The ZrNiAl type structure is a ternary ordered variant of the Fe₂P type structure. They can be derived from the aristotype AlB₂ (Fig. 14A) via a two-step symmetry reduction. The respective group-subgroup considerations along with the crystal chemical consequences have been discussed in a series of articles that should serve as a reference for further reading.^{43–45,279} Over 100 entries regarding Mg intermetallics are found in the Pearson data base.⁶⁷ Besides one report, all of them are rare-earth compounds. MgAuGa, the non-rare earth representative, however, should be rather listed in the gallium Section 4.06.4.5.2.3 since the Mg atoms occupy the cavities within the [AuGa]^{δ-} polyanion.²⁸⁰ For the remaining compounds, two variants are observed. The first with a transition metal according to *RETMg* with *RE* = Y, La-Nd, Sm, Gd-Tm and *T* = Cu, Zn, Rh, Pd, Ag, Pt,

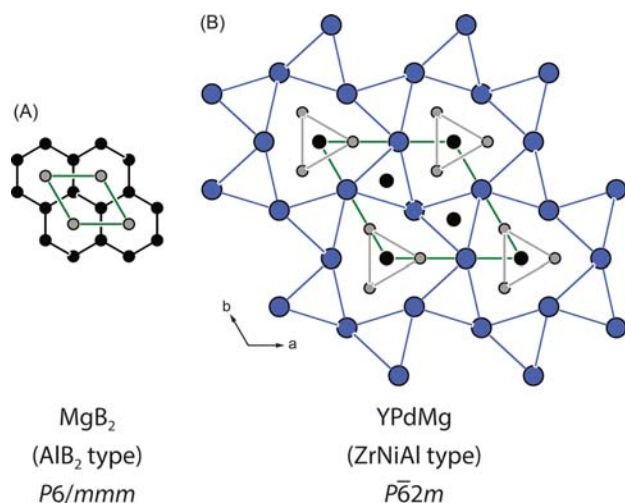


Fig. 14 Comparison of the (A) MgB_2 (AlB_2 type) and (B) YPdMg (ZrNiAl type) structures. The Y atoms are depicted in blue, Mg atoms in gray, B or Pd atoms in black.

Au ,^{281–285} the second, REMMg , with a main group element ($\text{RE} = \text{Y, La-Nd, Sm, Gd-Lu, M} = \text{Al-Tl, Sn, Pb}$). In both series, the T/M and the Mg atoms form the polyanion with the RE cations located in cavities of the framework (Fig. 14B).

Next in line, with respect to their reported elemental combinations are the RE_4TMg ($F43m$, Gd_4RhIn type) and the RET_2Mg ($Fm\bar{3}m$, MnCu_2Al type) compounds. However, these structure types will be introduced later as they are not only specific for Mg. Therefore, some peculiarities of Mg intermetallics shall be mentioned. With the Er_2RuMg_2 ,²⁸⁶ the Er_2RuMg_3 ,²⁸⁷ the $\text{Sc}_3\text{Ru}_2\text{Mg}$,²⁸⁷ the $\text{Lu}_3\text{Ru}_2\text{Mg}_2$,²⁸⁸ and the Pt_2ZnCd ²⁸⁹ type structures a series of compounds with great similarities can be described. All of the aforementioned structure types exhibit building blocks that can be described by different patterns of stacked cubes (Fig. 15). Therefore, these compounds can be derived either from the CsCl or the W type structure. The crystal chemical relations are well documented in the original articles.^{286–289}

4.06.4.5.1.3 Zinc

Zinc as a constituent element for the respective intermetallics has some advantages with respect to their synthesis, as elemental Zn has a low melting point of 692 K⁸³ and can therefore be used as a metal flux (see Section 4.06.3.4). This, however, usually yields

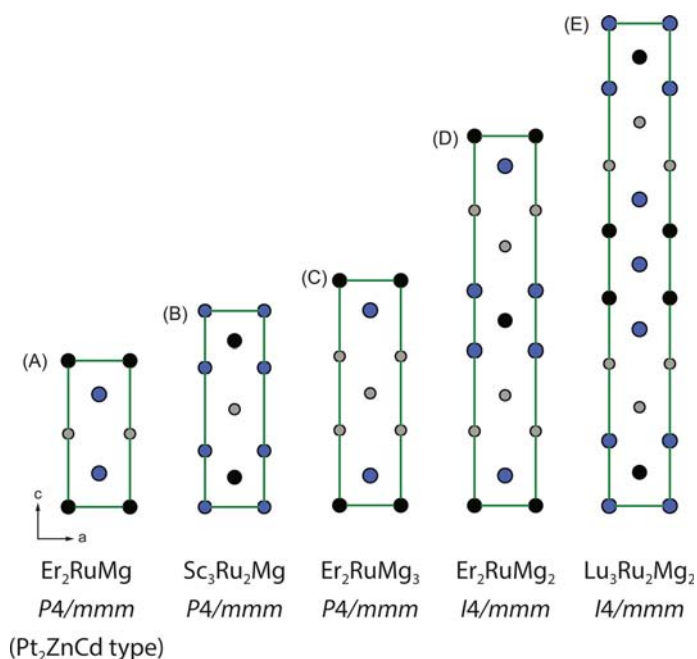


Fig. 15 Comparison of the (A) Er_2RuMg (Pt_2ZnCd type), (B) $\text{Sc}_3\text{Ru}_2\text{Mg}$, (C) Er_2RuMg_3 , (D) Er_2RuMg_2 and (E) $\text{Lu}_3\text{Ru}_2\text{Mg}_2$ structures as examples for ternary Mg-intermetallics (see text). The Mg atoms are depicted in gray, T atoms in black and RE atoms in blue.

zinc-rich phases. An experimental difficulty arises for the synthesis of compounds where one (or more) components, with respect to Zn, exhibit fairly high melting points, since arc-melting is not a good option due to the low boiling point of Zn (1180 K). These difficulties can be overcome using gas-tight metal ampoules (see Section 4.06.3.2).

In combination with the alkali metals, Li forms the equiatomic LiZn crystallizing in the NaTl type structure (Fig. 9A), while for the heavier homologs only one composition, MZn_{13} ($M = Na-Cs$)²⁹⁰ with the NaZn₁₃ type structure (Fig. 11B), is reported. The alkaline earth metals in contrast form a wide variety of compositions. As for the alkali metals, also the NaZn₁₃ type structure is observed for $AE = Ca$ and Sr.^{291,292} This is the most Zn rich composition in the system $AE-Zn$, followed by the BaCd₁₁ type structure ($I4_1/amd$; Fig. 16A),²⁹³ the Th₂Zn₁₇ type ($R\bar{3}m$; Fig. 16B)²⁹⁴ and three different structure types for the general composition $AEZn_5$. CaZn₁₁²⁹¹ and SrZn₁₁²⁹⁵ adopt the BaCd₁₁ type structure, while CaZn₅²⁹⁶ forms the CaCu₅ type structure ($P6/mmm$; Fig. 16B),²⁹⁶ SrZn₅ ($Pnma$; Fig. 16C)²⁹⁷ and BaZn₅ ($Cmcm$; Fig. 16D)²⁹⁷ in contrast exhibit their own respective structure types. For SrZn₅, also a high-temperature form has been reported,²⁹⁸ which crystallizes in the CaCu₅ type structure. In the BaCd₁₁ type structure, similar to the MnTh₁₂ and NaZn₁₃ type structures, the Ba atoms exhibit a large coordination number of $CN(Ba) = 22$. The structure can be described by the packing of these spherical polyhedra. In the M_2Zn_{17} compounds ($M = Y, La-Nd, Sm, Gd-Lu, Th, U, Pu$),^{291,299,300} crystallizing in the Th₂Zn₁₇ type structure, the atoms occupying the Th position are surrounded spherically by 19 Zn atoms. A lot of these binaries were studied with respect to their magnetic properties,³⁰¹ as the Zn atoms carry no magnetic moment. This leads to the magnetic properties arising solely from the rare earth elements, which is helpful for the understanding of the complex magnetic properties of other Th₂Zn₁₇ type compounds such as the important RE_2Fe_{17} ³⁰²⁻³⁰⁴ and RE_2Co_{17} ³⁰³⁻³⁰⁵ series. In CaZn₅, the Ca atoms exhibit a sixfold capped hexagonal prismatic surrounding ($CN = 18$), LT-SrZn₅ and BaZn₅ exhibit even higher coordination numbers of 21, however in all cases, the Zn atoms form a complex polyanion with the alkaline earth atoms in the respective cavities. For the equiatomic binaries finally, the CsCl type structure (Fig. 13A) is widely represented e.g., for the rare earth metals (Sc, Y, La-Nd, Sm-Lu)³⁰⁶⁻³⁰⁹ as well as several transition metals (e.g., Mn,³¹⁰ Ni,³¹¹ Rh,³¹² Pd³¹³ and the Cu group^{314,315}).

The most observed structure type for ternary zinc intermetallics is the cubic CeCr₂Al₂₀ type structure ($Fd\bar{3}m$, Fig. 17A). In the MT_2Zn_{20} compounds,³¹⁶⁻³¹⁹ the Zn atoms replace the Al atoms, while the Ce atoms get replaced by a rare earth ($M = Sc, Y, La-Nd, Sm, Gd-Lu$), U or an early transition metal ($M = Zr, Nb, Hf$). The Cr atoms in the prototype can finally remain Cr or be replaced

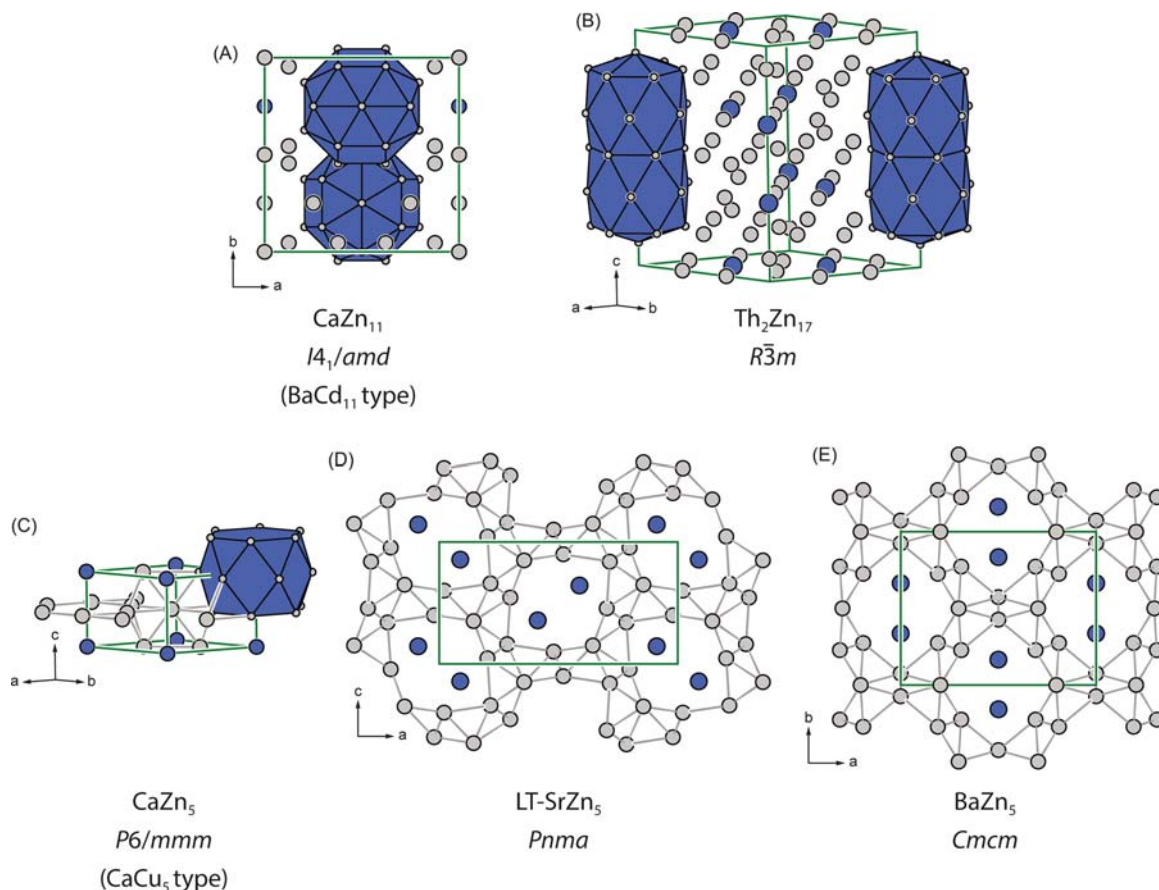


Fig. 16 Comparison of the (A) CaZn₁₁ (BaCd₁₁ type), (B) Th₂Zn₁₇ (own type), (C) CaZn₅ (CaCu₅ type), (D) LT-SrZn₅ (own type) and (E) BaZn₅ (own type) structures. The AE atoms are depicted in blue, Zn atoms in gray.

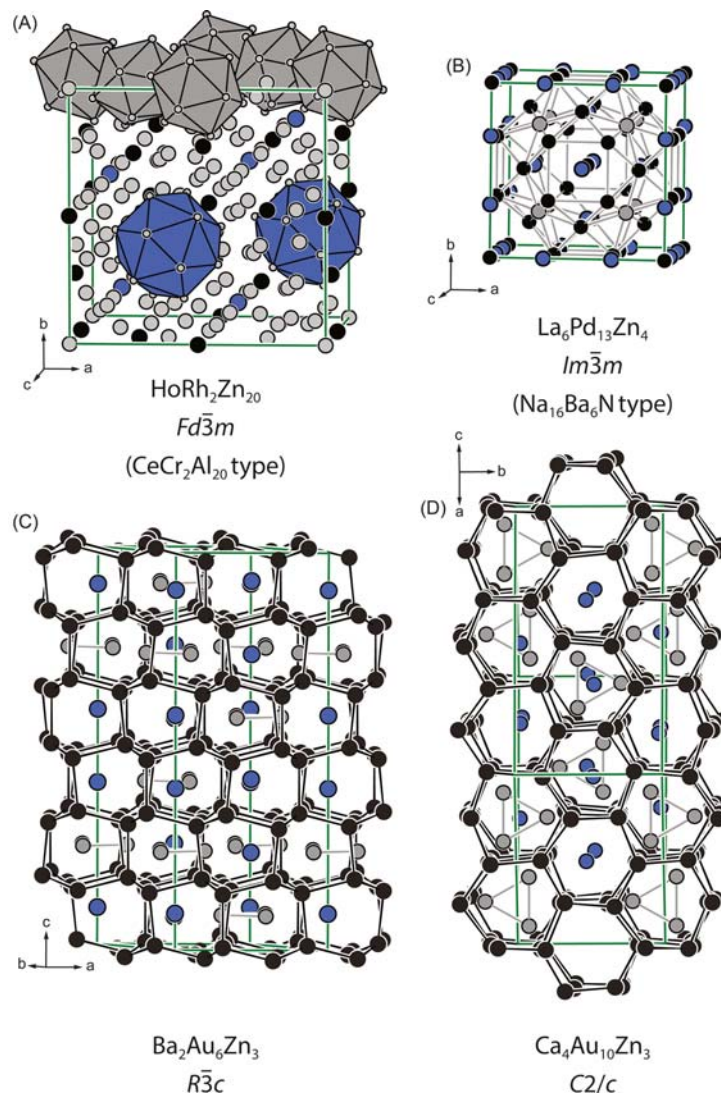


Fig. 17 Comparison of the structures of (A) $\text{HoRh}_2\text{Zn}_{20}$, (B) $\text{La}_6\text{Pd}_{13}\text{Zn}_4$, (C) $\text{Ba}_2\text{Au}_6\text{Zn}_3$ and (D) $\text{Ca}_4\text{Au}_{10}\text{Zn}_3$ as examples for ternary $MTZn$ intermetallics (see text). The Zn atoms are depicted in gray, the M atoms in blue, the T atoms in black.

by $T = \text{Mn}$, elements of the Fe or Co group, as well as Ni and Cu. Similar to the zinc-rich binaries, here also the tendency to separate the other metallic components can be observed, along with high coordination numbers. Both the M and the T atoms are solely surrounded by Zn atoms in the shape of a 16-vertex Frank-Kasper polyhedra (M) and an icosahedra (T), respectively. Another Zn-rich structure is formed by the $RE_2T_3\text{Zn}_{14}$ ($RE = \text{La-Nd, Sm, Gd-Lu}$; $T = \text{Fe, Co, Rh, Ni, Pd, Pt}$) ($R\bar{3}m$, Fig. 17B),³²⁰ which adopts an ordered $\text{Th}_2\text{Zn}_{17}$ type structure. Besides the Zn-rich ternary representatives, some equiatomic $RETZn$ ($RE = \text{Y, La-Nd, Sm, Gd-Tm, Lu}$, $T = \text{Ni, Pd, Au}$,^{321,322}) compounds have been observed. Under high-pressure conditions, the hexagonal $REPdZn$ series (ZrNiAl type, Fig. 14B) can be transformed to the orthorhombic TiNiSi type structure.³²³ Additionally, rather few examples of T -rich compounds, e.g., the $M_2\text{Au}_6\text{Zn}_3$ ($M = \text{Sr, Ba, Eu}$; $\text{Ba}_2\text{Au}_6\text{Zn}_3$ type, $R\bar{3}c$, Fig. 17C)³²⁴⁻³²⁶ series, the AlB_2 derivative $\text{Ca}_4\text{Au}_{10}\text{Zn}_3$ (own type, $C2/c$)³²⁷ or the $RE_6\text{Pd}_{13}\text{Zn}_4$ ($RE = \text{La-Nd, Sm, Gd, Tb}$; $\text{Na}_{16}\text{Ba}_6\text{N}$ type, $Im\bar{3}m$, Fig. 17D) series.³²⁸ In the structures of the first series and $\text{Ca}_4\text{Au}_{10}\text{Zn}_3$, the Zn atoms form Zn_3 triangles, located in cavities of an extended Au-network exhibiting tetrahedrally coordinated Au-atoms. In the latter series, the Zn atoms are part of the polyanionic $[\text{Pd}_{13}\text{Zn}_4]^{6-}$ network (Fig. 17B). In all cases, the M atoms occupy additional cavities in the respective structures.

4.06.4.5.1.4 Cadmium

As mentioned for zinc, also cadmium exhibits a fairly low melting point (594 K),⁸³ which on one hand can again be utilized for flux reactions, on the other hand, however, makes syntheses via arc-melting nearly impossible due to the low boiling point (1040 K).⁸³ As for many other binary systems, also for the Cd intermetallics, the simple cubic CsCl type structure ($Pm\bar{3}m$, Fig. 14A) with the MCd ($M = \text{Li, Ca-Ba, Sc, Y, La-Nd, Sm-Lu, Pd, Ag, Au}$)^{306,307,329-335} representatives is among the most common structure type

observed. The also cubic YCd_6 type structure ($Im\bar{3}$, Fig. 18B) with the MCd_6 ($M = Ca, Sr, Y, Ce-Nd, Sm-Lu, Np, Pu$)^{335–341} members, however, exhibits a significantly more complex crystal structure. Its structure is closely related to the icosahedral Tsai type quasicrystals and represents an 1/1 approximant, which can be described by different spheres of atoms that get stacked into each other. The most inner sphere consists of a Cd atom located on the 24g position, however, only with an occupation of 1/3 (Fig. 18C). This disordered polyhedron is surrounded by a pentagon dodecahedron (Fig. 18D) also formed by Cd, which is enwrapped by a Y_{12} icosahedron (Fig. 18E) followed by an icosidodecahedron (Fig. 18F). It has to be mentioned, that although these spherical arrangements can be used as a cut-out of the structure, still significant bonding between the different “shells” is present. The structure of $ErCd_3$ ($Cmcm$, Fig. 18A) and its isostructural representatives $RECD_3$ ($RE = Y, Tb-Tm, Lu$) can also be described based on the connection of polyhedra. Here, empty face-sharing Cd_6 octahedra are observed forming strands along the c -axis. Within the ab -plane they are connected to a network via all corners. The Er cations are located in the cavities of the polyanion.

For the ternary Cd intermetallics, a number of well-known structure types, e.g., the $TiNiSi$ or the $ZrNiAl$ type can be observed. Also, the ternary $MgCu_4Sn$ type, a derivative of the cubic Laves phase (see Section 4.06.4.2) can be observed. The most representatives, however, have been reported for the cubic Gd_4RhIn ($F\bar{4}3m$),³⁴² the tetragonal Mo_2FeB_2 ($P4/mbm$)³⁴³ and the hexagonal $Y_{10}RuCd_3$ ($P6_3/mmc$)³⁴⁴ type structures. The Gd_4RhIn type structure has been reported for a wide range of elemental combinations M_4TX (Fig. 19A), with $M = Ca, Y, La-Nd, Sm-Lu$ and $T = Co-Cu, Ru-Ag$ and $Ir-Au$, not only with $X = Cd$ ^{345–347} but also for $X = Mg$,^{348–358} Al ^{359,360} and In .^{342,359,361,362} Similar to the $ErCd_3$ type structure, empty Cd polyhedra, but this time Cd_4 tetrahedra, can be found. The transition metal atoms are located inside trigonal prisms ($T@RE_6$) which are interconnected via corners and edges to form a network. The Cd_4 units along with RE_6 octahedra reside in cavities of the network. Trigonal prismatic $T@RE_6$ entities, however, connected via faces and edges, can be observed on the RE_2T_2Cd representatives ($RE = Y, La-Nd, Sm, Gd-Lu; T = Ni,$

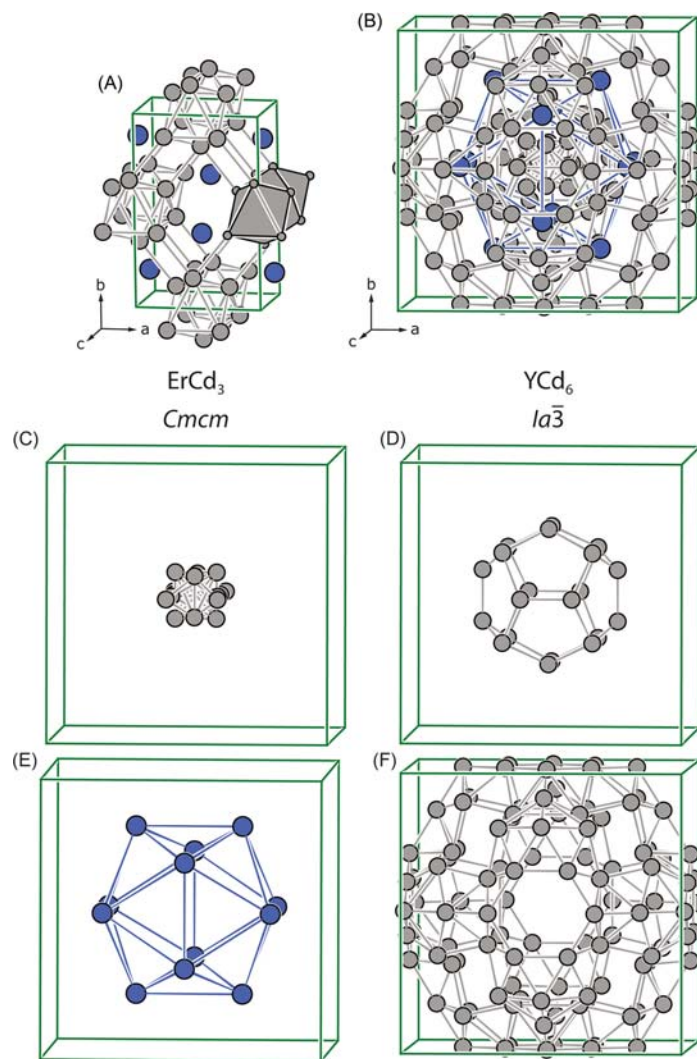


Fig. 18 Crystal structures of (A) $ErCd_3$ and (B) YCd_6 . The different observed “shells” are shown in (C–F) (see text). The Cd atoms are depicted in gray, the M atoms in blue.

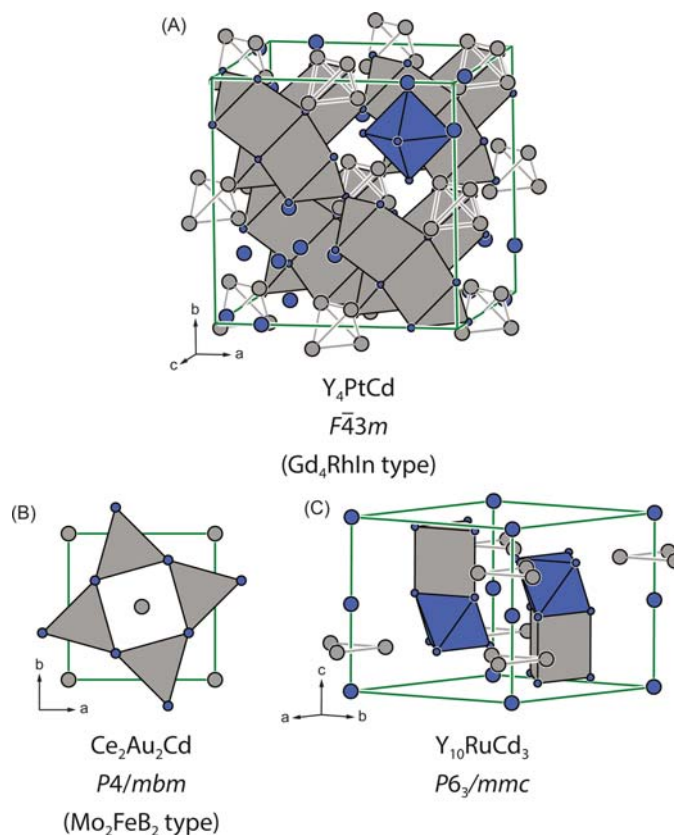


Fig. 19 Crystal structures of (A) Y_4PtCd (Gd_4RhIn type), (B) Ce_2Au_2Cd (Mo_2FeB_2 type) and (C) $Y_{10}RuCd_3$. The Cd atoms are depicted in gray, T atoms in black and the M atoms in blue.

Cu, Rh, Pd, Pt, Au; **Fig. 19B**),^{363–369} adopting the Mo_2FeB_2 type structure (ordered U_3Si_2 type). Due to the low Cd content, no polyhedra solely formed by Cd can be observed. They reside in RE_8 cubes, that condense to strands via trans-faces. Finally, in the $Y_{10}RuCd_3$ type structure, which is an ordered variant of the Co_2Al_5 type structure, also different polyhedra can be found and used for the description of the structure. Several Cd intermetallics $RE_{10}TCd_3$ ($RE = Y, Sm, Gd-Tm, Lu; T = Fe, Co, Ni, Ru, Rh, Pd, Os$; **Fig. 19C**)^{344,370,371} have been reported to crystallize in this structure type and also some Al representatives.³⁷² As for the compounds reported before, the transition metal atoms are located in $T@RE_6$ surroundings, while the Cd atoms for Cd_3 triangles. The $T@RE_6$ prisms get alternately stacked with empty RE_6 octahedra along the c -axis. More information on ternary rare earth transition metal cadmium intermetallics can also be found in a review article from 2011.³⁷³

4.06.4.5.1.5 Mercury

The synthesis of Hg-intermetallics, also called amalgams, like for the lighter homologues, is challenging due to the low boiling point of mercury (630 K). This requires sealed ampoules, however, even sealing is difficult due to the high vapor pressure of Hg. Alternative synthetic techniques, e.g., electrocrystallization (see **Section 4.06.3.5**) can be utilized to synthesize these compounds. As for the Zn- and Cd-intermetallics, numerous Hg-rich compounds have been prepared. As for the equiatomic compounds, the simple CsCl type structure (**Fig. 13A**) is observed for quite a number of main group (MHg with $M = Li,^{160} Mg-Ba^{329,374}$) and rare earth element ($REHg$ with $RE = Sc, Y, La-Nd, Eu-Lu$)^{306,375–378} containing compounds. The alkali metal containing amalgam NaHg forms its own structure type ($Cmcm$, **Fig. 20A**) with double-strands formed by zigzag-chains, while the KHg type structure ($P\bar{1}$, **Fig. 20B**) is also found for CsHg. In this triclinic structure, Hg_4 squares can be observed that connect via trans corners to form chains. For the equiatomic transition metal compounds THg, the representatives with $T = Mn^{379}$ (CsCl type), $T = Ti,^{380} Zr,^{380} Pd,^{381} Pt^{382}$ (CuAu type, $P4/mmm$, **Fig. 20C**) and $NiHg^{383}$ (CuTi type, $P4/mmm$) have been investigated. As for the Hg-rich compounds, e.g., the UHg_2 , the KHg_2 and the $BaHg_{11}$ type structures have been reported. All of these structure types are also found for a wide variety of other intermetallics. The UHg_2 type structure ($P6/mmm$, **Fig. 20E**) exhibits the same space group and is isopointal to the AlB_2 type structure ($P6/mmm$, **Fig. 14A**). The U atoms are located on the Al sites, while the Hg atoms occupy the B positions with respect to the aristotype. However, due to the different atomic sizes and the bonding situation these should be considered different structure types. Caused by the larger Hg-atoms, the honeycomb nets in the ab -plane get significantly enlarged. Thus, in turn the U atoms can move towards the Hg-nets, leading to a significantly shortened c -axis and a reduced c/a ratio of 0.65 ($c/a(AlB_2) = 1.08$). The rare earth elements ($M = Y, La, Ce, Eu, Dy-Er$)^{377,378,384–386} and U³⁸⁷ form this structure type for the MHg₂ compounds alongside

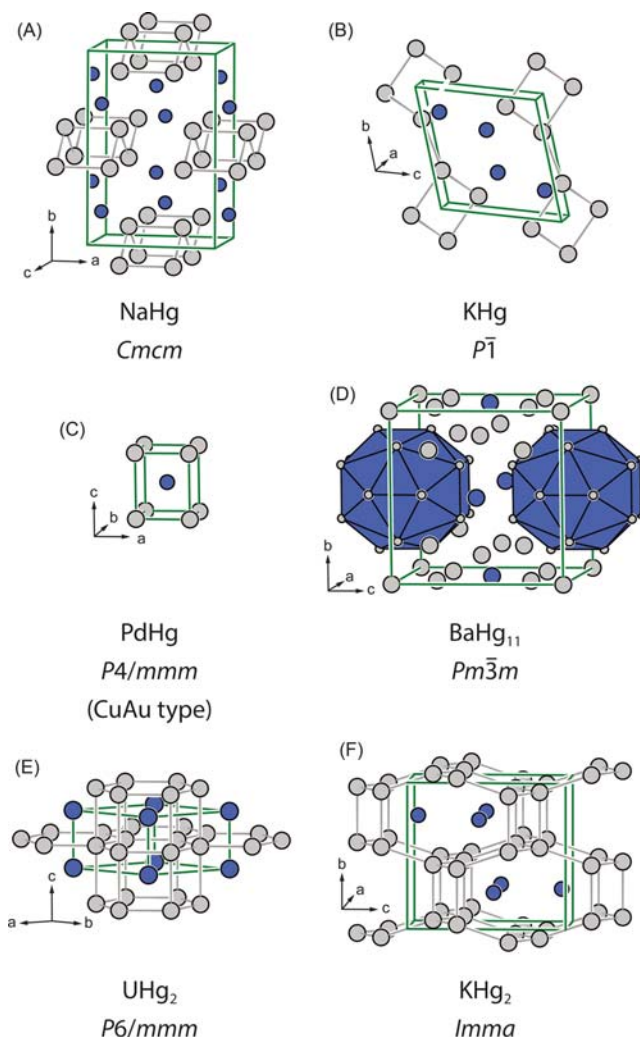


Fig. 20 Comparison of the structures of equiatomic (A) NaHg, (B) KHg and (C) CuAu type PdHg along with (D) Hg-rich BaHg₁₁ and (E) UHg₂ and (F) KHg₂, two AlB₂ related structures. The Hg atoms are depicted in gray, the main group, transition metal or actinide atoms in blue.

with NaHg₂³⁸⁸ and the high-pressure form of KHg₂.³⁸⁹ The orthorhombic KHg₂ type structure (*Imma*, Fig. 20F)³⁹⁰ can be derived from the AlB₂/UHg₂ type by a *klassengleiche* symmetry reduction of index 2. Here, a doubling of the *c*-axis takes place along with the introduction of additional degrees of freedom (variable atomic coordinates) allowing for a distortion of the honeycomb nets. This structure type is formed by the alkali (AHg₂; A = K, Rb, Cs)^{390,391} and alkaline earth (AEHg₂; AE = Sr, Ba)³⁹² amalgams. A comprehensive view of the plethora of super structures of the AlB₂/UHg₂ type structures based on group-subgroup relations has been given by Hoffmann and Pöttgen.⁴³ Finally, in the Hg-rich BaHg₁₁ type structure (*P6/mmm*, Fig. 20D),³⁹³ the Ba atoms exhibit a large coordination number of 20 and are exclusively surrounded by Hg atoms, similar to the BaCd₁₁ (Fig. 16A), the ThMn₁₂ (Fig. 11A) or the NaZn₁₃ (Fig. 11B) type structures. With mercury, this structure type is, besides Ba, also realized for KHg₁₁³⁹⁴ and RbHg₁₁³⁹⁴ as well as CaHg₁₁³⁹⁵ and SrHg₁₁.³⁹⁶

4.06.4.5.2 Group 13

4.06.4.5.2.1 Boron

Boron containing compounds are important in a number of different applications. FeB for example is used as a coating material for cutting tools and drills and is also formed in ferroboration (iron with 17–20 at.% boron). TiB₂ is the most important diboride due to its high oxidation resistance, the high melting point and its exceptional hardness and elastic modulus.³⁹⁷ LaB₆, crystallizing in the CaB₆ type structure, is used as electrode material for electron microscopy or as (internal) standard for powder X-ray diffraction. Furthermore, boron-rich materials can be used in moderator or control rods in nuclear reactors due to the high neutron cross section of ¹⁰B.

The most important binary compounds in the diverse field of *M/B* compounds are probably the ones crystallizing in the AlB₂ type structure³⁹⁸ (*P6/mmm*). While for the main group metals only MgB₂,³⁹⁹ BaB₂ and AlB₂³⁹⁸ are known, the AlB₂ type structure is

found for the transition metals Sc-Fe,⁴⁰⁰⁻⁴⁰⁴ Y-Mo,^{401,405,406} Ag,⁴⁰⁷ Hf-W^{401,408} and Au⁴⁰⁷ as well as the rare-earth metals Sm, Gd-Lu⁴⁰⁹⁻⁴¹¹ and finally the actinides U,⁴¹² Np⁴¹³ and Pu.⁴¹⁴ The structure is fairly simple, the B atoms form graphite like layers with the M atoms located above and below the center of every six-membered ring (Fig. 14A). What makes these borides so extremely interesting are their physical properties. MgB₂, and to a certain extent also other diborides, shows superconductivity below $T_C = 39$ K.^{415,416} This surprising discovery exceeded the previously highest critical temperature of thin film of Nb₃Ge with $T_C \sim 23$ K.^{417,418} Among the other binary borides, a rich versatility regarding the respective structures is observed. These range from isolated B atoms, e.g., in the Re₃B⁴¹⁹ or the NaCl⁴²⁰ type structure representatives, to both isolated atoms and dumbbells (Cr₅B₃⁴²¹ type), to dumbbells (U₃Si₂⁴²² type), to linear (NiAs⁴²³ or CuAl₂⁸⁹ type), corrugated (CrB,⁴²⁴ FeB⁴²⁵ or α -MoB⁴²⁶ type) or branched (Ru₁₁B₈⁴²⁷ type) chains further to double (Ta₃B₄⁴⁰⁸ type) or even triple (V₂B₃⁴²⁸ type) chains. Boron rich compounds finally exhibit B₆ octahedra (UB₄⁴²⁹ or CaB₆⁴³⁰ type), B₁₂ cubooctahedra (UB₁₂ type⁴²⁹) or B₁₂ icosahedra (YB₆₆ type⁴³¹). These can be directly connected or bridged via B₂ dumbbells. Due to the vast number of compounds reported along with the structural manifold, it should be referred to the Pearson data base⁶⁷ for detailed structural information and elemental combinations. Some of the mentioned structure types are graphically compiled in Figs. 21 and 22.

The number of entries in the Pearson data base⁶⁷ regarding ternary borides exceeds 4000. Therefore, only some selected structure types should be presented. In analogy to the AlB₂ type representatives in the binary systems, the most entries are found for the Nd₂Fe₁₄B (*P4₂/mmm*, Fig. 23A) and the YCrB₄ (*Pbam*, Fig. 23B) type structure among the ternary borides. The neodymium compound is widely used as hard magnetic material in various applications (wind turbines, electric motors, hard disk drives, speakers, headphones etc.) due to its high remnant and saturation magnetization. Its crystal structure is dominated by the Fe atoms with distances in the range of the sum of their covalent radii, indicating Fe-Fe bonding and coordination numbers of 12-14. The Nd and B atoms are located in voids of the Fe substructure. The latter are surrounded by six Fe and one Nd atom in the shape of

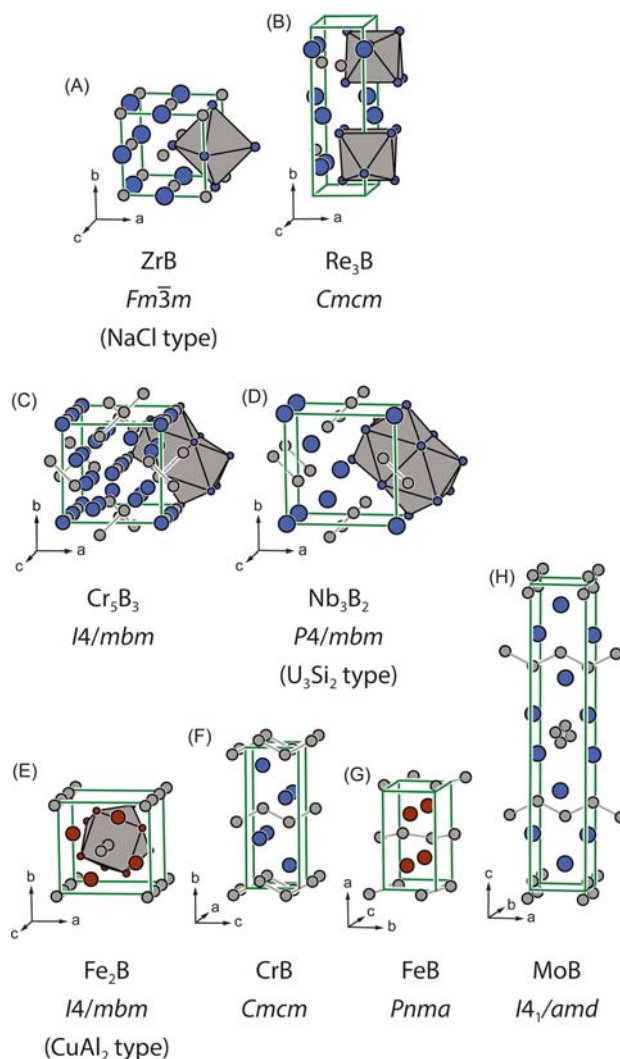


Fig. 21 Comparison of different binary borides with (A) and (B) isolated boron atoms, (C) isolated atoms and dumbbells, (D) solely dumbbells, and different types of chains (E–H) (see text). The B atoms are depicted in gray, Fe atoms in orange and T atoms in blue.

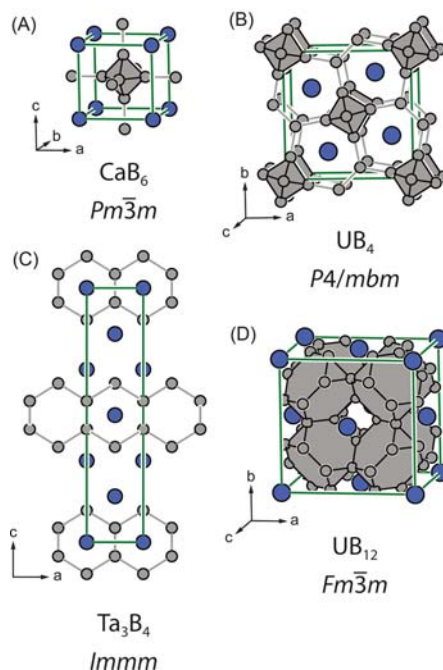


Fig. 22 Comparison of different binary borides with (A) and (B) octahedral B_6 entities, (C) bands and (D) cuboctahedral B_{12} building blocks (see text). The B atoms are depicted in gray, T atoms in blue.

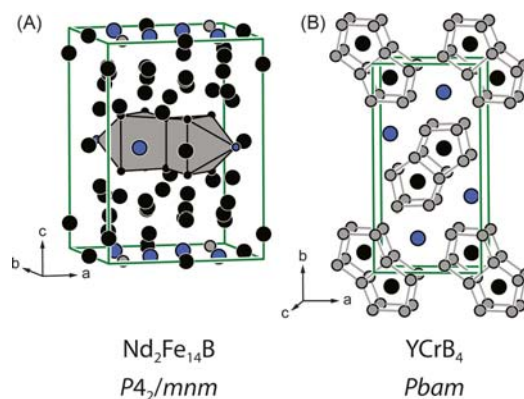


Fig. 23 Crystal structures of (A) tetragonal $Nd_2Fe_{14}B$ and (B) orthorhombic $YCrB_4$. Nd and Y atoms are shown in blue, Fe and Cr in black and B atoms in gray, respectively.

a monocapped trigonal prism ($B@Fe_6Nd$). Two of these prisms are condensed over a common edge. Both Nd sites exhibit spherical surroundings with high coordination numbers of 20. Besides $Nd_2Fe_{14}B$, numerous other 2-14-1 compounds according to $M_2T_{14}B$ have been observed with $M = Y, La-Nd, Sm, Gd-Tm, Lu, Th$ and $T = Fe, Co$.^{67,432-441} The $YCrB_4$ type structure has also been reported for a number of elemental combinations ($M = Sc, Y, Ce-Nd, Sm-Lu, Th, U$ and $T = V-Ni, Mo, Ru, Rh, W-Os$ ^{67,442-448}). Here, extended B-B bonding can be observed. The B atoms form pentagonal prisms that encapsulate the transition metal atoms according to $T@B_{10}$. Two of these prisms condense via a rectangular face forming double units. These entities are packed in a herring-bone pattern, separated by the M atoms.

4.06.4.5.2.2 Aluminum

Aluminum based alloys are used in almost every part of industry and everyday modern life due to their versatility paired with their outstanding physical and mechanical properties (e.g., low density, corrosion resistance). In order to form usable materials, pure aluminum is too ductile, a variety of elements can be alloyed to the main component Al. The typical light-weight alloys are based on the addition of Mg, Si, Mn, Cu and Zn, but also a variety of other metals can be added for specific applications. The extensive use of these alloys has led to a detailed investigation of the respective phase diagrams and the microstructure of these materials. In many of the copper-based so called 2XXX alloys, different precipitates are observed, e.g., the S-phase $MgCuAl_2$ or the T-phase Mg_4CuAl_4 (vide infra).⁴⁴⁹

Binary aluminum intermetallics represent a large group of compounds with over 2000 entries (just for the binaries between Al and an element of groups 1-12) in the Pearson data base.⁵⁷ Nearly all transition metals and rare-earth elements, exceptions are Cd and Hg as well as Pm, have been reported to form a binary aluminum compound. Interestingly, among the alkali metals, only the Li compounds LiAl (dimorphic, LT: $I4_1/amd$, LiIn type; RT: $Fd\bar{3}m$, NaTl type), Li_3Al_2 ($R\bar{3}m$, own type), Li_9Al_4 ($C2/m$, own type) and Li_2Al ($Cmcm$, Li_2Ga type) have been reported (Fig. 24A–D),^{161,450–453} while for the alkaline earth metals a significantly larger number of binaries has been reported. As selected examples, for $AE = Mg$ -Ba the $AEAl_2$ composition can be observed, while Ca, Sr and Ba also form the 1:4 composition $AEAl_4$. It is interesting to mention, that $MgAl_2$ adopts the $HfGa_2$ type structure ($I4_1/amd$),⁴⁵⁴ while $CaAl_2$ forms the cubic Laves phase ($MgCu_2$ type, Fig. 6A).⁴⁵⁵ The next heavier homolog $SrAl_2$ crystallizes in the orthorhombic KHg_2 type structure ($Imma$, Fig. 20F)⁴⁵⁶ and $BaAl_2$ is not existent under normal synthetic conditions. However high-temperature (HT)/high-pressure (HP) experiments allow the formation of $MgCu_2$ type $BaAl_2$ ⁴⁵⁷ and also $SrAl_2$ can be transformed into this cubic phase under HT/HP.⁴⁵⁸ For the $AEAl_4$ representatives with $AE = Ca$, Sr and Ba, the tetragonal $BaAl_4$ type structure ($I4/mmm$, Fig. 24F) can be found.^{455,459–461} In the case of $CaAl_4$, it is the high-temperature phase, while at room temperature, monoclinic $CaAl_4$ ($CaGa_4$ type structure, $C2/m$, Fig. 24E) is formed.⁴⁵⁹ The orthorhombic La_3Al_{11} type structure ($Immm$, Fig. 24G)⁴⁶² seems to be closely related to the $BaAl_4$ type structure and for a long time, this was not recognized.^{257,463,464} One of the reasons could be attributed to the relationship of the lattice parameters: $a(La_3Al_{11}) \approx a(BaAl_4)$, $b(La_3Al_{11}) \approx 3 \times a(BaAl_4)$, $c(La_3Al_{11}) \approx c(BaAl_4)$. Upon analysis of the structural relations between $BaAl_4$ and La_3Al_{11} , it becomes clear that these structures, although visually very similar, are not related by a group subgroup-relation.⁴⁵ Among the transition metal and rare earth aluminum intermetallics, the cubic Laves phase ($MgCu_2$, Fig. 6A) type structure plays an important role along with the CsCl (Fig. 13A) and the Cu_3Au (Fig. 13B) type structures. Although the majority of the binary representatives are reported for these structure types, the industrially relevant ones should also be mentioned. Probably one of the most investigated binaries for application purposes is Ni_3Al (Cu_3Au type, Fig. 13B). Due to its corrosion and chemical resistance, it is utilized as coating material for turbines or in different automotive applications. But also, titanium-aluminum based materials exhibit interesting mechanical properties. TiAl (Cu_3Au type, Fig. 20C) and Ti_3Al (Ni_3Sn , Fig. 24E) are probably the central compounds here. They can be chemically modified (alloying, substitution, introduction of vacancy filling elements) to further improve their respective properties. Finally, the compounds from the Ce-Al system should be explicitly mentioned. Most of the existing binaries show interesting physical

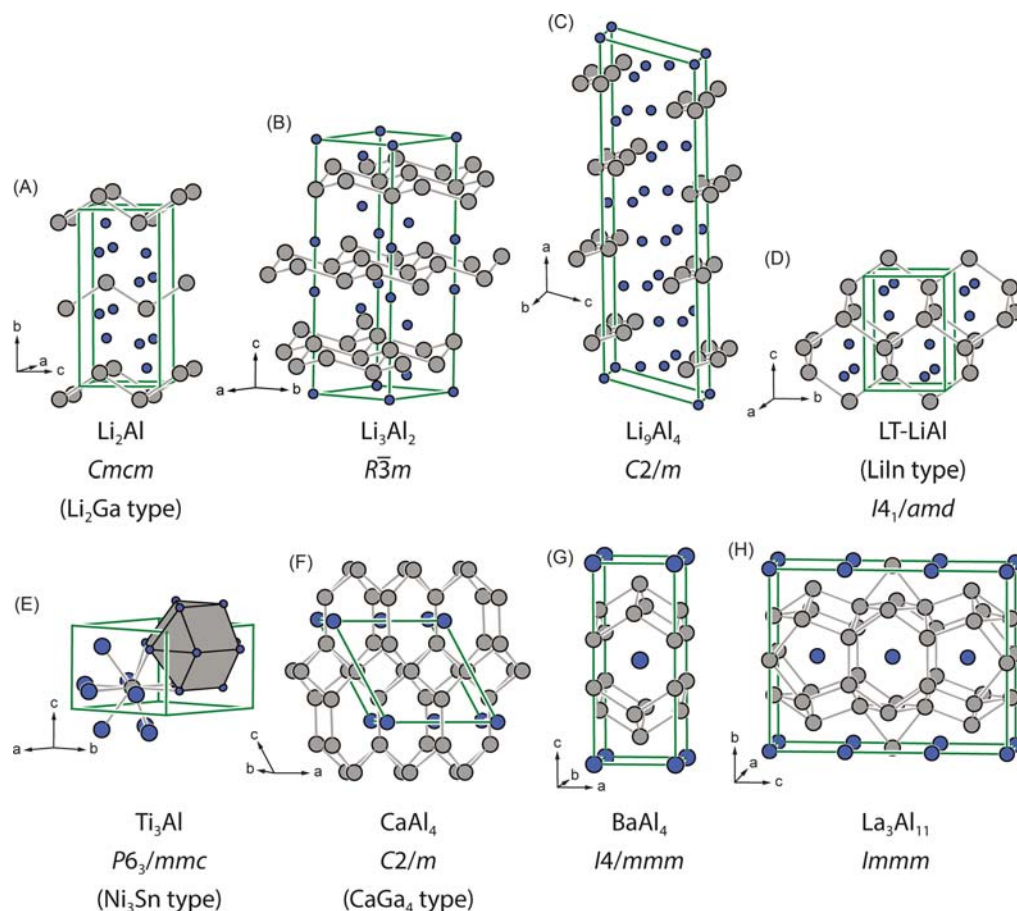


Fig. 24 Comparison of different binary aluminum intermetallics. (A) Li_2Al , (B) Li_3Al_2 , (C) Li_9Al_4 , (D) LT-LiAl, (E) Ti_3Al , (F) $CaAl_4$, (G) $BaAl_4$ and (H) La_3Al_{11} . The Al atoms are depicted in gray, A, AE, T or RE atoms in blue.

properties. CeAl_2 (MgCu_2 , Fig. 6A) for example is a Kondo compound with an incommensurate magnetic structure at low temperatures and a significant crystal field splitting of over 200 K.^{465–469} Also Ce_3Al (Cu_3Au type, Fig. 13B) and CeAl_3 (Ni_3Sn , Fig. 24E) have been characterized as dense Kondo systems.^{470–475}

As for the ternary aluminum intermetallics, the equiatomic ZrNiAl type structure ($P\bar{6}2m$, Fig. 14B) is, besides the TiNiSi type structure ($Pnma$, Fig. 25D), one of the most prominent equiatomic ternary structure types. With aluminum as a main group metal, it is formed for the 3d transition metals Fe–Cu, as well as Ru, Rh, Pd and Ir, Pt and Au in combination with Zr and Hf as well as the rare earth metals Y, Ce–Nd, Sm, Gd–Lu and the actinides Th, U and Pu.^{67,476–482} The TiNiSi type is mostly observed for rare earth elements (Sc, Y, La–Nd, Sm–Lu) as well as Mg and Ca with Rh, Pd, Ir, Pt and Au as transition metals.^{67,476–482} As stated before, orthorhombic MnCuAl_2 ($Cmcm$, Fig. 25E) is an important intermetallic precipitate found in Al based alloys. Its structure was first determined on Weissenberg film data.⁴⁸³ Due to its industrial importance, it has been extensively studied by diffraction experiments and electron microscopy.^{484–486} Both the space group and the magnesium/copper ordering were discussed readily,^{487,488} until a redetermination of the crystal structure based on high-quality single crystal X-ray diffraction data confirmed both, the atomic positions and the space group symmetry.⁴⁸⁹ The structure of MgCuAl_2 can be derived from binary Re_3B by a group-subgroup relation.⁴⁹⁰ Within the aluminum compounds, the MTAl_2 representatives with $M = \text{Ca, Sr, Ba, Sc, Y, La–Nd, Sm, Gd–Lu}$; $T = \text{Co, Ni, Cu, Pd, Pt}$ ^{491–501} have been prepared and investigated not only by diffractometry but also with respect to their physical and ^{27}Al NMR and ^{151}Eu Mössbauer spectroscopic properties.^{500,501} The peculiarity of this structure type, that has also been observed for other main group

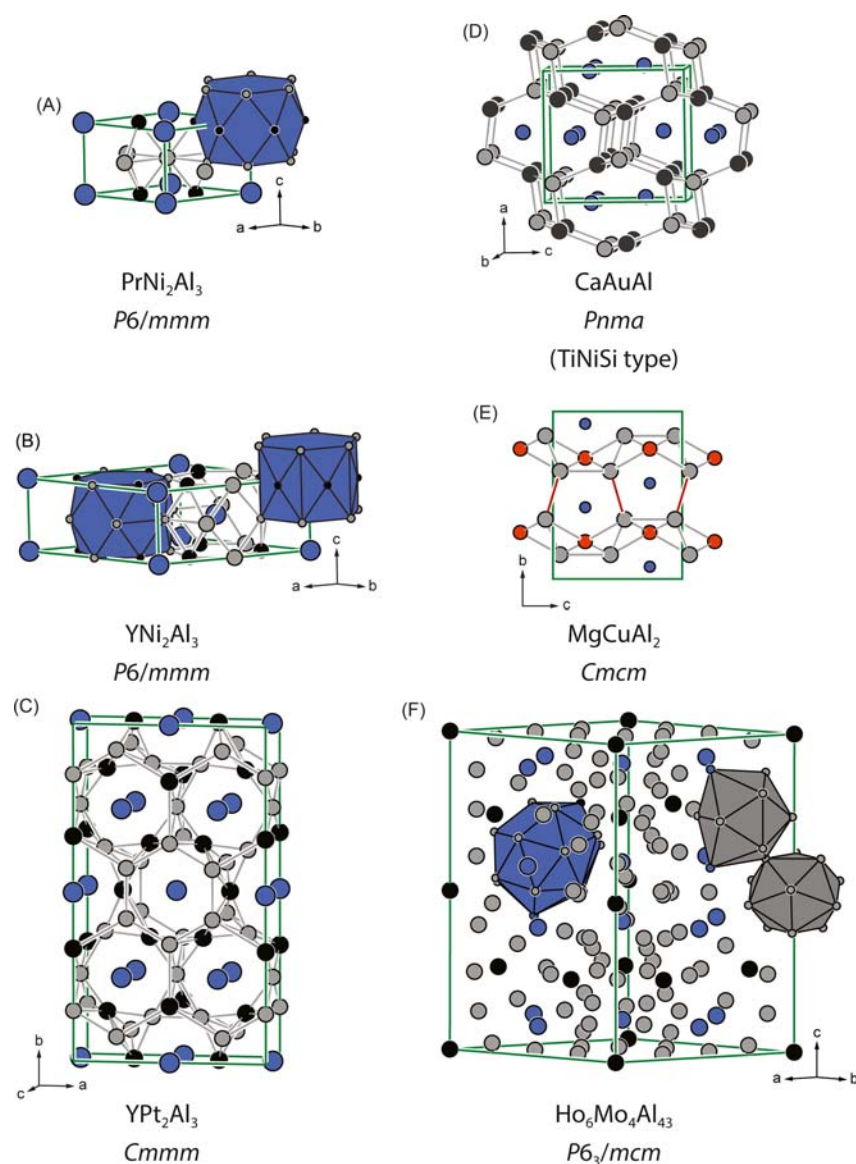


Fig. 25 Comparison of different ternary aluminum intermetallics. (A) PrNi_2Al_3 , (B) YNi_2Al_3 , (C) YPt_2Al_3 , (D) CaAuAl , (E) MgCuAl_2 and (F) $\text{Ho}_6\text{Mo}_4\text{Al}_{43}$. The Al atoms are depicted in gray, A, AE, or RE atoms in blue, T atoms in black, Cu in orange.

elements (X) besides Al, is the possibility for a significant distortion of the $[TX_2]^{6-}$ polyanion, depending on the M element. This leads, especially in the cases of the heavy alkaline earth metals to a reduction of the dimensionality from 3D towards 2D.^{501,502} While the latter compounds have only been reported with late transition metals so far, the $Ho_6Mo_4Al_{43}$ type structure ($P6_3/mcm$, Fig. 25F) is predominantly observed for the early transition metals, namely Ti, the V group, the Cr group and Mn along with Ca, Y, Nd, Sm, Gd-Lu, Th and U as replacements for Ho in the aristotype.^{503–507} As seen for many other compounds containing one element in a large excess, also in $Ho_6Mo_4Al_{43}$ the Al atoms encapsulate the Ho and Mo atoms leading to a stacking of polyhedra rather than the formation of a pronounced polyanionic network. Finally, the $PrNi_2Al_3$ ($P6/mmm$, Fig. 25A) and YNi_2Al_3 ($P6/mmm$, Fig. 16B) type structures should be mentioned. Their structures that can be derived from the $CaCu_5$ type structure ($P6/mmm$, Fig. 16B). $PrNi_2Al_3$ can be considered a coloring variant of $CaCu_5$, in which the two Cu positions $2c$ and $3g$ get occupied by Ni and Al, respectively. YNi_2Al_3 in contrast forms an isomorphic super structure ($i3$) with an enlarged unit cell ($2a + b, -a + b, c$), in which the rare earth position splits from $1a$ to $1a$ and $2c$. The $1a$ position (0,0,0), however, does not get occupied but the $1b$ position (0,0,1/2). This leads to two different coordination polyhedra for the Y atoms. Upon investigations of the $REPd_2Al_3$ series an $i7$ super structure of $PrNi_2Al_3$ was observed for $ErPd_2Al_3$ ($P6/m$).⁵⁰⁸ Within the $REPt_2Al_3$ series, surprisingly an orthorhombic super structure of $PrNi_2Al_3$ was found and characterized for YPt_2Al_3 ($Cmmm$, Fig. 25C).⁵⁰⁹ $YbPd_2Al_3$ (YNi_2Al_3 type) exhibits an interesting physical phenomena, a temperature induced valence phase transition around 110 K.⁵¹⁰ Below this temperature the Yb atoms exhibit a divalent state, while above they are trivalent. $Eu_2Pt_6Al_{15}$ ($P2/m$, $Sc_2Pt_6Al_{15}$ type structure) exhibits the invers phenomena around 45 K.⁵¹¹ Above, the Eu are divalent, while below they are trivalent. In both cases, a severe expansion/contraction of the unit cell is observed along with a dramatic change of the magnetic properties.

4.06.4.5.2.3 Gallium

For the Ga intermetallics, the AlB_2 ($P6/mmm$, Fig. 14A), CrB ($Cmcm$, Fig. 21F), and Cu_3Au ($Pm\bar{3}m$, Fig. 13B) type structures are again prominent representatives for binary compounds mentioned numerous times before. The AlB_2 type structure MGa_2 is found for the alkaline earth elements Ca, Sr and Ba as well as the rare earth elements Y, La-Nd, Sm-Tm and the actinides U, Np and Pu.^{512–517} For some of these, the magnetocaloric properties have been studied in detail.⁵¹⁸ The equiatomic CrB type structure is found for Ca, Sc, Y, La-Nd, Sm, Gd-Tm and Lu^{257,516,519–524} while finally the Cu_3Au type structure is observed for the rare earth elements Sc, La-Nd, Sm, Tb-Tm and Lu as well as for the transition metals Fe, Ni and Pt and the actinides U and Np. It is interesting to note, that of these, Sc, Tb-Tm, Lu, U and Np form the composition MGa_3 ,^{525–529} while the early lanthanides La-Nd, Sm along with Pu, Fe, Ni and Pt exhibit the M_3Ga composition.^{516,530–533} The Cr_3Si type structure is observed for V_3Ga , Nb_3Ga , Cr_3Ga and Mo_3Ga .⁵³⁴ It crystallizes in the cubic crystal system with space group $Pm\bar{3}n$ and can be described based on the coordination polyhedra surrounding the Ga atoms (Fig. 26A). The Ga atoms are located on the $2a$ site and therefore on the corners and in the center of the unit cell. They are surrounded by 12 T atoms in the shape of an icosahedron. The hexagonal Mn_5Si_3 type structure ($P6_3/mcm$, Fig. 26B) has been reported for the early transition metals of the Ti and V group as well as the small rare earth elements (Sc, Y, Ho-Tm and Lu).^{535–539} The Ti_2 atoms are surrounded by the Ga atoms in the shape of a distorted octahedron linked via common faces forming strands along the c axis. The Ti_1 atoms form empty octahedra also forming chains along $[001]$.

Among the ternary gallides, the most prominent structure type is the $MnCu_2Al$ type structure ($Fm\bar{3}m$, Fig. 27A), also known as Heusler phase with the general composition X_2YZ . This is observed for a wide range of elemental combinations listed in the Pearson

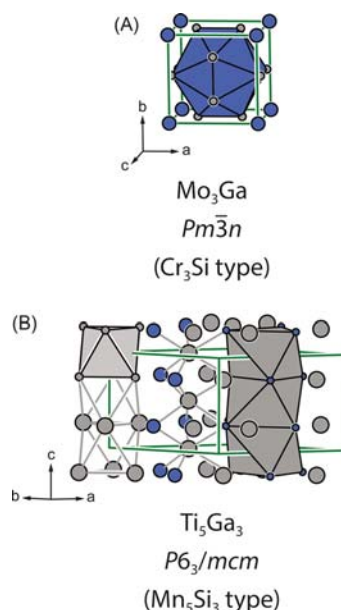


Fig. 26 Crystal structures of (A) Mo_3Ga and (B) Ti_5Ga_3 . Mo and Ti atoms are shown in gray, Ga atoms in blue.

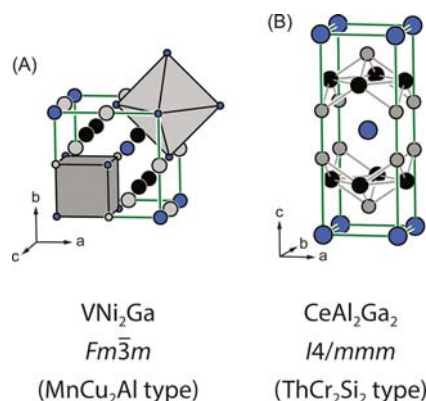


Fig. 27 Crystal structures of (A) VNi_2Ga (Heusler phase, MnCu₂Al type) and (B) CeAl_2Ga_2 (ThCr₂Si₂ type). V and Ce atoms are shown in blue, Ni or Al atoms in black, the Ga atoms in gray.

database.⁶⁷ It is followed by the equiatomic $MTGa$ compounds crystallizing in the orthorhombic TiNiSi type structure ($Pnma$, Fig. 25D) for $M = \text{Sc, Y, La-Nd, Sm, Eu-Lu, U}$ and $T = \text{Co, Ni, Rh, Pd, Ir, Pt and Au}$ ^{67,540–543} or the hexagonal ZrNiAl type structure with $M = \text{Mg, Ti, Zr, Hf, Y, La-Nd, Sm, Gd-Tm, Lu, Th, U, Pu}$ and $T = \text{Mn, Fe, Co, Ni, Ru, Rh, Pd, Ir, Pt and Au}$ ^{67,544–548} ($P6_2m$, Fig. 14B). Finally, the tetragonal ThCr₂Si₂ type ($I4/mmm$, Fig. 27B) is observed for the elemental combinations of MT_2Ga_2 with $M = \text{Li-K, Ca-Ba, Y, La-Nd, Sm-Dy, Yb}$ and $T = \text{Co, Ni, Cu, Zn, Pd, Ag, Cd, Pt and Au}$ but also Zn, Cd, Al and In.^{67,549–555} In many cases, significant homogeneity ranges were observed. While the TiNiSi and the ZrNiAl type structures have been described in detail before, the MnCu₂Al and the ThCr₂Si₂ type structures should be briefly explained. The latter one can be derived from the BaAl₄ type structure by replacing Ba by Th, one of the two Al sites with Cr and the other one with Si, and in the case of the gallides by the element given above. The MnCu₂Al type structure, however, can be considered as an intergrowth of the NaCl (here formed by Mn and Al) and the CaF₂ type structure (Cu in the tetrahedral voids of the Al structure). Besides these more or less ordered structures, a number of solid solutions, crystallizing in typical binary structure types (CaIn₂, KHg₂, La₃Al₁₁, Th₂Zn₁₇) can be observed. These are compiled in the Pearson database.⁶⁷

4.06.4.5.2.4 Indium

As for the Ga intermetallics also for the indium ones the Cu₃Au type structure ($Pm\bar{3}m$, Fig. 13B) is observed, and, as stated before, two different compositions can be observed. With Sc, Zr, Ni, Ag, Pt and La-Nd, Sm, Gd as well as Pu the $M_3\text{In}$ compounds are reported, while for Li, Mg, Sc, Y, La-Nd, Sm, Gd-Lu and the actinides Th, U, Np and Pu also the $M\text{In}_3$ compounds were synthesized. Furthermore, the equiatomic compounds $M\text{In}$ with $M = \text{Li, Ca, Ni, Rh, Pd, Sc, Y, La, Pr, Nd, Sm, Gd, Dy-Yb}$, some of them reported only as high-temperature modification, crystallize in the CsCl type structure (Fig. 13A).^{512,556–561} For the transition metals Ni, Cu and Pt, the main group elements Sb and Bi and for the rare earth metals Sc, Y, La-Nd, Sm, Gd-Tm and Lu, the hexagonal Ni₂In type structure ($P6_3/mmc$, Fig. 28A) is observed.^{67,560–564} The structure can be derived from the NiAs type structure by filling the empty trigonal prisms by additional Ni atoms. Consequently, chains of trigonal prisms that are alternatively filled by In and Ni are formed, running along the c axis. Finally, the CaIn₂ type structure ($P6_3/mcm$, Fig. 28B) should be mentioned. It can be understood as a Zintl phase in which the Ca atoms transfer two electrons onto the indium polyanion. Each In atom therefore exhibits one additional electron making them isoelectronic to group 14, hence forming a structure related to this group. In CaIn₂, the In atoms arrange like the carbon atoms in the hexagonal diamond, also known as Lonsdalite structure. For indium, it is reported for the divalent elements Ca, Sr, Eu and Yb.^{559,565}

Within the field of ternary indium compounds, the hexagonal ZrNiAl, the tetragonal Mo₂FeB₂, and the cubic MgCu₄Sn type structures are observed for numerous elemental combinations. The most compounds have been reported for equiatomic $MT\text{In}$

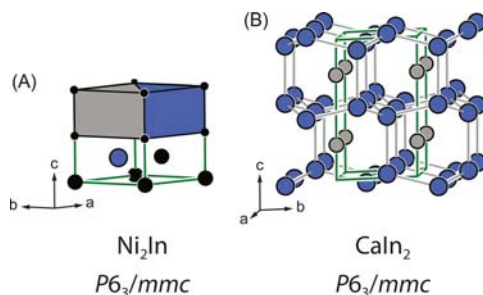


Fig. 28 Crystal structures of hexagonal (A) Ni_2In and (B) CaIn_2 . Ni atoms are shown in black, Ca atoms in gray and In atoms in blue.

compounds (ZrNiAl type, Fig. 14B) with $M = \text{Sc, Y, La-Nd, Sm, Gd-Lu, Th, U}$ and $T = \text{Mg, Ni, Cu, Rh, Pd, Ir, Pt}$ and Au,^{67,544,566-571} followed by the $M_2T_2\text{In}$ members (Mo_2FeB_2 type, Fig. 19B) with $M = \text{Sc, Y, Zr, Hf, La-Nd, Sm, Gd-Lu, Th, U-Pu}$ and $T = \text{Si, Ge, Co-Cu, Rh, Pd, Ir-Au}$.^{67,572-583} For the MgCu_4Sn type structures ($F\bar{4}3m$, Fig. 29A) finally, the elemental combinations $MT_4\text{Ga}$ with $M = \text{Mg, Ca, Sc, Y, La-Nd, Sm-Lu, U}$ and $T = \text{Co, Ni, Cu, Pt}$ have been reported.^{67,568,584-586} This cubic structure type can be derived from the cubic MgCu_2 type structure. While the Cu atoms still form corner-connected empty tetrahedra, within the Mg substructure, now two distinct atomic positions arise. Upon the characterization of the magnetic and transport properties of these compounds,^{587,588} a first-order valence phase transition was observed in YbCu_4In and investigated in great detail.⁵⁸⁹⁻⁵⁹⁷ Finally, the $\text{Lu}_5\text{Ni}_2\text{In}_4$ (*Pbam*, Fig. 29B) and the $\text{Nd}_{11}\text{Pd}_4\text{In}_9$ (*Cmmm*, Fig. 29C) type structures should be mentioned. In the case of the $M_5T_2\text{In}_4$ composition, these exist for $M = \text{Sc, Y, Zr, Hf, La-Nd, Sm, Gd-Tm, Lu}$ and $T = \text{Co, Ni, Rh, Pd, Ir, Pt}$,⁵⁹⁸⁻⁶⁰³ while the $M_{11}T_4\text{In}_9$ stoichiometry has been reported for $M = \text{Sc, Y, La-Nd, Sm, Gd-Tm, Lu}$ and $T = \text{Co, Ni, Ru, Pd}$.^{67,604-610} In both cases, the transition metal atoms exhibit trigonal prismatic surroundings by the rare earth atoms, while the In atoms reside in distorted square prisms. Only the connections between the two coordination environments differ.

4.06.4.5.2.5 Thallium

For the binary thallium intermetallics, finally, the Cu_3Au type structure (Fig. 13B) is the most prominent for both the $M_3\text{Tl}$ ($M = \text{La-Nd, Np}$ ⁶¹¹⁻⁶¹³) and MTl_3 ($M = \text{Ca, Y, La-Nd, Sm-Lu, Th, U}$ ^{67,331,332,512,565,613-617}) compositions, followed by compounds adopting the CsCl ($M\text{Tl}$ with $M = \text{Li, Ca, Sc, Y, La, Pr, Nd, Sm, Gd, Dy-Yb}$,^{67,160,306,512,558} Fig. 13A), the Pu_3Pd_5 ($M_3\text{Tl}_5$ with $M = \text{Y, La-Nd, Sm, Gd-Er, Th}$ ^{67,618-621}), and the Mn_5Si_3 type structures ($M_5\text{Tl}_3$ with $M = \text{Y, Ho-Tm, Lu}$,^{67,622} Fig. 26B). The Pu_3Pd_5 type structure, like many other intermetallic structures, can be described based on coordination environments or, if applicable, based on distinct metal-metal bonding. In both, the indium and the thallium compounds, In-In and Tl-Tl bonds can be observed. In Nd_3Tl_5 , the Tl atoms form a polyanion with extensive Tl-Tl bonding, resulting in slightly distorted empty square pyramids that are connected via all the top and two trans-oriented basal corners. The Nd atoms reside inside the cavities of this polyanion.

For the ternary representatives, only a few have been reported, most likely due to the toxicity of thallium compounds. The ones reported crystallize in the ZrNiAl for $MT\text{Tl}$ ($M = \text{Y, La-Nd, Sm, Gd-Lu, T} = \text{Mg, Pd}$,^{623,624} Fig. 14B) or MgCuAl_2 type structures (Fig. 25E), the latter $MT\text{Tl}_2$ compounds with $M = \text{Sr, Eu}$ and $T = \text{Pd}$ and Pt ^{623,625,626} show the previously mentioned Tl-Tl bonding.

4.06.4.5.3 Group 14

4.06.4.5.3.1 Carbon

Finally, the group 14 intermetallics should be summarized. While the heavier homologs form typical intermetallics with other metallic elements, for carbon, three different cases can be observed: (1) together with alkali- and alkaline earth elements, ionic salt-like carbides are formed (e.g., CaC_2 or Mg_2C_3), (2) covalent carbides, for example SiC, are observed in combination with elements bearing a similar electron negativity and finally (3) metallic carbides formed with transition metals, the rare earth elements or the actinides. The most prominent and also probably industrially most important carbides are observed in the Fe/C phase diagram. Here, C atoms are either incorporated into the Fe structure, strengthening the metal due to extensive Fe-C bonding, forming so called "interstitial carbides." These, by definition after Hägg, are only considered interstitial if the structure of the metal is

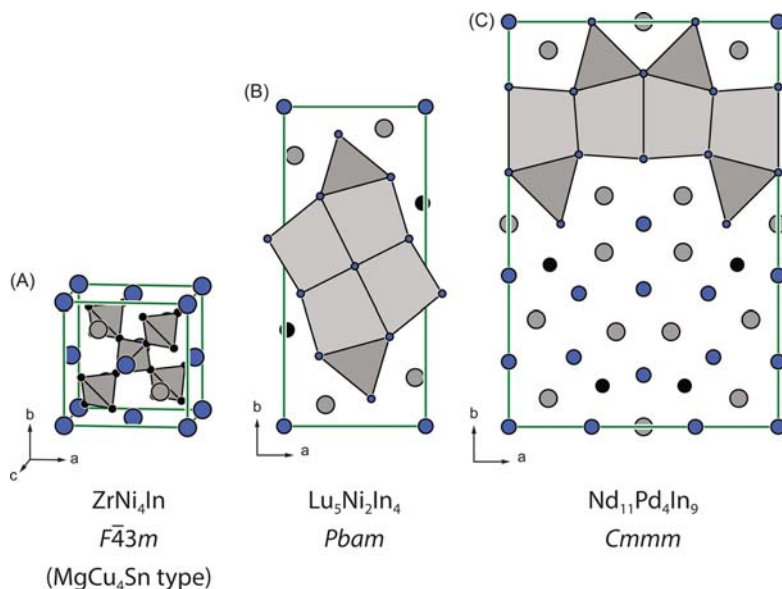


Fig. 29 Crystal structures of the (A) cubic MgCu_4Sn , (B) orthorhombic $\text{Lu}_5\text{Ni}_2\text{In}_4$ and (C) orthorhombic $\text{Nd}_{11}\text{Pd}_4\text{In}_9$ type structures. Mg, Lu and Nd atoms are shown in blue, Ni and Pd atoms in black and In atoms in gray.

retained in the binary carbide. WC for example crystallizes in the hexagonal crystal system with space group $P\bar{6}m2$, while elemental W exhibits a cubic body centered structure ($Im\bar{3}m$). Therefore, WC is no interstitial carbide.

From an industrial point of view, TiC, WC and Fe_3C are just three of the important carbides used in various applications, e.g., drill and cutting tools, as abrasive materials etc. or formed during the formation of steel. Along with the hardness of these materials comes a brittleness that hampers in many cases the direct use in technical applications. This problem can be overcome e.g., in the case of WC by the formation of a composite of WC along with elemental Co, supplying the necessary toughness. TiC crystallizes in the cubic crystal system with Ti on (0,0,0) and C on (1/2, 1/2, 1/2) and therefore adopts a structure that seems to be identical to the one of NaCl in the first place. From a crystallographic point of view, these structures are identical, thus a lot of times the structure of TiC is described to be of NaCl type. From a chemical point of view, the bonding situation is totally different. While NaCl is a salt, in TiC significant metal-carbon bonding is observed. Hence, the structural relationship should be described as isopointal rather than isostructural. The structures of TiC ($Fm\bar{3}m$), WC ($P\bar{6}m2$) and Fe_3C ($Pnma$) are shown in Fig. 30A–C. As in most of the carbides, that exhibit isolated C atoms, these are sixfold coordinated by the metal atoms, either in the shape of an octahedron (see TiC or Fe_3C) or in a trigonal prismatic fashion (see WC). The rare earth and actinide metal carbides also exhibit octahedral coordination environments for the C atoms, with varying compositions, e.g., RE_2C ($RE = Y, Gd-Ho$, ^{627,628} $R\bar{3}m$, $CdCl_2$ type, Fig. 30E). With increasing C content, the formation of C–C bonds occurs. The most prominent structure type is the Pu_2C_3 type formed for a large variety of elements (M_2C_3 with $M = Sc, Y, La-Nd, Sm, Gd-Lu, Th, U-Cm$, ^{629–632} $I\bar{4}3d$, Fig. 30D). The C–C distances are about 125 pm and therefore in the range of a triple bond. These dumbbells are surrounded by eight M atoms in the shape of a dodecahedron. In the Sc_3C_4 type structure (M_3C_4 with $M = Sc, Y, Tb-Lu$, ^{633–636} $P4/nmc$, Fig. 30F), finally, isolated C atoms, C_2 dumbbells and also linear triatomic propadiene analog entities are observed.

With respect to ternary carbides, the Mn_3AlC , $CeNiC_2$ and $UMoC_2$ type structures are the ones with the most entries in the Pearson data base.⁶⁷ The Mn_3AlC type (Fig. 31A) is isopointal to the perovskite type structure and has been reported for a number of elemental combinations M_3TC that cannot be listed here in a structured fashion, therefore it is referred to the Pearson data base.⁶⁷

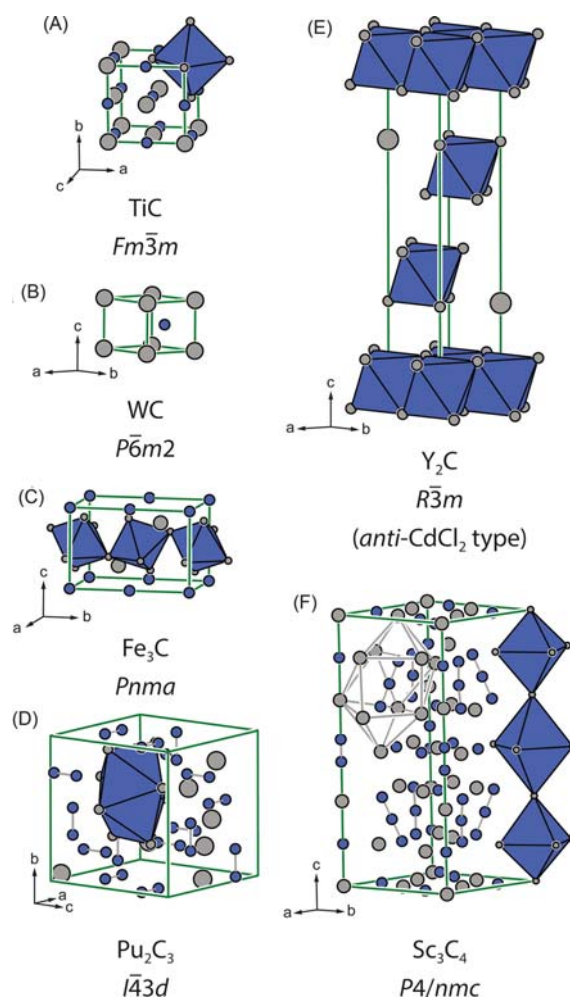


Fig. 30 Comparison of six binary intermetallic carbides. (A) Cubic TiC, (B) hexagonal WC, (C) orthorhombic Fe_3C , (D) cubic Pu_2C_3 , (E) trigonal Y_2C and (F) tetragonal Sc_3C_4 . M atoms are depicted in gray, C atoms in blue.

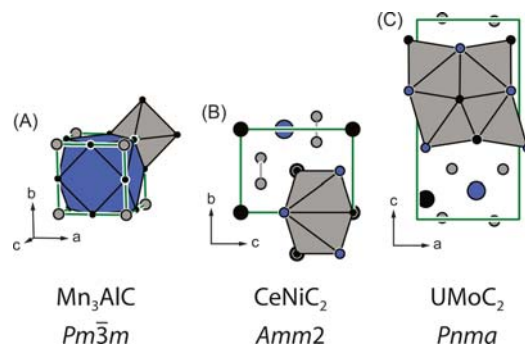


Fig. 31 Comparison of three ternary intermetallic carbides. (A) Cubic Mn_3AlC and orthorhombic (B) $CeNiC_2$ as well as (C) $UMoC_2$. Mn, Ce and U atoms are depicted in blue, Al, Ni and Mo atoms in black, C atoms in gray.

However, regardless of the respective elemental combinations, the carbon atoms always occupy the octahedral voids formed by the M atoms, while the T atoms are located in the cuboctahedral voids. For the MTC_2 compositions, the orthorhombic A -centered $CeNiC_2$ ($Amm2$, $M = Y, La-Nd, Sm, Gd-Lu, Th, Pu, T = Fe, Co, Ni, Rh$,^{67,637-639} Fig. 31B) and the orthorhombic primitive $UMoC_2$ ($Pnma$, $M = Y, Gd-Tm, U, Pu, T = V, Cr, Mn, Mo, Tc, Ru, W, Re$,^{67,640-643} Fig. 31C) type structures can be observed. The major difference between the two structure types is the coordination of the C atoms. While in the latter structure, the carbon atoms are surrounded in an octahedral fashion, in the $CeNiC_2$ type structure, C_2 dumbbells with C-C distances around 140 pm are observed. Several of the $CeNiC_2$ type compounds have been investigated with respect to their magnetism and magnetic structures.⁶⁴⁴⁻⁶⁴⁶

4.06.4.5.3.2 Silicon

For the binary silicides, the Mn_5Si_3 type structure ($P6_3/mmc$, Fig. 26B), already introduced for the gallides, has been reported for several early transition metals (T_5Si_3 , $T = Ti, V, Mn, Fe, Zr, Nb, Mo, Hf, Ta$ ^{67,647-651}) and a large number of rare earth elements (RE_5Si_3 , $RE = Sc, Y, La, Nd, Sm, Gd-Lu$ ^{67,652-656}). As for the equiatomic compounds, the orthorhombic FeB type structure (MSi , $M = Ti-Hf, La-Nd, Sm, Gd-Er, Th, U-Cm$,^{67,522,657-661} $Pnma$, Fig. 21G) and the cubic FeSi type structure ($P2_13$, Fig. 32C) with $M = Cr-Ni, Tc-Rh, Re$ and Os have been observed.^{67,660,662-666} While in the FeB type structure the Si atoms form corrugated chains with Si-Si bonds, in the FeSi type structure, both Fe and Si exhibit a coordination number of 13 in the shape of a pseudo Frank-

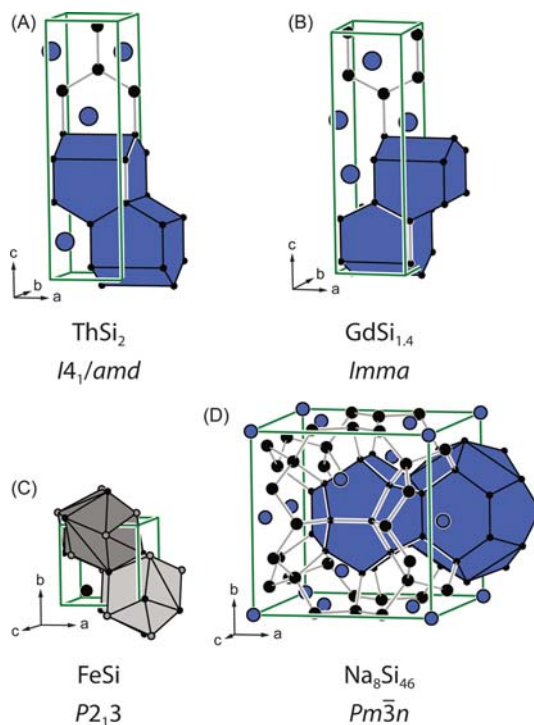


Fig. 32 Comparison of four different binary silicides. (A) Tetragonal $ThSi_2$, (B) orthorhombic $GdSi_{1.4}$, a distorted $ThSi_2$ type structure, (C) the cubic FeSi and (D) cubic clathrate type-I (Na_8Si_{46} type structure). Th, Gd, Na atoms are depicted in blue, Fe atoms in gray and Si atoms in black.

Kasper polyhedra according to $\text{Si}@\text{Fe}_7\text{Si}_6$ and $\text{Fe}@\text{Si}_7\text{Fe}_6$. With respect to the MSi_2 composition, the hexagonal AlB_2 ($P6/mmm$, Fig. 14A), the tetragonal ThSi_2 ($I4_1/amd$, Fig. 32A) and the orthorhombic $\text{GdSi}_{1.4}$ ($Imma$, Fig. 32B) type structures have been reported for $M = \text{Ca-Ba, Sc, Y, La-Nd, Sm-Lu, Th, U-Cm}$.^{67,657,661,667-673} For the rare earth elements, either the ThSi_2 or the $\text{GdSi}_{1.4}$ type structure is formed, depending on the respective element. The large and early rare earth metals form the tetragonal ThSi_2 type structure, while the late and small ones exhibit the $\text{GdSi}_{1.4}$ type structure, that can be described as a distorted ThSi_2 type. Additionally, a deficit on the Si2 site was observed, leading to the off-stoichiometry. A transition between the three structure types can be achieved by either quenching at high temperatures or by HT-HP experiments, which in many cases leads to the AlB_2 type structure. Another important structural arrangement is observed for the so-called clathrates. One of the prototypes for this class of compounds in the intermetallic field is the sodium silicide $\text{Na}_8\text{Si}_{46}$ ($Pm\bar{3}n$, Fig. 32D). The Si atoms in this crystal structure form an extended network, while the alkali or alkaline earth atoms reside in two different cavities: a 20-vertex pentagonal dodecahedron and a 24-vertex polyhedron consisting of 12 pentagons and 2 hexagons. Depending on the elemental combination or the synthesis conditions, a deficit can be observed on the cationic sites, leading to compositions with a general composition of $\text{M}_{8-x}\text{Si}_{46}$. Within this structure type, several variations with respect to the atoms occupying the cavities and also the network (e.g., $\text{Ba}_8\text{Al}_x\text{Si}_{46-x}$) can be achieved, making these compounds interesting materials for thermoelectric applications due to their low thermal conductivity caused by the atoms in the cavities (rattling atoms).^{674,675}

With respect to ternary silicides, the Pearson data base⁶⁷ contains more than 5000 entries in combination with alkali, alkaline earth, rare earth and transition metals. Of these, over 1000 entries belong to the MT_2Si_2 compounds that adopt to the tetragonal body centered ThCr_2Si_2 type structure ($I4/mmm$, Fig. 27B), existing for a wide range of elemental combinations ($M = \text{Ca-Ba, Sc, Y, La-Nd, Sm-Lu, Th, U, Np, Ac}$ and $T = \text{Mg, Cr-Zn, Tc-Ag, Os-Au}$; references are exemplarily^{67,676-683}). Besides the respective structural parameters, their properties have furthermore been studied by a wide range of techniques. Magnetic measurements, and neutron studies, and also e.g., NMR spectroscopic and XPS investigations have been conducted.⁶⁸⁴⁻⁶⁹² In addition to the solid solutions crystallizing in the AlB_2 ($P6/mmm$, Fig. 14A) and MgZn_2 (Fig. 6B) type structure, the TiNiSi (MTSi with $M =$ and $T =$; $Pnma$, Fig. 25D) and the CeNiSi_2 type structure (MTSi_2 , $M = \text{Ca, Y, La-Nd, Sm-Lu, Th, U, Np}$; $T = \text{Mn-Zn, Rh, Ir, Pt}$,⁶⁹³⁻⁷⁰⁰ Cmcm , Fig. 33) are observed. The CeNiSi_2 type structure can be described as a layer-like structure of zigzag-chains formed by Si atoms that connect layers that are similar to PbO . In between these building blocks, the Ce atoms are located.

4.06.4.5.3.3 Germanium

As for the silicides, also the binary germanides crystallize in a variety of already mentioned structure types. Among them are the Mn_5Si_3 (M_5Ge_3 , $M = \text{Ti-Hf, V-Ta, Mn, Mo, Sc, Y, La-Nd, Sm, Gd-Lu, U}$,^{67,647,701-708} $P6_3/mmc$, Fig. 26B), the CrB (MGe , $M = \text{Ca-Ba, S, Y, Pr, Nd, Sm-Tm}$,^{67,522,660,701,709,710} Cmcm , Fig. 9F), the ThSi_2 (MGe_2 , $M = \text{Ba, Y, La-Nd, Sm, Gd-Ho, Th, Np}$,^{67,257,711,712} $I4_1/amd$, Fig. 32A) the Cr_3Si (M_3Ge , $M = \text{V, Cr, Mo, Nb}$,^{67,713-715} $Pm\bar{3}n$, Fig. 26A) and finally the Sm_5Ge_4 (M_5Ge_4 , $M = \text{Ti, Hf, Sc, Y, La-Nd, Sm, Gd-Lu}$,^{67,716,717} $Pnma$, Fig. 34) type structures. Besides the Sm_5Ge_4 type structure, all other mentioned prototypes have been described and discussed before, therefore it is referred to the respective sections. The compounds that adopt the Sm_5Ge_4 type structure crystallizes in the orthorhombic crystal system with space group $Pnma$. The crystal structure can be described best based on the coordination polyhedra surrounding the Sm atoms. The three crystallographically independent Sm sites exhibit spherical coordination environments with coordination numbers of 14–16. Two of the Ge sites form dumbbells with short Ge–Ge distances (266 pm), indicating substantial bonding contributions, while the third site remains isolated.

For the ternary equiatomic germanides, the TiNiSi (MTGe , $M = \text{Ca-Ba, Ti-Hf, V-Ta, Sc, Y, La-Nd, Sm-Lu, U, Np}$, $T = \text{Li, Mg, Mo, Mn-Cu, Ru-Pd, Cd, Ir-Au}$,^{67,540,718-723} $Pnma$, Fig. 25D) and ZrNiAl (MTGe , $M = \text{Ca, Ti-Hf, Nb, Ta, Sc, Y, La, Pr, Nd, Sm, Gd-Lu}$, $T = \text{Cr-Co, Cu, Zn, Ru-Cd, Os}$,^{67,526,724-731} $P\bar{6}2m$, Fig. 14B) type structures are observed. Furthermore, as for the respective silicides, a plethora of compounds adopting the ThCr_2Si_2 type structure ($M = \text{Ca-Ba, Zr, Hf, Y, La-Nd, Sm-Lu, Th, U, Np}$, $T = \text{Cr-Zn, Ru-Cd}$,

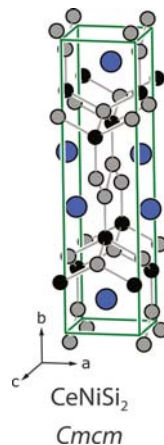


Fig. 33 Unit cell of the orthorhombic CeNiSi_2 type structure. Ce atoms are depicted in blue, Ni atoms in black, Ge atoms in gray.

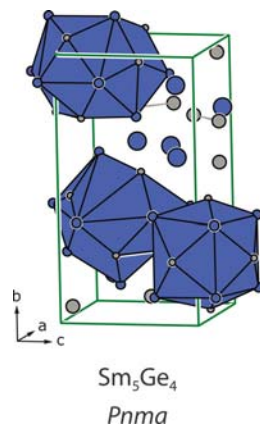


Fig. 34 Unit cell of the orthorhombic Sm_5Ge_4 type structure. Sm atoms are depicted in blue, Ge atoms in gray.

Os-Au,^{67,679,681–683,698,732–736} $I4/mmm$, Fig. 27B) along with their magnetic properties and magnetic structures have been reported.^{735,737–742} CaBe_2Ge_2 ($P4/nmm$, Fig. 35A) is another 1-2-2 composition that forms its own structure type with various elements ($M = \text{Ca, Sr, La-Nd, Sm, Eu, Dy, Th, U, T = \text{Be, Co, Ni, Zn, Rh, Ir, Pt, Au}$).^{67,689,743–747} Like ThCr_2Si_2 , it can also be derived from the BaAl_4 type structure, however, adopts a tetragonal primitive unit cell. The crystallographic relations between BaAl_4 , ThCr_2Si_2 and CaBe_2Ge_2 can be found in the literature.⁴⁵ The crystal structure of CaBe_2Ge_2 is very similar to the one of ThCr_2Si_2 , with the distinct difference, that between the layers now heteroatomic bonding arises compared to homoatomic bonds in the body-centered ThCr_2Si_2 type (Fig. 27B). Finally, the hexagonal MgFe_6Ge_6 type structure ($P6/mmm$, Fig. 35B) and the orthorhombic CeCu_2Ge_6 ($Amm2$, Fig. 35C) type structures should be mentioned. In the latter structure type zigzag-chains of Ge atoms along with slabs formed by the transition metal and additional Ge atoms are observed. The M atoms, as usual, occupy cavities in the framework. In the MgFe_6Ge_6 type structure, the transition metal atoms form Kagomé nets (6^3 nets) with Ge atoms located over the triangular and hexagonal meshes of the layer. The Mg atoms reside in cavities formed by 20 atoms ($\text{Mg@Fe}_{12}\text{Ge}_8$) forming an eightfold capped hexagonal prism. The CeCu_2Ge_6 type structure was observed for the elemental combinations with $M = \text{Y, La-Nd, Sm, Gd-Lu}$ and $T = \text{Mn, Co-Cu, Rh-Ag, Pt, Au}$ and Al,^{67,748–754} while the MgFe_6Ge_6 type structure was reported for $M = \text{Li, Mg, Ti, Zr-Hf, Nb, Sc, Y, Gd-Lu, U}$ and $T = \text{Cr-Co}$.^{67,755–760}

4.06.4.5.3.4 Tin

For the binary stannides, the most represented structure types have been already discussed before. The Cu_3Au type ($Pm\bar{3}m$, Fig. 13B) is observed both for $M_3\text{Sn}$ ($M = \text{Ti, Fe, Ni, Pd, Pt, La-Pr, Np}$ ^{67,611,612,761–763}) and MSn_3 ($M = \text{Ca, La-Nd, Sm-Er, Yb, Th, U-Pu}$ ^{67,257,387,614,615,764}) compounds, with the majority being reported for the latter composition. The $M_3\text{Sn}$ representatives with $M = \text{Ti, Fe}$ and Ni , only form during high-temperature/high-pressure experiments.⁷⁶⁵ The hexagonal Mn_5Si_3 type structure ($P6_3/mcm$, Fig. 26B) has been reported for the elements $M = \text{Ti-Hf, Sc, Y, La-Nd, Sm, Gd-Lu}$ and Th .^{647,766–769} Finally, several stannides

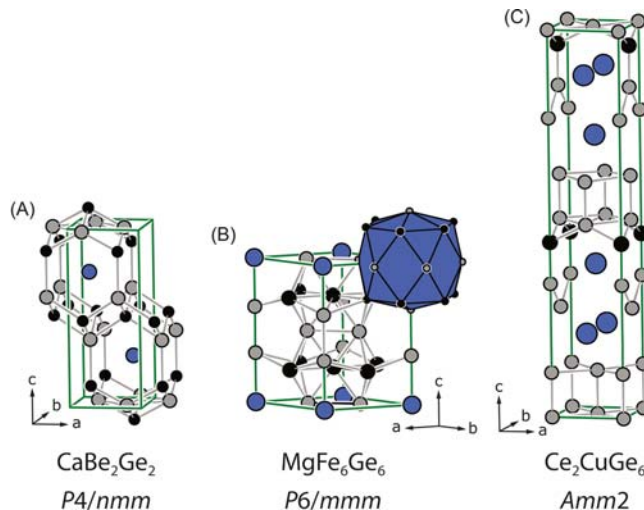


Fig. 35 Comparison of three ternary intermetallic germanides. (A) The tetragonal CaBe_2Ge_2 , (B) the hexagonal MgFe_6Ge_6 and (C) the Ce_2CuGe_6 type structure. Ca, Mg and Ce atoms are depicted in blue, Be, Fe and Cu atoms in black and Ge atoms in gray.

have been reported to crystallize with the compositions M_2Sn ($M = Ti, Mn-Cu, Rh, Pd, Yb$ ^{67,770-772}) and M_3Sn ($M = V, Zr-Mo, Ta$ ^{67,713,773-775}) in the Ni_2In ($P6_3/mmc$, Fig. 28A) and the Cr_3Si ($Pm\bar{3}n$, Fig. 26A) type structure, respectively. For the ternary tin-containing intermetallics, also a wide range of elemental combinations are reported, for example the Heusler phases MT_2Sn ($MnCu_2Al$ type, $Fm\bar{3}m$, Fig. 27A),⁶⁷ the orthorhombic $TiNiSi$ ($M = Na, Ca-Ba, Zr, Sc, Y, La-Nd, Sm-Lu, Np, T = Cu-Zn, Ru, Pd, Ir-Au$,^{150,776-782} $Pnma$, Fig. 25D) and $CeNiSi_2$ ($M = Li, Sr, Ba, Y, La-Nd, Sm-Tm, Lu, Th, T = Mn-Zn, Ru-Pd, Ir, Au, Si, Cmcm$; Fig. 33) or the hexagonal $ZrNiAl$ ($M = Ca, Zr, Hf, Sc, Y, Y, La-Nd, Sm, Gd-Lu, Th, U, Np, T = Co, Ni, Ru-Cd, Ir, Pt$,^{67,546,783,784} $P\bar{6}2m$, Fig. 14B) type representatives. Detailed investigations of the physical properties and the pressure dependence of their crystal structures have been reported for the $TiNiSi$ ⁷⁸⁵⁻⁷⁹⁰ and $ZrNiAl$ ⁷⁹¹⁻⁷⁹⁶ representatives. The $MgAgAs$ type structure, also known as “half-Heusler” phase crystallizes, like the regular Heusler phases, in the cubic crystal system but with space group $F\bar{4}3m$ (Fig. 36A). In this space group, the Cu position (8c) of the $MnCu_2Al$ type structure splits into two independent positions (4c and 4d) of which only one is occupied. For the stannides, the $MTSn$ phases with $M = T = Li, Mg, Sc, Ti-Hf, Nb, Ta, Mn-Cu, Rh, Pd, Ir-Au, Ho-Tm, Lu, Th$ and U ^{67,546,784,794,797-801} are reported. Since these half-Heusler phases often exhibit semiconducting properties, the investigation of their various physical properties has been vivid.⁸⁰²⁻⁸⁰⁸ The cubic $Yb_3Rh_4Sn_{13}$ ($Pm\bar{3}m$, Fig. 36B) and orthorhombic $Gd_3Cu_4Ge_4$ ($Immm$, Fig. 36C), finally, are also reported for a variety of different elemental combinations. While the $M_3T_4Sn_{13}$ compounds have been synthesized with $M = Ca, Sr, La-Nd, Sm-Gd, Yb, Th, U$ and $T = Co, Ru, Rh, Os-Pt$,^{67,809-818} the $M_3T_4Sn_4$ members exist with $M = Y, La-Nd, Sm-Yb$ and $T = Mg, Mn, Cu$ and Ag .^{67,819-824} In both cases the T and Sn atoms form a polyanionic network, the M atoms reside in cavities of said network. In both cases $Sn-Sn$ bonding is observed along with $T-Sn$ interactions. The T atoms reside in trigonal prismatic coordination by Sn atoms in the $Yb_3Rh_4Sn_{13}$ type structure, the M atoms are spherically surrounded by a 14-vertex Frank-Kasper polyhedra. The physical properties of compounds crystallizing in this structure type have been investigated in detail as some compounds exhibit superconductivity. In the $Gd_3Cu_4Ge_4$ type members, the M atoms reside in pentagonal or distorted hexagonal prismatic voids. For numerous of these structures, the magnetic properties along with the magnetic structures have been investigated.^{819,825-828} Finally, the Hf_5CuSn_3 type structure (M_5TSn_3 , $M = Ti-Hf, Ta, Y, La-Pr, Gd, Tb, Yb, U, T = Li, Mg, Mn-Ga, Ag, Au$,^{819,829-834} $P6_3/mcm$, Fig. 36D) should be mentioned. It can be considered either as a filled Mn_5Si_3 type structure or as ordered ternary variant of the Sm_5Ge_4/Ti_5Ge_4 type structure. The Cu atoms, in the case of the prototype, get inserted in the octahedral voids formed by the Hf atoms. Rieger and coworkers describe in their initial publication on this structure type that the Ni and Cu atoms play the same role as non-metal atoms. Recently, the insertion of Li and Mg into M_5Sn_3 compounds has been achieved by electrochemical reactions.⁸³⁵⁻⁸³⁷

4.06.4.5.3.5 Lead

For the binary lead intermetallics, also known as plumbides, the Cu_3Au , the Mn_5Si_3 and the Sm_5Ge_4 type structures have been reported. Overall, one should mention, that, compared to the lighter elements of group 14, significantly less compounds have been reported. Especially the lead-rich representatives exhibit an increased sensitivity towards moisture, which makes preparation and characterization of these compounds more difficult. For the Cu_3Au type structure ($Pm\bar{3}m$, Fig. 13B), as shown numerous times before, two compositions have been reported. The M_3Pb representatives for $M = Ca, Nb, Rh, Pd, Pt, Ce, Pr$ and Pu ^{67,611,838-843} and the lead-rich MPb_3 composition with $M = Na, Ca, Y, La-Nd, Sm-Lu, Th, U$ and Pu .^{257,331,614,615,764,844,845} The Mn_5Si_3 type structure ($P6_3/mcm$, Fig. 26B), M_5Pb_3 in the case of the plumbides, has been reported for the elements $M = Sc, Y, Zr, La-Nd, Sm, Gd-Lu$ and Th . Here, as for the lighter homologs only one composition is observed.^{766,767,769,846,847} The Sm_5Ge_4 type structure ($Pnma$, Fig. 34) finally has been reported with the composition M_5Pb_4 for $M = Sr, La-Nd, Sm, Gd-Tm$.^{67,848-852} For the ternary plumbides, again some previously mentioned structure types are observed. The ternary rare earth plumbides have been summarized

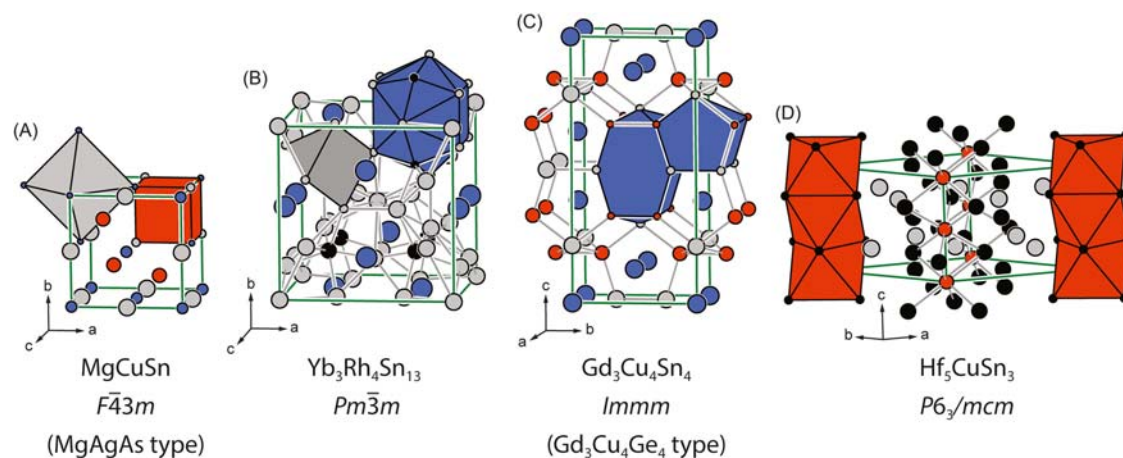


Fig. 36 Structures of four ternary intermetallic stannides. (A) Cubic $MgAgAs$ type $MgCuSn$, (B) cubic $Yb_3Rh_4Sn_{13}$, (C) orthorhombic $Gd_3Cu_4Sn_4$ ($Gd_3Cu_4Ge_4$ type) and (D) hexagonal Hf_5CuSn_3 . Mg, Yb, Gd and Hf atoms are depicted in blue, Cu atoms in orange, Rh atoms in black and Sn atoms in gray.

in a review in 2008⁸⁵³ followed by an update in 2020.⁸⁵⁴ The most prominent are the hexagonal Hf₅CuSn₃ (M_5TPb_3 , $M = Ca, Zr, Hf, Y, La-Nd, Sm, Gd-Tm, Lu$, $T = V-Zn, Ru, Ag, Cd$,^{67,829,830,855–860} $P6_3/mcm$, Fig. 36D) and ZrNiAl ($M = Ca, Y, La-Nd, Sm, Gd-Lu$, $T = Ni, Rh-Cd, Pt$,^{67,282,861–865} $P\bar{6}2m$, Fig. 14B) type structures along with the cubic MnCu₂Al type structure representatives (MT_2Pb , $M = T = Li, Mg, Sc, Y, Ti, V, Mn, Rh, Pd, Pr, Sm, Gd-Lu, Th, U$, $Fm\bar{3}m$, Fig. 27A).

References

- Holden, N. E.; Coplen, T. B.; Böhlke, J. K.; Tarbox, L. V.; Benefield, J.; de Laeter, J. R.; Mahaffy, P. G.; O'Connor, G.; Roth, E.; Tepper, D. H.; Walczyk, T.; Wieser, M. E.; Yoneda, S. *Pure Appl. Chem.* **2018**, *90*, 1833.
- Gazzara, C. P.; Middleton, R. M.; Weiss, R. J.; Hall, E. O. *Acta Crystallogr.* **1967**, *22*, 859.
- Pöttgen, R.; Jöhrendt, D. *Intermetallics: Synthesis, Structure, Function*, De Gruyter: Berlin, Boston, 2014.
- Pöttgen, R.; Jöhrendt, D. *Intermetallics: Synthesis, Structure, Function*, De Gruyter: Berlin, Boston, 2019.
- Dshemuchadse, J.; Steurer, W. *Intermetallics* In: *Union of Crystallography*, Oxford University Press: Oxford, 2016.
- Ferro, R.; Saccone, A. *Intermetallic Chemistry*, Pergamon: Oxford, Amsterdam, 2008.
- Gille, P.; Grin, Y. *Crystal Growth of Intermetallics*, De Gruyter: Berlin, Boston, 2019.
- Sikka, V. K. *Intermetallic-Based High-Temperature Materials* In: *Metals and Ceramics Division*, Oak Ridge National Lab: Oak Ridge, TN, 1999.
- Sikka, V. K.; Stoloff, N. S. *Physical Metallurgy and Processing of Intermetallic Compounds*, Chapman & Hall: New York, NY, 1996.
- Artini, C. *Alloys and Intermetallic Compounds—From Modeling to Engineering*, CRC Press: Boca Raton, 2017.
- Szytula, A.; Leciejewicz, J. *Handbook of Crystal Structures and Magnetic Properties of Rare Earth Intermetallics*, CRC Press: Boca Raton, 1994.
- Gschneidner, K. A., Jr.; Eyring, L. *Handbook on the Physics and Chemistry of Rare Earths*, North-Holland Publishing Co., 1978.
- Bünzli, J.-C. G.; Pecharsky, V. K. *Handbook on the Physics and Chemistry of Rare Earths*, North-Holland Publishing Co., 2020.
- Lotfi, S.; Brgoch, J. *Chem. A Eur. J.* **2020**, *26*, 8689.
- Lattner, S. E. *Acc. Chem. Res.* **2018**, *51*, 40.
- Lin, Q.; Miller, G. J. *Acc. Chem. Res.* **2018**, *51*, 49.
- Wang, J.; Dolyniuk, J.-A.; Kovnir, K. *Acc. Chem. Res.* **2018**, *51*, 31.
- Smetana, V.; Rhodehouse, M.; Meyer, G.; Mudring, A.-V. *Acc. Chem. Res.* **2017**, *50*, 2633.
- Walsh, J. P. S.; Freedman, D. E. *Acc. Chem. Res.* **2018**, *51*, 1315.
- Steinberg, S.; Dronskowski, R. *Crystals* **2018**, *8*, 225.
- Li, J.; Sun, S. *Acc. Chem. Res.* **2019**, *52*, 2015.
- Zhou, M.; Li, C.; Fang, J. *Chem. Rev.* **2020**.
- Kim, H. Y.; Joo, S. H. *J. Mater. Chem. A* **2020**, *8*, 8195.
- Rößner, L.; Armbrüster, M. *ACS Catal.* **2019**, *9*, 2018.
- Armbrüster, M. *Sci. Technol. Adv. Mater.* **2020**, *21*, 303.
- Pöttgen, R.; Janka, O.; Chevalier, B. *Z. Naturforsch.* **2016**, *71b*, 165.
- Janka, O.; Niehaus, O.; Pöttgen, R.; Chevalier, B. *Z. Naturforsch.* **2016**, *71b*, 737.
- Pöttgen, R.; Chevalier, B. *Z. Naturforsch.* **2015**, *70b*, 695.
- Pöttgen, R.; Chevalier, B. *Z. Naturforsch.* **2015**, *70b*, 289.
- Li, L. *Chin. Phys. B* **2016**, *25*, 037502.
- Gupta, S.; Suresh, K. G. *J. Alloys Compd.* **2015**, *618*, 562.
- Benndorf, C.; Eckert, H.; Janka, O. *Acc. Chem. Res.* **2017**, *50*, 1459.
- Hull, A. W. *Phys. Rev.* **1917**, *10*, 661.
- Eilers-Rethwisch, M.; Niehaus, O.; Janka, O. *Z. Anorg. Allg. Chem.* **2014**, *640*, 153.
- Niehaus, O.; Rodewald, U. C.; Abdala, P. M.; Touzani, R. S.; Fokwa, B. P. T.; Janka, O. *Inorg. Chem.* **2014**, *53*, 2471.
- Niehaus, O.; Janka, O. *Z. Anorg. Allg. Chem.* **2015**, *641*, 1792.
- Klenner, S.; Heletta, L.; Pöttgen, R. *Dalton Trans.* **2019**, *48*, 3648.
- Wondratschek, H.; Müller, U. *International Tables for Crystallography, Volume A1: Symmetry Relations Between Space Groups*, John Wiley & Sons: Chichester, Großbritannien, 2011.
- Bärnighausen, H. *MATCH, Commun. Math. Comput. Chem.* **1980**, *9*, 139.
- Bärnighausen, H.; Müller, U. *Symmetriebeziehungen zwischen den Raumgruppen als Hilfsmittel zur straffen Darstellung von Strukturzusammenhängen in der Kristallchemie*, Universität Karlsruhe und Universität-Gh Kassel: Germany, 1996.
- Müller, U. *Z. Anorg. Allg. Chem.* **2004**, *630*, 1519.
- Müller, U. *Symmetry Relationships Between Crystal Structures*, Oxford University Press, 2013.
- Hoffmann, R.-D.; Pöttgen, R. *Z. Kristallogr.* **2001**, *216*, 127.
- Zumdick, M. F.; Pöttgen, R. *Z. Kristallogr.* **1999**, *214*, 90.
- Pöttgen, R. *Z. Anorg. Allg. Chem.* **2014**, *640*, 869.
- Leon-Escamilla, E. A.; Corbett, J. D. *J. Alloys Compd.* **1998**, *265*, 104.
- Henning, R. W.; Leon-Escamilla, E. A.; Zhao, J.-T.; Corbett, J. D. *Inorg. Chem.* **1997**, *36*, 1282.
- Pöttgen, R.; Janka, O. In *High-Temperature Methods in Handbook of Solid State Chemistry*; Dronskowski, R., Kikkawa, S., Stein, A., Eds.; vol. 2; Wiley-VCH, 2017.
- Niepmann, D.; Prots, Y. M.; Pöttgen, R.; Jeitschko, W. *J. Solid State Chem.* **2000**, *154*, 329.
- Kanatzidis, M. G.; Pöttgen, R.; Jeitschko, W. *Angew. Chem. Int. Ed.* **2005**, *44*, 6996.
- Bugaris, D. E.; Loye, H.-C. Z. *Angew. Chem. Int. Ed.* **2012**, *51*, 3780.
- Kaner, R.; Castro, C. A.; Gruska, R. P.; Wold, A. *Mater. Res. Bull.* **1977**, *12*, 1143.
- Baghdadi, A.; Finley, A.; Russo, P.; Arnott, R. J.; Wold, A. *J. Less-Common Met.* **1974**, *34*, 31.
- Jeitschko, W.; Reehuis, M. *J. Phys. Chem. Solid* **1987**, *48*, 667.
- Wurth, A.; Löhken, A.; Mewis, A. *Z. Anorg. Allg. Chem.* **2002**, *628*, 661.
- Okada, S.; Kudou, K.; Mori, T.; Iizumi, K.; Shishido, T.; Tanaka, T.; Rogl, P. *J. Cryst. Growth* **2002**, *244*, 267.
- Okada, S.; Kudou, K.; Mori, T.; Iizumi, K.; Shishido, T.; Tanaka, T.; Nakajima, K.; Rogl, P. *Jpn. J. Appl. Phys.* **2002**, *41*, L555.
- Jeitschko, W.; Foecker, A. J.; Paschke, D.; Dewalsky, M. V.; Evers, C. B. H.; Künnen, B.; Lang, A.; Kotzyba, G.; Rodewald, U. C.; Möller, M. H. *Z. Anorg. Allg. Chem.* **2000**, *626*, 1112.
- Ozawa, T. C.; Kauzlarich, S. M. *Inorg. Chem.* **2003**, *42*, 3183.

60. Broll, S.; Jeitschko, W. *J. Alloys Compd.* **1995**, *229*, 233.
61. Pletcher, D.; Walsh, F. C. *Industrial Electrochemistry*, Springer: Netherlands, 1993.
62. Botte, G. G. *Electrochem. Soc. Interface* **2014**, *23*, 49.
63. Tambornino, F.; Sappl, J.; Pultar, F.; Cong, T. M.; Hübner, S.; Gifftthaler, T.; Hoch, C. *Inorg. Chem.* **2016**, *55*, 11551.
64. Hoch, C.; Simon, A. *Angew. Chem. Int. Ed.* **2012**, *51*, 3262.
65. Tambornino, F.; Hoch, C. *Z. Anorg. Allg. Chem.* **2015**, *641*, 537.
66. Donohue, J. *The Structures of the Elements*, Wiley: New York, USA, 1974.
67. Villars, P.; Cenzual, K. *Pearson's Crystal Data: Crystal Structure Database for Inorganic Compounds*, ASM International®: Materials Park, Ohio (USA), 2021.
68. Bragg, W. L. *Philos. Mag.* **1914**, *28*, 355.
69. Herrmann, K. W. *Iowa State Coll. J. Sci.* **1955**, *31*, 439.
70. Ellinger, F. H.; Zachariasen, W. H. *J. Am. Chem. Soc.* **1953**, *75*, 5650.
71. Jagodzinski, H. *Acta Crystallogr.* **1949**, *2*, 201.
72. Hull, A. W. *Trans. Am. Inst. Electr. Eng.* **1919**, *38*, 1445.
73. Bredig, G.; Allolio, R.; *Phys. Z. Chem* **1927**, *126U*, 41.
74. Teitel, R. J.; Cohen, M. *Trans. Am. Inst. Min. Metall. Pet. Eng.* **1949**, *185*, 285.
75. Hull, A. W. *Science* **1920**, *52*, 227.
76. Hull, A. W. *Phys. Rev.* **1921**, *17*, 571.
77. Häussermann, U.; Simak, S. I. *Phys. Rev. B* **2001**, *64*, 245114.
78. Debye, P. *Phys. Z.* **1917**, *18*, 483.
79. Beamer, W. H.; Maxwell, C. R. *J. Chem. Phys.* **1946**, *14*, 569.
80. Bradley, A. J. *Z. Kristallogr.* **1935**, *91*, 302.
81. Häussermann, U.; Simak, S. I.; Ahuja, R.; Johansson, B.; Lidin, S. *Angew. Chem. Int. Ed.* **1999**, *38*, 2017.
82. Häussermann, U.; Simak, S. I.; Ahuja, R.; Johansson, B. *Angew. Chem. Int. Ed.* **2000**, *39*, 1246.
83. Emsley, J. *The Elements*, Clarendon Press, Oxford University Press: Oxford, New York, 1998.
84. Frank, F. C.; Kasper, J. S. *Acta Crystallogr.* **1959**, *12*, 483.
85. Frank, F. C.; Kasper, J. S. *Acta Crystallogr.* **1958**, *11*, 184.
86. Shoemaker, C. B.; Shoemaker, D. P.; Hopkins, T. E.; Yindepit, S. *Acta Crystallogr.* **1978**, *B34*, 3573.
87. Fischer, W. *Z. Kristallogr.* **2006**, *221*, 305.
88. Parthé, E. *Z. Kristallogr.* **2006**, *221*, 301.
89. Friauf, J. B. *J. Am. Chem. Soc.* **1927**, *49*, 3107.
90. Tarschisch, L.; Titow, A. T.; Garjanow, F. K. *Phys. Z. Sowjetunion* **1934**, *5*, 503.
91. Lieser, K. H.; Witte, H. *Z. Metallkd.* **1952**, *43*, 396.
92. Laves, F.; Witte, H. *Metallwirtschaft* **1936**, *15*, 840.
93. Fukui, H.; Hirao, N.; Ohishi, Y.; Baron, A. Q. R. *J. Phys. Condens. Matter* **2010**, *22*, 095401.
94. Johnston, R. L.; Hoffmann, R. *Z. Anorg. Allg. Chem.* **1992**, *616*, 105.
95. Liu, C. T.; Zhu, J. H.; Brady, M. P.; McKamey, C. G.; Pike, L. M. *Intermetallics* **2000**, *8*, 1119.
96. Stein, F.; Palm, M.; Sauthoff, G. *Intermetallics* **2004**, *12*, 713.
97. Stein, F.; Palm, M.; Sauthoff, G. *Intermetallics* **2005**, *13*, 1056.
98. Zhu, J. H.; Liaw, P. K.; Liu, C. T. *Mater. Sci. Eng. A* **1997**, *239-240*, 260.
99. Nesper, R.; Miller, G. J. *J. Alloys Compd.* **1993**, *197*, 109.
100. Ormeci, A.; Simon, A.; Grin, Y. *Angew. Chem. Int. Ed.* **2010**, *49*, 8997.
101. Gschneidner, K. A., Jr.; Pecharsky, V. K. *Z. Kristallogr.* **2006**, *221*, 375.
102. Steglich, F.; Aarts, J.; Bredl, C. D.; Lieke, W.; Meschede, D.; Franz, W.; Schafer, H. *J. Magn. Magn. Mater.* **1980**, *15-8*, 889.
103. Ross, J. W.; Crangle, J. *Phys. Rev.* **1964**, *133*, A509.
104. Ren, W.-J.; Zhang, Z.-D. *Chin. Phys. B* **2013**, *22*, 077507.
105. Gratz, E.; Markosyan, A. S. *J. Phys. Condens. Matter* **2001**, *13*, R385.
106. Eriksson, O.; Johansson, B.; Brooks, M. S. S.; Skriver, H. L. *Phys. Rev. B* **1989**, *40*, 9519.
107. Gschneidner, K. A., Jr.; Pecharsky, V. K.; Tsokol, A. O. *Rep. Prog. Phys.* **2005**, *68*, 1479.
108. Pathak, A. K.; Paudyal, D.; Gschneidner, K. A., Jr.; Pecharsky, V. K. *J. Appl. Phys.* **2014**, *115*, 17E109.
109. Witte, H. *Z. Angew. Mineral.* **1938**, *1*, 255.
110. Kotur, B. Y. *Dopov. Akad. Nauk Ukr. RSR* **1977**, *A39*, 164.
111. Bardos, D. I.; Gupta, K. P.; Beck, P. A. *Trans. Metall. Soc. AIME* **1961**, *221*, 1087.
112. Hoffmann, R.-D.; Pöttgen, R.; Chevalier, B.; Gaudin, E.; Matar, S. F. *Solid State Sci.* **2013**, *21*, 73.
113. Soudé, A.; Tougait, O.; Pasturel, M.; Kaczorowski, D.; Noël, H.; Roisnel, T. *J. Alloys Compd.* **2011**, *509*, 5447.
114. Kuz'ma, Y. B.; Gladyshevskii, E. I. *Dopov. Akad. Nauk Ukr. RSR* **1963**, *A25*, 205.
115. Teslyuk, M. Y.; Gladyshevskii, E. I. *Visn. Lviv. Derzh. Univ., Ser. Khim.* **1963**, *6*, 42.
116. Blazina, Z.; Ban, Z. *Z. Naturforsch.* **1981**, *35b*, 1162.
117. Zelinskii, A. V.; Fedorchuk, A. O.; Zelinska, O. Y. *Visn. Lviv. Derzh. Univ., Ser. Khim.* **2013**, *54*, 92.
118. Sichevych, O.; Prots, Y.; Schnelle, W.; Schmidt, M.; Grin, Y. *Z. Kristallogr. - New Cryst. Struct.* **2006**, *221*, 263.
119. Hirai, D.; Kawakami, R.; Magdysyuk, O. V.; Dinnebier, R. E.; Yaresko, A.; Takagi, H. *J. Physical Soc. Japan* **2014**, *83*, 103703.
120. Mishra, T.; Hoffmann, R.-D.; Schwickert, C.; Pöttgen, R. *Z. Naturforsch.* **2011**, *66b*, 771.
121. Seidel, S.; Pöttgen, R. *Z. Anorg. Allg. Chem.* **2017**, *643*, 261.
122. Eustermann, F.; Pominov, A.; Pöttgen, R. *Z. Anorg. Allg. Chem.* **2018**, *644*, 1297.
123. Eustermann, F.; Stegmann, F.; Radzieowski, M.; Janka, O. *Inorg. Chem.* **2019**, *58*, 16211.
124. Witte, H. *Metallwirtsch. Metallwiss. Metalltech.* **1939**, *18*, 459.
125. Gladyshevskii, E. I.; Krypyakevych, P. I.; Teslyuk, M. Y. *Dokl. Akad. Nauk SSSR* **1952**, *85*, 81.
126. Osamura, K.; Murakami, Y. *J. Less-Common Met.* **1978**, *60*, 311.
127. Seidel, S.; Janka, O.; Benndorf, C.; Mausolf, B.; Haarmann, F.; Eckert, H.; Heletta, L.; Pöttgen, R. *Z. Naturforsch.* **2017**, *72b*, 289.
128. Kauzlarich, S. M. *Chemistry, Structure, and Bonding of Zintl Phases and Ions*, VCH Publishers, 1996.
129. Kniep, R. Introduction Eduard Zintl: His Life and Scholarly Work. In *Chemistry, Structure, and Bonding of Zintl Phases and Ions*; Kauzlarich, S. M., Ed., VCH Publishers, Inc: New York, 1996; p xvii.
130. Corbett, J. D. *Angew. Chem. Int. Ed.* **2000**, *39*, 671.
131. Fässler, T. F. *Zintl Phases: Principles and Recent Developments*, Springer-Verlag: Berlin, 2011.

132. Scharfe, S.; Kraus, F.; Stegmaier, S.; Schier, A.; Fässler, T. F. *Angew. Chem. Int. Ed.* **2011**, *50*, 3630.
133. Toberer, E. S.; May, A. F.; Snyder, G. J. *Chem. Mater.* **2010**, *22*, 624.
134. Snyder, G. J.; Toberer, E. S. *Nat. Mater.* **2008**, *7*, 105.
135. Hodge, K. L.; Goldberger, J. E. *J. Am. Chem. Soc.* **2019**, *141*, 19969.
136. Loaiza, L. C.; Monconduit, L.; Seznec, V. *Small* **2020**, *16*, 1905260.
137. Janka, O.; Kauzlarich, S. M. *Zintl Compounds, Encyclopedia of Inorganic and Bioinorganic Chemistry*, John Wiley & Sons, Ltd, 2021.
138. Wilson, R. J.; Lichtenberger, N.; Weinert, B.; Dehnen, S. *Chem. Rev.* **2019**, *119*, 8506.
139. Wilson, R. J.; Weinert, B.; Dehnen, S. *Dalton Trans.* **2018**, *47*, 14861.
140. Whitmire, K. H. *Coord. Chem. Rev.* **2018**, *376*, 114.
141. Shuai, J.; Mao, J.; Song, S.; Zhang, Q.; Chen, G.; Ren, Z. *Mater. Today Phys.* **2017**, *1*, 74.
142. Kauzlarich, S. M.; Zevalkink, A.; Toberer, E.; Snyder, G. J. *Zintl Phases: Recent Developments in Thermoelectrics and Future Outlook in Thermoelectric Materials and Devices*, The Royal Society of Chemistry, 2017.
143. Owen, E. A.; Preston, G. D. *Proc. Phys. Soc. Lond.* **1923**, *36*, 341.
144. Zintl, E.; Kaiser, H. *Z. Anorg. Allg. Chem.* **1933**, *211*, 113.
145. Eckerlin, P.; Leicht, E.; Wölfel, E. Z. *Anorg. Allg. Chem.* **1961**, *307*, 145.
146. Eckerlin, P.; Wölfel, E. Z. *Anorg. Allg. Chem.* **1955**, *280*, 321.
147. Bruzzzone, G.; Franceschi, E. *J. Less-Common Met.* **1978**, *57*, 201.
148. Bruzzzone, G.; Franceschi, E. *J. Less-Common Met.* **1977**, *52*, 211.
149. Turban, K.; Schäfer, H. *Z. Naturforsch.* **1973**, *28b*, 220.
150. Eisenmann, B.; Schäfer, H.; Turban, K. *Z. Naturforsch.* **1975**, *30b*, 677.
151. Widera, A.; Schäfer, H. *Z. Naturforsch.* **1976**, *31b*, 1434.
152. Widera, A.; Eisenmann, B.; Schäfer, H. *Z. Naturforsch.* **1976**, *31b*, 520.
153. Zintl, E.; Brauer, G. Z. *Elektrochem. Angew. Phys. Chem.* **1935**, *41*, 297.
154. Brauer, G.; Zintl, E. Z. *Phys. Chem.* **1937**, *37*, 323.
155. von Stackelberg, M.; Paulus, R. Z. *Phys. Chem.* **1933**, *22*, 305.
156. Zintl, E.; Husemann, E. Z. *Phys. Chem.* **1933**, *21*, 138.
157. Juza, R.; Kroebel, R. Z. *Anorg. Allg. Chem.* **1964**, *331*, 187.
158. Maass, K. E. Z. *Anorg. Allg. Chem.* **1970**, *374*, 19.
159. Zintl, E.; Dullenkopf, W. Z. *Phys. Chem.* **1932**, *16*, 195.
160. Zintl, E.; Brauer, G. Z. *Phys. Chem.* **1933**, *20*, 245.
161. Levinson, D. W.; McPherson, D. J. *Trans. Am. Soc. Metal* **1956**, *48*, 689.
162. Evers, J.; Oehlinger, G. *Inorg. Chem.* **2000**, *39*, 628.
163. Witte, J.; Schnering, H. G.; Klemm, W. Z. *Anorg. Allg. Chem.* **1964**, *327*, 260.
164. Busmann, E. Z. *Anorg. Allg. Chem.* **1961**, *313*, 90.
165. Hoch, C.; Röhr, C. Z. *Anorg. Allg. Chem.* **2002**, *628*, 1541.
166. Marsh, R. E.; Shoemaker, D. P. *Acta Crystallogr.* **1953**, *6*, 197.
167. Müller, W.; Volk, K. Z. *Naturforsch.* **1977**, *32b*, 709.
168. Hewaidy, I. F.; Busmann, E.; Klemm, W. Z. *Anorg. Allg. Chem.* **1964**, *328*, 283.
169. Cromer, D. *Acta Crystallogr.* **1959**, *12*, 36.
170. Hönle, W.; von Schnering, H. G. Z. *Kristallogr.* **1981**, *155*, 307.
171. Cromer, D. *Acta Crystallogr.* **1959**, *12*, 41.
172. Eisenmann, B.; Jordan, H.; Schäfer, H. *Angew. Chem. Int. Ed.* **1981**, *20*, 197.
173. Eisenmann, B.; Jordan, H.; Schäfer, H. *Mater. Res. Bull.* **1982**, *17*, 95.
174. Eisenmann, B.; Jordan, H.; Schäfer, H. Z. *Anorg. Allg. Chem.* **1981**, *475*, 74.
175. Eisenmann, B.; Somer, M. Z. *Naturforsch.* **1984**, *39b*, 736.
176. Eisenmann, B.; Klein, J. *J. Less-Common Met.* **1991**, *175*, 109.
177. Hurng, W. M.; Peterson, E. S.; Corbett, J. D. *Inorg. Chem.* **1989**, *28*, 4177.
178. Wolf, J.; Weber, D.; von Schnering, H. G. Z. *Naturforsch.* **1986**, *41b*, 731.
179. Cordier, D.; Schäfer, H.; Stelter, M. Z. *Naturforsch.* **1984**, *39*, 727.
180. Cordier, D.; Schäfer, H.; Stelter, M. Z. *Naturforsch.* **1985**, *40*, 1100.
181. Cordier, G.; Savelsberg, G.; Schäfer, H. Z. *Naturforsch.* **1982**, *37*, 975.
182. Cordier, G.; Schäfer, H.; Stelter, M. Z. *Naturforsch.* **1984**, *39b*, 727.
183. Cordier, G.; Schäfer, H.; Stelter, M. Z. *Naturforsch.* **1985**, *40b*, 1100.
184. Gerhard, C.; Herbert, S.; Michael, S. Z. *Naturforsch.* **1985**, *40*, 1100.
185. Cordier, G.; Schäfer, H.; Stelter, M. Z. *Naturforsch.* **1985**, *40b*, 5.
186. Johnson, S. I.; Zevalkink, A.; Snyder, G. J. *J. Mater. Chem. A* **2013**, *1*, 4244.
187. Verdier, P.; L'Haridon, P.; Maunay, M.; Laurent, Y. *Acta Crystallogr.* **1976**, *B32*, 726.
188. Verdier, P.; Maunay, M.; Marchand, R.; Lang, J. C. R. *Seances Acad. Sci., Ser. C* **1975**, *281C*, 457.
189. Cordier, G.; Steher, M. Z. *Naturforsch.* **1988**, *43b*, 463.
190. Chanakian, S.; Zevalkink, A.; Aydemir, U.; Gibbs, Z. M.; Pomrehn, G.; Fleurial, J.-P.; Bux, S.; Snyder, G. J. *J. Mater. Chem. A* **2015**, *3*, 10289.
191. Sun, Z.-M.; Mao, J.-G.; Pan, D.-C. *J. Alloys Compd.* **2006**, *421*, 190.
192. Zevalkink, A.; Takagiwa, Y.; Kitahara, K.; Kimura, K.; Snyder, G. J. *Dalton Trans.* **2014**, *43*, 4720.
193. Aydemir, U.; Zevalkink, A.; Ormeci, A.; Wang, H.; Ohno, S.; Bux, S.; Snyder, G. J. *Dalton Trans.* **2015**, *44*, 6767.
194. Todorov, I.; Chung, D. Y.; Ye, L.; Freeman, A. J.; Kanatzidis, M. G. *Inorg. Chem.* **2009**, *48*, 4768.
195. Fornasini, M. L.; Manfrinetti, P. Z. *Kristallogr. - New Cryst. Struct.* **2009**, *224*, 345.
196. Radzieowski, M.; Block, T.; Fickenscher, T.; Zhang, Y.; Fokwa, B. P. T.; Janika, O. *Mater. Chem. Front.* **2017**, *1*, 1563.
197. Radzieowski, M.; Stegemann, F.; Klenner, S.; Zhang, Y.; Fokwa, B. P. T.; Janika, O. *Mater. Chem. Front.* **2020**, *4*, 1231.
198. Park, S.-M.; Choi, E. S.; Kang, W.; Kim, S.-J. *J. Mater. Chem.* **2002**, *12*, 1839.
199. Childs, A. B.; Baranets, S.; Bobev, S. J. *Solid State Chem.* **2019**, *278*, 120889.
200. Lin, J.; Lv, W.; Gu, Y.; Guo, K.; Yang, X.; Zhao, J. *Materials* **2019**, *12*, 1.
201. Lv, W.; Yang, C.; Lin, J.; Hu, X.; Guo, K.; Yang, X.; Luo, J.; Zhao, J.-T. *J. Alloys Compd.* **2017**, *726*, 618.
202. Chanakian, S.; Aydemir, U.; Zevalkink, A.; Gibbs, Z. M.; Fleurial, J.-P.; Bux, S.; Jeffrey Snyder, G. J. *Mater. Chem. C* **2015**, *3*, 10518.
203. Cordier, G.; Schäfer, H.; Stelter, M. Z. *Anorg. Allg. Chem.* **1984**, *519*, 183.

204. Kuromoto, T. Y.; Kauzlarich, S. M.; Webb, D. J. *Mol. Cryst. Liq. Cryst.* **1990**, *181*, 349.
205. Kauzlarich, S. M.; Thomas, M. M.; Odink, D. A.; Olmstead, M. M. *J. Am. Chem. Soc.* **1991**, *113*, 7205.
206. Gallup, R. F.; Fong, C. Y.; Kauzlarich, S. M. *Inorg. Chem.* **1992**, *31*, 115.
207. Kuromoto, T. Y.; Kauzlarich, S. M.; Webb, D. J. *Chem. Mater.* **1992**, *4*, 435.
208. Chan, J. Y.; Wang, M. E.; Rehr, A.; Kauzlarich, S. M.; Webb, D. J. *Chem. Mater.* **1997**, *9*, 2131.
209. Ratal, E.; Bruins, P.; Hernandez, C. J.; Kauzlarich, S. M.; Augustine, M. P. *Chem. Mater.* **2002**, *14*, 2467.
210. Sanchez-Portal, D.; Martin, R. M.; Kauzlarich, S. M.; Pickett, W. E. *Phys. Rev. B* **2002**, *65*.
211. Kim, H.; Huang, Q.; Lynn, J. W.; Kauzlarich, S. M. *J. Solid State Chem.* **2002**, *168*, 162.
212. Kim, H.; Kauzlarich, S. M. *J. Solid State Chem.* **2005**, *178*, 1935.
213. Hu, Y.; Cerretti, G.; Kunz Wille, E. L.; Bux, S. K.; Kauzlarich, S. M. *J. Solid State Chem.* **2019**, *271*, 88.
214. Radziejowski, M.; Block, T.; Klenner, S.; Zhang, Y.; Fokwa, B. P. T.; Janka, O. *Inorg. Chem. Front.* **2019**, *6*, 137.
215. Siemens, D. P.; Delcastillo, J.; Potter, W.; Webb, D. J.; Kuromoto, T. Y.; Kauzlarich, S. M. *Solid State Commun.* **1992**, *84*, 1029.
216. Delcastillo, J.; Webb, D. J.; Kauzlarich, S. M.; Kuromoto, T. Y. *Phys. Rev. B* **1993**, *47*, 4849.
217. Rehr, A.; Kuromoto, T. Y.; Kauzlarich, S. M.; Delcastillo, J.; Webb, D. J. *Chem. Mater.* **1994**, *6*, 93.
218. Webb, D. J.; Cohen, R.; Klavins, P.; Shelton, R. N.; Chan, J. Y.; Kauzlarich, S. M. *J. Appl. Phys.* **1998**, *83*, 7192.
219. Fisher, I. R.; Wiener, T. A.; Bud'ko, S. L.; Canfield, P. C.; Chan, J. Y.; Kauzlarich, S. M. *Phys. Rev. B* **1999**, *59*, 13829.
220. Hu, Y.; Chen, C.-W.; Cao, H.; Makhmudov, F.; Grebenkemper, J. H.; Abdusalyamova, M. N.; Morosan, E.; Kauzlarich, S. M. *J. Am. Chem. Soc.* **2016**, *138*, 12422.
221. Carrillo-Cabrera, W.; Somer, M.; Peters, K.; von Schnering, H. G. *Chem. Ber.* **1996**, *129*, 1015.
222. Holm, A. P.; Kauzlarich, S. M.; Morton, S. A.; Waddill, G. D.; Pickett, W. E.; Tobin, J. G. *J. Am. Chem. Soc.* **2002**, *124*, 9894.
223. Holm, A. P.; Ozawa, T. C.; Kauzlarich, S. M.; Morton, S. A.; Waddill, G. D.; Tobin, J. G. *J. Solid State Chem.* **2005**, *178*, 262.
224. Rehr, A.; Kauzlarich, S. M. *J. Alloys Compd.* **1994**, *207*, 424.
225. Chan, J. Y.; Kauzlarich, S. M.; Klavins, P.; Shelton, R. N.; Webb, D. J. *Chem. Mater.* **1997**, *9*, 3132.
226. Payne, A. C.; Olmstead, M. M.; Kauzlarich, S. M.; Webb, D. J. *Chem. Mater.* **2001**, *13*, 1398.
227. Kim, H.; Chan, J. Y.; Olmstead, M. M.; Klavins, P.; Webb, D. J.; Kauzlarich, S. M. *Chem. Mater.* **2002**, *14*, 206.
228. Hermann, R. P.; Grandjean, F.; Kauzlarich, S. M.; Jiang, J.; Brown, S.; Long, G. J. *Inorg. Chem.* **2004**, *43*, 7005.
229. Hermann, R. P.; Grandjean, F.; Kafle, D.; Brown, D. E.; Johnson, C. E.; Kauzlarich, S. M.; Long, G. J. *Inorg. Chem.* **2007**, *46*, 10736.
230. Paik, J.-A.; Brandon, B.; Caillat, T.; Ewell, R.; Fleurial, J. P. *Proc. Nucl. Emerg. Tech. Space*, 2011; p 1. Paper 3695.
231. Grebenkemper, J. H.; Hu, Y.; Barrett, D.; Gogna, P.; Huang, C.-K.; Bux, S. K.; Kauzlarich, S. M. *Chem. Mater.* **2015**, *27*, 5791.
232. Kastbjerg, S.; Uvarov, C. A.; Kauzlarich, S. M.; Chen, Y.-S.; Nishibori, E.; Spackman, M. A.; Iversen, B. B. *Dalton Trans.* **2012**, *41*, 10347.
233. Uvarov, C. A.; Ortega-Alvarez, F.; Kauzlarich, S. M. *Inorg. Chem.* **2012**, *51*, 7617.
234. Yi, T.; Abdusalyamova, M. N.; Makhmudov, F.; Kauzlarich, S. M. *J. Mater. Chem.* **2012**, *22*, 14378.
235. Toberer, E. S.; Cox, C. A.; Brown, S. R.; Ikeda, T.; May, A. F.; Kauzlarich, S. M.; Snyder, G. J. *Adv. Funct. Mater.* **2008**, *18*, 2795.
236. Cox, C. A.; Toberer, E. S.; Levchenko, A. A.; Brown, S. R.; Snyder, G. J.; Navrotsky, A.; Kauzlarich, S. M. *Chem. Mater.* **2009**, *21*, 1354.
237. Uvarov, C. A.; Abdusalyamova, M. N.; Makhmudov, F.; Star, K.; Fleurial, J. P.; Kauzlarich, S. M. *Sci. Adv. Mater.* **2011**, *3*, 652.
238. Yu, C.; Chen, Y.; Xie, H. H.; Snyder, G. J.; Fu, C. G.; Xu, J. S.; Zhao, X. B.; Zhu, T. J. *Appl. Phys. Express* **2012**, *5*, 031801.
239. Brown, S. R.; Kauzlarich, S. M.; Gascoin, F.; Snyder, G. J. *Chem. Mater.* **2006**, *18*, 1873.
240. Chan, J. Y.; Olmstead, M. M.; Kauzlarich, S. M.; Webb, D. J. *Chem. Mater.* **1998**, *10*, 3583.
241. Fisher, I. R.; Bud'ko, S. L.; Song, C.; Canfield, P. C.; Ozawa, T. C.; Kauzlarich, S. M. *Phys. Rev. Lett.* **2000**, *85*, 1120.
242. Janka, O.; Pöttgen, R. *Z. Naturforsch.* **2020**, *75b*, 421.
243. Baker, T. W.; Williams, J. *Acta Crystallogr.* **1955**, *8*, 519.
244. Klemm, W.; Kunze, D. *Systems of Alkali and Alkaline Earth Metals*; vol. 2; The Chemical Society: London, 1967.
245. Baenziger, N. C.; Rundle, R. E. *Acta Crystallogr.* **1949**, *2*, 258.
246. Krypyakevych, P. I.; Tylkina, M. A.; Savitskii, E. M. *Sov. Phys. Crystallogr.* **1961**, *6*, 94.
247. Laube, E.; Nowotny, H. *Monatsh. Chem.* **1962**, *93*, 681.
248. Gladyshevskii, E. I.; Krypyakevych, P. I.; Frankevich, D. P. *Sov. Phys. Crystallogr.* **1964**, *8*, 628.
249. Raeuchle, R. F.; Rundle, R. E. *Acta Crystallogr.* **1952**, *5*, 85.
250. Zalkin, A.; Sands, D. E.; Bedford, R. G.; Krikorian, O. H. *Acta Crystallogr.* **1961**, *14*, 63.
251. Krypyakevych, P. I.; Gladyshevskii, E. I. *Dokl. Akad. Nauk SSSR* **1955**, *104*, 82.
252. Gladyshevskii, E. I.; Krypyakevych, P. I. *Sov. Phys. Crystallogr.* **1957**, *2*, 730.
253. Raeuchle, R. F.; von Batchelder, F. W. *Acta Crystallogr.* **1955**, *8*, 691.
254. von Batchelder, F. W.; Raeuchle, R. F. *Acta Crystallogr.* **1957**, *10*, 648.
255. von Batchelder, F. W.; Raeuchle, R. F. *Acta Crystallogr.* **1958**, *11*, 122.
256. Rodewald, U. C.; Chevalier, B.; Pöttgen, R. *J. Solid State Chem.* **2007**, *180*, 1720.
257. Landelli, A. *Natl. Phys. Lab. U.K., Symp.* 1951; p 3F2.
258. Peterson, D. T.; Diljak, P. F.; Vold, C. L. *Acta Crystallogr.* **1956**, *9*, 1036.
259. Krypyakevych, P. I.; Terekhova, V. F.; Zarechnyuk, O. S.; Burov, I. V. *Sov. Phys. Crystallogr.* **1963**, *8*.
260. Krypyakevych, P. I.; Evdokimenko, V. I.; Zalutskii, I. I. *Dopov. Akad. Nauk Ukr. RSR* **1964**, *5*, 766.
261. Krypyakevych, P. I.; Evdokimenko, V. I.; Gladyshevskii, E. I. *Sov. Phys. Crystallogr.* **1964**, *9*, 330.
262. Krypiakewytsch, P. I.; Evdokimenko, V. I. *Z. Anorg. Allg. Chem.* **1967**, *355*, 104.
263. Caro, P. J. *Less-Common Met.* **1965**, *8*, 235.
264. Hellnet, E.; Laves, F. *Z. Kristallogr.* **1943**, *105*, 134.
265. Nowotny, H. *Metallforschung* **1946**, *1*, 31.
266. Buschow, K. H. J. *Solid State Commun.* **1975**, *17*, 891.
267. Hlukhyy, V.; Pöttgen, R. *Z. Naturforsch.* **2004**, *59b*, 943.
268. Akhtar, D.; Gopalan, R.; Rajasekharan, T. P. *Z. Metallkd.* **1987**, *78*, 201.
269. Rossi, A.; Landelli, A. *Atti Accad. Naz. Lincei Cl. Sci. Fis. Mat. Nat. Rend.* **1934**, *19*, 415.
270. Range, K.-J.; Hafner, P. *J. Alloys Compd.* **1992**, *183*, 430.
271. Range, K.-J.; Hafner, P. *J. Alloys Compd.* **1993**, *191*, L5.
272. Hlukhyy, V.; Rodewald, U. C.; Hoffmann, R.-D.; Pöttgen, R. *Z. Naturforsch.* **2004**, *59b*, 251.
273. Makongo, J. P. A.; Kudla, C.; Prots, Y.; Niewa, R.; Burkhardt, U.; Kreiner, G. *Z. Kristallogr. - New Cryst. Struct.* **2005**, *220*, 309.
274. Haucke, W. *Naturwissenschaften* **1938**, *26*, 577.
275. Buckley, R. A.; Axon, H. J.; Conacher, J. *J. Inst. Met.* **1960**, *88*, 225.
276. Bronger, W.; Klemm, W. *Z. Anorg. Allg. Chem.* **1962**, *319*, 58.

277. Kohlmann, H.; Renaudin, G.; Yvon, K.; Wannek, C.; Harbrecht, B. *J. Solid State Chem.* **2005**, *178*, 1292.
278. Liu, G.; Xi, S.; Ran, G.; Zuo, K.; Li, P.; Zhou, J. *J. Alloys Compd.* **2008**, *448*, 206.
279. Zumdick, M. F.; Hoffmann, R.-D.; Pöttgen, R. *Z. Naturforsch.* **1999**, *54b*, 45.
280. Smetana, V.; Corbett, J. D.; Miller, G. J. *Acta Crystallogr.* **2014**, *C70*, 355.
281. Kinzhibalo, V. V.; Tyvanchuk, A. T.; Mel'nyk, E. V.; Rykhal', R. M. *Visn. Lviv. Derzh. Univ., Ser. Khim.* **1988**, *29*, 17.
282. Iandelli, A. *J. Alloys Compd.* **1994**, *203*, 137.
283. Pöttgen, R.; Hoffmann, R.-D.; Renger, J.; Rodewald, U. C.; Möller, M. H. *Z. Anorg. Allg. Chem.* **2000**, *626*, 2257.
284. Fickenscher, T.; Pöttgen, R. *J. Solid State Chem.* **2001**, *161*, 67.
285. Gibson, B. J.; Das, A.; Kremer, R. K.; Hoffmann, R.-D.; Pöttgen, R. *J. Phys. Condens. Matter* **2002**, *14*, 5173.
286. Kersting, M.; Niehaus, O.; Hoffmann, R.-D.; Pöttgen, R. *Z. Kristallogr.* **2013**, *228*, 643.
287. Kersting, M.; Niehaus, O.; Hoffmann, R.-D.; Rodewald, U. C.; Pöttgen, R. *Z. Kristallogr.* **2014**, *229*, 285.
288. Stein, S.; Kersting, M.; Heletta, L.; Pöttgen, R. *Z. Naturforsch.* **2017**, *72b*, 447.
289. Kersting, M.; Rodewald, U. C.; Pöttgen, R. *Z. Kristallogr.* **2015**, *230*, 151.
290. Zintl, E.; Haucke, W. *Z. Elektrochem. Angew. Phys. Chem.* **1938**, *44*, 104.
291. Iandelli, A.; Palenzona, A. *J. Less-Common Met.* **1967**, *12*, 333.
292. Bruzzone, G.; Ferretti, M.; Merlo, F. *J. Less-Common Met.* **1985**, *114*, 305.
293. Sanderson, M. J.; Baenziger, N. C. *Acta Crystallogr.* **1953**, *6*, 627.
294. Makarov, E. S.; Vinogradov, S. I. *Sov. Phys. Crystallogr.* **1956**, *1*, 499.
295. Kal, S.; Stoyanov, E.; Groy, T. L.; Haussermann, U. *Acta Crystallogr.* **2007**, *C63*, i96.
296. Haucke, W. *Z. Anorg. Allg. Chem.* **1940**, *244*, 17.
297. Baenziger, N. C.; Conant, J. W. *Acta Crystallogr.* **1956**, *9*, 361.
298. Bruzzone, G.; Merlo, F. *J. Less-Common Met.* **1983**, *92*, 75.
299. Laube, E. *Monatsh. Chem.* **1966**, *97*, 1568.
300. Siegrist, T.; Le Page, Y. *J. Less-Common Met.* **1987**, *127*, 189.
301. Olivier, M.; Siegrist, T.; McAlister, S. P. *J. Magn. Magn. Mater.* **1987**, *66*, 281.
302. Buschow, K. H. J. *J. Less-Common Met.* **1966**, *11*, 204.
303. Deryagin, A.; Ulyanov, A.; Kudrevatykh, N.; Barabanova, E.; Bashkov, Y.; Andreev, A.; Tarasov, E. *Phys. Status Solidi A* **1974**, *23*, K15.
304. Ray, A.; Strnat, K. *IEEE Trans. Magn.* **1972**, *8*, 516.
305. Ostertag, W.; Strnat, K. L. *Acta Crystallogr.* **1966**, *21*, 560.
306. Iandelli, A.; Palenzona, A. *J. Less-Common Met.* **1965**, *9*, 1.
307. Iandelli, A.; Botti, E. *Gazz. Chim. Ital.* **1937**, *67*, 638.
308. Laube, E.; Nowotny, H. *Monatsh. Chem.* **1963**, *94*, 162.
309. Chao, C. C.; Luo, H. L.; Duwez, P. *J. Appl. Phys.* **1964**, *35*, 257.
310. Hori, T.; Nakagawa, Y. *J. Physical Soc. Japan* **1964**, *19*, 1255.
311. Heike, W.; Schramm, J.; Vaupel, O. *Metallwirtsch. Metallwiss. Metalltech.* **1936**, *15*, 655.
312. Gross, N.; Kotzyba, G.; Künnen, B.; Jeitschko, W. *Z. Anorg. Allg. Chem.* **2001**, *627*, 155.
313. Nowotny, H.; Bauer, E.; Stempf, A. *Monatsh. Chem.* **1951**, *82*, 1086.
314. Owen, E. A.; Preston, G. D. *Lond. Edinb. Dubl. Phil. Mag.* **1926**, *2*, 1266.
315. Iwasaki, H.; Fujimura, T.; Ichikawa, M.; Endo, S.; Wakatsuki, M. *J. Phys. Chem. Solid* **1985**, *46*, 463.
316. Daszkiewicz, M.; Swatek, P.; Kaczorowski, D. *J. Alloys Compd.* **2012**, *517*, 26.
317. Nasch, T.; Jeitschko, W.; Rodewald, U. C. *Z. Naturforsch.* **1997**, *52b*, 1023.
318. Gross, N.; Nasch, T.; Jeitschko, W. *J. Solid State Chem.* **2001**, *161*, 288.
319. Jia, S.; Ni, N.; Samolyuk, G. D.; Safa-Sefat, A.; Dennis, K.; Ko, H.; Miller, G. J.; Bud'ko, S. L.; Canfield, P. C. *Phys. Rev. B* **2008**, *77*, 104408.
320. Gross, N.; Block, G.; Jeitschko, W. *Chem. Mater.* **2002**, *14*, 2725.
321. Iandelli, A. *J. Alloys Compd.* **1992**, *182*, 87.
322. Mishra, T.; Pöttgen, R. *Intermetallics* **2011**, *19*, 947.
323. Mishra, T.; Heymann, G.; Huppertz, H.; Pöttgen, R. *Intermetallics* **2012**, *20*, 110.
324. Mishra, T.; Lin, Q.; Corbett, J. D. *Inorg. Chem.* **2013**, *52*, 13623.
325. Lin, Q.; Mishra, T.; Corbett, J. D. *J. Am. Chem. Soc.* **2013**, *135*, 11023.
326. Gerke, B.; Hoffmann, R.-D.; Pöttgen, R. *Z. Anorg. Allg. Chem.* **2013**, *639*, 2444.
327. Gerke, B.; Hoffmann, R.-D.; Pöttgen, R. *Z. Anorg. Allg. Chem.* **2015**, *641*, 2174.
328. Gerke, B.; Janka, O.; Pöttgen, R. *Z. Anorg. Allg. Chem.* **2014**, *640*, 2747.
329. Ferro, R. *Acta Crystallogr.* **1954**, *7*, 781.
330. Iandelli, A.; Ferro, R. *Gazz. Chim. Ital.* **1954**, *84*, 463.
331. Iandelli, A.; Rolla, S. L. *Atti Accad. Naz. Lincei Cl. Sci. Fis. Mat. Nat. Rend.* **1960**, *29*, 62.
332. Bruzzone, G.; Ruggiero, A. F.; Bonino, G. B. *Atti Accad. Naz. Lincei Cl. Sci. Fis. Mat. Nat. Rend.* **1962**, *33*.
333. Kuz'ma, Y. B.; Uhryn, N. S. *Dopov. Akad. Nauk Ukr. RSR* **1966**, *8*, 1025.
334. Chao, C. C.; Duwez, P. E. *J. Appl. Phys.* **1966**, *37*, 2631.
335. Köster, W.; Meixner, J. *Z. Metallkd.* **1965**, *56*, 695.
336. Johnson, I.; Schablaske, R. V.; Tani, B.; Anderson, K. D. *Trans. Metall. Soc. AIME* **1964**, *230*, 1485.
337. Krumpelt, M.; Johnson, I.; Heiberger, J. J. *J. Less-Common Met.* **1969**, *18*, 35.
338. Bruzzone, G. *Gazz. Chim. Ital.* **1972**, *102*, 234.
339. Piao, S. Y.; Gómez, C. P.; Lidin, S. *Z. Naturforsch.* **2006**, *60b*, 644.
340. Xia, S.; Bobev, S. *Intermetallics* **2007**, *15*, 550.
341. Gómez, C. P.; Lidin, S. *Phys. Rev. B* **2003**, *68*, 024203.
342. Zaremba, R.; Rodewald, U. C.; Hoffmann, R.-D.; Pöttgen, R. *Monatsh. Chem.* **2007**, *138*, 523.
343. Gladyshevskii, E. I.; Fedorov, T. F.; Kuz'ma, Y. B.; Skolozdra, R. V. *Sov. Powder Metall. Met. Ceram.* **1966**, *5*, 305.
344. Johnscher, M.; Block, T.; Pöttgen, R. *Z. Anorg. Allg. Chem.* **2015**, *641*, 369.
345. Schappacher, F. M.; Pöttgen, R. *Monatsh. Chem.* **2008**, *139*, 1137.
346. Schappacher, F. M.; Rodewald, U. C.; Pöttgen, R. *Z. Naturforsch.* **2008**, *63b*, 1127.
347. Doğan, A.; Rayaprol, S.; Pöttgen, R. *J. Phys. Condens. Matter* **2007**, *19*, 076213.
348. Tuncel, S.; Rodewald, U. C.; Chevalier, B.; Pöttgen, R. *Z. Naturforsch.* **2007**, *62b*, 642.
349. Tuncel, S.; Hoffmann, R.-D.; Chevalier, B.; Matar, S. F.; Pöttgen, R. *Z. Anorg. Allg. Chem.* **2007**, *633*, 151.

350. Tuncel, S.; Chevalier, B.; Matar, S. F.; Pöttgen, R. *Z. Anorg. Allg. Chem.* **2007**, *633*, 2019.
351. Tuncel, S.; Chevalier, B.; Pöttgen, R. *Z. Naturforsch.* **2008**, *63b*, 600.
352. Li, L.; Niehaus, O.; Kersting, M.; Pöttgen, R. *Appl. Phys. Lett.* **2014**, *104*, 092416.
353. Rodewald, U. C.; Tuncel, S.; Chevalier, B.; Pöttgen, R. *Z. Anorg. Allg. Chem.* **2008**, *634*, 1011.
354. Solokha, P. G.; De Negri, S.; Pavlyuk, V. V.; Saccone, A. *Chem. Met. Alloys* **2009**, *2*, 39.
355. Couillaud, S.; Linsinger, S.; Duée, C.; Rougier, A.; Chevalier, B.; Pöttgen, R.; Bobet, J.-L. *Intermetallics* **2010**, *18*, 1115.
356. Tuncel, S.; Roquefère, J. G.; Stan, C.; Bobet, J.-L.; Chevalier, B.; Gaudin, E.; Hoffmann, R.-D.; Rodewald, U. C.; Pöttgen, R. *J. Solid State Chem.* **2009**, *182*, 229.
357. Linsinger, S.; Hermes, W.; Chevalier, B.; Couillaud, S.; Bobet, J.-L.; Eul, M.; Pöttgen, R. *Intermetallics* **2009**, *17*, 1028.
358. Kersting, M.; Matar, S. F.; Schwickert, C.; Pöttgen, R. *Z. Naturforsch.* **2012**, *67b*, 61.
359. Tappe, F.; Schwickert, C.; Linsinger, S.; Pöttgen, R. *Monatsh. Chem.* **2011**, *142*, 1087.
360. Engelbert, S.; Janka, O. *Intermetallics* **2018**, *96*, 84.
361. Zaremba, R.; Rodewald, U. C.; Pöttgen, R. *Z. Anorg. Allg. Chem.* **2006**, *632*, 2106.
362. Zaremba, R.; Rodewald, U. C.; Pöttgen, R. *Z. Naturforsch.* **2007**, *62b*, 1574.
363. Pöttgen, R.; Fugmann, A.; Hoffmann, R.-D.; Rodewald, U. C.; Niepmann, D. *Z. Naturforsch.* **2000**, *55b*, 155.
364. Stadler, F.; Fickenschner, T.; Pöttgen, R. *Z. Naturforsch.* **2001**, *56b*, 1241.
365. Fickenschner, T.; Rodewald, U. C.; Niepmann, D.; Mishra, R.; Eschen, M.; Pöttgen, R. *Z. Naturforsch.* **2005**, *60b*, 271.
366. Doğan, A.; Rayaprol, S.; Pöttgen, R. *J. Phys. Condens. Matter* **2006**, *19*, 026209.
367. Schappacher, F. M.; Hermes, W.; Pöttgen, R. *J. Solid State Chem.* **2009**, *182*, 265.
368. Guo, S.-P.; Meyers, J. J.; Tobash, P. H.; Bobev, S. J. *Solid State Chem.* **2012**, *192*, 16.
369. Rayaprol, S.; Doğan, A.; Pöttgen, R. *J. Phys. Condens. Matter* **2006**, *18*, 5473.
370. Block, T.; Pöttgen, R. *Monatsh. Chem.* **2019**, *150*, 975.
371. Niehaus, O.; Johnscher, M.; Block, T.; Gerke, B.; Pöttgen, R. *Z. Naturforsch.* **2016**, *71b*, 57.
372. Benndorf, C.; Eckert, H.; Janka, O. *Dalton Trans.* **2017**, *46*, 1083.
373. Tappe, F.; Pöttgen, R. *Rev. Inorg. Chem.* **2011**, *31*, 5.
374. Brauer, G.; Haucke, W. *Z. Phys. Chem.* **1936**, *33B*, 304.
375. Iandelli, A.; Ferro, R. *Atti Accad. Naz. Lincei Cl. Sci. Fis. Mat. Nat. Rend.* **1951**, *10*, 48.
376. Laube, E.; Nowotny, H. *Monatsh. Chem.* **1963**, *94*, 851.
377. Iandelli, A.; Palenzona, A.; Bonino, G. B. *Atti Accad. Naz. Lincei Cl. Sci. Fis. Mat. Nat. Rend.* **1964**, *37*, 165.
378. Kirchmayr, H. R. *Monatsh. Chem.* **1964**, *95*, 1667.
379. Lihl, F. *Monatsh. Chem.* **1955**, *86*, 186.
380. Pietrowsky, P. *Trans. Am. Inst. Min. Metall. Eng.* **1954**, *200*, 219.
381. Bittner, H.; Nowotny, H. *Monatsh. Chem.* **1952**, *83*, 287.
382. Bauer, E.; Nowotny, H.; Stempf, A. *Monatsh. Chem.* **1953**, *84*, 211.
383. Pušelj, M.; Ban, Z. *Z. Naturforsch.* **1977**, *32b*, 479.
384. Iandelli, A.; Ferro, R.; Rolla, S. L. *Atti Accad. Naz. Lincei Cl. Sci. Fis. Mat. Nat. Rend.* **1951**, *11*, 85.
385. Olcese, G. L.; Bonino, G. B. *Atti Accad. Naz. Lincei Cl. Sci. Fis. Mat. Nat. Rend.* **1963**, *35*, 48.
386. Laube, E.; Kusma, J. B. *Monatsh. Chem.* **1964**, *95*, 1504.
387. Rundle, R. E.; Wilson, A. S. *Acta Crystallogr.* **1949**, *2*, 148.
388. Nielsen, J. W.; Baenziger, N. C. *Acta Crystallogr.* **1954**, *7*, 277.
389. Beister, H.-J.; Syassen, K.; Deiseroth, H.-J.; Toelstede, D. *Z. Naturforsch.* **1993**, *48b*, 11.
390. Duwell, E. J.; Baenziger, N. C. *Acta Crystallogr.* **1955**, *8*, 705.
391. Deiseroth, H. J.; Strunck, A.; Bauhofer, W. *Z. Anorg. Allg. Chem.* **1988**, *558*, 128.
392. Bruzzone, G.; Bonino, G. B. *Atti Accad. Naz. Lincei Cl. Sci. Fis. Mat. Nat. Rend.* **1970**, *48*, 235.
393. Peyronel, G. *Gazz. Chim. Ital.* **1952**, *82*, 679.
394. Biehler, E.; Deiseroth, H. J. *Z. Anorg. Allg. Chem.* **1999**, *625*, 1073.
395. Pušelj, M.; Ban, Z. *Croat. Chem. Acta* **1978**, *51*, 75.
396. Bruzzone, G.; Merlo, F. *J. Less-Common Met.* **1974**, *35*, 153.
397. Basu, B.; Raju, G. B.; Suri, A. K. *Int. Mater. Rev.* **2006**, *51*, 352.
398. Hofmann, W.; Jäniche, W. *Naturwissenschaften* **1935**, *23*, 851.
399. Jones, M. E.; Marsh, R. E. *J. Am. Chem. Soc.* **1954**, *76*, 1434.
400. Kiessling, R. *Acta Chem. Scand.* **1949**, *3*, 595.
401. Norton, J. T.; Blumenthal, H.; Sindeband, S. J. *JOM* **1949**, *1*, 749.
402. Zhuravlev, N. N.; Stepanova, A. A. *Sov. Phys. Crystallogr.* **1958**, *3*, 76.
403. Binder, I.; Post, B. *Acta Crystallogr.* **1960**, *13*, 356.
404. Voroshnin, L. G.; Lyakhovich, L. S.; Panich, G. G.; Protasevich, G. F. *Met. Sci. Heat Treat.* **1970**, *12*, 732.
405. Kiessling, R. *Acta Chem. Scand.* **1949**, *3*, 90.
406. Steinitz, R.; Binder, I.; Moskowit, D. *JOM* **1952**, *4*, 983.
407. Obrowski, W. *Naturwissenschaften* **1961**, *48*, 428.
408. Kiessling, R. *Acta Chem. Scand.* **1949**, *3*, 603.
409. Castellano, R. N. *Mater. Res. Bull.* **1972**, *7*, 261.
410. Bauer, J.; Debuigne, J. *C.R. Acad. Sci., Ser. C* **1973**, *277*, 851.
411. Cannon, J. F.; Cannon, D. M.; Tracy Hall, H. *J. Less-Common Met.* **1977**, *56*, 83.
412. Howlett, B. *J. Inst. Met.* **1959**, *88*, 91.
413. Chipaux, R.; Larroque, J.; Beauvy, M. *J. Less-Common Met.* **1989**, *153*, 1.
414. McDonald, B. J.; Stuart, W. I. *Acta Crystallogr.* **1960**, *13*, 447.
415. Nagamatsu, J.; Nakagawa, N.; Muranaka, T.; Zenitani, Y.; Akimitsu, J. *Nature* **2001**, *410*, 63.
416. Mudgel, M.; Awana, V. P. S.; Kishan, H.; Felner, I.; Alvarez, D. G. A.; Bhalla, G. L. *J. Appl. Phys.* **2009**, *105*, 07E313.
417. Gavaler, J. R.; Janocko, M. A.; Jones, C. K. *J. Appl. Phys.* **1974**, *45*, 3009.
418. Testardi, L. R.; Wernick, J. H.; Royer, W. A. *Solid State Commun.* **1974**, *15*, 1.
419. Aronsson, B.; Stenberg, E.; Åselius, J. *Acta Chem. Scand.* **1960**, *14*, 733.
420. Bragg, W. L. *Proc. R. Soc. Lond.* **1914**, *89*, 468.
421. Bertaut, F.; Blum, P. *C. R. Acad. Sci.* **1953**, *236*, 1055.
422. Zachariasen, W. *Acta Crystallogr.* **1948**, *1*, 265.

423. Aminoff, G. Z. *Kristallogr.* **1923**, *58*, 203.
424. Frueh, A., Jr. *Acta Crystallogr.* **1951**, *4*, 66.
425. Bjurström, T.; Arnfelt, H. Z. *Phys. Chem.* **1929**, *4B*, 469.
426. Kiessling, R. *Acta Chem. Scand.* **1947**, *1*, 893.
427. Åselius, J. *Acta Chem. Scand.* **1960**, *14*, 2169.
428. Spear, K. E.; Gilles, P. W. *High Temp. Sci.* **1969**, *1*, 86.
429. Bertaut, F.; Blum, P. C. R. *Acad. Sci.* **1949**, *229*, 666.
430. Pauling, L.; Weinbaum, S. Z. *Kristallogr.* **1934**, *87*, 181.
431. Richards, S. M.; Kaspar, J. S. *Acta Crystallogr.* **1969**, *B25*, 237.
432. Oesterreicher, H.; Spada, F.; Abache, C. *Mater. Res. Bull.* **1984**, *19*, 1069.
433. Herbst, J. F.; Croat, J. J.; Pinkerton, F. E.; Yelon, W. B. *Phys. Rev. B* **1984**, *29*, 4176.
434. Sinnema, S.; Radwanski, R. J.; Franse, J. J. M.; de Mooij, D. B.; Buschow, K. H. J. *J. Magn. Magn. Mater.* **1984**, *44*, 333.
435. Spada, F.; Abache, C.; Oesterreicher, H. *J. Less-Common Met.* **1984**, *99*, L21.
436. Abache, C.; Oesterreicher, H. *J. Appl. Phys.* **1985**, *57*, 4112.
437. Herbst, J. F.; Croat, J. J.; Yelon, W. B. *J. Appl. Phys.* **1985**, *57*, 4086.
438. Herbst, J. F.; Yelon, W. B. *J. Appl. Phys.* **1985**, *57*, 2343.
439. Buschow, K. H. J.; de Mooij, D. B.; Sinnema, S.; Radwanski, R. J.; Franse, J. J. M. *J. Magn. Magn. Mater.* **1985**, *51*, 211.
440. Hirose, S.; Matsuura, Y.; Yamamoto, H.; Fujimura, S.; Sagawa, M.; Yamauchi, H. *J. Appl. Phys.* **1986**, *59*, 873.
441. Huang, M. Q.; Boltich, E. B.; Wallace, W. E.; Oswald, E. *J. Magn. Magn. Mater.* **1986**, *60*, 270.
442. Sobczak, R.; Rogl, P. *J. Solid State Chem.* **1979**, *27*, 343.
443. Rogl, P. *Mater. Res. Bull.* **1978**, *13*, 519.
444. Rogl, P.; Nowotny, H. *Monatsh. Chem.* **1975**, *106*, 381.
445. Stepanchikova, G. F.; Kuz'ma, Y. B. *Visn. Lviv. Derzh. Univ., Ser. Khim.* **1977**, *19*, 37.
446. Kuz'ma, Y. B.; Svarichevska, S. I. *Dopov. Akad. Nauk Ukr. RSR* **1972**, *10*, 166.
447. Kuz'ma, Y. B. *Sov. Phys. Crystallogr.* **1970**, *15*, 312.
448. Kuz'ma, Y. B. *Dopov. Akad. Nauk Ukr. RSR* **1970**, *8*, 756.
449. Ostermann, F. *Anwendungstechnologie Aluminium*, Springer Vieweg: Berlin, Heidelberg, 2014.
450. Puhakainen, K.; Boström, M.; Groy, T. L.; Häussermann, U. *J. Solid State Chem.* **2010**, *183*, 2528.
451. Tebbe, K.-F.; Schnering, H. G.; Rüter, B.; Rabeneck, G. *Z. Naturforsch.* **1973**, *28b*, 600.
452. Hansen, D. A.; Smith, J. F. *Acta Crystallogr.* **1968**, *B24*, 913.
453. Ehrenberg, H.; Pauly, H.; Knapp, M.; Gröbner, J.; Mirkovic, D. *J. Solid State Chem.* **2004**, *177*, 227.
454. Suryanarayana, C.; Tiwari, S. K.; Anantharaman, T. R. *Z. Metallkd.* **1978**, *69*, 155.
455. Nowotny, H.; Wormnes, E.; Mohrheim, A. *Z. Metallkd.* **1940**, *32*, 39.
456. Nagorsen, G.; Posch, H.; Schäfer, H.; Weiss, A. *Z. Naturforsch.* **1969**, *24b*, 1191.
457. Cordier, G.; Czech, E.; Schäfer, H. *Z. Naturforsch.* **1984**, *39b*, 421.
458. Cordier, G.; Czech, E.; Schäfer, H. *Z. Naturforsch.* **1982**, *37b*, 1442.
459. Miller, G. J.; Li, F.; Franzen, H. F. *J. Am. Chem. Soc.* **1993**, *115*, 3739.
460. Andress, K. R.; Alberti, E. *Z. Metallkd.* **1935**, *27*, 126.
461. Nowotny, H.; Wesenberg, H. *Z. Metallkd.* **1939**, *31*, 363.
462. Buschow, K. H. J.; Van Vucht, J. H. N. *Philips Res. Rep.* **1967**, *22*, 233.
463. Nowotny, H. N. *Z. Metallkd.* **1942**, *34*, 22.
464. Buschow, K. H. J. *Philips Res. Rep.* **1965**, *20*, 337.
465. Cattaneo, E. *Z. Phys. B: Condens. Matter* **1986**, *64*, 305.
466. Walker, E.; Purwins, H. G.; Landolt, M.; Hulliger, F. *J. Less-Common Met.* **1973**, *33*, 203.
467. Buschow, K. H. J.; van Daal, H. J. *Phys. Rev. Lett.* **1969**, *23*, 408.
468. Forgan, E. M.; Rainford, B. D.; Lee, S. L.; Abell, J. S.; Bi, Y. *J. Phys. Condens. Matter* **1990**, *2*, 10211.
469. White, J. A.; Williams, H. J.; Wernick, J. H.; Sherwood, R. C. *Phys. Rev.* **1963**, *131*, 1039.
470. Berton, A.; Chaussy, J.; Cornut, B.; Lasjaunias, J. L.; Odin, J.; Peyrard, J. *J. Magn. Magn. Mater.* **1980**, *15–18, Part 1*, 379.
471. Borchi, E.; De Gennaro, S.; Taddel, C. *Phys. Rev. B* **1977**, *15*, 4528.
472. Sera, M.; Satoh, T.; Kasuya, T. *J. Magn. Magn. Mater.* **1987**, *63–64*, 82.
473. Mader, K. H.; Swift, W. M. *J. Phys. Chem. Solid* **1968**, *29*, 1759.
474. Buschow, K. H. J.; Vandall, H. J. *Solid State Commun.* **1970**, *8*, 363.
475. Andres, K.; Graebner, J. E.; Ott, H. R. *Phys. Rev. Lett.* **1975**, *35*, 1779.
476. Dwight, A. E. *J. Less-Common Met.* **1984**, *102*, L9.
477. Hulliger, F. *J. Alloys Compd.* **1995**, *218*, 44.
478. Hulliger, F. *J. Alloys Compd.* **1995**, *229*, 265.
479. Hulliger, F. *J. Alloys Compd.* **1993**, *200*, 75.
480. Hulliger, F. *J. Alloys Compd.* **1993**, *196*, 225.
481. Xue, B.; Schwer, H.; Hulliger, F. *Acta Crystallogr.* **1994**, *C50*, 338.
482. Schwer, H.; Hulliger, F. *J. Alloys Compd.* **1997**, *259*, 249.
483. Perltz, H.; Westgren, A. *Arkiv Kemi Min. Geol.* **1943**, *16B*, 1.
484. Kilaas, R.; Radmilovic, V.; Dahmen, U. *Mater. Res. Soc. Symp. Proc.* **2001**, *589*, 273.
485. Mondolfo, L. F. *Al-Cu-Mg Aluminum-Copper-Magnesium system*, Butterworths: London, Boston, 1976.
486. Laves, F.; Witte, H. *Metallwirtschaft* **1936**, *15*, 15.
487. Cuisiat, F.; Duval, P.; Graf, R. *Scr. Metall.* **1984**, *18*, 1051.
488. Yan, J.; Chunzhi, L.; Minggao, Y. *J. Mater. Sci. Lett.* **1990**, *9*, 421.
489. Heying, B.; Hoffmann, R.-D.; Pöttgen, R. *Z. Naturforsch.* **2005**, *60b*, 491.
490. Pöttgen, R.; Lukachuk, M.; Hoffmann, R.-D. *Kristallogr.* **2006**, *221*, 435.
491. Rykhal', R. M.; Zarechnyuk, O. S. *Dopov. Akad. Nauk Ukr. RSR* **1971**, 854.
492. Rykhal', R. M.; Zarechnyuk, O. S.; Pyshchuk, A. V. *Visn. Lviv. Derzh. Univ., Ser. Khim.* **1972**, *14*, 13.
493. Rykhal', R. M.; Zarechnyuk, O. S.; Yarmolyuk, Y. P. *Sov. Phys. Crystallogr.* **1972**, *17*, 453.
494. Rykhal', R. M.; Zarechnyuk, O. S.; Pyshchuk, A. V. *Dopov. Akad. Nauk Ukr. RSR* **1973**, 568.
495. Rykhal', R. M.; Zarechnyuk, O. S. *Dopov. Akad. Nauk Ukr. RSR* **1977**, 375.

496. Bruzzone, G.; Ferretti, M.; Merlo, F.; Olcese, G. L. *Lanthanide and Actinide Res.* **1986**, *1*, 153.
497. Gladyshevskii, R. E.; Parthé, E. Z. *Kristallogr.* **1992**, *198*, 291.
498. Gladyshevskii, R. E.; Parthé, E. Z. *Kristallogr.* **1993**, *203*, 349.
499. Tang, C.; Du, Y.; Xu, H. H.; Xiong, W.; Zhang, L. J.; Zheng, F.; Zhou, H. Y. *Intermetallics* **2008**, *16*, 432.
500. Radziejowski, M.; Stegemann, F.; Doerenkamp, C.; Matar, S. F.; Eckert, H.; Dosche, C.; Wittstock, G.; Janka, O. *Inorg. Chem.* **2019**, *58*, 7010.
501. Stegemann, F.; Block, T.; Klenner, S.; Zhang, Y.; Fokwa, B. P. T.; Timmer, A.; Mönig, H.; Doerenkamp, C.; Eckert, H.; Janka, O. *Chem. A Eur. J.* **2019**, *25*, 10735.
502. Hoffmann, R.-D.; Pöttgen, R. *Chem. A Eur. J.* **2001**, *7*, 382.
503. Zarechnyuk, O. S.; Yanson, T. I.; Ostrovska, O. I.; Shevchuk, L. P. *Visn. Lviv. Derzh. Univ., Ser. Khim* **1988**, *29*, 44.
504. Niemann, S.; Jeitschko, W. Z. *Metallkd.* **1994**, *85*, 345.
505. Yanson, T. I.; Manyako, M. B.; Bodak, O.; Cerny, R.; Pacheco, J. V.; Yvon, K. Z. *Kristallogr.* **1994**, *209*, 922.
506. Thiede, V. M. T.; Jeitschko, W.; Niemann, S.; Ebel, T. J. *Alloys Compd.* **1998**, *267*, 23.
507. Kangas, M. J.; Treadwell, L. J.; Haldolaarachchige, N.; McAlpin, J. D.; Young, D. P.; Chan, J. Y. *J. Solid State Chem.* **2013**, *197*, 523.
508. Eustermann, F.; Hoffmann, R.-D.; Janka, O. Z. *Kristallogr.* **2017**, *232*, 573.
509. Eustermann, F.; Gausebeck, S.; Dosche, C.; Haensch, M.; Wittstock, G.; Janka, O. *Crystals* **2018**, *8*, 169.
510. Stegemann, F.; Stahl, J.; Bartsch, M.; Zacharias, H.; Johrendt, D.; Janka, O. *Chem. Sci.* **2019**, *10*, 11086.
511. Radziejowski, M.; Stegemann, F.; Block, T.; Stahl, J.; Johrendt, D.; Janka, O. *J. Am. Chem. Soc.* **2018**, *140*, 8950.
512. Baenziger, N. C.; Moriarty, J. L., Jr. *Acta Crystallogr.* **1961**, *14*, 948.
513. Haszko, S. E. *Trans. Metall. Soc. AIME* **1961**, *221*, 201.
514. Makarov, E. S.; Levdik, V. A. *Sov. Phys. Crystallogr.* **1956**, *1*, 506.
515. Bruzzone, G. *Boll. Sci. Fac. Chim. Ind. Bologna* **1966**, *24*, 113.
516. Yatsenko, S. P.; Semyannikov, A. A.; Semenov, B. G.; Chuntanov, K. A. *J. Less-Common Met.* **1979**, *64*, 185.
517. Kimmel, G.; Dayan, D.; Grill, A.; Pelleg, J. *J. Less-Common Met.* **1980**, *75*, 133.
518. dos Reis, R. D.; da Silva, L. M.; dos Santos, A. O.; Medina, A. M.; Cardoso, L. P.; Gandra, F. G. *J. Phys. Condens. Matter* **2010**, *22*, 486002.
519. Baenziger, N. C.; Moriarty, J. L., Jr. *Acta Crystallogr.* **1961**, *14*, 946.
520. Cable, J. W.; Koehler, W. C.; Wollan, E. O. *Phys. Rev.* **1964**, *136*, A240.
521. Schob, O.; Parthe, E. *Acta Crystallogr.* **1965**, *19*, 214.
522. Parthé, E.; Hohnke, D.; Jeitschko, W.; Schob, O. *Naturwissenschaften* **1965**, *52*, 155a.
523. Dwight, A. E.; Downey, J. W.; Conner, R. A., Jr. *Acta Crystallogr.* **1967**, *23*, 860.
524. Rieger, W.; Parthé, E. *Monatsh. Chem.* **1967**, *98*, 1935.
525. Krypyakevych, P. I.; Markiv, V. Y.; Dzyana, D. I. *Ukr. Fiz. Zh. Ukr. Ed.* **1964**, *9*, 908.
526. A. E. Dwight, Proc. 7th Rare Earth Res. Conf 1969, vol. 1.
527. Havinga, E. E.; Damsma, H.; Van Maaren, M. H. *J. Phys. Chem. Solid* **1970**, *31*, 2653.
528. Buschow, K. H. J. *J. Less-Common Met.* **1973**, *31*, 165.
529. Russell, A. M.; Roof, R. B.; Elliott, R. O.; Giessen, B. C. *J. Appl. Cryst.* **1976**, *9*, 244.
530. Schubert, K.; Bhan, S.; Burkhardt, W.; Gohle, R.; Meissner, H. G.; Pötzschke, M.; Stolz, E. *Naturwissenschaften* **1960**, *47*, 303.
531. Yatsenko, S. P.; Semenov, B. G.; Chuntanov, K. A. *Russ. Metall.* **1977**, *6*, 149.
532. Manory, R.; Pelleg, J.; Grill, A. *J. Less-Common Met.* **1978**, *61*, 293.
533. Mishima, Y.; Ochiai, S.; Suzuki, T. *Acta Metall.* **1985**, *33*, 1161.
534. Wood, E. A.; Compton, V. B.; Matthias, B. T.; Corenzwit, E. *Acta Crystallogr.* **1958**, *11*, 604.
535. Anderko, K. Z. *Metallkd.* **1958**, *49*, 165.
536. Schubert, K.; Meissner, H. G.; Pötzschke, M.; Rossteutscher, W.; Stolz, E. *Naturwissenschaften* **1962**, *49*, 57.
537. Pötzschke, M.; Schubert, K. Z. *Metallkd.* **1962**, *53*, 474.
538. Palenzona, A.; Franceschi, E. *J. Less-Common Met.* **1968**, *14*, 47.
539. Dzyana, D. I.; Krypyakevych, P. I. *Dopov. Akad. Nauk Ukr. RSR* **1969**, *3*, 247.
540. Hovestreydt, E.; Engel, N.; Klepp, K.; Chabot, B.; Parthé, E. *J. Less-Common Met.* **1982**, *85*, 247.
541. Rossi, D.; Mazzone, D.; Marazza, R.; Ferro, R. Z. *Anorg. Allg. Chem.* **1983**, *507*, 235.
542. Penc, B.; Hofmann, M.; Leciejewicz, J.; Szytula, A.; Zygmunt, A. *J. Alloys Compd.* **2000**, *305*, 24.
543. Hulliger, F. *J. Alloys Compd.* **1996**, *239*, 131.
544. Dwight, A. E.; Mueller, M. H.; Conner, R. A., Jr.; Downey, J. W.; Knott, H. W. *Trans. Metall. Soc. AIME* **1968**, *242*, 2075.
545. Andreev, A. V.; Bartashevich, M. I. *Phys. Met. Metallogr.* **1986**, *62*, 50.
546. Dwight, A. E. *J. Less-Common Met.* **1974**, *34*, 279.
547. Brabers, J. H. V. J.; de Boer, F. R.; Buschow, K. H. J. *J. Alloys Compd.* **1992**, *179*, 227.
548. Kraft, R.; Valldor, M.; Pöttgen, R. Z. *Naturforsch.* **2003**, *58b*, 827.
549. Dzyana, D. I.; Zarechnyuk, O. S. *Visn. Lviv. Derzh. Univ., Ser. Khim.* **1969**, *11*, 8.
550. Grin, Y. *Dopov. Akad. Nauk Ukr. RSR* **1982**, *2*, 76.
551. Sampathkumaran, E. V.; Gupta, L. C.; Vijayaraghavan, R.; Hatwar, T. K.; Ghatikar, M. N.; Padalia, B. D. *Mater. Res. Bull.* **1980**, *15*, 939.
552. Grin, Y. N.; Hiebl, K.; Rogl, P.; Noël, H. *J. Less-Common Met.* **1990**, *162*, 361.
553. Grin, Y. N.; Hiebl, K.; Rogl, P.; Eibler, R. *J. Less-Common Met.* **1986**, *115*, 367.
554. Grin, Y. N.; Rogl, P.; Hiebl, K.; Wagner, F. E.; Noël, H. *J. Solid State Chem.* **1987**, *70*, 168.
555. Grin, Y. N.; Rogl, P.; Hiebl, K. *J. Less-Common Met.* **1988**, *136*, 329.
556. Hellner, E.; Laves, F. Z. *Naturforsch.* **1947**, *2a*, 177.
557. Schubert, K.; Breimer, H.; Burkhardt, W.; Günzel, E.; Hauffler, R.; Lukas, H. L.; Vetter, H.; Wegst, J.; Wilkens, M. *Naturwissenschaften* **1957**, *44*, 229.
558. Moriarty, J. L., Jr.; Gordon, R. O.; Humphreys, J. E. *Acta Crystallogr.* **1965**, *19*, 285.
559. Bruzzone, G.; Ruggiero, A. F. *J. Less-Common Met.* **1964**, *7*, 368.
560. Palenzona, A. *J. Less-Common Met.* **1968**, *16*, 379.
561. Yatsenko, S. P.; Semyannikov, A. A.; Shakarov, H. O.; Fedorova, E. G. *J. Less-Common Met.* **1983**, *90*, 95.
562. Laves, F.; Wallbaum, H. J. Z. *Angew. Mineral.* **1942**, *4*, 17.
563. Kubiak, R. Z. *Anorg. Allg. Chem.* **1977**, *431*, 261.
564. Baela, W.; Szytula, A. *J. Less-Common Met.* **1988**, *138*, 123.
565. Iandelli, A. Z. *Anorg. Allg. Chem.* **1964**, *330*, 221.
566. Ferro, R.; Marazza, R.; Rambaldi, G. Z. *Metallkd.* **1974**, *65*, 37.
567. Rossi, D.; Ferro, R.; Contardi, V.; Marazza, R. Z. *Metallk.* **1977**, *68*, 493.
568. Sysa, L. V.; Zaremba, V. I.; Kalychak, Y. M.; Baranyak, V. M. *Visn. Lviv. Derzh. Univ., Ser. Khim.* **1988**, *29*, 32.

569. Zaremba, V. I.; Rodewald, U. C.; Lukachuk, M. Y.; Dubenskiy, V. P.; Heying, B.; Katoh, K.; Niide, Y.; Ochiai, A.; Pöttgen, R. *Monatsh. Chem.* **2006**, *137*, 249.
570. Ferro, R.; Marazza, R.; Rambaldi, G. *Z. Anorg. Allg. Chem.* **1974**, *410*, 219.
571. Buschow, K. H. J. *J. Less-Common Met.* **1975**, *39*, 185.
572. Kalychak, Y. M.; Bakar, A. M.; Gladyshevskii, E. I. *Izv. Vyssh. Uchebn. Zaved., Tsvetn. Metall.* **1989**, *3*, 95.
573. Kalychak, Y. M.; Zaremba, V. I.; Baranyak, V. M.; Zavali, P. Y.; Bruskov, V. A.; Sysa, L. V.; Dmytrakh, O. V. *Inorg. Mater.* **1990**, *26*, 74.
574. Peron, M. N.; Kergadallan, Y.; Rebizant, J.; Meyer, D.; Winand, J. M.; Zwirner, S.; Havela, L.; Nakotte, H.; Spirlet, J. C.; Kalvius, G. M.; Colineau, E.; Oddoue, J. L.; Jeandey, C.; Sanchez, J. P. *J. Alloys Compd.* **1993**, *201*, 203.
575. Pöttgen, R. *Z. Naturforsch.* **1994**, *49b*, 1525.
576. Nakotte, H.; Prokeš, K.; Brück, E.; Tang, N.; de Boer, F. R.; Svoboda, P.; Sechovsky, V.; Havela, L.; Winand, J. M.; Seref, A.; Rebizant, J.; Spirlet, J. C. *Physica B* **1994**, *201*, 247.
577. Hulliger, F.; Xue, B. Z. *J. Alloys Compd.* **1994**, *215*, 267.
578. Hulliger, F. *J. Alloys Compd.* **1995**, *217*, 164.
579. Pöttgen, R.; Kotzyba, G. *Z. Naturforsch.* **1996**, *51b*, 1248.
580. Hulliger, F. *J. Alloys Compd.* **1996**, *232*, 160.
581. Pereira, L. C. J.; Wastin, F.; Winand, J. M.; Kanellakopoulos, B.; Rebizant, J.; Spirlet, J. C.; Almeida, M. *J. Solid State Chem.* **1997**, *134*, 138.
582. Giovannini, M.; Michor, H.; Bauer, E.; Hilscher, G.; Rogl, P.; Ferro, R. *J. Alloys Compd.* **1998**, *280*, 26.
583. Zaremba, V. I.; Kaczorowski, D.; Nychyporuk, G. P.; Rodewald, U. C.; Pöttgen, R. *Solid State Sci.* **2004**, *6*, 1301.
584. Gladyshevskii, E. I.; Krypyakevych, P. I.; Teslyuk, M. Y.; Zarechnyuk, O. S.; Kuz'ma, Y. B. *Sov. Phys. Crystallogr.* **1961**, *6*, 207.
585. Blažina, Ž.; Drašner, A.; Ban, Z. *J. Nucl. Mater.* **1981**, *96*, 141.
586. Zaremba, V. I.; Baranyak, V. M.; Kalychak, Y. M. *Visn. Lviv. Derzh. Univ., Ser. Khim.* **1984**, *25*, 18.
587. Malik, S. K.; Vijayaraghavan, R.; Adroja, D. T.; Padalia, B. D.; Edelstein, A. S. *J. Magn. Magn. Mater.* **1990**, *92*, 80.
588. Nakamura, H.; Uenishi, A.; Ito, K.; Shiga, M.; Kuwai, T.; Sakurai, J. *J. Magn. Magn. Mater.* **1995**, *140-144*, 923.
589. Moriyoshi, C.; Shimomura, S.; Itoh, K.; Kojima, K.; Hiraoka, K. *J. Magn. Magn. Mater.* **2003**, *260*, 206.
590. Schmidt, S.; Hüfner, S.; Reinert, F.; Assmus, W. *Phys. Rev. B* **2005**, *71*, 195110.
591. Müller, H.; Bauer, E.; Gratz, E.; Yoshimura, K.; Nitta, T.; Mekata, M. *J. Magn. Magn. Mater.* **1988**, *76*, 159.
592. Felner, I.; Nowik, I.; Vaknin, D.; Potzel, U.; Moser, J.; Kalvius, G. M.; Wortmann, G.; Schmiester, G.; Hilscher, G.; Gratz, E.; Schmitzer, C.; Pillmayr, N.; Prasad, K. G.; de Waard, H.; Pinto, H. *Phys. Rev. B* **1987**, *35*, 6956.
593. Felner, I.; Nowik, I. *Phys. Rev. B* **1986**, *33*, 617.
594. Sarrao, J. L.; Immer, C. D.; Fisk, Z.; Booth, C. H.; Figueroa, E.; Lawrence, J. M.; Modler, R.; Cornelius, A. L.; Hundley, M. F.; Kwei, G. H.; Thompson, J. D.; Bridges, F. *Phys. Rev. B* **1999**, *59*, 6855.
595. Mito, T.; Nakamura, M.; Otani, M.; Koyama, T.; Wada, S.; Ishizuka, M.; Forthaus, M. K.; Lengsdorf, R.; Abd-Elmeguid, M. M.; Sarrao, J. L. *Phys. Rev. B* **2007**, *75*, 134401.
596. Severing, A.; Givord, F.; Boucherle, J. X.; Willers, T.; Rotter, M.; Fisk, Z.; Bianchi, A.; Fernandez-Diaz, M. T.; Stunault, A.; Rainford, B. D.; Taylor, J.; Goremychkin, E. *Phys. Rev. B* **2011**, *83*, 155112.
597. Hiraoka, K.; Yabuta, H.; Kojima, K.; Oikawa, K.; Kamiyama, T. *J. Magn. Magn. Mater.* **2007**, *310*, 380.
598. Zaremba, V. I.; Kalychak, Y. M.; Zavali, P. Y.; Bruskov, V. A. *Sov. Phys. Crystallogr.* **1991**, *36*, 801.
599. Lukachuk, M. Y.; Pöttgen, R. *Z. Naturforsch.* **2002**, *57b*, 1353.
600. Lukachuk, M. Y.; Heying, B.; Rodewald, U. C.; Pöttgen, R. *Heteroat. Chem.* **2005**, *16*, 364.
601. Tursina, A. I.; Kurenbaeva, Z. M.; Shtepa, D. V.; Nesterenko, S. N.; Noel, H. *Acta Crystallogr.* **2006**, *E62*, i80.
602. Zaremba, R.; Rodewald, U. C.; Pöttgen, R. *Monatsh. Chem.* **2007**, *138*, 819.
603. Zaremba, R.; Hermes, W.; Eul, M.; Pöttgen, R. *Z. Naturforsch.* **2008**, *63b*, 1447.
604. Provino, A.; Gschneidner, K. A., Jr.; Dhar, S. K.; Ferdeghini, C.; Mudryk, Y.; Manfrinetti, P.; Paudyal, D.; Pecharsky, V. K. *Acta Mater.* **2015**, *91*, 128.
605. Pustovoychenko, M.; Tyvanchuk, Y.; Hayduk, I.; Kalychak, Y. *Intermetallics* **2010**, *18*, 929.
606. Sojka, L.; Demchyna, M.; Belan, B.; Manyako, M.; Kalychak, Y. *Intermetallics* **2014**, *49*, 14.
607. Sojka, L.; Manyako, M.; Černý, R.; Ivanyk, M.; Belan, B.; Gladyshevskii, R.; Kalychak, Y. *Intermetallics* **2008**, *16*, 625.
608. Y. B. Tyvanchuk, V. I. Zaremba, V. I. Zaremba, V. I. Zaremba, R. Y. Serkiz, Abstr. 11th Int. Conf. Crystal Chem. Internet. Compd 2010, 139.
609. B. D. Belan, L. Sojka, M. B. Manyako, M. Ivanyk, R. Černý, R. E. Gladyshevskii, Y. M. Kalychak, Abstr. 10th Int. Conf. Crystal Chem. Internet. Compd 2007, 118.
610. Tyvanchuk, Y. B.; Dzevenko, M. V.; Kalychak, Y. M. *Visn. Lviv. Derzh. Univ., Ser. Khim.* **2012**, *53*, 127.
611. Jeitschko, W.; Nowotny, H.; Benesovsky, F. *Monatsh. Chem.* **1964**, *95*, 1040.
612. Haschke, H.; Nowotny, H.; Benesovsky, F. *Monatsh. Chem.* **1966**, *97*, 716.
613. Mitchell, A. W.; Lam, D. J. *J. Nucl. Mater.* **1974**, *52*, 125.
614. Zintl, E.; Neumayr, S. *Z. Elektrochem. Angew. Phys. Chem.* **1933**, *39*, 86.
615. Ferro, R. *Acta Crystallogr.* **1958**, *11*, 737.
616. Palenzona, A. *J. Less-Common Met.* **1966**, *10*, 290.
617. Moriarty, J. L., Jr.; Humphreys, J. E.; Gordon, R. O.; Baenziger, N. C. *Acta Crystallogr.* **1966**, *21*, 840.
618. Kim, S.-J.; Fässler, T. F. *Z. Anorg. Allg. Chem.* **2009**, *635*, 1925.
619. Palenzona, A.; Cirafici, S.; Canepa, F. *J. Less-Common Met.* **1985**, *114*, 311.
620. Delfino, S.; Saccone, A.; Mazzone, D.; Ferro, R. *J. Less-Common Met.* **1981**, *81*, 45.
621. Delfino, S.; Saccone, A.; Borzone, G.; Ferro, R. *J. Less-Common Met.* **1978**, *59*, 69.
622. Franceschi, E.; Palenzona, A. *J. Less-Common Met.* **1969**, *18*, 93.
623. Kraft, R.; Pöttgen, R. *Z. Anorg. Allg. Chem.* **2004**, *630*, 1738.
624. Kraft, R.; Pöttgen, R. *Z. Naturforsch.* **2005**, *60b*, 265.
625. Liu, S.; Corbett, J. D. *Inorg. Chem.* **2003**, *42*, 4898.
626. Kraft, R.; Rayaprol, S.; Sebastian, C. P.; Pöttgen, R. *Z. Naturforsch.* **2006**, *61b*, 159.
627. Lallement, R.; Lorenzelli, R.; Pascard, R. *C. R. Acad. Sci.* **1964**, *259*, 2442.
628. Atoji, M.; Kikuchi, M. *J. Chem. Phys.* **1969**, *51*, 3863.
629. Zachariasen, W. *Acta Crystallogr.* **1952**, *5*, 17.
630. Atoji, M.; Gschneidner, K. A., Jr.; Daane, A. H.; Rundle, R. E.; Spedding, F. H. *J. Am. Chem. Soc.* **1904**, *1958*, 80.
631. Brewer, L.; Krikorian, O. *J. Electrochem. Soc.* **1956**, *103*, 38.
632. Burdick, M. D.; Parker, H. S.; Roth, R. S.; McGandy, E. L. *J. Res. Natl. Bur. Stand.* **1955**, *54*, 217.
633. Pöttgen, R.; Jeitschko, W. *Inorg. Chem.* **1991**, *30*, 427.
634. Button, T. W.; McColm, I. J. *J. Less-Common Met.* **1984**, *97*, 237.
635. Hüfken, T.; Jeitschko, W. *J. Alloys Compd.* **1998**, *278*, 161.
636. Bauer, J.; Nowotny, H. *Monatsh. Chem.* **1971**, *102*, 1129.

637. Bodak, O. I.; Marusin, E. P. *Dopov. Akad. Nauk Ukr. RSR* **1979**, *12*, 1048.
638. Semenenko, K. N.; Putyatin, A. A.; Nikol'skaya, I. V.; Burnasheva, V. V. *Russ. J. Inorg. Chem.* **1983**, *28*, 943.
639. Jeitschko, W.; Gerss, M. H. *J. Less-Common Met.* **1986**, *116*, 147.
640. Jeitschko, W.; Behrens, R. K. *Z. Metallkd.* **1986**, *77*, 788.
641. Clark, N. J.; Mountford, R.; McColm, I. J. *J. Inorg. Nucl. Chem.* **1972**, *34*, 2729.
642. Nowotny, H.; Kieffer, R.; Benesovsky, F.; Laube, E. *Monatsh. Chem.* **1958**, *89*, 692.
643. J. D. Farr, M. G. Bowman, Carbides in Nuclear Energy Proc. Symp 1964, 1, 184.
644. Kotsanidis, P.; Yakinthos, J. K.; Gamari-Seale, E. *J. Less-Common Met.* **1989**, *152*, 287.
645. Schäfer, W.; Will, G.; Kotsanidis, P. A.; Yakinthos, J. K. *J. Magn. Magn. Mater.* **1990**, *88*, 13.
646. Schäfer, W.; Will, G.; Yakinthos, J. K.; Kotsanidis, P. A. *J. Alloys Compd.* **1992**, *180*, 251.
647. Pietrokowsky, P.; Duwez, P. E. *Nature* **1951**, *191*, 772.
648. Weill, A. R. *Nature* **1943**, *152*, 413.
649. Nowotny, H.; Lux, B.; Kudielka, H. *Monatsh. Chem.* **1956**, *87*, 447.
650. Schachner, H.; Cerwenka, E.; Nowotny, H. *Monatsh. Chem.* **1954**, *85*, 245.
651. Åmark, K.; Borén, B.; Westgren, A. *Metallwirtsch. Metallwiss. Metalltech.* **1936**, *15*, 835.
652. Parthe, E. *Acta Crystallogr.* **1960**, *13*, 868.
653. Mayer, I.; Shidlovsky, I. *Inorg. Chem.* **1969**, *8*, 1240.
654. Tchernev, D. I.; Narasimhan, K. S. V. L.; Steinfink, H. *IEEE Trans. Magn.* **1969**, *5*, 222.
655. Gladyshevskii, E. I. *Inorg. Mater.* **1965**, *1*, 868.
656. Gladyshevskii, E. I.; Krypyakevych, P. I. *Inorg. Mater.* **1965**, *1*, 644.
657. Zachariasen, W. *Acta Crystallogr.* **1949**, *2*, 94.
658. Brukl, C.; Nowotny, H.; Schob, O.; Benesovsky, F. *Monatsh. Chem.* **1961**, *92*, 781.
659. Gladyshevskii, E. I.; Krypyakevych, P. I. *J. Struct. Chem.* **1964**, *5*, 789.
660. Hohnke, D.; Parthe, E. *Acta Crystallogr.* **1966**, *20*, 572.
661. Benesovsky, F.; Nowotny, H.; Rieger, W.; Rassaerts, H. *Monatsh. Chem.* **1966**, *97*, 221.
662. Borén, B. *Arkiv Kemi Min. Geol.* **1934**, *11A*, 1.
663. McNeese, R. A.; Searcy, A. W. *J. Am. Chem. Soc.* **1955**, *77*, 5290.
664. Korst, W. L.; Finnie, L. N.; Searcy, A. W. *J. Phys. Chem.* **1957**, *61*, 1541.
665. Geller, S.; Wood, E. A. *Acta Crystallogr.* **1954**, *7*, 441.
666. Buddery, J. H.; Welch, A. J. E. *Nature* **1951**, *167*, 362.
667. Perri, J. A.; Binder, I.; Post, B. *J. Phys. Chem.* **1959**, *63*, 616.
668. Mayer, I. P.; Post, B.; Banks, E. *J. Phys. Chem.* **1962**, *66*, 693.
669. Mayer, I.; Felner, I. *J. Less-Common Met.* **1972**, *29*, 25.
670. Mayer, I.; Yanir, E.; Shidlovsky, I. *Inorg. Chem.* **1967**, *6*, 842.
671. Perri, J. A.; Banks, E.; Post, B. *J. Phys. Chem.* **1959**, *63*, 2073.
672. Brown, A.; Norreys, J. J. *Nature* **1959**, *183*, 673.
673. Jacobson, E. L.; Freeman, R. D.; Tharp, A. G.; Searcy, A. W. *J. Am. Chem. Soc.* **1956**, *78*, 4850.
674. Lindroth, D. O.; Brorsson, J.; Fransson, E.; Eriksson, F.; Palmqvist, A.; Erhart, P. *Phys. Rev. B* **2019**, *100*, 045206.
675. Baitinger, M.; Böhme, B.; Wagner, F. R.; Schwarz, U. *Z. Anorg. Allg. Chem.* **2020**, *646*, 1034.
676. Ban, Z.; Sikirica, M. *Acta Crystallogr.* **1965**, *18*, 594.
677. Bodak, O. I.; Gladyshevskii, E. I.; Krypyakevych, P. I. *Inorg. Mater.* **1961**, *1966*, 2.
678. Mayer, I.; Cohen, J.; Felner, I. *J. Less-Common Met.* **1973**, *30*, 181.
679. Rieger, W.; Parthe, E. *Monatsh. Chem.* **1969**, *100*, 444.
680. Ballestracci, R. *C. R. Seances Acad. Sci.* **1976**, *282*, 291.
681. Rossi, D.; Marazza, R.; Ferro, R. *J. Less-Common Met.* **1978**, *58*, 203.
682. Rossi, D.; Marazza, R.; Mazzone, D.; Ferro, R. *J. Less-Common Met.* **1978**, *59*, 79.
683. Marazza, R.; Ferro, R.; Rambaldi, G.; Zanicchi, G. *J. Less-Common Met.* **1977**, *53*, 193.
684. Hiebl, K.; Horvath, C.; Rogl, P.; Sienko, M. *J. Magn. Magn. Mater.* **1983**, *37*, 287.
685. Ślaski, M.; Leciejewicz, J.; Szytuła, A. *J. Magn. Magn. Mater.* **1983**, *39*, 268.
686. Höting, C.; Eckert, H.; Matar, S. F.; Rodewald, U. C.; Pöttgen, R. *Z. Naturforsch.* **2014**, *69b*, 305.
687. Barandiaran, J. M.; Gignoux, D.; Schmitt, D.; Sal, J. C. G.; Fernandez, J. R. *J. Magn. Magn. Mater.* **1987**, *69*, 61.
688. Abd-Elmeguid, M. M.; Sauer, C.; Köbler, U.; Zinn, W.; Röhler, J.; Keulzer, K. *J. Magn. Magn. Mater.* **1985**, *47-48*, 417.
689. Shelton, R. N.; Braun, H. F.; Musick, E. *Solid State Commun.* **1984**, *52*, 797.
690. Leciejewicz, J.; Siek, S.; Szytuła, A. *J. Magn. Magn. Mater.* **1984**, *40*, 265.
691. Lawrence, J. M.; den Boer, M. L.; Parks, R. D.; Smith, J. L. *Phys. Rev. B* **1984**, *29*, 568.
692. Hiebl, K.; Horvath, C.; Rogl, P.; Sienko, M. *Solid State Commun.* **1983**, *48*, 211.
693. Bodak, O. I.; Gladyshevskii, E. I. *Inorg. Mater.* **1969**, *5*, 1754.
694. Lukaszewicz, K.; Bodak, O. I. *Bull. Acad. Pol. Sci., Ser. Sci. Chim.* **1969**, *17*, 63.
695. Gil, A.; Szytuła, A.; Tomkowicz, Z.; Wojciechowski, K.; Zygmunt, A. *J. Magn. Magn. Mater.* **1994**, *129*, 271.
696. Morozkin, A. V.; Seropegin, Y. D.; Gribanov, A. V.; Sviridov, I. A.; Kurenbaeva, J. M.; Kurenbaev, A. L. *J. Alloys Compd.* **1998**, *264*, 190.
697. Pelizzone, M.; Braun, H. F.; Müller, J. *J. Magn. Magn. Mater.* **1982**, *30*, 33.
698. Bodak, O. I.; Gladyshevskii, E. I. *Sov. Phys. Crystallogr.* **1970**, *14*, 859.
699. Bodak, O. I.; Gladyshevskii, E. I. *Inorg. Mater.* **1970**, *6*, 1037.
700. Bodak, O. I.; Gladyshevskii, E. I.; Kardash, A. V.; Cherkashin, E. E. *Inorg. Mater.* **1970**, *6*, 1069.
701. Buschow, K. H. J.; Fast, J. F. *Phys. Status Solidi B* **1967**, *21*, 593.
702. Jeitschko, W.; Nowotny, H.; Benesovsky, F. *Monatsh. Chem.* **1964**, *95*, 1242.
703. Arbuckle, J.; Parthe, E. *Acta Crystallogr.* **1962**, *15*, 1205.
704. Gladyshevskii, E. I. *J. Struct. Chem.* **1964**, *5*, 852.
705. Parthe, E.; Norton, J. T. *Acta Crystallogr.* **1958**, *11*, 14.
706. Nowotny, H.; Searcy, A. W.; Orr, J. E. *J. Phys. Chem.* **1956**, *60*, 677.
707. Carlson, O. N.; Armstrong, P. E.; Wilhelm, H. A. *Trans. Am. Soc. Met.* **1956**, *48*, 843.
708. Castelliz, L. *Monatsh. Chem.* **1953**, *84*, 765.
709. Eckerlin, P.; Meyer, H. J.; Wölfel, E. *Z. Anorg. Allg. Chem.* **1955**, *281*, 322.

710. Gladyshevskii, E. I.; Uhryn, N. S. *Dopov. Akad. Nauk Ukr. RSR* **1965**, 1326.
711. Gladyshevskii, E. I. *J. Struct. Chem.* **1964**, 5, 523.
712. Raman, A.; Steinfink, H. *Inorg. Chem.* **1967**, 6, 1789.
713. Pauling, L. *Acta Crystallogr.* **1957**, 10, 374.
714. Carpenter, J. H.; Searcy, A. W. *J. Am. Chem. Soc.* **1956**, 78, 2079.
715. Wallbaum, H. J. *Naturwissenschaften* **1944**, 32, 76.
716. Smith, G. S.; Tharp, A. G.; Johnson, W. *Acta Crystallogr.* **1967**, 22, 940.
717. Smith, G. S.; Johnson, Q.; Tharp, A. G. *Acta Crystallogr.* **1967**, 22, 269.
718. Ganglberger, E.; Nowotny, H.; Benesovsky, F. *Monatsh. Chem.* **1967**, 98, 95.
719. Yarmolyuk, Y. P.; Markiv, V. Y.; Gladyshevskii, E. I. *Visn. Lviv. Derzh. Univ., Ser. Khim.* **1969**, 11, 14.
720. Jeitschko, W.; Jordan, A. G.; Beck, P. A. *Trans. Metall. Soc. AIME* **1969**, 245, 335.
721. Dwight, A. E.; Vaishnav, P. P.; Kimball, C. W.; Matykiewicz, J. L. *J. Less-Common Met.* **1986**, 119, 319.
722. Johnson, V.; Jeitschko, W. *J. Solid State Chem.* **1972**, 4, 123.
723. Morozkin, A. V.; Sviridov, I. A. *J. Alloys Compd.* **2000**, 296, L4.
724. Heying, B.; Haverkamp, S.; Rodewald, U. C.; Eckert, H.; Peter, S. C.; Pöttgen, R. *Solid State Sci.* **2015**, 39, 15.
725. Baran, S.; Hofmann, M.; Leciejewicz, J.; Penc, B.; Slaski, M.; Szytula, A. *J. Alloys Compd.* **1998**, 281, 92.
726. Gibson, B.; Pöttgen, R.; Kremer, R. K.; Simon, A.; Ziebeck, K. R. A. *J. Alloys Compd.* **1996**, 239, 34.
727. Masumoto, H.; Watanabe, K.; Mitera, M. *J. Physical Soc. Japan* **1973**, 34, 1414.
728. Grund, I.; Zwiener, G.; Schuster, H.-U. *Z. Anorg. Allg. Chem.* **1986**, 535, 7.
729. Jeitschko, W. *Acta Crystallogr.* **1970**, B26, 815.
730. Jeitschko, W. *Metal. Trans. A* **1970**, 1, 2963.
731. Roy Montreuil, J.; Deyris, B.; Fruchart, R.; Michel, A. C. R. *Seances Acad. Sci., Ser. C* **1968**, 266C.
732. Sikirica, M.; Ban, Z. *Croat. Chem. Acta* **1964**, 36, 151.
733. McCall, W. M.; Narasimhan, K. S. V. L.; Butera, R. A. *J. Appl. Cryst.* **1973**, 6, 301.
734. Eisenmann, B.; May, N.; Müller, W.; Schäfer, H.; Weiss, A.; Winter, J.; Ziegler, G. Z. *Naturforsch.* **1970**, 25b, 1350.
735. Rossi, D.; Marazza, R.; Ferro, R. *J. Less-Common Met.* **1979**, 66, P17.
736. Dörrscheidt, W.; Niess, N.; Schäfer, H. Z. *Naturforsch.* **1976**, 31b, 890.
737. Ban, Z.; Ormeje, L.; Szytula, A.; Tomkowicz, Z. *Phys. Status Solidi A* **1975**, 27, 333.
738. Narasimhan, K. S. V. L.; Rao, V. U. S.; Bergner, R. L.; Wallace, W. E. *J. Appl. Phys.* **1975**, 46, 4957.
739. Joshi, D. A.; Nigam, A. K.; Dhar, S. K.; Thamizhavel, A. *J. Magn. Magn. Mater.* **2010**, 322, 3363.
740. Venturini, G.; Malaman, B.; Pontonnier, L.; Bacmann, M.; Fruchart, D. *Solid State Commun.* **1988**, 66, 597.
741. Szytula, A.; Leciejewicz, J.; Baźela, W.; Ptasiwicz-Bąk, H.; Zygmunt, A. *J. Magn. Magn. Mater.* **1987**, 69, 299.
742. Francois, M.; Venturini, G.; Marêché, J. F.; Malaman, B.; Roques, B. *J. Less-Common Met.* **1985**, 113, 231.
743. Eisenmann, B.; May, N.; Müller, W.; Schäfer, H. Z. *Naturforsch.* **1972**, 27b, 1155.
744. Lloret, B.; Buffat, B.; Chevalier, B.; Etourneau, J. *J. Magn. Magn. Mater.* **1987**, 67, 232.
745. Niepmann, D.; Pöttgen, R. *Intermetallics* **2001**, 9, 313.
746. Dommann, A.; Hulliger, F.; Ott, H. R.; Gramlich, V. *J. Less-Common Met.* **1985**, 110, 331.
747. Morozkin, A. V.; Seropegin, Y. D.; Gribanov, A. V.; Barakatova, J. M. *J. Alloys Compd.* **1997**, 256, 175.
748. Konyk, M.; Romaka, L.; Gignoux, D.; Fruchart, D.; Bodak, O.; Gorelenko, Y. *J. Alloys Compd.* **2005**, 398, 8.
749. Morozkin, A. V.; Seropegin, Y. D.; Bodak, O. I. *J. Alloys Compd.* **1996**, 234, 143.
750. Sologub, O.; Hiebl, K.; Rogl, P.; Bodak, O. I. *J. Alloys Compd.* **1995**, 227, 37.
751. Oleksyn, O. Y.; Fedyna, M. F.; Koterlyn, G. M. *Visn. Lviv. Derzh. Univ., Ser. Khim.* **1991**, 31, 19.
752. Konyk, M. B.; Salamakha, P. S.; Bodak, O. I.; Pecharsky, V. K. *Sov. Phys. Crystallogr.* **1988**, 33, 494.
753. Salamakha, P. S. *Visn. Lviv. Derzh. Univ., Ser. Khim.* **1988**, 29, 62.
754. Fedyna, M. F.; Pecharsky, V. K.; Bodak, O. I. *Dopov. Akad. Nauk Ukr. RSR* **1987**, 2, 50.
755. Venturini, G.; Welter, R.; Malaman, B. *J. Alloys Compd.* **1992**, 185, 99.
756. Skolozdra, R. V.; Kotur, B. Y.; Andrusyak, R. I.; Gorelenko, Y. K. *Inorg. Mater.* **1991**, 27, 1371.
757. Buchholz, W.; Schuster, H.-U. *Z. Anorg. Allg. Chem.* **1981**, 482, 40.
758. Andrusyak, R. I. *Visn. Lviv. Derzh. Univ., Ser. Khim.* **1986**, 27, 24.
759. Buchholz, W.; Schuster, H.-U. *Z. Naturforsch.* **1978**, 33b, 877.
760. Olenych, R. R.; Akselrud, L. G.; Yarmolyuk, Y. P. *Dopov. Akad. Nauk Ukr. RSR* **1981**, 2, 84.
761. Harris, I. R.; Raynor, G. V.; Winstanley, C. J. *J. Less-Common Met.* **1967**, 12, 69.
762. Haschke, H.; Nowotny, H.; Benesovsky, F. *Monatsh. Chem.* **1966**, 97, 1045.
763. Pfisterer, H.; Schubert, K. *Naturwissenschaften* **1950**, 37, 112.
764. Rossi, A. *Gazz. Chim. Ital.* **1934**, 64, 832.
765. Cannon, J. F. *Mater. Res. Soc. Symp. Proc.* **1984**, 22, 113.
766. Nowotny, H.; Auer-Welsbach, H.; Bruss, J.; Kohl, A. *Monatsh. Chem.* **1959**, 90, 15.
767. Jeitschko, W.; Parthé, E. *Acta Crystallogr.* **1965**, 19, 275.
768. Palenzona, A.; Merlo, F.; Bonino, G. B. *Atti Accad. Naz. Lincei Cl. Sci. Fis. Mat. Nat. Rend.* **1966**, 40, 617.
769. Jeitschko, W.; Parthé, E. *Acta Crystallogr.* **1967**, 22, 551.
770. Nial, O. *Z. Anorg. Allg. Chem.* **1938**, 238, 287.
771. Lihl, F.; Kimbauer, H. *Monatsh. Chem.* **1955**, 86, 745.
772. Schubert, K. *Z. Naturforsch.* **1947**, 2a, 120.
773. Geller, S.; Matthias, B. T.; Goldstein, R. *J. Am. Chem. Soc.* **1955**, 77, 1502.
774. Schubert, K.; Anantharaman, T. R.; Ata, H. O. K.; Meissner, H. G.; Pötschke, M.; Rossteutscher, W.; Stolz, E. *Naturwissenschaften* **1960**, 47, 512.
775. Holleck, H.; Benesovsky, F.; Nowotny, H. *Monatsh. Chem.* **1962**, 93, 996.
776. Axel, H.; Eisenmann, B.; Schäfer, H.; Weiss, A. *Z. Naturforsch.* **1969**, 24b, 815.
777. Eisenmann, B.; Schäfer, H.; Weiss, A. *Z. Anorg. Allg. Chem.* **1972**, 391, 241.
778. Wrobel, G.; Schuster, H. U. *Z. Anorg. Allg. Chem.* **1977**, 432, 95.
779. Skolozdra, R. V.; Koretskaya, O. E.; Gorelenko, Y. K. *Ukr. Fiz. Zh. (Russ. Ed.)* **1982**, 27, 263.
780. Skolozdra, R. V.; Koretskaya, O. E.; Gorelenko, Y. K. *Inorg. Mater.* **1984**, 20, 520.
781. Dwight, A. E. *J. Less-Common Met.* **1983**, 93, 411.
782. Rossi, D.; Marazza, R.; Ferro, R. *J. Less-Common Met.* **1985**, 107, 99.

783. Dwight, A. E.; Harper, W. C.; Kimball, C. W. *J. Less-Common Met.* **1973**, *30*, 1.
784. Buschow, K. H. J.; De Mooij, D. B.; Palstra, T. T. M.; Nieuwenhuys, G. J.; Mydosh, J. A. *Philips Res. Rep.* **1985**, *40*, 313.
785. Adroja, D. T.; Malik, S. K. *Phys. Rev. B* **1992**, *45*, 779.
786. Zygmunt, A.; Szytula, A. *J. Alloys Compd.* **1995**, *219*, 185.
787. Canepa, F.; Cirafici, S. *J. Alloys Compd.* **1996**, *232*, 71.
788. Riecken, J. F.; Heymann, G.; Hermes, W.; Rodewald, U. C.; Hoffmann, R.-D.; Huppertz, H.; Pöttgen, R. *Z. Naturforsch.* **2008**, *63b*, 695.
789. Ritter, C.; Provino, A.; Manfrinetti, P.; Gschneidner, K. A., Jr. *J. Alloys Compd.* **2011**, *509*, 9724.
790. Lemoine, P.; Vernière, A.; Venturini, G.; Capelli, S.; Malaman, B. *J. Magn. Magn. Mater.* **2012**, *324*, 961.
791. Heymann, G.; Heying, B.; Rodewald, U. C.; Janka, O.; Huppertz, H.; Pöttgen, R. *J. Solid State Chem.* **2016**, *236*, 138.
792. Sechovský, V.; Havela, L.; Neužil, L.; Andreev, A. V.; Hilscher, G.; Schmitzer, C. *J. Less-Common Met.* **1986**, *121*, 169.
793. Routsis, C. D.; Yakinthos, J. K.; Gamari-Seale, H. *J. Magn. Magn. Mater.* **1992**, *117*, 79.
794. Palstra, T. T. M.; Nieuwenhuys, G. J.; Vlastuin, R. F. M.; van den Berg, J.; Mydosh, J. A.; Buschow, K. H. J. *J. Magn. Magn. Mater.* **1987**, *67*, 331.
795. Szytula, A.; Penc, B.; Kolenda, M.; Leciejewicz, J.; Stüsser, N.; Zygmunt, A. *J. Magn. Magn. Mater.* **1996**, *153*, 273.
796. Mishra, R.; Pöttgen, R.; Hoffmann, R.-D.; Trill, H.; Mosel, B. D.; Piotrowski, H.; Zumdieck, M. F. *Z. Naturforsch.* **2001**, *56b*, 589.
797. Nowotny, H.; Holub, F. *Monatsh. Chem.* **1960**, *91*, 877.
798. Jeitschko, W. *Metal. Trans. A* **1970**, *1*, 3159.
799. Gladyshevskii, E. I.; Krypyakevych, P. I. *Dokl. Akad. Nauk SSSR* **1955**, *102*, 743.
800. Marazza, R.; Ferro, R.; Rambaldi, G. *J. Less-Common Met.* **1975**, *39*, 341.
801. Eberz, U.; Seelentag, W.; Schuster, H.-U. *Z. Naturforsch.* **1980**, *35b*, 1341.
802. Gülrth, M.; Rogl, G.; Romaka, V. V.; Grytsiv, A.; Bauer, E.; Rogl, P. *Acta Mater.* **2016**, *104*, 210.
803. Jung, D.-Y.; Kurosaki, K.; Kim, C.-E.; Muta, H.; Yamanaka, S. *J. Alloys Compd.* **2010**, *489*, 328.
804. Romaka, V. A.; Stadyk, Y. V.; Fruchart, D.; Romaka, L. P.; Goryn, A. M.; Gorelenko, Y. K.; Dominuk, T. I. *Semiconductors* **2009**, *43*, 278.
805. Grykalowska, A.; Wochowski, K.; Nowak, B. *Intermetallics* **2005**, *13*, 756.
806. Kuentzler, R.; Clad, R.; Schmerber, G.; Dossmann, Y. *J. Magn. Magn. Mater.* **1992**, *104-107*, 1976.
807. Kawanaka, H.; Fujii, H.; Nishi, M.; Takabatake, T.; Motoya, K.; Uwatoko, Y.; Ito, Y. *J. Physical Soc. Japan* **1989**, *58*, 3481.
808. Otto, M. J.; Feil, H.; Van Woerden, R. A. M.; Wijngaard, J.; Van Der Valk, P. J.; Van Bruggen, C. F.; Haas, C. *J. Magn. Magn. Mater.* **1987**, *70*, 33.
809. Cooper, A. S. *Mater. Res. Bull.* **1980**, *15*, 799.
810. Vandenberg, J. M. *Mater. Res. Bull.* **1980**, *15*, 835.
811. Espinosa, G. P.; Cooper, A. S.; Barz, H.; Remeika, J. P. *Mater. Res. Bull.* **1980**, *15*, 1635.
812. Remeika, J. P.; Espinosa, G. P.; Cooper, A. S.; Barz, H.; Rowell, J. M.; McWhan, D. B.; Vandenberg, J. M.; Moncton, D. E.; Fisk, Z.; Woolf, L. D.; Hamaker, H. C.; Maple, M. B.; Shirane, G.; Thonlinson, W. *Solid State Commun.* **1980**, *34*, 923.
813. Espinosa, G. P.; Cooper, A. S.; Barz, H. *Mater. Res. Bull.* **1982**, *17*, 963.
814. Hodeau, J. L.; Marezio, M.; Remeika, J. P.; Chen, C. H. *Solid State Commun.* **1982**, *42*, 97.
815. Miraglia, S.; Hodeau, J. L.; Marezio, M.; Laviron, C.; Ghedira, M.; Espinosa, G. P. *J. Solid State Chem.* **1986**, *63*, 358.
816. Hayamizu, H.; Kase, N.; Akimitsu, J. *Phys. C* **2010**, *470*, S541.
817. Mishra, R.; Schwickert, C.; Langer, T.; Pöttgen, R. *Z. Naturforsch.* **2011**, *66b*, 664.
818. Ślebarski, A.; Goraus, J. *Phys. Rev. B* **2013**, *88*, 155122.
819. Boulet, P.; Mazzone, D.; Noël, H.; Riani, P.; Rogl, P.; Ferro, R. *Intermetallics* **1999**, *7*, 931.
820. Romaka, V. V.; Davydov, V.; Gladyshevskii, R.; Melnychenko, N. *J. Alloys Compd.* **2007**, *443*, 68.
821. O. V. Zaplatynsky, L. P. Salamakha, O. L. Sologub, Abstr. 6th Int. Conf. Crystal Chem. Internet. Compd 1995, 105.
822. Weitzer, F.; Hiebl, K.; Rogl, P.; Noël, H. *Ber. Bunsen. Phys. Chem* **1992**, *96*, 1715.
823. Thirion, F.; Steinmetz, J.; Malaman, B. *Mater. Res. Bull.* **1983**, *18*, 1537.
824. Skolozdra, R. V.; Komarovskaya, L. P.; Akselrud, L. G. *Ukr. Fiz. Zh. (Russ. Ed.)* **1984**, *29*, 1395.
825. Wawrzyńska, E.; Hernández-Velasco, J.; Penc, B.; Sikora, W.; Szytula, A.; Zygmunt, A. *J. Phys. Condens. Matter* **2003**, *15*, 5279.
826. Wawrzyńska, E.; Hernández-Velasco, J.; Penc, B.; Szytula, A.; Tomala, K. *J. Phys. Condens. Matter* **2004**, *16*, 7535.
827. Wawrzyńska, E.; Hernández-Velasco, J.; Penc, B.; Szytula, A. *J. Phys. Condens. Matter* **2003**, *16*, 45.
828. Singh, S.; Dhar, S. K.; Manfrinetti, P.; Palenzona, A. *J. Magn. Magn. Mater.* **2002**, *250*, 190.
829. Rieger, W.; Parthé, E. *Monatsh. Chem.* **1968**, *99*, 291.
830. Rieger, W.; Nowotny, H.; Benesovsky, F. *Monatsh. Chem.* **1965**, *96*, 232.
831. Schuster, J. C.; Naka, M.; Shibayanagi, T. *J. Alloys Compd.* **2000**, *305*, L1.
832. Riani, P.; Mazzone, D.; Zanichchi, G.; Marazza, R.; Ferro, R. *Intermetallics* **1997**, *5*, 507.
833. Marazza, R.; Riani, P.; Mazzone, D.; Zanichchi, G.; Ferro, R. *Intermetallics* **1996**, *4*, 131.
834. Kwon, Y. U.; Corbett, J. D. *Chem. Mater.* **1992**, *4*, 1348.
835. Stetskiv, A. O.; Kordan, V.; Tarasiuk, I. I.; Zelinska, O. Y.; Pavlyuk, V. V. *Chem. Met. Alloys* **2014**, *7*, 106.
836. Kowalczyk, G.; Kordan, V.; Stetskiv, A.; Pavlyuk, V. *Intermetallics* **2016**, *70*, 53.
837. Balińska, A.; Kordan, V.; Misztal, R.; Pavlyuk, V. *J. Solid State Electrochem.* **2015**, *19*, 2481.
838. Nowotny, H.; Schubert, K.; Dettinger, U. *Metallforschung* **1946**, *1*, 137.
839. Helleis, O.; Kandler, H.; Leicht, E.; Quiring, W.; Wölfel, E. *Z. Anorg. Allg. Chem.* **1963**, *320*, 86.
840. Griffin, R. B.; Gschneidner, K. A., Jr. *Metal. Trans. A* **1971**, *2*, 2517.
841. Wood, D. H.; Cramer, E. M.; Wallace, P. L.; Ramsey, W. J. *J. Nucl. Mater.* **1969**, *32*, 193.
842. El Boragy, M.; Jain, K. C.; Mayer, H. W.; Schubert, K. *Z. Metallkd.* **1972**, *63*, 751.
843. Leger, J.-M.; Hall, H. T. *J. Less-Common Met.* **1974**, *34*, 17.
844. Teitel, R. J. *Trans. Am. Inst. Min. Metall. Pet. Eng.* **1952**, *194*, 397.
845. Kuz'ma, Y. B.; Skolozdra, R. V.; Markiv, V. Y. *Dopov. Akad. Nauk Ukr. RSR* **1964**, 1070.
846. Nowotny, H.; Schachner, H. *Monatsh. Chem.* **1953**, *84*, 169.
847. Palenzona, A.; Fornasini, M. L.; Bonino, G. B. *Atti Accad. Naz. Lincei Cl. Sci. Fis. Mat. Nat. Rend.* **1966**, *40*, 1040.
848. McMasters, O. D.; O'Keefe, T. J.; Gschneidner, K. A., Jr. *Trans. Metall. Soc. AIME* **1968**, *242*, 936.
849. Merlo, F.; Fornasini, M. L.; Bonino, G. B. *Atti Accad. Naz. Lincei Cl. Sci. Fis. Mat. Nat. Rend.* **1969**, *46*, 265.
850. Guloy, A.; Corbett, J. D. *J. Solid State Chem.* **2005**, *178*, 1112.
851. Bruzzone, G.; Franceschi, E.; Merlo, F. *J. Less-Common Met.* **1981**, *81*, 155.
852. McMasters, O. D.; Gschneidner, K. A., Jr. *J. Less-Common Met.* **1976**, *45*, 275.
853. Pöttgen, R.; Rodewald, U. C. In *Chapter 237—Rare Earth—Transition Metal—Plumbides*; Gschneidner, K. A., Bünzli, J.-C. G., Pecharsky, V. K., Eds.; vol. 38; Elsevier, 2008.

854. Klenner, S.; Pöttgen, R. In *Chapter 312—Rare Earth Transition Metal Plumbides—An Update in Handbook on the Physics and Chemistry of Rare Earths*; Bünzli, J.-C. G., Pecharsky, V. K., Eds.; vol. 57; Elsevier, 2020.
855. Gulay, L. D. *J. Alloys Compd.* **2005**, *392*, 165.
856. Guloy, A. M.; Mudring, A.-V.; Corbett, J. D. *Inorg. Chem.* **2003**, *42*, 6673.
857. Gulay, L. D. *J. Alloys Compd.* **2002**, *347*, 124.
858. Gulay, L. D.; Stepiel-Damm, J.; Wolcyrz, M. *J. Alloys Compd.* **2001**, *314*, 209.
859. Gulay, L. D. *J. Alloys Compd.* **2000**, *313*, 144.
860. Guloy, A. M.; Corbett, J. D. *J. Solid State Chem.* **1994**, *109*, 352.
861. Merlo, F.; Pani, M.; Fornasini, M. L. *J. Alloys Compd.* **1993**, *196*, 145.
862. Merlo, F.; Pani, M.; Fornasini, M. L. *J. Less-Common Met.* **1991**, *171*, 329.
863. Hermes, W.; Rayaprol, S.; Pöttgen, R. *Z. Naturforsch.* **2007**, *62b*, 901.
864. Gulay, L. D. *J. Alloys Compd.* **2001**, *314*, 219.
865. Marazza, R.; Mazzone, D.; Riani, P.; Zanocchi, G. *J. Alloys Compd.* **1995**, *220*, 241.

4.07 Critical charge transfer pairs in intermetallic superconductors

Ranuri S. Dissanayaka Mudiyansele^a, Tomasz Klimczuk^b, and Weiwei Xie^a, ^a Department of Chemistry and Chemical Biology, Rutgers University, Piscataway, NJ, United States; and ^b Faculty of Applied Physics and Mathematics and Advanced Materials Center, Gdansk University of Technology, Gdansk, Poland

© 2023 Elsevier Ltd. All rights reserved.

4.07.1	Introduction to the background of superconductivity	217
4.07.2	Critical charge transfer pairs in representative superconductors	218
4.07.2.1	Fe-As	219
4.07.2.2	Ir-Ge	220
4.07.2.3	Ru-P	221
4.07.2.4	Co/Rh/Ir-Sn	222
4.07.3	Three basic characterizations when reporting new superconductors	223
4.07.3.1	Electrical resistivity	223
4.07.3.2	Magnetic susceptibility	225
4.07.3.3	Heat capacity	227
4.07.4	Summary	232
Acknowledgment		232
References		232

Abstract

Superconductors which expel magnetic flux field and provide zero-resistance are critical to current and future quantum information technology. In this article, we focus on several superconducting families and analyze the correlations among their crystal structures, specific chemical bonding, and superconductivity from chemistry perspectives. We connect superconducting materials with the critical charge transfer pairs based on their chemical bonding interactions. Moreover, we elucidate our empirical chemistry approaches to new superconductors from structural connections and electron counting rules. Furthermore, the basic but critical characterizations are described for chemists when reporting new superconductors. In the end, we provide our chemically intuitive thoughts on novel superconducting materials design.

4.07.1 Introduction to the background of superconductivity

Superconductors are the materials that enter a state that offer no resistance to the passage of electric current below a certain temperature called critical temperature (T_c).¹ When the resistance falls to zero at T_c , electricity can circulate inside the superconducting material without any energy dissipation. Another unique property of the superconductors is their ability to expel an external magnetic field given it is sufficiently weak. This phenomenon is named the Meissner effect after the physicist who first observed in 1933.¹ Energy losses associated with the electric current is harnessed in everyday life spanning from simple devices like light bulbs to all kinds of motions and transportations.^{2,3} Therefore, superconductivity at high temperatures is a remarkable phenomenon that could lead to faster, more efficient electronic devices and long-distance, low-voltage electric grids that can transmit power without energy loss and ultra-fast levitating trains that ride frictionless magnets instead of rails.⁴ Superconducting magnets have become a natural choice in applications that need strong magnetic fields. For example, medical diagnosis devices like magnetic resonance imaging (MRI), magnetic separations in the mineral industry, or particle accelerators.^{5,6}

The superconducting phenomenon was first observed by Dutch physicist Heike Kamerlingh Onnes in 1911, when he was studying the properties of solid mercury at liquid helium temperatures. Since then, scientists continue to make discoveries on superconductors; however, until the discovery of superconductivity in cuprates, the T_c was always below 35 K.^{1,7,8} Meanwhile, in the 1950s, the Bardeen-Cooper-Schrieffer theory (BCS) successfully explained the observed phenomena of superconductivity. The BCS theory fundamentally explains that electron-phonon coupling induces a superconducting state by pairing up electrons (Cooper pair) with the opposite crystal momenta.^{1,7} The superconductivity that can be explained by the BCS theory are now known as the "conventional superconductors." In 1986, superconductivity with $T_c \sim 30$ K was found in the Ba-doped antiferromagnetic insulator La_2CuO_4 , which unveiled the era of high T_c cuprate superconductors.⁸ After that, scientists continue fabricating new superconducting materials that contain functional CuO_2 that exhibit specific interlayer distances, for example, $\text{HgBa}_2\text{Ca}_2\text{Cu}_3\text{O}_{8+\delta}$ (Hg-1223, $T_c = 133$ K) and $\text{TlBa}_2\text{Ca}_2\text{Cu}_3\text{O}_{8+\delta}$ (Tl-1223, $T_c = 138$ K).^{9–11} The situation remained unchanged for more than 30 years until layered Fe-based superconductors and other unconventional high-temperature superconductors were found in 2008. Even though superconductivity was a well-understood phenomenon in the 1960s, expansion of research on superconductivity later revealed that there is a wealth of more complicated forms of superconductivity which is still elusive. However, superconductivity is impossible without quantum mechanics whereas it is also an interesting case where quantum effects are visible at the macroscopic scale.⁴

The common challenge in the superconductor field is to discover a room-temperature superconductor that can be used at ambient conditions which can simply revolutionize the future based on their superefficient applications. Despite that, each class of materials has its pros and cons when it comes to real-world applications. Starting from the discovery of superconducting properties in solid mercury, different classes of materials, including elements, ceramics/cuprates, pnictides, organic materials, and alloys, have been widely explored and discovered. Followed by the discovery of superconductivity of mercury in 1911, other elemental superconductors were found where lead and niobium at the highest T_c of 9.3 and 7 K and tungsten with the lowest T_c of 0.01 K. However, scientists immediately realized that elemental superconductors are of no practical use as their ordinary resistivity reappeared when certain current limits (critical current, J_c) and certain magnetic fields (the critical field, H_c) were surpassed. The superconductors with this behavior are referred to as type-I superconductors. Drawbacks of elemental superconductors mentioned above led to explore and discover novel compound superconductors with better performances. During the 1950s niobium-based materials were discovered with relatively high T_c (~ 10 – 20 K) that were able to conduct large amounts of currents and withstand high magnetic fields without being quenched to the normal metal state. These compounds and alloys are called the type-II superconductors where they possess a lower critical field (H_{c1}) that allows the penetration of the magnetic field retaining the zero resistance of the material and an upper critical field (H_{c2}), a higher magnetic field that fully destroyed the superconductivity.

Another family of intermetallic “Chevrel phase” chalcogenide superconductors was also found to have a very large H_{c2} where PbMo_6S_8 was reported as the compound with the highest $T_c \sim 14$ K. Superconductivity in oxides have been widely studied at the same period where the discovery of the 1-2-3 superconductor, $\text{YBa}_2\text{Cu}_3\text{O}_7$, initiated the era of the high- T_c superconductivity having the potential for commercial applications. The superconductors that have a T_c higher than the boiling temperature of the liquid nitrogen (77 K) are known as high- T_c superconductors. Considering the cuprate superconductors in terms of their T_c , the family has almost fully explored through conventional synthesis leading to the maximum $T_c \sim 138$ K in the family. The limitations of the practical applications are not solely the T_c of the available superconductors as this can be resolved using closed-cycle refrigeration systems.¹² For example, the widely studied cuprate high- T_c superconductors are brittle that limits their potential applications in various fields like electric power transmission/aircraft.^{5,12,13} Moreover, other factors, such as the behavior of superconductors in high magnetic fields and currents, need to be addressed through innovative processing and chemical manipulation. Understanding the fundamental rules on designing and developing high-temperature intermetallic superconductors is important in exploring new superconductors with exotic properties to overcome above challenges. This review summarizes the main families of intermetallic superconductors while discussing the chemical perspective on predicting and synthesis of novel superconductors (Fig. 1).

4.07.2 Critical charge transfer pairs in representative superconductors

Superconductivity in materials can be considered as a property that arises from the instabilities of the electronic system that are balanced along with other factors such as electron-lattice coupling or magnetism.¹ Despite fascinating properties of superconductors, the most challenging aspect in the field is the difficulty to predict the new compounds with exotic superconducting properties. Only a few predictive rules seem to work while others fail.¹⁴ In this section, we will be discussing some of the empirical rules derived

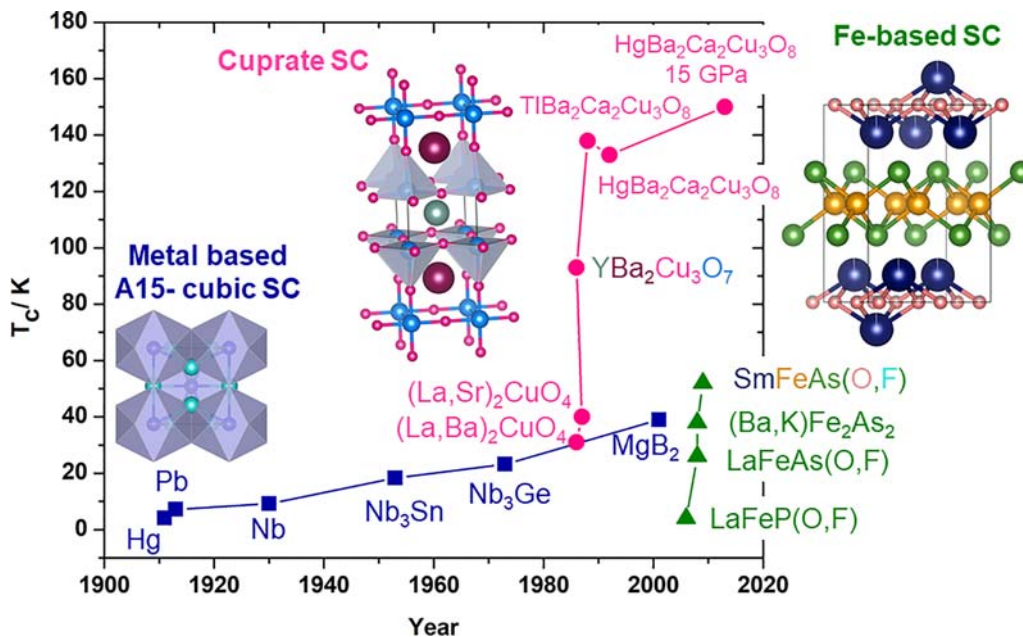


Fig. 1 Discovery progress of superconductors in different structural families. From Hosono, H.; Yamamoto, A.; Hiramatsu, H.; Ma, Y. Recent Advances in Iron-Based Superconductors toward Applications. *Mater. Today* **2018**, *21* (3), 278–302, <https://doi.org/10.1016/j.mattod.2017.09.006>.

from a chemical perspective of previously studied superconducting compounds that are useful in designing, predicting, and synthesis of novel intermetallic superconductors. While the condensed matter physicists understand the superconductivity through the “*k*-space” based on the fermi surfaces and other particle interactions like electron-phonon coupling, the synthetic chemists use a distinct viewpoint based on real space features such as chemical compositions and atomic structures which also plays a significant role in superconductivity. Extensive analysis of the main superconducting families exhibits that critical charge transfer pairs in the periodic table such as Cu-O and Fe-As are a significant factor in these superconducting materials. Critical charge transfer pairs can be assumed as the balance between covalent and ionic bonding that leads to a proper charge transfer between the atoms so that the bond valence responds to perturbations from other forces present leading to a superconductor.¹⁴ The Fermi surface or the *k*-space view is a quantitative approach used for the discovery of novel superconductors whereas the critical charge transfer pairs is a qualitative viewpoint which is equally important from a synthetic chemist’s standpoint.¹⁴ One of the most important properties observed in the large families of cuprates and Fe-based superconductors is that they are layered compounds with critical charge transfer pairs of Cu-O and Fe-As respectively. The discovery of new superconducting materials can be promoted by this chemical approach of manipulating critical charge transfer pairs in various structural families. Therefore, a discussion on the well-established critical charge transfer pairs and other potential pairs are of great interest.

4.07.2.1 Fe-As

Starting from the iron-based superconductor, LaFeAsO_{0.9}F_{0.1} with a $T_c \sim 26$ K in 2008, scientists keep looking for new superconductors in this family. By revealing the concept of designing the new superconductors manipulating the effective FeAs layers and tuning the valence electrons in the interlayers, several families of Fe-based superconducting materials have been discovered such as (122-(AE)Fe₂As₂ (AE)-Ba/Sr/Ca/Eu),¹⁵ 1111-LnFeAsO (Ln-La/Ce/Pr/Nd/Sm/Gd/Tb),^{15,16} and 111-AFeAs (A-Li/Na/La).¹⁷ Current record of the $T_c = 56$ K has reported for NdFeAsO_{0.9}F_{0.1} in the family. All iron-based superconductors share the common Fe₂X₂ (X = As/Se) layered structural component and these layers are composed of edge shared FeX₄ distorted tetrahedra. The FeX₄ tetrahedra alternate with the other intermediary layers as shown in Fig. 2. Furthermore, incorporating effective PtAs layers with FeAs layers led to the discovery of 10-3-8 Ca₁₀(Pt₃As₈)(Fe₂As₂)₅ and 10-4-8 Ca₁₀(Pt₄As₈)(Fe₂As₂)₅ superconductors. The structural features related to superconductivity, doping induced superconductivity, and interplay between magnetism and superconductivity in these iron-based superconductors have been thoroughly discussed and summarized in several review papers.^{18,19}

Although Fe-As and Cu-O are well known critical charge transfer pairs that play an important role in superconductivity, there is a big periodic table that allows us to systematically examine other potential charge transfer pairs that can give rise to new superconducting families with exotic properties. Some of those potential pairs such as Ir-Ge, Ru-P/Sb, Co/Rh/Ir-Sn will be discussed here. Iridium and ruthenium are 5*d* and 4*d* transition metals with strong spin-orbit coupling effects. Recently, theoretical predictions have been made on the unconventional Mott insulating states assisted via the spin-orbit coupling effects. That has been experimentally confirmed in the compounds such as Sr₂IrO₄ and α -RuCl₃.^{20,21} Furthermore, this fragile nature of the magnetic orderings observed in Ir and Ru are susceptible to be suppressed inducing superconductivity as a result, which is similar to the magnetic instabilities seen in Fe-based superconductors. Moreover, other metalloids like As in Fe-As critical charge transfer pair are Ge and P. Ge and P have similar chemical properties in terms of electronegativity and size where they can be replaced to develop a new family of superconductors. Atomic radii and Pauli electronegativity of As, Ge, and P are 1.11 Å, 1.09 Å, 0.98 Å and 2.18, 2.01, 2.19, respectively.^{22,23} Thus, we identify the Ir-Ge and Ru-P pairs as other potential critical charge transfer pairs.

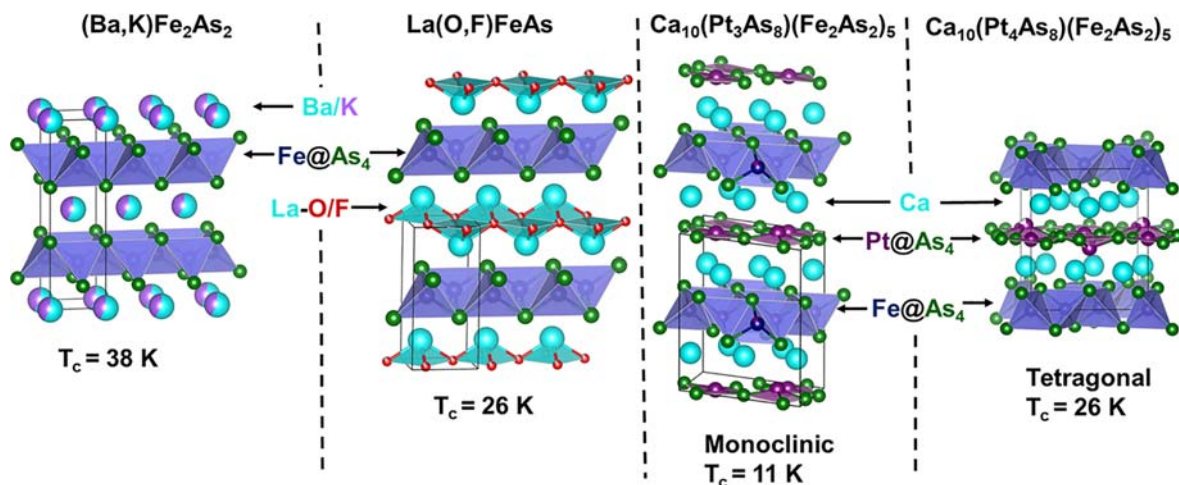


Fig. 2 Layered structural features of Fe-based superconductors: LaOFeAs, BaFe₂As₂, Ca₁₀(Pt₄As₈)(Fe₂As₂)₅, and Ca₁₀(Pt₃As₈)(Fe₂As₂)₅.

4.07.2.2 Ir-Ge

According to the valence balance concept, the Fe-based superconducting materials LaOFeAs and BaFe₂As₂ can be formulated as La³⁺O²⁻Fe²⁺As³⁻ and Ba²⁺(Fe²⁺)₂(As³⁻)₂. The number of valence electrons can be tuned such that Fe²⁺ and Fe³⁺ can coexist in the compound inducing superconductivity through Fe-As pairs in the pnictide superconductors. Similar to this trend, Ir which has common oxidation states +3 and +4 can be paired with Ge with its stable -4 oxidation state to form the Ir-Ge pair which gives rise to superconductivity in materials. In addition, both Fe-As (Fe:8e- and As:5e-) and Ir-Ge (Ir:9e- and As:4e-) has the same number of valence electron count of 13e-. The binary IrGe is one such material with exceptional high $T_c \sim 5.2$ K, compared to other late-metal germanides resulting from the strong electron-phonon coupling.^{24,25} Relatively large number of ternary intermetallic germanides with rare earth elements are known while some of them like LaIr₂Ge₂ and La₃Ir₂Ge₂ have shown superconductivity at ambient pressure with T_c at ~ 1.5 K and 4.7 K respectively.^{26,27} The Ca₃Ir₄Ge₄ is one of the few compounds in the ternary phase diagram of the Ca-Ir-Ge system that shows superconductivity at low temperatures of about 1.8 K.²⁸ The compound La₃Ir₄Ge₄ crystallizes in orthorhombic La₃Ni₂Ge₂-structure type in the space group *Pbcm* (No. 57) and detailed structural analysis is not reported for the La₃Ir₄Ge₄.²⁶ The Ca₃Ir₄Ge₄ compound crystallizes in the cubic, non-centrosymmetric Na₃Pt₄Ge₄-structure type in the space group *I-43m* (No. 217). The structural analysis of the Ca₃Ir₄Ge₄ shows that the Ir atoms are arranged in tetrahedral coordination with Ge atoms such a way these edge-sharing and corner-sharing IrGe₄ tetrahedra form a three-dimensional network as shown in Fig. 3A. The channels in the structure are filled by the Ca atoms and the Ir₄Ge₄ polyanions in the Ir-Ge framework and the Ir tetrahedron in the center of the unit cell are shown in Fig. 3B and C.²⁸ The compound is a paramagnetic metal with a fermi liquid behavior above the T_c while the Stoner enhancement factor suggests that there is a significant electron-electron correlation.²⁸

Another example where the Ir-Ge critical charge transfer pair involved in superconductivity is TaIr₂Ge₂, which is a type-II BCS superconductor at $T_c = 3.5$ K.²⁹ The less electropositive Ta element has led to endohedral cluster fragments unlike the layered features commonly observed in tetragonal 122 ThCr₂Si₂ and CaBe₂Ge₂ structure type.²⁹ The compound crystallizes in centrosymmetric, orthorhombic space group *Pnmm* (NO. 58). The TaIr₂Ge₂ can be expressed as Ta-centered 11 Ir and Ge atoms coordinated polyhedral, Ta@Ir₇Ge₄. The 3D network of the structure extends via vertex sharing and face sharing endohedral clusters as shown in Fig. 3D. However, BaIr₂Ge₂ that crystallized in BaRh₂Si₂-structure type is non-superconducting down to 1.8 K which is consistent with the non-superconductivity observed in isovalent BaFe₂As₂ in the pnictide family. Another superconducting compound is SrIrGe₃ with a $T_c = 0.5$ K, which has a non-centrosymmetric tetragonal structure with space group *I4mm* (No. 107). It has layers of GeIr₂Ge tetrahedra which are connected via Ge-Ge and Ir-Ge bonds.^{30,31} Interestingly, the isostructural and isovalent BaIrGe₃ is not superconducting down to 1.8 K.³²

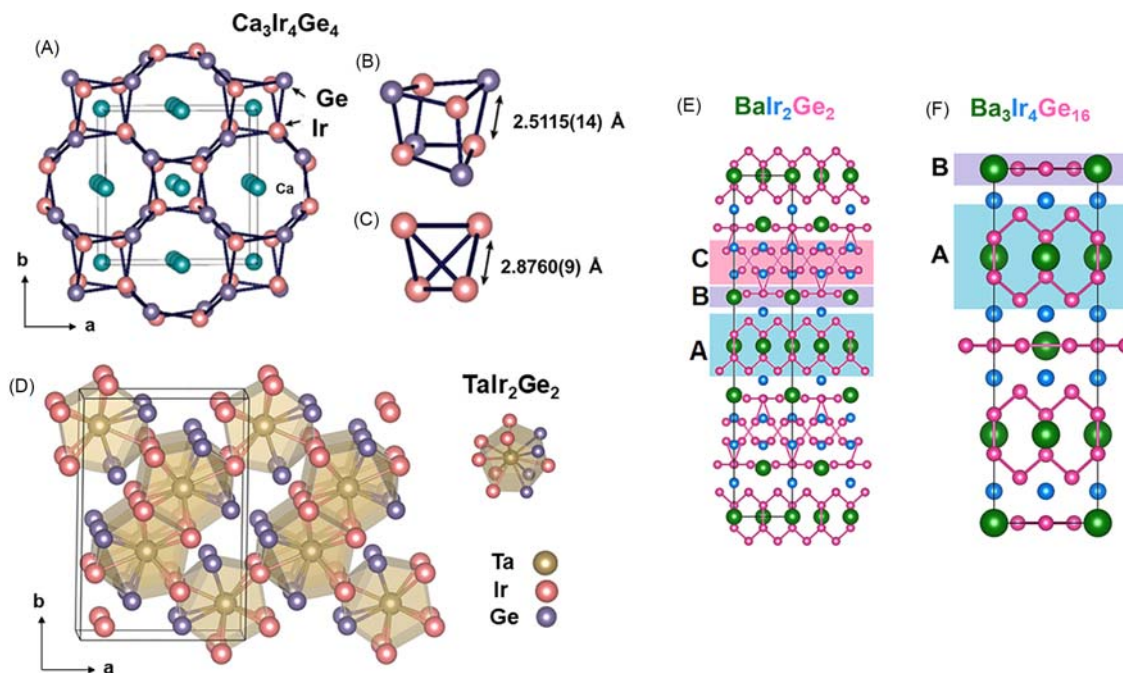


Fig. 3 (A) Crystal structure of Ca₃Ir₄Ge₄. (B) Ir₄Ge₄ polyanion in the shape of a tetrahedral star. (C) Ir tetrahedron in the center of the unit cell. (D) Crystal structure of TaIr₂Ge₂ showing vertex and edge sharing Ta@Ir₇Ge₄ clusters. (E) Assembly of building blocks in superconductors, BaIr₂Ge₂ and Ba₃Ir₄Ge₁₆ (F). (A–C) From Von Rohr, F.; Luo, H.; Ni, N.; Wörle, M.; Cava, R. J. Superconductivity and Correlated Fermi Liquid Behavior in Noncentrosymmetric Ca₃Ir₄Ge₄. *Phys. Rev. B* **2014**, *89* (22), 224504. (D) From Srivichitranond, L. C.; Seibel, E. M.; Xie, W.; Sobczak, Z.; Klimczuk, T.; Cava, R. J. Superconductivity in a New Intermetallic Structure Type Based on Endohedral Ta@Ir₇Ge₄ Clusters. *Phys. Rev. B* **2017**, *95* (17), 174521, <https://doi.org/10.1103/PhysRevB.95.174521>.

Another two representative candidates in Ir/Ge-based superconductors are $\text{Ba}_3\text{Ir}_4\text{Ge}_{16}$ and BaR_2Ge_7 with $T_c \sim 5.2$ and 2.5 K, respectively.³³ Detailed single crystal structural studies have shown that BaR_2Ge_7 and $\text{Ba}_3\text{Ir}_4\text{Ge}_{16}$ consist of unique quasi-two-dimensional networks with edge-shared crown-shaped BaGe_{16} polyhedra. Furthermore, there are Ge-Ge pairs/Ge-Ge dimers with the interatomic distances shorter than 3.0 Å connected with each other leading to a layered material in terms of the Ge network.^{33,34} On the other hand, these two materials can be seen as multiple layered networks of Ir-Ge pair as shown in Fig. 3E. $\text{Ba}_3\text{Ir}_4\text{Ge}_{16}$ can be interpreted as a combination of layers A and B, while BaR_2Ge_7 can be considered as a combination of layers A, B, and C, where C is a two-dimensional zigzag IrGe_2 framework. From this structural point of view, these compounds suggest that there is a lot of room to explore the new compounds based on multiple networks of Ir-Ge building blocks with unconventional superconductivity. Especially, $\text{R}_2\text{R}_2\text{Ge}_7$ and $\text{R}_3\text{Ir}_4\text{Ge}_{16}$ (R-rare-earth elements) with the 4f magnetically active rare-earth elements can be an important structural motif to study the competition between magnetism and superconductivity.

4.07.2.3 Ru-P

Ru-P (Ru:8e- and P:5e-) charge transfer pair is isovalent to Fe-As (Fe:8e- and As:5e-) pair observed in pnictide superconductors family. Ru has the common oxidation states of +2, +3, and +4 which can pair with the oxidation state of P^{3-} . As discussed above in the Ir-Ge case, the number of electrons in compounds can be tuned in a way that the different Ru oxidation states coexists consequently inducing the superconductivity via Ru-P charge transfer pair in materials. The possibility of the occurrence of high T_c superconductivity in ternary transition metal phosphide compounds can be traced back to the 1980s when ZrRuP superconductor was discovered.³⁵ Even though other ternary transition metal phosphides ($\text{MM}'\text{P}$) with 3d metals such as Co, Ni, Fe, Mn, and Cr have been known before, these compounds ordered ferromagnetically with no superconducting properties, presumably due to the magnetic nature of these elements.³⁵ Interestingly, the ZrRuP compound crystallizes in two modifications of hexagonal phase and orthorhombic phase each with T_c of 13 K and 3.5 K respectively.^{36,37} Hexagonal ZrRuP is a layered compound, each layer occupied either by Zr and P or Ru and P atoms (Fig. 4A). The Ru atoms form a two-dimensional triangular cluster of Ru_3 that are linked with each other via Ru-P bonds in the basal plane. In contrast, the orthorhombic phase is composed of layers filled with Zr and Ru where all the layers are equivalent. The similarity is that both phases have Zr-Zr chains with similar bond distances. While detailed structural comparison is reported in previous reports cited here, ZrRuP is an interesting candidate for studying the effect of the

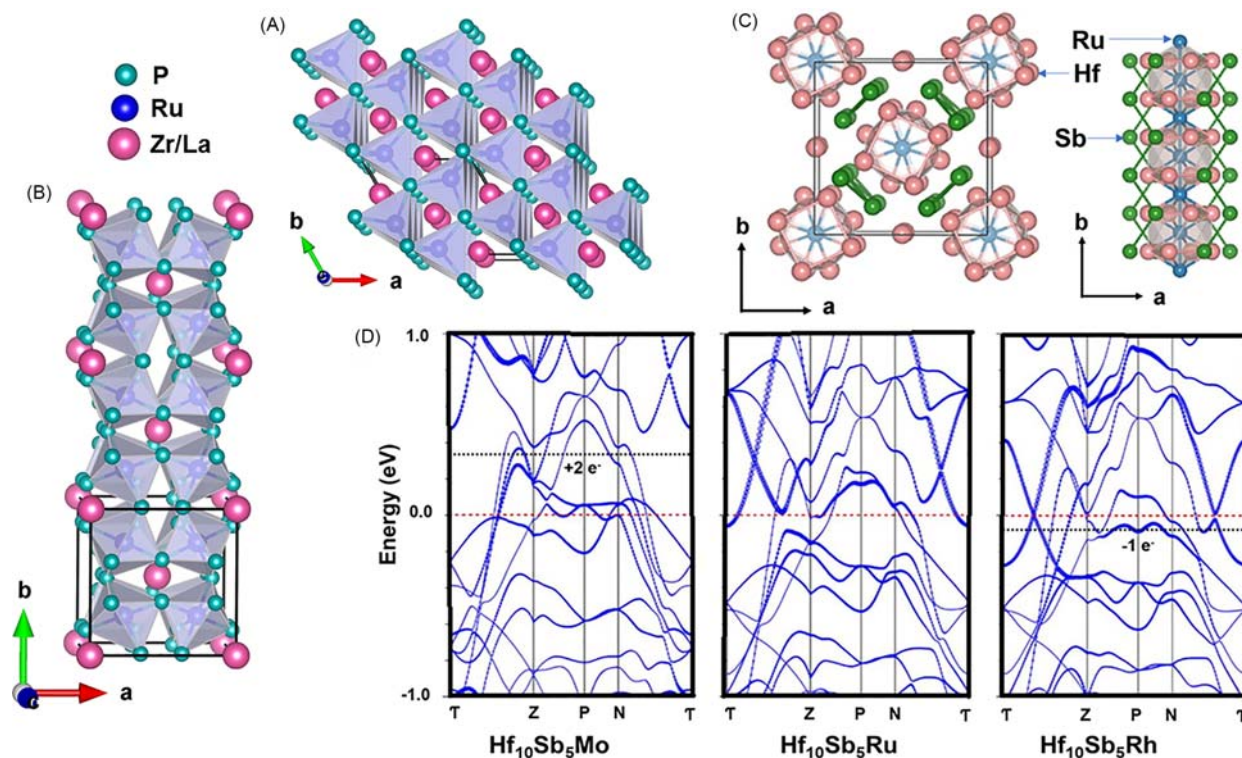


Fig. 4 The crystal structure of (A) ZrRuP -hexagonal type (B) $\text{LaRu}_4\text{P}_{12}$ showing the Ru-P network by the polyhedral. The crystal structure of $\text{Hf}_5\text{Sb}_{2.5}\text{Ru}_{0.5}$ (C) showing the Hf square antiprisms around the Ru/Sb chains in 011 direction (left) and (right) column of Hf with imbedded Ru-Sb chains (Green:Sb, blue: Ru/Sb mixed chains, pink:Hf) (D) Band structure calculations of model compound $\text{Hf}_{10}\text{Sb}_5\text{M}$ ($\text{M} = \text{Mo}, \text{Ru}, \text{Rd}$) obtained from non-spin-polarized LDA calculations. (C, D) From Xie, W.; Luo, H.; Seibel, E. M.; Nielsen, M. B.; Cava, R. J. Superconductivity in $\text{Hf}_5\text{Sb}_3\text{-xRu}_x$: Are Ru and Sb a Critical Charge-Transfer Pair for Superconductivity? *Chem. Mater.* **2015**, *27* (13), 4511–4514, <https://doi.org/10.1021/acs.chemmater.5b01655>.

crystal structure on the superconducting properties when the formal electron counts remain unchanged in the system.^{36,37} The intensive studies followed by the discovery of ZrRuP superconductivity has led to a large family of TT'X (T, T'-transition metal element, X-Si, Ge, P, As) where more than 10 compounds are superconducting above 10 K.³⁸ Interestingly, orthorhombic MoRuP has shown the highest $T_c = 16$ K among all of them and TRuP materials have shown relatively high T_c compared to others suggesting the Ru-P critical charge transfer pair may play an important role in it.^{38,39} In addition, there are three different structure types found in this family; Fe₂P-type hexagonal (*h*-TT'X), Co₂P-type orthorhombic (*o*-TT'X), and TiFeSi-type orthorhombic (*o*-TT'X) structures.³⁸ The *h*-TT'X type has displayed higher T_c compared to the other structure types; most of *h*-TT'X type compounds have T_c above 10 K.³⁸ Moreover, the upper critical fields of the ZrRuP and HfRuP compounds synthesized by high pressure are found to be 16 T and 14 T, respectively, which are significantly large.⁴⁰ This paves the path to employ the Ru-P as a charge transfer pair to explore other intermetallic compounds with interesting properties.

The ternary metal pnictide RT₄P₁₂ (R-rare earth elements, T-Fe/Os/Ru) is another interesting intermetallic class of compounds that crystallize in a CoAs₃ skutterudite structure type.⁴¹ LaRu₄P₁₂ is the candidate with the highest superconducting $T_c = 7.2$ K in the family. La atoms locate at (000) and ($\frac{1}{2}$, $\frac{1}{2}$, $\frac{1}{2}$) of a cubic structure and the transition metal atoms are in the center of a distorted octahedral environment of six P atoms (Fig. 4B). This structure is well defined by the P₄⁴⁻ groups.^{42,43} Other members of the same class LaFe₄P₁₂ and LaOs₄P₁₂ show superconducting properties at 4.1 and 1.8 K, lower T_c compared to the Ru counterpart suggesting that the Ru-P pair is an important factor in the superconducting properties.⁴³ In addition, arsenide compounds LaRu₄As₁₂ and PrRu₄As₁₂ are superconducting at 10 K and 2.4 K where PrRu₄As₁₂ being the only known superconducting magnetic rare-earth filled skutterudite.⁴² LaRu₄As₁₂ has a higher T_c than its isostructural phosphide counterpart, which is not the general case for other arsenide compounds such as HfRuAs and ZrRuAs. HfRuAs and ZrRuAs become superconducting at 4.5 K and 12 K, in which the critical temperatures are much lower than their relative phosphide compounds.^{44,45} In general, the T_c tends to decrease with the increasing As concentration. Overall, these observations indicate that Ru-P could be another choice of critical charge transfer pair where synthetic chemists can use to explore novel superconductors in combination together with other factors such as formal electron counts and crystal structural features. Furthermore, Ru-As could also be a potential candidate.

Similarly, LaRu₄Sb₁₂ and PrRu₄Sb₁₂ with the same skutterudite structures are superconductors at 3.58 K and 1.04 K.^{46,47} However, isoelectronic and isostructural other transition metal skutterudite antimonides LaOs₄Sb₁₂, LaFe₄Sb₁₂ or LaRh₄Sb₈Sn₄ do not show superconductivity down to 1.8 K.⁴⁸⁻⁵⁰ In further support of this claim, Xie et al. has reported a detailed study by systematically modifying the W₅Si₃ structure type to test the effectiveness Ru-Sb critical charge transfer pair.¹⁴ W₅Si₃ is itself a superconductor at 2.7 K.⁵¹ In this study, they have looked at the (Hf/Zr)₅(Sb_{3-x}M_x) type compounds where M is a transition metal and $x \sim 0.5$. The doping of M stabilizes this structure type giving the opportunity to elucidate the effect of the element identity of M only. The crystal structure shows that M and Sb forms a bonded chain inside a column of Hf shown in the Fig. 4C. The Hf₅Sb_{2.5}Ru_{0.5} has been found to be superconducting at 3.2 K whereas Mo, Rh, Pd, or Pt variants are not superconducting.¹⁴ Not only that, but another study has also shown that the compounds with 3d elements V, Mn, Co, Fe, Ni and Cu in place of Ru atom are not superconductors.⁵² Furthermore, the attempts of co-substituting minor constituents of different atoms to obtain isoelectronic (described in detail using electronic band structure calculations) and isostructural compounds such as (Hf_{4.5}Y_{0.5})Sb_{2.5}Ru_{0.5} are also non-superconducting.¹⁴ The electronic band structure calculations for these compounds have shown that the Ru variant has a saddle point located close to the Fermi energy level at *N* point in the Brillouin zone which is sensitive to the element M where it splits into two bands for Rh and Mo species (Fig. 4). The saddle point is a characteristic of band structure that always relates to the electronic instability and a tendency toward some exotic properties, such as charge-density waves, structural transitions, or superconductivity.⁵³ Furthermore, the compound Zr₅Sb_{2.5}Ru_{0.5} is superconducting at 5 K while no reports on superconductivity on Fe, Co or Ni variants in place of Ru.^{54,55} The fact that only Ru variants from 11 different elements tested is superconducting in (Hf/Zr)₅(Sb_{3-x}M_x) system along with the non-superconducting behavior of the LaOs₄Sb₁₂ and LaRh₄Sb₈Sn₄ suggests the importance of the chemical identity of Ru-Sb pair in the superconducting materials (Table 1).

4.07.2.4 Co/Rh/Ir-Sn

The ternary stannide R₃T₄Sn₁₃ where R-rare earth elements and T-transition metals, belongs to an interesting group of intermetallic compounds due to the occurrence of superconductivity and or magnetism with the replacement of various rare earth elements. Many members of this family belong to the so-called phase I, derived from cubic space group *Pm-3n* (No.223) crystallize in

Table 1 The superconducting family of Fe/Ru/Os-P/As compounds (T_c /K).

Compound	T_c	Compound	T_c	Compound	T_c	Compound	T_c
LaFe ₄ P ₁₂	4.1	LaRu ₄ P ₁₂	7.2	LaOs ₄ P ₁₂	1.8	ZrRuP	13
LaFe ₄ As ₁₂	–	LaRu ₄ As ₁₂	10.3	LaOs ₄ As ₁₂	3.2 ⁵⁶	ZrRuAs	11
PrFe ₄ P ₁₂	–	PrRu ₄ P ₁₂	–	PrOs ₄ P ₁₂	–	HfRuP	14
PrFe ₄ As ₁₂	–	PrRu ₄ As ₁₂	2.4	PrOs ₄ As ₁₂	–	HfRuAs	4.5
CeFe ₄ P ₁₂	–	CeRu ₄ P ₁₂	–	CeOs ₄ P ₁₂	–	MoRuP	16
CeFe ₄ As ₁₂	–	CeRu ₄ As ₁₂	–	CeOs ₄ As ₁₂	–	MoRuAs	–

$\text{Yb}_3\text{Rh}_4\text{Sn}_{13}$ -structure type containing 40 atoms per unit cell. This system was first discovered in the 1980s by Remeika et al.^{57–60} In general, the compounds with divalent or tetravalent R cations were found to be in phase I while the trivalent cations occur in phase II. Even though the detailed structural information on phase II is not known precisely, diffraction studies clearly interpret it as a distortion of S_{12} cages.^{61,62} In other words, phase II is a superlattice distortion of phase I with a twice original lattice constant.⁶³ Specifically, the compounds $\text{R}_3\text{T}_4\text{Sn}_{13}$ with $\text{R}=\text{La}/\text{Ca}/\text{Sr}$ and $\text{T}=\text{Co}/\text{Rh}/\text{Ir}$ are a large group of compounds with a quasi-skutterudite structure that show superconductivity with interesting properties such as peak effects.⁶⁴ Especially, the $\text{La}_3\text{M}_4\text{Sn}_{13}$ compounds provide an avenue to better understand the relationship between superconductivity and magnetism in the presence of strong electron correlations.^{65,66} The $\text{Ca}/\text{Sr}_3\text{Ir}_4\text{Sn}_{13}$ are candidates with a correlated electron system with a superlattice quantum critical point which has emerged due to chemical or physical pressure.⁶³ Moreover, another class of stannides $\text{R}_5\text{Rh}_6\text{Sn}_{18}$ discovered more than 30 years ago, the compounds where $\text{R}=\text{Sc}, \text{Y}, \text{Lu}$ has become an interesting system recently in terms of studying their superconducting states.^{58,67–71} They crystallize in a tetragonal structure with a space group of $I4_1/acd$ (No: 142). The R atom occupies two sites with different symmetries.

Table 2 summarizes the reported superconductors in both families with their superconducting transition temperatures. Furthermore, the Co/Rh/Ir with 9e- and Sn with 4e- valence electrons make a total of 13e- valence electrons in a related manner to Fe-As critical charge transfer pair in the intermetallic pnictide superconductors. Supporting this claim, the observation of superconductivity in a large family of these stannides discussed above helps to conclude that Co-Sn, Rh-Sn, and Ir-Sn are other potential critical charge transfer pairs that provide a lot of room to explore new superconductors with the rational design based on other factors like electronic counts and structure types.

4.07.3 Three basic characterizations when reporting new superconductors

In this chapter, we will describe the methods used for obtaining the most important superconducting (and some other) parameters. There are three measurement techniques commonly used for proving and fully describing properties of a superconducting compound: electrical resistivity, magnetic susceptibility, and heat capacity. Below, we will describe them one by one with the experimental results obtained for CaRh_2 ⁷³ and Nblr_2B_2 .⁷⁴

4.07.3.1 Electrical resistivity

Lack of resistance at liquid helium temperatures in a tested mercury sample was first observed by Prof. Onnes and his collaborators. For many years, observation of zero-resistance below critical temperature was the only method used for proving the presence of superconductivity. The method requires a properly prepared sample, diligence, and experience. It should be pointed out, that resistivity measurement may be deceptive, i.e., thin film of remaining indium, tin or lead flux on the surface of crystals will show superconducting transition at 3.4 K, 3.7 K, and 7.2 K, respectively.^{75,76} Superconductors are materials that—in most cases—reveal a metallic-like character below room temperature down to the superconducting transition. The residual resistivity ratio (RRR) defined as the ratio of resistivity at (usually) room temperature to residual resistivity—gives information about quality of a tested sample.⁷⁷ The RRR parameter can be as small as 1–2 (disordered polycrystalline materials), and as large as several thousand (ultra-pure crystals). A resistance of the sample is typically low and using an ordinary ohmmeter is not a good idea. It is because the resistance of the cables would be comparable with the resistance of the sample. Therefore, a four-probe (contact) method, schematically shown in Fig. 5 (inset), was developed, and is widely used in practice. The resistance (R) is given by a formula: $R = \rho \frac{l}{A}$, in which ρ is resistivity of the measured sample, and l is a distance between voltage contacts and A is a cross-section area ($A = t * w$). We are interested in the resistivity ρ , which is a fundamental property of a material: $\rho = R \frac{A}{l} = \frac{U}{I} \frac{tw}{l}$. The measured voltage signal (U) is small and for very good metallic samples at low temperature it can be comparable with a background (noise). To make U larger, one can increase applied current (I). However, the current you can use is limited by a current source (up to 5–7 mA in the Quantum Design PPMS system) and increasing current should be done with caution. The electrical current flowing through a sample can increase its temperature. A common problem with a low temperature resistivity measurement (below 1.8 K) is the inability to lower and stabilize the temperature due to the sample heating effect. The other way to increase measured U is making a geometric factor ($t * w / l$) as small as possible, which means large l and small t and w . In short, your sample should be thin, thick, and long.

Table 2 The reported superconductors in ternary stannides (T_c/K).

Compound	T_c	Compound	T_c
$\text{Ca}_3\text{Co}_4\text{Sn}_{13}$	6.0 ⁵⁷	$\text{Ca}_3\text{Ir}_4\text{Sn}_{13}$	7.6 ^{57,63}
$\text{La}_3\text{Co}_4\text{Sn}_{13}$	2.7 ^{66,72}	$\text{Sr}_3\text{Ir}_4\text{Sn}_{13}$	5.0 ⁶³
$\text{Ca}_3\text{Rh}_4\text{Sn}_{13}$	8.3 ⁵⁷	$\text{La}_3\text{Ir}_4\text{Sn}_{13}$	2.5 ⁶⁰
$\text{Sr}_3\text{Rh}_4\text{Sn}_{13}$	4.2 ⁶⁰	$\text{Lu}_5\text{Rh}_6\text{Sn}_{18}$	4.0 ^{67,71}
$\text{La}_3\text{Rh}_4\text{Sn}_{13}$	3.1 ⁶⁶	$\text{Y}_5\text{Rh}_6\text{Sn}_{18}$	3.0 ^{68,70,71}
$\text{Yb}_3\text{Rh}_4\text{Sn}_{13}$	8.0 ⁶⁴	$\text{Sc}_5\text{Rh}_6\text{Sn}_{18}$	5.0 ⁶⁹

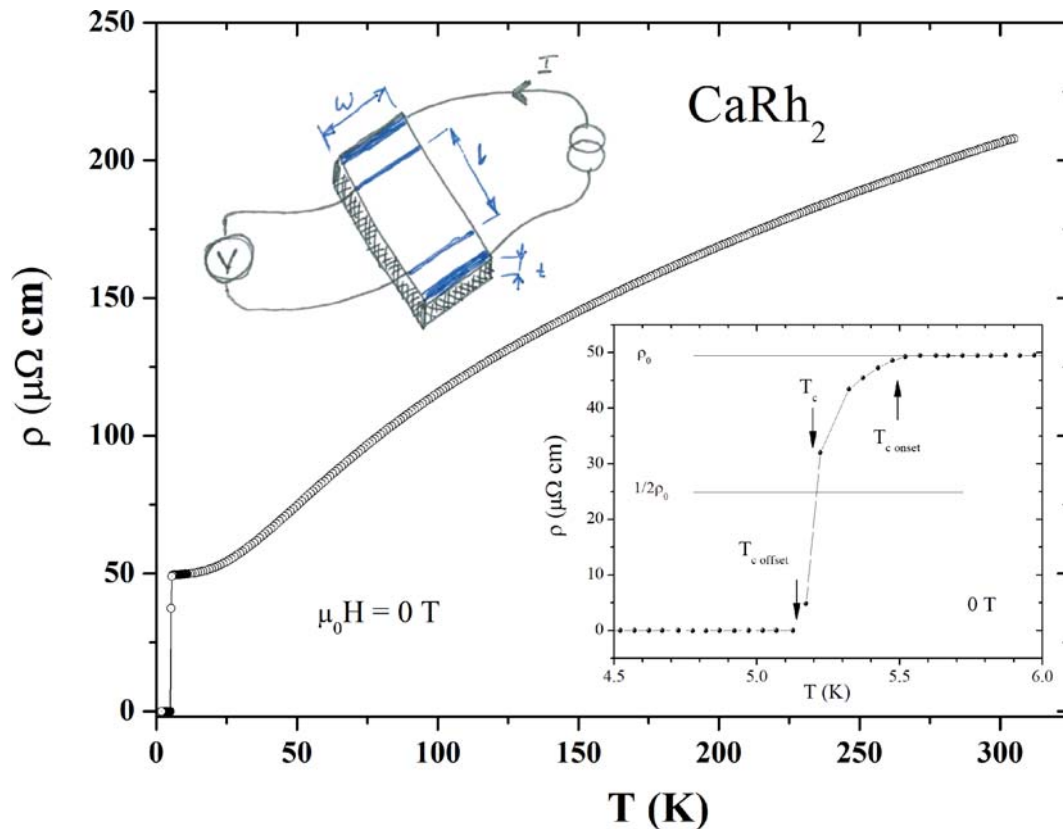


Fig. 5 *Main panel:* resistivity for CaRh₂ over a wide temperature range. *Inset* shows transition to superconducting state. Upper inset is a sketch of the 4-probe contact resistance technique. The contacts are represented by a parallel stripe. The external and internal contacts are called *current* and *voltage* contacts, respectively. A rectangular sample has thickness t and width w . Distance between *voltage* contacts is l . From Górnicka, K.; Cava, R. J.; Klimczuk, T. The Electronic Characterization of the Cubic Laves-Phase Superconductor CaRh₂. *J. Alloys Compd.* **2019**, 793, 393–399, <https://doi.org/10.1016/j.jallcom.2019.04.199>.

A typical temperature dependent resistivity for a superconducting compound CaRh₂ is shown in Fig. 5. The sample reveals metallic-like behavior with the residual resistivity ratio $RRR = 210/50 \sim 4$. An inset shows a transition to the superconducting state. The ρ_0 stands for residual resistivity—resistivity caused by crystal structure imperfections, while $T_{c\text{ onset}}$ and $T_{c\text{ offset}}$ are temperatures at which resistivity starts to decrease and reaches zero, respectively. The critical temperature (T_c) is usually defined as a temperature of the 50% drop of the $\rho(T)$. An observed character of the transition provides information concerning homogeneity of the superconducting phase. For a *not so good* sample, i.e., sample containing two superconducting phases, the transition will be broad, or step-like, see for example: La₃Ni₄P₄O₂⁷⁸ and La₃Co.⁷⁹

As expected, when the magnetic field is applied, T_c shifts to lower temperature and the transition becomes broader—as is shown in Fig. 6A. The upper critical field depends on temperature and this is shown in panel B. The $H_{c2}(T)$ data points were taken from the upper panel—see two vertical arrows for the zero field and 2.4 T measurement. In fact, at this moment we only assume that the obtained data points represent the *upper* critical field. In case of the first type superconductor, those points should be treated as the critical field. A field dependent magnetization $M(H)$ measurement—that will be explained below—will give an answer concerning type-I or type-II superconductivity. However, having the critical field in order of tesla, strongly suggests type-II superconductivity for CaRh₂.

The zero-temperature upper critical field $H_{c2}(0)$ is an important parameter that can be estimated from $H_{c2}(T)$ plot. For CaRh₂ it was obtained by using the Ginzburg-Landau (GL) relation: $\mu_0 H_{c2}(T) = \mu_0 H_{c2}(0) \frac{(1-t^2)}{(1+t^2)}$, where $t = T/T_c$ and T_c is a superconducting critical temperature at zero applied magnetic field. If the critical field is very large, or T_c is small, we can see only a small part of the $H_{c2}(T)$ diagram, which is the case of recently reported NbIr₂B₂ (see Fig. 7). This problem is caused by limitations of the measurement system. In a basic Physical Property Measurement System (PPMS) the lowest temperature is 1.8 K and the largest magnetic field 9 T. Hence, our data can be obtained for $T > 1.8$ K and $\mu_0 H < 9$ T—a yellow area in Fig. 7. In such a case, the formula provided by Werthamer-Helfand-Hohenberg (WHH) [Ref.^{80,81}] can be used: $\mu_0 H_{c2}(0) = -A \left(\frac{d(\mu_0 H_{c2})}{dT} \right)_{T=T_c} T_c$, where T_c is a zero-field critical temperature and $d(\mu_0 H_{c2})/dT$ is a $\mu_0 H_{c2}(T)$ slope near T_c —see Fig. 7. In the clean limit $A = 0.73$, whereas in the dirty limit $A = 0.69$. Dirty/clean limit is a comparison of the coherence length (ξ_0) and the carriers mean free path (l). In a clean limit the ratio ξ_0/l is

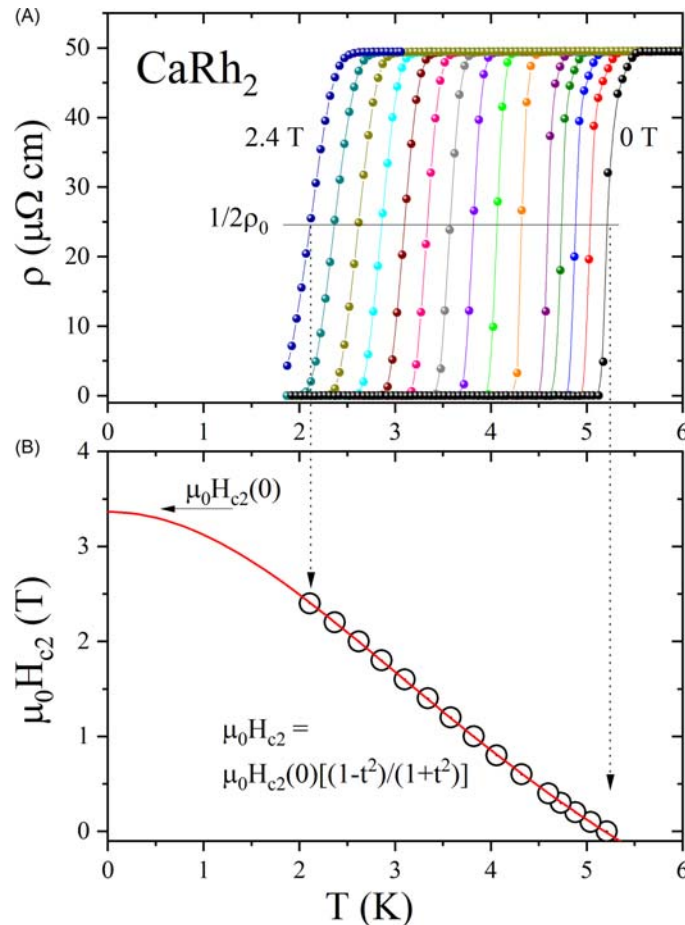


Fig. 6 (A) Low temperature resistivity under various magnetic field (0–2.4 T) for CaRh_2 . (B) The temperature dependence of the upper critical field with the data fitted with the Ginzburg-Landau formula. (A, B) From Górnicka, K.; Cava, R. J.; Klimczuk, T. The Electronic Characterization of the Cubic Laves-Phase Superconductor CaRh_2 . *J. Alloys Compd.* **2019**, *793*, 393–399, <https://doi.org/10.1016/j.jallcom.2019.04.199>.

smaller than one, which means that l is larger than ξ_0 . One should remember that this formula was derived for a single band type-II superconductors. A detailed discussion of the orbital upper critical field generalized to two-band, cleaned materials and anisotropic superconductors can be found in a Kogan and Prozorov paper.⁸²

In summary, resistivity is a rather simple technique from which we can get basic information concerning superconducting temperature and an upper critical field value (or critical field for type-I superconductor).

4.07.3.2 Magnetic susceptibility

The Meissner-Ochsenfeld effect was first observed in 1933, more than 20 years after discovering the superconductivity in mercury. Expulsion of the magnetic field from a superconductor—perfect diamagnetism—is the second feature of a superconducting material.

Even a one (superconducting) part of the sample per few thousands can give a detectable diamagnetic signal. In the past several new superconducting compounds were found ($\text{LnNi}_2\text{B}_2\text{C}$,⁸³ $\text{Mg}_{10}\text{Ir}_{19}\text{B}_2$,⁸⁴ NbRh_2B_2 ,⁸⁵ NbIr_2B_2 ⁷⁴) starting from a sample in which a very tiny diamagnetism was observed. It usually took us several weeks (or months) to establish the exactly accurate stoichiometry of new compounds and then study their physical properties.

Temperature-dependent magnetization is usually the first test we perform in the search for new superconducting materials. A tested sample can be in form of powder or a solid piece. Depending on your magnetometer (SQUID, VSM, or ACMS) a typical sample mass is from a few mg to 100 mg. The volume of a sample is a factor that should be considered.

The test starts from cooling with no field (zero-field-cooling) to the lowest available temperature and then a small magnetic field is applied H_{app} . The H_{app} value cannot be too large. Magnetic field decreases critical temperature (suppresses superconductivity)—that is why T_c estimated by magnetic susceptibility is often slightly lower than T_c obtained from zero-field resistivity or heat capacity studies. In an extreme case if the field H_{app} was greater than a critical field (H_c), a superconducting signal would not be observed. A typical H_{app} field is 10 Oe or 20 Oe. It is worth noting that the field-cooling measurement should not be used in search for

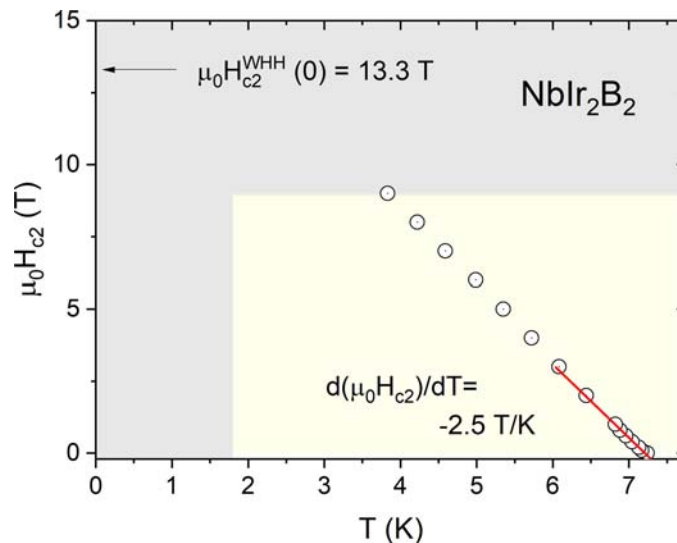


Fig. 7 Temperature dependence of the upper critical field for Nblr_2B_2 .

superconductivity, especially for sample in polycrystalline form. It is because the signal in polycrystalline material can be much weaker (still diamagnetic) which is caused by trapping magnetic field in inter-grain space. Now we will present and discuss the experimental magnetic results obtained for CaRh_2 . **Fig. 8** presents temperature dependent volume magnetic susceptibility (multiplied by 4π) measured in ZFC and FC mode. A volume susceptibility was calculated from $\chi_v = M_v/H_{\text{app}}$, where M_v is measured magnetization (in emu unit) divided by a sample volume (in cm^3). A drop of $\chi_v(T)$ starts at around 5.3 K, but the superconducting critical temperature is usually estimated as a temperature at which the steepest slope $\chi_v(T)$ line in a superconducting state intersects the extrapolation of the normal-state susceptibility.⁸⁶ In the CGS system for a perfect diamagnetism, full shielding volume fraction, the volume susceptibility reaches $\chi_v = -1/4\pi$. For CaRh_2 , below 4.5 K $\chi_v(T)$ is constant and $4\pi\chi_v = -2.2$, which is more than twice larger than expected value $4\pi\chi_v = -1$. The discrepancy is caused by a demagnetization effect.

The magnetic field inside a sample with elliptical shape is given by $H = H_{\text{app}} - H_{\text{d}}$, where H_{app} is the applied magnetic field, $H_{\text{d}} = -NM$ is the demagnetization field and N is a demagnetization factor. For a long sample oriented parallel to H_{app} , a demagnetization factor $N = 0$, whereas for a flat sample oriented perpendicular to H_{app} , N approaches 4π (in CGS) or 1 (in SI). The value of N can be roughly calculated knowing the shape of a sample and its alignment with the magnetic field, see for example Ref.,⁸⁷ more practical is estimation of the N value from the virgin part of the $M(H)$ curve measured at $T < T_c$ —see inset in **Fig. 9**. Besides temperature dependent $M_v(T)$, a field dependent volume magnetization $M_v(H)$ can be measured. The measurement should be done below T_c i.e., at the lowest stable temperature. **Fig. 9** shows $M(H)$ plot measured at 1.7 K for CaRh_2 . The shape of $M(H)$ provides an

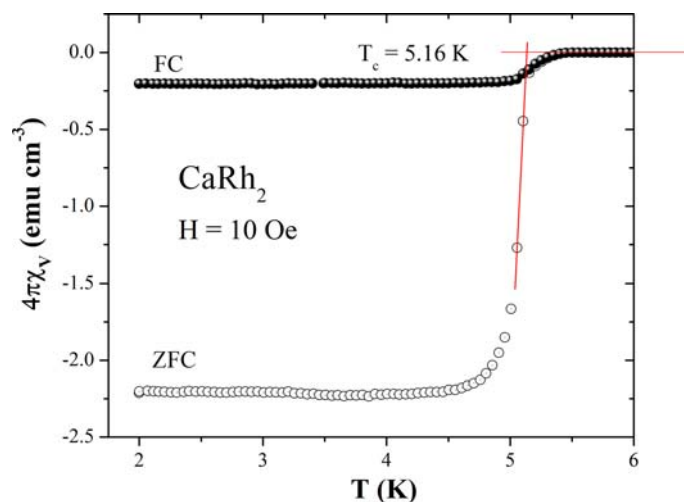


Fig. 8 Temperature dependence of the zero-field cooling (ZFC) and field cooling (FC) volume susceptibility for CaRh_2 . From Górnicka, K.; Cava, R. J.; Klimczuk, T. The Electronic Characterization of the Cubic Laves-Phase Superconductor CaRh_2 . *J. Alloys Compd.* **2019**, *793*, 393–399, <https://doi.org/10.1016/j.jallcom.2019.04.199>.

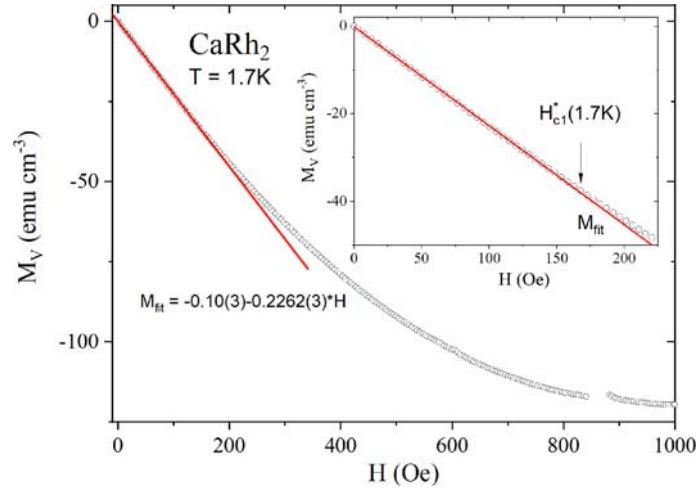


Fig. 9 Volume magnetization M_V vs applied magnetic field $M_V(H)$ measured at 1.7 K. An inset shows a linear response of M_V and a deviation from the full Meissner state.

information if a tested compound is type-I or type-II superconductor. The initial linear behavior of $M(H)$ was fitted by a simple $M_{\text{fit}} = a + bH$ relation. Fitting parameter a should be close to zero. A finite value of a is a direct information concerning a remnant field in the magnetometer. Having b allows us to calculate N value because the slope $b = 1/[4\pi(1 - N)]$. For CaRh_2 a linear fit gives $b = -0.2262$ and hence $N = 0.65$.

As can be seen in the inset of **Fig. 9**, above a certain field the $M_V(H)$ starts to deviate from linearity. The value of the lower critical field H^*_{c1} can be obtained from a field dependent $M_V - M_{\text{fit}}$ plot—see **Fig. 10B**. A dashed horizontal line is marking H^*_{c1} at each temperature. It should be noted that the criterion for the position of the line is not given explicitly and although this construction greatly helps to calculate H^*_{c1} , its value will be always slightly overestimated. Very recently a method of extraction of H^*_{c1} from the fit of the $M(H)$ dataset to the power law, with the threshold criterion H^*_{c1} , was proposed by Talantsev.⁸⁸

Having the H^*_{c1} estimated at several temperatures $T < T_c$ we can plot $H^*_{c1}(T)$ which is shown in **Fig. 11**. There is an extra point ($H = 0$) obtained from zero-field resistivity or heat capacity measurement. Then using a fit, $H^*_{c1}(T) = \mu_0 H^*_{c1}(0) \left[1 - \left(\frac{T}{T_c} \right)^2 \right]$, the zero temperature lower critical field value $H^*_{c1}(0)$ can be obtained. For CaRh_2 $H^*_{c1}(0) = 146$ Oe. The reason we use * is simple—the estimated value must be corrected by a demagnetization factor and hence $\mu_0 H^*_{c1}(0) = \mu_0 H^*_{c1}(0)/(1 - N) = 418$ Oe.

4.07.3.3 Heat capacity

This is typically a final method used for testing superconductivity and the only one that proves a volume effect of a superconducting state. How important this method is in confirming superconductivity can be found in a Ref. by Carnicom et al.⁸⁹ The method brings several important parameters, i.e., Sommerfeld coefficient (γ), Debye temperature (Θ_D), a normalized heat capacity jump at T_c ($\Delta C/(\gamma T_c)$), a superconducting gap value (ΔE), electron-phonon coupling strength (λ_{ep}). The method is relatively simple, though time consuming. It requires a small piece of a sample with one polished face that will be in contact with a platform of the calorimeter. More details concerning the most common—relaxation, two- τ method—can be found elsewhere.⁹⁰ Low temperature specific heat vs temperature for CaRh_2 is presented in **Fig. 12**. Transition to the superconducting state is manifested by a λ -shape anomaly at around 5.1 K. An exact T_c is obtained by an equal entropy construction which is shown in a **Fig. 12**. The construction is also useful for calculating a specific heat jump at T_c and for CaRh_2 we estimated $\Delta C/T_c = 44 \text{ mJ mol}^{-1} \text{ K}^{-2}$. It should be noted that superconductivity (in zero field) is a 2-nd order transition and therefore the λ -shape behavior of $C_p(T)$ is observed.

External magnetic field suppresses superconductivity which is shown in **Fig. 13A**. The transition shifts to lower temperature and a jump decreases as magnetic field is increased. However, for a type-I superconductors, an observed $\Delta C/T_c$ jump measured under low magnetic field can be larger than a zero-field $\Delta C/T_c$. This effect is caused by a fact that the first order transition is expected for a type-I superconductor tested under non-zero magnetic field. Note that in zero-field a second order transition is observed no matter if it is type-I or type-II superconductor. Since $M(H)$ measurement is sometimes not a conclusive if the superconductor is type-I or type-II, measuring C_p under a small magnetic field might be an additional test that shed light on this problem, see for example Ref. YbSb_2 ,⁹¹ ScGa_3 , and LuGa_3 ,⁹² LiBi .⁹³

An important parameter that can be estimated from the low temperature heat capacity measurement is an electronic specific heat coefficient (γ), sometimes called the Sommerfeld constant. In absence of magnetic ordering state, the heat capacity is given by

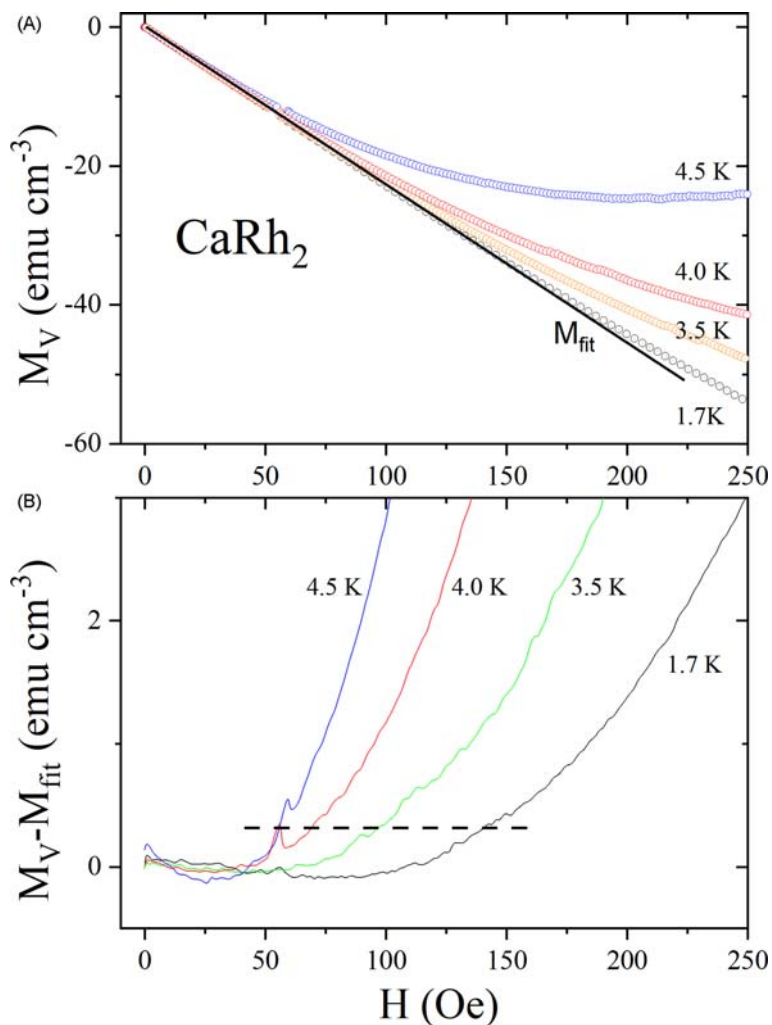


Fig. 10 (A) Volume magnetization versus applied magnetic field at constant temperature $T = 1.7$ K, 3.5 K, 4 K and 4.5 K. (B) Deviation from a fitted linear dependence on H . A dashed horizontal line is used for estimating a lower critical field $H_{c1}^*(T)$. (A) From Górnicka, K.; Cava, R. J.; Klimczuk, T. The Electronic Characterization of the Cubic Laves-Phase Superconductor CaRh₂. *J. Alloys Compd.* **2019**, 793, 393–399, <https://doi.org/10.1016/j.jallcom.2019.04.199>.

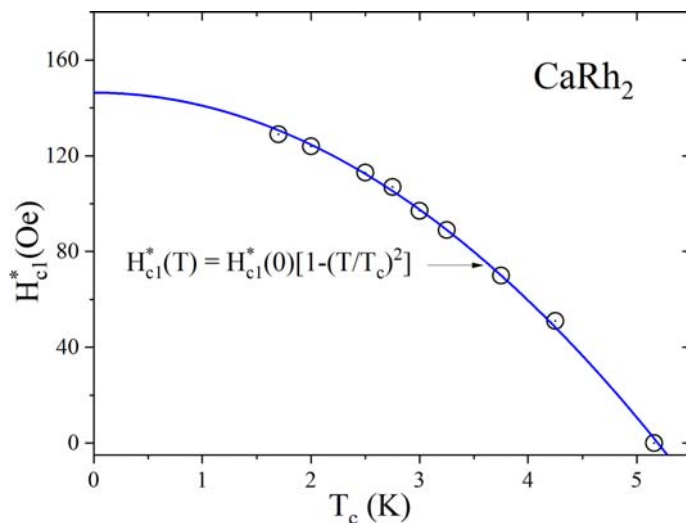


Fig. 11 Lower critical field H_{c1}^* versus temperature for CaRh₂. The last point for $T = 5.25$ K ($H = 0$ Oe) was obtained from zero-field resistivity measurement. From Górnicka, K.; Cava, R. J.; Klimczuk, T. The Electronic Characterization of the Cubic Laves-Phase Superconductor CaRh₂. *J. Alloys Compd.* **2019**, 793, 393–399, <https://doi.org/10.1016/j.jallcom.2019.04.199>.

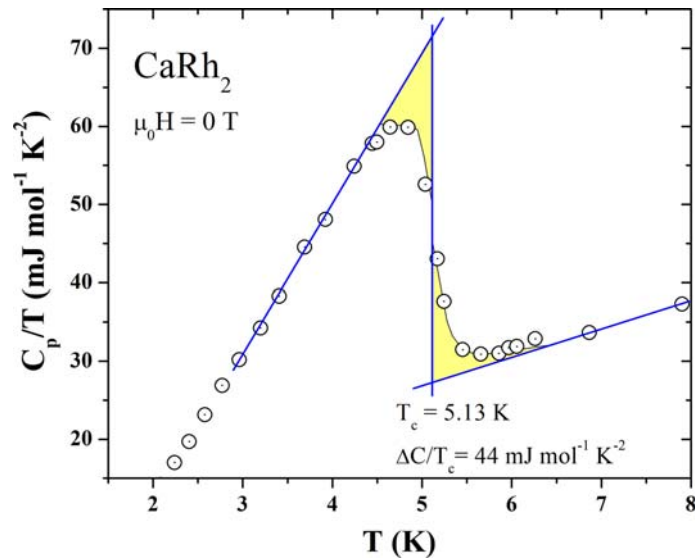


Fig. 12 The specific heat (C_p/T) versus temperature for CaRh₂ in vicinity of the superconducting transition. The entropy conservation construction is shown which gives $T_c = 5.13 \text{ K}$ and $\Delta C/T_c = 44 \text{ mJ mol}^{-1} \text{ K}^{-2}$. From Górnicka, K.; Cava, R. J.; Klimczuk, T. The Electronic Characterization of the Cubic Laves-Phase Superconductor CaRh₂. *J. Alloys Compd.* **2019**, *793*, 393–399, <https://doi.org/10.1016/j.jallcom.2019.04.199>.

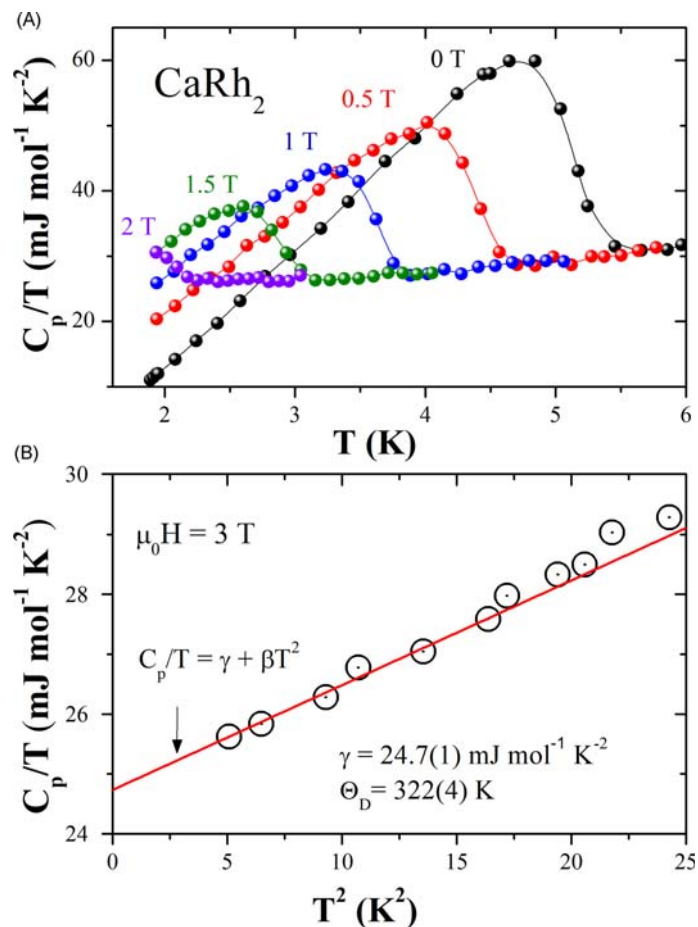


Fig. 13 The specific heat (C_p/T) versus temperature for CaRh₂ in vicinity of the superconducting transition. The entropy conservation construction is shown which gives $T_c = 5.13 \text{ K}$ and $\Delta C/T_c = 44 \text{ mJ mol}^{-1} \text{ K}^{-2}$. (A, B) From Górnicka, K.; Cava, R. J.; Klimczuk, T. The Electronic Characterization of the Cubic Laves-Phase Superconductor CaRh₂. *J. Alloys Compd.* **2019**, *793*, 393–399, <https://doi.org/10.1016/j.jallcom.2019.04.199>.

electronic (C_{el}) and phonon (C_{ph}) heat capacity. Both terms are temperature dependent. The first one is given by $C_{el}(T) = \gamma T \left[1 - \frac{3\pi^2}{10} \left(\frac{T}{T_F} \right)^2 \right]$, and since the Fermi temperature is $\sim 10^5$ K, $C_{el}(T)$ is linearly dependent on temperature: $C_{el}(T) = \gamma T$. There are two models—Debye and Einstein—that are used for modeling the phonon (lattice) specific heat C_{ph} . At sufficiently low temperature the Debye T^3 law is observed: $C_{ph}(T) = \beta T^3$, with β parameter related to the Debye temperature (Θ_D) by: $\Theta_D = \left(\frac{12\pi^4}{5\beta} nR \right)^{1/3}$. In this formula R is a gas constant and n is a number of atoms per formula unit. The total heat capacity, in absence of magnetic contribution, is given by: $C_p = C_{el}(T) + C_{ph}(T) = \gamma T + \beta T^3$, which can be written as: $\frac{C_p}{T} = \gamma + \beta T^2$. Fig. 13B presents C_p/T vs T^2 for CaRh_2 under 3 T field below 5 K. The applied magnetic field exceeds the upper critical field and hence the sample is in a normal state. The estimated $\gamma = 24.7(1)$ mJ mol $^{-1}$ K $^{-2}$ and $\beta = 0.18(1)$ mJ mol $^{-1}$ K $^{-4}$. Knowing β value the Debye temperature is calculated $\Theta_D = 322$ K. Experiments show that the validity of T^3 law is restricted to $\sim 2\%$ of Θ_D , in other words the fit should be done for $T < \Theta_D/50$. If the Debye temperature is low—often observed for compounds with heavy elements—then the phonon specific heat term can be extended and $C_{ph}(T) = \beta_3 T^3 + \beta_5 T^5$ formula should be used for the fit, see for example Ref.⁷⁹

Another parameter that can be directly obtained from the experimental results of C_p is a superconducting gap (Δ_0). For weak-coupling BCS superconductors, the expected gap value can be calculated from: $2\Delta_0 = 3.52k_B T_c$. In the superconducting state, the electronic specific heat part $C_{el} \sim \exp(-\Delta_0/k_B T)$, and hence a log scale C_{el} is plotted vs $1/T$ or T_c/T . One should note that even a small fraction of non-superconducting metallic impurity can greatly influence the fit. Therefore, the fitting formula usually includes $\gamma_0 T$ term with the residual γ_0 coming from an impurity phase. An example is shown in Fig. 14 for CaBi_2 :

The fit cannot be done up to T_c and instead an accurate BCS model should be used: $C_{BCS} = t \frac{d}{dT} \int_0^\infty dy \left(\frac{-6\gamma \Delta_0}{k_B \pi} \right) [f \ln f + (1-f) \ln(1-f)]$, where $t = T/T_c$, f is the Fermi function $f = 1/(e^{E/k_B T} + 1)$, $E = \sqrt{\varepsilon^2 + \Delta^2}$, $\gamma = \varepsilon/\Delta_0$, and $\Delta(T)/\Delta_0$ can be taken from the tabulated values of Mühlischlegel.⁹⁴

The additional important parameters can be calculated from the one gathered in the Table 3, particularly from the heat capacity measurement. Having γ and knowing $\Delta C/T_c$ a normalized specific heat jump at T_c can be obtained $\Delta C/\gamma T_c$. The Bardeen-Cooper-Schrieffer (BCS) theory for the weak-coupling superconductors predicts $\Delta C/\gamma T_c = 1.43$. For CaRh_2 we obtained $\Delta C/\gamma T_c = 1.78$ suggesting moderate or strong-coupling superconductivity. If the estimated value is lower than 1.43, it usually suggests presence of non-superconducting impurities. However, the observed jump value is much lower for the materials in which weak ferromagnetism is coexisting with superconductivity: UGe_2 ($\Delta C/\gamma T_c = 0.29$),⁹⁵ UCoGe ($\Delta C/\gamma T_c = 1.0$),⁹⁶ URhGe ($\Delta C/\gamma T_c = 0.6$).⁹⁷ It is worth noting that $\Delta C/\gamma T_c$ can be sometimes reduced by a multigap superconductivity [see for example $\text{Lu}_2\text{Fe}_3\text{Si}_5$ ^{98,99}].

The next important parameter that can be calculated is the electron-phonon coupling constant λ_{ep} given by an inverted McMillan's formula¹⁰⁰:

$$\lambda_{ep} = \frac{1.04 + \mu^* \ln(\Theta_D/1.45T_c)}{(1 - 0.62\mu^*) \ln(\Theta_D/1.45T_c) - 1.04}$$

In this formula T_c is the critical temperature, Θ_D is the Debye temperature obtained from heat capacity measurements, and μ^* is the Coulomb repulsion. The μ^* value is assigned between 0.1 and 0.15 as suggested by theory.¹ The choice of μ^* value is arbitrary and usually $\mu^* = 0.13$ which is located in the middle of the proposed range.^{101–103}

For CaRh_2 an obtained electron-phonon coupling constant $\lambda_{ep} = 0.63$ and this value indicate that CaRh_2 is a moderate or strong-coupling superconductor. The McMillan's equation was derived for a BCS weak-coupling superconductors and hence should be

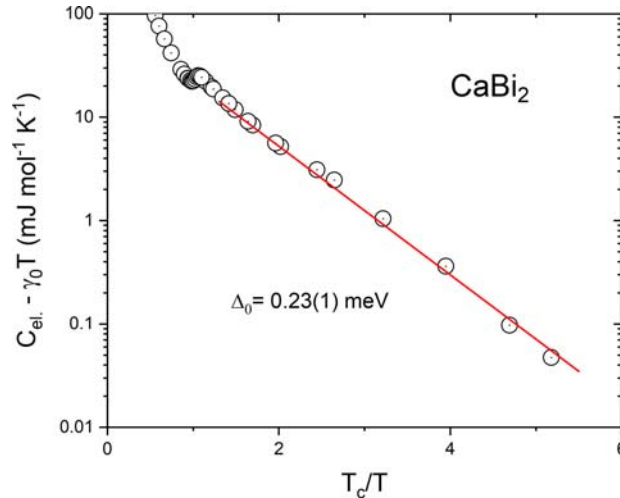


Fig. 14 The electronic specific heat C_{el} versus T_c/T for CaBi_2 . The $\gamma_0 T$ term originates from the impurity phase.

Table 3 The physical parameters that can be estimated from resistivity, magnetic susceptibility and heat capacity measurements.

	Resistivity	Magnetic susceptibility	Heat capacity
T_c	×	×	×
H_{c1}		×	
H_{c2}	×	×	×
γ			×
Θ_D			×
$\Delta C/T_c$			×
Δ_0			×

used with caution. If the specific heat anomaly jump $\Delta C/\gamma T_c$ is large (suggesting strong coupling), then more appropriate Allen-Dynes equation¹⁰⁴ should be use:

$$T_c = \left(\frac{\omega_{ln}}{1.2}\right) \exp \left[-\frac{1.04(1 + \lambda_{ep})}{\lambda_{ep} - \mu^*(1 + 0.62\lambda_{ep})} \right]$$

in which ω_{ln} is the logarithmic averaged phonon frequency. The value of ω_{ln} can be calculated from a formula proposed by F. Marsiglio and J. P. Carbotte for strong-coupling superconductors¹⁰⁵:

$$\frac{\Delta C}{\gamma T_c} = 1.43 \left[1 + 53 \left(\frac{T_c}{\omega_{ln}} \right)^2 \ln \left(\frac{\omega_{ln}}{3T_c} \right) \right]$$

For CaRh₂ the ω_{ln} value is 105 K and hence λ_{ep} is 0.89, larger than derived from the inverted McMillan's formula.

Having calculated electron-phonon coupling constant and the Sommerfeld coefficient, the non-interacting density of states at the Fermi level $N(E_F)$ can be obtained from

$$N(E_F) = \frac{3\gamma}{\pi^2 k_B^2 (1 + \lambda_{ep})}$$

Where k_B is the Boltzmann constant. Taking $\lambda_{ep} = 0.89$ we get $N(E_F) = 5.54$ states eV⁻¹ per f.u.

Now we go back to the lower and upper critical field derived from magnetic susceptibility and resistivity measurements. Assuming that the upper critical field is purely orbital, the superconducting coherence length ξ_{GL} can be obtained from the Ginzburg-Landau formula¹⁰⁶ $H_{c2} = \Phi_0/2\pi\xi_{GL}^2$ where $\Phi_0 = hc/2e$ is the quantum flux. For CaRh₂ the estimated upper critical field is $\mu_0 H_{c2} = 3.37$ T and hence $\xi_{GL} = 98$ Å.

Knowing the coherence length we can compare it with the mean free path l and the ξ_0/l ratio gives an information if the sample is clean or dirty limit. A very useful equation for calculating the mean free path was derived by Singh et al.¹⁰⁷

$$l = 2.372 \times 10^{-14} \left[\frac{\left(\frac{m^*}{m_e}\right)^2 V_M^2}{N(E_F)^2 \rho} \right],$$

where V_M is the molar volume (cm³ per mole), $N(E_F)$ is the density of states at the Fermi energy for both spin directions (states/eV f.u.), ρ is resistivity (Ω cm) and m^* is an effective mass of the charge carriers.

Having lower critical field and coherence length, we can get the superconducting penetration depth λ_{GL} by using a formula:

$$H_{c1} = \frac{\Phi_0}{4\pi\lambda_{GL}^2} \ln \frac{\lambda_{GL}}{\xi_{GL}},$$

For CaRh₂ we obtained $\lambda_{GL} = 942$ Å. The next parameter in a chain of our calculations is the Ginzburg-Landau parameter $\kappa_{GL} = \lambda_{GL}/\xi_{GL}$ which for CaRh₂ is $\kappa_{GL} = 9.5 > 1/\sqrt{2}$, supporting the type-II nature of the superconductivity. Finally, the thermodynamic critical field can be obtained from κ_{GL} , H_{c1} and H_{c2} using the formula $H_{c1}H_{c2} = H_c^2 \ln \kappa_{GL}$ and for CaRh₂ it yields $\mu_0 H_c = 0.25$ T.

We would like to point out that this short overview does not describe all aspects related to derivation of the superconducting parameters. For example, we did not discuss the single-band α -model of superconductivity¹⁰⁸ derived from the BCS theory and often used for the data analysis.¹⁰⁹ An useful elaboration of this model can be found in ref. 110.

4.07.4 Summary

In this review article, we focus on several superconducting family compounds and interpret them from structural and chemical bonding aspects, in particular, we emphasized the concept of critical charge transfer pairs such as Fe-As, Ir-Ge, Rh-Sn and Ru-P in superconductors. Moreover, three basic but important measurements to characterize the superconductivity have been explained in detail. The empirical rules to find new superconductivity from chemistry viewpoint could provide a different approach to novel superconductors.

Acknowledgment

The work at Rutgers was supported by Beckman Young Investigator Award and NSF-DMR-2053287. T.K. was supported by the National Science Centre (Poland) grant (UMO-2018/30/M/ST5/00773).

References

1. Poole, C. K.; Farach, H. A.; Creswick, R. J. *Handbook of Superconductivity*, Elsevier, 1999.
2. Holmes, L. Practical Applications of Superconductivity. *Electron Power* **1980**, *26* (3), 247–250. <https://doi.org/10.1049/ep.1980.0136>.
3. Seidel, P. *Applied Superconductivity: Handbook on Devices and Applications*, John Wiley & Sons, 2015.
4. Emergent Superconductivity. *Nat. Phys.* **2020**, *16* (7), 705. <https://doi.org/10.1038/s41567-020-0969-7>.
5. Superconductors Enable Lower Cost MRI Systems | NASA Spinoff n.d. https://spinoff.nasa.gov/Spinoff2012/hm_6.html (accessed 21 Nov 2020).
6. Preuss, P. n.d. Superconductors Face the Future. <https://newscenter.lbl.gov/2010/09/10/superconductors-future/> (accessed 20 Nov 2020).
7. Williams, J. E. C. Superconductors. In *Modern Materials*; Gonser, B. W., Ed.; vol. 6; Elsevier, 1968; pp 187–245. <https://doi.org/10.1016/B978-1-4831-9655-8.50010-1>.
8. Bednorts, I.; Myuller, K. Perovskite-Type Oxides the New Approach to High-Tc Superconductivity. *Usp. Fiz. Nauk* **1988**, *156* (2), 323–346.
9. Meng, R. L.; Beauvais, L.; Zhang, X. N.; Huang, Z. J.; Sun, Y. Y.; Xue, Y. Y.; Chu, C. W. Synthesis of the High-Temperature Superconductors $\text{HgBa}_2\text{CaCu}_2\text{O}_{6+\delta}$ and $\text{HgBa}_2\text{Ca}_2\text{Cu}_3\text{O}_{8+\delta}$. *Phys. C* **1993**, *216* (1), 21–28. [https://doi.org/10.1016/0921-4534\(93\)90629-5](https://doi.org/10.1016/0921-4534(93)90629-5).
10. Mikusu, S.; Takami, S.; Tokiwa, K.; Takeuchi, K.; Iyo, A.; Tanaka, Y.; Watanabe, T. Neutron Powder Diffraction of the Superconductor $\text{TlBa}_2\text{Ca}_2\text{Cu}_3\text{O}_{8+\delta}$ with Different Maximum T_C Values ($T_C = 120\text{--}132\text{ K}$). *Supercond. Sci. Technol.* **2008**, *21* (8), 085014. <https://doi.org/10.1088/0953-2048/21/8/085014>.
11. Ihara, H.; Sugise, R.; Hirabayashi, M.; Terada, N.; Jo, M.; Hayashi, K.; Negishi, A.; Tokumoto, M.; Kimura, Y.; Shimomura, T. A New High-Tc $\text{TlBa}_2\text{Ca}_3\text{Cu}_4\text{O}_{11}$ Superconductor with $T_C > 120\text{K}$. *Nature* **1988**, *334* (6182), 510–511. <https://doi.org/10.1038/334510a0>.
12. Cava, R. J. Oxide Superconductors. *J. Am. Ceram. Soc.* **2000**, *83* (1), 5–28.
13. Rahman, A.; Rahaman, Z.; Samsuddoha, N. A Review on Cuprate Based Superconducting Materials Including Characteristics and Applications. *Am. J. Phys.* **2015**, *3* (2), 39–56.
14. Xie, W.; Luo, H.; Seibel, E. M.; Nielsen, M. B.; Cava, R. J. Superconductivity in $\text{Hf}_6\text{Sb}_{3-x}\text{Ru}_x$: Are Ru and Sb a Critical Charge-Transfer Pair for Superconductivity? *Chem. Mater.* **2015**, *27* (13), 4511–4514. <https://doi.org/10.1021/acs.chemmater.5b01655>.
15. Dai, P.; Hu, J.; Dagotto, E. Magnetism and Its Microscopic Origin in Iron-Based High-Temperature Superconductors. *Nat. Phys.* **2012**, *8* (10), 709–718. <https://doi.org/10.1038/nphys2438>.
16. Chen, X. H.; Wu, T.; Wu, G.; Liu, R. H.; Chen, H.; Fang, D. F. Superconductivity at 43 K in $\text{SmFeAsO}_{1-x}\text{F}_x$. *Nature* **2008**, *453* (7196), 761–762. <https://doi.org/10.1038/nature07045>.
17. Parker, D. R.; Pitcher, M. J.; Baker, P. J.; Franke, I.; Lancaster, T.; Blundell, S. J.; Clarke, S. J. Structure, Antiferromagnetism and Superconductivity of the Layered Iron Arsenide NaFeAs . *Chem. Commun.* **2009**, *16*, 2189–2191. <https://doi.org/10.1039/B818911K>.
18. Hosono, H.; Yamamoto, A.; Hiramatsu, H.; Ma, Y. Recent Advances in Iron-Based Superconductors Toward Applications. *Mater. Today* **2018**, *21* (3), 278–302. <https://doi.org/10.1016/j.mattod.2017.09.006>.
19. Chen, X.; Dai, P.; Feng, D.; Xiang, T.; Zhang, F.-C. Iron-Based High Transition Temperature Superconductors. *Natl. Sci. Rev.* **2014**, *1* (3), 371–395. <https://doi.org/10.1093/nsr/nwu007>.
20. Watanabe, H.; Shirakawa, T.; Yunoki, S. Monte Carlo Study of an Unconventional Superconducting Phase in Iridium Oxide $\text{J}_{\text{eff}} = 1/2$ Mott Insulators Induced by Carrier Doping. *Phys. Rev. Lett.* **2013**, *110* (2), 027002.
21. Plumb, K.; Clancy, J.; Sandilands, L.; Shankar, V. V.; Hu, Y.; Burch, K.; Kee, H.-Y.; Kim, Y.-J. $\alpha\text{-RuCl}_3$: A Spin-Orbit Assisted Mott Insulator on a Honeycomb Lattice. *Phys. Rev. B* **2014**, *90* (4), 041112.
22. Dunbar, I. H.; MacLagan, R. G. A. R.; Parr, R. G. Concerning Atomic Radii. *J. Mol. Struct.* **1974**, *23* (1), 121–129. [https://doi.org/10.1016/0022-2860\(74\)85061-1](https://doi.org/10.1016/0022-2860(74)85061-1).
23. Allred, A. L. Electronegativity Values from Thermochemical Data. *J. Inorg. Nucl. Chem.* **1961**, *17* (3), 215–221. [https://doi.org/10.1016/0022-1902\(61\)80142-5](https://doi.org/10.1016/0022-1902(61)80142-5).
24. Tütüncü, H.; Uzunok, H.; Karaca, E.; Bağcı, S.; Srivastava, G. Ab Initio Investigation of Spin Orbit Coupling Effect on the Physical Properties of IrGe Superconductor. *Intermetallics* **2019**, *106*, 107–114.
25. Hirai, D.; Ali, M. N.; Cava, R. J. Strong Electron–Phonon Coupling Superconductivity Induced by a Low-Lying Phonon in IrGe. *J. Phys. Soc. Jpn.* **2013**, *82* (12), 124701.
26. Li, D.; Nimori, S.; Homma, Y.; Shiohara, Y.; Tobo, A.; Onodera, H.; Haga, Y.; Onuki, Y. Short-Range Magnetic Correlation with Kondo-Lattice Behavior in $\text{Ce}_3\text{Ir}_2\text{Ge}_2$ and Superconductivity in $\text{La}_3\text{Ir}_2\text{Ge}_2$. *J. Appl. Phys.* **2005**, *97* (7), 073903.
27. Francois, M.; Venturini, G.; Mareche, J.; Malaman, B.; Roques, B. De Nouvelles Séries de Germaniures, Isotopes de $\text{U}_4\text{Re}_7\text{Si}_6$, ThCr_2Si_2 et CaBe_2Ge_2 , Dans Les Systèmes Ternaires R–T–Ge Où R Est Un Élément Des Terres Rares et T ≡ Ru, Os, Rh, Ir: Supraconductivité de LaIr_2Ge_2 . *J. Less Common Met.* **1985**, *113* (2), 231–237.
28. Von Rohr, F.; Luo, H.; Ni, N.; Wörle, M.; Cava, R. J. Superconductivity and Correlated Fermi Liquid Behavior in Noncentrosymmetric $\text{Ca}_3\text{Ir}_4\text{Ge}_4$. *Phys. Rev. B* **2014**, *89* (22), 224504.
29. Srivichitrarond, L. C.; Seibel, E. M.; Xie, W.; Sobczak, Z.; Klimczuk, T.; Cava, R. J. Superconductivity in a New Intermetallic Structure Type Based on Endohedral $\text{Ta@Ir}_7\text{Ge}_4$ Clusters. *Phys. Rev. B* **2017**, *95* (17), 174521. <https://doi.org/10.1103/PhysRevB.95.174521>.
30. Kakihana, M.; Akamine, H.; Tomori, K.; Nishimura, K.; Teruya, A.; Nakamura, A.; Honda, F.; Aoki, D.; Nakashima, M.; Amako, Y.; Matsubayashi, K.; Uwatoko, Y.; Takeuchi, T.; Kida, T.; Hagiwara, M.; Haga, Y.; Yamamoto, E.; Harima, H.; Hedo, M.; Nakama, T.; Onuki, Y. Superconducting, Fermi Surface, and Magnetic Properties in SrTGe_3 and EuTGe_3 (T: Transition Metal) With the Rashba-Type Tetragonal Structure. *J. Alloys Compd.* **2017**, *694*, 439–451. <https://doi.org/10.1016/j.jallcom.2016.09.287>.
31. Fujii, H.; Sato, A. BaNiSn_3 -Type Ternary Germanides SrMGe_3 (M = Ir; Pd and Pt). *J. Alloys Compd.* **2010**, *508* (2), 338–341. <https://doi.org/10.1016/j.jallcom.2010.08.150>.
32. Gui, X.; Chang, T.-R.; Kong, T.; Pan, M. T.; Cava, R. J.; Xie, W. Monoclinic 122-Type BaIr_2Ge_2 With a Channel Framework: A Structural Connection between Clathrate and Layered Compounds. *Materials* **2017**, *10* (7), 818. <https://doi.org/10.3390/ma10070818>.

33. Falmbigl, M.; Grytsiv, A.; Rogl, P.; Giester, G. Clathrate Formation in the Systems Ba–Ir–Ge and Ba–Rh, Ir–Si: Crystal Chemistry and Phase Relations. *Intermetallics* **2013**, *36*, 61–72. <https://doi.org/10.1016/j.intermet.2012.12.010>.
34. Ishida, S.; Yanagi, Y.; Oka, K.; Kataoka, K.; Fujihisa, H.; Kito, H.; Yoshida, Y.; Iyo, A.; Hase, I.; Gotoh, Y.; Eisaki, H. Crystal Structure and Superconductivity of BaIr_2Ge_7 and $\text{Ba}_3\text{Ir}_4\text{Ge}_{16}$ with Two-Dimensional Ba–Ge Networks. *J. Am. Chem. Soc.* **2014**, *136* (14), 5245–5248. <https://doi.org/10.1021/ja5011527>.
35. Barz, H.; Ku, H. C.; Meisner, G. P.; Fisk, Z.; Matthias, B. T. Ternary Transition Metal Phosphides: High-Temperature Superconductors. *PNAS* **1980**, *77* (6), 3132–3134. <https://doi.org/10.1073/pnas.77.6.3132>.
36. Müller, R.; Shelton, R. N.; Richardson, J. W.; Jacobson, R. A. Superconductivity and Crystal Structure of a New Class of Ternary Transition Metal Phosphides $\text{TT}'\text{P}$ ($\text{T} = \text{Zr}, \text{Nb}, \text{Ta}$ and $\text{T}' = \text{Ru}, \text{Rh}$). *J. Less Common Met.* **1983**, *92* (1), 177–183. [https://doi.org/10.1016/0022-5088\(83\)90240-0](https://doi.org/10.1016/0022-5088(83)90240-0).
37. Shirovani, I.; Ichihashi, N.; Nozawa, K.; Kinoshita, M.; Yagi, T.; Suzuki, K.; Enoki, T. Superconductivity of ZrRuP . *Jpn. J. Appl. Phys.* **1993**, *32* (S3), 695. <https://doi.org/10.7567/JJAPS.32S3.695>.
38. Hase, I. Electronic Structure of the Superconducting Compounds O-ZrRuP and MoRuP . *Phys. Rev. B* **2003**, *68* (6), 064506. <https://doi.org/10.1103/PhysRevB.68.064506>.
39. Wong-Ng, W.; Ching, W. Y.; Xu, Y.-N.; Kaduk, J. A.; Shirovani, I.; Swartzendruber, L. Structure and Electronic Properties of the Orthorhombic MoRuP Superconductor Prepared at High Pressure. *Phys. Rev. B* **2003**, *67* (14), 144523. <https://doi.org/10.1103/PhysRevB.67.144523>.
40. Shirovani, I.; Tachi, K.; Konno, Y.; Todo, S.; Yagi, T. Superconductivity of the Ternary Ruthenium Compounds HfRuP and ZrRuX ($\text{X} = \text{P}, \text{As}, \text{Si}$ or Ge) Prepared at a High Pressure. *Philos. Mag. B* **1999**, *79* (5), 767–776. <https://doi.org/10.1080/13642819908205748>.
41. Meisner, G. P. Superconductivity and Magnetic Order in Ternary Rare Earth Transition Metal Phosphides. *Physica B* **1981**, *108* (1), 763–764. [https://doi.org/10.1016/0378-4363\(81\)90686-0](https://doi.org/10.1016/0378-4363(81)90686-0).
42. Shirovani, I.; Uchiyumi, T.; Ohno, K.; Sekine, C.; Nakazawa, Y.; Kanoda, K.; Todo, S.; Yagi, T. Superconductivity of Filled Skutterudites $\text{LaRu}_4\text{As}_{12}$ and $\text{PrRu}_4\text{As}_{12}$. *Phys. Rev. B* **1997**, *56* (13), 7866–7869. <https://doi.org/10.1103/PhysRevB.56.7866>.
43. Jeitschko, W.; Braun, D. $\text{LaFe}_4\text{P}_{12}$ with Filled CoAs_3 -Type Structure and Isotypic Lanthanoid–Transition Metal Polyphosphides. *Acta Crystallogr. B* **1977**, *33* (11), 3401–3406. <https://doi.org/10.1107/S056774087701108X>.
44. Meisner, G. P. Superconductivity and Structural Transformation in HfRuAs . *Phys. Lett. A* **1983**, *96* (9), 483–486. [https://doi.org/10.1016/0375-9601\(83\)90171-8](https://doi.org/10.1016/0375-9601(83)90171-8).
45. Meisner, G. P.; Ku, H. C.; Barz, H. Superconducting Equiatomic Ternary Transition Metal Arsenides. *Mater. Res. Bull.* **1983**, *18* (8), 983–991. [https://doi.org/10.1016/0025-5408\(83\)90010-7](https://doi.org/10.1016/0025-5408(83)90010-7).
46. Takeda, N.; Ishikawa, M. Superconducting and Magnetic Properties of Filled Skutterudite Compounds $\text{RERu}_4\text{Sb}_{12}$ ($\text{RE} = \text{La}, \text{Ce}, \text{Pr}, \text{Nd}$ and Eu). *J. Phys. Soc. Jpn.* **2000**, *69* (3), 868–873. <https://doi.org/10.1143/JPSJ.69.868>.
47. Uchiyumi, T.; Shirovani, I.; Sekine, C.; Todo, S.; Yagi, T.; Nakazawa, Y.; Kanoda, K. Superconductivity of $\text{LaRu}_4\text{X}_{12}$ ($\text{X} = \text{P}, \text{As}$ and Sb) with Skutterudite Structure. *J. Phys. Chem. Solids* **1999**, *60* (5), 689–695. [https://doi.org/10.1016/S0022-3697\(98\)00292-3](https://doi.org/10.1016/S0022-3697(98)00292-3).
48. Luo, H.; Krizan, J. W.; Muechler, L.; Haldolaarachchige, N.; Klimczuk, T.; Xie, W.; Fuccillo, M. K.; Felser, C.; Cava, R. J. A Large Family of Filled Skutterudites Stabilized by Electron Count. *Nat. Commun.* **2015**, *6* (1), 6489. <https://doi.org/10.1038/ncomms7489>.
49. Yasumoto, Y.; Yamaguchi, A.; Yanagisawa, T.; Nemoto, Y.; Goto, T.; Ochiai, A. Off-Center Rattling and Tunneling in Filled Skutterudite $\text{LaOs}_4\text{Sb}_{12}$. *J. Phys. Soc. Jpn.* **2008**, *77*, 242–244. <https://doi.org/10.1143/JPSJS.77SA.242>.
50. Nouneh, K.; Reshak, A. H.; Auluck, S.; Kityk, I. V.; Viennois, R.; Benet, S.; Charar, S. Band Energy and Thermoelectricity of Filled Skutterudites $\text{LaFe}_4\text{Sb}_{12}$ and $\text{CeFe}_4\text{Sb}_{12}$. *J. Alloys Compd.* **2007**, *437* (1), 39–46. <https://doi.org/10.1016/j.jallcom.2006.07.114>.
51. Kawashima, K.; Muranaka, T.; Kousaka, Y.; Akutagawa, S.; Akimitsu, J. Superconductivity in Transition Metal–Silicide W_5Si_3 . *J. Phys. Conf. Ser.* **2009**, *150* (5), 052106. <https://doi.org/10.1088/1742-6596/150/5/052106>.
52. Kleinke, H.; Ruckert, C.; Felser, C. Mixed Linear (M,Sb) Chains in the New Antimonides $\text{Hf}_{10}\text{M}_3\text{Sb}_{6-\delta}$ ($\text{M} = \text{V}, \text{Cr}, \text{Mn}, \text{Fe}, \text{Co}, \text{Ni}, \text{Cu}$): Crystal and Electronic Structures, Phase Ranges, and Electrical and Magnetic Properties. *Eur. J. Inorg. Chem.* **2000**, *2000* (2), 315–322. [https://doi.org/10.1002/\(SICI\)1099-0682\(200002\)2000:2<315::AID-EJIC315>3.0.CO;2-Q](https://doi.org/10.1002/(SICI)1099-0682(200002)2000:2<315::AID-EJIC315>3.0.CO;2-Q).
53. Simon, A. Superconductivity and Chemistry. *Angew. Chem. Int. Ed. Eng.* **1997**, *36* (17), 1788–1806. <https://doi.org/10.1002/anie.199717881>.
54. Garcia, E.; Corbett, J. D. Chemistry in the Polar Intermetallic Host Zirconium Antimonide, Zr_5Sb_3 . Fifteen Interstitial Compounds. *Inorg. Chem.* **1990**, *29* (18), 3274–3282. <https://doi.org/10.1021/ic00343a004>.
55. Xie, W.; Luo, H.; Phelan, B. F.; Cava, R. J. $\text{Zr}_5\text{Sb}_{3-x}\text{Ru}_x$, a New Superconductor in the W_5Si_3 Structure Type. *J. Mater. Chem. C* **2015**, *3* (31), 8235–8240. <https://doi.org/10.1039/C5TC01818H>.
56. Juraszek, J.; Henkie, Z.; Cichorek, T. Specific Heat of the Filled Skutterudite Superconductor $\text{LaOs}_4\text{As}_{12}$. *Acta Phys. Pol. A* **2016**. <https://doi.org/10.12693/APHYSPOLA.130.597>.
57. Hayamizu, H.; Kase, N.; Akimitsu, J. Superconducting Properties of $\text{Ca}_3\text{T}_4\text{Sn}_{13}$ ($\text{T} = \text{Co}, \text{Rh}$, and Ir). *J. Phys. Soc. Jpn.* **2011**, *80*, SA114. <https://doi.org/10.1143/JPSJS.80SA.SA114>.
58. Remeika, J. P.; Espinosa, G. P.; Cooper, A. S.; Barz, H.; Rowell, J. M.; McWhan, D. B.; Vandenberg, J. M.; Moncton, D. E.; Fisk, Z.; Woolf, L. D.; Hamaker, H. C.; Maple, M. B.; Shirane, G.; Tholinson, W. A New Family of Ternary Intermetallic Superconducting/Magnetic Stannides. *Solid State Commun.* **1980**, *34* (12), 923–926. [https://doi.org/10.1016/0038-1098\(80\)91099-6](https://doi.org/10.1016/0038-1098(80)91099-6).
59. Hodeau, J. L.; Chenavas, J.; Marezio, M.; Remeika, J. P. The Crystal Structure of $\text{SnYb}_3\text{Rh}_4\text{Sn}_{12}$, a New Ternary Superconducting Stannide. *Solid State Commun.* **1980**, *36* (10), 839–845. [https://doi.org/10.1016/0038-1098\(80\)90125-8](https://doi.org/10.1016/0038-1098(80)90125-8).
60. Kase, N.; Hayamizu, H.; Akimitsu, J. Superconducting State in the Ternary Stannide Superconductors $\text{R}_3\text{T}_4\text{Sn}_{13}$ ($\text{R} = \text{La}, \text{Sr}; \text{T} = \text{Rh}, \text{Ir}$) with a Quasiskutterudite Structure. *Phys. Rev. B* **2011**, *83* (18), 184509. <https://doi.org/10.1103/PhysRevB.83.184509>.
61. Hodeau, J. L.; Marezio, M.; Remeika, J. P.; Chen, C. H. Structural Distortion in the Primitive Cubic Phase of the Superconducting/Magnetic Ternary Rare-Earth Rhodium Stannides. *Solid State Commun.* **1982**, *42* (2), 97–102. [https://doi.org/10.1016/0038-1098\(82\)90360-X](https://doi.org/10.1016/0038-1098(82)90360-X).
62. Miraglia, S.; Hodeau, J. L.; Marezio, M.; Laviron, C.; Ghedira, M.; Espinosa, G. P. Nature of the Structural Distortion and of the Chemical Bonding in $\text{SnM}_3\text{Rh}_4\text{Sn}_{12}$ ($\text{M} = \text{La}, \text{Gd}, \text{Yb}, \text{Ca}, \text{Sr}$, and Th). *J. Solid State Chem.* **1986**, *63* (3), 358–368. [https://doi.org/10.1016/0022-4596\(86\)90192-1](https://doi.org/10.1016/0022-4596(86)90192-1).
63. Klintberg, L. E.; Goh, S. K.; Alireza, P. L.; Saines, P. J.; Tompsett, D. A.; Logg, P. W.; Yang, J.; Chen, B.; Yoshimura, K.; Grosche, F. M. Pressure- and Composition-Induced Structural Quantum Phase Transition in the Cubic Superconductor $\text{Ca}_3\text{Ir}_4\text{Sn}_{13}$. *Phys. Rev. Lett.* **2012**, *109* (23), 237008. <https://doi.org/10.1103/PhysRevLett.109.237008>.
64. Sato, H.; Aoki, Y.; Sugawara, H.; Fukuhara, T. Peak Effect in the Superconducting Mixed State of $\text{Yb}_3\text{Rh}_4\text{Sn}_{13}$ Single Crystals. *J. Phys. Soc. Jpn.* **1995**, *64* (9), 3175–3178. <https://doi.org/10.1143/JPSJ.64.3175>.
65. Bordet, P.; Miraglia, S.; Hodeau, J. L.; Marezio, M. Competition between Magnetism and Superconductivity in Erbium Rhodium Stannide. *J. Solid State Chem.* **1999**, *147* (1), 399–409. <https://doi.org/10.1006/jssc.1999.8405>.
66. Ślebarski, A.; Fijałkowski, M.; Maška, M. M.; Mierzejewski, M.; White, B. D.; Maple, M. B. Superconductivity of $\text{La}_3\text{Co}_4\text{Sn}_{13}$ and $\text{La}_3\text{Rh}_4\text{Sn}_{13}$: A Comparative Study. *Phys. Rev. B* **2014**, *89* (12), 125111. <https://doi.org/10.1103/PhysRevB.89.125111>.
67. Bhattacharyya, A.; Adroja, D. T.; Quintanilla, J.; Hillier, A. D.; Kase, N.; Strydom, A. M.; Akimitsu, J. Broken Time-Reversal Symmetry Probed by Muon Spin Relaxation in the Caged Type Superconductor $\text{Lu}_5\text{Rh}_6\text{Sn}_{18}$. *Phys. Rev. B* **2015**, *91* (6), 060503. <https://doi.org/10.1103/PhysRevB.91.060503>.
68. Kase, N.; Kittaka, S.; Sakakibara, T.; Akimitsu, J. Anisotropic Superconductivity of the Caged Compound $\text{Y}_5\text{Rh}_6\text{Sn}_{18}$ with Unusual Normal-State Electrical Resistivity. Proceedings of the International Conference on Strongly Correlated Electron Systems (SCES2013); JPS Conference Proceedings. *J. Phys. Soc. Jpn.*; p 3. <https://doi.org/10.7566/JSPSC.3.015042>.

69. Kase, N.; Kittaka, S.; Sakakibara, T.; Akimitsu, J. Superconducting Gap Structure of the Cage Compound $\text{Sc}_5\text{Rh}_6\text{Sn}_{18}$. *J. Phys. Soc. Jpn.* **2012**, *81* (Suppl.B), SB016. <https://doi.org/10.1143/JPSJS.81SB.SB016>.
70. Kase, N.; Inoue, K.; Hayamizu, H.; Akimitsu, J. Highly Anisotropic Gap Function in a Nonmagnetic Superconductor $\text{Y}_5\text{Rh}_6\text{Sn}_{18}$. *J. Phys. Soc. Jpn.* **2011**, *80* (Suppl.A), SA112. <https://doi.org/10.1143/JPSJS.80SA.SA112>.
71. Zhang, Z.; Xu, Y.; Kuo, C. N.; Hong, X. C.; Wang, M. X.; Cai, P. L.; Dong, J. K.; Lue, C. S.; Li, S. Y. Nodeless Superconducting Gap in the Caged-Type Superconductors $\text{Y}_5\text{Rh}_6\text{Sn}_{18}$ and $\text{Lu}_5\text{Rh}_6\text{Sn}_{18}$. *Supercond. Sci. Technol.* **2015**, *28* (10), 105008. <https://doi.org/10.1088/0953-2048/28/10/105008>.
72. Neha, P.; Srivastava, P.; Shrutti; Saha, J.; Patnaik, S. Synthesis and Characterization of $\text{La}_3\text{Co}_4\text{Sn}_{13}$ Superconductor. *AIP Conf. Proc.* **2015**, *1665* (1), 130034. <https://doi.org/10.1063/1.4918182>.
73. Górnicka, K.; Cava, R. J.; Klimczuk, T. The Electronic Characterization of the Cubic Laves-Phase Superconductor CaRh_2 . *J. Alloys Compd.* **2019**, *793*, 393–399. <https://doi.org/10.1016/j.jallcom.2019.04.199>.
74. Górnicka, K.; Gui, X.; Wiendlocha, B.; Nguyen, L. T.; Xie, W.; Cava, R. J.; Klimczuk, T. NbIr_2B_2 and TaIr_2B_2 —New Low Symmetry Noncentrosymmetric Superconductors with Strong Spin–Orbit Coupling. *Adv. Funct. Mater.* **2020**, *31*, 2007960.
75. Jennings, L. D.; Swenson, C. A. Effects of Pressure on the Superconducting Transition Temperatures of Sn, In, Ta, Tl, and Hg. *Phys. Rev.* **1958**, *112* (1), 31–43. <https://doi.org/10.1103/PhysRev.112.31>.
76. Townsend, P.; Sutton, J. Investigation by Electron Tunneling of the Superconducting Energy Gaps in Nb, Ta, Sn, and Pb. *Phys. Rev.* **1962**, *128* (2), 591–595. <https://doi.org/10.1103/PhysRev.128.591>.
77. Cabrera, G. G.; Falicov, L. M. Theory of the Residual Resistivity of Bloch Walls I. Paramagnetic Effects. *Phys. Status Solidi B* **1974**, *61* (2), 539–549. <https://doi.org/10.1002/pssb.2220610219>.
78. Klimczuk, T.; McQueen, T. M.; Williams, A. J.; Huang, Q.; Ronning, F.; Bauer, E. D.; Thompson, J. D.; Green, M. A.; Cava, R. J. Superconductivity at 2.2 K in the Layered Oxypnictide $\text{La}_3\text{Ni}_4\text{P}_4\text{O}_{22}$. *Phys. Rev. B* **2009**, *79* (1), 012505. <https://doi.org/10.1103/PhysRevB.79.012505>.
79. Strychalska, J.; Roman, M.; Sobczak, Z.; Wiendlocha, B.; Winiarski, M. J.; Ronning, F.; Klimczuk, T. Physical Properties and Electronic Structure of La_3Co and La_3Ni Intermetallic Superconductors. *Phys. C* **2016**, *528*, 73–83. <https://doi.org/10.1016/j.physc.2016.07.017>.
80. Helfand, E.; Werthamer, N. R. Temperature and Purity Dependence of the Superconducting Critical Field, H_{c2} . *Phys. Rev. Lett.* **1964**, *13* (23), 686–688. <https://doi.org/10.1103/PhysRevLett.13.686>.
81. Werthamer, N. R.; Helfand, E.; Hohenberg, P. C. Temperature and Purity Dependence of the Superconducting Critical Field, H_{c2} . III. Electron Spin and Spin–Orbit Effects. *Phys. Rev.* **1966**, *147* (1), 295–302. <https://doi.org/10.1103/PhysRev.147.295>.
82. Kogan, V. G.; Prozorov, R. Orbital Upper Critical Field of Type-II Superconductors with Pair Breaking. *Phys. Rev. B* **2013**, *88* (2), 024503. <https://doi.org/10.1103/PhysRevB.88.024503>.
83. Cava, R. J.; Takagi, H.; Zandbergen, H. W.; Krajewski, J. J.; Peck, W. F.; Siegrist, T.; Batlogg, B.; van Dover, R. B.; Felder, R. J.; Mizuhashi, K.; Lee, J. O.; Eisaki, H.; Uchida, S. Superconductivity in the Quaternary Intermetallic Compounds $\text{LnNi}_2\text{B}_2\text{C}$. *Nature* **1994**, *367* (6460), 252–253. <https://doi.org/10.1038/367252a0>.
84. Klimczuk, T.; Xu, Q.; Morosan, E.; Thompson, J. D.; Zandbergen, H. W.; Cava, R. J. Superconductivity in Noncentrosymmetric $\text{Mg}_{10}\text{Ir}_9\text{B}_{16}$. *Phys. Rev. B* **2006**, *74* (22), 220502. <https://doi.org/10.1103/PhysRevB.74.220502>.
85. Carnicom, E. M.; Xie, W.; Klimczuk, T.; Lin, J.; Górnicka, K.; Sobczak, Z.; Ong, N. P.; Cava, R. J. TaRh_2B_2 and NbRh_2B_2 : Superconductors with a Chiral Noncentrosymmetric Crystal Structure. *Sci. Adv.* **2018**, *4* (5), eaar7969. <https://doi.org/10.1126/sciadv.aar7969>.
86. Klimczuk, T.; Cava, R. J. Carbon Isotope Effect in Superconducting MgCNi_3 . *Phys. Rev. B* **2004**, *70* (21), 212514. <https://doi.org/10.1103/PhysRevB.70.212514>.
87. Sato, M.; Ishii, Y. Simple and Approximate Expressions of Demagnetizing Factors of Uniformly Magnetized Rectangular Rod and Cylinder. *J. Appl. Phys.* **1989**, *66* (2), 983–985. <https://doi.org/10.1063/1.343481>.
88. Talantsev, E. F. Method to extracting the penetration field in superconductors from DC magnetization data. *Rev. Sci. Instrum.* **2021**, *93* (5), 053912. <https://doi.org/10.1063/5.0081288>.
89. Carnicom, E. M.; Xie, W.; Yang, Z.; Górnicka, K.; Kong, T.; Klimczuk, T.; Cava, R. J. Importance of Specific Heat Characterization When Reporting New Superconductors: An Example of Superconductivity in LiGa_2Rh . *Chem. Mater.* **2019**, *31* (6), 2164–2173. <https://doi.org/10.1021/acs.chemmater.9b00258>.
90. Klaasse, J. C. P.; Brück, E. H. Heat-Capacity Measurements on Small Samples: The Hybrid Method. *Rev. Sci. Instrum.* **2008**, *79* (12), 123906. <https://doi.org/10.1063/1.3043430>.
91. Zhao, L. L.; Lausberg, S.; Kim, H.; Tanatar, M. A.; Brando, M.; Prozorov, R.; Morosan, E. Type-I Superconductivity in YbSb_2 Single Crystals. *Phys. Rev. B* **2012**, *85* (21), 214526. <https://doi.org/10.1103/PhysRevB.85.214526>.
92. Svanidze, E.; Morosan, E. Type-I Superconductivity in ScGa_3 and LuGa_3 Single Crystals. *Phys. Rev. B* **2012**, *85* (17), 174514. <https://doi.org/10.1103/PhysRevB.85.174514>.
93. Górnicka, K.; Gutowska, S.; Winiarski, M. J.; Wiendlocha, B.; Xie, W.; Cava, R. J.; Klimczuk, T. Superconductivity on a Bi Square Net in LiBi . *Chem. Mater.* **2020**, *32* (7), 3150–3159. <https://doi.org/10.1021/acs.chemmater.0c00179>.
94. Mühlischlegel, B. Die Thermodynamischen Funktionen des Supraleiters. *Z. Physik* **1959**, *155* (3), 313–327. <https://doi.org/10.1007/BF01332932>.
95. Tateiwa, N.; Kobayashi, T. C.; Amaya, K.; Haga, Y.; Settai, R.; Ōnuki, Y. Heat-Capacity Anomalies at T_{sc} and T^* in the Ferromagnetic Superconductor UGe_2 . *Phys. Rev. B* **2004**, *69* (18), 180513. <https://doi.org/10.1103/PhysRevB.69.180513>.
96. Huy, N. T.; Gasparini, A.; de Nijs, D. E.; Huang, Y.; Klaasse, J. C. P.; Gortenmulder, T.; de Visser, A.; Hamann, A.; Görlach, T.; Löhneysen, H.; v. Superconductivity on the Border of Weak Itinerant Ferromagnetism in UCoGe . *Phys. Rev. Lett.* **2007**, *99* (6), 067006. <https://doi.org/10.1103/PhysRevLett.99.067006>.
97. Aoki, D.; Huxley, A.; Ressouche, E.; Braithwaite, D.; Flouquet, J.; Brison, J.-P.; Lhotel, E.; Paulsen, C. Coexistence of Superconductivity and Ferromagnetism in URhGe . *Nature* **2001**, *413* (6856), 613–616. <https://doi.org/10.1038/35098048>.
98. Biswas, P. K.; Balakrishnan, G.; Paul, D. M. K.; Lees, M. R.; Hillier, A. D. Two-Gap Superconductivity in $\text{Lu}_2\text{Fe}_3\text{Si}_5$: A Transverse-Field Muon Spin Rotation Study. *Phys. Rev. B* **2011**, *83* (5), 054517. <https://doi.org/10.1103/PhysRevB.83.054517>.
99. Zehetmayer, M. A Review of Two-Band Superconductivity: Materials and Effects on the Thermodynamic and Reversible Mixed-State Properties. *Supercond. Sci. Technol.* **2013**, *26* (4), 043001. <https://doi.org/10.1088/0953-2048/26/4/043001>.
100. McMillan, W. L. Transition Temperature of Strong-Coupled Superconductors. *Phys. Rev.* **1968**, *167* (2), 331–344. <https://doi.org/10.1103/PhysRev.167.331>.
101. Barker, J. A. T.; Breen, B. D.; Hanson, R.; Hillier, A. D.; Lees, M. R.; Balakrishnan, G.; Paul, D. McK.; Singh, R. P. Superconducting and normal-state properties of the noncentrosymmetric superconductor. *Phys. Rev. B* **2018**, *98* (10), 104506. <https://doi.org/10.1103/PhysRevB.98.104506>.
102. Amon, A.; Svanidze, E.; Cardoso-Gil, R.; Wilson, M. N.; Rosner, H.; Bobnar, M.; Schnelle, W.; Lynn, J. W.; Gumenuk, R.; Hennig, C.; Luke, G. M.; Borrmann, H.; Leithe-Jasper, A.; Grin, Yu. Noncentrosymmetric Superconductor BeAu . *Phys. Rev. B* **2018**, *97* (1), 014501. <https://doi.org/10.1103/PhysRevB.97.014501>.
103. Srivichitraranond, L. C.; Seibel, E. M.; Xie, W.; Sobczak, Z.; Klimczuk, T.; Cava, R. J. Superconductivity in a New Intermetallic Structure Type Based on Endohedral $\text{Ta@Ir}_7\text{Ge}_4$ Clusters. *Phys. Rev. B* **2017**, *95* (17), 174521. <https://doi.org/10.1103/PhysRevB.95.174521>.
104. Allen, P. B.; Dynes, R. C. Transition Temperature of Strong-Coupled Superconductors Reanalyzed. *Phys. Rev. B* **1975**, *12* (3), 905–922. <https://doi.org/10.1103/PhysRevB.12.905>.
105. Marsiglio, F.; Carbotte, J. P. Strong-Coupling Corrections to Bardeen-Cooper-Schrieffer Ratios. *Phys. Rev. B* **1986**, *33* (9), 6141–6146. <https://doi.org/10.1103/PhysRevB.33.6141>.
106. Tinkham, M. *Introduction to Superconductivity*, Courier Corporation, 1996.
107. Singh, Y.; Martin, C.; Bud'ko, S. L.; Ellern, A.; Prozorov, R.; Johnston, D. C. Multigap Superconductivity and Shubnikov–de Haas Oscillations in Single Crystals of the Layered Boride OsB_2 . *Phys. Rev. B* **2010**, *82* (14), 144532. <https://doi.org/10.1103/PhysRevB.82.144532>.

108. Padamsee, H.; Neighbor, J. E.; Shiffman, C. A. Quasiparticle phenomenology for thermodynamics of strong-coupling superconductors. *J. Low Temp. Phys.* **1973**, *12*, 387–411. <https://doi.org/10.1007/BF00654872>.
109. Anand, V. K.; Kim, H.; Tanatar, M. A.; Prozorov, R.; Johnston, D. C. Superconductivity and Physical Properties of CaPd₂Ge₂ Single Crystals. *J. Phys. Condens. Matter.* **2014**, *26* (40), 405702.
110. Johnston, D. C. Elaboration of the α -Model Derived from the BCS Theory of Superconductivity. *Supercond. Sci. Technol.* **2013**, *26* (11), 115011.

4.08 Magnetic materials

Michael Shatruk and Judith K. Clark, Department of Chemistry and Biochemistry, Florida State University, Tallahassee, FL, United States

© 2023 Elsevier Ltd. All rights reserved.

4.08.1	Introduction	236
4.08.2	Definitions, units, and equations	237
4.08.2.1	Magnetization and susceptibility	237
4.08.2.2	Magnetic units	237
4.08.2.3	Diamagnetism and paramagnetism	237
4.08.2.4	Curie-Weiss law	238
4.08.2.5	Magnetic ordering	238
4.08.3	Magnetic oxides	239
4.08.3.1	Ferromagnetic oxides	239
4.08.3.2	Antiferromagnetic oxides	240
4.08.3.3	Ferrimagnetic oxides	243
4.08.4	Intermetallic magnets	246
4.08.4.1	General considerations	246
4.08.4.2	Binary intermetallics	247
4.08.4.3	Heusler and Half-Heusler compounds	248
4.08.4.4	ThCr ₂ Si ₂ -type intermetallics	249
4.08.5	Noncollinear magnetic ordering	249
4.08.5.1	General considerations	249
4.08.5.2	Materials with noncollinear magnetic structures	250
4.08.6	Applications of magnetic materials	253
4.08.6.1	Permanent magnets	253
4.08.6.2	Colossal magnetoresistance	254
4.08.6.3	Magnetocaloric materials	255
References		257
Further reading		261

Abstract

This chapter aims to familiarize the reader with a rich and burgeoning area of magnetism and magnetic materials. After introduction to the fundamental concepts of magnetism, specific examples of magnetic materials and behaviors are considered, being divided in two general subgroups—oxides and intermetallics. The conventional magnetic behavior associated with collinear ordering of magnetic moments is contrasted with complex magnetic structures characterized by non-collinear spin textures that arise from competing magnetic interactions. The chapter concludes with discussion of several properties that are paramount to technological uses of magnetic materials, such as permanent magnetism, colossal magnetoresistance, and magnetocaloric effect.

4.08.1 Introduction

Magnetism is a fascinating area of knowledge that crosses disciplinary boundaries between physics, chemistry, materials science, mathematics, engineering, and biology. Yet the coverage of magnetism and magnetic materials in undergraduate and graduate chemistry courses remains rather limited. This status-quo is somewhat surprising, taking into account the central role of chemistry in the synthesis and discovery of new materials and the paramount importance that magnetic materials play in many modern technologies, including information processing, data storage, cell phones, loudspeakers, wind turbines, and electric vehicles, to name a few.

This Chapter aims to provide a brief introduction to the main concepts of solid-state magnetism, followed by a discussion of various types and examples of magnetic materials. The coverage will not include a broad area of molecular magnetism and molecule-based magnetic materials, for which the reader is referred to excellent existing monographs.^{1,2} In Section 4.08.2, we provide the main definitions and units that will become useful for understanding the phenomena and materials discussed in this Chapter. To keep this account concise, we do not provide a comprehensive introduction to the fundamentals of magnetism that can be found in textbooks on solid-state physics^{3,4} or in more specialized texts on magnetism.^{5,6} Instead, we focus on the

most important principles and equations that are of practical use in the everyday research carried out by solid-state and materials chemists. In Sections 4.08.3 and 4.08.4, we consider representative examples of conventional magnetically ordered materials, while in Section 4.08.5 we cover less conventional types of magnetic behavior that are currently of great interest in solid-state sciences. Finally, Section 4.08.6 briefly discusses some current and emerging applications of magnetic materials.

We would like to emphasize that the coverage of specific examples is rather limited and selective, as our goal is to maintain a balance between the length of this account, the discussion of representative examples, and the necessity to reflect the great diversity of magnetic materials. Thus, this Chapter aims to introduce our readers to the fascinating and constantly expanding field of magnetism and magnetic materials. Those, who find this area of knowledge intriguing, can continue exploring its realm by using Further readings suggested in the end of the Chapter.

4.08.2 Definitions, units, and equations

4.08.2.1 Magnetization and susceptibility

A typical first step in the study of any magnetic material is the measurement of its response to an external magnetic field (H). This response is defined as magnetic induction (B). (Hereafter, the bold symbols indicate vectors or operators.) In vacuum, H and B are related by a constant known as the magnetic permeability of vacuum ($\mu_0 = 4\pi \times 10^{-7} \text{ T}\cdot\text{m/A}$):

$$B = \mu_0 H \quad (1)$$

In the presence of a material, however, the magnetic induction is modified as

$$B = \mu_0 (H + M) \quad (2)$$

where M is the magnetization of the material. The relationship between the magnetization and the applied magnetic field is given by

$$M = \chi_v H \quad (3)$$

which allows us to re-write Eq. (2) as

$$B = \mu_0 (1 + \chi_v) H \quad (4)$$

where χ_v is the volume magnetic susceptibility, an intrinsic property that characterizes the influence of the material on the magnetic induction produced by the applied field. This quantity, however, is of little practical value, as one typically prefers to describe the magnetic behavior of materials in terms of mass (χ_m) or molar (χ_{mol}) magnetic susceptibility:

$$\chi_m = \frac{\chi_v}{\rho} \quad (5)$$

$$\chi_{\text{mol}} = \frac{\chi_m}{FW} \quad (6)$$

where ρ is the density of the material and FW is its molar mass. Analogous conversions can be performed for the magnetization values.

4.08.2.2 Magnetic units

The units of magnetism are a common area of confusion, due to the long-term usage of cgs units alongside the SI units in this area of research. Without going into the historic details, suffice is to say that the cgs units appear to be strongly preferred by chemists, while the physics community has been progressively adhering more and more to the SI system. For that reason, we will not make an effort to follow one specific system of units, but would rather stick with whatever was reported in the original literature related to the specific examples of magnetic materials considered in this Chapter. Table 1 summarizes the SI and cgs units of magnetism and gives the conversion between the two systems.

4.08.2.3 Diamagnetism and paramagnetism

According to Lenz's law, an increasing magnetic field acting on a charged particle produces a current that in turn generates magnetic field in the opposite direction. Consequently, the applied magnetic field is weakened. This phenomenon is true of any interaction between a magnetic field and a charged particle and is the basis for *diamagnetism*. An electron also carries an angular momentum and acts as an elementary bearer of magnetism, or an elementary magnetic dipole. Such a magnetic dipole tends to align with the applied magnetic field. The presence of unpaired electrons, thus, results in the enhancement of the applied field, or *paramagnetism*.

The total magnetic susceptibility of any compound consists of diamagnetic and paramagnetic contributions, $\chi = \chi^{\text{dia}} + \chi^{\text{para}}$. While the paramagnetic contribution is not necessarily present, diamagnetism is an underlying property of all matter, and, therefore $\chi^{\text{dia}} \neq 0$ for any sample, even the one that exhibits paramagnetic behavior or magnetic ordering. Nevertheless, the diamagnetic contribution usually is very small, on the order of $-(1 \div 100) \cdot 10^{-6} \text{ emu/mol}$. Typically, if this value is less than 1% of the observed magnetic response, it can be ignored, but it should be taken into account when measuring samples with weaker magnetic signals.²

Table 1 The SI and cgs units of magnetism and the conversion factors.

Quantity (symbol)	SI units	cgs units	cgs → SI conversion
Magnetic induction (B)	T	G	$\times 10^{-4}$
Magnetic field strength (H)	A/m	Oe	$\times 10^3/(4\pi)$
Magnetization (M)	A/m	Oe	$\times 10^3$
Magnetic moment (m) ^a	A m ² or J/T	emu or erg/G	$\times 10^{-3}$
Mass susceptibility (χ_m)	m ³ /kg	emu/g	$\times 4\pi \cdot 10^{-3}$
Molar susceptibility (χ_{mol})	m ³ /mol	emu/mol	$\times 4\pi \cdot 10^{-6}$

^aThe elementary magnetic moment of a free electron equals 1 Bohr magneton, $\mu_B = 9.274 \cdot 10^{-24}$ J/T.

4.08.2.4 Curie-Weiss law

A magnetic atom or ion is characterized by the total angular momentum (J), which consists of the orbital (L) and spin (S) angular momenta, $J = L + S$. For lighter elements (e.g., the 3d metal ions), the orbital contribution is often (but not always) small and $J \approx S$. For heavier elements, such as 4d, 5d, 4f, and 5f metal ions, the orbital contribution cannot be ignored.

For a paramagnet, the value of J is related to the molar susceptibility through the Curie law:

$$\chi_{mol} = \frac{N_A \mu_B^2 g^2 J(J+1)}{3k_B T} = \frac{C}{T} \quad (7)$$

where N_A is Avogadro's number, μ_B is the Bohr magneton, g is the Lande g -factor (gyromagnetic ratio) of the electron, and k_B is Boltzmann's constant. Combining all constants and numeric values in this equation gives the Curie constant, C , which characterizes the magnetic behavior of species in the paramagnetic region. In the cgs units, $\frac{N_A \mu_B^2}{3k_B} \approx 1/8$, and Eq. (7) can be re-written as

$$\chi_{mol} T = \frac{g^2 J(J+1)}{8} = C \quad (8)$$

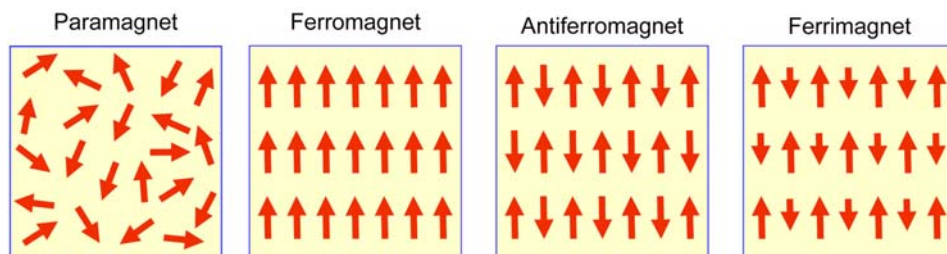
Eqs. (7) and (8), however, are only valid for dilute paramagnets, i.e., the systems where interactions between spin centers are negligible. In the presence of magnetic exchange interactions, these equations have to be modified to account for the deviation from the Curie law:

$$\chi_{mol} = \frac{C}{T - \theta} \quad (9)$$

where θ is the Weiss constant, and Eq. (9) is the Curie-Weiss law. This equation is frequently used to characterize magnetic substances in the paramagnetic regime. A common practice is to fit the temperature dependence of inverse magnetic susceptibility to a linear relationship, to extract the values of C and θ that characterize the single-site magnetism and the inter-site coupling, respectively. The effective magnetic moment (μ_{eff}) is related to the Curie constant as $\mu_{eff} = \sqrt{8C}$ in the cgs units or $\mu_{eff} = 797.8\sqrt{C}$ in the SI units. Note that, while the values of magnetic susceptibility are linearly additive, and so are Curie constants, the values of μ_{eff} are not. Therefore, average or cumulative effective magnetic moments should be calculated through sum of squares.

4.08.2.5 Magnetic ordering

When the exchange interactions between magnetic moments are sufficiently strong to overcome the paramagnetic disorder caused by thermal fluctuations, a material can develop an ordered magnetic phase (Scheme 1). In the ordered state, the magnetic moments

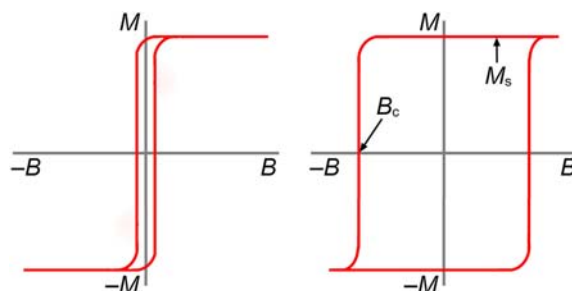


Scheme 1 A comparison of the magnetic moment arrangement in the paramagnetic state and the three conventional magnetically ordered states.

exhibit long-range alignment below a certain ordering temperature, typically referred to as the Curie temperature (T_C) for ferromagnetic (FM) ordering or the Neel temperature (T_N) for antiferromagnetic (AFM) ordering. These most conventional types of magnetic ordering correspond, respectively, to the parallel and antiparallel alignments of magnetic moments. In the ideally ordered state, the net magnetization of a ferromagnet is maximized while that of an antiferromagnet is equal to zero. If the antiparallel ordering takes place in a material that contains sites with different magnetic moments, one can observe ferrimagnetic (FiM) behavior, with a non-zero net magnetization. Materials that exhibit these three types of magnetic ordering will be discussed in Sections 4.08.3 and 4.08.4. In the case of competing magnetic interactions, more complex spin textures can emerge in the ordered state, e.g., stripe, helical, spiral, cycloid, or fan ordering. These types of magnetic behavior will be discussed in Section 4.08.5.

Although magnetic measurements in the presence of an applied magnetic field represent the most common approach to characterize magnetic materials, it should be emphasized that the true magnetically ordered state develops even in the absence of applied field, i.e., the magnetic ordering is spontaneous. It can be detected from a lambda-shaped anomaly in the heat capacity measurements or by observation of changes in the neutron diffraction pattern caused by coherent scattering from the ensemble of long-range-ordered magnetic moments.⁷

Immediately below the ordering temperature, the magnetic moments spontaneously align within small regions known as domains, although the moments of adjacent domains remain mis-aligned with respect to each other. Application of an external magnetic field and lowering of temperature cause gradual fusion of domains in the direction of preferred orientation of magnetization, via domain wall movement. The size of the domains, the thickness of domain walls, and the ease with which they propagate through the material are dictated by a delicate balance between different energy contributions,⁸ i.e., the exchange energy due to interaction between magnetic moments, the magnetocrystalline energy (magnetic anisotropy) due to the coupling between magnetic moments and the crystalline lattice, and the magnetostatic energy due to stray magnetic fields generated just outside the magnetic material. The resistance of domain walls to moving under applied magnetic field leads to the emergence of a hysteresis loop expressed as an irreversible change in magnetization as a function of applied field. Based on the character of the hysteresis, magnetically ordered materials can be classified as soft magnets, which show a facile response to the applied field and easy fusion of domains, and hard magnets, which show a strong resistance to the applied field and wide hysteresis loops (Scheme 2). The



Scheme 2 A schematic depiction of hysteresis loops for soft (left) and hard (right) magnets. The definitions of the saturation magnetization (M_s) and coercivity (B_c) are indicated for the hard magnet.

important parameters used to characterize magnetic properties are the maximum value of magnetization reached under applied magnetic field (known as the saturation magnetization, M_s) and the value of the applied field required to bring the magnetization of a material to zero (known as the coercive field, or coercivity, B_c).

4.08.3 Magnetic oxides

4.08.3.1 Ferromagnetic oxides

Due to their ubiquitous nature, oxides have been one of the most extensively investigated classes of magnetic materials. The oxide bridge is an effective mediator of exchange interactions between magnetic ions. These interactions have been thoroughly investigated from the theoretical perspective, and a set of semi-empirical rules has been developed to identify FM and AFM exchange pathways.^{9–11} The FM exchange requires orthogonality (zero overlap) of magnetic orbitals. Such a scenario is far less common than the AFM exchange. As a result, the majority of oxides exhibit AFM or FiM ordering, while FM ordered oxides are relatively rare (Table 2). It was also pointed out that AFM oxides, in general, are insulating or semiconducting, while FM oxides tend to exhibit metallic properties.¹²

CrO_2 is the only binary 3d metal oxide that shows FM ordering. This rutile-type oxide exhibits T_C of 396 K and the magnetic moment (m) of $2.0 \mu_B$ per formula unit (f.u.), as expected for the Cr^{4+} ion with the $3d^2$ electronic configuration and the spin state $S = 1$. The most remarkable property of CrO_2 is its half-metallicity, i.e., the presence of electrons with only one spin direction at the Fermi level and the opening of a band gap for the other spin direction. The half-metallic nature of CrO_2 spurred a high interest to this material for applications in spintronic devices.^{13,14} Unfortunately, investigation of this oxide is challenging, as the phase is

Table 2 Examples of ferromagnetic oxides with characteristic magnetic parameters.

Compound	Structure type	T_C , K	m , μ_B/atom
CrO ₂	Rutile (TiO ₂)	396	2.0
EuO	Rock salt (NaCl)	69	7.0
La _{0.7} Sr _{0.3} MnO ₃	Perovskite (CaTiO ₃)	370	3.7
Pr _{0.7} Sr _{0.3} MnO ₃	Perovskite (CaTiO ₃)	311	0.27 (Pr), 3.4 (Mn)
Nd _{0.7} Sr _{0.3} MnO ₃	Perovskite (CaTiO ₃)	195	
Sm _{0.7} Sr _{0.3} MnO ₃	Perovskite (CaTiO ₃)	70	
SrRuO ₃	Perovskite (CaTiO ₃)	160	0.77
La ₂ MnIrO ₆	Perovskite (CaTiO ₃)	100	4.0
In ₂ Mn ₂ O ₇	Pyrochlore (Ca ₂ Nb ₂ O ₇)	129	3.0
Tl ₂ Mn ₂ O ₇	Pyrochlore (Ca ₂ Nb ₂ O ₇)	124	3.0

metastable and readily decomposes to form a more stable oxide, Cr₂O₃. The only other binary FM oxide is EuO,¹⁵ with the rock-salt structure type. This insulating material exhibits FM ordering at 69 K, with $m = 7.0 \mu_B/\text{f.u.}$, as expected for the Eu²⁺ ion ($4f^7$, $S = 7/2$).

A large class of magnetic oxides is represented by compounds based on the perovskite structure, AMO₃. The adaptability of this structure to a broad range of electropositive (A) and transition (M) metal ions offers a wide chemical space for systematic investigation and tuning of magnetic properties. Similar to the binary oxides, ternary oxides exhibit FM ordering much less frequently as compared to AFM ordering. One of the most notable examples of ferromagnetism is offered by La_{1-x}Sr_xMnO₃. At the optimal value of $x = 0.3$, it exhibits half-metallicity and FM ordering at $T_C = 380$ K. The magnetic moment of $3.7 \mu_B/\text{f.u.}$ is in agreement with the presence of a mixture of Mn³⁺ ($3d^4$, $S = 2$) and Mn⁴⁺ ($3d^3$, $S = 3/2$) ions. The reason for the optimal FM behavior at this composition will be discussed in Section 4.08.3.2, while in Section 4.08.6.2 we will mention some examples of uses of La_{0.7}Sr_{0.3}MnO₃ and related manganites due to the colossal magnetoresistance (CMR) effect.

In principle, it was shown that ferromagnetism is achieved at $x = 0.3$ value for a broad range of lanthanide (Ln) – alkaline earth (A) manganites of the Ln_{1-x}A_xMnO₃ stoichiometry, where Ln = La, Pr, Nd, Sm and A = Ca, Sr, Ba, Pb.¹⁶ The T_C value showed a systematic increase with the increasing ionic radius of the Ln³⁺ ions (Table 2). This finding was attributed to the larger size of the electropositive cation in the perovskite structure causing less deviation from linearity of the Mn–O–Mn bridges that propagate superexchange coupling between the Mn sites.¹⁷

Pyrochlore-type manganites In₂Mn₂O₇ and Tl₂Mn₂O₇ show FM ordering with $T_C = 129$ K and 124 K, respectively.¹⁸ In contrast to the mixed-valent perovskite-type La_{0.7}Sr_{0.3}MnO₃, these materials contain only Mn⁴⁺ ions ($3d^3$, $S = 3/2$), which justifies the moment of $3 \mu_B$ per Mn site. Tl₂Mn₂O₇ was reported to exhibit half-metallicity and CMR.¹⁹ The observation of the CMR effect was explained by the increase in the charge carrier density with lowering the temperature or increasing the magnetic field near T_C .²⁰

An interesting variant of manganite ferromagnets are mixed 3d–5d metal oxides, such as La₂MnIrO₆. Here, the magnetic exchange between Mn³⁺ ions (high-spin $3d^4$, $S = 2$) mediated by the diamagnetic Ir³⁺ ions (low-spin $5d^6$, $S = 0$) leads to FM ordering at 100 K, with the experimental saturation moment of $4.0 \mu_B$. DFT calculations confirmed that the majority of unpaired spin density resides on the Mn site ($3.888 \mu_B$) while the Ir site carries only a small induced spin density oriented in the opposite direction ($-0.097 \mu_B$).

The 4d metal oxide, SrRuO₃, which also possesses the perovskite structure, shows FM ordering at rather high temperature of 160 K, despite the relatively low magnetic moment of the formally low-spin Ru⁴⁺ ion ($4d^4$, $S = 1$). The strong magnetic exchange between the Ru sites is mediated by conduction electrons, i.e., SrRuO₃ behaves as itinerant magnet.²¹ Indeed, the saturation moment is only $\sim 0.77 \mu_B$ per Ru atom, i.e., much lower than could be expected for the formal $S = 1$ state of the Ru⁴⁺ ion. (A more detailed discussion of itinerant magnetism is provided in Section 4.08.4.1.)

4.08.3.2 Antiferromagnetic oxides

Oxides that exhibit AFM ordering (Table 3) are much more common than those that show FM ordering. The prototypical simplest oxide antiferromagnets are represented by 3d metal monoxides, MO ($M = \text{Mn, Fe, Co, Ni}$), which were among the first materials subjected to magnetic structure determination by neutron diffraction.²² In these NaCl-type structures, the magnetic moments of M²⁺ ions are coupled FM in the (111) crystallographic planes, but the direction of moments alternates in the adjacent planes, causing the overall AFM ordering.^{23–25}

A more complex magnetic behavior is observed in α -Fe₂O₃, commonly known as hematite, which shows a collinear AFM order below 259 K. The moments are aligned nearly parallel to the rhombohedral axis of the corundum-type structure, alternating their direction in the hexagonal planes perpendicular to this axis (Fig. 1a). Above 259 K, a Morin transition takes place,²⁶ associated with reorientation of the magnetic moments perpendicular to the rhombohedral axis (Fig. 1b). Nevertheless, the moments are slightly canted out of the hexagonal planes, due to a weak Dzyaloshinskii–Moriya interaction, creating the overall canted AFM structure, with a small residual magnetization.²⁷

Table 3 Examples of antiferromagnetic oxides with characteristic magnetic parameters.

Compound	Structure type	T_N , K	m , μ_B/atom^a
MnO	Rock salt (NaCl)	118	5.6
FeO	Rock salt (NaCl)	200	3.3
CoO	Rock salt (NaCl)	290	4.0
NiO	Rock salt (NaCl)	525	2.5
Cr ₂ O ₃	Corundum (Al ₂ O ₃)	308	2.4
α -Fe ₂ O ₃	Corundum (Al ₂ O ₃)	960	4.1
CaCrO ₃	Perovskite (CaTiO ₃)	90	1.2
α -Sr ₂ CrO ₄	K ₂ NiF ₄	110	1.0
LaMnO ₃	Perovskite (CaTiO ₃)	140	3.9
La _{0.33} Ca _{0.67} MnO ₃	Perovskite (CaTiO ₃)	140	2.9
LaSr ₂ Mn ₂ O ₇	Sr ₃ Ti ₂ O ₇	210	2.8
Ca ₃ Ru ₂ O ₇	Ca ₃ Mn ₂ O ₇	56	1.6
La ₂ CoTiO ₆	Double perovskite (Ba ₂ LaRuO ₆)	25	5.8
La ₂ NiTiO ₆	Double perovskite (Ba ₂ LaRuO ₆)	25	4.1
Ca ₂ LaRuO ₆	Double perovskite (Ba ₂ LaRuO ₆)	12	2.0
Ba ₂ LaRuO ₆	Double perovskite (Ba ₂ LaRuO ₆)	30	2.0
Ba ₂ MnTeO ₆	Double perovskite (Ba ₂ LaRuO ₆)	20	4.8
Ba ₂ MnWO ₆	Double perovskite (Ba ₂ LaRuO ₆)	8	4.5

^aThese values are typically found by magnetic structure determination from neutron scattering data.

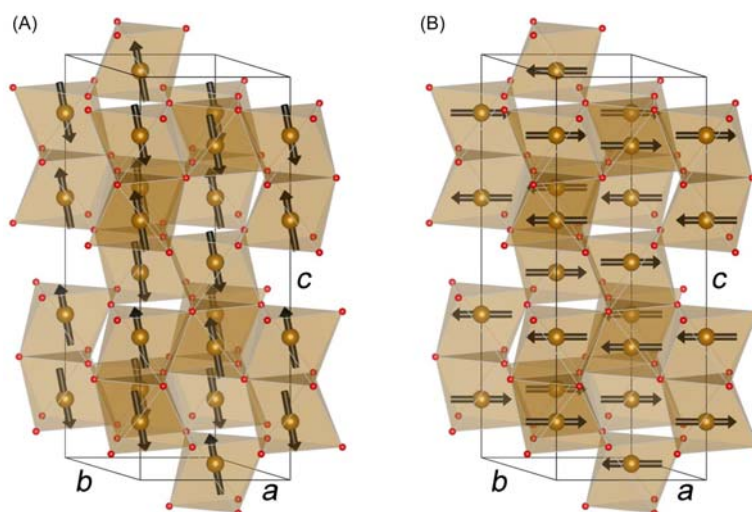


Fig. 1 The magnetic structures of α -Fe₂O₃ determined at 10 K (a) and 300 K (b), i.e., below and above the Morin transition temperature. Color scheme: Fe = gold, O = red.

Cr₂O₃, which also possesses the corundum structure, exhibits AFM ordering at 308 K, with the Cr moments aligning parallel to the rhombohedral axis.²⁸ Under applied magnetic field of 5.8 T and below 90 K, the material undergoes a first-order spin-flop transition that causes the Cr moments to orient perpendicular to the rhombohedral axis while maintaining the AFM order.²⁹ Another interesting aspect of Cr₂O₃ is its magnetoelectric behavior. The AFM ordering causes the loss of the inversion center in the crystal structure and leads to nonlinear optical effects that stem from coupling between nonlinear electric susceptibility and magnetic susceptibility.³⁰

CaCrO₃, Ca₃Ru₂O₇, and LaSr₂Mn₂O₇ represent rare examples of metallic AFM oxides. In CaCrO₃,¹² the high formal oxidation state of Cr⁴⁺ leads to substantial *pd* hybridization, i.e., covalent contribution to Cr–O bonding, which is also evidenced in the Cr magnetic moment of 1.2 μ_B being substantially lower than the expectation value of 2 μ_B for the Cr⁴⁺ ion (3d², *S* = 1). The result is that both the nearest-neighbor (NN) and next-nearest-neighbor (NNN) magnetic exchange interactions are quite strong. Competition between these interactions (spin frustration) leads to a C-type AFM structure, in which stripes of Cr moments are aligned FM along the *b* axis but AFM within the *ac* plane of the orthorhombic perovskite-type structure (Fig. 2).

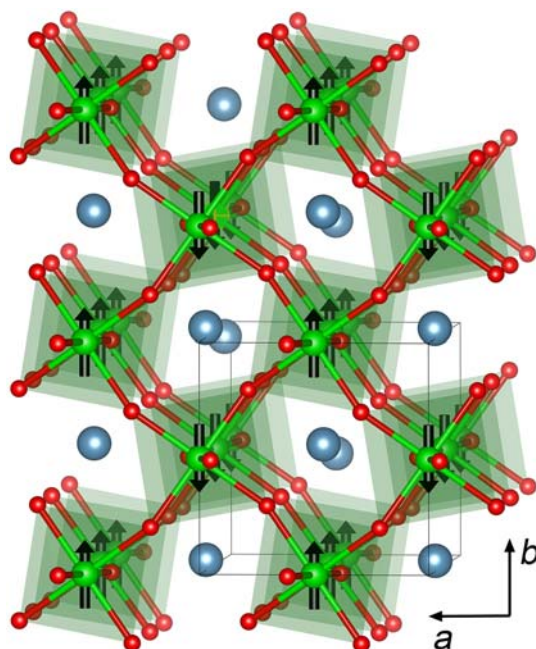


Fig. 2 The magnetic structure of CaCrO_3 viewed approximately down the c axis and showing the FM and AFM arrangement of Cr magnetic moments in the bc and ab planes, respectively. Color scheme: Ca = teal, Cr = green, O = red.

Interestingly, $\alpha\text{-Sr}_2\text{CrO}_4$, which also contains Cr^{4+} ions, is an AFM insulator with $T_N = 110$ K.³¹ The insulating behavior of this material vs. the metallic behavior of CaCrO_3 , most likely, stems from the decreased dimensionality of the Cr–O bonding, which forms a 3D perovskite-type framework in CaCrO_3 but a 2D K_2NiF_4 -type structure in $\alpha\text{-Sr}_2\text{CrO}_4$. The other polymorph, $\beta\text{-Sr}_2\text{CrO}_4$, also shows insulating behavior. It possesses a honeycomb structure that leads to a much lower AFM ordering temperature of 3.2 K.³²

$\text{Ca}_3\text{Ru}_2\text{O}_7$ belongs to the Ruddlesden-Popper type phases and exhibits a structure built of bilayers of vertex-sharing RuO_6 octahedra, separated by Ca^{2+} ions.³³ This material shows metallic behavior and undergoes AFM ordering at 56 K. The Ru moments show in-plane FM ordering within the bilayers, but the adjacent bilayers are coupled AFM.³⁴ At 48 K, however, a metal-to-insulator transition takes place, and the material becomes a more common non-metallic antiferromagnet.³³

Similar behavior was observed in another family of Ruddlesden-Popper structures, $\text{La}_{1-x}\text{Sr}_x\text{Mn}_2\text{O}_7$.³⁵ Both metallic behavior and AFM ordering were observed at $x = 1$, corresponding to the composition $\text{LaSr}_2\text{Mn}_2\text{O}_7$. The Mn moments also show in-plane FM orientation, but the AFM structure is present already within each bilayer, with antiparallel arrangement of two FM planes. Quite interestingly, a slight change in the La/Sr ratio leads to a rich variety of magnetic structures, with weakly canted in-plane FM ordering at $x = 0.9$, collinear in-plane FM ordering at $x = 0.8$, axial FM ordering at $x = 0.7$, and, finally, to the in-plane AFM ordering with FM ordering within each bilayer at $x = 0.6$ (Fig. 3).

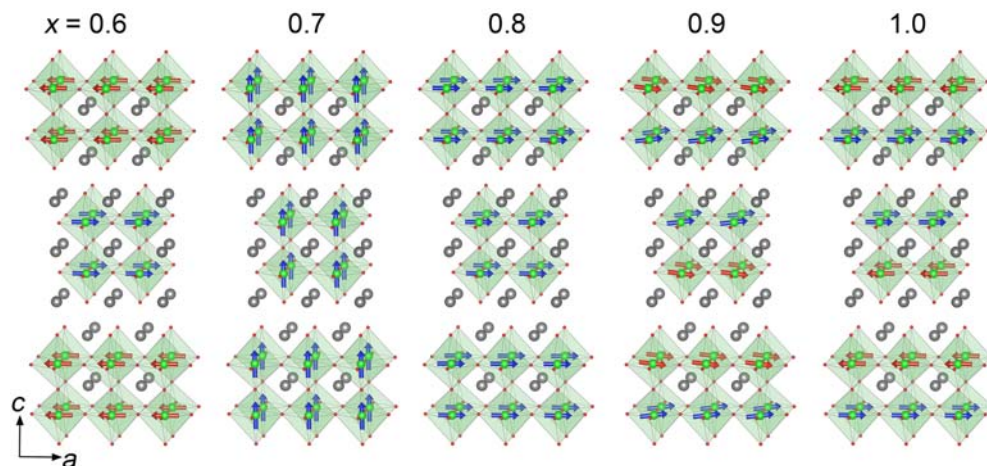


Fig. 3 A series of magnetic structures observed for $\text{La}_{1-x}\text{Sr}_x\text{Mn}_2\text{O}_7$ as a function of x . Color scheme: La/Sr = gray, Mn = green, O = red.

Such variation of magnetic structures with the change in the valence electron count is typical for many manganites.³⁶ In Section 4.08.3.1, we have already mentioned that the $\text{Ln}_{1-x}\text{A}_x\text{MnO}_3$ perovskites ($\text{Ln} = \text{La, Pr, Nd, Sm}$; $\text{A} = \text{Ca, Sr, Ba, Pb}$) exhibit metallic behavior and FM ordering at the optimal value of $x = 0.3$. The pure LaMnO_3 contains exclusively Mn^{3+} ions ($3d^4, S = 2$) and shows AFM ordering at 140 K.³⁷ It was shown that the FM exchange constant (0.83 meV) within the MnO_2 layers in the ab plane exceeds by a factor of 1.4 the AFM exchange coupling (-0.58 meV) between these layers along the c axis.³⁸ Doping Ca^{2+} (or other A^{2+} ions) for Ln^{3+} leads to a mixture of Mn^{3+} and Mn^{4+} ions and strengthens FM coupling through double exchange, eventually leading to the FM ordering at $x = 0.3$. At other values of x , corresponding to different degree of hole-doping, i.e., different $\text{Mn}^{3+}/\text{Mn}^{4+}$ ratios, rich magnetic behavior can be observed as a function of temperature and applied magnetic field. As an example, we consider the series $\text{La}_{1-x}\text{Ca}_x\text{MnO}_3$, the terminal members of which, LaMnO_3 and CaMnO_3 , are pure antiferromagnets. At small levels of Ca for La substitution ($x < 0.15$), the Mn spins begin to cant away from the ab plane, creating an uncompensated magnetic moment along the c axis,³⁹ but at higher doping levels ($x > 0.15$) FM ordering is observed.⁴⁰ As the Ca content is further increased, the competition between the FM and AFM states is observed as a function of temperature: $\text{La}_{0.5}\text{Ca}_{0.5}\text{MnO}_3$ exhibits FM ordering at 225 K but then converts to an AFM phase at 170 K.⁴¹ At $x = 0.67$, only AFM ordering is observed below 140 K, with the formation of both crystallographic and magnetic superstructures. The latter shows a complex noncollinear AFM structure.⁴²

A large group of AFM oxides is represented by double perovskites, $\text{A}_2\text{MM}'\text{O}_6$. The most common magnetic structures adopted by such compounds show AFM coupling between either (111) or (001) planes. The former takes place when the NN interactions are stronger than the NNN interactions, while the latter occurs when the NNN interactions are stronger than the NN ones. When these interactions are of comparable strength, spin frustration often leads to the formation of striped AFM structure, with the rows of FM-coupled magnetic moments aligning antiparallel to each other. The balance between the NN and NNN magnetic exchange constants can be tuned by changing the size of the A site, thus varying the distances between the M and M' sites and the corresponding angles at the oxide bridges. For example, both $\text{Ca}_2\text{LaRuO}_6$ and $\text{Ba}_2\text{LaRuO}_6$ show AFM ordering, but the Ru moments align FM in the (001) planes or along the b axis, respectively,⁴³ which suggests that the NN and NNN exchange constant become comparable in $\text{Ba}_2\text{LaRuO}_6$. On the other hand, both $\text{Ba}_2\text{MnTeO}_6$ and Ba_2MnWO_6 show AFM structures with FM alignment of Mn moments in the (001) or (111) planes, respectively,^{44,45} indicating that a crossover in the relative strength of the NN and NNN interactions takes place between these two compositions. The difference in the magnetic structures was attributed to the presence of completely filled 4d orbitals in the formally Te^{6+} ion and completely empty 5d orbitals in the formally W^{6+} ion.

The competition between the NN and NNN interactions can be seen in $\text{La}_2\text{CoTiO}_6$ and $\text{La}_2\text{NiTiO}_6$; both of them show AFM transition at 25 K.⁴⁶ The magnetic structure reveals stripe-type AFM ordering, with the transition metal moments coupled FM along the b axis and AFM along the a and c axes. The moments are slightly tilted with respect to the ab plane, but the overall AFM structure is collinear.

When substantially different magnetic elements are introduced in the M and M' sites, they can behave nearly independently of each other. For example, $\text{Sr}_2\text{CoOsO}_6$ exhibits two AFM transitions, with the magnetic moments of Os^{6+} ions ($5d^2, S = 1$) ordering AFM at 108 K and the moments of Co^{2+} ions ($3d^7, S = 3/2$) ordering AFM at 70 K.⁴⁷ The Os moments couple FM along the c axis and AFM in the ab plane, while the Co moments couple FM along the b axis and AFM in the ac plane (Fig. 4). The independent ordering of the two magnetic sublattices was justified by DFT calculations, which revealed that the NN Os–Co interactions were substantially weaker than the NNN Os–Co–Os or Co–Os–Co interactions.

4.08.3.3 Ferrimagnetic oxides

Ferrimagnetic (FiM) ordering arises from AFM coupling between spins of different magnitude, which results in the total uncompensated magnetic moment in the ordered state. Consequently, ferrimagnetism emerges in the structures that contain either different magnetic elements or the same magnetic element in different oxidation states and/or different coordination environments (Table 4). In both situations, the spins of the same magnitude should couple FM to each other and AFM to the spins of different magnitude. Perhaps, the most well-known example of FiM ordering is provided by magnetite, Fe_3O_4 , with the inverse spinel structure. The Fe^{2+} and a half of Fe^{3+} ions occupy octahedral interstices in the cubic close packing of O^{2-} ions, while the other half of Fe^{3+} ions occupy tetrahedral interstices. The ions located in the octahedral and tetrahedral sites are coupled AFM to each other, resulting in the overall FiM order.⁴⁸ Interestingly, a γ -polymorph of Fe_2O_3 (maghemite), although containing only Fe^{3+} ions, also exhibits ferrimagnetism. Similar to Fe_3O_4 , this material has a spinel-type structure, but 1/6 of Fe^{3+} ions are missing from the octahedral sites, i.e., its formula can be written as $[\text{Fe}]_t[\text{Fe}_{5/3}\square_{1/3}]_o$, where \square represents a vacancy. The uneven distribution of the Fe^{3+} ions between the octahedral and tetrahedral sites results in FiM ordering.⁴⁹

Fe_3O_4 is a parent representative of other magnetic ferrites, MFe_2O_4 ($\text{M} = \text{Mn, Co, Ni}$), with the inverse spinel structure. The degree of inversion, i.e., the concentration of the M^{2+} ions in the octahedral sites, depends strongly on the synthetic conditions,⁵⁰ which, therefore, also affect the observed magnetic properties.⁵¹ NiFe_2O_4 is a nearly perfect inverse spinel, due to the substantial ligand field stabilization energy for the Ni^{2+} ion ($3d^8, t_{2g}^6e_g^2, S = 1$) in the octahedral ligand field, as compared to the Fe^{3+} ion ($3d^5, t_{2g}^3e_g^2, S = 5/2$). The AFM coupling between the Fe^{3+} ions distributed equally among the tetrahedral and octahedral sites leads to the cancellation of their moments, leaving the net magnetic moment equal to the moment of the Ni^{2+} ion ($2.2 \mu_B$) located nearly exclusively in the octahedral sites. The preference for the octahedral coordination of the M^{2+} ion remains strong in CoFe_2O_4 , although this material tends to contain from 5% to 25% of Co^{2+} ions in the tetrahedral sites. Quenching the samples annealed at high temperature leads to a higher concentration of Co^{2+} in the tetrahedral sites, while slow cooling allows the formation of

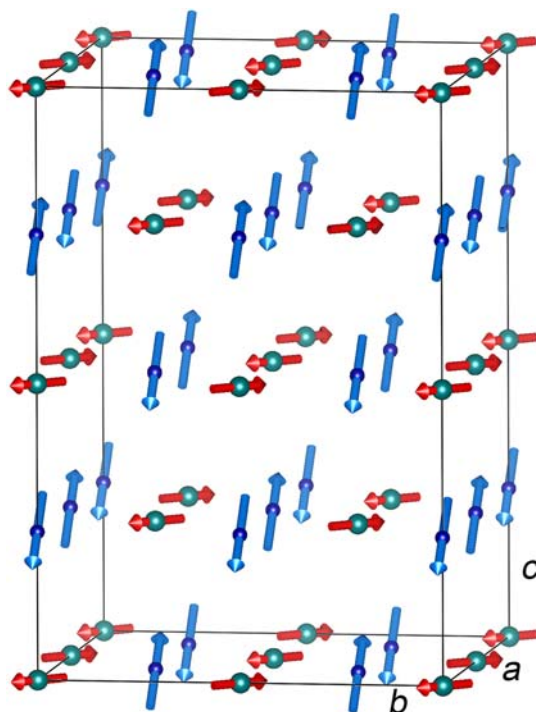


Fig. 4 The magnetic structure of $\text{Sr}_2\text{CoOsO}_6$. The Co and Os magnetic moments are shown with blue and red arrows, respectively. The non-magnetic atoms are not shown.

Table 4 Examples of ferrimagnetic oxides with characteristic magnetic parameters.

Compound	Structure type	T_C , K	m , $\mu_B/\text{f.u.}$
Fe_3O_4	Spinel (MgAl_2O_4)	860	4.0
$\gamma\text{-Fe}_2\text{O}_3$	Spinel (MgAl_2O_4)	950	2.5
MnFe_2O_4	Spinel (MgAl_2O_4)	573	4.5–4.8 ^a
CoFe_2O_4	Spinel (MgAl_2O_4)	793	3.5–4.0 ^a
NiFe_2O_4	Spinel (MgAl_2O_4)	868	2.2
$\text{SrFe}_{12}\text{O}_{19}$	$\text{PbFe}_{12}\text{O}_{19}$	750	19.7
$\text{BaFe}_{12}\text{O}_{19}$	$\text{PbFe}_{12}\text{O}_{19}$	740	19.3
$\text{Y}_3\text{Fe}_5\text{O}_{12}$	$\text{Y}_3\text{Al}_5\text{O}_{12}$	560	5.0
$\text{Gd}_3\text{Fe}_5\text{O}_{12}$	$\text{Y}_3\text{Al}_5\text{O}_{12}$	545	16.0
$\text{Sr}_2\text{CrMoO}_6$	Double perovskite ($\text{Ba}_2\text{LaRuO}_6$)	450	0.20
$\text{Sr}_2\text{FeMoO}_6$	Double perovskite ($\text{Ba}_2\text{LaRuO}_6$)	415	2.9
$\text{Sr}_2\text{CrOsO}_6$	Double perovskite ($\text{Ba}_2\text{LaRuO}_6$)	725	1.3
$\text{Ca}_2\text{FeOsO}_6$	Double perovskite ($\text{Ba}_2\text{LaRuO}_6$)	310	1.2

^aThe net magnetic moment depends on the thermal treatment regime used to synthesize a specific sample.

more inverted spinel structures.⁵² Similar mixing of Mn^{2+} and Fe^{3+} ions in the tetrahedral and octahedral sites takes place in MnFe_2O_4 .⁵³ The reported FiM ordering temperature gradually decreases from NiFe_2O_4 to CoFe_2O_4 to MnFe_2O_4 .⁵⁴

An interesting variant of 3d metal ferrites, MnFe_3O_5 was synthesized recently under high-pressure and high-temperature conditions.⁵⁵ This material is isostructural to Fe_4O_5 . It shows AFM ordering of Fe magnetic moments at 350 K, but the subsequent ordering of Mn moments at 150 K causes the formation of an FiM structure.⁵⁶ An opposite situation was reported for MnFeO_3 , obtained by mechanochemical synthesis.⁵⁷ This material shows ferrimagnetism at 300 K but then undergoes AFM ordering at 36 K.

Alkaline-earth ferrites $\text{AFe}_{12}\text{O}_{19}$ exhibit FiM ordering at 750 K for $\text{A} = \text{Sr}$ and 740 K for $\text{A} = \text{Ba}$.⁵⁸ In their hexagonal magnetoplumbite structures, the Fe magnetic moments are aligned with the c axis.⁵⁹ There are 24 Fe^{3+} ions per unit cell, of which 16 have their moments oriented in one direction and the other 8 have the moments oriented in the opposite direction (Fig. 5). The resulting FiM structure exhibits remarkably strong resistance to deviation from the c axis under applied magnetic field. This high

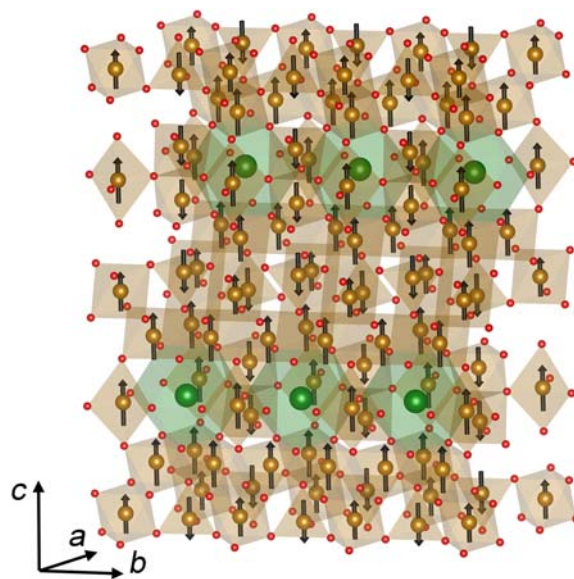


Fig. 5 The magnetic structure of $\text{BaFe}_{12}\text{O}_{19}$, showing ferrimagnetic arrangement of the Fe moments. Color scheme: Ba = green, Fe = gold, O = red.

magnetocrystalline anisotropy makes $\text{AFe}_{12}\text{O}_{19}$ ferrites practically useful permanent magnets, especially since they do not contain expensive lanthanide ions.⁶⁰

Another technologically important group of ferrimagnets is represented by lanthanide ferrite garnets, with the general formula $\text{Ln}_3\text{Fe}_5\text{O}_{12}$. The Fe^{3+} ions are coordinated by O^{2-} ions either tetrahedrally or octahedrally (in the 3:2 ratio), and the Fe magnetic moments in the tetrahedral sites are aligned antiparallel to the moments in the octahedral sites. The uneven distribution of the Fe^{3+} ions among the two crystallographic sites results in ferrimagnetism. The prototypical ferrite garnet, $\text{Y}_3\text{Fe}_5\text{O}_{12}$ (YIG), exhibits FiM ordering at 545 K and the saturation magnetization of $5 \mu_{\text{B}}$ per f.u.,⁶¹ as expected from the antiparallel alignment of the Fe moments in the 3:2 ratio. The Fe moments are aligned along the body diagonal of the cubic structure.⁶² YIG is an insulating material with a very narrow FM resonance linewidth, which explains its wide application in radio-frequency communication technologies.

With the introduction of magnetic Ln^{3+} ions, the total magnetization of the Fe sublattice remains approximately equal to $5 \mu_{\text{B}}$ per f.u., and the coupling between the two magnetic sublattices is relatively weak.⁶³ The stronger magnetic exchange between the Fe^{3+} ions leads to the Fe moments ordering at substantially higher temperatures than the Ln moments. As a result, an interesting situation is observed due to the magnetization of some Ln^{3+} ions exceeding the total magnetization of the Fe^{3+} ions. The coupling between the total magnetic moment of the Ln and Fe sublattices is FM for the Ln^{3+} ions with a less than half-filled 4f shell and AFM for the Ln^{3+} ions with a half or higher filling of the 4f shell. Thus, for heavier lanthanide ferrite garnets, starting with $\text{Gd}_3\text{Fe}_5\text{O}_{12}$, as the Ln moments undergo FM ordering but align antiparallel to the total moment of the Fe sublattice, the magnetization changes sign with decreasing temperature. This phenomenon is known as magnetic pole reversal, and the temperature at which the magnetization reverses is referred to as the compensation point.⁴⁸ Magnetic measurements on single crystals showed that the compensation point for $\text{Ln}_3\text{Fe}_5\text{O}_{12}$ decreases from 286 K for Gd to 246 K for Tb to 226 K for Dy to 137 K for Ho and to 83 K for Er.⁶⁴ In the recent past, the presence of the compensation point was leveraged in the application of lanthanide ferrite garnets in magneto-optical recording technology.⁶⁵

We conclude our discussion of FiM oxides with double-perovskite structures, $\text{A}_2\text{MM}'\text{O}_6$. Similar to spinels and garnets, the presence of different crystallographic sites for incorporation of magnetic ions provides a convenient framework for the design of FiM materials. Interestingly, however, double-perovskite ferrimagnets are relatively rare, and AFM ordering is more commonly observed due to the complete compensation of the magnetic moments if they are present only in the M and/or M' sites.⁶⁶ A notable group of double-perovskite ferrimagnets contains a 3d metal in the M sites and a 4d or 5d metal in the M' sites (the substantially different nature of the M and M' elements is essential for achieving an ordered arrangement of the corresponding magnetic ions). Thus, compounds Sr_2MMoO_6 were reported to undergo FiM ordering at 450 K for $\text{M} = \text{Cr}$ ⁶⁷ and 415 K for $\text{M} = \text{Fe}$,⁶⁸ due to AFM coupling between the M^{3+} ions ($3d^3$, $S = 3/2$ for Cr and $3d^5$, $S = 5/2$ for Fe) and Mo^{5+} ions ($4d^1$, $S = 1/2$). While the magnetic ordering takes place at similar temperatures in these Mo-containing materials, the Os-containing $\text{Ca}_2\text{FeOsO}_6$ and $\text{Sr}_2\text{CrOsO}_6$ show FiM ordering at 320 K⁶⁹ and 725 K,⁷⁰ respectively. The drastic difference in the T_{C} values might stem from the monoclinic distortion in $\text{Ca}_2\text{FeOsO}_6$, as compared to the tetragonal structure of $\text{Sr}_2\text{CrOsO}_6$. As a result, the M–O–M' bridges in the former show strong deviation from linearity ($\sim 152^\circ$), thus weakening the AFM exchange between the Fe^{3+} and Os^{5+} ions. The linear bridges in $\text{Sr}_2\text{CrOsO}_6$ lead to much stronger coupling between the Cr^{3+} and Os^{5+} ions and one of the highest ordering temperatures among perovskite and double-perovskite magnets.⁷¹

4.08.4 Intermetallic magnets

4.08.4.1 General considerations

Although only five elemental metals, Cr, Fe, Co, Ni, and Gd, exhibit magnetic ordering under ambient pressure, there are numerous FM, AFM, and FiM intermetallics (Table 5). It should be emphasized that an intermetallic compound implies a structure that contain two or more types of metal atoms distributed over distinct crystallographic sites, which distinguishes them from alloys—typically statistically disordered structures formed by two or more metals.⁷² Stoner proposed a simple criterion⁷³ to predict the possibility of FM ordering in a metallic system: $J \cdot n(E_F) > 1$, where J is the nearest-neighbor magnetic exchange constant and $n(E_F)$ is the density of states (DOS) at the Fermi level (E_F). Despite the relative simplicity of the Stoner criterion, which follows from the mean-field theory, it often serves as effective means for justification or even prediction of FM ordering in intermetallic materials.^{74–76}

An interesting approach—rooted in chemical principles—to interpretation of magnetic properties of metallic materials was proposed by Dronskowski and Landrum, who showed that FM ordering correlates with pronounced antibonding interactions between the magnetic metal atoms at the Fermi level.^{77,78} The nature of chemical bonding can be assessed by crystal orbital Hamilton population (COHP) analysis, according to which the positive, near-zero, and negative regions of the $-COHP$ function correspond, respectively, to bonding, nonbonding, and antibonding interactions.⁷⁹ A combined use of the Stoner and Dronskowski-Landrum criteria offers a powerful approach to analyzing and predicting magnetic behavior of metallic (itinerant)

Table 5 Examples of magnetic intermetallics with characteristic magnetic parameters.

Compound	Structure type	Ordering	T_C or T_N , K	m , $\mu_B/f.u.^a$
MnBi	NiAs	FM	613-627 ^b	3.0
FePt	CuAu	FM	750	2.8
YMn ₂	MgCu ₂	AFM	116	2.7
YFe ₂	MgCu ₂	FM	545	2.9
PrMn ₂	MgZn ₂	AFM	115	2.6 (Pr), 2.8 (Mn)
NdMn ₂	MgZn ₂	AFM	104	2.9 (Nd), 2.7 (Mn)
PrFe ₂	MgCu ₂	FiM		
NdFe ₂	MgCu ₂	FiM		
GdFe ₂	MgCu ₂	FiM	785	2.8
TbFe ₂	MgCu ₂	FiM	711	4.7
SmCo ₅	CaCu ₅	FM	1020	6.3
YCo ₅	CaCu ₅	FM	987	
Cu ₂ MnAl	Heusler (Cu ₂ MnAl)	FM	603	3.6
Co ₂ FeSi	Heusler (Cu ₂ MnAl)	FM	1100	6.0
Co ₂ FeGe	Heusler (Cu ₂ MnAl)	FM	1073	6.1
CoVSb	Half-Heusler (LiAlSi)	FM	48	0.17
CoMnSb	Half-Heusler (LiAlSi)	FM	478	4.2
NiMnSb	Half-Heusler (LiAlSi)	FM	728	4.2
PtMnSb	Half-Heusler (LiAlSi)	FM	572	4.0
AuMnSb	Half-Heusler (LiAlSi)	FM	72	3.5
CuMnSb	Half-Heusler (LiAlSi)	AFM	55	3.9
LaMn ₂ Si ₂	ThCr ₂ Si ₂	AFM/FM	470/310	1.6 (FM)
LaMn ₂ Ge ₂	ThCr ₂ Si ₂	AFM/FM	415/325	1.5 (FM)
YMn ₂ Si ₂	ThCr ₂ Si ₂	AFM	514	
YMn ₂ Ge ₂	ThCr ₂ Si ₂	AFM	427	
GdMn ₂ Ge ₂	ThCr ₂ Si ₂	AFM/FiM	365/97	
TbMn ₂ Ge ₂	ThCr ₂ Si ₂	AFM/FiM	414/95	
LaCo ₂ P ₂	ThCr ₂ Si ₂	FM	132	0.9
CeCo ₂ P ₂	ThCr ₂ Si ₂	AFM	440	
PrCo ₂ P ₂	ThCr ₂ Si ₂	AFM	309	
NdCo ₂ P ₂	ThCr ₂ Si ₂	AFM	307	
LaCo ₂ As ₂	ThCr ₂ Si ₂	FM	205	1.0
CeCo ₂ As ₂	ThCr ₂ Si ₂	FM	147	1.3
PrCo ₂ As ₂	ThCr ₂ Si ₂	FM/FiM	140/50	2.9
NdCo ₂ As ₂	ThCr ₂ Si ₂	FM/FiM	62/35	1.7

^aIn the case of AFM ordering, the value corresponds to the moment per magnetic atom.

^bThe MnBi phase is immediately FM upon formation by decomposition of paramagnetic Mn_{1.08}Bi at 613 K (see the text). The phase remains stable and FM when heated till 627 K, at which point it converts to Mn_{1.08}Bi.

magnets.⁸⁰ For example, they provide a clear explanation for the AFM behavior of Cr, in which the Fermi level crosses nonbonding states, and FM behavior of Fe, Co, and Ni, in which it crosses antibonding states.⁷⁷

4.08.4.2 Binary intermetallics

Compositionally, intermetallics that consist of two elements represent the simplest magnetic materials beyond the elementary magnets. Nevertheless, their magnetic behavior can be rather complex, due to the variation of magnetic exchange interactions caused by changes in the crystal structure and stoichiometry, which can be used to vary the concentration and topology of magnetic centers. MnBi and FePt are among the most prominent binary ferromagnets. Both are hard magnets, and the large coercivity values can be attributed to the presence of non-magnetic heavy elements, Bi and Pt, respectively, which contribute to strong magnetocrystalline anisotropy through spin-orbit coupling. Besides, in both cases, the non-magnetic atoms carry a substantial non-zero spin density,^{81,82} thus facilitating the strong magnetic exchange that leads to high FM ordering temperatures.

The high-temperature (HT) paramagnetic phase of MnBi shows a slight non-stoichiometry, with an approximate composition $\text{Mn}_{1.08}\text{Bi}$. When cooled below 613 K, the HT phase decomposes with the release of excess manganese and the formation of low-temperature (LT) stoichiometric MnBi. The LT phase is already ordered FM at the decomposition temperature.⁸³ Although this material is very interesting as an inexpensive permanent magnet, its formation mechanism, obviously, poses a challenge for the synthesis of a pure LT phase. Nevertheless, the studies of MnBi are quite extensive. Besides its remarkable magnetic properties, MnBi also shows a large linear non-saturation magnetoresistance in applied magnetic fields up to 70 T and high charge-carrier mobilities.⁸⁴ These properties can be beneficial for spintronic applications.

FePt also forms as two different polymorphs. The disordered alloy with a face-centered cubic (FCC) structure can be converted to an ordered tetragonal L1_0 -FePt structure (Fig. 6) when heated above 700 K. The ordered polymorph of FePt shows the coercive field of ~ 1 T at room temperature.⁸⁵ This hard magnet has been extensively investigated vis-à-vis its potential uses in magnetic recording⁸⁶ and biomedical applications.⁸⁷

Compounds AT_2 ($A = \text{Sc, Y, Ti, Zr, Hf, Nb, Ta, or lanthanide (Ln)}$; $T = \text{Mn, Fe, Co}$) are a prominent family of binary intermetallic magnets. They crystallize in one of the two Laves structures, of either the cubic MgCu_2 type or the hexagonal MnZn_2 type.⁸⁸ Similar to the evolution of magnetic ordering from AFM in Cr metal to FM in Fe, Co, and Ni metals, associated with the gradual filling of the non-bonding and then antibonding states (according to the Dronskowski-Landrum criterion), the transition-metal sublattice in the AT_2 materials also shows the change from paramagnetism to AFM and then to FM ordering as the d -band becomes more filled. Thus, YMn_2 is an antiferromagnet,⁸⁹ YFe_2 is a ferromagnet,^{90,91} and YCo_2 is a paramagnet.⁹² The antiferromagnetism of YMn_2 is in contrast with paramagnetic behavior of the other AMn_2 materials with non-magnetic A atoms,⁹³ although compounds LnMn_2 with $\text{Ln} = \text{Pr, Nd, or Sm}$, also exhibit collinear AFM ordering in both the Ln and Mn sublattices.⁸⁹ Decreasing the size of the Ln elements leads to canted or helimagnetic ordering in LnMn_2 with $\text{Ln} = \text{Gd, Tb, or Dy}$.^{94,95} On the other hand, nearly all LnFe_2 and LnCo_2 compounds show FM ordering in the transition metal sublattice,⁹³ except for superconducting CeCo_2 ⁹⁶ and paramagnetic LuCo_2 .⁹⁷ The coupling between the 3d and 4f moments in these intermetallics is FM for the lanthanides with less than half-filled 4f shell and AFM for Gd and those with more than half-filled 4f shell. This common observation for binary 3d-4f intermetallics was justified by Brooks and Johansson.⁹⁸ Consequently, the LnFe_2 and LnCo_2 phases exhibit FM ordering for $\text{Ln} = \text{La-Sm}$ and FiM ordering for $\text{Ln} = \text{Gd-Yb}$.^{90,99,100} The strength of the magnetic exchange coupling in these materials varies systematically with the size of the lanthanide ion. For example, the FiM ordering temperature decreases from 785 K to 590 K in the LnFe_2 series with $\text{Ln} = \text{Gd-Er}$.⁹⁰

The effect of the FM or AFM coupling between the 3d and 4f moments is evident in one of the strongest permanent magnets, SmCo_5 , which finds extensive commercial usage due to the high values of ordering temperature (1020 K), coercivity, and

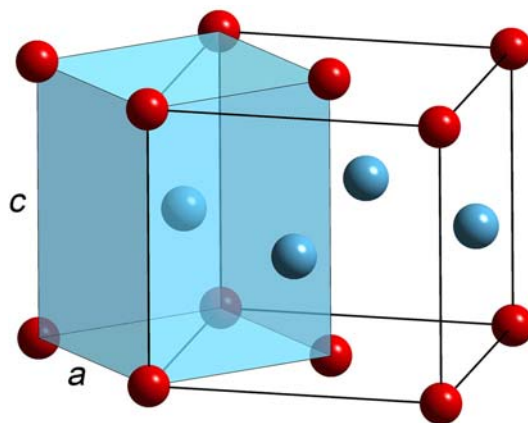


Fig. 6 The ordered tetragonal unit cell of L1_0 -FePt (highlighted as a blue translucent polyhedron) vs. the FCC unit cell of the disordered FePt alloy (solid black lines). Color scheme: Fe = red, Pt = blue.

magnetization.¹⁰¹ This compound has a hexagonal CaCu_5 -type structure, in which Co atoms are stacked in honeycomb and kagomé layers that alternate along the c axis. The Sm atoms fill hexagonal channels formed by the Co atoms (Fig. 7). The Sm and Co moments are ordered FM parallel to the c axis, with the respective values of $1.0 \mu_{\text{B}}$ and $2.2 \mu_{\text{B}}$ at 5 K.¹⁰² The fact that an isostructural compound, YCo_5 , shows FM ordering at similar temperature, 987 K,¹⁰³ indicates that the high coercivity of SmCo_5 stems from high magnetocrystalline anisotropy of the Sm atoms,¹⁰⁴ while the high T_{C} value is due to the strong magnetic exchange between the Co atoms. Interestingly, the magnetic structure of this material was determined by neutron diffraction only recently,¹⁰² as the enormously high neutron absorption cross-section of the natural Sm precluded such studies. The magnetic structure was determined on the sample enriched with the ^{200}Sm isotope ($\sim 99\%$).

Recently, a substantial attention has been paid to metallic antiferromagnets that can be used in spintronic devices. AFM materials are resistant to applied magnetic fields and do not produce stray fields that can be detrimental to the device performance. At the same time, they have been shown to exhibit ultrafast dynamics and large magnetotransport effects.¹⁰⁵ In particular, FeRh and Mn_2Au have been incorporated in AFM memory resistor devices, which use reorientation of magnetic moments of the material to readout electrical current. FeRh exhibits a CsCl-type structure and AFM order at room temperature, with the moment of $\sim 3.0 \mu_{\text{B}}$ per Fe atom. At 340 K, however, this material shows a transition to FM ordering, which is sustained up to the Curie temperature of 670 K.¹⁰⁶ These properties of FeRh were leveraged for heat-assisted magneto-recording,¹⁰⁷ where the moments in the AFM state were aligned in one of the two directions, depending on the writing magnetic field, and the “memory” of the direction could be erased by heating the material above the AFM-to-FM transition temperature.

Mn_2Au is an antiferromagnet with the high ordering temperature of ~ 1500 K.¹⁰⁸ It has a tetragonal crystal structure of the Cr_2Al type, where double layers of Mn atoms alternate with layers of Au atoms along the c axis. Within each double-layer, the Mn moments exhibit AFM ordering in the ab plane, but the orientation of the moments can be switched on an ultrafast timescale. For example, switching with current pulses of THz frequency has been demonstrated.¹⁰⁹

4.08.4.3 Heusler and Half-Heusler compounds

The first ferromagnetic metals prepared from non-magnetic elements were reported by Heusler.¹¹⁰ Cu_2MnAl , which shows FM ordering of Mn moments at 603 K,¹¹¹ became a prototype for a large class of compounds known as “Heusler” and “half-Heusler” alloys, with stoichiometries X_2YZ and XYZ , respectively. The half-Heusler structure (Fig. 8a) is characterized by a NaCl-type arrangement of the Y and Z atoms, in which four out of eight octants of a cubic unit cell are centered by X atoms. The Heusler structure (Fig. 8b) is obtained by filling all eight octants with X atoms.

In general, the half-Heusler compounds carry magnetic moments only in the Y sites, while the Heusler compounds have magnetic moments in both Y and X sites. Therefore, more diverse magnetic behavior can be expected for Heusler structures. Indeed, ferromagnetism is common for Heusler compounds but far less common for half-Heusler compounds. As an example, weak itinerant ferromagnetism was reported in CoVSb , with the maximum magnetic moment of $0.17 \mu_{\text{B}}$ per f.u..¹¹² A series of half-Heusler antimonides, XMnSb , are ferromagnets with $T_{\text{C}} = 478$ K, 728 K, 572 K, and 72 K for $\text{X} = \text{Co}$, Ni, Pt, and Au, respectively.¹¹³ Obviously, the change in the valence electron count has a dramatic impact on the ordering temperature. Interestingly, CuMnSb shows AFM ordering at 55 K.

The Heusler compound Co_2FeSi shows one of the highest FM ordering temperatures among intermetallics, $T_{\text{C}} = 1100$ K.¹¹⁴ In addition, it shows half-metallic behavior. A very similar T_{C} value of 1073 K was reported for Co_2FeGe ,¹¹⁵ but replacing Fe with Mn

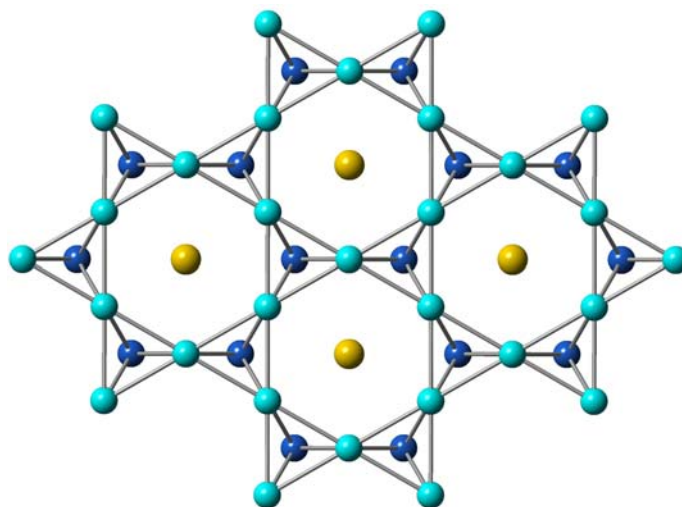


Fig. 7 The crystal structure of SmCo_5 viewed down the hexagonal c axis. The Co atoms that form the honeycomb and kagomé layers are highlighted with different shades of blue. The Sm atoms (gold) are located in the hexagonal channels.

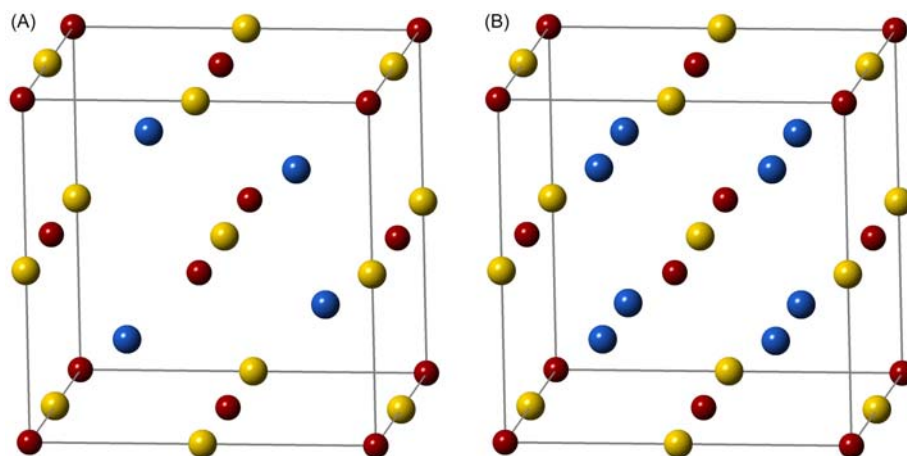


Fig. 8 The crystal structures of half-Heusler (a) and Heusler (b) compounds. The X, Z, and Y atoms are shown with blue, garnet, and gold, respectively.

leads to notably lower T_C values of 985 K for Co_2MnSi and 905 K for Co_2MnGe .¹¹¹ A large compilation of the T_C values for Heusler intermetallics was provided in the latter work.

It was demonstrated that the Heusler compounds follow quite well the Slater-Pauling plot,¹¹⁶ which relates the observed magnetic moment to the average number of valence electrons per atom. Likewise, the magnetic ordering temperature also might show a clear trend for chemically related compounds. For example, in the series Co_2MAl , the T_C increases from 134 K to 310 K to 334 K to 693 K for $M = \text{Ti}, \text{V}, \text{Cr}, \text{Mn}$, respectively.¹¹¹

4.08.4.4 ThCr_2Si_2 -type intermetallics

Among ternary intermetallic compounds, the ThCr_2Si_2 structure type is one of the most abundant,¹¹⁷ due to its remarkable adaptability to a variety of elemental compositions, AT_2X_2 , where, in general, A is an alkali, alkaline-earth, lanthanide, or actinide metal, T is a transition metal, and X is a main-group element. These compounds exhibit magnetism when either T is a 3d metal or A is an f-metal, or both. For example, rich magnetic behavior is observed in the series of tetrelides, LnMn_2Tt_2 ($\text{Tt} = \text{Si}, \text{Ge}$), and pnictides, LnCo_2Pn_2 ($\text{Pn} = \text{P}, \text{As}$). The behavior of LaMn_2Si_2 and LaMn_2Ge_2 is very similar. Both undergo AFM ordering at 470 K/415 K, followed by spin reorientation that leads to FM ordering at 310 K/325 K.^{118,119} In contrast, YMn_2Si_2 and YMn_2Ge_2 , which also contain a diamagnetic A element, exhibit only AFM ordering at 514 K¹²⁰ and 427 K.¹²¹

When a magnetic 4f element is used in place of La, the magnetic behavior of silicides and germanides becomes drastically different. In the case of LnMn_2Si_2 , AFM ordering of Mn moments is observed for $\text{Ln} = \text{Ce-Nd}$,¹²² while compounds with heavier lanthanides, starting with Gd, also show AFM ordering of Mn moments at higher temperatures, but at lower temperatures FM ordering of Ln moments causes reorientation of the Mn moments in the opposite direction, to create the overall FiM structure.^{123–125} For the LnMn_2Ge_2 series, in the case of $\text{Ln} = \text{Ce-Nd}$, AFM ordering of Mn moments at ~ 400 K is followed by spin reorientation to the FM-ordered state at 320–335 K.¹²⁶ This behavior is similar to that observed for LaMn_2Ge_2 . Nevertheless, the Pr- and Nd-containing compounds show another phase transition at 40 K, caused by the FM alignment of the 4f moments with respect to the Mn moments, to achieve FM ordering in both sublattices. In compounds with $\text{Ln} = \text{Gd-Er}$, the Mn moments order AFM at higher temperatures and undergo reorientation antiparallel to the Ln moments that order at lower temperatures (Table 5), thus creating the overall FiM structure.¹²⁷

In the LnCo_2Pn_2 series, FM ordering of Co 3d moments is observed for both LaCo_2P_2 ¹²⁸ and LaCo_2As_2 .¹²⁹ Similar to the LnMn_2Tt_2 series, the behavior of phosphides and arsenides formed with magnetic lanthanides differs substantially. In LnCo_2P_2 with $\text{Ln} = \text{Ce-Sm}$, the magnetic phase transitions in the 3d and 4f sublattices are completely decoupled,¹³⁰ as the AFM ordering of Co moments at higher temperatures (440 K for $\text{Ln} = \text{Ce}$ and ~ 300 K for $\text{Ln} = \text{Pr-Sm}$) is followed by AFM ordering of the Ln moments at much lower temperatures (< 30 K). In contrast, in LnCo_2As_2 ($\text{Ln} = \text{Ce-Nd}$), the Co moments order FM at higher temperatures, which drives the FM ordering of Ln moments in an opposite direction, for the overall FiM ordering.¹³¹ Unfortunately, a full comparison between the magnetic properties in these series of tetrelides and pnictides cannot be made, because the LnCo_2P_2 compounds are not known for lanthanides beyond Eu.

4.08.5 Noncollinear magnetic ordering

4.08.5.1 General considerations

There are several general scenarios that lead to the emergence of noncollinear magnetic ordering:

- (1) A competition between AFM and FM exchange interactions: with the increasing complexity of magnetic exchange pathways, one should expect that some magnetic configurations will require a compromise between the two types of collinear orderings. In some cases, such competition might even prevent the long-range magnetic ordering and lead to the formation of spin glass, in which magnetic moments are “frozen” in random orientations below the spin-glass transition temperature.¹³²
- (2) Geometric frustration of AFM interactions between spin centers: it is easy to show that pairwise AFM interactions cannot be satisfied simultaneously when an odd number of atoms with the same magnetic moment are arranged on a regular polygon.^{133–135} This so-called spin frustration typically counteracts system’s tendency to form an ordered arrangement of magnetic moments, and the magnetic ordering temperature (T_N) is suppressed. The extent of spin frustration can be evaluated by the frustration factor, $f = T_N/\theta$, where θ is the Weiss constant (see **Section 4.08.2.4**). Systems that exhibit $f > 5$ are typically considered to be strongly frustrated.¹³⁶ The formation of a noncollinear magnetic structure offers a pathway to resolve the spin frustration.
- (3) Magnetic exchange in the absence of inversion symmetry: the magnetic moments that are not related by an inversion center are coupled by the Dzyaloshinskii-Moriya (DM) interaction,^{137,138} which is described by the vector product of the magnetic moments. The minimization of the total energy resulting from such interaction forces the moments to become perpendicular to each other. Therefore, systems with DM interactions tend to develop noncollinear spin textures (magnetic structures). The DM exchange constants are enhanced by spin-orbit coupling effects.^{139,140}

The noncollinear magnetic structures that form due to the above-mentioned conditions exhibit spin arrangements that can be very sensitive to external perturbations, i.e., several magnetic configurations with comparable energies can exist close to the ground state. In other words, the ground state of such systems might show a high degree of degeneracy. Such behavior can be leveraged for switching the magnetic configurations by minor changes in the applied magnetic or electric fields. Therefore, there is a high current interest to materials with noncollinear spin textures for the development of next-generation electronic devices that can be operated with lower power consumption.^{141–144}

4.08.5.2 Materials with noncollinear magnetic structures

In **Section 4.08.3.2**, we have already mentioned how the competition between the AFM and FM ordering leads to a variety of magnetic structures in $\text{La}_{1-x}\text{Sr}_{2+x}\text{Mn}_2\text{O}_7$, depending on the La/Sr ratio.³⁵ In particular, at $x = 0.9$, the FM ordered Mn moments exhibit slight canting out of plane, revealing the action of an AFM exchange component in the perpendicular direction, along the c axis (Fig. 3). Likewise, the competing magnetic interactions lead to canted or helimagnetic ordering in LnMn_2 with Ln = Gd, Tb, or Dy,^{94,95} as described in **Section 4.08.4.2**. Here, we provide further examples of materials that exhibit noncollinear spin textures. Their main magnetic parameters are listed in **Table 6**. We will proceed from the discussion of cases with competing magnetic interactions to the examples of spin-frustrated structures and, finally, to the noncollinear spin textures that emerge in non-centrosymmetric crystal structures. In addition, we attempt to consider diverse classes of materials, to demonstrate that complex spin textures can be achieved in various crystal structures and to reveal the common ingredients of such magnetic behavior.

One of the simpler scenarios for the emergence of helimagnetic ordering appears in structures that contain chains of magnetic atoms. In such cases, the collinear AFM or FM exchange along the chain can be perturbed by the weaker magnetic coupling between the chains to create a noncollinear magnetic state, especially if the magnetic atoms in neighbor chains are offset along the direction of chain propagation (Fig. 9a). An example of such behavior is provided by compounds MnM_2X_4 , where M = Sb or Bi and X = S or Se.^{145–147} Their crystal structures feature chains of edge-sharing $[\text{MnX}_6]$ octahedra separated by M atoms, and the neighbor chains are offset by a half-translation. The AFM *intra*chain coupling is perturbed by a weaker AFM *inter*chain coupling, causing the formation of incommensurate magnetic helices with the Mn moments rotating perpendicular to the chain propagation direction (Fig. 9b).

Table 6 Examples of materials with noncollinear magnetic structures.

Compound	Structure Type	Ordering	T_C or T_N , K	m , μ_B/atom
MnSb_2S_4	HgBi_2S_4	AFM	25	4.6
MnSb_2Se_4	HgBi_2S_4	AFM	20	4.2
MnBi_2Se_4	HgBi_2S_4	AFM	15	3.3
$\text{Co}_2\text{V}_2\text{O}_7$	$\text{Co}_2\text{V}_2\text{O}_7$	AFM	6.0	2.1–2.7
$\text{Mn}_2\text{FeSbO}_6$	$\text{Ba}_2\text{LaRuO}_6$	AFM	60	4.9 (Mn), 4.3 (Fe)
$\text{Sr}_3\text{Fe}_2\text{O}_7$	$\text{Sr}_3\text{Ti}_2\text{O}_7$	AFM	115	4.8
CrB_2	AlB_2	AFM	88	0.5
MnPtGa	Ni_2In	FM/canted/AFM	236/186/140	3.1/2.7/3.0
Mn_3Sn	Ni_3Sn	AFM	420	3.0
Mn_3Ir	Cu_3Au	AFM	960	2.45
HfMnSb_2	NiAs	AFM	270	2.8
MnSi	FeSi	AFM	30	0.4
Cu_2OSeO_3	Cu_2OSeO_3	FIM	60	0.6

^aThe moment is given per magnetic atom.

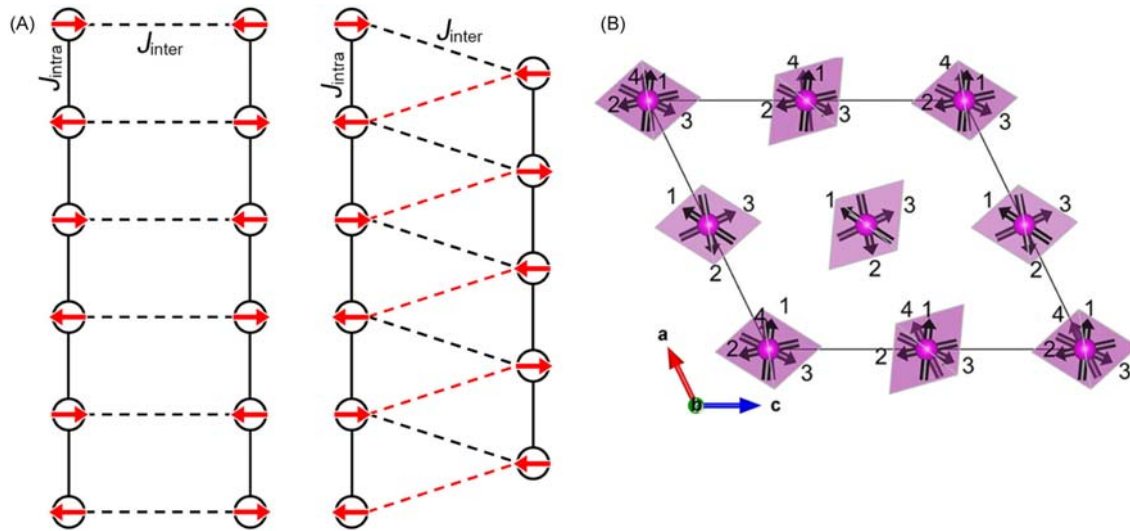


Fig. 9 (a) The scheme of coupling between two AFM chains. The structure with mis-matched atomic arrangement along the chain propagation direction necessarily results in the competing AFM and FM exchange interactions that are highlighted, respectively, with black and red dashed lines. (b) The view of the helimagnetic structure of MnSb_2S_4 in the chain propagation direction. The numbers indicate the position of consecutive Mn^{2+} ions along the chain, to visualize the rotation of the magnetic moments.

A more complicated chain structure is observed for $\text{Co}_2\text{V}_2\text{O}_7$, in which the CoO_6 octahedra fuse to form zigzag chains separated by VO_4 tetrahedra.¹⁴⁸ Such structural arrangement also leads to multiple competing magnetic interactions, resulting in noncollinear AFM ordering. Interestingly, the tendency to form the noncollinear spin texture was proposed as the source of magnetoelectric coupling in this material, which also showed ferroelectric behavior induced by applied magnetic field.¹⁴⁹

The double perovskite structure of $\text{Mn}_2\text{FeSbO}_6$ contains Mn^{2+} and Fe^{3+} ions (both $3d^5$, $S = 5/2$) that are involved in competing magnetic interactions, due to the lower symmetry of this substantially distorted monoclinic structure.¹⁵⁰ Similar to the previous cases, the presence of the competing magnetic exchange pathways leads to a noncollinear spin texture, in which the Mn and Fe moments form a helimagnetic arrangement by rotating around the b axis, within the ac plane.

An interesting example of a helimagnetic structure formed by competing magnetic interactions is provided by the tetragonal bilayer perovskite $\text{Sr}_3\text{Fe}_2\text{O}_7$. This material shows a metal-to-insulator transition upon cooling below 340 K, followed by AFM ordering at 115 K.¹⁵¹ The magnetically ordered state shows a helimagnetic structure, with the spins of Fe^{4+} ions ($3d^4$, $S = 2$) rotating in the (110) lattice planes.¹⁵² The noncollinear magnetic spin texture was attributed to competition between double-exchange and AFM superexchange interactions of comparable strength.

CrB_2 exhibits a rather simple crystal structure of the AlB_2 type, in which the metal atoms form triangular layers that alternate with honeycomb layers of B atoms in such a way that the Cr atoms center the hexagonal channels formed by the B atoms.¹⁵³ Based on the graphene-like structure of the boron sheets, one could assume formal oxidation states of -1 for B and $+2$ for Cr ($3d^4$, $S = 2$). Nevertheless, the magnetic moment on Cr is only $0.5 \mu_B$, which is much lower than the expectation value of $4 \mu_B$ for an $S = 2$ ion. The reason for this discrepancy is the strongly delocalized bonding in this material, which causes metallic behavior and itinerant magnetism.¹⁵⁴ The triangular arrangement of Cr sites leads to strong spin frustration, as can be judged from the Weiss constant, $\theta = -750$ K, substantially exceeding the observed AFM ordering temperature, $T_N = 88$ K. Moreover, the nearest distances between Cr atoms within the plane (2.983 \AA) and between the planes (3.078 \AA) are similar, which might be the reason for the observation of a cycloidal magnetic structure with incommensurate propagation vector.¹⁵⁵

A related structural arrangement is found in MnPtGa , which belongs to the Ni_2In structure type. The Pt and Ga atoms form honeycomb layers, which alternate with triangular layers of Mn atoms.¹⁵⁶ In this case, however, due to very different atomic sizes as compared to the CrB_2 structures, the nearest in-plane Mn-Mn distance (4.328 \AA) is substantially longer than the interplane Mn-Mn distance (2.788 \AA). The material undergoes collinear FM ordering at $T_C = 236$ K, with the Mn moments aligning parallel to the c axis.¹⁵⁷ At 186 K, however, a transition to a noncollinear canted FM phase is observed, with the moments deviating by 24° from the c axis, in the $+b$ or $-b$ direction. Finally, below 140 K, an incommensurate AFM structure with spin-density wave is formed, in which the propagation vector evolves with temperature.

The kagomé lattice, which can be viewed as a layer of vertex sharing triangles (see the structure formed by light-blue atoms in Fig. 7), is probably the most well-investigated atomic arrangement that leads to spin frustration in the case of AFM interactions.^{178–180} An example of such a structure is provided by Mn_3Sn , which contains kagomé layers of Mn atoms, with Sn atoms centering the hexagons of those layers. The spin frustration due to AFM exchange causes the Mn moments to adopt a noncollinear magnetic structure within the hexagonal ab plane (Fig. 10).¹⁵⁸ Despite spin frustration, this material still exhibits a rather high AFM ordering temperature, $T_N = 420$ K, which, together with semi-metallic behavior, attracted extensive interest to the potential use of Mn_3Sn in AFM spintronic devices. For example, a recent work showed the possibility to read and write well-defined magnetic domains in Mn_3Sn thin films by heat-assisted magnetic recording.¹⁵⁹

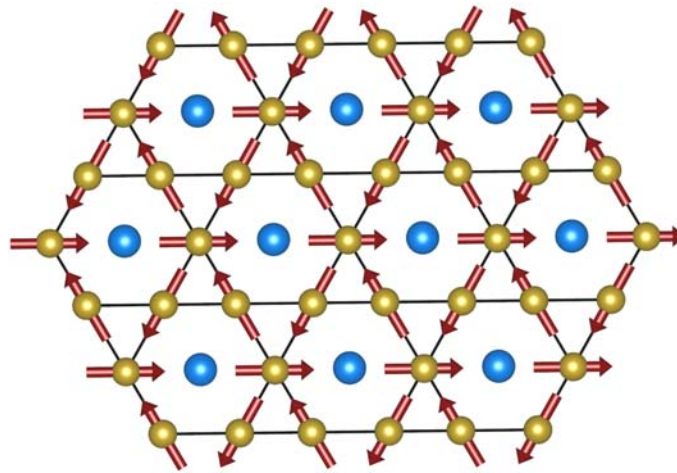


Fig. 10 The noncollinear AFM ordering of Mn moments (garnet arrows) in the kagomé layers observed in the crystal structure of Mn_3Sn (Mn = gold, Sn = blue) viewed down the hexagonal c axis. The kagomé lattice of Mn atoms is emphasized with black lines.

Another binary intermetallic with the same stoichiometry, Mn_3Ir , exhibits either a disordered or an ordered cubic structure of the Cu_3Au type. Annealing a disordered alloy with the face-centered cubic lattice leads to gradual ordering, with the Mn and Ir atoms locating, respectively, in the face centers and corners of the cubic unit cell. This atomic ordering also causes the increase in T_N from 730 K to 960 K.¹⁶⁰ In the atomically ordered structure, the Mn moments exhibit noncollinear AFM ordering within the (111) planes.¹⁶¹ The arrangement of the Mn and Ir atoms in these planes is analogous to the arrangement of Mn and Sn atoms in the hexagonal planes of the Mn_3Sn structure. Thus, the structures of Mn_3Sn and Mn_3Ir are closely related, as both of them are built the Sn/Ir-filled kagomé layers of Mn atoms and exhibit noncollinear in-plane ordering of Mn moments. Given its very high AFM ordering temperature, Mn_3Ir also has been extensively investigated as potential material for spintronic devices.^{162,163}

The intermetallic compound HfMnSb_2 is a colored variant of the hexagonal NiAs-type structure, with layers of Hf- and Mn-centered Sb_6 octahedra alternating along the c axis. The material undergoes magnetic ordering at 270 K, and the magnetization saturates at $2.95 \mu_B$ per Mn atom at 5 K and 7 T.¹⁶⁴ The field dependence of magnetization, however, exhibits an inclined plateau with an inflection point, suggesting that the material behaves quite different from a typical ferromagnet. Indeed, neutron powder diffraction analysis revealed a conical incommensurate magnetic structure, with the Mn moments deviating by $\sim 75^\circ$ from the c axis. The noncollinear magnetic structure, yet again, might be a result of spin frustration caused by the triangular arrangement of Mn sites.

Skyrmionic materials are a rapidly emerging class of noncentrosymmetric magnets. In such structures, the lack of inversion symmetry activates the DM exchange interactions, which favors perpendicular alignment of interacting magnetic moments, thus competing with the classical exchange interactions that favor parallel alignment of spins. The combination of these competing interactions, when their strengths are comparable, leads to noncollinear magnetic structures. A distinct difference of the skyrmion phase from the other noncollinear spin textures considered above is that magnetic skyrmions emerge as spin whirls (Fig. 11) that cannot be converted into collinear states through a continuous transformation.^{184,165,166}

The first experimental demonstration of magnetic skyrmions was achieved in small-angle neutron scattering (SANS) studies of MnSi ,¹⁶⁷ which revealed a consistent formation of a lattice of spin whirls (skyrmions) driven by applied magnetic field. This material belongs to the FeSi structure type, characterized by the noncentrosymmetric cubic space group $P2_13$. In zero field, MnSi shows AFM ordering at 29.5 K, with the formation of a helimagnetic structure with a repeat distance of 19 nm (more than 40 times larger than the lattice constant) in the [111] direction.¹⁶⁸ Under applied magnetic field, the material develops a conical spin arrangement

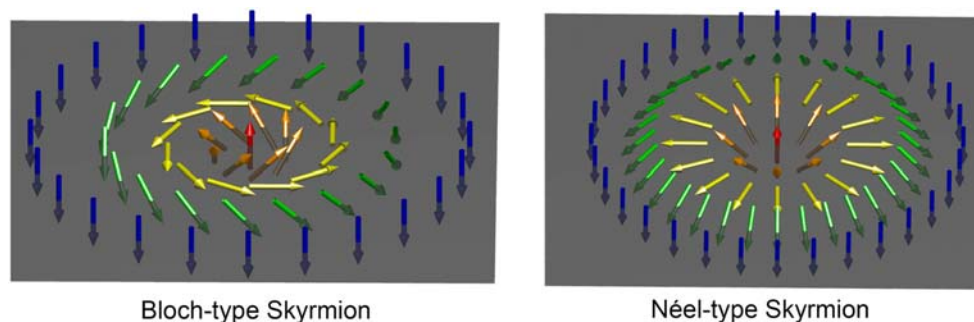


Fig. 11 Two types of skyrmions that can be observed in noncentrosymmetric magnets.

above 0.1 T, and the formation of the skyrmion lattice (Fig. 11) is observed in a narrow range of applied magnetic fields (from 0.1 to 0.2 T) and temperatures (from 29.5 to 27.5 K).¹⁶⁷ The discovery of the unusual behavior of MnSi has prompted active studies of other noncentrosymmetric magnets, in the search for new magnetic skyrmion materials.¹⁶⁶

Following the detection of skyrmions in the itinerant helimagnet MnSi and structurally related metallic materials,¹⁶⁵ magnetic skyrmions were observed in the multiferroic insulating copper(II) oxo-selenite, Cu_2OSeO_3 , which also crystallizes in the space group $P2_13$.¹⁶⁹ In the absence of magnetic fields, Cu_2OSeO_3 exhibits FiM ordering at $T_C = 60$ K due to antiparallel alignment of $S = 1/2$ moments in inequivalent Cu sites present in the 2:1 ratio.¹⁷⁰ However, a more careful study of this material by Lorentz transmission electron microscopy showed that the magnetic structure is helically modulated along the [110] direction, with the modulation period of 50 nm.¹⁷¹ The emergence of magnetic skyrmions was observed under applied magnetic field of ~ 0.05 T at 5 K and ~ 0.02 T at 45 K, with a nearly linear relationship between the critical field and temperature. The skyrmion phase is suppressed in favor of the FiM phase under fields above 0.2 T.

Without a doubt, we will see further expansion of research on magnetic materials with noncollinear spin textures in the nearest years, and new magnetic phenomena still will be discovered in this area. The prospects of low-power electronic devices and new types of magnetic memories and information processing schemes will continue to drive fundamental research on these materials and their potential applications.

4.08.6 Applications of magnetic materials

4.08.6.1 Permanent magnets

Permanent magnets are essential to many technologies, such as information storage, hybrid and electric vehicles, and transducers in speakers and microphones.^{101,172} As clean-energy technologies and modes of transportation are rapidly developing as alternatives to fossil-fuel based economy, permanent magnet consumption is predicted to grow at a rate of 36% annually over the next decade.¹⁷³ The traditional magnets used in these technologies have been optimized with coatings to prevent corrosion, and the manufacturing process has been streamlined. Nevertheless, extensive research to discover more sustainable permanent magnets continues.^{174–176}

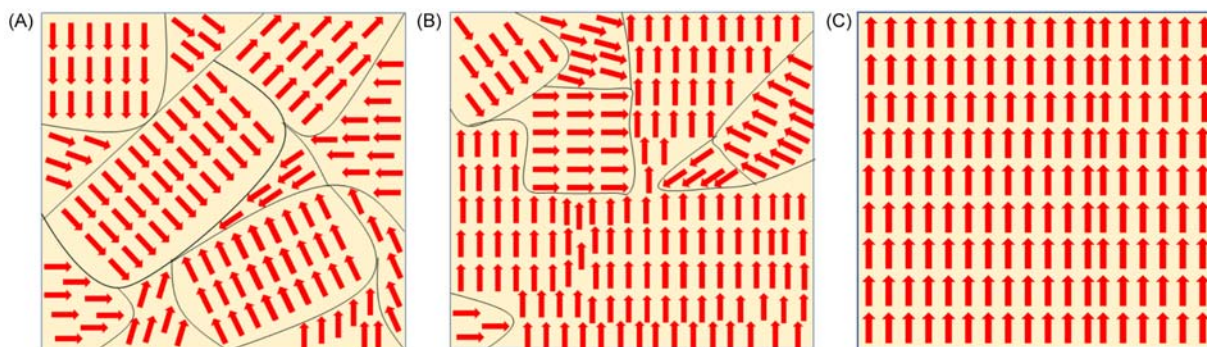
The strongest and most popular practical permanent magnets are lanthanide-containing $\text{Nd}_2\text{Fe}_{14}\text{B}$ and SmCo_5 . The increased demand for the rare-earth based materials is exacerbated by their highly concentrated production and risks of supply-chain disruption, which lead to very volatile market prices of rare-earth metals. As an example, Dy is often incorporated into $\text{Nd}_2\text{Fe}_{14}\text{B}$ to raise the T_C and sustain a large energy product to higher operating temperatures encountered in electric motor vehicles.¹⁷⁶ In 2009, the average price of Dy was near 100 \$/kg, but in 2011 the price soared to 3400 \$/kg. The inflated prices of Dy and other lanthanides resulted in the European Union, Japan, and the United States filing a formal complaint with the World Trade Organization. In 2014, the average price for Dy was near 625 \$/kg, and in 2019 it was down to 380 \$/kg.

As the need for permanent magnets continues to grow, the demand, cost, and risks of supply-chain disruption for rare-earth elements are also expected to persist. In the remainder of this section, we discuss examples of research efforts aimed at addressing the sustainability of permanent-magnet materials. As was mentioned in the introduction to this chapter, the distinct characteristic of hard (permanent) magnets is the large coercive field required to demagnetize them (Scheme 2). Combined with the high saturation (M_s) and remanent (M_r) magnetization, the high coercivity (B_c) produces a large energy product, defined as the maximum MB product achievable for a specific magnetic material. The magnetization is defined by the combined values of coupled magnetic moments, while coercivity depends on the interplay of magnetocrystalline anisotropy, magnetic exchange strength, and magneto-static energy.⁸ Additionally, for a permanent magnet to be useful, its T_C needs to be well above the expected working temperature. At today's level of technology, all these factors are optimal in the $\text{Nd}_2\text{Fe}_{14}\text{B}$ and SmCo_5 magnets. The high values of M_s and T_C are warranted by the presence of a large fraction of 3d metals and strong magnetic exchange coupling between them, while the high value of B_c is due to remarkably strong magnetic anisotropy of the 4f metals. The parameters of the most popular permanent magnets in use today and their applications are summarized in Table 7.

In zero magnetic field, any non-magnetized magnetic material will break into domains to minimize the magnetostatic energy. Even though the magnetic moments within each domain become ordered below the Curie temperature, the total magnetization is zero, due to the random average orientation of the total magnetization vectors of different domains (Scheme 3a). Under applied

Table 7 The parameters and applications of the most important permanent magnets.

Magnet	T_C (K)	B_c (T)	M_r (T)	$(MB)_{max}$ (kJ/m ³)	Applications
Alnico	823	0.07	1.35	55	Aerospace components, rotating machinery, sensors, military radar equipment, bearings
$\text{BaFe}_{12}\text{O}_{19}$	453	0.36	0.36	25	Fridge magnets, whiteboards, breaks, clamps, switches, crafts and home projects, guitar pick-ups
SmCo_5	523	1.0	0.83	160	Drilling, wind turbines, missile components, robotic arms, gyroscopes, particle accelerators, motors
$\text{Nd}_2\text{Fe}_{14}\text{B}$	353–473	1.2	1.2	260	Hard-disc drives, audio equipment, headphones and loudspeakers, MRI scanners, electric motors and generators, medical devices



Scheme 3 The microstructure of a magnet is broken into domains (a) that anneal through the motion of domain walls under applied magnetic field (b), until all moments point in the same direction to reach the saturation magnetization (c).

magnetic field, the domains tend to orient their moments in the same direction. This process takes place through the motion of domain walls (Scheme 3b), until all magnetic moments point in the same direction (Scheme 3c) above certain saturation field or below certain temperature, when cooled under applied field. In best permanent magnets, the removal of the applied field should have a negligible effect on the remanent magnetization (M_r), as all magnetic moments tend to remain co-aligned. The process of demagnetization requires application of a magnetic field in the opposite direction, to nucleate domain walls and initiate their motion through the material, until the total magnetization goes to zero at B_c .

Recent research efforts have focused on eliminating the 4f elements from permanent-magnet formulations, by taking advantage of the magnetocrystalline anisotropy due to specific symmetry of the underlying crystal structure and strong spin-orbit coupling of heavier transition and main-group elements. Thus, Fe_3Sn is one of the recent candidates for a permanent magnet composed of earth-abundant materials. It has $T_C = 743$ K and $M_s = 2.3 \mu_B$ per Fe atom. This material, however, shows an easy-plane anisotropy, as opposed to an easy-axis anisotropy desirable for permanent magnets.¹⁷⁷ A partial substitution of Mn for Fe and Sb for Sn allows for more desirable anisotropic parameters but decreases the T_C to 425 K. This is still a desirable range for permanent magnets, but, obviously, the elemental substitution is not without caveats. It is difficult to produce a stable pure phase and the material is prone to decomposition into the substituent elements, making it a large-scale manufacturing nightmare.¹⁷⁸ Continued investigation of varying substitutions may lead to a more promising lanthanide-free hard magnet.

Another interesting permanent-magnet candidate is MnAl. This material, also composed of earth-abundant elements, has strong magnetocrystalline anisotropy, good resistance to corrosion, and low density. The magnetism for the tetragonal structure of interest is still under debate. The compound has been identified both as ferromagnet and antiferromagnet. The discrepancy seems to be due to the antisite disorder of Mn and Al atoms, which strongly depends on the thermal treatment. It has been shown that AFM ordering is associated with Mn atoms occupying Al sites. The ordering temperature is increased to 650 K with the addition of carbon, but these inclusions are known to alter the tetragonal phase at elevated temperatures.¹⁷⁹

Preservation of the high magnetic anisotropy afforded by 4f elements is the major challenge in the design of lanthanide-free permanent magnets.¹⁸⁰ The ongoing efforts in this direction focus not only on the search for new compounds but also on the micro- and nanostructuring engineered to preserve the high magnetic anisotropy while minimizing or eliminating the expensive 4f elements.^{174,181,182} Other notable materials that have been envisioned or even predicted through artificial intelligence¹⁸³ as good candidates for lanthanide-free permanent magnets are Co_3N , Co_3Si , $\text{Mn}_{50}\text{Bi}_{45}\text{Sn}_5$, $\text{Zr}_2\text{Co}_{11}$, and $\text{Fe}_3\text{Co}_3\text{Ti}_2$, to name a few.

4.08.6.2 Colossal magnetoresistance

Anisotropic magnetoresistance (AMR) has been used for writing, storing, and reading information since 1991, when IBM introduced the first hard-disk drives (HDD). The introduction of AMR at the time only increased the relative magnetoresistance by 1%, but this improvement sufficed to increase the capacity of the HDD storage density from 25% to 60%. Pursuing a larger change in relative resistance goes hand in hand with increasing the storage capacity for everyday electronic devices.¹⁸⁴ Colossal magnetoresistance (CMR) refers to an orders-of-magnitude change in electrical resistivity under an applied magnetic field. The application of CMR allows our electronics to be considerably smaller with the ability to store a much larger volume of data.¹⁸⁵

Many perovskite manganites, $\text{Ln}_{1-x}\text{A}_x\text{MnO}_3$, are known to exhibit CMR. In 1993, von Helmolt et al. reported a 60% resistance drop under 6-T applied magnetic field in a thin film of $\text{La}_{0.67}\text{Ba}_{0.33}\text{MnO}_3$ grown epitaxially on a SrTiO_3 substrate.¹⁸⁶ Shortly after that, $\text{Pr}_{0.5}\text{Sr}_{0.5}\text{MnO}_3$ was shown to offer a resistance change of over 2 orders of magnitude, giving the rise to the term “colossal magnetoresistance”.¹⁸⁷ CMR of a similar magnitude was reported for a double perovskite, $\text{NdBaMn}_2\text{O}_6$. The resistance changes more than two orders of magnitude around 300 K when a magnetic field of ~ 2 T was applied.¹⁸⁸ An even more dramatic effect was observed for $(\text{La}_{0.4}\text{Pr}_{0.6})_{1.2}\text{Sr}_{1.8}\text{Mn}_2\text{O}_7$, where the change in resistance is over 6 orders of magnitude at 5 K and 3 T.¹⁸⁹

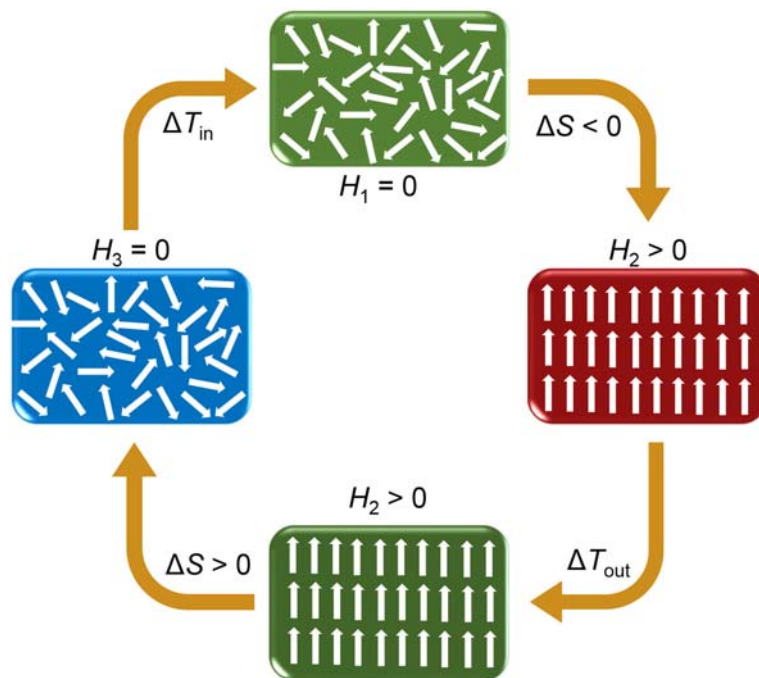
Although CMR is found mainly in doped FM perovskites, it was also reported for non-oxide materials. Thus, an AFM orthorhombic Zintl phase, $\text{Eu}_5\text{In}_2\text{Sb}_6$, shows the decrease in resistance by 5 orders of magnitude at 15 K and 9 T. This is one of the largest CMR effects observed in a stoichiometric AFM compound.¹⁹⁰ The magnetic structure of this compound is complicated, with

consecutive AFM transitions at 14 K and 7 K. The material is anisotropic, with the magnetic moments ordering in the *ab* plane of the orthorhombic crystal structure. Another example of CMR in a non-oxide material is provided by insulating $\text{Mn}_3\text{Si}_2\text{Te}_6$, which shows FiM ordering at 78 K. Under applied magnetic field of 9 T, the resistivity drops by seven orders of magnitude, causing an insulator-to-metal transition at 130 K.¹⁹¹

Despite many promising results, it must be noted that current limitations in the applications of CMR are the low temperatures at which the practically useful effect is observed and the large magnetic fields required to achieve practically appealing CMR values. Ideally, the materials should operate around room temperature and under relatively low magnetic fields (< 2 T).

4.08.6.3 Magnetocaloric materials

The magnetocaloric effect (MCE), discovered by Weiss and Piccard in 1917,¹⁹² is a thermodynamic phenomenon arising from the change in the magnetic component of the total entropy upon application or removal of the magnetic field (Scheme 4). Under adia-



Scheme 4 A schematic of the magnetic refrigeration cycle that relies on the magnetocaloric effect. Application of the magnetic field ($H_1 \rightarrow H_2$) causes the magnetic ordering and the increase in material's temperature. After the heat is removed (ΔT_{out}), the material is demagnetized ($H_2 \rightarrow H_3$), to cause the disorder of magnetic moments followed by the decrease in temperature (ΔT_{in}).

batic conditions (zero heat exchange with the environment, $\delta Q = 0$), removal of the magnetic field (demagnetization of the material) results in a temperature drop—an effect that can be harvested for refrigeration technology.

According to the thermodynamic theory,¹⁹³ the MCE is calculated as an adiabatic temperature change associated with the change in the magnetic field (dH): $dT = -\frac{T}{C_{H,p}} \left(\frac{\partial M}{\partial T} \right)_{H,p} dH$. The calculation takes into account the change in the magnetization (M) of the material and its heat capacity $C_{H,p}$ at constant magnetic field and pressure. The largest temperature change in ferro- or ferrimagnets should be achieved in the vicinity of the magnetic phase transition, at which point the magnetic moment of the compound experiences the most drastic changes. The direct measurement of the temperature change during demagnetization is difficult, and a more practical (although far less accurate) estimate of MCE by measuring the change in entropy, $-\Delta S = \left(\frac{\partial M}{\partial T} \right)_{H,p} dH$, is commonly used upon initial evaluation of magnetocaloric materials.¹⁹⁴

An ideal MCE material should exhibit a negligible magnetic hysteresis, to avoid work losses due to rotating domains in the refrigeration cycle, and a low heat capacity, to maximize the change in temperature. For practical purposes, the material also should be inexpensive and harmless to the environment. Additionally, the material should exhibit large changes in entropy and temperature under practical applied magnetic field (< 2 T). Despite more than the hundred-year-old history of the phenomenon, until recently, its investigation has been limited to attainment of sub-Kelvin temperatures by means of adiabatic demagnetization of paramagnetic salts.^{195–198} The situation changed drastically in 1997 when Pecharsky and Gschneidner discovered a “colossal” MCE in the system $\text{Gd}_5(\text{Si}_{4-x}\text{Ge}_x)$ near room temperature.¹⁹⁹ This discovery opened the way to magnetic refrigeration for practical purposes.²⁰⁰

A 1st-order magnetic transition results in an abrupt change of the magnetization value and, therefore, leads to larger changes in entropy and temperature as compared to a 2nd-order transition.²⁰¹ A 1st-order transition is usually observed as a transition between two magnetically ordered phases. On the other hand, a 2nd-order transition is associated with a disorder-order magnetic transition, and the MCE at such transitions is reduced by short-range order and spin fluctuations in the disordered state. These effects are absent in the order-order transitions. Moreover, the order-order transitions are often accompanied by structural phase transitions, which increase the change in magnetization and enhance the MCE. For example, $\text{Gd}_5\text{Si}_2\text{Ge}_2$, one of the benchmark magnetocaloric materials, exhibits simultaneous 1st-order magnetic and structural phase transitions. The FM ordering of Gd moments at 276 K is accompanied by a reversible breaking or making of bonds between Si/Ge sites, which leads to a large entropy change.²⁰² Therefore, coupling the magnetic and structural phase transitions is one of the desired features of magnetic refrigerants. Below we will discuss the most promising of such materials, which are summarized in **Table 8**. Noteworthy, all of them are itinerant magnets. This observation might be connected to the facile magnetization changes due to rapid dynamics of domain wall propagation in soft magnets with partially delocalized magnetic electrons. On the other hand, such delocalization unavoidably suppresses the magnetic moment, thus decreasing the maximum magnetization value and, consequently, lowering the attainable MCE. All these factors have to be taken into account when designing novel magnetic refrigerants.

With regard to coupling the structural and magnetic phase transition, martensitic magnets are of apparent interest, as long as the temperature of the martensitic transition (T_m) can be matched with that of magnetic ordering (T_C). One of the most promising examples of such behavior is MnCoGe, which exists as high-temperature hexagonal (HT, the Ni_2In type) and low-temperature orthorhombic (LT, the TiNiSi type) polymorphs.²⁰³ Unfortunately, the structural phase transition takes place at 420 K, while FM ordering in the LT polymorph is observed at 260 K. Hole doping (i.e., the decrease in the number of valence electrons) is expected to increase the stability of the hexagonal (HT) polymorph.²⁰⁴ Therefore, chemical modification was used to match the temperatures of the martensitic transformation and FM ordering. For example, creating vacancies in the Mn site led to both transitions occurring around 290 K in $\text{Mn}_{0.965}\text{CoGe}$, causing a large entropy change of 26 J/(kg·K) under applied field of 5 T.²⁰⁵ A similar effect was achieved by hole doping through substitution of Ga for Ge; $\text{MnCoGe}_{0.95}\text{Ga}_{0.05}$ showed $-\Delta S = 34$ J/(kg·K) under applied field of 5 T at 318 K.²⁰⁶ The drawback of these materials, however, is the relatively large thermal hysteresis of the 1st-order phase transition, which has an adverse impact on the MCE values.

AlFe_2B_2 shows FM ordering near RT, with T_C varying from 278 to 310 K depending on the synthetic conditions.²⁰⁷ The change in T_C was traced to minor antisite disorder between the Al and Fe atoms.²⁰⁸ In addition to the practical range of the FM transition, the recent interest to magnetocaloric properties of this material is explained by its low cost and a relatively large cooling capacity,⁷⁶ due to the smaller molar mass, as compared to the majority of other magnetic refrigerants operating near RT. Multiple attempts at chemical substitutions and variable processing conditions have failed to raise the MCE value to become comparable to those observed in some other prominent magnetocaloric materials (Table 7), although some promising results were obtained with partial substitution of Ga for Al.²⁰⁹

Tegus *et al.* reported a large MCE of 18 J/(kg·K) at 5 T for $\text{MnFeP}_{0.45}\text{As}_{0.55}$ around RT.²¹⁰ This material crystallizes in the hexagonal Fe_2P structure type and exhibits a 1st-order magnetostructural transition under applied magnetic field at 305 K. This field-induced transition is the reason for the large MCE. Attempts to increase the MCE value by chemical substitution, in general, led either to the of the 1st-order character of the magnetic phase transition or to the deviation of T_C from the desired near-RT range, even if the MCE value was improved.²¹¹

The $\text{LaFe}_{13-x}\text{Si}_x$ composition, perhaps, has shown the most promise among near-RT magnetic refrigerants. This material belongs to the NaZn_{13} structure type with a face-centered cubic lattice.²¹² The first report on the magnetocaloric behavior in this series showed $-\Delta S = 20$ J/(kg·K) for the sample with $x = 1.4$ under applied field of 5 T at 210 K. Similar to the previous example, the large MCE was explained by field-induced 1st-order metamagnetic transition.²¹³ The T_C and MCE can be tuned by varying the Fe/Si ratio, but they appear to show opposite trends. For example, T_C decreased to 190 K and MCE increased to 29 J/(kg·K) for $x = 1.3$, while the corresponding values of $x = 2.2$ were 240 K and 10 J/(kg·K). These findings, together with the relatively low cost of the material due to the dominant Fe content, prompted extensive studies on optimizing the MCE in $\text{LaFe}_{13-x}\text{Si}_x$ by chemical substitutions. Initially, raising both T_C and MCE proved to be difficult,²¹⁴ but eventually hydrogenation was found as a reliable way to bring the T_C close to RT with relatively small losses in the MCE.²¹⁵ Unfortunately, the stability of such hydrides is low,²¹⁶ especially under the condition of the repeating magnetostructural transition associated with cycling of the magnetic field required for the refrigeration process.

Table 8 Examples of promising magnetocaloric materials and their magnetic properties.

Compound	T_C (K)	$-\Delta S$ (J/(kg K))	$\Delta\mu_0H$ (T)
$\text{Gd}_5\text{Si}_2\text{Ge}_2$	276	30	5
$\text{Mn}_{0.965}\text{CoGe}$	290	26	5
$\text{MnCoGe}_{0.95}\text{Ga}_{0.05}$	318	34	5
AlFe_2B_2	307	7.7	5
$\text{MnFeP}_{0.45}\text{As}_{0.55}$	305	18	5
$\text{Ni}_{50}\text{Mn}_{37}\text{Sn}_{13}$	320	18	5
$\text{LaFe}_{11.6}\text{Si}_{1.4}$	210	20	5

Despite the challenges associated with the optimization of MCE and discovery of useful and sustainable magnetocaloric materials, the rapid progress taking place in this research area over the last 25 years promises to bring practical magnetic refrigeration to fruition in the nearest decades.

References

1. Carlin, R. L. *Magnetochemistry*, Springer: Berlin, 1989.
2. Kahn, O. *Molecular Magnetism*, Wiley-VCH: New York, 1993.
3. Ashcroft, N. W.; Mermin, N. D. *Solid State Physics*, Thomson Press Ltd, 2003.
4. Kittel, C. *Introduction to Solid State Physics*, 8th ed.; Wiley: Weinheim, 2005.
5. Getzlaff, M. *Fundamentals of Magnetism*, Springer: Berlin, 2008.
6. Stöhr, J.; Siegmann, H. C. *Magnetism. From Fundamentals to Nanoscale Dynamics*, Springer: Berlin, 2006.
7. Garlea, V. O.; Chakoumakos, B. C. Magnetic Structures. In *Experimental Methods in The Physical Sciences*; Fernandez-Alonso, F., Price, D. L., Eds.; vol. 48; Elsevier, 2015; pp 203–290.
8. Spaldin, N. *Magnetic Materials: Fundamentals and Device Applications*, Cambridge University Press: Cambridge, 2003.
9. Goodenough, J. B. Theory of the Role of Covalence in the Perovskite-Type Manganites $[\text{La}, \text{M}(\text{II})]\text{MnO}_3$. *Phys. Rev.* **1955**, *100*, 564–573.
10. Goodenough, J. B. An Interpretation of the Magnetic Properties of the Perovskite-Type Mixed Crystals $\text{La}_{1-x}\text{Sr}_x\text{CoO}_{3-x}$. *J. Phys. Chem. Solid* **1958**, *6*, 287–297.
11. Kanamori, J. Superexchange Interaction and Symmetry Properties of Electron Orbitals. *J. Phys. Chem. Solid* **1959**, *10*, 87–98.
12. Komarek, A. C.; Streltsov, S. V.; Isobe, M.; et al. CaCrO_3 : An Anomalous Antiferromagnetic Metallic Oxide. *Phys. Rev. Lett.* **2008**, *101*, 167204.
13. Anguelouch, A.; Gupta, A.; Xiao, G.; et al. Near-Complete Spin Polarization in Atomically-Smooth Chromium-Dioxide Epitaxial Films Prepared Using a CVD Liquid Precursor. *Phys. Rev. B* **2001**, *64*, 180408.
14. Parker, J. S.; Watts, S. M.; Ivanov, P. G.; Xiong, P. Spin Polarization of CrO_2 at and across an Artificial Barrier. *Phys. Rev. Lett.* **2002**, *88*, 196601.
15. Matthias, B. T.; Bozorth, R. M.; Van Vleck, J. H. Ferromagnetic Interaction in EuO . *Phys. Rev. Lett.* **1961**, *7*, 160–161.
16. Coey, J. M. D.; Viret, M.; Von Molnar, S. Mixed-Valence Manganites. *Adv. Phys.* **1999**, *48*, 167–293.
17. Thomas, R. M.; Ranno, L.; Coey, J. M. D. Transport Properties of $(\text{Sm}_{1-x}\text{A}_x)_3\text{MnO}_3$ ($\text{A} = \text{Ca}^{2+}, \text{Sr}^{2+}, \text{Ba}^{2+}, \text{Pb}^{2+}$). *J. Appl. Phys.* **1997**, *81*, 5763–5765.
18. Shimakawa, Y.; Kubo, Y.; Hamada, N.; et al. Crystal Structure, Magnetic and Transport Properties, and Electronic Band Structure of $\text{A}_2\text{Mn}_2\text{O}_7$ Pyrochlores ($\text{A} = \text{Y}, \text{In}, \text{Lu}, \text{and Ti}$). *Phys. Rev. B* **1999**, *59*, 1249–1254.
19. Subramanian, M. A.; Toby, B. H.; Ramirez, A. P.; et al. Colossal Magnetoresistance without $\text{Mn}^{3+}/\text{Mn}^{4+}$ Double Exchange in the Stoichiometric Pyrochlore $\text{Ti}_2\text{Mn}_2\text{O}_7$. *Science* **1996**, *273*, 81–84.
20. Imai, H.; Shimakawa, Y.; Sushko, Y. V.; Kubo, Y. Carrier Density Change in the Colossal-Magnetoresistance Pyrochlore $\text{Ti}_2\text{Mn}_2\text{O}_7$. *Phys. Rev. B* **2000**, *62*, 12190–12194.
21. Kiyama, T.; Yoshimura, K.; Kosuge, K.; et al. Invar Effect of SrRuO_3 : Itinerant electron Magnetism of Ru $4d$ Electrons. *Phys. Rev. B* **1996**, *54*, R756–R759.
22. Shull, C. G.; Strauser, W. A.; Wollan, E. O. Neutron Diffraction by Paramagnetic and Antiferromagnetic Substances. *Phys. Rev.* **1951**, *83*, 333–345.
23. Goodwin, A. L.; Tucker, M. G.; Dove, M. T.; Keen, D. A. Magnetic Structure of MnO at 10 K from Total Neutron Scattering Data. *Phys. Rev. Lett.* **2006**, *96*, 047209.
24. Ressouche, E.; Kernavainis, N.; Regnault, L.-P.; Henry, J.-Y. Magnetic Structures of the Metal Monoxides NiO and CoO Re-Investigated by Spherical Neutron Polarimetry. *Phys. B Condens. Matter* **2006**, *385-386*, 394–397.
25. Roth, W. L. Magnetic Structures of MnO , FeO , CoO , and NiO . *Phys. Rev.* **1958**, *110*, 1333–1341.
26. Morin, F. J. Magnetic Susceptibility of $\alpha\text{-Fe}_2\text{O}_3$ and $\alpha\text{-Fe}_2\text{O}_3$ with Added Titanium. *Phys. Rev.* **1950**, *78*, 819–820.
27. Hill, A. H.; Jiao, F.; Bruce, P. G.; et al. Neutron Diffraction Study of Mesoporous and Bulk Hematite, $\alpha\text{-Fe}_2\text{O}_3$. *Chem. Mater.* **2008**, *20*, 4891–4899.
28. Corliss, L. M.; Hastings, J. M.; Nathans, R.; Shirane, G. Magnetic Structure of Cr_2O_3 . *J. Appl. Phys.* **1965**, *36*, 1099–1100.
29. Fiebig, M.; Fröhlich, D.; Thiele, H. J. Determination of Spin Direction in the Spin-Flop Phase of Cr_2O_3 . *Phys. Rev. B* **1996**, *54*, R12681–R12684.
30. Fiebig, M.; Fröhlich, D.; Krichevstov, B. B.; Pisarev, R. V. Second Harmonic Generation and Magnetic-Dipole-Electric-Dipole Interference in Antiferromagnetic Cr_2O_3 . *Phys. Rev. Lett.* **1994**, *73*, 2127–2130.
31. Jeanneau, J.; Toulemonde, P.; Remenyi, G.; et al. Magnetism and Anomalous Apparently Inverse Jahn-Teller Effect in Sr_2CrO_4 . *EPL (Europhys. Lett.)* **2019**, *127*, 27002.
32. Rani, M.; Sakurai, H.; Okubo, S.; et al. Antiferromagnetic Ordering in Sr_2CrO_4 . *J. Phys. Condens. Matter* **2013**, *25*, 226001.
33. Cao, G.; McCall, S.; Crow, J. E.; Guertin, R. P. Observation of a Metallic Antiferromagnetic Phase and Metal to Nonmetal Transition in $\text{Ca}_3\text{Ru}_2\text{O}_7$. *Phys. Rev. Lett.* **1997**, *78*, 1751–1754.
34. Yoshida, Y.; Ikeda, S.-I.; Matsuhata, H.; et al. Crystal and Magnetic Structure of $\text{Ca}_3\text{Ru}_2\text{O}_7$. *Phys. Rev. B* **2005**, *72*, 054412.
35. Kubota, M.; Fujioaka, H.; Hirota, K.; et al. Relation between Crystal and Magnetic Structures of Layered Manganite $\text{La}_{2-2x}\text{Sr}_{1+2x}\text{Mn}_2\text{O}_7$ ($0.30 \leq x \leq 0.50$). *J. Physical Soc. Japan* **2000**, *69*, 1606–1609.
36. Coey, J. M. D.; Viret, M.; von Molnar, S. Mixed-Valence Manganites. *Adv. Phys.* **2009**, *58*, 571–697.
37. Wollan, E. O.; Koehler, W. C. Neutron Diffraction Study of the Magnetic Properties of the Series of Perovskite-Type Compounds $[(1-x)\text{La}_x\text{Ca}]\text{MnO}_3$. *Phys. Rev.* **1955**, *100*, 545–563.
38. Moussa, F.; Hennion, M.; Rodríguez-Carvajal, J.; et al. Spin Waves in the Antiferromagnet Perovskite LaMnO_3 : A Neutron-Scattering Study. *Phys. Rev. B* **1996**, *54*, 15149–15155.
39. Elemans, J. B. A. A.; Van Laar, B.; Van Der Veen, K. R.; Loopstra, B. O. The Crystallographic and Magnetic Structures of $\text{La}_{1-x}\text{Ba}_x\text{Mn}_{1-x}\text{Me}_x\text{O}_3$ ($\text{Me} = \text{Mn}$ or Ti). *J. Solid State Chem.* **1971**, *3*, 238–242.
40. Huang, Q.; Santoro, A.; Lynn, J. W.; et al. Structure and Magnetic Order in $\text{La}_{1-x}\text{Ca}_x\text{MnO}_3$ ($0 < x < \sim 0.33$). *Phys. Rev. B* **1998**, *58*, 2684–2691.
41. Radaelli, P. G.; Cox, D. E.; Marezio, M.; et al. Simultaneous Structural, Magnetic, and Electronic Transitions in $\text{La}_{1-x}\text{Ca}_x\text{MnO}_3$ with $x = 0.25$ and 0.50 . *Phys. Rev. Lett.* **1995**, *75*, 4488–4491.
42. Radaelli, P. G.; Cox, D. E.; Capogna, L.; et al. Wigner-Crystal and Bi-Stripe Models for the Magnetic and Crystallographic Superstructures of $\text{La}_{0.333}\text{Ca}_{0.667}\text{MnO}_3$. *Phys. Rev. B* **1999**, *59*, 14440–14450.
43. Battle, P. D.; Goodenough, J. B.; Price, R. The Crystal Structures and Magnetic Properties of $\text{Ba}_2\text{LaRuO}_6$ and $\text{Ca}_2\text{LaRuO}_6$. *J. Solid State Chem.* **1983**, *46*, 234–244.
44. Mustonen, O. H. J.; Pugh, C. E.; Walker, H. C.; et al. Diamagnetic d -Orbitals Drive Magnetic Structure Selection in the Double Perovskite $\text{Ba}_2\text{MnTeO}_6$. *Chem. Mater.* **2020**, *32*, 7070–7079.
45. Mutch, H.; Mustonen, O.; Walker, H. C.; et al. Long- and Short-Range Magnetism in the Frustrated Double Perovskite Ba_2MnWO_6 . *Phys. Rev. Mater.* **2020**, *4*, 014408.
46. Rodríguez, E.; López, M. L.; Campo, J.; et al. Crystal and Magnetic Structure of the Perovskites La_2MTiO_6 ($\text{M} = \text{Co}, \text{Ni}$). *J. Mater. Chem.* **2002**, *12*, 2798–2802.
47. Morrow, R.; Mishra, R.; Restrepo, O. D.; et al. Independent Ordering of Two Interpenetrating Magnetic Sublattices in the Double Perovskite $\text{Sr}_2\text{CoOsO}_6$. *J. Am. Chem. Soc.* **2013**, *135*, 18824–18830.
48. Néel, L. Magnetic Properties of Ferrites; Ferrimagnetism and Antiferromagnetism. *Ann. Phys.* **1948**, *3*, 137–198.
49. Dronskowski, R. The Little Maghemite Story: A Classic Functional Material. *Adv. Funct. Mater.* **2001**, *11*, 27–29.

50. Mazen, S. A.; Sabrah, B. A. Thermal Effect on Formation and Conduction Mechanism of MnFe_2O_4 . *Thermochim. Acta* **1986**, *105*, 1–8.
51. Sawatzky, G. A.; Van Der Woude, F.; Morrish, A. H. Mössbauer Study of Several Ferrimagnetic Spinels. *Phys. Rev.* **1969**, *187*, 747–757.
52. Sawatzky, G. A.; Van Der Woude, F.; Morrish, A. H. Recoilless-Fraction Ratios for Fe^{57} in Octahedral and Tetrahedral Sites of a Spinel and a Garnet. *Phys. Rev.* **1969**, *183*, 383–386.
53. Hastings, J. M.; Corliss, L. M. Neutron Diffraction Study of Manganese Ferrite. *Phys. Rev.* **1956**, *104*, 328–331.
54. Wickham, D. G.; Mark, J.; Knox, K. Metal iron(III) Oxides. *Inorg. Synth.* **1967**, *9*, 152–156.
55. Hong, K. H.; McNally, G. M.; Coduri, M.; Atfield, J. P. Synthesis, Crystal Structure, and Magnetic Properties of MnFe_3O_5 . *Z. Anorg. Allg. Chem.* **2016**, *642*, 1355–1358.
56. Hong, K. H.; Arevalo-Lopez, A. M.; Coduri, M.; et al. Cation, Magnetic, and Charge Ordering in MnFe_3O_5 . *J. Mater. Chem. C* **2018**, *6*, 3271–3275.
57. Rayaprol, S.; Kaushik, S. D.; Babu, P. D.; Siruguri, V. Structure and Magnetism of FeMnO_3 . *AIP Conf. Proc.* **2013**, *1512*, 1132–1133.
58. Shirik, B. T.; Buessens, W. R. Temperature Dependence of M_s and K_1 of $\text{BaFe}_{12}\text{O}_{19}$ and $\text{SrFe}_{12}\text{O}_{19}$ Single Crystals. *J. Appl. Phys.* **1969**, *40*, 1294–1296.
59. Collomb, A.; Wolfers, P.; Obradors, X. Neutron Diffraction Studies of Some Hexagonal Ferrites: $\text{BaFe}_{12}\text{O}_{19}$, $\text{BaMg}_2\text{-W}$ and $\text{BaCo}_2\text{-W}$. *J. Magn. Magn. Mater.* **1986**, *62*, 57–67.
60. Granados-Miralles, C.; Jenuš, P. On the Potential of Hard Ferrite Ceramics for Permanent Magnet Technology—A Review on Sintering Strategies. *J. Phys. D Appl. Phys.* **2021**, *54*, 303001.
61. Geller, S.; Gilleo, M. A. The Crystal Structure and Ferrimagnetism of Yttrium-Iron Garnet, $\text{Y}_3\text{Fe}_2(\text{FeO}_4)_3$. *J. Phys. Chem. Solid* **1957**, *3*, 30–36.
62. Rodic, D.; Mitric, M.; Tellgren, R.; et al. True Magnetic Structure of the Ferrimagnetic Garnet $\text{Y}_3\text{Fe}_5\text{O}_{12}$ and Magnetic Moments of iron Ions. *J. Magn. Magn. Mater.* **1999**, *191*, 137–145.
63. Pauthenet, R. Spontaneous Magnetization of some Garnet Ferrites and the Aluminum-Substituted Garnet Ferrites. *J. Appl. Phys.* **1958**, *29*, 253–255.
64. Geller, S.; Remeika, J. P.; Sherwood, R. C.; et al. Magnetic Study of the Heavier Rare-Earth iron Garnets. *Phys. Rev.* **1965**, *137*, A1034–A1038.
65. Eppler, W. R.; Kryder, M. H. Garnets for Short Wavelength Magneto-Optic Recording. *J. Phys. Chem. Solid* **1995**, *56*, 1479–1490.
66. Vasala, S.; Karppinen, M. $\text{A}_2\text{B}'\text{B}''\text{O}_6$ Perovskites: A Review. *Prog. Solid State Chem.* **2015**, *43*, 1–36.
67. Arulraj, A.; Ramesha, K.; Gopalakrishnan, J.; Rao, C. N. R. Magnetoresistance in the Double Perovskite $\text{Sr}_2\text{CrMoO}_6$. *J. Solid State Chem.* **2000**, *155*, 233–237.
68. Kobayashi, K. I.; Kimura, T.; Sawada, H.; et al. Room-Temperature Magnetoresistance in an Oxide Material with an Ordered Double-Perovskite Structure. *Nature* **1998**, *395*, 677–680.
69. Feng, H. L.; Arai, M.; Matsushita, Y.; et al. High-Temperature Ferrimagnetism Driven by Lattice Distortion in Double Perovskite $\text{Ca}_2\text{FeOsO}_6$. *J. Am. Chem. Soc.* **2014**, *136*, 3326–3329.
70. Krockenberger, Y.; Mogare, K.; Reehuis, M.; et al. $\text{Sr}_2\text{CrOsO}_6$: End Point of a Spin-Polarized Metal-Insulator Transition by $5d$ Band Filling. *Phys. Rev. B* **2007**, *75*, 020404.
71. Serrate, D.; Teresa, J. M. D.; Ibarra, M. R. Double Perovskites with Ferromagnetism above Room Temperature. *J. Phys. Condens. Matter* **2006**, *19*, 023201.
72. Pöttgen, R.; Johrendt, D. *Intermetallics: Synthesis, Structure, Function*, De Gruyter, 2019.
73. Stoner, E. C. Collective Electron Ferromagnetism. *Proc. R. Soc. Lond. A Math. Phys. Sci.* **1938**, *165*, 372–414.
74. Gourdon, O.; Bud'ko, S. L.; Williams, D.; Miller, G. J. Crystallographic, Electronic, and Magnetic Studies of ζ_2 -GaM ($M = \text{Cr, Mn or Fe}$): Trends in Itinerant Magnetism. *Inorg. Chem.* **2004**, *43*, 3210–3218.
75. Kovnir, K.; Thompson, C. M.; Zhou, H. D.; et al. Tuning Ferro- and Metamagnetic Transitions in Rare-Earth Cobalt Phosphides $\text{La}_{1-x}\text{Pr}_x\text{Co}_2\text{P}_2$. *Chem. Mater.* **2010**, *22*, 1704–1713.
76. Tan, X.; Chai, P.; Thompson, C. M.; Shatruk, M. Magnetocaloric Effect in AlFe_2B_2 : Toward Magnetic Refrigerants from Earth-Abundant Elements. *J. Am. Chem. Soc.* **2013**, *135*, 9553–9557.
77. Landrum, G. A.; Dronskowski, R. Ferromagnetism in Transition Metals: A Chemical Bonding Approach. *Angew. Chem. Int. Ed.* **1999**, *38*, 1390–1393.
78. Landrum, G. A.; Dronskowski, R. The Orbital Origins of Magnetism: From Atoms to Molecules to Ferromagnetic Alloys. *Angew. Chem. Int. Ed.* **2000**, *39*, 1560–1585.
79. Dronskowski, R.; Blochl, P. E. Crystal Orbital Hamilton Populations (COHP)—Energy-Resolved Visualization of Chemical Bonding in Solids Based on Density-Functional Calculations. *J. Phys. Chem.* **1993**, *97*, 8617–8624.
80. Shatruk, M. Chemical Aspects of Itinerant Magnetism. In *Encyclopedia of Inorganic and Bioinorganic Chemistry*; Scott, R. A., Ed., Wiley-VCH: Chichester, 2017; p eibc2494.
81. Antoniák, C.; Spasova, M.; Trunova, A.; et al. Correlation of Magnetic Moments and Local Structure of FePt Nanoparticles. *J. Phys. Conf. Ser.* **2009**, *190*, 012118.
82. Coehoorn, R.; Groot, R. A. D. The Electronic Structure of MnBi. *J. Phys. F* **1985**, *15*, 2135–2144.
83. Tu, C.; Stutius, W. The Phase Transformation and Physical Properties of the MnBi and $\text{Mn}_{1.08}\text{Bi}$ Compounds. *IEEE Trans. Magn.* **1974**, *10*, 581–586.
84. He, Y.; Gayles, J.; Yao, M.; et al. Large Linear Non-saturating Magnetoresistance and High Mobility in Ferromagnetic MnBi. *Nat. Commun.* **2021**, *12*, 4576.
85. Lipson, H.; Shoenberg, D.; Stupart, G. V. The Relation between Atomic Arrangement and Coercivity in an Alloy of iron and Platinum. *J. Inst. Met.* **1941**, *67*, 333–340.
86. Wang, F.; Xing, H.; Xu, X. Overcoming the Trilemma Issues of Ultrahigh Density Perpendicular Magnetic Recording Media by $\text{L}_{10}\text{-Fe}(\text{Co})\text{Pt}$ Materials. *SPIN* **2015**, *5*, 1530002.
87. Lee, H.; Shin, T.-H.; Cheon, J.; Weissleder, R. Recent Developments in Magnetic Diagnostic Systems. *Chem. Rev.* **2015**, *115*, 10690–10724.
88. Wells, A. F. *Structural Inorganic Chemistry*, 5th ed.; Oxford University Press, 1983.
89. Labroo, S.; Willis, F.; Ali, N. Influence of Mn Moments on the Properties of RMn_2 Compounds ($R = \text{Y}$ and Light Rare Earths). *J. Appl. Phys.* **1990**, *67*, 5295–5297.
90. Buschow, K. H. J.; van Stepele, R. P. Magnetic Properties of some Cubic Rare-Earth-iron Compounds of the Type RFe_2 and $\text{R}_x\text{Y}_{1-x}\text{Fe}_2$. *J. Appl. Phys.* **1970**, *41*, 4066–4069.
91. Ilarraz, J.; del Moral, A. Magnetic Ordering Temperatures in Rare Earth-Fe₂ Laves Phases Determined by DTA. *Phys. Status Solidi A* **1979**, *51*, K41–K43.
92. Burzo, E.; Gratz, E.; Pop, V. On the Magnetic Behaviour of ACo_2 ($A = \text{Y, Lu, Zr, Sc}$ and Hf) Compounds. *J. Magn. Magn. Mater.* **1993**, *123*, 159–164.
93. Duc, N. H.; Brommer, P. E. Formation of 3d-Moments and Spin Fluctuations in some Rare-Earth-Cobalt Compounds. In *Handbook of Magnetic Materials*; Buschow, K. H. J., Ed.; vol. 12; Elsevier, 1999; pp 259–394.
94. Inoue, K.; Nakamura, Y.; Yamaguchi, Y.; et al. Neutron Diffraction Study of C14-Laves-Phase, TbMn_2 and DyMn_2 . *Phys. B Condens. Matter* **1997**, *237-238*, 579–580.
95. Ouladidaf, B.; Ritter, C.; Ballou, R.; Deportes, J. Magnetic Ordering of GdMn_2 . *Phys. B Condens. Matter* **2000**, *276-278*, 670–671.
96. Allen, J. W.; Oh, S. J.; Lindau, I.; et al. CeRu_2 and CeCo_2 : Superconductors with $4f$ Electrons. *Phys. Rev. B* **1982**, *26*, 445–448.
97. Ohta, M.; Fujita, A.; Fukamichi, K.; et al. Effect of Spin Fluctuations on Thermal Expansion Characteristics in Paramagnetic Laves-Phase $\text{Lu}(\text{Co}_{1-x}\text{Ga}_x)_2$ Compounds. *Phys. Rev. B* **2005**, *71*, 054412.
98. Brooks, M. S. S.; Johansson, B. Density Functional Theory of the Ground-State Magnetic Properties of Rare Earths and Actinides. In *Handbook of Magnetic Materials*; Buschow, K. H. J., Ed.; vol. 7; Elsevier, 1993; pp 139–230.
99. Burzo, E. Magnetic and Crystallographic Properties of Rare-Earth and Yttrium-iron Laves Phases. *Z. Angew. Phys.* **1971**, *32*, 127–132.
100. Burzo, E. Crystallographic, Magnetic, and EPR Studies of Rare-Earth and Yttrium-Cobalt Laves Phases. *Int. J. Magn.* **1972**, *3*, 161–170.
101. Gutfleisch, O.; Willard, M. A.; Brück, E.; et al. Magnetic Materials and Devices for the 21st Century: Stronger, Lighter, and More Energy Efficient. *Adv. Mater.* **2011**, *23*, 821–842.
102. Kohlmann, H.; Hansen, T. C.; Nassif, V. Magnetic Structure of SmCo_5 from 5 K to the Curie Temperature. *Inorg. Chem.* **2018**, *57*, 1702–1704.
103. Buschow, K. H. J. Intermetallic Compounds of Rare-Earth and 3d Transition Metals. *Rep. Prog. Phys.* **1977**, *40*, 1179–1256.
104. Buschow, K. H. J.; Van Diepen, A. M.; De Wijn, H. W. Crystal-Field Anisotropy of Sm^{3+} in SmCo_5 . *Solid State Commun.* **1974**, *15*, 903–906.
105. Baltz, V.; Manchon, A.; Tsoi, M.; Moriyama, T.; Ono, T.; Tserkovnyak, Y. Antiferromagnetic Spintronics. *Rev. Mod. Phys.* **2018**, *90*, 015005.
106. Moruzzi, V. L.; Marcus, P. M. Antiferromagnetic-Ferromagnetic Transition in FeRh. *Phys. Rev. B* **1992**, *46*, 2864–2873.
107. Martí, X.; Fina, I.; Frontera, C.; Liu, J.; Wadley, P.; He, Q.; Paull, R. J.; Clarkson, J. D.; Kudrnovsky, J.; Turek, I.; Kuneš, J.; Yi, D.; Chu, J. H.; Nelson, C. T.; You, L.; Arenholz, E.; Salahuddin, S.; Fontcuberta, J.; Jungwirth, T.; Ramesh, R. *Room-Temperature Antiferromagnetic Memory Resistor*. *Nat. Mater.* **2014**, *13*, 367–374.

108. Barthem, V. M. T. S.; Colin, C. V.; Mayaffre, H.; Julien, M. H.; Givord, D. Revealing the Properties of Mn_2Au for Antiferromagnetic Spintronics. *Nat. Commun.* **2013**, *4*, 2892.
109. Olejnik, K.; Seifert, T.; Kašpar, E.; Novák, V.; Wadley, P.; Campion, R. P.; Baumgartner, M.; Gambardella, P.; Němec, P.; Wunderlich, J.; Sinova, J.; Kužel, P.; Müller, M.; Kampfrath, T.; Jungwirth, T. Terahertz Electrical Writing Speed in an Antiferromagnetic Memory. *Sci. Adv.* **2018**, *4*, eaar3566.
110. Heusler, F. Manganese Bronze and the Synthesis of Magnetizable Alloys from Non-magnetic Metals. *Angew. Chem.* **1904**, *17*, 260–264.
111. Buschow, K. H. J.; Vanengen, P. G.; Jongebreur, R. Magneto-Optical Properties of Metallic Ferromagnetic Materials. *J. Magn. Magn. Mater.* **1983**, *38*, 1–22.
112. Heyne, L.; Igarashi, T.; Kanomata, T.; et al. Atomic and Magnetic Order in the Weak Ferromagnet $CoVsb$: Is it a Half-Metallic Ferromagnet? *J. Phys. Condens. Matter* **2005**, *17*, 4991–4999.
113. Otto, M. J.; Van Woerden, R. A. M.; Van der Valk, P. J.; et al. Half-Metallic Ferromagnets. I. Structure and Magnetic Properties of $NiMnSb$ and Related Inter-Metallic Compounds. *J. Phys. Condens. Matter* **1989**, *1*, 2341–2350.
114. Wurmehl, S.; Fecher, G. H.; Kandpal, H. C.; et al. Investigation of Co_2FeSi : The Heusler Compound with Highest Curie Temperature and Magnetic Moment. *Appl. Phys. Lett.* **2006**, *88*, 032503.
115. Mitra, S.; Ahmad, A.; Chakrabarti, S.; et al. Investigation on Structural, Electronic and Magnetic Properties of Co_2FeGe Heusler Alloy: Experiment and Theory. *J. Magn. Magn. Mater.* **2022**, *552*, 169148.
116. Graf, T.; Felsler, C.; Parkin, S. S. P. Simple Rules for the Understanding of Heusler Compounds. *Prog. Solid State Chem.* **2011**, *39*, 1–50.
117. Shatruk, M. $ThCr_2Si_2$ Structure Type: The “Perovskite” of Intermetallics. *J. Solid State Chem.* **2019**, *272*, 198–209.
118. Nowik, I.; Levi, Y.; Felner, I.; Bauminger, E. R. New Multiple Magnetic Phase Transitions and Structures in RMn_2X_2 , $X = Si$ or Ge , $R =$ Rare Earth. *J. Magn. Magn. Mater.* **1995**, *147*, 373–384.
119. Venturini, G.; Welter, R.; Ressouche, E.; Malaman, B. Neutron Diffraction Studies of $LaMn_2Ge_2$ and $LaMn_2Si_2$ Compounds: Evidence of Dominant Antiferromagnetic Components within the Mn planes. *J. Alloys Compd.* **1994**, *210*, 213–220.
120. Kido, H.; Hoshikawa, T.; Shimada, M.; Koizumi, M. Synthesis and Magnetic Properties of RMn_2Si_2 ($R = Y, Nd, Gd$) and YNi_2Si_2 . *Funtai Oyobi Funmatsu Yakin* **1984**, *31*, 67–69.
121. Venturini, G. Magnetic Study of the Compounds RMn_2Ge_2 ($R = La-Sm, Gd$) and $R_xY_{1-x}Mn_2Ge_2$ ($R = La, Lu; 0 < x < 1$) above Room Temperature. *J. Alloys Compd.* **1996**, *232*, 133–141.
122. Szytula, A.; Leciejewicz, J. Magnetic Properties of Ternary Intermetallic Compounds of the RT_2X_2 Type. In *Handbook on the Physics and Chemistry of Rare Earths*; Gschneidner K. A. Jr., Eyring, L., Eds.; vol. 12; Elsevier, 1989; pp 133–211 (Reprinted from: NOT IN FILE).
123. Kolda, M.; Leciejewicz, J.; Szytula, A.; et al. Magnetic Transition in $TbMn_2Si_2$. *J. Alloys Compd.* **1996**, *241*, L1–L3.
124. Łątka, K. Magnetic Ordering in $GdMn_2Si_2$. *Acta Phys. Pol. A* **1987**, *A72*, 73–75.
125. Ohashi, M.; Onodera, H.; Ono, T.; et al. Magnetic Order in the Competing Interaction State of Ternary Intermetallics $DyMn_2Si_2$ and $DyMn_2Ge_2$. Proceedings of 5th International Symposium in Advances Nuclear Energy Research; pp 404–409.
126. Welter, R.; Venturini, G.; Ressouche, E.; Malaman, B. Neutron Diffraction Study of $CeMn_2Ge_2$, $PrMn_2Ge_2$ and $NdMn_2Ge_2$: Evidence of Dominant Antiferromagnetic Components within the (001) Mn planes in Ferromagnetic $ThCr_2Si_2$ -Type Manganese Ternary Compounds. *J. Alloys Compd.* **1995**, *218*, 204–215.
127. Narasimhan, K. S. V. L.; Rao, V. U. S.; Bergner, R. L.; Wallace, W. E. Magnetic Properties of RMn_2Ge_2 Compounds ($R = La, Ce, Pr, Nd, Gd, Tb, Dy, Ho, Er$, and Th). *J. Appl. Phys.* **1975**, *46*, 4957–4960.
128. Reehuis, M.; Ritter, C.; Ballou, R.; Jeitschko, W. Ferromagnetism in the $ThCr_2Si_2$ -Type Phosphide $LaCo_2P_2$. *J. Magn. Magn. Mater.* **1994**, *138*, 85–93.
129. Thompson, C. M.; Kovnir, K.; Eveland, S.; et al. Synthesis of $ThCr_2Si_2$ -Type Arsenides from Bi Flux. *Chem. Commun.* **2011**, *47*, 5563–5565.
130. Reehuis, M.; Jeitschko, W. Structure and Magnetic Properties of the Phosphides $CaCo_2P_2$ and LnT_2P_2 with $ThCr_2Si_2$ Structure and LnT_2P_2 with $PbCl_2$ Structure ($Ln =$ Lanthanoides, $T = Fe, Co, Ni$). *J. Phys. Chem. Solid* **1990**, *51*, 961–968.
131. Thompson, C. M.; Tan, X. Y.; Kovnir, K.; et al. Synthesis, Structures, and Magnetic Properties of Rare-Earth Cobalt Arsenides, RCo_2As_2 ($R = La, Ce, Pr, Nd$). *Chem. Mater.* **2014**, *26*, 3825–3837.
132. Mydosh, J. A. Spin Glasses: An Experimental Introduction, Taylor & Francis: Washington, DC, 1993.
133. Moessner, R.; Ramirez, A. P. Geometrical Frustration. *Phys. Today* **2006**, *9*, 24–29.
134. Greedan, J. E. Geometrically Frustrated Magnetic Materials. *J. Mater. Chem.* **2001**, *11*, 37–53.
135. Ramirez, A. P. Strongly Geometrically Frustrated Magnets. *Annu. Rev. Mater. Sci.* **1994**, *24*, 453–480.
136. Balents, L. Spin Liquids in Frustrated Magnets. *Nature* **2010**, *464*, 199–208.
137. Dzyaloshinsky, I. A Thermodynamic Theory of “Weak” Ferromagnetism of Antiferromagnetics. *J. Phys. Chem. Solids* **1958**, *4*, 241–255.
138. Moriya, T. Anisotropic Superexchange Interaction and Weak Ferromagnetism. *Phys. Rev.* **1960**, *120*, 91–98.
139. Kanazawa, N.; Seki, S.; Tokura, Y. Noncentrosymmetric Magnets Hosting Magnetic Skyrmions. *Adv. Mater.* **2017**, *29*, 1603227.
140. Shibata, K.; Yu, X. Z.; Hara, T.; Morikawa, D.; Kanazawa, N.; Kimoto, K.; Ishiwata, S.; Matsui, Y.; Tokura, Y. Towards Control of the Size and Helicity of Skyrmions in Helimagnetic Alloys by Spin–Orbit Coupling. *Nat. Nanotechnol.* **2013**, *8*, 723–728.
141. Tokura, Y.; Seki, S. Multiferroics with Spiral Spin Orders. *Adv. Mater.* **2010**, *22*, 1554–1565.
142. Chai, Y. S.; Kwon, S.; Chun, S. H.; Kim, I.; Jeon, B.-G.; Kim, K. H.; Lee, S. Electrical Control of Large Magnetization Reversal in a Helimagnet. *Nat. Commun.* **2014**, *5*, 4208.
143. Yu, X. Z.; Kanazawa, N.; Zhang, W. Z.; Nagai, T.; Hara, T.; Kimoto, K.; Matsui, Y.; Onose, Y.; Tokura, Y. Skyrmion Flow near Room Temperature in an Ultralow Current Density. *Nat. Commun.* **2012**, *3*, 988.
144. Ishiwata, S.; Taguchi, Y.; Murakawa, H.; Onose, Y.; Tokura, Y. Low-Magnetic-Field Control of Electric Polarization Vector in a Helimagnet. *Science* **2008**, *319*, 1643–1646.
145. Léone, P.; Doussier-Brochard, C.; André, G.; Moëlo, Y. Magnetic Properties and Neutron Diffraction Study of Two Manganese Sulfosalts: Monoclinic $MnSb_2S_4$ and Benavidesite ($MnPb_4Sb_6S_{14}$). *Phys. Chem. Miner.* **2008**, *35*, 201–206.
146. Djeutedjeu, H.; Makongo, J. P. A.; Rotaru, A.; Palasyuk, A.; Takas, N. J.; Zhou, X.; Ranmohotti, K. G. S.; Spinu, L.; Uher, C.; Poudeu, P. F. P.; of $MnSb_2Se_4$. Crystal Structure, Charge Transport, and Magnetic Properties. *Eur. J. Inorg. Chem.* **2011**, *2011*, 3969–3977.
147. Clark, J. K.; Pak, C.; Cao, H.; Shatruk, M. Helimagnetism in $MnBi_2Se_4$ Driven by Spin-Frustrating Interactions between Antiferromagnetic Chains. *Crystals* **2021**, *11*, 242.
148. Ji, W. H.; Yin, L.; Zhu, W. M.; Kumar, C. M. N.; Li, C.; Li, H. F.; Jin, W. T.; Nandi, S.; Sun, X.; Su, Y.; Brückel, T.; Lee, Y.; Harmon, B. N.; Ke, L.; Ouyang, Z. W.; Xiao, Y. Noncollinear Magnetic Structure and Anisotropic Magnetoelastic Coupling in Cobalt Pyrovanadate $Co_2V_2O_7$. *Phys. Rev. B* **2019**, *100*, 134420.
149. Chen, R.; Wang, J. F.; Ouyang, Z. W.; He, Z. Z.; Wang, S. M.; Lin, L.; Liu, J. M.; Lu, C. L.; Liu, Y.; Dong, C.; Liu, C. B.; Xia, Z. C.; Matsuo, A.; Kohama, Y.; Kindo, K. Magnetic Field Induced Ferroelectricity and Half Magnetization Plateau in Polycrystalline $R_2V_2O_7$ ($R = Ni, Co$). *Phys. Rev. B* **2018**, *98*, 184404.
150. Dos Santos-García; Ritter, C.; Solana-Madruga, E.; Sáez-Puche, R. Magnetic and Crystal Structure Determination of Mn_2FeSbO_6 Double Perovskite. *J. Phys. Condens. Matter* **2013**, *25*, 206004.
151. Peets, D. C.; Kim, J. H.; Dosanjh, P.; Reehuis, M.; Maljuk, A.; Aliouane, N.; Ulrich, C.; Keimer, B. Magnetic Phase Diagram of $Sr_3Fe_2O_{7-d}$. *Phys. Rev. B* **2013**, *87*, 214410.
152. Kim, J. H.; Jain, A.; Reehuis, M.; Khaliullin, G.; Peets, D. C.; Ulrich, C.; Park, J. T.; Faulhaber, E.; Hoser, A.; Walker, H. C.; Adroja, D. T.; Walters, A. C.; Inosov, D. S.; Maljuk, A.; Keimer, B. Competing Exchange Interactions on the Verge of a Metal-Insulator Transition in the Two-Dimensional Spiral Magnet $Sr_3Fe_2O_7$. *Phys. Rev. Lett.* **2014**, *113*, 147206.
153. Post, B.; Glaser, F. W.; Moskowitz, D. Transition Metal Diborides. *Acta Metall* **1954**, *2*, 20–25.
154. Funahashi, S.; Hamaguchi, Y.; Tanaka, T.; Bannai, E. Helical Magnetic Structure in CrB_2 . *Solid State Commun.* **1977**, *23*, 859–862.
155. Park, P.; Park, K.; Kim, T.; Kousaka, Y.; Lee, K. H.; Perring, T. G.; Jeong, J.; Stuhr, U.; Akimitsu, J.; Kenzelmann, M.; Park, J.-G. Momentum-Dependent Magnon Lifetime in the Metallic Noncollinear Triangular Antiferromagnet CrB_2 . *Phys. Rev. Lett.* **2020**, *125*, 027202.

156. Buschow, K. H. J.; De Mooij, D. B. Crystal Structure and Magnetic Properties of PtMnGa and PtMnAl. *J. Less-Common Met.* **1984**, *99*, 125–130.
157. Cooley, J. A.; Bocarsly, J. D.; Schueller, E. C.; Levin, E. E.; Rodriguez, E. E.; Huq, A.; Lapidus, S. H.; Wilson, S. D.; Seshadri, R. Evolution of Noncollinear Magnetism in Magnetocaloric MnPtGa. *Phys. Rev. Mater.* **2020**, *4*, 044405.
- [158] Brown, P. J.; Nunez, V.; Tasset, F.; Forsyth, J. B.; Radhakrishna, P. Determination of the Magnetic Structure of Mn₃Sn Using Generalized Neutron Polarization Analysis. *J. Phys. Condens. Matter* **1990**, *2*, 9409–9422.
159. Reichlova, H.; Janda, T.; Godinho, J.; Markou, A.; Kriegner, D.; Schlitz, R.; Zelezny, J.; Soban, Z.; Bejarano, M.; Schultheiss, H.; Nemeč, P.; Jungwirth, T.; Felser, C.; Wunderlich, J.; Goennenwein, S. T. B. Imaging and Writing Magnetic Domains in the Non-Collinear Antiferromagnet Mn₃Sn. *Nat. Commun.* **2019**, *10*, 5459.
160. Yamaoka, T. Antiferromagnetism in Γ -Phase Mn-Ir Alloys. *J. Phys. Soc. Jpn.* **1974**, *36*, 445–450.
161. Tomeno, I.; Fuke, H. N.; Iwasaki, H.; Sahashi, M.; Tsunoda, Y. Magnetic Neutron Scattering Study of Ordered Mn₃Ir. *J. Appl. Phys.* **1999**, *86*, 3853–3856.
162. Kohn, A.; Kovács, A.; Fan, R.; McIntyre, G. J.; Ward, R. C. C.; Goff, J. P. The Antiferromagnetic Structures of IrMn₃ and Their Influence on Exchange-Bias. *Sci. Rep.* **2013**, *3*, 2412.
163. Arpacı, S.; Lopez-Dominguez, V.; Shi, J.; Sánchez-Tejerina, L.; Garesci, F.; Wang, C.; Yan, X.; Sangwan, V. K.; Grayson, M. A.; Hersam, M. C.; Finocchio, G.; Khalili Amiri, P. Observation of Current-Induced Switching in Non-Collinear Antiferromagnetic IrMn₃ by Differential Voltage Measurements. *Nat. Commun.* **2021**, *12*, 3828.
- [164] Murakami, T.; Yamamoto, T.; Tassel, C.; Takatsu, H.; Ritter, C.; Ajiro, Y.; Kageyama, H. HfMnSb₂: A Metal-Ordered Nias-Type Pnictide with a Conical Spin Order. *Angew. Chem. Int. Ed.* **2016**, *55*, 9877–9880.
165. Felser, C. Skyrmions. *Angew. Chem. Int. Ed.* **2013**, *52*, 1631–1634.
166. Tokura, Y.; Kanazawa, N. Magnetic Skyrmion Materials. *Chem. Rev.* **2021**, *121*, 2857–2897.
167. Mühlbauer, S.; Binz, B.; Jonietz, F.; Pfleiderer, C.; Rosch, A.; Neubauer, A.; Georgii, R.; Böni, P. Skyrmion Lattice in a Chiral Magnet. *Science* **2009**, *323*, 915–919.
168. Ishikawa, Y.; Tajima, K.; Bloch, D.; Roth, M. Helical Spin Structure in Manganese Silicide MnSi. *Solid State Commun.* **1976**, *19*, 525–528.
169. Effenberger, H.; Pertlik, F. The Crystal Structures of Copper(II) Oxo-Selenite Cu₂O(SeO₃) (Cubic and Monoclinic) and Cu₄O(SeO₃)₃ (Monoclinic and Triclinic). *Monatsh. Chem.* **1986**, *117*, 887–896.
170. Bos, J.-W. G.; Colin, C. V.; Palstra, T. T. M. Magnetolectric Coupling in the Cubic Ferrimagnet Cu₂OSeO₃. *Phys. Rev. B* **2008**, *78*, 094416.
171. Seki, S.; Yu, X. Z.; Ishiwata, S.; Tokura, Y. Observation of Skyrmions in a Multiferroic Material. *Science* **2012**, *336*, 198–201.
172. Coey, J. M. D. Permanent Magnet Applications. *J. Magn. Magn. Mater.* **2002**, *248*, 441–456.
173. Kramer, D. US Government Acts to Reduce Dependence on China for Rare-Earth Magnets. *Phys. Today* **2021**, *74*, 20–24.
174. Coey, J. M. D. Perspective and Prospects for Rare Earth Permanent Magnets. *Engineering* **2020**, *6*, 119–131.
175. Kuz'min, M. D.; Skokov, K. P.; Jian, H.; et al. Towards High-Performance Permanent Magnets without Rare Earths. *J. Phys. Condens. Matter* **2014**, *26*, 064205.
176. McCallum, D. J.; Lewis, L. H.; Skomski, R.; et al. Practical Aspects of Modern and Future Permanent Magnets. *Annu. Rev. Mat. Res.* **2014**, *44*, 451–477.
177. Sales, B. C.; Saporov, B.; McGuire, M. A.; et al. Ferromagnetism of Fe₃Sn and Alloys. *Sci. Rep.* **2014**, *4*, 7024.
178. Vekilova, O. Y.; Fayyazi, B.; Skokov, K. P.; et al. Tuning the Magnetocrystalline Anisotropy of Fe₃Sn by Alloying. *Phys. Rev. B* **2019**, *99*, 024421.
179. Cui, J.; Kramer, M.; Zhou, L.; et al. Current Progress and Future Challenges in Rare-Earth-Free Permanent Magnets. *Acta Mater.* **2018**, *158*, 118–137.
180. Carnevale, D. J.; Shatruk, M.; Strouse, G. F. Ligand Passivated Core-Shell FePt@Co Nanomagnets Exhibiting Enhanced Energy Product. *Chem. Mater.* **2016**, *28*, 5480–5487.
181. Liu, J. P. Exchange-Coupled Nanocomposite Permanent Magnets. In *Nanoscale Magnetic Materials and Applications*; Liu, J. P., Fullerton, E., Gutfleisch, O., Sellmeyer, D. J., Eds., Springer, 2009; pp 309–335 (Reprinted from: NOT IN FILE).
182. Zeng, H.; Li, J.; Liu, J. P.; et al. Exchange-Coupled Nanocomposite Magnets by Nanoparticle Self-Assembly. *Nature* **2002**, *420*, 395–398.
183. Sakurai, M.; Wang, R.; Liao, T.; et al. Discovering Rare-Earth-Free Magnetic Materials through the Development of a Database. *Phys. Rev. Mater.* **2020**, *4*, 114408.
184. Chappert, C.; Fert, A.; Van Dau, F. N. The Emergence of Spin Electronics in Data Storage. *Nat. Mater.* **2007**, *6*, 813–823.
185. Fontcuberta, J. Colossal Magnetoresistance. *Phys. World* **1999**, *12*, 33–38.
186. von Helmolt, R.; Wecker, J.; Holzapfel, B.; et al. Giant Negative Magnetoresistance in Perovskitelike La_{2/3}Ba_{1/3}MnO_x Ferromagnetic Films. *Phys. Rev. Lett.* **1993**, *71*, 2331–2333.
187. Tomioka, Y.; Asamitsu, A.; Moritomo, Y.; et al. Collapse of a Charge-Ordered State under a Magnetic Field in Pr_{1/2}Sr_{1/2}MnO₃. *Phys. Rev. Lett.* **1995**, *74*, 5108–5111.
188. Yamada, S.; Abe, N.; Sagayama, H.; et al. Room-Temperature Low-Field Colossal Magnetoresistance in Double-Perovskite Manganite. *Phys. Rev. Lett.* **2019**, *123*, 126602.
189. Wagner, P.; Wackers, G.; Cardinaletti, I.; et al. From Colossal Magnetoresistance to Solar Cells: An Overview on 66 Years of Research into Perovskites. *Phys. Status Solidi A* **2017**, *214*, 1700394.
190. Rosa, P.; Xu, Y.; Rahn, M.; et al. Colossal Magnetoresistance in a Nonsymmorphic Antiferromagnetic Insulator. *npj Quantum Mater.* **2020**, *5*, 52.
191. Ni, Y.; Zhao, H.; Zhang, Y.; et al. Colossal magnetoresistance via avoiding fully polarized magnetization in the ferrimagnetic insulator Mn₃Si₂Te₆. *Phys. Rev. B* **2021**, *103*, L161105.
192. Weiss, P.; Piccard, A. Le phénomène Magnétocalorique. *J. Phys.* **1917**, *7*, 103–109.
193. Tishin, A. M.; Spichkin, Y. I. *The Magnetocaloric Effect and its Applications*, Bristol-Philadelphia Institute of Physics Publishing, 2003.
194. Pecharsky, V. K.; Gschneidner, K. A. Magnetocaloric Effect from Indirect Measurements: Magnetization and Heat Capacity. *J. Appl. Phys.* **1999**, *86*, 565–575.
195. de Haas, W. J.; Wiersma, E. C.; Kramers, H. A. The Attainment of a Very Low Temperature by Adiabatic Demagnetization of a Salt of a Rare Earth. *Naturwissenschaften* **1933**, *21*, 467.
196. Giaque, W. F.; MacDougall, D. P. Attainment of Temperatures below 1° Absolute By Demagnetization of Gd₂(SO₄)₃·8H₂O. *Phys. Rev.* **1933**, *43*, 768.
197. Giaque, W. F.; MacDougall, D. P. The Production of Temperatures below One Degree Absolute by Adiabatic Demagnetization of Gadolinium Sulfate. *J. Am. Chem. Soc.* **1935**, *57*, 1175–1185.
198. Kurti, N.; Simon, F. Production of Very Low Temperature by the Magnetic Method: Superconductivity of Cadmium. *Nature* **1934**, *133*, 907–908.
199. Pecharsky, V. K.; Gschneidner, K. A., Jr. Giant Magnetocaloric Effect in Gd₅(Si₂Ge₂). *Phys. Rev. Lett.* **1997**, *78*, 4494–4497.
200. Brück, E. Magnetocaloric Refrigeration at Ambient Temperature. In *Handbook of Magnetic Materials*; Buschow, K. H. J., Ed.; vol. 17; Elsevier, 2007; pp 235–291.
201. Pecharsky, V. K.; Gschneidner, K. A., Jr.; Pecharsky, A. O.; Tishin, A. M. Thermodynamics of the Magnetocaloric Effect. *Phys. Rev. B: Condens. Matter Mater. Phys.* **2001**, *64*, 144406/144401–144406/144413.
202. Choe, W.; Pecharsky, V. K.; Pecharsky, A. O.; et al. Making and Breaking Covalent Bonds across the Magnetic Transition in the Giant Magnetocaloric Material Gd₅(Si₂Ge₂). *Phys. Rev. Lett.* **2000**, *84*, 4617–4620.
203. Jeitschko, W. A High-Temperature X-Ray Study of the Displacive Phase Transition in MnCoGe. *Acta Crystallogr. Sect. B* **1975**, *31*, 1187–1190.
204. Wang, Y.; Yannello, V.; Graterol, J.; Zhang, H.; Long, Y.; Shatruk, M. Theoretical and Experimental Insights into the Effects of Zn Doping on the Magnetic and Magnetocaloric Properties of MnCoGe. *Chem. Mater.* **2020**, *32*, 6721–6729.
205. Liu, E. K.; Zhu, W.; Feng, L.; Chen, J. L.; Wang, W. H.; Wu, G. H.; Liu, H. Y.; Meng, F. B.; Luo, H. Z.; Li, Y. X. Vacancy-Tuned Paramagnetic/Ferromagnetic Martensitic Transformation in Mn-Poor Mn_{1-x}CoGe Alloys. *Europhys. Lett.* **2010**, *91*, 17003.
206. Zhang, D.; Nie, Z.; Wang, Z.; Huang, L.; Zhang, Q.; Wang, Y.-d. Giant Magnetocaloric Effect in MnCoGe with Minimal Ga Substitution. *J. Magn. Magn. Mater.* **2015**, *387*, 107–110.
207. Mann, D. K.; Wang, Y.; Marks, J. D.; Strouse, G. F.; Shatruk, M. Microwave Synthesis and Magnetocaloric Effect in AlFe₂B₂. *Inorg. Chem.* **2020**, *59*, 12625–12631.
208. Lejeune, B. T.; Schlagel, D. L.; Jensen, B. A.; Lograsso, T. A.; Kramer, M. J.; Lewis, L. H. Effects of Al and Fe Solubility on the Magnetofunctional Properties of AlFe₂B₂. *Phys. Rev. Mater.* **2019**, *3*, 094411.

209. Barua, R.; Lejeune, B. T.; Jensen, B. A.; Ke, L.; McCallum, R. W.; Kramer, M. J.; Lewis, L. H. Enhanced Room-Temperature Magnetocaloric Effect and Tunable Magnetic Response in Ga- and Ge-Substituted AlFe_2B_2 . *J. Alloys Compd.* **2019**, *777*, 1030–1038.
210. Tegus, O.; Brueck, E.; Buschow, K. H. J.; de Boer, F. R. Transition-Metal-Based Magnetic Refrigerants for Room-Temperature Applications. *Nature* **2002**, *415*, 150–152.
211. Franco, V.; Blázquez, J. S.; Ipus, J. J.; Law, J. Y.; Moreno-Ramírez, L. M.; Conde, A. Magnetocaloric Effect: From Materials Research to Refrigeration Devices. *Prog. Mater. Sci.* **2018**, *93*, 112–232.
212. Rosca, M.; Balli, M.; Fruchart, D.; Gignoux, D.; Hill, E. K.; Miraglia, S.; Ouladdiaf, B.; Wolfers, P. Neutron Diffraction Study of $\text{LaFe}_{11.31}\text{Si}_{1.69}$ and $\text{LaFe}_{11.31}\text{Si}_{1.69}\text{H}_{1.45}$ Compounds. *J. Alloys Compd.* **2010**, *490*, 50–55.
213. Hu, F.-x.; Shen, B.-g.; Sun, J.-r.; Cheng, Z.-h.; Rao, G.-h.; Zhang, X.-x. Influence of Negative Lattice Expansion and Metamagnetic Transition on Magnetic Entropy Change in the Compound $\text{LaFe}_{11.4}\text{Si}_{1.6}$. *Appl. Phys. Lett.* **2001**, *78*, 3675–3677.
214. Jia, L.; Sun, J. R.; Shen, J.; Dong, Q. Y.; Zou, J. D.; Gao, B.; Zhao, T. Y.; Zhang, H. W.; Hu, F. X.; Shen, B. G. Magnetocaloric Effects in the $\text{La}(\text{Fe,Si})_{13}$ Intermetallics Doped by Different Elements. *J. Appl. Phys.* **2009**, *105*, 07A924.
215. Wang, J.; Chen, Y.; Tang, Y.; Xiao, S.; Liu, T.; Zhang, E. The Hydrogenation Behavior of $\text{LaFe}_{11.44}\text{Si}_{1.56}$ Magnetic Refrigerating Alloy. *J. Alloys Compd.* **2009**, *485*, 313–315.
216. Zheng, H.; Tang, Y.; Chen, Y.; Wu, J.; Wang, H.; Xue, X.; Wang, J.; Pang, W. The High-Temperature Hydrogenation Behavior of $\text{LaFe}_{11.6}\text{Si}_{1.4}$ and Splitting of $\text{LaFe}_{11.6}\text{Si}_{1.4}\text{H}_\gamma$ Magnetocaloric Transition. *J. Alloys Compd.* **2015**, *646*, 124–128.

Further reading

1. Buschow, K. H. J. Intermetallic Compounds of Rare-Earth and 3d Transition Metals. *Rep. Prog. Phys.* **1977**, *40*, 1179–1256.
2. Coey, J. M. D., Venkatesan, M. & Xu, H. (2013). Introduction to Magnetic Oxides. In Ogale, S. B., Venkatesan, T. V. & Blamire, M. G. (Eds.) *Functional Metal Oxides: New Science and Novel Applications*, Ch. 1, 1st ed., pp. 3–49. Wiley-VCH.
3. Graf, T., Winterlik, J., MÜchler, L., Fecher, G. H., Felser, C. & Parkin, S. S. P. (2013). Magnetic Heusler Compounds. In Buschow, K. H. J. (Ed.) *Handbook of Magnetic Materials*, ch. 1, Vol. 21, pp. 1–75. Amsterdam: Elsevier.
4. Buschow, K. H. J.; de Boer, F. R. *Physics of Magnetism and Magnetic Materials*, Kluwer Academic: New York, 2004.
5. Carlin, R. L. *Magnetochemistry*, Springer: Berlin, 1989.
6. Coey, J. M. D. Permanent Magnet Applications. *J. Magn. Magn. Mater.* **2002**, *248*, 441–456.
7. Coey, J. M. D.; Viret, M.; von Molnár, S. Mixed-Valence Manganites. *Adv. Phys.* **2009**, *58*, 571–697.
8. Gutfleisch, O.; Willard, M. A.; Brück, E.; Chen, C. H.; Sankar, S. G.; Liu, J. P. Magnetic Materials and Devices for the 21st Century: Stronger, Lighter, and More Energy Efficient. *Adv. Mater.* **2011**, *23*, 821–842.
9. Kahn, O. *Molecular Magnetism*, Wiley-VCH: New York, 1993.
10. Spaldin, N. *Magnetic Materials: Fundamentals and Device Applications*, Cambridge University Press: Cambridge, 2003.
11. Stöhr, J.; Siegmann, H. C. *Magnetism. From Fundamentals to Nanoscale Dynamics*, Springer: Berlin, 2006.
12. Tokura, Y.; Kanazawa, N. Magnetic Skyrmion Materials. *Chem. Rev.* **2021**, *121*, 2857–2897.

4.09 Luminescence in the solid state

Shruti Hariyani and Jakoah Brgoch, Department of Chemistry and the Texas Center for Superconductivity, University of Houston, Houston, TX, United States

© 2023 Elsevier Ltd. All rights reserved.

4.09.1	Introduction	263
4.09.2	Electronic transitions in inorganic solids	264
4.09.2.1	Jablonski diagram	264
4.09.2.1.1	Absorption	264
4.09.2.1.2	Non-radiative relaxation	265
4.09.2.1.3	Fluorescence and phosphorescence	265
4.09.2.2	Interactions between the activator ion and the host structure	265
4.09.3	Luminescent transition metal and main group materials	267
4.09.3.1	Absorption in transition metal complexes	267
4.09.3.2	Emission from d^0 transition metals	269
4.09.3.3	Emission from d^n ($0 < n < 10$) transition metals	270
4.09.3.4	Emission from d^{10} transition metals	272
4.09.3.5	Emission from s^2 transition metals	272
4.09.4	Rare-earth substituted materials	273
4.09.4.1	Emission from a $4f \leftrightarrow 4f$ transition in rare-earth activators	273
4.09.4.1.1	Emission from Eu^{3+}	273
4.09.4.1.2	Emission from Dy^{3+}	276
4.09.4.1.3	Emission from Tb^{3+}	276
4.09.4.2	Emission from Ce^{3+} and Eu^{2+} ($4f^{n-1}5d^1 \rightarrow 4f^n$ transitions)	279
4.09.4.3	Thermal stability of $4f \leftrightarrow 5d$ electronic transitions	280
4.09.4.4	Notable rare-earth substituted phosphors families	282
4.09.4.4.1	Garnets	282
4.09.4.4.2	Silicates	283
4.09.4.4.3	UCr_4C_4 -type materials	284
4.09.5	Upconversion materials	284
4.09.5.1	Mechanisms of upconversion emission	284
4.09.5.2	Familiar upconversion systems	285
4.09.6	The role of defects and the rise of persistent luminescence	286
4.09.7	Application of rare-earth and transition metal substituted phosphors	288
4.09.7.1	Phosphors for LED-based white lighting	288
4.09.7.2	Phosphors for display panels	289
4.09.7.3	Phosphors for promoting plant growth	290
4.09.7.4	Upconversion materials for temperature sensing	290
4.09.7.5	Persistent luminescent phosphors for lateral flow assays	292
4.09.8	Scintillators	292
4.09.8.1	Mechanism of gamma-ray conversion to light production	292
4.09.8.2	Notable scintillators and their applications	294
4.09.9	Semiconductors	294
4.09.9.1	LEDs	295
4.09.9.2	Quantum dots	296
4.09.10	Discovery of new luminescent materials	298
4.09.10.1	Rational synthesis through atomic substitution	298
4.09.10.2	Identification of new host crystal structures	299
4.09.10.2.1	The single particle diagnosis approach	299
4.09.10.2.2	Combinatorial chemistry approach	300
4.09.10.3	Data-driven approaches	301
4.09.11	Conclusion and outlook	302
Acknowledgments		302
References		303

Abstract

Luminescent inorganic materials have become a mainstay in modern life. These solid-state compounds are essential for applications ranging from solid-state LED-based lighting and display applications to bioimaging and temperature sensing. The diversity of their uses has required researchers to expand beyond investigating luminescence in naturally occurring minerals to developing a host of synthetic materials. The success of this field has been driven first and foremost by a fundamental understanding of the physics dictating an inorganic solid's optical properties. This chapter introduces the origin of luminescence in the solid state discussing the various electronic transitions in transition metal and rare-earth substituted materials. Examples of essential materials systems are covered, including the luminescence of inorganic phosphors, scintillators, semiconductors, and quantum dots. Additionally, current applications of rare-earth and transition metal substituted phosphors are discussed in detail. Finally, recent advances in applying combinatorial, computational, and data-driven chemistry to discover new luminescent materials are highlighted.

4.09.1 Introduction

It was only ~140 years ago that our surroundings were illuminated purely by black-body radiation. Like the sun or a candle, a black-body radiator emits energy at all wavelengths of the electromagnetic spectrum once that body (or surface) surpasses a temperature unique to that material. Now, the world is continually illuminated by luminescent materials in the form of LED light bulbs, televisions, and computer screens. Luminescence is different from black-body radiation because light is generated by converting an external stimulus (energy) into photons through a series of electronic transitions.¹

The earliest records of humans *using* luminescence involved naturally occurring minerals. In 10th-century Japan and China, a painting of a cow was found to emit visible light after mixing ink with a special kind of pearl shell. In India, legend said that cobras would carry a luminescent stone in their mouth at night to lure fireflies as prey. The first artificial luminescent material, however, was not “discovered” until 1603. Vincenzo Cascariolo, a shoemaker and alchemist, attempted to use the mineral barite (BaSO_4) to create gold. His method involved grinding and heating barite that was found near Bologna in modern-day Italy. The compound he made did not produce gold, but it did yield a material that emitted a surprising yellow-orange afterglow when subjected to sunlight. This “Stone of Bologna” would become famous and be the center of many studies to identify the origin of its luminescent properties.¹ In 1671, Athanasius Kirchner strengthened the observed yellow-orange luminescence by heating BaSO_4 with carbon. We now know that a reaction upon heating caused the formation of BaS, which was the source of the observed light emission. Similar studies across Europe stemming from the exciting discovery of emission in BaS uncovered numerous other light-emitting stones, eventually called *phosphors*, and catalyzed research into solid-state luminescence for centuries to come.

The first breakthroughs that would allow for the practical application of luminescent materials would not occur until the end of the 19th century.² The realization of gas discharge and electron beams by Geissler and Braun (1858) and the discovery of X-rays by Röntgen (1895) spurred the search for materials that could convert these various forms of energy.^{3–5} Approximately 1 year later, Pupin (1896) showed that calcium tungstate, CaWO_4 , could convert X-rays with energies between 20 and 100 keV to blue light (≈ 430 nm).² This discovery led to the creation of X-ray intensifying screens that lasted for 75 years until the advent of rare-earth substituted phosphors. Edison and Braun shortly thereafter used CaWO_4 to develop the Hg gas fluorescent lamp and cathode ray tube, respectively.⁶ Colored light was made possible by combining the neon or argon gas discharge with colored glass bulbs or, more interestingly, phosphors that emitted different colors. Indeed, this phosphor conversion methodology was the basis for the first colored television sets, which combined a cathode ray tube and blue (ZnS:Ag^+), red ($(\text{Zn,Cd})\text{S:Cu}^+, \text{Ag}^+$), and green-emitting ($(\text{Zn,Cd})\text{S:Cu}^+, \text{Al}^{3+}$) phosphors. The synthesis of rare-earth (i.e., Ce^{3+} , Eu^{2+} , Tb^{3+} , etc.) element-based phosphors suggested by Koedam and Opstelten⁷ in 1971 and quantum dots by Alexey Ekimov⁸ in 1981 would yield highly efficient luminescent materials and mark the second and current major milestone in the application of luminescence.

Before delving into the mechanisms governing luminescence, it is instructive to briefly discuss the origin and classification of the various types of luminescence. The word luminescence was coined by German physicist Eilhardt Wiedemann in 1888 and originated from the Latin word *lumen*, meaning light.¹ Here, luminescence is defined as the phenomenon of light production through the absorption and conversion of external excitation energy. Light includes visible radiation (400–700 nm) and the ultraviolet and infrared regions of the electromagnetic spectrum. Wiedemann also classified luminescence into six different categories depending on its form of excitation: photoluminescence, thermoluminescence, electroluminescence, crystalloluminescence, triboluminescence, and chemiluminescence.¹ Photoluminescence is the specific focus of this chapter and involves excitation upon exposure to higher energy (often ultraviolet or visible) electromagnetic radiation followed by the re-emission of a photon. This process can be broken down into two subsets, phosphorescence or fluorescence, which is discussed later. Thermoluminescence is light produced from gentle heating (not to be confused with black-body radiation), whereas electroluminescence is generated by excitation following the application of an electric field. Crystalloluminescence occurs when a solution crystalizes; in contrast, triboluminescence occurs when a crystal is crushed and ground. Finally, chemiluminescence occurs as the byproduct of a chemical reaction and is often observed in nature, like in fireflies and jellyfish. Many other types of luminescence have also been identified, like cathodoluminescence, where light is produced from the bombardment of electrons. However, these generally fall into one of the six main categories.

This chapter is divided into four sections. The first describes the general mechanisms involved in photoluminescence (hereafter referred to generally as luminescence) that apply to all materials. Indeed, inorganic and organic systems exhibit all forms of

luminescence, but this chapter will focus on inorganic luminescent materials. The second section will discuss the influence of the crystal structure on the observed luminescence. The third section covers the specific mechanisms governing luminescence in transition metal and rare-earth substituted phosphors, up-conversion materials, scintillators, and semi-conductors. Notable examples in the literature back each type of material and their optical properties are discussed in detail. Finally, strategies to identify novel luminescent materials with enhanced optical properties, such as first-principles calculations and machine learning, are highlighted. This chapter will provide a thorough review of the history of luminescent materials and the mechanisms by which their optical properties are governed, and the innovative strategies currently being implemented to expedite the discovery of these fascinating materials.

4.09.2 Electronic transitions in inorganic solids

4.09.2.1 Jablonski diagram

Luminescence occurs through the absorption of incident energy that is converted to a different energy photon upon relaxation. The mechanism of light production is best illustrated through a modified Jablonski diagram, shown in Fig. 1. The Jablonski diagram is composed of columns, where each column represents a singlet ($S_0, S_1, S_2, \dots, S_n$) or triplet ($T_0, T_1, T_2, \dots, T_n$) spin multiplicity. Within each column, black horizontal lines represent the various eigenstates. The vertical axis qualitatively describes the energy difference between the eigenstates.⁹ The transitions in a Jablonski diagram follow the various *selection rules* that constrain the electronic transitions. The two most important electronic-dipole selection rules that govern optical transitions are the spin selection rule and the parity selection rule.¹⁰ The spin selection rule forbids electronic transitions that involve a change in the spin multiplicity ($\Delta S = 0$). The parity (orbital) selection rule ($\Delta L = \pm 1$) forbids electronic transitions between energy levels with the same parity in centrosymmetric compounds, i.e., transitions within the d shell, within the f shell, and within the s shells. Transitions between s and p and p to d are allowed. The word “forbidden” to describe transitions is a bit of a misnomer because the transitions can still occur due to perturbations from spin-orbit coupling, electron-vibration coupling, and uneven crystal fields.¹¹ As a result, singly forbidden transitions can still be observed, although the transitions are weak. A complete discussion of all selection rules can be found in *The Basics of Spectroscopy*.¹⁰

4.09.2.1.1 Absorption

The first electronic transition in any Jablonski diagram is photon absorption, shown by the vertical blue lines in Fig. 1. The photon’s energy is transferred to an electron, causing the electron to be excited from the ground state (S_0), to a higher energy level (S_n), called an excited state. The absorption process occurs on the order of 10^{-15} s.¹² The Franck-Condon principle governs the specific eigenstates populated upon the electron transition to the excited state. The absorption spectrum of solid-state materials can be measured experimentally using diffuse reflectance spectroscopy. Diffuse reflectance spectroscopy measures the reflection (back-scatter) and transmission of light by a material. The back-reflected light, in which the sample absorbs some light, is then collected by a detector. The portion of the light that is scattered and returns to the sample surface is the diffuse reflectance. The raw diffuse reflectance spectrum is often converted to absorbance through the Kubelka-Munk function, Eq. (1), where R_∞ is absolute reflectance, K is the absorption coefficient, and S is the scattering coefficient.¹³ The resulting spectrum upon transformation can then be analyzed using a Tauc plot, which can provide information on the optical bandgap of the sample. Here, Eq. (2) is used to evaluate a plot of the measured absorbance, $F(R_\infty)$, against Planck’s constant (h), the photon frequency (ν), and n is either $\frac{1}{2}$ for a direct band gap material or 2 for an indirect band gap material. A is a constant, and E_g is the measured band gap.^{14,15}

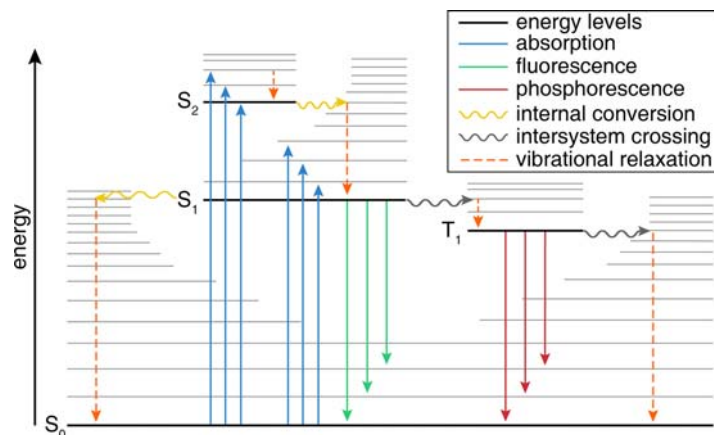


Fig. 1 The Jablonski diagram illustrating the process of absorption (blue), fluorescence (green), phosphorescence (red), internal conversion (yellow), intersystem crossing (gray), and vibrational relaxation (orange).

$$F(R_\infty) = \frac{(1 - R_\infty)^2}{2R_\infty} = \frac{K}{S} \quad (1)$$

$$F(h\nu F(R_\infty))^{1/n} = A(h\nu - E_g) \quad (2)$$

4.09.2.1.2 Non-radiative relaxation

Once the electron is in the excited state, many pathways exist to dissipate the absorbed energy, and this may not always be the form of a photon re-emission. Indeed, the first pathway of energy loss is non-radiative relaxation, represented by the orange dashed line in Fig. 1. The electron loses energy through vibrations (kinetic energy) as it relaxes down the various eigenstates.⁹ Non-radiative relaxation is a very fast process, between 10^{-14} and 10^{-11} s, and occurs immediately after absorption.¹² By definition, non-radiative relaxation occurs within the same excited state. This process is called internal conversion if the relaxation transitions from a higher (S_n) to a lower electronic excited state (S_{n-1}). Internal conversion is mechanistically identical to vibrational relaxation and is caused by a substantial overlap between excited states. In Fig. 1, internal conversion is shown by the yellow squiggly line. It is important to note that these non-radiative pathways are not the final transition (relaxation) to the ground state. Because there is a significant energy difference between the first excited state and the ground state, internal conversion to the ground state is prolonged. Therefore, once the electron reaches the lowest energy, first excited state (S_1), there are competing processes for relaxation.

4.09.2.1.3 Fluorescence and phosphorescence

Fluorescence is one of the competing relaxation processes from the first excited state to the ground state within the same eigenstate and is represented by the straight green line in Fig. 1. The energy of the emitted photon is the energy difference between the eigenstates of the transition after subtracting the energy lost through non-radiative pathways. Fluorescence is a quantum-mechanically allowed transition that occurs on the order of 10^{-9} to 10^{-7} s and competes with other non-radiative processes occurring on similar timescales. Fluorescence from a higher energy excited state, for example, the second excited state (S_2), is not often observed because it occurs on a much slower timescale than non-radiative relaxation, meaning vibrational relaxation and internal conversion dominate.

The alternative radiative relaxation pathway is called phosphorescence, and it occurs in two steps. The first step, known as inter-system crossing, occurs when the electron changes its excited state spin multiplicity. As illustrated by the gray squiggly line in Fig. 1, the electron transitions from the singlet to the triplet excited state. This transition is quantum-mechanically forbidden due to the requirement of the conservation of spin angular momentum, but spin-orbit coupling makes it a weakly allowed process. As a result, this process is slow (10^{-8} to 10^{-3} s) and can compete with fluorescence, especially in systems containing heavy elements. Once the system is in the triplet state, the electron can non-radiatively relax to the lowest energy triplet excited state (T_1) and finally relax to the singlet ground state (S_0) through the emission of a photon termed phosphorescence, represented by the red line in Fig. 1. Phosphorescence is the slowest electronic transition and occurs on a timescale of 10^{-4} to 10^{-1} s because this relaxation process is also a quantum-mechanically forbidden process.⁹

There are many other methods of non-radiative relaxation between the first excited state and ground state, which is why most systems do not exhibit luminescence. The two most common processes are external conversion, where energy is lost through collisions and quenching from the Stokes' shift.¹¹ Non-radiative relaxation through external conversion is not a concern for solid-state inorganic materials where the atoms are constrained and no collisions occur. On the other hand, the Stokes' shift, which is defined as the energy difference between the excitation and emission maxima, dramatically impacts inorganic materials since the emission energy is inherently lower than excitation energy in down-converting materials. The position of these maxima is related to the equilibrium position offset ΔR and the phonon energy, which is detailed in the next section. Recent studies by Wang et al. determined that the magnitude of the Stokes shift is proportional to the average bond length for compounds with the same structure and anion type. Moreover, there is no apparent correlation between the magnitude of the Stokes shift and the cation coordination number.¹⁶ To reduce non-radiative relaxation, current research is focused on reducing the Stokes shift. One strategy includes preventing access to non-radiative relaxation pathways in highly rigid crystal structures, which is further discussed in Section 4.09.10.3.

4.09.2.2 Interactions between the activator ion and the host structure

The original solid-state inorganic materials that led to the entire field of phosphor chemistry were based on naturally occurring compounds. Research eventually showed that most of these materials demonstrate *extrinsic* luminescence. They are compounds composed of a solid-state host crystal structure containing a small concentration of an "activator ion." The host crystal structure is often an oxide, nitride, halide, or any combination therein, whereas the activator is an impurity ion that has been introduced into the crystal structure. The observed photoluminescence is considered extrinsic because the luminescence would not occur without the activator ion. The most common activators include rare-earth ions, like Ce^{3+} , Eu^{3+} , Tb^{3+} , and transition metals such as Cr^{3+} or Mn^{4+} .¹¹ The most intense photoluminescence occurs for elements that have allowed transitions, like the $4f \leftrightarrow 5d$ transitions of Ce^{3+} or Eu^{2+} .¹⁷ In cases where the emission from the activator ion is weak, the presence of a secondary activator ion, called a sensitizer, can also be intentionally introduced into the host structure.¹⁸ The role of the sensitizer is to absorb and transfer the excitation energy to the activator. It is also possible to have *intrinsic* luminescent materials where the activator ion is

a fundamental part of the crystal structure, such as in CaWO_4 , where the tungstate $(\text{WO}_4)^{2-}$ polyanion acts as the luminescent center.

A luminescent material will only emit radiation after the incident excitation energy is absorbed by the phosphor. The absorption spectrum is composed of several components. Examining the absorption spectrum of a well-known extrinsic luminescent material, $\text{Y}_2\text{O}_3:\text{Eu}^{3+}$, a widely used red-emitter in gas-discharge lamps, illustrates multiple components of the absorption spectrum in these materials.¹⁹ Fig. 2A shows many notable features, including an intense broad absorption peak in the ultraviolet region spanning from 180 nm to 230 nm, a second broad absorption peak centered at 250 nm, and a region of narrow absorption lines at lower energy. The highest energy absorption band from the host lattice (HL) arises purely from the host, Y_2O_3 , caused by the electronic transition from the valence band to the conduction band. The other two features, the broad charge transfer (CT) band and the cluster of narrower line emission, stem from the presence of the Eu^{3+} activator ion substituted in the structure.¹¹

The excitation spectrum of $\text{Y}_2\text{O}_3:\text{Eu}^{3+}$, plotted in Fig. 2B, can now be compared to the phosphor's absorption spectrum. The absorption and excitation spectra look nearly identical in $\text{Y}_2\text{O}_3:\text{Eu}^{3+}$. These data demonstrate that Eu^{3+} can be excited in one of two ways. The first is a direct method by utilizing ultraviolet and or visible radiation that corresponds to the wavelength of the narrow Eu^{3+} absorption/excitation lines. The second, and less obvious method, is to excite the phosphor using a 180–230 nm excitation source. The host lattice will absorb this excitation energy and transfer it to the Eu^{3+} activator to produce the material's characteristic red emission. This energy transfer process from the second broad excitation band centered at 250 nm is the origin of the charge-transfer terminology.¹¹ It is important to note that high-energy excitation, such as fast electrons, γ -rays, and X-rays, will always excite the host lattice.

The varying linewidths of the different features in the absorption band, narrow lines versus a broad excitation band, can be explained using a configurational coordinate diagram.¹¹ These plots classically depict potential energy curves of the activator ion as a function of the configurational coordinate and assume the configurational coordinate describes one vibrational mode, a symmetric stretching mode, between the activator ion and the ligands from the host crystal structure. An example configurational coordinate diagram (Fig. 3A) shows the energy versus the activator-ligand distance, R , which is the only structural parameter that varies upon stretching. The lowest energy parabolic curve, centered at $R = 0$, represents the ground state. The ground state has vibrational energy levels $\nu = 0, 1, 2 \dots$, where ν is the frequency of a harmonic oscillator. In the lowest vibrational level, $\nu = 0$, the probability of finding an electron at R_0 is the highest, whereas, at higher vibrational levels, $\nu \geq 1$, the highest probability of finding the electron is at the edge of the parabola. Like the Jablonski diagram, an electron can be excited from the ground state to an excited state parabola. As chemical bonds are slightly weaker in the excited state, the excited state configurational diagram has a slightly different equilibrium distance, R_0' . Therefore, a transition between the ground state and excited state can be qualitatively understood as $\Delta R = R - R_0'$ and can be visualized as starting from R_0 and ending at the edge of the excited state parabola. It is also possible for absorption to begin at $R \neq R_0$, leading to a broad absorption band. In fact, the larger the value of ΔR , the wider the absorption band tends to appear. Narrow absorption bands result from the excited state parabola lying nearly directly above the ground state, or $\Delta R \approx 0$.

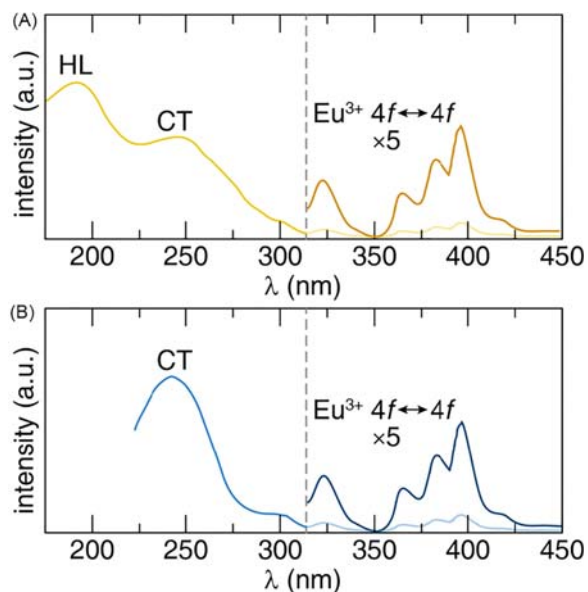


Fig. 2 (A) The absorption spectrum of $\text{Y}_2\text{O}_3:\text{Eu}^{3+}$ consists of three components: a host lattice absorption (HL) band, a charge transfer band (CT), and sharp absorption bands from the electronic transitions of Eu^{3+} . (B) The excitation spectrum does not show any contribution from the host crystal structure. The intensity of the absorption bands from the $\text{Eu}^{3+} 4f \leftrightarrow 4f$ transitions are multiplied by 5 for ease of viewing. Panel (A): Modified from Blasse G.; Grabmaier, B. C. *Luminescent Materials*. Springer-Verlag: **1994**. Panel (B): modified from Wan, J.; Wang, Z.; Chen, X.; Mu, L.; Qian, Y., Shape-Tailored Photoluminescent Intensity of Red Phosphor $\text{Y}_2\text{O}_3:\text{Eu}^{3+}$. *J. Cryst. Growth* **2005**, *284* (3), 538–543.

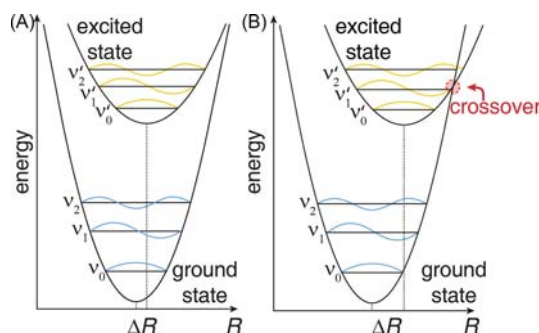


Fig. 3 (A) A small ΔR between the ground and excited-state potential energy surfaces indicates less electron-phonon coupling. Narrow emission bands are expected. (B) Strong electron-phonon coupling causes ΔR to be large, where a phonon-assisted non-radiative relaxation can occur through the crossover point. Wide emission bands are expected. Reproduced with permission from Hermus, M.; Phan, P.-C.; Duke, A. C.; Brgoch, J., Tunable Optical Properties and Increased Thermal Quenching in the Blue-Emitting Phosphor Series: $\text{Ba}_2(\text{Y}_{1-x}\text{Lu}_x)_5\text{B}_5\text{O}_{17}:\text{Ce}^{3+}$ ($x = 0 - 1$). *Chem. Mater.* **2017**, *29* (12), 5267–5275.

The value of ΔR is also a measure of electron-phonon coupling in a system. Electron-phonon coupling describes the scattering of electrons by lattice vibrations where the electrons become paired with a phonon to overcome the repulsive forces from electron-electron interactions. Therefore, when $\Delta R = 0$, there is weak electron-phonon coupling that occurs, and $\Delta R > 0$ and $\Delta R \gg 0$ represent intermediate and strong electron-phonon coupling, respectively.¹¹ The magnitude of electron-phonon coupling can be estimated by determining a materials Huang-Rhys factor, S .^{20,21} The Huang-Rhys parameter of a luminescent material can be experimentally calculated by measuring the full width at half maximum (fwhm) of the emission band as a function of temperature and fitting the data following Eq. (3).^{11,22} Here, $\hbar\omega$ is the average phonon energy, k_B is the Boltzmann constant, and T is temperature. A measure of strong electron-phonon coupling is indicated by a value of $S > 5$, whereas weak electron-phonon coupling yields $S < 1$.²³ It can now be immediately inferred that the differences in ΔR and chemical bonding control the width of the absorption band.

$$\text{fwhm} = \sqrt{8\ln(2)} \hbar\omega \sqrt{\text{Scoth} \frac{\hbar\omega}{2k_B T}} \quad (3)$$

Non-radiative relaxation can also be reasoned using configurational coordinate diagrams. If the magnitude of ΔR is large, caused, for example, by exposing the activator-ligand pair to high temperatures, which increases the bond lengths, there can be a point where the excited state parabola intersects with the ground state parabola. This intersection is known as the cross-over point and can serve as a pathway for non-radiative relaxation to the ground state.²⁴ The cross-over point is illustrated in Fig. 3B. The excitation energy is completely lost in the form of heat. This mechanism explains the significant losses in emission intensity at elevated temperatures. It may come as a surprise, but non-radiative relaxation can also occur when the excited and ground state parabolas are parallel. Although there is no clear cross-over point, if the energy difference between the ground and excited states is less than or equal to ≈ 5 times the highest frequency vibration, this energy is also sufficient to excite the vibrations. The energy is then lost in the form of heat.¹¹ This process is known as multi-phonon emission. The last configuration that must be considered is the case of three parabolas: the ground state, a parallel excited state, and a displaced excited state. According to Blasse, the parallel excited state belongs to the same configuration and is connected to the ground state through forbidden transitions.¹¹ The displaced excited state arises from a different configuration where relaxation to the ground state occurs through allowed transitions. In this situation, upon absorption, an electron is promoted to the displaced excited state through an allowed transition where non-radiative relaxation can occur from the displaced excited state to the parallel excited state. Relaxation to the ground state occurs in the form of line emission from the parallel excited state. This situation is commonly seen in Eu^{3+} substituted crystal structures, which is discussed further in Section 4.09.4.1.1.

Returning to the example of the $\text{Y}_2\text{O}_3:\text{Eu}^{3+}$ absorption spectrum. The host lattice (HL) absorption feature is broad; therefore, it can be concluded that there is a large ΔR between the ground and excited states of the host. The charge-transfer band is also broad. This is a consequence of electron transfer from O^{2-} to Eu^{3+} , also causing a large ΔR . The narrow absorption lines are due to electronic transitions within the non-bonding $4f^6$ shell of Eu^{3+} , leading to a $\Delta R = 0$. Finally, the $4f \leftrightarrow 4f$ transition is also forbidden by the parity rule, causing the weak intensity of the transition.

4.09.3 Luminescent transition metal and main group materials

4.09.3.1 Absorption in transition metal complexes

Synthetic solid-state luminescent research efforts are frequently concentrated on the transition metal and main group-containing materials. Four main types of luminescent compounds are usually studied, and they are classified based on their electron configuration. They include d^0 , d^n where $0 < n < 10$, d^{10} , and s^2 elements. Little was understood about the excited states of these ions,

particularly the transition metal systems, until 1954 when Yukito Tanabe and Satoru Sugano systematically used crystal field theory and the Racah parameters to plot the calculated energy of the electronic states of each electron configuration.^{25–28}

Crystal field theory and its counterpart ligand field theory are reliable models for interpreting the bonding interactions between a transition metal and its coordinating ligands. It is capable of explaining the body color, magnetic properties, structure, and reactivity of transition metal compounds.²⁹ Crystal field theory operates on a basic assumption that the transition metal and ligands can be treated as a simple positive and negative point charge, respectively.³⁰ The positive and negative ions are assumed to be non-overlapping spheres at some inter-nuclear distance apart. Coulomb's Law can describe this interaction, provided in Eq. (4), where E is the bond energy between the positive and negative ions, q_1 and q_2 are the charges of the ions, and r is the distance that separates each point charge.

$$E \propto \frac{q_1 q_2}{r} \quad (4)$$

This equation supports that cations with a low charge, like the alkali and alkali earth metals, tend to form few coordination compounds. Transition metals, however, have differing numbers of d electrons in their orbitals, which are also not spherical. Therefore, the bonding energy and properties of the transition metal compound are more accurately described when accounting for the shape and occupation of the d orbitals.

A free transition metal M^{n+} cation has five degenerate nd orbitals. Placing this metal ion in the center of a uniform, spherical negative charge increases the overall energy of the orbitals but they remain degenerate.²⁸ This degeneracy is lost when the metal becomes coordinated by other ions following ligand field theory. As the distance between the ligand and the ion decreases, the repulsion between the two relieves the degeneracy, known as ligand field splitting. Taking the example of a high symmetry octahedrally coordinated transition metal ion (Fig. 4), as the ligands approach the ion, the electrons in the d_{z^2} and $d_{x^2-y^2}$ orbitals will experience greater repulsion than the d_{xy} , d_{xz} , and d_{yz} orbitals. As a consequence, the d_{z^2} and $d_{x^2-y^2}$ orbitals are pushed higher in energy relative to the other three orbitals. The d_{z^2} and $d_{x^2-y^2}$ remain doubly degenerate, whereas the d_{xy} , d_{xz} , and d_{yz} are triply degenerate, following the O_h point group of the octahedral coordination environment.³⁰ The energy difference between the orbitals for octahedral complexes is commonly referred to Δ_{oct} . Similarly, the energy difference between the d orbitals in tetrahedral complexes is $4/9 \Delta_{\text{oct}}$.

Giulio Racah used crystal (ligand) field theory to develop the Racah parameters, which described inter-electron repulsion within the metal complex.²⁸ The amount of repulsion between the electrons varies from ion to ion and depends on the number and spin of the electrons and orbitals they occupy. The parameters A , B , and C describe the total repulsion. A is generally the same for any metal, B is an approximation of the bond strength between ligand and metal, and C is simplified to $1/4B$. Interestingly, there is a decrease in the B parameter when a free transition-metal ion forms a complex with ligands. The decrease in the B Racah parameter for transition-metal complexes indicates less inter-electron repulsion relative to free transition-metal ions and suggests the size of the d -orbital electron cloud is larger in the complex. This is known as the nephelauxetic effect, based on the Greek word for cloud-expanding, and was proposed by K. C. Jorgensen.³¹ This expansion is theorized to occur due to one or both of the following two reasons. (i) The effective positive charge on the transition-metal is reduced by the negative charge of the ligands or (ii) overlap between the d -orbitals of the transition-metal and ligand forms covalent bonds. The reduction of B is normally reported as the ratio: $\beta = B(\text{complex})/B(\text{free ion})$. It has experimentally been observed that the magnitude of the nephelauxetic effect experienced by a transition-metal complex is dependent upon the ligand and metal following^{28,31}:

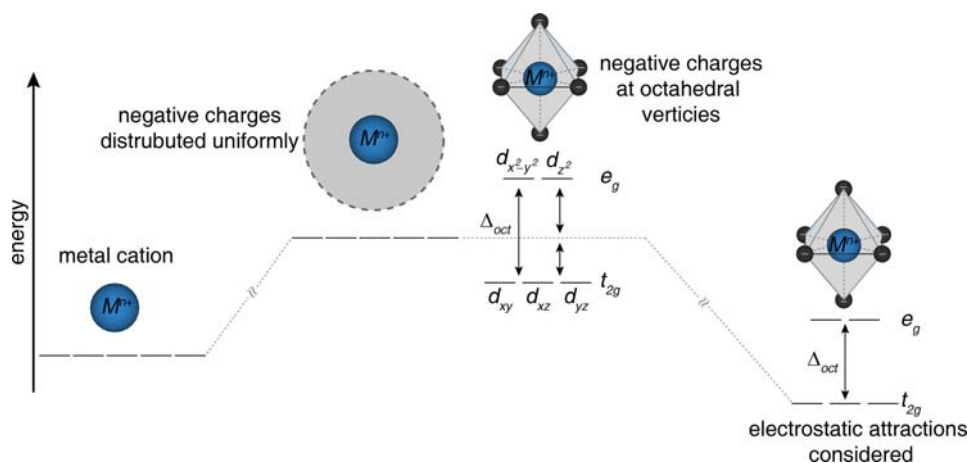


Fig. 4 A free metal cation, M^{n+} , has five degenerate nd orbitals. Distributing a negative charge uniformly around a metal cation causes the energy of the orbitals to increase due to electrostatic repulsion. The d orbitals remain degenerate. If the negative charge is distributed across the vertices of an octahedron surrounding the metal cation causes the $5d$ orbitals to split. The d_{z^2} and $d_{x^2-y^2}$ orbitals will be higher in energy while the d_{xy} , d_{xz} , and d_{yz} orbitals lower in energy. Attractive electrostatic interactions between the negative ligands and the positive metal cause the energy of the $5d$ orbitals to decrease while maintaining the splitting.

ligand : $F^- < H_2O < NH_3 < en \text{ (ethylenediamine)} < [ox]^{2-} \text{ (oxalate)} \approx H_2O < [NCS]^- < Cl^- < [CN]^- < Br^- < I^-$

metal : $Mn(II) < Ni(II) \approx Co(II) < Mo(II) < Re(IV) < Fe(III) < Ir(III) < Co(III) < Mn(IV)$

The nephelauxetic effect can thus be used to tune the absorption bands (and the color) of transition-metal compounds. For example, the absorption in $V(H_2O)_6^{3+}$ could be shifted to higher energy or blue-shifted, by exchanging H_2O for any of the ligands to the right of H_2O in the series. In contrast, if a lower absorption energy and thus red body color is desired, then ligands to the left of H_2O should be used. The absorptivity can also be shifted by replacing the transition metal in the same manner; $Mn(II)$ will experience the smallest nephelauxetic effect, whereas $Mn(IV)$ will experience the largest effect.

Tanabe and Sugano compiled the research on crystal (ligand) field theory and considered the mutual interactions between the d electrons to develop the famous Tanabe-Sugano diagrams.^{25–27} The x -axis of the diagram is in terms of the crystal field (Δ) divided by the Racah Parameter (B). The left side of the diagram at $\Delta/B = 0$, lists the energy levels of the free ion. The energy levels may split into two or more levels when $\Delta/B \neq 0$. The lowest energy level, the ground state, lies on the x -axis at $\Delta/B = 0$. The free ion energy levels are marked following ^{2S+1}L where S and L are the total spin and orbital angular momentum, respectively. The values of the total orbital angular momentum can be 0 (S), 1 (P), 2 (D), 3 (F), G (4), etc. The degeneracy of these levels is $2L + 1$. Crystal field levels are represented by ^{2S+1}X where X can be A (singly degenerate), E (doubly degenerate), or T (triply degenerate), and the subscript indicates symmetry properties.

There are seven Tanabe-Sugano diagrams to predict the absorption spectrum of d^{2-8} transition metal ions with octahedral symmetry usually considered. In terms of luminescence, Cr^{3+} containing materials provide an excellent example of using Tanabe-Sugano diagrams. Cr^{3+} requires a d^3 diagram. The ground state term symbol when the d^3 ion is in octahedral coordination is 4F . There are three spin-allowed transitions from the 4A_2 ground state: $^4A_2 \rightarrow ^4T_2$, $^4A_2 \rightarrow ^4T_1$ (4F), and $^4A_2 \rightarrow ^4T_1$ (4P). These three transitions can be seen in an absorption spectrum of a Cr^{3+} -containing transition metal material.

In the d^{4-7} Tanabe-Sugano diagrams, a vertical line at specific values of Δ/B represents discontinuities in the slopes of the excited states' energy levels. The discontinuity occurs when the spin pairing energy equals the ligand field splitting energy. Therefore, complexes with a smaller Δ/B ratio are known as low-spin, and higher Δ/B ratios represent high-spin complexes. The d^5 diagram allows the analysis of the transitions in both a high-spin and low-spin case. The slopes of the excited states' energies change when $\Delta/B \approx 2.9$. In high-spin complexes, there are two spin-allowed transitions from the ground state 2T_2 : $^2T_2 \rightarrow ^2T_1$ and $^2T_2 \rightarrow ^2A_2$. The ground state term of low-spin complexes is 6A_1 , and all optical transitions from this ground state violate either the spin or parity selection rules. Despite the forbidden nature of these transitions, there are still small (weak) peaks observed in a d^5 absorption spectrum. Interestingly, the width of the absorption bands can differ between transitions, such as in MnF_2 where the $^6A_1 \rightarrow ^4A_1$ and $^6A_1 \rightarrow ^4E$ bands are very narrow compared to the broad $^6A_1 \rightarrow ^4T_1$ and $^6A_1 \rightarrow ^4T_2$ transitions. Similar to the width of the emission bands, this phenomenon is associated with perturbations from electron-phonon coupling. If the energy level upon absorption is parallel with the ground-state (the x -axis), there is minimal change in ΔR , and a narrow absorption band can be expected; however, if there is a considerable change in the excited state slope relative to the ground state, then a variation in ΔR is expected, leading to broader absorption bands.

It is worth mentioning that the d^1 , d^9 , and d^{10} Tanabe-Sugano diagrams are not needed to predict the absorption spectrum.^{25–27} There is no electron repulsion in a d^1 complex. The single electron's ground state term symbol is 2D with fivefold degeneracy. The degeneracy is lifted by splitting the orbitals into two- and threefold degenerate orbitals, 2E and 2T_2 , respectively, in octahedral symmetry. Both terms are doublets because the spin multiplicity is equal to $2S + 1$ where $S = 1/2$. The only possible optical transition is from 2T_2 to 2E , which is consistent with the single absorption band seen in UV-Vis experiments of d^1 transition metals like $[Ti(H_2O)_6]^{3+}$. The energy difference between the two states is $20,000 \text{ cm}^{-1}$ or $10\Delta_{oct}$. Because this transition violates the parity selection rule, the intensity of the absorption band is weak. The term symbol for d^9 transition metal complexes is identical to the d^1 complexes, 2D . The transition occurs from the 2E state to the 2T_2 state in the same magnitude of Δ_{oct} , with an opposite sign. Finally, d^{10} transition metal complexes have a filled d -shell, and therefore, no Tanabe-Sugano diagrams are available.

4.09.3.2 Emission from d^0 transition metals

Materials containing d^0 transition metals tend to exhibit broad photoluminescence emission bands with large Stokes shifts of $10,000\text{--}20,000 \text{ cm}^{-1}$.¹¹ The excitation band of these systems is primarily composed of a charge transfer (CT) band arising from the transfer of electrons from the ligand to the metal center. Luminescent d^0 transition metal polyanions include TiO_4^{4-} , MoO_4^{2-} , VO_3^{4-} , NbO_6^{7-} , WO_4^{2-} , and TaO_4^{3-} . Two of the most popular d^0 transition metal complexes, WO_4^{2-} and NbO_4^{2-} , will be discussed here to illustrate the properties of these materials. For a more in-depth review on all of the luminescent d^0 transition metal complexes, the reader is directed to Blasse's *The Luminescence of Closed-Shell Transition-Metal Complexes. New Developments*.³²

Scheelite, or $CaWO_4$, is a naturally occurring luminescent material that can also be synthesized in laboratory settings. This compound has been studied for decades and was once considered a vital intrinsic scintillator used as a counter and laser host material. Additionally, $CaWO_4$ was thought to be a suitable material in the search for dark matter. Detectors utilizing $CaWO_4$ as an absorbing medium could differentiate between electrons and nuclei through the simultaneous detection of scintillation photons and phonons.³³ The excitation and emission band of $CaWO_4$ are shown in Fig. 5. When monitored at an emission wavelength of 380 nm, the excitation band spans the region from 220 to 325 nm. The excitation band has a maximum at 269 nm, with

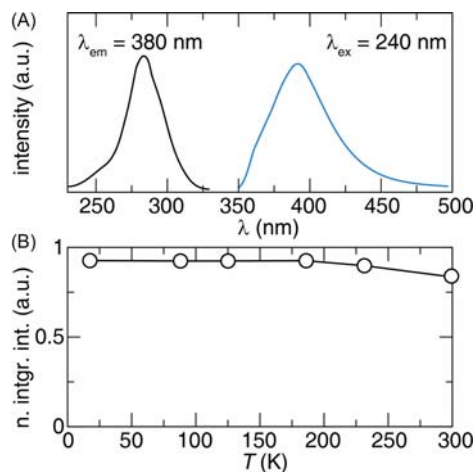


Fig. 5 (A) The excitation and emission spectrum of CaWO_4 and the (B) normalized, integrated emission intensity as a function of temperature. Modified from: Treadaway, M.J.; Powell, R.C., Luminescence of Calcium Tungstate Crystals. *J. Chem. Phys.* **1974**, *61* (10), 4003–4011.

a shoulder located at approximately 250 nm.³⁴ Exciting CaWO_4 with 240 nm (short wavelength ultra-violet radiation), X-rays, or cathode rays generates a broad emission band centered at ≈ 420 nm resulting from charge transfer in the WO_4^{2-} groups.³⁵ This material exhibits a massive Stokes shift of $\approx 16,000$ cm^{-1} . The emission intensity of CaWO_4 as a function of temperature was also investigated by Powell et al. by monitoring the emission from 10 K to 300 K upon 240 nm excitation. This result showed that the emission in CaWO_4 is incredibly robust against quenching with increasing temperature, making it a popular material for various applications.³⁴

Another popular phosphor containing a d^0 transition metal is YNbO_4 . YNbO_4 crystallizes in the Fergusonite structure and is considered a distorted Scheelite structure. YNbO_4 shows an efficient, intrinsic blue emission ($\lambda_{\text{em}} = 405$ nm) under 260 nm excitation.³⁶ The quantum yield, or the ratio of photons absorbed to photons emitted, at this excitation wavelength is 50% at room temperature, while the luminescent decay time at 77 K is 15 μs .³² Intentionally introducing Ca^{2+} and Zr^{4+} into the YNbO_4 structure showed that the presence of these impurities did not change the position of the excitation and emission bands. However, these ions did dramatically quench the observed emission.

4.09.3.3 Emission from d^n ($0 < n < 10$) transition metals

The electronic transitions and ensuing absorption/emission spectra of d^n ($0 < n < 10$) transition metal compounds are well described following the Tanabe Sugano diagrams. Starting first with d^3 transition metals, the most familiar example is likely the characteristic red color seen in rubies, which comes from the presence of Cr^{3+} (d^3) in Al_2O_3 . The emission spectrum of $\text{Al}_2\text{O}_3:\text{Cr}^{3+}$ consists of two sharp lines, called R-lines (Raman lines R_1 and R_2), located at ≈ 700 nm (Fig. 6A).^{11,37} The presence of two R-lines is caused by the splitting of the ${}^2\text{E}$ excited state due to spin-orbit coupling. The emission stems from the ${}^2\text{E} \rightarrow {}^4\text{A}_2$ transition, corresponding to the transition from the lowest energy excited state to the ground state. Since the parity and spin selection rules are allowed, the lifetime of the emission decay is on the order of milliseconds.

The ${}^4\text{T}_2 \rightarrow {}^4\text{A}_2$ transition exhibits strong coupling to the lattice generating broad emission bands for many of the Cr^{3+} -substituted structures.³⁸ This transition also represents relaxation from the lowest excited state to the ground state, specifically for systems with relatively lower energy crystal fields. An example where these optical properties are found is in the double perovskite, $\text{La}_2\text{MgZrO}_6:\text{Cr}^{3+}$.³⁹ The excitation spectrum is composed of two distinct transitions, located at 460 nm and 650 nm, that correspond to the two spin-allowed transitions of Cr^{3+} , ${}^4\text{A}_2 \rightarrow {}^4\text{T}_1$ and ${}^4\text{A}_2 \rightarrow {}^4\text{T}_2$, respectively. The red emission is attributed to the transition from the lowest energy excited state, ${}^4\text{T}_2$, to the ${}^4\text{A}_2$ ground state. The emission band, provided in Fig. 6B, is extremely broad and has a full width at half maximum of 210 nm (2796 cm^{-1}). The broad emission band was reported to arise from the substitution of Cr^{3+} on two crystallographically independent sites, Zr^{4+} and Mg^{2+} . This was corroborated by fitting the luminescent decay curve to a bi-exponential with lifetimes of 47 and 159 μs . The long lifetimes are typical for the spin-allowed ${}^4\text{T}_2 \rightarrow {}^4\text{A}_2$ transition. From these examples, we now know that the magnitude of crystal field splitting on the Cr^{3+} atom controls the resulting optical properties of the luminescent material.

The emission in these complexes stems from the relaxation of the lowest energy excited state to the ground state. High temperature can yield sufficient energies to thermally occupy the second lowest energy excited state in some cases. For example, in Fig. 6C, the line emission in $\text{Y}_3\text{Ga}_5\text{O}_{12}:\text{Cr}^{2+}$ at 10 K represents the ${}^2\text{E} \rightarrow {}^4\text{A}_2$ transition, but at higher temperatures (> 180 K), the emission spectrum broadens due to the prevalence for the ${}^4\text{T}_2 \rightarrow {}^4\text{A}_2$ transition.⁴⁰

The d^5 transition metals, specifically Mn^{2+} , do not exhibit a line emission and instead have a broad emission that stems from the different slopes of the excited states indicating ΔR is > 0 .¹¹ The emission wavelength depends on the host crystal structure, but the

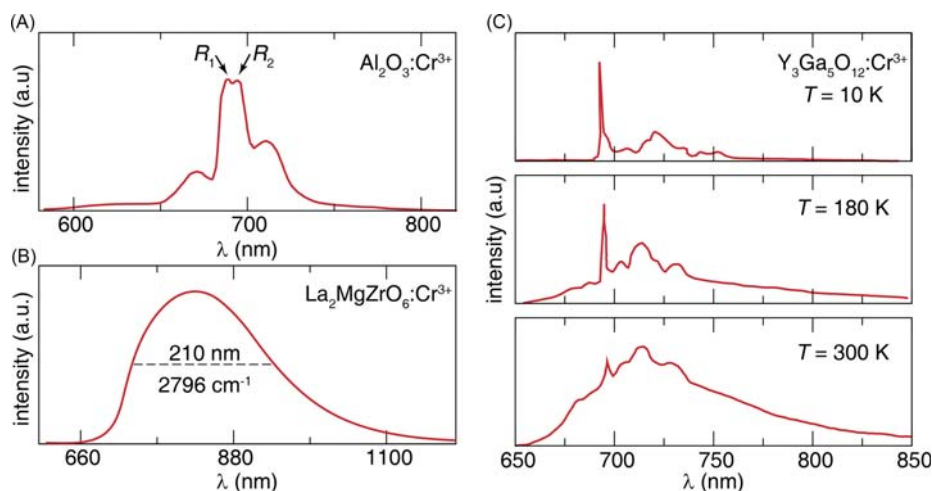


Fig. 6 (A) The room temperature emission spectrum of $\text{Al}_2\text{O}_3:\text{Cr}^{3+}$ from the ${}^2\text{E} \rightarrow {}^4\text{A}_2$. (B) The room temperature emission spectrum of $\text{La}_2\text{MgZrO}_6:\text{Cr}^{3+}$ from the ${}^4\text{T}_2 \rightarrow {}^4\text{A}_2$ transition. (C) The temperature-dependent emission spectrum of $\text{Y}_3\text{Ga}_5\text{O}_{12}:\text{Cr}^{3+}$ at 10, 180, and 300 K. Panel (A): Modified from Kusuma, H. H.; Astuti, B.; Ibrahim, Z., Absorption and Emission Properties of Ruby ($\text{Cr}:\text{Al}_2\text{O}_3$) Single Crystal. *J. Phys. Conf. Ser.* **2019**, *1170*, 012054. Panel (B): Modified from Zeng, H.; Zhou, T.; Wang, L.; Xie, R.-J., Two-Site Occupation for Exploring Ultra-Broadband Near-Infrared Phosphor—Double-Perovskite $\text{La}_2\text{MgZrO}_6:\text{Cr}^{3+}$. *Chem. Mater.* **2019**, *31* (14), 5245–5253. Panel (C) Modified from Henderson, B.; Marshall, A.; Yamaga, M.; O'Donnell, K. P.; Cockayne, B., The Temperature Dependence of Cr^{3+} Photoluminescence in Some Garnet Crystals. *J. Phys. C Solid State Phys.* **1988**, *21* (36), 6187–6198.

emission typically varies between green and deep red. The emission color is dictated by the crystal field splitting of the Mn^{2+} ion. A weak crystal field around Mn^{2+} occurs in tetrahedral coordination environments and usually gives rise to green emission, whereas a stronger crystal field in an octahedral coordination environment results in a more pronounced red emission. The radiative transition in Mn^{2+} containing systems corresponds to ${}^4\text{T}_1 \rightarrow {}^6\text{A}_1$.

One notable example is $\text{SrMgAl}_{10}\text{O}_{17}:\text{Mn}^{2+}$. This compound crystallizes in the hexagonal space group $P6_3/mmc$ in the β -alumina structure type. The structure is layered and alternates between $\text{MgAl}_{10}\text{O}_{16}$ spinel blocks composed of $[\text{AlO}_6]$ octahedra and $[(\text{Al}/\text{Mg})\text{O}_4]$ tetrahedra and conduction planes consisting of $[\text{AlO}_4]$ tetrahedra where the Sr^{2+} atoms lie in ninefold coordination.⁴¹ The iso-valent substitution site for Mn^{2+} is the MgO_4 tetrahedra within the crystal structure. As a result, a green emission is expected due to the weak crystal field from tetrahedral coordination. The excitation band of $\text{SrMgAl}_{10}\text{O}_{17}:\text{Mn}^{2+}$ has four distinct maxima located at 361, 381, 428, and 453 nm, which stem from the transitions between the ground state, ${}^6\text{A}_1$, and the ${}^4\text{E}$, ${}^4\text{T}_2$, ${}^4\text{A}_1$, ${}^4\text{E}$, and ${}^4\text{T}_2$ excited states, respectively. Non-radiative relaxation occurs from these excited states to the lowest energy excited state, ${}^4\text{T}_1$. Radiative relaxation down to the ground state results in green emission centered at 515 nm.⁴²

Placing Mn^{2+} in octahedral coordination, such as in $\text{Cs}_2\text{NaBiCl}_6:\text{Mn}^{2+}$, results in red emission.⁴³ $\text{Cs}_2\text{NaBiCl}_6$ crystallizes in the cubic $Fm\bar{3}m$ space group, which is typical for double perovskites with the $\text{A}_2\text{B}^{\text{I}}\text{B}^{\text{III}}\text{X}_6$ general formula, where $\text{A} = \text{Cs}, \text{Rb}$, $\text{B}^{\text{I}} = \text{Ag}, \text{K}, \text{Na}, \text{Li}$, $\text{B}^{\text{III}} = \text{Bi}, \text{Sb}, \text{In}$, and $\text{X} = \text{Cl}, \text{Br}, \text{I}$. Substituting Mn^{2+} into the double perovskite occurs on the octahedral $[\text{BX}_6]$ site. It is assumed that Mn^{2+} substitutes on both the Na^+ and Bi^{3+} site following $\text{Na}^+ + \text{Bi}^{3+} \rightarrow 2\text{Mn}^{2+}$ to maintain charge balancing. The excitation band of $\text{Cs}_2\text{NaBiCl}_6:\text{Mn}^{2+}$ consists of two prominent emission peaks and one low-intensity peak located at 294, 354, and 428 nm. The two more intense peaks correspond to the ${}^1\text{S}_0 \rightarrow {}^3\text{P}_2$ (294 nm) and ${}^1\text{S}_0 \rightarrow {}^3\text{P}_1$ (354 nm) transitions. Exciting at these maxima results in red-orange emission centered at 590 nm as expected from Mn^{2+} in octahedral coordination. Considering UV-A ($\lambda_{\text{em}} = 320\text{--}400$ nm) emitting LED chips are not as efficient as violet/blue LEDs ($\lambda_{\text{em}} = 405\text{--}450$ nm), Majher et al. attempted to substitute Br^- for Cl^- to manipulate the nephelauxetic effect and red-shift the excitation and emission bands of $\text{Cs}_2\text{NaBiCl}_6:\text{Mn}^{2+}$. Substituting 10% of Br^- for Cl^- resulted in a 21 nm red-shift of the prominent excitation band to 375 nm but had a negligible effect on the emission spectrum. This result suggested that the bromide ions did not coordinate the Mn^{2+} activator ion.

It is worth noting that there are also instances in which tetrahedral coordination can give rise to red emission. MgSiN_2 substituted with Mn^{2+} exhibits red emission despite tetrahedral coordination around the activator.⁴⁴ MgSiN_2 crystallizes in $Pna2_1$ and is composed of MgN_4 and SiN_4 tetrahedra. The Mn^{2+} atoms are predicted to substitute for Mg^{2+} due to their isovalency. Exciting this phosphor using ultraviolet radiation produces a broad emission band from 550 to 800 nm with a maximum centered at ≈ 626 nm. This red emission was ultimately attributed to the presence of the N atoms. The N^{3-} coordination around Mn^{2+} caused a stronger nephelauxetic effect due to its smaller electronegativity and larger formal charge. As a result, the magnitude of crystal field splitting on Mn^{2+} was larger and resulted in a red-shifted emission. The same phenomenon was seen in the isostructural Mn^{2+} substituted ZnGeN_2 and ZnSiN_2 .⁴⁵

4.09.3.4 Emission from d^{10} transition metals

Luminescent d^{10} transition metals are typically divided into two different classes, monovalent and multivalent transition metals. The monovalent transition metals include Cu^+ and Ag^+ , with the optical properties nearly identical between these two ions. Complexes containing these transition metals often show efficient emission at room temperature stemming from the $3d^9 4s^1 \rightarrow 3d^{10}$ transition. The excitation spectra of Cu^+ -substituted phosphors, for example, contain two emission bands assigned to the ${}^1\text{A}_{1g} \rightarrow {}^1\text{E}_g$ and ${}^1\text{A}_{1g} \rightarrow {}^1\text{T}_{2g}$ transitions.⁴⁶ The emission bands tend to be broad due to the two inherent transitions and larger magnitudes of electron-phonon coupling. In addition, the emission color is strongly dependent on the host crystal structure and can be tuned across the visible region. For example, the larger the alkaline earth metal in alkaline-earth sulfide phosphors, the more blue-shifted the emission becomes, as seen in $\text{CaS}:\text{Cu}^+$ ($\lambda_{\text{em}} = 413 \text{ nm}$), $\text{SrS}:\text{Cu}^+$ ($\lambda_{\text{em}} = 478 \text{ nm}$), and $\text{BaS}:\text{Cu}^+$ ($\lambda_{\text{em}} = 585 \text{ nm}$).⁴⁷ The luminescence lifetimes of these phosphors are typically on the order of tens of microseconds.⁴⁶ The natural abundance of Cu makes it an exciting activator for various applications, including $\text{LiF}:\text{Mg}^{2+}$, Cu^+ for thermoluminescence dosimetry, $\text{NaCl}:\text{Cu}^+$ for two-dimensional X-ray imaging sensors in computed radiography, and $\text{Sr}:\text{Cu}^+$ blue-emitting thin films for electroluminescent displays.⁴⁸ The main drawback of these materials is the difficulty in identifying host structures capable of Cu^+ substitution. Researchers have focused primarily on developing sulfide,⁴⁷ sulfate,⁴⁹ or halosulfate⁴⁸ phosphors, which can be readily prepared using wet chemical processes.

The multivalent d^{10} transition metals include Zn^{2+} , Ge^{4+} , Sb^{5+} , and Te^{6+} . These ions tend to show intense, broad absorption bands in the UV region. The absorption and emission bands arise from charge-transfer transitions from the $2p$ orbitals of oxygen to an antibonding orbital which lie partly on the d^{10} ion and partly on the ligand. Intrinsic violet luminescence ($\lambda_{\text{em}} = 440 \text{ nm}$) can be observed in $\text{Zn}_4\text{B}_6\text{O}_{13}$ from the $\text{Zn}(\text{II})\text{O}_4$ complex under 250 nm excitation at 4.2 K.⁵⁰ At room temperature, the emission shifts to 435 nm. At 4.2 K, emission can also be seen in KSbOSiO_4 from the $\text{Sb}(\text{V})\text{O}_6$ complex. Exciting KSbOSiO_4 at 240 nm produces cyan emission ($\lambda_{\text{em}} = 470$, Stokes shift = $20,000 \text{ cm}^{-1}$), which becomes quenched at room temperature.⁵¹ RbSbOGeO_4 shows intrinsic luminescence from both Sb^{3+} and Ge^{4+} where the emission band has the green emission band from Sb^{3+} and a weak red emission band from Ge^{4+} .⁵¹ Finally, $\text{Li}_2\text{ZrTeO}_6$ also exhibits luminescence at low temperatures. Exciting at 305 nm produces yellow emission from the tellurite octahedron, $\text{Te}(\text{VI})\text{O}_6$, centered at 610 nm with a Stokes shift of $17,000 \text{ cm}^{-1}$.⁵²

4.09.3.5 Emission from s^2 transition metals

Activators with $ns^2 np^0$ configurations like Pb^{2+} , Bi^{3+} , Sn^{2+} , and Sb^{3+} are often utilized in various luminescent materials. The ground state term for a free $ns^2 np^0$ ion is ${}^1\text{S}_0$. The first excited state is split into four levels: ${}^3\text{P}_0$, ${}^3\text{P}_1$, ${}^3\text{P}_2$, and ${}^1\text{P}_1$ (arranged from lowest to highest energy) due to spin-orbit coupling and Jahn-Teller interactions.⁵³ Typically, the transitions from ${}^1\text{S}_0$ to the ${}^3\text{P}_0$ and ${}^3\text{P}_2$ excited states are forbidden, whereas the ${}^1\text{S}_0$ transition to the low energy ${}^3\text{P}_1$ state and high energy ${}^1\text{P}_1$ state is parity-allowed due to spin-orbit coupling. The low energy ${}^1\text{S}_0 \rightarrow {}^3\text{P}_1$ transition typically exhibits higher intensity than the high energy ${}^1\text{S}_0 \rightarrow {}^1\text{P}_1$ transition at room temperature. The high intensity of ${}^1\text{S}_0 \rightarrow {}^3\text{P}_1$ is attributed to spin-orbit mixing between the ${}^3\text{P}_1$ and ${}^1\text{P}_1$ states. The emission from the triplet ${}^3\text{P}_n$ ($n = 1, 2, 3$) states and ${}^1\text{P}_1$ results in two distinct emission peaks that can be tuned across the visible spectrum and selectively excited. Typically, the intensity of spin-orbit coupling interactions increases with nuclear charge, and the stronger the spin-orbit coupling interactions, the less influence Jahn-Teller effects tend to have.

Decades of research on these materials have revealed the dramatic influence the host crystal structure plays on the resulting optical properties. The full width at half maximum of the emission band is dictated by the Huang Rhys factor, S , which describes the magnitude of electron-phonon coupling.⁵³ A large Huang Rhys parameter, and thus a large magnitude of electron-phonon coupling, usually results in a wide ($> 100 \text{ nm}$) emission band with an approximately Gaussian shape. The host crystal structure also dictates the magnitude of the Stokes shift. The extent of reorganization that occurs in the excited state, and thus the magnitude of the Stokes shift, is directly related to the host crystal structure.⁵⁴ A short Stokes shift can be achieved by minimizing the amount of excited state reorganization by targeting substitution sites smaller than the preferred activator environment. This minimizes the probability of relaxation to different equilibrium distances and leads to narrow emission spectra. Large octahedral activator environments allow the activator ion to off-center from its equilibrium position due to coupling with vibrational modes known as a pseudo-Jahn-Teller effect. The Jahn-Teller effect can be observed from the splitting of the ${}^1\text{S}_0 \rightarrow {}^3\text{P}_1$, ${}^1\text{P}_1$ absorption transitions and, in rare cases, the presence of two emission bands due to different minima on the potential energy surfaces of the excited states.

The emission from Sb^{3+} , Sn^{2+} , Bi^{3+} , and Pb^{2+} typically share three common characteristics. Luminescence from these activators is due to the ${}^3\text{P}_1 \rightarrow {}^1\text{S}_0$ transition and the luminescence usually has a large Stokes' shift, leading to considerably broad emission spectra. Finally, the luminescence decay is on the order of microseconds due to the spin-forbidden transitions.⁴¹ One of the most famous Sb^{3+} -substituted phosphors used in commercial fluorescent lamps for decades is $\text{Ca}_{10}(\text{PO}_4)_6(\text{F},\text{Cl}):\text{Sb}^{3+},\text{Mn}^{2+}$. The combination of the blue emission from Sb^{3+} and the yellow emission from Mn^{2+} under 254 nm excitation appears as white light.⁵⁵ Double perovskites and vacancy ordered double perovskites are popular host crystal structures for Sb^{3+} including the blue-emitting $\text{Cs}_2\text{NaNCl}_6:\text{Sb}^{3+}$ (fwhm = 80 nm) and cyan-emitting $\text{Rb}_3\text{InCl}_6:\text{Sb}^{3+}$ (fwhm = 129 nm), which both show promise in near-UV LED driven devices.^{54,56} Bi^{3+} has also been successfully incorporated into double perovskites, where the Bi^{3+} cation fully occupies a crystallographic position within the crystal structure and acts as an intrinsic luminescent center. For example, in $\text{Cs}_2\text{NaBiCl}_6:\text{Mn}^{2+}$, the Bi^{3+} acts as a sensitizer that absorbs UV radiation and transfers the energy to Mn^{2+} to produce orange emission.⁴³ Sn^{2+} has also been used as a sensitizer to improve Mn^{2+} luminescence in $\text{Sr}_2\text{P}_2\text{O}_7:\text{Sn}^{2+}, \text{Mn}^{2+}$.⁵⁷ On the other hand, luminescence from Pb^{2+} usually occurs in the UV to the blue region of the visible spectrum. Both $\text{Li}_6\text{CaB}_3\text{O}_{8.5}:\text{Pb}^{2+}$ and

$\text{LiSr}_4(\text{BO}_3)_3:\text{Pb}^{2+}$ emit in the UV at 307 and 328 nm upon excitation at ≈ 275 nm.^{58,59} $\text{BaAl}_2\text{B}_2\text{O}_7:\text{Pb}^{2+}$ has a blue emission ($\lambda_{\text{em}} = 423$ nm) upon 266 nm excitation with a very large Stokes shift of $13,953$ cm^{-1} .⁶⁰

4.09.4 Rare-earth substituted materials

The optical properties of luminescent materials depend on both the activator ion and the host crystal structure. The energy levels of the activator ions upon substitution into the host determine the excitation and emission properties of the material. Focusing first on rare-earth activated materials that contain at least one of the lanthanides (La–Lu), the optical properties are dictated by one of two optical transitions: a $4f \leftrightarrow 4f$ transition or a transition between $4f^{n-1}5d^1$ and $4f^n5d^0$ energy levels.

4.09.4.1 Emission from a $4f \leftrightarrow 4f$ transition in rare-earth activators

In the $4f \leftrightarrow 4f$ transition, the host crystal structure (usually) does not heavily influence the activator's emission energy since the $5d$ and $6s$ electrons shield the $4f$ electrons. As a result, the excitation energies of these activators have been predicted and represented in a Dieke diagram. When displaying these energies as a potential energy surface, the excited state lies directly above the ground state, meaning the emission is observed as sharp, narrow lines. The $4f \leftrightarrow 4f$ transitions are parity forbidden and are only observed as weak magnetic-dipole and induced electric-dipole transitions. The host crystal structure has a negligible effect on the intensities of the magnetic dipole transitions, whereas the crystal structure heavily influences the electric dipole transitions. The intensities arising from the electric dipole transitions have been successfully predicted using Judd-Ofelt theory, introduced in 1962. Nowadays, programs exist to automate the process of calculating the Judd-Ofelt intensity parameters; RELIC can calculate the intensity parameters from the absorption spectrum of any lanthanide, whereas JOES can calculate the intensity parameter, oscillator strengths, excited-state lifetimes, and estimates of the quantum efficiencies from the emission spectrum of Eu^{3+} doped compounds. Because the $4f \leftrightarrow 4f$ transitions are forbidden, they tend to have long decay times ranging from microseconds to milliseconds.

4.09.4.1.1 Emission from Eu^{3+}

Eu^{3+} substitution in a host lattice usually results in red emission. The emission spectrum consists of sharp lines since $\Delta R \approx 0$. Each line seen in the emission spectrum corresponds to a transition between the $^5\text{D}_0$ excited state and $^7\text{F}_J$ ($J = 0, 1, 2, 3, 4, 5, 6$) ground state levels of the $4f^6$ configuration (Fig. 7). The transitions most commonly observed are $^7\text{F}_J$ ($J = 0, 1, 2, 4$, and 6).⁶¹ The observation (or lack of observation) of these transitions has been extensively studied. Using the Judd-Ofelt approximation, it has been determined that (1) $^5\text{D}_0 \rightarrow ^7\text{F}_0$ is an electric dipole transition forbidden by the selection rule, (2) the transition between $^5\text{D}_0 \rightarrow ^7\text{F}_1$ is spin forbidden but is allowed from magnetic-dipole interactions due to spin-orbit coupling, and (3) the $^5\text{D}_0 \rightarrow ^7\text{F}_2$ transition is a forced electric-dipole transition since the electric-dipole transition is not strictly forbidden due to spin-orbit coupling and appear as weak lines in the spectra whose intensity is heavily influenced by the odd-parity character of the $4f^6$ wavefunctions.⁶² The weaker transitions (usually not seen because the intensity is too weak) are $^5\text{D}_0 \rightarrow ^7\text{F}_{4,6}$ which are electric-dipole transitions, and $^5\text{D}_0 \rightarrow ^7\text{F}_{3,5}$ which are forbidden transitions.

Specific trends have been observed regarding the intensity of the most commonly observed transitions. For example, the intensity of the $^5\text{D}_0 \rightarrow ^7\text{F}_1$ is not influenced by the host structure. The intensity of a transition may also be used to probe the site symmetry of the activator. In this case, the ratio of the intensity of the $^5\text{D}_0 \rightarrow ^7\text{F}_2$ transition to the $^5\text{D}_0 \rightarrow ^7\text{F}_1$ transition is called the "asymmetry ratio" and helps estimate the noncentrosymmetric nature of the Eu^{3+} substitution site within the host crystal

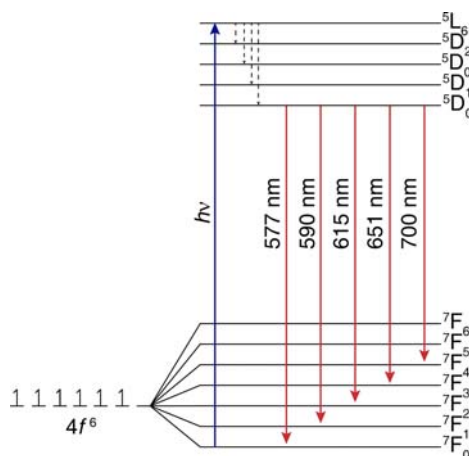


Fig. 7 Schematic of the possible electronic transitions in Eu^{3+} .

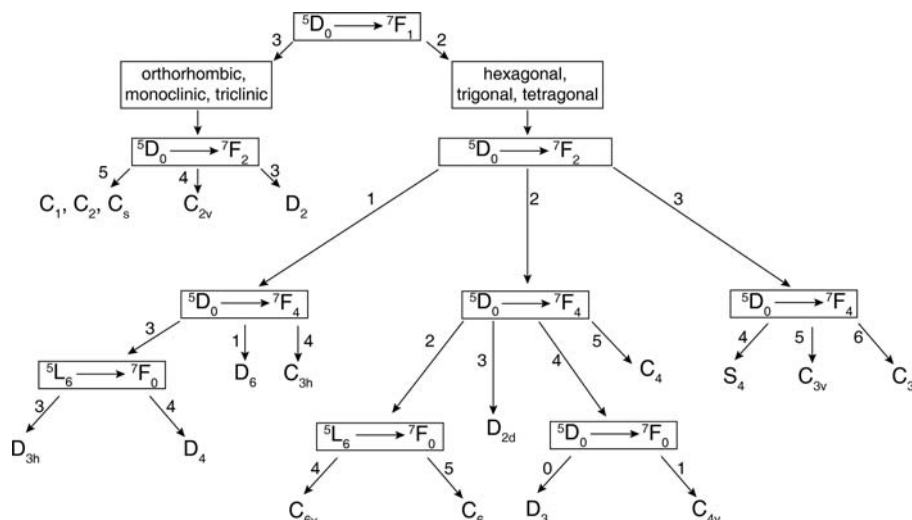


Fig. 8 Flow chart to determine the point group symmetry of Eu^{3+} based on the observed transitions. Modified from Koen Binnemans; Gorller-Walrand, C., Application of the Eu^{3+} Ion for Site Symmetry Determination. *J. Rare Earths* **1996**, *14*, 173–180.

structure. Similarly, the crystal system of the host crystal structure and point group of the activator ion can be determined by correlating the number of observed emission peaks, as seen in Fig. 8.⁶³

One of the most popular Eu^{3+} -substituted phosphors, $\text{Y}_2\text{O}_3:\text{Eu}^{3+}$, has been traditionally used in fluorescent lamps, display applications, cathode ray tubes, field emission displays, and lasers. Y_2O_3 crystallizes in the cubic $\text{Ia}\bar{3}$ space group, provided in Fig. 9A, and is composed of two crystallographically independent $[\text{YO}_6]$ octahedra. The Eu^{3+} substitutes on each Y^{3+} site in C_2 and S_6 symmetry to produce an emission band composed of an intense peak at 611 nm from the ${}^5\text{D}_0 \rightarrow {}^7\text{F}_2$ transition and weak bands from ${}^5\text{D}_0 \rightarrow {}^7\text{F}_{0,1,3,4}$, respectively (Fig. 9B).^{64,65} Like many host crystal structures, a range of Eu^{3+} concentrations (0.5–20 at.%) can be substituted into Y_2O_3 with the optimal concentration near 5 at.% for micro-scale powders and 9 at.% for the nanophosphor. The phosphor also has excellent thermal stability by retaining over 50% of its room-temperature emission intensity at 810 K, making it an attractive material for application.⁶⁶

Considering Eu^{3+} phosphors are standard red emitters in applications like LED light bulbs where the operating temperature is >420 K, these materials must retain their optical properties even at high temperatures. As a result, researchers have utilized experimental observations and data science to predict the effect of temperature on a phosphor's emission. In 1983, Van Dijk and Schuurmans developed an equation to quantify the rate of non-radiative relaxation as a function of temperature.¹¹ The rate of temperature-dependent non-radiative relaxation is heavily influenced by the offset between the ground state and excited state

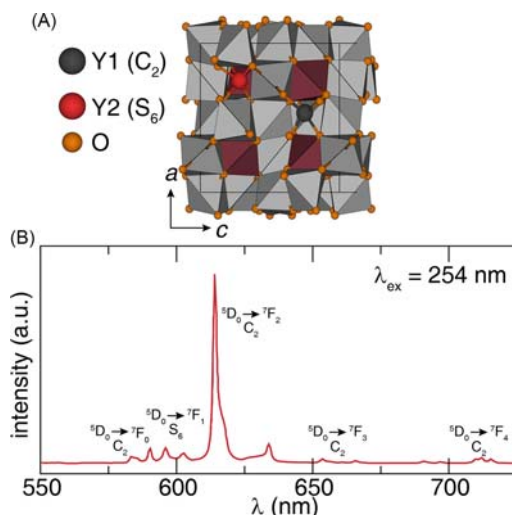


Fig. 9 (A) The crystal structure of Y_2O_3 is composed of two crystallographically independent Y^{3+} sites. 75% of the sites sit in C_2 symmetry and 25% in S_6 . (B) The emission spectrum of $\text{Y}_2\text{O}_3:\text{Eu}^{3+}$ under 254 nm excitation. (B) Modified from Marinkovic, K.; Mancic, L.; Gomez, L. S.; Rabanal, M. E.; Dramicanin, M.; Milosevic, O., Photoluminescent Properties of Nanostructured $\text{Y}_2\text{O}_3:\text{Eu}^{3+}$ Powders Obtained Through Aerosol Synthesis. *Opt. Mater.* **2010**, *32* (12), 1606–1611.

configurational coordinate diagrams (ΔR). As a result, the magnitude of non-radiative relaxation can only be reasonably calculated for crystal structures with weak electron-phonon coupling.¹¹ The rate of temperature-dependent non-radiative relaxation of the transitions that occur between the $4f$ energy levels can be described by Eq. (5).

$$W(T) = W(0)(n + 1)^\rho \quad (5)$$

where

$$W(0) = \beta \exp[-(\Delta E - 2h\nu_{\max})\alpha] \quad (6)$$

$$n = \exp\left[\left(\frac{h\nu}{kT}\right) - 1\right]^{-1} \quad (7)$$

$$\rho = \frac{\Delta E}{h\nu} \quad (8)$$

Here, $W(T)$ is the rate of non-radiative relaxation at a specific temperature, T . In the determination of $W(0)$ using Eq. (6), α and β are constants, and ν_{\max} represents the highest available vibrational frequency surrounding the activator ion. Small ΔE or higher vibrational frequencies lead to larger values of $W(0)$. Finally, the energy difference between the energy levels, ΔE , contributes to the exponential term. The values of n and ρ in Eq. (5) are determined through Eqs. (7) and (8), respectively. This series of equations represents a leap in understanding non-radiative decay processes as it is possible to calculate the rate of temperature-dependent non-radiative relaxation with an accuracy of one order of magnitude.

Researchers have more recently attempted to further understand the thermal quenching of Eu^{3+} -substituted phosphors with higher accuracy by employing machine learning models.⁶⁶ A support vector regression (SVR) machine learning model was constructed by Zhuo et al. to predict the thermal response of Eu^{3+} -substituted phosphors. The training set data used in the model was collected from the peer-reviewed literature and resulted in 134 compounds, while 51 compositional features were used to describe the data. The final model had a coefficient of determination, $r^2 = 0.71$, with a mean absolute error of 31 K. This model was then used to predict the T_{50} , or temperature at which the room temperature emission intensity of a phosphor is decreased by 50%, of 1337 oxide compounds compiled in Pearson's Crystal Database. The predictions were then experimentally validated by synthesizing five new Eu^{3+} -substituted phosphors and experimentally determining the thermal quenching temperature. The five compounds selected, $\text{Sr}_2\text{ScO}_3\text{F}$, $\text{Cs}_2\text{MgSi}_5\text{O}_{12}$, $\text{Ba}_2\text{P}_2\text{O}_7$, $\text{LiBaB}_9\text{O}_{15}$, and $\text{Y}_3\text{Al}_5\text{O}_{12}$, represent a diverse chemical space and differing structural motifs. The excitation spectra of all materials are very similar and indicate that the phosphors can be effectively excited between 350 and 450 nm, while the different emission spectra vary, as expected, due to the different activator site symmetries in the host crystal structure (Fig. 10). The predicted and experimentally determined thermal quenching temperatures show excellent agreement and differ by a maximum of 21% for $\text{Ba}_2\text{P}_2\text{O}_7:\text{Eu}^{3+}$ and a minimum of 1% for $\text{LiBaB}_9\text{O}_{15}:\text{Eu}^{3+}$. The percent difference for all of the compounds can be seen in Table 1. Overall, this data-driven approach allows for a rapid and accurate prediction of the thermal quenching temperature of Eu^{3+} -substituted phosphors.

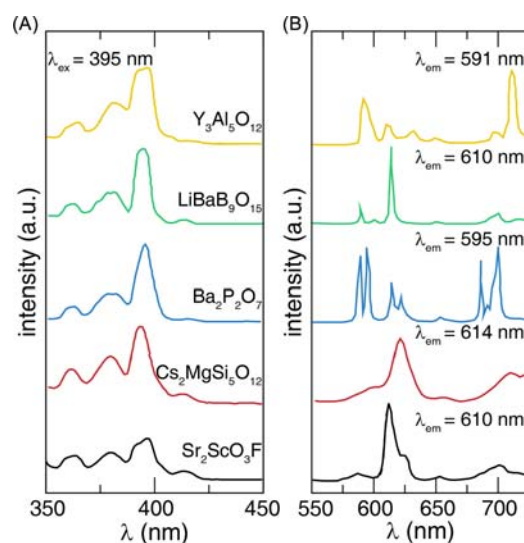


Fig. 10 The excitation and emission spectra of $\text{Y}_3\text{Al}_5\text{O}_{12}:\text{Eu}^{3+}$, $\text{LiBaB}_9\text{O}_{15}:\text{Eu}^{3+}$, $\text{Ba}_2\text{P}_2\text{O}_7:\text{Eu}^{3+}$, $\text{Cs}_2\text{MgSi}_5\text{O}_{12}:\text{Eu}^{3+}$, and $\text{Sr}_2\text{ScO}_3\text{F}:\text{Eu}^{3+}$. Reproduced with permission from Zhuo, Y.; Hariyani, S.; Armijo, E.; Abolade Lawson, Z.; Brgoch, J., Evaluating Thermal Quenching Temperature in Eu^{3+} -Substituted Oxide Phosphors via Machine Learning. *ACS Appl. Mater. Interfaces* 2019.

Table 1 The composition, space group, predicted thermal quenching temperature, experimental thermal quenching temperature, and the percent difference of $\text{Y}_3\text{Al}_5\text{O}_{12}:\text{Eu}^{3+}$, $\text{LiBaB}_9\text{O}_{15}:\text{Eu}^{3+}$, $\text{Ba}_2\text{P}_2\text{O}_7:\text{Eu}^{3+}$, $\text{Cs}_2\text{MgSi}_5\text{O}_{12}:\text{Eu}^{3+}$, and $\text{Sr}_2\text{ScO}_3\text{F}:\text{Eu}^{3+}$.

Composition	Space group	Pred. T_{50} (K)	exp. T_{50} (K)	% diff.
$\text{Y}_3\text{Al}_5\text{O}_{12}:\text{Eu}^{3+}$	$Ia\bar{3}d$	681	760	-10
$\text{LiBaB}_9\text{O}_{15}:\text{Eu}^{3+}$	$R\bar{3}c$	643	650	-1
$\text{Ba}_2\text{P}_2\text{O}_7:\text{Eu}^{3+}$	$P6_2m$	575	475	21
$\text{Cs}_2\text{MgSi}_5\text{O}_{12}:\text{Eu}^{3+}$	$Ia\bar{3}d$	553	540	2
$\text{Sr}_2\text{ScO}_3\text{F}:\text{Eu}^{3+}$	$I4/mmm$	479	450	6

Reproduced with permission from Zhuo, Y.; Hariyani, S.; Armijo, E.; Abolade Lawson, Z.; Brgoch, J., Evaluating Thermal Quenching Temperature in Eu^{3+} -Substituted Oxide Phosphors via Machine Learning. *ACS Appl. Mater. Interfaces* **2019**, *12*, 5244–5250.

4.09.4.1.2 Emission from Dy^{3+}

Emission from Dy^{3+} consists of two dominating transitions, ${}^6\text{H}_{15/2} \rightarrow {}^4\text{F}_{9/2}$ and ${}^6\text{H}_{13/2} \rightarrow {}^4\text{F}_{9/2}$, which results in blue ($\lambda_{\text{em}} \approx 470$ nm) and yellow ($\lambda_{\text{em}} \approx 570$ nm) emission, respectively, and two weaker transitions, ${}^4\text{I}_{15/2} \rightarrow {}^6\text{H}_{15/2}$ and ${}^4\text{F}_{9/2} \rightarrow {}^6\text{H}_{11/2}$ that produce a blue and red emission, respectively.⁶⁷ A schematic illustrating the relaxation mechanism is provided in Fig. 11. The combination of the intense blue and yellow emission appears as white light, but because the ${}^4\text{F}_{9/2} \rightarrow {}^6\text{H}_{13/2}$ transition is more heavily influenced by the host crystal structure the emission may appear more yellow in color. This difference in the intensity of the emission peaks is commonly referred to as the yellow-to-blue intensity ratio. As Dy^{3+} -substituted phosphors with an appropriate blue to yellow emission intensity ratio can produce white light, these materials are targeted to produce a white-light-emitting device with a single phosphor. As a result, Zou and co-workers have synthesized various Dy^{3+} -substituted borate, vanadate, niobate, antimonite, titanite, zirconate, and sulfide phosphors to understand the effect of the host crystal structure on the yellow-to-blue intensity ratio.⁶⁸ It was found that the yellow-to-blue intensity ratio increases with a decreasing charge to ionic radius (Z/r) ratio and with decreasing electronegativity of the next-nearest neighbor atom (M), Dy-O- M , in the oxides, as listed in Table 2. The site symmetry of the Dy^{3+} also highly influences the yellow-to-blue intensity ratio, where Dy^{3+} occupying a symmetric crystallographic site with an inversion center causes no luminescence to be observed. Finally, the concentration of Dy^{3+} substituted into the host crystal structure has a negligible effect on the yellow-to-blue intensity ratio when the substitution is isovalent; however, the defect states generated from aliovalent substitutions will impact the observed emission due to changes in the local site symmetry of Dy^{3+} (Table 3).

4.09.4.1.3 Emission from Tb^{3+}

Tb^{3+} typically generates green emission from one dominant, sharp emission peak centered at 545 nm from the ${}^5\text{D}_4 \rightarrow {}^7\text{F}_5$ transition, with many lower intensity peaks from weaker transitions. Borates have shown excellent promise as host crystal structures for Tb^{3+} substitution because borates tend to possess near-UV absorption, generate an intense green emission, and produce higher color purities than other host structures. For example, the recently discovered NaSrB_5O_9 crystal structure, which adopts the monoclinic $P2_1/c$ spacegroup, has been reported as a host for Tb^{3+} substitution. The crystal structure is composed of a boron framework of three $[\text{BO}_3]$ trigonal planes and two $[\text{BO}_4]$ tetrahedra that form a pentaborate group, $[\text{B}_5\text{O}_9]^{3-}$. The Na^+ and Sr^{2+} cations are

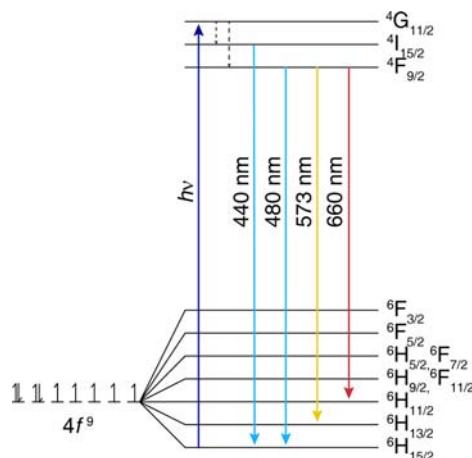


Fig. 11 Schematic of the possible electronic transitions in Dy^{3+} .

Table 2 Influence of the charge to ionic radius (Z/r) and electronegativity (E) of the next-nearest neighbor atom (M) in Dy-O-M on the yellow-to-blue intensity ratio (Y/B).

M	Z/r	E	Y/B			
			$M_3La_2(BO_3)_4$	$M_3Gd_2(BO_3)_4$	$M_3Y_2(BO_3)_4$	$M_2B_2O_5$
Ca	2.02	1.0	0.82	0.96	0.86	2.11
Sr	1.79	1.0	1.05	1.17	1.00	2.46
Ba	1.49	0.9	1.21	1.25	1.35	2.62

Modified from Su, Q.; Pei, Z.; Chi, L.; Zhang, H.; Zhang, Z.; Zou, F., The Yellow-to-Blue Intensity Ratio (Y/B) of Dy^{3+} Emission. *J. Alloys Compd.* **1993**, *192* (1), 25–27.

Table 3 Influence of the dysprosium concentration (mol%) on the yellow-to-blue intensity ratio (Y/B) in systems with isovalent substitution ($La_2Ti_2O_7$, $Gd_2Zr_2O_7$, $LaZrSbO_6$) and aliovalent substitution (CaS).

Dy^{3+} (mol%)	Y/B			
	$La_2Ti_2O_7$	$Gd_2Zr_2O_7$	$LaZrSbO_6$	CaS
0.5	1.2	1.7	—	—
1	1.1	1.7	1.4	3.0
2	1.1	1.7	—	—
3	1.1	—	1.4	—
5	1.2	—	1.3	3.33
7.5	—	—	—	3.61
9	—	1.8	1.5	—
10	—	—	—	4.20

Modified from Su, Q.; Pei, Z.; Chi, L.; Zhang, H.; Zhang, Z.; Zou, F., The Yellow-to-Blue Intensity Ratio (Y/B) of Dy^{3+} Emission. *J. Alloys Compd.* **1993**, *192* (1), 25–27.

coordinated by 8 oxygen atoms, and both cations are replaced with a single Tb^{3+} cation to maintain charge balance. The excitation spectrum of $NaSrB_5O_9:Tb^{3+}$ consists of several sharp emission peaks from the ground state to various excited states: ${}^7F_6 \rightarrow {}^5H_6$ (303 nm), ${}^7F_6 \rightarrow {}^5H_7$ (317 nm), ${}^7F_6 \rightarrow {}^5D_2$ (348 nm), ${}^7F_6 \rightarrow {}^5L_{10}$ (368 nm), ${}^7F_6 \rightarrow {}^5G_6$ (379 nm), and ${}^7F_6 \rightarrow {}^5D_4$ (485 nm). The most intense peak arises from the ${}^7F_6 \rightarrow {}^5G_6$ (379 nm) transition and was used to excite the phosphor to produce the characteristic green emission from 425 to 650 nm. The green emission results from the combination of the weak ${}^5D_3 \rightarrow {}^7F_4$ (442 nm), ${}^5D_4 \rightarrow {}^7F_6$ (490 nm), ${}^5D_4 \rightarrow {}^7F_4$ (587 nm), and ${}^5D_4 \rightarrow {}^7F_3$ (622 nm) transitions and the intense ${}^5D_4 \rightarrow {}^7F_5$ (545 nm) transition.⁶⁹ Moreover, the phosphor with 1 at.% Tb^{3+} substitution has a photoluminescent quantum yield of 35% and retains 54% of the room temperature emission intensity at 483 K.

In Tb^{3+} and other trivalent rare-earth substituted systems, concentration quenching can occur in the form of cross-relaxation, which is non-radiative relaxation due to energy transfer between an activator in the excited state to the same activator in the ground state.⁷⁰ This process is illustrated in Fig. 12. The occurrence of cross-relaxation in a system is evident by the domination of one transition over another. For example, in Tb^{3+} , cross-relaxation occurs in the ${}^5D_3 \rightarrow {}^7F_6$ transition meaning the blue emission from Tb^{3+} becomes preferentially quenched, and the green emission from the ${}^5D_4 \rightarrow {}^7F_5$ transition dominates. Therefore, the emission color of Tb^{3+} can be shifted from blue-white at low Tb^{3+} concentrations to bright green at high Tb^{3+} concentrations by manipulating cross-relaxation to simultaneously reduce the population of Tb^{3+} ions in the 5D_3 excited state and increasing the population in the 5D_4 state.²⁸

The major drawback of Tb^{3+} -substituted materials is that the $4f \leftrightarrow 4f$ forbidden transitions cause sharp, weak absorption peaks in the UV region, which makes it difficult to sufficiently excite the phosphor with a nearly monochromatic LED.⁷¹ Fortunately, the broad emission bands of Ce^{3+} phosphors (discussed in the next section) that emit in the UV region can serve as an excitation source for Tb^{3+} phosphors. As a result, researchers have focused on developing Ce^{3+}/Tb^{3+} co-substituted phosphors. Here, the Ce^{3+} serves as a sensitizer to increase the absorption of Tb^{3+} in the near-UV region. This strategy was utilized in the $Sr_2LiScB_4O_{10}$ system, where Ce^{3+} substitution results in an asymmetric and broad emission band centered at 385 nm under 347 nm excitation. The excitation band of $Sr_2LiScB_4O_{10}:Tb^{3+}$, as shown in Fig. 13, overlaps with the emission spectrum of $Sr_2LiScB_4O_{10}:Ce^{3+}$, indicating that co-doping may be an effective strategy to produce green emission. Generally, more overlap indicates higher rates of energy transfer. Indeed, the emission spectrum of $Sr_2LiScB_4O_{10}:Ce^{3+}, Tb^{3+}$ is composed of two main features, the broad band emission from 235 to 375 nm from the Ce^{3+} and the sharp emission peak at 544 nm from the ${}^5D_4 \rightarrow {}^7F_5$ transition along with the weaker transitions ${}^5D_4 \rightarrow {}^7F_j$ ($J = 6, 4, 3$) producing emission peaks at 488, 585, and 625 nm, respectively.⁷²

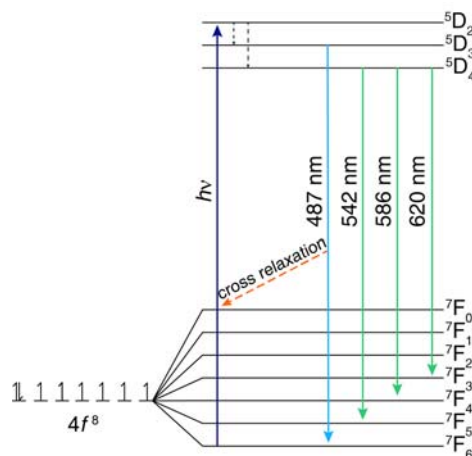


Fig. 12 Schematic of the possible electronic transitions in Tb^{3+} .

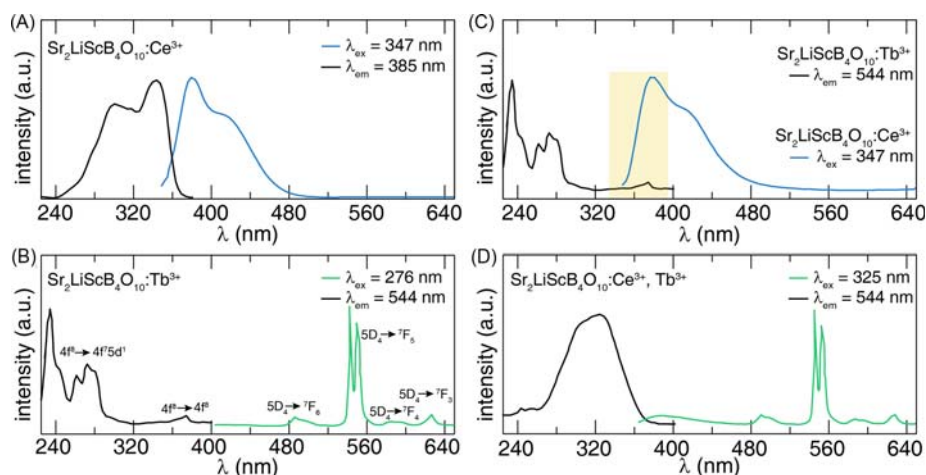


Fig. 13 (A) Photoluminescent excitation (black) and emission (blue) spectra of $\text{Sr}_2\text{LiScB}_4\text{O}_{10}:\text{Ce}^{3+}$. (B) Photoluminescent excitation (black) and emission (green) spectra of $\text{Sr}_2\text{LiScB}_4\text{O}_{10}:\text{Tb}^{3+}$. (C) The emission spectrum of $\text{Sr}_2\text{LiScB}_4\text{O}_{10}:\text{Ce}^{3+}$ (blue) and the excitation spectrum of $\text{Sr}_2\text{LiScB}_4\text{O}_{10}:\text{Tb}^{3+}$ (black) overlap, indicating potential for charge transfer. (D) Photoluminescent excitation (black) and emission (green) spectra of $\text{Sr}_2\text{LiScB}_4\text{O}_{10}:\text{Ce}^{3+}, \text{Tb}^{3+}$. Modified from Chen, H.; Wang, Y., $\text{Sr}_2\text{LiScB}_4\text{O}_{10}:\text{Ce}^{3+}/\text{Tb}^{3+}$: A Green-Emitting Phosphor With High Energy Transfer Efficiency and Stability for LEDs and FEDs. *Inorg. Chem.* **2019**, *58* (11), 7440–7452.

Understanding the mechanism of charge transfer within co-substituted systems is vital for optimizing these systems. Energy transfer may occur through electronic multipolar interactions or other exchange interactions. These interactions have a critical distance, R_c , where an R_c less than 5 Å means energy transfer is the dominating interaction, and an R_c greater than 5 Å favors electronic multipolar interactions. The critical distance may be calculated following Eq. (9),

$$R_c = 2 \left(\frac{3V}{4\pi\chi N} \right)^{1/3} \quad (9)$$

where χ represents the optimal Tb^{3+} doping concentration, which in the $\text{Sr}_2\text{LiScB}_4\text{O}_{10}$ example was determined to be $\chi = 0.023$, V is the volume of the unit cell, and N is the number of molecules in one unit cell. The critical distance of Tb^{3+} ions in $\text{Sr}_2\text{LiScB}_4\text{O}_{10}$ was determined to be 11.83 Å using these values, indicating electronic multipolar interactions dominate. The multipolar interactions can be further understood by examining the relationship between Dexter's energy transfer formula using Reisfeld's approximation in Eq. (10).⁷³

$$\frac{\eta_0}{\eta_s} \propto C_{\text{Ce}^{3+} + \text{Tb}^{3+}}^{n/3} \quad (10)$$

Here, η_0 and η_s are the photoluminescent quantum yields of $\text{Sr}_2\text{LiScB}_4\text{O}_{10}:\text{Ce}^{3+}$ and $\text{Sr}_2\text{LiScB}_4\text{O}_{10}:\text{Ce}^{3+}, \text{Tb}^{3+}$, respectively, and C is the sum of the activator concentrations. The values of η_0 and η_s can be approximated by the ratio of relative emission intensities of $\text{Sr}_2\text{LiScB}_4\text{O}_{10}:\text{Ce}^{3+}$ and $\text{Sr}_2\text{LiScB}_4\text{O}_{10}:\text{Ce}^{3+}, \text{Tb}^{3+}$, I_{s0}/I_s . From here, it is possible to determine if exchange interactions or multipolar

interactions are favored. A linear relationship between C and I_{50}/I_5 represents exchange interactions, whereas a linear relationship between I_{50}/I_5 and C^n/I_5 with $n = 6, 8,$ and 10 , corresponding to dipole-dipole, dipole-quadrupole, and quadrupole-quadrupole interactions. In $\text{Sr}_2\text{LiScB}_4\text{O}_{10}:\text{Ce}^{3+}, \text{Tb}^{3+}$, the exchange interaction can automatically be ruled out due to the critical distance, with the most linear relationship stemming from the dipole-dipole interactions.⁷² Knowledge of the charge transfer mechanism allowed the phosphor's emission color to be tuned from the UV/blue region of the visible spectrum (Ce^{3+} -substitution) to the green region of the visible spectrum ($\text{Ce}^{3+}\text{-Tb}^{3+}$ co-substitution), demonstrating the value of co-substitution in phosphors.

4.09.4.2 Emission from Ce^{3+} and Eu^{2+} ($4f^n-15d^1 \rightarrow 4f^n$ transitions)

The two most common rare-earth ions that exhibit transitions between the $4f^{n-1}5d^1 \leftrightarrow 4f^n5d^0$ energy levels are Ce^{3+} and Eu^{2+} . The energy levels of a free, gaseous rare-earth ion differ significantly compared to substituting the ion into a host structure. For example, the energy difference between the $4f$ and $5d$ levels of a gaseous Ce^{3+} ion is approximately 6.2 eV ($50,000 \text{ cm}^{-1}$), meaning this electronic transition occurs in the UV region.¹⁷ However, incorporating this ion in a crystal structure results in inter-electron repulsion that stabilizes and lowers the energy of the rare-earth $5d$ energy levels, known as the centroid shift. The magnitude of the centroid shift is directly proportional to anion polarizability and is inversely proportional with the covalency of the composition of the host. As the degree of covalency between the activator and its coordination anions increases, the activator's $5d$ orbitals become further stabilized. When the $5d$ orbitals undergo the centroid shift, they are degenerate, as illustrated in Fig. 14. This degeneracy is lifted by a second phenomenon, crystal field splitting. The well-shielded $4f$ orbitals are unaffected and remain nearly constant in energy. As a result, the combination of the centroid shift and crystal field splitting defines the energy difference between the $4f$ and the lowest energy $5d$ orbital, known as the Stokes' shift. The magnitude of the crystal field splitting depends on the bond lengths between the rare-earth ion and coordinating anion, the coordination environment, and the symmetry of the activator site, all determined by the host structure. Crystal field splitting can be approximated following Eq. (11),

$$Dq = \frac{Ze^2r^4}{6R^5} \quad (11)$$

where Dq is the crystal field splitting, e is the charge of an electron, r is the radius of the $5d$ wavefunction, and R is the distance between activator and coordinating anion.⁷⁴ It is important to note that this equation was derived from a point charge model and is, therefore, somewhat inaccurate. It is simply an approximation to describe crystal field splitting trends as a function of different bond lengths. In addition, the magnitude of crystal field splitting depends on polyhedral distortion, which can be described by the bond length distortion index, D , calculated using Eq. (12),

$$D = \frac{1}{n} \sum_{i=1}^n \frac{|l_i - l_{av}|}{l_{av}} \quad (12)$$

where l_i is the distance between the central and coordinating i th atom and l_{av} is the average bond length. A more distorted polyhedron would result in increased crystal field splitting. Finally, Dorenbos also noted that the shape of the polyhedral environment is correlated to the magnitude of crystal field splitting; Dorenbos determined that octahedral, cubic, and dodecahedral coordination yields the largest crystal field splitting, and the smallest crystal field splitting is found for activators in tricapped trigonal prisms and cuboctahedral coordination.⁷⁵ As a result, if one wanted to red-shift an emission spectrum by increasing the

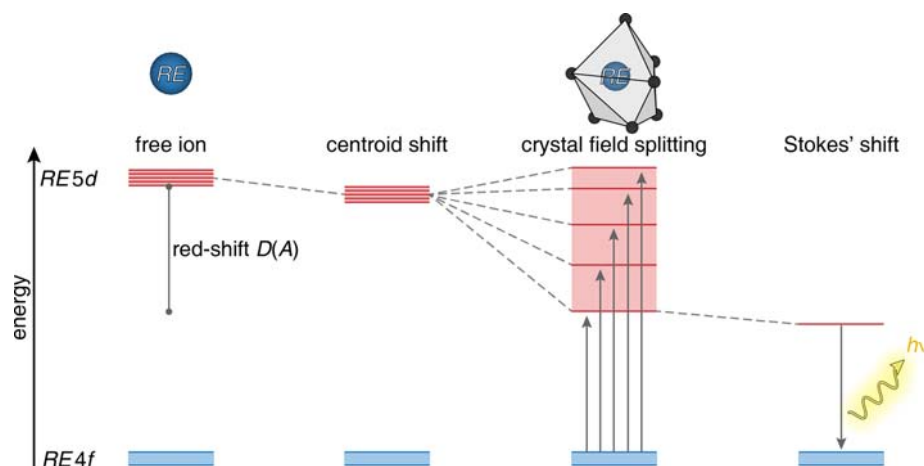


Fig. 14 A schematic energy level diagram for a rare-earth ion (RE) shows the effect of the centroid shift and crystal field splitting. These phenomena ultimately decrease the energy difference between the $4f$ and $5d$ orbitals, known as the red-shift, $D(A)$. Emission results from the lowest energy excited $5d$ orbital to the $4f$ ground state where the energy difference between these orbitals is known as the Stokes' shift. Modified from George, N. C.; Denault, K. A.; Seshadri, R., Phosphors for Solid-State White Lighting. *Annu. Rev. Mat. Res.* **2013**, *43* (1), 481–501.

crystal field splitting, one would have to choose a host that contain highly symmetric polyhedra with short bond lengths and/or small coordination numbers.

The electronic transitions in Ce^{3+} and Eu^{2+} give rise to broad emission and excitation bands, in contrast to the $4f \leftrightarrow 4f$ line transitions. This is due to the large ΔR between the ground and excited states and the radiative transitions between vibrational levels.¹¹ Past research has also shown that highly rigid structures can reduce non-radiative relaxation and electron-phonon coupling in the excited state, which leads to a narrower emission spectrum. Moreover, multiple luminescent centers produce an emission spectrum with multiple peaks of different shapes and positions. Overlap of these emission bands would cause an overall broadening of the emission band. Finally, host structures substituted with Ce^{3+} tend to have broader emission bands than those substituted with Eu^{2+} . This arises because the degeneracy of the $4f$ levels is lifted and causes spin-orbit coupling of the $4f$ ground state into two levels, $^2F_{5/2}$ and $^2F_{7/2}$. The result is the observed dual emission from the lowest energy $5d$ state ($^2D_{3/2}$) to the two separate 2F levels giving rise to a broader emission band.¹⁷ It is important to note that the emission band of any rare-earth substituted system undergoing $4f^{n-1}5d^1 \rightarrow 4f^n5d^0$ transitions may also be broadened by choosing a host structure with multiple luminescent centers with different crystal field splitting parameters.

The luminescence from rare-earth activator ions can be described in the simplest terms as an exponential decay.¹⁷ The number of terms in the exponential function used to fit the decay curve and the number of unique luminescence lifetimes typically correspond to the number of crystallographic independent substitution sites in the host crystal structure. The transition between $4f$ and $5d$ energy levels occurs on a nanosecond time scale due to the transition's spin and parity allowed nature. Non-radiative relaxation from higher energy $5d$ energy levels to the lowest energy excited state takes only 1 ns, or 1/10 of the time required for radiative relaxation, due to strong electron-phonon coupling. Generally, Ce^{3+} has the fastest radiative decay time, on the order of 10–100 ns, making it the shortest lifetime of all rare-earth activator ions. Eu^{2+} tends to have slower decay times, $\approx 1 \mu\text{s}$, because the multiplicity of the excited spin state can be either an octet or sextet, but the ground state is an octet spin state (8S_0), meaning the excited state relaxation is spin-forbidden, yielding longer decay times.^{11,76} The fast decay rates of Ce^{3+} phosphors make them attractive for general lighting applications, which require short decay times. Further, the fast decay times limit absorption saturation effects that can negatively influence the optical properties. In general, however, the decay rates of phosphors tend to shorten upon exposure to elevated temperatures, which are typically experienced in lighting devices. The high temperature promotes non-radiative pathways causing shorter decay times.

4.09.4.3 Thermal stability of $4f \leftrightarrow 5d$ electronic transitions

The emergence of the high brightness InGaN blue LED triggered a search for new phosphors that can be effectively excited by blue ($\lambda_{\text{ex}} = 450 \text{ nm}$) light. However, the small compact size of modern LED chips generates a sufficient amount of heat that can negatively impact the phosphor's optical properties. Indeed, the heat activates the phonon modes of the phosphor, which increases the probability of phonon-assisted non-radiative relaxation, effectively reducing the observed luminescence intensity. Moreover, the increased temperature changes the local coordination environment that can cause a shift in the phosphor's emission color. The ability of a phosphor to resist changes in emission intensity as a function of increasing temperature is known as thermal stability. The thermal stability of a phosphor is greatly influenced by the position of the activator's energy levels with respect to the host conduction and valence band. If the activator's $5d$ orbitals energy levels are too close to the host conduction band, an electron may be promoted from the ground state and into the conduction band, which effectively quenches the emission. This phenomenon, known as photoionization, may be avoided by choosing a host crystal structure with a band gap in the UV so that it is far from the activator absorption energy.

The energy barrier, ΔE , between the activator's excited state orbitals and the conduction band of the host determines whether the electron may be thermally promoted and trapped in the conduction band, thereby quenching the emission. It has been proposed that choosing a host structure with a sufficiently wide band gap may help prevent temperature-induced photoionization. In fact, machine learning models have been developed to predict host structures that are ideal for producing a thermally robust emission (discussed in Section 4.09.10.3). Another proposed theory of thermal quenching is known as the cross-over mechanism. This mechanism describes the non-radiative relaxation of an excited state electron through an intersection point between the $4f$ (ground) and lowest excited $5d$ state. The probability of thermal quenching through this mechanism depends strongly on the quenching barrier, ΔE . Research has shown that host structures that undergo minimal electron-phonon coupling (small magnitudes of ΔR) are structures that contain rigid bonding networks and should be sought when developing new phosphors for LED and laser-based applications.

The quantitative value of ΔE can be experimentally determined by investigating the relationship between $5d \leftrightarrow 4f$ rare-earth emission intensity, $I(T)$, and the temperature, T , following the Arrhenius equation (Eq. 13).

$$I_T = \frac{I_0}{1 + \frac{\Gamma_v}{\Gamma_r} \exp\left(\frac{-\Delta E}{k_B T}\right)} \quad (13)$$

Here, Γ_v is the radiative decay rate, Γ_0 is the attempt rate of the thermal quenching process, k_B is Boltzmann's constant, and ΔE describes the thermal quenching barrier.⁷⁷ The value of ΔE can be determined directly by fitting the normalized, integrated emission intensity versus temperature decay curve to the Arrhenius equation or by approximating the relationship following Eq. (14).

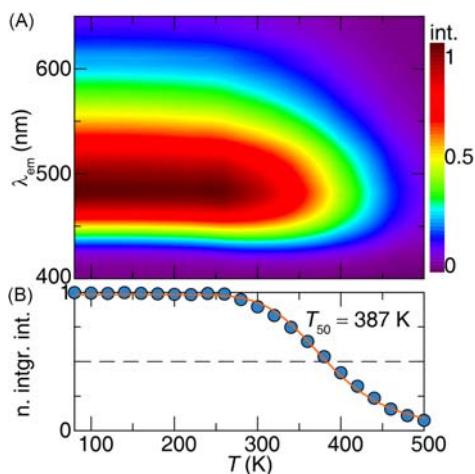


Fig. 15 (A) Contour plot of the normalized temperature-dependent emission spectra of BaScO₂F:Eu²⁺ under 340 nm excitation. (B) Normalized, integrated intensity of the emission as a function of temperature. The orange line is the Arrhenius fit, which yields an activation energy of 0.32 eV. Reproduced with permission from Hariyani, S.; Brgoch, J., Local Structure Distortion Induced Broad Band Emission in the All-Inorganic BaScO₂F:Eu²⁺ Perovskite. *Chem. Mater.* **2020**, *32* (15), 6640–6649.

$$\Delta E = \frac{T_{50}}{680} \quad (14)$$

This equation contains the crucial T_{50} quenching temperature or the temperature at which the emission intensity decreases to 50% of its initial intensity. The T_{50} can be experimentally determined by incrementally heating the sample from liquid nitrogen or room temperature to elevated temperatures using a cryostat/heater coupled with a spectrofluorometer. From this data, it is possible to plot the normalized, integrated emission intensity versus temperature to determine T_{50} . The higher the value of the T_{50} , the more thermally robust a phosphor is considered. Current LEDs can reach operating temperatures approaching 450 K; thus, a minimum T_{50} of 450 K is considered essential before a phosphor can be used in conjunction with an LED. The advent of laser-based lighting has even more stringent T_{50} requirements.

Fig. 15 depicts an example of a temperature-dependent photoluminescence measurement for BaScO₂F:Eu²⁺.⁷⁸ The emission spectrum of BaScO₂F:Eu²⁺ was collected incrementally from 80 K to 500 K with an excitation wavelength of 340 nm. **Fig. 15A** illustrates a contour plot of the emission spectrum. The dark red regions depict the maximum intensity, which is retained until ~300 K. Quenching begins once the temperature is increased beyond 300 K. The normalized, integrated emission intensity from each emission scan is plotted in **Fig. 15B**. The T_{50} was determined to be 387 K by extrapolating the temperature that would yield a normalized integrated emission intensity of 0.5 (dashed line). This decay curve was fit to the Arrhenius equation (Eq. 13) shown by the orange line to return an energy barrier of 0.32 eV. Using Eq. (14), the value of the energy barrier is 0.57 eV. This example highlights the caution in approximating the value of ΔE .

Temperature-dependent lifetime measurements can also be conducted in a similar manner to determine the T_{50} . A material's luminescence lifetime is known to be proportional to the photoluminescent quantum yield of a phosphor. These measurements can be utilized to corroborate the value of the T_{50} or determine the T_{50} if the temperature-dependent emission intensity is ambiguous. For example, the temperature-dependent emission intensity of Na₂MgPO₄F:Eu²⁺ does not decay as a function of temperature as one would expect.⁷⁹ As shown in **Fig. 16A**, the emission intensity increases as a function of temperature until 460 K, where the emission intensity is almost double the 80 K intensity. Increasing the temperature further causes luminescence quenching to set in by 580 K, and the T_{50} is finally reached at 634 K. The origin of this odd response is clear from studying the emission spectra as a function of temperature provided in **Fig. 16B**. At 80 K, two distinct emission peaks correspond to two Eu²⁺ atoms substituting on two crystallographically independent Na⁺ sites. As the temperature increases, the higher energy peak starts to increase in intensity. This abnormal increase in the emission intensity is likely due to the depopulation of defect trap states at high temperatures, illustrated in **Fig. 16C**. The trap states are a charge compensation mechanism arising from the aliovalent substitution of Eu²⁺ for Na⁺. The enhanced emission intensity improves the phosphor's thermal stability but makes determining an accurate T_{50} difficult. However, temperature-dependent lifetime measurements are not affected by defect trap states and thus allow for a reliable determination of T_{50} for this phosphor.⁸⁰ In this case, the material's T_{50} was found to be 520 K, which surpasses the minimum of 423 K and makes this phosphor appropriate for lighting applications.

Previous research has uncovered other strategies to improve the thermal quenching resistance if a phosphor system does not have a T_{50} above the threshold. The first strategy involves managing the local activator environment to manage thermal quenching.⁸¹ The local activator environment can be manipulated through cationic substitution. This strategy is commonly employed to tailor the crystal field splitting of the activator to shift a phosphor's emission color to the desired wavelength. However, it has recently been determined that a large degree of cation disorder can enhance a phosphor's thermal stability. For example, Liu and co-workers reported that cation disorder, which can be calculated by the variance of cation size, r , in a structure by

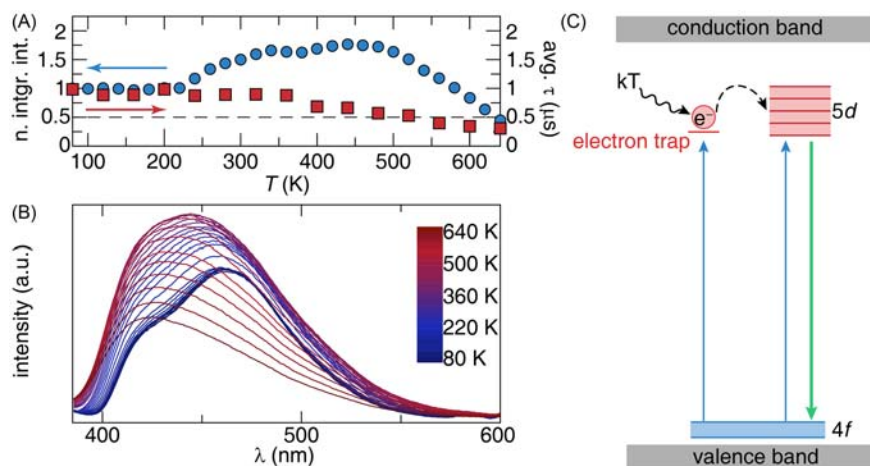


Fig. 16 (A) Normalized, integrated emission intensity (blue circle) and photoluminescent lifetime (red square) as a function of temperature for $\text{Na}_2\text{MgPO}_4\text{F}:\text{Eu}^{2+}$. (B) Temperature-dependent emission spectra of $\text{Na}_2\text{MgPO}_4\text{F}:\text{Eu}^{2+}$. (C) The mechanism of electron de-trapping upon exposure to thermal energy (kT). Reduced with permission from Hariyani, S.; Brgoch, J., *Advancing Human-Centric LED Lighting Using $\text{Na}_2\text{MgPO}_4\text{F}:\text{Eu}^{2+}$* . *ACS Appl. Mater. Interfaces* **2021**, 13 (14), 16669–16676.

$\sigma^2 = \langle r^2 \rangle - \langle r \rangle^2$, can induce deep trap states that disrupt the inherent lattice vibration of a host structure.⁸² These trap states will confine and release electrons at high temperatures, thereby enhancing a phosphor's thermal stability. This was seen in the $\text{Ba}_2\text{Sr}_x\text{SiO}_4:\text{Eu}^{2+}$ system, where the thermal stability improves as a function of increasing cation disorder. The main consequence of employing this strategy is determining the correct balance between the creation of trap states and hindering the structural rigidity of the host structure.

Thermal stability may also be improved through post-processing techniques after the material is already synthesized. One such post-processing technique is to apply a surface coating on the phosphor. The coating material should be homogenous and transparent to the excitation and emission energy. Examples of popular coating materials include MgO, ZnO, Al_2O_3 , TiO_2 , and SiO_2 . The surface coating is usually carried out in solution. For example, coating $\text{Ca}_2\text{BO}_3\text{Cl}:\text{Eu}^{2+}$ involved dispersing the phosphor powder in a $\text{C}_2\text{H}_5\text{OH}$, H_2O , and tetraethylorthosilicate (TEOS). TEOS is a common silicon source to produce a SiO_2 coating. The solution was then heated at 60 °C for 1 h at a pH of 9–10. The amount of tetraethylorthosilicate is varied during the coating process to identify the optimal coating weight percent. In this case, the optimal SiO_2 coating percentage for $\text{Ca}_2\text{BO}_3\text{Cl}:\text{Eu}^{2+}$ was 8 wt%. Measuring the temperature-dependent emission revealed that at 473 K, the pristine $\text{Ca}_2\text{BO}_3\text{Cl}:\text{Eu}^{2+}$ retained 41% of the room temperature intensity, whereas the coated phosphor was more thermally robust and retained 91% of the room-temperature emission intensity.⁸³ There are two mechanisms proposed to explain the improved thermal stability. The first hypothesis is that a surface coating may reduce the number of surface defects that contribute to non-radiative relaxation. The second theory suggests that a surface coating minimizes the phosphor's contact to air to prevent oxidation of the activator (Eu^{2+} to Eu^{3+}) at high temperatures.

4.09.4.4 Notable rare-earth substituted phosphors families

4.09.4.4.1 Garnets

The most popular class of phosphors are garnets that crystallize in the general formula $\text{X}_3\text{Y}_2\text{Z}_3\text{O}_{12}$ where X, Y, and Z represent the three cationic sites that can accommodate various cations with differing radii. Garnets crystallize in the cubic space group $Ia\bar{3}d$ and are composed of an intricate network of $[\text{YO}_4]$ tetrahedra and $[\text{ZO}_6]$ octahedra known as a double gyroid, with 8-coordinate X^{3+} cations filling the voids.⁸⁴ In mineralogy, garnets are referred to as a group of naturally occurring silicate minerals that occur in a variety of species such as $\text{Mg}_3\text{Al}_2\text{Si}_3\text{O}_{12}$ (Pyrope), $\text{Ca}_3\text{Fe}_2\text{Si}_3\text{O}_{12}$ (Andradite), and $\text{Ca}_3\text{Cr}_2\text{Si}_3\text{O}_{12}$ (Uvarovite). Garnet materials have been used since the Bronze age as gemstones due to their brilliant color when substituted with transition metal ions and abrasives due to their high hardness.⁸⁵ However, they were not used as luminescent materials until 1967. The first artificial garnets were synthesized at that time, including the solid solution $(\text{Mn}_{1-x}\text{Y}_x)_3\text{Al}_2(\text{Si}_{1-x}\text{Al}_x)_3\text{O}_{12}$, where the end member $\text{Y}_3\text{Al}_5\text{O}_{12}$ was first successfully prepared.⁸⁶ Blasse and Brill found that substituting Ce^{3+} in $\text{Y}_3\text{Al}_5\text{O}_{12}$ produced a yellow emission upon excitation with blue light ($\lambda_{\text{ex}} \approx 450$ nm), which in combination, appears as white light to the human eye.⁸⁷ The distorted eight-fold coordinated environment around the small Y^{3+} cation induces a large crystal field splitting of the Ce^{3+} 5d levels, where the energy difference between the highest and lowest energy 5d orbitals is ~ 3.3 eV or $26,600$ cm^{-1} . Combining the large crystal field splitting and large centroid shift from covalent bonding leads to an energy difference of ~ 4000 cm^{-1} , resulting in the observed yellow emission. Exciting $\text{Y}_3\text{Al}_5\text{O}_{12}:\text{Ce}^{3+}$ (YAG: Ce^{3+}) from the ground state $^2F_{5/2}$ state to the 5d orbitals produces a broad excitation band centered at ~ 460 nm.¹⁷ The broad emission band is centered at 540 nm and is the result of relaxation from the lowest excited 5d state to the two 4f levels in the ground state split by spin-orbit coupling. The compatibility with a blue LED and the yellow emission makes YAG: Ce^{3+} one of the most widely used phosphors in commercial applications. This is further discussed in Section 4.09.7.2.

Despite its discovery almost 50 years ago, researchers are still attempting to improve YAG:Ce³⁺ and tune its emission to be suitable for a myriad of applications. For example, researchers are attempting to improve the red spectral rendering of YAG:Ce³⁺ by incorporating Tb³⁺, Gd³⁺, and even substituting Si-N with the goal of red-shifting the Ce³⁺ emission.⁸⁸ For example, an attempt to red-shift the emission involved replacing Y³⁺ ($r_{8\text{-coordinate}} = 0.90 \text{ \AA}$) with Lu³⁺ ($r_{8\text{-coordinate}} = 0.86 \text{ \AA}$) because the smaller size of Lu³⁺ should result in shorter bond distances that increase the magnitude of crystal field splitting around the activator and red-shift the emission.⁸⁹ Surprisingly, Lu₃Al₅O₁₂ emits bright green, with an emission band centered at 511 nm.⁹⁰ Indeed, it was found that the magnitude of crystal field splitting in Ce³⁺-substituted garnets increases when the radius of the cation on the eight-fold coordinate site *increases* and shifts the emission to longer wavelengths.⁹¹ On the other hand, when the radius of the cations occupying the tetrahedral and octahedral sites increase, the emission wavelength decreases. These trends are due to large local distortions of the eight-fold coordinated site, which greatly influences the crystal field splitting. This fundamental understanding of the YAG:Ce³⁺ crystal chemistry led researchers to substitute the larger La³⁺ ($r_{8\text{-coordinate}} = 1.03 \text{ \AA}$), Gd³⁺ ($r_{8\text{-coordinate}} = 0.94 \text{ \AA}$), and Tb³⁺ ($r_{8\text{-coordinate}} = 0.92 \text{ \AA}$) ions to successfully red-shift the emission, but these derivatives show worse photoluminescent quantum yields and thermal stabilities.

4.09.4.4.2 Silicates

Silicates are crystal structures containing silicon atoms coordinated by oxygen that compose one of the largest classes of naturally abundant minerals. The family of silicate crystal structures are classified by the bonding of the [SiO₄] tetrahedra through the [SiO₄^{4-2x}]_n general formula where $0 \leq x < 2$. Orthosilicates, also known as nesosilicates, are crystal structures composed of isolated SiO₄⁴⁻ tetrahedra ($x = 0$), metasilicate crystal structures contain SiO₃²⁻ groups ($x = 1$), and pyrosilicates contain Si₂O₇⁶⁻ ($x = 0.5$, $n = 2$) groups.⁹² Recent literature is dominated by orthosilicate phosphors due to their tunable emission, allowing them to cover most of the visible spectrum. The most popular orthosilicate crystal structures are M₂SiO₄ and M₃SiO₅, where $M = \text{Ca, Sr, and Ba}$.⁹³ In 1968, Blasse and Barry simultaneously investigated the orthosilicates and other silicates such as M₂MgSi₂O₇ and M₃MgSi₂O₈ as Eu²⁺-substituted phosphors.⁹⁴

M₂SiO₄ crystallizes in different space groups depending on the choice of M -site cation. When $M = \text{Ba}$, the compound will only crystallize in the orthorhombic space group *Pmcn*.⁹⁵ Sr₂SiO₄ has two polymorphs. The first is a low-temperature phase (< 85 °C) where Sr₂SiO₄ crystallizes in the β -type monoclinic *P2₁/n* structure and above 85 °C, Sr₂SiO₄ is isostructural to Ba₂SiO₄. Ca₂SiO₄ is also polymorphic and can crystallize in the γ -type, which has an orthorhombic olivine structure (space group *Pbnm*) and is stable at room temperature, and also forms a metastable room temperature β -phase, which is also isostructural to Ba₂SiO₄.⁹⁶ The M₂SiO₄:Eu²⁺ phosphors emit in the 500–600 nm region upon excitation from 300 to 400 nm, where the emission can be further tuned through solid solutions between the alkaline earth cations. One of the drawbacks of this structure type is that the compound contains two crystallographically independent M sites, one 10-coordinate and one 9-coordinate. As a result, the crystal structure produces a broad emission band that can be observed at low (77 K) temperatures.¹⁷ The photoluminescent quantum yield depends on the choice of M -site cation; Ba₂SiO₄:Eu²⁺ has the highest room-temperature quantum yield of 75%, whereas the Ca and Sr-containing derivatives have a quantum yield of only 30%. The thermal stability of these materials, on the other hand, is quite similar, where the emission intensity is 50% of the room temperature intensity at 150 °C. Interestingly, making a 50:50 solid solution between Sr and Ba, (BaSr)SiO₄:Eu²⁺, improves the thermal stability by retaining 50% of the room temperature emission intensity at 225 °C, making it the most thermally stable of the M₂SiO₄:Eu²⁺ phosphors.

The substitution of Ce³⁺ into the M₂SiO₄ structure results in violet or blue emission, consistent with crystal field splitting around the smaller Ce³⁺.⁹⁷ Interestingly, Ce³⁺-substituted Ca₂SiO₄ in the γ -type polymorph can also exhibit yellow emission ($\lambda_{\text{em}} = 575 \text{ nm}$) under near-UV and blue light excitation. The olivine crystal structure comprises two crystallographically independent, highly distorted [CaO₆] octahedra, where one octahedron has inversion symmetry, and the other possesses mirror symmetry. Cheetham and co-workers proposed that Ce³⁺ substitutes on both [CaO₆] sites where the Ce³⁺ sitting on the site with inversion symmetry produced a yellow emission based on past research that showed this substitution site yielded a larger crystal field splitting in olivine structures.⁹⁶ The second Ce³⁺ with mirror symmetry yields a blue emission that is fully absorbed by the Ce³⁺ ion occupying the inversion symmetry site, resulting in only the yellow emission.

The M₃SiO₅ orthosilicates also crystallize in a different space group depending on the choice of M -site cation. Here, the general trend is that as the M -site cation becomes larger in ionic size, the symmetry of the crystal structure increases where Ca₃SiO₅, Sr₃SiO₅, and Ba₃SiO₅ crystallize in the monoclinic *Cm*, tetragonal *P4/ncc*, and tetragonal *I4/mmm*, respectively.¹⁷ Substituting Eu²⁺ in these materials results in a broad emission peak centered between 500 and 600 nm under 254 nm excitation. Moreover, the emission band can be tuned to higher energy by increasing the size of the alkaline earth cation, following crystal field splitting. Substituting Ce³⁺ in these crystal structures results in a 30 nm red-shifted emission compared to the Eu²⁺ emission.⁶ Unfortunately, Sr₃SiO₅:Ce³⁺ loses 50% of its room-temperature emission intensity by 170 °C.⁹⁸

In the M₂SiO₄ and M₃SiO₅ orthosilicates, the crystal structures contain isolated SiO₄ tetrahedra. The M₂MgSi₂O₇ structures, on the other hand, are composed of corner-connected SiO₄ and MgO₄ tetrahedra. M₂MgSi₂O₇ ($M = \text{Ca and Sr}$) crystallizes in the Åkermanite-type structure, *P42₁m*. Ba₂MgSi₂O₇ crystallizes in the monoclinic *C2/c*. Each crystal structure has only one crystallographic site for rare-earth substitution. Surprisingly, the emission from these orthosilicates deviates from the expected trend where the Ca, Sr, and Ba derivatives emit at 575, 470, and 500 nm, respectively.^{99,100} Preparing a 50:50 solid solution between Sr and Ba, or SrBaMgSi₂O₇, does follow the expected crystal field splitting trends where the emission blue shifts to 440 nm. The photoluminescent quantum yield of these Eu²⁺-substituted phosphors is only 40% at liquid nitrogen temperatures, and the emission becomes

fully quenched by 350 K, indicating poor thermal stability.¹⁰¹ The poor efficiency and thermal stability may be due to the proximity between the excited state $5d$ orbitals and the host conduction band, allowing photoionization to occur.

Finally, $M_3\text{MgSi}_2\text{O}_8$ crystallizes in the trigonal $P\bar{3}$ when $M = \text{Ba}$ and the monoclinic $P2_1/c$ when $M = \text{Sr}$ and Ca .¹⁷ These compounds are still structurally similar as they both contain two-dimensional sheets of SiO_4 and MgO_4 tetrahedra with three M sites that are 6-, 9-, and 10-fold coordinated. These materials have a wide excitation band that spans the UV to near-UV with a maximum near 400 nm. The emission in these compounds follows crystal field splitting trends where $\text{Ba}_3\text{MgSi}_2\text{O}_8:\text{Eu}^{2+}$ emits at 440 nm, and $\text{Ca}_3\text{MgSi}_2\text{O}_8:\text{Eu}^{2+}$ emits at 475 nm. The quantum yields of these phosphors also increase as the average alkaline earth cation size increases, where the 40% efficiency of $\text{Ca}_3\text{MgSi}_2\text{O}_8:\text{Eu}^{2+}$ improves to 80% by full Ba substitution.

4.09.4.4.3 UCr_4C_4 -type materials

The UCr_4C_4 type crystal structures are fascinating structures that follow the $A[\text{B}_2\text{C}_2\text{X}_4]$ and $A[\text{BC}_3\text{X}_4]$ general formulas. This structure type was first investigated by Schnick and co-workers in $\text{Sr}[\text{LiAl}_3\text{N}_4]:\text{Eu}^{2+}$. This phosphor possesses a narrow full width at half maximum of 50 nm (1180 cm^{-1}) despite the presence of two crystallographically independent Sr sites for rare-earth substitution owing to the highly condensed and rigid backbone of $[\text{AlN}_4]$ and $[\text{LiN}_4]$ tetrahedra and the symmetric cuboid environment around the Sr atoms.¹⁰² $\text{Sr}[\text{LiAl}_3\text{N}_4]:\text{Eu}^{2+}$ emits at 649 nm under 440 nm excitation and possesses a photoluminescent quantum yield of 74%. In addition, the phase retains 95% of its room-temperature emission intensity at 500 K. This symmetric eight-fold coordination environment is extremely favorable for narrow emission bands and has inspired the discovery of a number of derivatives including red-emitting $\text{Sr}[\text{Mg}_3\text{SiN}_4]:\text{Eu}^{2+}$ (fwhm = 43 nm, 1170 cm^{-1}),¹⁰³ $M[\text{Mg}_2\text{Al}_2\text{N}_4]:\text{Eu}^{2+}$ ($M = \text{Ca}, \text{Sr}, \text{Ba}$) (fwhm = 1815, 1823, and 2331 cm^{-1} for $M = \text{Ca}, \text{Sr},$ and Ba , respectively), and $\text{Ba}[\text{Mg}_2\text{Ga}_2\text{N}_4]:\text{Eu}^{2+}$ (fwhm = 2168 cm^{-1}).¹⁰⁴ Synthesizing these phases require oxygen and water-free gloveboxes and high temperature and pressure sintering; therefore, researchers have turned to oxide-based UCr_4C_4 phases called alkali lithosilicates. In addition to the easier synthesis, these phases are also more chemically stable than their nitride counterparts. A number of these phases have been reported in the $A[\text{BC}_3\text{X}_4]$ general formula where $A = \text{Rb}, \text{Cs}, \text{K}, \text{Na},$ and Li , $B = \text{Na}$ and Li , $C = \text{Ti}, \text{Ge}, \text{Si}, \text{Al},$ and X is O with either Eu^{2+} or Ce^{3+} substitution.¹⁰⁵ Notable phosphors from this class of materials include $\text{RbNa}_3(\text{Li}_3\text{SiO}_4)_2:\text{Eu}^{2+}$ which has a cyan emission ($\lambda_{\text{em}} = 471\text{ nm}$), an ultra-narrow full width at half maximum of 22.4 nm (980 cm^{-1}), and retains over 96% of the room temperature emission intensity at $150\text{ }^\circ\text{C}$.¹⁰⁶ $\text{CsNa}_2\text{K}(\text{Li}_3\text{SiO}_4)_4:\text{Ce}^{3+}$ has two distinct emission bands at 418 nm and 450 nm with full width at half maxima of 22 and 45 nm, respectively, in addition to zero thermal quenching and impressive chemical stability by retaining 97% of its original photoluminescent intensity after 90 days of exposure to ambient atmosphere.¹⁰⁷

4.09.5 Upconversion materials

4.09.5.1 Mechanisms of upconversion emission

Another class of luminescent materials includes photon up-converting materials. Photon upconversion is a non-linear optical process that produces high-energy photons through the sequential absorption of two or more low-energy photons.¹⁰⁸ Upconverting materials were envisioned by Bloembergen in 1959 due to a need for detecting and counting infrared (IR) photons through the interaction of IR photons with phosphors.¹⁰⁹ Unfortunately, due to a lack of pumping (excitation) sources, the first upconverting material was not developed until 1966 by F. Auzel.¹¹⁰ Advances in lasers and optical technology made it possible to experimentally observe IR to visible photon upconversion in $\text{Er}^{3+}\text{-Yb}^{3+}$ and $\text{Tm}^{3+}\text{-Yb}^{3+}$ systems. Improvements in the synthesis of these phases lead to various advancements, including resistance to photobleaching, wide excitation bands, outstanding penetration depth in biological systems, and less sensitivity to particle size. However, upconverting materials still require improvements in efficiency, color output, and identifying the appropriate energy transfer pathway for the desired emission for specific applications.

There are many mechanisms identified that are either independently or cooperatively involved in the upconversion process. Time-resolved photoluminescence measurements are often conducted to determine which upconversion mechanism is occurring. The first mechanism, shown in Fig. 17A, depicts the most straightforward mechanism known as excited-state absorption (ESA). This mechanism involves multi-step excitation from the ground state to an intermediate state through the sequential absorption of one or more low-energy photons.¹⁰⁸ The photons populate the intermediate state where upconversion occurs. The second pump photon can be absorbed by the absorption cross-section of the excited ion. The ESA process generally occurs at low activator concentration, typically less than 1%, as higher activator concentrations have a higher probability of quenching the up-conversion emission through non-radiative relaxation. However, the drawback to this mechanism is that it occurs in single rare-earth substituted systems, and the efficiency becomes suppressed due to weak absorption from parity-forbidden $4f \leftrightarrow 4f$ transitions.

Another mechanism is energy-transfer upconversion (ETUC). This mechanism is more efficient than ESA because it involves two luminescent centers: an activator and a sensitizer.¹⁰⁸ Here, the sensitizer is excited and emits photons that are subsequently absorbed by the nearest-neighbor activator within a certain photon travel distance, shown in Fig. 17B. Emission from upconversion occurs from the relaxation of the activator to the ground state or a lower excited state.

It may seem counter-intuitive that an energy-transfer mechanism is more efficient than a direct approach like ESA. In this situation, the sensitizer provides access to new excitation wavelengths with reduced efficiency since it is the product of two processes with an efficiency inherently less than 100%. This process's high efficiency depends on the degree of overlap between the emission band of the sensitizer and absorption band of the activator, the activator concentration dependence of the sensitizer emission

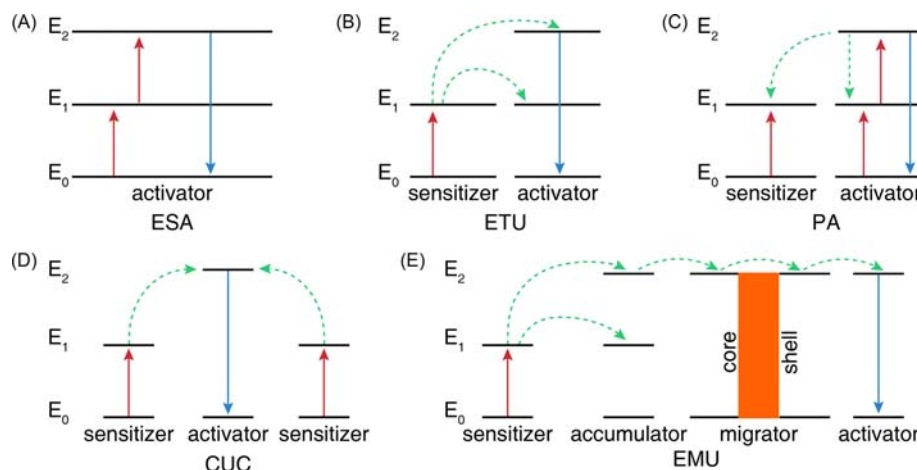


Fig. 17 Upconversion mechanisms of rare-earth substituted materials where E_0 is the ground state, E_1 and E_2 are excited states, ESA is excited-state absorption, ETU is energy-transfer upconversion, PA is photon avalanche, CUC is cooperative upconversion, and EMU is energy migration-mediated up-conversion. Reproduced with permission from Mahata, M. K.; Hofsass, H. C.; Vetter, U., *Photon-Upconverting Materials: Advances and Prospects for Various Emerging Applications*. In *Luminescence—An Outlook on the Phenomena and Their Applications*, InTech: 2016.

spectrum, and the sensitizer lifetime, which is independent of the activator concentration. The probability of energy transfer between two ions at a distance, R , can be determined by these factors. At even more considerable distances (larger R), the resonant radiative transfer may permit long-range energy diffusion. This can lead to photon-trapping effects, increasing the lifetime and ultimately increasing the probability of upconversion. In fact, this process is so efficient that it can be obtained from black-body excitation or spontaneous diode emission before lasers were readily available.

Although useful, ETUC is not the most efficient upconversion process. Photon avalanche (PA) is the most efficient way of producing upconversion emission, and the mechanism is illustrated in Fig. 17C.¹⁰⁸ The photon avalanche process is more complex than the previous two mechanisms as it only occurs after surpassing a specific critical pump density. The pump density must be sufficiently large to populate the immediate energy levels, known as the intermediate reservoir levels, through the non-resonant ground state process. This is followed by excited-state absorption or energy-transfer up-conversion of the excited electron to the up-conversion emitting level. Once in the upconversion energy state, relaxation to the ground state occurs. This causes an increase in the reservoir and upconversion emission energy levels, leading to an “avalanche” effect that generates excited electrons. This feedback loop process explains why the photon avalanche mechanism is the most efficient method to produce upconversion emission.

The cooperative upconversion (CUC) process, illustrated in Fig. 17D, is similar but not as efficient as the energy-transfer upconversion process because it also utilizes an activator and sensitizer. In this process, two adjacent sensitizers populate the upconversion emission level through cooperative energy transfer. This differs from energy transfer upconversion as cooperative upconversion does not have long-lasting intermediate energy levels compatible with the sensitizer. As a result, cooperative upconversion is most commonly observed in systems that have been substituted with Yb^{3+} . Yb^{3+} acts as the cooperative sensitizer, while the sensitizer can be any of the rare-earth ions.

The final mechanism to produce upconversion emission is through energy migration-mediated upconversion (EMMUC). This mechanism, provided in Fig. 17E, was proposed by Liu et al. based on their observation of the energy transfer that occurred in the $\text{NaGdF}_4:\text{Yb}^{3+}, \text{Tm}^{3+}@\text{NaGdF}_4:\text{Ln}^{3+}$ ($\text{Ln} = \text{Tb}^{3+}, \text{Eu}^{3+}, \text{Dy}^{3+}, \text{and Sm}^{3+}$) core-shell nanostructures.¹¹¹ This process is the most complex as it involves four types of luminescent centers: activator, sensitizer, accumulator, and migrator. The sensitizer/accumulator and the activator are separated in separate layers of the core-shell and are connected through the migrator. First, the sensitizer is excited through ground-state absorption, where it transfers its energy to the accumulator. This promotes the accumulator to a higher excited state. The accumulator should reside in energy levels with longer lifetimes to accept the sensitizer’s energy transfer. Next, the energy is shifted from the accumulator to the migrator, followed by energy transfer through the core-shell interface by utilizing the migrators. Finally, the energy is trapped by an activator in the shell and emits the upconversion luminescence during the relaxation process.

4.09.5.2 Familiar upconversion systems

Inorganic upconversion systems may contain multiple activators and produce emission through resonance energy transfer. The choice of activator, however, is crucial and can result in tunable emissive properties. One popular upconversion system capable of a tunable emission is lanthanide-substituted core-shell NaGdF_4 nanoparticles. $\text{NaGdF}_4:\text{Yb}^{3+}, \text{Tm}^{3+}@\text{NaGdF}_4:\text{Eu}^{3+}$ produces upconversion emission from Eu^{3+} upon excitation at 976 nm. In this system, the Yb^{3+} and Tm^{3+} ions in the core act as double sensitizers to promote the Eu^{3+} emission. The Eu^{3+} activator can also be replaced with Tb^{3+} , Dy^{3+} , or Sm^{3+} to tune the emission to the green, yellow, and orange regions of the visible spectrum.¹¹¹ Wang et al. also investigated the effect of varying the

upconversion activator ion and the emitting activator ion. For example, the emission spectrum of $\text{NaYbF}_4@(\text{Na}(\text{Yb}, \text{Gd})\text{F}_4)_n@(\text{NaGdF}_4)_m$ produces a blue or green emission depending on whether Tm^{3+} or Ho^{3+} and Er^{3+} are chosen as the upconverting ions in the inner shell layer. However, if the emitting activator ions Dy^{3+} , Eu^{3+} , or Tb^{3+} are substituted in the outermost shell and Tm^{3+} is utilized as the upconverting ion in the inner shell, the emission can be tuned in the green to red region of the visible spectrum by extracting energy from the UV emission of Tm^{3+} .¹¹² It is important to note, there have been no other examples of effective energy migration in other lanthanide-substituted upconversion nanoparticles.

The presence of multiple activators in upconverting systems means the color purity of the emission is often low. $\text{NaYF}_4: \text{Yb}^{3+}, \text{Er}^{3+}$ is one of the most popular upconverting systems. NaYF_4 can exist as one of two polymorphs, a metastable, high-temperature cubic phase or the thermodynamically stable low-temperature hexagonal phase. The hexagonal polymorph typically shows higher upconversion emission efficiency than the cubic phase. Hexagonal $\text{NaYF}_4: \text{Yb}^{3+}, \text{Er}^{3+}$ typically shows multiple narrow emission lines in the red and green region of the visible spectrum.¹¹³ This emission is not ideal for many applications such as anti-counterfeiting, color display, and bioimaging, where a high color purity emission is desired. One solution to enhance color purity is through manipulating the chemical composition of the host. For example, $\text{KMnF}_3: \text{Yb}^{3+}, \text{Er}^{3+}$ yields pure red emission at 660 nm because the Mn^{2+} ions quench the green Yb^{3+} emission. In addition, the Mn^{2+} emission can transfer its energy to the Er^{3+} excited state to promote the production of the red emission.¹¹⁴ Substituting Mn^{2+} in $\text{NaYF}_4: \text{Yb}^{3+}, \text{Er}^{3+}$ yields a similar result of enhanced red emission.¹¹⁵ Another popular red-emitting upconversion material is $\text{Na}_3\text{ZrF}_7: \text{Yb}^{3+}, \text{Er}^{3+}$ which is reported to have five times the upconversion emission intensity of $\text{NaYF}_4: \text{Yb}^{3+}, \text{Er}^{3+}$ which was attributed to the formation of lanthanide-lanthanide clusters in the nanoparticles. This shortened distance between the activators increases the probability of cross-relaxation to promote the quenching and energy transfer of the green Yb^{3+} emission to Er^{3+} .¹¹⁶

4.09.6 The role of defects and the rise of persistent luminescence

The radiative recombination time, or luminescence lifetime, of Ce^{3+} is typically on the order of ~ 10 – 100 ns, whereas Eu^{2+} phosphors decay on the order of microseconds due to the larger degeneracy of the excited state. However, some phosphors exhibit a unique optical response where the radiative relaxation occurs on a time scale exceeding the typical decay times. This anomalous radiative decay can last anywhere from seconds to days and is often referred to in the literature as persistence luminescence, afterglow, or long-lasting phosphorescence.

The prototypical use of persistent luminescence materials is in modern glow-in-the-dark toys, which typically utilize $\text{SrAl}_2\text{O}_4:\text{Eu}^{2+}$. SrAl_2O_4 crystallizes in the monoclinic space group $P2_1$ and is composed of $[\text{AlO}_4]$ tetrahedra that form a corner connected three-dimensional backbone with two crystallographically independent octahedrally coordinated Sr^{2+} atoms.¹¹⁷ The substitution of Eu^{2+} produces a broad emission peak composed of two distinct emissions. The first emission is centered at 450 nm, but is thermally quenched at 150 K. The second and far more dominant emission, is centered at 520 nm, and produces the characteristic green emission.¹¹⁸ When exposed to UV to blue light, $\text{SrAl}_2\text{O}_4:\text{Eu}^{2+}$ can emit for ≈ 70 min.¹¹⁹ Interestingly, the addition of a second activator, notably Dy^{3+} , can push the lifetime to 30 h.¹²⁰ While many proposed mechanisms attempt to rationalize the observation of persistent luminescence, each mechanism agrees that some form of electron trapping/de-trapping gives rise to the optical phenomenon.

The earliest proposed mechanism for persistent luminescence was by Matsuzawa based on his observations of the famous $\text{SrAl}_2\text{O}_4:\text{Eu}^{2+}$.¹²⁰ This mechanism, illustrated in Fig. 18A, proposed that electron trap states and charge carrier holes arose from lattice defects. Photoconductivity measurements suggested that Sr^{2+} vacancies in $\text{SrAl}_2\text{O}_4:\text{Eu}^{2+}$ acted as hole donors. The hypothesis that electron holes would act as the primary charge carrier was further supported through additional photoconductivity measurements on $\text{SrAl}_2\text{O}_4:\text{Eu}^{2+}, \text{Dy}^{3+}$. Matsuzawa suggested that when Dy^{3+} is co-substituted with Eu^{2+} in SrAl_2O_4 , the Eu^{2+} is reduced to Eu^+ when an electron from Eu^{2+} is promoted to the $5d$ orbitals. This causes Dy^{3+} to oxidize to Dy^{4+} since the resulting hole is carried through the valence band of the Dy^{3+} $4f$ orbitals. The Dy^{4+} oxidation state was accepted due to the presence of Nd^{4+} in fluoride phosphors.¹²¹ Applying thermal energy causes electron-hole recombination to occur where the electron is released from its trap state and recombines with Eu^+ to produce Eu^{2+} and a photon. This model was believed to have been experimentally validated through thermoluminescence and photoconductivity measurements and, as a result, was accepted for many years. However, recent investigations into the oxidation states of Eu^{2+} and Dy^{3+} using X-ray absorption spectroscopy (XAS) and electron paramagnetic resonance spectroscopy (EPR) have not provided any evidence of Eu^{2+} reduction or Dy^{3+} oxidation.

The main drawback of this model was that Matsuzawa could not explain how $\text{SrAl}_2\text{O}_4:\text{Eu}^{2+}$ exhibited a long luminescence lifetime without a co-activator. To further investigate the validity of Matsuzawa's proposed mechanism, the lanthanide energy levels of many well-known phosphors were calculated to establish localized activator energy levels. It was found that the Eu^{2+} $4f$ orbitals were not energetically favorable to act as a charge carrier hole since the Dy^{3+} $4f$ orbitals lay just below the valence band. Using this new information, Dorenbos proposed another mechanism (Fig. 18B).¹²² It was proposed that an electron may be photoionized into the conduction band where the co-dopant can trap the electron. This would cause Eu^{2+} to oxidize and the co-activator to become reduced, which is the opposite of the Matsuzawa model.¹²⁴ This model successfully verifies the location of the Eu^{2+} $5d$ orbitals but unfortunately failed to explain the presence of trap states in a system with a single activator.

Clabau provided further understanding of these materials by considered persistent luminescence in the absence of a co-activator. This mechanism was based on the results of EPR on $\text{SrAl}_2\text{O}_4:\text{Eu}^{2+}$ upon continuous UV excitation.¹²³ The EPR measurement revealed that Eu^{2+} may be oxidized and can independently partake in the electron trapping and de-trapping process. Clabau placed

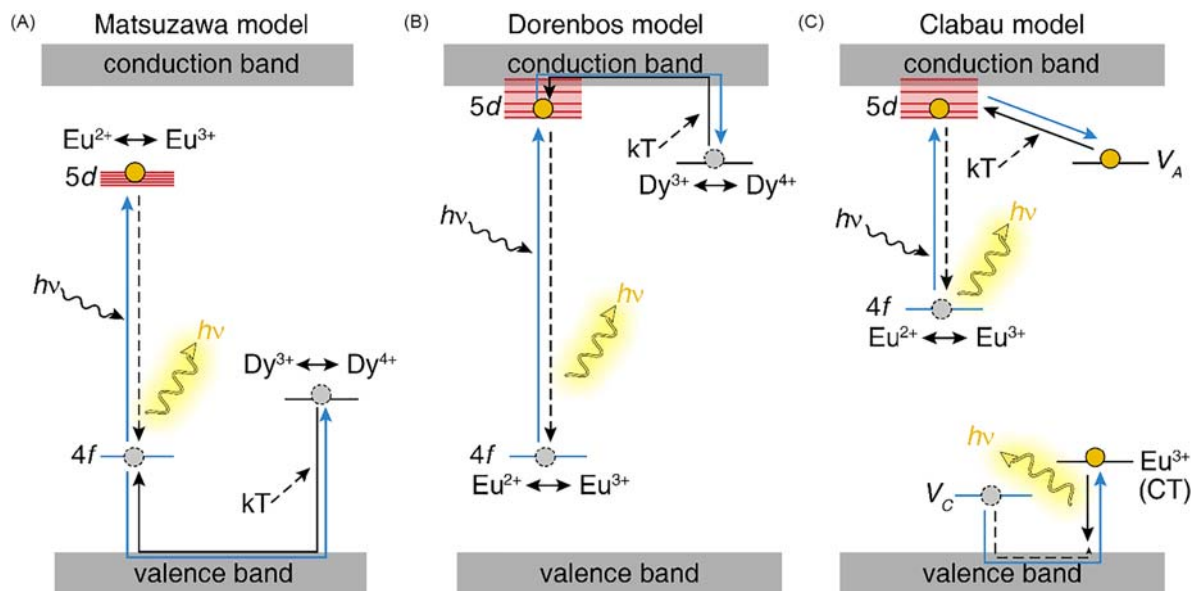


Fig. 18 (A) Schematic representing the mechanism of persistent luminescence proposed by Matsuzawa where an electron from Eu^{2+} is excited from the $4f$ to the $5d$ orbitals. The resulting hole is conducted through the valence band and is trapped by a $4f$ orbital of Dy^{3+} . Thermal energy, kT , releases the hole where it recombines with the relaxed electron to form a photon.¹²⁰ (B) Dorenbos proposed that the excited electron from Eu^{2+} is photoionized into the conduction band where it remains trapped in the $5d$ orbital of the rare-earth (in this case, Dy^{3+}) co-activator. Thermal energy releases the electron where it recombines with the hole that remained in the $4f$ orbital to produce a photon.¹²² (C) Clabau suggested that the excited electron from Eu^{2+} becomes trapped in an anion vacancy (V_A) and the hole remains in the $4f$ orbital. Thermal energy releases the electron where it recombines with the hole to produce a photon. A different electron from Eu^{3+} is excited through charge transfer (CT) and its hole trapped in a cation vacancy (V_C). Charge transfer releases the hole and it recombines with the electron to produce a photon.¹²³ Excitation and trapping are blue lines, thermal release and relaxation are black lines. Electrons are yellow circles, and holes are gray circles. Modified from Finley, E. *Structure-Composition Relationships and Their Influence on Long Luminescent Lifetimes in Persistent Luminescent Phosphor*. Houston, TX: University of Houston, 2019.

the Eu^{2+} $5d$ orbitals near the bottom of the conduction band in his model, similar to the Dorenbos model. The approach of Clabau differs from the Dorenbos model by suggesting that an electron from Eu^{2+} may be excited, not photoionized, into the conduction band, and the presence of Eu^{3+} arises from the failure to fully reduce Eu^{2+} during synthesis. The Eu^{3+} also participates in the trapping and de-trapping through charge transfer to emit photons (Fig. 18C). This suggests that the second, low-temperature emission peak observed in $\text{SrAl}_2\text{O}_4:\text{Eu}^{2+}$, centered at 450 nm, arises from the recombination of a Eu^{3+} hole trapped by a cation (Sr^{2+}) vacancy. Simultaneously, an electron from Eu^{2+} is trapped and released from an anion vacancy, resulting in the dominant emission peak centered at 520 nm. Unfortunately, extensive crystallographic studies have confirmed that the second, low-temperature emission peak arises from $\text{SrAl}_2\text{O}_4:\text{Eu}^{2+}$ having two crystallographically independent Sr^{2+} sites. The Clabau model successfully constructed a mechanism that involves a second activator by showing the influential role of lattice defects on persistent luminescence.

More recently, density functional theory calculations have provided more clarity on the energetics driving the formation of vacancies in these systems. Calculations by Qu et al. show that cation and anion vacancies form simultaneously in $\text{CaAl}_2\text{O}_4:\text{Eu}^{2+}$, Nd^{3+} .¹²⁵ The oxygen vacancies form close to the bottom of the conduction band and act as trap states, whereas the calcium vacancies lie close to the top of the valence band, which is consistent with EPR measurements. These cation vacancies observed in $\text{CaAl}_2\text{O}_4:\text{Eu}^{2+}$, Nd^{3+} are likely occurring in $\text{SrAl}_2\text{O}_4:\text{Eu}^{2+}$, Dy^{3+} , which was observed in photoconductivity experiments. Ultimately, the *ab initio* calculations were able to show that the oxygen vacancies and co-activator $5d$ orbitals form near the bottom of the conduction band and possess the appropriate energies to act as electron traps. The cation vacancies are not energetically favored to act as trap states but rather stabilized the anionic vacancies. If a co-activator is in a system, it may act as an electron trap and an electron donor.

It is now clear that trap states control the ability to produce a long luminescent lifetime in a persistent luminescent phosphor. The depopulation of these trap states at room temperature is dependent upon the trap state and host structure. Depopulation of a trap state requires a certain amount of energy, known as the activation energy or trap depth.¹¹⁷ Shallow traps, which have activation energy less than 0.4 eV from the bottom of the conduction band depopulate immediately at room temperature. In contrast, deeper traps with energies greater than 1.0 eV require more energy than available at room temperature and remain trapped indefinitely. As a result, the ideal trap depth is at 0.65 eV.¹²⁶ Extensive research has been done to classify these trap states as either Schottky defects, which are unoccupied cationic or anionic sites, Frenkel defects, in which an atom occupies an interstitial site, leaving a vacancy, or an anti-site defect, where two atoms of different type exchange sites. Computational studies were able to show that Schottky defects are the most energetically favorable and that these Schottky defect sites have favorable activation energies with respect to the conduction band minimum.

4.09.7 Application of rare-earth and transition metal substituted phosphors

Rare-earth and transition metal-substituted phosphors are used in a variety of applications such as general and display lighting, medical imaging, and temperature sensing, among others. Optical properties such as excitation and emission maximum, quantum efficiency, thermal stability, and lifetime dictate which application a luminescent material is appropriate for. It should be noted that a plethora of both rare-earth and transition metal-substituted phosphors can be used in each application, but for brevity, we will highlight some of the most famous phosphors used in diverse applications that we interact with on a daily basis.

4.09.7.1 Phosphors for LED-based white lighting

The development of the first efficient blue LED brought upon white light-emitting devices by coupling the LED with $\text{Y}_3\text{Al}_5\text{O}_{12}:\text{Ce}^{3+}$ (YAG: Ce^{3+}), which is the technology that can now be found in smartphone flashlights, car headlights, and LED light bulbs. YAG: Ce^{3+} is used in most devices due to its impressive (>90%) photoluminescent quantum yield and its ability to retain 50% of its room temperature emission intensity up to 550 K.⁹¹ Nevertheless, these devices were classically known to have a high correlated color temperature (CCT \approx 5000 K) with a low general color rendering index, $R_a > 70$, meaning the light has a blue hue that appears harsh to the eye. This similar problem plagued fluorescent lighting. The correlated color temperature of these lights can be lowered by adding a second, red-emitting phosphor such as $\text{Sr}_2\text{Si}_5\text{N}_8:\text{Eu}^{2+}$.¹²⁷ This material crystallizes in the orthorhombic $Pmn2_1$ and is composed of corner connected Si_3N_4 tetrahedra with 8-coordinate Sr atoms in the voids. The red emission is due to large crystal field splitting and a strong nephelauxetic effect from the nitrogen coordination. $\text{Sr}_2\text{Si}_5\text{N}_8:\text{Eu}^{2+}$ has a broad excitation band centered at 450 nm, indicating good compatibility with blue LEDs, and 86% of the emission intensity is retained at 150 °C, the temperature regarded as the maximum operating temperature of LED light bulbs.¹²⁸ The addition of a red-emitter improves the general color rendering index, R_a , of these devices from 63 to \approx 72, but offers limited color tunability.^{128,129} Color tunability is more readily achieved through the addition of an explicit green-emitter. Substituting Y^{3+} for Lu^{3+} in $\text{Y}_3\text{Al}_5\text{O}_{12}:\text{Ce}^{3+}$ results in bright green emission upon blue light excitation. The green emission band from $\text{Lu}_3\text{Al}_5\text{O}_{12}:\text{Ce}^{3+}$, centered at \approx 550 nm, is very broad and covers the region from 500 to 750 nm, making it suitable for full coverage of the visible spectrum in the production of white light. Increasing the Ce^{3+} concentration causes a red-shift in the emission spectrum, so the emission can be tuned from the green to yellow region of the visible spectrum. In addition, $\text{Lu}_3\text{Al}_5\text{O}_{12}:\text{Ce}^{3+}$ retains over 85% of its room temperature emission intensity up to 250 K, making it compatible with LEDs that generate heat during operation.¹³⁰ In addition, the emission peak does not drastically shift, indicating excellent chromatic stability. Utilizing both $\text{Lu}_3\text{Al}_5\text{O}_{12}:\text{Ce}^{3+}$ and $\text{Sr}_2\text{Si}_5\text{N}_8:\text{Eu}^{2+}$ in a device yields a $R_a > 80$ while improving the overall gamut of available colors.

Another strategy to improve the color tunability and color rendering index of lighting devices is to utilize a UV or near-UV LED ($\lambda_{\text{em}} = 365\text{--}400$ nm) and red, green, and blue-emitting phosphors. This approach has the added advantage of covering the UV to the blue region, which is lost when using a blue LED. The aforementioned green and red-emitting phosphors can be utilized with UV and near-UV LEDs. The most famous blue emitter for UV LED-driven devices is $\text{BaMgAl}_{10}\text{O}_{17}:\text{Eu}^{2+}$. While this phosphor has been historically used in plasma display devices, years of optimization have improved the UV and near-UV absorption to yield photoluminescent quantum yields nearing 100% under 365 nm excitation and 90% 400 nm excitation. In addition, commercially produced $\text{BaMgAl}_{10}\text{O}_{17}:\text{Eu}^{2+}$ has a thermally robust emission with excellent chemical stability.⁷⁹ Prototype devices containing a phosphor blend of $\text{BaMgAl}_{10}\text{O}_{17}:\text{Eu}^{2+}$, $\text{Lu}_3\text{Al}_5\text{O}_{12}:\text{Ce}^{3+}$, and $\text{Sr}_2\text{Si}_5\text{N}_8:\text{Eu}^{2+}$ can produce a cold white light that can be tuned to a warm white light by manipulating the ratio of each luminescent material. These devices tend to have a $R_a > 90$. Unfortunately, these devices have not been widely commercialized due to the higher cost of UV and near-UV LEDs compared to blue-emitting LEDs.

The many advantages of LED lighting, including affordable cost, wide material availability, and long lifespans, have helped them gain a significant share of the commercial and residential lighting sector. Unfortunately, the reliance on blue LEDs ($\lambda_{\text{em}} = 450$ nm) as the excitation source in these devices overstimulates human's intrinsic photosensitive retinal ganglion cells, which overproduces dopamine and suppresses melatonin production. This has been shown to cause macular degeneration, cataract formation, mood disorders, and circadian disruption.¹³¹ Therefore, switching to violet LEDs ($\lambda_{\text{em}} = 405$ nm) to create "human-centric" lighting is one approach that minimizes blue light exposure at nighttime to reduce melatonin suppression.¹³² Devices utilizing violet LEDs have been reported to have higher color rendering indexes and luminous efficacies.¹³³ The most straightforward way to produce a human-centric light is to identify a yellow-emitting phosphor that can be efficiently excited by a violet LED rather than a blue LED to produce white light. $(\text{Ca}_{1-x-y}\text{Sr}_x\text{Eu}_y)_7(\text{SiO}_3)_6\text{Cl}_2$ fulfills this need by producing a bright yellow emission centered at 580 nm upon 400 nm excitation.¹³⁴ The crystal structure contains two crystallographically independent sites for rare-earth substitution. Eu^{2+} can substitute onto the $M(1)$ site, which is coordinated by seven oxygen atoms and one chlorine atom to produce a blue emission. Yellow emission is obtained when Eu^{2+} is substituted onto the $M(2)$ site which is asymmetrically coordinated by a single bridging and four non-bridging oxygen ions and two chlorine ions which gives rise to a large crystal field splitting. Increasing the Ca content in the crystal structure changes the local structure around the $M(2)$ site causing a red-shift of the emission where the yellow emission dominates. $(\text{Ca}_{0.37}\text{Sr}_{0.53}\text{Eu}_{0.10})_7(\text{SiO}_3)_6\text{Cl}_2$ possess an impressive 91% photoluminescent quantum yield and retains 75% of its emission intensity at 423 K. Most importantly, fabricating a prototype LED light bulb utilizing a violet LED, blue-emitting $(\text{Ca,Sr})_5(\text{PO}_4)_3\text{Cl}:\text{Eu}^{2+}$ and yellow-emitting $(\text{Ca}_{0.37}\text{Sr}_{0.53}\text{Eu}_{0.10})_7(\text{SiO}_3)_6\text{Cl}_2$ produces a white light with less blue light intensity. Additionally, the device retains 96% of its emission intensity after 3000 h of operation and the correlated color temperature of the light can be tuned from 3010 to 5070 K by varying the fraction of Ca within the host crystal structure.¹³⁴ The lack

of a red spectral component, however, will still hinder the color rendering of the device. Therefore, a device can also be constructed using a violet LED and blue-, green-, and red-emitting phosphors. While many green-, yellow-, and red-emitting materials are highly efficient under 405 nm excitation, there is a noticeable gap of blue phosphors with this capability due to the short Stokes shift required. $\text{Na}_2\text{MgPO}_4\text{:Eu}^{2+}$ is a new blue-emitting phosphor that has been reported with 70% quantum yield under 405 nm excitation, zero thermal quenching, and moderate chemical stability in high moisture environments.⁷⁹ Fabricating a prototype LED light bulb resulted in a device with a correlated color temperature of ≈ 2700 K and an Ra of 93. Comparing this device to a commercial "Soft White" Sylvania light bulb, which uses a blue LED, revealed a similar correlated color temperature but a poor Ra of 83. In addition, the commercial bulb had significantly higher blue light intensity than the violet LED device, meaning melatonin suppression will not be significantly disrupted using a violet LED. Therefore, the future of LED lighting consists of human-centric light that can be produced by utilizing violet LEDs and compatible blue-emitting phosphors such as $\text{Na}_2\text{MgPO}_4\text{:Eu}^{2+}$.

4.09.7.2 Phosphors for display panels

Luminescent phosphors are also used in display panels to produce color images. The first color cathode ray tube television display screens were developed in the 1960s after researchers found that the materials like Zn_2SiO_4 and CaWO_4 produced luminescence in a gas discharge environment. The resulting televisions used the semi-conducting ZnS host crystal structure substituted with different activators to produce blue, green, and red emissions.¹³⁵ Substituting Ag^+ in ZnS generated a blue emission reported to have an efficiency of 21–25%. Substituting Cd^{2+} for Zn^{2+} in ZnS shifted the emission to the red region of the visible spectrum. $(\text{Zn}, \text{Cd})\text{S}:\text{Ag}^+$ produced a broad emission band centered at ≈ 675 nm and was quickly replaced with Eu^{3+} -substituted phosphors once it was determined a narrow line emission would be more beneficial for color rendering. Substituting Cu^+ and Al^{3+} instead in $(\text{Zn}, \text{Cd})\text{S}$ resulted in a green emission that could be tuned from 530 nm to 560 nm by varying the Zn:Cu ratio. The combination of these three phosphors produced a functional picture in the first cathode ray tube television, but they quickly became antiquated upon the transition to rare-earth and transition metal luminescent phosphors in 1972.²

The switch to flat panel displays was driven by the rise of rare-earth and transition metal luminescent phosphors that could be excited by plasma-based technologies. These panels were made up of millions of cells containing a mixture of Xe and Ne gas that generate a plasma. The Xe and Ne gas plasma discharge is used to generate vacuum ultraviolet radiation used as the excitation source for red, green, and blue-emitting phosphors coated on the surface of the cells. In general, plasma display panels required luminescent materials that perform this visible-light conversion process efficiently, can withstand constant exposure to vacuum ultraviolet radiation, and are thermally robust to the heat treatment used during panel processing. Generally, plasma display panels utilized $\text{BaMgAl}_{10}\text{O}_{17}:\text{Eu}^{2+}$ as the blue emitter, $\text{ZnSiO}_4:\text{Mn}^{2+}$ as the green emitter, and $(\text{Y}, \text{Gd})\text{BO}_3:\text{Eu}^{3+}$ as the red emitter. Under vacuum ultraviolet excitation ($\lambda_{\text{ex}} = 147$ nm), the emission spectra of these phosphors consisted of two broad band peaks, one at 450 nm from the $4f^65d^1$ to $4f^7$ transition in Eu^{2+} in $\text{BaMgAl}_{10}\text{O}_{17}$, and the second centered at 525 nm originating from the ${}^4\text{T}_1 \rightarrow {}^6\text{A}_1$ transition from Mn^{2+} in ZnSiO_4 . The emission spectrum from $(\text{Y}, \text{Gd})\text{BO}_3:\text{Eu}^{3+}$ consisted of three sharp lines at 595 nm (${}^5\text{D}_0 \rightarrow {}^7\text{F}_1$), 611 nm (${}^5\text{D}_0 \rightarrow {}^7\text{F}_2$), and 626 nm (${}^5\text{D}_0 \rightarrow {}^7\text{F}_2$).¹³⁶ $\text{BaMgAl}_{10}\text{O}_{17}:\text{Eu}^{2+}$ was the most unstable phosphor among the three used in plasma display panels. The blue emission degraded drastically due to oxidation of the rare-earth under prolonged use and the intercalation of water into the host crystal structure during panel processing, which resulted in a loss of efficiency and color purity. Despite these drawbacks, $\text{BaMgAl}_{10}\text{O}_{17}:\text{Eu}^{2+}$ was 1.5 times more efficient than $\text{Y}_2\text{SiO}_5:\text{Ce}^{3+}$ and had better chromaticity and efficiency under vacuum ultraviolet excitation compared to $\text{CaWO}_4:\text{Pb}^{2+}$ and $\text{Y}_2\text{SiO}_5:\text{Ce}^{3+}$, making it widely used as the blue-emitter in plasma display lighting.¹³⁷ The green-emitting $\text{ZnSiO}_4:\text{Mn}^{2+}$ was far more stable in plasma display panels than $\text{BaMgAl}_{10}\text{O}_{17}:\text{Eu}^{2+}$, but it suffered from emission degradation through ion bombardment but not in the same magnitude as the blue-emitter. The main drawback of this material was the long decay time from the ${}^4\text{T}_1 \rightarrow {}^6\text{A}_1$ transition. It was found that substituting a small percentage of Ba^{2+} in the host crystal structure can decrease the decay time from 17 to 10 ms, but this decrease was accompanied by a 20% drop in emission efficiency.¹³⁶ Tb^{3+} -activated lanthanide phosphates were also considered as the green emitter in plasma displays. $\text{YPO}_4:\text{Tb}^{3+}$ and $(\text{Gd}_{0.74}\text{Y}_{0.11})\text{P}_{1.15}\text{O}_8:\text{Tb}^{3+}$ were brighter and had shorter decay times than $\text{ZnSiO}_4:\text{Mn}^{2+}$, but poorer color purity.^{138,139} Red-emitting $(\text{Y}, \text{Gd})\text{BO}_3:\text{Eu}^{3+}$ possessed high efficiency under vacuum ultraviolet excitation and remained unaffected from the heat treatment in panel processing. Unfortunately, the strong orange emission from the ${}^5\text{D}_0 \rightarrow {}^7\text{F}_1$ transition resulted in subpar color purity and required a filter to remove this emission. This dramatically reduced the light output from this phosphor. To counteract this, research focused on improving the quantum efficiency of the phosphor. Successful techniques include co-substituting $(\text{Y}, \text{Gd})\text{BO}_3:\text{Eu}^{3+}$ with Bi^{3+} to enhance absorption in the ultraviolet region or by incorporating Lu^{3+} into the host crystal structure.¹⁴⁰ Plasma display technology dominated the market from 1980 to the early 2000s, with extensive research being conducted to improve the stability and efficiency of these phosphors. However, plasma displays have become obsolete with the advent of low-cost liquid crystal, LED displays, OLED, and most recently, QLED displays, which provide higher color quality and resolution.

Modern LED displays require luminescent materials with specific optical properties to meet the industrial demand. The reproducibility of the color of an object, for example, should be high. The color reproducibility is directly impacted by the gamut available in the device, as the color gamut represents all available colors in a display device. The required color gamut is regulated through national standards such as the Advanced Television System Committee (ATSC) utilized in North America, Integrated Services Digital Broadcasting (ISDB-T) used in South America, and Digital Terrestrial Multimedia Broadcast (DVB-T) used in much of Europe, Africa, and Asia, among others. The goal is to maximize the available color gamut of a device to access the widest range of colors. This is most easily done by utilizing narrow, highly saturated red, green, and blue-emitters in the display device. The

blue-emitter commonly used in displays is a blue LED, which gives rise to the name of an LED display. Not only does the LED act as the blue emitter, but it also acts as the excitation source for the green and red-emitters. The most popular green-emitting phosphor for display applications is β -SiAlON:Eu²⁺. β -SiAlON is a structural derivative of Si₃N₄, which is a precursor often used to synthesize oxynitride and nitride phosphors. This phase crystallizes in the hexagonal $P6_3$ or $P6_3/m$ space group. The structure is composed of continuous channels of (Si/Al)N₄ tetrahedra along the c direction, and the Eu²⁺ atoms sit in the voids present in the crystal structure. This phosphor produces an intense green emission centered at 538 nm upon blue light excitation. The phosphor is thermally robust, has a photoluminescent quantum yield approaching 100%, and is the narrowest commercial green phosphor available today after approximately 20 years of optimization. Finally, the choice of red-emitter is crucial as the emission should occur solely in the visible region, as near-IR emission can significantly hinder the color rendering index and gamut. As a result, the U. S. Department of Energy had set the goal of developing a red-emitter, from 615 nm to 635 nm, with a narrow emission (< 40 nm). The most popular phosphor that meets these requirements is K₂SiF₆:Mn⁴⁺ (KSF:Mn⁴⁺). K₂SiF₆ crystallizes in the cubic $Fm\bar{3}m$ and is composed of [SiF₆] octahedra and [KF₁₂] cuboctahedra. KSF:Mn⁴⁺ has a narrow line emission at 630 nm with a full width at half maximum of 30 nm and is highly efficient due to its strong absorption of blue light. The added advantages of KSF:Mn⁴⁺ over more traditional red-emitting nitride phosphors include that this phosphor emits purely in the red region as the emission does not overlap in the orange or near-IR region of the visible spectrum, and secondly, the phosphor does not absorb past 510 nm, meaning there is no absorption of green emission or self-absorption.¹⁴¹ Most importantly, these luminescent materials have highly saturated color coordinates, meaning the color gamut created from these devices is large and can cover upwards of 70% of the desired color gamut.¹⁴² The future of television will always look towards expanding the available display color gamut, meaning research on the discovery of viable ultra-narrow emitting luminescent materials will continue to be a dominating field in materials science and chemistry.

4.09.7.3 Phosphors for promoting plant growth

The color tunability of LED lights allows these devices to be used in numerous applications beyond traditional display and indoor lighting. LED light bulbs have also been used to facilitate indoor plant growth by tuning the emission wavelength and intensity of the light to the photoreceptors in plants that control photosynthesis and flowering. It has been found that blue light (410–500 nm) influences chlorophyll production, leaf morphogenesis, flower-bud formation, stomatal opening, and phototropism, red light (610–700 nm) may improve vegetative flowering, budding, and intermodal elongation, and near-infrared light (720 nm) promotes plant growth and photosynthesis.¹⁴³

Co-substituting Mn²⁺ in blue-emitting phosphors with an octahedral substitution site may produce dual blue and red-emitting phosphors for promoting plant growth. For example, NaSrPO₄ crystallizes in $P\bar{3}m1$ and is composed of face sharing [NaO₆], [SrO₁₂], and [(Na/Sr)O₁₀] polyhedra units. Substituting Eu²⁺ produces a broad emission band from 400 to 650 nm ($\lambda_{\text{ex}} = 365$ nm) that can be deconvoluted into two Gaussian peaks centered at approximately 450 and 500 nm. These peaks overlap nicely with the photoreceptors that control chlorophyll production. The two bands arise from the substitution of Eu²⁺ on both Sr²⁺ sites. NaSrPO₄:Eu²⁺ has a moderate quantum yield of $\approx 34\%$ and retains 95% of room temperature emission intensity at 150 °C under UV excitation, making it a good candidate for Mn²⁺ substitution on the octahedral site to produce a dual-emitting phosphor.^{144,145} Choi et al. successfully synthesized NaSr_{0.5}Ba_{0.5}PO₄:Eu²⁺, Mn²⁺, which has a broad excitation band from 200 to 400 nm and an emission band with two distinct emission peaks located at 450 nm from the $4f^65d^1$ to $4f^7$ transition in Eu²⁺ and 600 nm from the ⁴T₁ to ⁶A₁ transition in Mn²⁺. The addition of the Mn²⁺ has a negligible effect on the thermal stability of the phosphor. This material possessed the required optical properties to promote plant growth, so Choi et al. fabricated a prototype LED-drive light to test its effect on the growth of oats and onions. The experiment consisted of exposing plants to sunlight only and the second set of plants to sunlight during the day and the prototype LED light at night. It was found that both the onions and oats with the continual light simulation experienced germination faster, allowing them to grow more quickly. In addition, the prototype appeared to enhance photosynthesis in oats since the oats grew taller and seemed greener than the control group. Therefore, using phosphor-converted LED lights that overlap with the photoreceptors in plants effectively improves crop yields and facilitates growth in areas with poor light.

4.09.7.4 Upconversion materials for temperature sensing

Upconversion materials have been commonly used in solid-state lasers,^{146–148} three-dimensional flat panel displays,¹⁴⁹ and wavelength amplification,^{150,151} as well as temperature sensing and fluorescence imaging. Fluorescence imaging is a widespread technique for biological and medical applications due to its high image resolution. Conventional fluorescence imaging typically utilizes down-conversion luminescent materials, i.e., phosphors, to convert high-energy radiation into visible light. Unfortunately, the high-energy excitation light required for down-conversion phosphors has been reported to damage DNA and cause cell death from long-term irradiation.¹⁵² In addition, these excitation wavelengths can readily excite biological tissue, which, in combination with low penetration depths, causes low signal-to-noise ratios. Upconversion materials are better suited for fluorescence imaging because they are excited by infra-red wavelengths that cannot excite the tissue in the body, meaning higher resolution images can be obtained by minimizing auto-fluorescence. In addition, upconversion materials are resistant to photobleaching and have excellent photostability. The upconversion materials must be synthesized as nanoparticles and be biologically compatible to be

used in imaging applications. Recently, $\text{NaYF}_3: \text{Yb}^{3+}, \text{Er}^{3+}$ nanoparticles were synthesized and coated with polyethyleneimine, a thermally stable and hydrophilic polymer that makes the nanoparticles soluble in water and buffers for in vivo imaging and can be used to conjugate biomolecules to the nanoparticles.¹⁵² The coated nanoparticles were injected intradermally and intramuscularly into the tissue of rats at various penetration depths and showed intense red ($\lambda_{\text{em}} = 653 \text{ nm}$) and green ($\lambda_{\text{em}} = 540 \text{ nm}$) emission with narrow full width at half maxima of 24 nm and 16 nm, respectively, when exposed to the NIR laser. Moreover, nanoparticle concentrations of $1 \mu\text{g}/\text{mL}^{-1}$ did not affect cell viability after 48 h, and increasing the concentration to $25 \mu\text{g}/\text{mL}^{-1}$ caused cell viability to remain above 90%. The nanoparticles were also found to be non-toxic to bone marrow cells, where no significant increase in cell death was observed after an incubation period of 5 days. Most importantly, the nanoparticles were undetectable in the rats 7 days after injection.

Upconversion materials have also been applied in the field of temperature sensing. Temperature sensing is widely used in many industries, including meteorology, aerodynamics, medicine, military technology, and in our daily lives as air conditioning and refrigeration.¹⁵³ Instead of more conventional thermometers, such as those based on thermal expansion and the Seebeck coefficient, upconversion materials can also be used as optical thermometric sensors. These materials rely on the temperature dependence of upconversion materials and allow for contactless measurement and large-scale imaging, which is helpful in medical applications that require sterile environments. There are three methods of temperature sensing based on changes in fluorescence intensity, changes in fluorescence decay lifetime, and the differences in fluorescence intensity of two activators' emission bands with different responses to temperature. The fluorescence intensity ratio method of temperature sensing is widely regarded as the most promising because it reduces the dependence on measurement conditions.¹⁵⁴ Upconversion materials are popular for this method of temperature sensing since the most efficient upconversion materials contain two rare-earths, one as an activator and one as a sensitizer. Typically, Er^{3+} and Yb^{3+} co-substituted upconverting materials are used in temperature sensing because Yb^{3+} strongly absorbs at 980 nm and transfers this energy to Er^{3+} to produce intense green emission bands from the $^2\text{H}_{11/2} \rightarrow ^4\text{I}_{15/2}$ and $^4\text{S}_{3/2} \rightarrow ^4\text{I}_{15/2}$ transitions.¹⁵⁵ $\beta\text{-NaYF}_4: \text{Yb}^{3+}, \text{Er}^{3+}$ is one of the most popular upconversion materials capable of temperature sensing.¹⁵⁶ The changes in the fluorescence intensity ratio can be seen by exciting $\beta\text{-NaYF}_4: \text{Yb}^{3+}, \text{Er}^{3+}$ with a 29 mW 980 nm laser from 160 to 300 K. As the temperature increases, the fluorescence intensity ratio of the two emission transitions increase, as seen in Fig. 19A. Plotting the temperature (T) versus the ratio (R) of the integrated emission intensity (Fig. 19B) shows the data can be well fit with an exponential function:

$$R = 8.06\exp(-1082.1/T) \quad (15)$$

The effective energy difference can be obtained from fitting the data following Eq. (15). This value is 752 cm^{-1} , which is within the range of splitting between $^2\text{H}_{11/2}$ and $^4\text{S}_{3/2}$ ($700\text{--}800 \text{ cm}^{-1}$). Furthermore, the relative sensitivity (S) can be derived for a temperature range of 50–500 K by:

$$S = \left| \frac{1}{R} \frac{dR}{dT} \right| = \frac{\Delta E}{kT^2} \quad (16)$$

Eq. (16) shows that a more significant energy difference yields better sensitivity at a given temperature, meaning smaller temperature variations can be detected using the fluorescence intensity ratio. In $\beta\text{-NaYF}_4: \text{Yb}^{3+}, \text{Er}^{3+}$ the large energy difference of 752 cm^{-1} yields a sensitivity of $1.2\% \text{ K}^{-1}$. This impressive sensitivity shows that $\beta\text{-NaYF}_4: \text{Yb}^{3+}, \text{Er}^{3+}$ can be readily used as an upconversion temperature sensing material.

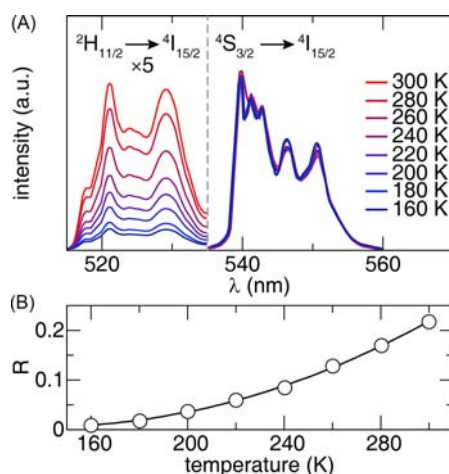


Fig. 19 (A) The temperature-dependent emission intensity of the $^2\text{H}_{11/2} \rightarrow ^4\text{I}_{15/2}$ (magnified $\times 5$ for ease of viewing) and $^4\text{S}_{3/2} \rightarrow ^4\text{I}_{15/2}$ transitions of $\beta\text{-NaYF}_4: \text{Yb}^{3+}, \text{Er}^{3+}$ from 160 to 300 K. (B) The temperature versus the ratio, R , of the integrated emission intensity can be fit by an exponential function, as seen by the black line. Modified from Zhou, S.; Deng, K.; Wei, X.; Jiang, G.; Duan, C.; Chen, Y.; Yin, M., Upconversion Luminescence of $\text{NaYF}_4: \text{Yb}^{3+}, \text{Er}^{3+}$ for Temperature Sensing. *Opt. Commun.* **2013**, *291*, 138–142.

4.09.7.5 Persistent luminescent phosphors for lateral flow assays

The bright green emission and incredibly long lifetime of $\text{SrAl}_2\text{O}_4:\text{Eu}^{2+}, \text{Dy}^{3+}$ enables the phosphor to be used in various applications stemming from emergency signage, novelty toys, and luminescent paints.^{28,120} More recently, these phosphors have been considered for bioanalytical applications because the lifetime of these materials is significantly longer than the spin-forbidden transitions of transition-metal-based complexes.^{157,158} However, bioanalytical applications require high quality, high purity, and chemically stable submicron-sized particles. As a result, various synthetic routes have been employed to produce $\text{SrAl}_2\text{O}_4:\text{Eu}^{2+}, \text{Dy}^{3+}$ including sol-gel,^{159,160} combustion,^{161,162} hydrothermal,¹⁶³ and reverse micelle routes.¹⁶⁴ Unfortunately, the products of these methods often include a blue-emitting $\text{Sr}_4\text{Al}_{14}\text{O}_{25}:\text{Eu}^{2+}, \text{Dy}^{3+}$ impurity.¹⁶⁵ A pure phase product can most readily be obtained by sintering at temperatures greater than 1300 °C, which unfortunately produces large, agglomerated particles. These large particles can be milled to reduce their size and then encapsulated in a water-resistant silica shell before being used in bioanalytical applications.

The search for a replacement for $\text{SrAl}_2\text{O}_4:\text{Eu}^{2+}, \text{Dy}^{3+}$ in biological applications led researchers to $\text{Sr}_2\text{MgSi}_2\text{O}_7:\text{Eu}^{2+}$. This material crystallizes in the tetragonal space group $P4_21m$ in the Åkermanite structure type.¹⁶⁶ The excitation band of $\text{Sr}_2\text{MgSi}_2\text{O}_7:\text{Eu}^{2+}$ spans the UV to the near-UV region with a maximum at 365 nm. Excitation of this phosphor produces a broad emission band centered at 472 nm that can be blue-shifted by substituting Ba^{2+} for Sr^{2+} following $(\text{Sr}_{1-x}\text{Ba}_x)_2\text{MgSi}_2\text{O}_7:\text{Eu}^{2+}$ ($x = 0, 0.125, 0.25, 0.375$).¹²⁶ The substitution of Ba^{2+} has little effect on the luminescent lifetime as all of the phosphors have a lifetime of ≈ 10 min. Co-substituting the phosphors with Dy^{3+} increases the average lifetime by approximately 3 min. The trap depths of these materials were determined through thermoluminescence measurements and were found to be between 0.4 and 0.89 eV, which is near the ideal value of 0.65 eV.

With seemingly ideal optical properties, $\text{Sr}_2\text{MgSi}_2\text{O}_7:\text{Eu}^{2+}, \text{Dy}^{3+}$ and $\text{SrAl}_2\text{O}_4:\text{Eu}^{2+}, \text{Dy}^{3+}$ were further investigated for bioanalytical applications by utilizing the phosphors as an optical reporter in a point-of-care diagnostic. As $\text{Sr}_2\text{MgSi}_2\text{O}_7:\text{Eu}^{2+}, \text{Dy}^{3+}$ and $\text{SrAl}_2\text{O}_4:\text{Eu}^{2+}, \text{Dy}^{3+}$ emit in distinctly different wavelengths, there was a unique opportunity to utilize both phosphors in a multiplex lateral flow assay, capable of detecting both prostate-specific antigens (PSA) and human chorionic gonadotropin (hCG). Lateral flow assays require nanoparticles to allow the particles to flow freely through the membrane. Therefore, the phosphors are first milled to produce their desired nanometer particle size and then fractionated using differential centrifugal sedimentation to get monodisperse particles. The particles are then encapsulated with a silica shell using the Stöber process to make the nanophosphors moisture resistant. Then the prostate-specific antigen (PSA) was conjugated to $\text{SrAl}_2\text{O}_4:\text{Eu}^{2+}, \text{Dy}^{3+}$, and human chorionic gonadotropin (hCG) antibodies were conjugated to $\text{Sr}_2\text{MgSi}_2\text{O}_7:\text{Eu}^{2+}, \text{Dy}^{3+}$ using reductive amination chemistry.¹⁶⁷ The ability to conjugate two different antibodies to two nanophosphors with distinct emissions allows the development of a multiplex assay to detect multiple analytes simultaneously. The antibody-conjugated $\text{Sr}_2\text{MgSi}_2\text{O}_7:\text{Eu}^{2+}, \text{Dy}^{3+}$ and $\text{SrAl}_2\text{O}_4:\text{Eu}^{2+}, \text{Dy}^{3+}$ were tested for binding with a dilute mixture of hCG and PSA antigens, respectively, in a lateral flow assay. This assay was coupled to an iPhone 5S smartphone through a custom attachment and the “Luminostics” application that operates the phone’s LED flash, which acts as the excitation source for the phosphors and the camera for image capture.¹⁶⁸ The nanophosphors could be efficiently excited by the smartphone and produced three distinct bands on the lateral flow assay strip. The first band contains only $\text{SrAl}_2\text{O}_4:\text{Eu}^{2+}, \text{Dy}^{3+}$ particles binding to the anti-PSA antibodies evidenced by the green emission. $\text{Sr}_2\text{MgSi}_2\text{O}_7:\text{Eu}^{2+}, \text{Dy}^{3+}$ particles were bound only to the second test region containing anti-hCG antibodies, which was seen as a blue band. The third band at the control region appears blue-green because both nanophosphors are bound with anti-mouse antibodies, proving that these two compounds can be successfully used to detect two different analytes simultaneously. This new point-of-care diagnostic test allows for rapid, low cost, readily accessible, and a reliable multiplex diagnostic test.

4.09.8 Scintillators

4.09.8.1 Mechanism of gamma-ray conversion to light production

Scintillation, like luminescence, is a mechanism to produce photons. These materials convert high-energy X-ray or gamma-ray photons that arise from nuclear decay processes into lower-energy visible or near-visible radiation. Scintillators operate by promoting an electron from the valence band into the conduction band or the exciton band creating electron-hole pairs. The ensuing relaxation process involving electron-hole recombination results in a photon of visible light with energy less than the band gap, as seen in Fig. 20A.¹⁶⁹

Like phosphors, activators may also be intentionally introduced to shift the photons’ emission wavelength to the visible region. The addition of the activator creates localized sites, as seen in Fig. 20B, that act as defect states. Energy is transferred to the luminescent center by the electron-hole pairs resulting in radiative relaxation from the activator ion.¹⁷⁰ The amount of energy transferred to the luminescent centers from the electron-hole pair is known as the transfer efficiency.¹⁷¹ In ideal situations, no energy is lost during this transfer; however, in reality, some energy is lost when electrons or holes migrate through the crystal structure or from non-radiative relaxation, impurity quenching, concentration quenching, and electron-phonon coupling. The activator should also be homogeneously substituted into the scintillator as small variations in the light output can directly impact the resolution of the scintillator. Further, research has shown that ideal scintillators possess emission bands that do not overlap with the absorption band; otherwise, the material can suffer from self-absorption. Self-absorption can also occur due to quenching from unwanted impurities.

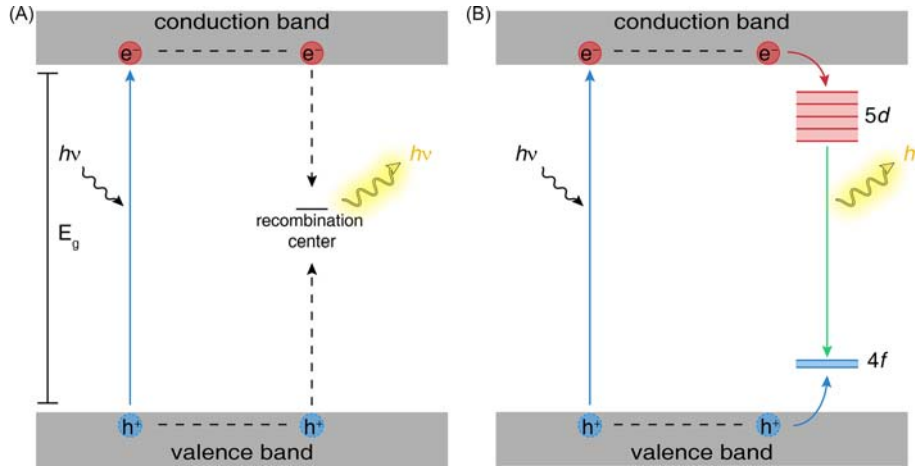


Fig. 20 Schematics representing the mechanism of scintillation in an (A) intrinsic and (B) extrinsic scintillator.

The wavelength of the scintillator's emission is dictated by the energy difference between the host band gap (E_g) and the activator ions. As a result, scintillators can emit at wavelengths across the visible spectrum. For instance, NaI:Tl^+ emits blue light ($E_{g,\text{PBE}} = 3.5$ eV; $\lambda_{\text{em}} = 415$ nm) and CsI:Tl^+ emits green light ($E_{g,\text{PBE}} = 3.9$ eV; $\lambda_{\text{em}} = 540$ nm).¹⁶⁹ These scintillators are known as extrinsic scintillators because they are doped with a small percentage of thulium. Examples of intrinsic scintillators include CdWO_4 and BaF_2 .^{33,172} There are many advantages of intrinsic scintillators, including higher thermal stability and avoiding the inherent non-uniform distribution of the activator in a large single crystal. It is important to note that the optical properties of scintillators do not depend on the orientation of the single crystal; the orientation will only have a significant influence if significant impurities hinder the crystal. In addition, the presence of a significant number of impurities can cause additional defects within the crystal structure that can act as electron traps. Relaxation of trapped electrons to the ground state causes undesirable persistent luminescence, whereas the allowed transitions typically occur within 10^{-8} s after excitation to produce fluorescence.

The observed emission's quantum efficiency depends on the incident photon energy that is converted into electron-hole pairs and eventually into scintillation. The conversion efficiency has been determined by Lempicki¹⁷³ following Eq. (17),

$$L = \frac{10^6}{2.3 E_g} \beta S Q \quad (17)$$

where L is known as the light output in photons per million electron volts, β is the conversion efficiency in electron-hole pairs created per million electron volts of incident radiation, S is the efficiency of energy transfer from electron-hole pairs to luminescent center, and Q is the quantum efficiency of the luminescent center in the excited state. The total scintillation efficiency is described by $\beta S Q$ and indicates that the ideal scintillator must (1) efficiently create electron-hole pairs, (2) possess enough electron-hole mobility to allow recombination, and (3) undergo minimal thermal quenching of the excited state. In theory, the scintillation efficiency is inversely related to the width of the band gap. However, it has been reported that as the band gap decreases, Q also decreases with non-radiative transitions dominating the energy transfer process, causing the scintillator to undergo self-absorption. In addition, extrinsic scintillators show an activator concentration dependence with respect to the quantum efficiency. Finally, the activator concentration must surpass a certain threshold to enhance electron mobility and provide uniform light output. The quantum efficiency of the luminescence is also temperature-dependent. The amount of thermal energy present in the system influences the energy levels of the luminescent center. As more thermal energy penetrates a crystalline system, the equilibrium quantum states shift, causing an increase in the thermal quenching rates.

There are several components to the light pulse emitted from a scintillator. Each pulse has a distinct rise, decay time, and amplitude. The shape of the pulse can be approximated by the sum of the rise and decay times. The rise time of the light pulse follows Eq. (18), where λ_r is the characteristic time required to occupy the luminescent centers in a given crystalline material.

$$I_A(t) = -I_0 e^{-\lambda_r t} \quad (18)$$

The decay time for scintillators is larger in magnitude than the rise time and can be described by Eq. 19,

$$I_B(t) = -I_0 e^{-\lambda_d t} \quad (19)$$

where λ_d is the characteristic transition probability for the same material. The decay time is also dependent upon the ambient temperature and activator concentration. For instance, the decay time of NaI:Tl decreases by a factor of four as the temperature increases, and the decay time can vary as much as 50% depending on the thallium concentration. The amplitude of the light pulse is dependent upon several parameters: (1) the amount of incident radiation, (2) the conversion efficiency, (3) the light collection efficiency of the device coupled to the scintillator, and (4) the signal processing capability of the device.¹⁶⁹ Specific applications

require specific rise and decay times. For example, in positron emission tomography (PET), scintillators with fast rise and decay times and narrower pulse widths allow for faster data acquisition to occur at higher rates. These qualities are ideal for reducing imaging time and, consequently, producing higher-quality images due to less patient motion and discomfort.

4.09.8.2 Notable scintillators and their applications

The scintillators used in devices for particle detection are typically large crystals. One of the most famous applications for scintillators is gamma-ray attenuation. Scintillators attenuate gamma-ray radiation following the pencil beam equation, given in Eq. (20).

$$I(x) = I_0 e^{-\mu \rho x} \quad (20)$$

The intensity of the gamma-ray is reduced by an exponential correction factor which is dependent upon the mass attenuation coefficient (μ), the density of the material (ρ), and the thickness of the material (x). A scintillator's relative stopping power can be determined through the effective atomic number. A larger atomic number yields a higher probability that a photon will be absorbed in the photoelectric process, where an incident photon gives up all of its energy to a bound electron.¹⁶⁹ Small increases in a material's density or thickness cause substantial increases in a material's stopping power as a more significant electron density increases the probability that a gamma-ray photon will be attenuated by Compton scattering. One famous scintillator used in this application is NaI:Tl⁺. This scintillator can attenuate 90% of a 140 keV gamma-ray of ^{99m}Tc, a metastable nuclear isomer of technetium-99.¹⁶⁹ Unfortunately, NaI:Tl⁺ is hygroscopic, which limits its long term use.¹⁷⁴

One of the most spectacular applications of scintillators is in electromagnetic calorimeters. One of the largest calorimeters was built at CERN (The European Organization for Nuclear Research) in Geneva and it contains 12,000 Bi₄Ge₃O₁₂ crystals that are used to count electrons and photons ejected from high-energy experiments.¹⁷⁵ Bi₄Ge₃O₁₂ crystallizes in the cubic Eulytite structure and contains isolated GeO₄ tetrahedra and distorted BiO₆ octahedra.¹⁷⁶ The emission from Bi₄Ge₃O₁₂ is centered at \approx 480 nm, and the large Stokes shift implies that the emission is easily thermally quenched. In fact, at room temperature, approximately 66% of the low-temperature emission intensity is quenched. The room temperature conversion efficiency is 2%. This conversion efficiency may seem low, but it is sufficient for its application at CERN because the energy of the particles involved in the experiments is so high that the conversion efficiency of the scintillator can be low (0.08%). In addition, Bi₄Ge₃O₁₂ is suitable for this application due to its high density, good chemical stability, and short luminescent lifetime.¹⁷⁵

Finally, one of the most extensive uses of scintillation detectors is in medical imaging. The most commonly used scintillation materials for medical imaging are CdWO₄, Lu₂SiO₅:Ce³⁺, and the previously mentioned NaI:Tl⁺ and Bi₄Ge₃O₁₂.¹⁶⁹ These detectors have been successfully used in isotope preparation, investigating biological samples, *in vivo* counting, and anatomical imaging. SPECT, or Single Photon Emission Computed Tomography, is a functional imaging technique where radioisotopes are injected into the body usually as a labeled isotope. The most common isotope is ^{99m}Tc. The emitted radiation (120–150 keV) is then measured by a γ -ray camera which contains NaI:Tl⁺. The camera is rotated around the patient to construct a three-dimensional image of the radioisotope distribution.¹⁷⁵ Unfortunately, this method does not allow for accurate corrections for radiation attenuation, meaning high-quality images of low-lying organs cannot be obtained. PET imaging utilizes the measurement of annihilated positrons by an array of scintillator detectors. The imaging technique used positron-emitting radioisotopes, which are injected into the patient. The emission of the 511 eV photons is detected by either NaI:Tl⁺, Bi₄Ge₃O₁₂, or Lu₂SiO₅:Ce³⁺, where the signals can be processed, corrected for radiation attenuations, and an image reconstructed. The first PET imaging systems used NaI:Tl⁺ crystals, but eventually, Bi₄Ge₃O₁₂ and Lu₂SiO₅:Ce³⁺ became more popular due to their higher densities and light output.¹⁶⁹

4.09.9 Semiconductors

Thus far, nearly all of the materials discussed here have been based on wide band gap insulators that are generally substituted with a small percentage of an activator ion substituted into the crystal structure or that have structural units that generate charge-transfer bands. The electronic transitions of the activator ion occur between the host valence and conduction band, and by varying the crystal chemistry, it is possible to tune to optical properties. On the other hand, semiconductors have an intrinsically narrower band gap than insulators, typically less than 3 eV, meaning that electronic transitions from the valence to the conduction band occur in the (near) visible region. The smaller band gap allows the promotion of an electron into the conduction band, where it exists in a metastable state and can freely move around since it has separated from the positive nucleus of an atom. This electron is known as a negative charge carrier and causes electrical conductivity in a solid. The charge compensation mechanism for creating this negative charge carrier is the presence of a positive charge carrier in the valence band, or a hole. The hole represents the lack of an electron and plays an essential role in the conductivity of a semiconductor. Once the electrons begin to continually cross into the conduction band, neighboring electrons are pulled into the newly created holes. These holes become filled while new neighboring holes are created.¹⁷⁷

Relaxation to the ground state first involves the electron and hole binding to form an exciton (Fig. 21A). When the exciton relaxes back to the ground state, an energy equivalent to the energy difference between the electron and hole is released. This process is known as recombination or band to band recombination. Radiative recombination occurs if the energy released through recombination is in the form of a photon with a characteristic energy similar to the material's band gap.¹⁷⁸ Photon emission is a result of a large energy difference between the electron and the hole. Radiative recombination is typically associated with band-to-band

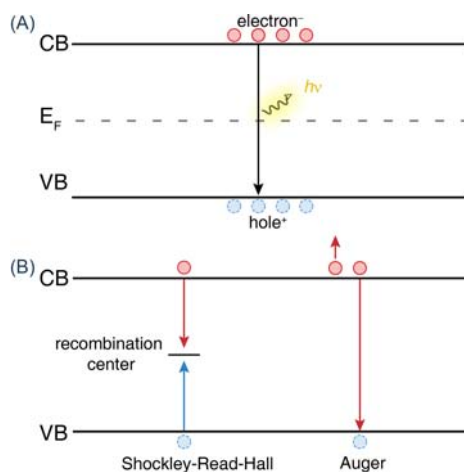


Fig. 21 (A) Radiative relaxation, or band to band recombination, through electron-hole recombination. (B) Non-radiative relaxation through recombination centers (Shockley-Read-Hall defect states) and Auger recombination.

recombination, which occurs in crystal structures with extremely low defect concentrations. Defects can impact interatomic distances and electron interaction density which can alter the band structure of a material. Additionally, defects can also introduce intermediate energy levels, which can trap the charge carriers. The trapped carrier is unable to recombine and will eventually return to its initial state. High concentrations of carrier traps reduce carrier mobility and increase the probability of non-radiative recombination.¹⁷⁹

Besides intermediate energy levels, some energy levels are located equidistant from the conduction and valence bands known as recombination centers. Recombination centers act similarly to intermediate states since they can trap a charge carrier.¹⁸⁰ The difference between the two states is that there is a small probability that a carrier of an opposite charge can also occupy the recombination center, leading to a form of recombination known as Shockley-Read-Hall or defect level recombination, as illustrated in Fig. 21B.^{181,182} This recombination, however, is not in the form of a photon because the energy difference between the electron and hole is small. The energy is released through thermal vibration (phonons) in the form of heat, which negatively impacts the efficiency since electron mobility decreases with increasing phonon concentration.

The final form of recombination is known as non-radiative Auger recombination (Fig. 21B). Auger recombination involves three carriers. Here, an electron and hole recombine, and the energy released is transferred to an electron within the conduction band rather than being lost to thermal vibrations. The electron becomes promoted to a higher energy level within the conduction band and relaxes down to the lowest energy level in the conduction band in the form of thermal vibrations.¹⁸³ This recombination method is detrimental to the efficiency of semiconductors with a high concentration of electron donor atoms. In addition, the probability of Auger recombination increases as a function of increased electron concentration in the conduction band.

There are two distinct types of semiconductors: intrinsic and extrinsic semiconductors.¹⁸⁴ Intrinsic semiconductors are also known as pure or un-doped semiconductors and consist of crystalline structures free from defects and impurities. All intrinsic semiconductors are group 14 elements, with the most common and widely studied intrinsic semiconductors being elemental Si and Ge. Here, the number of electrons and holes in the conduction and valence bands, respectively, is equal. Therefore, intrinsic semiconductors are often called *i*-type. It is challenging to grow intrinsic semiconductor crystals free of impurity. As impurities negatively impact the electronic structure, band gap, and recombination rates of semiconductors, purification is conducted to minimize impurity concentrations to less than a few parts per billion. Purification can be expensive and tedious; therefore, industry prefers the use of extrinsic semiconductors, which is a semiconductor substituted with another element.

There are two types of extrinsic semiconductors: *p*-type and *n*-type. The presence of the dopant atom, known as an acceptor, draws electrons from the valence band. The acceptor is typically a trivalent atom such as B, Ga, In, and Al that replaces Si or Ge. The trivalent atom will be bonded to four silicon atoms while accepting an electron from an adjacent atom into its covalent bond, creating a hole. As the concentration of the acceptor increases, the number of holes will exceed the number of mobile electrons, which will lead to an overwhelming positive charge in the system. These semiconductors are thus known as *p*-type or positive type. Negative type semiconductors (*n*-type) possess a negative charge through a large number of electron donor elements that donate electrons to the conduction band.¹⁷⁷ The extra electron comes from the substitution of P, As, Sb, or Bi for one Si or Ge atom. These acceptor and donor atoms allow electrons to conduct more efficiently in extrinsic semiconductors than intrinsic semiconductors.

4.09.9.1 LEDs

One of the most famous semiconducting materials is the gallium nitride (GaN) light-emitting diode (LED). Gallium nitride is a direct band gap (3.4 eV) semiconductor used as the emitter in blue LEDs. Pure GaN crystallizes in the wurtzite crystal structure

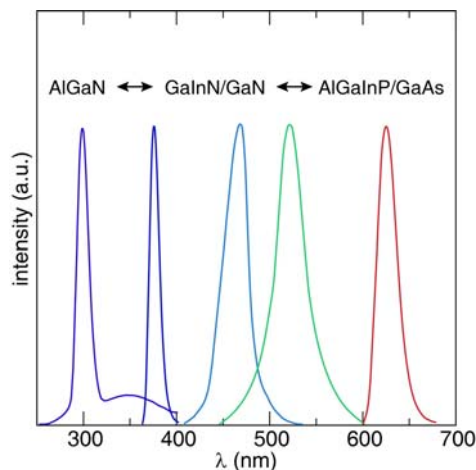


Fig. 22 The tunable emission spectrum of GaN through Al, In, P, and As substitution.¹⁸⁶

(hexagonal $P6_3mc$). The addition of magnesium or silicon as a dopant shifts GaN from *i*-type to *p*-type or *n*-type, respectively.¹⁸⁵ Unfortunately, this substitution causes a high degree of dislocation density within the crystal structure and results in tensile stress making the material brittle. It also causes the luminescence to be inefficient due to many recombination centers arising from strain fields absorbing and releasing the energy through vibrations. Instead, a buffer layer can be added when depositing GaN on a sapphire substrate using molecular beam epitaxy. This allows for the relaxation of the stresses and results in a high-performance blue-emitting LED. The band gap of GaN can also be tuned to shift the emission from the ultraviolet region to red in the visible region by adding certain ratios of In, Al, P, or As.¹⁸⁶ This can be seen in Fig. 22, where the blue GaN emission can be blue shifted to the UV and deep UV regions of the visible spectrum by inserting In and Al for Ga, respectively. As the emission color of the LED is so dependent upon the band gap of the material, it is instructive to discuss the electronic structure of GaN. The top of the valence band is set by the N $2p$ orbitals and Ga $4p$ orbitals. The core of the valence band is composed of the Ga $3s$ orbitals with a minor contribution from N $2s$ orbitals, which sit between -10 and -15 eV. The bottom of the conduction band is set by both Ga and N, where the PBE-DFT calculated band gap was determined as 1.74 eV.¹⁸⁷ For more information on LEDs, the reader is encouraged to refer to *Light-Emitting Diodes*.¹⁸⁶

4.09.9.2 Quantum dots

Another fascinating class of luminescent semiconductors is quantum dots. Quantum dots are nanostructured materials with optical and electronic properties that change as a function of particle size. The particle size of these nanostructures is typically less than 100 nm, which allows for quantum confinement to occur. When an electron and hole combine, they form an exciton. The distance between the electron and hole is known as the exciton Bohr radius. If the radius of a quantum dot approaches the exciton Bohr radius, then the electrons and holes are confined to the dimension of the quantum dot. The confinement causes the particle's energy levels to become discrete and results in the band gap's size dependence.¹⁸⁸ As a result, there is a blue shift in the emission wavelength as a function of decreasing particle size, where the absorption and emission energy can be tuned by manipulating the particle size during synthesis. Larger quantum dots with a 5–6 nm diameter have lower confinement energies and typically emit red, whereas small quantum dots (2–3 nm diameter) usually emit blue. A schematic of this phenomenon can be seen in Fig. 23. It is important to note that the emission color also depends on the composition of the quantum dot.

Typical quantum dots are binaries such as CdSe, PbS, InAs. Ternary quantum dots have also been synthesized, such as CuIn_5Se_8 . CdSe quantum dots have been synthesized with particle sizes in the range of ≈ 1 to ≈ 10 nm. This offers a tunable emission from the blue to red region of the visible spectrum.¹⁸⁸ In particular, CdSe quantum dots with particle sizes of 4.6, 5.4, and 6.8 nm yield 509, 554, and 605 nm emissions, respectively, corresponding to emission from the green to orange-red region, under 365 nm excitation.¹⁸⁹ PbS quantum dots are popular materials for optoelectronic devices such as solar cells and photodetectors. These quantum dots have been synthesized within a particle size range of 2.5–6 nm, corresponding to band gaps of 0.8–1.6 eV, respectively. The emission of these particles falls within the IR region and can be tuned between 990, 1280, and 1600 nm for the small, medium, and large quantum dots, and they have impressive photoluminescent quantum yields between 40% and 70%.¹⁹⁰ The ternary quantum dots such as CuIn_5Se_8 can also emit in the red to IR region, 650–975 nm, by tuning the size from ≈ 2.0 to 3.5 nm.¹⁹¹

Quantum dots are zero-dimensional nanostructures with respect to bulk materials. This means that the material has well separated energy levels due to the small number of atoms in the quantum dot.¹⁸⁸ As a result, quantum dots are referred to as “artificial atoms” because the wavefunctions of each electronic state mimic those of atoms. In actuality, quantum dots are energetically somewhere between a discrete atom and bulk materials. This phenomenon affects the resulting optical properties because the emission is atom-like, meaning sharp peaks are observed. The most common mechanism of radiative relaxation in quantum dots is band-to-band relaxation, where the electron from the conduction band combines with the hole in the valence band. The full width at half

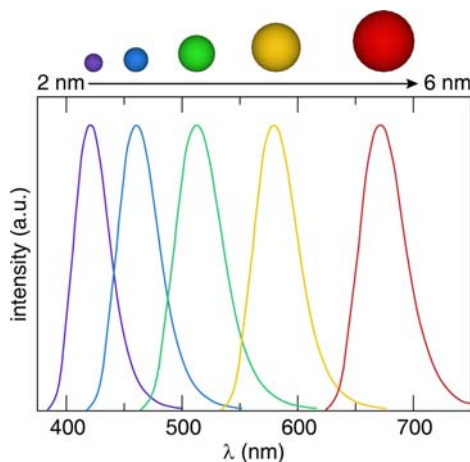


Fig. 23 Schematic representing the relationship between emission color and the size of a quantum dot.

maximum of emission from room temperature band-to-band relaxation varies from 15 to 30 nm depending on the average particle size. Interestingly, Pron et al. have reported a new synthetic route to reduce the emission full width at half maximum of ZnSe quantum dots to 12.7–16.9 nm that emit from 390 to 440 nm.¹⁹²

In addition to the incredibly narrow emission, quantum dots can also produce very bright emission with high photoluminescent quantum yields. CdSe is one of the most popular red-emitting quantum dots due to its high photoluminescent quantum yield of 85%. In addition, it has a narrow full width at half maximum of 23 nm and is stable upon aging for several months.¹⁹³ The photoluminescent quantum yield of quantum dots can also be drastically improved by coating the particles with a wide band-gap semiconductor. For example, ZnSe was coated with ZnS, which has 5% lattice mismatch with ZnSe. In its pristine form, ZnSe has a room temperature photoluminescent quantum yield of $\approx 10\%$, but adding the outer shell improved the quantum yield to 32%.¹⁹⁴

In some cases, activator ions such as transition metals or rare-earth elements have been intentionally substituted into a quantum dot. The predominant mechanism for radiative relaxation is still through electron-hole recombination. However, radiative relaxation can still occur through the activator. If orbitals are mixed due to relaxed selection rules, then $d-d$ transitions in transition metals (Mn^{2+}) and $f-f$ transitions of rare-earth elements (Eu^{3+} , Tb^{3+} , Er^{3+} , Tm^{3+}) are allowed.¹⁹⁵ Many studies have been conducted on the effect of the activator inclusion on the optical properties of ZnO quantum dots. Tb^{3+} -substituted ZnO quantum dots exhibited two distinct emissions. It was found that increasing the concentration of Tb^{3+} improved the emission from the rare-earth while simultaneously quenching the ZnO emission. On the other hand, substituting Mn^{2+} causes preferred orientation of nanorods to the substrate and the resulting optical properties strongly depend on the synthetic conditions.¹⁹⁶ There are reports of Mn^{2+} causing the ZnO emission to quench, while others state that the transition metal causes a blue shift in the emission.^{197,198} In other cases, the inclusion of the activator was found to increase the photoluminescent quantum yield through charge transfer.¹⁹⁹

The nearly monochromatic and incredibly bright emission observed from these materials makes them excellent candidates for display lighting. For example, in quantum dot light-emitting diode (Q-LED) televisions, a blue LED is used to excite green and red-emitting quantum dots which are placed in front of the LED. The quantum dots in these devices produce only the necessary colors required for the image on the screen, making the image brighter, clearer, and more energy-efficient. In 2016, researchers from Samsung Electronics revealed the first Q-LED display that was brighter than liquid-crystal displays while consuming less than one-fifth of the power. The commercial product utilized InP-based quantum dots as their green and red emitters.²⁰⁰

Quantum dots are also popular materials for biological applications due to the ability to functionalize and assay multiple quantum dots in a single device with minimal interference. Generally, the intensity, emission spectrum, and lifetime dictate the application of the quantum dot. High photoluminescent quantum yields are required for intensity-based imaging. Devices that require assayed quantum dots require that the emission bands are narrow enough to prevent overlap.^{201,202} Finally, quantum dots with fluorescent lifetimes of tens of nanoseconds such as CdSe possess a lifetime longer than the autofluorescence seen from tissue (1 ns), meaning a high signal to noise ratio image can be obtained.¹⁸⁸ In some studies, luminescent activators have been substituted into the quantum dot to elongate the lifetime. The activators create local quantum states within the band gap and act as trap states to delay radiative relaxation to the ground state. As a result, researchers have used quantum dots for in vivo and in vitro imaging. For example, CdTe/CdSe quantum dots have been used to image cancerous lymph nodes through in vivo fluorescence. The near-infrared (NIR) emission from these quantum dots is advantageous since hemoglobin and water have lower absorption coefficients and scattering in the NIR region.²⁰³ These recent advances in quantum dots have led to predictions that these materials will be able to provide unparalleled sensitivity and selectivity in biomedical imaging, disease detection, drug discovery, and protein tracking over traditional organic dyes.

Unfortunately, the above applications require that the quantum dot be biologically compatible with the human body. The majority of quantum dots with exceptional optical properties contain heavy toxic metals such as Cd, Se, and Pb. Son et al. reported that ion exchange could occur at the surface of a CdSe quantum dot, which causes the release of Cd^{2+} into the bloodstream.²⁰⁴ To

help counteract this phenomenon, some quantum dots are coated with a biocompatible shell. Current research also suggests that these toxic metals may accumulate in organs and tissues for weeks or months after exposure. Finally, recent *in vitro* studies have shown that quantum dots may be cytotoxic. CdTe quantum dots coated with a biocompatible shell of mercaptopropionic acid and cysteamine were cytotoxic to rats at concentrations of 10 $\mu\text{g}/\text{mL}$. The same CdTe quantum dots without the shell were cytotoxic at just 1 $\mu\text{g}/\text{mL}$. Interestingly, smaller quantum dots (2.2 ± 0.1 nm) were found to have higher rates of cytotoxicity than larger quantum dots (5.2 ± 0.1 nm) at an equal concentration.²⁰⁵ The concerns with safety and the toxicity of heavy metals have led to the development of the Restriction of Hazardous Substances Directive 2002/95/EC (RoHS), which sets guidelines for the allowed levels of each metal. The amount of Cd and Pb, for example, used in each device or procedure is limited to less than 0.01 and 0.1 wt %, respectively, to ensure the safety of those exposed.^{206,207}

Quantum dots also exhibit intermittent photoluminescence known as “blinking” in which the quantum dot emits light for a period of time followed by a dark period. This blinking effect was first observed by Nirmal et al. who saw the switch between radiative and non-radiative states from a single CdSe quantum dot at room temperature.²⁰⁸ Further work by Kagan et al. realized that a single quantum dot spends a significant time (≈ 100 s) in the dark period despite constant exposure to an excitation source. This observed fluctuation in photoluminescent intensity can interfere with time-lapse imaging for tracking involving quantum dots. The most widely accepted mechanism for blinking involves illumination-induced charging (luminescence \rightarrow dark period) followed by reneutralization (dark period \rightarrow luminescence) of the quantum dot.²⁰⁹ This process is hypothesized to occur due to the interaction of an exciton and an excess charge (electron or hole) that resides in deep-trap states and produces an electric field. This electric field triggers non-radiative Auger recombination. Since Auger recombination can occur on orders of magnitudes faster than radiative recombination, the observed emission from a charged quantum dot can be severely quenched. Thus, the current goal of quantum dot research is to eliminate blinking in quantum dots. Current work in this effort has shown that surface-bound ligands and thicker shells can significantly reduce blinking by eliminating trap-states.^{210,211} Complete blinking suppression was achieved by Wang et al. who synthesized alloyed CdZnSe-ZnSe core-shell quantum dots that continually emitted.²¹² While this advance is critical for fluorescence detection, the quantum dot has several distinct, broad emission peaks, which makes it unsuitable for techniques involving monitoring several fluorophores.

4.09.10 Discovery of new luminescent materials

The diversity of applications that require luminescent materials means that researchers are continually trying to discover new materials with appropriate optical properties for each application. As a result, there are many strategies commonly utilized to expedite the process of phosphor discovery.

4.09.10.1 Rational synthesis through atomic substitution

One of the most popular strategies in the design and discovery of new phosphors is to form a solid solution through atomic substitution. The Hume-Rothery rules for atomic substitution state that atomic substitution can occur between two atoms with a similar oxidation state, electronegativity, and whose radii differ by no more than 15%.²¹³ In addition, the preliminary crystal structures must be structurally similar. The differences in atomic radii influence the crystal field splitting around the activator ion by manipulating the distance between activator and ligand, R (recall: Eq. 11). This allows the emission of a phosphor to be tuned to a specific, desired wavelength by carefully modifying the host crystal structure using atomic substitution. The most common method using this approach is to modify an existing phosphor with an outstanding photoluminescent quantum yield and thermal stability in an effort to shift the emission wavelength. Because there is a noticeable gap between the number of reported blue- and cyan-emitting materials compared to green-emitting materials, an effective strategy is to form a solid solution based on an outstanding blue-emitting phosphor and shift the emission to the green region of the electromagnetic spectrum. For example, $\text{BaSi}_2\text{O}_2\text{N}_2:\text{Eu}^{2+}$ is a cyan-emitting phosphor ($\lambda_{\text{em}} = 494$ nm) that crystallizes in the orthorhombic $Cmcm$ with the Ba^{2+} in a 12-fold coordinate cuboid-like environment that gives rise to a narrow full width at half maximum of 35 nm.^{214,215} The phosphor also has an impressive T_{50} of 600 K and a quantum yield of 71%. Sr^{2+} ($r_{12\text{-coord}} = 1.44$ Å) may be substituted for Ba^{2+} ($r_{12\text{-coord}} = 1.61$ Å) due to the 11% difference in the size of these two cations in 12-fold coordination.^{89,214} Substituting 100% of Sr^{2+} for Ba^{2+} into this structure, $\text{SrSi}_2\text{O}_2\text{N}_2:\text{Eu}^{2+}$, follows the expected crystal field splitting trends and shifts the emission maximum by almost 40–537 nm, producing a green-emitting phosphor. The smaller size of Sr^{2+} compared to Ba^{2+} induces a larger magnitude of crystal field splitting around Eu^{2+} , causing the observed red-shift in the emission. Further, the quantum yield of this phosphor improves to 91% while the T_{50} remains 600 K, indicating that $\text{SrSi}_2\text{O}_2\text{N}_2:\text{Eu}^{2+}$ is a viable green-emitting phosphor for lighting applications.²¹⁴

Solid solutions may also show unexpected improvement in the optical properties of a phosphor. For example, Lu^{3+} was incrementally substituted for Y^{3+} following $\text{Ba}_2(\text{Y}_{1-x}\text{Lu}_x)_5\text{B}_5\text{O}_{17}:\text{Ce}^{3+}$ ($x = 0, 0.25, 0.5, 0.75, 1$) in an effort to red-shift the blue emission of the borate phosphor. $\text{Ba}_2\text{Y}_5\text{B}_5\text{O}_{17}:\text{Ce}^{3+}$ emits blue ($\lambda_{\text{em}} = 457$ nm) under UV excitation and has a moderate quantum yield of 70% with a T_{50} of 403 K.²¹⁶ Interestingly, incrementally substituting Y^{3+} for Lu^{3+} blue-shifts the emission maximum by 10–447 nm. This is unexpected due to crystal field splitting and is likely due to a subtle local structural distortion of the substitution site from incorporating the smaller Lu^{3+} into the crystal structure.⁷⁴ The phosphor’s quantum yield and thermal stability also improve as Lu^{3+} was incrementally added to the crystal structure. Upon 100% Lu^{3+} substitution, the quantum yield increases to 87%, and the T_{50} improves by 50–452 K. This improvement was attributed to increased structural rigidity stemming from the

replacement of the larger Y^{3+} ($r_{7\text{-coord}} = 0.90 \text{ \AA}$) for the smaller Lu^{3+} ($r_{7\text{-coord}} = 0.86 \text{ \AA}$).⁸⁹ An increase in local rigidity may improve the quantum yield by limiting the number of accessible non-radiative pathways and increase the phosphor's thermal stability by minimizing the potential for crossover points between the excited and ground states.²¹⁷ This was corroborated by calculating the Debye temperature, which is a proxy for structural rigidity, using *ab initio* calculations; the Debye temperature of $Ba_2Y_5B_5O_{17}$ is only 336 K, whereas $Ba_2Lu_5B_5O_{17}$ has a Debye temperature of 355 K.^{216,218} Therefore, solid solutions, where a larger atom is replaced with a smaller, chemically harder atom, may be a useful strategy in improving the optical properties of a phosphor.

There are some rare instances where a solid solution may improve the optical properties by enhancing the chemical stability of the host crystal structure. $Sr_{1.975-x}Ba_xCe_{0.025}AlO_4F:Ce^{3+}$ emits bright green with a maximum at 502 nm and a quantum yield approaching 100% when excited by 400 nm radiation.²¹⁹ The main drawback of this phosphor is that it degrades upon contact with moisture, effectively preventing it from any real-world application. Interestingly, a solid solution can be formed with the nearly isostructural $Sr_3SiO_5:Ce^{3+}$ following $Sr_2Ba(AlO_4F)_{1-x}(SiO_5)_x:Ce^{3+}$.⁹⁸ It was found that the emission red-shifts with each incremental addition of $Sr_3SiO_5:Ce^{3+}$, reaching a maximum red-shift to 552 nm when $x = 0.9$. The quantum yield also steadily decreases from near unity to 67% when $x = 0.9$. The main improvement seen in the phosphor was increased resistance to moisture, where the compositions when $x \geq 0.5$ are stable under ambient conditions. This is likely due to the decrease of fluoride character in the system, which is commonly known to be susceptible to moisture degradation. Therefore, the composition of the phosphor can be tuned to balance the loss of quantum yield and improvement in the chemical stability to yield a phosphor suitable for applications.

4.09.10.2 Identification of new host crystal structures

Traditionally, phosphors are discovered by screening inorganic crystal structure databases such as ICSD (Inorganic Crystal Structure Database), PCD (Pearson's Crystal Database) or Materials Project, and substituting activators in a trial-and-error method. This practice is time-intensive, laborious, and becoming more difficult with most of the obvious candidates having already been investigated. Instead, new methods should be developed to rapidly screen chemical spaces to identify completely new crystal structures that can then be substituted with activators to produce photoluminescence. We will discuss two processes that have successfully expedited the discovery of new phosphors.

4.09.10.2.1 The single particle diagnosis approach

Phosphors are typically synthesized as polycrystalline powders rather than large single crystals. The size of the particles in the powder varies from several to several tens of micrometers, where the larger particulates could be considered as small single crystals. In theory, the large particles that exhibit bright luminescence can be isolated and further characterized, but structure determination from small single crystals is exceptionally challenging due to irregular particle morphology or other imperfections. The single particle diagnosis approach circumvents this difficulty by performing crystal structure analysis using a high-resolution single-crystal X-ray diffractometer with a charge-coupled device (CCD) area detector and utilizing multilayer focusing mirrors for structural analysis and a single-particle fluorescence spectrophotometer to evaluate the optical properties.²²⁰ The workflow typically consists of five steps (Fig. 24). The first step involves choosing a chemical space and synthesizing numerous compositions (50+) substituted with Ce^{3+} or Eu^{2+} through traditional high-temperature sintering. This forms the "powder library." The second is to identify and isolate particles with the desired optical properties and appropriate particle size, morphology, and growth under an optical microscope. The third step involves determining the lattice parameters of the particle using the single crystal X-ray diffractometer and

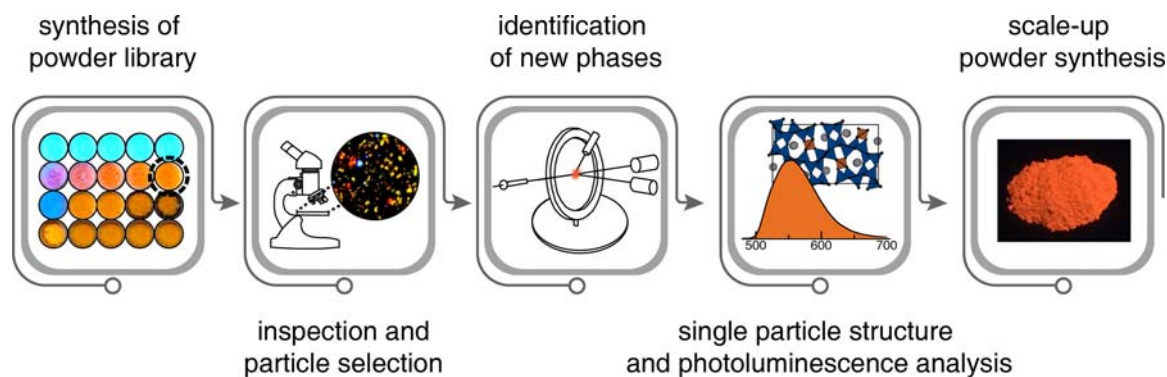


Fig. 24 Workflow of the single particle diagnosis approach. First, a chemical space should be identified and a powder library synthesized. A particle of appropriate size and desired luminescence should be identified for single-crystal X-ray diffraction where the lattice parameters will be indexed against known compositions from inorganic structural databases. If unknown, the composition and photoluminescence properties of the particle are characterized. Finally, the phase is attempted to be synthesized as a powder. Modified from Wang, X.-J.; Xie, R.-J., Screening and Discovery of Phosphors by the Single-Particle-Diagnosis Approach. *J. Appl. Phys.* **2021**, *129* (12), 123106, Wang, X.; Takeda, T.; Hirotsaki, N.; Funahashi, S.; Xie, R.-J., Single-Particle-Diagnosis Approach: An Efficient Strategy for Discovering New Nitride Phosphors. *J. Rare Earths* **2018**, *36* (1), 42–48.

screening the data against the known compounds listed in the crystal structure databases. The particles whose parameters cannot be matched in the database are treated as new phosphors. The fourth step is characterization, including crystal structure and composition identification and measuring the optical properties of the phosphor, such as the emission spectrum, photoluminescent quantum yield, and thermal quenching resistance. Finally, the last step is determining the appropriate synthetic route to obtain phase pure powders and scale up the sample size.²²¹

This methodology has successfully identified many new phosphors from various compositional spaces, including oxynitridosilicates,²²² nitridoaluminosilicates,²²³ nitridolithoaluminates,²²⁴ and oxonitridoaluminosilicates.²²⁵ A particularly exciting system, $\text{Ba}_2\text{LiAlSi}_7\text{N}_{12}$, was identified from the $\text{Ba}_3\text{N}_2\text{-Li}_3\text{N-Si}_3\text{N}_4\text{-AlN}$ phase space. The particle of $\text{Ba}_2\text{LiAlSi}_7\text{N}_{12}$ was chosen from the powder library due to the plate-like shape and large particle size ($46 \times 31 \times 11 \mu\text{m}$), making it suitable for single crystal analysis. Other particles were also investigated, but lattice parameter analysis revealed that the particles were known phosphors, namely $\text{BaSi}_7\text{N}_{10}:\text{Eu}^{2+}$, $\text{Ba}_2\text{Si}_5\text{N}_8:\text{Eu}^{2+}$, and $\text{BaSi}_6\text{N}_8:\text{Eu}^{2+}$.^{226–228} $\text{Ba}_2\text{LiAlSi}_7\text{N}_{12}$ crystallizes in the orthorhombic $Pnmm$ and the structure is composed of corner connected $(\text{Si,Al})\text{N}_4$ and LiN_4 tetrahedra and the single Ba atom sites in the one-dimensional tunnel formed by the tetrahedra along the b direction.²²⁴ The Ba atom is coordinated by 11 N atoms. Exciting this phosphor at 405 nm produces a narrow green emission with a full width at half maximum of 61 nm and a photoluminescent quantum yield of 79%. The phosphor retains 95% and 91% of the room temperature integrated intensities at 200 °C and 300 °C, respectively. The high thermal stability was attributed to the rigid backbone in the crystal structure from the $(\text{Si,Al})\text{N}_4$ and LiN_4 tetrahedra. Synthesis of polycrystalline $\text{BaSi}_7\text{N}_{10}:\text{Eu}^{2+}$ resulted in several impurities such as $\text{Ba}_2\text{Si}_5\text{N}_8:\text{Eu}^{2+}$ and $\text{BaSi}_6\text{N}_8:\text{Eu}^{2+}$ due to the loss of Li during synthesis. The impurities interfere with the observed luminescence of the polycrystalline sample, but they can be removed through careful control of the synthetic conditions. It is clear from this example that the single particle diagnosis approach is a successful method to quickly identify new phosphors.

4.09.10.2.2 Combinatorial chemistry approach

The single particle diagnosis approach, while successful, still relies on extensive trial-and-error. This process could be simplified by screening composition spaces using combinatorial chemistry to identify new and promising host crystal structures as potential phosphors. The Sohn group has implemented a new strategy that combines heuristics optimization with high-throughput experimentation to identify novel phosphors.²²⁹ The workflow is presented in Fig. 25. In their work, a non-dominated-sorting genetic algorithm (NSGA) is first used to search multi-dimensional compositional spaces. Then a particle swarm optimization (PSO) is conducted to reduce the compositional phase space by considering a new parameter called the structural rank, which describes the novelty of the phosphor. This approach is combined with a solid-state high-throughput experimentation to identify new materials. This process can be broken down into three steps. The first is to determine the composition space of interest, called the decision parameter, based on current literature, chemical intuition, and industry demand. The next step is to identify a new phosphor using an NSGA and PSO-assisted combinatorial materials search based on high-throughput experimentation and the structural rank

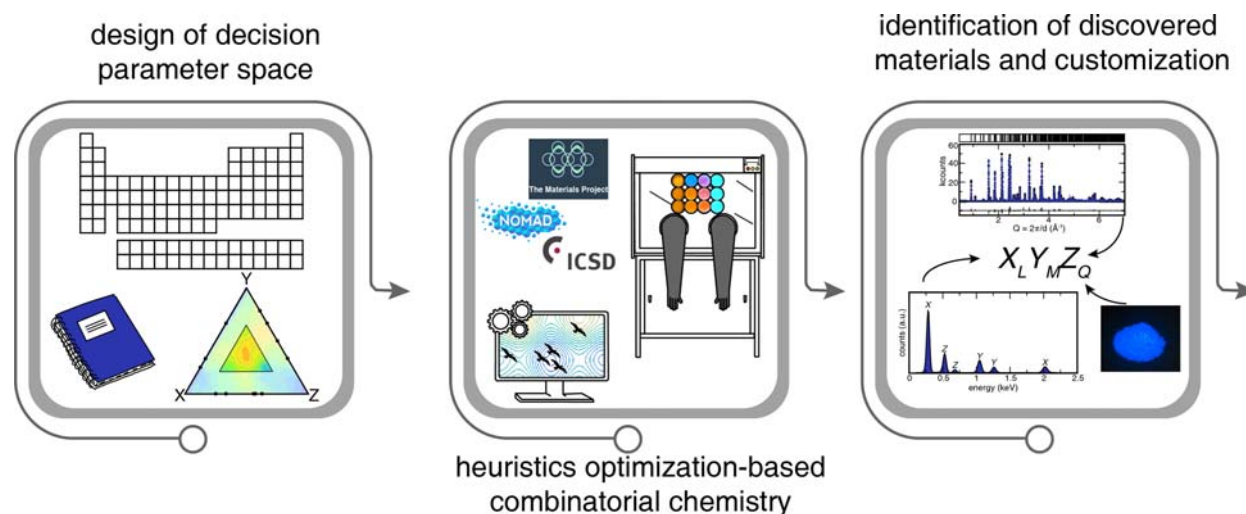


Fig. 25 Workflow of the combinatorial chemistry approach to identify new phosphors. First, the composition space of interest should be narrowed down based on literature, patents, chemical intuition, and industry needs. Next, a heuristic optimization-based combinatorial approach involving optimization algorithms, experimental evaluation through high-throughput synthesis and characterization, and parameterization of the material novelty by indexing against known compositions from inorganic structural databases is conducted. Finally, the new phase is identified through compositional analysis and structural determination and a large-scale phase pure synthesis is attempted. Modified from Park, W. B.; Shin, N.; Hong, K.-P.; Pyo, M.; Sohn, K.-S., A New Paradigm for Materials Discovery: Heuristics-Assisted Combinatorial Chemistry Involving Parameterization of Material Novelty. *Adv. Funct. Mater.* **2012**, 22 (11), 2258–2266, Park, W. B.; Singh, S. P.; Sohn, K.-S., Discovery of a Phosphor for Light Emitting Diode Applications and Its Structural Determination, $\text{Ba}(\text{Si,Al})_5(\text{O,N})_8:\text{Eu}^{2+}$. *J. Am. Chem. Soc.* **2014**, 136 (6), 2363–2373.

parameter. The last step is to realize the new material through synthesis, characterization, and identifying the appropriate synthesis for scale up.

This methodology was applied to identify a new phosphor in the AEO ($AE = \text{Mg, Ca, Sr, Ba}$)- Al_2O_3 - AlN - Si_3N_4 phase space.²³⁰ This phase space was chosen based on what would likely yield a new phosphor immediately applicable in industrial use. Such a large, seemingly infinite composition space requires a two-step feedback loop to screen the composition space properly. First, the phase space was confined to Si_3N_4 -rich compositions based on preliminary high-throughput experimentation, which showed that compositions outside the specific region often melted at temperatures above 1600°C and compositions rich in $\text{AlN}/\text{Al}_2\text{O}_3$ and Si_3N_4 would often produce already known SiAlON phosphors. The resulting phase space was reduced to 16,256 compositions. While hundreds of phosphor samples were synthesized using high-throughput experimentation, the phase space cannot be sufficiently screened using this brute-force methodology. Applying the NSGA through five generations, where each generation contained the results of the preliminary experiments, each optimization narrowed the composition space by converging around a specific composition space of $\text{BaO}/\text{SrO}-\text{Al}_2\text{O}_3-\text{Si}_3\text{N}_4$. Then, a PSO combinatorial material search was employed to fine-tune the results from the NSGA by further narrowing the phase space to the Si_3N_4 rich region. With only photoluminescence intensity as an objective function in the PSO process, five consecutive swarms were able to isolate around the unknown composition. Structural identification first involved matching the powder diffraction to those reported in inorganic structural databases, similar to the lattice parameter search done in single-particle diagnosis. After determining that the new phase, $\text{Ba}(\text{Si}/\text{Al})_5(\text{O}/\text{N})_8$, did not match any known phase, the space group was determined as being $A2_1am$ through indexing, space group determination, and Rietveld refinements. This new phosphor has an AB_5X_8 structure type, which had never been reported before. The compound contains a three-dimensional network of corner-connected $(\text{Al}/\text{Si})(\text{O}/\text{N})_4$ tetrahedra where the Ba^{2+} lies inside the voids created by the network. The phosphor emits a bright blue-green light under near-UV excitation. This new combinatorial approach has proven successful in identifying this new structure type and new compositions such as yellow-emitting $\text{Ca}_{1.5}\text{Ba}_{0.5}\text{Si}_5\text{O}_3\text{N}_6:\text{Eu}^{2+}$ and red-emitting $\text{Ca}_{15}\text{Si}_{20}\text{O}_{10}\text{N}_{30}:\text{Eu}^{2+}$, which can be immediately used in industrial applications.^{231,232}

4.09.10.3 Data-driven approaches

Machine learning algorithms may also be utilized to screen inorganic structural databases to predict crystal structures that will produce phosphors with thermally stable and efficient emission upon rare-earth substitution. A workflow of the process of constructing and evaluating a machine learning model is provided in Fig. 26.²³³ First, data are collected from literature, crystal structure databases, figures, or laboratory notebooks. The data are then translated into a numerical representation so that data can be interpreted by a computer. Models are then constructed by applying various algorithms on the data set. The algorithm that yields the best performance is chosen for further optimization. Finally, the predictive power of the model is evaluated on unseen data.

The Debye temperature (Θ_D) represents the highest temperature that can be achieved due to a single vibration. Recently, the DFT calculated Debye temperature has been used as a proxy for structural rigidity as materials with a higher Θ_D tend to have higher-energy phonon modes, which inhibit access to non-radiative pathways and lead to higher quantum efficiencies. In contrast, lower Debye temperatures signify the presence of softer phonon modes that increase the probability of non-radiative relaxation.²¹ As a result, the Debye temperature has been used as a screening tool to identify potential host structures with predicted high efficiencies. The only drawback to this approach is that these calculations are computationally expensive. Zhuo et al. proposed an alternate methodology to expedite the identification process. They developed a machine learning model that could predict, rather than calculate, the Debye temperature of a host structure within a matter of seconds.²³ A support vector machine regression model was trained based on the calculated Debye temperatures of 2610 compounds. The model had a coefficient of determination (r^2) of 0.89 with a mean absolute error of 37.9 K, meaning there is excellent agreement with the calculated Debye temperature values and the machine learning predicted value of the Debye temperature. Once the model had been successfully trained, the model was used to predict the Debye temperature of $>100,000$ compounds from the Pearson's Crystal Database. The Debye temperature was

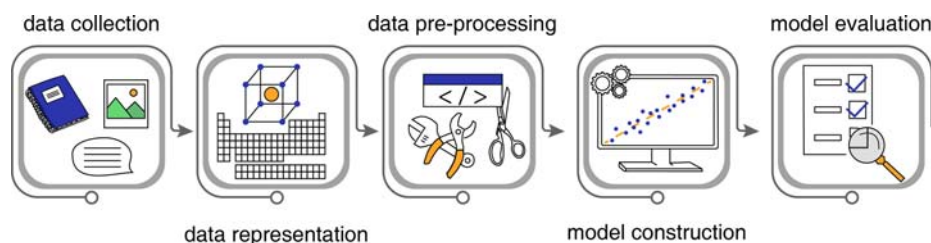


Fig. 26 Workflow of the machine learning approach. Data are collected from literature, crystal structure databases, and figures. Next, numerical representations of the data are created to be interpreted by a computer. The data is then analyzed and cleaned during data pre-processing to remove irrelevant, redundant, noisy, or unreliable information. The data are then utilized in model construction, where a number of machine learning algorithms are applied and the highest performing model is chosen. The model is trained using these algorithms, and its predictive power is finally evaluated on an unseen data set. Modified from Zhuo, Y.; Tehrani, A. M.; Brgoch, J., *A New Era of Inorganic Materials Discovery Powered by Data Science In Machine Learning in Chemistry: The Impact of Artificial Intelligence* Cartwright, H. M., (ed.) The Royal Society of Chemistry 2020; pp. 311–339.

plotted against its band gap, extracted from the Materials Project, to construct a tool for identifying the most promising host materials. Recall, crystal structures with wide band gaps tend to minimize temperature-induced photoionization. Therefore, plotting each compound's predicted Debye temperature versus the calculated band gap through a sorting diagram can be used to identify and group classes of host crystal structures with predicted high quantum yields and high thermal quenching resistance, respectively. Sorting diagrams revealed some general trends between classes of materials. For example, nitrides tend to have band gaps > 4.5 eV and generally high Debye temperatures that arise from covalently bonded, corner connecting tetrahedra present within the structure. Fluorides have very wide band gaps, between 4 and 8 eV, but low Debye temperatures (< 500 K) likely due to the ionic bonding in these crystal structures. Finally, borates tend to have wide band gaps, between 4 and 8 eV, and very high Debye temperatures, greater than 500 K, owing to boron's small size that promotes dense polyhedral packing. The sorting diagram revealed that borates are an ideal class of materials that will increase the probability of discovering a phosphor with a high quantum yield. This led to the identification of $\text{NaBaB}_9\text{O}_{15}:\text{Eu}^{2+}$ which has a high Θ_D of 729 K and a calculated band gap of 5.5 eV. The hypothesis that $\text{NaBaB}_9\text{O}_{15}:\text{Eu}^{2+}$ would have enhanced optical properties based on these two descriptors was validated by the phosphor producing purple emission ($\lambda_{\text{em}} = 416$ nm) upon 315 nm excitation with a quantum yield of 95% and zero thermal quenching up to 500 K. Nowadays, researchers have also utilized machine learning to predict thermal quenching temperature,⁶⁶ centroid shift,²³⁴ and excitation wavelength,²³⁵ among other properties, to rapidly identify phosphors for specialized applications.

Finally, data-driven techniques may also aid in identifying new phosphor hosts with predicted desired optical properties. In this approach, host structures are predicted by density functional theory calculations and experimentally validated. The Ong group recently performed a high-throughput screening of the $\text{SrO}-\text{Al}_2\text{O}_3-\text{SiO}_2-\text{SiN}_3$ phase space using a data-mined substitution algorithm on the prototype structures the ICSD.¹³⁷ A total of 496 structures were generated as a result. To narrow the phase space, the thermodynamic stability of each phase with respect to the elements at 0 K was determined. Compositions with energies ≤ 50 meV above the convex hull, the linear combination of stable phases in a phase diagram, were identified as potentially thermodynamically stable phases. As mentioned previously, host crystal structures should also possess wide enough band gaps to prevent photoionization and other quenching mechanisms. Therefore the compositions with a calculated band gap of 3.0–5.5 eV were allowed to remain as a potential structure. Finally, the Debye temperature was calculated to estimate the rigidity of the remaining host structures. These parameters narrowed the phase space from 496 structures to 3. $\text{Sr}_3\text{AlSi}_3\text{O}_9\text{N}$ and $\text{SrAl}_2\text{Si}_3\text{O}_4\text{N}$ were predicted to be metastable, meaning synthesis would likely be challenging, whereas $\text{Sr}_2\text{AlSi}_2\text{O}_6\text{N}$ was identified as a thermodynamically stable crystal structure with a large band gap ($E_{\text{g,HSE}} = 5.41$ eV) and high Debye temperature ($\Theta_D = 525$ K). $\text{Sr}_2\text{AlSi}_2\text{O}_6\text{N}$ crystallizes in the tetragonal space group $P42_1m$ which is derived from $\text{Ba}_2\text{ZnGe}_6\text{O}$. The structure is composed of alternating layers of $[\text{SrO}_8]$ and $[(\text{Si}/\text{Al})\text{O}_4]$ tetrahedra. Substituting Eu^{2+} into the crystal structure produces an unprecedented broad band emission from 400 to 850 nm with a maximum at 600 nm and—full width at half maximum of 230 nm. This broad emission, which appears as white light, was reported to stem from local disorder around the activator stemming from the Al/Si and O/N disorder present in the crystal structure. The emission is also thermally stable as 88% of the 80 K emission intensity is retained at 420 K. Fabricating a prototype device using a 375 nm LED and the single, white-emitting phosphor produced a white light with excellent color quality ($R_a = 97$). This shows that data-driven approaches can successfully screen compositional spaces by targeting thermodynamically stable structures predicted to yield phosphors with excellent optical properties.

4.09.11 Conclusion and outlook

In the last century, luminescent materials have gained unprecedented attention due to its facile and ubiquitous integration in general lighting and display lighting and, more recently, biomedicine for disease detection, imaging, and temperature sensing. The luminescent materials discussed in this chapter represent only a fraction of the total reported luminescent materials, a field that is growing exponentially by the day. As illustrated throughout the chapter, luminescence from transition metal and rare-earth substituted phosphors, semiconductors, and scintillators are dictated by structure-property relationships, which allow researchers to manipulate these relationships and fine-tune their optical properties for specific applications. The luminescent materials used today to illuminate our living rooms and create images on our television sets have been studied for decades. Yet, some of these materials are still not optimal for the application. Therefore, new approaches involving multiple disciplines, including computer science, data science, and materials engineering, should and are being developed to increase the number of novel luminescent materials and identify materials with the ideal optical properties to meet a specific industrial need. There is no doubt that luminescent materials have revolutionized the way we see and interact with the world, and the future impact of these materials is bright.

Acknowledgments

The authors are grateful for the generous financial support provided by the National Science Foundation (CER 19-11311 and DMR-1847701) and Welch Foundation (E-1981).

References

- Virk, H. S. History of Luminescence From Ancient to Modern Times. *Defect Diffus. Forum* **2015**, *361*, 1–13.
- Feldmann, C.; Jüstel, T.; Ronda, C. R.; Schmidt, P. J. Inorganic Luminescent Materials: 100 Years of Research and Application. *Adv. Funct. Mater.* **2003**, *13* (7), 511–516.
- Braun, F. *Ann. Phys. (Leipzig)* **1897**, *60*, 552.
- Röntgen, W. C. On a New Kind of Rays. *Science* **1896**, *3* (59), 227–231. <https://doi.org/10.1126/science.3.59.227>.
- Röntgen, W. C. Weiter Beobachtungen über die Eigenschaften der X-Strahlen. *Sitzungsber. Konig. Preus. Akad. Wiss. Berlin* **1897**, *26*, 576.
- Jang, H. S.; Won, Y.-H.; Vaidyanathan, S.; Kim, D. H.; Jeon, D. Y. Emission Band Change of $(\text{Sr}_{1-x}\text{M}_x)_3\text{SiO}_5:\text{Eu}^{2+}$ ($M=\text{Ca},\text{Ba}$) Phosphor for White Light Sources Using Blue/Near-Ultraviolet LEDs. *J. Electrochem. Soc.* **2009**, *156* (6), J138.
- Koedam, M.; Opstellen, J. J. Measurement and Computer-Aided Optimization of Spectral Power Distributions. *Light. Rec. Technol.* **1971**, *3* (3), 205–210.
- Ekimov, A. I.; Onushchenko, A. A. Quantum Size Effect in Three-Dimensional Microscopic Semiconductor Crystals. *JETP Lett.* **1981**, *34* (6), 345–349.
- Frackowiak, D. The Jablonski Diagram. *J. Photochem. Photobiol. B* **1988**, *2* (3), 399.
- Ball, D. W. *The Basics of Spectroscopy*, vol. TT49; SPIE Publications, 2001.
- Blasse, G.; Grabmaier, B. C. *Luminescent Materials*, Springer-Verlag, 1994.
- Jaffe, H. H.; Miller, A. L. The Fates of Electronic Excitation Energy. *J. Chem. Educ.* **1966**, *43* (9), 469–473.
- Tandon, S. P.; Gupta, J. P. Measurement of Forbidden Energy Gap of Semiconductors by Diffuse Reflectance Technique. *Phys. Status Solidi B* **1970**, *38* (1), 363–367.
- Tauc, J.; Grigorovici, R.; Vancu, A. Optical Properties and Electronic Structure of Amorphous Germanium. *Phys. Status Solidi B* **1966**, *15* (2), 627–637.
- Makula, P.; Pacia, M.; Macyk, W. How To Correctly Determine the Band Gap Energy of Modified Semiconductor Photocatalysts Based on UV–Vis Spectra. *J. Phys. Chem. Lett.* **2018**, *9* (23), 6814–6817.
- Zhao, M.; Zhang, Q.; Xia, Z. Structural Engineering of Eu^{2+} -Doped Silicates Phosphors for LED Applications. *Acc. Mater. Res.* **2020**, *1* (2), 137–145.
- George, M. C.; Denault, K. A.; Seshadri, R. Phosphors for Solid-State White Lighting. *Annu. Rev. Mat. Res.* **2013**, *43* (1), 481–501.
- DeLuca, J. A. An Introduction to Luminescence in Inorganic Solids. *J. Chem. Educ.* **1980**, *57* (8), 541–545.
- Wan, J.; Wang, Z.; Chen, X.; Mu, L.; Qian, Y. Shape-Tailored Photoluminescent Intensity of Red Phosphor $\text{Y}_2\text{O}_3:\text{Eu}^{3+}$. *J. Cryst. Growth* **2005**, *284* (3), 538–543.
- de Jong, M.; Seijo, L.; Meijerink, A.; Rabouw, F. T. Resolving the Ambiguity in the Relation Between Stokes Shift and Huang–Rhys Parameter. *Phys. Chem. Chem. Phys.* **2015**, *17* (26), 16959–16969.
- Huang, K.; Rhys, A. Theory of Light Absorption and Non-Radiative Transitions in F-Centres. *Proc. R. Soc. London, Ser. A* **1950**, *204*, 406–423. https://doi.org/10.1142/9789812793720_0007.
- Cooke, D. W.; Bennett, B. L.; McClellan, K. J.; Roper, J. M.; Whittaker, M. T. Oscillator Strengths, Huang–Rhys Parameters, and Vibrational Quantum Energies of Cerium-Doped Gadolinium Oxyorthosilicate. *J. Appl. Phys.* **2000**, *87* (11), 7793–7797.
- Zhuo, Y.; Mansouri Tehrani, A.; Olynyk, A. O.; Duke, A. C.; Brgoch, J. Identifying an Efficient, Thermally Robust Inorganic Phosphor Host via Machine Learning. *Nat. Commun.* **2018**, *9* (1), 4377.
- Hermus, M.; Phan, P.-C.; Duke, A. C.; Brgoch, J. Tunable Optical Properties and Increased Thermal Quenching in the Blue-Emitting Phosphor Series: $\text{Ba}_2(\text{Y}_{1-x}\text{Lu}_x)_5\text{B}_5\text{O}_{17}:\text{Ce}^{3+}$ ($x = 0 - 1$). *Chem. Mater.* **2017**, *29* (12), 5267–5275.
- Tanabe, Y.; Sugano, S. On the Absorption Spectra of Complex Ions. I. *J. Physical Soc. Japan* **1954**, *9* (5), 753–766.
- Tanabe, Y.; Sugano, S. On the Absorption Spectra of Complex Ions. II. *J. Physical Soc. Japan* **1954**, *9* (5), 766–779.
- Tanabe, Y.; Sugano, S. On the Absorption Spectra of Complex Ions. III The Calculation of the Crystalline Field Strength. *J. Physical Soc. Japan* **1956**, *11* (8), 864–877.
- Yen, W. M.; Shinonoya, S.; Yamamoto, H. *The Phosphor Handbook*, 2nd ed.; Taylor and Francis Group: Raton, FL, 2007; p 1056.
- Companion, A. L.; Komarynsky, M. A. Crystal Field Splitting Diagrams. *J. Chem. Educ.* **1964**, *41* (5), 257.
- Cotton, F. A. Ligand Field Theory. *J. Chem. Educ.* **1964**, *41* (9), 466.
- Tchougréeff, A. L.; Dronskowski, R. Nephelauxetic Effect Revisited. *Int. J. Quantum Chem.* **2009**, *109* (11), 2606–2621.
- Blasse, G. The Luminescence of Closed-Shell Transition-Metal Complexes. New Developments. In *Structure and Bonding*, vol. 42; Springer: Berlin, Heidelberg, 1980.
- Mikhailik, V. B.; Bauliff, I. K.; Kraus, H.; Rodnyi, P. A.; Ninkovic, J. Two-Photon Excitation and Luminescence of a CaWO_4 Scintillator. *Radiat. Meas.* **2004**, *38* (4), 585–588.
- Treadaway, M. J.; Powell, R. C. Luminescence of Calcium Tungstate Crystals. *J. Chem. Phys.* **1974**, *61* (10), 4003–4011.
- Grasser, R.; Scharmann, A. Luminescent Sites in CaWO_4 and $\text{CaWO}_4:\text{Pb}$ Crystals. *JOL* **1976**, *12–13*, 473–478.
- Buth, A. H.; Blasse, G. Luminescence and Energy Transfer in Yttrium Niobate (YNbO_4). *Phys. Status Solidi A* **1981**, *64* (2), 669–676.
- Kusuma, H. H.; Astuti, B.; Ibrahim, Z. Absorption and Emission Properties of Ruby ($\text{Cr}:\text{Al}_2\text{O}_3$) Single Crystal. *J. Phys. Conf. Ser.* **2019**, *1170*, 012054.
- Malysa, B.; Meijerink, A.; Jüstel, T. Temperature Dependent Luminescence Cr^{3+} -Doped $\text{GdAl}_3(\text{BO}_3)_4$ and $\text{YAl}_3(\text{BO}_3)_4$. *JOL* **2016**, *171*, 246–253.
- Zeng, H.; Zhou, T.; Wang, L.; Xie, R.-J. Two-Site Occupation for Exploring Ultra-Broadband Near-Infrared Phosphor—Double-Perovskite $\text{La}_2\text{MgZrO}_6:\text{Cr}^{3+}$. *Chem. Mater.* **2019**, *31* (14), 5245–5253.
- Henderson, B.; Marshall, A.; Yamaga, M.; O'Donnell, K. P.; Cockayne, B. The Temperature Dependence of Cr^{3+} Photoluminescence in Some Garnet Crystals. *J. Phys. C Solid State Phys.* **1988**, *21* (36), 6187–6198.
- Amidani, L.; Korthout, K.; Joos, J. J.; van der Linden, M.; Sijbom, H. F.; Meijerink, A.; Poelman, D.; Smet, P. F.; Glatzel, P. Oxidation and Luminescence Quenching of Europium in $\text{BaMgAl}_{10}\text{O}_{17}$ Blue Phosphors. *Chem. Mater.* **2017**, *29* (23), 10122–10129.
- Singh, V.; Chakradhar, R. P. S.; Rao, J. L.; Kim, D.-K. Mn^{2+} Activated $\text{MgSrAl}_{10}\text{O}_{17}$ Green-Emitting Phosphor—A Luminescence and EPR Study. *JOL* **2008**, *128* (9), 1474–1478.
- Majher, J. D.; Gray, M. B.; Strom, T. A.; Woodward, P. M. $\text{Cs}_2\text{NaBiCl}_6:\text{Mn}^{2+}$ —A New Orange-Red Halide Double Perovskite Phosphor. *Chem. Mater.* **2019**, *31* (5), 1738–1744.
- Duan, C. J.; Delsing, A. C. A.; Hintzen, H. T. Red Emission From Mn^{2+} on a Tetrahedral Site in MgSiN_2 . *JOL* **2009**, *129* (6), 645–649.
- Zhang, Q. H.; Wang, J.; Yeh, C. W.; Ke, W. C.; Liu, R. S.; Tang, J. K.; Xie, M. B.; Liang, H. B.; Su, Q. Structure, Composition, Morphology, Photoluminescence and Cathodoluminescence Properties of ZnGeN_2 and $\text{ZnGeN}_2:\text{Mn}^{2+}$ for Field Emission Displays. *Acta Mater.* **2010**, *58* (20), 6728–6735.
- Yamashita, N.; Ebisumori, K.; Nakamura, K. Photoluminescence Properties of the $(\text{Ca},\text{Sr})\text{S}:\text{Cu}^+$ Powder Phosphors. *JOL* **1994**, *62* (1), 25–31.
- Yamashita, N. Photoluminescence Properties of Cu^+ Centers in MgS , CaS , SrS and BrS . *Jpn. J. Appl. Phys.* **1991**, *30*, 3335–3340. Part 1, No. 12A.
- Dhoble, S. J.; Gedam, S. C.; Nagpure, I. M.; Godbole, S. V.; Bhide, M. K.; Moharil, S. V. Luminescence of Cu^+ in Halosulphate Phosphor. *J. Mater. Sci.* **2008**, *43* (9), 3189–3196.
- Sahare, P. D.; Bakare, J. S.; Dhole, S. D.; Kumar, P. Effect of Phase Transition and Particle Size on Thermoluminescence Characteristics of Nanocrystalline $\text{K}_2\text{Ca}_2(\text{SO}_4)_3:\text{Cu}^+$ Phosphor. *Radiat. Meas.* **2012**, *47* (11), 1083–1091.
- Meijerink, A.; Blasse, G.; Glasbeek, M. Photoluminescence, Thermoluminescence and EPR Studies on $\text{Zn}_4\text{B}_6\text{O}_{13}$. *J. Phys. Condens. Matter* **1990**, *2* (29), 6303–6313.
- Hamoumi, M.; Wiegel, M.; Blasse, G.; Favard, J. F.; Piffard, Y. Luminescence of Ions With d^0 Configuration in Compositions With the KTiPO_4 Structure. *Mater. Res. Bull.* **1992**, *27* (6), 699–703.
- De Bruin, T. J. M.; Wiegel, M.; Dirksen, G. J.; Blasse, G. Luminescence of $\text{Li}_2\text{ZrTeO}_6$. *J. Solid State Chem.* **1993**, *107* (2), 397–400.
- Jing, Y.; Liu, Y.; Li, M.; Xia, Z. Photoluminescence of Singlet/Triplet Self-Trapped Excitons in Sb^{3+} -Based Metal Halides. *Adv. Opt. Mater.* **2021**, *9* (8), 2002213.

54. Gray, M. B.; Hariyani, S.; Strom, T. A.; Majher, J. D.; Brgoch, J.; Woodward, P. M. High-Efficiency Blue Photoluminescence in the $\text{Cs}_2\text{NaNCl}_6\text{:Sb}^{3+}$ Double Perovskite Phosphor. *J. Mater. Chem. C* **2020**, *8* (20), 6797–6803.
55. Boutinaud, P. Luminescence of Sb^{3+} in Closed Shell Transition Metal Oxides. *JOL* **2019**, *208*, 394–401.
56. Majher, J. D.; Gray, M. B.; Liu, T.; Holzapfel, N. P.; Woodward, P. M. Rb_3InCl_6 : A Monoclinic Double Perovskite Derivative With Bright Sb^{3+} -Activated Photoluminescence. *Inorg. Chem.* **2020**, *59* (19), 14478–14485.
57. Gao, Y.; Cheng, Y.; Huang, F.; Lin, H.; Xu, J.; Wang, Y. $\text{Sn}^{2+}/\text{Mn}^{2+}$ Codoped Strontium Phosphate ($\text{Sr}_2\text{P}_2\text{O}_7$) Phosphor for High Temperature Optical Thermometry. *J. Alloys Compd.* **2018**, *735*, 1546–1552.
58. Pekgözü, İ.; Erdoğan, E.; Demirel, B.; Sabri Gök, M.; Karabulut, H.; Başak, A. S. A Novel UV-Emitting Phosphor: $\text{Li}_6\text{CaB}_3\text{O}_{8.5}\text{Pb}^{2+}$. *JOL* **2011**, *131* (11), 2290–2293.
59. Pekgözü, İ. A Novel UV-Emitting Phosphor: $\text{LiSr}_4(\text{BO}_3)_3\text{:Pb}^{2+}$. *JOL* **2013**, *143*, 93–95.
60. Pekgözü, İ.; Seyidoğlu, S.; Taşcıoğlu, S. A Novel Blue-Emitting Phosphor: $\text{BaAl}_2\text{B}_2\text{O}_7\text{:Pb}^{2+}$. *JOL* **2008**, *128* (9), 1541–1543.
61. Gschneidner, K. A., Jr.; LeRoy, E. *Handbook on the Physics and Chemistry of Rare Earths*, vol. 23; Elsevier, 1996. North Holland.
62. Souza, A. S.; Oliveira, Y. A. R.; Couto dos Santos, M. A. Enhanced Approach to the Eu^{3+} Ion $^5\text{D}_0 \rightarrow ^7\text{F}_0$ Transition Intensity. *Opt. Mater.* **2013**, *35* (9), 1633–1635.
63. Binnemans, K.; Gorler-Walrand, C. Application of the Eu^{3+} Ion for Site Symmetry Determination. *J. Rare Earths* **1996**, *14*, 173–180.
64. Buijs, M.; Meyerink, A.; Blasse, G. Energy Transfer Between Eu^{3+} Ions in a Lattice With Two Different Crystallographic Sites: $\text{Y}_2\text{O}_3\text{:Eu}^{3+}$, $\text{Gd}_2\text{O}_3\text{:Eu}^{3+}$ and Eu_2O_3 . *JOL* **1987**, *37* (1), 9–20.
65. Marinkovic, K.; Mancic, L.; Gomez, L. S.; Rabanal, M. E.; Dramicanin, M.; Milosevic, O. Photoluminescent Properties of Nanostructured $\text{Y}_2\text{O}_3\text{:Eu}^{3+}$ Powders Obtained Through Aerosol Synthesis. *Opt. Mater.* **2010**, *32* (12), 1606–1611.
66. Zhuo, Y.; Hariyani, S.; Armijo, E.; Abolade Lawson, Z.; Brgoch, J. Evaluating Thermal Quenching Temperature in Eu^{3+} -Substituted Oxide Phosphors via Machine Learning. *ACS Appl. Mater. Interfaces* **2019**, *12*, 5244–5250.
67. Lokeswara Reddy, G. V.; Rama Moorthy, L.; Packiyaraj, P.; Jamalalah, B. C. Optical Characterization of $\text{YAl}_3(\text{BO}_3)_4\text{:Dy}^{3+}\text{--Tm}^{3+}$ Phosphors Under Near UV Excitation. *Opt. Mater.* **2013**, *35* (12), 2138–2145.
68. Su, Q.; Pei, Z.; Chi, L.; Zhang, H.; Zhang, Z.; Zou, F. The Yellow-to-Blue Intensity Ratio (Y/B) of Dy^{3+} Emission. *J. Alloys Compd.* **1993**, *192* (1), 25–27.
69. Ramesh, B.; Dillip, G. R.; Raju, B. D. P.; Somasundaram, K.; Peddi, S. P.; de Carvalho dos Anjos, V.; Joo, S. W. Facile One-Pot Synthesis of Hexagons of $\text{NaNb}_5\text{O}_9\text{:Tb}^{3+}$ Phosphor for Solid-State Lighting. *Mater. Res. Express* **2017**, *4* (4), 046201.
70. Nakazawa, E.; Shionoya, S. Relaxation Between Excited Levels of Tb^{3+} Ion Due to Resonance Energy Transfer. *J. Physical Soc. Japan* **1970**, *28* (5), 1260–1265.
71. Geng, W.; Zhou, X.; Ding, J.; Wang, Y. $\text{NaBaY}(\text{BO}_3)_2\text{:Ce}^{3+}, \text{Tb}^{3+}$: A Novel Sharp Green-Emitting Phosphor Used for WLED and FEDs. *J. Am. Ceram. Soc.* **2018**, *101* (10), 4560–4571.
72. Chen, H.; Wang, Y. $\text{Sr}_2\text{LiScB}_4\text{O}_{10}\text{:Ce}^{3+}/\text{Tb}^{3+}$: A Green-Emitting Phosphor With High Energy Transfer Efficiency and Stability for LEDs and FEDs. *Inorg. Chem.* **2019**, *58* (11), 7440–7452.
73. Zhong, J.; Zhuo, Y.; Hariyani, S.; Zhao, W.; Zhuang, W.; Brgoch, J. Thermally Robust and Color-Tunable Blue-Green-Emitting $\text{BaMgSi}_4\text{O}_{10}\text{:Eu}^{2+}, \text{Mn}^{2+}$ Phosphor for Warm-White LEDs. *Inorg. Chem.* **2020**, *59* (18), 13427–13434.
74. Rack, P. D.; Holloway, P. H. The Structure, Device Physics, and Material Properties of Thin Film Electroluminescent Displays. *Mater. Sci. Eng. R* **1998**, *21* (4), 171–219.
75. Dorenbos, P. Crystal Field Splitting of Lanthanide $4f^{-1}5d$ -Levels in Inorganic Compounds. *J. Alloys Compd.* **2002**, *341* (1), 156–159.
76. Yen, W. M.; Shinoya, S.; Yamamoto, H. *Fundamentals of Phosphors*, Taylor and Francis Group: Boca Raton, FL, 2006.
77. Qin, X.; Liu, X.; Huang, W.; Bettinelli, M.; Liu, X. Lanthanide-Activated Phosphors Based on $4f-5d$ Optical Transitions: Theoretical and Experimental Aspects. *Chem. Rev.* **2017**, *117* (5), 4488–4527.
78. Hariyani, S.; Brgoch, J. Local Structure Distortion Induced Broad Band Emission in the All-Inorganic $\text{BaScO}_2\text{:Eu}^{2+}$ Perovskite. *Chem. Mater.* **2020**, *32* (15), 6640–6649.
79. Hariyani, S.; Brgoch, J. Advancing Human-Centric LED Lighting Using $\text{Na}_2\text{MgPO}_4\text{:Eu}^{2+}$. *ACS Appl. Mater. Interfaces* **2021**, *13* (14), 16669–16676.
80. Müller, M.; Jüstel, T. On the Luminescence and Energy Transfer of White Emitting $\text{Ca}_3\text{Y}_2(\text{Si}_3\text{O}_9)_2\text{:Ce}^{3+}, \text{Mn}^{2+}$ Phosphor. *JOL* **2014**, *155*, 398–404.
81. Qiao, J.; Zhao, J.; Liu, Q.; Xia, Z. Recent Advances in Solid-State LED Phosphors With Thermally Stable Luminescence. *J. Rare Earths* **2019**, *37* (6), 565–572.
82. Tsai, Y.-T.; Chiang, C.-Y.; Zhou, W.; Lee, J.-F.; Sheu, H.-S.; Liu, R.-S. Structural Ordering and Charge Variation Induced by Cation Substitution in $(\text{Sr,Ca})\text{AlSi}_3\text{Eu}$ Phosphor. *J. Am. Chem. Soc.* **2015**, *137* (28), 8936–8939.
83. Liu, H.; Xia, Z.; Zhuang, J.; Zhang, Z.; Liao, L. Surface Treatment Investigation and Luminescence Properties of SiO_2 -Coated $\text{Ca}_2\text{BO}_3\text{Cl:0.02Eu}^{2+}$ Phosphors via Sol–Gel Process. *J. Phys. Chem. Solid* **2012**, *73* (1), 104–108.
84. Ueda, J.; Tanabe, S. Review of Luminescent Properties of Ce^{3+} -Doped Garnet Phosphors: New Insight Into the Effect of Crystal and Electronic Structure. *Opt. Mater. X* **2019**, *1*, 100018.
85. Xia, Z.; Meijerink, A. Ce^{3+} -Doped Garnet Phosphors: Composition Modification, Luminescence Properties and Applications. *Chem. Soc. Rev.* **2017**, *46* (1), 275–299.
86. Yoder, H. S.; Keith, M. L. Complete Substitution of Aluminum for Silicon: The system $3\text{MnO} \cdot \text{Al}_2\text{O}_3 \cdot 3\text{SiO}_2\text{--}3\text{Y}_2\text{O}_3 \cdot 5\text{Al}_2\text{O}_3$. *Am. Mineral.* **1951**, *36* (7-8), 519–533.
87. Blasse, G.; Brill, A. A New Phosphor for Flying-Spot Cathode-Ray Tubes for Color Televisions: Yellow-Emitting $\text{Y}_3\text{Al}_5\text{O}_{12}\text{:Ce}^{3+}$. *Appl. Phys. Lett.* **1967**, *11* (2), 53–55.
88. Lin, Y. S.; Liu, R. S.; Cheng, B. M. Investigation of the Luminescent Properties of Tb^{3+} -Substituted YAG:Ce, Gd Phosphors. *J. Electrochem. Soc.* **2005**, *152* (6), J41.
89. Shannon, R. D. Revised Effective Ionic Radii and Systematic Studies of Interatomic Distances in Halides and Chalcogenides. *Acta Crystallogr., Sect. A: Found. Crystallogr.* **1976**, *A32* (5), 751–767.
90. Chen, Y.; He, J.; Zhang, X.; Rong, M.; Xia, Z.; Wang, J.; Liu, Z.-Q. Dual-Mode Optical Thermometry Design in $\text{Lu}_3\text{Al}_5\text{O}_{12}\text{:Ce}^{3+}/\text{Mn}^{4+}$ Phosphor. *Inorg. Chem.* **2020**, *59* (2), 1383–1392.
91. Bachmann, V.; Ronda, C.; Meijerink, A. Temperature Quenching of Yellow Ce^{3+} Luminescence in YAG:Ce. *Chem. Mater.* **2009**, *21* (10), 2077–2084.
92. Liebau, F. *Structural Chemistry of Silicates: Structure, Bonding, and Classification*, Springer-Verlag: Heidelberg, 1985.
93. Kieffer, S. W. Thermodynamics and Lattice Vibrations of Minerals: 4. Application to Chain and Sheet Silicates and Orthosilicates. *Rev. Geophys.* **1980**, *18* (4), 862–886.
94. Barry, T. L. Fluorescence of Eu^{2+} -Activated Phases in Binary Alkaline Earth Orthosilicate Systems. *J. Electrochem. Soc.* **1968**, *115* (11), 1181.
95. Poort, S. H. M.; Janssen, W.; Blasse, G. Optical Properties of Eu^{2+} -Activated Orthosilicates and Orthophosphates. *J. Alloys Compd.* **1997**, *260* (1), 93–97.
96. Kalaji, A.; Mikami, M.; Cheetham, A. K. Ce^{3+} -Activated $\gamma\text{-Ca}_2\text{SiO}_4$ and Other Olivine-Type ABXO_4 Phosphors for Solid-State Lighting. *Chem. Mater.* **2014**, *26* (13), 3966–3975.
97. Kelsey, P. V.; Brown, J. J. Ce^{3+} -Activated Photoluminescence in the BaO-SrO-SiO_2 System: I. Crystalline Phases. *J. Electrochem. Soc.* **1976**, *123* (9), 1384–1388.
98. Im, W. B.; George, N.; Kurzman, J.; Brinkley, S.; Mikhailovsky, A.; Hu, J.; Chmelka, B. F.; DenBaars, S. P.; Seshadri, R. Efficient and Color-Tunable Oxyluoride Solid Solution Phosphors for Solid-State White Lighting. *Adv. Mater.* **2011**, *23* (20), 2300–2305.
99. Aitasalo, T.; Hreniak, D.; Hölsä, J.; Laamanen, T.; Lastusaari, M.; Niittykoski, J.; Pellé, F.; Strek, W. Persistent Luminescence of $\text{Ba}_2\text{MgSi}_2\text{O}_7\text{:Eu}^{2+}$. *JOL* **2007**, *122–123*, 110–112.
100. Poort, S. H. M.; Reijnhoud, H. M.; van der Kuip, H. O. T.; Blasse, G. Luminescence of Eu^{2+} in Silicate Host Lattices With Alkaline Earth Ions in a Row. *J. Alloys Compd.* **1996**, *241* (1), 75–81.
101. Birkel, A.; Darago, L. E.; Morrison, A.; Lory, L.; George, N. C.; Mikhailovsky, A. A.; Birkel, C. S.; Seshadri, R. Microwave Assisted Preparation of Eu^{2+} -Doped $\text{Åkermanite Ca}_2\text{MgSi}_2\text{O}_7$. *Solid State Sci.* **2012**, *14* (6), 739–745.
102. Pust, P.; Weiler, V.; Hecht, C.; Tücks, A.; Wochnik, A. S.; Henß, A.-K.; Wiechert, D.; Scheu, C.; Schmidt, P. J.; Schnick, W. Narrow-Band Red-Emitting $\text{Sr}[\text{LiAl}_3\text{N}_4]\text{:Eu}^{2+}$ as a Next-Generation LED-Phosphor Material. *Nat. Mater.* **2014**, *13*, 891–896.

103. Schmiechen, S.; Schneider, H.; Wagatha, P.; Hecht, C.; Schmidt, P. J.; Schnick, W. Toward New Phosphors for Application in Illumination-Grade White PC-LEDs: The Nitridomagnesiumsilicates $\text{Ca}[\text{Mg}_3\text{SiN}_4]:\text{Ce}^{3+}$, $\text{Sr}[\text{Mg}_3\text{SiN}_4]:\text{Eu}^{2+}$, and $\text{Eu}[\text{Mg}_3\text{SiN}_4]$. *Chem. Mater.* **2014**, *26* (8), 2712–2719.
104. Pust, P.; Hintze, F.; Hecht, C.; Weiler, V.; Locher, A.; Zitnanska, D.; Harm, S.; Wiechert, D.; Schmidt, P. J.; Schnick, W. Group (III) Nitrides $M[\text{Mg}_2\text{Al}_2\text{N}_4]$ ($M = \text{Ca}, \text{Sr}, \text{Ba}, \text{Eu}$) and $\text{Ba}[\text{Mg}_2\text{Ga}_2\text{N}_4]$ —Structural Relation and Nontypical Luminescence Properties of Eu^{2+} -Doped Samples. *Chem. Mater.* **2014**, *26* (21), 6113–6119.
105. Wang, W.; Tao, M.; Liu, Y.; Wei, Y.; Xing, G.; Dang, P.; Lin, J.; Li, G. Photoluminescence Control of UCr_4C_4 -Type Phosphors with Superior Luminous Efficiency and High Color Purity via Controlling Site Selection of Eu^{2+} Activators. *Chem. Mater.* **2019**, *31* (21), 9200–9210.
106. Liao, H.; Zhao, M.; Molokeyev, M. S.; Liu, Q.; Xia, Z. Learning From a Mineral Structure Toward an Ultra-Narrow-Band Blue-Emitting Silicate Phosphor $\text{RbNa}_3(\text{Li}_3\text{SiO}_4)_4:\text{Eu}^{2+}$. *Angew. Chem. Int. Ed.* **2018**, *57* (36), 11728–11731.
107. Viswanath, N. S. M.; Krishnamurthy Grandhi, G.; Tran Huu, H.; Choi, H.; Jun Kim, H.; Min Kim, S.; You Kim, H.; Park, C.-J.; Bin Im, W. Zero-Thermal-Quenching and Improved Chemical Stability of a UCr_4C_4 -Type Phosphor via Crystal Site Engineering. *Chem. Eng. J.* **2020**, *420*, 127664.
108. Mahata, M. K.; Hofsass, H. C.; Vetter, U. Photon-Upconverting Materials: Advances and Prospects for Various Emerging Applications. In *Luminescence—An Outlook on the Phenomena and Their Applications*, InTech, 2016.
109. Bloembergen, N. Solid State Infrared Quantum Counters. *Phys. Rev. Lett.* **1959**, *2* (3), 84–85.
110. Auzel, F. Upconversion and Anti-Stokes Processes With f and d Ions in Solids. *Chem. Rev.* **2004**, *104* (1), 139–174.
111. Wang, F.; Deng, R.; Wang, J.; Wang, Q.; Han, Y.; Zhu, H.; Chen, X.; Liu, X. Tuning Upconversion Through Energy Migration in Core-Shell Nanoparticles. *Nat. Mater.* **2011**, *10* (12), 968–973.
112. Wen, H.; Zhu, H.; Chen, X.; Hung, T. F.; Wang, B.; Zhu, G.; Yu, S. F.; Wang, F. Upconverting Near-Infrared Light Through Energy Management in Core-Shell-Shell Nanoparticles. *Angew. Chem. Int. Ed.* **2013**, *52* (50), 13419–13423.
113. Zhou, J.; Liu, Q.; Feng, W.; Sun, Y.; Li, F. Upconversion Luminescent Materials: Advances and Applications. *Chem. Rev.* **2015**, *115* (1), 395–465.
114. Wang, J.; Wang, F.; Wang, C.; Liu, Z.; Liu, X. Single-Band Upconversion Emission in Lanthanide-Doped KMnF_3 Nanocrystals. *Angew. Chem. Int. Ed.* **2011**, *50* (44), 10369–10372.
115. Chan, E. M.; Han, G.; Goldberg, J. D.; Gargas, D. J.; Ostrowski, A. D.; Schuck, P. J.; Cohen, B. E.; Milliron, D. J. Combinatorial Discovery of Lanthanide-Doped Nanocrystals With Spectrally Pure Upconverted Emission. *Nano Lett.* **2012**, *12* (7), 3839–3845.
116. Chen, D.; Lei, L.; Zhang, R.; Yang, A.; Xu, J.; Wang, Y. Intrinsic Single-Band Upconversion Emission in Colloidal $\text{Yb/Er(Tm):Na}_3\text{Zr(Hf)F}_7$ Nanocrystals. *Chem. Commun.* **2012**, *48* (86), 10630–10632.
117. Finley, E.; Mansouri Tehrani, A.; Brgoch, J. Intrinsic Defects Drive Persistent Luminescence in Monoclinic $\text{SrAl}_2\text{O}_4:\text{Eu}^{2+}$. *J. Phys. Chem. C* **2018**, *122* (28), 16309–16314.
118. Aitasalo, T.; Hölsä, J.; Jungner, H.; Krupa, J.-C.; Lastusaari, M.; Legendziewicz, J.; Niittykoski, J. Effect of Temperature on the Luminescence Processes of $\text{SrAl}_2\text{O}_4:\text{Eu}^{2+}$. *Radiat. Meas.* **2004**, *38* (4), 727–730.
119. Abbruscato, V. Optical and Electrical Properties of $\text{SrAl}_2\text{O}_4:\text{Eu}^{2+}$. *J. Electrochem. Soc.* **1971**, *118* (6), 930.
120. Matsuzawa, T.; Aoki, Y.; Takeuchi, N.; Murayama, Y. A New Long Phosphorescent Phosphor With High Brightness, $\text{SrAl}_2\text{O}_4:\text{Eu}^{2+}, \text{Dy}^{3+}$. *J. Electrochem. Soc.* **1996**, *143* (8), 2670–2673.
121. Varga, L. P.; Asprey, L. B. Electronic Spectra of Weak-Field Fluoride Complexes of Tetravalent Neodymium. *J. Chem. Phys.* **1968**, *49* (10), 4674–4679.
122. Dorenbos, P. Mechanism of Persistent Luminescence in Eu^{2+} and Dy^{3+} Codoped Aluminate and Silicate Compounds. *J. Electrochem. Soc.* **2005**, *152* (7), H107.
123. Clabau, F.; Rocquefelte, X.; Jobic, S.; Deniard, P.; Whangbo, M. H.; Garcia, A.; Le Mercier, T. Mechanism of Phosphorescence Appropriate for the Long-Lasting Phosphors Eu^{2+} -Doped SrAl_2O_4 With Co-Dopants Dy^{3+} and B^{3+} . *Chem. Mater.* **2005**, *17* (15), 3904–3912.
124. Finley, E. *Structure-Composition Relationships and Their Influence on Long Luminescent Lifetimes in Persistent Luminescent Phosphors*, University of Houston: Houston, TX, 2019.
125. Qu, B.; Zhang, B.; Wang, L.; Zhou, R.; Zeng, X. C. Mechanistic Study of the Persistent Luminescence of $\text{CaAl}_2\text{O}_4:\text{Eu}, \text{Nd}$. *Chem. Mater.* **2015**, *27* (6), 2195–2202.
126. Finley, E.; Cobb, A.; Duke, A.; Paterson, A.; Brgoch, J. Optimizing Blue Persistent Luminescence in $(\text{Sr}_{1-x}\text{Ba}_x)_2\text{MgSi}_2\text{O}_7:\text{Eu}^{2+}, \text{Dy}^{3+}$ via Solid Solution for Use in Point-of-Care Diagnostics. *ACS Appl. Mater. Interfaces* **2016**, *8* (40), 26956–26963.
127. Xie, R.-J.; Hirotsaki, N.; Suehiro, T.; Xu, F.-F.; Mitomo, M. A Simple, Efficient Synthetic Route to $\text{Sr}_2\text{Si}_5\text{N}_8:\text{Eu}^{2+}$ -Based Red Phosphors for White Light-Emitting Diodes. *Chem. Mater.* **2006**, *18* (23), 5578–5583.
128. Brinkley, S. E.; Pfaff, N.; Denault, K. A.; Zhang, Z.; Hintzen, H. T.; Seshadri, R.; Nakamura, S.; DenBaars, S. P. Robust Thermal Performance of $\text{Sr}_2\text{Si}_5\text{N}_8:\text{Eu}^{2+}$: An Efficient Red Emitting Phosphor for Light Emitting Diode Based White Lighting. *Appl. Phys. Lett.* **2011**, *99* (24), 241106.
129. Xie, R.-J.; Hirotsaki, N.; Mitomo, M.; Takahashi, K.; Sakuma, K. Highly Efficient White-Light-Emitting Diodes Fabricated With Short-Wavelength Yellow Oxynitride Phosphors. *Appl. Phys. Lett.* **2006**, *88* (10), 101104.
130. Park, K.; Kim, T.; Yu, Y.; Seo, K.; Kim, J. Y/Gd-Free Yellow $\text{Lu}_2\text{Al}_5\text{O}_{12}:\text{Ce}^{3+}$ Phosphor for White LEDs. *JOL* **2016**, *173*, 159–164.
131. Prayag, A. S.; Munch, M.; Aeschbach, D.; Chellappa, S. L.; Gronfier, C. Light Modulation of Human Clocks, Wake, and Sleep. *Clocks Sleep* **2019**, *1* (1), 193–208.
132. Cupkova, D.; Kajati, E.; Mocnej, J.; Papcun, P.; Koziorek, J.; Zolotova, I. Intelligent Human-Centric Lighting for Mental Wellbeing Improvement. *Int. J. Distrib. Sens. Netw.* **2019**, *15* (9), 1550147719875878.
133. Nakamura, S.; Senoh, M.; Iwasa, N.; Nagahama, S. I. High-Power InGaN Single-Quantum-Well-Structure Blue and Violet Light-Emitting Diodes. *Appl. Phys. Lett.* **1995**, *67* (13), 1868–1870.
134. Daicho, H.; Iwasaki, T.; Enomoto, K.; Sasaki, Y.; Maeno, Y.; Shinomiya, Y.; Aoyagi, S.; Nishibori, E.; Sakata, M.; Sawa, H.; Matsuishi, S.; Hosono, H. A Novel Phosphor for Glareless White Light-Emitting Diodes. *Nat. Commun.* **2012**, *3* (1), 1132.
135. Hase, T.; Kano, T.; Nakazawa, E.; Yamamoto, H. Phosphor Materials for Cathode-Ray Tubes. In *Advances in Electronics and Electron Physics*; Hawkes, P. W., Ed.; vol. 79; Academic Press, 1990; pp 271–373.
136. Shuxiu, Z. Vacuum-Ultraviolet/Visible Conversion Phosphors for Plasma Display Panels. *IEEE Trans. Plasma Sci.* **2006**, *34* (2), 294–304.
137. Koike, J.; Kojima, T.; Toyonaga, R.; Kagami, A.; Hase, T.; Inaho, S. New Tricolor Phosphors for Gas Discharge Display. *J. Electrochem. Soc.* **1979**, *126* (6), 1008–1010.
138. Rao, R. P.; Devine, D. J. RE-Activated Lanthanide Phosphate Phosphors for PDP Applications. *JOL* **2000**, *87–89*, 1260–1263.
139. Sohn, K.-S.; Mun Lee, J.; Woon Jeon, I.; Dong Park, H. Combinatorial Searching for Tb^{3+} -Activated Phosphors of High Efficiency at Vacuum UV Excitation. *J. Electrochem. Soc.* **2003**, *150* (8), H182.
140. Veenis, A. W.; Bril, A. On the VUV Excitation Spectra and Quantum Efficiencies of Luminescent Powders, Mainly Rare Earth Activated Borates. *Philips J. Res.* **1978**, *33* (3–4), 124–132.
141. Murphy, J. E.; Garcia-Santamaria, F.; Setlur, A. A.; Sista, S. 62.4: PFS, K2SiF6:Mn4+: The Red-Line Emitting LED Phosphor Behind GE's TriGain Technology™ Platform. *SID Symp. Dig. Tech. Pap.* **2015**, *46* (1), 927–930.
142. Zhuo, Y.; Hariyani, S.; Zhong, J.; Brgoch, J. Creating a Green-Emitting Phosphor through Selective Rare-Earth Site Preference in $\text{NaBaB}_9\text{O}_{15}:\text{Eu}^{2+}$. *Chem. Mater.* **2021**, *33* (9), 3304–3311.
143. Fang, S.; Lang, T.; Han, T.; Cai, M.; Cao, S.; Peng, L.; Liu, B.; Zhong, Y.; Yakovlev, A. N.; Korepanov, V. I. A Novel Efficient Single-Phase Dual-Emission Phosphor With High Resemblance to the Photosynthetic Spectrum of Chlorophyll A and B. *J. Mater. Chem. C* **2020**, *8* (18), 6245–6253.
144. Zhang, S.; Nakai, Y.; Tsuboi, T.; Huang, Y.; Seo, H. J. The Thermal Stabilities of Luminescence and Microstructures of Eu^{2+} -Doped KBaPO_4 and NaSrPO_4 With $\beta\text{-K}_2\text{SO}_4$ Type Structure. *Inorg. Chem.* **2011**, *50* (7), 2897–2904.
145. Bandi, V. R.; Jeong, J.; Shin, H.-J.; Jang, K.; Lee, H.-S.; Yi, S.-S.; Jeong, J. H. Thermally Stable Blue-Emitting $\text{NaSrPO}_4:\text{Eu}^{2+}$ Phosphor for Near UV White LEDs. *Opt. Commun.* **2011**, *284* (19), 4504–4507.

146. Chou, H.; Jenssen, H. P. Upconversion Processes in Er-Activated Solid State Laser Materials. In *Advanced Solid State Lasers*; Shand, M., Jenssen, H., Eds., Optical Society of America: Cape Cod, Massachusetts, 1989; p DD5. Cape Cod, Massachusetts, 1989/05/01.
147. Joubert, M.-F. Photon Avalanche Upconversion in Rare Earth Laser Materials. *Opt. Mater.* **1999**, *11* (2), 181–203.
148. Zhang, F.; Wan, Y.; Yu, T.; Zhang, F.; Shi, Y.; Xie, S.; Li, Y.; Xu, L.; Tu, B.; Zhao, D. Uniform Nanostructured Arrays of Sodium Rare-Earth Fluorides for Highly Efficient Multicolor Upconversion Luminescence. *Angew. Chem. Int. Ed.* **2007**, *46* (42), 7976–7979.
149. Zhang, C.; Yang, L.; Zhao, J.; Liu, B.; Han, M.-Y.; Zhang, Z. White-Light Emission From an Integrated Upconversion Nanostructure: Toward Multicolor Displays Modulated by Laser Power. *Angew. Chem. Int. Ed.* **2015**, *54* (39), 11531–11535.
150. Blixt, P.; Nilsson, J.; Carnas, T.; Jaskorzynska, B. Concentration-Dependent Uconversion in Er³⁺ Doped Fiber Amplifiers: Experiments and Modeling. *IEEE Photon. Technol. Lett.* **1991**, *3* (11), 996–998.
151. Ohtsuki, T.; Honkanen, S.; Najafi, S. I.; Peyghambarian, N. Cooperative Upconversion Effects on the Performance of Er³⁺-Doped Phosphate Glass Waveguide Amplifiers. *J. Opt. Soc. Am. B* **1997**, *14* (7), 1838–1845.
152. Chatterjee, D. K.; Rufaihah, A. J.; Zhang, Y. Upconversion Fluorescence Imaging of Cells and Small Animals Using Lanthanide Doped Nanocrystals. *Biomaterials* **2008**, *29* (7), 937–943.
153. Wang, X.-D.; Wolfbeis, O. S.; Meier, R. J. Luminescent Probes and Sensors for Temperature. *Chem. Soc. Rev.* **2013**, *42* (19), 7834–7869.
154. Zhao, Y.; Wang, X.; Zhang, Y.; Li, Y.; Yao, X. Optical Temperature Sensing of Up-Conversion Luminescent Materials: Fundamentals and Progress. *J. Alloys Compd.* **2020**, *817*, 152691.
155. Li, Z.; Zhang, Y.; Jiang, S. Multicolor Core/Shell-Structured Upconversion Fluorescent Nanoparticles. *Adv. Mater.* **2008**, *20* (24), 4765–4769.
156. Zhou, S.; Deng, K.; Wei, X.; Jiang, G.; Duan, C.; Chen, Y.; Yin, M. Upconversion Luminescence of NaYF₄: Yb³⁺, Er³⁺ for Temperature Sensing. *Opt. Commun.* **2013**, *291*, 138–142.
157. Liu, J.; Lécuyer, T.; Seguin, J.; Mignet, N.; Scherman, D.; Viana, B.; Richard, C. Imaging and Therapeutic Applications of Persistent Luminescence Nanomaterials. *Adv. Drug Deliv. Rev.* **2019**, *138*, 193–210.
158. Maldiney, T.; Richard, C.; Seguin, J.; Wattier, N.; Bessodes, M.; Scherman, D. Effect of Core Diameter, Surface Coating, and PEG Chain Length on the Biodistribution of Persistent Luminescence Nanoparticles in Mice. *ACS Nano* **2011**, *5* (2), 854–862.
159. Aitasalo, T.; Hölsä, J.; Jungner, H.; Lastusaari, M.; Niittykoski, J. Sol-Gel Processed Eu²⁺-Doped Alkaline Earth Aluminates. *J. Alloys Compd.* **2002**, *341* (1), 76–78.
160. Chen, I. C.; Chen, T.-M. Effect of Host Compositions on the Afterglow Properties of Phosphorescent Strontium Aluminate Phosphors Derived From the Sol-Gel Method. *J. Mater. Res.* **2001**, *16* (5), 12.
161. Fu, Z.; Zhou, S.; Yu, Y.; Zhang, S. Combustion Synthesis and Luminescence Properties of Nanocrystalline Monoclinic SrAl₂O₄:Eu²⁺. *Chem. Phys. Lett.* **2004**, *395* (4), 285–289.
162. Tanaka, H.; Gubarevich, A. V.; Wada, H.; Odawara, O. Process Stages During Solution Combustion Synthesis of Strontium Aluminates. *Int. J. Self-Propag. High-Temp. Synth.* **2013**, *22* (3), 151–156.
163. Xiao, Q.; Xiao, L.; Liu, Y.; Chen, X.; Li, Y. Synthesis and Luminescence Properties of Needle-Like SrAl₂O₄:Eu, Dy Phosphor via a Hydrothermal Co-Precipitation Method. *J. Phys. Chem. Solid* **2010**, *71* (7), 1026–1030.
164. Finley, E.; Paterson, A. S.; Cobb, A.; Willson, R. C.; Brgoch, J. Reducing Particle Size of Persistent Luminescent SrAl₂O₄:Eu²⁺, Dy³⁺ via Microwave-Assisted, Reverse Micelle Synthesis. *Opt. Mater. Express* **2017**, *7* (7), 2597–2616.
165. Rojas-Hernandez, R. E.; Rubio-Marcos, F.; Rodriguez, M.Á.; Fernandez, J. F. Long Lasting Phosphors: SrAl₂O₄:Eu, Dy as the Most Studied Material. *Renew. Sustain. Energy Rev.* **2018**, *81*, 2759–2770.
166. Blasse, G.; Wanmaker, W. L.; ter Vrugt, J. W. Some New Classes of Efficient Eu²⁺-Activated Phosphors. *J. Electrochem. Soc.* **1968**, *115* (6), 673.
167. Danthararajana, A. N.; Finley, E.; Vu, B.; Kourentzi, K.; Willson, R. C.; Brgoch, J. A Multicolor Multiplex Lateral Flow Assay for High-Sensitivity Analyte Detection Using Persistent Luminescent Nanophosphors. *Anal. Methods* **2020**, *12* (3), 272–280.
168. Paterson, A. S.; Raja, B.; Mandadi, V.; Townsend, B.; Lee, M.; Buell, A.; Vu, B.; Brgoch, J.; Willson, R. C. A Low-Cost Smartphone-Based Platform for Highly Sensitive Point-of-Care Testing With Persistent Luminescent Phosphors. *Lab Chip* **2017**, *17* (6), 1051–1059.
169. Wilkinson, F. CHAPTER 13—Scintillators. In *Emission Tomography*; Wernick, M. N., Aarsvold, J. N., Eds., Academic Press: San Diego, 2004; pp 229–254.
170. Faderl, N. *Fast Decay Solid-State Scintillators for High-Speed X-Ray Imaging*; vol. 11159; SPIE, 2019.
171. Weber, M. J. Inorganic Scintillators: Today and Tomorrow. *JOL* **2002**, *100* (1), 35–45.
172. Novotny, R.; Riess, R.; Hingmann, R.; Ströher, H.; Fischer, R. D.; Koch, G.; Kühn, W.; Metag, V.; Mühlhans, R.; Kneissl, U.; Wilke, W.; Haas, B.; Vivien, J. P.; Beck, R.; Schoch, B.; Schutz, Y. Detection of Hard Photons with BaF₂ Scintillators. *Nucl. Instrum. Methods Phys. Res., Sect. A* **1987**, *262* (2), 340–346.
173. Lempicki, A.; Wojtowicz, A. J. Fundamental Limitations of Scintillators. *JOL* **1994**, *60-61*, 942–947.
174. Krämer, K. W.; Dorenbos, P.; Güdel, H. U.; van Eijk, C. W. E. Development and Characterization of Highly Efficient New Cerium Doped Rare Earth Halide Scintillator Materials. *J. Mater. Chem.* **2006**, *16* (27), 2773–2780.
175. Blasse, G. Scintillator Materials. *Chem. Mater.* **1994**, *6* (9), 1465–1475.
176. Zou, G.; Liu, Z.; Wang, L.; Zhao, Y.; Cui, Q.; Li, D. Pressure-Induced Amorphization of Crystalline Bi₄Ge₃O₁₂. *Phys. Lett. A* **1991**, *156* (7), 450–454.
177. (a) Neamen, D. *An Introduction to Semiconductor Devices*, 1st ed.; McGraw-Hill, 2006; (b) Housecroft, C. E.; Sharpe, A. G. *Inorganic Chemistry*, 3rd ed.; Pearson Education Limited, 2008.
178. Dumke, W. P. Spontaneous Radiative Recombination in Semiconductors. *Phys. Rev.* **1957**, *105* (1), 139–144.
179. Tongay, S.; Suh, J.; Ataca, C.; Fan, W.; Luce, A.; Kang, J. S.; Liu, J.; Ko, C.; Raghunathanan, R.; Zhou, J.; Ogletree, F.; Li, J.; Grossman, J. C.; Wu, J. Defects Activated Photoluminescence in Two-Dimensional Semiconductors: Interplay Between Bound, Charged and Free Excitons. *Sci. Rep.* **2013**, *3* (1), 2657.
180. Sugahara, T.; Sato, H.; Hao, M.; Naoi, Y.; Kurai, S.; Tottori, S.; Yamashita, K.; Nishino, K.; Romano, L. T.; Sakai, S. Direct Evidence that Dislocations are Non-Radiative Recombination Centers in GaN. *Jpn. J. Appl. Phys.* **1998**, *37* (Part 2, 4A), L398–L400.
181. Schenk, A.; Krumbein, U. Coupled Defect-Level Recombination: Theory and Application to Anomalous Diode Characteristics. *J. Appl. Phys.* **1995**, *78* (5), 3185–3192.
182. Shockley, W.; Read, W. T. Statistics of the Recombinations of Holes and Electrons. *Phys. Rev.* **1952**, *87* (5), 835–842.
183. Haug, A. Band-to-Band Auger Recombination in Semiconductors. *J. Phys. Chem. Solid* **1988**, *49* (6), 599–605.
184. Kasap, S. O.; Capper, P. *Springer Handbook of Electronic and Photonic Materials*, Springer: New York, 2006.
185. Isamu, A.; Hiroshi, A.; Masahiro, K.; Kazumasa, H. Photoluminescence of Mg-Doped p-Type GaN and Electroluminescence of GaN p-n Junction LED. *JOL* **1991**, *48-49*, 666–670.
186. Schubert, E. F.; Cho, J.; Kim, J. K. Light-Emitting Diodes. In *Kirk-Othmer Encyclopedia of Chemical Technology*, John Wiley & Sons, Inc., 2015; pp 1–20.
187. Persson, C.; Ahuja, R.; Ferreira da Silva, A.; Johansson, B. First-Principle Calculations of Optical Properties of Wurtzite AlN and GaN. *J. Cryst. Growth* **2001**, *231* (3), 407–414.
188. Bera, D.; Qian, L.; Tseng, T.-K.; Holloway, P. H. Quantum Dots and Their Multimodal Applications: A Review. *Materials* **2010**, *3* (4), 2260–2345.
189. Thomas, D.; Lee, H. O.; Santiago, K. C.; Pelzer, M.; Kuti, A.; Jenrette, E.; Bahoura, M. Rapid Microwave Synthesis of Tunable Cadmium Selenide (CdSe) Quantum Dots for Optoelectronic Applications. *J. Nanomater.* **2020**, *2020*, 5056875.
190. Chan, S.; Liu, M.; Latham, K.; Haruta, M.; Kurata, H.; Teranishi, T.; Tachibana, Y. Monodisperse and Size-Tunable PbS Colloidal Quantum Dots via Heterogeneous Precursors. *J. Mater. Chem. C* **2017**, *5* (8), 2182–2187.
191. Allen, P. M.; Bawendi, M. G. Ternary I–III–VI Quantum Dots Luminescent in the Red to Near-Infrared. *J. Am. Chem. Soc.* **2008**, *130* (29), 9240–9241.

192. Reiss, P.; Quemard, G.; Carayon, S.; Bleuse, J.; Chandezon, F.; Pron, A. Luminescent ZnSe Nanocrystals of High Color Purity. *Mater. Chem. Phys.* **2004**, *84* (1), 10–13.
193. Qu, L.; Peng, X. Control of Photoluminescence Properties of CdSe Nanocrystals in Growth. *J. Am. Chem. Soc.* **2002**, *124* (9), 2049–2055.
194. Chen, H.-S.; Lo, B.; Hwang, J.-Y.; Chang, G.-Y.; Chen, C.-M.; Tasi, S.-J.; Wang, S.-J. J. Colloidal ZnSe, ZnSe/ZnS, and ZnSe/ZnS Quantum Dots Synthesized From ZnO. *J. Phys. Chem. B* **2004**, *108* (44), 17119–17123.
195. Sun, B.; Marx, E.; Greenham, N. C. Photovoltaic Devices Using Blends of Branched CdSe Nanoparticles and Conjugated Polymers. *Nano Lett.* **2003**, *3* (7), 961–963.
196. Hirate, T.; Sasaki, S.; Li, W.; Miyashita, H.; Kimpara, T.; Satoh, T. Effects of Laser-Abated Impurity on Aligned ZnO Nanorods Grown by Chemical Vapor Deposition. *Thin Solid Films* **2005**, *487* (1), 35–39.
197. Zhang, X. T.; Liu, Y. C.; Zhang, J. Y.; Lu, Y. M.; Shen, D. Z.; Fan, X. W.; Kong, X. G. Structure and Photoluminescence of Mn-Passivated Nanocrystalline ZnO Thin Films. *J. Cryst. Growth* **2003**, *254* (1), 80–85.
198. Xu, C. X.; Sun, X. W.; Dong, Z. L.; Tan, S. T.; Cui, Y. P.; Wang, B. P. Manganese-Doped Zinc Oxide Tetrahedra and Their Photoluminescent Properties. *J. Appl. Phys.* **2005**, *98* (11), 113513.
199. Bhargava, R. N.; Gallagher, D.; Hong, X.; Nurmikko, A. Optical Properties of Manganese-Doped Nanocrystals of ZnS. *Phys. Rev. Lett.* **1994**, *72* (3), 416–419.
200. Kim, T.-H.; Jun, S.; Cho, K.-S.; Choi, B. L.; Jang, E. Bright and Stable Quantum Dots and their Applications in Full-Color Displays. *MRS Bull.* **2013**, *38* (9), 712–720.
201. Michalet, X.; Pinaud, F. F.; Bentolila, L. A.; Tsay, J. M.; Doose, S.; Li, J. J.; Sundaresan, G.; Wu, A. M.; Gambhir, S. S.; Weiss, S. Quantum Dots for Live Cells, In Vivo Imaging, and Diagnostics. *Science* **2005**, *307* (5709), 538–544.
202. Medintz, I. L.; Uyeda, H. T.; Goldman, E. R.; Mattoussi, H. Quantum Dot Bioconjugates for Imaging, Labelling and Sensing. *Nat. Mater.* **2005**, *4* (6), 435–446.
203. Kim, S.; Lim, Y. T.; Soltesz, E. G.; de Grand, A. M.; Lee, J.; Nakayama, A.; Parker, J. A.; Mihaljevic, T.; Laurence, R. G.; Dor, D. M.; Cohn, L. H.; Bawendi, M. G.; Frangioni, J. V. Near-Infrared Fluorescent Type II Quantum Dots for Sentinel Lymph Node Mapping. *Nat. Biotechnol.* **2004**, *22* (1), 93–97.
204. Son, D. H.; Hughes, S. M.; Yin, Y.; Paul Alivisatos, A. Cation Exchange Reactions in Ionic Nanocrystals. *Science* **2004**, *306* (5698), 1009–1012.
205. Hardman, R. A Toxicologic Review of Quantum Dots: Toxicity Depends on Physicochemical and Environmental Factors. *Environ. Health Perspect.* **2006**, *114* (2), 165–172.
206. Goosey, M. Implementation of the RoHS Directive and Compliance Implications for the PCB Sector. *Circuit World* **2007**, *33* (1), 47–50.
207. Saha, A.; Figueroba, A.; Konstantatos, G. Ag₂ZnSnS₄ Nanocrystals Expand the Availability of RoHS Compliant Colloidal Quantum Dots. *Chem. Mater.* **2020**, *32* (5), 2148–2155.
208. Nirmal, M.; Dabbousi, B. O.; Bawendi, M. G.; Macklin, J. J.; Trautman, J. K.; Harris, T. D.; Brus, L. E. Fluorescence Intermittency in Single Cadmium Selenide Nanocrystals. *Nature* **1996**, *383* (6603), 802–804.
209. Efros, A. L.; Nesbitt, D. J. Origin and Control of Blinking in Quantum Dots. *Nat. Nanotechnol.* **2016**, *11* (8), 661–671.
210. Chen, Y.; Vela, J.; Htoon, H.; Casson, J. L.; Werder, D. J.; Bussian, D. A.; Klimov, V. I.; Hollingsworth, J. A. “Giant” Multishell CdSe Nanocrystal Quantum Dots With Suppressed Blinking. *J. Am. Chem. Soc.* **2008**, *130* (15), 5026–5027.
211. Fomenko, V.; Nesbitt, D. J. Solution Control of Radiative and Nonradiative Lifetimes: A Novel Contribution to Quantum Dot Blinking Suppression. *Nano Lett.* **2008**, *8* (1), 287–293.
212. Mahler, B.; Spinicelli, P.; Buil, S.; Quelin, X.; Hermier, J.-P.; Dubertret, B. Towards Non-Blinking Colloidal Quantum Dots. *Nat. Mater.* **2008**, *7* (8), 659–664.
213. Wang, Z.; Huang, Y.; Liu, C. T.; Li, J.; Wang, J. Atomic Packing and Size Effect on the Hume-Rothery Rule. *Intermetallics* **2019**, *109*, 139–144.
214. Bachmann, V.; Ronda, C.; Oeckler, O.; Schnick, W.; Meijerink, A. Color Point Tuning for (Sr,Ca,Ba)Si₂O₇:Eu²⁺ for White Light LEDs. *Chem. Mater.* **2009**, *21* (2), 316–325.
215. Strobel, P.; de Boer, T.; Weiler, V.; Schmidt, P. J.; Moewes, A.; Schnick, W. Luminescence of an Oxonitridoberyllate: A Study of Narrow-Band Cyan-Emitting Sr[Be₆ON₄]:Eu²⁺. *Chem. Mater.* **2018**, *30* (9), 3122–3130.
216. Hermus, M.; Phan, P.-C.; Brgoch, J. Ab Initio Structure Determination and Photoluminescent Properties of an Efficient, Thermally Stable Blue Phosphor, Ba₂Y₅B₅O₁₇:Ce³⁺. *Chem. Mater.* **2016**, *28* (4), 1121–1127.
217. Settler, A.; Shiang, J.; Hannah, M.; Happek, U. *Phosphor Quenching in LED Packages: Measurements, Mechanisms, and Paths Forward*; vol. 7422; SPIE, 2009.
218. Brgoch, J.; DenBaars, S. P.; Seshadri, R. Proxies from Ab Initio Calculations for Screening Efficient Ce³⁺ Phosphor Hosts. *J. Phys. Chem. C* **2013**, *117* (35), 17955–17959.
219. Im, W. B.; Brinkley, S.; Hu, J.; Mikhailovsky, A.; DenBaars, S. P.; Seshadri, R. Sr_{2.975-x}Ba_xCe_{0.025}AlO₄F: A Highly Efficient Green-Emitting Oxyluoride Phosphor for Solid State White Lighting. *Chem. Mater.* **2010**, *22* (9), 2842–2849.
220. Wang, X.-J.; Xie, R.-J. Screening and Discovery of Phosphors by the Single-Particle-Diagnosis Approach. *J. Appl. Phys.* **2021**, *129* (12), 123106.
221. Wang, X.; Takeda, T.; Hirotsaki, N.; Funahashi, S.; Xie, R.-J. Single-Particle-Diagnosis Approach: An Efficient Strategy for Discovering New Nitride Phosphors. *J. Rare Earths* **2018**, *36* (1), 42–48.
222. Zhang, Y.; Li, S.; Takeda, T.; Funahashi, S.; Hirotsaki, N.; Xie, R.-J. Realizing Red/Orange Emission of Eu²⁺/Ce³⁺ in La_{26-x}Sr_xSi₄₁O_{x+1}N_{80-x} (x = 12.72–12.90) Phosphors for High Color Rendition White LEDs. *J. Mater. Chem. C* **2020**, *8* (38), 13458–13466.
223. Hirotsaki, N.; Takeda, T.; Funahashi, S.; Xie, R.-J. Discovery of New Nitridosilicate Phosphors for Solid State Lighting by the Single-Particle-Diagnosis Approach. *Chem. Mater.* **2014**, *26* (14), 4280–4288.
224. Takeda, T.; Hirotsaki, N.; Funahashi, S.; Xie, R.-J. Narrow-Band Green-Emitting Phosphor Ba₂LiSi₇AlN₁₂:Eu²⁺ With High Thermal Stability Discovered by a Single Particle Diagnosis Approach. *Chem. Mater.* **2015**, *27* (17), 5892–5898.
225. Wang, C.-Y.; Takeda, T.; Melvin ten Kate, O.; Funahashi, S.; Xie, R.-J.; Takahashi, K.; Hirotsaki, N. New Deep-Blue-Emitting Ce-Doped A_{4-m}B_nC_{19+2m}X_{29+m} (A = Sr, La; B = Li; C = Si, Al; X = O, N; 0 ≤ m ≤ 1; 0 ≤ n ≤ 1) Phosphors for High-Color-Rendering Warm White Light-Emitting Diodes. *ACS Appl. Mater. Interfaces* **2019**, *11* (32), 29047–29055.
226. Shioi, K.; Hirotsaki, N.; Xie, R.-J.; Takeda, T.; Li, Y. Luminescence Properties of SrSi₆N₈:Eu²⁺. *J. Mater. Sci.* **2008**, *43* (16), 5659–5661.
227. Li, Y. Q.; Delsing, A. C. A.; Metslaar, R.; de With, G.; Hintzen, H. T. Photoluminescence Properties of Rare-Earth Activated BaSi₇N₁₀. *J. Alloys Compd.* **2009**, *487* (1), 28–33.
228. Li, Y. Q.; van Steen, J. E. J.; van Krevel, J. W. H.; Botly, G.; Delsing, A. C. A.; DiSalvo, F. J.; de With, G.; Hintzen, H. T. Luminescence Properties of Red-Emitting M₂Si₆N₈:Eu²⁺ (M = Ca, Sr, Ba) LED Conversion Phosphors. *J. Alloys Compd.* **2006**, *417* (1), 273–279.
229. Park, W. B.; Shin, N.; Hong, K.-P.; Pyo, M.; Sohn, K.-S. A New Paradigm for Materials Discovery: Heuristics-Assisted Combinatorial Chemistry Involving Parameterization of Material Novelty. *Adv. Funct. Mater.* **2012**, *22* (11), 2258–2266.
230. Park, W. B.; Singh, S. P.; Sohn, K.-S. Discovery of a Phosphor for Light Emitting Diode Applications and Its Structural Determination, Ba(Si,Al)₅(O,N)₈:Eu²⁺. *J. Am. Chem. Soc.* **2014**, *136* (6), 2363–2373.
231. Park, W. B.; Kim, H.; Park, H.; Yoon, C.; Sohn, K.-S. The Composite Structure and Two-Peak Emission Behavior of a Ca_{1.5}Ba_{0.5}Si₆O₃N₆:Eu²⁺ Phosphor. *Inorg. Chem.* **2016**, *55* (5), 2534–2543.
232. Park, W. B.; Singh, S. P.; Yoon, C.; Sohn, K.-S. Eu²⁺ Luminescence From 5 Different Crystallographic Sites in a Novel Red Phosphor, Ca_{1.5}Si_{2.0}O_{1.0}N_{3.0}:Eu²⁺. *J. Mater. Chem.* **2012**, *22* (28), 14068–14075.
233. A New Era of Inorganic Materials Discovery Powered by Data Science. In *Machine Learning in Chemistry: The Impact of Artificial Intelligence*; Zhuo, Y., Tehrani, A. M., Brgoch, J., Cartwright, H. M., Eds., The Royal Society of Chemistry, 2020; pp 311–339.
234. Zhuo, Y.; Hariyani, S.; You, S.; Dorenbos, P.; Brgoch, J. Machine Learning 5d-Level Centroid Shift of Ce³⁺ Inorganic Phosphors. *J. Appl. Phys.* **2020**, *128* (1), 013104.
235. Barai, V. L.; Dhoble, S. J. Prediction of Excitation Wavelength of Phosphors by Using Machine Learning Model. *JOL* **2019**, *208*, 437–442.

4.10 Battery materials

Zachery W.B. Iton^a, Seong Shik Kim^b, Eshaan S. Patheria^b, Michelle D. Qian^b, Skyler D. Ware^b, and Kimberly A. See^b,

^aDepartment of Applied Physics and Materials Science, California Institute of Technology, Pasadena, CA, United States; and

^bDivision of Chemistry and Chemical Engineering, California Institute of Technology, Pasadena, CA, United States

© 2023 Elsevier Ltd. All rights reserved.

4.10.1	Introduction	309
4.10.1.1	Battery basics	309
4.10.1.2	The first battery	311
4.10.1.3	The lithium-ion battery	312
4.10.1.4	Battery performance metrics	313
4.10.1.4.1	Gravimetric vs volumetric capacity	313
4.10.1.4.2	Power vs energy	314
4.10.1.5	Electrochemical data	314
4.10.1.5.1	C rates	314
4.10.1.5.2	Galvanostatic cycling	315
4.10.2	Early battery chemistry	318
4.10.2.1	High-temperature batteries	318
4.10.2.2	Alkaline/Ni-based batteries	318
4.10.2.3	Pb-acid battery	319
4.10.3	Intercalation chemistry and the lithium revolution	319
4.10.3.1	Intercalation cathode materials	320
4.10.3.1.1	Sulfides	321
4.10.3.1.2	Oxides	323
4.10.3.1.3	Polyanion cathode materials	331
4.10.3.1.4	Mixed anion cathode materials	335
4.10.3.1.5	Li-rich cathode materials involving multi-electron redox	336
4.10.4	Anode materials for LIBs	339
4.10.4.1	Intercalation anode materials	339
4.10.4.1.1	Graphite as an intercalation host	339
4.10.4.2	Other intercalation-based anode structures	341
4.10.5	Conversion batteries	343
4.10.5.1	Conversion cathodes	343
4.10.5.1.1	Sulfur	343
4.10.5.1.2	Oxygen	345
4.10.5.2	Conversion anodes	347
4.10.5.2.1	Lithium metal	347
4.10.5.2.2	Silicon	348
4.10.5.2.3	Conversion oxides	348
4.10.6	Beyond Li	348
4.10.6.1	Na and K ion batteries	349
4.10.6.1.1	Na and K intercalation cathodes	349
4.10.6.1.2	Na and K intercalation anodes	351
4.10.6.1.3	Commercial Na ⁺ batteries	351
4.10.6.2	Multivalent intercalation	351
4.10.6.2.1	Sulfides	352
4.10.6.2.2	Oxides	354
References		356

Abstract

Batteries have become a ubiquitous part of life thanks to their ability to power portable electronic devices from cell phones and laptops to electric vehicles. Batteries also have the potential to play an essential role in enabling a greener transportation industry and large scale use of intermittent renewable energy such as solar and wind. This chapter is focused on the solid-state materials chemistry that enables energy storage in battery systems. The concepts and terminology required to understand the content are explained in the first section. The chapter briefly discusses early battery technology including high temperature

batteries, alkaline batteries, and Pb-Acid batteries. We then discuss more contemporary chemistry including the significant conceptual discoveries, such as intercalation chemistry, that led to the successful commercialization of lithium-ion batteries (LIBs). A comparative review of a variety of significant intercalation cathode and anode materials is presented, with emphasis on material structure and how it affects their electrochemical properties. In each section a brief history of each material, as well as a detailed description of its structure, advantageous properties, drawbacks, and current electrochemical research directions on similar materials is provided. This chapter also covers next-generation battery chemistry including Li-rich cathode materials, electrodes based on conversion chemistry, such as S_8 or O_2 cathodes, and Li and Si anodes. The section concludes with a discussion of development of battery materials for next-generation systems based on other monovalent working ions, Na^+ and K^+ , and multivalent working ions, Mg^{2+} , Zn^{2+} , and Ca^{2+} .

4.10.1 Introduction

A battery converts between electrical energy and chemical energy. The currency of electrical energy is electrons and, in a battery, the currency of chemical energy is ions. Solid materials often serve as sources and sinks of electrons and ions. Examples of charge storage in solution are also of interest, however, this chapter will focus on only the solid materials in battery systems. The properties of electrons or holes are determined by a material's electronic structure, which is shaped by the chemical bonding environments of its constituent atoms. In an electrochemical reaction that is confined to the solid-state, the insertion or removal of electrons is concomitantly charge balanced by the introduction or removal of ions. The latter can result in significant perturbations to the chemical structure. Thus, electrochemical reactions in materials are described by a dynamic interplay between electronic and chemical structure. To explain mechanisms of charge storage in solid-state materials, it is first necessary to introduce the basic anatomy of a battery and some relevant terminology.

4.10.1.1 Battery basics

A battery toggles between electrical and chemical energy via electrochemical reactions that occur concomitantly at two electrodes termed the anode and cathode. An oxidation reaction at the anode releases electrons into the external circuit and is accompanied by a reduction reaction at the cathode that consumes the electrons. The gain and loss of electrons is charge balanced by ions that conduct across the electronically insulating electrolyte as depicted in Fig. 1.¹

A schematic of a generalized battery during discharge is shown in Fig. 1a. Chemical energy is converted into electrical energy spontaneously and current flows from the cathode to the anode. By convention, the direction of current flow is opposite to the flow of electrons. The electrode nomenclature is defined during the discharge when oxidation occurs at the anode and reduction occurs at the cathode. An easy way to remember this convention is the mnemonic "An Ox" and "Red Cat." Thermodynamically speaking, the potential energy of the anode is higher than that of the cathode and thus the reaction is spontaneous.

A schematic of a general battery during charge is shown in Fig. 1b. Analogously, electrical energy is converted into chemical energy upon applying a voltage across the cell to drive the uphill reaction. Now, the oxidation reaction occurs at the cathode and the reduction reaction at the anode. Although the opposite reaction is occurring at each electrode, the battery community colloquially conserves designation of the electrodes (anode vs cathode) as it was defined for the discharge (spontaneous) reactions.

The reduction and oxidation reactions that occur at the electrodes are called half reactions. The corresponding half reaction at each electrode is indicated below the electrode in Fig. 1. If the half reactions are irreversible, the battery can only be discharged once and is called a primary battery/cell. Alternatively, if the half reactions are reversible, the battery is rechargeable and is called a secondary battery/cell. The two half reactions together give the full redox reaction of the battery. For example, the half reactions and full reaction for the battery in Fig. 1 are



Although the equations are written with cations j^+ and i^+ and indicate a single electron transfer, j^+ and i^+ could be replaced by anions, and the electron transfer could involve multiple electrons. The standard reduction potentials of many half reactions are tabulated and can be used to estimate the thermodynamic cell potential. The standard reduction potential E^0 describes a reduction reaction at standard conditions and thus the potential of the full cell described above is calculated by $E_{cell}^0 = E_c^0 - E_a^0$ where E_c^0 is the standard reduction potential of the cathodic half reaction and E_a^0 is the standard reduction potential of the anodic half reaction. Positive cell potentials yield negative Gibbs free energy (ΔG^0) and thus spontaneous reactions:

$$\Delta G^0 = -nFE_{cell}^0 \quad (4)$$

$$\Delta G = -nFE_{cell}$$

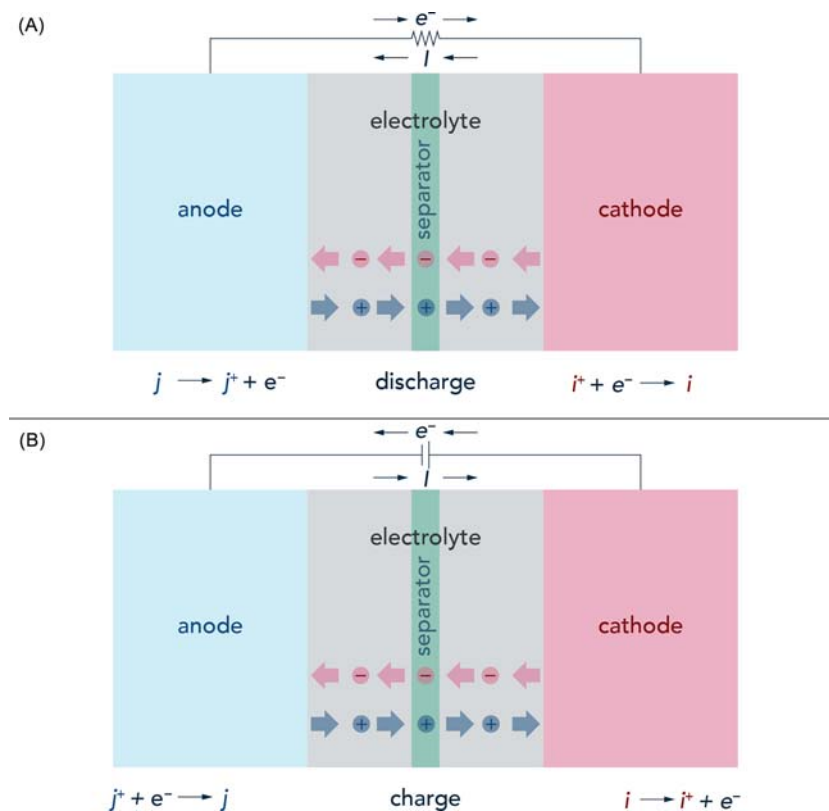


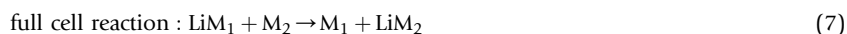
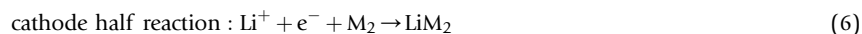
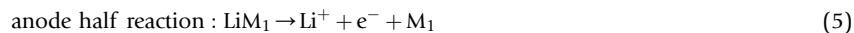
Fig. 1 All batteries contain an anode, electrolyte, and cathode. An electrolyte-permeable, electronically-insulating separator between the anode and cathode prevents electrical contact between the electrodes. The electrolyte is electronically insulating and ionically conducting. In the schematics, electrons are indicated as e^- , the anode material as j , and the cathode material as i . The solvated ions in the electrolyte are indicated as $+$ and $-$. (a) During discharge, j is oxidized to j^+ at the anode and i^+ is reduced to i at the cathode. Discharge is spontaneous. (b) During charge, j^+ is reduced to j and i is oxidized to i^+ . The names of the two electrodes, anode vs. cathode, are defined for the spontaneous reaction. Charging the battery requires an applied voltage across the cell. For both charge and discharge the direction of e^- and current I flow through the external circuit is indicated.

where n is the number of electrons transferred and F is Faraday's constant ($96,485 \text{ C mol}^{-1}$). In the second equation, we drop the superscript 0 implying that the same relationship holds in non-standard conditions.

The species j and i are called the electrochemically active species. That is, the electrochemically active species are the species in the anode and cathode which change oxidation state in the half reactions and store charge. Discrete changes in formal oxidation state are often used to describe the charge compensation mechanisms in battery materials, however, such a description becomes less accurate in materials with delocalized electrons or holes and/or covalent bonds. It is more accurate to say the electrochemically active species are the species on which changes in charge density are most localized during the half reactions. In other words, the electrochemically active species are the species that have occupied density of states near the Fermi level.

The ions $+$ and $-$ in the electrolyte in Fig. 1 conduct the ionic component of the full cell reaction. As written above, $+$ and $-$ are generalized and could refer to any cation or anion. At least one or more of the ions in the electrolyte will also appear in the half reactions (consider, for instance, if $+$ = j^+). Such ions are called working ions. The working ion can undergo reduction and oxidation itself or simply act as a charge compensating ion, as is the case for Li^+ in a Li-ion battery (LIB).

To illustrate the relationship between electrical and chemical energy in a battery, we turn to a thermodynamic analysis of a simple model system with a single working ion: the LIB. The materials and mechanisms in a LIB will be given considerable detail later in the chapter. For now, however, to explain the relationship between electrical and chemical energy in a battery, we can modify the half-reactions above to include a Li^+ working ion. The Li^+ is both in the electrolyte and reacts at the electrodes; the ion $+$ in Fig. 1 is taken to be Li^+ for this analysis. The half reactions and full cell reaction for a LIB can be generalized as:



Note that the formal oxidation state of Li^+ remains unchanged and M_1 and M_2 are the electrochemically active species. In a LIB, M_1 is often graphite and M_2 is a metal oxide. More detail on these materials can be found later in the chapter. For now, we start from the general thermodynamic identity for the electrochemical Gibbs free energy.

$$d\bar{G} = \sum_{\alpha} \sum_{\beta} \bar{\mu}_{\beta}^{\alpha} dN_{\beta}^{\alpha} \quad (8)$$

where \bar{G} is the electrochemical Gibbs free energy, and $\bar{\mu}_{\beta}^{\alpha}$ is the electrochemical potential of species α in phase β , and N_{β}^{α} is the number of particles of species α in phase β . We assume constant temperature and pressure such that the SdT and VdP terms in the thermodynamic identity are equal to 0.

Recall that the electrochemical potential $\bar{\mu}_{\beta}^{\alpha}$ is the partial molar Gibbs free energy of a given species β in phase α , composed of the sum of its chemical potential μ_{β}^{α} , which determines diffusive equilibrium, and electrostatic potential ϕ_{β}^{α} , which determines electrostatic equilibrium.²

$$\bar{\mu}_{\beta}^{\alpha} = \left(\frac{\partial \bar{G}^{\alpha}}{\partial N_{\beta}^{\alpha}} \right)_{T,P} = \mu_{\beta}^{\alpha} + z_{\beta} F \phi_{\beta}^{\alpha} \quad (9)$$

z_{β} is the signed charge number of β (e.g., +1, -1, +2, -2), and F is the Faraday constant (96485 C mol⁻¹).

In the LIB model system, we have only the Li^+ working ion and electrons e^- , so the thermodynamic identity simplifies as below:

$$(d\bar{G})_{T,P} = \sum_{\alpha} \bar{\mu}_{\text{Li}^+}^{\alpha} dN_{\text{Li}^+}^{\alpha} + \bar{\mu}_{e^-}^{\alpha} dN_{e^-}^{\alpha} \quad (10)$$

The derivative in the electrochemical Gibbs free energy of the cell can be written in terms of the Li^+ and e^- concentrations in all phases; the three major phases indicated in Fig. 1 are the anode, electrolyte, and cathode.³

$$(d\bar{G})_{T,P} = \bar{\mu}_{\text{Li}^+}^{\text{anode}} dN_{\text{Li}^+}^{\text{anode}} + \bar{\mu}_{e^-}^{\text{anode}} dN_{e^-}^{\text{anode}} + \bar{\mu}_{\text{Li}^+}^{\text{cathode}} dN_{\text{Li}^+}^{\text{cathode}} + \bar{\mu}_{e^-}^{\text{cathode}} dN_{e^-}^{\text{cathode}} + \bar{\mu}_{\text{Li}^+}^{\text{electrolyte}} dN_{\text{Li}^+}^{\text{electrolyte}} \quad (11)$$

Note that the electrolyte, unlike the anode and cathode, conducts only Li^+ and other dissolved ions. The electrolyte (typically an organic solvent with a Li salt in an LIB) is highly insulating with respect to e^- or hole (h^+) species.

From Eq. (11), it is possible to invoke Eq. (4) $\Delta G^0 = -nFE_{\text{cell}}^0$ at equilibrium and $\Delta G = -nFE_{\text{cell}}$ at non-equilibrium states (i.e., during charge and discharge) to derive expressions for E_{cell}^0 and E_{cell} , respectively.^{2,4,5} We leave this derivation as an exercise for the reader.

$$E_{\text{cell}}^0 = -\frac{\bar{\mu}_{e^-}^{\text{cathode}} - \bar{\mu}_{e^-}^{\text{anode}}}{e} \quad (12)$$

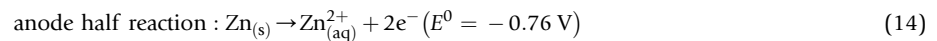
$$E_{\text{cell}} = -\frac{\left[\bar{\mu}_{\text{Li}^+}^{\text{cathode}} + \bar{\mu}_{e^-}^{\text{cathode}} \right] + \left[-\bar{\mu}_{\text{Li}^+}^{\text{anode}} - \bar{\mu}_{e^-}^{\text{anode}} \right]}{e} \quad (13)$$

Thus, at equilibrium, the total electrical energy per charge E_{cell}^0 is solely the difference in the electrochemical potential of electrons e^- at the cathode versus the anode, i.e., the net electrochemical potential difference of e^- between the electrodes. Whereas, in non-equilibrium states, the total electrical energy per charge E_{cell} is the difference in the electrochemical potential of the working ion Li^+ at the cathode versus the anode, minus the difference in electrochemical potential of electrons e^- at the cathode versus the anode, i.e., the net electrochemical potential difference of all charge species between the cathode and the anode.

4.10.1.2 The first battery

The first battery was built by the Italian scientist Alessandro Volta in 1800. The battery was composed of alternating electrodes of dissimilar metals, for example Zn and Cu, separated by a saltwater electrolyte. It is worth noting here that the term “battery” technically refers to many cells in series, like the one Volta made. However, single cells are commonly referred to as batteries in the literature. Volta was prompted to construct the battery to probe a hypothesis inspired by an experiment by his contemporary, Luigi Galvani. Galvani observed that the legs of a frog hung from an Fe hook twitched when touched by a Cu probe. While Galvani suggested the twitch came from electricity intrinsic to the frog, Volta hypothesized the electricity was intrinsic to the metals. To test his hypothesis, Volta constructed the voltaic pile—the first battery (Fig. 2).⁶

Volta observed that current could be generated from the repetitive stack of two different metals separated by a salt-water soaked pasteboard. Volta also used Sn in place of Zn and brass or Ag in place of Cu.⁶ Later study of the voltaic pile by others after Volta found that the cathode metal is inert and the reaction at the cathode is reduction of protons (H^+) to hydrogen gas ($\text{H}_{2(\text{g})}$) with the electrons delivered via Cu (Fig. 2).⁷ The half reactions, full redox reaction, and equation for the EMF for the voltaic pile are as follows. The potentials below are standard reduction potentials and are thus referenced to the normal hydrogen electrode (NHE).



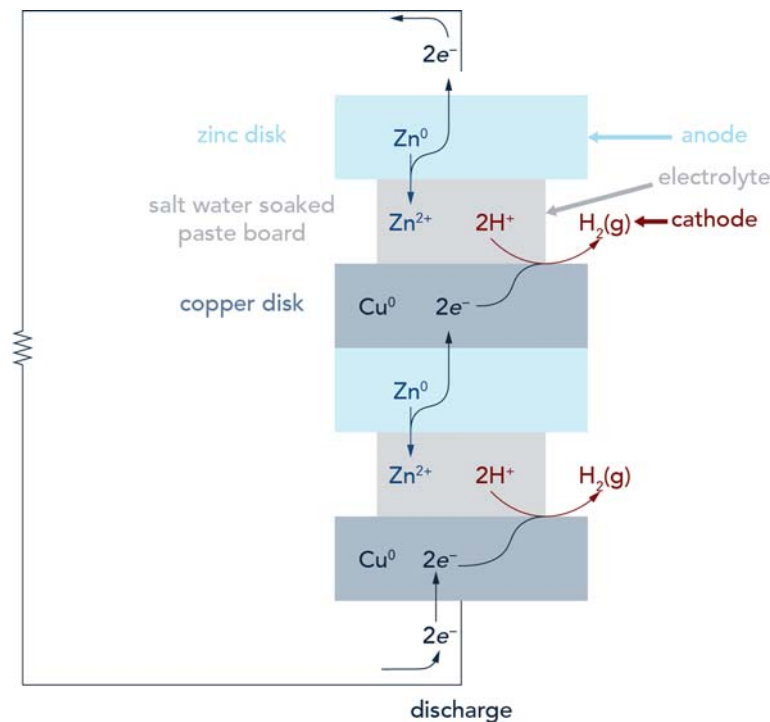
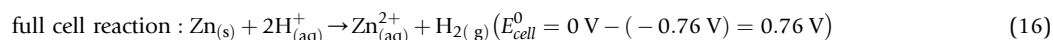
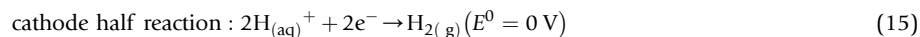


Fig. 2 A diagram of the voltaic pile as described by Volta. It consisted of several electrochemical cells in series. Each cell consists of a Zn disk anode, saltwater electrolyte (pasteboard soaked in saltwater), and a $\text{H}_2(\text{g})$ cathode. The Cu disks are inert electron conductors now called current collectors. The cell is drawn discharging, when oxidation occurs at the Zn anode and reduction of protons in the electrolyte evolves $\text{H}_2(\text{g})$ at the surface of the Cu disk.



$$\Phi = - \frac{\mu_{2\text{H}^+}^{\text{H}_{2(\text{g})}} - \mu_{\text{Zn}^{2+}}^{\text{Zn}_{(\text{s})}}}{2\text{e}^-} \quad (17)$$

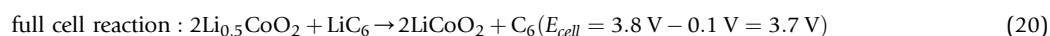
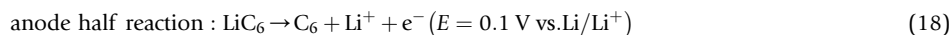
In practice, the voltage across a single cell of the voltaic pile in Fig. 2 is not equal to the thermodynamic value Φ because the voltage is perturbed by extraneous factors like side reactions at the anode to form ZnSO_4 and ZnO . The voltaic pile consists of several cells in series so the total voltage is the sum of the individual cells.⁷

Initial challenges with Volta's cell included the formation of insulating Zn compounds at the anode and the adherence of $\text{H}_{2(\text{g})}$ to the Cu disks.⁷ Regardless, Volta's battery set the stage for future development and study of similar electrochemical cells. Any electrochemical cell can be viewed as the sum of its half reactions, and the brief discussion of the voltaic pile introduces the overall mode of operation of a battery.

4.10.1.3 The lithium-ion battery

The most ubiquitous battery today is the LIB. As an additional example to help frame the next sections, and since it will be a key focus of the chapter, the LIB is briefly introduced now. A far more detailed discussion follows later in the chapter.

Despite greater chemical complexity compared to the voltaic pile, the LIB can still be defined by its half reactions. The half reactions, full reaction, and equation for the EMF for the LIB during discharge are as follows⁸:



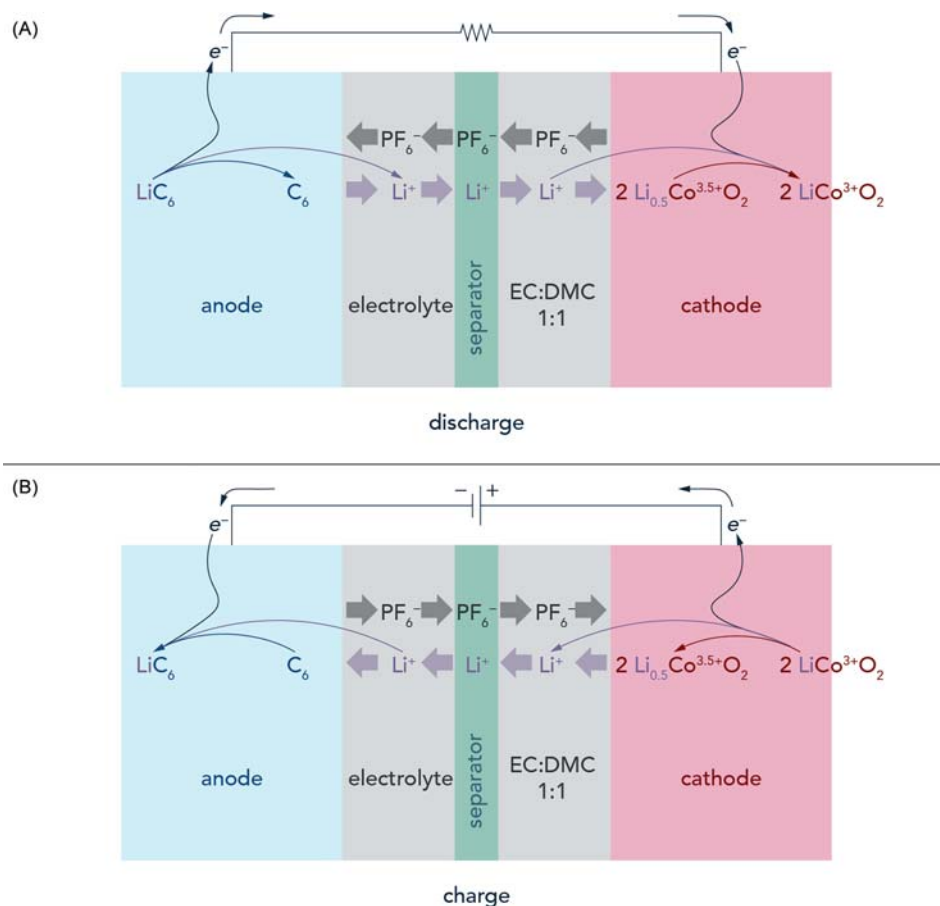


Fig. 3 (a) The archetypal LIB consists of a graphite (C_6) anode, Li salt (LiPF_6) in organic carbonate solvent electrolyte, and lithium cobalt oxide (LiCoO_2) cathode. During discharge, the $\text{Li}_{0.5}\text{CoO}_2$ cathode is lithiated and reduced and the lithiated graphite (LiC_6) is delithiated and oxidized. (b) During charge, the LiCoO_2 cathode is delithiated and oxidized, and the C_6 anode is lithiated and reduced. In its pristine state as assembled, the LIB is fully discharged. The causes for and consequences of the pristine state of the Li-ion being the discharged state, as opposed to charged, will be discussed later in the chapter.

$$\Phi = -\frac{\mu_{\text{Li}^+}^{\text{LiCoO}_2} - \mu_{\text{Li}^+}^{\text{C}_6}}{e} \quad (21)$$

During charge (Fig. 3b) LiCoO_2 loses half an equivalent of the working ion, Li^+ , whilst the C_6 anode incorporates Li from the electrolyte. The anodic electrochemically active species is C_6 , and the cathodic electrochemically active species is the Co in LiCoO_2 .

Why only half an equivalent of Li is removed from and inserted into LiCoO_2 will be explained in Section 4.10.3.1.2.1.2. However, to accurately represent the redox in the LIB it is taken as a fact for now.

4.10.1.4 Battery performance metrics

One paramount figure of merit for a battery is its energy density. That is, the quantity of electrical energy it can store as chemical energy per unit weight or unit volume. While the factors that determine energy density in a battery are numerous, a principal component of the energy density includes the intrinsic energy density of the anode and cathode materials. However, as suggested in Figs. 1 and 2, the total weight or volume of a battery, and overall battery energy density, will depend on the relative voltage between the anode and cathode materials, weight/volume of the electrolyte, any other insulators/separators (e.g. the pasteboard in Fig. 2), metal current collectors (connected to the anode and cathode), overall cell design etc. Thus, while energy density is important for practical purposes, it is not an intrinsic property of a material. For chemists concerned solely with the impact of the electrode materials on the energy density it is useful to define an intrinsic gravimetric (by weight) and volumetric (by volume) capacity, as opposed to energy density, as a metric to easily compare the capacity of various materials.

4.10.1.4.1 Gravimetric vs volumetric capacity

As the energy stored in a battery depends on the relative voltage between specific anode and cathode materials, the intrinsic capacity of a material on its own cannot be defined in terms of energy. Thus, the capacity is defined in terms of charge stored per unit weight

(gravimetric capacity) or volume (volumetric capacity) as opposed to energy. By convention, the units of gravimetric capacity are mA h g⁻¹ and the units of volumetric capacity are mA h cm⁻³. It is intuitive to see how mA h are units of charge as follows:

$$1 \text{ mA} \cdot \text{h} = 10^{-3} \text{ A} \cdot \text{h} = 10^{-3} \frac{\text{C}}{\text{s}} \cdot \text{h} = 10^{-3} \cdot 3.6 \cdot 10^3 \frac{\text{C}}{\text{s}} \cdot \text{s} = 3.6 \text{ C} \quad (22)$$

where mA and A are milliamps and amps, respectively, h is hours, s is seconds and C is Coulombs. Recall that Coulombs are the International System of Units (SI) unit of electrical charge where 1 C = 6.242 × 10¹⁸ e where e = elementary charge.

The gravimetric and volumetric capacity of a compound used as an electrode are defined as follows:

$$\text{Gravimetric Capacity (mA} \cdot \text{h} \cdot \text{g}^{-1}) = \frac{n \cdot x \cdot F}{mw \cdot 3.6} \quad (23)$$

$$\text{Volumetric Capacity (mA} \cdot \text{h} \cdot \text{cm}^{-3}) = \frac{n \cdot x \cdot F}{V \cdot 3.6} \quad (24)$$

where n = Units of charge per working ion, x = theoretical electrochemically accessible equivalents of working ion, F = Faraday's constant ≈ 96485 (C mol⁻¹), mw = molecular weight (g mol⁻¹), V = volume of 1 mole of unit cells (cm³ mol⁻¹) and 3.6 is a unit conversion factor (C mA⁻¹ h⁻¹).

Table 1 shows the gravimetric and volumetric capacities of the anode and cathode materials from the voltaic pile (**Fig. 2**) and LIB (**Fig. 3**).

Note that the volumes of 1 mol of unit cells (cm³ mol⁻¹) are scaled to match the stoichiometry. The volumetric capacity for H_{2(g)} is undefined as it depends drastically on its container, pressure and temperature.

The formulae above define the quantity x , the "Theoretical Electrochemically Accessible Equivalents of Working Ion." In practice, not all of the equivalents of working ion in a given material may be electrochemically accessible. For example, for LiCoO₂, the theoretical capacity calculated in the table above is based on $x = 1$. However, in practice, only 0.5 equiv. of Li⁺ are accessible and so the experimental gravimetric and volumetric capacities are 137 mA h g⁻¹ and 692 mA h cm⁻³, respectively.

4.10.1.4.2 Power vs energy

Another important distinction in the figures of merit for a battery is between power and energy. For many practical uses not only is the battery energy density important but also how quickly the battery can convert between electrical and chemical energy, i.e. the power. At the chemical level, power is determined by the kinetics of the redox reactions where higher (lower) power density corresponds to faster (slower) redox reactions. As the redox kinetics are complex and depend on the specific interface and/or any interphase between an electrode and electrolyte, the power density, like energy density, is not an intrinsic property. Thus, both energy and power densities cannot be globally defined from first principles. Nonetheless, both metrics are often measured at the device level in units of W h kg⁻¹ or W h m⁻³ for gravimetric and volumetric energy densities, respectively, and W kg⁻¹ or W m⁻³ for gravimetric and volumetric power densities, respectively.

4.10.1.5 Electrochemical data

Many electrochemical techniques are used to characterize battery materials. In any electrochemical experiment, either the voltage or the current can be controlled, but not both. A common experiment used to evaluate materials is executed by controlling the current flow, i.e. the rate of electron flow, between the electrodes and measuring the voltage response. The direction of current is switched when either a time cutoff or voltage cutoff is reached. This is a charge/discharge experiment that is also called chronopotentiometry or galvanostatic cycling.

4.10.1.5.1 C rates

With the definitions of capacity above, it is possible to describe the current applied in a galvanostatic cycling experiment in terms of the capacity of the compound. By convention, the rate of charge/discharge is called a C rate and it reflects the time it will take to exhaust the full capacity of the compound. A cell discharged at a rate of n C will exhaust its full capacity in $1/n$ hours. For instance, a cell cycled at 2 C will exhaust the capacity in 30 min and a cell cycled at C/2 will exhaust the capacity in two hours. The rate is controlled by varying the current applied to the cell. To determine the current corresponding to a given C rate, the following equation can be used:

Table 1 The gravimetric (Q_{Grav}) and volumetric capacities (Q_{Vol}) of the anode and cathode materials of the voltaic pile and LIB.

Electrode material	Working ion	n	x	mw (g mol ⁻¹)	V (cm ³ mol ⁻¹)	Q_{Grav} (Theoretical) mA h g ⁻¹	Q_{Vol} (Theoretical) mA h cm ⁻³
LiCoO ₂	Li ⁺	1	1	97.87	38.75	274	1384
LiC ₆	Li ⁺	1	1	79.01	35.95	339	746
H _{2(g)}	H ⁺	1	2	2.016	-	26589	-
Zn(s)	Zn ²⁺	2	1	65.38	9.150	820	5858

$$|I| = m \cdot Q_{th} \cdot n \quad (25)$$

where I is current in mA, m is the mass of the active material in g, Q_{th} is the theoretical gravimetric capacity of the active material in mA h g⁻¹, and n is taken from nC and has units of h⁻¹. The current is shown as an absolute value because if the material is oxidized, then positive current will be applied and if it is reduced, then negative current will be applied. In practice, battery electrodes consist of a mix of the electrochemically active material and conductive carbons, binders etc. Thus, to calculate the current for a given C rate, we specify the mass of only the active material. The C rate discussed here is based on the theoretical capacity, but very often materials cannot reach the theoretical capacity due to inherent material limitations, electrode fabrication issues, or myriad other issues and thus the actual time to full discharge or charge is less than the targeted C rate. Thus, a practical C rate can also be defined by measuring the time required for full discharge or charge at a given current.

The definition above is written in terms of gravimetric capacity, but it could have as easily been written in terms of volumetric capacity by substituting the mass of the active material for the volume of the active material, and the gravimetric capacity for the volumetric capacity. In practice, however, the mass of active material is much easier to measure than the volume. Various C rates to charge 5 mg of the LIB cathode compound LiCoO₂ with theoretical gravimetric capacity 137 mA h g⁻¹ are shown in **Table 2**.

4.10.1.5.2 Galvanostatic cycling

As described above, a constant current is applied in the galvanostatic cycling experiment between the electrodes and the voltage response is measured. A typical experimental setup resembles **Fig. 2b**, except often a Li(s) metal anode is used instead of C₆. The setup is called a half cell because the limiting processes occur at the cathode making it easier to study the reactions at the cathode. Thus, the cathode is the working electrode and the Li anode serves as both the counter and reference electrodes, such that the voltage between the anode and cathode is relative to Li ⇌ Li⁺ + e⁻ at 0 V (vs Li/Li⁺). Three electrode experiments are also useful to decouple processes at the working vs the counter electrode, however, the Li metal counter/reference provides a relatively stable potential and so utilizing a 3rd electrode is often unnecessary. In an example experiment, suppose we have 5 mg of LiCoO₂ in the cathode and wish to cycle it at a rate of 2 C. The material is already lithiated, so the Li⁺ is first removed from the cathode. Thus, a positive current of 1.37 mA will be applied to the electrode to drive the oxidation reaction. Even though LiCoO₂ is first oxidized, LiCoO₂ sits at a high voltage, or low chemical potential, and is thus defined as the cathode of the battery and the cell is thus in the discharged state as assembled. Once the capacity is exhausted, ostensibly after 30 min, the current is reversed to reduce the LiCoO₂ and the material is again fully discharged (lithiated) after 30 min.

The most obvious way to plot the voltage response in a galvanostatic cycling experiment would be as a function of time, since the only independent variable that can be directly measured is the time since the constant current was first applied. However, if the mass (or volume) of the active material, m , is known, then the gravimetric (or volumetric) capacity can be calculated with the time elapsed as follows:

$$Q = \frac{|I| \cdot \Delta t}{m} \quad (26)$$

where Q is the measured capacity in units of mA h g⁻¹, I is the applied current applied in units of mA, Δt is the time elapsed in units of h, and m is the mass of active material in units of g. From the measured capacity, the moles of Li⁺, x , exhausted per formula unit (e.g. Li_{1-x}CoO₂) can be calculated as follows:

$$x = \frac{Q \cdot mw \cdot 3.6}{F} \quad (27)$$

where mw is the molecular weight of the active material in units of g mol⁻¹, 3.6 is a conversion factor from Coulombs to mA h (i.e. units of C mA⁻¹ h⁻¹) and F = Faraday's constant ≈ 96485 C mol⁻¹. Thus, in a galvanostatic cycling experiment, the moles of working ion exhausted per formula unit x is linearly increased or decreased by the current applied between the electrodes, and the voltage response is measured.

It follows from **Section 4.10.1.1** that x directly relates to the chemical potential by the equation below.

$$\left(\frac{\partial G}{\partial x} \right)_{T,P} = \mu_x^{\text{active material}} \quad (28)$$

Table 2 The current applied for various C rates to charge 5 mg of the LIB cathode compound LiCoO₂.

Rate (nC)	Current (mA)	Time to full charge (hh:mm)
0.1 C	0.0685	10:00
0.5 C	0.343	02:00
1 C	0.685	01:00
2 C	1.370	00:30
10 C	6.850	00:06

Here the subscript x denotes the working ion, and the superscript denotes the active material, whether anode or cathode. Also recall that the voltage between the electrodes is a function of the chemical potential in Eq. (18). Thus, the voltage response in a galvanostatic cycling experiment provides insight into the Gibbs free energy landscape of the electrochemical activity of a battery via the chemical potential of the working ion in the active material. Of course, the measured curve also captures kinetic factors but the thermodynamic factors tend to dominate the overall shape of galvanostatic curves. In fact, we can mathematically derive the shape of the voltage response based on simple models of the Gibbs free energy landscape. Here, we will consider the single-phase reaction model and two-phase reaction model, with example materials, both of which explain a great deal of experimental results.

It is worth noting that there are experimental techniques that can be used to decouple thermodynamic contributions to the voltage response from kinetic contributions such as galvanostatic intermittent titration technique. Such techniques are beyond the scope of this chapter.

4.10.1.5.2.1 Single-phase reaction—LiCoO₂

Fig. 4a shows representative galvanostatic cycling data for the discharge of a cell with an LiCoO₂ cathode, starting from Li_{0.5}CoO₂. The curve is characterized by its shallow slope vs x . It is possible to derive the shape mathematically if we assume a single-phase discharge mechanism. In other words, we assume that for any and all x , the compound is a thermodynamically ideal mixture⁹ of Li_{1-x}CoO₂. The mixing entropy of a thermodynamically ideal mixture is given as below⁹:

$$\Delta S = k_B(x \ln x + (1-x) \ln (1-x)) \quad (29)$$

Thus, the Gibbs free energy as a function of x is as below.¹⁰

$$\Delta G(x) = G(0.5) + \varepsilon x + k_B T(x \ln x + (1-x) \ln (1-x)) \quad (30)$$

Here, $G(0.5)$ is the free energy of the fully discharged active material when $x = 0.5$ (i.e. the energy of Li_{0.5}CoO₂), εx is the energy change per Li atom sans any entropic component, and the third term is the entropic contribution to the energy of the ideal mixture at x . Taking the derivative of $G(x)$ with respect to x yields the chemical potential:

$$\left(\frac{\partial G}{\partial x}\right)_{T,P} = \mu_{\text{Li}^+}^{\text{LiCoO}_2} = \varepsilon + k_B T \ln\left(\frac{x}{1-x}\right) \quad (31)$$

Next, we can plug the above expression into our general equation for the voltage between the electrodes, assuming a Li metal anode, as follows:

$$\Phi = -\frac{\mu_{\text{Li}^+}^{\text{LiCoO}_2} - \mu_{\text{Li}^+}^{\text{Li(s)}}}{e} = \frac{\varepsilon + k_B T \ln\left(\frac{x}{1-x}\right) - \mu_{\text{Li}^+}^{\text{Li(s)}}}{e} \quad (32)$$

Indeed, the shape of the curve in Fig. 4a resembles Eq. (37). Note that $\mu_{\text{Li}^+}^{\text{Li(s)}}$, the chemical potential of Li⁺ in the Li metal anode, is a constant. The Li metal anode is treated as an infinite source/sink of Li⁺, so there is no change in Gibbs free energy as Li⁺ is inserted or removed from the metal. One aspect of the voltage response that is apparently unexplained by the above treatment is the sharp transition in the potential near $x \approx 0$. In general, if current is still applied once the material available for a certain redox reaction is exhausted, the cell will polarize until a voltage is reached at which a new reaction can occur or until the experiment is

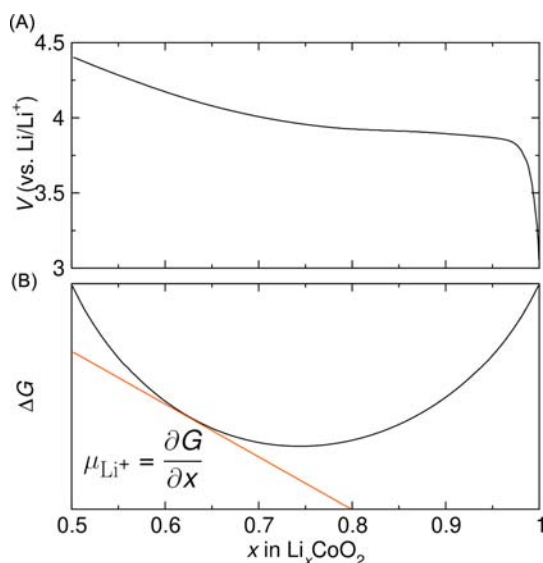


Fig. 4 (a) Representative galvanostatic discharge curve for LiCoO₂.⁸ (b) The Gibbs free energy landscape for Li_{1-x}CoO₂ vs x .¹⁰

stopped at a specified potential limit. If the cell is being charged, for example, eventually the voltage will reach a regime in which the electrolyte can be irreversibly oxidized (decomposed) and thus potential limits are set on the experiment to avoid electrolyte decomposition. Mathematically, the transition is best understood via the Nernst Eq. (15), rewritten below for the LiCoO_2 half cell.

$$\Phi = E_{\text{LiCoO}_2}^0 - E_{\text{Li}^{\oplus}(\text{s})}^0 - \frac{RT}{F} \ln Q \quad (33)$$

where Q is the reaction quotient. Near $x \approx 0$, $Q \approx 0$ as there is mostly reactant and little to no product near $x \approx 0$. Thus, Φ is dominated by the natural logarithm term. While the value of $\ln Q$ tends to $-\infty$ for $Q \approx 0$, it practically manifests as a sharp transition of several hundred mV. The single-phase reaction in LiCoO_2 ends at $x = 0.5$, so a similar sharp transition is not observed at the end of charge (or equivalently at the start of discharge i.e. $x = 0.5$) as $Q \approx 1$ and so $\ln Q \approx 0$ (as there are equal parts as many reactants as products at $x = 0.5$). In the next example, we will see that the divergent behavior of the voltage is observed at both the start and end of charge.

4.10.1.5.2.2 Two-phase reaction— LiFePO_4

The canonical two-phase LIB cathode is LiFePO_4 . For now, we will consider how a two-phase reaction mechanism manifests in the galvanostatic charge/discharge curves. A more detailed discussion of LiFePO_4 can be found in Section 4.10.3.1.3.1. As opposed to the $\text{Li}_{1-x}\text{CoO}_2$ thermodynamically ideal mixture, $\text{Li}_{1-x}\text{FePO}_4$ forms two distinct and physically separate phases of $x \cdot \text{LiFePO}_4$ and $(1-x) \cdot \text{FePO}_4$ during charge.

Fig. 5a shows representative galvanostatic charge curve for LiFePO_4 . The curve is flat vs x between x_1 and x_2 , i.e. the chemical potential of Li^+ remains constant as a function of x . Again, it is possible to derive the shape mathematically if we assume a two-phase mechanism. The two distinct phases manifest as local minima at $(x_1, G(x_1))$ and $(x_2, G(x_2))$ in the Gibbs free energy landscape shown in Fig. 5b. Note that the thermodynamic minima fall slightly less than and greater than $x = 1$ and $x = 0$, respectively. As we explained above, the reason for the rise in the Gibbs free energy and sharp transition of the voltage near $x = 1$ and $x = 0$ arises from the off-equilibrium logarithm term in the Nernst equation. Since there is no mixing of the lithiated and delithiated phases for LiFePO_4 , we observe the sharp transition in the voltage at both the start and end of charge.

Since none of the intermediate compounds $\text{Li}_{1-x}\text{FePO}_4$ at any x are more stable than the compositions at x_1 and x_2 , the energy falls along the tangent between the two minima during charge/discharge. We start with a slope-intercept equation of the form $y = m \cdot x + b$ to get a general formula for $G(x)$. Based on Fig. 5, $m = \frac{G(x_1) - G(x_2)}{x_1 - x_2}$ and $G(0) = b$.

$$G(x) = \frac{G(x_1) - G(x_2)}{x_1 - x_2} \cdot x + b \quad (34)$$

We take the derivative of $G(x)$ with respect to x to get the chemical potential as below.

$$\left(\frac{\partial G}{\partial x} \right)_{T,P} = \mu_{\text{Li}^+}^{\text{LiFePO}_4} = \frac{G(x_1) - G(x_2)}{x_1 - x_2} \approx G(x_1) - G(x_2) \quad (35)$$

where in the last step above we invoked the approximation $x_1 - x_2 \approx 1$ because the regions between 1 and x_1 and x_2 and 0 are small compared to $x_1 - x_2$.

Next, as we did previously, we plug the above expression into our general equation for the voltage as follows:

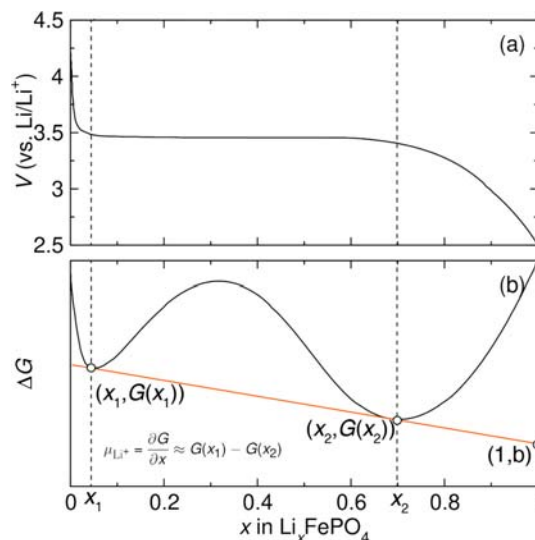


Fig. 5 (a) Representative galvanostatic charge curve for LiFePO_4 .⁸ (b) The Gibbs free energy landscape for LiFePO_4 vs x .¹⁰

$$\Phi = -\frac{\mu_{\text{Li}^+}^{\text{LiFeO}_4} - \mu_{\text{Li}^+}^{\text{Li(s)}}}{e} = \frac{G(x_2) - G(x_1) - \mu_{\text{Li}^+}^{\text{Li(s)}}}{e} \quad (36)$$

Indeed, the shape of the curve in Fig. 5 resembles the above equation - it is constant between x_1 and x_2 . The slope at values of x greater than x_1 and less than x_2 are kinetic artifacts from the electrode/electrolyte interface or other factors.

While LiCoO_2 and LiFePO_4 are close to model materials for single-phase and two-phase behavior, respectively, most materials exhibit a complex mix of both. Nonetheless, galvanostatic cycling is a powerful tool to characterize and determine the practical viability of battery materials. Not only because it gives fundamental insight into the charge/discharge mechanisms, but because galvanostatic cycling can provide insight into the material's performance under load in a practical cell.

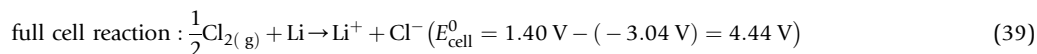
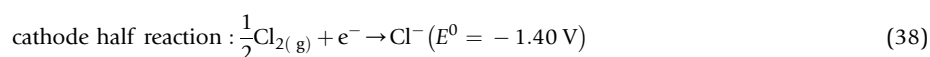
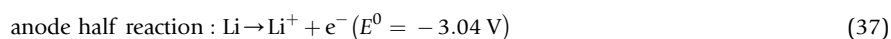
4.10.2 Early battery chemistry

Between the voltaic pile and the modern LIB, several primary and secondary batteries were developed, and some used in industrial applications. Below, we briefly introduce some of these batteries, their half reactions, and practical applications and limitations.

4.10.2.1 High-temperature batteries

High-temperature batteries became popular in the second half of the twentieth century due to their high energy and power density. High temperatures are required due to the use of molten-salt or solid ceramic electrolytes. These electrolytes can have much lower resistances than liquid, aqueous or organic electrolytes. However, this requires temperatures above the melting point of the salt (typically between 100 and 650 °C) or elevated temperatures at which fast solid-state ion conductivity is enabled in ceramics.¹¹

A typical example of a high-temperature battery is the Li-Cl battery, which consists of a Li metal anode, molten fused-salt LiCl electrolyte, and $\text{Cl}_{2(\text{g})}$ cathode as below:

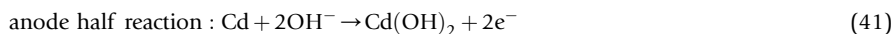
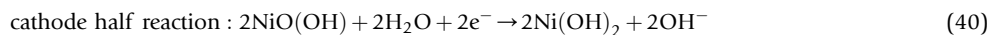


The high-temperature batteries were mostly based on elemental electrodes and binary salt electrolytes. The use of elemental electrodes instead of composite electrodes, composed of conductive additives and binders in addition to the active materials, yields high energy density batteries. The entire weight/volume of the electrode consists of only the working ions and no other elements, resembling Fig. 1.

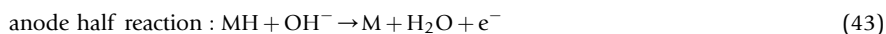
However, the practical viability of high-temperature batteries is limited. Firstly, the high temperature requirement precludes its application in low or moderate temperature applications. Additionally, for the Li-Cl battery, the delivery of $\text{Cl}_{2(\text{g})}$ into the battery presents an engineering challenge. Although a porous carbon electrode enables $\text{Cl}_{2(\text{g})}$ to be removed/introduced in a controlled manner, the accumulation of inert impurities in the $\text{Cl}_{2(\text{g})}$ (such as CO_2 and N_2) at the pores hinders the diffusion of $\text{Cl}_{2(\text{g})}$ to the electrode-electrolyte interface. Additionally, many materials are unstable when in contact with Li, LiCl, and $\text{Cl}_{2(\text{g})}$ at high temperatures. Despite attempts to coat cell components with inert materials, the need for specific materials at different interfaces further complicates long-term high-temperature battery stability.¹¹ Although only the Li-Cl battery is discussed here as an example, the key difficulties associated with most of the high-temperature batteries resemble the problems above: chemical contamination of the cell over time degrading reversibility, and the instability and high reactivity of elemental components at high temperatures.

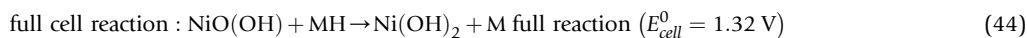
4.10.2.2 Alkaline/Ni-based batteries

The alkaline/Ni-based batteries are named for their use of a highly alkaline KOH electrolyte and a Ni oxide cathode. The cell chemistry was pioneered by Waldemar Jungner in Sweden and Thomas Edison in the United States in the late nineteenth century/early twentieth century.¹² Various anodes are combined with the Ni oxide cathode, most popularly an elemental metal (Cd, Zn or Fe) or metal hydride anode as below^{13,14}:



or



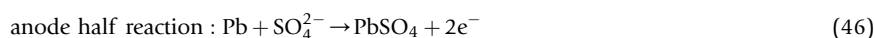
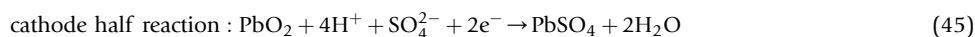


The principal drawbacks of alkaline/Ni-based batteries are their toxicity and limited long-term reversibility. For example, the low natural abundance of Cd and its high toxicity make the Cd anode-based cell expensive and hazardous. Furthermore, the Cd cell exhibits a memory effect. If the cell is not fully charged/discharged, the capacity on future cycles is limited to that of the incomplete cycle. The origin of the memory effect is uncertain, but it likely has to do with irreversible morphological changes of unused active material at intermediate states of charge/discharge. While the Fe and Zn analogs are cheaper, they similarly lack reversibility. For example, the Fe anode corrodes over time as the open circuit voltage of the charged battery is outside the stability window of the electrolyte. Thus, the battery slowly self-discharges about 1–2% of its nominal capacity per day in ambient conditions via $\text{H}_{2(\text{g})}$ evolution and/or O reduction.¹³

The metal hydride anode-based cell resolves most of the cost and toxicity problems associated with Cd. However, the alloys that store H are prone to crack or even dissolve in the electrolyte over cycling. Moreover, the pressure management necessary to mitigate such damage is expensive.¹³ Despite this challenge, the Ni metal-hydride battery saw some success in commercial vehicles and was implemented in early versions of mass-market hybrid electric vehicles like the Toyota Prius.¹⁴

4.10.2.3 Pb-acid battery

Pb-acid batteries were developed by Gaston Planté in France in 1859.¹² They consist of a metallic Pb anode, concentrated H_2SO_4 electrolyte, and PbO_2 cathode as follows¹⁴:



The cell chemistry is exceedingly elegant with the product of both the anodic and cathodic reactions being PbSO_4 . The relatively high cell voltage (at time of invention), low cost of Pb, and overall high stability at ambient temperatures have ensured the popularity of Pb-acid batteries over decades. Their main shortcomings are low energy density due to the heavy atomic weight of Pb and short lifetime. Pb-acid batteries are acutely affected by deep discharge, when the build-up of PbSO_4 can render the electrode surfaces inert.¹⁵ Nonetheless, Pb-acid batteries play an important role in most internal combustion engine vehicles as an intermittent high power density power source. Their industrial maturity and low cost allowed for optimization for many different applications, including (albeit rarely) storage of energy from intermittent renewable sources.¹⁴

Ultimately, the early batteries that preceded the LIB lacked the energy density and chemical reversibility for economically viable, portable and rechargeable energy storage devices.

4.10.3 Intercalation chemistry and the lithium revolution

Many of the early secondary battery chemistries were based on so-called conversion mechanisms in which the phase of the active material is converted to a new phase upon redox. The Pb-acid battery, for example, converted Pb metal to dissolved PbSO_4 as described above. Conversion mechanisms, however, elicit significant structural perturbations of the electrodes upon charge and discharge causing rapid capacity loss as substantial energy is required to facilitate extensive bond breaking and structural reorganization. Thus, a new paradigm that permitted reversible charge and discharge with minimal changes to the structure was needed. In the 1970s, Whittingham demonstrated that reversible cycling of electrochemical cells could be achieved through an intercalation mechanism.¹⁶ Intercalation is a topotactic reaction in which a guest species, in this case an ion, is reversibly inserted into a host structure. During intercalation, the host structure undergoes minimal structural changes, and thus the space group of the host and that of the resulting intercalation compound are related.¹⁷ Generically speaking, an intercalation reaction can be described as:



where G is the guest molecule/ion, L is the host lattice and G_xL is the resulting intercalated compound. Intercalation can occur into one-, two- and three-dimensional structures, as shown in Fig. 6. Intercalation has been extensively studied for two-dimensional, layered structures. These structures have been shown to facilitate intercalation of guest ions due to the weakly bonded van der Waals gaps between the strongly bonded metal-containing layers. In three-dimensional materials, intercalation can occur once interstitial sites are accessible to the guest species. Thus, in such structures there is a constraint on the size of potential guest species.¹⁸

The first demonstration of intercalation chemistry was the intercalation of SO_4^{2-} ions into graphite in 1841.¹⁷ In the 1960s, intercalation reactions became the focus of extensive investigation, as it was discovered that this reaction type could alter the electronic and optical properties of materials.¹⁹

In the 1970's, there was growing interest in high-energy rechargeable batteries for electric vehicles and stationary storage of renewable energy. Initially, high-temperature batteries, discussed in Section 4.10.2.1, were proposed as a solution but safety issues

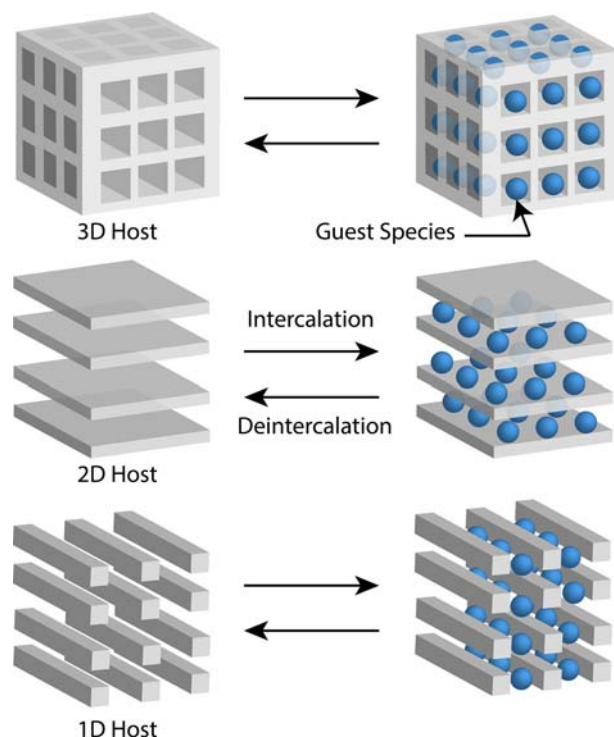


Fig. 6 3D, 2D, and 1D host materials before and after intercalation of guest species.

prevented application.¹¹ Utilizing intercalation chemistry provided an opportunity to design energy-dense batteries that could operate at ambient temperature. Li^+ emerged as the ideal candidate for the working ion in high-energy batteries as it has the most negative reduction potential of any metal (-3.04 V vs NHE). Additionally, Li^+ is an ideal guest species for intercalation chemistry; it is a very small monovalent ion, allowing it to fit into interstitial sites in three-dimensional structures. It also has a relatively low charge density, which permits facile transport through host lattices. The fortuitous combination of these characteristics enabled the development of low-weight, energy-dense, high-power batteries.

Modern LIBs utilize intercalation chemistry at both the graphite anode and the LiCoO_2 cathode. Notably, the realization of this technology resulted from nearly half a century of developments in basic solid-state chemistry of materials that are worth exploring in more detail. The following sections will provide an overview of several critical intercalation electrode materials that played a role in enabling state-of-the-art secondary battery technology, beginning with intercalation cathodes.

4.10.3.1 Intercalation cathode materials

Cathodes are currently the energy-limiting or potential-limiting electrodes in a LIB. Additionally, in modern commercial LIBs, the cathode accounts for more than 20% of the battery cost, and the raw materials used account for more than 50% of the cathode's cost.²⁰ Thus, further development on cathode materials will play a key role in decreasing battery technology costs, and ultimately making batteries more economically viable for use in electric cars and grid-scale energy storage applications.

The requirements for effective cathode materials in secondary batteries are as follows:

- (1) The host material must contain an ion that can readily participate in redox reactions, e.g. a transition metal.
- (2) The host material must support reversible redox reactions—intercalation mechanisms are ideal to limit structural changes and irreversibility.
- (3) The host material must be structurally stable.
- (4) The voltage of the host material should be positive relative to the desired anode material. Greater positive voltages yield higher energy density—in modern systems a potential around 4 V vs the anode is preferable.
- (5) The material should have a high ionic and electronic conductivity to support fast electrochemical processes, although modifications can be made to accommodate sluggish mobility for either carrier.

The ideal cathode material is composed of abundant, inexpensive, environmentally benign elements. The majority of the reported and commercialized cathode materials for modern LIBs fall into one of two categories: layered materials in which Li^+ can be inserted and occupy the empty layers or materials with more open structures.²¹ The latter has an inherent disadvantage in energy density because the structure itself is denser. The following sections will provide a detailed account of notable materials used as

intercalation cathodes for LIBs. The focus will be on their structure, advantageous/disadvantageous properties, mechanisms of electrochemical processes, and practical uses. The section will conclude with a discussion of cathode materials for next-generation LIBs.

4.10.3.1.1 Sulfides

4.10.3.1.1.1 Layered transition metal disulfides (TiS_2)

Building on the development of intercalation chemistry in transition metal disulfides, at Exxon Corporation, Whittingham demonstrated the first rechargeable battery employing Li^+ working ions and intercalation chemistry in 1976.¹⁶ The structure of TiS_2 is shown in Fig. 7a. It is a layered material with a trigonal crystal structure ($P\bar{3}m1$). Each layer comprises an arrangement of hexagonally close-packed Ti atoms sandwiched between hexagonal close-packed arrangements of S atoms. Thus, the Ti^{4+} atoms are octahedrally coordinated by S^{2-} ions, forming edge-sharing octahedra. The S atoms decorate the van der Waals gap.²² TiS_2 is designated as an O1 structure, meaning Li is octahedrally coordinated ("O") and the stacking of the metal and Li layers are directly on top of each other resulting in a sum of one metal layer in the unit cell ("1"). O1, O2, and O3 structures are discussed in more detail in Section 4.10.3.1.2.1.2 (pictured for LiCoO_2 in Fig. 15 in Section 4.10.3.1.2.1.2).

TiS_2 was the lightest of the layered transition metal dichalcogenides being investigated, making it a particularly appealing option for battery applications. Additionally, it is electronically conducting, so no conducting additive is needed. This maximizes the amount of active material that can be packed into the cell, resulting in a higher energy density. Initially, it was thought that TiS_2 was a semi-metal²³; however, later studies attribute the electronic conductivity to the presence of conducting electrons that are produced by a slight excess of Ti in the van der Waals gap,²⁴ meaning TiS_2 is an extrinsic semiconductor and not a semi-metal. It should be noted that extensive interlayer Ti (1% or more) has been shown to pin the layers together and drastically inhibit, or even prohibit, the intercalation of guest molecules.²⁵ Thus, it is essential to avoid high-temperature synthesis routes as they provide sufficient energy for the formation of Ti-vacancy-interstitial pairs that result in interlayer Ti. The most effective phase of this material for intercalation cathode applications is the ordered structure, which can be prepared at 600 °C.

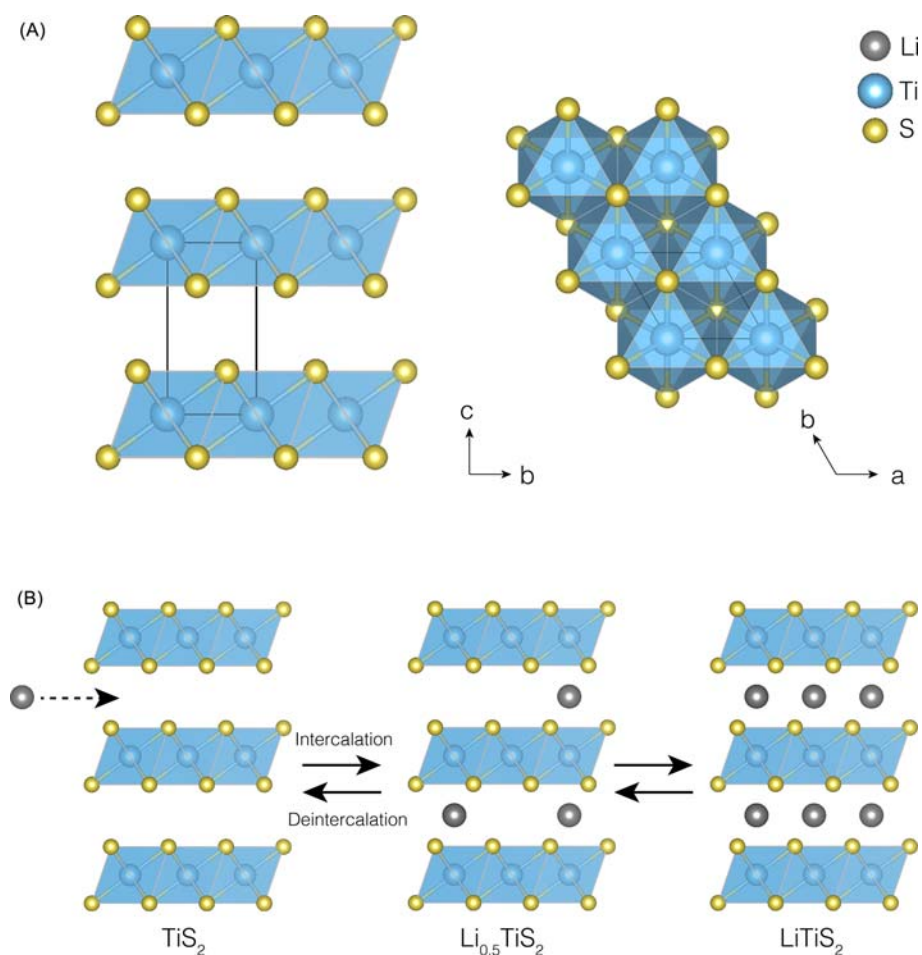


Fig. 7 (a) The structure of TiS_2 ($P\bar{3}m1$) in the bc plane (left) and ab plane (right). (b) A cartoon illustrating the intercalation mechanism by which Li^+ is reversibly inserted into TiS_2 , ultimately resulting in LiTiS_2 .

Crucially, TiS_2 was shown to form a single-phase across the entire range $\text{Li}_{1-x}\text{TiS}_2$. Thus, up to one equivalent of Li^+ can be reversibly inserted and removed from the TiS_2 structure without the structure undergoing a phase change as shown in Fig. 7b, resulting in minimal capacity loss and high cycling reversibility.



Intercalated Li^+ occupies octahedral vacancies in the van der Waals gap (Fig. 7b). During intercalation, an electron is drawn from the external circuit to maintain charge neutrality through the reduction of TiS_2 . A simple way to understand the charge compensation mechanism is the reduction of Ti^{4+} to Ti^{3+} . However, the Ti–S bond is partially covalent, due to overlap between the Ti d band and the S p band, which suggests that S^{2-} may be active in the redox processes in TiS_2 . For accounting purposes, we will imagine the formal charge of Ti is reduced from Ti^{4+} to Ti^{3+} during intercalation. The impact of transition metal-anion covalency on redox processes will be explained further in Section 4.10.3.1.4.1. Whittingham demonstrated a battery using a TiS_2 cathode paired with a Li metal anode resulting in a potential of < 2.5 V. The reversibility of the intercalation reaction with Li allowed for nearly 1000 cycles without significant capacity loss.²¹

Although this was an important milestone in the development of high-capacity, long-lasting secondary batteries, it was not without fault. Shortcomings of Li batteries with TiS_2 cathodes included reduction of the electrolyte at the Li metal anode, internal shorts, thermal runaway, and potentially catastrophic failure (discussed in detail in Section 4.10.5.2.1). These issues, in combination with the relatively low cell voltage, led researchers to investigate different materials for future LIB cathodes.

In recent work, TiS_2 has been proposed as a high performance cathode for K batteries,²⁶ a cathode for Mg^{2+} intercalation,²⁷ and TiS_2 nanoplates as high-rate cathodes for Na-ion batteries.²⁸ The first two applications will be discussed in more detail in later sections of this chapter.

4.10.3.1.1.2 Thiospinels (CuM_2S_4)

Another early sulfide-based material that showed promise as a potential cathode for LIBs was the CuM_2S_4 ($M = \text{Ti}, \text{V}, \text{Cr}, \text{Co}$) thiospinel phase. This material family was first suggested for battery applications in 1981.²⁹

The structure of CuTi_2S_4 is shown in (Fig. 8). It forms in a spinel structure ($\text{Fd}\bar{3}\text{m}$) with cubic close-packed S anions and Cu cations occupying the 8a tetrahedral sites. The tetrahedra are not connected themselves but are corner-sharing with the Ti octahedra that occupy the 16d sites. In contrast with layered TiS_2 , the thiospinel phase is an example of intercalation into a non-layered structure. One equivalent of Li^+ can reversibly intercalate into CuTi_2S_4 and occupy the vacant 16c octahedral sites.²⁹ The arrangement of Li sites enables a 3D diffusion pathway in the material.

instead of the 2D pathways in layered materials. Additionally, intercalation into a non-layered structure results in isotropic expansion and the size selectivity eliminates water or solvent intercalation from the electrolyte. Li^+ mobility in CuTi_2S_4 is slow because the Cu atoms block the principal diffusion pathway in the material. The 8a tetrahedral sites share all four faces with the 16c sites (which Li^+ comes to occupy); therefore removing the Cu atoms from the 8a sites would facilitate the formation of an accessible 3D conduction pathway in the material. A secondary pathway exists through the 48f sites, but this pathway requires much higher activation energy because it shares two faces with occupied 16d sites. The 8b tetrahedral sites share all four faces with occupied 16d sites and are thus inaccessible to inserted Li^+ . Goodenough attempted to synthesize a material that could utilize the primary, low energy diffusion pathway by extracting Cu from the structure through chemical oxidation with iodine in dry acetonitrile³⁰:



A greater amount of Li could be reversibly inserted into the $\text{Cu}_{0.007}\text{Ti}_2\text{S}_4$ defect thiospinel material (up to 1.93 equiv). Neutron diffraction studies showed that the Li only occupies the 16c sites and not the 8a sites.³¹ The remnant Cu atoms occupying the 8a sites still increase the impedance for Li diffusion through the material. The Cu can be removed entirely, and 1.95 equiv. of Li can be

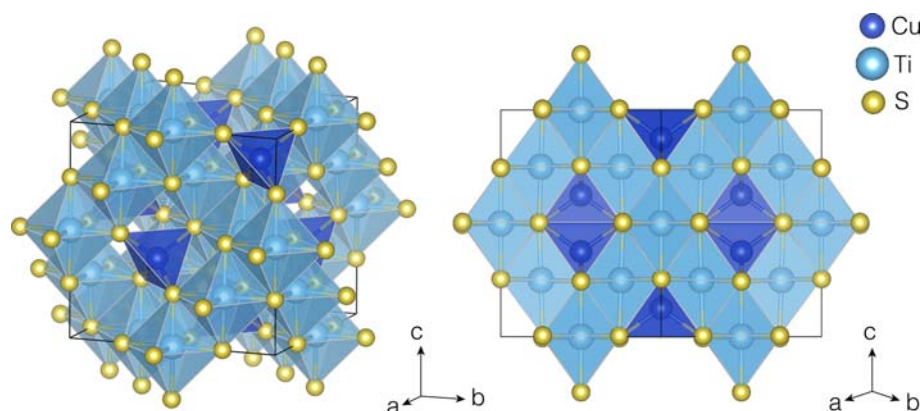


Fig. 8 The structure of CuTi_2S_4 ($\text{Fd}\bar{3}\text{m}$) rotated 22.5° off the a axis and 12.25° off the c axis (left) and along the $[110]$ direction (right).

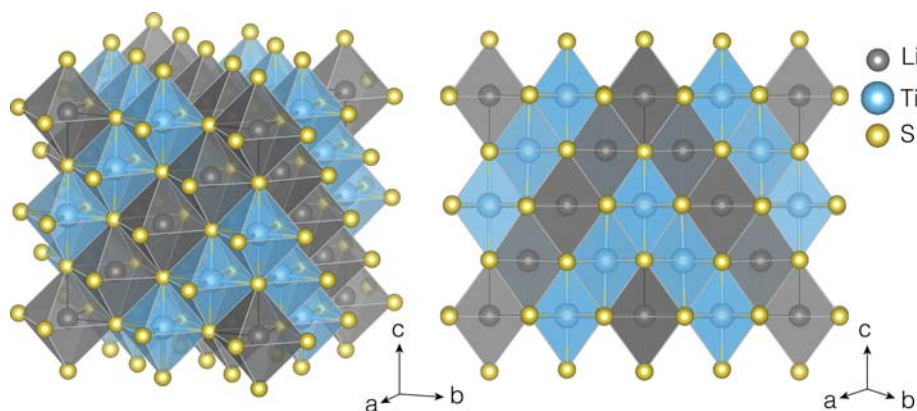


Fig. 9 The structure of $\text{Li}_2\text{Ti}_2\text{S}_4$ ($\text{Fd}\bar{3}\text{m}$) rotated 22.5° off the a axis and 12.25° off the c axis (left) and along the $[110]$ direction (right).

reversibly inserted into the resulting cubic titanium sulfide ($c\text{-Ti}_{2.05}\text{S}_4$), as illustrated in Fig. 9. This represents a substantial increase over the capacity obtained with CuTi_2S_4 . The redox couple is still $\text{Ti}^{3+/4+}$, so the material's voltage is comparable to that of layered TiS_2 over the entire Li-composition range. Additionally, the diffusion coefficient of Li in ($c\text{-Ti}_{2.05}\text{S}_4$) is less than that of the layered form. Thus, although this material has some benefits over the layered TiS_2 phase, its practical application is limited by its low diffusivity and the necessary pairing with a Li metal anode as a Li^+ source and to ensure sufficient voltage.

Current electrochemical research areas for thiospinel phases are primarily centered around using tertiary Mg thiospinels like MgSc_2S_4 as a potential solid-state electrolyte for all-solid-state Mg-ion batteries,³² and materials like MgTi_2S_4 as cathodes in Mg-ion batteries.³³

4.10.3.1.2 Oxides

4.10.3.1.2.1 Layered transition metal oxides

Although the layered oxide materials have a similar structure to the sulfides, there was initially minimal interest in the oxides, as it was thought that Li^+ could not be easily removed from them.²¹ However, to overcome the low voltage associated with the sulfide cathode materials, the research focus shifted to layered oxide-based materials. A higher cell potential can be attained if there is a greater negative free energy change for an intercalation reaction, as seen in Eq. 18. The achievable voltage in layered sulfide materials is limited due to the position of the S 3p band (Fig. 10).

The top of the S 3p band limits the potential of these materials to < 2.5 V vs Li/Li^+ , as seen in TiS_2 . Attempts to stabilize a sulfide based structure with access to a redox couple at a higher potential e.g. $\text{Co}^{3+/4+}$ would result in the oxidation of S^{2-} into disulfide ions (S_2)²⁻ and lead to the formation of a pyrite structure instead of the desired layered structure (Fig. 11). The subject of anion redox, i.e. charge compensation mechanisms that involves the anion, is a discussed in Section 4.10.3.1.5.

However, in an oxide, the top of the O 2p band is at a much lower energy than the S 3p in a sulfide, due to the higher electronegativity of oxygen, and thus in oxides lower-lying metal ion energy bands that can facilitate a higher cell potential are accessible.

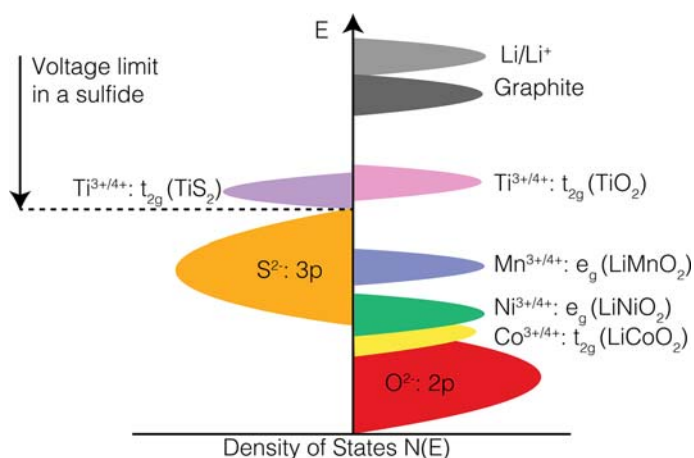


Fig. 10 Positions of the redox energies relative to the top of anion p bands. Adapted from Manthiram, A. A Reflection on Lithium-Ion Battery Cathode Chemistry. *Nat Commun* 2020, 11, 1550.

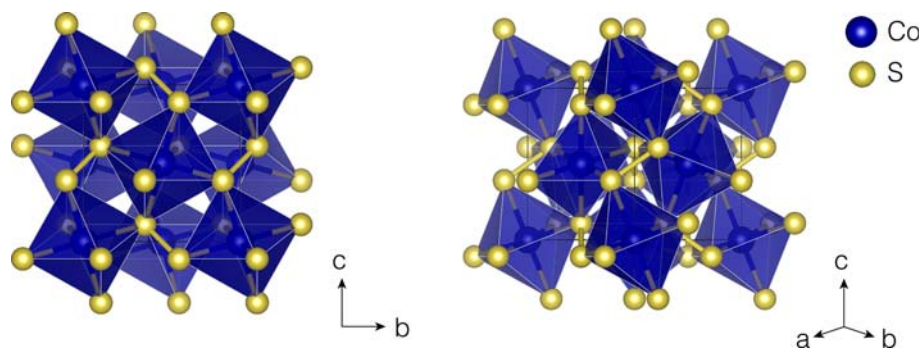


Fig. 11 The structure of CoS_2 ($\text{Pa}\bar{3}$) in the bc plane (left) and along the $[110]$ direction (right). CoS_2 adopts a pyrite structure with disulfide ions $(\text{S}_2)^{2-}$.

4.10.3.1.2.1.1 Early binary transition metal oxides (oxides of Mo and V)

Two of the earliest oxides studied as potential cathode materials for secondary LIBs were MoO_3 and V_2O_5 . MoO_3 is a layered material consisting of Mo octahedra that are corner-sharing in the $[100]$ direction and edge-sharing in a zigzag line along the $[010]$ direction (Fig. 12).

While the elements within a layer are covalently bonded together, the double-layers are held together by van der Waals forces. The weak bonding combined with an interlayer spacing of 6.929 Å make MoO_3 a good intercalation cathode candidate. Although initial studies claimed MoO_3 underwent a disproportionation type reaction with Li^+ ,³⁴ later studies showed that the introduction of Li^+ is a surprisingly reversible intercalation reaction.^{35,36} About 1.5 equiv. of Li^+ can reversibly intercalate into MoO_3 through the multielectron reduction of Mo^{6+} to Mo^{5+} and subsequently Mo^{4+} :



However, the rate capability of MoO_3 is poor compared to V_2O_5 and TiS_2 due to slow kinetics. Thus, MoO_3 is less suitable for practical applications.

V_2O_5 has several polymorphs including orthorhombic $\alpha\text{-V}_2\text{O}_5$, monoclinic $\beta\text{-V}_2\text{O}_5$ obtained through exposing $\alpha\text{-V}_2\text{O}_5$ to high temperature and pressure, and γ - and $\varepsilon\text{-V}_2\text{O}_5$ produced by chemical removal of metals from vanadium oxide bronzes.³⁷ Fig. 13a and b shows $\alpha\text{-V}_2\text{O}_5$ —the polymorph which was considered to be a promising candidate for battery cathodes—in the bc plane and the ab plane, respectively. $\alpha\text{-V}_2\text{O}_5$ also has a layered structure in an orthorhombic crystal system (Fig. 13). It consists of chains of edge-sharing VO_5 square pyramids. The chains themselves are corner-sharing. Very weak V–O bonds separate the layers. Thus, the structure can also be described as having distorted VO_6 octahedra, as shown in Fig. 13c, but for this discussion, the former description is more useful. The weak sixth V–O bond affords the ability to insert guest species into the interlayer space. However, Li^+

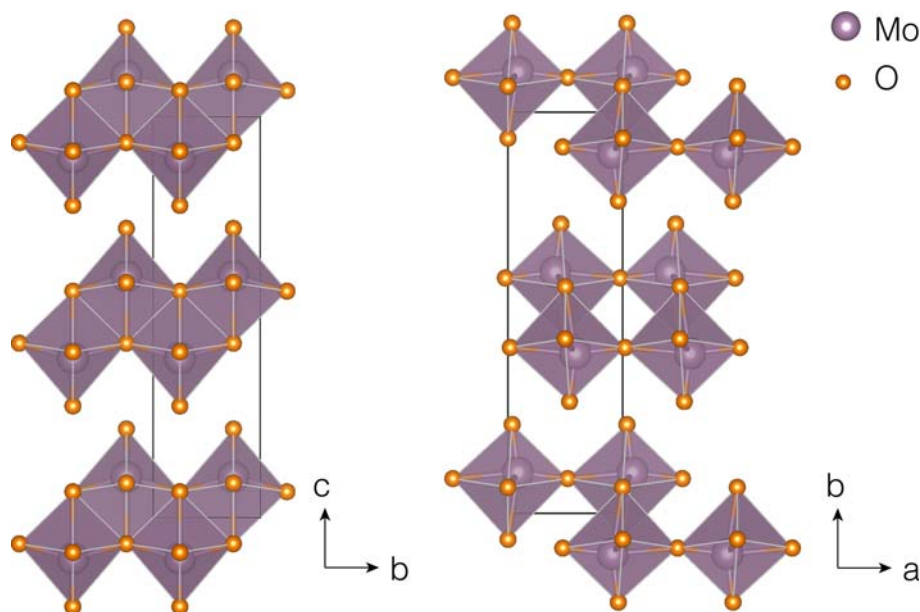


Fig. 12 The structure of layered MoO_3 (Pbnm) in the bc plane (left) and in the ab plane (right).

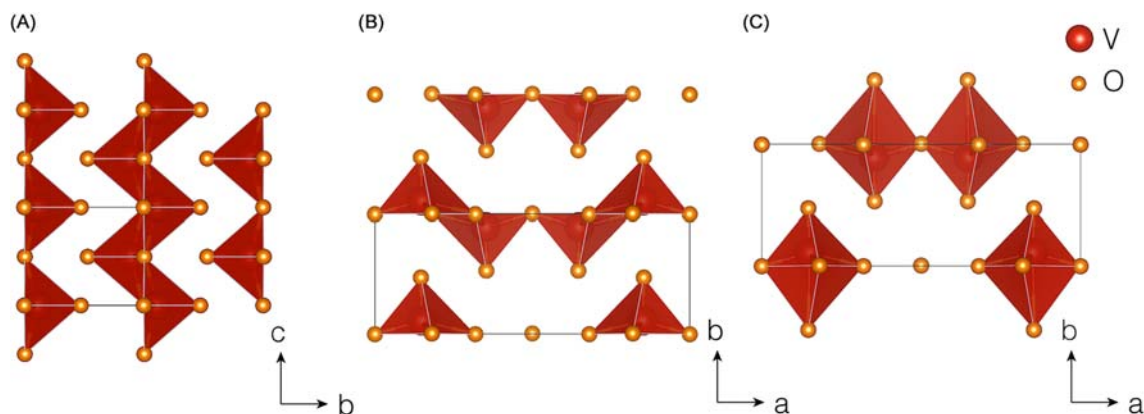


Fig. 13 (a) The structure of layered α - V_2O_5 (Pmnm) in the bc plane and (b) in the ab plane. (c) A visualization of α - V_2O_5 with VO_6 polyhedra completed by long V–O bond.

intercalation/deintercalation in V_2O_5 is more complicated than previously discussed materials, with numerous phases forming throughout the process.

The intercalation of Li^+ in V_2O_5 can be simply described as:



The α phase is maintained for ($x < 0.1$), the ϵ phase forms for ($0.35 < x < 0.7$) and the δ phase for ($0.9 < x < 1$) as V^{5+} is reduced to V^{4+} . The three phases form reversibly upon intercalation of less than one equivalent of Li^+ . The α - and ϵ -phases are very similar, with the ϵ -phase having puckered layers. The formation of the δ -phase corresponds to the shifting of alternating layers by half a unit cell along the b direction. Minimal energy is required for this process as no strong V–O bonds are broken. In practice, up to 3 equiv. of Li^+ can be inserted. However, irreversible structural changes begin to occur upon intercalation of more than one equivalent of Li^+ . Initially, the γ -phase is formed in which the organization of the VO_5 pyramids changes from up up down down to up down up down. Upon insertion of 3 equiv. of Li, the ω -phase, which has a rock-salt structure, is formed.^{38,39} X-ray absorption spectroscopy (XAS) data determined that capacity fade in the γ - and ω -phases is a result of the irreversible formation of compounds like $LiVO_3$ and Li_3VO_4 . If cycled at $x < 1$, then V_2O_5 can perform as a suitable intercalation cathode for a LIB. However, while it may offer long cycle life, V_2O_5 proved to be a low voltage and low energy density relative to other cathode materials.

4.10.3.1.2.1.2 Lithium cobalt oxide (LiCoO₂ or LCO)

In 1980, Goodenough demonstrated that Li^+ could be reversibly removed from $LiCoO_2$ electrochemically. Replacing the sulfide-based cathode with $LiCoO_2$ facilitated access to low-lying energy bands. The increase in the cell voltage achieved with $LiCoO_2$ made it feasible to replace the problematic Li metal anode with a safer material despite the inevitability that the replacement anode would have a slightly less negative reduction potential. Additionally, since Li^+ is already present in $LiCoO_2$, the cathode could serve as a Li^+ source, permitting the use of a delithiated anode such as graphite. Thus, $LiCoO_2$ emerged as an ideal cathode material that satisfied all the desired criteria.⁴⁰ $LiCoO_2$ became the prototypical cathode material in LIBs, which swiftly dominated the secondary battery market after Sony's commercialization in 1991. Even today, the cathode materials in state-of-the-art LIBs stem from $LiCoO_2$.

Depending on the synthesis temperature, $LiCoO_2$ can form phases with different crystal structures. A low-temperature synthesis (< 400 °C) results in a cubic spinel phase, while a high-temperature synthesis (around 750 °C) results in a trigonal layered structure, similar to that of the layered sulfides. The layered structure exhibits superior electrochemical performance compared to the cubic spinel phase. Thus, high-temperature synthesis is vital for practical applications.

The structure of the layered form is shown in Fig. 14. It adopts an α - $NaFeO_2$ -type ($R\bar{3}m$) crystal structure of cubic close-packed O^{2-} ions in the 6c sites, and ordered Li^+ and Co^{3+} ions in the octahedral interstitial sites (3a and 3b, respectively) in alternate (111) planes. The octahedra are edge-sharing, and each layer is displaced by one third of the lattice parameter to minimize ionic interactions between the cations. The structure is termed an O3-type structure, in which the Li^+ is octahedrally coordinated ("O"), and "3" sets of Co and Li layers are in the unit cell. $LiCoO_2$ can also form a stable O2-type structure, in which 2 of each metal layer are present in each unit cell, and every second layer is rotated by 60°. The two structures are compared in Fig. 15. Although the O2-type is capable of similar electrochemical performance as the O3-type, it is more challenging to synthesize, making it inconvenient for commercial applications.⁴² Therefore, the focus of the following discussion will be the O3-type material.

Since this cathode material is prepared in the lithiated state, the cell must be charged on assembly. During charge, shown in forward reaction of Eq. (58), Li^+ is extracted from the cathode. The removal of Li^+ is charge balanced nominally by oxidation of Co^{3+} to Co^{4+} . At the same time, Li^+ is intercalated into the anode, a process which will be discussed in more detail in Section 4.10.4.1.1. Upon discharge, shown in the back reaction of Eq. (58), the Li^+ is intercalated into $LiCoO_2$, and Co^{4+} is reduced to Co^{3+} .

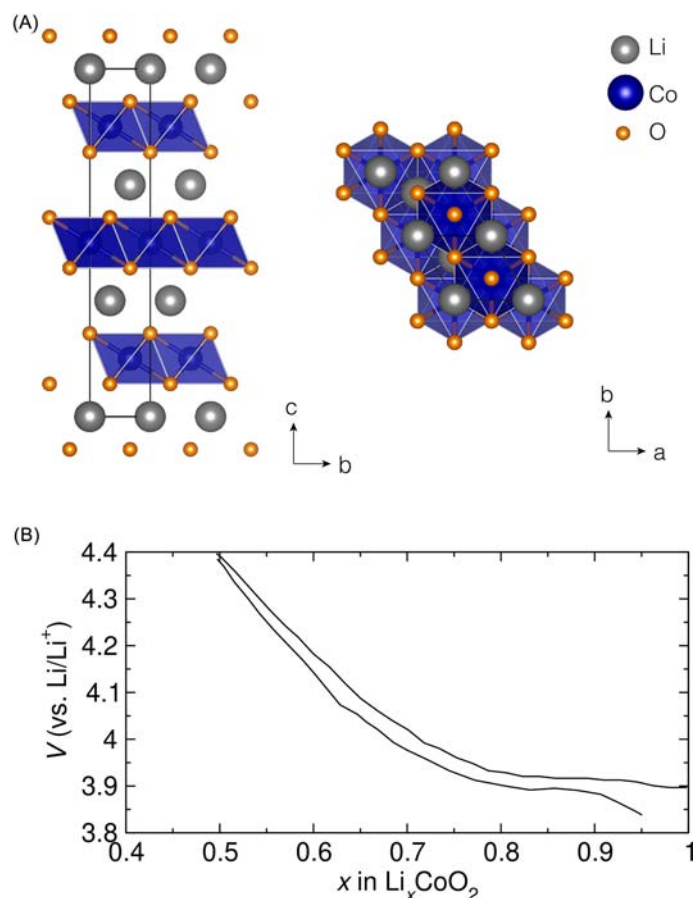


Fig. 14 (a) The structure of layered LiCoO₂ (R $\bar{3}m$) in the bc plane (left) and in the ab plane (right). (b) Representative galvanostatic cycling of LiCoO₂ with a 1 M LiBF₄ in propylene carbonate electrolyte and an Li_{0.1}V₂O₅ anode and a rate of 1 mA cm⁻². The electrochemistry data is from Ref. 41



LiCoO₂ experiences several structural changes during the removal of Li⁺ from the lattice.⁴³ The severity of the structural change can be separated into two regions, $x < 0.5$ and $0.5 \leq x < 1$, where x is the amount of Li⁺ removed from the structure. As shown in Fig. 4, the removal of the first 0.5 equiv. of Li⁺ occurs through a single-phase mechanism. Within this region the structural changes are minimal and are attributed to the increasing electronic delocalization of Li_{1-x}CoO₂, which will be discussed in greater detail later in this section.⁴⁴ In the region of $0.5 < x < 1$, Li_{1-x}CoO₂ undergoes transformations that are detrimental to its electrochemical performance. Around $x = 0.5$, Li_{1-x}CoO₂ undergoes a phase transformation to a monoclinic phase.⁴⁵ The formation of the monoclinic phase causes dramatic capacity fade. Additional transformations occur after the formation of the monoclinic phase. The completely delithiated end member CoO₂ is a hexagonal O1 phase that was reported by Amatucci et al. using in situ X-ray diffraction (XRD). About 95% of the removed Li⁺ can be reinserted into the CoO₂ end member on the first discharge⁴⁶ suggesting that the drastic capacity fade experienced during deep delithiation is due to iterative phase transitions that likely induce particle cracks and lead to bulk structural degradation.⁴³ Furthermore, claims have been made that a surface impedance increase occurs around $x = 0.5$ due to side reactions involving the electrolyte and surface species at the cathode, which would also contribute to capacity fade.⁴⁷ Additionally, the covalent nature of the Co–O bond, which manifests as an overlap of the O p band with the Co d band in the pDOS (as shown pictorially in Fig. 10), causes the O²⁻ to play a role in charge compensation. At high degrees of delithiation, O²⁻ is oxidized leading to O_{2(g)} evolution and contributing further to the structural instability. As a result of these complications, the practical capacity of an LiCoO₂ cathode is limited to half that of the theoretical capacity, or $\sim 140 \text{ mA h g}^{-1}$, to avoid rapid capacity fade. Notably, the practical capacity is lower than that of LiTiS₂ at 210 mA h g⁻¹. However, the energy density of a cell with a LiCoO₂ cathode is greater than that of a cell with a TiS₂ cathode since the voltage LiCoO₂, which can simply be thought of as the potential of the Co^{3+/4+} couple ($\sim 4 \text{ V vs Li/Li}^+$), is about twice that of a TiS₂ cathode.

Solid-state diffusion of the working ion, Li⁺, in the host material is important when considering the rate at which the material can be cycled. The diffusivity of Li⁺ in Li_xCoO₂ was determined to be $5 \times 10^{-9} \text{ cm}^2 \text{ s}^{-1}$ across the entire composition range,⁴⁸ which is comparable to the Li⁺ diffusivity in LiTiS₂ of $10^{-8} \text{ cm}^2 \text{ s}^{-1}$.²¹ High diffusivities enable these cathodes to cycle at relatively high current densities, 4 and 10 mA cm⁻², respectively.⁴⁹ On the other hand, the electronic conductivity of LiCoO₂ is variable. The

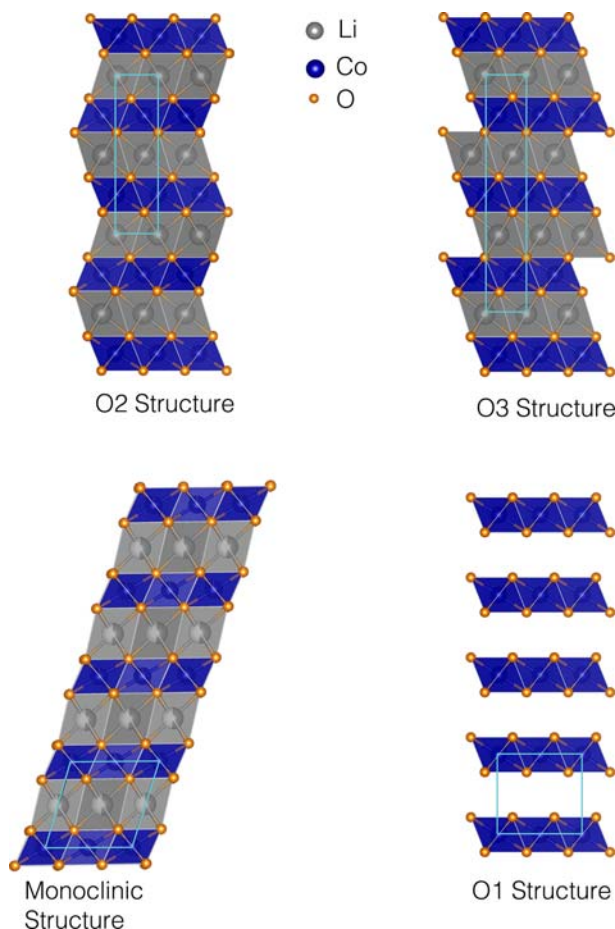


Fig. 15 A comparison of O2 and O3 LiCoO₂, monoclinic LiCoO₂ formed by the phase transition after removing 1/2 of the Li⁺ in the structure, and the O1 structure of the CoO₂ end member. The unit cells for each structure are shown in cyan.

electronic conductivity has been shown to vary significantly with both temperature and Li⁺ content. Pristine LiCoO₂ behaves as a semiconductor; the conductivity increases three orders of magnitude (10^{-6} to 10^{-3} S cm⁻¹) as the temperature increases from 150 K to 300 K. Notably, the Co³⁺ ions have a low spin $t_{2g}^6e_g^0$ configuration and therefore should not contribute to the electronic conductivity. The observed conductivity likely arises from small amounts of Co⁴⁺ in the pristine material due to deviations from ideal Li⁺ stoichiometry during the high-temperature synthesis.⁴⁴ The Co⁴⁺ ions have a low spin $t_{2g}^5e_g^0$ electron configuration, so the t_{2g} band is no longer full. The presence of edge-sharing octahedra leads to the possibility of direct overlap of the t_{2g} orbitals. According to Goodenough, delocalization of electronic carriers through overlapping t_{2g} orbitals in metal oxides is expected if the metal-metal distance is smaller than the critical value R_C , an empirical value that can be calculated for 3d elements using the following equation:

$$R_C(3d) = 3.20 - 0.05m - 0.03(Z - Z_{Ti}) - 0.04S(S + 1) \quad (54)$$

where m is the valence of M^{m+} , Z is the atomic number of M , and S is the effective spin of M .⁵⁰ Ménétiér et al. demonstrated that the metal-metal distance in LiCoO₂ is smaller than R_C regardless of how much Li⁺ has been removed from the structure.⁴⁴ Thus, the direct overlap of the t_{2g} orbitals can account for the unexpected conductivity in the pristine material. Furthermore, LiCoO₂ was shown to be a p-type semiconductor.⁵¹ However, at high Li⁺ contents, the concentration of Co⁴⁺ is too small to result in enough holes in the t_{2g} band for significant conductivity through electronic delocalization. Upon delithiation, during charging of the cell, a hole is created in the t_{2g} band every time a Li⁺ vacancy is formed. Early in the deintercalation process, the holes are pinned to the Li⁺ vacancies to maintain local charge neutrality. Thus, the material still behaves as a semiconductor with relatively low electronic conductivity. After more substantial delithiation ($0.50 < x < 0.74$), both the number of holes and Li⁺ vacancies is significantly larger, leading to delocalization and a metal-insulator transition that increases the electronic conductivity by up to 6 orders of magnitude.⁴⁴ The change in conductivity at different levels of delithiation is much more concerning for battery applications than the change with temperature. As such, unlike TiS₂, an LiCoO₂ cathode must be mixed with a conductive additive to ensure optimal electronic conductivity causing a decrease in the overall energy density and power capability of the cell.

Catastrophic failure associated with thermal runaway is a major concern in practical battery applications. At elevated temperatures ($> 200\text{ }^\circ\text{C}$), LiCoO_2 will decompose to release O_2 which can react exothermically with organic compounds in the cell resulting in thermal runaway. In fact, LiCoO_2 exhibits the lowest thermal stability of any commercialized cathode material.⁵² However, it is the most stable of the layered transition metal oxides that were reasonable candidates for cathode materials. The stability of LiCoO_2 stems from the large octahedral-site stabilization energy (OSSE). The OSSE measures the difference in crystal field stabilization energy of an element in an octahedral vs a tetrahedral site. Thus, a high OSSE implies that the element will not readily migrate out of the octahedral site through a tetrahedral site. Since the Co and Li layers are separated by a tetrahedral site, the Co does not migrate into the Li layer under slight thermal excitation.⁵³ This property ensures the structural stability of LiCoO_2 , another property making it suitable for long life practical battery applications.

Although LiCoO_2 proved to be an excellent choice as a cathode material in commercial LIBs, it still has some limitations. In addition to a limited practical capacity of 50% of theoretical, utilizing LiCoO_2 also results in a relatively expensive battery. Co is the least abundant and most expensive component of standard LIBs. Additionally, nearly 65% of Co mining occurs in the Democratic Republic of Congo (DRC). The geographic isolation of the resource raises reasonable concerns about the possibility of supply disruptions caused by government policy or socio-political instability as has occurred in the past.⁵⁴ Humanitarian issues are also of concern; the mining of Co in the DRC is largely unregulated, leading to thousands of child laborers working in unsafe conditions.⁵⁵ Thus, an effective cathode material that utilizes less Co, or none at all, would prove to be a more secure, sustainable, long term option for LIBs. This will be especially important for large scale applications, such as electric vehicles and grid-scale energy storage, which are of growing importance and is the current focus of much contemporary cathode research. Efforts in this vein have resulted in cathodes with Ni, Mn, or Al substituted for Co and these materials will be discussed in following sections.

4.10.3.1.2.1.3 Other layered transition metal oxides

After successful demonstration of LiCoO_2 as a cathode material in LIBs, many other layered LiMO_2 compounds were investigated. The $M=\text{Mn}$ and Fe analogs must be synthesized through ion-exchange with the appropriate NaMO_2 phases, which are easily synthesized.^{56,57} However, like LiCoO_2 , the $M=\text{Ti}$, V, Cr, and Ni analogs can be synthesized directly through high-temperature solid-state synthesis. In the case of LiTiO_2 the operating potential is too low for practical batteries.

LiCrO_2 is generally known to be electrochemically inactive because the one electron oxidation of $\text{Cr}^{3+/4+}$ that would occur upon Li^+ deintercalation during charging is thermodynamically difficult. Cr^{3+} has a very stable $t_{2g}^3e_g^0$ configuration and oxidation would result in the less stable Cr^{4+} ($t_{2g}^2e_g^0$), which as a result tends to disproportionate into $2/3 \text{Cr}^{3+}$ (d^3) and $1/3 \text{Cr}^{6+}$ (d^0). A unique three electron oxidation of Cr^{3+} to Cr^{6+} has been observed in LiCrO_2 , but Li^+ cannot reintercalate into the structure because the Cr^{6+} preferentially migrates to the smaller tetrahedral interstitial, resulting in irreversible capacity loss.⁵⁸

Similarly, LiVO_2 presents challenges as a potential cathode material. LiVO_2 exhibits a negligible discharge capacity because of a phase change that occurs upon extraction of more than $1/3$ of the Li^+ , during which $1/3$ of the V migrate to the empty sites in the Li layer.⁵⁹ Unlike Co, V (d^2) has a low OSSE and can easily migrate through the tetrahedral interstitial into the Li layer. Recent studies have tried to address this problem by substituting some of the V with electrochemically inactive $3+$ elements like Cr to stabilize the structure.⁶⁰ This has proven to enable cycling, but some minor structural changes still impede long-term capacity retention. Other recent studies concerning LiVO_2 have been focused on the cubic phase with a distorted rock-salt structure, which unexpectedly shows a capacity of approximately 130 mA h g^{-1} and capacity retention over 100 cycles.⁶¹

The LiFeO_2 phases were extensively studied due to the abundance and non-toxicity of Fe. The $\alpha\text{-NaFeO}_2$ -type Fe phase did not show Li deintercalation, making it unsuitable as a Li-ion cathode. Other phases of LiFeO_2 have since been investigated, including a corrugated layered phase, those with ramsdellite and hollandite structures, and an $\beta\text{-NaFeO}_2$ -type phase, with tetrahedral Fe^{3+} instead of octahedral.⁵⁷ None of these phases proved to be capable of sustaining long term cycling mainly due to structural transformations upon deintercalation.⁶²

Besides LiCoO_2 , LiMnO_2 and LiNiO_2 are the two phases that garnered the most interest for practical applications. Ni is cheaper than Co and still offers a similar theoretical capacity and voltage as LiCoO_2 . The Mn phase was presented as the “green” option because it is cheaper and less toxic than Co or Ni. Unfortunately, both materials have several similar drawbacks that preclude them from being used as cathodes in practical devices.

Firstly, well-ordered LiNiO_2 is difficult to synthesize. Instead, during the high-temperature synthesis ($700\text{--}800\text{ }^\circ\text{C}$), Ni^{2+} tends to form and Li^+ is volatile, resulting in $\text{Li}_{1-y}\text{Ni}_{1+y}\text{O}_2$ stoichiometries. The additional y equivalents of Ni tend to occupy the Li layer (3b sites).⁶³ In LiMnO_2 , Mn is prone to leaching out of the electrode during cycling due to a disproportionation reaction of Mn^{3+} to Mn^{4+} and Mn^{2+} . Mn^{2+} leaches from the material and is soluble in the electrolyte,⁶⁴ which is a challenge for all cathodes containing Mn. Furthermore, both materials exhibit Jahn-Teller distortions. The Ni^{3+} , low spin d^7 ($t_{2g}^6e_g^1$), and Mn^{3+} , high spin d^4 ($t_{2g}^3e_g^1$), are both stabilized by the elongation of one $M\text{--O}$ bond along the octahedral axis. The Jahn-Teller distortions are thought to be partially responsible for the structural instabilities and observed irreversible phase transformations that occur during delithiation.⁶⁵ After removing 0.5 equiv. of Li^+ , LiMnO_2 undergoes an irreversible transformation to the spinel phase, LiMn_2O_4 . Nearly stoichiometric LiNiO_2 undergoes phase changes upon removing around 0.25 and 0.50 equiv. of Li^+ . However, in the non-stoichiometric phases that readily form at high temperatures, the Ni present in the Li layer anchors the structure and helps prevent these structural changes. Unfortunately, this is accompanied by inhibition of Li^+ diffusion in the layer and thus reduces the power capability.

Finally, both Ni^{3+} and Mn^{3+} , like V^{3+} , have low OSSE, and thus suffer from transition metal migration through the tetrahedral site into the Li layer during cycling.¹⁹ This results in poor electrochemical performance and correlates to a lower thermal stability than LiCoO_2 .

Thus, neither pure LiNiO_2 nor LiMnO_2 are suitable materials for commercial LIB cathodes. However, strategic combinations of these layered transition metal oxides enables the development of cathode materials with an agglomeration of their individual beneficial properties. Many mixed-metal layered transition metal oxides have been investigated, including $\text{LiNi}_{1-y}\text{Co}_y\text{O}_2$, $\text{LiMn}_{1-y}\text{Co}_y\text{O}_2$, $\text{LiNi}_{1-y}\text{Mn}_y\text{O}_2$, and several combinations of three different metals. In general, the substitutions affect the structural stability or chemical stability, impacting the available capacity and retention of capacity on cycling. The following section will focus on materials that have proven to be most promising and successful for practical applications, those containing Ni, Mn, and Co (NMC), and those containing Ni, Co, and Al (NCA).

4.10.3.1.2.1.4 $\text{LiNi}_{x-y-z}\text{Mn}_y\text{Co}_z\text{O}_2$ (NMC or NCM)

Mixing Ni, Mn, and Co on the transition metal sites of LiCoO_2 has beneficial effects on the electrochemistry and economics. As previously discussed, Mn is the most abundant and least toxic of the three, thus increasing Mn content leads to a cheaper and more environmentally safe cathode. Additionally, since the Mn d band lies above the O 2p band, cathodes with higher Mn content are more chemically stable as no O^{2-} oxidation occurs during Li^+ removal. Although Co is the least abundant, most toxic, and least chemically stable, Co has the most significant impact on structural integrity since it has the highest OSSE. Co also produces the phase with the highest electronic conductivity. Interestingly, Ni falls between Mn and Co in all of these categories.¹⁹ Thus, current research directions seek to increase the Ni content and decrease the Co content to increase the capacity and lower the cost.

Based on these characteristics, it is unsurprising that $\text{LiNi}_{x-y}\text{Mn}_y\text{O}_2$ (NMO) was one of the phases of intense interest due to its potential to be the cheapest phase with a high capacity. Since the Mn d band lies above the Ni, Mn^{3+} tends to reduce Ni^{3+} during synthesis. It follows then that NMO tends to form with Mn^{4+} , which is electrochemically inactive in an octahedral site due to the stable electron configuration $t_{2g}^3e_g^0$. Thus, Ni^{2+} is stabilized in the structure. This eliminates problems associated with Jahn-Teller distortions in the single metal materials. Since the Ni allows for deeper cycling of the material without an irreversible phase change, NMO can reach higher capacities than LiCoO_2 . However, as expected, NMO is prone to cation mixing which will significantly affect the Li^+ diffusivity, and thus, the power capabilities.⁶⁶ More recent studies of this material have suggested making $\text{LiNi}_{0.5}\text{Mn}_{0.5}\text{O}_2$ through an ion exchange process produces a low defect material that can be reversibly cycled with a capacity of 180 mA h g^{-1} at high rates.⁶⁷ However, this phase suffers from low thermal stability, insufficient cycle life, and the use of expensive synthesis procedures.

Logically, Co substitution into NMO can further improve the structural stability. The material $\text{LiNi}_{1/3}\text{Mn}_{1/3}\text{Co}_{1/3}\text{O}_2$ (known as NMC 111 or NMC 333, where the numbers indicate the Ni:Mn:Co ratio) demonstrated about 200 mA h g^{-1} of reversible capacity for the first 30 cycles at a similar voltage to LiCoO_2 .⁶⁸ In practical application, due to voltage limitations required to increase the lifetime, NMC 111 is limited to about $150\text{--}160 \text{ mA h g}^{-1}$. This material also exhibits higher thermal stability than LiCoO_2 or LiNiO_2 and is cheaper than LiCoO_2 . NMC 111 was the earliest of these phases and remains the most common for practical applications today. It is used for electric vehicles, electric bikes, medical devices, and power tools.

In the last decade, propelled by the goal of enabling widespread adoption of EVs, the field has moved toward developing inexpensive, high energy NMC materials with greater Ni content including NMC 442, 532, 622, and 811. The US Department of Energy estimates that by 2030, batteries for automotive applications will need to deliver a 300 mile driving range at a pack level cost of $\$80 \text{ kWh}^{-1}$.⁶⁹ The average current cost is $\$143 \text{ kWh}^{-1}$.⁶⁹ A 300 mile driving range could be achieved with a $60\text{--}70 \text{ kWh}$ pack.⁷⁰ To obtain this energy density, the energy density of the cell must be about 350 Wh kg^{-1} , which corresponds to about 800 Wh kg^{-1} for the cathode active material.⁷¹ For reference, a LIB with an LiCoO_2 cathode has an energy density of about 550 Wh kg^{-1} . Increasing Ni content in these materials is the logical way to achieve cost effective, high energy density packs. However, increasing the Ni content decreases the percentage of Ni that is Ni^{2+} instead of Ni^{3+} . In NMC 111, Ni^{3+} accounts for approximately 100% of Ni and it decreases to about 60% in 811. Consequently, although these phases are sequentially cheaper and provide a higher capacity (811 can deliver capacities around 200 mA h g^{-1}), NMC 111 is still the most stable.⁷² Other reports suggest that these high Ni content materials are not inherently less stable but that the instability comes from the degree of Li utilization.⁷¹ The NMCs with less than 80% Ni content have all been commercialized. NMC 811 has entered the early stages of commercialization. Improvements with regards to rapid capacity and voltage fade can still be made. Thus, current studies are focused on post-processing steps to realize the commercialization of very high Ni content materials including optimized annealing to control the amount of Li/Ni disorder and improve electrochemical performance,⁷³ doping the structure with electrochemically inactive elements, for instance adding inexpensive metals like Al or Mg to act as structural stabilizers, pursuing surface modifications, and employing concentration gradients using core-shell structures to protect the more vulnerable Ni-rich core.⁷⁴ Kim et al. extensively outlines these approaches in a review paper.⁷⁵

4.10.3.1.2.1.5 $\text{LiNi}_{x-y-z}\text{Co}_y\text{Al}_z\text{O}_2$ (NCA)

The most common composition of NCA is $\text{LiNi}_{0.8}\text{Co}_{0.15}\text{Al}_{0.05}\text{O}_2$. Similar to NMC 811, NCA is another high-Ni content cathode material that promises the associated benefits: high capacity (200 mA h g^{-1}) and relatively low cost. The development of NCA materials resulted from the optimization of $\text{LiNi}_{0.8}\text{Co}_{0.2}\text{O}_2$. Although introducing Co into LiNiO_2 effectively reduces cation disorder, $\text{LiNi}_{0.8}\text{Co}_{0.2}\text{O}_2$ nonetheless suffers from a rapid fade due to the formation of a high impedance solid electrolyte interphase (SEI). The SEI formation occurs due to oxidation of the electrolyte likely fueled by the large amounts of high valent Ni after charging.

Substitution of 5% Al was shown to decrease the amount of high-oxidation state Ni at a given SOC. Thus, it reduces the formation of the SEI by reducing oxidation of the electrolyte thereby stabilizing the cathode-electrolyte interface.⁷⁶ However, it should be noted that NCA suffers from high capacity fade at temperatures above 40 °C.⁷⁷ Nonetheless, the high capacity, calendar life, and power capacities of NCA led to its commercialization. For example, NCA has since seen widespread use in Tesla vehicles.⁷⁸

4.10.3.1.2.2 Spinel oxides (LiMn_2O_4)

The second class of promising oxide materials for Li-ion intercalation cathodes are spinel oxides. After the demonstration of Li^+ insertion into the spinel magnetite,⁷⁹ the spinels were further investigated for use as potential high-voltage cathode materials. The structure of LiMn_2O_4 , shown in Fig. 16a, is similar to the thiospinels discussed earlier, but S is replaced by O. Furthermore, the structure is related to the $\alpha\text{-NaFeO}_2$ structure of the layered oxides, but the cations are distributed between the tetrahedral and octahedral voids in the cubic close-packed O structure. Unlike in $\text{Li}_2\text{Ti}_2\text{S}_4$, Li occupies the tetrahedral 8a sites in LiMn_2O_4 instead of the 16c sites and a mixed 3+/4+ metal occupies the 16d octahedral sites. The transition metals in period 4 that can form this phase are Ti, V, and Mn. Again, the low potential afforded by the LiTi_2O_4 makes it unsuitable as a LIB cathode material. LiV_2O_4 suffered from kinetic limitations and had to be cycled at low C rates to avoid substantial capacity loss.⁸⁰ As such, the rest of this section will focus on LiMn_2O_4 , the prominent spinel oxide employed in LIBs.

LiMn_2O_4 was identified as an ideal non-toxic, inexpensive cathode material for LIBs. When using a LiMn_2O_4 cathode and a non-lithiated anode, the battery must first be charged on assembly, as is the case with LiCoO_2 .



During charging the Mn^{3+} is oxidized to Mn^{4+} , and Li^+ is removed from LiMn_2O_4 . The spinel structure offers a three-dimensional diffusion pathway for Li^+ in one 8a tetrahedral site to hop to another through an empty neighboring 16c octahedral site, as shown schematically in (Fig. 16b).

Although the structure is mostly maintained during intercalation, the LiMn_2O_4 cathode discharges in a two-phase, two-step mechanism. One plateau appears around 4 V and the other around 3 V. The 4 V plateau encompasses the intercalation of about 1 equivalent of Li^+ and is associated with the reverse reaction shown in Eq. (60) above. Continued intercalation of Li^+ into the structure beyond one equivalent results in the insertion of Li^+ into the octahedral 16c sites. This is accompanied by the

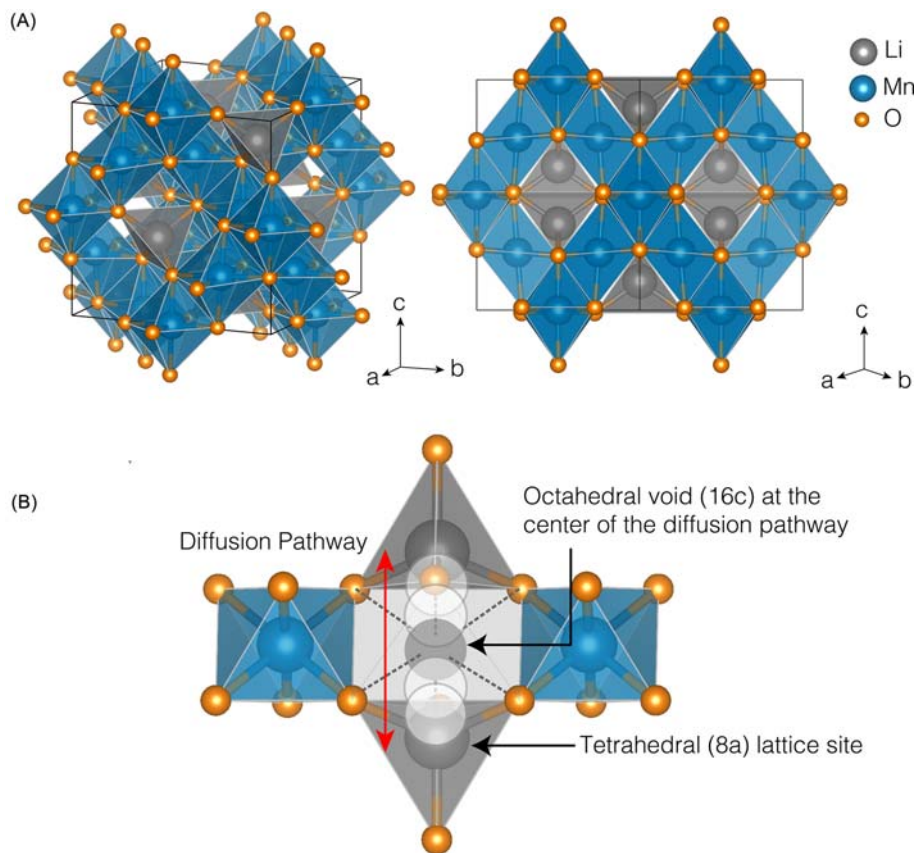
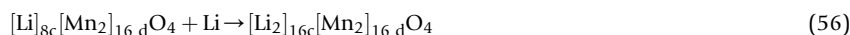


Fig. 16 (a) The structure of spinel LiMn_2O_4 ($\text{Fd}\bar{3}\text{m}$) rotated 22.5° off the a axis and 12.25° off the c axis (left) and along the [110] (right). (b) An illustration of the Li diffusion pathway in LiMn_2O_4 from 8a lattice site through 16c octahedral void.

simultaneous displacement of the existing 8a Li into the 16c sites as well. The 3 V plateau is thus correlated with the generation of the rock-salt phase $[\text{Li}_2]_{16c}[\text{Mn}_2]_{16d}\text{O}_4$.⁸¹



The Mn^{4+} is reduced to Mn^{3+} upon intercalation of Li. As in previously discussed materials, Jahn-Teller distortions associated with Mn^{3+} in this rock-salt phase decrease the cubic symmetry to tetragonal. The distortion causes a 16% increase in the unit cell's c/a ratio, which is not sustainable for prolonged cycling. Thus, in practical applications, cycling is usually limited to the 4 V plateau, producing a specific capacity of $< 130 \text{ mA h g}^{-1}$. Still, the tetragonal phase has been shown to form at the surface of this cathode under high-rate cycling at 4 V. Most of the capacity fade experienced by this material is due to Mn dissolution. These issues can be mitigated, and cycle-life improved by substituting 0.05 equiv. of Li for Mn. Only 0.85 equiv. of Li^+ can be removed from the resulting $\text{Li}_{1.05}\text{Mn}_{1.95}\text{O}_4$ (one for each Mn^{3+} that can be oxidized), resulting in $\text{Li}_{0.2}\text{Mn}_{1.95}\text{O}_4$ when fully charged. The remaining Li^+ helps to stabilize the fully charged structure. Increasing the concentration of Mn^{4+} reduces Mn^{3+} dissociation and the impact of Jahn-Teller distortions associated with Mn^{3+} .⁸² Unlike LiCoO_2 , this material remains semiconducting throughout Li^+ intercalation and thus also requires the use of a conducting additive in the electrode. LiMn_2O_4 is still an attractive choice for applications that require inexpensive, long-lasting cells, such as medical devices and equipment, power tools, and electric bikes. Although it was initially an option for EVs, it has since been replaced with NCA and NMC.

Recent investigations into spinel materials for electrochemical applications include developing high-voltage phases (approaching 5 V) through the substitution of Mn with other ions like Cr, Co, and Ni. $\text{LiMn}_{1.5}\text{Ni}_{0.5}\text{O}_4$ has been demonstrated with Mn^{4+} and Ni^{2+} as in NMC materials. This material can be cycled at 4.7 V due to the $\text{Ni}^{2+/4+}$ couple and has a capacity of 135 mA h g^{-1} . However, it has not been commercialized because of the absence of an electrolyte stable at this high voltage.^{83,84} In addition to being suitable cathodes for LIBs, spinel oxides have recently been suggested as potential candidates for both high-voltage high-capacity Zn and Mg battery cathodes.^{85,86}

4.10.3.1.3 Polyanion cathode materials

4.10.3.1.3.1 Phosphates (LiFePO_4)

In addition to the oxide materials, polyanion materials including phosphates, sulfates, and silicates, have also proven to be promising cathode material candidates for LIBs. The use of phospho-olivines as LIB cathode materials was first reported in 1997 by Goodenough.⁸⁷ The first reported material, LiFePO_4 , continues to be the best-performing in this family. LiFePO_4 is made from abundant, inexpensive, and environmentally benign elements and has so far played a niche role in energy storage. LiFePO_4 is touted as a cheaper, safer, and less-toxic alternative to the commonly utilized LiCoO_2 and its derivatives, and boasts a higher thermal stability than several prominent oxide cathode materials including LiCoO_2 , LiNiO_2 , and LiMn_2O_4 .^{88,89} Additionally, its stability in common organic electrolytes and relatively facile synthesis also contribute to its appeal as a cathode material.⁹⁰

LiFePO_4 crystallizes as in an olivine structure, which has an orthorhombic lattice (Pnma). The structure is shown in Fig. 17 and is characterized by a slightly disordered hexagonal close packed (HCP) array of O atoms, in which the P occupies the 4c tetrahedral sites and the metals occupy two distinct types of octahedral sites: the Li in the 4a site and Fe in the 4c site. The Fe octahedra are

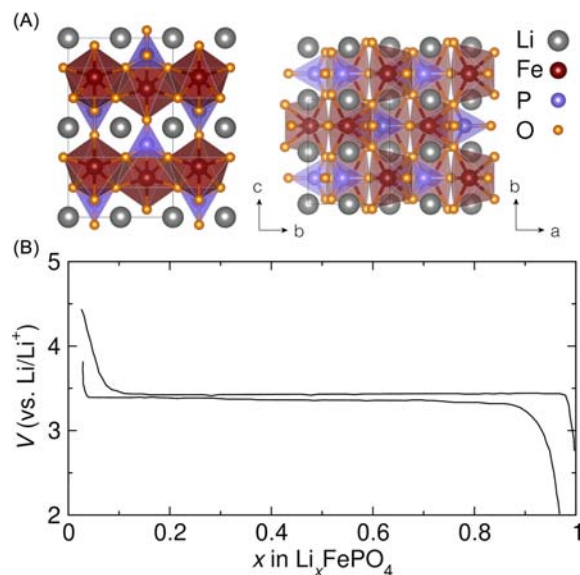
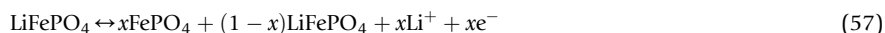


Fig. 17 (a) The structure of olivine LiFePO_4 (Pnma) in the bc plane (left) and in the ab plane (right). (b) The first charge and discharge cycles of LiFePO_4 at 0.12 mA cm^{-2} with a Li metal anode and 1 M LiPF_6 electrolyte (1:1 propylene carbonate:dimethyl carbonate). The galvanostatic cycling data is from Yamada et al., 2001.⁹¹

corner-sharing forming zigzag chains running parallel to the *c*-axis, and share an edge with only one PO₄ tetrahedron. The Li octahedra are edge sharing in the *b* direction and separate layers of Li octahedra are linked by PO₄ tetrahedra which are corner-sharing on one end and edge-sharing on the other.⁹² The olivine structure can be considered as a hexagonal analog of the spinel structure, which was previously discussed in detail. Both structure types are stoichiometrically A₂BX₄ compounds, in the case of LiFePO₄, A=Fe & Li (oct), B=P (tet) and X=O. The olivine phase is comparatively less stable than the spinel due to the corner sharing between octahedra and tetrahedra in the olivine vs the edge sharing octahedra in the spinel.²¹ Furthermore, under pressure, the olivine phase converts to the spinel-like phase,²¹ however, the high pressure spinel-like phase LiFePO₄ is electrochemically inactive.⁹³

In the seminal study by Padhi et al., reversible extraction of 0.6 equiv. of Li⁺ from olivine LiFePO₄ was demonstrated using LiClO₄ as the electrolyte, yielding a specific capacity of 100–110 mA h g⁻¹ compared to a theoretical value of 170 mA h g⁻¹.^{87,88} LiFePO₄ could not be fully delithiated electrochemically in this study. Full delithiation was achieved via chemical oxidation but the product, FePO₄, is a new phase isostructural to heterosite (Fe_{0.65}Mn_{0.35}PO₄).⁸⁷ Later work enabled utilization of >95% of the theoretical capacity of LiFePO₄ through optimization of the synthesis parameters.⁹¹ A moderate synthesis temperature of 500 °C < *T* < 600 °C eliminated undesirable particle growth at *T* > 600 °C and the presence of noncrystalline residual Fe³⁺ at *T* < 500 °C.⁹¹ Electrochemical intercalation/deintercalation of Li⁺ in LiFePO₄ proceeds in a two-phase reaction with the following forward reaction occurring during extraction (charge):



and the reverse reaction upon insertion (discharge). Studies with neutron and X-ray diffraction have identified monophasic regions at the beginning of charge and discharge where the phases Li_{0.5}FePO₄ and Li_{0.98}FePO₄ are present, respectively.⁹⁴

The physical manifestation of the two-phase reaction may proceed in a variety of ways. Two mechanisms are depicted schematically in Fig. 18. In the shrinking core model, Li⁺ diffuses through the outer shells of LiFePO₄/FePO₄ particles. Transport limitations within each particle may prevent full particle conversion, resulting in multiple phase boundaries within a particle that make the full capacity of the material inaccessible.⁹⁵ Delmas et al. suggest that the shrinking core model dominates at an agglomerate scale. A second mechanism called the domino cascade model is likely to dominate in nanoparticles. In the domino cascade model, the interfacial zone in individual crystallites contains a high concentration of Li⁺ vacancies and Fe²⁺/Fe³⁺ polarons due to structural mismatch between LiFePO₄ and FePO₄. This destabilizes the interfacial zone and allows for rapid propagation of the phase front through the crystal.⁹⁶

A critical factor in the commercial success of LiFePO₄ is that the operating voltage is higher than that which is seen in simple iron oxides using the same Fe³⁺/Fe²⁺ redox couple. In binary iron oxides, e.g. Fe₂O₃, the potential of the Fe³⁺/Fe²⁺ redox couple is < 2.5 V vs Li/Li⁺, which is too low for practical applications. The average potential of the Fe³⁺/Fe²⁺ redox couple in LiFePO₄, however, is increased to about 3.5 V vs Li/Li⁺ due to inductive effects and structural factors.^{19,87} The degree of covalency in the Fe–O bond determines the energy of the Fe³⁺/Fe²⁺ redox couple. Decreasing the covalency of the Fe–O bonds increases the energy of bonding orbitals and decreases the energy of the corresponding antibonding orbitals. In an octahedral high-spin Fe³⁺ (t_{2g}³e_g²) compound, the reduction potential is dependent on the energy of the t_{2g} antibonding orbital, since this is the orbital that the electron occupies after reduction to Fe²⁺. Decreasing the energy of the t_{2g} antibonding orbital corresponds to a more facile reduction of Fe³⁺, and thus, a more positive standard reduction potential of Fe³⁺/Fe²⁺ and a higher cell voltage.

Via the inductive effect, the neighboring counteraction *X* (common counteractions being Mo, W, or S) in an Fe–O–*X* linkage will influence the Fe–O covalency: stronger (more covalent) X–O bonding results in weaker (less covalent) Fe–O bonding and vice-versa (Fig. 19). Therefore, stronger X–O bonds result in weaker Fe–O bonds and a more positive Fe³⁺/Fe²⁺ redox couple, which corresponds to a larger cell voltage. Consequently, as the covalent bonding strength of the polyanion trends as SO₄²⁻ > WO₄²⁻ > MoO₄²⁻, the potential of the Fe³⁺/Fe²⁺ redox couple, and thus the cell voltage, decreases in the same order.^{97,98}

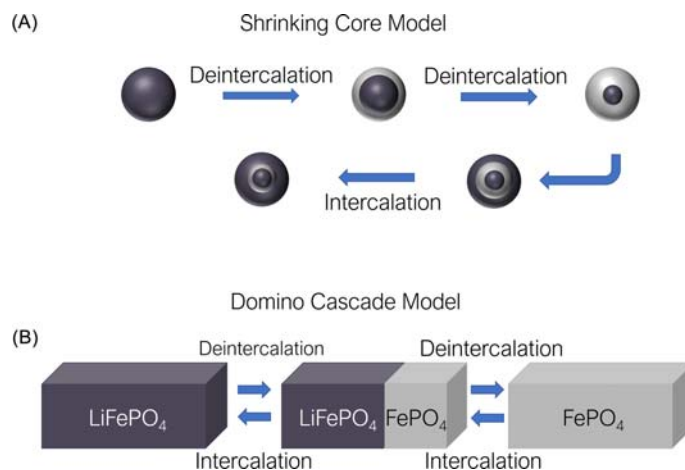


Fig. 18 Schematic showing two proposed two-phase mechanisms for deintercalation and intercalation of LiFePO₄.

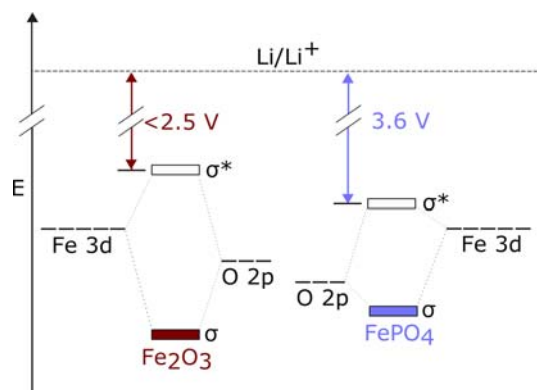


Fig. 19 Orbital diagram depicting the inductive effect of polyanions on the $\text{Fe}^{3+}/\text{Fe}^{2+}$ redox potential.

The demonstration of this effect in $\text{Fe}_2(\text{MO}_4)_3$ materials inspired the investigation of phosphate materials, eventually leading to the discovery of the LiFePO_4 cathode.¹⁹

Other studies have noted that the potential of the $\text{Fe}^{3+}/\text{Fe}^{2+}$ redox couple is different in materials with the same polyanions, such as $\text{Li}_3\text{Fe}_2(\text{PO}_4)_3$, LiFePO_4 , LiFeP_2O_7 , and $\text{Fe}_4(\text{P}_2\text{O}_7)_3$. Thus, the structure of these materials must also affect the potential of the redox couple.⁹² While these structures have either the phosphate $[\text{PO}_4]^{3-}$ or diphosphate $[\text{P}_2\text{O}_7]^{4-}$ polyanion, differences in the crystal structure and in P–O connectivity resulted in different electrochemical behavior.⁹² The different P–O connectivity in each structure is shown in Fig. 20.

Both $\text{Li}_3\text{Fe}_2(\text{PO}_4)_3$ and LiFeP_2O_7 have a framework of corner-sharing, slightly distorted FeO_6 octahedra and PO_4 tetrahedra. In $\text{Li}_3\text{Fe}_2(\text{PO}_4)_3$, the FeO_6 octahedra share corners with six PO_4 tetrahedra, and in turn the PO_4 tetrahedra is connected to four FeO_6 octahedra. In LiFeP_2O_7 , as shown in Fig. 20b, each FeO_6 octahedra is linked to six PO_4 tetrahedra belonging to five different diphosphate groups. Two of the PO_4 tetrahedra connected to a given FeO_6 belong to the same diphosphate group, leading to a $[\text{FeP}_2\text{O}_{11}]$ unit. Each P in the $[\text{P}_2\text{O}_7]^{4-}$ group contains one long P–O bond to the bridging O (O_b) and three shorter P–O bonds to terminal oxygens (O_t) coordinated to different Fe atoms. In LiFeP_2O_7 , each PO_4 tetrahedron is coordinated to three FeO_6 octahedra and one PO_4 tetrahedron, resulting in shorter P– O_t bonds than $\text{Li}_3\text{Fe}_2(\text{PO}_4)_3$ and consequently weaker Fe–O bonds and thus a higher cell voltage. $\text{Fe}_4(\text{P}_2\text{O}_7)_3$ consists of two distinct kinds of face shared FeO_6 octahedra resulting in Fe_2O_9 groups, and P_2O_7 groups, shown in Fig. 20c. The FeO_6 octahedra are distorted and have $\text{Fe}(1)\text{--O--Fe}(1)\text{--O}_t\text{--P--O}_b\text{--P--O}_t\text{--Fe}(2)\text{--O--Fe}(2)$ bonding, with even weaker Fe– O_t bonds than in LiFeP_2O_7 due to the bonding in $\text{Fe}_4(\text{P}_2\text{O}_7)_3$ and the strength of the P– O_t bond.

In the ordered olivine LiFePO_4 structure, the phosphate polyanions are isolated from each other, the Fe atoms only share one edge with a PO_4 tetrahedron, and two Fe^{2+} and one P share the same O, which further decreases the Fe–O bond strength. These structural factors result in ordered olivine structure having a more negative redox potential compared to other similar Li materials with $[\text{PO}_4]^{2-}$ polyanions.⁹²

The primary drawbacks of LiFePO_4 as a cathode material are irreversible capacity loss and its relatively low energy density compared to other LIB cathodes.^{87,88} The irreversible capacity loss results from diffusion-limited transfer of Li across the two-

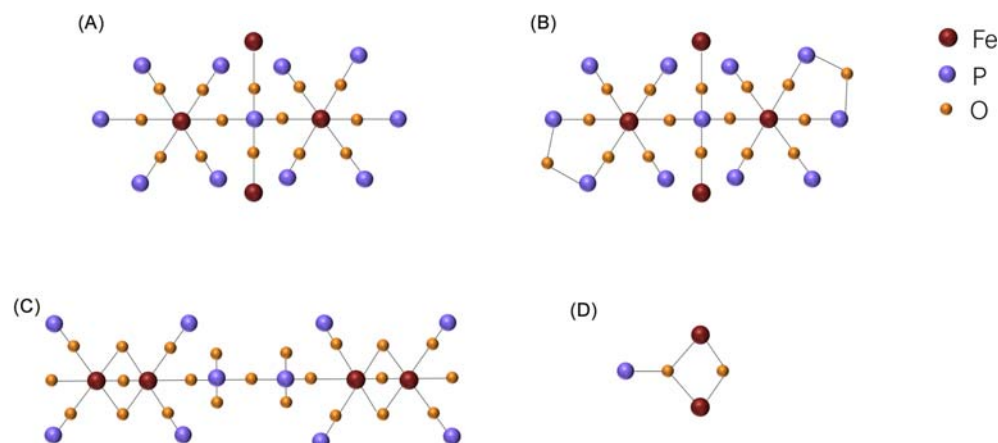


Fig. 20 An illustration of P–O connectivity in (a) $\text{Li}_3\text{Fe}_2(\text{PO}_4)_3$, (b) LiFeP_2O_7 , (c) $\text{Fe}_4(\text{P}_2\text{O}_7)_3$, and (d) LiFePO_4 . Adapted from Padhi, A. K.; Nanjundaswamy, K. S.; Masquelier, C.; Okada, S.; Goodenough, J. B. Effect of Structure on the Fe³⁺/Fe²⁺ Redox Couple in Iron Phosphates. *J. Electrochem. Soc.* **1997**, *144*, 6.

phase interface, as well as the low electronic conductivity of FePO_4 .^{87,99} The diffusion coefficients of Li^+ in LiFePO_4 and FePO_4 are in the range of 1.8×10^{-14} to $2 \times 10^{-16} \text{ cm}^2 \text{ s}^{-1}$, respectively.¹⁰⁰ Consequently, decreasing the particle size results in increased capacity.⁸⁷ Several studies have shown that smaller LiFePO_4 particle sizes can result in near 100% capacity utilization, and further evidence of diffusion-limited capacity was shown with elevated temperature cycling studies.^{89,91,101,102} In addition, carbon-coating LiFePO_4 particles has also allowed the access of higher capacities by improving electrical conductivity.^{101,102}

In an effort to improve the capacities of olivine-based cathode materials, the use of transition metals other than Fe have been explored in $M=\text{Mn, Co, and Ni}$, all of which have higher redox potentials vs Li^+/Li .⁸⁸ Reversible extraction and insertion of Li^+ in LiMnPO_4 has been demonstrated at 4.1 V vs Li/Li^+ initially reported to reach reversible capacities of 140 mA h g^{-1} ,¹⁰³ but a reversible capacity of 168 mA h g^{-1} was achieved by utilizing nanoplates.¹⁰⁴ Despite Li_xMnPO_4 boasting a higher theoretical energy density due to the higher redox potential and similar capacity, in practical devices it has a lower energy density than Li_xFePO_4 since the lower electronic conductivity of LiMnPO_4 necessitates the use of a greater amount of conductive additives.^{105,106} An initial study of the olivine material LiCoPO_4 yielded charge and discharge capacities of 86 and 70 mA h g^{-1} , respectively at 4.8 V vs Li/Li^+ .¹⁰⁷ It has been hypothesized that the charge and discharge mechanisms of LiCoPO_4 differ from its Fe and Mn counterparts by proceeding via an intermediate phase $\text{Li}_{0.7}\text{CoPO}_4$.¹⁰⁸ Similar to LiFePO_4 , high capacities (167 mA h g^{-1}) were achieved in LiCoPO_4 by reducing the particle size.¹⁰⁹ Development of both LiCoPO_4 and LiMnPO_4 as cathode materials is also hindered by their high operating voltages and corresponding need for electrolytes with more positive anodic stability windows.¹¹⁰ More recent work on LiNiPO_4 has shown improvements in synthesis techniques and electrical conductivity leading to discharge capacities of 175 mA h g^{-1} , 150 mA h g^{-1} , and 125 mA h g^{-1} with corresponding capacity retention of 82.7%, 84.1%, and 82.2% after 100 cycles at 0.05 C, 0.1 C and 1 C rates, respectively.¹¹¹

4.10.3.1.3.2 Sulfates

Following the discovery of LiFePO_4 as a stable, low cost cathode material, several additional cathode materials based on polyanion frameworks comprised of Earth-abundant elements have been developed. Among these are a family of sulfate compounds, including $\text{Li}_2\text{Fe}(\text{SO}_4)_2$, LiFeSO_4F , and LiFeSO_4OH . Both $\text{Li}_2\text{Fe}(\text{SO}_4)_2$ and LiFeSO_4OH crystallize in the monoclinic $\text{P}2_1/\text{c}$ space group. $\text{Li}_2\text{Fe}(\text{SO}_4)_2$ is comprised of FeO_6 octahedra that share corners with SO_4 tetrahedra, with Li atoms in distorted octahedral sites between SO_4 tetrahedra.¹¹² LiFeSO_4OH is composed of FeO_6 octahedra that share edges in the [010] direction and corners in the [001] direction to form a layered structure. SO_4 tetrahedra share vertices with the FeO_6 octahedra on each side of the layer, and Li atoms are tetrahedrally coordinated to O atoms and rest in the space between layers.¹¹³ LiFeSO_4F can be synthesized in two polymorphs. The triclinic tavorite phase ($\text{P}\bar{1}$) is composed of a network of FeO_4F_2 octahedra that share corners through F atoms in trans positions. The FeO_4F_2 octahedra are cross-linked by SO_4 tetrahedra along the a and b axes, and Li atoms occupy tetrahedral holes. The monoclinic triplite phase ($\text{C}2/\text{c}$) is similar to that of the tavorite, but the Fe and Li atoms both occupy MO_4F_2 octahedra, and the F atoms adopt a cis arrangement.¹¹⁴

Sulfate-based cathode materials were proposed as alternatives to LiFePO_4 due to their higher voltage vs Li/Li^+ . LiFeSO_4OH and tavorite LiFeSO_4F both exhibit an open circuit voltage (OCV) of 3.6 V vs Li/Li^+ , while $\text{Li}_2\text{Fe}(\text{SO}_4)_2$ shows an OCV of 3.83 V vs Li/Li^+ ,¹¹² and LiFeSO_4F shows an OCV of 3.9 V vs Li/Li^+ . Up to 0.86 equiv. of Li^+ can be reversibly (de)inserted into the $\text{Li}_2\text{Fe}(\text{SO}_4)_2$ structure by 1D migration along the [100] direction.^{112,115} Similarly, up to 0.8 equiv. of Li^+ can be reversibly (de)inserted into triplite LiFeSO_4F , though the Li migration pathway is restricted to the ac plane.¹¹⁶

Despite the high voltages vs Li/Li^+ and the low cost of manufacturing sulfate-based cathode materials, the lower experimental capacities (approx. 150 mA h g^{-1}) and moisture sensitivity preclude the sulfate materials from replacing current cathodes. Current research on sulfate cathodes examines mixed-alkali materials (ex. $\text{LiNaFe}(\text{SO}_4)_2$) and their utility in Na-based batteries.^{112,117}

4.10.3.1.3.3 Silicates

Polyanion cathodes based on orthosilicates (Li_2MSiO_4 ; $M=\text{Fe}^{2+}, \text{Mn}^{2+}, \text{Co}^{2+}$) have attracted attention for many of the same reasons as phosphate-based cathode materials. Silicates offer lattice stabilization due to the strong Si–O bonds, while the lower electronegativity of Si compared to P yields a lower band gap and higher electronic conductivity.¹¹⁸ Furthermore, silicates offer the potential to remove two Li^+ per formula unit, leading to greater theoretical capacities.¹¹⁸

Silicates generally adopt a structure in which the oxide anions are tetragonally packed and half of the tetrahedral holes are occupied by cations. Various polymorphs can be generated by altering the cation ordering within the tetrahedral holes or by introducing structural distortions (see Fig. 21).¹¹⁹ The polymorphs can generally be classified into two categories: β , in which only corner-sharing tetrahedra are present, and γ , in which tetrahedra share both corners and edges.¹¹⁹ The electrochemical properties of $\text{Li}_2\text{FeSiO}_4$ in particular are affected by the Fe–O bond distance as dictated by the structure—similarly to LiFePO_4 as described above, the shorter and more covalent Fe–O bonds in γ polymorphs increase the energy of the antibonding states, lowering the voltage at which $\text{Fe}^{2+/3+}$ redox occurs.¹²⁰

Electrochemical cycling and XRD reveal that $\gamma\text{-Li}_2\text{FeSiO}_4$ undergoes a structural change to a β polymorph during the first two discharge/charge cycles. One equivalent of Li^+ can be reversibly (de)inserted to generate LiFeSiO_4 (isostructural with $\text{Li}_2\text{FeSiO}_4$). Typical capacities range from 140 to 160 mA h g^{-1} , or 80–100% of the theoretical maximum.¹²¹

$\text{Li}_2\text{MnSiO}_4$ and $\text{Li}_2\text{CoSiO}_4$ both exhibit high initial capacities but rapid irreversible capacity fade upon further cycling.^{122,123} Li extraction from $\text{Li}_2\text{MnSiO}_4$ proceeds through an amorphous phase, in contrast to the two-phase reaction evident in $\text{Li}_2\text{FeSiO}_4$. The poor intercalation kinetics, low rate capability, and irreversible capacity fade in $\text{Li}_2\text{MnSiO}_4$ preclude its use as an independent

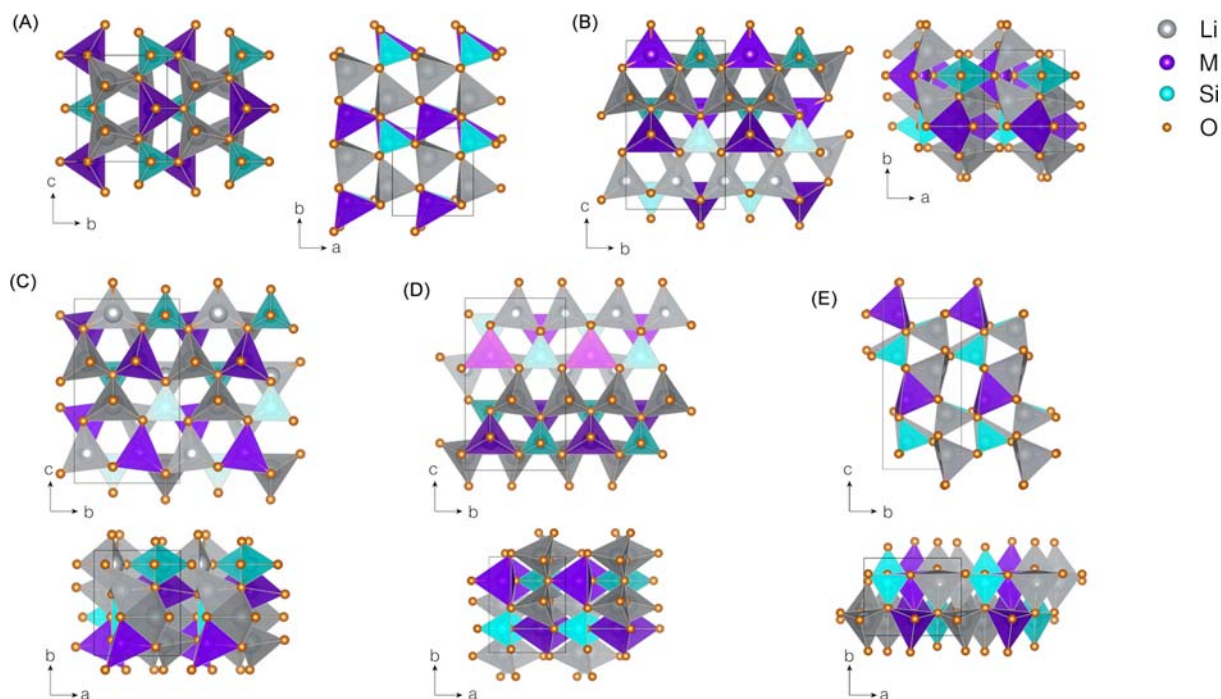


Fig. 21 Structures of various silicate cathode materials Li_2MSiO_4 : the (a) β_{II} polymorph of $\text{Li}_2\text{FeSiO}_4$, (b) β_I polymorph of $\text{Li}_2\text{MnSiO}_4$, (c) γ_s polymorph of $\text{Li}_2\text{FeSiO}_4$, (d) γ_0 polymorph of $\text{Li}_2\text{MnSiO}_4$, and (e) γ_{II} polymorph of $\text{Li}_2\text{FeSiO}_4$. Adapted from Islam, M. S.; Dominko, R.; Masquelier, C.; Sirisopanaporn, C.; Armstrong, A. R.; Bruce, P. G. Silicate Cathodes for Lithium Batteries: Alternatives to Phosphates? *J. Mater. Chem.* **2011**, *21*, 9811–9818.

cathode material, but a solid solution of $\text{Li}_2\text{Fe}_x\text{Mn}_{1-x}\text{SiO}_4$ has been synthesized to stabilize the tetrahedral Mn^{3+} formed upon discharge.¹²⁴ The mixed-cation material $\text{Li}_2\text{Fe}_{0.5}\text{Mn}_{0.5}\text{SiO}_4$ exhibits high capacity (214 mA h g^{-1}) and a wide voltage window but significant capacity fade over time.¹²⁴

Current research on silicate cathodes focuses on mixed-alkali configurations (ex. $\text{Li}_x\text{Na}_{1-x}\text{FeSiO}_4$) and on nanostructuring composites with carbon to improve electronic conductivity.

4.10.3.1.4 Mixed anion cathode materials

4.10.3.1.4.1 Oxyfluorides

Oxyfluoride cathode materials were developed to improve upon both metal fluorides and transition metal oxide cathodes. Fluorides, such as FeF_3 , offer high specific capacity and high voltage due to the ionic nature of the M–F bond. However, the higher ionicity also results in a wider band gap, so most metal fluorides are electronic insulators and require the formation of a nanocomposite with a conductive matrix to measure electrochemical activity. Transition metal oxide cathode materials can be electronic conductors and exhibit long cycle life but offer lower specific capacities than the corresponding metal fluoride. Oxyfluoride cathode materials were investigated to improve cycling stability and electronic conductivity by introducing more covalent M–O bonds into the M–F framework.¹²⁵ Several metal oxyfluorides have been investigated, including VO_2F ,^{126,127} BiOF ,^{128,129} and FeOF ,^{125,130–133} but FeOF has garnered the most attention due to the abundance of Fe in the Earth’s crust and to the success of other Fe-based cathodes such as LiFePO_4 .

FeOF adopts a rutile-type tetragonal structure ($P4_2/nmn$). Starting from the precursor FeF_2 , O can be introduced into the material by annealing in air. O is directly substituted onto the anion lattice, and the anion ordering is random due to the similar ionic radii of F and O. The full solid solution $\text{FeO}_x\text{F}_{2-x}$ can be synthesized, with longer annealing times or higher temperatures yielding higher oxygen content.^{125,131}

Discharge of the oxyfluoride cathode proceeds through a two-step mechanism. At potentials above 2 V vs Li/Li^+ , Fe^{3+} is reduced to Fe^{2+} and Li^+ is intercalated into the rutile-type FeOF phase.¹²⁵ Below 2 V, a conversion reaction occurs in which the fluoride component is reduced to LiF and Fe^0 and a Li–Fe–O rock salt phase is formed. Upon recharging, the composite material does not return to the original FeOF rutile-type phase; rather, it forms a F-rich rutile phase and an O-rich rock salt phase.^{125,131}

Despite their high specific capacities, the discussed oxyfluoride materials exhibit an average working potential of just 2.2 V, which limits their applicability in commercial and industrial settings.¹³⁴ Current research on oxyfluoride cathodes focuses on mixed transition metal systems and on incorporating oxyfluorides into Na-ion batteries.^{135–137}

4.10.3.1.5 Li-rich cathode materials involving multi-electron redox

The term “Li-rich” is used to describe materials that contain more than one equivalent of Li per transition metal. Most of the materials discussed thus far are limited to removal and insertion of up to one Li per transition metal, but Li-rich materials can go beyond this limit to achieve higher theoretical capacities. Removal of more than one equivalent of Li necessitates oxidation of more than one electron per transition metal which is termed multielectron redox.¹³⁸ For simplicity’s sake, we can again account for charge compensation considering formal oxidation states. Multielectron oxidation on the transition metal would result in high-valent metals. Metals with multiple stable oxidation states, like V, are capable of multielectron redox. Alternatively, the anions could also participate in charge compensation and this mechanism is termed anion redox. An ideal multielectron cathode material would demonstrate increased capacity without compromising desirable characteristics such as high operating voltage, high reversibility, good compatibility with electrolytes, and safe operation.

4.10.3.1.5.1 Li-rich metal sulfides

The idea of anion redox was first conceptualized in metal sulfides in the 1980s by the pioneering works of Rouxel et al.^{139,140} Rouxel explained that the anionic sp band of oxides generally lies below the transition metal d band (except for metals in the highest oxidation states), which reduces the interaction between the two bands (Fig. 22a) and results in highly ionic character. However, the sp bands in later-group chalcogenides are higher in energy and may interact with certain transition metal d bands. The interaction between an appropriate transition metal-anion combination is characterized by increased covalency. If empty transition metal d levels energetically overlap with the anionic levels, the states with majority metal d character will be filled at the expense of the states with majority anion character. The resulting hole in the anion states enables the redox participation of the anion (Fig. 22b).^{139,140} An example of this is the transition from the layered structure to the pyrite structure in metal sulfides that was discussed in Section 4.10.3.1.2. Interestingly, although the high energy sulfur p states initially limited the voltage of intercalation compounds, it is now of interest to leverage this property to engage anion redox. As will be discussed in the next section, electrochemical analysis of oxides for anion redox is difficult because anion redox in oxides often occurs outside the electrochemical stability window of established electrolytes.

A few metal sulfides have emerged based on TiS_2 that exhibit reversible (de)lithiation of more than one equivalent of Li. LiTiS_2 , the lithiated form of TiS_2 , adopts an equivalent structure to that of oxides with the O1 structural designation.^{141,142} This structure can be made “Li-rich” as Li can occupy 1/3 of the transition metal sites to yield Li_2TiS_3 , or $\text{Li}(\text{Li}_{0.33}\text{Ti}_{0.66})\text{S}_2$. Li_2TiS_3 adopts the same O3-type structure as the commercial LiCoO_2 .¹⁴³ The oxidation state of Ti in the fully lithiated Li_2TiS_3 is 4+ which makes the Ti d^0 and renders the material redox inactive if only transition metal redox was to be considered. Solid-solutions of $\text{Li}(\text{Li}_x\text{Ti}_{1-x})\text{S}_2$ from the end members LiTiS_2 and Li_2TiS_3 yield mixed $\text{Ti}^{3+/4+}$ and exhibit capacities higher than those obtained through utilization of the $\text{Ti}^{3+/4+}$ redox couple only (based on the amount of Ti in the material). The excess capacity may be enabled by anion redox.¹⁴³ Two different regions are observed in the voltage profile -an initial sloping region followed by a long plateau at 2.8 V. X-ray photoelectron spectroscopy (XPS) is used to assign the initial sloping region to the $\text{Ti}^{3+/4+}$ couple, and the subsequent long plateau at 2.8 V to $2\text{S}^{2-}/(\text{S}_2)^{2-}$ couple.¹⁴³ Several polymorphs of Li_2TiS_3 , including $\text{Fm}\bar{3}\text{m}$ and an amorphous phase, also exhibit reversible electrochemical cycling within a similar voltage window.^{144,145}

The $3d^0$ electronic configuration of Ti^{4+} in Li_2TiS_3 can also be altered through aliovalent substitution of the transition metal. Saha et al. introduced Fe^{2+} to form $\text{Li}_{1.33-2x/3}\text{Ti}_{0.67-x/3}\text{Fe}_x\text{S}_2$ (Ti^{4+} and Fe^{2+}) via solid-state reaction of Li_2S , TiS_2 , and FeS , and demonstrated the feasibility of anion redox.¹⁴⁶ Not only is the Fe^{2+} ($3d^6$) capable of oxidation, but it is also more covalent in nature with the S 3p band compared to that of $\text{Ti}^{3+/4+}$. Since this entire family of materials is isostructural to LiCoO_2 , direct comparison between oxides and sulfides can be achieved. Fe substitution of 10% results in a significantly larger capacity than what would be expected from the $\text{Fe}^{2+/3+}$ redox couple, and, for $0.3 \leq x \leq 0.5$, the capacity observed is very close to the theoretical capacity.

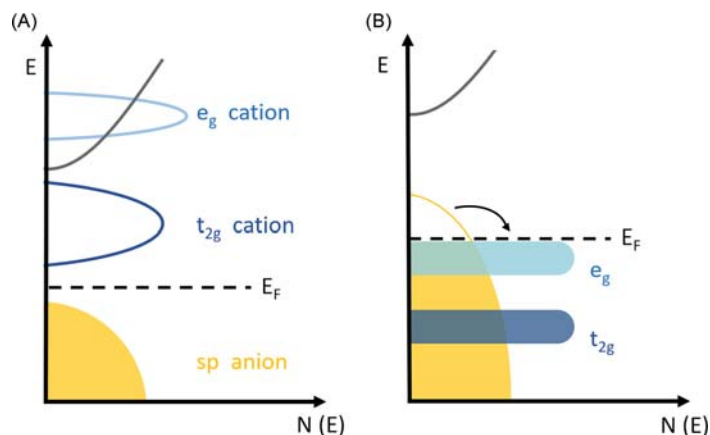


Fig. 22 Density of states schematics for (a) ionic and (b) covalent chalcogenides. Adapted from Rouxel, J. Anion–Cation Redox Competition and the Formation of New Compounds in Highly Covalent Systems. *Chem. Eur. J.* **1996**, *2*, 1053–1059.

$\text{Li}_{1.13}\text{Ti}_{0.57}\text{Fe}_{0.3}\text{S}_2$ shows the highest capacity of 245 mA h g^{-1} . Voltage profiles of $\text{Li}_{1.33-2x/3}\text{Ti}_{0.67-x/3}\text{Fe}_x\text{S}_2$ also resemble those of $\text{Li}(\text{Li}_x\text{Ti}_{1-x})\text{S}_2$ in that an initial sloping region is followed by a long plateau at 2.8 V. Synchrotron XRD data suggest that both the Ti–S and S–S bond lengths are shorter at the end of charge, although that of S–S at the end of charge (3.344 Å) is much larger than the (S–S)²⁻ bond length reported for TiS_3 (2.04 Å) suggesting that there is no S–S dimerization.¹⁴⁷ Nonetheless, partial Density of States (pDOS) calculations as well as S K-edge XAS data strongly suggest S²⁻ oxidation to Sⁿ⁻, which explains why the observed capacity is higher than that which would be produced through cation redox alone.

Li_2FeS_2 is another metal sulfide material that shows redox contributions from the anions.^{139,148} Li_2FeS_2 , first reported by Sharma et al. in 1976, exhibited signs of anion redox as reported by Rouxel.¹³⁹ The structure, solved by Batchelor et al., has a different layered structure compared to aforementioned sulfides.^{148,149} Layers of edge-sharing Li octahedra are separated by layers of mixed Li/Fe edge-sharing tetrahedral sites.^{149,150}

The charge profile for Li_2FeS_2 is characterized by an initial sloping region followed by a long plateau at $\sim 2.5\text{ V}$ (Fig. 23b). Li_2FeS_2 accommodates the removal of ~ 1.8 equiv. of Li^+ in cycle 1, achieving a capacity of 350 mA h g^{-1} . Li_2FeS_2 also exhibits high Coulombic efficiencies.^{151,152} Fe and S K-edge XAS data of Li_2FeS_2 provided direct evidence of cation and anion oxidation during charge.¹⁵¹ The rising Fe K-edge shifts to higher energy after the initial sloping region, suggesting Fe^{2+} oxidation upon charge. The plateau region is mostly defined by sulfide oxidation to persulfides, as evidenced by a new pre-edge feature in the S K-edge spectrum that matches the pre-edge feature associated with persulfides in pyrite FeS_2 . The shapes of the Fe and S K-edge X-ray absorption near edge structure (XANES) resemble those of pristine material at the end of discharge, suggesting high reversibility. Hansen et al. demonstrated that Li_2FeS_2 not only invokes anion redox, but also involves reversible redox on the $2\text{S}^{2-}/(\text{S}_2)^{2-}$ couple during cycling. From Li_2FeS_2 , the position of the anion sp bands can be modulated by introducing Se in the S sites and creating the chalcogenide solid solution $\text{Li}_2\text{FeS}_{2-y}\text{Se}_y$.¹⁵³ As Se is titrated into $\text{Li}_2\text{FeS}_{2-y}\text{Se}_y$, the voltage of the long plateau during which anion oxidation occurs systematically shifts to more negative potentials. Changes in the electronic structure affect the contribution of the cation and anion during cycling, presenting direct control over the functional properties of multielectron redox materials.¹⁵³ Further discussion of anion redox in sulfides can be found in our recent perspective article.¹⁵⁴

4.10.3.1.5.2 Li-rich metal oxides

Although the concept of anion redox was first developed in metal sulfides, anion redox in oxides is of great interest to produce materials with higher energy densities. However, because oxides are intrinsically more ionic in nature due to the lower lying sp band of oxygen, the operating voltage needs to be drastically higher to invoke anion redox. The required voltages tend to be outside of the electrochemical stability window of common electrolytes; therefore, many undesirable side reactions are encountered.

Efforts to understand anion redox in oxides emerged in the 1990s. A study in 1996 characterized fully delithiated LiCoO_2 , which suggested that Co was not fully oxidized to 4+ and that something besides Co must have been oxidized to compensate for Li removal.⁴⁶ Synchrotron XRD also suggested that the O–O interplanar distance decreased upon oxidation, making the participation of lattice anions more plausible.¹⁵⁵ Li_2RuO_3 , developed by James and Goodenough in 1987, is a thermodynamically stable Li-rich layered structure capable of reversible cycling, although only the transition metal redox couple was utilized.^{156,157} Subsequently, it was demonstrated that Li_2MnO_3 showed electrochemical activity, despite the octahedral Mn^{4+} being electrochemically

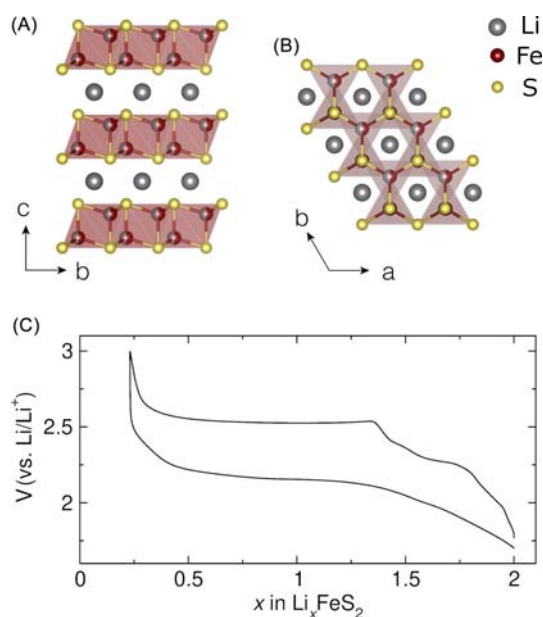


Fig. 23 (a) The structure of layered Li_2FeS_2 ($\text{P}\bar{3}\text{m}1$) in the bc plane and (b) ab plane. (c) Representative galvanostatic cycling of Li_2FeS_2 with LP100 electrolyte and a Li anode at C/10. The electrochemistry data is from Ref. 151.

inactive.^{158,159} Li_2MnO_3 is isostructural to Li_2TiS_3 and the layered transition metal oxides. Li_2MnO_3 does not show any capacity in the conventional voltage window used for LiCoO_2 and NMCs. At voltages higher than 4 V vs Li/Li^+ , Li_2MnO_3 can be oxidized resulting in O_2 gas evolution from oxide oxidation. The large structural changes and loss of O_2 gas renders the anion redox irreversible.^{159,160}

Efforts to improve the electrochemistry of Li_2MnO_3 focused on substituting Mn with redox-active transition metals. Substitution of Ni^{2+} for Mn^{4+} and Li^+ enabled oxidation below 4 V and increased the capacity contributions above 4 V to yield 230 mA h g^{-1} .¹⁶¹ Substitution of other transition metals followed in the form of $x\text{LiMO}_2 + (1-x)\text{Li}(\text{Li}_{1/3}\text{Mn}_{2/3})\text{O}_2$, where $M = \text{Mn, Co, Cr}$, and so on, among which $\text{Li}(\text{Li}_{0.2}\text{Ni}_{0.13}\text{Mn}_{0.54}\text{Co}_{0.13})\text{O}_2$ exhibited high capacities of over 250 mA h g^{-1} .^{138,162} However, so-called Li-rich NMCs suffered from a large capacity loss in the first cycle accompanied by irreversible $\text{CO}_{2(\text{g})}$ and $\text{O}_{2(\text{g})}$ release.^{138,163,164} The initial capacity loss as a result of cycling at high voltages permanently affects the electrochemical activity, irreversibly changing charge and discharge shapes. With continued cycling, voltage decay is observed during discharge, which decreases the energy efficiency of the cell. Because of these puzzling results, researchers needed more concrete evidence to assign bulk cationic and anionic redox processes as the main contributors to the charge compensation mechanism in Li-rich oxides.

Metals in the 4d and 5d blocks are able to form more covalent $M\text{-O}$ interactions than 3d metals, because the spatial expansion of the 4d and 5d orbitals allows for better orbital overlap with O, and they are more electronegative than 3d metals due to the poor shielding of the nucleus by the diffuse d orbitals. Thus, isostructural materials based on these 4d and 5d metals serve as good model systems to study anion redox. Building upon Goodenough's structural work on Li_2RuO_3 that exhibited reversible cation redox couple below 4 V, Sathiya et al. synthesized $\text{Li}_2\text{Ru}_{1-y}\text{Sn}_y\text{O}_3$ materials with redox-inactive Sn^{4+} that provided strong evidence for anion redox.^{156,157,165} Ru–Sn materials exhibited minimal gas release in the first cycle and showed no gas evolution on further cycling, compared to Li-rich NMCs or even isostructural Ru–Mn materials that released 3–6 times more O_2 gas. The authors attribute this reduction in O_2 gas release to the enhanced flexibility of the Sn–O bonds.¹⁶⁵ Also, Sn-containing Li-rich materials exhibit minimal voltage capacity fade compared to Li-rich NMCs or isostructural Ru–Ti materials, which suggested that the larger, less mobile Sn^{4+} ions are less likely to migrate into the tetrahedral sites.^{138,165,166} In addition, XPS and electron paramagnetic resonance spectroscopy (EPR) provided evidence of the presence of oxidized O species in $\text{Li}_2\text{Ru}_{0.5}\text{Sn}_{0.5}\text{O}_3$. This led the authors to propose a reductive coupling mechanism in which peroxy- and superoxy- moieties form that result in the reduction of surrounding metal centers. A similar model system, $\text{Li}_2\text{Ir}_{1-y}\text{Sn}_y\text{O}_3$, directly showed the deformation of the IrO_6 octahedra as a result of anion oxidation, which was also supported by DFT calculations.¹³⁸

Building upon insights from characterization techniques that provided direct evidence of anion redox in these model systems, recent measurement techniques as well as theoretical works further confirmed the bulk anionic redox activity in Li-rich NMCs. For instance, XPS and hard-XPS of Li-rich NMCs suggest a quantitative contribution of 34% of oxidized lattice oxygen to the capacity, and the constant intensity of the oxidized lattice oxygen feature with increased penetration depth suggested the presence of O^{n-} ($n < 2$) in the bulk.¹⁶⁷ Also, resonant inelastic X-ray scattering (RIXS) is suggested to provide direct observation of oxidized lattice O in $\text{Li}_{1.2}\text{Ni}_{0.2}\text{Mn}_{0.6}\text{O}_2$,¹⁶⁸ although the origins of the RIXS features are still under debate. Alternatively, first principles calculations proposed that the oxidation of Mn^{4+} to Mn^{7+} accompanied by migration from octahedral to tetrahedral sites may trigger spontaneous formation of O_2 molecules or peroxide ions and also account for some experimental results such as the observation of tetrahedral occupancy at the end of charge through X-ray diffraction.^{169,170}

Although reversible bulk cationic and anionic redox activities have been confirmed in Li-rich NMC materials, they still face some hurdles that need to be overcome before they can be used commercially. Firstly, stable electrolytes that support reversible cation and anion redox activities must be developed. Anion redox in oxides occurs at high voltages ($> 4 \text{ V vs Li}/\text{Li}^+$), subjecting conventional carbonate electrolytes to degradation reactions. For example, alkyl-carbonate-based electrolytes can undergo oxidation leading to H^+ generation.¹⁵⁹

Electrolyte degradation can also lead to $\text{CO}_{(\text{g})}$ and $\text{O}_{2(\text{g})}$ evolution.^{159,171} Different combinations of solvents or additives are under investigation to mitigate electrolyte degradation. Secondly, voltage fade is observed in Li-rich NMCs, which is promoted at high potentials.¹⁶⁷ The comparison between Sn- and Ti-substituted Li_2RuO_3 materials have shown that Ti-substituted materials exhibit more rapid voltage fade due to the higher mobility of Ti that allows it to readily migrate to the tetrahedral site.¹⁶⁶ In Li-rich NMCs, migration of Mn to the tetrahedral site has been shown lead to a phase transition to the spinel.^{172,173} To that end, chemical modifications, especially on the particle level, have been pursued.^{174,175} Next, the initial irreversible capacity loss that occurs mostly in the first charge must be addressed. The capacity loss likely stems from lattice anion oxidation and leads to $\text{O}_{2(\text{g})}$ evolution. Different coating methods and materials have been applied and can mitigate the irreversible capacity loss to a certain extent.^{176,177} Lastly, the challenge of voltage hysteresis, which results in decreasing energy efficiency, has not yet been fully addressed. Cation migration is correlated with voltage hysteresis, but it is unclear whether anion redox or structural instability associated with cation migration is the direct cause.^{178–180}

There is ongoing research in the field of anion redox in Li-rich oxides to mitigate these drawbacks and to ultimately reach optimal performances for practical applications. In doing so, lessons learned throughout the journey are motivating different systems such as the aforementioned Li-rich sulfides and materials with different mobile ions such as Na^+ or divalent ions which will be discussed in more detail later in the chapter.

4.10.4 Anode materials for LIBs

4.10.4.1 Intercalation anode materials

Next, we will discuss the negative electrode for LIBs in detail. The crucial requirements for successful anode materials in secondary batteries that ensure high energy, high power densities, and safety are as follows:

- (1) utilization of light-weight materials with a high degree of Li accommodation per formula unit to maximize the gravimetric capacity;
- (2) constant, very negative reduction potential (as close to the reduction potential of Li/Li^+ as possible) to optimize the overall voltage of the cell;
- (3) high electronic and ionic conductivity to ensure fast transport of Li^+ and electrons;
- (4) innately safe structural designs to prevent thermal runaway of the battery.

We will first explore the development of graphite as the most widely used anode material, focusing on its mechanism and characteristics, and then discuss other intercalation-based anode candidates.

4.10.4.1.1 Graphite as an intercalation host

The first commercial LIBs used LiCoO_2 as the cathode and graphite as the anode. Both electrode materials act as intercalation hosts for Li^+ . However, graphite was not the first material to be proposed for use as an anode in secondary Li batteries. Li metal was often used as an anode in early Li-based batteries to achieve the highest voltage for a Li battery system with any given cathode material. However, problems related to the reactivity of Li metal, short circuiting, and thermal runaway hindered the commercialization of these batteries. These issues are discussed in detail in Section 4.10.5.2.1. In fact, shortly after the first rechargeable Li-metal batteries were introduced in the 1980s, there were reports of catastrophic failure resulting in fires. These safety concerns ultimately led to an end of efforts to commercialize Li metal batteries at the time.

Initially, intercalation-based materials did not receive attention as anode candidates because of their compromised capacity and voltage compared to pure Li metal. However, following the challenges with employing Li metal anodes, the high reversibility of intercalation materials made them promising candidates despite the lower voltages and capacities. In addition, the balance between energy density and reversibility is tunable in intercalation materials because the chemical interaction between the host material and Li^+ affects the reactivity of Li^+ and thus the electrode potential.

Graphite consists of layers of graphene sheets held together by van der Waals forces. Graphite is by far the most common and commercially used intercalation material for the anode (Fig. 24).¹⁸² During battery discharge, the C in the anode is oxidized spontaneously:



During charge, external voltage is applied to reverse the above half reaction, and graphite is reduced. In fact, the term “Li-ion battery” gained its name after implementing a carbonaceous anode host, to emphasize the fact that the cell is free of pure Li

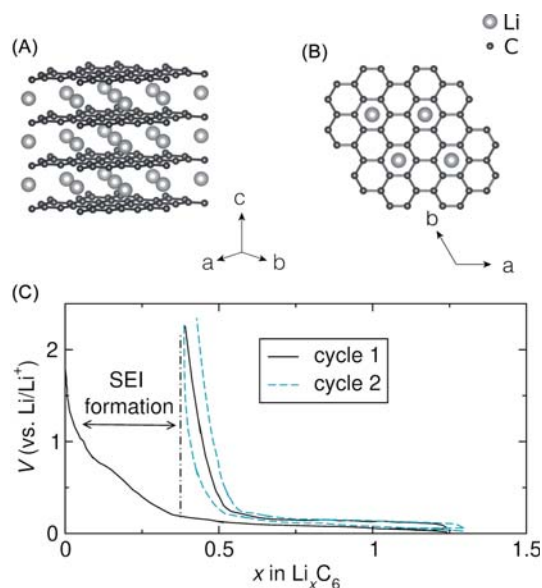


Fig. 24 Structure of lithiated C_6 (a) along the [110] direction and (b) in the ab plane. (c) Charging/discharging profiles of graphite between 0.01 and 2.5 V at a rate of C/5. The irreversible capacity on the first cycle is due to electrolyte decomposition to form the solid electrolyte interphase. The electrochemical data is from Ref. 181

metal.¹⁸³ Carbonaceous hosts exhibit reduction potentials very close to that of Li metal (0.1 V vs Li/Li⁺), thus minimizing voltage loss incurred by moving away from pure Li metal. The higher natural abundance of graphite over Li metal results in a substantial reduction in cost. Furthermore, Li intercalated graphite is less prone to dendrite formation and is thus a safer alternative to Li metal. These advantages made the lower capacity of graphite (372 mA h g⁻¹), compared to that of Li metal (3856 mA h g⁻¹), an acceptable trade off. However, several challenges arose during the development of graphite as the standard anode host due to its reactivity with prominent electrolytes.

4.10.4.1.1.1 Solid electrolyte interphase (SEI)

Challenges associated with developing graphite as the anode stemmed from its strong reducing potential. The reduction potential of LiC₆ lies below the reductive stability window of common electrolytes. Therefore, the electrolyte was prone to decomposition when in contact with the graphite anode. In the initial investigations of graphite as a potential anode material, unbeknownst to the investigators, propylene carbonate (PC) solvent molecules co-intercalated along with Li⁺ during reduction and subsequently decomposed. As the solvent molecules decomposed, they destroyed the structure of graphite and caused the graphene layers to separate in a process called exfoliation. Exfoliation led to poor electrochemical performance, minimal discharge current, and ultimately the investigation of graphite as an anode was abandoned (Fig. 25).¹⁸⁴ It was not until 20 years after first reports of different organic electrolytes for carbonaceous anodes that researchers discovered that the simple substitution of PC with a similar molecule, ethylene carbonate (EC), solved the problem.

Although EC was first evaluated in 1958 as a solvent candidate for electrolytes, PC had been preferred over EC mainly due to the higher melting point of EC (34 °C), which made it solid at room temperature, and the general assumption in the field that the small structural difference of a methyl group would not dramatically impact the electrochemical results.¹⁸⁵ In fact, the effects of EC were not studied extensively until after the first generation of commercial LIBs was made available by Sony in 1991.¹⁸⁶ EC did not induce the destructive exfoliation process; instead, EC irreversibly decomposed into an interfacial layer on the surface of graphite. This protective layer formed as a result of controlled EC co-intercalation and decomposition is known as a solid-electrolyte interphase (SEI).¹⁸⁷

The SEI, first proposed by Peled in 1979, helps the graphitic anode maintain the structural integrity by preventing further intercalation of solvent molecules.¹⁸⁷ Li⁺ is able to diffuse through the SEI without the solvent molecules, leading to stable, reversible charge/discharge cycles. Furthermore, the SEI is electronically insulating such that the potential at the graphite electrode does not drop to values at which electrolyte decomposition occurs and thus, the electrolyte decomposition becomes self-limiting. Many experimental and computational efforts aimed at elucidating the composition of the layer revealed that SEI consists of lithium salts of alkylcarbonates as a result of carbonate reduction.^{188–195} The layer is formed when a negative potential is applied to the graphite electrode immersed in the electrolyte. In the electrochemistry, SEI formation is observed as irreversible capacity on cycle 1 discharge (Fig. 24b). Products of the reduction of salt anions such as LiF, LiCl, and Li₂O precipitate on the electrode surface and prevent electrolytes from further contact with the electrode (Fig. 25).¹⁹⁶ Reduction of solvent is followed by the formation of both insoluble components such as Li₂CO₃ and partially soluble semi-carbonates and polymers. These materials exist as a mosaic of microphases, as depicted in Fig. 25.¹⁹⁷ The current understanding of the diffusion of Li⁺ is that solvated Li⁺ lose their solvation shells while penetrating the SEI and enter the graphite in a solvent-free form.¹⁹⁶ The SEI conducts Li⁺ through vacancies and interstitial lattice defects.

Because the SEI formed in the initial cycle is permanent, the formation of SEI must be done in a controlled manner. In modern LIB-manufacturing facilities, cells are assembled in the discharged configuration and deliberately charged during the “formation cycle” to ensure safe and optimized SEI formation prior to use. The cell must be assembled in a discharged configuration, with a fully lithiated cathode and delithiated graphite as the anode. Assembling the cell in a discharged state avoids both economic and safety challenges, as manufacturing lithiated graphite is more costly, and LiC₆ is not only reactive to moisture, but also to electrolytes, especially in the absence of the stable SEI.¹⁸² The discovery of the spontaneous formation of an SEI that serves as a protective layer enabled the proliferation of LIBs, and efforts are ongoing to transfer this concept to other battery systems.

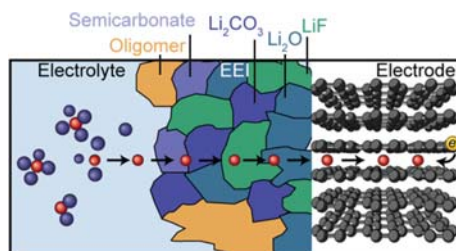


Fig. 25 SEI components and Li⁺ intercalation during reduction. Adapted from Gauthier, M.; Carney, T. J.; Grimaud, A.; Giordano, L.; Pour, N.; Chang, H.-H.; Fen-ning, D. P.; Lux, S. F.; Paschos, O.; Bauer, C.; Maglia, F.; Lupart, S.; Lamp, P.; Shao-Horn, Y. Electrode-Electrolyte Interface in Li-Ion Batteries: Current Understanding and New Insights. *J. Phys. Chem. Lett.* **2015**, *6*, 4653–4672.

4.10.4.1.1.2 Electrochemical Li^+ intercalation mechanism in graphite

Li^+ intercalates into the interlayer spacing between graphite layers during charging. The theoretical capacity of 372 mA h g^{-1} is based on full lithiation to LiC_6 , in which up to one Li atom is intercalated per six carbon atoms which leaves the adjacent sites empty (Fig. 24). During reduction, Li^+ maintain their cationic form while the six sp^2 -hybridized Cs share the negative charge, with the electron density being higher near the Li^+ ion.¹⁹⁸ Intercalation of more than one Li atom per six carbon atoms at ambient pressure and temperature would lead to shorter Li—Li distance and eventually Li with an unstable metallic nature.

During intercalation, Li^+ initially enters the graphite lattice via the prismatic surface and diffuses between two basal planes (Fig. 24). As intercalation of Li^+ continues, the Li^+ preferentially intercalates between certain layers of graphite and leaves some interlayer spaces unoccupied in a process called ‘staging’. Staging occurs because the repulsive Coulombic interactions between Li^+ are lower in energy than the energy that is required to expand the van der Waals gap between two layers. Therefore, Li^+ atoms accumulate in one layer until a threshold is reached. After the threshold is reached, a new layer ordering is established. As the Li^+ concentration increases during charging, the number of periodic unoccupied carbon layers between two nearest Li^+ layers decreases. This process is denoted by the stage index. For instance, fully occupied LiC_6 is described as stage I as two Li^+ layers are separated by only one carbon layer. Stage II denotes separation by two carbon layers, and so forth. The exact ordering mechanism of inserted Li^+ is still under debate, but it is largely determined by minimizing the free energy based on different factors such as the strain energy as a function of Li^+ concentration and the charging rate.^{181,199–202} The presence of stage I, II, III, and IV have been supported by characterization techniques such as XRD and Raman spectroscopy.^{203–207}

The staging behavior of graphite can be shown in an electrochemical potential curve as a function of capacity, or degree of Li^+ intercalation in Li_xC_6 during reduction. After an initial sloping region, multiple plateaus are observed (Fig. 26). The plateau indicates two stages are present at the same time. These two-phase regions are liquid-like and disordered, i.e. there is no in-plane ordering.^{201,208} In these plateau regions, the pre-existing stage undergoes phase transformation and becomes more dense and ordered. Though the exact staging mechanism is still unknown, some structural changes have been identified during the progression from stage II to stage I. The stacking of graphene sheets changes from ABAB to AAA to fully accommodate all Li^+ and becomes highly ordered and crystalline.^{181,208,209} Also, the interlayer spacing increases by 10.3% when fully lithiated.^{208,210,211} Interestingly, the first charge cycle exhibits a capacity higher than the theoretical capacity of LiC_6 , which is then followed by subsequent cycles with high Coulombic efficiencies. The initial irreversible capacity that exceeds the theoretical capacity is attributed to the solvent cointercalation and SEI formation as discussed in the previous section.²¹²

LiC_6 is a successful anode material, and research efforts have discovered unique characteristics such as the formation of the protective SEI and the staging mechanism. Applying what has been discovered in graphite intercalation compounds to different families of materials in the future will offer insights to ultimately develop design rules for next-generation anode materials that enable higher energy and power density while ensuring safety.

4.10.4.2 Other intercalation-based anode structures

Although graphite is the most widely used anode material, researchers are developing other intercalation-based anode materials that can overcome disadvantages associated with graphite or that are tailored for specific applications in which graphite anodes perform poorly. For instance, TiO_2 , which has a theoretical capacity of 335 mA h g^{-1} , exhibits high thermal stability. TiO_2 has many stable polymorphs that are shown in Fig. 27 and each displays different electrochemical behavior. The most suitable TiO_2 phase for anode applications is anatase. The anatase phase crystallizes in a body-centered tetragonal phase with interstitial sites available for Li^+ intercalation.⁴² TiO_2 can be lithiated and delithiated above 1 V vs Li/Li^+ . While more positive redox potential (lower operating

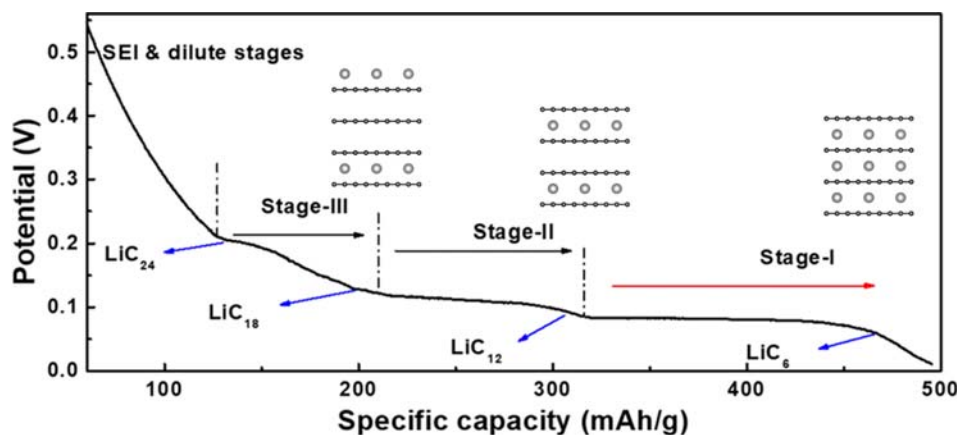


Fig. 26 Different stages of Li_xC_6 shown with the reduction profile during charge. Adapted from Liu, Q.; Li, S.; Wang, S.; Zhang, X.; Zhou, S.; Bai, Y.; Zheng, J.; Lu, X. Kinetically Determined Phase Transition From Stage II (LiC_{12}) to Stage I (LiC_6) in a Graphite Anode for Li-Ion Batteries. *J. Phys. Chem. Lett.* 2018, 9, 5567–5573.

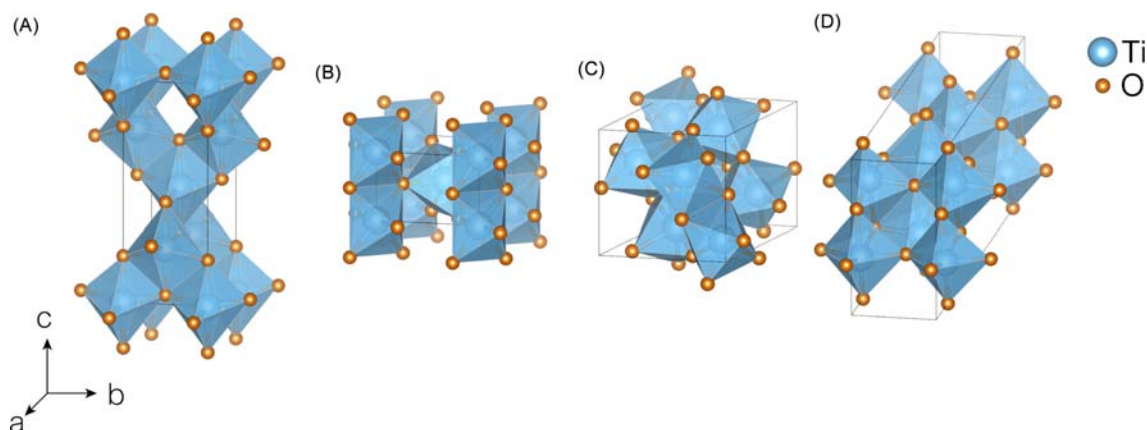


Fig. 27 Polymorphs of TiO_2 include (a) anatase, (b) rutile, (c) brookite, and (d) bronze.

voltage) results in safer operations by avoiding electrolyte decomposition and dendrite formation, it also means decreased energy density. The prioritization of these characteristics must be considered for different applications. Notably, the use of nanocomposites of TiO_2 led to improved electrochemical behavior.^{42,213–216}

Another Ti-based oxide material is $\text{Li}_4\text{Ti}_5\text{O}_{12}$ (or $\text{Li}_{1.33}\text{Ti}_{1.67}\text{O}_4$) (LTO), which crystallizes in a spinel structure in which 1/6 of the total Ti ions in octahedral sites are replaced Li. LTO utilizes the $\text{Ti}^{3+/4+}$ redox couple at 1.55 V vs Li/Li^+ , again avoiding both the electrolyte decomposition and dendrite formation that occur at low potentials.^{217–219} The lithiation of LTO occurs via a two-phase reaction with minimal hysteresis, and the structural stability of LTO is maintained. Similarly to TiO_2 , LTO also benefits from nano-scaling.^{220,221} Additionally, the interplanar distance in LTO doesn't change upon (de)intercalation. This unique zero-strain property of LTO makes it a good candidate to be utilized with other materials, as surface coating for cathodes or as nanocrystals of dual-phase LTO and TiO_2 .²²² Also, recent efforts showed that LTO aliovalently substituted with Y exhibits improved electrochemical properties. Y-doped LTO delivers $141.3 \text{ mA h g}^{-1}$ after 1800 cycles at a rate of 10 C.^{42,223} LTO has the potential to be particularly useful in applications in which safety is integral, such as EV applications.

The last example of an intercalation-based anode material that will be discussed is Nb_2O_5 . Nb_2O_5 has gained attention for its high-rate Li intercalation similar to nanostructured electrodes, which can be useful in high-rate cycling and intercalation pseudocapacitance.^{224,225} Operating between 1 and 2 V vs Li/Li^+ , Nb_2O_5 does not cause unstable electrolyte decomposition that generally occurs below 1 V vs Li/Li^+ and, thus, avoids dendrite formation as well.^{226–228} Nb_2O_5 also exists in multiple polymorphs, such as TT-, T-, and B- Nb_2O_5 , whose formation depend on synthesis conditions such as the temperature and choice of precursor compounds. Consequently, the differences in inherent crystallographic properties affect their corresponding electrochemical performance. Of the different polymorphs, bulk TT- and T- Nb_2O_5 perform similar to nanostructured Nb_2O_5 .^{225,229} T- Nb_2O_5 , shown in Fig. 28, is composed of primarily highly distorted octahedral and pentagonal bipyramidal Nb environments and partially occupied Nb sites, while the TT-phase is a metastable structure whose structural details are not fully understood.²²⁵ The structure of T- Nb_2O_5 can be described as layers of Nb polygons bridged by O, with the interlayer with a distance of 3.93 Å creating room for facile Li^+ diffusion. Nearly degenerate 2D diffusion pathways perpendicular to the *c* axis without obvious minima to trap Li^+ throughout the structure can be visualized (Fig. 28).²²⁵ The activation barrier in T- Nb_2O_5 , 58 meV as T- $\text{Li}_2\text{Nb}_2\text{O}_5$, is significantly lower than those of other LIB materials.²²⁵ Unlike TiO_2 whose electrochemical performance is highly dependent on the particle size, Nb_2O_5 shows optimal performance even on the micrometer scale.

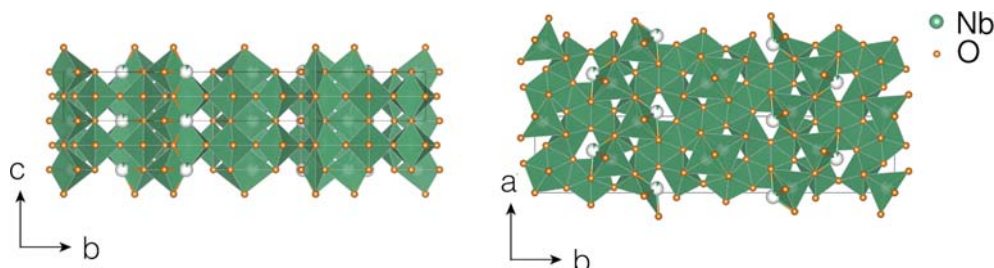


Fig. 28 Structure of T- Nb_2O_5 in the bc plane (left) and ab plane (right).

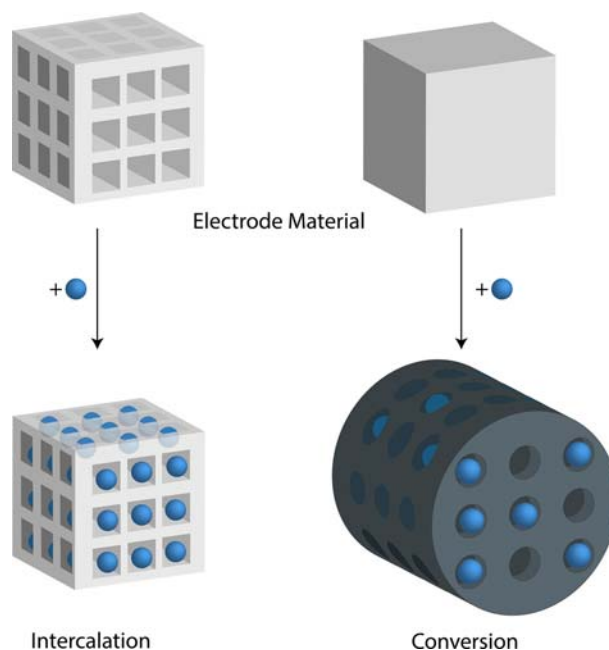


Fig. 29 Illustration of crystallographic changes during intercalation of guest species into a host lattice (left) and conversion reactions (right), in which a new phase is formed.

4.10.5 Conversion batteries

4.10.5.1 Conversion cathodes

Much of the discussion so far has focused on intercalation mechanisms for charge storage in which the delithiated structure is crystallographically related to the lithiated one. Conversion electrodes, on the other hand, undergo a significant phase change upon charging or discharging. Fig. 29 schematically demonstrates the difference between conversion and intercalation reactions. Because conversion electrodes are not limited by the number of crystallographic sites which can accommodate an intercalated ion, they offer much higher gravimetric and volumetric capacities than intercalation-based electrodes.

4.10.5.1.1 Sulfur

S_8 is a promising conversion cathode material for next generation Li-based batteries. S_8 is inexpensive, lightweight, nontoxic, and readily available as a product of petroleum refining, and S_8 cathodes offer high theoretical capacities of 1672 mA h g^{-1} . S_8 cathodes are often paired with Li metal anodes, and Li–S batteries offer theoretical energy densities of 2600 Wh kg^{-1} —approximately five times greater than that of a conventional LIB.²³⁰

Elemental S is stable in many polymorphs; the most stable structure at room temperature is orthorhombic α - S_8 which is composed of eight-membered S rings. The monoclinic β - and γ - S_8 can be prepared at elevated temperatures.

The half reaction at the cathode of a Li–S battery during discharge is:



The Li–S convex hull (Fig. 30) suggests that Li_2S , S_8 , and Li are the only stable crystalline solid-state phases in the Li–S phase diagram.^{231,232} A solid-state reduction would then involve a single two-phase reduction resulting in a single plateau in the discharge curve around 2 V vs Li/Li⁺ (Fig. 30b).²³¹ However, in practice, the Li–S discharge is characterized by two discrete plateaus (Fig. 31). The multi-step mechanism arises because the reduction produces dissolved intermediate lithium polysulfides (Li_xS_y) via a solution-mediated mechanism. The polysulfide intermediates can undergo several disproportionation reactions and are difficult to conclusively identify. Therefore, assigning each plateau in the discharge profile is exceedingly difficult. At first, the discharge was suggested to involve a cascading reduction from S_8 to Li_2S via Li_2S_8 , then Li_2S_6 , etc. The first discharge plateau, near 2.3 V vs Li/Li⁺, was suggested to correspond to cleavage of the S_8 ring and reduction of solid S_8 to solution-phase long-chain polysulfides such as Li_2S_8 and subsequently Li_2S_6 through the disproportionation reaction



and the second plateau near 2.1 V vs Li/Li⁺ indicates reduction of long-chain polysulfides to shorter-chain polysulfides like Li_2S_4 , Li_2S_2 , and the final solid discharge product Li_2S .^{234,235} However, evidence for solid Li_2S earlier in the discharge pathway suggests a different mechanism. The first plateau can be understood as reduction of S_8 to soluble Li_xS_y and Li_2S in a three-phase mechanism. The potential drops when S_8 is consumed and dissolved Li_xS_y are reduced to Li_2S .²³¹

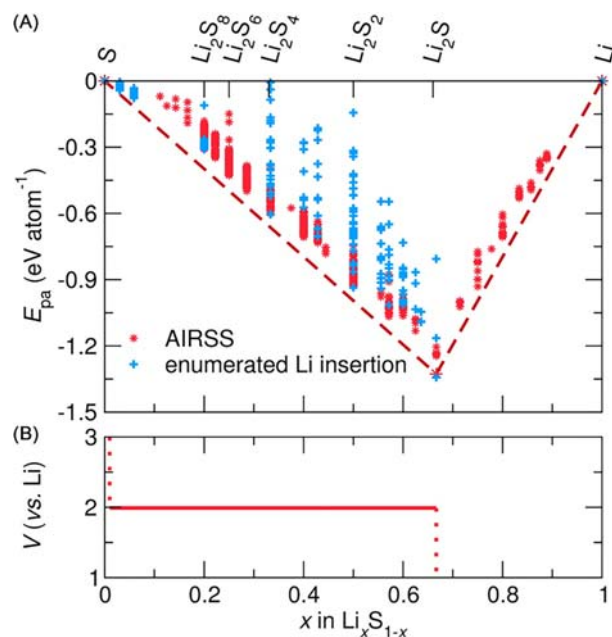


Fig. 30 (a) The Li-S convex hull reveals only one thermodynamically stable solid-state product: Li_2S . (b) If the discharge of a Li-S battery followed a solid-state conversion reaction pathway to form Li_2S , a single plateau would be observed around 2 V vs Li/Li^+ . Adapted from See, K. A.; Leskes, M.; Griffin, J. M.; Britto, S.; Matthews, P. D.; Emly, A.; Van der Ven, A.; Wright, D. S.; Morris, A. J.; Grey, C. P.; Seshadri, R. Ab Initio Structure Search and in Situ ^7Li NMR Studies of Discharge Products in the Li-S Battery System. *J. Am. Chem. Soc.* **2014**, *136*, 16368–16377.

Saturation of the electrolyte with polysulfide species has also been proposed to limit S_8 reduction beyond the first plateau²³⁵; the second discharge plateau then consists of further reduction of dissolved polysulfides to solid Li_2S .²³¹ Early works hypothesized the existence of a secondary solid discharge product Li_2S_2 , but Li_2S_2 falls above the convex hull and is thus thought to be unstable, and experimental evidence has since confirmed that solid Li_2S_2 is not formed during discharge.^{231,232}

The charge mechanism in a Li-S battery is similarly convoluted by the simultaneous presence of several polysulfide species undergoing multiple disproportionation reactions and by the transient nature of polysulfide oxidation intermediates. A typical charge curve exhibits one sloping plateau (Fig. 31, black trace).²³³ In general, solid Li_2S is thought to be oxidized first to solution-phase short-chain polysulfides such as Li_2S_4 , which are then oxidized further to longer-chain polysulfides ($\text{Li}_2\text{S}_\gamma$, $\gamma > 4$). The long-chain polysulfides exist in equilibrium through complex disproportionation reactions until solid elemental S (S_8) is recovered at potentials above 2.9 V vs Li/Li^+ .^{235,236}

Due to the solubility of polysulfide intermediates, S_8 cathodes must contend with rapid failure as a result of the polysulfide shuttle effect. Li polysulfides, formed during S_8 reduction on discharge, can dissolve into the organic liquid electrolyte, diffuse away from the cathode, and reduce further at the Li anode to form insoluble Li_2S (Fig. 32).²³⁰ The loss of active material at the cathode leads to significant capacity fade over time, as well as poor Coulombic efficiency. As the ionic conductivity of Li_2S is approximately $10^{-14} \text{ S cm}^{-1}$,²³⁷ the insulating Li_2S formed at the Li anode also passivates the Li surface and leads to degradation of the anode and increased internal resistance of the cell.

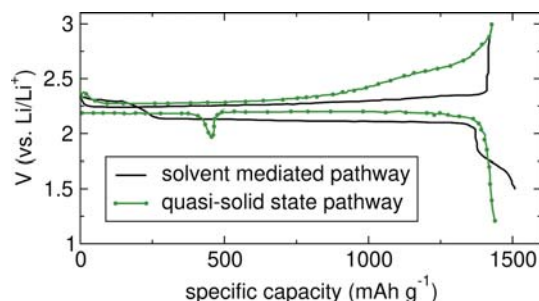


Fig. 31 Discharge/charge profiles of a Li-S battery with different electrolytes. In a conventional electrolyte such as 1 M LiTFSI in DOL/DME (black trace), the discharge reaction proceeds through a solution-mediated pathway with two distinct plateaus, while a concentrated solvate electrolyte such as 4.2 M LiTFSI in acetonitrile (green trace, fluorinated ether cosolvent added to reduce viscosity) forces a quasi-solid-state S reduction pathway. Electrochemical data is from Lee et al.²³³ Cells were cycled at C/30 and 55 °C.

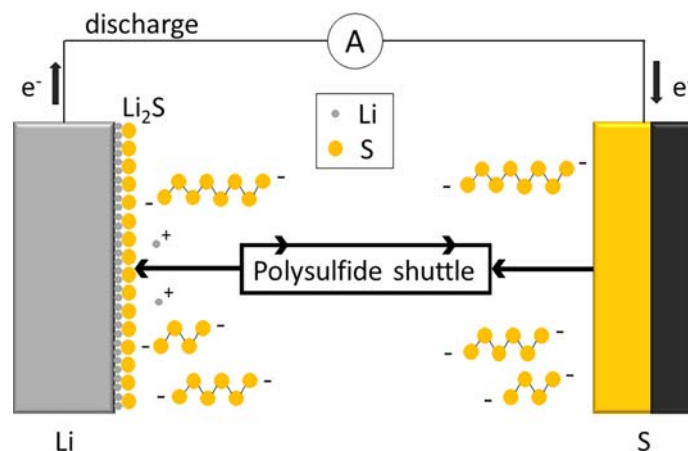


Fig. 32 Schematic of the polysulfide shuttle in Li-S batteries. Adapted from Bresser, D.; Passerini, S.; Scrosati, B. Recent Progress and Remaining Challenges in Sulfur-Based Lithium Secondary Batteries—A Review. *Chem. Commun.* **2013**, 49, 10545–10562.

New electrolyte systems are being developed to reduce the solubility of Li polysulfides. Highly concentrated electrolytes known as solvate electrolytes employ stoichiometric ratios of salt:solvent to generate unique coordination structures.^{238–240} The high concentrations force coordination of most solvent molecules to the electrolyte salt, leaving little free solvent available to dissolve polysulfide compounds. The low solubility of intermediate polysulfide species alters the S_8 reduction pathway, yielding an “equi-potential bi-plateau” in the discharge trace (Fig. 31).²³⁹ The mechanism of S_8 reduction is thought to proceed through a quasi-solid-state pathway in which S_8 is first reduced to Li_2S_4 , which is enabled by the very slight solubility of polysulfide species in the solvate electrolyte. Following a dip in the discharge profile ascribed to a nucleation overpotential for Li_2S , the slightly soluble polysulfides are reduced to solid Li_2S . Solvate electrolytes have the added benefit of reducing catastrophic solvent decomposition at the Li anode,²³⁸ but the high viscosity and low conductivity associated with such concentrated solutions require the addition of cosolvents or increased temperatures to achieve high capacities during operation.

Despite their many advantages over conventional Li battery cathodes, S_8 cathodes are subject to several limitations that have prevented commercialization to date. S_8 and its reduction products are ionically and electronically insulating, and S_8 cathodes must include conductive additives such as carbon to facilitate charge transfer over a large surface area. S_8 can be infiltrated into the pores of high surface area mesoporous carbons such as CMK-3 (cubic ordered mesoporous carbon) to improve the electrochemical accessibility of the S_8 as was done in the seminal work by Ji et al.²⁴¹ Such infiltration is one of the most commonly employed methods of establishing high conductivity in S_8 cathodes, but the addition of the carbon matrix limits the energy density of the cell. It is additionally challenging to cycle cathodes of high areal loading for similar reasons. Furthermore, because the mechanism involves solution phase intermediates, the performance of the cell depends on factors like the S_8 -to-electrolyte ratio. Cycling cells without excess electrolyte in so-called “lean” conditions is challenging.

S_8 cathodes are being actively investigated as a promising next generation energy storage solution. Current research focuses on addressing many of the challenges described above as well as incorporating S_8 cathodes into new electrochemical systems. Nanostructured conductive matrices are being developed to inhibit polysulfide dissolution while maintaining good electrical contact. These nanostructures typically constrain active S_8 within hollow carbon nanospheres or other frameworks with high tortuosity to prevent polysulfides from migrating away from the cathode surface.^{242–244} Recently, solid-state electrolytes have been incorporated into Li-S cells.^{245,246} Though solid electrolytes are mainly employed to mitigate dendrite growth at the Li anode, the controlled diffusion pathways can also prevent dissolution and diffusion of long-chain polysulfides away from the cathode surface. S_8 electrodes are also being incorporated into emerging Na^+ batteries due to their potential as an exceptionally low cost energy storage system.^{247,248} Na^+ batteries will be discussed further in Section 4.10.5.

4.10.5.1.2 Oxygen

O_2 -based cathodes are the only cathode materials capable of competing with liquid fuels on an energy density scale. When used in concert with a Li metal anode, O_2 -based batteries offer the highest theoretical energy density of any currently known system at 11.4 kW h g^{-1} —since O_2 can be obtained from ambient air, the energy density of the battery is limited by the amount of Li in the anode.²⁴⁹ Due to the added mass of the electrolyte and cell components, the practical energy density of a Li- O_2 battery is around 3600 Wh kg^{-1} ,²⁵⁰ which is comparable to that of gasoline (1700 Wh kg^{-1}). The best-performing batteries also offer discharge capacities above 5500 mA h g^{-1} , well above the capacities of current Li^+ batteries (around 150 mA h g^{-1}).²⁵¹

O_2 -based batteries were first investigated in the 1970s,²⁵² but research in the Li- O_2 system accelerated beginning in the mid-1990s when Abraham et al. developed a reversible Li- O_2 battery using a nonaqueous electrolyte.²⁵³ Nonaqueous electrolytes have since dominated research on Li- O_2 batteries due to their greater compatibility with the Li anode, but aqueous, hybrid, and solid-state electrolytes have also been employed.²⁵⁴

The discharge mechanism for a Li–O₂ battery relies on the O₂ reduction reaction (ORR). Li and O₂ combine to form Li₂O₂ in an overall two electron reduction mechanism. The formation of Li₂O₂ proceeds through a thermodynamically unstable LiO₂ intermediate. First LiO₂ is formed by a one electron reduction of O₂:



LiO₂ can then be converted to Li₂O₂ via another single electron reduction:



or by disproportionation^{222,255,256}:



During charge, Li₂O₂ is oxidized to form Li⁺ and O₂ but does not form the LiO₂ intermediate.^{222,255,256}

A catalyst is required to capture and reduce O₂. Several properties must be considered when selecting a catalyst (Fig. 33).²⁵⁷ The material must exhibit high electronic conductivity, high ORR and oxygen evolution reaction (OER) activity, and sufficient chemical and electrochemical stability. Li oxidation occurs much more quickly than O₂ reduction, so the rate capability of the battery is limited by the ORR/OER activity of the cathode. The catalyst must also have a large surface area, since O₂ reduction occurs only at the surface of the electrode, and it must be porous to allow O₂ to permeate the full depth of the electrode. The pore size must be carefully selected to be large enough to prevent clogging as Li₂O₂ is plated during discharge while remaining small enough to maximize the available surface area without sacrificing volumetric energy density.²⁵⁷

Such limitations to the catalyst composition present a significant barrier to further development of Li–O₂ batteries. Porous carbon frameworks are often used as substrates due to their high surface areas and permeability, but C exhibits intrinsically low ORR/OER activity. Several metallic catalysts such as Ni foam also offer high porosity but only act as catalysts for either the discharge or charge reaction, not both.²⁵⁸ Metal surfaces are also prone to oxidation under the highly oxidative conditions of the cathode and to decomposition following reaction with O₂^{•−} formed during the initial one electron reduction of O₂, limiting their conductivity and imposing large overpotentials. However, C and metal systems can also function as supports for more appropriate catalysts. Noble metals such as Au²⁵⁹ and Pd²⁶⁰ can be effective electrode materials if supported on a conductive and porous framework, as can transition metal oxides such as MnO₂ or Co₃O₄.^{261/262}

Other issues have also hindered commercialization of Li–O₂ batteries. While several systems that rely on pure, dry O₂ have been developed, fewer exist that can utilize environmental O₂. To utilize O₂ from the air, the O₂ must first be separated from the N₂, H₂O, CO₂, and other gases that can reduce the efficiency of the battery or react unfavorably with either the cathode or the anode. Li in the electrolyte can easily and irreversibly react with H₂O to form LiOH or with CO₂ to form Li₂CO₃ at the cathode surface. These side products can passivate the cathode surface, limiting the number of active sites available for ORR/OER and preventing the diffusion of O₂ through the catalyst pores. O₂-selective membranes can prevent a significant fraction of external gases from reaching the cathode and forming unwanted side products, or from reaching the anode and passivating the Li metal surface. Commonly employed membranes include Si oil or silicate zeolites immobilized in a polytetrafluoroethylene (PTFE) matrix,²⁴⁹ polysiloxanes,²⁶³ and high density polyethylene (HDPE).²⁶⁴

Addressing the above challenges with O₂ cathodes is an active area of research. Development of O₂-selective membranes with low water permeability is of particular importance, as the best membranes to date exhibit O₂/H₂O selectivities < 4.²⁴⁹ Significant quantities of H₂O therefore still enter the catalyst framework and passivate the electrode through undesirable side reactions, and membranes with higher O₂ selectivity are necessary to extend the lifetime of the cathode. Improvements in catalyst design, such

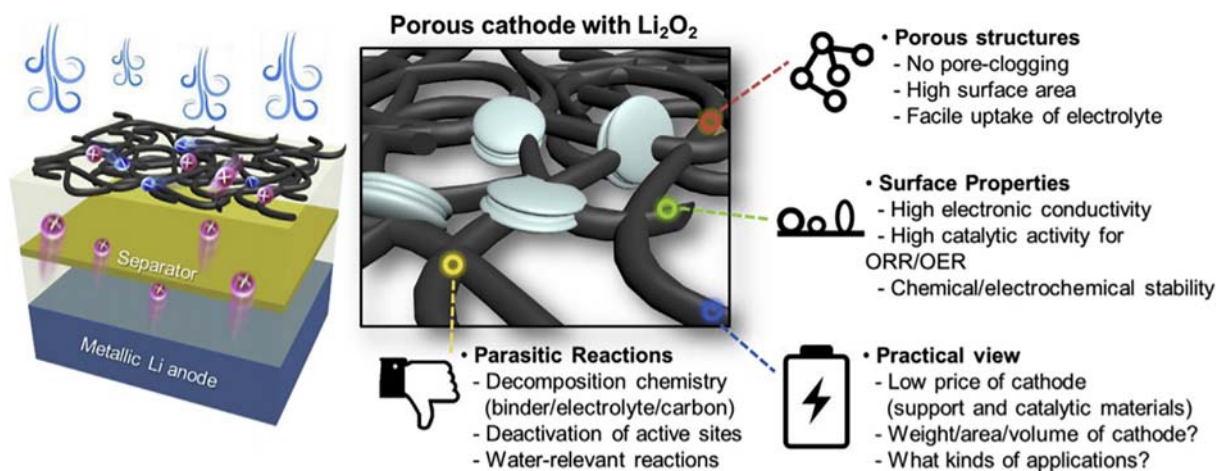


Fig. 33 Major challenges in the design of cathodes for metal-air batteries. Adapted from Jung, J.-W.; Cho, S.-H.; Nam, J. S.; Kim, I.-D. Current and Future Cathode Materials for Non-Aqueous Li-Air (O₂) Battery Technology—A Focused Review. *Energy Storage Materials* 2020, 24, 512–528.

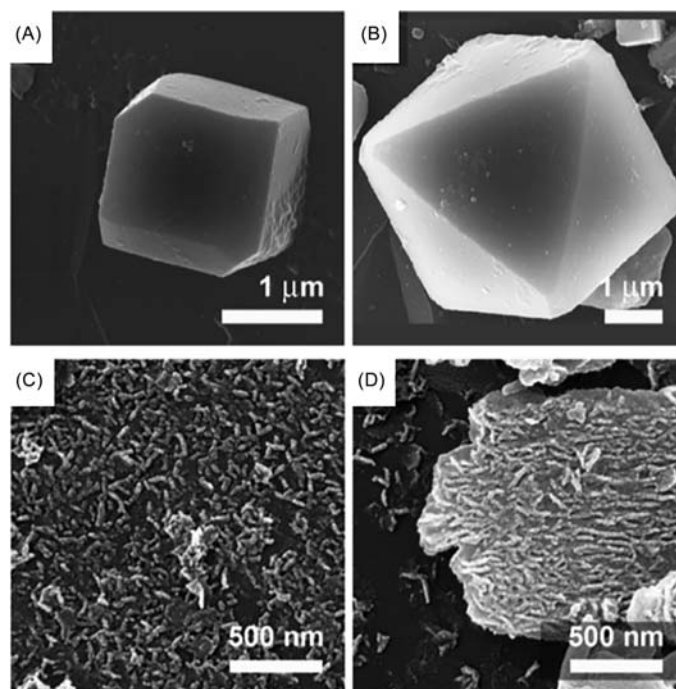


Fig. 34 Various deposition morphologies of Li_2O_2 . Adapted from Yang, Y.; Zhang, T.; Wang, X.; Chen, L.; Wu, N.; Liu, W.; Lu, H.; Xiao, L.; Fu, L.; Zhuang, L. *Tuning the Morphology and Crystal Structure of Li_2O_2 : A Graphene Model Electrode Study for $\text{Li}-\text{O}_2$ Battery*. *ACS Appl. Mater. Interfaces* **2016**, *8*, 21350–21357.

as new morphologies and composite materials will enable greater capacity, cyclability, and chemical stability at the O_2 cathode. Furthermore, parasitic side reactions as well as variable Li_2O_2 crystallinity and morphology (see examples in Fig. 34) lead to complications in interpreting the charge profile and a consequent poor understanding of the true OER mechanism on charge.^{250,257,260} Developing in situ characterization techniques to elucidate the charge mechanism will inform future catalyst design.

4.10.5.2 Conversion anodes

Conversion anodes offer significantly higher capacities than state-of-the-art, intercalation-based graphite anodes, making them suitable for use with high-capacity cathodes such as S_8 and O_2/air in potential next-generation batteries.

4.10.5.2.1 Lithium metal

Li metal is often regarded as the “holy grail” of anode materials due to its high theoretical capacity (3862 mA h g^{-1}) and highly negative reduction potential (-3.04 V vs NHE). Li anodes have been investigated in many energy storage systems, including in $\text{Li}-\text{S}$ and $\text{Li}-\text{O}_2$ batteries.²⁶⁵ The processes and mechanisms at a Li metal electrode will only be touched on briefly here.

The plating and stripping of Li metal is enabled by the SEI formed on the anode surface during cycling. The low reduction potential of Li is outside the electrochemical stability window of most organic electrolytes, and the electrolyte decomposes upon contact with the Li metal surface to form Li_2O , LiOH , and other inorganic Li species, as well as Li_2CO_3 and LiOR , similar to the SEI formed on lithiated graphite anodes. The ionically conductive, electronically insulating SEI protects the electrolyte from further decomposition at the Li metal surface and can enable reversible Li plating and stripping at low current densities. At high current densities, however, the SEI is subject to breakage during Li deposition due to the large volume change at the anode and the formation of dendrites.

Dendrites are needle-like structures formed at metal anodes following uneven deposition on a rough surface during charging (i.e. electrodeposition of Li^+ at the anode) at high current density. The uneven deposition morphology can be caused by inhomogeneities in the SEI and by a high barrier to self-diffusion of adsorbed ions at the Li surface.²⁶⁶ The electric field (and thus local current density) at peaks formed from uneven deposition is greater than the field at smooth surfaces, lowering the energetic barrier for metal deposition at peaks and propagating further uneven deposition. After several cycles of plating and stripping, dendrites grow to such an extent that they can pierce the separator between the anode and cathode, providing a low-resistance pathway for electron transfer directly between the two electrodes and short-circuiting the cell (Fig. 35). Electrons will flow through the low-resistance pathway, generating a large electrical current that rapidly increases the temperature within the cell and ignites the organic electrolyte. High operating temperatures or current densities exacerbate the effects of uneven metal deposition and increase the likelihood of dendrite

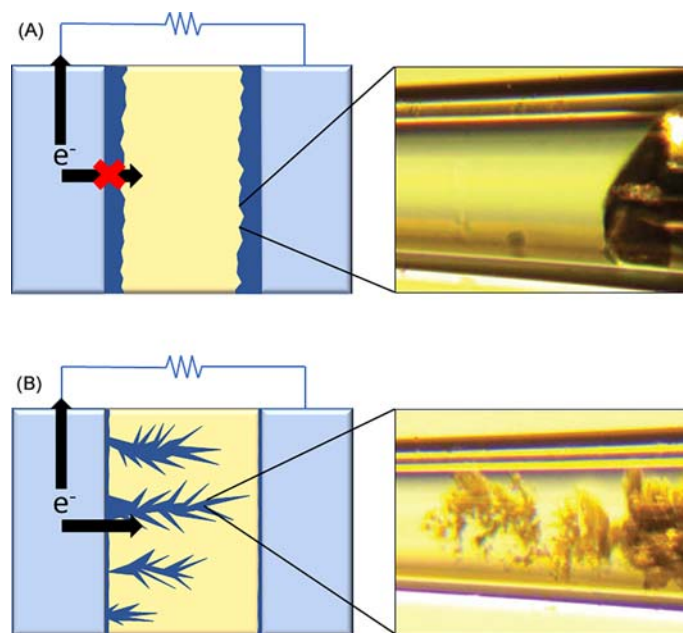


Fig. 35 (a) A smooth deposition morphology prevents short circuits and forces electrons through the external load, powering a device during discharge. (b) Dendrites provide a low-resistance path between electrodes that can lead to rapid Joule heating. Adapted from Bai, P.; Li, J.; Brushett, F. R.; Bazant, M. Z. Transition of Lithium Growth Mechanisms in Liquid Electrolytes. *Energy Environ. Sci.* **2016**, *9*, 3221–3229.

formation. Several strategies are currently being employed to mitigate dendrite growth, including modifying electrolyte chemistry,^{238,267} introducing artificial SEIs,^{268–270} and nanostructuring the Li anode to spatially restrict dendrite growth.^{271,272}

4.10.5.2.2 Silicon

Safety concerns over dendritic deposition of Li have led researchers to investigate other high capacity anode materials. Among these, Si possesses the highest theoretical gravimetric capacity of 4200 mA h g^{-1} , corresponding to the fully lithiated alloy $\text{Li}_{22}\text{Si}_5$.²⁷³ In high temperature systems with molten salt electrolytes, several distinct crystalline phases can be formed during discharge, including $\text{Li}_{12}\text{Si}_7$, Li_7Si_3 , $\text{Li}_{13}\text{Si}_4$, and $\text{Li}_{22}\text{Si}_5$.²⁷⁴ At room temperature, an amorphous phase is formed on discharge and crystallizes into cubic $\text{Li}_{15}\text{Si}_4$ at low potentials vs Li/Li^+ ,²⁷⁵ with a theoretical capacity of 3579 mA h g^{-1} , approximately 10 times higher than that of the graphite anodes currently used in Li^+ batteries. Si is also abundant and nontoxic, and it exhibits a low electrochemical reduction potential of 0.37 V vs Li/Li^+ . However, due to the large volume increase of 300–400% upon alloying with Li, batteries with Si anodes are subject to repeated breakage of the SEI and severe electrolyte decomposition, leading to poor cyclability.^{276,277} Several nanostructures have been developed to mitigate the mechanical strain caused by volume expansion, but improvements in strain tolerance often come at the expense of lowered density and reduced volumetric capacity.^{278–282} Current research on Si anodes focuses on designing artificial SEIs to better accommodate the large volume changes during cycling.^{283–285}

4.10.5.2.3 Conversion oxides

Several transition metal oxides have also been investigated as anode materials for LIBs due to their high theoretical capacities, which are often 2–3 times larger than that of graphite anodes (372 mA h g^{-1}). During the discharge conversion reaction, the metal oxide is reduced to the corresponding metal and Li_2O :



As with Si anodes, the large volume changes associated with the conversion reactions, as well as irreversible capacity fade during initial cycles, lead to low cyclability and electrolyte depletion as the SEI deforms and fresh electrode surface is exposed to the electrolyte. Nanostructuring the metal oxide materials can help to mitigate large volume changes, and forming composite electrodes with conductive carbon improves the conductivity and mechanical flexibility of the electrode even after several discharge/charge cycles.^{286,287}

4.10.6 Beyond Li

Despite the success of the modern Li^+ battery and the promise of next-generation batteries based on Li^+ chemistry, there are also current significant research efforts to develop beyond-Li chemistry. Such research is motivated by several factors, perhaps the most

prominent of which is Li resource criticality that could limit the mass proliferation of Li-based batteries. The global reserves of Li are highly concentrated in a few regions, and despite efforts to expand current mining and develop new methods to mine previously untapped sources of Li, the Li supply will likely fall short of demand for extended periods of time over the 21st century.²⁸⁸ Alternatives like monovalent Na and K; divalent Mg, Zn and Ca; and even trivalent Al are far more abundant and do not have the same natural resource limitations as Li. The possibility of higher energy density batteries based on multivalent elements due to the greater charge stored and transferred per ion is also an attractive quality for higher energy density next-generation batteries. We briefly overview some of these research directions below.

4.10.6.1 Na and K ion batteries

Na and K batteries are attractive candidates for next-generation batteries because of the higher natural abundance and lower cost of Na and K compared to Li. However, in current Li batteries, the low natural abundances of Co and Ni are the limiting factors rather than the natural abundance of Li.²⁸⁹ Nonetheless, competitive Na and K batteries could make a large impact on the economic viability and ubiquity of battery-based energy storage.

Although Na and K are similar to Li in that they are all monovalent, they each differ significantly in atomic radii and charge density as shown below in Table 3.²⁹⁰ Thus, the three alkali metals each demand unique properties of their host structure/material to enable its use as a working ion.

4.10.6.1.1 Na and K intercalation cathodes

The principal challenge with developing intercalation cathodes for Na and K compared to Li is the larger radii of the former compared to the latter. Next-generation Na⁺ and K⁺ cathodes need to accommodate greater structural distortions than their current Li counterparts. Here, three types of cathodes will be briefly discussed: oxides, polyanions, and Prussian blue analogs.

4.10.6.1.1.1 Oxides

Because of the success of metal oxide cathodes in the Li battery field, several ternary Na_xMO₂ and K_xMO₂ phases have been explored for Na and K batteries where M = Ti, V, Cr, Mn, Fe, Co, Ni. Of greatest importance are those phases which crystallize in the O3 ($x = 1$) and P2 ($x \approx 0.67$) structures. The O3 phase is isostructural to LiCoO₂, in which the alkali layer consists of octahedrally-coordinated Na or K connected by tetrahedral voids. The P2 phase consists of prismatically-coordinated Na or K that share rectangular faces. As it is more difficult for Na or K to migrate through a tetrahedral interstitial site as opposed to through a shared rectangular face, the P2 phases generally outperform the O3 ones.²⁸⁹

The larger radii of Na and K relative to Li leads to more weakly coordinated alkali ions, i.e. the O²⁻ to Na⁺/K⁺ bond distances are longer, and so the interlayer spacing in the Na and K materials is larger. Thus, the O²⁻ less effectively screens Na⁺/K⁺ compared to Li⁺. As a result, the alkali-alkali repulsion in the Na and K materials is stronger than in the Li materials, and so the former have lower energy densities and steeper charge/discharge curves as in Fig. 36.

4.10.6.1.1.2 Polyanions

Cathodes with polyanions, similar in stoichiometry to LiFePO₄, are posited to better screen alkali ions and increase the distance between working ions. Such an effect would reduce the slope of the charge curves of Na and K materials. The most well-studied of the polyanionic materials are the Na superionic conductors (NASICONs), which have the general chemical formula Na_xNM(PO₄)₃ where x is between 0 and 4 and N and M are metals such as Ti, V, Cr, Mn. The general structure of the NASICONs is an open three-dimensional framework that enables fast Na⁺ migration. The structure of Na₃V₂(PO₄)₃ with the R3c space group is shown in Fig. 37 and reversibly cycles up to two Na equivalents.²⁹¹

As in LiFePO₄, the inductive effect in polyanionic Na and K materials raises the redox voltage compared to their pure oxide counterparts. The inductive effect can be further enhanced in the structurally related Na fluorophosphates, in which the presence of fluorine further increases the voltage.²⁹² The charge/discharge voltage of Na₃V₂(PO₄)₂F_{3-γ}O_γ continuously increases as γ decreases.²⁹³

Table 3 Atomic properties of Li, Na, and K and theoretical capacities of their respective elemental anodes.

	Li	Na	K
Relative atomic mass	6.94	23.00	39.10
Shannon-Prewitt ionic radii for coordination number of 6 (Å)	0.76	1.02	1.38
Standard reduction potential vs NHE (V)	-3.04	-2.71	-2.93
Theoretical gravimetric capacity (mA h g ⁻¹)	3861	1166	685
Theoretical volumetric capacity (mA h cm ⁻³)	2062	1131	591

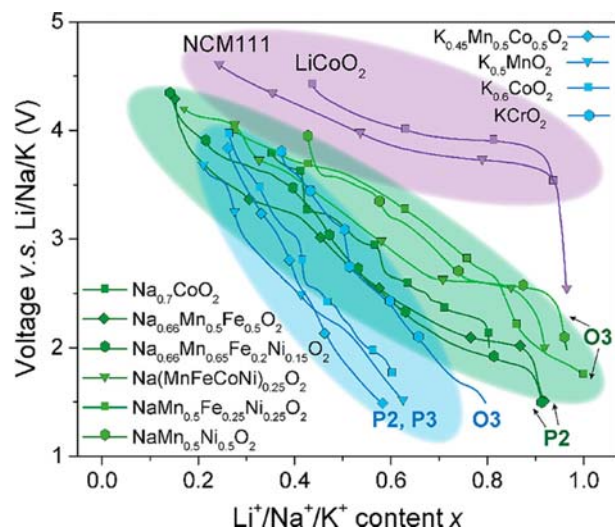


Fig. 36 Charge curves of several of Li, Na and K layered oxides. The slopes of the charge curves generally increase from Li to Na to K. Unlike in LiCoO_2 , the Na and K metal oxide curves are not as smooth, implying that the mid-charge phases are not thermodynamically ideal mixtures. This may be due to vacancies and alkali ion ordering at different x caused by stronger alkali-alkali interactions. Adapted from Tian, Y.; Zeng, G.; Rutt, A.; Shi, T.; Kim, H.; Wang, J.; Koettgen, J.; Sun, Y.; Ouyang, B.; Chen, T.; Lun, Z.; Rong, Z.; Persson, K.; Ceder, G. Promises and Challenges of Next-Generation “Beyond Li-Ion” Batteries for Electric Vehicles and Grid Decarbonization. *Chem. Rev.* **2021**, *121*, 1623–1669.

4.10.6.1.1.3 Prussian blue analogs

The flexible structures and large voids of Prussian blue analogs (PBAs) enable high Na^+ and K^+ mobility and make them candidates for Na and K cathodes. PBAs have a general formula of $A_{2-x}M_A[M_B(\text{CN})_6]_{1-y}\square_y \cdot z\text{H}_2\text{O}$ where A is either Na or K, M_A and M_B are transition metals, \square is a $M(\text{CN})_6$ vacancy, and z is typically between 1 and 5. The metals form a network of corner-sharing octahedra bridged by cyano ligands. The voids formed by the bridged octahedra are cubic and form an open, cage-like structure that facilitates Na^+ or K^+ diffusion.²⁹²

While the charge/discharge voltages for Na and K oxides and polyanionic materials are generally lower compared to those of their Li counterparts, the discharge voltages for Na and K Prussian blue analogs are higher compared to those of their Li analogs. This is likely due to the stronger interaction of the larger Na^+ and K^+ with the metal organic framework compared to the smaller Li^+ .²⁹⁴ The crystal structure of hexacyanoferrate Prussian blue is shown in Fig. 38.

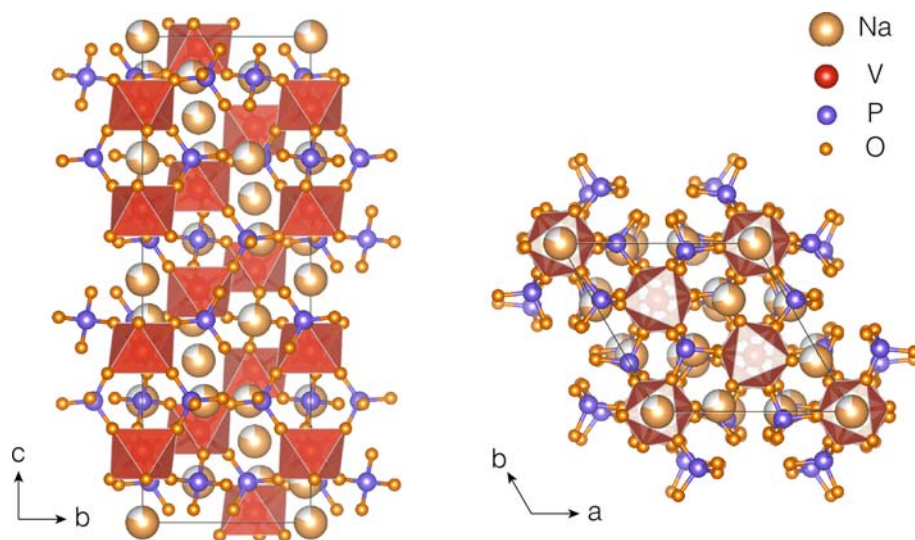


Fig. 37 The structure of $\text{Na}_3\text{V}_2(\text{PO}_4)_3$ ($R\bar{3}c$), in the bc plane (left) and the ab plane (right). The open pathways between Na sites enable high Na^+ conductivity even at room temperature.

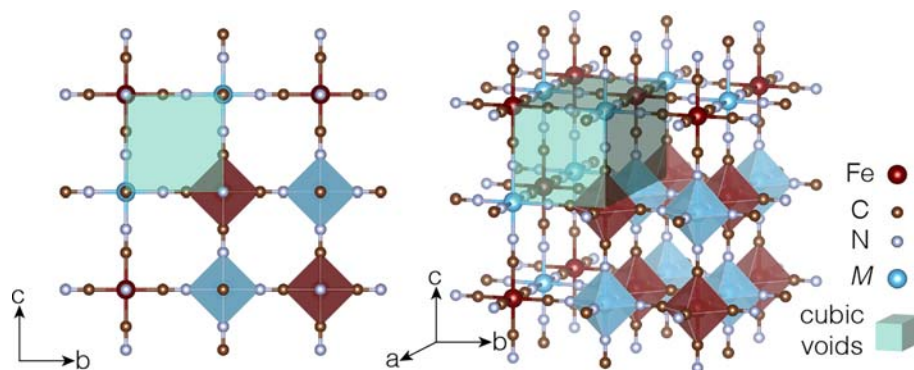


Fig. 38 The annotated crystal structure of hexacyanoferrate Prussian blue. Adapted from Kundu, D.; Talaie, E.; Duffort, V.; Nazar, L. F. *The Emerging Chemistry of Sodium Ion Batteries for Electrochemical Energy Storage. Angew. Chem. Int. Ed.* **2015**, *54*, 3431–3448.

4.10.6.1.2 Na and K intercalation anodes

The principal challenge for Na and K anodes echoes the challenge for cathodes: the large atomic radii relative to Li. Overall research efforts toward Na and K anodes are less extensive than toward cathodes.²⁸⁹ Thus, three types of Na and K anodes will be discussed very briefly here: Na and K metals, carbonaceous anodes (hard carbon for Na, graphite for K), and other intercalation anodes.

Metallic Na and K develop dendrites over cycling just as metallic Li does, for similar physicochemical reasons related to the activation energy for self-diffusion of Na^+ and K^+ on the surface of the metal electrode.²⁹⁵ While significant efforts have been made to suppress dendrite growth, it remains an unsolved problem.

Curiously, Na cannot intercalate into graphite at comparable levels to Li and K.²⁹⁶ Two main arguments have been put forward as to why. The first suggests that Li and K are able to intercalate into graphite because their atomic radii match the lattice parameters of graphite, whereas the atomic radius of Na does not. The mismatch induces stress that delaminates the graphite layers before high levels of Na^+ can intercalate.²⁹⁷ The second argument suggests that the difference in ionization energy of Na relative to Li and K prevents Na intercalation into graphite.²⁹⁸ Regardless, the extremely low capacity of graphite as an Na anode led to the development of an alternative carbon-based anode for Na: hard carbon. Hard carbon consists of graphite flakes with curvature created by sp^3 -hybridized C–C bonds that are absent in graphite. The intercalation mechanism for Na into hard carbon is mostly unknown, but its high capacity of nearly 350 mA h g^{-1} for Na has led to its use in commercial Na-ion batteries.^{299,300}

Lastly, a few low-voltage intercalation anodes for Na and K are reported. For example, $\text{Na}_2\text{Ti}_3\text{O}_7$ can host up to two Na^+ reversibly with a demonstrated capacity of approximately 180 mA h g^{-1} (617 mA h cm^{-3}) at $\sim 0.3 \text{ V}$ vs Na/Na^+ .³⁰¹ Most other intercalation anodes cannot achieve such low voltages, resulting in lower overall cell energy density.

4.10.6.1.3 Commercial Na^+ batteries

Despite limited study compared to Li, Na and K have the potential for large commercial impacts due to their high natural abundances and low costs. Commercial battery progress for K is limited, but several companies have commercialized Na^+ batteries based on hard carbon anodes paired with oxide or Prussian blue analog cathodes and the Na analog of organic carbonate-based electrolytes in commercial Li^+ cells. That said, the overall performance, life-time, energy density and market share of Na^+ cells pale in comparison to Li^+ cells.³⁰⁰ Nonetheless, recent advancements in Na^+ electrolytes have shown improved performance with oxide cathodes and perhaps a pathway to competitive Na batteries.³⁰²

4.10.6.2 Multivalent intercalation

Multivalent batteries offer additional alternatives to Li with the potential of being more cost-effective and environmentally friendly. The higher density of the corresponding metals also allows for higher volumetric capacities—3833, 5848, 8046, and $2072 \text{ mA h cm}^{-3}$ for Mg, Zn, Al, and Ca, respectively, compared to $2046 \text{ mA h cm}^{-3}$ for Li metal anodes.^{303,304} The primary obstacles in the development of multivalent intercalation batteries stem from challenges associated with the electrochemistry of charge-dense multivalent ions including solvating the working ion in electrolyte, achieving reversible multielectron redox, and conducting the working ion in the solid-state. Multivalent ion conduction in solids is discussed at length in our recent perspective article.^[305]

Cathodes for multivalent batteries must accommodate the higher charge density while maintaining structural integrity for reversibility. Both chemical and electrochemical multivalent cation intercalation were first studied in the 1980s and 1990s. Mg is the most studied divalent working ion in electrochemical systems and this section will focus primarily on Mg batteries. By 1991, chemical incorporation of Mg into V_6O_{13} ; V_2O_5 ; WO_3 ; layered and cubic TiS_2 ; β -, γ -, and λ - MnO_2 ; and MoO_2 had all been demonstrated.³⁰⁶

Anodes for multivalent batteries are primarily the metals themselves. Advantages for the use of Mg metal over Li metal include its low cost, high theoretical volumetric capacity, and relatively smooth deposition morphology.²⁷ Mg batteries may provide safer, more environmentally friendly alternatives to Pb-acid and Ni-Cd batteries. They may also be useful in heavy load applications where Li is not practical.³⁰⁷ Advancement of Mg batteries has been hindered by the lack of suitable electrolytes that support Mg

electrodeposition and stripping and a dearth of intercalation cathode materials.³⁰⁷ A fundamental understanding of electrolytes that dissolve Mg^{2+} , are compatible with the Mg metal anode and the intercalation cathode, and facilitate Mg electrodeposition and stripping is an active area of research. In this chapter, however, we will focus on what is currently known for cathode materials.

4.10.6.2.1 Sulfides

The slow rate of Mg diffusion and conversion in oxides has led to a focus on softer lattices like sulfides and selenides.²⁷ The softer anions generate a weaker Coulombic attraction between Mg^{2+} and the host lattice than harder anions, resulting in increased ion mobility.³³

4.10.6.2.1.1 Mo_6S_8

Electrochemical Mg^{2+} intercalation was first demonstrated in 2000 with a Chevrel phase cathode material, Mo_6S_8 (R $\bar{3}$).³⁰⁷ Zn^{2+} , Cd^{2+} , Ni^{2+} , Mn^{2+} , Co^{2+} , and Fe^{2+} have all also been successfully electrochemically inserted into this material.³⁰⁸⁻³¹⁰ The Chevrel phase has a unique structure, shown in Fig. 39, where eight S anions form the corners of a cube whose faces are populated by six Mo cations, forming Mo_6 octahedra. The Mo_6S_8 clusters pack in quasi-simple-cubic packing, leaving 3D channels that support ion diffusion.³¹¹

The Chevrel phase can accommodate Mg^{2+} in two different sites, shown as Mg1 and Mg2 in Fig. 39a. Intercalation into the distinct lattice sites manifest as two distinct plateaus around 1.2 V and 1 V vs Mg RE in the discharge profile shown in Fig. 39b. In $\text{Mg}_2\text{Mo}_6\text{S}_8$, one Mg^{2+} per formula unit is located in the inner sites, and another in the outer sites.³¹² Aurbach et al. suggested that the 1.2 V vs Mg RE plateau represents magnesiation of the inner site, Mg1, and the second 1 V vs Mg RE plateau indicates magnesiation of the outer site, Mg2.³⁰⁷ Consequently, intercalation into Mo_6S_8 occurs in two steps:



and



The diffusion of Mg^{2+} in Chevrel phase occurs between tetrahedral sites, crossing through an intermediate three-coordinate site. The deformation and polarizability of the anionic framework affect the activation energy for Mg^{2+} diffusion, along with the polarizing power of the cation defined by the ratio of the cation charge to its ionic radius. Mg has about twice the polarizing power of Li, making the polarizability of the anionic framework a significant factor in Mg diffusion kinetics. This explains, and is corroborated by, the more facile diffusion of Mg^{2+} in Mo_6Se_8 than Mo_6S_8 , as the ionic radii of S^{2-} and Se^{2-} are 1.82 and 1.92 Å, respectively.³¹³

At moderate-to-high intercalation levels in the Chevrel phase, mobility of Mg^{2+} is comparable to that of Li^+ . In contrast, the lower Mg^{2+} mobility at low intercalation levels is due to trapping of Mg^{2+} in the Mo_6S_8 matrix and is likely due to the larger activation energy required for Mg^{2+} to be removed from the more stable inner sites, Mg1.³¹³ When Mg^{2+} are present in both the inner and outer sites, the repulsive force between them aids bulk diffusion.³¹² The facile diffusion of Mg^{2+} in the Chevrel phase contrasts dramatically with the sluggish Mg^{2+} diffusion typically seen in transition metal oxides and sulfides.³¹³

Sluggish Mg^{2+} diffusion is not only due to strong ionic interactions, but also to difficulties distributing the extra charge upon intercalation in the host material. The high density of redox active atoms in the clusters of the Chevrel phase allow the material to easily accommodate the divalent cation. A more recent XPS study has shed light on the charge-transfer mechanism of Mg^{2+} insertion into the Chevrel phase. The two Mg insertion sites (inner and outer) were identified by their different polarizations, and a two-

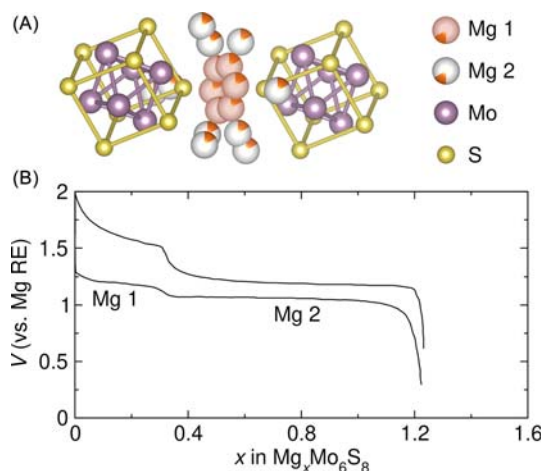


Fig. 39 (a) Structure of $\text{Mg}_2\text{Mo}_6\text{S}_8$ and (b) discharge and charge curves of Mo_6S_8 at 0.3 mA cm^{-2} with an Mg metal anode and $0.25 \text{ M Mg}(\text{AlCl}_2\text{BuEt})_2$ in tetrahydrofuran (THF) electrolyte. The two discharge plateaus and their corresponding intercalation sites are also shown. The electrochemistry is adapted from Aurbach et al. (2000).³⁰⁷

step Mg insertion process was confirmed. The first step involves the redistribution of charge toward axial S, while the Mo₆ cluster helps to stabilize electron deficiency during the second galvanostatic plateau.³¹⁴

While the Chevrel phase has excellent reversibility and a theoretical capacity of 122 mA h g⁻¹, it has a relatively low operating voltage of between 1 and 1.3 V vs Mg/Mg²⁺.^{307,314,315} Subsequent material investigations have sought to increase operating voltages while retaining the reversibility and high ionic mobility of the working ion.

4.10.6.2.1.2 TiS₂

The cubic and layered forms for TiS₂ were described and shown in Sections 4.10.3.1.1.1 and 4.10.3.1.1.2. Chemical intercalation of Mg²⁺ into both cubic and layered TiS₂ was demonstrated in the early 1990s by Bruce et al.^{306,316} However, while Li⁺ had been electrochemically intercalated into TiS₂ by the late 1970s,³¹⁷ electrochemical intercalation of Mg²⁺ in TiS₂ was not shown until 2004 in layered TiS₂ nanotubes.³¹⁸

The first paper on TiS₂ as a Mg cathode material reported a maximum capacity of 236 mA h g⁻¹ at a discharge rate of 10 mA g⁻¹ for a total of 0.49 Mg²⁺ intercalated per formula unit of TiS₂ at 20 °C. An inverse relationship between capacity and temperature was also observed, in addition to roughly 22% capacity fade over 80 cycles.³¹⁸ Mg²⁺ intercalation into cubic TiS₂ was reported by Amir et al. in 2007.³¹⁹ In a system with Mg(AlCl₂BuEt)₂/THF electrolyte, first discharge capacities of approximately 87 and 15 mA h g⁻¹ were reported for cubic and layered TiS₂, respectively. Capacity fading was also observed to such an extent that Amir et al. dismissed TiS₂ as a viable cathode for Mg entirely.³¹⁹ Interest in TiS₂ as an Mg cathode material was only renewed by a combination of theoretical and experimental studies in the mid-2010s, although these studies also indicated Mg²⁺ diffusion would be difficult and required elevated temperatures. A computational study from Emly et al. predicted substantial migration barriers for Mg²⁺, on the order of 1 eV higher than Li, and suggested that transition metals more amenable to changes in valence state such as Mo would be better chalcogenide cathode candidates. Such metals would be likely to rehybridize more easily, allowing for lower migration barriers.³²⁰ The same study predicted octahedral occupation in both forms of TiS₂ with diffusion through the surrounding tetrahedral sites, with the energy difference between tetrahedral and octahedral occupancy decreasing with increasing *c* lattice parameter.³²⁰

Sun et al. first demonstrated discharge capacities of over 100 mA h g⁻¹ in both layered and cubic TiS₂ with 2PhMgCl-AlCl₃ (all-phenyl complex, or APC)/THF at 60 °C.^{27,33} In layered TiS₂, Mg first preferentially intercalates into octahedral sites in an electrochemically irreversible step, followed by the reversible occupation of both octahedral and tetrahedral sites at sufficiently high Mg concentrations. This manifests in the galvanostatic cycling profiles as plateaus around 1.0 V and 0.5 V vs Mg/Mg²⁺. Using operando XRD, four phases were observed over the course of cycling. The second and third phases show larger *c* parameters than their respective prior phases, and appear at Mg_{0.05}TiS₂ and Mg_{0.17}TiS₂, respectively. The fourth phase has a significantly expanded *a* parameter compared to the third phase, and is present at the end of discharge (Mg_{0.56}TiS₂).²⁷ In contrast, cubic TiS₂ exhibits a sloping discharge curve indicative of a single-phase insertion mechanism. Similar to layered TiS₂, cubic TiS₂ (containing trace Cu, as discussed in Section 4.10.3.1.1.2) also promotes multi-step intercalation with the filling of octahedral sites first, followed by redistribution across both octahedral and tetrahedral sites past 0.6 Mg per Cu_{0.1}Ti₂S₄ unit.³³ This finding of multiple-site occupancy was corroborated by later first-principle studies.³²¹

Although our understanding of Mg-TiS₂ electrochemistry has improved greatly in recent years, many improvements are necessary before it can become a viable Mg cathode material. At the present, more work is required to improve the low operating voltage (1 V vs Mg/Mg²⁺), combat pronounced capacity fade, and reduce the high operating temperatures.^{27,318}

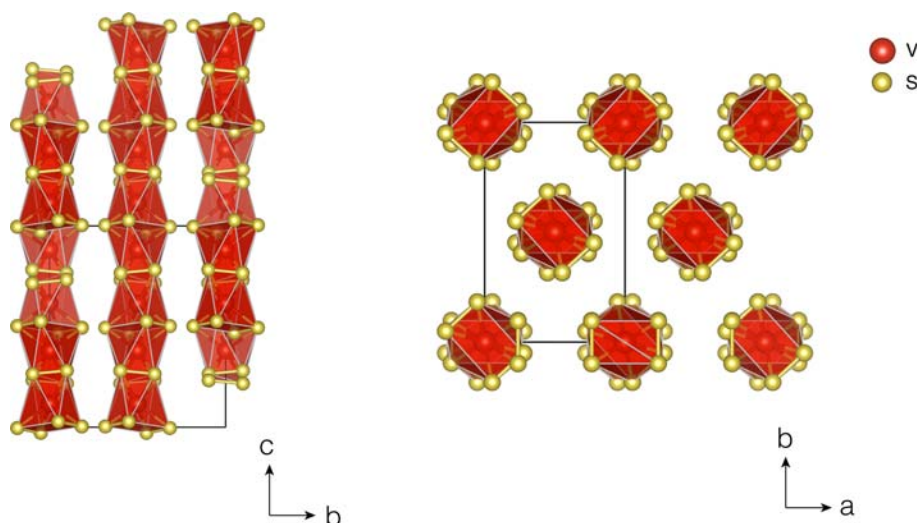


Fig. 40 Structure of VS₄ (I2/c) in the bc plane (left) and in the ab plane (right).

4.10.6.2.1.3 VS₄

VS₄ is a linear chain compound in which V⁴⁺ is octahedrally coordinated to S dimers (S₂²⁻), and crystallizes in the monoclinic I2/c space group (Fig. 40). The chains are spaced 5.38 Å apart and weakly bonded together by van der Waals forces, potentially offering facile diffusion paths between chains. Combined with a relatively small bandgap close to 1.0 eV and consequently, a high electronic conductivity, VS₄ is an attractive multivalent cathode candidate.³²²

VS₄ was first explored as an Mg cathode material in 2018. Wang et al. used highly-branching nanostructured VS₄ in composite cathodes to achieve capacities of 251 mA h g⁻¹ at 100 mA g⁻¹ in coin cells assembled with 0.4 M APC electrolyte in THF.³²² Cyclic voltammograms taken between 0.2 V and 2.2 V vs Mg/Mg²⁺ showed a cathodic wave around 0.35 V. Subsequent cycles show coupled reduction and oxidation waves at 1.18 V and 1.25 V vs Mg/Mg²⁺, respectively. The assembled cells displayed remarkable cyclability, with a maximum discharge capacity of 177 mA h g⁻¹ achieved after 133 cycles and 150 mA h g⁻¹ after 180 cycles at 100 mA g⁻¹. The authors credit the weak VS₄/Mg²⁺ interactions, linear open channels of VS₄, and large Mg²⁺ storage capacity for the observed cycling stability. Through Raman and XPS studies, they determined that the VS₄ structure remained relatively undisturbed after discharge up to Mg_{0.875}VS₄ and that both cation and anion redox occurred throughout the cycling process. They concluded that during discharge, some S₂²⁻ is reduced to S²⁻ and, interestingly, some V⁴⁺ is oxidized to V⁵⁺. No evidence for MgS or elemental V is observed.³²²

A more recent study improved the capacity of the Mg-VS₄ system with the Mg tetrakis(hexafluoroisopropoxy)borate (Mg[B(hfp)₄]₂) electrolyte and demonstrated reversible electrochemistry of VS₄ in a Ca cell with a Ca[B(hfp)₄]₂ electrolyte.³²³ Removal of Mg²⁺ was confirmed with XPS and both *ex-situ* and *operando* Raman.³²³ The bulk structural changes of a 0.25 M Mg(AlCl₂EtBu)₂/THF based Mg-VS₄ system were investigated in 2020.³²⁴ Using XANES, pair distribution function (PDF), and ⁵⁴V NMR studies, Dey et al. identified the intermediate phase Mg₃V₂S₈. In contrast with the previous two studies, MgS and V metal were also characterized in the reduction products.³²⁴ The exact reaction mechanism of this material is still under debate, and may depend heavily on the electrolyte. For example, desolvation of Mg²⁺ in chloride-containing electrolytes is difficult, resulting in incorporation of species like MgCl⁺ which can alter the reaction pathway.³²⁵

4.10.6.2.2 Oxides

Although oxides have been relatively successful Li-ion cathodes and are desirable for their higher energy densities, advancements in multivalent oxide cathodes have been hindered by decreased ionic mobility.^{313,315} While reducing particle size may help improve oxide diffusion kinetics, the resulting increase in electrode surface area also increases capacitive contributions.³¹⁵ Some reports have suggested that water incorporated into the crystal can facilitate multivalent ion diffusion, but it is unclear if the resulting capacity increases are due to increases in Mg intercalation or proton or hydronium intercalation. In general, water in Mg batteries is undesirable due to its passivating effect on Mg metal anodes and low anodic and cathodic stability.³¹⁵ Another barrier in the development of Mg oxide cathode materials is the low free energy of formation of MgO, which may form as an undesired reduction product. Mg is extremely oxophilic. At one electron reduction stages, MgO formation is generally not expected and intercalation is favored over conversion. However, the kinetic challenges imposed by low Mg²⁺ ion mobility cause local regions of high Mg²⁺ concentration, leading to a higher number of electrons transferred locally and increasing the chance of conversion to MgO.³¹⁵

Despite these challenges, oxides remain appealing cathode candidates for several reasons: the wealth of prior knowledge about structure and intercalation mechanisms in LIBs, high intercalation voltage compared to sulfides, and large capacities.^{324,326}

4.10.6.2.2.1 V₂O₅

The structure of V₂O₅ and its various polymorphs were detailed in Section 4.10.3.1.2.1.1. As previously discussed, V₂O₅ is a well-known intercalation material from LIB studies with a theoretically high capacity of 440 mA h g⁻¹. However, while roughly 3 equiv. of Li⁺ can be inserted into V₂O₅, the insertion limit for Mg²⁺ is much lower at around 0.5 or 0.6 equivalents with high-surface area morphologies.^{327,328} In Li systems, V₂O₅ experiences a series of transitions between polymorphs as Li⁺ is incorporated, but in Mg systems, primarily the α, δ, and ε phases are relevant. The α and δ phases are very similar with alternating layers along the *b* axis shifted by *a*/2 in the δ phase compared to α-V₂O₅. In both phases, the Mg sites are located between layers close to the middle of the VO₅ pyramids, though the Mg sites are 8-coordinate in α-V₂O₅ and 6-coordinate in δ-V₂O₅.^{327,328} While the fully-magnesiated phase MgV₂O₅ is chemically synthesized as the δ phase, theory has predicted and experiments have shown that electrochemically-cycled V₂O₅ produces the partially-magnesiated, Mg-ordered ε phase. Electrochemical products can be different from chemically synthesized products due to the kinetic effects allowing for the preparation of metastable phases. If the magnesiation reaction of V₂O₅ were to proceed via a two-phase nucleation and growth of δ-V₂O₅ mechanism, there should be no barrier to magnesiation up to one equivalent of Mg. However, the reaction instead appears to proceed through the development of the metastable ε-V₂O₅ phase, likely because the former pathway requires kinetically unfavorable structural rearrangement and the generation of high interfacial energies. Gautam et al. have suggested that cycling δ-V₂O₅, which has higher Mg-mobility than α-V₂O₅, may allow for the access of higher intercalation limits and capacities (the calculated migration barriers are 600–760 meV and 975–1120 meV, respectively).³²⁸

As mentioned, the use of water-rich electrolytes has been suggested to improve the performance of V₂O₅ as a Mg cathode; however, such an electrolyte presents significant challenges for use with Mg metal anodes. Significantly higher capacities have been achieved in wet compared to dry electrolyte systems. In an Mg|Mg(TFSI)₂/G2|V₂O₅ cell, Sa et al. observed more than a four-fold increase in capacity between a system with 2600 ppm H₂O and one with 15 ppm H₂O (~260 mA h g⁻¹ vs ~60 mA h g⁻¹,

respectively).³²⁹ However, subsequent ¹H NMR studies confirmed the involvement of proton intercalation. The change in V valence state in dry electrolyte as determined through Extended X-ray Absorption Fine Structure (EXAFS) corresponds to the intercalation of 0.2 equivalents of Mg²⁺ per unit V₂O₅.³²⁹ These results provide more evidence of limited Mg intercalation, and emphasize the importance of differentiating proton and Mg contributions to capacities in Mg-V₂O₅ systems.

4.10.6.2.2.2 MoO₃

The structure of MoO₃ was detailed in Section 4.10.3.1.2.1.1. In 1995, Spahr et al. were the first to demonstrate Mg²⁺ intercalation MoO₃. In contrast with monovalent Li⁺ and Na⁺, Mg²⁺ failed to demonstrate electrochemical insertion in dry polycarbonate-based electrolytes. However, using a molten salt mixture of 41 wt% 1-ethyl-3-methylimidazolium chloride (EMIC), 56 wt% AlCl₃, and 3 wt% MgCl₂, Mg²⁺ insertion was suggested by both cyclic voltammetry and galvanostatic cycling. Initial discharge achieved a capacity of 150 mA h g⁻¹ corresponding to 0.76 electrons or 0.38 Mg²⁺ per f.u. MoO₃.³³⁰

Mg intercalation sites are located within and between the layers along the c axis.³¹¹ Magnesiumation occurs in two steps at 1.80 V and 1.74 V, while demagnesiumation is a single oxidation event at 2.15 V.³³¹ During slow galvanostatic titration (0.3 μA cm⁻²), thin film MoO₃ can achieve reversible capacities of 220 mA h g⁻¹ corresponding to 0.59 equivalents of Mg per f.u. MoO₃, and 95% Coulombic reversibility.^{311,331} However, electrochemical conditioning in the form of initial intercalation with a small galvanostatic current is necessary for reversible cycling, and the overpotential for demagnesiumation of MoO₃ increases with decreasing Mg content. Both effects may result from changes in the electronic conductivity as Mg²⁺ content changes. Increasing Mg content enhances the electronic conductivity and promotes favorable kinetics upon insertion while decreasing Mg content reduces electronic conductivity and hinders de-insertion. However, the overpotential increases during demagnesiumation may also indicate voltage-induced structural damage.³³¹ The conditional reversibility and sluggish kinetics of Mg²⁺ intercalation into MoO₃ require further attention before it can be a feasible cathode material in Mg batteries.

4.10.6.2.2.3 MnO₂

MnO₂ has a wide variety of polymorphs that have been studied as Mg cathode materials to varying degrees. α-MnO₂, also known as hollandite MnO₂, as shown in Fig. 41 crystallizes in the I4/m space group and has a 2 × 2 tunnel structure with both corner- and edge-sharing MnO₆ octahedra. λ-MnO₂ takes on a spinel structure (Fd $\bar{3}$ m) with edge-sharing MnO₆ octahedra.^{261,315} R-MnO₂, or ramsdellite MnO₂ (Pbnm), has both corner- and edge-sharing MnO₆ octahedra in a 2 × 1 tunnel structure, and δ-MnO₂, or birnessite MnO₂ (C2/m) shown in Fig. 42 consists of stacked MnO₂ planes with or without interlayer water.^{315,332,333}

α-MnO₂ when cycled in a 0.2 M magnesium bis(hexamethyldisilazide), or Mg(HMDS)₂, in THF electrolyte has promising first charge and discharge capacities at 280 and 240 mA h g⁻¹, respectively.²⁶¹ However, similar to the case for LIBs, Mg batteries with MnO₂ cathodes experience severe capacity fade during subsequent cycling, initially attributed to structural changes resulting from Jahn-Teller distortions as the concentration of d⁴ Mn³⁺ ions increase. EXAFS data suggest that the MnO₆ octahedra corner links are broken during Mg²⁺ insertion, which may cause the ion diffusion pathways to collapse.²⁶¹ Later studies have suggested a conversion mechanism rather than an intercalation mechanism for several forms of MnO₂. The conversion pathway is likely favored due to the high stability of the MgO product.³³⁴ Evidence for the conversion pathway is the strong correlation between achievable capacity and available surface area. Cathodes with surface areas above 70 m² g⁻¹ had initial capacities of 250 mA h g⁻¹, regardless of which MnO₂ polymorph was used. If an intercalation mechanism were in operation, a capacity dependence on tunnel size would be expected, but none was observed.³³⁵ Several possible conversion reactions occur, including conversion to Mn₂O₃, MgO, and (MgMn)O.

In δ-MnO₂, structural water also participates in the conversion reaction. While pristine, as-synthesized δ-Mg_{0.15}MnO₂ · 0.9 H₂O in 0.25 M Mg(TFSI)₂ in diglyme shows an initial capacity of 80 mA h g⁻¹, the capacity increases to 135 mA h g⁻¹ after conditioning for 20 cycles.

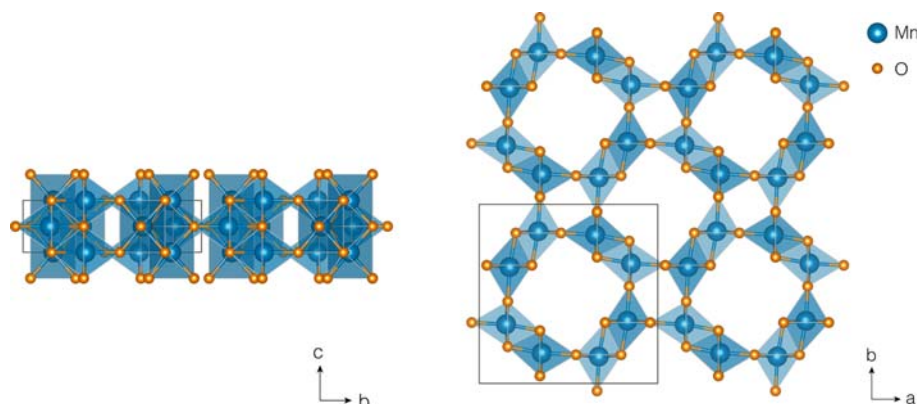


Fig. 41 The structure of α-MnO₂ (I4/m) in the bc plane (left) and in the ab plane (right).

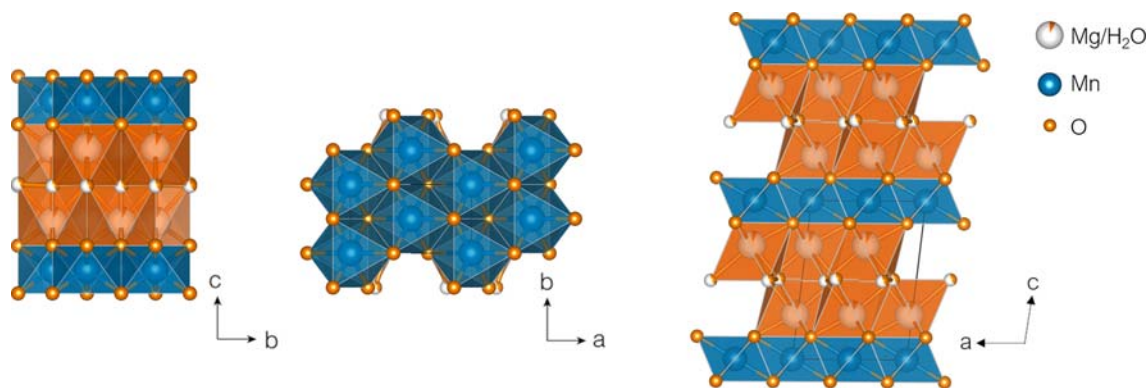
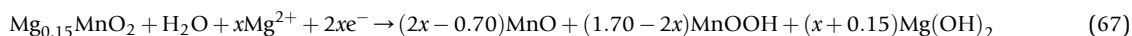


Fig. 42 Structure of birnessite-MnO₂ (C2/m) in the bc plane (left) and in the ab plane (right).

Electrolyte water content increases during conditioning and the XRD reflection corresponding to structural water at (001) disappears, confirming the release of structural water into the electrolyte where it may participate in the following reaction³³⁶:



Notably, although conversion reactions appear to dominate in both dry and wet organic electrolytes, different mechanisms have been observed in aqueous electrolytes. When Mg_{0.15}MnO₂ · 0.9 H₂O is cycled in aqueous 0.5 M Mg(ClO₄)₂, an initial capacity of 150 mAh g⁻¹ is obtained. Subsequent capacity fade is attributed to dissolution of the active material as determined by SEM images of precipitated Mn-containing particles. A contraction of the interlayer spacing from 7 Å to 4.86 Å is observed via XRD, corresponding to a transformation to the octahedral plane spacing in spinel MgMn₂O₄.³³⁶ Annular bright-field (ABF) Scanning transmission electron microscopy (STEM) images also showed direct evidence of Mg²⁺ intercalation in an aqueous electrolyte with a spinel MnO₂ cathode.³³⁷

The various polymorphs of MnO₂ have also received special interest as cathodes for Zn-ion batteries. Zn metal anodes are compatible with aqueous electrolytes because although the standard reduction potential is negative of NHE, the kinetics for H₂O reduction on Zn metal are very slow. Zn²⁺ intercalation in MnO₂ yields a high theoretical capacity of 616 mAh g⁻¹ assuming a two electron reduction of Mn⁴⁺.³³⁸



However, while several Zn/MnO₂ systems with capacities on the order of 200 mAh g⁻¹ have been studied, their reaction mechanisms remain under debate with the possibilities of H⁺, Zn²⁺, or both H⁺ and Zn²⁺ insertion contributing to the observed capacities. The mechanism may also differ between the varying crystal structures.³³⁸

References

1. Goodenough, J. B. Evolution of Strategies for Modern Rechargeable Batteries. *Acc. Chem. Res.* **2013**, *46*, 1053–1061.
2. Boettcher, S. W.; Oener, S. Z.; Loneragan, M. C.; Surendranath, Y.; Ardo, S.; Brozek, C.; Kempler, P. A. Potentially Confusing: Potentials in Electrochemistry. *ACS Energy Lett.* **2021**, *6* (1), 261–266. <https://doi.org/10.1021/acseenergylett.0c02443>.
3. Inzelt, G. Crossing the Bridge Between Thermodynamics and Electrochemistry. From the Potential of the Cell Reaction to the Electrode Potential. *ChemTexts* **2014**, *1*, 2.
4. Van der Ven, A.; Deng, Z.; Banerjee, S.; Ong, S. P. Rechargeable Alkali-Ion Battery Materials: Theory and Computation. *Chem. Rev.* **2020**. <https://doi.org/10.1021/acs.chemrev.9b00601>.
5. Usiskin, R.; Maier, J. Interfacial Effects in Lithium and Sodium Batteries. *Advanced Energy Materials* **2021**, *11* (2), 2001455. <https://doi.org/10.1002/aenm.202001455>.
6. Volta, A.; Banks, J. I. On the Electricity Excited by the Mere Contact of Conducting Substances of Different Kinds. *Null* **1800**, *7*, 289–311.
7. Brockman, C. J. Primary Cells—A Brief Historical Sketch. *J. Chem. Educ.* **1927**, *4*, 770.
8. Nitta, N.; Wu, F.; Lee, J. T.; Yushin, G. Li-Ion Battery Materials: Present and Future. *Mater. Today* **2015**, *18*, 252–264.
9. Schroeder, D. V. *Thermal Physics*, Addison Wesley Longman: United States, 2000.
10. Van der Ven, A.; Bhattacharya, J.; Belak, A. A. Understanding Li Diffusion in Li-Intercalation Compounds. *Acc. Chem. Res.* **2013**, *46*, 1216–1225.
11. Cairns, E. J.; Shimotake, H. High-Temperature Batteries. *Science* **1969**, *164*, 1347–1355.
12. Gupta, S. D. The Search for Portable Electricity. In *Electrochemistry, Past and Present*, ACS Symposium Series; American Chemical Society, 1989, vol. 390; pp 543–553. Chapter 37.
13. Shukla, A. K.; Venugopalan, S.; Hariprakash, B. Nickel-Based Rechargeable Batteries. *J. Power Sources* **2001**, *100*, 125–148.
14. Cook, T. R.; Dogutan, D. K.; Reece, S. Y.; Surendranath, Y.; Teets, T. S.; Nocera, D. G. Solar Energy Supply and Storage for the Legacy and Nonlegacy Worlds. *Chem. Rev.* **2010**, *110*, 6474–6502.
15. Linden, D.; Reddy, T. B. *Handbook of Batteries*, 3rd ed.; McGraw-Hill: New York, NY, 2002.
16. Whittingham, M. S. Electrical Energy Storage and Intercalation Chemistry. *Science* **1976**, *192*, 1126–1127.
17. Stanley Whittingham, M. Intercalation Chemistry: An Introduction. In *Intercalation Chemistry*, Elsevier, 1982; pp 1–18.
18. Jacobson, A. J.; Nazar, L. F. Intercalation Chemistry. In *Encyclopedia of Inorganic and Bioinorganic Chemistry*; Scott, R. A., Ed.; John Wiley & Sons, Ltd: Chichester, UK, 2011; p eibc0093.
19. Manthiram, A. A Reflection on Lithium-Ion Battery Cathode Chemistry. *Nat. Commun.* **2020**, *11*, 1550.

20. Schmuck, R.; Wagner, R.; Hörpel, G.; Placke, T.; Winter, M. Performance and Cost of Materials for Lithium-Based Rechargeable Automotive Batteries. *Nat. Energy* **2018**, *3*, 267–278.
21. Whittingham, M. S. Lithium Batteries and Cathode Materials. *Chem. Rev.* **2004**, *104*, 4271–4302.
22. Chianelli, R.; Scanlon, J.; Thompson, A. Structure Refinement of Stoichiometric TiS₂. *Materials Research Bulletin* **1975**, *10*, 1379–1382.
23. Thompson, A. H. Electron-Electron Scattering in Ti S₂. *Phys. Rev. Lett.* **1975**, *35*, 1786–1789.
24. McKelvy, M.; Glaunsinger, W. Synthesis and Characterization of Nearly Stoichiometric Titanium Disulfide. *Journal of Solid State Chemistry* **1987**, *66*, 181–188.
25. Thompson, A.; Gamble, F.; Symon, C. The Verification of the Existence of TiS₂. *Materials Research Bulletin* **1975**, *10*, 915–919.
26. Wang, L.; Zou, J.; Chen, S.; Zhou, G.; Bai, J.; Gao, P.; Wang, Y.; Yu, X.; Li, J.; Hu, Y.-S.; Li, H. TiS₂ as a High Performance Potassium Ion Battery Cathode in Ether-Based Electrolyte. *Energy Storage Materials* **2018**, *12*, 216–222.
27. Sun, X.; Bonnick, P.; Nazar, L. F. Layered TiS₂ Positive Electrode for Mg Batteries. *ACS Energy Lett.* **2016**, *1*, 297–301.
28. Liu, Y.; Wang, H.; Cheng, L.; Han, N.; Zhao, F.; Li, P.; Jin, C.; Li, Y. TiS₂ Nanoplates: A High-Rate and Stable Electrode Material for Sodium Ion Batteries. *Nano Energy* **2016**, *20*, 168–175.
29. Eisenberg, M. Performance of Ambient Temperature Sulfospinel and TiS₂—Lithium Secondary Cells. *Electrochim. Acta* **1981**, *26*, 955–956.
30. James, A.; Goodenough, J. Lithium Ion Diffusion in the Defect Thiospinel Li_xCu_{0.07}Ti₂S₄ (0.1 < x < 1.85). *Solid State Ionics* **1988**, *27*, 37–43.
31. James, A.; Goodenough, J.; Clayden, N. Structural and NMR Study of the Lithiated Defect Thiospinels Li_xCu_{0.07}[Ti₂S₄] (0 < x < 2). *J. Solid State Chem.* **1988**, *77*, 356–365.
32. Canepa, P.; Bo, S.-H.; Sai Gautam, G.; Key, B.; Richards, W. D.; Shi, T.; Tian, Y.; Wang, Y.; Li, J.; Ceder, G. High Magnesium Mobility in Ternary Spinel Chalcogenides. *Nat. Commun.* **2017**, *8*, 1759.
33. Sun, X.; Bonnick, P.; Duffort, V.; Liu, M.; Rong, Z.; Persson, K. A.; Ceder, G.; Nazar, L. F. A High Capacity Thiospinel Cathode for Mg Batteries. *Energy Environ. Sci.* **2016**, *9*, 2273–2277.
34. Gabano, J. P.; Jumel, Y.; Gomis, J. P. Abstr. 144th Meet. *Electrochem. Soc. Boston* **1973**, 134.
35. Whittingham, M. S.; Dines, M. B. N-Butyllithium—An Effective, General Cathode Screening Agent. *J. Electrochem. Soc.* **1977**, *124*, 1387–1388.
36. Whittingham, M. S. The Role of Ternary Phases in Cathode Reactions. *J. Electrochem. Soc.* **1976**, *123*, 315–320.
37. Smirnov, M. B.; Roginskii, E. M.; Smirnov, K. S.; Baddour-Hadjean, R.; Pereira-Ramos, J.-P. Unraveling the Structure–Raman Spectra Relationships in V₂O₅ Polymorphs via a Comprehensive Experimental and DFT Study. *Inorg. Chem.* **2018**, *57*, 9190–9204.
38. Mansour, A. N.; Smith, P. H.; Baker, W. M.; Balasubramanian, M.; McGreen, J. In Situ XAS Investigation of the Oxidation State and Local Structure of Vanadium in Discharged and Charged V₂O₅ Aerogel Cathodes. *Electrochim. Acta* **2002**, *11*.
39. Zhu, J.; Shen, H.; Shi, X.; Yang, F.; Hu, X.; Zhou, W.; Yang, H.; Gu, M. Revealing the Chemical and Structural Evolution of V₂O₅ Nanoribbons in Lithium-Ion Batteries Using in Situ Transmission Electron Microscopy. *Anal. Chem.* **2019**, *91*, 11055–11062.
40. Mizushima, K.; Jones, P.; Wiseman, P.; Goodenough, J. Li_xCoO₂. *Mater. Res. Bull.* **1980**, *15*, 783–789.
41. Cho, J.; Kim, Y. J.; Park, B. Novel LiCoO₂ Cathode Material With Al₂O₃ Coating for a Li Ion Cell. *Chem. Mater.* **2000**, *12*, 3788–3791.
42. Julien, C.; Mauger, A.; Vjih, A.; Zaghbi, K. *Lithium Batteries*, Springer International Publishing: Cham, 2016.
43. Lyu, Y.; Wu, X.; Wang, K.; Feng, Z.; Cheng, T.; Liu, Y.; Wang, M.; Chen, R.; Xu, L.; Zhou, J.; Lu, Y.; Guo, B. An Overview on the Advances of LiCoO₂ Cathodes for Lithium-Ion Batteries. *Adv. Energy Mater.* **2021**, *11*, 2000982.
44. Ménétrier, M.; Saadouni, I.; Levasseur, S.; Delmas, C. The Insulator-Metal Transition Upon Lithium Deintercalation From LiCoO₂: Electronic Properties and ⁷Li NMR Study. *J. Mater. Chem.* **1999**, *9*, 1135–1140.
45. Venkatraman, S.; Shin, Y.; Manthiram, A. Phase Relationships and Structural and Chemical Stabilities of Charged Li[Sub 1-x]CoO[Sub 2-δ] and Li[Sub 1-x]Ni[Sub 0.85]Co[Sub 0.15]O[Sub 2-δ] Cathodes. *Electrochem. Solid-State Lett.* **2003**, *6*, A9.
46. Amatucci, G. G.; Tarascon, J. M.; Klein, L. C. CoO₂, The End Member of the Li_xCoO₂ Solid Solution. *J. Electrochem. Soc.* **1996**, *143*, 1114–1123.
47. Chen, Z.; Dahn, J. Methods to Obtain Excellent Capacity Retention in LiCoO₂ Cycled to 4.5 V. *Electrochim. Acta* **2004**, *49*, 1079–1090.
48. Kikkawa, S.; Miyazaki, S.; Koizumi, M. Electrochemical Aspects of the Deintercalation of Layered AMO₂ Compounds. *J. Power Source* **1985**, *14*, 231–234.
49. Whittingham, M.; Gamble, F. R. The Lithium Intercalates of the Transition Metal Dichalcogenides. *Mater. Res. Bull.* **1975**, *10*, 363–371.
50. Goodenough, J. Metallic Oxides. *Progr. Solid State Chem.* **1971**, *5*, 145–399.
51. Tukamoto, H.; West, A. R. Electronic Conductivity of LiCoO₂ and Its Enhancement by Magnesium Doping. *J. Electrochem. Soc.* **1997**, *144*, 3164–3168.
52. Doughty, D.; Roth, E. P. A General Discussion of Li Ion Battery Safety. *Electrochem. Soc. Interface* **2012**, *8*.
53. Chebiam, R. V.; Prado, F.; Manthiram, A. Structural Instability of Delithiated Li[Sub 1-x]Ni[Sub 1-y]Co[Sub y]O[Sub 2] Cathodes. *J. Electrochem. Soc.* **2001**, *148*, A49.
54. Olivetti, E. A.; Ceder, G.; Gaustad, G. G.; Fu, X. Lithium-Ion Battery Supply Chain Considerations: Analysis of Potential Bottlenecks in Critical Metals. *Joule* **2017**, *1*, 229–243.
55. Sovacool, B. K. The Precarious Political Economy of Cobalt: Balancing Prosperity, Poverty, and Brutality in Artisanal and Industrial Mining in the Democratic Republic of the Congo. *Extract. Indus. Soc.* **2019**, *6*, 915–939.
56. Fuchs, B.; Kemmler-Sack, S. Synthesis of LiMnO₂ and LiFeO₂ in Molten Li Halides. *Solid State Ionics* **1994**, *68*, 279–285.
57. Armstrong, A. R.; Tee, D. W.; La Mantia, F.; Novák, P.; Bruce, P. G. Synthesis of Tetrahedral LiFeO₂ and Its Behavior as a Cathode in Rechargeable Lithium Batteries. *J. Am. Chem. Soc.* **2008**, *130*, 3554–3559.
58. Komaba, S.; Takei, C.; Nakayama, T.; Ogata, A.; Yabuuchi, N. Electrochemical Intercalation Activity of Layered NaCrO₂ vs. LiCrO₂. *Electrochem. Commun.* **2010**, *12*, 355–358.
59. de Picciotto, L.; Thackeray, M.; David, W.; Bruce, P.; Goodenough, J. Structural Characterization of Delithiated LiVO₂. *Mater. Res. Bull.* **1984**, *19*, 1497–1506.
60. Ma, X.; Hautier, G.; Jain, A.; Doe, R.; Ceder, G. Improved Capacity Retention for LiVO₂ by Cr Substitution. *J. Electrochem. Soc.* **2013**, *160*, A279–A284.
61. Baur, C.; Chable, J.; Klein, F.; Chakravadhanula, V. S. K.; Fichtner, M. Reversible Delithiation of Disordered Rock Salt LiVO₂. *ChemElectroChem* **2018**, *5*, 1484–1490.
62. Chable, J.; Baur, C.; Chang, J. H.; Wenzel, S.; Garcia-Lastra, J. M.; Vegge, T. From Trigonal to Cubic LiVO₂: A High-Energy Phase Transition toward Disordered Rock Salt Materials. *J. Phys. Chem. C* **2020**, *124*, 2229–2237.
63. Hirano, A. Relationship between Non-Stoichiometry and Physical Properties in LiNiO₂. *Solid State Ionics* **1995**, *78*, 123–131.
64. Tu, J.; Zhao, X.; Cao, G.; Zhuang, D.; Zhu, T.; Tu, J. Enhanced Cycling Stability of LiMn₂O₄ by Surface Modification With Melting Impregnation Method. *Electrochim. Acta* **2006**, *51*, 6456–6462.
65. Zhu, X.; Meng, F.; Zhang, Q.; Xue, L.; Zhu, H.; Lan, S.; Liu, Q.; Zhao, J.; Zhuang, Y.; Guo, Q.; Liu, B.; Gu, L.; Lu, X.; Ren, Y.; Xia, H. LiMnO₂ Cathode Stabilized by Interfacial Orbital Ordering for Sustainable Lithium-Ion Batteries. *Nat. Sustain.* **2021**, *4*, 392–401.
66. Rossen, E.; Jones, C. D. W.; Dahn, J. R. Structure and Electrochemistry of Li_xMn_{1-y}O₂. *Solid State Ionics* **1992**, *8*.
67. Kang, K.; Meng, Y. S.; Bréger, J.; Grey, C. P.; Ceder, G. Electrodes With High Power and High Capacity for Rechargeable Lithium Batteries. *Science* **2006**, *311*, 977.
68. Yabuuchi, N.; Ohzuku, T. Novel Lithium Insertion Material of LiCo_{1/3}Ni_{1/3}Mn_{1/3}O₂ for Advanced Lithium-Ion Batteries. *Journal of Power Sources* **2003**, *119–121*, 171–174.
69. Spitsen, P. *Energy Storage Grand Challenge Roadmap*, 2020; p 157.
70. Battery University. *BU-1003: Electric Vehicle (EV)*, Battery University, 2019. https://batteryuniversity.com/learn/article/electric_vehicle_ev.
71. Li, W.; Erickson, E. M.; Manthiram, A. High-Nickel Layered Oxide Cathodes for Lithium-Based Automotive Batteries. *Nat. Energy* **2020**, *5*, 26–34.
72. Sun, H.; Zhao, K. Electronic Structure and Comparative Properties of LiNi_xMn_yCo_zO₂ Cathode Materials. *J. Phys. Chem. C* **2017**, *121*, 6002–6010.
73. Wang, T.; Ren, K.; Xiao, W.; Dong, W.; Qiao, H.; Duan, A.; Pan, H.; Yang, Y.; Wang, H. Tuning the Li/Ni Disorder of the NMC811 Cathode by Thermally Driven Competition Between Lattice Ordering and Structure Decomposition. *J. Phys. Chem. C* **2020**, *124*, 5600–5607.

74. Sun, Y.-K.; Myung, S.-T.; Park, B.-C.; Prakash, J.; Belharouak, I.; Amine, K. High-Energy Cathode Material for Long-Life and Safe Lithium Batteries. *Nat. Mater* **2009**, *8*, 320–324.
75. Kim, J.; Lee, H.; Cha, H.; Yoon, M.; Park, M.; Cho, J. Prospect and Reality of Ni-Rich Cathode for Commercialization. *Adv. Energy Mater.* **2018**, *8*, 1702028.
76. Chen, C.; Liu, J.; Stoll, M.; Henriksen, G.; Vissers, D.; Amine, K. Aluminum-Doped Lithium Nickel Cobalt Oxide Electrodes for High-Power Lithium-Ion Batteries. *J. Power Sources* **2004**, *128*, 278–285.
77. Bloom, I.; Jones, S. A.; Battaglia, V. S.; Henriksen, G. L.; Christophersen, J. P.; Wright, R. B.; Ho, C. D.; Belt, J. R.; Motloch, C. G. Effect of Cathode Composition on Capacity Fade, Impedance Rise and Power Fade in High-Power, Lithium-Ion Cells. *J. Power Sources* **2003**, *124*, 538–550.
78. Sun, Y.-K. High-Capacity Layered Cathodes for Next-Generation Electric Vehicles. *ACS Energy Lett.* **2019**, *4*, 1042–1044.
79. Thackeray, M.; David, W.; Goodenough, J. Structural Characterization of the Lithiated Iron Oxides $\text{Li}_x\text{Fe}_3\text{O}_4$ and $\text{Li}_x\text{Fe}_2\text{O}_3$. *Mater. Res. Bull.* **1982**, *17*, 785–793.
80. Pistoia, G.; Pasquali, M.; De Picciotto, L.; Thackeray, M. Behaviour of the Spinel LiV_2O_4 as a Positive Electrode for Secondary Li Cells. *Solid State Ionics* **1988**, *28–30*, 879–885.
81. Thackeray, M. M. Spinel Electrodes for Lithium Batteries. *J. Am. Ceram. Soc.* **2004**, *82*, 3347–3354.
82. Thackeray, M. M.; Shao-Horn, Y.; Kahaian, A. J.; Kepler, K. D.; Skinner, E.; Vaughey, J. T.; Hackney, S. A. Structural Fatigue in Spinel Electrodes in High Voltage (4 V) $\text{Li}_x\text{Mn}_2\text{O}_4$. *Cells* **1998**, *4*.
83. Zhong, Q.; Bonakdarpour, A.; Zhang, M.; Gao, Y.; Dahn, J. R. Synthesis and Electrochemistry of $\text{LiNi}_x\text{Mn}_{2-x}\text{O}_4$. *J. Electrochem. Soc.* **1997**, *144*, 205–213.
84. Manthiram, A.; Chemelewski, K.; Lee, E.-S. A Perspective on the High-Voltage $\text{LiMn}_{1.5}\text{Ni}_{0.5}\text{O}_4$ Spinel Cathode for Lithium-Ion Batteries. *Energy Environ. Sci.* **2014**, *7*, 1339.
85. Pan, C.; Zhang, R.; Nuzzo, R. G.; Gewirth, A. A. $\text{ZnNi}_x\text{Mn}_x\text{Co}_{2-2x}\text{O}_4$ Spinel as a High-Voltage and High-Capacity Cathode Material for Nonaqueous Zn-Ion Batteries. *Adv. Energy Mater.* **2018**, *8*, 1800589.
86. Kwon, B. J.; et al. High Voltage Mg-Ion Battery Cathode via a Solid Solution Cr-Mn Spinel Oxide. *Chem. Mater.* **2020**, *32*, 6577–6587.
87. Padhi, A. K. Phospho-Olivines as Positive-Electrode Materials for Rechargeable Lithium Batteries. *J. Electrochem. Soc.* **1997**, *144*, 1188.
88. Mauger, A.; Julien, C. Olivine Positive Electrodes for Li-Ion Batteries: Status and Perspectives. *Batteries* **2018**, *4*, 39.
89. Takahashi, M. Reaction Behavior of LiFePO_4 as a Cathode Material for Rechargeable Lithium Batteries. *Solid State Ion* **2002**, *148*, 283–289.
90. Chung, S.-Y.; Bloking, J. T.; Chiang, Y.-M. Electronically Conductive Phospho-Olivines as Lithium Storage Electrodes. *Nature Mater* **2002**, *1*, 123–128.
91. Yamada, A.; Chung, S. C.; Hinokuma, K. Optimized LiFePO_4 for Lithium Battery Cathodes. *J. Electrochem. Soc.* **2001**, *148*, A224.
92. Padhi, A. K.; Nanjundaswamy, K. S.; Masquelier, C.; Okada, S.; Goodenough, J. B. Effect of Structure on the Fe_3/Fe_2 Redox Couple in Iron Phosphates. *J. Electrochem. Soc.* **1997**, *144*, 6.
93. García-Moreno, O.; Alvarez-Vega, M.; García-Jaca, J.; Gallardo-Amores, J. M.; San-juán, M. L.; Amador, U. Influence of the Structure on the Electrochemical Performance of Lithium Transition Metal Phosphates as Cathodic Materials in Rechargeable Lithium Batteries: A New High-Pressure Form of LiMPO_4 ($M = \text{Fe}$ and Ni). *Chem. Mater.* **2001**, *13*, 1570–1576.
94. Yamada, A.; Koizumi, H.; Nishimura, S.-I.; Sonoyama, N.; Kanno, R.; Yonemura, M.; Nakamura, T.; Kobayashi, Y. Room-temperature miscibility gap in Li_xFePO_4 . *Nat. Mater.* **2006**, *5*, 357–360.
95. Srinivasan, V.; Newman, J. Discharge Model for the Lithium Iron-Phosphate Electrode. *J. Electrochem. Soc.* **2004**, *151*, A1517.
96. Delmas, C.; Maccario, M.; Croguennec, L.; Le Cras, F.; Weill, F. Lithium Deintercalation in LiFePO_4 Nanoparticles via a Domino-Cascade Model. *Nat. Mater.* **2008**, *7*, 665–671.
97. Manthiram, A.; Goodenough, J. B. Lithium Insertion Into $\text{Fe}_2(\text{MO}_4)_3$ Frameworks: Comparison of $M = \text{W}$ with $M = \text{Mo}^*$. *J. Solid State Chem.* **1987**, *71*, 349–360.
98. Manthiram, A.; Goodenough, J. B. Lithium Insertion Into $\text{Fe}_2(\text{SO}_4)_3$ Frameworks. *J. Power Sources* **1989**, *26*, 403–408.
99. Andersson, A. S.; Thomas, J. O. The Source of First-Cycle Capacity Loss in LiFePO_4 . *J. Power Sources* **2001**, *5*.
100. Prossini, P. P.; Lisi, M.; Zane, D.; Pasquali, M. Determination of the Chemical Diffusion Coefficient of Lithium in LiFePO_4 . *Solid State Ion* **2002**, *148*, 45–51.
101. Huang, H.; Yin, S. C.; Nazar, L. F. Approaching Theoretical Capacity of LiFePO_4 at Room Temperature at High Rates. *ECS Solid-State Lett.* **2001**, *4*, A170.
102. Ravet, N.; Chouinard, Y.; Magnan, J.; Besner, S.; Gauthier, M.; Armand, M. Electroactivity of Natural and Synthetic Triphylite. *Journal of Power Sources* **2001**, *97–98*, 503–507.
103. Li, G.; Azuma, H.; Tohma, M. LiMnPO_4 as the Cathode for Lithium Batteries. *ECS Solid-State Lett.* **2002**, *5*, A135.
104. Choi, D.; Wang, D.; Bae, I.-T.; Xiao, J.; Nie, Z.; Wang, W.; Viswanathan, V. V.; Lee, Y. J.; Zhang, J.-G.; Graff, G. L.; Yang, Z.; Liu, J. LiMnPO_4 Nanoplate Grown via Solid-State Reaction in Molten Hydrocarbon for Li-Ion Battery Cathode. *Nano Lett.* **2010**, *10*, 2799–2805.
105. Yonemura, M.; Yamada, A.; Takei, Y.; Sonoyama, N.; Kanno, R. Comparative Kinetic Study of Olivine Li_xMPO_4 ($M = \text{Fe}, \text{Mn}$). *J. Electrochem. Soc.* **2004**, *151*, A1352.
106. Delacourt, C.; Laffont, L.; Bouchet, R.; Wurm, C. Toward Understanding of Electrical Limitations (Electronic, Ionic) in LiMPO_4 ($M = \text{Fe}, \text{Mn}$) Electrode Materials. *J. Electrochem. Soc.* **2005**, *152*, A913.
107. Amine, K.; Yasuda, H.; Yamachi, M. Olivine LiCoPO_4 as 4.8 V Electrode Material for. *Lithium Batteries* **2000**, *3*.
108. Bramnik, N. N.; Nikolowski, K.; Baehtz, C.; Bramnik, K. G.; Ehrenberg, H. Phase Transitions Occurring upon Lithium Insertion-Extraction of LiCoPO_4 . *Chem. Mater.* **2007**, *19*, 908–915.
109. Llorís, J. M.; Pérez Vicente, C.; Tirado, J. L. Improvement of the Electrochemical Performance of $\text{LiCoPO}_4[\text{Sub } 4]$ 5 V Material Using a Novel Synthesis Procedure. *Electrochem. Solid-State Lett.* **2002**, *5*, A234.
110. Fisher, C. A. J.; Hart Prieto, V. M.; Islam, M. S. Lithium Battery Materials LiMPO_4 ($M = \text{Mn}, \text{Fe}, \text{Co},$ and Ni): Insights into Defect Association, Transport Mechanisms, and Doping Behavior. *Chem. Mater.* **2008**, *20*, 5907–5915.
111. Nasir, M. H.; Janjua, N. K.; Santoki, J. Electrochemical Performance of Carbon Modified LiNiPO_4 as Li-Ion Battery Cathode: A Combined Experimental and Theoretical Study. *J. Electrochem. Soc.* **2020**, *167*, 130526.
112. Reynaud, M.; Ati, M.; Melot, B. C.; Sougrati, M. T.; Rousse, G.; Chotard, J.-N.; Tarascon, J.-M. $\text{Li}_2\text{Fe}(\text{SO}_4)_2$ as a 3.83V Positive Electrode Material. *Electrochem. Commun.* **2012**, *21*, 77–80.
113. Subban, C. V.; Ati, M.; Rousse, G.; Abakumov, A. M.; Van Tendeloo, G.; Janot, R.; Tarascon, J.-M. Preparation, Structure, and Electrochemistry of Layered Poly-anionic Hydroxy-Sulfates: LiMSO_4OH ($M = \text{Fe}, \text{Co}, \text{Mn}$) Electrodes for Li-Ion Batteries. *J. Am. Chem. Soc.* **2013**, *135*, 3653–3661.
114. Chung, S. C.; Barpanda, P.; Nishimura, S.-I.; Yamada, Y.; Yamada, A. Polymorphs of LiFeSO_4F as Cathode Materials for Lithium Ion Batteries—A First Principle Computational Study. *Phys. Chem. Chem. Phys.* **2012**, *14*, 8678–8682.
115. Clark, M. J.; Eames, C.; Reynaud, M.; Rousse, G.; Chotard, J.-N.; Tarascon, J.-M.; Saiful Islam, M. High Voltage Sulphate Cathodes $\text{Li}_2\text{M}(\text{SO}_4)_2$ ($M = \text{Fe}, \text{Mn}, \text{Co}$): Atomic-Scale Studies of Lithium Diffusion, Surfaces and Voltage Trends. *J. Mater. Chem. A* **2014**, *2*, 7446–7453.
116. Lee, S.; Park, S. S. Comparative Study of Tavorite and Triphylite LiFeSO_4F as Cathode Materials for Lithium Ion Batteries: Structure, Defect Chemistry, and Lithium Conduction Properties from Atomistic Simulation. *J. Phys. Chem. C* **2014**, *118*, 12642–12648.
117. Yao, G.; Zhang, X.; Yan, Y.; Zhang, J.; Song, K.; Shi, J.; Mi, L.; Zheng, J.; Feng, X.; Chen, W. Facile Synthesis of Hierarchical $\text{Na}_2\text{Fe}(\text{SO}_4)_2@\text{rGO}/\text{C}$ as High-Voltage Cathode for Energy Density-Enhanced Sodium-Ion Batteries. *J. Energy Chem.* **2020**, *50*, 387–394.
118. Nyttén, A.; Abouimrane, A.; Armand, M.; Gustafsson, T.; Thomas, J. O. Electrochemical Performance of $\text{Li}_2\text{FeSiO}_4$ as a New Li-Battery Cathode Material. *Electrochem. Commun.* **2005**, *7*, 156–160.
119. Islam, M. S.; Dominko, R.; Masquelier, C.; Sirisopanaporn, C.; Armstrong, A. R.; Bruce, P. G. Silicate Cathodes for Lithium Batteries: Alternatives to Phosphates? *J. Mater. Chem.* **2011**, *21*, 9811–9818.

120. Sirisopanorn, C.; Masquelier, C.; Bruce, P. G.; Armstrong, A. R.; Dominko, R. Dependence of $\text{Li}_2\text{FeSiO}_4$ Electrochemistry on Structure. *J. Am. Chem. Soc.* **2011**, *133*, 1263–1265.
121. Nyttén, A.; Kamali, S.; Häggström, L.; Gustafsson, T.; Thomas, J. O. The Lithium Extraction/Insertion Mechanism in $\text{Li}_2\text{FeSiO}_4$. *J. Mater. Chem.* **2006**, *16*, 2266–2272.
122. Dominko, R.; Arçon, I.; Kodre, A.; Hanžel, D.; Gabersček, M. In-Situ XAS Study on $\text{Li}_2\text{MnSiO}_4$ and $\text{Li}_2\text{FeSiO}_4$ Cathode Materials. *J. Power Source* **2009**, *189*, 51–58.
123. Lyness, C.; Delobel, B.; Armstrong, A. R.; Bruce, P. G. The Lithium Intercalation Compound $\text{Li}_2\text{CoSiO}_4$ and Its Behaviour as a Positive Electrode for Lithium Batteries. *Chem. Commun.* **2007**, 4890–4892.
124. Deng, C.; Zhang, S.; Yang, S. Y. Effect of Mn Substitution on the Structural, Morphological and Electrochemical Behaviors of $\text{Li}_2\text{Fe}_{1-x}\text{Mn}_x\text{SiO}_4$ Synthesized via Citric Acid Assisted Sol-Gel Method. *J. Alloys Compounds* **2009**, *487*, L18–L23.
125. Pereira, N.; Badway, F.; Wartelsky, M.; Gunn, S.; Amatucci, G. G. Iron Oxyfluorides as High Capacity Cathode Materials for Lithium Batteries. *J. Electrochem. Soc.* **2009**, *156*, A407.
126. Cambaz, M. A.; Vinayan, B. P.; Clemens, O.; Munnangi, A. R.; Chakravadhanula, V. S. K.; Kübel, C.; Fichtner, M. Vanadium Oxyfluoride/Few-Layer Graphene Composite as a High-Performance Cathode Material for Lithium Batteries. *Inorg. Chem.* **2016**, *55*, 3789–3796.
127. Carlos Pérez-Flores, J.; Villamor, R.; Ávila-Brandé, D.; Amores, J. M. G.; Morán, E.; Kuhn, A.; García-Alvarado, F. VO₂F: A New Transition Metal Oxyfluoride With High Specific Capacity for Li Ion Batteries. *J. Mater. Chem. A* **2015**, *3*, 20508–20515.
128. Bervas, M.; Klein, L. C.; Amatucci, G. G. Reversible Conversion Reactions With Lithium in Bismuth Oxyfluoride Nanocomposites. *J. Electrochem. Soc.* **2005**, *153*, A159.
129. Bervas, M.; Yakshinsky, B.; Klein, L. C.; Amatucci, G. G. Soft-Chemistry Synthesis and Characterization of Bismuth Oxyfluorides and Ammonium Bismuth Fluorides. *J. Am. Ceram. Soc.* **2006**, *89*, 645–651.
130. Kitajou, A.; Komatsu, H.; Nagano, R.; Okada, S. Synthesis of FeOF Using Roll-Quenching Method and the Cathode Properties for Lithium-Ion Battery. *J. Power Sources* **2013**, *243*, 494–498.
131. Kim, S.-W.; Pereira, N.; Chernova, N. A.; Omenya, F.; Gao, P.; Whittingham, M. S.; Amatucci, G. G.; Su, D.; Wang, F. Structure Stabilization by Mixed Anions in Oxyfluoride Cathodes for High-Energy Lithium Batteries. *ACS Nano* **2015**, *9*, 10076–10084.
132. Sina, M.; Nam, K.-W.; Su, D.; Pereira, N.; Yang, X.-Q.; Amatucci, G.; Cosandey, F. Structural Phase Transformation and Fe Valence Evolution in $\text{FeO}_x\text{F}_{2-x}\text{C}$ Nanocomposite Electrodes During Lithiation and de-Lithiation Processes. *J. Mater. Chem. A* **2013**, *1*, 11629–11640.
133. Wiaderek, K. M.; Borkiewicz, O. J.; Castillo-Martínez, E.; Robert, R.; Pereira, N.; Amatucci, G. G.; Grey, C. P.; Chupas, P. J.; Chapman, K. W. Comprehensive Insights into the Structural and Chemical Changes in Mixed-Anion FeOF Electrodes by Using Operando PDF and NMR Spectroscopy. *J. Am. Chem. Soc.* **2013**, *135*, 4070–4078.
134. Zhang, L.; Dambournet, D.; Iadecola, A.; Batuk, D.; Borkiewicz, O. J.; Wiaderek, K. M.; Salager, E.; Shao, M.; Chen, G.; Tarascon, J.-M. Origin of the High Capacity Manganese-Based Oxyfluoride Electrodes for Rechargeable Batteries. *Chem. Mater.* **2018**, *30*, 5362–5372.
135. Takeda, N.; Ikeuchi, I.; Natsui, R.; Nakura, K.; Yabuuchi, N. Improved Electrode Performance of Lithium-Excess Molybdenum Oxyfluoride: Titanium Substitution With Concentrated Electrolyte. *ACS Appl. Energy Mater.* **2019**, *2*, 1629–1633.
136. House, A. R.; Jin, L.; Maitra, U.; Tsuruta, K.; Somerville, W. J.; Förstermann, P. D.; Massel, F.; Duda, L.; Roberts, R. M.; Bruce, P. G. Lithium Manganese Oxyfluoride as a New Cathode Material Exhibiting Oxygen Redox. *Energy Environ. Sci.* **2018**, *11*, 926–932.
137. Kitajou, A.; Zhao, L.; Nagano, R.; Inoishi, A.; Kobayashi, E.; Okada, S. Electrochemical Performance and Thermal Stability of Iron Oxyfluoride (FeOF) for Sodium-Ion Batteries. *Batteries* **2018**, *4*, 68.
138. Assat, G.; Tarascon, J.-M. Fundamental Understanding and Practical Challenges of Anionic Redox Activity in Li-Ion Batteries. *Nat. Energy* **2018**, *3*, 373–386.
139. Rouxel, J. Anion–Cation Redox Competition and the Formation of New Compounds in Highly Covalent Systems. *Chem. Eur. J.* **1996**, *2*, 1053–1059.
140. Rouxel, J. Some Solid State Chemistry With Holes: Anion–Cation Redox Competition in Solids. *Curr. Sci.* **1997**, *73*, 31–39.
141. Delmas, C.; Fouassier, C.; Hagenmuller, P. Structural Classification and Properties of the Layered Oxides. *Phys. B+C* **1980**, *99*, 81–85.
142. Selte, K.; Bjerkelund, E.; Kjekshus, A. J. Intermediate Phases in the Systems Niobium–Selenium Niobium–Tellurium, Tantalum–Selenium, and Tantalum–Tellurium. *Less Common Metals* **1966**, *11*, 14–30.
143. Flamarly-Mespoullie, F.; Boulineau, A.; Martínez, H.; Suchomel, M. R.; Delmas, C.; Pec-quenard, B.; Le Cras, F. Lithium-Rich Layered Titanium Sulfides: Cobalt- and Nickel-Free High Capacity Cathode Materials for Lithium-Ion Batteries. *Energy Storage Mater.* **2020**, *26*, 213–222.
144. Sakuda, A.; Takeuchi, T.; Okamura, K.; Kobayashi, H.; Sakaebe, H.; Tatsumi, K.; Ogumi, Z. Rock-Salt-Type Lithium Metal Sulphides as Novel Positive-Electrode Materials. *Sci. Rep.* **2015**, *4*, 4883.
145. Cras, F. L.; Pecquenard, B.; Dubois, V.; Phan, V.-P.; Guy-Bouyssou, D. All-Solid-State Lithium-Ion Microbatteries Using Silicon Nanofilm Anodes: High Performance and Memory Effect. *Adv. Energy Mater.* **2015**, *5*, 1501061.
146. Saha, S.; Assat, G.; Sougrati, M. T.; Foix, D.; Li, H.; Vergnet, J.; Turi, S.; Ha, Y.; Yang, W.; Cabana, J.; Rousse, G.; Abakumov, A. M.; Tarascon, J.-M. Exploring the Bottlenecks of Anionic Redox in Li-Rich Layered Sulfides. *Nat. Energy* **2019**, *4*, 977–987.
147. Furuseth, S.; Brattas, L.; Kjekshus, A.; Andresen, A. F.; Fischer, P. On the Crystal Structures of TiS_3 , ZrS_3 , ZrSe_3 , ZrTe_3 , HfS_3 , HfSe_3 . *Acta Chem. Scand.* **1975**, *29A*, 623–631.
148. Sharma, R. A. Equilibrium Phases Between Lithium Sulfide and Iron Sulfides. *J. Electrochem. Soc.* **1976**, *123*, 448–453.
149. Batchelor, R. J.; Einstein, F. W. B.; Jones, C. H. W.; Fong, R.; Dahn, J. R. Crystal Structure of Li_2FeS_2 . *Phys. Rev. B* **1988**, *37*, 3699–3702.
150. Gard, P.; Sourisseau, C.; Ouvrard, G.; Brec, R. Infrared Study of Lithium Intercalated Phases in the Li_xFeS_2 System ($0 \leq x \leq 2$). Characterization of a New Iron Disulfide. *Solid State Ionics* **1986**, *20*, 231–238.
151. Hansen, C. J.; Zak, J. J.; Martinolich, A. J.; Ko, J. S.; Bashian, N. H.; Kaboudvand, F.; Van der Ven, A.; Melot, B. C.; Nelson Weker, J.; See, K. A. Multielectron, Cation and Anion Redox in Lithium-Rich Iron Sulfide Cathodes. *J. Am. Chem. Soc.* **2020**, *142*, 6737–6749.
152. Fong, R.; Dahn, J. R.; Jones, C. H. W. Electrochemistry of Pyrite-Based Cathodes for Ambient Temperature Lithium Batteries. *J. Electrochem. Soc.* **1989**, *136*, 3206–3210.
153. Martinolich, A. J.; Zak, J. J.; Agyeman-Budu, D. N.; Kim, S. S.; Bashian, N. H.; Irshad, A.; Narayan, S. R.; Melot, B. C.; Nelson Weker, J.; See, K. A. Controlling Covalency and Anion Redox Potentials Through Anion Substitution in Li-Rich Chalcogenides. *Chem. Mater.* **2021**, *33*, 378–391.
154. Zak, Joshua J.; Kim, Seong Shik; Laskowski, Forrest A. L.; See, Kimberly A. An Exploration of Sulfur Redox in Lithium Battery Cathodes. *Journal of the American Chemical Society* **2022**, *144* (23), 10119–10132. In this issue.
155. Tarascon, J.; Vaughan, G.; Chabre, Y.; Seguin, L.; Anne, M.; Strobel, P.; Amatucci, G. In Situ Structural and Electrochemical Study of $\text{Ni}_{1-x}\text{Co}_x\text{O}_2$ Metastable Oxides Prepared by Soft Chemistry. *J. Solid State Chem.* **1999**, *147*, 410–420.
156. James, A. C. W. P.; Goodenough, B. Structure and Bonding in Lithium Ruthenate, Li_2RuO_3 . *J. Solid State Chem.* **1987**, *74*, 287–294.
157. Kobayashi, H.; Kanno, R.; Kawamoto, Y.; Tabuchi, M.; Nakamura, O.; Takano, M. Structure and Lithium Deintercalation of $\text{Li}_{2-x}\text{RuO}_3$. *Solid State Ion.* **1995**, *82*, 25–31.
158. Kalyani, P.; Chitra, S.; Mohan, T.; Gopukumar, S. Lithium Metal Rechargeable Cells Using Li_2MnO_3 as the Positive Electrode. *J. Power Sources* **1999**, *80*, 103–106.
159. Robertson, A. D.; Bruce, P. G. Mechanism of Electrochemical Activity in Li_2MnO_3 . *Chem. Mater.* **2003**, *15*, 1984–1992.
160. Yu, D. Y. W.; Yanagida, K.; Kato, Y.; Nakamura, H. Electrochemical Activities in Li_2MnO_3 . *J. Electrochem. Soc.* **2009**, *9*.
161. Lu, Z.; Dahn, J. R. Understanding the Anomalous Capacity of $\text{Li/Li}[\text{Ni}_x\text{Li}_{(1/3-2x/3)}\text{Mn}_{(2/3-x/3)}\text{O}_2]$ Cells Using In Situ X-Ray Diffraction and Electrochemical Studies. *J. Electrochem. Soc.* **2002**, *9*.
162. Thackeray, M. M.; Kang, S.-H.; Johnson, C. S.; Vaughey, J. T.; Benedek, R.; Hackney, S. A. Li_2MnO_3 -Stabilized LiMO_2 (M = Mn, Ni, Co) Electrodes for Lithium-Ion Batteries. *J. Mater. Chem.* **2007**, *17*, 3112.
163. Luo, K.; Roberts, M. R.; Hao, R.; Guerrini, N.; Pickup, D. M.; Liu, Y.-S.; Edström, K.; Guo, J.; Chadwick, A. V.; Duda, L. C.; Bruce, P. G. Charge-Compensation in 3d-Transition-Metal-Oxide Intercalation Cathodes Through the Generation of Localized Electron Holes on Oxygen. *Nat. Chem.* **2016**, *8*, 684–691.

164. Strehle, B.; Kleiner, K.; Jung, R.; Chesneau, F.; Mendez, M.; Gasteiger, H. A.; Piana, M. The Role of Oxygen Release From Li- and Mn-Rich Layered Oxides During the First Cycles Investigated by On-Line Electrochemical Mass Spectrometry. *J. Electrochem. Soc.* **2017**, *164*, A400–A406.
165. Sathya, M.; Rousse, G.; Ramesha, K.; Laisa, C. P.; Vezin, H.; Sougrati, M. T.; Doublet, M.-L.; Foix, D.; Gonbeau, D.; Walker, W.; Prakash, A. S.; Ben Hassine, M.; Dupont, L.; Tarascon, J.-M. Reversible Anionic Redox Chemistry in High-Capacity Layered-Oxide Electrodes. *Nat. Mater.* **2013**, *12*, 827–835.
166. Sathya, M.; Abakumov, A. M.; Foix, D.; Rousse, G.; Ramesha, K.; Saubanère, M.; Doublet, M. L.; Vezin, H.; Laisa, C. P.; Prakash, A. S.; Gonbeau, D.; VanTendeloo, G.; Tarascon, J.-M. Origin of Voltage Decay in High-Capacity Layered Oxide Electrodes. *Nat. Mater.* **2015**, *14*, 230–238.
167. Assat, G.; Foix, D.; Delacourt, C.; Iadecola, A.; Dedryvère, R.; Tarascon, J.-M. Fundamental Interplay Between Anionic/Cationic Redox Governing the Kinetics and Thermodynamics of Lithium-Rich Cathodes. *Nat. Commun.* **2017**, *8*, 2219.
168. Xu, J.; Sun, M.; Qiao, R.; Renfrew, S. E.; Ma, L.; Wu, T.; Hwang, S.; Nordlund, D.; Su, D.; Amine, K.; Lu, J.; McCloskey, B. D.; Yang, W.; Tong, W. Elucidating Anionic Oxygen Activity in Lithium-Rich Layered Oxides. *Nat. Commun.* **2018**, *9*, 947.
169. Radin, M. D.; Vinckeviciute, J.; Seshadri, R.; Van der Ven, A. Manganese Oxidation as the Origin of the Anomalous Capacity of Mn-Containing Li-Excess Cathode Materials. *Nat. Energy* **2019**, *4*, 639–646.
170. Kleiner, K.; Strehle, B.; Baker, A. R.; Day, S. J.; Tang, C. C.; Buchberger, I.; Chesneau, F.-F.; Gasteiger, H. A.; Piana, M. Origin of High Capacity and Poor Cycling Stability of Li-Rich Layered Oxides: A Long-Duration In Situ Synchrotron Powder Diffraction Study. *Chem. Mater.* **2018**, *30*, 3656–3667.
171. Moshkovich, M.; Cojocar, M.; Gottlieb, H.; Aurbach, D. The Study of the Anodic Stability of Alkyl Carbonate Solutions by In Situ FTIR Spectroscopy, EQCM, NMR and MS. *J. Electroanal. Chem.* **2001**, *497*, 84–96.
172. Wu, Y.; Ma, C.; Yang, J.; Li, Z.; Allard, L. F.; Liang, C.; Chi, M. Probing the Initiation of Voltage Decay in Li-Rich Layered Cathode Materials at the Atomic Scale. *J. Mater. Chem. A* **2015**, *3*, 5385–5391.
173. Gu, M.; Belharouak, I.; Zheng, J.; Wu, H.; Xiao, J.; Genc, A.; Amine, K.; Thevuthasan, S.; Baer, D. R.; Zhang, J.-G.; Browning, N. D.; Liu, J.; Wang, C. Formation of the Spinel Phase in the Layered Composite Cathode Used in Li-Ion Batteries. *ACS Nano* **2013**, *7*, 760–767.
174. Qiu, B.; Zhang, M.; Wu, L.; Wang, J.; Xia, Y.; Qian, D.; Liu, H.; Hy, S.; Chen, Y.; An, K.; Zhu, Y.; Liu, Z.; Meng, Y. S. Gas–Solid Interfacial Modification of Oxygen Activity in Layered Oxide Cathodes for Lithium-Ion Batteries. *Nat. Commun.* **2016**, *7*, 12108.
175. Kim, S.; Cho, W.; Zhang, X.; Oshima, Y.; Choi, J. W. A Stable Lithium-Rich Surface Structure for Lithium-Rich Layered Cathode Materials. *Nat. Commun.* **2016**, *7*, 13598.
176. Yan, P.; Zheng, J.; Zhang, X.; Xu, R.; Amine, K.; Xiao, J.; Zhang, J.-G.; Wang, C.-M. Atomic to Nanoscale Investigation of Functionalities of an Al₂O₃ Coating Layer on a Cathode for Enhanced Battery Performance. *Chem. Mater.* **2016**, *28*, 857–863.
177. Zhao, Y.; Liu, J.; Wang, S.; Ji, R.; Xia, Q.; Ding, Z.; Wei, W.; Liu, Y.; Wang, P.; Ivey, D. G. Surface Structural Transition Induced by Gradient Polyanion-Doping in Li-Rich Layered Oxides: Implications for Enhanced Electrochemical Performance. *Adv. Funct. Mater.* **2016**, *26*, 4760–4767.
178. Dees, D. W.; Abraham, D. P.; Lu, W.; Gallagher, K. G.; Bettge, M.; Jansen, A. N. Electrochemical Modeling and Performance of a Lithium-and Manganese-Rich Layered Transition-Metal Oxide Positive Electrode. *J. Electrochem. Soc.* **2015**, *162*, A559–A572.
179. Dogan, F.; Long, B. R.; Croy, J. R.; Gallagher, K. G.; Iddir, H.; Russell, J. T.; Balasubramanian, M.; Key, B. Re-Entrant Lithium Local Environments and Defect Driven Electrochemistry of Li- and Mn-Rich Li-Ion Battery Cathodes. *J. Am. Chem. Soc.* **2015**, *137*, 2328–2335.
180. Rinaldo, S. G.; Gallagher, K. G.; Long, B. R.; Croy, J. R.; Bettge, M.; Abraham, D. P.; Bareño, J.; Dees, D. W. Physical Theory of Voltage Fade in Lithium-and Manganese-Rich Transition Metal Oxides. *J. Electrochem. Soc.* **2015**, *162*, A897–A904.
181. Liu, Q.; Li, S.; Wang, S.; Zhang, X.; Zhou, S.; Bai, Y.; Zheng, J.; Lu, X. Kinetically Determined Phase Transition From Stage II (LiC₁₂) to Stage I (LiC₆) in a Graphite Anode for Li-Ion Batteries. *J. Phys. Chem. Lett.* **2018**, *9*, 5567–5573.
182. Winter, M.; Barnett, B.; Xu, K. Before Li Ion Batteries. *Chem. Rev.* **2018**, *118*, 11433–11456.
183. Nagaura, T.; Tozawa, K. Lithium Ion Rechargeable Battery. *Prog. Batteries Sol. Cells* **1990**, *9*, 209–217.
184. Wagner, M. R.; Raimann, P. R.; Trifonova, A.; Moeller, K.-C.; Besenhard, J. O.; Winter, M. Electrolyte Decomposition Reactions on Tin-and Graphite-Based Anodes Are Different. *Electrochem. Solid-State Lett.* **2004**, *7*, A201.
185. Harris, W. S. *Electrochemical Studies in Cyclic Esters*, 1958.
186. Takehara, Z.-I.; Kanamura, K. Historical Development of Rechargeable Lithium Batteries in Japan. *Electrochim. Acta* **1993**, *38*, 1169–1177.
187. Peled, E. The Electrochemical Behavior of Alkali and Alkaline Earth Metals in Nonaqueous Battery Systems—The Solid Electrolyte Interphase Model. *J. Electrochem. Soc.* **1979**, *126*, 2047–2051.
188. Aurbach, D.; Ein-Eli, Y.; Markovsky, B.; Zaban, A.; Lusk, S.; Carmeli, Y.; Yamin, H. The Study of Electrolyte Solutions Based on Ethylene and Diethyl Carbonates for Rechargeable Li Batteries: II. Graphite Electrodes. *J. Electrochem. Soc.* **1995**, *142*, 2882–2890.
189. Aurbach, D.; Ein-Eli, Y. The Study of Li-Graphite Intercalation Processes in Several Electrolyte Systems Using In Situ X-Ray Diffraction. *J. Electrochem. Soc.* **1995**, *142*, 1746–1752.
190. Xu, K. "Charge-Transfer" Process at Graphite/Electrolyte Interface and the Solvation Sheath Structure of Li⁺ in Nonaqueous Electrolytes. *J. Electrochem. Soc.* **2007**, *7*.
191. Xu, K.; Lam, Y.; Zhang, S. S.; Jow, T. R.; Curtis, T. B. Solvation Sheath of Li⁺ in Nonaqueous Electrolytes and Its Implication of Graphite/Electrolyte Interface Chemistry. *J. Phys. Chem. C* **2007**, *111*, 7411–7421.
192. von Cresce, A.; Xu, K. Preferential Solvation of Li⁺ Directs Formation of Interphase on Graphitic Anode. *Electrochem. Solid-State Lett.* **2011**, *14*, A154.
193. Bogle, X.; Vazquez, R.; Greenbaum, S.; Cresce, A. V. W.; Xu, K. Understanding Li⁺–Solvent Interaction in Nonaqueous Carbonate Electrolytes With ¹⁷O NMR. *J. Phys. Chem. Lett.* **2013**, *4*, 1664–1668.
194. von Wald Cresce, A.; Borodin, O.; Xu, K. Correlating Li⁺ Solvation Sheath Structure With Interphasial Chemistry on Graphite. *J. Phys. Chem. C* **2012**, *116*, 26111–26117.
195. Xu, K.; von Cresce, A. Interfacing Electrolytes With Electrodes in Li Ion Batteries. *J. Mater. Chem.* **2011**, *21*, 9849.
196. Peled, E.; Menkin, S. Review—SEI: Past, Present, and Future. *J. Electrochem. Soc.* **2017**, *164*, A1703–A1719.
197. Gauthier, M.; Carney, T. J.; Grimaud, A.; Giordano, L.; Pour, N.; Chang, H.-H.; Fen-ning, D. P.; Lux, S. F.; Paschos, O.; Bauer, C.; Maglia, F.; Lupart, S.; Lamp, P.; Shao-Horn, Y. Electrode-Electrolyte Interface in Li-Ion Batteries: Current Understanding and New Insights. *J. Phys. Chem. Lett.* **2015**, *6*, 4653–4672.
198. Dresselhaus, M. D. G. Intercalation compounds of graphite. *Adv. Phys.* **1981**, *30* (2), 139–326.
199. Dresselhaus, M. D. G. Intercalation compounds of graphite. *Adv. Phys.* **1981**, *51* (1), 1–186.
200. Safran, S. A.; Hamann, D. R. Long-Range Elastic Interactions and Staging in Graphite Intercalation Compounds. *Phys. Rev. Lett.* **1979**, *42*, 1410–1413.
201. Heß, M.; Novák, P. Shrinking Annuli Mechanism and Stage-Dependent Rate Capability of Thin-Layer Graphite Electrodes for Lithium-Ion Batteries. *Electrochim. Acta* **2013**, *106*, 149–158.
202. Safran, S. A.; Hamann, D. R. Electrostatic Interactions and Staging in Graphite Intercalation Compounds. *Phys. Rev. B* **1980**, *22*, 606–612.
203. Dahn, J. R.; Fong, R.; Spoon, M. J. Suppression of Staging in Lithium-Intercalated Carbon by Disorder in the Host. *Phys. Rev. B* **1990**, *42*, 6424–6432.
204. Billaud, D.; Henry, F.; Willmann, P. Electrochemical Synthesis of Binary Graphite-Lithium Intercalation Compounds. *Mater. Res. Bull.* **1993**, *28*, 477–483.
205. Dahn, J. R. Phase Diagram of Li_xC₆. *Phys. Rev. B* **1991**, *44*, 9170–9177.
206. Huang, W.; Frech, R. In Situ Raman Studies of Graphite Surface Structures During Lithium Electrochemical Intercalation. *J. Electrochem. Soc.* **1998**, *145*, 765–770.
207. Inaba, M.; Yoshida, H.; Ogumi, Z.; Abe, T.; Mizutani, Y.; Asano, M. In Situ Raman Study on Electrochemical Li Intercalation into Graphite. *J. Electrochem. Soc.* **1995**, *142*, 20–26.
208. Nazri, G.; Pistoia, G., Eds.; *Lithium Batteries: Science and Technology*, Kluwer Academic Publishers: Boston, 2004.
209. Song, M. K.; Hong, S. D.; No, K. T. The Structure of Lithium Intercalated Graphite Using an Effective Atomic Charge of Lithium. *J. Electrochem. Soc.* **2001**, *148*, A1159.
210. Billaud, D.; McRae, E.; Hold, A. Synthesis and Electrical Resistivity of Lithium-Pyrographite Intercalation Compounds (Stages I, II and 111). *Mater. Res. Bull.* **1979**, *14*, 8.

211. Song, X. Y.; Kinoshita, K.; Tran, T. D. Microstructural Characterization of Lithiated Graphite. *J. Electrochem. Soc.* **1996**, *143*, L120–L123.
212. Yazami, R. Surface Chemistry and Lithium Storage Capability of the Graphite–Lithium Electrode. *Electrochim. Acta* **1999**, *45*, 87–97.
213. Chen, J.; Yang, L.; Tang, Y. Electrochemical Lithium Storage of TiO₂ Hollow Microspheres Assembled by Nanotubes. *Journal of Power Sources* **2010**, *195*, 6893–6896.
214. Gnanasekar, K. I.; Subramanian, V.; Robinson, J.; Gnanasekar, K. I.; Gnanasekar, K. I.; Gnanasekar, K. I.; Jiang, J. C.; Posey, F. E.; Rambabu, B. Direct Conversion of TiO₂ Sol to Nanocrystalline Anatase at 85 °C. *J. Mater. Res.* **2002**, *17*, 1507–1512.
215. Beuvier, T.; Richard-Plouet, M.; Mancini-Le Granvalet, M.; Brousse, T.; Crosnier, O.; Brohan, L. TiO₂ (B) Nanoribbons As Negative Electrode Material for Lithium Ion Batteries With High Rate Performance. *Inorg. Chem.* **2010**, *49*, 8457–8464.
216. Reddy, M.; Jose, R.; Teng, T.; Chowdari, B.; Ramakrishna, S. Preparation and Electrochemical Studies of Electrospun TiO₂ Nanofibers and Molten Salt Method Nanoparticles. *Electrochim. Acta* **2010**, *55*, 3109–3117.
217. Thackeray, M. M. Structural Considerations of Layered and Spinel Lithiated Oxides for Lithium Ion Batteries. *J. Electrochem. Soc.* **1995**, *142*, 2558–2563.
218. Nakahara, K.; Nakajima, R.; Matsushima, T.; Majima, H. Preparation of Particulate Li₄Ti₅O₁₂ Having Excellent Characteristics as an Electrode Active Material for Power Storage Cells. *J. Power Sources* **2003**, *117*, 131–136.
219. Cheng, L.; Liu, H.-J.; Zhang, J.-J.; Xiong, H.-M.; Xia, Y.-Y. Nanosized Li₄Ti₅O₁₂ Prepared by Molten Salt Method as an Electrode Material for Hybrid Electrochemical Supercapacitors. *J. Electrochem. Soc.* **2006**, *7*.
220. Borghols, W. J. H.; Wagemaker, M.; Lafont, U.; Kelder, E. M.; Mulder, F. M. Size Effects in the Li_{4+x}Ti₅O₁₂ Spinel. *J. Am. Chem. Soc.* **2009**, *131*, 17786–17792.
221. Liu, W.; Zhang, J.; Wang, Q.; Xie, X.; Lou, Y.; Xia, B. The Effects of Li₂CO₃ Particle Size on the Properties of Lithium Titanate as Anode Material for Lithium-Ion Batteries. *Ionics* **2014**, *20*, 1553–1560.
222. Li, X.; Lai, C.; Xiao, C.; Gao, X. Enhanced High Rate Capability of Dual-Phase Li₄Ti₅O₁₂-TiO₂ Induced by Pseudocapacitive Effect. *Electrochim. Acta* **2011**, *56*, 9152–9158.
223. Bai, Y.-J.; Gong, C.; Lun, N.; Qi, Y.-X. Yttrium-Modified Li₄Ti₅O₁₂ as an Effective Anode Material for Lithium Ion Batteries With Outstanding Long-Term Cyclability and Rate Capabilities. *J. Mater. Chem. A* **2013**, *1*, 89–96.
224. Augustyn, V.; Come, J.; Lowe, M. A.; Kim, J. W.; Taberna, P.-L.; Tolbert, S. H.; Abruña, H. D.; Simon, P.; Dunn, B. High-Rate Electrochemical Energy Storage Through Li+ Intercalation Pseudocapacitance. *Nat. Mater.* **2013**, *12*, 518–522.
225. Griffith, K. J.; Forse, A. C.; Griffin, J. M.; Grey, C. P. High-Rate Intercalation Without Nanostructuring in Metastable Nb₂O₅ Bronze Phases. *J. Am. Chem. Soc.* **2016**, *138*, 8888–8899.
226. Reddy, M. A.; Varadaraju, U. V. Lithium Insertion into Niobates With Columbite-Type Structure: Interplay Between Structure-Composition and Crystallite Size. *J. Phys. Chem. C* **2011**, *115*, 25121–25124.
227. Han, J.-T.; Goodenough, J. B. 3-V Full Cell Performance of Anode Framework TiNb₂O₇/Spinel LiNi_{0.5}Mn_{1.5}O₄. *Chem. Mater.* **2011**, *23*, 3404–3407.
228. Han, J.-T.; Liu, D.-Q.; Song, S.-H.; Kim, Y.; Goodenough, J. B. Lithium Ion Intercalation Performance of Niobium Oxides: KNb₅O₁₃ and K₆Nb₁₀₋₈O₃₀. *Chem. Mater.* **2009**, *21*, 4753–4755.
229. Wei, M.; Wei, K.; Ichihara, M.; Zhou, H. Nb₂O₅ Nanobelts: A Lithium Intercalation Host with Large Capacity and High Rate Capability. *Electrochem. Commun.* **2008**, *10*, 980–983.
230. Bresser, D.; Passerini, S.; Scrosati, B. Recent Progress and Remaining Challenges in Sulfur-Based Lithium Secondary Batteries—A Review. *Chem. Commun.* **2013**, *49*, 10545–10562.
231. See, K. A.; Leskes, M.; Griffin, J. M.; Britto, S.; Matthews, P. D.; Emly, A.; Van der Ven, A.; Wright, D. S.; Morris, A. J.; Grey, C. P.; Seshadri, R. Ab Initio Structure Search and In Situ ⁷Li NMR Studies of Discharge Products in the Li–S Battery System. *J. Am. Chem. Soc.* **2014**, *136*, 16368–16377.
232. Yang, G.; Shi, S.; Yang, J.; Ma, Y. Insight into the Role of Li₂S₂ in Li–S Batteries: A First-Principles Study. *J. Mater. Chem. A* **2015**, *3*, 8865–8869.
233. Lee, C.-W.; Pang, Q.; Ha, S.; Cheng, L.; Han, S.-D.; Zavadil, K. R.; Gallagher, K. G.; Nazar, L. F.; Balasubramanian, M. Directing the Lithium-Sulfur Reaction Pathway via Sparingly Solvating Electrolytes for High Energy Density Batteries. *ACS Cent. Sci.* **2017**, *3*, 605–613.
234. Kumaresan, K.; Mikhaylik, Y.; White, R. E. A Mathematical Model for a Lithium-Sulfur Cell. *J. Electrochem. Soc.* **2008**, *155*, A576.
235. Cuisinier, M.; Cabelguen, P.-E.; Evers, S.; He, G.; Kolbeck, M.; Garsuch, A.; Bolin, T.; Balasubramanian, M.; Nazar, L. F. Sulfur Speciation in Li-S Batteries Determined by Operando X-Ray Absorption Spectroscopy. *J. Phys. Chem. Lett.* **2013**, *4*, 3227–3232.
236. Zheng, D.; Liu, D.; Harris, J. B.; Ding, T.; Si, J.; Andrew, S.; Qu, D.; Yang, X.-Q.; Qu, D. Investigation of the Li-S Battery Mechanism by Real-Time Monitoring of the Changes of Sulfur and Polysulfide Species During the Discharge and Charge. *ACS Appl. Mater. Interfaces* **2017**, *9*, 4326–4332.
237. Lorgner, S.; Usiskin, R. E.; Maier, J. Transport and Charge Carrier Chemistry in Lithium Sulfide. *Adv. Funct. Mater.* **2019**, *29*, 1807688.
238. Yamada, Y.; Furukawa, K.; Sodeyama, K.; Kikuchi, K.; Yaegashi, M.; Tateyama, Y.; Yamada, A. Unusual Stability of Acetonitrile-Based Superconcentrated Electrolytes for Fast-Charging Lithium-Ion Batteries. *J. Am. Chem. Soc.* **2014**, *136*, 5039–5046.
239. Pang, Q.; Shyamsunder, A.; Narayanan, B.; Kwok, C. Y.; Curtiss, L. A.; Nazar, L. F. Tuning the Electrolyte Network Structure to Invoke Quasi-Solid State Sulfur Conversion and Suppress Lithium Dendrite Formation in Li-S Batteries. *Nat. Energy* **2018**, *3*, 783–791.
240. Seo, D. M.; Borodin, O.; Han, S.-D.; Boyle, P. D.; Henderson, W. A. Electrolyte Solvation and Ionic Association II. Acetonitrile-Lithium Salt Mixtures: Highly Dissociated Salts. *J. Electrochem. Soc.* **2012**, *159*, A1489–A1500.
241. Ji, X.; Lee, K. T.; Nazar, L. F. A Highly Ordered Nanostructured Carbon-Sulphur Cathode for Lithium-Sulphur Batteries. *Nat. Mater.* **2009**, *8*, 500–506.
242. Osada, N.; Bucur, B. C.; Aso, H.; Muldoon, J. The Design of Nanostructured Sulfur Cathodes Using Layer by Layer Assembly. *Energy Environ. Sci.* **2016**, *9*, 1668–1673.
243. Yang, Y.; Zheng, G.; Cui, Y. Nanostructured Sulfur Cathodes. *Chem. Soc. Rev.* **2013**, *42*, 3018–3032.
244. Li, W.; Zheng, G.; Yang, Y.; Seh, Z. W.; Liu, N.; Cui, Y. High-Performance Hollow Sulfur Nanostructured Battery Cathode Through a Scalable, Room Temperature, One-Step, Bottom-up Approach. *Proc. Natl. Acad. Sci. U. S. A.* **2013**, *110*, 7148–7153.
245. Zhao, Q.; Liu, X.; Stalin, S.; Khan, K.; Archer, L. A. Solid-State Polymer Electrolytes With in-Built Fast Interfacial Transport for Secondary Lithium Batteries. *Nat. Energy* **2019**, *4*, 365–373.
246. Chiochan, P.; Yu, X.; Sawangphruk, M.; Manthiram, A. A Metal Organic Framework Derived Solid Electrolyte for Lithium-Sulfur Batteries. *Adv. Energy Mater.* **2020**, *10*, 2001285.
247. Yan, Z.; Liang, Y.; Xiao, J.; Lai, W.; Wang, W.; Xia, Q.; Wang, Y.; Gu, Q.; Lu, H.; Chou, S.-L.; Liu, Y.; Liu, H.; Dou, S.-X. A High-Kinetics Sulfur Cathode with a Highly Efficient Mechanism for Superior Room-Temperature Na–S Batteries. *Adv. Mater.* **2020**, *32*, 1906700.
248. Hu, X.; Ni, Y.; Wang, C.; Wang, H.; Matios, E.; Chen, J.; Li, W. Facile-Processed Nanocarbon-Promoted Sulfur Cathode for Highly Stable Sodium-Sulfur Batteries. *Cell Rep. Phys. Sci.* **2020**, *1*, 100015.
249. Zhang, J.; Xu, W.; Liu, W. Oxygen-Selective Immobilized Liquid Membranes for Operation of Lithium-Air Batteries in Ambient Air. *J. Power Sources* **2010**, *195*, 7438–7444.
250. Yang, S.; He, P.; Zhou, H. Research Progresses on Materials and Electrode Design Towards Key Challenges of Li-Air Batteries. *Energy Storage Mater.* **2018**, *13*, 29–48.
251. Kim, H.; Lee, H.; Kim, M.; Bae, Y.; Baek, W.; Park, K.; Park, S.; Kim, T.; Kwon, H.; Choi, W.; Kang, K.; Kwon, S.; Im, D. Flexible Free-Standing Air Electrode With Bimodal Pore Architecture for Long-Cycling Li–O₂ Batteries. *Carbon* **2017**, *117*, 454–461.
252. Littauer, E. L.; Tsai, K. C. Anodic Behavior of Lithium in Aqueous Electrolytes: II. Mechanical Passivation. *J. Electrochem. Soc.* **1976**, *123*, 964.
253. Abraham, K. M.; Jiang, Z. A Polymer Electrolyte-Based Rechargeable Lithium/Oxygen Battery. *J. Electrochem. Soc.* **1996**, *143*, 1.
254. Ma, Z.; Yuan, X.; Li, L.; Ma, Z.-F.; Wilkinson, D. P.; Zhang, L.; Zhang, J. A Review of Cathode Materials and Structures for Rechargeable Lithium–Air Batteries. *Energy Environ. Sci.* **2015**, *8*, 2144–2198.
255. Yoon, K. R.; Jung, J.-W.; Kim, I.-D. Recent Progress in 1D Air Electrode Nanomaterials for Enhancing the Performance of Nonaqueous Lithium–Oxygen Batteries. *Chem-NanoMat* **2016**, *2*, 616–634.

256. Lim, H.-D.; Lee, B.; Bae, Y.; Park, H.; Ko, Y.; Kim, H.; Kim, J.; Kang, K. Reaction Chemistry in Rechargeable Li–O₂ Batteries. *Chem. Soc. Rev.* **2017**, *46*, 2873–2888.
257. Jung, J.-W.; Cho, S.-H.; Nam, J. S.; Kim, I.-D. Current and Future Cathode Materials for Non-Aqueous Li-Air (O₂) Battery Technology—A Focused Review. *Energy Storage Mater.* **2020**, *24*, 512–528.
258. Veith, G. M.; Dudney, N. J. Current Collectors for Rechargeable Li-Air Batteries. *J. Electrochem. Soc.* **2011**, *158*, A658.
259. Peng, Z.; Freunberger, S. A.; Chen, Y.; Bruce, P. G. A Reversible and Higher-Rate Li–O₂ Battery. *Science* **2012**, *337*, 563–566.
260. Yang, Y.; Zhang, T.; Wang, X.; Chen, L.; Wu, N.; Liu, W.; Lu, H.; Xiao, L.; Fu, L.; Zhuang, L. Tuning the Morphology and Crystal Structure of Li₂O₂: A Graphene Model Electrode Study for Li–O₂ Battery. *ACS Appl. Mater. Interfaces* **2016**, *8*, 21350–21357.
261. Zhang, R.; Yu, X.; Nam, K.-W.; Ling, C.; Arthur, T. S.; Song, W.; Knapp, A. M.; Ehrlich, S. N.; Yang, X.-Q.; Matsui, M. α -MnO₂ as a Cathode Material for Rechargeable Mg Batteries. *Electrochem. Commun.* **2012**, *23*, 110–113.
262. Lee, H.; Kim, Y.-J.; Lee, D. J.; Song, J.; Lee, Y. M.; Kim, H.-T.; Park, J.-K. Directly Grown Co₃O₄ Nanowire Arrays on Ni-Foam: Structural Effects of Carbon-Free and Binder-Free Cathodes for Lithium-Oxygen Batteries. *J. Mater. Chem. A* **2014**, *2*, 11891–11898.
263. Crowther, O.; Salomon, M. Oxygen Selective Membranes for Li-Air (O₂) Batteries. *Membranes* **2012**, *2*, 216–227.
264. Zhang, J.-G.; Wang, D.; Xu, W.; Xiao, J.; Williford, R. E. Ambient Operation of Li/Air Batteries. *J. Power Sources* **2010**, *195*, 4332–4337.
265. Cheng, X.-B.; Zhang, R.; Zhao, C.-Z.; Zhang, Q. Toward Safe Lithium Metal Anode in Rechargeable Batteries: A Review. *Chem. Rev.* **2017**, *117*, 10403–10473.
266. Jäckle, M.; Groß, A. Microscopic Properties of Lithium, Sodium, and Magnesium Battery Anode Materials Related to Possible Dendrite Growth. *J. Chem. Phys.* **2014**, *141*, 174710.
267. Chen, J.; Yang, H.; Zhang, X.; Lei, J.; Zhang, H.; Yuan, H.; Yang, J.; Nuli, Y.; Wang, J. Highly Reversible Lithium-Metal Anode and Lithium–Sulfur Batteries Enabled by an Intrinsic Safe Electrolyte. *ACS Appl. Mater. Interfaces* **2019**.
268. Shen, X.; Li, Y.; Qian, T.; Liu, J.; Zhou, J.; Yan, C.; Goodenough, J. B. Lithium Anode Stable in Air for Low-Cost Fabrication of a Dendrite-Free Lithium Battery. *Nat. Commun.* **2019**, *10*, 900.
269. Liu, F.; Wang, L.; Zhang, Z.; Shi, P.; Feng, Y.; Yao, Y.; Ye, S.; Wang, H.; Wu, X.; Yu, Y. A Mixed Lithium-Ion Conductive Li₂S/Li₂Se Protection Layer for Stable Lithium Metal Anode. *Adv. Funct. Mater.* **2020**, *30*, 2001607.
270. Fan, L.; Guo, Z.; Zhang, Y.; Wu, X.; Zhao, C.; Sun, X.; Yang, G.; Feng, Y.; Zhang, N. Stable Artificial Solid Electrolyte Interphase Films for Lithium Metal Anode via Metal–Organic Frameworks Cemented by Polyvinyl Alcohol. *J. Mater. Chem. A* **2020**, *8*, 251–258.
271. Yoon, B.; Park, J.; Lee, J.; Kim, S.; Ren, X.; Lee, Y. M.; Kim, H.-T.; Lee, H.; Ryou, M.-H. High-Rate Cycling of Lithium-Metal Batteries Enabled by Dual-Salt Electrolyte-Assisted Micropatterned Interfaces. *ACS Appl. Mater. Interfaces* **2019**, *11*, 31777–31785.
272. Peng, Z.; Wang, S.; Zhou, J.; Jin, Y.; Liu, Y.; Qin, Y.; Shen, C.; Han, W.; Wang, D. Volumetric Variation Confinement: Surface Protective Structure for High Cyclic Stability of Lithium Metal Electrodes. *J. Mater. Chem. A* **2016**, *4*, 2427–2432.
273. Bie, Y.; Yang, J.; Lu, W.; Lei, Z.; Nuli, Y.; Wang, J. A Facile 3D Binding Approach for High Si Loading Anodes. *Electrochim. Acta* **2016**, *212*, 141–146.
274. Wen, C. J.; Huggins, R. A. Chemical Diffusion in Intermediate Phases in the Lithium-Silicon System. *J. Solid State Chem.* **1981**, *37*, 271–278.
275. Obrovac, M. N.; Christensen, L. Structural Changes in Silicon Anodes During Lithium Insertion/Extraction. *Electrochem. Solid-State Lett.* **2004**, *7*, A93.
276. Zhu, J.; Wang, T.; Fan, F.; Mei, L.; Lu, B. Atomic-Scale Control of Silicon Expansion Space as Ultrastable Battery Anodes. *ACS Nano* **2016**, *10*, 8243–8251.
277. Tian, H.; Xin, F.; Wang, X.; He, W.; Han, W. High Capacity Group-IV Elements (Si, Ge, Sn) Based Anodes for Lithium-Ion Batteries. *J. Mater.* **2015**, *1*, 153–169.
278. Chan, C. K.; Peng, H.; Liu, G.; McIlwrath, K.; Zhang, X. F.; Huggins, R. A.; Cui, Y. High-Performance Lithium Battery Anodes Using Silicon Nanowires. *Nat. Nanotechnol.* **2008**, *3*, 31–35.
279. Franco Gonzalez, A.; Yang, N.-H.; Liu, R.-S. Silicon Anode Design for Lithium-Ion Batteries: Progress and Perspectives. *J. Phys. Chem. C* **2017**, *121*, 27775–27787.
280. Profatilova, I. A.; Stock, C.; Schmitz, A.; Passerini, S.; Winter, M. Enhanced Thermal Stability of a Lithiated Nano-Silicon Electrode by Fluoroethylene Carbonate and Vinylene Carbonate. *J. Power Source* **2013**, *222*, 140–149.
281. Szczech, R. J.; Jin, S. Nanostructured Silicon for High Capacity Lithium Battery Anodes. *Energy Environ. Sci.* **2011**, *4*, 56–72.
282. Schroder, K. W.; Celio, H.; Webb, L. J.; Stevenson, K. J. Examining Solid Electrolyte Interphase Formation on Crystalline Silicon Electrodes: Influence of Electrochemical Preparation and Ambient Exposure Conditions. *J. Phys. Chem. C* **2012**, *116*, 19737–19747.
283. Jiménez, A. R.; Nölle, R.; Wagner, R.; Hüsker, J.; Kolek, M.; Schmich, R.; Winter, M.; Placke, T. A Step towards Understanding the Beneficial Influence of a LiPON-Based Artificial SEI on Silicon Thin Film Anodes in Lithium-Ion Batteries. *Nanoscale* **2018**, *10*, 2128–2137.
284. Ai, Q.; Li, D.; Guo, J.; Hou, G.; Sun, Q.; Sun, Q.; Xu, X.; Zhai, W.; Zhang, L.; Feng, J.; Si, P.; Lou, J.; Ci, L. Artificial Solid Electrolyte Interphase Coating to Reduce Lithium Trapping in Silicon Anode for High Performance Lithium-Ion Batteries. *Adv. Mater. Interfaces* **2019**, *6*, 1901187.
285. Ai, Q.; Fang, Q.; Liang, J.; Xu, X.; Zhai, T.; Gao, G.; Guo, H.; Han, G.; Ci, L.; Lou, J. Lithium-Conducting Covalent–Organic–Frameworks as Artificial Solid–Electrolyte–Interphase on Silicon Anode for High Performance Lithium Ion Batteries. *Nano Energy* **2020**, *72*, 104657.
286. Yu, S.-H.; Lee, S. H.; Lee, D. J.; Sung, Y.-E.; Hyeon, T. Conversion Reaction-Based Oxide Nanomaterials for Lithium Ion Battery Anodes. *Small* **2016**, *12*, 2146–2172.
287. Yang, Z.; Shen, J.; Archer, A.; L. An in Situ Method of Creating Metal Oxide—Carbon Composites and Their Application as Anode Materials for Lithium-Ion Batteries. *J. Mater. Chem.* **2011**, *21*, 11092–11097.
288. Greim, P.; Solomon, A. A.; Breyer, C. Assessment of Lithium Criticality in the Global Energy Transition and Addressing Policy Gaps in Transportation. *Nat. Commun.* **2020**, *11*, 4570.
289. Tian, Y.; Zeng, G.; Rutt, A.; Shi, T.; Kim, H.; Wang, J.; Koettgen, J.; Sun, Y.; Ouyang, B.; Chen, T.; Lun, Z.; Rong, Z.; Persson, K.; Ceder, G. Promises and Challenges of Next-Generation “Beyond Li-Ion” Batteries for Electric Vehicles and Grid Decarbonization. *Chem. Rev.* **2021**, *121*, 1623–1669.
290. Yabuuchi, N.; Kubota, K.; Dahbi, M.; Komaba, S. Research Development on Sodium-Ion Batteries. *Chem. Rev.* **2014**, *114*, 11636–11682.
291. Jian, Z.; Han, W.; Lu, X.; Yang, H.; Hu, Y.-S.; Zhou, J.; Zhou, Z.; Li, J.; Chen, W.; Chen, D.; Chen, L. Superior Electrochemical Performance and Storage Mechanism of Na₃V₂(PO₄)₃ Cathode for Room-Temperature Sodium-Ion Batteries. *Adv. Energy Mater.* **2013**, *3*, 156–160.
292. Kundu, D.; Talaie, E.; Duffort, V.; Nazar, L. F. The Emerging Chemistry of Sodium Ion Batteries for Electrochemical Energy Storage. *Angew. Chem. Int. Ed.* **2015**, *54*, 3431–3448.
293. Broux, T.; Bamine, T.; Fauth, F.; Simonelli, L.; Olszewski, W.; Marini, C.; Ménétrier, M.; Carlier, D.; Masquelier, C.; Croguennec, L. Strong Impact of the Oxygen Content in Na₃V₂(PO₄)₂F_{3–y}O_y (0 ≤ y ≤ 0.5) on Its Structural and Electrochemical Properties. *Chem. Mater.* **2016**, *28*, 7683–7692.
294. Ling, C.; Chen, J.; Mizuno, F. First-Principles Study of Alkali and Alkaline Earth Ion Intercalation in Iron Hexacyanoferrate: The Important Role of Ionic Radius. *J. Phys. Chem. C* **2013**, *117*, 21158–21165.
295. Lee, B.; Paek, E.; Mitlin, D.; Lee, S. W. Sodium Metal Anodes: Emerging Solutions to Dendrite Growth. *Chem. Rev.* **2019**, *119*, 5416–5460.
296. Komaba, S.; Hasegawa, T.; Dahbi, M.; Kubota, K. Potassium Intercalation into Graphite to Realize High-Voltage/High-Power Potassium-Ion Batteries and Potassium-Ion Capacitors. *Electrochem. Commun.* **2015**, *60*, 172–175.
297. Nobuhara, K.; Nakayama, H.; Nose, M.; Nakanishi, S.; Iba, H. First-Principles Study of Alkali Metal-Graphite Intercalation Compounds. *J. Power Source* **2013**, *243*, 585–587.
298. Liu, Y.; Merinov, B. V.; Goddard, W. A. Origin of Low Sodium Capacity in Graphite and Generally Weak Substrate Binding of Na and Mg among Alkali and Alkaline Earth Metals. *Proc. Natl. Acad. Sci. U. S. A.* **2016**, *113*, 3735–3739.
299. Hasegawa, G.; Kanamori, K.; Kannari, N.; Ozaki, J.-I.; Nakanishi, K.; Abe, T. Hard Carbon Anodes for Na-Ion Batteries: Toward a Practical Use. *ChemElectroChem* **2015**, *2*, 1917–1920.
300. Bauer, A.; Song, J.; Vail, S.; Pan, W.; Barker, J.; Lu, Y. The Scale-up and Commercialization of Nonaqueous Na-Ion Battery Technologies. *Adv. Energy Mater.* **2018**, *8*, 1702869.

301. Rudola, A.; Sharma, N.; Balaya, P. Introducing a 0.2 V Sodium-Ion Battery Anode: The $\text{Na}_2\text{Ti}_3\text{O}_7$ to $\text{Na}_3\text{xTi}_3\text{O}_7$ Pathway. *Electrochem. Commun.* **2015**, *61*, 10–13.
302. Song, J.; Wang, K.; Zheng, J.; Engelhard, M. H.; Xiao, B.; Hu, E.; Zhu, Z.; Wang, C.; Sui, M.; Lin, Y.; Reed, D.; Sprenkle, V. L.; Yan, P.; Li, X. Controlling Surface Phase Transition and Chemical Reactivity of O_3 -Layered Metal Oxide Cathodes for High-Performance Na-Ion Batteries. *ACS Energy Lett.* **2020**, *5*, 1718–1725.
303. Tang, H.; Peng, Z.; Wu, L.; Xiong, F.; Pei, C.; An, Q.; Mai, L. Vanadium-Based Cathode Materials for Rechargeable Multivalent Batteries: Challenges and Opportunities. *Electrochem. Energ. Rev.* **2018**, *1*, 169–199.
304. Shyamsunder, A.; Blanc, L. E.; Assoud, A.; Nazar, L. F. Reversible Calcium Plating and Stripping at Room Temperature Using a Borate Salt. *ACS Energy Lett.* **2019**, *4*, 2271–2276.
305. Iton, Zachery W. B.; See, Kimberly A. Multivalent Ion Conduction in Inorganic Solids. *Chemistry of Materials* **2022**, *34* (3), 881–898. In this issue.
306. Bruce, P. G.; Krok, F.; Nowinski, J.; Gibson, V. C.; Tavakkoli, K. Chemical Intercalation of Magnesium into Solid Hosts. *J. Mater. Chem.* **1991**, *1*, 705.
307. Aurbach, D.; Lu, Z.; Schechter, A.; Gofer, Y.; Gizbar, H.; Turgeman, R.; Cohen, Y.; Moshkovich, M.; Levi, E. Prototype Systems for Rechargeable Magnesium Batteries. *Nature* **2000**, *407*, 724–727.
308. Levi, E.; Levi, M. D.; Chasid, O.; Aurbach, D. A Review on the Problems of the Solid State Ions Diffusion in Cathodes for Rechargeable Mg Batteries. *J. Electroceram.* **2009**, *22*, 13–19.
309. Gocke, E.; Schramm, W.; Dolscheid, P.; Schollhorn, R. Molybdenum Cluster Chalcogenides Mo_6S_8 : Electrochemical Intercalation of Closed Shell Ions Zn^{2+} , Cd^{2+} , and Na^+ . *J. Solid State Chem.* **1987**, *70*, 71–81.
310. Schöllhorn, R.; Kümpers, M.; Besenhard, J. Topotactic Redox Reactions of the Channel Type Chalcogenides Mo_3S_4 and Mo_3Se_4 . *Mater. Res. Bull.* **1977**, *12*, 781–788.
311. Mao, M.; Gao, T.; Hou, S.; Wang, C. A Critical Review of Cathodes for Rechargeable Mg Batteries. *Chem. Soc. Rev.* **2018**, *47*, 8804–8841.
312. Levi, E.; Lancry, E.; Mitelman, A.; Aurbach, D.; Ceder, G.; Morgan, D.; Isnard, O. Phase Diagram of Mg Insertion into Chevrel Phases, $\text{Mg}_x\text{Mo}_6\text{T}_8$ (T = S, Se). 1. Crystal Structure of the Sulfides. *Chem. Mater.* **2006**, *18*, 5492–5503.
313. Levi, M.; Lancry, E.; Levi, E.; Gizbar, H.; Gofer, Y.; Aurbach, D. The Effect of the Anionic Framework of MoX Chevrel Phase (X = S, Se) on the Thermodynamics and the Kinetics of the Electrochemical Insertion of Mg Ions. *Solid State Ionics* **2005**, *176*, 1695–1699.
314. Richard, J.; Benayad, A.; Colin, J.-F.; Martinet, S. Charge Transfer Mechanism Into the Chevrel Phase Mo_6S_8 During Mg Intercalation. *J. Phys. Chem. C* **2017**, *121*, 17096–17103.
315. Canepa, P.; Sai Gautam, G.; Hannah, D. C.; Malik, R.; Liu, M.; Gallagher, K. G.; Persson, K. A.; Ceder, G. Odyssey of Multivalent Cathode Materials: Open Questions and Future Challenges. *Chem. Rev.* **2017**, *117*, 4287–4341.
316. Bruce, P. Multivalent Cation Intercalation. *Solid State Ionics* **1992**, *53–56*, 351–355.
317. Whittingham, M. Chemistry of Intercalation Compounds: Metal Guests in Chalcogenide Hosts. *Progr. Solid State Chem.* **1978**, *12*, 41–99.
318. Tao, Z.-L.; Xu, L.-N.; Gou, X.-L.; Chen, J.; Yuan, H.-T. TiS_2 Nanotubes as the Cathode Materials of Mg-Ion Batteries. *Chem. Commun.* **2004**, 2080.
319. Amir, N.; Vestfrid, Y.; Chusid, O.; Gofer, Y.; Aurbach, D. Progress in Nonaqueous Magnesium Electrochemistry. *J. Power Sources* **2007**, *174*, 1234–1240.
320. Emly, A.; Van der Ven, A. Mg Intercalation in Layered and Spinel Host Crystal Structures for Mg Batteries. *Inorg. Chem.* **2015**, *54*, 4394–4402.
321. Kolli, S. K.; Van der Ven, A. First-Principles Study of Spinel MgTiS_2 as a Cathode Material. *Chem. Mater.* **2018**, *30*, 2436–2442.
322. Wang, Y.; Liu, Z.; Wang, C.; Yi, X.; Chen, R.; Ma, L.; Hu, Y.; Zhu, G.; Chen, T.; Tie, Z.; Ma, J.; Liu, J.; Jin, Z. Highly Branched VS_4 Nanodendrites With 1D Atomic-Chain Structure as a Promising Cathode Material for Long-Cycling Magnesium Batteries. *Adv. Mater.* **2018**, *30*, 1802563.
323. Li, Z.; Vinayan, B. P.; Jankowski, P.; Njel, C.; Roy, A.; Vegge, T.; Maibach, J.; Lastra, J. M. G.; Fichtner, M.; Zhao-Karger, Z. Multi-Electron Reactions Enabled by Anion-Based Redox Chemistry for High-Energy Multivalent Rechargeable Batteries. *Angew. Chem. Int. Ed.* **2020**, *59*, 11483–11490.
324. Dey, S.; Lee, J.; Britto, S.; Stratford, J. M.; Keyzer, E. N.; Dunstan, M. T.; Cibin, G.; Cassidy, S. J.; Elgami, M.; Grey, C. P. Exploring Cation-Anion Redox Processes in One-Dimensional Linear Chain Vanadium Tetrasulfide Rechargeable Magnesium Ion Cathodes. *J. Am. Chem. Soc.* **2020**, *142*, 19588–19601.
325. Pei, C.; Yin, Y.; Sun, R.; Xiong, F.; Liao, X.; Tang, H.; Tan, S.; Zhao, Y.; An, Q.; Mai, L. Interchain-Expanded Vanadium Tetrasulfide With Fast Kinetics for Rechargeable Magnesium Batteries. *ACS Appl. Mater. Interfaces* **2019**, *11*, 31954–31961.
326. Aydinol, M. K.; Kohan, A. F.; Ceder, G.; Cho, K.; Joannopoulos, J. *Ab Initio* Study of Lithium Intercalation in Metal Oxides and Metal Dichalcogenides. *Phys. Rev. B* **1997**, *56*, 1354–1365.
327. Mukherjee, A.; Sa, N.; Phillips, P. J.; Burrell, A.; Vaughey, J.; Klie, R. F. Direct Investigation of Mg Intercalation Into the Orthorhombic V_2O_5 Cathode Using Atomic-Resolution Transmission Electron Microscopy. *Chem. Mater.* **2017**, *29*, 2218–2226.
328. Sai Gautam, G.; Canepa, P.; Abdellahi, A.; Urban, A.; Malik, R.; Ceder, G. The Intercalation Phase Diagram of Mg in V_2O_5 From First-Principles. *Chem. Mater.* **2015**, *27*, 3733–3742.
329. Sa, N.; Wang, H.; Proffitt, D. L.; Lipson, A. L.; Key, B.; Liu, M.; Feng, Z.; Fister, T. T.; Ren, Y.; Sun, C.-J.; Vaughey, J. T.; Fenter, P. A.; Persson, K. A.; Burrell, A. K. Is Alpha- V_2O_5 a Cathode Material for Mg Insertion Batteries? *J. Power Sources* **2016**, *323*, 44–50.
330. Spahr, M.; Novák, P.; Haas, O.; Nesper, R. Electrochemical Insertion of Lithium, Sodium, and Magnesium in Molybdenum(VI) Oxide. *J. Power Sources* **1995**, *54*, 346–351.
331. Gershinsky, G.; Yoo, H. D.; Gofer, Y.; Aurbach, D. Electrochemical and Spectroscopic Analysis of Mg^{2+} Intercalation into Thin Film Electrodes of Layered Oxides: V_2O_5 and MoO_3 . *Langmuir* **2013**, *29*, 10964–10972.
332. Shin, J.; Seo, J. K.; Yaylian, R.; Huang, A.; Meng, Y. S. A Review on Mechanistic Understanding of MnO_2 in Aqueous Electrolyte for Electrical Energy Storage Systems. *Int. Mater. Rev.* **2020**, *65*, 356–387.
333. Ling, C.; Zhang, R. Manganese Dioxide As Rechargeable Magnesium Battery Cathode. *Front. Energy Res.* **2017**, *5*, 30.
334. Ling, C.; Zhang, R.; Arthur, T. S.; Mizuno, F. How General Is the Conversion Reaction in Mg Battery Cathode: A Case Study of the Magnesian of $\alpha\text{-MnO}_2$. *Chem. Mater.* **2015**, *27*, 5799–5807.
335. Zhang, R.; Arthur, T. S.; Ling, C.; Mizuno, F. Manganese Dioxides as Rechargeable Magnesium Battery Cathode; Synthetic Approach to Understand Magnesian Process. *J. Power Sources* **2015**, *282*, 630–638.
336. Sun, X.; Duffort, V.; Mehdi, B. L.; Browning, N. D.; Nazar, L. F. Investigation of the Mechanism of Mg Insertion in Birnessite in Nonaqueous and Aqueous Rechargeable Mg-Ion Batteries. *Chem. Mater.* **2016**, *28*, 534–542.
337. Kim, C.; Phillips, P. J.; Key, B.; Yi, T.; Nordlund, D.; Yu, Y.-S.; Bayliss, R. D.; Han, S.-D.; He, M.; Zhang, Z.; Burrell, A. K.; Klie, R. F.; Cabana, J. Direct Observation of Reversible Magnesium Ion Intercalation Into a Spinel Oxide Host. *Adv. Mater.* **2015**, *27*, 3377–3384.
338. Ming, J.; Guo, J.; Xia, C.; Wang, W.; Alshareef, H. N. Zinc-Ion Batteries: Materials, Mechanisms, and Applications. *Mater. Sci. Eng. R Rep.* **2019**, *135*, 58–84.

4.11 The chemistry of quantum materials

Tyrel M. McQueen, Department of Chemistry, Johns Hopkins University, Baltimore, MD, United States; Department of Materials Science and Engineering, Johns Hopkins University, Baltimore, MD, United States; and William H. Miller III Department of Physics and Astronomy, Johns Hopkins University, Baltimore, MD, United States

© 2023 Elsevier Ltd. All rights reserved.

4.11.1	A chemical definition of “quantum material”	364
4.11.2	A short history of quantum materials	365
4.11.3	Classification of quantum materials: Scheme I	367
4.11.4	Classification of quantum materials: Scheme II	369
4.11.5	Ideality meets reality	371
4.11.6	Preparation of quantum materials	372
4.11.7	Other frontiers	372
Acknowledgments		372
References		373

Abstract

Quantum materials have emerged as an exciting interface between materials chemistry, materials science, and condensed matter physics. A quantum material is one in which the structure, behavior, or reactivity arise from quantum mechanical interactions that are not adequately captured by classical models and calculations. The chapter gives a brief history of the field and sets the context for understanding recent advances by giving two different classification schemes by which to organize different quantum materials and phenomena. Drawing on exemplars of the behavior, the connections between chemistry and quantum materials is discussed and explored. Real compounds and real materials are then discussed in the context of these classifications, and limitations of existing approaches evaluated. The frontiers of the field – covering synthesis, characterization, and theory – and involving convergences with data science and quantum information science and engineering are proposed. The scalable atomic control of synthesis is identified as a particular urgent need, and will be enabled by the development of a comprehensive understanding of solid state reactivity in the vein of retrosynthetic analysis familiar to most molecular chemists. The content of the chapter is particularly targeted at chemists of all education levels interested in joining the worldwide efforts in quantum materials to further fundamental knowledge and society.

4.11.1 A chemical definition of “quantum material”

In this chapter, an overview of the history, recent progress, and potential future directions of quantum materials is presented. First, a definition is needed: what is a quantum material? A survey of the literature over the past decade^{1–6} gives a variety of definitions, **Table 1**. Several features from these definitions are apparent:

1. Quantum materials are related to strongly correlated electronic systems
2. Quantum materials are related to emergent phenomena
3. Quantum materials exhibit macroscopic behaviors that uniquely arise from quantum mechanics (e.g., entanglement)

Given these obviously strong roots and connections of quantum materials to open questions within condensed matter physics, it is natural to ask: what are the connections to chemistry, and particularly inorganic and materials chemistry? A search of current top chemistry journals in October 2021 including *Journal of the American Chemical Society*, *Nature Chemistry*, *Chemical Science*, and *Angewandte Chemie* for the keyword “quantum materials” yields results primarily related to quantum dots. Certainly quantum dots would seem to fit under the definitions in **Table 1** – with emergent phenomena arising from a combination of dimensional confinement with the quantum mechanical nature of electrons – but is the chemistry connection limited to this one class of quantum material?

We answer this question in the negative, finding strong connections between outstanding chemical questions – including about the transformation of matter, the making and breaking of chemical bonds, and descriptions of the configuration of electrons in matter. This leads to our inorganic chemist’s definition of a quantum material:

A quantum material is one in which the structure, behavior, or reactivity arise from quantum mechanical interactions that are not adequately captured by classical models and calculations.

Table 1 Definitions of “quantum material.”

“Quantum materials is a label that has come to signify the area of condensed-matter physics formerly known as strongly correlated electronic systems. Although the field is broad, a unifying theme is the discovery and investigation of materials whose electronic properties cannot be understood with concepts from contemporary condensed-matter textbooks.”	Orenstein ⁶
“Emergent phenomena are common in condensed matter. Their study now extends beyond strongly correlated electron systems, giving rise to the broader concept of quantum materials.”	Nat. Phys. uncredited ¹
“Quantum materials are solids with exotic physical properties, arising from the quantum mechanical properties of their constituent electrons; such materials have great scientific and/or technological potential.”	Broholm, et al. ²
“[W]hile quantum mechanics ultimately determines materials properties at the macroscale, matter wave characteristics generally fade from view through decoherence in a quantum to classical cross-over regime. In quantum materials on the other hand, the veil is lifted on the quantum world and the deeply confounding features of quantum mechanics including entanglement, coherence, and quantum fluctuations directly impact materials properties and thus can be harnessed to create exotic and/or powerful new phenomena.”	Broholm, et al. ³
“This rather broad class of materials has its roots in everything we rely on in lives and occupations that include everything from electronics and computational technologies to energy usage and storage. These materials can generally be defined as being shown to exhibit exotic properties where electron correlations are at the forefront for these properties to be manifested.”	Tobash and Bobev ⁴
“For chemists, we would say that the simplest of definitions is that a quantum material is one whose electronic or magnetic properties are best described as having a nontrivial quantum mechanical origin—in other words materials where classical particles or calculations that do not take into account the full character of the system do not adequately describe the electronic or magnetic properties displayed.”	Cava, et al. ⁵
“A quantum material is one in which the structure, behavior, or reactivity arise from quantum mechanical interactions that are not adequately captured by classical models and calculations.”	This work

Crucially, simply having quantum mechanics present (as all matter does) is not sufficient; instead, quantum materials are those in which behavior does not degenerate to that describable by classical models, and instead require direct consideration of quantum entanglement, quantum coherence, and/or quantum fluctuations.

4.11.2 A short history of quantum materials

The term quantum material is a relatively recent invention, coming into mainstream lingo around 2012.⁶ But scientific fields, unlike say electron-positron pairs, do not spontaneously appear out of a vacuum.⁷ They are evolutions – merges, branches, or otherwise – of earlier areas of research. Of course quantum mechanics itself began with unexpected observations – from the photoelectric effect

to the discovery of cathode rays and black body radiation – and the field properly born in the 1920s by luminaries Born, Heisenberg, Pauli, and others.

A line of inquiry developed in parallel involves emergence. A term perhaps first used in its modern form by philosopher G.H. Lewis in the 1870s,⁸ the central observation was that many physical phenomena – be it the flocking of birds, schooling of fish, or maybe even life itself – could not seemingly be broken down into smaller parts, instead appearing to behave as greater than the sum of the individual constituents. Emergence was being found in virtually every system built of a large number of parts – i.e. complex systems – whether in nature or in human constructions (economies, etc.). And this extended to the behavior of materials, Fig. 1.

In order to apply the then new theories of quantum mechanics to condensed matter (i.e. solid/liquid) systems, it was not generally possible to fully solve the underlying equations because of the great complexity arising from a large number of identical, and interacting, particles. Solutions to this soon appeared from Landau¹⁰ and others,¹¹ in the form of recognizing that in some cases the problem could be transformed into a simpler one by replacing the real particles by fictitious ones – known as quasiparticles – and the real (complex) interactions by simpler effective interactions. That is, the collective behaviors between many constituents as specified by quantum mechanics could be rewritten in terms of new, emergent objects (the quasiparticles) and correspondingly distinct (and emergent) interactions. This led to a band description/theory of electron states in metals/insulators that provided both a physical model explaining discoveries of classical semiconductor behavior such as the photovoltaic effect and the foundation on which new devices – such as the transistor – would be built, thus beginning the new field known as semiconductor physics.

The union of quantum mechanics and emergence also led to natural explanations for other discoveries. For example, the celebrated BCS theory^{12,13} in 1957 provided a quantum mechanical, microscopic description of the phenomenon known as superconductivity (itself discovered in mercury in 1911),¹⁴ with pairs of electrons – Cooper pairs – as the emergent object. At the same time, a whole zoo of new behaviors was being observed in condensed matter materials – charge and spin density waves, heavy fermion physics, the fractional quantum hall effect, and more – each of which seemingly represented a different type of emergence from the underlying quantum mechanics, and requiring different treatment to explain and predict. The common theme, microscopically, was that the interactions between the electrons are not weak and cannot be simplified into a simple effective interaction, and hence this area of research became known as strongly correlated electron physics.

Within the domain of strongly correlated electron physics, many phenomena that could not be readily extracted via simpler effective models of the underlying quantum mechanics were also found. The most famous is high temperature superconductivity,¹⁵ Fig. 2. Phenomenologically the same as all other known superconductors, the microscopic BCS model is unable to account for the observed transition temperatures – $T_c = 93$ K for $\text{YBa}_2\text{Cu}_3\text{O}_7$ ^{16,17} (an application of BCS theory using classical band models of electron behavior gives a predicted T_c of only a few kelvins). On the theoretical front, an example is the quantum spin liquid,^{18–22} in which strongly interacting spins produce a long range entangled state with no magnetic order at $T = 0$ K. What sets these examples apart from, e.g., the magnetic order of a ferromagnet, or the electrical conductivity of a metal, is that they are not reducible to an effective single particle picture. With the recognition that the underlying origin of the difficulty in such a reduction is rooted in the indistinguishable and quantum mechanical nature of the microscopic particles, the field of quantum materials was born.

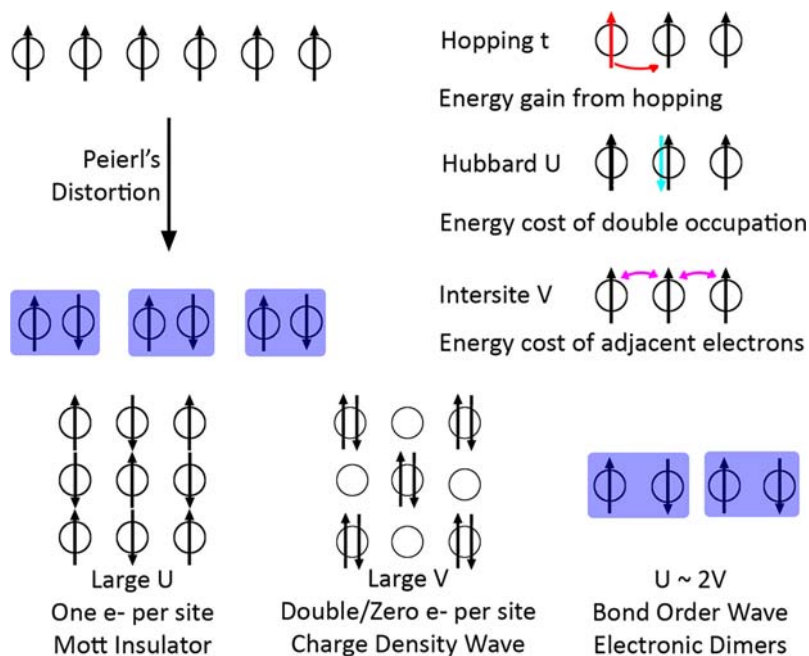


Fig. 1 Complexity emerges from simple microscopic interactions. Electrons are attracted to nuclei; there is an energy gain for electrons from being able to move (hop) between nuclear (sites) [or, equivalently, it takes energy to confine an electron – as anyone who has solved particle in a box knows], but there is an electrostatic energy cost of doing so due to electron-electron repulsion and Pauli exclusion. Out of these simple interactions, a variety of complex, emergent, states can appear, including dimerization (a la H_2), Mott insulators (a la antiferromagnetism), spontaneous charge disproportionation (a la charge density wave), or electronic – without nuclear – dimerization (a bond order wave⁹).

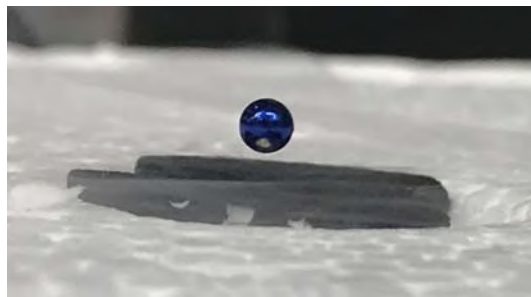


Fig. 2 A $\text{Nd}_2\text{Fe}_{14}\text{B}$ magnet suspended over a piece of the high temperature superconductor $\text{YBa}_2\text{Cu}_3\text{O}_7$. The high temperature superconductor is an example of a quantum material.

4.11.3 Classification of quantum materials: Scheme I

Since the defining characteristic of a quantum material is that quantum mechanical behavior is directly manifest, it is useful to categorize quantum materials based on the specific quantum phenomena present. This in turn requires classification based on the labels used to describe the underlying particles and quantum states. **Table 2** gives examples of each of these types of labels. For example, consider a pair of entangled photons that have been physically separated in space. In such a system, the underlying particles are photons of light, the phenomena is that of entanglement, and the quantum states are defined by the observable set in the preparation of the entangled state – e.g. the polarization of the photons. Despite this system’s apparent simplicity, and perhaps not even being a real quantum material (because it is made of photons, not matter), it is one of few examples where quantum mechanical entanglement has been directly verified by tests of violation of Bell’s Inequality,^{23–30} and thus serves as an important benchmark example in understanding the progress of the study of quantum materials.

Using the general classification labels of **Table 2**, mainstream quantum materials exhibit various combinations of all of the listed phenomena. At the same time, they almost exclusively involve electrons as the underlying particle. It is thus useful to further distinguish the behaviors of quantum matter based on the specific electron states. To do so, there are two helpful limits to consider:

1. **Fully Localized (“Real Space”) Limit:** good quantum numbers, i.e. good descriptors of the electron states, come from the total spin of the electrons combined with the spatial position of the nuclei. A canonical example is a reaction coordinate diagram, which shows the energy of electron states as a function of nuclear positions. In this limit, electrons are well localized in real space.
2. **Fully Delocalized (“Reciprocal Space”) Limit:** good quantum numbers come from the total spin of the electrons combined with the periodicity of the nuclei. A canonical example is an electronic band structure, which shows the energy of electron states as a function of crystal momentum (which is defined by the atomic periodicity). In this limit, electrons are delocalized over a periodic pattern of nuclei that extends infinitely.

A good quantum number is the eigenvalue of an operator that commutes with the Hamiltonian (that is, it is possible to know both this quantum number and the energy from the Hamiltonian precisely and simultaneously). Roald Hoffmann has an excellent set of works describing these limits and their connections.^{31–33} There are also online tools including the Bilbao Crystallographic Server^{34–36} and ISODISTORT^{37,38} that help visualize the connections between real and reciprocal space. In addition to these limits, the symmetries that are present play a key role in defining the underlying electronic states.

Utilizing this classification scheme, **Fig. 3** diagrams a non-exhaustive list of behavior associated with quantum materials. It is immediately apparent that in many cases there is a correspondence between behaviors in the real and reciprocal space limits. For example, conical intersections, or places where two electronic energy surfaces of appropriate symmetry intersect with an avoided crossing in a molecular electronic structure, are pivotal in accurately describing the excited state dynamics and reactivity of molecules.^{39–41} In particular, they are responsible for non-adiabatic relaxation processes in which classical models that do not take into account the quantum mechanical nature of the states, and the resultant π Berry phase around these intersections, fail to describe.

Table 2 General classification labels for quantum materials based on the phenomena, the underlying particles, and their states.

<i>Phenomena</i>	<i>Particles</i>	<i>States</i>
Entanglement	Nuclei	Momentum
Coherence	Electrons	Spin (Angular Momentum)
Fluctuations	Photons	Position
Continuity		Polarization

A single quantum material can involve more than one label from each column, and some combinations of labels describe quantum systems that are not considered quantum materials.

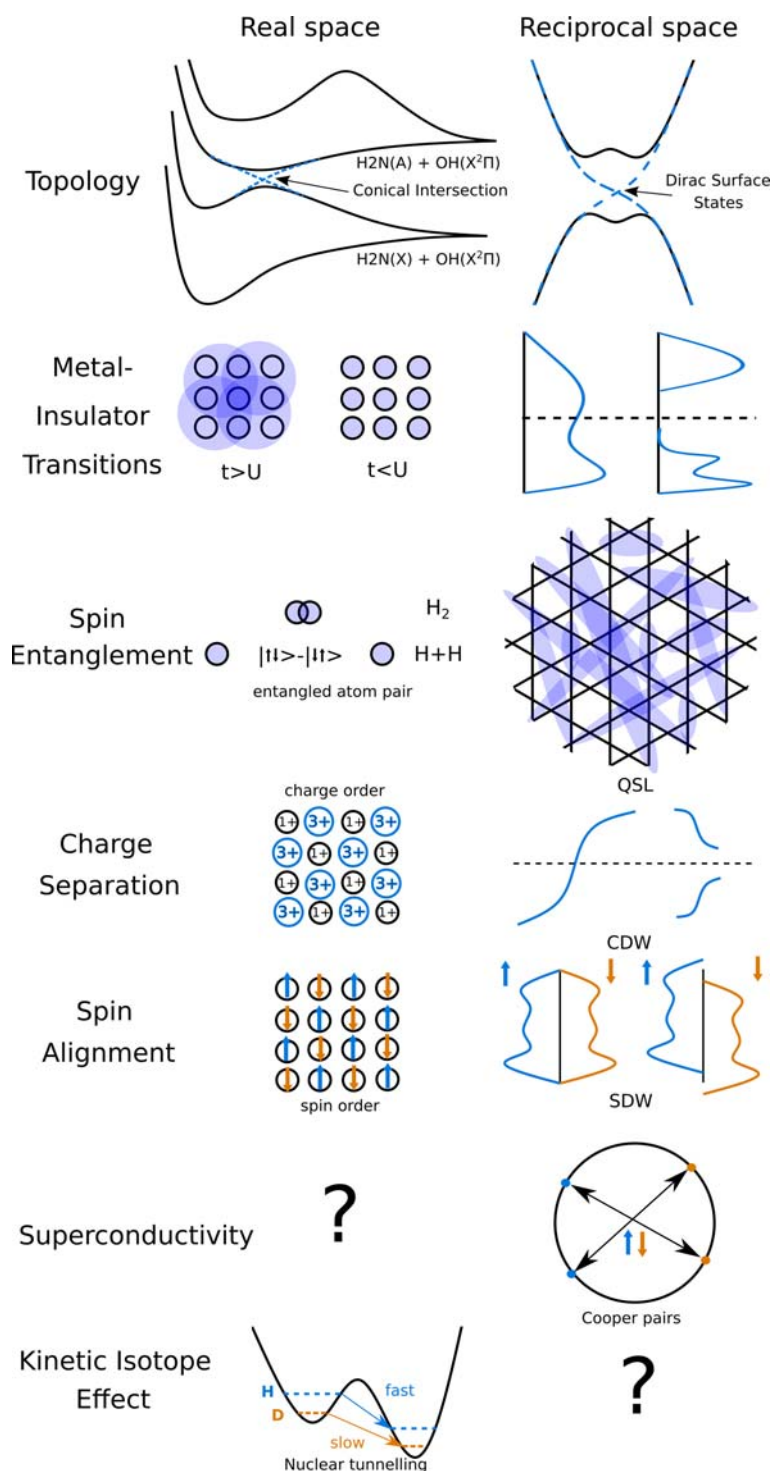


Fig. 3 Sample quantum behaviors. Electron states that cross will mix and form avoided crossings. Due to continuity and smoothness requirements of the wavefunctions, these crossings can leave residual effects in the potential energy surfaces, specifically the wave function picking up a “Berry phase” of π (i.e. if a system is moved in a closed circle enclosing the point, instead of returning to the original state, the wavefunction inverts).³⁹ In real space, these are known as conical intersections and result in non-adiabatic relaxation between states.^{40,41} In reciprocal space, these are known as Dirac crossings and result in metallic surface states between normal and topological insulators.^{42–45} Metal insulator transitions occur due to electron localization on atoms (real space) or electron localization in energy to open an energy gap (reciprocal space).^{46,47} Electrons in an H₂ molecule form a fully entangled singlet state. If the two H atoms are then separated in space, without a measurement occurring to keep the quantum coherence, a pair of spatially separated electrons result. If different configurations of electron spin are similarly paired across many atomic sites, as in a periodic solid like a kagomé lattice, and mixed to form a single quantum state, the result is a quantum spin liquid.^{18–22} Separation of charge in real space results in charge order. Separation of charge in reciprocal space results in a charge density wave.⁴⁸ Ordering of electron spins in real space results in magnetic (spin) order.⁴⁹ Ordering of spins in reciprocal space results in a spin density wave. Some quantum behaviors have no obvious real/reciprocal space pairs, for example: What is the real space analog of a superconductor?^{12–14} What is the reciprocal space analog of the kinetic isotope effect from atomic tunneling?^{50,51}

The corresponding behavior in reciprocal space is known as a topological insulator; at the interface between a normal insulator, such as vacuum, and a topological insulator there are cone-like, linearly dispersing, metallic surface states that also have a π Berry phase around the crossing point; as with conical intersections, such surface states are not expected without considering the quantum mechanical nature of the electrons.^{42–45}

In other cases, the correspondence of behavior between these two limits is not as clear. For example, superconductivity, discovered in 1911,¹⁴ arises from the entanglement of pairs of electrons to form Cooper pairs that adopt phase coherence below T_c . The celebrated BCS theory defines a microscopic mechanism based on the electron pairing in reciprocal space.^{12,13} While such pairing can readily occur between electrons well described in the real-space limit, it is also not obvious what phenomena results.⁵² As a second example, the kinetic isotope effect, in which the rate of a chemical reaction varies with nuclear mass, experimentally known since at least the 1940s and invaluable in the elucidation of reaction mechanisms, is easily described as arising from the change in vibrational frequencies driven by the nuclear mass change in a real space picture combined with quantum mechanical tunneling.^{50,51} While such changes in vibrational frequencies in the reciprocal space limit are well known, and underlie the isotope effect on superconducting T_c , what new phenomena this produces is not known.⁵³

It is outside the scope of this work to provide a comprehensive description of the chemistry of each of these classes of quantum material, and the reader is instead referred to the excellent books and review articles referenced above for more detailed discussion.

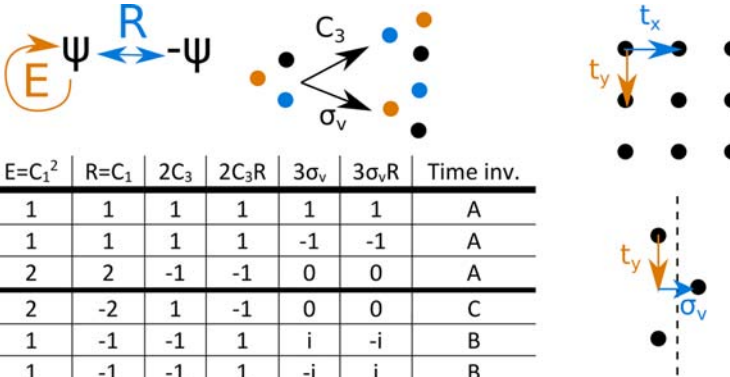
4.11.4 Classification of quantum materials: Scheme II

The prior section classified quantum materials based on the underlying particles, states involved, and quantum-specific behavior present. An alternative classification scheme is based on the chemical constituents – i.e. what atoms, in what arrangement, with what bonds – and then what quantum materials phenomena are possible within that space. For example, most theoretical models for a quantum spin liquid (QSL) state start with the assumption that electrons are fully localized on individual atomic or molecular sites, with specific geometric connectivity between sites (often based on triangles). So a dense packing of atoms like in iron metal, or arranging atoms on squares, are unlikely to yield a QSL.

The formal language used to describe the arrangement of atoms are based on symmetry and the application of group theory. All chemists are familiar with these in the context of molecular symmetry and point groups. For quantum materials, two additional ingredients are needed. The first, not familiar to all chemists, is that a proper treatment of electron spin requires use of double groups. A double group, as the name implies, has twice the symmetry operators of a normal group, and arises because rotating the wavefunction (ψ) of a half-integer spin particle (like an electron) by 2π (360°) can be said to return not ψ but $-\psi$. This has no effect on observables (which depend on quantities that go like $|\psi|^2$), but is of course essential for proper treatment of electron spin.^{54–56} The second additional ingredient is that there are also translational symmetry elements, Fig. 4.

Table 3 gives this author's attempt at a representative but non-exhaustive list of how atom identities, electron counts, and symmetry/connectivity conspire to produce known families of quantum materials and phenomena, and the reader is encouraged to consult the given references for details.

Several trends are immediately apparent. High temperature superconductivity is clustered in materials with strong two dimensional connectivity, and mostly derived from common structure types – e.g. perovskites and ThCr_2Si_2 .^{97,98} Quantum spin liquid candidates are also clustered in materials with strong two dimensional connectivity, but often less prevalent structure types and with triangles as a common motif. Topological states, being a direct consequence of symmetry, draw from multiple structural



C_{3v}	$E=C_1^2$	$R=C_1$	$2C_3$	$2C_3R$	$3\sigma_v$	$3\sigma_vR$	Time inv.
$a_1=\Gamma_1$	1	1	1	1	1	1	A
$a_2=\Gamma_2$	1	1	1	1	-1	-1	A
$e=\Gamma_3$	2	2	-1	-1	0	0	A
Γ_4	2	-2	1	-1	0	0	C
Γ_5	1	-1	-1	1	i	-i	B
Γ_6	1	-1	-1	1	-i	i	B

Fig. 4 Symmetry and group theory classify quantum materials. The symmetry element of a rotation by 360° ($C_1=R$) returns atoms to their original places but inverts the wavefunction. Applying this operation twice returns both atoms and the wavefunction to the original configuration and is the identity operator ($C_1^2=E$). The closed set of allowed symmetry operations (group) for a system with C_{3v} symmetry gives rise to a set of orthogonal irreducible representations. Time reversal symmetry can require additional equivalencies (case B: $\Gamma_5=\Gamma_6$) or not (cases A and C). Periodic solids add translational symmetries to these point groups, which can also give rise to combined symmetry operations that are independent objects (e.g. glide plane, shown).

Table 3 Representative atomic connectivity, electron counts, and observed quantum behaviors.

Connectivity	Electron Count	Behavior	References
fcc/bcc and A15 structure CuO ₂ /NiO ₂ planes	4.5 or 7 valence electrons d ⁹ d ⁷	superconductivity antiferromagnetic insulator or nonmagnetic metal MIT, charge and spin ordering	57,58 59–61 62–64
M ₂ X ₂ layers	d ^{9-δ} 28-δ e/layer 28 e/layer	superconductivity superconductivity antiferromagnetism	65–68 69–71 72
Kagomé (corner sharing triangles) MX _x layers	33–34 e/layer Integer	charge density wave 120° magnetic order or quantum spin liquid or valence bond order	73,74 18–22
Honeycomb MX _x layers	Non-Integer	Dirac Metal	75–77
Triangular MX _x layers	Integer	magnetic order or quantum spin liquid	78,79
Pyrochlore M ₂ X (corner sharing tetrahedra)	Integer	magnetic order or classical spin liquid or superconductor	80–82
M ₂ X ₃ quintuple layers	Non-Integer	Superconductor or charge/spin density wave	83,84
MX-M ₂ Y ₃ heterostructures	Integer or Non-Integer	Spin ice or topological insulator/semimetal or superconductor	85–87
fcc (Half-)Heusler X ₂₋₃ YZ	Integer	Topological insulator	88,89
Defect centers (e.g. NV center in diamond, Si vacancy center in SiC, Rare earth in host)	Integer	Magnetic Topological insulator	90,91
Molecular Complexes	Various	Various	92
	Various	Spin qubit or optical mixing (e.g. laser) or scintillation	93,94
	Various	Various (most recently, qubit centers)	95,96

classes, but unified based on the space group of the material. Some structural families, e.g. Heusler, encompass sufficient chemical and structural flexibility to exhibit nearly any quantum state depending on the details. Single spin centers, as used in qubits and quantum sensing are unified by being well-separated objects in a semiconducting/insulating host lattice.

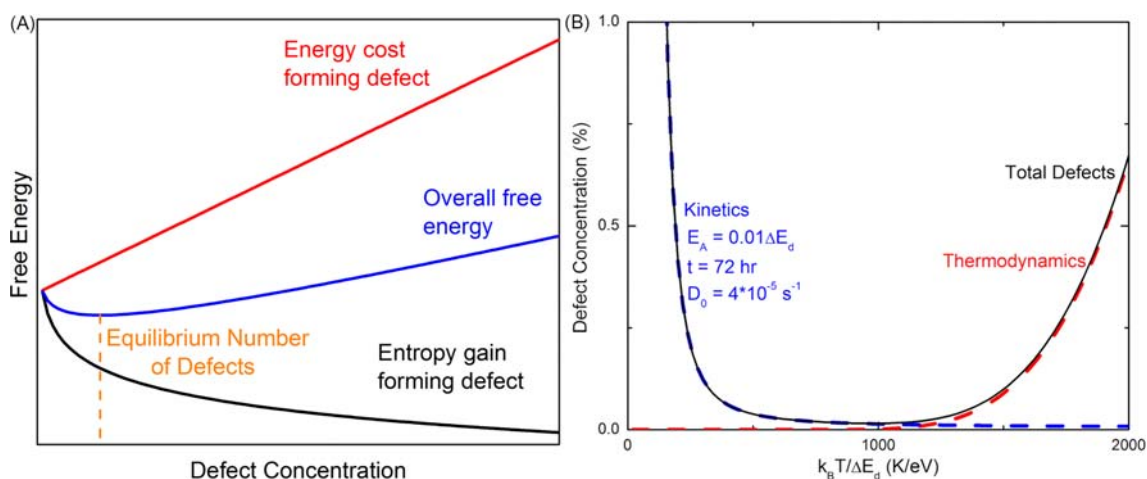


Fig. 5 (A) The internal energy cost (ΔU or ΔH) of forming a defect (imperfection) is positive since by definition it stretches and or breaks/makes chemical bonds that are not at their (local) energy minima (red line). However, adding an imperfection at any temperature $T > 0$ K is entropically favorable because it adds configurational entropy (so $-T\Delta S = -k_B T \ln \Omega$, black line). The result is that the total thermodynamic energy (blue line) minimum, and hence equilibrium number of defects, is greater than zero (yellow dashed lines). Thus, at equilibrium, all materials have defects. (B) Kinetics do not improve the matter. While the thermodynamic number of defects reduces when T is small, the number of kinetically stabilized defects rises as atoms form bonds to what they encounter first, and then are unable to diffuse/move to the ideal/optimum locations. For any synthesis carried out in finite time, this results in a “bathtub” shaped curve where the number of defects is minimized (not zero) at some intermediate temperature. The only way to make a material defect free is to carry out the synthesis at absolute zero, and to wait infinite time for its completion.

4.11.5 Ideality meets reality

The forgoing sections have a built-in assumption: that the compounds/materials being considered have a well-defined (and often periodic) structure and composition. Is this rigorously true? For any synthesis carried out at a temperature greater than absolute zero, the answer is sadly “probably not,” as described in Fig. 5.

While thermodynamic and kinetic considerations dictate defects in general, that does not necessarily mean that it applies in all situations. For example, if the system size is very small, then the entropic energy gain of forming a single defect might not in fact outweigh the energy cost. For example, consider the case of a benzene molecule, C_6H_6 , and its “defect” version pyridine C_5H_5N , where a C–H has been replaced by N. The enthalpic energy cost is the energy difference between the two molecules⁹⁹: $100 \text{ kJ/mol} - 49 \text{ kJ/mol} = 51 \text{ kJ/mol}$, or about $\Delta H_{\text{defect}} = 0.5 \text{ eV/molecule}$. The entropic energy gain from such a substitution is $-T\Delta S = -T k_B \ln(6) = -T(1.5 \times 10^{-4} \text{ eV/molecule})$ since there are six equivalent choices of C–H to replace with N. So as long as the synthesis temperature stays below $\sim 3300 \text{ K}$ (a highly likely event), then a defect free material is possible. This explains the existence of well-defined, defect free, single molecules.

But now consider a single mL of liquid benzene. At a density of 0.88 g/mL and a molecular weight of 78.1 g/mol , there are 6.8×10^{21} molecules. Starting with a solution of perfect benzene molecules, the energy cost of introducing a single pyridine defect is still 0.5 eV/molecule . But the entropic energy gain is now $-T\Delta S = -T k_B \ln(6 \cdot 6.8 \times 10^{21}) = -T(5 \times 10^{-3} \text{ eV/molecule})$, so a defect free solution is only possible when prepared below $\sim 100 \text{ K}$. This explains the non-existence of 100% pure reagents.

What does this mean for quantum materials? It means that all real quantum materials have defects, and including them – from theoretical treatment to data interpretation is essential. A large suite of experimental and theoretical methods to detect and quantify defects in materials have been developed, Table 4.

Some of these methods (e.g. photoluminescence) have been used for decades in the fields leading up to quantum materials. Others (e.g. X-ray micro Computed Tomography) are only more recently being deployed for the understanding of quantum materials. Of course the full range of techniques available is much broader than Table 4 as there are many variations on the techniques listed (e.g. hyperspectral imaging blends UV/Vis emission and optical imaging or numerical simulations) and nearly any observable is directly or indirectly coupled to defects that are present. For example, electrical measurements in the presence of thermal or optical excitation or detection are often used for defect characterization in semiconductors, and “simple” quantities such as density can put bounds on the type and number of defects present.

Table 4 Select methods for observing and quantifying defects in quantum materials.

<i>(Scanning) Transmission electron microscopy</i> ¹⁰⁰	<i>UV/Vis/IR/THz Absorption/emission</i> ^{101,102}	<i>Photoluminescence or fluorescence</i> ¹⁰³
X-ray/Neutron/Electron Diffraction ¹⁰⁴	Diffuse Scattering/Pair Distribution Function ¹⁰⁵	Inductively Coupled Plasma or Glow Discharge – Mass or Emission Spectroscopy (ICP-MS/GDMS) ¹⁰⁶
X-ray micro computed tomography ¹⁰⁷	Defect etching ¹⁰⁸	(Polarized) Optical Imaging ¹⁰⁹
Scanning Tunneling Microscopy / Atomic Force Microscopy ¹¹⁰	Electron Paramagnetic or Nuclear Magnetic Resonance ¹¹¹	Raman/Inelastic Scattering/Microscopy ¹¹²
Density Functional Theory Supercells ¹¹³	Quantum Monte Carlo ¹¹⁴	Quantum Oscillations ¹¹⁵

Table 5 Frontiers in quantum materials synthesis.

<i>Direction</i>	<i>Innovations needed</i>	<i>Potential outcomes</i>
New extremes (higher pressures, temperatures, rates) ^{128,129}	Stronger materials Better (thermal) insulators	New kinds of bonding involving “core” electrons Higher temperature superconductors
Synthesis methods at intermediate temperatures ¹¹⁸	Methods to tailor bond strength/specific bond breaking in the solid state	Nearly defect free quantum behaviors and all new phenomena that will result
Lithography in three dimensions	Extremely rapid (kHz rate) single atomic layer patterning techniques	Moore’s law continues Lossless photonics Defect free quantum spin liquids
Atomic scale 3D printing	Single atom deposition Universal elemental feedstocks	New quantum sensors and qubits High performance catalysts

4.11.6 Preparation of quantum materials

Many excellent books, reviews, and perspectives exist on methods to design and synthesize quantum materials and the reader is directed to them.^{116–127} For our purposes, it is most useful to consider what is not currently possible, but might become possible with sufficient chemical and community innovations. A selection of key directions, necessary chemical innovations, and likely outcomes if successful, are given in Table 5.

Although quite varied, a common ingredient is evident: advances in preparation revolve around greater (and, ideally, atomic level) control over where atoms are placed and how they are bonded to their neighbors. This is essential because while it is not possible to remove all defects, control over the type, number, and distribution of defects *is possible*, and essential to preparing new quantum materials with novel and superior properties and performance.^{130,131} Another unifying theme is that the field of quantum materials synthesis is where organic synthesis was ca. 50 years ago: a large zoo of reactions and known reactivity, but without the connective tissue – the understanding of reactivity – to enable nearly limitless control over what structures are produced. Developing this connective tissue – a coherent understanding of chemical reactivity – is imperative, but will not be easy given little progress has been made over the past 20 years.¹²⁰ It also extends beyond quantum materials to all other areas of solid state inorganic materials.

4.11.7 Other frontiers

In addition to developing methods to put every atom in its place (scalably), there are a number of other prospective future directions with quantum materials that may come to fruition over the next decade, particularly in the chemical space. These include:

- *Developing the connection between topology and chemical reactivity.* Existing models of chemical reactivity rely heavily on consideration of orbital overlaps and electron transfer to decide (in the absence of experimental or computational thermodynamic or kinetic data) whether a given chemical transformation will occur or not. Recent work has shown that there are unexpected connections between topology and some classical rules of chemical reactivity.¹³² This perhaps suggests that there is more to be learned in the “real space” limit for this type of quantum material. Relatedly, there are efforts to understand whether topological states can be used to improve catalysis and catalyst design.¹³³
- *Extended defects/structures as design elements.* Compared to a decade ago, there is much activity now in the control and use of point defects in tailoring the behavior (and indeed building) quantum materials. Compared to the ceramics or metallurgy communities however, extended defects – e.g. antiphase domain boundaries, or aperiodic but locally constrained atomic displacements – are only rarely quantified, and even more rarely considered as sources of quantum phenomena in materials. With the rise of layered heterostructures, this is changing in the context of controlled interfacial materials. It is natural to expand this to more general extended structures in materials across multiple length scales and dimensions.
- *The intersection with Quantum Information Science and Engineering (QISE).* Born out of lasers and atomic clocks, QISE is seeing the development of the first practical quantum computers, and the first practical quantum sensors. Both of these have the potential to greatly influence the future of quantum materials – enabling new regimes of predictive power and enabling quantification of defect structures and probing of entanglement that are not possible today.¹³⁴ QISE will also likely be substantially impacted by chemical quantum materials advances, as sources of improved materials for single site or superconducting qubits and sensors, as current state of the art materials in QISE (e.g. NV centers in diamond, Nb/Ta/Al superconductors) are likely too simple on the materials complexity – performance scale.^{135,136}
- *The intersection with data science.* Computing power has advanced to the level that theoretical tools first described more than 50 years ago, such as convolutional neural networks, are now possible to implement and apply to real data and real systems. These tools excel at identifying patterns and relationships when there is a high dimensionality (ie. large number of) inputs indirectly linked to outputs, exactly as found in quantum materials – both theoretically (from the underlying quantum mechanics to the emergent phenomena), and experimentally (from the large number of known and unknown synthesis variables to behavior of the material so produced). These tools will certainly lead to advances in our understanding and control over synthesis and design of quantum materials in individual laboratories.^{137–139} If the community can come together to pool (i.e. publish) data, they may have an even more transformative impact.^{140–145}

Acknowledgments

This chapter was made possible as part of the broader outreach component of NSF-DMR Award #1905411. The author thanks Gregory Bassen, Thomas Whorisky, and Courtney McQueen for feedback on an earlier draft of this chapter.

References

1. The rise of quantum materials *Nat. Phys.* **2016**, *12*, 105.
2. Broholm, C.; Fisher, I.; Moore, J.; Murnane, M. *Quantum Materials for Energy Relevant Technologies BRN*, DOE-BES, 2016.
3. Broholm, C.; Awschalom, D.; Dessau, D.; Greene, L. *Workshop Report on Midscale Instrumentation to Accelerate Progress in Quantum Materials*, NSF-DMR, 2018.
4. Tobash, P. H.; Bobev, S. Chemical Bonding and Structural Relationships in Extended Solids. In *Fundamentals of Quantum Materials*; Paglione, J., Butch, N. P., Rodriguez, E. E., Eds., World Scientific Publishing, 2021; pp 19–47. Chapter 2.
5. Cava, R.; de Leon, N.; Xie, W. Introduction: Quantum Materials. *Chem. Rev.* **2021**, *121*, 2777–2779.
6. Orenstein, J. Ultrafast Spectroscopy of Quantum Materials. *Phys. Today* **2012**, *65*, 44.
7. The astute reader will note that creating such a pair spontaneously would not conserve energy, and thus even these do not in fact appear out of a vacuum. In vacuum fluctuations, virtual pairs of such particles are allowed by Heisenberg uncertainty to appear, for a very short time ($\Delta E \Delta t \geq \hbar/2$, so if Δt is very small, ΔE can be large).
8. Lewes, G. H. *Problems of Life and Mind. First Series: The Foundations of a Creed*, vol. 2; Osgood: Boston, 1875; p 369.
9. McQueen, T. M.; Ho, D. M.; Jiménez Cahua, C.; Cava, R. J.; Pascal, R. A., Jr.; Soos, Z. G. Realization of the Bond Order Wave (BOW) Phase of Extended Hubbard Models in Rb-TCNQ(I). *Chem. Phys. Lett.* **2009**, *475*, 44–48.
10. Landau, L. D. über Die Bewegung der Elektronen in Kristallgitter. *Phys. Z. Sowjet.* **1933**, *3*, 644–645.
11. Kozhevnikov, A. B. *Stalin's Great Science: The Times and Adventures of Soviet Physicists*, Imperial College Press: London, 2004.
12. Bardeen, J.; Cooper, L. N.; Schrieffer, J. R. Microscopic Theory of Superconductivity. *Phys. Rev.* **1957**, *106*, 162.
13. Bardeen, J.; Cooper, L. N.; Schrieffer, J. R. Theory of Superconductivity. *Phys. Rev.* **1957**, *108*, 1175.
14. Onnes, H. K. The Superconductivity of Mercury. *Comm. Phys. Lab. Univ. Leiden* **1911**, *122*, 122–124.
15. Bednorz, J. G.; Müller, K. A. Possible high- T_c Superconductivity in the Ba-La-cu-O System. *Zeitschrift für Physik B Condens. Matter* **1986**, *64*, 189–193.
16. Wu, M. K.; Ashburn, J. R.; Torng, C. J.; Hor, P. H.; Meng, R. L.; Gao, L.; Huang, Z. J.; Wang, Y. Q.; Chu, C. W. Superconductivity at 93 K in a New Mixed-Phase Y-Ba-cu-O Compound System at Ambient Pressure. *Phys. Rev. Lett.* **1987**, *58*, 908.
17. Schneemeyer, L. F.; Waszczak, J. V.; Siegrist, T.; van Dover, R. B.; Rupp, L. W.; Batlogg, B.; Cava, R. J.; Murphy, D. W. Superconductivity in YBa₂Cu₃O₇ Single Crystals. *Nature* **1987**, *328*, 601–603.
18. Anderson, P. W. Resonating Valence Bonds: A New Kind of Insulator? *Mater. Res. Bull.* **1973**, *8*, 153–160.
19. Savary, L.; Balents, L. Quantum Spin Liquids: A Review. *Rep. Prog. Phys.* **2017**, *80*, 016502.
20. Knolle, J.; Moessner, R. A Field Guide to Spin Liquids. *Ann. Rev. Condens. Matter Phys.* **2019**, *10*, 451–472.
21. Chamorro, J. R.; McQueen, T. M.; Tran, T. T. Chemistry of Quantum Spin Liquids. *Chem. Rev.* **2021**, *121*, 2898–2934.
22. Broholm, C.; Cava, R. J.; Kivelson, S. A.; Nocera, D. G.; Norman, M. R.; Senthil, T. Quantum spin liquids. *Science* **2020**, *367*, eaay0668.
23. Bell, J. S. On the Einstein Podolsky Rosen Paradox. *Physics Physique Fizika* **1964**, *1*, 195.
24. Freedman, S. J.; Clauser, J. F. Experimental Test of Local Hidden-Variable Theories. *Phys. Rev. Lett.* **1972**, *28*, 938.
25. Aspect, A.; Dalibard, J.; Roger, G. Experimental Test of Bell's Inequalities Using Time-Varying Analyzers. *Phys. Rev. Lett.* **1804**, *1982*, 49.
26. Tittel, W.; Brendel, J.; Zbinden, H.; Gisin, N. Violation of Bell Inequalities by Photons More than 10 km Apart. *Phys. Rev. Lett.* **1998**, *81*, 3563.
27. Weihs, G.; Jennewein, T.; Simon, C.; Weinfurter, H.; Zeilinger, A. Violation of Bell's Inequality under Strict Einstein Locality Conditions. *Phys. Rev. Lett.* **1998**, *81*, 5039.
28. Pan, J.-W.; Bouwmeester, D.; Daniell, M.; Weinfurter, H.; Zeilinger, A. Experimental Test of Quantum Nonlocality in Three-Photon Greenberger-Horne-Zeilinger Entanglement. *Nature* **2000**, *403*, 515–519.
29. Rowe, M. A.; Kłypinski, D.; Meyer, V.; Sackett, C. A.; Itano, W. M.; Monroe, C.; Wineland, D. J. Experimental Violation of a Bell's Inequality with Efficient Detection. *Nature* **2001**, *409*, 791–794.
30. Salart, D.; Baas, A.; van Houwelingen, J. A. W.; Gisin, N.; Zbinden, H. Spacelike Separation in a Bell Test Assuming Gravitationally Induced Collapses. *Phys. Rev. Lett.* **2008**, *100*, 220404.
31. Hoffmann, R. *Solids and Surfaces: A Chemist's View of Bonding in Extended Structures*, Wiley, 1991.
32. Hoffmann, R. A Chemical and Theoretical Way to Look at Bonding on Surfaces. *Rev. Mod. Phys.* **1988**, *60*, 601.
33. Hoffmann, R. How Chemistry and Physics Meet in the Solid State. *Angew. Chem. Int. Ed.* **1987**, *26*, 846–878.
34. Aroyo, M. I.; Perez-Mato, J. M.; Orobengoa, D.; Tasci, E.; de la Flor, G.; Kirov, A. Crystallography Online: Bilbao Crystallographic Server. *Bulg. Chem. Commun.* **2011**, *43* (2), 183–197. <https://www.cryst.ehu.es/>.
35. Aroyo, M. I.; Perez-Mato, J. M.; Capillas, C.; Kroumova, E.; Ivantchev, S.; Madariaga, G.; Kirov, A.; Wondratschek, H. Bilbao Crystallographic Server I: Databases and Crystallographic Computing Programs. *Z. Krist.* **2006**, *221* (1), 15–27. <https://doi.org/10.1524/zkri.2006.221.1.15>.
36. Aroyo, M. I.; Kirov, A.; Capillas, C.; Perez-Mato, J. M.; Wondratschek, H. Bilbao Crystallographic Server II: Representations of Crystallographic Point Groups and Space Groups. *Acta Cryst.* **2006**, *A62*, 115–128. <https://doi.org/10.1107/S0108767305040286>.
37. Stokes, H. T.; Hatch, D. M.; Campbell, B. J. ISODISTORT. *ISOTROPY Software Suite*, **2006**. <https://iso.byu.edu>.
38. Campbell, B. J.; Stokes, H. T.; Tanner, D. E.; Hatch, D. M. ISODISPLACE: An Internet Tool for Exploring Structural Distortions. *J. Appl. Cryst.* **2006**, *39*, 607–614. <https://doi.org/10.1107/S0021889806014075>.
39. Berry, M. V. Quantal Phase Factors Accompanying Adiabatic Changes. *Proc. Royal Soc. A* **1984**, *392*, 45–57.
40. Yarkony, D. R. Diabolical Conical Intersections. *Rev. Mod. Phys.* **1996**, *68*, 985.
41. Bunker, P. R.; Jensen, P. *Molecular Symmetry and Spectroscopy*, 2nd edn; NRC Research Press: Ottawa, 1998.
42. König, M.; Wiedmann, S.; Brüne, C.; Roth, A.; Bühmann, H.; Molenkamp, L. W.; Qi, X.-L.; Zhang, S.-C. Quantum Spin Hall Insulator State in HgTe Quantum Wells. *Science* **2007**, *318*, 766–770.
43. Fu, L.; Kane, C. L. Topological Insulators with Inversion Symmetry. *Phys. Rev. B* **2007**, *76*, 045302.
44. Kane, C. L.; Moore, J. E. Topological insulators. *Phys. World* **2011**, *24*, 32–36.
45. Armitage, N. P.; Mele, E. J.; Vishwanath, A. Weyl and Dirac Semimetals in Three-Dimensional Solids. *Rev. Mod. Phys.* **2018**, *90*, 015001.
46. Mott, N. F. Metal-Insulator Transition. *Rev. Mod. Phys.* **1968**, *40*, 677.
47. Imada, M.; Fujimori, A.; Tokura, Y. Metal-Insulator Transitions. *Rev. Mod. Phys.* **1998**, *70*, 1039.
48. Chen, C.-W.; Choe, J.; Morosan, E. Charge Density Waves in Strongly Correlated electron Systems. *Rep. Prog. Phys.* **2016**, *79*, 084505.
49. Hurd, C. M. Varieties of Magnetic Order in Solids. *Contemp. Phys.* **1982**, *23*, 469–493.
50. Karandashev, K.; Xu, Z.-H.; Meuwly, M.; Vaniček, J.; Richardson, J. O. Kinetic Isotope Effects and how to Describe them. *Struct. Dyn.* **2017**, *4*, 061501.
51. Bigeleisen, J. Theory of isotope effects in chemical reaction rates. *Conference on Isotopic Exchange Reactions and Chemical Kinetics*, Brookhaven National Laboratory and Associated Universities Incorporated, 1948.
52. Simon, A. Superconductivity and Chemistry. *Angew. Chem. Int. Ed.* **1997**, *36*, 1788–1806.
53. Bigeleisen, J.; Lee, M. W.; Mandel, F. Equilibrium Isotope Effects. *Annu. Rev. Phys. Chem.* **1973**, *24*, 407–440.
54. Hamermesh, M. *Group Theory and its Application to Physical Problems*, Dover Books on Physics: New York, 1989.
55. Tinkham, M. *Group Theory and Quantum Mechanics*, Dover Books on Chemistry: New York, 2003.
56. Cotton, F. A. *Chemical Applications of Group Theory*, 3rd edn.; Wiley, 1991.

57. Matthias, B. T. Empirical Relation between Superconductivity and the Number of Valence Electrons per Atom. *Phys. Rev.* **1955**, *97*, 74.
58. Stewart, G. R. Superconductivity in the A15 Structure. *Phys. C* **2015**, *514*, 28–35.
59. Yamaguchi, Y.; Yamaguchi, H.; Ohashi, M.; Yamamoto, H.; Shimoda, N.; Kikuchi, M.; Syono, Y. Observation of the Antiferromagnetic Ordering in La_2CuO_4 . *Jpn. J. Appl. Phys.* **1987**, *26*, L447.
60. Mitsuda, S.; Shirane, G.; Sinha, S. K.; Johnston, D. C.; Alvarez, M. S.; Vaknin, D.; Moncton, D. E. Confirmation of Antiferromagnetism in $\text{La}_2\text{CuO}_{4-y}$ with Polarized Neutrons. *Phys. Rev. B* **1987**, *36*, 822(R).
61. Hayward, M. A.; Green, M. A.; Rosseinsky, M. J.; Sloan, J. Sodium Hydride as a Powerful Reducing Agent for Topotactic Oxide Deintercalation: Synthesis and Characterization of the Nickel(II) Oxide LaNiO_2 . *J. Am. Chem. Soc.* **1999**, *121*, 8843–8854.
62. Mitchell, J. F. A Nickelate Renaissance. *Front. Phys.* **2021**. fphy.2021.813483.
63. Zheng, H.; Zhang, J.; Wang, B.; Phelan, D.; Krogstad, M. J.; Ren, Y.; Phelan, W. A.; Chmaissem, O.; Poudel, B.; Mitchell, J. F. High pO₂ Floating Zone Crystal Growth of the Perovskite Nickelate PrNiO_3 . *Crystals* **2019**, *9*, 324.
64. Freeland, J. W.; van Veenendaal, M.; Chakhalian, J. Evolution of Electronic Structure across the Rare-Earth RNiO_3 Series. *J. Electron Spectrosc. Relat. Phenom.* **2016**, *208*, 56–62.
65. Cava, R. J. Oxide superconductors. *J. Am. Ceram. Soc.* **2000**, *83*, 5–28.
66. Cava, R. J. Introduction to the Structure and Chemistry of Superconducting Materials. *Physica C: Superconductivity* **1997**, *282-287*, 27–33.
67. Li, D.; Lee, K.; Wang, B. Y.; Osada, M.; Crossley, S.; Lee, H. R.; Cui, Y.; Hikita, Y.; Hwang, H. Y. Superconductivity in an Infinite-Layer Nickelate. *Nature* **2019**, *572*, 624–627.
68. Pan, G. A.; Segedin, D. F.; LaBollita, H.; Song, Q.; Nica, E. M.; Goodge, B. H.; Pierce, A. T.; Doyle, S.; Novakov, S.; Carrizales, D. C.; N'Diaye, A. T.; Shafer, P.; Paik, H.; Heron, J. T.; Mason, J. A.; Yacoby, A.; Kourkoutis, L. F.; Erten, O.; Brooks, C. M.; Botana, A. S.; Mundy, J. A. Superconductivity in a Quintuple-Layer Square-Planar Nickelate. *Nat. Mater.* **2021**, *21*, 160–164.
69. Pickett, W. E. The Other High-Temperature Superconductors. *Phys. B: Condens. Matter* **2001**, *296*, 112–119.
70. Ishida, K.; Nakai, Y.; Hosono, H. To What Extent iron-Pnictide New Superconductors Have Been Clarified: A Progress Report. *J. Physical Soc. Japan* **2009**, *78*, 062001.
71. Cava, R. J.; Takagi, H.; Batlogg, B.; Zandbergen, H. W.; Krajewski, J. J.; Peck, W. F., Jr.; van Dover, R. B.; Felder, R. J.; Siegrist, T.; Mizuhashi, K.; Lee, J. O.; Eisaki, H.; Carter, S. A.; Uchida, S. Superconductivity at 23 K in Yttrium Palladium Boride Carbide. *Nature* **1994**, *367*, 146–148.
72. Huang, Q.; Qiu, Y.; Bao, W.; Green, M. A.; Lynn, J. W.; Gasparovic, Y. C.; Wu, T.; Wu, G.; Chen, X. H. Neutron-Diffraction Measurements of Magnetic Order and a Structural Transition in the Parent BaFe_2As_2 Compound of FeAs-Based High-Temperature Superconductors. *Phys. Rev. Lett.* **2008**, *101*, 257003.
73. Neilson, J. R.; Llobet, A.; Stier, A. V.; Wu, L.; Wen, J.; Tao, J.; Zhu, Y.; Tesanovic, Z. B.; Armitage, N. P.; McQueen, T. M. Mixed-Valence-Driven Heavy-Fermion Behavior and Superconductivity in KNi_2Se_2 . *Phys. Rev. B* **2012**, *86*, 054512.
74. Tiedje, O.; Krasovskii, E. E.; Schattke, W.; Stoll, P.; Näther, C.; Bensch, W. Bridging from ThCr_2Si_2 -Type Materials to Hexagonal Dichalcogenides: An Ab Initio and Experimental Study of KCu_2Se_2 . *Phys. Rev. B* **2003**, *67*, 134105.
75. Kida, T.; Fenner, L. A.; Dee, A. A.; Terasaki, I.; Hagiwara, M.; Wills, A. S. The Giant Anomalous Hall Effect in the Ferromagnet Fe_3Sn_2 – A Frustrated Kagome Metal. *J. Phys. Condens. Matter* **2011**, *23*, 112205.
76. Ye, L.; Kang, M.; Liu, J.; von Cube, F.; Wicker, C. R.; Suzuki, T.; Jozwiak, C.; Bostwick, A.; Rotenberg, E.; Bell, D. C.; Fu, L.; Comin, R.; Checkelsky, J. G. Massive Dirac Fermions in a Ferromagnetic Kagome Metal. *Nature* **2018**, *555*, 638–642.
77. Ortiz, B. R.; Gomes, L. C.; Morey, J. R.; Winiarski, M. J.; Bordelon, M.; Mangum, J. S.; Oswald, I. W. H.; Rodriguez-Rivera, J. A.; Neilson, J. R.; Wilson, S. D.; Ertekin, E.; McQueen, T. M.; Toberer, E. S. New Kagome Prototype Materials: Discovery of KV_3Sb_5 , RbV_3Sb_5 , and CsV_3Sb_5 . *Phys. Rev. Mater.* **2019**, *3*, 094407.
78. Jackeli, G.; Khomskii, D. I. Classical Dimers and Dimerized Superstructure in an Orbital Degenerate Honeycomb Antiferromagnet. *Phys. Rev. Lett.* **2008**, *100*, 147203.
79. Kitaev, A. Anyons in an Exactly Solved Model and Beyond. *Ann. Phys. Rehabil. Med.* **2006**, *321*, 2–111.
80. Kalmeyer, V.; Laughlin, R. B. Theory of the Spin Liquid State of the Heisenberg Antiferromagnet. *Phys. Rev. B* **1989**, *39*, 11879.
81. Collins, M. F.; Petrenko, O. A. Review/Synthese: Triangular Antiferromagnets. *Can. J. Phys.* **1997**, *75*, 605–655.
82. Van Maaren, M. H.; Schaeffer, G. M. Superconductivity in Group Va Dichalcogenides. *Phys. Lett.* **1966**, *20*, 131.
83. Jin, R.; Sales, B. C.; Khalifah, P.; Mandrus, D. Observation of Bulk Superconductivity in $\text{Na}_x\text{CoO}_2 \cdot y\text{H}_2\text{O}$ and $\text{Na}_x\text{CoO}_2 \cdot y\text{D}_2\text{O}$ Powder and Single Crystals. *Phys. Rev. Lett.* **2003**, *91*, 217001.
84. Shekellon, J. P.; Neilson, J. R.; Soltan, D. G.; McQueen, T. M. Possible Valence-Bond Condensation in the Frustrated Cluster Magnet $\text{LiZn}_2\text{Mo}_3\text{O}_8$. *Nat. Mater.* **2012**, *11*, 493–496.
85. Subramanian, M. A.; Aravamudan, G.; Subba Rao, G. V. Oxide Pyrochlores – A Review. *Prog. Solid State Chem.* **1983**, *15*, 55–143.
86. Gardner, J. S.; Gingras, J. P.; Greedan, J. E. Magnetic Pyrochlore Oxides. *Rev. Mod. Phys.* **2010**, *82*, 53.
87. She, J.-H.; Kim, C. H.; Fennie, C. J.; Lawler, M. J.; Kim, E.-A. Topological Superconductivity in Metal/Quantum-Spin-Ice Heterostructures. *npj Quantum Mater.* **2017**, *2*, 64.
88. Heremans, J. P.; Cava, R. J.; Samarth, N. Tetradymites as Thermoelectrics and Topological Insulators. *Nat. Rev. Mater.* **2017**, *2*, 17049.
89. Yan, B.; Zhang, S.-C. Topological Materials. *Rep. Prog. Phys.* **2012**, *75*, 096501.
90. Li, J.; Li, Y.; Du, S.; Wang, Z.; Gu, B.-L.; Zhang, S.-C.; He, K.; Duan, W.; Xu, Y. Intrinsic Magnetic Topological Insulators in Van der Waals Layered MnBi_2Te_4 -Family Materials. *Sci. Adv.* **2019**, *5*, aaw5685.
91. Zeugner, A.; Nietschke, F.; Wolter, A. U. B.; Gaß, S.; Vidal, R. C.; Peixoto, T. R. F.; Pohl, D.; Damm, C.; Lubk, A.; Hentrich, R.; Moser, S. K.; Fornari, C.; Min, C. H.; Schatz, S.; Kifßner, K.; Unzelmann, M.; Kaiser, M.; Scaravaggi, F.; Rellinghaus, B.; Nielsch, K.; Hess, C.; Büchner, B.; Reinert, F.; Bentmann, H.; Deckler, O.; Doert, T.; Ruck, M.; Iseva, A. Chemical Aspects of the Candidate Antiferromagnetic Topological Insulator MnBi_2Te_4 . *Chem. Mater.* **2019**, *31*, 2795–2806.
92. Graf, T.; Felser, C.; Parkin, S. S. P. Simple Rules for the Understanding of Heusler Compounds. *Prog. Solid State Chem.* **2011**, *39*, 1–50.
93. Schirhagl, R.; Chang, K.; Lorez, M.; Degen, C. L. Nitrogen-Vacancy Centers in Diamond: Nanoscale Sensors for Physics and Biology. *Annu. Rev. Phys. Chem.* **2014**, *65*, 83–105.
94. Wolfowicz, G.; Heremans, F. J.; Anderson, C. P.; Kanai, S.; Seo, H.; Gali, A.; Galli, G.; Awschalom, D. D. Quantum Guidelines for Solid-State Spin Defects. *Nat. Rev. Mater.* **2021**, *6*, 906–925.
95. DeMille, D. Quantum Computation with Trapped Polar Molecules. *Phys. Rev. Lett.* **2002**, *88*, 067901.
96. Gaita-Ariño, A.; Luis, F.; Hill, S.; Coronado, E. Molecular Spins for Quantum Computation. *Nat. Chem.* **2019**, *11*, 301–309.
97. King, R. B. Chemical Structure and Superconductivity. *J. Chem. Inf. Comput. Sci.* **1999**, *39*, 180–191.
98. Gui, X.; Lv, B.; Xie, W. Chemistry in Superconductors. *Chem. Rev.* **2021**, *121*, 2966–2991.
99. $\text{C}_6\text{H}_6 + \frac{1}{2} \text{N}_2 \rightarrow \text{C}_5\text{H}_5\text{N} + \text{C}_{(\text{graphite})} + \frac{1}{2} \text{H}_2(\text{g})$, all other components have $\Delta H_f = 0$. The numbers change considering different possible end products for the C and H, but this provides a crude estimate of the cost of substituting an N for a C-H.
100. Bianco, E.; Kourkoutis, L. F. Atomic-Resolution Cryogenic Scanning Transmission Electron Microscopy for Quantum Materials. *Acc. Chem. Res.* **2021**, *54*, 3277–3287.
101. Förster, H. UV/VIS spectroscopy. In *Characterization I. Molecular Sieves – Science and Technology*; Kage, H. G., Weitcamp, J., Eds.; vol. 4; Springer: Berlin, 2004; pp 337–426.
102. Zhong, S. Progress in Terahertz Nondestructive Testing: A Review. *Front. Mech. Eng.* **2019**, *14*, 273–281.
103. Pavesi, L. Photoluminescence of $\text{Al}_x\text{Ga}_{1-x}\text{As}$ Alloys. *J. Appl. Phys.* **1994**, *73*, 4779.
104. Cheetham, A. K.; Wilkinson, A. P. Synchrotron X-Ray and Neutron Diffraction Studies in Solid-State Chemistry. *Angew. Chem. Int. Ed.* **1992**, *31*, 1557–1570.
105. Egami, T.; Billinge, S. J. L. *Underneath the Bragg Peaks*; Elsevier Pergamon: New York, 2003.
106. Becker, J. S.; Dietze, H.-J. Inorganic Trace Analysis by Mass Spectrometry. *Spectrochim. Acta, Part B* **1998**, *53*, 1475–1506.

107. Withers, P. J.; Bouman, C.; Carmignato, S.; Cnudde, V.; Grimaldi, D.; Hagen, C. K.; Maire, E.; Manley, M.; Plessis, A. D.; Stock, S. R. X-Ray Computed Tomography. *Nat. Rev. Methods Primers* **2021**, *1*, 18.
108. Abbadie, A.; Hartmann, J.-M.; Brunier, F. A Review of Different and Promising Defect Etching Techniques: From Si to Ge. *ECS Trans.* **2007**, *10*, 3.
109. Nellist, P. D. Electron-Optical Sectioning for Three-Dimensional Imaging of Crystal Defect Structures. *Mater. Sci. Semicond. Process.* **2017**, *65*, 18–23.
110. Venables, J. A.; Smith, D. J.; Cowley, J. M. HREM, STEM, REM, SEM – and STM. *Surf. Sci.* **1987**, *181*, 235–249.
111. Watkins, G. D. EPR of Defects in Semiconductors: Past, Present, Future. *Phys. Solid State* **1999**, *41*, 746–750.
112. Orlando, A.; Franceschini, F.; Muscas, C.; Pidkova, S.; Bartoli, M.; Rovere, M.; Tagliaferro, A. A Comprehensive Review on Raman Spectroscopy Applications. *Chemosensors* **2021**, *9*, 262.
113. Freysoldt, C.; Grabowski, B.; Hickel, T.; Neugebauer, J.; Kresse, G.; Janotti, A.; Van de Walle, C. G. First-Principles Calculations for Point Defects in Solids. *Rev. Mod. Phys.* **2014**, *86*, 253.
114. Parker, W. D.; Wilkins, J. W.; Hennig, R. G. Accuracy of Quantum Monte Carlo Methods for Point Defects in Solids. *Phys. Status Solidi B* **2011**, *248*, 267–274.
115. Ibach, H.; Lüth, H. *Solid-State Physics: An Introduction to Principles of Materials Science*, Springer-Verlag: Berlin, 1995.
116. Paglione, J.; Butch, N. P.; Rodriguez, E. E. *Fundamentals of Quantum Materials*, World Scientific Publishing, 2021.
117. Schoop, L. M.; Pielhofer, F.; Lotsch, B. V. Chemical Principles of Topological Semimetals. *Chem. Mater.* **2018**, *30*, 3155–3176.
118. Chamorro, J. R.; McQueen, T. M. Progress toward Solid State Synthesis by Design. *Acc. Chem. Res.* **2018**, *51*, 2918–2925.
119. Aykol, M.; Montoya, J. H.; Hummelshøj, J. Rational Solid-State Synthesis Routes for Inorganic Materials. *J. Am. Chem. Soc.* **2021**, *143*, 9244–9259.
120. Jansen, M. A Concept for Synthesis Planning in Solid-State Chemistry. *Angew. Chem. Int. Ed.* **2002**, *41*, 3746–3766.
121. Yaghi, O. M.; O’Keeffe, M.; Kanatzidis, M. Design of Solids from Molecular Building Blocks: Golden Opportunities for Solid State Chemistry. *J. Solid State Chem.* **2000**, *152*, 1–2.
122. Kohlmann, H. Looking in to the Black Box of Solid-State Synthesis. *Eur. J. Inorg. Chem.* **2019**, *39–40*, 4174–4180.
123. Hulliger, J. Chemistry and Crystal Growth. *Angew. Chem. Int. Ed.* **1994**, *33*, 143–162.
124. Alcouffe, R. E. Review of Flux Synthesis Methods. In *Los Alamos Technical Report LA-4472*; 1970.
125. Koohpayeh, S. M.; Fort, D.; Abell, J. S. The Optical Floating Zone Technique: A Review of Experimental Procedures with Special Reference to Oxides. *Prog. Cryst. Growth Charact. Mater.* **2008**, *54*, 121–137.
126. Samarth, N. Quantum Materials Discovery from a Synthesis Perspective. *Nat. Mater.* **2017**, *16*, 1068–1076.
127. Canfield, P. C.; Fisk, Z. Growth of Single Crystals from Metallic Fluxes. *Philos. Mag. B* **1992**, *65*, 1117–1123.
128. Schmeier, J. L.; Aling, M.; Zoghlin, E.; Wilson, S. D. High-Pressure Laser Floating Zone Furnace. *Rev. Sci. Instrum.* **2019**, *90*, 043906.
129. Phelan, W. A.; Zahn, J.; Kennedy, Z.; McQueen, T. M. Pushing Boundaries: High Pressure, Supercritical Optical Floating Zone Materials Discovery. *J. Solid State Chem.* **2019**, *705–709*.
130. Ahn, C.; Cavalleri, A.; Georges, A.; Ismail-Beigi, S.; Millis, A. J.; Triscone, J.-M. Designing and Controlling the Properties of Transition Metal Oxide Quantum Materials. *Nat. Mater.* **2021**, 1462–1468.
131. Ko, W.; Gai, Z.; Puzetzy, A. A.; Liang, L.; Berlijn, T.; Hachtel, J. A.; Xiao, K.; Ganesh, P.; Yoon, M.; Li, A.-P. Understanding Heterogeneities in Quantum Materials. *Adv. Mater.* **2022**, 2106909.
132. Muechler, L. Topological Classification of Molecules and Chemical Reactions with a Perplectic Structure. *Phys. Rev. B* **2020**, *101*, 045123.
133. Kumar, N.; Guin, S. N.; Manna, K.; Shekhar, C.; Felser, C. Topological Quantum Materials from the Viewpoint of Chemistry. *Chem. Rev.* **2021**, *121*, 2780–2815.
134. Cao, Y.; Romero, J.; Olson, J. P.; Degroote, M.; Johnson, P. D.; Kieferová, M.; Kivlichan, I. D.; Menke, T.; Peropadre, B.; Sawaya, N. P. D.; Sim, S.; Veis, L.; Aspuru-Guzik, A. Quantum Chemistry in the Age of Quantum Computing. *Chem. Rev.* **2019**, *119*, 10856–10915.
135. de Leon, N. P.; Itoh, K. M.; Kim, D.; Mehta, K. K.; Northup, T. E.; Paik, H.; Palmer, B. S.; Samarth, N.; Sangtawesin, S.; Steuerman, D. W. Materials Challenges and Opportunities for Quantum Computing Hardware. *Science* **2021**, *372*, abb2823.
136. Gilbert, M. J. Topological electronics. *Commun. Phys.* **2021**, *4*, 70.
137. Quinn, M. R.; McQueen, T. M. Identifying New Classes of High Temperature Superconductors with Convolutional Neural Networks. *Front. Electron. Mater.* **2022**, femat.2022.893797.
138. Schmidt, J.; Marques, M. R. G.; Botti, S.; Marques, M. A. L. Recent Advances and Applications of Machine Learning in Solid-State Materials Science. *npj Comput. Mater.* **2019**, *5*, 83.
139. Braham, E. J.; Davidson, R. D.; Al-Hashimi, M.; Arróyave, R.; Banerjee, S. Navigating the Design Space of Inorganic Materials Synthesis Using Statistical Methods and Machine Learning. *Dalton Trans.* **2020**, *49*, 11480–11488.
140. Scheffler, M.; Aeschlimann, M.; Albrecht, M.; Bereau, T.; Bungartz, H.-J.; Felser, C.; Greiner, M.; Groß, A.; Koch, C. T.; Kremer, K.; Nagel, W. E.; Scheidgen, M.; Wöll, C.; Draxl, C. FAIR Data Enabling New Horizons for Materials Research. *Nature* **2022**, *604*, 635–642.
141. McQueen, T. M.; Berry, T.; Chamorro, J. R.; Ghasemi, A.; Phelan, W. A.; Pogue, E. A.; Pressley, L. A.; Sinha, M.; Stewart, V. J.; Tran, T. T.; Vivanco, H. K.; Winiarski, M. J. Future Directions in Quantum Materials Synthesis. In *Fundamentals of Quantum Materials*; Paglione, J., Butch, N. P., Rodriguez, E. E., Eds., World Scientific Publishing, 2021; pp 239–259. Chapter 11.
142. Brinson, L. C.; Bartolo, L. M.; Blaiszik, B.; Elbert, D.; Foster, I.; Strachan, A.; Voorhees, P. W. *FAIR Data will Fuel a Revolution in Materials Research*. *arXiv:2204.02881*, 2022.
143. Zunger, A.; Malý, O. I. Understanding Doping of Quantum Materials. *Chem. Rev.* **2021**, *121*, 3031–3060.
144. Giustino, F.; Lee, J. H.; Trier, F.; Bibes, M.; Winter, S. M.; Valenti, R.; Son, Y.-W.; Taillefer, L.; Heil, C.; Figueroa, A. I.; Placais, B.; Wu, Q.-S.; Yazayev, O. V.; Bakkers, E. P. A. M.; Nygard, J.; Forn-Diaz, P.; Francescho, S. D.; McIver, J. W.; Torres, L. E. F. F.; Low, T.; Kumar, A.; Galceran, R.; Valenzuela, S. O.; Costache, M. V.; Manchon, A.; Kim, E.-A.; Schleder, G. R.; Fazio, A.; Roche, S. The 2021 Quantum Materials Roadmap. *J. Phys. Mater.* **2020**, *3*, 042006.
145. An Accelerated, Data-Driven, Materials Discovery Future: Challenges and Opportunities in Two Dimensional, Interfacial, and Layered Materials to Advance Science and Engineering and Impact Society; 2022. Accessed 22 June 2022.

4.12 High pressure chemistry

Ulrich Schwarz^a, Kristina Spektor^b, and Ulrich Häussermann^c, ^aChemische Metallkunde, MPI-CPS, Dresden, Germany;

^bInorganic Chemistry, Faculty for Chemistry and Mineralogy, Leipzig University, Leipzig, Germany; and ^cDepartment of Materials and Environmental Chemistry, Stockholm University, Stockholm, Sweden

© 2023 Elsevier Ltd. All rights reserved.

4.12.1	Introduction	377
4.12.1.1	Background	377
4.12.1.2	Devices for high pressure chemistry	378
4.12.1.3	Challenges compared to “ambient pressure” chemistry and strategies	380
4.12.2	Inorganic materials from high pressure synthesis	381
4.12.2.1	Intermetallic compounds	381
4.12.2.1.1	Borides, carbides and nitrides of transition metals	381
4.12.2.1.2	Silicides	382
4.12.2.1.3	Germanides	383
4.12.2.1.4	Intermetallic clathrates	383
4.12.2.1.5	Bismuthides	384
4.12.2.2	Hydrides	385
4.12.2.2.1	Transition metal hydrides	385
4.12.2.2.2	Active metal hydrides	387
4.12.2.2.3	p-element hydrides	388
4.12.2.3	Carbides and nitrides	389
4.12.2.3.1	Salt-like carbides and nitrides MN ... MN ₂	390
4.12.2.3.2	Compounds with N ₂ species: diazenides (N ₂) ²⁻ vs pernitrides (N ₂) ⁴⁻	392
4.12.2.3.3	Unsaturated moieties as precursors for carbon and nitrogen based materials	394
4.12.2.4	Oxides	397
4.12.2.4.1	Non-metal oxides	397
4.12.2.4.2	Binary metal oxides	399
4.12.2.4.3	Mixed metal (multinary) transition metal oxides	399
4.12.2.5	Exotic halide and noble gas compounds	403
4.12.2.5.1	Halides	403
4.12.2.5.2	Noble gas compounds	404
4.12.2.6	Multi-anion systems	405
4.12.2.6.1	Oxynitrides	406
4.12.2.6.2	Transition metal oxyfluorides	408
4.12.2.6.3	Transition metal oxyhydrides	408
4.12.2.6.4	Miscellaneous	410
4.12.2.7	Molecular anion and tetrahedron-based network compounds	410
4.12.2.7.1	Borates, carbonates, silicates, phosphates	410
4.12.2.7.2	Nitridosilicates and oxonitridosilicates	412
4.12.2.7.3	Nitridophosphates and oxonitridophosphates	413
4.12.2.8	Open framework materials	415
4.12.2.8.1	High pressure as synthesis tool for open frameworks	415
4.12.2.8.2	(Structural) response of porous materials to high pressure conditions	415
4.12.2.8.3	Porous frameworks as reaction containers for pressure induced reactions	415
4.12.3	Conclusions and outlook	415
Acknowledgments		416
References		416

Abbreviations

1D One-dimensional

2D Two-dimensional

3D Three-dimensional

A Alkali (metal)

ADOR Assembly-disassembly-organization-reassembly

Ae Alkaline earth (metal)
 BCS Bardeen–Cooper–Schrieffer
 CTMH Complex transition metal hydrides
 DAC Diamond anvil cell
 DFT Density functional theory
 EELS Electron energy loss spectroscopy
 FIB Focused ion beam
 FM, AFM Ferromagnetic, antiferromagnetic
 GC–MS Gas chromatography–mass spectrometry
 HPHT High pressure, high temperature
 LH-DAC Laser heated diamond anvil cell
 LVP Large volume press
 MA Multi-anvil
 MD Molecular dynamics
 MOF Metal-organic framework
 PC Piston cylinder
 PIA Pressure-induced amorphization
 PIP Pressure-induced polymerization
 PTM Pressure-transmitting medium
 RE Rare-earth
 SSP Single source precursor
 T Transition metal
 XAS X-ray absorption spectroscopy
 XRD X-ray diffraction
 ZIF Zeolitic imidazolate framework

Abstract

High pressure chemistry—employing pressures from 1 to beyond 100 GPa for chemical synthesis in large volume press and laser heated diamond anvil cell devices—has developed into a highly active and broad field. Here we give an overview of recent trends along with a presentation of diverse inorganic compounds produced during the past decade.

4.12.1 Introduction

4.12.1.1 Background

Over the past 25–30 years high pressure chemistry has developed from a niche area into a highly active and diverse field, with a seemingly rapid increasing number of players. This development has been promoted by a better accessibility of and major technological advances in high pressure instrumentation, but also—and foremost—by recognizing the potential of high pressures to expand into completely new families of compounds.

Pressure in high pressure chemistry is typically specified in GPa, $1 \text{ GPa} = 10 \text{ kbar} = 9869 \text{ atm}$. Accordingly, atmospheric pressure corresponds to 10^{-4} GPa , and to relate, the pressure at the deepest part of the ocean (10 km) is about 10^{-1} GPa (1.1 kbar), and the pressure at the Earth's core is 360 GPa (Fig. 1). The influence of pressure to thermodynamic relations (chemical equilibria) and

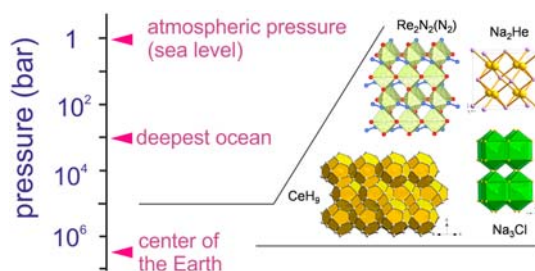


Fig. 1 Pressure scale (logarithmic) with markers relevant to the Earth and “exotic” materials recently synthesized at pressures around 1 Mbar.

kinetics for simple reactions or transformations is $-\partial \Delta G / \partial p = \partial \ln k / \partial p \times RT = -\Delta V^\circ$ and $\partial \ln k / \partial p \times RT = -\Delta V^\ddagger$ (with ΔV° being the difference of molar volumes for products and reactants (reaction volume) and ΔV^\ddagger being the volume of activation). A pressure range 1–100 GPa is routinely accessed with current devices. Depending on the compressibility of a material, ΔG may change (increase) by 1–200 kJ/mol upon pressurization from atmospheric pressure to 10 GPa.¹ In principle, whereas temperature influences the distribution of phonons and electrons on energy levels, pressure induced density changes alter a material's vibrational and electronic energy levels. As a consequence, when approaching Mbar pressures, previously unconceivable compound classes may emerge (cf. Fig. 1).

The effect of pressure may be illustrated from E - V curves from which H - p relations can be extracted (Fig. 2, note that the effect of temperature is neglected in this presentation). Per se, compounds formed or transformed at high pressure conditions have a higher H (or G at finite temperature) than the normal pressure ground state and—unless prevented by kinetic barriers—will revert when pressure is released. It is, however, not uncommon that high pressure phases—or more general, compounds/materials obtained at high pressures—can be retained in a metastable state at ambient pressure. The high pressure form of carbon, diamond, serves as a most prominent example. For chemists it is usually highly desirable not only to detect nonambient phases but also isolate kinetically stabilized phases at ambient pressure. This enables detailed structure and property characterizations of new materials and also gives the opportunity to subject them to further chemical modifications. Thus, synthesis efforts will be targeting “kinetic” phases where a substantial energy barrier prevents transformation into the normal pressure ground state.² Pathways for reversion to the normal pressure ground state may depend on p, T conditions during recovery and/or the choice of precursor materials in the synthesis experiment, which can be exploited in order to isolate metastable phases at ambient pressure.

Importantly, the effect of high pressure is not only to reach into metastable compounds. High pressure will also help accessing new materials that are thermodynamically stable at ambient pressure by enabling kinetics (through shortened diffusion paths) and by raising thermal stability (beyond the reaction/synthesis temperature) with respect to decomposition.^{2,3} As a matter of fact, a great deal of compounds from high pressure synthesis, for which pressures up to 10 GPa were applied, do not correspond to metastable high pressure phases, but thermodynamic ground state phases. A good example is β -SiB₃, which is a thermodynamical stable compound in the binary B-Si phase diagram. Yet its synthesis from the elements is impeded by the kinetically driven formation of α -SiB_{3-x}. When using pressures in a range 5.5–8 GPa the refractory semiconductor β -SiB₃ forms quantitatively within hours.⁴

There are numerous excellent reviews addressing various aspects of high pressure chemistry, often highlighting the potential of high pressure for obtaining new materials and/or emphasizing on new or improved properties, or specific compound classes obtained from high pressure synthesis.^{5–16} Here we attempt an overview of recent trends in high pressure chemistry and the manifold of new chemical compounds from high pressure synthesis across the periodic table. Importantly, our focus is on experimentally corroborated results. Computational predictions, which have become numerous—and are invaluable for directing synthesis efforts—will be only addressed if they closely relate to (or extend) experimental findings.

4.12.1.2 Devices for high pressure chemistry

Chemists have a long tradition in exploiting lower pressures ($p < 1$ GPa) in synthesis by developing and using autoclave devices (and also continuous flow apparatuses) for solid-gas and hydro/solvothermal reactions. In this review, however, we will not consider results from this technology, but report on chemistry performed at gigapascal pressures. For achieving gigapascal pressures, high pressure methodology is typically divided into large volume press (LVP) and diamond anvil cell (DAC) branches, for each of which there are excellent reviews.^{17–20} Clearly, since $p = F/A$ one faces small sample volumes at high pressures (“pressure-volume dilemma”) which is of concern to chemists since it limits the prospects for extensive and detailed property investigations of new compounds as well as their further chemical modification by ambient pressure post processing.

Highest pressures can be achieved with DACs. The basic principle of these cells is to drive two (large) single crystal diamonds into the sample space confined by a metal gasket with a circular hole (Fig. 3A). The diamonds are cut so that they have a circular facet (culet facet) at the pavillon facing the sample. The culet size may range from 0.1 to 1 mm in diameter, the former allowing for pressures exceeding hundred GPa. Naturally, multiple Mbar pressures will imply very small sample volumes, $< 10^{-3}$ mm³. Pressure can be increased manually by simply tightening screws or, more conveniently, remotely using a gas pressure-driven metal membrane device. For pressure determination, calibrants (gauges) have to be included. Also, if (close to-) hydrostatic conditions are desired in

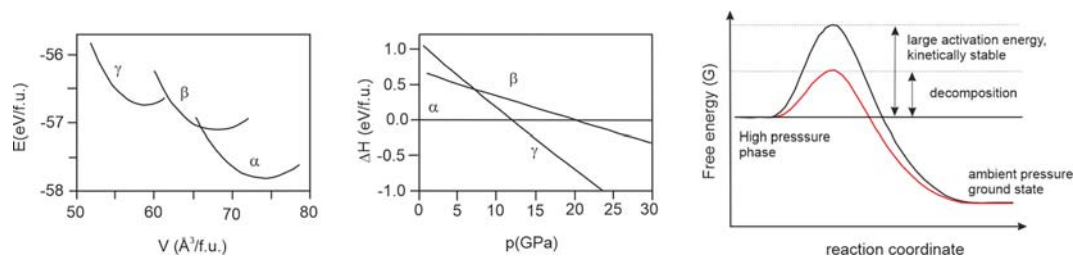


Fig. 2 E - V and H - p relations for a compound exhibiting three polymorphs α , β , γ . With pressure a transition $\alpha \rightarrow \gamma$ will be observed at around 10 GPa. The sketch to the right depicts the difference between a metastable and non-recoverable high pressure phase.

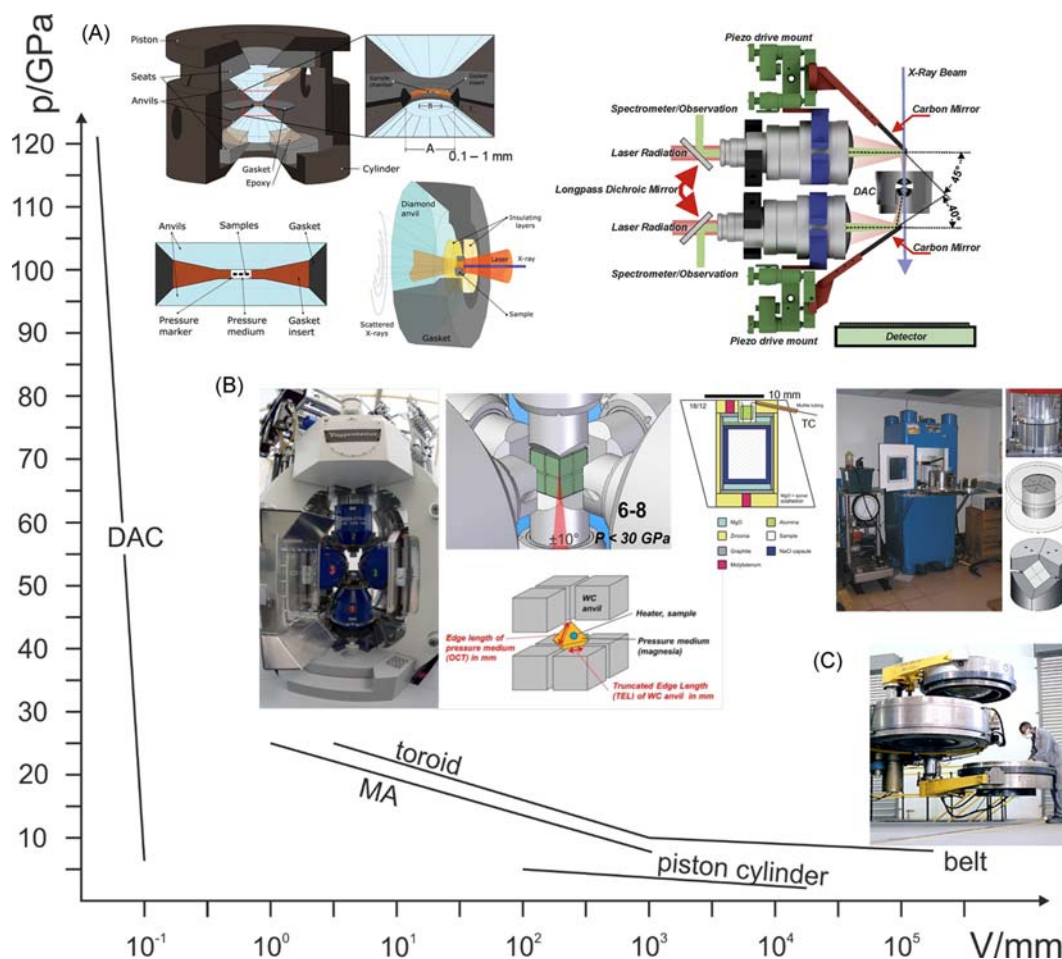


Fig. 3 Pressure-sample volume capability of high pressure devices used for inorganic materials synthesis. (A) Basic components of a DAC, according to Ref. 20 (and reproduced from Shen, G.; Mao, H.K. High-Pressure Studies with x-Rays Using Diamond Anvil Cells. *Rep. Prog. Phys.* **2017**, *80* (1), <https://doi.org/10.1088/1361-6633/80/1/016101>): opposing anvils, a confining gasket, and sample chamber. A beveled-anvil geometry is shown with culet size A beveled to B at a bevel angle θ . The lower part shows a typical sample configuration and the configuration for double-sided laser heating. Insulating layers are essential for efficient heating and minimizing temperature gradients. To the right is shown a scheme of the laser beam targeting on the DAC in experiments with synchrotron X-ray radiation at ID15B (ESRF) (reproduced from Fedotenko, T.; Dubrovinsky, L.; Aprilis, G.; Koemets, E.; Snigireva, I.; Barannikov, A.; Ershov, P.; Cova, F.; Hanfland, M.; Dubrovinskaia, N. Laser Heating Setup for Diamond Anvil Cells for *in Situ* Synchrotron and in House High and Ultra-High Pressure Studies. *Rev. Sci. Instrum.* **2019**, *90* (10), 104501. <https://doi.org/10.1063/1.5117786>). (B) Aspects of MA-LVP activities. To the left is shown the LVP at the beamline P61B (PETRA III) with cubic geometry (Refs. 22, 23) and to the right a laboratory press operating a Walker-type module. The middle part shows sketches of a pressure cell, the built up of a 6–8 assembly, and the positioning of a 6–8 assembly in an in-situ experiment at a synchrotron. (C) Belt-type LVP equipment as used in industrial processing of e.g., hard materials (Ref. 24).

the sample space, a pressure transmitting medium (PTM) has to be added. This may be an inert gas (He, Ar, N₂) condensed into the sample space, or salt (e.g., NaCl or MgO). Oftentimes when pursuing chemical reactions the presence of a PTM leads to undesired side effects. Therefore, chemists will frequently tolerate pressure gradients and exclude the PTM, unless the PTM is intentionally used as one of the reactants (“reactive” PTM) or is needed for isolation purposes. Chemical reactions are mostly induced by heating. Resistive heater designs provide reasonably uniform temperatures in the sample space, but diamonds have to be protected from burning and achievable temperatures are typically below 1273 K. Using laser heating (LH-DAC),^{21,25} much higher temperatures (in excess of 5000 K) can be reached in the local area of the sample space hit by the laser beam, which can be variably focused. As we will see later, many spectacular results were produced from LH-DAC experiments. When pursuing laser heating, it is important to isolate the sample from the highly thermally conducting diamond anvils by a ceramic/salt with a high melting point, like NaCl or MgO, which then at the same time will act as a PTM. The accurate determination of the actual p, T conditions in LH-DAC experiments is challenging. Especially T may be off by hundreds of K, and there are large T gradients.

The transparency of diamonds allows in-situ investigations of compressed samples by a variety of spectroscopy and diffraction methods. Although small-sized DACs are conveniently handled in a laboratory environment, the number of possible in-house investigations is rather limited. Preferably, DAC investigations are performed at X-ray synchrotron diffraction and spectroscopy beamlines, which would also provide the complex infrastructure for laser heating.

LVP methods are based on hydraulic presses driving piston cylinder (PC) or anvil devices.^{17,18,26} Anvil devices come in different flavors: belt, multi-anvil (MA), toroid. Compared to DACs, maximal attainable pressures are reduced by an order of magnitude (typically 20–25 GPa in routine applications) whereas sample volumes are drastically increased (10–10³ mm³ in laboratory settings). Importantly, sample temperatures (up to 2500 °C) are uniform and reaction environments at high p,T conditions can be stably maintained and controlled over long times (up to several days, if necessary). LVP techniques are also used in industrial settings for e.g., the synthesis of hard materials.²⁷ The principle of MA-LVP methodology, which is wide-spread in laboratory settings, is illustrated in Fig. 3B. One distinguishes two modes of operation, MA6-6 and MA6-8. The former allows for pressures up to 10 GPa, the latter up to 25 GPa. In both cases a cylindrical reaction volume is confined within a pressure cell that is shaped into either a cube (MA6-6) or an octahedron (MA6-8). The MA6-8 octahedron is enclosed by an assembly of 8 tungsten carbide cubic anvils with truncated corners, which then yields the shape of a cube. In the cubic apparatus, the sample is isotropically compressed along the cube's [100] directions. However, in laboratory settings the most popular LVP-MA design employs uniaxial compression along the [111] direction and pressure distributes through a cluster of steel wedges, which are situated in a confinement ring.^{28,29} High temperatures are produced using a cylindrical resistance heater contained within the pressure cell and measured accurately with thermocouples. The pressure is determined from load calibrations. In contrast with DACs, direct observation of the sample during an experiment is virtually impossible. In-situ diffraction experiments are feasible at some synchrotron facilities, such as the ESRF and PETRA III, which are equipped with LVP-MA beamlines (cubic design) and/or toroid based Paris-Edinburgh presses.^{22,23,30}

LVP devices have been traditional tools in geosciences, but are now increasingly employed by inorganic chemists as a tool for exploratory synthesis. Industrial settings would prefer belt-type methodology, since it offers the largest pressure-volume capability up to 10 GPa (Fig. 3C).²⁷ Assembly parts, gaskets, and anvils have been standardized and are nowadays commercially available.³¹ The same holds true for DACs and accessories for changing and measuring pressure as well as for resistive heating. FIB techniques allow the highly precise and reproducible machining of miniature parts for DACs.

Considering the various devices, what would be most useful for (inorganic) chemistry? As mentioned before, the size of sample volume and the recoverability of products are very important aspects. Then arguably, LVP based methods are most useful for high pressure chemistry as they provide precise p,T control of larger reaction volumes over prolonged periods of time. This allows setup of more complex, multicomponent, reaction schemes. It is noteworthy that the moderate pressure achievable with simple PC devices (~3 GPa) can already give access to variety of metastable inorganic materials.³² LVP based methods also provide the possibility to adjoin to industrial processing (based on belt-type methodology which is restricted to $p < 10$ GPa).²⁴ At the same time pressures are limited, and explorations at $p > 15$ –20 GPa will require the application of LH-DACs.

4.12.1.3 Challenges compared to “ambient pressure” chemistry and strategies

What kind of reactions can be performed at gigapascal pressures? Traditionally, since high pressure chemistry using gigapascal pressures evolved from geosciences, the focus has been primarily on the transformation of solids and solid-solid reactions. Still, most of the current activities are in the realm of solid state chemistry, but there are increasing efforts toward the application of more diverse reaction schemes, like methathesis reactions or using elaborate precursor strategies. Furthermore, solid-gas(fluid) reactions and reactions including volatile species (flux-mediated or hydrothermal reactions) at gigapascal pressures are emerging (Table 1).

Compared to ambient pressure synthesis there are a number of differences and certainly challenges. Apart from the smallness of sample volumes, adding an additional dimension to phase relations complicates considerably the task of finding compositions and formation conditions for new materials. Exploration of the multi-dimensional p,T , composition phase space is a daunting task. High throughput investigations at high pressures are severely limited. LH-DAC experiments may offer an opening, since with the combination of a highly focused X-ray and laser beam (at synchrotron facilities) different regions of sample space can be heated and probed independently and at different pressures, yielding many data points during a single experiment.

Importantly, and as initially mentioned, isolated products at ambient pressure from laboratory LVP experiment may not have originally formed at the applied high pressure, high temperature (HPHT) conditions but during the recovery process. Insight from

Table 1 Diversification of reaction schemes in high pressure chemistry.

Reaction scheme	Reactions/products	Pressures	Examples
Solid-gas/fluid	Hydrogenations, nitridations, oxidations	1– >100 GPa	$3 \text{ MgH}_2 + \text{Cr} + \text{H}_2 \rightarrow \text{Mg}_3\text{CrH}_8$ $\text{Re} + 2 \text{ N}_2 \rightarrow \text{Re}(\text{N}_2)\text{N}_2$
Hydrothermal	Oxides, oxyhydroxides	1–10 GPa	$\text{SiO}_2 \text{ (glass)} \rightarrow \text{Si}_{0.99}\text{O}_2\text{H}_{0.04}$ (hydrous stishovite)
Single source precursor	Intermetallics, nitrides, mixed-anion systems	4– >100 GPa	$(\text{NH}_4)_2[\text{Os}_x\text{Pt}_{1-x}\text{Cl}_6] \rightarrow \text{Os}_x\text{Pt}_{1-x}$ alloys $\text{Sn}_3\text{N}_4\text{-O} \rightarrow \text{Sn}_2\text{O}_2\text{N}$
Reactive precursor	Nitrides, mixed-anion systems	4–15 GPa	$2 (\text{PNCI}_2)_3 + 3 \text{ NH}_4\text{N}_3 + 2 \text{ BN} \rightarrow 2 \text{ BP}_3\text{N}_6 + 12 \text{ HCl} + 4 \text{ N}_2$
Metathesis	Nitrides	4–15 GPa	$\text{ZnF}_2 + \text{SnF}_4 + 2 \text{ Li}_3\text{N} \rightarrow \text{ZnSnN}_2 + 6 \text{ LiF}$ $\text{Na}_2\text{MO}_4 + 2 \text{ BN} \rightarrow \text{MoN}_2 + 2 \text{ NaBO}_2$ $2 \text{ PrF}_3 + 3 \text{ LiPN}_2 + \text{Li}_3\text{N} \rightarrow \text{Pr}_2\text{P}_3\text{N}_7 + 6 \text{ LiF}$

in-situ experiments is invaluable for determining p,T reaction conditions and to identify reaction pathways/intermediates, and for elucidating $p-T$ pathways for their recovery. The great majority of in-situ experiments is done at X-ray synchrotron facilities and as powder diffraction studies. As a major challenge, the quality of in-situ diffraction patterns is frequently insufficient for the unambiguous characterization of products or intermediates. A recent advancement is the coupling of the LH-DAC sample environment with single crystal diffraction from which reliable data for structure solution and refinement can be obtained even at Mbar pressures.³³

Lastly, high pressure chemistry has received a great stimulus from computational simulations. During the past 10 years crystal structure prediction methods based on first-principles calculations have become a robust tool to explore emergent behavior under pressure.^{34–36} The goal of structure prediction is to determine unit cell parameters and atomic coordinates that correspond to the global minimum on the potential energy surface. Structure prediction allows envisioning thermodynamically stable compositions and structures at high pressures, which can then guide synthesis efforts. The pool of predicted structures is often of great help for the experimentalist to identify products or transients in in-situ experiments. Also, theory may give reasonable suggestions for reaction pathways and can help to consolidate crystal structures where experimental data are insufficient to do so.

4.12.2 Inorganic materials from high pressure synthesis

4.12.2.1 Intermetallic compounds

The synthesis of intermetallic phases at high pressures covers a wide field from exploration of phase stability,^{37,38} crystal growth^{39,40} or manufacture of new modifications^{41–43} to enhanced reactivity in binary systems, e.g., compression stimulated compound formation in the system.⁴⁴ Although some studies report the manufacture of new ternary phases like the cluster compound $\text{Ce}_7\text{Au}_{13+x}\text{Ge}_{10-x}$,⁴⁵ the majority of studies concerns (pseudo-) binary phases of a few main group elements. Here, we rather focus on new compounds like B_6Se ⁴⁶ or Mn_3Ge_5 ,⁴⁷ which have been manufactured roughly within the past 10 years, and the selection presented below is grouped into larger classes according to their constituents.

4.12.2.1.1 Borides, carbides and nitrides of transition metals

Recently manufactured high pressure phases of boron and transition metals exhibit predominantly extended networks of the main group element and not the otherwise typical icosahedral units. While Fe_2B_7 forms a unique boron network,⁴⁸ the crystal structure of FeB_4 is isotypic to CrB_4 and features a boron network with channels filled by iron atoms (Fig. 4). Alternatively, this arrangement may be described as columns of FeB_{12} polyhedra, which are condensed along the c direction by common edges.⁴⁹ FeB_4 is a superhard material which becomes superconducting at low temperatures. A similar arrangement is adopted by MnB_4 , but the distortion of the 3D boron network is subtly different.⁵⁰

In contrast to the boron compounds, the selection of carbides and nitrides will be restricted to phases in which the non-metal atoms of carbon or nitrogen are positioned on interstitial sites. Several of the transition metal carbides have been synthesized using LH-DACs, e.g., the synthesis of rocksalt-type PtC and cementite-type Ni_3C requires extreme conditions with regards to temperature and pressure which can currently only be realized in such setups.^{51,52} The phase is of some importance for high pressure research as it represents a side product in laser heating experiments with platinum being added for pressure calibration. Even higher pressures demands the manufacture of ReC with an atomic arrangement isotypic to tungsten carbide, and state-of-the-art techniques are needed for generating sufficiently high pressures.⁵³ Laser heating is also required for the synthesis of Ru_2C .⁵⁴ In contrast, the manufacture of the metal-rich rhenium carbide Re_2C ,⁵⁵ manganese carbide MnC with zinc blende structure,⁵⁶ and the iron carbide Fe_7C_3 ⁵⁷ requires moderate pressure only and can be accessed with LVP devices.

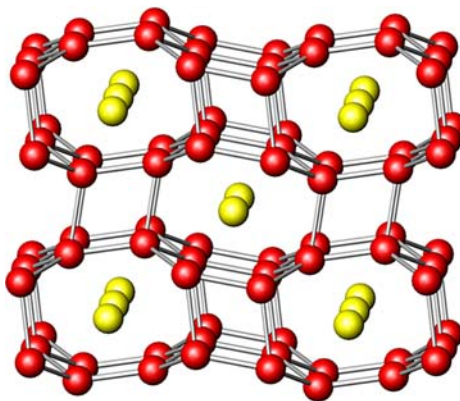


Fig. 4 Crystal structure of FeB_4 (CrB_4 type) in a projection along the c -axis. The four-connected boron atoms (red spheres) form a 3D network with [001] oriented channels accommodating transition-metal atoms (yellow).

Although alternative synthesis routes have been reported for molybdenum and tungsten nitride,^{58,59} LH-DACs are often the method of choice in the manufacture of new transition metal nitrides. The reason is that in the device nitrogen can be provided in pure form by compression into the liquid or solid state. The method yielded new compounds in the system rhenium—nitrogen, and by combining X-ray diffraction experiments and DFT model calculations their composition and structure were determined. The concerted study showed that the yielded phases Re_3N and Re_2N involve the same metal arrangement as in elemental rhenium with nitrogen in interstitial positions.⁶⁰ In contrast, the nitride Re_7N_3 adopts the more complex Th_7Fe_3 -type arrangement comprising units of condensed NRe_6 trigonal prisms.⁶¹ The combination of laser heating with Moessbauer spectroscopy on the ^{57}Fe nucleus as a local probe led to the discovery of NiAs-type iron nitride, FeN .⁶²

4.12.2.1.2 Silicides

Silicon forms a number of intermetallic compounds in which the interdependence of electron count and connectivity of the anionic tetrel partial structure is established by the 8-N rule and the Zintl concept. The spectrum of compositions, which is accessible at ambient pressure, is somewhat limited as the binary systems of silicon with alkaline earth metals like calcium or strontium and the related rare-earth metal europium are characterized by the absence of compounds with a higher silicon content than AeSi_2 ($\text{Ae} = \text{Ca}, \text{Sr}, \text{Eu}$). Compounds with silicon-richer compositions often require high pressure synthesis techniques. Following the investigation of mixtures Eu-Ga-Si , which evidenced the formation of the binary compound EuSi_6 upon compression,⁶³ analogous binary alkaline-earth compounds CaSi_6 , SrSi_6 and BaSi_6 were discovered.^{64–67} The silicides exhibit a EuGa_2Ge_4 -type crystal structures in which irregular polyhedra constituted by 18 silicon atoms accommodate the enclosed metal atoms (Fig. 5A). The resulting framework comprises solely four-bonded silicon atoms. Electrons, which are transferred from the cationic metal atoms onto the silicon polyanion, are located in antibonding states. In line with this picture of excess electrons occupying states in the conduction band, metal-type electrical conductivity is observed for the high pressure phases AeSi_6 .

The related framework compound MgSi_5 of the lighter alkaline-earth metal magnesium forms at a slightly different composition.⁶⁸ Here, the silicon partial structure exhibits 15 atom cages enclosing the Mg cations. Two types of smaller cages remain empty. While the silicon framework exhibits conventional two-center two-electron (2c-2e) bonds, the magnesium-silicon interaction is procured by quite unusual multi-center bonding. Recent in-situ laser-heating experiments evidenced a second high pressure phase, Mg_2Si_7 . The silicon atoms form 8 to 12 Si–Si contacts and the total coordination sphere comprises 11 or 12 next neighbors. The magnesium atoms are located in [001] oriented channels of the silicon framework.⁶⁹

The same composition, but a different spatial organization is realized by phases of the rare earth metals cerium and gadolinium.⁷⁰ The structure pattern of compounds RESi_5 ($\text{RE} = \text{Ce}, \text{Gd}$) is isotypic to that of earlier characterized LaGe_5 ⁷¹ and contains puckered silicon layers comprising five- and eight-coordinated silicon (Fig. 5B). Chemical bonding analysis of CeSi_5 indicates that the silicon atoms realize three covalent two-center bonds within the corrugated layers plus a silicon-cerium interaction, which is similar to a stereochemically active electron pair. The eight-coordinated silicon shows multicenter bonding between the silicon framework and the cerium atoms. The pronounced non-spherical symmetry (structuring) of the fifth shell of cerium evidences a participation of the semi-core states in the chemical bonding. In addition, the system Ce-Si features a second compound of composition Ce_2Si_7 with a unique silicon framework showing 4 to 6 Si–Si contacts per silicon atoms. The complete coordination spheres of the silicon atoms comprise 8, 9 or 10 next neighbors.⁷⁰

The binary system La-Si holds two polymorphic forms of LaSi_5 , which are structurally different.⁷² They consist of unique frameworks formed by three- and four-bonded silicon atoms. The silicon-richer compound LaSi_{10} features condensed polyhedra of 18 silicon atoms similar to those in the alkaline earth metal hexasilicides. LaSi_{10} and one modification of LaSi_5 are metallic conductors, which become superconducting at low temperatures.

Continued systematic exploration of binary silicon systems also resulted in the discovery of high pressure phases MSi_3 ($\text{M} = \text{Ca}, \text{Y}, \text{Lu}$).⁷³ The remarkable crystal structure is characterized by layers of condensed molecule-like Si_2 dimers (Fig. 5C). The alkaline

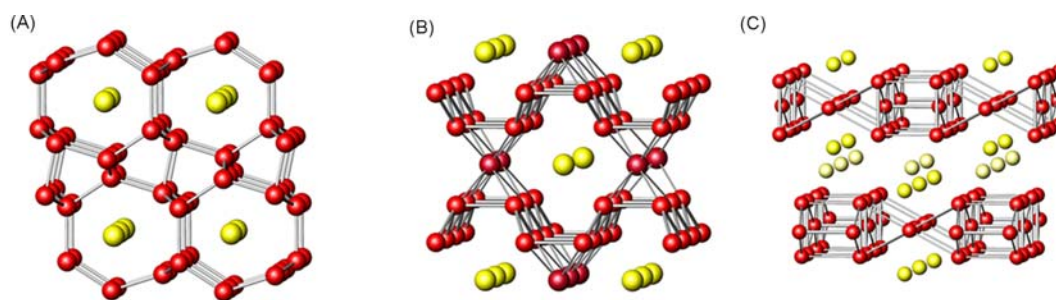


Fig. 5 (A) Crystal structure of compounds MSi_6 ($\text{M} = \text{Ca}, \text{Sr}, \text{Ba}; \text{Eu}$) in a projection along the c -axis. Four-bonded silicon atoms (red spheres) form a 3D framework. Channels in [001] orientation contain the metal atoms (yellow). (B) Crystal structure of silicides MSi_5 ($\text{M} = \text{Ce}, \text{Gd}; \text{LaGe}_5$ -type). Corrugated layers of silicon atoms (smaller red spheres) with (001) orientation enclose the rare-earth metal (yellow) and a second type of silicon atoms (larger red spheres). (C) Crystal structure of silicides MSi_3 ($\text{M} = \text{Ca}, \text{Y}; \text{Ho}, \text{Yb}, \text{Lu}; \text{CaGe}_3$ -type). Silicon dumbbells oriented parallel to [001] form tetragonal prisms, which are connected by other Si_2 -units into (001) oriented slabs. Metal atoms are located between these 2D structure segments. Silicon atoms are shown as red spheres, metal atoms are displayed in yellow.

earth element adopts the usual oxidation state +2, while the rare earth and transition metals realize +3. Independent from these differences in electron count, the compounds exhibit BCS-type superconductivity with weak electron–phonon coupling. GdSi₃, HoSi₃ and YbSi₃ adopt isotypic crystal structures,^{74–76} while the larger barium causes a unique distortion of the framework.⁷⁷

4.12.2.1.3 Germanides

The high pressure chemistry of germanium is closely related to that of the lighter homologue silicon, e.g., BaGe₆ is isotypic to the silicides MSi₆ (M = Ca, Sr, Ba; Eu) with EuGa₂Ge₄-type crystal structures, cf. Fig. 5A.⁷⁸ Yet, SrGe₆ adopts a unique atomic arrangement and is an electron precise Zintl phase comprising three- and four-bonded silicon atoms.⁷⁹ Moreover, partial disintegration of network segments by defect formation has been observed in the phase SrGe_{5.5}.⁸⁰ Later experiments evidenced incommensurate modulations of both atomic positions and site occupancy in the phases SrGe_{6–x} and BaGe_{6–x}.^{78,81} The finding of defect varieties is in line with the tendency that silicides often tolerate an excess of electrons while germanium (and tin) compounds are inclined to reduce the surplus by formation of vacancies. According to the bonding analysis of BaGe_{6–x} the defect formation is associated with the establishment of free electron pairs around the defects resulting in an electron precise composition for x = 0.5.⁷⁸ In agreement with this result, physical measurements evidence semiconducting electron transport properties for this defect concentration.

Compounds REGe₅ (RE = La, Nd, Sm, Gd, Tb)^{71,82–84} adopt the same atomic arrangement as silicides RESi₅ (RE = Ce, Gd), cf. Fig. 5B, but the defect varieties MGe_{4.5} (M = Nd, Sm, usually labelled as M₂Ge₉) are only observed for the germanium phases.⁸⁵ Finally, barium forms the compound BaGe₅ containing special double layers of germanium,⁸⁶ and the composition has no equivalent in the silicon chemistry of barium and its lighter homologues strontium and calcium.

At composition 1:3, compounds like CaGe₃, SrGe₃ and one modification of BaGe₃ exhibit the same atomic patterns as the corresponding silicon phases (cf. Fig. 5C), i.e., they contain intricate layers of condensed Ge₂ dumbbells and become superconducting at low temperatures.^{87–89} Barium germanide BaGe₃ exists in a second modification, which is isotypic to BaSn₃ (Ni₃Sn type representing a hexagonal variant of Cu₃Au) and exhibits superconductivity as well.⁹⁰

Phases REGe₃ (RE = La, Ce, Sm, Eu and Lu) exhibit a remarkable structural diversity. Triangular cluster units Ge₃ are a common feature of LaGe₃ and EuGe₃,^{91,92} while neighboring SmGe₃ forms a third variety resembling a unique distortion of the densest-packed Cu₃Au type,⁹³ which is formed by CeGe₃.⁹⁴ Yet another combination of building units is found for LuGe₃.⁹⁵ The crystal structure of the DyGe₃-type features layers of condensed Ge₂-dumbbells as well as germanium zigzag chains as building units. The same type of folded strings is observed in the high pressure phase LuGe.⁹⁶ Here, 2c Ge–Ge bonds in the 1D germanium polyanion go along with 4c bonds between the lutetium atoms. This is a very rare situation as polyanionic and polycationic species are realized in the same crystal structure.

At ambient pressure, magnesium and germanium form only the CaF₂-type Zintl phase Mg₂Ge. High pressure synthesis yields a compound of approximate composition Mg₉Ge₅, which has a cotunnite-related modulated crystal structure with incommensurate modulations.⁹⁷ A recent investigation essentially confirmed these findings, but described the phase as a filled UCl₃ variety with options for a precise electron balance.⁹⁸ Similar phases Mg₉Si₅ and Mg₉Sn₅ are formed by the homologues elements silicon and tin.^{97,99,100}

4.12.2.1.4 Intermetallic clathrates

Silicon and germanium form a number of intermetallic clathrates. These fascinating materials comprise frameworks of typically four-bonded host atoms, which enclose a minority of guest species in polyhedral cages (Fig. 6). The role of substitution atoms and defects in the covalent network has been reviewed recently.¹⁰¹

Despite early efforts to incorporate rare-earth metals¹⁰² into the cages, it was the pioneering synthesis of superconducting clathrate-I barium silicide Ba_{8–x}Si₄₆^{103–106} which stimulated broader interest and diverse efforts to expand the spectrum of

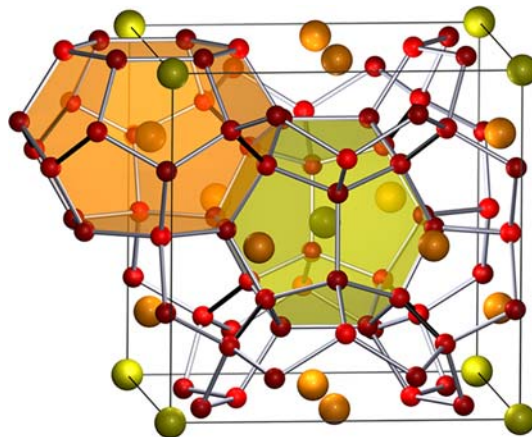


Fig. 6 The crystal structure of type-I clathrates comprises a network of four-bonded host atoms (mainly Si, Ge or Sn). The atomic arrangement provides polyhedral cages surrounded by 24 (orange) and 20 atoms (yellow) encapsulating the host atoms of the minority metals.

accessible compositions by application of HPHT synthesis. Thus, the corresponding clathrate $\text{Sr}_8\text{Si}_{46}$ was successfully synthesized only recently, and resistivity measurements clearly show that the strontium compound is also a type-II superconductor.¹⁰⁷ An even more important issue of the compound is revealed by the analysis of its chemical bonding behavior. The quantum chemical tools evidence that the conventional covalent bonding within the silicon network is accompanied by previously unnoticed multi-center bonding interactions between silicon framework and strontium atoms in the cages.

High pressure methods also paved the way for the manufacture of new alkali metal clathrates. While high pressure experiments in the binary systems germanium—sodium indicate only the formation of $\text{Na}_4\text{Ge}_{13}$,¹⁰⁸ investigations in the corresponding silicon system evidenced a complex behavior involving clathrate formation. At low temperatures (or as a precursor phase), clathrate-II $\text{Na}_{24+x}\text{Si}_{136}$ ¹⁰⁹ is formed while clathrate-I type $\text{Na}_8\text{Si}_{46}$ requires higher temperatures.¹¹⁰ The corresponding section of the phase diagram including NaSi_6 has been established by in-situ large volume techniques.¹¹¹

Application of high pressure also opened a promising route to clathrates of the heavier and, thus, bigger alkali metals. The expanded framework of $\text{Cs}_{8-x}\text{Si}_{46}$ ¹¹² and the analogous, defect-bearing germanium network of $\text{Cs}_{8-x}\text{Ge}_{46-y}$ require compression for synthesis.¹¹³ Lately, heavy alkali metals were incorporated in even smaller boron-substituted silicon clathrates like $\text{Rb}_8\text{B}_8\text{Si}_{38}$ and $\text{Cs}_8\text{B}_8\text{Si}_{38}$.^{114,115} With the same approach, the even more demanding synthesis of carbon-based clathrates was achieved recently and compounds SrB_3C_6 and LaB_3C_6 with a clathrate VII structure adopting the cubic bipartite sodalite structure have been synthesized.^{38,116} The framework of sp^3 -bonded atoms comprises the metal atoms in truncated octahedral $\text{C}_{12}\text{B}_{12}$ cages. According to band structure calculations, the electron-precise lanthanum compound is a semiconductor with an indirect band gap of approximately 1.3 eV.

4.12.2.1.5 Bismuthides

Heavy p-block metals like bismuth or lead exhibit exceptional chemical properties which manifest, e.g., in immiscibility with 3d transition metals even in the liquid state. The unusual properties can be traced back to the characteristic sequence of electronic energy levels caused by the pronounced spin-orbit splitting commonly ascribed to relativistic effects. Motivated by the quest for new superconducting intermetallic phases of bismuth, the constructive synthesis of superconducting CoBi_3 ¹¹⁷ laid the basis for ongoing preparation activities in other binary systems of bismuth and revealed that the state variable pressure is suited to overcome the barriers of compound formation in some systems.

High pressure synthesis granted access to the phases MnBi_2 , FeBi_2 and MoBi_2 , which adopt crystal structures of the Al_2Cu type (Fig. 7A).^{118–120} Interestingly, this atomic arrangement is closely related to one of the high pressure modifications of elemental bismuth.¹²¹

The neighboring metal cobalt forms the compound CoBi_3 with a NiBi_3 -like motif of 1D building units (Fig. 7B), which is also adopted by the corresponding compound RhBi_3 of the heavier group homologue of cobalt.¹¹⁷ Prototypic NiBi_3 undergoes at elevated pressure a phase transformation into NiBi_2 (Fig. 7C), which can also be synthesized directly from the elements.¹²² Further increase of pressure stabilizes β - NiBi .¹²³ The crystal structures of the nickel compounds can be rationalized as increasingly condensed atomic arrangements of the 1D segments.

Copper forms two quenchable phases with bismuth upon compression. The crystal structure of $\text{Cu}_{11}\text{Bi}_7$ is a unique defect variant of the NiAs structure type.¹²⁴ Temperature-dependent electrical resistivity and heat capacity measurements reveal a bulk superconducting transition at low temperatures. In accordance with the experimental findings, density functional theory calculations confirm that $\text{Cu}_{11}\text{Bi}_7$ is stabilized (relative to decomposition into the elements) at HPHT.¹²⁵ The second compound in the binary system, CuBi , comprises slabs of puckered Cu layers sandwiched between Bi planes.¹²⁶ Bonding analysis reveals negligible charge transfer between the metals, and the interactions within the Bi—Cu—Bi slabs have multicenter nature. Additional lone-pair interactions of the van der Waals type interconnect the 2D entities. CuBi exhibits metal-type electrical conductivity with superconductivity below $T_c = 1.3$ K. Moreover, copper is the first mid to late first-row transition metal for which the pressure-induced formation of a binary lead compound is reported. The crystal structure of Cu_3Pb (Mn_3Sn type) can be envisioned as a direct mixture of the

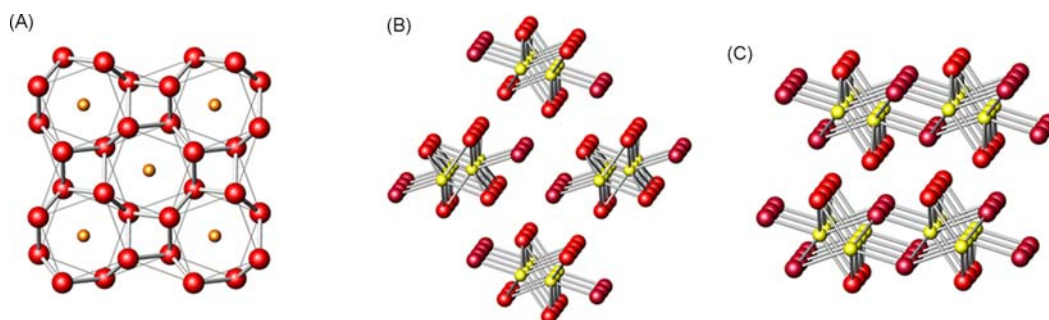


Fig. 7 (A) The atomic patterns of MnBi_2 and FeBi_2 (CuAl_2 type) consist of condensed tetragonal antiprisms of bismuth atoms (red spheres). The resulting channels in direction [001] are centered by transition metal atoms (orange). (B) The crystal structure of CoBi_3 (isotypic to NiBi_3 and RhBi_3) comprises [010] oriented columns of Co atoms (yellow spheres) which are connected and enclosed by bismuth atoms (red). (C) In the structure of NiBi_2 the columns are condensed into layers by bridging bismuth atoms.

elemental lattices of its constituents.¹²⁷ Computations of its electronic structure evidence band crossings near the Fermi level, suggesting that Cu₃Pb may qualify as a topologically nontrivial material.

4.12.2.2 Hydrides

Inorganic chemistry textbooks divide hydrides into ionic (in conjunction with active metals A (alkali), Ae (alkaline earth), RE (rare earth)), covalent (in conjunction with p-elements), and interstitial hydrides (for transition metals). The application of high pressures has been revolutionary for both metal and nonmetal hydride chemistry. Especially, the finding of high temperature superconductivity in highly compressed H₂S in 2015¹²⁸ caused a tremendous surge of activity, which in turn has led to the discovery of unprecedented hydrogen-rich hydrides.^{129–132} These hydrides, also called super- or polyhydrides, exhibit stunning hydrogen structures and compositions beyond conventional valence and bonding concepts.

For high pressure hydride synthesis both DAC and LVP techniques have been employed. H₂ can be loaded into DACs (together with the precursor to be hydrogenated (elements and/or ambient pressure stable hydrides)) and compound formation of compressed samples is induced by laser heating. In contrast, hydrogenation reactions using LVPs have to be performed with an internal hydrogen source. This source (e.g., ammonia borane, BH₃NH₃) is a material that releases hydrogen irreversibly at slightly elevated temperatures and leaves a chemically inert decomposition residual behind. Many times structural characterization, and especially locating H atoms, is a formidable challenge, especially in DAC synthesis experiments. Here a fruitful synergy between theory and experiment has evolved. Theory would predict hydride phases potentially stable at high pressure conditions, which are then matched against experimental data (mostly diffraction patterns or Raman spectra), or helps establishing the H content of phases and the location of H atoms in case unit cell and heavy atom positions can be extracted from experiment.

This chapter focuses on compounds from gigapascal hydrogenations (or from high pressure induced decompositions of molecular hydrides).

4.12.2.2.1 Transition metal hydrides

Early transition metals from the Sc–V (3–5) groups react readily with elemental hydrogen to form binary hydrides (e.g., TiH₂, V₂H). In contrast, with the exception of Pd, late transition metals (group 6–10) require gigapascal pressure conditions (1–5 GPa), which yields solid solution phases TH_{1–x} with sizeable homogeneity ranges. The *p*, *T* dependence of TH_{1–x} phase relations of the late transition metals were investigated up to 7–8 GPa already in the 1990s using LVP methodology.^{133,134} For *x* ≈ 0 TH_{1–x} phases attain structures based on close packings of metal atoms in which octahedral voids are preferentially occupied by H (i.e., anti-NiAs and NaCl structures for hcp and fcc metal arrangements, respectively). These phases can be retained at ambient pressure when decompression is performed at liquid N₂ temperature. Recent LH-DAC research showed that binary transition metal hydrides can be considerably extended when applying pressures in the range 20–150 GPa (Table 2). The emerging phases depart the classification of interstitial hydrides.

For Zr and Hf, hydrides with the Th₄H₁₅ structure were established¹³⁵ and for T = Nb and Tb a phase was found with the composition TH_{2+x} (*x* = 0.2–0.5).^{136,137} This phase is based on an hcp arrangement of metal atoms and hosts H atoms in all octahedral and a little more than half of the tetrahedral holes.¹³⁸ Above 55–60 GPa Nb and Ta hydrides attain a more hydrogen-rich composition, TH₃, which adopts the body centered cubic domeyite (Cu₃As) structure.^{136,139} New Cr hydrides, extending previously known ε-hcp-CrH, form above 10 GPa (Cr₂H₃) and 30 GPa (CrH₂).¹⁴⁰ The structures of Cr hydrides are all based on a hcp metal structure with completely filled octahedral and increasingly filled tetrahedral voids (Fig. 8). Most complex and interesting is the situation with the Fe group, and especially Fe itself, for which the row of phases FeH₂–FeH₃–FeH₅ (Fig. 9) extends previously known dhcp-FeH.^{141,142} FeH₂ and FeH₃ were discovered at 67 and 86 GPa, respectively. The tetragonal structure of FeH₂ does

Table 2 Binary transition metal hydrides obtained from gigapascal pressure hydrogenations.

Group 4	Group 5	Group 6	Group 7	Group 8	Group 9	Group 10
Ti	V	Cr	Mn	Fe	Co	Ni
		CrH	MnH	FeH	CoH	NiH
		Cr ₂ H ₃		FeH ₂	CoH ₂	Ni ₂ H ₃
		CrH ₂		FeH ₃	CoH ₃	
				FeH ₅		
Hf	Nb	Mo	Tc	Ru	Rh	Pd
Hf ₄ H ₁₅	NbH _{2.5}	MoH		RuH	RhH	PdH
	NbH ₃			Ru ₃ H ₈	RhH ₂	
				RuH ₄		
Zr	Ta	W	Re	Os	Ir	Pt
Zr ₄ H ₁₅	TaH _{2.2}	WH _{1.3}	ReH _{0.85}	OsH	IrH ₃	PtH
	TaH ₃					

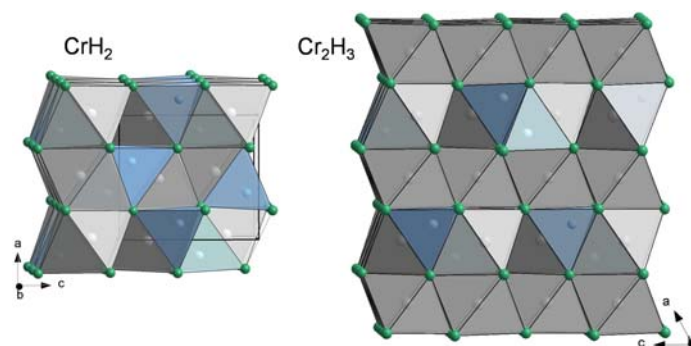


Fig. 8 Hcp based structures of CrH_2 and Cr_2H_3 with both octahedral and tetrahedral voids filled by H (grey and light blue, respectively). CrH_2 corresponds to the cotunnite structure where all octahedral and 50% of the tetrahedral voids in a hcp layer (defined by two consecutive 3^6 metal atom nets) are filled. In Cr_2H_3 layers with exclusively filled octahedral voids alternate with cotunnite-like ones.

not relate to the hcp derived structures of CrH_2 , NbH_2 and TaH_2 . Instead, H atoms are arranged in square nets, which alternate with layers of Fe atoms (Fig. 9A). Fe is coordinated by 8 H atoms whereas H attains a tetrahedral coordination by 4 Fe atoms. FeH_3 adopts a simple primitive cubic structure which is analogous to auriferite AuCu_3 (Fig. 9B). Fe is cuboctahedrally surrounded by 12 H atoms and H tetrahedrally by four Fe atoms (Fig. 9C). Tetragonal FeH_5 was synthesized at 130 GPa and exhibits a structure in which corrugated 4^4 layers of H are inserted between quasicubic slabs of FeH_3 structure (Fig. 9D). The inserted H atoms increase the coordination of Fe to 13 H atoms and cap a square face of each cuboctahedron in FeH_3 (Fig. 9E). The distances between the capping and cuboctahedron H atoms are very short, 1.32 Å. For the heavier congener Ru the previously unknown monohydride RhH was established (NaCl structure) at 14 GPa.¹⁴³ The compositions RuH_2 and RuH_3 do not seem to be stable. Instead Ru_3H_8 and RuH_4 were obtained which both have complex H substructures.¹⁴⁴ Moving to the Co group, hydrides display a simpler structural chemistry. CoH_2 and RhH_2 were discovered above 44 and 8 GPa, respectively, and adopt both the cubic fluorite structure.^{145,146} At higher pressures, above 75 GPa, CoH_3 with the $Pm\bar{3}m$ structure of FeH_3 was found stable.^{145,147} This phase has not been reported for Rh, but for Ir as a distorted cubic variant (at about 55 GPa).¹⁴⁸ Neither IrH nor IrH_2 have been reported until today.

With a few exceptions (e.g., RhH_2) binary group 10–16 transition metal hydrides T_mH_n with $n/m > 1$ are not recoverable at ambient pressure but decompose into monohydrides even at 1-N₂ temperatures. A few of these superhydrides display superconducting properties. E.g., CoH_3 has a T_c of 23 K above 18 GPa.¹⁴⁷

Compared to their lighter congeners the 5d metals W, Re, and Os appear more difficult to hydrogenate. Os would produce fcc (NaCl) OsH only at hydrogen pressures far beyond 100 GPa and upon laser heating,¹⁴⁹ Re accepts some H into its hcp structure at

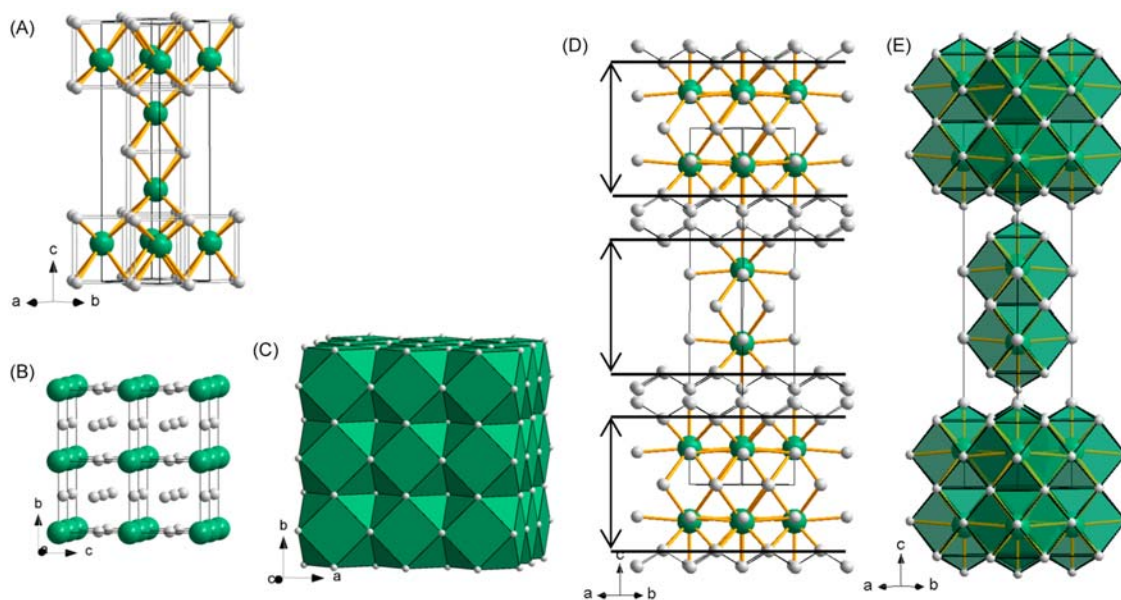


Fig. 9 (A) Crystal structure of tetragonal FeH_2 ($I4/mmm$). AuCu_3 -type structure of FeH_3 shown as atom arrangement (B) and arrangement of cuboctahedral FeH_{12} polyhedra (C). Structure of FeH_5 , again represented as atom arrangement (D) and arrangement of FeH_{13} polyhedra (E). The arrows in (D) indicate blocks corresponding to the FeH_3 structure. Fe and H atoms are depicted in green and grey, respectively.

a few GPa, $x \approx 0.22$, which at 15 GPa increases to ~ 0.5 . At pressures above 23 GPa and when heated to temperatures above 420 K hydrogen solubility saturates at $x \approx 0.85$.¹⁵⁰ W requires hydrogen pressures in excess of 25 GPa to form the anti-NiAs-type monohydride WH. Above 25 GPa a gradual occupation of tetrahedral interstitial sites was observed, which saturated at a composition $WH_{\sim 1.3}$.¹⁵¹ As for group 10, Ni_2H_3 with a monoclinic structure was discovered as post-NiH phase. Ni_2H_3 is stable above 20 GPa.^{152,153} Prototypic palladium hydride PdH_x would not absorb hydrogen beyond $x \approx 1$ even at hydrogen pressures approaching 100 GPa and while applying laser heating.¹⁵⁴ Pt forms trigonal PtH at a pressure of 27 GPa (PtH-I). At higher pressures this phase transitions into hexagonal PtH with the conventional anti-NiAs structure (PtH-II), which is stable up to at least 53 GPa.¹⁵⁵

The difficulty to obtain binary hydrides of late transition metals is contrasted by the ease with which these metals form ternary/multinary complex transition metal hydrides (CTMHs) when combined with active metals. CTMHs consist of negatively charged homoleptic hydrido complexes $[TH_m]^{n-}$ and active metal cations. Occasionally, CTMHs also contain interstitial H which is exclusively coordinated by metal cations. Typically, the transition metal T is from groups 7 to 10. The complex anions $[TH_m]^{n-}$, in which hydridic H is covalently bonded to T, exhibit a perplexing range of coordination numbers and geometries, which rivals that of carbonyl complexes. CTMHs are conventionally prepared from reactive sintering of mixtures of transition metal and active metal hydrides in a hydrogen atmosphere employing autoclave techniques.¹⁵⁶

It has been long believed that group 7 represents a sharp boundary between complex hydride forming late T and interstitial/ionic hydride forming early T (Fig. 10).¹⁵⁷ This boundary was attributed to the fact that early T are less electronegative and thus would favor interstitial bonding scenarios with H, leading to metallic hydrides as opposed to semiconducting complex hydrides. However, recently it has been shown that the application of high pressures, in the range 4–5 GPa, affords CTMHs also for all group 6 metals, the heavier group 5 metals Nb and Ta, and even group 4 Ti. The corresponding compounds are Mg_3CrH_8 with pentagonal bipyramidal $[CrH_7]^{5-}$,¹⁵⁸ Li_5TH_{11} (T = Mo, W) and Li_6TH_{11} (T = Nb, Ta) with tricapped trigonal prismatic complexes $[TH_9]^{3-/4-}$ ¹⁵⁹ and $BaCa_2Ti_2H_{14}$ with a binuclear titanium hydride complex $Ti_2H_{14}^{6-}$ with ninefold coordination.¹⁶⁰ $Ti_2H_{14}^{6-}$ is composed of two face-sharing monocapped square antiprisms and features Ti in the oxidation state IV (cf. Fig. 10). The sharing H atoms are involved in bent 3c-2e Ti–H–Ti bonds. Furthermore, high pressure synthesis employing 8–10 GPa established H-rich complexes also for first-row transition metals, e.g., in Na_3FeH_7 , Na_3CoH_6 , Na_3NiH_5 , as well as the perovskite compound $NaNiH_3$ ^{161,162} ($LiNiH_3$ can be obtained at much lower pressure, between 2 and 3 GPa¹⁶³). These results not only demonstrate the shift of the previously assumed CTMH boundary, but also emphasize the versatility of the H^- ligand for transition metals.^{157,164}

In contrast with the binary transition metal superhydrides, the described examples of hydrogen-rich ternary/multinary CTMHs were afforded by LVP synthesis and represent ambient pressure thermodynamically stable compounds, although they may occur as a different (high pressure) phase at the conditions of formation. High pressure is however needed for their synthesis for overcoming kinetics and thermal lability. Importantly, when pursuing LVP synthesis, H-structures of recovered hydrides—and even of in-situ products¹⁶⁵—can be ascertained by neutron diffraction.

4.12.2.2 Active metal hydrides

Analogous to transition metal hydrides, the application of high pressure—through LH-DAC experiments—also extended significantly hydrides of active metals in surprising ways. Following computational predictions for the systems A-H and Ae-H¹⁶⁶ the compounds LiH_2 ($2LiH \times H_2$) and $Ca_2H_5 = (2CaH_2) \times H_2$, CaH_4 ($CaH_2 \times H_2$) were discovered.^{167–170} At first sight their structures may be described as insertion of H_2 units in the salt like structures of AH and AeH₂. However, the H–H bond appears elongated, as indicated in the red shift of the H_2 stretching mode, which signals substantial charge transfer into the antibonding σ^* molecular orbital ($H_2^{\delta-}$). Ca_2H_5 was obtained at 20 GPa and CaH_4 was found stable above 25 GPa.¹⁷⁰ Its tetragonal structure relates to the intermetallic $BaAl_4$ ($ThCr_2Si_2$) structure (Fig. 11A). The formation of Li polyhydrides was shown in the pressure range

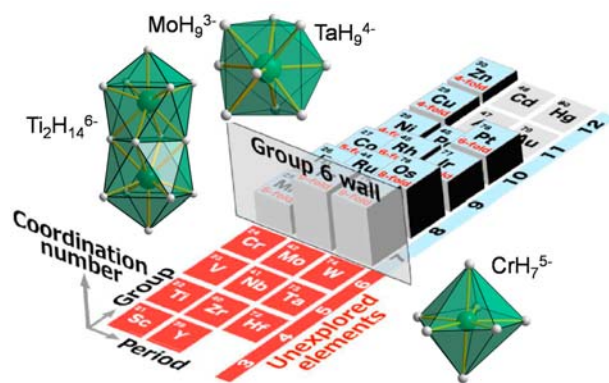


Fig. 10 Depiction of the traditional group 6 barrier for complex transition metal hydrides with the coordination number for TH_m^{n-} complexes indicated. Recent examples from high pressure synthesis breaking the barrier are grouped around. In addition, high pressure synthesis led to coordination increases for Ni (NiH_5^{3-}), Co (CoH_6^{3-}) and Fe (FeH_7^{3-}). The figure is adapted from reference Takagi, S.; Orimo, S. New Functionalities of Hydride Complexes with High Hydrogen Coordination. *J. Phys. Soc. Japan* **2020**, *89* (5), 051010. <https://doi.org/10.7566/JPSJ.89.051010> ((c) (2020) The Physical Society of Japan).

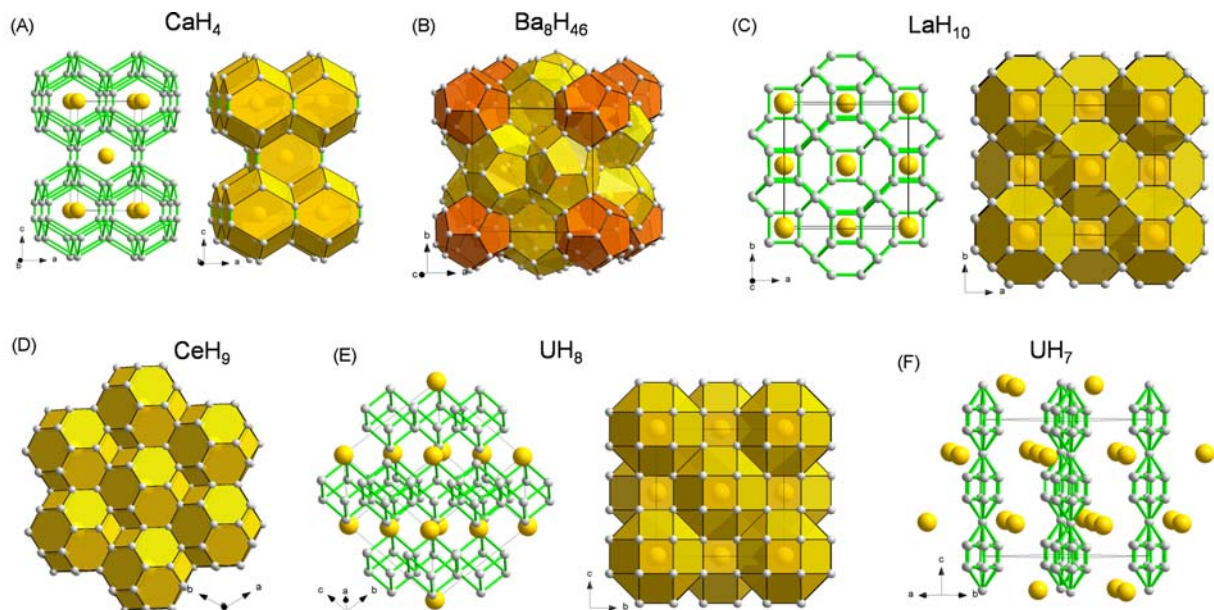


Fig. 11 Crystal structures of CaH_4 (A), Ba_8H_{46} (B), LaH_{10} (C), CeH_9 (D), UH_8 (E), and UH_7 (F). Metal and H atoms are depicted in golden and grey, respectively.

30–180 GPa.^{167,168} Presumably with increasing pressure four phases develop with increasing (but experimentally unknown) H composition.¹⁶⁸ Polyhydrides for Na with compositions NaH_3 and NaH_7 were discovered at pressure above 40 GPa.¹⁷¹ Whereas NaH_3 may be considered as insertion compound $\text{NaH} \times \text{H}_2$, the structure of NaH_7 indicates the development of hypervalently ($3c4e$) bonded H_3^- units ($\text{NaH}_3 \times 2\text{H}_2$).

Be makes an insertion polyhydride compound $\text{Be}_2\text{H}_4(\text{H}_2)$ at remarkably low pressures, 5–8 GPa.¹⁷² The hexagonal ($P6_3/mmc$) structure of $\text{Be}_2\text{H}_4(\text{H}_2)$ constitutes corner-sharing BeH_4 tetrahedra and H_2 molecules occupying an interstitial site. At substantially higher pressures polyhydrides of Ae adopt clathrate-like cage structures. Ca forms CaH_6 at pressures of 160–190 GPa which has a H substructure that is topologically equivalent to sodalite.¹⁷³ Its measured superconducting critical temperature T_c is 215 K at 172 GPa. Ba forms Ba_8H_{46} at 50 GPa and pseudocubic BaH_{12} above 100 GPa.¹⁷⁴ The former compound adopts the cubic type I clathrate structure which is prolific among Zintl phase clathrates and clathrate hydrates (Fig. 11B, cf. Fig. 6).

Similar to Ae metals a common trend for RE and actinides is the formation of a tetrahydride phase MH_4 with the tetragonal CaH_4 structure ($M = \text{Ce}, \text{Pr}, \text{Nd}, \text{Th}$) in the pressure range 30–70 GPa, which at higher pressures, in the Mbar range, is superseded by clathrate-like structures (cubic $Fm-3m$ MH_{10} for $M = \text{La}, \text{Ce}, \text{Pr}, \text{Th}$ (Fig. 11C) and hexagonal $P6_3/mmc$ MH_9 for $M = \text{Ce}, \text{Pr}, \text{Nd}, \text{Th}$ (Fig. 11D)).^{175–182} In the $Fm-3m$ structure metal atoms are encapsulated in H_{32} cages, in the $P6_3/mmc$ structure in H_{29} cages. As a common feature clathrate-like hydride phases are high temperature superconductors, with T_c values approaching room temperature. Uranium forms the sequence of hydrides $\beta\text{-UH}_3$, hcp- UH_7 and fcc- UH_8 when compressed in excess hydrogen.^{183,184} In the structures of $P6_3/mmc$ UH_7 and $Fm-3m$ UH_8 H atoms are arranged as cubes. The UH_8 structure corresponds to a NaCl-like arrangement of U and H_8 cubes (Fig. 11E), whereas in the UH_7 structure U atoms display a hcp arrangement and H_8 cubes, centered at the position of the octahedral voids, form chains by sharing corners across the body diagonal (Fig. 11F). The (calculated) H–H distances in clathrate-like polyhydrides are in a range 1.5–1.8 Å and these phases are typically only stable at pressures in excess of 50 GPa, similar to transition metal superhydrides T_mH_n with $n/m > 2$.

4.12.2.2.3 p-element hydrides

The discovery of superconductivity with T_c values of 203 K in highly compressed H_2S at 155 GPa marked a decisive advance toward room-temperature superconductivity.¹²⁸ The high T_c superconducting species has been identified to be H_3S , which forms, even below room temperature, from the pressure-induced decomposition of H_2S ($3\text{H}_2\text{S} = 2\text{H}_3\text{S} + \text{S}$).^{185,186} Recently, also pure H_3S was prepared by direct in-situ synthesis from the elements in a LH-DAC experiment at pressures above 150 GPa.¹⁸⁷ H_3S is polymorphic. The $Im-3m$ phase has a simple structure which can be considered as two interpenetrating ReO_3 -type substructures built from corner-connected SH_6 octahedra (Fig. 12A). Hypervalently coordinated S by H is a new feature, which also has been related to the superconducting properties of H_3S . At pressures below 150 GPa a rhombohedral distortion of the $Im-3m$ phase takes place, and at even lower pressures H_3S dissociates intrinsically into a non-metallic orthorhombic phase with intercalated H_2 molecules ($2\text{H}_2\text{S} \times \text{H}_2$). Intricate S–H chemistry is further revealed by the discovery of exotic compounds with S/H ratios 1:1.2–1:1.4 when heating S in LH-DAC experiments with PTMs that only provide a limited hydrogen reservoir (e.g., paraffin oil).¹⁸⁸ The substoichiometric sulfur hydride compounds have large unit cell structures which feature hypervalently bonded S, involving coordination to both H and neighboring S atoms (Fig. 12B).

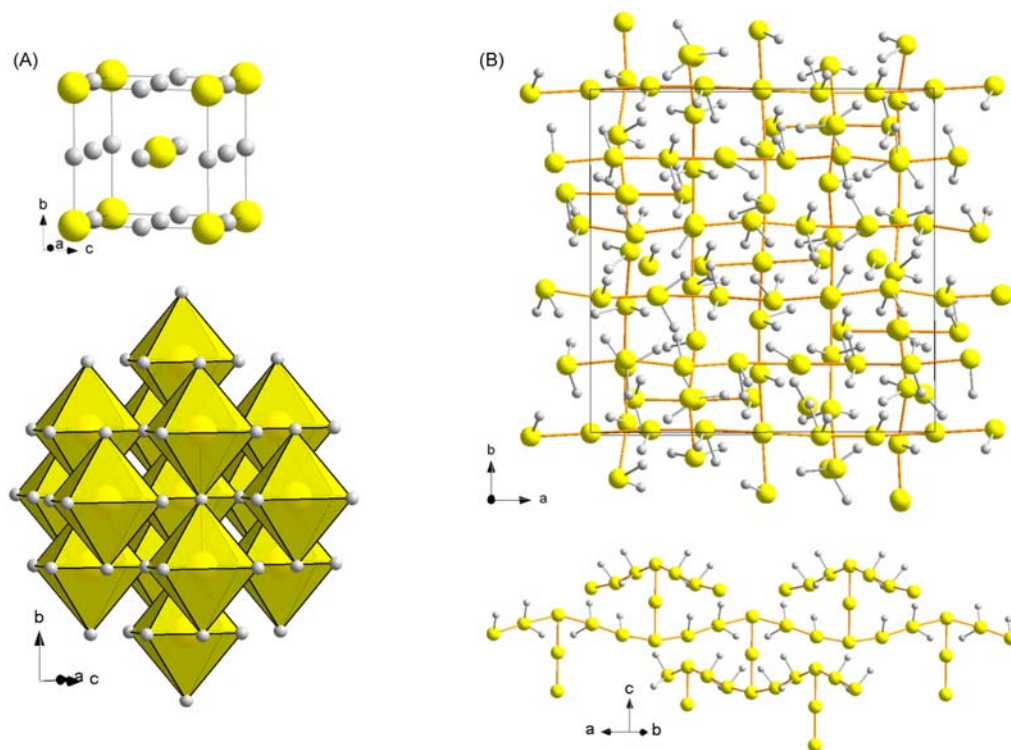


Fig. 12 Crystal structure of H_3S (A) and tetragonal (tI140) $\text{S}_{140}\text{H}_{176}$ (B). S and H atoms are depicted in yellow and grey, respectively. The lower row shows H_3S as two interpenetrating ReO_3 -type substructures and a strand of hypervalently bonded S in $\text{S}_{140}\text{H}_{176}$, respectively.

The high pressure chemistry of phosphor hydrides is experimentally less explored and hypervalent (and superconducting) species PH_2 and PH_3 have been merely predicted.^{189–191} As for Si hydrides, the recoverable ternary compounds K_2SiH_6 and Rb_2SiH_6 with hypervalent SiH_6^{2-} complexes were synthesized at 4–9 GPa.¹⁹² It is interesting to note that although p-element hydrides (e.g., H_3S) and clathrate-like active metal hydrides (e.g., LaH_{10}) are chemically very different they both represent BCS type superconductors.¹⁹³

4.12.2.3 Carbides and nitrides

Analogous to hydrides, carbides and nitrides may be classified as interstitial, covalent and ionic, depending on the electronegativity of the counter element(s). Interstitial carbides and nitrides are mostly associated with intermetallic compounds and therefore addressed in Section 4.12.2.1.1. Carbide and especially nitride materials represent an important class of solid state compounds with useful functional properties ranging from refractory ceramics (Si_3N_4 , AlN , SiC) to widegap semiconductors (GaN), superconductors (NbN) and high-hardness metals (WC , MoN , TiN). Accordingly, carbides and nitrides have been intensely investigated.

Similar to hydrides, the aim of high pressure synthesis is to increase the C or N content in binary/ternary compounds and/or to achieve compound formation with elemental combinations not previously known. Nitrides are frequently thermally rather labile and an important aspect is their stabilization at high pressures in order to achieve sufficiently high temperatures for initiating the often kinetically hindered formation reactions. Again, similar to hydrides, high pressure chemistry has significantly expanded carbide and nitride compounds, based on both main group and transition metals.

Synthesis efforts into nitrides have been broad and also quite involved. Various reaction schemes have been devised for LVP synthesis, using single component and reactive precursor strategies, metathesis reactions, or nitrogen sources such as NaN_3 and NH_4Cl , which at the same time may act as a flux or mineralizer for promoting crystal growth. A single source precursor (SSP) contains all elements of the targeted product, with an identical or similar stoichiometry. The SSP may represent a molecular species, such as $[\text{Rh}(\text{NH}_3)_6]_3(\text{N}_3)_5\text{Cl}_4$ which has been employed for the synthesis of rhodium pernitride, RhN_2 (see below), polymers from condensation reactions, or amorphous/nanocrystalline binary or multinary metal nitride ceramic materials prepared by ammonolysis reactions. Reactive precursors are metastable, high energy materials which are supposed to provide reduced kinetic barriers in high pressure nitridation reactions. For example, polymeric $(\text{PNCl}_2)_n$ or trimeric $(\text{PNCl}_2)_3$ have been shown to be versatile precursors for the synthesis of a range of P–N materials. LH-DAC experiments are ideally suited for exploring the formation of nitrides at highly extreme conditions because N_2 can be conveniently loaded as reactive PTM. And alike to hydrides, quite spectacular results were obtained. At very high pressures, in the megabar range, high reaction temperatures can be applied which enabled the synthesis of exotic nitrogen-rich high energy density materials. Carbide synthesis efforts primarily employed reactions involving elements, or

transformations of ambient pressure stable carbides. Because of their broad significance as materials, the high pressure chemistry of nitrides has been the subject to several reviews, e.g., Ref. 194,195. Further, the assessment of the chemical potential of N₂ at HPHT by Alkhalidi and Kroll represents an important contribution to understanding the high pressure synthesis of nitrides.¹⁹⁶

4.12.2.3.1 Salt-like carbides and nitrides MN ... MN₂

4.12.2.3.1.1 Carbides

The heavier alkaline earth metals Ca–Ba form acetylide carbides AeC₂ from direct reaction of the elements. This is not the case for Mg. Instead, MgC₂ is obtained when reacting Mg and acetylene C₂H₂. Above 770 K, MgC₂ transforms into a mixture of Mg₂C₃ possessing allylenide anions, C₃^{4−}, and graphite. In contrast with the acetylide carbides of Ca–Ba, both MgC₂ and Mg₂C₃ are thermodynamically metastable with respect to their formation from the elements. High pressure synthesis revealed the existence of a third Mg carbide, Mg₂C (with the anti-fluorite structure) which was obtained in a LVP device at 15 GPa and temperatures between 1770 and 2000 K by reacting stoichiometric elemental mixtures.¹⁹⁷ Mg₂C can be recovered to ambient pressure and is metastable up to 500 K. At higher temperature it decomposes to Mg₂C₃ and Mg.¹⁹⁸ The so obtained Mg₂C₃ is analogous to the phase obtained from the decomposition of MgC₂ (orthorhombic, *Pnmm*). From high pressure synthesis another form of Mg₂C₃ (β -Mg₂C₃) could then be obtained.¹⁹⁹ In the Mg–C phase diagram β -Mg₂C₃ is stable at pressures above 19 GPa. However, as Mg₂C, β -Mg₂C₃ can be retained metastably at ambient pressure. In the monoclinic crystal structure (*C2/c*) trimeric C₃^{4−} units are aligned parallel whereas they are mutually canted (by about 70°) in the α polymorph.

4.12.2.3.1.2 Main group nitrides

The technologically significant III–N semiconductors AlN, GaN, and InN crystallize with the hexagonal wurtzite structure and transform at pressures between 5 and 25 GPa into the cubic rocksalt (rs) structure with 6-coordinated ions. Typically the rs forms cannot be retained at ambient conditions, with the exception of rs-AlN for which recovery succeeded when w-AlN nanopowders were used as precursors.²⁰⁰ Similar to the chalcopyrite variations of III–V semiconductors ternary II–IV–N₂ materials provide an inherently greater variety of electronic/band gap properties compared to binary III–N materials. Famura et al. reported on the successful high pressure synthesis of ZnSnN₂ and MgSnN₂ attaining cation disordered average wurtzite and rocksalt structures, respectively.^{201,202} They applied an interesting metathesis strategy which employed the metals as fluoride precursors, according to MgF₂ + SnF₄ + 6 NaN₃ = MgSnN₂ + 6 NaF + 8 N₂ and ZnF₂ + SnF₄ + 2 Li₃N = ZnSnN₂ + 6 LiF. Reactions were performed in an LVP belt apparatus. MgSnN₂ was synthesized at pressures above 5.5 GPa and 1023 K, whereas ZnSnN₂ was obtained in a broad *p,T* wedge from 2.5 GPa to 7 GPa and temperatures 873–1273 K. Further compositional variations include II-(II')₂-N₂ systems. Among these is CaZn₂N₂ with a direct band gap of 1.8 eV which was synthesized at 5 GPa and 1473 K from a stoichiometric mixture of Ca₃N₂ and Zn₃N₂.²⁰³

The synthesis of the group 14 nitrides γ -Si₃N₄, γ -Ge₃N₄ and Sn₃N₄ in the years 1999–2000 represented a milestone as these compounds represented the first nitride spinels. Cubic γ -Si₃N₄ was originally obtained by a direct reaction of the elements using a LH-DAC (at about 15 GPa and 2200 K)²⁰⁴ and later also from conversion of the ambient pressure forms of Si₃N₄ using a MA-LVP device.²⁰⁵ The synthesis of γ -Ge₃N₄ is possible at lower *p,T* (above 10 GPa and 1473 K)²⁰⁶ and spinel structured Sn₃N₄ can even be obtained at ambient pressure, through a low temperature route from SnI₄ and KNH₂ in liquid NH₃. Spinel-Si₃N₄ revealed for the first time octahedrally coordinated Si by N. Recent investigations related to group 14 3:4 nitrides resulted in the discovery of the ternary nitride spinel BeP₂N₄ (obtained from the transformation of phenakite BeP₂N₄ at 47 GPa in a LH-DAC) featuring elusive PN₆ octahedra (Fig. 13A)²⁰⁹ and the solid solution phase Si_{3-x}Ti_xN_{4- δ} (with *x* about 0.18, 8 at.% Ti) from conversion of SSP Si– \ominus Ti–N ceramics at 15–20 GPa and 2073–2273 K.²¹⁰

Similar to Si₃N₄ also the group 15 nitride P₃N₅ adopts a tetrahedra based structure at ambient conditions which above 10 GPa transforms to a high pressure form.²¹¹ This phase, termed γ -P₃N₅, features a network of PN₄ tetrahedra and square pyramidal PN₅. Recent investigations produced the remarkable double nitride BP₃N₆ (BN \times P₃N₅), which was obtained from reactive precursor strategy in which PNCl₂ was reacted with h-BN and N-source NH₄N₃ at 8 GPa and 1373 K in a MA-LVP apparatus, according to 2 (PNCl₂)₃ + 3 NH₄N₃ + 2 BN = 2 BP₃N₆ + 12 HCl + 4 N₂.²⁰⁷ In the presence of NH₄Cl, acting as a mineralizer, BP₃N₆ is afforded as bladed single crystals with 10 \times 100 μ m size. The monoclinic crystal structure (*P2₁/c*) blends features of the α -P₃N₅ and c-BN structures by being composed of pairs of edge-sharing PN₄ tetrahedra and all-side corner-sharing BN₄ tetrahedra, yielding a highly condensed B–P–N framework (Fig. 13B). A high pressure modification of BP₃N₆ (β -BP₃N₆) with a 23% reduced volume was obtained when laser heating α -BP₃N₆ crystals at 42 GPa. β -BP₃N₆ can be retained at ambient pressure.²⁰⁸ The orthorhombic structure relates to a hexagonal close packing of N atoms with B and P atoms in tetrahedral and octahedral voids, respectively (Fig. 13C). β -BP₃N₆ was the first example of a nitride with P in a sixfold, octahedral, N-coordination. Further advances within the P–N theme refer to phosphorous nitride imides. A high pressure form of PN(NH) with a cristobalite-like structure was synthesized at 6 GPa and 1273 K,²¹² and β -P₄N₆(NH) with a unique tetrahedral framework topology was obtained when reacting α -P₃N₅ and NH₄Cl at 6 GPa and 1073 K.²¹³ Targeting a double silicon phosphorous nitride (SiPN₃) by reacting Si₃N₄ with the reactive precursor PNCl₂ and using NH₄N₃ as N-source (analogous to the synthesis of α -BP₃N₆, see above) resulted instead in the binary nitride imide SiP₂N₄(NH).²¹⁴ The compound was obtained at 8 GPa and 1373 K. The orthorhombic crystal structure (*Pnma*) combines octahedral SiN₆ and tetrahedral PN₄ units, with the NH group coordinating to P.

At ambient pressure sulfur forms a ring-like tetrameric nitride S₄N₄ which can be polymerized into metallic polythiazyl [(SN)_x] with a 1D chain structure.²¹⁵ In LH-DAC experiments sulfur-nitrogen mixtures react to SN₂ at pressures above 65 GPa. SN₂ was

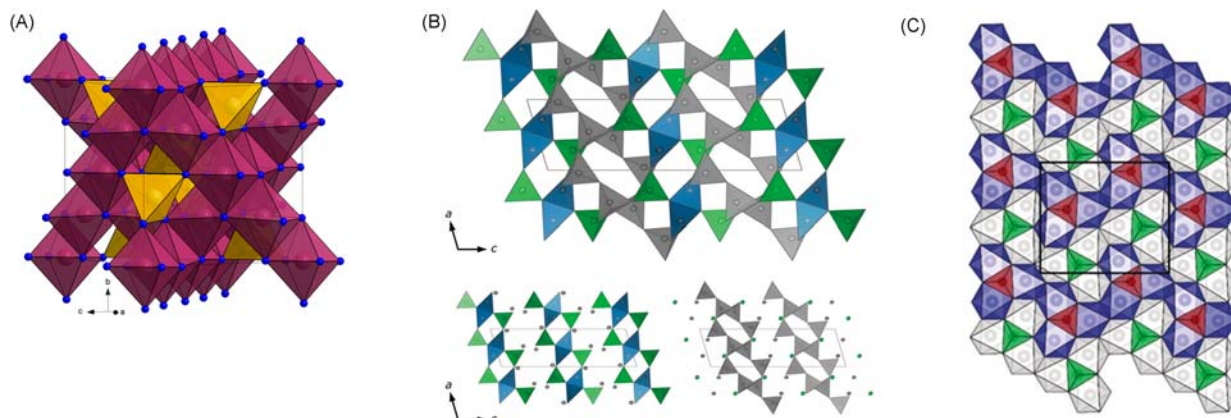


Fig. 13 (A) Ternary spinel structure of BeP_2N_4 . Be, Si and N atoms are drawn as golden, plum, and blue circles. (B) Monoclinic structure of $\alpha\text{-BP}_3\text{N}_6$ (representing a highly condensed tetrahedron framework) and (C) orthorhombic structure of $\beta\text{-BP}_3\text{N}_6$ (containing octahedrally coordinated P). (B) and (C) are taken from Vogel, S.; Bykov, M.; Bykova, E.; Wendl, S.; Kloß, S. D.; Pakhomova, A.; Dubrovinskaia, N.; Dubrovinsky, L.; Schnick, W. Nitride Spinel: An Ultrincompressible High-Pressure Form of BeP_2N_4 . *Angew. Chem. Int. Ed.* **2020**, *59* (7), 2730–2734, <https://doi.org/10.1002/anie.201910998> and Bhat, S.; Lale, A.; Bernard, S.; Zhang, W.; Ishikawa, R.; Haseen, S.; Kroll, P.; Wiehl, L.; Farla, R.; Katsura, T.; Ikuhara, Y.; Riedel, R. Discovery of Ternary Silicon Titanium Nitride with Spinel-Type Structure. *Sci. Rep.* **2020**, *10* (1), 7372. <https://doi.org/10.1038/s41598-020-64101-5>, respectively.

characterized by in-situ single crystal X-ray diffraction. It attains the orthorhombic CaCl_2 structure ($Pnmm$) in which S is octahedrally coordinated by N. S assumes an oxidation state VI and bonding is assumed highly polar covalent. SN_2 is sustained down to 20 GPa, below which it decomposes spontaneously into the constituting elements.²¹⁶

4.12.2.3.1.3 Transition metal nitrides

The discovery of $\gamma\text{-Si}_3\text{N}_4$ stimulated high pressure synthesis efforts also for the group 4 (Ti–Hf) nitrides. Nitrides for these early transition metals had been known only as MN compounds and it was expected that with pressure also the highest oxidation state with composition 3:4 becomes accessible. Indeed, similar to the initial synthesis of $\gamma\text{-Si}_3\text{N}_4$, direct reaction of the elements in a LH-DAC at about 18 GPa and temperatures up to 3000 K produced Zr_3N_4 and Hf_3N_4 with the cubic Th_3P_4 structure in which the metal attains an eightfold N coordination (Fig. 14A).²¹⁷ Recent work showed that $c\text{-Zr}_3\text{N}_4$ can be actually obtained at considerably lower pressures, in the 6–8 GPa region, and at temperatures around 1750 K when using a nanocrystalline $\text{Zr}_3\text{N}_4 + x$ precursor.²¹⁸ The synthesis was achieved in a belt-type LVP which suggests that production of $c\text{-Zr}_3\text{N}_4$ and its oxygen-bearing variants can be performed on an industrial scale. Finally the existence of long-sought $c\text{-Ti}_3\text{N}_4$ was also shown experimentally in a LH-DAC experiment when applying 75 GPa and 2400 K.²¹⁹ In contrast with the heavier congeners, the formation of $c\text{-Ti}_3\text{N}_4$ from the elements requires highly extreme conditions and the compound is accessible only in a very narrow p, T wedge. Experiments at very similar conditions produced the pernitride TiN_2 (see below). In contrast with Zr_3N_4 and Hf_3N_4 , Ti_3N_4 is not recoverable to ambient pressure but decomposes to TiN and N_2 below 10 GPa upon depressurization.

Transition metals beyond group 4 do not realize their highest possible oxidation states as nitrides, apart from Ta_3N_5 , which is a well-known semiconductor and photocatalyst that can be synthesized from Ta_2O_5 by high temperature ammonolysis. A mixture of two new dense and metallic polymorphs of Ta_3N_5 with the U_3Se_5 and U_3Te_5 structures was obtained from an amorphous Ta_3N_5 precursor upon laser heating at 22 GPa.²²⁰ Previous attempts to access these computationally predicted polymorphs by high pressure synthesis from the elements or other forms of Ta_2N_5 only produced Ta_2N_3 with Ta in a mixed IV/V oxidation state.²²¹ A range of nitrogen-rich binary nitrides ($\text{N}/\text{M} \geq 1$) were obtained for group 5 and 6 transition metals when employing the highly versatile metathesis reaction between metallates (e.g., NaVO_3 and Na_2MO_4 ($\text{M} = \text{Cr}, \text{Mo}, \text{W}$)) and BN, yielding transition metal nitride and alkali metal borate.²²² For example, the formation of CrN can be envisioned as a two-step reaction, according to (1) $\text{Na}_2\text{CrO}_4 + \text{BN} \rightarrow \text{NaCrO}_2 + \text{NaBO}_2 + \frac{1}{2} \text{N}_2$ and (2) $\text{NaCrO}_2 + \text{BN} \rightarrow \text{CrN} + \text{NaBO}_2$.²²³ Apart from bulk CrN, also W_3N_4 , W_2N_3 ,²²⁴ the superconductors γ - and δ - MoN ,²²⁵ and even MoN_2 with Mo in the highest attainable oxidation state (VI)²²⁶ were produced through this metathesis route. MoN_2 is isostructural to MoS_2 with Mo in a trigonal prismatic environment by 6 N atoms. Metallate–BN metathesis reactions have been performed using LVP devices and take place at moderate pressures, at around 5 GPa. Although versatile, their inherent disadvantage is the co-product NaBO_2 whose removal from the nitride requires lengthy washing protocols involving HCl or HNO_3 . More unconventional N-sources are melamin and NH_4Cl which afforded pure samples of WC and MoC-type WN, respectively at pressures between 5 and 6 GPa.^{58,227} Although Re(VI)N_2 (with the MoS_2 structure, analogous to MoN_2) was synthesized from a metathesis reaction between ReCl_5 and Li_3N at 7.7 GPa,²²⁸ transition metals beyond group 6 generally require pressures above 10 GPa for nitride formation. For example FeN with the NiAs structure was found at pressures between 10 and 45 GPa when reacting elemental iron with N_2 PTM in a LH-DAC at 1300 K (see Section 4.12.2.1.1).⁶²

An interesting territory for high pressure synthesis are ternary active metal/transition metal nitrides (nitridometallates) which are characterized by complex ions or polyanionic arrangements $[\text{TN}_m]^{n-}$.²²⁹ Typically the transition metal does not attain a high

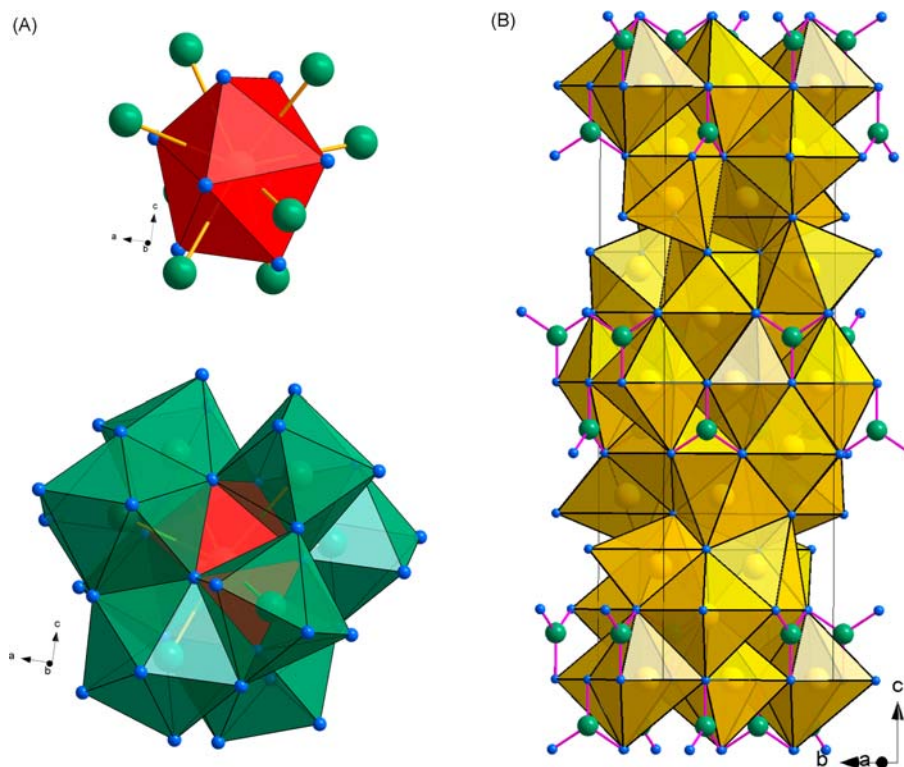


Fig. 14 (A) Cubic structure of T_3N_4 ($T = \text{Ti, Zr, Hf}$). M atoms (green) are coordinated by 8 N atoms (blue) in a triangle dodecahedral (disphenoidal) fashion. These polyhedra are connected via common edges and faces to 8 neighboring ones. (B) Orthorhombic structure of Ca_4FeN_4 ($Ibca$) exhibiting trigonal planar FeN_3^{5-} complexes and isolated nitride N^{3-} ions. Ca, Fe, and N atoms are represented in golden, green and blue, respectively.

oxidation state ($> \text{III}$) in nitridometallates. High pressure synthesis afforded Ca_4FeN_4 which features trigonal planar $[\text{FeN}_3]^{5-}$ ions with low spin Fe(IV) (d^4) and antiferromagnetic ordering below 25 K (Fig. 14B). The synthesis employed a precursor mixture Ca_3N_2 and Fe_2N and was performed in a LVP device at 6 GPa and 1473 K. NaN_3 was utilized as N-source, with the added benefit that molten Na metal promoted growth of single crystals.²³⁰ In a similar reaction the nitrido perovskite LaReN_3 was obtained from LaN and Re (at 8 GPa and 1273–1473 K).²³¹ This compound is a metal and has a triclinic $2 \times 2 \times 2$ superstructure with respect to the basic cubic perovskite cell. The low symmetry has been attributed to orbital ordering with strong spin-orbit coupling distortions. LaReN_3 is a metal and can be topotactically reduced above 773 K to layered tetragonal LaReN_2 .

4.12.2.3.2 Compounds with N_2 species: diazenides (N_2^{2-}) vs pernitrides (N_2^{4-})

Nitrogen-rich compounds containing N_2 species are divided into diazenides (N atoms are linked by a double bond, $(\text{N}_2)^{2-}$) and pernitrides (N atoms are linked by a single bond, $(\text{N}_2)^{4-}$). These N_2 species can be distinguished by their characteristic interatomic distance and associated vibron frequency which can be monitored by Raman spectroscopy: the N–N distance is about 1.4 Å in the pernitride species (800 cm^{-1}) and in the range 1.2–1.3 Å ($1300\text{--}1550 \text{ cm}^{-1}$) for the diazenide ones (the corresponding values for neutral dinitrogen are 1.1 Å and 2400 cm^{-1}).

4.12.2.3.2.1 Diazenides

Diazenides were first obtained for Sr and Ba when subjecting the metals to N_2 pressures of 5.5 kbar in an autoclave.²³² Their crystal structures relate to the corresponding alkaline earth metal acetylide carbides, AeC_2 . Recently it was shown that AeN_2 ($\text{Ae} = \text{Ca--Ba}$) can be conveniently obtained by controlled decomposition of the corresponding azides $\text{Ae}(\text{N}_3)_2$ at gigapascal pressures (12, 9, 3 GPa at 1073, 823, 723 K for $\text{Ae} = \text{Ca, Sr, Ba}$) in a LVP device.²³³ Further examples include Li_2N_2 (obtained from the decomposition of LiN_3 at 9 GPa and 750 K)²³⁴ and ternary, metallic, $\text{Li}_2\text{Ca}_3(\text{N}_2)_3$, which was synthesized from mixtures of LiN_3 and $\text{Ca}(\text{N}_3)_2$ at 9 GPa and 973 K.²³⁵ Interestingly, Li_2N_2 was also observed when laser heating a mixture of $\text{Li}(\text{Li}_3\text{N})$ and N_2 in a LH-DAC between 25 and 74 GPa.²³⁶ However, in this case Li_2N_2 crystallizes in a $Cmcm$ structure with differently aligned N_2 dumbbells and represents a high pressure polymorph. Moreover, in the same experiment LiN_2 (with N_2^-) was identified above 10 GPa and appears to be the thermodynamically stable compound in the Li–N system between 9 and 45 GPa. LiN_2 crystallizes in the hexagonal NiAs structure with Li on the position of Ni and the center of gravity of the N_2 dumbbell corresponding to As. The laser-heating initiated decomposition of NaN_3 at 4 GPa yielded NaN_2 which is isostructural to tetragonal FeSi_2 ($P4/mmm$).²³⁷ At higher pressures (around 30 GPa) $\text{Na}_3(\text{N}_2)_4$ with obviously a non-integer formal charge (-0.75) on the N_2 units was obtained. The structure of this

compound relates to the α -ThSi₂ structure type (*I4₁/amd*). Na₃(N₂)₄ decomposes to NaN₂ upon pressure release, at around 7 GPa, and NaN₂ decomposes into the elements below 3 GPa.

4.12.2.3.2.2 Pernitrides

The discovery of Pt nitride, the first noble metal nitride, received a lot of attention. Its synthesis was achieved in a LH-DAC at about 50 GPa and 2000 K using elemental N₂ as (reactive) PTM.²³⁸ The compound was initially believed to be a mononitride, but later identified as pernitride PtN₂ with the cubic pyrite structure and Pt in the oxidation state IV. With similar conditions also IrN₂, which adopts the monoclinic arsenopyrite structure, was synthesized. Both pernitrides are recoverable to ambient conditions. The metastable behavior in conjunction with interesting materials properties, such as outstanding hardness, fueled a systematic investigation of transition metal pernitrides. Today about a dozen representatives are known, in particular for all elements from groups 8, 9, 10 as well as for the early transition metals Ti and Cr and the late transition metal Cu.^{239–248} Their structures distribute over 6 different structure types: pyrite (PtN₂, PdN₂), arsenopyrite (IrN₂, RhN₂-I), marcasite (FeN₂, CoN₂, NiN₂, RuN₂, RhN₂-II, OsN₂), CuAl₂ (TiN₂), anti-NiAs (CrN₂), as well as NiAs (CuN₂) (Fig. 15). Some of them are polymorphic. For example, LH-DAC synthesis of RhN₂ from the elements at 43 GPa produced marcasite, whereas using an SSP yielded the arsenopyrite structure at somewhat milder conditions (39 GPa, 1600 K).²⁴⁹ Both structures are closely related.²⁵⁰ The first row transition metals pernitrides from FeN₂ to CuN₂ should be rather considered as diazenides, (N₂)²⁻, because of the otherwise unrealistically high oxidation state of the transition metal. As a matter of fact it has been suggested that Cu in CuN₂ corresponds to Cu⁺ (d¹⁰) (balanced by N₂⁻), making it isoelectronic to LiN₂.²⁴⁸ As LiN₂ (see above), CuN₂ adopts the NiAs structure with Cu in an undistorted octahedral environment of 6 N₂ units. In this context it is interesting to note that marcasite NiN₂ transforms upon pressure release at around 4 GPa into a tetragonal, layered structured, polymorph with diazenide moieties.²⁵¹ CrN₂ crystallizes with an anti-NiAs structure in which N₂ moieties are aligned one-dimensionally along the hexagonal *c* direction.²⁴⁷ The pressure range for the synthesis of transition metal pernitrides ranges from just above 30 GPa (Co, Ru) to about 70 GPa (Ti, Cr, Fe). Most pernitrides are recoverable to ambient pressure with the exception of PdN₂, NiN₂, CoN₂ and CuN₂.

To conclude pernitrides, we discuss peculiar ReN₂ which actually corresponds to Re₂(N₂)₄⁴⁻ (N³⁻)₂ containing both nitride and pernitride units and Re in the oxidation state V (Fig. 16).²⁵² ReN₂ can be obtained by reacting Re and N₂ in a LH-DAC above 40 GPa, but has been also synthesized in a LVP at 33 GPa and 2273 K (i.e., at the limit of conventional LVP pressure capability) and using NH₄N₃ as N-source. The material has been described as an ultra-incompressible and very hard metal. Finally, a pernitride

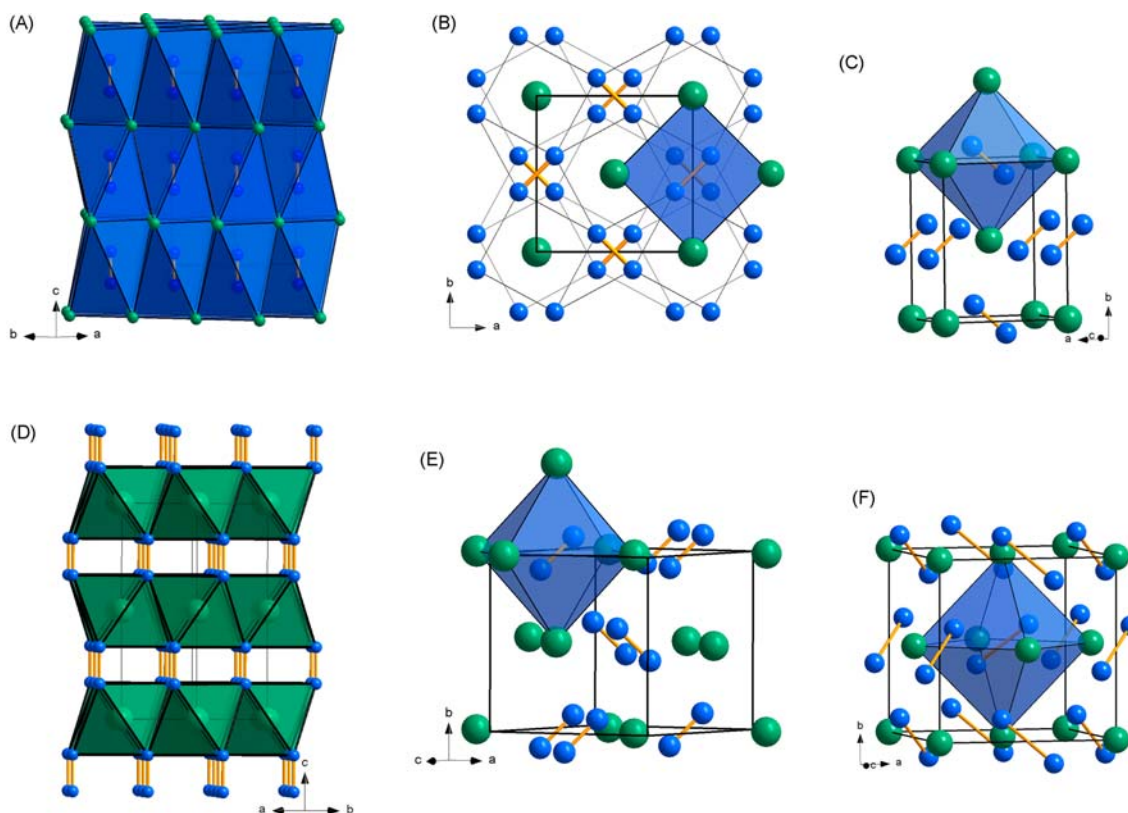


Fig. 15 Structure types adopted by transition metal TN₂ compounds. (A) Hexagonal anti-NiAs (CrN₂), (B) tetragonal CuAl₂ (TiN₂), (C) orthorhombic marcasite (FeN₂, CoN₂, NiN₂, RuN₂, RhN₂-II, OsN₂), (D) hexagonal NiAs (CuN₂), (E) monoclinic arsenopyrite (IrN₂, RhN₂-I), and (F) cubic pyrite (PtN₂, PdN₂). T and N atoms are depicted in green and blue, respectively. N dimer units are connected by light orange bonds.

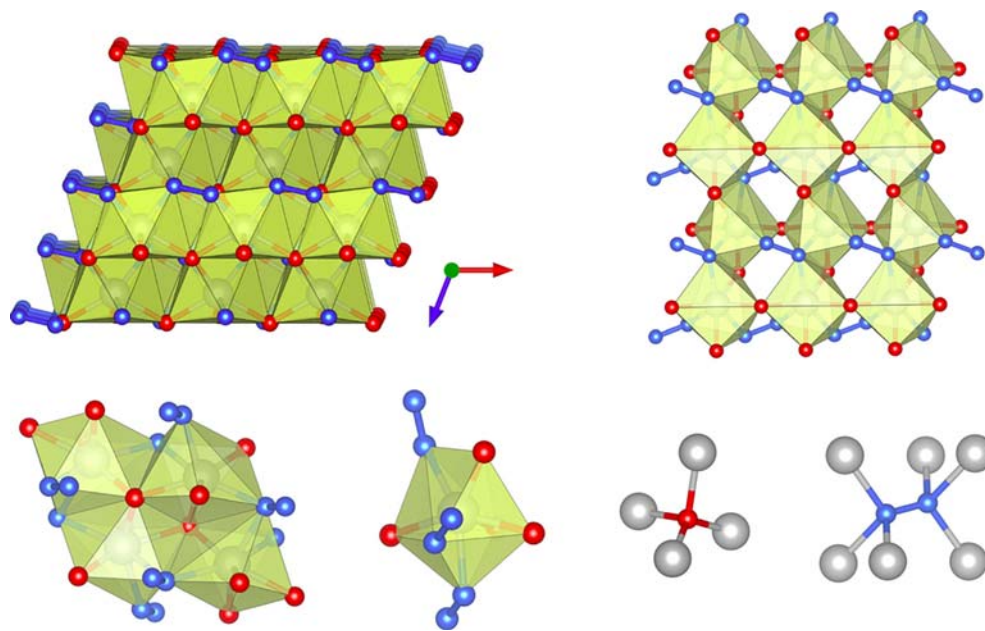


Fig. 16 Fragments of the crystal structure of $\text{Re}_2(\text{N}_2)(\text{N})_2$ ($P2_1/c$), Re atoms—grey, N1 atoms—blue, N2 atoms—red. Upper row: Projection of the crystal structure along the b -axis and connection of ReN_7 polyhedra with each other. Lower row: ReN_7 coordination polyhedra and coordination of N2 atoms and N1–N1 dumbbells. Figure taken from reference Bykov, M.; Chariton, S.; Fei, H.; Fedotenko, T.; Aprilis, G.; Ponomareva, A. V.; Tasnádi, F.; Abrikosov, I. A.; Merle, B.; Feldner, P.; Vogel, S.; Schnick, W.; Prakapenka, V. B.; Greenberg, E.; Hanfland, M.; Pakhomova, A.; Liermann, H.-P.; Katsura, T.; Dubrovinskaia, N.; Dubrovinsky, L. High-Pressure Synthesis of Ultraincompressible Hard Rhenium Nitride Pernitride $\text{Re}_2(\text{N}_2)(\text{N})_2$ Stable at Ambient Conditions. *Nat. Commun.* **2019**, *10* (1), 2994. <https://doi.org/10.1038/s41467-019-10995-3>.

was also reported for Si. As previously mentioned (Section 4.12.2.3.1.2), LH-DAC synthesis experiments yielded spinel $\gamma\text{-Si}_3\text{N}_4$ above 15 GPa. When increasing pressures above 60 GPa SiN_2 with the pyrite structure forms.²⁵³

4.12.2.3.3 Unsaturated moieties as precursors for carbon and nitrogen based materials

A lot of recent synthesis activities into new carbon and nitrogen based materials can be attributed to the idea of achieving pressure-induced oligo- or polymerization (PIP) of triple-bonded moieties isoelectronic to N_2 (as occurring in precursors containing, e.g., acetylide carbide C_2^{2-} or cyanide CN^- ions), or double-bonded moieties isoelectronic to CO_2 (as occurring in precursors containing, e.g., BN_2^{3-} , CN_2^{2-} , or C_3^{4-} ions), see Fig. 17.²⁵⁴ The idea is fueled by the large negative reaction volumes. Yet the energetics for PIP may be unfavorable when considering the relative strength of σ and π contributions to bonding between the 2nd period low Z elements. Also, PIP will result in negatively charged (polyanionic) low Z substructures, which need to be stabilized by electrostatic interactions from the environment of counteranions.

4.12.2.3.3.1 Carbon and carbide materials

PIP is well established for neutral unsaturated hydrocarbon molecules, such as acetylene, which can react at pairs of carbons to form well-known ordered, linear polymers such as crystalline polyethylene. At the same time there is a strong tendency to form extended amorphous carbon networks which are challenging to characterize.²⁵⁵ This is especially the case with aromatic molecules/precursors. Therefore it came as a surprise when Fitzgibbons et al. reported the pressure (or possibly rather stress) induced conversion of benzene to 1D nanothreads composed of sp^3 carbon and terminated by H.^{256,257} This conversion occurs at 20–23 GPa and at room temperature. Polymerized benzene samples are recoverable to ambient pressure and can be produced in macroscopic quantities using LVPs. The nanothreads have a length of >100 nm and assemble as crystalline packings from which they can be exfoliated. They display extraordinary strength and stiffness.²⁵⁸ Recently PIP of highly oriented π -stacked co-crystals of arenes and perfluoroarene resulted in a more systematic approach to thread-like columnar hydro(fluoro)carbons.²⁵⁹

A range of acetylide carbides, such as Li_2C_2 , CaC_2 , BaC_2 , for which theory predicted various polycarbide phases (with superconducting properties) from PIP, were investigated.^{260,261} Room temperature compression would typically yield high pressure phases of the acetylides based on closer packings of dumbbell anions and cations, and eventually lead to amorphization above ~ 25 GPa. This also holds for NaC_2H containing C_2H^- ions, for which, however, the amorphization pressure appears to be substantially lower (at around 15 GPa).²⁶² An exception is ThC_2 for which dimerization to tetrameric, trans-butadiene shaped, moieties was observed during a crystal-crystal transition at around 10 GPa.²⁶³ The pressure induced amorphized products of CaC_2 , Li_2C_2 , and NaC_2H were recovered.^{264,265} Their hydrolysis products, analyzed by GC–MS, showed the presence of a wider range of hydrocarbon molecules, including benzene, which proved the occurrence of PIP. Li_2C_2 and reaction mixtures Ca–C were also subjected to LH-DAC experiments which produced the new carbide phases Ca_2C_3 (an allylenide carbide with linear C_3^{4-} ions, at 17 GPa), Ca_2C (with a “quasi-

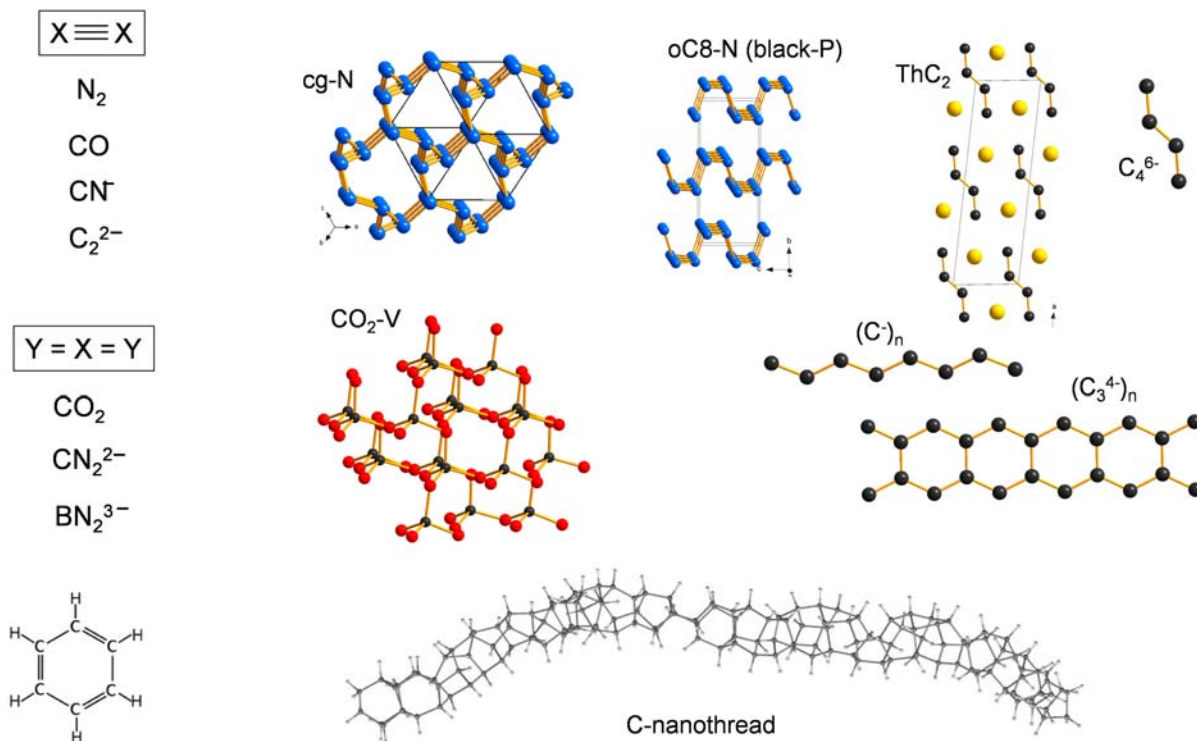


Fig. 17 Examples of unsaturated species prone to undergo PIP (left) and observed and computationally predicted polymeric species (right). Nanotthread figure adapted from reference Fitzgibbons, T. C.; Guthrie, M.; Xu, E.; Crespi, V. H.; Davidowski, S. K.; Cody, G. D.; Alem, N.; Badding, J. V. Benzene-Derived Carbon Nanotthreads. *Nat. Mater.* **2015**, *14* (1), 43–47. <https://doi.org/10.1038/nmat4088>.

2D-metal" structure, at 22 GPa),²⁶⁶ LiC₂ (a completely intercalated graphite with the AlB₂ structure, at 23 GPa), and Li₃C₄ with a polyazinide structure (at 37 GPa).²⁶⁷

4.12.2.3.3.2 C–N materials

C–N materials have attracted great interest ever since the prediction of super hard c-C₃N₄ with sp³ bonded C and N from high pressure synthesis.²⁶⁸ Despite many efforts and using a wide range of molecular and polymeric C–N precursors, the formation of this material remains elusive.²⁶⁹ However, a number of interesting and important discoveries have been made. Using dicyandiamide, C₂N₄H₄, as a precursor produced at 27 GPa and above 443 K crystalline carbon nitride dimide, C₂N₂(NH), with all tetrahedral coordination of C and N in a defect wurtzite structure.²⁷⁰ Using layered polytriazine imide, C₆N₉H₃, resulted in a family of pillared-layered solids,²⁷¹ whereas laser heating of layered "graphitic" g-C₃N₄ compressed to 40 GPa produced open framework C–N structures with mixed sp² and sp³ environments.²⁷² Tetracyanomethane, C(CN)₄, has been only investigated by room temperature compression, during which it transforms above 7 GPa into a disordered network which is recoverable to ambient pressure.²⁷³ Lastly, analogous to the PIP of benzene, carbon nitride derived nanotthreads were obtained from pyridine when pressurizing to 23 GPa at room temperature.²⁷⁴ Molecular precursors toward modified C–N materials include phosphorus tricyanide, P(CN)₃. Its polymerization at 12 GPa and 1273 K in a LVP device resulted in an ambient pressure recoverable sp² s-triazin network C₃N₃P in which P substitutes the bridging N atoms in layered g-C₃N₄.²⁷⁵ Glassy C₃N₃P is a semiconductor with a considerably higher hardness and thermal stability compared to g-C₃N₄. Salt like precursors, such as cyanides or cyanamides, undergo pressure induced amorphizations in a similar pressure range as acetylides when compressing at room temperature. The amorphous phases are recoverable to ambient conditions. They exhibit a broad and strong Raman band at around 1550 cm⁻¹, which indicates the presence of sp² hybridized C–N bonds and a layer-structured arrangement.^{276,277}

4.12.2.3.3.3 Nitrogen and nitride materials

Turning to nitrogen materials, the synthesis of crystalline polymeric "cubic-gauge" nitrogen, cg-N, from molecular nitrogen was achieved at temperatures above 2000 K and pressures above 110 GPa using a laser-heated diamond cell and reported in 2004.²⁷⁸ Cg-N attains a structure of three-bonded N and bond lengths are the same for all pairs of atoms, 1.35 Å at 115 GPa. Cg-N is metastable down to about 42 GPa below which dissociation occurs into a molecular nitrogen. An allotrope isostructural to orthorhombic black P was recently obtained at 140 GPa after laser heating and corresponds to the structure of rhombohedral black phosphorus.²⁷⁹ In contrast with the 3D structure of cg-N, 3-bonded N atoms are arranged in corrugated hexagon layers (armchair conformation), attaining a similar bond length as in cg-N. Several strategies have been discussed to recover polymeric

nitrogen to ambient pressure. From computations it was suggested that a composite with the noble gas He, HeN_4 , is stable (with respect to decomposition into elements) down to 8.5 GPa. In the proposed tetragonal structure of the composite phase N forms a 3D framework (built of 3-bonded N atoms), which is isostructural to the Si framework in LiSi (built of 3b Si^- moieties).²⁸⁰

A range of metal polynitride compounds have been prepared by LH-DAC synthesis using nitrogen as reactive PTM. The procedure is analogous to the synthesis of polyhydrides/hydrogen-rich hydrides, and polynitrides are on a similar trajectory in producing astonishing novel compounds. In contrast with polycarbides, polynitrides are more prone to form crystalline products which allow for unambiguous structure characterization. MgN_4 and Mg_2N_4 were obtained simultaneously when reacting Mg and N_2 above 53 GPa and 1773 K.²⁸¹ Orthorhombic MgN_4 (*lbam*) features N_4^{2-} polyanions with a 1D chain structure that resembles isolectronic polythiazyl $[(\text{SN})_x]$ (Fig. 18A). Mg_2N_4 constitutes tetrameric N_4^{4-} entities which can be regarded as *cis* $(^{2-})\text{N}=\text{N}=\text{N}=\text{N}(^{2-})$, which is isolectronic to *(cis)* N_2F_2 . Mg_2N_4 undergoes a phase transition upon decompression and is recoverable to ambient pressure as low pressure polymorph $\alpha\text{-Mg}_2\text{N}_4$ phase (MgN_4 is not). Similarly, BeN_4 was obtained at 84 GPa and 1973 K. This compound features also 1D polythiazyl-like N-chains but crystallizes in the triclinic structure of FeN_4 (described below).²⁸² BeN_4 undergoes a phase transition to a layered van der Waals bonded polymorph upon decompression. The low pressure polymorph decomposes slowly to $\alpha\text{-Be}_3\text{N}_2$ and N_2 at ambient pressure.

Laser heating of CsN_3 in an N_2 environment at 60 GPa produced CsN_5 featuring the N_5^- pentazolate ion.²⁸³ Upon pressure release CsN_5 decomposes below 18 GPa. Further, the pentazolates LiN_5 and NaN_5 were prepared at pressures above 45 GPa (Fig. 18B).^{284,285} In contrast with NaN_5 and CsN_5 , LiN_5 can be recovered as a metastable phase to ambient pressure. Yet the detailed characterization of its crystal structure is still outstanding. Cyclo N_5^- , which is the N-analogue of the aromatic cyclopentadienyl (C_5H_5^-) anion, has been a long sought-after and elusive species. Interestingly, coinciding with the high pressure synthesis of pentazolates organic chemists succeeded with the (ambient pressure) bulk synthesis of N_5^- via selective C–N bond cleavage in multi-substituted arylpentazole by oxidative dearylation.²⁸⁶ Accordingly, the ligand behavior of N_5^- toward metals could be more broadly explored which even enabled the preparation of Na pentazolate in an open framework zeolitic architecture.²⁸⁷

Nitrides of transition metals were extended from pernitrides (which typically form below 100 GPa, see above) to polynitrides when performing LH-DAC experiments above 100 GPa. The 1D chain of the polyanionic N_4^{2-} moiety present in MgN_4 appears as a recurring theme also for transition metal polynitrides. In $\text{ReN}_8 \times x\text{N}_2$ these trans-1,4 N chains run along the [100] direction in the orthorhombic structure and are mutually tilted by 45 degrees (Fig. 18C). Re(IV) is coordinated as in spirocycles by N atoms from 4 chains.²⁸⁸ The intersecting perpendicular planes of Re and N atoms give rise to square channels along the chain direction. The

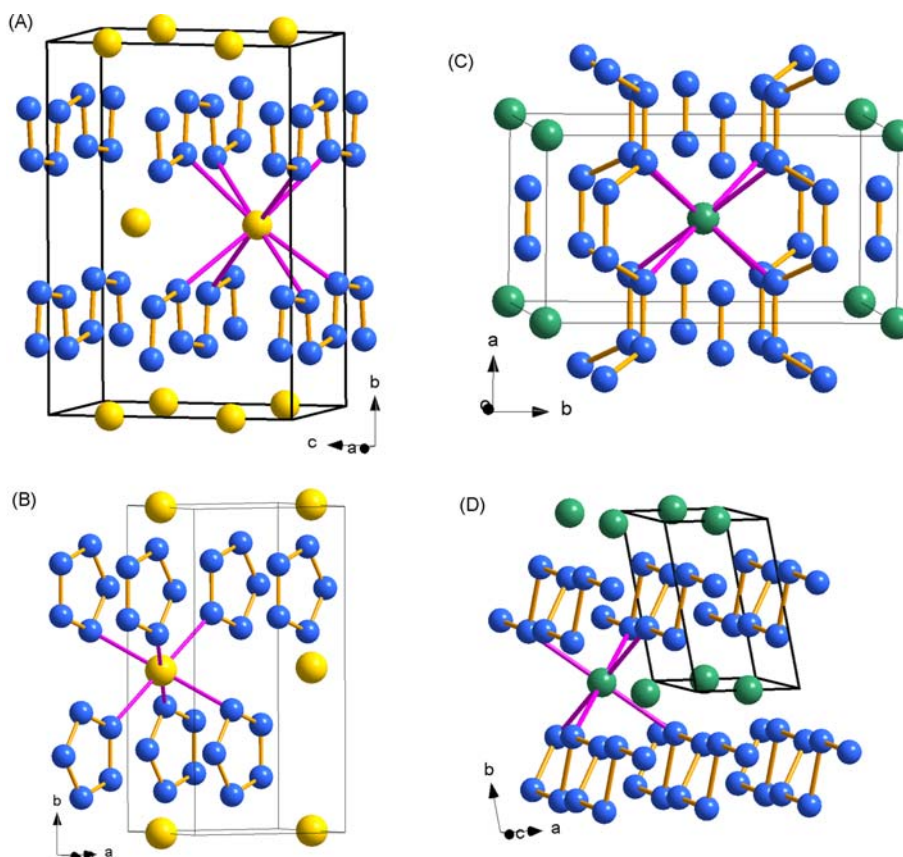


Fig. 18 Crystal structures of the polynitride compounds MgN_4 (A), LiN_5 (B), $\text{ReN}_8 \times x\text{N}_2$ (C), and FeN_4 (D). Li, Mg—golden, T—green, N—blue.

channels host extra molecular N_2 . $ReN_8 \times xN_2$ was synthesized at 105 and 121 GPa using laser heating to 2300–2700 K. The amount of extra N_2 depends on the synthesis pressure. Below 90 GPa $ReN_8 \times xN_2$ crystals deteriorate, which may relate to a release of included N_2 , and the compound is not recoverable to ambient pressure. Non-recoverable open metal-poly-nitride frameworks were also obtained for W, Hf, and Os using similar synthesis conditions as for $ReN_8 \times xN_2$.²⁸⁹ $W(IV)N_8 \times N_2$ is isostructural to $ReN_8 \times xN_2$. $Os_5N_{28} \times 3 N_2$ and $Hf_4N_{20} \times N_2$ can be expressed as $Os(IV)_5(N_4^{2-})_4(N_2^{2-})_6 \times 3 N_2$ and $Hf(IV)_4(N_4^{2-})_4(N_2^{2-})(N^{3-})_2 \times N_2$, respectively. Their metal-N frameworks contain in addition to the N_4^{2-} chain diazenide and nitride species. In contrast, the 3d metal Fe produces FeN_4 at 106 GPa. In the triclinic structure Fe(II) is octahedrally coordinated by 4 N atoms from two parallel running N_4^{2-} chains, and 2 N from perpendicular ones (Fig. 18D). The FeN_4 structure is considerably more compact than the MgN_4 one. In the latter Mg is coordinated by 8 N atoms from 4 different chains. FeN_4 can be decompressed down to 23 GPa.²⁹⁰ $R\bar{3}m$ -structured WN_6 was obtained at 126–165 GPa after laser heating to 3500 K.²⁹¹ In contrast with $W(IV)N_8 \times N_2$ the oxidation state of W is VI in WN_6 and nominally singly charged (2-bonded) N ions form armchair-like hexazine (N_6) rings. The calculated N–N bond length is 1.46 Å at ambient pressure and 1.39 Å at 130 GPa, which compares well with singly bonded pernitride N_2^{4-} species. Below 69 GPa WN_6 decomposes into $W(IV)N_8 \times N_2$ and cg-N. Another interesting transition metal polynitride is orthorhombic ($Fdd2$) TaN_5 featuring branched all-single bonded N chains.²⁹² This compound was formed at around 100 GPa and 2200 K as a mixture with TaN_4 . TaN_4 is built of tetrameric N units.

4.12.2.4 Oxides

Oxide compounds are certainly very diverse, ranging from apparently simple molecular non-metal oxides to complex structured multinary metal oxides with a broad range of compositions, chemical and physical properties. Aims of high pressure chemistry include new polymeric low Z materials from PIP of molecular nonmetal oxides and locking unusual oxidation states or coordination environment in metal oxides into dense phases that are metastable upon recovery to ambient pressure. Because of their high relevance to Earth sciences, the high pressure synthesis of metal oxides and investigations into the phase stability of metal oxides at HPHT conditions has a long tradition.

High pressure reactions typically employ component (binary) oxides as precursors.²⁹³ Sometimes (e.g., if high oxidation states are aspired) reactions are performed in the presence of oxidants, which may be peroxides, chlorates, or perchlorates.²⁹⁴ Peroxides are also called “self-oxidizers” since the metal constituent will be participating in the reaction.²⁹⁵ Chlorates and perchlorates would decompose into inert chlorides. Note that oxygen gas loading of DACs is rarely performed so that LH-DAC investigations also would employ solid oxidants, if desired.

4.12.2.4.1 Non-metal oxides

CO and CO_2 are low Z molecules with multiple bonded atoms and thus expected to undergo PIP. CO is isoelectronic to dinitrogen but much more reactive due to its polarity. In room temperature DAC investigations PIP into a black solid phase I is already observed at around 5.5 GPa and at room temperature.²⁹⁶ This phase is succeeded by a translucent phase II at 7.8 GPa and a transparent phase III above 50 GPa.²⁹⁷ Phases I and II were also prepared in an LVP device utilizing liquid CO which was loaded at liquid N_2 temperature.²⁹⁷ The polymeric forms of CO (pCO) are afforded as amorphous materials and their characterization is challenging, not at least because of their high photosensitivity. It is thought that the polymerization occurs stepwise, with phase I possessing a low-density chain or a 2D conjugated ladder structure.²⁹⁸ Translucent phase II corresponds to a high-density 3D network whereas transparent phase III adopts a 2D layer structure that metallizes above 150 GPa. The latter trend would mirror that of dinitrogen where cg-N obtained at 118 GPa possesses a (crystalline) 3D structure which at high pressures turns into the more compressible black phosphorus 2D layer structure.^{278,279} Similar to N_2 , nonpolar CO_2 is very resistant to PIP. Compression to above 40 GPa and heating to moderate temperatures (around 673 K) produces amorphous carbonia glass containing carbon that is 3- and 4-coordinated by oxygen.²⁹⁹ Upon (laser)heating to between 1500 and 3000 K the crystalline polymeric phase V is obtained (phases II–IV are denser molecular forms).³⁰⁰ The crystal structure of phase V corresponds to a 3D network of corner sharing CO_4 tetrahedra and resembles that of tetragonal β -cristobalite (Fig. 19A).³⁰² Phase V is stable over a wide p,T range (up to at least 120 GPa and 2700 K) and can be retained down to 8 GPa, where dissociation into molecular phase I takes place³⁰³ (note that polymeric cg-N can only be retained down to 42 GPa).

Remarkably, molecular CO_2 and polymeric SiO_2 (in the form of porous silicalite) react when pressurizing modestly to 16–22 GPa and heating at 600–900 K.³⁰⁴ The so-obtained silicon carbonate phase cannot be retained at ambient pressure. The possibility of carbon dioxide reacting with dense silica and forming a solid solution at similar pressures and higher temperatures (above 2000 K) by laser heating has, however, been ruled out by direct characterization of the thermodynamically stable phases of CO_2 and SiO_2 at those p,T conditions.^{305,306} This characterization revealed at the same time a remarkable reactivity of CO_2 and carbonates at HPHT to oxidize the 5d transition metals W, Re, Pt, and Au.^{306,307}

Dense forms of silica containing SiO_6 octahedra are stable at pressures above ~ 9 GPa. Stishovite with the rutile structure is the lowest pressure polymorph of this type (Fig. 20A). The pressure induced transition from tetrahedrally to octahedrally coordinated Si in silica is well studied. An analogous transition has been expected for the heavier homologue SiS_2 but not been observed until recently. At room temperature SiS_2 transforms sluggishly in the pressure range 15–22 GPa into a polymorph with the CdI_2 structure in which SiS_6 octahedra form 2D layers (Fig. 20B).³⁰⁸ CdI_2 -type SiS_2 is stable up to at least 65 GPa and Raman spectroscopy indicates a band gap closure at about 57 GPa. In contrast with rutile SiO_2 , CdI_2 -type SiS_2 cannot be retained at ambient pressure. It can also be synthesized directly from the elements in a DAC at 7.5–9 GPa upon laser heating (1300–1700 K).³⁰⁹ The quartz homeotype

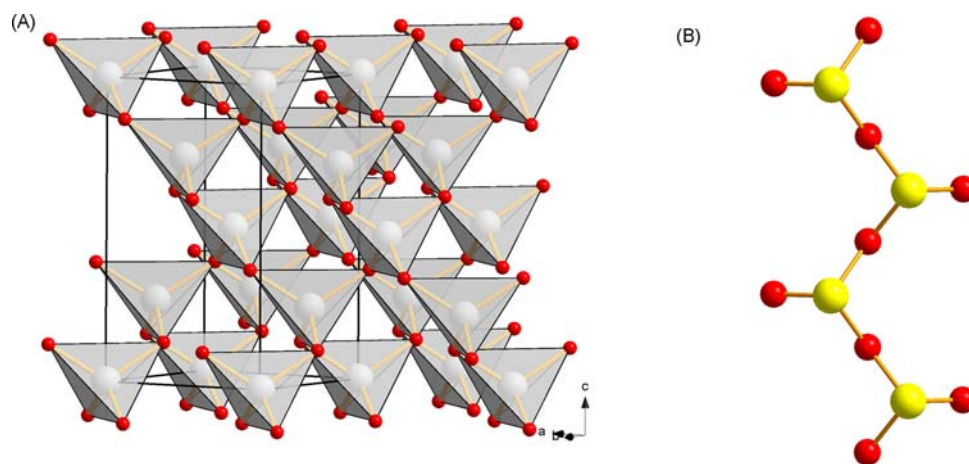


Fig. 19 (A) Crystal structure of polymeric CO₂ (CO₂-V, β -crystalbite). (B) Fragment of polymeric SO₂ according to ab initio molecular dynamics simulations (Ref. 301). C—light grey, S—yellow, O—red.

AlPO₄ undergoes a two-stage transition toward six-coordination of cations, first assuming an octahedral coordination for Al at around 14 GPa by adopting the CrVO₄ structure type (Fig. 20C), and then transforming at above 50 GPa to the CaCl₂-type in which also P attains an octahedral coordination by O (Fig. 20D).³¹⁰ Both transitions are kinetically hindered and were initiated by laser heating. The CaCl₂ structure is very similar to rutile and is also known for SiO₂ as a post-stishovite phase.³¹¹ The sixfold coordination of P by O is extremely rare.

The hypervalent (molecular) oxides P₂O₅ and SO₂ also possess double bonds and thus are expected to undergo PIP. However, they have been rarely studied because of their extreme hygroscopicity.³¹² P₂O₅ has been predicted to convert to dense forms with 5- and 6-coordinated P at 20–30 GPa.³¹³ SO₂ has been investigated in room and low temperature (77–210 K) DAC experiments using

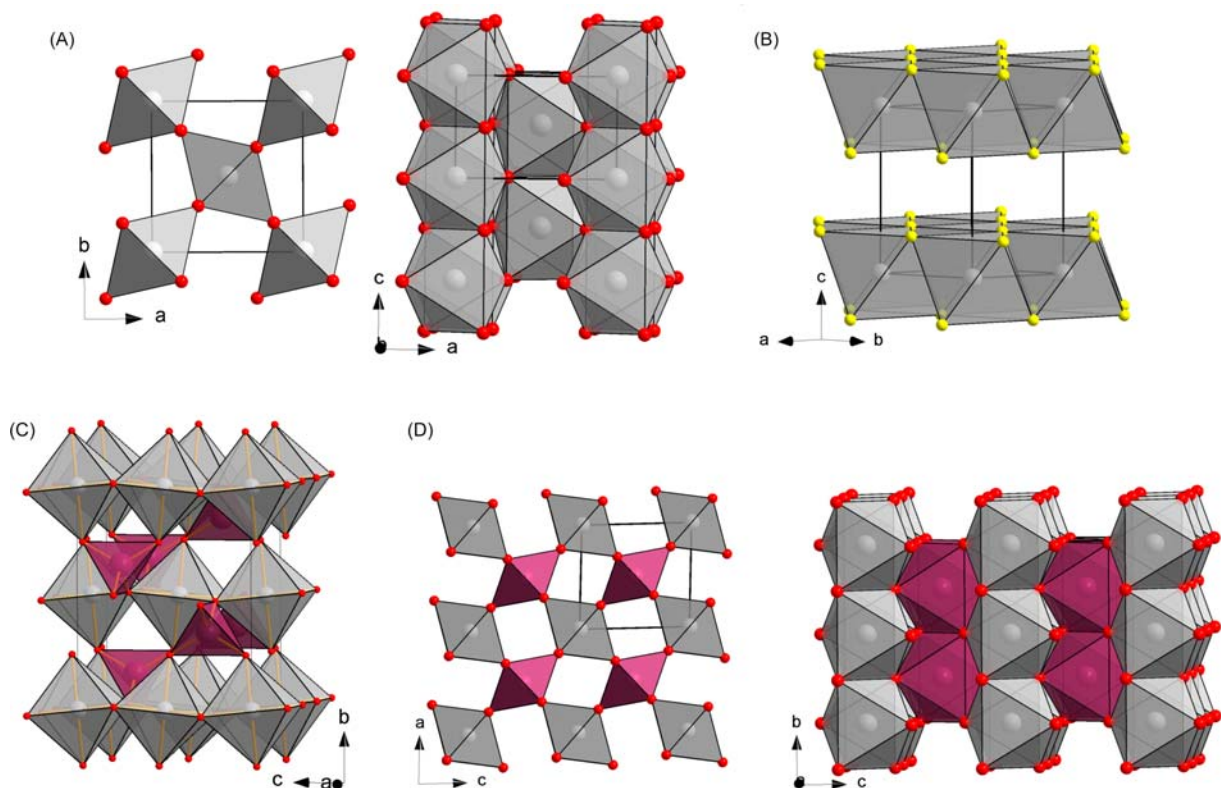


Fig. 20 (A) Stishovite SiO₂ with octahedrally coordinated Si (rutile structure). (B) High pressure form of SiS₂ with octahedrally coordinated Si (CdI₂ structure). High pressure forms of AlPO₄ with octahedrally coordinated Al (CrVO₄ structure) (C) and with both Al and P octahedrally coordinated (CaCl₂ structure) (D). Al, Si—light grey, P—plum, O—red, S—yellow.

Raman and synchrotron X-ray diffraction.³⁰¹ SO₂ undergoes first a crystalline to amorphous molecular transition in the pressure range 5–10 GPa, and then transforms to a polymeric amorphous form at around 26 GPa (polyamorphism). The transition between the amorphous forms is reversible. From MD simulations it is suggested that the amorphous polysulfite corresponds to intertwined chains in which S is 3-coordinated by O atoms (Fig. 19B).

4.12.2.4.2 Binary metal oxides

First-row transition metal monoxides constitute a well studied class of materials. Due to their many interesting properties they represent functional materials in catalysis, magnetic and optoelectronic applications, as well as gas-sensing. The interplay between the energetically close lying wurtzite (tetrahedrally coordinated M) and rocksalt (octahedrally coordinated M) forms is an important feature as it allows altering the properties. Earlier transition metal oxides (e.g., CoO) adopt the rocksalt structure and the metastable wurtzite form may be obtained under hydrothermal synthesis conditions.³¹⁴ ZnO has a wurtzite ground state structure. At pressures above 6 GPa rocksalt ZnO is the stable polymorph, which, however, persistently reverts to the wurtzite form upon pressure release.³¹⁵ Recoverable, ambient pressure metastable rs-ZnO was obtained when employing as precursor w-ZnO nanocrystals with sizes below 45 nm and a narrow size distribution. Quantitative conversion was achieved in a LVP device at 7.7 GPa and low enough temperatures (773–823 K) for not coarsening the precursor crystals.³¹⁶ The finding relates closely to the earlier described synthesis of recoverable rs-AlN from w-AlN nanopowders (Section 4.12.2.3.1.2).²⁰⁰ It exploits the particle size-dependence of the kinetic barrier for reversal and underlines the significance of precursor strategies in high pressure chemistry.

Turning to metal sesquioxides, M₂O₃, the rhombohedral corundum structure (e.g., for Al₂O₃, Cr₂O₃, Mn₂O₃, Fe₂O₃) and cubic bixbyite structure (e.g., for RE₂O₃) are most prolific. Also these oxides have a range of interesting properties and display complex *p, T* phase diagrams. In₂O₃ is a transparent conducting oxide and, similar to ZnO, an interesting material in optoelectronic applications. The ambient form is cubic bixbyite phase. Two quenchable high pressure polymorphs were synthesized using LVP devices. Using the bixbyite as precursor, corundum-In₂O₃ was produced at 12 GPa and 1650 K^{317,318} whereas an orthorhombic form with the Rh₂O₃-II structure was obtained when treating the corundum phase at 8–9 GPa and 873–1373 K.³¹⁹

Mn₂O₃ is a rare example of a binary oxide that can adopt a complex distorted perovskite structure. The perovskite polymorph (ζ -Mn₂O₃) was obtained when heating bixbyite structured Mn₂O₃ at pressures above 20 GPa to between 900 and 1300 K.³²⁰ Lower pressures would produce corundum structured Mn₂O₃, and at higher temperatures decomposition to Mn₃O₄ occurs. Both corundum and perovskite structured Mn₂O₃ are quenchable to ambient pressure. The triclinic structure of ζ -Mn₂O₃ displays heavily tilted MnO₆ octahedra and corresponds to a 4 × 4 × 4 supercell of the simple cubic perovskite ABO₃ (Fig. 21). In perovskites, typically the B-cation is small and highly charged whereas the A-cation is large and possesses a lower charge. In peculiar binary perovskites both A and B-type cations correspond to the same element but in different oxidation states. From EELS spectroscopy it was revealed that the charge separation of Mn in ζ -Mn₂O₃ should be according to Mn(II)Mn(III)₃[(Mn(III)_{0.75}/Mn(IV)_{0.25}]₄O₁₂. The binary oxide perovskite is also realized for Fe₂O₃ and obtained when compressing corundum structured hematite at room temperature to 54 GPa.³²¹ The triclinic structure is similar to ζ -Mn₂O₃ and develops into a monoclinic structure upon further increase of pressure (65 GPa). In contrast with ζ -Mn₂O₃, ζ -Fe₂O₃ is not quenchable to ambient pressure but reverts to hematite.

Dwelling more on Fe oxides, during the years 2011–2016 a surprising homologous series of mixed valence Fe oxides nFeO × m-Fe₂O₃ was established (Fig. 22). LH-DAC experiments in the pressure range 10–26 GPa produced about half a dozen of new Fe oxides, many of them structurally relating to the calcium ferrite family CaFe²⁺_nFe³⁺₂O_{4+n} (with Ca replaced by Fe²⁺).^{321–324} The great majority is quenchable to ambient pressure and Fe₄O₅ and Fe₅O₆ were also prepared in a LVP which provided sufficiently large samples for a detailed characterization of magnetic properties.^{325,326} It has been argued that high pressures and temperatures promote mixed-valence state phases for iron oxides.³²⁴ This may also hold true for rare earth metal oxides for which mixed-valence state scenarios M(III)₂O₃-M(IV)O₂ are known, e.g., for M = Ce, Tb.³²⁷

Another interesting discovery with respect to Fe oxides was the formation of pyrite type Fe(II)O₂ from α -Fe(III)OOH (goethite) at 92 GPa and 2050 K.³²⁸ However, later studies questioned the existence of pyrite FeO₂ and instead proposed that also FeOOH is able to realize the pyrite structure at megabar pressure conditions.³²⁹ Related to the cubic pyrite structure is the isomorphous PdF₂ structure, which is realized in some high pressure polymorphs of transition metal(IV) dioxides. This was the first time reported for RuO₂ and caused excitement because of the extraordinary hardness of PdF₂-type RuO₂.^{330,331} PdF₂-type RuO₂ does not contain O₂²⁻ dumbbell units (as in the pyrite structure) but separated O²⁻ ions which surround octahedrally the transition metal (Fig. 23). Each corner of an MO₆ octahedron is shared with two neighboring ones which creates a very rigid network. Shirako et al. extended PdF₂-type transition metal dioxides for M = Rh, Os, Ir, Pt.³³² The new MO₂ phases were obtained from transforming rutile structured RhO₂, OsO₂, IrO₂ and amorphous PtO₂ at pressures above 15 GPa (which are still accessible with LVPs) and temperatures around 1273 K. Later work by Chen et al. suggested that PtO₂ rather corresponds to a pyrite (containing O₂²⁻ dumbbells).³³³ As a matter of fact, PtO₂ may occur in both forms, pyrite Pt(II)O₂ and PdF₂-type Pt(IV)O₂. The reaction conditions applied by Chen et al. were rather unconventional: the formation of Pt(II)O₂ was observed in LH-DAC experiments when either oxidizing Pt or reducing amorphous PtO₂ in a water environment at around 60 GPa and 1800 K (Pt oxidation) or 1300–1500 K (PtO₂ reduction).

4.12.2.4.3 Mixed metal (multinary) transition metal oxides

Multinary transition metal oxides in conjunction with active metals A, Ae, RE are an extremely broad area and are distributed over a variety of prolific and important compound classes. Most notable are perovskites with the general formula ABO₃, which are one of the most adaptive structures in inorganic chemistry. From the ideal primitive cubic SrTiO₃ structure with a \approx 4 Å numerous

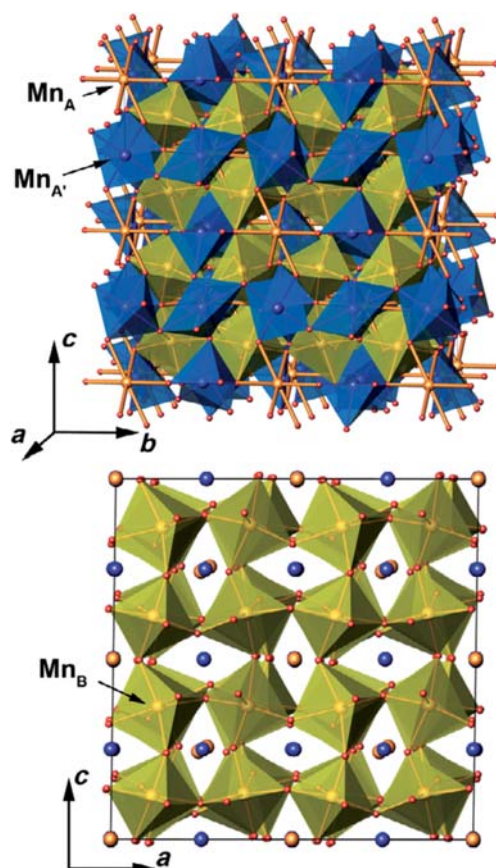


Fig. 21 Top: The crystal structure of ζ - Mn_2O_3 . The Mn_B cations are situated in the light green octahedra, Mn_A cations are at the centers of the blue tetragonal pyramids and octahedra, Mn_A cations are shown as brown spheres. O atoms are shown as small red spheres. Bottom: The framework of corner-sharing MnBO_6 octahedra demonstrating the in-phase cooperative tilting distortion. The figure is reproduced from reference Ovsyannikov, S. V.; Abakumov, A. M.; Tsirlin, A. A.; Schnelle, W.; Egoavil, R.; Verbeeck, J.; Van Tendeloo, G.; Glazyrin, K. V.; Hanfland, M.; Dubrovinsky, L. Perovskite-Like Mn_2O_3 : A Path to New Manganites. *Angew. Chem. Int. Ed.* **2013**, 52 (5), 1494–1498. <https://doi.org/10.1002/anie.201208553>.

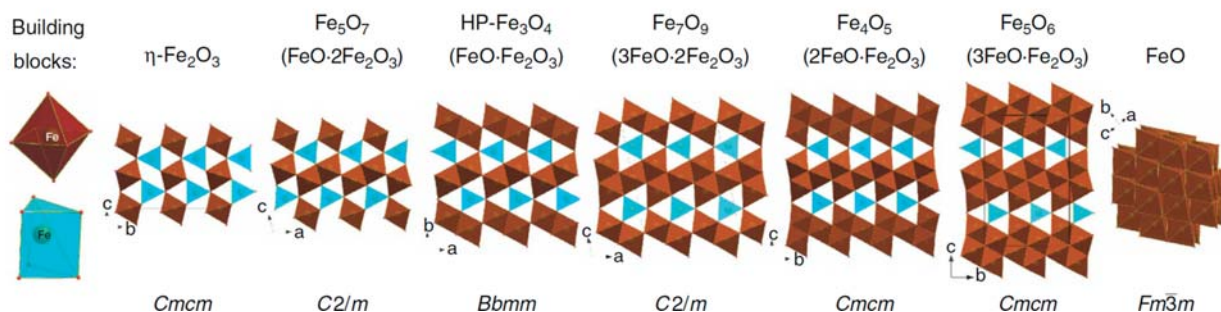


Fig. 22 Homologous series of iron oxides described by the common formula $n\text{FeO} \times m\text{Fe}_2\text{O}_3$. The figure is reproduced from reference Bykova, E.; Dubrovinsky, L.; Dubrovinskaja, N.; Bykov, M.; McCammon, C.; Ovsyannikov, S. V.; Liermann, H.-P.; Kuppenko, I.; Chumakov, A. I.; Ruffer, R.; Hanfland, M.; Prakapenka, V. Structural Complexity of Simple Fe_2O_3 at High Pressures and Temperatures. *Nat. Commun.* **2016**, 7 (1), 10661. <https://doi.org/10.1038/ncomms10661>.

subfamilies evolve, such as O-deficient $\text{ABO}_{3-\delta}$ and double (e.g., $\text{A}_2\text{BB}'\text{O}_6$, $\text{AA}'\text{BB}'\text{O}_6$), triple (e.g., $\text{A}_2\text{A}'\text{B}_2\text{B}'\text{O}_9$), and quadruple perovskites (e.g., $\text{AA}'_3\text{B}_4\text{O}_{12}$, $\text{A}_2\text{A}'\text{A}''\text{B}_4\text{O}_{12}$), describing various scenarios of cation/charge ordering (Fig. 24 and Fig. 25A).³³⁴ Related to perovskites are Ruddlesden-Popper phases $(\text{AO})_{n+1}(\text{BO}_2)_n$ and the hexagonal BaMnO_3 -type structure. The ubiquitous ABO_3 composition is also represented in the rhombohedral ilmenite (FeTiO_3) and LiNbO_3 structures and their variants, whereas brownmillerite $\text{ABO}_{2.5}$ and pyrochlore $\text{A}_2\text{B}_2\text{O}_7$ phases possess lower and higher O/M ratios, respectively.

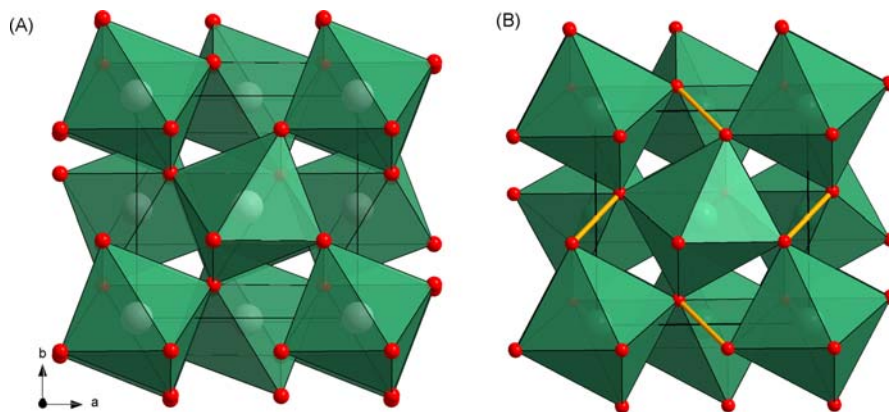


Fig. 23 Comparison of the cubic PdF₂ (A) and pyrite type structures (*Pa-3*) (B). Ru, Fe—green; F, S—red.

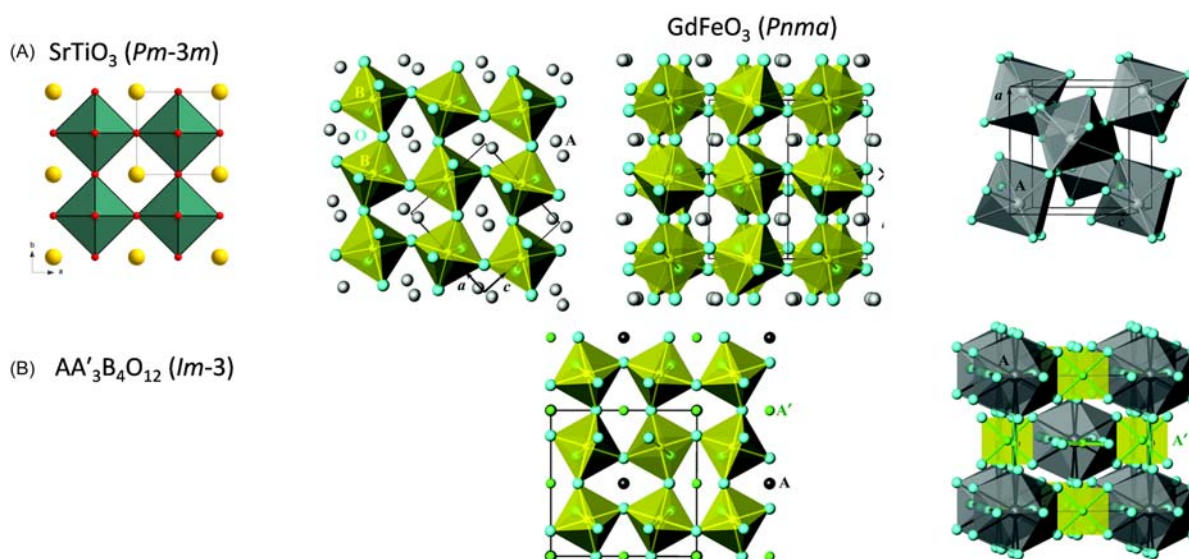


Fig. 24 Connections of BO₆ octahedra and fragments of structures with polyhedra for the A and A' sites in (A) ABO₃ simple perovskites and (B) AA₃B₄O₁₂ quadruple perovskites. A and A' sites are shown by spheres. The figure is adapted from reference Belik, A. A. Rise of A-Site Columnar-Ordered A₂A'A''B₄O₁₂ Quadruple Perovskites with Intrinsic Triple Order. *Dalton Trans.* **2018**, 47 (10), 3209–3217. <https://doi.org/10.1039/C7DT04490A>.

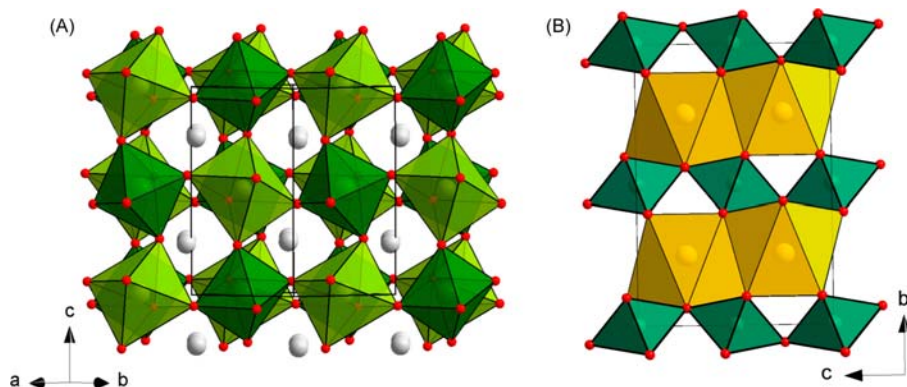


Fig. 25 (A) Crystal structure of the distorted A₂BB'O₆ double perovskite Mn₂MnReO₆ (ref. 340). Light and dark green octahedra indicate the coordination around the B and B' sites. A atoms are represented as grey spheres. (B) Crystal structure of CaIrO₃, also termed “post-perovskite” structure. Ca—golden, Ir—green, O—red.

HPHT reactions have been used since the 1970s as a route to synthesize mixed metal transition metal oxides and numerous compounds have been reported.²⁹³ The research has been essentially driven by the broad range of physical properties associated with mixed metal transition metal oxides, including ferroelectricity, ion conductivity, magnetism, superconductivity, catalytic activity. The necessity of detailed property characterization and also the prospect of tapping into technologically useful materials demands large sample volumes. Therefore, activities have almost exclusively been based on LVPs and utilized a pressure range 1–10 GPa. Although rarely examined, it can be suspected that the majority of recovered products obtained at these pressures are thermodynamically stable and HPHT conditions merely serve as a means to increase the rate of reactions between binary precursor oxides. LH-DAC investigations into multinary transition metal oxides using pressures above 20 GPa have been reported only recently. In the context of this review it is impossible to account for the broad high pressure synthesis activities in this area of materials, and we restrict ourselves to some representative examples.

To a first approximation the stability of perovskites is determined by the ratio of A–O to B–O bond lengths, expressed as the Goldschmidt tolerance factor $t = (r_A + r_B) / \sqrt{(r_B + r_O)}$ where r_i are the ionic radii. Materials with $0.85 < t < 1$ are usually stable. The different compressibilities of A–O and B–O bonds enables perovskites with lower (ambient pressure) t to be stabilized at high pressure and quenched to ambient conditions. As reviewed by Belik and Yi in 2014,³³⁵ pressures of about 6 GPa allowed for the synthesis of a larger number of perovskites with small cations on the A side ($A = \text{Sc}^{3+}$, In^{3+} , Mn^{2+} and $B = \text{Al}^{3+}$, transition metal M^{3+}). For all t is between 0.7 and 0.8. Consequently, they exhibit large structural distortions.

Perovskites with magnetically active A-type cations opened up for new functional materials and are a rapidly developing area. The A sites can now be an integral part of the electronic system (instead of just contributing to charge balance and the fine-tuning of B–O interactions), giving rise to intricate properties based on charge, orbital and spin ordering phenomena.³³⁶ There is an extended compound family $\text{AMn}_3\text{Mn}_4\text{O}_{12}$ (where $A = \text{Na}$, Ca , Sr , Cd , La , Nd) with mixed valence Mn(III) and Mn(IV) which has been synthesized from stoichiometric mixtures of A-oxide, Mn_2O_3 and MnO_2 at 4–8 GPa and 1273–1473 K.³³⁷ Further, there are now several perovskites which have exclusively transition metals on the A site, like MnVO_3 (GdFeO₃ structure, Fig. 24A),³³⁸ the double perovskites ($\text{A}_2\text{BB}'\text{O}_6$) $\text{Mn}_2\text{MnReO}_6$ and $\text{Mn}_2\text{FeReO}_6$ (which were produced from the stoichiometric reactions $3 \text{MnO} + \text{ReO}_3 + 2 \text{MnO} + \frac{1}{2} \text{Fe}_2\text{O}_3 + \frac{1}{2} \text{Re} + \frac{1}{2} \text{ReO}_3$, respectively, at 5 GPa and 1623 K),^{339,340} Fig. 25A, and the cubic quadruple perovskites ($\text{AA}'_3\text{B}_4\text{O}_{12}$) $\text{MnCu}_3\text{V}_4\text{O}_{12}$ and $\text{Cu}^{2+}\text{Cu}^{2+}_3\text{V}^{4+}_4\text{O}_{12}$ (*Im-3*), cf. Fig. 24B.^{341,342} $\text{MnCu}_3\text{V}_4\text{O}_{12}$ was prepared at 12 GPa and 1373 K according to $\text{MnO} + 3 \text{CuO} + 4 \text{VO}_2$, and $\text{CuCu}_3\text{V}_4\text{O}_{12}$ at 15 GPa and 1423 K from a binary mixture $4 \text{CuO} + 4 \text{VO}_2$ (lower pressures, around 6 GPa, yield CuVO_3 with the ilmenite structure³⁴³). In the quadruple perovskite structure A cations are coordinated by 12 O^{2-} ions in an icosahedral fashion. The small sized Cu^{2+} ions appear loosely coordinated and undergo rattling, as concluded from heat capacity measurements.³⁴² Lastly, also earlier mentioned Mn_2O_3 can be regarded as exotic binary representative of quadruple perovskites $\text{AA}'_3\text{B}_4\text{O}_{12}$ when considering charge separation (cf. Fig. 21).³²⁰

ScFeO_3 adopts a “non-perovskite” (bixbyite) structure at ambient conditions which is attributed to the small size of Sc^{3+} as A component. Kawamoto et al. showed in a LVP in-situ diffraction experiment that bixbyite ScFeO_3 transforms at 15 GPa and temperatures above 1073 K to an orthorhombic perovskite which, however, is not quenchable but converts to the LiNbO_3 structure upon pressure release.³⁴⁴ ScFeO_3 with the polar LiNbO_3 structure (*R3c*) is a weak ferromagnet with $T_N = 545$ K. In some cases the perovskite structure can be retained at ambient pressure despite a large size mismatch. For example, high pressure synthesis afforded stoichiometric NaWO_3 and KWO_3 from $\text{A}_2\text{WO}_4/\text{WO}_2/\text{WO}_3$ ($A = \text{Na}$, K) mixtures at pressures between 5 and 8 GPa and heating at 1273 K (Na) and 1973 K (K).^{345,346} Using high pressure techniques alkali metal evaporation during synthesis can be avoided, which is crucial for obtaining completely filled tungsten bronze oxides. NaWO_3 crystallizes with a $2 \times 2 \times 2$ superstructure of the simple cubic perovskite which is related to the quadruple perovskite ($\text{AA}'_3\text{B}_4\text{O}_{12}$) structure (cf. Fig. 24B) but displays different octahedral rotations.³⁴⁵ KWO_3 adopts the simple cubic perovskite structure (cf. Fig. 24A) although the tolerance factor is extremely high, $t = 1.06$, meaning that the potassium is too large.³⁴⁶

An interesting series of perovskites constitute Bi^{3+} as A cation and $M^{3+} = \text{Sc}$, Cr , Mn , Fe , Co , Ni as B cations.^{347–349} The lone pair of Bi^{3+} bears the potential for polar distortion and (anti)ferroelectric behavior of these compounds. Simultaneously, electronic spins on the M^{3+} ions may couple magnetically giving rise to magneto-electronic properties. BiMO_3 perovskites display different structural distortions of the perovskite structure and all of them, apart from BiFeO_3 , were prepared by high pressure synthesis in LVP devices at around 6 GPa from mixtures of Bi_2O_3 and M_2O_3 (or M) and sometimes in the presence of an oxygen source (KClO_4 , KClO_3). Recently also BiVO_3 has been added to this series. This compound was obtained from reacting elemental Bi with V_2O_5 in a DAC at 25 GPa and laser heating to 1500 K, which represent considerably harsher conditions compared to the preparation of the other members.³⁵⁰ BiVO_3 is quenchable to ambient pressure and in contrast to the other BiMO_3 members it attains the simple undistorted cubic perovskite structure. Computations predict the unusual combination of antiferromagnetic and metallic properties, which makes this compound a likely target for further investigations. Although the synthesis pressure is rather high, for detailed structure and physical property characterization it would be important to also achieve the preparation of BiVO_3 in a LVP device and, moreover, considering the stoichiometric reaction $\text{Bi}_2\text{O}_3 + \text{V}_2\text{O}_3 = 2 \text{BiVO}_3$ in order to minimize the propensity for side reactions.

Like Bi , also Pb affords a small sized A cation, and both may occur in two different oxidation states, $\text{Pb}^{2+}/\text{Pb}^{4+}$, $\text{Bi}^{3+}/\text{Bi}^{5+}$. For example, triclinic BiNiO_3 actually corresponds to charge separated $\text{Bi(III)}_{0.5}\text{Bi(V)}_{0.5}\text{Ni(II)O}_3$ and undergoes reversible intermetallic charge transfer to $\text{Bi}^{3+}\text{Ni}^{3+}\text{O}_3$ at 3.5 GPa in room temperature compression experiments. The pressure-induced charge transfer is accompanied with a structural change to the orthorhombic GdFeO_3 -type.^{351,352} Similarly, PbCoO_3 which was obtained from LVP synthesis by reacting a mixture of $\text{PbO} + 2 \text{PbO}_2 + \text{Co}_3\text{O}_4$ at 12 GPa and 1373–1473 K, represents a charge ordered quadruple perovskite $\text{AA}'_3\text{B}_2\text{B}'_2\text{O}_{12}$, which undergoes pressure-induced spin state transitions and intermetallic charge transfer.³⁵³

Generally the B site in perovskites allows transition metals to attain high oxidation states, e.g., Cu(III) in LaCuO_3 , or Fe(IV) in AeFeO_3 (Ae = Ca, Sr, Ba). HPHT reactions in the presence of an oxidizing agent can considerably enhance the ability to tap into compounds with unusual oxidation states. Prominent examples include the synthesis of NaOsO_3 at 6 GPa and 1473–1973 K from OsO_2 and Na_2O_2 , using Na_2O_2 as self-oxidizing agent.³⁵⁴ NaOsO_3 adopts an orthorhombic perovskite structure related to the GdFeO_3 -type. The octahedral environment of $5d^3$ Os(V) implies a half filled t_{2g} band. NaOsO_3 undergoes a continuous metal-insulator-transition with magnetic ordering at 410 K. Reaction mixtures $\text{Li}_2\text{O}/\text{OsO}_2/\text{LiClO}_4$ treated at 6 GPa and 1473 K yielded LiOsO_3 with the LiNbO_3 structure, which displays a ferroelectric-like $R-3c$ to $R3c$ transition at around 140 K despite being a metal.³⁵⁵ Highly oxidized cubic perovskite $\text{Ba}_{0.5}\text{Sr}_{0.5}\text{Co}_{0.8}\text{Fe}_{0.2}\text{O}_{3-\delta}$ ($\delta \approx 0.12$) was synthesized at 8 GPa and 773 K using NaClO_3 or KClO_4 as oxidizing agents.³⁵⁶ NaIrO_3 with d^4 Ir(V) was obtained at rather moderate pressures, 4.5 GPa, and 1073 K using Na_2O_2 , Ir and NaClO_3 as reactant mixture.³⁵⁷ Note that self-oxidizing Na_2O_2 oxidizes Ir from the metal to the pentavalent state. NaIrO_3 adopts the orthorhombic CaIrO_3 structure, which is also called post perovskite (Fig. 25B). In contrast with perovskite structures IrO_6 octahedra are arranged into layers in which they are connected via both shared corners and edges. The AeCoO_3 (Ae = Ca, Sr) perovskites with Co(IV) can be obtained from brownmillerite $\text{AeCoO}_{2.5}$ precursors and $\text{KClO}_4/\text{NaClO}_3$ oxidants at 7–8 GPa.^{358–360} SrCoO_3 attains the simple cubic perovskite structure whereas CaCoO_3 appear to be dimorphic. Low synthesis temperatures (at around 750 K) yield the orthorhombic GdFeO_3 structure, whereas high temperatures (1500 K) produce the simple cubic structure. The AeCoO_3 phases display interesting magnetic properties. In addition, exceptional oxygen evolution reactivities were recently reported for the cubic forms.³⁶⁰ Lastly, the superconductor $\text{Ba}_2\text{CuO}_{4-\delta}$, $\delta \approx 0.8$, was synthesized at 18 GPa and 1273 K and employing the oxidant BaO_2 .³⁶¹ $\text{Ba}_2\text{CuO}_{3.2}$ has a T_c above 70 K which is more than 30 K higher than that of isostructural counterparts based on the K_2NiF_4 -structured La_2CuO_4 parent cuprate.

4.12.2.5 Exotic halide and noble gas compounds

As described in Sections 4.12.2.2 and 4.12.2.3.3.3, high pressure chemistry in the 70–150 GPa region opened up for previously unimaginable families of hydride and nitride compounds. In this section we summarize exotic halide and noble gas compounds from LH-DAC experiments.

4.12.2.5.1 Halides

In 2013 sodium chloride with stoichiometries deviating from archetypal NaCl was reported.³⁶² Computation predicted that at pressures above 20 GPa NaCl_3 and at pressures above 70 GPa Na_3Cl should represent stable compounds in the Na–Cl phase diagram. Their existence could be subsequently confirmed from LH-DAC experiments loaded with NaCl pellets to which additional Cl_2 was condensed (when targeting NaCl_3) or Na added (when targeting Na_3Cl). Reactions were initiated at pressures above 60 GPa and observed at temperatures near and above 2000 K. At formation conditions NaCl_3 was obtained as metallic polymorph in a cubic structure, which upon pressure release transitioned into an insulating orthorhombic form ($Pnma$) at 54 GPa. $Pnma$ - NaCl_3 is isostructural to CsI_3 and features hypervalent linear Cl_3^- ions (Fig. 26A). It can be retained to 18 GPa below which decomposition into NaCl and Cl_2 occurs. Na_3Cl was found to exist in the pressure range 27 to 70 GPa. Its structure is tetragonal ($P4/mmm$) and corresponds to a layered ($\dots[\text{NaCl}][\text{Na}_2][\text{NaCl}][\text{Na}_2]\dots$) superstructure of the CsCl type with both Na and Cl in the eightfold coordination, i.e., $\text{Cl}@Na_8$, $\text{Na}@Na_8$, $\text{Na}@(\text{Na}_4\text{Cl}_4)$, Fig. 26B. Interestingly, using another form of extreme conditions, surfaces, Shi et al. produced (under ambient conditions) Na_2Cl and Na_3Cl compositions as 2D crystals on reduced graphene oxide membranes and on surfaces of natural graphite powders from undersaturated salt solutions.³⁶³

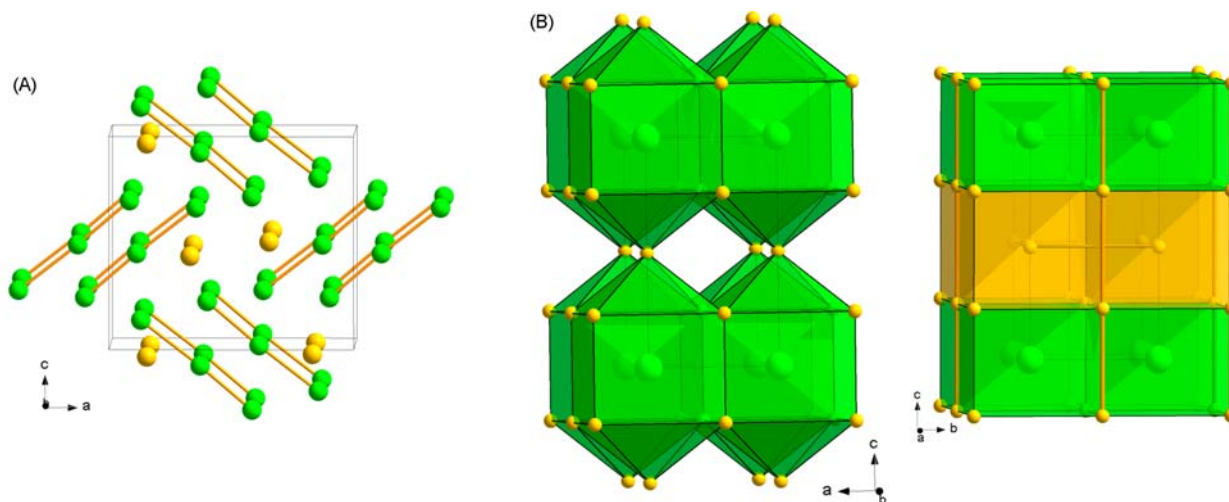


Fig. 26 (A) Crystal structure of NaCl_3 ($Pnma$) containing linear Cl_3^- ions. (B) Crystal structure of Na_3Cl ($P4/mmm$), emphasizing the coordination of Cl (left) and the relation to the CsCl -type structure (right). Na—golden, Cl—bright green.

The Na–Cl study was followed up by a computational prediction of numerous K–Cl compounds and the actual synthesis of KCl_3 .³⁶⁴ The formation reaction was initiated at pressures above 20 GPa. As NaCl_3 , KCl_3 is polymorphic. Above 40 GPa a cubic form isostructural to metallic NaCl_3 was obtained, whereas synthesis in the region 20–40 GPa afforded semiconducting trigonal KCl_3 ($P\bar{3}c1$) with discrete Cl_3^- ions. Upon pressure release the trigonal phase could be retained to about 10 GPa, below which a transition occurred to a phase with a yet unknown structure. This phase appeared to be stable down to 2 GPa.

High pressure promotes also the polyhalide chemistry of bromium. In contrast with Na–Cl and K–Cl, reactions take already place at room temperature and at considerably lower pressures. It has been speculated that the reaction of monohalides with halogen to form polyhalide occurs only if the monohalide is present in the B2 (CsCl) structure. For KI, CsBr, CsI and RbI this is already the case at ambient pressure, whereas the majority of monohalides would undergo a NaCl to CsCl type transition at high pressures.³⁶⁵ The formation of KBr_3 was observed in a DAC loaded with a KBr/Br_2 mixture at 2 GPa. Further compression to about 6 GPa produced monoclinic KBr_5 which remained stable up to 24 GPa.³⁶⁵ KBr_3 attains the orthorhombic ($Pnma$) CsI_3 structure. KBr_5 features a V-shaped Br_5^- anion. This geometry is well-known from polyiodide chemistry, e.g., $\text{N}(\text{CH}_3)_4\text{I}_5$. When laser heating KBr_5 in the pressure range 14–20 GPa it decomposes into trigonal KBr_3 and Br_2 . Upon pressure release at room temperature KBr_5 can be retained down to 5 GPa, and KBr_3 is stable to below 1 GPa.

4.12.2.5.2 Noble gas compounds

Among the notoriously non-reactive noble gases Xe actually has a well developed chemistry, comprising several dozens of compounds in which Xe assumes the oxidation states II, IV, VI, and VIII and of which fluorides and oxides meanwhile are considered classical.^{366,367} In contrast, the chemistry of Kr is restricted to the oxidation state II, and Ar compounds are virtually unknown. From computations it has been predicted that with pressure ArF_2 and KrF_4 should become stable above 60 and 15 GPa, respectively.^{368,369} Since chemistry involving fluorine is difficult to perform, there are no experimental results yet to support these predictions. More feasible is the study of reactions between noble gases and oxygen. Gas mixtures with well defined compositions can be prepared in high pressure vessels and subsequently loaded in DACs.³⁷⁰

The direct reaction between Xe and O_2 yielded two new oxides.³⁷¹ Laser heating mixtures $\text{O}_2/\text{Xe} > 50$ mol% above 77 GPa resulted in a single phase product Xe_2O_5 , which was characterized by in-situ powder diffraction, Raman spectroscopy and Xe K-edge XAS experiments. The tetragonal structure ($P4/ncc$) was ascertained by theoretical calculations and represents a 3D framework of corner sharing XeO_4 squares ($d = 1.98$ Å (calculated)), Fig. 27A. Every second Xe atom is bonded to a 5th O atom to form a XeO_5 square pyramid ($d = 1.83$ Å), which results in a unique mixed valance situation $\text{Xe(IV)O}_2\text{Xe(VI)O}_3$. Xe_2O_5 could be preserved down to around 30 GPa. At lower pressures the compound amorphizes. Raman spectroscopy indicated that Xe–O bonds are preserved in the amorph. Xe_3O_2 was observed when laser heating mixtures $\text{O}_2/\text{Xe} < 25$ mol% at pressures between 90 and 100 GPa. Xe_3O_2 could only be obtained in the presence of Xe_2O_5 , irrespective of the chosen O_2/Xe ratio, which was attributed to the initial formation of the O_2 rich van der Waals compound $\text{Xe}(\text{O}_2)_2$ prior laser heating.³⁷⁰ The structure of Xe_3O_2 (tetragonal, $Immm$) contains planar chains of XeO_4 squares sharing (opposite) edges (composition XeO_2) which are arranged as layers in the bc plane (Fig. 27B). Additional Xe—not bonded to O—is intercalated between layers, which again results in a mixed valance situation $\text{Xe(0)}_2\text{Xe(IV)O}_2$.

A most notable recent discovery is that of a stable compound of helium and sodium, Na_2He .³⁷² Again, similar to the discovery of Na–Cl compounds, initial crystal structure search computations predicted an exothermic formation enthalpy for $2 \text{Na} + \text{He} \rightarrow \text{Na}_2\text{He}$ above 160 GPa which was then confirmed in subsequent LH-DAC experiments. He (PTM) was loaded into a DAC containing thin plates of Na and the mixture was compressed up to 155 GPa. The sample was monitored using synchrotron X-ray diffraction (XRD), Raman spectroscopy and visual observations. A reaction occurred upon prolonged laser heating at 140 GPa at about

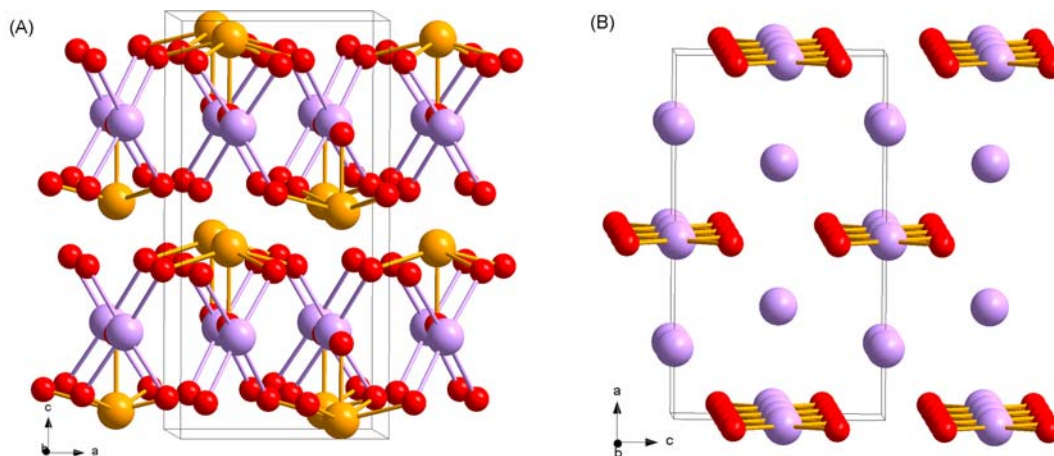


Fig. 27 (A) Crystal structure of tetragonal Xe_2O_5 constituting square planar XeO_4 and square pyramidal XeO_5 units. (B) Crystal structure of Xe_3O_2 constituting chains of square planar XeO_4 units and isolated Xe atoms. Xe—violet and light brown, O—red.

1500 K, close to or above the melting point of He. It is assumed that Na_2He has a melting point around 1500 K and crystallizes from a Na–He melt. Upon pressure release (at room temperature), Na_2He decomposes into its constituents below 113 GPa. The crystal structure of Na_2He corresponds to the simple anti-fluorite structure (Fig. 28A) and its electronic structure to that of a semiconducting electride involving an electron pair, i.e., $\text{Na}_2\text{He}(e_2)$. The electron pair is localized at the octahedral void position of the He fcc close packing, or alternatively, considering the anti-fluorite structure as a superstructure of the CsCl (B2) structure, Na_8 cubes of the simple cubic arrangement of Na atoms are filled by alternating He and e_2 (Fig. 28B). The (calculated) direct band gap of Na_2He exceeds 1.8 eV above 200 GPa.

The reactivity of He at high pressures was further investigated in a theoretical study, which revealed that He has a high propensity to react with a broad range of ionic compounds at pressures as low as 30 GPa.³⁷³ These products are stabilized by long range Coulomb interactions. In particular, it was predicted that CaF_2 (with the fluorite structure) accepts He in octahedral interstices at pressures above 30 GPa, which yields an analogous arrangement to $\text{Na}_2\text{He}(e_2)$. As a general trend, He will be preferably incorporated in salts that constitute uneven numbers of cations and anions and possess a larger number of anions than cations.

The formation of noble gas compounds at high pressures has large implications to Earth and planetary sciences as it indicates that He (and other noble gases) can be stored in the Earth's lower mantle.³⁷⁴ Particularly it has been stated that Xe is underabundant in the atmosphere of the Earth and in order to address the "missing Xe" paradox several theories were launched on how Xe may have been lost to space or been trapped in the depths of the Earth.³⁷⁴ As described above, pressure increases the reactivity of Xe with respect to oxygen and the stability of Xe oxides. Surprisingly, recent LH-DAC experiments and using synchrotron X-ray diffraction and Raman spectroscopy showed that Xe also fully reacts with Ni and Fe to form the compounds XeFe_3 and XeNi_3 , respectively.³⁷⁵ The reaction with Fe required pressures above 200 GPa and 2000 K and resulted in a dimorphic mixture of cubic Cu_3Au and orthorhombic ($Pm\bar{m}n$) NbPd_3 type phases. XeNi_3 forms at lower pressures (above 155 GPa) and temperatures, 1500 K, and was afforded in the orthorhombic CrNi_3 structure type, although, depending on heating/temperature quenching conditions, also the Cu_3Au form may be stabilized.³⁷⁶ Both NbPd_3 and CrNi_3 structures may be considered as fcc based superstructures in which all atoms attain a 12-fold coordination. On pressure release the XeFe_3 phases are stable down to about 120 GPa and XeNi_3 to at least 100 GPa, followed by a decomposition into the elements at lower pressures. Although XeNi_3 and XeFe_3 form at thermodynamic conditions relevant to the Earth core, it was deemed an unlikely explanation for the "missing Xe" paradox.³⁷⁵ Nevertheless, similar to the discovery of Na_2He the existence of XeFe_3 and XeNi_3 is surprising and emphasizes the significance of high pressures to tap into previously unimaginable compound classes.

4.12.2.6 Multi-anion systems

Multi-anion systems refer to compounds composed of two or more different anion species. Traditionally they derive from oxides in which substantial concentrations of oxide anions are replaced by other ions, such as in oxynitrides and oxyfluorides. The structures of multi-anion system often relate to that of parent oxides (e.g., perovskites), but may also reveal decisive variations in the case of strong anion ordering tendency, which can give rise to new and unusual coordination geometries for the metal atoms. Multi-anion systems can display unique structural and chemical states and possess a broad spectrum of interesting physical properties with the possibility of extensive tuning.^{377,378} Not too surprising, interest in multi-anion systems is rapidly increasing and the number of representatives has been grown vastly over the past decade. Oxynitrides are certainly most established, whereas others, like transition metal oxyhydrides, have been discovered more recently, and multi-anion compounds involving mixed molecular and simple ions are just emerging. Similar to nitrides and oxides, the application of high pressure is an important route to synthesize mixed-anion systems as it improves the kinetics of solid-solid reactions, prevents reagents from dissociation or evaporation, and stabilizes dense structures.

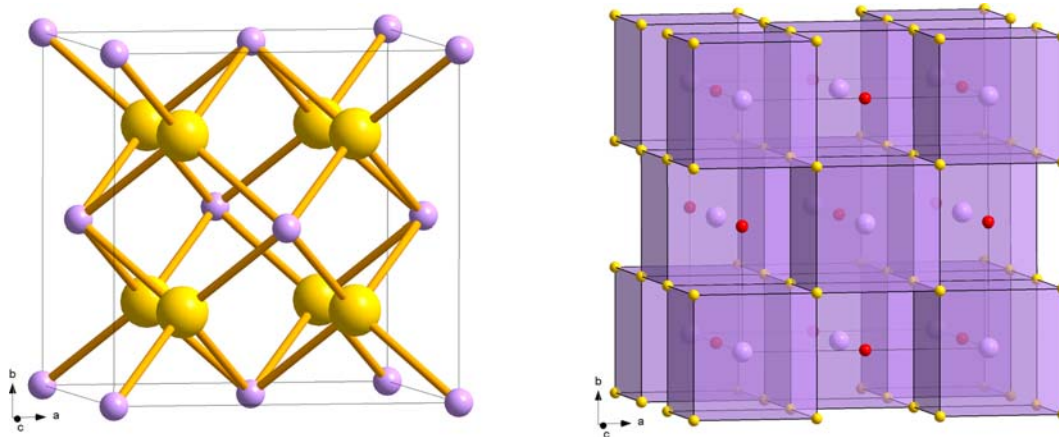


Fig. 28 Fluorite-type crystal structure of Na_2He . The location of electron pairs is indicated as red circles (right). Na—golden, He—violet.

4.12.2.6.1 Oxynitrides

4.12.2.6.1.1 Main group oxynitrides

Among the oxynitrides of group 13 elements AlON is a well known ceramic material which combines exceptional mechanical and optical properties. AlON ceramics adopts the cubic (*Fd-3m*) spinel structure (γ -AlON). Accordingly, the chemical formula is usually expressed as $\text{Al}_{(8+x)/3}\text{O}_{4-x}\text{N}_x$ (accounting for the two boundary compositions Al_2O_3 and $\text{Al}_3\text{O}_3\text{N}$), with x ranging from 0.45 to 0.55.³⁷⁹ The tetrahedral site ($8a$) is virtually fully occupied, whereas the octahedral one ($16d$) accommodates a variable concentration of Al^{3+} ions. γ -AlON is produced by reactive sintering of Al_2O_3 and AlN at ambient pressure. The synthesis of corresponding GaON from GaN and Ga_2O_3 requires high pressures and was achieved in LVP devices at 5 GPa.^{380,381} The reactivity of monoclinic β - Ga_2O_3 appears superior to corundum structured α - Ga_2O_3 , and the optimal synthesis protocol implies heating a β - Ga_2O_3 /GaN mixture (molar ratio 2:3) to 1523 K, followed by slow cooling to 1073 K and subsequent temperature quenching. From this protocol GaON is afforded as $\text{Ga}_{2.79}\square_{0.21}\text{O}_{3.05}\text{N}_{0.76}\square_{0.19}$ (where \square is vacancy), i.e., there are simultaneous Ga^{3+} (octahedral) vacancies and anionic vacancies in the GaON spinel structure.³⁸²

High pressure synthesis also afforded an oxynitride of boron, $\text{B}_6\text{N}_4\text{O}_3$ ($\text{B}_2\text{O}_3 \times 4\text{BN}$, "BON"), when sintering a ball milled mixture of *h*-BN and B_2O_3 (molar ratio 6:1) at 15.6 GPa and 2173 K in a MA-LVP device.³⁸³ BON is recoverable and its rhombohedral crystal structure relates closely to the cubic sphalerite structure (which is also the crystal structure of cubic BN), Fig. 29A. With respect to the sphalerite structure one seventh of the boron atoms are missing. DFT modeling of vacancy distributions revealed a strong tendency of ordering in BON, where O positions next to B vacancies are preferred over direct B–O contacts. BON is assumed to possess the highest bulk modulus among all oxynitrides.

Moving to group 14, the oxynitrides $\text{Si}_2\text{N}_2\text{O}$ and $\text{Ge}_2\text{N}_2\text{O}$ have been known for more than 50 years.³⁸⁴ They can be prepared by nitriding silicon/silica mixtures at 1723 K and ammonolysis of GeO_2 above 1123 K, respectively. In the orthorhombic crystal structure Si and Ge atoms are tetrahedrally coordinated by 3 N and 1 O atoms in an ordered fashion; in the tetrahedral framework N and O corners are shared with 3 and 2 neighboring tetrahedra, respectively. The tin oxynitride $\text{Sn}_2\text{N}_2\text{O}$ has been obtained from high pressure synthesis when reacting a mixture of crystalline Sn_3N_4 (spinel structure) and amorphous SnO_2 at 20 GPa and 1473–1773 K. $\text{Sn}_2\text{N}_2\text{O}$ is recoverable and crystallizes with the orthorhombic Rh_2S_3 structure (*Pbcn*).³⁸⁵ In this structure type S atoms distribute over two crystallographic sites with a ratio 2:1 which for $\text{Sn}_2\text{N}_2\text{O}$ are occupied by N and O atoms, respectively (Fig. 29B). In contrast with the lighter congeners, $\text{Si}_2\text{N}_2\text{O}$ and $\text{Ge}_2\text{N}_2\text{O}$, Sn attains an octahedral coordination (to 4 N and 2 O atoms) and in the dense $\text{Sn}_2\text{N}_2\text{O}$ structure octahedra share edges as well as faces, which results in short Sn–Sn distances comparable to those in β -Sn (3–3.2 Å). From DFT calculations it was concluded that Rh_2S_3 -type $\text{Sn}_2\text{N}_2\text{O}$ is metastable at ambient pressure.

Phosphorous displays an extraordinary rich oxynitride chemistry which especially has been revealed from high pressure synthesis. Phosphorous oxynitride PON is isolectronic with SiO_2 and displays similar chemical and structural properties, which is summarized in Fig. 30. PON may be synthesized from thermal decomposition of phosphoryl triamide ($\text{PO}(\text{NH}_2)_3$) in a stream of dry ammonia. Initially amorphous PON crystallizes above 973 K and adopts a tetragonal structure which corresponds virtually to β -cristobalite with O and N distributed randomly over the anion sites.³⁸⁶ The α -quartz phase of PON, again with randomly distributed O and N atoms, was prepared by submitting the β -cristobalite phase to 4.5 GPa and 1023 K in a belt type LVP apparatus.³⁸⁷ Upon compressing α -quartz PON at room temperature in a DAC, a transition to an α -quartz II phase occurs around 20 GPa, which then is followed by progressive and irreversible amorphization above 30 GPa.³⁸⁸ This behavior is parallel to SiO_2 . Further similarities to SiO_2 are seen in the high pressure behavior at elevated temperatures: When heating β -cristobalite PON to 1573 K at 15.5 GPa and at 20 GPa a coesite analogue (coe-PON)³⁸⁹ and a stishovite-related form (pc-PON),³⁹⁰ respectively, are formed. Both phases are recoverable to ambient pressure and, as for the low pressure forms, N and O atoms appear randomly distributed. The pc-PON structure relates closely to the rutile structure. However, the P atoms are significantly displaced from the center of the ON_6 octahedra and are described with a split position. Thus, the P atoms attain a fivefold square-pyramidal coordination. At ambient pressure the distance to the basal ligands is 1.70 Å and that to the axial one is 1.75 Å. The distance to the second axial atom, referring to the

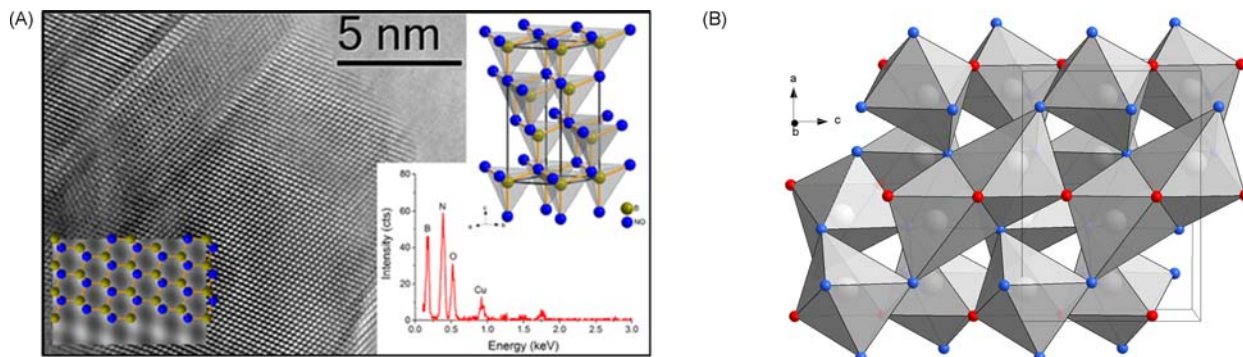


Fig. 29 (A) Boron oxynitride $\text{B}_6\text{N}_4\text{O}_3$ with a (boron defect) sphalerite type structure. The figure is reproduced from reference Bhat, S.; Wiehl, L.; Molina-Luna, L.; Mugnaioli, E.; Lauterbach, S.; Siculo, S.; Kroll, P.; Duerrschnebel, M.; Nishiyama, N.; Kolb, U.; Albe, K.; Kleebe, H.-J.; Riedel, R. High-Pressure Synthesis of Novel Boron Oxynitride $\text{B}_6\text{N}_4\text{O}_3$ with Sphalerite Type Structure. *Chem. Mater.* **2015**, *27* (17), 5907–5914. <https://doi.org/10.1021/acs.chemmater.5b01706>. (B) Crystal structure of Rh_2S_3 -type $\text{Sn}_2\text{N}_2\text{O}$. Sn—light grey, N—blue, O—red.

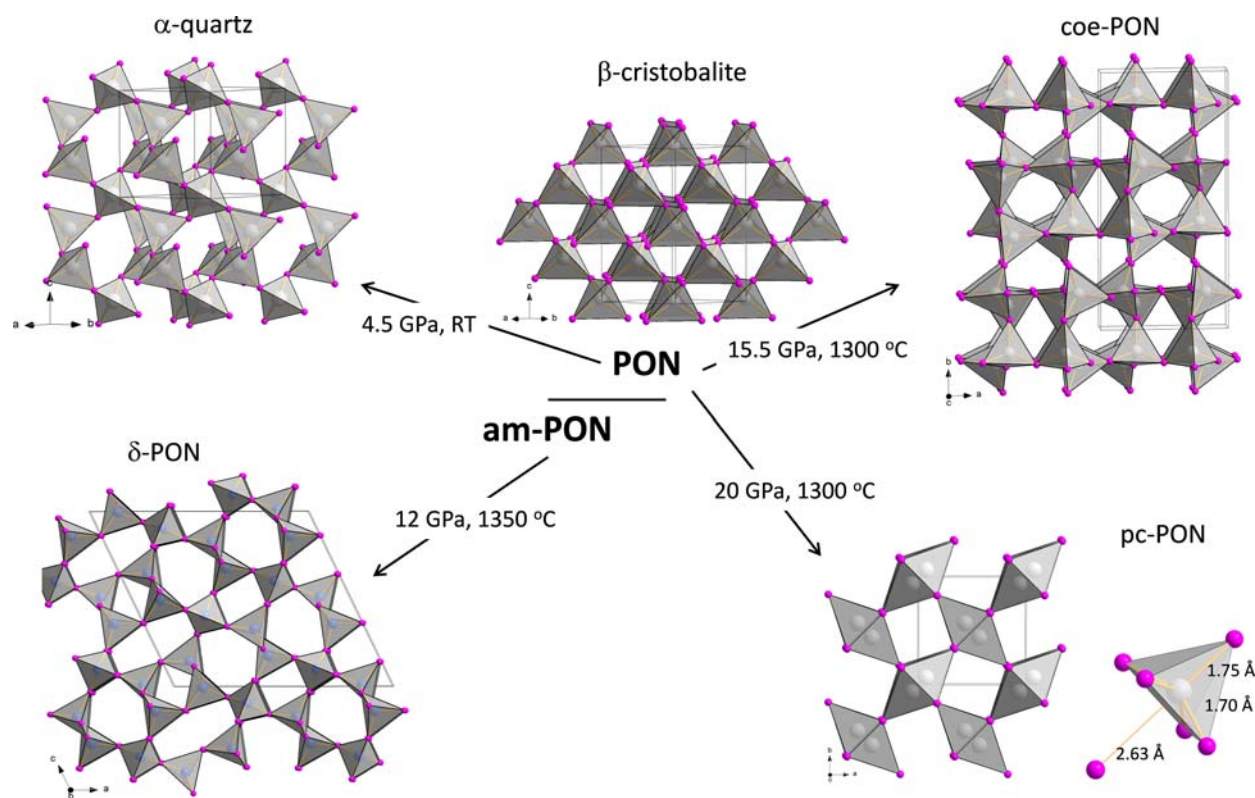


Fig. 30 High pressure transformations of crystalline PON (β -cristobalite structure) and amorphous PON ($\text{PO}_{0.88}\text{N}_{1.24}\text{H}_{0.56}$).

octahedral coordination in rutile, is 2.63 Å. Compressing pc-PON in a DAC at room temperature revealed a reversible tetragonal-to-orthorhombic phase transition at 20 GPa, which is similar to the stishovite- CaCl_2 transition in silica.³⁹⁰ Yet the P atoms maintain their 5-coordination in the orthorhombic polymorph and it has been speculated that pressures beyond 40 GPa are required in order to stabilize PON with P in a regular sixfold coordination (Fig. 30).

When using amorphous PON instead of crystalline β -cristobalite PON as precursor, LVP experiments at 1623 K and 12 GPa produced δ -PON with a new tetrahedral framework structure unknown to silica (Fig. 30).³⁹¹ δ -PON is recoverable and metastable with respect to coe-PON. Amorphous PON with an approximate composition $\text{PO}_{0.88}\text{N}_{1.24}\text{H}_{0.56}$ is obtained when carrying out the thermal decomposition of phosphoryl triamide at 900 K. Since the condensation process toward PON is not completed, the material is still hydrogenous and somewhat rich in N. Compared to the crystalline β -cristobalite form, amorphous PON is considered a reactive precursor. Simultaneous condensation processes and/or the presence of NH_3 at HPHT conditions open for pathways with lower activation energies. At the same time also imides may be produced. Heating amorphous PON precursor at 12 GPa to lower temperatures (1023 K) results in the phosphorus oxynitride imide $\text{P}_8\text{O}_8\text{N}_6(\text{NH})_3$ with an "interrupted" (high-density) tetrahedral framework structure that is composed of all-vertex sharing and three-vertex sharing tetrahedra in a ratio 3:1.³⁹² The imide ligands are associated with three-vertex tetrahedra.

4.12.2.6.1.2 Transition metal oxynitrides

Transition metal oxynitrides are a large and versatile family of compounds. The various synthesis approaches for oxynitrides have recently been reviewed by Fuertes.³⁹³ The most wide-spread route is the ammonolysis of oxides. The highly reducing atmosphere during thermal ammonolysis typically does not permit oxynitrides with middle and late transition metals. High pressure synthesis has been shown to be very effective in producing mixed metal oxynitrides through solid state reactions without the use of nitriding atmospheres. These reactions would typically employ mixtures of active metal oxide and transition metal nitride or oxynitride. With respect to the nitride/oxynitride precursor component, choices are limited since essentially only group 4 and 5 metals easily afford nitrides and oxynitrides (e.g., Ta_3N_5 , TaON, Zr_2ON_2). The role of high pressure is to prevent N-loss at the rather high reactions temperatures (> 1273 K) that are required for efficient diffusion of the metal atoms. Experiments were mostly executed with LVP devices and using a pressure range 2–10 GPa. The reported products were all quenchable to ambient pressure. In their structures O and N atoms are assumed to be randomly disordered.

An early example for mixed metal oxynitrides from high pressure synthesis are the perovskites REZrO_2N (RE = Pr, Nd, Sm) with orthorhombic $Pnma$ structure which combine magnetic RE^{3+} and non-magnetic d^0 transition metal ions.³⁹⁴ The compounds were prepared by direct sintering of 1:1 M mixtures of RE_2O_3 and Zr_2ON_2 at 2–3 GPa and 1473–1773 K. More recent examples include MnTaO_2N obtained from MnO and TaON mixtures at 6 GPa and 1673 K and ZnTaO_2N prepared from ZnO and TaON at 6 GPa

and 1873 K.³⁹⁵ MnTaO_2N adopts the polar LiNbO_3 structure ($R3c$, Fig. 31A) and possesses a complex helical magnetic structure below 25 K. In contrast, diamagnetic ZnTaO_2N was afforded in the centrosymmetric $R-3c$ space group with the Zn ions on a split position.³⁹⁶ For the solid solution $\text{Zn}_{1-x}\text{Mn}_x\text{TaO}_2\text{N}$ ($0 < x < 1$) the stabilization of the centrosymmetric structure was observed already at very low Zn concentrations, $x = 0.03$.³⁹⁶ Similar conditions produced also LiNbO_3 -structured $\text{Mn}(\text{Mn}_{1/6}\text{Ta}_{5/6})\text{O}_{2.5}\text{N}_{0.5}$ in which 1/6 of Ta(V) is replaced by Mn(II).³⁹⁷ Lastly, high pressure synthesis also uncovered mixed main group/transition metal oxynitrides. The phase $(\text{Nb}_2\text{O}_5)_{0.84}(\text{NbO}_2)_{0.32}(\text{GaN})_{0.82}$ was obtained in a rutile- and a α - PbO_2 -related structure when reacting GaN and Nb_2O_5 at 1 GPa and 1173 K and above 2.8 GPa and 1273 K, respectively.³⁹⁸ The structures are both cation and anion disordered. The discovery of this mixed main group/transition metal oxynitride phase was assisted by in-situ diffraction studies at a LVP synchrotron beamline as well as computational structure prediction in parallel.

4.12.2.6.2 Transition metal oxyfluorides

As oxynitrides also oxyfluorides have been the subject of considerable research efforts. With respect to transition metal oxyfluorides this was certainly fueled by the discovery of superconductivity in layer-structured copper oxyfluorides, e.g., $\text{Sr}_2\text{CuO}_2\text{F}_{2+x}$.³⁹⁹ Similar to oxynitrides there are various routes for the synthesis of oxyfluorides. LVP high pressure synthesis has played an important role early on, as e.g., manifested in the series of rutile-structured transition metal oxyfluorides TiOF , VOF , FeOF which were obtained from stoichiometric mixtures of the transition metal trifluoride and sesquioxide at 6–6.5 GPa and 1273–1473 K.⁴⁰⁰ Using similar conditions, high pressure synthesis also produced VO_2F (from mixtures of V_2O_5 and VOF_3) with the rhombohedral FeF_3 structure⁴⁰¹ and expanded the family of mixed metal ABO_2F and ABOF_2 perovskites with the representatives KTiO_2F , PbMO_2F ($M = \text{Sc}, \text{Mn}, \text{Fe}$) and AgFeOF_2 .^{402–407} Apart from tetragonal PbMnO_2F they all adopt the simple cubic perovskite structure in which O and F ions are randomly distributed. Further examples include the new layer-structured $\text{Sr}_2\text{MO}_3\text{F}$ ($M = \text{Co}, \text{Mn}$) compounds (with the K_2NiF_4 -type) which were synthesized from $\text{SrF}_2 + 3 \text{SrO} + \text{Mn}_2\text{O}_3$ ⁴⁰⁸ and $3 \text{SrO}_2 + \text{Co} + \text{SrF}_2$ (i.e., using peroxide SrO_2 as O source),⁴⁰⁹ respectively, at similar pressure conditions as the perovskites (around 6 GPa) but employing higher temperatures (up to 2000 K). In the $\text{Sr}_2\text{MO}_3\text{F}$ compounds fluorine ions appear segregated on the apical position (Fig. 31B).

4.12.2.6.3 Transition metal oxyhydrides

Mixed metal transition metal oxyhydrides have been established rather recently, with $\text{LaSrCoO}_3\text{H}_{0.7}$ as the first representative.⁴¹⁰ Generally the combination of the unlike O^{2-} and H^- ions in a joint substructure is rather uncommon. The majority of transition metal oxyhydrides have been obtained through soft chemistry where mixed metal oxides are reduced by metal hydrides (e.g., CaH_2) at low temperatures (typically below 773 K) under simultaneous hydride insertion. In recent years, however, high pressure synthesis has been increasingly successful in producing new representatives. Applied precursors were mixtures of binary metal hydrides and oxides with the metals in the same oxidation state as in the targeted oxyhydride product. Specifically, SrCrO_2H was obtained from stoichiometric mixtures $\text{SrO} + \text{SrH}_2 + \text{Cr}_2\text{O}_3$ which were sintered at 4–8 GPa and 973–1273 K.⁴¹¹ SrCrO_2H is afforded in the simple cubic perovskite structure with randomly distributed O and H ions. This is in contrast with H-ordered tetragonal SrVO_2H , which is obtained from hydride reduction of SrVO_3 at ambient pressure.⁴¹² Both compounds are antiferromagnetic insulators for which spin order persists far beyond room temperature ($T_N > 400$ K). The diamagnetic representative BaScO_2H was obtained from Sc_2O_3 and BaH_2 at pressures above 7 GPa and T around 1273 K.⁴¹³ Further, K_2NiF_4 -structured $\text{LaSrMnO}_{3.3}\text{H}_{0.7}$ with mixed valence Mn(III) and Mn(II) were synthesized from a mixture $\text{La}_2\text{O}_3/\text{SrO}/\text{SrH}_2/\text{MnO}/\text{Mn}_2\text{O}_3$ at 5 GPa and 1273 K.⁴¹⁴ $\text{LaSrMnO}_{3.3}\text{H}_{0.7}$

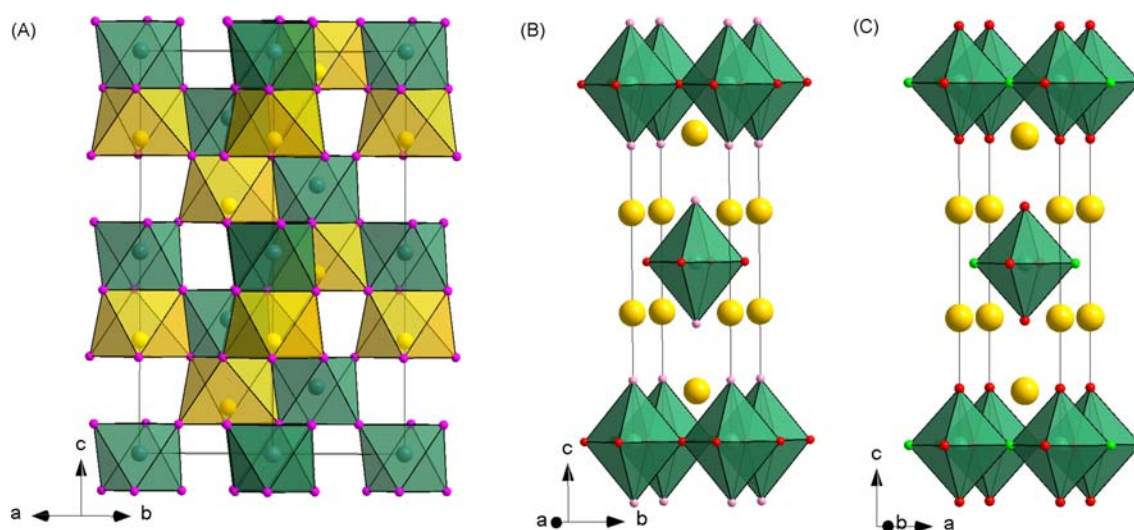


Fig. 31 (A) LiNbO_3 -type crystal structure ($R3c$) of MnTaO_2N and $\text{Mn}(\text{Mn}_{1/6}\text{Ta}_{5/6})\text{O}_{2.5}\text{N}_{0.5}$ in which 1/6 of Ta(V) is replaced by Mn(II). K_2NiF_4 -type related structures of $\text{Sr}_2\text{MnO}_3\text{F}$ with F segregated into the axial position (B) and orthorhombic $\text{Sr}_2\text{VO}_{4-x}\text{H}_x$ with H segregated into the equatorial position (C).

displays a spin glass transition at 24 K, which was attributed to competing FM and AFM interactions between unlike and like valent Mn species. Structurally related to $\text{LaSrMnO}_{3.3}\text{H}_{0.7}$, and prepared at similar conditions, is $\text{Sr}_2\text{VO}_{4-x}\text{H}_x$ ($0 < x < 1$) for which the H/O ratio can be controlled over a wide range. At highest H concentrations H segregates into the equatorial position in the VO_6 layers, which causes a change to orthorhombic ($Immm$) symmetry, Fig. 31C.⁴¹⁵

Transition metal oxyhydrides could be recently extended to double perovskite $\text{A}_2\text{B}'\text{BO}_{6-x}\text{H}_x$ phases with $\text{A} = \text{Na}$, $\text{B} = \text{Ba}$, $\text{B}' = \text{Ti}$, Cr , V .⁴¹⁶ $\text{Na}_2\text{BaTiO}_3\text{H}_3$, $\text{Ba}_2\text{NaVO}_{6-x}\text{H}_x$ ($x = 3-3.6$), and $\text{Na}_2\text{BaCrO}_3\text{H}_3$ with a cubic $2 \times 2 \times 2$ superstructure of the basic perovskite were obtained from molar ratios of BaO , BaH_2 , TiO_2 , V_2O_3 , Cr_2O_3 and using $2 \times$ molar excess of NaH . Reaction conditions were 4 GPa and 1100 K. Notably, the H-content in the anion sites of the double perovskite phases (50–63%) is substantially larger than those of phases deriving from the simple perovskite structure (<0.33%) and the bonding character of the transition metal hydride bond is more covalent.

We conclude with the single metal oxyhydride LaOH , which can be obtained as three different quenchable polymorphs when pressurizing reaction mixtures $\text{LaH}_3 + \text{La}_2\text{O}_3$ in the rather narrow range 1–5 GPa and heating to 1173 K (Fig. 32).⁴¹⁷ At lowest pressures α - LaOH with a fluorite-related structure is afforded (tetrahedrally coordinated H^- ions, HLa_4 (Fig. 32A)). At medium pressures LaOH is produced as PbCl_2 -structured phase (γ - LaOH) which implies a coordination number increase for H^- from 4 to 5 (HLa_5 , Fig. 32B). At higher pressures LaOH is afforded with the anti- Fe_2P type structure (δ - LaOH) in which the H coordination by La is switched back to tetrahedral and instead the one for O is increased to 5 (Fig. 32C). Yet the density of δ - LaOH is about 12% higher than that of γ - LaOH . The unique coordination reversal in δ - LaOH has been attributed to the high compressibility of the H^- ion.

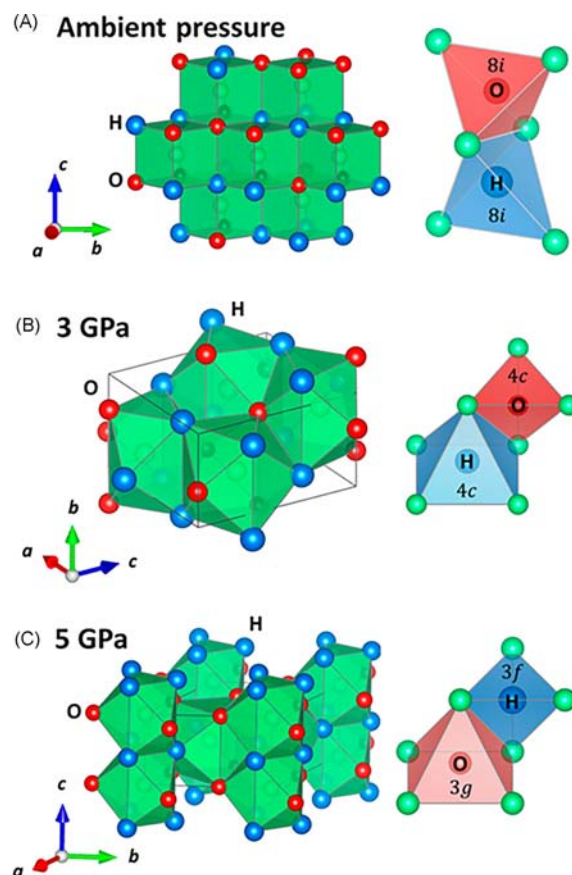


Fig. 32 Crystal structures of (A) α - LaOH synthesized at ambient pressure (and 1 GPa) crystallizing in an anion-ordered fluorite structure ($P4/nmm$) with LaO_4H_4 local coordination, (B) γ - LaOH ($Pnma$) synthesized at 3 GPa with LaO_5H_5 , and (C) δ - LaOH ($p-62m$) synthesized at 5 GPa with LaO_5H_4 local coordinations. The right panels represent the corresponding coordination geometry around the hydride and oxide anions: (A) HLa_4 and OLa_4 , (B) HLa_5 and OLa_4 , and (C) HLa_4 and OLa_5 . Red, blue, and green spheres denote O, H, and La atoms, respectively. The figure is reproduced from reference Broux, T.; Ubukata, H.; Pickard, C. J.; Takeiri, F.; Kobayashi, G.; Kawaguchi, S.; Yonemura, M.; Goto, Y.; Tassel, C.; Kageyama, H. High-Pressure Polymorphs of LaOH with Anion Coordination Reversal. *J. Am. Chem. Soc.* **2019**, *141* (22), 8717–8720. <https://doi.org/10.1021/jacs.9b03320> (web archive link,).

4.12.2.6.4 Miscellaneous

Multi-anion systems are extremely diverse with dozens of anion combinations. In this review we focused primarily on the rather established ones derived from oxides. Yet, as initially mentioned, multi-anion materials are a rapidly developing area in solid state chemistry. Here we collect a few examples where LVP high pressure synthesis in the pressure range 2–13 GPa enabled expanding into new anion combinations. For example, dense oxyhydroxides were obtained from hydrothermal conversions at gigapascal pressure (e.g., $\text{LiAlSiO}_3(\text{OH})_2$ ⁴¹⁸). A combination of molecular and simple ions was realized in fluoride borates, e.g., $\text{CeB}_2\text{O}_4\text{F}$ ⁴¹⁹ and apatite-related $\text{Pr}_5(\text{BO})_{3-x}(\text{BO}_3)_x(\text{F},\text{OH})_{2.67}\text{O}_{0.28}$ ($x \approx 1.6$),⁴²⁰ and hydroxide borates (e.g., $\text{In}_{19}\text{B}_{34}\text{O}_{74}(\text{OH})_{11}$ and $\text{DyB}_5\text{O}_8(\text{OH})_2$ ^{421,422}). Further, high pressure synthesis afforded new mixed anion systems combining two types of molecular anions, such as tetrahedral PO_4^{3-} and BO_4^{5-} in $\text{U}_2(\text{BO}_4)(\text{PO}_4)$ ⁴²³ and produced layer-structured oxychalcogenides $\text{Ae}_2\text{MO}_2\text{Ag}_2\text{X}_2$ (Ae = Sr, Ba, M = Co, Ni, X = Se, Te) which constitute alternate stacks of square planar MO_2 and Ag_2X_2 layers separated by Ae atoms.^{424,425}

4.12.2.7 Molecular anion and tetrahedron-based network compounds

The combination of acidic oxides such as B_2O_3 , SiO_2 , P_2O_5 with basic (active) metal oxides opens the world of borates, silicates, phosphates, etc., which are characterized by negatively charged substructures built from tetrahedrally coordinated B, Si, P, etc. (T) atoms. Typically, TO_4 tetrahedra share corners, and there is a rich structural chemistry depending on the extent and kind of linking. We will refer to these substructures generically as “networks”. Further diversity is introduced by mixed variants with two (or even more) kinds of T atoms (e.g., borosilicates, borophosphates, aluminosilicates, aluminophosphates). When applying the concept to nitrides, by combining active metal nitrides with Si_3N_4 and P_3N_5 as parents for the T atoms, the families of nitrosilicates and—phosphates emerge, which can be further expanded to oxonitridosilicates and oxonitridophosphates. There are seemingly endless variations for compositions and structures of tetrahedron-based networks. The degree of condensation of a tetrahedron framework is the ratio of tetrahedron centers to vertices in a framework. The low end is always 0.25 and corresponds to the “ortho” form (isolated tetrahedra). The stoichiometry of the constituent carrying the T atom, i.e., SiO_2 , PON , P_3N_5 , Si_3N_4 , P_2O_5 represents the upper limit. High pressure typically promotes the formation of denser frameworks, the edge-sharing of tetrahedra, and eventually the coordination change of T atoms to five- and even sixfold. Certainly, the investigation and synthesis of silicates at HPHT is most established given their significance to Earth sciences. But also borates have been studied to a great extent. Further, high pressure synthesis advanced especially the materials family of (oxo)nitridophosphates, again benefiting from devising various precursor strategies and/or the application of mineralizers.

4.12.2.7.1 Borates, carbonates, silicates, phosphates

Borates are distinguished in that both trigonal planar BO_3 and tetrahedral BO_4 units can occur which enriches their structural chemistry. In addition, the feature of (high pressure promoted) edge-linked tetrahedra is rather pronounced. HPHT synthesis reactions typically employed mixtures of metal oxides and B_2O_3 (or H_3BO_3) and were performed in LVP devices in a pressure range 3–14 GPa. The high pressure synthesis of borates have been reviewed earlier,⁹ and we restrict ourselves to some recent key findings.

$\text{YbB}_7\text{O}_{12}$ with an extraordinary high degree of condensation of the borate framework was obtained from stoichiometric reactions $\text{Y}_2\text{O}_3 + 7 \text{B}_2\text{O}_3$ at 10 GPa and 1473 K.⁴²⁶ The orthorhombic borate framework (*Pccn*) is exclusively built from BO_4 units and each tetrahedron is connected via two corners to three neighboring ones. Y is located in narrow channels and coordinated by 10 O atoms (Fig. 33A). High pressure expanded the range of transition metal borates (e.g., $\beta\text{-NiB}_4\text{O}_7$, $\beta\text{-HfB}_2\text{O}_5$, $\beta\text{-FeB}_2\text{O}_4$).^{427–431} In isostructural HP- CoB_2O_4 , HP- NiB_2O_4 and $\beta\text{-FeB}_2\text{O}_4$ the borate framework is exclusively built from pairs of edge-sharing BO_4 tetrahedra, which are corner connected via the terminal O atoms into 2D-herring bone patterned slabs (Fig. 33B). Divalent transition metals are located between borate slabs and attain an octahedral environment. $\text{Mo}_2\text{B}_4\text{O}_9$ was obtained from MoO_3 and B_2O_3 under the simultaneous presence of reducing $\text{B}_2(\text{OH})_4$ (tetrahydroxydiboron) at 12.3 GPa and 1573 K.⁴³² The compound contains tetrahedral $\text{Mo}(\text{III})_4$ cluster units and links borate and transition metal cluster chemistry. The Mo_4 clusters are embedded in a 4-ring arrangement of BO_4 tetrahedra (Fig. 33C). Each d^3 $\text{Mo}(\text{III})$ has an octahedral environment by 6 O atoms, of which four take a terminal coordination and two cap tetrahedron faces. All d electrons of $\text{Mo}(\text{III})$ are involved in cluster skeleton bonding and $\text{Mo}_2\text{B}_4\text{O}_9$ represents an electron precise, diamagnetic compound. Further, the actinide borates ThB_4O_8 and UB_4O_8 were manufactured at 5.5 GPa/1373 K and 10.5 GPa/1373 K, respectively, from mixtures of actinide dioxide and B_2O_3 .⁴³³ The borate framework corresponds to a 2D layer built from corner-condensed BO_4 tetrahedra. One fourth of the O atoms connect three tetrahedra. The actinide ions are situated between borate layers and are coordinated by 10 O atoms. The high pressure synthesized borates HP- KB_3O_5 and HP- CsB_5O_8 are distinguished by their extraordinary framework complexity.^{434,435} In the latter both structural units of borates, i.e., trigonal planar BO_3 and tetrahedral BO_4 , occur and multiple linkage possibilities (i.e., corner sharing to two or three neighboring units as well as edge-sharing of tetrahedra) are realized at the same time.

The usage of hygroscopic B_2O_3 and H_3BO_3 may give rise to serendipitous products, such as mixed anion borate hydroxides and hydrates. Examples for borate hydroxides with small contents of (OH) include $\text{NiB}_3\text{O}_5(\text{OH})$, acentric $\text{La}_3\text{B}_6\text{O}_{13}(\text{OH})$ with a borate framework containing edge-sharing tetrahedra (*P2*₁) and tetragonal $\text{M}_5\text{B}_{12}\text{O}_{25}(\text{OH})$ with M = Ga, In in an octahedral environment.^{436–438} Further, the presence of water may induce reactivity toward the BN container material which can lead to the release of $\text{NH}_3/\text{NH}_4^+$. For example, $(\text{NH}_4)\text{YB}_8\text{O}_{14}$ was obtained (although not as phase pure sample) when treating 1:8 M mixtures of Y_2O_3 and H_3BO_3 at 12.8 GPa and 1573 K.⁴³⁹ In the orthorhombic crystal structure (*Pnma*) 6-ring units of BO_4 tetrahedra form channels along the *c* direction which are linked through 3-connected tetrahedron corners to neighboring units (Fig. 33D). Thus

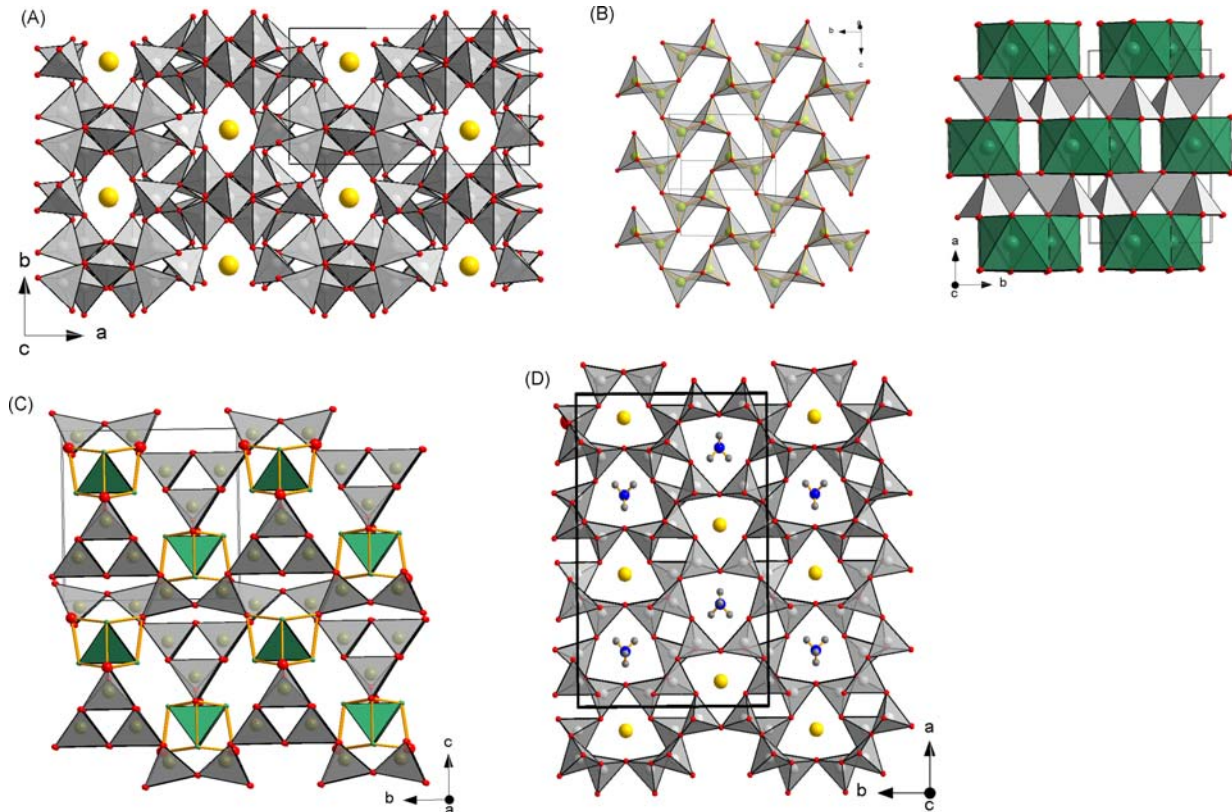


Fig. 33 (A) Highly condensed borate framework in YB_7O_{12} ($Pccn$). (B) Crystal structure of $\beta\text{-FeB}_2\text{O}_4$ ($C2/c$) constituting layers of edge-sharing BO_4 tetrahedra (B_2O_6 units) (left) and octahedrally coordinated Fe (right). (C) Crystal structure of $\text{Mo}_2\text{B}_4\text{O}_9$ ($P4_2/nmc$). (D) Crystal structure of $(\text{NH}_4)\text{YB}_8\text{O}_{14}$ ($Pnma$). Y—yellow, Mo—green, B—light grey, O—red, N—blue.

“channel walls” appear highly dense. The channels host NH_4^+ and Y^{3+} ions in alternating rows. Finally, also the incorporation of hydronium ions (H_3O^+) may occur, as e.g., observed in $\text{HP-Cs}_{1-x}(\text{H}_3\text{O}^+)_x\text{B}_3\text{O}_5$ ($x = 0.5\text{--}0.7$).⁴⁴⁰

There is certainly a large potential for high pressure synthesis to expand also borophosphates and emerging borosulfates which may possess interesting material properties. As an example we mention ion-conducting $\beta\text{-Li}_3\text{BP}_2\text{O}_8$ which was obtained when reacting mixtures of Li_3PO_4 and BPO_4 at 2–4 GPa and 873 K.⁴⁴¹

Carbonates are characterized by their trigonal planar CO_3^{2-} anions. Theoretical studies predicted the formation of CO_4 -bearing carbonates at pressures ranging from 80 to 150 GPa, depending on the chemical composition.⁴⁴² Different network scenarios, from isolated tetrahedra to pyroxene-like chains, were anticipated and it has been suggested that carbonates based on condensed CO_4 tetrahedra could show broad analogies with silicates, although C–O–C angles were expected to be much more rigid than Si–O–Si angles in silicates. Expectations into a tetrahedral carbonate chemistry were further fueled by the discovery of cristobalite-like polymeric $\text{CO}_2\text{-V}$ (cf. Section 4.12.2.4.1).

LH-DAC experiments were performed with Fe-bearing MgCO_3 ($\text{Mg}_{0.85}\text{Fe}_{0.15}\text{O}_3$), siderite $\text{Fe}_{0.7}\text{Mg}_{0.3}\text{CO}_3$, FeCO_3 , and (Fe substituted) dolomite CaCO_3 because of their relevance to Earth sciences and because the presence of Fe allows for convenient laser heating. On heating to 1500 K at pressures ~ 50 GPa FeCO_3 partially dissociates to form various iron oxides (cf. Section 4.12.2.4.2).⁴⁴³ At higher pressures, above 75 GPa, two new phases, tetrairon(III) orthocarbonate $(\text{Fe}^{3+})_4(\text{CO}_4^{4-})_3$ and diiron(II) diiron(III) tetracarbonate $(\text{Fe}^{2+})_2(\text{Fe}^{3+})_2\text{C}_4\text{O}_{13}$, evolved from redox decomposition (yielding diamond as reduced component). The structure (and composition) of both phases was determined from single crystal diffraction data of temperature quenched samples. Both phases contain CO_4 tetrahedra. In particular, the orthocarbonate $\text{Fe}_4\text{C}_3\text{O}_{12}$ was found at 1700 K in a multiphase mixture with Fe oxides. There are two crystallographically different Fe^{3+} ions in the rhombohedral crystal structure ($R3c$) which attain a trigonal prismatic and bicapped trigonal prismatic environment by 6 and 8 O atoms, respectively (Fig. 34A). Both types of d^5 Fe ions are assumed to be in a high spin state. $\text{Fe}_4\text{C}_4\text{O}_{13}$ is closely located in p,T space and was observed at slightly higher temperatures (1750 K). In the monoclinic crystal structure ($C2/c$) four CO_4^{4-} groups are linked together in a zigzag fashion by corner sharing (Fig. 34B). The iron ions have mono- and bi-capped prismatic coordination environments and are assumed to be in a mixed valence state. $\text{Mg}_{1.6}\text{Fe}_{2.4}\text{C}_4\text{O}_{13}$, which was obtained at 141 GPa and 2650 K from $\text{Fe}_{0.7}\text{Mg}_{0.3}\text{CO}_3$ (siderite), attains the same structure⁴⁴⁴ and there is an entire family of tetrasilicates with “zigzag-shaped” $\text{Si}_4\text{O}_{13}^{10-}$ units. $\text{Mg}_{0.85}\text{Fe}_{0.15}\text{CO}_3$ (and magnesite) transforms to $\text{MgCO}_3\text{-II}$ ($\text{Mg}_3(\text{C}_3\text{O}_9)$) without a compositional change.⁴⁴⁵ The transformation is observed at pressures 80–115 GPa upon laser heating. The rhombohedral crystal structure ($R-3c$) contains $\text{C}_3\text{O}_9^{6-}$ ring anions which constitute three

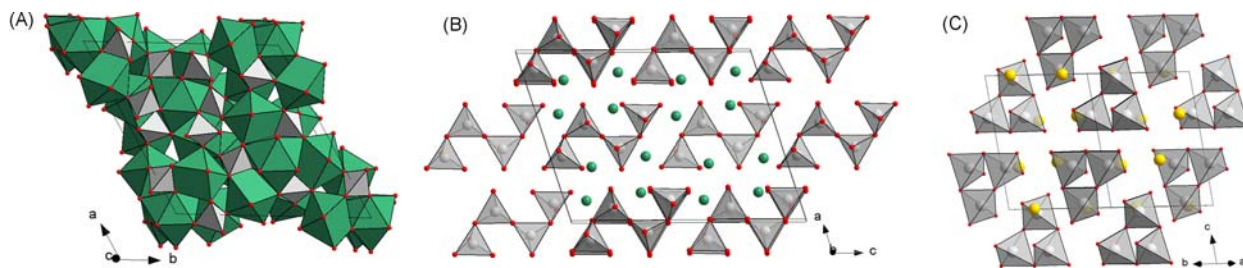


Fig. 34 (A) Distribution of tetrahedral CO_4 units and trigonal prismatic and bicapped trigonal prismatic coordinated Fe ions in the crystal structure of $\text{Fe}_4(\text{CO}_4)_3$ ($R3c$). Corner-linked CO_4 tetrameric (B) and trimeric units (C) in the crystal structures of $\text{Fe}_4\text{C}_4\text{O}_{13}$ and $\text{MgCO}_3\text{-II}$, respectively. Fe—green, Mg—golden, C—light grey, O—red.

corner-sharing CO_4 tetrahedra (Fig. 34C).⁴⁴⁶ Again, the motif is well-known for silicates. The metal ions have six and eightfold coordinations with O. It is interesting to note that upon compression to 98 GPa and prior laser heating the C—O bond length decreased by just 7% (to 1.195 Å), which reflects the incompressible nature of the CO_3^{2-} anion. C—O bond lengths in the $\text{C}_3\text{O}_9^{6-}$ ring unit are in a range of 1.29–1.41 Å. The 3-ring tetrahedral unit is also observed for Ca—Fe dolomite (in dolomite IV, $\text{Ca}(\text{Fe,Mg})_3\text{C}_3\text{O}_9$) after laser heating at 115 GPa.⁴⁴⁷ However, the crystal structure of dolomite IV is orthorhombic ($Pnma$) and topologically different from $\text{MgCO}_3\text{-II}$ due to the different coordination of the larger Ca ions. CO_4 bearing iron and magnesium carbonates are not quenchable but amorphize or sluggishly back-transform upon decompression.

Tetrahedral carbonate chemistry was recently extended by targeted synthesis experiments using reaction mixtures $\text{AeO} + \text{AeCO}_3$ and $\text{AeCO}_3 + \text{CO}_2$ ($\text{Ae} = \text{Ca, Sr}$) in LH-DAC experiments. In these experiments sp^3 hybridized carbonate moieties were already obtained at pressures in the range 20–50 GPa and the obtained products exhibited broader structural (silicate-like) variability.^{448–452} Reactions $\text{SrO} + \text{SrCO}_3$ afforded the orthocarbonates Sr_2CO_4 and $\text{Sr}_3[\text{CO}_4]\text{O}$ featuring isolated CO_4^{4-} units. Remarkably, these carbonates could be recovered at ambient conditions. The tetragonal structure of $\text{Sr}_3[\text{CO}_4]\text{O}$ can be considered as antiperovskite with a framework of corner-connected OSr_6 octahedra and CO_4^{4-} anions taking the position of the perovskite A-site. Reactions $\text{CaO} + \text{CaCO}_3$ afforded Ca_2CO_4 which is isostructural to Sr_2CO_4 and reactions $\text{CaCO}_3 + \text{CO}_2$ yielded tetragonal ($I-42d$) CaC_2O_5 in which CO_4^{4-} units form a tetrameric supertetrahedron $[\text{C}_4\text{O}_{10}]^{4-}$ by corner sharing. CaC_2O_5 persists on pressure release down to ~ 18 GPa where it decomposes into calcite and CO_2 . Reactions $\text{SrCO}_3 + \text{CO}_2$ also produced SrC_2O_5 which, however, forms a completely different structure with dimers of corner-sharing conventional sp^2 CO_3^{2-} units. SrC_2O_5 is the first inorganic pyrocarbonate salt, with $\text{C}_2\text{O}_5^{2-}$ bridging the gap between pyroborate $\text{B}_2\text{O}_5^{4-}$ and N_2O_5 . With these discoveries it seems likely that it is possible to obtain numerous novel carbonates, thus moving toward the rich chemistry of silicates. This includes quenchable ones which could be in the reach of LVP synthesis experiments.

Ternary silicates usually show transitions from tetrahedron-based networks to perovskite-like phases with six-coordinated Si at 20–30 GPa.⁴⁵³ The presence of Ti can afford new types of structures with octahedral Si—O frameworks at lower pressures. For example, reactions between MgO, SiO_2 and TiO_2 at 15 GPa and 1873 K in a MA LVP device produced $\text{MgTiSi}_2\text{O}_7$ in the trigonal weberite-type structure which is related to pyrochlore.⁴⁵⁴

Five-coordinated Si is not known for silicates but has been envisioned to occur in intermediate phases along pressure-induced transitions from four to sixfold coordination. Indeed such intermediate phases with 5-coordinated Si have now been observed in room temperature DAC experiments in a range of boro- and aluminosilicates, such as $\text{CaBSiO}_4(\text{OH})$ (datolite), $\text{BaAl}_2\text{Si}_2\text{O}_8$ (paracelsian), $\text{CaB}_2\text{Si}_2\text{O}_8$ (danburite).^{455–457} The transitions follow a similar pattern in that the tetrahedron network undergoes a continuous (isosymmetric) anisotropic distortion during which rings become so elliptically distorted that O atoms from tetrahedra oppositely situated in the ring become 5th ligands for T atoms, which then attain a trigonal bipyramidal coordination (Fig. 35A). Despite the isosymmetric nature of these transitions, the network topology is decisively changed through the creation of new T—O bonds. In danburite the transition to 5-coordination takes place above 23 GPa and affects only Si atoms, in paracelsian it is already observed above 6 GPa and involves both Al and Si T atoms. Above 33 GPa these silicates undergo transition to octahedral coordination, which is of reconstructive nature. A remarkable sequence of transitions was revealed for the beryllophosphate $\text{CaBe}_2\text{P}_2\text{O}_8$, which shows a concomitant stepwise increase of coordination for both Be and P from tetrahedral to octahedral through trigonal bipyramidal (Fig. 35B).⁴⁵⁸ The phase providing octahedral coordination is realized above 90 GPa after a reconstructive phase transition. The trigonal bipyramidal 5-coordination of P by O has also been observed in TiPO_4 upon room temperature compression to 56 GPa ($\text{TiPO}_4\text{-V}$).⁴⁵⁹ The only other example for sixfold coordinated P by O is earlier described AlPO_4 when adopting the CaCl_2 -type structure above 50 GPa.³¹⁰

4.12.2.7.2 Nitridosilicates and oxonitridosilicates

The structural chemistry of nitridosilicates is more diverse than that of oxosilicates because of the more varied crosslinking patterns. While O in SiO_4 units can only be terminally bonding or linking two tetrahedral units, N can connect up to 4 tetrahedral units, giving rise to highly condensed frameworks.⁴⁶⁰ As frequently observed for silicates (and also silicon nitride), employing pressures above 15 GPa leads to the formation of phases with 6-coordinated Si. For example, when prepared at ambient pressure MgSiN_2 possesses a wurtzite-like structure with Mg and Si in a tetrahedral coordination ($\alpha\text{-MgSiN}_2$). Treating $\alpha\text{-MgSiN}_2$ at about 20 GPa

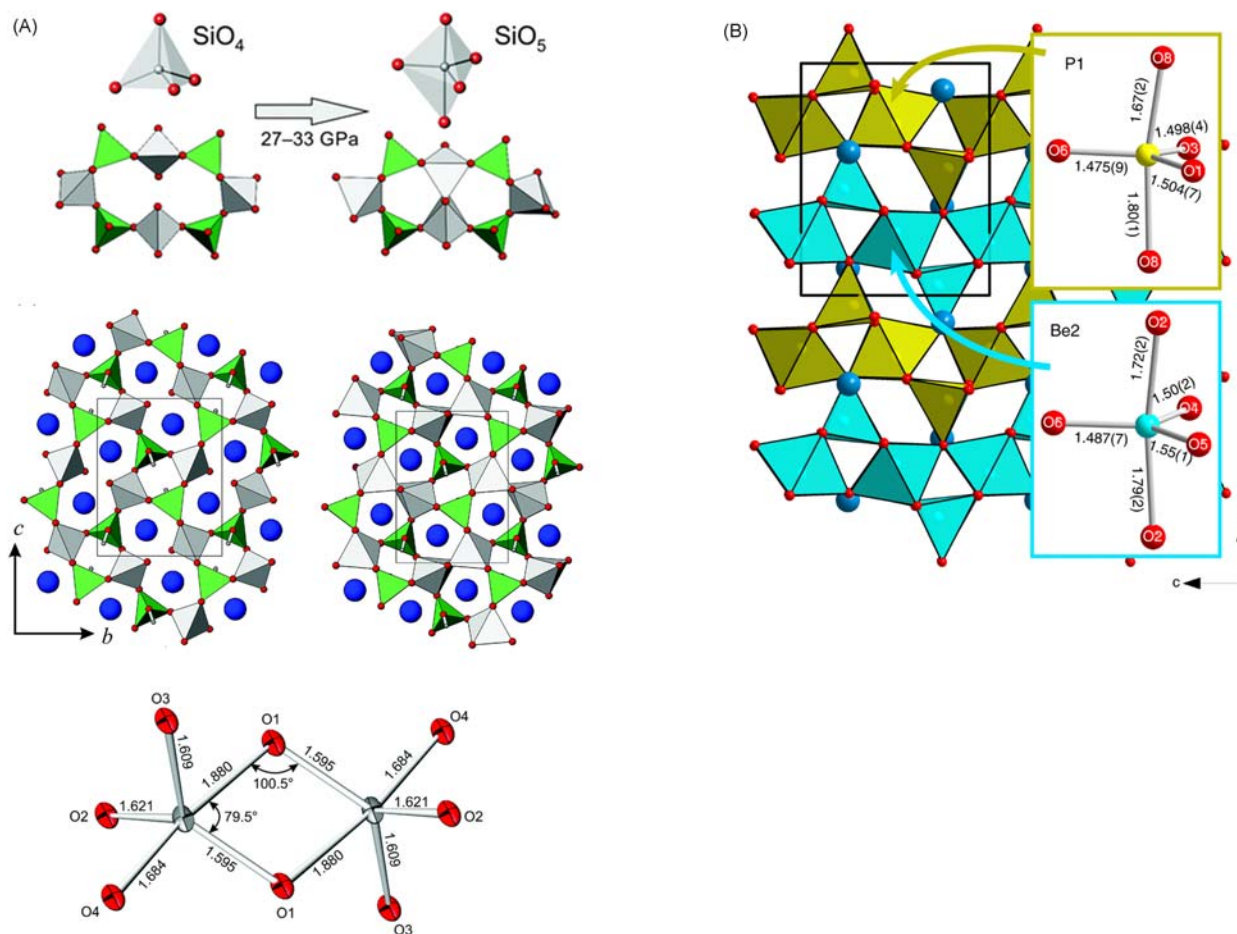


Fig. 35 (A) Crystal structure of $\text{CaBSiO}_4(\text{OH})$ datolite-I (left) and datolite-II (right). BO_4 and SiO_n ($n = 4, 5$) polyhedra are given in green and grey, respectively. Ca and O atoms are presented as blue and red spheres, respectively. The lower part of the figure highlights the edge condensed trigonal bipyramidal SiO_5 structural unit. (B) Crystal structure of hurlbutite-III ($\text{CaBe}_2\text{P}_2\text{O}_8$) at 83.2 GPa. BeO_n and PO_n polyhedra are given in blue and yellow. Ca and O atoms are given as blue and red spheres, respectively. Insets represent the trigonal bipyramidal geometry of PO_5 and BeO_5 groups. (A) The figure has been taken from reference Gorelova, L. A.; Pakhomova, A. S.; Aprilis, G.; Dubrovinsky, L. S.; Krivovichev, S. V. Pentacoordinated Silicon in the High-Pressure Modification of Datolite, $\text{CaBSiO}_4(\text{OH})$. *Inorg. Chem. Front.* **2018**, *5* (7), 1653–1660. <https://doi.org/10.1039/C8QI00257F>. (B) This figure has been taken from reference Pakhomova, A.; Aprilis, G.; Bykov, M.; Gorelova, L.; Krivovichev, S. S.; Belov, M. P.; Abrikosov, I. A.; Dubrovinsky, L. Penta- and Hexa-Coordinated Beryllium and Phosphorus in High-Pressure Modifications of $\text{CaBe}_2\text{P}_2\text{O}_8$. *Nat. Commun.* **2019**, *10* (1), 2800. <https://doi.org/10.1038/s41467-019-10589-z>.

and 1973 K yields rhombohedral $\beta\text{-MgSiN}_2$ ($R\text{-}3m$) which can be retained at ambient pressure.⁴⁶¹ It adopts the caswellsilverite structure with both types of cations in an octahedral coordination. A further interesting example is the polar ordered oxynitride perovskite YSiO_2N , which was obtained in a LH-DAC experiment using a mixture of YN and SiO_2 as reactants.⁴⁶² Quenchable YSiO_2N formed at pressures as low as 4 GPa and above 1473 K. Its tetragonal structure ($P4mm$) derives from the simple cubic perovskite. Second harmonic generation shows a strong non-linear optical signal, which confirms the polar properties of YSiO_2N . The formations conditions suggest that YSiO_2N can be also afforded using LVP devices, which would allow the unambiguous determination of structure and physical properties on bulk samples.

4.12.2.7.3 Nitridophosphates and oxonitridophosphates

Although (oxo)nitridosilicates constitute a large class of inorganic materials, comparatively few examples are reported from high pressure synthesis. This is rather different for (oxo)nitridophosphates, for which high pressures played an important role in uncovering this compound family. P can become easily reduced in the presence of nitride ions and redox decompositions can be effectively suppressed in a high pressure environment. A broad selection of precursors and the application of mineralizers, fluxes, and metathesis reaction schemes enabled then broad exploration of the compositional range of quenchable nitridophosphates in LVP experiments at pressures below 10 GPa. There has been a recent review,⁴⁶³ and we restrict ourselves to present some key findings.

A range of nitridophosphates (such as BeP_2N_4 , CuPN_2 and ZnP_2N_3) were obtained from the reaction of stoichiometric mixtures of active metal nitrides and P_3N_5 , according to e.g., $\text{Zn}_3\text{N}_2 + 2 \text{P}_3\text{N}_5 = 3 \text{ZnP}_2\text{N}_4$, at pressures 5–8 GPa and temperatures 1273–

1773 K.^{464–466} This route is restricted because of the limited number of active metal nitrides. Li_3N may in addition serve as a flux (as for the synthesis of $\text{Li}_{18}\text{P}_6\text{N}_{16}$ exhibiting unique tricyclic $[\text{P}_6\text{N}_{16}]^{18-}$ ions (Fig. 36A)⁴⁶⁷ and Li-nitridophosphates obtained from ambient pressure synthesis may be reacted at high pressures to yield new Li-nitridophosphates (e.g., $3 \text{LiPN}_2 + \text{Li}_7\text{PN}_4 = 2 \beta\text{-Li}_5\text{P}_2\text{N}_5$ at 9 GPa, 1273 K).⁴⁶⁸ $\beta\text{-Li}_5\text{P}_2\text{N}_5$ has a layered structure in which corner-sharing PN_4 tetrahedra are arranged as in the black phosphorous structure (Fig. 36B). $\beta\text{-Li}_5\text{P}_2\text{N}_5$ is metastable at ambient pressure and converts upon heating to $\alpha\text{-Li}_5\text{P}_2\text{N}_5$ ($\text{Li}_{10}\text{P}_4\text{N}_{10}$) with adamantane-like (tetrameric) structure (isoelectronic to P_4O_{10}) (Fig. 36C). $\beta\text{-Li}_5\text{P}_2\text{N}_5$ may also be obtained from compressing $\text{Li}_{10}\text{P}_4\text{N}_{10}$ (pressure induced polymerization of $\text{P}_4\text{N}_{10}^{10-}$ units). Another class of precursors are azides, for which a larger variety exists (i.e., all A, Ae, and Cd). Reactions with P_3N_5 yielded highly condensed, silicate-like frameworks as in MP_2N_4 ($M = \text{Ca}, \text{Sr}, \text{Ba}, \text{Cd}$) and NaPN_2 or layers with triply connecting N (as in $\text{SrP}_8\text{N}_{14}$).^{469,470} Most versatile are metathesis reactions, which opened for rare earth and transition metal nitridophosphates, e.g., $2 \text{REF}_3 + 3 \text{LiPN}_2 + \text{Li}_3\text{N} = \text{RE}_2\text{P}_3\text{N}_7 + 6 \text{LiF}$ at 5 GPa and 1573 K.⁴⁷¹ Open shell 3d transition metal nitridophosphates MP_8N_{14} (with $M(\text{II}) = \text{Fe}, \text{Co}, \text{Ni}$) were produced from mixtures metal halide, LiPN_2 and P_3N_5 .⁴⁷² Here relatively high pressures, 9 GPa, were required to suppress decomposition into transition metal phosphides and allow crystallization temperatures of 1473 K. The structure of MP_8N_{14} is closely related to that of $\text{SrP}_8\text{N}_{14}$ ⁴⁷⁰ and consists of highly condensed layers built from triply connecting N (Fig. 36D). Transition metal ions are located in an octahedral N environment. From electron spectra it was concluded that the N ligand is a “stronger” field ligand than the oxo ligand.

Substitution of P_3N_5 by $\text{PON/P}_2\text{O}_5$ and/or introduction of Li_2O yields oxonitridophosphates according to e.g., $3 \text{Sr}(\text{N}_3)_2 + 6 \text{PON} \rightarrow \text{Sr}_3\text{P}_6\text{O}_6\text{N}_8 + 8 \text{N}_2$, $\text{ZrCl}_4 + \text{PON} + 2 \text{Li}_2\text{O} \rightarrow \text{ZrPO}_3\text{N} + 4 \text{LiCl}$ (ZrSiO_4 structure), $2 \text{PrF}_3 + 3 \text{LiPN}_2 + \text{PON} + 2 \text{Li}_2\text{O} \rightarrow \text{LiPr}_2\text{P}_4\text{N}_7\text{O}_3 + 6 \text{LiF}$.^{473–475}

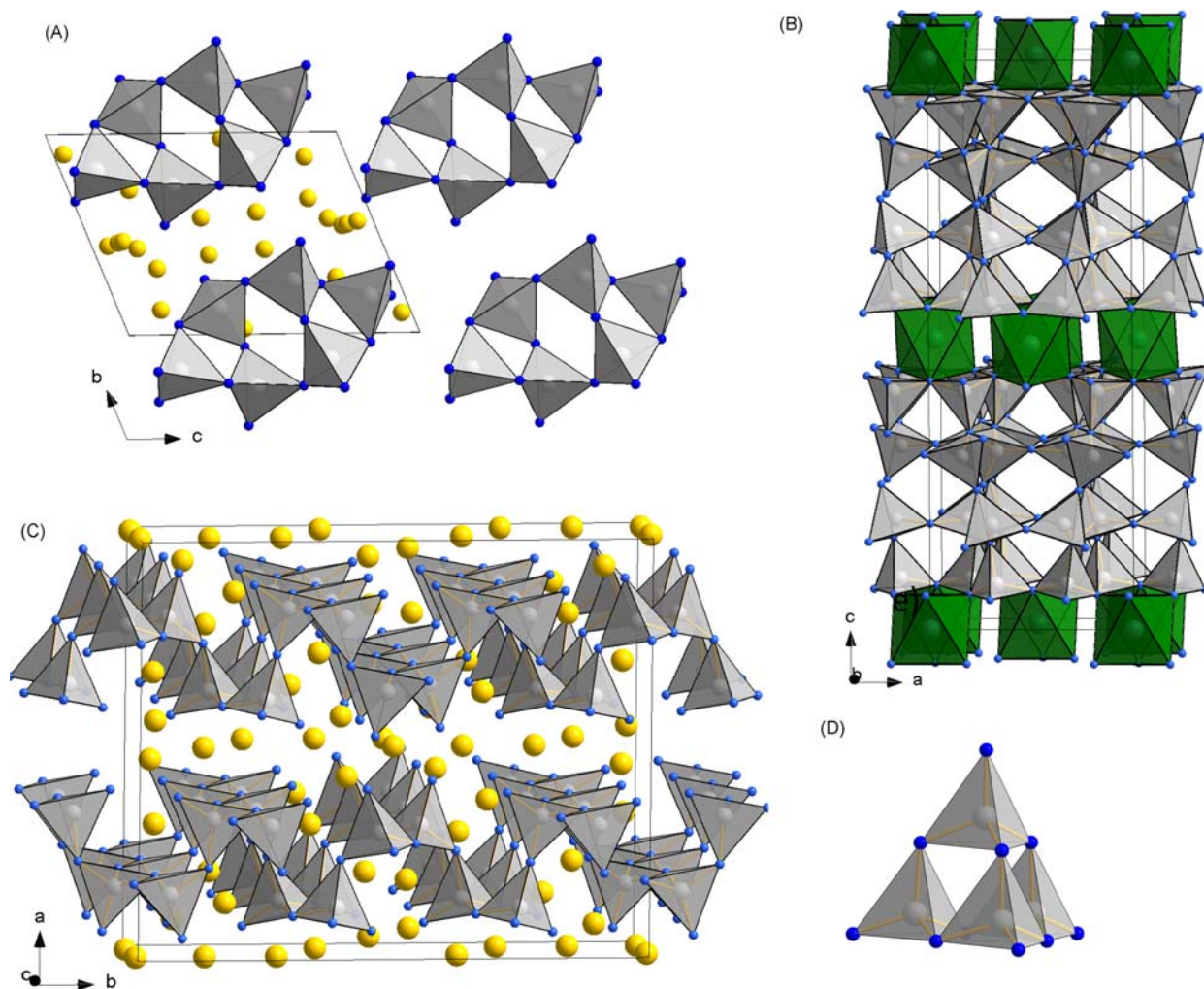


Fig. 36 Crystal structures of $\text{Li}_{18}\text{P}_6\text{N}_{16}$ with tricyclic $[\text{P}_6\text{N}_{16}]^{18-}$ ions (A) and $\beta\text{-Li}_5\text{P}_2\text{N}_5$ with PN_4 tetrahedra connected and arranged as atoms in black P (B). (C) Adamantane arrangement of tetrahedra in $\alpha\text{-Li}_5\text{P}_2\text{N}_5$. (d) Crystal structure of $\text{FeP}_8\text{N}_{14}$ ($Cmca$). Li—yellow, Fe—green, P—grey, N—blue.

4.12.2.8 Open framework materials

As open framework materials we consider porous materials such as zeolites, mesoporous silica, metal organic frameworks (MOFs), zinc imidazolate frameworks (ZIFs) and related coordination compounds.

4.12.2.8.1 High pressure as synthesis tool for open frameworks

High pressure synthesis typically leads to a dense or a denser form of a material, so high pressure conditions are not expected to play a large role in the synthesis of open framework materials. Yet there are some interesting developments. Landskron et al. introduced the concept of nanocasting at high pressures⁴⁷⁶ which allowed the preparation of periodic mesoporous quartz and coesite.⁴⁷⁷ Nanocasting at high pressures implies that HPHT conditions are applied to a periodic mesostructured composite with filled pores (e.g., SBA-16/carbon). The filler phase would prevent pressure induced pore collapse and, depending on p, T conditions, transition to high pressure forms can occur for either of the phases. The periodic mesoporous high pressure phase can then be isolated by selective removal of the non-transformed phase. However, a filler phase does not appear always necessary since it was shown that mesoporous coesite can also be obtained directly from SBA-16 at 12 GPa and 573 K⁴⁷⁸ and mesoporous *c*-BN was obtained from mesoporous *h*-BN at 10 GPa and 1273 K.⁴⁷⁹ Performing the conversion at higher temperatures resulted in nanocrystalline stishovite⁴⁸⁰ and *c*-BN, respectively.⁴⁷⁹

Recently high pressure was also identified as an interesting parameter for the synthesis of zeolites. Tan et al. investigated and found a unique crystallization behavior when applying pressures up to 0.9 GPa in the hydrothermal synthesis of zeolites.⁴⁸¹ With pressure zeolite synthesis was completed within hours (instead of days when using conventional autogenous pressure) and the obtained products depended on the applied pressure. This indicates that pressure strongly influences both the kinetics and thermodynamics of zeolite formation. Further, Mazur et al. reported pressure induced ADOR reassembly of 2D zeolite precursor into crystalline 3D zeolite.⁴⁸² In the ADOR approach a 3D zeolite with weak links (e.g., Ge double 4-rings) is sliced into layered precursors by hydrolysis. Controlled reassembly of the 2D layers can then produce new zeolites in a directed way. The pressure assisted ADOR reassembly was performed solvent-free in a LVP at 1 GPa and 473 K and led unexpectedly to a lower density (higher porosity) material than the product obtained from ambient pressure transformation.

4.12.2.8.2 (Structural) response of porous materials to high pressure conditions

The exertion of high pressures to porous materials typically leads to a pressure induced collapse (PIA) resulting in amorphous materials. The explicit behavior will depend on the kind of PTM, either being able to penetrate the porous structure or not. If penetrating (and non-interacting), porous materials can withstand quite high pressure (10–20 GPa). Zeolite materials were reviewed by Gatta et al.⁴⁸³ and Vezzalini et al.⁴⁸⁴ Specifically, penetrating PTM strongly reduce compressibility and crystal-fluid interactions (e.g., superhydration) may chance decisively elastic behavior and induce structural rearrangements (including PIA). In this respect, $\text{AlPO}_4\text{-54}$ ^{485,486} and also TON ⁴⁸⁷ have been studied extensively. Similarly, zeolites filled with a guest, i.e., CO_2 , can be stable up to 20 GPa and reveal exceptionally high loadings.^{488,489} Amorphous/glassy materials obtained from PIA of zeolites may be topologically ordered, i.e., the basic topology of the framework is retained (“intermediate” range structure/“low” entropy glasses)^{490,491} and also may show polyamorphism, i.e., undergo an amorphous low-density to high-density transformation at higher pressures.⁴⁹²

CN^- based coordination polymers (i.e., Prussian Blue analogues) show a similar behavior as zeolites^{493,494} and also the high pressure response of MOFs and ZIFs may resemble that of zeolites, eventually leading to PIA. However, their frameworks are mechanically and chemically much more flexible and their pressure response—prior to PIA—will frequently yield transitions to high pressure phases,⁴⁹⁵ including reconstructive connectivity changes,⁴⁹⁶ and a broader range of chemical interactions with PTMs (for details we refer to a recent review by Collings et al.⁴⁹⁷). An interesting recent observation is the pressure promoted low-temperature melting of MOFs and ZIFs yielding distinct high and low-density amorphs over different regions of the p, T phase diagram (1–6 GPa, 373–673 K). The strongly negative Clapeyron-slope melting behavior opens for new functional MOF/ZIF glasses which retain porosity.⁴⁹⁸

4.12.2.8.3 Porous frameworks as reaction containers for pressure induced reactions

The porous structure of micro- and mesoporous aluminosilicates can be exploited as reaction containers for high pressure reactions. Santoro et al. showed the pressure-induced polymerization of ethylene in the channels of the all- SiO_2 zeolite silicalite which results in a nanocomposite with isolated chains of non-conducting polyethylene confined in the pores.⁴⁹⁹ The nanocomposite shows interesting mechanical properties including zero thermal expansion. Pressure induced acetylene polymerization leads to conjugated chains confined within pores, with the possibility of manipulating electronic properties.⁵⁰⁰ The polymerization of CO produces all-transoid polycarbonyl chains.^{501,502} In contrast to the low dimensional phase I of pCO obtained by polymerizing CO in the absence of confinement (cf. Section 4.12.2.4.1),^{296,297} pCO in silicalite has a high degree of orientational and structural order. In the described examples polymerizations were performed at pressures below 10 GPa.

4.12.3 Conclusions and outlook

Extreme conditions involving the application of high pressures ($p > 1$ GPa) and high temperatures are increasingly employed in the synthesis of inorganic materials. This development has been promoted by recognizing the potential of extreme conditions to induce

unexpected chemical compositions, atom arrangements and electronic structures, leading to new classes of chemical compounds with unique properties. Here, unexpected noble gas compounds, polynitrides as well as transition metal bismuth binaries serve as excellent examples, and the synthesis of peculiar polyhydride phases has even opened a perspective for room-temperature superconductivity.¹³⁰

LH-DAC experiments expanded chemical synthesis to conditions far beyond 100 GPa. These experiments are primarily performed at synchrotron facilities and benefited from the symbiotic progress in X-ray beam properties (especially its focusing), detectors and analysis tools (i.e., the combination of LH-DAC experiments with single-crystal X-ray diffraction).³³ The advent of fourth generation radiation sources and further development of high pressure methodology (e.g., in the direction of dynamic compression) will allow for further breakthroughs in studying matter at extreme conditions. At the same time one has to be aware that sample sizes in DACs are minute and DAC experiments addressing chemical synthesis should be considered curiosity driven, i.e., exploring potential chemical compositions at highly extreme conditions.²⁰

Systematic synthesis efforts targeting metastable (recoverable) compounds employ LVP based methodology, e.g., for superconducting silicon and germanium compounds or quenchable oxides, nitrides and oxynitrides. The frequently used pressure limit of about 10 GPa provides the possibility to interface with industrial processing. Advances in the synthesis of metastable materials will not necessarily come from an increased pressure capability but rather from embracing a broader range of precursor strategies and reaction schemes at gigapascal pressures. These include solid-gas reactions, hydrothermal/solvothermal processing and flux-assisted methods.

Acknowledgments

We acknowledge support from the Swedish Research Council (2016-04413, 2019-06063) and the Knut and Alice Wallenberg Foundation (KAW 2018.0019).

References

- Badding, J. V.; Parker, L. J.; Nesting, D. C. High Pressure Synthesis of Metastable Materials. *J. Solid State Chem.* **1995**, *117* (2), 229–235. <https://doi.org/10.1006/jssc.1995.1268>.
- Brazhkin, V. V. High-Pressure Synthesized Materials: Treasures and Hints. *High Pressure Res.* **2007**, *27* (3), 333–351. <https://doi.org/10.1080/08957950701546956>.
- Demazeau, G. High Pressures and Chemical Reactivity: An Approach to the Synthesis of Novel Materials. *High Pressure Res.* **2008**, *28* (4), 483–489. <https://doi.org/10.1080/08957950802492134>.
- Eklöf, D.; Fischer, A.; Ektarawong, A.; Jaworski, A.; Pell, A. J.; Grins, J.; Simak, S. I.; Alling, B.; Wu, Y.; Widom, M.; Scherer, W.; Häussermann, U. Mysterious SiB₃: Identifying the Relation Between α - and β -SiB₃. *ACS Omega* **2019**, *4* (20), 18741–18759. <https://doi.org/10.1021/acsomega.9b02727>.
- Badding, J. V. High-Pressure Synthesis, Characterization, and Tuning of Solid State Materials. *Annu. Rev. Mater. Sci.* **1998**, *28* (1), 631–658. <https://doi.org/10.1146/annurev.matsci.28.1.631>.
- van Eldik, R.; Hubbard, C. D. Effect of Pressure on Inorganic Reactions: Introduction and Mechanistic Applications. In *High Pressure Chemistry: Synthetic, Mechanistic, and Supercritical Applications*; van Eldik, R., Klärner, F.-G., Eds., Wiley-VCH, 2002; pp 3–40. <https://doi.org/10.1002/9783527612628.ch01>.
- Demazeau, G.; Huppertz, H.; Alonso, J. A.; Pöttgen, R.; Moran, E.; Atfield, J. P. Materials Chemistry under High Pressures—Some Recent Aspects. *Z. Naturforsch. B* **2006**, *61* (12), 1457–1470. <https://doi.org/10.1515/znB-2006-1201>.
- Grochala, W.; Hoffmann, R.; Feng, J.; Ashcroft, N. W. The Chemical Imagination at Work in Very Tight Places. *Angew. Chem. Int. Ed.* **2007**, *46* (20), 3620–3642. <https://doi.org/10.1002/anie.200602485>.
- Huppertz, H. New Synthetic Discoveries via High-Pressure Solid-State Chemistry. *Chem. Commun.* **2011**, *47* (1), 131–140. <https://doi.org/10.1039/C0CC02715D>.
- Demchyna, R.; Leoni, S.; Rosner, H.; Schwarz, U. High-Pressure Crystal Chemistry of Binary Intermetallic Compounds. *Z. Kristallogr.* **2006**, *221* (5–7), 420–434. <https://doi.org/10.1524/zkri.2006.221.5-7.420>.
- Zhang, L.; Wang, Y.; Lv, J.; Ma, Y. Materials Discovery at High Pressures. *Nat. Rev. Mater.* **2017**, *2* (4), 17005. <https://doi.org/10.1038/natrevmats.2017.5>.
- Walsh, J. P. S.; Freedman, D. E. High-Pressure Synthesis: A New Frontier in the Search for Next-Generation Intermetallic Compounds. *Acc. Chem. Res.* **2018**, *51* (6), 1315–1323. <https://doi.org/10.1021/acs.accounts.8b00143>.
- Lin, J.; Du, X.; Yang, G. Pressure-Induced New Chemistry. *Chin. Phys. B* **2019**, *28* (10), 106106. <https://doi.org/10.1088/1674-1056/ab3f91>.
- Miao, M.; Sun, Y.; Zurek, E.; Lin, H. Chemistry under High Pressure. *Nat. Rev. Chem.* **2020**, *4* (10), 508–527. <https://doi.org/10.1038/s41570-020-0213-0>.
- Yoo, C.-S. Chemistry under Extreme Conditions: Pressure Evolution of Chemical Bonding and Structure in Dense Solids. *Matter Radiat. Extrem.* **2020**, *5* (1), 018202. <https://doi.org/10.1063/1.5127897>.
- Wang, X.; Liu, X. High Pressure: A Feasible Tool for the Synthesis of Unprecedented Inorganic Compounds. *Inorg. Chem. Front.* **2020**, *7* (16), 2890–2908. <https://doi.org/10.1039/D0QI00477D>.
- Huppertz, H. Multianvil High-Pressure/High-Temperature Synthesis in Solid State Chemistry. *Z. Kristallogr.* **2004**, *219* (6), 330–338. <https://doi.org/10.1524/zkri.219.6.330.34633>.
- Liebermann, R. C. Multi-Anvil, High Pressure Apparatus: A Half-Century of Development and Progress. *High Pressure Res.* **2011**, *31* (4), 493–532. <https://doi.org/10.1080/08957959.2011.618698>.
- Bassett, W. A. Diamond Anvil Cell, 50th Birthday. *High Pressure Res.* **2009**, *29* (2), 163–186. <https://doi.org/10.1080/08957950802597239>.
- Shen, G.; Mao, H. K. High-Pressure Studies with x-Rays Using Diamond Anvil Cells. *Rep. Prog. Phys.* **2017**, *80* (1), 016101. <https://doi.org/10.1088/1361-6633/80/1/016101>.
- Fedotenko, T.; Dubrovinsky, L.; Aprilis, G.; Koemets, E.; Snigirev, A.; Snigireva, I.; Barannikov, A.; Ershov, P.; Cova, F.; Hanfland, M.; Dubrovinskaia, N. Laser Heating Setup for Diamond Anvil Cells for *In Situ* Synchrotron and in House High and Ultra-High Pressure Studies. *Rev. Sci. Instrum.* **2019**, *90* (10), 104501. <https://doi.org/10.1063/1.5117786>.
- Farla, R.; Bhat, S.; Sonntag, S.; Chanyshv, A.; Ma, S.; Ishii, T.; Liu, Z.; Néri, A.; Nishiyama, N.; Faria, G. A.; Wroblewski, T.; Schulte-Schrepping, H.; Drube, W.; Seck, O.; Katsura, T. Extreme Conditions Research Using the Large-Volume Press at the P61B Endstation, PETRA III. *J. Synchrotron Radiat.* **2022**, *29* (2), 409–423. <https://doi.org/10.1107/S1600577522001047>.

23. *P61B Large Volume Press (DESY)*. https://photon-science.desy.de/facilities/petra_iii/beamlines/p61_high_energy_wiggler_beamline_lvp/p61b_large_volume_press_desy/index_eng.html (accessed 07 June 2022).
24. Powder Metallurgy Review. *Element Six Wins Award for 3-D Percussive Diamond Inserts*, Powder Metallurgy Review, 2014. <https://www.pm-review.com/element-six-wins-award-for-3-d-percussive-diamond-inserts/> (accessed 03 June 2022).
25. Anzellini, S.; Boccato, S. A Practical Review of the Laser-Heated Diamond Anvil Cell for University Laboratories and Synchrotron Applications. *Crystals* **2020**, *10* (6), 459. <https://doi.org/10.3390/cryst10060459>.
26. Khvostantsev, L. G.; Slesarev, V. N.; Brazhkin, V. V. Toroid Type High-Pressure Device: History and Prospects. *High Pressure Res.* **2004**, *24* (3), 371–383. <https://doi.org/10.1080/08957950412331298761>.
27. Element Six. *Competitive Advantage Through Innovation; Oil and Gas Capabilities; Brochure*, Element Six US Corporation: Spring, TX, USA, 2017.
28. Walker, D.; Carpenter, M. A.; Hitch, C. M. Some Simplifications to Multianvil Devices for High Pressure Experiments. *Am. Mineral.* **1990**, *75* (9–10), 1020–1028.
29. Walker, D. Lubrication, Gasketing, and Precision in Multianvil Experiments. *Am. Mineral.* **1991**, *76* (7–8), 1092–1100.
30. Guignard, J.; Crichton, W. A. The Large Volume Press Facility at ID06 Beamline of the European Synchrotron Radiation Facility as a High Pressure-High Temperature Deformation Apparatus. *Rev. Sci. Instrum.* **2015**, *86* (8), 085112. <https://doi.org/10.1063/1.4928151>.
31. Leinenweber, K. D.; Tyburczy, J. A.; Sharp, T. G.; Soignard, E.; Diedrich, T.; Petuskey, W. B.; Wang, Y.; Mosenfelder, J. L. Cell Assemblies for Reproducible Multi-Anvil Experiments (the COMPRES Assemblies). *Am. Mineral.* **2012**, *97* (2–3), 353–368. <https://doi.org/10.2138/am.2012.3844>.
32. Gainza, J.; Serrano-Sánchez, F.; Rodrigues, J. E. F. S.; Nemes, N. M.; Martínez, J. L.; Alonso, J. A. Metastable Materials Accessed under Moderate Pressure Conditions ($P \leq 3.5$ GPa) in a Piston-Cylinder Press. *Materials* **2021**, *14* (8), 1946. <https://doi.org/10.3390/ma14081946>.
33. Bykova, E.; Aprilis, G.; Bykov, M.; Glazyrin, K.; Wendt, M.; Wenz, S.; Liermann, H.-P.; Roeh, J. T.; Ehnes, A.; Dubrovinskaia, N.; Dubrovinsky, L. Single-Crystal Diffractometer Coupled with Double-Sided Laser Heating System at the Extreme Conditions Beamline P02.2 at PETRAIII. *Rev. Sci. Instrum.* **2019**, *90* (7), 073907. <https://doi.org/10.1063/1.5108881>.
34. Oganov, A. R.; Pickard, C. J.; Zhu, Q.; Needs, R. J. Structure Prediction Drives Materials Discovery. *Nat. Rev. Mater.* **2019**, *4* (5), 331–348. <https://doi.org/10.1038/s41578-019-0101-8>.
35. Wang, Y.; Lv, J.; Zhu, L.; Lu, S.; Yin, K.; Li, Q.; Wang, H.; Zhang, L.; Ma, Y. Materials Discovery via CALYPSO Methodology. *J. Phys. Condens. Matter* **2015**, *27* (20), 203203. <https://doi.org/10.1088/0953-8984/27/20/203203>.
36. Zurek, E.; Grochala, W. Predicting Crystal Structures and Properties of Matter under Extreme Conditions via Quantum Mechanics: The Pressure Is On. *Phys. Chem. Chem. Phys.* **2015**, *17* (5), 2917–2934. <https://doi.org/10.1039/C4CP04445B>.
37. Zeng, T.; Hoffmann, R.; Nesper, R.; Ashcroft, N. W.; Strobel, T. A.; Proserpio, D. M. Li-Filled, B-Substituted Carbon Clathrates. *J. Am. Chem. Soc.* **2015**, *137* (39), 12639–12652. <https://doi.org/10.1021/jacs.5b07883>.
38. Zhu, L.; Borstad, G. M.; Liu, H.; Guñka, P. A.; Guerette, M.; Dolyuniuk, J.-A.; Meng, Y.; Greenberg, E.; Prakapenka, V. B.; Chaloux, B. L.; Epshteyn, A.; Cohen, R. E.; Strobel, T. A. Carbon-Boron Clathrates as a New Class of Sp^3 -Bonded Framework Materials. *Sci. Adv.* **2020**, *6* (2), eaay8361. <https://doi.org/10.1126/sciadv.aay8361>.
39. Niewa, R.; Rau, D.; Wosylus, A.; Meier, K.; Hanfland, M.; Wessel, M.; Dronskowski, R.; Dzivenko, D. A.; Riedel, R.; Schwarz, U. High-Pressure, High-Temperature Single-Crystal Growth, Ab Initio Electronic Structure Calculations, and Equation of State of ϵ - Fe_2N_{1+x} . *Chem. Mater.* **2009**, *21* (2), 392–398. <https://doi.org/10.1021/cm802721k>.
40. Heymann, G.; Heying, B.; Rodewald, U. C.; Janka, O.; Huppertz, H.; Pöttgen, R. High-Pressure High-Temperature Crystal Growth of Equiatomic Rare Earth Stannides $RENiSn$ and $RPdSn$. *J. Solid State Chem.* **2016**, *236*, 138–146. <https://doi.org/10.1016/j.jssc.2015.06.044>.
41. Zeng, Z.; Zeng, Q.; Liu, N.; Oganov, A. R.; Zeng, Q.; Cui, Y.; Mao, W. L. A Novel Phase of $Li_{15}Si_4$ Synthesized under Pressure. *Adv. Energy Mater.* **2015**, *5* (12), 1500214. <https://doi.org/10.1002/aenm.201500214>.
42. Petermüller, B.; Neun, C.; Wurst, K.; Bayarjargal, L.; Zimmer, D.; Morgenroth, W.; Avalos-Borja, M.; Becerril-Juarez, I. G.; Mühlbauer, M. J.; Winkler, B.; Huppertz, H. High-Pressure Synthesis of β - Ir_4B_5 and Determination of the Compressibility of Various Iridium Borides. *Inorg. Chem.* **2018**, *57* (16), 10341–10351. <https://doi.org/10.1021/acs.inorgchem.8b01541>.
43. Cabrera, R. Q.; Salamat, A.; Barkalov, O. I.; Leynaud, O.; Hutchins, P.; Daisenberger, D.; Machon, D.; Sella, A.; Lewis, D. W.; McMillan, P. F. Pressure-Induced Structural Transformations of the Zintl Phase Sodium Silicide. *J. Solid State Chem.* **2009**, *182* (9), 2535–2542. <https://doi.org/10.1016/j.jssc.2009.06.037>.
44. Binns, J.; Dalladay-Simpson, P.; Wang, M.; Gregoryanz, E.; Howie, R. T. Enhanced Reactivity of Lithium and Copper at High Pressure. *J. Phys. Chem. Lett.* **2018**, *9* (11), 3149–3153. <https://doi.org/10.1021/acs.jpclett.8b01350>.
45. Heymann, G.; Heying, B.; Riecken, J. F.; Huppertz, H.; Pöttgen, R. One-Dimensional Gold Clusters in HP - $Ce_7Au_{13+x}Ge_{10-x}$. *Z. Naturforsch. B* **2013**, *68* (8), 871–876. <https://doi.org/10.5560/znb.2013-3158>.
46. Cherednichenko, K. A.; Mukhanov, V. A.; Wang, Z.; Oganov, A. R.; Kalinko, A.; Dovgaliuk, I.; Solozhenko, V. L. Discovery of New Boron-Rich Chalcogenides: Orthorhombic B_6X ($X=S, Se$). *Sci. Rep.* **2020**, *10* (1), 9277. <https://doi.org/10.1038/s41598-020-66316-y>.
47. Castillo, R.; Schnelle, W.; Bobnar, M.; Cardoso-Gil, R.; Schwarz, U.; Grin, Y. Structural, Magnetic and Thermoelectric Properties of hp - Mn_3Ge_5 . *Z. Anorg. Allg. Chem.* **2020**, *646* (4), 256–262. <https://doi.org/10.1002/zaac.201900342>.
48. Bykova, E.; Gou, H.; Bykov, M.; Hanfland, M.; Dubrovinsky, L.; Dubrovinskaia, N. Crystal Structures and Compressibility of Novel Iron Borides Fe_2B_7 and Fe_4B_{50} Synthesized at High Pressure and High Temperature. *J. Solid State Chem.* **2015**, *230*, 102–109. <https://doi.org/10.1016/j.jssc.2015.06.040>.
49. Gou, H.; Dubrovinskaia, N.; Bykova, E.; Tsirlin, A. A.; Kasinathan, D.; Schnelle, W.; Richter, A.; Merlini, M.; Hanfland, M.; Abakumov, A. M.; Batuk, D.; Van Tendeloo, G.; Nakajima, Y.; Kolmogorov, A. N.; Dubrovinsky, L. Discovery of a Superhard Iron Tetraboride Superconductor. *Phys. Rev. Lett.* **2013**, *111* (15), 157002. <https://doi.org/10.1103/PhysRevLett.111.157002>.
50. Gou, H.; Tsirlin, A. A.; Bykova, E.; Abakumov, A. M.; Van Tendeloo, G.; Richter, A.; Ovsyannikov, S. V.; Kurnosov, A. V.; Trots, D. M.; Konôpková, Z.; Liermann, H.-P.; Dubrovinsky, L.; Dubrovinskaia, N. Peierls Distortion, Magnetism, and High Hardness of Manganese Tetraboride. *Phys. Rev. B* **2014**, *89* (6), 064108. <https://doi.org/10.1103/PhysRevB.89.064108>.
51. Ono, S.; Kikegawa, T.; Ohishi, Y. A High-Pressure and High-Temperature Synthesis of Platinum Carbide. *Solid State Commun.* **2005**, *133* (1), 55–59. <https://doi.org/10.1016/j.ssc.2004.09.048>.
52. Fedotenko, T.; Khandarkhaeva, S.; Dubrovinsky, L.; Glazyrin, K.; Sedmak, P.; Dubrovinskaia, N. Synthesis and Compressibility of Novel Nickel Carbide at Pressures of Earth's Outer Core. *Minerals* **2021**, *11* (5), 516. <https://doi.org/10.3390/min11050516>.
53. Khandarkhaeva, S.; Fedotenko, T.; Bykov, M.; Bykova, E.; Chariton, S.; Sedmak, P.; Glazyrin, K.; Prakapenka, V.; Dubrovinskaia, N.; Dubrovinsky, L. Novel Rhenium Carbides at 200 GPa. *Eur. J. Inorg. Chem.* **2020**, *2020* (22), 2186–2190. <https://doi.org/10.1002/ejic.202000252>.
54. Sanjay Kumar, N. R.; Chandra Shekar, N. V.; Chandra, S.; Basu, J.; Divakar, R.; Sahu, P. C. Synthesis of Novel Ru_2C under High Pressure–High Temperature Conditions. *J. Phys. Condens. Matter* **2012**, *24* (36), 362202. <https://doi.org/10.1088/0953-8984/24/36/362202>.
55. Yasui, N.; Sougawa, M.; Hirai, M.; Yamamoto, K.; Okada, T.; Yamazaki, D.; Kojima, Y.; Ohfuji, H.; Kunitsugu, S.; Takarabe, K. High-Pressure and High-Temperature Synthesis of Rhenium Carbide Using Rhenium and Nanoscale Amorphous Two-Dimensional Carbon Nitride. *Cogent Phys.* **2015**, *2* (1), 1076702. <https://doi.org/10.1080/23311940.2015.1076702>.
56. Arpita Aparajita, A. N.; Sanjay Kumar, N. R.; Chandra, S.; Amirthapandian, S.; Chandra Shekar, N. V.; Sridhar, K. High-Pressure Synthesis of Manganese Monocarbide: A Potential Superhard Material. *Inorg. Chem.* **2018**, *57* (22), 14178–14185. <https://doi.org/10.1021/acs.inorgchem.8b02148>.
57. Gromilov, S.; Chepurov, A.; Sonin, V.; Zhimulev, E.; Sukhikh, A.; Chepurov, A.; Shcheglov, D. Formation of Two Crystal Modifications of Fe_7C_3-x at 5.5 GPa. *J. Appl. Cryst.* **2019**, *52* (6), 1378–1384. <https://doi.org/10.1107/S1600576719013347>.

58. Sasaki, T.; Ikoma, T.; Sago, K.; Liu, Z.; Niwa, K.; Ohsuna, T.; Hasegawa, M. High-Pressure Synthesis and Crystal Structure of MoC-Type Tungsten Nitride by Nitridation with Ammonium Chloride. *Inorg. Chem.* **2019**, *58* (24), 16379–16386. <https://doi.org/10.1021/acs.inorgchem.9b01945>.
59. Inumaru, K.; Nishikawa, T.; Nakamura, K.; Yamanaka, S. High-Pressure Synthesis of Superconducting Molybdenum Nitride δ -MoN by in Situ Nitridation. *Chem. Mater.* **2008**, *20* (14), 4756–4761. <https://doi.org/10.1021/cm800820d>.
60. Friedrich, A.; Winkler, B.; Bayarjargal, L.; Morgenroth, W.; Juarez-Arellano, E. A.; Milman, V.; Refson, K.; Kunz, M.; Chen, K. Novel Rhenium Nitrides. *Phys. Rev. Lett.* **2010**, *105* (8), 085504. <https://doi.org/10.1103/PhysRevLett.105.085504>.
61. Dubrovinsky, L.; Khandarkhaeva, S.; Fedotenko, T.; Laniel, D.; Bykov, M.; Giacobbe, C.; Lawrence Bright, E.; Sedmak, P.; Chariton, S.; Prakashenka, V.; Ponomareva, A. V.; Smirnova, E. A.; Belov, M. P.; Tasnádi, F.; Shulumba, N.; Trybel, F.; Abrikosov, I. A.; Dubrovinskaja, N. Materials Synthesis at Terapascal Static Pressures. *Nature* **2022**, *605* (7909), 274–278. <https://doi.org/10.1038/s41586-022-04550-2>.
62. Clark, W. P.; Steinberg, S.; Dronskowski, R.; McCammon, C.; Kuppenko, I.; Bykov, M.; Dubrovinsky, L.; Akselrud, L. G.; Schwarz, U.; Niewa, R. High-Pressure NiAs-Type Modification of FeN. *Angew. Chem. Int. Ed.* **2017**, *56* (25), 7302–7306. <https://doi.org/10.1002/anie.201702440>.
63. Wosylus, A.; Prots, Y.; Burkhardt, U.; Schnelle, W.; Schwarz, U.; Grin, Y. Breaking the Zintl Rule: High-Pressure Synthesis of Binary EuSi_6 and Its Ternary Derivative $\text{EuSi}_{6-x}\text{Ga}_x$ ($0 \leq x \leq 0.6$). *Solid State Sci.* **2006**, *8* (7), 773–781. <https://doi.org/10.1016/j.solidstatesciences.2006.04.003>.
64. Wosylus, A.; Prots, Y.; Burkhardt, U.; Schnelle, W.; Schwarz, U. High-Pressure Synthesis of the Electron-Excess Compound CaSi_6 . *Sci. Technol. Adv. Mater.* **2007**, *8* (5), 383–388. <https://doi.org/10.1016/j.stam.2007.06.005>.
65. Wosylus, A.; Prots, Y.; Burkhardt, U.; Schnelle, W.; Schwarz, U.; Grin, Y. High-Pressure Synthesis of Strontium Hexasilicide. *Z. Naturforsch. B* **2006**, *61* (12), 1485–1492. <https://doi.org/10.1515/znb-2006-1204>.
66. Yamanaka, S.; Maekawa, S. Structural Evolution of the Binary System Ba-Si under High-Pressure and High-Temperature Conditions. *Z. Naturforsch. B* **2006**, *61* (12), 1493–1499. <https://doi.org/10.1515/znb-2006-1205>.
67. Wosylus, A.; Demchyra, R.; Prots, Y.; Schnelle, W.; Schwarz, U. Refinement of the Crystal Structure of Barium Hexasilicide, BaSi_6 . *Z. Kristallogr. New Cryst. Struct.* **2009**, *224* (3), 347–348. <https://doi.org/10.1524/ncrs.2009.0154>.
68. Hübner, J.-M.; Carrillo-Cabrera, W.; Prots, Y.; Bobnar, M.; Schwarz, U.; Grin, Y. Unconventional Metal–Framework Interaction in MgSi_5 . *Angew. Chem. Int. Ed.* **2019**, *58* (37), 12914–12918. <https://doi.org/10.1002/anie.201907432>.
69. Koemets, I.; Ishii, T.; Hanfland, M.; Dubrovinsky, L. Equations of State of α -SiC (6H) and β' - $\text{Mg}_2\text{Si}_{1.1}$ from Single-Crystal X-Ray Diffraction Data and Novel High-Pressure Magnesium Silicide Mg_2Si_7 . *Phys. Chem. Miner.* **2022**, *49* (5), 12. <https://doi.org/10.1007/s00269-022-01189-3>.
70. Wosylus, A.; Meier, K.; Prots, Y.; Schnelle, W.; Rosner, H.; Schwarz, U.; Grin, Y. Unusual Silicon Connectivities in the Binary Compounds GdSi_5 , CeSi_5 , and Ce_2Si_7 . *Angew. Chem. Int. Ed.* **2010**, *49* (47), 9002–9006. <https://doi.org/10.1002/anie.201003490>.
71. Fukuoka, H.; Yamanaka, S. High-Pressure Synthesis and Superconductivity of LaGe_5 Containing a Tunnel Germanium Network. *Phys. Rev. B* **2003**, *67* (9), 094501. <https://doi.org/10.1103/PhysRevB.67.094501>.
72. Yamanaka, S.; Izumi, S.; Maekawa, S.; Umamoto, K. Phase Diagram of the La–Si Binary System Under High Pressure and the Structures of Superconducting LaSi_5 and LaSi_{10} . *J. Solid State Chem.* **2009**, *182* (8), 1991–2003. <https://doi.org/10.1016/j.jssc.2009.05.010>.
73. Schwarz, U.; Wosylus, A.; Rosner, H.; Schnelle, W.; Ormeci, A.; Meier, K.; Baranov, A.; Nicklas, M.; Leipe, S.; Müller, C. J.; Grin, Y. Dumbbells of Five-Connected Silicon Atoms and Superconductivity in the Binary Silicides MSi_3 ($M = \text{Ca}, \text{Y}, \text{Lu}$). *J. Am. Chem. Soc.* **2012**, *134* (33), 13558–13561. <https://doi.org/10.1021/ja3055194>.
74. Meier, K.; Cardoso-Gil, R.; Schwarz, U. Crystal Structure of Holmium Trisilicide, HoSi_3 . *Z. Kristallogr. New Cryst. Struct.* **2011**, *226* (3), 297–298. <https://doi.org/10.1524/ncrs.2011.0131>.
75. Wosylus, A.; Prots, Y.; Schwarz, U. Crystal Structure of Ytterbium Trisilicide, YbSi_3 . *Z. Kristallogr. New Cryst. Struct.* **2011**, *226* (3), 295–296. <https://doi.org/10.1524/ncrs.2011.0130>.
76. Neziraj, T.; Meier-Kirchner, K.; Schnelle, W.; Wirth, S.; Grin, Y.; Schwarz, U. Gadolinium Trisilicide—A Paramagnetic Representative of the YbSi_3 Type Series. *Z. Naturforsch. B* **2022**, *77* (4–5), 323–329. <https://doi.org/10.1515/znb-2022-0024>.
77. Hübner, J.-M.; Akselrud, L.; Schnelle, W.; Burkhardt, U.; Bobnar, M.; Prots, Y.; Schwarz, U. High-Pressure Synthesis and Chemical Bonding of Barium Trisilicide BaSi_3 . *Materials* **2019**, *12* (1), 145. <https://doi.org/10.3390/ma12010145>.
78. Akselrud, L.; Wosylus, A.; Castillo, R.; Aydemir, U.; Prots, Y.; Schnelle, W.; Grin, Y.; Schwarz, U. BaGe_6 and BaGe_{6-x} : Incommensurately Ordered Vacancies as Electron Traps. *Inorg. Chem.* **2014**, *53* (24), 12699–12705. <https://doi.org/10.1021/ic5021065>.
79. Schwarz, U.; Castillo, R.; Hübner, J. M.; Wosylus, A.; Prots, Y.; Bobnar, M.; Grin, Y. The Untypical High-Pressure Zintl Phase SrGe_6 . *Z. Naturforsch. B* **2020**, *75* (1–2), 209–216. <https://doi.org/10.1515/znb-2019-0197>.
80. Fukuoka, H.; Yamanaka, S.; Matsuoka, E.; Takabatake, T. High-Pressure Synthesis and Transport Properties of a New Binary Germanide, $\text{SrGe}_{6-\delta}$ ($\delta \approx 0.5$), with a Cagelike Structure. *Inorg. Chem.* **2005**, *44* (5), 1460–1465. <https://doi.org/10.1021/c0485615>.
81. Schwarz, U.; Castillo, R.; Wosylus, A.; Akselrud, L.; Prots, Y.; Wahl, B.; Doert, T.; Bobnar, M.; Grin, Y. Modulated Vacancy Ordering in SrGe_{6-x} ($x \approx 0.45$). *Z. Naturforsch. B* **2019**, *74* (1), 137–145. <https://doi.org/10.1515/znb-2018-0200>.
82. Meier, K.; Koz, C.; Kerkau, A.; Schwarz, U. Crystal Structure of Samarium Pentagermanide, SmGe_5 . *Z. Kristallogr. New Cryst. Struct.* **2009**, *224* (3), 349–350. <https://doi.org/10.1524/ncrs.2009.0155>.
83. Meier, K.; Kerkau, A.; Schwarz, U. Crystal Structures of Gadolinium Pentagermanide, GdGe_5 and Neodymium Pentagermanide, NdGe_5 . *Z. Kristallogr. New Cryst. Struct.* **2009**, *224* (3), 373–374. <https://doi.org/10.1524/ncrs.2009.0163>.
84. Meier, K.; Cardoso-Gil, R.; Schnelle, W.; Rosner, H.; Burkhardt, U.; Schwarz, U. Thermal, Magnetic, Electronic, and Superconducting Properties of Rare-Earth Metal Pentagermanides REGe_5 ($\text{RE} = \text{La}, \text{Nd}, \text{Sm}, \text{Gd}$) and Synthesis of TbGe_5 . *Z. Anorg. Allg. Chem.* **2010**, *636* (8), 1466–1473. <https://doi.org/10.1002/zaac.201000065>.
85. Meier, K.; Wosylus, A.; Cardoso-Gil, R.; Burkhardt, U.; Curfs, C.; Hanfland, M.; Grin, Y.; Schwarz, U. New Rare-Earth Metal Germanides RE_2Ge_9 ($\text{RE} = \text{Nd}, \text{Sm}$) by Thermal Decomposition of High-Pressure Phases REGe_5 . *Z. Anorg. Allg. Chem.* **2012**, *638* (10), 1446–1451. <https://doi.org/10.1002/zaac.201200146>.
86. Castillo, R.; Carrillo-Cabrera, W.; Schwarz, U.; Grin, Y. Classical and Nonclassical Germanium Environments in High-Pressure BaGe_5 . *Inorg. Chem.* **2015**, *54* (3), 1019–1025. <https://doi.org/10.1021/ic502396p>.
87. Schnelle, W.; Ormeci, A.; Wosylus, A.; Meier, K.; Grin, Y.; Schwarz, U. Dumbbells of Five-Connected Ge Atoms and Superconductivity in CaGe_3 . *Inorg. Chem.* **2012**, *51* (10), 5509–5511. <https://doi.org/10.1021/c300576a>.
88. Nishikawa, T.; Fukuoka, H.; Inumaru, K. High-Pressure Synthesis and Electronic Structure of a New Superconducting Strontium Germanide (SrGe_3) Containing Ge_2 Dumbbells. *Inorg. Chem.* **2015**, *54* (15), 7433–7437. <https://doi.org/10.1021/acs.inorgchem.5b00989>.
89. Castillo, R.; Baranov, A. I.; Burkhardt, U.; Cardoso-Gil, R.; Schnelle, W.; Bobnar, M.; Schwarz, U. Germanium Dumbbells in a New Superconducting Modification of BaGe_3 . *Inorg. Chem.* **2016**, *55* (9), 4498–4503. <https://doi.org/10.1021/acs.inorgchem.6b00299>.
90. Fukuoka, H.; Tomomitsu, Y.; Inumaru, K. High-Pressure Synthesis and Superconductivity of a New Binary Barium Germanide BaGe_3 . *Inorg. Chem.* **2011**, *50* (13), 6372–6377. <https://doi.org/10.1021/c200826d>.
91. Fukuoka, H.; Suekuni, K.; Onimaru, T.; Inumaru, K. High-Pressure Synthesis and Superconductivity of a New Binary Lanthanum Germanide LaGe_3 with Triangular Ge_3 Cluster Units. *Inorg. Chem.* **2011**, *50* (9), 3901–3906. <https://doi.org/10.1021/ic102077k>.
92. Castillo, R.; Baranov, A. I.; Burkhardt, U.; Grin, Y.; Schwarz, U. Triangular Ge_3 Units in a New Modification of EuGe_3 . *Z. Anorg. Allg. Chem.* **2015**, *641* (2), 355–361. <https://doi.org/10.1002/zaac.201400585>.
93. Hübner, J.-M.; Carrillo-Cabrera, W.; Cardoso-Gil, R.; Koželj, P.; Burkhardt, U.; Etter, M.; Akselrud, L.; Grin, Y.; Schwarz, U. High-Pressure Synthesis of SmGe_3 . *Z. Kristallogr.* **2020**, *235* (8–9), 333–339. <https://doi.org/10.1515/zkri-2020-0058>.

94. Fukuoka, H.; Yamanaka, S. High-Pressure Synthesis and Properties of a Cerium Germanide CeGe_3 with the Cubic Cu_3Au Type Structure. *Chem. Lett.* **2004**, *33* (10), 1334–1335. <https://doi.org/10.1246/cl.2004.1334>.
95. Hübner, J.-M.; Bobnar, M.; Akselrud, L.; Prots, Y.; Grin, Y.; Schwarz, U. Lutetium Trigermanide LuGe_3 : High-Pressure Synthesis, Superconductivity, and Chemical Bonding. *Inorg. Chem.* **2018**, *57* (16), 10295–10302. <https://doi.org/10.1021/acs.inorgchem.8b01510>.
96. Freccero, R.; Hübner, J.-M.; Prots, Y.; Schnelle, W.; Schmidt, M.; Wagner, F. R.; Schwarz, U.; Grin, Y. "Excess" Electrons in LuGe . *Angew. Chem. Int. Ed.* **2021**, *60* (12), 6457–6461. <https://doi.org/10.1002/anie.202014284>.
97. Bolotina, N. B.; Dyuzheva, T. I.; Bendeliani, N. A.; Petricek, V.; Petrova, A. E.; Simonov, V. I. Growth of Crystals, Composite Crystal Structures and Electrical Resistance of High-Pressure Phases of $\text{Mg}_2\text{B}_{1+x}$ ($\text{B}=\text{Sn,Ge}$). *J. Alloys Compd.* **1998**, *278* (1–2), 29–33. [https://doi.org/10.1016/S0925-8388\(98\)00552-0](https://doi.org/10.1016/S0925-8388(98)00552-0).
98. Akselrud, L.; Prots, Y.; Hübner, J.-M.; Burkhardt, U.; Schnelle, W.; Grin, Y.; Schwarz, U. Order and Disorder in the Modulated Phase $hp\text{-Mg}_9\text{Ge}_{5.1}$. *Z. Anorg. Allg. Chem.* **2022**, *648* (10), e202100381. <https://doi.org/10.1002/zaac.202100381>.
99. Fong, A. Y.; Xu, H.; Page, K.; Dirmyer, M. R.; Kodera, Y.; Obrey, S. J.; Garay, J. E. Synthesis and Structural Characterization of Dense Polycrystalline Mg_9Sn_5 , a Metastable Mg-Sn Phase. *J. Alloys Compd.* **2014**, *616*, 333–339. <https://doi.org/10.1016/j.jallcom.2014.07.122>.
100. Imai, M.; Ibuka, S.; Isoda, Y. Phase Relationship of Mg_2Si at High Pressures and High Temperatures and Thermoelectric Properties of Mg_9Si_5 . *Inorg. Chem.* **2021**, *60* (15), 11394–11400. <https://doi.org/10.1021/acs.inorgchem.1c01386>.
101. Baitinger, M.; Böhme, B.; Wagner, F. R.; Schwarz, U. Zintl Defects in Intermetallic Clathrates. *Z. Anorg. Allg. Chem.* **2020**, *646* (14), 1034–1041. <https://doi.org/10.1002/zaac.202000107>.
102. Demchyna, R.; Köhler, U.; Prots, Y.; Schnelle, W.; Baenitz, M.; Burkhardt, U.; Paschen, S.; Schwarz, U. High-Pressure Synthesis and Physical Properties of the Europium-Substituted Barium Clathrate $\text{Ba}_{8-x}\text{Eu}_x\text{Ge}_{13}$ ($x \leq 0.6$). *Z. Anorg. Allg. Chem.* **2006**, *632* (1), 73–78. <https://doi.org/10.1002/zaac.200500343>.
103. Yamanaka, S.; Enishi, E.; Fukuoka, H.; Yasukawa, M. High-Pressure Synthesis of a New Silicon Clathrate Superconductor, $\text{Ba}_8\text{Si}_{46}$. *Inorg. Chem.* **2000**, *39* (1), 56–58. <https://doi.org/10.1021/ic990778p>.
104. Fukuoka, H.; Kiyoto, J.; Yamanaka, S. Superconductivity of Metal Deficient Silicon Clathrate Compounds, $\text{Ba}_{8-x}\text{Si}_{46}$ ($0 < x \leq 1.4$). *Inorg. Chem.* **2003**, *42* (9), 2933–2937. <https://doi.org/10.1021/ic020676q>.
105. Liang, Y.; Böhme, B.; Reibold, M.; Schnelle, W.; Schwarz, U.; Baitinger, M.; Lichte, H.; Grin, Y. Synthesis of the Clathrate-I Phase $\text{Ba}_{8-x}\text{Si}_{46}$ via Redox Reactions. *Inorg. Chem.* **2011**, *50* (10), 4523–4528. <https://doi.org/10.1021/ic2001859>.
106. Castillo, R.; Schnelle, W.; Bobnar, M.; Burkhardt, U.; Böhme, B.; Baitinger, M.; Schwarz, U.; Grin, Y. The Clathrate $\text{Ba}_{8-x}\text{Si}_{46}$ Revisited: Preparation Routes, Electrical and Thermal Transport Properties. *Z. Anorg. Allg. Chem.* **2015**, *641* (2), 206–213. <https://doi.org/10.1002/zaac.201500001>.
107. Hübner, J.-M.; Prots, Y.; Schnelle, W.; Bobnar, M.; König, M.; Baitinger, M.; Simon, P.; Carrillo-Cabrera, W.; Ormeci, A.; Svanidze, E.; Grin, Y.; Schwarz, U. In-Cage Interactions in the Clathrate Superconductor $\text{Sr}_8\text{Si}_{46}$. *Chem. A Eur. J.* **2020**, *26* (4), 830–838. <https://doi.org/10.1002/chem.201904170>.
108. Stefanoski, S.; Finkelstein, G. J.; Ward, M. D.; Zeng, T.; Wei, K.; Bullock, E. S.; Beavers, C. M.; Liu, H.; Nolas, G. S.; Strobel, T. A. Zintl Ions within Framework Channels: The Complex Structure and Low-Temperature Transport Properties of $\text{Na}_4\text{Ge}_{13}$. *Inorg. Chem.* **2018**, *57* (4), 2002–2012. <https://doi.org/10.1021/acs.inorgchem.7b02914>.
109. Yamanaka, S.; Komatsu, M.; Tanaka, M.; Sawa, H.; Inumaru, K. High-Pressure Synthesis and Structural Characterization of the Type II Clathrate Compound $\text{Na}_{30.5}\text{Si}_{136}$ Encapsulating Two Sodium Atoms in the Same Silicon Polyhedral Cages. *J. Am. Chem. Soc.* **2014**, *136* (21), 7717–7725. <https://doi.org/10.1021/ja502733e>.
110. Kurakevych, O. O.; Strobel, T. A.; Kim, D. Y.; Muramatsu, T.; Struzhkin, V. V. Na-Si Clathrates Are High-Pressure Phases: A Melt-Based Route to Control Stoichiometry and Properties. *Cryst. Growth Des.* **2013**, *13* (1), 303–307. <https://doi.org/10.1021/cg3017084>.
111. Jouini, Z.; Kurakevych, O. O.; Moutaabbid, H.; Le Godec, Y.; Mezouar, M.; Guignot, N. Phase Boundary between Na-Si Clathrates of Structures I and II at High Pressures and High Temperatures. *J. Superhard Mater.* **2016**, *38* (1), 66–70. <https://doi.org/10.3103/S106345761601010X>.
112. Wosylus, A.; Veremchuk, I.; Schnelle, W.; Baitinger, M.; Schwarz, U.; Grin, Y. $\text{Cs}_{8-x}\text{Si}_{46}$: A Type-I Clathrate with Expanded Silicon Framework. *Chem. A Eur. J.* **2009**, *15* (24), 5901–5903. <https://doi.org/10.1002/chem.200900307>.
113. Veremchuk, I.; Wosylus, A.; Böhme, B.; Baitinger, M.; Borrmann, H.; Prots, Y.; Burkhardt, U.; Schwarz, U.; Grin, Y. Preparation and Crystal Structure of the Clathrate-I $\text{Cs}_{8-x}\text{Ge}_{44+y}\text{O}_{2-y}$. *Z. Anorg. Allg. Chem.* **2011**, *637* (10), 1281–1286. <https://doi.org/10.1002/zaac.201100187>.
114. Hübner, J.-M.; Jung, W.; Schmidt, M.; Bobnar, M.; Kozelj, P.; Böhme, B.; Baitinger, M.; Etter, M.; Grin, Y.; Schwarz, U. Cage Adaptation by High-Pressure Synthesis: The Clathrate-I Borosilicide $\text{Rb}_8\text{B}_8\text{Si}_{38}$. *Inorg. Chem.* **2021**, *60* (4), 2160–2167. <https://doi.org/10.1021/acs.inorgchem.0c02357>.
115. Hübner, J.-M.; Jung, W.; Kozelj, P.; Bobnar, M.; Cardoso-Gil, R.; Burkhardt, U.; Böhme, B.; Baitinger, M.; Schwarz, U.; Grin, Y. Mastering Extreme Size Constraints in the Clathrate-I Borosilicide $\text{Cs}_8\text{B}_8\text{Si}_{38}$. *Z. Anorg. Allg. Chem.* **2021**, *647* (2–3), 119–125. <https://doi.org/10.1002/zaac.202000400>.
116. Strobel, T. A.; Zhu, L.; Guñka, P. A.; Borstad, G. M.; Guerette, M. A Lanthanum-Filled Carbon-Boron Clathrate. *Angew. Chem. Int. Ed.* **2021**, *60* (6), 2877–2881. <https://doi.org/10.1002/anie.202012821>.
117. Schwarz, U.; Tencé, S.; Janson, O.; Koz, C.; Krellner, C.; Burkhardt, U.; Rosner, H.; Stiglich, F.; Grin, Y. CoBi_2 : A Binary Cobalt-Bismuth Compound and Superconductor. *Angew. Chem. Int. Ed.* **2013**, *52* (37), 9853–9857. <https://doi.org/10.1002/anie.201302397>.
118. Walsh, J. P. S.; Clarke, S. M.; Puggioni, D.; Tamerius, A. D.; Meng, Y.; Rondinelli, J. M.; Jacobsen, S. D.; Freedman, D. E. MnBi_2 : A Metastable High-Pressure Phase in the Mn-Bi System. *Chem. Mater.* **2019**, *31* (9), 3083–3088. <https://doi.org/10.1021/acs.chemmater.9b00385>.
119. Walsh, J. P. S.; Clarke, S. M.; Meng, Y.; Jacobsen, S. D.; Freedman, D. E. Discovery of FeBi_2 . *ACS Cent. Sci.* **2016**, *2* (11), 867–871. <https://doi.org/10.1021/acscentsci.6b00287>.
120. Altman, A. B.; Tamerius, A. D.; Koocher, N. Z.; Meng, Y.; Pickard, C. J.; Walsh, J. P. S.; Rondinelli, J. M.; Jacobsen, S. D.; Freedman, D. E. Computationally Directed Discovery of MoBi_2 . *J. Am. Chem. Soc.* **2021**, *143* (1), 214–222. <https://doi.org/10.1021/jacs.0c09419>.
121. McMahon, M. I.; Degtyareva, O.; Nelmes, R. J.; van Smaalen, S.; Palatinus, L. Incommensurate Modulations of Bi-III and Sb-II. *Phys. Rev. B* **2007**, *75* (18), 184114. <https://doi.org/10.1103/PhysRevB.75.184114>.
122. Clarke, S. M.; Powderly, K. M.; Walsh, J. P. S.; Yu, T.; Wang, Y.; Meng, Y.; Jacobsen, S. D.; Freedman, D. E. Controlling Dimensionality in the Ni-Bi System with Pressure. *Chem. Mater.* **2019**, *31* (3), 955–959. <https://doi.org/10.1021/acs.chemmater.8b04412>.
123. Powderly, K. M.; Clarke, S. M.; Amsler, M.; Wolverton, C.; Malliakas, C. D.; Meng, Y.; Jacobsen, S. D.; Freedman, D. E. High-Pressure Discovery of $\beta\text{-NiBi}$. *Chem. Commun.* **2017**, *53* (81), 11241–11244. <https://doi.org/10.1039/C7CC06471C>.
124. Clarke, S. M.; Walsh, J. P. S.; Amsler, M.; Malliakas, C. D.; Yu, T.; Goedecker, S.; Wang, Y.; Wolverton, C.; Freedman, D. E. Discovery of a Superconducting Cu-Bi Intermetallic Compound by High-Pressure Synthesis. *Angew. Chem. Int. Ed.* **2016**, *55* (43), 13446–13449. <https://doi.org/10.1002/anie.201605902>.
125. Clarke, S. M.; Amsler, M.; Walsh, J. P. S.; Yu, T.; Wang, Y.; Meng, Y.; Jacobsen, S. D.; Wolverton, C.; Freedman, D. E. Creating Binary Cu-Bi Compounds via High-Pressure Synthesis: A Combined Experimental and Theoretical Study. *Chem. Mater.* **2017**, *29* (12), 5276–5285. <https://doi.org/10.1021/acs.chemmater.7b01418>.
126. Guo, K.; Akselrud, L.; Bobnar, M.; Burkhardt, U.; Schmidt, M.; Zhao, J.-T.; Schwarz, U.; Grin, Y. Weak Interactions under Pressure: $hp\text{-CuBi}$ and Its Analogues. *Angew. Chem. Int. Ed.* **2017**, *56* (20), 5620–5624. <https://doi.org/10.1002/anie.201700712>.
127. Tamerius, A. D.; Clarke, S. M.; Gu, M.; Walsh, J. P. S.; Esters, M.; Meng, Y.; Hendon, C. H.; Rondinelli, J. M.; Jacobsen, S. D.; Freedman, D. E. Discovery of Cu_2Pb . *Angew. Chem.* **2018**, *130* (39), 12991–12995. <https://doi.org/10.1002/ange.201807934>.
128. Drozdov, A. P.; Erements, M. I.; Troyan, I. A.; Ksenofontov, V.; Shylin, S. I. Conventional Superconductivity at 203 Kelvin at High Pressures in the Sulfur Hydride System. *Nature* **2015**, *525* (7567), 73–76. <https://doi.org/10.1038/nature14964>.
129. Wang, H.; Li, X.; Gao, G.; Li, Y.; Ma, Y. Hydrogen-Rich Superconductors at High Pressures. *Wiley Interdiscip. Rev. Comput. Mol. Sci.* **2018**, *8* (1), e1330. <https://doi.org/10.1002/wcms.1330>.

130. Flores-Livas, J. A.; Boeri, L.; Sanna, A.; Profeta, G.; Arita, R.; Eremets, M. A Perspective on Conventional High-Temperature Superconductors at High Pressure: Methods and Materials. *Phys. Rep.* **2020**, *856*, 1–78. <https://doi.org/10.1016/j.physrep.2020.02.003>.
131. Zurek, E.; Bi, T. High-Temperature Superconductivity in Alkaline and Rare Earth Polyhydrides at High Pressure: A Theoretical Perspective. *J. Chem. Phys.* **2019**, *150* (5), 050901. <https://doi.org/10.1063/1.5079225>.
132. Zhang, X.; Zhao, Y.; Yang, G. Superconducting Ternary Hydrides under High Pressure. *Wiley Interdiscip. Rev.: Comput. Mol. Sci.* **2022**, *12* (3), e1582. <https://doi.org/10.1002/wcms.1582>.
133. Antonov, V. Phase Transformations, Crystal and Magnetic Structures of High-Pressure Hydrides of *d*-Metals. *J. Alloys Compd.* **2002**, *330–332*, 110–116. [https://doi.org/10.1016/S0925-8388\(01\)01532-8](https://doi.org/10.1016/S0925-8388(01)01532-8).
134. Fukai, Y. *The Metal-Hydrogen System: Basic Bulk Properties*, 2nd ed.; In: *Springer Series in Materials Science*, vol. 21; Springer: Berlin, 2005. <https://doi.org/10.1007/3-540-28883-X>.
135. Kuzovnikov, M. A.; Tkacz, M. High-Pressure Synthesis of Novel Polyhydrides of Zr and Hf with a Th_4H_{15} -Type Structure. *J. Phys. Chem. C* **2019**, *123* (50), 30059–30066. <https://doi.org/10.1021/acs.jpcc.9b07918>.
136. Liu, G.; Besedin, S.; Irodova, A.; Liu, H.; Gao, G.; Eremets, M.; Wang, X.; Ma, Y. Nb-H System at High Pressures and Temperatures. *Phys. Rev. B* **2017**, *95* (10), 104110. <https://doi.org/10.1103/PhysRevB.95.104110>.
137. Kuzovnikov, M. A.; Tkacz, M.; Meng, H.; Kapustin, D. I.; Kulakov, V. I. High-Pressure Synthesis of Tantalum Dihydride. *Phys. Rev. B* **2017**, *96* (13), 134120. <https://doi.org/10.1103/PhysRevB.96.134120>.
138. Kuzovnikov, M. A.; Antonov, V. E.; Ivanov, A. S.; Hansen, T.; Sawin, S.; Kulakov, V. I.; Tkacz, M.; Kolesnikov, A. I.; Gurev, V. M. Neutron Scattering Study of Tantalum Dihydride. *Phys. Rev. B* **2020**, *102* (2), 024113. <https://doi.org/10.1103/PhysRevB.102.024113>.
139. Ying, J.; Li, X.; Greenberg, E.; Prakapenka, V. B.; Liu, H.; Struzhkin, V. V. Synthesis and Stability of Tantalum Hydride at High Pressures. *Phys. Rev. B* **2019**, *99* (22), 224504. <https://doi.org/10.1103/PhysRevB.99.224504>.
140. Marizy, A.; Geneste, G.; Loubeyre, P.; Guigue, B.; Garbarino, G. Synthesis of Bulk Chromium Hydrides Under Pressure of up to 120 GPa. *Phys. Rev. B* **2018**, *97* (18), 184103. <https://doi.org/10.1103/PhysRevB.97.184103>.
141. Pépin, C. M.; Dewaele, A.; Geneste, G.; Loubeyre, P.; Mezouar, M. New Iron Hydrides under High Pressure. *Phys. Rev. Lett.* **2014**, *113* (26), 265504. <https://doi.org/10.1103/PhysRevLett.113.265504>.
142. Pépin, C. M.; Geneste, G.; Dewaele, A.; Mezouar, M.; Loubeyre, P. Synthesis of FeH_5 : A Layered Structure with Atomic Hydrogen Slabs. *Science* **2017**, *357* (6349), 382–385. <https://doi.org/10.1126/science.aan0961>.
143. Kuzovnikov, M. A.; Tkacz, M. Synthesis of Ruthenium Hydride. *Phys. Rev. B* **2016**, *93* (6), 064103. <https://doi.org/10.1103/PhysRevB.93.064103>.
144. Binns, J.; He, Y.; Donnelly, M.-E.; Peña-Alvarez, M.; Wang, M.; Kim, D. Y.; Gregoryanz, E.; Dalladay-Simpson, P.; Howie, R. T. Complex Hydrogen Substructure in Semimetallic RuH_4 . *J. Phys. Chem. Lett.* **2020**, *11* (9), 3390–3395. <https://doi.org/10.1021/acs.jpclett.0c00688>.
145. Wang, M.; Binns, J.; Donnelly, M.-E.; Peña-Alvarez, M.; Dalladay-Simpson, P.; Howie, R. T. High Pressure Synthesis and Stability of Cobalt Hydrides. *J. Chem. Phys.* **2018**, *148* (14), 144310. <https://doi.org/10.1063/1.5026535>.
146. Li, B.; Ding, Y.; Kim, D. Y.; Ahuja, R.; Zou, G.; Mao, H.-K. Rhodium Dihydride (RhH_2) with High Volumetric Hydrogen Density. *Proc. Natl. Acad. Sci. U. S. A.* **2011**, *108* (46), 18618–18621. <https://doi.org/10.1073/pnas.1114680108>.
147. Peña-Alvarez, M.; Li, B.; Kelsall, L. C.; Binns, J.; Dalladay-Simpson, P.; Hermann, A.; Howie, R. T.; Gregoryanz, E. Synthesis of Superconducting Cobalt Trihydride. *J. Phys. Chem. Lett.* **2020**, *11* (15), 6420–6425. <https://doi.org/10.1021/acs.jpclett.0c01807>.
148. Scheler, T.; Marqués, M.; Konôpková, Z.; Guillaume, C. L.; Howie, R. T.; Gregoryanz, E. High-Pressure Synthesis and Characterization of Iridium Trihydride. *Phys. Rev. Lett.* **2013**, *111* (21), 215503. <https://doi.org/10.1103/PhysRevLett.111.215503>.
149. Kuzovnikov, M. A.; Minkov, V. S.; Chariton, S.; Prakapenka, V. B.; Eremets, M. I. Synthesis of Osmium Hydride under High Hydrogen Pressure. *Phys. Rev. B* **2020**, *102* (21), 214109. <https://doi.org/10.1103/PhysRevB.102.214109>.
150. Scheler, T.; Degtyareva, O.; Gregoryanz, E. On the Effects of High Temperature and High Pressure on the Hydrogen Solubility in Rhenium. *J. Chem. Phys.* **2011**, *135* (21), 214501. <https://doi.org/10.1063/1.3652863>.
151. Scheler, T.; Peng, F.; Guillaume, C. L.; Howie, R. T.; Ma, Y.; Gregoryanz, E. Nanocrystalline Tungsten Hydrides at High Pressures. *Phys. Rev. B* **2013**, *87* (18), 184117. <https://doi.org/10.1103/PhysRevB.87.184117>.
152. Binns, J.; Donnelly, M.-E.; Wang, M.; Hermann, A.; Gregoryanz, E.; Dalladay-Simpson, P.; Howie, R. T. Synthesis of Ni_2H_3 at High Temperatures and Pressures. *Phys. Rev. B* **2018**, *98* (14), 140101(R). <https://doi.org/10.1103/PhysRevB.98.140101>.
153. Ying, J.; Liu, H.; Greenberg, E.; Prakapenka, V. B.; Struzhkin, V. V. Synthesis of New Nickel Hydrides at High Pressure. *Phys. Rev. Mater.* **2018**, *2* (8), 085409. <https://doi.org/10.1103/PhysRevMaterials.2.085409>.
154. Guigue, B.; Geneste, G.; Leridon, B.; Loubeyre, P. An X-Ray Study of Palladium Hydrides up to 100 GPa: Synthesis and Isotopic Effects. *J. Appl. Phys.* **2020**, *127* (7), 075901. <https://doi.org/10.1063/1.5138697>.
155. Scheler, T.; Degtyareva, O.; Marqués, M.; Guillaume, C. L.; Proctor, J. E.; Evans, S.; Gregoryanz, E. Synthesis and Properties of Platinum Hydride. *Phys. Rev. B* **2011**, *83* (21), 214106. <https://doi.org/10.1103/PhysRevB.83.214106>.
156. Bronger, W.; Auffermann, G. New Ternary Alkali-Metal – Transition-Metal Hydrides Synthesized at High Pressures: Characterization and Properties. *Chem. Mater.* **1998**, *10* (10), 2723–2732. <https://doi.org/10.1021/cm980344c>.
157. Takagi, S.; Orimo, S. New Functionalities of Hydride Complexes with High Hydrogen Coordination. *J. Physical Soc. Japan* **2020**, *89* (5), 051010. <https://doi.org/10.7566/JPSJ.89.051010>.
158. Takagi, S.; Iijima, Y.; Sato, T.; Saitoh, H.; Ikeda, K.; Otomo, T.; Miwa, K.; Ikeshoji, T.; Aoki, K.; Orimo, S. True Boundary for the Formation of Homoleptic Transition-Metal Hydride Complexes. *Angew. Chem. Int. Ed.* **2015**, *54* (19), 5650–5653. <https://doi.org/10.1002/anie.201500792>.
159. Takagi, S.; Iijima, Y.; Sato, T.; Saitoh, H.; Ikeda, K.; Otomo, T.; Miwa, K.; Ikeshoji, T.; Orimo, S. Formation of Novel Transition Metal Hydride Complexes with Ninefold Hydrogen Coordination. *Sci. Rep.* **2017**, *7* (1), 44253. <https://doi.org/10.1038/srep44253>.
160. Yajima, T.; Nakajima, H.; Honda, T.; Ikeda, K.; Otomo, T.; Takeda, H.; Hiroi, Z. Titanium Hydride Complex $\text{BaCa}_2\text{Ti}_2\text{H}_{14}$ with 9-Fold Coordination. *Inorg. Chem.* **2020**, *59* (7), 4228–4233. <https://doi.org/10.1021/acs.inorgchem.9b02810>.
161. Spektor, K.; Crichton, W. A.; Filippov, S.; Klarbring, J.; Simak, S. I.; Fischer, A.; Häussermann, U. Na–Ni–H Phase Formation at High Pressures and High Temperatures: Hydrido Complexes $[\text{NiH}_3]^{3-}$ Versus the Perovskite NaNiH_3 . *ACS Omega* **2020**, *5* (15), 8730–8743. <https://doi.org/10.1021/acsomega.0c00239>.
162. Spektor, K.; Crichton, W. A.; Filippov, S.; Simak, S. I.; Fischer, A.; Häussermann, U. Na_3FeH_7 and Na_3CoH_6 : Hydrogen-Rich First-Row Transition Metal Hydrides from High Pressure Synthesis. *Inorg. Chem.* **2020**, *59* (22), 16467–16473. <https://doi.org/10.1021/acs.inorgchem.0c02294>.
163. Sato, R.; Saitoh, H.; Endo, N.; Takagi, S.; Matsuo, M.; Aoki, K.; Orimo, S. Formation Process of Perovskite-Type Hydride LiNiH_3 : In Situ Synchrotron Radiation X-Ray Diffraction Study. *Appl. Phys. Lett.* **2013**, *102* (9), 091901. <https://doi.org/10.1063/1.4794067>.
164. Takagi, S.; Orimo, S. Recent Progress in Hydrogen-Rich Materials from the Perspective of Bonding Flexibility of Hydrogen. *Scr. Mater.* **2015**, *109*, 1–5. <https://doi.org/10.1016/j.scriptamat.2015.07.024>.
165. Machida, A.; Saitoh, H.; Sugimoto, H.; Hattori, T.; Sano-Furukawa, A.; Endo, N.; Katayama, Y.; Iizuka, R.; Sato, T.; Matsuo, M.; Orimo, S.; Aoki, K. Site Occupancy of Interstitial Deuterium Atoms in Face-Centred Cubic Iron. *Nat. Commun.* **2014**, *5* (1), 5063. <https://doi.org/10.1038/ncomms6063>.
166. Zurek, E. Hydrides of the Alkali Metals and Alkaline Earth Metals Under Pressure. *Comments Inorg. Chem.* **2017**, *37* (2), 78–98. <https://doi.org/10.1080/02603594.2016.1196679>.

167. Matsuoka, T.; Kuno, K.; Ohta, K.; Sakata, M.; Nakamoto, Y.; Hirao, N.; Ohishi, Y.; Shimizu, K.; Kume, T.; Sasaki, S. Lithium Polyhydrides Synthesized under High Pressure and High Temperature. *J. Raman Spectrosc.* **2017**, *48* (9), 1222–1228. <https://doi.org/10.1002/jrs.5183>.
168. Pépin, C.; Loubeyre, P.; Occelli, F.; Dumas, P. Synthesis of Lithium Polyhydrides above 130 GPa at 300 K. *Proc. Natl. Acad. Sci. U. S. A.* **2015**, *112* (25), 7673–7676. <https://doi.org/10.1073/pnas.1507508112>.
169. Mishra, A. K.; Muramatsu, T.; Liu, H.; Geballe, Z. M.; Somayazulu, M.; Ahart, M.; Baldini, M.; Meng, Y.; Zurek, E.; Hemley, R. J. New Calcium Hydrides with Mixed Atomic and Molecular Hydrogen. *J. Phys. Chem. C* **2018**, *122* (34), 19370–19378. <https://doi.org/10.1021/acs.jpcc.8b05030>.
170. Wu, G.; Huang, X.; Xie, H.; Li, X.; Liu, M.; Liang, Y.; Huang, Y.; Duan, D.; Li, F.; Liu, B.; Cui, T. Unexpected Calcium Polyhydride CaH₄: A Possible Route to Dissociation of Hydrogen Molecules. *J. Chem. Phys.* **2019**, *150* (4), 044507. <https://doi.org/10.1063/1.5053650>.
171. Struzhkin, V. V.; Kim, D. Y.; Stavrou, E.; Muramatsu, T.; Mao, H.; Pickard, C. J.; Needs, R. J.; Prakapenka, V. B.; Goncharov, A. F. Synthesis of Sodium Polyhydrides at High Pressures. *Nat. Commun.* **2016**, *7* (1), 12267. <https://doi.org/10.1038/ncomms12267>.
172. Matsuoka, T.; Fujihisa, H.; Ishikawa, T.; Nakagawa, T.; Kuno, K.; Hirao, N.; Ohishi, Y.; Shimizu, K.; Sasaki, S. Beryllium Polyhydride Be₄H₂(H₂)₂ Synthesized at High Pressure and Temperature. *Phys. Rev. Mater.* **2020**, *4* (12), 125402. <https://doi.org/10.1103/PhysRevMaterials.4.125402>.
173. Ma, L.; Wang, K.; Xie, Y.; Yang, X.; Wang, Y.; Zhou, M.; Liu, H.; Yu, X.; Zhao, Y.; Wang, H.; Liu, G.; Ma, Y. High-Temperature Superconducting Phase in Clathrate Calcium Hydride CaH₆ up to 215 K at a Pressure of 172 GPa. *Phys. Rev. Lett.* **2022**, *128* (16), 167001. <https://doi.org/10.1103/PhysRevLett.128.167001>.
174. Peña-Alvarez, M.; Binns, J.; Martínez-Canales, M.; Monserrat, B.; Ackland, G. J.; Dalladay-Simpson, P.; Howie, R. T.; Pickard, C. J.; Gregoryanz, E. Synthesis of Weaire–Phelan Barium Polyhydride. *J. Chem. Phys. Lett.* **2021**, *12* (20), 4910–4916. <https://doi.org/10.1021/acs.jpclett.1c00826>.
175. Geballe, Z. M.; Liu, H.; Mishra, A. K.; Ahart, M.; Somayazulu, M.; Meng, Y.; Baldini, M.; Hemley, R. J. Synthesis and Stability of Lanthanum Superhydrides. *Angew. Chem. Int. Ed.* **2018**, *57* (3), 688–692. <https://doi.org/10.1002/anie.201709970>.
176. Zhou, D.; Semenok, D. V.; Xie, H.; Huang, X.; Duan, D.; Aperis, A.; Oppeneer, P. M.; Galasso, M.; Kartsev, A. I.; Kvashnin, A. G.; Oganov, A. R.; Cui, T. High-Pressure Synthesis of Magnetic Neodymium Polyhydrides. *J. Am. Chem. Soc.* **2020**, *142* (6), 2803–2811. <https://doi.org/10.1021/jacs.9b10439>.
177. Peña-Alvarez, M.; Binns, J.; Hermann, A.; Kelsall, L. C.; Dalladay-Simpson, P.; Gregoryanz, E.; Howie, R. T. Praseodymium Polyhydrides Synthesized at High Temperatures and Pressures. *Phys. Rev. B* **2019**, *100* (18), 184109. <https://doi.org/10.1103/PhysRevB.100.184109>.
178. Zhou, D.; Semenok, D. V.; Duan, D.; Xie, H.; Chen, W.; Huang, X.; Li, X.; Liu, B.; Oganov, A. R.; Cui, T. Superconducting Praseodymium Superhydrides. *Sci. Adv.* **2020**, *6* (9), eaax6849. <https://doi.org/10.1126/sciadv.aax6849>.
179. Li, X.; Huang, X.; Duan, D.; Pickard, C. J.; Zhou, D.; Xie, H.; Zhuang, Q.; Huang, Y.; Zhou, Q.; Liu, B.; Cui, T. Polyhydride CeH₉ with an Atomic-like Hydrogen Clathrate Structure. *Nat. Commun.* **2019**, *10* (1), 3461. <https://doi.org/10.1038/s41467-019-11330-6>.
180. Salke, N. P.; Davari Eshfahani, M. M.; Zhang, Y.; Kruglov, I. A.; Zhou, J.; Wang, Y.; Greenberg, E.; Prakapenka, V. B.; Liu, J.; Oganov, A. R.; Lin, J.-F. Synthesis of Clathrate Cerium Superhydride CeH₈ at 80–100 GPa with Atomic Hydrogen Sublattice. *Nat. Commun.* **2019**, *10* (1), 4453. <https://doi.org/10.1038/s41467-019-12326-y>.
181. Semenok, D. V.; Kvashnin, A. G.; Ivanova, A. G.; Svilyk, V.; Fominski, V. Y.; Sadakov, A. V.; Sobolevskiy, O. A.; Pudalov, V. M.; Troyan, I. A.; Oganov, A. R. Superconductivity at 161 K in Thorium Hydride ThH₁₀: Synthesis and Properties. *Mater. Today* **2020**, *33*, 36–44. <https://doi.org/10.1016/j.matmod.2019.10.005>.
182. Chen, W.; Semenok, D. V.; Huang, X.; Shu, H.; Li, X.; Duan, D.; Cui, T.; Oganov, A. R. High-Temperature Superconducting Phases in Cerium Superhydride with a T_c up to 115 K below a Pressure of 1 Megabar. *Phys. Rev. Lett.* **2021**, *127* (11), 117001. <https://doi.org/10.1103/PhysRevLett.127.117001>.
183. Kruglov, I. A.; Kvashnin, A. G.; Goncharov, A. F.; Oganov, A. R.; Lobanov, S. S.; Holtgrewe, N.; Jiang, S.; Prakapenka, V. B.; Greenberg, E.; Yanilkin, A. V. Uranium Polyhydrides at Moderate Pressures: Prediction, Synthesis, and Expected Superconductivity. *Sci. Adv.* **2018**, *4* (10), eaat9776. <https://doi.org/10.1126/sciadv.aat9776>.
184. Guigüe, B.; Marizy, A.; Loubeyre, P. Synthesis of UH₇ and UH₈ Superhydrides: Additive-Volume Alloys of Uranium and Atomic Metal Hydrogen down to 35 GPa. *Phys. Rev. B* **2020**, *102* (1), 014107. <https://doi.org/10.1103/PhysRevB.102.014107>.
185. Bernstein, N.; Stephen Hellberg, C.; Johannes, M. D.; Mazin, I. I.; Mehl, M. J. What Superconducts in Sulfur Hydrides under Pressure and Why. *Phys. Rev. B* **2015**, *91* (6), 060511. <https://doi.org/10.1103/PhysRevB.91.060511>.
186. Goncharov, A. F.; Lobanov, S. S.; Kruglov, I.; Zhao, X.-M.; Chen, X.-J.; Oganov, A. R.; Konôpková, Z.; Prakapenka, V. B. Hydrogen Sulfide at High Pressure: Change in Stoichiometry. *Phys. Rev. B* **2016**, *93* (17), 174105. <https://doi.org/10.1103/PhysRevB.93.174105>.
187. Minkov, V. S.; Prakapenka, V. B.; Greenberg, E.; Eremets, M. I. A Boosted Critical Temperature of 166 K in Superconducting D₃S Synthesized from Elemental Sulfur and Hydrogen. *Angew. Chem. Int. Ed.* **2020**, *59* (43), 18970–18974. <https://doi.org/10.1002/anie.202007091>.
188. Laniel, D.; Winkler, B.; Bykova, E.; Fedotenko, T.; Chariton, S.; Milman, V.; Bykov, M.; Prakapenka, V.; Dubrovinsky, L.; Dubrovinskaya, N. Novel Sulfur Hydrides Synthesized at Extreme Conditions. *Phys. Rev. B* **2020**, *102* (13), 134109. <https://doi.org/10.1103/PhysRevB.102.134109>.
189. Flores-Livas, J. A.; Amsler, M.; Heil, C.; Sanna, A.; Boeri, L.; Profeta, G.; Wolverton, C.; Goedecker, S.; Gross, E. K. U. Superconductivity in Metastable Phases of Phosphorus-Hydride Compounds under High Pressure. *Phys. Rev. B* **2016**, *93* (2), 020508(R). <https://doi.org/10.1103/PhysRevB.93.020508>.
190. Bi, T.; Miller, D. P.; Shamp, A.; Zurek, E. Superconducting Phases of Phosphorus Hydride Under Pressure: Stabilization by Mobile Molecular Hydrogen. *Angew. Chem. Int. Ed.* **2017**, *56* (34), 10192–10195. <https://doi.org/10.1002/anie.201701660>.
191. Shamp, A.; Terpstra, T.; Bi, T.; Falls, Z.; Avery, P.; Zurek, E. Decomposition Products of Phosphine Under Pressure: PH₂ Stable and Superconducting? *J. Am. Chem. Soc.* **2016**, *138* (6), 1884–1892. <https://doi.org/10.1021/jacs.5b10180>.
192. Puhakainen, K.; Benson, D.; Nylén, J.; Konar, S.; Stoyanov, E.; Leinenweber, K.; Häussermann, U. Hypervalent Octahedral SiH₆²⁻ Species from High-Pressure Synthesis. *Angew. Chem. Int. Ed.* **2012**, *51* (13), 3156–3160. <https://doi.org/10.1002/anie.201108713>.
193. Drozdov, A. P.; Kong, P. P.; Minkov, V. S.; Besedin, S. P.; Kuzovnikov, M. A.; Mozaffari, S.; Balicas, L.; Balakirev, F. F.; Graf, D. E.; Prakapenka, V. B.; Greenberg, E.; Knyazev, D. A.; Tkacz, M.; Eremets, M. I. Superconductivity at 250 K in Lanthanum Hydride under High Pressures. *Nature* **2019**, *569* (7757), 528–531. <https://doi.org/10.1038/s41586-019-1201-8>.
194. Horvath-Bordon, E.; Riedel, R.; Zerr, A.; McMillan, P. F.; Auffermann, G.; Prots, Y.; Bronger, W.; Knipr, R.; Kroll, P. High-Pressure Chemistry of Nitride-Based Materials. *Chem. Soc. Rev.* **2006**, *35* (10), 987–1014. <https://doi.org/10.1039/b517778m>.
195. Salamat, A.; Hector, A. L.; Kroll, P.; McMillan, P. F. Nitrogen-Rich Transition Metal Nitrides. *Coord. Chem. Rev.* **2013**, *257* (13–14), 2063–2072. <https://doi.org/10.1016/j.ccr.2013.01.010>.
196. Alkhalidi, H.; Kroll, P. Chemical Potential of Nitrogen at High Pressure and High Temperature: Application to Nitrogen and Nitrogen-Rich Phase Diagram Calculations. *J. Phys. Chem. C* **2019**, *123* (12), 7054–7060. <https://doi.org/10.1021/acs.jpcc.9b00476>.
197. Kurakevych, O. O.; Strobel, T. A.; Kim, D. Y.; Cody, G. D. Synthesis of Mg₂C: A Magnesium Methanide. *Angew. Chem. Int. Ed.* **2013**, *52* (34), 8930–8933. <https://doi.org/10.1002/anie.201303463>.
198. Stefanoski, S.; Liu, H.; Yao, Y.; Strobel, T. A. Ambient-Pressure Polymerization of Carbon Anions in the High-Pressure Phase Mg₂C. *Inorg. Chem.* **2015**, *54* (22), 10761–10765. <https://doi.org/10.1021/acs.inorgchem.5b01780>.
199. Strobel, T. A.; Kurakevych, O. O.; Kim, D. Y.; Le Godec, Y.; Crichton, W.; Guignard, J.; Guignot, N.; Cody, G. D.; Oganov, A. R. Synthesis of β-Mg₂C₃: A Monoclinic High-Pressure Polymorph of Magnesium Sesquicarbide. *Inorg. Chem.* **2014**, *53* (13), 7020–7027. <https://doi.org/10.1021/ic500960d>.
200. Schwarz, M. R.; Antlauf, M.; Schermer, S.; Keller, K.; Schlothauer, T.; Kortus, J.; Heide, G.; Kroke, E. Formation and Properties of Rocksalt-Type AlN and Implications for High Pressure Phase Relations in the System Si–Al–O–N. *High Pressure Res.* **2014**, *34* (1), 22–38. <https://doi.org/10.1080/08957959.2013.857020>.
201. Kawamura, F.; Yamada, N.; Imai, M.; Taniguchi, T. Synthesis of ZnSnN₂ Crystals via a High-Pressure Metathesis Reaction. *Cryst. Res. Technol.* **2016**, *51* (3), 220–224. <https://doi.org/10.1002/crat.201500258>.
202. Kawamura, F.; Imura, M.; Murata, H.; Yamada, N.; Taniguchi, T. Synthesis of a Novel Rocksalt-Type Ternary Nitride Semiconductor MgSnN₂ Using the Metathesis Reaction under High Pressure. *Eur. J. Inorg. Chem.* **2020**, *2020* (5), 446–451. <https://doi.org/10.1002/ejic.201901059>.

203. Hinuma, Y.; Hatakeyama, T.; Kumagai, Y.; Burton, L. A.; Sato, H.; Muraba, Y.; Iimura, S.; Hiramatsu, H.; Tanaka, I.; Hosono, H.; Oba, F. Discovery of Earth-Abundant Nitride Semiconductors by Computational Screening and High-Pressure Synthesis. *Nat. Commun.* **2016**, *7* (1), 11962. <https://doi.org/10.1038/ncomms11962>.
204. Zerr, A.; Mieke, G.; Serghiou, G.; Schwarz, M.; Kroke, E.; Riedel, R.; Fueß, H.; Kroll, P.; Boehler, R. Synthesis of Cubic Silicon Nitride. *Nature* **1999**, *400* (6742), 340–342. <https://doi.org/10.1038/22493>.
205. Schwarz, M.; Mieke, G.; Zerr, A.; Kroke, E.; Poe, B. T.; Fuess, H.; Riedel, R. Spinel-Si₃N₄: Multi-Anvil Press Synthesis and Structural Refinement. *Adv. Mater.* **2000**, *12* (12), 883–887. [https://doi.org/10.1002/1521-4095\(200006\)12:12<883::AID-ADMA883>3.0.CO;2-C](https://doi.org/10.1002/1521-4095(200006)12:12<883::AID-ADMA883>3.0.CO;2-C).
206. Leinenweber, K.; O'Keeffe, M.; Somayazulu, M.; Hubert, H.; McMillan, P. F.; Wolf, G. H. Synthesis and Structure Refinement of the Spinel, γ -Ge₃N₄. *Chem. A Eur. J.* **1999**, *5* (10), 3076–3078. [https://doi.org/10.1002/\(SICI\)1521-3765\(19991001\)5:10<3076::AID-CHEM3076>3.0.CO;2-D](https://doi.org/10.1002/(SICI)1521-3765(19991001)5:10<3076::AID-CHEM3076>3.0.CO;2-D).
207. Vogel, S.; Buda, A. T.; Schnick, W. United in Nitride: The Highly Condensed Boron Phosphorus Nitride BP₃N₆. *Angew. Chem. Int. Ed.* **2018**, *57* (40), 13202–13205. <https://doi.org/10.1002/anie.201808111>.
208. Vogel, S.; Bykov, M.; Bykova, E.; Wendl, S.; Kloß, S. D.; Pakhomova, A.; Chariton, S.; Koemets, E.; Dubrovinskaia, N.; Dubrovinsky, L.; Schnick, W. Boron Phosphorus Nitride at Extremes: PN₆ Octahedra in the High-Pressure Polymorph β -BP₃N₆. *Angew. Chem. Int. Ed.* **2019**, *58* (27), 9060–9063. <https://doi.org/10.1002/anie.201902845>.
209. Vogel, S.; Bykov, M.; Bykova, E.; Wendl, S.; Kloß, S. D.; Pakhomova, A.; Dubrovinskaia, N.; Dubrovinsky, L.; Schnick, W. Nitride Spinel: An Ultracompressible High-Pressure Form of BeP₂N₄. *Angew. Chem. Int. Ed.* **2020**, *59* (7), 2730–2734. <https://doi.org/10.1002/anie.201910998>.
210. Bhat, S.; Lale, A.; Bernard, S.; Zhang, W.; Ishikawa, R.; Haseen, S.; Kroll, P.; Wiehl, L.; Farla, R.; Katsura, T.; Ikuhara, Y.; Riedel, R. Discovery of Ternary Silicon Titanium Nitride with Spinel-Type Structure. *Sci. Rep.* **2020**, *10* (1), 7372. <https://doi.org/10.1038/s41598-020-64101-5>.
211. Landskron, K.; Huppertz, H.; Senker, J.; Schnick, W. High-Pressure Synthesis of γ -P₃N₅ at 11 GPa and 1500 °C in a Multianvil Assembly: A Binary Phosphorus(V) Nitride with a Three-Dimensional Network Structure from PN₄ Tetrahedra and Tetragonal PN₅ Pyramids. *Angew. Chem. Int. Ed.* **2001**, *40* (14), 2643–2645. [https://doi.org/10.1002/1521-3773\(20010716\)40:14<2643::AID-ANIE2643>3.0.CO;2-T](https://doi.org/10.1002/1521-3773(20010716)40:14<2643::AID-ANIE2643>3.0.CO;2-T).
212. Marchuk, A.; Pucher, F. J.; Karau, F. W.; Schnick, W. A High-Pressure Polymorph of Phosphorus Nitride Imide. *Angew. Chem. Int. Ed.* **2014**, *53* (9), 2469–2472. <https://doi.org/10.1002/anie.201309020>.
213. Baumann, D.; Schnick, W. High-Pressure Polymorph of Phosphorus Nitride Imide HP₄N₇ Representing a New Framework Topology. *Inorg. Chem.* **2014**, *53* (15), 7977–7982. <https://doi.org/10.1021/ic500767f>.
214. Vogel, S.; Buda, A. T.; Schnick, W. Rivalry under Pressure: The Coexistence of Ambient-Pressure Motifs and Close-Packing in Silicon Phosphorus Nitride Imide SiP₂N₄NH. *Angew. Chem. Int. Ed.* **2019**, *58* (11), 3398–3401. <https://doi.org/10.1002/anie.201813789>.
215. Mikulski, C. M.; Russo, P. J.; Saran, M. S.; MacDiarmid, A. G.; Garito, A. F.; Heeger, A. J. Synthesis and Structure of Metallic Polymeric Sulfur Nitride, (SN)_x, and Its Precursor, Disulfur Dinitride, S₂N₂. *J. Am. Chem. Soc.* **1975**, *97* (22), 6358–6363. <https://doi.org/10.1021/ja00855a012>.
216. Laniel, D.; Bykov, M.; Fedotenko, T.; Ponomareva, A. V.; Abrikosov, I. A.; Glazyrin, K.; Svitylyk, V.; Dubrovinsky, L.; Dubrovinskaia, N. High Pressure Investigation of the S–N₂ System up to the Megabar Range: Synthesis and Characterization of the SN₂ Solid. *Inorg. Chem.* **2019**, *58* (14), 9195–9204. <https://doi.org/10.1021/acs.inorgchem.9b00830>.
217. Zerr, A.; Mieke, G.; Riedel, R. Synthesis of Cubic Zirconium and Hafnium Nitride Having Th₃P₄ Structure. *Nat. Mater.* **2003**, *2* (3), 185–189. <https://doi.org/10.1038/nmat836>.
218. Taniguchi, T.; Dzivenko, D.; Riedel, R.; Chauveau, T.; Zerr, A. Synthesis of Cubic Zirconium(IV) Nitride, c-Zr₃N₄, in the 6–8 GPa Pressure Region. *Ceram. Int.* **2019**, *45* (16), 20028–20032. <https://doi.org/10.1016/j.ceramint.2019.06.263>.
219. Bhadram, V. S.; Liu, H.; Xu, E.; Li, T.; Prakash, V. B.; Hrubik, R.; Lany, S.; Strobel, T. A. Semiconducting Cubic Titanium Nitride in the Th₃P₄ Structure. *Phys. Rev. Mater.* **2018**, *2* (1), 011602. <https://doi.org/10.1103/PhysRevMaterials.2.011602>.
220. Salamat, A.; Woodhead, K.; Shah, S. I. U.; Hector, A. L.; McMillan, P. F. Synthesis of U₃Se₅ and U₃Te₅ Type Polymorphs of Ta₃N₅ by Combining High Pressure–Temperature Pathways with a Chemical Precursor Approach. *Chem. Commun.* **2014**, *50* (70), 10041–10044. <https://doi.org/10.1039/C4CC05147E>.
221. Zerr, A.; Mieke, G.; Li, J.; Dzivenko, D. A.; Bulatov, V. K.; Höfer, H.; Bolfan-Casanova, N.; Fialin, M.; Brey, G.; Watanabe, T.; Yoshimura, M. High-Pressure Synthesis of Tantalum Nitride Having Orthorhombic U₂S₃ Structure. *Adv. Funct. Mater.* **2009**, *19* (14), 2282–2288. <https://doi.org/10.1002/adfm.200801923>.
222. Lei, L.; Yin, W.; Jiang, X.; Lin, S.; He, D. Synthetic Route to Metal Nitrides: High-Pressure Solid-State Metathesis Reaction. *Inorg. Chem.* **2013**, *52* (23), 13356–13362. <https://doi.org/10.1021/ic401483a>.
223. Chen, M.; Wang, S.; Zhang, J.; He, D.; Zhao, Y. Synthesis of Stoichiometric and Bulk CrN Through a Solid-State Ion-Exchange Reaction. *Chem. A Eur. J.* **2012**, *18* (48), 15459–15463. <https://doi.org/10.1002/chem.201202197>.
224. Wang, S.; Yu, X.; Lin, Z.; Zhang, R.; He, D.; Qin, J.; Zhu, J.; Han, J.; Wang, L.; Mao, H.; Zhang, J.; Zhao, Y. Synthesis, Crystal Structure, and Elastic Properties of Novel Tungsten Nitrides. *Chem. Mater.* **2012**, *24* (15), 3023–3028. <https://doi.org/10.1021/cm301516w>.
225. Wang, S.; Antonio, D.; Yu, X.; Zhang, J.; Cornelius, A. L.; He, D.; Zhao, Y. The Hardest Superconducting Metal Nitride. *Sci. Rep.* **2015**, *5* (1), 13733. <https://doi.org/10.1038/srep13733>.
226. Wang, S.; Ge, H.; Sun, S.; Zhang, J.; Liu, F.; Wen, X.; Yu, X.; Wang, L.; Zhang, Y.; Xu, H.; Neuefeind, J. C.; Qin, Z.; Chen, C.; Jin, C.; Li, Y.; He, D.; Zhao, Y. A New Molybdenum Nitride Catalyst with Rhombohedral MoS₂ Structure for Hydrogenation Applications. *J. Am. Chem. Soc.* **2015**, *137* (14), 4815–4822. <https://doi.org/10.1021/jacs.5b01446>.
227. Wang, C.; Tao, Q.; Dong, S.; Wang, X.; Zhu, P. Synthesis and Mechanical Character of Hexagonal Phase δ -WN. *Inorg. Chem.* **2017**, *56* (7), 3970–3975. <https://doi.org/10.1021/acs.inorgchem.6b03041>.
228. Kawamura, F.; Yusa, H.; Taniguchi, T. Synthesis of Rhenium Nitride Crystals with MoS₂ Structure. *Appl. Phys. Lett.* **2012**, *100* (25), 251910. <https://doi.org/10.1063/1.4729586>.
229. Niewa, R.; Jacobs, H. Group V and VI Alkali Nitridometalates: A Growing Class of Compounds with Structures Related to Silicate Chemistry. *Chem. Rev.* **1996**, *96* (6), 2053–2062. <https://doi.org/10.1021/cr9405157>.
230. Kloß, S. D.; Haffner, A.; Manuel, P.; Goto, M.; Shimakawa, Y.; Atfield, J. P. Preparation of Iron(IV) Nitridoferrate Ca₄FeN₄ Through Azide-Mediated Oxidation Under High-Pressure Conditions. *Nat. Commun.* **2021**, *12* (1), 571. <https://doi.org/10.1038/s41467-020-20881-y>.
231. Kloß, S. D.; Weidemann, M. L.; Atfield, J. P. Preparation of Bulk-Phase Nitride Perovskite LaReN₃ and Topotactic Reduction to LaNiO₂-Type LaReN₂. *Angew. Chem. Int. Ed.* **2021**, *60* (41), 22260–22264. <https://doi.org/10.1002/anie.202108759>.
232. Auffermann, G.; Prots, Y.; Kniep, R. SrN and SrN₂: Diazenides by Synthesis under High N₂-Pressure. *Angew. Chem. Int. Ed.* **2001**, *40* (3), 547–549. [https://doi.org/10.1002/1521-3773\(20010202\)40:3<547::AID-ANIE547>3.0.CO;2-X](https://doi.org/10.1002/1521-3773(20010202)40:3<547::AID-ANIE547>3.0.CO;2-X).
233. Schneider, S. B.; Frankovsky, R.; Schnick, W. Synthesis of Alkaline Earth Diazenides M_{AE}N₂ (M_{AE} = Ca, Sr, Ba) by Controlled Thermal Decomposition of Azides Under High Pressure. *Inorg. Chem.* **2012**, *51* (4), 2366–2373. <https://doi.org/10.1021/ic2023677>.
234. Schneider, S. B.; Frankovsky, R.; Schnick, W. High-Pressure Synthesis and Characterization of the Alkali Diazenide Li₂N₂. *Angew. Chem. Int. Ed.* **2012**, *51* (8), 1873–1875. <https://doi.org/10.1002/anie.201108252>.
235. Schneider, S. B.; Seibald, M.; Deringer, V. L.; Stoffel, R. P.; Frankovsky, R.; Friederichs, G. M.; Laqua, H.; Duppel, V.; Jeschke, G.; Dronskowski, R.; Schnick, W. High-Pressure Synthesis and Characterization of Li₂Ca₃[N₂]₃—An Uncommon Metallic Diazenide with [N₂]²⁻ Ions. *J. Am. Chem. Soc.* **2013**, *135* (44), 16668–16679. <https://doi.org/10.1021/ja408816t>.
236. Laniel, D.; Weck, G.; Loubeyre, P. Direct Reaction of Nitrogen and Lithium up to 75 GPa: Synthesis of the Li₃N, LiN, LiN₂, and LiN₅ Compounds. *Inorg. Chem.* **2018**, *57* (17), 10685–10693. <https://doi.org/10.1021/acs.inorgchem.8b01325>.

237. Bykov, M.; Tasca, K. R.; Batyrev, I. G.; Smith, D.; Glazyrin, K.; Chariton, S.; Mahmood, M.; Goncharov, A. F. Dinitrogen as a Universal Electron Acceptor in Solid-State Chemistry: An Example of Uncommon Metallic Compounds $\text{Na}_3(\text{N}_2)_4$ and NaN_2 . *Inorg. Chem.* **2020**, *59* (20), 14819–14826. <https://doi.org/10.1021/acs.inorgchem.0c01863>.
238. Crowhurst, J. C.; Goncharov, A. F.; Sadigh, B.; Evans, C. L.; Morrall, P. G.; Ferreira, J. L.; Nelson, A. J. Synthesis and Characterization of the Nitrides of Platinum and Iridium. *Science* **2006**, *311* (5765), 1275–1278. <https://doi.org/10.1126/science.1121813>.
239. Young, A. F.; Sanloup, C.; Gregoryanz, E.; Scandolo, S.; Hemley, R. J.; Mao, H. Synthesis of Novel Transition Metal Nitrides IrN_2 and OsN_2 . *Phys. Rev. Lett.* **2006**, *96* (15), 155501. <https://doi.org/10.1103/PhysRevLett.96.155501>.
240. Crowhurst, J. C.; Goncharov, A. F.; Sadigh, B.; Zaug, J. M.; Aberg, D.; Meng, Y.; Prakapenka, V. B. Synthesis and Characterization of Nitrides of Iridium and Palladium. *J. Mater. Res.* **2008**, *23* (1), 1–5. <https://doi.org/10.1557/JMR.2008.0027>.
241. Niwa, K.; Suzuki, K.; Muto, S.; Tatsumi, K.; Soda, K.; Kikegawa, T.; Hasegawa, M. Discovery of the Last Remaining Binary Platinum-Group Pernitride RuN_2 . *Chem. A Eur. J.* **2014**, *20* (43), 13885–13888. <https://doi.org/10.1002/chem.201404165>.
242. Niwa, K.; Dzivenko, D.; Suzuki, K.; Riedel, R.; Troyan, I.; Eremets, M.; Hasegawa, M. High Pressure Synthesis of Marcasite-Type Rhodium Pernitride. *Inorg. Chem.* **2014**, *53* (2), 697–699. <https://doi.org/10.1021/ic402885k>.
243. Bhadram, V. S.; Kim, D. Y.; Strobel, T. A. High-Pressure Synthesis and Characterization of Incompressible Titanium Pernitride. *Chem. Mater.* **2016**, *28* (6), 1616–1620. <https://doi.org/10.1021/acs.chemmater.6b00042>.
244. Niwa, K.; Terabe, T.; Kato, D.; Takayama, S.; Kato, M.; Soda, K.; Hasegawa, M. Highly Coordinated Iron and Cobalt Nitrides Synthesized at High Pressures and High Temperatures. *Inorg. Chem.* **2017**, *56* (11), 6410–6418. <https://doi.org/10.1021/acs.inorgchem.7b00516>.
245. Laniel, D.; Dewaele, A.; Garbarino, G. High Pressure and High Temperature Synthesis of the Iron Pernitride FeN_2 . *Inorg. Chem.* **2018**, *57* (11), 6245–6251. <https://doi.org/10.1021/acs.inorgchem.7b03272>.
246. Niwa, K.; Fukui, R.; Terabe, T.; Kawada, T.; Kato, D.; Sasaki, T.; Soda, K.; Hasegawa, M. High-Pressure Synthesis and Phase Stability of Nickel Pernitride. *Eur. J. Inorg. Chem.* **2019**, *2019* (33), 3753–3757. <https://doi.org/10.1002/ejic.201900489>.
247. Niwa, K.; Yamamoto, T.; Sasaki, T.; Hasegawa, M. High-Pressure Synthesis, Crystal Growth, and Compression Behavior of Hexagonal CrN_2 Having One-Dimensionally Aligned Nitrogen Dimer. *Phys. Rev. Mater.* **2019**, *3* (5), 053601. <https://doi.org/10.1103/PhysRevMaterials.3.053601>.
248. Binns, J.; Donnelly, M.-E.; Peña-Alvarez, M.; Wang, M.; Gregoryanz, E.; Herrmann, A.; Dalladay-Simpson, P.; Howie, R. T. Direct Reaction Between Copper and Nitrogen at High Pressures and Temperatures. *J. Phys. Chem. Lett.* **2019**, *10* (5), 1109–1114. <https://doi.org/10.1021/acs.jpclett.9b00070>.
249. Bykov, M.; Yuseenko, K. V.; Bykova, E.; Pakhomova, A.; Kraus, W.; Dubrovinskaja, N.; Dubrovinsky, L. Synthesis of Arsenopyrite-Type Rhodium Pernitride RhN_2 from a Single-Source Azide Precursor. *Eur. J. Inorg. Chem.* **2019**, *2019* (32), 3667–3671. <https://doi.org/10.1002/ejic.201900488>.
250. Yu, R.; Zhan, Q.; De Jonghe, L. C. Crystal Structures of and Displacive Transitions in OsN_2 , IrN_2 , RuN_2 , and RhN_2 . *Angew. Chem. Int. Ed.* **2007**, *46* (7), 1136–1140. <https://doi.org/10.1002/anie.200604151>.
251. Bykov, M.; Bykova, E.; Ponomareva, A. V.; Tasnádi, F.; Chariton, S.; Prakapenka, V. B.; Glazyrin, K.; Smith, J. S.; Mahmood, M. F.; Abrikosov, I. A.; Goncharov, A. F. Realization of an Ideal Cairo Tessellation in Nickel Diazenide NiN_2 : High-Pressure Route to Pentagonal 2D Materials. *ACS Nano* **2021**, *15* (8), 13539–13546. <https://doi.org/10.1021/acsnano.1c04325>.
252. Bykov, M.; Chariton, S.; Fei, H.; Fedotenko, T.; Aprilis, G.; Ponomareva, A. V.; Tasnádi, F.; Abrikosov, I. A.; Merle, B.; Feldner, P.; Vogel, S.; Schnick, W.; Prakapenka, V. B.; Greenberg, E.; Hanfland, M.; Pakhomova, A.; Liermann, H.-P.; Katsura, T.; Dubrovinskaja, N.; Dubrovinsky, L. High-Pressure Synthesis of Ultracompressible Hard Rhenium Nitride Pernitride $\text{Re}_2(\text{N}_2)(\text{N}_2)$ Stable at Ambient Conditions. *Nat. Commun.* **2019**, *10* (1), 2994. <https://doi.org/10.1038/s41467-019-10995-3>.
253. Niwa, K.; Ogasawara, H.; Hasegawa, M. Pyrite Form of Group-14 Element Pernitrides Synthesized at High Pressure and High Temperature. *Dalton Trans.* **2017**, *46* (30), 9750–9754. <https://doi.org/10.1039/C7DT01583F>.
254. Yang, X.; Wang, X.; Wang, Y.; Li, K.; Zheng, H. From Molecules to Carbon Materials—High Pressure Induced Polymerization and Bonding Mechanisms of Unsaturated Compounds. *Crystals* **2019**, *9* (10), 490. <https://doi.org/10.3390/cryst9100490>.
255. Ward, M. D.; Huang, H.-T.; Zhu, L.; Popov, D.; Strobel, T. A. High-Pressure Behavior of C_{22} and Polymerization to a Conductive Polymer. *J. Phys. Chem. C* **2019**, *123* (18), 11369–11377. <https://doi.org/10.1021/acs.jpcc.8b12161>.
256. Fitzgibbons, T. C.; Guthrie, M.; Xu, E.; Crespi, V. H.; Davidowski, S. K.; Cody, G. D.; Alem, N.; Badding, J. V. Benzene-Derived Carbon Nanotubes. *Nat. Mater.* **2015**, *14* (1), 43–47. <https://doi.org/10.1038/nmat4088>.
257. Li, X.; Baldini, M.; Wang, T.; Chen, B.; Xu, E.; Vermilyea, B.; Crespi, V. H.; Hoffmann, R.; Molaison, J. J.; Tulk, C. A.; Guthrie, M.; Sinogeikin, S.; Badding, J. V. Mechanochemical Synthesis of Carbon Nanotube Single Crystals. *J. Am. Chem. Soc.* **2017**, *139* (45), 16343–16349. <https://doi.org/10.1021/jacs.7b09311>.
258. Juhl, S. J.; Wang, T.; Vermilyea, B.; Li, X.; Crespi, V. H.; Badding, J. V.; Alem, N. Local Structure and Bonding of Carbon Nanotubes Probed by High-Resolution Transmission Electron Microscopy. *J. Am. Chem. Soc.* **2019**, *141* (17), 6937–6945. <https://doi.org/10.1021/jacs.8b13405>.
259. Friedrich, A.; Collings, I. E.; Dziubek, K. F.; Fanetti, S.; Radacki, K.; Ruiz-Fuertes, J.; Pellicer-Porres, J.; Hanfland, M.; Sieh, D.; Bini, R.; Clark, S. J.; Marder, T. B. Pressure-Induced Polymerization of Polycyclic Arene—Perfluoroarene Cocrystals: Single Crystal X-Ray Diffraction Studies, Reaction Kinetics, and Design of Columnar Hydrofluorocarbons. *J. Am. Chem. Soc.* **2020**, *142* (44), 18907–18923. <https://doi.org/10.1021/jacs.0c09021>.
260. Nylén, J.; Konar, S.; Lazor, P.; Benson, D.; Häussermann, U. Structural Behavior of the Acetylide Carbides Li_2C_2 and CaC_2 at High Pressure. *J. Chem. Phys.* **2012**, *137* (22), 224507. <https://doi.org/10.1063/1.4770268>.
261. Efthimiopoulos, I.; Kunc, K.; Vazhenin, G. V.; Stavrou, E.; Syassen, K.; Hanfland, M.; Liebig, S.; Ruschewitz, U. Structural Transformation and Vibrational Properties of BaC_2 at High Pressure. *Phys. Rev. B* **2012**, *85* (5), 054105. <https://doi.org/10.1103/PhysRevB.85.054105>.
262. Han, J.; Tang, X.; Wang, Y.; Wang, Y.; Han, Y.; Lin, X.; Dong, X.; Lee, H. H.; Zheng, H.; Li, K.; Mao, H. Pressure-Induced Polymerization of Monosodium Acetylide: A Radical Reaction Initiated Topochemically. *J. Phys. Chem. C* **2019**, *123* (50), 30746–30753. <https://doi.org/10.1021/acs.jpcc.9b09698>.
263. Guo, Y.; Yu, C.; Lin, J.; Wang, C.; Ren, C.; Sun, B.; Huai, P.; Xie, R.; Ke, X.; Zhu, Z.; Xu, H. Pressure-Induced Structural Transformations and Polymerization in ThC_2 . *Sci. Rep.* **2017**, *7* (1), 45872. <https://doi.org/10.1038/srep45872>.
264. Dong, X.; Wang, L.; Li, K.; Zheng, H.; Wang, Y.; Meng, Y.; Shu, H.; Mao, H.; Feng, S.; Jin, C. Tailored Synthesis of the Narrowest Zigzag Graphene Nanoribbon Structure by Compressing the Lithium Acetylide under High Temperature. *J. Phys. Chem. C* **2018**, *122* (35), 20506–20512. <https://doi.org/10.1021/acs.jpcc.8b04081>.
265. Zheng, H.; Wang, L.; Li, K.; Yang, Y.; Dong, X.; Wang, C.-H.; Tulk, C. A.; Molaison, J. J.; Ivanov, I. N.; Feyngenson, M.; Yang, W.; Guthrie, M.; Zhao, Y.; Mao, H.-K.; Jin, C. Pressure Induced Polymerization of Acetylide Anions in CaC_2 and 10^7 Fold Enhancement of Electrical Conductivity. *Chem. Sci.* **2017**, *8* (1), 298–304. <https://doi.org/10.1039/C6SC02830F>.
266. Li, Y.-L.; Wang, S.-N.; Oganov, A. R.; Gou, H.; Smith, J. S.; Strobel, T. A. Investigation of Exotic Stable Calcium Carbides Using Theory and Experiment. *Nat. Commun.* **2015**, *6* (1), 6974. <https://doi.org/10.1038/ncomms7974>.
267. Wang, L.; Dong, X.; Wang, Y.; Zheng, H.; Li, K.; Peng, X.; Mao, H.; Jin, C.; Meng, Y.; Huang, M.; Zhao, Z. Pressure-Induced Polymerization and Disproportionation of Li_2C_2 Accompanied with Irreversible Conductivity Enhancement. *J. Phys. Chem. Lett.* **2017**, *8* (17), 4241–4245. <https://doi.org/10.1021/acs.jpclett.7b01779>.
268. Liu, A. Y.; Cohen, M. L. Prediction of New Low Compressibility Solids. *Science* **1989**, *245* (4920), 841–842. <https://doi.org/10.1126/science.245.4920.841>.
269. McMillan, P. F. New Nitrides: From High Pressure–High Temperature Synthesis to Layered Nanomaterials and Energy Applications. *Philos. Trans. R. Soc. A* **2019**, *377* (2147), 20180244. <https://doi.org/10.1098/rsta.2018.0244>.
270. Horvath-Bordon, E.; Riedel, R.; McMillan, P. F.; Kroll, P.; Mieke, G.; van Aken, P. A.; Zerr, A.; Hoppe, P.; Shebanova, O.; McLaren, I.; Lauterbach, S.; Kroke, E.; Boehler, R. High-Pressure Synthesis of Crystalline Carbon Nitride Imide, $\text{C}_2\text{N}_2(\text{NH})$. *Angew. Chem. Int. Ed.* **2007**, *46* (9), 1476–1480. <https://doi.org/10.1002/anie.200603851>.

271. Salamat, A.; Deifallah, M.; Quesada Cabrera, R.; Corà, F.; McMillan, P. F. Identification of New Pillared-Layered Carbon Nitride Materials at High Pressure. *Sci. Rep.* **2013**, *3* (1), 2122. <https://doi.org/10.1038/srep02122>.
272. Pickard, C. J.; Salamat, A.; Bojdys, M. J.; Needs, R. J.; McMillan, P. F. Carbon Nitride Frameworks and Dense Crystalline Polymorphs. *Phys. Rev. B* **2016**, *94* (9), 094104. <https://doi.org/10.1103/PhysRevB.94.094104>.
273. Keefer, D. W.; Gou, H.; Wang, Q.; Purdy, A.; Epshteyn, A.; Juhl, S. J.; Cody, G. D.; Badding, J.; Strobel, T. A. Tetracyanomethane Under Pressure: Extended CN Polymers from Precursors with Built-in sp^3 Centers. *J. Phys. Chem. A* **2018**, *122* (11), 2858–2863. <https://doi.org/10.1021/acs.jpca.7b10729>.
274. Li, X.; Wang, T.; Duan, P.; Baldini, M.; Huang, H.-T.; Chen, B.; Juhl, S. J.; Koeplinger, D.; Crespi, V. H.; Schmidt-Rohr, K.; Hoffmann, R.; Alem, N.; Guthrie, M.; Zhang, X.; Badding, J. V. Carbon Nitride Nanowire Crystals Derived from Pyridine. *J. Am. Chem. Soc.* **2018**, *140* (15), 4969–4972. <https://doi.org/10.1021/jacs.7b13247>.
275. Wang, Q.; Gou, H.; Zhu, L.; Huang, H.-T.; Biswas, A.; Chaloux, B. L.; Epshteyn, A.; Yesinowski, J. P.; Liu, Z.; Cody, G.; Ma, M.; Zhao, Z.; Fei, Y.; Prescher, C.; Greenberg, E.; Prakash, V. B.; Strobel, T. A. Modifying Carbon Nitride Through Extreme Phosphorus Substitution. *ACS Mater. Lett.* **2019**, *1* (1), 14–19. <https://doi.org/10.1021/acsmaterlett.9b00010>.
276. Chen, J.-Y.; Yoo, C.-S. Physical and Chemical Transformations of Sodium Cyanide at High Pressures. *J. Chem. Phys.* **2009**, *131* (14), 144507. <https://doi.org/10.1063/1.3245861>.
277. Keefer, D. W.; Gou, H.; Purdy, A. P.; Epshteyn, A.; Kim, D. Y.; Badding, J. V.; Strobel, T. A. Pressure-Induced Polymerization of $\text{LiN}(\text{CN})_2$. *J. Phys. Chem. A* **2016**, *120* (47), 9370–9377. <https://doi.org/10.1021/acs.jpca.6b06780>.
278. Eremets, M. I.; Gavriluk, A. G.; Trojan, I. A.; Dzivenko, D. A.; Boehler, R. Single-Bonded Cubic Form of Nitrogen. *Nat. Mater.* **2004**, *3* (8), 558–563. <https://doi.org/10.1038/nmat1146>.
279. Laniel, D.; Winkler, B.; Fedotenko, T.; Pakhomova, A.; Chariton, S.; Milman, V.; Prakash, V.; Dubrovinsky, L.; Dubrovinskaia, N. High-Pressure Polymeric Nitrogen Allotrope with the Black Phosphorus Structure. *Phys. Rev. Lett.* **2020**, *124* (21), 216001. <https://doi.org/10.1103/PhysRevLett.124.216001>.
280. Li, Y.; Feng, X.; Liu, H.; Hao, J.; Redfern, S. A. T.; Lei, W.; Liu, D.; Ma, Y. Route to High-Energy Density Polymeric Nitrogen *t*-N via He–N Compounds. *Nat. Commun.* **2018**, *9* (1), 722. <https://doi.org/10.1038/s41467-018-03200-4>.
281. Laniel, D.; Winkler, B.; Koemets, E.; Fedotenko, T.; Bykov, M.; Bykova, E.; Dubrovinsky, L.; Dubrovinskaia, N. Synthesis of Magnesium-Nitrogen Salts of Polynitrogen Anions. *Nat. Commun.* **2019**, *10* (1), 4515. <https://doi.org/10.1038/s41467-019-12530-w>.
282. Bykov, M.; Fedotenko, T.; Chariton, S.; Laniel, D.; Glazyrin, K.; Hanfland, M.; Smith, J. S.; Prakash, V. B.; Mahmood, M. F.; Goncharov, A. F.; Ponomareva, A. V.; Tasnádi, F.; Abrikosov, I. A.; Bin Masood, T.; Hotz, I.; Rudenko, A. N.; Katsnelson, M. I.; Dubrovinskaia, N.; Dubrovinsky, L.; Abrikosov, I. A. High-Pressure Synthesis of Dirac Materials: Layered van Der Waals Bonded BeN_4 Polymorph. *Phys. Rev. Lett.* **2021**, *126* (17), 175501. <https://doi.org/10.1103/PhysRevLett.126.175501>.
283. Steele, B. A.; Stavrou, E.; Crowhurst, J. C.; Zaug, J. M.; Prakash, V. B.; Oleynik, I. I. High-Pressure Synthesis of a Pentazolate Salt. *Chem. Mater.* **2017**, *29* (2), 735–741. <https://doi.org/10.1021/acs.chemmater.6b04538>.
284. Laniel, D.; Weck, G.; Gaiffe, G.; Garbarino, G.; Loubeyre, P. High-Pressure Synthesized Lithium Pentazolate Compound Metastable Under Ambient Conditions. *J. Phys. Chem. Lett.* **2018**, *9* (7), 1600–1604. <https://doi.org/10.1021/acs.jpclett.8b00540>.
285. Bykov, M.; Bykova, E.; Chariton, S.; Prakash, V. B.; Batyrev, I. G.; Mahmood, M. F.; Goncharov, A. F. Stabilization of Pentazolate Anions in the High-Pressure Compounds Na_2N_5 and NaN_5 and in the Sodium Pentazolate Framework $\text{NaN}_5\cdot\text{N}_2$. *Dalton Trans.* **2021**, *50* (21), 7229–7237. <https://doi.org/10.1039/D1DT00722J>.
286. Xu, Y.; Wang, Q.; Shen, C.; Lin, Q.; Wang, P.; Lu, M. A Series of Energetic Metal Pentazolate Hydrates. *Nature* **2017**, *549* (7670), 78–81. <https://doi.org/10.1038/nature23662>.
287. Zhang, W.; Wang, K.; Li, J.; Lin, Z.; Song, S.; Huang, S.; Liu, Y.; Nie, F.; Zhang, Q. Stabilization of the Pentazolate Anion in a Zeolitic Architecture with $\text{Na}_{20}\text{N}_{60}$ and $\text{Na}_{24}\text{N}_{60}$ Nanocages. *Angew. Chem. Int. Ed.* **2018**, *57* (10), 2592–2595. <https://doi.org/10.1002/anie.201710602>.
288. Bykov, M.; Bykova, E.; Koemets, E.; Fedotenko, T.; Aprilis, G.; Glazyrin, K.; Liermann, H.-P.; Ponomareva, A. V.; Tidholm, J.; Tasnádi, F.; Abrikosov, I. A.; Dubrovinskaia, N.; Dubrovinsky, L. High-Pressure Synthesis of a Nitrogen-Rich Inclusion Compound $\text{ReN}_x\cdot x\text{N}_2$ with Conjugated Polymeric Nitrogen Chains. *Angew. Chem. Int. Ed.* **2018**, *57* (29), 9048–9053. <https://doi.org/10.1002/anie.201805152>.
289. Bykov, M.; Chariton, S.; Bykova, E.; Khandarkhaeva, S.; Fedotenko, T.; Ponomareva, A. V.; Tidholm, J.; Tasnádi, F.; Abrikosov, I. A.; Sedmak, P.; Prakash, V.; Hanfland, M.; Liermann, H.; Mahmood, M.; Goncharov, A. F.; Dubrovinskaia, N.; Dubrovinsky, L. High-Pressure Synthesis of Metal-Inorganic Frameworks $\text{Hf}_4\text{N}_{20}\cdot\text{N}_2$, $\text{WN}_8\cdot\text{N}_2$, and $\text{Os}_5\text{N}_{28}\cdot 3\text{N}_2$ with Polymeric Nitrogen Linkers. *Angew. Chem. Int. Ed.* **2020**, *59* (26), 10321–10326. <https://doi.org/10.1002/anie.202002487>.
290. Bykov, M.; Bykova, E.; Aprilis, G.; Glazyrin, K.; Koemets, E.; Chuvashova, I.; Kuppenko, I.; McCammon, C.; Mezouar, M.; Prakash, V.; Liermann, H.-P.; Tasnádi, F.; Ponomareva, A. V.; Abrikosov, I. A.; Dubrovinskaia, N.; Dubrovinsky, L. Fe-N System at High Pressure Reveals a Compound Featuring Polymeric Nitrogen Chains. *Nat. Commun.* **2018**, *9* (1), 2756. <https://doi.org/10.1038/s41467-018-05143-2>.
291. Salke, N. P.; Xia, K.; Fu, S.; Zhang, Y.; Greenberg, E.; Prakash, V. B.; Liu, J.; Sun, J.; Lin, J.-F. Tungsten Hexanitride with Single-Bonded Armchairlike Hexazine Structure at High Pressure. *Phys. Rev. Lett.* **2021**, *126* (6), 065702. <https://doi.org/10.1103/PhysRevLett.126.065702>.
292. Bykov, M.; Bykova, E.; Ponomareva, A. V.; Abrikosov, I. A.; Chariton, S.; Prakash, V. B.; Mahmood, M. F.; Dubrovinsky, L.; Goncharov, A. F. Stabilization of Polynitrogen Anions in Tantalum–Nitrogen Compounds at High Pressure. *Angew. Chem. Int. Ed.* **2021**, *60* (16), 9003–9008. <https://doi.org/10.1002/anie.202100283>.
293. Rodgers, J. A.; Williams, A. J.; Atfield, J. P. High-Pressure/High-Temperature Synthesis of Transition Metal Oxide Perovskites. *Z. Naturforsch. B* **2006**, *61* (12), 1515–1526. <https://doi.org/10.1515/znb-2006-1208>.
294. Demazeau, G.; Baranov, A.; Presniakov, I.; Sobolev, A. High Oxygen Pressures and the Stabilization of the Highest Oxidation States of Transition Metals—Mössbauer Spectroscopic Characterization of the Induced Electronic Phenomena. *Z. Naturforsch. B* **2006**, *61* (12), 1527–1540. <https://doi.org/10.1515/znb-2006-1209>.
295. Jin, C. Q. Using Pressure Effects to Create New Emergent Materials by Design. *MRS Adv.* **2017**, *2* (48), 2587–2596. <https://doi.org/10.1557/adv.2017.495>.
296. Evans, W. J.; Lipp, M. J.; Yoo, C.-S.; Cynn, H.; Herberg, J. L.; Maxwell, R. S.; Nicol, M. F. Pressure-Induced Polymerization of Carbon Monoxide: Disproportionation and Synthesis of an Energetic Lactonic Polymer. *Chem. Mater.* **2006**, *18* (10), 2520–2531. <https://doi.org/10.1021/cm0524446>.
297. Ryu, Y.-J.; Kim, M.; Lim, J.; Dias, R.; Klug, D.; Yoo, C.-S. Dense Carbon Monoxide to 160 GPa: Stepwise Polymerization to Two-Dimensional Layered Solid. *J. Phys. Chem. C* **2016**, *120* (48), 27548–27554. <https://doi.org/10.1021/acs.jpcc.6b09434>.
298. Xia, K.; Sun, J.; Pickard, C. J.; Klug, D. D.; Needs, R. J. Ground State Structure of High-Energy-Density Polymeric Carbon Monoxide. *Phys. Rev. B* **2017**, *95* (14), 144102. <https://doi.org/10.1103/PhysRevB.95.144102>.
299. Santoro, M.; Gorelli, F. A.; Bini, R.; Ruocco, G.; Scandolo, S.; Crichton, W. A. Amorphous Silica-Like Carbon Dioxide. *Nature* **2006**, *441* (7095), 857–860. <https://doi.org/10.1038/nature04879>.
300. Iota, V.; Yoo, C. S.; Cynn, H. Quartzlike Carbon Dioxide: An Optically Nonlinear Extended Solid at High Pressures and Temperatures. *Science* **1999**, *283* (5407), 1510–1513. <https://doi.org/10.1126/science.283.5407.1510>.
301. Zhang, H.; Tóth, O.; Liu, X.-D.; Bini, R.; Gregoryanz, E.; Dalladay-Simpson, P.; Panfilis, S. D.; Santoro, M.; Gorelli, F. A.; Martoňák, R. Pressure-Induced Amorphization and Existence of Molecular and Polymeric Amorphous Forms in Dense SO_2 . *Proc. Natl. Acad. Sci. U. S. A.* **2020**, *117* (16), 8736–8742. <https://doi.org/10.1073/pnas.1917749117>.
302. Datchi, F.; Mallick, B.; Salamat, A.; Ninet, S. Structure of Polymeric Carbon Dioxide $\text{CO}_2\cdot\text{V}$. *Phys. Rev. Lett.* **2012**, *108* (12), 125701. <https://doi.org/10.1103/PhysRevLett.108.125701>.
303. Dziubek, K. F.; Ende, M.; Scelta, D.; Bini, R.; Mezouar, M.; Garbarino, G.; Miletich, R. Crystalline Polymeric Carbon Dioxide Stable at Megabar Pressures. *Nat. Commun.* **2018**, *9* (1), 3148. <https://doi.org/10.1038/s41467-018-05593-8>.
304. Santoro, M.; Gorelli, F.; Haines, J.; Cambon, O.; Levelut, C.; Garbarino, G. Silicon Carbonate Phase Formed from Carbon Dioxide and Silica under Pressure. *Proc. Natl. Acad. Sci. U. S. A.* **2011**, *108* (19), 7689–7692. <https://doi.org/10.1073/pnas.1019691108>.

305. Santamaría-Pérez, D.; McGuire, C.; Makhluif, A.; Kavner, A.; Chulía-Jordan, R.; Jorda, J. L.; Rey, F.; Pellicer-Porres, J.; Martínez-García, D.; Rodríguez-Hernández, P.; Muñoz, A. Correspondence: Strongly-Driven Re + CO₂ Redox Reaction at High-Pressure and High-Temperature. *Nat. Commun.* **2016**, *7* (1), 13647. <https://doi.org/10.1038/ncomms13647>.
306. Santamaría-Pérez, D.; McGuire, C.; Makhluif, A.; Kavner, A.; Chulía-Jordán, R.; Pellicer-Porres, J.; Martínez-García, D.; Doran, A.; Kunz, M.; Rodríguez-Hernández, P.; Muñoz, A. Exploring the Chemical Reactivity between Carbon Dioxide and Three Transition Metals (Au, Pt, and Re) at High-Pressure, High-Temperature Conditions. *Inorg. Chem.* **2016**, *55* (20), 10793–10799. <https://doi.org/10.1021/acs.inorgchem.6b01858>.
307. Chulía-Jordán, R.; Santamaría-Pérez, D.; Marqueño, T.; Ruiz-Fuertes, J.; Daisenberger, D. Oxidation of High Yield Strength Metals Tungsten and Rhenium in High-Pressure High-Temperature Experiments of Carbon Dioxide and Carbonates. *Crystals* **2019**, *9* (12), 676. <https://doi.org/10.3390/cryst9120676>.
308. Evers, J.; Möckl, L.; Oehlinger, G.; Köppe, R.; Schnöckel, H.; Barkalov, O.; Medvedev, S.; Naumov, P. More than 50 Years After Its Discovery in SiO₂ Octahedral Coordination Has Also Been Established in SiS₂ at High Pressure. *Inorg. Chem.* **2017**, *56* (1), 372–377. <https://doi.org/10.1021/acs.inorgchem.6b02294>.
309. Wang, Y.; Jiang, S.-Q.; Goncharov, A. F.; Gorelli, F. A.; Chen, X.-J.; Płašienka, D.; Martoňák, R.; Tosatti, E.; Santoro, M. Synthesis and Raman Spectroscopy of a Layered SiS₂ Phase at High Pressures. *J. Chem. Phys.* **2018**, *148* (1), 014503. <https://doi.org/10.1063/1.5011333>.
310. Pellicer-Porres, J.; Saitta, A. M.; Polian, A.; Itié, J. P.; Hanfland, M. Six-Fold-Coordinated Phosphorus by Oxygen in AlPO₄ Quartz Homeotype Under High Pressure. *Nat. Mater.* **2007**, *6* (9), 698–702. <https://doi.org/10.1038/nmat1966>.
311. Teter, D. M.; Hemley, R. J.; Kresse, G.; Hafner, J. High Pressure Polymorphism in Silica. *Phys. Rev. Lett.* **1998**, *80* (10), 2145–2148. <https://doi.org/10.1103/PhysRevLett.80.2145>.
312. Brazhkin, V. V.; Gromnitskaya, E. L.; Danilov, I. V.; Katayama, Y.; Lyapin, A. G.; Popova, S. V. High Pressure Behavior of P₂O₅ Crystalline Modifications: Compressibility, Elastic Properties and Phase Transitions. *Mater. Res. Express* **2015**, *2* (2), 025201. <https://doi.org/10.1088/2053-1591/2/2/025201>.
313. Salvadó, M. A.; Pertierra, P. Theoretical Study of P₂O₅ Polymorphs at High Pressure: Hexacoordinated Phosphorus. *Inorg. Chem.* **2008**, *47* (11), 4884–4890. <https://doi.org/10.1021/ic8001543>.
314. Liu, J. F.; Yin, S.; Wu, H. P.; Zeng, Y. W.; Hu, X. R.; Wang, Y. W.; Lv, G. L.; Jiang, J. Z. Wurtzite-to-Rocksalt Structural Transformation in Nanocrystalline CoO. *J. Phys. Chem. B* **2006**, *110* (43), 21588–21592. <https://doi.org/10.1021/jp0648238>.
315. Decremps, F.; Zhang, J.; Liebermann, R. C. New Phase Boundary and High-Pressure Thermoelasticity of ZnO. *Europhys. Lett.* **2000**, *51* (3), 268–274. <https://doi.org/10.1209/epl/i2000-00347-0>.
316. Baranov, A. N.; Sokolov, P. S.; Tafeenko, V. A.; Lathe, C.; Zubavichus, Y. V.; Veligzhanin, A. A.; Chukichev, M. V.; Solozhenko, V. L. Nanocrystallinity as a Route to Metastable Phases: Rock Salt ZnO. *Chem. Mater.* **2013**, *25* (9), 1775–1782. <https://doi.org/10.1021/cm400293j>.
317. Bekheet, M. F.; Schwarz, M. R.; Lauterbach, S.; Kleebe, H.-J.; Kroll, P.; Stewart, A.; Kolb, U.; Riedel, R.; Gurlo, A. *In Situ* High Pressure High Temperature Experiments in Multi-Anvil Assemblies with Bixbyite-Type In₂O₃ and Synthesis of Corundum-Type and Orthorhombic In₂O₃ Polymorphs. *High Pressure Res.* **2013**, *33* (3), 697–711. <https://doi.org/10.1080/08957959.2013.834896>.
318. García-Domene, B.; Sans, J. A.; Manjón, F. J.; Ovsyannikov, S. V.; Dubrovinsky, L. S.; Martínez-García, D.; Gomis, O.; Errandonea, D.; Moutaabbid, H.; Le Godec, Y.; Ortíz, H. M.; Muñoz, A.; Rodríguez-Hernández, P.; Popescu, C. Synthesis and High-Pressure Study of Corundum-Type In₂O₃. *J. Phys. Chem. C* **2015**, *119* (52), 29076–29087. <https://doi.org/10.1021/acs.jpcc.5b06939>.
319. Bekheet, M. F.; Schwarz, M. R.; Lauterbach, S.; Kleebe, H.-J.; Kroll, P.; Riedel, R.; Gurlo, A. Orthorhombic In₂O₃: A Metastable Polymorph of Indium Sesquioxide. *Angew. Chem. Int. Ed.* **2013**, *52* (25), 6531–6535. <https://doi.org/10.1002/anie.201300644>.
320. Ovsyannikov, S. V.; Abakumov, A. M.; Tsirlin, A. A.; Schnelle, W.; Egoavil, R.; Verbeeck, J.; Van Tendeloo, G.; Glazyrin, K. V.; Hanfland, M.; Dubrovinsky, L. Perovskite-Like Mn₂O₃: A Path to New Manganites. *Angew. Chem. Int. Ed.* **2013**, *52* (5), 1494–1498. <https://doi.org/10.1002/anie.201208553>.
321. Bykova, E.; Dubrovinsky, L.; Dubrovinskaia, N.; Bykov, M.; McCammon, C.; Ovsyannikov, S. V.; Liermann, H.-P.; Kuppenko, I.; Chumakov, A. I.; Rüffer, R.; Hanfland, M.; Prakapenka, V. Structural Complexity of Simple Fe₂O₃ at High Pressures and Temperatures. *Nat. Commun.* **2016**, *7* (1), 10661. <https://doi.org/10.1038/ncomms10661>.
322. Lavina, B.; Dera, P.; Kim, E.; Meng, Y.; Downs, R. T.; Weck, P. F.; Sutton, S. R.; Zhao, Y. Discovery of the Recoverable High-Pressure Iron Oxide Fe₄O₅. *Proc. Natl. Acad. Sci. U. S. A.* **2011**, *108* (42), 17281–17285. <https://doi.org/10.1073/pnas.1107573108>.
323. Lavina, B.; Meng, Y. Unraveling the Complexity of Iron Oxides at High Pressure and Temperature: Synthesis of Fe₅O₆. *Sci. Adv.* **2015**, *1* (5), e1400260. <https://doi.org/10.1126/sciadv.1400260>.
324. Sinmyo, R.; Bykova, E.; Ovsyannikov, S. V.; McCammon, C.; Kuppenko, I.; Ismailova, L.; Dubrovinsky, L. Discovery of Fe₇O₉: A New Iron Oxide with a Complex Monoclinic Structure. *Sci. Rep.* **2016**, *6* (1), 32852. <https://doi.org/10.1038/srep32852>.
325. Ovsyannikov, S. V.; Bykov, M.; Bykova, E.; Kozlenko, D. P.; Tsirlin, A. A.; Karkin, A. E.; Shchennikov, V. V.; Kichanov, S. E.; Gou, H.; Abakumov, A. M.; Egoavil, R.; Verbeeck, J.; McCammon, C.; Dyadkin, V.; Chernyshov, D.; van Smaalen, S.; Dubrovinsky, L. S. Charge-Ordering Transition in Iron Oxide Fe₄O₅ Involving Competing Dimer and Trimer Formation. *Nat. Chem.* **2016**, *8* (5), 501–508. <https://doi.org/10.1038/nchem.2478>.
326. Ovsyannikov, S. V.; Bykov, M.; Medvedev, S. A.; Naumov, P. G.; Jesche, A.; Tsirlin, A. A.; Bykova, E.; Chuvashova, I.; Karkin, A. E.; Dyadkin, V.; Chernyshov, D.; Dubrovinsky, L. S. A Room-Temperature Verwey-Type Transition in Iron Oxide, Fe₅O₆. *Angew. Chem. Int. Ed.* **2020**, *59* (14), 5632–5636. <https://doi.org/10.1002/anie.201914988>.
327. Glätzle, M.; Janka, O.; Svítlyk, V.; Chernyshov, D.; Bartsch, M.; Zacharias, H.; Pöttgen, R.; Huppertz, H. The High-Pressure Oxide Tb₃O₅ and Its Non-Centrosymmetric Low-Temperature Polymorph—A Comprehensive Study. *Chem. A Eur. J.* **2018**, *24* (57), 15236–15245. <https://doi.org/10.1002/chem.201804006>.
328. Hu, Q.; Kim, D. Y.; Yang, W.; Yang, L.; Meng, Y.; Zhang, L.; Mao, H.-K. Fe₂O and FeOOH under Deep Lower-Mantle Conditions and Earth's Oxygen–Hydrogen Cycles. *Nature* **2016**, *534* (7606), 241–244. <https://doi.org/10.1038/nature18018>.
329. Nishi, M.; Kuwayama, Y.; Tsuchiya, J.; Tsuchiya, T. The Pyrite-Type High-Pressure Form of FeOOH. *Nature* **2017**, *547* (7662), 205–208. <https://doi.org/10.1038/nature22823>.
330. Haines, J.; Léger, J. M.; Schulte, O. *Pa*-3 Modified Fluorite-Type Structures in Metal Dioxides at High Pressure. *Science* **1996**, *271* (5249), 629–631. <https://doi.org/10.1126/science.271.5249.629>.
331. Tse, J. S.; Klug, D. D.; Uehara, K.; Li, Z. Q.; Haines, J.; Léger, J. M. Elastic Properties of Potential Superhard Phases of RuO₂. *Phys. Rev. B* **2000**, *61* (15), 10029. <https://doi.org/10.1103/PhysRevB.61.10029>.
332. Shirako, Y.; Wang, X.; Tsujimoto, Y.; Tanaka, K.; Guo, Y.; Matsushita, Y.; Nemoto, Y.; Katsuya, Y.; Shi, Y.; Mori, D.; Kojitani, H.; Yamaura, K.; Inaguma, Y.; Akaogi, M. Synthesis, Crystal Structure, and Electronic Properties of High-Pressure PdF₂-Type Oxides MO₂ (M = Ru, Rh, Os, Ir, Pt). *Inorg. Chem.* **2014**, *53* (21), 11616–11625. <https://doi.org/10.1021/ic501770g>.
333. Chen, H.; Zhou, S.; Morgan, D.; Prakapenka, V.; Greenberg, E.; Leinenweber, K.; Shim, S.-H. The O–O Bonding and Hydrogen Storage in the Pyrite-Type PtO₂. *Inorg. Chem.* **2019**, *58* (13), 8300–8307. <https://doi.org/10.1021/acs.inorgchem.9b00046>.
334. Belik, A. A. Rise of A-Site Columnar-Ordered A₂A'A''B₄O₁₂ Quadruple Perovskites with Intrinsic Triple Order. *Dalton Trans.* **2018**, *47* (10), 3209–3217. <https://doi.org/10.1039/C7DT04490A>.
335. Belik, A. A.; Yi, W. High-Pressure Synthesis, Crystal Chemistry and Physics of Perovskites with Small Cations at the A Site. *J. Phys. Condens. Matter* **2014**, *26* (16), 163201. <https://doi.org/10.1088/0953-8984/26/16/163201>.
336. Prodi, A.; Gilioli, E.; Gauzzi, A.; Licci, F.; Marezio, M.; Bolzoni, F.; Huang, Q.; Santoro, A.; Lynn, J. W. Charge, Orbital and Spin Ordering Phenomena in the Mixed Valence Manganite (NaMn³⁺)(Mn³⁺₂Mn⁴⁺₂)O₁₂. *Nat. Mater.* **2004**, *3* (1), 48–52. <https://doi.org/10.1038/nmat1038>.
337. Glazkova, Y. S.; Terada, N.; Matsushita, Y.; Katsuya, Y.; Tanaka, M.; Sobolev, A. V.; Presniakov, I. A.; Belik, A. A. High-Pressure Synthesis, Crystal Structures, and Properties of CdMn₇O₁₂ and SrMn₇O₁₂ Perovskites. *Inorg. Chem.* **2015**, *54* (18), 9081–9091. <https://doi.org/10.1021/acs.inorgchem.5b01472>.

338. Markkula, M.; Arevalo-Lopez, A. M.; Kusmartseva, A.; Rodgers, J. A.; Ritter, C.; Wu, H.; Atfield, J. P. Incommensurate Spin Order in the Metallic Perovskite MnVO_3 . *Phys. Rev. B* **2011**, *84* (9), 094450. <https://doi.org/10.1103/PhysRevB.84.094450>.
339. Li, M.-R.; Retuerto, M.; Deng, Z.; Stephens, P. W.; Croft, M.; Huang, Q.; Wu, H.; Deng, X.; Kotliar, G.; Sánchez-Benítez, J.; Hadermann, J.; Walker, D.; Greenblatt, M. Giant Magnetoresistance in the Half-Metallic Double-Perovskite Ferrimagnet $\text{Mn}_2\text{FeReO}_6$. *Angew. Chem. Int. Ed.* **2015**, *54* (41), 12069–12073. <https://doi.org/10.1002/anie.201506456>.
340. Li, M.-R.; Hodges, J. P.; Retuerto, M.; Deng, Z.; Stephens, P. W.; Croft, M. C.; Deng, X.; Kotliar, G.; Sánchez-Benítez, J.; Walker, D.; Greenblatt, M. $\text{Mn}_2\text{MnReO}_6$: Synthesis and Magnetic Structure Determination of a New Transition-Metal-Only Double Perovskite Canted Antiferromagnet. *Chem. Mater.* **2016**, *28* (9), 3148–3158. <https://doi.org/10.1021/acs.chemmater.6b00755>.
341. Akizuki, Y.; Yamada, I.; Fujita, K.; Nishiyama, N.; Irifune, T.; Yajima, T.; Kageyama, H.; Tanaka, K. A-Site-Ordered Perovskite $\text{MnCu}_3\text{V}_4\text{O}_{12}$ with a 12-Coordinated Manganese(II). *Inorg. Chem.* **2013**, *52* (19), 11538–11543. <https://doi.org/10.1021/ic401855j>.
342. Akizuki, Y.; Yamada, I.; Fujita, K.; Taga, K.; Kawakami, T.; Mizumaki, M.; Tanaka, K. Rattling in the Quadruple Perovskite $\text{CuCu}_3\text{V}_4\text{O}_{12}$. *Angew. Chem. Int. Ed.* **2015**, *54* (37), 10870–10874. <https://doi.org/10.1002/anie.201504784>.
343. Chamberland, B. L. The Synthesis of New Ilmenite-Type Derivatives, CuVO_3 and CoVO_3 . *J. Solid State Chem.* **1970**, *1* (2), 138–142. [https://doi.org/10.1016/0022-4596\(70\)90004-6](https://doi.org/10.1016/0022-4596(70)90004-6).
344. Kawamoto, T.; Fujita, K.; Yamada, I.; Matoba, T.; Kim, S. J.; Gao, P.; Pan, X.; Findlay, S. D.; Tassel, C.; Kageyama, H.; Studer, A. J.; Hester, J.; Irifune, T.; Akamatsu, H.; Tanaka, K. Room-Temperature Polar Ferromagnet ScFeO_3 Transformed from a High-Pressure Orthorhombic Perovskite Phase. *J. Am. Chem. Soc.* **2014**, *136* (43), 15291–15299. <https://doi.org/10.1021/ja507958z>.
345. Ikeuchi, Y.; Takatsu, H.; Tassel, C.; Goto, Y.; Murakami, T.; Kageyama, H. High-Pressure Synthesis of Fully Occupied Tetragonal and Cubic Tungsten Bronze Oxides. *Angew. Chem. Int. Ed.* **2017**, *56* (21), 5770–5773. <https://doi.org/10.1002/anie.201701732>.
346. Ikeuchi, Y.; Takatsu, H.; Tassel, C.; Brown, C. M.; Murakami, T.; Okamoto, Y.; Kageyama, H. Rattling Behavior in a Simple Perovskite NaWO_3 . *Inorg. Chem.* **2019**, *58* (10), 6790–6795. <https://doi.org/10.1021/acs.inorgchem.9b00248>.
347. Ishiwata, S.; Azuma, M.; Takano, M.; Nishibori, E.; Takata, M.; Sakata, M.; Kato, K. High Pressure Synthesis, Crystal Structure and Physical Properties of a New Ni(II) Perovskite BiNiO_3 . *J. Mater. Chem.* **2002**, *12* (12), 3733–3737. <https://doi.org/10.1039/B206022A>.
348. Belik, A. A. Solid Solutions between BiMnO_3 and BiCrO_3 . *Inorg. Chem.* **2016**, *55* (23), 12348–12356. <https://doi.org/10.1021/acs.inorgchem.6b02237>.
349. Belik, A. A.; Iikubo, S.; Kodama, K.; Igawa, N.; Shamoto, S.; Niitaka, S.; Azuma, M.; Shimakawa, Y.; Takano, M.; Izumi, F.; Takayama-Muromachi, E. Neutron Powder Diffraction Study on the Crystal and Magnetic Structures of BiCoO_3 . *Chem. Mater.* **2006**, *18* (3), 798–803. <https://doi.org/10.1021/cm052334z>.
350. Klein, R. A.; Altman, A. B.; Saballos, R. J.; Walsh, J. P. S.; Tamerius, A. D.; Meng, Y.; Puggioni, D.; Jacobsen, S. D.; Rondinelli, J. M.; Freedman, D. E. High-Pressure Synthesis of the BiVO_3 Perovskite. *Phys. Rev. Mater.* **2019**, *3* (6), 064411. <https://doi.org/10.1103/PhysRevMaterials.3.064411>.
351. Azuma, M.; Carlsson, S.; Rodgers, J.; Tucker, M. G.; Tsujimoto, M.; Ishiwata, S.; Isoda, S.; Shimakawa, Y.; Takano, M.; Atfield, J. P. Pressure-Induced Intermetallic Valence Transition in BiNiO_3 . *J. Am. Chem. Soc.* **2007**, *129* (46), 14433–14436. <https://doi.org/10.1021/ja074880u>.
352. Azuma, M.; Chen, W.; Seki, H.; Czapski, M.; Smirnova, O.; Oka, K.; Mizumaki, M.; Watanuki, T.; Ishimatsu, N.; Kawamura, N.; Ishiwata, S.; Tucker, M. G.; Shimakawa, Y.; Atfield, J. P. Colossal Negative Thermal Expansion in BiNiO_3 Induced by Intermetallic Charge Transfer. *Nat. Commun.* **2011**, *2* (1), 347. <https://doi.org/10.1038/ncomms1361>.
353. Liu, Z.; Sakai, Y.; Yang, J.; Li, W.; Liu, Y.; Ye, X.; Qin, S.; Chen, J.; Agrestini, S.; Chen, K.; Liao, S.-C.; Haw, S.-C.; Baudelet, F.; Ishii, H.; Nishikubo, T.; Ishizaki, H.; Yamamoto, T.; Pan, Z.; Fukuda, M.; Ohashi, K.; Matsuno, K.; Machida, A.; Watanuki, T.; Kawaguchi, S. I.; Arevalo-Lopez, A. M.; Jin, C.; Hu, Z.; Atfield, J. P.; Azuma, M.; Long, Y. Sequential Spin State Transition and Intermetallic Charge Transfer in PbCoO_3 . *J. Am. Chem. Soc.* **2020**, *142* (12), 5731–5741. <https://doi.org/10.1021/jacs.9b13508>.
354. Shi, Y. G.; Guo, Y. F.; Yu, S.; Arai, M.; Belik, A. A.; Sato, A.; Yamaura, K.; Takayama-Muromachi, E.; Tian, H. F.; Yang, H. X.; Li, J. Q.; Varga, T.; Mitchell, J. F.; Okamoto, S. Continuous Metal-Insulator Transition of the Antiferromagnetic Perovskite NaOsO_3 . *Phys. Rev. B* **2009**, *80* (16), 161104(R). <https://doi.org/10.1103/PhysRevB.80.161104>.
355. Shi, Y.; Guo, Y.; Wang, X.; Princep, A. J.; Khalyavin, D.; Manuel, P.; Michiue, Y.; Sato, A.; Tsuda, K.; Yu, S.; Arai, M.; Shirako, Y.; Akaogi, M.; Wang, N.; Yamaura, K.; Boothroyd, A. T. A Ferroelectric-Like Structural Transition in a Metal. *Nat. Mater.* **2013**, *12* (11), 1024–1027. <https://doi.org/10.1038/nmat3754>.
356. Yamada, I.; Otake, T.; Asai, K.; Oka, K.; Kawaguchi, S.; Wada, K.; Yagi, S. High-Pressure Synthesis of Highly Oxidized $\text{Ba}_{0.5}\text{Sr}_{0.5}\text{Co}_{0.8}\text{Fe}_{0.2}\text{O}_{3-\delta}$ Cubic Perovskite. *Mater. Chem. Front.* **2019**, *3* (6), 1209–1217. <https://doi.org/10.1039/C9QM00067D>.
357. Brehmholm, M.; Dutton, S. E.; Stephens, P. W.; Cava, R. J. NaIrO_3 —A Pentavalent Post-Perovskite. *J. Solid State Chem.* **2011**, *184* (3), 601–607. <https://doi.org/10.1016/j.jssc.2011.01.028>.
358. Osaka, T.; Takahashi, H.; Sagayama, H.; Yamasaki, Y.; Ishiwata, S. High-Pressure Synthesis of an Unusual Antiferromagnetic Metal CaCoO_3 with GdFeO_3 -Type Perovskite Structure. *Phys. Rev. B* **2017**, *95* (22), 224440. <https://doi.org/10.1103/PhysRevB.95.224440>.
359. Xia, H.; Dai, J.; Xu, Y.; Yin, Y.; Wang, X.; Liu, Z.; Liu, M.; McGuire, M. A.; Li, X.; Li, Z.; Jin, C.; Yang, Y.; Zhou, J.; Long, Y. Magnetism and the Spin State in Cubic Perovskite CaCoO_3 Synthesized Under High Pressure. *Phys. Rev. Mater.* **2017**, *1* (2), 024406. <https://doi.org/10.1103/PhysRevMaterials.1.024406>.
360. Li, X.; Wang, H.; Cui, Z.; Li, Y.; Xin, S.; Zhou, J.; Long, Y.; Jin, C.; Goodenough, J. B. Exceptional Oxygen Evolution Reactivities on CaCoO_3 and SrCoO_3 . *Sci. Adv.* **2019**, *5* (8), eaav6262. <https://doi.org/10.1126/sciadv.aav6262>.
361. Li, W. M.; Zhao, J. F.; Cao, L. P.; Hu, Z.; Huang, Q. Z.; Wang, X. C.; Liu, Y.; Zhao, G. Q.; Zhang, J.; Liu, Q. Q.; Yu, R. Z.; Long, Y. W.; Wu, H.; Lin, H. J.; Chen, C. T.; Li, Z.; Gong, Z. Z.; Guguchia, Z.; Kim, J. S.; Stewart, G. R.; Uemura, Y. J.; Uchida, S.; Jin, C. Q. Superconductivity in a Unique Type of Copper Oxide. *Proc. Natl. Acad. Sci. U. S. A.* **2019**, *116* (25), 12156–12160. <https://doi.org/10.1073/pnas.1900908116>.
362. Zhang, W.; Oganov, A. R.; Goncharov, A. F.; Zhu, Q.; Bouffeffel, S. E.; Lyakhov, A. O.; Stavrou, E.; Somayazulu, M.; Prakapenka, V. B.; Konôpková, Z. Unexpected Stable Stoichiometries of Sodium Chlorides. *Science* **2013**, *342* (6165), 1502–1505. <https://doi.org/10.1126/science.1244989>.
363. Shi, G.; Chen, L.; Yang, Y.; Li, D.; Qian, Z.; Liang, S.; Yan, L.; Li, L. H.; Wu, M.; Fang, H. Two-Dimensional Na–Cl Crystals of Unconventional Stoichiometries on Graphene Surface from Dilute Solution at Ambient Conditions. *Nat. Chem.* **2018**, *10* (7), 776–779. <https://doi.org/10.1038/s41557-018-0061-4>.
364. Zhang, W.; Oganov, A. R.; Zhu, Q.; Lobanov, S. S.; Stavrou, E.; Goncharov, A. F. Stability of Numerous Novel Potassium Chlorides at High Pressure. *Sci. Rep.* **2016**, *6* (1), 26265. <https://doi.org/10.1038/srep26265>.
365. Patel, N. N.; Verma, A. K.; Mishra, A. K.; Sunder, M.; Sharma, S. M. The Synthesis of Unconventional Stoichiometric Compounds in the K–Br System at High Pressures. *Phys. Chem. Chem. Phys.* **2017**, *19* (11), 7996–8007. <https://doi.org/10.1039/C7CP00340D>.
366. Grochala, W. Atypical Compounds of Gases, Which Have Been Called 'Noble'. *Chem. Soc. Rev.* **2007**, *36* (10), 1632–1655. <https://doi.org/10.1039/B702109G>.
367. Mazej, Z. Noble-Gas Chemistry More than Half a Century after the First Report of the Noble-Gas Compound. *Molecules* **2020**, *25* (13), 3014. <https://doi.org/10.3390/molecules25133014>.
368. Kurzydowski, D.; Zaleski-Egijerd, P. High-Pressure Stabilization of Argon Fluorides. *Phys. Chem. Chem. Phys.* **2016**, *18* (4), 2309–2313. <https://doi.org/10.1039/C5CP05725F>.
369. Kurzydowski, D.; Sołtysiak, M.; Džoleva, A.; Zaleski-Egijerd, P. High-Pressure Reactivity of Kr and F_2 —Stabilization of Krypton in the +4 Oxidation State. *Crystals* **2017**, *7* (11), 329. <https://doi.org/10.3390/cryst7110329>.
370. Weck, G.; Dewaele, A.; Loubeyre, P. Oxygen/Noble Gas Binary Phase Diagrams at 296 K and High Pressures. *Phys. Rev. B* **2010**, *82* (1), 014112. <https://doi.org/10.1103/PhysRevB.82.014112>.
371. Dewaele, A.; Worth, N.; Pickard, C. J.; Needs, R. J.; Pascarelli, S.; Mathon, O.; Mezouar, M.; Irifune, T. Synthesis and Stability of Xenon Oxides Xe_2O_5 and Xe_3O_2 under Pressure. *Nat. Chem.* **2016**, *8* (8), 784–790. <https://doi.org/10.1038/nchem.2528>.

372. Dong, X.; Oganov, A. R.; Goncharov, A. F.; Stavrou, E.; Lobanov, S.; Saleh, G.; Qian, G.-R.; Zhu, Q.; Gatti, C.; Deringer, V. L.; Dronskowski, R.; Zhou, X.-F.; Prakapenka, V. B.; Konôpková, Z.; Popov, I. A.; Boldyrev, A. I.; Wang, H.-T. A Stable Compound of Helium and Sodium at High Pressure. *Nat. Chem.* **2017**, *9* (5), 440–445. <https://doi.org/10.1038/nchem.2716>.
373. Liu, Z.; Botana, J.; Hermann, A.; Valdez, S.; Zurek, E.; Yan, D.; Lin, H.; Miao, M. Reactivity of He with Ionic Compounds under High Pressure. *Nat. Commun.* **2018**, *9* (1), 951. <https://doi.org/10.1038/s41467-018-03284-y>.
374. Sanloup, C. Noble Gas Reactivity in Planetary Interiors. *Front. Phys.* **2020**, *8*, 157. <https://doi.org/10.3389/fphy.2020.00157>.
375. Stavrou, E.; Yao, Y.; Goncharov, A. F.; Lobanov, S. S.; Zaig, J. M.; Liu, H.; Greenberg, E.; Prakapenka, V. B. Synthesis of Xenon and Iron-Nickel Intermetallic Compounds at Earth's Core Thermodynamic Conditions. *Phys. Rev. Lett.* **2018**, *120* (9), 096001. <https://doi.org/10.1103/PhysRevLett.120.096001>.
376. Dewaele, A.; Pépin, C. M.; Geneste, G.; Garbarino, G. Reaction between Nickel or Iron and Xenon Under High Pressure. *High Pressure Res.* **2017**, *37* (2), 137–146. <https://doi.org/10.1080/08957959.2016.1267165>.
377. Kageyama, H.; Hayashi, K.; Maeda, K.; Atfield, J. P.; Hiroi, Z.; Rondinelli, J. M.; Poeppelmeier, K. R. Expanding Frontiers in Materials Chemistry and Physics with Multiple Anions. *Nat. Commun.* **2018**, *9* (1), 772. <https://doi.org/10.1038/s41467-018-02838-4>.
378. Kageyama, H.; Yajima, T.; Tsujimoto, Y.; Yamamoto, T.; Tassel, C.; Kobayashi, Y. Exploring Structures and Properties through Anion Chemistry. *Bull. Chem. Soc. Jpn.* **2019**, *92* (8), 1349–1357. <https://doi.org/10.1246/bcsj.20190095>.
379. Tu, B.; Liu, X.; Wang, H.; Wang, W.; Zhai, P.; Fu, Z. Combining 27Al Solid-State NMR and First-Principles Simulations To Explore Crystal Structure in Disordered Aluminum Oxynitride. *Inorg. Chem.* **2016**, *55* (24), 12930–12937. <https://doi.org/10.1021/acs.inorgchem.6b02360>.
380. Soignard, E.; Machon, D.; McMillan, P. F.; Dong, J.; Xu, B.; Leinenweber, K. Spinel-Structured Gallium Oxynitride (Ga₃O₃N) Synthesis and Characterization: An Experimental and Theoretical Study. *Chem. Mater.* **2005**, *17* (22), 5465–5472. <https://doi.org/10.1021/cm051224p>.
381. Huppertz, H.; Hering, S. A.; Zvoriste, C. E.; Lauterbach, S.; Oeckler, O.; Riedel, R.; Kinski, I. High-Pressure Synthesis, Electron Energy-Loss Spectroscopy Investigations, and Single Crystal Structure Determination of a Spinel-Type Gallium Oxonitride Ga_{2.79} □_{0.21}(O_{3.05}N_{0.76} □_{0.19}). *Chem. Mater.* **2009**, *21* (10), 2101–2107. <https://doi.org/10.1021/cm803371k>.
382. Boyko, T. D.; Zvoriste, C. E.; Kinski, I.; Riedel, R.; Hering, S.; Huppertz, H.; Moewes, A. Anion Ordering in Spinel-Type Gallium Oxonitride. *Phys. Rev. B* **2011**, *84* (8), 085203. <https://doi.org/10.1103/PhysRevB.84.085203>.
383. Bhat, S.; Wiehl, L.; Molina-Luna, L.; Magnaioli, E.; Lauterbach, S.; Sicolo, S.; Kroll, P.; Duerschnebel, M.; Nishiyama, N.; Kolb, U.; Albe, K.; Kleebe, H.-J.; Riedel, R. High-Pressure Synthesis of Novel Boron Oxynitride B₆N₄O₃ with Sphalerite Type Structure. *Chem. Mater.* **2015**, *27* (17), 5907–5914. <https://doi.org/10.1021/acs.chemmater.5b01706>.
384. Idrestedt, I.; Brosset, C.; Ledaal, T.; Seip, H. M. Structure of Si₂N₂O. *Acta Chem. Scand.* **1964**, *18*, 1879–1886. <https://doi.org/10.3891/acta.chem.scand.18-1879>.
385. Bhat, S.; Wiehl, L.; Haseen, S.; Kroll, P.; Glazyrin, K.; Gollé-Leidreiter, P.; Kolb, U.; Farla, R.; Tseng, J.-C.; Ionescu, E.; Katsura, T.; Riedel, R. A Novel High-Pressure Tin Oxynitride Sn₂N₂O. *Chem. A Eur. J.* **2020**, *26* (10), 2187–2194. <https://doi.org/10.1002/chem.201904529>.
386. Boukbir, L.; Marchand, R.; Laurent, Y.; Bacher, P.; Roult, G. Preparation and Time-of-Flight Neutron Diffraction Study of the Cristobalite-Type PON Phosphorus Oxynitride. *Ann. Chim. Fr.* **1989**, *14*, 475–481.
387. Léger, J. M.; Haines, J.; de Oliveira, L. S.; Chateau, C.; Sauze, A. L.; Marchand, R. High Pressure Behaviour of the β-Cristobalite-Type Phase of Phosphorus Oxynitride, PON. *J. Phys. Condens. Matter* **1996**, *8* (50), L773–L777. <https://doi.org/10.1088/0953-8984/8/50/001>.
388. Léger, J.-M.; Haines, J.; de Oliveira, L. S.; Chateau, C.; Le Sauze, A.; Marchand, R.; Hull, S. Crystal Structure and High Pressure Behaviour of the Quartz-Type Phase of Phosphorus Oxynitride PON. *J. Phys. Chem. Solid* **1999**, *60* (2), 145–152. [https://doi.org/10.1016/S0022-3697\(98\)00282-0](https://doi.org/10.1016/S0022-3697(98)00282-0).
389. Baumann, D.; Niklaus, R.; Schnick, W. A High-Pressure Polymorph of Phosphorus Oxynitride with the Coesite Structure. *Angew. Chem. Int. Ed.* **2015**, *54* (14), 4388–4391. <https://doi.org/10.1002/anie.201410526>.
390. Vogel, S.; Baumann, D.; Niklaus, R.; Bykova, E.; Bykov, M.; Dubrovinskaja, N.; Dubrovinsky, L.; Schnick, W. Stishovite's Relative: A Post-Coesite Form of Phosphorus Oxynitride. *Angew. Chem. Int. Ed.* **2018**, *57* (22), 6691–6695. <https://doi.org/10.1002/anie.201803610>.
391. Baumann, D.; Sedlmaier, S. J.; Schnick, W. An Unprecedented AB₂ Tetrahedra Network Structure Type in a High-Pressure Phase of Phosphorus Oxynitride (PON). *Angew. Chem. Int. Ed.* **2012**, *51* (19), 4707–4709. <https://doi.org/10.1002/anie.201200811>.
392. Sedlmaier, S. J.; Celinski, V. R.; Schmedt auf der Günne, J.; Schnick, W. High-Pressure Synthesis and Structural Investigation of H₃P₈O₈N₉: A New Phosphorus(V) Oxynitride Imide with an Interrupted Framework Structure. *Chem. A Eur. J.* **2012**, *18* (14), 4358–4366. <https://doi.org/10.1002/chem.201103010>.
393. Fuertes, A. Synthetic Approaches in Oxynitride Chemistry. *Prog. Solid State Chem.* **2018**, *51*, 63–70. <https://doi.org/10.1016/j.progsolidstchem.2017.11.001>.
394. Yang, M.; Rodgers, J. A.; Middle, L. C.; Oró-Solé, J.; Jorge, A. B.; Fuertes, A.; Atfield, J. P. Direct Solid-State Synthesis at High Pressures of New Mixed-Metal Oxynitrides: RZrO₂N (R = Pr, Nd, and Sm). *Inorg. Chem.* **2009**, *48* (24), 11498–11500. <https://doi.org/10.1021/ic902020r>.
395. Tassel, C.; Kuno, Y.; Goto, Y.; Yamamoto, T.; Brown, C. M.; Hester, J.; Fujita, K.; Higashi, M.; Abe, R.; Tanaka, K.; Kobayashi, Y.; Kageyama, H. MnTaO₂N: Polar LiNbO₃-Type Oxynitride with a Helical Spin Order. *Angew. Chem. Int. Ed.* **2015**, *54* (2), 516–521. <https://doi.org/10.1002/anie.201408483>.
396. Katsumata, T.; Ohba, C.; Tohe, A.; Takeda, A.; Shoji, M.; Aimi, A.; Mori, D.; Inaguma, Y. Synthesis of New LiNbO₃-Type Oxynitrides, Mn(Mn_{1/6}Ta_{5/6})O_{2.5}N_{0.5} Under High Pressure and at High Temperature. *Chem. Lett.* **2018**, *47* (1), 37–39. <https://doi.org/10.1246/cl.170851>.
397. Kuno, Y.; Tassel, C.; Fujita, K.; Batuk, D.; Abakumov, A. M.; Shitara, K.; Kuwabara, A.; Moriwake, H.; Watabe, D.; Ritter, C.; Brown, C. M.; Yamamoto, T.; Takeiri, F.; Abe, R.; Kobayashi, Y.; Tanaka, K.; Kageyama, H. ZnTaO₂N: Stabilized High-Temperature LiNbO₃-Type Structure. *J. Am. Chem. Soc.* **2016**, *138* (49), 15950–15955. <https://doi.org/10.1021/jacs.6b08635>.
398. Woerner, W. R.; Qian, G.-R.; Oganov, A. R.; Stephens, P. W.; Dharmagunawardhane, H. A. N.; Sinclair, A.; Parise, J. B. Combined Theoretical and in Situ Scattering Strategies for Optimized Discovery and Recovery of High-Pressure Phases: A Case Study of the GaN–Nb₂O₅ System. *Inorg. Chem.* **2016**, *55* (7), 3384–3392. <https://doi.org/10.1021/acs.inorgchem.5b02791>.
399. Al-Mamouri, M.; Edwards, P. P.; Greaves, C.; Slaski, M. Synthesis and Superconducting Properties of the Strontium Copper Oxy-Fluoride Sr₂CuO₂F_{2+δ}. *Nature* **1994**, *369* (6479), 382–384. <https://doi.org/10.1038/369382a0>.
400. Chamberland, B. L.; Sleight, A. W. Preparation of First-Row Transition Metal Oxyfluorides of the Composition MOF. *Solid State Commun.* **1967**, *5* (9), 765–767. [https://doi.org/10.1016/0038-1098\(67\)90369-9](https://doi.org/10.1016/0038-1098(67)90369-9).
401. Pérez-Flores, J. C.; Villamor, R.; Ávila-Brandé, D.; Gallardo Amores, J. M.; Morán, E.; Kuhn, A.; García-Alvarado, F. VO₂F: A New Transition Metal Oxyfluoride with High Specific Capacity for Li Ion Batteries. *J. Mater. Chem. A* **2015**, *3* (41), 20508–20515. <https://doi.org/10.1039/C5TA05434F>.
402. Chamberland, B. L. A New Oxyfluoride Perovskite, KTiO₂F. *Mater. Res. Bull.* **1971**, *6* (5), 311–315. [https://doi.org/10.1016/0025-5408\(71\)90164-4](https://doi.org/10.1016/0025-5408(71)90164-4).
403. Troyanchuk, I. O.; Kasper, N. V.; Mantyskaya, O. S.; Shapovalova, E. F. High-Pressure Synthesis of Some Perovskite-Like Compounds with a Mixed Anion Type. *Mater. Res. Bull.* **1995**, *30* (4), 421–425. [https://doi.org/10.1016/0025-5408\(95\)00015-1](https://doi.org/10.1016/0025-5408(95)00015-1).
404. Inaguma, Y.; Greneche, J.-M.; Crosnier-Lopez, M.-P.; Katsumata, T.; Calage, Y.; Fourquet, J.-L. Structure and Mössbauer Studies of F–O Ordering in Antiferromagnetic Perovskite PbFeO₂F. *Chem. Mater.* **2005**, *17* (6), 1386–1390. <https://doi.org/10.1021/cm048125g>.
405. Katsumata, T.; Nakashima, M.; Inaguma, Y.; Tsurui, T. Synthesis of New Perovskite-Type Oxyfluoride, PbMnO₂F. *Bull. Chem. Soc. Jpn.* **2012**, *85* (3), 397–399. <https://doi.org/10.1246/bcsj.20110295>.
406. Katsumata, T.; Nakashima, M.; Umemoto, H.; Inaguma, Y. Synthesis of the Novel Perovskite-Type Oxyfluoride PbScO₂F under High Pressure and High Temperature. *J. Solid State Chem.* **2008**, *181* (10), 2737–2740. <https://doi.org/10.1016/j.jssc.2008.06.048>.
407. Takeiri, F.; Yamamoto, T.; Hayashi, N.; Hosokawa, S.; Arai, K.; Kikkawa, J.; Ikeda, K.; Honda, T.; Otomo, T.; Tassel, C.; Kimoto, K.; Kageyama, H. AgFeOF₂: A Fluorine-Rich Perovskite Oxyfluoride. *Inorg. Chem.* **2018**, *57* (11), 6686–6691. <https://doi.org/10.1021/acs.inorgchem.8b00500>.

408. Tsujimoto, Y.; Li, J. J.; Yamaura, K.; Matsushita, Y.; Katsuya, Y.; Tanaka, M.; Shirako, Y.; Akaogi, M.; Takayama-Muromachi, E. New Layered Cobalt Oxyfluoride, $\text{Sr}_2\text{CoO}_3\text{F}$. *Chem. Commun.* **2011**, 47 (11), 3263–3265. <https://doi.org/10.1039/C0CC05482H>.
409. Su, Y.; Tsujimoto, Y.; Matsushita, Y.; Yuan, Y.; He, J.; Yamaura, K. High-Pressure Synthesis, Crystal Structure, and Magnetic Properties of $\text{Sr}_2\text{MnO}_3\text{F}$: A New Member of Layered Perovskite Oxyfluorides. *Inorg. Chem.* **2016**, 55 (5), 2627–2633. <https://doi.org/10.1021/acs.inorgchem.5b02984>.
410. Kobayashi, Y.; Hernandez, O.; Tassel, C.; Kageyama, H. New Chemistry of Transition Metal Oxyhydrides. *Sci. Technol. Adv. Mater.* **2017**, 18 (1), 905–918. <https://doi.org/10.1080/14686996.2017.1394776>.
411. Tassel, C.; Goto, Y.; Kuno, Y.; Hester, J.; Green, M.; Kobayashi, Y.; Kageyama, H. Direct Synthesis of Chromium Perovskite Oxyhydride with a High Magnetic-Transition Temperature. *Angew. Chem. Int. Ed.* **2014**, 53 (39), 10377–10380. <https://doi.org/10.1002/anie.201405453>.
412. Denis Romero, F.; Leach, A.; Möller, J. S.; Foronda, F.; Blundell, S. J.; Hayward, M. A. Strontium Vanadium Oxide-Hydrides: “Square-Planar” Two-Electron Phases. *Angew. Chem. Int. Ed.* **2014**, 53 (29), 7556–7559. <https://doi.org/10.1002/anie.201403536>.
413. Goto, Y.; Tassel, C.; Noda, Y.; Hernandez, O.; Pickard, C. J.; Green, M. A.; Sakaebe, H.; Taguchi, N.; Uchimoto, Y.; Kobayashi, Y.; Kageyama, H. Pressure-Stabilized Cubic Perovskite Oxyhydride BaScO_3H . *Inorg. Chem.* **2017**, 56 (9), 4840–4845. <https://doi.org/10.1021/acs.inorgchem.6b02834>.
414. Tassel, C.; Goto, Y.; Watabe, D.; Tang, Y.; Lu, H.; Kuno, Y.; Takeiri, F.; Yamamoto, T.; Brown, C. M.; Hester, J.; Kobayashi, Y.; Kageyama, H. High-Pressure Synthesis of Manganese Oxyhydride with Partial Anion Order. *Angew. Chem. Int. Ed.* **2016**, 55 (33), 9667–9670. <https://doi.org/10.1002/anie.201605123>.
415. Bang, J.; Matsuishi, S.; Hiraka, H.; Fujisaki, F.; Otomo, T.; Maki, S.; Yamaura, J.; Kumai, R.; Murakami, Y.; Hosono, H. Hydrogen Ordering and New Polymorph of Layered Perovskite Oxyhydrides: $\text{Sr}_2\text{VO}_4\cdot x\text{H}_2\text{O}$. *J. Am. Chem. Soc.* **2014**, 136 (20), 7221–7224. <https://doi.org/10.1021/ja502277r>.
416. Yajima, T.; Takahashi, K.; Nakajima, H.; Honda, T.; Ikeda, K.; Otomo, T.; Hiroi, Z. High-Pressure Synthesis of Transition-Metal Oxyhydrides with Double-Perovskite Structures. *Inorg. Chem.* **2022**, 61 (4), 2010–2016. <https://doi.org/10.1021/acs.inorgchem.1c03162>.
417. Broux, T.; Ubukata, H.; Pickard, C. J.; Takeiri, F.; Kobayashi, G.; Kawaguchi, S.; Yonemura, M.; Goto, Y.; Tassel, C.; Kageyama, H. High-Pressure Polymorphs of LaHO with Anion Coordination Reversal. *J. Am. Chem. Soc.* **2019**, 141 (22), 8717–8720. <https://doi.org/10.1021/jacs.9b03320>.
418. Spektor, K.; Fischer, A.; Häussermann, U. Crystallization of LiAlSiO_4 Glass in Hydrothermal Environments at Gigapascal Pressures—Dense Hydrated Aluminosilicates. *Inorg. Chem.* **2016**, 55 (16), 8048–8058. <https://doi.org/10.1021/acs.inorgchem.6b01181>.
419. Hinteregger, E.; Wurst, K.; Tribus, M.; Huppertz, H. High-Pressure Synthesis and Characterization of the First Cerium Fluoride Borate $\text{CeB}_2\text{O}_4\text{F}$. *J. Solid State Chem.* **2013**, 204, 47–52. <https://doi.org/10.1016/j.jssc.2013.05.013>.
420. Glätzle, M.; Pitscheider, A.; Oeckler, O.; Wurst, K.; Huppertz, H. A High-Pressure Praseodymium Fluoride Borate Linking Multiple Structural Features of Apatite-Type Compounds. *Chem. A Eur. J.* **2019**, 25 (7), 1767–1772. <https://doi.org/10.1002/chem.201805092>.
421. Zoller, M.; Heymann, G.; Saxer, A.; Huppertz, H. High-Pressure Synthesis of the Acentric Borate $\text{DyB}_5\text{O}_{14}(\text{OH})_2$. *Eur. J. Inorg. Chem.* **2020**, 2020 (4), 370–376. <https://doi.org/10.1002/ejic.201901285>.
422. Vitzthum, D.; Wurst, K.; Prock, J.; Brüggeller, P.; Huppertz, H. The Indium Borate $\text{In}_9\text{B}_{34}\text{O}_{74}(\text{OH})_{11}$ with T2 Supertetrahedra. *Inorg. Chem.* **2016**, 55 (21), 11473–11478. <https://doi.org/10.1021/acs.inorgchem.6b02029>.
423. Hinteregger, E.; Wurst, K.; Perfler, L.; Kraus, F.; Huppertz, H. High-Pressure Synthesis and Characterization of the Actinide Borate Phosphate $\text{U}_2[\text{BO}_4][\text{PO}_4]$. *Eur. J. Inorg. Chem.* **2013**, 2013 (30), 5247–5252. <https://doi.org/10.1002/ejic.201300662>.
424. Matsumoto, Y.; Yamamoto, T.; Nakano, K.; Takatsu, H.; Murakami, T.; Hongo, K.; Maezono, R.; Ogino, H.; Song, D.; Brown, C. M.; Tassel, C.; Kageyama, H. High-Pressure Synthesis of $\text{A}_2\text{NiO}_2\text{Ag}_2\text{Se}_2$ (A = Sr, Ba) with a High-Spin Ni^{2+} in Square-Planar Coordination. *Angew. Chem. Int. Ed.* **2019**, 58 (3), 756–759. <https://doi.org/10.1002/anie.201810161>.
425. Matsumoto, Y.; Nambu, Y.; Honda, T.; Ikeda, K.; Otomo, T.; Kageyama, H. High-Pressure Synthesis of $\text{Ba}_2\text{CoO}_2\text{Ag}_2\text{Te}_2$ with Extended CoO_2 Planes. *Inorg. Chem.* **2020**, 59 (12), 8121–8126. <https://doi.org/10.1021/acs.inorgchem.0c00429>.
426. Fuchs, B.; Schmitt, M. K.; Wurst, K.; Huppertz, H. High-Pressure Synthesis and Crystal Structure of the Highly Condensed Yttrium Borate YB_7O_{12} . *Eur. J. Inorg. Chem.* **2019**, 2019 (2), 271–276. <https://doi.org/10.1002/ejic.201801303>.
427. Schmitt, M. K.; Janka, O.; Niehaus, O.; Dresselhaus, T.; Pöttgen, R.; Pielhofer, F.; Wehrich, R.; Krzhizhanovskaya, M.; Filatov, S.; Bubnova, R.; Bayarjargal, L.; Winkler, B.; Glaum, R.; Huppertz, H. Synthesis and Characterization of the High-Pressure Nickel Borate $\gamma\text{-NiB}_4\text{O}_7$. *Inorg. Chem.* **2017**, 56 (7), 4217–4228. <https://doi.org/10.1021/acs.inorgchem.7b00243>.
428. Knyrim, J. S.; Huppertz, H. High-Pressure Synthesis, Crystal Structure, and Properties of the First Ternary Hafniumborate $\beta\text{-HfB}_2\text{O}_5$. *J. Solid State Chem.* **2007**, 180 (2), 742–748. <https://doi.org/10.1016/j.jssc.2006.12.005>.
429. Knyrim, J. S.; Roebner, F.; Jakob, S.; Johrendt, D.; Kinski, I.; Glaum, R.; Huppertz, H. Formation of Edge-Sharing BO_4 Tetrahedra in the High-Pressure Borate $\text{HP-NiB}_2\text{O}_4$. *Angew. Chem. Int. Ed.* **2007**, 46 (47), 9097–9100. <https://doi.org/10.1002/anie.200703399>.
430. Neumair, S. C.; Glaum, R.; Huppertz, H. Synthesis and Crystal Structure of the High-Pressure Iron Borate $\beta\text{-FeB}_2\text{O}_4$. *Z. Naturforsch. B* **2009**, 64 (8), 883–890. <https://doi.org/10.1515/znB-2009-0802>.
431. Neumair, S. C.; Kaindl, R.; Huppertz, H. Synthesis and Crystal Structure of the High-Pressure Cobalt Borate $\text{HP-CoB}_2\text{O}_4$. *Z. Naturforsch. B* **2010**, 65 (11), 1311–1317. <https://doi.org/10.1515/znB-2010-1104>.
432. Schmitt, M. K.; Janka, O.; Pöttgen, R.; Benndorf, C.; de Oliveira, M.; Eckert, H.; Pielhofer, F.; Tragl, A.-S.; Wehrich, R.; Joachim, B.; Johrendt, D.; Huppertz, H. $\text{Mo}_2\text{B}_4\text{O}_9$ —Connecting Borate and Metal-Cluster Chemistry. *Angew. Chem. Int. Ed.* **2017**, 56 (23), 6449–6453. <https://doi.org/10.1002/anie.201701891>.
433. Hinteregger, E.; Hofer, T. S.; Heymann, G.; Perfler, L.; Kraus, F.; Huppertz, H. High-Pressure Synthesis and Characterization of New Actinide Borates, AnB_4O_8 (An = Th, U). *Chem. A Eur. J.* **2013**, 19 (47), 15985–15992. <https://doi.org/10.1002/chem.201302378>.
434. Neumair, S. C.; Vanicek, S.; Kaindl, R.; Többs, D. M.; Martineau, C.; Taulelle, F.; Senker, J.; Huppertz, H. $\text{HP-KB}_3\text{O}_5$ Highlights the Structural Diversity of Borates: Corner-Sharing BO_3/BO_4 Groups in Combination with Edge-Sharing BO_4 Tetrahedra. *Eur. J. Inorg. Chem.* **2011**, 2011 (27), 4147–4152. <https://doi.org/10.1002/ejic.201100618>.
435. Sohr, G.; Többs, D. M.; Schmedt auf der Günne, J.; Huppertz, H. $\text{HP-CsB}_5\text{O}_8$: Synthesis and Characterization of an Outstanding Borate Exhibiting the Simultaneous Linkage of All Structural Units of Borates. *Chem. A Eur. J.* **2014**, 20 (51), 17059–17067. <https://doi.org/10.1002/chem.201404018>.
436. Schmitt, M. K.; Janka, O.; Pöttgen, R.; Huppertz, H. Structure Elucidation and Characterization of the High-Pressure Nickel Borate Hydroxide $\text{NiB}_3\text{O}_5(\text{OH})$. *Z. Anorg. Allg. Chem.* **2017**, 643 (21), 1344–1350. <https://doi.org/10.1002/zaac.201700130>.
437. Fuchs, B.; Heymann, G.; Wang, X.; Tudi, A.; Bayarjargal, L.; Siegel, R.; Schmutzler, A.; Senker, J.; Joachim-Mrosok, B.; Saxer, A.; Yang, Z.; Pan, S.; Huppertz, H. $\text{La}_3\text{B}_6\text{O}_{13}(\text{OH})$: The First Acentric High-Pressure Borate Displaying Edge-Sharing BO_4 Tetrahedra. *Chem. A Eur. J.* **2020**, 26 (30), 6851–6861. <https://doi.org/10.1002/chem.201905419>.
438. Vitzthum, D.; Wurst, K.; Pann, J. M.; Brüggeller, P.; Seibald, M.; Huppertz, H. Exploration into the Syntheses of Gallium- and Indiumborates under Extreme Conditions: $\text{M}_3\text{B}_2\text{O}_{25}(\text{OH})$: Structure, Luminescence, and Surprising Photocatalytic Properties. *Angew. Chem. Int. Ed.* **2018**, 57 (35), 11451–11455. <https://doi.org/10.1002/anie.201804083>.
439. Schmitt, M. K.; Podewitz, M.; Liedl, K. R.; Huppertz, H. High-Pressure Synthesis and Characterization of the Ammonium Yttrium Borate $(\text{NH}_4)\text{YB}_8\text{O}_{14}$. *Inorg. Chem.* **2017**, 56 (22), 14291–14299. <https://doi.org/10.1021/acs.inorgchem.7b02402>.
440. Sohr, G.; Neumair, S. C.; Heymann, G.; Wurst, K.; Schmedt auf der Günne, J.; Huppertz, H. Oxonium Ions Substituting Cesium Ions in the Structure of the New High-Pressure Borate $\text{HP-Cs}_1-x(\text{H}_3\text{O})_x\text{B}_3\text{O}_5$ ($x = 0.5\text{--}0.7$). *Chem. A Eur. J.* **2014**, 20 (15), 4316–4323. <https://doi.org/10.1002/chem.201303550>.
441. Hirose, E.; Kataoka, K.; Nagata, H.; Akimoto, J.; Sasaki, T.; Niwa, K.; Hasegawa, M. High-Pressure Synthesis, Crystal Chemistry, and Ionic Conductivity of a Structural Polymorph of $\text{Li}_3\text{BP}_2\text{O}_8$. *Inorg. Chem.* **2018**, 57 (24), 15048–15050. <https://doi.org/10.1021/acs.inorgchem.8b03155>.

442. Oganov, A. R.; Hemley, R. J.; Hazen, R. M.; Jones, A. P. Structure, Bonding, and Mineralogy of Carbon at Extreme Conditions. *Rev. Mineral. Geochem.* **2013**, *75* (1), 47–77. <https://doi.org/10.2138/rmg.2013.75.3>.
443. Cerantola, V.; Bykova, E.; Kuppenko, I.; Merlini, M.; Ismailova, L.; McCammon, C.; Bykov, M.; Chumakov, A. I.; Petitgirard, S.; Kantor, I.; Svitlyk, V.; Jacobs, J.; Hanfland, M.; Mezouar, M.; Prescher, C.; Rüffer, R.; Prakapenka, V. B.; Dubrovinsky, L. Stability of Iron-Bearing Carbonates in the Deep Earth's Interior. *Nat. Commun.* **2017**, *8* (1), 15960. <https://doi.org/10.1038/ncomms15960>.
444. Merlini, M.; Hanfland, M.; Salamat, A.; Petitgirard, S.; Müller, H. The Crystal Structures of $Mg_2Fe_2C_4O_{13}$, with Tetrahedrally Coordinated Carbon, and $Fe_{13}O_{19}$, Synthesized at Deep Mantle Conditions. *Am. Mineral.* **2015**, *100* (8–9), 2001–2004. <https://doi.org/10.2138/am-2015-5369>.
445. Boulard, E.; Pan, D.; Galli, G.; Liu, Z.; Mao, W. L. Tetrahedrally Coordinated Carbonates in Earth's Lower Mantle. *Nat. Commun.* **2015**, *6* (1), 6311. <https://doi.org/10.1038/ncomms7311>.
446. Chariton, S.; Bykov, M.; Bykova, E.; Koemets, E.; Fedotenko, T.; Winkler, B.; Hanfland, M.; Prakapenka, V. B.; Greenberg, E.; McCammon, C.; Dubrovinsky, L. The Crystal Structures of Fe-Bearing $MgCO_3$ sp^2 - and sp^3 -Carbonates at 98 GPa from Single-Crystal X-Ray Diffraction Using Synchrotron Radiation. *Acta Crystallogr. E* **2020**, *76* (5), 715–719. <https://doi.org/10.1107/S2056989020005411>.
447. Merlini, M.; Cerantola, V.; Gatta, G. D.; Gemmi, M.; Hanfland, M.; Kuppenko, I.; Lotti, P.; Müller, H.; Zhang, L. Dolomite-IV: Candidate Structure for a Carbonate in the Earth's Lower Mantle. *Am. Mineral.* **2017**, *102* (8), 1763–1766. <https://doi.org/10.2138/am-2017-6161>.
448. König, J.; Spahr, D.; Bayarjargal, L.; Gavryushkin, P. N.; Sagatova, D.; Sagatov, N.; Milman, V.; Liermann, H.-P.; Winkler, B. Novel Calcium sp^3 Carbonate Ca_2O_5 -I42d May Be a Carbon Host in Earth's Lower Mantle. *ACS Earth Space Chem.* **2021**, *6* (1), 73–80. <https://doi.org/10.1021/acsearthspacechem.1c00284>.
449. Spahr, D.; Binck, J.; Bayarjargal, L.; Luchitskaia, R.; Morgenroth, W.; Comboni, D.; Milman, V.; Winkler, B. Tetrahedrally Coordinated sp^3 -Hybridized Carbon in Sr_2CO_4 Orthocarbonate at Ambient Conditions. *Inorg. Chem.* **2021**, *60* (8), 5419–5422. <https://doi.org/10.1021/acs.inorgchem.1c00159>.
450. Spahr, D.; König, J.; Bayarjargal, L.; Gavryushkin, P. N.; Milman, V.; Liermann, H.-P.; Winkler, B. $Sr_3[CO_4]O$ Antiperovskite with Tetrahedrally Coordinated sp^3 -Hybridized Carbon and OSr_6 Octahedra. *Inorg. Chem.* **2021**, *60* (19), 14504–14508. <https://doi.org/10.1021/acs.inorgchem.1c01900>.
451. Spahr, D.; König, J.; Bayarjargal, L.; Milman, V.; Perlov, A.; Liermann, H.-P.; Winkler, B. $Sr[C_2O_5]$ is an Inorganic Pyrocarbonate Salt with $[C_2O_5]^{2-}$ Complex Anions. *J. Am. Chem. Soc.* **2022**, *144* (7), 2899–2904. <https://doi.org/10.1021/jacs.2c00351>.
452. Binck, J.; Laniel, D.; Bayarjargal, L.; Khandarkhaeva, S.; Fedotenko, T.; Aslandukov, A.; Glazyrin, K.; Milman, V.; Chariton, S.; Prakapenka, V. B.; Dubrovinskaja, N.; Dubrovinsky, L.; Winkler, B. Synthesis of Calcium Orthocarbonate, Ca_2CO_4 -Pnma at P - T Conditions of Earth's Transition Zone and Lower Mantle. *Am. Mineral.* **2022**, *107* (3), 336–342. <https://doi.org/10.2138/am-2021-7872>.
453. Prewitt, C. T.; Downs, R. T. High-Pressure Crystal Chemistry. *Rev. Mineral. Geochem.* **1998**, *37* (1), 283–317.
454. Bindi, L.; Sirotkina, E. A.; Bobrov, A. V.; Pushcharovsky, D.; Irifune, T. Discovery of $MgTiSi_2O_7$: A New High-Pressure Silicate with the Weberite Structure Synthesized at Transition-Zone Conditions. *Phys. Chem. Miner.* **2017**, *44* (6), 419–424. <https://doi.org/10.1007/s00269-016-0868-8>.
455. Pakhomova, A.; Bykova, E.; Bykov, M.; Glazyrin, K.; Gasharova, B.; Liermann, H.-P.; Mezouar, M.; Gorelova, L.; Krivovichev, S.; Dubrovinsky, L. A Closer Look into Close Packing: Pentacoordinated Silicon in a High-Pressure Polymorph of Danburite. *IUCrJ* **2017**, *4* (5), 671–677. <https://doi.org/10.1107/S2052252517010612>.
456. Gorelova, L. A.; Pakhomova, A. S.; Aprilis, G.; Dubrovinsky, L. S.; Krivovichev, S. V. Pentacoordinated Silicon in the High-Pressure Modification of Datolite, $CaBSiO_4(OH)$. *Inorg. Chem. Front.* **2018**, *5* (7), 1653–1660. <https://doi.org/10.1039/C8QI00257F>.
457. Gorelova, L. A.; Pakhomova, A. S.; Krivovichev, S. V.; Dubrovinsky, L. S.; Kasatkin, A. V. High Pressure Phase Transitions of Paracelsian $BaAl_2Si_2O_8$. *Sci. Rep.* **2019**, *9* (1), 12652. <https://doi.org/10.1038/s41598-019-49112-1>.
458. Pakhomova, A.; Aprilis, G.; Bykov, M.; Gorelova, L.; Krivovichev, S. S.; Belov, M. P.; Abrikosov, I. A.; Dubrovinsky, L. Penta- and Hexa-Coordinated Beryllium and Phosphorus in High-Pressure Modifications of $CaBe_2P_2O_8$. *Nat. Commun.* **2019**, *10* (1), 2800. <https://doi.org/10.1038/s41467-019-10589-z>.
459. Bykov, M.; Bykova, E.; Hanfland, M.; Liermann, H.-P.; Kremer, R. K.; Glaum, R.; Dubrovinsky, L.; van Smaalen, S. High-Pressure Phase Transformations in $TiPO_4$: A Route to Pentacoordinated Phosphorus. *Angew. Chem. Int. Ed.* **2016**, *55* (48), 15053–15057. <https://doi.org/10.1002/anie.201608530>.
460. Zeuner, M.; Pagano, S.; Schnick, W. Nitridosilicates and Oxonitridosilicates: From Ceramic Materials to Structural and Functional Diversity. *Angew. Chem. Int. Ed.* **2011**, *50* (34), 7754–7775. <https://doi.org/10.1002/anie.201005755>.
461. Andrade, M.; Dzivenko, D.; Miehle, G.; Boehler, R.; Hintzen, H. T.; Riedel, R. High-Pressure High-Temperature Synthesis and Structure of β - $MgSiN_2$. *Phys. Status Solidi RRL* **2011**, *5* (5–6), 196–198. <https://doi.org/10.1002/pssr.201105189>.
462. Vadapoo, R.; Ahart, M.; Somayazulu, M.; Holtgrewe, N.; Meng, Y.; Konopkova, Z.; Hemley, R. J.; Cohen, R. E. Synthesis of a Polar Ordered Oxynitride Perovskite. *Phys. Rev. B* **2017**, *95* (21), 214120. <https://doi.org/10.1103/PhysRevB.95.214120>.
463. Klob, S. D.; Schnick, W. Nitridophosphates: A Success Story of Nitride Synthesis. *Angew. Chem. Int. Ed.* **2019**, *58* (24), 7933–7944. <https://doi.org/10.1002/anie.201812791>.
464. Sedlmaier, S. J.; Eberspächer, M.; Schnick, W. High-Pressure Synthesis, Crystal Structure, and Characterization of Zn_2PN_3 —A New *Catena*-Polynitridophosphate. *Z. Anorg. Allg. Chem.* **2011**, *637* (3–4), 362–367. <https://doi.org/10.1002/zaac.201000403>.
465. Pucher, F. J.; Hummel, F.; Schnick, W. $CuPN_2$: Synthesis, Crystal Structure, and Electronic Properties. *Eur. J. Inorg. Chem.* **2015**, *2015* (11), 1886–1891. <https://doi.org/10.1002/ejic.201500009>.
466. Pucher, F. J.; Karau, F. W.; Schmedt auf der Günne, J.; Schnick, W. CdP_2N_4 and MnP_2N_4 —Ternary Transition-Metal Nitridophosphates. *Eur. J. Inorg. Chem.* **2016**, *2016* (10), 1497–1502. <https://doi.org/10.1002/ejic.201600042>.
467. Bertschler, E.-M.; Dietrich, C.; Janek, J.; Schnick, W. $Li_3P_8N_{16}$ —A Lithium Nitridophosphate with Unprecedented Tricyclic $[P_8N_{16}]^{18-}$ Ions. *Chem. A Eur. J.* **2017**, *23* (9), 2185–2191. <https://doi.org/10.1002/chem.201605316>.
468. Bertschler, E.-M.; Niklaus, R.; Schnick, W. Reversible Polymerization of Adamantane-Type $[P_4N_{10}]^{10-}$ Anions to Honeycomb-Type $[P_2N_5]^{5-}$ Layers under High-Pressure. *Chem. A Eur. J.* **2018**, *24* (3), 736–742. <https://doi.org/10.1002/chem.201704975>.
469. Pucher, F. J.; Marchuk, A.; Schmidt, P. J.; Wiechert, D.; Schnick, W. Luminescent Nitridophosphates $CaP_2N_4:Eu^{2+}$, $SrP_2N_4:Eu^{2+}$, $BaP_2N_4:Eu^{2+}$, and $BaSr_2P_8N_{12}:Eu^{2+}$. *Chem. A Eur. J.* **2015**, *21* (17), 6443–6448. <https://doi.org/10.1002/chem.201500047>.
470. Wendl, S.; Schnick, W. $SrH_4P_8N_{12}$ and SrP_8N_{14} : Insights into the Condensation Mechanism of Nitridophosphates Under High Pressure. *Chem. A Eur. J.* **2018**, *24* (59), 15889–15896. <https://doi.org/10.1002/chem.201803125>.
471. Klob, S. D.; Schnick, W. Rare-Earth-Metal Nitridophosphates Through High-Pressure Metathesis. *Angew. Chem. Int. Ed.* **2015**, *54* (38), 11250–11253. <https://doi.org/10.1002/anie.201504844>.
472. Klob, S. D.; Janka, O.; Block, T.; Pöttgen, R.; Glaum, R.; Schnick, W. Open-Shell 3d Transition Metal Nitridophosphates $M^II P_8N_{14}$ ($M^II = Fe, Co, Ni$) by High-Pressure Metathesis. *Angew. Chem. Int. Ed.* **2019**, *58* (14), 4685–4689. <https://doi.org/10.1002/anie.201809146>.
473. Klob, S. D.; Schnick, W. $LiPr_2P_4N_7O_3$: Structural Diversity of Oxonitridophosphates Accessed by High-Pressure Metathesis. *Inorg. Chem.* **2018**, *57* (7), 4189–4195. <https://doi.org/10.1021/acs.inorgchem.8b00455>.
474. Sedlmaier, S. J.; Schmedt auf der Günne, J.; Schnick, W. $Sr_3P_6O_8N_6$ —A Highly Condensed Layered Phosphate. *Dalton Trans.* **2009**, *21*, 4081–4084. <https://doi.org/10.1039/B905136H>.
475. Klob, S. D.; Weis, A.; Wandelt, S.; Schnick, W. High-Pressure Metathesis of the $M_{1-x}PO_{3+4x}N_{1-4x}$ ($x \approx 0.05$) and $M_{0.75}PO_4$ ($M = Zr, Hf$) Orthophosphates. *Inorg. Chem.* **2018**, *57* (7), 4164–4170. <https://doi.org/10.1021/acs.inorgchem.8b00373>.
476. Mandal, M.; Landskron, K. Synthetic Chemistry with Periodic Mesostructures at High Pressure. *Acc. Chem. Res.* **2013**, *46* (11), 2536–2544. <https://doi.org/10.1021/ar4000373>.

477. Mohanty, P.; Kokoszka, B.; Liu, C.; Weinberger, M.; Mandal, M.; Stagno, V.; Fei, Y.; Landskron, K. Large-Pore Periodic Mesoporous Silicas with Crystalline Channel Walls and Exceptional Hydrothermal Stability Synthesized by a General High-Pressure Nanocasting Route. *Microporous Mesoporous Mater.* **2012**, *152*, 214–218. <https://doi.org/10.1016/j.micromeso.2011.11.031>.
478. Mohanty, P.; Ortalan, V.; Browning, N. D.; Arslan, I.; Fei, Y.; Landskron, K. Direct Formation of Mesoporous Coesite Single Crystals from Periodic Mesoporous Silica at Extreme Pressure. *Angew. Chem. Int. Ed.* **2010**, *49* (25), 4301–4305. <https://doi.org/10.1002/anie.201001114>.
479. Mandal, M.; Liu, C.; Sanders, T.; Haso, F.; Bhadram, V.; Arslan, I.; Liu, T.; Fei, Y.; Landskron, K. Periodic Mesoporous Hexagonal Boron Nitride at High Pressure: A Route to Cubic Boron Nitride Nanocrystals and Mesoporous Cubic Boron Nitride. *ChemistrySelect* **2017**, *2* (2), 740–744. <https://doi.org/10.1002/slct.201601925>.
480. Mohanty, P.; Li, D.; Liu, T.; Fei, Y.; Landskron, K. Synthesis of Stishovite Nanocrystals from Periodic Mesoporous Silica. *J. Am. Chem. Soc.* **2009**, *131* (8), 2764–2765. <https://doi.org/10.1021/ja8075007>.
481. Tan, C.; Liu, Z.; Yonezawa, Y.; Sukenaga, S.; Ando, M.; Shibata, H.; Sasaki, Y.; Okubo, T.; Wakihara, T. Unique Crystallization Behavior in Zeolite Synthesis Under External High Pressures. *Chem. Commun.* **2020**, *56* (18), 2811–2814. <https://doi.org/10.1039/C9CC09966B>.
482. Mazur, M.; Arévalo-López, A. M.; Wheatley, P. S.; Bignami, G. P. M.; Ashbrook, S. E.; Morales-García, Á.; Nachtigall, P.; Attfield, J. P.; Čejka, J.; Morris, R. E. Pressure-Induced Chemistry for the 2D to 3D Transformation of Zeolites. *J. Mater. Chem. A* **2018**, *6* (13), 5255–5259. <https://doi.org/10.1039/C7TA09248B>.
483. Gatta, G. D.; Lotti, P.; Tabacchi, G. The Effect of Pressure on Open-Framework Silicates: Elastic Behaviour and Crystal–Fluid Interaction. *Phys. Chem. Miner.* **2018**, *45* (2), 115–138. <https://doi.org/10.1007/s00269-017-0916-z>.
484. Vezzalini, G.; Arletti, R.; Quartieri, S. High-Pressure-Induced Structural Changes, Amorphization and Molecule Penetration in MFI Microporous Materials: A Review. *Acta Crystallogr. B* **2014**, *70* (3), 444–451. <https://doi.org/10.1107/S2052520614008014>.
485. Alabarse, F. G.; Brubach, J.-B.; Roy, P.; Haidoux, A.; Levelut, C.; Bantignies, J.-L.; Cambon, O.; Haines, J. AlPO₄-54–AlPO₄-8 Structural Phase Transition and Amorphization under High Pressure. *J. Phys. Chem. C* **2015**, *119* (14), 7771–7779. <https://doi.org/10.1021/acs.jpcc.5b00318>.
486. Alabarse, F. G.; Joseph, B.; Lausi, A.; Haines, J. Effect of H₂O on the Pressure-Induced Amorphization of Hydrated AlPO₄-17. *Molecules* **2019**, *24* (16), 2864. <https://doi.org/10.3390/molecules24162864>.
487. Thibaud, J.-M.; Rouquette, J.; Hermet, P.; Dziubek, K.; Gorelli, F. A.; Santoro, M.; Garbarino, G.; Alabarse, F. G.; Cambon, O.; Di Renzo, F.; van der Lee, A.; Haines, J. High-Pressure Phase Transition, Pore Collapse, and Amorphization in the Siliceous 1D Zeolite, TON. *J. Phys. Chem. C* **2017**, *121* (8), 4283–4292. <https://doi.org/10.1021/acs.jpcc.6b11594>.
488. Santamaría-Pérez, D.; Marqueño, T.; MacLeod, S.; Ruiz-Fuertes, J.; Daisenberger, D.; Chulía-Jordan, R.; Errandonea, D.; Jordá, J. L.; Rey, F.; McGuire, C.; Mahkluf, A.; Kavner, A.; Popescu, C. Structural Evolution of CO₂-Filled Pure Silica LTA Zeolite Under High-Pressure High-Temperature Conditions. *Chem. Mater.* **2017**, *29* (10), 4502–4510. <https://doi.org/10.1021/acs.chemmater.7b01158>.
489. Marqueño, T.; Santamaría-Pérez, D.; Ruiz-Fuertes, J.; Chulía-Jordán, R.; Jordá, J. L.; Rey, F.; McGuire, C.; Kavner, A.; MacLeod, S.; Daisenberger, D.; Popescu, C.; Rodríguez-Hernández, P.; Muñoz, A. An Ultrahigh CO₂-Loaded Silicalite-1 Zeolite: Structural Stability and Physical Properties at High Pressures and Temperatures. *Inorg. Chem.* **2018**, *57* (11), 6447–6455. <https://doi.org/10.1021/acs.inorgchem.8b00523>.
490. Haines, J.; Levelut, C.; Isambert, A.; Hébert, P.; Kohara, S.; Keen, D. A.; Hammouda, T.; Andrault, D. Topologically Ordered Amorphous Silica Obtained from the Collapsed Siliceous Zeolite, Silicalite-1-F: A Step toward “Perfect” Glasses. *J. Am. Chem. Soc.* **2009**, *131* (34), 12333–12338. <https://doi.org/10.1021/ja904054v>.
491. Isambert, A.; Angot, E.; Hébert, P.; Haines, J.; Levelut, C.; Parc, R. L.; Ohishi, Y.; Kohara, S.; Keen, D. A. Amorphization of Faujasite at High Pressure: An X-Ray Diffraction and Raman Spectroscopy Study. *J. Mater. Chem.* **2008**, *18* (47), 5746–5752. <https://doi.org/10.1039/B809774G>.
492. Neville Greaves, G.; Meneau, F.; Kargl, F.; Ward, D.; Holliman, P.; Albergamo, F. Zeolite Collapse and Polyamorphism. *J. Phys. Condens. Matter* **2007**, *19* (41), 415102. <https://doi.org/10.1088/0953-8984/19/41/415102>.
493. Catafesta, J.; Haines, J.; Zorzi, J. E.; Pereira, A. S.; Perottoni, C. A. Pressure-Induced Amorphization and Decomposition of Fe[Co(CN)₆]. *Phys. Rev. B* **2008**, *77* (6), 064104. <https://doi.org/10.1103/PhysRevB.77.064104>.
494. Boström, H. L. B.; Collings, I. E.; Cairns, A. B.; Romao, C. P.; Goodwin, A. L. High-Pressure Behaviour of Prussian Blue Analogues: Interplay of Hydration, Jahn-Teller Distortions and Vacancies. *Dalton Trans.* **2019**, *48* (5), 1647–1655. <https://doi.org/10.1039/C8DT04463E>.
495. Widmer, R. N.; Lampronti, G. I.; Chibani, S.; Wilson, C. W.; Anzellini, S.; Farsang, S.; Kleppe, A. K.; Casati, N. P. M.; MacLeod, S. G.; Redfern, S. A. T.; Coudert, F.-X.; Bennett, T. D. Rich Polymorphism of a Metal–Organic Framework in Pressure–Temperature Space. *J. Am. Chem. Soc.* **2019**, *141* (23), 9330–9337. <https://doi.org/10.1021/jacs.9b03234>.
496. Su, Z.; Miao, Y. R.; Zhang, G.; Miller, J. T.; Suslick, K. S. Bond Breakage under Pressure in a Metal Organic Framework. *Chem. Sci.* **2017**, *8* (12), 8004–8011. <https://doi.org/10.1039/c7sc03786d>.
497. Collings, I. E.; Goodwin, A. L. Metal–Organic Frameworks Under Pressure. *J. Appl. Phys.* **2019**, *126* (18), 181101. <https://doi.org/10.1063/1.5126911>.
498. Widmer, R. N.; Lampronti, G. I.; Anzellini, S.; Gaillac, R.; Farsang, S.; Zhou, C.; Belonguer, A. M.; Wilson, C. W.; Palmer, H.; Kleppe, A. K.; Wharmby, M. T.; Yu, X.; Cohen, S. M.; Telfer, S. G.; Redfern, S. A. T.; Coudert, F.-X.; MacLeod, S. G.; Bennett, T. D. Pressure Promoted Low-Temperature Melting of Metal–Organic Frameworks. *Nat. Mater.* **2019**, *18* (4), 370–376. <https://doi.org/10.1038/s41563-019-0317-4>.
499. Santoro, M.; Gorelli, F. A.; Bini, R.; Haines, J.; van der Lee, A. High-Pressure Synthesis of a Polyethylene/Zeelote Nano-Composite Material. *Nat. Commun.* **2013**, *4* (1), 1557. <https://doi.org/10.1038/ncomms2564>.
500. Scelta, D.; Ceppatelli, M.; Santoro, M.; Bini, R.; Gorelli, F. A.; Perucchi, A.; Mezouar, M.; van der Lee, A.; Haines, J. High Pressure Polymerization in a Confined Space: Conjugated Chain/Zeelote Nanocomposites. *Chem. Mater.* **2014**, *26* (7), 2249–2255. <https://doi.org/10.1021/cm500061f>.
501. Santoro, M.; Dziubek, K.; Scelta, D.; Ceppatelli, M.; Gorelli, F. A.; Bini, R.; Thibaud, J.-M.; Di Renzo, F.; Cambon, O.; Rouquette, J.; Hermet, P.; van der Lee, A.; Haines, J. High Pressure Synthesis of All-Transoid Polycarbonyl [–(C=O)–]_n in a Zeolite. *Chem. Mater.* **2015**, *27* (19), 6486–6489. <https://doi.org/10.1021/acs.chemmater.5b02596>.
502. Santoro, M.; Scelta, D.; Dziubek, K.; Ceppatelli, M.; Gorelli, F. A.; Bini, R.; Garbarino, G.; Thibaud, J.-M.; Di Renzo, F.; Cambon, O.; Hermet, P.; Rouquette, J.; van der Lee, A.; Haines, J. Synthesis of 1D Polymer/Zeelote Nanocomposites Under High Pressure. *Chem. Mater.* **2016**, *28* (11), 4065–4071. <https://doi.org/10.1021/acs.chemmater.6b01639>.

4.13 Mixed anion materials

Tong Zhu, Daichi Kato, Shenghan Gao, and Hiroshi Kageyama, Department of Energy and Hydrocarbon Chemistry, Graduate School of Engineering, Kyoto University, Nishikyo-ku, Kyoto, Japan

© 2023 Elsevier Ltd. All rights reserved.

4.13.1	Introduction	431
4.13.2	Oxynitrides	432
4.13.2.1	Ammonolysis of oxides	432
4.13.2.2	Synthesis from solid nitridation sources	433
4.13.2.3	High pressure synthesis	434
4.13.2.4	Topochemical synthesis from oxyhydrides	434
4.13.2.5	Anion order in oxynitrides	434
4.13.3	Oxyhydrides	436
4.13.3.1	High temperature synthesis	436
4.13.3.2	Topochemical synthesis	436
4.13.3.3	High pressure synthesis	438
4.13.3.4	Anion order-disorder	438
4.13.3.5	Thin films	439
4.13.4	Oxyfluorides	439
4.13.4.1	Topochemical synthesis	440
4.13.4.2	Electrochemical synthesis	441
4.13.4.3	Solvothermal synthesis	442
4.13.4.4	High pressure synthesis	443
4.13.5	Oxychalcogenides and oxypnictides	443
4.13.6	Conclusion	444
References		444

Abstract

Inorganic oxide compounds have been the central focus of solid-state research in the past century, leading to the discovery of countless devices ranging from batteries to solid oxide fuel cells. The rapid development of modern society requires for additional materials with more superior functionalities, driving scientists to look for compounds beyond simple oxides.

A mixed-anion compound is a solid-state material with more than one anionic species. The combination of different anions in a single phase offers an opportunity not only to provide improved properties from compounds with single-anion species, but to emerge new functionalities which have not seen before. In this article, we will give a brief review of the current status of oxide-based mixed-anion compounds, including oxynitrides, oxyhydrides, oxyfluorides, oxychalcogenides and oxypnictides, with the former three types being our main focus. In order to demonstrate the crucial role of multiple anions, the synthetic aspects of these compounds towards desired structures and properties will be mainly discussed. It will be seen that although compounds with multiple anions indeed offer a platform towards advanced functional materials, their syntheses are normally beyond the simple 'heat-and-beat' method and require particular designing approaches. The area of mix-anion chemistry still remains largely unexplored, and this article only serves as an entry point to the field.

4.13.1 Introduction

Most natural minerals are oxides, and even in human-made products such as potteries and pigments, oxides have been used since ancient times. Most modern electronic devices, such as capacitors and cathode materials, are manufactured based on oxides. Most of these materials can be easily obtained by simply sintering raw materials at high temperatures, as humans (or the earth) have been doing since BC. The structures and properties of these oxides largely depend on the chemistry of the selected cations.

Mixed-anion compounds consisting of multiple anion species do exist, but in overwhelmingly small numbers. However, the blending of anions has the potential to essentially change the science, not just improve properties, and in recent years mixed-anion compounds are attracting a great deal of attention as next-generation materials for industry¹. Unlike oxides, which can be easily synthesized by simply firing at high temperatures, new synthetic chemistry is required for mixed-anion compounds. In oxides, metals are coordinated only to oxide ligands, whereas in mixed-anion compounds cations are coordinated to different ligands, from which innovative physical properties are expected to emerge. In this regard, mixed-anion science is just in its infancy, so it is not possible to give a complete and comprehensive description. Therefore, in this article, we will review the knowledge that is currently

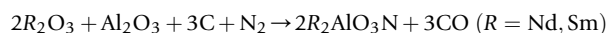
available, with a particular focus on mixed-anion compounds containing the oxide ion, such as oxynitrides, oxyhydrides, and oxyfluorides, and outline their syntheses and structural features.

4.13.2 Oxynitrides

Neighboring to each other in the periodic table, oxide and nitride anions have several similar chemical and electronic characteristics: they are isoelectronic, with a $[\text{He}]2s^22p^6$ electronic configuration; the electronegativities of both anions are relatively high (Mulliken electronegativities are 3.22 and 3.08 for O and N, respectively)²; they have similar ionic radii (1.38 Å for O^{2-} and 1.46 Å for N^{3-})³. These similarities imply that oxynitrides share close structural features with respect to their oxide analogues.

Nevertheless, in addition to the higher formal charge for nitride anion which gives a chance to combine it with more positively charged cations, higher polarizability and lower electronegativity of the nitride anion brings about important consequences to the bonding nature: a metal-nitride bond possesses more covalent character than a metal-oxide bond. In fact, oxynitrides are considered as a highly fascinating class of materials and possess some superior properties which are not seen in oxides. For example, the presence of higher energy N $2p$ orbitals relative to O $2p$ orbitals means that oxynitrides have a smaller band gap than oxides, making them suitable candidates for applications as visible light responsive photocatalysts and pigments^{4,5}.

The major challenge in the research of oxynitrides remains the synthesis. The higher bond energy of N_2 molecule (941 kJ mol^{-1} ; for O_2 the value is 500 kJ mol^{-1})⁶⁻⁹ and lower electron affinity of nitrogen¹⁰ means a lower free formation energy of oxynitrides, and the synthetic conditions of oxynitrides require a careful control in order to prevent the decomposition of oxynitrides into oxides and N_2 . In addition, the choice of nitridation source is also critical. N_2 is inert, with triple bonds too strong to be cleaved (the formation energy of nitride anion from its gas form is $+2300 \text{ kJ mol}^{-1}$)⁶⁻⁹. Therefore, N_2 is rarely used as a nitrogen source in the synthesis of oxynitrides, although there are some exceptions, such as the layered perovskites $\text{Nd}_2\text{AlO}_3\text{N}$ and $\text{Sm}_2\text{AlO}_3\text{N}$ that can be synthesized by the following reaction¹¹:



4.13.2.1 Ammonolysis of oxides

Reacting oxides or carbonates under flowing NH_3 at moderate to high temperatures is the most commonly used strategy for the synthesis of oxynitrides. Ammonolysis of oxides generates water as a by-product, which serves as one of the main thermodynamic driving forces towards the formation of oxynitrides¹². The toxic nature of NH_3 and its tendency to dissociate into H_2 and N_2 suggest that ammonolysis reactions must be dealt with great care. The dissociation reaction at high temperature can be explained by Le Chatelier's principle ($2\text{NH}_3(\text{g}) + \text{heat} \leftrightarrow \text{N}_2(\text{g}) + 3\text{H}_2(\text{g})$), indicating that increasing temperature shifts the equilibrium to the right. This dissociation reaction at elevated temperatures implies two consequences: the importance of controlling ammonia flow rate and the highly reducing reaction environment. During the dissociation reaction, active nitriding species (NH_2 , NH and atomic N) may be formed before fully converting to N_2 and H_2 , and these transient phases react with the oxide surface. However, to form bulk oxynitrides, nitride anions require a high diffusion activation energy¹³. Therefore, the reaction temperature and NH_3 flow rate are two important parameters involved in ammonolysis and should be adjusted delicately: the reaction temperature needs to be high enough to decompose NH_3 into active transient phases and for nitride anions to diffuse, while at the same time the flow rate must be controlled to provide fresh active nitriding species.

At times, different products are generated depending on NH_3 flow rates. A semiconducting β -TaON containing alternating oxide and nitride layers (Fig. 1A) is prepared by direct ammonolysis of Ta_2O_5 at 850°C with fast NH_3 flow^{14,17}. In contrast, γ -TaON polymorph (Fig. 1B) forms if a slower NH_3 flow rate is employed¹⁵. The γ -form is a metastable phase because a 900°C treatment results in the transformation into the β -form. Presumably, γ -TaON phase is kinetically accessible at mild conditions.

Due to the reducing environment provided by H_2 , high temperature ammonolysis is applicable to transition-metal oxynitrides containing metals with low electronegativities, such as Ti, Nb, and Ta. A series of perovskite oxynitrides with a general formula $A^{II}B^V\text{O}_2\text{N}$ ($A = \text{Ba, Sr, Ca}$; $B = \text{Nb, Ta}$) can be prepared by heating mixtures of ACO_3 and B_2O_5 under flowing ammonia¹⁸⁻²¹. An aliovalent substitution of oxide with nitride allows the use of cations with higher charges. The presence of nitride anions, more specifically its larger polarizability with respect to oxide, is responsible for large dielectric constants observed in BaTaO_2N and SrTaO_2N ²¹. Visible-light responsive photocatalytic activities such as water splitting are observed, e.g., in LaTiO_2N ^{5,22}, which is due to a lower electronegativity of nitrogen, resulting in the upward shift of the valence band maximum and a narrowing of the band gap. Such band-gap control is also utilized in non-toxic pigments $\text{Ca}_{1-x}\text{La}_x\text{TaO}_{3-x}\text{N}_x$ ⁴, with their colors tuned by adjusting x .

An appropriate choice of flux, e.g., KCl/NaCl , lowers the reaction temperature and thus can reduce the concentration of anion vacancies. It also provides a morphology control. LaTiO_2N ²³, BaTaO_2N ²⁴ and BaNbO_2N ²⁵ prepared from flux-assisted synthesis possess superior photocatalytic activities. BaTaO_2N crystals, grown with the assistance of molten BaCN_2 flux²⁶, exhibit ferroelectric switching. Most oxynitrides are semiconductors, but oxynitrides containing metals with partially filled d -orbitals can be obtained. For example, $\text{SrW}^{\text{IV/V}}\text{O}_2\text{N}$, $\text{SrMo}^{\text{IV/V}}\text{O}_{2.5}\text{N}_{0.5}$ and $\text{LaW}^{\text{V/VI}}\text{O}_{0.6}\text{N}_{2.4}$ are directly synthesized from $\text{SrW}^{\text{VI}}\text{O}_4$, $\text{SrMo}^{\text{VI}}\text{O}_4$ and $\text{La}_2\text{W}^{\text{VI}}\text{O}_9$ respectively²⁷⁻²⁹.

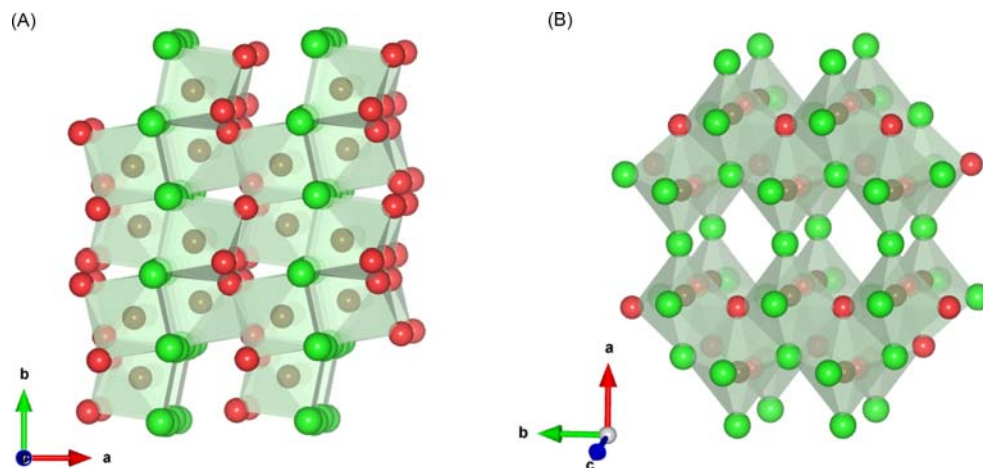


Fig. 1 Crystal structure of β -TaON¹⁴ (A) and γ -TaON¹⁵ (B). Ta, O and N are shown in brown, red and green, respectively. β -TaON contains edge-sharing TaO₃N₄ polyhedra with alternating oxide and nitride layers, while γ -TaON contains TaO₃N₃ and TaO₂N₄ octahedra sharing corners and edges. The crystal structures shown in this article are produced using VESTA software¹⁶.

4.13.2.2 Synthesis from solid nitridation sources

A recent progress in the oxynitride synthesis is the use of solid nitride sources. SrTaO₂N³⁰ and CaTaO₂N³¹ can be synthesized by reacting a low-cost solid nitridation source, C₃N₄, with Sr₂Ta₂O₇ and Ca₂Ta₂O₇ precursors, respectively. Their synthetic temperature (800 °C) is lower than that of conventional ammonolysis (1000 °C)^{32,33} or the solid-solid synthesis of SrTaO₂N using TaON and SrO (1500 °C)³⁴, which is attributed to the formation of a SrCN₂ intermediate (Fig. 2)³⁰. In addition to shorter reaction time, the obtained oxynitrides synthesized with C₃N₄ have better morphologies and smaller particle sizes. Likewise, reacting La₂Ti₂O₇ with urea produces a single-phase of LaTiO₂N³⁵.

MnO_xN_y, a potential catalyst for oxygen-reduction reaction, can be synthesized from manganese oxides and NaNH₂ at temperatures below 280 °C³⁶. Since the melting point of NaNH₂ is approximately 240 °C³⁷, it acts as both nitridation source and a flux, which explains the low reaction temperature. Simple metal nitrides can be used as nitridation sources. When a mixture of MoO₃ and NaN₃ is heated, polar Na₃MoO₃N is obtained³⁸. Both nitridation sources discussed here should be dealt with great care due to their explosive nature.

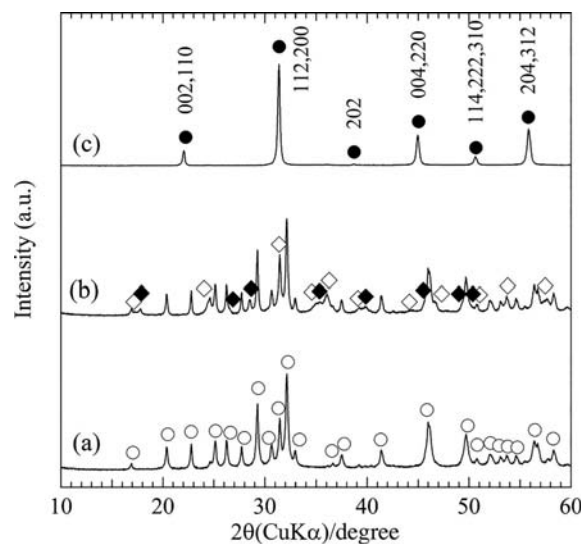


Fig. 2 X-ray diffraction patterns of the precursors (Sr₂Ta₂O₇ and amorphous C₃N₄) and products as a function of temperatures³⁰. (a) before the reaction; (b) 700 °C; (c) 800 °C. Unfilled circles, filled circles, unfilled diamonds and filled diamonds represent Sr₂Ta₂O₇, SrTaO₂N, Ta₃N₅ and SrCN₂, respectively. The formation of SrCN₂ intermediate is important for the low reaction temperature. Reprinted with permission from Masubuchi, Y.; Tadaki, M.; Kikkawa, S. Synthesis of the Perovskite SrTaO₂N Using C₃N₄ for Both Reduction and Nitridation. *Chem. Lett.* **2018**, 47 (1), 31–33. Copyright {2018} The Chemical Society of Japan.

4.13.2.3 High pressure synthesis

High pressure synthesis yields compounds that would not be available at ambient pressure. It is particularly suitable for the synthesis of perovskite and other closed-packed structures, which is also true for oxynitrides. In addition, the principal role of high pressure in synthesizing oxynitrides is to prevent nitrogen loss under reaction conditions. Perovskite oxynitrides $LnZrO_2N$ ($Ln = Pr, Nd$ and Sm) can only be synthesized under high pressure (2–3 GPa) from Ln_2O_3 and Zr_2ON_2 ³⁹. Here, it is important to use Zr_2ON_2 as a precursor instead of ZrN with a melting point of approximately 3000 °C⁴⁰.

Another advantage is that the non-reducing condition makes it possible to prepare oxynitrides with middle-to-late transition metals. $MnTaO_2N$ is prepared from MnO and $TaON$ at 6 GPa and 1400 °C⁴¹. It adopts a polar $LiNbO_3$ -type structure ($R3c$ space group) and exhibits a helical spin order as a result of competing nearest and next-nearest neighbor interactions due to extensive MnO_4N_2 octahedral tilting. Similar approach is applied to synthesize $ZnTaO_2N$ ⁴², which adopts a centrosymmetric, high-temperature $LiNbO_3$ -type structure ($R-3c$ space group) down to 20 K (Fig. 3). This non-polar structure is explained by the strong electrostatic repulsion between Zn^{2+} and Ta^{5+} , a situation only possible in perovskite oxynitrides with total negative formal charge of -7 .

4.13.2.4 Topochemical synthesis from oxyhydrides

The labile nature of hydride anions is utilized to topochemically synthesize oxynitrides at mild conditions. $BaTiO_{3-x}N_{2x/3}$, with the nitrogen content tuned up to 0.6, is synthesized from ammonolysis of $BaTiO_{2.4}H_{0.6}$ at 500 °C, a temperature which can only nitridize the surface of an oxide⁴³. During the whole synthesis route from tetragonal (polar) $BaTiO_3$, Ti^{4+} (d^0) is first reduced to $Ti^{3.4+}$ ($d^{0.6}$) in cubic $BaTiO_{2.4}H_{0.6}$, but then gradually oxidized while maintaining the cubic structure, and finally completely oxidized to Ti^{4+} (d^0) in tetragonal (polar) $BaTiO_{2.4}N_{0.4}$. More strikingly, the same material can be synthesized in nitrogen gas at 400 °C, which is unprecedented given the triple bond of N_2 molecule⁴⁴.

The topochemical nitridation from oxyhydrides reveals the importance of anion vacancy in facilitating anion diffusion. While direct ammonolysis of $EuTiO_3$ produces $EuTiO_{2.25}N_{0.75}$, ammonolysis of $EuTiO_{2.82}H_{0.18}$ leads to a fully nitridized product of $Eu^{III}-Ti^{IV}O_2N$ ⁴⁵. This contrasting result is attributed to the anion vacancy created during the early stage of ammonolysis: the presence of a small amount of anion vacancy (2%) in $EuTiO_{2.82}N_{0.12}\square_{0.06}$ (\square : anion vacancies) significantly reduces the kinetic barrier for further N^{3-} diffusion (or N/O exchange), leading to $EuTiO_2N$.

4.13.2.5 Anion order in oxynitrides

The order and disorder of anions in oxynitrides is an important research focus because the physical and chemical properties are quite sensitive to the anion distribution. However, the similarity between oxides and nitrides makes it difficult to distinguish between these two anions by X-ray diffraction. Advanced techniques such as neutron diffraction and polarized XANES are used to explore the possibility of anion ordering. As displayed in Fig. 4, there are different possibilities in anion arrangement: in addition to the well-known complete disorder (left) and complete order (middle), a correlated short-range order (right) is possible, which emerges by imposing the local bonding constraint on the $M(O/N)_6$ octahedron.

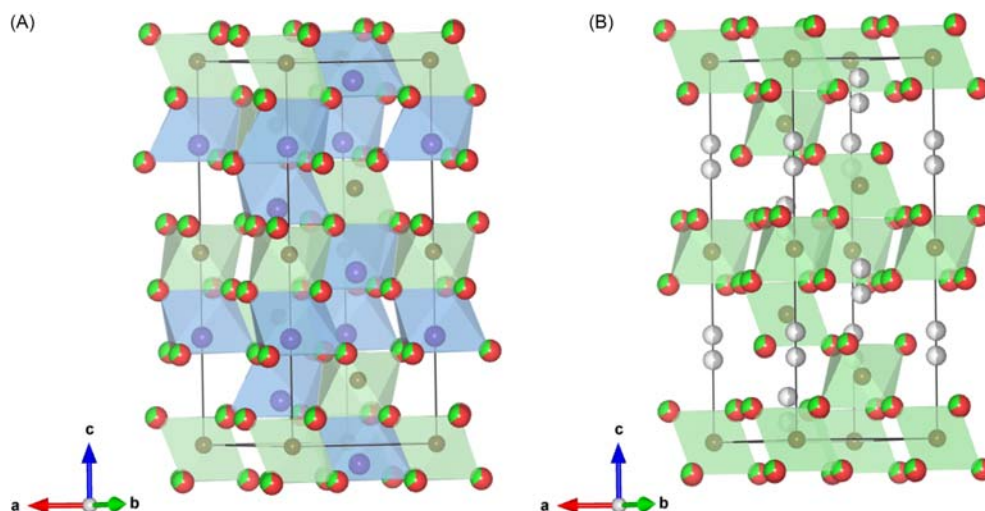


Fig. 3 Crystal structures of polar $MnTaO_2N$ ⁴¹ (A) and non-polar $ZnTaO_2N$ ⁴² (B). Mn, Zn, Ta, O and N are shown in purple, silver, brown, red and green, respectively. Zn adopts a disordered arrangement in its crystallographic site with 50% occupancy. The polar nature of $MnTaO_2N$ can be viewed by considering the collective polar displacements of Mn^{2+} and Ta^{5+} cations along the hexagonal c axis, and similar displacements are not observed in $ZnTaO_2N$.

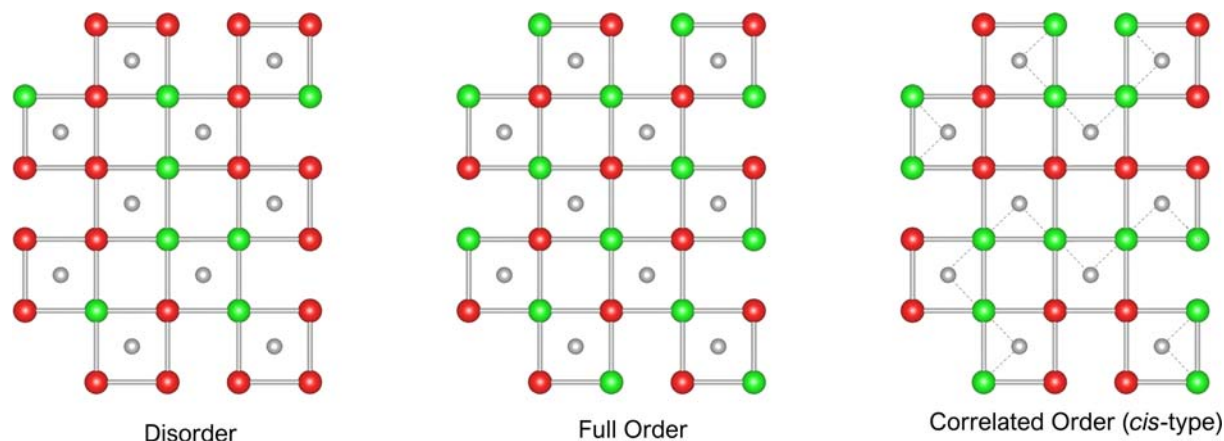


Fig. 4 Simplified scenarios for oxide (red)/nitride (green) anion order in oxynitride perovskites. Silver balls represent central metal cations. A random distribution of anions exists in the left figure, while a well-defined periodic arrangement exists in the middle figure. A correlated local *cis*-arrangement is observed in the right-hand-side figure, with the local *cis*-arrangement demonstrated by the dotted line.

From an energy point of view, the enthalpy (bonding) gain from anion order must be large enough to compensate for the entropy loss, since anion ordering comes with an entropy penalty. In perovskite AMO_2N oxynitrides without d electrons, a *cis*-configuration is energetically favored due to strong $M(d_\pi)-N(p_\pi)-M(d_\pi)$ interactions⁴⁶. This local bonding constraint, together with the entropy consideration, suggests the short-range order composed of various zigzag $N-M-N$ chains (rings). A combined neutron powder diffraction and electron diffraction study indicates a local *cis*-arrangement in $SrNbO_2N$ (Fig. 5A)⁴⁶. A similar local arrangement is also observed in $BaTaO_2N$ using PDF measurements and DFT calculations⁴⁸.

What complicates the structure of perovskite oxynitrides is that the perovskite structure is sensitive to octahedral tilting. When correlated anion order and tilting distortions occur simultaneously, the crystal structure can be complicated, especially when these two parameters are symmetrically incompatible with each other. For example, the octahedral tilting distortion in $LaTaON_2$ lowers the crystal symmetry from cubic to orthorhombic, but with the correlated O/N order, the true symmetry becomes monoclinic (Fig. 5B)⁴⁷. A metastable, *trans*-configurational $Ca_{1-x}Sr_xTaO_2N$ thin film can be partially stabilized by applying compressive strain from a substrate, as revealed by N and O K-edge linearly polarized X-ray absorption near-edge structure (LP-XANES) and TEM, together with first-principles calculations^{49,50}.

More recently, ammonolysis of $SrVO_3$ powders at $600^\circ C$ is found to yield $SrVO_{2.2}N_{0.6}\square_{0.2}$, with vacancy planes aligned along the $[111]$ direction with a five-fold periodicity⁵¹. When the epitaxial $SrVO_3$ film is subjected to the same treatment, the direction and periodicity of anion-vacancy planes change, resulting in different superstructures. These observations together suggest that strain engineering provides a new avenue to manipulate the structure as well as properties of oxynitrides, and may further be expanded to other mixed-anion compounds.

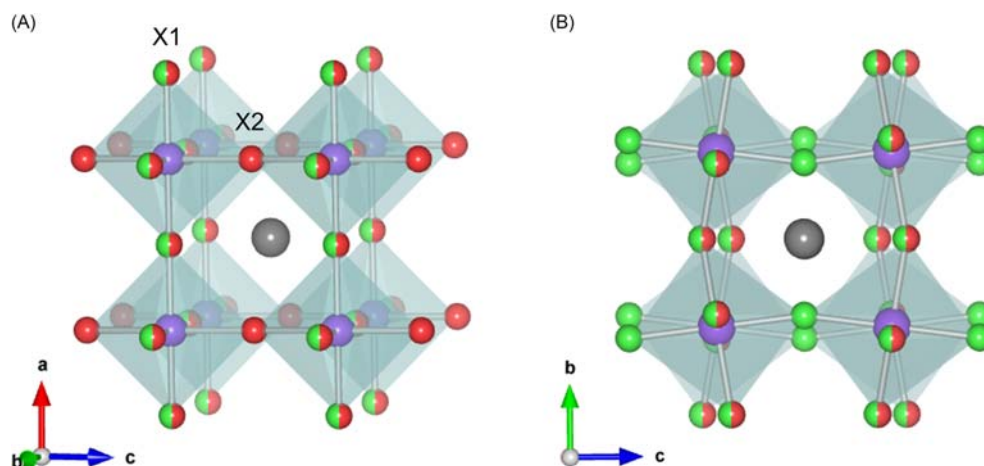


Fig. 5 Tetragonal $SrNbO_2N$ ⁴⁶ (A) and monoclinic $LaTaON_2$ ⁴⁷ (B). Sr/La, Nb/Ta, O and N are shown in grey, purple, red and green respectively. Nitride anions adopt local *cis*-order in the ab plane (only) in $SrNbO_2N$, but the lack of long-range order gives an average structure observed in (A), with half of the X1 site occupied by nitride, while X2 site is fully occupied by oxide. A similar local *cis*-order exists in $LaTaON_2$ with oxides only residing in the ab plane⁴⁷. Such local order combines with the octahedral tilting to generate an (average) monoclinic structure.

4.13.3 Oxyhydrides

4.13.3.1 High temperature synthesis

Ionic hydrogen usually exists as a proton (H^+) by losing one electron from the hydrogen atom, as can be imagined from its position in the periodic table of elements. Hydrogen can also become a hydride (H^-) by accepting another electron in the 1 s orbital to form the closed-shell electronic structure of helium. However, in the earth and biological environments where oxygen and water are abundant, hydrogen is almost exclusively protonic, owing to its moderate electronegativity ($H = 2.20$), which is close to C ($= 2.55$) and P ($= 2.19$). The synthesis of oxyhydrides therefore requires a reducing environment to avoid oxidation. One hypothetical approach to synthesize an oxyhydride is simply heating a mixture of binary oxides and hydrides at high temperature. However, the examples of high temperature synthesis are rare because the chemical properties of oxide and hydride anions are very different. Even in vacuum, the metal hydride precursor (e.g., SrH_2) will dissociate into an elemental metal and hydrogen gas, resulting in the formation of oxides, rather than an oxyhydride.

Nevertheless, as a successful example, Ba_3AlO_4H has been synthesized from a mixture of BaH_2 , BaO , and Al_2O_3 at $1100\text{ }^\circ\text{C}$ under H_2 atmosphere⁵². Ba_3AlO_4H can be viewed to adopt an anti-perovskite structure (Fig. 6A), in which the hydride appears to be stabilized by being located in the octahedral center surrounded by Ba with a low electronegativity of 0.89. Similarly, in $Rb_2Ba_6Sb_5HO$ (Fig. 6B), the hydride anion is located at the center of the *trans*- HBa_2Rb_4 octahedron, while $Ba_8Sb_4OH_2$ and $Ba_8Bi_4OH_2$ contain HBa_5 pyramids⁵³. In addition, hydride-rich suboxides such as $Ba_{21}M_2O_5H_{24}$ ($M = Ge, Si, Ga, Tl$)⁵⁴ and $LnHO$ ($Ln = \text{lanthanide}$)^{55–57} are known. $LaHO$ is synthesized by heating a mixture of $LaH_{2.5}$ and La_2O_3 at $900\text{ }^\circ\text{C}$ with flowing hydrogen gas. Other synthetic routes are reported, such as “ $2Nd + Nd(OH)_3 \rightarrow 3NdHO$ ” and “ $Nd_2O_3 + CaH_2 \rightarrow 3NdHO + CaO$ ”⁵⁶. $LnHO$ crystallizes in the fluorite structure, while YHO adopts an anti-LiMgN type structure⁵⁸.

4.13.3.2 Topochemical synthesis

In the case of transition metals with *d*-electrons, under high temperature conditions the hydride anions reduce the transition metal cations into elemental metals. One useful approach to avoid this is to use low-temperature topochemical reactions using metal hydrides such as CaH_2 and NaH . This method was first applied to a cobalt oxide with a layered perovskite structure according to the following reaction at $450\text{ }^\circ\text{C}$:



yielding $LaSrCoO_3H_{0.7}$, as shown in (Fig. 7)⁵⁹. Here, the byproduct CaO can be washed away with 0.1 M NH_4Cl in degassed methanol under a nitrogen atmosphere. In $LaSrCoO_3H_{0.7}$, the hydride anion is located exclusively in the equatorial site in a striped fashion (along the *a*-axis) with a 30% anion deficiency. The Co valence is quite low ($+1.7$), reflecting the strong reducing condition. However, the presence of electrons in the $3d\ e_g$ orbital of $Co^{1.7+}$ ($d^{7.3}$) helps stabilize the structure by forming a 180 degrees $Co-H-Co$ σ bond with the H 1 s orbital, as supported by DFT calculations⁶⁰. Later, this synthetic method was applied to obtain $BaTiO_{3-x}H_x$ from perovskite $BaTiO_3$ according to the following formula⁶¹,

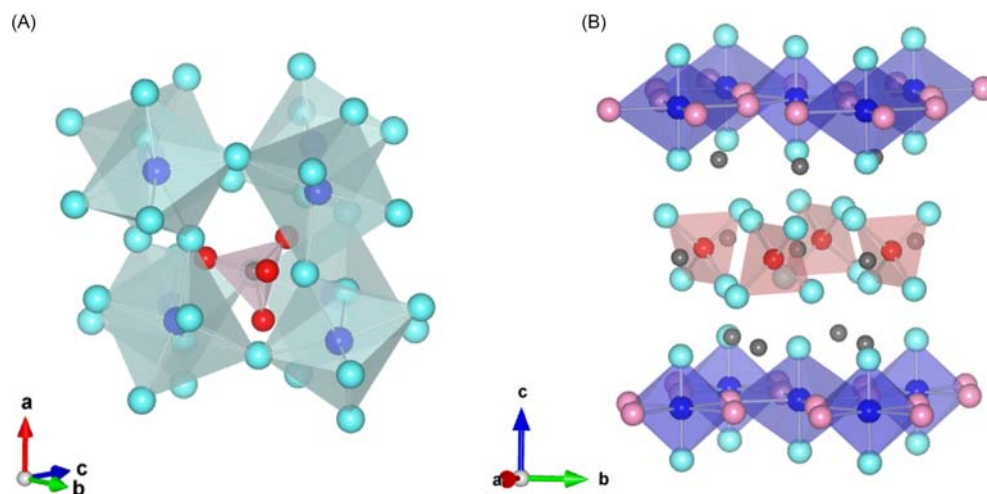


Fig. 6 Crystal structures of Ba_3AlO_4H ⁵² (A) and $Rb_2Ba_6Sb_5HO$ ⁵³ (B). In Ba_3AlO_4H the formula is better rearranged as $(AlO_4)HBa_3$ to describe its anti-perovskite structure with H locating in the center of Ba octahedra (to form HBa_6) and AlO_4 polyanions sitting in the A-site. In $Rb_2Ba_6Sb_5HO$, the structural framework can be viewed as alternating OBa_4 tetrahedron layers and corner-sharing (HBa_2Rb_4) octahedron layers separated by Sb (grey spheres) along *c*. OBa_4 tetrahedra are also separated by Sb within their layer. The formula may hence be written as $(OBa_4)Sb_5(HBa_2Rb_2)$ to emphasize its structural feature.

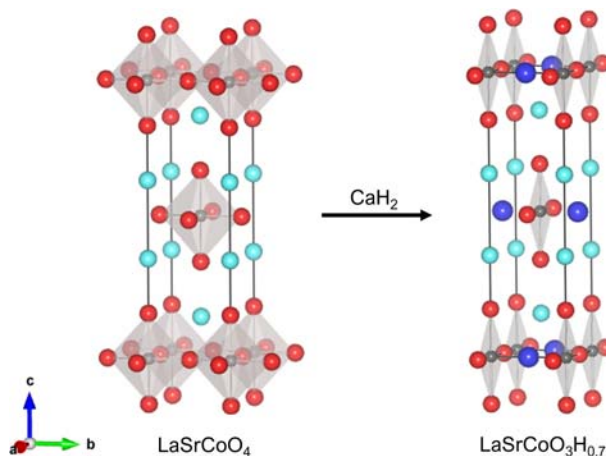


Fig. 7 Topochemical reaction of LaSrCoO_4 with CaH_2 to yield $\text{LaSrCoO}_3\text{H}_{0.7}$.⁵⁹ La/Sr, Co, O and H are shown in cyan, grey, red and blue respectively. Hydride anions occupy half of equatorial sites (with deficiency) and form stripes along *a*.

The parent BaTiO_3 is a tetragonal ferroelectric material at room temperature and is widely used in electronic devices such as multilayer transistors, but it changes into a non-polar, cubic structure ($Pm-3m$) as a result of hydrogen substitution (i.e., electron doping). Unlike the anion-ordered $\text{LaSrCoO}_3\text{H}_{0.7}$, anions (H^-/O^{2-}) are randomly distributed in $\text{BaTiO}_{3-x}\text{H}_x$, with the content of hydride being experimentally variable. Depending on the reaction conditions, up to 20% substitution ($x = 0.6$) can be achieved. While $\text{LaSrCoO}_3\text{H}_{0.7}$ is a Mott insulator, $\text{BaTiO}_{3-x}\text{H}_x$ is a Pauli paramagnetic metal⁶². In $\text{BaTiO}_{3-x}\text{H}_x$, *d* electrons only exist in the t_{2g} orbital even at the largest *x* composition, which results in important features. Unlike $\text{LaSrCoO}_3\text{H}_{0.7}$, the Ti 3*d* t_{2g} orbitals are orthogonal to the H 1*s* orbital and thus are nonbonding in nature. In addition, the hydride anion can undergo a rapid exchange reaction due to its smaller mass and charge (relative to O^{2-}) and is prone to reacting with oxidizers or acids due to its strong basicity. This means that hydrides in oxyhydrides can be regarded as labile ligands as used in coordination chemistry, and can be converted into new mixed-anion compounds (e.g., oxynitrides and oxyfluorides) through low-temperature anion-exchange reactions using oxyhydrides as precursors (Fig. 8)⁴⁴. Hydride diffusion has been investigated using deuterium exchange⁶¹. Besides, the hydride's lability makes $\text{BaTiO}_{3-x}\text{H}_x$ an excellent catalyst for ammonia synthesis. Ti has been considered a "dead" element for catalytic uses because of its strong binding to nitrogen (as seen in TiN as a coating material)⁶³. The introduction of hydrides, however, changes the well-known scaling rule in catalysis.

A series of $\text{Sr}_{n+1}\text{V}_n\text{O}_{2n+1}\text{H}_n$ ($n = 1, 2$ and ∞ for $\text{Sr}_2\text{VO}_3\text{H}$, $\text{Sr}_3\text{V}_2\text{O}_5\text{H}_2$ and SrVO_2H , respectively) are obtained from their corresponding precursors, the Ruddlesden-Popper (RP) perovskite oxides $\text{Sr}_{n+1}\text{V}_n\text{O}_{3n+1}$ ($\text{Sr}_3\text{V}_2\text{O}_7$, Sr_2VO_4 and SrVO_3)⁶⁴. Interestingly, $\text{Sr}_{n+1}\text{Fe}_n\text{O}_{2n+1}$ ($n = 1, 2$ and ∞ for Sr_2FeO_3 , $\text{Sr}_3\text{Fe}_2\text{O}_5$ and SrFeO_2 , respectively) obtained by hydride reduction of $\text{Sr}_{n+1}\text{Fe}_n\text{O}_{3n+1}$ (Sr_2FeO_4 , $\text{Sr}_3\text{Fe}_2\text{O}_7$, and SrFeO_3) exhibit a similar structural conversion, but hydride anions are replaced by oxygen vacancies⁶⁵⁻⁶⁷. SrVO_2H is a quasi-two-dimensional antiferromagnet (Mott insulator) because V–H–V along the *c*-axis is nonbonding due to the orthogonal geometry between V t_{2g} and H 1*s* orbitals. When high pressure is applied, a phase transition to metallic state can be achieved⁶⁸.

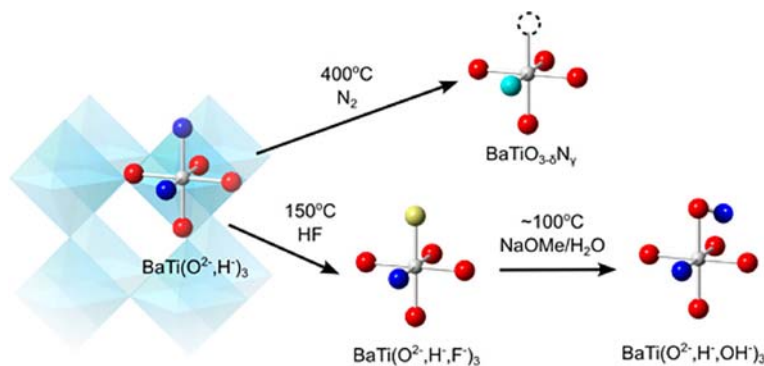


Fig. 8 The use of oxyhydride $\text{BaTiO}_{2.5}\text{H}_{0.5}$ as a starting material enables new multi-step low temperature topochemical routes to access new mixed-anion compounds⁴⁴. O^{2-} , H^- , N^{3-} and F^- anions are shown in red, blue, green and yellow, respectively. Reprinted with permission from Masuda, N.; Kobayashi, Y.; Hernandez, O.; Bataille, T.; Paofai, S.; Suzuki, H.; Ritter, C.; Ichijo, N.; Noda, Y.; Takegoshi, K.; Tassel, C.; Yamamoto, T.; Kageyama, H. Hydride in $\text{BaTiO}_{2.5}\text{H}_{0.5}$: A Labile Ligand in Solid State Chemistry. *J. Am. Chem. Soc.* **2015**, *137* (48), 15315–15321. Copyright (2015) American Chemical Society.

Strongly reduced oxides of 4*d* transition metals, e.g., SrRuO₂, are not accessible through hydride reduction, but SrFe_{0.5}Ru_{0.5}O₃ in combination with 3*d* metal cations can be reduced to SrFe_{0.5}Ru_{0.5}O₂⁶⁹. Similar strategies have been used to obtain oxyhydrides containing 4*d* and 5*d* transition metal cations, for example, LaSr₃NiRuO₄H₄^{70,71}, LaSr₃CoRuO₄H₄⁷², LaSr₃CoRhO₆H₂ and LaSr₃MnRhO₆H₂⁷³. Thus, topochemical hydride reduction approach has greatly expanded the repertoire of transition metal-containing oxyhydrides, together with the high-pressure synthesis described later.

In most of oxyhydrides presented here, the anion compositions are described to be stoichiometric, but the presence of an anion deficiency must be considered, at least during the reaction to allow oxygen and hydride anions to diffuse through the anion lattice. In this regard, the result on the reactivity of SrTiO₃ is suggestive; the amount of hydride content can be greatly increased by introducing oxygen deficiencies in SrTiO₃ through aliovalent cation substitution (Ti⁴⁺ → Sc³⁺)⁷⁴, similar to what is commonly applied to ionic conductors in solid-state ionics. In other words, the kinetic factor dominates the final product (i.e., hydride content).

4.13.3.3 High pressure synthesis

Despite the robust nature of Cr³⁺ against reduction, it is not possible to obtain SrCrO₂H through a conventional high-temperature reaction of "SrO + SrH₂ + Cr₂O₃ → 2SrCrO₂H" because SrH₂ decomposes to Sr and H₂ upon heating, as mentioned earlier. However, the target reaction can proceed by applying high pressure (1000 °C, 5 GPa), which suppresses the generation of gas species⁷⁵. Since SrCrO₂H perovskite is cubic and has no octahedral rotation, magnetic ordering occurs at much higher temperatures than that of the isoelectronic LnCrO₃ (Ln = lanthanide) with orthorhombic distortions. While reduction of LaSrMnO₄ using CaH₂ yields LaSrMnO_{3.5}, hydride anions are incorporated via high-pressure synthesis, yielding LaSrMnO_{3.3}H_{0.7}⁷⁶. High-pressure synthesis also provides access to oxyhydrides with other structures, in addition to perovskite with only corner-sharing octahedra. For example, the 6H-type perovskites BaVO_{3-x}H_x (x < 1) (Fig. 9) and BaCrO₂H consisting of corner-sharing and face-sharing octahedra can be stabilized at 6 GPa^{77,78}.

Topochemical reactions using metal hydrides are limited to oxyhydrides with reducible transition metals. From this point of view, high-pressure synthesis is an effective way to synthesize oxyhydrides with *s* and *p* block elements. The orthorhombic La₂LiHO₃ can be synthesized at 2 GPa⁷⁹, which is isostructural with Sr₂VO₃H. By lowering the synthesis pressure, a tetragonal structure La₂Li(O_{1.21}H_{0.53}□_{0.26})O₂ (□ = vacancy) can be obtained with hydride residing in the equatorial anion site, acquiring excellent hydride conductivity. In LaSrLiO₂H₂, the apical site is occupied by hydride. Sr₂LiOH₃ shows a hydride conduction of 3.2 × 10⁻⁵ S cm⁻¹ at 300 °C. High pressure synthesis has been widely employed to search for hydride ion conductors⁸⁰.

4.13.3.4 Anion order-disorder

Like other mixed-anion compounds, the anion order/disorder is an important topic in oxyhydrides. Here we show some cases where the characteristics of hydrides come into play. In SrV^{III}O₂H and its analogues, only *trans*-VO₄H₂ octahedra (Fig. 10A) are present, and these are aligned in the same direction to form a fully ordered structure⁸¹. The *trans* configuration is understood in

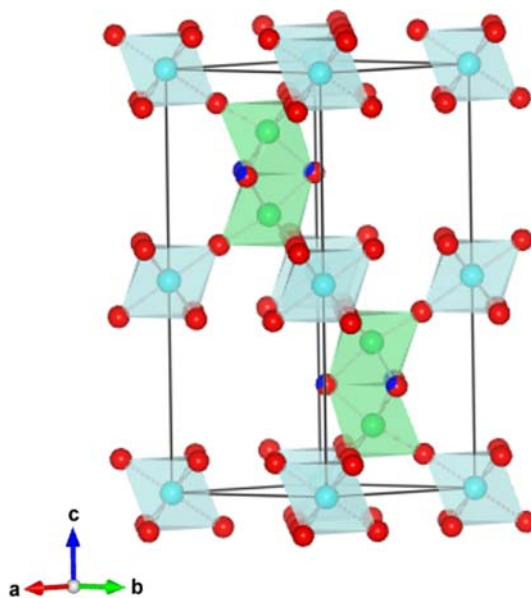


Fig. 9 Crystal structure of 6H-type BaVO_{3-x}H_x (x < 1)⁷⁷. V1, V2, O, and H are shown in cyan, green, red and blue respectively. Ba is omitted. Hydrides are found to preferentially (but not completely) occupy face-shared sites.

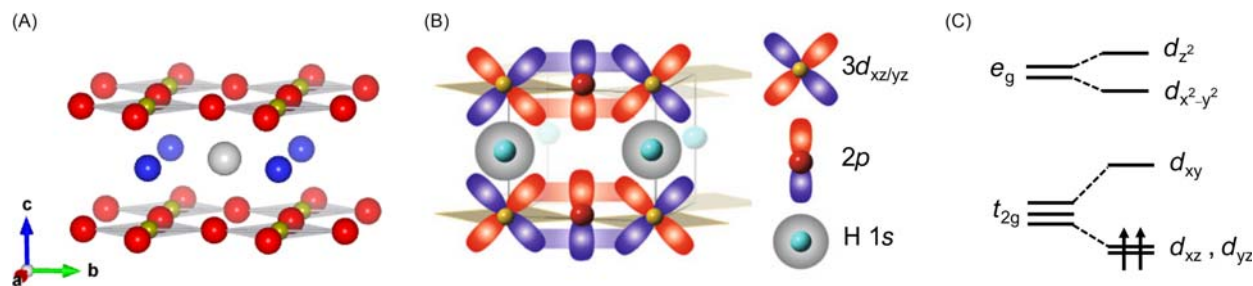


Fig. 10 Crystal structure of SrVO_2H ⁸¹ (A). Sr, V, O and H are shown in silver, grey-green, red and blue respectively. The inter- and intra-layer orbital overlapping (B) in the SrVO_2H . Low-lying d_{yz}/d_{xz} orbitals due to crystal field splitting (C). (B) is reproduced from Yamamoto, T.; Zeng, D.; Kawakami, T.; Arcisauskaitė, V.; Yata, K.; Patino, M. A.; Izumo, N.; McGrady, J. E.; Kageyama, H.; Hayward, M. A. The Role of π -Blocking Hydride Ligands in a Pressure-Induced Insulator-to-Metal Phase Transition in SrVO_2H . *Nat. Commun.* **2017**, *8* (1), an open access article under a CCA 4.0 license. No changes were made.

terms of electron count: two d electrons of V^{3+} are stabilized by occupying low-lying d_{yz}/d_{xz} orbitals due to crystal field splitting (Fig. 10C).

On the other hand, BaScO_2H (d^0), $\text{SrTiO}_{3-x}\text{H}_x$ ($d^{0\sim 0.6}$), and SrCrO_2H (d^3) are all known to have a cubic perovskite structure^{75,82-84}. However, anions may not be distributed in a strictly random manner. For BaScO_2H , *ab initio* random structure search suggests that the *cis*-configuration is more stable, possibly due to stabilization by the 90 degrees π -bond of O 2p in BaScO_2H , as shown in the section on oxynitrides⁸⁴. In fact, ¹H NMR results show a slight preference for the *cis*-configuration. On the other hand, in $6\text{H-BaVO}_{3-x}\text{H}_x$, theoretical calculations of the structures with over 1500 different anion configurations suggest that the *trans*-configuration is preferred⁷⁷. In this case, the number of d electrons is between 1 and 2 per vanadium, which means that the crystal field stabilization effect is at play (Fig. 10C), although not as effectively as in SrVO_2H with two d electrons. In support of this, no difference in *cis/trans* preference is seen in $6\text{H-BaTiO}_{3-x}\text{H}_x$ ($x < 1$) with the d electron less than 1.⁸⁵

Another important aspect in anion order of oxyhydrides is the size flexibility of hydride anions: XRD measurements of SrVO_2H under high pressure revealed that the compressibility of hydride anions is twice that of oxide ions (half the bulk modulus)⁸¹. The large difference in the compressibility of oxide and hydride anions can explain the anion order-disorder transition in the fluorite structure LnHO ⁵⁷. When Ln^{3+} is small ($\text{Ln} = \text{Sm} \sim \text{Er}$), the anions are disordered, but as the size of Ln^{3+} increases, the oxide ions become more underbonded, and anion ordering occurs for $\text{Ln} = \text{La-Nd}$, where the hydride anion expands, allowing the Ln-O distance to decrease. Thus, the underbonding effect of the oxide anion is eliminated. The use of large Ln^{3+} here corresponds to a negative “chemical pressure”.

Conversely, when physical pressure is applied to LaHO , the structure becomes PbCl_2 -type at 3 GPa and further changes to anti- Fe_2P -type at 5 GPa⁸⁶. In oxides, the local structures can usually be represented by placing metal cations in the center of polyhedron, but in mixed-anion compounds, reverse of this relationship and considering the local structure around the anions can provide important insights. For example, in LaHO with the PbCl_2 -type structure at 3 GPa, hydride is five-coordinated and oxide is four-coordinated, but in the anti- Fe_2P -type structure at 5 GPa, this relationship is reversed, with four-coordinated hydride and five-coordinated oxide. At high pressure, the coordination number usually increases because of an increase in density, but here the coordination number decreases due to the extraordinary compressibility of hydride anions. The size flexibility of the hydride anion also appears crucial in the anion ordering in $\text{LaSrCoO}_3\text{H}_{0.7}$ (Fig. 7)⁵⁹: by reducing the Co-H-Co distance, La/Sr becomes closer to the oxide anion and consequently avoids being underbonded.

4.13.3.5 Thin films

Single crystals are not easily accessible for mixed-anion compounds, but if available one can understand precise physical properties as well as reaction processes. For example, single crystal $\text{ATiO}_{3-x}\text{H}_x$ films ($A = \text{Ba}, \text{Sr}, \text{Ca}$) are obtained by hydride reduction of epitaxial thin films of ATiO_3 grown by pulsed laser deposition (PLD)⁸³. The $\text{ATiO}_{3-x}\text{H}_x$ films are found to be intrinsically metallic. For SrVO_2H , a single crystal film with a [001] alignment is obtained, which is isostructural with the bulk⁸⁷, but by applying stress to this thin film, a partially disordered phase of hydride and oxide anions is obtained as a transient phase⁸⁸. LnHO thin films are studied as photochromic materials⁸⁹. A YHO film is obtained by sputtering Y in an H_2 atmosphere to produce a YH_2 thin film and then exposing the film to an O_2 atmosphere⁹⁰. Although the control the O/H ratio is difficult in this method, it is possible to synthesize $\text{LnO}_x\text{H}_{3-2x}$ ($0.5 < x < 1.5$) by sputtering with gas mixtures of various O_2/H_2 ratios⁸⁹.

4.13.4 Oxyfluorides

Several features of fluorine, when incorporated into oxides, contribute to the emergence and enhancement of various functions. For example, metal-fluorine bonding lowers the energy level of the transition metal due to the high electronegativity of fluorine, leading

to a higher redox potential of oxyfluoride cathodes compared to corresponding oxides⁹¹. Since the valence of the F^- anion is lower than O^{2-} and its ionic radius is similar, electron doping is easily done via the solid solution formation with oxides⁹². Conversely, the similarity in ionic radii makes the anionic ordering in oxyfluorides difficult to control. However, if the metal is coordinated to both oxide and fluoride anions, the local symmetry around the metal center is reduced (e.g., from O_h symmetry in octahedral case), thus controlling anion ordering is important. Although such asymmetric local geometry does not necessarily guarantee overall asymmetry, it is the key to create structures without inversion symmetry, which is necessary for various functional properties such as enantiomorphism, circular dichroism, second-harmonic generation (SHG), piezoelectricity, and pyroelectricity⁹³.

High-temperature solid-state reactions are often used to synthesize oxyfluorides, and are especially effective when oxides and fluorides of the same structure are present. For example, a solid solution of $Ba(Zr_{1-x}Li_x)O_{3-3x}F_{3x}$ is synthesized by heating the mixture of $BaZrO_3$ and $BaLiF_3$ at 1250 °C, where the anion charge difference is compensated by the charge difference of cations⁹⁴. However, the high stability of binary fluorides such as AEF_2 (AE = alkaline earth) and LnF_3 (Ln = lanthanide) often inhibits the formation of oxyfluorides when these binary fluorides are used as starting materials. Therefore, attempts have been made to synthesize oxyfluorides by other methods, including low-temperature topochemical synthesis, high-pressure synthesis and hydrothermal synthesis.

4.13.4.1 Topochemical synthesis

In topochemical reactions, the similar ionic radii between oxide and fluoride anions are advantageous for acquiring solid solutions. The higher mobility of fluoride anions is another benefit in low temperature topochemical reactions where ion diffusion is limited. Depending on the choice of fluorinating reagents (and host oxides), the nature of topochemical fluorination reactions differs⁹². The simplest fluorination reagent is fluorine gas, but great care must be taken when handling. For example, when flowing F_2 gas, pipes and reaction vessels made of Ni should be used since other metals such as stainless steel are easily corroded by fluorine. Solid XeF_2 , which decomposes into Xe and F_2 at elevated temperatures, can also be used as a fluorine source in a sealed tube.

The most prominent feature of fluorine gas as fluorine source is its strong oxidizing ability, which provides access to higher oxidation states of transition metals via intercalation of fluoride anion into host oxides. For example, $Sr_3Fe_2O_6$ with an oxygen-deficient double-layered RP structure is oxidized to $Sr_3Fe_2O_6F_{0.87}$ containing an unusually high valent Fe^{5+} from a topochemical F^- intercalation at 140 °C (Fig. 11)⁹⁵. In $Sr_3Fe_2O_6$, oxygen vacancies are located at the middle apical site, but the F^- insertion reorganizes the anion configuration, with F^- occupying the terminal apical site and O^{2-} filling the vacant site (Fig. 11). The rearrangement of anions can be understood by Pauling's second rule: the lower valent F^- anions prefer to coordinate to the lower valent Sr^{2+} than to the $Fe^{3+/5+}$ cation^{95,96}.

Transition metal fluorides MF_2 (M = Cu, Zn, etc.) can also be used for oxidative intercalation of fluorine^{97,98}. Fluorination of the RP phase $Sr_3Ru^{IV}_2O_7$ occurs by heating with CuF_2 in air, yielding $Sr_3Ru^V_2O_7F_2$, where fluoride anions occupy the interstitial sites of

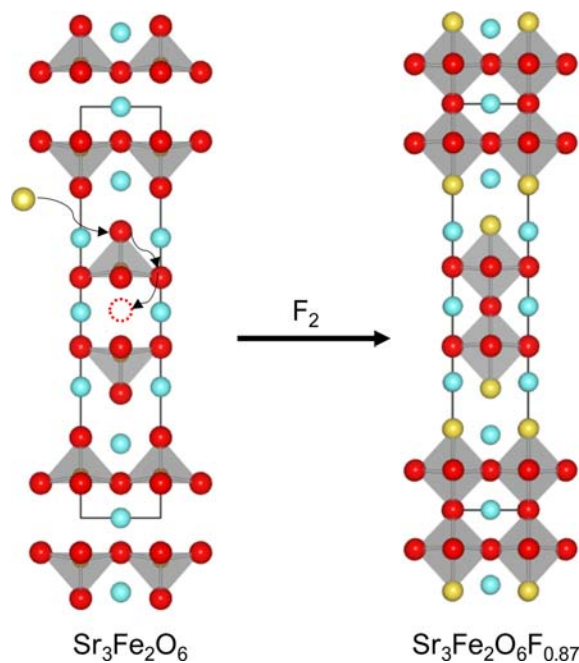
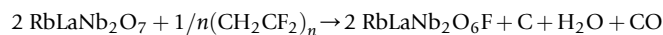
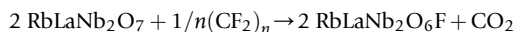


Fig. 11 Synthesis of $Sr_3Fe_2O_6F_{0.87}$ via oxidative fluorination⁹⁵. Sr, O and F are shown in cyan, red and yellow respectively. Grey octahedra represent the coordination of FeO_5 and FeO_5F in $Sr_3Fe_2O_6$ and $Sr_3Fe_2O_6F_{0.87}$, respectively. Dotted red circle represents oxygen vacancy. The migration of oxides occurs during fluorination.

the rock-salt block (Fig. 12)⁹⁹. The reaction mechanism is not clear, but it is likely that CuF_2 reacts with air to form CuO and F_2 , the latter being used for intercalation.

Despite the strong oxidizing nature of fluorine, reductive fluorination is possible with the appropriate choice of reactants. Fluorine-containing organic materials such as polyvinylidenedifluoride $[(\text{CH}_2\text{CF}_2)_n; \text{PVDF}]^{100}$ and polytetrafluoroethylene $[(\text{CF}_2)_n; \text{PTFE}]^{101}$ can reduce oxide precursors via 1:F/O exchange reaction. Here, the reducing ability is provided by carbon in the reactants, which can extract the oxygen from the host oxides. The examples using $\text{RbLaNb}_2\text{O}_7$ are shown below¹⁰¹:



Oxygen is extracted by carbon to produce CO or CO_2 , and the resulting vacancies are filled with fluorine. This exchange reaction causes the insulating $\text{RbLaNb}_2\text{O}_7$ precursor to become metallic and the formal valence of Nb^{5+} to be reduced to $+4.5$ ($d^{0.5}$). PTFE with a larger carbon content can reduce oxide hosts more extensively than PVDF. However, in both cases, there is a tendency that carbon remains on the sample surface.

Redox neutral fluorination, in which one oxygen is replaced by two fluorine without changing the valence state of transition metal, also exists. As shown in Fig. 13B, double-layered RP perovskite $\text{Sr}_3\text{Ti}_2\text{O}_7$ is converted to $\text{Sr}_3\text{Ti}_2\text{O}_5\text{F}_4$ by complete O/F exchange at the apical sites as well as fluorine-intercalation into the interstitial sites, and hence maintaining the Ti^{4+} oxidation state¹⁰³. In the case of the single-layered Sr_2TiO_4 , fluorine insertions proceed in an alternative fashion, as shown in Fig. 13A, yielding $\text{Sr}_2\text{TiO}_3\text{F}_2$. In these cases, various fluorinating agents are used, such as NH_4F , MF_2 ($M = \text{Zn}, \text{Cu}$), and PVDF ¹⁰².

4.13.4.2 Electrochemical synthesis

The oxidative fluorine intercalation can be carried out electrochemically. For example, the oxygen vacancy in $\text{YBa}_2\text{Cu}_3\text{O}_{7-x}$ is filled with fluorine using an all-solid-state electrochemical cell¹⁰⁴. Electrochemical fluorine (de)intercalation reactions have attracted recent attention as the next generation of rechargeable batteries. The reversible electrochemical intercalation of fluorine has been demonstrated using LaSrMnO_4 with the RP structure as a cathode material with gravimetric theoretical capacities of 132 mAh/g (i.e., $\text{LaSrMnO}_4 \rightleftharpoons \text{LaSrMnO}_4\text{F}_{1.7}$), comparable to the state-of-art lithium-ion batteries such as LiFePO_4 with 170 mAh/g¹⁰⁵. Fluoride ions, supplied from the PbF_2 anode, are intercalated to the LaSrMnO_4 cathode, through the electrolyte consisting of Ba-doped LaF_3 . The inserted fluoride anions are located at the interstitial site in the rock salt block. As seen in Fig. 14, in the first stage every second layer of anion interstitial sites is filled, followed by filling all the interstitial sites in the second stage.

Whereas the chemical potential of a material can be altered to some extents by pressure and other factors, electrochemical routes allow greater control over the electrochemical potential, and is hence suitable for the synthesis of metastable oxyfluorides, with reactions occurring even at room temperature. Electrochemical fluorination of La_2CuO_4 proceeds at room temperature, resulting in the composition of $\text{La}_2\text{CuO}_4\text{F}_x$ ($x \sim 0.18$)¹⁰⁶. This fluorine insertion significantly increases the c lattice parameter from 13.141 Å to

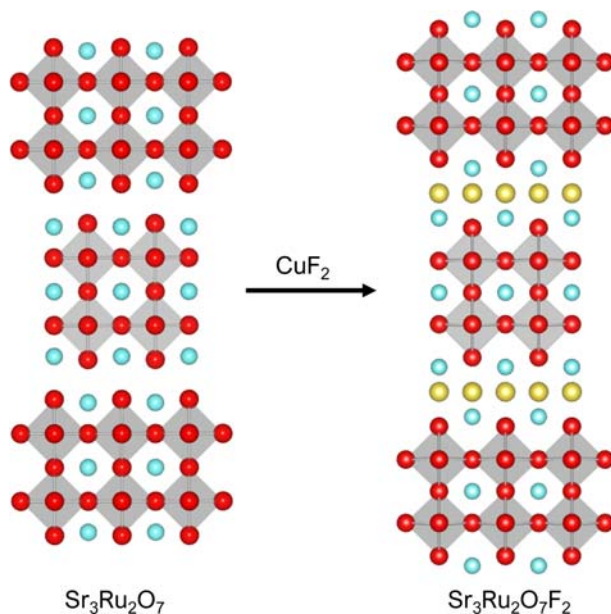


Fig. 12 Oxidative fluorination of $\text{Sr}_3\text{Ru}_2\text{O}_7$ ⁹⁹. Sr, O and F are shown in cyan, red and yellow respectively. Grey octahedra represent the coordination of RuO_6 . Fluorides occupy the interlayer interstitial sites, leading to an expansion of the crystal structure.

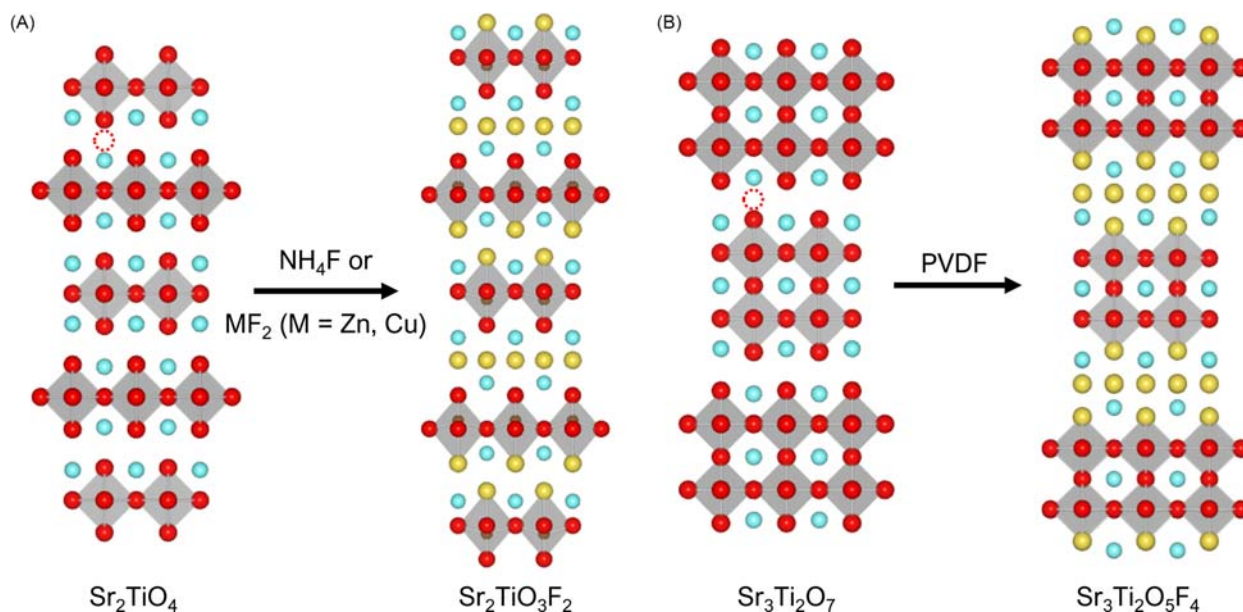


Fig. 13 Synthesis of $\text{Sr}_2\text{TiO}_3\text{F}_2$ ¹⁰² (A) and $\text{Sr}_3\text{Ti}_2\text{O}_5\text{F}_4$ ¹⁰³ (B). Sr, O and F are shown in cyan, red and yellow respectively. Grey octahedra represent the coordination of Ti. Red dotted circles represent interstitial sites. Fluorides are intercalated into alternating interlayers in $\text{Sr}_2\text{TiO}_3\text{F}_2$ as well as replacing half of apical oxides in adjacent layers. In $\text{Sr}_3\text{Ti}_2\text{O}_5\text{F}_4$, fluorides are inserted in the interlayer interstitial sites and replacing apical oxides in all layers.

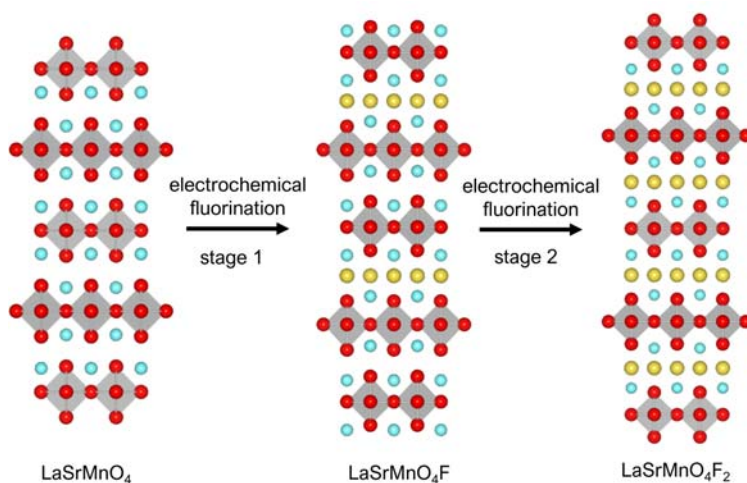


Fig. 14 Electrochemical fluorination of LaSrMnO_4 ¹⁰⁵. La/Sr, O and F are shown in cyan, red and yellow respectively. Grey octahedra represent the coordination of MnO_6 . The process involves two steps: 1. Fluorine-insertion for every second interlayer; 2. A complete fluorine-intercalation.

13.205 Å, which is similar to the change in topochemical fluorination with F_2 gas. $\text{La}_2\text{NiO}_3\text{F}_3$, which cannot be synthesized with F_2 gas, has been synthesized by electrochemical fluorination of $\text{La}_2\text{NiO}_3\text{F}_2$ ^{105,107}.

4.13.4.3 Solvothermal synthesis

Low-temperature solvothermal synthesis is a suitable synthetic approach to control O/F ordering around the transition metal, which is often difficult to achieve in high-temperature reactions. The produced heteroleptic polyhedra contain distortions due to differences in the bonding between central cations with O^{2-} and F^- . Fig. 15 illustrates how 'replaced' fluoride ligand in the octahedron leads to a displacement of metal center from its high symmetry position. Depending on the number and position of fluoride ligands, the metal cation in the octahedron is off-centered towards corner, edge, and face direction^{108,109}. Mixed oxide-fluoride octahedra are therefore promising acentric building units. Such an asymmetric coordination environment does not always break the inversion symmetry of a crystal, but it does increase its likelihood, as found in $\text{Cd}(\text{pyz})(\text{H}_2\text{O})_2\text{MoO}_2\text{F}_4$ (pyz = pyridine)¹¹⁰ and

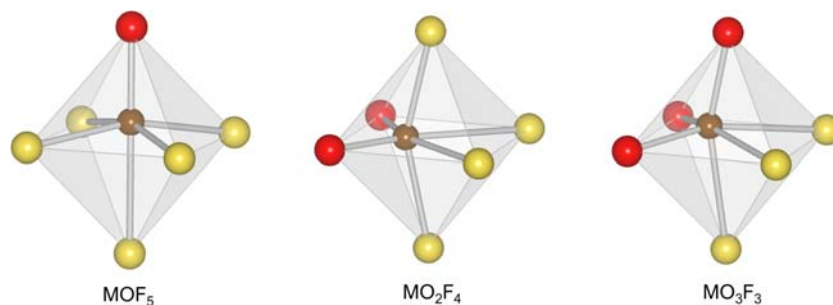


Fig. 15 The distortions in MO_nF_{6-n} polyhedra ($n = 1, 2$ and 3), where M represents transition metal cations (such as V^{5+} , Nb^{5+} and Mo^{6+})^{108–111}. M , O and F are shown in brown, red and yellow respectively. Displacement directions of central cations depend on the number and position of fluorides.

$CuVOF_4(H_2O)_7$ ¹⁰⁸. For this reason, hydrothermal synthesis has been extensively used to obtain materials such as nonlinear optical and piezoelectric materials that require non-centrosymmetric structures. Solvothermal synthesis is also a suitable method for growing large single crystals needed for practical applications.

4.13.4.4 High pressure synthesis

High pressure synthesis is particularly useful to synthesize oxyfluorides with high density structures, including $Tl^+Tl^{3+}OF_2$ ¹¹², $AgTiO_2F$ ¹¹³, $PbMnO_2F$ ¹¹⁴, and $AgFeOF_2$ ¹¹⁵. The O/F ordering are sometimes controlled by changing reaction conditions. The layered perovskite Sr_2FeO_3F , synthesized at 3 GPa and 1300 °C, has a fully O/F-ordered structure, with fluoride anions occupying the apical site of the perovskite layer, but when the same starting materials are treated at 1800 °C and 6 GPa, a phase with partially ordered anions is produced¹¹⁶. Single crystal oxyfluorides such as $Ba_2Ca_3Cu_4O_8(O_{1-x}F_x)_2$ ¹¹⁷ and Sr_2FeO_3F ¹¹⁶ can be grown by melt-growth method under high pressure. Both flux method and melt growth method can be used for single crystal growth, due to the highly packed and dense reaction environment under high pressure, compositional deviations are less likely to occur even at high temperatures^{116–119}.

4.13.5 Oxychalcogenides and oxypnictides

Oxychalcogenides and oxypnictides constitute two important families of oxide-containing mixed-anion compounds. Compared to oxide anions, chalcogenide (S^{2-} , Se^{2-} , Te^{2-}) and pnictide (P^{3-} , As^{3-} , Sb^{3-} , Bi^{3-}) anions are larger and more polarizable, and hence give rise to layered structures where chalcogenide/pnictide and oxide anions reside in separate layers. Fig. 16A shows the ZrSiCuAs-type crystal structure of $LaFeAsO$ ¹²⁰, which contains alternating antifluorite (Fe_2As_2)²⁻ and fluorite (La_2O_2)²⁺ building blocks. This structural feature can be explained by the hard-soft acid-base (HSAB) theory: lanthanide, a hard acid, forms layers with oxide which is a hard base; while two softer ions form the other type of layers. This situation is different from oxynitrides, oxyfluorides and

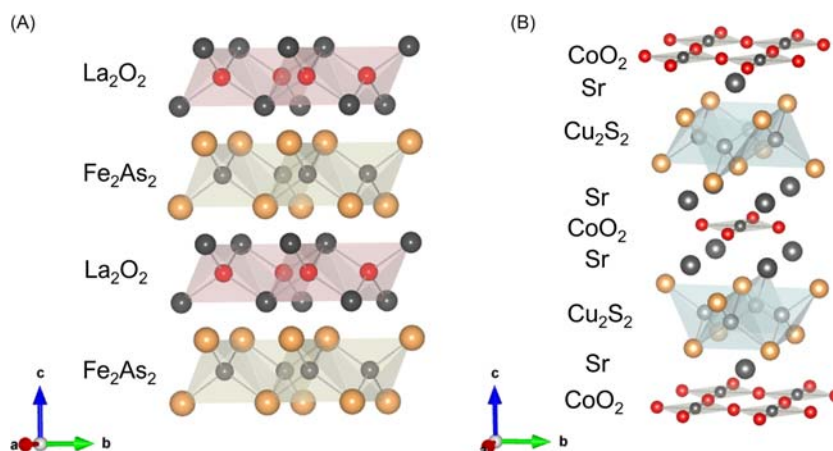


Fig. 16 Crystal structures of $LaFeAsO$ ¹²⁰ (A) and $Sr_2CoO_2Cu_2S_2$ ¹²¹ (B). $LaFeAsO$ adopts a ZrSiCuAs-type structure containing alternating antifluorite (Fe_2As_2)²⁻ and fluorite (La_2O_2)²⁺ layers. O and As are shown in red and light orange respectively. $Sr_2CoO_2Cu_2S_2$ contains antifluorite (Cu_2S_2)²⁻ layers and square-planar (CoO_2)²⁻ sheets, separated by Sr^{2+} cations. O and S are shown in red and light orange respectively.

oxyhydrides with heteroleptic coordination geometries discussed in previous sections¹²². The formation of chemically distinctive layers in oxychalcogenides and oxynitrides is responsible for many interesting properties observed, such as superconductivity^{123–125} and thermoelectricity^{126,127}.

LaFeAsO, prepared by a direct solid-state reaction from LaAs, Fe₃As₂ and La₂O₃ in a sealed tube, is an antiferromagnetic insulator, but electron doping by fluorine substitution at the oxide site induces superconductivity^{120,128}. BiCuSeO adopts a similar ZrSiCuAs-type crystal structure, with insulating (Bi₂O₂)²⁺ and conductive (Cu₂Se₂)²⁻ layers alternating along the stacking axis¹²⁹. This material, along with its Sr-substituted derivatives Bi_{1-x}Sr_xCuSeO, shows excellent thermoelectric properties^{130,131}.

There are many compounds with Sr₂Mn₃Sb₂O₂-type structure, such as Sr₂MO₂Cu₂S₂ (M = Mn, Co, Zn, Ni)¹³². Fig. 16B shows the structure of Sr₂CoO₂Cu₂S₂, which contains alternating antifluorite (Cu₂S₂)²⁻ layers and square-planar layers of (CoO₂)²⁻ separated by Sr²⁺ cations¹²¹. This is a rare example of high-spin Co²⁺ existing in a square-planar environment. In fact, incorporating transition metals into the square-planar layers is synthetically challenging and sometimes high pressure condition is required. For example, synthesis of A₂NiO₂Ag₂Se₂ (A = Sr, Ba) under ambient pressure is not possible due to the large size difference between (Ag₂Se₂)²⁻ and (NiO₂)²⁻ layers. However, such size-mismatch can be compensated under high pressure due to the higher compressibility of chalcogenide layers (versus oxide layers). Upon pressure releasing, the chalcogenide layers expand significantly and stretch the neighboring (NiO₂)²⁻ layers. This tensile strain leads to the first observation of high-spin Ni²⁺ state in square-planar coordination¹³³. A similar high-pressure induced effect is observed in Ba₂CoO₂Ag₂Te₂, in which the tensile strain gives rise to an unusual magnetic state for the Co²⁺ cation¹³⁴. Additionally, a recent study in Ba₂ZnO₂Ag₂Te₂, a material only accessible under high pressure, suggests a coexistence of *cis/trans* arrangement of O–Zn–O in [ZnO₂]²⁻ layer¹³⁵.

4.13.6 Conclusion

In summary, a wide range of oxide-based mixed-anion compounds shows diverse chemical and physical properties that are sometimes inaccessible in oxide materials. In terms of synthesis, there are various difficulties unique to mixed anion systems, and we have seen many strategies to remove them. It should be noted that it is impossible to give a full description of all types of mixed-anion compounds in this article, not even for oxide-containing ones. In addition, although this article focuses on oxide-containing mixed-anion compounds, non-oxide mixed-anion phases have also emerged to show useful properties, such as M₃HCh/M₃FCh (M = Li/Na, Ch = S, Se, Te)^{136,137} and Ba₂H₃X (X = Cl, Br, I)¹³⁸ as fast ionic conductors, and CoPS as a hydrogen evolution catalyst^{139,140}. The field of mixed-anion chemistry is still in its very early stage and a more extensive investigation from both chemical and physical sides is therefore necessary.

References

- Kageyama, H.; Hayashi, K.; Maeda, K.; Attfield, J. P.; Hiroi, Z.; Rondinelli, J. M.; Poeppelmeier, K. R. Expanding Frontiers in Materials Chemistry and Physics with Multiple Anions. *Nat. Commun.* **2018**, *9*, 772.
- Weller, M.; Overton, T.; Armstrong, F.; Rourke, J. *Inorganic Chemistry*, Oxford University Press, 2018.
- Shannon, R. D. Revised Effective Ionic Radii and Systematic Studies of Interatomic Distances in Halides and Chalcogenides. *Acta Crystallogr. A* **1976**, *32* (5), 751–767.
- Jansen, M.; Letschert, H. P. Inorganic Yellow-Red Pigments without Toxic Metals. *Nature* **2000**, *404* (6781), 980–982.
- Kasahara, A.; Nukumizu, K.; Hitoki, G.; Takata, T.; Kondo, J. N.; Hara, M.; Kobayashi, H.; Domen, K. Photoreactions on LaTiO₂N under Visible Light Irradiation. *Chem. A Eur. J.* **2002**, *106* (29), 6750–6753.
- Clarke, S. J.; DiSalvo, F. J. Synthesis and Structure of One-, Two-, and Three-Dimensional Alkaline Earth Metal Gallium Nitrides: Sr₃Ga₂N₄, Ca₃Ga₂N₄, and Sr₃Ga₃N₅. *Inorg. Chem.* **1997**, *36* (6), 1143–1148.
- Clarke, S. J.; Kowach, G. R.; DiSalvo, F. J. Synthesis and Structure of Two New Strontium Germanium Nitrides: Sr₃Ge₂N₂ and Sr₂GeN₂. *Inorg. Chem.* **1996**, *35* (24), 7009–7012.
- Clarke, S. J.; DiSalvo, F. J. Solid Solutions between LaN and Ca₃N₂: Defect Rock Salt Nitrides La_{1-x}Ca_xN_{1-x/3}. *J. Solid State Chem.* **1997**, *129* (1), 144–146.
- DiSalvo, F. J.; Clarke, S. J. Ternary Nitrides: A Rapidly Growing Class of New Materials. *Curr. Opin. Solid State Mater. Sci.* **1996**, *1* (2), 241–249.
- Pearson, R. G. Negative Electron Affinities of Nonmetallic Elements. *Inorg. Chem.* **1991**, *30* (14), 2856–2858.
- Chev r , F.; Pallu, A.; Ray, E.; Tessier, F. Characterization of Nd₂AlO₃N and Sm₂AlO₃N Oxynitrides Synthesized by Carbothermal Reduction and Nitridation. *J. Alloys Compd.* **2011**, *509* (19), 5839–5842.
- Ebbinghaus, S. G.; Abicht, H.-P.; Dronskowski, R.; M ller, T.; Reller, A.; Weidenkaff, A. Perovskite-Related Oxynitrides—Recent Developments in Synthesis, Characterisation and Investigations of Physical Properties. *Prog. Solid State Chem.* **2009**, *37* (2), 173–205.
- Wolff, H.; Dronskowski, R. Defect Migration in Fluorite-Type Tantalum Oxynitrides: A First-Principles Study. *Solid State Ion.* **2008**, *179* (21), 816–818.
- Armytage, D.; Fender, B. E. F. Anion Ordering in TaON: A Powder Neutron-Diffraction Investigation. *Acta Crystallogr. B* **1974**, *30* (3), 809–812.
- Schilling, H.; Stork, A.; Irran, E.; Wolff, H.; Bredow, T.; Dronskowski, R.; Lerch, M. γ-TaON: A Metastable Polymorph of Tantalum Oxynitride. *Angew. Chem. Int. Ed.* **2007**, *46* (16), 2931–2934.
- Momma, K.; Izumi, F. VESTA 3 for Three-Dimensional Visualization of Crystal, Volumetric and Morphology Data. *J. Appl. Cryst.* **2011**, *44* (6), 1272–1276.
- Brauer, G.; Weidlein, J. R. Synthesis and Properties of Tantalum Oxide Nitride, TaON. *Angew. Chem. Int. Ed.* **1965**, *4* (10), 875.
- Pors, F.; Marchand, R.; Laurent, Y.; Bacher, P.; Roult, G. Etude Structurale Des Perovskites Oxyazototes BaTaO₂N et BaNbO₂N: Structural Study of BaTaO₂N and BaNbO₂N Oxynitrided Perovskites. *Mater. Res. Bull.* **1988**, *23* (10), 1447–1450.
- G nther, E.; Hagenmayer, R.; Jansen, M. Strukturuntersuchungen an Den Oxidnitriden SrTaO₂N, CaTaO₂N Und LaTaO₂N Mittels Neutronen- Und R ntgenbeugung. *Z. Anorg. Allg. Chem.* **2000**, *626* (7), 1519–1525.
- Ebbinghaus, S. G.; Weidenkaff, A.; Rachel, A.; Reller, A. Powder Neutron Diffraction of SrNbO₂N at Room Temperature and 1.5K. *Acta Crystallogr. C* **2004**, *60* (9), i91–i93.
- Kim, Y.; Woodward, P. M.; Baba-Kishi, K. Z.; Tai, C. W. Characterization of the Structural, Optical, and Dielectric Properties of Oxynitride Perovskites AMO₂N (A = Ba, Sr, Ca; M = Ta, Nb). *Chem. Mater.* **2004**, *16* (7), 1267–1276.

22. Kasahara, A.; Nukumizu, K.; Takata, T.; Kondo, J. N.; Hara, M.; Kobayashi, H.; Domen, K. LaTiO_2N as a Visible-Light (≤ 600 nm)-Driven Photocatalyst (2). *J. Phys. Chem. B* **2003**, *107* (3), 791–797.
23. Kawashima, K.; Hojamberdiev, M.; Wagata, H.; Yubuta, K.; Vequizo, J. J. M.; Yamakata, A.; Oishi, S.; Domen, K.; Teshima, K. NH_3 -Assisted Flux-Mediated Direct Growth of LaTiO_2N Crystallites for Visible-Light-Induced Water Splitting. *J. Phys. Chem. C* **2015**, *119* (28), 15896–15904.
24. Hojamberdiev, M.; Yubuta, K.; Vequizo, J. J. M.; Yamakata, A.; Oishi, S.; Domen, K.; Teshima, K. NH_3 -Assisted Flux Growth of Cube-like BaTaO_2N Submicron Crystals in a Completely Ionized Nonaqueous High-Temperature Solution and Their Water Splitting Activity. *Cryst. Growth Des.* **2015**, *15* (9), 4663–4671.
25. Hojamberdiev, M.; Zahedi, E.; Nurlaela, E.; Kawashima, K.; Yubuta, K.; Nakayama, M.; Wagata, H.; Minegishi, T.; Domen, K.; Teshima, K. The Cross-Substitution Effect of Tantalum on the Visible-Light-Driven Water Oxidation Activity of BaNbO_2N Crystals Grown Directly by an NH_3 -Assisted Flux Method. *J. Mater. Chem. A* **2016**, *4* (33), 12807–12817.
26. Hosono, A.; Masubuchi, Y.; Yasui, S.; Takesada, M.; Endo, T.; Higuchi, M.; Itoh, M.; Kikkawa, S. Ferroelectric BaTaO_2N Crystals Grown in a BaCN_2 Flux. *Inorg. Chem.* **2019**, *58* (24), 16752–16760.
27. Fawcett, I. D.; Ramanujachary, K.; v; Greenblatt, M. Synthesis, Structure and Properties of the Oxynitrides SrWO_2N and $\text{SrMoO}_{2.5}\text{N}_{0.5}$. *Mater. Res. Bull.* **1997**, *32* (11), 1565–1570.
28. Antoine, P.; Marchand, R.; Laurent, Y.; Michel, C.; Raveau, B. On the Electrical Properties of the Perovskites $\text{LnWO}_3\text{N}_{3-x}$. *Mater. Res. Bull.* **1988**, *23* (7), 953–957.
29. Bacher, P.; Antoine, P.; Marchand, R.; L'Haridon, P.; Laurent, Y.; Roult, G. Time-of-Flight Neutron Diffraction Study of the Structure of the Perovskite-Type Oxynitride $\text{LaWO}_3\text{N}_{2.4}$. *J. Solid State Chem.* **1988**, *77* (1), 67–71.
30. Masubuchi, Y.; Tadaki, M.; Kikkawa, S. Synthesis of the Perovskite SrTaO_2N Using C_3N_4 for Both Reduction and Nitridation. *Chemistry Letters* **2018**, *47* (1), 31–33.
31. Yang, Q.; Masubuchi, Y.; Higuchi, M. Synthesis of Perovskite-Type Oxynitrides $\text{SrNb}(\text{O},\text{N})_3$ and $\text{CaTa}(\text{O},\text{N})_3$ Using Carbon Nitride. *Ceram. Int.* **2020**, *46* (9), 13941–13944.
32. Zhang, Y. R.; Motohashi, T.; Masubuchi, Y.; Kikkawa, S. Local Anionic Ordering and Anisotropic Displacement in Dielectric Perovskite SrTaO_2N . *J. Ceram. Soc. Jpn.* **2011**, *119* (1391), 581–586.
33. Masubuchi, Y.; Sun, S.-K.; Kikkawa, S. Processing of Dielectric Oxynitride Perovskites for Powders, Ceramics, Compacts and Thin Films. *Dalton Trans.* **2015**, *44* (23), 10570–10581.
34. Clarke, S. J.; Hardstone, K. A.; Michie, C. W.; Rosseinsky, M. J. High-Temperature Synthesis and Structures of Perovskite and $n = 1$ Ruddlesden–Popper Tantalum Oxynitrides. *Chem. Mater.* **2002**, *14* (6), 2664–2669.
35. Okada, R.; Katagiri, K.; Masubuchi, Y.; Inumaru, K. Preparation of LaTiO_2N Using Hydrothermally Synthesized $\text{La}_2\text{Ti}_2\text{O}_7$ as a Precursor and Urea as a Nitriding Agent. *Eur. J. Inorg. Chem.* **2019**, *2019* (9), 1257–1264.
36. Miura, A.; Rosero-Navarro, C.; Masubuchi, Y.; Higuchi, M.; Kikkawa, S.; Tadanaga, K. Nitrogen-Rich Manganese Oxynitrides with Enhanced Catalytic Activity in the Oxygen Reduction Reaction. *Angew. Chem. Int. Ed.* **2016**, *55* (28), 7963–7967.
37. Miura, A.; Takei, T.; Kumada, N. Synthesis of Wurtzite-Type InN Crystals by Low-Temperature Nitridation of LiInO_2 Using NaNH_2 Flux. *Cryst. Growth Des.* **2012**, *12* (9), 4545–4547.
38. Arumugam, N.; Hönnerscheid, A.; Jansen, M. A New Oxynitride Compound of Molybdenum, $\text{Na}_3\text{MoO}_3\text{N}$ —Synthesis via the Azide Route and Structure. *Z. Anorg. Allg. Chem.* **2003**, *629* (6), 939–941.
39. Yang, M.; Rodgers, J. A.; Middler, L. C.; Oró-Solé, J.; Jorge, A. B.; Fuertes, A.; Atfield, J. P. Direct Solid-State Synthesis at High Pressures of New Mixed-Metal Oxynitrides: RZrO_2N (R = Pr, Nd, and Sm). *Inorg. Chem.* **2009**, *48* (24), 11498–11500.
40. Rumble, J.; Bruno, T. J. *CRC Handbook of Chemistry and Physics: A Ready-Reference Book of Chemical and Physical Data; CRC Handbook of Chemistry and Physics*, Taylor & Francis, 2018.
41. Tassel, C.; Kuno, Y.; Goto, Y.; Yamamoto, T.; Brown, C. M.; Hester, J.; Fujita, K.; Higashi, M.; Abe, R.; Tanaka, K.; Kobayashi, Y.; Kageyama, H. MnTaO_2N : Polar LiNbO_3 -Type Oxynitride with a Helical Spin Order. *Angew. Chem. Int. Ed.* **2015**, *54* (2), 516–521.
42. Kuno, Y.; Tassel, C.; Fujita, K.; Batuk, D.; Abakumov, A. M.; Shitara, K.; Kuwabara, A.; Moriwake, H.; Watabe, D.; Ritter, C.; Brown, C. M.; Yamamoto, T.; Takeiri, F.; Abe, R.; Kobayashi, Y.; Tanaka, K.; Kageyama, H. ZnTaO_2N : Stabilized High-Temperature LiNbO_3 -Type Structure. *J. Am. Chem. Soc.* **2016**, *138* (49), 15950–15955.
43. Yajima, T.; Takeiri, F.; Aidzu, K.; Akamatsu, H.; Fujita, K.; Yoshimune, W.; Ohkura, M.; Lei, S.; Gopalan, V.; Tanaka, K.; Brown, C. M.; Green, M. A.; Yamamoto, T.; Kobayashi, Y.; Kageyama, H. A Labile Hydride Strategy for the Synthesis of Heavily Nitridized BaTiO_3 . *Nat. Chem.* **2015**, *7* (12), 1017–1023.
44. Masuda, N.; Kobayashi, Y.; Hernandez, O.; Bataille, T.; Paofai, S.; Suzuki, H.; Ritter, C.; Ichijo, N.; Noda, Y.; Takegoshi, K.; Tassel, C.; Yamamoto, T.; Kageyama, H. Hydride in $\text{BaTiO}_{2.5}\text{H}_{0.5}$: A Labile Ligand in Solid State Chemistry. *J. Am. Chem. Soc.* **2015**, *137* (48), 15315–15321.
45. Mikita, R.; Aharen, T.; Yamamoto, T.; Takeiri, F.; Ya, T.; Yoshimune, W.; Fujita, K.; Yoshida, S.; Tanaka, K.; Batuk, D.; Abakumov, A. M.; Brown, C. M.; Kobayashi, Y.; Kageyama, H. Topochemical Nitridation with Anion Vacancy-Assisted $\text{N}^{3-}/\text{O}^{2-}$ Exchange. *J. Am. Chem. Soc.* **2016**, *138* (9), 3211–3217.
46. Yang, M.; Oró-Solé, J.; Rodgers, J. A.; Jorge, A. B.; Fuertes, A.; Atfield, J. P. Anion Order in Perovskite Oxynitrides. *Nat. Chem.* **2011**, *3* (1), 47–52.
47. Clark, L.; Oró-Solé, J.; Knight, K. S.; Fuertes, A.; Atfield, J. P. Thermally Robust Anion-Chain Order in Oxynitride Perovskites. *Chem. Mater.* **2013**, *25* (24), 5004–5011.
48. Page, K.; Stoltzfus, M. W.; Kim, Y.-I.; Proffen, T.; Woodward, P. M.; Cheetham, A. K.; Seshadri, R. Local Atomic Ordering in BaTaO_2N Studied by Neutron Pair Distribution Function Analysis and Density Functional Theory. *Chem. Mater.* **2007**, *19* (16), 4037–4042.
49. Oka, D.; Hirose, Y.; Matsui, F.; Kamisaka, H.; Oguchi, T.; Maejima, N.; Nishikawa, H.; Muro, T.; Hayashi, K.; Hasegawa, T. Strain Engineering for Anion Arrangement in Perovskite Oxynitrides. *ACS Nano* **2017**, *11* (4), 3860–3866.
50. Oka, D.; Hirose, Y.; Kamisaka, H.; Fukumura, T.; Sasa, K.; Ishii, S.; Matsuzaki, H.; Sato, Y.; Ikuhara, Y.; Hasegawa, T. Possible Ferroelectricity in Perovskite Oxynitride SrTaO_2N Epitaxial Thin Films. *Sci. Rep.* **2014**, *4* (1), 4987.
51. Yamamoto, T.; Chikamatsu, A.; Kitagawa, S.; Izumo, N.; Yamashita, S.; Takatsu, H.; Ochi, M.; Maruyama, T.; Namba, M.; Sun, W.; Nakashima, T.; Takeiri, F.; Fujii, K.; Yashima, M.; Sugisawa, Y.; Sano, M.; Hirose, Y.; Sekiba, D.; Brown, C. M.; Honda, T.; Ikeda, K.; Otomo, T.; Kuroki, K.; Ishida, K.; Mori, T.; Kimoto, K.; Hasegawa, T.; Kageyama, H. Strain-Induced Creation and Switching of Anion Vacancy Layers in Perovskite Oxynitrides. *Nat. Commun.* **2020**, *11* (1), 5923.
52. Huang, B.; Corbett, J. D. $\text{Ba}_3\text{AlO}_4\text{H}$: Synthesis and Structure of a New Hydrogen-Stabilized Phase. *J. Solid State Chem.* **1998**, *141* (2), 570–575.
53. Boss, M.; Petri, D.; Pickhard, F.; Zörnchen, P.; Röhr, C. Neue Barium-Antimonid-Oxide Mit Den Zintl-Ionen $[\text{Sb}]^{3-}$, $[\text{Sb}_2]^{4-}$ Und $[\text{Sb}_3]^{5-}$. *Z. Anorg. Allg. Chem.* **2005**, *631* (6–7), 1181–1190.
54. Huang, B.; Corbett, J. D. $\text{Ba}_{21}\text{Ge}_2\text{O}_5\text{H}_{24}$ and Related Phases. A Corrected Structure Type and Composition for a Zintl Phase Stabilized by Hydrogen. *Inorg. Chem.* **1998**, *37* (8), 1892–1899.
55. Malaman, B.; Brice, J. F. Etude Structurale de l'hydrure-Oxyde LaHO Par Diffraction Des Rayons X et Par Diffraction Des Neutrons. *J. Solid State Chem.* **1984**, *53* (1), 44–54.
56. Widerøe, M.; Fjellvåg, H.; Norby, T.; Willy Poulsen, F.; Willestoft Berg, R. NdHO , a Novel Oxhydryde. *J. Solid State Chem.* **2011**, *184* (7), 1890–1894.
57. Yamashita, H.; Broux, T.; Kobayashi, Y.; Takeiri, F.; Ubukata, H.; Zhu, T.; Hayward, M. A.; Fujii, K.; Yashima, M.; Shitara, K.; Kuwabara, A.; Murakami, T.; Kageyama, H. Chemical Pressure-Induced Anion Order-Disorder Transition in LnHO Enabled by Hydride Size Flexibility. *J. Am. Chem. Soc.* **2018**, *140* (36), 11170–11173.
58. Zapp, N.; Auer, H.; Köhlmann, H. YHO , an Air-Stable Ionic Hydride. *Inorg. Chem.* **2019**, *58* (21), 14635–14641.
59. Hayward, M. A.; Cussen, E. J.; Claridge, J. B.; Bieringer, M.; Rosseinsky, M. J.; Kiely, C. J.; Blundell, S. J.; Marshall, I. M.; Pratt, F. L. The Hydride Anion in an Extended Transition Metal Oxide Array: $\text{LaSrCoO}_3\text{H}_{0.7}$. *Science* **2002**, *295* (5561), 1882–1884.
60. Bridges, C. A.; Darling, G. R.; Hayward, M. A.; Rosseinsky, M. J. Electronic Structure, Magnetic Ordering, and Formation Pathway of the Transition Metal Oxide Hydride $\text{LaSrCoO}_3\text{H}_{0.7}$. *J. Am. Chem. Soc.* **2005**, *127* (16), 5996–6011.

61. Kobayashi, Y.; Hernandez, O. J.; Sakaguchi, T.; Yajima, T.; Roisnel, T.; Tsujimoto, Y.; Morita, M.; Noda, Y.; Mogami, Y.; Kitada, A.; Ohkura, M.; Hosokawa, S.; Li, Z.; Hayashi, K.; Kusano, Y.; Kim, J. E.; Tsuji, N.; Fujiwara, A.; Matsushita, Y.; Yoshimura, K.; Takegoshi, K.; Inoue, M.; Takano, M.; Kageyama, H. An Oxyhydride of BaTiO_3 Exhibiting Hydride Exchange and Electronic Conductivity. *Nat. Mater.* **2012**, *11* (6), 507–511.
62. Ito, T. U.; Koda, A.; Shimomura, K.; Higemoto, W.; Matsuzaki, T.; Kobayashi, Y.; Kageyama, H. Excited Configurations of Hydrogen in the $\text{BaTiO}_{3-x}\text{H}_x$ Perovskite Lattice Associated with Hydrogen Exchange and Transport. *Phys. Rev. B* **2017**, *95* (2), 1–5.
63. Tang, Y.; Kobayashi, Y.; Masuda, N.; Uchida, Y.; Okamoto, H.; Kageyama, T.; Hosokawa, S.; Loyer, F.; Mitsuhashi, K.; Yamanaka, K.; Tamenori, Y.; Tassel, C.; Yamamoto, T.; Tanaka, T.; Kageyama, H. Metal-Dependent Support Effects of Oxyhydride-Supported Ru, Fe, Co Catalysts for Ammonia Synthesis. *Adv. Energy Mat.* **2018**, *8* (36), 1–9.
64. Denis Romero, F.; Leach, A.; Möller, J. S.; Foronda, F.; Blundell, S. J.; Hayward, M. A. Strontium Vanadium Oxide-Hydrides: "Square-Planar" Two-Electron Phases. *Angew. Chem. Int. Ed.* **2014**, *53* (29), 7556–7559.
65. Tsujimoto, Y.; Tassel, C.; Hayashi, N.; Watanabe, T.; Kageyama, H.; Yoshimura, K.; Takano, M.; Ceretti, M.; Ritter, C.; Paulus, W. Infinite-Layer Iron Oxide with a Square-Planar Coordination. *Nature* **2007**, *450* (7172), 1062–1065.
66. Tassel, C.; Seinerberg, L.; Hayashi, N.; Ganesanpotti, S.; Ajiro, Y.; Kobayashi, Y.; Kageyama, H. Sr_2FeO_3 with Stacked Infinite Chains of FeO_4 Square Planes. *Inorg. Chem.* **2013**, *52* (10), 6096–6102.
67. Kageyama, H.; Watanabe, T.; Tsujimoto, Y.; Kitada, A.; Sumida, Y.; Kanamori, K.; Yoshimura, K.; Hayashi, N.; Muranaka, S.; Takano, M.; Ceretti, M.; Paulus, W.; Ritter, C.; André, G. Spin-Ladder Iron Oxide: $\text{Sr}_3\text{Fe}_2\text{O}_5$. *Angew. Chem. Int. Ed.* **2008**, *47* (31), 5740–5745.
68. Yamamoto, T.; Morgan, H. W. T.; Zeng, D.; Kawakami, T.; Amano Patino, M.; Hayward, M. A.; Kageyama, H.; McGrady, J. E. Pressure-Induced Transitions in the 1-Dimensional Vanadium Oxyhydrides $\text{Sr}_2\text{VO}_3\text{H}$ and $\text{Sr}_3\text{V}_2\text{O}_5\text{H}_2$, and Comparison to 2-Dimensional SrVO_2H . *Inorg. Chem.* **2019**, *58* (22), 15393–15400.
69. Denis Romero, F.; Burr, S. J.; McGrady, J. E.; Gianolio, D.; Cibin, G.; Hayward, M. A. $\text{SrFe}_{0.5}\text{Ru}_{0.5}\text{O}_2$: Square-Planar Ru^{2+} in an Extended Oxide. *J. Am. Chem. Soc.* **2013**, *135* (5), 1838–1844.
70. Jin, L.; Lane, M.; Zeng, D.; Kirschner, F. K. K.; Lang, F.; Manuel, P.; Blundell, S. J.; McGrady, J. E.; Hayward, M. A. $\text{LaSr}_3\text{NiRuO}_4\text{H}_4$: A 4d Transition-Metal Oxide-Hydride Containing Metal Hydride Sheets. *Angew. Chem. Int. Ed.* **2018**, *57* (18), 5025–5028.
71. Jin, L.; Hayward, M. A. Hole and Electron Doping of the 4d Transition-Metal Oxyhydride $\text{LaSr}_3\text{NiRuO}_4\text{H}_4$. *Angew. Chem. Int. Ed.* **2020**, *59* (5), 2076–2079.
72. Jin, L.; Batuk, M.; Kirschner, F. K. K.; Lang, F.; Blundell, S. J.; Hadermann, J.; Hayward, M. A. Exsolution of SrO during the Topochemical Conversion of $\text{LaSr}_3\text{CoRuO}_8$ to the Oxyhydride $\text{LaSr}_3\text{CoRuO}_4\text{H}_4$. *Inorg. Chem.* **2019**, *58* (21), 14863–14870.
73. Jin, L.; Hayward, M. A. Rhodium-Containing Oxide-Hydrides: Covalently Stabilized Mixed-Anion Solids. *Chem. Commun.* **2019**, *55* (33), 4861–4864.
74. Takeiri, F.; Aidzu, K.; Yajima, T.; Matsui, T.; Yamamoto, T.; Kobayashi, Y.; Hester, J.; Kageyama, H. Promoted Hydride/Oxide Exchange in SrTiO_3 by Introduction of Anion Vacancy via Alivalent Cation Substitution. *Inorg. Chem.* **2017**, *56* (21), 13035–13040.
75. Tassel, C.; Goto, Y.; Kuno, Y.; Kuno, J.; Green, M.; Kobayashi, Y.; Kageyama, H. Direct Synthesis of Chromium Perovskite Oxyhydride with a High Magnetic-Transition Temperature. *Angew. Chem. Int. Ed.* **2014**, *53* (39), 10377–10380.
76. Tassel, C.; Goto, Y.; Watabe, D.; Tang, Y.; Lu, H.; Kuno, Y.; Takeiri, F.; Yamamoto, T.; Brown, C. M.; Hester, J.; Kobayashi, Y.; Kageyama, H. High-Pressure Synthesis of Manganese Oxyhydride with Partial Anion Order. *Angew. Chem. Int. Ed.* **2016**, *55* (33), 9667–9670.
77. Yamamoto, T.; Shitara, K.; Kitagawa, S.; Kuwabara, A.; Kuroe, M.; Ishida, K.; Ochi, M.; Kuroki, K.; Fujii, K.; Yashima, M.; Brown, C. M.; Takatsu, H.; Tassel, C.; Kageyama, H. Selective Hydride Occupation in $\text{BaVO}_{3-x}\text{H}_x$ ($0.3 \leq x \leq 0.8$) with Face- and Corner-Shared Octahedra. *Chem. Mater.* **2018**, *30* (5), 1566–1574.
78. Higashi, K.; Ochi, M.; Nambu, Y.; Yamamoto, T.; Murakami, T.; Yamashina, N.; Tassel, C.; Matsumoto, Y.; Takatsu, H.; Brown, C. M.; Kageyama, H. Enhanced Magnetic Interaction by Face-Shared Hydride Anions in $6\text{H-BaCrO}_2\text{H}$. *Inorg. Chem.* **2021**, *60* (16), 11957–11963.
79. Kobayashi, G.; Hinuma, Y.; Matsuoka, S.; Watanabe, A.; Iqbal, M.; Hirayama, M.; Yonemura, M.; Kamiyama, T.; Tanaka, I.; Kanno, R. Pure H^- Conduction in Oxyhydrides. *Science* **2016**, *351* (6279), 1314–1317.
80. Nawaz, H.; Takeiri, F.; Kuwabara, A.; Yonemura, M.; Kobayashi, G. Synthesis and H^- Conductivity of a New Oxyhydride Ba_2YHO_3 with Anion-Ordered Rock-Salt Layers. *Chem. Commun.* **2020**, *56* (71), 10373–10376.
81. Yamamoto, T.; Zeng, D.; Kawakami, T.; Arcisauskaitė, V.; Yata, K.; Patino, M. A.; Izumo, N.; McGrady, J. E.; Kageyama, H.; Hayward, M. A. The Role of π -Blocking Hydride Ligands in a Pressure-Induced Insulator-to-Metal Phase Transition in SrVO_2H . *Nat. Commun.* **2017**, *8* (1).
82. Sakaguchi, T.; Kobayashi, Y.; Yajima, T.; Ohkura, M.; Tassel, C.; Takeiri, F.; Mitsuoka, S.; Ohkubo, H.; Yamamoto, T.; Kim, J. E.; Tsuji, N.; Fujiwara, A.; Matsushita, Y.; Hester, J.; Avdeev, M.; Ohoyama, K.; Kageyama, H. Oxyhydrides of $(\text{Ca}, \text{Sr}, \text{Ba})\text{TiO}_3$ Perovskite Solid Solutions. *Inorg. Chem.* **2012**, *51* (21), 11371–11376.
83. Yajima, T.; Kitada, A.; Kobayashi, Y.; Sakaguchi, T.; Bouilly, G.; Kasahara, S.; Terashima, T.; Takano, M.; Kageyama, H. Epitaxial Thin Films of $\text{ATiO}_{3-x}\text{H}_x$ ($\text{A} = \text{Ba}, \text{Sr}, \text{Ca}$) with Metallic Conductivity. *J. Am. Chem. Soc.* **2012**, *134* (21), 8782–8785.
84. Goto, Y.; Tassel, C.; Noda, Y.; Hernandez, O.; Pickard, C. J.; Green, M. A.; Sakaebae, H.; Taguchi, N.; Uchimoto, Y.; Kobayashi, Y.; Kageyama, H. Pressure-Stabilized Cubic Perovskite Oxyhydride BaScO_2H . *Inorg. Chem.* **2017**, *56* (9), 4840–4845.
85. Sinclair, C. D.; Skakle, M. S. J.; Morrison, D. F.; Smith, I. R.; Beales, P. T. Structure and Electrical Properties of Oxygen-Deficient Hexagonal BaTiO_3 . *J. Mater. Chem.* **1999**, *9* (6), 1327–1331.
86. Broux, T.; Ubukata, H.; Pickard, J. C.; Takeiri, F.; Kobayashi, G.; Kawaguchi, S.; Yonemura, M.; Goto, Y.; Tassel, C.; Kageyama, H. High-Pressure Polymorphs of LaHO with Anion Coordination Reversal. *J. Am. Chem. Soc.* **2019**, *141* (22), 8717–8720.
87. Katayama, T.; Chikamatsu, A.; Yamada, K.; Shigematsu, K.; Onozuka, T.; Minohara, M.; Kumigashira, H.; Ikenaga, E.; Hasegawa, T. Epitaxial Growth and Electronic Structure of Oxyhydride SrVO_2H Thin Films. *J. Appl. Phys.* **2016**, *120* (8).
88. Namba, M.; Takatsu, H.; Yoshimune, W.; Daniel, A.; Itoh, S.; Terashima, T.; Kageyama, H. A Partial Anion Disorder in SrVO_2H Induced by Biaxial Tensile Strain. *Inorganics (Basel)* **2020**, *8* (4), 2–9.
89. Cornelius, S.; Colombi, G.; Nafezarefi, F.; Schreuders, H.; Heller, R.; Munnik, F.; Dam, B. Oxyhydride Nature of Rare-Earth-Based Photochromic Thin Films. *J. Phys. Chem. Lett.* **2019**, *10* (6), 1342–1348.
90. Montero, J.; Martinsen, F. A.; Garcia-Tecedor, M.; Karazhanov, S. Z.; Maestre, D.; Hauback, B.; Marstein, E. S. Photochromic Mechanism in Oxygen-Containing Yttrium Hydride Thin Films: An Optical Perspective. *Phys. Rev. B* **2017**, *95* (20), 1–4.
91. Fedotov, S. S.; Luchinin, N. D.; Aksyonov, D. A.; Morozov, A. V.; Ryazantsev, S. V.; Gaboardi, M.; Plaisier, J. R.; Stevenson, K. J.; Abakumov, A. M.; Antipov, E. V. Titanium-Based Potassium-Ion Battery Positive Electrode with Extraordinarily High Redox Potential. *Nat. Commun.* **2020**, *11* (1), 1484.
92. Clemens, O.; Slater, P. R. Topochemical Modifications of Mixed Metal Oxide Compounds by Low-Temperature Fluorination Routes. *Rev. Inorg. Chem.* **2013**, *33* (2–3), 105–117.
93. Halasyamani, P. S.; Poeppelmeier, K. R. Noncentrosymmetric Oxides. *Chem. Mater.* **1998**, *10* (10), 2753–2769.
94. Kerfah, A.; Taïbi, K.; Guehria-Laïdoudi, A.; Simon, A.; Ravez, J. New Oxyfluoride Lead-Free Ferroelectric Relaxors in the $\text{BaTiO}_3\text{-BaZrO}_3\text{-BaLiF}_3$ System. *Mater. Lett.* **2000**, *42* (3), 189–193.
95. Simon Case, G.; Hector, L. A.; Levason, W.; Needs, L. R.; Thomas, F. M.; Weller, T. M. Syntheses, Powder Neutron Diffraction Structures and Mössbauer Studies of Some Complex Iron Oxyfluorides: $\text{Sr}_3\text{Fe}_2\text{O}_6\text{F}_{0.87}$, $\text{Sr}_2\text{FeO}_3\text{F}$ and $\text{Ba}_2\text{InFeO}_5\text{F}_{0.68}$. *J. Mater. Chem.* **1999**, *9* (11), 2821–2827.
96. Tsujimoto, Y.; Yamaura, K.; Takayama-Muromachi, E. Oxyfluoride Chemistry of Layered Perovskite Compounds. *Appl. Sci.* **2012**, *2* (1), 206–219.
97. Slater, P. R.; Hodges, J. P.; Francesconi, M. G.; Edwards, P. P.; Greaves, C.; Gameson, I.; Slaski, M. An Improved Route to the Synthesis of Superconducting Copper Oxyfluorides $\text{Sr}_{2-x}\text{A}_x\text{CuO}_2\text{F}_{2+\delta}$ ($\text{A} = \text{Ca}, \text{Ba}$) Using Transition Metal Difluorides as Fluorinating Reagents. *Phys. C: Super.* **1995**, *253* (1), 16–22.

98. Zhang, R.; Read, G.; Lang, F.; Lancaster, T.; Blundell, S. J.; Hayward, M. A. $\text{La}_2\text{SrCr}_2\text{O}_7\text{F}_2$: A Ruddlesden–Popper Oxyfluoride Containing Octahedrally Coordinated Cr^{4+} Centers. *Inorg. Chem.* **2016**, *55* (6), 3169–3174.
99. Li, R. K.; Greaves, C. Double-Layered Ruthenate $\text{Sr}_3\text{Ru}_2\text{O}_7\text{F}_2$ Formed by Fluorine Insertion into $\text{Sr}_3\text{Ru}_2\text{O}_7$. *Phys. Rev. B Condens. Matter Mat. Phys.* **2000**, *62*, 3811–3815.
100. Slater, P. R. Poly(Vinylidene Fluoride) as a Reagent for the Synthesis of K_2NiF_4 -Related Inorganic Oxide Fluorides. *J. Fluor. Chem.* **2002**, *117* (1), 43–45.
101. Kobayashi, Y.; Tian, M.; Eguchi, M.; Mallouk, T. E. Ion-Exchangeable, Electronically Conducting Layered Perovskite Oxyfluorides. *J. Am. Chem. Soc.* **2009**, *131* (28), 9849–9855.
102. Slater, P. R.; Gover, R. K. B. Synthesis and Structure of the New Oxide Fluoride $\text{Sr}_2\text{TiO}_3\text{F}_2$ from the Low Temperature Fluorination of Sr_2TiO_4 : An Example of a Staged Fluorine Substitution/Insertion Reaction. *J. Mater. Chem.* **2002**, *12* (2), 291–294.
103. Wissel, K.; Vogel, T.; Dasgupta, S.; Fortes, A. D.; Slater, P. R.; Clemens, O. Topochemical Fluorination of $n = 2$ Ruddlesden–Popper Type $\text{Sr}_3\text{Ti}_2\text{O}_7$ to $\text{Sr}_3\text{Ti}_2\text{O}_5\text{F}_4$ and Its Reductive Defluorination. *Inorg. Chem.* **2020**, *59* (2), 1153–1163.
104. MacManus, J. L.; Fray, D. J.; Evetts, J. E. Fluorination of $\text{Y}_1\text{Ba}_2\text{Cu}_2\text{O}_{7-x}$ by a Solid State Electrochemical Method. *Phys. C: Super. Appl.* **1991**, *184* (1), 172–184.
105. Nowroozi, M. A.; Mohammad, I.; Molaiyan, P.; Wissel, K.; Munnangi, A. R.; Clemens, O. Fluoride Ion Batteries—Past, Present, and Future. *J. Mater. Chem. A* **2021**, *9* (10), 5980–6012.
106. Delville, M. H.; Barbut, D.; Wattiaux, A.; Bassat, J. M.; Ménétrier, M.; Labrugère, C.; Grenier, J. C.; Etourneau, J. Electrochemical Fluorination of La_2CuO_4 : A Mild “Chimie Douce” Route to Superconducting Oxyfluoride Materials. *Inorg. Chem.* **2009**, *48* (16), 7962–7969.
107. Wissel, K.; Malik, A. M.; Vasala, S.; Plana-Ruiz, S.; Kolb, U.; Slater, P. R.; da Silva, I.; Alff, L.; Rohrer, J.; Clemens, O. Topochemical Reduction of $\text{La}_2\text{NiO}_3\text{F}_2$: The First Ni-Based Ruddlesden–Popper $n = 1$ T' -Type Structure and the Impact of Reduction on Magnetic Ordering. *Chem. Mater.* **2020**, *32* (7), 3160–3179.
108. Donakowski, M. D.; Gautier, R.; Yeon, J.; Moore, D. T.; Nino, J. C.; Halasyamani, P. S.; Poeppelmeier, K. R. The Role of Polar, Lambda (λ)-Shaped Building Units in Noncentrosymmetric Inorganic Structures. *J. Am. Chem. Soc.* **2012**, *134* (18), 7679–7689.
109. Cantwell, J. R. *Fluorides and Oxyfluorides: Synthesis, Structural Characteristics, and Properties*, Northwestern University: Ann Arbor, 2018.
110. Maggard, P. A.; Kopf, A. L.; Stern, C. L.; Poeppelmeier, K. R.; Ok, K. M.; Halasyamani, P. S. From Linear Inorganic Chains to Helices: Chirality in the $\text{M}(\text{Pyz})(\text{H}_2\text{O})_2\text{MoO}_2\text{F}_4$ ($\text{M} = \text{Zn}, \text{Cd}$) Compounds. *Inorg. Chem.* **2002**, *41* (19), 4852–4858.
111. Gautier, R.; Donakowski, M. D.; Poeppelmeier, K. R. Orientational Order of $[\text{VOF}_5]^{5-}$ and $[\text{NbOF}_5]^{2-}$ Polar Units in Chains. *J. Solid State Chem.* **2012**, *195*, 132–139.
112. Demazeau, G.; Granneck, G.; Marbeuf, A.; Portier, J.; Hagenmull, P. An Oxyfluorinated Perovskite Ti_2OF_2 . *C. R. Hebd. Seances Acad.* **1969**, *269* (17), 987.
113. Inaguma, Y.; Sugimoto, K.; Ueda, K. Synthesis of the Perovskite-Type Oxyfluoride AgTiO_2F : An Approach Adopting the HSAB Principle. *Dalton Trans.* **2020**, *49* (21), 6957–6963.
114. Katsumata, T.; Nakashima, M.; Inaguma, Y.; Tsurui, T. Synthesis of New Perovskite-Type Oxyfluoride, PbMnO_2F . *Bull. Chem. Soc. Jpn.* **2012**, *85* (3), 397–399.
115. Takeiri, F.; Yamamoto, T.; Hayashi, N.; Hosokawa, S.; Arai, K.; Kikkawa, J.; Ikeda, K.; Honda, T.; Otomo, T.; Tassel, C.; Kimoto, K.; Kageyama, H. AgFeOF_2 : A Fluorine-Rich Perovskite Oxyfluoride. *Inorg. Chem.* **2018**, *57* (11), 6686–6691.
116. Tsujimoto, Y.; Matsushita, Y.; Hayashi, N.; Yamaura, K.; Uchikoshi, T. Anion Order-to-Disorder Transition in Layered Iron Oxyfluoride $\text{Sr}_2\text{FeO}_3\text{F}$ Single Crystals. *Cryst. Growth Des.* **2014**, *14* (9), 4278–4284.
117. Iyo, A.; Hirai, M.; Tokiwa, K.; Watanabe, T.; Tanaka, Y. Preparation of Polycrystals with Various T_c and Single Crystal Growth of $\text{Ba}_2\text{Ca}_3\text{Cu}_4\text{O}_8(\text{O}_{1-x}\text{F}_x)_2$ under High Pressure. *Phys. C: Super.* **2003**, *392–396*, 140–144.
118. Zhigadlo, N. D.; Katrych, S.; Bukowski, Z.; Weyeneth, S.; Puzniak, R.; Karpinski, J. Single Crystals of Superconducting $\text{SmFeAsO}_{1-x}\text{F}_x$ Grown at High Pressure. *J. Phys. Condens. Matter* **2008**, *20* (34), 342202.
119. Karpinski, J.; Zhigadlo, N. D.; Katrych, S.; Bukowski, Z.; Moll, P.; Weyeneth, S.; Keller, H.; Puzniak, R.; Tortello, M.; Daghero, D.; Gonnelli, R.; Maggio-Aprile, I.; Fasano, Y.; Fischer, Ø.; Rogacki, K.; Batlogg, B. Single Crystals of $\text{LnFeAsO}_{1-x}\text{F}_x$ ($\text{Ln} = \text{La}, \text{Pr}, \text{Nd}, \text{Sm}, \text{Gd}$) and $\text{Ba}_{1-x}\text{Rb}_x\text{Fe}_2\text{As}_2$: Growth, Structure and Superconducting Properties. *Phys. C: Super.* **2009**, *469* (9), 370–380.
120. Kamihara, Y.; Watanabe, T.; Hirano, M.; Hosono, H. Iron-Based Layered Superconductor $\text{La}[\text{O}_{1-x}\text{F}_x]\text{FeAs}$ ($x = 0.05–0.12$) with $T_c = 26$ K. *J. Am. Chem. Soc.* **2008**, *130* (11), 3296–3297.
121. Smura, C. F.; Parker, D. R.; Zbiri, M.; Johnson, M. R.; Gál, Z. A.; Clarke, S. J. High-Spin Cobalt(II) Ions in Square Planar Coordination: Structures and Magnetism of the Oxyfluorides $\text{Sr}_2\text{CoO}_2\text{Cu}_2\text{S}_2$ and $\text{Ba}_2\text{CoO}_2\text{Cu}_2\text{S}_2$ and Their Solid Solution. *J. Am. Chem. Soc.* **2011**, *133* (8), 2691–2705.
122. Clarke, S. J.; Adamson, P.; Herkelrath, S. J. C.; Rutt, O. J.; Parker, D. R.; Pitcher, M. J.; Smura, C. F. Structures, Physical Properties, and Chemistry of Layered Oxychalcogenides and Oxypnictides. *Inorg. Chem.* **2008**, *47* (19), 8473–8486.
123. Johrendt, D.; Pöttgen, R. Pnictide Oxides: A New Class of High- T_c Superconductors. *Angew. Chem. Int. Ed.* **2008**, *47* (26), 4782–4784.
124. Watanabe, T.; Yanagi, H.; Kamiya, T.; Kamihara, Y.; Hiramatsu, H.; Hirano, M.; Hosono, H. Nickel-Based Oxyphosphide Superconductor with a Layered Crystal Structure, LaNiOP . *Inorg. Chem.* **2007**, *46* (19), 7719–7721.
125. Kamihara, Y.; Hiramatsu, H.; Hirano, M.; Kawamura, R.; Yanagi, H.; Kamiya, T.; Hosono, H. Iron-Based Layered Superconductor: LaOFeP . *J. Am. Chem. Soc.* **2006**, *128* (31), 10012–10013.
126. Li, Y.; Liu, J.; Chen, Y.-F.; Wang, F.-N.; Zhang, X.-M.; Wang, X.-J.; Li, J.-C.; Wang, C.-L. Multiple-Valley Effect on Modulation of Thermoelectric Properties of n -Type ZrCuSiAs -Structure Oxyantimonides LnTSbO ($\text{Ln} = \text{Lanthanides}$ and $\text{T} = \text{Zn}, \text{Mn}$). *J. Materiomics* **2019**, *5* (1), 51–55.
127. Luu, S. D. N.; Vaqueiro, P. Layered Oxychalcogenides: Structural Chemistry and Thermoelectric Properties. *J. Materiomics* **2016**, *2* (2), 131–140.
128. Sato, T.; Nakayama, K.; Sekiba, Y.; Arakane, T.; Terashima, K.; Souma, S.; Takahashi, T.; Kamihara, Y.; Hirano, M.; Hosono, H. Doping Dependence of Pseudogap in $\text{LaFeAsO}_{1-x}\text{F}_x$. *J. Physical Soc. Japan* **2008**, *77* (Supplement C), 65–68.
129. Zhao, L.-D.; He, J.; Berardan, D.; Lin, Y.; Li, J.-F.; Nan, C.-W.; Dragoë, N. BiCuSeO Oxytellurides: New Promising Thermoelectric Materials. *Energ. Environ. Sci.* **2014**, *7* (9), 2900–2924.
130. Barreteau, C.; Bérardan, D.; Amzallag, E.; Zhao, L.; Dragoë, N. Structural and Electronic Transport Properties in Sr-Doped BiCuSeO . *Chem. Mater.* **2012**, *24* (16), 3168–3178.
131. Ren, G.-K.; Wang, S.; Zhou, Z.; Li, X.; Yang, J.; Zhang, W.; Lin, Y.-H.; Yang, J.; Nan, C.-W. Complex Electronic Structure and Compositing Effect in High Performance Thermoelectric BiCuSeO . *Nat. Commun.* **2019**, *10* (1), 2814.
132. Brechtel, E.; Cordier, G.; Schäfer, H. Über Oxidpnictide: Zur Kenntnis Von $\text{A}_2\text{Mn}_3\text{B}_2\text{O}_2$ Mit $\text{A} = \text{Sr}, \text{Ba}$ Und $\text{B} = \text{As}, \text{Sb}, \text{Bi}$. *Z. Naturforsch., B: J. Chem. Sci.* **1979**, *34*, 777–780.
133. Matsumoto, Y.; Yamamoto, T.; Nakano, K.; Takatsu, H.; Murakami, T.; Hongo, K.; Maezono, R.; Ogino, H.; Song, D.; Brown, C. M.; Tassel, C.; Kageyama, H. High-Pressure Synthesis of $\text{A}_2\text{NiO}_2\text{Ag}_2\text{Se}_2$ ($\text{A} = \text{Sr}, \text{Ba}$) with a High-Spin Ni^{2+} in Square-Planar Coordination. *Angew. Chem. Int. Ed.* **2019**, *58* (3), 756–759.
134. Matsumoto, Y.; Nambu, Y.; Honda, T.; Ikeda, K.; Otomo, T.; Kageyama, H. High-Pressure Synthesis of $\text{Ba}_2\text{CoO}_2\text{Ag}_2\text{Te}_2$ with Extended CoO_2 Planes. *Inorg. Chem.* **2020**, *59* (12), 8121–8126.
135. Yang, Y.; Zhu, T.; Matsumoto, Y.; Kageyama, H. High-Pressure Synthesis and Order–Disorder Transition of Layered Oxytelluride $\text{Ba}_2\text{ZnO}_2\text{Ag}_2\text{Te}_2$. *Inorg. Chem.* **2022**, *61* (18), 7026–7031.
136. Fujii, S.; Gao, S.; Tassel, C.; Zhu, T.; Broux, T.; Okada, K.; Miyahara, Y.; Kuwabara, A.; Kageyama, H. Alkali-Rich Antiperovskite M_3FCh ($\text{M} = \text{Li}, \text{Na}$; $\text{Ch} = \text{S}, \text{Se}, \text{Te}$): The Role of Anions in Phase Stability and Ionic Transport. *J. Am. Chem. Soc.* **2021**, *143* (28), 10668–10675.

137. Gao, S.; Broux, T.; Fujii, S.; Tassel, C.; Yamamoto, K.; Xiao, Y.; Oikawa, I.; Takamura, H.; Ubukata, H.; Watanabe, Y.; Fujii, K.; Yashima, M.; Kuwabara, A.; Uchimoto, Y.; Kageyama, H. Hydride-Based Antiperovskites with Soft Anionic Sublattices as Fast Alkali Ionic Conductors. *Nat. Commun.* **2021**, *12* (1), 1–10.
138. Ubukata, H.; Takeiri, F.; Shitara, K.; Tassel, C.; Saito, T.; Kamiyama, T.; Broux, T.; Kuwabara, A.; Kobayashi, G.; Kageyama, H. Anion Ordering Enables Fast H⁻ Conduction at Low Temperatures. *Sci. Adv.* **2021**, *7* (23).
139. Wu, T.; Stone, M. L.; Shearer, M. J.; Stolt, M. J.; Guzei, I. A.; Hamers, R. J.; Lu, R.; Deng, K.; Jin, S.; Schmidt, J. R. Crystallographic Facet Dependence of the Hydrogen Evolution Reaction on CoPS: Theory and Experiments. *ACS Catalysis* **2018**, *8* (2), 1143–1152.
140. Cabán-Acevedo, M.; Stone, M. L.; Schmidt, J. R.; Thomas, J. G.; Ding, Q.; Chang, H.-C.; Tsai, M.-L.; He, J.-H.; Jin, S. Efficient Hydrogen Evolution Catalysis Using Ternary Pyrite-Type Cobalt Phosphosulphide. *Nat. Mater.* **2015**, *14* (12), 1245–1251.

4.14 The zoology of two-dimensional van der waals materials

A.J. Williams and J.E. Goldberger, The Ohio State University, Columbus, OH, United States

© 2023 Elsevier Ltd. All rights reserved.

4.14.1	Introduction	450
4.14.2	Synthesis of 2D van der Waals compounds in crystal, monolayer, and thin film forms	450
4.14.2.1	Bulk crystals	450
4.14.2.2	Preparation of monolayer and few-layer 2D materials	451
4.14.2.2.1	Mechanical exfoliation of crystals	452
4.14.2.2.2	Dispersions of 2D materials in solution	452
4.14.2.2.3	Thin film growth methods	454
4.14.2.2.4	Lateral heterostructures	456
4.14.2.2.5	Vertical heterostructures via mechanical exfoliation	456
4.14.2.2.6	Vertical heterostructures via thin film growth	457
4.14.3	The canonical families of 2D materials	459
4.14.3.1	Graphene and hexagonal boron nitride (hBN)	460
4.14.3.2	Xenes/Xanes	463
4.14.3.3	MXenes	464
4.14.3.4	Transition metal dichalcogenides (TMDs)	465
4.14.3.5	PdS ₂ and PdSe ₂	467
4.14.3.6	The group 13 monochalcogenides (TrCh)	468
4.14.3.7	Transition metal halides (MX ₃)	469
4.14.3.8	Transition metal phospho-/silico-/germano- trichalcogenides (MXCh ₃)	470
4.14.4	Emerging families of 2D vdW compounds	471
4.14.4.1	Metal trichalcogenides	472
4.14.4.2	Tetradymites	473
4.14.4.3	Tetradymite derivatives	475
4.14.4.4	The octahedral APn ₂ Te ₄ family	475
4.14.4.5	The tetrahedral MTr ₂ Ch ₄ family	478
4.14.4.6	The iron germanium tellurides (Fe _n GeTe ₂)	478
4.14.4.7	The tantalum-nickel group chalcogenides	480
4.14.4.8	Mixed metal tellurides	481
4.14.4.9	The metal chalcogenides (MChX) and group 4 metal nitrohalides (MNX)	486
4.14.4.10	A ternary main group compound, GaGeTe	487
4.14.4.11	Alloys of van der Waals compounds	487
4.14.4.12	Intercalated 2D vdW materials	488
4.14.5	Conclusions	488
References		488

Abstract

Layered, or 2D materials refer to compounds in which the arrangement of atoms and bonding pathways along two dimensions are similar and much stronger than along the third dimension. Compounds in which the bonding along the third dimension is dominated by vdW interactions are referred to as 2D vdW materials. The focus of this chapter is to survey the zoology and breadth of two-dimensional (2D) van der Waals (vdW) compounds. We will start by describing synthetic techniques to grow 2D vdW compounds in bulk crystal, thin film and few-layer form, highlighting the various methodologies for the preparation of monolayers. We will also detail strategies that have been developed to prepare lateral, vertical, and twisted heterostructures of different 2D vdW compounds. We will then survey the structure, properties and applications of the most well-studied “canonical” families of 2D vdW materials, emphasizing known changes in properties once the materials are exfoliated to the monolayer and few-layer thicknesses. We end by describing the structure and properties of emerging families of 2D vdW compounds, and their changes upon exfoliation to the few layer form.

4.14.1 Introduction

Two-dimensional (2D) van der Waals (vdW) materials have long been one of the most captivating and well-studied families of inorganic materials, due to the wealth of unusual physical phenomena that occur when electronic, and thermal transport, or magnetic ordering, is confined to a plane. The exfoliation of monolayer graphene and the Nobel Prize winning discovery^{1,2} that it exhibits a quantized Hall effect at room temperature opened the door to the exploration of exotic phenomena that occur in monolayers of other 2D vdW materials. In recent years, there has been a massive worldwide investment in 2D materials research. Graphene and other 2D materials are starting to be explored for commercialization in a wide range of technologies including water and air filtration, flexible electronics, infrared photodetection, lubrication, aerospace ice protection, and medical sensing technologies, to name a few.^{3–6} Even in the decades following graphene's initial work, 2D vdW compounds remain an energetic and dynamic frontier of materials discovery.

Over the past century, solid-state and materials chemists have discovered many different 2D vdW compounds and are continuing to do so. Each new material system features its own unique properties and reactivity, and also expands the realm of possible building blocks and applications. It also requires investigation in how these properties change down to the monolayer limit. With the development of aberration corrected transmission electron microscopy, researchers can now visualize the atoms and defects in a single layer. Additionally, the proliferation of e-beam lithography has greatly accelerated the measurement and our understanding of the electronic properties of a single layer of atoms. With the continued improvement of methods to exfoliate 2D vdW materials to the monolayer and restack them in specific orders and twist angles, researchers can now address the questions posed by Richard Feynman in his famous 1959 lecture, *There's Plenty of Room at the Bottom*, "What could we do with layered structures with just the right layers? What would the properties of materials be if we could really arrange the atoms the way we want them?"⁷

This chapter surveys the zoology and breadth of 2D vdW compounds. To start, we will describe the various synthesis methods to grow 2D vdW compounds in bulk crystal, thin film and few-layer form, highlighting the various methodologies for the preparation of monolayers. We will also detail strategies that have been developed to prepare lateral, vertical, and twisted heterostructures of different 2D vdW compounds. We will then survey the structure, properties and applications of the most well-studied "canonical" families of 2D vdW materials, emphasizing known changes in properties once the materials are exfoliated to the monolayer and few-layer thicknesses. We end by describing the structure and properties of emerging families of 2D vdW compounds, and their changes upon exfoliation to the few layer form. Whenever possible, we will highlight the many illuminating in-depth reviews and tutorial articles that have been written on each topic or class of materials.

4.14.2 Synthesis of 2D van der Waals compounds in crystal, monolayer, and thin film forms

In this section, we will describe different synthetic strategies toward preparing macroscopic crystals of 2D vdW compounds. Then we discuss approaches to exfoliate and transfer monolayer and few-layer thickness of these compounds onto substrates, as well as prepare dispersions in solution. We review methods of thin film growth for the preparation of controlled thicknesses of 2D vdW compounds onto substrates. We end by discussing various techniques to prepare lateral and vertical heterostructures comprised of different vdW compounds, integrated in a precise arrangement.

4.14.2.1 Bulk crystals

The preparation of bulk single crystals of 2D vdW compounds is of paramount importance in this field, as they allow researchers to understand the intrinsic structures and properties of layered compounds in their natural form as well as upon exfoliation to few-layer forms.^{2,8,9} Indeed, the initial work, on the exotic electronic transport properties of monolayer graphene in the mid-2000s relied on kish graphite crystals, which are highly crystalline graphite flakes that form during steel production.^{1,2,9} Similarly, many studies on exfoliated MoS₂ used macroscopic geological specimens of molybdenite as their source.^{10–12} Evaluating the electronic, magnetic, thermal transport properties along different directions, requires the preparation of crystals with dimensions larger than 1 mm, and for many measurements, ideally > 3 mm.

2D vdW compounds have an intrinsic anisotropy in their chemical bonding, which leads to a large difference in the in-plane and cross-plane growth rates. Specifically, the lateral edges of a layered compound consists of coordinatively unsaturated atoms that have high sticking coefficients, whereas the top and bottom faces are coordinatively saturated due to the vdW bonding. Thus, 2D vdW compounds often crystallize into platelet like morphologies with much larger in-plane dimensions (typically mm-cm) than cross-plane dimensions (typically 10–100 μm). Here, we briefly discuss many common synthetic strategies for preparing these phases. For further detail on the crystal growth of vdW compounds we point the reader to these review articles.^{13–16}

There are multiple techniques that are used to grow bulk crystals of vdW compounds, which are illustrated in Fig. 1. First, *directional solidification* fosters crystal growth by the slow, directional cooling of a solid above its melting point (Fig. 1a). These approaches require the solid to be a congruently melting phase, that is, the stoichiometry of a material in its liquid and solid state at its melting point will be the same. Stoichiometric ratios of precursors are sealed in quartz tubes which often will have conical ends, to facilitate the crystallization of a single domain. Directional solidification techniques are often classified as dynamic or static approaches. In dynamic approaches, the tube is physically pulled through a furnace held at a constant temperature gradient during growth. In static approaches, the tube is fixed in position, and the furnace temperatures at different zones are changed during

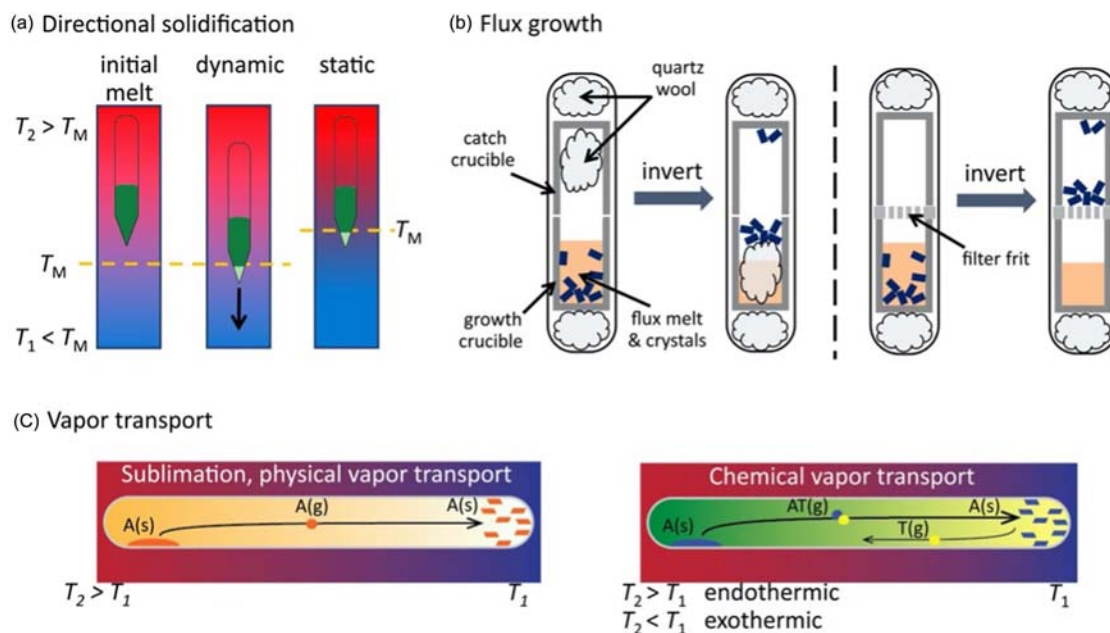


Fig. 1 Schematic diagrams of common growth techniques. (a) Directional solidification (in the Bridgman-Stockbarger method) in which the molten sample (dark green) moves relative to a temperature gradient so that freezing of the solid (light green) occurs first at the sharp tip. Two configurations are shown, dynamic and static. (b) The flux technique in which the crystals (blue) nucleate and grow from a liquid (orange). Upon inversion, the liquid flows through a filter allowing crystals to be easily isolated. Two configurations are shown, with quartz wool used as a filter and with an alumina frit filter. (c) Vapor transport reactions in which the source material, A, is transported through the gas phase(s) and recrystallized. Two example reactions are shown, sublimation and CVT. Reprinted with permission from May, A. F., Yan, J. & McGuire, M. A. A Practical Guide for Crystal Growth of van der Waals Layered Materials. *J. Appl. Phys.* **2020**, *128*, 051101. © AIP Publishing, 2020.

growth. Second, in *flux growth* (Fig. 1b) a crystal is grown at high temperatures in a molten element or salt “flux,” which acts as a solvent at these synthesis conditions.¹⁷ Similar to the growth of molecular crystals via recrystallization, this approach exploits the temperature dependent differences in solubility. The separation of the crystals from the molten flux often relies on inverting the tube at high temperature state, but using either quartz wool or specialized Canfield crucibles to catch the crystals. Finally, chemical vapor transport (CVT) techniques are often used to grow crystals of 2D materials. In this approach the 2D materials precursors are sealed into a tube, which is placed under a set thermal gradient, and the volatile metal-anion species will transport to the thermodynamically favorable side, and then nucleate and grow crystals. This has been one of the most prevalent approaches in the growth of vdW crystals, as most 2D vdW compounds have anions (chalcogens or halogens) and metal-anion high temperature species with high vapor pressures (Fig. 1c). In addition, external transport agents (I_2 , $AlCl_3$, $TeCl_4$ etc.) can be used as a carrier to repeatedly transport material of the desired phase to the crystallization region (Fig. 1d). Depending on the thermodynamics of the specific materials system, crystals may grow at either the hot or cold sides.

Different materials often require different growth techniques, and this is dictated by many factors including the binary and ternary phase diagrams, and the vapor pressures of the constituent elements. For example, single crystals of $PdSe_2$ can be prepared through a direction cooling allowing for crystallization from a Se flux. Here, rather than inverting the growth tube, the crystals are separated from the Se flux by volatilizing the excess Se away (Fig. 2a). As a second example, crystals of $NaSn_2Sb_2$ are grown directly from the melt (Fig. 2b). As a third example, crystals of CrI_3 are readily grown by chemical vapor transport (Fig. 2c),¹⁸ due to the volatility of I_2 , $CrI_3(g)$ and $CrI_4(g)$. Finally, careful control over the Fermi level and/or doping level is essential for realizing exotic physical phenomena in both metals and semiconductors, and thus many phases require significant synthetic¹⁶ and zone-refining efforts¹⁴ as well as the use of ultra-high purity reagents.

4.14.2.2 Preparation of monolayer and few-layer 2D materials

One of the defining structural features of vdW compounds is that they have strong covalent/ionic bonding in the two in-plane dimensions, along with vdW bonding in the third, cross-plane direction. For instance, the calculated adhesion energy between neighboring layers of van der Waals compounds are rather weak at $19.6 \text{ meV}/\text{\AA}^2$ in GaS, $33.4 \text{ meV}/\text{\AA}^2$ in $PtTe_2$, $22.5 \text{ meV}/\text{\AA}^2$ in graphene¹⁹ and $28.3 \text{ meV}/\text{\AA}^2$ in germanane.²⁰ This value is increased in $NaSn_2As_2$, $90.5 \text{ meV}/\text{\AA}^2$, a material which can be exfoliated but contains $\frac{1}{2}$ of a Sn–Sn bond across the van der Waals gap.²¹ When isolated as a monolayer, the electronic structure, chemical reactivity, and physical properties can be quite different compared to the bulk crystal. As a result, numerous strategies have been developed to isolate and study monolayer and few-layer derivatives of these compounds.

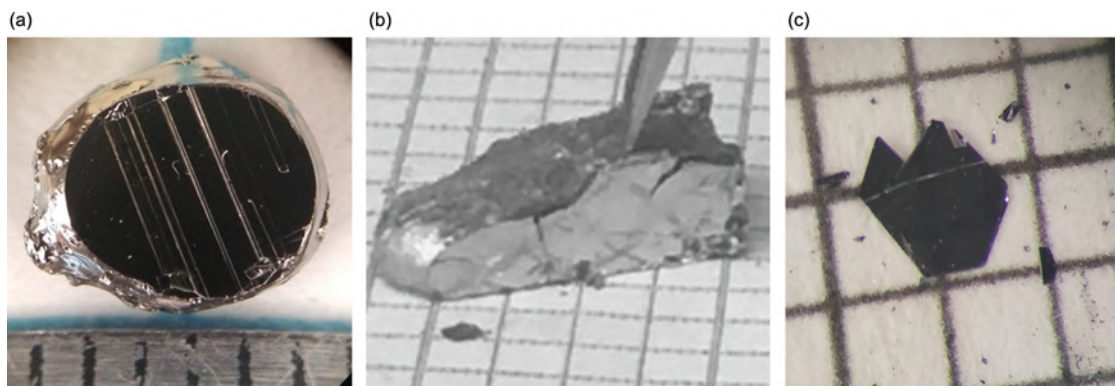


Fig. 2 Single crystals of (a) PdSe₂ grown from direction cooling, (b) NaSn₂Sb₂ grown from the melt, and (c) CrI₃ grown from chemical vapor transport.¹⁸

4.14.2.2.1 Mechanical exfoliation of crystals

The mechanical exfoliation of vdW compounds is one of the most well-known and powerful strategies to isolate monolayers from bulk crystals. Initial work focused on using adhesive tape to pull the vdW layers apart in a single crystal.^{2,11,22} Typically, micron-thick crystals are pressed between two pieces of tape, and then reduced in thickness by the repeated adhesion and deadhesion on fresh tape, until much thinner samples can be transferred onto a substrate, typically a dielectric SiO₂ coated Si chip. Early work by Frindt in the 1960s showed that few-layer films of MoS₂ could be isolated and visualized by transmission electron microscopy (TEM).²² As part of their Nobel prize winning work, Novoselov and Geim, showed that single layers of graphite could be prepared in a similar fashion.^{1,2} Exfoliated monolayers and few-layers of many different vdW compounds have been prepared this way, and many different adhesive materials can be used (Scotch tape, Kapton tape, Polydimethylsiloxane (PDMS)).¹⁹ The preparation of large domains via exfoliation is much easier in compounds that have appreciable mechanical strength, and that have flat van der Waals surfaces which allow neighboring layers to glide off each other. In addition, the electronic properties of mono and few-layer compounds prepared via mechanical exfoliation of crystals far exceed those synthesized using thin film growth techniques, or prepared via solution-based dispersion techniques, due to the reduced level of defects, dislocations, and dopants that can be controlled in these crystals. Still, these early approaches suffer from low yields and often lead to relatively small monolayer sizes.

In the last 15 years, numerous strategies have been developed to increase the yield, size, and success rate of monolayers exfoliated from bulk crystals, so much so that it has facilitated the preparation of multilayer heterostructures. First, it has been established that the cleanliness and flatness of the substrate- vdW material interface is essential to obtaining high yields of exfoliated materials (Fig. 3). Ultrasonic and plasma cleaning of the substrate immediately prior to interfacing the vdW crystals to the substrate is necessary to improving the yield.¹⁹ In addition, oftentimes trapped gas bubbles can form between the substrate and the vdW crystal, preventing the formation of strong vdW bonding between them. In addition, thermal annealing even at 100 °C before removing the adhesive tape causes trapped gas to diffuse out of the 2D material-substrate interface,²³ allowing a tighter, more uniform contact between the two materials. Second, this exfoliation and transfer process can be automated using a homebuilt transfer tool to allow much more precise distribution of forces and minimize trapped gas and wrinkling.^{24,25} In addition, these processes and tools are now often performed in ultraclean and O₂/H₂O free glovebox environments. One final set of strategies that have demonstrated the ability to transfer single layers of a crystal onto a substrate utilize the strong noncovalent interactions between vdW compounds and Au (Fig. 4a–g).¹⁹ In one example, entire cm-sized layers of a crystal are transferred using an ultraflat Au film. This ultraflat Au film is prepared by evaporating Au onto an ultraflat prime silicon wafer. Then a polyvinylpyrrolidone interfacial film is spun coat onto the Au, before a thermal release tape is adhered to the back side. The gold film is then peeled off the substrate and then adhered to the face of a single crystal. Because there exists a relatively strong non-covalent interaction between Au and many vdW compounds,¹⁹ especially chalcogen-terminated vdW compounds, the top monolayer binds more strongly to the Au than the neighboring layer. The top monolayer can be peeled off in its entirety, and then transferred to another substrate. The thermal release tape is removed upon annealing, and then the Au layer can be etched away using KI/I₂. Together, these techniques have transformed the often serendipitous exfoliation process into one which is reliable and deterministic.

4.14.2.2.2 Dispersions of 2D materials in solution

A second route to transform vdW solids into their monolayer and few-layer forms involves a group of strategies focused on preparing their dispersions in solution.^{26–30} These strategies enable the preparation of scalable quantities of solutions of isolated layers, which can be incorporated with other materials to form hybrid composites, or further processed into thin films using standard industrial techniques such as reel-to-reel manufacturing. There is immense interest in using such materials for applications including batteries,^{31,32} supercapacitors,^{32–35} water desalination membranes,^{36–38} and ion exchange membranes.^{39,40}

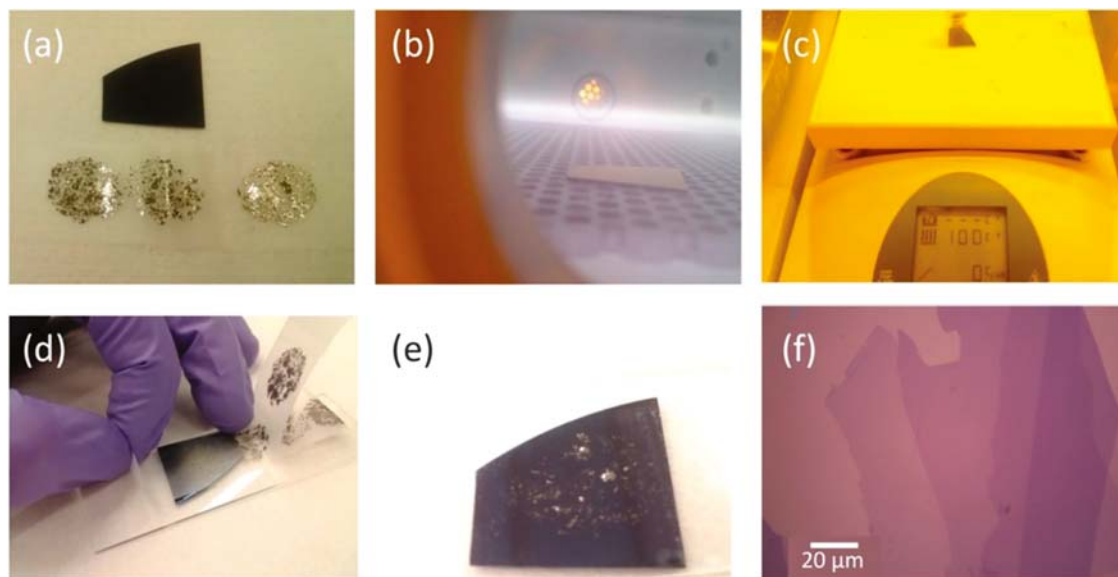


Fig. 3 Illustration of the modified exfoliation process for layered crystals (shown here for graphene). (a) Optical image of the SiO₂/Si substrate and adhesive tape with graphite flakes, which adhere after contact with a highly oriented pyrolytic graphite crystal. (b) Oxygen plasma cleaning of the SiO₂/Si substrate. (c) Contact between the graphite decorated tape and the substrate surface, followed by heating of the substrate (with tape) on a hot plate in air at ~100 °C for 2 min. (d) Removal of the substrate from the hot plate and peeling the tape off. (e) Optical image of the substrate after graphene exfoliation. (f) Optical micrograph of one of the graphene flakes on the substrate in (e). The flake has a thickness varying in steps between 1 and 4 layers. Reprinted with permission from Huang, Y., Sutter, E., Shi, N. N., Zheng, J., Yang, T., Englund, D., Gao, H.-J. & Sutter, P. Reliable Exfoliation of Large-Area High-Quality Flakes of Graphene and Other Two-Dimensional Materials. *ACS Nano*, 2015, 9, 10612–10620. © American Chemical Society, 2015.

The first of these strategies is the direct ultrasonication of bulk crystals in pure solvents that have the ideal surface energies to prevent reaggregation²⁷ (Fig. 5a)⁴¹. For instance, Coleman and collaborators²⁹ showed that a wide variety of vdW compounds, such as the transition metal dichalcogenides (TMDs), MoS₂, WS₂, MoSe₂, MoTe₂, TaSe₂, NbSe₂, NiTe₂, hexagonal boron nitride (h-BN), and Bi₂Te₃ can be readily dispersed in organic solvents. For each compound, the ideal solvent featured a specific range of dispersion, polar, H-bonding forces, as quantified by the Hansen solubility parameter.⁴² This strategy can be extended to the preparation of aqueous dispersions by ultrasonication of bulk crystals in H₂O with the presence of surfactants or polymers that can prevent reaggregation.⁴³ This approach parallels earlier surfactant-based approaches that were developed to disperse carbon nanotubes.⁴⁴

Oftentimes preparing the dispersions can be facilitated by first weakening the van der Waals forces in the layered crystals via chemically modifying the 2D layer (Fig. 5b). One such method is through oxidation or reduction of the 2D lattice. A classic example is the Hummers' method for oxidizing graphite to graphene oxide using KMnO₄, NaNO₃ and concentrated H₂SO₄.⁴⁵ This oxidation significantly disrupts the strong vdW forces of graphite by introducing epoxides, carboxylic acids, and alcohol substituents to the faces and edges, facilitating dispersion in water. Once films are formed, the graphene oxide can be reduced back to graphene, considering the strong thermodynamic driving force for reforming sp²-hybridized graphitic networks. Another example is the reduction of MoS₂ via intercalating Li into the vdW space, which expands the interlayer distance, substantially weakening the vdW forces and enabling dispersion in water. Selective etching techniques (Fig. 5c) rely on chemically dissolving away specific layers of a non-vdW compound with multiple components, converting it into a vdW compound that can be subsequently dispersed. This approach has been utilized to prepare dispersions of Xenes (Section 4.14.3.2) and MXenes (Section 4.14.3.3). Ion-exchange techniques (Fig. 5d) can be similarly utilized to prepare monolayer and few-layer dispersions of non-vdW layered compounds, whose structures consist of charged layers that are electrostatically held together via the presence of counterions.^{46–48} For instance, in many compounds monovalent cations are readily exchanged for larger monovalent cations in concentrated salt solutions. In one example, Ag⁺ cations in AgCrS₂ can be exchanged for a variety of bulky tetra-alkyl ammonium cations, which can then be dispersed in dimethyl formamide solvent.⁴⁹ As another example, carbonate counterions in the layer double hydroxide phase of Mg₆Al₂(OH)₁₆CO₃·4H₂O can be exchanged for dodecyl sulfate, greatly facilitating the formation of monolayer dispersions.⁵⁰

In general, all of these approaches represent powerful strategies to prepare large quantities of monolayer and few-layer dispersions. Very often a variety of layer thicknesses is produced in solution and multiple cycles of centrifugation, redispersion, and separation processes are required to isolate monolayers, if desired.²⁹ Finally, it is worth nothing that sonication and chemical modification often leads to the formation of a variety of defects that often disrupts the electronic properties and prevents the observation of the same exotic electronic behavior that can be observed in mechanically exfoliated layers.

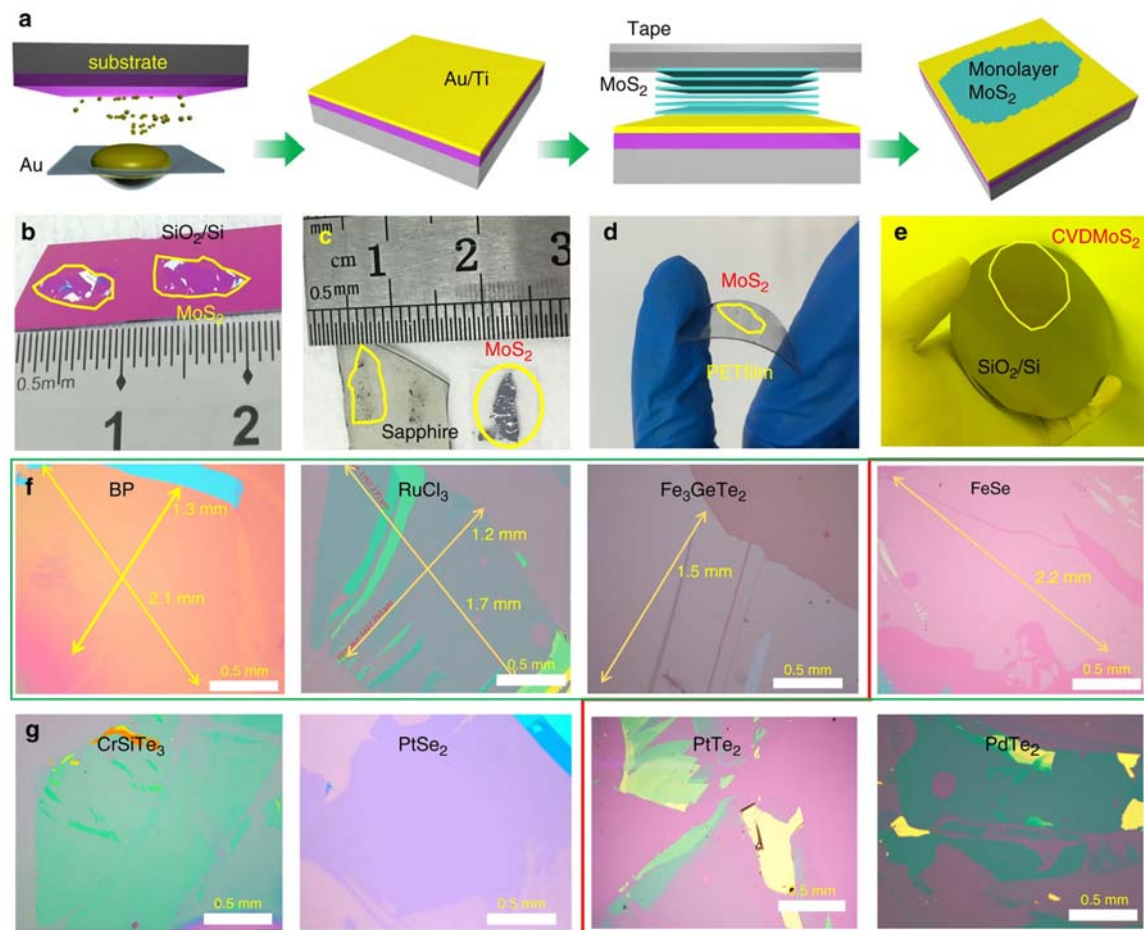


Fig. 4 (a) Schematic of the exfoliation process using the ultraflat Au film transfer method. (b-d) Optical images of exfoliated MoS₂ on SiO₂/Si, sapphire, and plastic film. (e) 2-in. CVD-grown monolayer MoS₂ film transferred onto a 4-in. SiO₂/Si substrate. (f, g) Optical images of large exfoliated 2D crystals: BP, FeSe, Fe₃GeTe₂, RuCl₃, PtSe₂, PtTe₂, PdTe₂, and CrSiTe₃. Those exfoliated monolayers highlighted in the red box are, so far, not accessible using other mechanical exfoliate methods. Reprinted with permission from Huang, Y., Pan, Y.-H., Yang, R., Bao, L.-H., Meng, L., Luo, H.-L., Cai, Y.-Q., Liu, G.-D., Zhao, W.-J., Zhou, Z., Wu, L.-M., Zhu, Z.-L., Huang, M., Liu, L.-W., Liu, L., Cheng, P., Wu, K.-H., Tian, S.-B., Gu, C.-Z., Shi, Y.-G., Guo, Y.-F., Cheng, Z. G., Hu, J.-P., Zhao, L., Yang, G.-H., Sutter, E., Sutter, P., Wang, Y.-L., Ji, W., Zhou, X.-J. & Gao, H.-J. Universal Mechanical Exfoliation of Large-Area 2D Crystals. *Nat. Commun.* **2020**, *11*, 2453. © 2020.

4.14.2.2.3 Thin film growth methods

A third approach to prepare monolayer and few-layer flakes of vdW crystals is to grow thin films of them directly onto substrates and wafers. It has been a long-standing goal to be able to prepare wafer-scale monodomain monolayer crystals of specific 2D materials and their heterostructures, as this thin film form factor has numerous advantages.^{51,52} It allows the ability to utilize semiconductor microfabrication technologies to evaluate their properties and integrate them into complex device technologies. Furthermore, the same transfer techniques that have been developed to exfoliate monolayers onto a substrate as discussed in Section 4.14.2.2.1, can be extended to transfer wafer-sized monolayer thin films onto other monolayers and materials. In addition, this bottom-up approach to the synthesis of thin films allows for greater control over the thickness and size of the grown flakes. In principle, thin film growth strategies may also allow for the direct preparation of vertical heterostructures of different 2D vdW materials by consecutive growth cycles upon the same substrate, providing these materials are resilient to the varying growth conditions.

Typical thin film growth methods include CVD reactions, chemical vapor deposition (CVD), and molecular beam epitaxy (MBE). The earliest route toward thin film preparation of 2D materials was CVD and is similar to the CVD approach described in the synthesis of bulk single crystals in Section 4.14.2.1. This method uses either temperature and/or a carrier gas to transform solid-state precursors of the constituent elements into volatile species and transport the reagents to a substrate where growth occurs (Fig. 6a).⁵³ Many TMDs (CrSe₂,⁵⁴ VSe₂,⁵⁵ MoS₂,^{56,57} MoSe₂,⁵⁸ TaSe₂,⁵⁹ WS₂,⁶⁰ PtSe₂⁶¹) and hexagonal BN⁶² (hBN) have been grown at wafer scale sizes using this method. For each structure, different precursors are selected as sources, for example, in the TMDs the highly volatile chalcogens are used in their elemental form while metal oxides or metal halides (i.e., MoCl₄) are common metal sources. For instance, the preparation of few-layer MoS₂ films on Al₂O₃ substrates can be accomplished by transporting S, and MoCl₅ at high temperatures using an inert carrier gas.⁵⁷ Next, CVD enables the growth of thin films by the controlled flow and

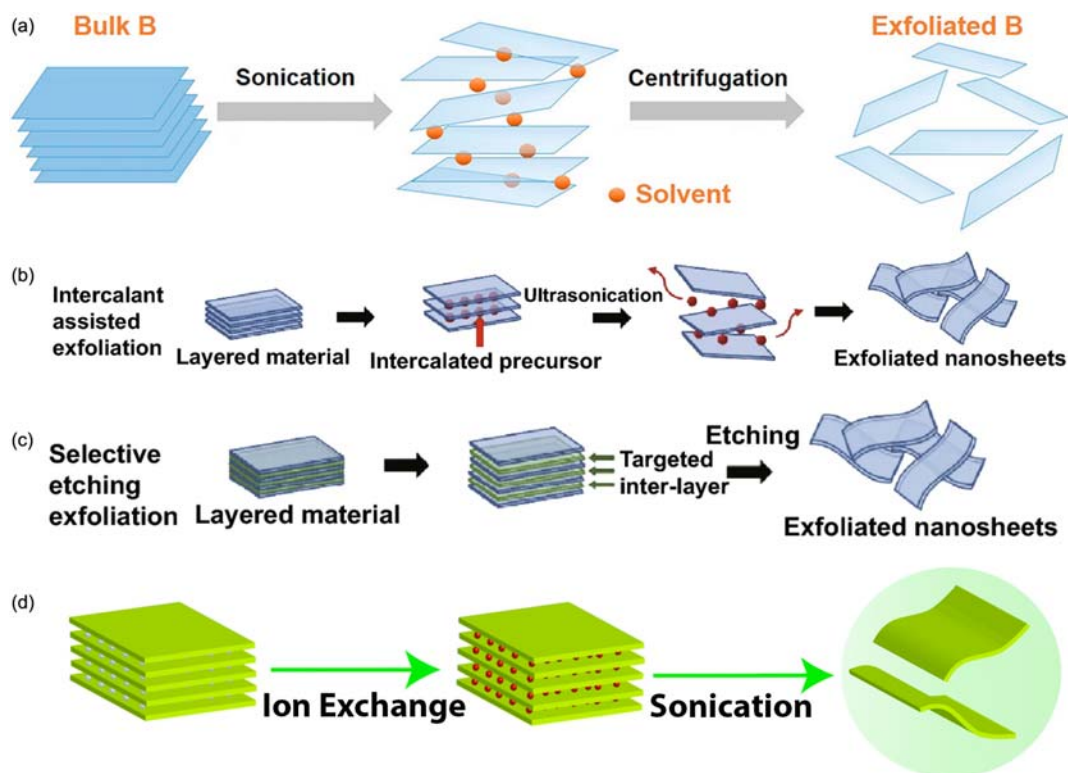


Fig. 5 (a) Schematic illustration of the sonication-assisted liquid-phase exfoliation process. (b) Intercalant-assisted exfoliation where a metal ion (usually Li^+) is used to intercalate into the bulk precursor in a liquid media coupled with ultrasonication, which shears the sheets apart. (c) Selective etching, in which an etchant (usually strong acids, e.g., HF) is used to remove one or more constituent atoms and results in the formation of sheets. (d) Ion exchange assisted exfoliation. Panel (a) reprinted with permission from Li, H., Jing, L., Liu, W., Lin, J., Tay, R. Y., Tsang, S. H. & Teo, E. H. T. Scalable Production of Few-Layer Boron Sheets by Liquid-Phase Exfoliation and Their Superior Supercapacitive Performance. *ACS Nano*, **2018a**, *12*, 1262–1272. © American Chemical Society, 2018. Panels (b and c) reprinted with permission from Mukherjee, S., Ren, Z. & Singh, G. Beyond Graphene Anode Materials for Emerging Metal Ion Batteries and Supercapacitors. *Nano-Micro Lett.* **2018**, *10*, 70. © 2018. Panel (d) reprinted with permission from Cai, X., Luo, Y., Liu, B. & Cheng, H.-M. Preparation of 2D Material Dispersions and Their Applications. *Chem. Soc. Rev.* **2018a**, *47*, 6224–6266. © 2018 Royal Society of Chemistry, 2018.

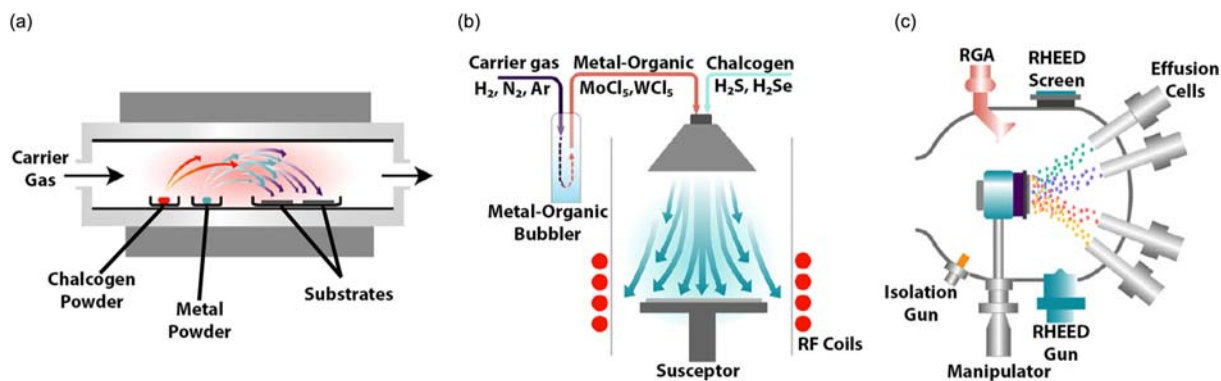


Fig. 6 Schematic of common techniques for synthesis of thin films of 2D materials. (a) Growth via CVD, (b) growth via metal-organic CVD (MOCVD), and (c) growth via MBE. Reprinted with permission from Briggs, N., Subramanian, S., Lin, Z., Li, X., Zhang, X., Zhang, K., Xiao, K., Geohegan, D., Wallace, R., Chen, L.-Q., Terrones, M., Ebrahimi, A., Das, S., Redwing, J., Hinkle, C., Momeni, K., Van Duin, A., Crespi, V., Kar, S. & Robinson, J. A. A roadmap for electronic grade 2D materials. *2D Mater.* **2019**, *6*, 022001. © Institute of Physics, 2019.

deposition of gas phase precursors over a target substrate. This approach introduces high vapor pressures of 2D material precursors at precise flow rates into a main growth chamber using mass flow controllers (Fig. 6b). CVD allows much more precise control of the concentrations of precursors in the gas phase over CVT, potentially allowing higher quality monolayer films with controlled doping levels. In one example, the growth of monolayer films of WSe_2 can be prepared using WCl_6 and $(\text{C}_2\text{H}_5)_2\text{Se}$ as precursors.⁶³

Finally, MBE growth of thin films offers a high level of control over the elemental composition of thin films (Fig. 6c). It utilizes the deposition of beams of the elements with precisely quantified fluxes in ultra-high vacuum chambers to grow 2D materials. One such example is the MBE growth of In_2Se_3 few-layer thin films.⁶⁴

4.14.2.2.4 Lateral heterostructures

The preparation of monolayer vdW materials in which the chemical composition of the crystalline material changes abruptly along the length and width without disruptions in the lattice connectivity, opens the door to designing complex architectures for advanced devices and applications. Two such strategies have been developed to prepare these lateral heterostructures. The first strategy relies on modifying existing thin film growth strategies to control the composition of the reactants in the vapor phase as a function of time. As discussed previously, vdW compounds have more reactive edge sites compared to the top and bottom faces, and thus, after nucleation, material growth typically occurs along the in-plane direction. Any change in the vapor phase reactants will lead to the growth of a different material along the growth front. This has been widely demonstrated in the preparation of lateral heterostructures of TMDs, which all have similar crystal structures and lattice constants, facilitating the seamless change in composition with the presence of additional grain boundaries.^{65–69} When the two materials grow optimally at drastically different temperatures for a given method, as is the case for WSe_2 which grows at 925 °C, and MoS_2 which grows at 775 °C, a crystal with a rather sharp interface can be grown in a two-step process. The higher temperature WSe_2 phase is nucleated and grown first, followed by the lower temperature growth of MoS_2 in a second step, allowing for the preparation of a single junction.⁷⁰ More recently, the preparation of vdW monolayers with multiple $\text{MoSe}_2/\text{WSe}_2$ sections can be prepared in a CVT-type process by changing the transport gas. (Fig. 7a–g).⁷¹ At the growth temperature of 1060 °C, in an $\text{N}_2 + \text{H}_2\text{O}$ gas mixtures, MoS_2 and MoSe_2 partially react to form volatile $\text{MoO}_2(\text{g})$ and $\text{H}_2\text{S}/\text{H}_2\text{Se}$ species, whereas the tungsten chalcogenides form nonvolatile $\text{WO}_{3-x}(\text{s})$ phases. When the vapor transport agent is switched to $\text{H}_2 + \text{Ar}$, the $\text{MoO}_2(\text{g})$ is reduced to nonvolatile $\text{Mo}(\text{s})$ which reacts with the chalcogen, and the $\text{WO}_{3-x}(\text{s})$ is reduced to volatile $\text{WO}_2(\text{g})$ species. The volatile species transport to the growing 2D flake and form either a Mo-rich or W-rich dichalcogenide, depending on the gas mixtures. By repeatedly swapping between the two gas mixtures, multiple domains of the two different metal sources can be grown in a single flake. A second strategy to prepare lateral heterostructures of vdW monolayer and few-layer materials relies on the lithographic patterning and chemical modification of an exfoliated flake. For instance, MoS_2 can be converted between a semiconducting MoS_2 two-layer per hexagonal unit cell polytype (2H) and a metallic one-layer per trigonal unit cell polytype (1T) via Li reduction and intercalation using n-butyl lithium.³³ Thus, lateral heterostructures can be prepared by lithographically patterning the region of the flakes that are exposed to n-butyl lithium.⁷²

4.14.2.2.5 Vertical heterostructures via mechanical exfoliation

Vertical heterostructures of semiconductors have been one of the most widely studied and technologically useful electronic platforms for over half a century.^{73–75} In traditional semiconductors these structures are created through the growth of one material on top of a second material that has a different composition and/or doping level. These heterostructures typically use different group IV, III-V, or II-VI semiconductors, that have similar zinc-blende or wurtzite structure types and lattice constants to facilitate epitaxy.^{76–79} Considerable efforts in controlling and grading the composition during growth are needed to minimize the strain that originates from the lattice mismatch of different materials. In contrast, vdW materials have coordinatively saturated top and bottom surfaces, which allows for the formation of vertical heterostructures from compounds with drastically different structures and properties, with minimal effects of strain.⁵¹ The two strategies for constructing such vertical heterostructures with 2D vdW materials involve exfoliation-based and thin film-based approaches.

The fabrication of vertical heterostructures using multistep exfoliation builds off the approaches discussed in Section 4.14.2.2.1 to prepare and transfer monolayer or few materials from single crystals onto different substrates. A wide variety of techniques have been investigated,^{80–88} and here we describe in detail a dry transfer exfoliation method utilizing PDMS (Fig. 8a–d).⁸² In this specific example, a top layer of a hBN dielectric material is mechanically exfoliated onto PDMS directly. Then the 2D material of interest is exfoliated onto a desired substrate. Mechanical exfoliation often produces a wide array of flakes with different sizes, thicknesses, and positions across a substrate. Once suitable flakes of each are identified, one must align the desired hBN flake on the PDMS with the target flake on the substrate. The hBN can be transferred to the substrate at high temperature by slowly peeling away the PDMS from the substrate. Alternatively, to pick up the exfoliated flake, the PDMS can be rapidly peeled away from the substrate yielding a heterostructure on the PDMS. This process can be repeated multiple times to prepare complex vertical heterostructures of many different 2D vdW materials (Fig. 8e)⁸⁹. Oftentimes this process is performed in a clean glovebox environment, using mechanized transfer tools.^{90,91}

This exfoliation procedure can be further used to alter the twist angle between different exfoliated layers. The relative twist angle between neighboring layers can significantly affect interlayer coupling and produce new heterostructures with unique Moiré patterns with exotic electronic phenomena that do not exist in the bulk or monolayer form.^{92,93} This has led to an emerging field of “twistronics” that has gathered considerable interest in recent years.^{94–97} For instance, superconductivity has been discovered in graphene bilayers twisted with the “magic angle” of 1.1°.^{98,99} One approach to prepare a twisted bilayer of a material is to exfoliate a monolayer onto a substrate and then tear and transfer half of the monolayer onto a holder, which is rotated by a desired angle using a goniometer, and then used to pick up the remaining half of the monolayer on the substrate (Fig. 9).¹⁰⁰ Because the two halves come from the same crystalline monolayer, the crystallographic angle between them after stacking is determined by the angle of the rotation. The holder can either be a hemispherical holder, a droplet of epoxy, or PDMS coated by an adhesion polymer which is first used to pick up a top hBN layer. Once the edge of the hBN flake is aligned halfway with the underlying 2D material, the 2D material can be torn by slowly peeling away the holder.

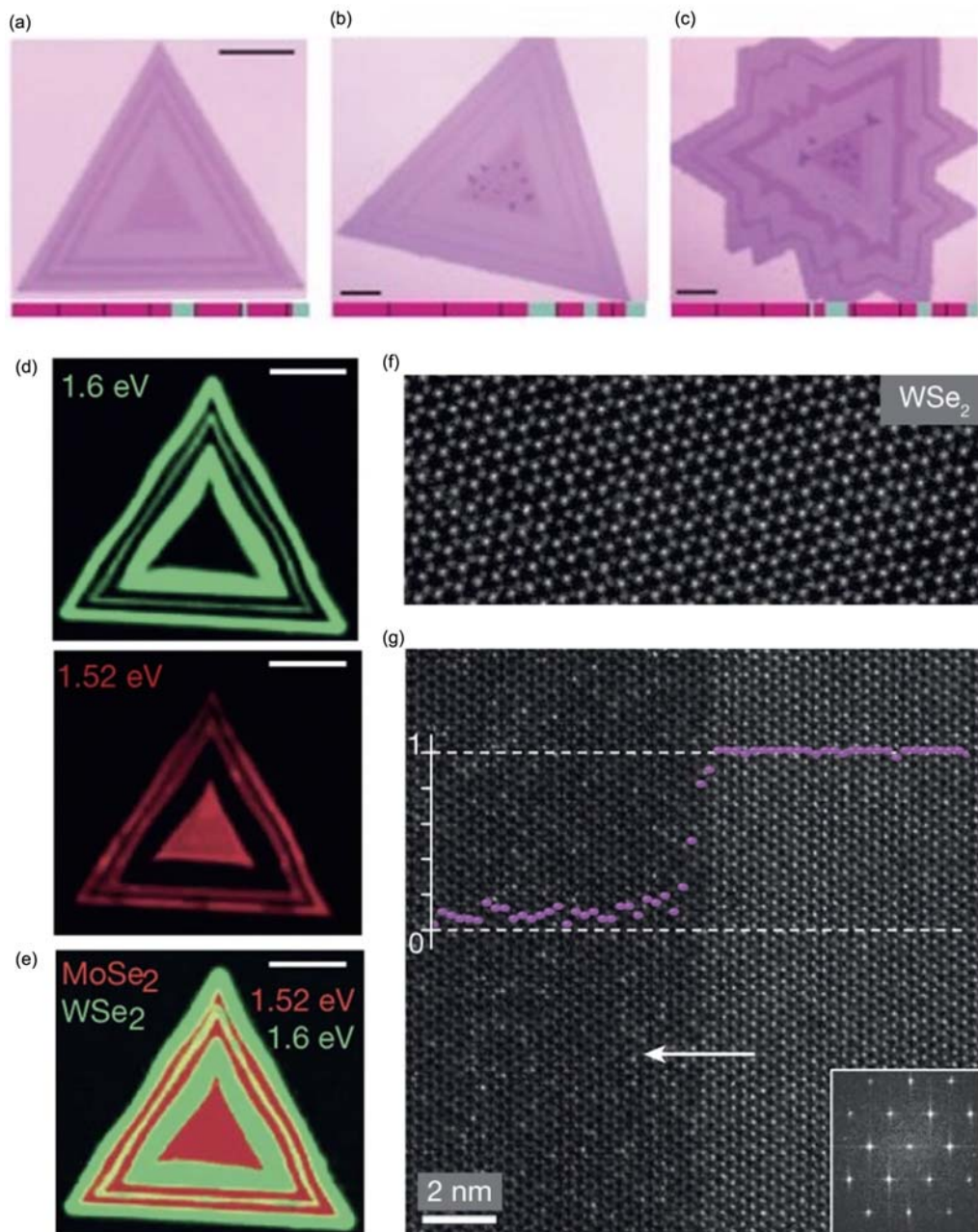


Fig. 7 (a–b) Optical images of five-junction heterostructures. The difference in thickness of the MoSe₂ layers in a and b is seen by the difference in thickness of the dark-contrast regions. (c) Seven-junction heterostructure with variable domain widths. The underlying color bars in a–c depicts the growth timescale: from left to right (pink, MoSe₂; green, WSe₂), each division (black line) corresponds to approximately 120 s. (d) Photoluminescence (PL) intensity maps for the WSe₂ (1.6 eV, top) and MoSe₂ (1.52 eV, bottom) domains and (e) composite photoluminescence map for the heterostructure in (a). (f) Z-contrast atomic-resolution high-angle annular dark field scanning transmission electron microscopy (HAADF-STEM) images of pure WSe₂ (g), Atomic-resolution HAADF-STEM images of the sharp interface, with the corresponding Fourier-transform pattern and composition profile (atomic fraction of tungsten per vertical atomic column). The sharp interface has an average interface width of 1 nm (4 atomic columns). Reproduced with permission from Sahoo, P. K., Memaran, S., Xin, Y., Balicas, L. & Gutiérrez, H. R. One-Pot Growth of Two-Dimensional Lateral Heterostructures Via Sequential Edge-Epitaxy. *Nature*, **2018**, 553, 63–67. © Springer Nature, 2018.

4.14.2.2.6 Vertical heterostructures via thin film growth

The preparation of vertical heterostructures of different 2D materials utilizing conventional thin film growth techniques has generated some initial examples of vertical heterostructure materials. The first approach is the sequential growth of each layer, wherein an initial vdW material is grown on a substrate followed by the growth of a second vdW material. This sequential growth has yielded multilayer stacks of TMDs grown on both graphene^{101–103} and other TMD layers.^{104–107} One example is the growth of NiTe₂ on

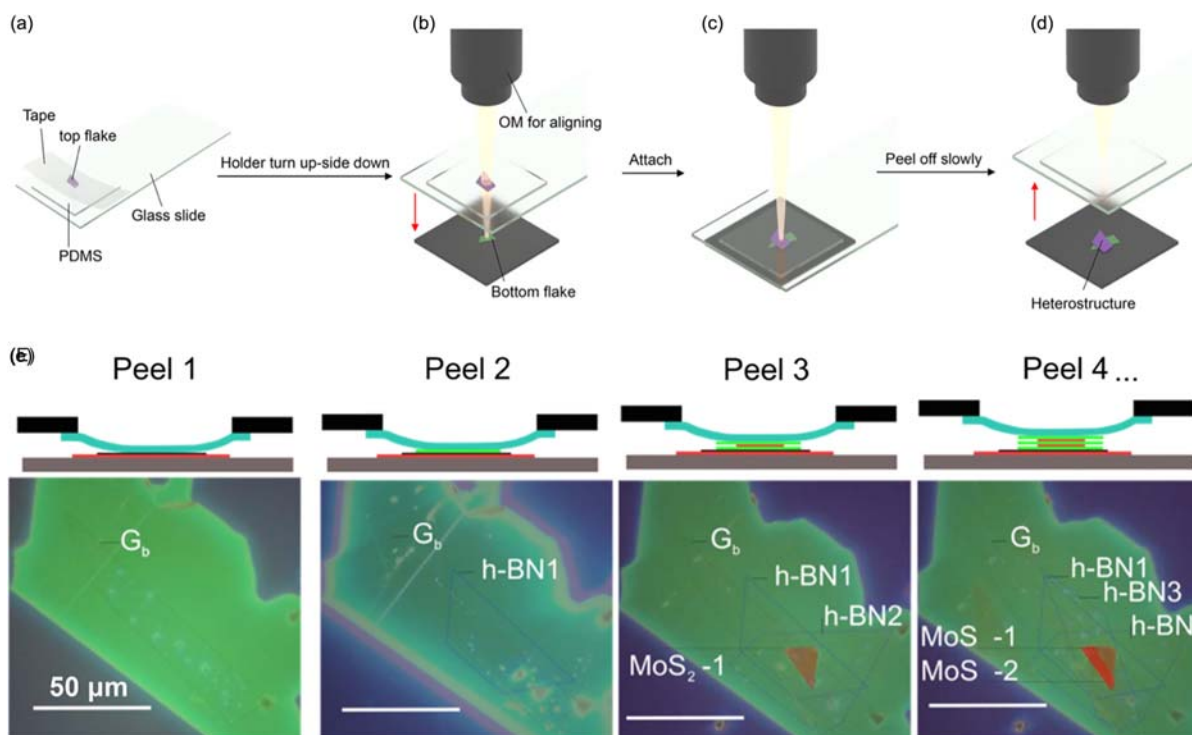


Fig. 8 PDMS exfoliation method. (a) The top flakes are directly exfoliated onto a PDMS stamp placed on the glass slide. (b) The holder is turned up-side down and mounted into the position followed by the precise alignment of the top desired flake to the bottom target one, which is prepared on the 300 nm SiO₂/Si wafer (c) The holder is brought down, pressing the PDMS against the substrate. (d) The PDMS is then lifted back together with the glass slide slowly, and the top flake is released from the stamp and attached onto the target position, yielding the heterostructure. (e) Schematics and the corresponding optical microscopy images illustrating the stacking process of graphene/hBN/MoS₂/hBN/MoS₂/hBN from the bottom-up approach by dry peeling with the highlighted flake edges observed in the semi-transparent dark field. The scale bar is 50 μm. Panel (a–d) reprinted with permission Fan, S., Vu, Q. A., Tran, M. D., Adhikari, S. & Lee, Y. H. Transfer Assembly for Two-Dimensional van der Waals Heterostructures. *2D Mater.* **2020**, *7*, 022005. © Institute of Physics, 2014. Panel (e) reprinted with permission from Withers, F., Del Pozo-Zamudio, O., Mishchenko, A., Rooney, A. P., Gholinia, A., Watanabe, K., Taniguchi, T., Haigh, S. J., Geim, A. K., Tartakovskii, A. I. & Novoselov, K. S. Light-Emitting Diodes by Band-Structure Engineering in van der Waals Heterostructures. *Nat. Mater.* **2015**, *14*, 301–306. © Springer Nature, 2015.

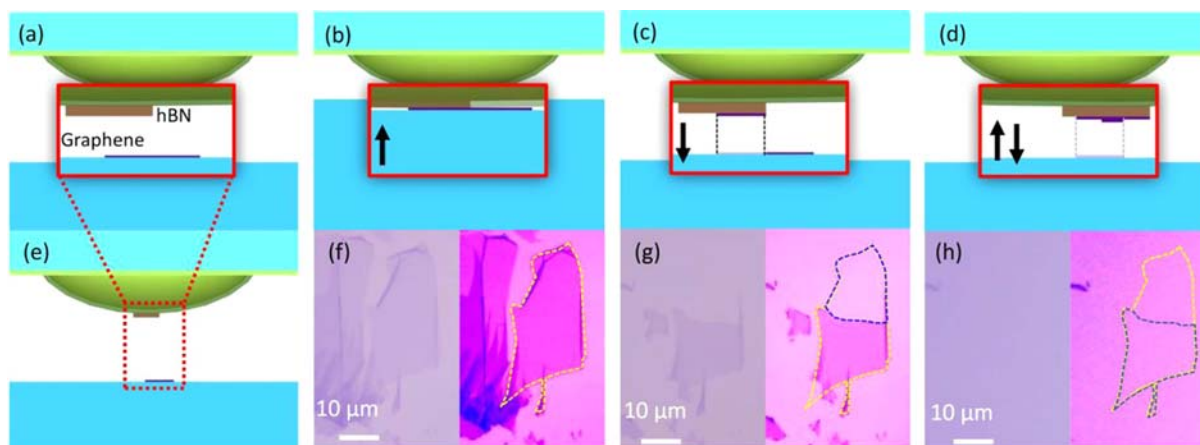


Fig. 9 Rotationally aligned graphene double layer realized by successive transfers from a monolayer graphene using a hemispherical handle substrate. (a,e) Schematic of layer pick-up. The red box represents a zoom-in view of the hemispherical handle substrate. (b–d) Schematics and (f–h) corresponding optical micrographs of successive stacking steps. Panels b and f illustrate a partial contact of the handle with the bottom graphene. Panels c and g show the handle substrate release with one graphene section detached. Panels d and h illustrate the second contact with the handle translated laterally to create an overlap region of the two graphene layers. The two images in panels f and h represent the same optical micrographs, with the contrast enhanced and the graphene contour marked in the right-hand image. Because the two graphene layers are obtained from a single grain, their principal crystal axes remain aligned if the handle is not rotated with respect to the bottom substrate. Reprinted with permission from Kim, K., Yankowitz, M., Fallahzad, B., Kang, S., Movva, H. C. P., Huang, S., Larentis, S., Corbet, C. M., Taniguchi, T., Watanabe, K., Banerjee, S. K., Leroy, B. J. & Tutuc, E. van der Waals Heterostructures with High Accuracy Rotational Alignment. *Nano Lett.*, **2016**, *16*, 1989–1995. © American Chemical Society, 2016.

a WSe₂ monolayer substrate, in which WSe₂ mono and bilayers were initially grown via CVD at 850 °C before the growth of micron sized, multilayer NiTe₂ multilayers at 600 °C.¹⁰⁴ It is important to realize that thin film growth techniques often require subsequent layers to be grown at lower temperatures than the initial layer material to minimize the interlayer diffusion of chemical species and maximize the stability of each layer (Fig. 10).¹⁰⁶ For instance, in a second approach, the growth of WSe₂ monolayers using different CVD precursors was optimized to occur at 950 °C, whereas the growth of MoS₂ occurs at 750 °C. Growing WSe₂, and then MoS₂ preserves stoichiometries of both monolayer compositions. Conversely, the growth of MoS₂ at 750 °C first, followed by the growth of WSe₂ at 950 °C, causes the S atoms in the MoS₂ to be replaced by Se.

A second approach that overcomes the diffusion of elements into neighboring layers that typically occur in high temperature CVD growth conditions, relies on the low temperature deposition of calibrated atomic layers of metals and chalcogen anions, followed by a single crystallization anneal at moderate temperatures.^{108–110} This process enables the deterministic growth of layers of vdW and even other non-vdW compounds across an entire 6" substrate with precise control of sequencing. For instance, Fig. 11 shows a cross-sectional TEM image of precise thicknesses of the vdW compound TiSe₂, separated by precise thicknesses of PbSe in the rock salt structure. These materials have a large crystallinity in the cross-plane direction but smaller in-plane domain sizes on the order of tens to hundreds of nanometers. In total, vertical heterostructures grown via thin film methods do not exhibit the same level of exotic electronic phenomena that can be accomplished via mechanical exfoliation.

4.14.3 The canonical families of 2D materials

We will give a brief overview of the structure and properties of the families of 2D vdW materials that have been the most well-studied compounds. We will highlight the unique aspects of each material system, as well as the changes in properties that occur when exfoliating down to a monolayer, and where each material system has attracted considerable attention for technological application.

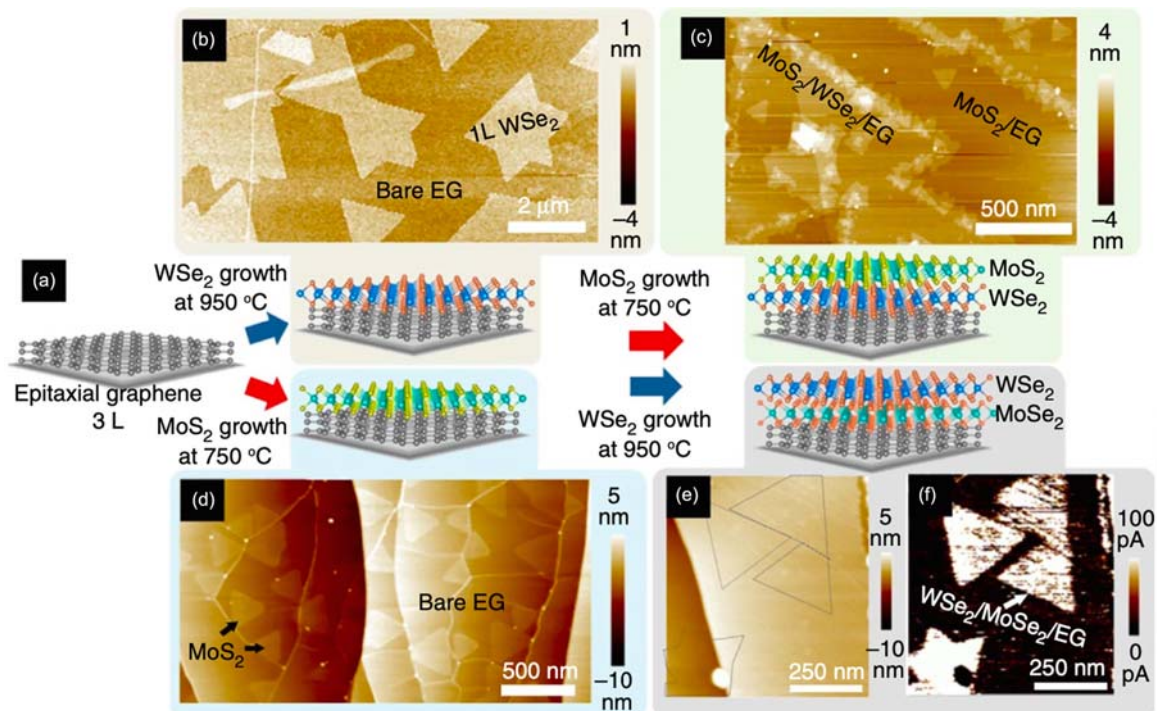


Fig. 10 MoS₂-WSe₂-epitaxial graphene vertical heterostructures begins with the synthesis of (a) 3 L epitaxial graphene from SiC followed by (b) vapor transport or MOCVD of WSe₂ and (c) vapor transport of MoS₂. WSe₂-MoSe₂-epitaxial graphene heterostructures are similarly grown, except when (d) MoS₂ is grown first on epitaxial graphene followed by (e) growth of the WSe₂, a Se-S ion exchange occurs, leading to the formation of MoSe₂ from the original MoS₂ layer. The MoSe₂ domains are difficult to topographically identify; however, (f) conductive atomic force microscopy (AFM) clearly delineates their location due to enhanced tunneling at the heterostructures. Reprinted with permission Lin, Y.-C., Ghosh, R. K., Addou, R., Lu, N., Eichfeld, S. M., Zhu, H., Li, M.-Y., Peng, X., Kim, M. J., Li, L.-J., Wallace, R. M., Datta, S. & Robinson, J. A. Atomically Thin Resonant Tunnel Diodes Built From Synthetic van der Waals Heterostructures. *Nat. Commun.* **2015**, *6*, 7311. © 2015.

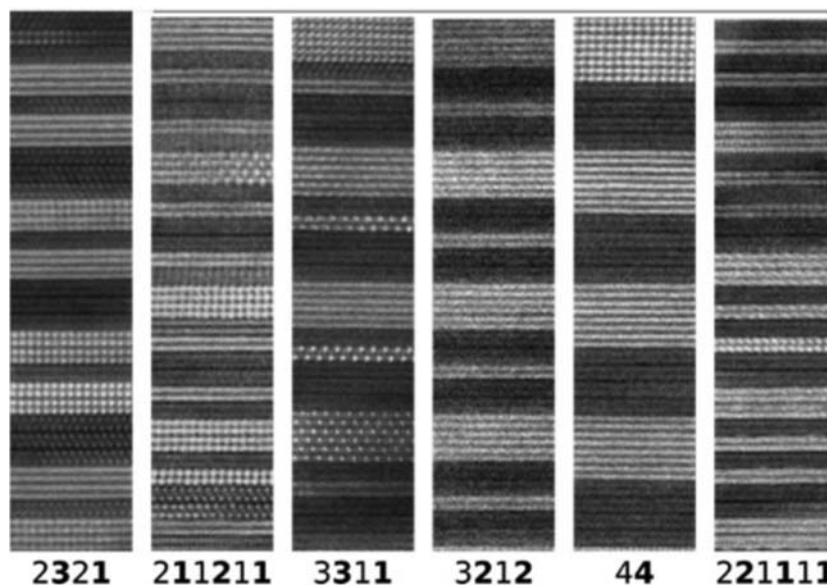


Fig. 11 HAADF-STEM images of structural isomers containing four bilayers of PbSe and four TiSe₂ trilayers. The notation on the bottom of the images provides the number of PbSe bilayers in bold and the number of TiSe₂ layers in normal font. The sequence of numbers matches the sequence of layers in each isomer. Reprinted with permission from Cordova, D. L. M. & Johnson, D. C. Synthesis of Metastable Inorganic Solids With Extended Structures. *ChemPhysChem*, 2020, 21, 1345–1368. © Wiley Online Library, 2020.

4.14.3.1 Graphene and hexagonal boron nitride (hBN)

The most well-studied and Nobel Prize winning example of 2D material research is graphene, a monolayer of graphite. Similarly, hBN, which is structurally similar to graphite, has proven to be one of the most important dielectric materials for 2D vdW research. The crystal structure of graphite consists of single atom thick layers of carbon atoms in a covalently bonded honeycomb arrangement in which the C atoms exist in sp² hybridization (Fig. 12a). These layers stack in a hexagonal unit cell consisting of two graphite layers that are held together by vdW forces. hBN crystallizes into a similar structure as graphite, such that every carbon atom in a layer is replaced alternately with boron and nitrogen atoms (Fig. 12b).

Graphite is a metallic material on account of the aromaticity and delocalization of the half-filled C 2p_z orbitals throughout each layer. The bulk band structure of graphite close to the Fermi level is shown in Fig. 12c,¹¹¹ where the bands close to the Fermi level are predominantly of C 2p_z origin. In contrast, hBN has a large 5.95 eV band gap. The large electronegativity difference between B and N induces a large energetic splitting between the 2p_z orbital bonding and antibonding bands (Fig. 12d).¹¹² The valence band has predominantly N 2p_z character whereas the empty conduction band is predominantly B 2p_z character.

The latest explosion in research interest on graphene was sparked in 2005, when Novoselov and Geim discovered that monolayer graphene remarkably exhibited a Quantum Hall effect that persisted to room temperature.^{1,2} A detectable quantized Hall effect at experimentally accessible magnetic fields (5–10 T) requires a material to exhibit high carrier mobilities (> > 1000 cm² V⁻¹ s⁻¹). This ultrahigh carrier mobility in graphene arises from a change in the band structure of graphene compared to graphite. In single layer graphene there exists a single pair of 2p_z orbitals with a conical linear dispersion at the Fermi level (Fig. 11e),¹¹³ meeting at a single energy point defined as a Dirac point. The conical linear dispersion of the bands at the Fermi level are thus known as Dirac cones. In graphene, electronic transport mathematically follows the relativistic Dirac equation because of this linear band dispersion near the Fermi level, and this causes the charge carriers in graphene to behave as though they are relativistic particles with close to zero rest mass, and a speed of ~1/300th the speed of light.¹

One method that can be utilized to approximate the band structure of a monolayer material from the band structure of the bulk is the “Zone-Folding Scheme,” which was originally popularized by.¹¹⁴ The principal idea behind this method is that only the electronic states that occur along particular wavevectors are confined. Thus, the electronic states of a monolayer can be approximated as a specific subset of the electronic states of the bulk vdW compound, assuming minimal changes in structure upon exfoliation. In essence, one can estimate the band structure of a 2D monolayer by identifying the appropriate 2D plane in the band structure of a parent 3D material. For vdW compounds with crystal structures consist of 1-layer per unit cell, this plane occurs at $k_z = \pi/2c$. For 2-layers per unit, it occurs at $k_z = \pi/c$, and for 3 or greater layers per unit cell, it lies outside of the first Brillouin zone and thus the monolayer band structure cannot be easily observed.

This “zone folding scheme” can be used to identify the monolayer graphene structure with Dirac cones based on the band structure of bulk 2-layer graphite (Fig. 13a).¹¹⁵ Here, we will illustrate the zone-folding scheme by examining the p_z orbital bands in graphite and graphene, using Roald Hoffmann’s methodology to merge molecular orbital theory and band structure.¹¹⁶ In graphite, each unit cell consists of two graphite layers that are offset in the xy plane leading to an “A” and “B” layer. Each layer has two carbon

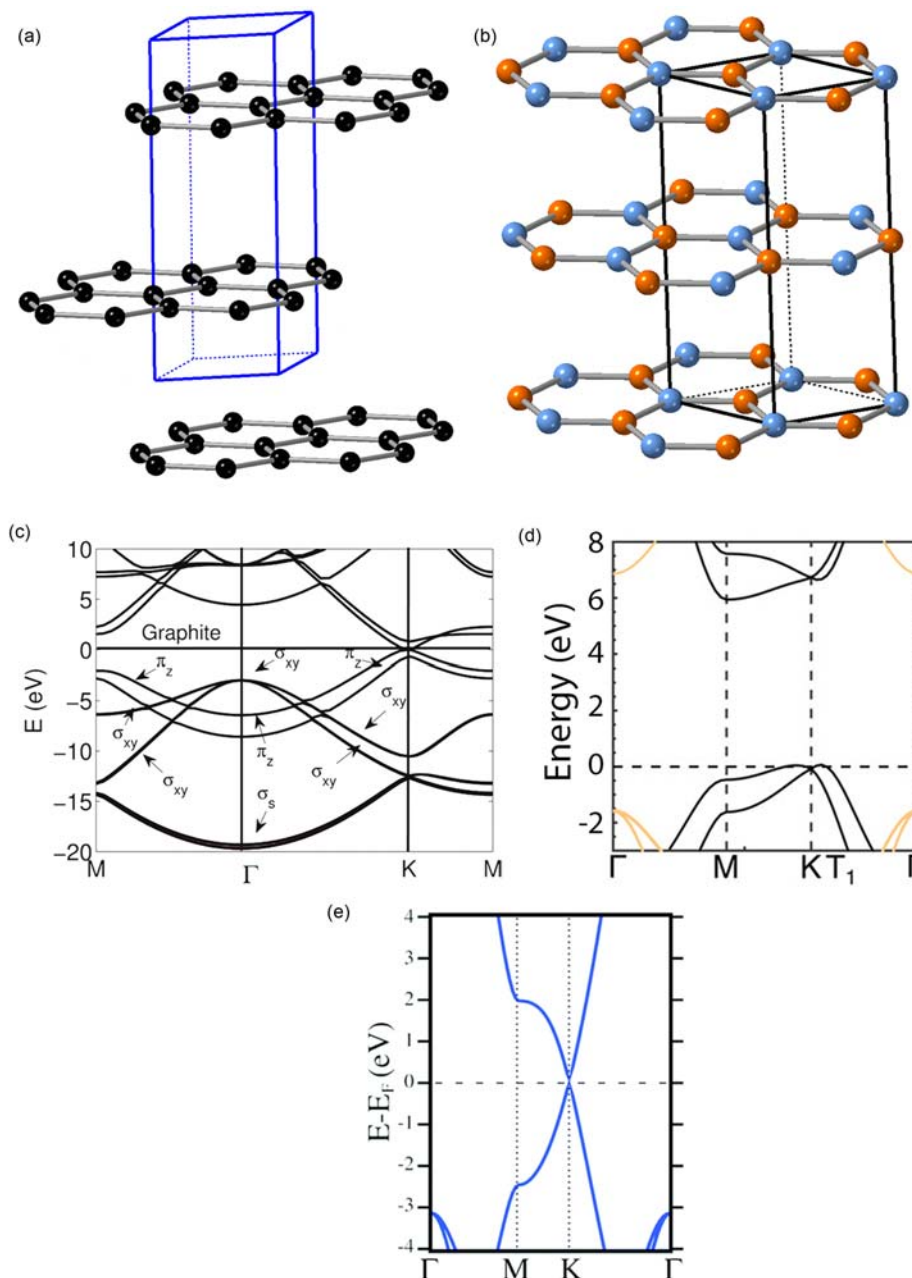


Fig. 12 Crystal structures of (a) graphene and (b) hexagonal boron nitride; orange spheres correspond to B atoms and blue spheres correspond to N atoms. Band structure of (c) bulk graphite, Band structure of (d) bulk hexagonal boron nitride. Band structure of (e) monolayer graphene. Panel (c) reprinted with permission from Rêgo, C. R. C., Oliveira, L. N., Tereshchuk, P. & Da Silva, J. L. F. Comparative Study of van der Waals Corrections to the Bulk Properties of Graphite. *J. Phys. Condens. Matter.* **2015**, 27, 415502. © Institute of Physics, 1989. Panel (d) reprinted with permission from Wickramaratne, D., Weston, L. & Van De Walle, C. G. Monolayer to Bulk Properties of Hexagonal Boron Nitride. *J. Phys. Chem. C* **2018**, 122, 25524–25529. © American Chemical Society, 2018. Panel (e) reprinted with permission from Roldán, R., Chirulli, L., Prada, E., Silva-Guillén, J. A., San-Jose, P. & Guinea, F. Theory of 2D Crystals: Graphene and Beyond. *Chem. Soc. Rev.* **2017**, 46, 4387–4399. © Royal Society of Chemistry, 2017.

atoms in the unit cell, thus there are four bands of p_z character: two bands that are bonding and two bands that are antibonding along the in-plane directions. In the $K\Gamma M$ plane (when $k_z = 0$), the orbital phase of the wavevector is constant between unit cells along the z -direction, thus, at the Γ point the phase of the p_z orbitals in layer A are the same (Fig. 13b). The phase of the p_z orbitals on layer B can either be the same or opposite of those in layer A. There are thus two bands, at the Γ point, one in which the phases are opposite, Γ_{π_1} , and one in the phases are the same as in layer A, Γ_{π_2} . At Γ_{π_1} , there is an interlayer bonding interaction between the A and B layers. At Γ_{π_2} , the interlayer interaction is antibonding. Thus, these two p_z orbital bands are split in energy, with Γ_{π_1} being lower in energy than Γ_{π_2} . At the HAL plane (where $k_z = \pi/c$), the splitting in energy between the bands caused by the

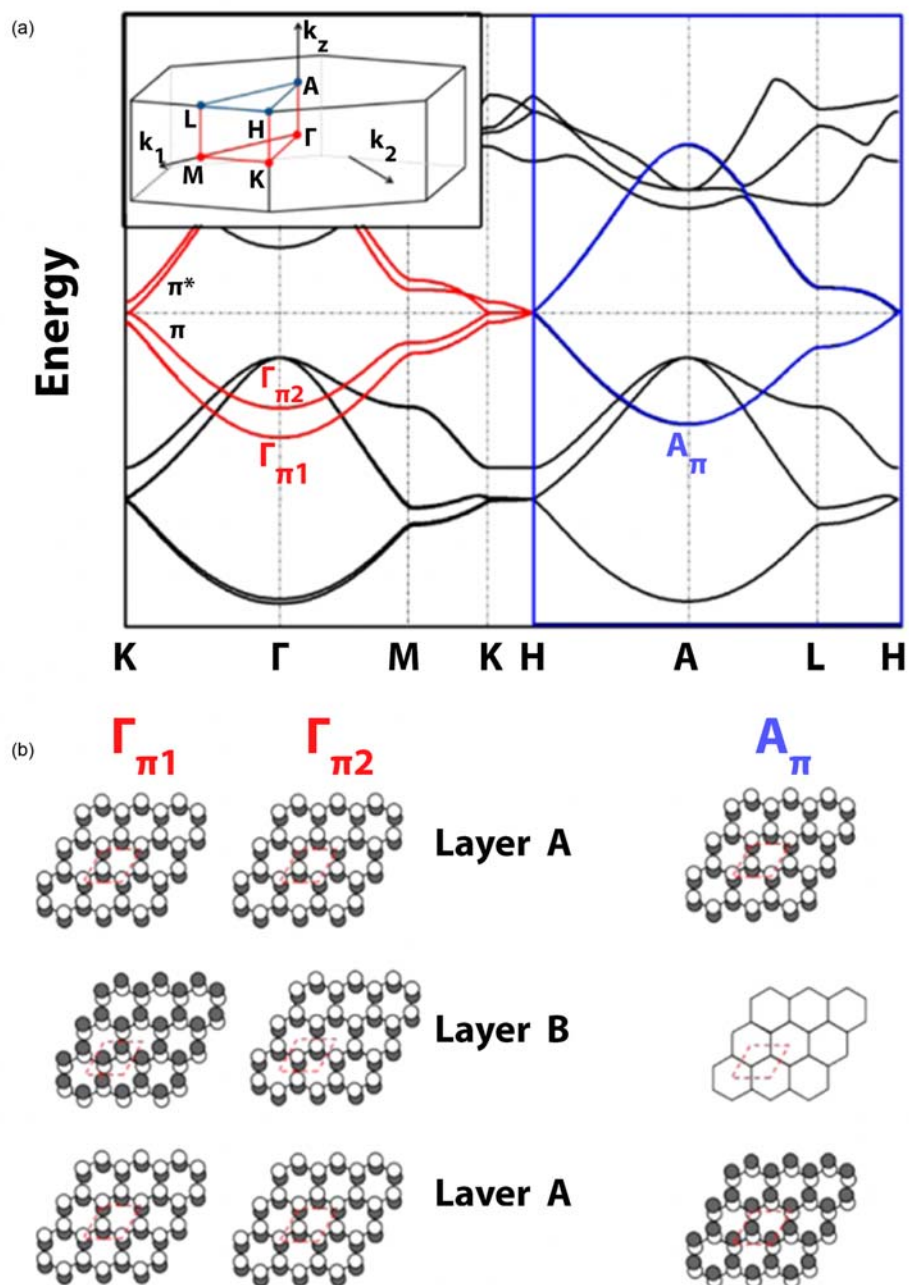


Fig. 13 Tight-binding band structure of graphite with the HAL plane outlined in blue (inset = Brillouin zone map). The bonding and antibonding π -bands comprised of the C $2p_z$ orbitals are highlighted in red for the $K\Gamma M$ plane and in blue for the HAL plane. (b) Real-space wave functions of the π -bonding bands at Γ and A. Reprinted with permission from Li, T. & Goldberger, J. E. Atomic-Scale Derivatives of Solid-State Materials. *Chem. Mater.* **2015**, *27*, 3549–3559. © American Chemical Society, 2015.

interlayer interactions is almost completely eliminated. At the A point, the phase of the p_z orbital wavefunctions must flip sign every unit cell, from layer A to the next layer A. Because of this sinusoidal change in orbital phase, there must exist a nodal plane of zero wavefunction density halfway between the two A layers, and coinciding with layer B. In other words, the wavefunctions at the HAL plane represent band structures with zero wavefunction density in neighboring layers. Thus, the HAL plane effectively approximates the monolayer band structure. Indeed, one can visualize the presence of Dirac cones at the H point in the graphite band structure.

In addition to its exotic electronic transport properties, graphene has other properties of interest. It has an incredibly high in-plane thermal conductivity of $>2000 \text{ W m}^{-1} \text{ K}^{-1}$. It is one of the strongest materials known, having a tensile strength of $>130 \text{ GPa}$. Graphene has attracted considerable interest in an overwhelming number of applications including as a flexible,

transparent conductor,^{117–119} as a supercapacitor,^{120,121} and as a filtration membrane.^{38,122} Despite having ultrahigh carrier mobilities, the inability to get large $I_{\text{on}}/I_{\text{off}}$ ratios on account of its Dirac cone-like electronic structure with no band gap limits application in high-speed electronics. Due to the Dirac cone-like electronic structure, one cannot simply just “open up a gap” and still maintain the ultrahigh mobility carriers.

It has been found that this exotic transport behavior in graphene is incredibly sensitive to the flatness and cleanliness of the substrate, the presence of residual polymers or e-beam resist, as well as any point defects or disruption of the lattice, all of which serve to reduce the carrier mobility.^{123–125} Thus, it has been found that hBN is an excellent substrate for graphene (and other 2D materials) due to its flatness and mechanical rigidity.^{126,127} It is truly the gold standard of dielectric materials. In addition, certain vacancies in hBN have been demonstrated to exhibit polarized and ultrabright single-photon emitters at room temperature, making them attractive candidates for quantum computing applications.^{128,129}

4.14.3.2 Xenes/Xanes

“Xenes,” and their covalently functionalized derivatives, “Xanes,” correspond to 2D materials built from a single composition of main group elements, as highlighted in these review articles.^{15,130,131} The Xenes can include group 13 elements like B, in borophene, group 14 elements such as Si, Ge, and Sn, in silicene, germanene, and stanene, group 15 elements such as P, As, Sb, and Bi. Unlike graphene, the group 13 and group 14 elements do not inherently form layered vdW compounds. Their 2D derivatives are typically only formed by evaporating precise quantities of elements in ultra-high vacuum onto surfaces, and, unless encapsulated, are typically only evaluated in surface science experiments. In contrast, the “Xanes” are systems that can be manipulated, studied, and processed under standard laboratory conditions.

The structures of these 2D materials can be quite diverse (Fig. 14a). First, boron is a very unique element, and the varied bonding possibilities of boron lead to at least 16 different polymorphs in the bulk, composed of interconnected icosahedrons. Similarly, borophene forms multiple related polymorphs depending on the growth substrate, and is built from a triangular lattice that is punctuated by vacancies termed hollow hexagons.¹³² The two most common polymorphs occur at a vacancy ratio of $\nu = 1/5$ and $\nu = 1/6$ where ν indicates the proportion of vacant sites, these structures can be described as lines of vacancies that order along one of the in-plane directions of the crystal structure. These different borophene derivatives grown on metal substrates have been found to be metallic, based on electronic structure calculations and scanning tunneling microscopy experiments.

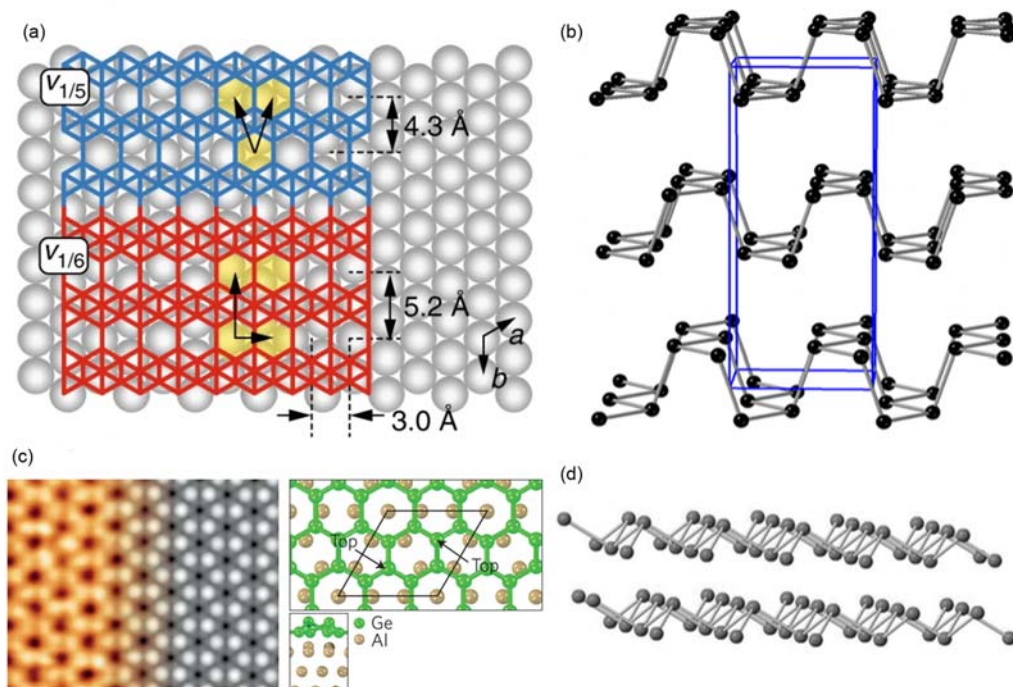


Fig. 14 (a) Model structure of $\nu_{1/5}$ and $\nu_{1/6}$ phases of borophene. (b) crystal structure of black phosphorus. (c) Model and structure of monolayer germanene on aluminum, (d) crystal structure of bilayer bismuthene. Panel (a) republished with permission Liu, X., Wang, L., Li, S., Rahn, M. S., Yakobson, B. I. & Hersam, M. C. Geometric Imaging of Borophene Polymorphs With Functionalized Probes. *Nat. Commun.* **2019**, *10*, 1642. © 2019. Panel (c) reprinted with permission from (Molle, A., Goldberger, J., Houssa, M., Xu, Y., Zhang, S.-C. & Akinwande, D. Buckled Two-Dimensional Xene Sheets. *Nat. Mater.* **2017**, *16*, 163–169. © Springer Nature, 2017. Panel (d) reprinted with permission from Pumera, M. & Sofer, Z. 2D Monoelemental Arsenene, Antimonene, and Bismuthene: Beyond Black Phosphorus. *Adv. Mater.* **2017**, *29*, 1605299. © John Wiley and Sons, 2017.

The group 14 Xenes based on Si, Ge, or Sn atoms are structurally similar to graphene. However instead of being flat, they form a buckled hexagonal honeycomb structure as π -bonding is considerably weaker in 3rd row elements and below since these atoms are larger and have much weaker p_z orbital overlap (Fig. 14c).¹³⁰ Thus, the honeycomb network of the group 14 Xenes tend to buckle, bringing the atoms closer and enabling a stronger overlap of their π -bonding p_z orbitals. This results in a mixed sp^2 - sp^3 hybridization, which stabilizes their hexagonal arrangement. These compounds all have similar electronic structures to graphene with Dirac cones at the K point but are proposed to form a variety of different topological states under strain, and with the application of external electric and magnetic fields.¹³⁰

The heavy group 15 elements (P, As, Sb, Bi) inherently form crystal structures in which each atom has three covalent bonds with its nearest neighbors and one lone pair of electrons. The structure of phosphorene consists of a single layer of black phosphorus from its bulk crystal structure and is shown in Fig. 14b.¹³³ It has an orthorhombic structure that is built from the connection of P_6 hexagons in chair conformations within each layer. In contrast As, Sb, and Bi, all crystallize into trigonal structures based on buckled honeycomb networks of these atoms, in which neighboring atoms alternately tilt upwards and downwards. (Fig. 14d).¹³³ Black phosphorus is a readily exfoliatable crystal which can be used to create monolayer phosphorene. Few-layer antimonene has also been prepared experimentally from both mechanical and liquid exfoliation.^{134,135} Thus far, few-layer As and Bi have only been prepared when grown on metal thin film supports and evaluated in surface science studies.¹³⁶⁻¹³⁸ Recently, nitrogen was also found to crystallize into the black phosphorus structure type at 146 GPa and 2200 K.¹³⁹ Bulk black phosphorus is a semiconductor that has a direct 0.3 eV band gap,¹⁴⁰ which increases to 1.7 eV in monolayer phosphorene, and depending on the in-plane direction, the 300 K bulk electron and hole mobilities can be $\sim 1000 \text{ cm}^2 \text{ V}^{-1} \text{ s}^{-1}$.¹⁴¹ While there are large number of computational predictions^{142,143} about potential layer-dependent properties of As, Sb, and Bi, there is very little experimentally assessed properties of these materials due to the inability to prepare these compounds on insulators.

The most well-studied covalently terminated Xenes are the covalently functionalized, Si, Ge, and Sn Xenes. These compounds require ligand termination on every atom to be stable under ambient conditions, and therefore are ideal 2D systems for understanding the influence of surface functionalization. Graphene consists of carbon atoms arranged in a honeycomb network, where each carbon atom has 3σ and 1π bond with its three nearest neighbors. In the Si, Ge, and Sn derivatives of graphene, the σ bond distances are much larger with significantly reduced π -orbital overlap, and consequently these analogues have much weaker π -bonds. As a result, there is a strong thermodynamic preference for these materials to have a fourth σ bond to a terminating ligand. In other words, the heavy group 14 graphane analogues are stabilized by the surface functionalization.

The synthesis of group 14 graphane analogues, Xenes, is accomplished via the direct transformation of precursor intermetallic layered Zintl phases (CaSi_2 , CaGe_2 , BaSn_2) that possess the same single atom thick puckered honeycomb structure as graphene. Zintl phases, or more precisely, phases that follow the Zintl-Klemm electron counting rules, correspond to compounds comprised of group 13-16 p-block elements combined with the electropositive elements (groups 1-3 or rare earth elements). The large electronegativity difference causes the p-block elements to accept electrons from the electropositive elements. In their crystal structures, the p-block elements form covalently bonded polyanion frameworks, in such a way as to create a formal octet. For instance, the structure of the layered Zintl phases CaSi_2 , CaGe_2 , and BaSn_2 consist of layers of Si^- , Ge^- , and Sn^- in a buckled graphene arrangement separated by Ca^{2+} or Ba^{2+} cations (Fig. 15).¹⁴⁴⁻¹⁴⁶ These materials react with electrophiles that bond with the Si/Ge/Sn framework to form covalently terminated SiR, GeR, and SnR. Specifically, they can react with acids to form $\text{R} = -\text{H}$ or $-\text{OH}$ Xenes,^{20,147-157} or can react with primary and some secondary organohalides to form organic terminated Xenes.^{20,147,148,152,158-164} These Xenes are semiconductors with band gaps that are centered around 2.7 eV,¹⁶⁵ 1.7 eV,^{161,163} and 0.3 eV¹⁶⁶ (theoretical) for Si, Ge, and Sn respectively, and can be tuned appreciably with ligand identity. In addition, the Sn derivatives have attracted considerable theoretical interest as potential topological insulating materials.

4.14.3.3 MXenes

"MXenes" compounds correspond to a family of layered transition metal carbides, carbonitrides and nitrides that are prepared via the topotactic deintercalation of either layered "MAX" phases or metal aluminum carbides/nitrides/carbonitrides. These

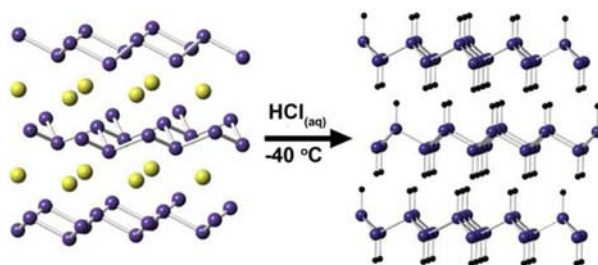


Fig. 15 Deintercalation of CaGe_2 in aqueous HCl at low temperatures results in GeH, yellow spheres correspond to Ca atoms, purple atoms correspond to Ge atoms and black spheres correspond to H atoms. Reprinted with permission from Bianco, E., Butler, S., Jiang, S., Restrepo, O. D., Windl, W. & Goldberger, J. E. Stability and Exfoliation of Germanane: A Germanium Graphane Analogue. *ACS Nano*, **2013**, 7, 4414-4421. © American Chemical Society, 2013.

compounds have been extensively reviewed.^{167–169} The “MXene” general chemical formula is $M_n + 1X_nT_x$ ($n = 1–3$), where M corresponds to an early transition metal (Sc, Ti, Zr, Hf, V, Nb, Ta, Cr, Mo), X is carbon and/or nitrogen and T_x stands is the surface terminating group, (for example, hydroxyl, oxygen, or fluorine). To prepare these phases, the aluminum in the MAX phases is etched away typically using hydrofluoric acid, and the resulting MXenes have a mix of ligand terminations that include -F, -OH, and -O. For instance, the single octahedral thick MAX phase Ti_2AlC is converted into MXenes with the stoichiometry of Ti_2CT (Fig. 16a and b), the double octahedral thick MAX phase Ti_3AlC_2 is converted to $Ti_3C_2T_x$ (Fig. 16c and d), and the triple octahedral thick phases transform from Ti_4AlC_3 to $Ti_4C_3T_x$ (Fig. 16e and f). The surface termination is very dependent on the processing conditions, and for instance, nuclear magnetic resonance (NMR) studies have shown that $Ti_3C_2T_x$ can have terminations ranging from $Ti_3C_2(OH)_{0.12(2)}F_{0.8(2)}O_{0.54(7)}$ to $Ti_3C_2(OH)_{0.06(2)}F_{0.25(8)}O_{0.84(6)}$ depending on the HF source.^{170,171}

MXenes have attracted considerable attention for a wide range of applications.^{168,172} Despite numerous computational predictions of being able to tune from the metal to semiconducting state, all experimental MXenes are metallic with high conductivities of up to 2.4×10^6 S cm^{-1} in $Ti_3C_2T_x$.¹⁷³ The only MXene-like family of compounds that is measured to have an optical band gap is Y_2CF_2 which has a 1.9 eV gap, however, this phase features strong Y-F ionic bonding between neighboring layers and is thus not a 2D vdW compound.¹⁷⁴ Regardless, the metallicity and 2D vdW nature of MXenes, which allows processing into clays and inks via swelling with different solvents, makes these compounds excellent supercapacitor electrodes,^{175,176} and coatings for electromagnetic shielding.¹⁷⁷

4.14.3.4 Transition metal dichalcogenides (TMDs)

After graphene, the second most well-studied family of 2D vdW compounds are the TMDs, which have the stoichiometry of MCh_2 where M is a transition metal, and Ch is a chalcogen (S, Se, Te). The solid-state chemistry, structure, and properties of this large family of compounds have been well studied and even extensively reviewed since the 1960s,^{178–183} and were the focus of the early exfoliation work by Frindt (MoS_2).²² Since then, they have repeatedly been the subject of scientific inquiry due to the prevalence of interesting phenomena such as superconductivity, charge density waves, as well as their ability to intercalate organic molecules as well as ions such as Li. Upon the discovery of monolayer graphene in 2004, there has been a resurgence in interest in the TMDs due to a combination of relative stability, simplicity of synthesis, as well as the presence of many exotic properties.^{179,184}

TMDs crystallize into structure types that consist of layers of transition metals, M, in sixfold coordination to chalcogen atoms (S, Se, Te). From an ionic bonding perspective, the chalcogen anions would have a formal charge of Ch^{2-} , and the metal would be M^{4+} . Depending on the d-electron count of the metal, its local coordination geometry can be either octahedral (d^0 , d^1 , d^3 , d^6), or trigonal prismatic (d^1 , d^2), and is connected to its six nearest neighbors within each layer in an edge-sharing fashion. When distortions away from ideal octahedral coordination are considered, this leads to four predominant structures commonly referred to as the 1T, 2H, $1T'$ and ReS_2 structure type (Fig. 17). The 1T structure type consists of layers of transition metal octahedra in a 1-layer per trigonal unit cell structure type. The 2H structure type consists of layers of transition metals in trigonal prismatic coordination, leading to a 2-layer per hexagonal unit cell structure type. Although technically the $1T'$ structure corresponds to layers of distorted octahedra in a 2-layer monoclinic unit cell, it is commonly referred to as the $1T'$ polytype. In the $1T'$ polytype two of the three M-M distances along the three *hki* directions in the hexagonal plane form long bonds, while the third forms a short bond. Finally, the ReS_2 structure type is a 1-layer per triclinic unit cell derivative of the 1T polytype in which the *Re-Re* distances along all three *hki* directions in the hexagonal plane have alternatingly long bonds and short bonds.

As alluded to earlier, the local coordination of the metal strongly depends on the d-electron count. This can be readily explained using molecular orbital theory arguments, when considering the differences in d-orbital splitting in trigonal prismatic and octahedral geometry. In an octahedral geometry, the d-orbitals split into a lower energy triply degenerate set, and a higher energy doubly degenerate set. Thus, d^0 (Ti, Zr, Hf),¹⁸² d^3 (Re)¹⁸⁵ and low spin d^6 (Pd in $PdTe_2$, and Pt)^{186,187} electron configurations are all stabilized in octahedral coordination. In a trigonal prismatic geometry, the d-orbitals split into a low energy singly degenerate state, along with two sets of doubly degenerate orbital states at higher energy. Thus, there is a strong preference for d^2 metals (Mo, W) to crystallize into a 2H structure type.^{180,188} The group 5 (Nb, Ta) d^1 compounds can crystallize into both polytypes.¹⁸³ Ligand field stabilization energy arguments based on electron count can also explain many of the structural changes that occur in this family. For example, Li-ion intercalation of MoS_2 (d^2) to form $LiMoS_2$ (d^3) causes a change from the 2H trigonal prismatic to 1T octahedral polytype.³³ Finally, Mn, and the Fe, and Co group dichalcogenides mostly crystallize into 3D pyrite and marcasite type structures rather than 2D vdW compounds.

These compounds can range from semiconductors to metal and host a wide variety of exotic electronic phenomena including charge density waves, superconductivity, and a wealth of topological phenomena. In general, the electronic structure of these transition metal dichalcogenides depends on the electron count and the chalcogenide present. Typically, the d^0 1T sulfides and selenides are semiconducting with bandgaps between 0.2 and 2.0 eV in the bulk,^{189,190} except in the case of $TiSe_2$, which is a semimetal with a 5 meV band overlap.¹⁹¹ The d^1 TMDs are all metallic as a consequence of the partial filling of the d-orbital bands.¹⁹² The d^2 2H phases in trigonal prismatic geometry are semiconducting with bulk band gaps around 1 eV.¹⁹³ The $1T'$ d^2 $MoTe_2$ and WTe_2 phases are semimetals.¹⁹⁴ The d^3 ReS_2 and $ReSe_2$ phases are Mott insulators with 1.5 and 1.3 eV band gaps.¹⁹⁵ The d^6 PtS_2 and $PtSe_2$ phases are semiconductors with 0.7 and 0.1 eV band gaps.¹⁹⁶ Finally, all transition metal ditellurides are metallic in nature, except for 2H $MoTe_2$ which has a band gap of 1.0 eV.¹⁹⁷ This is in part because the reduced electronegativity of Te causes its 5p orbital bands to be higher in energy compared to the S 3p and Se 4p orbital states, and close to the same energies as the transition metal d-orbital bands.

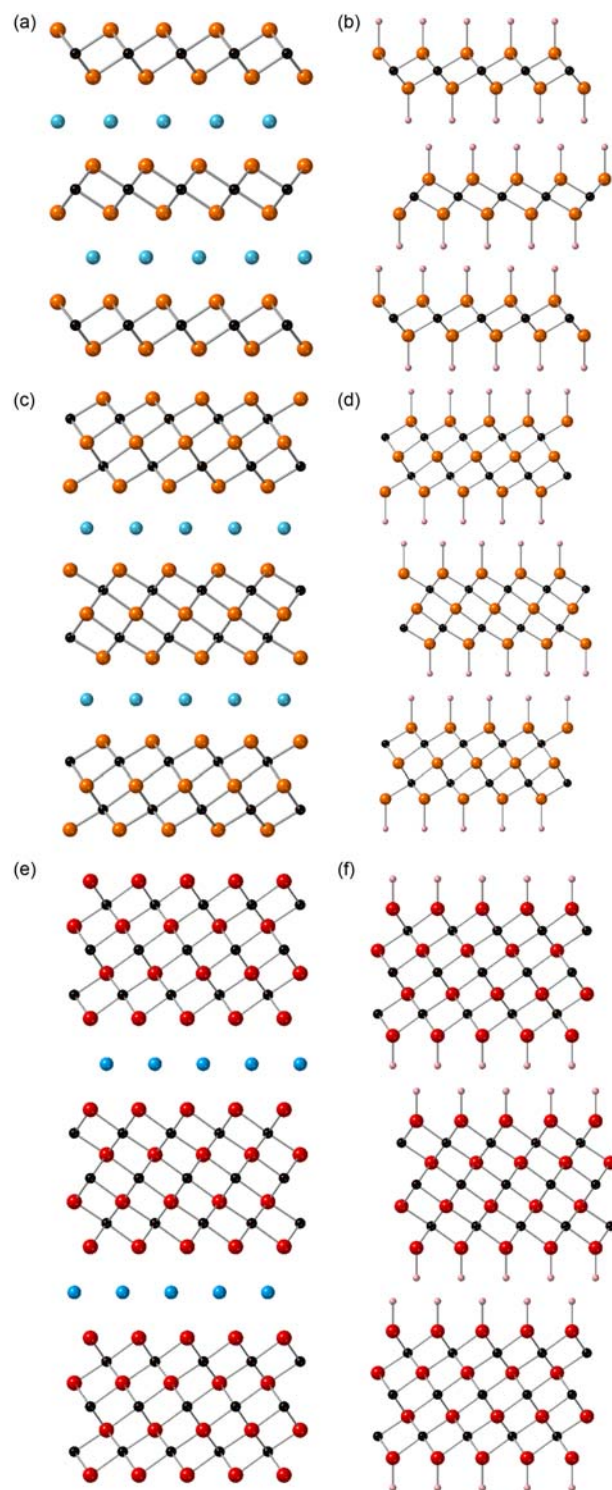


Fig. 16 (a) Structure of single layer Ti_2AlC MAX phase and (b) single layer MXene analogue, Ti_2CT_x . (c) Structure of double layer Ti_3AlC_2 MAX phase and (d) double layer MXene analogue $\text{Ti}_3\text{C}_2\text{T}_x$. $\text{Ti}_3\text{C}_2\text{X}$. (e) Structure of triple layer V_4AlC_3 MAX phase and (f) triple layer MXene analogue, $\text{V}_4\text{C}_3\text{T}_x$. In all figures black spheres correspond to C atoms, blue spheres correspond to Al in MAX form, and pink spheres correspond to terminating atoms. In (a–d) orange spheres correspond to Ti and in (e–f) red spheres correspond to V atoms.

Many of these undergo significant changes in electronic structure when exfoliating down to the monolayer. The most classic example is the change in band structure that occurs in the group 6 2H TMDs that have indirect band gaps in the bulk which shift to direct band gaps of greater magnitude at the monolayer. For instance, 2H-MoS₂ was discovered in 2010 to transition from an indirect band gap of 1.29 eV in the bulk to a direct band gap of 1.9 eV in the monolayer.^{198,199} Similar to the previous discussion

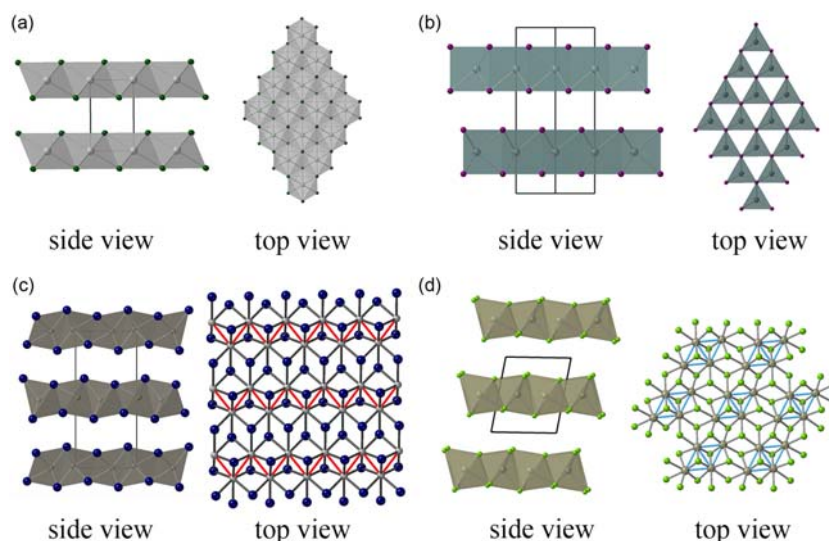


Fig. 17 Side view of the crystal structure and top-down view of a monolayer of (a) 1T-PtS₂, (b) 2H-NbSe₂, (c) 1T'-WTe₂, with the short W-W distances drawn in red, and (d) ReSe₂ with the short Re-Re distances drawn in light blue. In (a), Gray spheres correspond to Pt, green spheres correspond to S. In (b) green spheres correspond to Nb, purple spheres correspond to Se. In (c), gray spheres correspond to W, and blue spheres correspond to Te. In (d) beige spheres correspond to Re, and green spheres correspond to Se.

on graphite to graphene using zone folding (Section 4.14.3.1), a change in the energetic states in MoS₂ at the valence band minimum occurs due to the elimination of the cross-layer interactions between Mo d_{z^2} and S p_z orbital states.

A second change upon the exfoliation to the monolayer is the loss of inversion symmetry. This causes a splitting of the sixfold degeneracy of the K point in the Brillouin zone into two threefold degenerate points labeled, K and K' that have opposite Berry curvatures. In addition to the broken inversion symmetry, the spin-degenerate valence band maxima at the K and K' are split by ~ 160 meV by spin-orbit coupling in MoS₂, or 400 meV in WS₂ (Fig. 18e). This allows selective excitation of either the K or K' states with circularly polarized light. The large difference in the spin-orbit splitting of the electron-hole excited state forms an energetic barrier preventing interconversion between the K and K' excited states. As a consequence, there has been some interest in exploring the possibility of being able to perform computations using the selective excitation and transport through either the K or K' valleys, a proposition referred to as "valleytronics."^{95,200,201}

There has been immense research in transition metal dichalcogenides for a wide variety of applications, of which we will only briefly name a few. First, these compounds have been extensively studied as active field effect transistor elements even at the monolayer, due to their atomic scale thicknesses and like most 2D vdW compounds, they have naturally very few mobility-disrupting surface states.¹⁷⁹ However, because the conduction bands and, depending on the electron count, the valence bands in these compounds are typically comprised of the transition metal d-orbitals, which have much smaller band widths than p- or s-orbital bands, these compounds typically have carrier mobilities on the order of $100 \text{ cm}^2 \text{ V}^{-1} \text{ s}^{-1}$, which are much lower than traditional group IV, or III-V semiconductors.^{202,203} In addition, the 1T' WTe₂ and MoTe₂ phases have attracted considerable interest as quantum spin Hall materials,^{204,205} potentially allowing for dissipationless conduction in these materials similar to the quantum Hall effect. As another example, MoS₂ has attracted considerable interest in water splitting, and has shown to have a relatively small overpotential for the hydrogen evolution reaction, 150 meV in 1T polytype,²⁰⁶ achieved through Li intercalation. MoS₂ is also one of the most air and water stable TMDs. Almost all other members of this family have a strong propensity to oxidize in monolayer form. Finally, many of these compounds, such as NbSe₂ and PdTe₂ have been found to exhibit superconductivity both in the bulk and in monolayer form.^{207,208}

4.14.3.5 PdS₂ and PdSe₂

PdS₂ and PdSe₂, which by definition are transition metal dichalcogenides, exhibit a distinct 2D vdW structure. These compounds have a layered structure built from square planar Pd²⁺ in coordination with S₂²⁻ and Se₂²⁻ anions (Fig. 19). Pd²⁺ has a d^8 electron configuration, which explains the square planar coordination geometry. PdS₂ and PdSe₂ are semiconductors with bulk indirect band gaps of $E_g = 0.7$ eV and $E_g = 0.5$ eV, respectively,¹⁹⁶ and have a large layer dependent change in properties. Monolayer PdSe₂ has been found to have an indirect band gap of 1.37 eV,^{209,210} while monolayer PdS₂ has not been experimentally measured. PdSe₂ is air-stable even in the monolayer form, due to Pd's limited propensity for oxidation, and the relative strength of the softer Pd-chalcogen bonding interactions. These compounds have been studied for applications in optoelectronics^{211,212} and transistors.^{213,214}

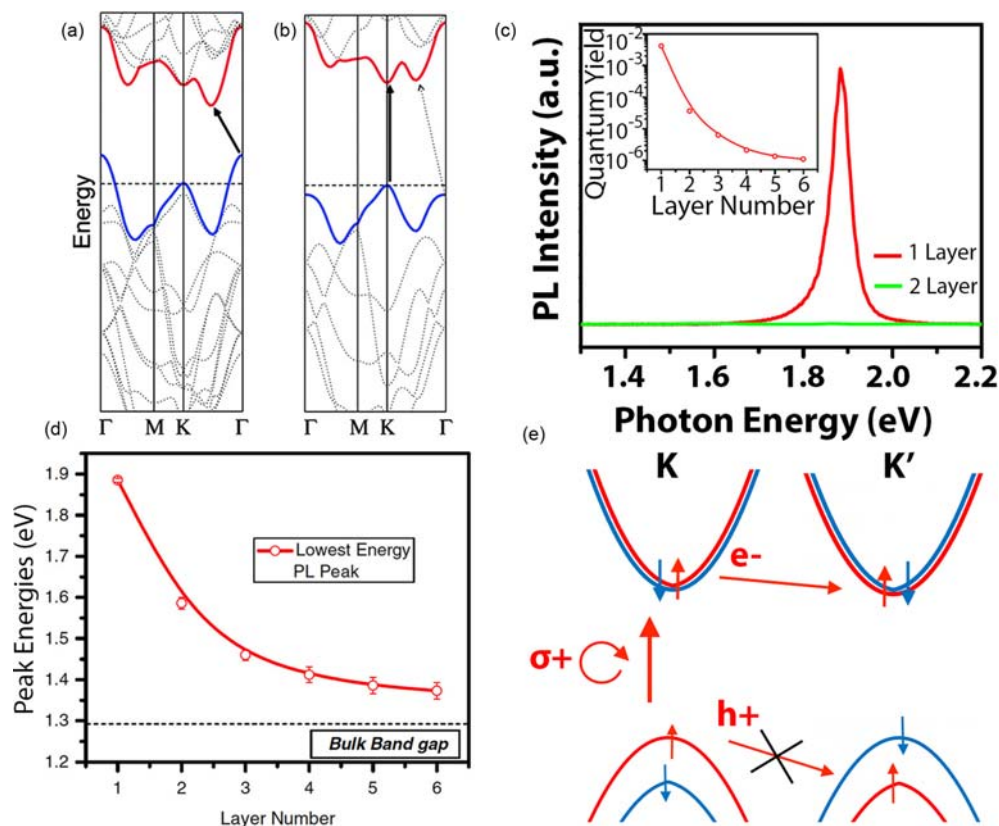


Fig. 18 Calculated band structures of (a) bulk and (b) monolayer MoS₂. The solid arrows indicate the lowest-energy transitions. (c) PL spectra for mono- and bilayer MoS₂ samples. The inset shows the PL quantum yield of thin layers of MoS₂ for number of layers $N = 1-6$ in log scale. (d) Band gap energy of thin layers of MoS₂ for $N = 1-6$. The band gap values were inferred from the energy of the indirect gap PL feature I for $N = 2-6$ and from the energy of the PL peak A for $N = 1$. As a reference, the (indirect) band gap energy of bulk MoS₂ is shown as dashed line. (e) Example of spin-valley locking seen in the monolayer upon splitting of the degeneracy of K and K' states. Red and blue correspond to bands with opposite spin character. Panel (a and b) reprinted with permission from Splendiani, A., Sun, L., Zhang, Y., Li, T., Kim, J., Chim, C.-Y., Galli, G. & Wang, F. Emerging Photoluminescence in Monolayer MoS₂. *Nano Lett.* **2010**, *10*, 1271–1275. © American Chemical Society, 2010. Panel (c and d) reprinted with permission from Mak, K. F., Lee, C., Hone, J., Shan, J. & Heinz, T. F. 2010. Atomically Thin MoS₂: A New Direct-Gap Semiconductor. *Phys. Rev. Lett.* **2010**, *105*, 136805. © American Physical Society, 2010.

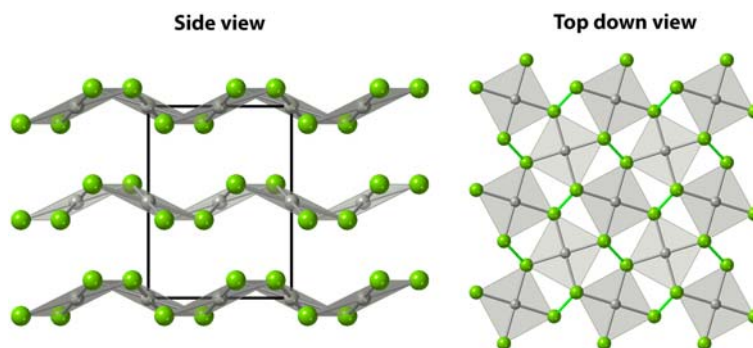


Fig. 19 Crystal structure of PdSe₂. Gray spheres correspond to Pd atoms, and green spheres correspond to Se atoms.

4.14.3.6 The group 13 monochalcogenides (TrCh)

The Group 13 monochalcogenides, TrCh, where Tr is a trivalent triel atom (Ga, In) and Ch is a chalcogen (S, Se) are of significant interest for their use as high mobility 2D vdW semiconductors. In the known compounds (GaS, GaSe, and InSe) the charge mismatch between the trivalent Tr^{3+} cations and the divalent Ch^{2-} anions causes these compounds to form vdW layers consisting of quadruple atomic Ch-Tr-Tr-Ch layers and feature a Tr–Tr covalent bond (Fig. 20). This covalent Tr–Tr bonding allows the layered structures to form an octet. The coordination environment of a Tr atom is tetrahedral, with three bonds to chalcogen atoms and one

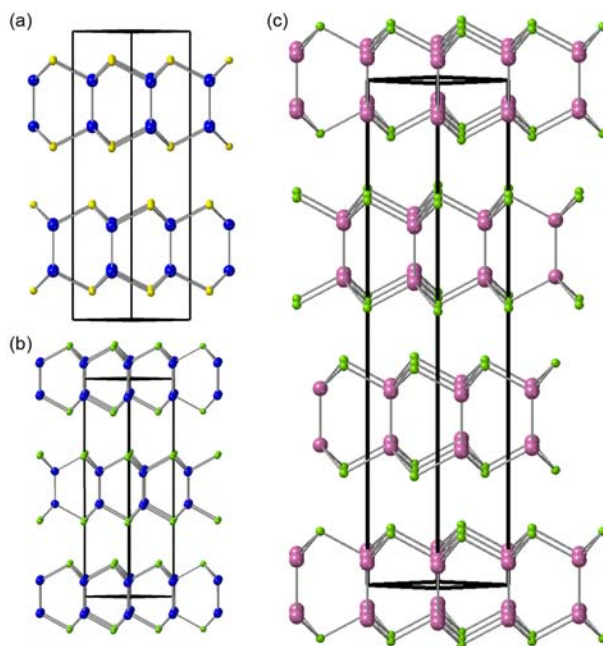


Fig. 20 Crystal structure of (a) $2H_c$ -GaS, (b) $2H_b$ -GaSe and (c) $3R$ -InSe. In (a) yellow spheres correspond to S atoms, in (a) and (b) blue spheres correspond to Ga atoms, in (b) and (c) green spheres correspond to Se and in (c) pink spheres correspond to In.

to a triel, and forms a corner-sharing between Tr-Tr dimers. Each isolated quadruple layer can be envisioned as two separate buckled honeycomb lattices that are connected through the Tr-Tr bonds.

There are three different stacking polytypes that are formed in this family of compounds, two of which are variants of the $2H$ polytype with different space groups, denoted as $2H_b$ ($P-6m2$) and $2H_c$ ($P6_3/mmc$) as well as a three-layer rhombohedral ($3R$) stacking sequence having an $R3m$ space group. In the $2H_b$ polytype, neighboring quadruple Ch-Tr-Tr-Ch layers are translated akin to an AB-type stacking sequence (Fig. 20a). In the $2H_c$ polytype, the second quadruple layer is rotated by 60° . The $3R$ polytype has a repeating ABC-type stacking sequence of the quadruple layers. InSe and GaSe can crystallize into all three polytypes, whereas GaS only crystallizes into the $2H_c$ polytype.^{215,216}

All these phases, GaS, GaSe, and InSe, are semiconductors with band gaps spanning a wide energy range. $2H_b$ -InSe, also denoted as ϵ -InSe, has a direct gap of 1.4 eV²¹⁷ with the CBM and VBM both at the Γ point while the $2H_c$ and $3R$ polytypes have smaller direct gaps of 1.28²¹⁸ and 1.29 eV.²¹⁹ $2H_c$ -GaS and $2H_c$ -GaSe have indirect gaps of 2.59 and 2.11 eV, respectively, due to a slight shift in the VBM away from Γ . The $2H_b$ and $3R$ forms of GaSe see a slightly reduced indirect gap of 2.07 eV.²²⁰ These compounds have much higher carrier mobilities in the bulk than the transition metal dichalcogenides, in part due to the Tr and Ch s/p orbital character of the band edges which leads to much larger band dispersions than the d-orbital nature of the TMDs. The $3R$ InSe polytype, denoted as γ -InSe, has been reported to have mobilities ranging from 500 to 2000 $\text{cm}^2 \text{V}^{-1} \text{s}^{-1}$ depending on synthetic condition.^{221,222} Bridgeman-Stockbarger syntheses have produced the best single crystal samples by minimizing stacking faults.²²² GaS and GaSe are similarly sensitive to synthesis conditions and have mobilities from 10 to 100 $\text{cm}^2 \text{V}^{-1} \text{s}^{-1}$.²²³ This high-mobility of InSe is preserved in the few layer regime, for instance 10-layer InSe with an electron-doped concentration of $8 \times 10^{12} \text{cm}^{-2}$, has room temperature carrier mobilities of $> 1000 \text{cm}^2 \text{V}^{-1} \text{s}^{-1}$, and increases to $12,700 \text{cm}^2 \text{V}^{-1} \text{s}^{-1}$ down to 50 K.²²⁴ In addition, the band gap of InSe blue shifts by 200 meV upon exfoliation from the bulk down to 5 quadruple layers thick.²¹⁷ The field effect mobility of monolayer InSe is surprisingly quite low, $< 0.1 \text{cm}^2 \text{V}^{-1} \text{s}^{-1}$ which is attributed to the much higher contact resistances, and highlights the possibility for mid-gap trap states with these higher band gap materials.²²⁴

4.14.3.7 Transition metal halides (MX_3)

The transition metal trihalides, MX_3 , where $M = \text{Ti, V, Cr, Fe, Mo, Ru, Rh, and Ir}$, and $X = \text{Cl, Br, and I}$ have attracted significant interest as magnetic 2D vdW compounds. This family of compounds are derivatives of the TMD structure type, but feature vacancies at every 3rd transition metal site, producing a honeycomb-shaped edge-sharing network of metal halide octahedra resulting in two closely related structure types: the $R-3$ BiI_3 crystal structure, and the monoclinic $C2/m$ AlCl_3 crystal structure (Fig. 21). In the BiI_3 structure type, the transition metal octahedra are distorted to have locally C_3 site symmetry, and in the AlCl_3 structure, the transition metal octahedra have locally C_2 symmetry. In addition, the layers have small translational differences between the structure types. Many of the compounds that have AlCl_3 symmetry undergo a low temperature structural phase transition to the BiI_3 structure type.

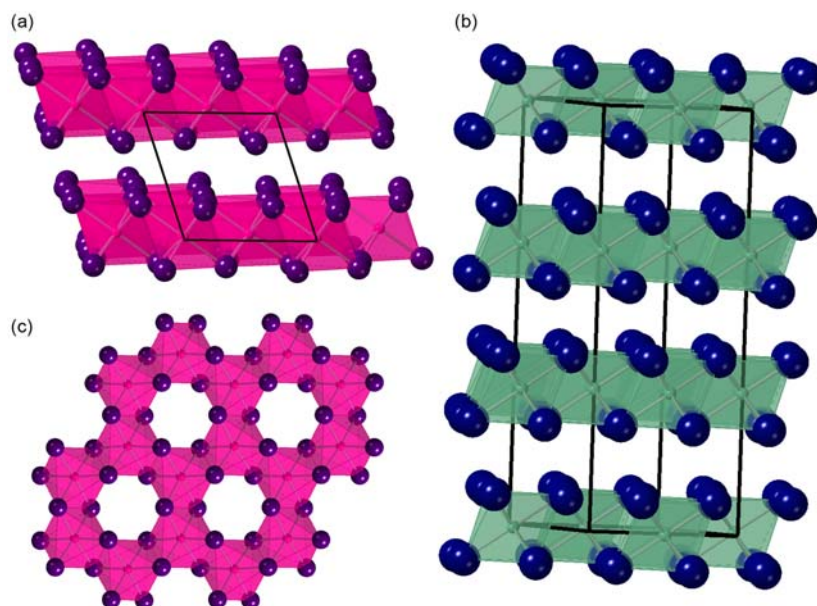


Fig. 21 Crystal structure of (a) AlCl₃-type CrI₃ and (b) BiI₃-type FeBr₃. (c) top-down view of honeycomb lattice of CrI₆ octahedra. In (a) pink spheres correspond to Cr atoms and purple spheres correspond to I atoms. In (b) green spheres correspond to Fe and blue spheres correspond to Br.

These have been one of the most well-studied families of compounds in the search for magnetic 2D materials.^{225–228} In particular, trivalent V³⁺, Cr³⁺/Mo³⁺, Fe³⁺ (high spin), and Ru³⁺ (low spin) have electron configurations of d², d³, high spin d⁵, and low spin d⁵, respectively, which in an octahedral crystal field gives rise to 2, 3, 5, and 1 unpaired electron(s). CrI₃ was the first 2D vdW material discovered to be ferromagnetic at the monolayer scale²²⁹ and has been extensively studied.^{230–233} CrI₃ is ferromagnetic in the bulk and monolayer with the Cr³⁺ d³ spins oriented along the out of plane direction. In few-layer samples, neighboring layers can be either ferromagnetically or antiferromagnetically aligned, depending on the strength of an applied magnetic field. Another well-studied system is RuCl₃, which has attracted considerable interest as a potential quantum spin liquid material.^{234–237} Additionally, despite having unpaired electrons, these transition metal halides are all semiconducting, which can be attributed to a Mott-Hubbard type mechanism by which electron-electron interactions produce a band gap due to Coulombic repulsion of localized electrons.^{238,239} Finally, the early transition metal halides are extremely air and water sensitive, both in the bulk, and much more so when exfoliated to few layers.¹⁸ It has been established that in CrI₃, ligand substitution is promoted via a photoactivated mechanism. These compounds must be handled in a glovebox and, at the few layer scale, are ideally encapsulated in hBN protective layers.

4.14.3.8 Transition metal phospho-/silico-/germano- trichalcogenides (MXCh₃)

The transition metal phosphorous trichalcogenides (TMPC), having the stoichiometry MPCCh₃, have shown interesting magnetic and ferroelectric properties. There are over 20 materials in this family of compounds, and they have been extensively reviewed.^{240–242} The structure of these compounds is shown in Fig. 22a. Each compound features a [P₂Ch₆]⁴⁻ anion which forms a staggered ethane-like geometry. Within each layer, the divalent transition metal is in octahedral coordination with the chalcogen atom from three different [P₂Ch₆]⁴⁻ anions. These metal-chalcogen octahedra form a honeycomb arrangement similar to the transition metal halides discussed in Section 4.14.3.7. However, the holes in the honeycomb lattice are occupied by the P₂ dimer. Oftentimes, M₂P₂Ch₆ is used to describe the stoichiometry of this family of compounds. Many different divalent cations can form this layered structure including alkali earths (Mg), transition metals (Mn, Fe, Ni, Zn, Cd, Hg) and even main group elements (Sn). This canonical formulation of the TMPC's with divalent cations can also be modified by cation site ordering, with 1/3rd site vacancies to accommodate trivalent cations (In³⁺) such as in In_{2/3}PSe₃ or by replacement of divalent cations with site ordered monovalent and trivalent cations such as in CuInP₂Se₆. Just as in the transition metal trihalides, these compounds also typically crystallize into R-3 or C2/m space groups, with the site ordered double transition metal variants (i.e., CuInP₂Se₆) crystallizing into the P-31c space group Fig. 22b. In addition, CrSiTe₃ and CrGeTe₃, were among the earliest families of 2D magnets, and form a nearly identical structure type, in this case built from [Si₂Te₆]⁶⁻ or [Ge₂Te₆]⁶⁻ anions.

These compounds have been extensively studied in part due to the wide range of interesting magnetic properties that emerge in this family of materials. These compounds are typically found to be antiferromagnetic with varying magnetically ordered superstructures that depend on the d-electron count of the transition metal. For instance, Fig. 23 shows the low temperature magnetic structure of FePS₃, and MnPS₃ and NiPS₃.²⁴¹ In FePS₃ and MnPS₃ the moments are pointed along the cross-plane direction, whereas in NiPS₃ the magnetic moments are pointed along the in-plane direction. In FePS₃, the Fe spins flip their orientation in each layer along the

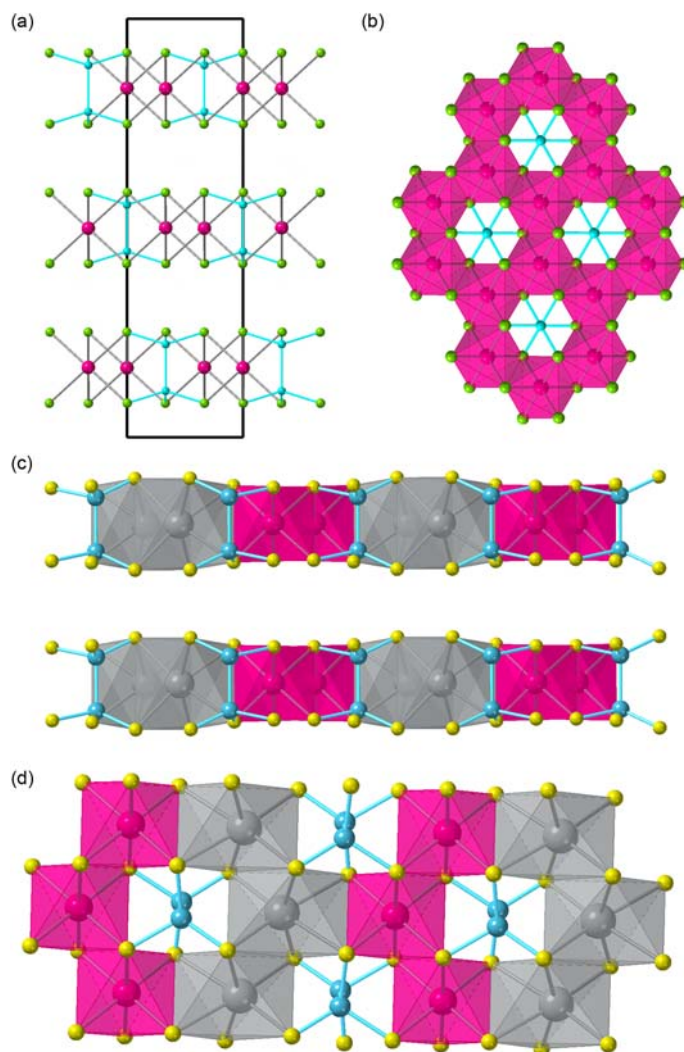


Fig. 22 Side view (a) and top-down view (b) of MnPS_3 . Side view (c) and top-down view (d) of AgCrP_2S_6 . In all structures, pink atoms correspond to Cr atoms and blue spheres correspond to P atoms. In (a) and (b) green spheres correspond to Se atoms and in (c) and (3d) gray atoms correspond to Ag atoms and yellow atoms correspond to S atoms.

zigzag direction, and neutron diffraction indicates that there is an incommensurate $[1/2 \ 1/2 \ 0.34]$ propagation vector. In MnPS_3 , the Mn spins are antiferromagnetically coupled with their nearest neighbors in-plane. In NiPS_3 , each Ni spin is ferromagnetically coupled to two nearest neighbors, and antiferromagnetically coupled to the third, and consequently form ferromagnetically coupled zigzag chains. The Neel temperature (T_N) can vary from 20 K in AgCrP_2S_6 ²⁴³ to 155 K in NiPS_3 .²⁴⁴ The CrSiTe_3 and CrGeTe_3 phases are ferromagnetic with bulk Curie temperatures (T_C) values of 33 K²⁴⁵ and 40 K,^{246,247} respectively. Additionally, these compounds are all measured to be insulating, with the lowest energy gaps corresponding to transition-metal based d-d transitions. Finally, the quaternary double transition metal Cu-containing analogues (i.e., CuInP_2S_6 , $\text{CuInP}_2\text{Se}_6$, CuCrP_2S_6 , and CuVP_2S_6 , $\text{CuBiP}_2\text{Se}_6$) as well as $\text{AgBiP}_2\text{Se}_6$ have been found to be ferroelectric or anti-ferroelectric with a vertically applied field.^{248–250} This ferroelectricity arises from a field-induced distortion of the Cu^{1+} or Ag^{1+} atoms away from the center of the octahedral and toward either the top or bottom face. The ferroelectric transition temperature can be as high as 315 K in $\text{CuInP}_2\text{Se}_6$.²⁴⁸ The non-magnetic compound $\text{Sb}_2\text{Si}_2\text{Te}_6$ has also recently been shown to have excellent p-type thermoelectric performance exhibiting a high ZT value of 1.65 at 823 K.²⁵¹ These compounds have been exfoliated to few layer form using mechanical exfoliation, as well as ultrasonication with surfactants, although the changes in magnetic properties at the monolayer are not fully established.

4.14.4 Emerging families of 2D vdW compounds

We will now highlight several additional families of 2D vdW materials with properties in the monolayer and few-layer form are only starting to be explored. Here we detail the chemical structure of these families and known phases that exist. Then we will

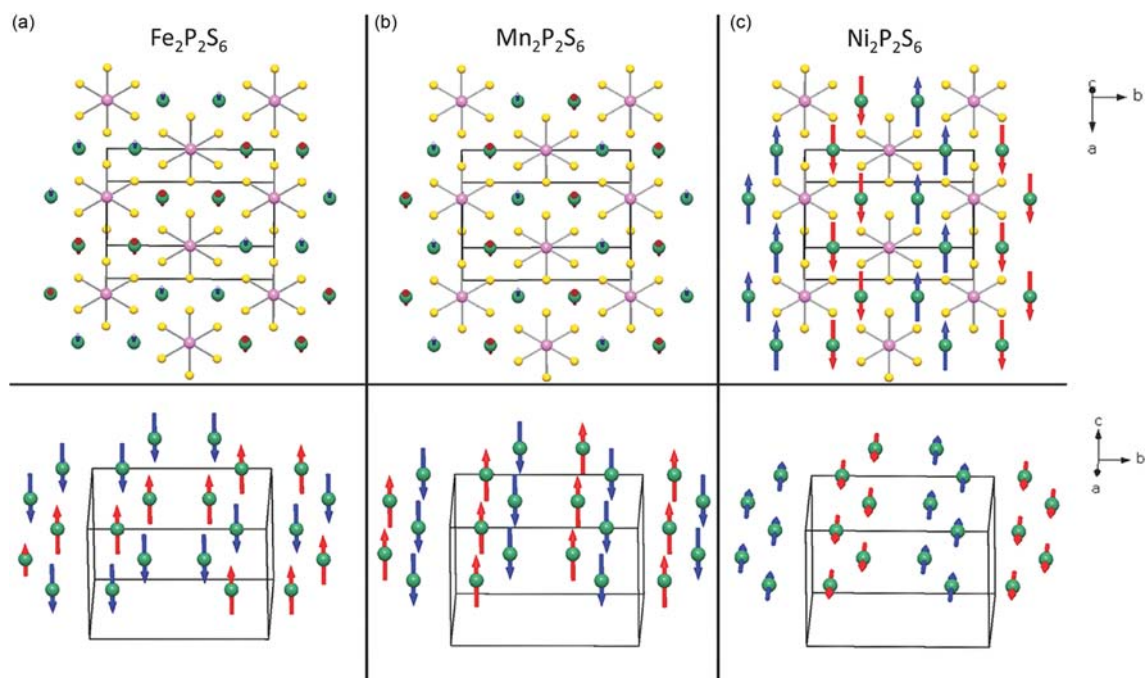


Fig. 23 Magnetic structures of (a) $\text{Fe}_2\text{P}_2\text{S}_6$, (b) $\text{Mn}_2\text{P}_2\text{S}_6$, and (c) $\text{Ni}_2\text{P}_2\text{S}_6$. The upper figures, where pink spheres correspond to P atoms, yellow spheres correspond to S atoms, and green spheres correspond to the metal site, show projections along the stacking direction. The lower panels show an isometric projection of just the metal cation sites. Reprinted with permission from Susner, M. A., Chyasnachyus, M., McGuire, M. A., Ganesh, P. & Maksymovych, P. Metal Thio- and Selenophosphates as Multifunctional van der Waals Layered Materials. *Adv. Mater.* **2017**, *29*, 1602852. © John Wiley and Sons, 2017.

discuss the unique properties of each material in the bulk form, and, when experimentally measured, their changes upon exfoliation.

4.14.4.1 Metal trichalcogenides

There are many layered vdW compounds that form with the stoichiometry of MCh_3 , where M is an early transition metal, lanthanide, or actinide. All of these compounds crystallize into closely related space groups of which two families are known, the monoclinic $\text{P}2_1/\text{m}$ compounds and the orthorhombic Cmcm compounds that exist almost exclusively with $\text{Ch} = \text{Te}$ (Fig. 24). The $\text{P}2_1/\text{m}$ compounds typically form with tetravalent $\text{M} = \text{Ti, Zr, Hf, U, or Th}$ and $\text{Ch} = \text{S, Se, or Te}$, in which one chalcogen is a dianion (e.g., S^{2-}), and two chalcogens form a dichalcogenide dianion (e.g., S_2^{2-}). The early work by Furusetz et al.²⁵² classified the $\text{P}2_1/\text{m}$ compounds as to having either A-type (or ZrSe_3 -type) or B-type (TiS_3 -type) crystal structures. (Fig. 24a and b) The biggest difference between the A-type and B-type structures is the distribution of M-M distances within the layers, in which the A-type compounds are more 2D with roughly equal distances along the two in-plane directions, whereas the B-type compounds are more chain-like with much larger M-M distances along one of the in-plane directions.²⁵³ A similar set of structures form for $\text{M} = \text{Nb, Ta}$, in which the extra electron in these structures breaks some of the Ch-Ch bonds in the dianions. This structural disruption yields multiple distinct chains of MCh_8 bicapped trigonal prisms that are offset from one another along the chain direction. The Cmcm MCh_3 compounds (Fig. 24c) are known to form with all trivalent lanthanide metals except Pm, Eu, and Yb, as well as with Y and certain trivalent actinides ($\text{M} = \text{Np, Pu, Am, and Cm}$).^{254,255} These Cmcm structures typically only form with tellurium, although one of the three equivalents of Te can be substituted with Se. The Te anions within each vdW layer are divalent, which is the one that can be substituted. The Te atoms capping each vdW layer form a slightly distorted square net arrangement with an overall valence of $[\text{Te}_2]^-$.

These compounds have attracted considerable interest due to the plethora of exotic physical phenomena in both the bulk and upon exfoliation.²⁵⁶ For instance, NbSe_3 and TaSe_3 , ZrTe_3 , and HfTe_3 , all exhibit superconductivity with T_C values typically < 2 K.^{257–260} The NbSe_3 compound also simultaneously undergoes a charge density wave transitions at 145 K²⁶¹ and 59 K.^{255,262} The d^0 compounds ($\text{M} = \text{Ti, Zr, and Hf, Ch} = \text{S, Se}$) are semiconducting with band gaps varying from 1.07 to 3.1 eV in TiS_3 and HfS_3 .^{263,264} All the lanthanide tritelluride compounds are metallic, and the compounds in which the spin orbit coupling $J \neq 0$ (Ce, Pr, Nd, Sm, Gd, Tb, Dy, Ho, and Er) show antiferromagnetic transitions all below 6 K except for GdTe_3 which has a $T_N \sim 12$ K.²⁵⁶ At 2 K in the antiferromagnetic ground state, GdTe_3 has incredibly large electron and hole Hall mobilities of $60,000$ and $15,000$ $\text{cm}^2\text{V}^{-1}\text{s}^{-1}$.²⁶⁵ This excellent mobility arises from the square net of Te atoms that leads to incredibly steep bands at the Fermi level. This compound is of special interest as it is the first magnetic 2D material exhibiting Dirac physics. Limited

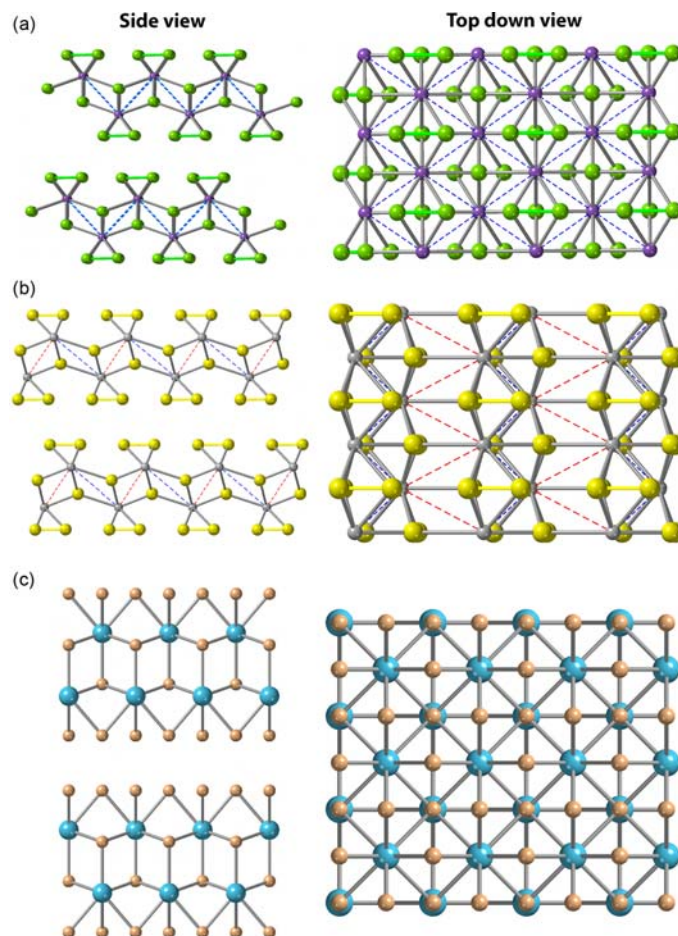


Fig. 24 Side view and top-down view on crystal structure of (a) A-type ZrSe_3 , (b) B-type TiS_3 , and (c) Cmc2h AmTe_3 . In (a) purple spheres correspond to Zr atoms and green spheres correspond to Se, Se–Se bonds are indicated in green, blue dotted lines illustrate equivalent Zr–Zr distances in each layer. In (b) gray spheres correspond to Ti atoms and yellow spheres correspond to S atoms, S–S bonds are indicated in yellow, blue dashed lines indicate short Ti–Ti distances while red dashed lines illustrate long Ti–Ti distances. In (c) light blue spheres correspond to Am atoms and cream spheres correspond to Te atoms.

work on the properties of exfoliated compounds has been investigated.^{266,267} It is noted that all compounds are all found to be extremely air-sensitive due to the thermodynamic propensity of forming metal oxides.

4.14.4.2 Tetradymites

One of the more well-studied families of 2D materials in the bulk are the tetradymites.^{268,269} This family gets its name from the geological mineral, Tetradymite, which exhibits fourfold twinning and has a formula of $\text{Bi}_2\text{Te}_2\text{S}$. Tetradymites have a chemical formula of M_2Ch_3 , in which M is pnictogen (As, Sb, and Bi) and Ch is chalcogen (S, Se, Te). Tetradymites crystallize into a 5-atom thick 2D vdW structure which consists of a double-octahedral thick networks of edge-sharing MCh_6 octahedra. The tetradyomite structure has rhombohedral symmetry, with space group $R\bar{3}m$, and three quintuple layers stacked along the long c axis of the crystallographic unit cell (Fig. 25a). The tetradyomite-type structure competes with stibnite- and orpiment-type structures which have lower symmetry (Fig. 25b and c). The occurrence of the orpiment, stibnite and tetradyomite structures in these binary M_2Ch_3 compounds is shown in Fig. 25d with the most stable binary tetradymites forming for $\text{M} = \text{Bi}$ and $\text{Ch} = \text{Se}$, Te , or $\text{M} = \text{Sb}$ and $\text{Ch} = \text{Te}$.

These compounds have attracted considerable interest in thermoelectrics and as topological insulators in the bulk. Typically, commercial thermoelectric modules that operate utilize Bi_2Te_3 as the n-type module and Sb_2Te_3 as the p-type module for operation under ambient conditions. Bi_2Se_3 has a direct gap of 0.30 eV,²⁷⁰ Sb_2Te_3 has an indirect band gap of 0.210 eV,²⁷¹ and Bi_2Te_3 has an indirect band gap of 0.13 eV,²⁷¹ all measured optically. The gap energy and transport properties are exceptionally dependent on the preparation method and doping level, and synthetic precautions are necessary to control the energetic position of the Fermi level. In these materials, the valence band maximum is predominantly comprised of Se or Te p_z orbitals, and the conduction minimum is comprised of Bi or Sb p_z orbitals. However, when spin-orbit splitting is factored in, the large spin-orbit splitting in the bismuth

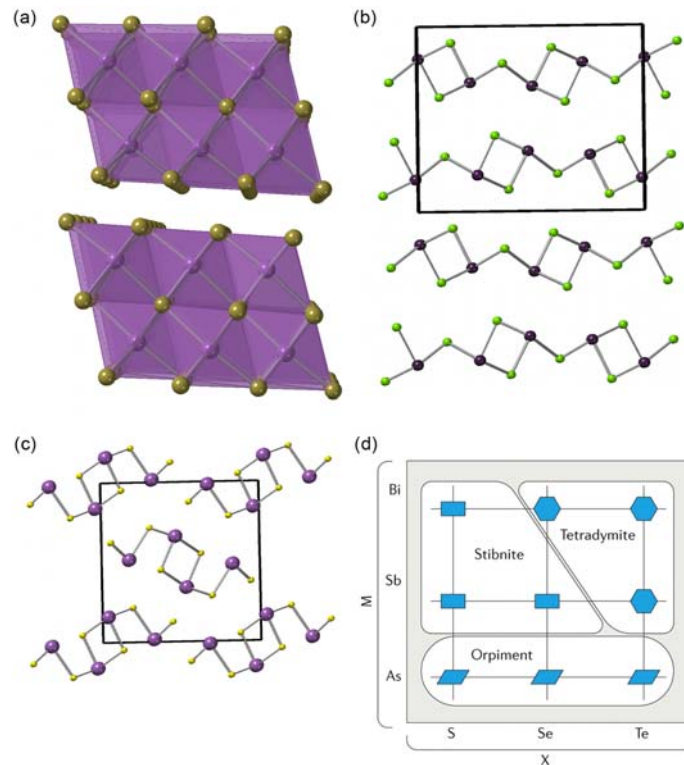


Fig. 25 Structure of (a) tetradymite Bi_2Te_3 , (b) Orpiment As_2Se_3 , (c) Stibnite Bi_2S_3 . (d) Schematic showing the crystallographic phases of M_2X_3 compounds. As the difference in electronegativity between M and X increases from the top right corner to the bottom left corner, these materials crystallize in progressively more distorted lattices. Panel (d) reprinted with permission from Heremans, J. P., Cava, R. J. & Samarth, N. Tetradymites as Thermoelectrics and Topological Insulators. *Nat. Rev. Mater.* **2017**, 2, 17049. © Springer Nature, 2017.

compounds results in a band inversion of the extrema, causing the valence band maximum to be predominantly Bi p_z in character, and the conduction band minimum to be predominantly Se or Te p_z in character (Fig. 26). This band inversion is evidenced by the emergence of a characteristic Mexican hat-shaped valence band maximum at the Γ point. Furthermore, this band inversion will result in the presence of topologically-protected Dirac-cone like metallic surface states with spin-momentum locking.²⁷² To summarize, the bulk of these topological materials are gapped, whereas the surface states are metallic.

There has been some early work on the exfoliation of these materials. For instance, Sb_2Te_3 , Bi_2Te_3 , and Bi_2Se_3 have all been prepared in few-layer form via mechanical exfoliation,^{273–275} and epitaxial growth.^{276–278} There have been some electronic transport studies on few-layer exfoliated flakes in which both the effect of the metallic surface through resistivity vs. temperature trends,

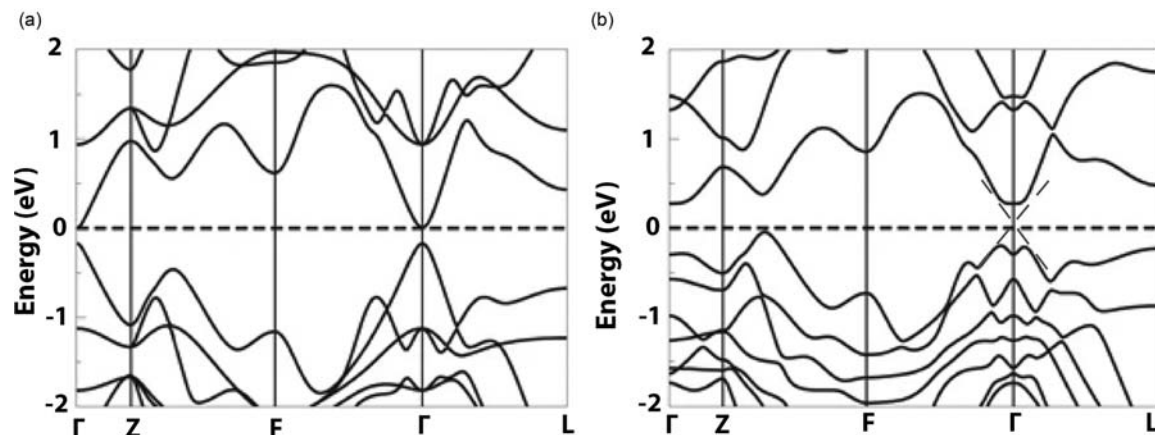


Fig. 26 Band structure for Bi_2Se_3 without (a) and with (b) SOC. The Dirac-cone shaped topologically protected surface states in (b) are drawn in blue. Reprinted with permission from Zhang, H., Liu, C.-X., Qi, X.-L., Dai, X., Fang, Z. & Zhang, S.-C. Topological Insulators in Bi_2Se_3 , Bi_2Te_3 and Sb_2Te_3 With a Single Dirac Cone on the Surface. *Nat. Phys.* **2009b**, 5, 438–442. © Springer Nature, 2009.

as well as the semiconducting bulk, through electrostatic gating, have been observed. In addition, studies on thermal conductivity in Bi_2Te_3 have shown that there was a reduction in the cross-plane and in-plane thermal conductivities from 0.5–0.6 and 1.5–2.0 $\text{W m}^{-1} \text{K}^{-1}$ respectively, to 0.1–0.3 and 1.1 $\text{W m}^{-1} \text{K}^{-1}$.²⁷⁹ Still, the monolayer properties have not been nearly as extensively studied compared to those described in Section 4.14.3.

4.14.4.3 Tetradymite derivatives

There are several binary and ternary compounds with crystal structures that are closely related to the tetradymite family but are not solely comprised of pnictogen and chalcogen atoms. In_2Se_3 is the only binary M_2Ch_3 derivative of this structure in which the trivalent pnictogen element is replaced with a trivalent group 13 triel element. Sn_4As_3 crystallizes into a 7-atom thick anti-tetradymite 2D vdW structure which consists of triple-octahedral thick layers of edge-sharing AsSn_6 octahedra.²⁸⁰ In addition, the layered Sn compounds, NaSn_2P_2 , NaSn_2As_2 , NaSn_2Sb_2 , SrSn_2As_2 , EuSn_2P_2 , and EuSn_2As_2 all have the same structure and consists of quintuple layers of $\text{Sn}-(\text{P}/\text{As}/\text{Sb})-(\text{Na}/\text{Eu}/\text{Sr})-(\text{P}/\text{As}/\text{Sb})-\text{Sn}$ (Fig. 27a). Analyzing EuSn_2As_2 using the formal Zintl-Klemm electron counting rules, upon donation of two electrons per Eu atom the Sn atoms would feature a full octet with a lone pair in the vdW space, and thus there is no interlayer bonding between neighboring Sn layers. In the case of NaSn_2As_2 , the donation of only one electron from each Na atom results in each Sn atom formally having 7.5 e^- , thus there would be $\frac{1}{2}$ a Sn-Sn interlayer bond between neighboring layers. There is a slight change in Sn-Sn distance between EuSn_2As_2 (3.33 Å²⁸¹) and NaSn_2As_2 (3.30 Å²¹) indicating this, which together are much longer than a Sn-Sn bond length of 3.1 Å. Next, the Ti_2PTE_2 , Zr_2PTE_2 and Hf_2PTE_2 compounds have the same quintuple layers of $\text{Te}-(\text{Ti}/\text{Zr}/\text{Hf})-\text{P}-(\text{Ti}/\text{Zr}/\text{Hf})-\text{Te}$, with large Te-Te bond distances of 3.8 Å,²⁸² indicative of a vdW gap. In these compounds, if one assumes the formal oxidation states of Te^{2-} and P^{3-} , then the group 4 element would have to have an oxidation of $\text{M}^{3.5+}$, which is indicative of a delocalized electron. Finally, the compounds Ta_2CS_2 , Ta_2CSe_2 , and Nb_2CS_2 also feature quintuple layers of $\text{S}-(\text{Nb}/\text{Ta})-\text{C}-(\text{Nb}/\text{Ta})-\text{S}$ (Fig. 27b). Here, assuming formal valences of C^{4-} and S^{2-} would require the transition metal to be tetravalent and have a d^1 configuration.

These compounds have a wide range of interesting properties. NaSn_2As_2 is a metal that was discovered to simultaneously exhibit p-type conductivity along the cross-plane direction and n-type along the in-plane direction, a phenomenon denoted as “goniopolarity.”²⁸³ The thermopower and Hall coefficients display opposite signs depending on whether the measurement occurs along the in-plane or cross-plane directions (Fig. 27c). The metallic EuSn_2As_2 and EuSn_2P_2 compounds have attracted considerable attention due to the combination of Eu^{2+} -based magnetism with topologically protected surface states, depending on the orientation of the magnetic moment (Fig. 27d).^{281,284} $\text{Hf}_2\text{Te}_2\text{P}$ is also a metal with topologically protected surface states.²⁸⁵ In addition, $\text{Nb}_2\text{S}_2\text{C}$ and $\text{Ta}_2\text{S}_2\text{C}$ are superconductors with transition temperatures of 7.6 and 3.6 K, respectively (Fig. 27e).^{286,287} To date, there are very few studies on the properties of exfoliated few layer versions of these materials.

4.14.4.4 The octahedral APn_2Te_4 family

Another family of compounds that can be thought of as derivatives of the tetradymite structure and have attracted considerable attention due to the combination of magnetism and topology are the APn_2Te_4 family, where A is either Mn, or a heavy group 14 element (Ge, Si, and Pb), and Pn is a pnictogen (As, Sb, and Bi). Currently MnBi_2Te_4 and its derivatives are the most well studied family of compounds. The members of this class include MnBi_2Te_4 ,²⁸⁸ and $\text{MnBi}_{2+2x}\text{Te}_{4+3x}$ derivatives including MnBi_4Te_7 ,²⁸⁹ $\text{MnBi}_6\text{Te}_{10}$,²⁸⁹ and $\text{MnBi}_8\text{Te}_{13}$,²⁹⁰ (Fig. 28) as well as the Sb derivatives MnSb_2Te_4 ,²⁹¹ and MnSb_4Te_7 .²⁹² MnBi_2Te_4 is a vdW compound comprised of layers of edge-sharing MnTe_6 octahedra sandwiched between BiTe_6 octahedra, thereby forming a septuple layer. In MnBi_4Te_7 , a Bi_2Te_3 layer is interdigitated or intergrown between neighboring MnBi_2Te_4 layers. In $\text{MnBi}_6\text{Te}_{10}$, two Bi_2Te_3 layers exist between the MnBi_2Te_4 . Single crystals of compounds up to $\text{MnBi}_8\text{Te}_{13}$ have been prepared. In addition, $\text{MnBi}_{2-x}\text{Sb}_x\text{Te}_4$ alloys of all compounds can be readily prepared.

MnBi_2Te_4 is antiferromagnetic with $T_N = 24.4 \text{ K}$ ²⁹³ in which the Mn^{2+} moments within each layer are ferromagnetically coupled and oriented along the cross-plane direction, with neighboring layers antiferromagnetically coupled. The magnetic ordering undergoes a change to a canted antiferromagnetic alignment with an applied field of $\sim 3.4 \text{ T}$, and changes again to ferromagnetic state at 7 T. The ferromagnetic state is a Weyl semimetal²⁹³ which has a pair of topologically protected Dirac nodes oriented along the Γ to Z direction. With no applied field, MnBi_2Te_4 is an insulator with a band gap of 150 meV, but also features topologically protected surface states. When exfoliated to five layers, MnBi_2Te_4 was found to exhibit the quantum anomalous Hall effect at 4.5 K,²⁹⁴ which is the highest temperature in which this phenomenon has been observed in any material. When additional Bi_2Te_3 layers are interdigitated between the MnBi_2Te_4 layers, T_N drops to 13 K in MnBi_4Te_7 and 11 K in $\text{MnBi}_6\text{Te}_{10}$. Numerous reviews on this family compound can be found.^{288,289,295}

The nonmagnetic derivatives of this structure type, in which A is a divalent group 14 element (Ge, Sn, Pb) also have attracted considerable interest as phase change materials and as topological insulators. There are many compounds that can form the same isostructural sequences in which multiple layers of Pn_2Te_3 are interdigitated in between APn_2Te_4 layers, thereby leading to stoichiometries of $\text{APn}_{2+2x}\text{Te}_{4+3x}$. These compounds also crystallize into another family of compounds in which the number of ATe_6 octahedra is increased sequentially within each vdW layer. For instance, $\text{A}_2\text{Pn}_2\text{Te}_5$ compounds such as $\text{Pb}_2\text{Bi}_2\text{Te}_5$ feature two octahedra thick edge sharing layers of ATe_6 , capped by edge-sharing octahedra of PnTe_6 (Fig. 29). These compounds form derivatives in which an additional ATe_6 is added into the middle, leading to a sequence of stoichiometries of $\text{A}_2 + y\text{Pn}_2\text{Te}_5 + y$ where remarkably,

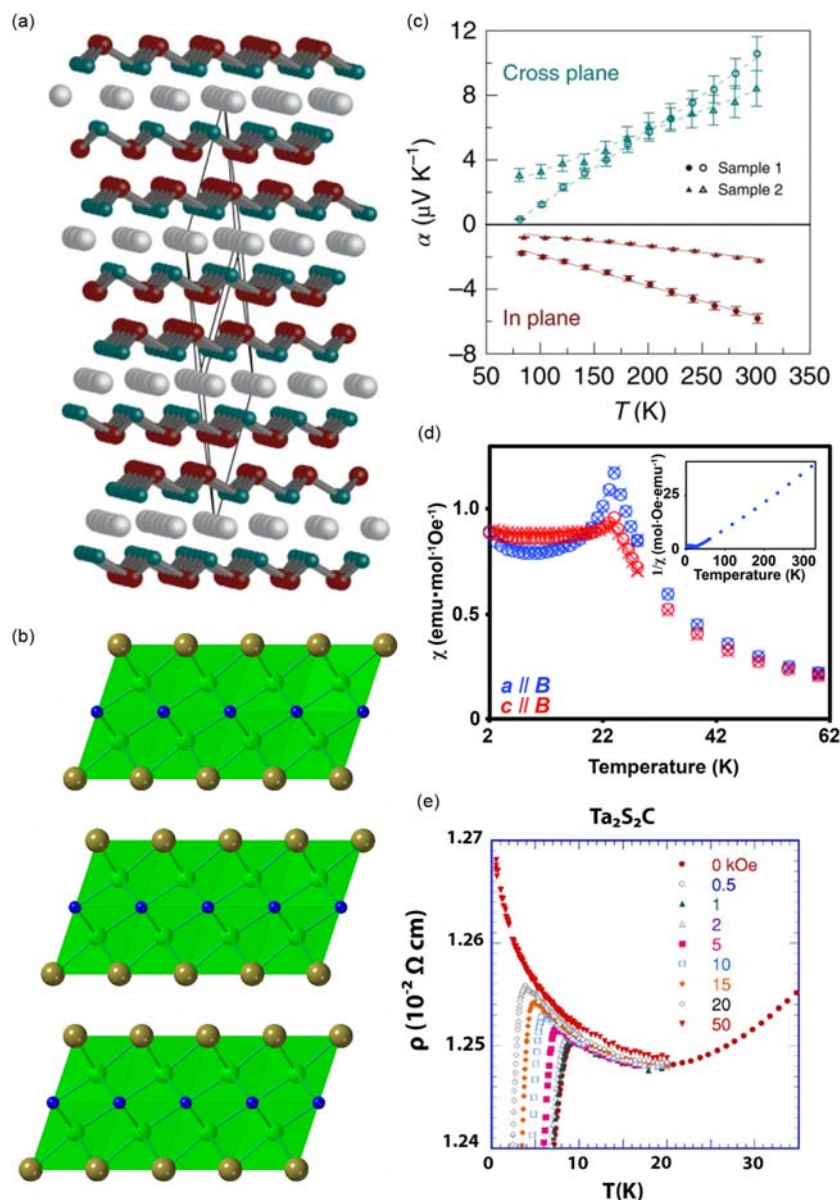


Fig. 27 (a) Crystal structure of NaSn₂As₂, gray spheres correspond to Na atoms, maroon spheres correspond to Sn atoms, and turquoise spheres correspond to As atoms. (b) Crystal structure of Zr₂PTe₂ where light green spheres correspond to Zr atoms, blue spheres correspond to P atoms and beige spheres correspond to Te atoms. (c) Experimental in-plane and cross-plane temperature-dependent thermopower in NaSn₂As₂ crystals. The triangles and circles correspond to measurements on two different single crystals. The lines are guides to the eye. (d) temperature-dependent magnetic susceptibility of EuSn₂As₂ oriented at different crystal orientations with respect to the measuring magnetic field of 0.01T. Inset is the Curie–Weiss fit corresponding to the inverse susceptibility of the crystal with its a-axis oriented parallel to the applied field. The blue data points correspond to measurements with the a-axis parallel to the field and the red data points correspond to measurements with c-axis oriented parallel to the field. (e) T dependence of ρ in Ta₂S₂C at fixed H = 0, 0.5, 1, 2, 5, 10, 15, 20, and 50 kOe. Panel (a and c) reprinted with permission from He, B., Wang, Y., Arguilla, M. Q., Cultrara, N. D., Scudder, M. R., Goldberger, J. E., Windl, W. & Heremans, J. P. The Fermi Surface Geometrical Origin of Axis-Dependent Conduction Polarity in Layered Materials. *Nat. Mater.* **2019**, *18*, 568–572. © Springer Nature, 2019. Panel (d) reprinted with permission from Arguilla, M. Q., Cultrara, N. D., Baum, Z. J., Jiang, S., Ross, R. D. & Goldberger, J. E. EuSn₂As₂: An Exfoliable Magnetic Layered Zintl–Klemm Phase. *Inorg. Chem. Front.* **2017**, *4*, 378–386. © Royal Society of Chemistry, 2014. Panel (e) reprinted with permission from Suzuki, M., Suzuki, I. S., Noji, T., Koike, Y. & Walter, J. Successive Superconducting Transitions in Ta₂S₂C Studied by Electrical Resistivity and Nonlinear ac Magnetic Susceptibility. *Phys. Rev. B: Condens. Matter Mater. Phys.* **2007**, *75*, 184536. © American Physical Society, 2007.

single crystal structures with up to $y = 5$ can be found in the Ge-As-Te system. Depending on the size matching of the A²⁺ and Pn³⁺ cation, site disorder can arise in the layers nearest the vdW gap. The compounds with the stoichiometry of APn₄Te₇ and A₂Pn₂Te₅ crystallize into the trigonal P-3m1 space group, and the other phases crystallize into R-3m. A comprehensive list of both the magnetic and non-magnetic compounds that have been crystallographically characterized is given in Table 1.

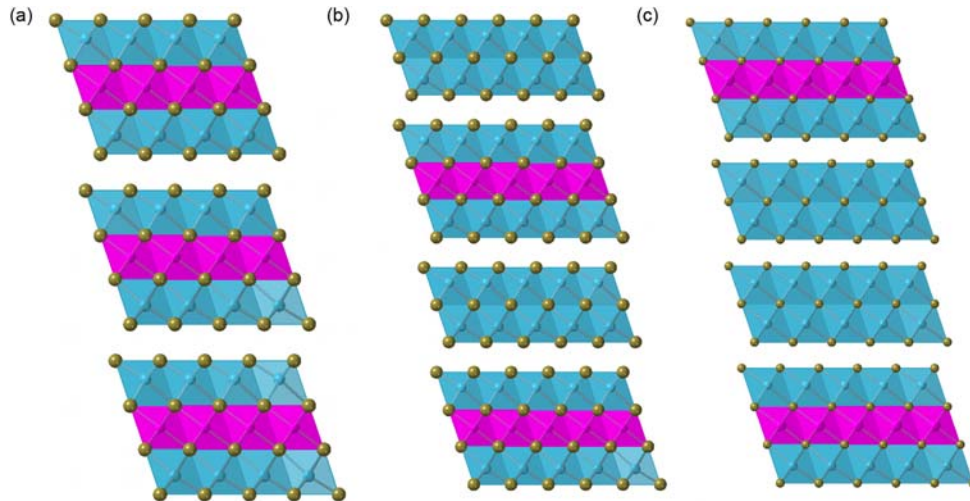


Fig. 28 Crystal Structure of (a) MnBi_2Te_4 , (b) MnBi_4Te_7 , (c) $\text{MnBi}_6\text{Te}_{10}$. Purple spheres correspond to Mn, blue spheres correspond to Bi and beige spheres correspond to Te.

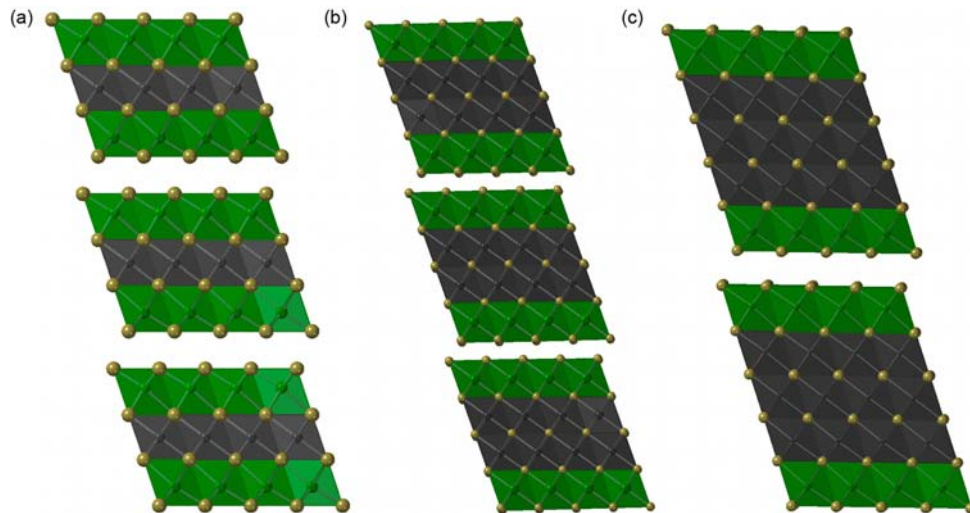


Fig. 29 Crystal structure of (a) GeSb_2Te_4 , (b) $\text{Ge}_2\text{Sb}_2\text{Te}_5$, and (c) $\text{Ge}_3\text{Sb}_2\text{Te}_6$. Black spheres correspond to Ge, green spheres correspond to Sb and beige spheres correspond to Te.

Table 1 List of known compounds in the octahedral APn_2Te_4 family.

Stoichiometry:	Known compounds		Refs.
APn_2Te_4	MnBi_2Te_4 MnSb_2Te_4 GeAs_2Te_4 GeSb_2Te_4	SnBi_2Te_4 SnSb_2Te_4 PbBi_2Te_4 PbSb_2Te_4	288, 291, 302
APn_4Te_7	MnBi_4Te_7 MnSb_4Te_7 GeAs_4Te_7 GeSb_4Te_7	GeBi_4Te_7 SnBi_4Te_7 PbBi_4Te_7	289, 292, 296, 303, 298, 299, 304
$\text{APn}_6\text{Te}_{10}$	$\text{MnBi}_6\text{Te}_{10}$	$\text{PbBi}_6\text{Te}_{10}$	289, 299
$\text{APn}_8\text{Te}_{13}$	$\text{MnBi}_8\text{Te}_{13}$	$\text{PbBi}_8\text{Te}_{13}$	290, 299
$\text{A}_2\text{Pn}_2\text{Te}_5$	$\text{Ge}_2\text{As}_2\text{Te}_5$ $\text{Ge}_2\text{Sb}_2\text{Te}_5$	$\text{Ge}_2\text{Bi}_2\text{Te}_5$ $\text{Pb}_2\text{Bi}_2\text{Te}_5$	296, 305, 298, 306
$\text{A}_3\text{Pn}_2\text{Te}_6$	$\text{Ge}_3\text{As}_2\text{Te}_6$ $\text{Ge}_3\text{Sb}_2\text{Te}_6$	$\text{Ge}_3\text{Bi}_2\text{Te}_6$	296, 307, 298
$\text{A}_4\text{Pn}_2\text{Te}_7$	$\text{Ge}_4\text{As}_2\text{Te}_7$		296
$\text{A}_5\text{Pn}_2\text{Te}_8$	$\text{Ge}_5\text{As}_2\text{Te}_8$		308
$\text{A}_7\text{Pn}_2\text{Te}_{10}$	$\text{Ge}_7\text{As}_2\text{Te}_{10}$		309

GePn_2Te_4 , $\text{Ge}_2\text{Pn}_2\text{Te}_5$, where $\text{Pn} = \text{As}, \text{Sb}$, have all shown considerable use as phase change materials technology whereby a reversible structural transition shows significant change in the resistivity of these materials.³¹⁰ In $\text{Ge}_2\text{Sb}_2\text{Te}_5$, this manifests as a six order of magnitude decrease in the resistivity from an amorphous phase, to a metastable 3D rock salt structure type, and finally to the thermodynamically stable crystalline layered phase. When this phase is heated above the melting point and cooled rapidly, it forms the amorphous solid. When the phase is annealed at a temperature below the melting point, it transforms to the rock salt structure type, and eventually the layered structure, both leading to a significant lowering of resistivity and refractive index. Thus, $\text{Ge}_2\text{Sb}_2\text{Te}_5$ is the most widely used phase change memory material and is used for memory storage and digital video disk (DVD) applications.^{311,312} However, to maximize data processing speed only the first transition from amorphous to the 3D metastable rock salt structure is exploited. Additionally, PbBi_2Te_4 and PbBi_4Te_7 have been experimentally confirmed to be topological insulators with bulk band gaps of 0.230 and ~ 0.20 eV, respectively.^{313,314} GeBi_2Te_4 has also been found to exhibit Dirac cone-like surface states.³¹⁵ Despite extensive exploration of the growth of thin films for memory storage, the exfoliation of thin flakes of these materials has yet to be experimentally realized and is complicated by the different kinds of vdW layers that are combined in compounds with the $\text{APn}_2 + 2x\text{Te}_4 + 3x$ stoichiometry.

4.14.4.5 The tetrahedral MTr_2Ch_4 family

The next family of 2D vdW compounds also originate from a similar MTr_2Ch_4 stoichiometry, but in this case, the Tr is in tetrahedral coordination. These can form derivatives with different thicknesses of the vdW layers, leading to stoichiometries of $\text{M}_{1+x}\text{Tr}_2\text{Ch}_{4+x}$. In these layered phases, M is a divalent first row transition metal (Mn, Fe, Ni, and Zn), Tr is a group 13 element (Ga, In) and Ch is either S or Se. Trivalent transition metals (Sc, V, Cr, and Co) have all been incorporated into analogous layered structures with a concomitant replacement of the Tr element or with a fractional stoichiometry.³¹⁶ The MTr_2Ch_4 compounds are structurally similar to the octahedral MPn_2Ch_4 family discussed in Section 4.14.4.4, with a single layer of edge-sharing MCh_6 octahedra, but differ in that this MCh_6 layer is sandwiched by corner sharing TrCh_4 tetrahedra (Fig. 30a). There are four known stacking polytypes in this stoichiometry, which are the 1T, 2T, 2H, and 3R polytype.³¹⁶ These compounds also form derivatives in which two layers of edge-sharing MCh_6 octahedra are terminated by TrCh_4 octahedra, leading to the $\text{M}_2\text{Tr}_2\text{Ch}_5$ stoichiometry, such as in $\text{Mn}_2\text{Ga}_2\text{S}_5$ (Fig. 30b).³¹⁷ In a small number of compounds, $\text{Zn}_2\text{In}_2\text{Se}_5$ and $\text{Fe}_2\text{In}_2\text{Se}_5$,³¹⁸ the additional Zn or Fe layer is in tetrahedral coordination with the chalcogen atoms. (Fig. 30d). Finally, $\text{Zn}_3\text{In}_2\text{S}_6$ is the only member known to have three transition metals per vdW layer, and whose vdW layers consists of ZnS_4 - ZnS_4 - InS_6 - ZnS_4 - InS_4 tetrahedra and octahedra (Fig. 30c). In many of these compounds the trivalent and transition metal sites have appreciable mixing due to similar ionic radii. In addition, there are a large number of quaternary alloy phases in which either both S and Se, divalent transition metals, or multiple trivalent metals, are alloyed on to the same site.^{316,319,320}

The properties of these materials have been explored when pure phases can be isolated. These materials are primarily semiconducting in the bulk with gaps of up to 2.39 eV for $\text{Zn}_3\text{In}_2\text{S}_6$.³²¹ FeGa_2S_4 and $\text{Fe}_2\text{Ga}_2\text{S}_5$ have very small transport gaps (30 meV for $\text{Fe}_2\text{Ga}_2\text{S}_5$).³²² The large surface areas and wide variety of band gaps have led to exploration of the use of this family of materials as photocatalysts. For instance, $\text{Zn}_3\text{In}_2\text{S}_6$ has been explored in the photocatalytic reduction of CO_2 .³²¹ In addition to their photocatalytic properties, the MTr_2Ch_4 Mn, Fe and Ni structures are all highly frustrated magnetic systems exhibiting antiferromagnetic and/or spin glass transitions below 20 K.^{323–325} The double octahedral thick $\text{Fe}_2\text{Ga}_2\text{S}_5$ is an exception that exhibits a much higher T_N of 110 K.³²⁶ The magnetic frustration seen in these compounds originates from the metal atoms arranging on a trigonal with significant antiferromagnetic direct exchange. In addition, site disorder also plays a crucial role in disrupting long range magnetic order. The properties of these compounds upon exfoliation have not yet been investigated.

4.14.4.6 The iron germanium tellurides (Fe_nGeTe_2)

The compounds Fe_3GeTe_2 , Fe_4GeTe_2 and Fe_5GeTe_2 , or more precisely $\text{Fe}_{3-x}\text{GeTe}_2$ to $\text{Fe}_{5-x}\text{GeTe}_2$ have attracted considerable interest as 2D vdW ferromagnetic metallic materials with T_C far above 100 K and even approaching room temperature. $\text{Fe}_{3-x}\text{GeTe}_2$ is by far the most extensively studied compound.^{327–330} The structure consists of slabs of Fe_{3-x}Ge layers bounded by Te atoms, as shown in Fig. 31a.³³¹ In general, there are two different Fe Wyckoff positions in the lattice, a Fe (1) position on the top of bottom of each layer, and an Fe (2) position in the center of each layer. The Fe (1) position has double the occupancy of the Fe (2) position. Careful single crystal X-ray and neutron diffraction studies as well as transmission electron microscopy studies indicated that the central Fe (2) position can have variable occupancies. When $x > 0.24$, or when the Fe stoichiometry is less than $\text{Fe}_{2.76}\text{GeTe}_2$, the Fe occupies the Fe (1) and Fe (2) positions only. With greater Fe stoichiometries, the additional Fe occupies the interlayer vdW space, having a profound effect on the magnetism of the compounds and limiting the exfoliation. Bulk $\text{Fe}_{2.76}\text{GeTe}_2$, has a T_C of 150 K,^{329,330} whereas Fe_3GeTe_2 has a T_C of 220 K.^{327,328} The higher transition temperature of Fe_3GeTe_2 is a consequence of the 3D interlayer magnetic coupling caused by Fe intercalation. In the monolayer form, $\text{Fe}_{3-x}\text{GeTe}_2$ is reported to have a transition temperature of 126 K.³³² There are some reports about an increase of the transition temperature to above 300 K with higher ionic liquid gating, however, these compounds are also prone to amorphization into various magnetic Fe_xGe_y phases with transition temperatures above room temperature.^{333,334} Finally, Ni_3GeTe_2 also has the same vdW crystal structure of $\text{Fe}_{3-x}\text{GeTe}_2$

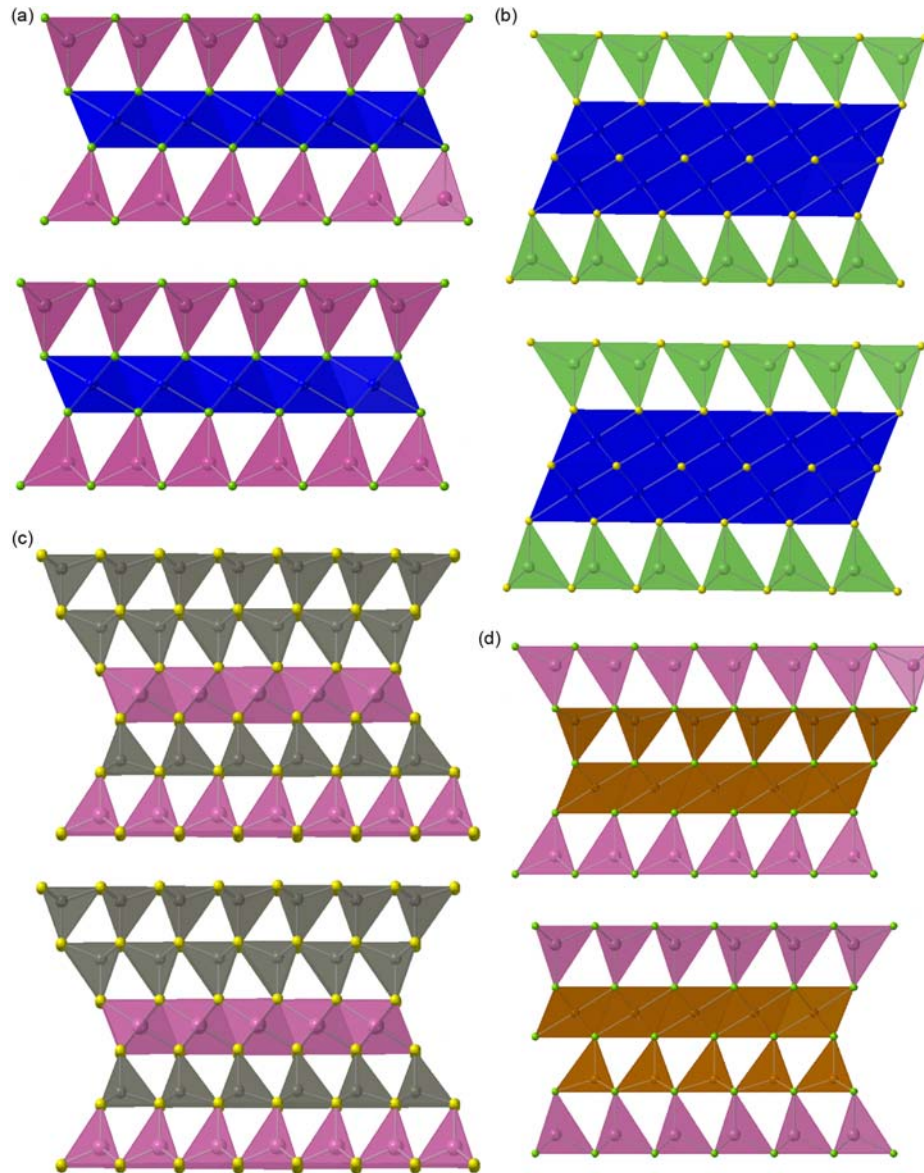


Fig. 30 Crystal Structure of (a) MnIn_2Se_4 , (b) $\text{Mn}_2\text{Ga}_2\text{S}_5$, (c) $\text{Zn}_3\text{In}_2\text{S}_6$, and (d) $\text{Fe}_2\text{In}_2\text{Se}_5$. Where in (a) blue spheres correspond to Mn atoms, pink spheres correspond to In, and green spheres correspond to S, in (b) Blue spheres correspond to Mn atoms, green spheres correspond to Ga atoms, and yellow spheres correspond to S atoms. In (c) gray spheres correspond to Zn, pink spheres correspond to In atoms and yellow spheres correspond to S, and in (d) orange spheres correspond to Fe atoms, pink spheres correspond to In atoms and green spheres correspond to Se.

and features the same propensity for nickel to partially occupy a position in the vdW space. Ni_3GeTe_2 is also metallic, however it is Pauli paramagnet.³³⁵

Fe_4GeTe_2 is structurally similar to $\text{Fe}_3-x\text{GeTe}_2$ but features an additional Fe atom per vdW layer (Fig. 31b). The magnetic transition in the bulk of this compound is 270 K, with the magnetic moments nominally aligned along the in-plane direction, although at 110 K, the orientation of the magnetic moments switches to the out of plane direction.³³⁶ The precise Fe stoichiometry of this compound and the influence on properties is not as extensively studied as $\text{Fe}_3-x\text{GeTe}_2$ or $\text{Fe}_5-x\text{GeTe}_2$. $\text{Fe}_5-x\text{GeTe}_2$ is structurally similar to $\text{Fe}_3-x\text{GeTe}_2$, with an additional 2 Fe atoms per vdW layer but has split-site Fe and Ge positions that lead to intrinsic site and spin disorder (Fig. 31c). This disorder partially arises from the fact that it is a metastable phase with crystals that must be synthesized via rapid quenching.³³⁷ This family of compounds have magnetic ordering temperatures between 270 and 310 K. Partial Fe-Co substitution has been reported for the Fe_4GeTe_2 and $\text{Fe}_5-x\text{GeTe}_2$ family of compounds, showing concomitant variation in transition temperatures and magnetic ordering type. For instance, $\text{Fe}_3\text{CoGeTe}_2$ has an antiferromagnetic structure with a T_N of 155 K, but still retains its metallicity.³³⁸

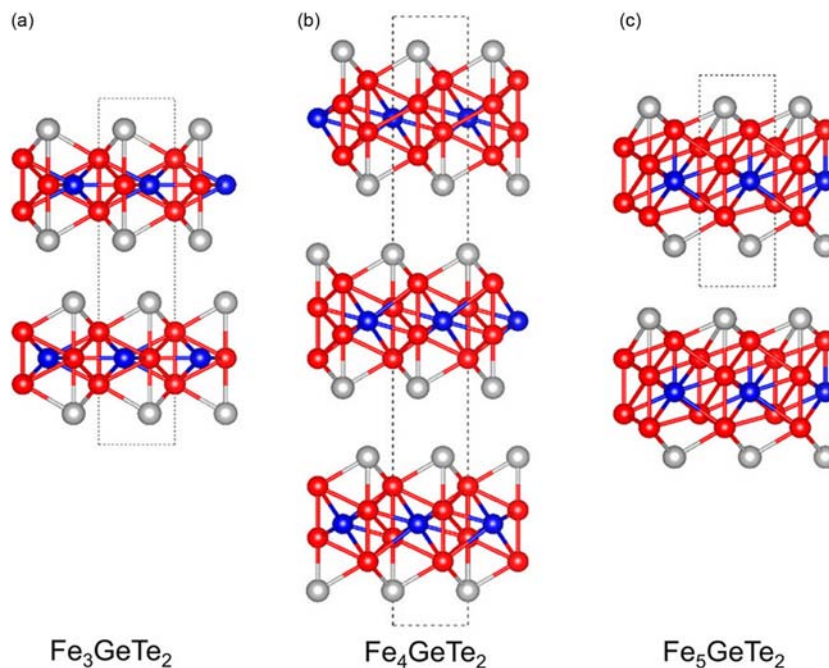


Fig. 31 Crystal structures of (a) Fe_3GeTe_2 , (b) Fe_4GeTe_2 , and (c) Fe_5GeTe_2 . Red spheres correspond to Fe atoms, blue spheres correspond to Ge atoms and white spheres correspond to Te atoms. Reprinted with permission Su, Y., Li, X., Zhu, M., Zhang, J., You, L. & Tsymbal, E. Y. Van der Waals Multiferroic Tunnel Junctions. *Nano Lett.*, **2021**, *21*, 175–181. © American Chemical Society, 2021.

4.14.4.7 The tantalum-nickel group chalcogenides

Ternary vdW compounds consisting of tantalum, a nickel group element, and a chalcogen, most notably Ta_2NiSe_5 , have attracted considerable recent interest due to the possibility of an exciton insulating ground state. TaNiS_5 and Ta_2NiSe_5 crystallize into vdW layers that are derivatives of the octahedral transition metal dichalcogenide structure type. The structure is comprised of chains of two edge-sharing TaCh_6 octahedra, separated on each side of the chain by one NiCh_4 tetrahedra (Fig. 32a). At high temperatures, both Ta_2NiS_5 and Ta_2NiSe_5 crystallize into an octahedral Cmcm structure type. In Ta_2NiSe_5 , below 325 K³³⁹ a phase transition to a monoclinic C2/m phase is seen, while no such transition is observed in Ta_2NiS_5 . Transport measurements have shown a concurrent transition from semimetallic behavior in the high temperature phase to semiconducting behavior in the low temperature phase. At room temperature, Ta_2NiS_5 is a narrow optical gap semiconductor with a ~ 0.25 eV gap, while Ta_2NiSe_5 has a 0.16 eV gap.³⁴⁰ This semiconducting behavior can be understood from an ionic bonding perspective, where one can formally consider the oxidation state of Ta^{5+} , Ni^0 , and $\text{S}^{2-}/\text{Se}^{2-}$. Thus, the conduction band minimum is comprised of empty Ta 5d orbitals, and the valence band maximum is composed of primarily filled Ni d¹⁰ orbitals but with some chalcogenide p-orbital mixing (Fig. 32b). The especially narrow band gap in Ta_2NiSe_5 has led to the discovery of an excitonic insulator phase due to the exciton binding energy exceeding that of the electronic band gap. Indeed, there is a growing body of evidence suggesting that the phase transition seen in this material is caused by the formation of excitons consisting of e^- on the Ta atoms, and h^+ on the Ni atoms.

There are numerous other tantalum-nickel group-chalcogenides that form 2D vdW structures that have been discovered. First, Ta_2PdS_6 and Ta_2PdSe_6 have structures that are nearly identical to Ta_2NiS_5 , except the Pd is in square planar coordination (Fig. 33a), which results an extra chalcogen per formula unit. Ta_2PdS_6 is semiconducting with a 40 meV band gap, whereas Ta_2PdSe_6 is metallic and has been discovered to become superconducting at 4.5 K when ethylenediamine is intercalated into the vdW gap.³⁴¹ Second, Ta_2NiSe_7 forms a chain-like structure that is closely related to Ta_2NiSe_5 . Here, the vdW layers consists of three chain-like components; there are chains of two TaCh_6 octahedra, separated on each side by NiCh_5 in square pyramidal geometry, connected to a double wide set of bicapped TaCh_8 trigonal prisms, reminiscent of the transition metal trichalcogenide structure type described in Section 4.14.4.1 (Fig. 33b). There are two sets of Se_2^{2-} anions per formula unit. Ta_2PtSe_7 is isostructural to Ta_2NiSe_7 , although in this case Pt is in an octahedral coordination due to its larger size. While the properties of the Ta_2PtSe_7 are not fully explored, Ta_2NiSe_7 is metallic and is reported to form charge density waves with a transition temperature of 52.5 K.³⁴² $\text{Ta}_2\text{Ni}_3\text{Te}_5$ is another 2D vdW compound that consists of chains of edge-sharing NiTe_4 tetrahedra, connected to chains of edge-sharing TaTe_5 square pyramids (Fig. 33c).³⁴³ As another example $\text{Ta}_4\text{Pd}_3\text{Te}_{16}$ ³⁴⁴ form layered compounds comprised of chains of double-octahedral wide TaTe_6 , followed by a PdTe_6 octahedra, followed by TaTe_8 bicapped trigonal prism, then PdTe_6 , then TaTe_8 , PdTe_6 before the next double-wide chain of TaTe_6 (Fig. 33d). $\text{Ta}_3\text{Pd}_3\text{Te}_{14}$ ³⁴⁵ forms a nearly identical sequence, although the double-octahedral wide chains of TaTe_6 are replaced with single octahedral wide chains. $\text{Ta}_4\text{Pd}_3\text{Te}_{16}$ and $\text{Ta}_3\text{Pd}_3\text{Te}_{14}$ have attracted considerable interest due to the observation of multiband superconductivity below 4.6 K³⁴⁴ and 1.0 K,³⁴⁵ respectively. One final 2D

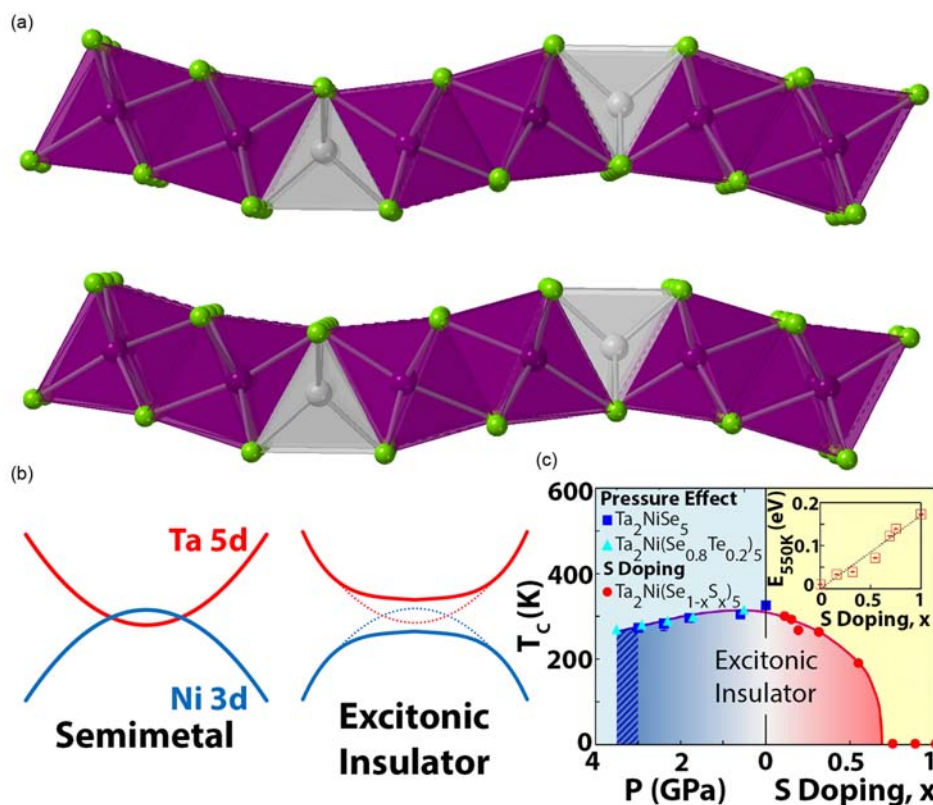


Fig. 32 (a) Crystal structure of Ta_2NiSe_5 , where purple spheres correspond to Ta atoms, gray spheres correspond to Ni atoms, and green spheres correspond to Se atoms. (b) Schematic of the high temperature semimetallic phase and the low temperature excitonic insulating state of Ta_2NiSe_5 . (c) Phase diagram of the excitonic insulator phase in Ta_2NiSe_5 given by the transition temperature T_c as a function of and concomitant pressure and Te doping (left), and S/Se alloying (right). These two halves correspond semimetallic and semiconducting regions of chemical composition and pressure phase space. Panel (c) reprinted with permission from Lu, Y. F., Kono, H., Larkin, T. I., Rost, A. W., Takayama, T., Boris, A. V., Keimer, B. & Takagi, H. Zero-Gap Semiconductor to Excitonic Insulator Transition in Ta_2NiSe_5 . *Nat. Commun.* **2017**, *8*, 14408. © 2017.

vdW compound in this family is TaNiTe_5 , which has a structure comprised of alternating chains of edge-sharing NiTe_6 octahedra coordinated to face-sharing chains of bicapped trigonal TaTe_8 prisms. TaNiTe_5 has been shown to have very anisotropic conductivity with a ρ ratio of 1:7:16 along the two in-plane and cross-plane directions, respectively, and has been explored for hosting Dirac Fermions.^{346,347}

4.14.4.8 Mixed metal tellurides

There exists a diverse family of structurally precise ternary layered compounds consisting of two different metals occupying unique Wyckoff sites and coordination environments, and a wide variety of stoichiometries. The first set of these have the stoichiometry of $\text{MM}'\text{Te}_4$ where $\text{M} = \text{Nb}, \text{Ta}$ and $\text{M}' = \text{Os}, \text{Rh}, \text{Ir}$. These crystallize into a site ordered $1T'$ TMD-type structure of space group $\text{Pmn}2_1$ with double octahedra wide chains of each metal (Fig. 34a and c), and lack inversion symmetry. These compounds typically feature short metal-metal distances between chains of different metals and long metal-metal distances between the same metal.^{101,348} These compounds stack into a 2-layer orthorhombic unit cell in which the rotation of the edge-sharing MTe_6 octahedra tilts in opposite direction in each layer (Fig. 34a). The Ta-Ru analogue is also known but typically forms as $\text{Ta}_{1+x}\text{Ru}_{1-x}\text{Te}_4$, with the excess Ta occupying the Ru sites.³⁴⁸ TaFeTe_4 is also very similar but crystallizes into two polytypes (Fig. 34b and c). The more stable structure, α - TaFeTe_4 consists of a 2-layer stacking sequence with an $I2/m$ space group and features a translational shift in neighboring layers, leading to the presence of inversion symmetry. The noncentrosymmetric $\text{Pmn}2_1$ β - TaFeTe_4 phase (34a,c) is metastable and is prepared by thermal quenching from 450 °C.³⁴⁹ All of these compounds are metallic either from transport measurements and/or theoretical calculations. In addition, TaFeTe_4 has been shown to have anisotropic in-plane electronic resistivities that are lower by up to a factor of 2–3 \times when measured along the chain direction compared to perpendicular to the chains.³⁴⁹ Many of these phases have been theorized to be Type-II Weyl semimetals but only TaIrTe_4 has been experimentally confirmed to be Type-II Weyl semimetals through pump-probe angle-resolved photoelectron spectroscopy (ARPES) measurements (Fig. 34d and e).^{350–352} TaIrTe_4 has additionally been shown to be superconducting at 0.57 K under 23.8 GPa, with an increasing transition temperature of up to 2.1 K with increasing pressure.³⁵³ Many of these compounds (TaFeTe_4 , TaIrTe_4 , NbIrTe_4 , TaRuTe_4 , and TaRhTe_4) have been

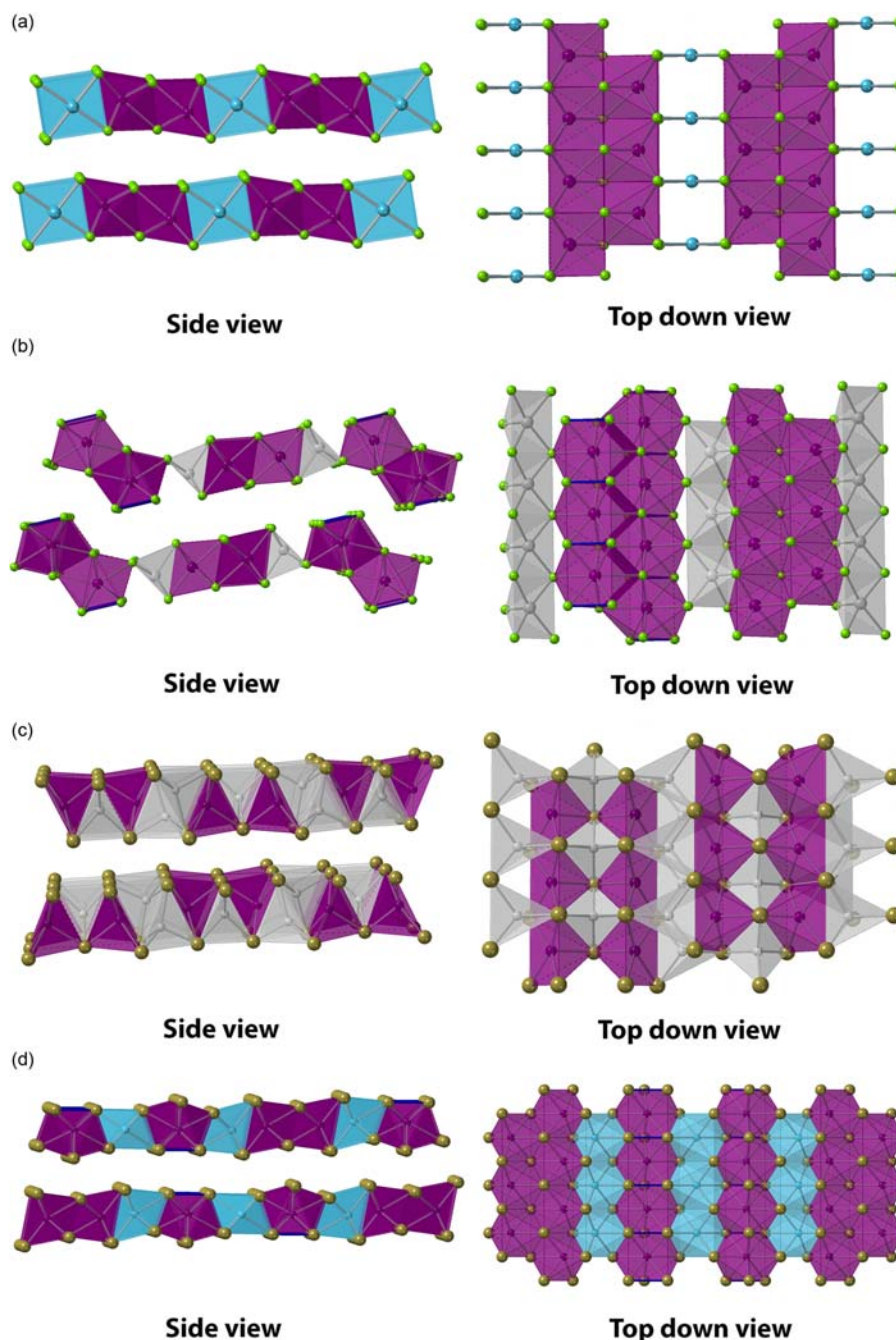


Fig. 33 Crystal structure in both side and top view of (a) Ta_2PdSe_6 , (b) Ta_2NiSe_7 , (c) $\text{Ta}_2\text{Ni}_3\text{Te}_5$, and (d) $\text{Ta}_4\text{Pd}_3\text{Te}_{16}$, where purple spheres correspond to Ta atoms, light blue spheres correspond to Pd atoms, gray spheres correspond to Ni atoms, light green spheres correspond to Se atoms, and beige spheres correspond to Te.

exfoliated down to few-layer form, and initial characterization of their stability and angle dependent Raman features have been explored.^{354–356} Thin flakes of TaIrTe_4 have been shown to host a nonlinear hall effect for radiofrequency rectification.³⁵⁷ A surface oxide is seen in exfoliation of TaIrTe_4 requiring either passivation such as has been performed via SiO_2 sputtering, or via the air free manipulation of thin flakes of this material. The stability of the other compounds in this family upon exfoliation have yet to be elucidated but are likely to be similar to TaIrTe_4 .^{357,358}

TaCo_2Te_2 is the only known mixed metal telluride with a $M:M':\text{Te}$ stoichiometry of 1:2:2. It crystallizes in an orthorhombic Pnma lattice where each vdW layer is constructed from an inner square lattice of Ta atoms, sandwiched between square lattices of Co atoms which are then terminated to a gap by Te atoms. The square nets of cobalt are distorted and undergo a Peierls distortion to form Co dimers (Fig. 35a).³⁵⁹ TaCo_2Te_2 is a nearly compensated semimetal in the bulk with high carrier mobilities of

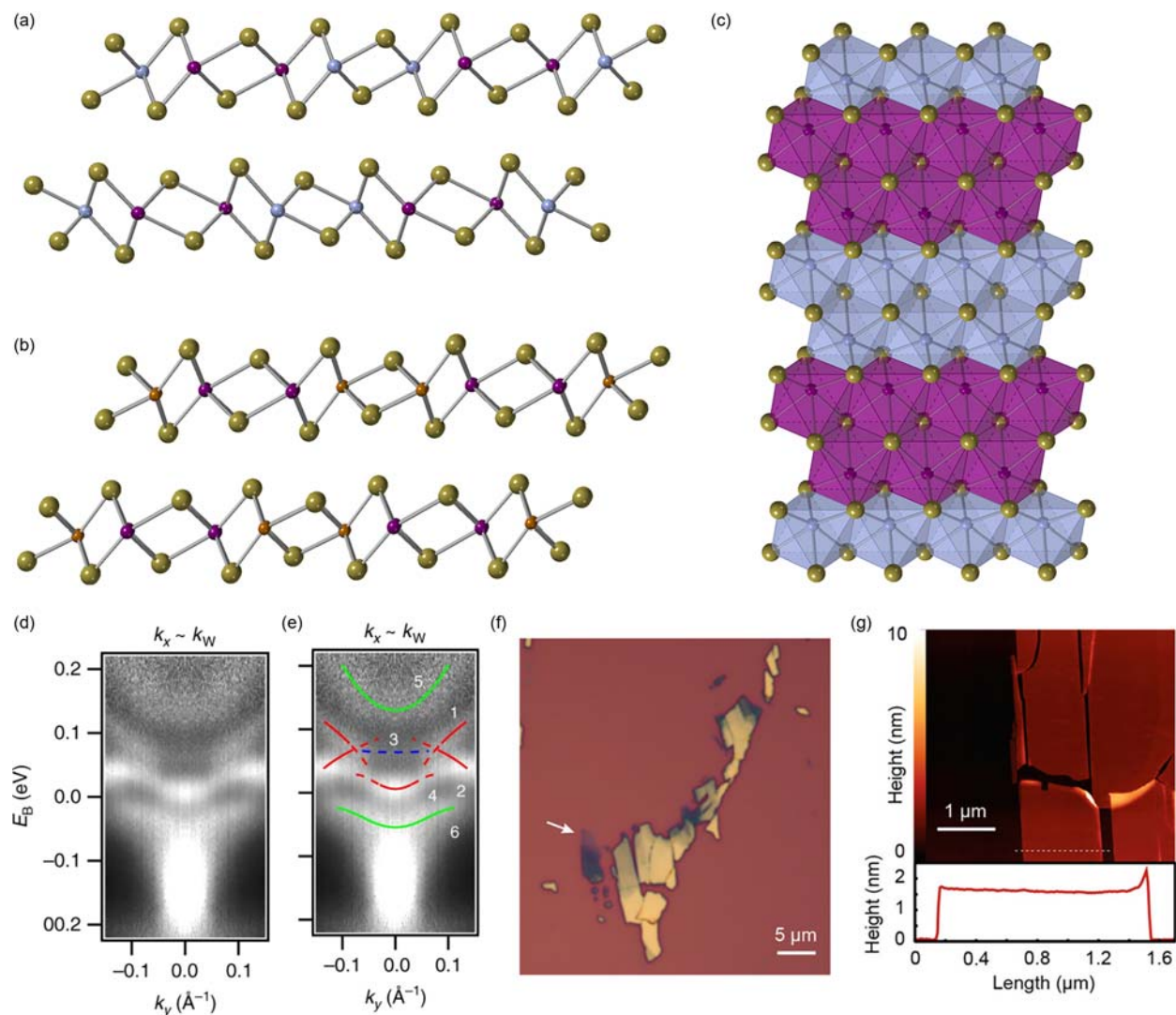


Fig. 34 Crystal structure of (a) side view of TaIrTe_4 , (b) side view of $\alpha\text{-TaFeTe}_4$, and (c) top-down view of TaIrTe_4 . Beige atoms correspond to Te atoms, purple spheres correspond to Ta atoms, light blue spheres correspond to Ir atoms and orange spheres correspond to Fe atoms. (d) Pump probe ARPES spectra of TaIrTe_4 , showing dispersion above E_F at fixed k_x expected to be near the Weyl points. (e) The same spectrum as (d) but with key features marked. The Weyl cone candidates are labeled 1 and 2, a Fermi arc candidate is labeled 3. (f) Optical microscope image of an exfoliated $\alpha\text{-TaFeTe}_4$ flake on a Si/SiO_2 substrate. The arrow highlights the bilayer flake imaged in (g). (g) AFM image of an exfoliated $\alpha\text{-TaFeTe}_4$ bilayer and height profile along a line cut (dashed white line) of the exfoliated $\alpha\text{-TaFeTe}_4$ flake. Panel (d and e) reprinted with permission from Belopolski, I., Yu, P., Sanchez, D. S., Ishida, Y., Chang, T.-R., Zhang, S. S., Xu, S.-Y., Zheng, H., Chang, G., Bian, G., Jeng, H.-T., Kondo, T., Lin, H., Liu, Z., Shin, S. & Hasan, M. Z. Signatures of a Time-Reversal Symmetric Weyl Semimetal With Only Four Weyl Points. *Nat. Commun.* **2017**, *8*, 942. © 2017. Panel (f and g) reprinted with permission from Wiscons, R. A., Cho, Y., Han, S. Y., Dismukes, A. H., Meirzadeh, E., Nuckolls, C., Berkelbach, T. C. & Roy, X. Polytypism, Anisotropic Transport, and Weyl Nodes in the van der Waals Metal TaFeTe_4 . *J. Am. Chem. Soc.* **2021**, *143*, 109–113. © American Chemical Society, 2021.

$1550 \text{ cm}^2\text{V}^{-1} \text{ s}^{-1}$ for holes and $2290 \text{ cm}^2\text{V}^{-1} \text{ s}^{-1}$ for electrons.³⁶⁰ In magnetic susceptibility this compound shows an atypical magnetic susceptibility with a decrease in susceptibility upon cooling before a significant increase below 14 K with no clear magnetic transition below 300 K.³⁶⁰ This magnetic order is thus posited to be antiferromagnetic with T_N above room temperature. This material has been exfoliated down to an 11-layer thickness and has shown to be robust in ambient conditions for 4 months.³⁶⁰

TaFeTe_3 is the only known mixed metal telluride with a $\text{M}:\text{M}':\text{Te}$ stoichiometry of 1:1:3. Non-stoichiometric $\text{TaFe}_{1+y}\text{Te}_3$ crystallizes into $\text{P2}_1/\text{m}$ in which the coordination of Fe is tetrahedral leading to a contraction in the double Fe polyhedra wide chain and shorter Fe-Fe distances than that of Fe-Ta (Fig. 35b).³⁶¹ The excess Fe occupies interstitial sites in the vdW space between layers. This material is metallic and orders antiferromagnetically between 160 and 200 K depending on the Fe content.³⁶² This material has also been explored to host a spin density wave transition.

Another family of three compounds is found at the further metal rich stoichiometry of $\text{MM}'\text{Te}_2$, where NbCoTe_2 , TaCoTe_2 , and NbFeTe_2 have been identified.^{363,364} These structures are built up from a significantly elongated honeycomb network of Nb/Ta

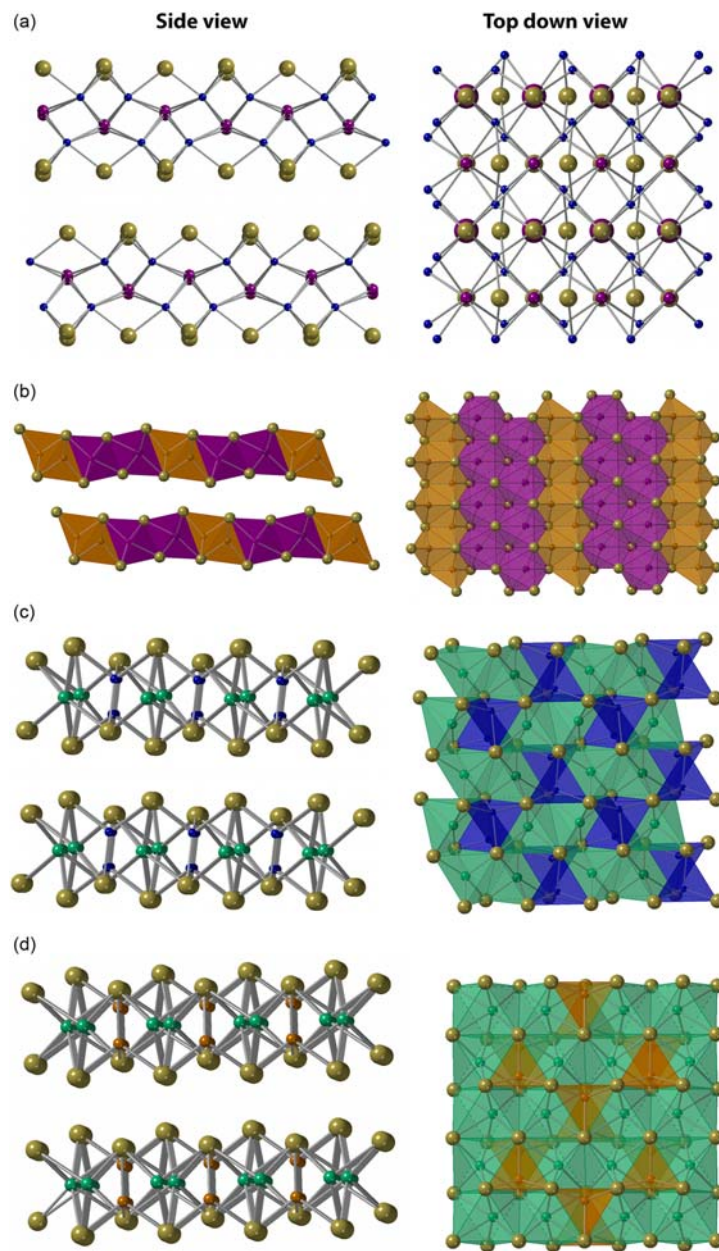


Fig. 35 Crystal structures from side and top view of (a) TaCo_2Te_2 , (b) TaFeTe_3 , (c) NbCoTe_2 , and (d) NbFeTe_2 . In all structures beige spheres correspond to Te atoms, purple spheres correspond to Ta atoms while green atoms correspond to Nb atoms and blue spheres correspond to Co atoms while orange spheres correspond to Fe atoms. In (a) only Co–Te and Co–Ta bonds are shown for simplicity, in the top-down view Ta atoms have been enlarged for illustrative purposes only. In (b–d) only metal–Te bonds are depicted.

atoms within each hexagon resides an Fe_2Te_6 dimer formed from two edge sharing tetrahedra. NbFeTe_2 crystallizes into Pnma with each Nb atom in a distorted geometry (Fig. 35c). In contrast NbCoTe_2 and TaCoTe_2 crystallize into $\text{P2}_1/\text{c}$ where one of the M–Te bonds is broken yielding a square pyramidal geometry (Fig. 35d). All of these materials are metallic, with TaFeTe_2 demonstrating spin glass behavior with $T_f = 44$ K and exhibits negative magnetoresistance of up to 1% at 14T while NbCoTe_2 is a Pauli paramagnet.^{363,365} The layer dependent properties of these novel stoichiometries have not yet been explored.

Finally, several mixed metal telluride phases form with a group 14 element (Si, Ge) substituted for the M' metal. For example, Nb_2SiTe_4 crystallizes into a monoclinic $\text{C2}/\text{c}$ structure that is formed from face sharing NbTe_6 trigonal prisms³⁶⁶ (Fig. 36a), albeit each Nb only has a 50% occupancy. The silicon atoms, which also have a 50% occupancy, reside in the middle of these shared faces forming square planar arrangements with tellurium atoms. Each NbTe_6 trigonal prism has 1/3rd of its faces capped by a Si atom. Nb_2SiTe_4 is semiconducting with a 0.39 eV band gap in the bulk and has been of interest as a photodetector in the mid IR.^{367,368} This material has also been exfoliated down to few layer thicknesses and shows stability in air on the order of hours,³⁶⁷ however the

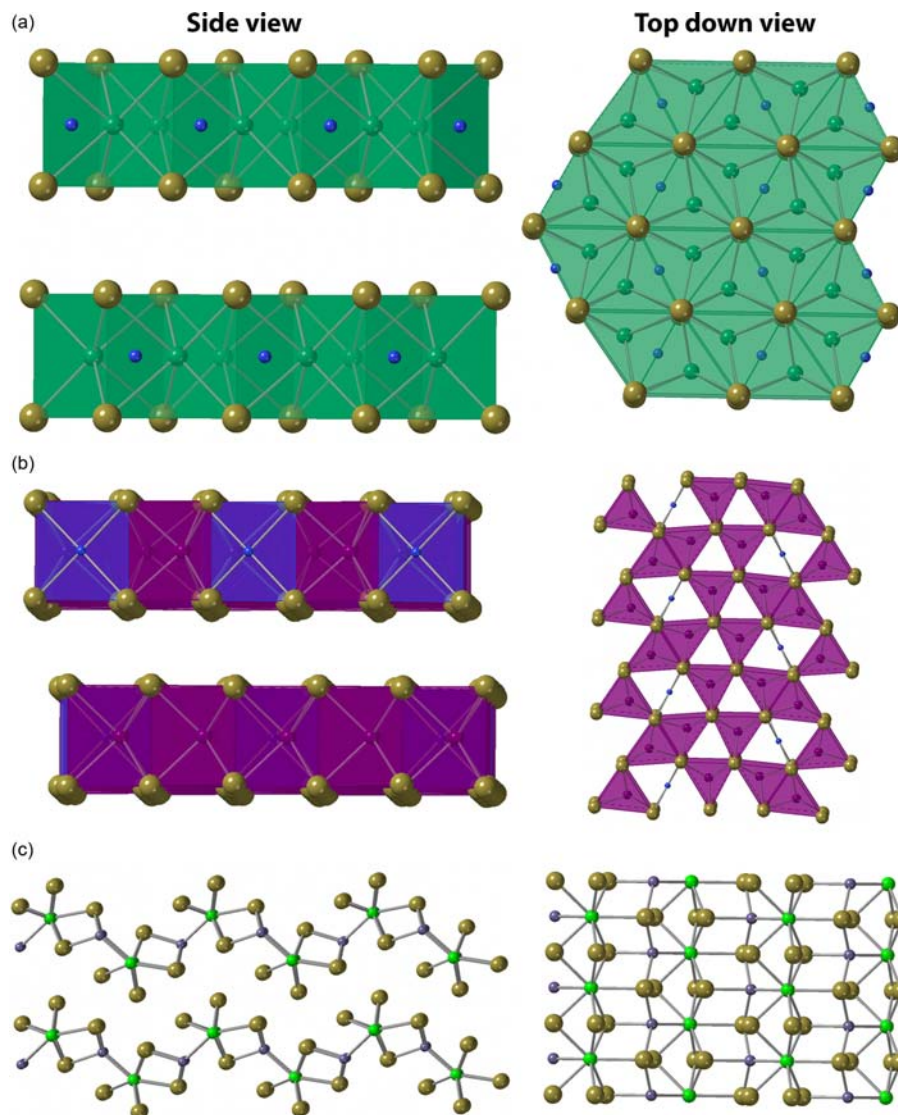


Fig. 36 Crystal structure from side and top view of (a) Nb_2SiTe_4 , (b) Ta_3SiTe_6 , and (c) ZrGeTe_4 . In all structures beige atoms correspond to Te, in (a) and (b) blue spheres correspond to Si atoms, in (c) purple spheres correspond to Ge. In (a) green spheres correspond to Nb atoms, in (b) purple atoms correspond to Ta atoms and in (c) bright green spheres correspond to Zr atoms. In (a), Nb_2SiTe_4 , the Nb and Si positions both have a 50% occupancy.

layer dependent properties have not yet been explored. Another set of compounds forms with a stoichiometry of $\text{M}_3\text{M}'\text{Te}_6$, where $\text{M} = \text{Nb}/\text{Ta}$ and $\text{M}' = \text{Si}/\text{Ge}$, and crystallize into a 2-layer orthorhombic Pnma unit cell (Fig. 36b). This structure is built up from $(\text{Nb}/\text{Ta})\text{Te}_6$ prisms that are connected together in both an edge-sharing and face-sharing network. Additionally, the Si/Ge atoms have fourfold coordination with Te, and are in fourfold coordination with the Nb atoms, leading to a distorted rectangular prism geometry.³⁶⁹ The Si members of this family are more well studied and have been predicted to be topological semimetals with hour-glass shaped Dirac dispersions in the bulk.³⁷⁰ Nb_3SiTe_6 has also been exfoliated down to the bilayer and novel 2D electron-electron interactions can be seen in an increase in resistivity at low temperatures (< 25 K) when the thickness is thinned to below 10 nm, while no exfoliation studies have been performed on the other materials in this family.³⁷¹ Thin flakes of this material are stable to ambient conditions on the order of weeks. A final family of 2D mixed metal tellurides, ZrGeTe_4 and HfGeTe_4 , crystallize into a $\text{Cmc}2_1$ space group where each vdW layer is characterized by alternating Zr/Hf and Ge chains (Fig. 36c).³⁷² The Zr/Hf atoms form bicapped trigonal prisms where one face is capped by germanium, all the other bonds are Te. The Ge is in tetrahedral coordination to three Te atom one Zr/Hf atom. These compounds are narrow gapped semiconductors with an indirect band gap of 0.5 eV in ZrGeTe_4 ³⁷³ and 0.18 eV in HfGeTe_4 ³⁷² and have been explored as near IR photodetectors. ZrGeTe_4 has been exfoliated down to thicknesses from 100 to 300 nm and is air sensitive in both bulk and after exfoliation to the few-layer regime.³⁷³

4.14.4.9 The metal chalcogenides (MChX) and group 4 metal nitrohalides (MNX)

The metal chalcogenides MChX where Ch = O, S and X = Cl, Br, I form with a wide variety of trivalent metal cations and have attracted interest as semiconducting 2D magnets. These compounds crystallize into the FeOCl structure type which is comprised of a rectangular network of MCh_4X_2 distorted octahedra (Fig. 37a). The M and Ch atoms form a rectangular network that buckles along one of the in-plane directions. The halogen atoms cap the M-Ch network above and below the layers, and bridge two neighboring M atoms within each layer. The interlayer vdW interactions occur between these halogen atoms. Three separate groups of trivalent cations form layered vdW compounds in the FeOCl structure type, trivalent first row transition metals (M = Sc, Ti, V, Cr, Fe), group 13 triel elements (M = Al, In), and trivalent late lanthanides (M = Gd-Lu).³⁷⁴ The first row transition metals form almost exclusively with Ch = O with the exception of CrSBr. Of the triel metals, only AlOCl, InOCl, and InOBr are known. The third family of trivalent cations to form this 2D vdW structure are late lanthanides (Gd-Lu) in which the MSI sulfiodides are the most well-known but ErSeI and DySBr are also known analogs.³⁷⁵ The titanium nitrohalides with stoichiometry $TiNX$, (X = Cl, Br, I) also crystallize into this structure type. In these compounds, the replacement of the trivalent metal with a tetravalent metal is counterbalanced by the substitution of a divalent chalcogen anion with the trivalent nitride.

A small number of metal chalcogenides and metal nitrohalides with larger metal radii (YbOCl, SmSI, ZrNX, and HfNX where X = Cl, Br, I) crystallize into the closely related SmSI structure type (Fig. 37b). These compounds consist of two-atom thick puckered honeycomb networks of alternating M and N or S atoms. The N or S atoms are in tetrahedral coordination with the metal atoms, which pucker outward and are each terminated with three halogens. This causes each metal to have a sevenfold coordination of $M(Ch/N)_4X_3$, in a capped octahedral coordination geometry.

The first-row transition metal derivatives of this structure type are the most well studied compounds with this stoichiometry and have been investigated for their electronic and magnetic properties. These compounds are all Mott insulators with gaps of 1–2 eV^{376–380} despite variable d-electron counts. The strong 180° super exchange coupling seen along the M-O-M axis dominates across all these compounds leading to strong antiferromagnetic coupling. Despite this, in TiOX at the ordering temperature, 67 K in TiOCl and 27 K in TiOBr, a spin-Peierls transition is seen where the $Ti^{3+} d^1$ ions dimerize along the flat in plane direction. Upon further cycling of temperature an incommensurate transition phase of incomplete Peierls distortion is seen between 67 and 91 K in TiOCl.^{381,382} With an even d electron count, VOCl d^2 is a collinear antiferromagnet below T_N of 80 K.³⁸³ CrOCl and CrOBr are low temperature antiferromagnets with a T_N of 13.6 K in CrOCl with a monoclinic distortion.^{376,384} In contrast CrSBr has a bulk antiferromagnetic transition of 132 K.³⁸⁵ Finally FeOCl is a bulk antiferromagnet at 92 K.³⁸⁶ CrSBr has been extensively studied and

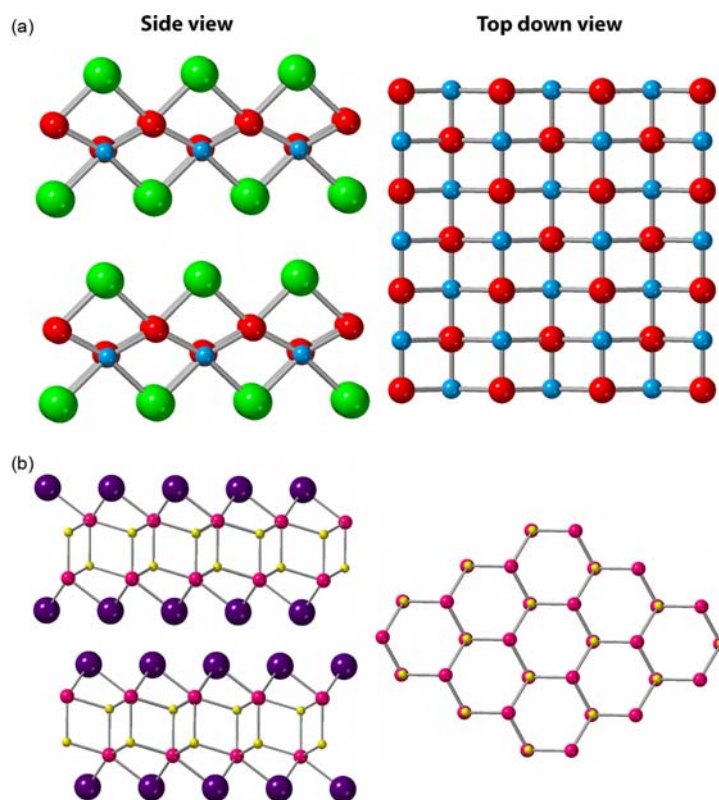


Fig. 37 Crystal structure of (a) AlOCl (FeOCl-type) and (b) SmSI (SmSI-type) in the side view and top-down view. In (a) blue spheres correspond to Al atoms, red spheres represent O atoms, and green spheres correspond to Cl atoms. In (b) pink spheres correspond to Sm atoms, yellow spheres correspond to S atoms, and purple spheres correspond to I atoms.

shows, surprisingly, an increasing transition temperature upon exfoliation with an antiferromagnetic transition of 149 K in the bilayer. This was determined by the presence of second harmonic generation upon breaking inversion symmetry in the antiferromagnetic state.³⁸⁷ The monolayer is reported to be ferromagnetic. FeOCl has also been exfoliated to the bilayer but the magnetic properties of isolated layers have not yet been measured due to the moisture sensitivity of thin flakes.³⁸⁸ AlOCl has been explored as a catalyst for ethyl and vinyl polymerization,³⁸⁹ and InOCl has been investigated as a gas sensor for formaldehyde.³⁹⁰ Thin films of the triel atom compounds have not been explored. The lanthanide derivatives are low temperature magnets with FM transitions below 15 K in TbSI, DySI, HoSI and antiferromagnetic transitions below 10 K in GdSI, ErSI, TmSI, and YbSI.³⁷⁴ In the SmSI structure type, the MNX family of compounds are d^0 wide band gap semiconductors,³⁹¹ with ZrNCl having a bulk band gap of 2.6 eV that increases to 3.3 eV below a thickness of 4 layers.³⁹² SmSI has been proposed as a Kitaev spin liquid with no magnetic ordering seen above 1.8 K.³⁹³

4.14.4.10 A ternary main group compound, GaGeTe

GaGeTe is a structurally unique 2D vdW material, that is built from an inner layer of Ge atoms in a buckled honeycomb lattice which is terminated by corner sharing GaTe₃ trigonal pyramids (Fig. 38). This material is p-type semiconductor in the bulk with an optical band gap of 1.12 eV.³⁹⁴ The material has been exfoliated down to the few layer, 6.4 nm, and retains the air stability of the bulk.³⁹⁵ However, the properties of exfoliated samples have not yet been extensively experimentally explored.

4.14.4.11 Alloys of van der Waals compounds

Many of these families of 2D materials can be modified by alloying multiple atoms onto a single Wyckoff position of the original lattice. These materials are site disordered alloys having the same structure as the parent material but with fractional occupancy of the alloy atom. The most well studied family of 2D vdW alloys are the TMDs, where a magnetic first row transition metal (V, Cr, Mn, Fe, Co, Ni) is substituted on the metal site of the lattice. This method of alloying has been shown in multiple examples, such as substituting $\leq 10\%$ Mn, Fe, Co, and Ni onto MoS₂, and substituting V into both WS₂ (12%) and WSe₂ (9%).^{396–399} The low levels of substitution in these compounds yields dilute magnetic semiconductors as seen in Mn_{0.03}Mo_{0.97}S₂ where $T_C = 350$ K but the magnetization of 1.06 μB per Mn atom is indicative of a fractional spin system with localized spins.⁴⁰⁰ This alloying has also been shown to persist down to the atomic limit where $\sim 2\%$ Fe has been alloyed into monolayers of MoS₂ and SnS₂.⁴⁰¹ One significant exception to the limited extent of alloying is the metallic Cr_xPt_{1-x}Te₂ system where single phases up to $x = 0.45$ are seen.⁴⁰² In Cr_{0.45}Pt_{0.55}Te₂, a T_C of 220 K is seen in the bulk with a magnetization of 2.37 μB per Cr atom, from both localized and itinerant spins. This material has been shown to be air stable in both single crystal and few layer forms due to the minimal propensity of Pt to form oxides. Beyond the TMD family, successful alloying has been confirmed in the Xanes where in GeH, up to 9% of the Ge atoms can be substituted with Sn atoms with concomitant introduction of OH groups capping Sn atoms. This substitution can be used to tune the band gap from 1.59 in GeH to 1.38 in Ge_{0.91}Sn_{0.09}H_{0.91}(OH)_{0.09}, however upon the incorporation of Sn into the structure the air stability of GeH is destroyed.¹⁵⁸ One final example is in septuple layer anti-tetradymite Sn₄As₃, where up to $\frac{1}{4}$ of the Sn atoms can be substituted with Pb.²⁸⁰

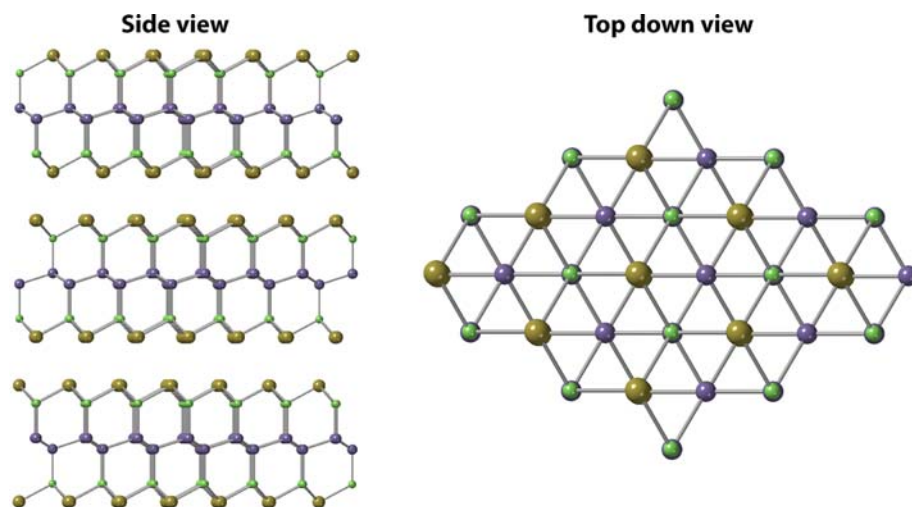


Fig. 38 Crystal structure of GaGeTe from side and top-down view. Green spheres correspond to Ga atoms, purple spheres correspond to Ge atoms and beige spheres correspond to Te atoms.

4.14.4.12 Intercalated 2D vdW materials

Van der Waals compounds inherently have void spaces in the gap between neighboring layers where a wide variety of chemical species can be introduced and form stable and distinct species. This incorporation of ions into the vdW gap is referred to as intercalation and has been extensively reviewed.^{403–408} It is of paramount importance for fine tuning electronic structure, and for a wide variety of properties and applications. For instance, the Nobel prize winning work by Stan Whittingham on the exploration of Li battery anodes initially focused on the reversible intercalation and deintercalation of Li atoms into TiS_2 .⁴⁰⁹

The intercalation of species into the vdW gap can lead to significant changes in the structure and properties. This is due to the fact that the intercalation of many chemical species is often accompanied with a reduction or oxidation of the 2D material. For instance, the intercalation of Li^+ into the vdW gap requires the framework to be reduced by one electron to maintain charge neutrality. One such example of a structural change is seen in the lithium intercalation of MoS_2 , in which the additional electron reduces molybdenum from Mo^{4+} (d^2) to Mo^{3+} (d^3). This reduction results in a structural transition from the 2H polytype in MoS_2 consisting of MoS_6 trigonal prisms to the 1T polytype consisting of MoS_6 octahedra.⁴¹⁰ A second structural change is seen upon intercalating $\text{Fe}_{2.76}\text{GeTe}_2$ with Na in which a metastable structure is formed. Above 100 °C it decomposes to form Na_2Te and various Fe_{2-x}Ge phases, increasing the measured magnetic transition temperature.³³⁴ Occasionally, the altered 2D framework can be retained through a low temperature deintercalation step, stabilizing these metastable structures. For instance, the 1T MoS_2 polytype can be stabilized by washing away Li in water from 1T-Li MoS_2 . These structural transitions can also be used to modulate the electronic properties, for example, the 2H MoS_2 is semiconducting due to the crystal field splitting of a trigonal prism, while both the d^3 1T-Li MoS_2 and the deintercalated d^2 1T- MoS_2 are metallic, as would be expected. As another example, intercalating metallic 2H-NbSe₂ with lithium causes a band gap to open up, as Nb is reduced from Nb^{4+} (d^1) to Nb^{3+} (d^2).¹⁹² Intercalation can also lead to the creation of superconducting phases such as in $\text{Mg}_{0.8}\text{ZrNCl}$ which has a superconducting transition temperature of 15 K,^{411,412} or in Cu_xTiSe_2 which has a transition of 4.15 K.⁴¹³ Superconductivity can also emerge upon intercalation of exfoliated 2D materials. The intercalation of bilayer graphene with Ca or Yb induces a superconducting phase transition to occur at 11.5 and 6.5 K, respectively.⁴¹⁴

The magnetic properties of these materials can also be modulated by introducing magnetic intercalant atoms such as in Fe-intercalated TaS_2 , $\text{Fe}_{0.25}\text{TaS}_2$, which undergoes a ferromagnetic transition at 160 K in the bulk.⁴¹⁵ Magnetism can also be introduced by the intercalation of magnetic compounds, for example, 2D FeCl_3 can be intercalated into bulk and thin film form of graphite in which the 2D nature of FeCl_3 is retained in the Fe atom lattice, however the Cl lattice is disordered due to significant lattice mismatch between FeCl_3 and graphene.^{416,417} In few layer graphene this leads to antiferromagnetic ordering in 2D at 30 K and in 3D at 3.8 K.^{418,419} Finally, intercalated 2D vdW materials have been explored in energy storage applications where cations can be reversibly intercalated and deintercalated providing a source of mobile charges. Two examples are the potassium intercalation of both graphene to form KC_8 which reaches a specific capacity of 273 mAh g^{-1} ⁴²⁰ for battery applications and MXene $\text{Ti}_3\text{C}_2\text{T}_2$ a capacitance of 500 F g^{-1} .⁴²¹

4.14.5 Conclusions

There are an incredible number of 2D vdW materials across the periodic table that have been discovered over the past century of inorganic and materials chemistry research. The cornucopia of fascinating phenomena and properties of these materials includes superconductivity, magnetism, goniopolarity, exciton insulators, and topological materials. The steady evolution of exfoliation techniques have improved to the point that complex heterostructures and devices can be designed at will from monolayers that combine a multitude of different 2D vdW materials. Further research into the layer-dependent properties of many families have yet to be explored and are likely to yield new surprises. The diversity of compounds combined with their ability to be restacked give chemists exquisite control over the arrangements of atoms on a small scale, leading to “an enormously greater range of possible properties that substances can have, and of different things that we can do.”⁷

References

- Novoselov, K. S.; Geim, A. K.; Morozov, S. V.; Jiang, D.; Katsnelson, M. I.; Grigorieva, I. V.; Dubonos, S. V.; Firsov, A. A. Two-Dimensional Gas of Massless Dirac Fermions in Graphene. *Nature* **2005**, *438*, 197–200.
- Novoselov, K. S.; Geim, A. K.; Morozov, S. V.; Jiang, D.; Zhang, Y.; Dubonos, S. V.; Grigorieva, I. V.; Firsov, A. A. Electric Field Effect in Atomically Thin Carbon Films. *Science* **2004**, *306*, 666.
- Castilla, S.; Vangelidis, I.; Pusapati, V.-V.; Goldstein, J.; Autore, M.; Slipchenko, T.; Rajendran, K.; Kim, S.; Watanabe, K.; Taniguchi, T.; Martín-Moreno, L.; Englund, D.; Tielrooij, K.-J.; Hillenbrand, R.; Lidorikis, E.; Koppens, F. H. L. Plasmonic Antenna Coupling to Hyperbolic Phonon-Polaritons for Sensitive and Fast Mid-Infrared Photodetection With Graphene. *Nat. Commun.* **2020**, *11*, 4872.
- Foley, T.; Diamante, L.; Waters, R.; Gomollón-Bel, F. In *Annual Report 2020*; Foley, T., Ed., Graphene Flagship, 2021.
- Poletti, F.; Scidà, A.; Zanfagnini, B.; Kovtun, A.; Parkula, V.; Favaretto, L.; Melucci, M.; Palermo, V.; Treossi, E.; Zanardi, C. Graphene-Paper-Based Electrodes on Plastic and Textile Supports as New Platforms for Amperometric Biosensing. *Adv. Funct. Mater.* **2022**, *32*, 2107941.
- Zhou, X.; Leng, T.; Pan, K.; Abdalla, M.; Novoselov, K. S.; Hu, Z. Conformal Screen Printed Graphene 4×4 Wideband MIMO Antenna on Flexible Substrate for 5G Communication and IoT Applications. *2D Mater.* **2021**, *8*, 045021.
- Feynman, R. P. *There's Plenty of Room at the Bottom. Annual Meeting of the American Physical Society, December 29, 1959*, California Institute of Technology, 1959.

8. Butler, S. Z.; Hollen, S. M.; Cao, L.; Cui, Y.; Gupta, J. A.; Gutiérrez, H. R.; Heinz, T. F.; Hong, S. S.; Huang, J.; Ismach, A. F.; Johnston-Halperin, E.; Kuno, M.; Plashnitsa, V. V.; Robinson, R. D.; Ruoff, R. S.; Salahuddin, S.; Shan, J.; Shi, L.; Spencer, M. G.; Terrones, M.; Windl, W.; Goldberg, J. E. Progress, Challenges, and Opportunities in Two-Dimensional Materials Beyond Graphene. *ACS Nano* **2013**, *7*, 2898–2926.
9. Liu, X.; Li, Q.; Ruan, Q.; Rahn, M. S.; Yakobson, B. I.; Hersam, M. C. Borophene Synthesis Beyond the Single-Atomic-Layer Limit. *Nat. Mater.* **2022**, *21*, 35–40.
10. Frisenda, R.; Niu, Y.; Gant, P.; Muñoz, M.; Castellanos-Gomez, A. Naturally occurring van der Waals materials. *NPJ 2D Mater. Appl.* **2020**, *4*, 38.
11. Savjani, N.; Lewis, E. A.; Patrick, R. A. D.; Haigh, S. J.; O'Brien, P. MoS₂ Nanosheet Production by the Direct Exfoliation of Molybdenite Minerals From Several Type-Localities. *RSC Adv.* **2014**, *4*, 35609–35613.
12. Zhao, W.; Jiang, T.; Shan, Y.; Ding, H.; Shi, J.; Chu, H.; Lu, A. Direct Exfoliation of Natural SiO₂-Containing Molybdenite in Isopropanol: A Cost Efficient Solution for Large-Scale Production of MoS₂ Nanosheets. *Nanomaterials* **2018**, *8*, 843. 30336546 PMC6215130.
13. Cai, Z.; Liu, B.; Zou, X.; Cheng, H.-M. Chemical Vapor Deposition Growth and Applications of Two-Dimensional Materials and Their Heterostructures. *Chem. Rev.* **2018**, *118*, 6091–6133.
14. Liu, C.; Wang, L.; Qi, J.; Liu, K. Designed Growth of Large-Size 2D Single Crystals. *Adv. Mater.* **2020**, *32*, 2000046.
15. Mannix, A. J.; Kiraly, B.; Hersam, M. C.; Guisinger, N. P. Synthesis and Chemistry of Elemental 2D Materials. *Nat. Rev. Chem.* **2017**, *1*, 0014.
16. May, A. F.; Yan, J.; Mcquire, M. A. A Practical Guide for Crystal Growth of van der Waals Layered Materials. *J. Appl. Phys.* **2020**, *128*, 051101.
17. Kanatzidis, M. G.; Pöttgen, R.; Jeitschko, W. The Metal Flux: A Preparative Tool for the Exploration of Intermetallic Compounds. *Angew. Chem. Int. Ed.* **2005**, *44*, 6996–7023.
18. Shcherbakov, D.; Stepanov, P.; Weber, D.; Wang, Y.; Hu, J.; Zhu, Y.; Watanabe, K.; Taniguchi, T.; Mao, Z.; Windl, W.; Goldberg, J.; Bockrath, M.; Lau, C. N. Raman Spectroscopy, Photocatalytic Degradation, and Stabilization of Atomically Thin Chromium Tri-iodide. *Nano Lett.* **2018**, *18*, 4214–4219.
19. Huang, Y.; Pan, Y.-H.; Yang, R.; Bao, L.-H.; Meng, L.; Luo, H.-L.; Cai, Y.-Q.; Liu, G.-D.; Zhao, W.-J.; Zhou, Z.; Wu, L.-M.; Zhu, Z.-L.; Huang, M.; Liu, L.-W.; Liu, L.; Cheng, P.; Wu, K.-H.; Tian, S.-B.; Gu, C.-Z.; Shi, Y.-G.; Guo, Y.-F.; Cheng, Z. G.; Hu, J.-P.; Zhao, L.; Yang, G.-H.; Sutter, E.; Sutter, P.; Wang, Y.-L.; Ji, W.; Zhou, X.-J.; Gao, H.-J. Universal Mechanical Exfoliation of Large-Area 2D Crystals. *Nat. Commun.* **2020**, *11*, 2453.
20. Bianco, E.; Butler, S.; Jiang, S.; Restrepo, O. D.; Windl, W.; Goldberg, J. E. Stability and Exfoliation of Germanane: A Germanium Graphene Analogue. *ACS Nano* **2013**, *7*, 4414–4421.
21. Arguilla, M. Q.; Katoch, J.; Krymowski, K.; Cultrara, N. D.; Xu, J.; Xi, X.; Hanks, A.; Jiang, S.; Ross, R. D.; Koch, R. J.; Ulstrup, S.; Bostwick, A.; Jozwiak, C.; McComb, D. W.; Rotenberg, E.; Shan, J.; Windl, W.; Kawakami, R. K.; Goldberg, J. E. NaSn₂As₂: An Exfoliatable Layered van der Waals Zintl Phase. *ACS Nano* **2016**, *10*, 9500–9508.
22. Frindt, R. F. Single Crystals of MoS₂ Several Molecular Layers Thick. *J. Appl. Phys.* **1966**, *37*, 1928–1929.
23. Huang, Y.; Sutter, E.; Shi, N. N.; Zheng, J.; Yang, T.; Englund, D.; Gao, H.-J.; Sutter, P. Reliable Exfoliation of Large-Area High-Quality Flakes of Graphene and Other Two-Dimensional Materials. *ACS Nano* **2015**, *9*, 10612–10620.
24. Kang, K.; Lee, K.-H.; Han, Y.; Gao, H.; Xie, S.; Muller, D. A.; Park, J. Layer-by-Layer Assembly of Two-Dimensional Materials Into Wafer-Scale Heterostructures. *Nature* **2017**, *550*, 229–233.
25. Liu, F.; Wu, W.; Bai, Y.; Chae, S. H.; Li, Q.; Wang, J.; Hone, J.; Zhu, X. Y. Disassembling 2D van der Waals Crystals Into Macroscopic Monolayers and Reassembling Into Artificial Lattices. *Science* **2020**, *367*, 903–906.
26. Cai, X.; Luo, Y.; Liu, B.; Cheng, H.-M. Preparation of 2D Material Dispersions and Their Applications. *Chem. Soc. Rev.* **2018**, *47*, 6224–6266.
27. Coleman, J. N.; Lotya, M.; O'Neill, A.; Bergin, S. D.; King, P. J.; Khan, U.; Young, K.; Gaucher, A.; De, S.; Smith, R. J.; Shvets, I. V.; Arora, S. K.; Stanton, G.; Kim, H.-Y.; Lee, K.; Kim, G. T.; Duesberg, G. S.; Hallam, T.; Boland, J. J.; Wang, J. J.; Donegan, J. F.; Grunlan, J. C.; Moriarty, G.; Shmeliov, A.; Nicholls, R. J.; Perkins, J. M.; Grievson, E. M.; Theuwissen, K.; McComb, D. W.; Nellist, P. D.; Nicolosi, V. Two-Dimensional Nanosheets Produced by Liquid Exfoliation of Layered Materials. *Science* **2011**, *331*, 568–571.
28. Hu, C.-X.; Shin, Y.; Read, O.; Casiraghi, C. Dispersant-Assisted Liquid-Phase Exfoliation of 2D Materials Beyond Graphene. *Nanoscale* **2021**, *13*, 460–484.
29. Nicolosi, V.; Chhowalla, M.; Kanatzidis, M. G.; Strano, M. S.; Coleman, J. N. Liquid Exfoliation of Layered Materials. *Science* **2013**, *340*, 1226419.
30. Tao, H.; Zhang, Y.; Gao, Y.; Sun, Z.; Yan, C.; Texter, J. Scalable Exfoliation and Dispersion of Two-Dimensional Materials—An Update. *Phys. Chem. Chem. Phys.* **2017**, *19*, 921–960.
31. Jena, N. K.; Araujo, R. B.; Shukla, V.; Ahuja, R. Borophene as a Benchmark of Graphene: A Potential 2D Material for Anode of Li and Na-Ion Batteries. *ACS Appl. Mater. Interfaces* **2017**, *9*, 16148–16158.
32. Mukherjee, S.; Ren, Z.; Singh, G. Beyond Graphene Anode Materials for Emerging Metal Ion Batteries and Supercapacitors. *Nano-Micro Lett.* **2018**, *10*, 70.
33. Acerce, M.; Voiry, D.; Chhowalla, M. Metallic 1T phase MoS₂ Nanosheets as Supercapacitor Electrode Materials. *Nat. Nanotechnol.* **2015**, *10*, 313–318.
34. Feng, J.; Sun, X.; Wu, C.; Peng, L.; Lin, C.; Hu, S.; Yang, J.; Xie, Y. Metallic Few-Layered VS₂ Ultrathin Nanosheets: High Two-Dimensional Conductivity for In-Plane Supercapacitors. *J. Am. Chem. Soc.* **2011**, *133*, 17832–17838.
35. Zhang, X.; Hou, L.; Ciesielski, A.; Samorì, P. 2D Materials Beyond Graphene for High-Performance Energy Storage Applications. *Adv. Energy Mater.* **2016**, *6*, 1600671.
36. Li, H.; Ko, T.-J.; Lee, M.; Chung, H.-S.; Han, S. S.; Oh, K. H.; Sadmani, A.; Kang, H.; Jung, Y. Experimental Realization of Few Layer Two-Dimensional MoS₂ Membranes of Near Atomic Thickness for High Efficiency Water Desalination. *Nano Lett.* **2019**, *19*, 5194–5204.
37. Safaei, J.; Xiong, P.; Wang, G. Progress and Prospects of Two-Dimensional Materials for Membrane-Based Water Desalination. *Mater. Today Adv.* **2020**, *8*, 100108.
38. You, Y.; Sahajwalla, V.; Yoshimura, M.; Joshi, R. K. Graphene and Graphene Oxide for Desalination. *Nanoscale* **2016**, *8*, 117–119.
39. Perez-Page, M.; Sahoo, M.; Holmes, S. M. Single Layer 2D Crystals for Electrochemical Applications of Ion Exchange Membranes and Hydrogen Evolution Catalysts. *Adv. Mater. Interfaces* **2019**, *6*, 1801838.
40. Zheng, Z.; Grünkler, R.; Feng, X. Synthetic Two-Dimensional Materials: A New Paradigm of Membranes for Ultimate Separation. *Adv. Mater.* **2016**, *28*, 6529–6545.
41. Li, H.; Jing, L.; Liu, W.; Lin, J.; Tay, R. Y.; Tsang, S. H.; Teo, E. H. T. Scalable Production of Few-Layer Boron Sheets by Liquid-Phase Exfoliation and Their Superior Supercapacitive Performance. *ACS Nano* **2018**, *12*, 1262–1272.
42. Hansen, C. M. *Hansen Solubility Parameters: A User's Handbook*, CRC Press: Boca Raton, FL, 2007.
43. Smith, R. J.; King, P. J.; Lotya, M.; Wirtz, C.; Khan, U.; De, S.; O'Neill, A.; Duesberg, G. S.; Grunlan, J. C.; Moriarty, G.; Chen, J.; Wang, J.; Minett, A. I.; Nicolosi, V.; Coleman, J. N. Large-Scale Exfoliation of Inorganic Layered Compounds in Aqueous Surfactant Solutions. *Adv. Mater.* **2011**, *23*, 3944–3948.
44. Kharisova, O. V.; Kharisov, B. I.; De Casas Ortiz, E. G. Dispersion of Carbon Nanotubes in Water and Non-Aqueous Solvents. *RSC Adv.* **2013**, *3*, 24812–24852.
45. Hummers, W. S.; Offeman, R. E. Preparation of Graphitic Oxide. *J. Am. Chem. Soc.* **1958**, *80*, 1339.
46. Kim, S. Y.; Kim, S.-I.; Kim, M. K.; Kim, J.; Mizusaki, S.; Ko, D.-S.; Jung, C.; Yun, D.-J.; Roh, J. W.; Kim, H.-S.; Sohn, H.; Lim, J.-H.; Oh, J.-M.; Jeong, H. M.; Shin, W. H. Ultrasonic Assisted Exfoliation for Efficient Production of RuO₂ Monolayer Nanosheets. *Inorg. Chem. Front.* **2021**, *8*, 4482–4487.
47. Ma, R.; Sasaki, T. Nanosheets of Oxides and Hydroxides: Ultimate 2D Charge-Bearing Functional Crystallites. *Adv. Mater.* **2010**, *22*, 5082–5104.
48. Tanaka, T.; Ebina, Y.; Takada, K.; Kurashima, K.; Sasaki, T. Oversized Titania Nanosheet Crystallites Derived from Flux-Grown Layered Titanate Single Crystals. *Chem. Mater.* **2003**, *15*, 3564–3568.
49. Peng, J.; Liu, Y.; Lv, H.; Li, Y.; Lin, Y.; Su, Y.; Wu, J.; Liu, H.; Guo, Y.; Zhuo, Z.; Wu, X.; Wu, C.; Xie, Y. Stoichiometric Two-Dimensional Non-van der Waals AgCrS₂ With Superionic Behaviour at Room Temperature. *Nat. Chem.* **2021**, *13*, 1235–1240.
50. Ma, R.; Liu, Z.; Li, L.; Iyi, N.; Sasaki, T. Exfoliating Layered Double Hydroxides in Formamide: A Method to Obtain Positively Charged Nanosheets. *J. Mater. Chem.* **2006**, *16*, 3809–3813.
51. Koma, A. Van der Waals Epitaxy—A New Epitaxial Growth Method for a Highly Lattice-Mismatched System. *Thin Solid Films* **1992**, *216*, 72–76.
52. Xu, X.; Guo, T.; Kim, H.; Hota, M. K.; Alsaadi, R. S.; Lanza, M.; Zhang, X.; Alshareef, H. N. Growth of 2D Materials at the Wafer Scale. *Adv. Mater.* **2021**, *34*, 2108258.

53. Briggs, N.; Subramanian, S.; Lin, Z.; Li, X.; Zhang, X.; Zhang, K.; Xiao, K.; Geoghegan, D.; Wallace, R.; Chen, L.-Q.; Terrones, M.; Ebrahimi, A.; Das, S.; Redwing, J.; Hinkle, C.; Momeni, K.; Van Duin, A.; Crespi, V.; Kar, S.; Robinson, J. A. A Roadmap for Electronic Grade 2D Materials. *2D Mater.* **2019**, *6*, 022001.
54. Li, B.; Wan, Z.; Wang, C.; Chen, P.; Huang, B.; Cheng, X.; Qian, Q.; Li, J.; Zhang, Z.; Sun, G.; Zhao, B.; Ma, H.; Wu, R.; Wei, Z.; Liu, Y.; Liao, L.; Ye, Y.; Huang, Y.; Xu, X.; Duan, X.; Ji, W.; Duan, X. Van der Waals Epitaxial Growth of Air-Stable CrSe₂ Nanosheets With Thickness-Tunable Magnetic Order. *Nat. Mater.* **2021**, *20*, 818–825.
55. Liu, Z.-L.; Wu, X.; Shao, Y.; Qi, J.; Cao, Y.; Huang, L.; Liu, C.; Wang, J.-O.; Zheng, Q.; Zhu, Z.-L.; Ibrahim, K.; Wang, Y.-L.; Gao, H.-J. Epitaxially grown Monolayer VSe₂: An Air-Stable Magnetic Two-Dimensional Material With Low Work Function at Edges. *Sci. Bull.* **2018**, *63*, 419–425.
56. Yu, H.; Liao, M.; Zhao, W.; Liu, G.; Zhou, X. J.; Wei, Z.; Xu, X.; Liu, K.; Hu, Z.; Deng, K.; Zhou, S.; Shi, J.-A.; Gu, L.; Shen, C.; Zhang, T.; Du, L.; Xie, L.; Zhu, J.; Chen, W.; Yang, R.; Shi, D.; Zhang, G. Wafer-Scale Growth and Transfer of Highly-Oriented Monolayer MoS₂ Continuous Films. *ACS Nano* **2017**, *11*, 12001–12007.
57. Yu, Y.; Li, C.; Liu, Y.; Su, L.; Zhang, Y.; Cao, L. Controlled Scalable Synthesis of Uniform, High-Quality Monolayer and Few-layer MoS₂ Films. *Sci. Rep.* **2013**, *3*, 1866.
58. Wang, X.; Gong, Y.; Shi, G.; Chow, W. L.; Keyshar, K.; Ye, G.; Vajtai, R.; Lou, J.; Liu, Z.; Ringe, E.; Tay, B. K.; Ajayan, P. M. Chemical Vapor Deposition Growth of Crystalline Monolayer MoSe₂. *ACS Nano* **2014**, *8*, 5125–5131.
59. Shi, J.; Wang, X.; Zhang, S.; Xiao, L.; Huan, Y.; Gong, Y.; Zhang, Z.; Li, Y.; Zhou, X.; Hong, M.; Fang, Q.; Zhang, Q.; Liu, X.; Gu, L.; Liu, Z.; Zhang, Y. Two-Dimensional Metallic Tantalum Disulfide as a Hydrogen Evolution Catalyst. *Nat. Commun.* **2017**, *8*, 958.
60. Okada, M.; Sawazaki, T.; Watanabe, K.; Taniguchi, T.; Hibino, H.; Shinohara, H.; Kitaura, R. Direct Chemical Vapor Deposition Growth of WS₂ Atomic Layers on Hexagonal Boron Nitride. *ACS Nano* **2014**, *8*, 8273–8277.
61. Gong, Y.; Lin, Z.; Chen, Y.-X.; Khan, Q.; Wang, C.; Zhang, B.; Nie, G.; Xie, N.; Li, D. Two-Dimensional Platinum Diselenide: Synthesis, Emerging Applications, and Future Challenges. *Nano-Micro Lett.* **2020**, *12*, 174.
62. Ahmed, K.; Dahal, R.; Weltz, A.; Lu, J. Q.; Danon, Y.; Bhat, I. B. Growth of Hexagonal Boron Nitride on (111) Si for Deep UV Photonics and Thermal Neutron Detection. *Appl. Phys. Lett.* **2016**, *109*, 113501.
63. Park, K.; Kim, Y.; Song, J.-G.; Kim, S. J.; Wan, L. C.; Hee, R. G.; Lee, Z.; Park, J.; Kim, H. Uniform, Large-Area Self-Limiting Layer Synthesis of Tungsten Diselenide. *2D Mater.* **2016**, *3*, 014004.
64. Poh, S. M.; Tan, S. J. R.; Wang, H.; Song, P.; Abidi, I. H.; Zhao, X.; Dan, J.; Chen, J.; Luo, Z.; Pennycook, S. J.; Castro Neto, A. H.; Loh, K. P. Molecular-Beam Epitaxy of Two-Dimensional In₂Se₃ and Its Giant Electroresistance Switching in Ferroresistive Memory Junction. *Nano Lett.* **2018**, *18*, 6340–6346.
65. Li, M.-Y.; Shi, Y.; Cheng, C.-C.; Lu, L.-S.; Lin, Y.-C.; Tang, H.-L.; Tsai, M.-L.; Chu, C.-W.; Wei, K.-H.; He, J.-H.; Chang, W.-H.; Suenaga, K.; Li, L.-J. Epitaxial Growth of a Monolayer WSe₂-MoS₂ Lateral p-n Junction With an Atomically Sharp Interface. *Science* **2015**, *349*, 524–528.
66. Zhang, R.; Li, M.; Li, L.; Wei, Z.; Jiao, F.; Geng, D.; Hu, W. The More, the Better—Recent Advances in Construction of 2D Multi-Heterostructures. *Adv. Funct. Mater.* **2021**, *31*, 2102049.
67. Zhang, X.-Q.; Lin, C.-H.; Tseng, Y.-W.; Huang, K.-H.; Lee, Y.-H. Synthesis of Lateral Heterostructures of Semiconducting Atomic Layers. *Nano Lett.* **2015**, *15*, 410–415.
68. Zhang, Y.; Yin, L.; Chu, J.; Shifa, T. A.; Xia, J.; Wang, F.; Wen, Y.; Zhan, X.; Wang, Z.; He, J. Edge-Epitaxial Growth of 2D NbS₂-WS₂ Lateral Metal-Semiconductor Heterostructures. *Adv. Mater.* **2018**, *30*, 1803665.
69. Zhang, Z.; Chen, P.; Duan, X.; Zang, K.; Luo, J.; Duan, X. Robust Epitaxial Growth of Two-Dimensional Heterostructures, Multiheterostructures, and Superlattices. *Science* **2017**, *357*, 788–792.
70. Huang, C.; Wu, S.; Sanchez, A. M.; Peters, J. J. P.; Beanland, R.; Ross, J. S.; Rivera, P.; Yao, W.; Cobden, D. H.; Xu, X. Lateral Heterojunctions Within Monolayer MoSe₂-WSe₂ Semiconductors. *Nat. Mater.* **2014**, *13*, 1096–1101.
71. Sahoo, P. K.; Memaran, S.; Xin, Y.; Balicas, L.; Gutiérrez, H. R. One-Pot Growth of Two-Dimensional Lateral Heterostructures Via Sequential Edge-Epitaxy. *Nature* **2018**, *553*, 63–67.
72. Voiry, D.; Fullon, R.; Yang, J.; De Carvalho Castro e Silva, C.; Kapper, R.; Bozkurt, I.; Kaplan, D.; Lagos, M. J.; Batson, P. E.; Gupta, G.; Mohite, A. D.; Dong, L.; Er, D.; Shenoy, V. B.; Asefa, T.; Chhowalla, M. The Role of Electronic Coupling Between Substrate and 2D MoS₂ Nanosheets in Electrocatalytic Production of Hydrogen. *Nat. Mater.* **2016**, *15*, 1003–1009.
73. Harame, D. L.; Comfort, J. H.; Cressler, J. D.; Crabbe, E. F.; Sun, J. Y.; Meyerson, B. S.; Tice, T. Si/SiGe Epitaxial-Base Transistors. I. Materials, Physics, and Circuits. *IEEE Trans. Electron Devices* **1995**, *42*, 455–468.
74. Heiblum, M.; Nathan, M. I.; Thomas, D. C.; Knodler, C. M. Direct Observation of Ballistic Transport in GaAs. *Phys. Rev. Lett.* **1985**, *55*, 2200–2203.
75. Yablonovitch, E.; Kane, E. O. Band Structure Engineering of Semiconductor Lasers for Optical Communications. *J. Lightwave Technol.* **1988**, *6*, 1292–1299.
76. Lei, T.; Fanciulli, M.; Molnar, R. J.; Moustakas, T. D.; Graham, R. J.; Scanlon, J. Epitaxial Growth of Zinc Blende and Wurtzitic Gallium Nitride Thin Films on (001) Silicon. *Appl. Phys. Lett.* **1991**, *59*, 944–946.
77. Matsuoka, T.; Okamoto, H.; Nakao, M.; Harima, H.; Kurimoto, E. Optical Bandgap Energy of Wurtzite InN. *Appl. Phys. Lett.* **2002**, *81*, 1246–1248.
78. Mizuguchi, M.; Akinaga, H.; Manago, T.; Ono, K.; Oshima, M.; Shirai, M.; Yuri, M.; Lin, H. J.; Hsieh, H. H.; Chen, C. T. Epitaxial Growth of Zinc-Blende CrAs/GaAs Multilayer. *J. Appl. Phys.* **2002**, *91*, 7917–7919.
79. Wang, L.; Liu, X.; Zan, Y.; Wang, J.; Wang, D.; Lu, D.-C.; Wang, Z. Wurtzite GaN Epitaxial Growth on a Si(001) Substrate Using γ -Al₂O₃ as an Intermediate Layer. *Appl. Phys. Lett.* **1998**, *72*, 109–111.
80. Cao, Y.; Wang, X.; Lin, X.; Yang, W.; Lv, C.; Lu, Y.; Zhang, Y.; Zhao, W. Movable-Type Transfer and Stacking of van der Waals Heterostructures for Spintronics. *IEEE Access* **2020**, *8*, 70488–70495.
81. Castellanos-Gomez, A.; Buscema, M.; Molenaar, R.; Singh, V.; Janssen, L.; Van Der Zant, H. S. J.; Steele, G. A. Deterministic Transfer of Two-Dimensional Materials by All-Dry Viscoelastic Stamping. *2D Mater.* **2014**, *1*, 011002.
82. Fan, S.; Vu, Q. A.; Tran, M. D.; Adhikari, S.; Lee, Y. H. Transfer Assembly for Two-Dimensional van der Waals Heterostructures. *2D Mater.* **2020**, *7*, 022005.
83. Lin, Z.; McCreary, A.; Briggs, N.; Subramanian, S.; Zhang, K.; Sun, Y.; Li, X.; Borys, N. J.; Yuan, H.; Fullerton-Shirey, S. K.; Chernikov, A.; Zhao, H.; McDonnell, S.; Lindenberg, A. M.; Xiao, K.; Leroy, B. J.; Drndić, M.; Hwang, J. C. M.; Park, J.; Chhowalla, M.; Schaak, R. E.; Javey, A.; Hersam, M. C.; Robinson, J.; Terrones, M. 2D Materials Advances: From Large Scale Synthesis and Controlled Heterostructures to Improved Characterization Techniques, Defects and Applications. *2D Mater.* **2016**, *3*, 042001.
84. Liu, Y.; Weiss, N. O.; Duan, X.; Cheng, H.-C.; Huang, Y.; Duan, X. Van der Waals Heterostructures and Devices. *Nat. Rev. Mater.* **2016**, *1*, 16042.
85. Novoselov, K. S.; Mishchenko, A.; Carvalho, A.; Castro Neto, A. H. 2D Materials and van der Waals Heterostructures. *Science* **2016**, *353*, aac9439.
86. Schranghamer, T. F.; Sharma, M.; Singh, R.; Das, S. Review and Comparison of Layer Transfer Methods for Two-Dimensional Materials for Emerging Applications. *Chem. Soc. Rev.* **2021**, *50*, 11032–11054.
87. Solís-Fernández, P.; Bissett, M.; Ago, H. Synthesis, Structure and Applications of Graphene-Based 2D Heterostructures. *Chem. Soc. Rev.* **2017**, *46*, 4572–4613.
88. Son, S.; Shin, Y. J.; Zhang, K.; Shin, J.; Lee, S.; Idzuchi, H.; Coak, M. J.; Kim, H.; Kim, J.; Kim, J. H.; Kim, M.; Kim, D.; Kim, P.; Park, J.-G. Strongly Adhesive Dry Transfer Technique for van der Waals Heterostructure. *2D Mater.* **2020**, *7*, 041005.
89. Withers, F.; Del Pozo-Zamudio, O.; Mishchenko, A.; Rooney, A. P.; Gholinia, A.; Watanabe, K.; Taniguchi, T.; Haigh, S. J.; Geim, A. K.; Tartakovsky, A. I.; Novoselov, K. S. Light-Emitting Diodes by Band-Structure Engineering in van der Waals Heterostructures. *Nat. Mater.* **2015**, *14*, 301–306.
90. Purdie, D. G.; Pugno, N. M.; Taniguchi, T.; Watanabe, K.; Ferrari, A. C.; Lombardo, A. Cleaning Interfaces in Layered Materials Heterostructures. *Nat. Commun.* **2018**, *9*, 5387.
91. Qi, H.; Wang, L.; Sun, J.; Long, Y.; Hu, P.; Liu, F.; He, X. Production Methods of Van der Waals Heterostructures Based on Transition Metal Dichalcogenides. *Crystals* **2018**, *8*, 35.
92. He, F.; Zhou, Y.; Ye, Z.; Cho, S.-H.; Jeong, J.; Meng, X.; Wang, Y. Moiré Patterns in 2D Materials: A Review. *ACS Nano* **2021**, *15*, 5944–5958.

93. Lau, C. N.; Bockrath, M. W.; Mak, K. F.; Zhang, F. Reproducibility in the Fabrication and Physics of Moiré Materials. *Nature* **2022**, *602*, 41–50.
94. Carr, S.; Massatt, D.; Fang, S.; Cazeaux, P.; Luskin, M.; Kaxiras, E. Twistronics: Manipulating the Electronic Properties of Two-Dimensional Layered Structures Through Their Twist Angle. *Phys. Rev. B* **2017**, *95*, 075420.
95. Ciarrocchi, A.; Tagarelli, F.; Avsar, A.; Kis, A. Excitonic Devices With van der Waals Heterostructures: Valleytronics Meets Twistronics. *Nat. Rev. Mater.* **2022**, 1–16.
96. Liu, M.; Wang, L.; Yu, G. Developing Graphene-Based Moiré Heterostructures for Twistronics. *Adv. Sci.* **2022**, *9*, 2103170.
97. Ren, Y.-N.; Zhang, Y.; Liu, Y.-W.; He, L. Twistronics in Graphene-Based van der Waals Structures. *Chin. Phys. B* **2020**, *29*, 117303.
98. Cao, Y.; Fatemi, V.; Demir, A.; Fang, S.; Tomarken, S. L.; Luo, J. Y.; Sanchez-Yamagishi, J. D.; Watanabe, K.; Taniguchi, T.; Kaxiras, E.; Ashoori, R. C.; Jarillo-Herrero, P. Correlated Insulator Behaviour at Half-Filling in Magic-Angle Graphene Superlattices. *Nature* **2018**, *556*, 80–84.
99. Cao, Y.; Fatemi, V.; Fang, S.; Watanabe, K.; Taniguchi, T.; Kaxiras, E.; Jarillo-Herrero, P. Unconventional Superconductivity in Magic-Angle Graphene Superlattices. *Nature* **2018**, *556*, 43–50.
100. Kim, K.; Yankowitz, M.; Fallahzad, B.; Kang, S.; Movva, H. C. P.; Huang, S.; Larentis, S.; Corbet, C. M.; Taniguchi, T.; Watanabe, K.; Banerjee, S. K.; Leroy, B. J.; Tutuc, E. van der Waals Heterostructures with High Accuracy Rotational Alignment. *Nano Lett.* **2016**, *16*, 1989–1995.
101. Agnoli, S.; Ambrosetti, A.; Mentes, T. O.; Sala, A.; Locatelli, A.; Silvestrelli, P. L.; Cattelan, M.; Eichfeld, S.; Deng, D. D.; Robinson, J. A.; Avila, J.; Chen, C.; Asensio, M. C. Unraveling the Structural and Electronic Properties at the WSe_2 -Graphene Interface for a Rational Design of van der Waals Heterostructures. *ACS Appl. Nano Mater.* **2018**, *1*, 1131–1140.
102. Hoang, A. T.; Katiyar, A. K.; Shin, H.; Mishra, N.; Forti, S.; Coletti, C.; Ahn, J.-H. Epitaxial Growth of Wafer-Scale Molybdenum Disulfide/Graphene Heterostructures by Metal–Organic Vapor-Phase Epitaxy and Their Application in Photodetectors. *ACS Appl. Mater. Interfaces* **2020**, *12*, 44335–44344.
103. Lin, Y.-C.; Chang, C.-Y. S.; Ghosh, R. K.; Li, J.; Zhu, H.; Addou, R.; Diaconescu, B.; Ohta, T.; Peng, X.; Lu, N.; Kim, M. J.; Robinson, J. T.; Wallace, R. M.; Mayer, T. S.; Datta, S.; Li, L.-J.; Robinson, J. A. Atomically Thin Heterostructures Based on Single-Layer Tungsten Diselenide and Graphene. *Nano Lett.* **2014**, *14*, 6936–6941.
104. Li, J.; Yang, X.; Liu, R.; Huang, B.; Wu, R.; Zhang, Z.; Zhao, B.; Ma, H.; Dang, W.; Wei, Z.; Wang, K.; Lin, Z.; Yan, X.; Sun, M.; Li, B.; Pan, X.; Luo, J.; Zhang, G.; Liu, Y.; Huang, Y.; Duan, X.; Duan, X. General Synthesis of Two-Dimensional van der Waals Heterostructure Arrays. *Nature* **2020**, *579*, 368–374.
105. Li, X.; Lin, M.-W.; Lin, J.; Huang, B.; Puzos, A. A.; Ma, C.; Wang, K.; Zhou, W.; Pantelides, S. T.; Chi, M.; Kravchenko, I.; Fowlkes, J.; Rouleau, C. M.; Geoghegan, D. B.; Xiao, K. Two-Dimensional GaSe/MoSe₂ Misfit Bilayer Heterojunctions by van der Waals Epitaxy. *Sci. Adv.* **2016**, *2*, e1501882.
106. Lin, Y.-C.; Ghosh, R. K.; Addou, R.; Lu, N.; Eichfeld, S. M.; Zhu, H.; Li, M.-Y.; Peng, X.; Kim, M. J.; Li, L.-J.; Wallace, R. M.; Datta, S.; Robinson, J. A. Atomically Thin Resonant Tunnel Diodes Built From Synthetic van der Waals Heterostructures. *Nat. Commun.* **2015**, *6*, 7311.
107. Zhang, K.; Ding, C.; Pan, B.; Wu, Z.; Marga, A.; Zhang, L.; Zeng, H.; Huang, S. Visualizing Van der Waals Epitaxial Growth of 2D Heterostructures. *Adv. Mater.* **2021**, *33*, 2105079.
108. Cordova, D. L. M.; Johnson, D. C. Synthesis of Metastable Inorganic Solids With Extended Structures. *ChemPhysChem* **2020**, *21*, 1345–1368.
109. Göhler, F.; Choffel, M. A.; Schmidt, C.; Zahn, D. R. T.; Johnson, D. C.; Seyller, T. Influence of Nanoarchitectures on Interlayer Interactions in Layered Bi–Mo–Se Heterostructures. *J. Phys. Chem. C* **2021**, *125*, 9469–9478.
110. Hadland, E.; Jang, H.; Falmbigl, M.; Fischer, R.; Medlin, D. L.; Cahill, D. G.; Johnson, D. C. Synthesis, Characterization, and Ultralow Thermal Conductivity of a Lattice-Mismatched SnSe₂(MoSe₂)_{1.32} Heterostructure. *Chem. Mater.* **2019**, *31*, 5699–5705.
111. Rêgo, C. R. C.; Oliveira, L. N.; Tereshchuk, P.; Da Silva, J. L. F. Comparative Study of van der Waals Corrections to the Bulk Properties of Graphite. *J. Phys. Condens. Matter* **2015**, *27*, 415502.
112. Wickramaratne, D.; Weston, L.; Van De Walle, C. G. Monolayer to Bulk Properties of Hexagonal Boron Nitride. *J. Phys. Chem. C* **2018**, *122*, 25524–25529.
113. Roldán, R.; Chirrolí, L.; Prada, E.; Silva-Guillén, J. A.; San-Jose, P.; Guinea, F. Theory of 2D Crystals: Graphene and Beyond. *Chem. Soc. Rev.* **2017**, *46*, 4387–4399.
114. Sato, K.; Saito, R.; Cong, C.; Yu, T.; Dresselhaus, M. S. Zone Folding Effect in Raman G-Band Intensity of Twisted Bilayer Graphene. *Phys. Rev. B: Condens. Matter Mater. Phys.* **2012**, *86*, 125414.
115. Li, T.; Goldberger, J. E. Atomic-Scale Derivatives of Solid-State Materials. *Chem. Mater.* **2015**, *27*, 3549–3559.
116. Hoffmann, R. How Chemistry and Physics Meet in the Solid State. *Angew. Chem. Int. Ed. Engl.* **1987**, *26*, 846–878.
117. Bae, S.; Kim, H.; Lee, Y.; Xu, X.; Park, J.-S.; Zheng, Y.; Balakrishnan, J.; Lei, T.; Ri Kim, H.; Song, Y. I.; Kim, Y.-J.; Kim, K. S.; Özyilmaz, B.; Ahn, J.-H.; Hong, B. H.; Iijima, S. Roll-to-Roll Production of 30-Inch Graphene Films for Transparent Electrodes. *Nat. Nanotechnol.* **2010**, *5*, 574–578.
118. Nair, R. R.; Blake, P.; Grigorenko, A. N.; Novoselov, K. S.; Booth, T. J.; Stauber, T.; Peres, N. M. R.; Geim, A. K. Fine Structure Constant Defines Visual Transparency of Graphene. *Science* **2008**, *320*, 1308.
119. Novoselov, K. S.; Fal'ko, V. I.; Colombo, L.; Gellert, P. R.; Schwab, M. G.; Kim, K. A Roadmap for Graphene. *Nature* **2012**, *490*, 192–200.
120. Liu, C.; Yu, Z.; Neff, D.; Zhamu, A.; Jang, B. Z. Graphene-Based Supercapacitor with an Ultrahigh Energy Density. *Nano Lett.* **2010**, *10*, 4863–4868.
121. Velasco, A.; Ryu, Y. K.; Boscá, A.; Ladrón-De-Guevara, A.; Hunt, E.; Zuo, J.; Pedrós, J.; Calle, F.; Martínez, J. Recent Trends in Graphene Supercapacitors: From Large Area to Microsupercapacitors. *Sustainable Energy Fuels* **2021**, *5*, 1235–1254.
122. Wu, W.; Shi, Y.; Liu, G.; Fan, X.; Yu, Y. Recent Development of Graphene Oxide Based Forward Osmosis Membrane for Water Treatment: A Critical Review. *Desalination* **2020**, *491*, 114452.
123. Nowak, D.; Clapa, M.; Kula, P.; Sochacki, M.; Stonio, B.; Galazka, M.; Pelka, M.; Kuten, D.; Niedzielski, P. Influence of the Interactions at the Graphene-Substrate Boundary on Graphene Sensitivity to UV Irradiation. *Materials (Basel, Switzerland)* **2019**, *12*, 3949.
124. Scarfe, S.; Cui, W.; Luican-Mayer, A.; Ménard, J.-M. Systematic THz Study of the Substrate Effect in Limiting the Mobility of Graphene. *Sci. Rep.* **2021**, *11*, 8729.
125. Tyagi, A.; Mišekis, V.; Martini, L.; Forti, S.; Mishra, N.; Gebeyehu, Z. M.; Giambra, M. A.; Zribi, J.; Frégnaux, M.; Aureau, D.; Romagnoli, M.; Beltram, F.; Coletti, C. Ultra-Clean High-Mobility Graphene on Technologically Relevant Substrates. *Nanoscale* **2022**, *14*, 2167–2176.
126. Ashworth, C. Growing Wafer-Scale Single-Crystal hBN. *Nat. Rev. Phys.* **2020**, *2*, 176.
127. Molaei, M. J.; Younas, M.; Rezakazemi, M. A Comprehensive Review on Recent Advances in Two-Dimensional (2D) Hexagonal Boron Nitride. *ACS Appl. Electron. Mater.* **2021**, *3*, 5165–5187.
128. Caldwell, J. D.; Aharonovich, I.; Cassabois, G.; Edgar, J. H.; Gil, B.; Basov, D. N. Photonics With Hexagonal Boron Nitride. *Nat. Rev. Mater.* **2019**, *4*, 552–567.
129. Zhang, K.; Feng, Y.; Wang, F.; Yang, Z.; Wang, J. Two Dimensional Hexagonal Boron Nitride (2D-hBN): Synthesis, Properties and Applications. *J. Mater. Chem. C* **2017**, *5*, 11992–12022.
130. Molle, A.; Goldberger, J.; Houssa, M.; Xu, Y.; Zhang, S.-C.; Akinwande, D. Buckled Two-Dimensional Xene Sheets. *Nat. Mater.* **2017**, *16*, 163–169.
131. Zhao, A.; Wang, B. Two-Dimensional Graphene-Like Xenos as Potential Topological Materials. *APL Mater.* **2020**, *8*, 030701.
132. Liu, X.; Wang, L.; Li, S.; Rahn, M. S.; Yakobson, B. I.; Hersam, M. C. Geometric Imaging of Borophene Polymorphs With Functionalized Probes. *Nat. Commun.* **2019**, *10*, 1642.
133. Pumera, M.; Sofer, Z. 2D Monoelemental Arsenene, Antimonene, and Bismuthene: Beyond Black Phosphorus. *Adv. Mater.* **2017**, *29*, 1605299.
134. Ares, P.; Aguilar-Galindo, F.; Rodríguez-San-Miguel, D.; Aldave, D. A.; Díaz-Tendero, S.; Alcamí, M.; Martín, F.; Gómez-Herrero, J.; Zamora, F. Mechanical Isolation of Highly Stable Antimonene under Ambient Conditions. *Adv. Mater.* **2016**, *28*, 6332–6336.
135. Gibaja, C.; Rodríguez-San-Miguel, D.; Ares, P.; Gómez-Herrero, J.; Varela, M.; Giller, R.; Maultzsch, J.; Hauke, F.; Hirsch, A.; Abellán, G.; Zamora, F. Few-Layer Antimonene by Liquid-Phase Exfoliation. *Angew. Chem. Int. Ed.* **2016**, *55*, 14345–14349.
136. Hu, Y.; Qi, Z.-H.; Lu, J.; Chen, R.; Zou, M.; Chen, T.; Zhang, W.; Wang, Y.; Xue, X.; Ma, J.; Jin, Z. van der Waals Epitaxial Growth and Interfacial Passivation of Two-Dimensional Single-Crystalline Few-Layer Gray Arsenic Nanoflakes. *Chem. Mater.* **2019**, *31*, 4524–4535.

137. Reis, F.; Li, G.; Dudy, L.; Bauerfeind, M.; Glass, S.; Hanke, W.; Thomale, R.; Schäfer, J.; Claessen, R. Bismuthene on a SiC Substrate: A Candidate for a High-Temperature Quantum Spin Hall Material. *Science* **2017**, *357*, 287–290.
138. Shah, J.; Wang, W.; Sohail, H. M.; Uhrberg, R. I. G. Experimental Evidence of Monolayer Arsenene: An Exotic 2D Semiconducting Material. *2D Mater.* **2020**, *7*, 025013.
139. Laniel, D.; Winkler, B.; Fedotenko, T.; Pakhomova, A.; Chariton, S.; Milman, V.; Prakupenka, V.; Dubrovinsky, L.; Dubrovinskaya, N. High-Pressure Polymeric Nitrogen Allotrope with the Black Phosphorus Structure. *Phys. Rev. Lett.* **2020**, *124*, 216001.
140. Warschauer, D. Electrical and Optical Properties of Crystalline Black Phosphorus. *J. Appl. Phys.* **1963**, *34*, 1853–1860.
141. Li, L.; Yu, Y.; Ye, G. J.; Ge, Q.; Ou, X.; Wu, H.; Feng, D.; Chen, X. H.; Zhang, Y. Black Phosphorus Field-Effect Transistors. *Nat. Nanotechnol.* **2014**, *9*, 372–377.
142. Guo, Y.; Pan, F.; Ye, M.; Sun, X.; Wang, Y.; Li, J.; Zhang, X.; Zhang, H.; Pan, Y.; Song, Z.; Yang, J.; Lu, J. Monolayer Bismuthene-Metal Contacts: A Theoretical Study. *ACS Appl. Mater. Interfaces* **2017**, *9*, 23128–23140.
143. Ye, X.-J.; Zhu, G.-L.; Liu, J.; Liu, C.-S.; Yan, X.-H. Monolayer, Bilayer, and Heterostructure Arsenene as Potential Anode Materials for Magnesium-Ion Batteries: A First-Principles Study. *J. Phys. Chem. C* **2019**, *123*, 15777–15786.
144. Nedumkandathil, R.; Benson, D. E.; Grins, J.; Spektor, K.; Häussermann, U. The 3R Polymorph of CaSi₂. *J. Solid State Chem.* **2015**, *222*, 18–24.
145. Tobash, P. H.; Bobev, S. Synthesis, Structure and Electronic Structure of a New Polymorph of CaGe₂. *J. Solid State Chem.* **2007**, *180*, 1575–1581.
146. Trout, A. H.; Hodge, K. L.; Scudder, M.; Goldberger, J. E.; Mccomb, D. W. Low-Pressure Induced Disproportionation of Barium Distannide. *J. Phys. Chem. C* **2021**, *125*, 15496–15502.
147. Amamou, W.; Odenthal, P. M.; Bushong, E. J.; O'hara, D. J.; Kelly Luo, Y.; Van Baren, J.; Pinchuk, I.; Wu, Y.; Ahmed, A. S.; Katoch, J.; Bockrath, M. W.; Tom, H. W. K.; Goldberger, J. E.; Kawakami, R. K. Large Area Epitaxial Germanene for Electronic Devices. *2D Mater.* **2015**, *2*, 035012.
148. Asel, T. J.; Yanchenko, E.; Yang, X.; Jiang, S.; Krymowski, K.; Wang, Y.; Trout, A.; Mccomb, D. W.; Windl, W.; Goldberger, J. E.; Brillson, L. J. Identification of Ge Vacancies as Electronic Defects in Methyl- and Hydrogen-Terminated Germanene. *Appl. Phys. Lett.* **2018**, *113*, 061110.
149. Coloyan, G.; Cultrara, N. D.; Katre, A.; Carrete, J.; Heine, M.; Ou, E.; Kim, J.; Jiang, S.; Lindsay, L.; Mingo, N.; Broid, D.; Heremans, J. P.; Goldberger, J.; Shi, L. Basal-Plane Thermal Conductivity of Nanocrystalline and Amorphized Thin Germanene. *Appl. Phys. Lett.* **2016**, *109*, 131907.
150. Cultrara, N. D.; Arguilla, M. Q.; Jiang, S.; Sun, C.; Scudder, M. R.; Ross, R. D.; Goldberger, J. E. Group-13 and Group-15 Doping of Germanene. *Beilstein J. Nanotechnol.* **2017**, *8*, 1642–1648.
151. Cultrara, N. D.; Wang, Y.; Arguilla, M. Q.; Scudder, M. R.; Jiang, S.; Windl, W.; Bobev, S.; Goldberger, J. E. Synthesis of 1T, 2H, and 6R Germanene Polytypes. *Chem. Mater.* **2018**, *30*, 1335–1343.
152. Jiang, S.; Bianco, E.; Goldberger, J. E. The Structure and Amorphization of Germanene. *J. Mater. Chem. C* **2014**, *2*, 3185–3188.
153. Ma, Y.; Chen, Y.; Ma, Y.; Jiang, S.; Goldberger, J.; Vogt, T.; Lee, Y. Inter- and Intralayer Compression of Germanene. *J. Phys. Chem. C* **2014**, *118*, 28196–28201.
154. Pinchuk, I. V.; Odenthal, P. M.; Ahmed, A. S.; Amamou, W.; Goldberger, J. E.; Kawakami, R. K. Epitaxial Co-Deposition Growth of CaGe₂ Films by Molecular Beam Epitaxy for Large Area Germanene. *J. Mater. Res.* **2014**, *29*, 410–416.
155. Restrepo, O. D.; Mishra, R.; Goldberger, J. E.; Windl, W. Tunable Gaps and Enhanced Mobilities in Strain-Engineered Silicene. *J. Appl. Phys.* **2014**, *115*, 033711.
156. Trout, A. H.; Wang, Y.; Esser, B. D.; Jiang, S.; Goldberger, J. E.; Windl, W.; Mccomb, D. W. Identification of Turbostratic Twisting in Germanene. *J. Mater. Chem. C* **2019**, *7*, 10092–10097.
157. Young, J. R.; Chitara, B.; Cultrara, N. D.; Arguilla, M. Q.; Jiang, S.; Fan, F.; Johnston-Halperin, E.; Goldberger, J. E. Water Activated Doping and Transport in Multilayered Germanene Crystals. *J. Phys. Condens. Matter* **2015**, *28*, 034001.
158. Arguilla, M. Q.; Jiang, S.; Chitara, B.; Goldberger, J. E. Synthesis and Stability of Two-Dimensional Ge/Sn Graphene Alloys. *Chem. Mater.* **2014**, *26*, 6941–6946.
159. Asel, T. J.; Huey, W. L. B.; Noesges, B.; Molotkaiete, E.; Chien, S.-C.; Wang, Y.; Barnum, A.; Mcpherson, C.; Jiang, S.; Shields, S.; D'andrea, C.; Windl, W.; Cinquanta, E.; Brillson, L. J.; Goldberger, J. E. Influence of Surface Chemistry on Water Absorption in Functionalized Germanene. *Chem. Mater.* **2020**, *32*, 1537–1544.
160. Cinquanta, E.; Sardar, S.; Huey, W. L. B.; Vozzi, C.; Goldberger, J. E.; D'andrea, C.; Gadermaier, C. Dynamics of Two Distinct Exciton Populations in Methyl-Functionalized Germanene. *Nano Lett.* **2022**, *22*, 1183–1189.
161. Huey, W. L. B.; Goldberger, J. E. Covalent Functionalization of Two-Dimensional Group 14 Graphene Analogues. *Chem. Soc. Rev.* **2018**, *47*, 6201–6223.
162. Jiang, S.; Arguilla, M. Q.; Cultrara, N. D.; Goldberger, J. E. Covalently-Controlled Properties by Design in Group IV Graphene Analogues. *Acc. Chem. Res.* **2015**, *48*, 144–151.
163. Jiang, S.; Butler, S.; Bianco, E.; Restrepo, O. D.; Windl, W.; Goldberger, J. E. Improving the Stability and Optical Properties of Germanene Via One-Step Covalent Methyl-Termination. *Nat. Commun.* **2014**, *5*, 3389.
164. Jiang, S.; Krymowski, K.; Asel, T.; Arguilla, M. Q.; Cultrara, N. D.; Yanchenko, E.; Yang, X.; Brillson, L. J.; Windl, W.; Goldberger, J. E. Tailoring the Electronic Structure of Covalently Functionalized Germanene Via the Interplay of Ligand Strain and Electronegativity. *Chem. Mater.* **2016**, *28*, 8071–8077.
165. Yamanaka, S.; Matsu-Ura, H.; Ishikawa, M. New Deintercalation Reaction of Calcium From Calcium Disilicide. Synthesis of Layered Polysilane. *Mater. Res. Bull.* **1996**, *31*, 307–316.
166. Xu, Y.; Yan, B.; Zhang, H.-J.; Wang, J.; Xu, G.; Tang, P.; Duan, W.; Zhang, S.-C. Large-Gap Quantum Spin Hall Insulators in Tin Films. *Phys. Rev. Lett.* **2013**, *111*, 136804.
167. Aslam, M. K.; Xu, M. A Mini-Review: MXene Composites for Sodium/Potassium-Ion Batteries. *Nanoscale* **2020**, *12*, 15993–16007.
168. Gogotsi, Y.; Anasori, B. The Rise of MXenes. *ACS Nano* **2019**, *13*, 8491–8494.
169. Lei, J.-C.; Zhang, X.; Zhou, Z. Recent Advances in MXene: Preparation, Properties, and Applications. *Front. Phys.* **2015**, *10*, 276–286.
170. Hart, J. L.; Hantanasirisakul, K.; Lang, A. C.; Anasori, B.; Pinto, D.; Pivak, Y.; Van Omme, J. T.; May, S. J.; Gogotsi, Y.; Taheri, M. L. Control of MXenes' Electronic Properties Through Termination and Intercalation. *Nat. Commun.* **2019**, *10*, 522.
171. Hope, M. A.; Forse, A. C.; Griffith, K. J.; Lukatskaya, M. R.; Ghidui, M.; Gogotsi, Y.; Grey, C. P. NMR Reveals the Surface Functionalisation of Ti₃C₂ MXene. *Phys. Chem. Chem. Phys.* **2016**, *18*, 5099–5102.
172. Anasori, B.; Lukatskaya, M. R.; Gogotsi, Y. 2D metal Carbides and Nitrides (MXenes) for Energy Storage. *Nat. Rev. Mater.* **2017**, *2*, 16098.
173. Shayesteh Zeraati, A.; Mirkhani, S. A.; Sun, P.; Naguib, M.; Braun, P. V.; Sundararaj, U. Improved Synthesis of Ti₃C₂T_x MXenes Resulting in Exceptional Electrical Conductivity, High Synthesis Yield, and Enhanced Capacitance. *Nanoscale* **2021**, *13*, 3572–3580.
174. Maeda, K.; Wakayama, H.; Washio, Y.; Ishikawa, A.; Okazaki, M.; Nakata, H.; Matsuishi, S. Visible-Light-Induced Photocatalytic Activity of Stacked MXene Sheets of Y₂CF₂. *J. Phys. Chem. C* **2020**, *124*, 14640–14645.
175. Couly, C.; Alhabeb, M.; Van Aken, K. L.; Kurra, N.; Gomes, L.; Navarro-Suárez, A. M.; Anasori, B.; Alshareef, H. N.; Gogotsi, Y. Asymmetric Flexible MXene-Reduced Graphene Oxide Micro-Supercapacitor. *Adv. Electron. Mater.* **2018**, *4*, 1700339.
176. Jiang, Q.; Kurra, N.; Alhabeb, M.; Gogotsi, Y.; Alshareef, H. N. All Pseudocapacitive MXene-RuO₂ Asymmetric Supercapacitors. *Adv. Energy Mater.* **2018**, *8*, 1703043.
177. Iqbal, A.; Sambyal, P.; Koo, C. M. 2D MXenes for Electromagnetic Shielding: A Review. *Adv. Funct. Mater.* **2020**, *30*, 2000883.
178. Lv, R.; Robinson, J. A.; Schaak, R. E.; Sun, D.; Sun, Y.; Mallouk, T. E.; Terrones, M. Transition Metal Dichalcogenides and Beyond: Synthesis, Properties, and Applications of Single- and Few-Layer Nanosheets. *Acc. Chem. Res.* **2015**, *48*, 56–64.
179. Manzelli, S.; Ovchinnikov, D.; Pasquier, D.; Yazev, O. V.; Kis, A. 2D Transition Metal Dichalcogenides. *Nat. Rev. Mater.* **2017**, *2*, 17033.
180. Meng, L.; Ma, Y.; Si, K.; Xu, S.; Wang, J.; Gong, Y. Recent Advances of Phase Engineering in Group VI Transition Metal Dichalcogenides. *Tungsten* **2019**, *1*, 46–58.
181. Voiry, D.; Mohite, A.; Chhowalla, M. Phase Engineering of Transition Metal Dichalcogenides. *Chem. Soc. Rev.* **2015**, *44*, 2702–2712.
182. Yan, C.; Gong, C.; Wangyang, P.; Chu, J.; Hu, K.; Li, C.; Wang, X.; Du, X.; Zhai, T.; Li, Y.; Xiong, J. 2D Group IVB Transition Metal Dichalcogenides. *Adv. Funct. Mater.* **2018**, *28*, 1803305.
183. Zhang, Z.; Yang, P.; Hong, M.; Jiang, S.; Zhao, G.; Shi, J.; Xie, Q.; Zhang, Y. Recent Progress in the Controlled Synthesis of 2D Metallic Transition Metal Dichalcogenides. *Nanotechnology* **2019**, *30*, 182002.

184. Fu, Q.; Han, J.; Wang, X.; Xu, P.; Yao, T.; Zhong, J.; Zhong, W.; Liu, S.; Gao, T.; Zhang, Z.; Xu, L.; Song, B. 2D Transition Metal Dichalcogenides: Design, Modulation, and Challenges in Electrocatalysis. *Adv. Mater.* **2021**, *33*, 1907818.
185. Hart, L.; Dale, S.; Hoyer, S.; Webb, J. L.; Wolverson, D. Rhenium Dichalcogenides: Layered Semiconductors with Two Vertical Orientations. *Nano Lett.* **2016**, *16*, 1381–1386.
186. Chen, E.; Xu, W.; Chen, J.; Warner, J. H. 2D Layered Noble Metal Dichalcogenides (Pt, Pd, Se, S) for Electronics and Energy Applications. *Mater. Today Adv.* **2020**, *7*, 100076.
187. Pi, L.; Li, L.; Liu, K.; Zhang, Q.; Li, H.; Zhai, T. Recent Progress on 2D Noble-Transition-Metal Dichalcogenides. *Adv. Funct. Mater.* **2019**, *29*, 1904932.
188. Reale, F.; Sharda, K.; Mattevi, C. From Bulk Crystals to Atomically Thin Layers of Group VI-Transition Metal Dichalcogenides Vapour Phase Synthesis. *Appl. Mater. Today* **2016**, *3*, 11–22.
189. Chen, C. H.; Fabian, W.; Brown, F. C.; Woo, K. C.; Davies, B.; Delong, B.; Thompson, A. H. Angle-Resolved Photoemission Studies of the Band Structure of TiSe_2 and TiS_2 . *Phys. Rev. B: Condens. Matter Mater. Phys.* **1980**, *21*, 615–624.
190. Moustafa, M.; Zandt, T.; Janowitz, C.; Manzke, R. Growth and Band Gap Determination of the $\text{ZrS}_x\text{Se}_{2-x}$ Single Crystal Series. *Phys. Rev. B: Condens. Matter Mater. Phys.* **2009**, *80*, 035206.
191. Pillo, T.; Hayoz, J.; Berger, H.; Lévy, F.; Schlapbach, L.; Aebi, P. Photoemission of Bands Above the Fermi level: The Excitonic Insulator Phase Transition in 1T- TiSe_2 . *Phys. Rev. B: Condens. Matter Mater. Phys.* **2000**, *61*, 16213–16222.
192. Beal, A. R.; Hughes, H. P.; Liang, W. Y. The Reflectivity Spectra of Some Group VA Transition Metal Dichalcogenides. *J. Phys. C Solid State Phys.* **1975**, *8*, 4236, 4234.
193. Kam, K. K.; Chang, C. L.; Lynch, D. W. Fundamental Absorption Edges and Indirect Band Gaps in $\text{W}_{1-x}\text{Mo}_x\text{Se}_2$ ($0 \leq x \leq 1$). *J. Phys. C Solid State Phys.* **1984**, *17*, 4031–4040.
194. Qi, Y.; Naumov, P. G.; Ali, M. N.; Rajamathi, C. R.; Schnelle, W.; Barkalov, O.; Hanfland, M.; Wu, S.-C.; Shekhar, C.; Sun, Y.; Süß, V.; Schmidt, M.; Schwarz, U.; Pippel, E.; Werner, P.; Hillebrand, R.; Förster, T.; Kampert, E.; Parkin, S.; Cava, R. J.; Felser, C.; Yan, B.; Medvedev, S. A. Superconductivity in Weyl Semimetal Candidate MoTe_2 . *Nat. Commun.* **2016**, *7*, 11038.
195. Jariwala, B.; Voiry, D.; Jindal, A.; Chalke, B. A.; Bapat, R.; Thamizhavel, A.; Chhowalla, M.; Deshmukh, M.; Bhattacharya, A. Synthesis and Characterization of ReS_2 and ReSe_2 Layered Chalcogenide Single Crystals. *Chem. Mater.* **2016**, *28*, 3352–3359.
196. Hulliger, F. Electrical Properties of Some Nickel-Group Chalcogenides. *J. Phys. Chem. Solid* **1965**, *26*, 639–645.
197. Grant, A. J.; Griffiths, T. M.; Pitt, G. D.; Yoffe, A. D. The Electrical Properties and the Magnitude of the Indirect Gap in the Semiconducting Transition Metal Dichalcogenide Layer Crystals. *J. Phys. C Solid State Phys.* **1975**, *8*, L17–L23.
198. Mak, K. F.; Lee, C.; Hone, J.; Shan, J.; Heinz, T. F. Atomically Thin MoS_2 : A New Direct-Gap Semiconductor. *Phys. Rev. Lett.* **2010**, *105*, 136805.
199. Splendiani, A.; Sun, L.; Zhang, Y.; Li, T.; Kim, J.; Chim, C.-Y.; Galli, G.; Wang, F. Emerging Photoluminescence in Monolayer MoS_2 . *Nano Lett.* **2010**, *10*, 1271–1275.
200. Pacchioni, G. Valleytronics With a Twist. *Nat. Rev. Mater.* **2020**, *5*, 480.
201. Schaubley, J. R.; Yu, H.; Clark, G.; Rivera, P.; Ross, J. S.; Seyler, K. L.; Yao, W.; Xu, X. Valleytronics in 2D Materials. *Nat. Rev. Mater.* **2016**, *1*, 16055.
202. Cui, Y.; Xin, R.; Yu, Z.; Pan, Y.; Ong, Z.-Y.; Wei, X.; Wang, J.; Nan, H.; Ni, Z.; Wu, Y.; Chen, T.; Shi, Y.; Wang, B.; Zhang, G.; Zhang, Y.-W.; Wang, X. High-Performance Monolayer WS_2 Field-Effect Transistors on High- κ Dielectrics. *Adv. Mater.* **2015**, *27*, 5230–5234.
203. Yu, Z.; Ong, Z.-Y.; Pan, Y.; Cui, Y.; Xin, R.; Shi, Y.; Wang, B.; Wu, Y.; Chen, T.; Zhang, Y.-W.; Zhang, G.; Wang, X. Realization of Room-Temperature Phonon-Limited Carrier Transport in Monolayer MoS_2 by Dielectric and Carrier Screening. *Adv. Mater.* **2016**, *28*, 547–552.
204. Kim, H.-J.; Kang, S.-H.; Hamada, I.; Son, Y.-W. Origins of the Structural Phase Transitions in MoTe_2 and WTe_2 . *Phys. Rev. B* **2017**, *95*, 180101.
205. Tang, S.; Zhang, C.; Wong, D.; Pedramrazi, Z.; Tsai, H.-Z.; Jia, C.; Moritz, B.; Claassen, M.; Ryu, H.; Kahn, S.; Jiang, J.; Yan, H.; Hashimoto, M.; Lu, D.; Moore, R. G.; Hwang, C.-C.; Hwang, C.; Hussain, Z.; Chen, Y.; Ugeda, M. M.; Liu, Z.; Xie, X.; Devereaux, T. P.; Crommie, M. F.; Mo, S.-K.; Shen, Z.-X. Quantum spin Hall State in Monolayer 1T'- WTe_2 . *Nat. Phys.* **2017**, *13*, 683–687.
206. Wang, Y.; Carey, B. J.; Zhang, W.; Chrimes, A. F.; Chen, L.; Kalantar-Zadeh, K.; Ou, J. Z.; Daeneke, T. Intercalated 2D MoS_2 Utilizing a Simulated Sun Assisted Process: Reducing the HER Overpotential. *J. Phys. Chem. C* **2016**, *120*, 2447–2455.
207. Hamill, A.; Heischmidt, B.; Sohn, E.; Shaffer, D.; Tsai, K.-T.; Zhang, X.; Xi, X.; Suslov, A.; Berger, H.; Forró, L.; Burnell, F. J.; Shan, J.; Mak, K. F.; Fernandes, R. M.; Wang, K.; Pribyl, V. S. Two-Fold Symmetric Superconductivity in Few-Layer NbSe_2 . *Nat. Phys.* **2021**, *17*, 949–954.
208. Leng, H.; Orain, J. C.; Amato, A.; Huang, Y. K.; De Visser, A. Type-I Superconductivity in the Dirac Semimetal PdTe_2 Probed by μSR . *Phys. Rev. B* **2019**, *100*, 224501.
209. Nishiyama, W.; Nishimura, T.; Ueno, K.; Taniguchi, T.; Watanabe, K.; Nagashio, K. Quantitative Determination of Contradictory Bandgap Values of Bulk PdSe_2 from Electrical Transport Properties. *Adv. Funct. Mater.* **2022**, *32*, 2108061.
210. Zhang, G.; Amani, M.; Chaturvedi, A.; Tan, C.; Bullock, J.; Song, X.; Kim, H.; Lien, D.-H.; Scott, M. C.; Zhang, H.; Javey, A. Optical and Electrical Properties of Two-Dimensional Palladium Diselenide. *Appl. Phys. Lett.* **2019**, *114*, 253102.
211. Oyedele, A. D.; Yang, S.; Liang, L.; Puzosky, A. A.; Wang, K.; Zhang, J.; Yu, P.; Pudasaini, P. R.; Ghosh, A. W.; Liu, Z.; Rouleau, C. M.; Sumpter, B. G.; Chisholm, M. F.; Zhou, W.; Rack, P. D.; Geoghegan, D. B.; Xiao, K. PdSe_2 : Pentagonal Two-Dimensional Layers with High Air Stability for Electronics. *J. Am. Chem. Soc.* **2017**, *139*, 14090–14097.
212. Seo, J. E.; Das, T.; Park, E.; Seo, D.; Kwak, J. Y.; Chang, J. Polarity Control and Weak Fermi-Level Pinning in PdSe_2 Transistors. *ACS Appl. Mater. Interfaces* **2021**, *13*, 43480–43488.
213. Dong, Z.; Yu, W.; Zhang, L.; Mu, H.; Xie, L.; Li, J.; Zhang, Y.; Huang, L.; He, X.; Wang, L.; Lin, S.; Zhang, K. Highly Efficient, Ultrabroad PdSe_2 Phototransistors from Visible to Terahertz Driven by Multiphysical Mechanism. *ACS Nano* **2021**, *15*, 20403–20413.
214. Fu, C.; Xiao, Y.-T.; Xing, Y.; Tong, X.-W.; Wang, J.; Zhang, Z.-X.; Wang, L.; Wu, D.; Luo, L.-B. Filterless Discrimination of Wavelengths in the Range from Ultraviolet to Near-Infrared Light Using Two PdSe_2 /Thin Si/PdSe_2 Heterojunction Photodetectors. *ACS Appl. Mater. Interfaces* **2021**, *13*, 43273–43281.
215. Bergeron, H.; Lebedev, D.; Hersam, M. C. Polymorphism in Post-Dichalcogenide Two-Dimensional Materials. *Chem. Rev.* **2021**, *121*, 2713–2775.
216. Terhell, J. C. J. M. Polyttypism in the III–VI Layer Compounds. *Prog. Cryst. Growth Charact. Mater.* **1983**, *7*, 55–110.
217. Lei, S.; Ge, L.; Najmaei, S.; George, A.; Kappera, R.; Lou, J.; Chhowalla, M.; Yamaguchi, H.; Gupta, G.; Vajtai, R.; Mohite, A. D.; Ajayan, P. M. Evolution of the Electronic Band Structure and Efficient Photo-Detection in Atomic Layers of InSe . *ACS Nano* **2014**, *8*, 1263–1272.
218. Gürbulak, B.; Şata, M.; Dogan, S.; Duman, S.; Ashkhasi, A.; Keskenler, E. F. Structural Characterizations and Optical Properties of InSe and InSe:Ag Semiconductors Grown by Bridgman/Stockbarger Technique. *Physica E* **2014**, *64*, 106–111.
219. Julien, C. M.; Balkanski, M. Lithium Reactivity With III–VI Layered Compounds. *Mater. Sci. Eng. B* **2003**, *100*, 263–270.
220. Mercier, A.; Mooser, E.; Voitchovsky, J. P. Near Edge Optical Absorption and Luminescence of GaSe , GaS and of Mixed Crystals. *JOL* **1973**, *7*, 241–266.
221. De Blasi, C.; Micocci, G.; Mongelli, S.; Tepore, A.; Zuanni, F. Growth and Characterization of High Quality InSe Single Crystals. *Mater. Chem. Phys.* **1983**, *9*, 55–64.
222. Imai, K.; Suzuki, K.; Haga, T.; Hasegawa, Y.; Abe, Y. Phase Diagram of In–Se System and Crystal Growth of Indium Monoselenide. *J. Cryst. Growth* **1981**, *54*, 501–506.
223. Mancini, A. M.; Micocci, G.; Rizzo, A. New Materials for Optoelectronic Devices: Growth and Characterization of Indium and Gallium Chalcogenide Layer Compounds. *Mater. Chem. Phys.* **1983**, *9*, 29–54.
224. Bandurin, D. A.; Tyurina, A. V.; Yu, G. L.; Mishchenko, A.; Zolyomi, V.; Morozov, S. V.; Kumar, R. K.; Gorbachev, R. V.; Kudrynskiy, Z. R.; Pezzini, S.; Kovalyuk, Z. D.; Zeitler, U.; Novoselov, K. S.; Patané, A.; Eaves, L.; Grigorieva, I. V.; Fal'ko, V. I.; Geim, A. K.; Cao, Y. High Electron Mobility, Quantum Hall Effect and Anomalous Optical Response in Atomically Thin InSe . *Nat. Nanotechnol.* **2017**, *12*, 223–227.
225. Jiang, X.; Liu, Q.; Xing, J.; Liu, N.; Guo, Y.; Liu, Z.; Zhao, J. Recent Progress on 2D Magnets: Fundamental Mechanism, Structural Design and Modification. *Appl. Phys. Rev.* **2021**, *8*, 031305.
226. Mcguire, M. A. Crystal and Magnetic Structures in Layered, Transition Metal Dihalides and Trihalides. *Crystals* **2017**, *7*, 7050121.
227. Yang, S.; Zhang, T.; Jiang, C. van der Waals Magnets: Material Family, Detection and Modulation of Magnetism, and Perspective in Spintronics. *Adv. Sci.* **2021**, *8*, 2002488.

228. Zhang, S.; Xu, R.; Luo, N.; Zou, X. Two-Dimensional Magnetic Materials: Structures, Properties and External Controls. *Nanoscale* **2021**, *13*, 1398–1424.
229. Huang, B.; Clark, G.; Navarro-Moratalla, E.; Klein, D. R.; Cheng, R.; Seyler, K. L.; Zhong, D.; Schmidgall, E.; McGuire, M. A.; Cobden, D. H.; Yao, W.; Xiao, D.; Jarillo-Herrero, P.; Xu, X. Layer-Dependent Ferromagnetism in a van der Waals Crystal Down to the Monolayer Limit. *Nature* **2017**, *546*, 270–273.
230. Li, T.; Jiang, S.; Sivadas, N.; Wang, Z.; Xu, Y.; Weber, D.; Goldberger, J. E.; Watanabe, K.; Taniguchi, T.; Fennie, C. J.; Fai Mak, K.; Shan, J. Pressure-Controlled Interlayer Magnetism in Atomically Thin CrI₃. *Nat. Mater.* **2019**, *18*, 1303–1308.
231. McCreary, A.; Mai, T. T.; Utermohlen, F. G.; Simpson, J. R.; Garrity, K. F.; Feng, X.; Shcherbakov, D.; Zhu, Y.; Hu, J.; Weber, D.; Watanabe, K.; Taniguchi, T.; Goldberger, J. E.; Mao, Z.; Lau, C. N.; Lu, Y.; Trivedi, N.; Valdés Aguilar, R.; Hight Walker, A. R. Distinct Magneto-Raman Signatures of Spin-Flip Phase Transitions in CrI₃. *Nat. Commun.* **2020**, *11*, 3879.
232. Xu, Y.; Ray, A.; Shao, Y.-T.; Jiang, S.; Lee, K.; Weber, D.; Goldberger, J. E.; Watanabe, K.; Taniguchi, T.; Muller, D. A.; Mak, K. F.; Shan, J. Coexisting Ferromagnetic–Antiferromagnetic State in Twisted Bilayer CrI₃. *Nat. Nanotechnol.* **2022**, *17*, 143–147.
233. Zhang, X.-X.; Li, L.; Weber, D.; Goldberger, J.; Mak, K. F.; Shan, J. Gate-Tunable Spin Waves in Antiferromagnetic Atomic Bilayers. *Nat. Mater.* **2020**, *19*, 838–842.
234. Baek, S. H.; Do, S. H.; Choi, K. Y.; Kwon, Y. S.; Wolter, A. U. B.; Nishimoto, S.; Van Den Brink, J.; Büchner, B. Evidence for a Field-Induced Quantum Spin Liquid in α -RuCl₃. *Phys. Rev. Lett.* **2017**, *119*, 037201.
235. Kim, H.-S.; Vijay, V. S.; Catuneanu, A.; Kee, H.-Y. Kitaev Magnetism in Honeycomb RuCl₃ With Intermediate Spin-Orbit Coupling. *Phys. Rev. B: Condens. Matter Mater. Phys.* **2015**, *91*, 241110.
236. Sears, J. A.; Zhao, Y.; Xu, Z.; Lynn, J. W.; Kim, Y.-J. Phase Diagram of α -RuCl₃ in an in-Plane Magnetic Field. *Phys. Rev. B* **2017**, *95*, 180411.
237. Weber, D.; Schoop, L. M.; Duppel, V.; Lippmann, J. M.; Nuss, J.; Lotsch, B. V. Magnetic Properties of Restacked 2D Spin 1/2 honeycomb RuCl₃ Nanosheets. *Nano Lett.* **2016**, *16*, 3578–3584.
238. McGuire, M. A.; Dixit, H.; Cooper, V. R.; Sales, B. C. Coupling of Crystal Structure and Magnetism in the Layered, Ferromagnetic Insulator CrI₃. *Chem. Mater.* **2015**, *27*, 612–620.
239. Son, S.; Coak, M. J.; Lee, N.; Kim, J.; Kim, T. Y.; Hamidov, H.; Cho, H.; Liu, C.; Jarvis, D. M.; Brown, P. A. C.; Kim, J. H.; Park, C.-H.; Khomskii, D. I.; Saxena, S. S.; Park, J.-G. Bulk Properties of the van der Waals Hard Ferromagnet V₁₃. *Phys. Rev. B* **2019**, *99*, 041402.
240. Samal, R.; Sanyal, G.; Chakraborty, B.; Rout, C. S. Two-Dimensional Transition Metal Phosphorous Trichalcogenides (MPX₃): A Review on Emerging Trends, Current State and Future Perspectives. *J. Mater. Chem. A* **2021**, *9*, 2560–2591.
241. Susner, M. A.; Chyavanichyus, M.; McGuire, M. A.; Ganesh, P.; Maksymovych, P. Metal Thio- and Selenophosphates as Multifunctional van der Waals Layered Materials. *Adv. Mater.* **2017**, *29*, 1602852.
242. Wang, F.; Shifa, T. A.; Yu, P.; He, P.; Liu, Y.; Wang, F.; Wang, Z.; Zhan, X.; Lou, X.; Xia, F.; He, J. New Frontiers on van der Waals Layered Metal Phosphorous Trichalcogenides. *Adv. Funct. Mater.* **2018**, *28*, 1802151.
243. Payen, C.; Mutka, H.; Soubeyroux, J. L.; Molinié, P.; Colombet, P. Static and Dynamic Properties of the Quasi-1D Heisenberg Antiferromagnets AgVP₂S₆ (S = 1) and AgCrP₂S₆ (S = 3/2). *J. Magn. Magn. Mater.* **1992**, *104–107*, 797–798.
244. Chandrasekharan, N.; Vasudevan, S. Magnetism and Exchange in the Layered Antiferromagnet NiPS₃. *J. Phys. Condens. Matter* **1994**, *6*, 4569–4579.
245. Carteaux, V.; Moussa, F.; Spiesser, M. 2D Ising-Like Ferromagnetic Behaviour for the Lamellar Cr₂Si₂Te₆ Compound: A Neutron Scattering Investigation. *Europhys. Lett.* **1995**, *29*, 251–256.
246. Gong, C.; Li, L.; Li, Z.; Ji, H.; Stern, A.; Xia, Y.; Cao, T.; Bao, W.; Wang, C.; Wang, Y.; Qiu, Z. Q.; Cava, R. J.; Louie, S. G.; Xia, J.; Zhang, X. Discovery of Intrinsic Ferromagnetism in Two-Dimensional van der Waals Crystals. *Nature* **2017**, *546*, 265–269.
247. Kang, S.; Kang, S.; Yu, J. Effect of Coulomb Interactions on the Electronic and Magnetic Properties of Two-Dimensional CrSiTe₃ and CrGeTe₃ Materials. *J. Electron. Mater.* **2019**, *48*, 1441–1445.
248. Banys, J.; Samulionis, V.; Cajipe, V. B.; Vysochanskii, Y. Dielectric Properties of Ferroelectrics CuInP₂Se₆ and CuCrP₂S₆. *Ferroelectrics* **2001**, *257*, 163–168.
249. Ju, L.; Shang, J.; Tang, X.; Kou, L. Tunable Photocatalytic Water Splitting by the Ferroelectric Switch in a 2D AgBiP₂Se₆ Monolayer. *J. Am. Chem. Soc.* **2020**, *142*, 1492–1500.
250. Susner, M. A.; Rao, R.; Pelton, A. T.; Mcleod, M. V.; Maruyama, B. Temperature-Dependent Raman Scattering and X-Ray Diffraction Study of Phase Transitions in Layered Multiferroic CuCrP₂S₆. *Phys. Rev. Mater.* **2020**, *4*, 104003.
251. Luo, Y.; Cai, S.; Hao, S.; Pielhofer, F.; Hadar, I.; Luo, Z.-Z.; Xu, J.; Wolverton, C.; Dravid, V. P.; Pfitzner, A.; Yan, Q.; Kanatzidis, M. G. High-Performance Thermoelectrics from Cellular Nanostructured Sb₂Si₂Te₆. *Joule* **2020**, *4*, 159–175.
252. Furuse, S.; Brattås, L.; Kjekshus, A.; Andresen, A. F.; Fischer, P. On the Crystal Structures of TiS₃, ZrS₃, ZrSe₃, ZrTe₃, HfS₃, and HfSe₃. *Acta Chem. Scand.* **1975**, *29a*, 623–631.
253. Guilmeau, E.; Berthebaud, D.; Misse, P. R. N.; Hébert, S.; Lebedev, O. I.; Chateigner, D.; Martin, C.; Maignan, A. ZrSe₃-Type Variant of TiS₃: Structure and Thermoelectric Properties. *Chem. Mater.* **2014**, *26*, 5585–5591.
254. Fokwa, B. P. T.; Doert, T. The Ternary Rare-Earth Polychalcogenides LaSeTe₂, CeSeTe₂, PrSeTe₂, NdSeTe₂, and SmSeTe₂: Syntheses, Crystal Structures, Electronic Properties, and Charge-Density-Wave-Transitions. *Solid State Sci.* **2005**, *7*, 573–587.
255. Malliakas, C.; Billinge, S. J. L.; Kim, H. J.; Kanatzidis, M. G. Square Nets of Tellurium: Rare-Earth Dependent Variation in the Charge-Density Wave of RETe₃ (RE = Rare-Earth Element). *J. Am. Chem. Soc.* **2005**, *127*, 6510–6511.
256. Yumigeta, K.; Qin, Y.; Li, H.; Blei, M.; Attarde, Y.; Kopas, C.; Tongay, S. Advances in Rare-Earth Tritelluride Quantum Materials: Structure, Properties, and Synthesis. *Adv. Sci.* **2021**, *8*, 2004762.
257. Lin, C.; Ochi, M.; Noguchi, R.; Kuroda, K.; Sakoda, M.; Nomura, A.; Tsubota, M.; Zhang, P.; Bareille, C.; Kurokawa, K.; Arai, Y.; Kawaguchi, K.; Tanaka, H.; Yaji, K.; Harasawa, A.; Hashimoto, M.; Lu, D.; Shin, S.; Arita, R.; Tanda, S.; Kondo, T. Visualization of the Strain-Induced Topological Phase Transition in a Quasi-One-Dimensional Superconductor TaSe₃. *Nat. Mater.* **2021**, *20*, 1093–1099.
258. Liu, Z. Y.; Li, J.; Zhang, J. F.; Yang, P. T.; Zhang, S.; Chen, G. F.; Uwatoko, Y.; Yang, H. X.; Sui, Y.; Liu, K.; Cheng, J. G. Quasi-One-Dimensional Superconductivity in the Pressurized Charge-Density-Wave Conductor HfTe₃. *NPJ Quantum Mater.* **2021**, *6*, 90.
259. Regueiro, M. N.; Mignot, J. M.; Castello, D. Superconductivity at High Pressure in NbSe₃. *Europhys. Lett.* **1992**, *18*, 53–57.
260. Zhu, X.; Lv, B.; Wei, F.; Xue, Y.; Lorenz, B.; Deng, L.; Sun, Y.; Chu, C.-W. Disorder-Induced Bulk Superconductivity in ZrTe₃ Single Crystals Via Growth Control. *Phys. Rev. B: Condens. Matter Mater. Phys.* **2013**, *87*, 024508.
261. Hodeau, J. L.; Marezio, M.; Roucau, C.; Ayroles, R.; Meerschaut, A.; Rouxel, J.; Monceau, P. Charge-Density Waves in NbSe₃ at 145K: Crystal Structures, X-Ray and Electron Diffraction Studies. *J. Phys. C Solid State Phys.* **1978**, *11*, 4117–4134.
262. Coleman, R. V.; Everson, M. P.; Lu, H.-A.; Johnson, A.; Falicov, L. M. Effects of High Magnetic Fields on Charge-Density Waves in NbSe₃. *Phys. Rev. B: Condens. Matter Mater. Phys.* **1990**, *41*, 460–489.
263. Molina-Mendoza, A. J.; Barawi, M.; Biele, R.; Flores, E.; Ares, J. R.; Sánchez, C.; Rubio-Bollinger, G.; Agrait, N.; D’agosta, R.; Ferrer, I. J.; Castellanos-Gomez, A. Electronic Bandgap and Exciton Binding Energy of Layered Semiconductor TiS₃. *Adv. Electron. Mater.* **2015**, *1*, 1500126.
264. Schairer, W.; Shafer, M. W. Growth and Optical Absorption Spectra of the Layer-Type Trichalcogenides ZrS₃ and HfS₃. *Phys. Status Solidi (a)* **1973**, *17*, 181–184.
265. Lei, S.; Lin, J.; Jia, Y.; Gray, M.; Topp, A.; Farahi, G.; Klemenz, S.; Gao, T.; Rodolakis, F.; Mcchesney, J. L.; Ast, C. R.; Yazdani, A.; Burch, K. S.; Wu, S.; Ong, N. P.; Schoop, L. M. High Mobility in a van der Waals Layered Antiferromagnetic Metal. *Sci. Adv.* **2020**, *6*, eaay6407.
266. Watanabe, M.; Nakamura, R.; Lee, S.; Asano, T.; Ibe, T.; Tokuda, M.; Taniguchi, H.; Ueta, D.; Okada, Y.; Kobayashi, K.; Niimi, Y. Shubnikov-de-Haas Oscillation and Possible Modification of Effective Mass in CeTe₃ Thin Films. *AIP Adv.* **2021**, *11*, 015005.

267. Xing, Y.; Li, Y.; Yang, Z.; Wang, Z.; Yang, P.; Ge, J.; Liu, Y.; Liu, Y.; Luo, T.; Tang, Y.; Wang, J. Extremely Large and Anisotropic Magnetoresistance in Rare-Earth Triteluride TbTe_3 . *J. Appl. Phys.* **2020**, *128*, 073901.
268. Heremans, J. P.; Cava, R. J.; Samarth, N. Tetradymites as Thermoelectrics and Topological Insulators. *Nat. Rev. Mater.* **2017**, *2*, 17049.
269. Wang, L.-L.; Johnson, D. D. Ternary Tetradymite Compounds as Topological Insulators. *Phys. Rev. B: Condens. Matter Mater. Phys.* **2011**, *83*, 241309.
270. Mazumder, K.; Shirage, P. M. A Brief Review of Bi_2Se_3 Based Topological Insulator: From Fundamentals to Applications. *J. Alloys Compd.* **2021**, *888*, 161492.
271. Sehr, R.; Testardi, L. R. The Optical Properties of p-Type Bi_2Te_3 - Sb_2Te_3 Alloys Between 2–15 Microns. *J. Phys. Chem. Solid* **1962**, *23*, 1219–1224.
272. Zhang, H.; Liu, C.-X.; Qi, X.-L.; Dai, X.; Fang, Z.; Zhang, S.-C. Topological Insulators in Bi_2Se_3 , Bi_2Te_3 and Sb_2Te_3 With a Single Dirac Cone on the Surface. *Nat. Phys.* **2009**, *5*, 438–442.
273. Hossain, M. Z.; Rumyantsev, S. L.; Shahil, K. M. F.; Teweldebrhan, D.; Shur, M.; Balandin, A. A. Low-Frequency Current Fluctuations in “Graphene-like” Exfoliated Thin-Films of Bismuth Selenide Topological Insulators. *ACS Nano* **2011**, *5*, 2657–2663.
274. Xu, Y.; Miotkowski, I.; Chen, Y. P. Quantum Transport of Two-Species Dirac Fermions in Dual-Gated Three-Dimensional Topological Insulators. *Nat. Commun.* **2016**, *7*, 11434.
275. Xu, Y.; Miotkowski, I.; Liu, C.; Tian, J.; Nam, H.; Alidoust, N.; Hu, J.; Shih, C.-K.; Hasan, M. Z.; Chen, Y. P. Observation of Topological Surface State Quantum Hall effect in an Intrinsic Three-Dimensional Topological Insulator. *Nat. Phys.* **2014**, *10*, 956–963.
276. Bansal, N.; Kim, Y. S.; Brahlek, M.; Edrey, E.; Oh, S. Thickness-Independent Transport Channels in Topological Insulator Bi_2Se_3 Thin Films. *Phys. Rev. Lett.* **2012**, *109*, 116804.
277. Richardella, A.; Zhang, D. M.; Lee, J. S.; Koser, A.; Rench, D. W.; Yeats, A. L.; Buckley, B. B.; Awschalom, D. D.; Samarth, N. Coherent Heteroepitaxy of Bi_2Se_3 on GaAs (111) B. *Appl. Phys. Lett.* **2010**, *97*, 262104.
278. Zhang, G.; Qin, H.; Teng, J.; Guo, J.; Guo, Q.; Dai, X.; Fang, Z.; Wu, K. Quintuple-Layer Epitaxy of Thin Films of Topological Insulator Bi_2Se_3 . *Appl. Phys. Lett.* **2009**, *95*, 053114.
279. Teweldebrhan, D.; Goyal, V.; Balandin, A. A. Exfoliation and Characterization of Bismuth Telluride Atomic Quintuples and Quasi-Two-Dimensional Crystals. *Nano Lett.* **2010**, *10*, 1209–1218.
280. Koster, K. G.; Wang, Y.; Scudder, M. R.; Moore, C. E.; Windl, W.; Goldberger, J. E. Synthesis and Characterization of a New Family Of Layered $\text{Pb}_x\text{Sn}_{4-x}\text{As}_3$ Alloys. *J. Mater. Chem. C* **2021**, *9*, 6477–6483.
281. Arguilla, M. Q.; Cultrara, N. D.; Baum, Z. J.; Jiang, S.; Ross, R. D.; Goldberger, J. E. EuSn_2As_2 : An Exfoliable Magnetic Layered Zintl–Klemm Phase. *Inorg. Chem. Front.* **2017**, *4*, 378–386.
282. Tschulik, K.; Ruck, M.; Binnewies, M.; Milke, E.; Hoffmann, S.; Schnelle, W.; Fokwa, B. P. T.; Gilleßen, M.; Schmidt, P. Chemistry and Physical Properties of the Phosphide Telluride Zr_2PTe_2 . *Eur. J. Inorg. Chem.* **2009**, *2009*, 3102–3110.
283. He, B.; Wang, Y.; Arguilla, M. Q.; Cultrara, N. D.; Scudder, M. R.; Goldberger, J. E.; Windl, W.; Heremans, J. P. The Fermi Surface Geometrical Origin of Axis-Dependent Conduction Polarity in Layered Materials. *Nat. Mater.* **2019**, *18*, 568–572.
284. Gui, X.; Pletikoscic, I.; Cao, H.; Tien, H.-J.; Xu, X.; Zhong, R.; Wang, G.; Chang, T.-R.; Jia, S.; Valla, T.; Xie, W.; Cava, R. J. A New Magnetic Topological Quantum Material Candidate by Design. *ACS Cent. Sci.* **2019**, *5*, 900–910.
285. Hosen, M. M.; Dimitri, K.; Nandy, A. K.; Aperis, A.; Sankar, R.; Dhakal, G.; Maldonado, P.; Kabir, F.; Sims, C.; Chou, F.; Kaczorowski, D.; Durakiewicz, T.; Oppeneer, P. M.; Neupane, M. Distinct Multiple Fermionic States in a Single Topological Metal. *Nat. Commun.* **2018**, *9*, 3002.
286. Sakamaki, K.; Wada, H.; Nozaki, H.; Ōnuki, Y.; Kawai, M. Van der Waals Type Carbosulfide Superconductor. *Solid State Commun.* **2001**, *118*, 113–118.
287. Suzuki, M.; Suzuki, I. S.; Noji, T.; Koike, Y.; Walter, J. Successive Superconducting Transitions in $\text{Ta}_2\text{S}_2\text{C}$ Studied by Electrical Resistivity and Nonlinear ac Magnetic Susceptibility. *Phys. Rev. B: Condens. Matter Mater. Phys.* **2007**, *75*, 184536.
288. He, K. MnBi_2Te_4 -Family Intrinsic Magnetic Topological Materials. *NPJ Quantum Mater.* **2020**, *5*, 90.
289. Souchay, D.; Nentwig, M.; Günther, D.; Keilholz, S.; De Boer, J.; Zeugner, A.; Isaeva, A.; Ruck, M.; Wolter, A. U. B.; Büchner, B.; Oeckler, O. Layered Manganese Bismuth Tellurides With GeBi_4Te_7 - and $\text{GeBi}_6\text{Te}_{10}$ -type Structures: Towards Multifunctional Materials. *J. Mater. Chem. C* **2019**, *7*, 9939–9953.
290. Hu, C.; Ding, L.; Gordon, K. N.; Ghosh, B.; Tien, H.-J.; Li, H.; Linn, A. G.; Lien, S.-W.; Huang, C.-Y.; Mackey, S.; Liu, J.; Reddy, P. V. S.; Singh, B.; Agarwal, A.; Bansil, A.; Song, M.; Li, D.; Xu, S.-Y.; Lin, H.; Cao, H.; Chang, T.-R.; Dessau, D.; Ni, N. Realization of an Intrinsic Ferromagnetic Topological State in $\text{MnBi}_8\text{Te}_{13}$. *Sci. Adv.* **2020**, *6*, eaba4275.
291. Murakami, T.; Nambu, Y.; Koretsune, T.; Xiangyu, G.; Yamamoto, T.; Brown, C. M.; Kageyama, H. Realization of Interlayer Ferromagnetic Interaction in MnSb_2Te_4 Toward the Magnetic Weyl Semimetal State. *Phys. Rev. B* **2019**, *100*, 195103.
292. Huan, S.; Zhang, S.; Jiang, Z.; Su, H.; Wang, H.; Zhang, X.; Yang, Y.; Liu, Z.; Wang, X.; Yu, N.; Zou, Z.; Shen, D.; Liu, J.; Guo, Y. Multiple Magnetic Topological Phases in Bulk van der Waals Crystal MnSb_4Te_7 . *Phys. Rev. Lett.* **2021**, *126*, 246601.
293. Hao, Y.-J.; Liu, P.; Feng, Y.; Ma, X.-M.; Schwier, E. F.; Arita, M.; Kumar, S.; Hu, C.; Lu, R. E.; Zeng, M.; Wang, Y.; Hao, Z.; Sun, H.-Y.; Zhang, K.; Mei, J.; Ni, N.; Wu, L.; Shimada, K.; Chen, C.; Liu, Q.; Liu, C. Gapless Surface Dirac Cone in Antiferromagnetic Topological Insulator MnBi_2Te_4 . *Phys. Rev. X* **2019**, *9*, 041038.
294. Zhao, Y.-F.; Zhou, L.-J.; Wang, F.; Wang, G.; Song, T.; Ovchinnikov, D.; Yi, H.; Mei, R.; Wang, K.; Chan, M. H. W.; Liu, C.-X.; Xu, X.; Chang, C.-Z. Even–Odd Layer-Dependent Anomalous Hall Effect in Topological Magnet MnBi_2Te_4 Thin Films. *Nano Lett.* **2021**, *21*, 7691–7698.
295. Lapano, J.; Nuckols, L.; Mazza, A. R.; Pai, Y.-Y.; Zhang, J.; Lawrie, B.; Moore, R. G.; Eres, G.; Lee, H. N.; Du, M.-H.; Ward, T. Z.; Lee, J. S.; Weber, W. J.; Zhang, Y.; Brahlek, M. Adsorption-Controlled Growth of $\text{MnTe}(\text{Bi}_2\text{Te}_3)_n$ by Molecular Beam Epitaxy Exhibiting Stoichiometry-Controlled Magnetism. *Phys. Rev. Mater.* **2020**, *4*, 111201.
296. Shu, H. W.; Jaulmes, S.; Flahaut, J. Système AsGeTe : III. Étude cristallographique d’une famille de composés à modèles structuraux communs: $\beta\text{-As}_2\text{Te}_3$, As_4GeTe_7 et $\text{As}_2\text{Ge}_n\text{Te}_{3+n}$ ($n = 1\text{ à }5$). *J. Solid State Chem.* **1988**, *74*, 277–286.
297. Matsunaga, T.; Yamada, N. Structural Investigation of GeSb_2Te_4 A High-Speed Phase-Change Material. *Phys. Rev. B: Condens. Matter Mater. Phys.* **2004**, *69*, 104111.
298. Karpinskii, O. G.; Shelimova, L. E.; Kretova, M. A.; Zemskov, V. S. X-ray Diffraction Study of Ge-Bi-Te Mixed-Layer Ternary Compounds. *Inorg. Mater.* **2000**, *36*, 1108–1113.
299. Karpinskii, O. G.; Shelimova, L. E.; Avilov, E. S.; Kretova, M. A.; Zemskov, V. S. X-ray Diffraction Study of Mixed-Layer Compounds in the $\text{PbTe-Bi}_2\text{Te}_3$ System. *Inorg. Mater.* **2002**, *38*, 17–24.
300. Nemov, S. A.; Ulashkevich, Y. V.; Povolotskii, A. V.; Khlamov, I. I. Reflectance of a PbSb_2Te_4 Crystal in a Wide Spectral Range. *Semiconductors* **2016**, *50*, 1322–1326.
301. Saxena, A.; Sharma, M. M.; Sharma, P.; Kumar, Y.; Rani, P.; Singh, M.; Patnaik, S.; Awana, V. P. S. Structural and Weak Antilocalization Analysis of Topological Single-Crystal SnSb_2Te_4 . *J. Alloys Compd.* **2022**, *895*, 162553.
302. Zou, Y.-C.; Chen, Z.-G.; Zhang, E.; Kong, F.; Lu, Y.; Wang, L.; Drennan, J.; Wang, Z.; Xiu, F.; Cho, K.; Zou, J. Atomic Disorders in Layer Structured Topological Insulator SnBi_2Te_4 Nanoplates. *Nano Res.* **2018**, *11*, 696–706.
303. Matsunaga, T.; Kojima, R.; Yamada, N.; Kifune, K.; Kubota, Y.; Takata, M. Structural Features of GeSb_4Te_7 , an Intermetallic Compound in the $\text{GeTe-Sb}_2\text{Te}_3$ Homologous Series. *Chem. Mater.* **2008**, *20*, 5750–5755.
304. Kuznetsov, V. L.; Kuznetsova, L. A.; Rowe, D. M. Electrical Transport Properties of SnBi_4Te_7 and PbBi_4Te_7 With Different Deviations From Stoichiometry. *J. Phys. D Appl. Phys.* **2001**, *34*, 700–703.
305. Urban, P.; Schneider, M. N.; Erra, L.; Welzmler, S.; Fahrnbauer, F.; Oeckler, O. Temperature Dependent Resonant X-ray Diffraction of Single-Crystalline $\text{Ge}_2\text{Sb}_2\text{Te}_5$. *CrstEngComm* **2013**, *15*, 4823–4829.
306. Chatterjee, A.; Biswas, K. Solution-Based Synthesis of Layered Intergrowth Compounds of the Homologous $\text{Pb}_m\text{Bi}_{2n}\text{Te}_{3n+m}$ Series as Nanosheets. *Angew. Chem. Int. Ed.* **2015**, *54*, 5623–5627.

307. Matsunaga, T.; Kojima, R.; Yamada, N.; Kifune, K.; Kubota, Y.; Takata, M. Structural Investigation of $\text{Ge}_2\text{Sb}_2\text{Te}_6$, an Intermetallic Compound in the $\text{GeTe}-\text{Sb}_2\text{Te}_3$ Homologous Series. *Appl. Phys. Lett.* **2007**, *90*, 161919.
308. Jaulmes, S.; Shu, H. W.; Mazurier, A. Structure de l'octatellure de diarsenic et de pentagermanium. *Acta Crystallogr. C* **1987**, *43*, 2268–2270.
309. Nentwig, M.; Fahrnbauer, F.; Kasprick, M.; Oeckler, O. Single Crystal Structure Elucidation and Thermoelectric Properties of a Long-Periodically Ordered Germanium Arsenic Telluride. *J. Alloys Compd.* **2017**, *694*, 1160–1164.
310. Guo, P.; Sarangan, A. M.; Agha, I. A Review of Germanium-Antimony-Telluride Phase Change Materials for Non-Volatile Memories and Optical Modulators. *Appl. Sci.* **2019**, *9*, 530.
311. Schumacher, M.; Weber, H.; J vari, P.; Tsuchiya, Y.; Youngs, T. G. A.; Kaban, I.; Mazzarello, R. Structural, Electronic and Kinetic Properties of the Phase-Change Material $\text{Ge}_2\text{Sb}_2\text{Te}_5$ in the Liquid State. *Sci. Rep.* **2016**, *6*, 27434.
312. Yamada, N.; Ohno, E.; Akahira, N.; Nishiuchi, K. I.; Nagata, K. I.; Takao, M. High Speed Overwritable Phase Change Optical Disk Material. *Jpn. J. Appl. Phys.* **1987**, *26*, 61.
313. Caillat, T.; Huang, C. K.; Fleurial, J.-P.; Snyder, G. J.; Borshchevsky, A. *Synthesis and Thermoelectric Properties of Some Materials With the PbBi_4Te_7 Crystal Structure*, 2004.
314. Kuroda, K.; Miyahara, H.; Ye, M.; Ereemeev, S. V.; Koroteev, Y. M.; Krasovskii, E. E.; Chulkov, E. V.; Hiramoto, S.; Moriyoshi, C.; Kuroiwa, Y.; Miyamoto, K.; Okuda, T.; Arita, M.; Shimada, K.; Namatame, H.; Taniguchi, M.; Ueda, Y.; Kimura, A. Experimental Verification of PbBi_2Te_4 as a 3D Topological Insulator. *Phys. Rev. Lett.* **2012**, *108*, 206803.
315. Neupane, M.; Xu, S. Y.; Wray, L. A.; Petersen, A.; Shankar, R.; Alidoust, N.; Liu, C.; Fedorov, A.; Ji, H.; Allred, J. M.; Hor, Y. S.; Chang, T. R.; Jeng, H. T.; Lin, H.; Bansil, A.; Cava, R. J.; Hasan, M. Z. Topological Surface States and Dirac Point Tuning in Ternary Topological Insulators. *Phys. Rev. B: Condens. Matter Mater. Phys.* **2012**, *85*, 235406.
316. Haeuseler, H.; Srivastava, S. K. Phase Equilibria and Layered Phases in the Systems $\text{A}_2\text{X}_3-\text{M}_2\text{X}_3-\text{M}'\text{X}$ (A = Ga, In; M = Trivalent Metal; M' = Divalent Metal; X = S, Se). *Z. Krist.* **2000**, *215*, 205–221.
317. Pardo, M.-P.; Fourcroy, P.-H.; Flahaut, J. Systeme $\text{Ga}_2\text{S}_3\text{MnS}$ Diagramme de Phase—Etude Cristallographique. *Mater. Res. Bull.* **1975**, *10*, 665–675.
318. Torres, T.; Sagredo, V.; De Chabaud, L.; Attolini, G.; Bolzoni, F. The Crystal Structure of $\text{Fe}_2\text{In}_2\text{Se}_5$, a FeIn_2Se_4 -Related Polytype. *J. Phys. Chem. Solid* **2013**, *66*, 2049–2051.
319. Haeuseler, H.; Cordes, W.; Reinen, D.; Kesper, U. Materials with Layered Structures. VIII. Subsolidus Phase Diagram of the System $\text{MnIn}_2\text{S}_4-\text{MnIn}_2\text{Se}_4$ and Characterization of the Layered Materials $\text{MnIn}_x\text{S}_{4-x}\text{Se}_{4-x}$ by Electrical Measurements and Diffuse Reflectance Spectroscopy. *J. Solid State Chem.* **1993**, *106*, 501–505.
320. Haeuseler, H.; Kwarteng-Acheampong, W. Materials With Layered Structures II: A New Quaternary Compound With $\text{ZnIn}_2\text{S}_4(\text{IIIa})$ -Type Structure in the System $\text{MnGa}_2\text{S}_4-\text{MnCr}_2\text{S}_4$. *Mater. Res. Bull.* **1989**, *24*, 939–943.
321. She, H.; Wang, Y.; Zhou, H.; Li, Y.; Wang, L.; Huang, J.; Wang, Q. Preparation of $\text{ZnIn}_2\text{S}_6/\text{TiO}_2$ for Enhanced CO_2 Photocatalytic Reduction Activity Via Z-scheme Electron Transfer. *ChemCatChem* **2019**, *11*, 753–759.
322. Tomita, T.; Nambu, Y.; Nakatsuji, S.; Koeda, S.; Hedo, M.; Uwatoko, Y. Pressure Dependence of Electrical Transport in the Triangular Antiferromagnetic Insulators FeGa_2S_4 and $\text{Fe}_2\text{Ga}_2\text{S}_5$. *J. Physical Soc. Japan* **2009**, *78*, 094603.
323. Mantilla Ochoa, J. C.; Bindilatti, V.; Ter Haar, E.; Coaquira, J. A. H.; De Souza Brito, G. E.; Grates, X.; Sagredo, V. Spin Glass Behavior in MnIn_2Se_4 and $\text{Zn}_{1-x}\text{Mn}_x\text{In}_2\text{Se}_4$ Magnetic Semiconductors. *J. Magn. Magn. Mater.* **2004**, *272-276*, 1308–1309.
324. Torres, T.; Sagredo, V.; De Chabaud, L. M.; Attolini, G.; Bolzoni, F. Magnetic and Structural Characterization of the Semiconductor FeIn_2Se_4 . *Phys. B Condens. Matter* **2006**, *384*, 100–102.
325. Zhao, S.; De R otier, P. D.; Yaouanc, A.; Maclaughlin, D. E.; Mackie, J. M.; Bernal, O. O.; Nambu, Y.; Higo, T.; Nakatsuji, S. Spin Dynamics and Spin Freezing in the Triangular Lattice Antiferromagnets FeGa_2S_4 and NiGa_2S_4 . *Phys. Rev. B: Condens. Matter Mater. Phys.* **2012**, *86*, 064435.
326. Nakatsuji, S.; Tonomura, H.; Onuma, K.; Nambu, Y.; Sakai, O.; Maeno, Y.; Macaluso, R. T.; Chan, J. Y. Spin Disorder and Order in Quasi-2D Triangular Heisenberg Antiferromagnets: Comparative Study of FeGa_2S_4 , $\text{Fe}_2\text{Ga}_2\text{S}_5$, and NiGa_2S_4 . *Phys. Rev. Lett.* **2007**, *99*, 157203.
327. Chen, B.; Yang, J.; Wang, H.; Imai, M.; Ohta, H.; Michioka, C.; Yoshimura, K.; Fang, M. Magnetic Properties of Layered Itinerant Electron Ferromagnet Fe_3GeTe_2 . *J. Physical Soc. Japan* **2013**, *82*, 124711.
328. Fei, Z.; Huang, B.; Malinowski, P.; Wang, W.; Song, T.; Sanchez, J.; Yao, W.; Xiao, D.; Zhu, X.; May, A. F.; Wu, W.; Cobden, D. H.; Chu, J.-H.; Xu, X. Two-Dimensional Itinerant Ferromagnetism in Atomically Thin Fe_3GeTe_2 . *Nat. Mater.* **2018**, *17*, 778–782.
329. Kong, X.; Nguyen, G. D.; Lee, J.; Lee, C.; Calder, S.; May, A. F.; Gai, Z.; Li, A.-P.; Liang, L.; Berlijn, T. Interlayer Magnetism in $\text{Fe}_{3-x}\text{GeTe}_2$. *Phys. Rev. Mater.* **2020**, *4*, 094403.
330. May, A. F.; Calder, S.; Cantoni, C.; Cao, H.; McGuire, M. A. Magnetic Structure and Phase Stability of the van der Waals Bonded Ferromagnet $\text{Fe}_{3-x}\text{GeTe}_2$. *Phys. Rev. B* **2016**, *93*, 014411.
331. Su, Y.; Li, X.; Zhu, M.; Zhang, J.; You, L.; Tsymal, E. Y. Van der Waals Multiferroic Tunnel Junctions. *Nano Lett.* **2021**, *21*, 175–181.
332. Roemer, R.; Liu, C.; Zou, K. Robust Ferromagnetism in Wafer-Scale Monolayer and Multilayer Fe_3GeTe_2 . *NPJ 2D Mater. Appl.* **2020**, *4*, 33.
333. Deng, Y.; Yu, Y.; Song, Y.; Zhang, J.; Wang, N. Z.; Sun, Z.; Yi, Y.; Wu, Y. Z.; Wu, S.; Zhu, J.; Wang, J.; Chen, X. H.; Zhang, Y. Gate-Tunable Room-Temperature Ferromagnetism in Two-Dimensional Fe_3GeTe_2 . *Nature* **2018**, *563*, 94–99.
334. Weber, D.; Trout, A. H.; McComb, D. W.; Goldberger, J. E. Decomposition-Induced Room-Temperature Magnetism of the Na-Intercalated Layered Ferromagnet $\text{Fe}_{3-x}\text{GeTe}_2$. *Nano Lett.* **2019**, *19*, 5031–5035.
335. Deiseroth, H.-J.; Aleksandrov, K.; Reiner, C.; Kienle, L.; Kremer, R. K. Fe_3GeTe_2 and Ni_3GeTe_2 —Two New Layered Transition-Metal Compounds: Crystal Structures, HRTEM Investigations, and Magnetic and Electrical Properties. *Eur. J. Inorg. Chem.* **2006**, *2006*, 1561–1567.
336. Seo, J.; Kim, D. Y.; An, E. S.; Kim, K.; Kim, G.-Y.; Hwang, S.-Y.; Kim, D. W.; Jang, B. G.; Kim, H.; Eom, G.; Seo, S. Y.; Stania, R.; Muntwiler, M.; Lee, J.; Watanabe, K.; Taniguchi, T.; Jo, Y. J.; Lee, J.; Min, B. I.; Jo, M. H.; Yeom, H. W.; Choi, S.-Y.; Shim, J. H.; Kim, J. S. Nearly Room Temperature Ferromagnetism in a Magnetic Metal-Rich van der Waals Metal. *Sci. Adv.* **2020**, *6*, 8912.
337. May, A. F.; Ovchinnikov, D.; Zheng, Q.; Hermann, R.; Calder, S.; Huang, B.; Fei, Z.; Liu, Y.; Xu, X.; McGuire, M. A. Ferromagnetism Near Room Temperature in the Cleavable van der Waals Crystal Fe_3GeTe_2 . *ACS Nano* **2019**, *13*, 4436–4442.
338. Seo, J.; An, E. S.; Park, T.; Hwang, S.-Y.; Kim, G.-Y.; Song, K.; Noh, W.-S.; Kim, J. Y.; Choi, G. S.; Choi, M.; Oh, E.; Watanabe, K.; Taniguchi, T.; Park, J. H.; Jo, Y. J.; Yeom, H. W.; Choi, S.-Y.; Shim, J. H.; Kim, J. S. Tunable High-Temperature Itinerant Antiferromagnetism in a van der Waals Magnet. *Nat. Commun.* **2021**, *12*, 2844.
339. Di Salvo, F. J.; Chen, C. H.; Fleming, R. M.; Waszczak, J. V.; Dunn, R. G.; Sunshine, S. A.; Ibers, J. A. Physical and Structural Properties of the New Layered Compounds Ta_2NiS_5 and Ta_2NiSe_5 . *J. Less-Common Met.* **1986**, *116*, 51–61.
340. Lu, Y. F.; Kono, H.; Larkin, T. I.; Rost, A. W.; Takayama, T.; Boris, A. V.; Keimer, B.; Takagi, H. Zero-Gap Semiconductor to Excitonic Insulator Transition in Ta_2NiSe_5 . *Nat. Commun.* **2017**, *8*, 14408.
341. Nakamura, S.; Noji, T.; Hatakeda, T.; Sato, K.; Kawamata, T.; Kato, M.; Koike, Y. New Ethylenediamine-Intercalated Superconductor $(\text{C}_2\text{H}_8\text{N}_2)_y\text{Ta}_2\text{PdSe}_6$ with $T_c = 4.5$ K. *J. Phys. Conf. Ser.* **2018**, *969*, 012076.
342. Fleming, R. M.; Sunshine, S. A.; Chen, C. H.; Schneemeyer, L. F.; Waszczak, J. V. Defect-Inhibited Incommensurate Distortion in Ta_2NiSe_7 . *Phys. Rev. B: Condens. Matter Mater. Phys.* **1990**, *42*, 4954–4959.
343. Tremel, W. Isolated and Condensed Ta_2Ni_2 Clusters in the Layered Tellurides $\text{Ta}_2\text{Ni}_2\text{Te}_4$ and $\text{Ta}_2\text{Ni}_3\text{Te}_5$. *Angew. Chem. Int. Ed. Engl.* **1991**, *30*, 840–843.
344. Jiao, W.-H.; Tang, Z.-T.; Sun, Y.-L.; Liu, Y.; Tao, Q.; Feng, C.-M.; Zeng, Y.-W.; Xu, Z.-A.; Cao, G.-H. Superconductivity in a Layered $\text{Ta}_4\text{Pd}_3\text{Te}_{16}$ With PdTe_2 Chains. *J. Am. Chem. Soc.* **2014**, *136*, 1284–1287.
345. Jiao, W.-H.; He, L.-P.; Liu, Y.; Xu, X.-F.; Li, Y.-K.; Zhang, C.-H.; Zhou, N.; Xu, Z.-A.; Li, S.-Y.; Cao, G.-H. Superconductivity in $\text{Ta}_3\text{Pd}_3\text{Te}_{14}$ With Quasi-One-Dimensional PdTe_2 Chains. *Sci. Rep.* **2016**, *6*, 21628.
346. Hu, J.; Dai, Z.; Kan, X.; Zheng, G.; Chen, Z.; Ma, Y. Transport and Thermal Properties of Single Crystal TaNiTe_5 . *J. Alloys Compd.* **2022**, *895*, 162563.

347. Xu, C.; Liu, Y.; Cai, P.; Li, B.; Jiao, W.; Li, Y.; Zhang, J.; Zhou, W.; Qian, B.; Jiang, X.; Shi, Z.; Sankar, R.; Zhang, J.; Yang, F.; Zhu, Z.; Biswas, P.; Qian, D.; Ke, X.; Xu, X. Anisotropic Transport and Quantum Oscillations in the Quasi-One-Dimensional TaNiTe₅: Evidence for the Nontrivial Band Topology. *J. Phys. Chem. Lett.* **2020**, *11*, 7782–7789.
348. Mar, A.; Jobic, S.; Ibers, J. A. Metal-Metal vs Tellurium-Tellurium Bonding in WTe₂ and its Ternary Variants TaIrTe₄ and NbIrTe₄. *J. Am. Chem. Soc.* **1992**, *114*, 8963–8971.
349. Wiscons, R. A.; Cho, Y.; Han, S. Y.; Dismukes, A. H.; Meirzadeh, E.; Nuckolls, C.; Berkelbach, T. C.; Roy, X. Polytypism, Anisotropic Transport, and Weyl Nodes in the van der Waals Metal TaFeTe₄. *J. Am. Chem. Soc.* **2021**, *143*, 109–113.
350. Belopolski, I.; Yu, P.; Sanchez, D. S.; Ishida, Y.; Chang, T.-R.; Zhang, S. S.; Xu, S.-Y.; Zheng, H.; Chang, G.; Bian, G.; Jeng, H.-T.; Kondo, T.; Lin, H.; Liu, Z.; Shin, S.; Hasan, M. Z. Signatures of a Time-Reversal Symmetric Weyl Semimetal With Only Four Weyl Points. *Nat. Commun.* **2017**, *8*, 942.
351. Haubold, E.; Koepfner, K.; Efremov, D.; Khim, S.; Fedorov, A.; Kushnirenko, Y.; Van Den Brink, J.; Wurmehl, S.; Büchner, B.; Kim, T. K.; Hoesch, M.; Sumida, K.; Taguchi, K.; Yoshikawa, T.; Kimura, A.; Okuda, T.; Borisenko, S. V. Experimental Realization of Type-II Weyl State in Noncentrosymmetric TaIrTe₄. *Phys. Rev. B* **2017**, *95*, 241108.
352. Koepfner, K.; Kasinathan, D.; Efremov, D. V.; Khim, S.; Borisenko, S.; Büchner, B.; Van Den Brink, J. TaIrTe₄: A Ternary Type-II Weyl Semimetal. *Phys. Rev. B* **2016**, *93*, 201101.
353. Cai, S.; Emmanouilidou, E.; Guo, J.; Li, X.; Li, Y.; Yang, K.; Li, A.; Wu, Q.; Ni, N.; Sun, L. Observation of Superconductivity in the Pressurized Weyl-Semimetal Candidate TaIrTe₄. *Phys. Rev. B* **2019**, *99*, 020503.
354. Liu, Y.; Gu, Q.; Peng, Y.; Qi, S.; Zhang, N.; Zhang, Y.; Ma, X.; Zhu, R.; Tong, L.; Feng, J.; Liu, Z.; Chen, J.-H. Raman Signatures of Broken Inversion Symmetry and In-Plane Anisotropy in Type-II Weyl Semimetal Candidate TaIrTe₄. *Adv. Mater.* **2018**, *30*, 1706402.
355. Shipunov, G.; Piening, B. R.; Wuttke, C.; Romanova, T. A.; Sadakov, A. V.; Sobolevskiy, O. A.; Guzovsky, E. Y.; Usoltsev, A. S.; Pudalov, V. M.; Efremov, D. V.; Subakti, S.; Wolf, D.; Lubk, A.; Büchner, B.; Aswartham, S. Layered van der Waals Topological Metals of TaTMTe₄ (TM = Ir, Rh, Ru) Family. *J. Phys. Chem. Lett.* **2021**, *12*, 6730–6735.
356. Shojaei, I. A.; Pournia, S.; Le, C.; Ortiz, B. R.; Jnawali, G.; Zhang, F.-C.; Wilson, S. D.; Jackson, H. E.; Smith, L. M. A Raman Probe of Phonons and Electron-Phonon Interactions in the Weyl Semimetal NbIrTe₄. *Sci. Rep.* **2021**, *11*, 8155.
357. Kumar, D.; Hsu, C.-H.; Sharma, R.; Chang, T.-R.; Yu, P.; Wang, J.; Eda, G.; Liang, G.; Yang, H. Room-Temperature Nonlinear Hall Effect and Wireless Radiofrequency Rectification in Weyl Semimetal TaIrTe₄. *Nat. Nanotechnol.* **2021**, *16*, 421–425.
358. Xing, Y.; Shao, Z.; Ge, J.; Luo, J.; Wang, J.; Zhu, Z.; Liu, J.; Wang, Y.; Zhao, Z.; Yan, J.; Mandrus, D.; Yan, B.; Liu, X.-J.; Pan, M.; Wang, J. Surface Superconductivity in the Type II Weyl Semimetal TaIrTe₄. *Natl. Sci. Rev.* **2020**, *7*, 579–587.
359. Tremel, W. TaNi₂Te₂, A Novel Layered Telluride, and TaCo₂Te₂, a Structural Variant With Peierls Distortion. *Angew. Chem. Int. Ed. Engl.* **1992**, *31*, 217–220.
360. Singha, R.; Yuan, F.; Cheng, G.; Salters, T. H.; Oey, Y. M.; Villalpando, G. V.; Jovanovic, M.; Yao, N.; Schoop, L. M. TaCo₂Te₂: An Air-Stable, High Mobility Van der Waals Material with Probable Magnetic Order. *Adv. Funct. Mater.* **2022**, *32*, 2108920.
361. Neuhausen, J.; Potthoff, E.; Tremel, W.; Ensling, J.; Güttlich, P.; Kremer, R. K. TaFe_{1.14}Te₃, A New Low-Dimensional Ternary Tantalum Telluride. *Z. Naturforsch. B* **1993**, *48*, 797–811.
362. Liu, R. H.; Zhang, M.; Cheng, P.; Yan, Y. J.; Xiang, Z. J.; Ying, J. J.; Wang, X. F.; Wang, A. F.; Ye, G. J.; Luo, X. G.; Chen, X. H. Spin-Density-Wave Transition of Fe1 Zigzag Chains and Metamagnetic Transition of Fe2 in TaFe_{1+y}Te₃. *Phys. Rev. B: Condens. Matter Mater. Phys.* **2011**, *84*, 184432.
363. Li, J.; Badding, M. E.; Disalvo, F. J. New Layered Ternary Niobium Tellurides: Synthesis, Structure, and Properties of Niobium Metal Telluride, NbMTe₂ (M = Iron, Cobalt). *Inorg. Chem.* **1992**, *31*, 1050–1054.
364. Li, J.; McCulley, F.; McDonnell, S. L.; Masciocchi, N.; Proserpio, D. M.; Sironi, A. X-Ray Powder Diffraction as a Tool for Facing Twins: The Case of the Monoclinic Niobium Cobalt Ditelluride and Tantalum Cobalt Ditelluride Phases. *Inorg. Chem.* **1993**, *32*, 4829–4833.
365. Zhang, J. H.; Chen, F.; Li, J.; O'Connor, C. J. Magnetic Property of Layered Compound NbFeTe₂. *J. Appl. Phys.* **1997**, *81*, 5283–5285.
366. Gareh, J. E.; Boucher, F.; Evain, M. Synthesis, Crystal and Electronic Structure of the Ternary Layered Compounds NbA_{1/2}Te₂ (A = Si, Ge). *Eur. J. Solid State Inorg. Chem.* **1996**, *33*, 355–369.
367. Zhao, M.; Xia, W.; Wang, Y.; Luo, M.; Tian, Z.; Guo, Y.; Hu, W.; Xue, J. Nb₂SiTe₄: A Stable Narrow-Gap Two-Dimensional Material with Ambipolar Transport and Mid-Infrared Response. *ACS Nano* **2019**, *13*, 10705–10710.
368. Zhou, K.; Deng, J.; Chen, L.; Xia, W.; Guo, Y.; Yang, Y.; Guo, J.-G.; Guo, L. Observation of Large in-Plane Anisotropic Transport in van der Waals Semiconductor Nb₂SiTe₄. *Chin. Phys. B* **2021**, *30*, 087202.
369. Li, J.; Badding, M. E.; Disalvo, F. J. Synthesis and Structure of Nb₃SiTe₆, a New Layered Ternary Niobium Telluride Compound. *J. Alloys Compd.* **1992**, *184*, 257–263.
370. Li, S.; Liu, Y.; Wang, S.-S.; Yu, Z.-M.; Guan, S.; Sheng, X.-L.; Yao, Y.; Yang, S. A. Nonsymmorphic-Symmetry-Protected Hourglass Dirac Loop, Nodal Line, and Dirac Point in Bulk and Monolayer X₃SiTe₆ (X = Ta, Nb). *Phys. Rev. B* **2018**, *97*, 045131.
371. Li, Y.; Ran, Z.; Jiang, W.; Jing, Q.; Hu, J.; Luo, W.; Qian, D. Anisotropic Surface State in a Topological Semimetal Candidate Ta₃SiTe₆. *Appl. Phys. Lett.* **2022**, *120*, 041602.
372. Mar, A.; Ibers, J. A. The Layered Ternary Germanium Tellurides ZrGeTe₄, HfGeTe₄, and TiGeTe₆: Structure, Bonding, and Physical Properties. *J. Am. Chem. Soc.* **1993**, *115*, 3227–3238.
373. Yan, W.; Johnson, B. C.; Balendhran, S.; Cadusch, J.; Yan, D.; Michel, J. I.; Wang, S.; Zheng, T.; Crozier, K.; Bullock, J. Visible to Short-Wave Infrared Photodetectors Based on ZrGeTe₄ van der Waals Materials. *ACS Appl. Mater. Interfaces* **2021**, *13*, 45881–45889.
374. Blaschkowski, B.; Rosner, H.; Schnelle, W.; Schleid, T. Sulfidiodide (MSI) der schweren Lanthanoide (M = Gd – Lu): Kristallstrukturen und Magnetische Eigenschaften. *Z. Anorg. Allg. Chem.* **2013**, *639*, 237–240.
375. Stöwe, K. Die Kristallstrukturen von ErSe₂ und NaErSe₂. *Z. Anorg. Allg. Chem.* **1997**, *623*, 1639–1643.
376. Coïc, L.; Spiesser, M.; Palvadeau, P.; Rouxel, J. Chromium (III) Oxyhalides: Magnetic and Optical Properties. Lithium Intercalation. *Mater. Res. Bull.* **1981**, *16*, 229–236.
377. Maule, C. H.; Tothill, J. N.; Strange, P.; Wilson, J. A. An Optical Investigation Into the 3d¹ and 3d² Transition-Metal Halides and Oxyhalides, Compounds Near to Delocalisation. *J. Phys. C Solid State Phys.* **1988**, *21*, 2153–2179.
378. Telford, E. J.; Dismukes, A. H.; Lee, K.; Cheng, M.; Wieteska, A.; Bartholomew, A. K.; Chen, Y.-S.; Xu, X.; Pasupathy, A. N.; Zhu, X.; Dean, C. R.; Roy, X. Layered Antiferromagnetism Induces Large Negative Magnetoresistance in the van der Waals Semiconductor CrSBr. *Adv. Mater.* **2020**, *32*, 2003240.
379. Vénien, J. P.; Palvadeau, P.; Schleich, D.; Rouxel, J. Vanadium (III) Oxychloride: Magnetic, Optical and Electrical Properties; Lithium and Molecular Intercalations. *Mater. Res. Bull.* **1979**, *14*, 891–897.
380. Zeng, Y.; Gu, P.; Zhao, Z.; Zhang, B.; Lin, Z.; Peng, Y.; Li, W.; Zhao, W.; Leng, Y.; Tan, P.; Yang, T.; Zhang, Z.; Song, Y.; Yang, J.; Ye, Y.; Tian, K.; Hou, Y. 2D FeOCl: A Highly In-Plane Anisotropic Antiferromagnetic Semiconductor Synthesized Via Temperature-Oscillation Chemical Vapor Transport. *Adv. Mater.* **2022**, *34*, 2108847.
381. Krimmel, A.; Stremfper, J.; Bohnenbuck, B.; Keimer, B.; Hoinkis, M.; Klemm, M.; Horn, S.; Loidl, A.; Sing, M.; Claessen, R.; Zimmermann, M. V. Incommensurate Structure of the Spin-Peierls Compound TiOCl in Zero and Finite Magnetic Fields. *Phys. Rev. B: Condens. Matter Mater. Phys.* **2006**, *73*, 172413.
382. Shaz, M.; Van Smaalen, S.; Palatinus, L.; Hoinkis, M.; Klemm, M.; Horn, S.; Claessen, R. Spin-Peierls Transition in TiOCl. *Phys. Rev. B: Condens. Matter Mater. Phys.* **2005**, *71*, 100405.
383. Wiedenmann, A.; Venien, J. P.; Palvadeau, P.; Rossat-Mignod, J. Magnetic Ordering of the Quasi-Two-Dimensional System VOCl. *J. Phys. C Solid State Phys.* **1983**, *16*, 5339–5350.
384. Zhang, T.; Wang, Y.; Li, H.; Zhong, F.; Shi, J.; Wu, M.; Sun, Z.; Shen, W.; Wei, B.; Hu, W.; Liu, X.; Huang, L.; Hu, C.; Wang, Z.; Jiang, C.; Yang, S.; Zhang, Q.-M.; Qu, Z. Magnetism and Optical Anisotropy in van der Waals Antiferromagnetic Insulator CrOCl. *ACS Nano* **2019**, *13*, 11353–11362.
385. Göser, O.; Paul, W.; Kahle, H. G. Magnetic Properties of CrSBr. *J. Magn. Magn. Mater.* **1990**, *92*, 129–136.
386. Grant, R. W. Magnetic Structure of FeOCl. *J. Appl. Phys.* **1971**, *42*, 1619–1620.

387. Lee, K.; Dismukes, A. H.; Telford, E. J.; Wiscons, R. A.; Wang, J.; Xu, X.; Nuckolls, C.; Dean, C. R.; Roy, X.; Zhu, X. Magnetic Order and Symmetry in the 2D Semiconductor CrSBr. *Nano Lett.* **2021**, *21*, 3511–3517.
388. Ferrenti, A. M.; Klemenz, S.; Lei, S.; Song, X.; Ganter, P.; Lotsch, B. V.; Schoop, L. M. Change in Magnetic Properties upon Chemical Exfoliation of FeOCl. *Inorg. Chem.* **2020**, *59*, 1176–1182.
389. Imai, H.; Saegusa, T.; Ohsugi, S.; Furukawa, J. Oxyaluminum Compound Catalysts for the Polymerizations of Cyclic Ethers and Vinyl Monomers. *Makromol. Chem.* **1965**, *81*, 119–128.
390. Bian, Y.; Nie, L.; Wang, A.; Zhang, L.; Yue, R.; Han, N.; Chen, Y. Facile Synthesis of Stoichiometric InOCl Mesoporous Material for High Performance Formaldehyde gas Sensors. *Sens. Actuators B* **2020**, *319*, 128078.
391. Felser, C.; Seshadri, R. Electronic Structures and Instabilities of ZnCl and HfCl: Implications for Superconductivity in the Doped Compounds. *J. Mater. Chem.* **1999**, *9*, 459–464.
392. Feng, F.; Guo, H.; Li, D.; Wu, C.; Wu, J.; Zhang, W.; Fan, S.; Yang, Y.; Wu, X.; Yang, J.; Ye, B.; Xie, Y. Highly Efficient Photothermal Effect by Atomic-Thickness Confinement in Two-Dimensional ZnCl Nanosheets. *ACS Nano* **2015**, *9*, 1683–1691.
393. Ji, J.; Sun, M.; Cai, Y.; Wang, Y.; Sun, Y.; Ren, W.; Zhang, Z.; Jin, F.; Zhang, Q. Rare-Earth Chalcogenides: A Family of van der Waals Layered Kitaev Spin Liquid Candidates. *Chin. Phys. Lett.* **2021**, *38*, 047502.
394. Kucek, V.; Drasar, C.; Navratil, J.; Benes, L.; Lostak, P. Optical and Transport Properties of GaGeTe Single Crystals. *J. Cryst. Growth* **2013**, *380*, 72–77.
395. Wang, W.; Li, L.; Zhang, Z.; Yang, J.; Tang, D.; Zhai, T. Ultrathin GaGeTe p-Type Transistors. *Appl. Phys. Lett.* **2017**, *111*, 203504.
396. Dau, M. T.; Vergnaud, C.; Gay, M.; Alvarez, C. J.; Marty, A.; Beigné, C.; Jalabert, D.; Jacquot, J. F.; Renault, O.; Okuno, H.; Jamet, M. van der Waals Epitaxy of Mn-Doped MoSe₂ on Mica. *APL Mater.* **2019**, *7*, 051111.
397. Martinez, L. M.; Delgado, J. A.; Saiz, C. L.; Cosio, A.; Wu, Y.; Villagrán, D.; Gandha, K.; Karthik, C.; Niebedim, I. C.; Singamaneni, S. R. Magnetic and Electrocatalytic Properties of Transition Metal Doped MoS₂ Nanocrystals. *J. Appl. Phys.* **2018**, *124*, 153903.
398. Pham, Y. T. H.; Liu, M.; Jimenez, V. O.; Yu, Z.; Kalappattil, V.; Zhang, F.; Wang, K.; Williams, T.; Terrones, M.; Phan, M.-H. Tunable Ferromagnetism and Thermally Induced Spin Flip in Vanadium-Doped Tungsten Diselenide Monolayers at Room Temperature. *Adv. Mater.* **2020**, *32*, 2003607.
399. Zhang, F.; Zheng, B.; Sebastian, A.; Olson, D. H.; Liu, M.; Fujisawa, K.; Pham, Y. T. H.; Jimenez, V. O.; Kalappattil, V.; Miao, L.; Zhang, T.; Pendurthi, R.; Lei, Y.; Elias, A. L.; Wang, Y.; Alem, N.; Hopkins, P. E.; Das, S.; Crespi, V. H.; Phan, M.-H.; Terrones, M. Monolayer Vanadium-Doped Tungsten Disulfide: A Room-Temperature Dilute Magnetic Semiconductor. *Adv. Sci.* **2020**, *7*, 2001174.
400. Tan, H.; Wang, C.; Hu, W.; Duan, H.; Guo, P.; Li, N.; Li, G.; Cai, L.; Sun, Z.; Hu, F.; Yan, W. Reversible Tuning of the Ferromagnetic Behavior in Mn-Doped MoS₂ Nanosheets Via Interface Charge Transfer. *ACS Appl. Mater. Interfaces* **2018**, *10*, 31648–31654.
401. Li, Q.; Zhao, X.; Deng, L.; Shi, Z.; Liu, S.; Wei, Q.; Zhang, L.; Cheng, Y.; Zhang, L.; Lu, H.; Gao, W.; Huang, W.; Qiu, C.-W.; Xiang, G.; Pennycook, S. J.; Xiong, Q.; Loh, K. P.; Peng, B. Enhanced Valley Zeeman Splitting in Fe-Doped Monolayer MoS₂. *ACS Nano* **2020**, *14*, 4636–4645.
402. Huey, W. L. B.; Ochs, A. M.; Williams, A. J.; Zhang, Y.; Kraguljac, S.; Deng, Z.; Moore, C. E.; Windl, W.; Lau, C. N.; Goldberger, J. E. Cr_xPt_{1-x}Te₂ (x ≤ 0.45): A FAMILY of Air-Stable and Exfoliable van der Waals Ferromagnets. *ACS Nano* **2022**, *16*, 3852–3860.
403. Cao, Q.; Grote, F.; Hußmann, M.; Eigler, S. Emerging Field of Few-Layered Intercalated 2D Materials. *Nanoscale Adv.* **2021**, *3*, 963–982.
404. Stark, M. S.; Kuntz, K. L.; Martens, S. J.; Warren, S. C. Intercalation of Layered Materials from Bulk to 2D. *Adv. Mater.* **2019**, *31*, 1808213.
405. Tributsch, H. Photo-Intercalation: Possible Application in Solar Energy Devices. *Appl. Phys.* **1980**, *23*, 61–71.
406. Wan, J.; Lacey, S. D.; Dai, J.; Bao, W.; Fuhrer, M. S.; Hu, L. Tuning Two-Dimensional Nanomaterials by Intercalation: Materials, Properties and Applications. *Chem. Soc. Rev.* **2016**, *45*, 6742–6765.
407. Wang, M.; Williams, D.; Lahti, G.; Teshima, S.; Aguilar, D. D.; Perry, R.; Koski, K. J. Chemical Intercalation of Heavy Metal, Semimetal, and Semiconductor Atoms Into 2D Layered Chalcogenides. *2D Mater.* **2018**, *5*, 045005.
408. Yoffe, A. Layer Compounds. *Annu. Rev. Mater. Sci.* **1973**, *3*, 147–170.
409. Whittingham, M. S. Intercalation Chemistry and Energy Storage. *J. Solid State Chem.* **1979**, *29*, 303–310.
410. Fan, X.; Xu, P.; Zhou, D.; Sun, Y.; Li, Y. C.; Nguyen, M. A. T.; Terrones, M.; Mallouk, T. E. Fast and Efficient Preparation of Exfoliated 2H MoS₂ Nanosheets by Sonication-Assisted Lithium Intercalation and Infrared Laser-Induced 1T to 2H Phase Reversion. *Nano Lett.* **2015**, *15*, 5956–5960.
411. Schurz, C. M.; Shlyk, L.; Schleid, T.; Niewa, R. Superconducting Nitride Halides MNX (M = Ti, Zr, Hf; X = Cl, Br, I). *Z. Kristallogr. - Cryst. Mater.* **2011**, *226*, 395–416.
412. Yagyu, H.; Kato, M.; Tezuka, H.; Noji, T.; Yamanaka, S.; Koike, Y. A new Family of Superconducting Intercalation Compound of Mg_xMnCl (M = Zr, Hf). *Phys. C* **2010**, *470*, S760–S761.
413. Morosan, E.; Zandbergen, H. W.; Dennis, B. S.; Bos, J. W. G.; Onose, Y.; Klimczuk, T.; Ramirez, A. P.; Ong, N. P.; Cava, R. J. Superconductivity in Cu_xTiSe₂. *Nat. Phys.* **2006**, *2*, 544–550.
414. Weller, T. E.; Ellerby, M.; Saxena, S. S.; Smith, R. P.; Skipper, N. T. Superconductivity in the Intercalated Graphite Compounds C₆Yb and C₆Ca. *Nat. Phys.* **2005**, *1*, 39–41.
415. Morosan, E.; Zandbergen, H. W.; Li, L.; Lee, M.; Checkelsky, J. G.; Heinrich, M.; Siegrist, T.; Ong, N. P.; Cava, R. J. Sharp Switching of the Magnetization in Fe_{1/4}TaS₂. *Phys. Rev. B: Condens. Matter Mater. Phys.* **2007**, *75*, 104401.
416. Caswell, N.; Solin, S. A. Vibrational Excitations of Pure FeCl₃ and Graphite Intercalated With Ferric Chloride. *Solid State Commun.* **1978**, *27*, 961–967.
417. Cowley, J. M.; Ibers, J. A. The Structures of Some Ferric Chloride–Graphite Compounds. *Acta Crystallogr.* **1956**, *9*, 421–431.
418. Bointon, T. H.; Khrapach, I.; Yakimova, R.; Shytov, A. V.; Craciun, M. F.; Russo, S. Approaching Magnetic Ordering in Graphene Materials by FeCl₃ Intercalation. *Nano Lett.* **2014**, *14*, 1751–1755.
419. Kim, N.; Kim, K. S.; Jung, N.; Brus, L.; Kim, P. Synthesis and Electrical Characterization of Magnetic Bilayer Graphene Intercalate. *Nano Lett.* **2011**, *11*, 860–865.
420. Jian, Z.; Luo, W.; Ji, X. Carbon Electrodes for K-Ion Batteries. *J. Am. Chem. Soc.* **2015**, *137*, 11566–11569.
421. Li, J.; Yuan, X.; Lin, C.; Yang, Y.; Xu, L.; Du, X.; Xie, J.; Lin, J.; Sun, J. Achieving High Pseudocapacitance of 2D Titanium Carbide (MXene) by Cation Intercalation and Surface Modification. *Adv. Energy Mater.* **2017**, *7*, 1602725.

4.15 A practical guide to Three-dimensional halide perovskites: Structure, synthesis, and measurement

Kurt P. Lindquist^a, Julian A. Vigil^{a,b}, Alexander C. Su^a, and Hemamala I. Karunadasa^{a,c}, ^a Department of Chemistry, Stanford University, Stanford, CA, United States; ^b Department of Chemical Engineering, Stanford University, Stanford, CA, United States; and ^c Stanford Institute for Materials and Energy Sciences, SLAC National Accelerator Laboratory, Menlo Park, CA, United States

© 2023 Elsevier Ltd. All rights reserved.

4.15.1	Introduction	500
4.15.2	A brief history	501
4.15.3	Structure and composition	501
4.15.3.1	Single perovskites	502
4.15.3.2	Double perovskites	503
4.15.3.3	Perovskites with unusual ordering	505
4.15.3.4	Alloyed perovskites	505
4.15.4	Electronic structure	506
4.15.4.1	Introduction and theory	506
4.15.4.2	Density functional theory	508
4.15.4.3	Computational approximations	510
4.15.4.3.1	Exchange-correlation functional	510
4.15.4.3.2	Basis functions and pseudopotentials	511
4.15.4.3.3	Relativistic effects and spin-orbit coupling	511
4.15.4.3.4	Alloyed systems	511
4.15.4.4	Case study: Band structure of CsPbBr ₃	512
4.15.4.5	Single perovskites	512
4.15.4.6	Double perovskites	514
4.15.5	Synthesis	516
4.15.5.1	Introduction	516
4.15.5.2	Solid-state synthesis and crystallization from a melt	518
4.15.5.2.1	High-temperature solid-state synthesis	518
4.15.5.2.2	Room-temperature mechanochemical methods	518
4.15.5.2.3	The Bridgman method: Bulk crystal growth from a melt	519
4.15.5.3	Solution-state synthesis	519
4.15.5.3.1	Temperature-controlled methods	521
4.15.5.3.2	Solvent evaporation methods	522
4.15.5.3.3	Mixed-solvent methods	522
4.15.5.3.4	Hydrothermal and solvothermal methods	523
4.15.5.3.5	Ultrasound- and microwave-assisted methods	523
4.15.5.4	Thin-film deposition	524
4.15.5.5	Post-synthetic transformations	525
4.15.6	Measurement	526
4.15.6.1	Introduction	526
4.15.6.2	Elemental analysis	526
4.15.6.3	X-ray and neutron scattering	527
4.15.6.3.1	Powder X-ray diffraction	527
4.15.6.3.2	Single-crystal X-ray diffraction	528
4.15.6.3.3	Neutron diffraction	529
4.15.6.3.4	Diffuse and total scattering	529
4.15.6.3.5	Inelastic X-ray and neutron scattering	530
4.15.6.3.6	Other X-ray scattering techniques	531
4.15.6.4	X-ray absorption spectroscopy	531
4.15.6.5	Photoemission spectroscopy	532
4.15.6.5.1	X-ray photoelectron spectroscopy	532
4.15.6.5.2	Ultraviolet photoelectron spectroscopy	533
4.15.6.5.3	Angle-resolved photoemission spectroscopy	534
4.15.6.6	Optical, vibrational, nuclear, and electronic spectroscopy	534
4.15.6.6.1	Ultraviolet-visible-near infrared spectroscopy	534
4.15.6.6.2	Photoluminescence spectroscopy	538
4.15.6.6.3	Vibrational spectroscopy	540

4.15.6.6.4	Nuclear magnetic resonance spectroscopy	542
4.15.6.7	Microscopy	542
4.15.6.7.1	Optical microscopy	542
4.15.6.7.2	Electron microscopy	544
4.15.6.8	Electronic and ionic conductivity	545
4.15.7	Some peculiar properties	546
4.15.7.1	Perovskites under high pressure	546
4.15.7.2	Hole doping and metallic transport in Sn ²⁺ -based perovskites	547
4.15.7.3	Halide conductivity and halogen loss	547
4.15.7.4	Light-induced halide segregation	548
Acknowledgements		549
References		550

Abstract

Halide perovskites, a diverse class of crystalline semiconductors, have recently been under intense study by numerous research communities owing primarily to their efficacy as solar-cell absorbers. With this surge in interest has come a plethora of reports, which are challenging to navigate, particularly as a new researcher in the field. Here, we offer a practical guide to the crystal and electronic structures, synthesis, and measurement and characterization of 3D halide perovskites. We do not attempt to provide a comprehensive review of any one topic; instead, we hope to offer the interested researcher who is unfamiliar with the field a tractable entry point into the vast and diverse field of 3D halide perovskites. We start with a brief history and then describe the crystal structure and composition, including multiple subtypes of 3D halide perovskites. We then discuss the electronic structure of 3D halide perovskites, providing both a working understanding of theoretical calculations of perovskite band structures as well as outlining a more intuitive symmetry-based approach that highlights the molecular orbitals that compose the bands. Next, we offer a practical guide to the synthesis of 3D halide perovskites, including some common techniques to prepare both bulk and thin-film samples. We then describe a selection of widely used methods of characterization, giving examples of each as applied to 3D halide perovskites. Finally, we discuss some intriguing properties of 3D halide perovskites to motivate exploratory studies.

4.15.1 Introduction

Halide perovskites offer a platform that can be tuned in composition, connectivity, and dimensionality, yielding a broad choice of physical and optoelectronic properties.^{1,2} Although these materials have been studied for well over a century,^{3–5} this class of crystalline semiconductors has recently come into the focus of researchers for its outstanding optoelectronic properties.^{6,7} Members of this family afford several advantages for optoelectronic applications, including strong band-edge optical absorption, low charge-carrier (electron/hole) recombination rates, and luminescent charge-carrier recombination.⁷ Halide perovskites can be synthesized as crystals or deposited as films from solution at ambient conditions, allowing for inexpensive and scalable manufacture.⁸ Although these materials have been assessed as components in light-emitting diodes,⁹ lasers,⁹ X-ray detectors,¹⁰ and data-storage devices,¹¹ they currently show most promise as photovoltaic absorbers.^{7,12,13} In just 6 years the power conversion efficiency (PCE) of halide-perovskite-based solar cells increased from 4% to over 20%—an increase that has taken several decades in other photovoltaic absorber materials, such as silicon.^{6,14,15} This feat has been enabled by a number of research communities working in tandem. Indeed, this rich field of research is propelled forward by those who design and optimize devices and by those who measure the fundamental properties of this diverse family of materials and further expand the family by synthesizing new members. Understanding the structural and electronic origins of the fundamental properties of halide perovskites is key to their continued development.

There are numerous reviews on halide perovskites, with most focused on technological applications or on a specific subset of materials, properties, or synthetic methods. The aim of this chapter is not to provide a comprehensive review of any particular topic, but rather to introduce the atomic and electronic structures and optical and physical properties of three-dimensional (3D) halide perovskites to a reader who has a background in chemistry but may be unfamiliar with the fast-moving research field of perovskites. To aid new investigators in this field, we describe common synthetic methods and well-established characterization methods along with case studies that show their utility for perovskites. We focus on the fundamental properties of 3D halide perovskites, with minimal discussion of device fabrication and characterization. For the purposes of this chapter, we will restrict our scope to bulk 3D perovskites with chloride, bromide, or iodide anions. Several pseudohalides (e.g., CN[−], SCN[−], N₃[−]) are also known to adopt derivatives of the 3D perovskite structure; these members are reviewed elsewhere.¹⁶ Changing the dimensionality of the 3D perovskite structure to lower-dimensional perovskites and to nanostructures has substantial effects on their optoelectronic properties. Two-dimensional (2D) perovskites have been extensively studied since the 1990s and we refer the reader to reviews by David

B. Mitzi, which provide an excellent overview of the foundational work.^{17,18} Perovskite nanoparticles have also been studied with fervor by numerous researchers and are reviewed elsewhere.^{19,20}

4.15.2 A brief history

The German mineralogist Gustav Rose first discovered the mineral perovskite, CaTiO_3 , in 1839 in a sample found in the Ural Mountains of Russia by his Russian colleague August Alexander Kämmerer. Kämmerer requested the mineral be named after Count Lev Alekseyevich von Perovski, a Russian nobleman who was a decorated veteran of the Napoleonic Wars, Minister of Internal Affairs, and a mineralogist.²¹ Early investigations were sparse and probed the composition and optical properties of perovskite, though the crystal structure was not yet known.³ Thomas Barth, a student of the Norwegian mineralogist Victor Goldschmidt, published a detailed structural study of CaTiO_3 in 1925.²² This was followed by the seminal publication by Goldschmidt in 1926 that introduced the tolerance factor, a predictor to determine whether a given composition will form a perovskite structure based on geometrical packing arguments.²³ In 1945, the Irish crystallographer Helen Dick Megaw solved the crystal structure of BaTiO_3 , a ferroelectric perovskite with multiple polymorphs that laid the foundation for further research into the diverse phase space and properties offered by perovskites.²⁴ Oxide perovskites remain under intense study for their desirable electronic, ion transport, and magnetic properties, as well as their geological importance: the perovskite $(\text{Mg,Fe})\text{SiO}_3$ is the primary constituent of the Earth's lower mantle.²¹ Further reading on oxide perovskites can be found in the following reference,²⁵ among countless others.

Similar to their oxide counterparts, the discovery and initial characterization of halide perovskites came in the 19th century, with an early study carried out in 1883 by C. Whitman Cross and William F. Hillebrand on the mineral elpasolite, K_2NaAlF_6 (named for its location of discovery, El Paso County, Colorado), a double perovskite.⁵ An early discussion of Cl-, Br-, and I-based perovskites was published by Horace Wells on CsPbX_3 ($X = \text{Cl}^-, \text{Br}^-, \text{I}^-$).⁴ Studies in this nascent field characterized the materials by visual observations and elemental analysis, though the crystal structures were yet unknown or unconfirmed. Crystal structures of halide perovskites came in the 1920s, with KMgF_3 and CsHgCl_3 as early examples.^{26,27} The mixed-valence double perovskite $\text{Cs}_2\text{AuAuCl}_6$ and its analog $\text{Cs}_2\text{AgAuCl}_6$ were also among the first halide perovskites to have their crystal structures elucidated by X-ray diffraction, first correctly described in 1938 by Norman Elliott and Linus Pauling.²⁸ A more detailed history of halide double perovskites (including elpasolites and K_2PtCl_6 -type perovskites) can be found here.²⁹

The first crystal structure of a lead-halide perovskite was published by Christian Møller in 1957, with the structure determination of the perovskite phase of CsPbCl_3 .³⁰ Importantly, Møller followed this publication with a report on the photoconductivity of CsPbX_3 ($X = \text{Cl}^-, \text{Br}^-, \text{I}^-$), a seminal study that predated the burst in interest in halide perovskite optoelectronics by decades.³¹ The crystal structure of the archetypal lead-halide hybrid perovskite $(\text{CH}_3\text{NH}_3)\text{PbI}_3$ was characterized in 1978 by Dieter Weber.³² Studies of halide perovskites prior to the late 2000s primarily focused on the fundamental structural, optical, and charge-transport properties,^{33–35} including the investigation of metallic transport in hole-doped Sn-based 3D perovskites (see Section 4.15.7.2).³⁶

The 2009 report by Tsutomu Miyasaka and coworkers established halide perovskites as a photosensitizer in a TiO_2 -based photovoltaic cell with a liquid electrolyte and a halogen redox couple.⁶ Nearly simultaneous 2012 reports by Nam-Gyu Park and coworkers and Henry Snaith and coworkers subsequently demonstrated the efficacy of halide perovskites as absorber layers in solid-state solar cells with power conversion efficiencies (PCEs) of 9.7% and 10.9%, respectively.^{37,38} These reports launched halide-perovskite photovoltaics into the multidisciplinary research prominence that continues into the 2020s. Compared with more established solar technologies such as Si and CdTe, the rise in PCE of perovskite-based solar cells has been meteoric, with the PCE record for a single-junction solar cell using a halide perovskite as the absorber now at 25.7%.¹⁵ Halide perovskites have also been combined with other absorber materials in a tandem configuration; among these, monolithic perovskite-Si tandem devices have been the focus, recently reaching a record PCE of 29.5%.¹⁵ Particularly appealing is the reduced sensitivity of the performance of halide-perovskite-based solar cells to defects, allowing for low-cost manufacture without significant detriment.⁷ Efforts to commercialize halide perovskites as photovoltaic technologies are well under way³⁹; however, roadblocks to their widespread application remain. Because most high-performing perovskite absorbers are based on lead-halide compositions, the toxicity of the water-soluble Pb^{2+} salt is a concern.⁴⁰ Additionally, the instability of hybrid halide perovskites to ambient moisture and heat is a concern as a cost-competitive solar cell must operate for more than 20 years.¹ Numerous efforts are underway to address these issues, including the development of superior device manufacturing processes and encapsulation strategies and the exploration of alternative, nontoxic, stable compositions for the next generation of absorbers.

4.15.3 Structure and composition

The 3D halide perovskites are ionic solids with corner-sharing halide (X site) octahedra, connected in three dimensions, with cations (A site) occupying the voids between octahedra. The center of each halide octahedron (the octahedral site; B site) may be occupied by a metal cation or may be vacant (Fig. 1). The remainder of this chapter will primarily focus on the Cl-, Br-, and I-based analogs, which tend to be easier to synthesize and have properties better suited for optoelectronic device applications than their F-based analogs. The term “perovskite” will hereafter refer to Cl-, Br-, and I-based 3D perovskites unless otherwise specified.

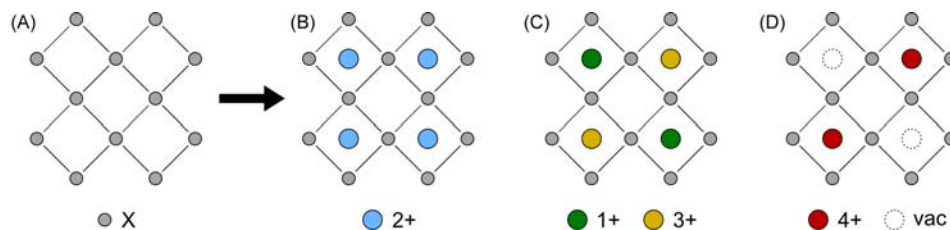


Fig. 1 (A) A 2D representation of the halide (X) framework of a perovskite. The octahedral sites (B sites) must have an average charge of 2+ and can contain, for example: (B) 2+ cations; (C) 1+ and 3+ cations; (D) 4+ cations and cation vacancies. A sites are not shown.

While the original definition of a perovskite was restricted to the CaTiO_3 (ABX_3) structure type, this class of materials encompasses more complex compositions. For instance, double perovskites have the doubled formula $\text{A}_2\text{BB}'\text{X}_6$, where B and B' are two distinct and crystallographically ordered B sites, as in the mineral elpasolite, $\text{K}_2\text{Na}^{\text{I}}\text{Al}^{\text{III}}\text{F}_6$,⁴¹ or the double perovskite $\text{K}_2\text{Pt}^{\text{IV}}\text{Cl}_6$, where one B site is vacant (see Section 4.15.3.2).⁴² In certain double perovskites, the same cation can occupy both the A and B sites, thus forming the cryolite structure with the formula A_2ABX_6 , as in the mineral cryolite, $\text{Na}_2\text{Na}^{\text{I}}\text{Al}^{\text{III}}\text{F}_6$ (see Section 4.15.3.2).⁴³

The simplest single perovskite structure has a cubic lattice with the crystallographic space group $Pm\bar{3}m$ and a lattice parameter equal to the length of a single octahedron, or the length of the linear X–B–X unit; an example of a perovskite with this structure is CsSnBr_3 , which has a lattice parameter of 5.80 Å at 300 K.⁴⁴ However, tilts/rotations between octahedra often occur to geometrically accommodate mismatches in ionic radii. These deviations can reduce the symmetry of the perovskite structure while maintaining the coordination numbers and atomic connectivity of the cubic structure. The Glazer system of nomenclature, named after its developer, A. Michael Glazer, was introduced in 1972 to describe octahedral tilting in oxide perovskites and this nomenclature has also been applied to halide perovskites.⁴⁵ Assuming perfect octahedral coordination of the X-site anions about each B-site cation, there are 15 different tilt systems that can occur in perovskites, resulting in various degrees of symmetry reduction from the ideal cubic $Pm\bar{3}m$ structure. The well-studied composition $(\text{CH}_3\text{NH}_3)\text{PbI}_3$, for instance, has octahedral tilting along with some minor octahedral distortion at room temperature, and has been assigned a tetragonal space group of $I4/mcm$.⁴⁶ More prominent octahedral distortion can result from the incorporation of transition metals into the perovskite structure; for instance, the mixed-valence double perovskite $\text{Cs}_2\text{Au}^{\text{I}}\text{Au}^{\text{III}}\text{Cl}_6$ has axially elongated octahedral coordination of the Au^{3+} center and axially compressed octahedral coordination of the Au^{I} center, resulting in a symmetry reduction from the expected cubic $Fm\bar{3}m$ space-group assignment for the archetypal double perovskite structure to the tetragonal space group $I4/mmm$.²⁸ The B-site vacancies in perovskites of the K_2PtCl_6 structure type may also distort away from octahedral symmetry, though we will consider as 3D perovskites only those that have approximate octahedral symmetry of the halides surrounding the vacant B site (Fig. 1D).

4.15.3.1 Single perovskites

Single perovskites have the formula ABX_3 with a single divalent B site. Although several cations across the periodic table exhibit stable 2+ oxidation states, only a smaller subset forms stable perovskite structures due to geometric constraints. The likelihood that a given composition will form a perovskite structure can be predicted by the octahedral factor and the tolerance factor. The octahedral factor is derived from the hard-sphere atomic packing model postulated by Linus Pauling in 1929: this factor uses ionic radii to determine whether a given B-site cation can accommodate octahedral coordination of a given anion.⁴⁷ The tolerance factor was developed by Victor Goldschmidt in 1926 and similarly uses ionic radii to test whether the A-site cation will fit within the cuboctahedral cavity formed by a given B–X framework.²³ Although these rules have strong predictive power for the oxide perovskites, where the more electronegative oxide anion (O^{2-}) and the higher charges of the metal cations (e.g., Ti^{4+}) results in more ionic character of the bonds, the significant covalency involved in metal-halide bonds reduces the efficacy of the octahedral and tolerance factors for the perovskites with the heavier halides (e.g., Br^- , I^-); nevertheless, they offer predictive guidelines and remain in use for analysis of new and hypothetical perovskite compositions.⁴⁸ Furthermore, attempts to adapt these guidelines for halide perovskites have offered enhanced predictive power by considering additional geometric parameters.^{49–51}

The perovskite structure can accommodate a remarkable swath of the periodic table: 3D single perovskites based on Cl, Br, or I have been shown to exist at room temperature with the divalent B-site cations Pb,³⁰ Sn,⁴⁴ Ge,⁵² Hg,^{53,54} Ca,⁵⁵ Dy,⁵⁶ Eu, Sm, Tm, Yb,⁵⁷ Sr,⁵⁸ and Mn⁵⁹ (Fig. 2). The smaller ionic radius and higher electronegativity of F^- allows F-based 3D single perovskites to form with an even wider selection of divalent B-site cations, additionally including Cr, Fe, Cu, Ni, Co,⁶⁰ Cd,⁶¹ Pd,⁶² Ag,⁶³ Mg,²⁷ Zn,^{64,65} and V.⁶⁶ Whereas the B-site cation often dictates the optoelectronic properties of a perovskite, the A-site cation often has a strong templating effect on the resulting crystal structure, and thus must also be judiciously selected. Typical choices for an A-site cation are the alkali metals, Tl^+ , Ag^+ , or small (organo)ammonium cations such as NH_4^+ , CH_3NH_3^+ , and $\text{NH}_2\text{CHNH}_2^+$. The ability of the metal-halide framework to accommodate small mismatches in ionic radii and adopt distorted structures at room temperature likely contributes to the observed structural diversity of 3D halide perovskites (Fig. 2).

The most-studied single perovskites are the Pb-based analogs, primarily due to their tendency to exhibit desirable semiconducting properties for optoelectronic applications. For example, $(\text{CH}_3\text{NH}_3)\text{PbI}_3$ was the primary composition used in the seminal reports of perovskites as solar absorbers, and this composition remains the basis for the champion solar cells with perovskite

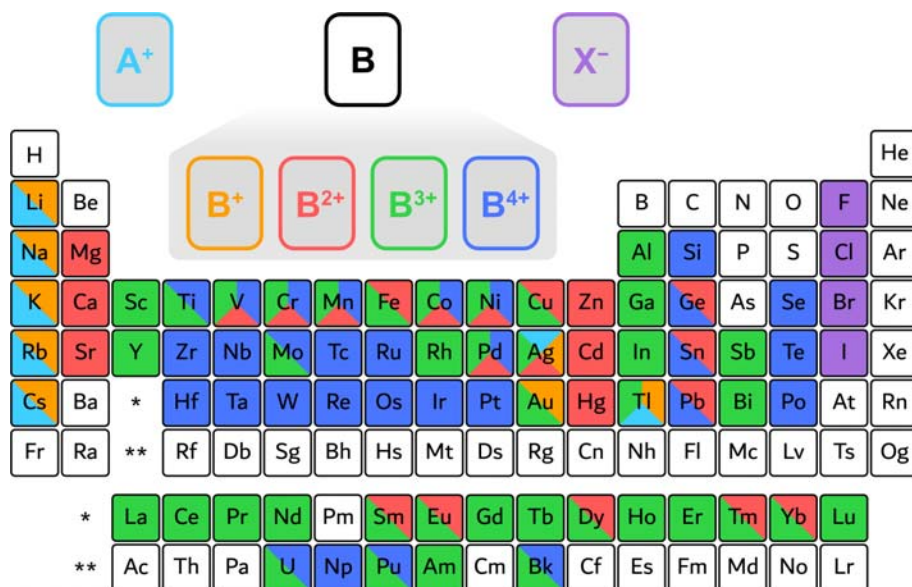


Fig. 2 A periodic table of the elements showing the various elements that form 3D halide perovskites. Cyan, orange, red, green, blue, and purple signify an element's reported incorporation in a 3D halide perovskite as A^+ , B^+ , B^{2+} , B^{3+} , B^{4+} , and X^- respectively. Elements not stoichiometrically incorporated into a perovskite structure are not included here. Adapted with permission from Wolf, N. R.; Connor, B. A.; Slavney, A. H.; Karunadasa, H. I., Doubling the Stakes: The Promise of Halide Double Perovskites. *Angew. Chem. Int. Ed.* **2021**, *60* (30), 16264–16278. 202016185. Copyright 2021 John Wiley and Sons Publishers.

absorbers.^{6,37,38} At room temperature, the single perovskite $(\text{CH}_3\text{NH}_3)\text{PbI}_3$ adopts a distorted perovskite structure in a tetragonal space group, whereas $(\text{CH}_3\text{NH}_3)\text{PbBr}_3$ and $(\text{CH}_3\text{NH}_3)\text{PbCl}_3$ are cubic perovskites at room temperature.⁶⁷ In contrast to the minimal structural effect of halide substitution in this composition, substitution of the A-site cation with the smaller Cs^+ gives a non-perovskite phase, denoted $\delta\text{-CsPbI}_3$, at room temperature.⁶⁸ Greek letters are sometimes used to distinguish polymorphs, or crystallographic phases, which share a formula yet differ in structure. This composition, $\delta\text{-CsPbI}_3$, undergoes a phase transition to a cubic perovskite phase, $\alpha\text{-CsPbI}_3$, at high temperature ($\sim 320^\circ\text{C}$). In addition, an orthorhombic perovskite structure, $\gamma\text{-CsPbI}_3$, that is metastable at room temperature can be isolated temporarily by thermal quenching or by inducing strain.⁶⁹ Upon cooling, transformation of the α to γ phase proceeds through a tetragonal perovskite intermediate, $\beta\text{-CsPbI}_3$. This high degree of polymorphism, with a dependence on synthetic conditions and post-synthetic treatment, is typical of perovskites and exemplifies the structural flexibility of these materials, even within a single composition.

4.15.3.2 Double perovskites

The impressive compositional diversity afforded by the ABX_3 single perovskite structure can be expanded even further by incorporating two distinct B sites to form the $\text{A}_2\text{BB}'\text{X}_6$ double perovskite structure. Here, the B–B' site pair bears an average charge of $2+$; thus, the B–B' pairs can consist of two distinct $2+$ cations, a $1+$ and a $3+$ cation, or a $4+$ cation and a B-site vacancy with zero charge (Fig. 1). Not all combinations of B sites will form perovskite structures, and the Pauling octahedral factor still offers a guideline for metal cation-halide combinations that can form octahedra⁴⁷; the Goldschmidt tolerance factor,²³ however, is not directly applicable to double perovskites, though various modifications of the tolerance factor have been proposed.^{48–50,70} Empirically, the monovalent cations Au,²⁸ Tl,⁷¹ Ag, and the alkali metals^{72,73} and the trivalent cations Au,²⁸ Cr,⁷⁴ Ti, Sb, Bi, In, Fe, Am, Bk, Pu,⁷⁵ U,⁷⁶ Ag,⁷⁷ and all the rare-earth metals^{72–75} (except Pm) have been incorporated into double perovskite structures with Cl, Br, or I at room temperature (Fig. 2). Similar to the single perovskites, F-based compositions allow for more B-site diversity, additionally including the trivalent cations Ga,⁷⁸ Co, Ni,⁷⁹ V,⁸⁰ Al,⁸¹ Cu, Mn,⁸² Mo,⁸³ Pd,⁸⁴ and Rh.⁸⁵ Here too, the A-site choice is primarily driven by structural, rather than electronic, considerations and includes the alkali metals, Tl^+ , Ag^+ , and some small ammonium cations.

All known halide double perovskites have rock-salt ordering of the B-site cations, where the B and B' cations alternate in all three dimensions,²⁹ similar to the ordering of Na^+ and Cl^- in the NaCl rock-salt structure (Fig. 3). Although other types of B-site ordering have been seen in the oxide double perovskites, such as layered and columnar arrangements,^{29,86} these structures have not yet been realized in the halides. The rock-salt ordering is likely driven by Coulombic forces that disfavor charge aggregation. In contrast, the pairing of two $2+$ B-site cations rarely results in B-site ordering: the only known composition with such ordering is the tetragonal double perovskite $\text{Cs}_2\text{Pd}^{\text{II}}\text{Hg}^{\text{I}}\text{Cl}_6$, where the axial elongation and compression of the $[\text{PdX}_6]^{4-}$ and $[\text{HgX}_6]^{4-}$ octahedra, respectively, drives the rock-salt B-site ordering.⁸⁷

Instead of pairing with another cation, a $4+$ B-site cation can pair with a vacant B site, as in the archetypal structure $\text{K}_2\text{Pt}^{\text{IV}}\text{Cl}_6$.⁸⁸ Despite being structurally zero dimensional (0D), consisting of isolated $[\text{BX}_6]^{2-}$ octahedra, their optoelectronic properties are often

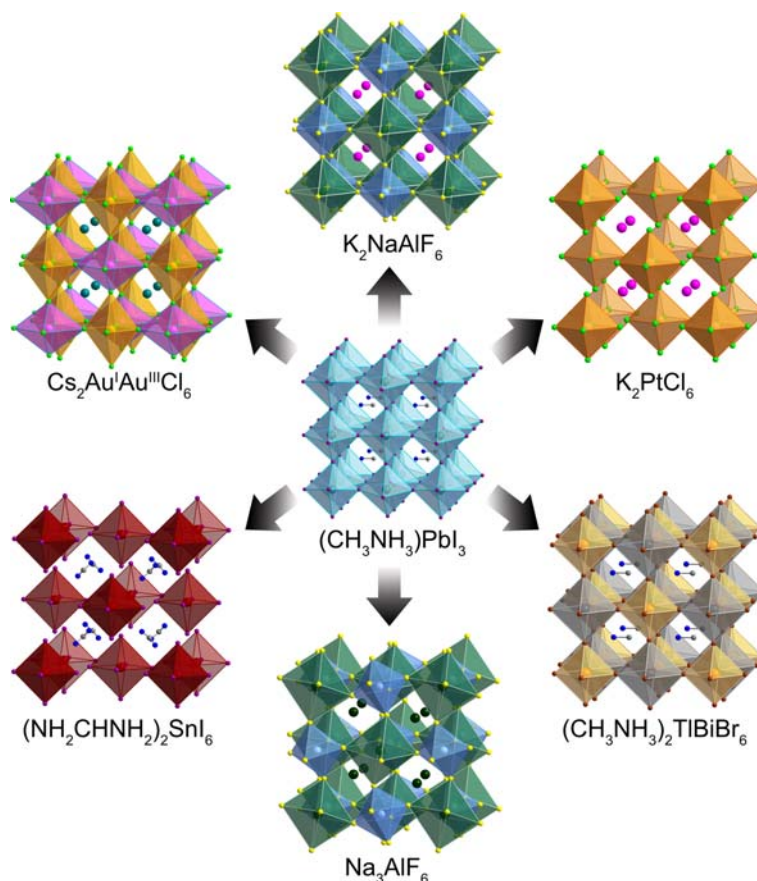


Fig. 3 Crystal structures of various 3D halide double perovskites highlighting the structural diversity of this class of materials. The hybrid single perovskite $(\text{CH}_3\text{NH}_3)\text{PbI}_3$ is shown at the center. Dark green = Na, light blue = Al, dark orange = Pt, light orange = Bi, black = Tl, dark red = Sn, light pink = Au^+ , gold = Au^{3+} , turquoise = Pb, teal = Cs, magenta = K, purple = I, brown = Br, green = Cl, yellow = F, gray = C, and dark blue = N. H atoms are omitted for clarity. Adapted with permission from Wolf, N. R.; Connor, B. A.; Slavney, A. H.; Karunadasa, H. I., Doubling the Stakes: The Promise of Halide Double Perovskites. *Angew. Chem. Int. Ed.* **2021**, *60* (30), 16264–16278. Copyright 2021 John Wiley and Sons Publishers.

more akin to those of 3D perovskites due to halide-halide interactions across the vacancies. Thus, we consider these K_2PtCl_6 -type perovskites, with approximately octahedral halide coordination at the vacant B sites, as 3D double perovskites. However, due to the lack of 3D connectivity, larger A-site cations can be accommodated in these structures to the point where the vacancies expand and adjacent octahedra lose electronic connectivity, thus forming a structurally and electronically 0D material, which is better described as a molecular salt (e.g., $((\text{CH}_3\text{CH}_2\text{CH}_2\text{CH}_2)_4\text{N})_2\text{Te}^{\text{IV}}\text{Br}_6$ ⁸⁹). Most metals with a stable 4+ oxidation state will form a K_2PtCl_6 -type perovskite.⁹⁰ Of interest to the photovoltaic research community is the composition Cs_2SnI_6 , which is stable to ambient conditions and exhibits strong optical absorption and high native *n*-type electronic conductivity.^{91–93}

In contrast to the single perovskites, nearly all 3D double perovskites adopt ideal octahedral symmetry about the B-site cations and exhibit no octahedral rotations in the cubic space group $Fm\bar{3}m$ at ambient conditions.⁹⁴ Notable exceptions to this trend are the tetragonal double perovskites Cs_2BAuX_6 ($\text{B} = \text{Ag}^+, \text{Au}^+$; $\text{X} = \text{Cl}^-, \text{Br}^-, \text{I}^-$)^{28,95} and $\text{Cs}_2\text{PdHgCl}_6$ (Fig. 4A),⁸⁷ the rhombohedral

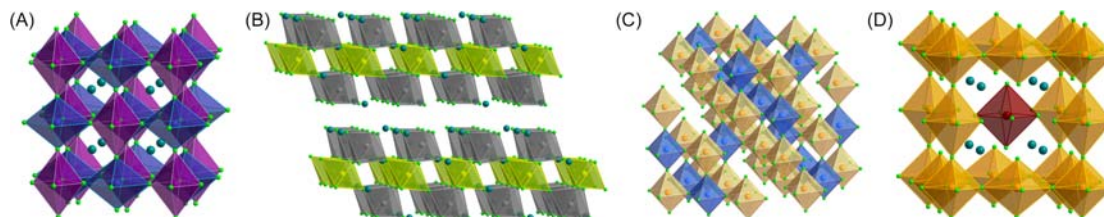


Fig. 4 Crystal structures of some unusual 3D perovskites: (A) $\text{Cs}_2\text{Pd}^{\text{II}}\text{Hg}^{\text{III}}\text{Cl}_6$; (B) $\text{Cs}_4\text{Cu}^{\text{III}}\text{Sb}^{\text{III}}\text{Cl}_{12}$; (C) $\text{Cs}_4\text{Cd}^{\text{II}}\text{Bi}^{\text{III}}\text{Cl}_{12}$; (D) $\text{Cs}_8\text{Au}^{\text{III}}\text{In}^{\text{III}}\text{Cl}_{23}$. Dark blue = Hg, violet = Pd, yellow-green = Cu, gray = Sb, light blue = Cd, light orange = Bi, gold = Au, red = In, teal = Cs, green = Cl. Cs atoms are omitted in (C) for clarity.

double perovskite $(\text{CH}_3\text{NH}_3)\text{KBiCl}_6$,⁹⁶ and some K_2PtCl_6 -type perovskites that exhibit enhanced structural flexibility due to their lack of 3D connectivity.^{97,98} In addition, cryolites are a subset of double perovskites that contain a cation that acts as both the A site and one of the B sites and commonly exhibit octahedral distortions and tilting; this is exemplified by the composition $\text{Na}_2\text{Na}^{\text{I}}\text{Gd}^{\text{III}}\text{Br}_6$.⁷²

4.15.3.3 Perovskites with unusual ordering

Some compositions with B-site vacancies form structures with nontrivial derivations from the archetypal perovskite structure. For example, the perovskites with the general formula $\text{Cs}_4\text{BB}'_2\text{X}_{12}$ (e.g., $\text{Cs}_4\text{Cu}^{\text{II}}\text{Sb}^{\text{III}}_2\text{Cl}_{12}$ and $\text{Cs}_4\text{Mn}^{\text{II}}\text{Sb}^{\text{III}}_2\text{Cl}_{12}$)^{99,100} have three distinct, crystallographically ordered B sites: B, B', and a vacancy. The $[\text{B}^{\text{II}}\text{X}_6]^{4-}$ and $[\text{B}'^{\text{III}}\text{X}_6]^{3-}$ octahedra align in alternating planes, with a layer of B-site vacancies separating the inorganic framework into slabs (Fig. 4B). Like the K_2PtCl_6 -type perovskites, here too we consider the octahedral vacancies, $[(\text{vac})\text{X}_6]^{6-}$, to be distinct B sites, and thus categorize this structure as a 3D perovskite. Indeed, these compositions exhibit optoelectronic properties (e.g., bandgap) more similar to those of a 3D perovskite than of a 2D perovskite. The $\text{Cs}_4\text{BB}'_2\text{X}_{12}$ family can accommodate additional divalent and trivalent cations, and includes the perovskites $\text{Cs}_4\text{Cd}^{\text{II}}\text{Sb}^{\text{III}}_2\text{Cl}_{12}$, $\text{Cs}_4\text{Cd}^{\text{II}}\text{Bi}^{\text{III}}_2\text{Cl}_{12}$, and $\text{Cs}_4\text{Mn}^{\text{II}}\text{Bi}^{\text{III}}_2\text{Cl}_{12}$.^{101,102}

Metals that adopt distorted octahedral geometries can drive unusual structural ordering in perovskites, as is the case with the double perovskite $\text{Cs}_2\text{Pd}^{\text{II}}\text{Hg}^{\text{II}}\text{Cl}_6$ that contains ordered homovalent B-site metals.⁸⁷ Ordering of homovalent B-site metals also occurs in the “gold-cage perovskites” with the general formula $\text{Cs}_8\text{Au}^{\text{III}}_4\text{M}^{\text{III}}\text{X}_{23}$.¹⁰³ This unusual structure can be derived from the ABX_3 single-perovskite lattice by conceptually removing the face-center B-site cations from a doubled $(2 \times 2 \times 2)$ unit cell, thus forming a hollow “cage” of corner-sharing distorted $[\text{AuX}_6]^{3-}$ octahedra around an isolated $[\text{MX}_6]^{3-}$ octahedron (Fig. 4D). Unlike all other halide perovskites of which we are aware, here the B sites (including vacancies) do not average to a 2+ charge. Thus, electrostatic charge balance is achieved through one halide vacancy per formula unit; this vacancy is disordered around the Au atom at the unit-cell corner, giving an apparent octahedral coordination to this Au^{3+} center. Pronounced octahedral distortions also occur in the double perovskite derivatives $\text{Cs}_2\text{In}^{\text{I}}\text{In}^{\text{III}}\text{X}_6$ ($\text{X} = \text{Cl}^-$, Br^-), which exhibit strong off-centering of the In^+ cation, resulting in a twisting of the octahedra relative to one another along one dimension leading to a highly distorted octahedral or pentagonal bipyramidal coordination of the In^+ center.^{104,105}

While A-site ordering is well documented in oxide perovskites,⁸⁶ it is comparatively rare in 3D halide perovskites, occurring in only four reported F-based perovskites: $(\text{Na}_3\text{Ba})\text{NaCu}_3\text{F}_{12}$,¹⁰⁶ $(\text{NaBa})\text{LiNiF}_6$,¹⁰⁷ $(\text{Na}_2\text{Ba})\text{Mn}_4\text{F}_{12}$,¹⁰⁸ and $(\text{Na}_2\text{Ba})\text{Fe}_4\text{F}_{12}$,^{108,109} where the A-site cations are grouped in parentheses in each formula. Unique in their structures, these compositions form perovskites with $1+/2+$ A-site cation pairings, allowing for $1+/2+$ B-site cation pairings or stoichiometric A-site vacancies to compensate for the charge imbalance. These A-site combinations exhibit crystallographic order, likely driven by the minimization of Coulombic forces as with the charge ordering of the $1+/3+$ B-site double perovskites.

With the already impressive diversity of known halide-perovskite structures, we expect future studies will reveal still more compositions and structures within this large family, especially with perovskites that incorporate A- or B-site vacancies to form quasi-pentenary structures.

4.15.3.4 Alloyed perovskites

Some perovskite compositions form alloys containing a mixture of components at a single crystallographic site. A solid solution is specifically an alloy that can accommodate the mixing of atomic constituents in any proportion without significantly changing its crystal structure. Like metallic alloys, such as brass (copper and zinc) or steel (iron and carbon), the properties of the resulting alloy differ from those of the parent compositions. With the exceptions of $\text{Cs}_2\text{PdHgCl}_6$ and the gold-cage perovskites,^{87,103} mixing homovalent (isovalent) ions in a single perovskite composition either results in crystallographic disorder of those ions, thus forming a solid solution, or results in the bulk phase segregation of two distinct compositions. A commonly used perovskite solid solution is the family of mixed Pb/Sn single perovskites, $\text{A}(\text{Sn}_x\text{Pb}_{1-x})\text{X}_3$.^{110,111} Members of this family form a solid solution wherein Pb and Sn have no long-range order, thus leaving the single-perovskite crystal structure intact, and can be mixed in any proportion ($0 \leq x \leq 1$).^{34,35} In this series, some members with an intermediate composition have a lower bandgap energy than either parent composition, referred to as “bandgap bowing,” thus distinguishing the alloy from its non-alloyed counterparts.¹¹² In double perovskites, the B and B' sites retain long-range order, even in an alloyed composition, to minimize Coulombic forces. For instance, including TlBr in the synthesis of $\text{Cs}_2\text{AgBiBr}_6$ under aerobic conditions results in the oxidation of Tl^+ to Tl^{3+} and its incorporation into the Bi^{3+} site, yielding the alloyed double perovskite $\text{Cs}_2\text{Ag}(\text{Tl}_x\text{Bi}_{1-x})\text{Br}_6$. Here, the Ag^+ site alternates with the alloyed $\text{Tl}^{3+}/\text{Bi}^{3+}$ site in the typical elpasolite structure. Similarly, including AgBr in the synthesis of $(\text{CH}_3\text{NH}_3)_2\text{TlBiBr}_6$ results in the partial substitution of Ag^+ for Tl^+ , forming $(\text{CH}_3\text{NH}_3)_2(\text{Ag}_x\text{Tl}_{1-x})\text{BiBr}_6$.¹¹³ The perovskites $\text{Cs}_4(\text{Mn}_x\text{Cd}_{1-x})\text{Bi}_2\text{Cl}_{12}$ and $\text{Cs}_4(\text{Mn}_x\text{Cu}_{1-x})\text{Sb}_2\text{Cl}_{12}$ also form solid solutions of any alloying proportion.^{100,102} The mixing of B sites can be used to improve the properties of a perovskite, for example, by decreasing the magnitude of the bandgap^{111,113} and increasing the stability¹¹⁴ of the parent perovskite.

Though much less common than homovalent alloying, heterovalent (aliovalent) alloying can also substantially alter the properties of perovskites. Although numerous studies have alloyed small concentrations of heterovalent cations into thin films to observe the effect of alloying on device performance, few studies have rigorously investigated the effects of heterovalent alloying on the crystal structure and electronic properties. In the Pb^{2+} perovskites, alloying Bi^{3+} has been proposed to create Pb^{2+} vacancies

for charge compensation, though the substitution mechanism has not yet been rigorously determined.¹¹⁵ Similarly, the double perovskite $\text{Cs}_2\text{AgBiBr}_6$ can be alloyed with a combination of Sn^{2+} and Sn^{4+} substituted at the Ag and Bi sites, respectively. Here, Ag^+ vacancies, evident in electron density difference maps, are thought to provide charge compensation.¹¹⁶ Simultaneous alloying of two heterovalent species, for example mixing equal amounts of Sb^{3+} and Sb^{5+} (with an average charge of $4+$) into $\text{Cs}_2\text{Sn}^{\text{IV}}\text{Cl}_6$, can provide charge balance without requiring the formation of a charge-compensating defect.¹¹⁷ In these systems, heterovalent alloying leads to a drastic change in the optical absorption with <1 atom% of the alloying cation, providing yet another means to modify the optoelectronic properties of perovskites.

Some alloys exhibit unusual phase behavior, such as the alloy $\text{Cs}_2\text{Ag}^{1-3x}\text{Au}^{\text{III}}_{1+x}\text{Cl}_6$, where six different crystallographic phases can form, dependent on the value of x that can be tuned via the stoichiometry of the crystallization solution during synthesis.¹¹⁸ The homovalent alloy $\text{Cs}_2(\text{Ag}^I_x\text{Au}^{1-x})\text{Au}^{\text{III}}\text{Cl}_6$ forms two different phases that can similarly be tuned.¹¹⁹

Unlike B-site alloying, A-site alloying typically only has an indirect effect on the electronic structure of a perovskite and is often used to stabilize a perovskite phase against thermodynamic instability or perturb the B–X sublattice to induce minor modulations to its optoelectronic properties. For instance, in the A-site-alloyed perovskite $(\text{Rb}_x\text{Cs}_{1-x})\text{PbX}_3$ ($X = \text{Cl}^-$, Br^-), the degree of alloying determines the extent of octahedral tilting, which can tune the bandgap energy over a range of 0.2 eV.¹²⁰ While modest, these effects can significantly boost the performance of a solar cell: indeed, many of the highest performing perovskite-based solar cells to date incorporate a mixture of Cs^+ , CH_3NH_3^+ , and $\text{NH}_2\text{CHNH}_2^+$, sometimes also including Rb^+ .^{121–123} High-performance solar cells often employ mixed-halide compositions, as the electronic structure of a perovskite is strongly dependent on the halide composition (see Section 4.15.4.5).¹²⁴ Many Pb-based perovskite compositions form solid solutions with mixtures of Cl/Br and Br/I across a wide range of ratios, for example in $(\text{CH}_3\text{NH}_3)\text{Pb}(\text{Br}_x\text{I}_{1-x})_3$ (Fig. 5), providing a facile synthetic approach to tuning the optoelectronic properties of a perovskite.^{125,126} However, halide conductivity in the lattice can lead to reversible, light-induced changes in the atomic structure of mixed-halide perovskites, particularly for many bromide-rich mixed bromide-iodide compositions (see Section 4.15.7.4).¹²⁷

4.15.4 Electronic structure

4.15.4.1 Introduction and theory

Much of the recent interest in halide perovskites is spurred by their remarkable optoelectronic properties. An understanding of the underlying electronic structure is necessary to explain how halide perovskites interact with light and the subsequent dynamics of the photogenerated charge carriers. In this section, we introduce the basic theory behind the electronic structure of extended solids, illustrate the key considerations of band-structure calculations, and discuss the most important information that can be gleaned from the band structures of perovskites. We then discuss, in more depth, key features and trends of band structures of single and double perovskites.

To understand the optoelectronic properties of these 3D crystalline solids, we first start with their basic building unit: the 0D molecular complex. In molecules, each electronic state consists of linear combinations of atomic orbitals (LCAOs). The allowed interactions between atomic orbitals are dictated by the point symmetry of the molecule. For an octahedral $[\text{BX}_6]^{n-}$ molecule

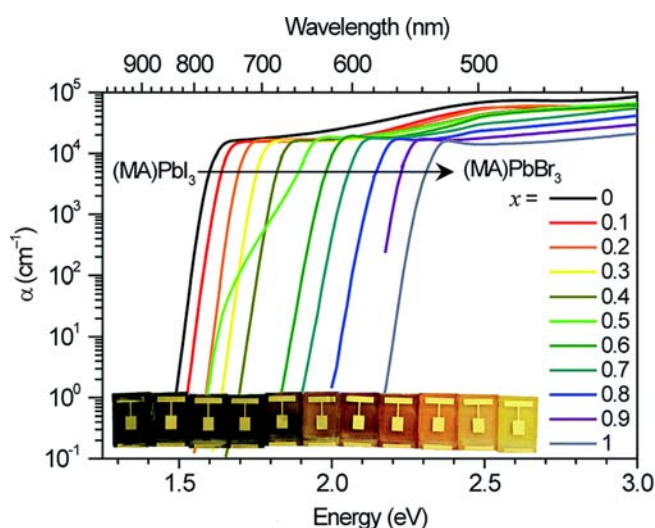


Fig. 5 Absorption coefficient of $(\text{MA})\text{Pb}(\text{Br}_x\text{I}_{1-x})_3$ measured by diffuse reflectance and transmission UV-vis-NIR spectroscopy of thin films and photocurrent spectroscopy of solar cells. Inset: photograph of $(\text{MA})\text{Pb}(\text{Br}_x\text{I}_{1-x})_3$ solar cells from $x = 0$ to $x = 1$. $\text{MA} = \text{CH}_3\text{NH}_3^+$. Reprinted from Hoke, E. T.; Slotcavage, D. J.; Dohner, E. R.; Bowring, A. R.; Karunadasa, H. I.; McGehee, M. D. Reversible Photo-Induced Trap Formation in Mixed-Halide Hybrid Perovskites for Photovoltaics. *Chem. Sci.* **2015**, *6* (1), 613–617 - Published by The Royal Society of Chemistry.

with σ -bonding ligands, the symmetry adapted linear combinations (SALCs) of ligand orbitals, also known as ligand group orbitals (LGOs), have A_{1g} , E_g , and T_{1u} symmetry under the O_h point group. These SALCs interact with orbitals on the central atom that have the same symmetry (typically represented as in-phase, bonding or out-of-phase, antibonding interactions) to yield molecular orbitals (MOs) which represent electronic states of the molecule (Fig. 6A). Mixing of states with the same symmetry, distortions away from ideal symmetry, and inclusion of additional orbital interactions (e.g., π interactions) can further tune the energy landscape.

The energies of optical transitions in a $[BX_6]^{n-}$ molecule are determined by the energy difference between filled and unfilled MOs, with the lowest-energy transition associated with the energy difference between the highest occupied molecular orbital (HOMO) and the lowest unoccupied molecular orbital (LUMO). The relative intensities of these transitions are governed by the overlap between wavefunctions of the initial and final electronic states and their point symmetries, leading to well-known selection rules such as the Laporte selection rule.¹²⁸ In octahedral complexes with inversion symmetry, MOs that are symmetric to inversion are denoted *gerade* (e.g., E_g) and MOs that are antisymmetric to inversion (changing phase upon inversion) are denoted as *ungerade* (e.g., T_{1u}). Optical transitions between two *gerade* states or two *ungerade* states are symmetry-forbidden, whereas transitions between *gerade* states and *ungerade* states are symmetry-allowed. For more information on the applications of group theory in inorganic chemistry, we refer the reader to several excellent textbooks.^{129–131}

In crystalline 3D solids, such as perovskites, the crystal structure forms a periodic arrangement of atomic orbitals. Therefore, in addition to considering the point symmetry of the molecular building units, construction of electronic wavefunctions requires consideration of the effects of translational symmetry between unit cells. Inclusion of translational symmetry converts the MOs to electronic bands, where orbital overlap between unit cells dictates the band curvature, or dispersion. We start with the MOs of the molecular $[BX_6]^{n-}$ unit within one unit cell, the smallest repeat unit of the crystal, as our building block. Translational symmetry between unit cells is described by Bloch's theorem:

$$\Psi(r+R) = e^{ik \cdot R} \Psi(r) \quad (1)$$

where $\psi(r)$ is the MO in the initial unit cell, R is a vector describing the position of a second unit cell with respect to the first, $\psi(r+R)$ is the MO in that second unit cell, and $e^{ik \cdot R}$ is a phase factor dependent on k , the wavevector of the electron. Note that this functional form includes two important approximations: first, the dependence of $\psi(r)$ only on r , the position of the electron, implies the Born-Oppenheimer approximation, where the electronic wavefunction is considered independent of the wavefunction of the nuclei due to the much slower motion of the more massive nuclei. Second, $\psi(r)$ is a wavefunction describing a single electron that is being considered independently of the other electrons in a multi-electron system. The many-particle interactions must be modeled by an exchange-correlation term in quantitative calculations (see Section 4.15.4.3.1).

According to Bloch's theorem, from one unit cell to the next, the wavefunction can only differ by a phase factor $e^{ik \cdot R}$, and interactions between atoms within each unit cell will remain the same. Thus, k can be considered a translational quantum number that describes the symmetry of the electronic state. For perovskites, k is a three-component vector with one component corresponding to each lattice vector of the unit cell. Each component corresponds to the phase shift in a lattice direction and can take a maximum value of $\pm \pi/a$ for a given unit-cell vector of length a ; this value corresponds to a maximally out-of-phase translation, while a component with a value of 0 corresponds to an in-phase translation. For example, the unit cell symmetry of the X k point in the $Fm\bar{3}m$ space group features out-of-phase translations along two unit-cell directions, but in-phase translations along the third unit-cell direction

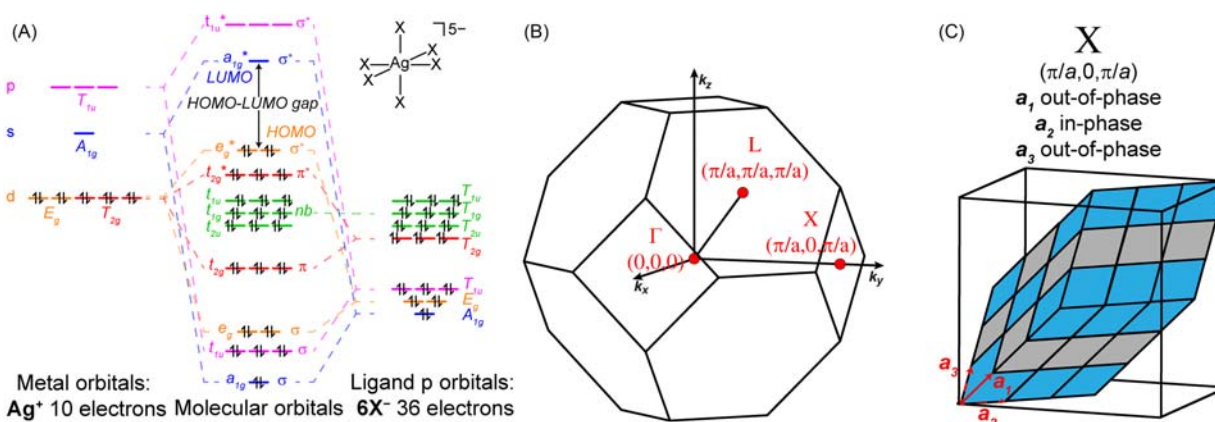


Fig. 6 (A) An octahedral $[BX_6]^{n-}$ molecular orbital diagram, using $[AgX_6]^{5-}$ as an example, showing σ and π interactions. (B) Brillouin Zone of the $Fm\bar{3}m$ lattice, highlighting high-symmetry k points Γ , X, and L. (C) Illustration of translational symmetry of the X point for the $Fm\bar{3}m$ lattice. Blue and gray rhombohedra represent the two phases of the unit cells. (A) and (C) adapted from Slavney, A. H.; Connor, B. A.; Leppert, L.; Karunadasa, H. I., A Pencil-and-Paper Method for Elucidating Halide Double Perovskite Band Structures. *Chem. Sci.* **2019**, *10* (48), 11041–11053 - Published by The Royal Society of Chemistry. (B) Reproduced from Aroyo, M. I.; Orobengoe, D.; de la Flor, G.; Tasci, E. S.; Perez-Mato, J. M.; Wondratschek, H., Brillouin-zone Databases on the Bilbao Crystallographic Server. *Acta Crystallogr. Sect. A: Found. Crystallogr.* **2014**, *70* (2), 126–137. Reproduced with permission of the International Union of Crystallography.

(Fig. 6C). The set of unique k vectors is defined by the (first) Brillouin Zone (BZ) of a solid, which is dependent on the space group of the crystal (Fig. 6B).¹³² Those k vectors or k points with high symmetry are assigned standard letters that serve as indices in band-structure diagrams. Different BZs have different letter assignments to k points; thus, care should be taken when comparing band structures from different space groups. This is particularly true for the single perovskites due to the previously discussed high degree of polymorphism for a given composition. The BZs of high-symmetry cubic space groups that are common for single and double perovskites, for example $Pm\bar{3}m$ and $Fm\bar{3}m$, respectively, have high degrees of degeneracy. Distortions due to crystal packing may significantly lower crystal symmetries and break degeneracies, which can introduce more complex electronic structures.

To fully derive the band structure of a crystalline material, we start with the energy levels of the MOs determined by the interactions within one unit cell of the crystal. We can then apply the translational symmetry dictated by each k point of interest and evaluate the inter-unit-cell interactions to determine the perturbation to the initial energy levels. For a 3D material, as k is gradually varied, the energy of a single MO will spread to cover a range of energies. Because k is a three-component vector, a plot of energy as a function of k is difficult to visualize; instead, a descriptive path through k space is chosen to include high-symmetry points of interest, where most energy maxima and minima occur. These plots of $E(k)$ vs k give rise to the commonly plotted bands of the band structure. Some calculations use a standardized path to fully illustrate all high-symmetry paths within the BZ.¹³³ Many band structures instead include a k -point path that does not cover the entire BZ, but illustrates all relevant energy features in the band.

For a more general discussion of applying group theoretical concepts to solid-state structures, please consult these references.^{134,135} For a symmetry-based approach to analyzing features of single- and double-perovskite band structures, see Sections 4.15.4.5 and 4.15.4.6 and the following references,^{136–138} respectively.

4.15.4.2 Density functional theory

Electronic-structure calculations of perovskites can be carried out with density functional theory (DFT). DFT uses the Hohenberg-Kohn theorem, which states that the electron density can replace the wavefunction as the central variable that determines all ground-state observables of the interacting many-electron system. In practice, DFT solves one-particle equations^{139,140}:

$$\left[-\frac{\hbar^2 \nabla^2}{2m} + v_{KS}[n](\mathbf{r}) \right] \varphi_i(\mathbf{r}) = \varepsilon_i \varphi_i(\mathbf{r}) \quad (2)$$

where i runs from 1 to N , the number of electrons in the system, $\varphi_i(\mathbf{r})$ are single-particle orbitals, ε_i are the corresponding energies, $-\frac{\hbar^2 \nabla^2}{2m}$ is the classical kinetic-energy component of the Hamiltonian, and $v_{KS}[n](\mathbf{r})$ is the Kohn-Sham potential. The Kohn-Sham potential is a functional dependent on the input electron density, $n(\mathbf{r})$, as indicated by the notation $v_{KS}[n](\mathbf{r})$, and defined as:

$$v_{KS}[n](\mathbf{r}) = v_{ext}(\mathbf{r}) + v_{Hartree}[n](\mathbf{r}) + v_{xc}[n](\mathbf{r}) \quad (3)$$

where v_{ext} is the external potential, which comes from the interaction of electrons with nuclei, $v_{Hartree}$ corresponds to classical electrostatic electron-electron interactions and is dependent on $n(\mathbf{r})$, and v_{xc} is the exchange-correlation potential, the functional derivative of the exchange-correlation energy $E_{xc}[n]$ with respect to electron density. $E_{xc}[n]$ accounts for all other energetic considerations and is generally unknown; thus, it must be approximated (see Section 4.15.4.3). In this context, each of the functionals $v_{KS}[n](\mathbf{r})$, $v_{Hartree}[n](\mathbf{r})$, and $v_{xc}[n](\mathbf{r})$ can be seen as a formula that takes the electron density (a function) as an input and outputs an energy based on the interaction it models. The Kohn-Sham orbitals, $\varphi_i(\mathbf{r})$, are then used to calculate the electron density:

$$n(\mathbf{r}) = \sum_i |\varphi_i(\mathbf{r})|^2 \quad (4)$$

Eqs. (2)–(4) are known as the Kohn-Sham equations. They are solved iteratively by first constructing $v_{KS}[n](\mathbf{r})$ based on a starting guess for the electron density, $n(\mathbf{r})$, then solving Eq. (2) and using the resulting $\varphi_i(\mathbf{r})$ to obtain a new $n(\mathbf{r})$. This process is iterated until the electron density is “self-consistent,” i.e., the input and output electron densities are equal (within some convergence criteria). The electron density obtained from this procedure can then be used to calculate the total energy of the system. By minimizing the total energy with respect to the atomic positions, one can also obtain the ground-state atomic structure of the material. Typically, the starting guess for such a structural “relaxation” comes from atomic coordinates obtained through X-ray diffraction (see Section 4.15.6.3). Even though the Kohn-Sham energy levels, ε_i , cannot be precisely equated with ionization energies and electron affinities, such as those obtained from photoemission and inverse photoemission spectroscopies (see Section 4.15.6.5.2), in practice they are routinely interpreted as such and used to obtain band structures by calculating the energy levels individually at each k point.¹⁴¹

The change in energy of a particular electronic state as a function of k is its dispersion relation, and the variation of each electronic state with k generates a band. Qualitatively, the dispersion may be described as the “spread” in energy of a band. Dispersion is strongly affected by structural dimensionality and the degree of orbital overlap. As a consequence, 3D perovskites have more dispersion than analogous lower-dimensional perovskites.

The energy states can be populated with electrons according to the Pauli exclusion principle. In typical intrinsic semiconductors like perovskites, bands that are occupied by electrons at $T = 0$ K are valence bands (VBs), whereas bands that are unoccupied at $T = 0$ K are conduction bands (CBs). The highest-energy occupied state is the valence band maximum (VBM), and the lowest-energy unoccupied state is the conduction band minimum (CBM). The difference in energy of the two states is the bandgap, E_g .

The position of the VBM and CBM in k space and the magnitude of E_g greatly influences the optical absorption and emission of perovskites. If the VBM and CBM occur at the same k point, the bandgap is direct, i.e., the initial and final electronic states of this transition have the same wavevector, and direct optical excitation of the electron from the VBM to the CBM via the absorption of a single photon of appropriate energy is possible. If the VBM and CBM do not share the same k point, the electronic transition from the VBM to the CBM is indirect and requires coupling of the photon absorption to a lattice phonon mode (a collective lattice vibration) to change the electronic wavevector. Just like in molecular systems, electronic transitions in extended solids are also governed by inversion symmetry, leading to symmetry-allowed or forbidden transitions. Direct-allowed transitions yield strong photon absorption, which is highly desirable for thin-film photovoltaic applications. Semiconductors with indirect or direct-forbidden bandgaps typically exhibit significantly weaker absorption near the bandgap energy and thus require thicker films for adequate light absorption compared to similar direct-gap absorbers.

Multiple definitions of bandgaps exist: the optical bandgap, as measured by optical spectroscopy, gives the lowest-energy electronic transition effected by the absorption of a photon (see Section 4.15.6.6.1). The transport, or fundamental bandgap, can be measured from photoelectron spectroscopies (see Section 4.15.6.5.2) and gives the difference between the first ionization energy and the first electron affinity. The Kohn-Sham bandgap calculated by DFT is similar to the fundamental bandgap but differs due to the KS energies being calculated based on an unchanging total electron number N , whereas the fundamental bandgap evaluates energies based on the removal (first ionization energy) and addition (first electron affinity) of one electron to the system. Furthermore, DFT has a self-interaction error between a calculated electron and its corresponding hole that increases occupied-state energies, which tends to decrease the calculated bandgap. In practice, these different definitions of bandgap produce similar values for a given 3D perovskite, and variations within each definition (e.g., due to experimental error) are often greater than those between different definitions; thus, the bandgap values are frequently directly compared to one another. For more information about the distinction between these bandgaps, we refer the reader to the following references.^{142,143} The agreement of bandgap values with experiment can be further improved with methods beyond DFT, such as GW methods, which use many-body perturbation theory to more accurately describe spectral properties upon excitation, at the cost of additional computational expense.¹⁴⁴ A discussion of perturbative methods is beyond the scope of this chapter; we instead refer the interested reader to the following comprehensive references.^{145,146}

The Fermi level, E_F , is defined as the energy that has a 50% probability of being occupied by an electron, as described by the Fermi-Dirac distribution:

$$f(E) = \frac{1}{1 + e^{(E-E_F)/k_B T}} \quad (5)$$

where k_B is the Boltzmann constant, T is absolute temperature (in Kelvin), and E is the energy of the electron. In intrinsic semiconductors, the Fermi level lies within the bandgap and there is no energy level at E_F that can be populated. n -type doping of a semiconductor will shift the position of E_F higher in energy, due to the higher concentration of electrons in the conduction band, whereas p -type doping of a semiconductor will shift the E_F lower in energy.¹⁴⁷

Carrier effective masses provide a simple metric to evaluate a material's charge-carrier mobility, which is important for high-performance optoelectronic devices. Carrier effective masses may be calculated from band dispersion. In crystalline solids, the movement of a charge carrier differs from its movement in a vacuum due to its interactions with the periodic potential of the crystalline lattice. In the simplest case, the band edge near the CBM is approximately parabolic, and the energy of the electron can be described as:

$$E(\mathbf{k}) = E_0 + \frac{\hbar^2 \mathbf{k}^2}{2m^*} \quad (6)$$

where E_0 is the energy level of the CBM, \mathbf{k} is the wavevector, and m^* is the electron effective mass. Under this approximation, we assume the behavior is equivalent and parabolic with respect to \mathbf{k} for all directions of \mathbf{k} space. Fitting the curvature of the band, i.e., numerically evaluating the second derivative of the energy with respect to \mathbf{k} , yields an electron effective mass. As a result, the effective mass is inversely proportional to band curvature under this approximation. Analogous formulas can be calculated for holes at the VBM. In real materials, the curvature may differ in different directions in \mathbf{k} space, and a unique carrier effective mass is typically reported along each high-symmetry direction.

The carrier mobility determines the ease with which the charge carrier moves through a material under the influence of an external electric field. Mobility can be probed experimentally, for example by Hall effect measurements (see Section 4.15.6.8), and can be related to effective mass by:

$$\mu = \frac{e\tau}{m^*} \quad (7)$$

where μ is the carrier mobility, e is the elementary charge, τ is the mean free time (between scattering events for the carrier), and m^* is carrier effective mass. For a more comprehensive treatment of factors affected by carrier effective mass, see the following reference.¹⁴⁸ Carrier effective mass and carrier mobility are typically inversely related, so computational identification of materials with low carrier effective masses effectively screens for absorber materials with high carrier mobilities. In general, I-based perovskites tend to have greater dispersion than corresponding Br- or Cl-based compositions, particularly with the heavier B-site metals—based on greater orbital overlap due to the large, diffuse I 5p orbitals—and thus exhibit lower effective masses and higher mobilities.

Finally, a density of states (DOS) plot formally describes the number of energy levels in the band structure in a given energy interval. To first approximation, the DOS can be thought of as inversely proportional to the slope of $E(\mathbf{k})$ vs \mathbf{k} .¹³⁴ The DOS is often accompanied by a projection onto individual atomic orbitals, allowing visualization of individual orbital contributions to different bands; this may be plotted as a projected DOS (PDOS). The crystal orbital overlap population (COOP) plot visualizes the DOS as weighted by bonding or antibonding interactions between pairs of basis orbitals, providing a footing for understanding the local orbital interactions in the electronic structure. These concepts are exemplified using CsPbBr₃ as a case study in [Section 4.15.4.4](#).

4.15.4.3 Computational approximations

Here, we give a brief overview of several important factors to consider for understanding calculated electronic structures of perovskites. The specifics of the DFT calculations, including the treatment of the exchange-correlation contribution to the electron-electron interaction, can greatly impact qualitative features of electronic structure, including atomic orbital contributions to electronic states or band dispersion, and quantitative results, such as the magnitude of the bandgap. Therefore, some experimental calibration is desirable to ensure the reliability of the results. We do not provide an exhaustive list of factors that affect electronic structure calculations, but instead highlight several important considerations when using band structures to evaluate optical and electronic properties of perovskites.

4.15.4.3.1 Exchange-correlation functional

The energy levels in Kohn-Sham DFT calculations are evaluated for a system of effectively non-interacting electrons. In order to properly account for quantum mechanical effects of electron-electron interactions, the exchange-correlation functional must be introduced. The exchange-correlation potential (v_{xc} ; see [Section 4.15.4.2](#)) may be defined by its relation to the exchange-correlation energy (E_{xc}) and the electron density function ($n(\mathbf{r})$):

$$v_{xc} = \frac{\delta E_{xc}}{\delta n(\mathbf{r})} \quad (8)$$

The exchange-correlation potential can also be split into the exchange potential, which describes the exchange interaction between two electrons governed by the Pauli principle, and the correlation potential, which describes all other corrections for the differences between a many-electron and one-electron system. In theory, DFT is an exact scheme; however, since the form of E_{xc} is not known, approximations must be used. The simplest approximation for the exchange-correlation term is the local density approximation (LDA), first introduced by Kohn and Sham,¹⁴⁹ where the exchange-correlation energy density at any given position \mathbf{r} is assumed to be the same as the exchange-correlation energy density for a uniform electron gas with electron density $n(\mathbf{r})$. LDA is the simplest exchange-correlation approximation and is therefore computationally inexpensive, yet still may give useful information; however, care should be taken when evaluating optical and electronic properties from calculations using LDA. For instance, calculations using LDA for (CH₃NH₃)PbI₃ not only severely underestimate the bandgap magnitude, but also poorly describe the dispersion of the valence bands.¹⁵⁰ Unlike LDA, a generalized gradient approximation (GGA) includes the dependence on the gradient of the electronic density to the exchange-correlation functional to account for the inhomogeneity of real systems.¹⁵¹ A hybrid functional mixes GGA with some fraction of exact exchange, which explicitly calculates the exchange interaction with calculated electron orbitals instead of electron density, and is typically implemented in a generalized Kohn-Sham framework that allows for a more accurate determination of bandgaps.¹⁵² Both GGA and hybrid methods of approximation are commonly used in calculations for solid-state materials, including for perovskites.

Some common functionals used in perovskite calculations include the PBE,¹⁵³ PBE0,¹⁵⁴ PBEsol,¹⁵⁵ and HSE06¹⁵⁶ functionals. The PBE functional, developed by John Perdew, Kieron Burke, and Matthias Ernzerhof,¹⁵³ is a GGA functional. Because the PBE functional is non-empirical and does not require fitting of parameters to experimental data sets, it has seen widespread use across a range of materials. It is well known that the PBE functional underestimates bandgaps due to electron self-interaction, in extreme cases predicting metallic behavior for semiconductors.¹⁴⁴ It is also known to overestimate lattice constants in solids.^{155,157} Despite underestimating bandgaps in perovskites, electronic structures calculated with PBE can often still capture qualitative trends in bandgap energy. For instance, comparison of calculated bandgaps of (CH₃NH₃)(Sn_xPb_{1-x})I₃ computed with PBE show a systematic underestimation of bandgaps, but the characteristic bandgap decrease for intermediate compositions (called bandgap bowing) is still observed.¹⁵⁸ The PBE functional may also be used for systems with large unit cells to maintain computational tractability, at the potential cost of quantitative bandgap accuracy.^{116,159} The PBEsol functional is a reformulation of PBE for solids that adjusts parameters to reduce errors in equilibrium lattice constants,¹⁵⁵ but still suffers from underestimation of bandgaps due to the inherent limitations of Kohn-Sham DFT.

PBE0 and HSE06 are commonly used functionals based on hybrid approximations. Like PBE, these functionals are widely applicable to many systems because the parameter for exact exchange is non-empirical. However, these functionals include the Hartree-Fock exact-exchange calculation, which is more computationally intensive than only evaluating GGA functionals.¹⁶⁰ These are commonly used functionals when quantitative bandgap calculations are desired, as they provide a closer match to experimental values. In all cases, care should be taken to choose a functional appropriate to the property of a material that is to be evaluated. Comparisons to other calculations and experimental results are necessary to ensure accuracy.

4.15.4.3.2 Basis functions and pseudopotentials

All features of the electronic structure will be greatly impacted by the chosen approximation for the exchange-correlation functional. However, steps may be taken to reduce computational complexity while maintaining accuracy. First, it is common to use plane waves rather than an atomic basis with spherical harmonic wavefunctions for calculations in solids. In atomic calculations, integrals are performed over all real space with Gaussian wavefunctions. For solids, this is impractical, and a Fourier transform is applied and the wavefunction is integrated over k space instead, using the periodicity of the crystal lattice to determine the electron density in k space. To practically perform these integrations, the Brillouin zone is quantized into a k -point mesh rather than taking a continuous integral over k , and a cutoff energy for the expansion in plane waves is applied. Second, in the regions close to atomic nuclei, wavefunctions oscillate rapidly due to the large potential energy of an electron at the nucleus. Augmented-wave methods divide the wavefunction into a core segment within a defined radius and an envelope function to treat bonding interactions. The common projector-augmented wave (PAW) method uses plane waves for the outer envelope in combination with pseudopotentials that smooth the core wavefunction into more computationally tractable functions. These pseudopotentials are less computationally intensive and represent core electrons that are treated as chemically inert. Typically, only the valence electrons are treated explicitly.

4.15.4.3.3 Relativistic effects and spin-orbit coupling

Einstein's theory of special relativity states that the mass of a moving particle, such as an electron, depends on its velocity. For an electron that experiences a nuclear charge of Z , relativistic corrections scale with Z^2 .¹⁶¹ Therefore, while negligible for lighter elements, this effect becomes significant for heavier elements, including elements commonly found in perovskites, such as the lanthanides, I, Au, Hg, Tl, Pb, and Bi. Several relativistic effects can be qualitatively observed in these elements, including the contraction and stabilization in energy of s and p orbitals, the expansion and destabilization of d and f orbitals, and spin-orbit coupling (SOC), which lifts the degeneracies of p and d orbitals.¹⁶² Relativistic quantum mechanical effects are described by the Dirac equation, but few DFT calculations currently implement relativistic DFT with this formalism. Instead, relativistic effects can be treated by modifying the kinetic-energy term in the Kohn-Sham equations to approximate the kinetic-energy term of the Dirac equation; this method is known as the zeroth-order regular approximation (ZORA).¹⁶³ This energy can then be split into a scalar relativistic term and an SOC term. Implementation of these approximations also requires relativistic pseudopotentials.

Calculations on perovskites can be greatly affected by the inclusion of relativistic effects. For example, inclusion of scalar relativistic effects in calculations of CsPbBr₃ increases the calculated bandgap from 0.3 eV to 2.1 eV due to a stabilization of the valence band that exhibits Pb 6s orbital character.¹³⁶ On the other hand, inclusion of spin-orbit coupling effects in calculations of (CH₃NH₃)PbX₃ (X = Br⁻, I⁻) leads to a reduction in calculated bandgap due to significant splitting of the conduction bands but little effect on the valence band.¹⁶⁴ Calculations of APbI₃ (A = Cs⁺, CH₃NH₃⁺, NH₂CHNH₂⁺) with PBE functionals that neglect SOC effects yield bandgaps close to experimental ones due to a fortuitous cancellation of errors between bandgap underestimation commonly observed with use of the PBE functional and overestimation of the bandgap due to omission of stabilizing SOC effects on the conduction band.¹⁶⁵ However, this is not true for AsN₃ perovskites, where SOC effects are less pronounced and similar calculations indeed show poor agreement with experimental values.¹⁶⁶ Inclusion of semi-core electrons in calculations of perovskites with SOC corrections can have a significant impact on the calculated bandgap¹⁴⁴: the inclusion of more valence electrons results in a larger predicted gap that is closer to the gap predicted by an all-electron full-potential linear augmented plane-wave calculation.

4.15.4.3.4 Alloyed systems

Alloying in perovskite compositions is a powerful tool to tune optoelectronic properties. However, accurately modeling disordered materials, especially materials with dilute impurities, introduces additional challenges.^{92,113,116,159} Such modeling requires the use of a supercell to capture the non-stoichiometric substitution and becomes more computationally intensive as the concentration of the impurity ion decreases and correspondingly increases the required size of the supercell. The use of hybrid functionals may become prohibitive for such cases due to the large number of atoms involved.¹¹⁶ Using a supercell that is too small may introduce artifacts from dopant interactions because the periodic boundary conditions generate dopant sites with long-range order. Another consequence of the use of a larger supercell is the introduction of band folding. As can be seen in Bloch's theorem (see Section 4.15.4.1), doubling of R will halve the maximum magnitude of k to maintain the same phase factor. This may be conceptualized as folding the band structure in half, thereby doubling the number of bands (Fig. 7).¹⁶⁷ Each k point in the folded band structure corresponds to two k points in the unfolded band structure, leading to a loss of information. Unfolding of these bands requires chemical intuition and knowledge of the symmetry of the system. For example, the band structure of Cs₂AgBiBr₆ calculated with its larger conventional face-centered-cubic cell (with four formula units) shows a VBM at Γ , but the band structure calculated with its smaller primitive rhombohedral unit cell (with one formula unit) reveals a VBM at X instead. Calculations on alloys with very dilute impurity concentrations are conducted on supercells and the band structures are then unfolded for accurate determination of k points at the band extrema. However, as the impurity concentrations increase and the impurity orbitals modify the perovskite host, the symmetry reduction caused by the impurity sites prevents straightforward band unfolding and both the folded and unfolded band structures contain useful aspects of the alloyed material's band structure.¹¹³

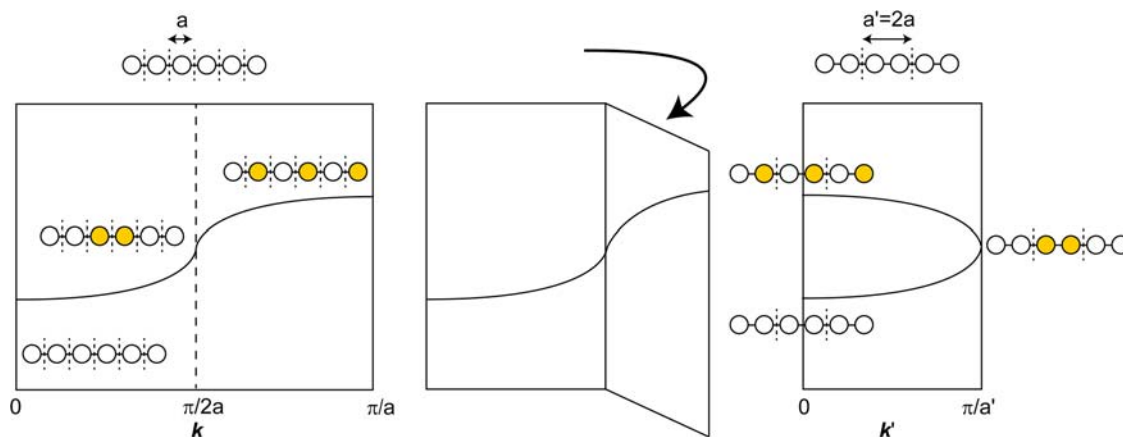


Fig. 7 Schematic of s-orbital band folding of a model system of 1D H atoms observed going from unit-cell vector a to $a' = 2a$. White and yellow circles represent the two phases of the s orbitals. Adapted with permission from Hoffmann, R., *How Chemistry and Physics Meet in the Solid State. Ang. Chem. Int. Ed.* **1987**, 26 (9), 846–878. Copyright 1987 John Wiley and Sons Publishers.

4.15.4.4 Case study: Band structure of CsPbBr₃

Here, we use representative results from electronic-structure calculations for cubic $Pm\bar{3}m$ CsPbBr₃¹³⁶ as a demonstration of typical lead-halide perovskite band structure and DOS plots (Fig. 8). The band structure is shown in triplicate to highlight the overall band structure and orbital contributions from both Pb and Br. In all plots, the energy is referenced to the vacuum energy level to compare absolute energies of the band edges with other materials. The energy may also be referenced to the energy of a flat band that is deep within the valence band, such as a band that has A-site character, for the purpose of comparing between analogous systems.¹⁵⁹ This is particularly important when evaluating perovskites for device applications, as aligning the energy levels of the absorber layer with those of the charge-transport layers and electrodes is key for optimal device performance. The energy is also commonly referenced to zero at the VBM or to zero at E_F . The x -axis shows a path through k space for the BZ of the $Pm\bar{3}m$ space group, including Γ (0, 0, 0), X (0, π/a , 0), M (π/a , π/a , 0), and R (π/a , π/a , π/a). As noted in Section 4.15.4.1, the X point in the BZ of the simple cubic $Pm\bar{3}m$ space group differs from the X point in the face-centered $Fm\bar{3}m$ space group. The VBM and CBM calculated for cubic $Pm\bar{3}m$ CsPbBr₃ both occur at R, and a direct bandgap of 2.1 eV is predicted when scalar relativistic effects are included, in reasonable agreement with the experimental bandgap of 2.39 eV (measured for the high-temperature cubic $Pm\bar{3}m$ phase at 435 K because the RT phase is orthorhombic).¹⁶⁸ The same calculation carried out without relativistic corrections significantly raises the energy of the uppermost VB and predicts a bandgap magnitude of 0.3 eV.¹³⁶

Orbital contributions to the band structure of CsPbBr₃ illustrate the local bonding interactions in the material. Halide 4p character is evident throughout the VBs and CBs, with particularly strong contributions to the VBs (Fig. 8C). This large contribution by halide np orbitals is characteristic of the band edges of perovskites, while the B-site frontier-orbital (HOMO/LUMO) contribution will depend on composition. For example, in CsPbBr₃, the two bands with significant Pb 6s contribution occur in a band deep in the VB and in the uppermost VB (Fig. 8B). The Pb 6p orbital contributions are found most strongly in the three CBs lowest in energy, as well as in VB states at intermediate energies (Fig. 8B). The DOS and COOP plots provide another means of visualizing this information (see Section 4.15.4.2). The spike in the DOS plot near -14 eV corresponds to a flat band assigned to the A-site cation, Cs⁺. This band lacks dispersion due to a dearth of orbital-orbital interactions, typical of A-site cations in perovskites. The COOP plot also illustrates the metal-halide interactions more clearly: the VBM states are dominated by Pb 6s-Br 4p antibonding character while the CB states are dominated by Pb 6p-Br 4p antibonding character. The corresponding Pb 6s-Br 4p bonding states and Pb 6p-Br 4p bonding states are found deeper in the VB. The band-edge transition can thus be assigned as a transition from a filled metal-halide antibonding state to an unfilled metal-halide antibonding state, similar to the HOMO-LUMO transition of an octahedrally coordinated molecular Pb complex.¹⁶⁹

4.15.4.5 Single perovskites

General trends across single perovskites with group 14 B sites (i.e., Ge, Sn, Pb) show that, regardless of composition or symmetry, the VBM is primarily composed of halide np and B-site ns orbital contributions, while the CBM is composed of halide np and B-site np orbital contributions. These observed electronic structure trends can be understood in the context of local chemical bonding through consideration of the molecular orbital (MO) units.¹³⁶ By taking combinations of frontier MOs of the B site, namely the ns and np orbitals for the VBs and CBs, respectively, with combinations of halide np orbitals, translation of the MOs along the lattice vectors according to Bloch's theorem allows for visualization of the local orbital symmetry at each k point. Evaluation of the relative energies of interaction between the halide np orbitals and the B-site ns and np orbitals explains the pattern of dispersion observed between the cubic high-symmetry k points. The COOPs (crystal orbital overlap populations) for CsPbBr₃ show how VB states are

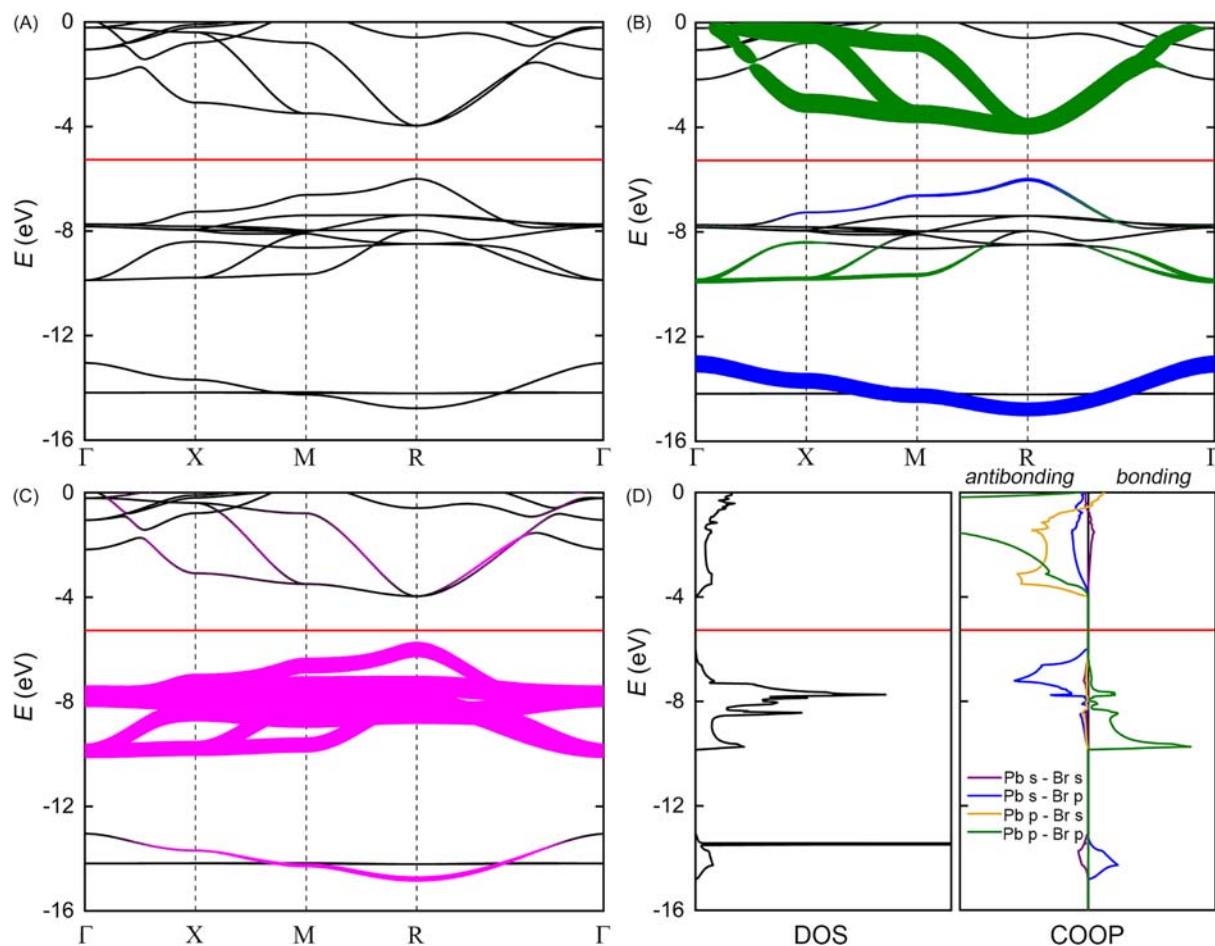


Fig. 8 Electronic structure of cubic $Pm\bar{3}m$ CsPbBr₃: (A) band structure computed at the ZORA-SCAN/TZ2P level of theory; (B) band structure with Pb 6s and 6p contributions to the bands in blue and green, respectively; (C) band structure with Br 4p contributions to the bands in magenta; (D) density of states and crystal orbital overlap population (decomposed into individual Pb–Br bonding contributions) plots. The energy is referenced to the vacuum level. The Fermi level, E_F , is given by the horizontal red line. Adapted with permission from Goesten, M. G.; Hoffmann, R., Mirrors of Bonding in Metal Halide Perovskites. *J. Am. Chem. Soc.* **2018**, *140* (40), 12996–13010. Copyright 2018 American Chemical Society.

dominated by Pb 6s–Br 4p antibonding interactions and the CB states are dominated by Pb 6p–Br 4p antibonding interactions, in line with both the MO analysis¹³⁶ and other reported results (Fig. 8D).¹⁷⁰ For CsGeBr₃, CsSnBr₃, and CsPbBr₃, the VBM is composed of B-site *ns*–Br 4p interactions. The closer the Br 4p orbital energy levels lie to the corresponding B-site *ns* orbital energy levels, the stronger the expected σ^* antibonding interaction, leading to a higher expected energy of the VBM. The Pb 6s energy levels lie below the Ge 4s energy levels, which in turn lie below the Sn 5s energy levels, and all B-site energy levels are below the Br 4p levels, as determined by B-site and CsBr₃ sublattice calculations.¹³⁶ The calculated VBM energies correlate monotonically to the B-site *ns* orbital energy level. While there are significant antibonding interactions in the CBs, the CBM at R is predicted to be B-site *np* nonbonding. This energy is expected to correlate to the B-site *np* orbital energy, which is observed as the CBM energy increases with increasing B-site *np* orbital energy.

Many of the characteristic features of the electronic structure of CsPbBr₃ in Section 4.15.4.4 are representative of other single perovskites. For example, the prototypical organoammonium perovskite, (CH₃NH₃)PbI₃, has a direct bandgap and strong band-edge optical absorption. Similar to CsPbBr₃, the VB states near the bandgap are dominated by I 5p and Pb 6s orbital antibonding contributions, while the lowest-energy CB states contain I 5p and Pb 6p orbital antibonding contributions.¹⁶⁹ Contributions from CH₃NH₃⁺ occur at much lower energies below the VBM.^{136,171} While the CH₃NH₃⁺ cation does not contribute electronically to the band extrema, its structural influence can still indirectly affect the electronic structure. The lowering of the symmetry of (CH₃NH₃)PbI₃ from the cubic ($Pm\bar{3}m$) to the tetragonal ($I4/mcm$) perovskite phase, for instance, moves the calculated bandgap from R to Γ , with an accompanying increase in magnitude by 0.13 eV.¹⁷² Calculations that fix the orientation of CH₃NH₃⁺ show how such orientations can also alter the calculated bandgap magnitude.¹⁷³

Substitutions to halide composition do not affect the orbital makeup of the band edges: the direct bandgap at R is preserved for cubic $Pm\bar{3}m$ band structures of CsPbF₃, CsPbCl₃, CsPbBr₃, and CsPbI₃, with the bandgap magnitude decreasing monotonically with

increasing halide atomic number.¹³⁶ Band structures computed on the lower-symmetry orthorhombic $Pnma$ phases of CsPbCl_3 , CsPbBr_3 , and CsPbI_3 show the same trend in bandgap magnitude with a direct bandgap preserved at Γ .¹⁷⁴

The search for Pb-free perovskite compositions that retain many of the optoelectronic properties of the Pb-based perovskites has led to significant work on the analogous Sn-based compositions. Calculations on cubic $Pm\bar{3}m$ CsSnCl_3 , CsSnBr_3 , and CsSnI_3 show a very similar pattern of band dispersion to their corresponding Pb-based counterparts: all three show a direct transition at R from Sn 5s, halide np -based VB states to Sn 5p, halide np -based CB states.¹⁷⁵ The VBM of cubic $Pm\bar{3}m$ CsSnBr_3 is calculated to be nearly 1 eV higher than that of CsPbBr_3 on an absolute energy scale,¹³⁶ which is in line with experimental observations of the instability of Sn^{2+} -based perovskites to oxidation of the high-energy 5s electrons of Sn^{2+} to form Sn^{4+} .¹¹⁴ This general VBM trend is consistent with experimental photoelectron spectroscopic measurements on Sn- and Pb-based perovskites (see Section 4.15.6.5.2).¹⁷⁶ Studies of ASnX_3 ($A = \text{Cs}^+$, CH_3NH_3^+ , $\text{NH}_2\text{CHNH}_2^+$; $X = \text{Cl}^-$, I^-)¹⁷⁷ have shown that a direct bandgap is maintained for CsSnI_3 through two perovskite phase transitions and that the orbital contributions remain the same for each phase. The VB shows contributions from Sn 5s and I 5p orbitals, and the CBs show contributions from Sn 5p and I 5p orbitals. The electronic structure of the cubic $Pm\bar{3}m$ phase of CsSnI_3 has similar PDOS contributions to those of $(\text{CH}_3\text{NH})\text{SnI}_3$ and $(\text{NH}_2\text{CHNH}_2)\text{SnI}_3$ and the same direct bandgap observed at R, with the bandgap increasing linearly with lattice parameter. The direct bandgap also occurs at R for cubic $Pm\bar{3}m$ CsSnCl_3 , but a phase transition to a non-perovskite monoclinic $P2_1/n$ structure results in an edge-sharing octahedral framework and significantly alters the dispersion of the calculated band structure. This significant change in band structure is generally true for transitions between perovskite and non-perovskite phases.

Moving further up the periodic table, calculations for the hypothetical cubic $Pm\bar{3}m$ CsGeI_3 predict a direct bandgap also at R but with a larger magnitude than that of CsSnI_3 .¹⁷⁸ PDOS calculations show analogous orbital contributions to the band edges: the VBs are dominated by I 5p and Ge 4s contributions, while the CBs are dominated by I 5p and Ge 4p contributions.¹⁷⁸ However, CsGeI_3 crystallizes in the rhombohedral space group $R\bar{3}m$. Despite this symmetry distortion, the calculated band-edge transition is still direct at Z, and PDOS calculations reveal that the orbital character is maintained from the undistorted cubic structure to the rhombohedral structure.¹⁷⁹

Computational studies can also reveal the origin of the optical and electronic effects of alloying perovskites. For instance, the aforementioned bandgap bowing, where intermediate compositions of $\text{A}(\text{Sn}_x\text{Pb}_{1-x})\text{X}_3$ have smaller bandgaps than the ternary parent compositions, has been investigated: a computational study on $(\text{CH}_3\text{NH}_3)(\text{Sn}_x\text{Pb}_{1-x})\text{I}_3$ has found the bandgap reduction to be largely chemical in nature, rather than primarily due to lattice mismatches or structural distortions.¹⁸⁰ As seen in the parent, non-alloyed perovskites, due to the greater relativistic stabilization of the 6s and 6p orbitals, the valence 5s orbitals of Sn are higher in energy than the Pb 6s orbitals, and the Pb 6p orbitals are both lower in energy than the Sn 5p orbitals and further stabilized by spin-orbit coupling effects, leading to a VBM character of Sn 5s/I 5p and a CBM character of Pb 6p/I 5p in the alloyed perovskites. Computational investigations of mixed-halide perovskites have also corroborated the experimentally observed trend of increasing bandgap magnitude with increasing Br content in the $(\text{CH}_3\text{NH}_3)\text{Pb}(\text{Br}_x\text{I}_{1-x})_3$ solid solution.¹⁸¹

4.15.4.6 Double perovskites

The electronic structures of double perovskites are significantly more diverse than those of single perovskites described in the previous section. Whereas the bandgap transition in Pb, Sn, and Ge single perovskites can be considered as an s-orbital to p-orbital transition within the same metal, the bandgap transition in double perovskites often takes the form of a metal-to-metal charge transfer (MMCT)^{137,182,183} or a ligand-to-metal charge transfer (LMCT),^{92,137} depending on B-site composition. Thus, the diversity of B and B' cations with a large range of frontier-orbital energies can allow bandgap magnitudes to vary widely across this family of materials. Calculations on double perovskites can show direct-allowed,⁷¹ direct-forbidden,^{92,182,184} and indirect bandgaps,^{96,185} also depending on B-site composition. In contrast to single perovskites, where the crystal symmetry varies widely with composition due to octahedral tilting, most elpasolites maintain the undistorted cubic $Fm\bar{3}m$ symmetry (from a doubling of the primitive-cubic single-perovskite unit cell) at or near ambient conditions. The maintenance of symmetry for most double perovskites reduces the difficulty in comparing calculated band structures of double perovskites to one another and in predicting the properties of compositions that have yet to be synthesized or characterized. However, other factors (e.g., functional choice and SOC) must still be considered for accurate comparison of distinct compositions and in the prediction of properties.^{186,187}

Double perovskites may deviate from cubic symmetry by tilting between the octahedral $[\text{BX}_6]^{n-}$ units, most often seen in the K_2PtCl_6 -type double perovskites, such as Rb_2SnI_6 ,⁹⁸ and in the cryolites, such as $\text{Na}_2\text{Na}^{\text{I}}\text{Cd}^{\text{III}}\text{Br}_6$,⁷² (Fig. 3), or by symmetry lowering of the local B-site coordination due to octahedral distortions driven by electronic configuration, as in the elpasolite $\text{Cs}_2\text{Au}^{\text{I}}\text{Au}^{\text{III}}\text{Cl}_6$.²⁸ Octahedral tilting causes only small changes to the band dispersion in K_2PtCl_6 -type double perovskites, likely due to the weaker interactions across the B-site vacancies. For example, calculations on the high-temperature tetragonal $P4/mnc$ and low-temperature monoclinic $P2_1/n$ structures of Rb_2SnI_6 show very little effect of symmetry lowering on the band dispersion or on the orbital composition of the bands and the direct-forbidden bandgap is maintained at Γ , with an increase in magnitude by 0.19 eV upon lowering symmetry.⁹⁸ The elpasolite $\text{Cs}_2\text{Au}^{\text{I}}\text{Au}^{\text{III}}\text{X}_6$ ($X = \text{Cl}^-$, Br^- , I^-) is calculated to be stable in a tetragonal $I4/mmm$ structure,¹⁸⁸ and calculations yield analogous band dispersion and an indirect bandgap for all three halide compositions. The PDOS shows the expected band-edge composition based on Au frontier orbitals, with contributions from Au 5d and X np valence orbitals.¹⁸⁸

Because of the greater variety in B-site orbital character, double-perovskite band structures have fewer overall trends that encompass all structures. Here, we examine two representative double perovskites, discuss specific material properties, and highlight how changes to composition may be reflected in the electronic structure. We then discuss a chemically intuitive method of predicting double-perovskite band-edge character, similar to the analysis for single perovskites.¹³⁶

The rock-salt-ordered $\text{Cs}_2\text{AgBiBr}_6$ crystallizes in a cubic $Fm\bar{3}m$ structure. Unlike the cubic Pb-based single perovskites, $\text{Cs}_2\text{AgBiBr}_6$ displays an indirect bandgap, with the VBM at X and the CBM at L. The VBM has Ag 4d, Bi 6s, and Br 4p character, while the CBM has Ag 5s, Bi 6p, and Br 4p character (Fig. 9A),^{113,183,185,189} corresponding to the frontier orbitals expected of Ag^+ , Bi^{3+} , and Br^- ions. It is worth noting that SOC effects will strongly affect the band structure of $\text{Cs}_2\text{AgBiBr}_6$, particularly with the CB, due to the stabilization and splitting of the Bi $p_{1/2}$ and Bi $p_{3/2}$ states.¹⁸⁹ The relative contributions of the two B-site orbitals are not equivalent: the VB is dominated by Ag 4d and Br 4p character, with Bi 6s character present at the VBM at X but not throughout the entire band. Similarly, the primarily Bi 6p- and Br 4p-based CB has Ag 5s character in the CBM solely about L.¹³⁷ Both the relative energies and the orbital symmetries of these frontier orbitals are important to determining the nature of the bandgap in these materials. This can be shown by substitution of the constituent elements: replacing Bi^{3+} with isoelectronic Sb^{3+} to form $\text{Cs}_2\text{AgSbBr}_6$ leads to a moderate (~ 0.3 eV) reduction in bandgap magnitude. The VBM is increased in energy due to the higher energy of the Sb 5s orbitals compared to the Bi 6s orbitals leading to increased dispersion in the VB.^{159,190} Furthermore, substitution of Bi^{3+} with Tl^{3+} to form $\text{Cs}_2\text{AgTlBr}_6$ leads to both a large (~ 1.0 eV) reduction in bandgap magnitude and a transition from an indirect to a direct bandgap (Fig. 10).¹⁸² The basis for these effects can be explained by a local bonding picture that allows for prediction of band-edge character, as discussed below.

The K_2PtCl_6 -type double perovskite, Cs_2SnBr_6 , has a VB with a maximum at Γ and with significantly less dispersion than the VB of $\text{Cs}_2\text{AgBiBr}_6$ (Fig. 9B). The CBM occurs at Γ , leading to a direct bandgap transition.¹³⁷ However, this bandgap transition is calculated to be parity-forbidden, similar to the iodide analog Cs_2SnI_6 .⁹² Whereas the CB shows Sn 5s orbital and Br 4p orbital contributions, the VBs consist solely of Br 4p orbitals without contributions from Sn orbitals, explaining its low dispersion. This is due to the relative energies of the Sn and Br frontier orbitals: the Sn 4d highest occupied orbital is too low in energy compared to the Br 4p ligand orbitals to contribute to the VB states. By contrast, replacing Sn^{4+} with Te^{4+} to form Cs_2TeI_6 , for example, introduces Te 5s orbital contributions to the VBM, and Te 5p character in the CB moves the CBM to L and makes the bandgap indirect.⁹² Despite being isostructural, the electronic structures of these two perovskites differ greatly.

A linear combination of atomic orbitals (LCAO) approach can also be used to analyze the local bonding of $\text{A}_2\text{BB}'\text{X}_6$ (B = metal; B' = metal or a vacancy) double perovskites.¹³⁷ In order to be generally applicable to all double perovskites, first, the Bloch waves of the halide-only framework can be generated. Here, the σ -bonding SALCs of the six halides octahedrally arranged around the B site (i.e., A_{1g} , 2E_g , and 3T_{1u}) and appropriate translational symmetry (depending on the k point) generate the halide SALCs around the B' site. The interactions between these halide-only SALCs and the metal orbitals can then be evaluated. A similar treatment can be applied to the π -bonding SALCs. Metal orbitals with symmetries matching those of the halide SALCs are expected to give the maximally bonding/antibonding MOs, corresponding to band extrema. In the absence of metal-halide bonding/antibonding interactions, the interactions between two adjacent halides that are 90 degrees apart are found to dictate the energy of the band. Thus, by energetically ranking bonding and anti-bonding interactions between nearest neighbors (B-X interactions) and next-nearest neighbors (90 degrees adjacent X-X interactions), the band dispersion can be determined at the high-symmetry k points. The VBM and CBM can be determined by the symmetry of the B- and B'-cation frontier orbitals (Table 1). Thus, the direct/indirect nature of the bandgap of a double perovskite may often be predicted from its chemical formula and some knowledge of the frontier

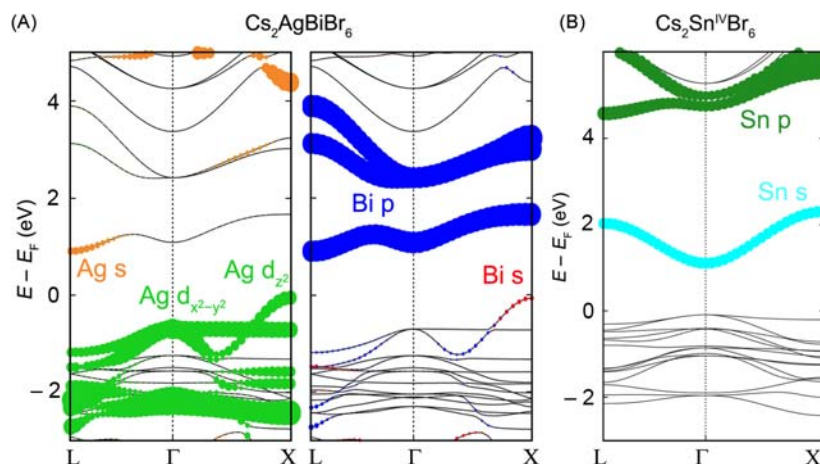


Fig. 9 Band structures of: (A) $\text{Cs}_2\text{AgBiBr}_6$; (B) Cs_2SnBr_6 . The band structure of $\text{Cs}_2\text{AgBiBr}_6$ in (A) is shown in duplicate and the B-site cation orbital contributions are proportionally shown in color. Bromide contributions are present but not shown. Adapted from Slavney, A. H.; Connor, B. A.; Leppert, L.; Karunadasa, H. I., A Pencil-and-Paper Method for Elucidating Halide Double Perovskite Band Structures. *Chem. Sci.* **2019**, *10* (48), 11041–11053 - Published by The Royal Society of Chemistry.

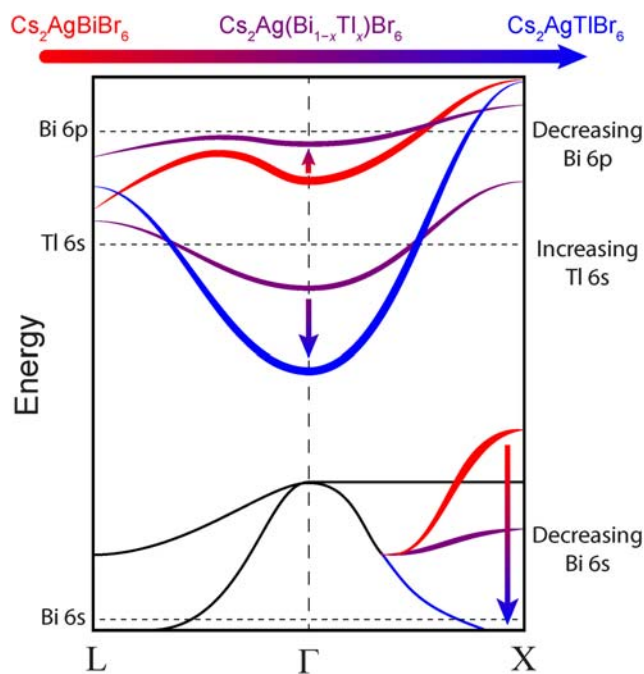


Fig. 10 Schematic band diagram showing the change in electronic structure over the composition range of the $\text{Cs}_2\text{Ag}(\text{Bi}_{1-x}\text{Tl}_x)\text{Br}_6$ solid solution. Only the bands or portions of bands that change with alloying are colored. Red and blue lines are the bands of $\text{Cs}_2\text{AgBiBr}_6$ and $\text{Cs}_2\text{AgTlBr}_6$, respectively, while purple shows an intermediate composition. Horizontal dashed black lines show the approximate energies of the isolated molecular orbitals. Reprinted with permission from Wolf, N. R.; Connor, B. A.; Slavney, A. H.; Karunadasa, H. I., Doubling the Stakes: The Promise of Halide Double Perovskites. *Angew. Chem. Int. Ed.* **2021**, *60* (30), 16264–16278. Copyright 2021 John Wiley and Sons Publishers.

orbital energies. This work applies to all cubic, non-distorted double perovskites, but can be adapted to include distorted structures such as Rb_2SnI_6 or $\text{Cs}_2\text{Au}^{\text{I}}\text{Au}^{\text{III}}\text{Cl}_6$. Knowledge of the relevant frontier orbitals for the B-site cations of interest is often chemically intuitive based on electronic configuration, but in some cases prior knowledge from calculations or experiments such as photoelectron spectroscopy is needed (see Section 4.15.6.5). For instance, tabulated X-ray photoelectron measurements were used to determine that the Sn 4d orbitals were too low in energy to interact with the Br 4p orbitals that make up the VB states in Cs_2SnBr_6 .

Both homovalent and heterovalent alloying of double perovskites can induce drastic changes in the optoelectronic properties (see Section 4.15.3.4). The $\text{Cs}_2\text{AgBiBr}_6$ host lattice, for instance, can accommodate a variety of alloyed species. Calculations for $\text{Cs}_2\text{Ag}(\text{Tl}_{0.06}\text{Bi}_{0.94})\text{Br}_6$ (where Tl^{3+} is homovalent but non-isoelectronic with Bi^{3+}) indicate a drastically decreased indirect bandgap because of a lowered CBM at Γ due to the introduction of empty Tl 6s orbitals that form an impurity band (Fig. 10).¹¹³ Calculations on $\text{Cs}_2\text{Ag}(\text{Sb}_{0.25}\text{Bi}_{0.75})\text{Br}_6$ (where Sb^{3+} is homovalent and isoelectronic with Bi^{3+}) also show a reduction in the magnitude of the indirect bandgap but to a lesser extent than for Tl^{3+} alloying.¹⁵⁹ Here, the bandgap reduction occurs due to the filled Sb 5s orbitals, which are higher in energy than the Bi 6s orbitals that are stabilized by relativistic effects, thus raising the energy of the VBM.

Theoretical treatments of heterovalent alloying are also possible, but care must be taken to ensure that the simulated charge-compensation mechanism is appropriate. Calculations show Sn^{2+} substitution at the Ag^+ site accompanied by charge-compensating Ag^+ vacancies in $\text{Cs}_2\text{AgBiBr}_6$ at 1.25 atom% Sn introduces Sn 5p character to the CB, resulting in a calculated direct bandgap that is reduced in magnitude by 0.09 eV.¹¹⁶ In contrast, Sn^{4+} substitution at the Bi^{3+} site, also with charge-compensating Ag^+ vacancies, leads to similar changes as for Tl^{3+} alloying at the Bi^{3+} site: the indirect bandgap is maintained but the Sn 5s orbitals form a new low-energy CB that decreases the bandgap by 0.44 eV. Similar calculations on Bi^{3+} -alloyed Cs_2SnCl_6 accompanied by charge-compensating Cl^- vacancies at 0.41 atom% Bi result in a bandgap reduction of 0.90 eV as a high-energy Bi 6s-based VB is introduced.¹⁹¹

4.15.5 Synthesis

4.15.5.1 Introduction

The ions in oxide perovskites ($\text{A}^{\text{I}}\text{B}^{\text{V}}\text{O}_3$, $\text{A}^{\text{II}}\text{B}^{\text{IV}}\text{O}_3$, or $\text{A}^{\text{III}}\text{B}^{\text{III}}\text{O}_3$) feature double the average charge seen in their halide congeners ($\text{A}^{\text{I}}\text{B}^{\text{II}}\text{X}_3$). The lattice energy in an ionic crystal increases quadratically with the charge of the ions; thus, this doubling of the average charge is reflected by an increase in the thermodynamic stability of an oxide perovskite crystal relative to its halide counterpart. Thermochemical measurements indeed confirm the difference in the formation enthalpy and free energy between oxides and halides (Table 2),^{192,193} where the halide perovskites and their precursors exhibit relatively modest thermodynamic stability.

Table 1 VBM and CBM predictions of double perovskites based on B and B' orbital character.

Orbitals		Prediction	
B	B'	VBM	CBM
σ -Bonding states ^a			
s	s	Γ	Γ
p	p	Γ	Γ
$d_{x^2-y^2}/d_{z^2}$	$d_{x^2-y^2}/d_{z^2}$	Γ & X	Γ & X
s	p	L	L
s	$d_{x^2-y^2}/d_{z^2}$	X	X
p	$d_{x^2-y^2}/d_{z^2}$	–	–
s	null	X	Γ
p	null	L	L
$d_{x^2-y^2}/d_{z^2}$	null	Γ & X	X
null	null	Γ & X	–
π -Bonding states ^a			
$d_{xy}/yz/xz$	$d_{xy}/yz/xz$	Γ & X	Γ & X
$d_{xy}/yz/xz$	null	X	Γ & X
null	null	Γ ^b	–
$d_{xy}/yz/xz$	$d_{xy}/yz/xz$	Γ & X	Γ & X

The VBM (CBM) of a given perovskite is determined by identifying the energetically appropriate HOMO (LUMO) of the B and B' cations of interest, then finding the corresponding line in the table.

^a π - and σ -bonding states involve orthogonal orbitals and cannot interact.

^bThe σ -bonding halide-only states (i.e., *null-null* combination) have more 90 degrees adjacent X–X interactions and will often form the band extrema. See text and reference for further details.

Reprinted from Slavney, A. H.; Connor, B. A.; Leppert, L.; Karunadasa, H. I., A Pencil-and-Paper Method for Elucidating Halide Double Perovskite Band Structures. *Chem. Sci.* **2019**, *10* (48), 11041–11053 - Published by The Royal Society of Chemistry.

Table 2 Comparison of the entropy, $S_{298\text{ K}}^0$, enthalpy of formation, $\Delta_f H_{298\text{ K}}^0$, and Gibbs free energy of formation, $\Delta_f G_{298\text{ K}}^0$, for CaTiO₃ and (CH₃NH₃)PbBr₃ perovskites and their precursors, with respect to pure elements.

Composition	$\Delta_f H_{298\text{ K}}^0$ (kJ mol ⁻¹)	$S_{298\text{ K}}^0$ (J mol ⁻¹ K ⁻¹)	$\Delta_f G_{298\text{ K}}^0$ (kJ mol ⁻¹)	Melting point (°C)
CaTiO _{3(s)} ^a	–1659	93.7	–1687	1970
CaO _(s) ^a	–635	38.2	–646	2613
TiO _{2(s)} ^{a,b}	–945	50.6	–960	1857
(CH ₃ NH ₃)PbBr _{3(s)} ^c	–543	349	–647	–
(CH ₃ NH ₃)Br _(s) ^c	–259	–	–	–
PbBr _{2(s)} ^c	–277	161	–325	373

^aThermodynamic and melting-point data from ref.¹⁹²

^bRutile.

^cThermodynamic data from ref.¹⁹³

The oxide perovskites are commonly synthesized using solid-state ceramic methods, for example, heating well-mixed component oxides (or carbonates) at high temperature (>2/3 of the melting point, often above 1000 °C) for a period of hours to days.^{194,195} More recently, methodologies including sol-gel, hydrothermal, and microwave-assisted syntheses have decreased reaction temperatures to below 500 °C for certain compositions.¹⁹⁴ By comparison, many halide salts are readily soluble in polar organic solvents and aqueous solutions including hydrohalic (HX) acids at room temperature (RT) and melt at temperatures well below 1000 °C (Table 2). Thus, in addition to solid-state syntheses at moderate temperatures (below 500 °C), a wide variety of solution-state and evaporation-based methods have been employed to synthesize halide perovskites at or near RT. Methods for the deposition of perovskite thin films are particularly attractive from a manufacturing perspective, a topic that was recently reviewed in detail by Nitin Padture and David Mitzi.¹⁹⁶

Here, we provide a survey of synthesis methods that produce 3D halide perovskite crystals, powders, and thin films. We place a particular emphasis on solution-state methods because within the perovskite family, solution-state self-assembly at or near RT is unique to the halides (and the pseudohalides; see Section 4.15.1). These syntheses are easily accessible without specialized equipment and they offer a range of conditions where desirable phases may be preferentially crystallized. For example, in a typical synthesis, the precursor stoichiometry can be tuned, spectator ions can be added to change solubilities,¹⁹⁷ and the solvent(s),

pH, and temperature of the reaction mixture can be varied. These self-assembly reactions can also be manipulated to afford the desired morphology: thin films, powders, and shape- and size-controlled single crystals can be formed for a range of applications. The ease and tunability of solution-state synthesis, combined with the relatively similar thermodynamic stabilities of competing products, has enabled researchers to screen conditions and discover a diverse range of compounds within the still-expanding halide perovskite family.

4.15.5.2 Solid-state synthesis and crystallization from a melt

Conventional solid-state ceramic methods, such as heating intimate mixtures of the solid precursors or crystallization from a melt, have been adapted to synthesize 3D halide perovskites. Widespread implementation of solid-state syntheses is impeded by particular characteristics of halide perovskites such as the decomposition and/or volatilization of organoammonium A-site cations and metal halides. There are, however, advantages in the solid-state methods: solubility differences among precursors and coordinating solvents complicate solution-state methods, whereas evaporation-based methods suffer from volatility differences among precursors and thermal and ablation-induced decomposition of precursor salts. Furthermore, increasing the number of components, such as with alloyed or double-perovskite compositions, increases the number of competing side phases during solution-state self-assembly. Solid-state techniques eliminate solvent and solubility complications and may offer enhanced stoichiometric control, in some cases proceeding at or near RT.

4.15.5.2.1 High-temperature solid-state synthesis

Christian Møller made first mention in 1957 that CsPbCl₃ may be prepared “simply by melting and sintering” CsCl and PbCl₂.³⁰ Mixtures of the binary halide precursors (e.g., CsBr and PbBr₂) can be held at elevated temperatures (typically below the melting point of the components) to obtain the desired perovskite, provided it is the thermodynamic product. This constraint can be circumvented, albeit temporarily: the perovskite phases of CsSnI₃,¹⁹⁸ CsPbI₃,¹⁹⁹ and (NH₂CHNH₂)PbI₃,^{111,200} for example, are not the thermodynamic product at RT but may in some cases be isolated as a nonequilibrium phase. Organoammonium perovskites are rarely prepared at elevated temperatures due to the facile release of gaseous small molecules such as CH₃NH₂ or HX. Thus, the high-temperature methods for perovskite synthesis will, in general, be limited to compositions where the precursor halide salts have a definite melting or sublimation point. This includes most inorganic and few organoammonium salts: (CH₃NH₃)X (X = Cl⁻, Br⁻, I⁻) salts have been utilized in solid-state syntheses,²⁰¹ though their behavior varies between the halides. Thermogravimetric analysis indicates a single sublimation step for both (CH₃NH₃)Cl and (CH₃NH₃)I with onset temperatures of approximately 195 °C and 247 °C, respectively²⁰²; differential thermal analysis (DTA) further suggests the sublimation coincides with an exothermic decomposition of (CH₃NH₃)I above 350 °C.²⁰³ We note that scanning thermogravimetric and related analyses sometimes fail to capture the long-term stability of a compound; isothermal heating of bulk (CH₃NH₃)PbX₃ (X = Br⁻, I⁻) at 60 °C (for 72 h²⁰⁴) and (CH₃NH₃)PbI₃ thin films at 85 °C (for 24 h²⁰⁵) causes the loss of CH₃NH₂ and HX (X = Br, I) gas at more modest temperatures, likely driven by Le Chatelier’s principle in open systems.

In contrast to a typical ceramic preparation in air, high-temperature solid-state syntheses of perovskites require an inert atmosphere to avoid reactivity with oxygen and water. Commonly, mixed or ground halide precursors are transferred to either: (i) fused silica, quartz, or inert (graphite or noble-metal) tubes to be evacuated and sealed before heating, or (ii) a crucible within a tube or flow-through furnace under inert gas flow. In some cases, a pellet of the mixed precursors is pressed prior to heating: the compacting of grains facilitates interdiffusion of the reacting species and often improves conversion in a solid-state reaction (Fig. 11A). Reaction mixtures are held at high temperature for a period of hours to days before cooling. The cooling rate is often dictated by the desire to allow for grain or crystal growth (slow cooling) or to isolate a fine-grained powder or nonequilibrium phase (rapid cooling). The product of a well-designed solid-state reaction often yields a phase-pure perovskite, presumably owing to relative instability of the precursors and sufficient ion diffusion. However, some studies, for example with (CH₃NH₃)Sn(Cl_xBr_{1-x})₃,²⁰¹ note a need to repeatedly grind and heat to obtain the desired solid solution, a common technique used in the ceramic community to achieve complete conversion.

4.15.5.2.2 Room-temperature mechanochemical methods

The application of mechanical energy to mixtures of precursor halide salts has also been used to produce phase-pure powders of single^{111,206,207} and double perovskites.^{208–210} Solvent-free mechanical mixing and grinding may be performed by hand (with a mortar and pestle) or with grinding media in a ball mill. Room-temperature mechanochemical syntheses allow for precise accounting of stoichiometry, avoid instabilities at elevated temperatures, and proceed due to favorable thermodynamics of formation and reasonable rates of ion diffusion. Although many of these syntheses have been performed with precautions to exclude moisture (e.g., in a glovebox), it is difficult to eliminate the possibility that slight surface dissolution and recrystallization of the solids helps to facilitate these reactions.

Mechanochemistry is well-suited to prepare organoammonium perovskite compositions, in particular to study the complex, mixed-halide and/or mixed-A-site perovskites that are increasingly found in high-performance optoelectronic devices. Compared to solution-state assembly, these solid-state syntheses have improved the stoichiometric precision and expanded the scope of compositions in (NH₂CHNH₂)Pb(Br_xI_{1-x})₃ and (NH₂CHNH₂)Pb(Cl_xBr_{1-x})₃,²¹¹ (CH₃NH₃)Pb(Br_xI_{1-x})₃ and (CH₃NH₃)Pb(Cl_xBr_{1-x})₃,²¹² and ((CH₃NH₃)_x(NH₂CHNH₂)_{1-x})PbI₃²¹³ alloys. Recently, the synthesis of Cs₂AgInBr₆, a double-perovskite composition predicted to be thermodynamically stable but previously unreported, was achieved using mechanochemistry.²⁰⁸

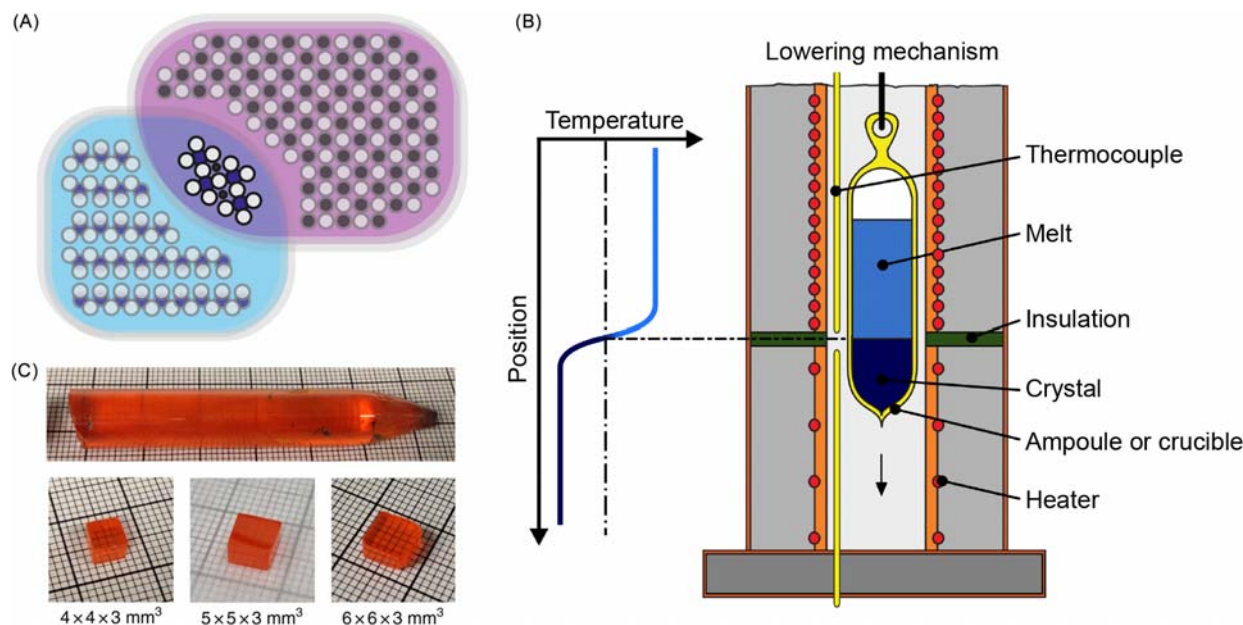


Fig. 11 Schematic representations of: (A) a solid-state reaction dependent on interdiffusion of ions between grains of the precursors; (B) a typical vertical Bridgman crystallization in a two-zone furnace, adapted with permission from Cepheiden, CC BY-SA 3.0 (<https://creativecommons.org/licenses/by-sa/3.0/>), via Wikimedia Commons; (C) (top) an 11-mm-diameter CsPbBr₃ ingot grown using the Bridgman method and (bottom) crystals cut from the ingot. Reprinted from He, Y.; Matei, L.; Jung, H. J.; McCall, K. M.; Chen, M.; Stoumpos, C. C.; Liu, Z.; Peters, J. A.; Chung, D. Y.; Wessels, B. W.; Wasielewski, M. R.; Dravid, V. P.; Burger, A.; Kanatzidis, M. G. High Spectral Resolution of Gamma-Rays at Room Temperature by Perovskite CsPbBr₃ Single Crystals. *Nat. Commun.* **2018**, *9* (1), 1609 - Published by Springer Nature under Creative Commons Attribution 4.0 International License: <http://creativecommons.org/licenses/by/4.0/>.

As-of-yet undiscovered perovskite compositions that have eluded synthesis due to small regions of thermodynamic stability, the formation of side-phases, or solubility mismatch of precursors may prove to be accessible via mechanochemistry.

4.15.5.2.3 The Bridgman method: Bulk crystal growth from a melt

The Bridgman method, among other melt crystallizations including the Czochralski and floating-zone methods, is the primary technique that has been used to grow large single crystals of perovskites. Solid halide precursors are ground together, typically in a moisture-free or oxygen-free atmosphere, then sealed in an ampoule under vacuum as described above for a solid-state powder synthesis (see Section 4.15.5.2.1). A vertical Bridgman crystallization with a multi-zone furnace (Fig. 11B) is typically guided by the results of a DTA measurement to target a desired temperature profile. For example, CsPbBr₃ melts at 567 °C and crystallizes at 514 °C and goes through two symmetry-lowering phase transitions upon cooling, around 130 °C and 88 °C.²¹⁴ In addition to the melting point, one must also consider the nature of these phase transitions, twin formation, and thermal expansion to obtain defect- and crack-free bulk single-crystal ingots.²¹⁵ For instance, despite a linear volumetric expansion relationship, the low-symmetry perovskite phases may exhibit non-linear expansion in distinct crystallographic axes, leading to anisotropic stresses.²¹⁴ Generally speaking, the Bridgman method suffers from induced stresses at the interface between the cooling perovskite ingot and the ampoule but offers excellent impurity-free conditions with an inert tube under static vacuum.

Further considerations include the translation rate of the ampoule through the furnace(s) and the cooling rate of the lower (cooler) zone once the ampoule has completed its pass through the upper (warmer) zone. The cooling rate from the cold zone to RT may be very slow, perhaps 2 °C h⁻¹,^{215,216} to further mitigate fracturing of the crystal. The translation rate may be similarly slow, for instance 0.5 mm h⁻¹.²¹⁵ To date, CsPbBr₃ has been the common composition among large, Bridgman-grown perovskite crystals (Fig. 11C), with ingot sizes reaching 40 cm³ (2.4 cm diameter).²¹⁶ Single crystals or polycrystals of CsPbX₃ (X = Cl⁻, Br⁻),^{217,218} KMnCl₃,²¹⁸ CsSnI₃,²¹⁹ and double perovskites such as Ce-alloyed Cs₂LiYCl₆²²⁰ and Cs₂NaInCl₆²²¹ have also been grown by this method. With the desire for large single crystals, particularly for fundamental studies and applications such as high-energy photon detection, the scope of compositions grown by the Bridgman method may continue to expand within the limits of non-volatile component halides with definite melting points.

4.15.5.3 Solution-state synthesis

In contrast to the precursors for sulfide and oxide perovskites, binary halide salts tend to exhibit high solubility in water (Table 3),²²² polar organic solvents, and aqueous hydrohalic acids (HX_(aq)); this presents a unique opportunity to self-assemble halide perovskites from solution. The earliest reports of the synthesis of halide perovskites by Wells in the 1890s⁴ and the organoammonium

Table 3 Comparison of the solubility product constant (K_{sp}) and measured solubility (20–30 °C) of various inorganic salts that are perovskite precursors.²²²

Precursor salt	K_{sp}	Saturation concentration (mol/100 g H ₂ O)	Perovskite
CsCl	–	1.11	CsPbCl ₃
PbCl ₂	1.70×10^{-5}	3.60×10^{-3}	
Ba(OH) ₂	2.55×10^{-4}	2.55×10^{-2}	BaTiO ₃
TiO(OH) ₂	1.0×10^{-29}	–	
Pb(OH) ₂	1.43×10^{-15}	–	Pb(Ti _x Zr _{1-x})O ₃
ZrO(OH) ₂	6.3×10^{-49}	–	
TiO(OH) ₂	1.0×10^{-29}	–	

compositions by Weber in the 1970s^{32,223} indeed describe their preparation from aqueous solution. Solution-state syntheses generally operate on the principle of supersaturation and allow a wide range of techniques to obtain polycrystalline powders or larger crystals of the desired perovskite. Temperature-controlled methods induce a rapid precipitation or slow crystallization based on the relationship between temperature and solubility. These, along with solvent evaporation, are often the simplest techniques available to the experimentalist. Mixed-solvent and vapor-diffusion methods take advantage of the varied solubility of perovskites between polar and non-polar solvents. Finally, hydrothermal, solvothermal, and ultrasound- and microwave-assisted techniques have also been applied in cases where the aforementioned methods are insufficient to obtain a desired composition or morphology.

Classical theory of nucleation and growth provides the basis for understanding the mechanisms of the solution-state methods, as well as some thin-film depositions, which we describe here. We briefly describe the salient points, particularly differentiating homogeneous and heterogeneous nucleation as a function of concentration, and note that a more detailed description can be found in review articles by Nitin Padture and David Mitzi and references therein.^{196,224} Homogeneous nucleation occurs within the precursor solution, whereas heterogeneous nucleation occurs at interfaces between the solution and the reaction vessel, colloidal particles, or the headspace gas-solution interface. For homogeneous nucleation, the change in free energy depends primarily on the radius of the nucleus, the interfacial energy between the nucleus and the solution, and the precursor concentration relative to the saturation limit. An intermediate value of the radius coincides with the maximum free energy change: this value is defined as the critical radius (Fig. 12A). Only above this critical radius is the nucleus stable and expected to grow. The change in free energy for heterogeneous nucleation follows a similar dependence, but its magnitude is diminished through a reduction in the interfacial energy. Thus, the barrier in free energy to reach a critical radius of the nuclei is expected to be lower for heterogeneous than homogeneous nucleation (inset of Fig. 12A). In a typical crystallization, this manifests as a higher likelihood (or rate) of heterogeneous nucleation compared to homogeneous nucleation, at low degrees of saturation. If the concentration, and hence degree of saturation, increases further, heterogeneous nucleation becomes limited by available nucleation sites and homogeneous nucleation will begin and eventually dominate (Fig. 12B). Furthermore, nucleation rates can exhibit a time dependence, which can be analyzed if the concentration is monitored as a function of time or varied in a controlled manner. Temporal analysis informs that minimizing the duration of the nucleation “window,” where the concentration exceeds saturation or supersaturation and nucleation rates are high, facilitates the growth of large single crystals from solution in the absence of a seed. Understanding the nucleation thermodynamics and the competing mechanisms helps predict the product(s) of the methods described below and informs improvements

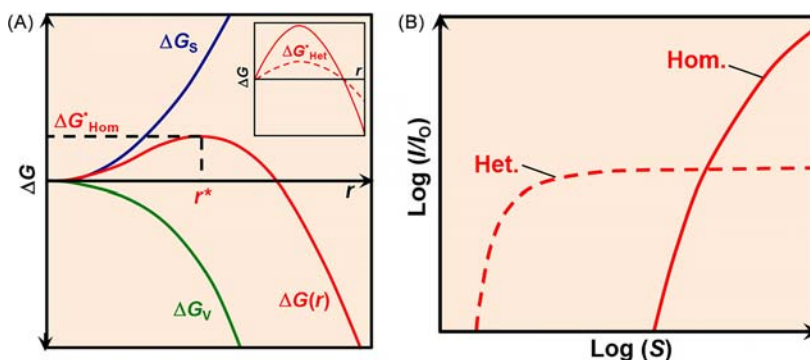


Fig. 12 (A) Gibbs free energy changes (ΔG) as a function of nucleus radius (r) for a homogeneous (ΔG_{Hom}^*) and heterogeneous (inset, dashed line, ΔG_{Het}^*) nucleation. ΔG_s and ΔG_v are the surface and volume Gibbs free energy change, respectively, and r^* is the critical nucleation radius. (B) Logarithmic plot of the normalized rate of nucleation (I/I_0) as a function of the saturation ratio ($S = C/C_s$, where C is the concentration and C_s is the saturation limit). Adapted with permission from Dunlap-Shohl, W. A.; Zhou, Y.; Padture, N. P.; Mitzi, D. B., Synthetic Approaches for Halide Perovskite Thin Films. *Chem. Rev.* **2019**, *119* (5), 3193–3295. Copyright 2018 American Chemical Society.

in synthetic design. For example, limiting the number of nucleation sites by filtering dust and other microparticles from the precursor solution can yield fewer heterogeneous nucleation sites, yielding larger crystals.

4.15.5.3.1 Temperature-controlled methods

Temperature-controlled crystallizations exploit the solubility-temperature relationship in solution to obtain the desired perovskite product. In a typical case, the dissociation equilibrium favors the dissociated (solvated) product as temperature increases; here, the halide precursors may be dissolved at high temperature and cooled to a lower temperature to induce supersaturation and the precipitation of a powder or the nucleation and growth of single crystals. Alternatively, specific precursor-solvent combinations can exhibit retrograde solubility, or a negative relationship between temperature and solubility (Fig. 13). Such systems enable an “inverse temperature crystallization” (ITC), wherein the temperature is raised to induce supersaturation. This behavior may be the result of solute-solvent complexation (e.g., $\text{PbI}_n\text{S}_m^{2-n}$, where S = solvent, $n = 2-6$) that dissociates at high temperature and is more likely to occur in systems where the solvent interacts weakly with the metal (e.g., Pb^{2+} in polar organic solvents), favoring higher halide coordination numbers.²²⁵ It is worth noting that the solubility-temperature relationship need not monotonically increase or decrease: in the case where solubility peaks at an intermediate temperature (Fig. 13A), supersaturation can often be achieved either by heating or cooling from this temperature. This is the case with some perovskites, which may be crystallized by either heating or cooling, depending on the combination of precursors and solvent. For example, $(\text{CH}_3\text{NH}_3)\text{PbX}_3$ ($\text{X} = \text{Cl}^-$, Br^- , I^-) crystallizes upon slow cooling from a solution of the aqueous HX acid⁴⁶ but requires heating to crystallize from polar organic solvents.²²⁶⁻²²⁹

Aqueous solutions of the halide salts, typically in the corresponding HX acid, tend to exhibit a positive relationship between solubility and temperature; thus, they are commonly used to synthesize the desired perovskite upon cooling from high temperature. The rate of cooling tends to correlate inversely with grain size. For example, the double perovskite $\text{Cs}_2\text{AgBiBr}_6$ precipitates as a powder upon cooling naturally from 110 °C to RT, but as small (μm) or large (mm) single crystals upon slow cooling at a rate of 2 °C h^{-1} or 1 °C h^{-1} , respectively, from 9 M HBr.²⁰⁴ Fast cooling results in a mass homogeneous nucleation and the precipitation of a powder; the rate may range from a rapid quench (for example, using liquid N_2 ¹⁸²) to simply removing the reaction from the heat source to cool to ambient temperature. Rapid cooling may also kinetically trap nonequilibrium crystallographic phases, albeit temporarily, in the isolated product.^{199,230} On the other hand, slow cooling often results in the nucleation and growth of single crystals. The nucleation and growth periods may be influenced by the cooling rate or the introduction of a seed crystal, as discussed below. Crystallization through cooling is simple, generally applicable to a range of perovskite compositions, and requires optimization of only precursor concentration and cooling rate.

The ITC method is based on the negative relationship between temperature and solubility (Fig. 13) in certain systems and it has been used for the growth of mm-scale $(\text{CH}_3\text{NH}_3)\text{PbX}_3$ ($\text{X} = \text{Cl}^-$, Br^- , I^-) single crystals.²²⁶⁻²²⁹ Organoammonium perovskite compositions, including $(\text{CH}_3\text{NH}_3)\text{PbX}_3$ ($\text{X} = \text{Cl}^-$, Br^- , I^-)²²⁶⁻²²⁹ and $(\text{NH}_2\text{CHNH}_2)\text{PbX}_3$ ²²⁷ ($\text{X} = \text{Br}^-$, I^-), and CsPbBr_3 ^{231,232} are notably crystallized using this method from polar organic solvents, including dimethylformamide (DMF), dimethylsulfoxide (DMSO), and γ -butyrolactone (GBL). Once supersaturation conditions are reached, the growth rate of nucleated crystals, or a single

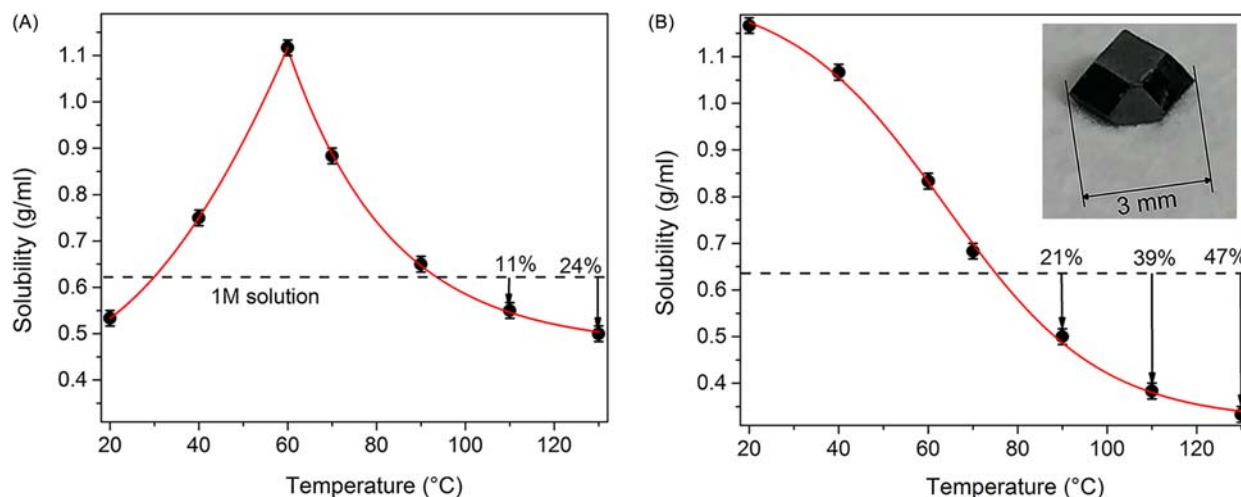


Fig. 13 Retrograde solubility of perovskites in γ -butyrolactone (GBL): (A) the solubility of $(\text{CH}_3\text{NH}_3)\text{PbI}_3$ in GBL exhibits a maximum at an intermediate temperature; (B) the solubility of $(\text{NH}_2\text{CHNH}_2)\text{PbI}_3$ in GBL decreases monotonically above RT. Inset is a mm-scale single crystal grown by the “inverse temperature crystallization” method. Arrows and numerical values represent the percentage of solubility at a given temperature relative to a 1 M solution (dashed horizontal line), equivalently indicating the mass percentage that may be isolated from solution during an isothermal inverse temperature crystallization at this temperature. Adapted with permission from Saidaminov, M. I.; Abdelhady, A. L.; Maculan, G.; Bakr, O. M., Retrograde Solubility of for Maminidinium and Methylammonium Lead Halide Perovskites Enabling Rapid Single Crystal Growth. *Chem. Commun.* **2015**, 51 (100), 17658–17661 - Published by The Royal Society of Chemistry.

seed crystal, is easily controlled via the heating rate or by isothermally approaching equilibrium. The solubility relationship required for the ITC method may be difficult to predict a priori; however, once a suitable solvent-solute system is identified, the ITC method can offer value in allowing the experimentalist to grow large single crystals within hours.

In a solution-state crystallization without a seed crystal, using temperature-controlled methods or the solvent-based methods described below, heterogeneous nucleation at interfaces will dominate. Multiple nucleation sites are commonly observed to form simultaneously and grow at the interfaces between the solution and either the headspace or the reaction vessel. A typical crystallization from solution commonly yields small single crystals suitable for studies such as structure determination via X-ray diffraction. These small crystals may also be used as seed crystals in subsequent crystallizations to form larger single crystals suitable for measurements such as neutron scattering. Seed crystals are commonly placed at the bottom of the vessel; however, top-seeded growth has also been reported.²³³ The ITC method is particularly amenable to seeded growth as, by its nature, the likelihood of re-dissolving the seed or inducing mass precipitation is quite low as the solution is heated to the point of supersaturation. Conversely, the addition of a seed to an already supersaturated solution may trigger a mass precipitation, or rapid nucleation, from the solution. Finally, shape-controlled crystallization methods—that is, confining the solution or influencing the crystallization mechanism to obtain a desired shape or aspect ratio—have been developed in concert with these solution-state methods and were recently reviewed.²³⁴ Careful choice of concentration, temperature, and additional surfactant recently yielded single crystals of CsPbBr₃ from solution with an anisotropy (or aspect) ratio of 10⁵, with thicknesses on the order of 100 nm and lateral dimensions approaching 1 cm.²³⁵

4.15.5.3.2 Solvent evaporation methods

Solvent evaporation from a saturated solution of the perovskite precursor(s) induces supersaturation and often the nucleation and growth of single crystals of the desired perovskite product. While technically not limited to organic solvents, this method is commonly employed using organic solvents with vapor pressures exceeding that of water at room temperature (Table 4). There is a tradeoff between vapor pressure and solubility that must be considered when choosing a solvent (or solvent system): a balance must be struck between the volatility of a solvent and the total solubility of the precursor(s) to obtain a reasonable yield of the product. The volatility of the solvent, along with the rate of exchange of the headspace vapor, will determine the crystallization rate: in the case of a volatile solvent (e.g., acetonitrile), a fine-grained powder may result from rapid evaporation. Mixed-solvent evaporations (see Section 4.15.5.3.3) may also be feasible, provided the perovskite is less soluble in the solvent with a lower vapor pressure. For instance, (CH₃NH₃)PbCl₃ crystallizes from a mixture of DMSO and GBL upon evaporation of DMSO within weeks.²³⁶ The evaporation rate can be controlled by the surface area of the exposed solution (e.g., by changing the diameter of the vial, loosely capping a vial, or using a cap with holes) or by the temperature of the solution. Small crystals are typically obtained, as discussed above, from a crystallization without a seed crystal. This method is less attractive for the seeded growth of a large single crystal because it may take days to months to obtain a comparable product to one obtained from an hours-long ITC method. It does, however, offer the experimentalist a number of solvent options and can be efficient for screening or small single-crystal growth.

4.15.5.3.3 Mixed-solvent methods

Mixed-solvent methods encompass a range of versatile solution-state techniques to obtain phase-pure perovskite powders and single crystals at constant temperature. The crux of these methods is the choice of at least two solvents: one that poorly solubilizes the perovskite (the “bad” solvent or “antisolvent”) and one that readily dissolves the perovskite. The ideal solvent system is often found with some intuition and candidate screening. In the simplest case, where a powder is desired, the direct addition of an antisolvent to the perovskite precursor solution (or vice versa) yields the product instantaneously as a powder. Single-crystal growth is typically achieved using two common methods: vapor-liquid diffusion and liquid-liquid diffusion (layering).

Table 4 Vapor pressure and density of common solvents used in bulk syntheses and thin-film processing of the perovskites, and water for comparison, at 20–25 °C.

Solvent	Vapor pressure (Torr)	Density (g cm ⁻³)
<i>N,N</i> -Dimethylformamide, (CH ₃) ₂ NC(O)H	2.7	0.94
Dimethylsulfoxide, (CH ₃) ₂ S(O)	0.6	1.1
Water, H ₂ O	18	0.99
Chlorobenzene, C ₆ H ₅ Cl	8.8	1.1
Toluene, C ₇ H ₈	28.5	0.87
2-propanol, (CH ₃) ₂ CHOH	33	0.79
Acetonitrile, CH ₃ CN	89	0.79
Methanol, CH ₃ OH	97	0.79
Acetone, (CH ₃) ₂ C(O)	190	0.78
Dichloromethane, CH ₂ Cl ₂	350	1.3
Diethyl ether, (C ₂ H ₅) ₂ O	440	0.71

A simple vapor-liquid diffusion crystallization involves placing a smaller, open vial containing the perovskite precursor solution inside a larger, closed vial containing the antisolvent (Fig. 14A). For a liquid-liquid diffusion, a typical procedure involves carefully layering the less-dense solvent or solution (usually the antisolvent) on top of the denser solvent or solution (usually the perovskite solution) in a narrow vial or tube (Fig. 14B). Minimizing the mixing of the two layers upon the initial layering is important and may be achieved by slowly pipetting the top solvent or solution along the inner wall of the vessel. In either case, the antisolvent diffuses into the solution that is at (or near) saturation with the perovskite to induce supersaturation. The choice of crystallization technique will largely be dictated by the physical properties of the two solvents: solvents with a large difference in vapor pressure may be more amenable to vapor-liquid diffusion whereas solvents with a large difference in density may be more successful in a liquid-liquid diffusion (Table 4). The two solvents are most often miscible, although solvent pairs with only minor mutual solubility have also been successfully used. Common laboratory solvents including diethyl ether, acetone, toluene, chlorobenzene, and dichloromethane tend to be effective antisolvents for crystallizing perovskites from saturated solutions in more polar “good” solvents, including DMF and DMSO. The wide range of vapor pressures among candidate antisolvents (Table 4) allows the experimentalist to tune the rate of diffusion, and hence crystallization, and target a growth rate of a seed or heterogeneously nucleated crystals. The vapor-liquid diffusion method was among the first reported methods to grow bulk (mm-cm) crystals of $(\text{CH}_3\text{NH}_3)\text{PbX}_3$ ($X = \text{Br}^-$, I^-)²³⁷ and CsPbBr_3 ²³¹ and continues to be a common method to grow perovskite crystals from solution at RT. In cases where a highly volatile antisolvent is required, rapid diffusion may result in the mass precipitation of a powder. In this case, the diffusion rate may be modulated by introducing a frit (or another physical barrier) between the nested vials to slow diffusion and form larger crystals.

4.15.5.3.4 Hydrothermal and solvothermal methods

There are cases where poor solubility of the precursor halide salts renders the temperature-controlled or mixed-solvent methods unsatisfactory. Instead, reactions in closed systems allow the experimentalist to heat a solution above the normal boiling point of the solvent due to the increased pressure in the sealed vessel. Such conditions tend to elevate the solubility and mobility of the reactants and, in the case of an aqueous solution, decrease the viscosity and dielectric constant of water.¹⁹⁵ These closed (sealed) reactions are typically performed in PTFE-lined stainless steel autoclaves or sealed ampoules over the course of days and termed hydrothermal or solvothermal reactions when the solubilizing medium is an aqueous or an organic solvent, respectively. Solvothermal reactions have been employed in the synthesis of nanomaterials but are less common than hydrothermal reactions, which often yield bulk materials as a powder or single crystals. The double perovskites $\text{Cs}_2\text{AgInCl}_6$ ^{238,239} and Cs_2SnCl_6 ^{191,240} crystallize from a hydrothermal reaction where the stoichiometric precursor salts are heated in aqueous HCl above its normal boiling point at atmospheric pressure. Similar to the design considerations for a reaction cooled from high temperature at atmospheric pressure, rapid cooling yields a powder of the phase-pure perovskite whereas slow cooling allows for single-crystal growth. Bulk single crystals of the above materials are obtained when slow cooling from an initial temperature of 150–180 °C at rates of 2–8 °C h⁻¹. The hydrothermal method is also amenable to alloying and doping a perovskite host lattice; such examples include alloying Bi^{3+} into $\text{Cs}_2(\text{Na}_x\text{Ag}_{1-x})\text{InCl}_6$ ²³⁹ and Bi^{3+} or Sb^{3+} into Cs_2SnCl_6 ^{191,240} to tune their photoluminescence by simple addition of the alloying precursor (see Section 4.15.6.6.2.2).

4.15.5.3.5 Ultrasound- and microwave-assisted methods

Applying ultrasound to a solution can induce local pressure and temperature gradients and cavitation within the solvent through the collapse of microbubbles, leading to unique effects on suspension, solubility, and the nucleation process. By manipulating such

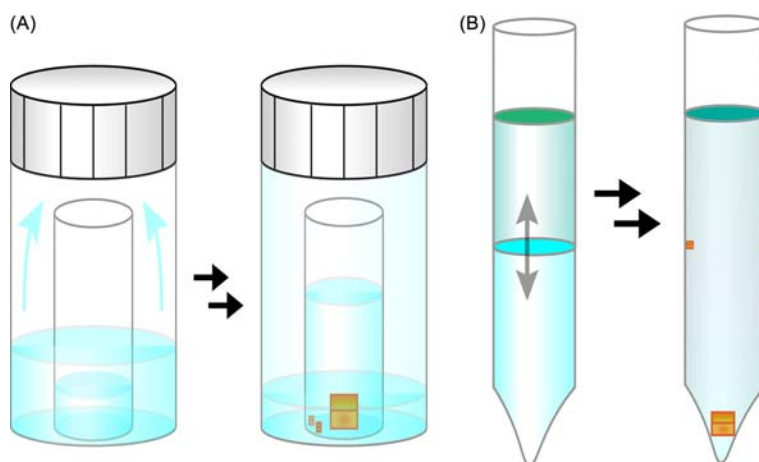


Fig. 14 Schematic representation of the mixed-solvent crystallization techniques: (A) the vapor-liquid diffusion method using nested vials, with the good solvent (which dissolves the perovskite) in the inner vial and the bad solvent (which does not dissolve the perovskite) in the outer vial; (B) the liquid-liquid diffusion, or layering, method.

effects, bulk and nanocrystalline oxide perovskites have been co-precipitated from solution near RT.²⁴¹ The synthesis of bulk halide perovskites at RT by similar techniques has recently been investigated. Upon addition of $(\text{CH}_3\text{NH}_3)\text{I}$ to a suspension of PbI_2 in isopropanol (an antisolvent of $(\text{CH}_3\text{NH}_3)\text{PbI}_3$), a powder of $(\text{CH}_3\text{NH}_3)\text{PbI}_3$ can be precipitated under continuous sonication.²⁴² The perovskite formation may be attributed to a “microsolubility” effect, where the insoluble precursors are finely dispersed and ultrasound-induced cavitation increases the local solubility of $(\text{CH}_3\text{NH}_3)\text{PbI}_3$ and nucleates a fine-grained powder. Ultrasound-induced cavitation has also been used to nucleate single-crystal growth on surfaces from a supersaturated solution of the perovskite: application of a single short ultrasonic pulse (< 1 s) to a supersaturated solution (achieved by vapor-liquid diffusion) nucleates the growth of $(\text{CH}_3\text{NH}_3)\text{PbBr}_3$ single crystal films on a variety of substrates.²⁴³ The growth is anisotropic, with resulting crystals having thicknesses of 10s of μm and lateral dimensions of 100 s of μm to 3 mm, notably in the absence of surfactants or other growth-directing components in the solution.

In the context of assisted solution-state crystallization techniques, microwave radiation offers rapid, precise, programmable, and scalable heating that exceeds the capabilities of traditional methods. Combining microwave heating and the ITC method, large (mm-sized) single crystals of $(\text{CH}_3\text{NH}_3)\text{PbX}_3$ and $(\text{NH}_2\text{CHNH}_2)\text{PbX}_3$ ($X = \text{Br}^-$, I^-) were grown from solution in an automated and reproducible fashion.²⁴⁴

4.15.5.4 Thin-film deposition

We direct the interested reader to comprehensive review articles for detailed discussions of the various thin-film deposition methods, including topics beyond the scope of this work such as scalable fabrication methods, post-processing, microstructural transformations, and device fabrication.^{196,224,245} Our intention here is to provide an overview of common methods while highlighting experimental considerations that appear to be specific to certain perovskite compositions.

The basic mechanisms of nucleation and growth introduced in Section 4.15.5.3 apply to many common thin-film deposition methods from solution. Deposition of the precursors from a single solution (or source) is termed “simultaneous” or a “one-step” approach.¹⁹⁶ After the simultaneous deposition of a precursor solution, supersaturation is usually achieved upon solvent removal by either: (i) evaporation induced by heating or convection from a gas stream (“gas-quenching”), or (ii) exchange of the solvent with an antisolvent.^{224,246} Perhaps the simplest deposition method is drop-casting: the precursor solution can be deposited on a variety of substrates and evaporation of the solvent occurs at RT or at elevated temperatures by casting onto a heated substrate. Spin-coating is a similarly simple method that has proven to be more effective and widely used in producing perovskite thin films both with and without a mesoporous support (Fig. 15A). Here, the precursor solution is deposited on a substrate, which is then spun at high rates of rotation (typically 1000s of rotations per minute). The centrifugal forces accelerate the evaporation of the solvent at rates controlled by the rotation rate. When the product of the optimized spin-coating procedure is a solvated precursor mixture or intermediate phase, annealing at temperatures in the range of 100–200 °C serves to remove the residual solvent and crystallize the perovskite. This annealing, typically over a duration of minutes to a few hours, may also lead to restructuring of the grains of the film. Several modifications to the basic spin-coating procedure described above have been implemented to address insufficient solvent removal: the most common are adding antisolvents and gas-quenching.

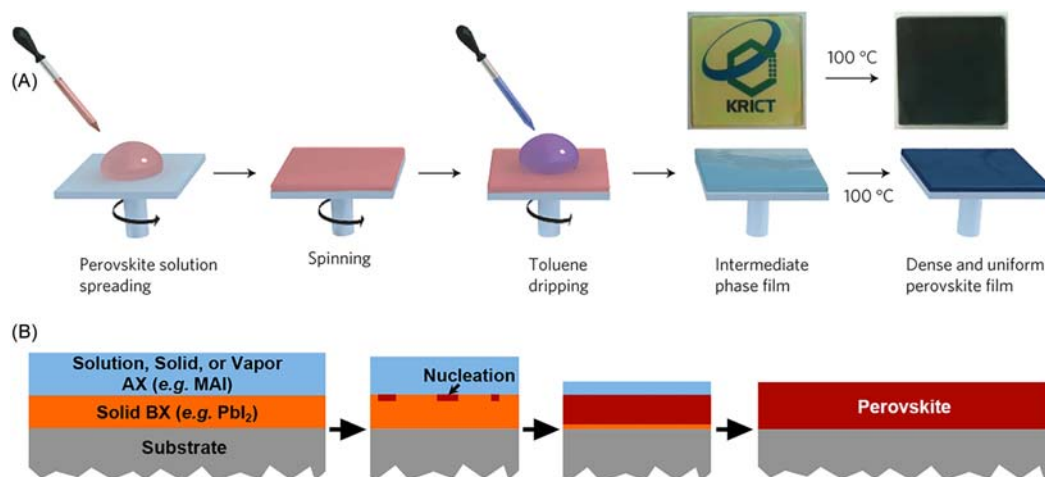


Fig. 15 (A) Schematic representation of a typical antisolvent-assisted spin-coating procedure, where the “intermediate phase” film is annealed to crystallize the perovskite thin film. Adapted with permission from Jeon, N. J.; Noh, J. H.; Kim, Y. C.; Yang, W. S.; Ryu, S.; Seok, S. I., Solvent Engineering for High-Performance Inorganic-Organic Hybrid Perovskite Solar Cells. *Nat. Mater.* **2014**, *13* (9), 897–903. Copyright 2014 Nature Publishing Group. (B) Schematic representation of a two-step thin film synthesis method wherein a solid PbI_2 film, for instance, is converted to the perovskite in a solid-solid, solid-liquid (solution), or solid-vapor reaction. MAI = $(\text{CH}_3\text{NH}_3)\text{I}$. Adapted with permission from Dunlap-Shohl, W. A.; Zhou, Y.; Padture, N. P.; Mitzi, D. B., Synthetic Approaches for Halide Perovskite Thin Films. *Chem. Rev.* **2019**, *119* (5), 3193–3295. Copyright 2018 American Chemical Society.

A unique and prevalent complication in depositions from solution arises from the use of polar aprotic solvents that coordinate Pb^{2+} , particularly DMF and DMSO. There exist many intermediate phases that are stable at RT or elevated temperatures that incorporate these solvents, notably Lewis adducts of lead iodides (e.g., $\text{PbI}_2\cdot\text{DMF}$, $\text{PbI}_2\cdot\text{DMSO}$, $\text{PbI}_2\cdot 2\text{DMSO}$) and quasi-quaternary compounds of the same or differing stoichiometry to the perovskite (e.g., $(\text{CH}_3\text{NH}_3)_2\text{Pb}_3\text{I}_8\cdot 2\text{DMSO}$, $(\text{CH}_3\text{NH}_3)\text{PbI}_3\cdot\text{DMF}$).¹⁹⁶ The quasi-quaternary intermediates often comprise motifs of one-dimensional (1D), edge-sharing lead-iodide octahedra. The 1D structure manifests macroscopically as a rod-like crystal habit in films of the intermediate phases and requires thermal annealing, solvent annealing (thermal annealing in the presence of solvent vapor), antisolvent techniques, or another post-processing approach to attain the perovskite phase. Furthermore, the nature of the intermediate-to-perovskite conversion has important implications on the ultimate film coverage and microstructure: grain size and boundary characteristics, for example, will have knock-on effects on optoelectronic properties such as charge-carrier recombination rates and diffusion lengths.

A simultaneous thin-film deposition may also be achieved under high vacuum following the evaporation or ablation of a single solid source (or matrix) comprised of a mixture of precursors. The benefits of evaporation-based deposition methods are numerous and attractive for optoelectronic device fabrication, including excellent coverage with pinhole-free films and a lack of sensitivity to substrate chemistry or defects. The limitations, however, are significant for perovskites, particularly affecting organoammonium- and/or Sn-containing compositions owing to large mismatches in the melting point, vapor pressure (volatility), and thermodynamic stability of the precursors. Even still, early work showed that a simple thermal co-evaporation led to densely packed films of $(\text{CH}_3\text{NH}_3)\text{Pb}(\text{Cl}_x\text{I}_{1-x})_3$ from a dual-source configuration when the more volatile $(\text{CH}_3\text{NH}_3)\text{I}$ precursor was evaporated in excess relative to PbCl_2 .²⁴⁷ More advanced one-step evaporation-based techniques may operate at atmospheric pressure or low vacuum; this is attractive as it retains the benefit of eliminating the use of solvents while providing energy savings by not requiring high-vacuum equipment.²⁴⁵ For instance, one-step chemical vapor deposition (CVD) under low vacuum (1 mTorr) yields $(\text{CH}_3\text{NH}_3)\text{Pb}(\text{Cl}_x\text{I}_{1-x})_3$ films after in situ annealing.²⁴⁸

In addition to these thermal evaporation techniques, energy may be transferred to the solid source or matrix through a monochromatic radiation source to induce evaporation or ablation. The source laser typically varies in energy/wavelength from infrared (IR) to ultraviolet (UV), depending on the technique. An emergent technique, resonant infrared matrix-assisted pulsed laser evaporation (RIR-MAPLE), is altogether less destructive than ablation techniques owing to the resonant excitation of a matrix solvent in the lower-energy IR. Because the precursors are transferred via a “plume” of the matrix solvent, the morphology of films deposited by the RIR-MAPLE technique resembles those deposited from solution. A major challenge associated with this technique is in the identification of a matrix solvent system that meets two critical criteria: (i) sufficient solubility of the perovskite, and (ii) the presence of functional groups necessary for strong absorption in resonance with the IR excitation (e.g., hydroxyl-containing solvents for an Er:YAG laser).¹⁹⁶ So, while advances have been made in the deposition of $(\text{CH}_3\text{NH}_3)\text{PbI}_3$ and a handful of other perovskite compositions using RIR-MAPLE, its generality and application in high-efficiency device fabrication are yet to be established.

The disparate physical characteristics of the halide precursor salts (including differences in solubility, vapor pressure, and stability) are often accommodated by a stepwise approach to tailor each processing step to a precursor, arranged in a logical sequence. Classified as “two-step” or “sequential” deposition methods, independent application of two precursors (or two precursor mixtures) yields the perovskite after a reaction occurring at a solid-solid, solid-liquid, or solid-vapor interface (Fig. 15B). Solid-vapor reactions are particularly well-suited towards volatile organoammonium halides and tin halides. For example, spin-coated PbI_2 films are converted to $(\text{CH}_3\text{NH}_3)\text{PbI}_3$ in the presence of $(\text{CH}_3\text{NH}_3)\text{I}$ vapor ($(\text{CH}_3\text{NH}_2\cdot\text{HI})$)²⁰² in a sealed container at 150°C .²⁴⁹ and thermally evaporated CsI films are converted to the double perovskite Cs_2SnI_6 in the presence of SnI_4 vapor in a sealed container at 190°C .⁹³ Such reactions exemplify the simplification of the overall process by taking advantage of the volatility of $(\text{CH}_3\text{NH}_3)\text{I}$ or SnI_4 : subliming these compounds near a film of the other precursor yields the desired perovskite. Techniques operating on similar principles, albeit with more controlled conditions suitable to scalable thin-film deposition or device fabrication, which are classified as physical vapor deposition (PVD) or two-step CVD, have also been developed.²⁴⁵

Common sequential solid-liquid thin-film reactions similarly proceed through the fabrication of a film of the metal-halide precursor followed by a reaction upon contact with a solution of the A-site-halide precursor. For example, $(\text{CH}_3\text{NH}_3)\text{BI}_3$ ($\text{B} = \text{Sn}^{2+}$, Pb^{2+}) thin films form upon dipping PbI_2 or SnI_2 films in isopropanol solutions of $(\text{CH}_3\text{NH}_3)\text{I}$.²⁵⁰ This approach allows for the metal-halide precursor to be deposited by any of the methods described above or by more specific techniques, including electro-deposition of PbO_2 (on a conductive substrate) followed by solution conversion to PbI_2 in aqueous HI solution.²⁵¹ Finally, and typically the most sluggish type of reaction, solid-solid reactions produce perovskite thin films from the sequential deposition of precursor layers. Albeit slow, the lack of solvent or solubility considerations makes solid-solid reactions valuable, and rates of thermally activated diffusion may be increased by holding the films at elevated temperatures. The precursor layers are typically deposited by the methods described above and subsequently annealed for a period of minutes to hours to achieve complete interdiffusion and conversion to the phase-pure perovskite.¹⁹⁶

4.15.5.5 Post-synthetic transformations

The 3D perovskites are non-porous crystalline solids, precluding many of the bulk intercalation, physisorption, chemisorption, and ion-exchange reactions that occur in the layered or low-dimensional perovskite congeners.²⁵² Reactions at the halide sites, however, do occur in the 3D perovskites owing to the halide redox chemistry and defect-mediated halide conductivity (see Section 4.15.7.3). The formation energies of halogen point defects, particularly halogen vacancies, and the associated activation energies of migration have consistently been measured (and calculated) in the range of 0.1–0.6 eV.^{253,254} The low barrier for defect-mediated halide

conductivity enables transport and reactions of halide ions in the bulk, including halide exchange and segregation (see Sections 4.15.7.3 and 4.15.7.4). Halide exchange is the predominant post-synthetic transformation observed in bulk perovskites. Comparison of the standard reduction potentials of the molecular halogen/halide couples²⁵⁵ ($\text{Cl}_2/\text{Cl}^- = 1.36 \text{ V vs. SHE}$; $\text{Br}_2/\text{Br}^- = 1.07 \text{ V vs. SHE}$; $\text{I}_2/\text{I}^- = 0.54 \text{ V vs. SHE}$) indicates spontaneous redox-mediated reactions may occur between the more oxidizing halogen gas and a more reducing halide lattice. That is, a Br-based lattice is converted to a Cl-based lattice in the presence of Cl_2 ($\text{Cl}_2 + 2\text{Br}^- \rightarrow \text{Br}_2 + 2\text{Cl}^-$; $E_{\text{cell}}^0 = 0.29 \text{ V}$) and an I-based lattice can be converted to a Cl- or Br-based lattice in the presence of Cl_2 or Br_2 , respectively. Post-synthetic, redox-mediated halide exchange was demonstrated with the conversion of $(\text{CH}_3\text{NH}_3)\text{PbI}_3$ thin films (Fig. 16), where the rate of conversion could be influenced by the concentration of X_2 ($\text{X} = \text{Cl}, \text{Br}$).²⁵⁵ Interestingly, the precursor film morphology was preserved in the resulting $(\text{CH}_3\text{NH}_3)\text{PbBr}_3$ and $(\text{CH}_3\text{NH}_3)\text{PbCl}_3$ films. Non-redox-driven halide exchange has also been shown from solid-liquid or solid-vapor reactions between perovskite thin films and solutions of $(\text{CH}_3\text{NH}_3)\text{X}$ ($\text{X} = \text{Cl}^-, \text{Br}^-, \text{I}^-$)²⁵⁶ or $(\text{CH}_3\text{NH}_3)\text{X}$ ($\text{X} = \text{Br}^-, \text{I}^-$) vapor,²⁵⁷ respectively. Exchange induced by HX ($\text{X} = \text{Cl}, \text{Br}, \text{I}$) vapor has also been reported.²⁵⁸ While there have been sporadic reports of post-synthetic incorporation of small molecules in bulk 3D perovskites, including NH_3 and CH_3NH_2 , the characterization and mechanistic interpretation of these processes has yet to be clarified.²⁵²

4.15.6 Measurement

4.15.6.1 Introduction

Since the study of solid-state semiconductors accelerated following the invention of the transistor in 1947, the suite of characterization techniques available to study these materials has grown in both breadth and depth. Modern-day instrumentation and measurement techniques offer insight into both micro- and macroscopic structure and properties that is crucial for developing a complete understanding of perovskites to drive the field forward. In this section, we will review some of the most common methods used to characterize perovskites. More advanced techniques are beyond the scope of this chapter, though a host of advanced characterization techniques have been and continue to be applied to study these complex materials.

4.15.6.2 Elemental analysis

Fundamental to the understanding of any solid is the determination of its elemental composition. Elemental analysis is particularly useful for solution-based synthesis and thin-film deposition, where the composition of the precipitate does not necessarily match that of the precursor solution. Elemental analysis is not only useful as a purity check; it is indispensable in the characterization and understanding of alloyed perovskites. Any report of a novel composition, in the bulk, would be incomplete without elemental analysis.

Historically, a variety of chemical techniques have been used to determine the metal and halogen content of solids; most techniques begin with the digestion of the solid in a suitable matrix. Because modern elemental analysis typically requires only a few mg of solid, the analysis is even applicable to thin films, where scraping or dissolving the solid from multiple large-area thin films can yield the necessary mass. For perovskites, which are typically insoluble in nonpolar organic solvents, the matrix is often an aqueous

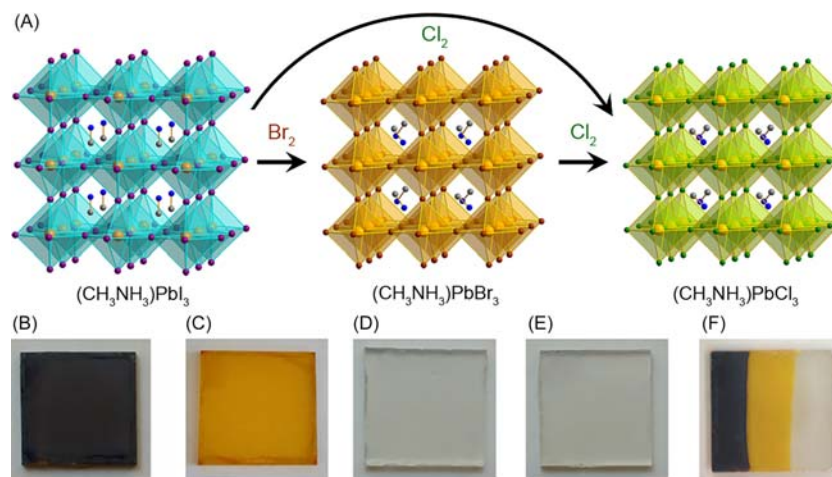


Fig. 16 (A) Schematic of the redox-mediated X_2/X^- halide exchange reactions between $(\text{CH}_3\text{NH}_3)\text{PbX}_3$ ($\text{X} = \text{Cl}^-, \text{Br}^-, \text{I}^-$) and gaseous molecular halogen. (B–F) Optical photographs of thin films of: (B) as-prepared $(\text{CH}_3\text{NH}_3)\text{PbI}_3$; (C) $(\text{CH}_3\text{NH}_3)\text{PbBr}_3$ prepared by exposure of $(\text{CH}_3\text{NH}_3)\text{PbI}_3$ to gaseous Br_2 ; (D) $(\text{CH}_3\text{NH}_3)\text{PbCl}_3$ prepared by sequential exposure of $(\text{CH}_3\text{NH}_3)\text{PbI}_3$ to gaseous Br_2 and Cl_2 ; (E) $(\text{CH}_3\text{NH}_3)\text{PbCl}_3$ prepared by exposure of $(\text{CH}_3\text{NH}_3)\text{PbI}_3$ to gaseous Cl_2 ; (F) $(\text{CH}_3\text{NH}_3)\text{PbI}_3$ partitioned and exposed to gaseous Br_2 and Cl_2 . Adapted with permission from Solis-Ibarra, D.; Smith, I. C.; Karunadasa, H. I., Post-Synthetic Halide Conversion and Selective Halogen Capture in Hybrid Perovskites. *Chem. Sci.* **2015**, *6* (7), 4054–4059 - Published by The Royal Society of Chemistry.

acid, such as nitric acid or hydrohalic acid. Some perovskites, such as those containing Ag, require aggressive digestion methods, such as microwave-assisted digestion and the addition of perchloric acid. Chemical methods of metal determination often involve the formation of a precipitate via addition of an anion or a redox reagent, followed by gravimetric analysis. Titration, also often to selectively form a precipitate with the element of interest, is another commonly used technique that is additionally suitable for determination of halogen content. Modern techniques used for metals analysis are flame-atomic absorption spectroscopy (flame-AAS) and inductively coupled plasma analysis that is paired with either atomic emission spectroscopy (ICP-AES) or mass spectrometry (ICP-MS). These analysis techniques provide high-throughput, high-precision, and low-cost determination of metal content, with less precise determination of halogen content. The low precision of halogen determination is due to a number of factors, including volatilization, interference from the Ar plasma source, and various complications involving the matrix, namely isobaric (from overlapping isotopes of different elements) and polyatomic (from molecular species with the same mass-to-charge ratio as the analyte) interferences. High-precision analysis of halogen content can be achieved using ion chromatography or chemical methods, such as gravimetric analysis following precipitation from solution (e.g., as AgX^{95}). Analysis of I is less sensitive to ICP interference effects than F, Cl, and Br and can yield reasonable precision with ICP analysis.²⁵⁹

Though chemical-based elemental analysis dominated the early perovskite literature,^{95,260} contemporary work routinely uses ICP for analysis of alloyed compositions,^{113,115,116,239} though it is often improperly omitted as an analysis for novel stoichiometric perovskite compositions. Owing to its high precision, ICP analysis has been employed to examine the stoichiometry of thermally evaporated thin films of $(\text{CH}_3\text{NH}_3)\text{PbI}_3$ to fine-tune slightly non-stoichiometric compositions.²⁶¹ Its sensitivity also has allowed ICP analysis to be used to detect the minute amount of Br_2 off-gassing from perovskites by using crotonic acid as a reactive trap for volatile Br_2 gas (see Section 4.15.7.3 and Fig. 32).¹⁸² ICP analysis has also revealed otherwise hidden B-site alloying in the gold-cage perovskites.¹⁰³

Determination of the organic content may be carried out via combustion analysis, often referred to as CHN, CHNO, or CHNS analysis, based on the elements being measured by the combustion analyzer. CHN analysis is primarily used for analysis of hybrid organic-inorganic perovskites²⁶² but can also be used for inorganic compositions as a confirmation that solvent has not been incorporated. Time-of-flight secondary ion mass spectrometry (ToF-SIMS) also provides a method for simultaneously determining the identity and abundance of both metals and organic content. Because this technique operates by using an ion beam to sputter a small portion of the sample into a mass spectrometer, ToF-SIMS can provide 3D spatial resolution, though the ion beam may also damage the sample and introduce artifacts into the measurement. ToF-SIMS is commonly used to determine the composition of perovskite thin films, particularly for alloyed perovskite compositions where the film composition may differ from the solution stoichiometry.²⁶³ For a more detailed discussion of elemental analysis, analytical chemistry textbooks are a good resource.²⁶⁴

4.15.6.3 X-ray and neutron scattering

4.15.6.3.1 Powder X-ray diffraction

X-rays represent one of the most valuable probes that the solid-state chemist has in their toolbox. The development of laboratory, synchrotron, and free-electron-laser X-ray sources has promoted the accessibility and utility of X-ray characterization for researchers. X-ray diffraction, a specific condition of an elastic X-ray scattering event (where “elastic” refers to an event with no net loss or gain of energy), results from the periodic atomic arrangement of a crystalline solid and thus provides information about the average crystal structure. Because X-rays have wavelengths on the order of the atomic or ionic radii in solids, a periodic atomic structure can act as a diffraction grating to incoming X-rays. When the scattered X-rays constructively interfere, this appears as a peak in the scattered X-ray intensity, sometimes referred to as a reflection. This condition is satisfied according to Bragg’s law:

$$n\lambda = 2d\sin\theta \quad (9)$$

where n is a positive integer, λ is the X-ray wavelength, d is the distance between crystallographic planes, and θ is the scattering angle. Most commonly, diffraction is measured by detecting the scattered X-ray intensity as a function of the angle, θ , at a fixed X-ray wavelength, λ . Further reading on X-ray diffraction, including both online and text-based resources, is available through the website of the International Union of Crystallography (IUCr).²⁶⁵

Powder X-ray diffraction (PXRD) is a routine, generally nondestructive measurement in the laboratory that often takes just minutes to complete. Preparation of a sample for PXRD can be as simple as arranging the powdered sample into a pile on a sample mount. The diffraction “pattern” given by PXRD provides a fingerprint of a polycrystalline powder that can be used for rapid crystallographic phase identification. By comparing the experimental data to simulated PXRD patterns from known compounds, the composition of a powder can be determined, even for a mixture of multiple phases. For these reasons, PXRD is often the first measurement carried out on a newly synthesized sample.

The applications of PXRD extend beyond simple phase identification: high-quality PXRD data, especially data collected from a synchrotron source, can be used to solve or refine a previously unknown crystal structure. Common methods to obtain or refine a structural model from experimental PXRD data are Pawley, Le Bail, and Rietveld analyses.²⁶⁶ Such analysis is particularly useful for compositions that cannot be grown as high-quality single crystals suitable for single-crystal X-ray diffraction (SCXRD): for example, the double-perovskite derivative $\text{Cs}_2\text{In}^{\text{III}}\text{In}^{\text{III}}\text{X}_6$ ($\text{X} = \text{Cl}^-$, Br^-) must be grown by high-temperature solid-state methods and single crystals have been difficult to produce. Its structure was therefore solved using high-resolution synchrotron PXRD and refined using Rietveld analysis.¹⁰⁴ A later study used single crystals, but due to the low quality of the SCXRD data, the structural analysis was complemented by PXRD data. Analyzing the breadth of PXRD reflections can provide an estimate of the crystallite size and lattice

strain in the solid. This analysis was used to study the strain and crystallite size in a thin film of $(\text{CH}_3\text{NH}_3)\text{Pb}(\text{Br}_{0.6}\text{I}_{0.4})_3$ under illumination to correlate structural changes to light-induced halide segregation (see Section 4.15.7.4).¹²⁷ Additionally, the angle of a given reflection is dependent on the dimensions of the unit cell and can therefore be used to estimate the degree of atomic mixing in an alloyed perovskite, as done for perovskite compositions with mixed Na/Ag²³⁹ (Fig. 17A and B, respectively), Sn/Pb,^{112,267} and Sn/Te⁹² B sites and mixed halides.¹²⁷

While determination of a new crystal structure using SCXRD data is typically more reliable, PXRD offers several advantages over SCXRD. The experiment is faster, easier, and employs more broadly accessible equipment. PXRD also provides data on a bulk sample, useful for purity checks and for heterogeneous samples. Finally, powder X-ray diffractometers can also be used to examine thin films or other sample morphologies, which can be useful to compare the effects of synthesis on the resulting structure, such as the manifestation of peak splitting as a function of cooling rate (Fig. 17C).¹⁰³ However, care must be taken to account for preferential orientation, or texture, where crystal grains orient along a preferred crystallographic axis, increasing the intensity of certain reflections. These effects may be mitigated during sample preparation by thoroughly pulverizing the powder and by using minimal pressure when placing the powder onto the sample holder, as mechanical force can cause the powder to orient. The powder may also be restrained in an amorphous paste (e.g., vacuum grease) to prevent preferential orientation. However, preferential orientation is nearly unavoidable in thin-film samples, thus reducing the quantity of information that can be gleaned from simple XRD measurements on thin films. Additionally, because amorphous impurities will not appear in PXRD measurements, thorough checks of purity should include techniques such as elemental analysis in addition to PXRD.

4.15.6.3.2 Single-crystal X-ray diffraction

Single crystals, with dimensions on the order of 10s to 100s of μm , can usually be characterized using laboratory diffractometers, whereas crystals as small as 1–2 μm can be measured using synchrotron sources. Fortunately, the solution-state syntheses of many perovskites (see Section 4.15.5.3) are easily tuned to form high-quality single crystals suitable for X-ray diffraction. Unlike PXRD, which measures a collection of many randomly oriented crystallites, SCXRD measures the diffraction of a single crystal, including the extra parameter of crystal orientation. This extra information provides for a reliable determination of a crystal structure with little or no prior knowledge, thus making it a valuable technique for characterizing novel structures, for example $\text{Cs}_2\text{AgBiX}_6$ ($\text{X} = \text{Cl}^-$, Br^-).^{204,268} Because SCXRD only requires a single crystal, the technique requires very little sample, and it can also be used to obtain data on a single phase selected from a phase-impure sample batch.¹¹⁶ However, this can occasionally result in mischaracterization, for instance if the chosen crystal is an impurity and not representative of the bulk sample. For this reason, analysis of perovskite structure is best carried out using both SCXRD and PXRD.

To obtain a crystal-structure solution, the crystallographer first determines the unit-cell parameters from the location of the reflections in reciprocal space. The unit-cell parameters are then used to identify the crystal system, of which there are seven, giving the translational symmetry of the unit cell. The symmetry of the unit cell can be further specified by examination of the pattern of systematically absent reflections, which is used to assign the Bravais lattice, of which there are 14. After this assignment, the raw data can be integrated, a process that involves correlating the index of each reflection (corresponding to its crystallographic plane) with its intensity. After correcting for X-ray absorption by the crystal, the processed, or reduced, data can then be used to specify the internal symmetry of the unit cell to give the space group, of which there exist 230 in 3D space. An atomic model is then produced and refined against the data until satisfactory agreement is achieved. Contemporary software allows for the rapid determination of space group and initial structure solution, after which careful manipulation of the initial solution by the crystallographer is performed to obtain a final solution. While, in an ideal scenario, raw data can be transformed into a crystal-structure solution within

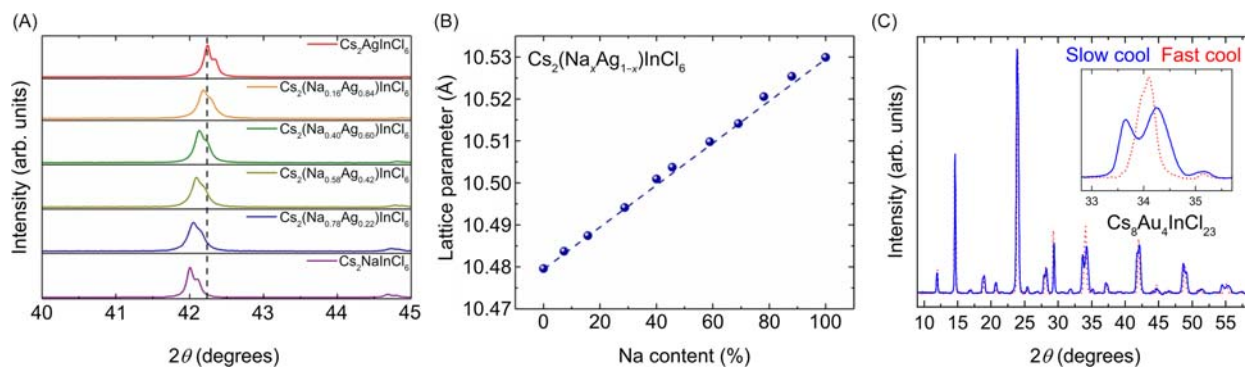


Fig. 17 (A) Powder X-ray diffraction (PXRD) of $\text{Cs}_2(\text{Na}_x\text{Ag}_{1-x})\text{InCl}_6$ showing the shift to lower angle with increasing Na content. (B) Lattice parameter of $\text{Cs}_2(\text{Na}_x\text{Ag}_{1-x})\text{InCl}_6$ plotted as a function of Na content, extracted from Rietveld fitting of the PXRD data. (C) PXRD of the gold-cage perovskite $\text{Cs}_8\text{Au}_4\text{InCl}_{23}$. PXRD allowed for comparison of rapidly precipitated powders to slowly cooled crystals of $\text{Cs}_8\text{Au}_4\text{InCl}_{23}$, leading to the observation of peak splitting and symmetry reduction that was not evident in the SCXRD solution¹⁰³ (unpublished data). Cu K_α radiation was used in all cases. (A) and (B) adapted by permission from: Springer Nature, *Nature*, Luo, J.; Wang, X.; Li, S.; Liu, J.; Guo, Y.; Niu, G.; Yao, L.; Fu, Y.; Gao, L.; Dong, Q.; Zhao, C.; Leng, M.; Ma, F.; Liang, W.; Wang, L.; Jin, S.; Han, J.; Zhang, L.; Etheridge, J.; Wang, J.; Yan, Y.; Sargent, E. H.; Tang, J., Efficient and Stable Emission of Warm-White Light From Lead-Free Halide Double Perovskites. *Nature* **2018**, 563 (7732), 541–545. Copyright 2018.

minutes, selection of space group and specific parameters of the solution must be carefully considered and may sometimes require further experiments for confirmation. For example, careful studies of the low-temperature tetragonal phase of $(\text{CH}_3\text{NH}_3)\text{PbCl}_3$ revealed the presence of previously unobserved reflections corresponding to the ordering of the CH_3NH_3^+ cations along one crystallographic axis with a repeat unit of incommensurate length to the repeat unit of the Pb–Cl sublattice.²⁶⁹

4.15.6.3.3 Neutron diffraction

Though less commonly used for perovskites, neutron diffraction provides a complementary probe of atomic structure to X-ray diffraction. X-rays primarily interact with the electron density through the electromagnetic interaction, which scales directly with atomic number; in contrast, neutrons interact with atomic nuclei through the weaker neutron-nucleon interaction, which does not directly scale with atomic number, making them more sensitive to many of the lighter elements to which X-rays are insensitive.²⁷⁰ Because they interact with the atomic nuclei and scattering factors do not decrease with increasing diffraction angle, as they do with X-rays, neutron diffraction gives better resolution of atomic position. Neutron diffraction can be performed on powders or single crystals. For these reasons, neutron diffraction has been used to examine the structural dynamics of the organic cation in organic-inorganic perovskites and its effects on phase transitions: while the weak X-ray scattering factors for the A-site cation relative to the B- and X-site ions in $(\text{CH}_3\text{NH}_3)\text{PbX}_3$ ($X = \text{Cl}^-, \text{Br}^-, \text{I}^-$) renders X-ray analysis largely insensitive to deviations of the A-site cation from a high-symmetry position, single-crystal neutron diffraction provides structural analysis that is sensitive to the symmetry and position of the A-site cation.^{271,272} However, producing neutrons at a sufficient flux for analysis is impractical at the laboratory scale; instead, nuclear reactors and spallation sources must be used, limiting the accessibility of neutron scattering facilities. Neutron scattering also requires a large sample mass that may be prohibitively expensive or difficult to obtain at the requisite size (often > 1 mm) by crystallization methods that are commonly employed for perovskites (see Section 4.15.5). Though not diffraction, strictly speaking, the incoherent scattering intensity at the “tails” of the elastic diffraction peak, corresponding to small values of energy transfer, has been modeled to understand the dynamics of CH_3NH_3^+ in $(\text{CH}_3\text{NH}_3)\text{PbI}_3$.²⁷³ The temperature dependence of these quasielastic neutron scattering (QENS) data was indicative of molecular reorientation (rather than ion diffusion) over 1–200ps timescales; such orientation of the CH_3NH_3^+ dipole results in ferroelectric polarization, or spontaneous electric polarization of the dipoles, in the perovskite. Ferroelectric domains have been proposed to play a role in screening the built-in electrical potential and hysteretic current-voltage responses following polarization, thereby reducing the performance of perovskite-based photovoltaic devices.²⁷³

4.15.6.3.4 Diffuse and total scattering

While X-ray and neutron diffraction arises from long-range atomic order, diffuse scattering can provide information about short-range atomic (dis)order, defects, and strain fields. The diffuse scattering intensity may be analyzed independently or in concert with the diffraction intensity, with the latter treatment being referred to as “total scattering” analysis. Diffuse scattering measurements are well-suited to probe the strain fields induced by a variety of point defects, bulk defects, and photoinduced structural dynamics. The development of pulsed, femtosecond-resolved X-ray sources and high-rate area detectors enables X-ray scattering measurements on the timescale of lattice and charge-carrier dynamics upon photoexcitation. Recently, photoinduced strain fields, attributed to polaron formation, were observed in the X-ray diffuse scattering from $(\text{CH}_3\text{NH}_3)\text{PbBr}_3$ upon photoexcitation.²⁷⁴ Though access to femtosecond-resolved X-ray sources for such diffuse scattering measurements is limited, total scattering measurements are generally accessible, and methods of analysis have been developed to interpret the data in terms of pair correlations.²⁷⁵

Referred to as pair distribution function (PDF) analysis, total scattering informs on local structure, making it useful for structures that may be partially disordered, amorphous, or exhibit anharmonicity. Structural anharmonicity refers to atomic displacements or phonons that deviate from the behavior of a simple harmonic oscillator in the lattice, instead exhibiting a double-well potential or other phenomena described by the anharmonic terms in the lattice energy. PDF analysis is a valuable complement to PXRD or SCXRD, where the structural model derived from these data represents long-range order that is spatially and temporally averaged. Local and dynamic coordination environments that deviate from the average structure manifest as diffuse scattering intensity that is modeled within PDF analysis.

Several studies have shown that the structural models derived from X-ray diffraction, often a high-symmetry cubic or tetragonal unit cell comprising a single formula unit, provide a poor fit of the PDF from X-ray and neutron total scattering measurements of single and double perovskites. In the high-temperature cubic phase of $(\text{CH}_3\text{NH}_3)\text{PbI}_3$, X-ray PDF at 350 K demonstrated that local structure (2–8 Å interatomic distances) was modeled more accurately upon symmetry-lowering to tetragonal space groups, while long-range structure (12–50 Å) showed averaging to the global cubic symmetry (Fig. 18).²⁷⁶ Indeed, a supercell model featuring local low-symmetry motifs that average to high symmetry was proposed for $(\text{CH}_3\text{NH}_3)\text{PbI}_3$ and resulted in an improved fit to the experimental X-ray PDF.²⁷⁷ Signatures of anharmonicity owing to A-site cation composition and orientation, tilting of the $[\text{BX}_6]^{n-}$ octahedra, and off-centering of the B-site cation have been investigated using X-ray and neutron PDF analysis of various single and double perovskites.^{277–281} The stereochemical activity of the ns^2 lone pair of Sn- and Pb-based perovskites, indiscernible in the average structure from diffraction measurements, was identified as a local distortion in analysis of the X-ray PDF.^{280,281} The local off-centering of Sn in the $[\text{SnBr}_6]^{4-}$ octahedron, as a result of the stereoactive lone pair, likely influences the material properties and functionality of CsSnBr_3 .²⁸⁰ This temperature-activated off-centering is observed most prominently in Sn–I and Pb–Br perovskites.²⁸¹

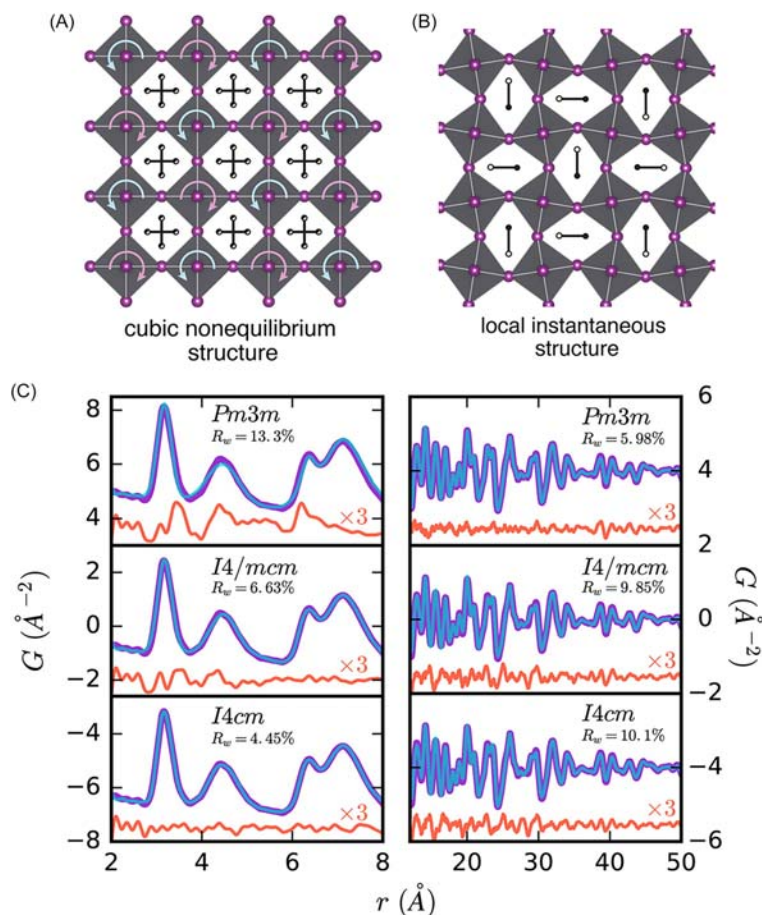


Fig. 18 Schematic representations of: (A) an average cubic perovskite structure with a methylammonium A-site cation disordered over multiple positions/orientations; (B) a local lower-symmetry perovskite structure, where the A-site cation is oriented along a single axis. (C) Experimental X-ray pair distribution functions from total scattering measurements of $(\text{CH}_3\text{NH}_3)\text{PbI}_3$ at 350 K (purple), cubic (space group $Pm\bar{3}m$) and tetragonal (space groups $I4/m\bar{c}m$ and $I4cm$) model fits (blue), and scaled residuals (orange); the data are separated into low- r (2–8 Å, left) and high- r (12–50 Å, right) to guide the eye and differentiate between local and long-range correlations. Adapted with permission from Beecher, A. N.; Semonin, O. E.; Skelton, J. M.; Frost, J. M.; Terban, M. W.; Zhai, H.; Alatas, A.; Owen, J. S.; Walsh, A.; Billinge, S. J. L., Direct Observation of Dynamic Symmetry Breaking above Room Temperature in Methylammonium Lead Iodide Perovskite. *ACS Energy Lett.* **2016**, *1* (4), 880–887, <https://doi.org/10.1021/acsenenergylett.6b00381>. Copyright 2016 American Chemical Society. Permissions related to this material should be directed to the ACS.

4.15.6.3.5 Inelastic X-ray and neutron scattering

Inelastic scattering occurs through the transfer of energy from the incident X-ray or neutron to the sample, or vice versa; energy loss or gain with respect to the incident X-ray (or neutron) corresponds to phonon emission or annihilation, respectively. Thus, the high resolution in energy and momentum enabled by modern neutron and synchrotron X-ray spectrometers allows for characterization of the phonon properties in solid-state materials. Strong coupling between these phonons and photoexcited charge carriers have been proposed to explain several of the unique optoelectronic properties of perovskites. Thus, the characterization of phonon dispersion and lifetimes affords an improved understanding of charge-carrier dynamics and scattering processes.^{276,282–284} Phonon lifetimes are also relevant to heat transport, and the observation of ultralow thermal conductivity in organoammonium perovskite compositions has motivated their application as thermoelectrics.^{282,283,285} Materials that exhibit the thermoelectric effect may efficiently convert temperature gradients to an electric potential, and vice versa. Specific phonon modes relevant to symmetry-lowering distortions and octahedral tilting instabilities have been studied for their relevance to phase transitions and ferroelectric polarization.^{286,287} The majority of the inelastic X-ray and neutron scattering studies on perovskites have been performed on $(\text{CH}_3\text{NH}_3)\text{PbI}_3$ and its deuterated counterpart, $(\text{CD}_3\text{ND}_3)\text{PbI}_3$. The choice between X-ray and neutron methods is a tradeoff between beam damage and composition considerations: neutron scattering is often preferred to mitigate X-ray-induced damage, particularly for organoammonium perovskites. For sufficient inelastic neutron scattering signal, however, a large (gram-scale) sample mass is required. The large incoherent scattering cross section of hydrogen yields significant background that further complicates the analysis of inelastic neutron scattering. Thus, deuteration of the organoammonium A-site cation is often required to minimize these effects, exacerbating cost and crystal-growth limitations. Inelastic neutron scattering can additionally provide information about the magnetic sublattice of a sample, though this has thus far seen little application in perovskites.

4.15.6.3.6 Other X-ray scattering techniques

The high flux of modern synchrotron and free-electron-laser X-ray sources, combined with high-rate area detectors, allows the collection of a 2D X-ray scattering pattern in a second or less. Thus, processes ranging from femtosecond-scale photoinduced structural dynamics²⁷⁴ (see Section 4.15.6.3.4) to crystallization that evolves over the course of hours can be monitored in a time-resolved fashion using X-ray scattering techniques. An X-ray scattering pattern collected on an area detector captures a range of reciprocal space, defined by the wavelength of the radiation, the detector position, and the sample geometry, and includes intensity contributions from diffraction and diffuse scattering. These measurements, often collected in grazing-incidence (GI) geometry, are classified as wide-angle X-ray scattering (WAXS) and small-angle X-ray scattering (SAXS) depending on the regime of scattered X-rays collected at the detector. The scattering vector, q , is defined by the difference in scattered and incident wavevectors, k_f and k_i , and its magnitude is related to the distance between scatterers (d), wavelength (λ), and the scattering angle (θ):

$$q = k_f - k_i \quad (10)$$

$$q = |q| = \frac{2\pi}{d} = \frac{4\pi\sin\theta}{\lambda} \quad (11)$$

At small q , generally $q < 0.5 \text{ \AA}^{-1}$ ($d > 12.6 \text{ \AA}$), the SAXS intensity is dominated by scattering from ordered superstructures and diffuse scattering at the nano- and microscale. The SAXS intensity, in addition to the structure factor, contains a morphological contribution and thus comprises information on particle (or grain) size and shape. For instance, the internal microstructure evolution and grain-size distribution within thin films of $(\text{CH}_3\text{NH}_3)\text{Pb}(\text{Cl}_x\text{I}_{1-x})_3$ has been monitored using in situ GISAXS during conversion and annealing steps for various deposition techniques, including a one-step deposition from a solution of the precursors²⁸⁸ and a two-step film conversion (see Section 4.15.5.4) from a PbI_2 layer to the perovskite.²⁸⁹ In contrast, the WAXS intensity comprises diffuse scattering and X-ray diffraction from crystalline order at the atomic scale ($q > 0.5 \text{ \AA}^{-1}$; $d < 12.6 \text{ \AA}$). GIWAXS has also been used to investigate thin-film formation and crystallization dynamics, particularly through analysis of: (i) in situ isothermal or variable temperature diffraction, or (ii) the degree of textured diffraction, indicating preferential orientation of crystallites. In situ diffraction has captured the transitions from solution to crystalline intermediate(s) to perovskite, as a function of time and temperature, informing on the optimal precursor and processing conditions.^{290,291} Texture analysis differentiates the mechanism of various two-step film deposition methods (see Section 4.15.5.4), where the orientation of the eventual perovskite film is dictated by the nature of the PbI_2 film conversion: a solid-vapor reaction with $(\text{CH}_3\text{NH}_3)\text{I}$ yields no preferential orientation, while reaction with a concentrated $(\text{CH}_3\text{NH}_3)\text{I}$ solution yields an oriented film.²⁹²

4.15.6.4 X-ray absorption spectroscopy

X-rays of sufficient energy can be absorbed by atoms to excite core-level electrons to unoccupied states; the transition energies are specific to each element and the ionization energies of its core electrons.²⁹³ As the incident X-ray energy approaches and reaches the transition energy, an abrupt absorption event is observed, often referred to as an absorption “edge” (Fig. 19A). Using monochromatic X-rays, such as those from a synchrotron source after passing through a monochromator, the absorption of a sample as a function of incident X-ray energy produces an X-ray absorption spectrum. Absorption is commonly measured either directly in a transmission geometry or from the fluorescence yield after an electron relaxes to fill the low-lying core hole and emits a photon.

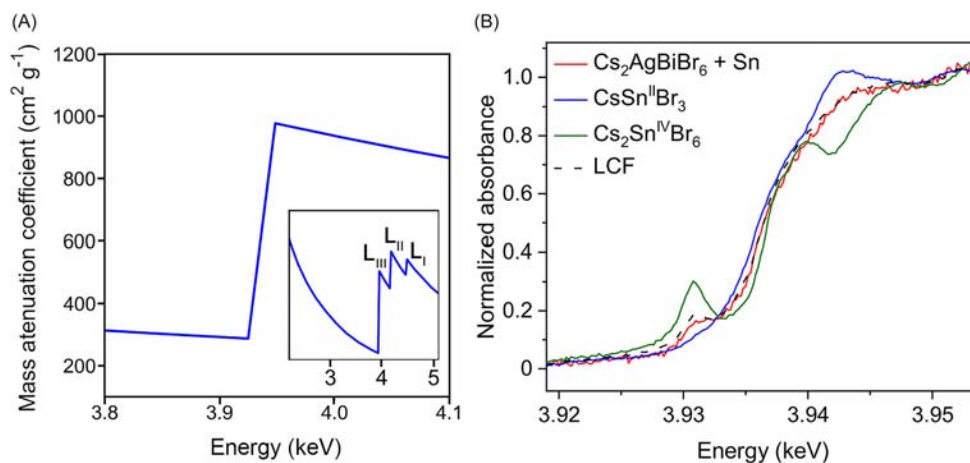


Fig. 19 (A) Calculated mass attenuation coefficient for Sn near the L_{III} edge, with the full L-edge energy range inset²⁹³. (B) Sn L_{III} -edge X-ray absorption near-edge structure (XANES) spectra of Sn-alloyed $\text{Cs}_2\text{AgBiBr}_6$ and $\text{CsSn}^{\text{III}}\text{Br}_3$ and $\text{Cs}_2\text{Sn}^{\text{IV}}\text{Br}_6$ standards. LCF denotes a linear-combination fit of the spectra of the two standards to that of Sn-alloyed $\text{Cs}_2\text{AgBiBr}_6$. Adapted from Lindquist, K. P.; Mack, S. A.; Slavney, A. H.; Leppert, L.; Gold-Parker, A.; Stebbins, J. F.; Salleo, A.; Toney, M. F.; Neaton, J. B.; Karunadasa, H. I., Tuning the Bandgap of $\text{Cs}_2\text{AgBiBr}_6$ Through Dilute Tin Alloying. *Chem. Sci.* **2019**, *10* (45), 10620–10628 - Published by The Royal Society of Chemistry.

Analysis of these characteristic emission lines, X-ray emission spectroscopy, is a complementary technique but so far not widely applied to the study of perovskites. The X-ray absorption spectrum is commonly treated in two energy ranges corresponding to distinct absorption phenomena: X-ray absorption near-edge structure (XANES) refers to energies at and near the atomic absorption edge, while energies above the edge are used for extended X-ray absorption fine structure (EXAFS) analysis. XANES data are most often compared to standards to give information about the oxidation state and coordination geometry of the absorber element in the sample. EXAFS data can be modeled to provide information about coordination geometry, bond lengths, and the identities of the coordinated atoms. More details regarding the principles of X-ray absorption spectroscopy (XAS) can be found in the following references.^{294,295}

XAS measurements are generally nondestructive and can be carried out on almost any element and a variety of sample morphologies, including crystals, powders, thin films, liquids, and gases, and held in various sample environments during measurement, including under inert or reactive gases and under variable temperature. The element specificity provided by XAS allows the technique to probe a specific component of the perovskite structure. For example, a small amount of Cl alloyed into Pb–I perovskites has been shown to improve their photovoltaic performance. XANES measurements at the Cl K edge on thin films of these alloyed perovskites gave insight into the reaction pathways occurring during film deposition and verified that Cl incorporates into the perovskite structure, helping to improve understanding of the effects of additives on photovoltaic performance.²⁹⁶ The utility of XAS for alloyed samples was further cemented when powders of $\text{Cs}_2\text{AgBiBr}_6$ alloyed with Sn were revealed to contain a mixture of Sn^{2+} and Sn^{4+} from XANES measurements, providing valuable information used to understand the electronic consequences of Sn alloying in $\text{Cs}_2\text{AgBiBr}_6$ (Fig. 19B).¹¹⁶ Similar to PDF analysis, EXAFS measurements excel where long-range atomic order is lacking or represents an average of multiple local configurations disordered over long range: for example, EXAFS measurements uncovered the local coordination environment of Au in the partially disordered gold-cage perovskites, $\text{Cs}_8\text{Au}_4\text{MX}_{23}$, allowing for an accurate description of the crystal structure of these compounds.¹⁰³ XAS measurements can also be coupled with a photoexcitation of the sample in an optical pump–X-ray probe scheme, giving structural information about the excited state. Measurements of this type have been used to study the dynamics of charge carriers in Pb-based perovskite nanocrystals.²⁹⁷

4.15.6.5 Photoemission spectroscopy

4.15.6.5.1 X-ray photoelectron spectroscopy

Like XAS, X-ray photoelectron spectroscopy (XPS) exploits the absorption of X-rays by core-level electrons in atoms. However, while XAS measures the attenuation of the incident X-rays, XPS measures the quantity and energies of the ejected photoelectrons, which are characteristic of the elemental identity, oxidation state, and coordination environment (Table 5). Approximations of relative elemental abundance within a sample are determined from the intensities of the signal from each element (corrected with relative sensitivity factors) with precision in the range of parts per hundred to parts per thousand. A distinguishing feature of XPS is its surface sensitivity: the escape depth of photoelectrons is in the range of 1–20 nm, depending on the nature of the sample. To probe below the surface of a sample, most XPS instruments are equipped with a sputtering gun that emits high-energy particles—such as single Ar^+ ions, ionized clusters of Ar atoms, or C_{60} —that can etch the sample surface.

XPS is commonly used for elemental quantification and to analyze the oxidation state of metals in perovskites, particularly in thin-film samples, where producing an adequate mass of sample for bulk elemental analysis may be labor intensive. The utility of XPS for bulk characterization of perovskites is severely limited because the composition of a surface often differs significantly from the interior and sputtering may damage the sample and alter its composition. Therefore, the measurements described in Section 4.15.6.2 are far more reliable for elemental analysis of bulk perovskites. However, the surface sensitivity of XPS is exploited to garner information about the elemental composition of the surface of a sample, for example to determine the species formed upon reaction of an electrode with the perovskite film.²⁹⁸ With sputtering, XPS can measure the composition of a sample as a function of depth, for example in an alloyed thin-film sample that may have an uneven distribution of elements or in a multilayer

Table 5 Summary of photoelectron spectroscopies.

Technique	Particles involved	Typical incident energy	Information content
X-ray photoelectron spectroscopy (XPS)	X-ray in; e^- out	1–4 keV	Chemical state, composition
Ultraviolet photoelectron spectroscopy (UPS)	UV photon in; e^- out	5–500 eV	Valence-band energy
Angle-resolved photoemission spectroscopy (ARPES)	UV photon or X-ray with known angle in; e^- out	5–4000 eV	Electronic band structure
Inverse photoelectron spectroscopy (IPS)	e^- in; photon out	8–20 eV	Energy of unoccupied states
Auger electron spectroscopy (AES)	e^- in; e^- out (Auger process)	1–5 keV	Chemical composition
Electron energy loss spectroscopy (EELS)	e^- in; e^- out	1–5 keV	Phonons, vibrations

Adapted with permission from Goncharova, L. V. Photoelectron spectroscopies. In *Basic Surfaces and Their Analysis*; Goncharova, L. V., Ed. Morgan & Claypool Publishers: San Rafael, CA, 2018. 6-1–6-17. Copyright 2018 Morgan & Claypool Publishers. All rights reserved.

optoelectronic device that may have interfacial atomic diffusion.^{299–301} While the binding energy of a signal can be compared to reported values to extract information about the oxidation state and coordination environment of an element, this value is subject to significant error due to difficulty in alignment.^{302,303} Because XPS involves photoionization of electrons, for electronically insulating samples like many perovskites, continuous X-ray flux will induce local charging which erroneously decreases the kinetic energy of ejected electrons due to attraction to the positively charged surface. Charge can be roughly compensated by using an electron flood gun, but the corrections are on the order of binding energy shifts due to changes in oxidation state and coordination environment. Additionally, the binding energy is relatively insensitive to oxidation state and coordination environment for some elements, such as Sn.³⁰⁴ Therefore, while XPS can provide an approximate characterization of the elemental abundance and chemical environments of the elements in a perovskite sample, other techniques such as ICP elemental analysis and XAS analysis of coordination environment are more suitable for precision studies.

4.15.6.5.2 Ultraviolet photoelectron spectroscopy

Ultraviolet photoelectron spectroscopy (UPS) relies on the same principles as XPS but operates using lower-energy ultraviolet excitation instead of X-ray excitation. Instead of exciting core electrons, ultraviolet light excites transitions of the valence electrons, providing information about the electronic structure of a semiconductor and the absolute energy of its valence band maximum. The information obtained from UPS can be complemented with inverse photoemission spectroscopy (IPES), a technique where electrons of a well-defined energy bombard the sample and couple to states well within the conduction band. These electrons subsequently decay to lower-energy states within the conduction band; some of these decay processes are accompanied by emission of photons, which are measured by the analyzer. Whereas UPS gives information about the valence band, IPES gives information about the conduction band (Table 5). Thus, combining UPS and IPES datasets, often along with modeling and computation, gives a complete picture of the density of states near the band extrema and their absolute energies.³⁰⁵ However, like XPS, UPS and IPES are highly surface-sensitive; therefore, great care must be taken to avoid contamination of the surfaces, for instance by maintaining an inert atmosphere above the sample. Like XPS, UPS also requires precise alignment of the spectrum onset. Many perovskites are too insulating to measure accurately in bulk materials (i.e., powder and crystal samples); instead, measurements must be carried out on thin-film samples deposited on sufficiently conductive substrates (e.g., ITO, FTO) to reduce charging effects.

For perovskite devices, the absolute energies of the band extrema are important values for choosing a device architecture, as each layer must have appropriate energy alignment to yield a high-efficiency device. UPS and IPES have been used to characterize the absolute energy positions of many of the most common perovskite absorber compositions (Fig. 20).^{37,176} UPS has been used to improve the performance of a photovoltaic cell by investigating the energy alignment of the perovskite layer with adjacent

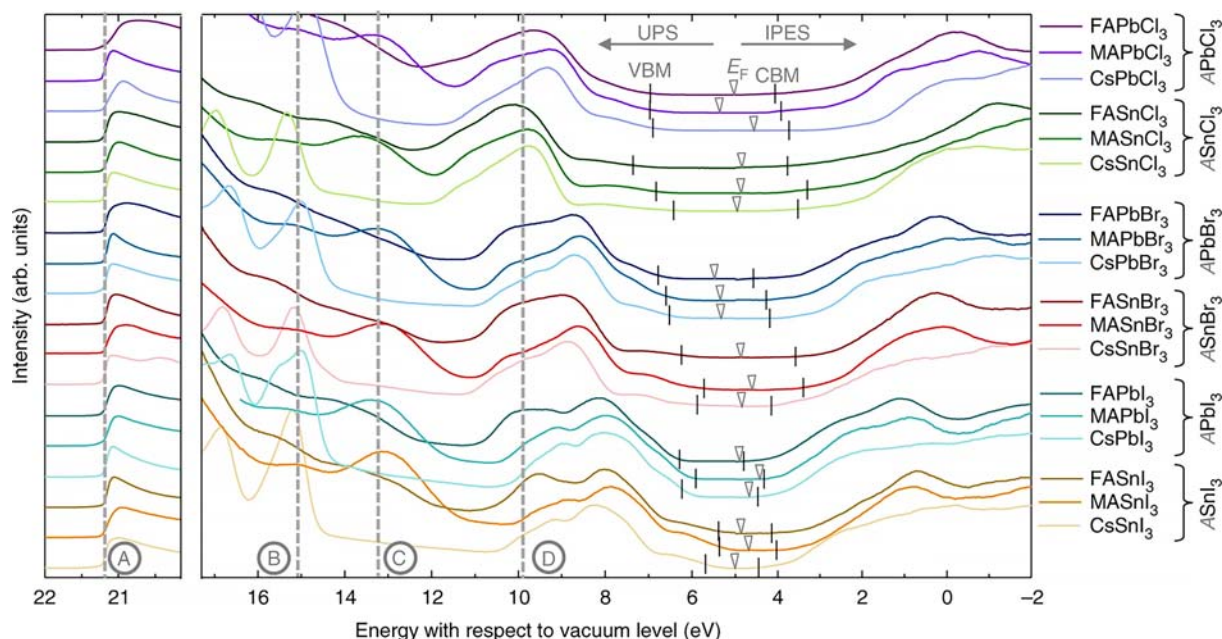


Fig. 20 Representative UPS and IPES spectra of 18 metal-halide perovskites. For easier comparison, the curves are vertically offset and the high-energy cutoffs are aligned at the excitation energy of 21.22 eV, marked by line (A). Lines (B–D) indicate characteristic features in the DOS, corresponding to the position of Cs⁺, MA, and FA related states, respectively. The extracted positions of the VBM and CBM are given by black vertical markers, and the Fermi level positions are marked by triangles. Note that for IPES measurements only the smoothed data trend is shown. MA = CH₃NH₃⁺, FA = NH₂CHNH₂⁺. Reprinted from Tao, S.; Schmidt, I.; Brocks, G.; Jiang, J.; Tranca, I.; Meerholz, K.; Olthof, S., Absolute Energy Level Positions in Tin- and Lead-Based Halide Perovskites. *Nat. Commun.* **2019**, *10* (1), 2560 - Published by Springer Nature under Creative Commons Attribution 4.0 International License: <http://creativecommons.org/licenses/by/4.0/>.

electron/hole transport layers in the device stack.³⁰⁶ The dependence of band extrema on the halide composition of perovskites has been studied with photoelectron spectroscopy, yielding experimental confirmation of computed electronic structures.³⁰⁷ Similarly, dopants can be used to tune the surface electronics of perovskite devices, as shown with UPS measurements, to improve the energy alignment with the adjacent layers.³⁰⁸

4.15.6.5.3 Angle-resolved photoemission spectroscopy

A further extension of XPS and UPS is realized by collecting angle-resolved data, a technique referred to as angle-resolved photoemission spectroscopy (ARPES). In contrast to the 1D estimation of the density of states provided by UPS, angle-resolved measurements can provide 2D band structures and represent the most direct experimental techniques available to probe electronic band structure. This can use either X-ray or ultraviolet excitation and is often named angle-resolved ultraviolet photoelectron spectroscopy (ARUPS) when ultraviolet excitation is used (Table 5).

For angle resolution to provide meaningful data, a single-crystalline sample with a known orientation must be measured. A clean, nearly atomically flat surface free of contaminants with a surface area of at least $\sim 1 \text{ mm} \times 1 \text{ mm}$ is also required. Samples that fulfill these requirements are typically large, freshly cleaved single crystals or epitaxially grown, single-crystalline films. While ARPES has not been extensively applied to perovskites, the technique has been used to map the electronic band structure of Pb-based perovskites and confirms computational predictions.³⁰⁹ More details on the principles of photoemission spectroscopy can be found in the following reference.³¹⁰

4.15.6.6 Optical, vibrational, nuclear, and electronic spectroscopy

4.15.6.6.1 Ultraviolet-visible-near infrared spectroscopy

4.15.6.6.1.1 Introduction

The ultraviolet-visible-near infrared (UV-vis-NIR) portion of the electromagnetic spectrum can excite valence electrons. The interaction of a semiconductor with UV-vis-NIR radiation not only determines its utility in an optoelectronic device but can also be used as a generally non-destructive probe of its fundamental characteristics. While UV-vis-NIR spectroscopy can reveal features such as excitonic and charge-transfer absorption, perhaps the most important characteristic of a perovskite that can be derived from UV-vis-NIR spectroscopy is its bandgap energy. A bandgap energy is often extracted from a Tauc plot, a common transformation of absorption data obtained from a variety of measurement techniques, some of which are described below. This method was introduced by Jan Tauc in 1966 and involves plotting $(\alpha h\nu)^{\frac{1}{r}}$ versus photon energy, $h\nu$, where α is the absorption coefficient of the absorbing material and r is a constant. The value of r differs based on the nature of the bandgap: $\frac{1}{2}$ for direct transitions and 2 for indirect transitions.³¹¹ In theory, the Tauc plot should give one linear region for a direct transition and two distinct linear regions for an indirect transition; the lower- and higher-energy linear regions for an indirect transition correspond to absorption of a photon coupled to the emission or absorption of a phonon, respectively. Therefore, linear fits to these two regions provide an estimate of the bandgap energy when extrapolated to $(\alpha h\nu)^{\frac{1}{r}} = 0$, where the average of the two values is taken as the bandgap energy for an indirect transition. Similarly, an extrapolation of a linear fit to $(\alpha h\nu)^2 = 0$ for the single linear region of a direct transition gives the bandgap energy. This method was originally developed for amorphous semiconductors and relies on several assumptions that do not necessarily hold true for crystalline semiconductors; therefore, improvements to the method have been attempted.^{312,313} However, the Tauc plot remains the most widely used method of bandgap energy determination for perovskites. UV-vis-NIR spectroscopy can also be performed at varied temperatures to get information about sub-bandgap-energy absorption, which may follow the Urbach rule:

$$\alpha(E) = \alpha_0 e^{\left(-\sigma \frac{E_0 - E}{k_B T}\right)} \quad (12)$$

where E is the photon energy, E_0 and α_0 are constants, and σ is the temperature-dependent steepness parameter which describes the steepness of the absorption edge.³¹⁴ Such analysis may help distinguish defect-based absorption from band-to-band absorption.¹⁸³ Low temperatures reduce the effects of thermal broadening and therefore help to distinguish nearby or overlapping absorption features. In addition, many UV-vis-NIR spectroscopy techniques can be combined with microscopy to provide spatially resolved information. Analytical chemistry textbooks, including the following reference,³¹⁵ offer more detailed discussions of optical spectroscopy.

4.15.6.6.1.2 Transmission

The most straightforward method to measure absorption as a function of photon energy is to directly measure the attenuation of monochromatic light as it transmits through a sample using a spectrophotometer (Fig. 21). To obtain quantitative data, the baseline absorption that arises from the instrument's optics and the sample mount must be subtracted from the spectrum. Transmission UV-vis-NIR spectra typically take only a few minutes to collect and require few assumptions for data analysis. Transmission UV-vis-NIR follows the general formula:

$$I_t = I_0 e^{-\alpha d} \quad (13)$$

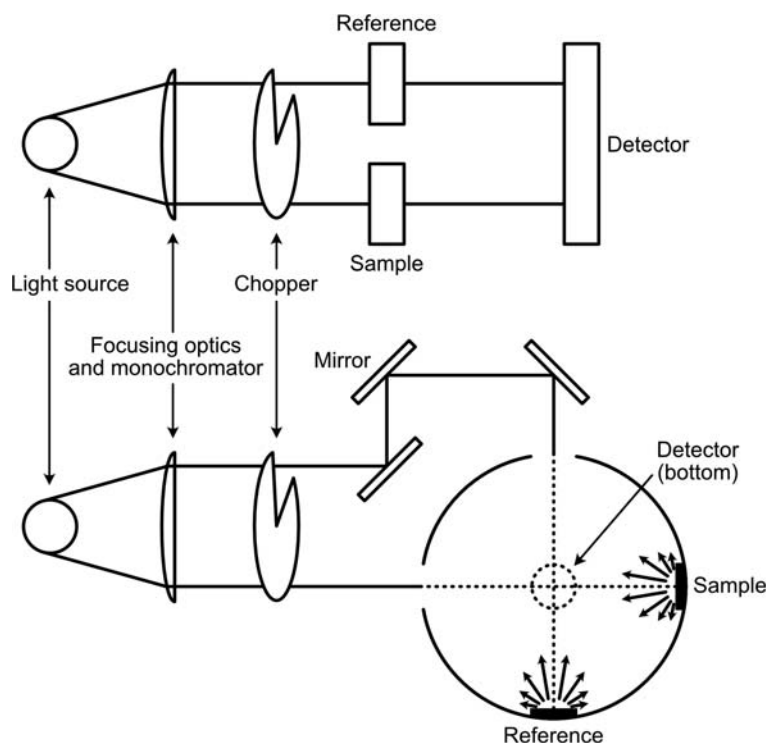


Fig. 21 Simplified diagram of the components and geometry for UV-vis-NIR measurements: transmission (top) and diffuse reflectance (bottom).

where I_t and I_0 are the intensity of the transmitted light and the intensity of the incident light, respectively, and d is the path length that light travels through the absorbing material. The percent transmittance, % T , is measured as $\frac{I_t}{I_0} \times 100\%$, and the commonly used unit of absorbance, A , is related to % T via the equation:

$$A = 2 - \log\%T \quad (14)$$

Dilute solutions follow the Beer-Lambert law:

$$A = \epsilon dc \quad (15)$$

where ϵ is the molar absorptivity and c is the concentration of the absorbing material.

Most halide-perovskite sample morphologies will not allow for adequate light transmission due to complete attenuation or scattering of the incident beam; however, thin films of thickness ~ 10 – 1000 nm can typically be measured using transmission UV-vis-NIR spectroscopy. The transmission is attenuated by absorption, reflection, and scattering of light; therefore, the obtained spectrum represents a convolution of these processes. For high-quality thin films, the contribution of scattering is negligible, and the contribution of reflectance can be minimized with a proper background subtraction, thus having a minimal effect if carried out properly. Transmission UV-vis-NIR spectroscopy is a routine measurement used to characterize the bandgap energies of perovskite thin films,³⁸ including alloyed compositions.^{110,316,317} Tests of long-term stability for devices may also utilize transmission UV-vis-NIR spectroscopy, though it should be considered as only one facet of a comprehensive examination of stability.^{110,316–318} The magnitude of UV-vis-NIR transmission can be used to qualitatively assess the surface coverage and overall quality of perovskite thin films.³¹⁹ High-bandgap perovskites have been considered for use as transparent and semitransparent photovoltaic devices, for which transmission UV-vis-NIR spectroscopy is an important test to measure the transparency of the device.^{320,321}

Transmission UV-vis-NIR spectra can also be collected on thin single crystals. In practice, bulk single crystals of perovskites of suitable lateral dimensions and mechanical stability will have a thickness of at least ~ 10 μm ; thus, the total absorption at photon energies above the bandgap energy will be too large for a spectrophotometer to measure. The data will therefore accurately represent only the low-energy, sub-bandgap-energy region where absorption coefficients are low, which provides information relevant to defect-based absorption (see Section 4.15.6.6.1.1). This analysis, carried out at various temperatures, has been used in perovskite single crystals to identify the source of weak sub-bandgap-energy absorption.¹⁸³

4.15.6.6.1.3 Diffuse reflectance

Solid powder samples typically cannot be measured using transmission UV-vis-NIR spectroscopy because they completely absorb and scatter the incident light. Instead of measuring the transmitted light, diffuse reflectance UV-vis-NIR spectroscopy measures the light scattered by the sample. This is measured by using an integrating sphere, a roughly spherical sample enclosure with a highly

scattering coating, such as a fine powder of polytetrafluoroethylene, and a detector that is positioned inside the sphere such that it is distant from the path of the incident beam (Fig. 21).

Ideally, the scattered light represents all the light that was not absorbed by the sample and can thus be used to calculate an absorption spectrum. The Kubelka-Munk transformation was developed in 1931 to transform diffuse reflectance UV-vis-NIR spectra from percent reflectance, %R, to a pseudo-absorption coefficient, α . The relationship is often simplified as follows:

$$\alpha = \frac{(1 - R)^2}{2R} \quad (16)$$

where R is the fractional reflectance. Like the Beer-Lambert law for solution-state transmission UV-vis-NIR spectroscopy, this transformation holds only for dilute samples with small particle sizes. Therefore, sample powders should be diluted in a mull with a highly scattering powder, such as BaSO₄. Samples that are too concentrated, such as neat powders, or samples with a large particle size will distort the resulting spectra (Fig. 22): features with low α will be overestimated and features with high α will be underestimated and have flattened peaks. There have been attempts to improve this transformation, but the original equation remains in use today.³²²

Because the synthesis of phase-pure powders is often easier than that of thin films, diffuse reflectance UV-vis-NIR spectroscopy is commonly used for bandgap determination for novel perovskite compositions,^{99,204,322} including alloyed compositions.¹¹² However, particular care must be taken for dilute alloys, as they often exhibit weak low-energy absorption that can be overestimated by diffuse reflectance UV-vis-NIR spectroscopy. Therefore, to distinguish between sub-bandgap trap states and a decreased bandgap in an alloyed perovskite, diffuse reflectance measurements should be complemented by other optical absorption techniques.^{115,116,323,324} Diffuse reflectance UV-vis-NIR spectra can be measured on thin-film samples to deconvolute absorption from scattering: because all scattered and transmitted light is collected by the detector in an integrating sphere, any decrease in measured light intensity relative to the reference can be ascribed to absorption by the perovskite film;³⁷ this is particularly useful when combined with transmission UV-vis-NIR spectra.^{127,318}

4.15.6.6.1.4 Single-crystal reflectance

Using a large single crystal with a highly reflective surface, UV-vis-NIR spectra can be collected by measuring the specular reflectance, as opposed to the diffuse reflectance from a highly scattering powder. Like a transmission measurement, the attenuation of the reflected light is measured as a function of photon energy to give a reflectance spectrum with units of %R. If polarized light is used, the incident beam can be oriented to probe specific interactions within a single crystal with a known structure and orientation. For example, the double perovskite Cs₂AuAu₆ has been examined with polarized single-crystal reflectance UV-vis-NIR spectroscopy to determine the atomic orbitals involved in the Au⁺ to Au³⁺ intervalence charge transfer.³²⁵

4.15.6.6.1.5 Spectroscopic ellipsometry

Whereas reflectance-based UV-vis-NIR spectroscopy is sensitive to the attenuation of the reflected light, spectroscopic ellipsometry measures the change in polarization of the specular reflection. The interaction of a reflective sample, such as a thin film or large single crystal, with the amplitude and phase of the polarized incident light must be modeled to obtain the thickness, surface

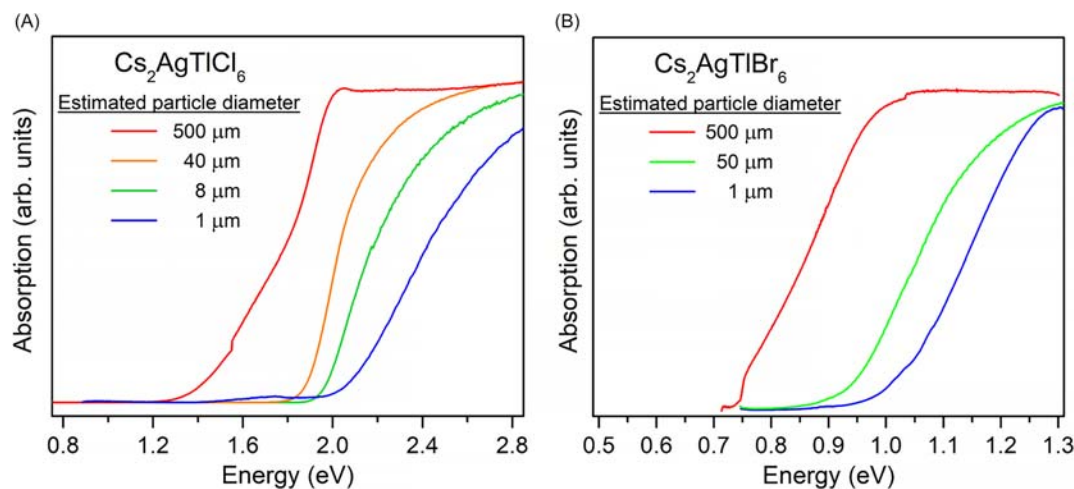


Fig. 22 UV-vis-NIR diffuse reflectance spectra of: (A) Cs₂AgTlCl₆; (B) Cs₂AgTlBr₆. The redshift of the absorption edge is due to the sensitivity of reflectance measurements to particle size and indicates the presence of a weakly absorbing defect species. It does not indicate significant differences in absorption properties between the samples. The smallest particle size was used to determine the bandgap. Reprinted with permission from Slavney, A. H.; Leppert, L.; Saldivar Valdes, A.; Bartesaghi, D.; Savenije, T. J.; Neaton, J. B.; Karunadasa, H. I., Small-Band-Gap Halide Double Perovskites. *Angew. Chem. Int. Ed.* **2018**, 57 (39), 12765–12770. Copyright 2018 John Wiley and Sons Publishers.

roughness, index of refraction, and absorption coefficient of a sample. Films of nearly any thickness, ranging from <1 nm to ~ 10 μm can be measured using spectroscopic ellipsometry. For perovskites, ellipsometry has found use as a probe of high-energy electronic transitions with strong absorption coefficients and to quantify the index of refraction and absorption coefficient, important parameters for device architecture.^{326–328} Because of its insensitivity to low-intensity absorption, ellipsometry has also been employed to distinguish bandgap shifts from sub-bandgap defect-based absorption in alloyed perovskites.³²³

4.15.6.6.1.6 Transient absorption

Transient absorption spectroscopy (TAS), also called flash photolysis, is a type of pump-probe spectroscopy that measures changes in light absorption, in the femtosecond to nanosecond time scales, after excitation. These measurements probe changes in the excited state of a material including vibrational and electronic processes. TAS measurements may be made as a function of time delay after initial excitation and as a function of wavelength. TAS has been applied to perovskites to study their charge-carrier dynamics: for instance, in the seminal 2012 report by Nam-Gyu Park and coworkers, femtosecond TAS was used to assess charge extraction and carrier dynamics in their devices to choose an appropriate architecture, a common application of the technique to perovskites.³⁷ TAS can also serve as a probe of charge-carrier trap density for alloyed or otherwise modified perovskite films and devices, or as a probe of degradation over time.^{329,330} The dynamics of charge carriers relaxing to the ground vibrational state of an excited electronic state have been studied extensively in perovskites using TAS: a phenomenon called “phonon bottleneck,” where the relaxation of charge carriers to the band extrema is prolonged at high concentrations of charge carriers, has been observed in perovskites and has implications for increased photovoltage in photovoltaic devices.³³¹ Additionally, mixed-halide perovskites have been examined with TAS to distinguish the segregated Br-rich and I-rich regions of the sample and to confirm that halide segregation has (or has not) occurred (see Section 4.15.7.4).^{332,333}

4.15.6.6.1.7 Advanced techniques

All crystalline semiconductors above 0 K exhibit a nonzero population of point defects, some of which may contribute electronic states within the bandgap. A photon of sufficient energy can excite an electron from the valence band into these defect states, resulting in optical absorption at energies below the bandgap energy. Photothermal³³⁴ and photoacoustic³³⁵ spectroscopies measure the heat produced from non-radiative recombination in semiconductors following an optical absorption and are highly sensitive to weak absorption. Here, all absorbed photons are assumed to convert into heat, which is a reasonable assumption for sub-bandgap absorption.³³⁴ Photothermal deflection spectroscopy (PDS) uses an optical probe to measure the change in the index of refraction of a sample, or of a deflection medium in thermal contact with the sample, as a function of wavelength (Fig. 23). Photoradiometry is a similar technique that directly measures the infrared (heat) emission following optical absorption. Photoacoustic spectroscopy (PAS) measures the pressure wave that propagates through a sample upon localized heating as a result of optical absorption. Fourier-transform photocurrent spectroscopy (FTPS) measures the photocurrent as a function of incident photon energy, relying on the assumption that all absorbed photons generate measurable photocurrent.

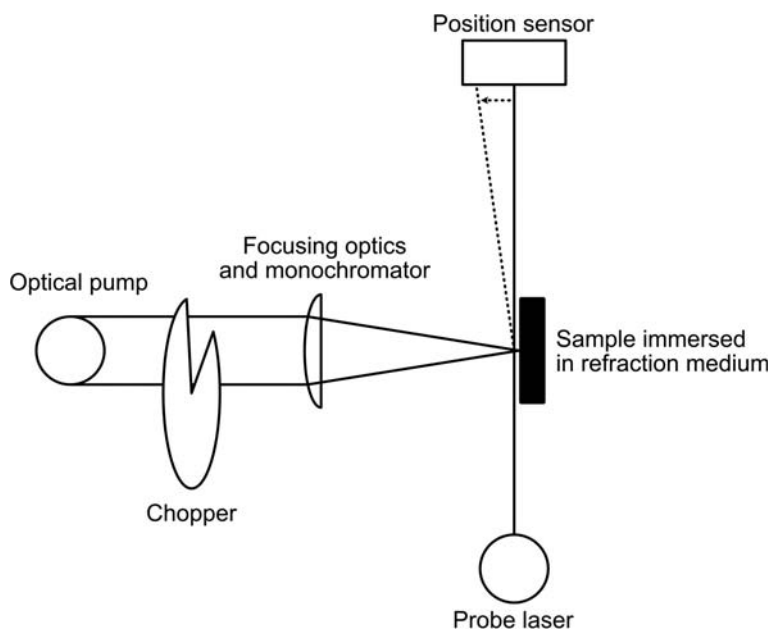


Fig. 23 Simplified diagram of a setup for transverse photothermal deflection spectroscopy. Adapted with permission from Jackson, W. B.; Amer, N. M.; Boccara, A. C.; Fournier, D., Photothermal Deflection Spectroscopy and Detection. *Appl. Opt.* **1981**, 20 (8), 1333–1344. Copyright 1981 The Optical Society.

These techniques boast superior sensitivity to transmission measurements: absorption coefficients as low as 10^{-3} cm^{-1} can be measured in an ideal case and coefficients of 1 cm^{-1} are routinely detected, a 1–4 order-of-magnitude improvement over transmission spectroscopy of solid samples. Additionally, they do not convolute absorption, scattering, and reflection, as with transmission spectroscopy. However, they rely on assumptions about the relaxation pathway of the photoexcitation that may not hold true for every sample. They require more in-depth sample preparation than transmission measurements, but some techniques can be used for both large single crystals and thin films. These techniques excel at measuring sub-bandgap-energy absorption events with low absorption coefficients but are inferior to transmission spectroscopy and spectroscopic ellipsometry for measuring absorption with strong absorption coefficients. Indeed, for perovskites, they have primarily been used to measure Urbach (defect) energies of thin films, an important parameter for device performance.³³⁶ PDS, for example, has been used to correlate Urbach energy with halide composition in mixed-halide perovskites.³³⁷ Similarly, the high sensitivity of photocurrent spectroscopy has been used to probe halide segregation in thin films of $(\text{CH}_3\text{NH}_3)\text{Pb}(\text{Br}_{0.4}\text{I}_{0.6})_3$ (Fig. 24; see Section 4.15.7.4).¹²⁷

4.15.6.6.2 Photoluminescence spectroscopy

4.15.6.6.2.1 Introduction

When a semiconductor absorbs a photon of energy greater than its bandgap, E_g , an electron may be excited to the conduction band (see Section 4.15.4.1). This excited electron may relax to the ground state by recombination with the hole left in the valence band; this process must be accompanied by a release of energy, e.g., as light or as heat. While UV-vis-NIR spectroscopy measures the light absorbed by a sample, photoluminescence (PL) spectroscopy measures the light emitted by a sample upon photoexcitation, thereby providing complementary information. Typically operating in the UV-vis-NIR portion of the electromagnetic spectrum, PL spectroscopy is an important probe of electronic structure and provides an early indication of a material's optoelectronic performance, particularly as a component in light-emitting devices. In 3D perovskites, the PL often arises from band-to-band recombination of charge carriers, thus PL spectroscopy can provide a rough measure of bandgap energy. However, some energy is lost to nonradiative pathways, most often to vibrational relaxation: this results in a decrease in the energy of the emitted photon relative to the energy of the absorption onset or bandgap. This energy difference between the absorption and emission processes is called the Stokes shift and is typically in the range of 10–100 meV for band-to-band PL in perovskites (Fig. 25A). In addition, more complex decay pathways can result in PL, such as defect-mediated luminescent recombination, excitonic (electrostatically bound electron-hole pair) emission (Fig. 25B), and emission from dopant species. Therefore, although PL spectroscopy can reveal much about the optoelectronic properties of perovskites, it should not be used as the sole method of bandgap determination. Many PL spectroscopy techniques can be combined with microscopy to provide spatially resolved information. PL intensity is commonly presented as a function of wavelength; units of energy (e.g., eV), however, are more appropriate for quantitative spectral analysis. In theory, a Gaussian lineshape, as a function of energy, is expected from emission resulting from band-to-band charge-carrier recombination. To convert between units of wavelength and energy, the Jacobian transformation must be used to account for the non-linear relationship between wavelength and energy.³³⁸ We note that the Jacobian transformation is only required for non-ratiometric techniques, such as steady-state PL spectroscopy. Ratiometric techniques, where the output signal is measured as a ratio of the input signal, such as UV-vis-NIR transmission spectroscopy or PL excitation spectroscopy, do not require this transformation. More information about PL spectroscopy may be found in the following reference.³³⁹

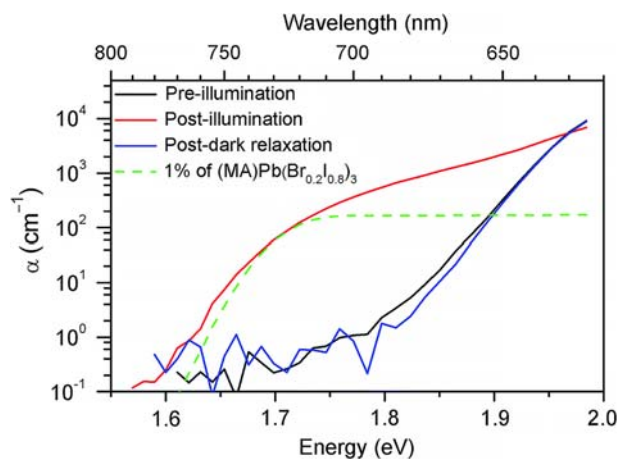


Fig. 24 Photocurrent spectra of a thin film of $(\text{MA})\text{Pb}(\text{Br}_{0.4}\text{I}_{0.6})_3$ before (black) and after (red) white-light soaking for 5 min at 100 mW cm^{-2} and post-light soaking after 1 h in the dark (blue). A scaled spectrum of a thin film of $(\text{MA})\text{Pb}(\text{Br}_{0.2}\text{I}_{0.8})_3$ is shown for comparison (dashed green). MA = CH_3NH_3^+ . Reprinted from Hoke, E. T.; Slotcavage, D. J.; Dohner, E. R.; Bowring, A. R.; Karunadasa, H. I.; McGehee, M. D., Reversible Photo-Induced Trap Formation in Mixed-Halide Hybrid Perovskites for Photovoltaics. *Chem. Sci.* **2015**, 6 (1), 613–617 - Published by The Royal Society of Chemistry.

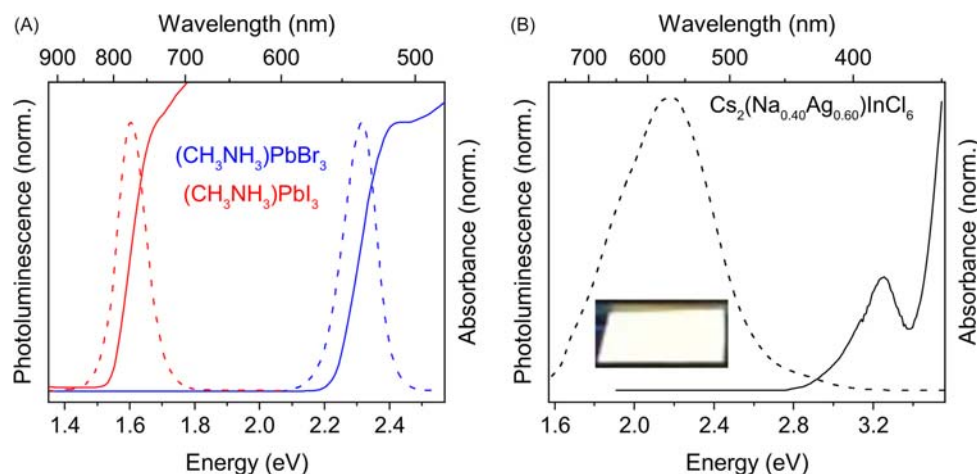


Fig. 25 Absorption spectra (solid lines) and steady-state photoluminescence spectra (dashed lines) for: (A) $(\text{CH}_3\text{NH}_3)\text{PbX}_3$ ($X = \text{Br}^-$, I^-); (B) $\text{Cs}_2(\text{Na}_{0.40}\text{Ag}_{0.60})\text{InCl}_6$. Inset: photograph of a thin film of $\text{Cs}_2(\text{Na}_{0.40}\text{Ag}_{0.60})\text{InCl}_6$ under UV excitation. (A) Adapted from Richter, J. M.; Abdi-Jalebi, M.; Sadhanala, A.; Tabachnyk, M.; Rivett, J. P. H.; Pazos-Outón, L. M.; Gödel, K. C.; Price, M.; Deschler, F.; Friend, R. H., Enhancing Photoluminescence Yields In Lead Halide Perovskites by Photon Recycling and Light Out-Coupling. *Nat. Commun.* **2016**, 7 (1), 13941 - Published by Springer Nature under Creative Commons Attribution 4.0 International License <http://creativecommons.org/licenses/by/4.0/>. (B) Adapted by permission from: Springer Nature, *Nature*, Luo, J.; Wang, X.; Li, S.; Liu, J.; Guo, Y.; Niu, G.; Yao, L.; Fu, Y.; Gao, L.; Dong, Q.; Zhao, C.; Leng, M.; Ma, F.; Liang, W.; Wang, L.; Jin, S.; Han, J.; Zhang, L.; Etheridge, J.; Wang, J.; Yan, Y.; Sargent, E. H.; Tang, J., Efficient and Stable Emission of Warm-White Light From Lead-Free Halide Double Perovskites. *Nature* **2018**, 563 (7732), 541–545. Copyright 2018.

4.15.6.6.2.2 Steady-state photoluminescence

A standard PL spectrometer uses two monochromators or sets of monochromators: one to select the photoexcitation wavelength from a broad-spectrum light source and another to measure the PL from the sample. To obtain a PL spectrum, the intensity of the emission from the sample is measured as a function of wavelength using the detector monochromator. In contrast, a PL excitation spectrum measures the intensity of PL emission from the sample at a single wavelength as a function of photoexcitation wavelength, i.e., the photoexcitation monochromator is scanned to give the spectrum. These techniques give complementary information that can help to reveal the origin of PL from a sample. In a straightforward case, the PL emission is a single, relatively narrow Gaussian peak with a small Stokes shift, and an excitation spectrum monitoring the emission at its maximum will match the absorption spectrum, as is the case for $(\text{CH}_3\text{NH}_3)\text{PbX}_3$ ($X = \text{Cl}^-$, Br^-) (Fig. 25A).^{340,341} In some impurity-doped perovskites, such as the double perovskite $\text{Cs}_2(\text{Na}_{0.40}\text{Ag}_{0.60})\text{InCl}_6$ alloyed with Bi^{3+} , the PL emission appears warm white and the radiative pathways are more complex (Fig. 25B).²³⁹ In Sb^{3+} -alloyed $\text{Cs}_2\text{NaInCl}_6$ and $\text{Cs}_2\text{KInCl}_6$, PL spectra have demonstrated how changing the local geometry of the host perovskite can shift the energy of the emission from the Sb^{3+} impurity.³⁴² PL excitation spectroscopy can also be used to investigate the origin of unusual PL, e.g., to show that the PL “blinking” in $(\text{CH}_3\text{NH}_3)\text{PbI}_3$ arises from photoinduced degradation of the perovskite.³⁴³

Though PL spectroscopy can be measured on both solid and liquid samples, special care must be taken when measuring solids to avoid artifacts from reflections, particularly with low-intensity emitters. For instance, the higher harmonics of the excitation source can lead to spurious features occurring in the PL spectrum at integer-multiple wavelengths of the excitation wavelength. Additionally, weak background fluorescence from components of the spectrometer or the sample mount can become competitive in intensity with the sample emission for low-intensity emitters. These issues can be mitigated by selection of non-luminescent sample mounts and judicious use of high-pass, low-pass, and band-pass optical filters.

4.15.6.6.2.3 Advanced techniques

PL spectra contain information beyond the emission energy and width. For instance, the dependence of PL intensity on excitation fluence offers insight into the origin of the PL emission: a sublinear dependence of intensity on excitation fluence suggests emission from defects, as the PL intensity should stop increasing as the defect-based trap states are saturated at high excitation fluences. A linear or superlinear dependence supports emission from the bulk material, although the lifetime of the PL and the magnitude of excitation fluence must be taken into account to eliminate a defect-based origin.^{344,345} Fluence-dependence analysis has been used to support the origin of the broad PL of the white-light emitting Bi-alloyed $\text{Cs}_2(\text{Na}_{0.40}\text{Ag}_{0.60})\text{InCl}_6$ as not arising from defects.²³⁹ Low-temperature measurements often take advantage of enhanced PL quantum yield (PLQY) owing to reduced contributions from nonradiative decay pathways involving phonons and molecular vibrations. However, varying temperature may also cause the PL features to change (e.g., narrowing of vibrationally broadened PL) or new PL features to arise (e.g., due to a crystallographic phase change). Indeed, vibrational broadening of the PL can be modeled to extract information about the lattice phonon modes that couple to the radiative electronic transition. At low temperatures, the Franck-Condon model of a phonon-coupled

electronic transition from the vibrational ground state of an electronic excited state can model the PL emission peak as a progression of peaks, separated by the vibrational energy of the ground electronic state. The relative intensities of these peaks are given by:

$$I(n) = I_0 \frac{S^n}{n!} \quad (17)$$

where n corresponds to the vibrational state in the electronic ground state, and S , the Huang-Rhys parameter, gives a measure of the distortion of the excited state with respect to the ground-state geometry.³⁴⁶ In the case of strong electron-phonon coupling, broadening of these peaks results in a smooth Gaussian PL emission lineshape, even at low temperatures.³⁴⁷ For example, the double perovskite $\text{Cs}_2\text{AgBiBr}_6$ has an indirect bandgap and thus no band-to-band PL is evident. A lower-energy PL band in this material has been attributed to defects.²⁰⁴ Fitting this PL band yields a value of $S = 11.7$, which can be used in combination with phonon-mode energies obtained from Raman spectroscopy (see Section 4.15.6.6.3) to reproduce the observed Stokes shift and PL emission spectrum, indicating that the emissive (intrinsic or extrinsic) defects have strong electron-phonon coupling.³⁴⁸ A broadened PL band in an extended solid can have homogenous and inhomogeneous contributions to line broadening.^{345,349} Assuming homogeneous line broadening, the Huang-Rhys parameter can be estimated by a fit to the full width at half maximum (fwhm) for an emission feature from a series of PL emission spectra taken at different temperatures, given by^{346,350}:

$$fwhm(T) = 2.36\sqrt{SE_{ph}} \sqrt{\coth\left(\frac{E_{ph}}{2k_B T}\right)} \quad (18)$$

where E_{ph} is the energy of the phonon mode that couples to the electronic transition, T is the temperature in Kelvin, and k_B is the Boltzmann constant. For example, in $\text{Cs}_2\text{AgInCl}_6$, the large S value of 37 supports the proposed model of distorted excited states in the Bi-alloyed $\text{Cs}_2(\text{Na}_x\text{Ag}_{1-x})\text{InCl}_6$ systems.²³⁹

In time-resolved (TR) PL spectroscopy, the PL intensity is measured as a function of time after photoexcitation, over timescales as short as femtoseconds. TRPL provides information about the radiative lifetime of electronically excited states, thus giving insight into the mechanisms of luminescence and the prevalence of charge-carrier trap states within the sample. Such PL lifetime studies help understand the effects of additives or film preparation techniques in perovskite devices.³⁵¹ In $(\text{CH}_3\text{NH}_3)\text{Pb}(\text{Br}_x\text{I}_{1-x})_3$, TRPL has been used to observe reversible, illumination-time-dependent growth in PL intensity of an additional emission feature, which has been attributed to reversible light-induced halide segregation (see Section 4.15.7.4).¹²⁷

Another important metric for assessing the viability of a perovskite for light-emitting applications is measurement of the PLQY, or the ratio of the number of photons emitted to the number of photons absorbed by the sample; this measurement can be accomplished using an integrating sphere (see Section 4.15.6.6.1.3). Calculation of the PLQY, Φ_f , by the direct method (i.e., without a reference standard for comparison) requires measurement of: E_c , the integrated emission of the sample; L_c , the scattered incident excitation light on the sample; E_a , the baseline emission of a blank; and L_a , the scattered incident excitation light on a blank:

$$\Phi_f = \frac{E_c - E_a}{L_a - L_c} \quad (19)$$

PLQY measurements can frequently vary between reports for a given material, and may be affected by sample morphology and individual detector efficiencies.³⁵² PLQY measurements are commonly used for assessing device viability. They have also been used in the Sb^{3+} -alloyed $\text{Cs}_2\text{MInCl}_6$ ($M = \text{Na}, \text{K}$) perovskites to demonstrate an inverse dependence of PLQY on Sb^{3+} concentration due to increasing self-quenching, reinforcing the mechanism of isolated Sb-based emission.³⁴²

4.15.6.6.3 Vibrational spectroscopy

Atomic bonds have characteristic strengths with corresponding vibrational frequencies that can be measured with vibrational spectroscopy. These frequencies typically occur in the IR region and thus can be excited by absorption of specific frequencies of IR light. Most modern IR spectrophotometers measure across a wide frequency range simultaneously and use a Fourier transform to convert the measured interference pattern, or interferogram, to a spectrum of absorbed intensity vs incident light frequency. Gaseous, liquid, solution-state, or thin or dilute solid samples can be measured with transmission IR spectroscopy, while concentrated solid samples must be measured using alternative techniques, such as attenuated total reflectance (ATR) IR spectroscopy. In ATR-IR, an IR light beam is reflected off the inner surface of a crystal, typically germanium or diamond, such that the wave propagates along the crystal and eventually reflects into the detector of the spectrophotometer. The evanescent wave in this crystal extends a small distance above the surface of the crystal, typically 0.5–2 μm ; if a sample is brought into close contact with the crystal, the evanescent wave will interact with the sample. This offers a facile method of obtaining IR spectra that is particularly useful for solid samples, such as perovskite powders.

A complementary technique, Raman spectroscopy, also probes atomic vibrations but does so by exploiting Raman scattering. When light, typically of UV-vis-NIR frequencies, is scattered off a sample, it may scatter elastically (with no change in the photon energy) or inelastically (with an increase or decrease in the photon energy). Raman scattering corresponds to inelastic scattering where the decrease or increase in photon energy is a result of the transfer of energy between the photon and a vibrational state of the sample. Thus, measurement of the intensity of the inelastically scattered light provides a spectrum with peaks that are characteristic of the vibrational modes of a sample, like with IR spectroscopy. However, the types of vibrations observed are distinct for IR and Raman spectroscopy: while IR-active vibrations must be associated with a change in the dipole moment, Raman-active modes require a change in electronic polarizability. Thus, the two techniques provide complementary information. Unlike

transmission measurements, scattering signals tend to be orders of magnitude weaker. Accurate determination of the energy difference between the scattered and incident photons also requires a monochromatic light source. Therefore, modern Raman measurements are typically carried out with laser excitation.

Standard IR and Raman spectroscopies are best suited for organic molecules, where the identification of functional groups is often simply correlated to the presence of a peak at a particular frequency; therefore, IR and Raman spectroscopies have found use in perovskites as probes of the organic component of organoammonium perovskite compositions. For example, IR and Raman spectra of $((\text{CH}_3\text{NH}_3)_x(\text{NH}_2\text{CHNH}_2)_{1-x})\text{PbX}_3$ ($X = \text{Cl}^-$, Br^- , I^-) have been used to probe the hydrogen-bonding strength between the ammonium group and X sites and how it is affected by the X-site identity.^{353,354} Separately, blueshifts of CH_3NH_3^+ rotational Raman modes under higher light fluence have been linked to photostriction, or a light-induced mechanical strain, in $(\text{CH}_3\text{NH}_3)\text{PbBr}_3$.³⁵⁵ While metal-halide bonds in perovskites can be probed with Raman and IR spectroscopy, they are typically at low frequencies ($< 500 \text{ cm}^{-1}$) and can be difficult to interpret without more advanced measurements and analysis, such as time-resolved and resonance Raman spectroscopies, or theoretical predictions. Higher-frequency Raman and IR modes can still provide useful information for perovskites: the evolution of Raman modes with pressure has been used to investigate the claimed comproportionation of Au^{3+} and Au^{1+} to Au^{2+} in $\text{Cs}_2\text{Au}^{\text{I}}\text{Au}^{\text{III}}\text{X}_6$ ($X = \text{Cl}^-$, Br^-) at high pressures.³⁵⁶ Additionally, measuring Raman spectra over time has served as a probe of moisture-induced degradation in $(\text{CH}_3\text{NH}_3)\text{PbX}_3$ ($X = \text{Cl}^-$, Br^-) thin films.³⁵⁷ Similarly, IR spectroscopy has been used to investigate the hydration of $(\text{CH}_3\text{NH}_3)\text{Pb}(\text{Br}_x\text{I}_{1-x})_3$ over time.³⁵⁸ Because the vibrational modes of metal-halide bonds can be relatively broad and occur at frequencies close to each other, fitting of vibrational modes requires accurate theoretical modeling of vibrations of the inorganic framework. Such work has been carried out to assign the symmetry and character of low-energy modes for the low-temperature orthorhombic phase of $(\text{CH}_3\text{NH}_3)\text{PbI}_3$, with the assignment confirmed by low-temperature (4 K) Raman measurements.³⁵⁹ Raman measurements have also been used in tandem with photoluminescence spectroscopy to identify the characteristic frequency of the vibration coupled to the color-center emission of $\text{Cs}_2\text{AgBiBr}_6$.³⁴⁸

Finally, Raman spectroscopy has proven valuable for investigating the phase transitions of perovskites. For instance, the low-frequency modes, corresponding to vibrations of the metal-halide framework, have been measured through the orthorhombic-tetragonal and tetragonal-cubic perovskite phase transitions of CsPbBr_3 and $(\text{CH}_3\text{NH}_3)\text{PbBr}_3$ (Fig. 26).³⁶⁰ The orthorhombic-

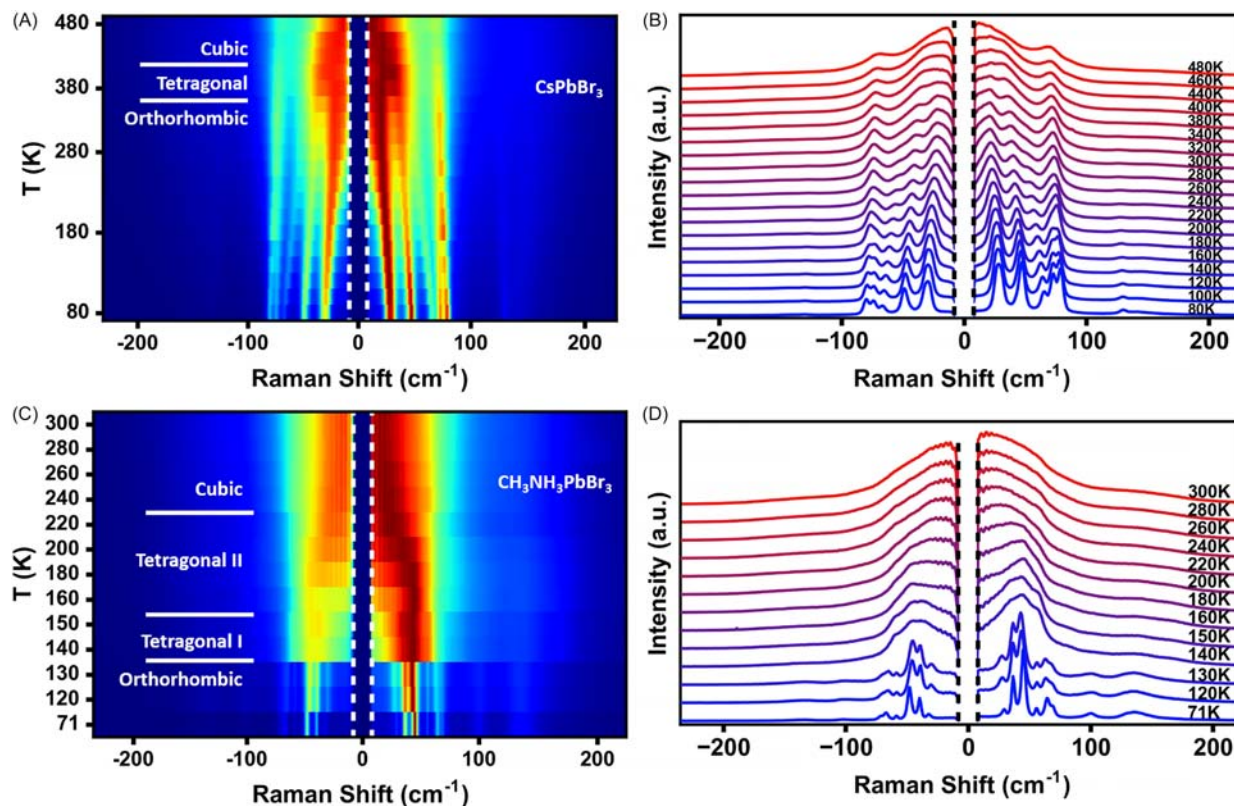


Fig. 26 Normalized temperature-dependent, low-frequency Raman spectra (sub-bandgap 633-nm excitation) collected from crystals of (A, B) CsPbBr_3 and (C, D) $(\text{CH}_3\text{NH}_3)\text{PbBr}_3$ through the crystallographic phase transitions: (A, C) color maps of intensity as a function of Raman shift and temperature; (B, D) offset Raman spectra for select temperatures. The phase-transition temperatures and the equilibrium phase at each temperature are indicated in (A, C) as white lines and text, respectively. Reprinted with permission from Guo, Y.; Yaffe, O.; Paley, D. W.; Beecher, A. N.; Hull, T. D.; Szpak, G.; Owen, J. S.; Brus, L. E.; Pimenta, M. A., Interplay Between Organic Cations and Inorganic Framework and Incommensurability in Hybrid Lead-Halide Perovskite $\text{CH}_3\text{NH}_3\text{PbBr}_3$. *Phys. Rev. Mater.* **2017**, 1 (4), 042401 <https://doi.org/10.1103/PhysRevMaterials.1.042401>. Copyright 2017 by the American Physical Society.

tetragonal phase transition in $(\text{CH}_3\text{NH}_3)\text{PbBr}_3$ is markedly more abrupt than for CsPbBr_3 , showing a loss of the discrete Raman modes and emergence of broad bands, suggesting the phase transition is coupled to the disorder of the methylammonium cation. Interestingly, both CsPbBr_3 and $(\text{CH}_3\text{NH}_3)\text{PbBr}_3$ show a broad “central peak” centered at $h\nu = 0$ (where h is Planck’s constant and ν is the frequency of a photon) in the cubic phase. This phenomenon is distinct from the central peak observed in inelastic neutron scattering measurements (see Section 4.15.6.3.5) of several perovskites, which is attributed to small, static, lower-symmetry domains in the average cubic structure of $(\text{CH}_3\text{NH}_3)\text{PbI}_3$.²⁸⁶

4.15.6.6.4 Nuclear magnetic resonance spectroscopy

In nuclear magnetic resonance (NMR), the interaction of a magnetic field with the nuclei in the sample is probed by pulsed radio-frequency radiation. Thus, the measurement is sensitive to the local environment surrounding a nucleus and the frequency of the resonant peaks and their splitting patterns yield valuable information about the chemical structure of a material. NMR spectra are commonly plotted using the chemical shift, δ , as the x -axis, where δ is a measure of the frequency of a resonance line that is normalized to the strength of the magnetic field used in the instrument and referenced to a standard compound. While 1D NMR of one or two nuclides is often sufficient to assign the structure of a small organic molecule, more advanced measurements and interpretation can be applied to yield further information needed for structural determination of more complicated molecules. In addition, NMR can serve as a probe of reaction dynamics and kinetics.

While solution-state NMR is the most readily accessible form, solid-state NMR can be used for extended structures such as perovskites that lose their structural identity when dissolved in solution. Solid samples are usually rotated at high (kHz) frequencies at the magic angle (54.7356°) to narrow the resonance bands sufficiently for observation, as multiple types of interactions in the solid state often broaden resonant bands beyond utility if measured without rotation or away from the magic angle. Further, not all nuclides are NMR-active or practicably measurable due to their isotopic abundance: to be NMR-active, a nuclide must have a nonzero spin-state. Additionally, practical considerations such as relaxation times and quadrupolar broadening mean that not every element can be measured or provide useful information by using NMR. The following reference³⁶¹ provides a detailed discussion of solid-state NMR of inorganic semiconductors.

Solution-state NMR is occasionally used for perovskites to determine composition. For instance, the ratio of oxidation states of Sn in Sn-alloyed $\text{Cs}_2\text{AgBiBr}_6$ was determined using ^{119}Sn NMR by dissolving the alloyed perovskite in dimethylsulfoxide.¹¹⁶ However, solid-state NMR is much more commonly used to characterize perovskites. Organoammonium perovskite compositions have been studied using ^1H and ^{13}C NMR to investigate the local chemical environment, dynamics, and phase segregation of the A-site cation.³⁶² Similar studies of various perovskite compositions have been carried out on the ^{133}Cs , ^{87}Rb , and ^{39}K nuclides, especially to determine the extent of incorporation of these cations in mixed-A-site structures and to study the rotational dynamics of A-site cations.³⁶² Other nuclides, such as ^{121}Sb and ^{119}Sn , have been used to study the B sites of perovskites, for example to determine the distribution of alloyed metals³⁶³ and to quantify ion mobility.³⁶⁴ The high sensitivity of NMR to changes in chemical environment has allowed for the X site to be indirectly studied using NMR of the B-site cation: occupancy of the X site by different halides leads to substantial shifts of the ^{207}Pb resonance in mixed-halide $(\text{CH}_3\text{NH}_3)\text{PbX}_3$ ($X = \text{Cl}^-$, Br^- , I^-) perovskites, thereby providing a probe for halide segregation (Fig. 27; see Section 4.15.7.4).³⁶⁵ While halides are practically more difficult to study directly with solid-state NMR, a combination of NMR and nuclear quadrupole resonance (NQR; a closely related spectroscopic technique³⁶⁶) has been successfully employed to examine halide-site disorder in CsPbX_3 ($X = \text{Cl}^-$, Br^- , I^-).³⁶⁷ Though perhaps not part of the standard characterization suite for perovskites, NMR has proven to be a valuable probe of local structure, particularly in alloyed perovskite compositions.³⁶⁸

4.15.6.7 Microscopy

The term “microscopy” covers a broad range of techniques that probe the sample with electromagnetic radiation with various wavelengths, including X-ray, UV, visible, and infrared as well as through physical interactions, such as scanning probe microscopy. In general, microscopy refers to techniques that image on the nm to mm length scale, thereby providing spatially resolved information that represents local, but not necessarily global, structure and dynamics.

4.15.6.7.1 Optical microscopy

As the adage goes, “a picture is worth a thousand words.” Indeed, optical microscopy offers a powerful means of materials characterization via direct visualization and can be combined with a variety of other experimental probes to achieve spatial resolution. Simple optical microscopy was particularly important to researchers who first studied perovskites in the late 19th and early 20th centuries, as they had no access to many of the characterization techniques that we take for granted today. Today, optical microscopy remains a rapid method to obtain information about phase identity, sample quality and purity, crystal symmetry, and even electronic properties.

Because microscopes are widely available, non-destructive, and quick to use, studying a sample under the microscope is often the first characterization technique employed on a freshly synthesized perovskite sample. The uniformity of the color and crystal habit of a polycrystalline sample can often distinguish between a phase-pure and impure sample. The color of a solid can also aid in phase identification and may provide a qualitative estimate of the bandgap energy (although trace impurities can dramatically change the color of a solid without any effect on the bandgap). Crystals with well-defined facets and uniform habit are more likely to have a well-ordered atomic structure and thin films with a uniform appearance are more likely to have a densely packed microstructure

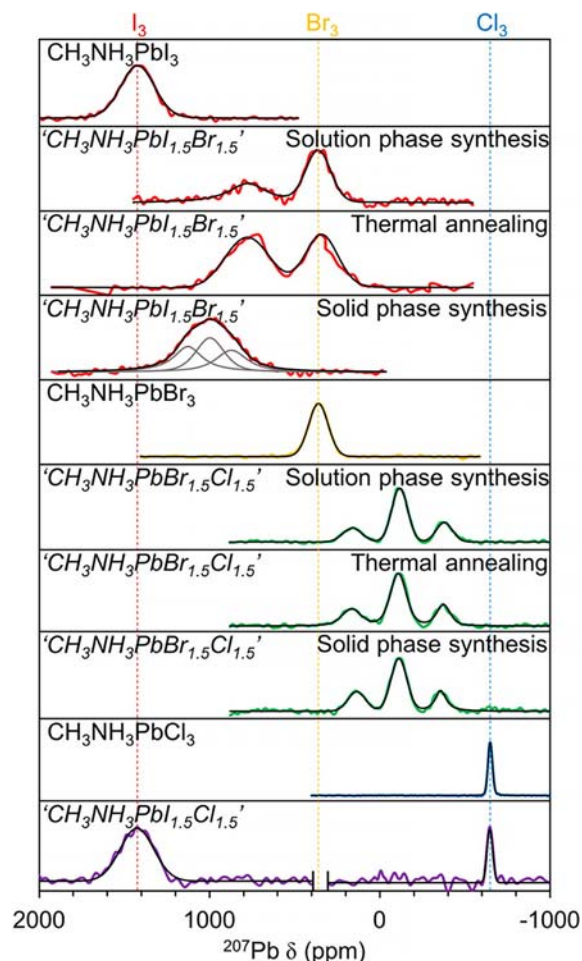


Fig. 27 Static ^{207}Pb solid-state NMR spectra (22 °C) of representative mixed-halide perovskites prepared by solution-phase synthesis, thermal annealing, and solid-phase synthesis. Black curves were fit to mixed Gaussian/Lorentzian peaks. Magic-angle spinning led to no substantial narrowing of the peaks. Italicized formulas in quotation marks are calculated from synthetic loading; formulas in regular script are compositional assignments made from experimental data. The peak splitting is indicative of halide segregation. Reprinted with permission from Rosales, B. A.; Men, L.; Cady, S. D.; Hanrahan, M. P.; Rossini, A. J.; Vela, J., Persistent Dopants and Phase Segregation in Organolead Mixed-Halide Perovskites. *Chem. Mater.* **2016**, *28* (19), 6848–6859. Copyright 2016 American Chemical Society.

with a uniform thickness that may ultimately perform better in a device. Depending on the power of the microscope optics, the habit of crystals with dimensions down to $\sim 10\ \mu\text{m}$ can be readily determined and the macroscopic crystal habit can provide information about the atomic structure. For example, crystals with a cubic habit (e.g., octahedra) are likely to be in a cubic space group (Fig. 28A) and crystals with one dimension much shorter than the other two are likely to have a 2D crystal structure. In addition, many microscopes are equipped with a set of rotatable plane polarizers. While crystals with cubic crystal symmetry will exhibit uniform rotation of polarized light, most crystals with any other crystal symmetry will not uniformly extinguish polarized light: this is known as dichroism or pleochroism. In addition to this test of cubic symmetry, polarized microscopy also provides a potent method to identify crystals that are composed of more than one domain, also known as twinned crystals, as their misaligned orientations will result in a non-uniform extinction of polarized light (Fig. 28B). This is especially useful when selecting crystals for single-crystal diffraction studies and has also been used to confirm the single-crystalline nature of mm-sized grains in $(\text{CH}_3\text{NH}_3)\text{PbCl}_x\text{I}_{3-x}$ thin films.³⁶⁹

The combination of optical microscopy with photoluminescence, absorption, and reflectance spectroscopies has offered microscopic information into the charge-carrier dynamics of perovskites, particularly when resolved in time. This has been used, for example, to extract the charge-carrier diffusion length for $(\text{CH}_3\text{NH}_3)\text{PbI}_3$ and to study the effects of grain boundaries on carrier transport.³⁷⁰ Some measurements may employ confocal microscopy, a technique that increases resolution and contrast and offers 3D spatial resolution by blocking out-of-focus light with a small pinhole. For example, in thin films of the mixed-halide composition $(\text{CH}_3\text{NH}_3)\text{Pb}(\text{Br}_x\text{I}_{1-x})_3$, confocal fluorescence microscopy has been used to visualize halide segregation and examine the effect of grain boundaries (Fig. 28C).³⁷¹ Traditional optical microscopy is limited in resolution by the wavelength of light used according to the equation:

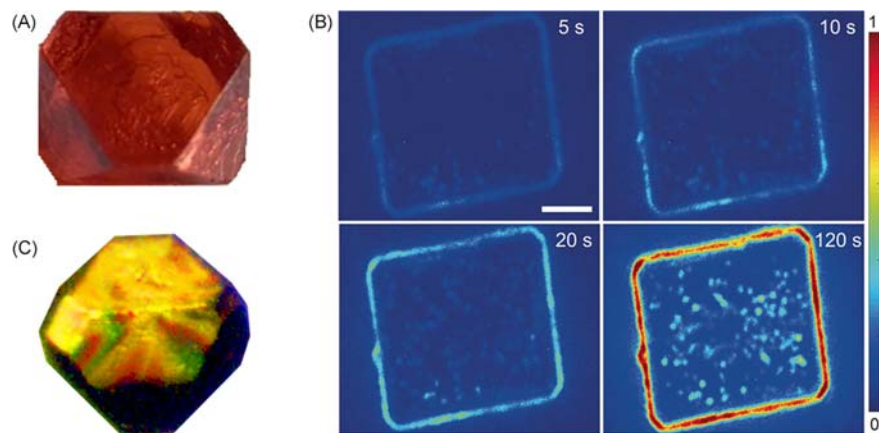


Fig. 28 (A) Photograph of a single crystal of the double perovskite $\text{Cs}_2\text{AgBiBr}_6$ showing the octahedral crystal habit resulting from the cubic crystal symmetry. Adapted with permission from Slavney, A. H.; Hu, T.; Lindenberg, A. M.; Karunadasa, H. I., A Bismuth-Halide Double Perovskite with Long Carrier Recombination Lifetime for Photovoltaic Applications. *J. Am. Chem. Soc.* **2016**, *138* (7), 2138–2141. Copyright 2016 American Chemical Society. (B) Photograph of a single crystal of the gold-cage perovskite $\text{Cs}_8\text{Au}_4\text{InCl}_{23}$ taken using a polarized microscope. The presence of multiple colors indicates that the crystal symmetry is not cubic. Adapted with permission from Lindquist, K. P.; Boles, M. A.; Mack, S. A.; Neaton, J. B.; Karunadasa, H. I., Gold-Cage Perovskites: A Three-Dimensional $\text{Au}^{\text{III}}\text{-X}$ Framework Encasing Isolated MX_6^{3-} Octahedra ($\text{M}^{\text{III}} = \text{In, Sb, Bi}$; $\text{X} = \text{Cl}^-, \text{Br}^-, \text{I}^-$). *J. Am. Chem. Soc.* **2021**, *143* (19), 7440–7448. Copyright 2021 American Chemical Society. (C) Widefield photoluminescence microscopy images collected over 120 s in the I-rich emission region (660–700 nm) of a crystal of $(\text{CH}_3\text{NH}_3)\text{Pb}(\text{Br}_{1-x}\text{I}_x)_3$, showing the I-rich domains at the edges of the crystal. Continuous blue light irradiation ($400\text{--}450\text{ nm}$, 5 mWcm^{-2}) was used as the excitation source. Scale bar: $5\ \mu\text{m}$. Adapted with permission from Mao, W.; Hall, C. R.; Chesman, A. S. R.; Forsyth, C.; Cheng, Y.-B.; Duffy, N. W.; Smith, T. A.; Bach, U., Visualizing Phase Segregation in Mixed-Halide Perovskite Single Crystals. *Angew. Chem. Int. Ed.* **2019**, *58* (9), 2893–2898. Copyright 2019 John Wiley and Sons Publishing.

$$d = \frac{\lambda}{2\text{NA}} \quad (20)$$

where d is the minimum resolvable distance and NA is the numerical aperture, which can reach ~ 1.5 with modern optics. However, advanced microscopy techniques, such as interferometry, can be used to obtain information beyond the theoretical limit of the wavelength of light employed. This has been exploited with the recently developed stroboSCAT method to visualize charge, exciton, and heat transport in $(\text{CH}_3\text{NH}_3)\text{PbBr}_3$ and double perovskites.^{372,373}

4.15.6.7.2 Electron microscopy

The use of electrons as an imaging probe offers greatly enhanced resolving power relative to conventional optical microscopy. Two common types of electron microscopy, scanning electron microscopy (SEM) and scanning transmission electron microscopy (STEM), operate by rastering a focused high-energy beam of electrons across the sample. Conventional TEM instead uses a less focused beam to illuminate the entire imaging area at once, like conventional optical microscopy. In TEM, the magnitude of electron transmission through the sample is measured; in SEM, what is usually detected are secondary electrons, which result from the inelastic interactions of the electron beam with the electrons of the sample within a limited depth. Both SEM and TEM give contrast images that are sensitive to factors such as atomic mass. However, TEM requires very thin samples ($< 200\text{ nm}$) and typically employs higher electron energies and currents than SEM, making sample damage more likely to occur. For these reasons, TEM has seen less widespread use than SEM for the relatively beam-sensitive perovskites, though methods have been developed to image with a reduced electron dose: researchers have successfully achieved atomic resolution measuring $(\text{NH}_2\text{CHNH}_2)\text{PbI}_3$ thin films with TEM.³⁷⁴ Cryoelectron microscopy has recently been applied to organoammonium perovskites, showing advantages versus conventional TEM in sample stability and establishing protocols for critical electron dose (rate).³⁷⁵

Because device performance is often related to grain size, film thickness, coverage, conformality, and composition, SEM is routinely used to characterize the morphology of perovskite thin-film samples at the nano- and microscale. Such measurements can be carried out in a normal geometry, thus imaging the plane of the thin film (Fig. 29A and B), or on a cross-section of a thin film or device stack, thus imaging perpendicular to the plane of the film (Fig. 29C).³⁷⁶ Such cross-sectional analysis is indispensable for characterizing devices, yielding information about the morphology of each layer in the device stack.³⁷⁷

Many advanced TEM- and SEM-based techniques are in use, one of which is energy-dispersive X-ray spectroscopy (EDS or EDX). This technique examines the X-ray emission from the sample following a process wherein a high-energy primary electron ejects a core electron in the sample. The X-ray emission energies are unique to each element and the integrated intensity of each feature can be examined to provide a quantitative elemental analysis of the sample area under electron bombardment, albeit with modest precision ($\sim 0.1\text{ wt\%}$ under ideal conditions) compared to bulk elemental analysis techniques such as ICP-MS. EDS therefore provides a high-resolution composition map that can be used to effectively determine the spatial distribution of elements within a sample. This technique has been used to study ion migration through grain boundaries in thin films of $(\text{CH}_3\text{NH}_3)\text{PbI}_3$,³⁷⁸ to determine the destination of additives used for improved perovskite photovoltaic device performance,³⁷⁹ and to investigate the

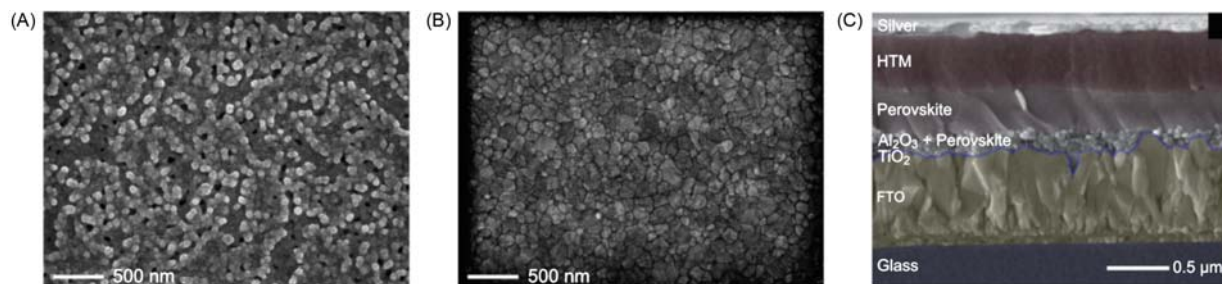


Fig. 29 SEM images of thin films of: (A) $\text{Cs}_2\text{AgBiBr}_6$; (B) Sn-alloyed $\text{Cs}_2\text{AgBiBr}_6$. Adapted from Lindquist, K. P.; Mack, S. A.; Slavney, A. H.; Leppert, L.; Gold-Parker, A.; Stebbins, J. F.; Salleo, A.; Toney, M. F.; Neaton, J. B.; Karunadasa, H. I., Tuning the Bandgap of $\text{Cs}_2\text{AgBiBr}_6$ Through Dilute Tin Alloying. *Chem. Sci.* **2019**, *10* (45), 10620–10628 - Published by The Royal Society of Chemistry. (C) A color-enhanced and annotated SEM cross-sectional image of a perovskite-based solar cell. Adapted with permission from Ball, J. M.; Lee, M. M.; Hey, A.; Snaith, H. J. Low-Temperature Processed Meso-Superstructured to Thin-Film Perovskite Solar Cells. *Energy Environ. Sci.* **2013**, *6*, 1739–1746. Copyright 2013 Royal Society of Chemistry Publishing.

spatial homogeneity of alloyed species such as Sn in Sn-alloyed $\text{Cs}_2\text{AgBiBr}_6$.¹¹⁶ Another advanced technique measures the electron backscatter diffraction (EBSD) to yield information about crystallographic phase and orientation. This has been applied to perovskites to differentiate morphological feature size observed with standard SEM from crystallographic grain size and reveal otherwise hidden local strain from the crystallographic misorientation of individual crystallites within a single morphological grain.^{380,381} For further reading, the following reference³⁸² focuses on the electron microscopy of polymers but offers a detailed discussion of the principles of electron microscopy.

4.15.6.8 Electronic and ionic conductivity

Because most optoelectronic devices require transport of charge across the active semiconducting layer, the electronic and ionic conductivity are crucial metrics to assess for a perovskite with potential device applications. Such measurements can indicate the degree of mixed ionic-electronic conductivity and the mechanisms of charge transport occurring in the perovskite; the transport mechanisms provide insight into chemical properties, such as atomic structure and composition, as well as point-defect reactions (see Section 4.15.7.3). Simple resistance measurements can be carried out using an ohmmeter, while more rigorous analysis typically employs a potentiostat or frequency response analyzer. Frequency response analysis, specifically electrochemical impedance spectroscopy (EIS), has been useful in analyzing mixed ionic-electronic conductors by applying an alternating current (AC) or AC potential differences at a range of frequencies. Equivalent circuits of varying complexity have been proposed to model the frequency-dependent response of mixed ionic-electronic conductors in EIS measurements,^{383–385} which has been discussed previously in the context of perovskites.³⁸⁶ An interpretation of the low- and high-frequency regions can also be made from the respective limits of the measurement (e.g., on a Nyquist or Bode plot). High-frequency processes are attributed to the bulk dielectric response, including relaxation contributions from the electron density, phonon modes, and dipolar reorientation; slower processes, such as free-charge redistribution and chemical diffusion, are encompassed in the low-frequency regime.³⁸⁷ Classical direct current (DC) measurements provide complementary information to AC measurements; for example, using cell designs and geometries such as DC reaction cells can allow identification of the dominant mobile defects.³⁸⁸ Further information is yielded by measuring resistance at various temperatures: resistivity increases with temperature for metals and decreases with temperature for semiconductors. The activation energy of conductance in a semiconductor can also be determined from the Arrhenius relationship. Furthermore, the temperature dependence of ionic conductivity may provide information on the energy of defects (relative to band extrema) and the thermodynamics of point-defect reactions.

Sample measurement cells, often home-built, may include temperature and atmospheric control and can be constructed to accommodate various sample morphologies, including single crystals and pressed pellets from polycrystalline solids. Samples should be uniform in thickness and free from large pinholes and other macroscopic defects. While single crystals are often preferable to avoid the contribution of grain boundaries to the measured resistance in polycrystalline samples, single crystals of appropriate geometry may not be accessible for all perovskites. Additionally, crystal orientation may affect the measured resistance in single crystals, though the effect may also be present in pressed pellets that have preferentially oriented grains. A further consideration for a measurement setup is the probe geometry: most commonly, either two points or four points of contact are made to a sample (Fig. 30).³⁸⁹ Two-point measurements can yield accurate results for more insulating materials and ideal sample geometries that are isotropic with high aspect ratios. If the sample conductivity approaches that of the leads and contacts, four-point contact is necessary to reduce error in the measurement. Multiple four-point contact geometries are used, including the van der Pauw method that is particularly useful for samples of small, defined thickness with arbitrary shape (thin plate).

The choice of material for making contact between the sample and electrical leads is especially important for perovskites: many commonly used metals, such as Cu^0 and Ag^0 , will react with halides to form electronically insulating layers of the corresponding metal halide. Non-reactive contact materials, such as graphitic carbon, are best used to measure electronic conductivities. To

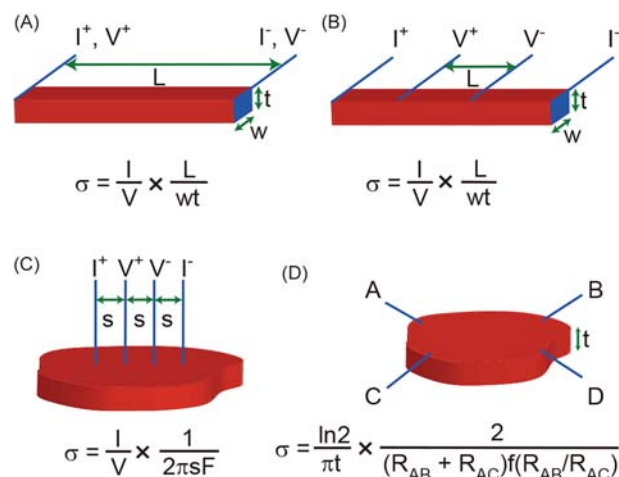


Fig. 30 Schematic representations, and the relationship between conductivity and measurable quantities, of common contact configurations for the conductivity measurement of a solid sample: (A) two-contact probe method; (B) four-contact probe method; (C) four-point probe method; (D) van der Pauw method, where σ is conductivity, R is resistance, I is current, V is voltage, L is length, t is thickness, w is width, s is distance, and F and f are correction factors. Adapted with permission from Sun, L.; Park, S. S.; Sheberla, D.; Dincă, M., Measuring and Reporting Electrical Conductivity in Metal-Organic Frameworks: $\text{Cd}_2(\text{TFTB})$ as a Case Study. *J. Am. Chem. Soc.* **2016**, *138* (44), 14772–14782. Copyright 2016 American Chemical Society.

measure ionic conductivity, an electronically insulating material that can accept or donate ions to the perovskite is used. For perovskites, AgX (X = halide of the perovskite composition) is often used in halide conductivity measurements: an AgX layer is placed between the perovskite and a Ag^0 layer, facilitating halide ion conductivity.²¹⁸ Ionic conductivity measurements are discussed in more detail below, including characterization of mixed ionic-electronic conduction and its implications towards hysteresis and space-charge polarization in devices (see Section 4.15.7.3).

Further information about charge-carrier characteristics in perovskites can be obtained from complementary techniques, including time-resolved microwave conductivity (TRMC) and the Hall effect. Measurement of the Hall effect, wherein a magnetic field applied perpendicular to a constantly flowing current produces a Hall voltage across the sample, yields the majority bulk charge-carrier density (concentration). From the measurement of electronic conductivity and charge-carrier concentration, the charge-carrier mobility can be calculated according to the relationship:

$$\sigma = ne\mu \quad (21)$$

where σ is the conductivity, n is the charge-carrier concentration, e is the elementary charge, and μ is the charge-carrier mobility. Another technique, photoconductivity, examines the effect of photoexcitation on electronic conductivity, an important parameter for a photovoltaic device that is necessarily under illumination during its operation. TRMC is a useful contactless technique that probes charge-carrier mobility, dynamics, and recombination upon photoexcitation by measuring the change in microwave reflectivity resulting from carrier dynamics. TRMC, Hall effect, and photoconductivity measurements have all been used to characterize the charge-transport properties of perovskites.^{31,36,390,391}

4.15.7 Some peculiar properties

4.15.7.1 Perovskites under high pressure

The behavior of materials can drastically change when subjected to pressures on the scale of gigapascals (GPa; 1 GPa \approx 10⁴ atm). Researchers routinely reach pressures of 10s and even 100 s of GPa, comparable to the pressures of the interior of the Earth, using diamond anvil cells (DACs), wherein two diamonds with microscopic culets are driven together with screws to compress a sample (Fig. 31).^{392–394} Diamonds provide high mechanical strength and reasonable transparency to X-rays and broadband optical light, allowing for a variety of characterization techniques, including X-ray diffraction and absorption spectroscopy, optical absorption and photoluminescence, vibrational spectroscopies such as Raman and infrared, and electronic conductivity and magnetoelectrical measurements.^{395,396} However, the low angular opening of DACs complicates certain types of X-ray studies, such as single-crystal diffraction. In addition, diffraction and scattering studies using neutrons cannot use DACs due to the small sample volume and must instead use alternative high-pressure cells that can accommodate larger sample volumes. To obtain diffraction data with a sufficient range in q (see Section 4.15.6.3.6) and penetration of the diamond, high-energy, high-flux X-ray beams are desired, thus typically requiring a synchrotron source. Pressures inside the DAC sample chamber are typically measured via one of two methods: by the X-ray diffraction of a standard calibrant, such as platinum or gold, or by the fluorescence energy of a microscopic ruby sphere.

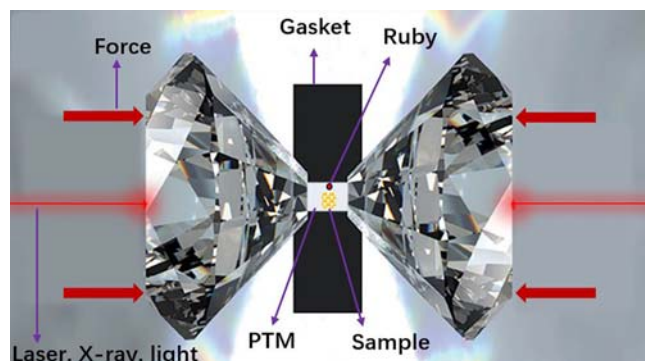


Fig. 31 Schematic representation of a diamond anvil cell. PTM = pressure transfer medium. Adapted from Li, M.; Liu, T.; Wang, Y.; Yang, W.; Lü, X., Pressure Responses of Halide Perovskites With Various Compositions, Dimensionalities, and Morphologies. *Matter Radiat. Extremes* **2020**, 5 (1), 018201 - Published by AIP publishing.

Though uniaxial force is supplied by compression of the diamonds relative to one another, a fluid pressure medium such as mineral oil or helium gas can be used to generate a hydrostatic or near-hydrostatic environment around the sample.

Perovskites are particularly amenable to high-pressure study because they are crystalline solids with soft lattices, meaning they exhibit strong structural responses to pressure that can be easily studied by X-ray diffraction. One of the most common and accessible measurements using DACs is powder X-ray diffraction, which has been used to study crystallographic phase changes in perovskites at high pressures.³⁹⁷ Commonly, perovskite lattice compression occurs with a mixture of bond compression and octahedral tilting, both of which impact electronic orbital overlap and band dispersion. In the case of $(\text{CH}_3\text{NH}_3)\text{PbI}_3$, single-crystal X-ray diffraction at high pressure has offered insight into the octahedral tilting and bond compression parameters, which have been correlated to changes in the photoluminescence.³⁹⁸ Further, infrared reflectivity and temperature-dependent electronic conductivity measurements have been used to demonstrate the metallization of $(\text{CH}_3\text{NH}_3)\text{PbI}_3$ above 60 GPa.³⁹⁹ Similarly, high pressure has been shown to reduce the octahedral distortion of the Au sites in the $\text{Cs}_2\text{Au}^{\text{I}}\text{Au}^{\text{III}}\text{I}_6$ double perovskite, eventually resulting in the comproportionation of Au^{3+} and Au^+ to Au^{2+} , as supported by powder X-ray diffraction,⁴⁰⁰ electronic conductivity,⁴⁰¹ and Mössbauer spectroscopy.⁴⁰² In some cases, the changes engendered by high pressure are retained and form a metastable structure after the release of pressure, as is the case with the comproportionated $\text{Cs}_2\text{Au}^{\text{I}}\text{Au}^{\text{II}}\text{I}_6$ perovskite.⁴⁰¹

4.15.7.2 Hole doping and metallic transport in Sn^{2+} -based perovskites

In contrast to Pb, the stability of the 2+ and 4+ oxidation states of Sn impart unique properties on Sn-based perovskites. Perovskites based on Sn^{2+} differ from those based on Pb^{2+} in several notable ways: they are significantly less toxic, they are typically more sensitive to atmospheric oxidation, their bandgaps are often lower than their Pb^{2+} -based analogs (see Section 4.15.4),¹¹² and they often exhibit metallic conductivity.^{36,198,403,404} The metallic *p*-type conductivity observed in several Sn^{2+} -based perovskites was revealed to be a result of spontaneous hole doping as a result of the facile oxidation of Sn^{2+} to Sn^{4+} . Indeed, intentional synthetic doping of Sn^{4+} increases the conductivity further.^{36,403,404} Electronic conductivity measurements, Hall effect measurements of the charge-carrier concentrations, infrared reflectivity measurements that show a plasma edge, thermopower measurements, and band-structure calculations were all used to confirm the origin of the metallic conductivity.^{36,198,403,404} While increasing the electronic conductivity, this spontaneous “self-doping” simultaneously serves to form carrier-recombination trap states that severely limit the efficiencies of Sn^{2+} -based perovskites in photovoltaic devices.⁴⁰⁵ To combat the self-doping, researchers have included additives such as Sn^0 and SnF_2 in syntheses of thin films.^{406,407} Photovoltaic devices with $((\text{NH}_2\text{CHNH}_2)_x((\text{NH}_2)_3\text{C})_{1-x})\text{SnI}_3$ absorbers created using such synthesis techniques and containing a small amount of $\text{INH}_3\text{CH}_2\text{CH}_2\text{NH}_3\text{I}$ additive have reached efficiencies of 9.6%.⁴⁰⁸

4.15.7.3 Halide conductivity and halogen loss

The degree of mixed ionic-electronic conductivity in semiconductors (measurements discussed in Section 4.15.6.8) has important implications for device performance, including but not limited to hysteresis in forward and reverse current-voltage scans, dielectric response, and the formation of space-charge regions.^{386,409,410} A significant contribution of ionic conductivity to the total conductivity of perovskites was established in the 1980s for CsPbX_3 ($X = \text{Cl}^-$, Br^-) and KMnCl_3 ;²¹⁸ halide conductivity was subsequently observed in methylammonium-based perovskites, particularly the high-temperature cubic phases of $(\text{CH}_3\text{NH}_3)\text{BCl}_3$ ($B = \text{Ge}^{2+}$, Sn^{2+})^{411,412} and $(\text{CH}_3\text{NH}_3)\text{PbX}_3$ ($X = \text{Cl}^-$, Br^-).⁴¹³ Low activation energies of conduction were reported and halogen vacancy point defects were proposed as the majority mobile defect in these perovskites based on the interfacial reactions in a reaction cell under bias.²¹⁸ Furthermore, the defect chemistry of thin films and pellets of $(\text{CH}_3\text{NH}_3)\text{PbI}_3$ has been recently investigated, thoroughly demonstrating the dominance of I^- vacancies as mobile charge carriers and the predominant defects in these

perovskites.^{386,409,410} Measurement of the dependency of conductivity on halogen partial pressure (e.g., $p(I_2)$) and electron-acceptor doping, in addition to complementary measurements including tracer diffusion and solid-state NMR,⁴¹⁴ have been instrumental in determining the relative contributions to ionic conductivity from the A-, B-, and X-site ions. Theoretical works have similarly predicted favorable energetics for the formation and migration of halogen defects, including both vacancies and interstitials;⁴¹⁵ the activation energy of halogen vacancy formation and migration is markedly lower than in the oxide perovskite congeners.^{254,416} Detailed investigations of the role of ionic conductivity in single crystals and at the interfaces of thin films are expected to further the understanding of defect chemistry, mechanisms, and the behavior of perovskite-based devices.^{386,409,415,417}

Perovskite defect chemistry, in addition to its contribution to ionic conductivity, plays a role in the bulk composition and charge-carrier concentration. A ubiquitous defect reaction in ceramics, including the oxide perovskite congeners, is the oxygen exchange equilibrium between the pristine structure and molecular oxygen, oxygen vacancies, and electrons. The reaction has important implications in oxide non-stoichiometry and various applications of the oxide perovskites; furthermore, manipulating $p(O_2)$ at elevated temperatures has enabled investigation of the thermodynamics of defects and dopants in the oxides.³⁸⁸ The analogous halogen exchange equilibrium was recently observed for the first time in the double perovskite $Cs_2AgTlBr_6$ at room temperature (Fig. 32).¹⁸² For any halide, the reaction is generally expressed in Kröger-Vink notation as:



where X_x represents the halogen in a halide lattice site, V_x^{\bullet} a positively charged halogen vacancy, e' is a conduction-band electron, and X_2 is the molecular halogen. The conductivity of $Cs_2AgTlBr_6$ crystals increases over time under inert-gas flow at room temperature and up to $\sim 60^\circ C$, indicative of n -type doping upon the introduction of charge-compensating mobile electrons as Br leaves the lattice (Fig. 32B). Under these conditions, the production of molecular Br_2 from "off-gassing" the crystal was confirmed by an alkene bromination reaction and quantified using mass spectrometry (Fig. 32A). The decreasing conductivity after exposing the crystal to a Br_2 -rich atmosphere demonstrated the reversibility of Br_2 off-gassing. Room-temperature halogen off-gassing is a noteworthy discovery and the extent (and rate) of this reaction across perovskite compositions, as well as its effects on device stability and interfacial reactivity, are important considerations in the field moving forward.

4.15.7.4 Light-induced halide segregation

The bandgap values of the perovskites vary widely between like compositions with differing halides owing to the contribution of the halide p-orbital character to the valence-band maximum (see Section 4.15.4). For example, the optical bandgap measured for $(CH_3NH_3)PbX_3$ is 3.0 eV for $X = Cl^-$, 2.3 eV for $X = Br^-$, and 1.6 eV for $X = I^-$.¹⁷⁶ It was thus expected that mixed-halide compositions, forming solid solutions, would offer tunable bandgaps and varying open-circuit potentials (V_{OC}) in perovskite-based photovoltaic devices. In particular, intermediate bandgaps are desirable for technologies including multi-junction solar cells⁴¹⁸ and blue-green light emitting diodes.⁴¹⁹

Monotonically increasing optical bandgap values upon Br incorporation, from 1.6 eV to 2.3 eV, were indeed measured for thin films of $(CH_3NH_3)Pb(Br_xI_{1-x})_3$.¹²⁵ Solar cells based on $(CH_3NH_3)Pb(Br_xI_{1-x})_3$ in the absorber layer, however, repeatedly failed to exhibit the larger V_{OC} values expected from their bandgaps for compositions with $x > 0.2$.^{125,420} Reversible, light-induced

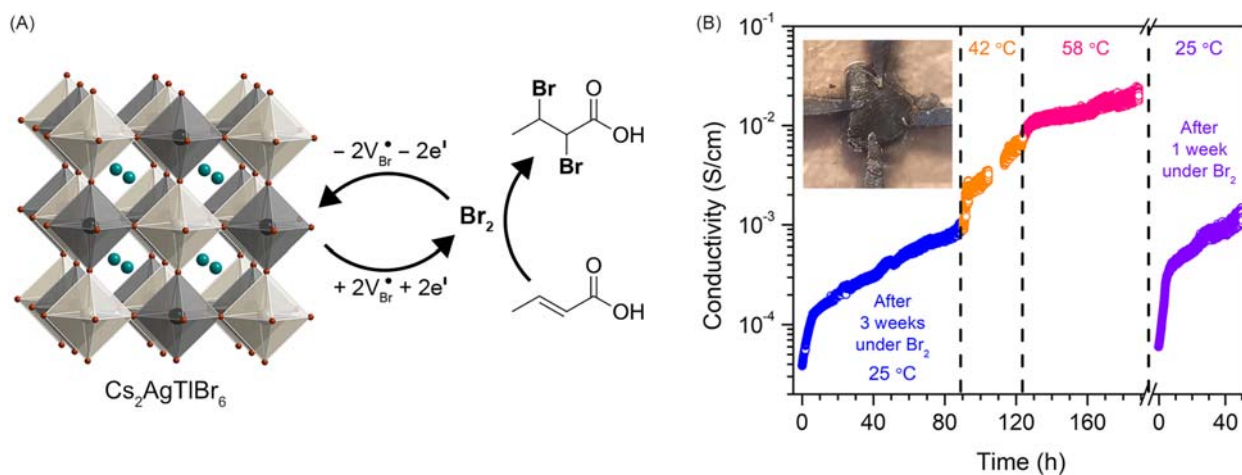


Fig. 32 (A) Schematic representation of Br_2 off-gassing from $Cs_2AgTlBr_6$ including the alkene bromination reaction and proposed point defect equilibrium, where V_{Br}^{\bullet} is a positively charged Br vacancy and e' is an electron. (B) Time evolution of the conductivity of a single crystal of $Cs_2AgTlBr_6$, measured in a four-point probe configuration with carbon contacts (inset), where time zero corresponds to the removal of the Br_2 atmosphere. Adapted with permission from Slavney, A. H.; Leppert, L.; Saldivar Valdes, A.; Bartesaghi, D.; Savenije, T. J.; Neaton, J. B.; Karunadasa, H. I., Small-Band-Gap Halide Double Perovskites. *Angew. Chem. Int. Ed.* **2018**, 57 (39), 12765–12770. Copyright 2018 John Wiley and Sons Publishing.

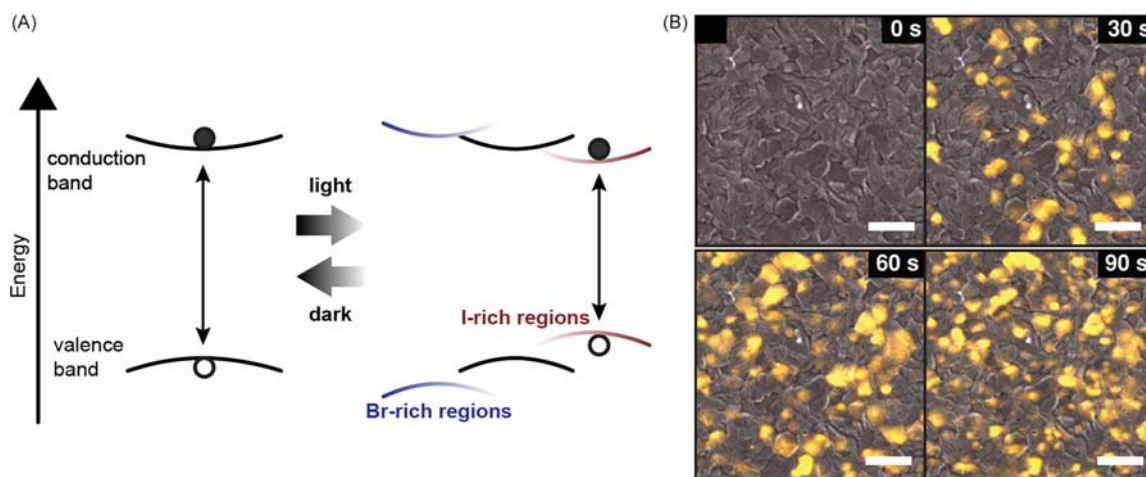


Fig. 33 (A) Schematic representation of reversible, light-induced halide segregation and the resulting low-energy photoluminescence from iodide-rich regions of a mixed bromide-iodide perovskite. Adapted from Hoke, E. T.; Slotcavage, D. J.; Dohner, E. R.; Bowring, A. R.; Karunadasa, H. I.; McGehee, M. D., Reversible Photo-Induced Trap Formation in Mixed-Halide Hybrid Perovskites for Photovoltaics. *Chem. Sci.* **2015**, *6* (1), 613–617 - Published by The Royal Society of Chemistry. (B) Cathodoluminescence imaging of a $(\text{CH}_3\text{NH}_3)\text{Pb}(\text{Br}_{0.9}\text{I}_{0.1})_3$ thin film, under 405-nm excitation, after successive 30-s time-soaking intervals, where iodide-rich domains appear bright in color; scale bar = 200 μm . Adapted with permission from Bischak, C. G.; Hetherington, C. L.; Wu, H.; Aloni, S.; Ogletree, D. F.; Limmer, D. T.; Ginsberg, N. S., Origin of Reversible Photoinduced Phase Separation in Hybrid Perovskites. *Nano Lett.* **2017**, *17* (2), 1028–1033. Copyright 2017 American Chemical Society.

transformations were subsequently discovered in thin films of $(\text{CH}_3\text{NH}_3)\text{Pb}(\text{Br}_x\text{I}_{1-x})_3$ ($x > 0.2$) from photoluminescence and X-ray diffraction measurements.¹²⁷ Light-soaking the pristine perovskite, a solid solution with mixed halides, led to a discretely redshifted photoluminescence peak at ca. 1.7 eV and splitting of Bragg peaks in powder X-ray diffraction patterns of thin films into two distinct peaks; both observations were indicative of the formation of two crystalline phases with distinct X-site compositions. The photogenerated electrons and holes were proposed to funnel into the lowest-bandgap iodide-rich domains, thereby lowering the photoluminescence emission energy and V_{OC} (Fig. 33A). This reversible phenomenon has since been widely corroborated in bromide-rich mixed bromide-iodide perovskites and is generally referred to as light-induced halide segregation. Luminescence measurements suggest light-induced segregation also occurs in mixed chloride-bromide perovskites, however a consensus has yet to be reached owing to the small number of studies and conflicting reports for similar compositions.^{419,421,422} Thus, we summarize the foundational work and recent advances only in the context of the mixed bromide-iodide perovskites.

Several models describing the origin of reversible, light-induced halide segregation have been proposed and are reviewed elsewhere in detail.^{423,424} Briefly, these include thermodynamic considerations of the bulk structural stability and halide segregation, polaron formation and polaron-induced strain, and charge-carrier trapping and induced fields from internal charge gradients. Despite a lack of consensus on the origin or mechanistic details, progress has been made towards monitoring halide segregation in situ, for example using cathodoluminescence imaging at the microscale (Fig. 33B), and preventing its detrimental effects on the V_{OC} of mixed-halide perovskite solar absorbers.⁴²¹ Forming more complex perovskite compositions, for example through A-site substitution or alloying, has proven successful in reducing halide segregation in absorber layers.⁴²³ The replacement of CH_3NH_3^+ at the A site, often with Cs^+ and/or $\text{NH}_2\text{CHNH}_2^+$, significantly slows halide segregation,⁴²³ and parallels have been drawn between the “chemical pressure” induced by A-site substitution and the effects of externally applied pressure (e.g., via a diamond anvil cell, see Section 4.15.7.1).^{398,424} Microstructure manipulation and surface passivation have also demonstrated influence on the kinetics of halide segregation, supporting models that include considerations of surface defects and interfacial effects.⁴²³ Reversible, light-induced halide segregation has proven to be an extraordinary and thought-provoking phenomenon and the various theoretical models and nano- and microscale tools developed to understand it serve to further our understanding of heterogeneities in the perovskites.

Acknowledgements

This work was supported by the Department of Energy, Office of Basic Energy Sciences, Division of Materials Sciences and Engineering, under contract DE-AC02-76SF00515 (J.A.V., A.C.S., H.I.K.) and the National Science Foundation, Division of Materials Research, under contract DMR-1904443 (K.P.L.). K.P.L. thanks the Center for Molecular Analysis and Design at Stanford University for a graduate fellowship and the Stanford Department of Chemistry for the William S. Johnson award. J.A.V. acknowledges fellowship support from the Stanford University Office of the Vice Provost of Graduate Education and the National Science Foundation Graduate Research Fellowship Program under Grant No. DGE-1656518. A.C.S. acknowledges support from a Stanford Graduate Fellowship. We gratefully acknowledge Dr. Linn Leppert for editorial assistance with Section 4.15.4 (Electronic structure), Dr. Maarten Goesten for assistance with Fig. 8, and Dr. Nathan R. Wolf for editorial assistance with Section 4.15.7.1 (Perovskites under high pressure).

References

- Slavney, A. H.; Smaha, R. W.; Smith, I. C.; Jaffe, A.; Uneyama, D.; Karunadasa, H. I. Chemical Approaches to Addressing the Instability and Toxicity of Lead-Halide Perovskite Absorbers. *Inorg. Chem.* **2017**, *56* (1), 46–55.
- Smith, M. D.; Crace, E. J.; Jaffe, A.; Karunadasa, H. I. The Diversity of Layered Halide Perovskites. *Annu. Rev. Mat. Res.* **2018**, *48* (1), 111–136.
- Bowman, H. L. On the Structure of Perovskite from the Burgumer Alp, Pflschthal, Tyrol. *Mineral. Mag. J. Mineral. Soc.* **1908**, *15* (69), 156–176.
- Wells, H. L. Über die Cäsium- und Kalium-Bleihalogenide. *Z. Anorg. Allg. Chem.* **1893**, *3* (1), 195–210.
- Cross, C. W.; Hillebrand, W. F. On Minerals of the Cryolite Group Recently Found in Colorado. *Am. J. Sci.* **1883**, *26* (154), 271–294.
- Kojima, A.; Teshima, K.; Shirai, Y.; Miyasaka, T. Organometal Halide Perovskites as Visible-Light Sensitizers for Photovoltaic Cells. *J. Am. Chem. Soc.* **2009**, *131* (17), 6050–6051.
- Green, M. A.; Ho-Baillie, A.; Snaith, H. J. The Emergence of Perovskite Solar Cells. *Nat. Photonics* **2014**, *8*, 506–514.
- Snaith, H. J. Present Status and Future Prospects of Perovskite Photovoltaics. *Nat. Mater.* **2018**, *17* (5), 372–376.
- Sutherland, B. R.; Sargent, E. H. Perovskite Photonic Sources. *Nat. Photonics* **2016**, *10* (5), 295–302.
- Wei, H.; Huang, J. Halide Lead Perovskites for Ionizing Radiation Detection. *Nat. Commun.* **2019**, *10* (1), 1066.
- Hwang, B.; Lee, J.-S. Recent Advances in Memory Devices with Hybrid Materials. *Adv. Electron. Mater.* **2019**, *5* (1), 1800519.
- Kazim, S.; Nazeeruddin, M. K.; Grätzel, M.; Ahmad, S. Perovskite as Light Harvester: A Game Changer in Photovoltaics. *Angew. Chem. Int. Ed.* **2014**, *53* (11), 2812–2824.
- Jena, A. K.; Kulkarni, A.; Miyasaka, T. Halide Perovskite Photovoltaics: Background, Status, and Future Prospects. *Chem. Rev.* **2019**, *119* (5), 3036–3103.
- Yang, W. S.; Noh, J. H.; Jeon, N. J.; Kim, Y. C.; Ryu, S.; Seo, J.; Seok, S. I. High-Performance Photovoltaic Perovskite Layers Fabricated through Intramolecular Exchange. *Science* **2015**, *348* (6240), 1234–1237.
- NREL Best-Research-Cell Efficiency Chart (n.d.) This plot is courtesy of the National Renewable Energy Laboratory, Golden, CO; <https://www.nrel.gov/pv/cell-efficiency.html>.
- Li, W.; Wang, Z.; Deschler, F.; Gao, S.; Friend, R. H.; Cheetham, A. K. Chemically Diverse and Multifunctional Hybrid Organic–Inorganic Perovskites. *Nat. Rev. Mater.* **2017**, *2* (3), 16099.
- Mitzi, D. B. Synthesis, structure, and properties of organic-inorganic perovskites and related materials. In *Progress in Inorganic Chemistry*, Wiley, 1999; pp 1–121.
- Saparov, B.; Mitzi, D. B. Organic–Inorganic Perovskites: Structural Versatility for Functional Materials Design. *Chem. Rev.* **2016**, *116* (7), 4558–4596.
- Akkerman, Q. A.; Rainò, G.; Kovalenko, M. V.; Manna, L. Genesis, Challenges and Opportunities for Colloidal Lead Halide Perovskite Nanocrystals. *Nat. Mater.* **2018**, *17* (5), 394–405.
- Huang, H.; Polavarapu, L.; Sichert, J. A.; Susa, A. S.; Urban, A. S.; Rogach, A. L. Colloidal Lead Halide Perovskite Nanocrystals: Synthesis, Optical Properties and Applications. *NPG Asia Mater.* **2016**, *8* (11), e328.
- Chakhmouradian, A. R.; Woodward, P. M. Celebrating 175 Years of Perovskite Research: A Tribute to Roger H. Mitchell. *Phys. Chem. Miner.* **2014**, *41* (6), 387–391.
- Barth, T. F. W. Die Kristallstruktur von Perowskit und verwandten Verbindungen. *Norsk Geol. Tidsskr.* **1925**, *8* (3), 201–216.
- Goldschmidt, V. M. Die Gesetze der Kristallochemie. *Naturwissenschaften* **1926**, *14* (21), 477–485.
- Megaw, H. D. Crystal Structure of Barium Titanate. *Nature* **1945**, *155* (3938), 484–485.
- Tilley, R. J. D. *Perovskites: Structure-Property Relationships*, John Wiley & Sons, Ltd, 2016.
- Natta, G.; Passerini, L. Isomorfismo, polimorfismo e morfotopia-I. Composti del tipo ABX₃. *Gazz. Chim. Ital.* **1928**, *58*, 472–484.
- van Arkel, A. E. Kristalstructuur van Magnesiumfluoride en Andere Verbindingen van Hetzelfde Kristalltype. *Physica* **1925**, *5*, 162–171.
- Elliott, N.; Pauling, L. The Crystal Structure of Cesium Aurous Auric Chloride, Cs₂AuAuCl₆, and Cesium Argentous Auric Chloride, Cs₂AgAuCl₆. *J. Am. Chem. Soc.* **1938**, *60* (8), 1846–1851.
- Wolf, N. R.; Connor, B. A.; Slavney, A. H.; Karunadasa, H. I. Doubling the Stakes: The Promise of Halide Double Perovskites. *Angew. Chem. Int. Ed.* **2021**, *60* (30), 16264–16278.
- Møller, C. K. A Phase Transition in Cæsium Plumbobichloride. *Nature* **1957**, *180* (4593), 981–982.
- Møller, C. K. Crystal Structure and Photoconductivity of Cæsium Plumbobichlorides. *Nature* **1958**, *182* (4647), 1436.
- Weber, D. CH₃NH₃PbX₃, ein Pb(II)-System mit kubischer Perowskitstruktur. *Z. Naturforsch. B* **1978**, *33* (12), 1443–1445.
- Clark, S. J.; Donaldson, J. D.; Harvey, J. A. Evidence for the Direct Population of Solid-State Bands by Non-bonding Electron Pairs in Compounds of the Type CsM^{II}X₃ (M^{II} = Ge, Sn, Pb; X = Cl, Br, I). *J. Mater. Chem.* **1995**, *5* (11), 1813–1818.
- Donaldson, J. D.; Laughlin, D.; Ross, S. D.; Silver, J. Phases Obtained from the Frozen Molten Systems Caesium–Tin–Halide and Caesium–Lead–Halide. *J. Chem. Soc., Dalton Trans.* **1973**, *19*, 1985–1988.
- Barrett, J.; Donaldson, J. D.; Silver, J.; Siew, N. P. Y. Mössbauer and Electronic-Reflectance Spectroscopic Studies and Resistivity Measurements on the Systems CsPb_{1–x}Sn_xBr₃, CsPb_{1–x}Sn_xBr₂Cl, M₁Cs_{1–x}SnBr₃, and M₂Cs_{1–x}SnBr₂Cl (M = Na, K, Rb, and NH₄). *J. Chem. Soc., Dalton Trans.* **1977**, *9*, 906–908.
- Mitzi, D. B.; Feild, C. A.; Schlesinger, Z.; Laibowitz, R. B. Transport, Optical, and Magnetic Properties of the Conducting Halide Perovskite CH₃NH₃SnI₃. *J. Solid State Chem.* **1995**, *114* (1), 159–163.
- Kim, H.-S.; Lee, C.-R.; Im, J.-H.; Lee, K.-B.; Moehl, T.; Marchioro, A.; Moon, S.-J.; Humphry-Baker, R.; Yum, J.-H.; Moser, J. E.; Grätzel, M.; Park, N.-G. Lead Iodide Perovskite Sensitized All-Solid-State Submicron Thin Film Mesoscopic Solar Cell with Efficiency Exceeding 9%. *Sci. Rep.* **2012**, *2* (1), 591.
- Lee, M. M.; Teuscher, J.; Miyasaka, T.; Murakami, T. N.; Snaith, H. J. Efficient Hybrid Solar Cells Based on Meso-Superstructured Organometal Halide Perovskites. *Science* **2012**, *338* (6107), 643–647.
- Roy, P.; Kumar Sinha, N.; Tiwari, S.; Khare, A. A Review on Perovskite Solar Cells: Evolution of Architecture, Fabrication Techniques, Commercialization Issues and Status. *Sol. Energy* **2020**, *198*, 665–688.
- Babayigit, A.; Ethirajan, A.; Muller, M.; Conings, B. Toxicity of Organometal Halide Perovskite Solar Cells. *Nat. Mater.* **2016**, *15*, 247–251.
- Frondel, C. New Data on Elpasolite and Hagemannite. *Am. Mineral.* **1948**, *33* (1–2), 84–87.
- Náray-Szabó, I.; Sigmond, G. A kryolith-káliumkryolith-rendszer olvadási görbéje. *Mat. Termesztud. Ert.* **1941**, *60* (2), 364–372.
- Náray-Szabó, S. V.; Sasvári, K. Die Struktur des Kryoliths Na₂AlF₆. *Z. Kristallogr.* **1938**, *99* (1), 27–31.
- Scaife, D. E.; Weller, P. F.; Fisher, W. G. Crystal Preparation and Properties of Cesium Tin(II) Trihalides. *J. Solid State Chem.* **1974**, *9* (3), 308–314.
- Glazer, A. M. The Classification of Tilted Octahedra in Perovskites. *Acta Crystallogr., Sect. B* **1972**, *28* (11), 3384–3392.
- Poglitisch, A.; Weber, D. Dynamic Disorder in Methylammoniumtrihalogenoplumbates (II) Observed by Millimeter-Wave Spectroscopy. *J. Chem. Phys.* **1987**, *87* (11), 6373–6378.
- Pauling, L. The Principles Determining the Structure of Complex Ionic Crystals. *J. Am. Chem. Soc.* **1929**, *51* (4), 1010–1026.
- Filip, M. R.; Giustino, F. The Geometric Blueprint of Perovskites. *Proc. Natl. Acad. Sci. U. S. A.* **2018**, *115* (21), 5397–5402.
- Travis, W.; Glover, E. N. K.; Bronstein, H.; Scanlon, D. O.; Palgrave, R. G. On the Application of the Tolerance Factor to Inorganic and Hybrid Halide Perovskites: A Revised System. *Chem. Sci.* **2016**, *7* (7), 4548–4556.
- Bartel, C. J.; Sutton, C.; Goldsmith, B. R.; Ouyang, R.; Musgrave, C. B.; Ghiringhelli, L. M.; Scheffler, M. New Tolerance Factor to Predict the Stability of Perovskite Oxides and Halides. *Sci. Adv.* **2019**, *5* (2), eaav0693.
- Kieslich, G.; Sun, S.; Cheetham, A. K. Solid-State Principles Applied to Organic–Inorganic Perovskites: New Tricks for an Old Dog. *Chem. Sci.* **2014**, *5* (12), 4712–4715.

52. Depmeier, W.; Möller, A.; Klaska, K.-H. The Structure of Antiferroelectric Tetramethylammonium Trichlorogermanate(II) at Room Temperature. *Acta Crystallogr., Sect. B* **1980**, *36* (4), 803–807.
53. Albarski, O.; Hillebrecht, H.; Rotter, H. W.; Thiele, G. Über Caesiumtrichloromercurat(II) CsHgCl₃: Lösung einer komplexen Überstruktur und Verhalten unter hohen Drücken. *Z. Anorg. Allg. Chem.* **2000**, *626* (6), 1296–1304.
54. Wells, H. L. Über die Cäsium-Mercuri-Halogenide. *Z. Anorg. Allg. Chem.* **1892**, *2* (1), 402–419.
55. Vaills, Y.; Buzaré, J. Y.; Gibaud, A.; Launay, C. X-Ray Investigations of the Cubic to Tetragonal Phase Transition in CsCaCl₃ at $T_c = 95$ K. *Solid State Commun.* **1986**, *60* (2), 139–141.
56. Hohnstedt, C.; Meyer, G. Metallothermische Reduktion des Tribromids und -Iodids von Dysprosium Mit Alkalimetallen. *Z. Anorg. Allg. Chem.* **1993**, *619* (8), 1374–1378.
57. Meyer, G. Neue Chlor-Perovskite Mit Zweiwertigen Lanthaniden: CsLn^{II}Cl₃ (Ln^{II} = Sm, Eu, Tm, Yb). *Naturwissenschaften* **1978**, *65* (5), 258.
58. Schilling, G.; Meyer, G. Ternäre Bromide und Iodide zweiwertiger Lanthanide und ihre Erdalkali-Analoga vom Typ AMX₃ und AM₂X₅. *Z. Anorg. Allg. Chem.* **1996**, *622* (5), 759–765.
59. Horowitz, A.; Amit, M.; Makovsky, J.; Dor, L. B.; Kalman, Z. H. Structure Types and Phase Transformations in KMnCl₃ and TiMnCl₃. *J. Solid State Chem.* **1982**, *43* (2), 107–125.
60. Knox, K. Perovskite-like fluorides. I. Structures of KMnF₃, KFeF₃, KNiF₃ and KZnF₃. Crystal Field Effects in the Series and in KCrF₃ and KCuF₃. *Acta Crystallogr.* **1961**, *14* (6), 583–585.
61. Hidaka, M.; Hosogi, S. The Crystal Structure of KCdF₃. *J. Phys. Paris* **1982**, *43* (8), 1227–1232.
62. Alter, E.; Hoppe, R. Über Fluoropalladate(II): KPdF₃, RbPdF₃, TIPdF₃ Und K₂PdF₄. *Z. Anorg. Allg. Chem.* **1974**, *408* (2), 115–120.
63. Odenthal, R. H.; Hoppe, R. Fluorargentate(II) der Alkalimetalle. *Monatsh. Chem.* **1971**, *102* (5), 1340–1350.
64. Ludekens, W. L. W.; Welch, A. J. E. Reactions between Metal Oxides and fluorides: Some New Double-Fluoride Structures of Type ABF₃. *Acta Crystallogr.* **1952**, *5* (6), 841.
65. Ludekens, W. L. W. *Studies in Reactions between Metal Oxides and fluorides*, University of London: London, 1950.
66. Williamson, R. F.; Boo, W. O. J. Lower Valence Fluorides of Vanadium. 1. Synthesis and Characterization of NaVF₃, KVF₃, and RbVF₃. *Inorg. Chem.* **1977**, *16* (3), 646–648.
67. Knop, O.; Wasylishen, R. E.; White, M. A.; Cameron, T. S.; Van Oort, M. J. M. Alkylammonium Lead Halides. Part 2. CH₃NH₃PbX₃ (X=Cl, Br, I) Perovskites: Cuboctahedral Halide Cages with Isotropic Cation Reorientation. *Can. J. Chem.* **1990**, *68* (3), 412–422.
68. Marronnier, A.; Roma, G.; Boyer-Richard, S.; Pedesseau, L.; Jancu, J.-M.; Bonnassieux, Y.; Katan, C.; Stoumpos, C. C.; Kanatzidis, M. G.; Even, J. Anharmonicity and Disorder in the Black Phases of Cesium Lead Iodide Used for Stable Inorganic Perovskite Solar Cells. *ACS Nano* **2018**, *12* (4), 3477–3486.
69. Straus, D. B.; Guo, S.; Cava, R. J. Kinetically Stable Single Crystals of Perovskite-Phase CsPbI₃. *J. Am. Chem. Soc.* **2019**, *141* (29), 11435–11439.
70. Rahim, W.; Cheng, A.; Lyu, C.; Shi, T.; Wang, Z.; Scanlon, D. O.; Palgrave, R. G. Geometric Analysis and Formability of the Cubic A₂BX₆ Vacancy-Ordered Double Perovskite Structure. *Chem. Mater.* **2020**, *32* (22), 9573–9583.
71. Deng, Z.; Wei, F.; Sun, S.; Kieslich, G.; Cheetham, A. K.; Bristowe, P. D. Exploring the Properties of Lead-Free Hybrid Double Perovskites Using a Combined Computational-Experimental Approach. *J. Mater. Chem. A* **2016**, *4* (31), 12025–12029.
72. Wickleder, M. S.; Meyer, G. Ternäre Halogenide vom Typ A₃MX₆. III. Synthese, Strukturen und Ionenleitfähigkeit der Halogenide Na₃MX₆ (X = Cl, Br). *Z. Anorg. Allg. Chem.* **1995**, *621* (3), 457–463.
73. Meyer, G. The Synthesis and Structures of Complex Rare-Earth Halides. *Prog. Solid State Chem.* **1982**, *14* (3), 141–219.
74. Baud, G.; Baraduc, L.; Gaille, P.; Cousseins, J.-C. Nouvelle perovskites chlorées du type Cs₂KB^{III}Cl₆. *C. R. Seances Acad. Sci., Ser. C* **1971**, *272*, 1328–1331.
75. Morss, L. R.; Siegal, M.; Stenger, L.; Edelstein, N. Preparation of Cubic Chloro Complex Compounds of Trivalent Metals: Cs₂NaMCl₆. *Inorg. Chem.* **1970**, *9* (7), 1771–1775.
76. Karbowiak, M.; Drożdżyński, J. Synthesis and Characterization of Caesium Tetrachlorouranate(III) and Dicaesium lithium Hexachlorouranate(III). *J. Alloys Compd.* **1998**, *275–277*, 848–851.
77. Bill, J.; Lerch, K.; Laqua, W. Cs₂Ag^IAg^{III}Cl₆. Eine gemischtvalente Verbindung mit dreiwertigem Silber. *Z. Anorg. Allg. Chem.* **1990**, *589* (1), 7–11.
78. Knox, K.; Mitchell, D. W. The Preparation and Structure of K₂NaCrF₆, K₂NaFeF₆ and K₂NaGaF₆. *J. Inorg. Nucl. Chem.* **1961**, *21* (3), 253–258.
79. Henkel, H.; Hoppe, R. Zur Kenntnis Des Kryolith-Typs. Über Na₃NiF₆ Und Andere Kryolithe. *Z. Anorg. Allg. Chem.* **1969**, *364* (5–6), 253–262.
80. Babel, D.; Haegele, R.; Pausewang, G.; Wall, F. Ueber Kubische Und Hexagonale Elpasolithe A^I₂B^{III}M^{III}F₆. *Mater. Res. Bull.* **1973**, *8* (12), 1371–1382.
81. Morss, L. R. Crystal Structure of Dipotassium Sodium Fluoroaluminat (Elpasolite). *J. Inorg. Nucl. Chem.* **1974**, *36* (12), 3876–3878.
82. Schneider, S.; Hoppe, R. Über neue Verbindungen Cs₂NaMF₆ und K₂NaMF₆ sowie über Cs₂KMnF₆. *Z. Anorg. Allg. Chem.* **1970**, *376* (3), 268–276.
83. Hoppe, R.; Lehr, K. Neue Hexafluoromolybdate(III). Cs₂MMoF₆, Rb₂MMoF₆, Tl₂MMoF₆ (M = K, Na) Und Cs₂TiMoF₆. Mit Einer Notiz über MoF₃. *Z. Anorg. Allg. Chem.* **1975**, *416* (3), 240–250.
84. Tressaud, A.; Khairoun, S.; Dance, J. M.; Hagenmuller, P. Palladium Compounds with +III Oxidation State. *Z. Anorg. Allg. Chem.* **1984**, *517* (10), 43–58.
85. Wilhelm, V.; Hoppe, R. Zur Kenntnis der Hexafluororhodate(III): Über Cs₂K[RhF₆], Rb₂K[RhF₆], K₂Na[RhF₆], Rb₂Na[RhF₆] und Tl₂Na[RhF₆]. *Z. Anorg. Allg. Chem.* **1975**, *414* (1), 91–96.
86. King, G.; Woodward, P. M. Cation Ordering in Perovskites. *J. Mater. Chem.* **2010**, *20* (28), 5785–5796.
87. Schröder, L.; Keller, H.-L. Darstellung und Kristallstruktur von Cs₂HgPdCl₆, eine Verzerrungsvariante der Chlorperovskite. *Z. Anorg. Allg. Chem.* **1991**, *603* (1), 69–76.
88. Scherrer, P.; Stoll, P. Bestimmung der von Werner abgeleiteten Struktur anorganischer Verbindungen vermittelst Röntgenstrahlen. *Z. Anorg. Allg. Chem.* **1922**, *121* (1), 319–320.
89. Couch, D. A.; Wilkins, C. J.; Rossman, G. R.; Gray, H. B. Electronic Energy Levels in Hexahalotellurate(IV) Complexes. *J. Am. Chem. Soc.* **1970**, *92* (2), 307–310.
90. Brik, M. G.; Kityk, I. V. Modeling of Lattice Constant and their Relations with Ionic Radii and Electronegativity of Constituting Ions of A₂XY₆ Cubic Crystals (A=K, Cs, Rb, Tl; X=Tetravalent Cation, Y=F, Cl, Br, I). *J. Phys. Chem. Solid* **2011**, *72* (11), 1256–1260.
91. Lee, B.; Stoumpos, C. C.; Zhou, N.; Hao, F.; Malliakas, C.; Yeh, C.-Y.; Marks, T. J.; Kanatzidis, M. G.; Chang, R. P. H. Air-Stable Molecular Semiconducting Iodosalts for Solar Cell Applications: Cs₂SnI₆ as a Hole Conductor. *J. Am. Chem. Soc.* **2014**, *136* (43), 15379–15385.
92. Maughan, A. E.; Ganose, A. M.; Bordelon, M. M.; Miller, E. M.; Scanlon, D. O.; Neilson, J. R. Defect Tolerance to Intolerance in the Vacancy-Ordered Double Perovskite Semiconductors Cs₂SnI₆ and Cs₂TeI₆. *J. Am. Chem. Soc.* **2016**, *138* (27), 8453–8464.
93. Saparov, B.; Sun, J.-P.; Meng, W.; Xiao, Z.; Duan, H.-S.; Gunawan, O.; Shin, D.; Hill, I. G.; Yan, Y.; Mitzi, D. B. Thin-Film Deposition and Characterization of a Sn-Deficient Perovskite Derivative Cs₂SnI₆. *Chem. Mater.* **2016**, *28* (7), 2315–2322.
94. Fierov, I. N.; Gorev, M. V.; Aleksandrov, K. S.; Tressaud, A.; Grannec, J.; Couzi, M. Phase Transitions in Elpasolites (Ordered Perovskites). *Mater. Sci. Eng., R* **1998**, *24* (3), 81–151.
95. Brauer, G.; Sleater, G. Preparation of Mixed Valent Aurate Halides. *J. Less-Common Met.* **1970**, *21* (3), 283–291.
96. Wei, F.; Deng, Z.; Sun, S.; Xie, F.; Kieslich, G.; Evans, D. M.; Carpenter, M. A.; Bristowe, P. D.; Cheetham, A. K. The Synthesis, Structure and Electronic Properties of a Lead-Free Hybrid Inorganic–Organic Double Perovskite (MA)₂KBiCl₆ (MA = Methylammonium). *Mater. Horiz.* **2016**, *3* (4), 328–332.
97. Brown, I. D. The Crystal Structure of K₂TeBr₆. *Can. J. Chem.* **1964**, *42* (12), 2758–2767.
98. Maughan, A. E.; Ganose, A. M.; Almaker, M. A.; Scanlon, D. O.; Neilson, J. R. Tolerance Factor and Cooperative Tilting Effects in Vacancy-Ordered Double Perovskite Halides. *Chem. Mater.* **2018**, *30* (11), 3909–3919.
99. Vargas, B.; Ramos, E.; Pérez-Gutiérrez, E.; Alonso, J. C.; Solís-Ibarra, D. A Direct Bandgap Copper–Antimony Halide Perovskite. *J. Am. Chem. Soc.* **2017**, *139* (27), 9116–9119.
100. Vargas, B.; Torres-Cadena, R.; Rodríguez-Hernández, J.; Gembicky, M.; Xie, H.; Jiménez-Mier, J.; Liu, Y.-S.; Menéndez-Proupin, E.; Dunbar, K. R.; Lopez, N.; Olalde-Velasco, P.; Solís-Ibarra, D. Optical, Electronic and Magnetic Engineering of (111) Layered Halide Perovskites. *Chem. Mater.* **2018**, *30* (15), 5315–5321.

101. Lin, Y.-P.; Hu, S.; Xia, B.; Fan, K.-Q.; Gong, L.-K.; Kong, J.-T.; Huang, X.-Y.; Xiao, Z.; Du, K.-Z. Material Design and Optoelectronic Properties of Three-Dimensional Quadruple Perovskite Halides. *J. Phys. Chem. Lett.* **2019**, *10* (17), 5219–5225.
102. Holzapfel, N. P.; Majher, J. D.; Strom, T. A.; Moore, C. E.; Woodward, P. M. Cs₄Cd_{1-x}Mn_xBi₂Cl₁₂—A Vacancy-Ordered Halide Perovskite Phosphor with High-Efficiency Orange-Red Emission. *Chem. Mater.* **2020**, *32* (8), 3510–3516.
103. Lindquist, K. P.; Boles, M. A.; Mack, S. A.; Neaton, J. B.; Karunadasa, H. I. Gold-Cage Perovskites: A Three-Dimensional Au^{III}-X Framework Encasing Isolated MX₆³⁻ Octahedra (M^{III} = In, Sb, Bi; X = Cl⁻, Br⁻, I⁻). *J. Am. Chem. Soc.* **2021**, *143* (19), 7440–7448.
104. Tan, X.; Stephens, P. W.; Hendrickx, M.; Hadermann, J.; Segre, C. U.; Croft, M.; Kang, C.-J.; Deng, Z.; Lapidus, S. H.; Kim, S. W.; Jin, C.; Kotliar, G.; Greenblatt, M. Tetragonal Cs_{1.17}In_{0.81}Cl₃: A Charge-Ordered Indium Halide Perovskite Derivative. *Chem. Mater.* **2019**, *31* (6), 1981–1989.
105. McCall, K. M.; Friedrich, D.; Chica, D. G.; Cai, W.; Stoumpos, C. C.; Alexander, G. C. B.; Deemyad, S.; Wessels, B. W.; Kanatzidis, M. G. Perovskites with a Twist: Strong In¹⁺ Off-Centering in the Mixed-Valent CsInX₃ (X = Cl, Br). *Chem. Mater.* **2019**, *31* (22), 9554–9566.
106. de Kozak, A.; Samouël, M.; Renaudin, J.; Ferey, G. Complex Copper(II) Fluorides: XII. Crystal Structure and Ferromagnetic Properties of Na₄BaCu₃F₁₂. *Eur. J. Solid State Inorg. Chem.* **1990**, *27*, 771–782.
107. Ducau, M.; Suh, K. S.; Senegas, J.; Darriet, J. Crystal Structure and NMR Studies of a Cubic Perovskite: The Fluoride NaBaLiNiF₆. *Mater. Res. Bull.* **1992**, *27* (9), 1115–1123.
108. Feist, M.; Ducau, M.; Grannec, J.; Darriet, J.; Tressaud, A.; Hagenmuller, P. New Type of Ordered Perovskite fluorides: Na₂BaM₄F₁₂ (M=Mn,Fe) and Na₂BaMF₆ (M=Co,Ni). *J. Fluorine Chem.* **1991**, *54* (1–3), 354.
109. Darriet, J.; Mayorga, S. G.; Tressaud, A. Crystal Structure of Na₂BaFe₄F₁₂: A New Ordered Perovskite-like Fluoride. *Eur. J. Solid State Inorg. Chem.* **1990**, *27* (6), 783–790.
110. Ogomi, Y.; Morita, A.; Tsukamoto, S.; Saitho, T.; Fujikawa, N.; Shen, Q.; Toyoda, T.; Yoshino, K.; Pandey, S. S.; Ma, T.; Hayase, S. CH₃NH₃Sn_xPb_(1-x)l₃ Perovskite Solar Cells Covering up to 1060 Nm. *J. Phys. Chem. Lett.* **2014**, *5* (6), 1004–1011.
111. Stoumpos, C. C.; Malliakas, C. D.; Kanatzidis, M. G. Semiconducting Tin and Lead Iodide Perovskites with Organic Cations: Phase Transitions, High Mobilities, and Near-Infrared Photoluminescent Properties. *Inorg. Chem.* **2013**, *52* (15), 9019–9038.
112. Hao, F.; Stoumpos, C. C.; Chang, R. P. H.; Kanatzidis, M. G. Anomalous Band Gap Behavior in Mixed Sn and Pb Perovskites Enables Broadening of Absorption Spectrum in Solar Cells. *J. Am. Chem. Soc.* **2014**, *136* (22), 8094–8099.
113. Slavney, A. H.; Leppert, L.; Bartesaghi, D.; Gold-Parker, A.; Toney, M. F.; Savenije, T. J.; Neaton, J. B.; Karunadasa, H. I. Defect-Induced Band-Edge Reconstruction of a Bismuth-Halide Double Perovskite for Visible-Light Absorption. *J. Am. Chem. Soc.* **2017**, *139* (14), 5015–5018.
114. Leijtens, T.; Prasanna, R.; Gold-Parker, A.; Toney, M. F.; McGehee, M. D. Mechanism of Tin Oxidation and Stabilization by Lead Substitution in Tin Halide Perovskites. *ACS Energy Lett.* **2017**, *2* (9), 2159–2165.
115. Abdelhady, A. L.; Saidaminov, M. I.; Murali, B.; Adinolfi, V.; Voznyy, O.; Katsiev, K.; Alarousu, E.; Comin, R.; Dursun, I.; Sinatra, L.; Sargent, E. H.; Mohammed, O. F.; Bakr, O. M. Heterovalent Dopant Incorporation for Bandgap and Type Engineering of Perovskite Crystals. *J. Phys. Chem. Lett.* **2016**, *7* (2), 295–301.
116. Lindquist, K. P.; Mack, S. A.; Slavney, A. H.; Leppert, L.; Gold-Parker, A.; Stebbins, J. F.; Salleo, A.; Toney, M. F.; Neaton, J. B.; Karunadasa, H. I. Tuning the Bandgap of Cs₂AgBiBr₆ through Dilute Tin Alloying. *Chem. Sci.* **2019**, *10* (45), 10620–10628.
117. Atkinson, L.; Day, P. Charge Transfer in Mixed-Valence Solids. Part IV. Electronic Spectra of Hexachloroantimonates(III,V). *J. Chem. Soc. A* **1969**, 2423–2431.
118. Berthold, H. J.; Ludwig, W. Präparative und röntgenographische Untersuchungen über Cäsium-Silber-Gold(III)-Chlorid. *Z. Naturforsch. B* **1980**, *35* (6), 651–656.
119. Berthold, H. J.; Ludwig, W. Thermische Zersetzung nichtstöchiometrischer Cäsium-Silber-Gold(III)-Chloride und Darstellung von Mischkristallen zwischen Cs₂AgAuCl₆ und Cs₂Au^{III}Cl₆. *Z. Naturforsch. B* **1980**, *35* (8), 970–975.
120. Linaburg, M. R.; McClure, E. T.; Majher, J. D.; Woodward, P. M. Cs_{1-x}Rb_xPbCl₃ and Cs_{1-x}Rb_xPbBr₃ Solid Solutions: Understanding Octahedral Tilting in Lead Halide Perovskites. *Chem. Mater.* **2017**, *29* (8), 3507–3514.
121. Greenland, C.; Shnier, A.; Rajendran, S. K.; Smith, J. A.; Game, O. S.; Wamwangi, D.; Turnbull, G. A.; Samuel, I. D. W.; Billing, D. G.; Lidzey, D. G. Correlating Phase Behavior with Photophysical Properties in Mixed-Cation Mixed-Halide Perovskite Thin Films. *Adv. Energy Mater.* **2020**, *10* (4), 1901350.
122. Saliba, M.; Matsui, T.; Seo, J.-Y.; Domanski, K.; Correa-Baena, J.-P.; Nazeeruddin, M. K.; Zakeeruddin, S. M.; Tress, W.; Abate, A.; Hagfeldt, A.; Grätzel, M. Cesium-Containing Triple Cation Perovskite Solar Cells: Improved Stability, Reproducibility and High Efficiency. *Energy Environ. Sci.* **2016**, *9* (6), 1989–1997.
123. Saliba, M.; Matsui, T.; Domanski, K.; Seo, J.-Y.; Ummadisingu, A.; Zakeeruddin, S. M.; Correa-Baena, J.-P.; Tress, W. R.; Abate, A.; Hagfeldt, A.; Grätzel, M. Incorporation of Rubidium Cations into Perovskite Solar Cells Improves Photovoltaic Performance. *Science* **2016**, *354* (6309), 206–209.
124. Ono, L. K.; Juarez-Perez, E. J.; Qi, Y. Progress on Perovskite Materials and Solar Cells with Mixed Cations and Halide Anions. *ACS Appl. Mater. Interfaces* **2017**, *9* (36), 30197–30246.
125. Noh, J. H.; Im, S. H.; Heo, J. H.; Mandal, T. N.; Seok, S. I. Chemical Management for Colorful, Efficient, and Stable Inorganic–Organic Hybrid Nanostructured Solar Cells. *Nano Lett.* **2013**, *13* (4), 1764–1769.
126. Comin, R.; Walters, G.; Thibau, E. S.; Voznyy, O.; Lu, Z.-H.; Sargent, E. H. Structural, Optical, and Electronic Studies of Wide-Bandgap Lead Halide Perovskites. *J. Mater. Chem. C* **2015**, *3* (34), 8839–8843.
127. Hoke, E. T.; Slotcavage, D. J.; Dohner, E. R.; Bowring, A. R.; Karunadasa, H. I.; McGehee, M. D. Reversible Photo-Induced Trap Formation in Mixed-Halide Hybrid Perovskites for Photovoltaics. *Chem. Sci.* **2015**, *6* (1), 613–617.
128. Laporte, O. Die Struktur des Eisenspektrums. *Z. Phys.* **1924**, *23* (1), 135–175.
129. Cotton, F. A. *Chemical Applications of Group Theory*, Wiley: New York, 1990.
130. Harris, D. C.; Bertolucci, M. D. *Symmetry and Spectroscopy: An Introduction to Vibrational and Electronic Spectroscopy*, New York: Dover Publications, 1989.
131. Albright, T. A.; Burdett, J. K.; Whangbo, M.-H. *Orbital Interactions in Chemistry*, 2nd Ed.; John Wiley & Sons, Inc.: Hoboken, NJ, 2013.
132. Aroyo, M. I.; Orobengoa, D.; de la Flor, G.; Tasci, E. S.; Perez-Mato, J. M.; Wondratschek, H. Brillouin-Zone Database on the Bilbao Crystallographic Server. *Acta Crystallogr. Sect. A* **2014**, *70* (2), 126–137.
133. Setyawan, W.; Curtarolo, S. High-Throughput Electronic Band Structure Calculations: Challenges and Tools. *Comput. Mater. Sci.* **2010**, *49* (2), 299–312.
134. Hoffmann, R. *Solids and Surfaces: A Chemist's View of Bonding in Extended Structures*, VCH Publishers, 1988.
135. Dresselhaus, M. S.; Dresselhaus, G.; Jorio, A. *Group Theory: Applications to the Physics of Condensed Matter*, Springer, 2008.
136. Goesten, M. G.; Hoffmann, R. Mirrors of Bonding in Metal Halide Perovskites. *J. Am. Chem. Soc.* **2018**, *140* (40), 12996–13010.
137. Slavney, A. H.; Connor, B. A.; Leppert, L.; Karunadasa, H. I. A Pencil-and-Paper Method for Elucidating Halide Double Perovskite Band Structures. *Chem. Sci.* **2019**, *10* (48), 11041–11053.
138. Quarti, C.; Katan, C.; Even, J. Physical Properties of Bulk, Defective, 2D and 0D Metal Halide Perovskite Semiconductors from a Symmetry Perspective. *J. Phys. Mater.* **2020**, *3* (4), 042001.
139. Nogueira, F.; Castro, A.; Marques, M. A. L. A tutorial on density functional theory. In *A Primer in Density Functional Theory*; Fiolhais, C., Nogueira, F., Marques, M. A. L., Eds., Springer Berlin Heidelberg: Berlin, Heidelberg, 2003; pp 218–256.
140. Capelle, K. A Bird's-Eye View of Density-Functional Theory. *Braz. J. Phys. Ther.* **2006**, *36* (4A), 1318–1343.
141. Baerends, E. J.; Gritsenko, O. V.; van Meer, R. The Kohn–Sham Gap, the Fundamental Gap and the Optical Gap: The Physical Meaning of Occupied and Virtual Kohn–Sham Orbital Energies. *Phys. Chem. Chem. Phys.* **2013**, *15* (39), 16408–16425.
142. Schlüter, M.; Sham, L. J. Density-functional theory of the band gap. In *Advances in Quantum Chemistry*; Löwdin, P.-O., Ed.; vol. 21; Academic Press, 1990; pp 97–112.
143. Shu, Y.; Truhlar, D. G. Relationships between Orbital Energies, Optical and Fundamental Gaps, and Exciton Shifts in Approximate Density Functional Theory and Quasiparticle Theory. *J. Chem. Theory Comput.* **2020**, *16* (7), 4337–4350.

144. Leppert, L.; Rangel, T.; Neaton, J. B. Towards Predictive Band Gaps for Halide Perovskites: Lessons from One-Shot and Eigenvalue Self-Consistent *GW*. *Phys. Rev. Mater.* **2019**, *3* (10), 103803.
145. Aryasetiawan, F.; Gunnarsson, O. The *GW* Method. *Rep. Prog. Phys.* **1998**, *61* (3), 237–312.
146. Golze, D.; Dvorak, M.; Rinke, P. The *GW* Compendium: A Practical Guide to Theoretical Photoemission Spectroscopy. *Front. Chem.* **2019**, *7*, 377.
147. Streetman, B. G.; Banerjee, S. Energy bands and charge carriers in semiconductors. In *Solid State Electronic Devices*, 7th Ed.; Prentice Hall: New Jersey, 2015; pp 84–142.
148. Kirchartz, T.; Rau, U. Linking Structural Properties with Functionality in Solar Cell Materials—The Effective Mass and Effective Density of States. *Sustainable Energy Fuels* **2018**, *2* (7), 1550–1560.
149. Kohn, W.; Sham, L. J. Self-Consistent Equations Including Exchange and Correlation Effects. *Phys. Rev.* **1965**, *140* (4A), A1133–A1138.
150. Brivio, F.; Butler, K. T.; Walsh, A.; van Schilfgaarde, M. Relativistic Quasiparticle Self-Consistent Electronic Structure of Hybrid Halide Perovskite Photovoltaic Absorbers. *Phys. Rev. B* **2014**, *89* (15), 155204.
151. Burke, K.; Wagner, L. O. DFT in a Nutshell. *Int. J. Quantum Chem.* **2013**, *113* (2), 96–101.
152. Seidl, A.; Göring, A.; Vogl, P.; Majewski, J. A.; Levy, M. Generalized Kohn-Sham Schemes and the Band-Gap Problem. *Phys. Rev. B* **1996**, *53* (7), 3764–3774.
153. Perdew, J. P.; Burke, K.; Ernzerhof, M. Generalized Gradient Approximation Made Simple. *Phys. Rev. Lett.* **1996**, *77* (18), 3865–3868.
154. Perdew, J. P.; Ernzerhof, M.; Burke, K. Rationale for Mixing Exact Exchange with Density Functional Approximations. *J. Chem. Phys.* **1996**, *105* (22), 9982–9985.
155. Perdew, J. P.; Ruzsinszky, A.; Csonka, G. I.; Vydrov, O. A.; Scuseria, G. E.; Constantin, L. A.; Zhou, X.; Burke, K. Restoring the Density-Gradient Expansion for Exchange in Solids and Surfaces. *Phys. Rev. Lett.* **2008**, *100* (13), 136406.
156. Krukau, A. V.; Vydrov, O. A.; Izmaylov, A. F.; Scuseria, G. E. Influence of the Exchange Screening Parameter on the Performance of Screened Hybrid Functionals. *J. Chem. Phys.* **2006**, *125* (22), 224106.
157. Wu, Z.; Cohen, R. E. More Accurate Generalized Gradient Approximation for Solids. *Phys. Rev. B* **2006**, *73* (23), 235116.
158. Guan, L.; Xu, X.; Liang, Y.; Han, S.; Guo, J.; Wang, J.; Li, X. Effect of Atomic Configuration on Band Gap Behaviour in $\text{CH}_3\text{NH}_3\text{Sn}_x\text{Pb}_{1-x}\text{I}_3$ Perovskites. *Phys. Lett. A* **2020**, *384* (8), 126173.
159. Du, K.-Z.; Meng, W.; Wang, X.; Yan, Y.; Mitzi, D. B. Bandgap Engineering of Lead-Free Double Perovskite $\text{Cs}_2\text{AgBiBr}_6$ through Trivalent Metal Alloying. *Angew. Chem. Int. Ed.* **2017**, *56* (28), 8158–8162.
160. Garza, A. J.; Scuseria, G. E. Predicting Band Gaps with Hybrid Density Functionals. *J. Phys. Chem. Lett.* **2016**, *7* (20), 4165–4170.
161. Autschbach, J. Perspective: Relativistic Effects. *J. Chem. Phys.* **2012**, *136* (15), 150902.
162. Norrby, L. J. Why Is Mercury Liquid? Or, why Do Relativistic Effects Not Get into Chemistry Textbooks? *J. Chem. Educ.* **1991**, *68* (2), 110–113.
163. van Lenthe, E.; Baerends, E. J.; Snijders, J. G. Relativistic Total Energy Using Regular Approximations. *J. Chem. Phys.* **1994**, *101* (11), 9783–9792.
164. Even, J.; Pedesseau, L.; Jancu, J.-M.; Katan, C. Importance of Spin–Orbit Coupling in Hybrid Organic/Inorganic Perovskites for Photovoltaic Applications. *J. Phys. Chem. Lett.* **2013**, *4* (17), 2999–3005.
165. Amat, A.; Mosconi, E.; Ronca, E.; Quarti, C.; Umari, P.; Nazeeruddin, M. K.; Grätzel, M.; De Angelis, F. Cation-Induced Band-Gap Tuning in Organohalide Perovskites: Interplay of Spin–Orbit Coupling and Octahedra Tilting. *Nano Lett.* **2014**, *14* (6), 3608–3616.
166. Even, J.; Pedesseau, L.; Jancu, J.-M.; Katan, C. DFT and $\mathbf{k} \cdot \mathbf{p}$ Modelling of the Phase Transitions of Lead and Tin Halide Perovskites for Photovoltaic Cells. *Phys. Status Solidi RRL* **2014**, *8* (1), 31–35.
167. Hoffmann, R. How Chemistry and Physics Meet in the Solid State. *Angew. Chem. Int. Ed.* **1987**, *26* (9), 846–878.
168. Mannino, G.; Deretzis, I.; Smecca, E.; La Magna, A.; Alberti, A.; Ceratti, D.; Cahen, D. Temperature-Dependent Optical Band Gap in CsPbBr_3 , MAPbBr_3 , and FAPbBr_3 Single Crystals. *J. Phys. Chem. Lett.* **2020**, *11* (7), 2490–2496.
169. Umebayashi, T.; Asai, K.; Kondo, T.; Nakao, A. Electronic Structures of Lead Iodide Based Low-Dimensional Crystals. *Phys. Rev. B* **2003**, *67* (15), 155405.
170. Fabini, D. H.; Seshadri, R.; Kanatzidis, M. G. The Underappreciated Lone Pair in Halide Perovskites Underpins their Unusual Properties. *MRS Bull.* **2020**, *45* (6), 467–477.
171. Filip, M. R.; Eperon, G. E.; Snaith, H. J.; Giustino, F. Steric Engineering of Metal-Halide Perovskites with Tunable Optical Band Gaps. *Nat. Commun.* **2014**, *5* (1), 5757.
172. Baikie, T.; Fang, Y.; Kadro, J. M.; Schreyer, M.; Wei, F.; Mhaisalkar, S. G.; Graetzel, M.; White, T. J. Synthesis and Crystal Chemistry of the Hybrid Perovskite $(\text{CH}_3\text{NH}_3)\text{PbI}_3$ for Solid-State Sensitized Solar Cell Applications. *J. Mater. Chem. A* **2013**, *1* (18), 5628–5641.
173. Leguy, A. M. A.; Azharhoosh, P.; Alonso, M. I.; Campoy-Quiles, M.; Weber, O. J.; Yao, J.; Bryant, D.; Weller, M. T.; Nelson, J.; Walsh, A.; van Schilfgaarde, M.; Barnes, P. R. F. Experimental and Theoretical Optical Properties of Methylammonium Lead Halide Perovskites. *Nanoscale* **2016**, *8* (12), 6317–6327.
174. Paul, T.; Chatterjee, B. K.; Maiti, S.; Sarkar, S.; Besra, N.; Das, B. K.; Panigrahi, K. J.; Thakur, S.; Ghorai, U. K.; Chattopadhyay, K. K. Tunable Cathodoluminescence over the Entire Visible Window from All-Inorganic Perovskite CsPbX_3 1D Architecture. *J. Mater. Chem. C* **2018**, *6* (13), 3322–3333.
175. Huang, L.-y.; Lambrecht, W. R. L. Electronic Band Structure, Phonons, and Exciton Binding Energies of Halide Perovskites CsSnCl_3 , CsSnBr_3 , and CsSnI_3 . *Phys. Rev. B* **2013**, *88* (16), 165203.
176. Tao, S.; Schmidt, I.; Brocks, G.; Jiang, J.; Tranca, I.; Meerholz, K.; Olthoff, S. Absolute Energy Level Positions in Tin- and Lead-Based Halide Perovskites. *Nat. Commun.* **2019**, *10* (1), 2560.
177. Borriello, I.; Cantele, G.; Ninno, D. Ab Initio Investigation of Hybrid Organic-Inorganic Perovskites Based on Tin Halides. *Phys. Rev. B* **2008**, *77* (23), 235214.
178. Krishnamoorthy, T.; Ding, H.; Yan, C.; Leong, W. L.; Baikie, T.; Zhang, Z.; Sherburne, M.; Li, S.; Asta, M.; Mathews, N.; Mhaisalkar, S. G. Lead-Free Germanium Iodide Perovskite Materials for Photovoltaic Applications. *J. Mater. Chem. A* **2015**, *3* (47), 23829–23832.
179. Stoumpos, C. C.; Frazer, L.; Clark, D. J.; Kim, Y. S.; Rhim, S. H.; Freeman, A. J.; Ketterson, J. B.; Jang, J. I.; Kanatzidis, M. G. Hybrid Germanium Iodide Perovskite Semiconductors: Active Lone Pairs, Structural Distortions, Direct and Indirect Energy Gaps, and Strong Nonlinear Optical Properties. *J. Am. Chem. Soc.* **2015**, *137* (21), 6804–6819.
180. Goyal, A.; McKechnie, S.; Pashov, D.; Tumas, W.; van Schilfgaarde, M.; Stevanović, V. Origin of Pronounced Nonlinear Band Gap Behavior in Lead–Tin Hybrid Perovskite Alloys. *Chem. Mater.* **2018**, *30* (11), 3920–3928.
181. Diez-Cabanes, V.; Even, J.; Beljonne, D.; Quarti, C. Electronic Structure and Optical Properties of Mixed Iodine/Bromine Lead Perovskites. To Mix or Not to Mix? *Adv. Opt. Mater.* **2021**, *9* (23), 2001832.
182. Slavney, A. H.; Leppert, L.; Saldivar Valdes, A.; Bartesaghi, D.; Savenije, T. J.; Neaton, J. B.; Karunadasa, H. I. Small-Band-Gap Halide Double Perovskites. *Angew. Chem. Int. Ed.* **2018**, *57* (39), 12765–12770.
183. Connor, B. A.; Leppert, L.; Smith, M. D.; Neaton, J. B.; Karunadasa, H. I. Layered Halide Double Perovskites: Dimensional Reduction of $\text{Cs}_2\text{AgBiBr}_6$. *J. Am. Chem. Soc.* **2018**, *140* (15), 5235–5240.
184. Meng, W.; Wang, X.; Xiao, Z.; Wang, J.; Mitzi, D. B.; Yan, Y. Parity-Forbidden Transitions and Their Impact on the Optical Absorption Properties of Lead-Free Metal Halide Perovskites and Double Perovskites. *J. Phys. Chem. Lett.* **2017**, *8* (13), 2999–3007.
185. McClure, E. T.; Ball, M. R.; Windl, W.; Woodward, P. M. $\text{Cs}_2\text{AgBiX}_6$ ($X = \text{Br}, \text{Cl}$): New Visible Light Absorbing, Lead-Free Halide Perovskite Semiconductors. *Chem. Mater.* **2016**, *28* (5), 1348–1354.
186. Cai, Y.; Xie, W.; Ding, H.; Chen, Y.; Thirumal, K.; Wong, L. H.; Mathews, N.; Mhaisalkar, S. G.; Sherburne, M.; Asta, M. Computational Study of Halide Perovskite-Derived A_2BX_6 Inorganic Compounds: Chemical Trends in Electronic Structure and Structural Stability. *Chem. Mater.* **2017**, *29* (18), 7740–7749.
187. Cai, Y.; Xie, W.; Teng, Y. T.; Harikesh, P. C.; Ghosh, B.; Huck, P.; Persson, K. A.; Mathews, N.; Mhaisalkar, S. G.; Sherburne, M.; Asta, M. High-Throughput Computational Study of Halide Double Perovskite Inorganic Compounds. *Chem. Mater.* **2019**, *31* (15), 5392–5401.
188. Bajorowicz, B.; Mikołajczyk, A.; Pinto, H. P.; Miodyńska, M.; Lisowski, W.; Klimczuk, T.; Kaplan-Ashiri, I.; Kazes, M.; Oron, D.; Zaleska-Medynska, A. Integrated Experimental and Theoretical Approach for Efficient Design and Synthesis of Gold-Based Double Halide Perovskites. *J. Phys. Chem. C* **2020**, *124* (49), 26769–26779.

189. Filip, M. R.; Hillman, S.; Haghighirad, A. A.; Snaith, H. J.; Giustino, F. Band Gaps of the Lead-Free Halide Double Perovskites $\text{Cs}_2\text{BiAgCl}_6$ and $\text{Cs}_2\text{BiAgBr}_6$ from Theory and Experiment. *J. Phys. Chem. Lett.* **2016**, *7* (13), 2579–2585.
190. Kavanagh, S.; Scanlon, D.; Walsh, A. Band alignment of antimony and bismuth Silver-bromide double Perovskites. Proceedings of Online Meetup - Beyond Lead Halide Perovskites: Syntheses and Applications of Metal Halide Semiconductors (MABP), Online, Spain, Online, Spain.
191. Tan, Z.; Li, J.; Zhang, C.; Li, Z.; Hu, Q.; Xiao, Z.; Kamiya, T.; Hosono, H.; Niu, G.; Lifshitz, E.; Cheng, Y.; Tang, J. Highly Efficient Blue-Emitting Bi-Doped Cs_2SnCl_6 Perovskite Variant: Photoluminescence Induced by Impurity Doping. *Adv. Funct. Mater.* **2018**, *28* (29), 1801131.
192. Binnewies, M.; Milke, E. *Thermochemical Data of Elements and Compounds*, 2nd Ed.; Wiley-VCH: Weinheim, 2002; p 928.
193. Ivanov, I. L.; Steparuk, A. S.; Bolyachkina, M. S.; Tsvetkov, D. S.; Safronov, A. P.; Zuev, A. Y. Thermodynamics of Formation of Hybrid Perovskite-Type Methylammonium Lead Halides. *J. Chem. Thermodyn.* **2018**, *116*, 253–258.
194. Bhalla, A. S.; Guo, R.; Roy, R. The Perovskite Structure—A Review of its Role in Ceramic Science and Technology. *Mater. Res. Innov.* **2000**, *4* (1), 3–26.
195. Corr, S. A.; Seshadri, R. 4.01: Synthetic methodologies. In *Comprehensive Inorganic Chemistry II*; Reedijk, J., Poeppelmeier, K., Eds., 2nd Ed.; Elsevier: Amsterdam, 2013; pp 1–15.
196. Dunlap-Shohl, W. A.; Zhou, Y.; Pature, N. P.; Mitzi, D. B. Synthetic Approaches for Halide Perovskite Thin Films. *Chem. Rev.* **2019**, *119* (5), 3193–3295.
197. Umeyama, D.; Leppert, L.; Connor, B. A.; Manupill, M. A.; Neaton, J. B.; Karunadasa, H. I. Expanded Analogs of Three-Dimensional Lead-Halide Hybrid Perovskites. *Angew. Chem. Int. Ed.* **2020**, *59* (43), 19087–19094.
198. Chung, I.; Song, J.-H.; Im, J.; Androulakis, J.; Malliakas, C. D.; Li, H.; Freeman, A. J.; Kenney, J. T.; Kanatzidis, M. G. CsSnI_3 : Semiconductor or Metal? High Electrical Conductivity and Strong Near-Infrared Photoluminescence from a Single Material. High Hole Mobility and Phase-Transitions. *J. Am. Chem. Soc.* **2012**, *134* (20), 8579–8587.
199. Sutton, R. J.; Filip, M. R.; Haghighirad, A. A.; Sakai, N.; Wenger, B.; Giustino, F.; Snaith, H. J. Cubic or Orthorhombic? Revealing the Crystal Structure of Metastable Black-Phase CsPbI_3 by Theory and Experiment. *ACS Energy Lett.* **2018**, *3* (8), 1787–1794.
200. Cordero, F.; Craciun, F.; Trequattrini, F.; Generosi, A.; Paci, B.; Paoletti, A. M.; Pennesi, G. Stability of Cubic FAPbI_3 from X-Ray Diffraction, Anelastic, and Dielectric Measurements. *J. Phys. Chem. Lett.* **2019**, *10* (10), 2463–2469.
201. Yamada, K.; Nakada, K.; Takeuchi, Y.; Nawa, K.; Yamane, Y. Tunable Perovskite Semiconductor $\text{CH}_3\text{NH}_3\text{SnX}_3$ (X: Cl, Br, or I) Characterized by X-Ray and DTA. *Bull. Chem. Soc. Jpn.* **2011**, *84* (9), 926–932.
202. Dualeh, A.; Gao, P.; Seok, S. I.; Nazeeruddin, M. K.; Grätzel, M. Thermal Behavior of Methylammonium Lead-Trihalide Perovskite Photovoltaic Light Harvesters. *Chem. Mater.* **2014**, *26* (21), 6160–6164.
203. Yu, H.; Wang, F.; Xie, F.; Li, W.; Chen, J.; Zhao, N. The Role of Chlorine in the Formation Process of “ $\text{CH}_3\text{NH}_3\text{PbI}_{3-x}\text{Cl}_x$ ” Perovskite. *Adv. Funct. Mater.* **2014**, *24* (45), 7102–7108.
204. Slavney, A. H.; Hu, T.; Lindenber, A. M.; Karunadasa, H. I. A Bismuth-Halide Double Perovskite with Long Carrier Recombination Lifetime for Photovoltaic Applications. *J. Am. Chem. Soc.* **2016**, *138* (7), 2138–2141.
205. Conings, B.; Drijkoningen, J.; Gauquelin, N.; Babayigit, A.; D’Haen, J.; D’Oleslaeger, L.; Ethirajan, A.; Verbeeck, J.; Manca, J.; Mosconi, E.; Angelis, F. D.; Boyen, H.-G. Intrinsic Thermal Instability of Methylammonium Lead Trihalide Perovskite. *Adv. Energy Mater.* **2015**, *5* (15), 1500477.
206. Prochowicz, D.; Franckevičius, M.; Cieślak, A. M.; Zakeeruddin, S. M.; Grätzel, M.; Lewiński, J. Mechanochemical Synthesis of the Hybrid Perovskite $\text{CH}_3\text{NH}_3\text{PbI}_3$: Characterization and the Corresponding Solar Cell Efficiency. *J. Mater. Chem. A* **2015**, *3* (41), 20772–20777.
207. Jana, A.; Mittal, M.; Singla, A.; Sapra, S. Solvent-Free, Mechanochemical Syntheses of Bulk Trihalide Perovskites and their Nanoparticles. *Chem. Commun.* **2017**, *53* (21), 3046–3049.
208. Breternitz, J.; Levchenko, S.; Hempel, H.; Gurieva, G.; Franz, A.; Hoser, A.; Schorr, S. Mechanochemical Synthesis of the Lead-Free Double Perovskite $\text{Cs}_2[\text{AgIn}]\text{Br}_6$ and its Optical Properties. *J. Phys. Energy* **2019**, *1* (2), 025003.
209. El Ajjouri, Y.; Locardi, F.; Gélvez-Rueda, M. C.; Prato, M.; Sessolo, M.; Ferretti, M.; Grozema, F. C.; Palazon, F.; Bolink, H. J. Mechanochemical Synthesis of Sn(II) and Sn(IV) Iodide Perovskites and Study of their Structural, Chemical, Thermal, Optical, and Electrical Properties. *Energ. Technol.* **2020**, *8* (4), 1900788.
210. Garcia-Espejo, G.; Rodríguez-Padrón, D.; Luque, R.; Camacho, L.; de Miguel, G. Mechanochemical Synthesis of Three Double Perovskites: $\text{Cs}_2\text{AgBiBr}_6$, $(\text{CH}_3\text{NH}_3)_2\text{TlBiBr}_6$ and $\text{Cs}_2\text{AgSbBr}_6$. *Nanoscale* **2019**, *11* (35), 16650–16657.
211. Askar, A. M.; Karmakar, A.; Bernard, G. M.; Ha, M.; Tersikh, V. V.; Wiltshire, B. D.; Patel, S.; Fleet, J.; Shankar, K.; Michaelis, V. K. Composition-Tunable Formamidinium Lead Mixed Halide Perovskites via Solvent-Free Mechanochemical Synthesis: Decoding the Pb Environments Using Solid-State NMR Spectroscopy. *J. Phys. Chem. Lett.* **2018**, *9* (10), 2671–2677.
212. Karmakar, A.; Askar, A. M.; Bernard, G. M.; Tersikh, V. V.; Ha, M.; Patel, S.; Shankar, K.; Michaelis, V. K. Mechanochemical Synthesis of Methylammonium Lead Mixed-Halide Perovskites: Unraveling the Solid-Solution Behavior Using Solid-State NMR. *Chem. Mater.* **2018**, *30* (7), 2309–2321.
213. Prochowicz, D.; Yadav, P.; Saliba, M.; Sasaki, M.; Zakeeruddin, S. M.; Lewiński, J.; Grätzel, M. Mechanochemical Synthesis of Pure Phase Mixed-Cation $\text{MA}_x\text{FA}_{1-x}\text{PbI}_3$ Hybrid Perovskites: Photovoltaic Performance and Electrochemical Properties. *Sustainable Energy Fuels* **2017**, *1* (4), 689–693.
214. Stoumpos, C. C.; Malliakas, C. D.; Peters, J. A.; Liu, Z.; Sebastian, M.; Im, J.; Chasapis, T. C.; Wibowo, A. C.; Chung, D. Y.; Freeman, A. J.; Wessels, B. W.; Kanatzidis, M. G. Crystal Growth of the Perovskite Semiconductor CsPbBr_3 : A New Material for High-Energy Radiation Detection. *Cryst. Growth Des.* **2013**, *13* (7), 2722–2727.
215. He, Y.; Matei, L.; Jung, H. J.; McCall, K. M.; Chen, M.; Stoumpos, C. C.; Liu, Z.; Peters, J. A.; Chung, D. Y.; Wessels, B. W.; Wasielewski, M. R.; Dravid, V. P.; Burger, A.; Kanatzidis, M. G. High Spectral Resolution of Gamma-Rays at Room Temperature by Perovskite CsPbBr_3 Single Crystals. *Nat. Commun.* **2018**, *9* (1), 1609.
216. Zhang, P.; Zhang, G.; Liu, L.; Ju, D.; Zhang, L.; Cheng, K.; Tao, X. Anisotropic Optoelectronic Properties of Melt-Grown Bulk CsPbBr_3 Single Crystal. *J. Phys. Chem. Lett.* **2018**, *9* (17), 5040–5046.
217. Kobayashi, M.; Omata, K.; Sugimoto, S.; Tamagawa, Y.; Kuroiwa, T.; Asada, H.; Takeuchi, H.; Kondo, S. Scintillation Characteristics of CsPbCl_3 Single Crystals. *Nucl. Instrum. Methods Phys. Res. A* **2008**, *592* (3), 369–373.
218. Mizusaki, J.; Arai, K.; Fueki, K. Ionic Conduction of the Perovskite-Type Halides. *Solid State Ion.* **1983**, *11* (3), 203–211.
219. Chung, I.; Lee, B.; He, J.; Chang, R. P. H.; Kanatzidis, M. G. All-Solid-State Dye-Sensitized Solar Cells with High Efficiency. *Nature* **2012**, *485* (7399), 486–489.
220. Higgins, W. M.; Glodo, J.; Shirwadkar, U.; Churilov, A.; Van Loef, E.; Hawrami, R.; Ciampi, G.; Hines, C.; Shah, K. S. Bridgman Growth of $\text{Cs}_2\text{LiYCl}_6$:Ce and ^6Li -Enriched $\text{Cs}_2^6\text{LiYCl}_6$:Ce Crystals for High Resolution Gamma Ray and Neutron Spectrometers. *J. Cryst. Growth* **2010**, *312* (8), 1216–1220.
221. Yurtavaeva, S. V.; Usachev, A. E.; Yablokov, Y. V. Spin-Spin Interactions of Ce^{3+} Ions in the Elpasolite Crystal $\text{Cs}_2\text{NaInCl}_6$. *Phys. Solid State* **1997**, *39* (7), 1075–1080.
222. Solubility and equilibrium constant. In *Lange’s Handbook of Chemistry*; Speight, J. G., Ed., 17th Ed.; McGraw-Hill Education: New York, 2017; p 1312.
223. Weber, D. $\text{CH}_3\text{NH}_3\text{SnBr}_{3-x}$ ($x = 0-3$), ein Sn(II)-System mit kubischer Perovskitstruktur. *Z. Naturforsch. B* **1978**, *33* (8), 862–865.
224. Zhou, Y.; Game, O. S.; Pang, S.; Pature, N. P. Microstructures of Organometal Trihalide Perovskites for Solar Cells: Their Evolution from Solutions and Characterization. *J. Phys. Chem. Lett.* **2015**, *6* (23), 4827–4839.
225. Hamill, J. C.; Schwartz, J.; Loo, Y.-L. Influence of Solvent Coordination on Hybrid Organic-Inorganic Perovskite Formation. *ACS Energy Lett.* **2018**, *3* (1), 92–97.
226. Saidaminov, M. I.; Abdelhady, A. L.; Murali, B.; Alarousu, E.; Burlakov, V. M.; Peng, W.; Dursun, I.; Wang, L.; He, Y.; Maculan, G.; Goriely, A.; Wu, T.; Mohammed, O. F.; Bakr, O. M. High-Quality Bulk Hybrid Perovskite Single Crystals within Minutes by Inverse Temperature Crystallization. *Nat. Commun.* **2015**, *6* (1), 7586.
227. Saidaminov, M. I.; Abdelhady, A. L.; Maculan, G.; Bakr, O. M. Retrograde Solubility of Formamidinium and Methylammonium Lead Halide Perovskites Enabling Rapid Single Crystal Growth. *Chem. Commun.* **2015**, *51* (100), 17658–17661.
228. Maculan, G.; Sheikh, A. D.; Abdelhady, A. L.; Saidaminov, M. I.; Haque, M. A.; Murali, B.; Alarousu, E.; Mohammed, O. F.; Wu, T.; Bakr, O. M. $\text{CH}_3\text{NH}_3\text{PbCl}_3$ Single Crystals: Inverse Temperature Crystallization and Visible-Blind UV-Photodetector. *J. Phys. Chem. Lett.* **2015**, *6* (19), 3781–3786.

229. Liu, Y.; Yang, Z.; Cui, D.; Ren, X.; Sun, J.; Liu, X.; Zhang, J.; Wei, Q.; Fan, H.; Yu, F.; Zhang, X.; Zhao, C.; Liu, S. Two-Inch-Sized Perovskite $\text{CH}_3\text{NH}_3\text{PbX}_3$ ($X = \text{Cl}, \text{Br}, \text{I}$) Crystals: Growth and Characterization. *Adv. Mater.* **2015**, *27* (35), 5176–5183.
230. Steele, J. A.; Jin, H.; Dovgaliuk, I.; Berger, R. F.; Braeckvelt, T.; Yuan, H.; Martin, C.; Solano, E.; Lejaeghere, K.; Rogge, S. M. J.; Notebaert, C.; Vandezande, W.; Janssen, K. P. F.; Goderis, B.; Debroye, E.; Wang, Y.-K.; Dong, Y.; Ma, D.; Saidaminov, M.; Tan, H.; Lu, Z.; Dyadkin, V.; Chernyshov, D.; Van Speybroeck, V.; Sargent, E. H.; Hofkens, J.; Roeffaers, M. B. J. Thermal Unequilibrium of Strained Black CsPbI_3 Thin Films. *Science* **2019**, *365* (6454), 679–684.
231. Rakita, Y.; Kedem, N.; Gupta, S.; Sadhanala, A.; Kalchenko, V.; Böhm, M. L.; Kulbak, M.; Friend, R. H.; Cahen, D.; Hodes, G. Low-Temperature Solution-Grown CsPbBr_3 Single Crystals and their Characterization. *Cryst. Growth Des.* **2016**, *16* (10), 5717–5725.
232. Dirin, D. N.; Cherniukh, I.; Yakunin, S.; Shynkarenko, Y.; Kovalenko, M. V. Solution-Grown CsPbBr_3 Perovskite Single Crystals for Photon Detection. *Chem. Mater.* **2016**, *28* (23), 8470–8474.
233. Dong, Q.; Fang, Y.; Shao, Y.; Mulligan, P.; Qiu, J.; Cao, L.; Huang, J. Electron-Hole Diffusion Lengths $> 175 \mu\text{m}$ in Solution-Grown $\text{CH}_3\text{NH}_3\text{PbI}_3$ Single Crystals. *Science* **2015**, *347* (6225), 967–970.
234. Liu, Y.; Yang, Z.; Liu, S. Recent Progress in Single-Crystalline Perovskite Research Including Crystal Preparation, Property Evaluation, and Applications. *Adv. Sci.* **2018**, *5* (1), 1700471.
235. Chen, Y.; Zeng, H.; Ma, P.; Chen, G.; Jian, J.; Sun, X.; Li, X.; Wang, H.; Yin, W.; Jia, Q.; Zou, G. Overcoming the Anisotropic Growth Limitations of Free-Standing Single-Crystal Halide Perovskite Films. *Angew. Chem. Int. Ed.* **2021**, *60* (5), 2629–2636.
236. Nandi, P.; Giri, C.; Swain, D.; Manju, U.; Topwal, D. Room Temperature Growth of $\text{CH}_3\text{NH}_3\text{PbCl}_3$ Single Crystals by Solvent Evaporation Method. *CrystEngComm* **2019**, *21* (4), 656–661.
237. Shi, D.; Adinolfi, V.; Comin, R.; Yuan, M.; Alarousu, E.; Buin, A.; Chen, Y.; Hoogland, S.; Rothenberger, A.; Katsiev, K.; Losovyj, Y.; Zhang, X.; Dowben, P. A.; Mohammed, O. F.; Sargent, E. H.; Bakr, O. M. Low Trap-State Density and Long Carrier Diffusion in Organolead Trihalide Perovskite Single Crystals. *Science* **2015**, *347* (6221), 519–522.
238. Zhou, J.; Xia, Z.; Molokchev, M. S.; Zhang, X.; Peng, D.; Liu, Q. Composition Design, Optical Gap and Stability Investigations of Lead-Free Halide Double Perovskite $\text{Cs}_2\text{AgInCl}_6$. *J. Mater. Chem. A* **2017**, *5* (29), 15031–15037.
239. Luo, J.; Wang, X.; Li, S.; Liu, J.; Guo, Y.; Niu, G.; Yao, L.; Fu, Y.; Gao, L.; Dong, Q.; Zhao, C.; Leng, M.; Ma, F.; Liang, W.; Wang, L.; Jin, S.; Han, J.; Zhang, L.; Etheridge, J.; Wang, J.; Yan, Y.; Sargent, E. H.; Tang, J. Efficient and Stable Emission of Warm-White Light from Lead-Free Halide Double Perovskites. *Nature* **2018**, *563* (7732), 541–545.
240. Li, J.; Tan, Z.; Hu, M.; Chen, C.; Luo, J.; Li, S.; Gao, L.; Xiao, Z.; Niu, G.; Tang, J. Antimony Doped Cs_2SnCl_6 with Bright and Stable Emission. *Front. Optoelectron.* **2019**, *12* (4), 352–364.
241. Colmenares, J. C.; Magdziarz, A.; Lisowski, P. Application of microwave and ultrasound irradiation in the synthesis of perovskite-type oxides ABO_3 . In *Perovskites and Related Mixed Oxides*; Granger, P., Parvulescu, V. I., Kaliaguine, S., Prellier, W., Eds., Wiley-VCH Verlag GmbH & Co: Weinheim, Germany, 2016; pp 91–112.
242. Kesari, Y.; Athawale, A. Ultrasound Assisted Bulk Synthesis of $\text{CH}_3\text{NH}_3\text{PbI}_3$ Perovskite at Room Temperature. *Mater. Lett.* **2015**, *159*, 87–89.
243. Peng, W.; Wang, L.; Murali, B.; Ho, K.-T.; Bera, A.; Cho, N.; Kang, C.-F.; Burlakov, V. M.; Pan, J.; Sinatra, L.; Ma, C.; Xu, W.; Shi, D.; Alarousu, E.; Goriely, A.; He, J.-H.; Mohammed, O. F.; Wu, T.; Bakr, O. M. Solution-Grown Monocrystalline Hybrid Perovskite Films for Hole-Transporter-Free Solar Cells. *Adv. Mater.* **2016**, *28* (17), 3383–3390.
244. Jancik, J.; Jancik Prochazkova, A.; Scharber, M. C.; Kovalenko, A.; Másilko, J.; Sariciftci, N. S.; Weiter, M.; Krajcovic, J. Microwave-Assisted Preparation of Organo-Lead Halide Perovskite Single Crystals. *Cryst. Growth Des.* **2020**, *20* (3), 1388–1393.
245. Raiford, J. A.; Oyakhire, S. T.; Bent, S. F. Applications of Atomic Layer Deposition and Chemical Vapor Deposition for Perovskite Solar Cells. *Energy Environ. Sci.* **2020**, *13* (7), 1997–2023.
246. Jeon, N. J.; Noh, J. H.; Kim, Y. C.; Yang, W. S.; Ryu, S.; Seok, S. I. Solvent Engineering for High-Performance Inorganic–Organic Hybrid Perovskite Solar Cells. *Nat. Mater.* **2014**, *13* (9), 897–903.
247. Liu, M.; Johnston, M. B.; Snaith, H. J. Efficient Planar Heterojunction Perovskite Solar Cells by Vapour Deposition. *Nature* **2013**, *501* (7467), 395–398.
248. Tavakoli, M. M.; Gu, L.; Gao, Y.; Reckmeier, C.; He, J.; Rogach, A. L.; Yao, Y.; Fan, Z. Fabrication of Efficient Planar Perovskite Solar Cells Using a One-Step Chemical Vapor Deposition Method. *Sci. Rep.* **2015**, *5* (1), 14083.
249. Chen, Q.; Zhou, H.; Hong, Z.; Luo, S.; Duan, H.-S.; Wang, H.-H.; Liu, Y.; Li, G.; Yang, Y. Planar Heterojunction Perovskite Solar Cells via Vapor-Assisted Solution Process. *J. Am. Chem. Soc.* **2014**, *136* (2), 622–625.
250. Liang, K.; Mitzi, D. B.; Prikas, M. T. Synthesis and Characterization of Organic–Inorganic Perovskite Thin Films Prepared Using a Versatile Two-Step Dipping Technique. *Chem. Mater.* **1998**, *10* (1), 403–411.
251. Chen, H.; Wei, Z.; Zheng, X.; Yang, S. A Scalable Electrodeposition Route to the Low-Cost, Versatile and Controllable Fabrication of Perovskite Solar Cells. *Nano Energy* **2015**, *15*, 216–226.
252. Smith, I. C.; Smith, M. D.; Jaffe, A.; Lin, Y.; Karunadasa, H. I. Between the Sheets: Postsynthetic Transformations in Hybrid Perovskites. *Chem. Mater.* **2017**, *29* (5), 1868–1884.
253. Eames, C.; Frost, J. M.; Barnes, P. R. F.; O'Regan, B. C.; Walsh, A.; Islam, M. S. Ionic Transport in Hybrid Lead Iodide Perovskite Solar Cells. *Nat. Commun.* **2015**, *6* (1), 7497.
254. De Souza, R. A.; Barboni, D. Iodide-Ion Conduction in Methylammonium Lead Iodide Perovskite: Some Extraordinary Aspects. *Chem. Commun.* **2019**, *55* (8), 1108–1111.
255. Solis-Ibarra, D.; Smith, I. C.; Karunadasa, H. I. Post-Synthetic Halide Conversion and Selective Halogen Capture in Hybrid Perovskites. *Chem. Sci.* **2015**, *6* (7), 4054–4059.
256. Pellet, N.; Teuscher, J.; Maier, J.; Grätzel, M. Transforming Hybrid Organic Inorganic Perovskites by Rapid Halide Exchange. *Chem. Mater.* **2015**, *27* (6), 2181–2188.
257. Li, G.; Ho, J. Y.-L.; Wong, M.; Kwok, H. S. Reversible Anion Exchange Reaction in Solid Halide Perovskites and its Implication in Photovoltaics. *J. Phys. Chem. C* **2015**, *119* (48), 26883–26888.
258. Chen, K.; Deng, X.; Goddard, R.; Tüysüz, H. Pseudomorphic Transformation of Organometal Halide Perovskite Using the Gaseous Hydrogen Halide Reaction. *Chem. Mater.* **2016**, *28* (15), 5530–5537.
259. Flores, E. M. M.; Mello, P. A.; Krzyzaniak, S. R.; Cauduro, V. H.; Picoloto, R. S. Challenges and Trends for Halogen Determination by Inductively Coupled Plasma Mass Spectrometry: A Review. *Rapid Commun. Mass Spectrom.* **2020**, *34* (S3), e8727.
260. Wells, H. L. Some Complex Chlorides Containing Gold. II. Cesium Triple Salts. *Am. J. Sci.* **1922**, *3* (17), 315–326.
261. Teuscher, J.; Ulianov, A.; Müntener, O.; Grätzel, M.; Tétreault, N. Control and Study of the Stoichiometry in Evaporated Perovskite Solar Cells. *ChemSusChem* **2015**, *8* (22), 3847–3852.
262. Peng, W.; Miao, X.; Adinolfi, V.; Alarousu, E.; El Tall, O.; Emwas, A.-H.; Zhao, C.; Walters, G.; Liu, J.; Ouellette, O.; Pan, J.; Murali, B.; Sargent, E. H.; Mohammed, O. F.; Bakr, O. M. Engineering of $\text{CH}_3\text{NH}_3\text{PbI}_3$ Perovskite Crystals by Alloying Large Organic Cations for Enhanced Thermal Stability and Transport Properties. *Angew. Chem. Int. Ed.* **2016**, *55* (36), 10686–10690.
263. Liu, Y.; Lorenz, M.; Ilev, A. V.; Ovchinnikova, O. S. Secondary Ion Mass Spectrometry (SIMS) for Chemical Characterization of Metal Halide Perovskites. *Adv. Funct. Mater.* **2020**, *30* (35), 2002201.
264. Christian, G. D.; Dasgupta, P. K.; Schug, K. A. *Analytical Chemistry*, 7th, John Wiley & Sons, Inc: Hoboken, NJ, 2014.
265. IUCR (n.d.) www.IUCr.org.
266. Le Bail, A. Whole Powder Pattern Decomposition Methods and Applications: A Retrospection. *Powder Diff.* **2005**, *20* (4), 316–326.
267. Xian, Y.; Zhang, Y.; Rahman, N. U.; Yin, H.; Long, Y.; Liu, P.; Li, W.; Fan, J. An Emerging All-Inorganic $\text{CsSn}_x\text{Pb}_{1-x}\text{Br}_3$ ($0 \leq x \leq 1$) Perovskite Single Crystal: Insight on Structural Phase Transition and Electronic Properties. *J. Phys. Chem. C* **2020**, *124* (24), 13434–13446.

268. Volonakis, G.; Filip, M. R.; Haghighirad, A. A.; Sakai, N.; Wenger, B.; Snaith, H. J.; Giustino, F. Lead-Free Halide Double Perovskites via Heterovalent Substitution of Noble Metals. *J. Phys. Chem. Lett.* **2016**, *7* (7), 1254–1259.
269. Kawamura, Y.; Mashiyama, H. Modulated Structure in Phase II of $\text{CH}_3\text{NH}_3\text{PbCl}_3$. *J. Korean Phys. Soc.* **1999**, *35*, 1437–1440.
270. X-ray and neutron scattering. In *Handbook of Nanophase and Nanostructured Materials*; Wang, Z. L., Liu, Y., Zhang, Z., Eds., Springer US: Boston, MA, 2002; pp 344–371.
271. Baikie, T.; Barrow, N. S.; Fang, Y.; Keenan, P. J.; Slater, P. R.; Piltz, R. O.; Gutmann, M.; Mhaisalkar, S. G.; White, T. J. A Combined Single Crystal Neutron/X-Ray Diffraction and Solid-State Nuclear Magnetic Resonance Study of the Hybrid Perovskites $\text{CH}_3\text{NH}_3\text{PbX}_3$ ($X = \text{I, Br and Cl}$). *J. Mater. Chem. A* **2015**, *3* (17), 9298–9307.
272. Mashiyama, H.; Kawamura, Y.; Kasano, H.; Asahi, T.; Noda, Y.; Kimura, H. Disordered Configuration of Methylammonium of $\text{CH}_3\text{NH}_3\text{PbBr}_3$ Determined by Single Crystal Neutron Diffraction. *Ferroelectrics* **2007**, *348* (1), 182–186.
273. Leguy, A. M. A.; Frost, J. M.; McMahon, A. P.; Sakai, V. G.; Kockelmann, W.; Law, C.; Li, X.; Foglia, F.; Walsh, A.; O'Regan, B. C.; Nelson, J.; Cabral, J. T.; Barnes, P. R. F. The Dynamics of Methylammonium Ions in Hybrid Organic–Inorganic Perovskite Solar Cells. *Nat. Commun.* **2015**, *6* (1), 7124.
274. Guzelurk, B.; Winkler, T.; Van de Goor, T. W. J.; Smith, M. D.; Bourelle, S. A.; Feldmann, S.; Trigo, M.; Teitelbaum, S. W.; Steinrück, H. G.; de la Pena, G. A.; Alonso-Mori, R.; Zhu, D.; Sato, T.; Karunadasa, H. I.; Toney, M. F.; Deschler, F.; Lindenberg, A. M. Visualization of Dynamic Polaronic Strain Fields in Hybrid Lead Halide Perovskites. *Nat. Mater.* **2021**, *20* (5), 618–623.
275. Egami, T.; Billinge, S. J. L. *Underneath the Bragg Peaks: Structural Analysis of Complex Materials*; vol. 16; Elsevier Ltd: Oxford, UK, 2012.
276. Beecher, A. N.; Semonin, O. E.; Skelton, J. M.; Frost, J. M.; Terban, M. W.; Zhai, H.; Alatas, A.; Owen, J. S.; Walsh, A.; Billinge, S. J. L. Direct Observation of Dynamic Symmetry Breaking above Room Temperature in Methylammonium Lead Iodide Perovskite. *ACS Energy Lett.* **2016**, *1* (4), 880–887.
277. Zhao, X.-G.; Dalpian, G. M.; Wang, Z.; Zunger, A. Polymorphous Nature of Cubic Halide Perovskites. *Phys. Rev. B* **2020**, *101* (15), 155137.
278. Maughan, A. E.; Ganose, A. M.; Candia, A. M.; Granger, J. T.; Scanlon, D. O.; Neilson, J. R. Anharmonicity and Octahedral Tilting in Hybrid Vacancy-Ordered Double Perovskites. *Chem. Mater.* **2018**, *30* (2), 472–483.
279. Maughan, A. E.; Paecklar, A. A.; Neilson, J. R. Bond Valences and Anharmonicity in Vacancy-Ordered Double Perovskite Halides. *J. Mater. Chem. C* **2018**, *6* (44), 12095–12104.
280. Fabini, D. H.; Laurita, G.; Bechtel, J. S.; Stoumpos, C. C.; Evans, H. A.; Kontos, A. G.; Raptis, Y. S.; Falaras, P.; Van der Ven, A.; Kanatzidis, M. G.; Seshadri, R. Dynamic Stereochemical Activity of the Sn^{2+} Lone Pair in Perovskite CsSnBr_3 . *J. Am. Chem. Soc.* **2016**, *138* (36), 11820–11832.
281. Laurita, G.; Fabini, D. H.; Stoumpos, C. C.; Kanatzidis, M. G.; Seshadri, R. Chemical Tuning of Dynamic Cation Off-Centering in the Cubic Phases of Hybrid Tin and Lead Halide Perovskites. *Chem. Sci.* **2017**, *8* (8), 5628–5635.
282. Gold-Parker, A.; Gehring, P. M.; Skelton, J. M.; Smith, I. C.; Parshall, D.; Frost, J. M.; Karunadasa, H. I.; Walsh, A.; Toney, M. F. Acoustic Phonon Lifetimes Limit Thermal Transport in Methylammonium Lead Iodide. *Proc. Natl. Acad. Sci. U. S. A.* **2018**, *115* (47), 11905–11910.
283. Ma, H.; Ma, Y.; Wang, H.; Sledobnick, C.; Alatas, A.; Urban, J. J.; Tian, Z. Experimental Phonon Dispersion and Lifetimes of Tetragonal $\text{CH}_3\text{NH}_3\text{PbI}_3$ Perovskite Crystals. *J. Phys. Chem. Lett.* **2019**, *10* (1), 1–6.
284. Manley, M. E.; Hong, K.; Yin, P.; Chi, S.; Cai, Y.; Hua, C.; Daemen, L. L.; Hermann, R. P.; Wang, H.; May, A. F.; Asta, M.; Ahmadi, M. Giant Isotope Effect on Phonon Dispersion and Thermal Conductivity in Methylammonium Lead Iodide. *Sci. Adv.* **2020**, *6* (31), eaaz1842.
285. Pisoni, A.; Jaćimović, J.; Barišić, O. S.; Spina, M.; Gaál, R.; Forró, L.; Horváth, E. Ultra-Low Thermal Conductivity in Organic–Inorganic Hybrid Perovskite $\text{CH}_3\text{NH}_3\text{PbI}_3$. *J. Phys. Chem. Lett.* **2014**, *5* (14), 2488–2492.
286. Weadock, N. J.; Gehring, P. M.; Gold-Parker, A.; Smith, I. C.; Karunadasa, H. I.; Toney, M. F. Test of the Dynamic-Domain and Critical Scattering Hypotheses in Cubic Methylammonium Lead Triiodide. *Phys. Rev. Lett.* **2020**, *125* (7), 075701.
287. Comin, R.; Crawford, M. K.; Said, A. H.; Herron, N.; Guise, W. E.; Wang, X.; Whitfield, P. S.; Jain, A.; Gong, X.; McGaughey, A. J. H.; Sargent, E. H. Lattice Dynamics and the Nature of Structural Transitions in Organolead Halide Perovskites. *Phys. Rev. B* **2016**, *94* (9), 094301.
288. Barrows, A. T.; Lilliu, S.; Pearson, A. J.; Babonneau, D.; Dunbar, A. D. F.; Lidzey, D. G. Monitoring the Formation of a $\text{CH}_3\text{NH}_3\text{PbI}_{3-x}\text{Cl}_x$ Perovskite during Thermal Annealing Using X-Ray Scattering. *Adv. Funct. Mater.* **2016**, *26* (27), 4934–4942.
289. Schlipf, J.; Docampo, P.; Schaffer, C. J.; Körstgens, V.; Bießmann, L.; Hanusch, F.; Giesbrecht, N.; Bernstorff, S.; Bein, T.; Müller-Buschbaum, P. A Closer Look into Two-Step Perovskite Conversion with X-Ray Scattering. *J. Phys. Chem. Lett.* **2015**, *6* (7), 1265–1269.
290. Stone, K. H.; Gold-Parker, A.; Pool, V. L.; Unger, E. L.; Bowring, A. R.; McGehee, M. D.; Toney, M. F.; Tassone, C. J. Transformation from Crystalline Precursor to Perovskite in PbCl_2 -Derived MAPbI_3 . *Nat. Commun.* **2018**, *9* (1), 3458.
291. Nenon, D. P.; Christians, J. A.; Wheeler, L. M.; Blackburn, J. L.; Sanehira, E. M.; Dou, B.; Olsen, M. L.; Zhu, K.; Berry, J. J.; Luther, J. M. Structural and Chemical Evolution of Methylammonium Lead Halide Perovskites during Thermal Processing from Solution. *Energy Environ. Sci.* **2016**, *9* (6), 2072–2082.
292. Oesinghaus, L.; Schlipf, J.; Giesbrecht, N.; Song, L.; Hu, Y.; Bein, T.; Docampo, P.; Müller-Buschbaum, P. Toward Tailored Film Morphologies: The Origin of Crystal Orientation in Hybrid Perovskite Thin Films. *Adv. Mater. Interfaces* **2016**, *3* (19), 1600403.
293. Hubbell, J. H.; Seltzer, S. M. *X-Ray Mass Attenuation Coefficients*, National Institute of Standards and Technology, 2004.
294. Bunker, G. *Introduction to XAFS: A Practical Guide to X-Ray Absorption Fine Structure Spectroscopy*, Cambridge University Press: Cambridge, 2010.
295. Calvin, S. *XAFS for Everyone*, CRC Press: Boca Raton, FL, 2013.
296. Pool, V. L.; Gold-Parker, A.; McGehee, M. D.; Toney, M. F. Chlorine in PbCl_2 -Derived Hybrid-Perovskite Solar Absorbers. *Chem. Mater.* **2015**, *27* (21), 7240–7243.
297. Santomauro, F. G.; Grilj, J.; Mewes, L.; Nedelcu, G.; Yakunin, S.; Rossi, T.; Capano, G.; Haddad, A. A.; Budarz, J.; Kinschel, D.; Ferreira, D. S.; Rossi, G.; Tovar, M. G.; Grolimund, D.; Samson, V.; Nachttegaal, M.; Smolentsev, G.; Kovalenko, M. V.; Chergui, M. Localized Holes and Delocalized Electrons in Photoexcited Inorganic Perovskites: Watching each Atomic Actor by Picosecond X-Ray Absorption Spectroscopy. *Struct. Dyn.* **2017**, *4* (4), 044002.
298. Back, H.; Kim, G.; Kim, J.; Kong, J.; Kim, T. K.; Kang, H.; Kim, H.; Lee, J.; Lee, S.; Lee, K. Achieving Long-Term Stable Perovskite Solar Cells Via Ion Neutralization. *Energy Environ. Sci.* **2016**, *9* (4), 1258–1263.
299. Deepa, M.; Salado, M.; Calio, L.; Kazim, S.; Shivaprasad, S. M.; Ahmad, S. Cesium Power: Low Cs^+ Levels Impart Stability to Perovskite Solar Cells. *Phys. Chem. Chem. Phys.* **2017**, *19* (5), 4069–4077.
300. Moghe, D.; Wang, L.; Traverse, C. J.; Redoute, A.; Sponseller, M.; Brown, P. R.; Bulović, V.; Lunt, R. R. All Vapor-Deposited Lead-Free Doped CsSnBr_3 Planar Solar Cells. *Nano Energy* **2016**, *28*, 469–474.
301. Matteocci, F.; Busby, Y.; Pireaux, J.-J.; Divitini, G.; Cacovich, S.; Ducati, C.; Di Carlo, A. Interface and Composition Analysis on Perovskite Solar Cells. *ACS Appl. Mater. Interfaces* **2015**, *7* (47), 26176–26183.
302. Greczynski, G.; Hultman, L. X-Ray Photoelectron Spectroscopy: Towards Reliable Binding Energy Referencing. *Prog. Mater. Sci.* **2020**, *107*, 100591.
303. Greczynski, G.; Hultman, L. Compromising Science by Ignorant Instrument Calibration—Need to Revisit half a Century of Published XPS Data. *Angew. Chem. Int. Ed.* **2020**, *59* (13), 5002–5006.
304. Wagner, C. D.; Muilenberg, G. E. *Handbook of X-Ray Photoelectron Spectroscopy: A Reference Book of Standard Data for Use in X-Ray Photoelectron Spectroscopy*, Perkin-Elmer, 1979.
305. Kahn, A. Fermi Level, Work Function and Vacuum Level. *Mater. Horiz.* **2016**, *3* (1), 7–10.
306. Correa Baena, J. P.; Steier, L.; Tress, W.; Saliba, M.; Neutzner, S.; Matsui, T.; Giordano, F.; Jacobsson, T. J.; Srimath Kandada, A. R.; Zakeeruddin, S. M.; Petrozza, A.; Abate, A.; Nazeeruddin, M. K.; Grätzel, M.; Hagfeldt, A. Highly Efficient Planar Perovskite Solar Cells through Band Alignment Engineering. *Energy Environ. Sci.* **2015**, *8* (10), 2928–2934.
307. Park, B.-W.; Philippe, B.; Jain, S. M.; Zhang, X.; Edvinsson, T.; Rensmo, H.; Zietz, B.; Boschloo, G. Chemical Engineering of Methylammonium Lead Iodide/Bromide Perovskites: Tuning of Opto-Electronic Properties and Photovoltaic Performance. *J. Mater. Chem. A* **2015**, *3* (43), 21760–21771.

308. Noel, N. K.; Habisreutinger, S. N.; Pellaroque, A.; Pulvirenti, F.; Wenger, B.; Zhang, F.; Lin, Y.-H.; Reid, O. G.; Leisen, J.; Zhang, Y.; Barlow, S.; Marder, S. R.; Kahn, A.; Snaith, H. J.; Arnold, C. B.; Rand, B. P. Interfacial Charge-Transfer Doping of Metal Halide Perovskites for High Performance Photovoltaics. *Energy Environ. Sci.* **2019**, *12* (10), 3063–3073.
309. Zu, F.; Amsalem, P.; Egger, D. A.; Wang, R.; Wolff, C. M.; Fang, H.; Loi, M. A.; Neher, D.; Kronik, L.; Duhm, S.; Koch, N. Constructing the Electronic Structure of $\text{CH}_3\text{NH}_3\text{PbI}_3$ and $\text{CH}_3\text{NH}_3\text{PbBr}_3$ Perovskite Thin Films from Single-Crystal Band Structure Measurements. *J. Phys. Chem. Lett.* **2019**, *10* (3), 601–609.
310. Goncharova, L. V. Photoelectron spectroscopies. In *Basic Surfaces and Their Analysis*; Goncharova, L. V., Ed., Morgan & Claypool Publishers: San Rafael, CA, 2018, 6–1–6–17.
311. Tauc, J.; Grigorovici, R.; Vancu, A. Optical Properties and Electronic Structure of Amorphous Germanium. *Phys. Status Solidi* **1966**, *15* (2), 627–637.
312. Dolgonos, A.; Mason, T. O.; Poeppelmeier, K. R. Direct Optical Band Gap Measurement in Polycrystalline Semiconductors: A Critical Look at the Tauc Method. *J. Solid State Chem.* **2016**, *240*, 43–48.
313. Murphy, A. B. Band-Gap Determination from Diffuse Reflectance Measurements of Semiconductor Films, and Application to Photoelectrochemical Water-Splitting. *Sol. Energy Mater. Sol. Cells* **2007**, *91* (14), 1326–1337.
314. Kurik, M. V. Urbach Rule. *Phys. Stat. Sol. (A)* **1971**, *8* (1), 9–45.
315. Skoog, D. A.; Holler, F. J.; Crouch, S. R. *Principles of Instrumental Analysis*, Cengage Learning, 2017.
316. Yi, C.; Luo, J.; Meloni, S.; Boziki, A.; Ashari-Astani, N.; Grätzel, C.; Zakeeruddin, S. M.; Röthlisberger, U.; Grätzel, M. Entropic Stabilization of Mixed A-Cation ABX_3 Metal Halide Perovskites for High Performance Perovskite Solar Cells. *Energy Environ. Sci.* **2016**, *9* (2), 656–662.
317. Isikgor, F. H.; Li, B.; Zhu, H.; Xu, Q.; Ouyang, J. High Performance Planar Perovskite Solar Cells with a Perovskite of Mixed Organic Cations and Mixed Halides, $\text{MA}_{1-x}\text{FA}_x\text{PbI}_{3-y}\text{Cl}_y$. *J. Mater. Chem. A* **2016**, *4* (32), 12543–12553.
318. Misra, R. K.; Ciannaruchi, L.; Aharon, S.; Mogilyansky, D.; Etgar, L.; Visoly-Fisher, I.; Katz, E. A. Effect of Halide Composition on the Photochemical Stability of Perovskite Photovoltaic Materials. *ChemSusChem* **2016**, *9* (18), 2572–2577.
319. Huang, Z.; Wang, D.; Wang, S.; Zhang, T. Highly Efficient and Stable MAPbI_3 Perovskite Solar Cell Induced by Regulated Nucleation and Ostwald Recrystallization. *Materials* **2018**, *11* (5), 778.
320. Liu, D.; Yang, C.; Lunt, R. R. Halide Perovskites for Selective Ultraviolet-Harvesting Transparent Photovoltaics. *Joule* **2018**, *2* (9), 1827–1837.
321. Jung, J. W.; Chueh, C.-C.; Jen, A. K.-Y. High-Performance Semitransparent Perovskite Solar Cells with 10% Power Conversion Efficiency and 25% Average Visible Transmittance Based on Transparent CuSCN as the Hole-Transporting Material. *Adv. Energy Mater.* **2015**, *5* (17), 1500486.
322. Christy, A. A.; Kvalheim, O. M.; Velapoldi, R. A. Quantitative Analysis in Diffuse Reflectance Spectrometry: A Modified Kubelka-Munk Equation. *Vib. Spectrosc.* **1995**, *9* (1), 19–27.
323. Nayak, P. K.; Sendner, M.; Wenger, B.; Wang, Z.; Sharma, K.; Ramadan, A. J.; Lovrinčić, R.; Pucci, A.; Madhu, P. K.; Snaith, H. J. Impact of Bi^{3+} Heterovalent Doping in Organic–Inorganic Metal Halide Perovskite Crystals. *J. Am. Chem. Soc.* **2018**, *140* (2), 574–577.
324. Meng, R.; Wu, G.; Zhou, J.; Zhou, H.; Fang, H.; Loi, M. A.; Zhang, Y. Understanding the Impact of Bismuth Heterovalent Doping on the Structural and Photophysical Properties of $\text{CH}_3\text{NH}_3\text{PbBr}_3$ Halide Perovskite Crystals with Near-IR Photoluminescence. *Chem. Eur. J.* **2019**, *25* (21), 5480–5488.
325. Kojima, N.; Kitagawa, H. Optical Investigation of the Intermolecular Charge-Transfer Interactions in the Three-Dimensional Gold Mixed-Valence Compounds $\text{Cs}_2\text{Au}_2\text{X}_6$ (X = Cl, Br or I). *J. Chem. Soc. Dalton Trans.* **1994**, *3*, 327–331.
326. Löper, P.; Stuckelberger, M.; Niesen, B.; Werner, J.; Filipčić, M.; Moon, S.-J.; Yum, J.-H.; Topić, M.; De Wolf, S.; Ballif, C. Complex Refractive Index Spectra of $\text{CH}_3\text{NH}_3\text{PbI}_3$ Perovskite Thin Films Determined by Spectroscopic Ellipsometry and Spectrophotometry. *J. Phys. Chem. Lett.* **2015**, *6* (1), 66–71.
327. Shirayama, M.; Kadowaki, H.; Miyadera, T.; Sugita, T.; Tamakoshi, M.; Kato, M.; Fujiseki, T.; Murata, D.; Hara, S.; Murakami, T. N.; Fujiwara, H. Optical Transitions in Hybrid Perovskite Solar Cells: Ellipsometry, Density Functional Theory, and Quantum Efficiency Analyses for $\text{CH}_3\text{NH}_3\text{PbI}_3$. *Phys. Rev. Appl.* **2016**, *5* (1), 014012.
328. Connor, B. A.; Biega, R.-I.; Leppert, L.; Karunadasa, H. I. Dimensional Reduction of the Small-Bandgap Double Perovskite $\text{Cs}_2\text{AgTlBr}_6$. *Chem. Sci.* **2020**, *11* (29), 7708–7715.
329. Leijtens, T.; Eperon, G. E.; Pathak, S.; Abate, A.; Lee, M. M.; Snaith, H. J. Overcoming Ultraviolet Light Instability of Sensitized TiO_2 with Meso-Superstructured Organometal Tri-Halide Perovskite Solar Cells. *Nat. Commun.* **2013**, *4* (1), 2885.
330. Li, W.; Zhang, W.; Van Reenen, S.; Sutton, R. J.; Fan, J.; Haghighirad, A. A.; Johnston, M. B.; Wang, L.; Snaith, H. J. Enhanced UV-Light Stability of Planar Heterojunction Perovskite Solar Cells with Caesium Bromide Interface Modification. *Energy Environ. Sci.* **2016**, *9* (2), 490–498.
331. Price, M. B.; Butkus, J.; Jellicoe, T. C.; Sadhanala, A.; Briane, A.; Halpert, J. E.; Broch, K.; Hodgkiss, J. M.; Friend, R. H.; Deschler, F. Hot-Carrier Cooling and Photoinduced Refractive Index Changes in Organic–Inorganic Lead Halide Perovskites. *Nat. Commun.* **2015**, *6* (1), 8420.
332. Yoon, S. J.; Draguta, S.; Manser, J. S.; Sharia, O.; Schneider, W. F.; Kuno, M.; Kamat, P. V. Tracking Iodide and Bromide Ion Segregation in Mixed Halide Lead Perovskites during Photoirradiation. *ACS Energy Lett.* **2016**, *1* (1), 290–296.
333. Yang, Z.; Rajagopal, A.; Jo, S. B.; Chueh, C.-C.; Williams, S.; Huang, C.-C.; Katahara, J. K.; Hillhouse, H. W.; Jen, A. K.-Y. Stabilized Wide Bandgap Perovskite Solar Cells by Tin Substitution. *Nano Lett.* **2016**, *16* (12), 7739–7747.
334. Jackson, W. B.; Amer, N. M.; Boccara, A. C.; Fournier, D. Photothermal Deflection Spectroscopy and Detection. *Appl. Optics* **1981**, *20* (8), 1333–1344.
335. Pao, Y.-H. *Optoacoustic Spectroscopy and Detection*, Academic Press, Inc: New York, NY, 1977.
336. De Wolf, S.; Holovsky, J.; Moon, S.-J.; Löper, P.; Niesen, B.; Ledinsky, M.; Haug, F.-J.; Yum, J.-H.; Ballif, C. Organometallic Halide Perovskites: Sharp Optical Absorption Edge and Its Relation to Photovoltaic Performance. *J. Phys. Chem. Lett.* **2014**, *5* (6), 1035–1039.
337. Sadhanala, A.; Deschler, F.; Thomas, T. H.; Dutton, S. E.; Goedel, K. C.; Hanusch, F. C.; Lai, M. L.; Steiner, U.; Bein, T.; Docampo, P.; Cahen, D.; Friend, R. H. Preparation of Single-Phase Films of $\text{CH}_3\text{NH}_3\text{Pb}(\text{I}_{1-x}\text{Br}_x)_3$ with Sharp Optical Band Edges. *J. Phys. Chem. Lett.* **2014**, *5* (15), 2501–2505.
338. Mooney, J.; Kambampati, P. Get the Basics Right: Jacobian Conversion of Wavelength and Energy Scales for Quantitative Analysis of Emission Spectra. *J. Phys. Chem. Lett.* **2013**, *4* (19), 3316–3318.
339. Lu, W.; Fu, Y. Photoluminescence. In *Spectroscopy of Semiconductors: Numerical Analysis Bridging Quantum Mechanics and Experiments*; Lu, W., Fu, Y., Eds., Springer International Publishing: Cham, 2018; pp 107–158.
340. Pazos-Outón, L. M.; Szumilo, M.; Lamboll, R.; Richter, J. M.; Crespo-Quesada, M.; Abdi-Jalebi, M.; Beeson, H. J.; Vrućinić, M.; Alsari, M.; Snaith, H. J.; Ehrler, B.; Friend, R. H.; Deschler, F. Photon Recycling in Lead Iodide Perovskite Solar Cells. *Science* **2016**, *351* (6280), 1430–1433.
341. Richter, J. M.; Abdi-Jalebi, M.; Sadhanala, A.; Tabachnyk, M.; Rivett, J. P. H.; Pazos-Outón, L. M.; Gödel, K. C.; Price, M.; Deschler, F.; Friend, R. H. Enhancing Photoluminescence Yields in Lead Halide Perovskites by Photon Recycling and Light out-Coupling. *Nat. Commun.* **2016**, *7* (1), 13941.
342. Noculak, A.; Morad, V.; McCall, K. M.; Yakunin, S.; Shynkarenko, Y.; Wörle, M.; Kovalenko, M. V. Bright Blue and Green Luminescence of Sb(III) in Double Perovskite Cs_2MnCl_6 (M = Na, K) Matrices. *Chem. Mater.* **2020**, *32* (12), 5118–5124.
343. Kiligardis, A.; Merdasa, A.; Rehermann, C.; Unger, E. L.; Scheblykin, I. G. Excitation Wavelength Dependence of Photoluminescence Flickering in Degraded MAPbI_3 Perovskite and its Connection to Lead Iodide Formation. *J. Lumin.* **2020**, *222*, 117129.
344. Schmidt, T.; Lischka, K.; Zulehner, W. Excitation-Power Dependence of the Near-Band-Edge Photoluminescence of Semiconductors. *Phys. Rev. B* **1992**, *45* (16), 8989–8994.
345. Dohner, E. R.; Jaffe, A.; Bradshaw, L. R.; Karunadasa, H. I. Intrinsic White-Light Emission from Layered Hybrid Perovskites. *J. Am. Chem. Soc.* **2014**, *136* (38), 13154–13157.
346. Solomon, E. I. Electronic Absorption Spectroscopy—Vibronic Coupling and Band Shape Analysis. *Comments Inorg. Chem.* **1984**, *3* (5), 300–318.
347. Pelant, I.; Valenta, J. *Luminescence Spectroscopy of Semiconductors*, OUP Oxford, 2012.

348. Zelewski, S. J.; Urban, J. M.; Surrente, A.; Maude, D. K.; Kuc, A.; Schade, L.; Johnson, R. D.; Dollmann, M.; Nayak, P. K.; Snaith, H. J.; Radaelli, P.; Kudrawiec, R.; Nicholas, R. J.; Plochocka, P.; Baranowski, M. Revealing the Nature of Photoluminescence Emission in the Metal-Halide Double Perovskite $\text{Cs}_2\text{AgBiBr}_6$. *J. Mater. Chem. C* **2019**, *7* (27), 8350–8356.
349. Fonoberov, V. A.; Alim, K. A.; Balandin, A. A.; Xiu, F.; Liu, J. Photoluminescence Investigation of the Carrier Recombination Processes in ZnO Quantum Dots and Nanocrystals. *Phys. Rev. B* **2006**, *73* (16), 165317.
350. Stadler, W.; Hofmann, D. M.; Alt, H. C.; Muschik, T.; Meyer, B. K.; Weigel, E.; Müller-Vogt, G.; Salk, M.; Rupp, E.; Benz, K. W. Optical Investigations of Defects in $\text{Cd}_{1-x}\text{Zn}_x\text{Te}$. *Phys. Rev. B* **1995**, *51* (16), 10619–10630.
351. Péan, E. V.; Dimitrov, S.; De Castro, C. S.; Davies, M. L. Interpreting Time-Resolved Photoluminescence of Perovskite Materials. *Phys. Chem. Chem. Phys.* **2020**, *22* (48), 28345–28358.
352. Fries, F.; Reineke, S. Statistical Treatment of Photoluminescence Quantum Yield Measurements. *Sci. Rep.* **2019**, *9* (1), 15638.
353. Glaser, T.; Müller, C.; Sendner, M.; Krekeler, C.; Semonin, O. E.; Hull, T. D.; Yaffe, O.; Owen, J. S.; Kowalsky, W.; Pucci, A.; Lovričić, R. Infrared Spectroscopic Study of Vibrational Modes in Methylammonium Lead Halide Perovskites. *J. Phys. Chem. Lett.* **2015**, *6* (15), 2913–2918.
354. Ruan, S.; McMeekin, D. P.; Fan, R.; Webster, N. A. S.; Eberndorff-Heidepriem, H.; Cheng, Y.-B.; Lu, J.; Ruan, Y.; McNeill, C. R. Raman Spectroscopy of Formamidinium-Based Lead Halide Perovskite Single Crystals. *J. Phys. Chem. C* **2020**, *124* (4), 2265–2272.
355. Wei, T.-C.; Wang, H.-P.; Li, T.-Y.; Lin, C.-H.; Hsieh, Y.-H.; Chu, Y.-H.; He, J.-H. Photostriction of $\text{CH}_3\text{NH}_3\text{PbBr}_3$ Perovskite Crystals. *Adv. Mater.* **2017**, *29* (35), 1701789.
356. Liu, X.; Moritomo, Y.; Nakamura, A.; Kojima, N. Broad Raman Band in the Single-Valence State of $\text{Cs}_2\text{Au}_2\text{X}_6$ ($X = \text{Cl}$ and Br). *J. Physical Soc. Japan* **1999**, *68* (10), 3134–3137.
357. Ledinský, M.; Löper, P.; Niesen, B.; Holovský, J.; Moon, S.-J.; Yum, J.-H.; De Wolf, S.; Fejfar, A.; Ballif, C. Raman Spectroscopy of Organic-Inorganic Halide Perovskites. *J. Phys. Chem. Lett.* **2015**, *6* (3), 401–406.
358. Gan, Z.; Yu, Z.; Meng, M.; Xia, W.; Zhang, X. Hydration of Mixed Halide Perovskites Investigated by Fourier Transform Infrared Spectroscopy. *APL Mater.* **2019**, *7* (3), 031107.
359. Pérez-Osorio, M. A.; Lin, Q.; Phillips, R. T.; Milot, R. L.; Herz, L. M.; Johnston, M. B.; Giustino, F. Raman Spectrum of the Organic-Inorganic Halide Perovskite $\text{CH}_3\text{NH}_3\text{PbI}_3$ from First Principles and High-Resolution Low-Temperature Raman Measurements. *J. Phys. Chem. C* **2018**, *122* (38), 21703–21717.
360. Guo, Y.; Yaffe, O.; Paley, D. W.; Beecher, A. N.; Hull, T. D.; Szpak, G.; Owen, J. S.; Brus, L. E.; Pimenta, M. A. Interplay between Organic Cations and Inorganic Framework and Incommensurability in Hybrid Lead-Halide Perovskite $\text{CH}_3\text{NH}_3\text{PbBr}_3$. *Phys. Rev. Mater.* **2017**, *1* (4), 042401.
361. Yesinowski, J. P. Solid-state NMR of inorganic semiconductors. In *Solid State NMR*; Chan, J. C. C., Ed., Springer Berlin Heidelberg: Berlin, Heidelberg, 2012; pp 229–312.
362. Kubicki, D. J.; Prochowicz, D.; Hofstetter, A.; Zakeeruddin, S. M.; Grätzel, M.; Emsley, L. Phase Segregation in Cs-, Rb- and K-Doped Mixed-Cation $(\text{MA})_x(\text{FA})_{1-x}\text{PbI}_3$ Hybrid Perovskites from Solid-State NMR. *J. Am. Chem. Soc.* **2017**, *139* (40), 14173–14180.
363. Karmakar, A.; Dodd, M. S.; Agnihotri, S.; Ravera, E.; Michaelis, V. K. Cu(II)-Doped $\text{Cs}_2\text{SbAgCl}_6$ Double Perovskite: A Lead-Free, Low-Bandgap Material. *Chem. Mater.* **2018**, *30* (22), 8280–8290.
364. Kubicki, D. J.; Prochowicz, D.; Salager, E.; Rakhmatullin, A.; Grey, C. P.; Emsley, L.; Stranks, S. D. Local Structure and Dynamics in Methylammonium, Formamidinium, and Cesium Tin(II) Mixed-Halide Perovskites from ^{119}Sn Solid-State NMR. *J. Am. Chem. Soc.* **2020**, *142* (17), 7813–7826.
365. Rosales, B. A.; Men, L.; Cady, S. D.; Hanrahan, M. P.; Rossini, A. J.; Vela, J. Persistent Dopants and Phase Segregation in Organolead Mixed-Halide Perovskites. *Chem. Mater.* **2016**, *28* (19), 6848–6859.
366. Suits, B. H. Nuclear Quadrupole Resonance Spectroscopy. In *Handbook of Applied Solid State Spectroscopy*; Vij, D. R., Ed., Springer US: Boston, MA, 2006; pp 65–96.
367. Piveteau, L.; Aebli, M.; Yazdani, N.; Millen, M.; Korosec, L.; Krieg, F.; Benin, B. M.; Morad, V.; Piveteau, C.; Shiroka, T.; Comas-Vives, A.; Copéret, C.; Lindenberg, A. M.; Wood, V.; Verel, R.; Kovalenko, M. V. Bulk and Nanocrystalline Cesium Lead-Halide Perovskites as Seen by Halide Magnetic Resonance. *ACS Cent. Sci.* **2020**, *6* (7), 1138–1149.
368. Franssen, W. M. J.; Kentgens, A. P. M. Solid-state NMR of hybrid halide perovskites. *Solid State Nucl. Magn. Reson.* **2019**, *100*, 36–44.
369. Nie, W.; Tsai, H.; Asadpour, R.; Blancon, J.-C.; Neukirch, A. J.; Gupta, G.; Crochet, J. J.; Chhowalla, M.; Tretiak, S.; Alam, M. A.; Wang, H.-L.; Mohite, A. D. High-Efficiency Solution-Processed Perovskite Solar Cells with Millimeter-Scale Grains. *Science* **2015**, *347* (6221), 522–525.
370. Delport, G.; Macpherson, S.; Stranks, S. D. Imaging Carrier Transport Properties in Halide Perovskites Using Time-Resolved Optical Microscopy. *Adv. Energy Mater.* **2020**, *10* (26), 1903814.
371. Mao, W.; Hall, C. R.; Chesman, A. S. R.; Forsyth, C.; Cheng, Y.-B.; Duffy, N. W.; Smith, T. A.; Bach, U. Visualizing Phase Segregation in Mixed-Halide Perovskite Single Crystals. *Angew. Chem. Int. Ed.* **2019**, *58* (9), 2893–2898.
372. Delor, M.; Weaver, H. L.; Yu, Q.; Ginsberg, N. S. Imaging Material Functionality through Three-Dimensional Nanoscale Tracking of Energy Flow. *Nat. Mater.* **2020**, *19* (1), 56–62.
373. Delor, M.; Slavney, A. H.; Wolf, N. R.; Filip, M. R.; Neaton, J. B.; Karunadasa, H. I.; Ginsberg, N. S. Carrier Diffusion Lengths Exceeding 1 μm Despite Trap-Limited Transport in Halide Double Perovskites. *ACS Energy Lett.* **2020**, *5* (5), 1337–1345.
374. Rothmann, M. U.; Kim, J. S.; Borchert, J.; Lohmann, K. B.; O'Leary, C. M.; Shearer, A. A.; Clark, L.; Snaith, H. J.; Johnston, M. B.; Nellist, P. D.; Herz, L. M. Atomic-Scale Microstructure of Metal Halide Perovskite. *Science* **2020**, *370* (6516), eabb5940.
375. Li, Y.; Zhou, W.; Li, Y.; Huang, W.; Zhang, Z.; Chen, G.; Wang, H.; Wu, G.-H.; Rolston, N.; Vila, R.; Chiu, W.; Cui, Y. Unravelling Degradation Mechanisms and Atomic Structure of Organic-Inorganic Halide Perovskites by Cryo-EM. *Joule* **2019**, *3* (11), 2854–2866.
376. Ball, J. M.; Lee, M. M.; Hey, A.; Snaith, H. J. Low-Temperature Processed Meso-Superstructured to Thin-Film Perovskite Solar Cells. *Energ. Environ. Sci.* **2013**, *6* (6), 1739–1743.
377. Salim, T.; Sun, S.; Abe, Y.; Krishna, A.; Grimsdale, A. C.; Lam, Y. M. Perovskite-Based Solar Cells: Impact of Morphology and Device Architecture on Device Performance. *J. Mater. Chem. A* **2015**, *3* (17), 8943–8969.
378. Shao, Y.; Fang, Y.; Li, T.; Wang, Q.; Dong, Q.; Deng, Y.; Yuan, Y.; Wei, H.; Wang, M.; Gruverman, A.; Shield, J.; Huang, J. Grain Boundary Dominated Ion Migration in Polycrystalline Organic-Inorganic Halide Perovskite Films. *Energ. Environ. Sci.* **2016**, *9* (5), 1752–1759.
379. Li, X.; Ibrahim Dar, M.; Yi, C.; Luo, J.; Tschumi, M.; Zakeeruddin, S. M.; Nazeeruddin, M. K.; Han, H.; Grätzel, M. Improved Performance and Stability of Perovskite Solar Cells by Crystal Crosslinking with Alkylphosphonic Acid ω -Ammonium Chlorides. *Nat. Chem.* **2015**, *7* (9), 703–711.
380. Jariwala, S.; Sun, H.; Adhyaksa, G. W. P.; Lof, A.; Muscarella, L. A.; Ehrlar, B.; Garnett, E. C.; Ginger, D. S. Local Crystal Misorientation Influences Non-radiative Recombination in Halide Perovskites. *Joule* **2019**, *3* (12), 3048–3060.
381. Sun, H.; Adhyaksa, G. W. P.; Garnett, E. C. The Application of Electron Backscatter Diffraction on Halide Perovskite Materials. *Adv. Energy Mater.* **2020**, *10* (26), 2000364.
382. Michler, G. H. *Electron Microscopy of Polymers*, Springer-Verlag: Berlin Heidelberg, 2008.
383. Jamnik, J.; Maier, J. Generalised Equivalent Circuits for Mass and Charge Transport: Chemical Capacitance and its Implications. *Phys. Chem. Chem. Phys.* **2001**, *3* (9), 1668–1678.
384. Jamnik, J.; Maier, J. Treatment of the Impedance of Mixed Conductors Equivalent Circuit Model and Explicit Approximate Solutions. *J. Electrochem. Soc.* **1999**, *146* (11), 4183–4188.
385. Lai, W.; Haile, S. M. Impedance Spectroscopy as a Tool for Chemical and Electrochemical Analysis of Mixed Conductors: A Case Study of Ceria. *J. Am. Ceram. Soc.* **2005**, *88* (11), 2979–2997.
386. Senocrate, A.; Maier, J. Solid-State Ionics of Hybrid Halide Perovskites. *J. Am. Chem. Soc.* **2019**, *141* (21), 8382–8396.
387. Wilson, J. N.; Frost, J. M.; Wallace, S. K.; Walsh, A. Dielectric and Ferroic Properties of Metal Halide Perovskites. *APL Mater.* **2019**, *7* (1), 010901.
388. Maier, J. Equilibrium thermodynamics of the real solid. In *Physical Chemistry of Ionic Materials*, Wiley, 2004; pp 108–267.

389. Sun, L.; Park, S. S.; Sheberla, D.; Dincă, M. Measuring and Reporting Electrical Conductivity in Metal-Organic Frameworks: Cd₂(TFTB) as a Case Study. *J. Am. Chem. Soc.* **2016**, *138* (44), 14772–14782.
390. Gottesman, R.; Haltzi, E.; Gouda, L.; Tirosh, S.; Bouhadana, Y.; Zaban, A.; Mosconi, E.; De Angelis, F. Extremely Slow Photoconductivity Response of CH₃NH₃PbI₃ Perovskites Suggesting Structural Changes under Working Conditions. *J. Phys. Chem. Lett.* **2014**, *5* (15), 2662–2669.
391. Savenije, T. J.; Guo, D.; Caselli, V. M.; Hutter, E. M. Quantifying Charge-Carrier Mobilities and Recombination Rates in Metal Halide Perovskites from Time-Resolved Microwave Photoconductivity Measurements. *Adv. Energy Mater.* **2020**, *10* (26), 1903788.
392. Weir, C. E.; Lippincott, E. R.; Van Valkenburg, A.; Bunting, E. N. Infrared Studies in the 1- to 15-Micron Region to 30,000 Atmospheres. *J. Res. Natl. Bur. Stand., Sect. A* **1959**, *63a* (1), 55–62.
393. Jamieson, J. C.; Lawson, A. W.; Nachtrieb, N. D. New Device for Obtaining X-Ray Diffraction Patterns from Substances Exposed to High Pressure. *Rev. Sci. Instrum.* **1959**, *30* (11), 1016–1019.
394. Li, M.; Liu, T.; Wang, Y.; Yang, W.; Lü, X. Pressure Responses of Halide Perovskites with Various Compositions, Dimensionalities, and Morphologies. *Matter Radiat. Extremes* **2020**, *5* (1), 018201.
395. Chapter 4: Optical properties of semiconductors under pressure. In *Semiconductors and Semimetals*; Goñi, A. R., Syassen, K., Suski, T., Paul, W., Eds.; vol. 54; Elsevier, 1998; pp 247–425.
396. Chapter 7: Diamond anvil cells in high-pressure studies of semiconductors. In *Semiconductors and Semimetals*; Yousuf, M., Suski, T., Paul, W., Eds.; vol. 55; Elsevier, 1998; pp 381–436.
397. Wang, Y.; Lü, X.; Yang, W.; Wen, T.; Yang, L.; Ren, X.; Wang, L.; Lin, Z.; Zhao, Y. Pressure-Induced Phase Transformation, Reversible Amorphization, and Anomalous Visible Light Response in Organolead Bromide Perovskite. *J. Am. Chem. Soc.* **2015**, *137* (34), 11144–11149.
398. Jaffe, A.; Lin, Y.; Beavers, C. M.; Voss, J.; Mao, W. L.; Karunadasa, H. I. High-Pressure Single-Crystal Structures of 3D Lead-Halide Hybrid Perovskites and Pressure Effects on their Electronic and Optical Properties. *ACS Cent. Sci.* **2016**, *2* (4), 201–209.
399. Jaffe, A.; Lin, Y.; Mao, W. L.; Karunadasa, H. I. Pressure-Induced Metallization of the Halide Perovskite (CH₃NH₃)PbI₃. *J. Am. Chem. Soc.* **2017**, *139* (12), 4330–4333.
400. Kitagawa, H.; Sato, H.; Kojima, N.; Kikegawa, T.; Shimomura, O. Metallization and Phase Transitions of the Three-Dimensional Halogen-Bridge Mixed-Valence Complex Cs₂Au₂I₆ under High Pressure. *Solid State Commun.* **1991**, *78* (11), 989–995.
401. Kojima, M.; Kitagawa, H.; Ban, T.; Amita, F.; Nakahara, M. Semiconductor-to-Metal and Metal-to-Metal Transitions in the Three-Dimensional Mixed-Valence Compound Cs₂Au₂I₆ under High Pressures. *Solid State Commun.* **1990**, *73* (11), 743–745.
402. Hafner, S. S.; Kojima, N.; Stanek, J.; Zhang, L. Divalent gold in perovskite type CsAuI₃. *Phys. Lett. A* **1994**, *192* (5), 385–388.
403. Miltz, D. B.; Liang, K. Synthesis, Resistivity, and Thermal Properties of the Cubic Perovskite NH₂CH=NH₂SnI₃ and Related Systems. *J. Solid State Chem.* **1997**, *134* (2), 376–381.
404. Takahashi, Y.; Hasegawa, H.; Takahashi, Y.; Inabe, T. Hall Mobility in Tin Iodide Perovskite CH₃NH₃SnI₃: Evidence for a Doped Semiconductor. *J. Solid State Chem.* **2013**, *205*, 39–43.
405. Noel, N. K.; Stranks, S. D.; Abate, A.; Wehrenfennig, C.; Guarnera, S.; Haghighirad, A.-A.; Sadhanala, A.; Eperon, G. E.; Pathak, S. K.; Johnston, M. B.; Petrozza, A.; Herz, L. M.; Snaith, H. J. Lead-Free Organic-Inorganic Tin Halide Perovskites for Photovoltaic Applications. *Energy Environ. Sci.* **2014**, *7* (9), 3061–3068.
406. Nakamura, T.; Yakumar, S.; Truong, M. A.; Kim, K.; Liu, J.; Hu, S.; Otsuka, K.; Hashimoto, R.; Murdey, R.; Sasamori, T.; Kim, H. D.; Ohkita, H.; Handa, T.; Kanemitsu, Y.; Wakamiya, A. Sn(IV)-Free Tin Perovskite Films Realized by In Situ Sn(O) Nanoparticle Treatment of the Precursor Solution. *Nat. Commun.* **2020**, *11* (1), 3008.
407. Handa, T.; Yamada, T.; Kubota, H.; Ise, S.; Miyamoto, Y.; Kanemitsu, Y. Photocarrier Recombination and Injection Dynamics in Long-Term Stable Lead-Free CH₃NH₃SnI₃ Perovskite Thin Films and Solar Cells. *J. Phys. Chem. C* **2017**, *121* (30), 16158–16165.
408. Jokar, E.; Chien, C.-H.; Tsai, C.-M.; Fathi, A.; Diau, E. W.-G. Robust Tin-Based Perovskite Solar Cells with Hybrid Organic Cations to Attain Efficiency Approaching 10%. *Adv. Mater.* **2019**, *31* (2), 1804835.
409. Kim, G. Y.; Senocrate, A.; Moia, D.; Maier, J. Ionically Generated Built-in Equilibrium Space Charge Zones—A Paradigm Change for Lead Halide Perovskite Interfaces. *Adv. Funct. Mater.* **2020**, *30* (31), 2002426.
410. Yang, T.-Y.; Gregori, G.; Pellet, N.; Grätzel, M.; Maier, J. The Significance of Ion Conduction in a Hybrid Organic-Inorganic Lead-Iodide-Based Perovskite Photosensitizer. *Angew. Chem. Int. Ed.* **2015**, *54* (27), 7905–7910.
411. Yamada, K.; Isobe, K.; Tsuyama, E.; Okuda, T.; Furukawa, Y. Chloride Ion Conductor CH₃NH₃GeCl₃ Studied by Rietveld Analysis of X-Ray Diffraction and ³⁵Cl NMR. *Solid State Ion.* **1995**, *79*, 152–157.
412. Yamada, K.; Kuranaga, Y.; Ueda, K.; Goto, S.; Okuda, T.; Furukawa, Y. Phase Transition and Electric Conductivity of AsnCl₃ (A = Cs and CH₃NH₃). *Bull. Chem. Soc. Jpn.* **1998**, *71* (1), 127–134.
413. Maeda, M.; Hattori, M.; Hotta, A.; Suzuki, I. Dielectric Studies on CH₃NH₃PbX₃ (X = Cl and Br) Single Crystals. *J. Phys. Soc. Jpn.* **1997**, *66* (5), 1508–1511.
414. Senocrate, A.; Moudrakovski, I.; Acartürk, T.; Merkle, R.; Kim, G. Y.; Starke, U.; Grätzel, M.; Maier, J. Slow CH₃NH₃⁺ Diffusion in CH₃NH₃PbI₃ under Light Measured by Solid-State NMR and Tracer Diffusion. *J. Phys. Chem. C* **2018**, *122* (38), 21803–21806.
415. Meggiolaro, D.; Mosconi, E.; De Angelis, F. Formation of Surface Defects Dominates Ion Migration in Lead-Halide Perovskites. *ACS Energy Lett.* **2019**, *4* (3), 779–785.
416. Walsh, A.; Scanlon, D. O.; Chen, S.; Gong, X. G.; Wei, S.-H. Self-Regulation Mechanism for Charged Point Defects in Hybrid Halide Perovskites. *Angew. Chem. Int. Ed.* **2015**, *54* (6), 1791–1794.
417. Xing, J.; Wang, Q.; Dong, Q.; Yuan, Y.; Fang, Y.; Huang, J. Ultrafast Ion Migration in Hybrid Perovskite Polycrystalline Thin Films under Light and Suppression in Single Crystals. *Phys. Chem. Chem. Phys.* **2016**, *18* (44), 30484–30490.
418. Eperon, G. E.; Hörantner, M. T.; Snaith, H. J. Metal Halide Perovskite Tandem and Multiple-Junction Photovoltaics. *Nat. Rev. Chem.* **2017**, *1* (12), 0095.
419. Sadhanala, A.; Ahmad, S.; Zhao, B.; Giesbrecht, N.; Pearce, P. M.; Deschler, F.; Hoyer, R. L. Z.; Gödel, K. C.; Bein, T.; Docampo, P.; Dutton, S. E.; De Volder, M. F. L.; Friend, R. H. Blue-Green Color Tunable Solution Processable Organolead Chloride–Bromide Mixed Halide Perovskites for Optoelectronic Applications. *Nano Lett.* **2015**, *15* (9), 6095–6101.
420. Suarez, B.; Gonzalez-Pedro, V.; Ripolles, T. S.; Sanchez, R. S.; Otero, L.; Mora-Sero, I. Recombination Study of Combined Halides (Cl, Br, I) Perovskite Solar Cells. *J. Phys. Chem. Lett.* **2014**, *5* (10), 1628–1635.
421. Bischak, C. G.; Hetherington, C. L.; Aloni, S.; Ogletree, D. F.; Limmer, D. T.; Ginsberg, N. S. Origin of Reversible Photoinduced Phase Separation in Hybrid Perovskites. *Nano Lett.* **2017**, *17* (2), 1028–1033.
422. Knight, A. J.; Herz, L. M. Preventing Phase Segregation in Mixed-Halide Perovskites: A Perspective. *Energy Environ. Sci.* **2020**, *13* (7), 2024–2046.
423. Brennan, M. C.; Ruth, A.; Kamat, P. V.; Kuno, M. Photoinduced Anion Segregation in Mixed Halide Perovskites. *Trends Chem.* **2020**, *2* (4), 282–301.
424. Slotcavage, D. J.; Karunadasa, H. I.; McGehee, M. D. Light-Induced Phase Segregation in Halide-Perovskite Absorbers. *ACS Energy Lett.* **2016**, *1* (6), 1199–1205.

4.16 Solid state inorganic color pigments: Ancient to modern

Jun Li, L. Sandhya Kumari, and M.A. Subramanian, Department of Chemistry, Oregon State University, Corvallis, OR, United States

© 2023 Elsevier Ltd. All rights reserved.

4.16.1	Introduction	560
4.16.2	Pigments through ages	561
4.16.3	Origin of color	562
4.16.3.1	Color due to <i>d-d</i> transitions	563
4.16.3.2	Color due to charge transfer transitions	564
4.16.3.3	Color due to band to band (band gap) transitions	567
4.16.3.4	Color due to defects (color centers)	569
4.16.3.5	Color due to other reasons	569
4.16.4	Structure, geometry and color of the inorganic chromophore ions	571
4.16.5	Inorganic pigments with transition metal chromophores at tetrahedral, octahedral, square pyramidal and square planar environments	572
4.16.6	Inorganic pigments with transition metal chromophores at trigonal bipyramidal coordination: YInMn blues and beyond	576
4.16.6.1	The Y(In,Mn)O ₃ blue	578
4.16.6.2	The Y(In,Mn/Ti/Zn/Al)O ₃ purple	580
4.16.6.3	The Y(In,Fe)O ₃ orange	583
4.16.6.4	The Y(In,Cu/Ti)O ₃ green	583
4.16.6.5	The Y(Al,M)O ₃ pigments	585
4.16.6.6	The Y(In,Mn)O ₃ blues and beyond	587
4.16.7	Rare earth oxides based pigments	589
4.16.8	Sulfides and oxynitrides	589
4.16.9	Concluding remarks	589
Acknowledgment		590
References		590

Abstract

Materials with various colors have always fascinated humans from prehistory to the present. They brought and continue to bring joy to our daily life by making the world a more beautiful place to live in and influence our feelings. The important factor that decides the color of a material is its interaction with light in the visible range (400–750 nm) sensitive to human eye. Compared with organic dyes, inorganic pigments exhibit better resistance to heat, light, weathering, solvents and chemicals, widely used as artist colors, exterior coatings and heat reflecting paints. Although fundamentals of the color science about gemstones and minerals are well-understood, it is difficult to predict the color of inorganic solids before they are prepared experimentally. Serendipity often plays a role in the discovery of many important colored compounds such as YInMn Blue. This chapter chronicles the historical importance of inorganic pigments, reviews the origin of color in solids and illustrates the correlation of the metal ion coordination/local environment and color. In general, transition metal chromophores with a coordination environment of less symmetry and more mixing between the *p* and *d* orbitals will have a greater probability of producing intense colors due to the relaxation of selection rules for the *d-d* transitions. Charge transfer transitions usually have high transition probabilities (laporte allowed), giving intense colors, and tend to dominate crystal field transition colors when both are present. The band to band transitions in sulfides and oxynitrides are perfect to give the desired pure color rather than in oxides. Designing durable, nontoxic and multifunctional inorganic pigments with brilliant colors is quite challenging, and a deep understanding of the structure-property relationship in this respect can be helpful.

4.16.1 Introduction

Although color is the most strikingly property of materials, it is often overlooked. It contributes to the value of gems and also provides an aid in mineral identification. In addition, color can provide useful information regarding their chemistry and crystal structure that underpin the observed fundamental properties. The quest for finding materials with intense and durable colors has preoccupied humans from prehistory to the present. Colored solids have always fascinated the scientists to explore the scientific facts behind the beauty and perfection. The color science in gemstones and minerals has been widely reviewed.^{1–3} Still it is difficult to predict the color in solids simply by any one of the known chemical and physical mechanisms which are responsible for observed

colors. Inorganic pigments are particularly interesting colored solids finding multifunctional applications especially as artist colors, exterior coatings and also as cool heat reflecting paints.^{4–6} Pigments are colored, black, white, or fluorescent solids (color effect) and they may be organic or inorganic. They are physically and chemically unaffected by the vehicle or substrate in which they are incorporated. They alter appearance by wavelength selective absorption and/or by scattering of light. Pigments can be classified by their chemical composition, and optical and/or technical properties. Organic dyes (sometimes referred to as pigments by non-specialists) are amazingly brilliant in their colors which arise from the charge transfer transitions in conjugated chromophore groups with π electrons.⁷ Even though, inorganic pigments lack the intensity and brightness of color of typical organic pigments, they are superior over the latter in terms of providing excellent resistance to heat, light, weathering, solvents and chemicals, and they are usually high refractive index materials providing high opacity.^{8,9} Generally, inorganic pigments are either oxides, sulfides, sulfoselenides or oxyhalides.¹⁰

This chapter chronicles the historical importance of inorganic pigments, the origin of color in solids and correlation of the metal ion coordination and color. It also demonstrates the challenges in developing a stable, nontoxic and bright colored pigments as it involves selective absorption according to wavelength—the result of various electronic transitions whose energies correspond to certain wavelengths of visible light—gives materials their distinctive colors. Although the origin of color in minerals are well understood, it is difficult to predict the precise color of a compound before it is made without knowing all the local crystal structural details. In fact, most of the pigments we come across today were discovered by “accident” or serendipity as the initial goal of the research has nothing to do with discovery of intensely colored compounds. Throughout history, such accidents have produced new coloring materials for artists and paint industry. Some pigments, it’s true, came from rationally designed experiments to make them—but given the limited understanding of chemical principles, and especially any real notion of how composition and crystal structure relates to color, the discovery of new pigments has mostly been a “chance” affair. Developing a stable, durable and brilliantly colored oxide is truly a challenging task and needs more scientific understanding of the crystal chemistry and the band structures. Solid state chemistry can play an important role in designing new colored oxides as many intense colors arise from the electronic transitions favored by structural distortions or asymmetry in the metal polyhedron.

4.16.2 Pigments through ages

Colored minerals, earths and ochres, have been used constantly used by all civilizations for art, decorations and outdoor coloring. Despite of their less brightness, they were formed naturally and offered wide range of tints and hues for artistic expressions and proved to be very stable. The first known pigments date to the early Paleolithic period, where they used red earths for cave paintings and ochres for other decorations.¹¹ Ochres are mixtures of quartz sand, clay (kaolin) and hematite (iron oxide, Fe_2O_3) also called, sanguine (the name is derived from Greek and French words for blood) with various hues ranging from brown, yellow, red and violet. Ochres with hematite crystals are red while the yellow ochre contains goethite (yellow iron oxide). Blacks are the manganese rich ochre. The red tints were sometimes made from yellow ochres by heating them. Cave paintings of Altamira in North Spain suggests that red color predominates in the prehistoric cave paintings. The walls of Lascaux caves in France (15,000 BCE) were found to be painted with red and yellow sandy ochres, manganese oxide browns and blacks and calcite white.¹¹ It is interesting to note that the colors like blue and green were absent in the ancient paintings and can be attributed to the scarcity of the blue minerals or the lack of luminosity of green especially in darker settings like in caves.^{12–14} The palette of the primitive artist was quite limited and contain only dull earth shades.

Ancient Blue pigments were lapis lazuli (now known as ultramarine) or $(\text{Na}_7\text{Al}_6\text{Si}_6\text{O}_{24}\text{S}_3)$ and Egyptian blue $(\text{CaCuSi}_4\text{O}_{10})$. Sometimes called “true blue,” ultramarine is made from the semiprecious gemstone lapis lazuli, which for centuries could only be found in the mountain ranges of Afghanistan.¹⁵ Egyptian traders began importing the stone as early as 6000 years ago, using it to adorn jewelry and head dresses. Yet they could never figure out how to synthesize a vibrant pigment from it. Mixed with minerals such as calcite, pyrite, augite, and mica, lapis loses its potency when it is ground up, turning from a bright blue to dull grey powder. This blue pigment derived from Lapis Lazuli was costlier than gold.¹¹ Egyptian blue—the first color to be synthetically produced—was invented in Ancient Egypt around 2200 BCE To create this pigment, Egyptians combined limestone and sand with a copper-containing mineral (such as azurite or malachite) and heated to high temperatures and the end result was an opaque turquoise blue colored solid which could be crushed up to make up the blue pigment.¹⁵

Ancient green pigments were Terra Verte $(\text{K}[(\text{Al}, \text{Fe}^{3+}), (\text{Fe}^{2+}, \text{Mg})](\text{AlSi}_3\text{Si}_4\text{O}_{10}(\text{OH})_2)$, malachite $(\text{Cu}_2\text{CO}_3(\text{OH})_2)$, and atacamite $(\text{Cu}_2\text{Cl}(\text{OH})_3)$.¹¹ Necessity for more colors for artistic expressions grew the innovative ideas of alchemists to excavate the minerals and study them for new possibilities. Egyptians added more colors to painting or art by introducing light and dark blue, green, violet and golden yellow. For red, they used arsenic sulfide, $\alpha\text{-As}_4\text{S}_4$ (realgar) and golden yellow of toxic arsenic sulfide (As_2S_3) instead of the dull yellow ochre. Apart from art, they explored the use of colored materials containing both natural and synthetic pigments as cosmetics.¹¹ Romans created many shades of violet by mixing Egyptian blue and red ochre, while green tone were made by layering yellow and blue. They also used cinnabar (HgS) red, in its mineral form which was one of the costly pigments in terms of the complication in getting the desired bright red with the correct fineness. The alchemists of ancient China artificially prepared mercuric sulfide which is known as vermilion from its elements and made it richer in color.¹⁶ More range of colors was available between 9th and 15th century and made important changes in the dyeing and painting techniques. The pottery and ceramic industry were flourished with art and colors and the famous “Iznik Pottery” used the colors of cobalt blue, emerald green and bole red (a mixture of hematite and clay containing hydrous silicates of aluminum) on colorless transparent lead glaze.¹⁷

With the advancement in pigment production, new techniques were tried to strengthen the saturation of colors by altering the relative refractive index of the medium in which pigments were dispersed.

When painting and dyeing techniques reached an advanced stage of development, new compounds were discovered like antimony sulfide and galena (lead sulfide) as black pigments. The pigment industry started flourishing with products such as Prussian blue ($\text{Fe}_4[\text{Fe}(\text{CN})_6]_3$), Scheele's green (CuHAsO_3), chrome yellow (PbCrO_4), better iron oxide pigments, and cadmium pigments.¹⁸ Bismuth oxychloride has been widely used as a pearlescent white pigment in 1960s for use in finger nail enamels, until new pearlescent pigments based on titanium dioxide were developed by research.¹⁰ Many synthetic colored pigments cadmium red ($\text{CdS}_{1-x}\text{Se}_x$), manganese blue [$\text{BaSO}_4 \cdot \text{Ba}_3(\text{MnO}_4)_2$], molybdenum red [$\text{Pb}(\text{Cr},\text{Mo},\text{S})\text{O}_4$], and mixed oxides with bismuth came onto the market.^{4,5}

Nowadays, research in the field of pigments is oriented toward the enlargement of the dichromatic set of colors together with an increased thermal and chemical stability and non-toxicity. This involves improving the color properties by optimizing through tuning the chemical compositions, crystal structures, band gap manipulation and preparative methods. There are several colored pigments discovered so far with many special properties like heat reflecting, photochromic, thermochromic, pearl/luster, and interference pigments.^{19–22} The pigments which give additional color effects like color travel, luster are called "effect pigments" and are demanding for decorative applications.²³

It is interesting to note that the pure red colored pigments are very limited to list in contrast to other colored pigments. Most of the reported oxide compositions in this category have hues far from pure red (either brown or vivid hues of reddish brown).^{24–28} Exceptions are the sulfides like cadmium sulfoselenide, vermilion (HgS) and molybdate red containing lead, all suffer from both toxicity and stability issues and are not currently used as pigments in large scale coatings.⁵ It is well known that the origin of red color in ruby (Cr^{3+} doped Al_2O_3) is *d-d* transitions arising from Cr^{3+} (d^3) occupying distorted octahedral sites of $\alpha\text{-Al}_2\text{O}_3$. However, since these *d-d* transitions are formally forbidden in the case of ideal octahedral symmetry; the transitions produce brilliant red color only in single crystals.^{4,29} Powdered ruby is pale red or pink and is not suitable as red pigment. Developing a brilliant red colored oxide is truly a challenging task and needs more scientific understanding of the crystal and the band structures.

The royal or beautiful purple color was used only in fabric dyeing during the ancient time. The alchemists played vital role in the development of vivid colors. A gold based pigment with rose-violet color was discovered in the 17th century by Andreas Cassius which became famous as purple Cassius. Similarly Prussian blue was discovered accidentally by Diesbach and Dieppel in 1704.¹⁴ The discovery of new elements like cobalt, nitrogen, manganese and chlorine, in the 18th century, engaged more chemists to involve in the search for new colored materials. Michel-Eugene Chevreul studied the psychology of colors and created the first chromatic color wheels and established the law of complementary colors.³⁰ The search for a good and bright yellow resulted in the discovery of lead chromate, by the isolation of chromium by Vauquelin in 1797.³¹ He also invented the brilliant viridian green (hydrated chromium (III) oxide). The ideal yellow chromate pigment was widely used for many applications including the road yellow markings due to their durability and temperature tolerance.³² But it was phased out of market for toxicity reasons. In fact, it is still a challenge to develop pigment that mimic lead chromate's color and ability to withstand the daily exposure to UV light for some special applications like the one stated above. Toxicity disfavored many brilliant colored pigments. There were many attempts by chemists to replace the lead based pigments due to the toxicity of lead and sulfurous fumes, which led to the invention of many other lead free pigments like zinc white, silicate pigments and copper chloride based green pigments. But, unfortunately, none of them offered the brilliant color of the lead based pigments. Many of the highly toxic pigments based on lead, arsenic and mercury were replaced by the cadmium family of pigments in the 19th century.¹¹ Vivid shades like orange, red and maroon were made from the yellow cadmium sulfide by adding selenium at varying concentrations for sulfur. Cadmium red was available as a commercial product from 1919. Although cadmium is less toxic than lead and mercury, it is still toxic and has an uncertain future due to regulatory concerns. Recently cadmium yellows were partly replaced by some azo organic pigments. Molybdate orange was first introduced as a commercial pigment in 1935. Solid solutions of lead molybdate and lead chromate were reported to give red hue following the finding that mineral wulfenite (PbMoO_4) was sometimes colored strongly red when it occurred near the mineral crocoite (PbCrO_4).³³

The recent discovery of intense blue colors due to Mn^{3+} in trigonal bipyramidal (TBP) coordination as a blue chromophore is a breakthrough¹⁹ since two centuries of efforts failed to rationally design highly durable inorganic blue pigments to replace CoAl_2O_4 (cobalt is classified as carcinogen) or less durable ultramarine ($\text{Na}_7\text{Al}_6\text{Si}_6\text{O}_{24}\text{S}_3$).

The science of pigments and dyes has an ancient and fascinating history. It is interesting to note that every other primary and secondary color is highly explored except red. Synthetic iron oxide is potentially used in industry which is refined from the red ochre known since antiquity. Vermilion or cinnabar (HgS) was another choice for red in art and other decorations. Several red dyes like cochineal, aniline and alizarin were invented for fabric dyeing, but they were unsuccessful as artists' colors or pigment applications. Remarkably cadmium red was the first essential innovation in red pigments. Many new red pigments like oxynitrides, oxysulfides, rare earth based reddish brown pigments, manganese based oxides have been reported since then, but they are not suitable for commercial use for reasons like poor stability, color quality and toxicity.^{4,26,34–36}

4.16.3 Origin of color

The cause of color in gems, minerals and inorganic solids has been extensively reviewed by many physicists and mineralogists. However, the quest for intense, stable and smart colored materials for multifunctional applications, makes it necessary to discuss

more in this topic to understand the origin of color. A deep understanding in this regard can be helpful in the exploration of new compounds with exciting and unanticipated properties. Nassau has stated 15 specific causes of color, arising from a variety of physical and chemical mechanisms.^{3,29} There are mainly four types of electronic transitions that can be used to explain the color in inorganic solids, i.e., crystal field or *d-d* transitions in transition metal oxides, charge transfer transitions in compounds with multi-centered ions, band to band transitions in semiconductors, metals and color centers in solids with a non-transition element impurity ion or a crystal defect. Different types of electronic transitions in inorganic compounds are shown schematically in Fig. 1.

4.16.3.1 Color due to *d-d* transitions

Visible light absorption in many oxides which contains transition metals as a major component or as an impurity is caused by *d-d* transition which is an electronic transition between atomic orbitals confined to a single atom. Red color of Cr^{3+} doped alumina as well as Mn^{3+} doped beryl ($\text{Be}_3\text{Al}_2\text{Si}_6\text{O}_{18}$), are the consequence of ligand field electronic absorption.^{37,38} Corundum or a pure crystal of $\alpha\text{-Al}_2\text{O}_3$ crystallizes in trigonal symmetry with the oxygen ions forming a hexagonal close-packed structure and aluminum cations filling two-thirds of the octahedral interstices. Each Al^{3+} center is in slightly distorted octahedron and no absorption of visible light takes place with all the paired electrons in it. When small concentration of Cr^{3+} (d^3) replaces Al^{3+} in corundum, partially filled *d* electrons of the chromophore ion can be excited to the high energy *d* orbitals by absorbing light in the violet (${}^4\text{A}_2\text{-}{}^4\text{T}_1$), and the yellow-green regions (${}^4\text{A}_2\text{-}{}^4\text{T}_2$), giving ruby its deep red color. These two electronic transitions are spin allowed, but forbidden by orbital (parity) selection rule and is relaxed by lowering the symmetry of the metal polyhedra or vibronic coupling.³⁹ However, the actual color of ruby is red with purple overtones, which is due to the characteristic red fluorescence emission (${}^2\text{E}\text{-}{}^4\text{A}_2$). The *d-d* transitions are usually weak and produce pale color if a chromophore ion with partially filled *d* electrons is present in a perfect octahedral environment. For example, Cr^{3+} doped in LaAlO_3 is not colored as the forbidden *d-d* transition is not relaxed in the AlO_6 octahedra of the perovskite, but it shows red luminescence.⁴⁰ In ruby, the weak forbidden *d-d* transitions are enhanced in intensity due to the distorted octahedral environment around chromium ions (Fig. 2). When the local environment around the same chromophore (Cr^{3+}) changes with the immediate neighbors around it as in beryl ($\text{Be}_3\text{Al}_2\text{Si}_6\text{O}_{18}$), it results in a large shift in visible absorption and transmission of light. Even though the extent of octahedral distortion and Al–O distances are the same in both hosts, the more open structure (Fig. 3) of beryl increases the covalency of metal-oxygen bonds and reduces the crystal field strength to blue shift the optical absorption and produce green color.¹ A similar effect of increased covalency changes the color from red to green, when the concentration of Cr^{3+} increases in Al_2O_3 . The concentration of chromophore ion is important in determining the hue as well as the purity of the color. The absorption bands are polarization dependent in alexandrite (Cr^{3+} containing BeAl_2O_4) that in blue-rich light, an intense blue-green color can be perceived, resembling that of emerald, while in red-rich candlelight a deep red color is observed, like that of ruby (alexandrite effect). Here Al^{3+} is in distorted octahedral sites of orthorhombic crystal structure and Cr^{3+} substitution produces color due to the *d-d* transition.² Vanadium (V^{3+}) causes the same “alexandrite” color change effect in natural and synthetic corundum. Mainly, the first row transition elements produce beautiful colors by the crystal field sensitive electronic transitions in most of the gems. Beryl containing Mn^{2+} exhibits a delicate pink hue (morganite), while Mn^{3+} containing beryl occurs as bright red.³⁸ Mn^{2+} and Fe^{3+} ions usually produce low-intensity absorptions in the visible range and pale colors as the *d-d* transitions in them are doubly forbidden (laporte and spin) in high spin states. On the other hand, Mn^{3+} and most of the other metal ions produce stronger absorptions and brighter colors.

But interestingly, the powders of these above oxides lack the intense color which they exhibit in the crystals. In the crystals, even slight distortion of the symmetric polyhedral can promote the weak symmetry forbidden *d-d* transitions to produce brilliant colors. The intense and dichroic color in gemstones or crystals can be attributed to the fact that different wavelengths of polarized light are absorbed in varying degrees along different crystallographic optic axes. In inorganic oxide powders, strong *d-d* absorptions are noted

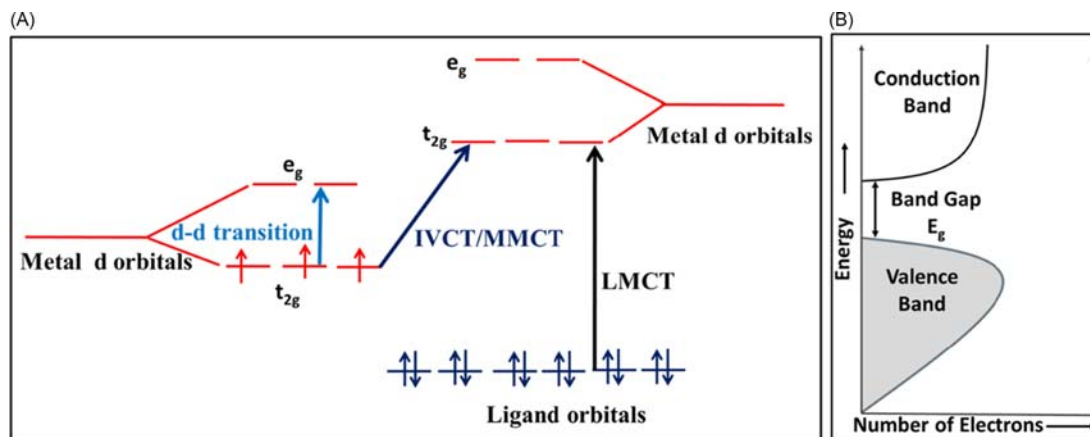


Fig. 1 Schematic representation of different types of electronic transitions: (a) *d-d* transition, intervalence charge transfer (IVCT), ligand to metal charge transfer (LMCT) and (b) band to band transitions, producing various colors in inorganic compounds.

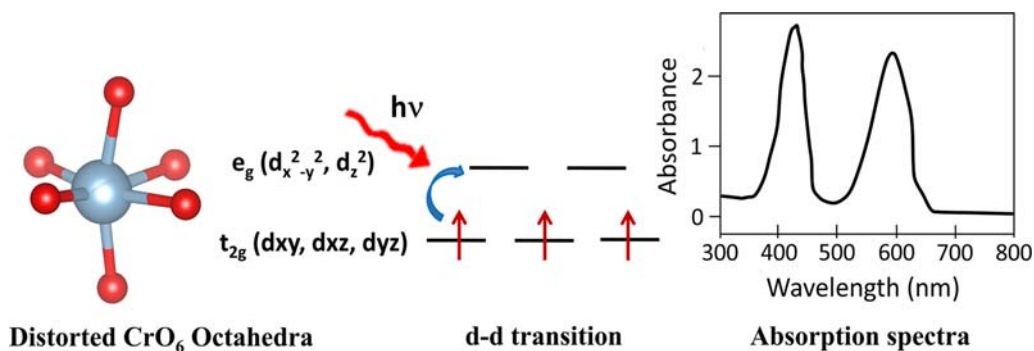


Fig. 2 The $d-d$ transition in ruby due to Cr^{3+} in distorted octahedra and the corresponding absorption spectra.

only in less symmetric environments like fivefold trigonal bipyramidal or square pyramidal geometries.^{19,41} The geometric distortions of the chromophore ions and the strength of bonding are key factors in the perfect allowed $d-d$ transitions giving bright colors. Sometimes, the color generated by the crystal field electronic transition is complicated that a same chromophore may occupy different site in the same compound, thus providing several sets of energy level schemes and resulting in superimposed absorption bands.

Like the $d-d$ transition in transition metal ions with partially filled d orbitals, $f-f$ transition in lanthanides with partially filled f orbitals can produce color in their solutions and solids. Because of the variable valency (+2 and +4 in addition to the stable +3) of the rare earths, they are known to give color effect.⁴² The color appears to depend on the number of f electrons. Light absorption by Ln^{3+} (lanthanide) ions and the resulting colors are most often due to $f-f$ transitions and less commonly, due to $f-d$ transitions. Since the electronic transitions within the f orbitals are Laporte forbidden, the intensities of the spectral bands associated within the $f-f$ transition may be low. Consequently, the spectra of lanthanide ions are rather weak and the absorption bands are narrow. While the lanthanide ions with unoccupied, half filled, or completely filled $4f$ shells (La^{3+} , Gd^{3+} , Lu^{3+}) are colorless, the remaining ions of the rare earth series exhibit characteristic colors depending on the number of available f electrons. In lanthanides, spin orbit coupling is more important than crystal field splitting and so the relaxation of forbidden transitions is rare. Rare earth based pigments like praseodymium yellow ($\text{ZrSiO}_4:\text{Pr}$) and reddish brown $\text{Ce}_{1-x}\text{Pr}_x\text{O}_2$ are widely used in the ceramic industry.^{43,44} In natural gems, rare earth metals are seldom found as the primary coloring agents. Neodymium and praseodymium usually occur together in natural gems, creating yellow and brown colors. Yellow sphen contains traces of iron (Fe^{3+}), neodymium (Nd^{3+}) and praseodymium (Pr^{3+}). Rare earth metals are also found as dopants in synthetic gems such as Ce^{3+} in yttrium aluminum garnet (yellow) and Er^{3+} and Ho^{3+} in Cubic Zirconia (pink). The radioactive metal ion, uranium (U^{4+}) in low concentration produces blue and green color in natural zircon (ZrSiO_4). The trioxide, UO_3 itself is yellow colored and are used to color glass and ceramics.⁴⁵

4.16.3.2 Color due to charge transfer transitions

Another electronic transition producing intense color in many inorganic solids and some gems with multiple centered ions or mixed valence ions is called charge transfer. Charge transfer transition can be of three different types: (a) Metal to metal charge transfer, (b) Ligand to metal charge transfer and (c) Ligand to ligand charge transfer. Metal to metal charge transfer can occur when two atoms are in close proximity to one another (i.e. transition metal ions in coordination sites sharing edges or faces) and the energy required to

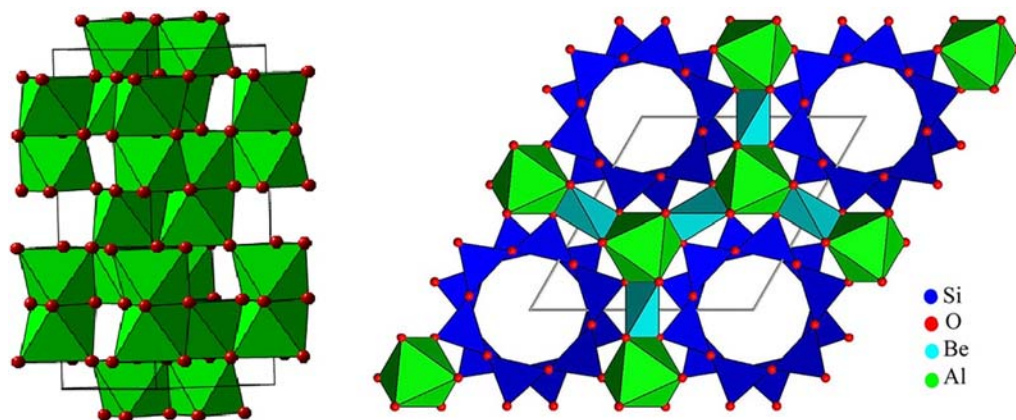


Fig. 3 Crystal structures of ruby (Al_2O_3 , Corundum, Cr^{3+} -doped) (left) and emerald ($\text{Be}_3\text{Al}_2\text{Si}_6\text{O}_{18}$, Beryl, Cr^{3+} -doped) (right).

transfer an electron from one atom to another within these compounds has been found to correspond to the energies of the visible light. Charge transfer that takes place between two different metal ions or between two similar metal ions of different oxidation state is called intervalence charge transfer (IVCT). For intervalence charge transfer to occur the metal ions should be able to adopt two different valence states. There occurs a momentary change of valences when an electron is transferred between two neighboring cations in adjacent coordination sites. A well-known example is blue sapphire, Al_2O_3 containing iron and titanium in adjacent face sharing octahedra as impurities.^{1,46} Fig. 4 shows the crystal structure of sapphire and the intervalence charge transfer from Fe^{2+} to Ti^{4+} where they occupy two adjacent face-sharing octahedra in Al_2O_3 . During this electronic transition a single electron is transferred between Fe and Ti to produce two pairs of ions in two valence states: (a) Fe^{2+} and Ti^{4+} and (b) Fe^{3+} and Ti^{3+} . This is possible as there is enough overlap between the outer orbitals of Fe^{2+} and Ti^{4+} to allow an electron to pass from one ion to another. The electron transfer involves the absorption of energy, producing a broad intense absorption band centered in the yellow-orange region and resulting in the deep blue color. The $\text{Fe}^{2+} \leftrightarrow \text{Ti}^{4+}$ intervalence transition causes green and brown color of many tourmalines (a boron silicate mineral) depending on the concentration of cation pairs. Manganese rich tourmalines are yellow green due to the charge transfer between Mn^{2+} and Ti^{4+} .⁴⁷ Most of the IVCT takes place between octahedrally coordinated cations. The intervalence charge transfer transitions are facilitated by short metal-metal interatomic distances and occur between cations located in the octahedra that are either face-sharing or edge-sharing. Very few examples with IVCT involving octahedral-tetrahedral (cordierite) and cubic-tetrahedral (garnet) pairs are known.³⁹ Garnets providing vivid geometric environments for its constituent ions are dramatically colored due to intervalence charge transfer transitions between $\text{Mn}^{2+} \leftrightarrow \text{Fe}^{3+}$, $\text{Mn}^{2+} \leftrightarrow \text{Ti}^{4+}$ etc. Many compounds with metal ions in mixed valence state are recognized for their unusual color by the typical intervalence charge transfer transitions.

In Prussian blue ($\text{Fe}_4^{3+}[\text{Fe}^{2+}(\text{CN})_6]_3$), the blue color arises from the spin allowed intervalence charge transfer between Fe^{2+} and Fe^{3+} ions.⁴⁸ Here, the Fe^{2+} and Fe^{3+} ions form a face centered cubic array with the CN^- ions octahedrally surrounding the metal ions. The two distinct iron cations are located in the octahedral voids formed by carbon ends of the cyanide ligands as well as those formed by the nitrogen ends of the cyanide ligands (Fig. 5). The color produced by the intervalence process also involves the change in the spin states of Fe^{2+} and Fe^{3+} ions. In this series, there are other compounds like Prussian green ($\text{Fe}^{3+}\text{Fe}^{3+}(\text{CN})_6$) and Prussian white ($\text{K}_2[\text{Fe}^{2+}\text{Fe}^{2+}(\text{CN})_6]$), where crystal field (*d-d*) transitions in Fe^{3+} produce the green color and the latter compound is colorless due to the absence of crystal field electronic transitions in the visible region.⁴⁵ The charge transfer between two adjacent Fe ions separated by oxygen atoms produces the greenish blue color in aquamarine ($\text{Be}_3\text{Al}_2\text{Si}_6\text{O}_{18}$) and vivianite [$\text{Fe}_3(\text{PO}_4)_2 \cdot 8\text{H}_2\text{O}$], where iron cations are present in two different sites.^{1,46} Many oxides containing mixed valence metal ions such as Fe_3O_4 (black), Pb_3O_4 (red) and Mn_3O_4 (black) have been used as pigments in ceramics and art.^{49,50} Cs_2SbCl_6 shows dark blue color where antimony is present in mixed valence states (+3/+5). Hydrated oxides of tungsten and molybdenum are blue-black in color due to the intervalence transition between metal ions in +5 and +6 valence states. Apart from the charge transfer involving mixed valence ions, another metal to metal charge transfer is also found to produce color in transition metal tungstates, molybdates and vanadates. The transition metal tungstates (AWO_4 , A = divalent transition metals) with wolframite structure are colored by low energy metal to metal charge transfer transitions rather than the *d-d* transitions. The metal to metal charge transfer from the occupied 3d orbitals of divalent transition metal to the unoccupied antibonding W 5d states produces various hues depending on the nature of the transition metal ion.⁵¹

The most common charge transfer in inorganic solids is the ligand to metal charge transfer (LMCT) which are broad absorptions in the near UV region extending to the visible part of the spectrum arising from the transfer of electrons from the neighboring oxygen ions to the central metal ion.³⁸ The oxygen to metal charge transfer absorption in most of the metal (d^0 or f^0) oxides (TiO_2 , CeO_2 ,

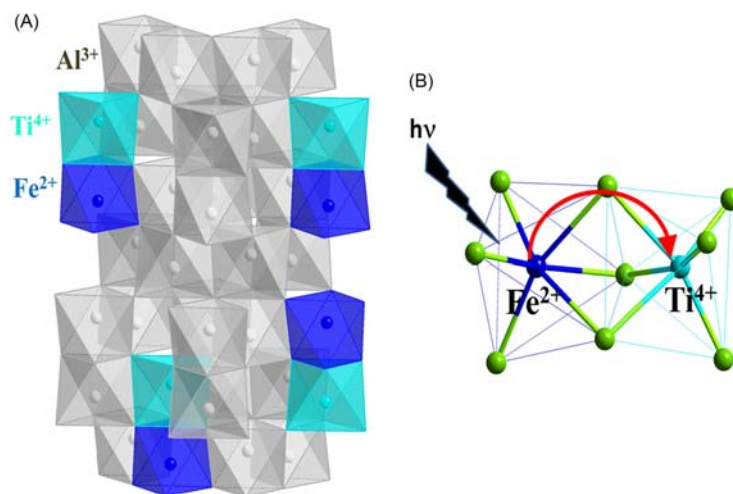


Fig. 4 (a) The crystal structure of sapphire and (b) the intervalence charge transfer from Fe^{2+} to Ti^{4+} which occupy two adjacent face-sharing octahedra in Al_2O_3 .

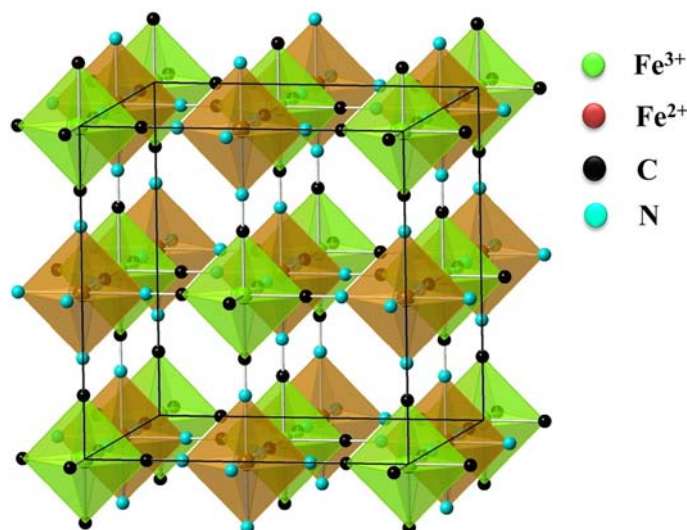


Fig. 5 The crystal structure of Prussian blue ($\text{Fe}_4^{3+}[\text{Fe}^{2+}(\text{CN})_6]_3$). Potassium ions are omitted for clarity.

MoO_3 , WO_3 etc.) are centered in the near UV region and are either white or pale colored. $\text{K}_2\text{Cr}_2\text{O}_7$ (orange) and KMnO_4 (violet) are strikingly colored by the ligand-to-metal (anion to cation) electron transfer (Fig. 6), where the effect of ligand fields can be ignored, as there are no unpaired electrons in the central metal ion (Cr^{6+} or Mn^{7+}). In golden beryl, the deep yellow color is caused mainly by $\text{O}^{2-} \rightarrow \text{Fe}^{3+}$ charge transfer.³⁷ The $\text{O}^{2-} \rightarrow \text{Fe}^{3+}$ charge transfer transitions produce similar absorption bands in corundum giving rise to a yellow color. The $\text{O}^{2-} \rightarrow \text{Fe}^{2+}$ charge transfer is centered mainly in ultraviolet and has minimal effect on color, unlike $\text{O}^{2-} \rightarrow \text{Fe}^{3+}$ charge transfer which extends into the visible region, causing yellow to brown hues in oxides. Many oxides including vanadates (VO_4^{3-}), chromates ($\text{Cr}_2\text{O}_7^{2-}$), and manganates (MnO_4^-) are colored by oxygen to metal charge transfer transitions in their tetrahedral coordinations.⁵² It is obvious that oxygen to metal charge transfer is common in all oxides and the corresponding absorption is mostly centered in the UV region. It becomes the cause of color based on the extent to which charge transfer absorption extends to the visible region. For example in ruby, there exist oxygen to metal charge transfer absorptions centered below 200 nm as well as $d-d$ transition absorptions in the visible range. Since the latter is in the visible region it is the main cause of the observed red color. The observed orange-yellow-brown colors of Fe_2O_3 (hematite) are due to presence of $d-d$ transitions and oxygen to metal charge transfer extends to the orange region of the visible spectrum transmitting only the orange-red wavelength. Also the $d-d$ transitions in Fe^{3+} (d^5) are forbidden by spin and orbital selection rules and hence charge transfer transition predominates. However, the cause of intense color displayed by Fe containing mineral is more complex than just charge transfer and will be described in later section.

There can be anion to anion charge transfer transitions which can produce color in certain minerals like lazurite (ultramarine blue), $(\text{Na,Ca})_8(\text{AlSi})_{12}\text{O}_{24}(\text{S}_2,\text{SO}_4)$. Lazurite contains sulfur molecular units (S_3^-) and transitions among the atoms in this grouping produce the deep blue color.⁵³ This mineral pigment is characterized by the sodalite structure which is composed of close-packed cuboctahedra ($\text{Al}_3\text{Si}_3\text{O}_{12}$)³⁻ called β cages.⁵⁴ The chromophore is polysulfide $[\text{S}_x]^-$ anions and are inserted in the β cages. Fig. 7 shows the sodalite crystal structure of ultramarine composed of β cages of $(\text{Al}_3\text{Si}_3\text{O}_{12})^{3-}$ and the sulfur molecular units (S_3^-) encapsulated inside the β cage. In fact, ultramarine contains the blue chromophore S_3^- and the yellow chromophore S_2^- which are tetrahedrally coordinated to the four Na^+ ions. In the bright blue ultramarine pigments, less than half of the sodalite

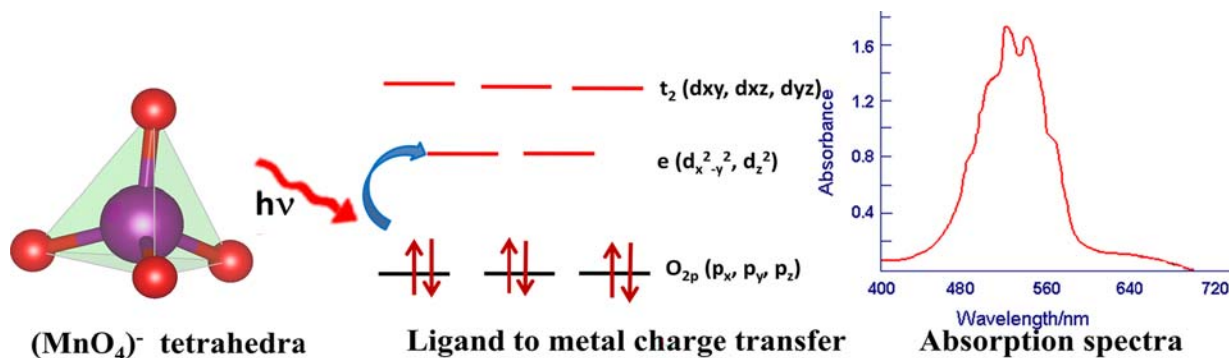


Fig. 6 Charge transfer transition in KMnO_4 from O_{2p} to Mn_{3d} (d^0) and the corresponding absorption spectra.

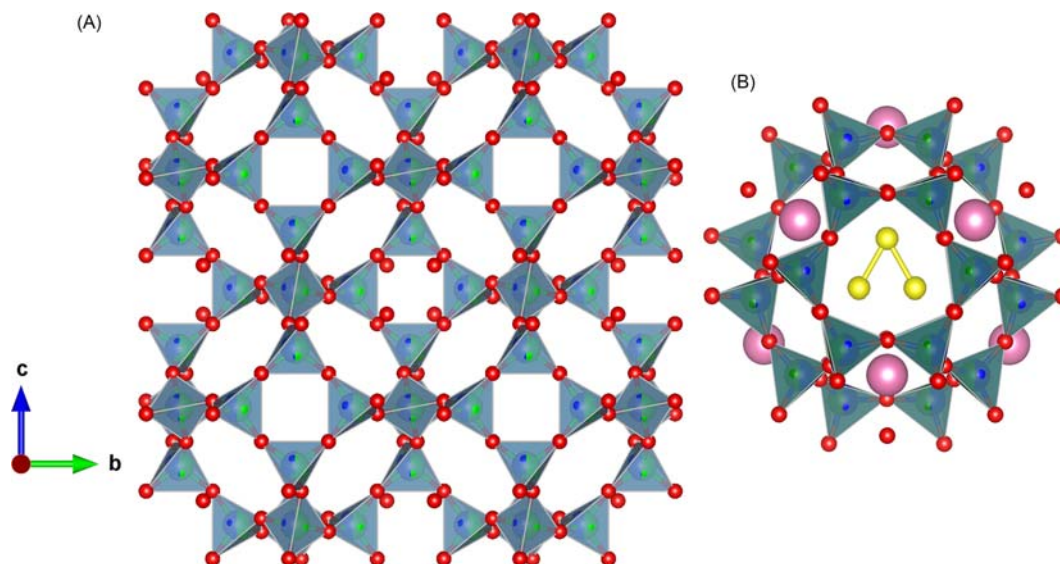


Fig. 7 (a) Sodalite structure of ultramarine composed of $(\text{Al}_3\text{Si}_3\text{O}_{12})^{3-}$ β cages and (b) the blue chromophore S_3^- anions (yellow spheres) encapsulated in the β cage surrounded by sodium cations (purple spheres).

cages are occupied by the blue chromophore S_3^- .⁵⁵ Depending on the content of sulfur in the polysulfide solid, the color varies from green, blue to pink and violet. Most organic gems like pearls and amber (a fossilized tree resin) show beautiful colors by the transition of delocalized electrons on the nonmetal molecular groups. Black color in graphite can be attributed to the movement of delocalized π -electrons between the sheets of connected six-membered rings of carbon atoms.¹ Charge transfer transitions have more transition probabilities governed by spin and parity selection rules compared to $d-d$ transitions which are transitions associated with a single metal ion. Hence charge-transfer colors are more intense, but of course the intensity of the color depends on the extent to which the charge-transfer absorption occurs in the visible portion of the spectrum. However, it is not really accurate to predict the origin of color in inorganic solids involving multiple atoms.

4.16.3.3 Color due to band to band (band gap) transitions

Color in metals and semiconductors can be explained by the band to band transition which arises from transitions of electrons localized on the entire crystal. In metals, semiconductors and crystalline solids, the distinct energy levels of numerous atoms are so close that they appear as bands.¹ These bands which are broadened by the individual energy levels are filled by available number of electrons in the band structure up to the Fermi level. The energy difference or the space between electron populated low energy band (valence band) and the empty high energy band (conduction band) is called the band gap (Fig. 8). The Fermi level is the most populated portion of the valence band and the energy separation between valence and conduction bands is crucial in determining the optical properties of many inorganic materials. The electrons on the valence band can be excited to the empty conduction band by the absorbed light and the minimum specific energy required for this electronic transition corresponds to the band gap energy (E_g) of that material.

If the band gap is smaller than the visible light range (Fig. 8), then all the light energies can be absorbed and black color results ($E_g \leq 1.7$ eV). So a dark colored material like PbS will have the absorption band starting from the UV region, extending to the entire visible range and finally falling to the near IR region. If a substance has larger band gap than 3 eV, all the visible wavelength will be transmitted and it appears colorless and the absorption band will be centered in the ultraviolet region. Colored materials will have band gap in the range 1.8–2.8 eV and exact energy of the band gap varies among different materials, so the transmitted color will also vary. In CdS, the valence band is composed of the filled 3p states of sulfur atoms and the conduction band is derived from the unoccupied 5s states of Cd. The energy difference ($E_g = 2.4$ eV) between these bands allows only the absorption of violet and some blue light and transmits all other wavelengths in the visible spectrum to produce the deep yellow color. That is, CdS will absorb all electromagnetic radiation with an energy of 2.4 eV or greater. On the other hand CdSe is a narrow band gap semiconductor with $E_g = 1.6$ eV and appears black with the absorption of entire visible light. A solid solution of these two semiconductors ($\text{CdS}_{1-x}\text{Se}_x$) can bring about beautiful red colors with a modified band structure, where only 2 eV energy is required for the inter band electronic transition (Fig. 9). The result is the transmission of only red wavelength with steep absorption edge absorbing all other colored wavelengths up to orange. Similar mechanism applies for red vermillion, HgS, with the electronic transition from S 3p valence band to Hg 6s conduction band. Recently, an interesting red metallic oxide based on $\text{Sr}_{1-x}\text{NbO}_3$ cubic perovskite is reported as an effective photocatalyst for water splitting.⁵⁶ It is quite attracting that metallic oxide without energy gap between the occupied and unoccupied bands is colored by exciting electrons within the band. Analyzing the absorption spectra of different colored compounds with unique origin of color will be helpful in understanding various causes of color.

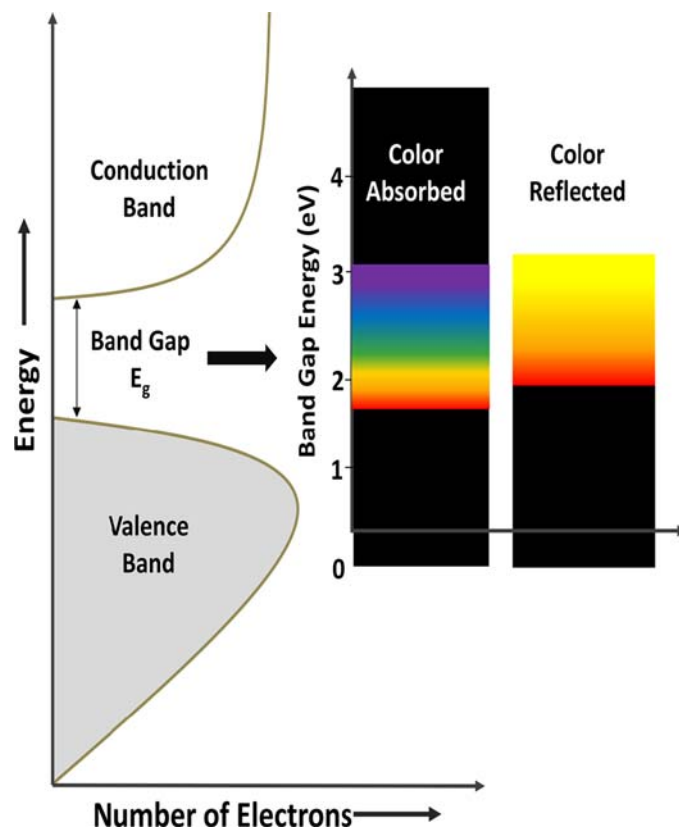


Fig. 8 Band gap energy and the color absorbed and reflected.

Some metals like gold, copper and silver have their characteristic colors and lusters due to the band to band transitions.⁵⁷ In metals, a single continuous band extends through to high energies and each energy level inside this band accommodates so many electrons. The surface of a metal can absorb all wavelengths of incident light, and excited electrons jump to a higher



Fig. 9 Band-gap colors in $\text{CdS}_{1-x}\text{Se}_x$ solid solutions. Pure cadmium sulfide (top left) has a band-gap energy of 2.6 eV, with the result that only violet light can be absorbed; the material has the color complementary to violet, namely yellow. In pure cadmium selenide (bottom left) the band-gap energy is 1.6 eV, so that all visible wavelengths are absorbed and the crystals are black. The other four materials are member of the solid solution samples showing a gradient in absorption, with colors from orange through red (2 eV).³

unoccupied energy level. The excited electrons return to the ground level rapidly and emit a photon of light of the same wavelength. So, most of the incident light is immediately re-emitted at the surface, creating the metallic luster in most of the metals. The number of available excited states may vary throughout the conduction band, so that some wavelengths are absorbed and re-emitted more efficiently than others, thus producing color. Gold owes its distinct yellow golden coloration to the ability of reflecting more yellow than other wavelengths, while silver and platinum absorb and emit all wavelengths with about the same efficiency and appear white. Different colors in metal alloys are due to the shift in energy levels relative to the Fermi level. The presence of certain impurities can affect the color as well other electronic properties of semiconductors. Striking examples are the yellow and blue color of diamond due to the presence of nitrogen and boron, respectively. Nitrogen possessing one more electron than the carbon atom, can act as a donor providing additional electronic level between the forbidden bands in diamond. The nitrogen impurity level is well below the conduction band and absorbs only violet and blue light leading to yellow color. The nitrogen donor level energy broadens into a band even if the concentration of nitrogen is very few per million carbon atoms due to thermal vibrations. Nitrogen-doped diamonds remain insulators as nitrogen is a deep impurity and an extremely rare green color can result from a higher nitrogen content of about 1 atom per 1000 atoms of carbon. Boron as an impurity in diamond forms an additional acceptor level because of shortage of one electron than carbon atom. This hole level which accepts electrons from the valence band is close to the valence band and less energy is required for the excitation of electrons between them, leading to blue color in diamond. The boron doped diamond can conduct electricity as the impurity acceptor level is shallow and ambient thermal excitation can raise electrons from the valence band into the acceptor level, and the resulting holes in the valence band act as carriers.¹ The “doping” of wide gap semiconductor by aliovalent metal species, is one of the most frequently adopted practices to provoke modifications of the bulk features of a material and its surface composition and reactivity.

4.16.3.4 Color due to defects (color centers)

Certain specimen of transparent crystals with coloration has been known for a long time. These inorganic substances without any impurity chromophore are colored due to the excitation of electrons located on non-transition element ion or on a crystal defect such as a missing ion. Color can be caused either by an electron color center (electron is present at a vacancy) or by a hole color center (electron is missing from a location). The purple color in fluorite (CaF_2) crystals is caused by the transition of electron trapped in the vacancy (Frenkel defect) created by the missing anion, F^- . Anion vacancy can be created during the growth of the crystal in presence of excess of cation or when interacted by energetic radiation. An electron usually occupies the empty position to produce the F-center (Farbe center) or electron color center to maintain electrical neutrality. This unpaired electron can then be raised to the available, higher energy levels by the absorption of energy in photons. The color generated by the transition of this single electron can be interpreted in terms of either crystal field rules of absorption or band theory.⁵⁸ As band theory applies to many crystalline inorganic solids, it is appropriate to view the single electron occupying the trap level within the wide band gap of the ionic solid. Upon excitation by ultraviolet radiation or high-energy X-rays or gamma rays, the electron is transferred to the conduction band and from there into the halide vacancy trap. The trap also contains excited energy levels as shown Fig. 10. Within the trap, the electronic transitions absorb particular wavelength depending on the ionic solid. The electronic transition due to F-centers in sodium chloride absorbs only blue light ($E_a = 2.7 \text{ eV}$), giving the solid a yellow-orange tinge. By heating the crystal, it acquires energy corresponding to E_b and the electron which is still within the trap returns to valence band via the conduction band, consequently the color is bleached. In some colored crystals the bleaching energy is smaller than the formation energy and hence exposure of such colored crystals containing F-centers to visible light bleaches the crystal to transparent when $E_a \sim E_b$.

In smoky quartz, the color is produced by the hole color center. Natural quartz containing one Al^{3+} ions per 10,000 Si^{4+} is colorless. The electrical neutrality is maintained by the presence of a nearby H^+ or Na^+ ion. Such a quartz on heating or irradiating, become smoky in color as one of a pair of electrons on an oxygen adjacent to each Al can be ejected from its position, leaving an unpaired electron (Fig. 11). The ejected electron is trapped by the H^+ electron precursor, producing the neutral H atom. The hole thus produced can have excited energy levels and light absorbing transitions. Quartz containing Fe^{3+} as an impurity, derives yellow color due to ligand field effect. The yellow crystal on heating turns purple (purple amethyst) because of the presence of hole color center. The color produced by color centers in many crystals is stable to light and those are discolored by heating can be restored by another irradiation. There are other color centers like V-centers produced by the vacancy due to missing cations, giving rise to an ultraviolet absorption band in alkali halides.

4.16.3.5 Color due to other reasons

Apart from the color in inorganic or organic solids caused by electronic transitions, there are other visual treats by natural colors arising from many other reasons. An interesting case is the faint blue color of water caused by vibrational transitions and it is the only known example of the kind. The absorbed photons promote transitions to high overtone and combination states of the nuclear motions of the molecule.⁵⁸ The intense colors of bird's plumages and butterfly can be termed as “structural color” as they are due to the presence of an array of nanostructures (organized layers or rods of a dense light scattering material) (Fig. 12). The size and spacing of these structures reflect only certain wavelengths of light, creating specific colors.⁵⁹ Color can also be caused by some physical optic effects like scattering, dispersion, interference, diffraction etc.¹ The brightness or intensity of the color of a powdered solid is governed by many factors like the specific cause of color, crystallinity etc. Especially for pigments, the refractive index of the compound and the particle size are so important in providing the perfect color for the specific application.

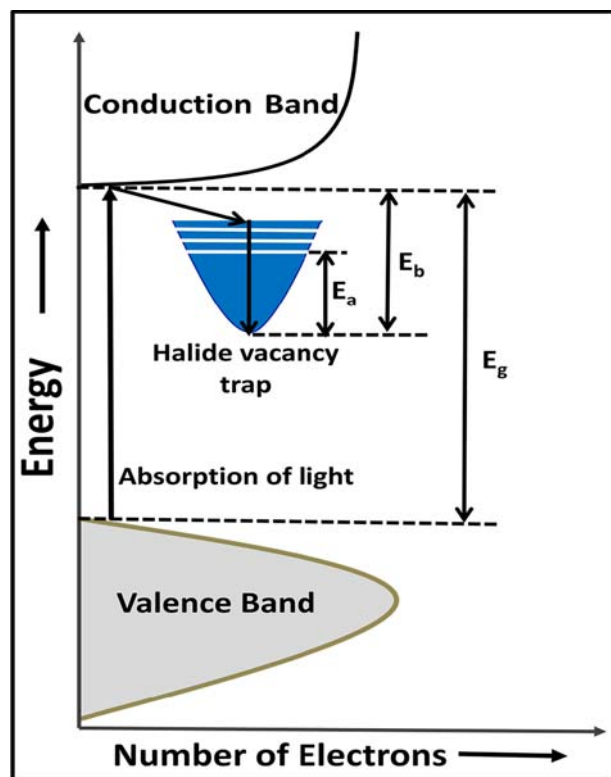


Fig. 10 Absorption due to electronic transitions within the vacancy trap (color center) in metal halide crystals due to defects.

Pigments with high refractive index are usually intensely bright colored and effectively scatter light in any medium. If a dark colored pigment is crushed and then sieved for various size ranging particles, as the particle size decreases, the amount of light scattered increases relative to the amount of light absorbed, so the smaller particles appear lighter in color. Sometimes too much grinding causes their colors to fade. The scattering power of pigment particles reaches a maximum when the particle size approaches half the wavelength of the incident light.⁶⁰

Table 1 lists all the above mentioned origins of colors in materials. They are classified under five broad types encompassing 14 different mechanisms. All but one mechanism (vibrations of the atoms in molecules) can be traced to changes in the state of electrons in matter. Electronic transitions are the most important causes of color because the energy needed to excite an electron falls in the range that corresponds to visible wavelengths of light reflecting the unabsorbed complementary color.

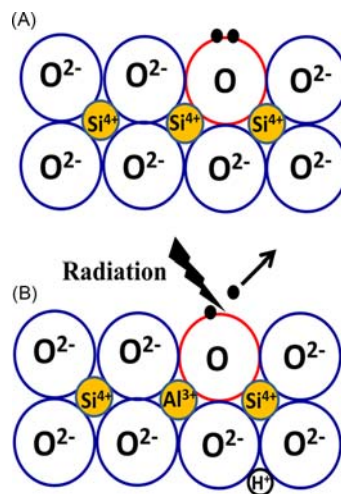


Fig. 11 The color center in smoky quartz.



Fig. 12 Structural color due to array of nanostructures on Lawes's parotia bird's feather (left) and the emerald swallowtail butterfly wings (right).⁵⁹

4.16.4 Structure, geometry and color of the inorganic chromophore ions

Although the causes of color in minerals and synthetic solid state compounds are well understood, it is difficult to predict the precise color of a compound before it is made. The current approaches to predict color transcend the conventional ideas, which attempt to attribute certain colors to certain elements in the solid: blue-green colors to copper, deep blue to cobalt, red or green to chromium, green to nickel and so on. However, this approach is not reliable. A well-known example is ruby vs. emerald. Both derive their colors from Cr^{3+} substitution into distorted AlO_6 octahedra. Dramatically different colors obtained with different hosts (Al_2O_3 and $\text{Be}_3\text{Al}_2\text{Si}_6\text{O}_{18}$) can be attributed to the differences in polyhedral distortions and covalency, which alter the $d-d$ transition absorption energies in the visible region.²⁹ Three types of metal ion coordination are common in oxides (especially in gemstones and minerals): tetrahedral (MO_4), octahedral (MO_6) and distorted cubic (MO_8). However, it should be noted that the highly idealized coordinations are rare and most of the silicate and oxide minerals have low symmetry coordination environments like distorted octahedra and tetrahedra. A metal ion with a coordination environment of less symmetry will have a greater probability of absorbing light than in a symmetric coordination site. The main reason is when a transition metal ion is not occupying a site with center of symmetry, Laporte selection rule is relaxed by the absence of center of symmetry. Also, there occurs more mixing between the ligand p and metal d orbitals and the allowed electronic transitions from p to d produce vibrant colors. Rather unusual five coordinated metal ions, MO_5 (trigonal bipyramidal and square pyramidal), can also produce intense color in oxides, where the $d-d$ transition is strong in the asymmetric environment.^{19,61} Fig. 13 shows the relative MO splitting in different metal ion coordination environments. Color due to particular chromophore dramatically changes when it occupies different coordination environment. A chromophore in single valence state can produce a variety of colors in different *gem* materials with the same metal-oxygen coordination. In such case, difference in the distance between the metal ion and the neighboring oxygen atoms matters a lot and the

Table 1 Origins of colors in materials are classified under five broad types encompassing 14 different mechanisms.²⁹

	<i>Electronic excitations</i>	<i>Incandescence flames, arcs, gas discharge</i>
<i>Electronic transitions in free atoms and ions; vibrational transitions in molecules</i>	<i>vibrations</i>	<i>Blue-green tint of pure water, icebergs</i>
Crystal-field colors	Transition-metal compounds Transition-metal impurities Color centers	Turquoise, most pigments like cobalt blue, lasers, phosphors, fluorescence Ruby, emerald, red sandstone, lasers, fluorescence Amethyst, smoky quartz, fluorescence
Electron transitions between molecular orbitals	Charge transfer Conjugated bonds	Blue sapphire, prussian blue, lapis lazuli Organic dyes, plant and animal colors, fireflies, dye lasers, fluorescence
Transitions in materials having energy bands	Metallic conductors Pure semiconductors Doped semiconductors	Copper, silver, gold, iron, brass. Silicon, galena, vermilion, diamond. cadmium yellow Blue diamond, yellow diamond, light-emitting diodes, phosphors
Geometrical physical optics structural	Dispersive refraction Scattering Interference Diffraction grating	The rainbow, "fire" in gemstones Blue sky, red of sunset, moonstone, star sapphire Oil film on water, lens coatings, bird feathers, butterfly wings Opal, liquid crystals, some insect colors

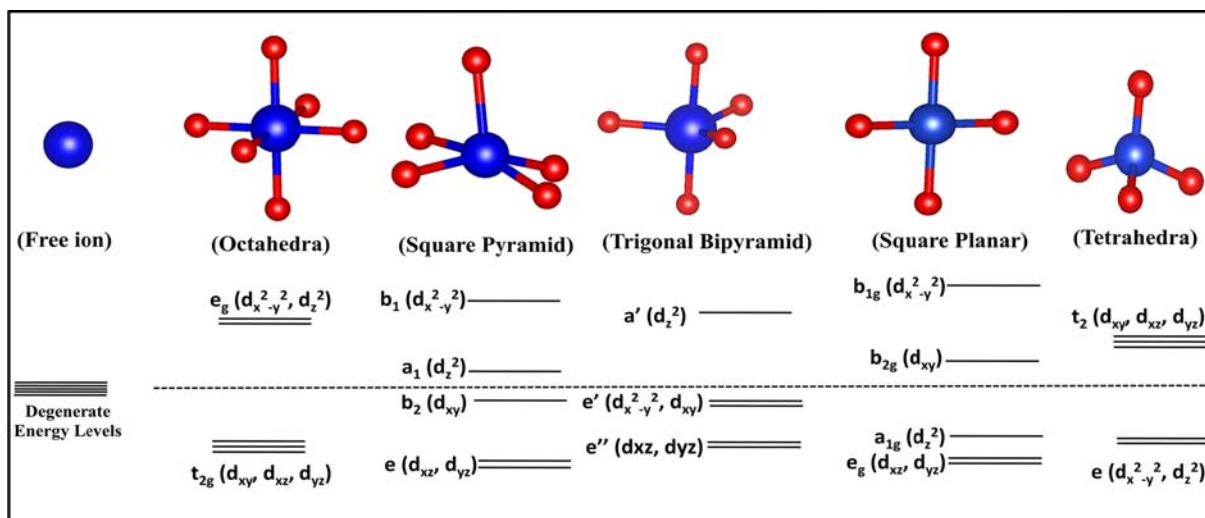


Fig. 13 Relative MO splitting levels for octahedral, square pyramidal, trigonal bipyramidal (TBP), square planar and tetrahedral coordination environments.

variation in electrostatic repulsion of the metal ions can bring about shift in the absorption spectra causing a contrast in color. The metal-oxygen bond length can be altered by the immediate neighboring cations as well as the concentration of the chromophore impurity. The preferred coordinations for various chromophore ions in different valence states are discussed below.

4.16.5 Inorganic pigments with transition metal chromophores at tetrahedral, octahedral, square pyramidal and square planar environments

Cr^{3+} prefers the octahedral site in most of the oxides like ruby, emerald and alexandrite and produces red and green colors. Cr^{3+} in octahedral coordination can also account for the purple or violet color in the rare gemstone like taaffeite ($\text{BeMg}_3\text{Al}_8\text{O}_{16}$).⁶² Large divalent chromium (Cr^{2+}) ions favor the distorted fivefold sites, which produce color in some phosphates. $\text{Cr}(\text{II})$ ions are found to give colors in phosphate single crystals like $\text{Cr}_3^{2+}\text{Ti}_4^{3+}(\text{PO}_4)_6$ (dark brown) and $\text{CrTi}_2(\text{P}_2\text{O}_7)_2$ -purple (pink powder).⁶³ In $\text{Cr}_3^{2+}\text{Ti}_4^{3+}(\text{PO}_4)_6$, Cr^{2+} ions share two independent sites like orthorhombically distorted octahedral coordination and a fivefold trigonal-bipyramidal environment whereas Ti^{3+} is in distorted octahedral environment. The absorption spectra of pink colored solid ($\text{CrTi}_2(\text{P}_2\text{O}_7)_2$) reveal the presence of $\text{Cr}^{\text{II}}\text{O}_4$ chromophore which is observed in some chromium containing silicates as well.⁶⁴ The Cr^{2+} ions occupy square pyramidal sites in SrCrP_2O_7 with isolated CrO_5 units and produce light blue color.⁶⁵ Cr^{6+} in tetrahedral coordination is mostly yellow or orange as in the case of PbCrO_4 and potassium dichromate $\text{K}_2\text{Cr}_2\text{O}_7$, respectively. Devoid of any d electrons, these solids are colored by the oxygen to metal charge transfer transitions. Charge transfer transitions usually have high transition probabilities (laporte allowed), giving intense colors, and tend to dominate crystal field transition colors when both are present.

As mentioned earlier, trivalent manganese is an interesting chromophore that gives intense blue colors when placed in the TBP coordination.¹⁹ In fact as a chromophore manganese can produce diverse colors from blue, violet, green to red and black.⁶⁶⁻⁷⁰ Most of the manganese oxides are black with di-, tri- or tetravalent manganese in octahedral coordination.^{66,71} Mn^{3+} in distorted octahedral site is responsible for the red hue in red beryl gems.³⁸ Bright orange color appears when divalent manganese is in the distorted cubic geometry in spessartine $\text{Mn}_3\text{Al}_2(\text{SiO}_4)_3$. The heat reflecting black pigment, $\text{Bi}_2\text{Mn}_4\text{O}_{10}$, contains Mn^{3+} in square pyramidal and Mn^{4+} in octahedral sites, respectively.⁷¹

Three oxo anions of manganese, blue (Mn^{5+}O_4)³⁻, green (Mn^{6+}O_4)²⁻ and purple (Mn^{7+}O_4)⁻ in tetrahedral sites are significant in colored crystalline solids. Manganese phosphate, $(\text{NH}_4)_2\text{Mn}_2(\text{P}_2\text{O}_7)_2$ known as manganese violet is a commercially used pigment.⁷² Pentavalent manganese produces turquoise or green color in tetrahedral coordination.^{73,74} Recently, intense turquoise color (Fig. 14) due to Mn^{5+} in apatite type compounds is reported.⁷⁵ Mostly, tetravalent manganese exhibits either brown or black color in octahedral coordination environments.^{72,76} Manganese (IV) oxide Li_2MnO_3 with honeycomb rock salt structure displays a red color,³⁶ where the honeycomb-ordered $[\text{LiMn}_6]$ units play a vital role in strengthening the spin allowed electronic transitions in Mn^{4+} and cause the red color as well as tunable emission in the red-yellow-green region (Fig. 15). If we make a comparison between colors produced by Cr^{3+} (d^3) and Mn^{4+} (d^3) in distorted octahedral coordination, the spin-forbidden ${}^4\text{A}_2\text{-}{}^2\text{E}$, ${}^2\text{T}_1$ transitions are likely to gain more intensity in the case of the latter due to the distortion in the edge-sharing MnO_6 and the Mn-Mn interaction in the honeycomb layered structure, which make Li_2MnO_3 a red-colored powder.

Iron oxide exists in various polymorphic forms like dark red hematite ($\alpha\text{-Fe}_2\text{O}_3$), brown yellow maghemite ($\gamma\text{-Fe}_2\text{O}_3$), and grey magnetite (Fe_3O_4).⁷⁷ Usually, minerals with dilute or isolated Fe^{3+} (d^5) are pale colored and the absorption is weak due to spin

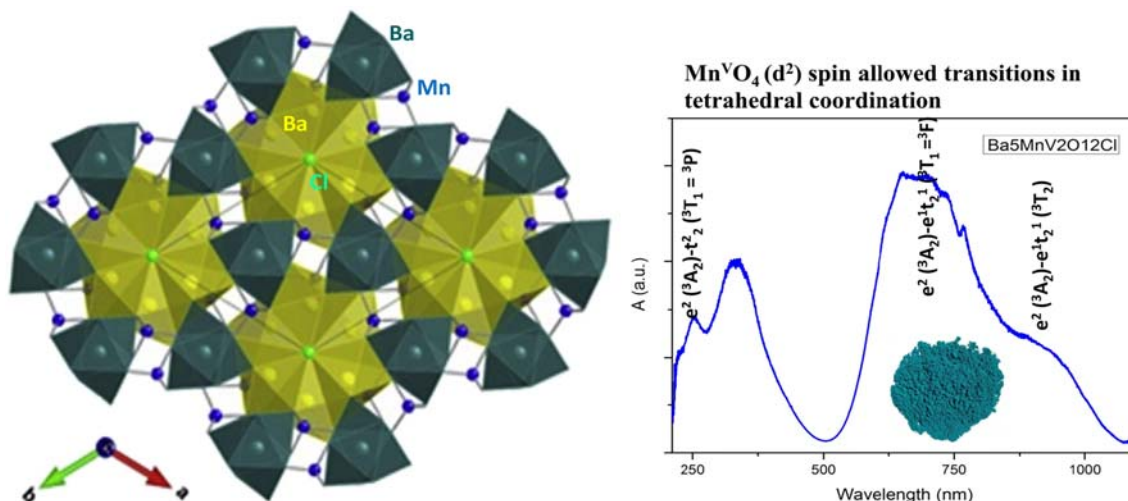


Fig. 14 Crystal structure of apatite type $\text{Ba}_5\text{Mn}_3\text{O}_{12}\text{Cl}$ and the spin allowed transitions of Mn^{5+} in tetrahedral coordination.⁷⁵

forbidden electronic transitions. The brightly yellow-orange-red colored oxides with Fe^{3+} ions are due to the O 2p-Fe 3d charge transfer transitions. As mentioned earlier, due to quantum mechanical considerations the $d-d$ transitions are forbidden by spin and orbital (Laporte) selection rules. It has been proposed that crystal-field absorption bands are greatly enhanced when Fe^{3+} cations occupy a pair of face- or edge-sharing octahedra (as in corundum structure). These Fe^{3+} ions can strongly interact magnetically and give rise to a revised selection rules that can lead to spin allowed transitions. This results in “electron pair transitions” corresponding to strong absorption band at about 475 nm which enhances the orange-yellow color of the material.^{45,78} Rossman⁷⁸ has listed the optical absorption wavelengths of iron containing oxides with respect to the geometry of Fe^{3+} ions. The oxo-linkages between Fe^{3+} provide the pathway for absorption band enhancement, leading to the deep red color in hematite, whereas green color is produced by the hydroxyl-linkages in $\text{Fe}(\text{OH})_3$.⁷⁹

Fe^{3+} can induce bright yellow to orange colors through substitution in trigonal bipyramidal sites in hexagonal YInO_3 .^[80] Dramatic modification of color can be seen in ferrous ion (Fe^{2+}) containing compounds also. The presence of ferrous iron in two slightly distorted octahedral sites produces green color in peridot $(\text{Mg}, \text{Fe})_2\text{SiO}_4$, but Fe^{2+} imparts a deep red color to almandine garnet $\text{Fe}_3\text{Al}_2(\text{SiO}_4)_3$ where it is in distorted cube.² A rare mineral Gillespite ($\text{BaFeSi}_4\text{O}_{10}$) is unusual in that it contains Fe^{2+} in a square planar four-coordinate ligand environment and is red in color.⁸¹ Fe^{2+} in more distorted site tends to have high absorption probabilities than in a more regular site.

Cobalt (Co^{2+}) is well detected for its blue or violet color in many oxides. Cobalt blue (CoAl_2O_4) is a well-known blue pigment through ages⁸² with a spinel crystal structure in which Co^{2+} ions occupy the tetrahedral sites. The crystal structure and absorption

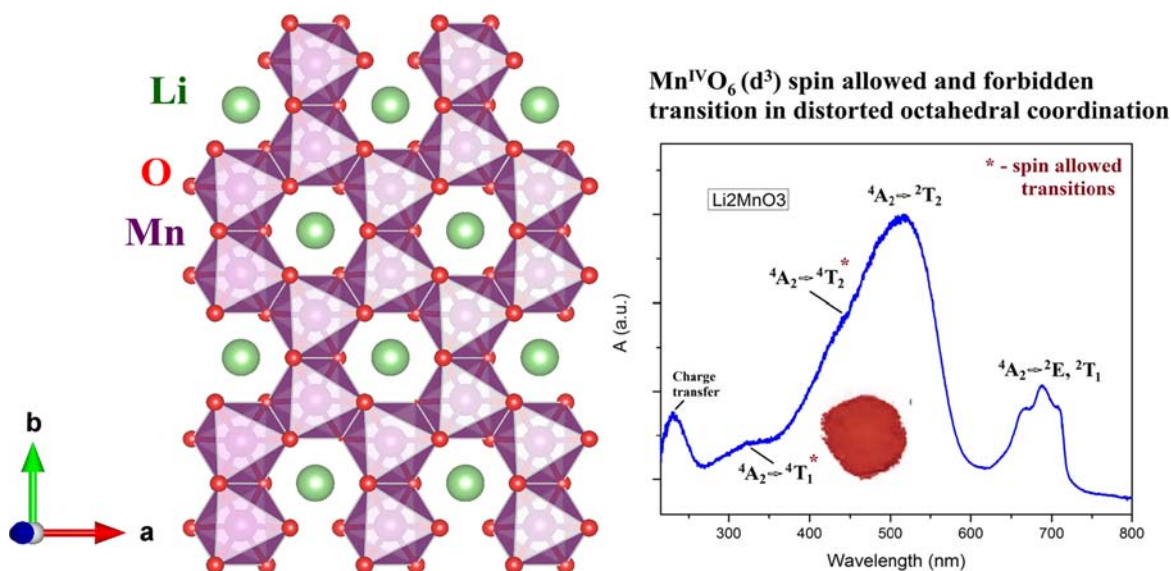


Fig. 15 Crystal structure, color and absorption spectrum of honeycomb layered Li_2MnO_3 .³⁶

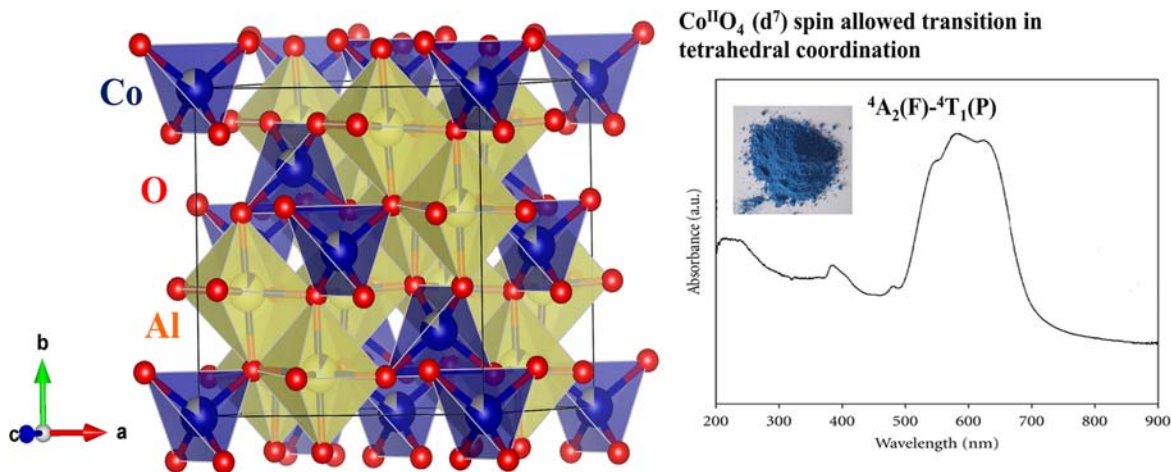


Fig. 16 Crystal structure and absorption spectrum of Cobalt blue (CoAl_2O_4) showing the spin allowed electronic transitions of Co^{2+} in tetrahedral coordination in spinel.

spectrum of cobalt blue spinel is shown in Fig. 16. In cerulean blue (Co_2SnO_4) with an inverse spinel structure Co^{2+} ions sit in both octahedral and tetrahedral sites. Cobalt blue gems have been mined from Luc Yen district of Vietnam which contain Co^{2+} as the major chromophore and also show the presence of Fe^{2+} . Hue differences like blue, skyblue and grey are controlled by the Co/Fe ratio, and the gems exhibit red luminescence under laser excitation due to Cr^{3+} impurities in the cobalt aluminate spinel.⁸³ The presence of absorption band due to Fe^{2+} can be used to distinguish between natural and synthetic spinel gems.⁸⁴ Co^{2+} appears pink in octahedral coordination of calcite known as cobaltocalcite $[(\text{Ca},\text{Co})\text{CO}_3]$. Various color hues ranging from violet, purple, blue through grey to black are observed for $\text{Co}_3(\text{PO}_4)_2$, $\text{SrCo}_2(\text{PO}_4)_2$, $\text{Co}_2\text{P}_2\text{O}_7$, BaCoP_2O_7 , SrCoP_2O_7 and $\text{LiMg}_{1-x}\text{Co}_x\text{BO}_3$ with four, five and six coordinated Co^{2+} .^{61,85} Fig. 17 shows the crystal structure of cobalt violet $\text{Co}_3(\text{PO}_4)_2$, having CoO_6 and CoO_5 in a ratio of 1:2, forming chains connected via edges. The optical transitions in these cobalt phosphates are very sensitive to the oxygen coordination and bright colors are observed for Co^{2+} in multiple geometries. Co^{2+} chromophores when tetrahedrally surrounded by sulfur atoms are green in sphalerite (ZnS), but produce blue color in blue spinel when connected to oxygens. Divalent nickel gives mostly green color in perfect octahedral sites of its oxides (NiO). But it can produce bright yellow and orange colors in distorted octahedral and fivefold square pyramidal coordination as in the case of LiNiPO_4 (olivine structure) and SrNiP_2O_7 (thortveitite structure type), respectively.^{41,86} The spinel NiAl_2O_4 is blue with the Ni^{2+} ions in both tetrahedral and octahedral sites. As already stated Cu^{2+} is prone to give blue or green color in their oxides in six or fivefold coordination.^{87,88} The first man-made blue pigment Egyptian blue, Han blue and Han purple pigments with CuO_4^{6-} chromophore unit are colored due to d-d transition in Cu^{2+} with square planar geometry.⁸⁹ The spin allowed transitions of Cu^{2+} in square planar geometry are shown in Fig. 18. Monovalent copper is reddish brown in its oxide Cu_2O due to band gap absorption with Cu^+ in octahedral symmetry.

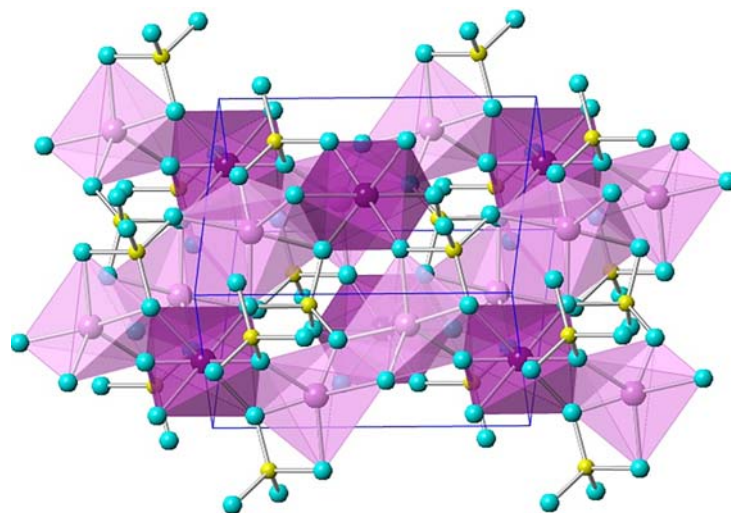


Fig. 17 The crystal structure of cobalt violet $\text{Co}_3(\text{PO}_4)_2$, containing Co^{2+} in octahedral (dark purple) and square pyramidal (light purple) polyhedra connected by PO_4 tetrahedral units.

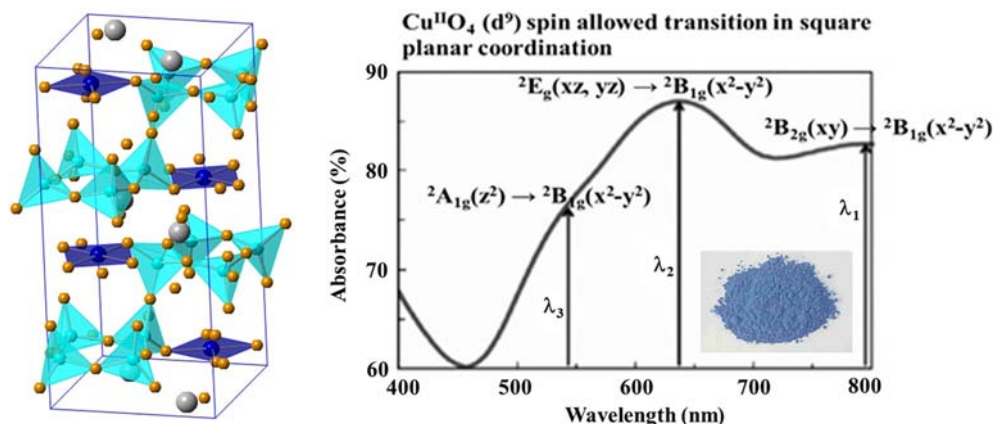


Fig. 18 Crystal structure and the spin allowed electronic transitions of Cu^{2+} in square planar coordination (blue) in Egyptian blue ($\text{CaCuSi}_4\text{O}_{10}$).

Addition of Ti^{3+} to the tetrahedral sites in silicate glass imparts a purple color.⁴⁵ Ti^{3+} in its octahedral coordination however shows only weak absorption and is easily overpowered by the absorption due to other transition metal ions in most minerals. Cohen et al. suggest Ti^{3+} gives color in rose quartz which is still under debate whether it is due to intervalence charge transfer between Fe^{2+} and Ti^{4+} .⁹⁰ When trivalent vanadium ions (V^{3+}) are the primary coloring chromophore they can create interesting green colors, as seen in mint green Merelani Garnet, lime-green vanadium Diopside and blue-green Zambian Emerald. Vanadium ions can also produce brown and yellow color in unheated Tanzanite (Zoisite, $\text{Ca}_2\text{Al}_3(\text{SiO}_4)(\text{Si}_2\text{O}_7)\text{O}(\text{OH})$), blue color in Tanzanite (V^{3+} ions are changed to V^{4+} ions with heat treatment), and blue color in Cavansite (V^{4+}). V^{3+} and V^{4+} favor the octahedral coordination in all these gemstones. Tetrahedrally coordinated V^{4+} is red in some doped silicate glasses. Vanadates with V^{5+} ions occupy tetrahedral coordination and provide mostly yellow hue by ligand to metal charge transfer transition.^{22,91}

Rare earth elements with partially filled f electrons are another choice of chromophores for colored solids. Ce, Pr, Nd, Tb, Er, and Yb in their tri- or tetravalent state occupy high coordination (6 or 8) environment and produce pink, lilac, yellow or reddish brown colors.⁹²⁻⁹⁴ Metals like Bi^{3+} and Sn^{2+} with s^2 lone pair reduce the band gap in many oxides (e.g. SnWO_4 , BiVO_4 , Bi_2WO_6) and produce yellow or orange color.^{22,95-97} Notably, the impact of lone pair electrons of the neighbor cation can produce a shift in the absorption edge and make them sharp enough to absorb the entire color and reflect others to give bright colors. In the two polymorphs of SnWO_4 , the Sn^{2+} cation is in the usual asymmetric environment favored by s^2 cations. In α - SnWO_4 the W is in octahedral coordination and produces a dark red ($E_g = 1.64$) color not attractive for pigment use whereas in β - SnWO_4 the W is in tetrahedral coordination and is almost colorless ($E_g = 2.68$). However, as in the case of α - SnWO_4 the quality of the color is poor due to a lack of sharpness of the optical band edge. The compounds $\text{Sn}_2\text{TiNbO}_6\text{F}$, $\text{Sn}_2\text{Ti}_{0.9}\text{Ta}_{1.1}(\text{O},\text{F})_7$, $\text{Sn}^{2+}_2(\text{Sn}^{4+}_{0.25}\text{W}_{1.22}\text{Sc}_{0.53})\text{O}_{6.96}$ and $\text{Sn}^{2+}_{1.4}(\text{Sn}^{4+}_{0.19}\text{Ti}_{1.06}\text{W}_{0.75})\text{O}_{6.15}$ with the pyrochlore structure (Fig. 19) are deep orange to reddish brown with band gaps in the range 2.3–1.9 eV.⁹⁸ In these cases, the band edges are sufficiently sharp to obtain bright colors. It has been shown that in oxides with Sn^{2+} the energy of the valence band based on Sn^{2+} is influenced by the degree of distortion around Sn^{2+} .⁹⁹

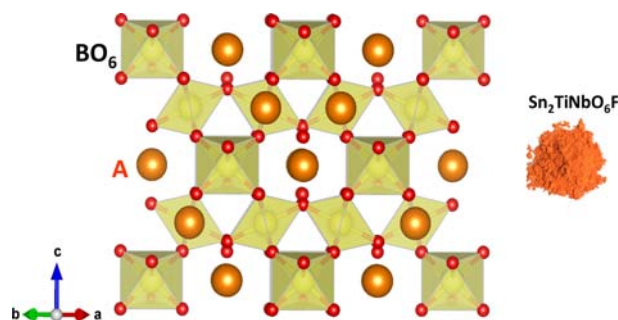


Fig. 19 Crystal structure of pyrochlore $\text{A}_2\text{B}_2\text{O}_7$ ($\text{A} = \text{Sn}$; $\text{B} = \text{Ti}, \text{Nb}$) shown as BO_6 octahedra and A cations. The color of $\text{Sn}_2\text{TiNbO}_6\text{F}$ is also shown.

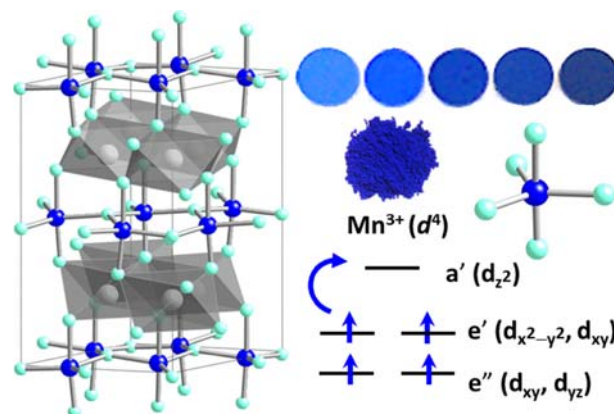


Fig. 20 Hexagonal structure of Y(In,Mn)O₃ showing In³⁺ and Mn³⁺ in blue TBP coordination, O in cyan spheres and Y in grey octahedra. Schematic energy diagram for TBP Mn³⁺ showing transitions from e' to a' that are formally dipole-allowed in this symmetry. Blue pellets from left to right are $x = 0.02, 0.05, 0.10, 0.25, 0.30$ of YIn_{1-x}Mn_xO₃ samples, indicating the resulting blue color varies with Mn content.

4.16.6 Inorganic pigments with transition metal chromophores at trigonal bipyramidal coordination: YInMn blues and beyond

While exploring a new class of manganese containing oxides for applications in electronics as magnetic capacitors, Subramanian et al.¹⁹ discovered a surprisingly intense blue color when introducing Mn³⁺ into the trigonal bipyramidal (TBP) sites of hexagonal YInO₃ (Fig. 20). Brilliant blue colors were found over much of the YIn_{1-x}Mn_xO₃ solid solution range, in spite of the fact that two end members YInO₃ and YMnO₃ are white and black, respectively. Both YInO₃ and YMnO₃ can crystallize in an acentric hexagonal structure consisting of alternating layers of edge-shared YO₆ octahedra and corner-shared MO₅ (M = In, Mn) trigonal bipyramids (Fig. 20).

Despite the large size mismatch between In³⁺ and Mn³⁺ an entire single-phase YIn_{1-x}Mn_xO₃ ($x = 0-1$) solid solution is easily fabricated by conventional solid state reactions. We attribute this complete miscibility to the similar In–O and Mn–O basal plane distances in isostructural hexagonal YInO₃ and YMnO₃. The large size difference between In³⁺ and Mn³⁺ is manifested only in the apical distances. The crystal field splitting of the d-orbital energies in TBP coordination is shown in Fig. 20. As indicated by DFT calculations of the densities of states and optical properties of the Y(In,Mn)O₃ compounds,¹⁹ the e' to a' energy excitation depends sensitively on the apical Mn–O bond length through its influence upon the energy of the d_{z²} orbital (Fig. 20).

This intense Y(In,Mn)O₃ blue is reported as “the first new inorganic blue created in more than two centuries”.^{100,101} The new blue pigments are safer to produce, much more durable and environmentally benign than any being used now or in the past. They can survive at extraordinarily high temperatures and do not fade after being treated with acids. As an added bonus, these pigments show unprecedented high heat reflectance ever seen in a blue pigment, i.e. strong reflection in near infrared region of the electromagnetic spectrum, making them ideal for painting energy efficient roofs of buildings and cars.¹⁰⁰⁻¹⁰² Moreover the increased UV absorbance, stability in QUV and outdoor weathering tests, and low HBU temperature values demonstrate that these materials offer a robust alternative to commercial blue pigments such as CoAl₂O₄.¹⁰³ The Y(In,Mn)O₃ pigment has now been labeled the new

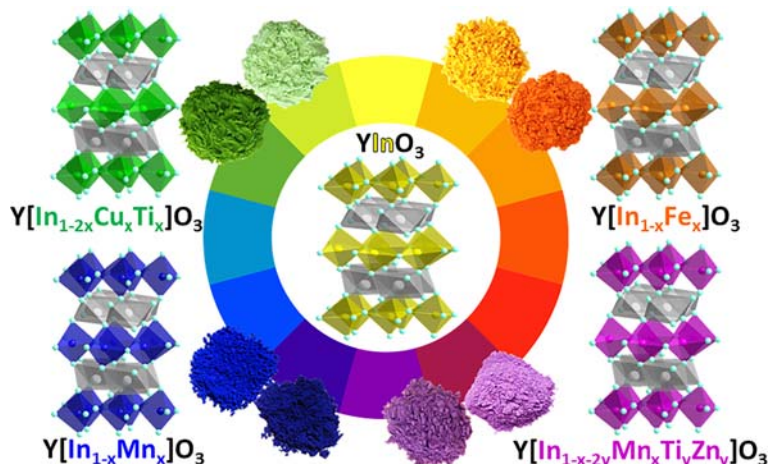


Fig. 21 A “rainbow” of colors is created through various substitutions into the TBP sites of hexagonal YInO₃.

“Blue Standard”.¹⁰⁴ A Y(In,Mn)O₃ blue sample sent to the Forbes Collection in the Straus Center for Conservation and Technical Studies at Harvard University is now kept together with 2500 other specimens that document the history of our longing for color.¹⁰⁵

So far the “happy accident” of Y(In,Mn)O₃ blue has led to discoveries of a “rainbow” of colors through rational design, as shown in Fig. 21. Starting from the hexagonal parent compound YInO₃, substituting a small amount of iron for indium produces intense orange colors, replacing some or all indium with titanium and copper generates green colors and swapping some of the manganese in blue pigments with a combination of zinc and titanium gives violet to purple colors.^{19,80,106,107} Most of these novel pigments show high durability and good heat reflecting property similar to the Y(In,Mn)O₃ blue.

Replacing Y³⁺ with other rare earth cations resulted in complete solid solutions of REIn_{1-x}Mn_xO₃ (RE = Dy, Ho, Er) with similar blue colors. Substitutions at the Y³⁺ site with small amount of Ca²⁺ or rare earth elements has little impact on the color. Crystals of YMn_{1-x}Ga_xO₃ ($x \leq 0.5$) grown by a floating zone technique have been studied for ferroelectric properties, but optical data were not reported.¹⁰⁸ Inspired by the success of intense Y(In,Mn)O₃ blue, Tamilarasan et al.⁶⁹ reported a series of metastable purple oxides YGa_{1-x}Mn_xO₃ that were prepared by a modified Pechini or sol-gel method.¹⁰⁹ Hexagonal solid solutions of InMn_{1-x}Ga_xO₃ prepared using a high-pressure technique show blue colors for compositions with low Mn content.¹¹⁰

Attempts to reduce the amount of indium led us to thorough study of the hexagonal YAlO₃-YMnO₃ solid solution synthesized by sol-gel method.⁶⁸ Although Mn-substitution did produce a navy blue color in hexagonal YAlO₃, it was not as bright as the expected color associated with TBP coordination. We found that the centric hexagonal structure of YAlO₃ reported in 1963, with Al in TBP coordination, cannot be correct based on its unit cell dimensions and bond-valence sums (BVS).¹¹¹ Our study indicated instead that all, or nearly all, of the Al in this compound has a coordination number of 6. The compound long assumed to be a hexagonal form of YAlO₃ is actually an oxycarbonate. The absence of bright color is presumably due to the destruction of TBP sites caused by carbonate substitution. This is also the case for the YAlO₃-YFeO₃ system with dull red brown colors.

It has been demonstrated that a blue color can also be obtained when Mn³⁺ is introduced into TBP sites of layered oxides other than hexagonal YInO₃ and YAlO₃. The YbFe₂O₄-related compounds contain double layers of trigonal bipyramids and are therefore potential hosts for Mn³⁺. The Mn substitution induced blue colors for ScGaZnO₄, LuGaZnO₄ and LuGaO₃(ZnO)₂ and bluish-purple colors for ScAlMgO₄, ScGaMgO₄ and LuGaMgO₄.⁶⁷

The YInMn blue discovery has motivated others to search for transition metal chromophores with TBP coordination in different structures.^{70,85,112,113} It is expected that the results will lead to routes for the development of inexpensive, environmentally benign and highly stable inorganic pigments.

Representative X-ray diffraction patterns are shown in Fig. 22 for hexagonal Y(In,M)O₃ ($M = \text{Mn, Mn/Ti/Zn, Fe, Cu/Ti}$) samples prepared by solid state reactions. All compounds crystallize in an acentric hexagonal structure (space group $P6_3cm$), a weak reflection near 20° 2θ indicating the 102 peak that arises from the ferroelectric form. The diffraction patterns for samples obtained by rapid microwave synthesis and the citrate route¹¹⁴ are similar to those in Fig. 22 with slight difference in the peak width due to particle size.

Substitution in the TBP sites of hexagonal YInO₃ always leads to perceivable contraction along the *c* axis while leaving the cell edge *a* essentially unchanged. In other words replacing In with *M* ($M = \text{Mn, Mn/Ti/Zn, Fe, Cu/Ti}$) has larger impact on the apical In(*M*)-O bond distances than on the basal-plane In(*M*)-O distances in the Y(In,*M*)O₃ solid solutions.

The optical property of a solid substance is associated with its crystal structure and composition, the local environment of chromophore ions, defects and so forth. There are many causes of color in inorganic solids²⁹: interatomic excitations or d-d transitions (CoAl₂O₄, azurite, ruby and emerald); charge transfer excitations (blue sapphire, ultramarine or Lapis Lazuli); valence to

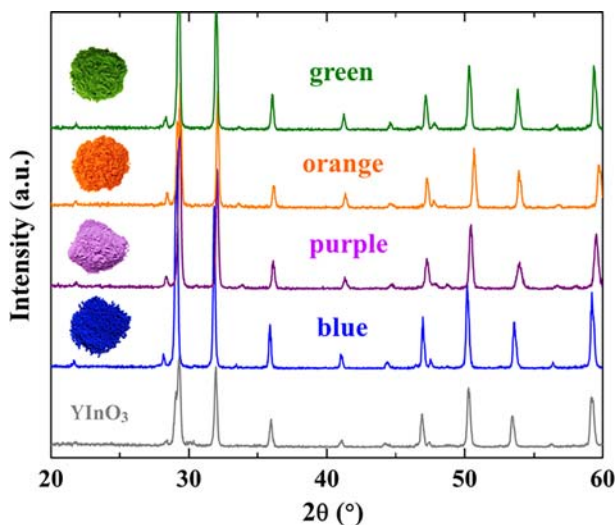


Fig. 22 Representative X-ray diffraction patterns of Y(In*M*)O₃ samples with various colors: blue ($M = \text{Mn}$), purple ($M = \text{Mn/Ti/Zn}$), orange ($M = \text{Fe}$), and green ($M = \text{Cu/Ti}$).

conduction band transitions ($\text{CdS}_{1-x}\text{Se}_x$ and HgS); color centers (smoky quartz, amethyst and topaz). Without carefully examining the crystal structures, the different color exhibited by ruby and emerald would be unexpected because both gemstones contain chromophore Cr^{3+} in a trigonally distorted octahedral environment at the Al^{3+} sites. As Orna put it: "The prediction of the coloring properties of yet unsynthesized compounds still remains in the realm of art rather than of science."⁷ For YInO_3 -based pigments it is proposed that the origin of color is associated with the crystal field splitting of the trigonal bipyramidal coordination, and the d-d energy excitation depends sensitively on the short apical $M\text{--O}$ bonds ($M = \text{Mn, Fe, Cu}$) through its impact upon the d_z^2 energy level (Fig. 20). The inverse relationship between crystal field splitting Δ_o and bond distance R proposed for octahedral coordination³⁹ presumably holds for trigonal bipyramidal coordination in a similar way as inferred by DFT calculations.¹⁹

All indium-containing pigments $\text{Y}(\text{In},M)\text{O}_3$ ($M = \text{Mn, Mn/Ti/Zn, Fe, Cu/Ti}$) exhibit higher near infrared (NIR) reflectance than Co blue. Especially those with relatively low concentration of chromophore M cations, the observed NIR reflectance is comparable to that of commercial TiO_2 , as shown in Fig. 23.

4.16.6.1 The $\text{Y}(\text{In},\text{Mn})\text{O}_3$ blue

The entire solid solutions of $\text{YIn}_{1-x}\text{Mn}_x\text{O}_3$ ($x = 0\text{--}1$) can be obtained through three synthetic routes: the conventional solid state reaction,¹⁹ the sol-gel method or CPM,¹¹⁴ and the microwave radiation. The color of the samples varies from vivid blue to dark blue as Mn content increasing (Fig. 24). For solid state synthesis, the formation of hexagonal blue pigments only occurs around 1300 °C. Heating the amorphous precursor from the solution method at 1000 °C, however, single phase of hexagonal $\text{YIn}_{1-x}\text{Mn}_x\text{O}_3$ can be obtained with grayish blue color. Further calcination to 1200 and 1300 °C gives rise to the same intense blue color as what was observed in solid state reactions. Blue pigments obtained from sol-gel precursors have smaller particle size due to low temperature preparation, providing advantages for applications and energy efficiency. Due to the design of our microwave setup, the microwave field is usually non-uniform, resulting in uneven absorption by the object being heated. Multiple heating with intermediate grindings are required to produce single phase samples.

The effect of Mn substitution on lattice parameters is illustrated in Fig. 25 for hexagonal $\text{YIn}_{1-x}\text{Mn}_x\text{O}_3$ solid solutions. Both the c lattice parameter and the c/a ratio decrease dramatically with x as a result of the short apical $\text{In}(\text{Mn})\text{--O}$ distances. It is clear that the similar basal-plane bond lengths in the end members (2.05 Å for YMnO_3 and 2.1 Å for YInO_3) give rise to a weak variation of cell edge a across the solid solution series. The apical Mn--O distance in YMnO_3 is only 1.86 Å, considerably shorter than those in the basal plane. While in YInO_3 , all of the In--O bonds are roughly the same length. Due to the considerable difference between apical Mn--O and In--O distances, the solid solution $\text{YIn}_{1-x}\text{Mn}_x\text{O}_3$ where Mn and In randomly occupy the same crystallographic site is no longer strictly periodic. The local relaxations around Mn and In will differ significantly. Both Raman and EPR studies reveal the existence of different apical bond distances for In and Mn.^{115,116} Analysis based on Bragg diffraction peaks is not normally expected to elucidate local structures. Techniques such as PDF (pair distribution function) and EXAFS (extended X-ray absorption fine structure) are commonly applied for this situation.

It has been shown that in favorable cases it is possible using Bragg diffraction peaks to accurately determine the detailed structures of different MO_x ($M = \text{In, Mn}$) polyhedra in a solid solution even though these polyhedra are not ordered.^{19,117} Structures of $\text{YIn}_{1-x}\text{Mn}_x\text{O}_3$ were refined for x values of 0.2, 0.5, and 0.8 by Rietveld analysis of neutron diffraction patterns, using both average and split models. For all three compositions, we could identify distinctly different positions for In/Mn and two apical O atoms using the structural model with split sites (Fig. 26). This was facilitated by the fact that the neutron scattering length of In is positive while that of Mn is negative. The relatively high scattering power of O in neutron diffraction improves the location accuracy of different apical O sites associated with In and Mn (Fig. 26). The refined bond distances are plotted in Fig. 27, together with the values of two end members.^{118,119} The distance between the refined Mn and In sites is as much as 0.40(4) Å, and the distance between the split

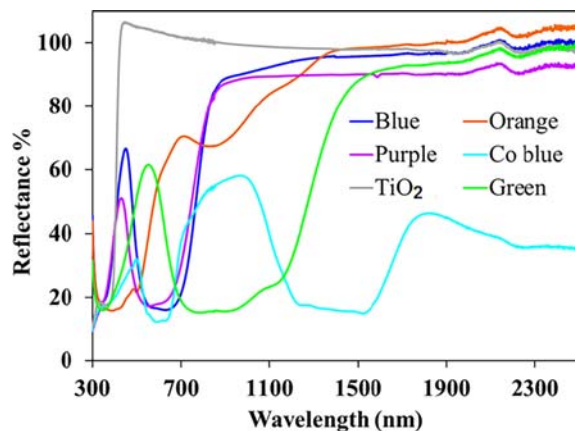


Fig. 23 NIR spectra of $\text{Y}(\text{In},M)\text{O}_3$ samples with various colors: blue ($M = \text{Mn}$), purple ($M = \text{Mn/Ti/Zn}$), orange ($M = \text{Fe}$), and green ($M = \text{Cu/Ti}$). Data of commercial TiO_2 and Co blue are plotted for comparison.

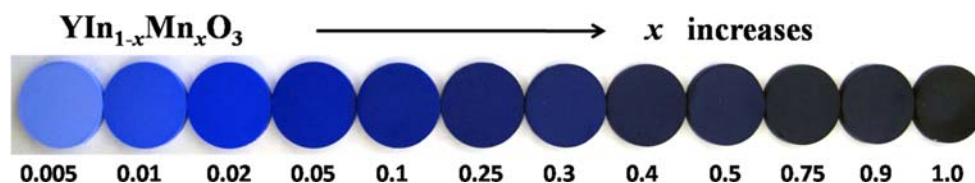


Fig. 24 Colors of pellets of $\text{YIn}_{1-x}\text{Mn}_x\text{O}_3$ showing change in intensity of blue color with increase in concentration of Mn^{3+} .

apical O sites is as much as $\sim 0.24(2)$ Å. The basal plane distances $\text{In}(\text{Mn})\text{--O}$ are nearly the same (~ 2.1 Å) regardless of the structural models, while the difference between apical In--O and Mn--O distances can be as much as 0.15 Å for the split model. The apical In--O distances in YInO_3 are about 11% longer than the apical Mn--O distances in YMnO_3 . However, after local relaxation these apical In--O distances are actually compressed no more than $\sim 3.5\%$ in $\text{YIn}_{1-x}\text{Mn}_x\text{O}_3$. And as the Mn content in the solid solution decreases the apical Mn--O distances actually only increase by $\sim 2.5\%$. The results are in agreement with previous XRD study¹⁹ and local structure analyses by XANES (X-ray absorption near edge structure) and EXAFS.¹²⁰ The TBP units become generally more distorted in the solid solution, something expected when combining TBP units with different sizes and shapes. Bond valence sums (BVS) of In and Mn are improved by using the split model.¹¹⁷

As shown in Fig. 20, the blue color of $\text{Y}(\text{In},\text{Mn})\text{O}_3$ pigments is dependent on an allowed $d-d$ transition ($e' \rightarrow a'$) for TBP Mn^{3+} , while the a' (d_{z^2}) energy level is associated with the apical Mn--O bond length. The little change in apical Mn--O distances, especially for the low Mn compositions of interest for their intense blue color, is consistent with the fact that as x increases in the $\text{YIn}_{1-x}\text{Mn}_x\text{O}_3$ series there is no significant change in the position of the absorption peak and hence the blue color. From the diffuse reflectance spectra in Fig. 28, we see that at low doping concentrations there is a strong, narrow (~ 1 eV width) absorption centered at ~ 2 eV that absorbs in the orange-green region of the visible spectrum. It is the absence of absorption in the 2.5–3 eV (blue) region of the spectrum that results in the blue color. As the concentration of Mn increases, the lower-energy absorption peak broadens and the higher-energy onset shifts to lower energy, consistent with the gradual darkening of the samples toward navy blue. We assign the higher-energy peak (3–3.5 eV) to the onset of the transition from the O 2p band to the Mn 3d_{z²} band. The blue color of the $\text{YIn}_{1-x}\text{Mn}_x\text{O}_3$ powders is evident even for very low values of x (Figs. 20 and 24). As the concentration of Mn is increased, the lower-energy absorption peak broadens and the higher-energy onset shifts to lower energy, consistent with the gradual darkening of the samples toward navy blue. In pure YMnO_3 , absorption occurs throughout the entire visible region, resulting in the black color.

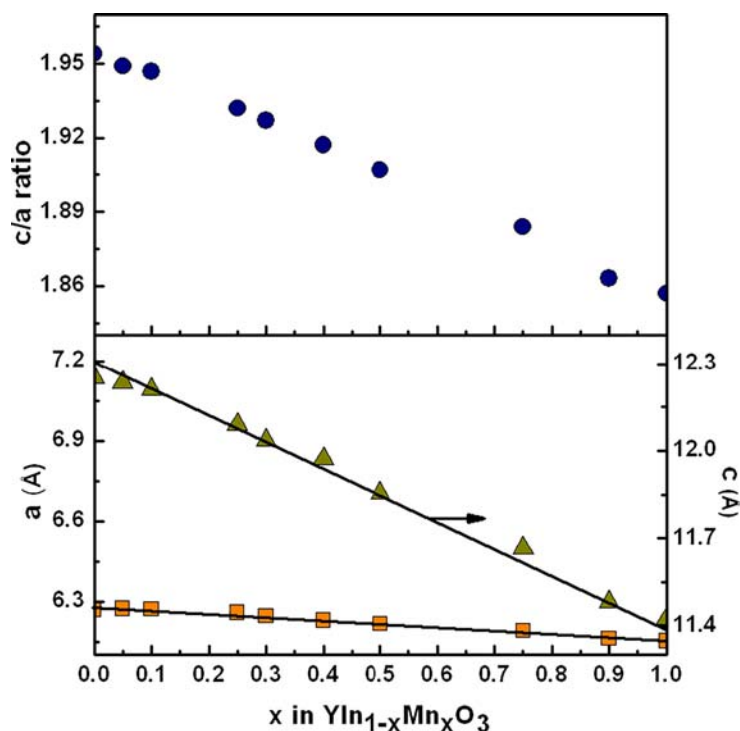


Fig. 25 The c/a ratio (top) and cell edges for the $\text{YIn}_{1-x}\text{Mn}_x\text{O}_3$ solid solutions.¹⁹ Trend lines are drawn to guide the eye. Estimated uncertainties are smaller than the plotted point size.

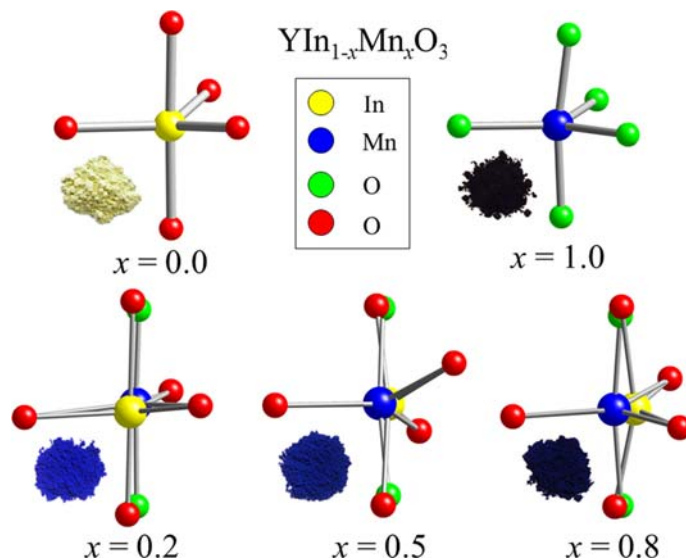


Fig. 26 The TBP polyhedra in $\text{YIn}_{1-x}\text{Mn}_x\text{O}_3$ ($x = 0.2, 0.5, 0.8$) showing distinct sites for Mn, In and apical oxygens.¹¹⁷ Basal plane O atoms are in the same positions in both InO_5 and MnO_5 polyhedra. The structures of two end members are drawn for comparison.^{118,119}

4.16.6.2 The $\text{Y}(\text{In},\text{Mn}/\text{Ti}/\text{Zn}/\text{Al})\text{O}_3$ purple

The discovery of $\text{Y}(\text{In},\text{Mn})\text{O}_3$ blue opened up a new field of research: rational design of novel inorganic pigments through cation substitution into the TBP sites of the host oxides. We now that an allowed d-d transition of TBP Mn^{3+} is responsible for the bright blue color of $\text{YIn}_{1-x}\text{Mn}_x\text{O}_3$ solid solutions and that the crystal field splitting between $a'(d_{z^2})$ and $e'(d_{x^2-y^2}, d_{xy})$ energy levels is sensitive to the apical Mn–O distance. When chemical pressure is applied to compress the apical Mn–O distance in $\text{YIn}_{1-x}\text{Mn}_x\text{O}_3$ the allowed d-d transition is moved to higher energy, and thereby tune the color from blue to violet/purple.¹⁰⁷ This was accomplished by substituting smaller cations such as $\text{Ti}^{4+}/\text{Zn}^{2+}$ and Al^{3+} onto the TBP In/Mn site, which yielded novel violet/purple phases (Fig. 29). The general formula is $\text{YIn}_{1-x-2y-z}\text{Mn}_x\text{Ti}_y\text{Zn}_y\text{Al}_z\text{O}_3$ ($x = 0.005-0.2$, $y = 0.1-0.4$ and $z \leq 0.1$), where the color darkens with the increasing amount of Mn. Higher y and/or small additions of Al provides a more reddish hue to the resulting purple colors. Substitutions for Y were attempted as well with Ca and rare earth elements (RE = La, Nd, Gd, Dy, Ho, Er, Eu, Yb,

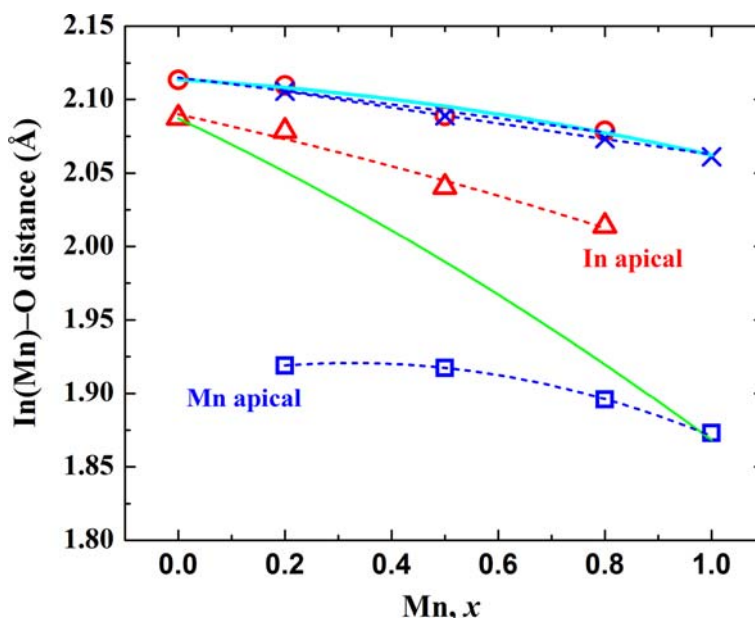


Fig. 27 Average bond distances $\text{In}(\text{Mn})-\text{O}$ for $\text{YIn}_{1-x}\text{Mn}_x\text{O}_3$ ($x = 0, 0.2, 0.5, 0.8, 1$).¹¹⁷ Literature reports are used for $x = 0$ and 1.^{118,119} Solid lines (apical: green; basal: turquoise) indicate expected behavior without local relaxation (average structural model). Symbols are for bond distances of In–O (apical: triangles; basal: circles) and Mn–O (apical: squares; basal: crosses) from Rietveld analysis with split atoms, with dashed lines showing the trends. Estimated uncertainties are smaller than the plotted point size.

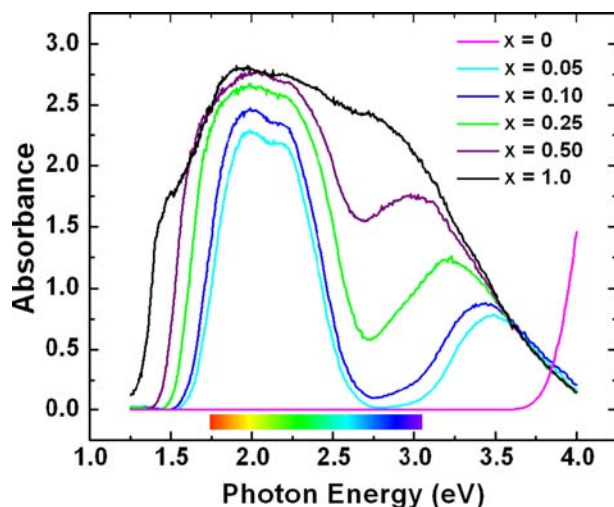


Fig. 28 Diffuse reflectance spectra of $\text{YIn}_{1-x}\text{Mn}_x\text{O}_3$ solid solutions.¹⁹

Sc), but there was little impact on the color. The same substitutions with Ti/Zn/Al in other hexagonal $\text{RE}(\text{In,Mn})\text{O}_3$ hosts (RE = Dy, Ho, Er) produce similar violet and purple colors.

Unit cell parameters a , c , c/a ratio and cell volume all decrease with increasing substitution (similar to Fig. 25) due to smaller $3+$ ionic radii of Mn/Ti/Zn/Al compared with that of In, which confirms the formation of the solid solution. Like the case of blue $\text{Y}(\text{In,Mn})\text{O}_3$ phases, we attribute this miscibility to the similar In–O and M –O ($M = \text{Mn, Ti, Zn, Al}$) basal-plane distances in hexagonal $\text{YIn}_{1-x}\text{M}_x\text{O}_3$. The large size difference between In^{3+} and M^{3+} is manifested only in the apical distances. Similar basal-plane bond distances lead to a weak variation of cell edge a over the whole range of the solid solution.

It has been found that for simple system like blue $\text{YIn}_{0.8}\text{Mn}_{0.2}\text{O}_3$ it is possible to refine In and Mn positions separately using neutron diffraction data, and refine as well the separate positions for the apical O atoms associate with In and Mn.¹¹⁷ Such an approach becomes much more challenging for the purple $\text{Y}(\text{In,Mn,Ti,Zn,Al})\text{O}_3$ compositions with relatively low Mn content. A split model was, however, successful for $\text{YIn}_{0.7}\text{Mn}_{0.1}\text{Ti}_{0.1}\text{Zn}_{0.1}\text{O}_3$. This was accomplished by refining the positions of Mn and its apical oxygens separately, leaving In, Ti, Zn, and Al at one site with occupancies fixed according to the nominal composition. Such a refinement is facilitated by the fact that Mn is the only atom in the structure with a negative scattering length. Fig. 29 displays a clear contraction of the apical bond distances with increasing substitution and a minor change in the basal plane distances. Without allowing local relaxation for Mn, the average apical Mn–O distance is refined to be 2.04 Å for $\text{YIn}_{0.7}\text{Mn}_{0.1}\text{Ti}_{0.1}\text{Zn}_{0.1}\text{O}_3$ ($x + 2y + z = 0.3$), but it becomes much shorter (1.86 Å) when refined with the split model. The same distance is 1.92 Å for

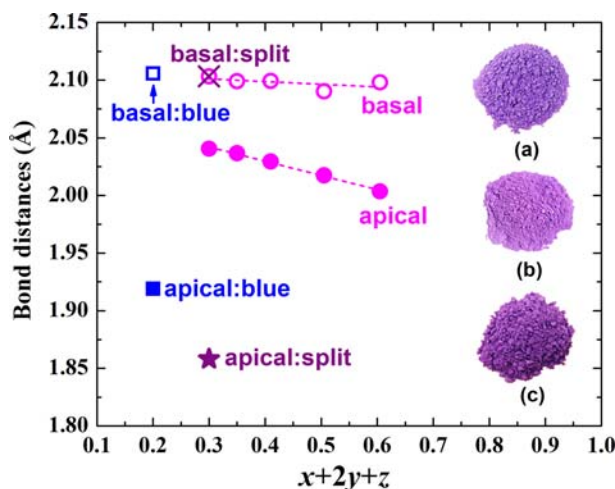


Fig. 29 Average bond distances of purple samples $\text{YIn}_{1-x-2y-z}\text{Mn}_x\text{Ti}_y\text{Zn}_z\text{Al}_z\text{O}_3$.¹⁰⁷ The value of $(x + 2y + z)$ is the total TBP site substitution for In. Open and filled circles are distances refined for samples without local relaxation. The cross sign and star (for purple sample $\text{YIn}_{0.7}\text{Mn}_{0.1}\text{Ti}_{0.1}\text{Zn}_{0.1}\text{O}_3$), the open and filled squares (for blue sample $\text{YIn}_{0.8}\text{Mn}_{0.2}\text{O}_3$), are distances refined with split sites for In and Mn and two apical oxygens. Dashed lines are drawn to guide the eye. Estimated uncertainties are smaller than the plotted point size. Compositions for selected samples (inset): (a) $x = 0.005$, $y = 0.1$; (b) $x = 0.01$, $y = 0.2$, $z = 0.1$; (c) $x = 0.03$, $y = 0.2$.

blue $\text{YIn}_{0.8}\text{Mn}_{0.2}\text{O}_3$ refined with local relaxation for Mn, indicating a decreasing apical Mn–O bond distance going from blue to purple. The actual difference between apical Mn–O distances of blue and purple samples might be even bigger if local relaxation could be applied for all the TBP cations of the purple samples, given the fact that Shannon radii (Å) for these cations in fivefold coordination are Mn^{3+} (0.58), Ti^{4+} (0.51), Zn^{2+} (0.68), Al^{3+} (0.48), and In^{3+} (0.723, estimated from the reported YInO_3 structure).^{118,121}

The decrease in apical Mn–O bond distance is presumably responsible for the color shift from blue to purple since the energy of the d_{z^2} state relative to the valence band maximum is determined by the Mn–O apical bond length (Fig. 20). More precisely, the crystal field splitting for Mn^{3+} is related to the ratio of the apical and basal plane Mn–O distances. Since the apical distances vary much more than the basal plane distances, it is primarily the apical Mn–O distances that correlate with the position of the allowed d-d transition. Similarly, using smaller Ga^{3+} (0.55 Å) to replace some In^{3+} in $\text{YIn}_{1-x}\text{Mn}_x\text{O}_3$ can also shift the color from blue to violet or purplish blue, but the successful substitution is limited to $x \sim 0.1$ by solid state synthesis. Adding more Ga to the hexagonal lattice would require a sol-gel precursor route that likely involves incorporation of carbonate groups into the crystal structure.^{68,69}

Diffuse reflectance spectra of selected purple and blue samples are compared in Fig. 30. For the purple solid solution $\text{YIn}_{1-x-2y}\text{Mn}_x\text{Ti}_y\text{Zn}_y\text{O}_3$, with increasing concentration of Ti/Zn, the lower-energy absorption peak is blue-shifted by 0.1–0.4 eV and the onsets of the higher-energy absorption peak is red-shifted by 0.1–0.4 eV with respect to the blue. We assign the lower energy absorption to the allowed d-d transition ($e'(d_{x^2-y^2}, d_{xy})$ to $a'(d_{z^2})$) as shown in Fig. 23 and the absorption in the near-UV to a charge-transfer transition from O to Mn. These peaks also broaden because of the disorder around Mn due to nearest neighbors like In, Ti and Zn. The color is defined by the minimum absorption, which shifts to higher energy with increasing y . In comparison to blue $\text{YIn}_{1-x}\text{Mn}_x\text{O}_3$ the shorter Mn–O distances impact both the d-d transition and the charge transfer peaks. It yields a larger ligand field splitting because it is mainly the apical Mn–O distance that decreases, which causes the d-d transition to move to a higher energy range of the visible (from orange to yellow-green). Also, the $\text{Mn}^{3+}-\text{O}^{2-}$ charge transfer becomes somewhat easier as the Mn–O distance decreases; consequently, the associated higher-energy absorption band moves to lower energy range. These two effects induced by the shorter Mn–O distances give rise to a slight increase in the absorption at the bottom of the valley (~ 2.7 eV). The same valley also rises in blue series $\text{YIn}_{1-x}\text{Mn}_x\text{O}_3$ with increasing amount of Mn due to the Mn–Mn charge transfer ($2\text{Mn}^{3+} \rightarrow \text{Mn}^{2+} + \text{Mn}^{4+}$) not shorter Mn–O distances.¹⁹ This is not as obvious in the purple $\text{YIn}_{1-x-2y}\text{Mn}_x\text{Ti}_y\text{Zn}_y\text{O}_3$ ($x \leq 0.2$) series due to the low Mn content.

Currently, manganese violet ($\text{NH}_4\text{MnP}_2\text{O}_7$) and cobalt violet ($\text{Co}_3(\text{PO}_4)_2$) are still commonly used pigments, along with ultramarine violet ($\text{Na}_{10}\text{Al}_6\text{Si}_6\text{O}_{24}\text{S}_4$) and Han purple ($\text{BaCuSi}_2\text{O}_6$). Han purple and ultramarine violet are chemically and thermally unstable. Manganese violet decomposes around 300 °C and cobalt violet has environmental issues. We performed heating and acid tests on our well-characterized purple pigments. The synthesis temperature is ~ 1300 °C but these pigments can endure even higher temperatures while maintaining their original colors. Treating our pigments with 10% $\sim 50\%$ of HNO_3 , HCl or H_2SO_4 solutions and stirring overnight resulted in negligible weight and color changes, and XRD patterns remain the same after the tests. Additionally, the lower indium content due to Ti/Zn/Al substitution reduces the cost of the pigments, and the simple preparation via solid state reaction offers advantages for industrial manufacturing process in contrast with the solution routes of some existing purple pigments.

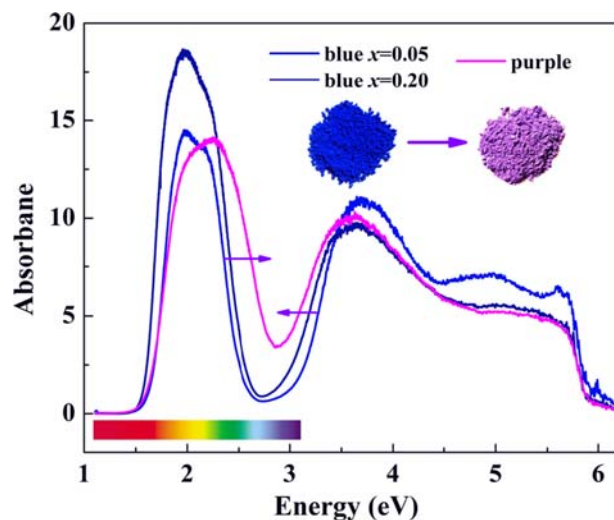


Fig. 30 Diffuse reflectance spectra for purple sample $\text{YIn}_{1-x-2y}\text{Mn}_x\text{Ti}_y\text{Zn}_y\text{O}_3$ ($x = 0.05$, $y = 0.3$) and blue samples $\text{YIn}_{1-x}\text{Mn}_x\text{O}_3$ ($x = 0.05$, 0.20).

4.16.6.3 The Y(In,Fe)O₃ orange

Introducing Fe³⁺ into the hexagonal YInO₃ system produced new solid solutions of YIn_{1-x}Fe_xO₃.⁸⁰ The color of these phases varies from yellow, orange to dark red with increasing Fe content x . A standard solid state high temperature method was used to prepare the In-rich YIn_{1-x}Fe_xO₃ phases. Since hexagonal YFeO₃ is metastable and normally prepared by a sol-gel method,¹⁰⁹ the Fe-rich YIn_{1-x}Fe_xO₃ phases were prepared by starting with metal nitrate solutions using citric acid as a chelating agent. The solid-state synthesis approach was successful for the preparation of yellow to bright orange YIn_{1-x}Fe_xO₃ powders from $x = 0.0$ to 0.3.

The solution route was successful for the preparation of dull red brown to dark red brown YIn_{1-x}Fe_xO₃ phases from $x = 0.7$ to 1.0. Neither approach was successful for intermediate x values (Fig. 31). X-ray diffraction profiles and SEM images indicate smaller crystallite/particle size for the Fe-rich samples. All phases appear to have the ferrielectric structure known for YInO₃. The hexagonal unit cell parameters versus x are shown in Fig. 31. Like other Y(In,M)O₃ systems, alteration along cell edge c still dominates when substituting chromophore ion Fe³⁺ into the In site.

For oxides containing Fe³⁺ there is strong optical absorption in the near UV based on a Fe³-O² charge transfer transition. This peak typically extends far enough into the visible to give a yellow color. The lower energy d-d transitions are forbidden, but they become allowed as the d states broaden into bands, i.e. a d-d transition is no longer restricted to occurring on one Fe atom. This broadening increases as Fe-Fe distances decrease with increasing Fe content. In Fig. 32 we see that for $x = 0.1$ the substituted Fe is so dilute that the color is essentially all due to the Fe³⁺-O²⁻ charge transfer. As the Fe concentration increases color derived from the lower energy d-d transitions becomes increasingly more evident.

4.16.6.4 The Y(In,Cu/Ti)O₃ green

Double substitution of Cu²⁺/Ti⁴⁺ into the TBP sites of hexagonal YMO₃ (M³⁺ = In, Al, Ga) resulted in solid solutions of the type YM_{1-x}(Cu_{0.5}Ti_{0.5})_xO₃ with green colors.¹⁰⁶ All showed impurity phases for $x < 0.8$, especially when M is Al and Ga. The green color of YCu_{0.5}Ti_{0.5}O₃ was found to be enhanced by small substitutions of In, Al and Ga. A range of vivid green colors, from light to dark, can be obtained by varying the x from 0 to 1 in YIn_{1-x}(Cu_{0.5}Ti_{0.5})_xO₃. The green color is perceptibly intensified by indium addition. Hexagonal RECu_{0.5}Ti_{0.5}O₃ (RE = Dy, Ho, Er, Tm, Yb and Lu) phases are also reported to show green colors.¹²²

The structure of YCu_{0.5}Ti_{0.5}O₃ is the same as that of hexagonal YMnO₃, but now we have equal amounts of Cu²⁺ and Ti⁴⁺ occupying the TBP sites in a disordered manner. Likewise in YM_{1-x}(Cu_{0.5}Ti_{0.5})_xO₃ (M³⁺ = In, Al, Ga) we have a random distribution of M³⁺/Cu²⁺/Ti⁴⁺ on the same TBP site. The d⁹ electronic configuration of Cu²⁺ favors the TBP position through crystal field stabilization. Our initial neutron diffraction study shows that Cu²⁺ has shorter apical distances than basal plane distances in the TBP coordination, despite the dilution of Cu²⁺ with Ti⁴⁺. Diffuse reflectance spectra are shown for selected YAl_{1-x}(Cu_{0.5}Ti_{0.5})_xO₃ samples in Fig. 33. There is a strong absorption centered at ~1.7 eV that absorbs in the red region of the visible spectrum, and the higher-energy absorption peak also shifting into the visible range. The color is determined by the minimum absorption (~2.3 eV) in the green region of the visible spectrum.

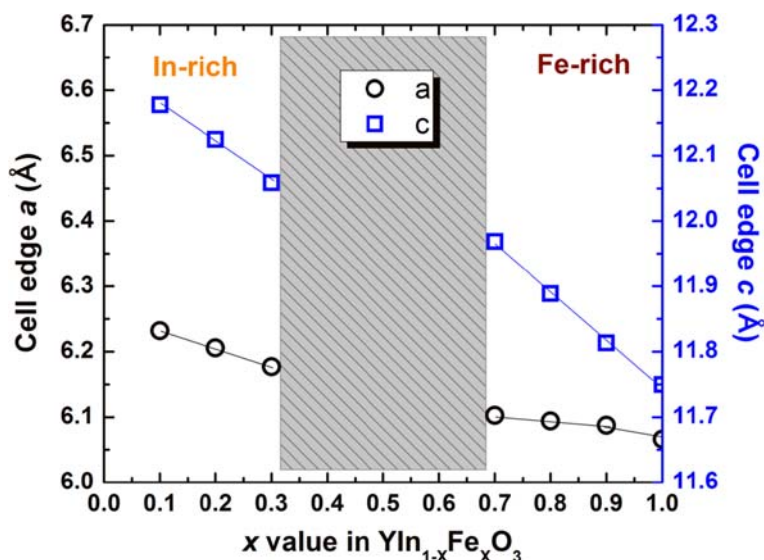


Fig. 31 Lattice parameters vs x in hexagonal YIn_{1-x}Fe_xO₃.⁸⁰ The shaded area indicating discontinuity of the lattice parameters due to missing phases with intermediate x values. Trend lines are drawn to guide the eye. Estimated uncertainties are smaller than the plotted point size.

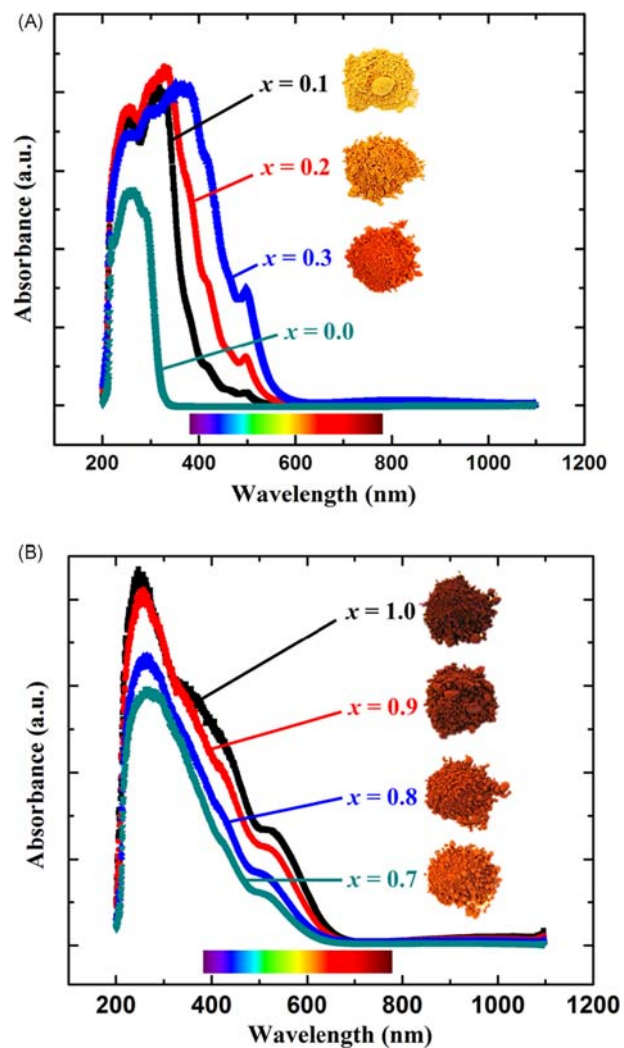


Fig. 32 Diffuse reflectance spectra of $\text{YIn}_{1-x}\text{Fe}_x\text{O}_3$ solid solutions: (a) $x = 0.1$ – 0.3 ; (b) $x = 0.7$ – 1.0 .⁸⁰ The selected samples (inset) showing the pigment color darkens with increasing Fe content x . Spectrum for $x = 0$ (hexagonal YInO_3 ; white) is shown for comparison.

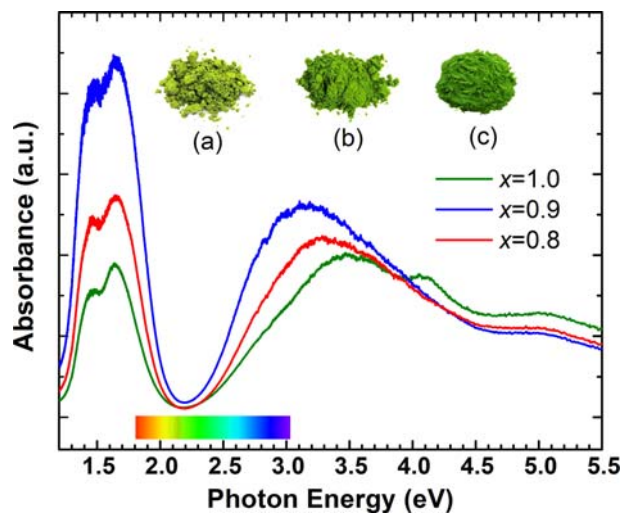


Fig. 33 Diffuse reflectance spectra of $\text{YAl}_{1-x}(\text{Cu}_{0.5}\text{Ti}_{0.5})_x\text{O}_3$ ($x = 1.0, 0.9, 0.8$) samples.¹⁰⁶ Compositions for selected samples (inset): (a) $\text{YCu}_{0.5}\text{Ti}_{0.5}\text{O}_3$; (b) $\text{YAl}_{0.1}(\text{Cu}_{0.5}\text{Ti}_{0.5})_{0.9}\text{O}_3$; (c) $\text{YIn}_{0.2}(\text{Cu}_{0.5}\text{Ti}_{0.5})_{0.8}\text{O}_3$.

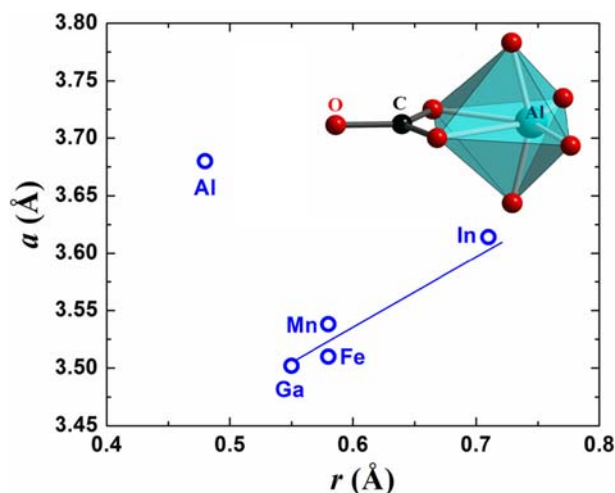


Fig. 34 Cell parameter a vs radius of the M cation in hexagonal YMO_3 ($M = \text{Al, Ga, Mn, Fe, In}$).⁶⁸ The small hexagonal pseudo cell is used. Trend lines are drawn to guide the eye. Estimated uncertainties are smaller than the plotted point size. Inset shows partial crystal structure of oxycarbonate “ $YAlO_3$ ” with the ideal composition $Y_3Al_3O_8CO_3$ and a coordination number of 6 for Al.

4.16.6.5 The $Y(\text{Al},M)\text{O}_3$ pigments

The discovery of $Y(\text{In},\text{Mn})\text{O}_3$ blue has led to a search for other hosts for Mn^{3+} in TBP coordination. An obvious choice would be $YAlO_3$. This compound, which has only been prepared through a citrate precursor route, has long been considered isostructural with $YInO_3$. The hexagonal structure proposed for $YAlO_3$ ¹¹¹ with Al in TBP coordination however is erroneous based on its unit cell dimensions and bond valence sums (BVS). Fig. 34 shows the plot of cell edge a values reported for hexagonal YMO_3 compounds where $M = \text{In, Fe, Mn, Ga}$ and Al, assuming that $YAlO_3$ has the centric structure ($P6_3/mmc$) and Al at the TBP position. The apparent deviation of $YAlO_3$ from the trend line suggests that the structure of hexagonal “ $YAlO_3$ ” is not the same as that for other YMO_3 phases. The reported z value of 0.077 gives BVSs of 1.95 for Al and 3.42 for Y, both of which are unreasonable deviations from the expected 3.0 value.¹¹¹

Our studies reveal instead that all, or nearly all, the Al in this compound has a coordination number (CN) of 6.⁶⁸ On heating in air this compound transforms to $YAlO_3$ with the perovskite structure liberating CO_2 . The compound long assumed to be a hexagonal form of $YAlO_3$ is actually an oxycarbonate with the ideal composition $Y_3Al_3O_8CO_3$ (Fig. 34, inset). We find that the hexagonal structures of $YGaO_3$ and $YFeO_3$ from the citrate route are also stabilized by small amounts of carbonate. The presence of carbonate in citrate-prepared $Y_3Ga_3O_9-x(\text{CO}_3)_x$ was also confirmed by IR data, and the cell edge analysis suggested an even higher carbonate concentration in the citrate-prepared hexagonal “ $REGaO_3$ ” phases ($RE = \text{La, Pr, Nd, Sm, or Eu}$) than in “ $YGaO_3$.”

The $YAlO_3$ - $YMnO_3$ system was explored in consideration of replacing indium with cheaper aluminum for making Mn-containing blue pigments. The standard solid-state synthesis approach however was successful only for the preparation of pure $YMnO_3$ and Al-poor phases $YAl_{1-x}Mn_xO_3$ ($x \geq 0.9$). A complete solid solution of $YAl_{1-x}Mn_xO_3$ ($x = 0-1$) was prepared by the

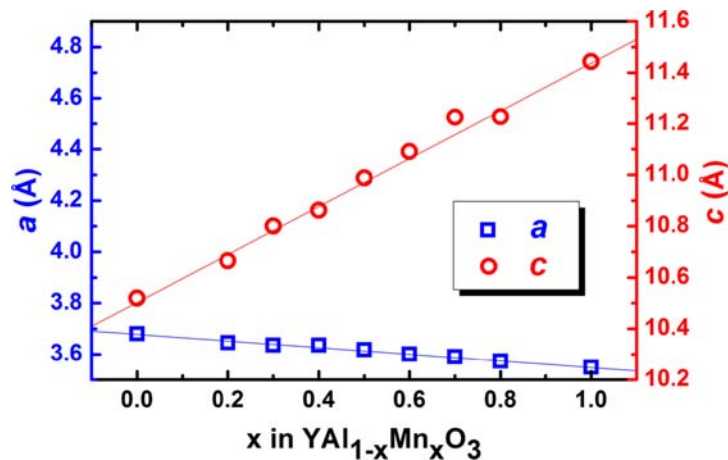


Fig. 35 Cell dimensions a and c vs x for solid solutions $YAl_{1-x}Mn_xO_3$.⁶⁸ Trend lines are drawn to guide the eye. Estimated uncertainties are smaller than the plotted point size.

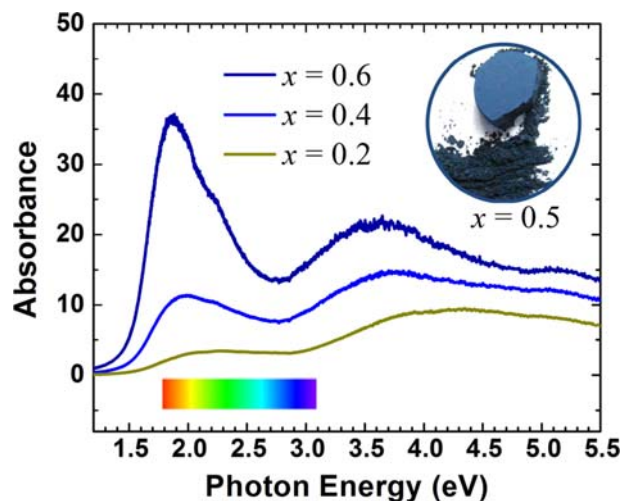


Fig. 36 Diffuse reflectance spectra of $\text{YAl}_{1-x}\text{Mn}_x\text{O}_3$ ($x = 0.2, 0.4, 0.6$) solid solutions. Inset shows a navy blue color exhibited by a $\text{YAl}_{1-x}\text{Mn}_x\text{O}_3$ ($x = 0.5$) sample.

citrate route.⁶⁸ XRD analysis shows that the superstructure reflections in YMnO_3 due to the ferroelectric distortion remain present at $x = 0.9$ but have disappeared for lower values of x . The disorder associated with the Al substitution for Mn has disrupted the long range forces required for the transition to the ferroelectric state. The variations of cell edges a and c with x are essentially linear (Fig. 35) suggesting a gradual decrease of carbonate with increasing x . Although a blue color develops with Mn substitution (Fig. 36), it is a dark navy blue rather than the brilliant-blue color observed for $\text{YIn}_{1-x}\text{Mn}_x\text{O}_3$ phases. The absence of bright color is presumably due to destruction of TBP sites caused by carbonate incorporation.^{68,123} A significant fraction of the Mn^{3+} will be on the highly distorted octahedral site that will produce color, but not the intense blue color associated with the TBP site.

Red brown phases of the type $\text{YAl}_{1-x}\text{Fe}_x\text{O}_3$ could only be prepared through the citrate route. The weak 102 reflection associated with ferroelectric distortion only appears in XRD patterns of Fe-rich samples. Lattice constants as a function of x are shown in Fig. 37. Unlike the $\text{YAl}_{1-x}\text{Mn}_x\text{O}_3$ solid solution, there is now a miscibility gap and the variation of a and c with x deviates strongly from linear. It would appear that for $\text{YAl}_{1-x}\text{Fe}_x\text{O}_3$ the carbonate level remains high on initial substitution of Fe up to the miscibility gap. Then there is an abrupt decrease in carbonate concentration of the Fe rich side of the gap, and this leads to the abrupt decrease in the a cell edge and the unit cell volume. This explanation is qualitatively supported by the infrared measurement for carbonate content.⁶⁸ Some carbonate is always present in hexagonal YFeO_3 itself. Again, the lack of intense red brown color (Fig. 37, inset) is likely related to the destruction of TBP sites caused by carbonate inclusion.

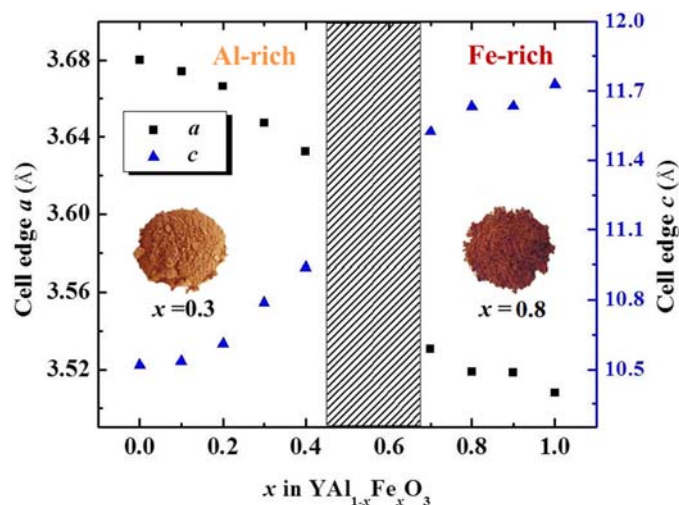


Fig. 37 Cell edges versus x for $\text{YAl}_{1-x}\text{Fe}_x\text{O}_3$ phases.⁶⁸ The shaded area indicating discontinuity of the lattice parameters due to missing phases with intermediate x values. Estimated uncertainties are smaller than the plotted point size. Inset shows dull red brown colors exhibited by selected $\text{YAl}_{1-x}\text{Fe}_x\text{O}_3$ samples.

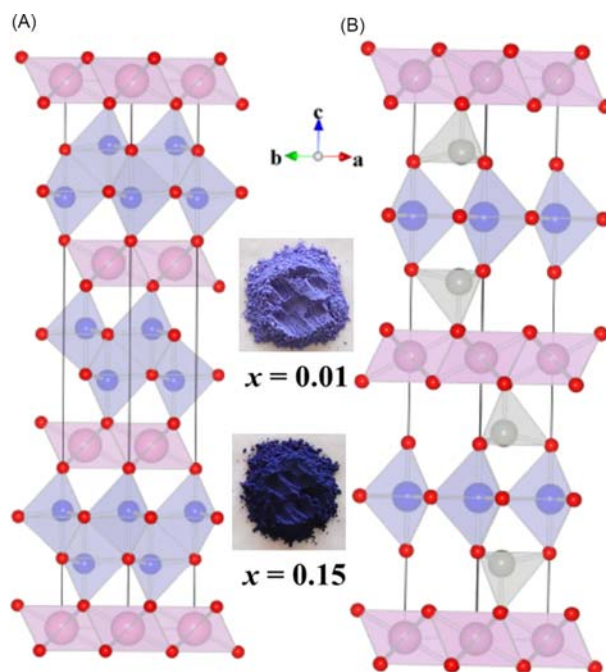


Fig. 38 Crystal structures of (a) YbFe_2O_4 and (b) $\text{LuFeO}_3(\text{ZnO})_2$ showing FeO_5 trigonal bipyramids in blue (Fe, blue spheres; O, red spheres; Yb/Lu, pink spheres; Zn, grey spheres).⁶⁷ Inset showing blue or bluish purple colors of two $\text{LuGa}_{1-x}\text{Mn}_x\text{MgO}_4$ ($x = 0.01, 0.15$) samples.

4.16.6.6 The $\text{Y}(\text{In},\text{Mn})\text{O}_3$ blues and beyond

The discovery of $\text{Y}(\text{In},\text{Mn})\text{O}_3$ blues is the first report on the synthesis of oxides with the chromophore based on a trigonal-bipyramidal (TBP)-coordinated Mn^{3+} ion.¹⁹ Many new colored inorganic compounds with chromophore ions at TBP coordination have been reported since then.^{67,70,85,112,113} We demonstrate in this section that blue pigments can be designed by introducing Mn^{3+} into various structures containing TBP coordination and the host oxide is not limited to hexagonal REMO_3 (RE = rare earth ion, $M = \text{In}, \text{Ga}, \text{Al}$) phases. Fig. 38a shows that the crystal structure of YbFe_2O_4 may be described as double-layered FeO_5 trigonal bipyramids sharing edges and sandwiched by YbO_6 octahedral layers along the c axis. The TBP polyhedron is distorted because of Coulomb repulsion between Fe ions. The Yb site is often occupied by In, Sc, Y, or smaller rare-earth ions. Fig. 38b shows that the structure of $\text{LuFeO}_3(\text{ZnO})_2$ contains single layers of FeO_5 trigonal bipyramids corner-shared with ZnO_4 tetrahedra that are sandwiched between layers of edge-sharing LuO_6 octahedra. Substitution of Mn^{3+} into the TBP sites of oxides with the YbFe_2O_4 -type structure produces an intense blue color because of an allowed d-d transition.⁶⁷ This has been demonstrated utilizing a variety of hosts including ScAlMgO_4 , ScGaMgO_4 , ScGaZnO_4 , LuGaMgO_4 , LuGaZnO_4 , and $\text{LuGaO}_3(\text{ZnO})_2$.⁶⁷ The hue of the blue color can be controlled by the choice of the host. All of the samples without Mn substitution are white, except for pale-yellow LuGaMgO_4 . Mn substitution causes a blue color for ScGaZnO_4 , LuGaZnO_4 , and $\text{LuGaO}_3(\text{ZnO})_2$ or a bluish-purple color for ScAlMgO_4 , ScGaMgO_4 , and LuGaMgO_4 . Colors of selected $\text{LuGa}_{1-x}\text{Mn}_x\text{MgO}_4$ samples are shown in Fig. 38 (inset).

Diffraction peaks due to impurity phases were not observed up to $x = 0.15$ for $\text{ScAl}_{1-x}\text{Mn}_x\text{MgO}_4$ and $\text{LuGa}_{1-x}\text{Mn}_x\text{MgO}_4$. Similarly, the formation of a solid solution up to 5% Mn was confirmed in $\text{ScGa}_{1-x}\text{Mn}_x\text{ZnO}_4$ and $\text{LuGa}_{1-x}\text{Mn}_x\text{O}_3(\text{ZnO})_2$. According to Shannon radii the evolution of unit cell parameters upon substitution confirmed the formation of solid solutions with Mn addition. Lattice refinements were based on the space group $R\bar{3}m$ (hexagonal setting).

Diffuse reflectance spectra for $\text{LuGa}_{1-x}\text{Mn}_x\text{MgO}_4$, $\text{ScAl}_{1-x}\text{Mn}_x\text{MgO}_4$, $\text{ScGa}_{1-x}\text{Mn}_x\text{ZnO}_4$ and $\text{LuGa}_{1-x}\text{Mn}_x\text{O}_3(\text{ZnO})_2$ show that band gaps in the undoped phases are evident only when Zn is present.⁶⁷ The band gaps for ScGaZnO_4 and $\text{LuGaO}_3(\text{ZnO})_2$ are estimated to be 4.5 and 3.7 eV, respectively. As Mn^{3+} is introduced, two new absorption bands appear for all of the samples. One of these bands is located at ~ 2 eV and is the origin of the bluish color. The other appears at about ~ 4 eV. As x increases, the intensity tends to saturate. However, these results clearly indicate that the newly formed absorption band at 2 eV originates from the TBP-coordinated Mn^{3+} ion. The small splitting of the absorption band at about 2 eV in these phases as well as in the $\text{YIn}_{1-x}\text{Mn}_x\text{O}_3$ phases can be attributed to the fact that the symmetry of the TBP site does not possess the full D_{3h} symmetry of an ideal TBP. The blue-colored $\text{ScGa}_{1-x}\text{Mn}_x\text{ZnO}_4$ and $\text{LuGa}_{1-x}\text{Mn}_x\text{O}_3(\text{ZnO})_2$ samples have a single absorption band at 1.9 eV. This is ascribed to an allowed transition from e' to a' in D_{3h} symmetry, the ideal symmetry for TBP coordination. A transition from e'' to a' is forbidden. The a' antibonding state originates from the Mn $3d_{z^2}$ and O_{apical} 2p interaction; thus, the position of the absorption band near 2 eV depends on the Mn– O_{apical} distances. All samples show a charge transfer from O 2p to Mn a' in the region 3.5–4.0 eV. As x increases, this absorption band broadens. Control of the Mn^{3+} ligand field via the Mn– O_{apical} bond distance can tune the color from blue to bluish-purple.

The melilite-type compounds with a general formula $\text{Sr}_2\text{MGe}_2\text{O}_7$ ($M = \text{Mg, Zn, Co, Mn}$) consist of M^{2+} and Ge^{4+} in tetrahedral coordinations. Using X-ray absorption spectroscopy, synchrotron X-ray diffraction and ab initio total energy calculations, it is found that the crystal structure of $\text{Sr}_2(\text{Mg}_{1-x}\text{Mn}_x)\text{Ge}_2\text{O}_7 + \delta$ contains MnO_5 trigonal bipyramids and the GeO_5 square pyramids, and that the oxidation state of Mn is mixed and close to 3+.¹¹² The DFT calculation suggests that the five coordinations around Mn^{3+} and Ge^{4+} ions result from the oxidation of Mn^{2+} ions induced by an interstitial oxygen atom. The Mn-substituted melilite-type $\text{Sr}_2\text{MgGe}_2\text{O}_7$ solid solutions exhibit a range of blue colors. The optical bandgap of the parent compound $\text{Sr}_2\text{MgGe}_2\text{O}_7$ is estimated to be 5.6 eV, and two absorption bands appear in the energy range of 1.6–2.8 eV and 3.5–6.0 eV due to Mn substitution. The blue hue of the compound is attributed to absorption in the visible light range resulted from the d–d electronic transition of Mn^{3+} in the trigonal bipyramidal geometry.

Germanate $\text{LaGaGe}_2\text{O}_7$ belongs to the $\text{AlNdGe}_2\text{O}_7$ structure type with a monoclinic space group of $P2_1/c$, in which the rare-earth ions are separated by GaO_5 and Ge_2O_7 polyhedra. Incorporating Mn^{3+} in the trigonal bipyramidal geometry produces blue solid solutions $\text{LaGa}_{1-x}\text{Mn}_x\text{Ge}_2\text{O}_7$ ($x = 0.1\text{--}0.4$).⁷⁰ The band gap of $\text{LaGaGe}_2\text{O}_7$ ($x = 0$) lies in the range of 3.3 eV. When introducing Mn^{3+} into the Ga site, two new absorption bands are observed in all substituted samples. The blue color is due to the absorption in the energy region of 1.7–2.5 eV. The absorption band located in the 3–4.5 eV region results from the transition taking place from O 2p to Mn d_{z^2} orbitals. The absorption centered around 2 eV arises presumably owing to the symmetry-allowed transition from $d_{x^2-y^2, xy} \rightarrow d_{z^2}$ (1.7 eV) and the formerly symmetry forbidden transition from $d_{xz, yz} \rightarrow d_{z^2}$ (2.1 eV). It is proposed that the longer Mn–O apical bond in $\text{LaGa}_{1-x}\text{Mn}_x\text{Ge}_2\text{O}_7$ results in a smaller ligand field around Mn^{3+} , thus decreasing the energy separation between the e' & e'' and a' orbitals.

Monoclinic LiMgBO_3 structure can be described as edge-shared MgO_5 TBP chains connected by trigonally coordinated B atoms and five-coordinated Li atoms to form a three-dimensional network.⁸⁵ Monoclinic $\alpha\text{-LiZnBO}_3$, the zinc analogue of LiMgBO_3 , has a crystal structure composed of ZnO_4 tetrahedra, LiO_5 TBPs, and BO_3 triangles.¹¹³ Some disorder is found between the Li and Zn atoms, and a long Zn–O bond associated with the ZnO_4 tetrahedral unit gives rise to a distorted-TBP geometry for ZnO_5 . Substitution in the TBP or distorted TBP sites of LiMgBO_3 ⁸⁵ and $\alpha\text{-LiZnBO}_3$ ¹¹³ with chromophore ions like Co, Ni or Cu creates a range of colors.

In addition to the above, there are crystal structures containing chromophores that occupy multiple coordination sites such as distorted octahedral, tetrahedral and trigonal bipyramidal. In these circumstances it is difficult to assign the causes of color unambiguously to a particular coordination. One of the examples is the hibonite structure with an ideal formula $\text{AM}_{12}\text{O}_{19}$ ($A = \text{Ca, Sr, RE}$; $M = \text{Al, Ni, Co, Mn, Fe, Cr, Cu}$), where the M cations are distributed over 5 crystallographic sites as shown in Fig. 39.^{124–126} A range of colors are generated through M-site substitution of aluminum with various di-, tri- and tetravalent cations ($M = \text{Ni, Fe, Mn}$,

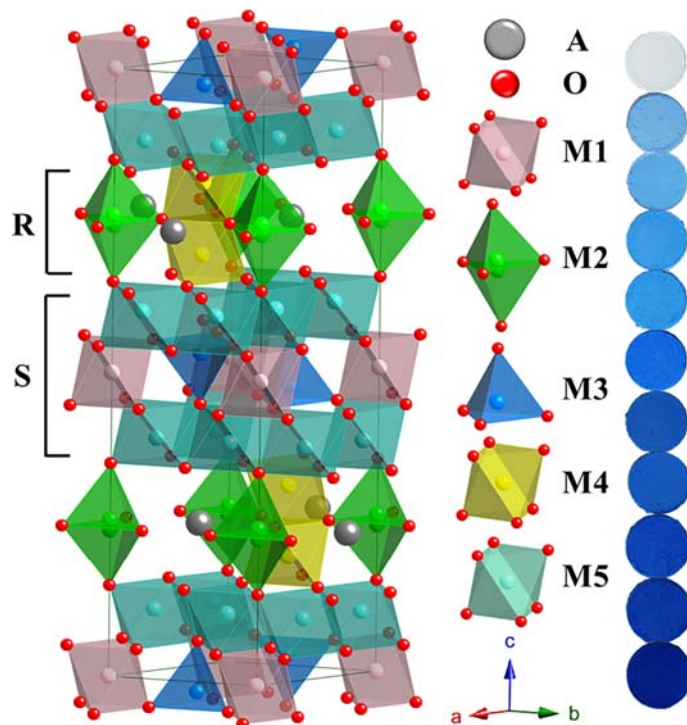


Fig. 39 Hexagonal crystal structure of hibonite $\text{AM}_{12}\text{O}_{19}$ ($A = \text{Ca, Sr, RE}$; $M = \text{Al, Ni, Co, Mn, Fe, Cr, Cu}$): 12 coordinated A atoms in grey; oxygen atoms in red; MO_6 octahedra in pink (M1), yellow (M4) and cyan (M5); MO_5 trigonal bipyramids in green (M2); and MO_4 tetrahedra in royal blue (M3). The framework can be viewed as S-block (spinel layers) and R-block (constituted by A ions, trigonal bipyramids and face-sharing octahedra) stacking alternatively along the c axis. (Right) Images of blue $\text{CaAl}_{12-2x}\text{Ni}_x\text{Ti}_x\text{O}_{19}$ ($x = 0\text{--}1.0$) solid solutions.¹²⁴

Cr, Cu, Ga, In, Ti, Ge, Sn or any combination thereof), where Ni, Fe, Mn, Cr and Cu are chromophores.^{124,126} Bright sky-blue to royal-blue colors are induced in the solid solutions of $\text{CaAl}_{12-2x}\text{Ni}_x\text{Ti}_x\text{O}_{19}$ ($x = 0-1.0$) and $\text{Ca}_{1-x}\text{La}_x\text{Al}_{12-x}\text{Ni}_x\text{O}_{19}$ ($x = 0-1.0$) with Ni^{2+} as the chromophore ion (Fig. 39). Although Ni^{2+} ions mostly occupy the octahedral sites in the NiAl_2O_4 spinel structure,¹²⁷ neutron diffraction studies indicate a preference of Ni^{2+} for the tetrahedral M3 site in the hibonite structure as a result of the longer than normal Al–O distances at the M3 site.¹²⁴ Less than 10% of the total amount of substituted Ni goes to the TBP sites. The optical absorption leading to the blue color primarily arises from d-d transitions of Ni^{2+} in tetrahedral coordination, nonetheless the impact of rest of the Ni^{2+} ions (in octahedral and TBP sites) on color may not be completely excluded.

4.16.7 Rare earth oxides based pigments

Rare earths with partially filled *f* electrons offer a vast opportunity to develop colored compounds for many optical applications including pigments. Among the several candidates for the alternative nontoxic red pigments, CeO_2 and its related materials have been attracted because of the opacity, low toxicity and high temperature stability.¹²⁸ Ln doped CeO_2 (Ln = Pr, Tb, Eu) and *M* doped CeO_2 solid solutions (*M* = Cr or In) have been reported as low toxicity red ceramic pigments.^{24,28} CeO_2 substituted with praseodymium as a chromophore is particularly known for the reddish brown color and several attempts were made to shift the absorption edge of Pr– CeO_2 to make it reddish in color by co-doping other rare earth and transition metal ions.^{35,76,129-134} In cerianite doped red pigments, the coloring mechanism is based on the shift of the charge transfer band of the semiconductor CeO_2 to higher wavelengths, introducing an additional electronic level by doping. The band gap between the anionic band and the cationic band is in CeO_2 is 3.01 eV. By doping CeO_2 with Pr^{4+} ions, the $4f^1$ electron of the praseodymium valence shell introduces an additional electronic level of energy between the O^{2-} valence band and Ce^{4+} conduction band and hence a reduced band gap of 1.88 eV is observed. The CeO_2 band gap falls in indigo region of visible wavelengths, and a complementary pale yellow color is observed. By contrast, Pr^{4+} -substituted CeO_2 absorbs in the wavelength region below 600 nm producing a red color.⁴⁴ In this series, other mixed metal oxides like $\text{TiCeO}_4:\text{Pr}^{4+}$ and $\text{RE}_2\text{Ce}_2\text{O}_7:\text{Pr}^{3+}$ (RE = Y, Sm) with near infrared reflectance are also known to give reddish brown hue by similar coloring mechanism.^{93,135,136}

Wendusu et al. has reported some non-toxic red pigments based on rare earths and bismuth ($(\text{Bi}_{0.72}\text{Er}_{0.28-x}\text{Y}_x)_{1-y}\text{Fe}_y)_2\text{O}_3$ and $\text{Ca}(\text{Bi}_{1-x}\text{RE}_x)_8\text{O}_{15}$ with improved redness (a^*) than iron oxide.^{26,137} However, the yellowness (b^*) is also an important factor in evaluating the pure red hue of a pigment. Pigments with b^* (yellow) dominating than a^* (red) can only be reddish orange or brownish orange in color rather than a real red colored material.

4.16.8 Sulfides and oxynitrides

Sulfides are specially noted for their brilliant color even from prehistoric times where realgar (AsS) and vermilion (HgS) were preferred for red color.¹¹ The invention of cadmium red, which is a solid solution of CdS and CdSe outdated many high toxic red pigments in the industry.¹⁶ However, this series also suffers from both toxicity and stability issues and is not currently used as pigments in large scale coatings. Most rare earth sesquisulfides are colored and especially cerium sulfide is promising in terms of color and purity. The low temperature $\alpha\text{-Ce}_2\text{S}_3$ is brownish black, while $\beta\text{-Ce}_2\text{S}_3$ with burgundy color is in fact an oxysulfide.⁵ The $\gamma\text{-Ce}_2\text{S}_3$ and its alkali-metal derivatives $\gamma\text{-Ce}_{2-x}\text{A}_{3x}\text{S}_3$ (A = alkali) with red and orange hue have been proposed as alternative to the toxic red pigments in use.¹³⁸⁻¹⁴⁰ The dark red color of Ce_2S_3 is due to the electronic transition from Ce 4f level to the Ce 5d conduction band corresponding to a band gap of 2.06 eV. The color range in this sulfide family can be enlarged by varying the ionicity of the Ce–S bond by introducing dopants. $\beta\text{-In}_2\text{S}_3$ is another promising candidate with orange red coloration similar to that of cadmium sulfide red with steep absorption edge.¹⁴¹ Jansen et al. developed a series of nontoxic red pigments based on solid solutions of CaTaO_2N and LaTaON_2 and $\text{Ta}_{3-x}\text{Zr}_x\text{N}_{5-x}\text{O}_x$.^{34,142} The fine tuning of the band gap is achieved with two different nonmetal ions in these perovskite oxynitrides to derive the red color. The band to band transitions in sulfides and oxynitrides are perfect to give the desired pure color rather than in oxides. However, these non-oxide based pigments are chemically not stable and their syntheses involve emission of toxic gases.

4.16.9 Concluding remarks

Designing a durable, non-toxic and intense inorganic pigments is a challenging research task and is dominated by many non-quantified uncertainties. All industrially commercialized colored pigments are colored inorganic solids. However, not all colored inorganic solids can be pigments. The colored solid to be qualified as pigments it has to undergo rigorous testing in real-world conditions such as lightfastness, sensitivity for damage from ultraviolet light, heat stability, toxicity, tinting strength, staining, dispersion, opacity or transparency, resistance to alkalis and acids. In spite of tremendous progress in understanding of chemistry and physics behind observation of colors, it is difficult to predict the color of the compound before it is synthesized in the lab. Hence, synthetic solid-state chemists will continue to play an important role in the future advancement in color science.

Acknowledgment

The work performed at Oregon State University is supported by grants from US National Science Foundation (DMR-0804167, DMR-1216479, DMR-1508527, DMR-2025615).

References

- Nassau, K. The Origins of Color in Minerals. *Am. Mineral.* **1978**, *63*, 219–229.
- Burns, R. G. Colours of Gems. *Chem. Br.* **1983**, 1004–1007.
- Nassau, K. The Fifteen Causes of Color. In *Color for Science, Art and Technology*; Nassau, K., Ed.; vol. 1; AZimuth, 1998; pp 123–168.
- Buxbaum, G., Pfaff, G., Eds.; *Industrial Inorganic Pigments*, 3rd ed.; Wiley-VCH, 2005.
- Smith, H. M., Ed.; *High Performance Pigments*, 1st ed.; Wiley-VCH Verlag-GmbH, 2002.
- Jeevanandam, P.; Mulukutta, R. S.; Phillips, M.; Chaudhuri, S.; Erickson, L. E.; Klabunde, K. J. Near Infrared Reflectance Properties of Metal Oxide Nanoparticles. *J. Phys. Chem. C* **2007**, *111*, 1912–1918.
- Orna, M. V. The Chemical Origins of Color. *J. Chem. Educ.* **1978**, *55* (8), 478–484.
- Furukawa, S.; Masui, T.; Imanaka, N. Synthesis of New Environment-Friendly Yellow Pigments. *J. Alloys Compd.* **2006**, *418*, 255–258.
- Christie, R. M. *Colour Chemistry*, 2nd ed.; The Royal Society of Chemistry, 2001.
- Lewis, P. A. Colorants: Organic and Inorganic Pigments. In *Color for Science, Art and Technology*; Nassau, K., Ed.; vol. 1; AZimuth, 1998; pp 283–312.
- Delemare, F.; Guineau, B. *Colors: The Story of Dyes and Pigments*, 60720th ed.; Harry N. Abrams, 2000.
- Coles, D. *Chromatopia: An Illustrated History of Color*, Thames & Hudson, 2019.
- Ruspoli, M. *The Cave of Lascaux: The Final Photographs*, Harry N. Abrams, 1987.
- Skelton, H. A Colour Chemist's History of Western Art. *Rev. Prog. Color. Relat. Top.* **1999**, *29*, 43–64.
- Berke, H. The Invention of Blue and Purple Pigments in Ancient Times. *Chem. Soc. Rev.* **2007**, *36*, 15–30.
- Ball, P. *The Colourful Science*, Chemistry World, 2014. <http://www.rsc.org/chemistryworld/2014/06/colour-chemistry>.
- Tulun, T.; Döner, G.; ÇALIŞIR F., ÇİNI N.; et al. An Archaeometric Study on Ancient Iznik Ceramics. *BAÜ Fen Bil. Enst. Dergisi* **2002**, *4* (2), 34–44.
- Taylor, P. J. Coloured Inorganic Pigments. *Rev. Prog. Color. Relat. Top.* **1973**, *4*, 37–43.
- Smith, A. E.; Mizoguchi, H.; Delaney, K.; Spaldin, N.; Sleight, A. W.; Subramanian, M. A. Mn^{3+} in Trigonal Bipyramidal Coordination: A New Blue Chromophore. *J. Am. Chem. Soc.* **2009**, *131*, 17084–17086.
- Tücks, A.; Beck, H. P. The Photochromic Effect of Bismuth Vanadate Pigments. Part I: Synthesis, Characterization and Lightfastness of Pigment Coatings. *J. Solid State Chem.* **2005**, *178*, 1145–1156.
- He, Y. P.; Wu, Z. Y.; Fu, L. M.; Li, C. R.; Miao, Y. M.; Cao, L.; Fan, H. M.; Zou, B. S. Photochromism and Size Effect of WO_3 and WO_3 - TiO_2 Aqueous Sol. *Chem. Mater.* **2003**, *15*, 4039–4045.
- Sandhya Kumari, L.; Prabhakar Rao, P.; Narayana Pillai Radhakrishnan, A.; James, V.; Sameera, S.; Koshy, P. Brilliant yellow color and enhanced NIR reflectance of monoclinic $BiVO_4$ through distortion in VO_4^{3-} tetrahedra. *Sol. Energy Mater. Sol. Cells* **2013**, *112*, 134–143.
- Pfaff, G. *Special Effect Pigments: Technical Basics and Applications*, 2nd ed.; Vincentz Network GmbH & Co KG, 2008.
- Garcia, A.; Llusar, M.; Calbo, J.; Tena, M. A.; Monrós, G. Low-Toxicity Red Ceramic Pigments for Porcelainised Stoneware from Lanthanide-Cerianite Solid Solutions. *Green Chem.* **2001**, *3*, 238–242.
- Candeia, R. A.; Souza, M. A. F.; Bernardi, M. I. B.; Maestrelli, S. C.; Santos, I. M. G.; Souza, A. G.; Longo, E. $MgFe_2O_4$ Pigment Obtained at Low Temperature. *Mater. Res. Bull.* **2006**, *41*, 183–190.
- Wendusu, M. T.; Imanaka, N. Novel Environment-Friendly Inorganic Red Pigments Based on $(Bi,Er,Y,Fe)_2O_3$ Solid Solutions. *J. Asian Ceramic Soc.* **2014**, *2*, 195–198.
- Lyubenova, T. S.; Carda, J. B.; Ocaña, M. Synthesis by Pyrolysis of Aerosols and Ceramic Application of Cr-Doped $CaYAlO_4$ Red–Orange Pigments. *J. Eur. Ceram. Soc.* **2009**, *29*, 2193–2198.
- Llusar, M.; Vitásková, L.; Šulcová, P.; Tena, M. A.; Badenes, J. A.; Monrós, G. Red Ceramic Pigments of Terbium-Doped Ceria Prepared through Classical and Non-conventional Coprecipitation Routes. *J. Eur. Ceram. Soc.* **2010**, *30*, 37–52.
- Nassau, K. *The Physics and Chemistry of Color*, 2nd ed.; Wiley- Interscience, 2001.
- Chevreul, M. E.; Birren, F. *The Principles of Harmony and Contrast of Colors and their Applications to the Arts*. revised ed., Schiffer Pub Ltd, 1987
- Cowley, A. C. D. Lead Chromate—That Dazzling Pigment. *Rev. Prog. Color. Relat. Top.* **1986**, *16*, 16–24.
- Kemsley, J. N. Road Markings. *Chem. Eng. News* **2010**, *88*, 67, 2010.
- Huckle, W. G.; Lalor, E. Inorganic Pigments. *Ind. Eng. Chem.* **1955**, *47* (8), 1501–1506.
- Jansen, M.; Letschert, H. P. Inorganic Yellow-Red Pigments without Toxic Metals. *Nature* **2000**, *404*, 980–982.
- Kumari, L. S.; Rao, P. P.; Reddy, M. L. Environment-Friendly Red Pigments from CeO_2 - Fe_2O_3 - Pr_6O_{11} Solid Solutions. *J. Alloys Compd.* **2008**, *461*, 509–515.
- Tamilarasan, S.; Laha, S.; Natarajan, S.; Gopalakrishnan, J. Li_2MnO_3 : A Rare Red-Coloured Manganese(IV) Oxide Exhibiting Tunable Red-Yellow-Green Emission. *J. Mater. Chem. C* **2015**, *3*, 4794–4800.
- Loeffler, B. M.; Burns, R. G. Shedding Light on the Color of Gems and Minerals. *Am. Sci.* **1976**, *64* (6), 636–647.
- Fritsch, B. E.; Rossmann, G. R. An Update on Color in Gems. Part 1: Introduction and Colors Caused by Dispersed Metal Ions. *Gems Gemol.* **1987**, 126–139.
- Burns, R. G. *Mineralogical Applications of Crystal Field Theory*, 2nd ed.; Cambridge University, 1993.
- Katayama, Y.; Kobayashi, H.; Tanabe, S. Deep-Red Persistent Luminescence in Cr^{3+} -Doped $LaAlO_3$ Perovskite Phosphor for In Vivo Imaging. *Appl. Phys. Express* **2015**, *8*, 012102-1–012102-3.
- El-bali, B.; Boukhar, A.; Aride, J.; Maaß, K.; Wald, D.; Glaum, R.; Abraham, F. Crystal Structure and Colour of $SrNiP_2O_7$ and $SrNi_3(P_2O_7)_2$. *Solid State Sci.* **2001**, *3*, 669–676.
- Binnemans, K.; Görller-Walrand, C. On the Color of the Trivalent Lanthanide Ions. *Chem. Phys. Lett.* **1995**, *235*, 163–174.
- Seabright, C. A. *Yellow Ceramic Pigments*. US2992123 A, 1961.
- Olazcuaga, R.; Le Polles, G.; El Kira, A.; Le Flem, G.; Maestro, P. Optical Properties of $Ce_{1-x}Pr_xO_2$ Powders and their Applications to the Coloring of Ceramics. *J. Solid State Chem.* **1987**, *71*, 570–573.
- Tilley, R. J. D. *Colour and the Optical Properties of Materials*, 2nd ed.; Wiley, 2011.
- Burns, R. G. Intervalence Transitions in Mixed-Valence Minerals of Iron and Titanium. *Annu. Rev. Earth Planet. Sci.* **1981**, *9*, 345–383.
- Rossmann, G. R.; Mattson, S. M. Yellow, Mn-Rich Elbaite with Mn-Ti Intervalence Charge Transfer. *Am. Mineral.* **1986**, *71*, 599–602.
- Robin, M. B. The Color and Electronic Configurations of Prussian Blue. *Inorg. Chem.* **1962**, *1* (2), 337–342.
- Best, S. P.; Clark, R. J. H.; Daniels, M. A. M.; Porter, C. A.; Withnall, R. Identification by Raman Microscopy and Visible Reflectance Spectroscopy of Pigments on an Icelandic Manuscript. *Stud. Conserv.* **1995**, *40* (1), 31–40.
- Clark, R. J. H. Pigment Identification on Medieval Manuscripts by Raman Microscopy. *J. Mol. Struct.* **1995**, *347*, 417–428.

51. Dey, S.; Ricciardo, R. A.; Cuthbert, H. L.; Woodward, P. M. Metal-to-Metal Charge Transfer in AWO_4 (A = Mg, Mn, Co, Ni, Cu, or Zn) Compounds with the Wolframite Structure. *Inorg. Chem.* **2014**, *53*, 4394–4399.
52. Woodward, P. M.; Mizoguchi, H.; Kim, Y. I.; Stoltzfus, M. W. The Electronic Structure of Metal Oxides. In *Metal Oxides: Chemistry and Applications*; Fierro, J. L. G., Ed., 1st ed.; Taylor and Francis Group, 2005; pp 133–194.
53. Fritsch, E.; Rossman, G. R. An Update on Color in Gems. Part 2: Colors Involving Multiple Atoms and Color Centers. *Gems Gemol.* **1988**, *24*, 3–15.
54. Demortier, A.; Lede, B.; Lelieur, J. P.; Duhayon, C. Occupancy of the Sodalite Cages in the Blue Ultramarine Pigments. *Inorg. Chem.* **2002**, *41*, 2848–2854.
55. Chivers, T.; Elder, P. J. W. Ubiquitous Trisulfur Radical Anion: Fundamentals and Applications in Materials Science, Electrochemistry, Analytical Chemistry and Geochemistry. *Chem. Soc. Rev.* **2013**, *42*, 5996–6005.
56. Xu, X. X.; Random, C.; Efstathiou, P.; Irvine, J. T. S. A Red Metallic Oxide Photocatalyst. *Nat. Mater.* **2012**, *11*, 595–598.
57. Nassau, K. The Fifteen Causes of Color: The Physics and Chemistry of Color. *Color Res. Appl.* **1987**, *12*, 4–26.
58. Shevell, S. K., Ed.; *The Science of Color*, 2nd ed.; Elsevier, 2003.
59. Ball, P. Nature's Color Tricks: Understanding Seven Clever Tactics Animals Use to Create Dazzling Hues May Lead to Sophisticated New Technologies. *Sci. Am.* **2012**, *306*, 74–79.
60. Orna, M. V. Chemistry and Artists' Colors: Part III. Preparation and Properties of Artists' Pigments. *J. Chem. Educ.* **1980**, *57* (4), 267–269.
61. Hunault, M.; Robert, J. L.; Newville, M.; Galoisy, L.; Calas, G. Spectroscopic Properties of Five-Coordinated Co^{2+} in Phosphates. *Spectrochim. Acta A Mol. Biomol. Spectrosc.* **2014**, *117*, 406–412.
62. Schmetzer, K. Crystal Chemistry of Natural be-mg-Al-Oxides: Taaffeite, Taprobanite, Musgravite. *Neues Jahrb. Mineral. Abh.* **1983**, *146*, 15–28.
63. Litterscheid, C.; Glaum, R. Mixed Chromium (II) Titanium (III) Phosphates: Crystal Growth, Structures and Electronic Absorption Spectra. *Phosphorus Res. Bull.* **2005**, *19*, 54–59.
64. Schmidt, A.; Glaum, R. $\text{Cr}_3\text{Si}_2\text{O}_7 \cdot \frac{1}{4}\text{MX}$ (MX = NaCl, NaBr, KCl, KBr): A Cage Structure Built from $[\text{Cr}^{\text{II}}\text{O}_4]$ and $[\text{Si}_2\text{O}_7]$ Units. *Inorg. Chem.* **1997**, *36*, 4883–4887.
65. Maaß, K.; Glaum, R. Strontium Chromium(II) Diphosphate, SrCrP_2O_7 . *Acta Crystallogr. C* **2000**, *56*, 404–406.
66. Swiller, D. R. *Manganese Vanadium Oxide Pigments*. EP 1170258 A2, 2002.
67. Mizoguchi, H.; Sleight, A. W.; Subramanian, M. A. New Oxides Showing an Intense Blue Color Based on Mn^{3+} in Trigonal-Bipyramidal Coordination. *Inorg. Chem.* **2011**, *50*, 10–12.
68. Li, J.; Smith, A. E.; Jiang, P.; Stalick, J. K.; Sleight, A. W.; Subramanian, M. A. True Composition and Structure of Hexagonal "YAlO₃", Actually $\text{Y}_3\text{Al}_3\text{O}_8\text{CO}_3$. *Inorg. Chem.* **2015**, *54*, 837–844.
69. Tamilarasan, S.; Sarma, D.; Reddy, M. L. P.; Natarajan, S.; Gopalakrishnan, J. $\text{YGa}_{1-x}\text{Mn}_x\text{O}_3$: A Novel Purple Inorganic Pigment. *RSC Adv.* **2013**, *3*, 3199–3202.
70. Saraswathy, D.; Rao, P. P.; Sameera, S.; James, V.; Raj, A. K. V. Monoclinic $\text{LaGa}_{1-x}\text{Mn}_x\text{Ge}_2\text{O}_7$: A New Blue Chromophore Based on Mn^{3+} in Trigonal Bipyramidal Coordination with Longer Apical Bond Lengths. *RSC Adv.* **2015**, *5*, 27278–27281.
71. Nguyen, N.; Legrain, M.; Doucuret, A.; Raveau, B. Distribution of Mn^{3+} and Mn^{4+} Species between Octahedral and Square Pyramidal Sites in $\text{Bi}_2\text{Mn}_4\text{O}_{10}$ -Type Structure. *J. Mater. Chem.* **1999**, *9*, 731–734.
72. Eastaugh, N.; Walsh, V.; Chaplin, T.; Siddall, R. *Pigment Compendium: A Dictionary and Optical Microscopy of Historical Pigments*, Elsevier, 2008.
73. Laha, S.; Sharma, R.; Bhat, S. V.; Reddy, M. L. P.; Gopalakrishnan, J.; Natarajan, S. $\text{Ba}_3(\text{P}_{1-x}\text{Mn}_x\text{O}_4)_2$: Blue/Green Inorganic Materials Based on Tetrahedral Mn(V). *Bull. Mater. Sci.* **2011**, *34* (6), 1257–1262.
74. Lachwa, H.; Reinen, D.; Color and Electronic Structure of Manganese(V) and Manganese(VI) in Tetrahedral Oxo Coordination. A Spectroscopic Investigation. *Inorg. Chem.* **1989**, *28* (6), 1044–1053.
75. Medina, E. A.; Li, J.; Stalick, J. K.; Subramanian, M. A. Intense Turquoise Colors of Apatite-Type Compounds with Mn^{5+} in Tetrahedral Coordination. *Solid State Sci.* **2016**, *52*, 97–105.
76. Kumari, L. S.; Rao, P. P.; Sameera, S.; Koshy, P. Synthesis and Optical Properties of $\text{Ce}_{0.95}\text{Pr}_{0.05-x}\text{M}_x\text{O}_2$ (M = Mn, Si) as Potential Ecological Red Pigments for Coloration of Plastics. *Ceram. Int.* **2012**, *38*, 4009–4016.
77. Morris, R. V.; Lauer, H. V.; Lawson, A. C.; Gibson, K. E.; Nace, G. A.; Stewart, C. Spectral and Other Physicochemical Properties of Submicron Powders of Hematite ($\alpha\text{-Fe}_2\text{O}_3$), Maghemite ($\gamma\text{-Fe}_2\text{O}_3$), Magnetite (Fe_3O_4), Goethite ($\alpha\text{-FeOOH}$), and Lepidocrocite ($\gamma\text{-FeOOH}$). *J. Geophys. Res.* **1985**, *90* (B4), 3126–3144.
78. Rossman, G. R. Why Hematite is Red: Correlation of Optical Absorption Intensities and Magnetic Moments of Fe^{3+} Minerals. *Miner. Spectrosc.* **1996**, *5*, 23–27.
79. Birch, W. D.; Pring, A.; Reller, A.; Schmale, H. W. Bernalite, $\text{Fe}(\text{OH})_3$, a New Mineral from Broken Hill, New South Wales: Description and Structure. *Am. Mineral.* **1993**, *78*, 827–834.
80. Jiang, P.; Li, J.; Sleight, A. W.; Subramanian, M. A. New Oxides Showing an Intense Orange Color Based on Fe^{3+} in Trigonal-Bipyramidal Coordination. *Inorg. Chem.* **2011**, *50*, 5858–5860.
81. Mackey, D. J.; McMeeking, R. F.; Hitchman, M. A. Magnetic Anisotropy and Electronic Structure of Gillespite, a Mineral Containing Planar, Four-Co-Ordinate, High-Spin Iron(II). *J. Chem. Soc. Dalton Trans.* **1979**, *2*, 299–305.
82. Melo, D. M. A.; Cunha, J. D.; Fernandes, J. D. G.; Bernardi, M. I.; Melo, M. A. F.; Martinelli, A. E. Evaluation of CoAl_2O_4 as Ceramic Pigments. *Mater. Res. Bull.* **2003**, *38*, 1559–1564.
83. Chauviré, B.; Rondeau, B.; Fritsch, E.; Ressigeac, P.; Devidal, J. L. Blue Spinel from the Luc Yen District of Vietnam. *Gems Gemol.* **2015**, *51*, 2–17.
84. Shigley, J. E.; Stockton, C. M. 'Cobalt Blue' Gem Spinels. *Gems Gemol.* **1984**, *20*, 34–41.
85. Tamilarasan, S.; Laha, S.; Natarajan, S.; Gopalakrishnan, J. Exploring the Colour of 3d Transition-Metal Ions in Trigonal Bipyramidal Coordination: Identification of Purple-Blue (CoO_5) and Beige-Red (NiO_5) Chromophores in LiMgBO_3 Host. *Eur. J. Inorg. Chem.* **2016**, *2*, 288–293.
86. Rossman, G. R.; Shannon, R. D.; Waring, R. K. Origin of the Yellow Color of Complex Nickel Oxides. *J. Solid State Chem.* **1981**, *39*, 277–287.
87. Jose, S.; Prakash, A.; Laha, S.; Natarajan, S.; Reddy, M. L. Green Colored Nano-Pigments Derived from Y_2BaCuO_5 : NIR Reflective Coatings. *Dyes Pigm.* **2014**, *107*, 118–126.
88. Chen, Y.; Zhang, Y.; Feng, S. H. Hydrothermal Synthesis and Properties of Pigments Chinese Purple $\text{BaCuSi}_2\text{O}_6$ and Dark Blue $\text{BaCu}_2\text{Si}_2\text{O}_7$. *Dyes Pigm.* **2014**, *105*, 167–173.
89. Moreno, M.; Aramburu, J. A. Origin of the Exotic Blue Color of Copper-Containing Historical Pigments. *Inorg. Chem.* **2015**, *54*, 192–199.
90. Cohen, A. J.; Makar, L. N. Dynamic Biaxial Absorption Spectra of Ti^{3+} and Fe^{2+} in a Natural Rose Quartz Crystal. *Mineral. Mag.* **1985**, *49*, 709–715.
91. Wendusu, I. K.; Masui, T.; Imanaka, N. Novel Environment-Friendly Yellow Pigments Based on (Bi, La) VO_4 . *Chem. Lett.* **2011**, *40*, 792–794.
92. Kumari, L. S.; Rao, P. P.; Sameera, S.; James, V.; Koshy, P. Effects of Rare Earth Substitution on the Optical Properties of Bi_2MoO_6 for Coloring Applications. *Mater. Res. Bull.* **2015**, *70*, 93–98.
93. Kumari, L. S.; George, G.; Rao, P. P.; Reddy, M. L. P. The Synthesis and Characterization of Environmentally Benign Praseodymium-Doped TiCeO_4 Pigments. *Dyes Pigm.* **2008**, *77*, 427–431.
94. Martos, M.; Julián-López, B.; Cordoncillo, E.; Escrbano, P. Structural and Spectroscopic Study of a New Pink Chromium-Free $\text{Er}_2(\text{Ti},\text{Zr})_2\text{O}_7$ Ceramic Pigment. *J. Am. Ceram. Soc.* **2009**, *92* (12), 2987–2992.
95. Zhang, L. W.; Man, Y.; Zhu, Y. F. Effects of Mo Replacement on the Structure and Visible-Light-Induced Photocatalytic Performances of Bi_2WO_6 Photocatalyst. *ACS Catal.* **2011**, *1*, 841–848.
96. Stoltzfus, M. W.; Woodward, P. M.; Seshadri, R.; Klepeis, J. H.; Bursten, B. Structure and Bonding in SnWO_4 , PbWO_4 , and BiVO_4 : Lone Pairs Vs Inert Pairs. *Inorg. Chem.* **2007**, *46*, 3839–3850.

97. Ghosh, M.; Pralong, V.; Wattiaux, A.; Sleight, A. W.; Subramanian, M. A. Tin (II) Doped Anatase (TiO₂) Nanoparticles: A Potential Route to "Greener" Yellow Pigments. *Chem. Asian J.* **2009**, *4*, 881–885.
98. Mizoguchi, H.; Wattiaux, A.; Kykyneshi, R.; Tate, J.; Sleight, A. W.; Subramanian, M. A. Synthesis and Characterization of Sn²⁺ Oxides with the Pyrochlore Structure. *Mater. Res. Bull.* **2008**, *43*, 1943–1948.
99. Chang, H. Y.; Ok, K. M.; Kim, J. H.; Halasyamani, P. S.; Stoltzfus, M.; Woodward, P. Synthesis, Structure, Characterization, and Calculations of Two New Sn²⁺-W⁶⁺-Oxides, Sn₂WO₅ and Sn₃WO₆. *Inorg. Chem.* **2007**, *46*, 7005–7011.
100. Stone, D. Coat d'Azur. *Natl. Geogr.* **2013**, *223* (2), 19.
101. Chang, K. *By Happy Accident, Chemists Produce a New Blue*, New York Times, 2009; p D3. November 24.
102. Bendiganavale, A. K.; Malshe, V. C. Infrared Reflective Inorganic Pigments. *Recent Pat. Chem. Eng.* **2008**, *1*, 67–79.
103. Smith, A. E.; Comstock, M. C.; Subramanian, M. A. Spectral Properties of the UV Absorbing and near-IR Reflecting Blue Pigment, YIn_{1-x}Mn_xO₃. *Dyes Pigm.* **2016**, *133*, 214–221.
104. Ball, P. *Blues Standard*, Royal Society of Chemistry Magazine, Chemistry World, 2012. September 27. <http://www.rsc.org/chemistryworld/2012/09/blue-pigment-paint-chemistry>.
105. Schama, S. *Blue as Can Be: A Color archive's Treasures Reveal a History of Pigment*, vol. 3; The New Yorker, Sept. 2018; pp 28–32.
106. Smith, A. E.; Sleight, A. W.; Subramanian, M. A. Synthesis and Properties of Solid Solutions of Hexagonal YCu_{0.5}Ti_{0.5}O₃ with YMO₃ (M = Mn, Cr, Fe, Al, Ga, and In). *Mater. Res. Bull.* **2011**, *46*, 1–5.
107. Li, J.; Lorger, S.; Stalick, J. K.; Sleight, A. W.; Subramanian, M. A. From Serendipity to Rational Design: Tuning the Blue Trigonal Bipyramidal Mn³⁺ Chromophore to Violet and Purple through Application of Chemical Pressure. *Inorg. Chem.* **2016**, *55*, 9798–9804.
108. Adem, U.; Nugroho, A. A.; Meetsma, A.; Palstra, T. T. M. Ferroelectric Displacements in Multiferroic Y(Mn,Ga)O₃. *Phys. Rev. B* **2007**, *75*, 014108.
109. Li, J.; Singh, U. G.; Schladt, T. D.; Stalick, J. K.; Scott, S. L.; Seshadri, R. Hexagonal YFe_{1-x}Pd_xO_{3-δ}: Nonperovskite Host Compounds for Pd²⁺ and their Catalytic Activity for CO Oxidation. *Chem. Mater.* **2008**, *20*, 6567–6576.
110. Rusakov, D. A.; Belik, A. A.; Kamba, S.; Savinov, M.; Nuzhnyy, D.; Kolodiaznyy, T.; Yamaura, K.; Takayama-Muromachi, E.; Borodavka, F.; Kroup, J. Structural Evolution and Properties of Solid Solutions of Hexagonal InMnO₃ and InGaO₃. *Inorg. Chem.* **2011**, *50*, 3559–3566.
111. Bertaut, F.; Mareschal, J. A New Type Hexagonal Structure: AlTO₃ (T = Y, Eu, Gd, Tb, Dy, Ho, Er). *C. R. Hebd. Seances Acad. Sci.* **1963**, *257*, 867–870.
112. Kim, T. G.; Kim, S. J.; Lin, C. C.; Liu, R. S.; Chan, T. S.; Im, S. J. Mellite-Type Blue Chromophores Based on Mn³⁺ in a Trigonal Bipyramidal Coordination Induced by Interstitial Oxygen. *J. Mater. Chem. C* **2013**, *1*, 5843–5848.
113. Tamilarasan, S.; Reddy, M. L. P.; Natarajan, S.; Gopalakrishnan, J. Developing Intense Blue and Magenta Colors in α-LiZnBO₃: The Role of 3d-Metal Substitution and Coordination. *Chem. Asian J.* **2016**, *11*, 3234–3240.
114. Gomes, Y. F.; Li, J.; Silva, K. F.; Santiago, A. A. G.; Bomio, M. R. D.; Paskocimas, C. A.; Subramanian, M. A.; Motta, F. V. Synthesis and Characterization of Y(In,Mn)O₃ Blue Pigment using the Complex Polymerization Method (CPM). *Ceram. Int.* **2018**, *44*, 11932–11939.
115. El Amrani, M.; Ta Phuoc, V.; Ammar, M. R.; Zaghioui, M.; Gervais, F. Structural Modifications of Disordered YMn_{1-x}In_xO₃ Solid Solutions Evidenced by Infrared and Raman Spectroscopies. *Solid State Sci.* **2012**, *14*, 1315–1320.
116. Krzystek, J.; Telsler, J.; Li, J.; Subramanian, M. A. Magnetic Properties and Electronic Structure of Manganese-Based Blue Pigments: A High-Frequency and -Field EPR Study. *Inorg. Chem.* **2015**, *54*, 9040–9045.
117. Li, J.; Sleight, A. W.; Subramanian, M. A. Determination of the Local Environment of Mn³⁺ and In³⁺ in the YInO₃-YMnO₃ Solid Solution, which Exhibits an Intense Blue Color. *Chem. Mater.* **2016**, *28*, 6050–6053.
118. Pistorius, C. W. F. T.; Kruger, J. G. Stability and Structure of Noncentrosymmetric Hexagonal LnInO₃ (Ln = Eu, Gd, Tb, Dy, Ho, Y). *J. Inorg. Nucl. Chem.* **1976**, *38*, 1471–1475.
119. Gibbs, A. S.; Knight, K. S.; Lightfoot, P. High-Temperature Phase Transitions of Hexagonal YMnO₃. *Phys. Rev. B* **2011**, *83*, 094111.
120. Mukherjee, S.; Ganegoda, H.; Kumar, A.; Pal, S.; Segre, C. U.; Sarma, D. D. Evolution of the Local Structure within Chromophoric Mn–O₅ Trigonal Bipyramids in YMn_{1-x}In_xO₃ with Composition. *Inorg. Chem.* **2018**, *57*, 9012–9019.
121. Shannon, R. D. Revised Effective Ionic Radii and Systematic Studies of Interatomic Distances in Halides and Chalcogenides. *Acta Crystallogr. Sect. A* **1976**, *A32*, 751–767.
122. Jiang, P.; Berthelot, R.; Li, J.; Sleight, A. W.; Subramanian, M. A. Topotactic Reduction and Reoxidation of Hexagonal RCu_{0.5}Ti_{0.5}O₃ (R = Y, Eu-Lu) Phases. *Mater. Res. Bull.* **2013**, *48*, 2237–2239.
123. Torres, M. Y.; Guerrero, N. A.; Díaz, T. D.; Macías, M. A.; Ospino, E. M.; Hernández, R. C.; Gauthier, G. H. Synthesis and Characterization of Pure and Mn-Substituted YA_{1.15}(CO₃)_{0.3}O_{3+δ}: A Variation from the Classical Hexagonal "YAlO₃". *J. Phys. Chem. Solid* **2019**, *124*, 199–204.
124. Li, J.; Medina, E. A.; Stalick, J. K.; Sleight, A. W.; Subramanian, M. A. Colored Oxides with Hibonite Structure: A Potential Route to Non-cobalt Blue Pigments. *Prog. Solid State Chem.* **2016**, *44*, 107–122.
125. Li, J.; Medina, E. A.; Stalick, J. K.; Sleight, A. W.; Subramanian, M. A. Structural Studies of CaAl₁₂O₁₉, SrAl₁₂O₁₉, La_{2/3+δ}Al_{12-δ}O₁₉, and CaAl₁₀NiTiO₁₉ with the Hibonite Structure; Indications of an Unusual Type of Ferroelectricity. *Z. Naturforsch. B* **2016**, *71* (5), 475–484.
126. Medina, E. A.; Li, J.; Subramanian, M. A. Colored Oxides with Hibonite Structure II: Structural and Optical Properties of CaAl₁₂O₁₉-Type Pigments with Chromophores Based on Fe, Mn, Cr and Cu. *Prog. Solid State Chem.* **2017**, *45–46*, 9–29.
127. O'Neill, H. S. C.; Dollase, W. A.; Rose, C. R., II Temperature Dependence of Cation Distribution in Nickel Aluminate (NiAl₂O₄) Spinel: A Powder XRD Study. *Phys. Chem. Miner.* **1991**, *18*, 302–310.
128. Nayak, R.; Rao, J. R.; Suryanarayana, A. Synthesis and Characterisation of Rare Earth Oxide Based Pigments. *J. Sci. Ind. Res. India* **2001**, *60*, 941–944.
129. Kumari, L. S.; Rao, P. P.; Koshy, P. Red Pigments Based on CeO₂-MO₂-Pr₆O₁₁ (M = Zr and Sn): Solid Solutions for the Coloration of Plastics. *J. Am. Ceram. Soc.* **2010**, *93* (5), 1402–1408.
130. Sulcova, P.; Trojan, M. The Synthesis of the Ce_{0.95-y}Pr_{0.05}La_yO_{2-y/2} Pigments. *Dyes Pigm.* **2000**, *44*, 165–168.
131. Sulcova, P.; Trojan, M. Thermal Analysis of Pigments Based on CeO₂. *J. Therm. Anal. Calorim.* **2001**, *65*, 399–403.
132. Sulcova, P.; Trojan, M. Study of Ce_{1-x}Pr_xO₂ Pigments. *Thermochim. Acta* **2003**, *395*, 251–255.
133. George, G.; Rao, P. P.; Reddy, M. L. P. Synthesis and Characterization of CeO₂-TiO₂-Pr₆O₁₁ Solid Solution for Environmentally Benign Nontoxic Red Pigments. *Chem. Lett.* **2006**, *35* (12), 1412–1413.
134. Sreeram, K. J.; Aby, C. P.; Nair, B. U.; Ramasami, T. Colored Cool Colorants Based on Rare Earth Metal Ions. *Sol. Energy Mater. Sol. Cells* **2008**, *92*, 1462–1467.
135. Vishnu, V. S.; George, G.; Reddy, M. L. P. Effect of Molybdenum and Praseodymium Dopants on the Optical Properties of Sm₂Ce₂O₇: Tuning of Band Gaps to Realize Various Color Hues. *Dyes Pigm.* **2010**, *85*, 117–123.
136. Sarasamma, V. V.; Lakshminpathi, R. M. Near-Infrared Reflecting Inorganic Pigments Based on Molybdenum and Praseodymium Doped Yttrium Cerate: Synthesis, Characterization and Optical Properties. *Sol. Energy Mater. Sol. Cells* **2011**, *95*, 2685–2692.
137. Wendusu, Y. T.; Masui, T.; Imanaka, N. Novel Environmentally Friendly Inorganic Red Pigments Based on Calcium Bismuth Oxides. *J. Adv. Ceram.* **2015**, *4* (1), 39–45.
138. Maestro, P. *Nouveaux pigments colorés à base de terres rares et leurs applications*. E.P. 0203838, 1985.

139. Gauthier, G.; Jobic, S.; Evain, M.; Koo, H.-J.; Whangbo, M.-H.; Fouassier, C.; Brec, R. Syntheses, Structures, and Optical Properties of Yellow Ce_2SiS_5 , $\text{Ce}_6\text{Si}_4\text{S}_{17}$, and $\text{Ce}_4\text{Si}_3\text{S}_{12}$ Materials. *Chem. Mater.* **2003**, *15* (4), 828–837.
140. Mauricot, R.; Gressier, P.; Evain, M.; Brec, R. Comparative Study of some Rare Earth Sulfides: Doped γ -[A] M_2S_3 (M = La, Ce and Nd, A = Na, K and Ca) and Undoped γ - M_2S_3 (M = La, Ce and Nd). *J. Alloys Compd.* **1995**, *223*, 130–138.
141. Gorai, S.; Guha, P.; Ganguli, D.; Chaudhuri, S. Chemical Synthesis of β - In_2S_3 Powder and its Optical Characterization. *Mater. Chem. Phys.* **2003**, *82*, 974–979.
142. Guenther, E.; Jansen, M. Optical Properties of $\text{Ta}_{(3-x)}\text{Zr}_{(x)}\text{N}_{(5-x)}\text{O}_{(x)}$ Semiconductor Pigments. *Mater. Res. Bull.* **2001**, *36*, 1399–1405.

4.17 Photoelectrochemical materials for solar energy conversion

Shaun O'Donnell, Jessica Chestnut, Magnus Pauly, and Paul A. Maggard, Department of Chemistry, North Carolina State University, Raleigh, NC, United States

© 2023 Elsevier Ltd. All rights reserved.

4.17.1	Introduction	595
4.17.1.1	Background	595
4.17.1.2	Key semiconductor parameters	596
4.17.2	Metal oxide semiconductors	597
4.17.2.1	Background	597
4.17.2.2	Crystal structures and photoelectrochemical properties	598
4.17.2.2.1	Perovskite type structures with 3D B-cation connectivity	598
4.17.2.2.2	Layered perovskite structures with 2D B-cation connectivity	599
4.17.2.2.3	Structures with 2D B-cation and extended A-cation connectivity	600
4.17.2.2.4	Structures with only 1D A-cation and B-cation connectivity	601
4.17.2.2.5	Structures with extended A-cation connectivity and isolated B-cations	602
4.17.2.3	Band gaps and band edge positions	602
4.17.2.3.1	Tuning the band gaps of oxide semiconductors	603
4.17.2.3.2	Tuning the conduction band energy of metal oxides	603
4.17.2.3.3	Tuning the valence band energy of metal oxides	605
4.17.2.4	Band dispersion and effective masses of charge carriers: Oxide semiconductors	607
4.17.2.4.1	General trends	608
4.17.2.4.2	Conduction band dispersion of metal oxides	610
4.17.2.4.3	Valence band dispersion of metal oxides	610
4.17.2.5	Summary of metal oxide semiconductors	612
4.17.3	Metal nitride semiconductors	612
4.17.3.1	Background	612
4.17.3.2	Crystal structures and photoelectrochemical properties	612
4.17.3.2.1	Perovskite-type oxynitride structures	613
4.17.3.2.2	Wurtzite-type oxynitride structures	614
4.17.3.2.3	Tantalum nitride and tantalum oxynitride	615
4.17.3.2.4	Layered carbon nitrides	616
4.17.3.3	Band gaps and band edge positions	617
4.17.3.3.1	Tuning the band gaps of nitride semiconductors	617
4.17.3.3.2	Tuning the conduction band energy of metal nitrides	618
4.17.3.3.3	Tuning the valence band energy of metal nitrides	619
4.17.3.4	Band dispersion and effective masses of charge carriers: Nitride semiconductors	620
4.17.3.4.1	General trends	620
4.17.3.4.2	Valence and conduction band dispersion of metal nitrides	621
4.17.3.4.3	Valence and conduction band dispersion of carbon nitrides	622
4.17.3.4.4	Summary of metal nitride semiconductors	623
4.17.4	Final summary and outlook	624
Acknowledgments		624
References		624

Abstract

Research and development on semiconductors for applications in solar energy conversion has witnessed rapid growth over the past several decades. With the aim of producing chemical fuels from sunlight, intense research efforts have focused on the discovery of semiconductors with crystalline structures and chemical compositions that have the potential to satisfy the complex set of required photoelectrochemical properties. This chapter focuses on the foundational structure-property relationships of selected oxide and nitride semiconductors relevant to their uses as n-/p-type photoelectrodes and as photocatalysts. Their solid-state structures and compositions are described, with a special emphasis on strategies proven effective at targeting suitable band gaps with strong visible-light absorption, efficient charge separation and diffusion of charge carriers, and optimal band edge energies for driving surface redox reactions for water splitting.

4.17.1 Introduction

4.17.1.1 Background

The development of commercially-viable semiconductors for the production of fuels from solar energy is a critical issue in the construction of artificial photosynthetic systems. Fuel-producing redox reactions targeted by current research efforts include the reduction of carbon dioxide to carbon monoxide and/or other carbon oxygenates (e.g., methanol or formic acid), or the reduction of water to H_2 . It is generally considered that the semiconductor must achieve efficiencies for solar-to-chemical conversion of $> 10\%$, have a functional lifetime that is 20–30 years and be economically competitive with fossil fuel energy sources. A complex combination of chemical and optoelectronic properties is required both within the bulk and at the surfaces of the semiconductor. As such, research within this field covers a large swath of disciplines such as surface corrosion, interfacial electron transfer, molecular reaction kinetics, crystalline structures and compositions, and defect states and defect energies. Thus, this chapter does not cover all possible aspects of relevant research in this field. Rather, the overarching theme addresses, specifically, the crystalline chemistry and physics of solid-state semiconductors that represent some of the most intensely studied materials in the field of solar energy conversion.

A nearly countless number of semiconducting solids have been investigated as n-/p-type photoelectrode films or as aqueous suspensions. Current reviews have highlighted that literally hundreds of them have been reported to exhibit high photocatalytic rates under irradiation, such as for the reduction of water to H_2 . Prominent systems include the metal-oxides, -chalcogenides, -nitrides, -oxynitrides, as well as elemental silicon and III-V and other semiconductors.^{1–5} However, no ideal semiconductor has yet been discovered, with prominent problems stemming from one or more of (a) inappropriate band gap for the broad-wavelength absorption of sunlight, (b) nonoptimal band edge energies to drive the fuel-producing redox reactions, (c) low charge carrier mobility and short minority carrier diffusion lengths, (d) high rates of bulk and surface recombination of charge carriers, (e) significant photo-corrosion problems in aqueous solutions under irradiation, and (f) non catalytically-active surface sites for facilitating multielectron redox reactions at high rates. The first four issues, (a) to (d), are amenable to modification by changes in the crystalline and electronic structure of the semiconductor. The remaining issues, (e) and (f), have been effectively moderated for many semiconductors with the use of surface coatings (e.g., TiO_2 , GaN, etc.) and co-catalysts (Pt nanoparticles, CoPi, etc.), respectively. The highest efficiencies for solar energy conversion will likely not be realized until after these post-synthetic surface modifications, which can add years of research and development for their optimization. Thus, a foundational challenge lies in the preparation of a semiconductor that has an optimal electronic structure for driving the surface redox reactions from photon-generated charge carriers.

The use of semiconductors as photoelectrodes for driving light-driven redox reactions can be traced back to original research on n-type TiO_2 and p-type GaP.^{6–9} While the relevant details of this process can only be briefly described, more in-depth discussions are provided in the Further Reading section. The fundamental mechanism is based upon the establishment of a semiconductor-to-liquid junction that functions as the underlying basis for charge separation and surface-driven catalysis,⁹ as illustrated in Fig. 1 for both n-type and p-type liquid junctions. Upon immersion of the semiconductor, a rectifying (Schottky) barrier forms with the equilibration of their electrochemical potentials and the surface depletion of the majority carriers. The absorption of bandgap photons (yellow arrows) generates electron-hole pairs that diffuse to this space charge layer near the interface. Charge carrier separation can then be driven by the potential gradient, i.e., band bending, within the space charge layer, with its width (W_{sc}) determined by the semiconductor's dielectric constant (ϵ), the doping density (N ; cm^{-3}), and the potential drop (ϕ_{sc}), given by Eq. (1):

$$W_{sc} = \sqrt{\frac{2\Delta\phi_{sc}\epsilon\epsilon_0}{eN}} \quad (1)$$

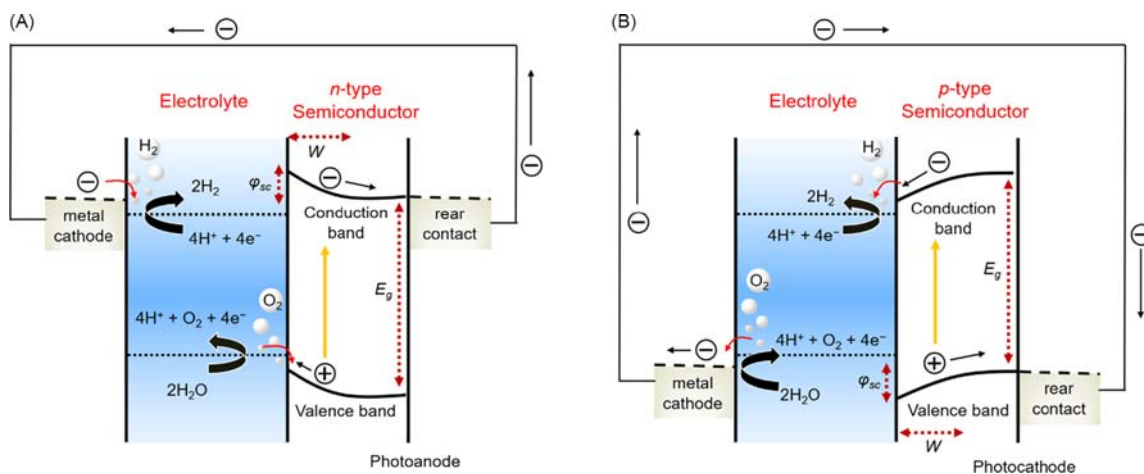


Fig. 1 Schematic of a photoelectrochemical cell for water-splitting using an (A) n-type and (B) p-type semiconductor photoelectrode.

where e is the charge on an electron ($1.6 \times 10^{-19} \text{C}$) and ϵ_0 is the permittivity of free space ($8.854 \times 10^{-12} \text{F m}^{-1}$). An upward band bending occurs for an n-type semiconductor which drives the holes in the valence band, i.e., the photon-generated minority carriers, to the interface for oxidation reactions. An n-type semiconductor thus functions as a photoanode. The situation is reversed for p-type semiconductors which function electrochemically as photocathodes. The majority carriers in each case diffuse to either a counter-electrode or to surface-attached metallic cocatalysts. A key requirement is that the conduction and valence bands be located at more negative and positive potentials, respectively, than the redox reactions they are intended to drive. This is as also called “band straddling,” as shown in Fig. 1 for the potentials for water oxidation and reduction to O_2 and H_2 . A relatively small band gap, needed for the absorption of lower-energy visible light, requires a closer approach of the band edges to these redox couples.

The photoelectrochemical properties of semiconductors can be probed either as photoelectrode films or as aqueous suspensions of particles. For the latter, as shown in Fig. 2A, a semiconductor-liquid junction again forms the basis for charge separation with the holes and electrons diffusing to separate surface sites for oxidation and reduction reactivity, respectively. The latter can arise from the attachment of surface cocatalyst, as shown in Fig. 2A for Pt, or from the different crystallographic facets of the particle. For overall water splitting, for example, the two half reactions combine to yield the thermodynamically-uphill reaction: $2\text{H}_2\text{O}(\text{g}) \rightarrow 2\text{H}_2(\text{g}) + \text{O}_2(\text{g})$; $\Delta G^\circ = 237.2 \text{ kJ/mol}$. This requires a minimum potential difference of 1.23 V and can be driven by the ultraviolet and visible wavelengths ($\lambda < 1008 \text{ nm}$) in sunlight. It is typically considered that band gaps in the range of $\sim 1.5\text{--}1.8 \text{ eV}$ are needed to provide suitable overpotentials for the half reactions to be driven at high rates of formation. However, relatively few semiconductor particles have been found to be active for overall water splitting, e.g., La-doped NaTaO_3 or Al-doped SrTiO_3 which have relatively large band gaps, as described below. Multijunction and tandem semiconductor configurations also show much promise,¹⁰ reducing the thermodynamic requirement for each semiconductor to straddle only a single band edge.

4.17.1.2 Key semiconductor parameters

The foregoing discussion on the functioning of semiconductor photoelectrodes reveals several critical physical properties that they should possess for attaining high solar-to-fuel efficiencies. This includes their band gaps, band edge energies, charge carrier separation and mobility, absence of defects which can act as charge recombination centers, and a functional diffusion length of the minority carriers. Clearly, the most effective research strategies will be those which leverage an in-depth understanding of the relationship between the above properties and the crystalline and electronic structures of the semiconductor.

The band edge energies as well as the band gap are primarily determined by the lowest unfilled and the highest filled crystal orbitals, Fig. 2(right). In many known oxide and nitride semiconductors, the states at their conduction band edges typically stem from the unfilled valence d -orbitals of an early transition-metal cation or unfilled p -orbitals of a main group cation (e.g., Ti(IV), Nb(V), Sn(IV)), while the states at their valence band edges often consist of the filled anion s/p -orbitals (e.g., O or N) or the filled d -orbitals of late transition-metal or main group cations (e.g., Cu(I) or Bi(III)). The simple oxides such as TiO_2 or Nb_2O_5 typically exhibit the largest band gaps as compared to the nitrides or mixed-metal oxides. This is because of the relatively low-energy valence band of oxides set by the O $2p$ valence orbitals, such as compared to the higher-energy valence bands of nitrides

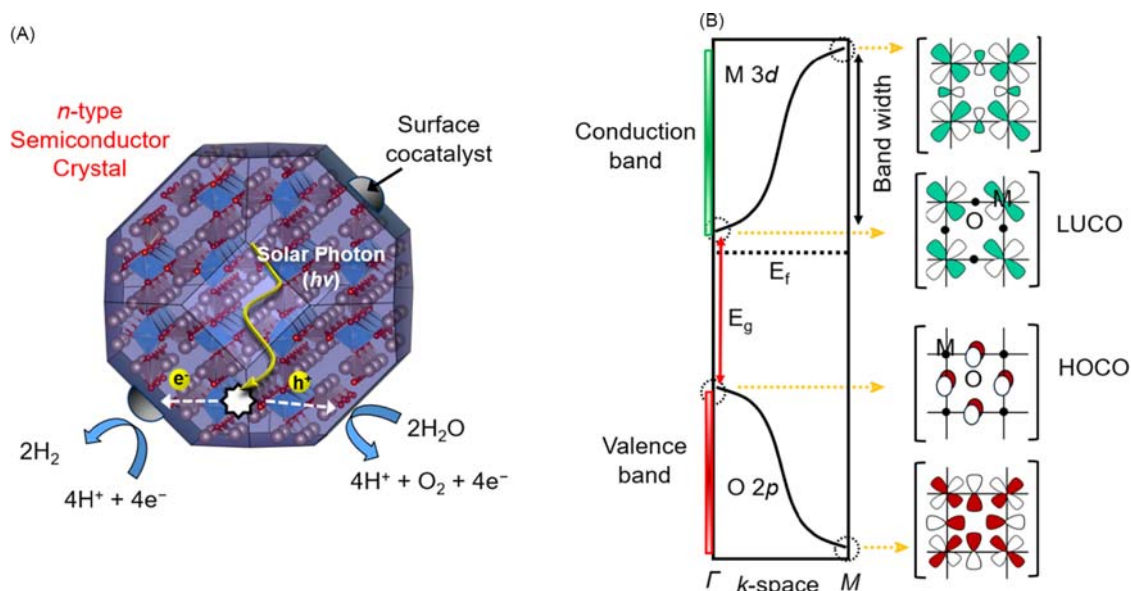


Fig. 2 (A) Representative schematic of the photocatalytic process on an n-type semiconductor particle. (B) The crystal orbitals (HOCO—highest occupied crystal orbital; LUCO—lowest unoccupied crystal orbital) constituting the valence and conduction band for a generic metal oxide semiconductor.

derived from the N 2*p* valence orbitals. For example, the band gaps of Ta₂O₅ and Ta₃N₅ are a respective ~ 3.8 eV and ~ 2.2 eV. The strategy to target small band gaps in mixed-metal oxides also involves the incorporation of a metal cation with a filled $d^{10}s^n$ electron configuration that forms a new metal-based valence band. An example here would be to compare the band gaps of BaTiO₃ and SnTiO₃ with respective band gaps of ~ 3.4 and ~ 2.0 eV. In addition to a small visible-light band gap, the energetic location of a semiconductor's band edges must be appropriately positioned with respect to the redox potentials for water oxidation and reduction. The dependence of the band edges on the structure and composition are discussed in the detailed sections below for each semiconductor system.

During irradiation of the semiconductor, a high minority-carrier diffusion length (*L*) is needed to enable the charge carriers to reach the surfaces for charge separation and interfacial charge transfer. Both the recombination lifetime (τ) and the charge mobility (μ) will determine the fraction of charge carriers which reach the surfaces before recombination, as defined by the following two equations:

$$L = \sqrt{\frac{\tau \mu k_B T}{e}} \quad (2)$$

$$\mu = \frac{e \tau_{\text{scatt}}}{m^*} \quad (3)$$

The τ_{scatt} is the average scattering time between collisions, *T* is temperature, k_B is the Boltzmann constant, and m^* is the effective mass. As shown by Eq. (3), the semiconductor should aim to have low effective masses for the photon-generated minority carriers and therefore high mobility (μ). The effective masses can be calculated based on the electronic band curvature as a function of *k*, i.e., by how fast the bands change in energy, as given by the following Eqs. (4) and (5):

$$\mu = \frac{e \tau_{\text{scatt}}}{h^2} \left(\frac{d^2 E}{dk^2} \right) \quad (4)$$

$$m^* = \left(\frac{h}{2\pi} \right)^2 \left(\frac{d^2 E}{dk^2} \right)^{-1} \quad (5)$$

The effective masses of electrons and holes are calculated from the band curvature of the respective conduction and valence band edges, as shown schematically in Fig. 2(right) from $k = \Gamma$ to *M*. A greater extent of band curvature, and thus decreasing effective mass, will be notably dependent upon the interaction strength between the metal and ligand valence orbitals. This interaction strength typically increases with overlap, e.g., with the linearity of the bond angle in Fig. 2 and with decreasing energetic separation of the valence atomic orbitals. As a result, the band dispersion of metal nitrides will typically be greater than for metal oxides because of the decreased *d*-orbital to *p*-orbital energetic separation. For more complex oxides, the precise details will depend upon the specific structural details as well as the valence orbitals involved, as described in the following sections.

4.17.2 Metal oxide semiconductors

4.17.2.1 Background

Metal oxides constitute one of the most well studied types of semiconductors for their application toward solar-driven water-splitting, as listed in Table 1 for many selected examples. This includes from the initial demonstration of water-splitting by Fujishima and Honda in 1972 using TiO₂,⁶ to the current investigations of the record-holder Al-doped SrTiO₃.¹¹ A key advantage of metal oxides is their generally greater stability against corrosion in aqueous solutions under photocatalytic reaction conditions. This is not the case for other semiconductors, i.e., based on metal pnictides, halides, and other chalcogenides, which can more easily corrode in aqueous solutions via hydrolysis or redox reactivity. In addition, their relative ease of synthesis makes metal oxides readily accessible with minimal resources. Despite their place as the most intensely investigated compounds, metal oxides also have a few inherent disadvantages. The first, and most obvious, drawback is the fact that most metal oxides tend to have relatively wide bandgaps ($E_g \geq 3.0$ eV) that greatly limit their ability to absorb photons across the majority of the solar spectrum. The wide bandgaps characteristic of many metal oxides are a result of a low-lying valence band that is formed by O 2*p* orbitals. In fact, the nature of the valence band also contributes to another common issue of metal oxides. The states comprising the valence band maximum are usually relatively localized O 2*p* states and result in low valence band dispersion and high hole effective masses. Finally, the defects that form in metal oxides, most commonly oxygen vacancies, tend to form deep-trap states that lead to fast charge recombination rates.

A deeper understanding of the impact of structure and composition on the physical properties of metal oxides has allowed researchers to address many of the challenges for their use as photoelectrodes or photocatalysts in solar energy conversion. What follows is a brief overview of some of the most prominent metal oxides that are currently being investigated as semiconductors for solar energy conversion and how their structures and compositions impact their photocatalytic properties. Key factors that will be included are their band gaps, the energies of the valence and conduction band edges, the charge-carrier effective masses, and the currently highest reported photocatalytic rates and efficiencies.

Table 1 Selection of metal oxide semiconductors used as photoelectrodes and/or suspension-based photocatalysts for solar-driven water splitting.

Composition	Structure type/Symmetry	Bandgap (eV)	Film/Powder	Efficiency/Activity
SrTiO ₃	Cubic Perovskite <i>Pm-3m</i>	3.1 (Indirect)	Powder	96% Overall Water-Splitting ($\lambda = 350\text{--}360\text{ nm}$) ¹¹
NaTaO ₃	Orthorhombic Perovskite <i>Pcmn</i>	4.0 (Direct)	Powder	20% Overall Water-Splitting ($\lambda = 270\text{ nm}$) ¹²
NaNbO ₃	Orthorhombic Perovskite <i>Pbcm</i>	3.4 (Indirect)	Powder	6.8% for H ₂ ($230\text{ nm} \leq \lambda \leq 350\text{ nm}$) ¹³
SrSnO ₃	Orthorhombic Perovskite <i>Pnma</i>	4.0 eV (Indirect)	Powder	227 $\mu\text{mol H}_2\text{ h}^{-1}\text{ g}^{-1}$ and 114 $\mu\text{mol O}_2\text{ h}^{-1}\text{ g}^{-1}$ Overall Water-Splitting (UV irradiation) ¹⁴
AgNbO ₃	Orthorhombic Perovskite <i>Pbcm</i>	2.8 (Indirect)	Powder	8.2 $\mu\text{mol H}_2\text{ h}^{-1}\text{ g}^{-1}$ and 37 $\mu\text{mol O}_2\text{ h}^{-1}\text{ g}^{-1}$ ($\lambda > 420\text{ nm}$) ¹⁵
LaFeO ₃	Orthorhombic Perovskite <i>Pbnm</i>	2.1 (Direct)	Powder	8.1% for H ₂ and O ₂ Separately ($\lambda > 420\text{ nm}$) ¹⁶
Ba ₅ Nb ₄ O ₁₅	111-Layered Perovskite <i>P-3m1</i>	3.9 (Indirect)	Powder	8.0% Overall Water-Splitting ($\lambda = 270\text{ nm}$) ¹⁷
BaLa ₄ Ti ₄ O ₁₅	111-Layered Perovskite <i>P-3c1</i>	3.9	Powder	16% Overall Water-Splitting ($\lambda = 270\text{ nm}$) ¹⁸
La ₂ Ti ₂ O ₇	110-Layered Perovskite <i>Pna2₁</i>	3.2 (Indirect)	Powder	27% Overall Water-Splitting (UV Irradiation) ¹⁹
Sr ₂ Nb ₂ O ₇	110-Layered Perovskite <i>Cmc2₁</i>	4.1 (Indirect)	Powder	32% for H ₂ (UV Irradiation) ²⁰
Bi ₂ WO ₆	Aurivillius <i>Pca2₁</i>	2.7 (Indirect)	Film	31% IPCE ($\lambda = 350\text{ nm}$) ²¹
BiVO ₄	Monoclinic Scheelite <i>I₂/b</i>	2.4 (Direct)	Film	2% quantum yield for O ₂ (AM 1.5G) ²²
Sn ₂ TiO ₄	Tetragonal <i>P4₂/mbc</i>	1.7 (Indirect)	Powder	151 $\mu\text{mol O}_2\text{ h}^{-1}\text{ g}^{-1}$ ($\lambda \geq 400\text{ nm}$) ²³
SnNb ₂ O ₆	Foordite <i>C2/c</i>	2.3 (Indirect)	Film, Powder	32% IPCE for O ₂ ($\lambda = 420\text{ nm}$), ²⁴ 0.43% quantum yield for H ₂ ($\lambda = 420\text{ nm}$) ²⁵
CuWO ₄	Distorted Wolframite <i>P2/c</i>	2.3 (Indirect)	Film	100% Faradaic Efficiency for O ₂ (AM 1.5G) ²⁶
CuFeO ₂	Delafossite <i>R-3 m</i>	1.5 (Indirect)	Film	96% Faradaic Efficiency Overall Water-Splitting (AM1.5G) ²⁷
CuBi ₂ O ₄	Tetragonal <i>P4/ncc</i>	1.8 (Indirect)	Film	~10% IPCE for H ₂ ($\lambda = 500\text{ nm}$) ²⁸
Ag ₃ VO ₄	Monoclinic <i>C2/c</i>	2.2 (Indirect)	Powder	17 $\mu\text{mol O}_2\text{ h}^{-1}\text{ g}^{-1}$ ($\lambda > 420\text{ nm}$) ²⁹
MnV ₂ O ₆	Brannerite <i>C2/m</i>	1.4 (Indirect)	Powder	9 $\mu\text{mol O}_2\text{ h}^{-1}\text{ g}^{-1}$ ($\lambda > 420\text{ nm}$) ³⁰

4.17.2.2 Crystal structures and photoelectrochemical properties

The crystal structures of the metal oxides are categorized below according to the extended connectivity of the metal cations that form the (a) conduction band states (B-cations; e.g., Ti(IV), Ta(V), Nb(V) cations) and (b) the valence band states (A-cations; e.g., Sn(II), Bi(III), Mn(II), Cu(I) cations). Typically, the presence of extended [-O-M-O-M-O-]_n connectivity is considered essential for establishing a high band dispersion and a high mobility of charge carriers in the conduction or valence band. However, this feature alone is not sufficient to attain high photon-to-fuel conversion efficiencies of a metal oxide as a photoelectrode film or photocatalyst suspension. Thus, while the crystal structures are organized according to this classification, the corresponding structure-property relationships are more complex and not easy to establish. These relationships will be explored further in subsequent sections.

4.17.2.2.1 Perovskite type structures with 3D B-cation connectivity

The perovskite-type structure is one of the most common for metal oxides and is also likely one of the most intensely investigated for solar water-splitting. Many of the highest efficiency photocatalysts and photoelectrodes are members of the perovskite family of compounds, such as given by the first several entries in Table 1. Perovskites have the general formula ABO₃, where the sum of the charges on the A- and B-cations is +6. The structure type contains the B-site cations coordinated in an octahedral environment that are condensed in a three-dimensional framework, as shown in Fig. 3A. The A-cation balances the charge on the octahedral "BO₃" framework and its relative ionic size determines whether the structure forms in a cubic or lower-symmetry distorted perovskite structure. Typically, the A-site cations are alkaline (Na, K) or alkaline-earth (Ca, Sr, Ba) cations, although larger transition metals cations such as Ag or La are also common. The B-site usually consists of transition-metal cations (Ti, Zr, Nb, Ta, W, etc.). The perovskite structure can be described as a face-centered cubic packing of the A-cations and oxide anions, with octahedral cavities partially filled by the B-site cations. As such, the A-site cation is typically relatively large and compatible for packing with the oxide anions, while the B-site cation must be sufficiently small to fill the octahedral cavity. Numerous types of distortions, such as octahedral tilting and A-site shifting, can occur in the perovskite structure and have key impacts on its band gaps, band edge energies, and effective masses.

The Goldschmidt tolerance factor, Eq. (6), has long been used to predict the formation of semiconductors with the ABO₃ composition in perovskite-type structures.

$$t = \frac{r_A + r_O}{\sqrt{2}(r_B + r_O)} \quad (6)$$

where r_A , r_B , and r_O are the radii of cation A, cation B, and oxygen, respectively. Typically, the Shannon radii values are referenced for the ion sizes as they not only account for the various oxidation states of each element but also calibrate for the coordination number. Additionally, while the accuracy of the tolerance factor in predicting perovskite stability for oxides and other highly ionic compounds is high, it is considered less reliable for structures with more covalent interactions. Revised versions of the Goldschmidt tolerance factor that show improved accuracy for more covalent materials have been developed.³¹ For example, the ideal cubic

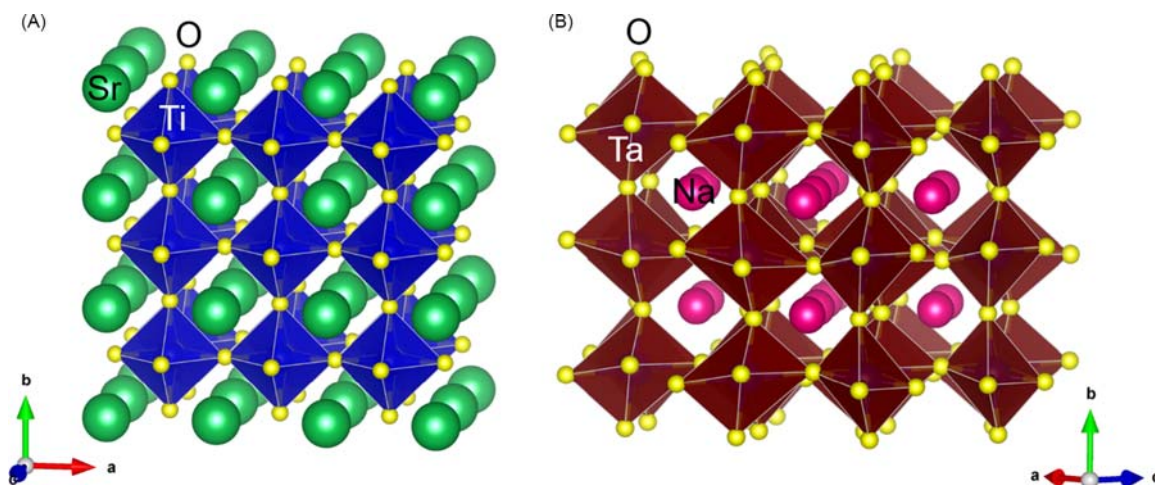


Fig. 3 Polyhedral drawings of the perovskite-type crystal structures of (A) SrTiO₃ and (B) NaTaO₃. Atom types are labeled.

perovskite will form typically when t is calculated to be between ~ 0.9 and 1.0 . A notable, current “gold standard” semiconductor for overall water splitting, Al-doped SrTiO₃ ($t = 1.00$), forms in the ideal cubic perovskite structure as shown in Fig. 3A. In this structure the Ti(IV) cation is octahedrally coordinated to O to form a 3D network of corner-shared TiO₆ octahedra with the charge-balancing Sr(II) cation located in a cuboctahedral environment. The TiO₆ octahedra have a linear Ti–O–Ti bond angle of 180° and six identical Ti–O bond lengths of ~ 1.95 Å. The band gap is found to be ~ 3.2 eV. As one of the best performing semiconductors for overall water-splitting, when loaded with suitable co-catalysts Al-doped SrTiO₃ can split water with a 96% efficiency within a wavelength range of 350–360 nm.¹¹ It also has a reported solar to H₂ conversion efficiency of 0.4%.³²

Unlike SrTiO₃, which forms in the ideal cubic perovskite structure, many more perovskites form as distorted versions and it is generally possible to forecast possible distortions from the tolerance factor. When $t > 1$, it means that either the A-site cation is too large or the B-site cation is too small. In such a case, a tetragonal or hexagonal structure will form to compensate for the incompatible ionic sizes. Conversely, if t is between 0.71 and 0.9 it means the A-cation is too small to fit into the interstices formed via the B–O sublattice and leading to either an orthorhombic or rhombohedral distortion. Many of the most studied metal oxide photocatalysts fall into the category of orthorhombically-distorted perovskites. These distortions usually occur via modulations of the BO₆ octahedra, such as octahedral tilting, which can have a profound effect on the band energies (and consequently bandgap) and charge carrier mobility. One prominent example is NaTaO₃ (Fig. 3B). The corner-sharing TaO₆ octahedra are highly distorted in NaTaO₃ with Ta–O–Ta bond angles of 160° – 166° and Ta–O bond lengths of ~ 2.23 , ~ 1.98 , and ~ 1.69 Å. While NaTaO₃ has a wideband gap of 4.0 eV, it can split water with a 20% efficiency at $\lambda = 270$ nm. The La-doped version of NaTaO₃ is capable of a higher 56% efficiency.^{12,33} Other examples of orthorhombic perovskites include NaNbO₃ with a bandgap of 3.4 eV and showing a 6.8% quantum yield for H₂ at $230 \text{ nm} \leq \lambda \leq 350 \text{ nm}$,¹³ SrSnO₃ with a bandgap of 4.0 eV with a high activity for overall-water splitting under UV irradiation,^{14,34} AgNbO₃ with a bandgap of 2.8 eV that has shown high activity for both H₂ and O₂ formation in the presence of sacrificial reagents,^{15,35} and LaFeO₃ with a 2.1 eV bandgap and 8.1% efficiency for H₂ and O₂, separately, under visible light ($\lambda > 420 \text{ nm}$).¹⁶

4.17.2.2 Layered perovskite structures with 2D B-cation connectivity

The highly common class of layered perovskite structures is also among the most photocatalytically-active known metal oxides. Their structures consist of two-dimensional perovskite slabs that have different thicknesses and that alternate with layers of A-site cations. Examples include the Dion-Jacobson, Ruddlesden-Popper, and Aurivillius phases, each having (100) orientations of their perovskite-type layer, as well as many having alternate orientations such as (110) and (111) layered perovskites. As in the perovskites, these layered structures typically have A-site cations consisting of alkaline (Na, K), alkaline-earth (Ca, Sr, Ba), or lanthanide cations. Conversely, the octahedrally-coordinated B-site commonly contains transition-metal cations (Ti, Zr, Nb, Ta, W, etc.). The structure of Ba₅Nb₄O₁₅, an example of a (111)-layered perovskite, is shown in Fig. 4A. Analogous to the perovskite-type structure, the structure consists of corner-shared NbO₆ octahedra that form layers in the ab -plane with charge balancing Ba²⁺ cations. The perovskite-like layers have a thickness of four octahedra and alternate with double layers of Ba²⁺ cations, resulting in the layered NbO₆ connectivity that has disrupted [–O–Nb–O–Nb–O–]_{*n*} bonding between the layers. The NbO₆ octahedra also exhibit a slight Jahn-Teller distortion with two different Nb–O bond lengths of ~ 1.94 Å and ~ 2.08 Å and a Nb–O–Nb bond angle of 171° . The band gap of Ba₅Nb₄O₁₅ is 3.9 eV and is also active for overall water splitting to H₂ and O₂ with an 8% quantum yield at $\lambda = 270 \text{ nm}$.^{17,36,37}

Many other layered perovskites have shown high photocatalytic efficiencies, mostly as n-type oxides loaded with surface cocatalysts such as Pt. For example, the related BaLa₄Ti₄O₁₅ also has a (111)-layered perovskite structure with a band gap of 3.9 eV. It has also exhibited similarly high efficiencies for overall water splitting with a 16% quantum yield at $\lambda = 270 \text{ nm}$.¹⁸ In the closely related

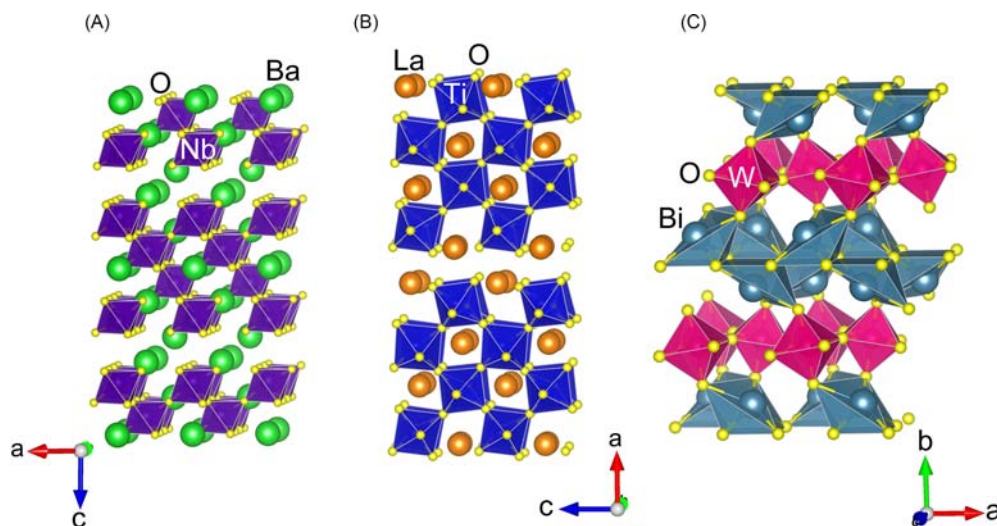


Fig. 4 Polyhedral drawings of layered perovskites of (A) $\text{Ba}_5\text{Nb}_4\text{O}_{15}$, (B) $\text{La}_2\text{Ti}_2\text{O}_7$, and (C) Bi_2WO_6 . Atom types are labeled.

(110)-layered perovskite $\text{La}_2\text{Ti}_2\text{O}_7$, Fig. 4B, the perovskite slabs are formed by taking a slice along the (110) plane of the perovskite structure, and is also one of the most active photocatalysts for water splitting. As in $\text{Ba}_5\text{Nb}_4\text{O}_{15}$, the connectivity of the TiO_6 octahedra is interrupted via a layer of La^{3+} cations and results in a two-dimensional $[-\text{O}-\text{Ti}-\text{O}-\text{Ti}-\text{O}-]_n$ connectivity. The Ti–O distances range from ~ 1.83 to ~ 2.20 Å, with Ti–O–Ti bond angles of $\sim 163^\circ$. The band gap of $\text{La}_2\text{Ti}_2\text{O}_7$ is 3.2 eV and has shown a 27% efficiency for overall water-splitting from UV light.¹⁹ $\text{Sr}_2\text{Nb}_2\text{O}_7$ is almost structurally identical to $\text{La}_2\text{Ti}_2\text{O}_7$ but with a much larger band gap of ~ 4.1 eV. It has been reported to have a 32% efficiency for the production of H_2 under UV irradiation, as well as being active for overall water-splitting.²⁰ However, all of these metal oxides possess relatively large band gaps that are not suitable for absorbing the visible-light energies of solar irradiation.

Very few examples are known wherein a layered perovskite exhibits a smaller visible-light band gap and has an appreciable photocatalytic efficiency. One example is the Aurivillius-type Bi_2WO_6 , Fig. 4C, which combines Bi^{3+} and W^{6+} cations in separate layers to produce a smaller band gap of only ~ 2.7 eV. Its structure consists of layers of edge-sharing BiO_6 polyhedra and corner-sharing WO_6 octahedra. The stereoactive lone pair on the Bi^{3+} cations leads to highly-distorted BiO_6 polyhedra with six different Bi–O bond lengths ranging from ~ 2.17 to ~ 2.54 Å. There are also six symmetry-unique W–O bond lengths that range from ~ 1.81 to ~ 2.15 Å and a layer connectivity with W–O–W bond angles of $\sim 161^\circ$ and $\sim 150^\circ$. Notably, photoelectrode films of Bi_2WO_6 have attained IPCE values reported to be $\sim 31\%$ for photoelectrochemical water splitting at $\lambda = 350$ nm.²¹

4.17.2.2.3 Structures with 2D B-cation and extended A-cation connectivity

Most of the metal oxides described to this point suffer from wide band gaps that are poorly suited for the longer-wavelength absorption of solar energy. The following examples are representative compounds which exhibit smaller, visible-light band gaps owing to the formation of higher-energy valence bands that do not predominantly stem from the O $2p$ -orbitals. These structures have been grouped according to the structural connectivity of their B-cations and A-cations that determine the dimensionalities of their extended connectivity as well as the anisotropy of their band dispersion.

The next examples are structures that consist of extended layers of the B-site cations together with extended chains or layers of the A-site cations. As shown in Fig. 5, these include SnNb_2O_6 , CuFeO_2 , and MnV_2O_6 . The crystal structures of SnNb_2O_6 and MnV_2O_6 are structurally similar, with both containing A-site and B-site cations with respective oxidation states of +2 and +5, i.e., Sn(II) and Mn(II) cations combined with Nb(V) and V(V) cations. Both structures also consist of 2D layers of NbO_6/VO_6 octahedra that condense via corner and edge-sharing modes, respectively. In SnNb_2O_6 , the NbO_6 octahedra are highly distorted with six different Nb–O bond lengths ranging from ~ 1.88 and ~ 2.17 Å and Nb–O–Nb bond angles ranging from 124° to 150° . In MnV_2O_6 , the VO_6 octahedra exhibit five symmetry-unique V–O distances that range from ~ 1.67 to ~ 2.52 Å and V–O–V bond angles from 106° to 144° . The condensed layers of NbO_6 and VO_6 octahedra within each are bridged together by 1D chains of distorted, edge-sharing SnO_4 square pyramids or MnO_6 octahedra, respectively. Their band gaps are located deep within the visible-light energies at ~ 2.3 eV (SnNb_2O_6) and ~ 1.4 eV (MnV_2O_6). Notably, MnV_2O_6 has one of the smallest known bandgaps that is still thermodynamically capable of driving overall water-splitting. Unlike many of the larger bandgap metal oxides, the initially reported photocatalytic efficiencies of both of these compounds are comparatively low. While SnNb_2O_6 has an IPCE value of 32% for the evolution of O_2 at $\lambda = 420$ nm as a photoanode, aqueous suspensions of its powders have shown only an $\sim 0.43\%$ quantum yield for the production of H_2 ($\lambda = 420$ nm).^{24,25} Aqueous suspensions of MnV_2O_6 are most active for O_2 evolution with rates of $\sim 9 \mu\text{mol h}^{-1} \text{g}^{-1}$ ($\lambda > 420$ nm).³⁰

In addition to the above two examples, a number of delafossite-type CuBO_2 (B = trivalent cation) compounds have been investigated as p-type photoelectrodes for the reduction of water to H_2 . Perhaps the most promising semiconductor of this group is

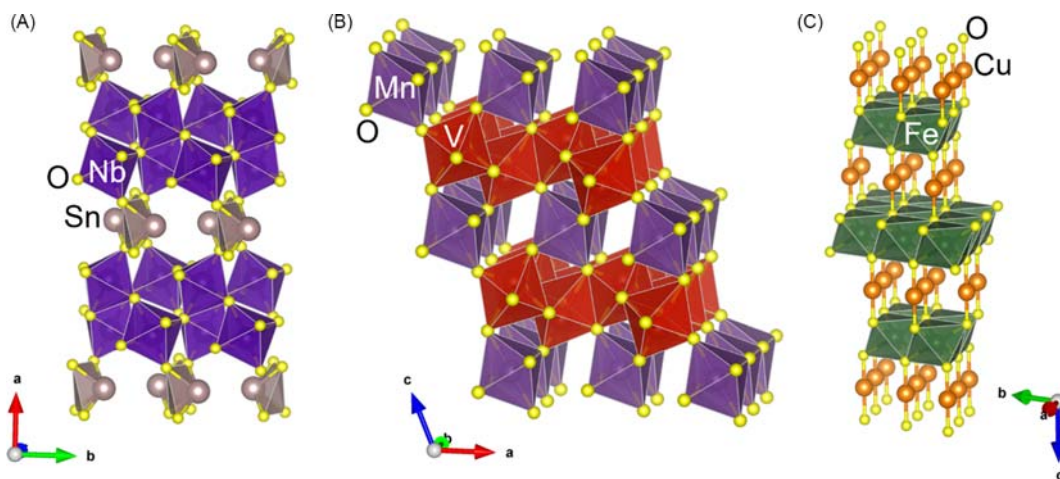


Fig. 5 Polyhedral drawings of metal oxide structures with 2D extended B-site connectivity and 1D extended A-site connectivity for (A) SnNb_2O_6 , (B) MnV_2O_6 , and (C) CuFeO_2 . Atom types are labeled.

CuFeO_2 , with the crystal structure shown in Fig. 5C, containing a combination of Cu(I) and Fe(III) cations. Its structure consists of layers of edge-shared FeO_6 octahedra in the ab -plane that are bridged by linearly coordinated Cu(I) cations. The FeO_6 octahedra have an Fe–O–Fe bond angle of 95° while the O–Cu–O bond angle is linear at 180° . Investigations into CuFeO_2 have received growing interest owing to its small band gap of only ~ 1.5 eV. As a photocathode, its Faradaic efficiency for driving overall water-splitting has been reported to be $\sim 96\%$ under AM 1.5G irradiation.²⁷

4.17.2.2.4 Structures with only 1D A-cation and B-cation connectivity

Several promising small bandgap semiconductors possess structures that consist of A-cations and B-cations with extended connectivity in only 1D. As shown in Fig. 6, three such examples include CuWO_4 , CuBi_2O_4 , and Sn_2TiO_4 . The simplest of these structures belongs to CuWO_4 , which forms in a distorted wolframite-type structure consisting of Cu(II) and W(VI) cations. Both cations are coordinated to oxide anions in octahedral environments and form extended 1D chains of CuO_6 and WO_6 that are bridged via their edges. The edge-shared CuO_6 and WO_6 octahedra exhibit M–O–M bond angles of 94° and 106° , respectively. The chains are arranged side-to-side in parallel as alternating layers of CuO_6 and WO_6 chains and bridged together via Cu–O–W connectivity. Under AM 1.5G irradiation, photoanodic films of CuWO_4 have shown a 100% Faradaic efficiency for the evolution of O_2 .²⁶

Similarly, both CuBi_2O_4 and Sn_2TiO_4 form structures that accommodate stereoactive lone pairs on the main group cations, i.e., the Bi(III) and Sn(II) cations. Like in CuWO_4 , the Sn_2TiO_4 structure consists of 1D chains of edge-sharing TiO_6 octahedra. However, the Sn(II) cations are single-side coordinated within SnO_3 trigonal pyramids that bridge via corner-sharing to form extended chains along the c -axis direction. Four neighboring SnO_3 chains orient their lone-pairs toward each other to form channels. The edge-shared TiO_6 octahedra exhibit a Ti–O–Ti bond angle of 96° , while the SnO_3 trigonal pyramids are condensed via Sn–O–Sn bond angles of 128° . A similar channel of lone-pairs is also found in CuBi_2O_4 . The structure is comprised of chains of edge-shared BiO_4 polyhedra with seesaw coordination geometries. Along the c -axis direction there are four neighboring BiO_4 chains with stereoactive lone-pairs on the Bi(III) cations directed at each other to form a channel. These chains are bridged by square planar CuO_4 polyhedra. However, extended $[-\text{O}-\text{Cu}-\text{O}-\text{Cu}-\text{O}-]$ connectivity does not occur in the structure. As a photocathode, polycrystalline films of CuBi_2O_4 have shown an IPCE for H_2 evolution of $\sim 10\%$ at $\lambda = 500$ nm.²⁸ Powders of Sn_2TiO_4 have been shown to

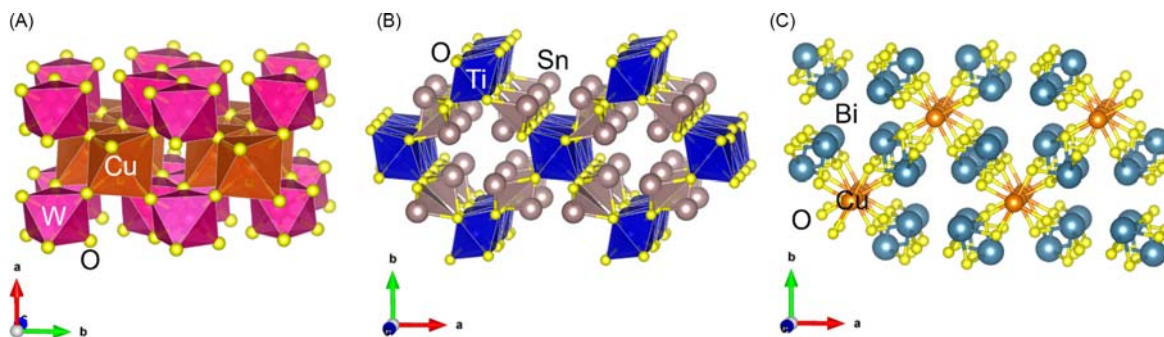


Fig. 6 Polyhedral drawings of metal oxide structures extended 1D A-site and B-site connectivity for (A) CuWO_4 , (B) Sn_2TiO_4 , and (C) CuBi_2O_4 . Atom types labeled.

be active for both H₂ and O₂, separately, with the highest activities measured for O₂ evolution at $\sim 151 \mu\text{mol h}^{-1} \text{g}^{-1}$ ($\lambda \geq 400 \text{ nm}$), corresponding to an apparent quantum yield of $\sim 1\%$.^{23,38}

4.17.2.2.5 Structures with extended A-cation connectivity and isolated B-cations

In many ternary and higher metal oxides, the A-cations commonly exhibit extended [O-A-O-A-O]_n connectivity while the B-cations occur as isolated BO₆ or BO₄ polyhedra. This especially occurs with A-rich compositions, e.g., with chemical compositions rich in Bi(III), Ag(I) or Pb(II) cations. In these structures the A-cation orbitals form the valence band states and show smaller visible-light band gaps. A relevant example is BiVO₄, which is perhaps the most intensely studied and best performing metal oxide for water oxidation in terms of efficiency and stability as a photoelectrode. The BiVO₄ composition, containing Bi(III) and V(V) cations, is known to have three different polymorphs, the zircon-tetragonal, scheelite-tetragonal, and scheelite-monoclinic structures. However, the monoclinic polymorph is known to show the best photocatalytic properties. The structure of monoclinic BiVO₄ is shown in Fig. 7A and consists of isolated VO₄ tetrahedra and edge-shared BiO₈ polyhedra, and together forming a 3D network. The BiO₈ polyhedra are highly distorted with four shorter ($\sim 2.36 \text{ \AA}$) and four longer Bi-O distances ($\sim 2.52 \text{ \AA}$ (x2) and $\sim 2.63 \text{ \AA}$ (x2)). The Bi-O-Bi bond angles all occur between $\sim 103^\circ$ and 106° . The VO₄ tetrahedron has a relatively more asymmetric coordination environment, with V-O distances of $\sim 1.76 \text{ \AA}$ (x2) and $\sim 1.70 \text{ \AA}$ (x2). The band gap of BiVO₄ is $\sim 2.4 \text{ eV}$. Its n-type photoelectrode films have reportedly shown $\sim 82\%$ of the theoretical maximum efficiency for O₂ evolution under simulated solar irradiation, and $>2\%$ efficiency for solar to O₂.^{22,39,40} A related example is Ag₃VO₄, shown in Fig. 7B, which also has three polymorphs that each contain Ag(I) and V(V) cations. However, only the α -phase has shown interesting photocatalytic properties. The structure of Ag₃VO₄ forms in a face-centered-cubic arrangement of cations along the (201) crystallographic direction, with the cations stacked in an "Ag₃V" sequence and the oxide anions located in the tetrahedral sites.⁴¹ This arrangement leads to the V(V) cations being tetrahedrally coordinated, while the Ag(I) cations are coordinated to oxide anions in both seesaw and square-planar geometries. The VO₄ tetrahedra occur as isolated polyhedra, with V-O distances of $\sim 1.71 \text{ \AA}$ (x2) and $\sim 1.73 \text{ \AA}$ (x2), but with no extended [O-V-O-V-O]_n connectivity. Conversely, the [-O-Ag-O-Ag-O]_n connectivity is three dimensional. The square planar Ag(I) coordination has Ag-O distances of $\sim 2.32 \text{ \AA}$ (x2) and $\sim 2.34 \text{ \AA}$ (x2) and Ag-O-Ag bond angles between 83° and 97° . The seesaw Ag(I) coordination has a greater range of Ag-O distances, from a short ~ 2.17 to $\sim 2.18 \text{ \AA}$ to a longer $\sim 2.56 \text{ \AA}$. The band gap for Ag₃VO₄ is $\sim 2.2 \text{ eV}$ and it exhibits a moderate activity for O₂ evolution at $\sim 17 \mu\text{mol h}^{-1} \text{g}^{-1}$ at $\lambda > 420 \text{ nm}$.²⁹

4.17.2.3 Band gaps and band edge positions

For driving photocatalytic reactions at the surfaces of a metal oxide it is essential that the band gap be suited to broadly absorb the ultraviolet and visible-light components of the solar spectrum, i.e., having a band gap in the range of ~ 1.5 to $\sim 2.4 \text{ eV}$. Further, the band edge positions need to be located at more positive and more negative redox potentials than the respective oxidation and reduction potentials, such as for the half reactions of water splitting. The sections below are organized by the solid-state strategies for tuning the band gaps and band edge energies of metal oxides for achieving efficient photocatalytic water splitting.

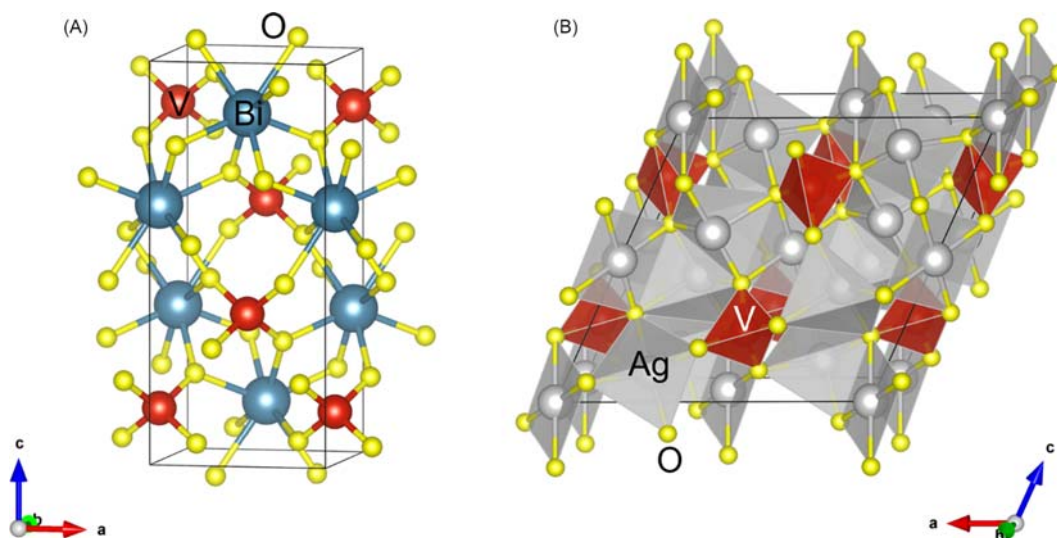


Fig. 7 Polyhedral drawings of metal oxide structures with 3D extended A-site connectivity and isolated B-sites for (A) BiVO₄ and (B) Ag₃VO₄. Atom types labeled.

4.17.2.3.1 Tuning the band gaps of oxide semiconductors

Many of the most well studied metal-oxide photocatalysts are ternary or higher metal oxides. For early transition-metal oxides that lack a valence-band-forming cation, e.g., Ag(I), Sn(II), or Bi(III), the valence band states derive primarily from the O 2*p* orbitals. Conversely, the edge of the conduction band is primarily formed by the empty *d*-orbitals of the early transition metal, e.g., Ti(IV), Nb(V) or V(V). These typically increasingly mix with the O 2*p*-orbitals in an antibonding fashion with higher energies in the conduction band. This situation typically yields only large band gaps, i.e., > 3.0 eV, as the valence band states on the O 2*p* orbitals are energetically distanced from the transition metal *d*-orbitals. The alkali or alkaline earth cations frequently present in metal oxides make no contribution to either of the bands at relevant energies, with their role being restricted to charge balancing and impacting the structure type.

Many of the aforementioned metal-oxide photocatalysts fall into the large band gap category, such as SrTiO₃, NaTaO₃, Ba₅Nb₄O₁₅, BaLa₄Ti₅O₁₅, and La₂Ti₂O₇. A densities-of-states (DOS) plot of SrTiO₃ is shown in Fig. 8A,^{42,43} which serves as a representative example. The top of its valence band is dominated by the O 2*p* states while the bottom of the conduction band is derived from Ti 3*d* orbital contributions, with some minor O 2*p* contributions in the conduction band at higher energies. Shown in Fig. 8B is a DOS plot for La₂Ti₂O₇, where the valence and conduction band states at the band edges are formed from O 2*p* and Ti 3*d* in a similar fashion as in SrTiO₃. The valence and conduction band energies of SrTiO₃ and La₂Ti₂O₇ are shown in Fig. 8C with respect to the redox couples for water splitting. Both SrTiO₃ (3.1 eV) and La₂Ti₂O₇ (3.2 eV) have very similar band gaps and band edge energies. These similarities arise from the fact that the band edge states in both compounds derive from the Ti 3*d* orbitals and O 2*p* orbitals. Thus, while SrTiO₃ crystallizes as a cubic perovskite and La₂Ti₂O₇ as a (110)-layered perovskite, the band edge energies are closely similar. This category of metal oxides typically have large overpotentials for water oxidation, providing a substantial thermodynamic driving force under ultraviolet irradiation for the evolution of O₂.

It can readily be anticipated that a reduction in the band gap, such as via raising the valence band edge, results in metal oxides that struggle to achieve the same rates and efficiencies for O₂ evolution. In contrast, high rates for the reduction of water to H₂ are found for many small bandgap metal oxides, especially when a sacrificial reagent or electrochemical cell are functioning to remove the photon-generated holes in the valence band. Thus, while the large bandgaps of metal oxides hinder their ability to efficiently utilize solar energy, they also frequently show excellent photoelectrochemical properties for water splitting reactions at their surfaces.

4.17.2.3.2 Tuning the conduction band energy of metal oxides

One strategy to reduce the band gap of metal oxides is by appropriate selection of the early transition metal cation. As described above, the energy of the conduction band edge for metal oxides is determined by the empty *d*-orbitals of the early transition metal cation. The general trend is that the conduction band energy will decrease in energy, i.e., shift to more positive potentials, when going up a group, i.e., from 5*d* to 4*d* to 3*d* transition metals. Accordingly, metal oxides with the lowest energy conduction bands are typically found for titanates and vanadates which have low lying, 3*d* orbitals. For example, the substitution of the Nb(V) cation for the Ta(V) cation in the NaMO₃ (M = Nb, Ta) orthorhombic perovskites shifts its conduction band edge to more positive potentials, Fig. 9C.^{42,44} The DOS of both NaNbO₃ and NaTaO₃ are also plotted in Fig. 9A and B. In both compounds the valence band is

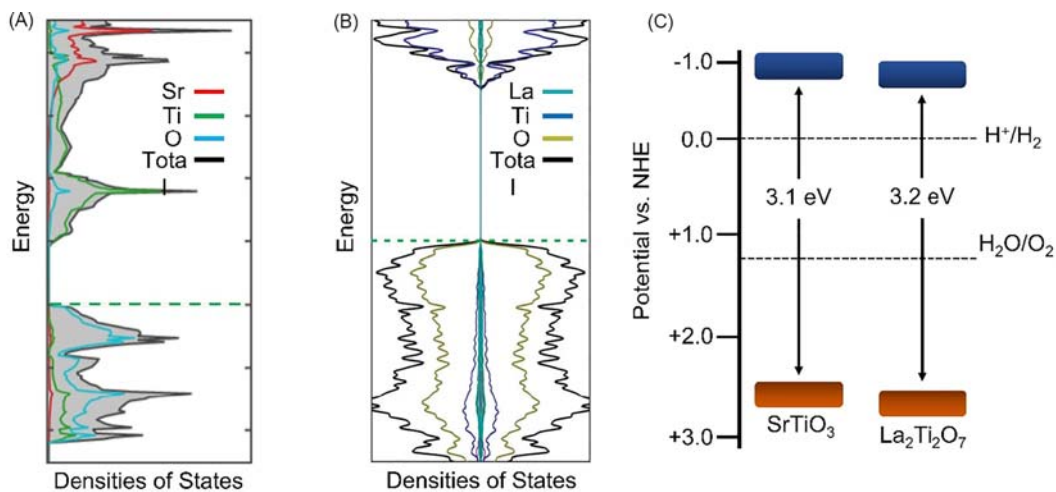


Fig. 8 Densities-of-states of (A) SrTiO₃ and (B) La₂Ti₂O₇. Valence and conduction band energies of SrTiO₃ and La₂Ti₂O₇ (C). Most metal oxides have valence bands comprised of relatively localized O 2*p* states and conduction bands formed from nonbonding transition metal *d* orbitals with higher energy states derived from TM *d*-O 2*p* antibonding interactions. Adapted with permission from (A) Jain, A.; Ong, S. P.; Hautier, G.; Chen, W.; Richards, W. D.; Dacek, S.; Cholia, S.; Gunter, D.; Skinner, D.; Ceder, G.; et al. Commentary: The Materials Project: A Materials Genome Approach to Accelerating Materials Innovation. *APL Mater.* **2013**, *1* (1) and (B) Zhang, J.; Dang, W.; Ao, Z.; Cushing, S. K.; Wu, N. Band Gap Narrowing in Nitrogen-Doped La₂Ti₂O₇ Predicted by Density-Functional Theory Calculations. *Phys. Chem. Chem. Phys.* **2015**, *17*(14), 8994–9000.

formed by the O $2p$ states. However, the conduction band in NaTaO₃ is formed by the empty Ta $5d$ orbitals while that in NaNbO₃ arises from the empty Nb $4d$ orbitals. The conduction band minimum of NaNbO₃ is located at -0.69 V vs. NHE, which is significantly lower in energy than the conduction band minimum of NaTaO₃ at -1.2 V vs. NHE.^{44,45} This results in a reduced band gap in NaNbO₃ compared to NaTaO₃ at ~ 3.4 and ~ 4.0 eV, respectively. A more continuous shifting of the energy of the conduction band edge and band gap has been found by investigations of mixed Nb(V)/Ta(V) cation solid solutions.⁴⁶

In addition to isovalent substitution, compositional changes involving post transition-metal cations can also be used to modulate the band gaps of metal oxides. Oxides containing the post transition-metal cations, with an electron configuration of $nd^{10}ns^0np^0$ ($n = 3, 4, \dots$; Sn(IV), Pb(IV), In(III), Sb(V), etc.), are often found to have lower conduction band energies than their transition metal analogs. An illustrative comparison can be found between the two cubic perovskites, BaZrO₃ and BaSnO₃. Unlike BaZrO₃, where the empty, nonbonding, $4d$ orbitals form the conduction band states, the conduction band of BaSnO₃ is formed from nonbonding, Sn $5s$ states. A substantially lower energy of the conduction band edge, i.e., at a more positive potential, is found in comparing BaZrO₃ (-1.8 V) vs. BaSnO₃ (-0.7 V).^{34,47} This difference is attributed to the increase in effective nuclear charge for the Sn $5s$ orbitals as compared to the Zr $4d$ orbitals, and yields a markedly decreased band gap for BaSnO₃ of ~ 3.1 eV as compared to BaZrO₃ of ~ 4.8 eV. These significant differences arise by simple changes in the chemical composition, but with the maintenance of the structure type.

In addition to changes in chemical composition, variations in the structure type are also known to play a key role in impacting the conduction band energy. An illustrative example can be found upon examining the differences between the cubic perovskite-type KTaO₃ and the NaTaO₃ perovskite with an orthorhombic distortion. Both structures are shown in Fig. 10. While KTaO₃ crystallizes in the cubic perovskite-type structure and has Ta-O-Ta bridging angles of 180° , the distorted NaTaO₃ perovskite has a more acute Ta-O-Ta angle of $\sim 163^\circ$. The measured band gaps for KTaO₃ and NaTaO₃ show a substantive shift, at a respective ~ 3.5 and ~ 4.0 eV. However, the energies of their valence (O $2p$) and conduction band edges (Ta $5d$ + O $2p$) are both comprised of the same orbital contributions. The change in band gap is directly related to the distortions of the TaO₆ octahedra that cause the conduction band edge to shift to a higher energy for NaTaO₃. For the undistorted KTaO₃, the lowest energy states in the conduction band are the non-bonding Ta d orbitals. Distortion of the perovskite structure away from the ideal 180° M-O-M angle breaks the cubic symmetry and allows antibonding interactions between the Ta $5d$ and O $2p$ orbitals, resulting in a raised energy of the conduction band edge for NaTaO₃. A monoclinic polymorph of NaTaO₃ has also been reported with Ta-O-Ta bond angles closer to 180° and a smaller band gap of ~ 3.9 eV.⁴⁸ An in-depth investigation of the effect of chemical composition and octahedral distortions on the electronic structure of perovskite oxides has been analyzed in much further detail.⁴⁷

It is generally considered that the smallest band gaps for metal oxides in this category occur when the oxide-bridged MO₆ octahedra have M-O-M bond angles as close to 180° as possible. Higher conduction band energies and larger band gaps are observed with increasing acuteness of the M-O-M bond angles. Similar electronic-structure arguments have been extended to the oxide connectivity of the post transition-metal cations, wherein their empty valence ns and/or np orbitals determine the energy and dispersion of the conduction band. For example, the orthorhombically-distorted perovskite SrSnO₃ has a much larger band gap of ~ 4.1 eV as compared to BaSnO₃ of ~ 3.1 eV, with respective Sn-O-Sn angles of $\sim 163^\circ$ and 180° . The more acute Sn-O-Sn

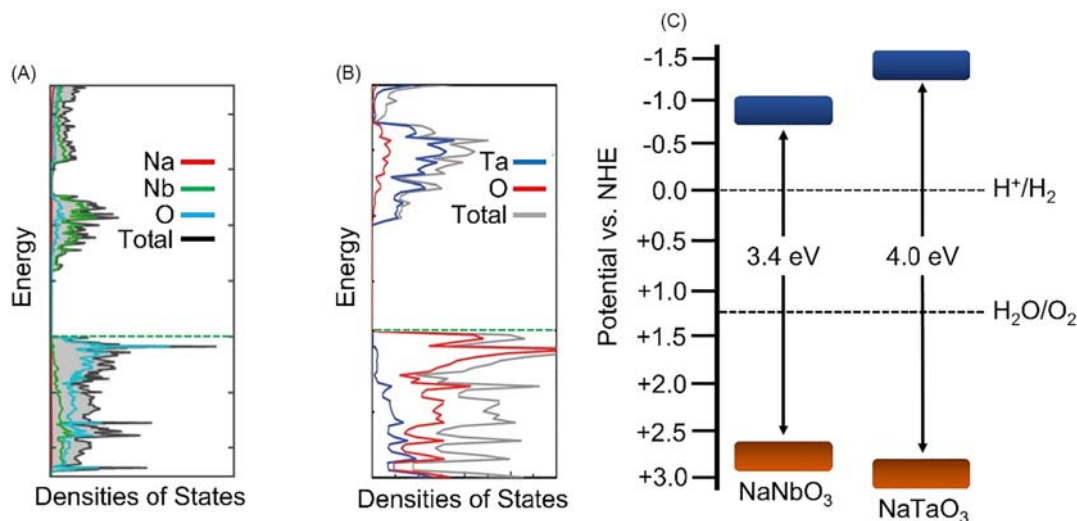


Fig. 9 DOS plots of (A) NaNbO₃ and (B) NaTaO₃. Band edge energies of NaNbO₃ and NaTaO₃ (C). The conduction band energy decreases from $5d > 4d > 3d$ metals, here demonstrated with Ta ($5d$) and Nb ($4d$). Adapted from (A) Jain, A.; Ong, S. P.; Hautier, G.; Chen, W.; Richards, W. D.; Dacek, S.; Cholia, S.; Gunter, D.; Skinner, D.; Ceder, G.; et al. Commentary: The Materials Project: A Materials Genome Approach to Accelerating Materials Innovation. *APL Mater.* **2013**, *1*(1) and (B) Modak, B.; Srinivasu, K.; Ghosh, S. K. Band Gap Engineering of NaTaO₃ Using Density Functional Theory: A Charge Compensated Codoping Strategy. *Phys. Chem. Chem. Phys.* **2014**, *16*(32), 17116–17124.

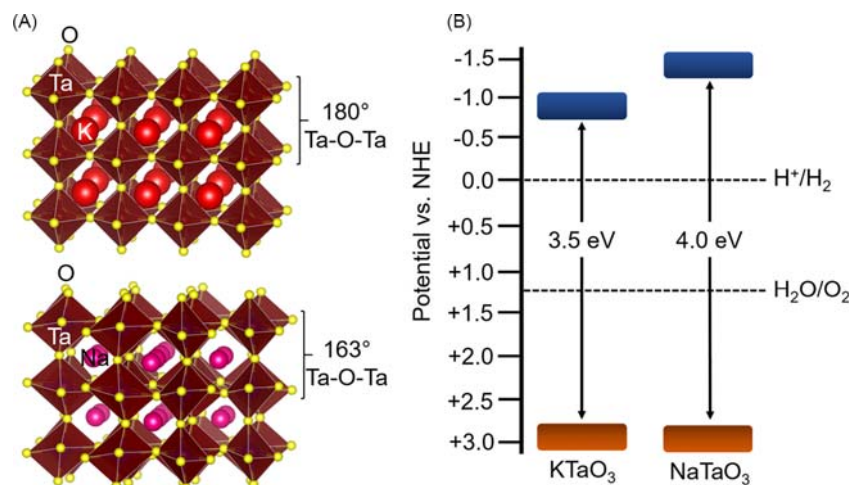


Fig. 10 (A) Crystal structures of KTaO₃ (top) and NaTaO₃ (bottom). Band energies of KTaO₃ and NaTaO₃ (B). Distortions of M–O–M bond angles away from the ideal 180° typically leads to a higher energy conduction band.

bond angle enables the antibonding mixing of the Sn *s* orbitals with the O 2*p* orbitals at the edge of the conduction band, and thus raising its energy.

4.17.2.3.3 Tuning the valence band energy of metal oxides

Tuning of the valence band energy of metal oxides has typically been considered more difficult as the valence band frequently stems from the more localized O 2*p* states. However, the optimal straddling of the redox couple for water oxidation requires that the valence band edge be sufficiently raised in energy, i.e., to more negative potentials, if metal oxides are to be capable of absorbing lower-energy visible light photons of the solar spectrum. Fortunately, several successful strategies have emerged over the past several years. These include the incorporation of late transition-metal cations with *nd*¹⁰ electron configurations, such as for the Cu(I) and Ag(I) cations, or the post-transition metal cations with *nd*¹⁰*ns*² electron configurations such as Sn(II), Pb(II), and Bi(III) cations. Less frequently, oxides have been investigated of the transition metal cations with partially filled *d*-orbital configurations, including for the Cu(II), Fe(II) and Mn(II) cations.

The oxides containing late transition-metal cations with *d*¹⁰ electron configurations leverage the fact that the filled *d* orbitals are located at a higher energy than the O 2*p* orbitals and can form a new valence band. The two cations commonly employed are Cu(I) and Ag(I). However, most of the Cu(I)- and Ag(I)-containing ternary and higher oxides are metastable with respect to decomposition to the simpler binary oxides. Thus, the number of known compositions are relatively few in number and limited in structural diversity as compared to the oxides containing alkali and alkaline earth cations. The Ag(I) cation has an ionic radius of ~1.15 Å (6-coordinate) that is intermediate between the Na cation at ~1.02 Å and the K cation of ~1.38 Å, and it shares some isostructural compositions. For example, AgNbO₃ crystallizes in an orthorhombically-distorted perovskite that is isostructural to NaNbO₃ with nearly identical Nb–O–Nb bond angles of 153°–164° and 155°–163°, respectively. Plotted in Fig. 11,⁴² the DOS shows the valence and conduction bands for NaNbO₃ is comprised of the O 2*p* orbitals and Nb 4*d* orbitals respectively, resulting in a band gap of ~3.4 eV. The conduction band of AgNbO₃ is similarly formed by the empty 4*d* orbitals of Nb, but the valence band edge is here comprised of states arising from the mixing of Ag 4*d* and O 2*p* orbitals in an antibonding fashion. The valence band maximum of AgNbO₃ is thus shifted to more negative potentials by ~0.6 V as compared to NaNbO₃, causing the band gap of AgNbO₃ to decrease to ~2.8 eV.⁴⁹ In addition, the valence band edge is raised but remains at a suitable energy to drive water oxidation, albeit at a smaller overpotential. Similar trends in the electronic structure are found for other Ag(I)- and Cu(I)-containing ternary oxides such as Ag₃VO₄ and CuFeO₂. In these cases, the raised valence band edges result in decreased band gaps of ~2.2 eV and ~1.5 eV, respectively.^{50,51}

Metal oxides containing post-transition metal cations with *d*¹⁰*ns*² electron configurations are among a growing group of semiconductors with small band gaps and favorable band edge energies, such as those containing the Sn(II), Pb(II), and Bi(III) cations. In analogy to oxides containing Cu(I) and Ag(I), their filled *ns*² orbitals are located at a higher energy, i.e., to more negative redox potentials, than the O 2*p* orbitals. This results in a higher energy valence band comprised of the *ns*² orbitals mixed with the O 2*p* orbitals in an antibonding fashion. The strength of this interaction, and thus the degree to which the valence band energy is raised, is determined by the energy match and orbital overlap between the post transition-metal *ns* orbital and the O 2*p* orbitals. The strength of this interaction has been found to decrease in the following order of Sn(II) > Pb(II) > Sb(III) > Bi(III).⁵² Further details on the electronic structures of this class of oxides can be found therein.⁵²

Currently, the best performing photocatalyst under visible light for water oxidation, BiVO₄, falls into this class. The DOS of BiVO₄ is plotted in Fig. 12A.^{53,54} The states which form the conduction band edge stem from the empty V 3*d* orbitals, and which are positioned below the redox potential for the reduction of water to H₂. Unlike most metal oxides, though, the edge of its valence

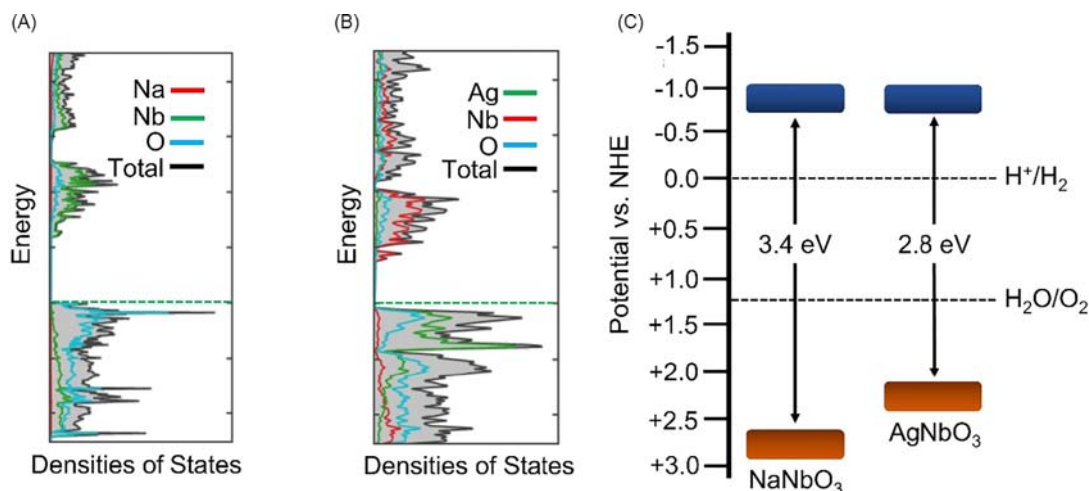


Fig. 11 DOS of (A) NaNbO_3 and (B) AgNbO_3 . Band energies of NaNbO_3 and AgNbO_3 (C). Higher energy valence bands and smaller bandgaps are found in mixed metal oxides that contain Ag(I) or Cu(I) as the filled d^{10} orbitals can form new, higher energy, states at the top of the valence band. (A) and (B) Adapted from Jain, A.; Ong, S. P.; Hautier, G.; Chen, W.; Richards, W. D.; Dacek, S.; Cholia, S.; Gunter, D.; Skinner, D.; Ceder, G.; et al. Commentary: The Materials Project: A Materials Genome Approach to Accelerating Materials Innovation. *APL Mater.* **2013**, *1*(1).

band is not derived predominantly from the O $2p$ orbitals but from strongly mixed Bi $6s$ orbitals as well. This leads to a higher energy valence band with significantly more band dispersion. The net density and contributions of Bi- $6s$ /O- $2p$ states at the valence band maximum is a consequence of the valence orbitals lying relatively close in energy. However, the combination of the low-lying V $3d$ conduction band and the raised valence band edge results in a reduced band gap of ~ 2.4 eV. This facilitates the absorption of a much larger fraction of visible-light energies by photoelectrode films of n-type BiVO_4 . As a result of the relatively higher-energy Bi $6s$ orbitals, many Bi(III)-containing oxides show reduced band gaps, e.g., Bi_2WO_6 with a band gap of ~ 2.7 eV.⁵⁵ While oxides which incorporate the Bi(III) cation typically yield smaller band gaps, it is typically a relatively modest reduction into the visible-light energies.

Perhaps the largest impact on the valence band energy and reduction in band gap can be found in the Sn(II)-containing oxides. One prominent example is Sn_2TiO_4 , with the calculated DOS as shown in Fig. 12B. In this case, the valence band maximum is

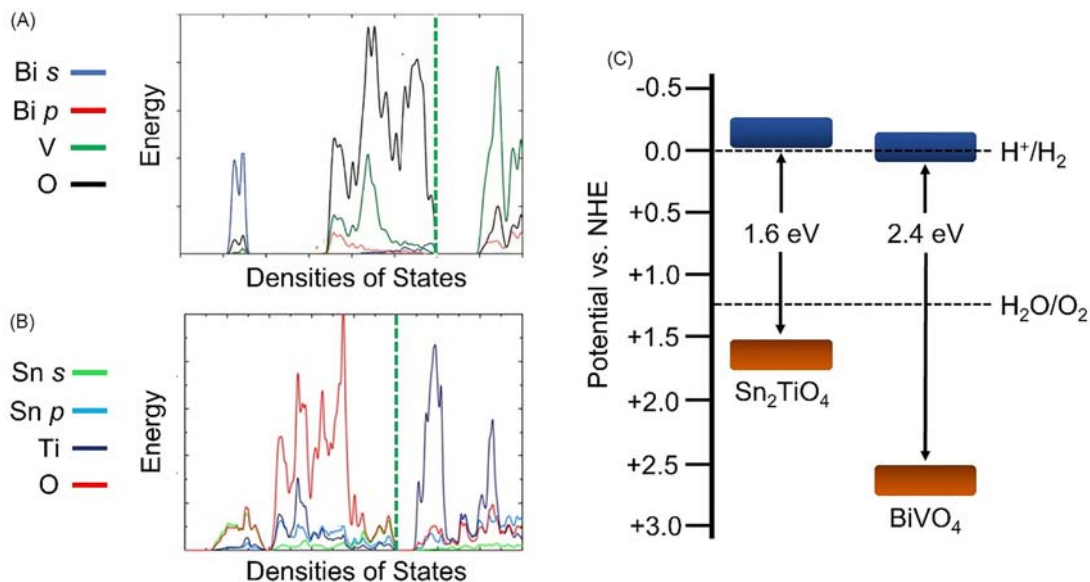


Fig. 12 DOS of (A) BiVO_4 and (B) Sn_2TiO_4 . Band energies of BiVO_4 and Sn_2TiO_4 (C). Metal oxides containing post-transition metals with $d^{10}ns^2$ electron configurations lead to higher energy valence bands and small bandgaps. The filled ns^2 orbitals have antibonding interactions with the O $2p$ orbitals in the valence band to form higher energy valence band states. Adapted with permission from (A) Walsh, A.; Yan, Y.; Huda, M. N.; Al-Jassim, M. M.; Wei, S. H. Band Edge Electronic Structure of BiVO_4 : Elucidating the Role of the Bi s and V d Orbitals. *Chem. Mater.* **2009**, *21*(3), 547–551 and (B) Burton, L. A.; Walsh, A. A Photoactive Titanate with a Stereochemically Active Sn Lone Pair: Electronic and Crystal Structure of Sn_2TiO_4 from Computational Chemistry. *J. Solid State Chem.* **2012**, *196*, 157–160.

formed from strongly mixed Sn-5s/O-2p orbitals in an antibonding fashion. The energy of its valence band edge is sufficiently raised, at a potential of +1.53 V, which closely approaches the redox potential for water oxidation. This yields a very small band gap ~ 1.6 eV, and nearly optimally straddles both redox potentials for water oxidation and reduction.^{23,56} Almost every known Sn(II)-containing oxide also containing an early transition-metal cation has a small band gap, including for SnNb₂O₆ (2.3 eV), Sn₂Nb₂O₇ (2.3 eV), and SnWO₄ (1.7 eV).^{57,58} However, Sn(II) cations can easily oxidize at their surfaces and many are metastable with respect to decomposition to simpler oxides. The joint issues of stability and photocatalytic efficiency represent some of the most prominent challenges for this group of semiconductor photocatalysts.

In the last category, oxides containing transition metal cations with partially-filled *d*-orbitals have also been investigated for their ability to effectuate changes in the valence band energy. For example, several known Cu(II)-containing oxides have shown promise as small bandgap photocatalysts, including CuWO₄ and CuBi₂O₄ with bandgaps of ~ 2.3 and ~ 1.8 eV, respectively. A comparative analysis reveals how chemical composition plays a critical role in determining their band gaps and band edge energies, as shown in Fig. 13.^{59,60} The valence band maxima for both CuWO₄ and CuBi₂O₄ are comprised of mixed Cu-3*d*/O-2*p* states in an antibonding fashion. An additional contribution for CuBi₂O₄ is that the Bi 6*s* orbitals mix with the O 2*p* orbitals in the valence band and further raise its energy. As a result, their valence band edges are starkly different in energy. In fact, the valence band energy of CuBi₂O₄ has been raised to such an extent that it no longer straddles the redox potential for the oxidation of water. The valence band of CuWO₄ is shifted positively by more than +1.5 eV by comparison and exhibits a large overpotential for water oxidation. These differences are reflected in their photocatalytic properties. While films of CuWO₄ are under investigation as photoanodes, films of CuBi₂O₄ are under investigation as photocathodes. The latter is facilitated by the substantial overpotential of the conduction band edge of CuBi₂O₄ for H₂ production. The antibonding interaction between the Cu-3*d*/O-2*p* orbitals in its conduction band raises its minimum above the proton reduction potential as compared to the non-interacting Cu 3*d* states in CuWO₄. An understanding of the origins of these band edge energies is critical to developing these metal oxides for solar energy conversion.

This category also includes several Fe(III)- and Mn(II)-containing oxides which possess electronic structures that follow analogous trends toward smaller band gaps. One example is the LaFeO₃ perovskite with a band gap of ~ 2.1 eV. Its valence band stems from mixed Fe-3*d*/O-2*p* orbitals, whereas the conduction band is formed almost exclusively from more localized Fe 3*d* orbitals. Another example is MnV₂O₆, which has partially-filled 3*d*⁵ orbitals on Mn(II) cations that strongly contribute to raising the valence band edge closer in energy to the water oxidation potential. It has a small band gap of ~ 1.4 eV that still maintains valence and conduction band energies capable of driving overall water-splitting. This result is surprising considering that its conduction band arises from the empty V 3*d* orbitals, in analogy with BiVO₄, Fig. 12A. As an aqueous suspension it shows moderate photocatalytic rates for the production of H₂ and O₂ under visible-light irradiation.³⁰

4.17.2.4 Band dispersion and effective masses of charge carriers: Oxide semiconductors

The mobility of the photon-generated minority carriers is a critical aspect of n-/p-type metal oxides for photocatalysis. Upon absorption of bandgap photons, minority charge-carriers are produced in the metal oxide which must have sufficient mobility to reach the

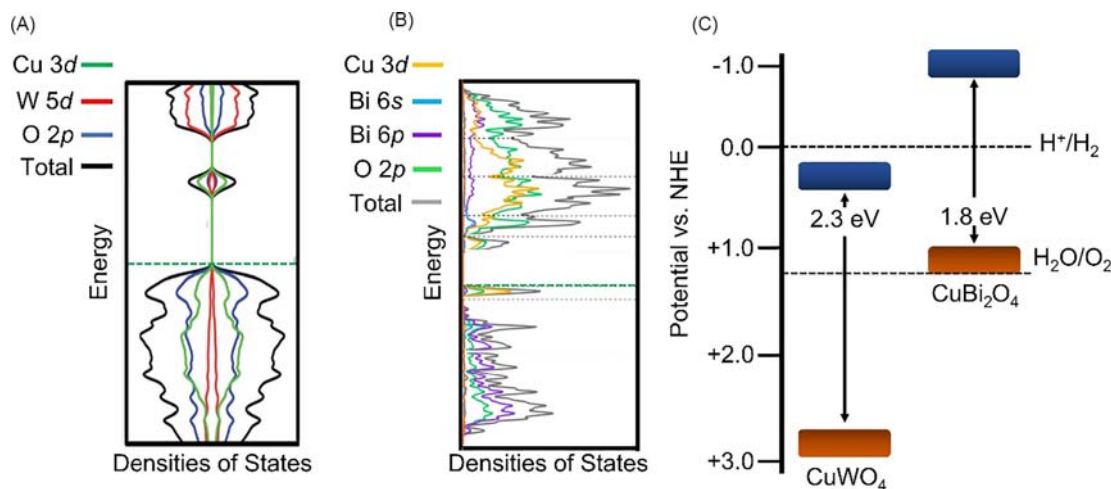


Fig. 13 DOS of (A) CuWO₄ and (B) CuBi₂O₄. Band energies of CuWO₄ and CuBi₂O₄ (C). Metal oxides with partially filled *d* orbitals can lead to significantly reduced bandgap energies. The bandgap reduction is typically a result of TM *d*-O 2*p* interactions that lead to a higher energy valence band. Adapted with permission from (A) Xie, X.; Liu, M.; Wang, C.; Chen, L.; Xu, J.; Cheng, Y.; Dong, H.; Lu, F.; Wang, W. H.; Liu, H.; et al. Efficient Photo-Degradation of Dyes Using CuWO₄ Nanoparticles With Electron Sacrificial Agents: A Combination of Experimental and Theoretical Exploration. *RSC Adv.* **2016**, 6(2), 953–959 and (B) Cooper, J. K.; Zhang, Z.; Roychoudhury, S.; Jiang, C.-M.; Gul, S.; Liu, Y.-S.; Dhall, R.; Ceballos, A.; Yano, J.; Prendergast, D.; et al. CuBi₂O₄: Electronic Structure, Optical Properties, and Photoelectrochemical Performance Limitations of the Photocathode. *Chem. Mater.* **2021**, 33(3), 934–945.

surfaces. Competing with this are charge-recombination events at the surfaces and in the bulk, which are mediated by bulk and surface defects with energies that fall within their band gap. It is critical then that the minority charge carriers have a maximal diffusion length and therefore a small effective mass. The effective masses are proportional to the dispersion of the conduction and valence bands for electrons and holes, respectively, or the rate of change of the band energies when moving through k -space. These relationships are evidenced by Eqs. (3)–(5) in the introduction. The below sections are thus organized according to the structural motifs which enable the attainment of the largest band dispersion in metal oxides.

4.17.2.4.1 General trends

Metal oxides routinely display relatively small electron effective masses. However, the opposite is generally true for the effective masses of holes. An analysis of ~ 3000 metal oxides has clearly demonstrated this trend, with the hole effective masses calculated from the band dispersions to be 3x to 5x larger, on average, as compared to the electron effective masses.⁶¹ An understanding of the structural and compositional aspects that determine the band dispersion in metal oxides is of critical importance in the development of metal oxide photocatalysts. The carrier effective masses, as well as the structural parameters that impact band dispersion, are listed in Table 2 for selected metal oxides which are discussed below.

One starting point is to analyze the electronic band structure diagram of a relatively simple and representative metal-oxide photocatalyst such as SrTiO₃. When suitably Al-doped, SrTiO₃ also exhibits the highest known rates with quantum efficiencies approaching unity for overall water splitting. Its band diagram is plotted in Fig. 14A.⁴² As a cubic perovskite, its $\langle 100 \rangle$ crystallographic directions are equivalent by symmetry and the carrier mobilities are isotropic. The conduction band minimum at the Γ -point is formed from the nonbonding Ti 3d orbitals, with the band dispersion increasing in energy from the antibonding interactions to the O 2p orbitals.

Table 2 Characteristic features of the crystal and electronic structures of metal oxides used as semiconductors for solar-driven water splitting.

Composition	Valence band states (connectivity)	Bond angles	Conduction band states (connectivity) ^a	Bond angles	Carrier effective masses (m_e , m_h)
SrTiO ₃	O 2p (3D)	–	Ti 3d (3D-corner shared octahedra)	180°	0.4 m_e , 1.2 m_h
NaTaO ₃	O 2p (3D)	–	Ta 5d (3D-corner shared octahedra)	166° and 160°	0.42–0.53 m_e , 3.93–4.84 m_h
NaNbO ₃	O 2p (3D)	–	Nb 4d (3D-corner-shared octahedra)	155°–163°	0.39–0.92 m_e , 2.84–5.62 m_h
			Sn 5s/p + O 2p (3D-corner shared octahedra)	160°	0.36–0.47 m_e , 2.12–2.85 m_h
SrSnO ₃	O 2p (3D)	–		160°	0.36–0.47 m_e , 2.12–2.85 m_h
AgNbO ₃	Ag 4d + O2p (3D-face-shared cuboctahedra)	91°–180°	Nb 4d (3D-corner-shared octahedra)	153°–164°	0.35–7.6 m_e , 2.75–7.01 m_h ⁶²
LaFeO ₃	Fe 3d + O2p (3D-corner-shared octahedra)	156°–157°	Fe 3d		1.49–1.93 m_e , 0.75–4.22 m_h
Ba ₅ Nb ₄ O ₁₅	O 2p (3D)	–	Nb 4d (2D-corner shared octahedra)	171°	0.91–8.85 m_e , 3.96–26.57 m_h
BaLa ₄ Ti ₄ O ₁₅	O 2p (3D)	–	Ti 3d (2D-corner shared octahedra)	162° and 164°	–
La ₂ Ti ₂ O ₇	O 2p (3D)	–	Ti 3d (2D-corner shared octahedra)	145°–174°	–
Sr ₂ Nb ₂ O ₇	O 2p (3D)	–	Nb 4d (2D-corner shared octahedra)	145°–174°	0.74–4.67 m_e , 1.29–182.70 m_h
Bi ₂ WO ₆	Bi 6s + O2p (2D-edge-shared polyhedra)	101°–114°	W 5d (2D-corner shared octahedra)	150° and 161°	0.49–510.40 m_e , 1.50–9.01 m_h
BiVO ₄	Bi 6s + O2p (3D-edge-shared polyhedra)	103° and 106°	V 3d (0D-isolated V-O tetrahedra)	–	0.3 m_e , 0.3 m_h ⁵³
Sn ₂ TiO ₄	Sn 5s + O2p (1D-corner shared polyhedra)	128°	Ti 3d (1D-edge-sharing octahedra)	96°	1.06–3.08 m_e , 0.96–1.44 m_h
SnNb ₂ O ₆	Sn 5s + O2p (1D-edge-shared polyhedra)	105°	Nb 4d (2D-corner shared octahedra)	124°–150°	1.83–4.67 m_e , 0.42–5.63 m_h
CuWO ₄	Cu 3d + O2p (1D-edge-shared octahedra)	94°	W 5d (1D-edge-shared octahedra) + Cu 3d	106°	59 m_e , 57 m_h ⁵⁹
CuFeO ₂	Cu 3d + O2p (0D-isolated O-Cu-O chain)	–	Fe 3d (2D-edge-shared octahedra)	95°	1.83 m_e , 1.35 m_h ⁵⁰
CuBi ₂ O ₄	Cu 3d + O2p (0D-isolated Cu-O square planes)	–	Cu 3d + O2p (0D-isolated Cu-O square planes)	–	–
Ag ₃ VO ₄	Ag 4d + O 2p (3D-polyhedra)	Varies	V 3d (0D-isolated V-O tetrahedra)	–	–
MnV ₂ O ₆	Mn 3d + O2p (1D-edge-shared octahedra)	105°	V3d (2D-edge-shared octahedra)	106° and 144°	–

^aCrystal structures were obtained from the Materials Project Database⁴² and cross-referenced with literature reports. Crystal structures from the Materials Project Database are the DFT optimized structures. All bond lengths and angles thus represent approximate values.

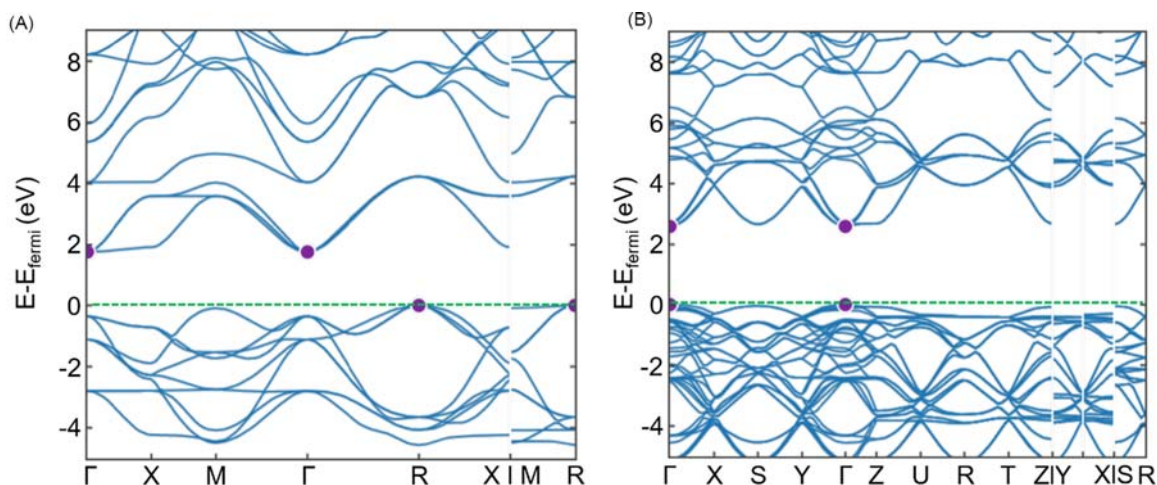


Fig. 14 Band diagrams of (A) SrTiO₃ and (B) NaTaO₃. Purple dots indicate the edges in k -space within the conduction and valence bands. Adapted from Jain, A.; Ong, S. P.; Hautier, G.; Chen, W.; Richards, W. D.; Dacek, S.; Cholia, S.; Gunter, D.; Skinner, D.; Ceder, G.; et al. Commentary: The Materials Project: A Materials Genome Approach to Accelerating Materials Innovation. *APL Mater.* **2013**, *1*(1).

For all other k -points, e.g., X , M , and R , the conduction bands are higher in energy. This antibonding interaction is what produces the dispersion of the conduction band and determines the electron effective mass. There is a much smaller band dispersion within the valence band because of the relatively more localized O $2p$ states and is responsible for the higher hole effective masses. This is reflected in the values in Table 2 for the calculated effective electron and hole masses of $0.4m_0$ and $1.2m_0$, respectively. Phonon coupling has been shown to increase these effective mass values for SrTiO₃.^{63,64} The experimentally measured effective masses in SrTiO₃ tend to be closer to $\sim 6m_0$.⁶⁵

For lower-symmetry perovskites, such as orthorhombic NaTaO₃, there can be significant differences in effective masses and carrier mobilities that depend upon the crystallographic direction, as shown in Fig. 14B and Table 2. For example, the electron effective masses in NaTaO₃ along the $\langle 100 \rangle$ set of crystallographic directions range between 0.42 and $0.53 m_e$, while the hole effective masses have a similarly narrow distribution between 3.93 and $4.84 m_e$. The impact on band dispersion is most severe in lower-dimensional perovskites that possess extended $[-O-M-O-M-O-]_n$ connectivity in only one or two dimensions. For example, in the layered Ba₅Nb₄O₁₅ shown in Fig. 15,⁴² the conduction band dispersion is largest from $\Gamma \rightarrow M$ and $\Gamma \rightarrow K$. These directions contain the (110) -plane of $[-O-Nb-O-Nb-O-]_n$ connectivity. Conversely, the bands are nearly flat along the $\Gamma \rightarrow A$ or the c -axis in a direction through the layers. This is the result of the loss of the crystal orbital interaction between the Nb $4d$ orbitals with the O $2p$ orbitals in the conduction band states. This anisotropy in band dispersion is reflected in the calculated electron effective masses, Table 2, which is $0.91 m_e$ along the a -axis and b -axis directions, but a much higher $8.85 m_e$ along the c -axis direction. When

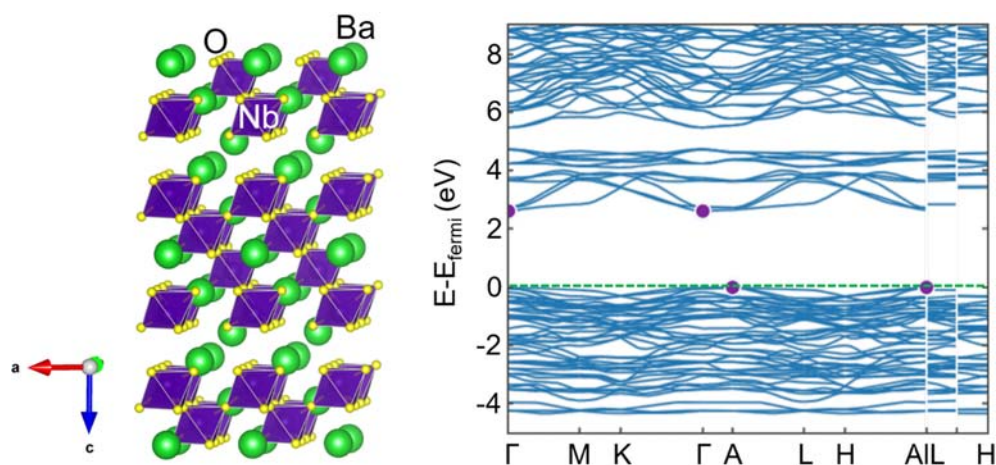


Fig. 15 Crystal structure (left) and band diagram (right) of Ba₅Nb₄O₁₅. The loss of extended $[-Nb-O-Nb-O-]_n$ connectivity down the c -axis leads to a smaller conduction band dispersion and higher electron effective mass in this crystallographic direction. The band diagram is adapted from Jain, A.; Ong, S. P.; Hautier, G.; Chen, W.; Richards, W. D.; Dacek, S.; Cholia, S.; Gunter, D.; Skinner, D.; Ceder, G.; et al. Commentary: The Materials Project: A Materials Genome Approach to Accelerating Materials Innovation. *APL Mater.* **2013**, *1*(1), with purple dots indicating the band edge extrema.

the metal-oxide connectivity is lowered to 1D, as for Sn_2TiO_4 , the band dispersion is also highly anisotropic with significant dispersion in only one direction. In this case, there is a high conduction band dispersion from $\Gamma \rightarrow Z$ along the direction of the titanate chains, but from $\Gamma \rightarrow X$ or $\Gamma \rightarrow M$ the bands are relatively flat. Down the titanate chains the electron effective mass is relatively small at $\sim 1.06 m_e$, while in directions between the chains it is a much larger $\sim 3.06 m_e$. Another example of the impact of disrupted $[-\text{O}-\text{M}-\text{O}-\text{M}-\text{O}-]_n$ connectivity can be found in BiVO_4 with conduction band states deriving from isolated VO_4 tetrahedra. Thus, one of the primary deficiencies of BiVO_4 as a photoanode is its poor carrier mobilities.⁴⁰ Careful tuning of the preparation conditions and n-type doping of BiVO_4 is required to greatly improve the diffusion of its conduction band electrons that has been postulated to occur via polaron hopping between adjacent tetrahedra.^{39,40}

Anisotropies in the carrier mobilities must be considered when preparing metal oxides as photoelectrodes, as reported for BiVO_4 and other metal oxides.³⁹ For optimal performance, the directions of highest mobilities for the charge carriers must be preferentially aligned for reaching the surfaces and/or back contact. Thus, the synthetic conditions of the crystallite growth and/or the fabrication techniques of the photoelectrode films can all play prominent roles in determining whether the maximal solar-to-fuel efficiencies are reached, and assuming that the surfaces can be functionalized to achieve efficient charge transfer and product formation.

4.17.2.4.2 Conduction band dispersion of metal oxides

One approach to effectively tune the band dispersions, and thus effective masses, in metal oxides is via changes in chemical composition. A large conduction band dispersion is regularly found for metal oxides containing main-group metal cations with $nd^{10}ns^0$ electron configurations, e.g., Sn(IV), Pb(IV), In(III), or Sb(IV) cations. Analogous to transition-metal oxides, their empty ns orbitals interact in an antibonding fashion with the O 2p orbitals at increasing energies in the conduction band. Their antibonding interactions can be larger than for d-orbitals because of the σ -type overlap and the closer energetic match, as shown schematically by the orbital interactions in Fig. 16. This situation yields a significantly larger band dispersion across their band structures in k -space, such as found in a comparison of BaZrO_3 vs. BaSnO_3 in Fig. 17.⁴² The conduction band minima of BaZrO_3 and BaSnO_3 are both located at Γ . The ~ 6 eV dispersion of the conduction band for BaSnO_3 is much larger than for BaZrO_3 of ~ 2 – 3 eV. The large conduction band dispersion in BaSnO_3 leads to very small electron effective masses calculated to be 0.03 – $0.09m_0$.⁶⁶ This comparison illustrates the substantial differences in conduction band dispersion that can occur simply through changes in composition.

An orthorhombic distortion of the perovskite-type structure, such as for SrSnO_3 shown in Fig. 17, results in a decrease of the Sn-5s/O-2p interaction as a result of the loss of orbital overlap for the more acute Sn–O–Sn bond angle of $\sim 160^\circ$. As these orbitals constitute the conduction band states, this yields a smaller band dispersion as compared to cubic BaSnO_3 . The situation is again analogous to that described above for the transition-metal oxide perovskites. The electron effective mass is calculated to be a relatively larger ~ 0.17 – $0.92m_0$. The electron effective mass for SrSnO_3 shows a finer-level dependence on crystallographic direction because of the lowered symmetry.⁶⁶ Conversely, the valence bands of both BaSnO_3 and SrSnO_3 still derive primarily from the O 2p orbitals and are relatively flat. This leads to relatively large effective masses for holes in the valence bands, a common limitation among the larger bandgap oxides. Particles of SrSnO_3 have nevertheless been demonstrated to split water stoichiometrically into H_2 and O_2 under UV-irradiation. The absence of similar photocatalytic activity for overall water splitting in BaSnO_3 has been attributed to higher rates of radiative recombination.³⁴

4.17.2.4.3 Valence band dispersion of metal oxides

Nearly all known metal oxides exhibit large hole effective masses in their valence bands, representing a longstanding limitation in this field. Similar to the conduction band, one of the most effective approaches to increasing the valence band dispersion has been via compositional modulations. For example, metal oxides containing main-group cations with electron configurations of $nd^{10}ns^2$,

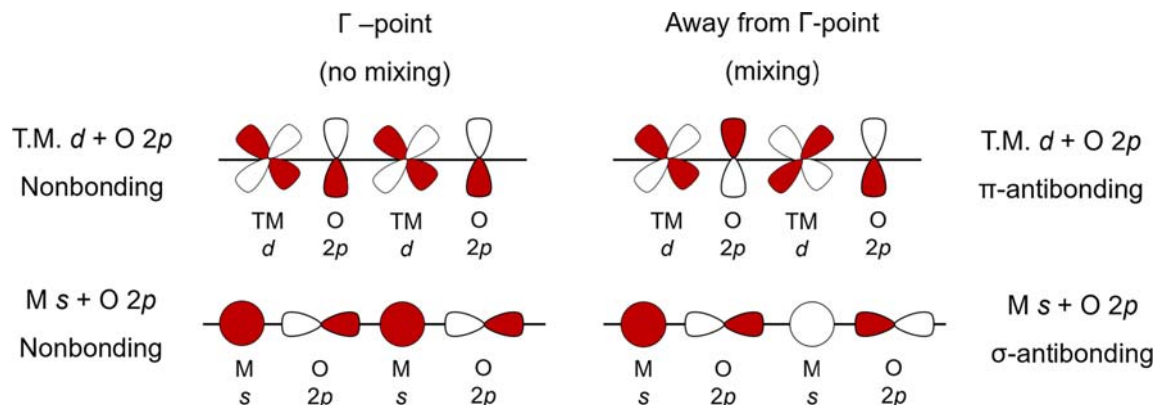


Fig. 16 Example of one set of valence atomic orbital interactions for a linear $[-\text{M}-\text{O}-\text{M}-\text{O}-]_n$ oxide chain containing a transition metal (top) or a post-transition metal (bottom), illustrated for the Γ -point (left; $k = 0$) and away from the Γ -point (right; $k = \pi/a$). At $k = 0$, the crystal orbitals are nonbonding, but at $k = \pi/a$ the crystal orbitals are both antibonding. The chain containing the transition metal has π^* interactions while the post-transition metal has larger σ^* interactions to the O 2p orbitals.

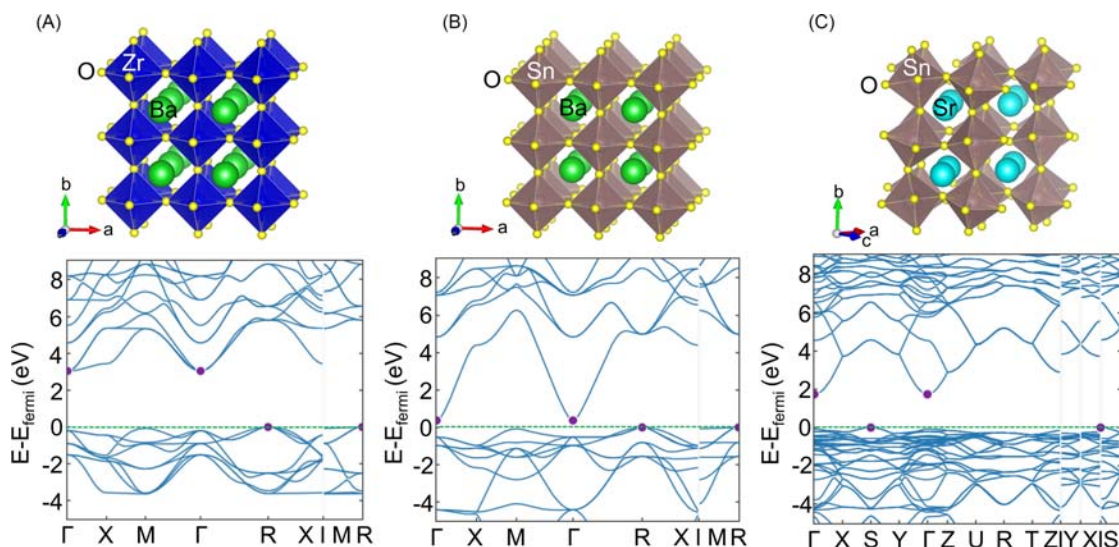


Fig. 17 Crystal structures and band diagrams of (A) BaZrO₃, (B) BaSnO₃, and (C) SrSnO₃. The post-transition metal on the B-site, i.e., Sn(IV), leads to a greater conduction band dispersion from the larger Sn-O σ^* -type interactions as compared to the smaller Zr-O π^* -type interactions. Band diagrams are adapted from Jain, A.; Ong, S. P.; Hautier, G.; Chen, W.; Richards, W. D.; Dacek, S.; Cholia, S.; Gunter, D.; Skinner, D.; Ceder, G.; et al. Commentary: The Materials Project: A Materials Genome Approach to Accelerating Materials Innovation. *APL Mater.* **2013**, 1(1).

e.g., Sn(II), Pb(II), or Bi(III) cations, can commonly exhibit a larger valence band dispersion. As described above, these types of cations possess filled ns^2 orbitals that are of suitable energy and symmetry to interact with the O $2p$ orbitals in an antibonding fashion. The extent of this interaction is based on the closeness of their energy match and the orbital overlap between the cation ns -orbital and O $2p$ -orbital. These crystal orbitals constitute a new higher-energy valence band with a more significant dispersion than found for transition-metal oxides. This interaction of the valence orbitals is found to decrease in the order Sn(II) > Pb(II) > Sb(III) > Bi(III). This has been investigated for Sn₂TiO₄, BiVO₄, and PbTiO₃ which have relatively smaller band gaps, as shown in Fig. 12 and Table 2.

It is illustrative to consider the crystal and electronic structures in Sn₂TiO₄ in deeper detail, Fig. 18.⁵⁴ Both the conduction and valence bands along $\Gamma \rightarrow Z$ show a relatively large dispersion and result in calculated effective masses as low as 0.96 m_e and 1.06 m_h for electrons and holes, respectively. This direction corresponds to the extended [-O-Sn-O-Sn-O]_n and [-O-Ti-O-Ti-O]_n chains within the crystal structure, drawn vertically in Fig. 18. However, in alternate crystallographic directions which lack extended connectivity, such as $Z \rightarrow R$ or $\Gamma \rightarrow M$, the bands show significantly less dispersion. The lack of extended structural connectivity in one or more directions within structures containing these cations is relatively common because of their ns^2 electron configurations and stereoactive lone-pairs. Further, while the strength of the $ns/O\ 2p$ orbital interaction is maximized when the M-O-M bond

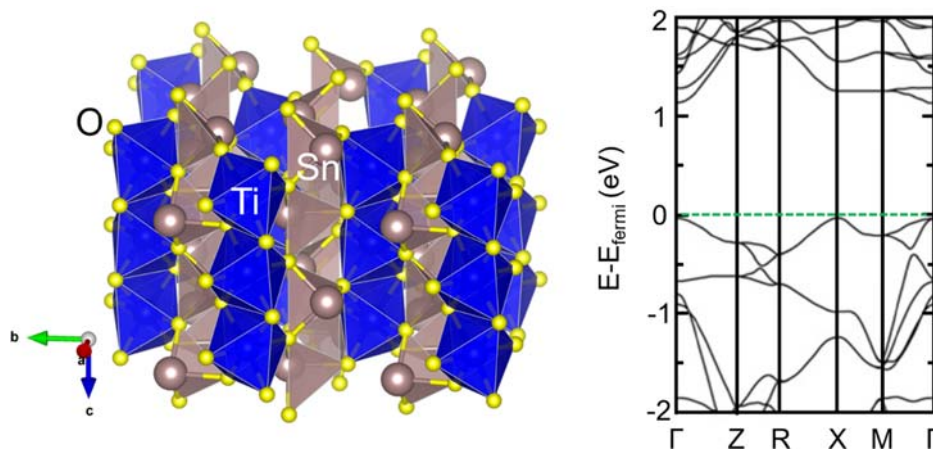


Fig. 18 Crystal structure (left) and band diagram (right) of Sn₂TiO₄. The filled Sn $5s$ orbitals interact with O $2p$ orbitals in the valence band and yielding in an increased valence band dispersion. Band diagram adapted with permission from Burton, L. A.; Walsh, A. A Photoactive Titanate With a Stereochemically Active Sn Lone Pair: Electronic and Crystal Structure of Sn₂TiO₄ From Computational Chemistry. *J. Solid State Chem.* **2012**, 196, 157–160.

angle is 180° , the stereoactive lone-pairs result in more acute, nonlinear, bond angles. In Sn_2TiO_4 , for instance, the Sn-O-Sn angle is a relatively acute $\sim 128^\circ$. New synthetic approaches to prepare metal oxides containing these cations with bond angles closer to 180° would be extremely useful in attaining the lowest possible hole effective masses. Similar structural and bonding situations occur for Pb(II)- and Bi(III)-containing oxides, e.g., for PbTiO_3 and BiFeO_3 .

4.17.2.5 Summary of metal oxide semiconductors

Many transition-metal oxides possess large band gaps because of their low-lying valence bands formed from the O $2p$ orbitals. Their conduction band edges have been found to be tunable by choice of the early transition-metal or main group cations, e.g., Ti(IV), Nb(V), Ta(V) or Sn(IV). Similarly, the nature of their valence bands can be modified by the selection of the late transition-metal or main group cations, e.g., Cu(I), Ag(I), Sn(II) or Bi(III). The crystal orbitals of the conduction and valence bands stem from the respective filled and empty valence orbitals of these cations with a corresponding admixture of the oxygen $2p$ orbital that is a function of the orbital overlap and energetic match. More specific band structure details are dependent upon the structure type, coordination environments, and the $[-\text{M-O-M-O}]_n$ connectivity, among other factors. Only metal oxides with wide band gaps and significant overpotentials for water reduction and oxidation have shown the capability to persistently split water with nearly quantum-unity efficiency under ultraviolet light, such as for Al-doped SrTiO_3 .

Extending high levels of photocatalytic performance to visible-light energies have currently met with limited success owing to a few factors. These include possessing an unsuitable energetic location of the valence band edge, low carrier mobilities and high effective masses in the valence band, as well as smaller overpotentials at the band edges to drive the redox reactions. To address these issues, the discovery of new mixed-metal oxides are needed which can enable the tuning of the valence band edge and the maximizing of the band dispersion for low hole effective masses. Several recent compounds have shown promising advances in this direction. These include metal oxides containing cations with nd^{10} or $nd^{10}ns^2$ electron configurations, such as BiVO_4 , CuBi_2O_4 , and Sn_2TiO_4 . Similarly, metal oxides containing partially filled d -orbitals have shown some promise. In some cases, such as Sn_2TiO_4 and MnV_2O_6 , metal oxides can possess small bandgaps with band edge energies that meet the thermodynamic requirements of overall water-splitting.

Other issues such as stability against corrosion, the ability to dope n-/p-type, and surface functionalization with protective layers and cocatalysts are critically important to attain stable and efficient solar-to-fuel energy conversion. However, full optimization and development of a metal oxide photocatalyst typically requires intense research efforts that are motivated by initial reports of its promising physical properties. A careful consideration of its electronic band structure represents a necessary first step in the identification of the most promising candidates. Many different chemical approaches can be used to tune the electronic structure of metal oxides and which yet offer much untapped potential for targeting required photoelectrochemical properties.

4.17.3 Metal nitride semiconductors

4.17.3.1 Background

Metal nitrides and oxynitrides have not been as extensively studied for photoelectrochemical (PEC) water splitting as metal oxides. Nitrides can often be difficult to synthesize with high crystallinity and typically require high reaction temperatures and a reactive nitrogen source such as ammonia. The most well-studied metal nitrides for photocatalytic applications in recent years have focused on GaN, TaON, Ta_3N_5 , MTaO_2N ($\text{M} = \text{Ca}, \text{Sr}, \text{Ba}$), MnNbO_2N ($\text{M} = \text{Sr}, \text{Ba}$), and LaTiO_2N , as listed in Table 3. These all tend to have smaller visible-light band gaps as compared to their metal oxide analogs and therefore absorb bandgap photons more broadly across the solar spectrum. Their band gaps are narrowed by the addition of high-energy nitrogen $2p$ orbitals within the valence band. The energetic position of their valence and conduction bands thus more closely straddle the redox potentials for water oxidation and reduction. Though, their n-type semiconducting character has made them most useful as photoelectrodes and photocatalysts for water oxidation.

Challenges in the use of metal nitrides include their typically higher levels of defects and oxygen impurities that are detrimental to the carrier mobility and recombination rates. Current approaches involve the development of the synthetic routes to enhance crystallinity and reduce defect densities. Another key issue is their stability, as the nitride anions commonly hydrolyze and oxidize at the surfaces during the photocatalytic production of O_2 . This leads to passivation of the nitride surface with an oxide layer that shuts down charge transfer. Therefore, stable photocurrents cannot be maintained for extended periods of time. In this section a brief overview is provided into the crystal structures of these metal nitrides and oxynitrides. It covers aspects of their crystal and electronic structures that determine their band gaps, band dispersion, energetic locations of their band positions, as well as a selection of their currently reported photocatalytic properties.

4.17.3.2 Crystal structures and photoelectrochemical properties

The range of investigated metal nitrides for photocatalytic water splitting is restricted to relatively fewer structure types as compared to the oxides. The coverage of this section, and its organization, focuses on the most notable examples having the perovskite type, wurtzite type, or their own structure type in a few cases. Similar to the oxides, the presence of extended $[-\text{N-M-N-M-N}]_n$ connectivity is considered fundamental to attaining the highest band dispersion and mobility of charge carriers in the valence band. While most

Table 3 Selection of metal nitride semiconductors used as photoelectrodes and/or suspension-based photocatalysts for solar-driven water splitting.

Composition	Structure type/ Symmetry	Band gap (eV)	Form	Photocurrent	Quantum efficiency
GaN	Wurtzite ⁶⁷ <i>P6₃mc</i>	3.4 ^{67,68} direct	Film ^{67–69}	20 ⁶⁸ ($\mu\text{A cm}^{-2}$), 0.6 ⁶⁷ –1.1 ⁶⁹ (mA cm^{-2})	7% overall water splitting (366 nm) ⁶⁷
In _x Ga _{1-x} N	Wurtzite	1.7 ⁷⁰ , 2.38 ⁷¹	Film ^{67,71}	1.8 ⁶⁷ , 40.6 ⁷⁰ (mA cm^{-2})	15% overall water splitting (366 nm) ⁶⁷ , 72.3% overall water splitting (AM 1.5G) ⁷⁰
GaN:ZnO	Wurtzite ^{72,73}	2.5–2.8 ⁷³	Powder ^{72–74} , Film	1.67 ⁷² (mA cm^{-2})	30.7% overall water splitting (360 nm) ⁷²
TaON	Monoclinic <i>P2₁/c</i>	2.5 ^{75,76} indirect	Powder ^{76–78} , Film ⁷⁵	4 ⁷⁵ (mA cm^{-2})	34% for O ₂ (>420 nm) ⁷⁶ , 76% overall water splitting (400 nm) ⁷⁵
Ta ₃ N ₅	Orthorhombic <i>Cmcm</i>	2.1 ^{79–83} indirect	Powder ⁷⁸ , Film ^{79–83}	4 ^{78,80} , 6.3 ⁸² , 8 ⁸³ , 12.1 ⁷⁹ (mA cm^{-2})	31% overall water splitting (500 nm) ⁷⁸ , 90% for O ₂ (400–550 nm) ⁷⁹
BaTaO ₂ N	Perovskite ^{84–88} <i>P4/mmm</i>	1.9 ^{84,86,87} , 2.1 ⁸⁸ direct	Powder ^{85,86,88} , Film ^{84,87}	6 ⁸⁶ (mA cm^{-2})	9% for O ₂ (600 nm) ⁸⁴
CaTaO ₂ N	Perovskite ^{89–91} <i>Pmc2₁</i>	2.43 ⁸⁹ direct	Powder ^{89,90} , Film ⁹¹	40 ⁹¹ , 50 ⁹⁰ ($\mu\text{A cm}^{-2}$)	0.003% overall water splitting (440 nm) ⁸⁹
SrTaO ₂ N	Perovskite ^{88,92,93} <i>Pmc2₁</i>	2.1 ⁸⁸ , 2.15 ⁹² , 2.23 ⁹⁴ direct	Powder ⁹² , Film ⁹³	0.01 ⁹² ($\mu\text{A cm}^{-2}$), 2.9 ⁹³ (mA cm^{-2})	40% overall water splitting (320–480 nm) ⁹³
LaTiO ₂ N	Perovskite ^{95–97} <i>I2₁2₁2₁</i>	2.1 ^{95–97} direct	Powder ^{95,97} , Film ⁹⁶	2 ⁹⁶ ($\mu\text{A cm}^{-2}$)	27.1% for O ₂ (440 nm) ⁹⁷
BaNbO ₂ N	Perovskite ^{85,88,98} <i>P4/mmm</i>	1.44 ⁹⁴ , 1.79 ⁸⁵ , 2.0 ⁸⁸ direct	Powder ^{85,88,98}	0.85 ⁹⁸ , 5.2 ⁸⁶ (mA cm^{-2})	6% for O ₂ (480–740 nm) ⁹⁸
SrNbO ₂ N	Perovskite ^{88,98–100} <i>P4/mmm</i>	1.47 ⁹⁴ , 1.8 ^{99,101} , 1.9 ⁸⁸ direct	Powder ^{88,98,100,101} , Film ⁹⁹	0.4 ¹⁰⁰ , 0.35 ⁹⁹ , 0.53 ⁹⁸ , 0.75 ¹⁰⁰ , 1.5 ¹⁰¹ (mA cm^{-2})	0.2% overall water splitting (400 nm) ⁹⁹

of the examples described herein contain structures with significant O/N disorder and defects, this aspect has surprisingly not precluded the attainment of potentially useful photocatalytic properties. This drawback has made it more challenging to establishing clear structure-property relationships. Described in each system are some of their highest known n/p-type photocurrent densities as films or photocatalytic activities as aqueous suspensions.

4.17.3.2.1 Perovskite-type oxynitride structures

Many of the most photocatalytically-active oxynitrides crystallize in the perovskite structure and are capable of water oxidation and reduction with high efficiencies. Several representative examples are listed near the bottom of **Table 3**. The ionic size requirements have been described for compounds to crystallize in this structure in **Section 4.17.2.2.1** above. However, a poorer reliability is found when using the Goldschmidt tolerance factor to predict the formation of metal-oxynitrides in the perovskite structure as a result of the more covalent metal-nitrogen interactions. Many of the most studied and promising metal-oxynitride perovskites crystallize with the chemical composition ABO₂N (A = Ca, Sr, Ba; B = Nb, Ta, Ti) with disordered O/N anions. These have been found to possess band gaps in the range of ~1.5–2.4 eV, with photocurrent densities and photocatalytic rates that can approach ~80–90% of their theoretical potential.

For the larger alkali-earth cations on the A-site and Nb(V)/Ta(V) cations on the B-site, a tetragonal perovskite structure forms in space group *P4/mmm*, shown in **Fig. 19**. The +2 and +5 oxidation states of the alkaline earth and early transition-metal cations are balanced by a 2:1 ratio of the oxide and nitride anions. The B-cations are octahedrally coordinated by both oxygen and nitrogen

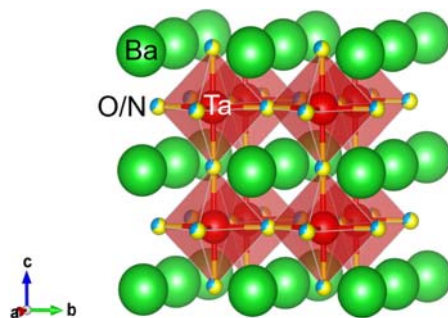


Fig. 19 Polyhedral drawing of the orthorhombically distorted perovskite BaTaO₂N. Atom types are labeled.

anions in a statistically random fashion, with M–O/N–M bond angles of 180° . Comparing BaTaO₂N and BaNbO₂N, the change in B-site cation causes changes in M–O/N bond lengths, from ~ 2.06 Å in BaTaO₂N to ~ 2.09 Å in BaNbO₂N. For SrNbO₂N, a shorter Sr–O/N bond length of ~ 2.04 Å is found owing to the smaller ionic radius of Sr as compared to of Ba. Though, the difference in their B-site cations has a significantly larger impact on the band gap than the M–O/N bond distances. While BaTaO₂N has a larger band gap of ~ 2.1 eV, the band gaps for BaNbO₂N and SrNbO₂N of ~ 1.4 and ~ 1.5 eV, respectively, are significantly smaller. All of these metal-oxynitrides show sizable photoanodic current densities for water oxidation under irradiation, **Table 3**, with theoretical limits of ~ 23 – 24 mA cm⁻² under AM 1.5G sunlight. Experimentally measured photoanodic current densities currently fall in the range of ~ 2 – 6 mA cm⁻² for films of BaTaO₂N, BaNbO₂N and SrNbO₂N. The highest current densities require annealing and other surface treatments to improve their crystallinity and to passivate defects. For example, BaTaO₂N photoelectrodes with a cobalt-oxide surface catalyst for water oxidation reach ~ 4.6 mA cm⁻² at 1.23 V vs. RHE, with a 9% efficiency at 600 nm.⁸⁴ Similar efficiencies are reported for BaNbO₂N and SrNbO₂N of $\sim 6\%$ and $\sim 0.2\%$ respectively.^{98,99} As the Nb(V) cation is more readily reduced to the +4 oxidation state as compared to Ta(V), the Nb(V)-based oxynitrides also tend to have more synthetic problems with anion deficiencies and oxygen impurities.^{85,86}

Several of the metal oxynitrides crystallize in orthorhombic space groups, i.e., *Pmc2₁* and *P2₁2₁2₁*, and have also shown promising photoelectrochemical properties as n-type semiconductors for water oxidation. The anion sites contain a disordered occupation of oxide and nitride anions in a 2:1 ratio. A representative orthorhombic perovskite, CaTaO₂N, is drawn in **Fig. 20**. The main structural difference compared to the tetragonal perovskites is octahedral tilting that causes deviations from 180° M–O/N–M bond angles. The relatively smaller ionic radius for Ca results in octahedral tilting with alternating bond angles of $\sim 141^\circ$ and $\sim 149^\circ$ for Ta–O/N–Ta and alternating Ta–O/N bond distances of 1.939–2.212 Å. These distances are $\sim 10\%$ longer as compared to those in the tetragonal perovskites. For LaTiO₂N, with a slightly different orthorhombic structure, the B-cation is Ti(IV) and the A-cation is La(III). This distorted perovskite also displays octahedral tilting with alternating Ti–O/N–Ti angles of $\sim 153^\circ$ and $\sim 159^\circ$ and Ti–O/N bonds that alternate between ~ 1.94 and ~ 2.11 Å. The band gaps of CaTaO₂N and LaTiO₂N are a respective ~ 2.43 and ~ 2.10 eV. Again, problems in preparing these metal oxynitrides in defect-free, highly crystalline forms has limited their photocurrents and photocatalytic rates for water oxidation. For example, LaTiO₂N with a surface CoO_x cocatalyst was found to be photocatalytically-active for water oxidation as an aqueous suspension of particles with a quantum efficiency of $\sim 27\%$ at a wavelength of 420 nm.⁹⁵ However, LaTiO₂N photoelectrode films have typically only shown very small photocurrents of ~ 1 – 3 μA cm⁻².⁹⁶ as a result of high recombination rates. Similarly, CaTaO₂N has shown a low photocatalytic activity for water splitting, with a reported 0.003% efficiency at 440 nm and photoanodic current density of only ~ 50 μA cm⁻².^{89,90}

4.17.3.2.2 Wurtzite-type oxynitride structures

Several metal oxynitrides have also been investigated that crystallize in the hexagonal wurtzite-type structure that show high photocatalytic activities for water oxidation. A few examples are listed for these types of semiconductors at the top of **Table 3**. For example, while GaN has been widely investigated for its properties in blue light-emitting diodes, it has also shown promising photocatalytic properties as a component in solid-solution metal oxynitrides. Shown in **Fig. 21A**, its structure is comprised of tetrahedrally-coordinated GaN₄ units, with a Ga–N distance of ~ 1.97 Å. These units condense via shared vertices to form a 3D network. Its band gap is relatively large at ~ 3.4 eV. It is a rare example of a metal nitride that is stable as a photoanode and has been shown to be active for water oxidation with an incident-photon-to-current efficiency of ~ 3 – 6% at ~ 355 nm.⁶⁷ Recent investigations have focused on mixing GaN with other wurtzite-type structures, such as InN and ZnO, to attain significantly lower band gaps that are more suitable for visible-light absorption of solar energy.

In In_xGa_{1-x}N solid solutions, the In(III) cations are randomly distributed over the tetrahedrally-coordinated Ga(III) cation sites. The Ga/In–N bonds have lengthened to ~ 2.18 Å, significantly longer than in GaN of 1.97 Å. As a result of the decreased overlap of the valence orbitals between Ga/In and N, i.e., ns^0np^0 and ns^2np^6 -orbitals, its band gap is redshifted substantially to ~ 1.7 eV for $\sim 50\%$ In(III) cations. The high-temperature preparation of In_xGa_{1-x}N typically suffers from deleterious defects and dislocations that can act as recombination centers. However, molecular beam epitaxy or metal-organic chemical vapor deposition are frequently

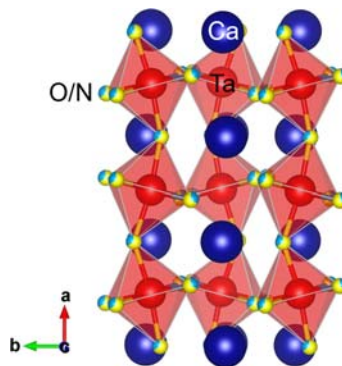


Fig. 20 Polyhedral drawing of the orthorhombically distorted perovskite CaTaO₂N. Atom types are labeled.

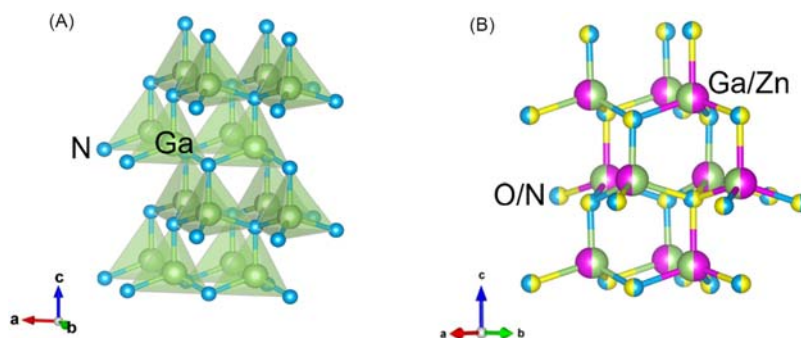


Fig. 21 Polyhedral drawing of the crystal structures of (A) wurtzite GaN and (B) GaN:ZnO solid solution. Atom types are labeled.

reported as techniques to prepare this metal oxynitride as high purity, defect free nanowires. The nanowire arrays exhibit a good photostability and have been extensively investigated as photoanodes.⁷⁰ These reach IPCE values of $\sim 10\text{--}30\%$ and reported quantum efficiencies for overall water splitting approaching $\sim 15\%$.⁷⁰ Remaining challenges include the growth of nanowire arrays with stable N-terminated facets and preparing compositions with up to 50% In(III) cations in order to reach the theoretically ideal band gap for a solar-to-hydrogen efficiency of $\sim 27\%$.

In the oxynitride GaN:ZnO solid solution both Zn(II) and Ga(III) cations are statistically disordered over the tetrahedral sites of the wurtzite-type structure, shown in Fig. 21B. These are charge balanced by a 1:1 statistical mixture of oxygen and nitrogen over the anion sites. In ZnO, the Zn–O distance is approximately 2.01 Å, which is slightly larger than the Ga–N bond distance. So, despite the differences in the four-coordinate ionic radii of Zn(II) and Ga(III) cations of 0.60 and 0.47 Å, respectively, the average metal-to-anion distance is within $\sim 2\%$ in the solid solution. Remarkably, the high degree of disorder apparently does not lead to a significant trapping of the charge carriers and high recombination rates. The GaN:ZnO solid solution exhibits a band gap of $\sim 2.5\text{--}2.8$ eV and represents the first reported example of total water splitting under visible-light irradiation. Its performance as a photocatalyst is highly dependent upon the preparation conditions and the attachment of surface cocatalysts because of the presence of bulk defects and surface corrosion problems. With the deposition of an RuO₂ surface co-catalyst, for example, it has been reported to show an apparent quantum efficiency of $\sim 0.14\%$ in a wavelength range of 300–480 nm for overall water splitting.⁷² As a photoanode film prepared using moisture-assisted annealing, and coated with a cobalt phosphate co-catalyst, a photocurrent of ~ 2 mA cm⁻² has been measured for water oxidation to O₂. This corresponds to an incident photon to current efficiency of $\sim 30.7\%$ under irradiation by photons within a wavelength range of $\sim 350\text{--}450$ nm.⁷²

4.17.3.2.3 Tantalum nitride and tantalum oxynitride

Other promising nitride semiconductors include TaON and Ta₃N₅, owing to their small band gaps and favorable band edge energies. The TaON semiconductor has the monoclinic crystal structure shown in Fig. 22A with a 3D edge-sharing polyhedral connectivity. The Ta(V) cation is coordinated to three oxygen and four nitrogen anions, with Ta–O distances ranging from ~ 2.02 to ~ 2.18 Å and Ta–N distances varying from ~ 2.07 to ~ 2.18 Å. The Ta–O–Ta and Ta–N–Ta bond angles are approximately 103–105°, i.e., far from the linear 180° needed for maximal band dispersion. The oxide and nitride anions segregate into alternating layers in the *a*-axis direction. This oxynitride semiconductor exhibits a band gap of ~ 2.5 eV. As a photoanode film it shows high photocurrents for water oxidation to O₂ of $\sim 1\text{--}4$ mA cm⁻², with an incident photon-to-current efficiency ranging from 20% to 80% that increases with the applied potential and shorter wavelengths.⁷⁵ Its main limitations include its tendency to photocorrode as well as its non-optimal band gap.

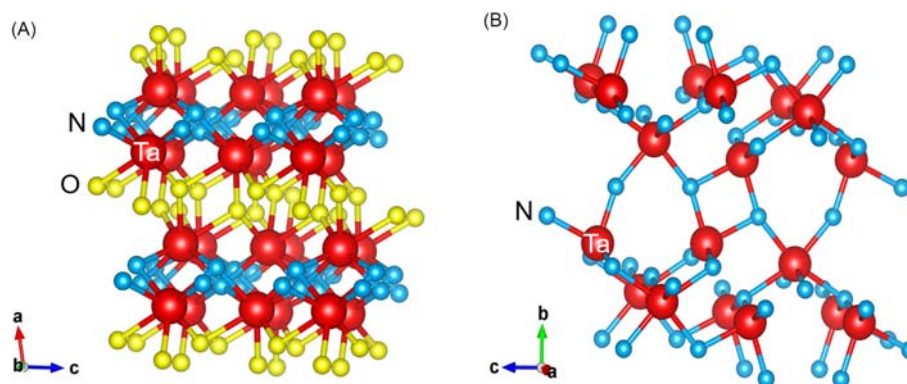


Fig. 22 Crystal structures and metal-anion bonding of (A) TaON and (B) Ta₃N₅. Atom types are labeled.

The fully-nitrided Ta₃N₅ semiconductor forms in an orthorhombic crystal system, as shown in Fig. 22B. The Ta(V) cations are bonded to six nitride anions to form highly-distorted TaN₆ octahedra that are, in turn, edge- and vertex-shared into a 3D framework. The Ta–N distances are all within a value of ~2.0 Å, with Ta–N–Ta bond angles ranging from 95° to 157°. As compared to TaON, powders and films of Ta₃N₅ show a relatively smaller band gap of ~2.1 eV. The bare, i.e., non-functionalized, films of n-type Ta₃N₅ exhibit photoanodic currents of > 1 mA cm⁻² that decay within minutes. However, films with an added blocking layer and molecular catalysts attached to its surfaces have reached close to the maximal theoretical limit for its photoanodic current of 12.1 mA cm⁻², with an incident photon-to-current efficiency approaching ~90–100% under 400–550 nm light irradiation.⁷⁹

4.17.3.2.4 Layered carbon nitrides

Semiconductors that have been intensely investigated in this field have been predominantly inorganic. However, an emerging class of semiconductors receiving growing attention is based on metal-free carbon nitrides. Carbon-nitride semiconductors are currently entirely based upon two-dimensional layer structures of alternating carbon and nitrogen, shown in Fig. 23. The two main types, i.e., imide linked and graphitic based, derive from the linkage of monomeric triazine or heptazine monomers which condense into extended layers. These layers in turn stack via Van der Waals interactions. The idealized layer structures of the graphitic carbon nitrides, g-C₃N₄, arising from the different monomers are illustrated in the righthand column of Fig. 23. Both have condensed layers containing small pores. These compounds are typically synthesized by heating to 400 °C to 550 °C in air or vacuum, or alternatively using salt-based flux or ionothermal reaction conditions.^{102–105}

Product purity and crystallinity of carbon nitrides are highly sensitive to the synthetic conditions, with most reported reaction conditions leading to impurities, variabilities in product distributions, and/or high amounts of amorphous content. The absence of high crystallinity has hindered their in-depth structural characterization. Crystalline carbon nitrides that have been discovered include poly(triazine imide) (PTI) and poly(heptazine imide) with imide-linked triazine and heptazine monomers. The PTI structure is obtained by crystallization in a sealed reaction vessel using a salt mixture such as KCl/LiCl. Its structure is the less dense analog of the graphitic carbon nitrides, as illustrated in the middle column of Fig. 23. The band gaps of the carbon nitride semiconductors most commonly fall between ~2.6–3.2 eV, within the upper energy ranges of visible-light wavelengths. Thus, much synthetic research has focused on dopants and other visible-light sensitizers to lower their band gaps. As aqueous suspensions, the carbon nitrides show a high photocatalytic activity for the reduction of water to H₂, with the highest reported quantum yields

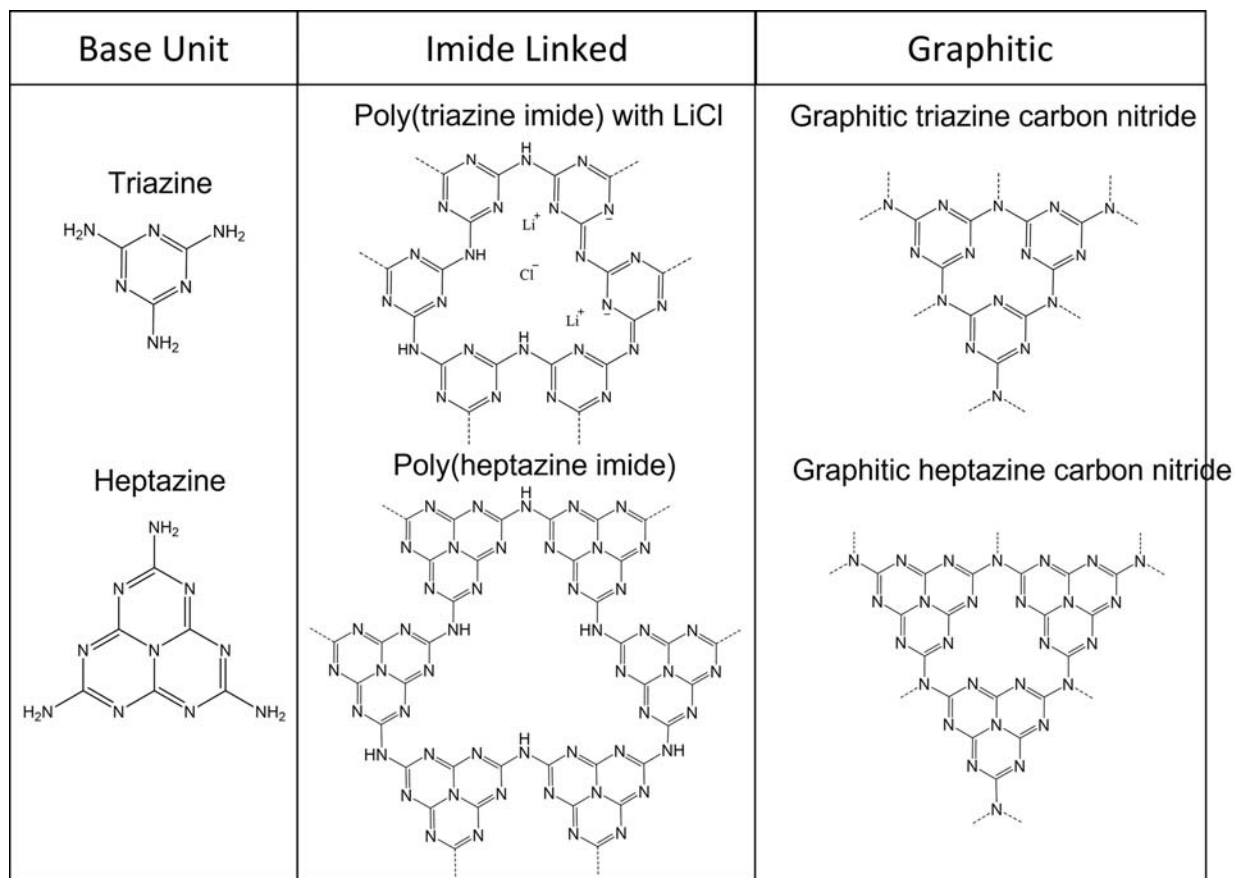


Fig. 23 Carbon nitride subunits triazine and heptazine (left) and their polymerized forms consisting of imide (middle) or graphitic (right) bridges.

approaching $\sim 60\%$ at 420 nm.¹⁰⁶ Conversely, these and other related carbon nitrides have not been found to be active for water oxidation to O₂ or for overall water splitting.

4.17.3.3 Band gaps and band edge positions

As described for the metal oxides, the band gaps and band edge positions of the semiconducting nitrides are critical for the broad absorption of solar energy and for the capability to drive redox reactions for water splitting at their surfaces. Generally, the incorporation of the nitride anion causes a significant change in the valence band energy, i.e., to more negative redox potentials, as compared to metal oxides. This feature of metal nitrides has resulted in a greater ability to achieve a suitable valence band energy to drive water oxidation to O₂ at significantly lower overpotentials.

4.17.3.3.1 Tuning the band gaps of nitride semiconductors

The majority of the metal nitride semiconductors described above share a few key features in their electronic structures, listed in Table 5. Similar to the metal oxides, the edges of their conduction band states are comprised predominantly of the nonbonding, empty transition-metal *d* orbitals. Higher energy states in the conduction band are formed by antibonding interactions to the nitrogen 2*p* orbitals, i.e., *nd-2p* orbital interactions. The valence bands are typically composed of N 2*p* orbitals that interact in a bonding fashion with the transition metal *d*-orbitals, with the O 2*p* orbitals located at lower energies for the metal oxynitrides. Shown in Fig. 24,⁴² for example, are the calculated densities-of-states (DOS) for Ta₃N₅ and BaTaO₂N. As shown for Ta₃N₅, the valence band maximum is comprised of N 2*p* orbitals while the conduction band minimum is composed of Ta 5*d* orbitals. A similar energetic positioning of the orbital contributions occurs in the case of the oxynitride BaTaO₂N, with the additional contributions from the O 2*p* orbitals at lower energies. Thus, the relatively higher energy N 2*p* orbitals are the primary reason for the smaller band gaps of metal nitrides and oxynitrides as compared to metal oxides. As listed in Table 3, the band gaps of the majority of the nitride and oxynitride semiconductors occur below about 2.3–2.4 eV, with several of them occurring below 2.0 eV, e.g., BaNbO₂N and SrNbO₂N. In general, their small band gaps have made them among the most intensely studied visible-light photocatalysts.

One promising approach for tuning the band gaps of nitride and oxynitride semiconductors has been via the formation of solid solutions, such as In_{*x*}Ga_{1-*x*}N and GaN:ZnO described above and shown in Fig. 21. These involve the formation of solid solutions containing GaN which is well-known to have a wide band gap of ~ 3.4 eV that is not capable of absorption of the visible-light photons of solar irradiation. The valence band of GaN is comprised primarily of N 2*p* orbitals while the conduction band is comprised primarily of Ga 4*s* and 4*p* orbitals. In contrast to octahedra-based frameworks, e.g., as in the perovskite structure type, tetrahedral coordination within its structure results in the edge states of the valence and conduction bands having bonding and antibonding character, respectively. The strong bonding and antibonding interactions between the Ga 4*s* and N 2*p* leads to its widely-split valence and conduction bands. The partial replacement of up to 50% of the Ga(III) for In(III) cations in In_{1-*x*}Ga_{*x*}N gives a significant reduction in the band gap to ~ 1.7 eV, Fig. 25. For this composition, i.e., In_{0.5}Ga_{0.5}N, the band gap has been reduced so that the individual band edges still straddle the H⁺/H₂ and O₂/H₂O redox potentials.⁷⁰ The full substitution by In(III) cations results in the InN semiconductor that also possesses a wurtzite-type structure with a much smaller band gap of ~ 0.6 eV. The significant reduction in band gap with increasing In(III) cations is attributable to the greater electronegativity difference between In 5*s* and N 2*p* as well as the reduced spatial orbital overlap.¹¹⁵ This leads to valence and conduction bands that are more closely-split energetically as compared to GaN by itself, Fig. 25.

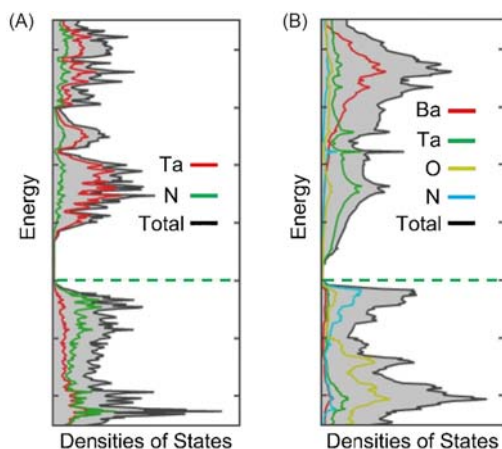


Fig. 24 DOS of (A) Ta₃N₅ and (B) BaTaO₂N. The higher energy N 2*p* orbitals comprise the top of the valence band in metal nitrides and oxynitrides and lead to a higher energy valence band compared to metal oxides. Adapted from Jain, A.; Ong, S. P.; Hautier, G.; Chen, W.; Richards, W. D.; Dacek, S.; Cholia, S.; Gunter, D.; Skinner, D.; Ceder, G.; et al. Commentary: The Materials Project: A Materials Genome Approach to Accelerating Materials Innovation. *APL Mater.* **2013**, *1*(1).

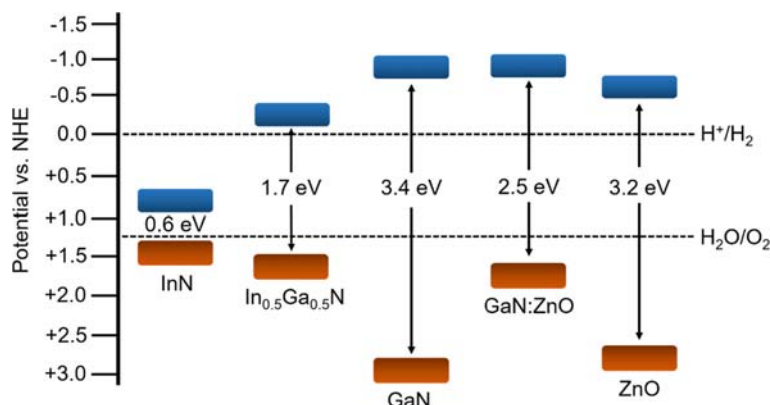


Fig. 25 Band energies for gallium-based solid solutions. GaN is shown to have a wide bandgap unsuitable for visible light absorption. Significantly reduced band gaps are shown for solid solutions with InN and ZnO.

Another effective strategy to reduce the band gap of GaN is found by forming a solid solution with ZnO. As with GaN, the ZnO semiconductor has a wurtzite-type structure and a relatively wide band gap of ~ 3.2 eV. Both pairs of cations (Ga/Zn) and anions (N/O) disorder over the same crystallographic sites of a resulting wurtzite-type structure. At a Zn(II):Ga(III) ratio of ~ 0.42 , the band gap is narrowed to ~ 2.5 eV, shown in Fig. 25. The band gap is shown to continuously decrease at up to this ZnO concentration in the solid solution. This is the result of the valence band edge being shifted to more negative potentials by ~ 1 eV, i.e., to higher energies, while the conduction band edge remains relatively constant. It is yet unclear why this shift in the valence band occurs, but it has been posited to result from the mixing of the Zn-3d/N-2p atomic orbitals. Nonetheless, the GaN:ZnO solid solution has been demonstrated to split water with an $\sim 0.29\%$ efficiency under 420 nm irradiation.⁷²

Current approaches to tuning the band gaps of carbon nitrides, listed in Table 4, have been met with relatively less success as compared to the metal-containing nitrides. The band gaps of crystalline carbon nitrides have shown a limited range from ~ 2.7 to > 3.2 eV. In general, decreasing the band gaps of these more covalent structures has proven challenging while also maintaining their crystallinity and well-defined structural features. Their valence band maximum is formed almost exclusively from N 2p orbitals, while the states at the conduction band minimum arise from C 2p-N 2p π^* interactions. Various stacking motifs, held together by Van der Waals interactions, have a relatively minor impact on their band gaps. The heptazine-based structures, e.g., poly(heptazine imide) and heptazine-g-C₃N₄ (H-g-C₃N₄), exhibit moderately smaller band gaps of ~ 2.7 – 2.9 eV. The calculated DOS for H-g-C₃N₄ is plotted in Fig. 26A,^{123,124} with a band gap of ~ 2.77 eV that is close to the experimentally measured value of ~ 2.7 eV.¹²¹ This compares to the larger band gap of ~ 3.1 eV for PTI, shown in Fig. 26B and C. For both, the conduction and valence band edges are located at potentials to drive the reduction and oxidation of water, although photocatalytic activity for only the former has been observed. Most current investigations have focused on the incorporation of additional elements which might lower their band gaps, such as through the coordination of metal cations or the exchange of anions. For example, poly(triazine imide)LiCl has a valence band edge comprised of Cl 2p orbitals, Fig. 26B. It is currently unclear whether these states play an active role in the electronic excitation responsible for its photocatalytic properties.¹²⁴

4.17.3.3.2 Tuning the conduction band energy of metal nitrides

Most investigations of metal nitrides have focused on the preparation of defect-free photoanode films and surface strategies to protect against corrosion. However, similar strategies to alter the conduction band energies have been adopted as described for

Table 4 Selection of carbon nitride semiconductors used as suspension-based photocatalysts for solar-energy driven water splitting.

Composition/Name	Structure type/Symmetry	Band gap	Film/Powder	Quantum efficiency (%)
Potassium poly(heptazine imide)	Triclinic $P1$ ¹⁰²	2.7 ¹⁰²	Powder ¹⁰²	0.000039 ¹¹⁶
Poly(heptazine imide)	Triclinic $P1$ ¹⁰²	2.7 ¹¹⁷	Powder ¹¹⁷	3.1 at 400 nm ¹¹⁷
Poly(triazine imide) LiCl	Orthorhombic $P2_12_12_1$ ¹⁰³	2.9 ¹⁰⁴ , 3.1 ¹⁰⁵	Powder ¹¹⁸	0.6 at 420 nm ¹¹⁸
Poly(triazine imide) HCl	–	3.2 ¹¹⁹	–	–
Poly(heptazine triazine) Na/K	–	2.58 ¹⁰⁶	Powder ¹⁰⁶	60 at 420 nm ¹⁰⁶
Triazine-g-C ₃ N ₄	–	3.19 ¹²⁰	Powder ¹²⁰	2.88 ¹²⁰
Heptazine-g-C ₃ N ₄	–	2.87 ^{120,121}	Powder ^{120,121}	–
COF-300	Tetragonal $I 41/a$ ¹²²	–	–	–
COF-303	–	–	–	–
LZU-79	Tetragonal $P 4_2/n$ ¹²²	–	–	–
LZU-111	Hexagonal $P 6_5$ ¹²²	–	–	–

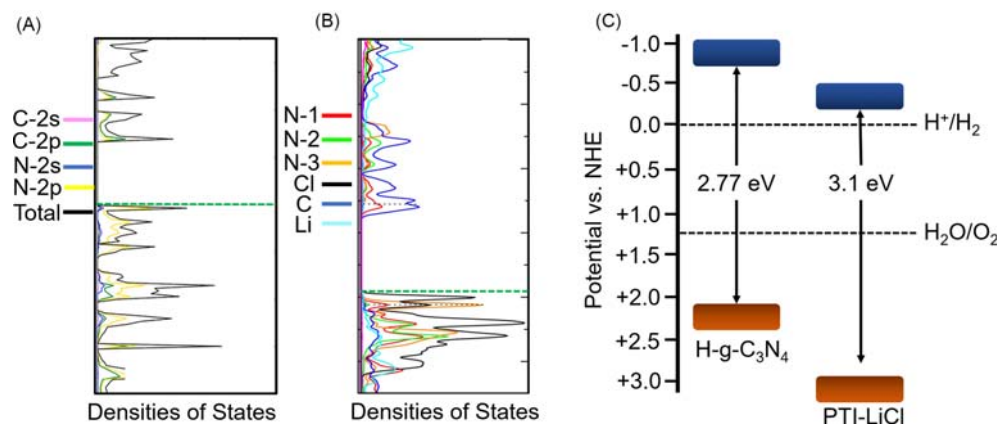


Fig. 26 Densities-of-states for H-g-C₃N₄ (A) and PTI-LiCl (B). The relative conduction and valence band energies are plotted in (C). The valence band of carbon nitrides are typically formed from N 2p states while the conduction band is derived from C-N antibonding interactions. Adapted with permission from (A) Makaremi, M.; Grixti, S.; Butler, K. T.; Ozin, G. A.; Singh, C. V. Band Engineering of Carbon Nitride Monolayers by N-Type, P-Type, and Isoelectronic Doping for Photocatalytic Applications. *ACS Appl. Mater. Interfaces* **2018**, *10*(13), 11143–11151 and (B) McDermott, E. J.; Wirthier, E.; Schnick, W.; Viridi, K. S.; Scheu, C.; Kauffmann, Y.; Kaplan, W. D.; Kurmaev, E. Z.; Moewes, A. Band Gap Tuning in Poly(Triazine Imide), a Nonmetallic Photocatalyst. *J. Phys. Chem. C* **2013**, *117*(17), 8806–8812.

the metal oxides in Section 4.17.2.3.2, though less extensively. For example, the conduction band energy of a series of related perovskite oxynitrides can be altered by selection of the early transition-metal cation, such as the Nb(V), Ta(V) or Ti(IV) cation. In the case of BaMO₂N, where M = Nb(V) or Ta(V) cation, the conduction band edge can be shifted to either more negative or positive potentials as a function of the corresponding *d*-orbital energies. The isovalent substitution of Ta(V) for Nb(V) yields a lower energy conduction band edge as a result of the lower-energy Nb 4*d* orbitals as compared to the Ta 5*d* orbitals. This trend is reflected in their conduction band energies plotted in Fig. 27. The lower-energy edge of the conduction band results in a decreased band gap for BaNbO₂N of ~1.44 eV as compared to ~2.17 eV for BaTaO₂N. An analogous trend is also found in a comparison of the conduction band energies and band gaps for SrTaO₂N and SrNbO₂N, Fig. 27. Further, in the case of both BaNbO₂N and SrNbO₂N, the conduction band edges are lowered to sufficiently positive potentials so as to not be thermodynamically capable of driving the reduction of protons to H₂. Thus, these have only been found to be active as photoanodes for water oxidation. The higher-energy conduction band edges for BaTaO₂N and SrTaO₂N are sufficiently negative to drive proton reduction, and together with their valence band edges for water oxidation, are capable of driving overall water splitting. Beyond these examples, relatively few metal-oxynitride semiconductors have been investigated as compared to the metal oxides owing to their difficulty in synthetic preparation.

4.17.3.3.3 Tuning the valence band energy of metal nitrides

Previously described in Section 4.17.2.3.3, modifying the valence band edge of metal oxides requires the introduction of a secondary metal cation, such as by adding Ag(I), Cu(I) or Sn(II) cations possessing a filled *nd*¹⁰*s*^{*n*} valence electron configuration. However, as the band gaps of most nitrides already fall within the visible-light energies owing to the N 2p orbitals, modification of their valence band energies has been much less investigated. One approach in nitrides and oxynitrides has been to alter the valence band edge by adjusting the nitrogen to oxygen ratio of their chemical compositions. A notable example can be found in

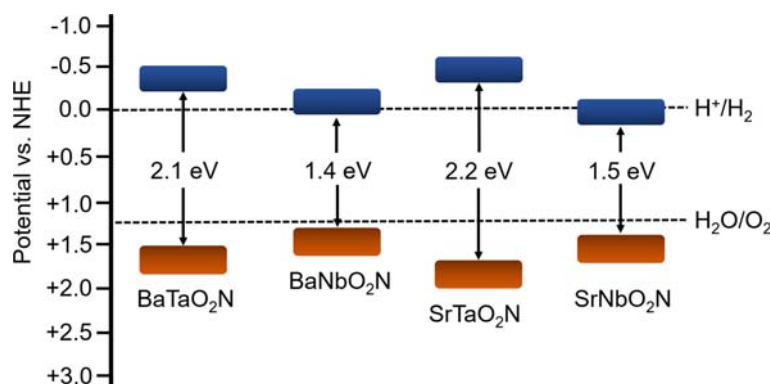


Fig. 27 Band energies for ABO₂N (A = Ba, Sr and B = Ta, Nb) oxynitride perovskites, showing the conduction band energy of the perovskite oxynitrides can be achieved via selection of the B-site transition metal cation.

a comparison of the semiconductors Ta_2O_5 , TaON , and Ta_3N_5 . The TaON semiconductor is typically synthesized by nitriding Ta_2O_5 , and because the N $2p$ orbitals are higher in energy than the O $2p$ orbitals, a smaller band gap occurs for TaON of ~ 2.5 eV than for Ta_2O_5 of ~ 3.9 eV. The band gap can be further redshifted by increasing the N/O ratio, with the fully nitrated Ta_3N_5 exhibiting the smallest band gap of ~ 2.1 eV. The band edge positions for all three compounds are plotted in Fig. 28. The trend of decreasing band gap with increasing nitrogen concentration arises because of the formation of a new, higher energy, N $2p$ -based valence band. As many metal nitrides and oxynitrides are synthesized from the ammonolysis of metal oxides, careful adjustment of the reaction conditions can allow for more or less nitrogen to be incorporated, providing a route to adjust the valence band edge and band gap.

The N/O ratio in the perovskite structure can also be altered by changing the oxidation states of the A-site or B-site cations. For example, in CaTaO_2N vs. LaTaON_2 the N/O ratio increases to compensate for the change in oxidation state of the A-site cation from +2 to +3. For LaTaON_2 , the band gap is ~ 2.04 eV and the valence band maximum is located at +0.94 V vs. NHE.¹²⁵ This contrasts with CaTaO_2N with a larger band gap of ~ 2.4 eV and a valence band maximum at +1.6 V. The higher nitrogen content leads to the higher valence band energies and smaller band gap of LaTaON_2 , which is among the smallest of the tantalum oxynitride perovskites. Recent research efforts have focused on the synthesis of solid solutions of LaTaON_2 and MTaO_2N , leading to an intermediate N/O molar ratio that has been used to tune the valence band energy and band gap of MTaO_2N .⁹⁰

The valence band energy of metal nitrides and oxynitrides is also highly sensitive to changes in the M–N–M bond angles. For the oxynitride perovskites with the composition MTaO_2N (M = Ca, Sr, Ba), the largest octahedral-tilting distortion is found for CaTaO_2N which has a Ta–N–Ta bond angle of $\sim 141^\circ$. It also has the largest band gap of ~ 2.4 eV. Conversely, the BaTaO_2N structure has linear 180° Ta–N–Ta bond angles and the smallest band gap of ~ 2.1 eV. The tilting distortion in SrTaO_2N falls intermediate between that of BaTaO_2N and CaTaO_2N and has an intermediate band gap of ~ 2.2 eV. The energies of the band edges for all three semiconductors are plotted for comparison in Fig. 29. The increased band gap is directly attributed to the lower valence band energies and higher conduction band energies that occur with a decreasing Ta–N–Ta bond angle. This dependence is a function of the increased bonding and antibonding character at the respective band edges. For BaTaO_2N , the highest-energy valence band states occur at Γ where the metal-to-anion interactions are nonbonding. However, the structural distortion and changes in bond angle breaks the underlying symmetry and allows orbital mixing at this point in k -space. Thus, the change in the alkaline-earth cation from Ca, to Sr, to Ba, indirectly causes subtle changes in the band edge positions and band gap.

4.17.3.4 Band dispersion and effective masses of charge carriers: Nitride semiconductors

As described above for metal-oxide semiconductors, the mobility of the photon-generated minority carriers is important in order for their efficient diffusion to the surfaces. This is especially critical for metal nitrides, which frequently suffer from the deleterious effects of poor crystallinity and high defect concentrations. Thus, small effective masses that achieve maximal diffusion lengths are crucial and can be assessed based upon the dispersion of the conduction and/or valence band, as given by Eqs. (3)–(5).

4.17.3.4.1 General trends

An analysis of the conduction band states for metal nitrides is analogous to that of metal-oxide semiconductors, and thus is only briefly discussed. Smaller electron effective masses are found for metal nitrides than as for metal oxides. Additionally, the relationships between band dispersion and lowered crystallographic symmetry and/or lowered dimensionality of extended $[-\text{M}-\text{N}-\text{M}-\text{N}]_n$ connectivity applies to the nitrides. One primary difference and advantage of metal nitride semiconductors is the increased valence band dispersion because of their greater covalent character and valence orbital interactions. The dispersion of the valence band for

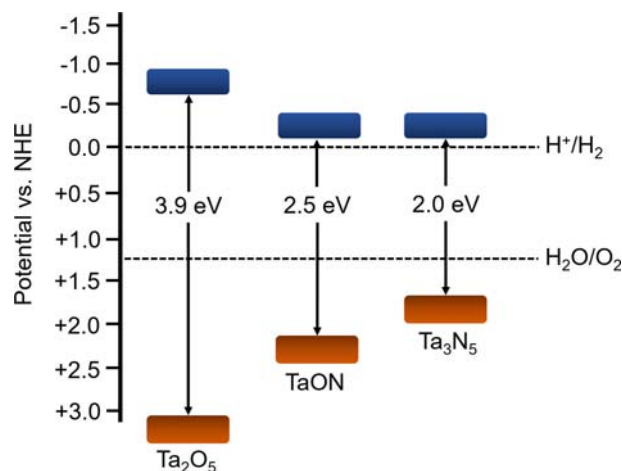


Fig. 28 Conduction and valence band energies for Ta_2O_5 , TaON , and Ta_3N_5 . The valence band energy increases with increasing amounts of N due to the presence of higher energy N $2p$ orbitals compared to O $2p$.

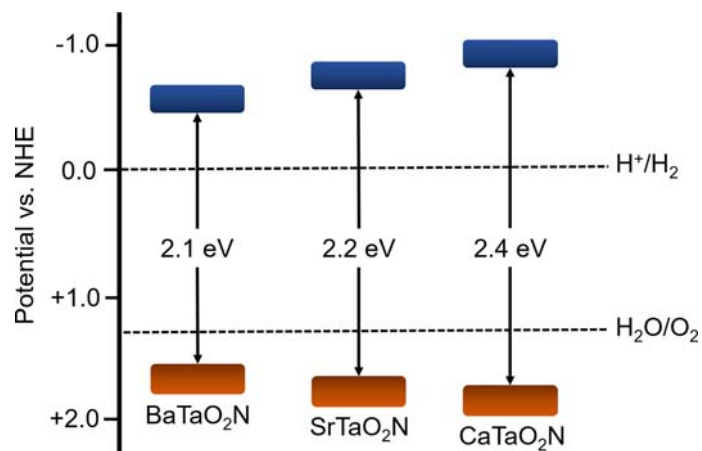


Fig. 29 Band energies of $ATaO_2N$ ($A = Ca, Sr, Ba$) oxynitride perovskites. Increasing structural distortions of the perovskite oxynitrides are seen with $A = Ba > Sr > Ca$. The structural distortions influence the valence and conduction band energies with increasing structural distortion leading to higher energy valence and conduction bands.

most metal oxides is relatively limited because of the weaker interactions between the oxygen $2p$ orbitals and the transition metal d orbitals. By contrast, the nitrogen $2p$ orbitals are located higher in energy, leading to a closer energetic match and greater orbital interactions.

4.17.3.4.2 Valence and conduction band dispersion of metal nitrides

Listed in **Table 5** are the carrier effective masses and structural parameters impacting on the band dispersion for selected metal nitrides. The effect of nitrogen on the band dispersion is illustrated by a comparison of Ta_2O_5 , $TaON$, and Ta_3N_5 , as shown in **Fig. 30**,¹⁰⁸ left to right. The three structures consist of 3D connected Ta-O/N polyhedra. For Ta_2O_5 , where the top of the valence band is formed predominantly by the more localized O $2p$ states, the band dispersion is limited and leads to high calculated hole effective masses of $\sim 3.67 m_h$. Relatively large electron effective masses of $\sim 2.31 m_e$ are also found for the conduction band. With the addition of N in $TaON$ the valence and conduction band dispersion increases, **Fig. 30B**, leading to lower carrier effective masses. For $TaON$, the effective hole and electron masses are calculated to be $2.40 m_h$ and $0.96 m_e$, respectively. After full nitridation to give Ta_3N_5 , **Fig. 30C**, the largest band dispersions and lowest carrier effective masses are achieved. The calculated hole and electron effective masses for Ta_3N_5 are $0.52 m_h$ and $0.64 m_e$. This trend reveals that the more covalent Ta–N orbital

Table 5 Characteristic features of the crystal and electronic structures of metal nitrides used as semiconductors for solar-energy driven water splitting.

Composition	Valence BAND States	Conduction band states ^a	Bond angles M-O/N-M	Mobility	Carrier effective masses (m_e, m_h)
GaN ¹⁰⁷	N 2p	Ga 3d	109°	150–650 cm^2/Vs	
InGaN	N 2p				
GaN:ZnO ¹⁰⁷	N 2p			1 cm^2/Vs	
TaON ¹⁰⁸	N 2p	Ta 5d			0.86 m_e , 1.22 m_h
Ta ₃ N ₅ ^{108–110}	N 2p	Ta 5d		1.3–1.9 cm^2/Vs	0.64 m_e , 0.52 m_h
BaTaO ₂ N ^{94,111,112}	N 2p	Ta 5d	180°		0.386 m_e 0.325 m_h
CaTaO ₂ N ^{94,113}	N 2p	Ta 5d	141°, 149°		0.47–0.93 m_e , 0.643 m_h 0.63–3.27 m_e , 0.964 m_h
SrTaO ₂ N ⁹⁴	N 2p	Ta 5d	164°		0.523 m_e 0.597 m_h
LaTiO ₂ N ^{94,114}	N 2p	Ti 3d	153°, 159°		0.5 m_e , 0.571 m_e 0.9 m_h , 0.827 m_h
BaNbO ₂ N ⁹⁴	N 2p	Nb 4d	180°		0.549 m_e 0.393 m_h
SrNbO ₂ N ⁹⁴	N 2p	Nb 4d	180°		0.635 m_e 0.375 m_h

^aCrystal structures were obtained from the Materials Project Database⁴² and cross-referenced with literature reports. Crystal structures from the Materials Project Database are the DFT optimized structures. All bond lengths and angles thus represent approximate values.

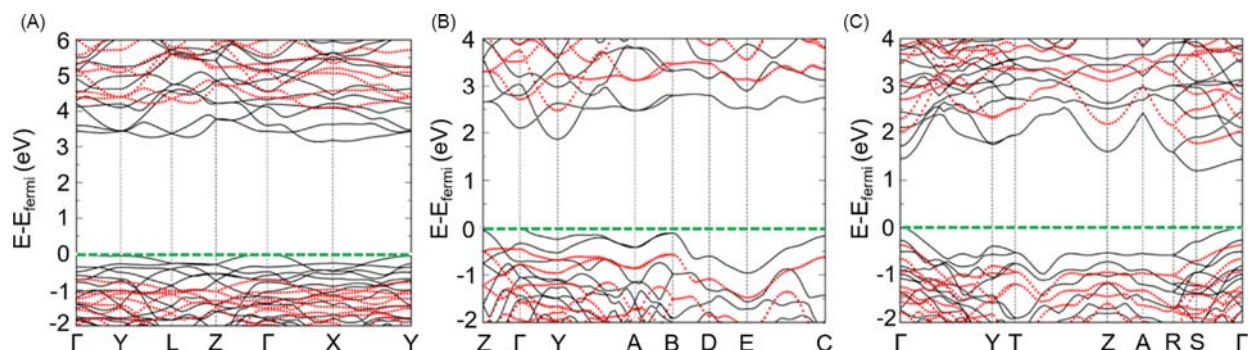


Fig. 30 Band diagrams for (A) Ta_2O_5 (B) TaON (C) Ta_3N_5 . The band dispersions are found to increase with increasing N content because of the stronger M-N interactions compared to M-O interactions. Adapted with permission from Cui, Z. H.; Jiang, H. Theoretical Investigation of Ta_2O_5 , TaON , and Ta_3N_5 : Electronic Band Structures and Absolute Band Edges. *J. Phys. Chem. C* **2017**, *121*(6), 3241–3251.

interactions leads to significantly reduced effective masses. The inherently lower effective masses for many of the metal nitrides and oxynitrides provides an underlying advantage in carrier mobilities as compared to metal oxides.

A high degree of crystallographic anisotropy is also found for many of the metal nitride and oxynitrides structures. For example, the crystal structure of Ta_3N_5 is orthorhombic with three symmetry-inequivalent axes with varying band dispersion and effective masses. The Ta–N bonds have less-extensive connectivity along the *b*-axis direction as compared to the *a*- and *c*-axis directions. The electron effective masses are $0.20 m_e$ and $0.83 m_e$ along the directions within the *ac* plane, but a larger $3.16 m_e$ down the *b*-axis direction. Consequently, a higher mobility of charge carriers is found to occur within the *ac* plane. The most efficient n-type Ta_3N_5 photoanodes have an optimal alignment of this crystallographic plane to enable the charge carriers to reach the surfaces. Experimentally, thin films of single-crystalline Ta_3N_5 nanorods aligned with the directions of the lowest effective masses exhibit a photocurrent onset potential that is negatively shifted by $+0.4 \text{ V}$ vs. RHE, which is about 400 mV lower than in randomly oriented Ta_3N_5 particles.¹²⁶

Metal oxynitrides with the perovskite-type structure are similarly susceptible to crystalline anisotropies owing to their symmetry-lowering distortions. This can be seen in Fig. 31 for the band structures of BaTaO_2N (a), CaTaO_2N (b) and LaTaON_2 (c).^{127,128} Both the valence and conduction bands for BaTaO_2N have a larger dispersion compared to CaTaO_2N . As expected, the calculated electron and hole effective masses for CaTaO_2N ($0.643 m_e$ and $0.964 m_h$) are higher than for BaTaO_2N ($0.386 m_e$ and $0.325 m_h$).¹²⁷ The lower dispersion for CaTaO_2N is directly attributed to the octahedral-tilting distortion described above and the longer Ta–N bond distances and reducing the N-2*p*/Ta-5*d* interactions. As a result, photoanodes of CaTaO_2N exhibit the smallest current densities at $\sim 50 \mu\text{A cm}^{-2}$.⁹⁰ For another example, LaTaON_2 has a similarly distorted perovskite structure and a calculated electron effective mass of $\sim 0.6 m_e$ and hole effective mass of $\sim 1.0 m_h^*/m_0$.¹²⁸ As was the case for perovskite-type oxides, the metal oxynitrides with cubic symmetry have the highest band dispersions.

4.17.3.4.3 Valence and conduction band dispersion of carbon nitrides

There is a relative paucity of studies regarding the band structures and band dispersions of carbon nitrides. The reason stems from the synthetic challenges of preparing highly crystalline structures with systematic changes in structure and chemical composition. One of the few crystalline carbon nitrides that has been the focus of electronic structure calculations is $g\text{-C}_3\text{N}_4$, with the band

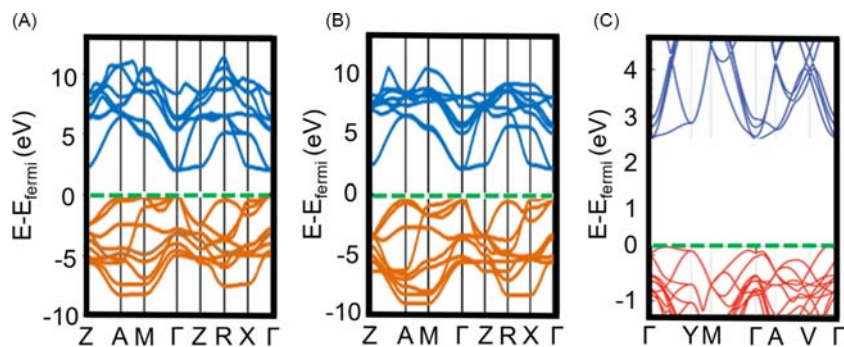


Fig. 31 Band diagrams of (A) BaTaO_2N (B) CaTaO_2N and (C) LaTaON_2 oxide perovskites. Increasing distortion of the perovskite structure leads to less band dispersion and higher effective masses. Adapted with permission from (A and B) Hafez, A. M.; Zedan, A. F.; AlQaradawi, S. Y.; Salem, N. M.; Allam, N. K. Computational Study on Oxynitride Perovskites for CO_2 Photoreduction. *Energy Convers. Manag.* **2016**, *122*, 207–214 and (C) Garcia-Esparza, A. T.; Tyminska, N.; Al Rahal Al Orabi, R.; Le Bahers, T. Full in Silico DFT Characterization of Lanthanum and Yttrium Based Oxynitride Semiconductors for Solar Fuels. *J. Mater. Chem. C* **2019**, (7), 1612–1621.

structure shown in Fig. 32.⁴² The lowest energy transition in $g\text{-C}_3\text{N}_4$ is calculated to be indirect, with the conduction band showing the greatest dispersion along the intralayer directions. While the band diagram and effective masses of other types of crystalline carbon nitrides are currently not well understood, experimental data have helped (indirectly) to elucidate upon some of their important photoelectrochemical properties. For example, when poly(heptazine-imide) (PHI) is irradiated with UV light in the presence of an electron donor, a long-lived photo-reduced state can exist for as long as 200 h in an oxygen free solution.^{102,129} This property has not been observed in other carbon nitrides such as PTI-LiCl. An explanation, based on electronic structure calculations, suggests that the electron density is delocalized over a greater number of carbon and nitrogen atoms of the heptazine-based units as compared to the smaller triazine-based units.¹³⁰ When bridged by imide functional groups, the conjugation can be further extended over multiple heptazine units and lead to even greater resonance stabilization. These long minority-carrier lifetimes have helped to explain the high photocatalytic activities for the production of H_2 .

4.17.3.4.4 Summary of metal nitride semiconductors

Nitride semiconductors have been found to predominantly exhibit smaller band gaps than metal oxides, usually falling well within the visible-light energies of $\sim 1.8\text{--}2.9$ eV. They also exhibit a greater valence band dispersion, and consequently smaller hole effective masses, as compared to most metal oxides. These key advantages occur because of the higher-energy $\text{N } 2p$ orbitals and its more covalent orbital interactions, resulting in a valence band edge that is raised in energy to more negative redox potentials. Control over the energetic positioning of the valence and conduction bands, and thus the band gap, requires different approaches as compared to the metal oxides. In metal oxynitrides a tuning of the valence band edge can be accomplished, for example, by modifying the N/O ratio in metal oxynitrides or by tuning the Ta-O/N-Ta bond angles in perovskite-type oxynitrides. Conversely, the conduction band edge can be modified by selection of the B-site cations, e.g., Ti(IV) , Nb(V) or Ta(V) , as found similarly for the metal oxides. Both the valence and conduction band energies can be simultaneously altered through the formation of solid solutions, and which typically involve more complex changes in electronic structure that are less well understood because of the multiple cations and anions that are disordered over the same crystallographic sites.

Together, the visible-light band gaps and small hole and electron effective masses for metal nitride and oxynitride semiconductors make them ideal candidates for solar-driven photocatalytic reactions. Their band edges are also well positioned, thermodynamically, to drive the water splitting reactions involving the production of H_2 and/or O_2 . However, some of the disadvantages of the nitride semiconductors include the synthetic difficulties of preparing defect-free, high-crystallinity thin films and powders, and their greater tendency to corrode under photoelectrochemical operation in aqueous solutions. Current research aimed at addressing these problems has been to use flux synthesis techniques to increase their crystallinity and to decrease defect concentrations. In addition, the application of surface coatings and cocatalysts have been used to achieve kinetically-stabilized surfaces. The carbon nitride semiconductors also show much promise as a relatively new class of semiconductors that are kinetically stabilized against corrosion. Further investigations are aimed at reducing their band gaps more deeply into the visible-light energies and in preparing these new materials as thin films. Relatively few studies have examined the carrier transport properties of carbon nitrides. Their high photocatalytic rates of H_2 production, together with their functionalizable 2D networks, suggest a promising potential for future scientific applications within this area.

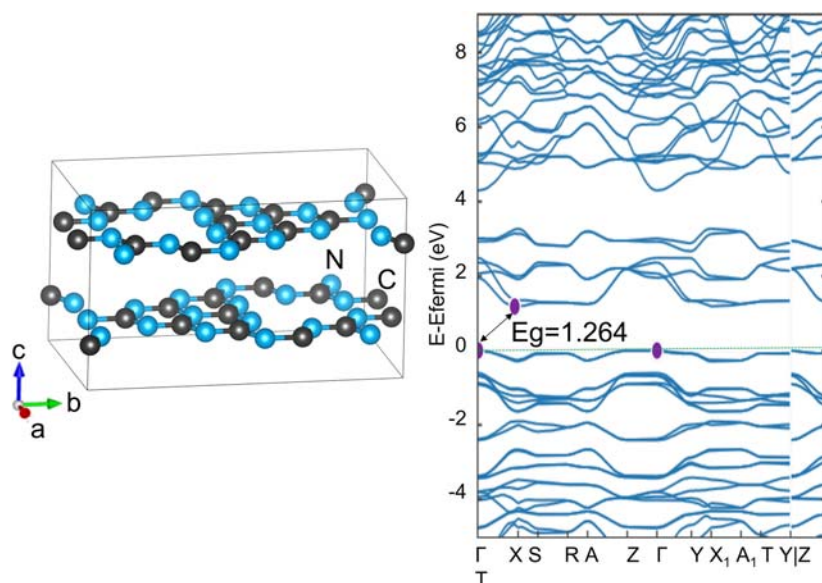


Fig. 32 Crystal structure of $g\text{-C}_3\text{N}_4$ (left) with the unit cell outlined and its calculated band structure (right). The band diagram is adapted from Jain, A.; Ong, S. P.; Hautier, G.; Chen, W.; Richards, W. D.; Dacek, S.; Cholia, S.; Gunter, D.; Skinner, D.; Ceder, G.; et al. Commentary: The Materials Project: A Materials Genome Approach to Accelerating Materials Innovation. *APL Mater.* **2013**, 1(1).

4.17.4 Final summary and outlook

The field of solar photocatalysis has undergone remarkable growth and developments since some of the earliest research in the 1970s. The many research advances are exemplified in the increased understanding of the compositional and structural features which determine many of the key photoelectrochemical properties. Some of the most fundamental aspects have comprised the main topics in this chapter, and which have been covered from the perspective of a solid-state scientist. These include the impact of chemical composition and crystalline structure on the band gap, band dispersion, and energetic positions of the conduction and valence band edges. While these aspects certainly do not cover all of the factors that lead to an efficient n-/p-type photoelectrode or particle photocatalyst, they are among the most primary and fundamental elements that form a beginning foundation. With a deeper understanding of these underlying structure-property relationships, further research may be aimed at understanding the many other factors that can dictate the resulting photoelectrochemical properties of a semiconductor. While these additional factors, such as defects, surface catalysts, and corrosion issues, are beyond the scope covered herein, they also constitute serious challenges that involve an investment of many years of research for each semiconductor under consideration. Accordingly, the identification of the most promising semiconductors is a critical first step that involves a careful understanding of the basic principles covered within this chapter.

Acknowledgments

The content of this work covering metal oxide semiconductors by S.O. is based upon support by the National Science Foundation under award number DMR-2004455, while the sections covering metal nitride and carbon nitride semiconductors by J.C. and M.P. are based upon support as part of the Center for Hybrid Approaches in Solar Energy to Liquid Fuels (CHASE), an Energy Innovation Hub funded by the U.S. Department of Energy, Office of Science, Office of Basic Energy Sciences under award number DE-SC0021173.

References

- Sivula, K.; Van De Krol, R. Semiconducting Materials for Photoelectrochemical Energy Conversion. *Nat. Rev. Mater.* **2016**, *1* (2).
- Li, J.; Wu, N. Semiconductor-Based Photocatalysts and Photoelectrochemical Cells for Solar Fuel Generation: A Review. *Cat. Sci. Technol.* **2015**, *5* (3), 1360–1384.
- Wang, Q.; Domen, K. Particulate Photocatalysts for Light-Driven Water Splitting: Mechanisms, Challenges, and Design Strategies. *Chem. Rev.* **2020**, *120* (2), 919–985.
- Rajeshwar, K.; Maggard, P. A.; O'Donnell, S. In Search of the "Perfect" Inorganic Semiconductor/Liquid Interface for Solar Water Splitting. *Electrochem. Soc. Interface* **2021**, *30*, 47–51.
- Rajeshwar, K. Hydrogen Generation at Irradiated Oxide Semiconductor–Solution Interfaces. *J. Appl. Electrochem.* **2007**, *37* (7), 765–787.
- Fujishima, A.; Honda, K. Electrochemical Photolysis of Water at a Semiconductor Electrode. *Nature* **1972**, *238* (5358), 37–38.
- Nozik, A. J. Photoelectrolysis Cells. *Appl. Phys. Lett.* **1976**, *29*, 150–153.
- Nozik, A. J. Photochemical Diodes. *Appl. Phys. Lett.* **1977**, *30* (11), 567–569.
- Nozik, A. J. Physical Chemistry of Semiconductor–Liquid Interfaces. *J. Phys. Chem.* **1996**, *100*, 13061–13078.
- Gerischer, H. Electrochemical Photo and Solar Cells Principles and Some Experiments. *J. Electroanal. Chem.* **1975**, *58* (1), 263–274.
- Takata, T.; Jiang, J.; Sakata, Y.; Nakabayashi, M.; Shibata, N.; Nandal, V.; Seki, K.; Hisatomi, T.; Domen, K. Photocatalytic Water Splitting With a Quantum Efficiency of Almost Unity. *Nature* **2020**, *581* (7809), 411–414.
- Kato, H.; Kudo, A. Water Splitting into H₂ and O₂ on Alkali Tantalate Photocatalysts ATaO₃ (A = Li, Na, and K). *J. Phys. Chem. B* **2001**, *105*, 4285–4292.
- Hamilton, A. M.; O'Donnell, S.; Zoellner, B.; Sullivan, I.; Maggard, P. A. Flux-Mediated Synthesis and Photocatalytic Activity of NaNbO₃ Particles. *J. Am. Ceram. Soc.* **2020**, *103* (1), 454–464.
- Zhang, W. F.; Tang, J.; Ye, J. Photoluminescence and Photocatalytic Properties of SrSnO₃ Perovskite. *Chem. Phys. Lett.* **2006**, *418* (1–3), 174–178.
- Kato, H.; Kobayashi, H.; Kudo, A. Role of Ag⁺ in the Band Structures and Photocatalytic Properties of AgMO₃ (M: Ta and Nb) With the Perovskite Structure. *J. Phys. Chem. B* **2002**, *106* (48), 12441–12447.
- Parida, K. M.; Reddy, K. H.; Martha, S.; Das, D. P.; Biswal, N. Fabrication of Nanocrystalline LaFeO₃: An Efficient Sol-Gel Auto-Combustion Assisted Visible Light Responsive Photocatalyst for Water Decomposition. *Int. J. Hydrogen Energy* **2010**, *35* (22), 12161–12168.
- Miseki, Y.; Kato, H.; Kudo, A. Water Splitting into H₂ and O₂ Over Ba₅Nb₄O₁₅ Photocatalysts With Layered Perovskite Structure Prepared by Polymerizable Complex Method. *Chem. Lett.* **2006**, *35* (9), 1052–1053.
- Kurashige, W.; Mori, Y.; Ozaki, S.; Kawachi, M.; Hossain, S.; Kawawaki, T.; Shearer, C. J.; Iwase, A.; Metha, G. F.; Yamazoe, S.; et al. Activation of Water-Splitting Photocatalysts by Loading With Ultrafine Rh–Cr Mixed-Oxide Cocatalyst Nanoparticles. *Angew. Chem. Int. Ed.* **2020**, *59* (18), 7076–7082.
- Kim, H. G.; Hwang, D. W.; Bae, S. W.; Jung, J. H.; Lee, J. S. Photocatalytic Water Splitting Over La₂Ti₂O₇ Synthesized by the Polymerizable Complex Method. *Catal. Lett.* **2003**, *91* (3–4), 193–198.
- Chen, D.; Ye, J. Selective-Synthesis of High-Performance Single-Crystalline Sr₂Nb₂O₇ Nanoribbon and SrNb₂O₆ Nanorod Photocatalysts. *Chem. Mater.* **2009**, *21*, 2327–2333.
- Dong, G.; Hu, H.; Wang, L.; Zhang, Y.; Bi, Y. Remarkable Enhancement on Photoelectrochemical Water Splitting Derived From Well-Crystallized Bi₂WO₆ and Co(OH)_x With Tunable Oxidation State. *J. Catal.* **2018**, *366*, 258–265.
- Kuang, Y.; Jia, Q.; Nishiyama, H.; Yamada, T.; Kudo, A.; Domen, K. A Front-Illuminated Nanostructured Transparent BiVO₄ Photoanode for > 2% Efficient Water Splitting. *Adv. Energy Mater.* **2016**, *6* (2), 2–8.
- O'Donnell, S.; Hamilton, A.; Maggard, P. A. Fast Flux Reaction Approach for the Preparation of Sn₂TiO₄: Tuning Particle Sizes and Photocatalytic Properties. *J. Electrochem. Soc.* **2019**, *166* (5), H3084–H3090.
- Niishiro, R.; Takano, Y.; Jia, Q.; Yamaguchi, M.; Iwase, A.; Kuang, Y.; Minegishi, T.; Yamada, T.; Domen, K.; Kudo, A. A CoO_x-Modified SnNb₂O₆ Photoelectrode for Highly Efficient Oxygen Evolution From Water. *Chem. Commun.* **2017**, *53* (3), 629–632.
- Zhou, C.; Zhao, Y.; Shang, L.; Shi, R.; Wu, L. Z.; Tung, C. H.; Zhang, T. Facile Synthesis of Ultrathin SnNb₂O₆ Nanosheets Towards Improved Visible-Light Photocatalytic H₂-Production Activity. *Chem. Commun.* **2016**, *52* (53), 8239–8242.
- Yourey, J. E.; Pyper, K. J.; Kurtz, J. B.; Bartlett, B. M. Chemical Stability of CuWO₄ for Photoelectrochemical Water Oxidation. *J. Phys. Chem. C* **2013**, *117* (17), 8708–8718.

27. Jang, Y. J.; Park, Y. B.; Kim, H. E.; Choi, Y. H.; Choi, S. H.; Lee, J. S. Oxygen-Intercalated CuFeO_2 Photocathode Fabricated by Hybrid Microwave Annealing for Efficient Solar Hydrogen Production. *Chem. Mater.* **2016**, *28* (17), 6054–6061.
28. Berglund, S. P.; Abdi, F. F.; Bogdanoff, P.; Chemseddine, A.; Friedrich, D.; Van De Krol, R. Comprehensive Evaluation of CuBi_2O_4 as a Photocathode Material for Photoelectrochemical Water Splitting. *Chem. Mater.* **2016**, *28* (12), 4231–4242.
29. Konta, R.; Kato, H.; Kobayashi, H.; Kudo, A. Photophysical Properties and Photocatalytic Activities Under Visible Light Irradiation of Silver Vanadates. *Phys. Chem. Chem. Phys.* **2003**, *5* (14), 3061–3065.
30. Zoellner, B.; Gordon, E.; Maggard, P. A. A Small Bandgap Semiconductor, P-Type MnV_2O_6 , Active for Photocatalytic Hydrogen and Oxygen Production. *Dalton Trans.* **2017**, *46* (32), 10657–10664.
31. Bartel, C. J.; Sutton, C.; Goldsmith, B. R.; Ouyang, R.; Musgrave, C. B.; Ghiringhelli, L. M.; Scheffler, M. New Tolerance Factor to Predict the Stability of Perovskite Oxides and Halides. *arXiv* **2018**, 1–10.
32. Zhao, Z.; Goncalves, R. V.; Barman, S. K.; Willard, E. J.; Byle, E.; Perry, R.; Wu, Z.; Huda, M. N.; Moulé, A. J.; Osterloh, F. E. Electronic Structure Basis for Enhanced Overall Water Splitting Photocatalysis With Aluminum Doped SrTiO_3 in Natural Sunlight. *Energ. Environ. Sci.* **2019**, *12* (4), 1385–1395.
33. Kato, H.; Asakura, K.; Kudo, A. Highly Efficient Water Splitting Into H_2 and O_2 over Lanthanum-Doped NaTaO_3 Photocatalysts With High Crystallinity and Surface Nanostructure. *J. Am. Chem. Soc.* **2003**, *125* (10), 3082–3089.
34. Zhang, W.; Tang, J.; Ye, J. Structural, Photocatalytic, and Photophysical Properties of Perovskite MSnO_3 ($M = \text{Ca}, \text{Sr}, \text{and Ba}$) Photocatalysts. *J. Mater. Res.* **2007**, *22* (7), 1859–1871.
35. Arney, D.; Hardy, C.; Greve, B.; Maggard, P. A. Flux Synthesis of AgNbO_3 : Effect of Particle Surfaces and Sizes on Photocatalytic Activity. *J. Photochem. Photobiol. A Chem.* **2010**, *214* (1), 54–60.
36. Miseki, Y.; Kato, H.; Kudo, A. Water Splitting Into H_2 and O_2 over Niobate and Titanate Photocatalysts With (111) Plane-Type Layered Perovskite Structure. *Energ. Environ. Sci.* **2009**, *2* (3), 306–314.
37. Hildebrandt, N. C.; Soldat, J.; Marschall, R. Layered Perovskite Nanofibers Via Electrospinning for Overall Water Splitting. *Small* **2015**, *11* (17), 2051–2057.
38. Boltersdorf, J.; Sullivan, I.; Shelton, T. L.; Wu, Z.; Gray, M.; Zoellner, B.; Osterloh, F. E.; Maggard, P. A. Flux Synthesis, Optical and Photocatalytic Properties of N-Type Sn_2TiO_4 : Hydrogen and Oxygen Evolution Under Visible Light. *Chem. Mater.* **2016**, *28* (24), 8876–8889.
39. Han, H. S.; Shin, S.; Kim, D. H.; Park, I. J.; Kim, J. S.; Huang, P. S.; Lee, J. K.; Cho, I. S.; Zheng, X. Boosting the Solar Water Oxidation Performance of a BiVO_4 Photoanode by Crystallographic Orientation Control. *Energ. Environ. Sci.* **2018**, *11* (5), 1299–1306.
40. Kim, J. H.; Lee, J. S. Elaborately Modified BiVO_4 Photoanodes for Solar Water Splitting. *Adv. Mater.* **2019**, *31* (20), 1–35.
41. Poeppelmeier, K. R.; et al.; et al. ChemInform Abstract: Structural, Optical, and Transport Properties of α - and β - Ag_3VO_4 . *ChemInform* **2012**, *43* (47).
42. Jain, A.; Ong, S. P.; Hautier, G.; Chen, W.; Richards, W. D.; Dacek, S.; Cholia, S.; Gunter, D.; Skinner, D.; Ceder, G.; et al. Commentary: The Materials Project: A Materials Genome Approach to Accelerating Materials Innovation. *APL Mater.* **2013**, *1* (1).
43. Zhang, J.; Dang, W.; Ao, Z.; Cushing, S. K.; Wu, N. Band Gap Narrowing in Nitrogen-Doped $\text{La}_2\text{Ti}_2\text{O}_7$ Predicted by Density-Functional Theory Calculations. *Phys. Chem. Chem. Phys.* **2015**, *17* (14), 8994–9000.
44. Modak, B.; Srinivasu, K.; Ghosh, S. K. Band Gap Engineering of NaTaO_3 Using Density Functional Theory: A Charge Compensated Codoping Strategy. *Phys. Chem. Chem. Phys.* **2014**, *16* (32), 17116–17124.
45. Chen, S.; Hu, Y.; Ji, L.; Jiang, X.; Fu, X. Preparation and Characterization of Direct Z-Scheme Photocatalyst $\text{Bi}_2\text{O}_3/\text{NaNbO}_3$ and its Reaction Mechanism. *Appl. Surf. Sci.* **2014**, *292*, 357–366.
46. Zoellner, B.; O'Donnell, S.; Wu, Z.; Itanze, D.; Carbone, A.; Osterloh, F. E.; Geyer, S.; Maggard, P. A. Impact of Nb(V) Substitution on the Structure and Optical and Photoelectrochemical Properties of the $\text{Cu}_3(\text{Ta}_{1-x}\text{Nb}_x)_{11}\text{O}_{30}$ Solid Solution. *Inorg. Chem.* **2019**, *58* (10), 6845–6857.
47. Yuan, Y.; Zhao, Z.; Zheng, J.; Yang, M.; Qiu, L.; Li, Z.; Zou, Z. Polymerizable Complex Synthesis of $\text{BaZr}_{1-x}\text{Sn}_x\text{O}_3$ Photocatalysts: Role of Sn^{4+} in the Band Structure and Their Photocatalytic Water Splitting Activities. *J. Mater. Chem.* **2010**, *20* (32), 6772–6779.
48. Hu, C. C.; Teng, H. Influence of Structural Features on the Photocatalytic Activity of NaTaO_3 Powders From Different Synthesis Methods. *Appl. Catal. A Gen.* **2007**, *331* (1), 44–50.
49. Li, G.; Yang, N.; Wang, W.; Zhang, W. F. Band Structure and Photoelectrochemical Behavior of AgNbO_3 - NaNbO_3 Solid Solution Photoelectrodes. *Electrochim. Acta* **2010**, *55* (24), 7235–7239.
50. Jiang, C. M.; Reyes-Lillo, S. E.; Liang, Y.; Liu, Y. S.; Liu, G.; Toma, F. M.; Prendergast, D.; Sharp, I. D.; Cooper, J. K. Electronic Structure and Performance Bottlenecks of CuFeO_2 Photocathodes. *Chem. Mater.* **2019**, *31* (7), 2524–2534.
51. Peng, C.; Liu, Y.; Cui, J.; Luo, K.; Shen, Y.; Li, X. First-Principle Calculation of the Electronic Structure of α - Ag_3VO_4 Using Two Different Exchange Correlation Functionals. *Mater. Chem. Phys.* **2021**, *262* (May 2020), 124307.
52. Walsh, A.; Payne, D. J.; Egdel, R. G.; Watson, G. W. Stereochemistry of Post-Transition Metal Oxides: Revision of the Classical Lone Pair Model. *Chem. Soc. Rev.* **2011**, *40* (9), 4455.
53. Walsh, A.; Yan, Y.; Huda, M. N.; Al-Jassim, M. M.; Wei, S. H. Band Edge Electronic Structure of BiVO_4 : Elucidating the Role of the Bi S and V d Orbitals. *Chem. Mater.* **2009**, *21* (3), 547–551.
54. Burton, L. A.; Walsh, A. A Photoactive Titanate With a Stereochemically Active Sn Lone Pair: Electronic and Crystal Structure of Sn_2TiO_4 From Computational Chemistry. *J. Solid State Chem.* **2012**, *196*, 157–160.
55. Moss, B.; Le, H.; Corby, S.; Morita, K.; Selim, S.; Sotelo-Vazquez, C.; Chen, Y.; Borthwick, A.; Wilson, A.; Blackman, C.; et al. Anisotropic Electron Transport Limits Performance of Bi_2WO_6 Photoanodes. *J. Phys. Chem. C* **2020**, *124* (35), 18859–18867.
56. Boltersdorf, J.; Sullivan, I.; Shelton, T. L.; Wu, Z.; Gray, M.; Zoellner, B.; Osterloh, F. E.; Maggard, P. A. Flux Synthesis, Optical and Photocatalytic Properties of N-Type Sn_2TiO_4 : Hydrogen and Oxygen Evolution Under Visible Light. *Chem. Mater.* **2016**, *28* (24), 8876–8889.
57. Cho, I. S.; Kwak, C. H.; Kim, D. W.; Lee, S.; Hong, K. S. Photophysical, Photoelectrochemical, and Photocatalytic Properties of Novel SnWO_4 Oxide Semiconductors With Narrow Band Gaps. *J. Phys. Chem. C* **2009**, *113* (24), 10647–10653.
58. Hosogi, Y.; Tanabe, K.; Kato, H.; Kobayashi, H.; Kudo, A. Energy Structure and Photocatalytic Activity of Niobates and Tantalates Containing Sn(II) With a $5s^2$ Electron Configuration. *Chem. Lett.* **2004**, *33* (1), 28–29.
59. Xie, X.; Liu, M.; Wang, C.; Chen, L.; Xu, J.; Cheng, Y.; Dong, H.; Lu, F.; Wang, W. H.; Liu, H.; et al. Efficient Photo-Degradation of Dyes Using CuWO_4 Nanoparticles With Electron Sacrificial Agents: A Combination of Experimental and Theoretical Exploration. *RSC Adv.* **2016**, *6* (2), 953–959.
60. Cooper, J. K.; Zhang, Z.; Roychoudhury, S.; Jiang, C.-M.; Gul, S.; Liu, Y.-S.; Dhall, R.; Ceballos, A.; Yano, J.; Prendergast, D.; et al. CuBi_2O_4 : Electronic Structure, Optical Properties, and Photoelectrochemical Performance Limitations of the Photocathode. *Chem. Mater.* **2021**, *33* (3), 934–945.
61. Hautier, G.; Miglio, A.; Ceder, G.; Rignanese, G. M.; Gonze, X. Identification and Design Principles of Low Hole Effective Mass P-Type Transparent Conducting Oxides. *Nat. Commun.* **2013**, *4*, 1–7.
62. Umezawa, N.; Shuxin, O.; Ye, J. Theoretical Study of High Photocatalytic Performance of Ag_3PO_4 . *Phys. Rev. B: Condens. Matter Mater. Phys.* **2011**, *83* (3), 1–8.
63. Lee, H.; Campbell, N.; Lee, J.; Asel, T. J.; Paudel, T. R.; Zhou, H.; Lee, J. W.; Noesges, B.; Seo, J.; Park, B.; et al. Direct Observation of a Two-Dimensional Hole Gas at Oxide Interfaces. *Nat. Mater.* **2018**, *17* (3), 231–236.
64. Anh, L. D.; Kaneta, S.; Tokunaga, M.; Seki, M.; Tabata, H.; Tanaka, M.; Ohya, S. High-Mobility 2D Hole Gas at a SrTiO_3 Interface. *Adv. Mater.* **2020**, *32* (14), 1–7.
65. Shirai, K.; Yamanaka, K. Mechanism Behind the High Thermoelectric Power Factor of SrTiO_3 by Calculating the Transport Coefficients. *J. Appl. Phys.* **2013**, *113* (5).

66. Moreira, E.; Henriques, J. M.; Azevedo, D. L.; Caetano, E. W. S.; Freire, V. N.; Albuquerque, E. L. Structural and Electronic Properties of $\text{Sr}_x\text{Ba}_{1-x}\text{SnO}_3$ From First Principles Calculations. *J. Solid State Chem.* **2012**, *187*, 186–194.
67. Ebaid, M.; Kang, J. H.; Ryu, S. W. Controlled Synthesis of GaN-Based Nanowires for Photoelectrochemical Water Splitting Applications. *Semicond. Sci. Technol.* **2017**, *32* (1).
68. Tyagi, P.; Ramesh, C.; Kaswan, J.; Dhua, S.; John, S.; Shukla, A. K.; Roy, S. C.; Kushvaha, S. S.; Muthusamy, S. K. Direct Growth of Self-Aligned Single-Crystalline GaN Nanorod Array on Flexible Ta Foil for Photocatalytic Solar Water-Splitting. *J. Alloys Compd.* **2019**, *805*, 97–103.
69. Kamimura, J.; Bogdanoff, P.; Abdi, F. F.; Lahnemann, J.; Van De Krol, R.; Riechert, H.; Geelhaar, L. Photoelectrochemical Properties of GaN Photoanodes With Cobalt Phosphate Catalyst for Solar Water Splitting in Neutral Electrolyte. *J. Phys. Chem. C* **2017**, *121* (23), 12540–12545.
70. Lin, J.; Wang, W.; Li, G. Modulating Surface/Interface Structure of Emerging InGaN Nanowires for Efficient Photoelectrochemical Water Splitting. *Adv. Funct. Mater.* **2020**, *30* (52), 1–20.
71. Alotaibi, B.; Nguyen, H. P. T.; Zhao, S.; Kibria, M. G.; Fan, S.; Mi, Z. Highly Stable Photoelectrochemical Water Splitting and Hydrogen Generation Using a Double-Band InGaN/GaN Core/Shell Nanowire Photoanode. *Nano Lett.* **2013**, *13* (9), 4356–4361.
72. Wang, Z.; Han, J.; Li, Z.; Li, M.; Wang, H.; Zong, X.; Li, C. Moisture-Assisted Preparation of Compact GaN:ZnO Photoanode Toward Efficient Photoelectrochemical Water Oxidation. *Adv. Energy Mater.* **2016**, *6* (20).
73. Hashiguchi, H.; Maeda, K.; Abe, R.; Ishikawa, A.; Kubota, J.; Domen, K. Photoresponse of GaN:ZnO Electrode on FTO Under Visible Light Irradiation. *Bull. Chem. Soc. Jpn.* **2009**, *82* (3), 401–407.
74. Maeda, K.; Takata, T.; Hara, M.; Saito, N.; Inoue, Y.; Kobayashi, H.; Domen, K. GaN:ZnO Solid Solution as a Photocatalyst for Visible-Light-Driven Overall Water Splitting. *J. Am. Chem. Soc.* **2005**, *127* (23), 8286–8287.
75. Abe, R.; Higashi, M.; Domen, K. Facile Fabrication of an Efficient Oxynitride TaON Photoanode for Overall Water Splitting into H_2 and O_2 Under Visible Light Irradiation. *J. Am. Chem. Soc.* **2010**, *132* (34), 11828–11829.
76. Yamasita, D.; Takata, T.; Hara, M.; Kondo, J. N.; Domen, K. Recent Progress of Visible-Light-Driven Heterogeneous Photocatalysts for Overall Water Splitting. *Solid State Ion.* **2004**, *172* (1–4 SPEC. ISS), 591–595.
77. Higashi, M.; Domen, K.; Abe, R. Highly Stable Water Splitting on Oxynitride TaON Photoanode System Under Visible Light Irradiation. *J. Am. Chem. Soc.* **2012**, *134* (16), 6968–6971.
78. Higashi, M.; Domen, K.; Abe, R. Fabrication of Efficient TaON and Ta_3N_5 Photoanodes for Water Splitting Under Visible Light Irradiation. *Energ. Environ. Sci.* **2011**, *4* (10), 4138–4147.
79. Liu, G.; Ye, S.; Yan, P.; Xiong, F.; Fu, P.; Wang, Z.; Chen, Z.; Shi, J.; Li, C. Enabling an Integrated Tantalum Nitride Photoanode to Approach the Theoretical Photocurrent Limit for Solar Water Splitting. *Energ. Environ. Sci.* **2016**, *9* (4), 1327–1334.
80. Ishikawa, A.; Takata, T.; Kondo, J. N.; Hara, M.; Domen, K. Electrochemical Behavior of Thin Ta_3N_5 Semiconductor Film. *J. Phys. Chem. B* **2004**, *108* (30), 11049–11053.
81. Nurlaela, E.; Sasaki, Y.; Nakabayashi, M.; Shibata, N.; Yamada, T.; Domen, K. Towards Zero Bias Photoelectrochemical Water Splitting: Onset Potential Improvement on a Mg:GaN Modified- Ta_3N_5 Photoanode. *J. Mater. Chem. A* **2018**, *6* (31), 15265–15273.
82. He, Y.; Thorne, J. E.; Wu, C. H.; Ma, P.; Du, C.; Dong, Q.; Guo, J.; Wang, D. What Limits the Performance of Ta_3N_5 for Solar Water Splitting? *Chem* **2016**, *1* (4), 640–655.
83. Zhong, M.; Hisatomi, T.; Sasaki, Y.; Suzuki, S.; Teshima, K.; Nakabayashi, M.; Shibata, N.; Nishiyama, H.; Katayama, M.; Yamada, T.; et al. Highly Active GaN-Stabilized Ta_3N_5 Thin-Film Photoanode for Solar Water Oxidation. *Angew. Chem.* **2017**, *129* (17), 4817–4821.
84. Nishimae, S.; Mishima, Y.; Nishiyama, H.; Sasaki, Y.; Nakabayashi, M.; Inoue, Y.; Katayama, M.; Domen, K. Fabrication of BaTaO₂N Thin Films by Interfacial Reactions of BaCO₃/ Ta_3N_5 Layers on a Ta Substrate and Resulting High Photoanode Efficiencies During Water Splitting. *Sol. RRL* **2020**, *4* (4), 2–9.
85. Hojamberdiev, M.; Zahedi, E.; Nurlaela, E.; Kawashima, K.; Yubuta, H.; Minegishi, T.; Domen, K.; Teshima, K. The Cross-Substitution Effect of Tantalum on the Visible-Light-Driven Water Oxidation Activity of BaNbO₂N Crystals Grown Directly by an NH₃-Assisted Flux Method. *J. Mater. Chem. A* **2016**, *4* (33), 12807–12817.
86. Seo, J.; Nakabayashi, M.; Hisatomi, T.; Shibata, N.; Minegishi, T.; Domen, K. Solar-Driven Water Splitting Over a BaTaO₂N Photoanode Enhanced by Annealing in Argon. *ACS Appl. Energy Mater.* **2019**, *2* (8), 5777–5784.
87. Wang, C.; Hisatomi, T.; Minegishi, T.; Wang, Q.; Zhong, M.; Katayama, M.; Kubota, J.; Domen, K. Synthesis of Nanostructured BaTaO₂N Thin Films as Photoanodes for Solar Water Splitting. *J. Phys. Chem. C* **2016**, *120* (29), 15758–15764.
88. Cordes, N.; Bräuniger, T.; Schnick, W. Ammonothermal Synthesis of EAMO₂N (EA = Sr, Ba; M = Nb, Ta) Perovskites and ¹⁴N Solid-State NMR Spectroscopic Investigations of AM(O,N)₃ (A = Ca, Sr, Ba, La). *Eur. J. Inorg. Chem.* **2018**, 5019–5026.
89. Xu, J.; Pan, C.; Takata, T.; Domen, K. Photocatalytic Overall Water Splitting on the Perovskite-Type Transition Metal Oxynitride CaTaO₂N Under Visible Light Irradiation. *Chem. Commun.* **2015**, *51* (33), 7191–7194.
90. Wang, Y.; Kang, Y.; Zhu, H.; Liu, G.; Irvine, J. T. S.; Xu, X. Perovskite Oxynitride Solid Solutions of LaTaO₂N-CaTaO₂N With Greatly Enhanced Photogenerated Charge Separation for Solar-Driven Overall Water Splitting. *Adv. Sci.* **2021**, *8* (2), 1–8.
91. Ma, Z.; Jaworski, A.; George, J.; Rokicinska, A.; Thersleff, T.; Budnyak, T. M.; Hautier, G.; Pell, A. J.; Dronskowski, R.; Kuśtrowski, P.; et al. Exploring the Origins of Improved Photocurrent by Acidic Treatment for Quaternary Tantalum-Based Oxynitride Photoanodes on the Example of CaTaO₂N. *J. Phys. Chem. C* **2019**, *124* (1), 152–160.
92. Zeng, W.; Bian, Y.; Cao, S.; Ma, Y.; Liu, Y.; Zhu, A.; Tan, P.; Pan, J. Phase Transformation Synthesis of Strontium Tantalum Oxynitride-Based Heterojunction for Improved Visible Light-Driven Hydrogen Evolution. *ACS Appl. Mater. Interfaces* **2018**, *10* (25), 21328–21334.
93. Fang, T.; Huang, H.; Feng, J.; Hu, Y.; Qian, Q.; Yan, S.; Yu, Z.; Li, Z.; Zou, Z. Reactive Inorganic Vapor Deposition of Perovskite Oxynitride Films for Solar Energy Conversion. *Research* **2019**, *2019*, 1–9.
94. Hafez, A. M.; Zedan, A. F.; AlQaradawi, S. Y.; Salem, N. M.; Allam, N. K. Computational Study on Oxynitride Perovskites for CO₂ Photoreduction. *Energ. Convers. Manage.* **2016**, *122*, 207–214.
95. Kasahara, A.; Nukumizu, K.; Hitoki, G.; Takata, T.; Kondo, J. N.; Hara, M.; Kobayashi, H.; Domen, K. Photoreactions on LaTiO₂N Under Visible Light Irradiation. *J. Phys. Chem. A* **2002**, *106* (29), 6750–6753.
96. Lawley, C.; Nachtegaal, M.; Stahn, J.; Roddatis, V.; Döbeli, M.; Schmidt, T. J.; Pergolesi, D.; Lippert, T. Examining the Surface Evolution of LaTiO_xN_x an Oxynitride Solar Water Splitting Photocatalyst. *Nat. Commun.* **2020**, *11* (1), 1–11.
97. Zhang, F.; Yamakata, A.; Maeda, K.; Moriya, Y.; Takata, T.; Kubota, J.; Teshima, K.; Oishi, S.; Domen, K. Cobalt-Modified Porous Single-Crystalline LaTiO₂N for Highly Efficient Water Oxidation Under Visible Light. *J. Am. Chem. Soc.* **2012**, *134* (20), 8348–8351.
98. Seo, J.; Moriya, Y.; Koderer, M.; Hisatomi, T.; Minegishi, T.; Katayama, M.; Domen, K. Photoelectrochemical Water Splitting on Particulate ANbO₂N (A = Ba, Sr) Photoanodes Prepared From Perovskite-Type ANbO₃. *Chem. Mater.* **2016**, *28* (19).
99. Maeda, K.; Higashi, M.; Siritanaratkul, B.; Abe, R.; Domen, K. SrNbO₂N as a Water-Splitting Photoanode With a Wide Visible-Light Absorption Band. *J. Am. Chem. Soc.* **2011**, *133* (32), 12334–12337.
100. Koderer, M.; Moriya, Y.; Katayama, M.; Hisatomi, T.; Minegishi, T.; Domen, K. Investigation on Nitridation Processes of Sr₂Nb₂O₇ and SrNbO₃ to SrNbO₂N for Photoelectrochemical Water Splitting. *Sci. Rep.* **2018**, *8* (1), 1–10.
101. Koderer, M.; Urabe, H.; Katayama, M.; Hisatomi, T.; Minegishi, T.; Domen, K. Effects of Flux Synthesis on SrNbO₂N Particles for Photoelectrochemical Water Splitting. *J. Mater. Chem. A* **2016**, *4* (20), 7658–7664.
102. Schlöberg, H.; Kröger, J.; Savasci, G.; Terban, M. W.; Bette, S.; Moudrakovski, I.; Duppel, V.; Podjaski, F.; Siegel, R.; Senker, J.; et al. Structural Insights Into Poly(Heptazine Imides): A Light-Storing Carbon Nitride Material for Dark Photocatalysis. *Chem. Mater.* **2019**, *31* (18), 7478–7486.

103. Mesch, M. B.; Bärwinkel, K.; Krysiak, Y.; Martineau, C.; Taulelle, F.; Neder, R. B.; Kolb, U.; Senker, J. Solving the Hydrogen and Lithium Substructure of Poly(Triazine Imide)/LiCl Using NMR Crystallography. *Chem. Eur. J.* **2016**, *22* (47), 16878–16890.
104. Ham, Y.; Maeda, K.; Cha, D.; Takanae, K.; Domen, K. Synthesis and Photocatalytic Activity of Poly(Triazine Imide). *Chem. Asian J.* **2013**, *8* (1), 218–224.
105. Wirmhier, E.; Döbbling, M.; Gunzelmann, D.; Senker, J.; Lotsch, B. V.; Schnick, W. Poly(Triazine Imide) With Intercalation of Lithium and Chloride Ions [(C₃N₃)₂(NH₂Li_{1-x})₃LiCl]: A Crystalline 2D Carbon Nitride Network. *Chem. Eur. J.* **2011**, *17* (11), 3213–3221.
106. Zhang, G.; Lin, L.; Li, G.; Zhang, Y.; Savateev, A.; Zafeiratos, S.; Wang, X.; Antonietti, M. Ionothermal Synthesis of Triazine–Heptazine-Based Copolymers With Apparent Quantum Yields of 60% at 420 nm for Solar Hydrogen Production From “Sea Water”. *Angew. Chem. Int. Ed.* **2018**, *57* (30), 9372–9376.
107. Luo, Y.; Suzuki, S.; Wang, Z.; Yubuta, K.; Vequizo, J. J. M.; Yamakata, A.; Shiiba, H.; Hisatomi, T.; Domen, K.; Teshima, K. Construction of Spatial Charge Separation Facets on BaTaO₂N Crystals by Flux Growth Approach for Visible-Light-Driven H₂ Production. *ACS Appl. Mater. Interfaces* **2019**, *11* (25), 22264–22271.
108. Cui, Z. H.; Jiang, H. Theoretical Investigation of Ta₂O₅, TaON, and Ta₃N₅: Electronic Band Structures and Absolute Band Edges. *J. Phys. Chem. C* **2017**, *121* (6), 3241–3251.
109. Wang, J.; Jiang, Y.; Ma, A.; Jiang, J.; Chen, J.; Li, M.; Feng, J.; Li, Z.; Zou, Z. Charge Compensation Doping to Improve the Photocatalytic and Photoelectrochemical Activities of Ta₃N₅: A Theoretical Study. *Appl. Catal. Environ.* **2019**, *244* (October 2018), 502–510.
110. Ziani, A.; Nurlaela, E.; Dhawale, D. S.; Silva, D. A.; Alarousu, E.; Mohammed, O. F.; Takanae, K. Carrier Dynamics of a Visible-Light-Responsive Ta₃N₅ Photoanode for Water Oxidation. *Phys. Chem. Chem. Phys.* **2015**, *17* (4), 2670–2677.
111. Hafez, A. M.; Salem, N. M.; Allam, N. K. Unravelling the Correlated Electronic and Optical Properties of BaTaO₂N With Perovskite-Type Structure as a Potential Candidate for Solar Energy Conversion. *Phys. Chem. Chem. Phys.* **2014**, *16* (34), 18418–18424.
112. Luo, Y.; Suzuki, S.; Wang, Z.; Yubuta, K.; Vequizo, J. J. M.; Yamakata, A.; Shiiba, H.; Hisatomi, T.; Domen, K.; Teshima, K. Construction of Spatial Charge Separation Facets on BaTaO₂N Crystals by Flux Growth Approach for Visible-Light-Driven H₂ Production. *ACS Appl. Mater. Interfaces* **2019**, *11* (25), 22264–22271.
113. Kubo, A.; Giorgi, G.; Yamashita, K. Anion Ordering in CaTaO₂N: Structural Impact on the Photocatalytic Activity. Insights From First-Principles. *Chem. Mater.* **2017**, *29* (2), 539–545.
114. Ninova, S.; Aschauer, U. Surface Structure and Anion Order of the Oxynitride LaTiO₂N. *J. Mater. Chem. A* **2017**, *5* (22), 11040–11046.
115. Carrier, P.; Wei, S. Theoretical Study of the Band-Gap Anomaly of InN. *J. Appl. Phys.* **2005**, *97* (3), 033707.
116. Savateev, A.; Tarakina, N. V.; Strauss, V.; Hussain, T.; ten Brummelhuis, K.; Sánchez Vadillo, J. M.; Markushyna, Y.; Mazzanti, S.; Tyutyunnik, A. P.; Walczak, R.; et al. Potassium Poly(heptazine imide): Transition Metal-Free Solid-State Triplet Sensitizer in Cascade Energy Transfer and [3+2]-Cycloadditions. *Angew. Chem. Int. Ed.* **2020**, *59* (35), 15061–15068.
117. Martin, D. J.; Qiu, K.; Shevlin, S. A.; Handoko, A. D.; Chen, X.; Guo, Z.; Tang, J. Highly Efficient Photocatalytic H₂ Evolution From Water Using Visible Light and Structure-Controlled Graphitic Carbon Nitride. *Angew. Chem. Int. Ed.* **2014**, *53* (35), 9240–9245.
118. Schwinghammer, K.; Tuffy, B.; Mesch, M. B.; Wirmhier, E.; Martineau, C.; Taulelle, F.; Schnick, W.; Senker, J.; Lotsch, B. V. Triazine-Based Carbon Nitrides for Visible-Light-Driven Hydrogen Evolution. *Angew. Chem. Int. Ed.* **2013**, *52* (9), 2435–2439.
119. Lin, L.; Wang, C.; Ren, W.; Ou, H.; Zhang, Y.; Wang, X. Photocatalytic Overall Water Splitting by Conjugated Semiconductors With Crystalline Poly(Triazine Imide) Frameworks. *Chem. Sci.* **2017**, *8* (8), 5506–5511.
120. Makaremi, M.; Grixti, S.; Butler, K. T.; Ozin, G. A.; Singh, C. V. Band Engineering of Carbon Nitride Monolayers by N-Type, P-Type, and Isoelectronic Doping for Photocatalytic Applications. *ACS Appl. Mater. Interfaces* **2018**, *10* (13), 11143–11151.
121. Wang, J.; Hao, D.; Ye, J.; Umezawa, N. Determination of Crystal Structure of Graphitic Carbon Nitride: Ab Initio Evolutionary Search and Experimental Validation. *Chem. Mater.* **2017**, *29* (7), 2694–2707.
122. Niu, J.; Li, L.; Wang, Y.; Su, J.; Li, J.; Wang, X. Single-Crystal X-ray Diffraction Structures of Covalent Organic Frameworks. *Science* **2018**, *52* (July), 48–52.
123. Makaremi, M.; Grixti, S.; Butler, K. T.; Ozin, G. A.; Singh, C. V. Band Engineering of Carbon Nitride Monolayers by N-Type, P-Type, and Isoelectronic Doping for Photocatalytic Applications. *ACS Appl. Mater. Interfaces* **2018**, *10* (13), 11143–11151.
124. McDermott, E. J.; Wirmhier, E.; Schnick, W.; Viridi, K. S.; Scheu, C.; Kauffmann, Y.; Kaplan, W. D.; Kurmaev, E. Z.; Moewes, A. Band Gap Tuning in Poly(Triazine Imide), a Nonmetallic Photocatalyst. *J. Phys. Chem. C* **2013**, *117* (17), 8806–8812.
125. Kato, H.; Ueda, K.; Kobayashi, M.; Kakihana, M. Photocatalytic Water Oxidation Under Visible Light by Valence Band Controlled Oxynitride Solid Solutions LaTaO₂N₂-SrTiO₃. **2015**, *3* (22), 11824–11829.
126. Pei, L.; Lv, B.; Wang, S.; Yu, Z.; Yan, S.; Abe, R.; Zou, Z. Oriented Growth of Sc-Doped Ta₃N₅ Nanorod Photoanode Achieving Low-Onset-Potential for Photoelectrochemical Water Oxidation. *ACS Appl. Energy Mater.* **2018**, *1*, 4150–4157.
127. Hafez, A. M.; Zedan, A. F.; AlQaradawi, S. Y.; Salem, N. M.; Allam, N. K. Computational Study on Oxynitride Perovskites for CO₂ Photoreduction. *Energ. Convers. Manage.* **2016**, *122*, 207–214.
128. Garcia-Esparza, A. T.; Tyminska, N.; Al Rahal Al Orabi, R.; Le Bahers, T. Full In Silico DFT Characterization of Lanthanum and Yttrium Based Oxynitride Semiconductors for Solar Fuels. *J. Mater. Chem. C* **2019**, *7*, 1612–1621.
129. Lau, V. W. H.; Klose, D.; Kasap, H.; Podjaski, F.; Pigní, M. C.; Reisner, E.; Jeschke, G.; Lotsch, B. V. Dark Photocatalysis: Storage of Solar Energy in Carbon Nitride for Time-Delayed Hydrogen Generation. *Angew. Chem. Int. Ed.* **2017**, *56* (2), 510–514.
130. Huang, C.; Wen, Y.; Ma, J.; Dong, D.; Shen, Y.; Liu, S.; Ma, H.; Zhang, Y. Unraveling Fundamental Active Units in Carbon Nitride for Photocatalytic Oxidation Reactions. *Nat. Commun.* **2021**, *12* (1), 1–8.

4.18 High temperature hydrothermal synthesis of inorganic compounds

Joseph W. Kolis and Colin D. McMillen, Department of Chemistry, Hunter Laboratories, Clemson University, Clemson, SC, United States

© 2023 Elsevier Ltd. All rights reserved.

4.18.1	Introduction and scope	629
4.18.1.1	Techniques	629
4.18.1.2	Advantages and disadvantages	630
4.18.1.3	Mineralizers	631
4.18.2	Early history and commercial efforts	631
4.18.2.1	Commercial development of quartz	632
4.18.2.2	Other commercial efforts	633
4.18.3	Oxides	634
4.18.3.1	Closed shell binary oxides	634
4.18.3.1.1	Divalent oxides	634
4.18.3.1.2	Trivalent oxides	635
4.18.3.1.3	Tetravalent oxides	636
4.18.3.2	Ternary mixed element oxides	637
4.18.3.2.1	Perovskites	637
4.18.3.2.2	Pyrochlores	638
4.18.3.2.3	Garnets	639
4.18.3.3	Open shell oxides	639
4.18.3.3.1	First row transition metal oxides	639
4.18.3.3.2	Heavy transition metal oxides	640
4.18.4	Metal oxyanion building blocks	641
4.18.4.1	Silicates	642
4.18.4.2	Phosphates	643
4.18.4.3	Germanates	643
4.18.4.4	Vanadates and molybdates	645
4.18.4.5	Carbonates	646
4.18.4.6	Borates	647
4.18.5	Halides	647
4.18.6	Chalcogenides	648
4.18.7	Hydrothermal synthesis of gems and minerals	649
4.18.8	Nitrides in supercritical ammonia	649
4.18.9	Summary	650
Acknowledgments		651
References		651

Abstract

The chemistry of inorganic materials in high temperature hydrothermal fluids is reviewed. The chemistry is generally restricted to reactions performed above 250 °C (typically between 400 °C and 750 °C). Some discussion of the technology is included. A brief historical background and a summary of the development of quartz growth is provided for perspective. The work focuses on the identity of the final crystalline products since almost nothing is known of the reaction intermediates or mechanisms. Two approaches are emphasized using hydrothermal fluids. One is the targeted growth of large single crystals and the other is the exploration of phase space of new materials. The work addresses primarily the chemistry of metal oxides across the periodic table, as well as metal complexes of oxyanions. These include silicates, phosphates, germanates, molybdates and vanadates. The chemistry of metal chalcogenides and metal fluorides are also reviewed. The chemistry of metal nitrides in supercritical ammonia is examined and comparisons to aqueous chemistry are provided. Throughout the review, attempts are made to identify the many opportunities for future work in the field.

4.18.1 Introduction and scope

The study of inorganic synthesis and crystal growth in hydrothermal fluids has been known in various guises for approximately 160 years. This review will focus on the use of higher temperature hydrothermal approaches specifically focusing on the thermal regime between 300 °C and 700 °C. The emphasis will be on synthesis, phase space exploration, and crystal growth, all of which are well-suited to be addressed by the high temperature hydrothermal approach. This temperature range is not an arbitrary choice, but rather represents the limits of fluoropolymer lined autoclaves, and thus requires inert metal (Ag, Au, Pt) liners. The reaction chemistry in the polymer lined autoclaves is immense and focuses on a wide range of topics including nanochemistry, microporous materials, and ceramics, and is beyond the scope of this review. The relatively low temperature hydrothermal technology has been used extensively to generate a wide range of new materials, including in the last decade, nano particles of many different systems, and this area has been well reviewed.¹⁻¹⁰

In this regard, the field of higher temperature hydrothermal synthesis has been the subject of a number of excellent reviews on the classical aspects of the field.¹¹⁻²⁴ In particular, Byrappa and co-workers have consistently provided excellent and timely reviews of various aspects of hydrothermal synthesis and crystal growth on a regular basis. They point out correctly that since the 1980s the general field of high temperature hydrothermal synthesis and crystal growth has undergone something of a retraction in interest, particularly in the United States. This was caused to a large degree by the demise of the large corporate research labs in the United States, especially Bell Labs, where much of the original hydrothermal research work took place. This is not to say however, that the situation is entirely without hope. There has been a massive expansion in the use of the relatively low temperature hydrothermal work with a focus on both nanoparticle growth as well as new phase exploration, particularly in timely areas like metal organic framework (MOF) synthesis. It is only a matter of time before the field will expand through this thermal barrier to attack new areas of inorganic materials. In particular we see a number of new and very exciting areas like quantum materials, exotic magnetic phases, highly refractory materials and unusual optical materials that demand a new approach to synthesis and processing. In that spirit, we endeavor to use this review to highlight some specific hydrothermal systems that serve as case studies of unique and interesting solutions for difficult materials problems. We will also try to point out current opportunities created by intricate emerging materials such as multiferroics and quantum spin liquids, where the use of hydrothermal synthesis can address some specific needs. Through these approaches we hope to entice new workers to enter the field and find new ways to use the hydrothermal method to attack some contemporary problems.

The high temperature hydrothermal approach that is often necessary for inorganic synthesis is a somewhat demanding technique that is neither standardized nor commercially addressed.²⁵⁻²⁸ Many details are also available in the patent literature.^{29,30} The high temperature fluid field is still too small to attract many commercial equipment suppliers. Valves, heaters, pressure sensors and temperature controllers are commercially accessible, but autoclaves, sealing mechanisms and assembled systems are not readily available. In our particular case, we design and manufacture all of our equipment in-house and are fortunate to have access to an excellent University machine shop which is both well-equipped and well-staffed with outstanding machinists. We feel that a detailed technical and experimental discussion is outside the scope of the review, but brief discussions of the approach and limitation of the methodology are presented when warranted. Generally any reactions *above* temperatures that can employ fluoropolymer lined autoclaves (≥ 250 °C) are called "high temperature" by us, although it should be noted that even the highest hydrothermal reaction conditions (ca. 750 °C) still employ very low reaction temperatures when compared to classical solid state melt-based methods. This experimental factor is emerging as an important dynamic in the preparation of optical and magnetic solids and will be highlighted where appropriate in the review. The overwhelming majority of superheated fluid reactions still employ water as a solvent. There is no intrinsic requirement for this limitation, and other solvents can and should be explored as reaction media. In the rigorous sense any solvent heated above its boiling point at 1 atm. is a solvothermal fluid, but the word "hydrothermal" has become a generic term for any solvent at high temperature. We will employ this ruse as well and refer to all the reactions in the review as "hydrothermal" and identify other solvents when appropriate. In general reaction temperatures above 350–400 °C will lead to the thermal decomposition of most organic species, which greatly limits the choice of organic solvents as well as reagents. For these reasons most of the work covered herein will focus on compounds recognized as "solid state compounds" rather than molecular based species. Most of the compounds resulting from high temperature hydrothermal fluids are condensed extended solids with oxide or halide building blocks. A very exciting emerging area involves the various oxyanion building blocks such as silicates, phosphates, vanadates and borates. For reasons discussed later the hydrothermal approach is well suited to these oxyanions, and this represents a massive opportunity for the hydrothermal field.

4.18.1.1 Techniques

The thermal regime of interest in this review can be accessed using autoclaves made of relatively well-known metals, either various stainless steels for use up to 450 °C, and nickel-based superalloys such as Inconel or Rene for use up to 750 °C. Higher temperatures are accessible using more specialized alloys but this range is not well explored and presents an increased number of experimental challenges. The alloy body is employed to retain the pressures generated within the reaction chamber, but these materials generally have almost no chemical resistance to the typical reaction conditions, especially aqueous based hydrothermal fluids containing halides or hydroxides (with one extremely important exception, as will be discussed below). An inert metal liner is thus also required to contain the reaction fluid to prevent corrosion of the structural autoclave wall. Such corrosion can both contaminate the samples and compromise the structural integrity of the autoclave. It should be kept in mind that high temperature supercritical

fluid states have very low viscosities, generally approaching those of gases. Any reaction chamber must be therefore completely sealed, generally by high quality welding, usually either pressure- or electro arc welding.³¹ There is really no shortcut or workaround to this step. Even the slightest compromise of the weld seal will lead to a failed reaction and often a destroyed autoclave. The inert metal liners are typically either silver, gold, or platinum. Fortunately, all of these inert metals weld very well and are easily workable. Silver is obviously the preferred material from a cost perspective but is the least inert. It is suitable for a number of reaction conditions, as it is stable to concentrated hydroxide and fluoride under almost all neutral or basic conditions. Fluids containing chlorides, acids and/or any oxidant require the use of gold or platinum liners. An alternative sealed tube material is fused silica which is quite stable to acids (except HF) and oxidants, but it is not flexible, so care must be taken to always maintain a slightly larger pressure on the outside of the tube than will occur at the ultimate reaction pressure on the inside of the tube.³²

It is important to understand the role of the high pressures involved in high temperature hydrothermal reactions. The pressures generated at the higher end of the reaction temperatures are usually on the order of 2–3 kbar, or 200–300 MPa. These pressures are intrinsic to the reaction solution and are generated by thermal expansion of the fluids. The pressures expand rapidly with the temperature and degree of fill and are well understood for water.³³ Thus the careful and demanding experimental techniques to accommodate pressure are employed only to contain the reaction fluid. It is rare that pressure is applied extrinsically for any reason. Although these pressures are high, they are quite low compared to the pressures employed as the thermodynamic factor to generate or stabilize particular phases. Generally, at least 3 GPa are required to access unique phases derived strictly from thermodynamic pressure stabilization. Since hydrothermal fluids are normally employed at pressures lower than this by more than order of magnitude, it is unlikely that pressure is a factor in the isolation of any specific phases. It is our experience that the pressure of a hydrothermal reaction is a minor contributor to the observed chemistry, and that temperature, mineralizer and starting materials are far more important factors.

4.18.1.2 Advantages and disadvantages

The relatively low reaction temperature has several advantages. Any crystal growth takes place in a fluid that is essentially isothermal near the growing crystal surface, so the level of thermal strain, inhomogeneity and defect density decreases dramatically compared to melt-solid type reactions. The reactions also occur in completely sealed systems so there are few external impurities that make their way into the product. If an ampule like platinum is used, it is completely sealed and generally has little if any activity, which leads to extremely pure samples. Another important advantage is that the growth takes place in a closed system so there are no problems with evaporation or loss of reactants. This greatly reduces the probability of forming oxide defects in lattices and minimizes the tendency to form nonstoichiometric compounds. The crystals that grow from these fluids typically have stoichiometric formulas with full occupancies and low displacement parameters. The closed system also inhibits decomposition of labile groups such as carbonates, nitrates and sulfates, enabling the growth of compounds not normally accessible by classical high temperature methods.

The closed aqueous systems also provided control of the chemical reaction conditions in the process. Thus stoichiometry, redox potential, acidity, polarity and other factors can be varied as needed to manage otherwise unstable systems. Of course, chemists are quite comfortable manipulating these experimental factors, and this can lead to rational design of desired materials. In the important case of refractory oxides, there are two advantages to the hydrothermal growth technique that are unique to this class of compounds. Because the materials, by definition, require extremely high temperatures to prepare by classical thermal methods, they are susceptible to loss of oxygen, and evaporation of element oxides. This can lead to a considerable number of lattice defects that can degrade the properties and lead to structural ambiguities. In addition, the high reaction temperatures can induce substantial site disorder, where ions of similar size can be dispersed over a range of crystallographic sites. This again introduces difficulties in structural and property measurements. The much lower reaction temperatures of the hydrothermal fluids generally minimize both defect densities and site disordering, making it a method deserving careful attention for the formation of demanding metal oxides.

There are obviously several disadvantages to the hydrothermal method as well. There are few if any commercial high temperature hydrothermal equipment vendors, so the technical expertise, design and fabrication of this demanding technology must generally be developed in-house. One significant limitation of the fundamental study of hydrothermal synthesis is the difficulty of obtaining in-situ or in-operando information about the chemical processes occurring during hydrothermal reactions. Any window material is subject to attack or breakage due to the pressures and it is very difficult to prevent leaks under actual operating conditions. This makes reaction design and observation of synthesis and growth nearly impossible. Experiments are generally run as closed systems and any speculations on the reaction process are handled in a postmortem fashion. As an example of this problem, the hydrothermal growth of quartz has been a resounding success as a result of thousands of man hours of detailed study (see below). Yet neither the identity of the soluble mobile species nor the mechanism of the transport reaction is known at all. A convenient solution to this difficult problem will undoubtedly result in rapid advances in the field of hydrothermal synthesis.

Another disadvantage of the method is the fact that growth is inherently a slow process. Growth of large single crystals in excess of 1 cm/edge is usually possible but can require considerable experimental exploration of growth conditions. The actual transport rate rarely exceeds 0.5 mm/day, so growth of large bulk samples may take several weeks. When a protocol has been optimized however, this is usually not a problem because once growth starts it continues as long as feedstock is present and the thermal gradient is maintained. Growth can proceed to the limits of the autoclave walls with no human input and multiple crystals can easily be grown in one vessel, so large-scale production and commercial growth is viable once a good recipe is established. Because of the large number of experimental variables and the closed nature of the reaction system however, the initial large-scale single

crystal growth may take some perseverance. This is in contrast to optical floating zone melt growth for example, where a 50 mm boule can be grown in several days aided by visible observation.

4.18.1.3 Mineralizers

A critical aspect of hydrothermal reactions is the use of mineralizers. These are usually small ionic species, most commonly nucleophilic anions such as OH^- , F^- , Cl^- , and CO_3^{2-} , whose primary role is to attack the feedstock and induce a small degree of solubility of the building blocks. These soluble species can migrate through the extremely low viscosity fluids to nucleate at a supersaturation site created by thermal differentials. Migration is driven by convection currents created by these modest thermal differentials (typically 5–50 degrees). Two types of hydrothermal reactions are generally performed. The most common is simply exploratory synthesis of some particular compound. This can be a known material or a new phase, but in either case, the material can be grown as relatively small single crystals without any pre-added seeds or large zones of thermal differential. In this case some reasonable starting materials are typically added to the reaction vessel along with an appropriate mineralizer, and a temperature with a modest thermal differential applied. The solubility and supersaturation processes are mostly random but often single crystals are obtained via spontaneous nucleation (SN). This high percentage formation of single crystals is one factor that makes this technique so attractive for phase exploration and new material synthesis. The crystals are often very high quality and can range in size up to several millimeters. It is rare to obtain crystals larger than 5 mm via the SN method but very often crystals suitable for single crystal diffraction are obtained. The mineralizer is usually essential to inducing the appropriate solubility and reactivity in the hydrothermal fluid even if it is not incorporated in the product. It almost always plays a critical role in the identity and quality of the final product and is often the most important variable in the chemistry.

If larger single crystals are desired for detailed physical property measurements, such as single crystal neutron scattering, multi-rank tensor transport or optical measurements, a transport growth process is required. In this case a small seed often obtained via the SN process is placed in a supersaturated growth zone in an autoclave with a suitable feedstock in a saturation zone. The zones can be separated by a baffle. The soluble molecules generated by the mineralizers can migrate to the growth (supersaturation) zone and deposit on the seed crystal steadily increasing its size. In principle once transport conditions are stabilized the crystal can grow to the size of the autoclave as long as feedstock remains available. Growth is generally slow (approximately an order of magnitude slower compared to Czochralski pulling for example) but requires little or no human input once the process is underway. It is this process that led to the growth of the famous photogenic quartz crystals in multikilogram sizes (vide infra). In order to maintain the growth-transport conditions, it is generally preferred that the mineralizer ions not be an integral chemical building block of the material being grown. Also, since more careful control over the solubility profile is needed during growth-transport reactions, these tend to benefit from lower mineralizer concentrations than SN reactions, as lower and moderate solubilities can limit parasitic nucleation to more efficiently direct growth onto the seed crystals.

4.18.2 Early history and commercial efforts

The original efforts that can reasonably be classified as hydrothermal growth came from geologists in the 19th century who sought to emulate natural growth conditions of various minerals.³⁴ They performed an array of reactions that were forebearers to modern work employing such hair-raising techniques as welded rifle barrels heated to red heat. The lack of reproducible results, not to mention numerous explosions, led to the development of the first true autoclaves that did indeed allow designed crystal growth of single crystal quartz for example in 1905, by Spezia.³⁵ Probably the first systematic phase exploration was performed by Morey at the US Geological Survey using autoclaves that are actually a close approximation of autoclave designs that bear his name to this day.³⁶ He reviewed the exploration of a range of minerals that can be prepared in the lab by emulating the presumed natural hydrothermal conditions and was able to prepare a wide range of mineral phases.³⁷ This work can be defined as the first modern phase exploration using the hydrothermal method. Subsequent work by Nacken³⁸ and others³⁹ was driven by the desire to form cultured quartz for commercial applications, as well as the growth of lab created gems such as sapphire and emeralds.⁴⁰

The post-WWII period saw a considerable increase in exploratory hydrothermal synthesis, led particularly but not exclusively, by workers in the United States, Britain, Japan and the USSR. The work was inspired by the tremendous successes in the growth of cultured quartz as well as the general one-upmanship of the cold war scientific establishments across the world. The advent of lasers led to the exploration of new laser hosts as well as need for frequency conversion across the entire electromagnetic spectrum from the visible to the radio frequency range. Of course, the emergence of the space age and the nuclear age required new materials, often as high quality single crystals, and these geopolitical factors served as the driver for inorganic synthesis using many techniques including the hydrothermal method. In many cases the hydrothermal method led to high quality single crystals of known phases, but the systematic exploration of these unusual experimental conditions also led to many new phases as well. The cooling of cold war tensions led to a decreased urgency to fund crystal materials research at national labs around the world, and the general demise of large corporate research labs such as Philips, Bell Labs and Dupont Central Research lead to a decrease in overall research and publications in the field of hydrothermal synthesis. Given the mandate of those labs, there was generally more emphasis on the targeted growth of technologically important single crystals. Until recently there has been relatively less work in academic labs where the emphasis is on more exploratory studies of new materials.

4.18.2.1 Commercial development of quartz

By far the most famous and important commercial success of hydrothermal synthesis is that of α -quartz (Fig. 1).^{41–47} Quartz found use because of its piezoelectric properties, and in particular its sensitive and narrow response window to high frequencies. It was used as a timer and frequency filter in numerous solid state and wireless applications including radios, receivers, and even color televisions (The fascinating history of the technological development of quartz in modern electronics is given in a detailed and compelling account by McGahey.⁴⁸). The early needs of α -quartz were readily accommodated using natural mineral sources, mostly from Brazil. With the supply of Brazilian material considered at risk by most parties (American, British and German) during and immediately after World War II however, various efforts were undertaken to grow synthetic α -quartz in laboratories. One challenge in the quartz system results from the phase transformation between low temperature α - and high temperature β -quartz at 573 °C. Although both are piezoelectric, the transformation between the two induces twinning that is impossible to control. Any useful growth must therefore take place below the transformation temperature, which is a significant experimental challenge for a refractory oxide with a considerable tendency to form glasses from the melt phase.

It was well known that natural α -quartz minerals grow well hydrothermally, and attempts were made to emulate the natural growth conditions in the lab as early as 1905, by Spezia in Italy,⁴⁹ who achieved some success in the targeted growth of the material. During WWII, Germany especially suffered from poor access to natural quartz due to naval blockade activities, as well as efforts by American agents to bribe Brazilian quartz miners to sell material to US rather than German buyers.⁵⁰ As a result of these factors, German researchers were very active in attempting to produce lab cultured quartz. In particular the work of Nacken led to some success in synthetic quartz crystal growth and this data was obtained at the end of the war by the Allies via the Technical Field Information Agency, later more well-known as Operation Paperclip.⁵¹ The information was subsequently forwarded to the Brush Engineering Company in Cleveland as well as to the Bell Telephone Labs. Both organizations were then well supported by contracts from the Army Signal Corps Labs to develop large scale commercial production of cultured quartz crystals.^{52,53} These efforts were immensely successful and massive amounts of high-quality quartz crystals were produced by these organizations and others until recent years when quartz filters and timers have begun to be replaced by semiconductor devices. The importance of readily available high quality α -quartz had a profound and largely unappreciated effect on the development of solid-state communication devices in the second half of the 20th century.^{54,55} The work by McGahey does an excellent job in highlighting the vital technological impact of inexpensive, high quality single crystals of α -quartz.

In addition to the commercial success of these efforts, several fundamental scientific aspects of this work emerged. The post war work by Hale and Sawyer at Brush, and Walker, Buehler and Laudise at Bell Labs, resulted in much greater understanding of hydrothermal chemistry and targeted crystal growth in general. These workers discovered the importance of mineralizers, thermal gradients, convection transport, seed orientation, high pressure autoclave design and many other factors. One important quirk unique to quartz growth that often goes without mention is the importance of the mineral acmite ($\text{NaFeSi}_2\text{O}_6$) or more properly aegirine, which readily forms on the walls of the steel autoclaves early in the hydrothermal growth process. The material is inert under the hydrothermal growth conditions and passivates the walls of the autoclaves preventing both corrosion of the autoclaves and contamination of the quartz product.⁵⁶ This fortuitous aspect allows for the use of unlined stainless steel autoclaves which makes the process much cheaper and technologically simpler. The ability to grow the materials under fairly benign thermal conditions without an expensive precious metal liner represents a perfect storm of experimental convenience for the large scale production of a vital material.



Fig. 1 Hydrothermally grown α -quartz (coffee travel mug for scale).

4.18.2.2 Other commercial efforts

It might appear that the successful commercial production of α -quartz would pave the way for other marketable materials to be grown hydrothermally, but relatively few materials came to market this way. The reasons are at least partially due to the issues described above, namely that quartz could be grown exceptionally well in inexpensive autoclaves that do not require costly liners. Few other synthesis procedures are that fortunate. One compound that was commercialized via hydrothermal growth was KTP (KTiOPO_4), which is an excellent frequency conversion material for 1- μm near IR to green laser light. It has excellent phase matching capabilities in the mid visible, so the ready availability of high power 1 μm laser light paved the way for this material to generate powerful lasers in the green region for a range of applications.^{57,58} The material was originally grown by more conventional flux methods,⁵⁹ but it was soon found that the hydrothermal technique could also lead to high quality crystals.^{60–65} Each method has its own advantages but the hydrothermal method in particular can be grown below the Curie temperature of the polar material (975 °C) so it is easy to obtain polar ordered crystals using ordered seeds. Its growth does require inert metal liners which increases cost. The material itself moves in and out of fashion in the markets, which impedes fuller large-scale development, but the hydrothermal growth method is well established to address any market needs as they evolve (Fig. 2).

Several other classical materials such as berlinite, AlPO_4 and its analogs (e.g., GaPO_4) have shown some commercial potential as pyroelectric, electrooptic and surface acoustic applications but few have achieved large market penetration like that of quartz. Like quartz, berlinite contains a number of low temperature phase transformations, meaning that a low temperature growth method is required to take advantage of its favorable electrooptic properties.^{66–68} As with quartz, it was also known early on that the material can be grown as high quality single crystals using a hydrothermal approach.^{69,70} This work led to more detailed investigation of growth conditions and development of good growth protocols.^{71–73} One unique problem that occurs for both AlPO_4 and GaPO_4 is that they have a negative solubility coefficient over much of their growth range. In this case the solubility of the material is actually higher at lower temperature.^{74,75} This is not an uncommon problem in hydrothermal growth and a number of materials display this curious behavior. It can be overcome by reversing the heating zones,⁷⁶ but the resultant complexity of the convection currents often leads to imperfections in the crystal growth. This partially accounts for the limited commercial penetration of this material.

Another class of crystals that received a spate of interest as potential photorefractive materials were the sillenites, with the formula $\text{Bi}_{12}\text{EO}_{20}$ (E = Ge, Si, Ti).⁷⁷ These can be grown a number of ways including by melt pulling methods,⁷⁸ but the hydrothermal approach provides a number of advantages especially as it leads to much lower defect density in the crystals compared to the higher temperature melt based methods.^{79,80} The complexity of the chemical and physical behavior of the material and the general loss of interest in photorefractive materials inhibited the further development of the hydrothermal growth of this class of compounds.

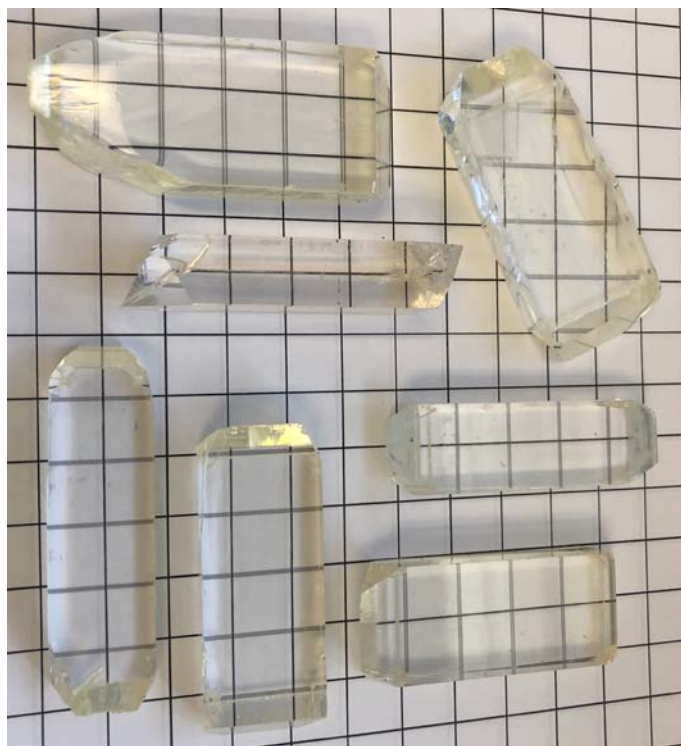


Fig. 2 Hydrothermally grown KTP (1 cm divisions).

4.18.3 Oxides

The oxides represent an enormous class of compounds, each subset of which presents its own series of demands and restrictions in terms of materials preparation. In the case of first row d-block transition metal oxides for example, the preparative toolbox is immense, so the hydrothermal approach has had a relatively minor impact on the vast number of known compounds. In contrast the rare earth oxides have a very limited range of synthetic approaches, which are even more limited if single crystals are desired because they are so extremely refractory. As the rare earth ions become more heavily investigated because of their magnetic and optical properties, we believe the hydrothermal approach will become increasingly more important. Perhaps the most deceptively intriguing class is the main group metal oxides from the middle of the periodic table, like those of gallium, tin, germanium, and indium. These oxides have many applications but are surprisingly under investigated compared to the transition metal oxides. Some of the resultant opportunities will be highlighted in this article.

Most of these various oxides have been traditionally synthesized as powders using some thermally driven method. Single crystal growth of most metal oxides usually involves some aspect of melting the feedstocks followed by crystallization. For the refractory oxides the growth temperatures are often in excess of 2000 °C, and can exceed 3000 °C. A wide range of exotic and elegant heating methods have been examined through the years but only a few received systematic development.⁸¹ These include arc melting, torch melting, RF induction and optical zone melting. More recently floating zone melting using optical heating is rapidly becoming the method of choice.^{82,83} This technique has several advantages including decent temperature control, atmosphere control (particularly in oxidizing environments) and growth of crystals of suitable size for property measurement, and it is now providing excellent results for a range of refractory oxides. These high temperature methods, however, often lead to some thermal strain in the product, lattice defects and site disorder.⁸⁴ These effects can be problematic given the detailed physical measurements required to study emergent properties such quantum magnetic behavior or multiferroicity.^{85,86}

Thus, in many cases experimentalists are forced to pick their poison. They can readily generate oxides in powder form, or they can employ high temperature methods to grow larger single crystals but risk the potential shortcomings described above, in particular lattice defects and site disorder. Not all systems suffer such limitations, but in general a versatile, relatively low temperature route to oxide single crystals would be of considerable utility in many cases. Here we take the opportunity to highlight the use of the hydrothermal approach to prepare a range of refractory oxides that specifically illustrate this advantage.

The best hydrothermal results are usually obtained for amphoteric oxides because oxides that are too acidic or too basic readily solubilize and do not transport and precipitate well. Fortunately, many useful oxides are suitably amphoteric, and suitable thermal conditions and mineralizers can be found for good chemical reactivity and crystal growth. Many of these amphoteric oxides also are extremely refractory and can be difficult to grow as high quality, low defect single crystals, so the availability of a hydrothermal route is often quite expedient. One interesting aspect of the hydrothermal methods is the formation of polymorphic phases that are not normally considered stable or accessible under ambient conditions. Several examples of structural polymorphs can be synthesized as single crystals that are not normally considered stable in the relatively low temperature (≤ 700 °C) hydrothermal conditions employ. For example, we isolated single crystals of BaTiO₃ in the cubic *Pm-3 m* space group, a phase which is normally only stable above 1200 °C.⁸⁷ It is not yet clear why the hydrothermal route stabilizes these phases, but we will highlight examples of this interesting area where appropriate.

4.18.3.1 Closed shell binary oxides

In this section we will first examine the hydrothermal chemistry of oxides that do not contain open shell d-block transition metals. These include main group ions, rare earths and early d-block, fully oxidized transition metal ions (e.g., Ti⁴⁺). For a variety of reasons these oxides have received considerably more studies than mid-valent transition metal oxides with open d-shells. We will attempt to choose illustrative examples that highlight some unique aspect where hydrothermal chemistry has an impact.

4.18.3.1.1 Divalent oxides

ZnO: Zinc oxide has been known to form high quality single crystals for many years. It is well studied because ZnO is a wide bandgap semiconductor but does not grow well as a high-quality single crystal via classical melt or flux methods. This drove the development of a hydrothermal method for the crystal growth. Interestingly it is a polar material and defects normally accrue on only one side of the polar crystal face. The use of a *c-face* seed often leads to a crystal with one highly transparent side and a side with a high density of defects that has a distinct yellow or green color. The growth process has been commercialized in Japan but difficulties in getting good doping protocols somewhat limits its use. The work has been comprehensively reviewed relatively recently.⁸⁸⁻⁹¹

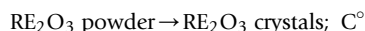
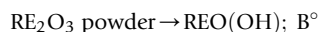
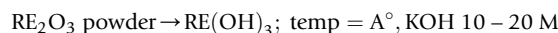
BeO: Beryllium oxide can also be grown readily via hydrothermal methods. It is of course an extremely toxic material which limits its commercial applications. At various points, however, it was of interest because of its use in nuclear reactors, its thermal conductivity, and its refractory nature. The extreme toxicity of vaporized BeO precludes traditional melt or vapor transport growth techniques. The hydrothermal method employs a sealed autoclave so the possibility of exposure at growth temperature is greatly minimized by this approach. Large, high quality single crystals of BeO were grown at 535 °C in 4 N KOH solutions, providing a convenient and relatively safe route to a material that will probably never be used.⁹² Despite these successes however, BeO has not seen any significant follow-on development due to its toxicity.

4.18.3.1.2 Trivalent oxides

Al_2O_3 : Single crystals of sapphire/corundum were reported to be grown hydrothermally relatively early.⁹³ The process was never studied extensively because of the well-established ability to grow very large high-quality crystals of sapphire using melt pulling methods. The growth process is of interest however because some detailed solubility experiments were performed, which led to the identification of very complex solubility curves that are highly dependent on the nature of mineralizer. Simple hydroxide is not suitable as a mineralizer because the difference in solubility across a thermal differential is not sufficient to induce a supersaturation zone for transport and crystal growth. In contrast the use of carbonate as a mineralizer proves to be quite satisfactory for growth. This subtle but inexplicable chemical behavior was one of the first examples of the challenges that exist in the hydrothermal process.

Rare Earth Sesquioxides, RE_2O_3 : This class of compounds is of considerable interest both for their technological importance but also because they were one of the first set of truly refractory oxides that were examined hydrothermally.^{94,95} All the rare earth oxides have melting points around 2400 °C. They have been the subject of intensive investigations through the years using some elegant and exotic high temperature growth techniques and display some complex structural chemistry at high temperatures.⁹⁶ High temperature growth reactions often lead to highly colored crystals because of impurities from the growth crucible, typically rhenium.⁹⁷ The products often also contain considerable numbers of oxide lattice defects suggesting the need for alternative crystal growth methods.

Early work showed interesting chemistry under hydrothermal conditions using only high temperature water with no mineralizer. Like aluminum, the trivalent lanthanides form a series of trihydroxides, oxyhydroxides and ultimately anhydrous sesquioxides as the reaction temperatures increase.^{98,99} We found that the trihydroxides and oxyhydroxides are often easy to grow as large high quality crystals in moderate aqueous base.



where $\text{C}^\circ > \text{B}^\circ > \text{A}^\circ$ and the values vary across the lanthanide series ranging from around 300–400 °C for A, 500–700 °C and 600-unknown for C.¹⁰⁰

Subsequent work by our group demonstrated that the anhydrous oxides can also be grown as high-quality single crystals in concentrated (10–20 M) hydroxides (Fig. 3).^{101–103}

The situation is complicated by the fact that as the metal ion gets larger the temperature for the conversion to the sesquioxides increases to beyond 750 °C. This thermal regime requires some more advanced technology for larger crystal growth but is ultimately achievable with appropriate resources. The important host materials Lu_2O_3 and Sc_2O_3 have the smallest ionic radii and can be readily grown at 600–700 °C using our existing methods. Lutetia is of particular interest for lasing applications because it has

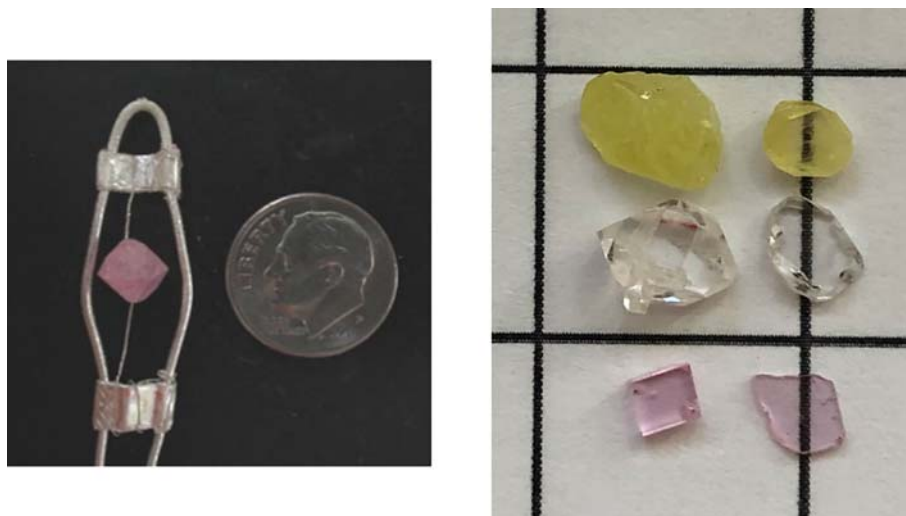


Fig. 3 Left: as-grown $\text{Er}:\text{Sc}_2\text{O}_3$ attached to the silver ladder used to suspend the crystal in the growth zone during hydrothermal growth. Right: $\text{Pr}:\text{Lu}_2\text{O}_3$, $\text{Yb}:\text{Lu}_2\text{O}_3$, and $\text{Er}:\text{Lu}_2\text{O}_3$ crystals in as-grown form and fabricated from a hydrothermally-grown boule for optical measurements (3–5 mm crystals).

very good thermal conductivity properties upon doping with lasing ions like Yb^{3+} so it has great interest as a host for high power laser applications. We recently demonstrated that every rare earth ion could be easily doped into Lu_2O_3 single crystals in any reasonable concentration, leading a huge number of new possibilities for new spectroscopic and lasing studies.¹⁰⁴ As our techniques develop for ever-higher temperature hydrothermal crystal growth, we anticipate that good quality single crystals of sesquioxides of increasing metal ion radius will be grown from hydrothermal media. At present however, it has proven difficult to form single crystals of any oxides containing rare earths larger than Yb, a factor which is inconvenient for the formation of technologically desirable oxides like Tb_2O_3 .

4.18.3.1.3 Tetravalent oxides

MO_2 ($M = \text{Ti, Zr, Hf}$): The Group 4 oxides, ZrO_2 and HfO_2 are among the most refractory materials in the periodic table with melting points exceeding 2700°C . As bulk crystals they are generally grown using extreme high temperature crucible free methods.^{105,106} There are a number of applications of these materials related either to their extreme hardness (commercial faux diamonds) or oxide defect structures (oxide conductors). There are also several purely scientific reasons to explore high quality single crystals of refractory oxides of Group 4. One is simply the lack of detailed information on the reactivity and properties of the materials since they are so inert their reaction chemistry and phase space is often poorly understood. As with the other refractive oxides they are usually prepared either as ceramics or defect-containing crystals, so a careful and detailed examination of their crystal structures is often not possible. As they often grow as defect forms of high symmetry cubic structures there are many subtle structural aspects that go unrealized. At room temperature the group 4 oxides adopt a low symmetry defect fluorite structure with the cubic phase only stable at very high temperatures. This is important because the cubic hafnia phase is an excellent oxide conductor. In order to stabilize the cubic structure the hafnia lattice must be doped with modest amounts of a larger ion such as a di- or trivalent ion. Given the technological significance and the scientific potential of these systems, a controlled route to well-defined stable cubic phases is desirable.

There are a number of reports of hydrothermal growth of the materials. In most of these cases, the refractory nature of the material precludes the use of hydroxide mineralizers, and fluorides must be used instead. The original work reported that moderate (1–5 M) alkali fluorides are suitable for solubility and transport of material over a reasonable temperature differential. In this way, high quality crystals can be prepared.^{107–109} This work showed that fluoride mineralizers, especially NH_4F induced high quality growth of lower symmetry (monoclinic and tetragonal) ZrO_2 and HfO_2 at reasonable rates. We extended that work to doped materials that led to single crystals of the cubic phase in hydrothermal fluids at 700°C .¹¹⁰ This is in marked contrast to the standard growth of cubic zirconia and cubic hafnia, which typically takes place via skull melting at $2500\text{--}3000^\circ\text{C}$ and requires significant amounts of dopants to stabilize the cubic phase. The discovery that such refractory oxides can be synthesized in hydrothermal fluids encouraged workers to look for other related refractory oxides. For example, zircon ZrSiO_4 could be prepared as single crystals.¹¹¹ As an extremely refractory, incongruently melting oxide, access of pure material is very limited. It was found, however, that 2–3 cm sized single crystals could be grown using KF mineralizer in water at 700°C .¹¹² The ability to grow single crystals of such extremely refractory materials at modest temperatures using the hydrothermal conditions suggests that there are few oxides that cannot succumb to a well-designed hydrothermal approach.

ThO_2 and UO_2 : One of the more intriguing refractory oxides to be examined was ThO_2 . This is the most refractory metal oxide known with a melting point of nearly 3400°C . Given its significance in the nuclear processing industry a number of attempts were made to grow single crystals using a variety of very high temperature melt techniques with mixed success, usually producing colored crystals containing considerable oxide lattice defects and thermal strain.¹¹³ We felt that this would be an excellent proof of concept because if we could demonstrate successful solubilization and growth of this material, there was no reason to think that any other oxides could withstand attack as well. We found that ThO_2 powder was completely inert to fluids with any concentration of hydroxide, even values approaching 30 M OH^- at 700°C . The oxide however is sufficiently soluble in 6–9 M CsF at $575\text{--}750^\circ\text{C}$ to transport to a growth zone and produce transparent high quality crystals sizes exceeding 6 mm/edge.¹¹⁴ This led to crystals large enough of suitable quality to enable bulk physical property measurements for the first time, such as thermal expansion and thermal conductivity.

We extended this approach to the analogous UO_2 and were able to grow single crystals of this material as well even though it is considerably less soluble than ThO_2 .¹¹⁵ This was particularly interesting because UO_2 is not well known as its absolute stoichiometry and tends to form nonstoichiometric compounds UO_{2-x} and UO_{2+x} when the traditional high temperature synthetic methods are employed. The hydrothermal method using concentrated fluoride mineralizers leads to low defect UO_2 as well as a series of U^{4+} doped ThO_2 host lattices $\text{U}_x\text{Th}_{1-x}\text{O}_2$. This enabled an extensive series of physical property measurements,¹¹⁶ as well as a recently issued patent on the growth process.¹¹⁷ The development of routes to these extremely refractory materials also provides an exploratory route to subsequent new materials and suggests that a wide range of new phases can be accessed via the hydrothermal approach.¹¹⁸ We recently extended this work with the tetravalent actinides to neptunium and plutonium, leading to single crystal growth of NpO_2 and PuO_2 in extremely concentrated hydroxide and fluoride mineralizers (mixed 20 M CsOH/5 M CsF).¹¹⁹

SnO_2 : The synthesis of heavier main group metal oxides as high quality single crystals is surprisingly difficult. They readily form pure ceramic powders but oxides like Ga_2O_3 , In_2O_3 and SnO_2 are particularly difficult to obtain as low defect single crystals. They generally have melting points approaching 2000°C and often are not congruently soluble in typical molten salt growth media. The primary problem with these oxides is they tend to extrude oxygen at the high temperatures near their melting points to form defect-ridden solids. Therefore, creative experimental conditions are often necessary to obtain bulk single crystals by traditional melt

techniques.¹²⁰ In contrast to the lighter group 13 and 14 element oxides (e.g., Al, Si), even the most fundamental chemistry is often not well developed for some heavy elements, particularly in terms of their single crystals. This is a significant shortcoming because these heavy group 13 and 14 oxides have a number of important applications such as transparent conductivity (ITO) and high power, wide bandgap rf technology (Ga_2O_3). To be sure many of the applications employ ceramics or, more commonly, thin films, but single crystals are also extremely useful as they provide access to the critical physical properties that can only be obtained from bulk crystals. They are also valuable as substrates for thin film epitaxial growth for device applications. As amphoteric oxides it seemed reasonable to examine whether these materials could undergo useful chemistry and can be grown as single crystals in hydrothermal fluids.^{121–123} We found that high quality SnO_2 single crystals can be prepared in hydrothermal conditions using 5 M CsF or 10 M CsOH at 650 °C (Fig. 4).

This work is still in its earliest stages and thus far only small (2–5 mm) single crystals have been produced but a dedicated growth program will undoubtedly lead to large high-quality crystals as desired. Interestingly SnO_2 behaves as the most inert of these oxides and requires relatively high concentration of fluoride mineralizer to solubilize and transport. The products in all cases, however, are colorless crystals, suggesting that they are essentially defect free.

The binary oxides with metals in higher oxidation states ($\geq 5+$) are probably too Lewis acidic to crystallize as simple oxides from hydrothermal fluids. Rather, they solubilize by forming stable oxyanions and if they do crystallize it is in the form of more complex oxyanions. For example, we made considerable efforts to grow crystals of Ta_2O_5 and WO_3 but they both invariably form complex structures of tantalates or tungstates. Several of these results will be discussed below. We are not aware of any successful results in growing these binary oxides hydrothermally.

4.18.3.2 Ternary mixed element oxides

A range of important alkali metal oxides have been prepared hydrothermally, especially involving Ta^{5+} and Nb^{5+} . Although probably too Lewis acidic to form binary oxides in hydrothermal fluids, they readily form high quality single crystals of ternary alkali metal group 5 oxides like LiTaO_3 , KNbO_3 and related materials.^{124,125} These materials are important nonlinear optical and piezoelectric materials and often have complex polymorph phase diagrams when prepared at high temperature melt reactions. Hydrothermal synthesis methods often display product distributions with unique phase stabilities, however. For example, the desired polar orthorhombic phase KNbO_3 can be grown directly as high quality stable single crystals at relatively low temperatures (≤ 500 °C).¹²⁵ Most other growth methods lead to cracked and twinned crystals as the material undergoes multiple phase changes as it cools. The material has a high NLO coefficient for the conversion of near IR to blue laser light but has not been extensively studied because of these crystal stability issues. The ability to access large high quality single crystals may provide impetus to examine them in more detail. The hydrothermal method is not a panacea unfortunately, and not all desired material can be accessed. For example, high quality magnesium free LiNbO_3 single crystals would be very attractive, but the material has an extremely narrow stability field in hydrothermal fluids. Even a slight excess of LiOH mineralizer leads to formation of Li_3NbO_4 at the expense of the target LiNbO_3 rendering the reaction difficult if not impossible in hydrothermal fluids.

4.18.3.2.1 Perovskites

The tetravalent metals represent a very attractive space for the hydrothermal chemistry of ternary oxides. A wide range of ternary oxides have been prepared and many of them are perovskite derivatives (ABO_3 A = Sr^{2+} , Ba^{2+} , Pb^{2+} , B = M^{4+}) with important technological ramifications. An early typical result is the synthesis and crystal growth of PbTiO_3 .¹²⁶ More recently we found that most of the tetravalent metal ions (Ti, Zr, Hf, Sn) can be prepared as high-quality single crystals in the perovskite structure using relatively high temperature hydrothermal conditions (600–700 °C).⁸⁷ This has some significance in that some of these compounds are

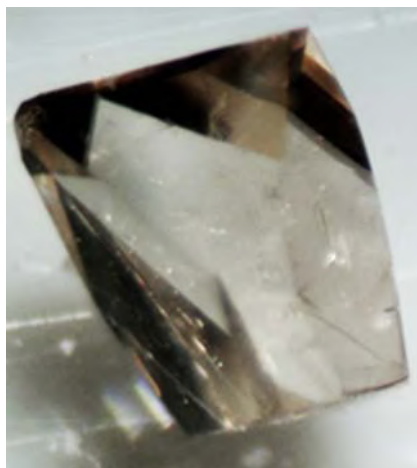


Fig. 4 SnO_2 single crystal obtained from hydrothermal synthesis (2–3 mm scale).

extremely refractory (e.g., SrHfO₃ mp > 2800 °C) making them very difficult to grow as single crystals. In several cases some very surprising results were obtained. For example, BaTiO₃ can be grown as single crystals in hydrothermal conditions at 650 °C but the cubic *Pm-3 m* phase is obtained. This is unexpected because the cubic phase is not considered stable below 1200 °C and this instability is the basis for its early widespread use in ferroelectric applications. Similarly, single crystal characterization of crystals of SrZrO₃ and SrHfO₃ grown hydrothermally reveals that they also grow in the cubic *Pm-3 m* space group whereas the traditional powders synthesized using the dry ceramic methods invariably produce materials in lower symmetry orthorhombic space groups.¹²⁷

Recently our group addressed the synthesis of BaSnO₃, a new material of considerable interest as a high power semiconducting transparent oxide.^{128,129} The wide bandgap, the rigorous cubic structure, and the ease of doping makes this a material of great promise. The problem, as with GaN, is that single crystals for homoepitaxial device production are very difficult to come by. The material has a high, indeterminate melting point and the tetravalent tin readily forms significant amounts of defects in the oxide lattice. We found however that high quality defect free single crystals in the desired cubic structure can be prepared under hydrothermal conditions using the simple reagents of barium hydroxide and SnO₂ and 5 M CsOH mineralizer at 650 °C.¹³⁰ This study is a good example of a major advantage of the hydrothermal method in that it is a relatively low temperature method so it provides access to oxides that might be otherwise difficult to obtain in suitable quality because of the instability of a metal ion in a high oxidation state (i.e., Sn⁴⁺), which tends to cause lattice defects at high growth temperatures. This concept can also be easily extended to a wide range of other refractory perovskites as well, like the rare earth orthoscatates REScO₃, which can be grown to exceptionally high quality in hydrothermal fluids with no detectable lattice defect or site disorder (Fig. 5, top row).¹³¹

4.18.3.2.2 Pyrochlores

With the rapid development of the hydrothermally grown perovskites, it became clear that other related ternary oxides can also be investigated. In this spirit several pyrochlores were synthesized recently using the hydrothermal method (Fig. 5, bottom row). The pyrochlores are well known oxides of course, with the formula A₂B₂O₇ and are reminiscent of perovskites in that both A and B sites can be readily substituted over a wide range metal ion sizes and oxidation states.¹³² The substitution menus are dependent on the A/B ratio of the ionic radii, with a number of lower symmetry structures known along with the ideal cubic parent structure. In that regard, the pyrochlores are also related to the perovskites in that the ideal cubic structures contain multiple trigonal axes leading to magnetic frustration with possible new quantum spin phases based on 3-D spin delocalization.^{133–135} These factors vaulted the rare earth pyrochlores to the forefront of research in the area of new quantum materials, especially those based on magnetic quantum spin liquids and other emergent phases. Although the pyrochlores can be synthesized and grown as single crystals in a number of ways, their refractory nature again typically requires high temperature and high-pressure techniques.¹³⁶ This leads to two significant problems, namely disorder among the A/B sites and defects within the oxide lattice. Both problems are widespread among the pyrochlores and a severe hinderance in the development of quantum materials, where sensitive control of physical property behavior is essential.^{86,137}

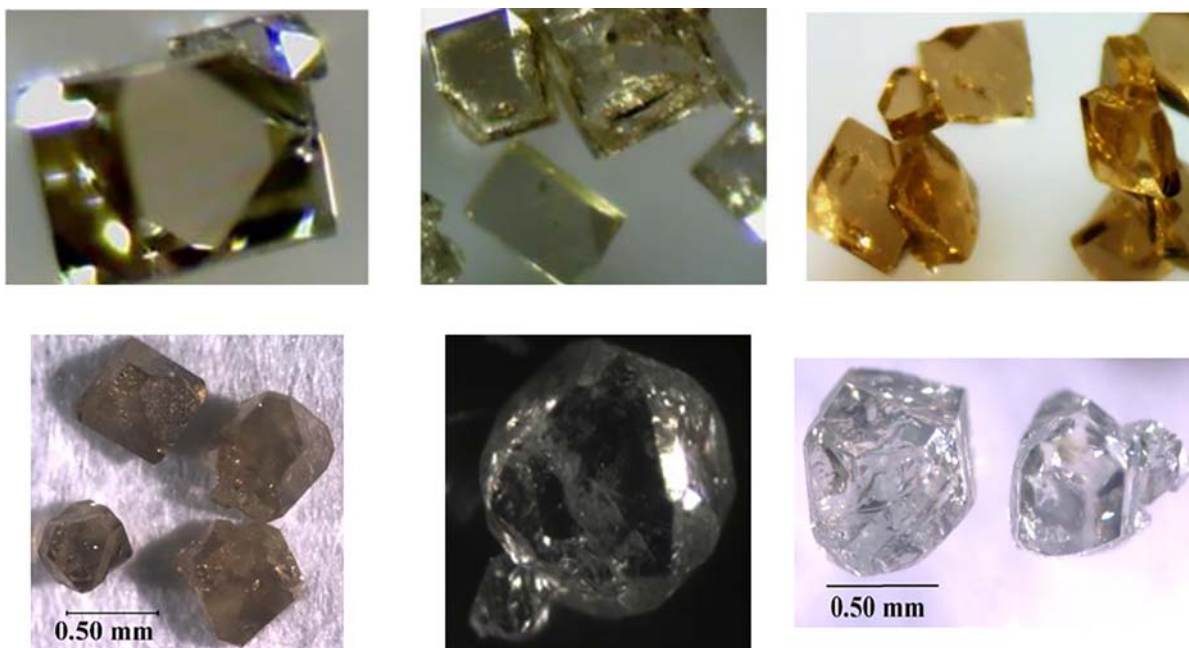


Fig. 5 Top row: perovskites EuScO₃, DyScO₃, HoScO₃. Bottom row: pyrochlores Pr₂Sn₂O₇, La₂Zr₂O₇, Gd₂Ti₂O₇.

To address these problems, our group recently began to explore the hydrothermal synthesis of various rare earth pyrochlores with two goals in mind. One was to prepare materials with minimal A/B site disorder and lattice defects, and the other was to be able to grow single crystals large enough to obtain single crystal neutron scattering data and oriented magnetic field measurements. The hydrothermal approach turned out to be suitable for both of these purposes and we were able to prepare a wide range of single crystals with all of the rare earths in the A site and various tetravalent ions in the B site (Sn, Ge, Ru, Zr, etc.).¹³⁸ We found that we could grow single crystals at a relatively modest temperature range of 650–700 °C to minimize site disorder and lattice defects. These did indeed prove to have crystallographically undetectable levels of A/B site disorder or lattice defects, while enabling a range of detailed neutron scattering and low temperature magnetic studies. These studies appear to open the door for a number of new quantum materials including quantum spin liquids and other emergent phases. This system provides an excellent example of one of the attributes of the hydrothermal method, whereby the target materials themselves are already well known, but employment of a low temperature method provides access to materials of significantly increased quality for subsequent measurements.^{139,140}

This study also provides another example where a high symmetry cubic phase is isolated even though it nominally considered to be thermodynamically unstable under the experimental conditions. Under normal circumstances, when germanium is used as the tetravalent B-site ion it is considered too small to stabilize the cubic phase for any of the rare earths, leading instead to lower symmetry tetragonal or monoclinic phases.^{141,142} It was believed that only extremely high pressures could drive the formation and stabilization of cubic RE₂Ge₂O₇ pyrochlores.¹⁴³ We found however that we could not only obtain the cubic phase for the smaller RE = Er, Yb, and Lu germanates, but that we could also grow fairly large single crystals of the cubic phase.¹⁴⁴ It is not clear to us why this cubic phase can be stabilized under hydrothermal conditions. It is true that the reactions are performed under some pressure, but the hydrothermal pressures (200 MPa) are lower by more than an order of magnitude (3–8 GPa) from those used to convert the germanate powders to cubic phases. We consider that to be too much of a thermodynamic differential, and postulate that the lower temperature crystal growth leads to some form of trapping and stabilization of the cubic phase. Access to these crystals is enabling some detailed examination of the quantum spin properties of these promising materials. It also suggests that the approach can be used to access a wide range of other phases with unusual quantum spin properties.

4.18.3.2.3 Garnets

Like the perovskites and pyrochlores, a wide range of garnets can also be synthesized hydrothermally and grown as high quality single crystals. The hydrothermal work is somewhat limited because many garnets melt congruently, so they can be synthesized straightforwardly using high temperature methods. There are several advantages to the hydrothermal approach, particularly in the design of novel dopants. The classical garnet, YAG (Y₃Al₅O₁₂) is a well-known host for laser applications and has been prepared in huge quantities using Czochralski methods. It does suffer from some twinning problems during growth and also displays some irregularities in dopant distribution when relatively large rare earth ions like Nd³⁺ are doped into the lattice in greater than 1% concentration. These problems can lead to a small but significant change in dopant concentration down the length of a typical commercial boule (ca. 20 cm). To address these issues the hydrothermal synthesis of various garnets was examined. A number of hosts were grown as single crystals, but the process is somewhat complicated by the large differences in solubility between Y₂O₃, Al₂O₃ and Y₃Al₅O₁₂.^{145,146} This necessitates the careful placement of the feedstocks and thermal zones within the growth autoclaves and limits the technique somewhat.¹⁴⁷ A number of other YAG analogs can be prepared this way as well.^{148,149} There are some specialized reasons to develop the methodology. In particular the technique is a good route to the epitaxial growth of heterogeneous layers to design multifunctional single crystals. The ability of garnet to accept a huge range of dopant ions enables the growth of garnets with multiple layers each with a different dopant and hence a different functionality. So gradient doping of lasing ions can be introduced along with end capping for thermal management, waveguides, and specialized applications such as amplified spontaneous emission.^{150,151} A number of patents were also issued on this topic.^{152–154}

4.18.3.3 Open shell oxides

In this section we specifically focus on transition metals with open shells containing valence d electrons, in contrast to materials such as perovskites like BaTiO₃, where the fully oxidized metal center acts mostly as a structural piece. There is a significant literature in this field over many years, but it is clear that it is only the tip of the iceberg and that a huge chemistry is still there to be explored. Given the array of oxidation states throughout the d-block metals and the wide range of coordination environments, the phase space of transition metal oxides still has enormous undeveloped areas. While a significant body of work has accrued in the area of hydrothermal synthesis of transition metal oxides, there has not really been a concerted and sustained effort to emulate the use of direct thermal approaches to transition metal oxide synthesis.

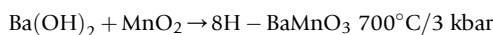
4.18.3.3.1 First row transition metal oxides

The earliest work in this area was mostly driven by the study of magnetism and a thorough review until 1978 is provided.¹⁵⁵ The classical magnetic material magnetite, Fe₃O₄, can be easily synthesized as large high quality single crystals under a wide range of modest hydrothermal conditions and in fact, this is probably the source of naturally occurring magnetite crystals.¹⁵⁶ Several other ferrites and spinels can also be prepared by similar methods.^{157,158} This work was extended to the hydrothermal growth of YIG, Y₃Fe₅O₁₂, which received intense examination for a period as a material for bubble memories in computers.^{159,160} This material was ultimately rendered obsolete for that application, but it did serve as an inspiration for a more detailed examination of magnetically active centers in hydrothermal conditions. One important aspect of this area is the ability to control the oxidation states of the

metal ions by varying the redox potential of the aqueous phase. This led to some very interesting investigations of magnetic transition metal oxides. This include a range of iron orthoferrites, manganates and other phases. Some recent work on the hydrothermal growth of SmFeO_3 at low hydrothermal temperatures finds intriguing suggestions of multiferroic behavior. This is a good example of the ability to synthesize materials below critical or Curie temperatures.^{161,162}

The readily availability of multiple oxidation states in transition metal ions can lead to a wide range of electronically and magnetically interesting phases, but it can also complicate the physical property measurements with significant defects in the oxide lattice. The high temperatures employed in classical synthesis for the oxides can often lead to mixed valence metal ions, creating difficulties in reproducibility and explanation of physical behavior. The hydrothermal approach can alleviate many of these difficulties because the reactions are performed at relatively low temperatures and are done in closed systems that prevent the escape of O_2 . Both of these factors stabilize the metal oxidation states and allow the synthesis of much more stoichiometrically controlled products. In the case of even mild oxidizing solutions, platinum liners are required to contain the fluids. Redox potential control can be done by exploiting the permeability of the inert metal walls to H_2 .¹⁶³ It is also easy to control the redox potential of the solution by the addition of simple chemical oxidants (e.g., ClO_3^-) or reductants (e.g., N_2H_4). Several systems are given below to highlight these aspects.

One fascinating older transition metal system is BaMnO_3 , which despite the simplicity of its formula, is not a classical perovskite structure. Rather it forms a complex series of unusual structures, the most well studied of which is called 8H- BaMnO_3 and contains tetrameric chains of face shared MnO_6 octahedra with corner shared kinks. This phase is only one of a series of related structures of various combinations of face sharing octahedral chains and kinks.^{164,165} The product distribution is very sensitive to the reaction conditions and in many cases, there are clearly nonstoichiometric oxygen sites, which also influence the product distribution and physical properties. A straightforward hydrothermal reaction



in gold tubing led to formation of stoichiometrically pure 8H- BaMnO_3 as high-quality single crystals that enabled the definitive structural study of the material (Fig. 6).¹⁶⁶ This work was revisited theoretically more recently and identified as a possible source of unusual bulk or thin film multiferroic materials.¹⁶⁷ The access to stoichiometrically pure single crystals of these and related materials may provide a route to their further experimental study to explore these theoretical studies.

4.18.3.3.2 Heavy transition metal oxides

Another example of the usefulness of hydrothermal synthesis of transition metal oxides focuses on the second and third row metal oxides. These are generally less well studied than the first row metal oxides but have some intriguing properties that make them very different from the first row d-block metals. Their hydrothermal chemistry in particular shows some exceptional promise. The metal ions are of interest because their ligand field splitting and spin orbit coupling are fairly comparable, which can lead to unusual nonclassical behavior. The heavier elements also can adopt a wide range of oxidation states, generally higher than the first row ions. These factors combine to make this part of the periodic table a rich hunting ground for nonclassical quantum emergent behavior.¹⁶⁸ The tendency of these metals to adopt a wide range of oxidation states makes the stoichiometric control of oxidation potential of the reaction conditions all the more important. One problem with traditional high temperature synthesis methods is

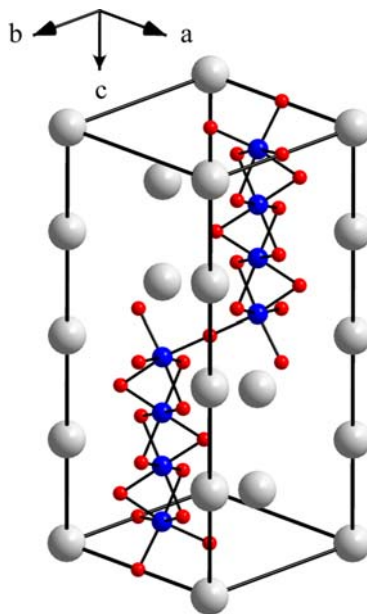


Fig. 6 Kinked chains of face-sharing MnO_6 units in 8-layer BaMnO_3 .

the tendency of the heavier d-block elements to extrude elemental oxides at reaction temperatures, leading to lattice oxide defects, nonstoichiometry and oxidation state irregularities. A recent article highlighted some of these challenges and provides “smoking gun” evidence of some of the advantages of performing hydrothermal synthesis and crystal growth in closed systems at relatively lower temperatures.¹⁶⁹ It compares the physical properties of a series of Ir and Ru pyrochlores prepared by classical thermal methods versus single crystals synthesized in hydrothermal fluids and makes explicit note of the difference in properties of the stoichiometrically pure hydrothermally prepared crystals.

The above article highlights work by an author (Sleight) who did some of the very earliest hydrothermal work with heavy d-block oxides. Sleight reported some of the first work with heavy d-block element oxides more than 50 years ago and discovered some beautiful examples of hydrothermal synthesis of new crystalline solids.^{170,171} Despite a long hiatus this work remains relevant to this day. It is being rediscovered and it is important in the investigation of emergent quantum spin materials. Longo and Sleight found that lanthanum oxide readily reacts with rhenium oxide to form large high quality single crystals of an interesting structure of $\text{La}_4\text{Re}_6\text{O}_{19}$, which has some very interesting physical properties.^{172,173} Subsequent work revealed a series of other interesting materials using hydrothermal conditions at 700 °C and 3 kbar.¹⁷⁴ Interestingly Sleight et al. found that for the metal rhenates no mineralizer is required, and large single crystals grow readily in the presence of only water, rare earth oxides and ReO_2 . This suggests that a soluble rhenate anion is itself a powerful mineralizer to engage the rare earth oxides. In our hands it appears that this property is unique to rhenium as most of the other metals require a mineralizer.

We recently began using this earlier work of Sleight as a jumping off point and prepared a wide range of phases as high quality single crystals of rare earth rhenates, suggesting that the original work was merely the tip of a very large iceberg.^{175,176} Extension of this work to the rare earth ruthenates suggests that the other heavy d-block elements also represent a very attractive area of research for new emergent nonclassical materials accessed by hydrothermal routes.^{177,178} It is also clear that the hydrothermal approach is a very promising way to minimize the problems that lurk for these materials. After a very promising start to this field, followed by a long period of relative dormancy it appears that the hydrothermal approach is well suited to make significant new contributions to this area.

It should be noted that the early second and third row transition metal oxides also appear to have a robust descriptive chemistry but in general they are not well explored. There is somewhat less of a driving force for these elements, because they tend to adopt their fully oxidized states and as such, display few magnetic or optical properties of interest, although some of their structural chemistry is both complex and interesting. In this regard we isolated such unusual species as $\text{Ln}_2\text{TaO}_5(\text{OH})$, and $\text{Ln}_3\text{Ta}_2\text{O}_9(\text{OH})$ (where Ln = rare earth ions) that have related structural motifs to the equally complex hydrothermal rare earth titanate $\text{Ln}_5\text{Ti}_4\text{O}_{15}(\text{OH})$.^{179–181} In many of these cases there is a hydroxide ion coordinated to the transition metal ion. This imparts some hydrogen bonding capability responsible for some of the structural complexity characteristic of these species.

4.18.4 Metal oxyanion building blocks

In this section we examine some of the progress made employing discrete oxyanion synthons (the so-called “ates”) as building blocks for new materials. These are typically small anions of amphoteric oxides that can be either main group- or transition metal-centered. Many are tetrahedral building blocks (SiO_4^{4-} , PO_4^{3-} , VO_4^{3-} , MoO_4^{2-} , etc.). In many cases of course it is not obvious where to define the line between an oxyanion building block (i.e., a discrete tetrahedral silicate) versus an element intrinsic to an oxide lattice (i.e., zircon ZrSiO_4). This is obviously an arbitrary call in many cases, and we will do our best identify the more obvious examples with the understanding that the gray line can shift with individual interpretation. Although the tetrahedra are the most common structural type, other building block options are available, such as trigonal planar groups (BO_3 , CO_3), trigonal bipyramids (GeO_5) and octahedra (SnO_6). In the latter case of species such as stannates with very large nominal formal charges, it is probably more accurate to view them as straightforward lattice elements as opposed to soluble discrete building blocks. The palette of structural options is also greatly increased by the capacity of many of these oxyanions to polymerize, forming an enormous selection of rings, chains and clusters. When this ability is combined with the variable coordination environments of the transition metal, there are an almost infinite variety of structural possibilities within this category. The silicates are obviously the most well-known polymeric anion building blocks, but other anions also form more complex structural varieties. For example, the vanadates also form short polymers, infinite chains, and many types of rings under hydrothermal conditions, and this leads to many beautiful new structures (Fig. 7).

It is well known of course that metal oxyanion compounds can be prepared by many different methods. The hydrothermal method is probably not as well explored as the flux method for example, but there is no question that it is an excellent approach to the problem. The amphoteric nature of the parent metal oxides, the flexibility of the metal counterions and the ability to control pH, stoichiometry, oxidation potential and temperature provide an enormous array of experimental variables. For common, earth-available oxyanions such as silicates and phosphates, the huge selection of mineral structures provides a hint of the range of possible materials that can form from these building blocks. These natural systems serve as an inspiration for the vast array of materials that can be prepared in the synthetic lab.¹⁸² Some isoelectronic and isostructural building blocks can show similar behavior to minerals, while other times the chemistry is very different. For example, PO_4^{3-} and VO_4^{3-} occasionally display isostructural chemistry but more often the chemistry is quite different.

Many, if not most of the well-formed single crystal silicate and phosphate minerals are the product of exposure to superheated aqueous fluids at some point in their genesis. It is well known that the phosphate and silicates form extremely viscous fluids in their

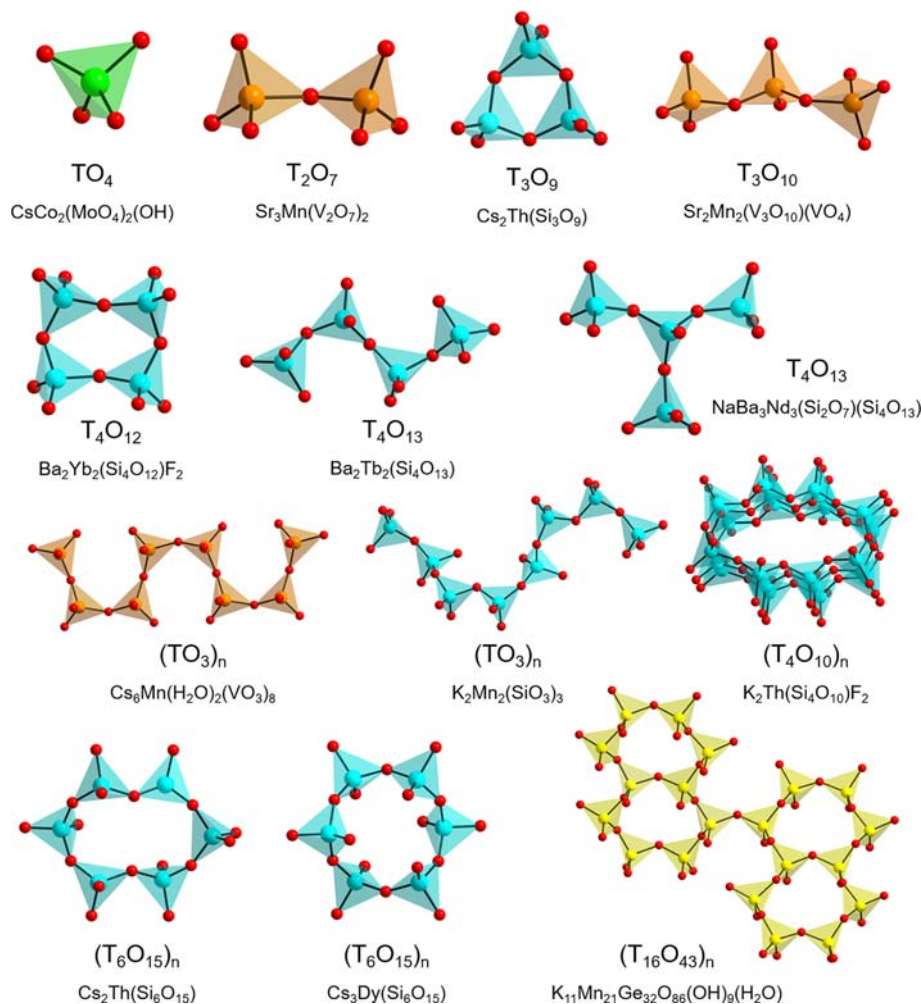


Fig. 7 Selected tetrahedral oxyanion building blocks recently observed from high temperature hydrothermal synthesis ($T = \text{Mo}^{6+}$, V^{5+} , P^{5+} , Ge^{4+} , Si^{4+} , B^{3+} , etc.).

melts with a tendency to form glasses rather than single crystals upon cooling. This has many technological advantages but limits the detailed study of the physical property of the materials as well formed single crystals from melts or fluxes. The weak basicity of the phosphates and silicates and their general stability in most aqueous conditions, however, makes them excellent candidates for hydrothermal chemistry.

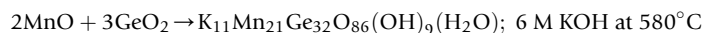
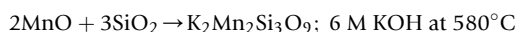
4.18.4.1 Silicates

Not surprisingly the hydrothermal chemistry of the silicates has a rich and robust history, due in part of course to its close ties to mineral geochemistry and the almost endless array of structural combinations of the polysilicate building blocks.¹⁸³ The silicates were among the original systems studied systematically in hydrothermal conditions. Morey published what is probably the first review on the area in 1913, and remained active in the field himself until the mid-1950s.^{36,37} Hydrothermal silicate research in the middle of the 20th century was dominated by the wholesale commercialization effort of quartz growth by nearly all parties interested in the area (see above). There are examples of more condensed silicon oxides where the arbitrarily defined role of silicon is as a lattice element rather than a “building block.” Zircon (ZrSiO_4) crystals can be grown at 700 °C in 3 M KF/LiF,¹¹² continuing the examples of fluorides as mineralizer for extremely refractory metal oxides. There was also enormous work on the growth of zeolite crystals via hydrothermal methods.^{184–187} Most of the work in microporous materials is performed at relatively low temperatures (<300 °C) because above those temperatures the structures begin to condense and form dense phases. This upper thermal limit to the microporous regime creates a distinct demarcation between that area and the denser packed oxides.¹⁸⁸

After somewhat of a hiatus in the field after the extensive efforts in quartz growth, a number of researchers began to revisit the metal silicate chemistry in the 1980s. Considerable work was reported on zirconium silicates in the Russian literature as potential ionic conductors and many new phases were partially identified, providing an excellent indication of the structural richness of the area.¹⁸⁹ An interesting extension of the field to the rare earth silicates was reported by Haile and Laudise in a series of papers in the

1990s describing a wide range of extremely complex alkali rare earth silicates as potential ionic conductors.^{190–194} Although only a few other follow up works were reported beyond this extensive work, it is clear that many other phases remain to be discovered in the broader system of rare earth silicates.^{195–200} As an example of the richness of this chemistry, making only modest changes in the protocols typical employed by Haile et al., we uncovered a very unusual new structure type with a long eight membered repeat unit in a chain creating a nearly incommensurate structure.²⁰¹ These results beg the question of how many other exciting new materials await discovery in this area using the hydrothermal method.

The analogous hydrothermal silicate chemistry with open-shell transition metal ions is not as well developed as might be expected for such important materials. This may possibly reflect the relatively high success rate of preparing metal silicates by flux and melt methods. The amphoteric nature of the silicates, their stability in high temperature hydrothermal fluids, and their tendency to form polymeric edge shared polysilicates makes them a likely target for hydrothermal reactions.²⁰² The potential of the field is indicated by a comparative study we did recently of a relatively simple pair of nearly identical reactions



The reaction using germanium oxide leads to a product with only MnO_6 octahedra and GeO_4 tetrahedra forming a bizarrely complex structure in surprisingly good yield and crystal quality. In contrast the identical reaction with silicon oxide leads to a much simpler formula $\text{K}_2\text{Mn}_2\text{Si}_3\text{O}_9$, but with a very unusual structure containing MnO_5 building blocks of both trigonal bipyramids and square pyramids.²⁰³ Several other reports of transition metal silicates have been reported containing open shell transition metals such as $\text{Rb}_4(\text{NbO})_2(\text{Si}_8\text{O}_{21})$ and $\text{Rb}_2(\text{VO})(\text{Si}_4\text{O}_{10})$,^{204,205} but a great deal more remains to be investigated. Of course, the structural and chemical opportunities for all of these building blocks increase exponentially when mixed components are introduced such as borosilicates.^{206,207} Under these circumstances the number of variants of possibilities is almost endless. The primary challenge confronting the investigator in these systems is the rational and/or systematic design of target materials.

Another interesting area of metal silicate work involves the exploration of U and Th silicates in high temperature aqueous fluids.^{118,208–211} In these cases, the study of hexavalent uranyl can often be done in low temperature ($\leq 220^\circ\text{C}$) hydrothermal solutions because of the good solubility of uranyl in water. When tetravalent uranium or thorium are being investigated, then high temperatures ($\geq 600^\circ\text{C}$) are generally required due to the extremely refractory and insoluble nature of the tetravalent actinide oxides. This work not only demonstrates the utility of the hydrothermal approach in inducing chemistry of the extremely refractory and insoluble tetravalent actinide oxides, but it also highlights a diversity and complexity of this area that indicates it is clearly only in infancy. Under appropriate circumstances the more radioactive elements like Pu^{4+} can probably form new silicates using the conditions developed above.

4.18.4.2 Phosphates

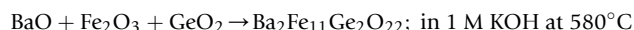
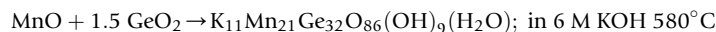
The phosphates have an interesting historical development. Despite their ubiquity in the mineral kingdom, they are not always treated with the same respect as the silicates. An amusing tongue-in-cheek account of these concerns was provided some time ago, but of course the phosphates are too important to be ignored.²¹² The elucidation of geological examples of metal phosphate serves as an inspiration for synthetic exploration exploiting hydrothermal methods, as some of the most remarkable structures in all of chemistry reside in the mineral phosphates and related arsenates.^{213–216} Work in the 1980s and 1990s by Haushalter targeted metal phosphates using hydrothermal methods.^{217,218} This research mostly employed relatively low ($\leq 220^\circ\text{C}$) reaction temperatures, but the array of beautiful new materials was remarkable, and in many ways this work can be viewed as one of the inspirations for the current massive field of hydrothermal MOFs. The open nature of many of these materials is reminiscent of many of the open framework metal phosphate minerals and highlights the importance of temperature in the preparation of the materials. As with the silicates, growth temperatures below about 300°C are probably necessary for the maintenance of open frameworks, especially if organic templates are involved. Higher growth temperatures ($\geq 500^\circ\text{C}$) almost always lead to condensed structures, and any organic templates are unlikely to survive temperatures above $400\text{--}500^\circ\text{C}$. There was a considerable degree of work done earlier on transition metal phosphates employing high temperature hydrothermal conditions. Much of this work was very systematic and thorough and led to a wide range of condensed metal phosphates.^{219–222} Phosphate work was also driven by the development of several commercially important metal phosphates, particularly KIP ($\text{KTiO}(\text{PO}_4)$) and berlinite AlPO_4 .^{62,69} Although the condensed phosphate and arsenate phases will probably never be as numerous as the organic templated MOFs, new phases continue to emerge, and the field is still ripe for further exploration.^{223–225}

4.18.4.3 Germanates

Among the elements beyond Si and P, even a modest perusal of the periodic table can identify some useful tendencies. It is well known for example, that silicates can only adopt the tetrahedral environment at any but the most extreme pressures. The larger stannates in contrast, are only known to adopt the octahedral environment. The intermediate sized germanate ion is much more structurally flexible and can adopt a range of coordination environments from four to six, and there are examples known where the germanate building block can adopt multiple coordination numbers within the same structure, as in $\text{Cs}_4\text{UGe}_8\text{O}_{20}$ and $\text{Cs}_3\text{U-Ge}_7\text{O}_{18}$.^{226,227} Since germanium is relatively rare within the earth's crust there are very few germanate minerals. Nevertheless, its

amphoteric nature, structural flexibility and aqueous stability make it an ideal oxyanion building block. Despite the dearth of naturally occurring metal germanate minerals, first row transition metals readily form a wide range of solids with germanates from hydrothermal solutions under even the simplest reaction conditions.^{20,228–231} Recently we and others have shown that it is an excellent building block, capable of forming an enormous array of interesting materials in hydrothermal fluids (Fig. 8).^{232–234}

Recently we found that even straightforward reactions of GeO_2 with simple first row transition metal oxides can lead to some spectacular results. As an illustration, the simple reaction of GeO_2 with Fe_2O_3 in the presence of Ba^{2+} leads to the growth of the interesting Y-type hexaferrite $\text{Ba}_2\text{Fe}_{11}\text{Ge}_2\text{O}_{22}$ as well-formed single crystals.²³⁵ The technologically important ferrites have been known since the 1950s but very few single crystals have been prepared. Some recent unusual examples of first row transition metal germanates prepared by hydrothermal chemistry are given below.



The complex structures formed as large high quality single crystals from such simple starting materials suggest that the phase space is extremely rich, with many exciting new materials awaiting discovery. It is clear that the surface is only being scratched in this area with enormous swaths of the periodic table essentially untouched. For example, there are few if any published reports on reactions involving second or third row transition metals with germanate oxyanions. The germanates also readily form a wide range of interesting complexes with rare earth ions, some of which are close analogs to silicates, but many of which are very different.^{236–240} In addition to the interesting structural results, some unusual chemical quirks emerge as well. We were able to isolate for example, a stable Tb^{4+} complex in high yield, using germanate building blocks.²⁴¹

The germanates seem to display a particular affinity for the hydrothermal medium. Although the subject has received some attention using classical melt based synthesis, the hydrothermal approach seems to be an ideal confluence of amphoteric solubility, phase stability and crystal growth for the metal germanates.²⁴² The early work in hydrothermal germanates suffered somewhat from lack of ready access to high quality single crystal diffraction,²⁰ but it left no question as to the wealth of new phases that await further exploration of phase space of metal germanates. In addition, the interesting behavior of magnetic germanates argues strongly for further exploratory development.²⁴³ A common characteristic that emerged from this chemistry is the sensitivity of the chemistry

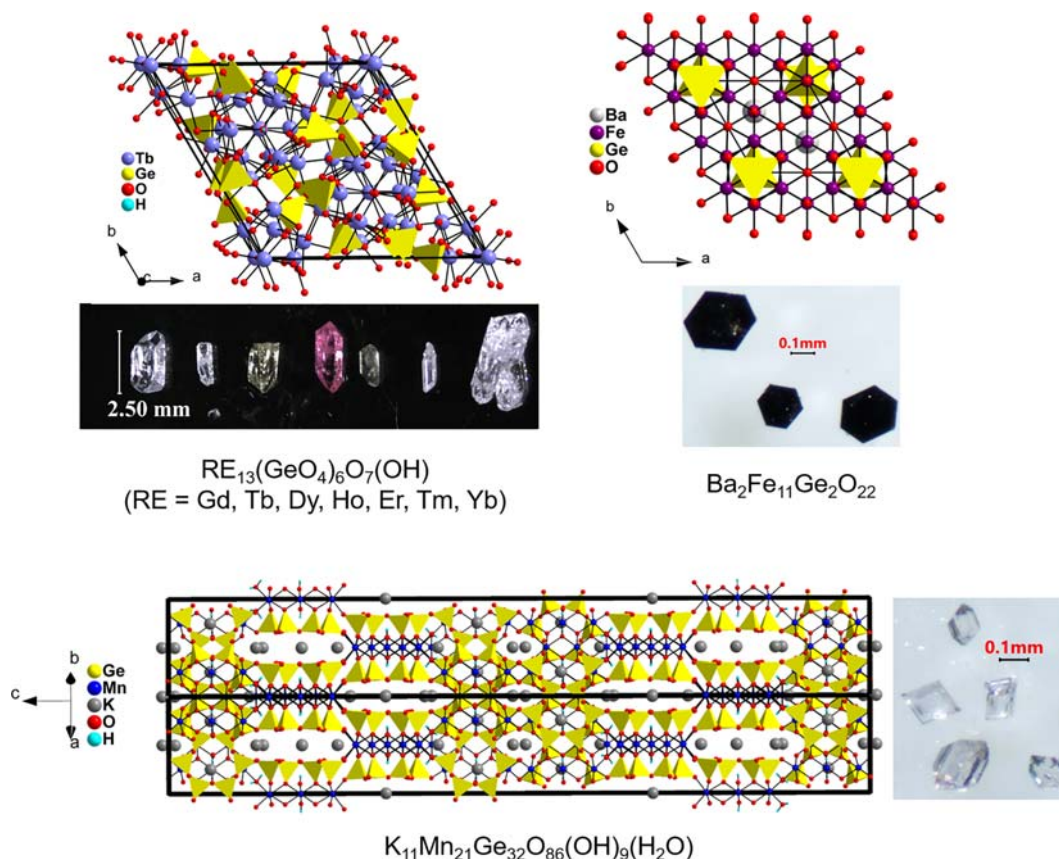


Fig. 8 Complex metal-germanate chemistry resulting from hydrothermal synthesis. Germanate oxyanions are shown as solid yellow tetrahedra.

to the reaction conditions, especially the identity and concentration of the mineralizer and the stoichiometry of the starting materials. It is clear that even small variations of the reaction conditions can lead to significant variations of the products. In most cases these variations are highly reproducible and lead to good yields, which suggests that the chemistry is truly a function of reaction conditions, rather than any fortuitous one-time selection of a "lucky" crystal. The implication of these observations is that the intermediate fluid chemistry is exceptionally complex. Additionally, the extension from germanate to stannate under hydrothermal conditions was essentially unknown until recently. We found that stannate is very refractory but can be mineralized to act as an octahedral building block in basic mineralizers to form both alkaline earth stannate perovskites and a wide range of rare earth stannate pyrochlores, as described above.

4.18.4.4 Vanadates and molybdates

Vanadates and molybdates show considerable promise as building blocks in hydrothermal fluids. They generally adopt tetrahedral structural environments and hence can be compared to their phosphate and sulfate main group cousins. They are very flexible in adopting other oxidation states but are generally quite stable in their highest (d^0) oxidation states particularly in the high temperature ($> 400\text{ }^\circ\text{C}$) hydrothermal environments. In this regard they are excellent building blocks for more complex structural motifs. The ability to study comparative systems such as phosphates versus vanadates, or molybdates versus sulfates is also interesting in regard to magnetic behavior. When the bridging element is a metal with empty d-orbitals, like V^{5+} or Mo^{6+} , versus the empty p-orbitals in P or S, there can be a significant change in the magnetic coupling, which is the source of considerable theoretical and practical interest.^{244,245}

The original work on hydrothermal chemistry of the molybdates and tungstates was performed by the Russian groups led by Lobachev and Demianets.²⁴⁶ The initial work was done on the growth of a number of scheelite analogs MMoO_4 and MWO_4 , where M is a wide range of divalent metal ions. Some but not all of the scheelite analogs can also be grown conveniently by CZ pulling methods, but some of those are also plagued by twinning issues, so the hydrothermal methods can be a useful alternative for specialty applications. Similarly, the growth of the $\text{ARE}(\text{MO}_4)_2$ (A = alkali ion, RE = rare earth ion, M = Mo, W) class of crystals was also explored by these workers.²⁴⁷ These compounds have been examined as hosts for a number of solid state laser applications. Many of these crystals can also be grown from melt and flux methods, but they can have complex structures and also suffer from twinning and disorder issues, so the hydrothermal method may be useful in some instances. Some very thorough work by Demianets and others led to a number of other more complex molybdate phases from hydrothermal fluids, although some of these were not completely structurally characterized.^{15,20} After that work the field once again seemed to fall into obscurity and very few other exploratory efforts were described until recently.

Compared to the extensive hydrothermal chemistry of the phosphates, the corresponding hydrothermal exploration of the vanadates is significantly less developed. The early historical work by Demianets et al. on molybdates and germanates is not really mirrored for the vanadates. Vanadates do have an extensive mineralogical chemistry, though not nearly as broad as the phosphates,^{248,249} and much of that probably derives from natural hydrothermal fluids. These structural studies provide an excellent comparative database for the laboratory synthesis of corresponding metal vanadates. There was also, like the phosphates, some considerable early work done in low temperature hydrothermal fluids.^{250–252} Vanadates can adopt a wide range of coordination environments beyond the tetrahedron, although tetrahedral generally appears to be the preferred environment in higher temperature hydrothermal fluids. They also appear to have a considerably greater tendency to form polymeric building block in hydrothermal conditions than the phosphates. These factors greatly increase the structural possibilities of vanadate building blocks. The degree of condensation and branching of the polyvanadates can be controlled by the traditional factors such as temperature, pH and nucleophilicity of the reaction medium. These factors are easy to control in the closed superheated aqueous phases, leading to a very rich coordination chemistry. The stability of trivalent, tetravalent, and pentavalent vanadium (though not all as tetrahedral building blocks) in hydrothermal systems is also a useful source of chemical variety.

Our initial efforts in this area were the result of trying to prepare YVO_4 single crystals as hosts for lasing ions,²⁵³ following up on earlier work by Byrappa.²⁵⁴ The material is well known as an excellent laser host but has some problems in its bulk growth because of the tendency of the V^{5+} ion to destabilize at the growth temperatures (ca. $1250\text{ }^\circ\text{C}$) and become reduced, with concomitant oxide defects in the lattice. The defects lead to the characteristic pale green-brown color of flux grown YVO_4 and diminish the effectiveness of the laser performance of the doped crystals. We found that high quality YVO_4 single crystals can be grown, including those doped with suitable lasing ions, via the hydrothermal method. Interestingly this approach also can lead to good quality single crystals of YNbO_4 and related materials.^{181,255} These phases are not isostructural with their vanadate analogs but may still serve as hosts for detectors and lasers. Subsequently we found that the rare earth vanadates have an extensive chemistry beyond the tetragonal YVO_4 structure type, including the glaserite structure which has a trigonal 2-D Kagome net structure displaying frustrated magnetism.^{256–259} Encouraged by these results we extended our investigations to the open shell first row transition metal ions with particular emphasis on magnetic properties of new phases. Performing reactions in aqueous fluids between $500\text{ }^\circ\text{C}$ and $700\text{ }^\circ\text{C}$ in the presence of 1–5 M alkali or alkaline earth OH^- ions leads to very good crystallization of an extensive array of new phases. In many cases high quality single crystals of sufficient size can be obtained from simple spontaneous nucleation, suitable for single crystal neutron and magnetic studies.^{260–263} We also found that simple addition of various halide ions in various concentrations also leads to new phases.^{264–268} In some cases the halide simply serves as a different mineralizer and induces formation of new phases. In other cases, the halide becomes incorporated into the lattice acting as a structural component creating an entirely new series of different phases. Most of the new phases thus far have complex low dimensional

structures, usually either 1-D or 2-D interactions, with many different vanadate building blocks, either single vanadates, dimers, trimers, more complex rings, or infinite chains, often mixed within the same lattice (Fig. 9). The large number of chemical variables in these systems, (alkali ion, mineralizer type and concentration, halide, redox factors, stoichiometry and many others) and the high sensitivity of the product distribution to these factors, makes this descriptive chemistry very extensive and still emerging rapidly. The interesting structural and magnetic properties of many of these new compounds makes the continued development of great interest.

Our group recently also started to revisit earlier work examining the transition metal molybdates, in particular open shell transition metal complexes, where previous work highlighted the use of the MoO_4^{2-} tetrahedral building blocks to form magnetically frustrated systems in analogy to metal sulfates.^{269–272} We found that, like the vanadates the molybdates are quite stable in hydrothermal fluids at 400–650 °C, and their descriptive chemistry appears to be very robust. The chemistry is not as well developed as that of the vanadates yet, but product formation is highly sensitive to the reaction conditions, especially the mineralizer identity and concentration.²⁷³ We found that the tetrahedral molybdates can serve as building blocks to form interesting low dimensional species with unusual magnetic properties.²⁷⁴ Tetrahedral molybdate and vanadate building blocks provide useful templates for Kagome layers of open shell transition metal species (Fig. 10).

4.18.4.5 Carbonates

One useful quality of the hydrothermal approach is in the examination of components that have limited thermal stability, like CO_3^{2-} and SO_4^{2-} . Both important building blocks tend to decompose in open systems above about 400 °C with loss of CO_2 and SO_2 respectively. This significantly limits their synthetic access from traditional high temperature solid state synthetic approaches. Reactions in sealed hydrothermal conditions solves a number of these problems. The sealed reaction vessels inhibit the loss of the volatile decomposition products, keeping them as part of the reaction equilibrium. At the same time the relatively low reaction temperatures of the hydrothermal fluids will allow for suitable solubility and crystal growth to lead to new products.

Hydrothermal growth of the MCO_3 class of compound was explored rather thoroughly by Ikomikova et al.²⁷⁵ and considerable insight was obtained into the growth of the various carbonates but relatively few new carbonates were obtained. It can be speculated however, that the employment of carbonate as a reagent in hydrothermal fluids can lead to new phases since the carbonate equilibrium should be maintained in the pressurized sealed autoclave, preventing loss of CO_2 and providing an ample source of CO_3^{2-} even at high temperatures.²⁷⁶ An excellent example of the potential of this area is $\text{K}_2\text{Mn}_3(\text{VO}_4)_2(\text{CO}_3)$ which has beautiful structure first prepared at relatively low temperature hydrothermal conditions (280 °C),²⁷⁷ and then as much larger single crystals at higher hydrothermal conditions (650 °C) for detailed neutron scattering experiments.^{278,279} The structure is very symmetrical and attractive but also displays an exceptionally complex magnetic behavior than only could be ascertained because of the growth of the large single crystals.

Oddly enough, the corresponding high temperature hydrothermal exploration of sulfates is almost unknown. This is somewhat surprising given the useful results obtained for magnetic systems at low temperature hydrothermal conditions, and the attractive properties of the sulfate dianion tetrahedral building block. It would not be surprising to see more high temperature hydrothermal work emerge from the $\text{SO}_4^{2-}/\text{MoO}_4^{2-}$ building blocks in the near future.

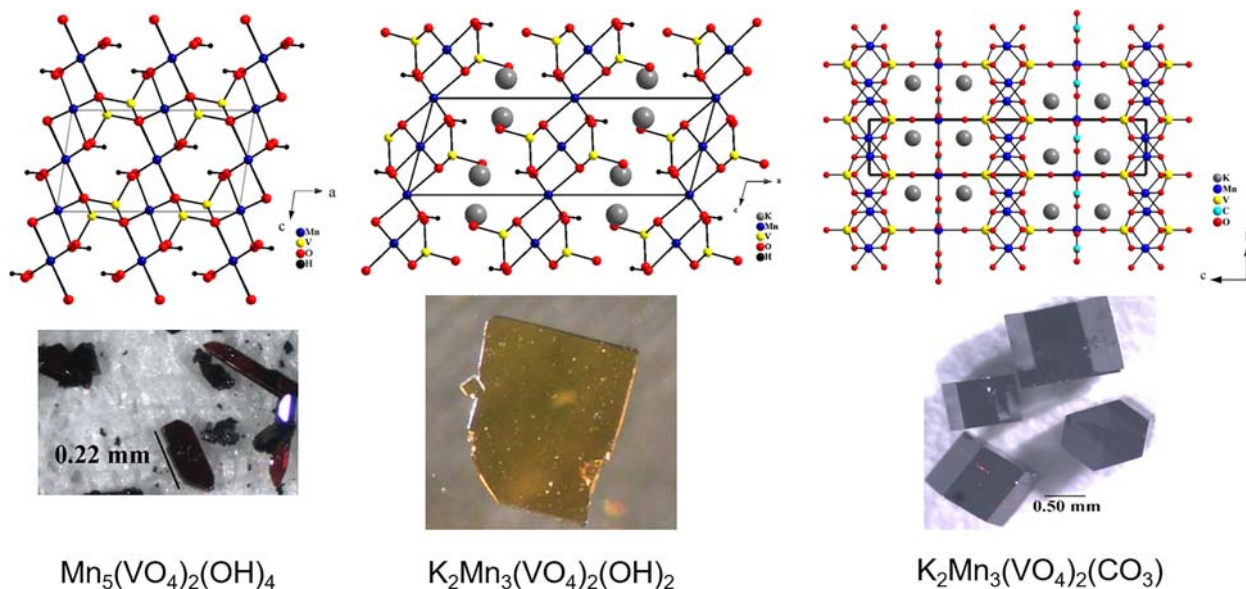


Fig. 9 Transition metal vanadates having low dimensional features. Vanadates can act as terminal decorations on chains and sheets, or as bridging groups between chains and sheets.

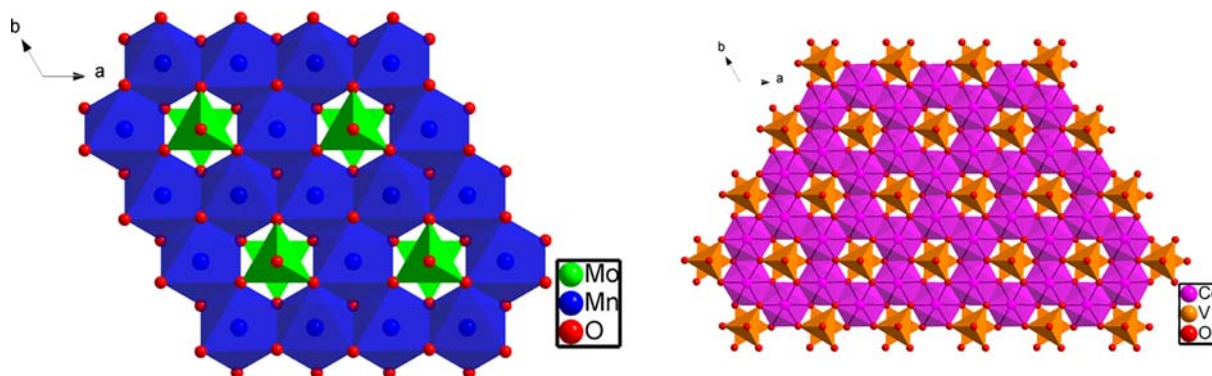


Fig. 10 Molybdate- and vanadate-templated Kagome layers in $\text{KMn}_3(\text{MoO}_4)_2\text{O}(\text{OH})$ (left) and $\text{K}_2\text{Co}_3(\text{VO}_4)_2(\text{CO}_3)$ (right).

4.18.4.6 Borates

Another interesting class of compounds that is very amenable to hydrothermal synthesis is the borates. Like the silicates, borate melts tend to be very viscous and tend not to grow good crystals directly from the melt. Also like the silicates, they do form interesting single crystals using the appropriate fluxes. Early work described in the Russian literature did describe the synthesis of several borates from high temperature hydrothermal fluids, but the literature was not readily available to western workers.²⁸⁰ The work was subsequently taken up by Byrappa and co-workers specifically looking at the synthesis of lithium borates such as polar acentric $\text{Li}_2\text{B}_4\text{O}_7$, which have potential ferroelectric, piezoelectric and nonlinear properties.^{281–284}

We entered this field to address a specific need for wide bandgap materials, particularly in deep UV optical applications. There are relatively few functional materials with bandgaps greater than 4 eV (300 nm) and even fewer with bandgaps of 6 eV (200 nm) or more. In particular there is a strong need for acentric materials capable of frequency manipulation for nonlinear optical applications in deep-UV solid state lasers. Borates are one of the only classes that fill this need admirably since they typically have very wide bandgaps (4–7 eV) while still maintaining decent nonlinear optical coefficients. Thus, there has been a major development effort to synthesize and grow new borate single crystals for advanced UV optics.^{285–287} Most of this work employs various fluxes as the reaction medium but the early success of the Russian groups²⁸⁸ and the amphoteric nature of borate suggested that hydrothermal reaction media could lead to acentric wide bandgap borates. A wide range of borates are stable and crystallize well from aqueous phase under relatively modest conditions. Borates typically can be mineralized using 0.1–1 M mineralizers, either OH^- or F^- , at reasonable temperatures, usually between 400 °C and 550 °C. They are generally more soluble than the refractory metal oxides, making them easier and cheaper to grow at commercial scale. A number of new borates were isolated from hydrothermal fluids, usually with alkali or alkaline earth cations in the lattice,^{289–298} but we particularly focused on two materials ABBF ($\text{ABe}_2(\text{BO}_3)_2\text{F}_2$ where A = K, Rb) and SBBO ($\text{Sr}_2\text{Be}_2\text{B}_2\text{O}_7$).^{299–303} These were both originally synthesized in flux media but both suffered from crystal quality issues. They do both show exceptional properties in deep UV optical applications, potentially enabling the development of all solid state lasers emitting between 175 nm and 355 nm. We began to examine hydrothermal protocols for the scale up growth of these promising materials as a possible route to commercial production of laser quality crystals. Other groups also were able to grow high quality single crystals of these classes of materials using the hydrothermal approach as well.^{304–306} This work shows considerable technological promise but is still in progress. We reported good commercial scale growth of the ABBF class of material, but that class of materials is exceptionally soft and layered in its bulk form (Fig. 11). Because of this, the primary limitation in the development of this important material is not the chemistry or crystal growth, but rather the post growth processing, which is exceptionally difficult.

4.18.5 Halides

Halide systems offer a bit of both extremes in hydrothermal systems. Many halides have high solubilities in water under ambient conditions, so high temperature hydrothermal approaches do not provide a particular advantage to their preparation or growth. However, there are several examples of systems where simple halides can be grown hydrothermally, as well as some more complex halide systems where hydrothermal conditions provide access to a variety of new phases having interesting structures and potential applications. Ideally, there would be enough solubility to impart dissolution and reactivity, but not so much solubility to provide a barrier to crystallization. Importantly, a given halide system must also sufficiently resist hydrolysis to promote crystallization of the halide species instead of OH^- -containing species. Even in high halide concentration aqueous solutions this is not guaranteed, as oxide or hydroxide groups can provide competition for the halide anions. A few binary halides appear to fit these requirements in acidic solutions, including CuI and PbI_2 .³⁰⁷ The alkaline earth metal fluorides have also been shown to be amenable to high temperature hydrothermal methods.³⁰⁸ We have actually found the formation of large SrF_2 and BaF_2 crystals can be somewhat of a barrier



Fig. 11 Hydrothermally grown $\text{RbBe}_2(\text{BO}_3)\text{F}_2$ (RBBF) crystals. Left: multiple crystals grown on a gold ladder from a single hydrothermal autoclave. Right: As-grown RBBF crystals (1 cm divisions).

to synthesizing new compounds in the presence of high fluoride concentrations, as the stability of the binary fluorides can cause a significant amount of the Sr^{2+} or Ba^{2+} ions to be partitioned into these phases making them unavailable for further reaction.

Of the halides, the fluorides appear to have the richest descriptive chemistry in hydrothermal systems. As with the perovskite oxides, perovskite fluorides, ABF_3 , provide systems with potentially interesting optical and magnetic properties. Somiya and coworkers found that fluoride ions from the KF mineralizer would out-compete chloride ions from the transition metal reagent to form crystals of KMnF_3 , KFeF_3 , KCoF_3 , KNiF_3 , and KZnF_3 at 600°C .^{309,310} Other transition metal fluoride salts such as NH_4MnF_3 , NaFeF_4 , $\text{NH}_4\text{Fe}_2\text{F}_6$, NH_4CrF_4 , BaZnF_4 , BaVF_5 , $\text{Ba}_6\text{Zn}_7\text{F}_{26}$ have been reported as relatively large crystals from acidic mineralizers of high HF concentrations.^{311–313} Double perovskite fluorides, analogous to the mineral elpasolite, can also be grown hydrothermally, and the lanthanide-based elpasolites such as $\text{Cs}_2\text{NaLnF}_6$ ($\text{Ln} = \text{Sc}, \text{Y}, \text{lanthanides}$) have been studied for their potential spectroscopic and scintillation properties.^{314–318} These are typically synthesized by the hydrothermal reaction of alkali fluorides with lanthanide oxide or fluoride precursors. A wide range of other alkali lanthanide fluorides have been grown hydrothermally, including ALnF_4 , A_2LnF_5 , AA'LnF_5 , and ALn_2F_7 ($\text{A} = \text{alkali metal}; \text{Ln} = \text{lanthanide}$) with complex relationships between their stoichiometries and structures.^{189,319–323} In this vein, we recently identified some systematic limits relating the phase distribution and polymorphism in ALn_2F_7 and $\text{ALn}_3\text{F}_{10}$ phases.³²⁴ Others have also used high temperature hydrothermal approaches to prepare complex fluoride crystals for spectroscopic studies.^{325–329} Such fluorides are attractive optical materials due to their low phonon energies, long lifetimes, and efficient luminescence due to reduced concentration quenching.

In addition to the lanthanide fluorides, a particularly stable class of fluoride compounds resulting from high temperature hydrothermal systems are those based on tetravalent metal ions such as Zr^{4+} , Hf^{4+} , Ce^{4+} , Th^{4+} , and U^{4+} . Much like the lanthanides, the metal-fluorine bond resists hydrolysis to a reasonable extent to enable considerable descriptive chemistry. Hydrothermal reactions of HfF_4 with alkali fluorides, AF ($\text{A} = \text{Li}, \text{Na}, \text{K}, \text{Rb}, \text{Cs}, \text{NH}_4$) produced several fluoride phases, including A_2HfF_6 , $\text{A}_5\text{Hf}_2\text{F}_{13}$, and A_3HfF_7 , as well as oxyfluorides $\text{A}_2\text{Hf}_3\text{OF}_{12}$ and A_3HfOF_5 , indicating some degree of hydrolytic reaction.³³⁰ Especially rich fluoride chemistry was observed from the reactions of ThF_4 with aqueous alkali fluoride mineralizers which produced crystals of ATHf_5 , $\text{ATH}_3\text{F}_{13}$, $\text{ATH}_6\text{F}_{25}$, ATH_2F_9 , and $\text{A}_7\text{Th}_6\text{F}_{31}$ ($\text{A} = \text{Na}, \text{K}, \text{NH}_4, \text{Rb}, \text{Cs}$) phases.^{331–335} In similar reactions that also contained $\text{Ba}(\text{OH})_2$, we obtained another series of thorium fluorides, $\text{A}_3\text{Ba}_2\text{Th}_3\text{F}_{19}$ ($\text{A} = \text{Na}, \text{K}, \text{Rb}$).³³⁶ Thorium is often used as a surrogate for approximating the chemical behavior of U^{4+} and the later actinides, and some recent studies suggest that mild and moderate hydrothermal synthesis will play an important role in understanding the chemical speciation and properties of these systems.^{337–340} In many instances, a vast array of these actinide-containing fluorides are accessible using both fluoride and oxide precursors, further opening this interesting area.^{341–344}

4.18.6 Chalcogenides

Chalcogenides are of interest in a variety of fields due to their potential electronic, optical, magnetic, and catalytic properties, as well as their propensity to form a variety of interesting structural features, including complex polyanions, clusters and open frameworks.^{345–348} A wealth of chalcogenide species have been prepared using low temperature hydrothermal/solvothermal approaches, and these are nicely reviewed elsewhere.^{349–353} Mild hydrothermal conditions are often quite suitable for the vast majority of exploratory studies, as well as the formation of nanostructured materials. High temperature hydrothermal approaches begin to gain traction when large single crystals are desired. The search for, and development of II/VI semiconductors led to a concerted chalcogenide synthesis effort involving high temperature hydrothermal approaches.³⁵⁴ Much of that work came as a direct extension of the approach developed by the Bell Laboratories group to grow ZnO. Sphalerite-type ZnS has appreciable solubility in aqueous hydroxide and chloride solutions, and was grown as large crystals at 350°C in aqueous KOH.³⁵⁵ Shortly after this, the growth of cubic ZnSe, cubic ZnTe, hexagonal CdSe, and cubic CdTe was demonstrated in aqueous hydroxide,³⁵⁶ with the growth conditions of ZnSe optimized using NaOH and LiOH mineralizers.³⁵⁷ Concurrent with that work, Rau and Rabenau approached the

chalcogenide systems using acidic hydrothermal conditions around 450 °C in quartz ampoules. A number of chalcogenide and chalcogenide-halide phases, including some that were subject to hydrolysis under basic conditions, were obtained as relatively large crystals using 2–12 M HCl, HBr, or HI including CuS, Cu₉S₅, CuSe, CdS, HgS, PbS, PbSe, MnS, Sb₂S₃, SbSI, Hg₃S₂Cl₂, Pb₅S₂I₆, Pb₇S₂Br₁₀, CuSe₂, AuTe, and AuBrTe₂.^{307,358–361} Strong acids have also been used to obtain HgSe and HgTe from 200 °C to 350 °C.³⁶² Chalcopyrite-type CuInSe₂ was also prepared from HCl solutions around 375–425 °C.³⁶³ The utility of alkali chloride solutions in synthesizing and transporting sulfides has also been demonstrated in several other studies. Of note, the synthesis of FeS₂ and CuFeS₂ was demonstrated at 300–500 °C using aqueous brines having modest alkali chloride concentrations.^{364–366}

The geochemical significance of many of these phases is a good example of the overlap between synthetic and natural systems, where synthetic hydrothermal approaches can emulate the hot sulfur-rich fluids that occur where magma and water coincide. This relationship has produced interesting studies aimed at understanding mineral formation and speciation of chalcogenides.³⁶⁷ For example, synthesis in the Cu–Fe–S system has produced a significant amount of synthetic data that informs on the stability fields and formation of pyrite, chalcopyrite, bornite, marcasite, pyrrhotite, arsenopyrite, and nukundamite, among other phases.^{368–374} In other studies, synthetic routes have been developed to other sulfosalt minerals such as Ag₃AsS₃, Ag₃SbS₃, Ag₇SbS₆, Cu₁₂Sb₄S₁₃, CuInS₂, and FeIn₂S₄.³⁷⁵ Although almost all exploratory hydrothermal chalcogenide synthesis occurs at low temperatures, or in other solvents such as supercritical ammonia or ethylenediamine, we have found high temperature hydrothermal methods to be occasionally useful. Some examples formed in aqueous solutions at 375 °C include the low-dimensional compound (NH₄)BaAs₄·2H₂O using a (NH₄)₂S mineralizer,³⁷⁶ Pb₆Sb₆Se₁₇ using NH₄Cl,³⁷⁷ and orthorhombic MnSb₂S₄ using NaCl.³⁷⁸

4.18.7 Hydrothermal synthesis of gems and minerals

One intriguing potential application of the hydrothermal technique, and a natural extension of its mineralogical prevalence, is in the growth of man-made gems. Naturally the first question on this topic will always regard the hydrothermal synthesis of diamond. This has been demonstrated in principle but will almost certainly never be more than a laboratory curiosity compared to the rapid advances made in other methods of diamond synthesis.^{379–382} There is a bit more promise in oxide-based gems. This world is one with a long history of feints and misinformation where actual growth methods are often, and understandably, closely held secrets. Much of the beguiling history of man-made gems is painstakingly spelled out by Nassau and others in a series of fascinating publications that read like a detective story.^{40,383} In most cases the hydrothermal method is not competitive to other growth methods such as flux growth, melt growth or melt pulling, but there are some interesting exceptions.

Obviously, any quartz based *gems* (i.e., citrine, amethyst) can be prepared via hydrothermal routes employing careful doping with various transition metal ions to obtain the desired color centers.^{40,384,385} Tourmaline was grown by hydrothermal methods, initially by a number of Russian groups, during the middle of the 20th century using boric acid and borate chlorides as a mineralizer.^{386,387} Despite considerable efforts however, it does not appear to be a commercially or scientifically viable approach to the material in the lab. This is somewhat surprising given that large well-formed natural tourmaline crystals are almost certainly grown in naturally occurring hydrothermal fluids.

One of the more intriguing hydrothermal related synthetic gem stories is that of emeralds (Cr³⁺ doped Be₃Al₂Si₆O₁₈).³⁸⁸ It was originally believed that Nacken grew synthetic emerald using a hydrothermal approach, but this is almost certainly not the case. Rather he probably used an unidentified flux method to obtain small samples of intermediate quality. The first truly successfully commercial method of outstanding synthetic emerald growth was perfected by Carroll Chatham of Chatham Emeralds, again using a closely held flux method.³⁸⁹ The first hydrothermal “synthesis” of emeralds was probably done by Lichleitner, but these were actually formed by using colorless beryl crystals as substrates with a thin coating of green emerald hydrothermally deposited in the surface to impart the characteristic color. The first well established hydrothermal growth of emeralds was performed by Flanagan et al. at Union Carbide.^{390–392} This work led to single crystal emeralds, but they were too small to compete with the existing flux methods. The primary problem with hydrothermal emerald growth is the same as with all Cr³⁺ hydrothermal reactions, namely the complete insolubility of trivalent chromium in aqueous base, necessitating the use of more experimentally challenging acid mineralizers. This approach led to commercially viable products, but they still do not compete well with flux grown material.³⁹³ The hydrothermal growth of beryls not doped with Cr³⁺ is much easier, but the resulting products are generally less valuable than emeralds.^{394–396} The one outstanding exception is the beautiful red beryl, where the red color can be achieved by doping with various combinations of Fe²⁺, Co²⁺, and Mn²⁺. This color is very rare in nature but can be synthesized as outstanding *gem* quality crystals in the hydrothermal lab.³⁹⁷

4.18.8 Nitrides in supercritical ammonia

Although the overwhelming majority of work in superheated solvents involves aqueous fluids, there is an interesting body of work on the use of ammonia to grow metal nitrides as a direct analogy to growing oxides in water. The pioneering work in this area was done by Jacobs and co-workers,³⁹⁸ and a review of this work provides considerable detail in handling super-pressurized ammonia and growing metal nitrides.³⁹⁹ The work shows the similarity to water in the formation of a wide range of metal amides (e.g., Ca(NH₂)₂ analogous to metal hydroxides Ca(OH)₂) from growth at relatively low temperatures.⁴⁰⁰ A series of nitrides (EuN, Cu₃N, Mn₃N₂) can be formed in supercritical ammonia at higher temperatures.⁴⁰¹ This reaction chemistry and crystal growth of

nitrides and amides in supercritical ammonia is still in its infancy.^{402–404} The chemistry is very complex and experimentally demanding but it appears to be extremely exciting and worthy of further effort.^{405–408}

Without a doubt the most intense effort involving supercritical ammonia involves the growth of single crystals of gallium nitride. Despite the enormous technological demand for GaN wide bandgap devices there are no convenient routes to bulk single crystals of the material for use as substrates. Once it was shown that single crystals of GaN could be grown in supercritical ammonia (again in analogy to the single crystal growth of quartz in water),^{409–417} an enormous effort was put forth to scale up growth of single crystals of GaN to commercial levels.^{418–420} This effort led to the successful commercial development of GaN single crystals for blue lasers and bright LEDs.^{421,422} The growth of GaN and other nitrides has been successful using NH_2^- as a mineralizer in supercritical ammonia, again as a direct analog to OH^- mineralizer for oxides in supercritical water. There is evidence, however, that some metal nitride feedstocks may be more soluble and mobile in acidic supercritical ammonia using NH_4X ($\text{X} = \text{F}, \text{Cl}$) as mineralizer.^{423–428}

4.18.9 Summary

The use of high temperature hydrothermal fluids as a synthetic medium for inorganic compounds has enjoyed considerable success especially since the late 1940s. The commercial development of single crystal α -quartz inspired researchers around the world to begin to examine the possibilities of the environment as a synthesis medium. In particular, Laudise in the United States, Somiya in Japan, Rabenau in Europe, and Lobachev and Demianets in the USSR, worked hard to highlight the uses of the medium in inorganic synthesis. The method can be used in two general ways, as a route to grow large single crystals of specifically targeted materials, and as a medium for the exploratory synthesis of new compounds. A primary attribute of the method is the low temperature of the reactions, typically less than 750 °C. This enables the growth of single crystals with relatively low phase transitions (such as α -quartz) that can probably not be accessed by any other method. With the proper selection of mineralizers, the technique also provides low temperature access to otherwise extremely refractory materials. Such materials can require such high reaction temperatures employing traditional melt based methods (often > 2500 °C) that they lead to lattice defects and impurities. The hydrothermal method provides a convenient access to high-purity, high-quality single crystals of some otherwise extremely recalcitrant materials. The technique is rarely competitive as a crystal growth method when materials are well behaved in traditional growth techniques such as Czochralski or Bridgeman methods. It has applications as a complimentary niche method when subtle factors need to be addressed regarding crystal quality or specialty doping for example.

In addition, the ability to vary and control experimental parameters such as redox potential, stoichiometry, counterion presence, pH and similar factors makes the technique very attractive for synthesis of new materials. Control of such factors are very much in the comfort zone of chemists, so the technique is very attractive for the exploration of new phase space. The technique also has the advantage of yielding good quality single crystals in a relatively high percentage of reactions. These initial crystals are not usually large enough for bulk physical property measurements, but they are often sufficient for single crystal X-ray diffraction which can provide the structural identity critical for a new phase. In many cases they can be manually separated and oriented for subsequent spectroscopic and magnetic studies for example. This relatively easy access to reliable structural data of some potentially complex materials at an early stage of their discovery makes this technique a very promising one for exploration of phase space and synthesis of new compounds.

The “high temperature” hydrothermal method (as opposed to the massive field involving aqueous reactions below 225 °C) has been known in its present incarnation since the early 20th century. The work by Morey to explore the geochemical growth of silicates was quickly followed by an extensive effort by many countries to exploit the method to grow single crystals of quartz, which is a somewhat underappreciated contribution to the development of modern wireless technology. The widespread success of this project led a number of workers to make the logical leap to exploit the technique as a synthetic medium to discover a wide range of new phases. The simultaneous evolution of X-ray diffraction to a routine method to obtain single crystal structures provides encouragement for the use of the method for exploratory synthesis. The fact that these refractory compounds can be grown as single crystals at relatively low temperatures is emerging as an important feature of the process. It is especially important as an access route to new quantum materials and other complex multifunctional solids like magnetoelectrics and topological materials. As the interest in new forms of matter and quantum materials increases, the requirements of exceptional crystal quality with minimal lattice defects or site disorder make this low temperature technique very attractive a route to new materials.

The technology to perform these reactions has not evolved very much over the last century. Variations of Morey vessels (from the 1920s) and Tuttle vessels (from the 1950s) are still the primary tools of the trade. There is no true commercial supplier of high temperature autoclaves right now, although fittings valves and other ancillary pieces of equipment are readily available. This is somewhat of an impediment to the development of the field. A possible field of significant advancement would be the ability to do *in situ* or *in operando* measurements of the hydrothermal process in real time. Such an effort will require considerable experimental ingenuity, and the initial developments are only in their infancy, but the potential payoff is very high.^{429–432}

The choice of solvent is worthy of some discussion. Obviously, the term hydrothermal itself implies an aqueous fluid, and water has been the predominant solvent in most high temperature superheated fluid reactions. The original hydrothermal reactions were investigated as a model for geochemical fluid reactions with particular emphasis on metal silicates. Water has many advantages as a high temperature fluid. It is stable, amenable to oxidizing and reducing conditions and capable of supporting a wide range of pH values. Most importantly it is a good solvent for most of the useful mineralizers. It works particularly well for reactions involving oxides and oxyanions but is also suitable for other types of products such as chalcogenides and some halides, particularly fluorides.

In principle the choice of solvent can be extended to a wide range of other fluids but there are several limitations. The fluid must be thermally stable to the high temperatures, which precludes most common organic solvents. With inorganic materials as the target, the solvent generally must also possess some polarity and must itself be inert to the reactants and mineralizers. These demands usually eliminate some otherwise interesting fluids such as CO₂ and SO₂. This still leaves a number of potentially intriguing solvents such as HX, SOF₂, and POCl₃. Most of these are entirely unexplored (except for some work in HX). Perhaps the most intriguing nonaqueous solvent is NH₃, whose chemistry is similar to water under supercritical conditions. It has been used for the targeted growth of the important GaN single crystals as well as a number of other metal nitrides. It is stable, polar, relatively easy to use and amenable to both acidic and basic mineralizers. Ammonia is restricted to about 600 °C due to its thermal decomposition to H₂ and N₂ at higher temperatures. Since most of the inert metal liners (Pt, Au, Ag) are permeable to H₂, there can be a gradual loss of ammonia and buildup of internal pressure of N₂ during reactions at higher temperatures.⁴³³ There is no reason that the solvent cannot continue to be explored for the development of new inorganic materials, however, especially metal nitrides and imides, which are generally refractory and difficult to prepare otherwise. There is no indication that supercritical water will not become obsolete any time soon, however. It continues to yield a steady stream of exciting results and shows no indication of slowing down in this regard. The hydrothermal approach to new materials and high-quality single crystals is still rich with potential.

Acknowledgments

The authors acknowledge generous support from the various funding agencies throughout the years and these are listed in the cited papers. In particular we acknowledge NSF DMR-1808371 and DoE DE-SC0020071, which provided support during the preparation of this review. The authors also express gratitude to their many outstanding co-workers, whose hard labor bore the fruit of the publications cited herein. The authors also gratefully acknowledge Dr. Art Ballato, who enthusiastically furnished much of the historical information regarding the synthesis of α -quartz. JWK would also like to acknowledge the memory of Dr. Bob Laudise, who unstintingly provided generous amounts of time, mentorship and encouragement to the author in his early attempts at hydrothermal chemistry.

References

1. Yoshimura, M.; Byrappa, K. *J. Mater. Sci.* **2008**, 2085–2103.
2. Sheldrick, W. S.; Wachhold, M. *Angew. Chem. Int. Ed. Engl.* **1997**, *36*, 206–224.
3. Walton, R. I. *Chem. Soc. Rev.* **2002**, *31*, 230–238.
4. Modeshia, D. R.; Walton, R. I. *Chem. Soc. Rev.* **2010**, *39*, 4303–4325.
5. Byrappa, K.; Adschiari, T. *Progress in Crystal Growth and Characterization of Materials*; vol. 53; Elsevier, 2007; pp 117–166.
6. Riman, R. E.; Suchanek, W. L.; Lencka, M. M. *Annal. Chim. Sci. Mater.* **2002**, *27*, 15–36.
7. Walton, R. I. *Chem. A Eur. J.* **2020**, *26*, 9041–9069.
8. Brunner, G. *Supercrit Fluid Sci and Tech.* **2014**, *5*, 559–589.
9. Clearfield, A. *Progress in Crystal Growth and Characterization of Materials*; Vol 21; Elsevier, 1980; pp 1–28.
10. Feng, S.; Ruren, X. *Acc. Chem. Res.* **2001**, *34*, 239–247.
11. Laudise, R. A. *Prog. Inorg. Chem. (F.A. Cotton Ed.)* **1962**, *3*, 1–47.
12. Laudise, R. A.; Nielson, J. W. *Solid St. Phys.* **1961**, *12*, 149–222.
13. Rabenau, A. *Angew. Chem. Int. Ed. Engl.* **1985**, *24*, 1026–1040.
14. Ballman, A. A.; Laudise, R. A. In *The Art and Science of Growing Crystals*; Gilman, J. J., Ed., John Wiley and Sons: New York, 1963; p 231.
15. Byrappa, K.; Yoshimura, M. *Handbook of Hydrothermal Technology*, Elsevier: Amsterdam, 2013.
16. Byrappa, K.; Keerthiraj, N.; Byrappa, S. M. *Handbook of Crystal Growth*, 2nd Ed.; Elsevier: Amsterdam, 2015; pp 535–575.
17. Laudise, R. A. *Chem. Eng. News* **1987**, *65* (39), 30.
18. Somiya, S., Ed.; *Hydrothermal Reactions for Materials Science and Engineering: An Overview of Research in Japan*, Elsevier Applied Science: London, 1989.
19. Lobachev, A. N. *Hydrothermal Synthesis of Crystals*, Consultants Bureau: New York, 1971.
20. Demianets, L. N.; Lobachev, A. N. *Curr. Top. Mat. Sci.* **1981**, *7*, 483–586.
21. Demazeau, G.; Largeau, A. Z. *Anorg. Allg. Chem.* **2015**, *641*, 159–163.
22. McMillen, C. D.; Kolis, J. W. *Phil. Mag.* **2012**, *92*, 2686–2711.
23. Kolis, J. W.; Korzenski, M. B. In *Reactions in SCF. Synthesis of Inorganic Solids. Hydrothermal Chemistry in Chemical Synthesis Using Supercritical Fluids*; Jessop, G., Leitner, W., Eds., Wiley-VCH: Weinheim, 1999; pp 226–234.
24. Demianets, L. N. *Progress in Crystal Growth and Characterization of Materials*; vol. 21; Elsevier, 1980; pp 299–355.
25. Rabenau, A. *Phys. Chem. Earth* **1981**, *13–14*, 361–374.
26. Ulmer, G. C.; Barnes, H. L. *Hydrothermal Experimental Techniques*, Wiley-Interscience: New York, 1987.
27. Ulmer, G. C. *Research Techniques for High Pressure and High Temperatures*, Springer Verlag US: New York, 1971.
28. Roy, R.; Tuttle, O. F. *Phys. Chem. Earth* **1956**, *1*, 138–180.
29. Ferretti, A.; Van Buskirk, O. R. *US Patent # 5,533, 465*, 1996.
30. Caporaso, A. J.; Kolb, E. D.; Laudise, R. A. *US Patent # 4,579, 622*, 1986.
31. Belt, R. F.; Ings, J. B. *J. Cryst. Growth* **1993**, *128*, 956–962.
32. Laudise, R. A.; Bridenbaugh, P. M.; Iradi, T. *J. Cryst. Growth* **1994**, *140*, 51–56.
33. Kennedy, G. C. *Am. J. Sci.* **1950**, *248*, 540–564.
34. de Senarmont, H. *Ann. Chim. Phys.* **1851**, *32*, 129.
35. Spezia, G. *Accad. Sci. Torino Atti.* **1905**, *40*, 254.
36. Morey, G. W. *J. Am. Ceram. Soc.* **1953**, *36*, 279–285.
37. Morey, G. W.; Niggli, P. *J. Am. Chem. Soc.* **1913**, *35*, 1086–1130.
38. Nacken, R. *Chem. Zietung* **1950**, *74*, 745.

39. Kerr, P. F.; Armstrong, E. *Bull. Geological Soc. Am.* **1943**, *54* (suppl. 1), 1–31.
40. Nassau, K. *Gems Made by Man* Gemological Institute of America, Santa Monica CA. (1980).
41. Laudise, R. A.; Barns, R. L. *IEEE Trans. Ultrason. Ferroelectr. Freq. Control* **1988**, *35*, 277–287.
42. Iwasuki, F.; Iwasuki, H. *J. Cryst. Growth* **2002**, *237–239*, 820–827.
43. Brown, C. S.; Kell, R. C.; Thomas, L. A.; Wooster, N.; Wooster, W. A. *Nature* **1951**, *167*, 940.
44. Buehler, E.; Walker, A. C. *Sci. Mon.* **1949**, *69*, 148.
45. Brown, C. S. *Inst. Elec. Engineers* **1961**. Paper 3620.
46. Walker, A. C. *Ind. Eng. Chem.* **1954**, *46*, 1670.
47. Armington, A. F. *Progress in Crystal Growth and Characterization of Materials*; Vol 21; Elsevier, 1991; pp 97–111.
48. McGahey, C. S. Georgia Institute of Technology, Ph.D. (2009).
49. Trossarelli, C. *J. Gemmol. Proc.* **1984**, *19*, 240–260.
50. Anon Proceedings of the Chicago Crystal Conference 1944.
51. Swinnerton, A. C. *Interrogation of German Scientists Regarding Quartz Crystals and Other Piezoelectronic Materials*. FIAT Final Report 641, 1945.
52. Hale, D. R. *Science* **1948**, *107*, 393.
53. Sawyer, C. B. 13th Frequency Control Symposium US Army Signal Laboratory (1959) Vol. 462.
54. Taki, S. *Prog. Crystal Growth and Charact.* **1991**, *23*, 313–339.
55. Corwin, J. F. *J. Chem. Ed.* **1960**, *37*, 11–14.
56. Bailey, D. K. *Am. J. Sci.* **1969**, *267-A*, 1–16.
57. Bierlein, J. D.; Vanherzeele, H. *J. Opt. Soc. Am. B* **1989**, *6*, 622–633.
58. Cheng, L. K.; Bierlein, J. D. *Ferroelectrics* **1993**, *142*, 209–228.
59. Roth, M.; Tseitlin, M. *J. Cryst. Growth* **2010**, *312*, 1059–1064.
60. Zumsteg, F. C.; Bierlein, J. D.; Gier, T. *E. J. Appl. Phys.* **1976**, *47*, 4980.
61. Laudise, R. A.; Cava, R. J.; Caporaso, A. J. *J. Cryst. Growth* **1986**, *74*, 275–280.
62. Laudise, R. A.; Sunder, W. A.; Belt, R. F.; Gashurov, G. *J. Cryst. Growth* **1990**, *102*, 427–433.
63. Zhang, C. L.; Hu, Z. G.; Huang, L. X.; Zhou, W. N.; Zhang, G.; Liu, Y. C.; Zou, Y. B.; Lu, F. H.; Hou, H. D.; Qin, S. J.; Zhang, H. X. *J. Cryst. Growth* **2008**, *310*, 2010–2014.
64. Zhang, C. L.; Huang, L. X.; Zhou, W. N.; Zhang, G.; Ruan, Q. F.; Lei, W.; Qin, S. J.; Lu, F. H.; Zuo, Y. B.; Shen, H. Y.; Wang, G. F. *J. Cryst. Growth* **2006**, *292*, 364–367.
65. Belt, R. F.; Gashurov, G.; Liu, Y. S. *Laser Focus/Electro-Optics* **1985**, *10*, 110–124.
66. Beck, W. *J. Am. Ceram. Soc.* **1949**, *32*, 147–151.
67. Morency, D. G.; Soluch, W.; Vetelino, J. F.; Mittleman, S. D.; Harmon, D.; Surek, S.; Field, J. C.; Lehmann, G. *Appl. Phys. Lett.* **1978**, *33*, 117–119.
68. Gualitieri, J.; Ballato, A. *DTIC US Army ERACDOM DELET-TR-81-15*, 1981.
69. Stanley, J. M. *Ind. Eng. Chem.* **1954**, *46*, 1684–1689.
70. Cambon, O.; Haines, J. *Crystals* **2017**, *7*, 38.
71. Kolb, E. D.; Laudise, R. A. *J. Cryst. Growth* **1978**, *43*, 313–319.
72. Hasegawa, K.; Minigishi, K.; Somya, S. In *Hydrothermal Reactions for Materials Science and Engineering*; Somya, S., Ed., Springer: Dordrecht, 1989.
73. Laudise, R. A. In *Crystal Growth of Electronic Materials*; Kaldis, E., Ed., Elsevier, 1985; pp 159–174.
74. Kolb, E. D.; Barns, R. L.; Laudise, R. A.; Grenier, J. C. *J. Cryst. Growth* **1980**, *50*, 404–418.
75. Barz, R. U.; Grassl, M.; Gille, P. *Cryst. Res. Technol.* **1999**, *34*, 1121–1127.
76. Jumas, J. C.; Goffon, A.; Capelle, B.; Zarka, A.; Doukhan, J. C.; Schwartzel, J.; Detaint, J.; Philippot, E. *J. Cryst. Growth* **1987**, *80*, 133–148.
77. Barsukova, M. L.; Kuznetsov, V. A.; Lobachev, A. N.; Shaldin, Y. V. *J. Cryst. Growth* **1972**, *13*, 530–534.
78. Skorikov, V. M.; Kargin, Y. F.; Egorysheva, A. V.; Volkov, V. V.; Gospodinov, M. *Inorg. Mater.* **2005**, *41*, S24–S46.
79. Harris, M.; Larkin, J.; Cormier, J. E.; Armington, A. F. *J. Cryst. Growth* **1994**, *137*, 128–131.
80. Larkin, J.; Harris, M.; Cormier, J. E.; Armington, A. F. *J. Cryst. Growth* **1993**, *128*, 871–875.
81. Müller-Buschbaum, H.-G. *Angew. Chem. Int. Ed. Engl.* **1981**, *20*, 22–33.
82. Dabkowska, H. A.; Dabkowski, A. B. In *Springer Handbook of Crystal Growth*; Dhanaraj, G., Byrappa, K., Prasad, V., Dudley, M., Eds., Springer: Berlin, Heidelberg, 2010. Springer Handbooks.
83. Koohpayeh, S. M.; Fort, D.; Abell, J. S. *Progress Crystal Growth and Characterization of Materials*; Vol 54; Elsevier, 2008; pp 121–137.
84. Koohpayah, S. M.; Wen, J.-J.; Trump, B. A.; Broholm, C. L.; McQueen, T. M. *J. Cryst. Growth* **2014**, *402*, 291–298.
85. Trump, B. A.; Koohpayeh, K. J.; Livi, K. J. T.; Wen, J.-J.; Arpino, K. E.; Ramasse, Q. M.; Brydson, R.; Feyngenson, M.; Takeda, H.; Takigawa, M.; Kimura, K.; Nakatsuji, S.; Broholm, C. L.; McQueen, T. M. *Nature Comm.* **2018**, *9*, 2619.
86. Ross, K. A.; Dabkowska, P. T.; Quilliam, J. A.; Yaraskavitch, L. R.; Kycia, J. B.; Gaulin, B. D. *Phys. Rev. B* **2012**, *86*, 174424.
87. Mann, J. M. Ph.D. Thesis, Clemson University, (2009).
88. Ehrentraut, D.; Sato, H.; Kagamitani, Y.; Sato, H.; Yoshikawa, A.; Fukuda, T. *Cryst. Growth Charact. Mat.* **2006**, *52*, 280–335.
89. Demyanets, L. N.; Lyutin, V. I. *J. Cryst. Growth* **2008**, *310*, 993–999.
90. Lin, W.; Chen, D.; Zhang, J.; Lin, Z.; Huang, J.; Li, W.; Wang, Y.; Huang, F. *Cryst. Growth Design* **2009**, *9*, 4378–4383.
91. Avrutin, V.; Cantwell, G.; Zhang, J.; Song, J. J.; Silversmith, D. J.; Morkoç, H. *Proc. IEEE* **2010**, *98*, 1339–1350.
92. Hill, V. G.; Harker R. I. (1966) Air Force Technical Report AFML-TR-66-343.
93. Laudise, R. A.; Ballman, A. A. *J. Am. Chem. Soc.* **1958**, *80*, 2655–2657.
94. Shafer, M. W.; Roy, R. *J. Am. Ceram. Soc.* **1959**, *42*, 563–570.
95. Christensen, A. N. *Acta Chem. Scand.* **1965**, *19*, 1391.
96. Adachi, G.; Imanaka, N. *Chem. Rev.* **1998**, *98*, 1479–1514.
97. Peters, V.; Bolz, A.; Petermann, K.; Huber, G. *J. Cryst. Growth* **2002**, *237–239*, 879–883.
98. Mroczkowski, S.; Eckert, J. *J. Cryst. Growth* **1972**, *13–14*, 549–551.
99. Shafer, W.; Roy, R. *Z. Anorg. Allg. Chem.* **1954**, *276*, 275–288.
100. Yang, S.; Powell, M.; Kolis, J. W.; Navrotsky, A. *J. Solid State Chem.* **2020**, *287*, 121344.
101. McMillen, C. D.; Thompson, D.; Tritt, T.; Kolis, J. W. *Cryst. Growth Design* **2011**, *11*, 4386–4391.
102. McMillen, C. D.; Sanjeeva, L. D.; Moore, C. A.; Brown, D. C.; Kolis, J. W. *J. Cryst. Growth* **2016**, *452*, 146–150.
103. McMillen, C. D.; Kolis, J. W. *J. Cryst. Growth* **2008**, *310*, 1939–1942.
104. Moore, C. A.; Brown, D. C.; Sanjeeva, L. D.; McMillen, C. D.; Kolis, J. W. *JOL* **2016**, *174*, 29–35.
105. Wenckus, J. F.; Menashi, W. P.; Castonguay, R. A. *USPTO #US4049384A*, 1977.
106. Alexandrov, V. I.; Osiko, V. V.; Tatarintsev, V. M.; Udovenchik, V. T. *USPTO #3984524A*, 1976.
107. Kuznetsov, V. A. *J. Cryst. Growth* **1968**, *3–4*, 405–410.
108. Sōmiya, S.; Akiba, T. *J. Eur. Ceram. Soc.* **1999**, *19*, 81–87.
109. Izumi, F.; Fujiki, Y. *Bull. Chem. Soc. Japan* **1976**, *49*, 709–712.

110. Mann, J. M.; Kolis, J. W. *J. Cryst. Growth* **2010**, *312*, 461–465.
111. Dharmarajan, R.; Belt, R. F.; Puttbach, R. C. *J. Cryst. Growth Des.* **1972**, *13* (14), 535–539.
112. Uhrin, R.; Belt, R. F.; Puttbach, R. C. *J. Cryst. Growth* **1974**, *21*, 65–68.
113. Wanklyn, B. M.; Garrard, B. J. *J. Cryst. Growth* **1984**, *66*, 346–350.
114. Mann, J. M.; Thompson, D.; Serivalsait, K.; Tritt, T. M.; Ballato, J.; Kolis, J. W. *Cryst. Growth Design* **2010**, *10*, 2146–2151.
115. Castilow, J.; Zens, T. W.; Mann, J. M.; Kolis, J. W.; McMillen, C. D.; Petrosky, J. *MRS Online Proc.* **2013**, *1576*, 1–6.
116. Turner, D. B.; Kelly, T. D.; Peterson, G. R.; Reding, J. D.; Hengehold, R. L.; Mann, J. M.; Kolis, J. W.; Zhang, X.; Dowben, P. A.; Petrosky, J. C. *Phys. Status Solidi B* **2016**, *253*, 1970–1976.
117. Mann, J. M.; Hunter, E. M.; Kolis, J. W. *USPTO # 9,903,041*, 2018.
118. Mann, J. M.; McMillen, C. D.; Kolis, J. W. *Cryst. Growth Design* **2015**, *15*, 2643–2651.
119. Powell, M. P.; Powell, B.; Kolis, J. W. Unpublished Results (n.d.).
120. Galazka, Z.; Irmischer, K.; Pietsch, M.; Schulz, T.; Uecker, R.; Klimm, D.; Fornari, R. *CrstEngComm* **2013**, *15*, 2220–2226.
121. Fujiki, Y.; Suzuki, Y. *J. Jap. Assoc. Min., Petrol. Econ. Geol.* **1973**, *68*, 277–283.
122. Harvill, M. L., Ph.D. Thesis, The Pennsylvania State University (1966).
123. Hill, V. G.; Chang, L. L. *Am. Mineral.* **1968**, *53*, 1744–1748.
124. Marshall, D. J.; Laudise, R. A. *Int. Conf. Cryst. Growth* **1966**, 557–561.
125. Mann, J. M.; Jackson, S.; Kolis, J. W. *J. Solid State Chem.* **2010**, *183*, 2675–2680.
126. Kuznetsov, V. A. In *Crystallization Under Hydrothermal Conditions*; Lobachev, A. N., Ed., Consultants Bureau: New York, 1973; pp 81–93.
127. Mann, J. M.; McMillen, C. D.; Kolis, J. W. Manuscript in preparation (n.d.).
128. Ismail-Beigi, S.; Walker, F. J.; Cheong, S.-W.; Rabe, K. M.; Ahn, C. H. *APL Mater.* **2015**, *3*, 062510.
129. Kim, H. J.; Kim, U.; Kim, T. H.; Kim, J.; Kim, H. M.; Jeon, B. G.; Lee, W. J.; Mun, H. S.; Hong, K. T.; Yu, J.; Char, K.; Kim, K. H. *Phys. Rev. B* **2012**, *86*, 165205.
130. Terry, R. J.; Combs, N.; McMillen, C. D.; Stemmer, S.; Kolis, J. W. *J. Cryst. Growth* **2020**, *536*, 125529.
131. Powell, M.; McMillen, C. D.; Kolis, J. W. Manuscript in preparation (n.d.).
132. Subramanian, M. A.; Aravamudan, G.; Subba Rao, G. V. *Prog. Solid St. Chem.* **1983**, *15*, 55–143.
133. Gardner, J. S.; Gingras, M. J. P.; Greedan, J. E. *Rev. Mod. Phys.* **2010**, *82*, 54–102.
134. Ross, K. A.; Savary, L.; Gaulin, B. D.; Balents, L. *Phys. Rev. X* **2011**, *1*, 021002.
135. Zhou, H. G.; Cheng, J. G.; Hallas, A. M.; Wiebe, C. R.; Li, G.; Balicas, L.; Zhou, J. S.; Goodenough, J. B.; Gardner, J. S.; Choi, E. S. *Phys. Rev. Lett.* **2012**, *108*, 207206.
136. Wiebe, C. R.; Hallas, A. M. *APL Mater.* **2015**, *3*, 041519.
137. Wen, J. J.; Koohpayeh, S. M.; Ross, K. A.; Trump, B. A.; McQueen, T. M.; Kimura, K.; Nakatsuji, K. S.; Qiu, Y.; Pajeroski, D. M.; Copley, J. R. D.; Broholm, C. L. *Phys. Rev. Lett.* **2017**, *118*, 107206.
138. Powell, M.; Sanjeeva, L. D.; McMillen, C. D.; Ross, K. A.; Sarkis, C.; Kolis, J. W. *Cryst. Growth Design* **2019**, *19*, 4920–4926.
139. Sarkis, C. L.; Rau, J. G.; Sanjeeva, L. D.; Powell, M.; Kolis, J. W.; Marbey, J.; Hill, S.; Rodriguez-Rivera, J. A.; Nair, H. A.; Gingras, M. J. P.; Ross, K. A. *Phys. Rev. B* **2020**, *102*, 134418.
140. Yahne, D. R.; Pereira, D.; Jaubert, L. D. C.; Sanjeeva, L. D.; Powell, M.; Kolis, J. W.; Xu, G.; Gingras, M. J. P.; Ross, K. A. *Phys. Rev. Lett.* **2021**. In Revision.
141. Pajeroski, D. M.; Taddei, K. M.; Sanjeeva, L. D.; Savici, A. T.; Stone, M. B.; Kolis, J. W. *Phys. Rev. B* **2020**, *101*, 014420.
142. Taddei, K. M.; Sanjeeva, L. D.; Kolis, J. W.; Sefat, A. S.; de la Cruz, C.; Pajeroski, D. M. *Phys. Rev. Mater.* **2019**, *3*, 014405.
143. Dun, Z. L.; Lee, M.; Choi, E. S.; Hallas, A. M.; Wiebe, C. R.; Gardner, J. S.; Arrighi, E.; Freitas, R. S.; Arevalo-Lopez, A. M.; Atfield, J. P.; Zhou, H. D.; Cheng, J. G. *Phys. Rev. B* **2014**, *89*, 064401.
144. Sanjeeva, L. D.; Ross, K. A.; Sarkis, C. L.; Nair, H. S.; McMillen, C. D.; Kolis, J. W. *Inorg. Chem.* **2018**, *57*, 12456–12460.
145. Puttbach, R. C.; Monchamp, R. R.; Nielsen, J. W. In *Crystal Growth*; Peiser, H. S., Ed., Pergamon: Oxford, 1967; pp 569–573.
146. Kolb, E. D.; Laudise, R. A. *J. Cryst. Growth* **1975**, *29*, 29–39.
147. McMillen, C. D.; Mann, J. M.; Fan, J.; Zhu, L.; Kolis, J. W. *J. Cryst. Growth* **2012**, *356*, 58–64.
148. Brown, D. C.; McMillen, C. D.; Moore, C. A.; Kolis, J. W.; Envid, V. *JOL* **2014**, *148*, 26–32.
149. Moore, C. A.; McMillen, C. D.; Kolis, J. W. *Cryst. Growth Design* **2013**, *13*, 2298–2306.
150. Kim, W.; Bayya, S.; Shaw, B.; Myers, J.; Qadri, S. N.; Thapa, R.; Gibson, D.; McLain, C.; Kolis, J. W.; Stadlerman, B. J. *Sanghera J. Optical Mater.* **2019**, *9*, 2716–2728.
151. McMillen, C. D.; Moore, C. A.; Kolis, J. W. *Advances in Optical Materials* In: *OSA Technical Digest*, 2012. IW5D.2.
152. Kolis, J. W.; McMillen, C. D. *USPTO #9,469,915 B2*, 2016.
153. Kolis, J. W.; McMillen, C. D.; Mann, J. M. *USPTO #9,506,166*, 2016.
154. Kolis, J. W.; McMillen, C. D. *USPTO #10,156,025 B2*, 2018.
155. Demianets, L. N. In *Crystals for Magnetic Applications*; Rooijmans, C. J. M., Ed.; *Crystals (Growth, Properties, and Applications)* vol. 1; Springer: Berlin, Heidelberg, 1978.
156. Kolb, E. D.; Caporaso, A. J.; Laudise, R. A. *J. Cryst. Growth* **1973**, *19*, 242–246.
157. Rogers, D. B.; Gilson, J. L.; Gier, T. E. *Solid St. Comm.* **1967**, *5*, 263–265.
158. Okamoto, S.; Sekizawa, H.; Okamoto, S. I. *J. Phys. Chem. Solid* **1973**, *36*, 591.
159. Kolb, E. D.; Laudise, R. A. *J. Appl. Phys.* **1971**, *42*, 1552.
160. Kolb, E. D.; Wood, D. L.; Laudise, R. A. *J. Appl. Phys.* **1968**, *39*, 1362.
161. Zhang, C.; Shang, M.; Liu, M.; Zhang, T.; Ge, L.; Yuan, H.; Feng, S. *J. Alloys Compd.* **2016**, *665*, 152–157.
162. Yoshimura, S.; Yamasawa, K.; Somiya, S. Proceeding of the International Meeting on Chemical Sensors (Kodansha Japan) 1983, 198–202.
163. Gunter, W. D.; Myer, J.; Girsberger, S. In *In Hydrothermal Experimental Technique*; Ulmer, G. C., Barnes, H. L., Eds., Wiley and Sons: New York, 1987; pp 100–120.
164. Chamberland, B. L.; Sleight, A. W.; Weiher, J. F. *J. Solid State Chem.* **1970**, *1*, 506–511.
165. Cussen, E. J.; Battle, P. D. *Chem. Mater.* **2000**, *12*, 831–838.
166. Potoff, A. D.; Chamberland, B. L.; Katz, L. *J. Solid State Chem.* **1973**, *8*, 234–237.
167. Rondinelli, J. M.; Eidelson, A. S.; Spaldin *Phys. Rev. B* **2009**, *79*, 2053119.
168. Khalifah, P.; Nelson, K. D.; Jin, R.; Mao, Z. Q.; Liu, Y.; Huang, Q.; Gao, X. P. A.; Ramirez, A. P.; Cava, R. J. *Nature* **2001**, *411*, 669–671.
169. Sleight, A. W.; Ramirez, A. W. *Solid State Commun.* **2018**, *275*, 12–15.
170. Longo, J. M.; Sleight, A. W. *Inorg. Chem.* **1968**, *7*, 108–111.
171. Sleight, A. W. *Mater. Res. Bull.* **1974**, *9*, 1177–1184.
172. Suzuki, H.; Ozawa, H.; Sato, H. *J. Physical Soc. Japan* **2007**, *76*, 044805.
173. Sasaki, A.; Wakeshima, M.; Hinatsu, Y. *J. Phys. Condens. Matter* **2006**, *18*, 9031.
174. Torardi, C.; Sleight, A. W. *J. Less-Common Met.* **1986**, *116*, 293–299.
175. Kolambage, M. T. K.; McGuire, K. A.; Sanjeeva, L. D.; Wen, E.; McMillen, C. D.; Kolis, J. W. *J. Solid State Chem.* **2019**, *275*, 149–158.
176. Kolambage, M. T. K.; McMillen, C. D.; Kolis, J. W. *J. Solid State Chem.* **2021**. Submitted.
177. Sanjeeva, L. D.; Liu, Y.; Xing, J.; Fishman, R. S.; Kolambage, M. T. K.; McGuire, M.; McMillen, C. D.; Kolis, J. W.; Sefat, A. S. *Phys. Status Solidi B* **2021**, *258*, 2000197.
178. Kolambage, M. T. K.; McMillen, C. D.; Kolis, J. W. *J. Alloys Compd.* **2021**. Submitted.

179. Sanjeeva, L. D.; Fulle, K.; McMillen, C. D.; Kolis, J. W. *Dalton Trans.* **2019**, *48*, 7704–7713.
180. Fulle, K.; Sanjeeva, L. D.; McMillen, C. D.; Kolis, J. W. *Dalton Trans.* **2018**, *47*, 6754–6762.
181. Fulle, K.; McMillen, C. D.; Sanjeeva, L. D.; Kolis, J. W. *Cryst. Growth Des.* **2016**, *16*, 4910–4917.
182. McMillen, C. D.; Kolis, J. W. *Dalton Trans.* **2016**, *45*, 2772–2784.
183. Day, M. C.; Hawthorne, F. C. *Mineral. Mag.* **2020**, *84*, 165–244.
184. Barrer, R. M. *Zeolites* **1981**, *1*, 129–140.
185. Barrer, R. M. *Hydrothermal Chemistry of Zeolites*, Academic Press, 1982.
186. Flanigen, E. N.; Patton, R. L.; Wilson, S. T. *Stud. Surf. Sci. Cat.* **1988**, *37*, 13.
187. Cundy, C. S.; Cox, P. A. *Micropor. Mesopor. Mat.* **2005**, *28*, 1–78.
188. Weller, M. T. *Dalton Trans.* **2000**, 4227–4240.
189. Demianets, L. N. *Progress Crystal Growth and Characterization of Materials*, Vol 21; Elsevier, 1991; pp 299–344.
190. Haile, S. M.; Wuensch, B. J.; Laudise, R. A. *J. Cryst. Growth* **1993**, *131*, 352–372.
191. Haile, S. M.; Wuensch, B. J.; Laudise, R. A. *J. Cryst. Growth* **1993**, *131*, 373–386.
192. Haile, S. M.; Wuensch, B. J. *Am. Mineral.* **1993**, *82*, 1141–1149.
193. Haile, S. M.; Wuensch, B. J.; Siegrist, T.; Laudise, R. A. *Solid State Ion.* **1992**, *53*, 1292–1301.
194. Haile, S. M.; Wuensch, B. J. *Acta Crystallogr. B* **2000**, *2000* (6), 773–779.
195. Zhao, X.; Li, J.; Chen, P.; Li, Y.; Chu, Q.; Liu, X.; Yu, J.; Xu, R. *Inorg. Chem.* **2010**, *49*, 9833–9838.
196. Aksenov, S. M.; Mackley, S. A.; Deyneko, D. V.; Taroev, V. K.; Tauson, V. L.; Rastsvetaeva, R. K.; Burns, P. C. *Micropor. Mesopor. Mat.* **2019**, *284*, 25–35.
197. Fulle, K.; Sanjeeva, L. D.; McMillen, C. D.; Kolis, J. W. *Acta Crystallogr. B* **2017**, *B73*, 907–915.
198. Sanjeeva, L. D.; Fulle, K.; McMillen, C. D.; Wang, F.; Liu, Y.; He, J.; Anker, J. N.; Kolis, J. W. *Solid State Sci.* **2015**, *48*, 256–262.
199. Huang, M. Y.; Chen, Y. H.; Chang, B. C.; Lii, K. H. *Chem. Mater.* **2005**, *17*, 5743–5747.
200. McMillen, C. D.; Emirdag-Eanes, M.; Stritzinger, J. T.; Kolis, J. W. *J. Solid State Chem.* **2012**, *195*, 155–160.
201. Terry, R.; Vinton, R. D.; McMillen, C. D.; Kolis, J. W. *Angew. Chem. Int. Ed. Engl.* **2018**, *75*, 2077–2080.
202. Johnson-McDaniel, D.; Comer, S.; Kolis, J. W.; Salguero, T. T. *Chem. A Eur. J.* **2015**, *21*, 17560–17564.
203. Smart, M.; McMillen, C. D.; Ivey, K.; Kolis, J. W. *Inorg. Chem.* **2020**, *59*, 16804–16808.
204. Kao, H. M.; Lii, K. H. *Inorg. Chem.* **2002**, *41*, 5644.
205. Li, C. Y.; Hsieh, C. Y.; Lin, H. M.; Kao, H. M.; Lii, K. H. *Inorg. Chem.* **2002**, *41*, 4208.
206. Heyward, C. C.; McMillen, C. D.; Kolis, J. W. *Inorg. Chem.* **2015**, *54*, 905–913.
207. Heyward, C. C.; Kimani, M. M.; Moore, C. A.; McMillen, C. D.; Kolis, J. W. *J. Alloys Compd.* **2016**, *656*, 206–212.
208. Chen, C.-S.; Lee, S.-F.; Lii, K.-H. *J. Am. Chem. Soc.* **2005**, *127*, 12208–12209.
209. Lee, C.-S.; Wang, S.-L.; Lii, K. W. *J. Am. Chem. Soc.* **2009**, *131*, 15116–15117.
210. Lee, C. S.; Lin, C. H.; Wang, S. L.; Lii, K. W. *Angew. Chem. Int. Ed. Engl.* **2010**, *49*, 4254–4256.
211. Chen, C.-L.; Nguyen, Q. B.; Chan, C.-S.; Lii, K.-W. *Inorg. Chem.* **2012**, *51*, 7463–7465.
212. Fisher, D. J. *Am. Mineral.* **1958**, *43*, 181–207.
213. Moore, P. B.; Shen, J. *Nature* **1983**, *306*, 356–358.
214. Moore, P. B. *Am. Mineral.* **1989**, *74*, 918–926.
215. Moore, P. B. *Aust. J. Chem.* **1992**, *45*, 1335–1354.
216. Moore, P. B. *Science* **1969**, *164*, 1063–1064.
217. Soghomonian, V.; Chen, Q.; Haushalter, R. C.; Zubieta, J.; O'Connor, C. J. *Science* **1993**, *259*, 1596.
218. Haushalter, R. C.; Mundi, L. *Chem. Mater.* **1992**, *4*, 31–48.
219. Moring, J.; Kostiner, E. *J. Solid State Chem.* **1986**, *61*, 379–383.
220. Shoemaker, G. L.; Anderson, J. B.; Kostiner, E. *Acta Crystallogr. B* **1977**, *B33*, 2969–2972.
221. Byrappa, K.; Litvin, B. N. *J. Mat. Sci.* **1983**, *18*, 703–708.
222. Byrappa, K. *Prog. Cryst. Growth Charact. Mater.* **1986**, *13*, 163–196.
223. Boudin, S.; Lii, K. H. *Inorg. Chem.* **1998**, *37*, 799–803.
224. Korzenski, M. B.; Kolis, J. W.; Long, G. J. *J. Solid State Chem.* **1999**, *147*, 390–398.
225. Mann, M.; Kolis, J. W. *J. Chem. Crystallogr.* **2010**, *40*, 337–342.
226. Nguyen, Q. B.; Lii, K. H. *Inorg. Chem.* **2011**, *50*, 9936–9938.
227. Nguyen, Q. B.; Chen, C. L.; Chiang, Y. W.; Lii, K. H. *Inorg. Chem.* **2012**, *51*, 3879–3882.
228. Emirdag-Eanes, M.; Kolis, J. W. *Mater. Res. Bull.* **2004**, *39*, 557–567.
229. Emirdag-Eanes, M.; Kolis, J. W. *J. Alloys Compd* **2004**, *370*, 90–93.
230. Kuzmina, I. P.; Melnikov, O. K.; Litvin, B. N. In *Hydrothermal Synthesis of Crystals*; Lobachev, A. N., Ed., Consultants Bureau: New York, 1971.
231. Kuzmina, I. P.; Litvin, B. N. In *Kuraszkovskaya in Crystallization Processes Under Hydrothermal Conditions*; Lobachev, A. N., Ed., Consultants Bureau: New York, 1973.
232. Lin, C. H.; Lii, K. H. *Angew. Chem. Int. Ed. Engl.* **2008**, *47*, 8711–8713.
233. Lin, C. H.; Chiang, R. K.; Lii, K. H. *J. Am. Chem. Soc.* **2009**, *131*, 2068–2069.
234. Sanjeeva, L. D.; McGuire, M. A.; McMillen, C. D.; Kolis, J. W. *Chem. Mater.* **2017**, *29*, 1404–1411.
235. Smart, M. M.; Smith Pellizzeri, T. M.; Morrison, G.; McMillen, C. D.; Zur Loye, H.-C.; Kolis, J. W. *Chem. Mater.* **2021**, *33*, 2258–2266.
236. Fulle, K.; Sanjeeva, L. D.; McMillen, C. D.; De Silva, C. R.; Ruehl, K.; Wen, Y.; Chumanov, G.; Kolis, J. W. *J. Alloys Compd* **2019**, *786*, 489–497.
237. Emirdag-Eanes, M.; Krawiec, M.; Kolis, J. W. *J. Chem. Cryst* **2001**, *31*, 281–285.
238. Emirdag-Eanes, M.; Pennington, W. T.; Kolis, J. W. *J. Alloys Compd* **2004**, *366*, 76–80.
239. Liu, W.; Yang, M.; Ji, Y.; Liu, F.; Wang, Y.; Wang, X.; Zhao, X.; Liu, X. *RSC Adv.* **2014**, *2014* (4), 26951–26955.
240. Golavastikov, N. I.; Belov, N. V. *Sov. Phys. Cryst.* **1982**, *27*, 650.
241. Fulle, K.; Sanjeeva, L. D.; McMillen, C. D.; Wen, Y.; Chumanov, G.; Kolis, J. W. *Inorg. Chem.* **2017**, *56*, 6044–6047.
242. Demianets, L. N.; Lobachev, A. N.; Emelchenko, G. A. *Prog. Cryst. Growth Charact. Mater.* **1990**, *21*, 295–355.
243. Hase, M.; Terasaki, I.; Uchinokura, K. *Phys. Rev. Lett.* **1993**, *70*, 3651–3654.
244. Koo, H.-J.; Whangbo, M.-H.; Lee, K.-S. *Inorg. Chem.* **2003**, *42*, 5932–5937.
245. Whangbo, M.-H.; Koo, H.-J.; Dai, D. *J. Solid State Chem.* **2003**, *176*, 417–481.
246. Demianets, L. M. In *Hydrothermal Synthesis of Crystals*; Lobachev, A. N., Ed., Consultants Bureau: New York, 1971; pp 65–79.
247. Byrappa, K.; Jain, A. *J. Mater. Res.* **1996**, *11*, 2869–2875.
248. Schindler, M.; Hawthorne, F. C.; Baur, W. H. *Can. Mineral.* **2000**, *38*, 1443–1456.
249. Schindler, M.; Hawthorne, F. C.; Baur, W. H. *Chem. Mater.* **2000**, *12*, 1248–1259.
250. Whittingham, M. S.; Song, Y.; Lutttta, S. L.; Zavalij, P. Y.; Chernova, N. *J. Mater. Chem.* **2005**, *15*, 3362–3379.
251. Chirayil, T.; Zavalij, P. Y.; Whittingham, M. S. *Chem. Mater.* **1998**, *10*, 2629–2640.

252. Zavaliy, P. Y.; Whittingham, M. S. *Acta Crystallogr. B* **1999**, *B55*, 627–663.
253. Forbes, A. R.; McMillen, C. D.; Giesber, H. G.; Kolis, J. W. *J. Cryst. Growth* **2008**, *310*, 4472–4476.
254. Byrappa, K.; Chandrashekar, C. K.; Basavalingu, B.; Lokanatharai, K. M.; Ananda, S.; Yoshimura, M. *J. Cryst. Growth* **2007**, *306*, 94–101.
255. Yang, M.; Zhao, X.; Ji, Y.; Liu, F.; Liu, W.; Sun, J.; Liu, X. *New J. Chem.* **2014**, *38*, 4249–4257.
256. Kimani, M. M.; Thompson, L.; Snider, W.; McMillen, C. D.; Kolis, J. W. *Inorg. Chem.* **2012**, *51*, 13271–13280.
257. Kimani, M. M.; Kolis, J. W. *JOL* **2014**, *145*, 492–497.
258. Yahne, D. R.; Sanjeewa, L. D.; Sefat, A. S.; Stadlerman, B.; Kolis, J. W.; Calder, S.; Ross, K. A. *Phys Rev B* **2020**, *102*, 104423.
259. Sanjeewa, L. D.; McGuire, M. A.; Garlea, V. O.; Hu, L.; Chumanov, G.; McMillen, C. D.; Kolis, J. W. *Inorg. Chem.* **2015**, *54*, 7014–7020.
260. Sanjeewa, L. D.; Garlea, O. V.; McGuire, M.; Frontzek, M.; McMillen, C. D.; Fulle, K.; Kolis, J. W. *Inorg. Chem.* **2017**, *56*, 14842–14849.
261. Sanjeewa, L. D.; McGuire, M. A.; McMillen, C. D.; Willett, D.; Chumanov, G.; Kolis, J. W. *Inorg. Chem.* **2016**, *55*, 9240–9249.
262. Sanjeewa, L. D.; Garlea, O. V.; McGuire, M. A.; McMillen, C. D.; Cao, H. B.; Kolis, J. W. *Phys. Rev. B* **2016**, *93*, 224407.
263. Sanjeewa, L. D.; McMillen, C. D.; Kolis, J. W. *J. Solid State Chem.* **2016**, *236*, 61–68.
264. Smith Pellizzeri, T. M.; McMillen, C. D.; Pellizzeri, S.; Wen, Y.; Getman, R. B.; Chumanov, G.; Kolis, J. W. *J. Solid State Chem.* **2017**, *255*, 225–233.
265. Smith Pellizzeri, T. M.; McMillen, C. D.; Kolis, J. W. *Inorg. Chem.* **2017**, *56*, 4206–4216.
266. Sanjeewa, L. D.; McMillen, C. D.; McGuire, M. A.; Kolis, J. W. *Inorg. Chem.* **2016**, *55*, 12512–12515.
267. Sanjeewa, L. D.; McGuire, M. A.; Smith Pellizzeri, T. M.; McMillen, C. D.; Garlea, V. O.; Willett, D.; Chumanov, G.; Kolis, J. W. *J. Solid State Chem.* **2016**, *241*, 30–37.
268. Sanjeewa, L. D.; McGuire, M. A.; McMillen, C. D.; Garlea, V. O.; Kolis, J. W. *Chem. Mater.* **2017**, *29*, 1404–1412.
269. Rapposch, M. H.; Anderson, J. B.; Kostiner, E. *Inorg. Chem.* **1980**, *19*, 3531–3539.
270. Svistov, L. E.; Smirnov, A. I.; Prozorova, L. A.; Petrenko, O. A.; Demianets, L. N.; Shapiro, A. Y. *Phys. Rev. B* **2003**, *67*, 094434.
271. Nocera, D. G.; Bartlett, B. M.; Grohol, D.; Papoutsakis, D.; Shores, M. P. *Chem. A Eur. J.* **2004**, *10*, 3850–3859.
272. Long, G. J.; Longworth, G.; Battle, P.; Cheatham, A. K.; Thundathil, R. V.; Beveridge, D. *Inorg. Chem.* **1979**, *18*, 624–632.
273. Pellizzeri, T. M.; McMillen, C. D.; Kolis, J. W. *Chem. A Eur. J.* **2020**, *26*, 597–600.
274. Liu, Y.; Sanjeewa, L. D.; Garlea, V. O.; Smith Pellizzeri, T. M.; Kolis, J. W.; Sefat, A. S. *Phys. Rev. B* **2020**, *101*, 064423.
275. Ikonnikova, N. Y. In *Hydrothermal Synthesis of Crystals*; Lobachev, A. N., Ed., Consultants Bureau: New York, 1971; pp 80–98.
276. Ruzsala, F.; Kostiner, E. *J. Cryst. Growth* **1974**, *26*, 155–156.
277. Yakubovich, O. V.; Yakovleva, E. V.; Golovanov, A. N.; Volkov, A. S.; Volkova, O. S.; Zvereva, E. A.; Dimitrova, O. V.; Vasiliev, A. N. *Inorg. Chem.* **2013**, *52*, 538–1543.
278. Garlea, V. O.; Sanjeewa, L. D.; McGuire, M. A.; Batista, C. D.; Samarakoon, A. M.; Graf, D.; Winn, B.; Ye, F.; Hoffmann, C.; Kolis, J. W. *Phys. Rev. X* **2019**, *9*, 011038.
279. Smith Pellizzeri, T. M.; Sanjeewa, L. D.; Pellizzeri, S.; McMillen, C. D.; Garlea, V. O.; Ye, F.; Sefat, A. S.; Kolis, J. W. *Dalton Trans.* **2020**, *49*, 4323–4335.
280. Belov, N. V.; Ivaschenko, A. I.; Bondareva, O. S.; Lobachev, A. N.; Yu, A.; Malinovskii, Y. A.; Melnikov, O. K.; Simonov, K. A. In *Hydrothermal Synthesis and Growth of Single Crystals*; Lobachev, A. N., Ed.; 158; Nauka: Moscow, 1982.
281. Byrappa, K.; Shekar, K. V. K.; Rodriguez-Clemente, R. *J. Mater. Res.* **1993**, *8*, 2319–2326.
282. Byrappa, K.; Shekar, K. V. K.; Rodriguez-Clemente, R. *Mater. Res. Bull.* **1993**, *28*, 709–718.
283. Byrappa, K.; Shekar, K. V. K. *J. Mater. Res.* **1993**, *8*, 864–870.
284. Byrappa, K.; Shekar, K. V. H. *J. Mater. Chem.* **1992**, *2*, 13–18.
285. Chen, C.; Lin, Z.; Wang, Z. S. *Appl. Phys. B* **2005**, *80*, 1–25.
286. Chen, C.; Sasaki, T.; Li, R.; Wu, Y.; Lin, Z.; Mori, Y.; Hu, Z.; Wang, J.; Aka, G.; Yoshimura, M.; Kaneda, Y. *Nonlinear Optical Borate Crystals: Principals and Applications*, John Wiley & Sons, 2012.
287. Tran, T. T.; Hongwei, Y.; Rondinelli, J. M.; Poepelmeier, K. R.; Halasyamani, P. S. *Chem. Mater.* **2016**, *28*, 5238–5258.
288. Leonyuk, N. I.; Leonyuk, L. I. *Progr. Cryst. Growth Charact.* **1995**, *31*, 179.
289. Jen, I. H.; Lee, Y. C.; Tsai, C. E.; Lii, K. H. *Inorg. Chem.* **2019**, *58*, 4085–4088.
290. Liao, C. J.; Wen, Y. S.; Lii, K. H. *Inorg. Chem.* **2018**, *57*, 11492–11497.
291. Kuo, Y. C.; Liu, H. K.; Wang, S. L.; Lii, K. H. *Dalton Trans.* **2020**, *49*, 6220–6226.
292. Heyward, C. C.; McMillen, C. D.; Kolis, J. W. *Inorg. Chem.* **2012**, *51*, 3956–3962.
293. McMillen, C. D.; Stritzinger, J.; Kolis, J. W. *Inorg. Chem.* **2012**, *51*, 3953–3955.
294. McMillen, C. D.; Kolis, J. W. *Inorg. Chem.* **2011**, *50*, 6809–6813.
295. McMillen, C. D.; Heyward, C. C.; Giesber, H. G.; Kolis, J. W. *J. Solid State Chem.* **2011**, *184*, 2966–2971.
296. McMillen, C. D.; Giesber, H. G.; Kolis, J. W. *J. Cryst. Growth* **2008**, *310*, 299–305.
297. Giesber, H. G.; Ballato, J.; Pennington, W. T.; Kolis, J. W.; Dejneka, M. *Glass Technol.* **2003**, *44*, 1.
298. Giesber, H. G.; Ballato, J.; Pennington, W. T.; Kolis, J. W. *Inform. Sci.* **2003**, *149*, 61.
299. Kolis, J. W.; Franco, T.; McMillen, C. D. *Mater. Res. Soc. Proc.* **2005**, *848*, 1–6.
300. McMillen, C. D.; Kolis, J. W. *J. Cryst. Growth* **2008**, *310*, 2033–2038.
301. McMillen, C. D.; Vanderveer, D.; Kolis, J. W. *Acta Crystallogr. B* **2009**, *B65*, 445–449.
302. McMillen, C. D.; Kolis, J. W. *Proc. OSA Front. Opt.* **2009**, *93*, AWC1.
303. McMillen, C. D.; Kolis, J. W.; Ballato, J. M.; Kaminski, A.; Liu, C. OSA Proceedings: Renewable Energy Optics and Photonics Congress (2010) NthC6.
304. Ye, N.; Tang, D. *J. Cryst. Growth* **2006**, *293*, 233–235.
305. Liu, L.; Zhou, H.; He, X.; Zhang, X.; Wang, X.; Lu, F.; Zhang, C.; Zhou, W.; Chen, C. *J. Cryst. Growth* **2012**, *348*, 60–64.
306. Sang, Y.; Yu, D.; Avdeev, M.; Piltz, R.; Sharma, N.; Ye, N.; Liu, H.; Wang, J. *CrystEngComm* **2012**, *14*, 6079–6084.
307. Rabenau, A.; Rau, H. *Philips Tech. Rev.* **1969**, *30*, 89–96.
308. Yoshimura, M.; Kim, K. J.; Somyia, S. *J. Mater. Sci. Lett.* **1984**, *3*, 1097–1098.
309. Somyia, S.; Hirano, S.-I.; Yoshimura, M.; Yanagisawa, K. *J. Mater. Sci.* **1981**, *16*, 813–816.
310. Yanagisawa, K.; Yoshimura, M.; Somyia, S. *J. Mater. Sci.* **1982**, *17*, 177–182.
311. Leblanc, M.; Ferey, G.; de Pape, R. *Mater. Res. Bull.* **1984**, *19*, 1581–1590.
312. Ferey, G.; Leblanc, M.; de Pape, R.; Passaret, M.; Bothorel-Razazi, M. P. *J. Cryst. Growth* **1975**, *29*, 209–211.
313. Renaudin, J.; Samouel, M.; Leblanc, M.; de Kozak, A.; Ferey, G. *J. Solid State Chem.* **1985**, *59*, 103–110.
314. Loiko, P. A.; Khaidukov, N. M.; Mendez-Ramos, J.; Vilejshikova, E. V.; Skoptsov, N. A.; Yumashev, K. V. *JOL* **2016**, *175*, 260–266.
315. Pytalev, D. S.; Jaffres, A.; Aschehoug, P.; Ryabochkina, P. A.; Malov, A. V.; Khaidukov, N. M.; Popova, M. N. *JOL* **2014**, *153*, 125–129.
316. Malkin, B. Z.; Pytalev, D. S.; Popova, M. N.; Baibekov, E. I.; Falin, M. L.; Gerasimov, K. I.; Khaidukov, N. M. *Phys. Rev. B* **2012**, *86*, 134110.
317. Tanner, P. A.; Duan, C.-K.; Makhov, V. N.; Kirm, M.; Khaidukov, N. M. *Opt. Mater.* **2009**, *31*, 1729–1734.
318. Tanner, P. A.; Yulong, L.; Edelstein, N. M.; Murdoch, K. M.; Khaidukov, N. M. *J. Phys. Condens. Matter* **1997**, *9*, 7817–7836.
319. Kaminskii, A. A.; Khaidukov, N. M. *Phys. Stat. Sol.* **1992**, *129*, K65.
320. Goryunov, A. V.; Popov, A. I.; Khaidukov, N. M.; Fedorov, P. P. *Mater. Res. Bull.* **1992**, *27*, 213–220.
321. Le Fur, Y.; Khaidukov, N. M.; Aleonard, S. *Acta Crystallogr.* **1992**, *C48*, 2062–2064.
322. Comer, S.; McMillen, C. D.; Kolis, J. W. *Solid State Sci.* **2013**, *17*, 90–96.

323. Bridenbaugh, P. M.; Eckert, J. O.; Nykolak, G.; Thomas, G.; Wilson, W.; Demianets, L. M.; Riman, R.; Laudise, R. A. *J. Cryst. Growth* **1994**, *144*, 243–252.
324. McMillen, C. D.; Comer, S.; Fulle, K.; Sanjeewa, L. D.; Kolis, J. W. *Acta Crystallogr. Sect. B Struct. Sci. Cryst. Engin. Mater.* **2015**, *71*, 768–776.
325. Faria, L. O.; Lo, D.; Kui, H. W.; Khaidukov, N. M.; Nogueira, M. S. *Radiat. Prot. Dosimetry* **2004**, *112*, 435–438.
326. Kaminskii, A. A.; Mironov, V. S.; Bagaev, S. N.; Khaidukov, N. M.; Joubert, M. F.; Jacquier, B.; Boulon, G. *Phys. Stat. Solidi* **1994**, *145*, 177–195.
327. Makhov, V. N.; Khaidukov, N. M.; Kirm, M.; Zimmerer, G.; Lam, S. K.; Lo, D.; Suetin, N. V. *Surf. Rev. Lett.* **2002**, *9*, 271–276.
328. Li, Y.; Yin, M.; Guo, H.; Makhov, V. N.; Khaidukov, N. M.; Krupa, J. C. *J. Phys. Condens. Matter* **2003**, *15*, 7117–7125.
329. de Barros, C. L. M.; Barthem, R. B.; Khaidukov, N. M. *JOL* **1999**, *82*, 307–314.
330. Underwood, C. C.; McMillen, C. D.; Chen, H.; Anker, J. N.; Kolis, J. W. *Inorg. Chem.* **2013**, *52*, 237–244.
331. Underwood, C. C.; Mann, M.; McMillen, C. D.; Musgraves, J. D.; Kolis, J. W. *Solid State Sci.* **2012**, *14*, 574–579.
332. Underwood, C. C.; Mann, M.; McMillen, C. D.; Kolis, J. W. *Inorg. Chem.* **2011**, *50*, 11825–11831.
333. Underwood, C. C.; McMillen, C. D.; Kolis, J. W. *J. Chem. Crystallogr.* **2012**, *42*, 606–610.
334. Underwood, C. C.; McMillen, C. D.; Kolis, J. W. *J. Chem. Crystallogr.* **2014**, *44*, 493–500.
335. Grzechnik, A.; Underwood, C. C.; Kolis, J. W.; Friese, K. *J. Fluorine Chem.* **2013**, *150*, 8–13.
336. Stritzinger, J.; McMillen, C. D.; Kolis, J. W. *J. Chem. Crystallogr.* **2012**, *42*, 366–371.
337. Felder, J.; Yeon, J.; Smith, M.; Zur Loye, H. C. *Inorg. Chem. Front.* **2017**, *4*, 368–377.
338. Klepov, V. V.; Felder, J. B.; Zur Loye, H.-C. *Inorg. Chem.* **2018**, *57*, 4497–5606.
339. Yeon, J.; Smith, M. D.; Tapp, J.; Moeller, A.; Zur Loye, H.-C. *Inorg. Chem.* **2014**, *53*, 6289–6298.
340. Klepov, V. V.; Morrison, G.; Zur Loye, H.-C. *Cryst. Growth Des.* **2019**, *19*, 1347–1355.
341. Chemey, A. T.; Sperling, J. M.; Windorff, C. J.; Hobart, D. E.; Albrecht-Schmitt, T. E. *Cryst. Growth Des.* **2020**, *20*, 2998–3006.
342. Pace, K. A.; Klepov, V. V.; Deason, T. K.; Smith, M. D.; Ayer, G. B.; Diprete, D. P.; Amoroso, J. W.; Zur Loye, H.-C. *Chem. A Eur. J.* **2020**, *26*, 12941–12944.
343. Chemey, A. T.; Celis-Barros, C.; Sperling, J. M.; Paez-Hernandez, D.; Albrecht-Schmitt, T. E. *Inorg. Chem.* **2019**, *58*, 14790–14799.
344. Windorff, C. J.; Chemey, A. T.; Sperling, J. M.; Klamm, B. E.; Albrecht-Schmitt, T. E. *Inorg. Chem.* **2020**, *59*, 4176–4180.
345. Kanatzidis, M. G. *Encyclopedia of Inorganic Chemistry*, John Wiley and Sons, 2006.
346. Kanatzidis, M. G. *Inorg. Chem.* **2017**, *56*, 3158–3173.
347. Brant, J. A.; Brunetta, C. D.; Aitken, J. A. *Comprehensive Inorganic Chemistry II*, Elsevier, 2013. ch. 10.
348. Xiong, W.-W.; Zhang, G.; Zhang, Q. *Inorg. Chem. Front.* **2014**, *1*, 292–301.
349. Sheldrick, W. S.; Wachold, M. *Coord. Chem. Rev.* **1998**, *176*, 211–322.
350. Dorhout, P. K.; Ford, N. B.; Raymond, C. C. *Coord. Chem. Rev.* **2017**, *352*, 537–550.
351. Sheldrick, W. S. *Z. Anorg. Allg. Chem.* **2012**, *638*, 2401–2424.
352. Zhou, J.; Dai, J.; Bian, G.-Q.; Li, C.-Y. *Coord. Chem. Rev.* **2009**, *253*, 1221–1247.
353. Kanatzidis, M. G.; Das, B. K. *Comm. Inorg. Chem.* **1999**, *21*, 29–51.
354. Pajaczkowska, A. *Prog. Cryst. Growth Charact.* **1978**, *1*, 289–326.
355. Laudise, R. A.; Kolb, E. D.; DeNeufville, J. P. *Am. Mineral.* **1965**, *50*, 382–391.
356. Kolb, E. D.; Caporaso, A. J.; Laudise, R. A. *J. Cryst. Growth* **1968**, *3–4*, 422–425.
357. Kolb, E. D.; Laudise, R. A. *J. Cryst. Growth* **1970**, *7*, 199–202.
358. Rau, H.; Rabenau, A. *Mater. Res. Bull.* **1967**, *2*, 609–614.
359. Rau, H.; Rabenau, A. *Solid State Commun.* **1967**, *5*, 331–332.
360. Pajaczkowska, A.; Rabenau, A. *J. Solid State Chem.* **1977**, *21*, 43–48.
361. Rabenau, A.; Rau, H.; Rosenstein, G. J. *Less-Common Metals* **1970**, *21*, 395–401.
362. Pajaczkowska, A. *J. Cryst. Growth* **1971**, *8*, 137–138.
363. Hurd, J. L.; Ciszek, T. F. *J. Cryst. Growth* **1984**, *70*, 415–419.
364. Barnard, W. M. *Econ. Geol.* **1967**, *62*, 138–147.
365. Barnard, W. M.; Christopher, P. A. *Econ. Geol.* **1966**, *61*, 897–902.
366. Barnard, W. M.; Christopher, P. A. *Econ. Geol.* **1966**, *61*, 1287–1290.
367. Putnis, A. *Rev. Mineral. Geochem.* **2009**, *70*, 87–124.
368. Sugaki, A.; Kitakaze, A.; Ueno, T. *Jpn. Assoc. Mineral. Petrol. Econ. Geol.* **1982**, *77*, 257–269.
369. Schoonen, M. A. A.; Barnes, H. L. *Geochem. Cosmochim. Acta* **1991**, *55*, 3491–3504.
370. Zhao, J.; Brugger, J.; Chen, G.; Ngothai, Y.; Pring, A. *Am. Mineral.* **2014**, *99*, 343–354.
371. Zhao, J.; Brugger, J.; Ngothai, Y.; Pring, A. *Am. Mineral.* **2014**, *99*, 2389–2397.
372. Qian, G.; Brugger, J.; Skinner, W. M.; Chen, G.; Pring, A. *Geochim. Cosmochim. Acta* **2010**, *74*, 5610–5630.
373. Hu, X.; Cai, Y.; Zhang, Y. *Appl. Geochem.* **2017**, *77*, 102–115.
374. Sugaki, A.; Shima, H.; Kitakaze, A.; Mizota, T. *Am. Mineral.* **1981**, *66*, 398–402.
375. Korzenski, M. B.; Kolis, J. W. *Inorg. Synth.* **2002**, *33*, 130–138.
376. Korzenski, M. B.; Schimek, G. L.; Kolis, J. W. *Solid State Sci.* **2000**, *2*, 379–383.
377. Emirdag-Eanes, M.; Kolis, J. W. *Z. Anorg. Allg. Chem.* **2002**, *628*, 10–11.
378. Kolis, J. W.; Korzenski, M. B. *MRS Proc.* **1996**, *453*, 35.
379. DeVries, R. C.; Roy, R.; Somya, S.; Yamada, S. In *Advanced Materials 1993*; Somya, S., Ed.; *Transactions of the Materials Research Society of Japan* vol. 19B; Elsevier: Amsterdam, 1994; pp 641–663.
380. Gogotsi, Y. G.; Nickel, K. G.; Kofstad, P. J. *Mater. Chem.* **1995**, *51*, 2313–2314.
381. DeVries, R. C. *Nature* **1997**, *385*, 485.
382. Zhao, X.-J.; Roy, R.; Cherian, K. A.; Badzian, A. *Nature* **1997**, *385*, 513–515.
383. Sunagawa, I. *Curr. Top. Mat. Sci* **1982**, *10*, 353–497.
384. Nassau, K. *Lap. J.* **1964**, 313–316.
385. Balitsky, V. S. *J. Cryst. Growth* **1977**, *41*, 100–102.
386. Setkova, T.; Shapovalov, Y.; Balitsky, V. *J. Cryst. Growth* **2011**, *318*, 904–907.
387. von Goerne, G.; Franz, G.; Wirth, R. *Eur. J. Mineral.* **1999**, *11*, 1061–1077.
388. Nassau, K. *J. Cryst. Growth* **1976**, *35*, 211–222.
389. Anon (n.d.) Private Conversations of JK with Thomas Chatham.
390. Flanagan, E. M.; Brack, D. W.; Mumbach, N. R.; Taylor, A. M. *Am. Mineral.* **1967**, *52*, 744–772.
391. Flanagan, E. M. *US Patent 3,567,642*, 1971.
392. Flanagan, E. M.; Mumbach, N. R. *US Patent 3,567,643*, 1971.
393. Schmetzer, K.; Kiefert, L.; Bernhardt, H.-J.; Beili, Z. *Gems Gemol.* **1997**, 276–291.
394. Yancey, P. J. *US Patent 3,723,337*, 1973.

395. Furusaki, T.; Bando, Y.; Kodaira, K.; Matsushita, T. *Mater. Res. Bull.* **1989**, *24*, 967–972.
396. Demianets, L. N.; Ivanov-Shitz, A. K.; Gainutdinov, R. V. *Inorg. Mat.* **2006**, *42*, 989–995.
397. Shigley, J. E.; McClure, S. F.; Cole, J.-C.; Koivula, J. I.; Lu, T.; Elen, S.; Demianets, L. M. *Gems Gemol.* **2001**, 41–55.
398. Jacobs, H.; Niewa, R.; Sichla, T.; Tenten, A.; Zachwieja, U. *J. Alloys Compd.* **1997**, *246*, 91–100.
399. Jacobs, H.; Schmidt, D. *Curr. Top. Mat. Sci.* **1981**, *8*, 381.
400. Richter, T. M. M.; Niewa, R. *Inorganics* **2014**, *2*, 29–78.
401. Jacobs, H.; Stüve, C. J. *Less Comm. Met.* **1984**, *96*, 323–329.
402. Häusler, J.; Schnick, W. *Chem.-Eur. J.* **2018**, *24*, 11864–11879.
403. Griffiths, S.; Pimpitkar, S.; Speck, J. S.; Nakamura, S. *J. Cryst. Growth* **2016**, *456*, 5–14.
404. Häusler, J.; Neudert, L.; Mallmann, M.; Niklaus, R.; Kimmel, A. C. L.; Alt, N. S.; Schlücker, E.; Oeckler, O.; Schnick, W. *Chem.-Eur. J.* **2017**, *23*, 2583–2590.
405. Cordes, N.; Nentwig, M.; Eisenburger, L.; Oeckler, O.; Schnick, W. *Eur. J. Inorg. Chem.* **2019**, 2304–2311.
406. Wendl, S.; Mallmann, M.; Strobel, P.; Schmidt, P. J.; Schnick, W. *Eur. J. Inorg. Chem.* **2020**, 841–846.
407. Cordes, N.; Niklaus, R.; Schnick, W. *Cryst. Growth Design* **2019**, *19*, 3484–3490.
408. Adekore, B. T.; Rakes, K.; Wang, B.; Callahan, M. J.; Pendurti, S.; Sitar, Z. *J. Elec. Mat.* **2006**, *35*, 1104–1111.
409. Ehrentraut, D.; Bockowski, M. *Handbook of Crystal Growth*, 2nd ed.; Elsevier, 2015; pp 577–619.
410. Dwilinski, R.; Baranowski, J. M.; Kaminska, M.; Doradzinski, R.; Garczynski, J.; Sierzputowski, L. *Acta Phys. Pol. A* **1996**, *90*, 763.
411. Kolis, J. W.; Wilcinski, S. W.; Laudise, R. A. *Mat. Res. Soc. Sym.* **1998**, *495*, 367.
412. Dwilinski, R.; Wyszomolek, A.; Baranowski, J.; Kamińska, M.; Doradziński, R.; Garczyński, J.; Sierzputowski, L.; Jacobs, H. *Acta Phys. Pol. A* **1995**, *88*, 833–836.
413. Ketchum, D. R.; Kolis, J. W. *J. Cryst. Growth* **2001**, *222*, 431.
414. Jiang, W.; Ehrentraut, D.; Downey, B. C.; Kamber, D. S.; Pakalapati, R. T.; Do Yoo, H.; D'Evelyn, M. P. *J. Cryst. Growth* **2014**, *403*, 18–21.
415. Zajac, M.; Kucharski, R.; Grabianska, K.; Gwardys-Bak, A.; Puchalski, A.; Wasik, D.; Litwin-Staszewska, E.; Piotrkowski, R.; Domagala, J. Z.; Bockowski, M. *Progress Crystal Growth and Characterization of Materials*; vol. 64; Elsevier, 2018; pp 63–74.
416. Wang, B.; Callahan, M. J. *J. Cryst. Growth* **2006**, *291*, 455–460.
417. Callahan, M. J.; Wang, B.; Bouthillette, L. O.; Wang, S. Q.; Kolis, J. W.; Bliss, D. F. *MRS Online Proc.* **2003**, 798.
418. Ehrentraut, D.; Kagamitani, Y.; Fukuda, T.; Orito, F.; Kawabata, S.; Katano, K.; Terada, S. *J. Cryst. Growth* **2008**, *310*, 3902–3906.
419. Wang, B.; Callahan, M. J. *Cryst. Growth Design* **2006**, *6*, 1227–1246.
420. Wang, B.; Callahan, M. J.; Rakes, K. D.; Bouthillette, L. O.; Wang, S. Q.; Bliss, D. F.; Kolis, J. W. *J. Cryst. Growth* **2006**, *287*, 376–380.
421. Stevenson, R. *IEEE Spectrum* **2010**, 40–45.
422. Ehrentraut, D.; Pakalapati, R. T.; Kamber, D. S.; Jiang, W.; Pocius, D. W.; Downey, B. C.; McLaurin, M.; D'Evelyn, M. P.; Jap, J. *Appl. Phys.* **2013**, *52*, 08JA01.
423. Zhang, S.; Hintze, F.; Schnick, W.; Niewa, R. *Eur. J. Inorg. Chem.* **2013**, 5387–5399.
424. Tomida, D.; Kuroda, K.; Hoshino, N.; Suzuki, K.; Kagamitani, Y.; Ishiguro, T.; Fukuda, T.; Yokoyama, C. *J. Cryst. Growth* **2010**, *312*, 3161–3164.
425. Bao, Q.; Saito, M.; Hazu, K.; Furusawa, K.; Kagamitani, Y.; Kayano, R.; Tomida, D.; Qiao, K.; Ishiguro, T.; Yokoyama, C.; Chichibu, S. F. *Cryst. Growth Design* **2013**, *13*, 4158–4161.
426. Schimmel, S.; Lindner, M.; Steigerwald, T. G.; Hertweck, B.; Richter, T. M.; Künecke, U.; Alt, N. S.; Niewa, R.; Schlücker, E.; Wellmann, P. J. *J. Cryst. Growth* **2015**, *418*, 64–69.
427. Ehrentraut, D.; Kagamitani, Y.; Yokoyama, C.; Fukuda, T. *J. Cryst. Growth* **2008**, *310*, 891–895.
428. Ketchum, D. R.; Schimek, G. L.; Pennington, W. T.; Kolis, J. W. *Inorg. Chim. Acta* **1999**, *294*, 200.
429. Ok, K. M.; O'Hare, D.; Smith, R. I.; Chowdhury, M.; Fikremariam, H. *Rev. Sci. Instrum.* **2010**, *81*, 25107.
430. Walton, R. I.; Francis, R. J.; Halasyamani, P. S.; O'Hare, D.; Smith, R. I.; Done, R.; Humphreys, R. J. *Rev. Sci. Instrum.* **1999**, *70*, 3391–3396.
431. Brugger, J.; Etschmann, B. E.; Grundler, P. V.; Liu, W.; Testemale, D.; Pring, A. *Am. Mineral.* **2012**, *97*, 1519–1522.
432. Xia, F.; Brugger, J.; Qian, G.; Ngothai, Y.; O'Neill, B.; Zhao, J.; Pullen, S.; Olsen, S.; Pring, A. *J. Appl. Cryst.* **2012**, *45*, 166–173.
433. Seward, T. M.; Hishima, N. In *Hydrothermal Experimental Technique*; Ulmer, G. C., Barnes, H. L., Eds., Wiley and Sons: New York, 1987; pp 141–156.

4.19 Solid-state electrolytes for lithium-ion batteries

Sanoop Palakkathodi Kammampata, Mohammad Akbari Garakani, Zheyu Zhang, and Venkataraman Thangadurai,
Department of Chemistry, University of Calgary, Calgary, AB, Canada

© 2023 Elsevier Ltd. All rights reserved.

4.19.1	Introduction	658
4.19.2	Fundamentals of solid-state electrolytes	658
4.19.2.1	Desired functional properties of solid state (ceramic) electrolytes	658
4.19.2.2	Ion transport mechanism in solid-state electrolytes	659
4.19.3	Inorganic solid electrolytes for all-solid-state batteries	661
4.19.3.1	Oxide based solid Li ion electrolytes	661
4.19.3.1.1	Perovskite-type solid electrolytes	661
4.19.3.1.2	NASICON-type solid electrolytes	663
4.19.3.1.3	LISICON-type solid electrolytes	664
4.19.3.1.4	Garnet-type solid electrolytes	665
4.19.3.2	Sulfide based solid electrolytes	668
4.19.3.3	Halide based solid electrolytes	669
4.19.3.3.1	Halide solid electrolytes with metal element	669
4.19.3.3.2	Halide solid electrolytes with non-metallic element	670
4.19.4	All-solid-state Li batteries (ASSLBs)	672
4.19.5	Conclusions	676
Acknowledgments		676
References		676

Abstract

This chapter aims to provide a systematic overview of the current state of the research in the field of solid-state electrolytes for all-solid-state Li batteries. The desired functional properties and ion transport mechanism of solid-state electrolytes are explained, followed by a detailed survey on the existing understanding of the metal oxides, sulfides, and halides for fast Li ion conduction. Emphasis is also given on the oxide-based Li ion solid electrolyte, covering the structures of perovskites, Na super ionic conductors (NASICONs)-type, Li super ionic conductors (LISICONs) and Li-stuffed garnets with their chemical composition-crystal structure-ionic conductivity relationships and electrochemical stability discussed. Examples of all-solid-state Li batteries and the evaluation of their performance in terms of capacity and cycle numbers are reported.

4.19.1 Introduction

Solid-state batteries based on ceramic fast ion conductors are foreseen as the future state of energy storage technology due to their higher energy and power density, safety and wide electrochemical stability window as compared to the present organic polymer electrolyte batteries.^{1,2} Solid-state batteries also have other advantages, such as absence of electrolyte leakage and vaporization of liquid electrolytes, ease of miniaturization and long cycle life. In an ideal solid-state (ceramic) electrolyte, only one-type of species are mobile, unlike organic electrolytes, and thus, solid-state batteries anticipated to have a superior performance over liquid electrolyte-based batteries.³ However, the present solid-state batteries exhibit moderate performances due to poor ionic conductivity of electrolytes, about an order of magnitude lower conductivity to that of liquid electrolytes, and chemical stability of electrode and electrolyte interfaces during the preparation and operation of batteries. Volume change of the electrodes and the formation of undesired products lead to high interfacial resistance, which affect the electrochemical performance of the battery.^{4,5} Thus, a better understanding of functional properties of solid electrolytes and electrodes are critical to develop next generation robust solid-state Li batteries for transportation and grid-scale applications.

4.19.2 Fundamentals of solid-state electrolytes

4.19.2.1 Desired functional properties of solid state (ceramic) electrolytes

A typical solid-state Li ion conductor should meet the following basic requirements for their use in all-solid-state Li batteries (ASSLBs):

- High total Li ion conductivity (bulk and grain boundary) in the order of $10^{-2} \text{ S cm}^{-1}$ and negligible electrode and electrolyte charge transfer interface impedance.
- Negligible electronic conductivity (with Li ion transference number (t_{Li^+}) ~ 1) at the entire range of Li activity between the cathode and anode.
- High chemical stability against the applied electrode materials, especially elemental Li and Li-metal alloys.
- High electrochemical decomposition voltage to apply high voltage positive electrodes, and
- Environmentally safe, and easy to prepare large amounts by cost effective methods.

Although Li ion conduction has been reported for a wide range of solid electrolytes with different types of crystal structures, most of them do not fulfill all the above requirements simultaneously. **Table 1** lists the room temperature conductivity (σ) of well-known solid electrolytes and their disadvantages when being used as electrolytes in ASSLBs.^{6–9}

4.19.2.2 Ion transport mechanism in solid-state electrolytes

Ions move in all directions in solid electrolytes even without applying an electric field due to thermal energy, and it is known as Brownian motion, like in liquids.³ Due to the random ion migrations, point defects are disordered in the structure. Under the application of electric potential, the ions move towards their opposite charged electrode. For example, positively charged cations and holes move towards negative electrode, and negatively charged ions and electrons move towards a positive electrode. The ionic conduction in solids is based on diffusion and migration of ions via defects.³ For ionic conductivity to occur in the crystal, it is important to have partial occupancy of energetically equivalent or near-equivalent sites in the structure which are randomly distributed.

Schottky and Frenkel are the two types of defects that are most important for ion mobility in solids. A Schottky defect is a stoichiometric defect, which occurs when paired cation and anion vacancies are present. In a material with a monovalent cation and anion, e.g., NaCl, there will be an equal number of cation and anion vacancies in the structure. These vacancies are distributed randomly in the lattice. Adjacent ions can jump to vacancy site leaving its own site vacant. This process leads to movement of ions through the solid resulting in conductivity which is called vacancy migration. A Frenkel defect is also a stoichiometric defect, which arises when an ion is displaced from its lattice site into an interstitial site. These intrinsic defects are rather small in concentration, and hence, extrinsic chemical substitution is generally used to increase the defect concentration. This ion can jump into an adjacent vacant interstitial site, resulting in a long-range conduction. **Fig. 1** shows the schematic representation of vacancy and interstitial mechanisms for ionic conduction in solids.¹⁰

Table 1 Common solid-state Li ion electrolytes, their room temperature (RT) conductivity (σ) and their limitation to use them in ASSLBs.^{6–9}

<i>Solid electrolytes</i>	σ (S cm^{-1})	<i>Strengths and issues to be solved for use in ASSLBs</i>
Li_3N	10^{-3}	Chemically stable with elemental Li anode, poor electrochemical stability window, decompose at about 0.445 V at room temperature
Li- β -alumina	10^{-4}	Chemically stable with elemental Li anode, high electrochemical stability, highly hygroscopic, not suitable for battery production
$\text{Li}_{14}\text{ZnGe}_4\text{O}_{16}$ (LISICON)	10^{-6}	Highly reactive with Li metal anode, and atm CO_2 ; poor conductivity stability with time
$\text{Li}_{1.3}\text{Ti}_{1.7}\text{Al}_{0.3}(\text{PO}_4)_3$ (NASICON)	10^{-3}	Reactive with elemental Li anode, low operating voltage due to facile Ti reduction, large grain-boundary impedance
$\text{Li}_{3x}\text{La}_{2/3-x}\square_{1/3-2x}\text{TiO}_3$	10^{-3}	Chemically not stable in contact with Li anode, low operating voltage due to Ti reduction, excellent bulk ionic conductivity, difficult to control the Li content due to high temperature synthesis and exhibit large grain boundary resistance
$\text{Li}_{2.88}\text{PO}_{3.86}\text{N}_{0.14}$ (LiPON)	10^{-6}	Stable to elemental Li anode, moderate Li ion conductivity, very hard to control Li and N content using sputtering condition (thin film application)
Sulfide glass (Ga_2S_3 - La_2S_3)	10^{-3}	Good bulk Li ion conductivity, highly hygroscopic, reactive to moisture and CO_2 , lack of long-term stability with elemental Li anode
$\text{Li}_7\text{La}_3\text{Zr}_2\text{O}_{12}$	10^{-4}	Exhibit the highest electrochemical stability window of 6 V/Li, stable to elemental Li, found to be reactive with CO_2 in presence of moisture, and intrinsic doping with Al may be required to establish the high conducting cubic phase

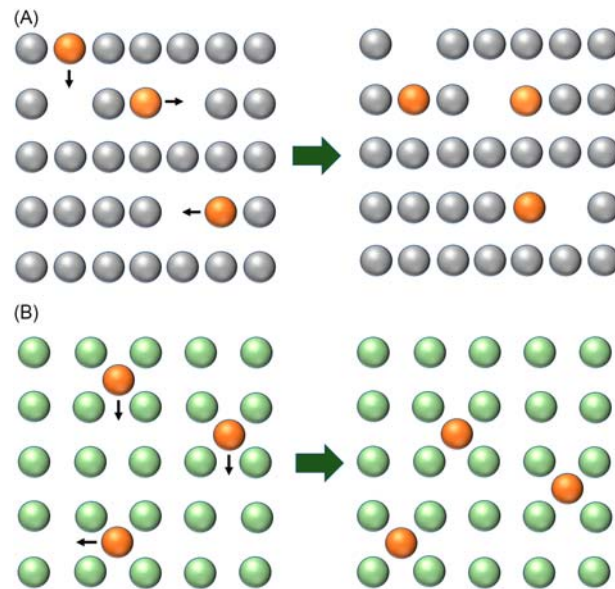


Fig. 1 Schematic representation of a (A) vacancy and (B) an interstitial ionic migration in solids.¹⁰ Redrawn by permission from Ref. Palakkathodi Kammampata, S.; Thangadurai, V. Cruising in Ceramics—Discovering New Structures for All-Solid-State Batteries—Fundamentals, Materials, and Performances. *Ionics (Kiel)* **2018**, *24* (3), 639–660. <https://doi.org/10.1007/s11581-017-2372-7>, Copyright (2018), Springer Nature.

Ionic conductivity (σ) of species (e.g., $i \cong \text{Li}^+$) can be represented as:

$$\sigma_i = n_i q \mu_i \quad (1)$$

where n_i is the number of charge carriers per unit volume, q is the elementary charge ($1.6 \times 10^{-19} \text{C}$), and μ_i is the electrical mobility of species (i). The concentration of mobile ion charge carriers is typically in the order of about 10^{21} – 10^{22} ions cm^{-3} in the solid-state structures.

The relation between temperature and mobility of ions (μ) can be expressed as:

$$\mu_i = \mu_0 \exp\left(\frac{-E_a}{kT}\right) \quad (2)$$

where μ_0 is a proportionality constant known as pre-exponential factor. μ_0 depends on the jump frequency, ν , which is the number of times per second the ion attempts the move and k is Boltzmann's constant. The relationship between the ionic conductivity of a solid and the diffusion coefficient of ions (D) is expressed by Nernst-Einstein equation:¹¹

$$\sigma_i = \frac{n_i q^2 D_i}{kT} \quad (3)$$

If we combine all the information in Eq. (1), a temperature-dependent conductivity equation is obtained and that can be expressed using the Arrhenius equation:

$$\sigma_i T = A \exp\left(\frac{-E_a}{kT}\right) \quad (4)$$

where E_a is the activation energy and A is the pre-exponential factor. For typical fast ion conductors, the activation energy for ionic conduction is about 0.1 eV. The fact that multiple species could carry charge in solid electrolytes drives the interest to understand the relative conductivities of different species. The fraction of the electrical conductivity through the electrolyte by a particular species is known as transference number (t_i) of that species (i):¹²

$$t_i = \frac{\sigma_i}{\sigma_{total}} \quad (5)$$

The sum of the transference numbers of all charge carrying species in an electrolyte is unity. i.e.,

$$t_i + t_e = 1 \quad (6)$$

Ionic transference number in fast solid ion electrolytes are estimated using experimental techniques such as Hittorf, Tubandt, and Hebb-Wagner polarization methods.^{13–17}

4.19.3 Inorganic solid electrolytes for all-solid-state batteries

A large number of inorganic structures have been investigated as the solid Li ion electrolyte for all-solid-state batteries due to their impressive room temperature ionic conductivity of 10^{-6} – 10^{-2} S cm^{-1} and the Li ion transference number of unity.^{10,18} These solids can be generally classified as either crystalline or amorphous glasses based on their structural properties. Among them, crystalline oxides, sulfides, and halide-based compounds have been widely investigated.^{8,19–21} While the amorphous materials show interesting functional physical and chemical properties, research and development is dominated by studies of crystalline materials, as it is rather easy to establish the crystal structure–chemical composition–ionic conductivity relationships. The physical and chemical properties of typical oxide, sulfide and halide based solid electrolytes are compared in Fig. 2. In the following sections, some examples of these three families of solid electrolytes are presented.

4.19.3.1 Oxide based solid Li ion electrolytes

Among the various oxide-based Li ion electrolytes, the perovskite-type, Na super ionic conductors (NASICONs)-type, Li super ionic conductors (LISICONs)-type, and Li-stuffed garnet-type structured materials have been studied extensively.^{10,23,29–31}

4.19.3.1.1 Perovskite-type solid electrolytes

Li ion conducting perovskite structure solid electrolytes were first reported by Latie et al.³² They investigated the ion conduction mechanism of $\text{Li}_x\text{M}_{1/3}\text{Nb}_{1-x}\text{Ti}_x\text{O}_3$ ($\text{M} = \text{La}, \text{Nd}$) using the NMR technique. Belous et al.³³ reported the fast Li ion conducting perovskite-type oxides $\text{Li}_{3x}\text{La}_{2/3-x}\square_{(1/3)-2x}\text{TiO}_3$ and investigated the change of crystal structure and ionic conductivity with Li content in the structure. Since then, several groups have been studied these Li ion conductors and the highest room temperature Li ion conductivity of $\sim 10^{-3}$ S cm^{-1} has been reported for $\text{Li}_{3x}\text{La}_{2/3-x}\square_{(1/3)-2x}\text{TiO}_3$ ($x = 0.1$).³⁴ Stramare et al. have reviewed the composition–structure–ionic conductivity property relationships of perovskite-type $\text{Li}_{3x}\text{La}_{2/3-x}\square_{(1/3)-2x}\text{TiO}_3$ ceramics.²³ Table 2 shows the ionic conductivity and activation energies of selected perovskite-type materials with and without La.²³

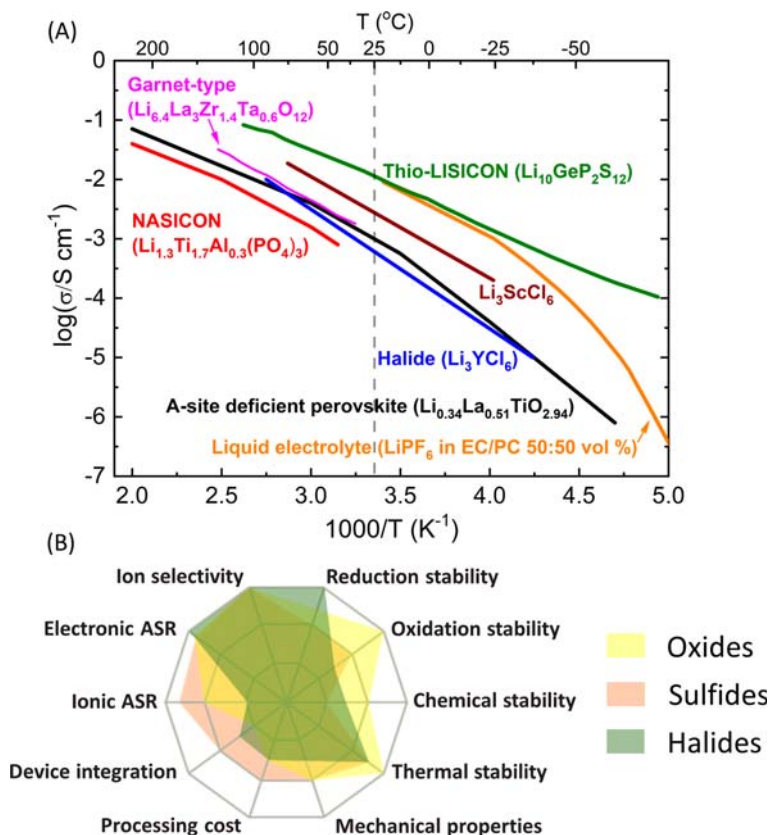


Fig. 2 (A) Ionic conductivity of Li solid electrolytes and organic electrolyte as a function of temperature^{22–27} and (B) radar plots of the performance properties of oxide, sulfide, and halide solid electrolytes (ASR = area specific resistance).²⁸ Redrawn by permission from Ref. Manthiram, A.; Yu, X.; Wang, S. Lithium Battery Chemistries Enabled by Solid-State Electrolytes. *Nat. Rev. Mater.* **2017**, 2 (4), 16103. <https://doi.org/10.1038/natrevmats.2016.103>, Copyright (2017), Springer Nature.

Table 2 Bulk Li ion conductivities (σ_{bulk}) at room temperature and activation energies (E_a) of selected perovskite-type structure materials.^{23,35}

Compound	σ_{bulk} (S cm^{-1})	E_a (eV)
$\text{Li}_{0.34}\text{La}_{0.51}\text{TiO}_{2.94}$	1.0×10^{-3}	0.40
$\text{Li}_{0.27}\text{La}_{0.59}\text{TiO}_3$	6.8×10^{-4}	0.36
$\text{Li}_{0.34}\text{La}_{0.56}\text{TiO}_3$	1.53×10^{-3}	0.33
$\text{Li}_{0.10}\text{La}_{0.63}\text{TiO}_3$	7.9×10^{-5}	0.36
$\text{Li}_{0.36}\text{La}_{0.53}\text{Sr}_{0.03}\text{TiO}_3$	2.54×10^{-3}	0.39
$\text{Li}_{0.36}\text{La}_{0.56}\text{Ti}_{0.97}\text{Al}_{0.03}\text{O}_3$	2.95×10^{-3}	0.38
$(\text{Li}_{0.1}\text{La}_{0.63})(\text{Mg}_{0.5}\text{W}_{0.5})\text{O}_3$	$\sim 10^{-6}$	0.39
$\text{Li}_{0.5}(\text{La}_{0.4}\text{Nd}_{0.1})\text{TiO}_3$	$\sim 10^{-3}$	0.33
$\text{La}_{0.58}\text{Li}_{0.36}\text{Ti}_{0.95}\text{Mg}_{0.05}\text{O}_3$	2.1×10^{-4}	0.29
$\text{La}_{0.55}\text{Li}_{0.36}\text{Ti}_{0.95}\text{Mn}_{0.05}\text{O}_3$	1.9×10^{-4}	0.29
$\text{La}_{0.55}\text{Li}_{0.36}\text{Ti}_{0.95}\text{Ge}_{0.05}\text{O}_3$	3.6×10^{-4}	0.29
$\text{La}_{0.55}\text{Li}_{0.36}\text{Ti}_{0.95}\text{Ru}_{0.05}\text{O}_3$	5.2×10^{-5}	0.28
$\text{La}_{0.51}\text{Li}_{0.36}\text{Ti}_{0.95}\text{W}_{0.05}\text{O}_3$	7.3×10^{-4}	0.27
$\text{La}_{0.55}\text{Li}_{0.36}\text{Ti}_{0.995}\text{Al}_{0.005}\text{O}_3$	1.1×10^{-3}	0.28
$\text{La}_{0.29}\text{Li}_{0.12}\text{NbO}_3$	4.25×10^{-5}	0.37
$\text{Li}_{0.34}\text{Pr}_{0.56}\text{TiO}_3$	10^{-6}	0.47
$\text{Sm}_{0.52}\text{Li}_{0.34}\text{TiO}_3$	$< 10^{-7}$	0.64
$\text{Nd}_{0.55}\text{Li}_{0.34}\text{TiO}_3$	$< 10^{-7}$	0.53
$\text{Nd}_{0.25}\text{Li}_{0.25}\text{TaO}_3$	$< 10^{-9}$	0.60
$\text{Y}_{0.25}\text{Li}_{0.25}\text{TaO}_3$	$< 10^{-10}$	0.85
$\text{Li}_{0.5}\text{Sr}_{0.56}\text{Fe}_{0.25}\text{Ta}_{0.75}\text{O}_3$	1.0×10^{-4}	0.36
$\text{Li}_{0.33}\text{Sr}_{0.56}\text{Co}_{0.225}\text{Ta}_{0.775}\text{O}_3$	5.1×10^{-6}	0.41
LiCaTiNbO_6	$< 10^{-7}$	0.68
LiSrTiNbO_6	$\sim 10^{-6}$	0.42
LiSrTiTaO_6	5.5×10^{-4}	0.33
$\text{LiSr}_2\text{Ti}_2\text{NbO}_9$	$< 10^{-6}$	0.37
$\text{LiBa}_2\text{Ti}_2\text{NbO}_9$	$< 10^{-7}$	0.74

Reprinted (adapted) with permission from Ref. Stramare, S.; Thangadurai, V.; Weppner, W. Lithium Lanthanum Titanates: A Review. *Chem. Mater.* **2003**, *15* (21), 3974–3990. doi: 10.1021/cm0300516, Copyright (2003) American Chemical Society.

The general chemical formula for perovskite oxides is ABO_3 (SrTiO_3) and its structure is shown in Fig. 3A, in which, A consists of alkaline, alkaline-earth, or rare-earth cations and B consists of transition metal ions.³⁶ The ideal cubic perovskite structure has the cubic space group of $Pm\bar{3}m$ in which A and B cations are 12-fold and 6-fold coordinated with O.³⁸ Depend on the compositions and synthesis methods, tetragonal, cubic, and or orthogonal perovskite structure can be obtained.³⁸ Fig. 3B schematically shows the bottleneck of the Li ion conduction in a perovskite-type $\text{Li}_{3-x}\text{La}_{2/3-x}\square_{(1/3)-2x}\text{TiO}_3$.³⁷ Considering an ideal perovskite crystal, the diameter of the bottleneck is estimated to be about 1.07 \AA .³⁷ It has been shown that the ionic conductivity of this structure changes with Li concentration as demonstrated in Fig. 3C, with a maximum conductivity (σ) at $x \approx 0.1$.²³ Also, substitution of La with other rare earth elements including Pr, Nd and Sm with different ionic radius affects the lattice parameter, activation energy (E_a) and ionic conduction of the material. As shown in Fig. 3D, La^{3+} shows the highest Li conduction and lowest activation energy.²³

It was found that the Li conductivity properties of the perovskite is mainly dictated by the A-site cations determining the size of Li diffusion channels. La-based LLTO exhibits the highest bulk ionic conductivity compared to other rare-earth containing perovskites (Fig. 3D). A-site vacancy concentration has a critical role in the conductivity of LLTO. Sr-doped LLTO with about 8% A-site vacancy concentration exhibited the highest ionic conductivity of $2.54 \times 10^{-3} \text{ S cm}^{-1}$.³⁵ Similarly, B-site substituted $\text{Li}_{0.36}\text{La}_{0.56}\text{Ti}_{0.97}\text{Al}_{0.03}\text{O}_3$ also showed the highest conductivity of $2.95 \times 10^{-3} \text{ S cm}^{-1}$ with an optimized A-site vacancy concentration of 8%.³⁵ One of the major concerns in Ti-based perovskite solid electrolytes, is the low grain boundary ionic conductivity (a large grain-boundary resistance) in the range of $10^{-5} \text{ S cm}^{-1}$ at room temperature which results in a low total ionic conductivity.³⁹ Blending and optimizing the synthesis route have been investigated to overcome this concern by optimizing the chemical composition and grain boundary fraction in the structure.⁴⁰

4.19.3.1.1 Chemical/electrochemical stability of perovskite-type Li ion electrolytes

It is found that this class of oxides are not suitable against elemental Li or intercalated electrodes due to the reduction of Ti^{4+} to Ti^{3+} at voltages below 2 V vs. Li/Li^+ leading to electronic conduction that will short circuit the cell.^{18,28,34,41,42} Zheng et al.⁴³ investigated the Ti^{4+} reduction in $\text{Li}_{0.35}\text{La}_{0.55}\text{TiO}_3$ and identified two lithiation steps at 1.8–1.1 V and 0.6–0 V vs. Li/Li^+ . They found that ~ 0.75 –0.9 Li could be inserted into this compound during the 1st lithiation step, but only 0.48 Li was reversibly inserted/extracted. They also proposed the formation of a monoclinic phase with 0.24 Li insertion. Elemental substitutions/interfacial modifications have

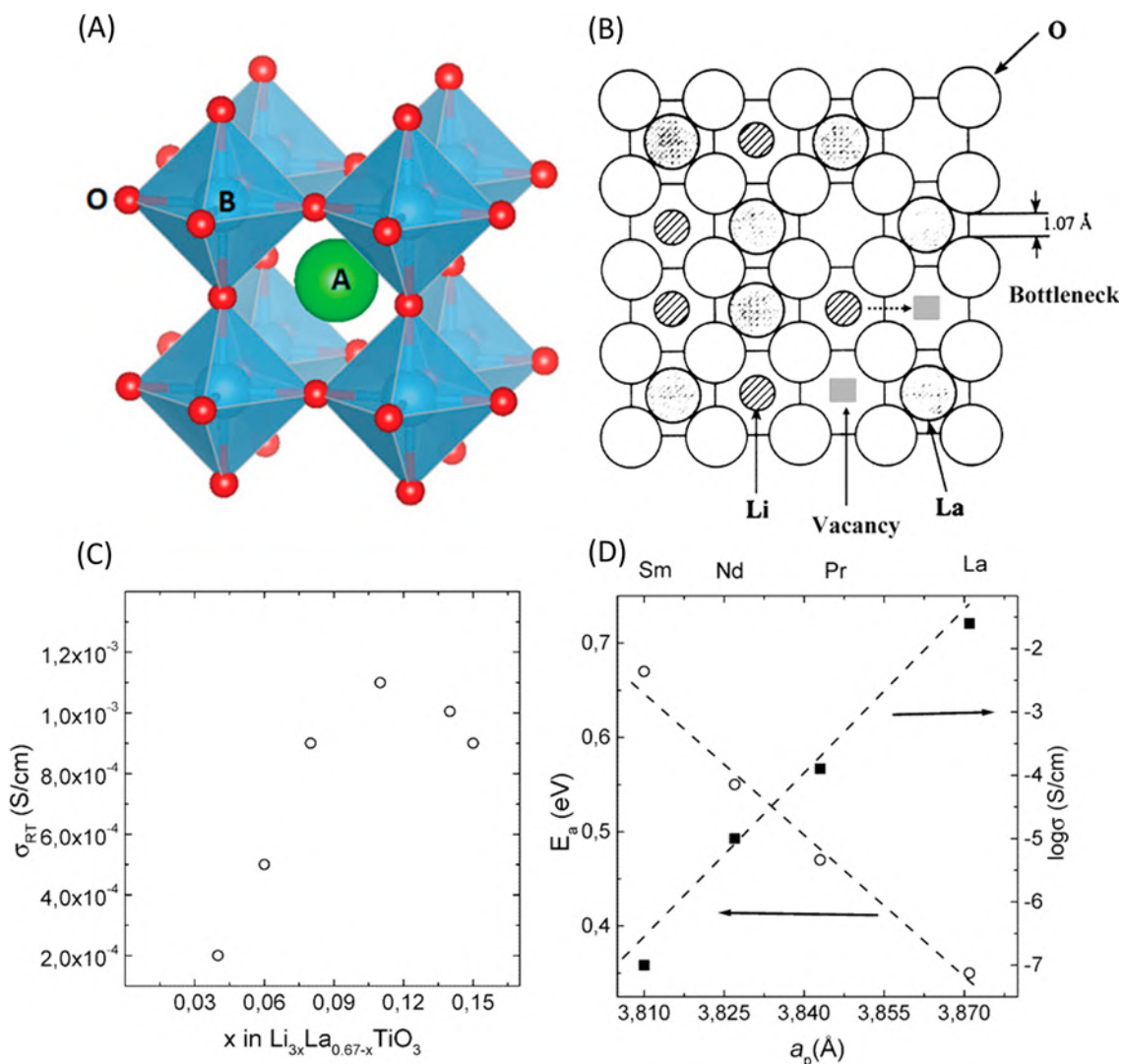


Fig. 3 (A) Schematic illustration of ideal cubic perovskite crystal structure;³⁶ (B) schematic illustration of Li ion conduction bottleneck in $\text{Li}_{3x}\text{La}_{2/3-x}\square_{(1/3)-2x}\text{TiO}_3$ structure;³⁷ (C) ionic conductivity vs. Li concentration at room temperature for $\text{Li}_{3x}\text{La}_{2/3-x}\square_{(1/3)-2x}\text{TiO}_3$;²³ and (D) change of ionic conductivity and activation energy versus lattice parameter in $\text{Li}_{0.34}\text{La}_{0.51}\text{TiO}_{2.94}$, $\text{Li}_{0.34}\text{Pr}_{0.51}\text{TiO}_{3.01}$, $\text{Li}_{0.34}\text{Nd}_{0.55}\text{TiO}_3$ and $\text{Li}_{0.38}\text{Sm}_{0.52}\text{TiO}_{2.97}$ at 27 °C.²³ (A) Reproduced with permission from Ref. Sun, C.; Alonso, J. A.; Bian, J. *Recent Advances in Perovskite-Type Oxides for Energy Conversion and Storage Applications*. *Adv. Energy Mater.* **2021**, *11* (2): 1–21. doi: 10.1002/aenm.202000459, Copyright (2021), John Wiley and Sons; (B) Reproduced with permission from Ref. Inaguma, Y.; Yu, J.; Shan, Y.; Itoh, M.; Nakamura, T. The Effect of the Hydrostatic Pressure on the Ionic Conductivity in a Perovskite Lanthanum Lithium Titanate. *J. Electrochem. Soc.* **1995**, *142* (1), L8–L11. doi: 10.1149/1.2043988, Copyright (1995), IOP Publishing Ltd.; (D) Reprinted with permission from Ref. Stramare, S.; Thangadurai, V.; Weppner, W. Lithium Lanthanum Titanates: A Review. *Chem. Mater.* **2003**, *15* (21): 3974–3990. <https://doi.org/10.1021/cm0300516>, Copyright (2003) American Chemical Society.

been proposed to solve this problem.³⁴ For example, it is shown that by substituting Ti^{4+} with Mn^{4+} and Ge^{4+} , ionic conductivity can be improved but full substitution is not possible due to the formation of a second phase.⁴⁴ So further effort is necessary to find cost-effective substitutions for Ti while maintaining a high ionic conductivity.

4.19.3.1.2 NASICON-type solid electrolytes

The first study on the crystal structure of a NASICON-type oxide was published in 1968 investigating the $\text{NaM}_2(\text{PO}_4)_3$ ($M = \text{Ge}, \text{Ti}, \text{Zr}$) compound.⁴⁵ In 1976, Goodenough et al. reported the first Na^+ ion conducting $\text{Na}_{1+x}\text{Zr}_2\text{Si}_x\text{P}_{3-x}\text{O}_{12}$.⁴⁶ The $x = 2$ member of NASICON exhibits relatively high sodium ion conductivity of $10^{-3} \text{ S cm}^{-1}$ at room temperature.⁴⁷ This family phase is popularly called as Na superionic conductors, NASICONs. Attempts have been made to prepare corresponding Li analogue of NASICON structure. Unlike the Na-phase, $\text{LiM}_2(\text{PO}_4)_3$ shows a higher conductivity than that of Li-stuffed NASICON phases. A room temperature ionic conductivity of $7.9 \times 10^{-8} \text{ S cm}^{-1}$ was reported for $\text{LiTi}_2(\text{PO}_4)_3$ (LTP).⁴⁸ Doping Ti with trivalent elements was found to improve the ionic conductivity and values as high as $\sim 10^{-3} \text{ S cm}^{-1}$ have been reported.⁴⁹ For example, elemental substitution

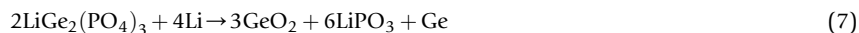
involved partial or complete replacement of Ti with cations of Al (e.g., $\text{Li}_{1+x}\text{Al}_x\text{Ti}_{2-x}(\text{PO}_4)_3$ (LATP)) or Al–Ge (e.g., $\text{Li}_{1+x}\text{Al}_x\text{Ge}_{2-x}(\text{PO}_4)_3$ (LAGP)).³⁴ Thangadurai et al. investigated Li ion conductivity of NASICON-type structure materials and Table 3 shows some of the examples of Li ion conducting NASICON ceramics.⁵⁰

Fig. 4A shows a schematic illustration of the NASICON crystal structure.⁵¹ NASICON type oxides have the general formula of $\text{AM}_2(\text{BO}_4)_3$ with a space group of $R\bar{3}c$ where A is a monovalent alkali atom (e.g., Li^+ , Na^+ , K^+), M consists of multivalent cations (e.g., Ge^{4+} , Ti^{4+} , Zr^{4+}) and B sites are occupied by P making PO_4 tetrahedra.³⁸ A 3D framework is made by corner-sharing PO_4 tetrahedra and MO_6 octahedra, generating the diffusion channels for A cations. Ion transfer is conducted by jumping between two types of A sites including A(I) octahedral vacancies and A(II) tetrahedral vacancies.^{38,56}

Fig. 4B shows the bulk ionic conductivity versus temperature for different NASICON compositions^{52–55} and Fig. 4C shows the effect of unit cell size on activation energy.⁷ To improve the ionic conduction, tuning the size of the channel by elemental substitution and improving the synthesis process have been proposed.^{38,57} Addition of Li compounds such as Li_2O has been reported to effectively improve the density and ionic conductivity of the ceramic as shown in Fig. 4D.^{10,58} NASICON type materials generally show large grain-boundary impedance. Li volatilization during synthesis and density of ceramics are crucial for conductivity.

4.19.3.1.2.1 Chemical/electrochemical stability of NASICON-type Li ion electrolytes

NASICON-type solid electrolytes are stable in air and water, however, their stability towards Li metal has been controversial.⁴⁹ Similar to perovskites, Ti-containing compounds show poor stability against metallic Li due to the reduction of Ti^{4+} .^{18,56} However, Li–Ge–P-based compositions have shown a high electrochemical stability window of 6 V vs. Li/Li^+ .^{24,59,60} Recent studies based on first-principles calculations showed that the electrochemical stability window of LATP and LAGP crystals are 2.17–4.21 V and 2.7–4.21 V, respectively.^{61,62} Other studies showed that the reaction between LAGP and Li metal is a conversion reaction with a high barrier energy while in case of LATP, the reaction is a single-electron transfer with lower energy barrier (according to Eqs. 7 and 8).^{49,57}



In general, to improve the stability of the NASICON against Li metal anode, using an intermediate layer between Li and NASICON has been proposed.^{49,57}

4.19.3.1.3 LISICON-type solid electrolytes

LISICON-type oxide solid electrolytes were firstly introduced in 1972 by the West group,⁶³ investigating the ionic conductivity of Li–Si–O system, and reported ionic conductivity of $\sim 2 \times 10^{-9} \text{ S cm}^{-1}$ at room temperature.^{48,64} Later in 1978, new compositions of $\text{Li}_{14}\text{Zn}(\text{GeO}_4)_4$ and $\text{Li}_{16-2x}\text{M}_x(\text{XO}_4)_4$ ($\text{M} = \text{Mg}, \text{Zn}, \text{X} = \text{Si}, \text{Ge}$) were reported with a high ionic conductivity of 8 S cm^{-1} for the former compound at 300°C .⁶⁵ Other important LISICON-type compounds include $\text{Li}_{3+x}\text{Ge}_x\text{V}_{1-x}\text{O}_4$ ⁶⁶ and $\text{Li}_{3+x}(\text{P}_{1-x}\text{Si}_x)\text{O}_4$.¹⁸ Doping has been used to improve the ionic conductivity of LISICON compound and the highest room temperature conductivity of $5.1 \times 10^{-5} \text{ S cm}^{-1}$ has been achieved in $\text{Li}_{3.53}(\text{Ge}_{0.75}\text{P}_{0.25})_{0.7}\text{V}_{0.3}\text{O}_4$ composition using a co-doping strategy.⁶⁷ Due to the lower Li conductivity of LISICON-type materials at room temperature, there are few reports on the application of these compounds in solid-state batteries.

The crystal structure of LISICON-type oxides is like $\gamma\text{-Li}_3\text{PO}_4$ structure and is schematically shown in Fig. 5 for a $\text{Li}_3\text{Zn}_{0.5}\text{GeO}_4$ which crystalize in an orthorhombic lattice with a space group of $Pnma$.⁶⁵ The crystal comprises of a close-packed distorted hexagonal arrangement of O anions while cations occupy tetrahedral interstices. Li ions in LiO_4 tetrahedra diffuse between these tetrahedra and interstitial sites located in the PO_4 network.^{18,68} Generating excess Li using elemental doping, improves the Li conduction by decreasing diffusion distance since the excess Li will occupy the interstitial sites.¹⁸ It is reported that doping of

Table 3 Chemical composition, cell volume, total ionic conductivity (σ), and activation energy (E_a) for NASICON-type phosphates $\text{LiM}^{\text{V}}\text{-M}^{\text{III}}(\text{PO}_4)_3$ ($\text{M}^{\text{V}} = \text{Nb}, \text{Ta}; \text{M}^{\text{III}} = \text{Al}, \text{Cr}, \text{Fe}$).

Composition	V/A^3	$\sigma_{30^\circ\text{C}} (\text{S cm}^{-1})$	$E_a (\text{eV})$
$\text{LiNbFe}(\text{PO}_4)_3$	1388	$< 10^{-8}$	0.85 (210–600 °C)
$\text{LiTaAl}(\text{PO}_4)_3$	1315	6.5×10^{-7}	0.47 (30–250 °C)
$\text{LiTaCr}(\text{PO}_4)_3$	1360	$< 10^{-7}$	0.49 (80–300 °C)
$\text{LiTaFe}(\text{PO}_4)_3$	1395	$< 10^{-7}$	0.86 (150–350 °C)
$\text{Li}_{1.2}\text{Ta}_{0.9}\text{Al}_{1.1}(\text{PO}_4)_3$	1332	6.5×10^{-7}	0.51 (30–250 °C)
$\text{LiTi}_2(\text{PO}_4)_3$	1310	2.0×10^{-6}	0.30 (30–200 °C)
$\text{LiZr}_2(\text{PO}_4)_3$	1508	3.2×10^{-10}	0.43 (300–400 °C)

Reproduced from Ref Thangadurai, V.; K.A Shukla; Gopalakrishnan, J. New Lithium-Ion Conductors Based on the NASICON Structure. *J. Mater. Chem.* **1999**, 9 (3), 739–741. doi: 10.1039/A807007E with permission from the Royal Society of Chemistry.

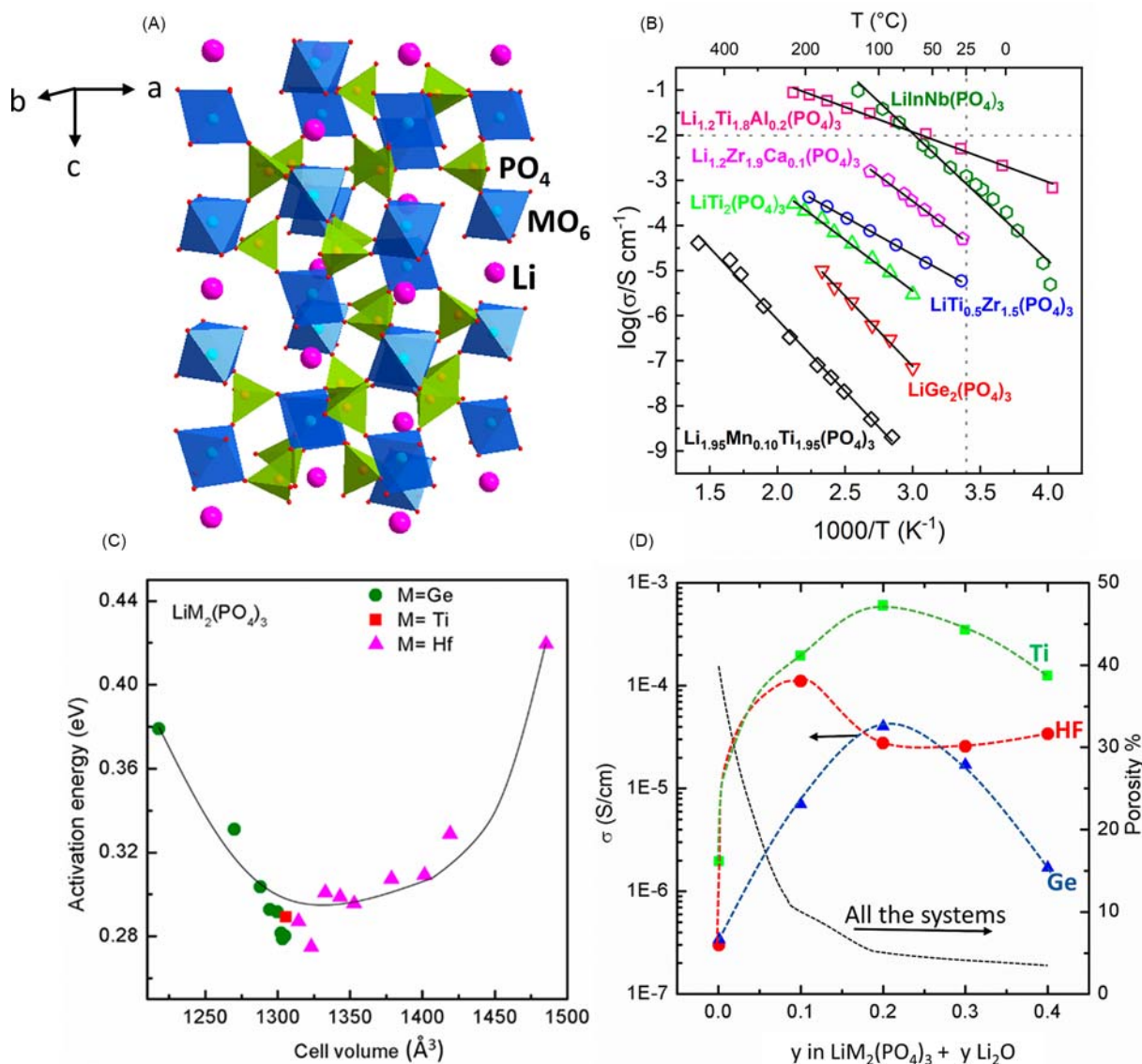


Fig. 4 Schematic illustration of (A) general NASICON structure;⁵¹ (B) bulk conductivity versus temperature for different NASICON compounds;^{52–55} (C) activation energy versus unit cell volume;¹⁰ and (D) effect of addition of Li_2O on densification and ionic conductivity.¹⁰ Figures C & D reprinted by permission from Ref. Palakkathodi Kammampata, S.; Thangadurai, V. *Cruising in Ceramics—Discovering New Structures for All-Solid-State Batteries—Fundamentals, Materials, and Performances. Ionics (Kiel)*. **2018**, 24 (3), 639–660. <https://doi.org/10.1007/s11581-017-2372-7>, Copyright (2018), Springer Nature.

Li_4SiO_4 with Li_3PO_4 can effectively improve the ionic conductivity as shown in Fig. 5B.^{10,69} In this case, SiO_4 tetrahedra are replaced with PO_4 tetrahedra changing the size of the unit cell and concentration of Li ions.⁶⁹

4.19.3.1.3.1 Chemical/electrochemical stability of LISICONs

Different LISICON compositions have shown different degrees of stability in air or against Li metal. For example, $\text{Li}_{3+x}\text{Y}_{1-x}\text{X}_x\text{O}_4$ compositions in which ($X = \text{Si, Ge, Ti}$ and $Y = \text{P, As, V, Cr}$) show good stability in atmospheric condition, however, long exposure in air can lead to degradation in compositions containing Ge or Ti.⁷⁰ The chemical stability of $\text{Li}_{3.4}\text{Si}_{0.4}\text{V}_{0.6}\text{O}_4$ composition has also been evaluated showing a good stability with Li/molten Li.⁷¹ Computational methods have also been used as a strong tool to predict the phase stability window of different solid electrolytes. Recent computational studies showed good stability of $\text{Li}_{3.42}\text{Zr}_{0.29}\text{GeO}_4$ compound with an oxidation potential of 3.39 V and reduction potential of 1.44 V.^{62,72}

4.19.3.1.4 Garnet-type solid electrolytes

The ideal garnet-type structures containing Li were first reported in 1969 by Kasper⁷³ with the chemical composition of $\text{Li}_3\text{Ln}_3\text{M}_2\text{O}_{12}$ ($M = \text{W, Te}$). However, the potential application of garnet as a solid electrolyte in Li rechargeable batteries was not

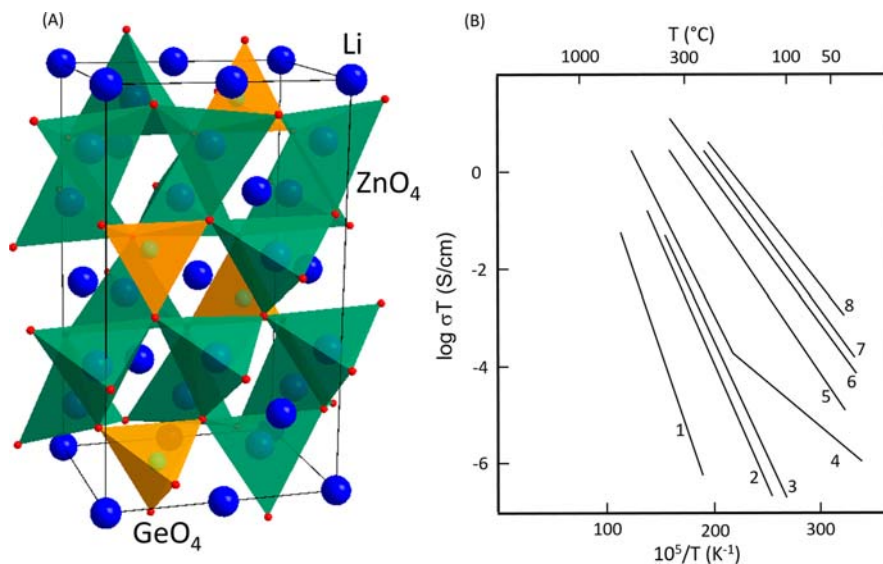


Fig. 5 (A) Crystal structure of a LISICON-type $\text{Li}_3\text{Zn}_{0.5}\text{GeO}_4$ composition,⁶⁵ (B) variation of ionic conductivity with temperature for Li_4SiO_4 - Li_3PO_4 system. (1) Li_3PO_4 ; (2) 50-mol% Li_3PO_4 ; (3) Li_4SiO_4 ; (4) Li_4SiO_4 ; (5) 9.1-mol% Li_3PO_4 ; (6) 20-mol% Li_3PO_4 ; (7) 30-mol% Li_3PO_4 ; and (8) 40-mol% Li_3PO_4 .¹⁰ Reprinted by permission from Ref. Palakkathodi Kammampata, S.; Thangadurai, V. *Cruising in Ceramics—Discovering New Structures for All-Solid-State Batteries—Fundamentals, Materials, and Performances. Ionics (Kiel)* **2018**, *24* (3), 639–660. <https://doi.org/10.1007/s11581-017-2372-7>, Copyright (2018), Springer Nature.

been introduced until 2003 when the Li ion conduction of $\text{Li}_5\text{La}_3\text{M}_2\text{O}_{12}$, where $\text{M} = \text{Ta}, \text{Nb}$, was reported showing a Li conductivity of $\sim 10^{-6} \text{ S cm}^{-1}$ at 25°C .³¹ In attempts to improve the ionic conductivity, garnets with higher Li content per formula unit have been introduced. Examples include $\text{Li}_6\text{BaLa}_2\text{Ta}_2\text{O}_{12}$ and $\text{Li}_7\text{La}_3\text{Zr}_2\text{O}_{12}$ (LLZO) with improved Li conductivities of $4 \times 10^{-5} \text{ S cm}^{-1}$ and $3 \times 10^{-4} \text{ S cm}^{-1}$ at ambient temperature.^{74,75} Several chemical compositions of garnets have been introduced based on LLZO type structure. Many research works focused on improving the physical, chemical, and/or electrochemical properties of this class of ceramics have been performed to achieve a high performance and highly safe all-solid-state Li battery.⁸

Ideal garnets are a group of orthosilicates having the general chemical formula of $\text{A}_3\text{B}_2\text{Si}_3\text{O}_{12}$ with a general cubic structure of $Ia\bar{3}d$ space group in which A and B occupy the 8 and 6 coordination sites.⁸ Li-containing garnets have been derived from the structural prototype of $\text{Ca}_3\text{Al}_2\text{Si}_3\text{O}_{12}$ in which Li occupies the Si sites to form $\text{Li}_3\text{La}_3\text{Te}_2\text{O}_{12}$.⁸ Fig. 6A show more details on the crystal structure of the cubic garnet (LLZO) in which the garnet framework consists of dodecahedral LaO_8 and octahedral ZrO_6 . Li cations occupy two different sites as Li_1 in the tetrahedral (24 d) sites and Li_2 in octahedral (48 g and 96 h) sites. The arrangement of Li ions in these sites is a key factor to determine the Li ion conduction.⁷⁶ It has been shown that LLZO has two polymorphs; one is a room temperature stable tetragonal phase in which Li ions form an ordered sub-lattice and the second phase is a cubic structure which is not stable at low temperatures and shows a disordered Li cation distribution. It is shown that partial occupancy of Li atoms in Li_2 sites in the cubic phase leads to an ionic conductivity two orders of magnitude higher than the tetragonal phase.^{76,77} In a garnet crystal, three-dimensional (3D) Li ion migration occurs via a hopping mechanism.⁷⁸ In recent years, several works have been carried out to dope different elements at different sites of the cubic LLZO to further enhance the Li ion conduction and stability of this ceramic.⁸

To achieve a high Li ion conductive LLZO garnet, initially it was necessary to stabilize the cubic phase at RT. Studies showed that by doping supervalent cations such as Al^{3+} and Ga^{3+} , Li vacancies will be generated, leading to disorder of the Li sublattice and stabilization of the cubic LLZO.^{79,80} Moreover, there are Coulombic interactions between the ions in the migration pathway due to their small separation distance and it was revealed that the Coulombic repulsion between dopants, such as Al^{3+} , Zn^{2+} and Ga^{3+} , and Li^+ is stronger than that between pairs of Li ions. So Li ions can be activated by proper doping, which affects the concentration and mobility of charge carriers.⁸⁰ Extensive experimental and computational studies confirmed that the maximum ionic conductivity in a cubic LLZO can be achieved when the Li content is ~ 6.4 Li per formula.⁸¹ Other dopants such as Ta^{5+} , Nb^{5+} , Te^{6+} , and W^{6+} cations occupying the Zr^{4+} site, or Sr^{2+} , Ba^{2+} , Ca^{2+} , Rb^+ on the La^{3+} sites have also been investigated.^{8,80} Fig. 6B–D show the effect of elemental substitution in different sites on the ionic conductivity and lattice parameter of LLZO.²¹ The ionic conductivity of garnet-type electrolytes can be further improved by increasing the concentration and mobility of Li ions, which can be achieved by choosing a suitable combination of dopants with optimum amount.

4.19.3.1.4.1 Chemical/electrochemical stability of garnet

The chemical stability of garnet in the presence of water, CO_2 and against Li metal has been widely studied. In water, Li^+/H^+ exchange can occur depending on the temperature, duration of exposure, and pH of the solution. Experimental studies have revealed that garnet can maintain its crystal structure even at a high Li^+/H^+ exchange rate of 63.6%.⁸² However, a phase transition

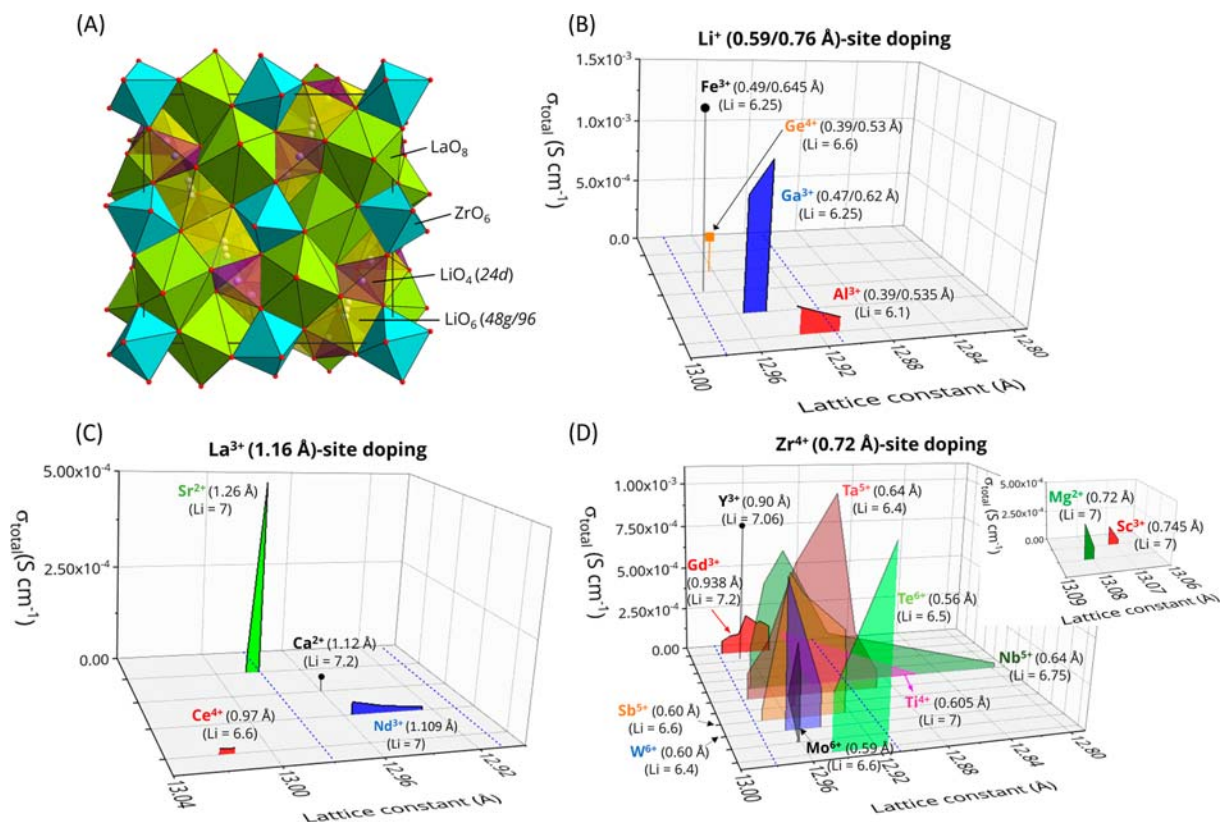


Fig. 6 (A) Crystal structure of a cubic LLZO. Effect of elemental doping in (B) Li; (C) La; and (D) Zr sites on the ionic conductivity and lattice parameter of LLZO.²¹ Reproduced from Ref Samson, A. J.; Hofstetter, K.; Bag, S.; Thangadurai, V. A Bird's-Eye View of Li-Stuffed Garnet-Type $\text{Li}_7\text{La}_3\text{Zr}_2\text{O}_{12}$ Ceramic Electrolytes for Advanced all-Solid-State Li Batteries. *Energ. Environ. Sci.* **2019**, *12* (10): 2957–2975. <https://doi.org/10.1039/C9EE01548E> with permission from the Royal Society of Chemistry.

had occurred in the garnet crystal structure when the Li^+/H^+ exchange was 75%.⁸³ Garnet also reacts with atmospheric CO_2 which can be accelerated by humidity and forms a Li_2CO_3 layer on the surface of the garnet structures. The formation of Li_2CO_3 impurity layer decreases the ionic conductivity of garnet electrolyte and increases charge transfer resistance between garnet electrolyte and elemental Li electrode.⁸⁴ Therefore, processing and storage of garnet in atmospheric environment is challenging. Garnet electrolytes have a very good chemical stability when in contact with molten Li. Also, the electrochemical stability studies of garnets shows a wide electrochemical stability up to 6 V vs. Li/Li^+ making it a promising candidate to use in Li-metal batteries.^{8,74} Fig. 7 compares the properties of the four different solid oxide electrolytes discussed in this chapter. Although ionic conductivity and chemical/electrochemical stability are critically important to develop a high-performance solid oxide electrolyte, other parameters such as the cost and processability of the material play very important roles on the supply chain and should be considered.

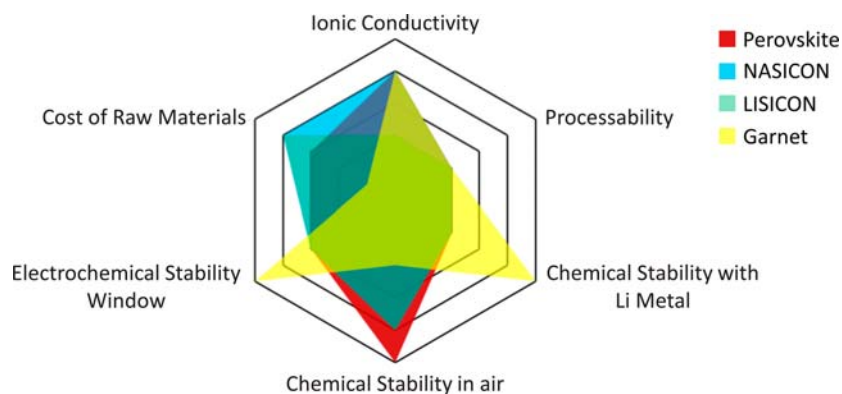


Fig. 7 Comparison of the properties of different solid oxide electrolytes.^{8,34,48,49,85}

4.19.3.2 Sulfide based solid electrolytes

Sulfide inorganic solid electrolytes are attracting much consideration, owing to their highest room temperature ionic conductivity among the inorganic solid electrolytes (10^{-3} – 10^{-2} S cm $^{-1}$), which is comparable to that of liquid electrolytes, and a remarkable electrochemical stability up to 5 V vs. Li/Li $^{+}$.^{24,86} Sulfide solid electrolytes originate by the replacement of oxygen ions with sulfur ion in oxides. Sulfide solid electrolytes have lower electronegativity and bonding strength to Li ions compared with oxides. Additionally, the higher ionic radius of S $^{2-}$ compared with O $^{2-}$ greatly increase the size of Li $^{+}$ transport bottlenecks and allows for more facile Li ion conduction.⁸⁷ Thio-LISICON-type solid electrolytes are derived from LISICON-type γ -Li $_3$ PO $_4$ structure by replacing oxygen with sulfur. The thio-LISICON electrolytes, with chemical composition Li $_{3.25}$ Ge $_{0.25}$ P $_{0.75}$ S $_4$, exhibits a room temperature Li $^{+}$ conductivity of 2.2×10^{-3} S cm $^{-1}$, which is about four orders of magnitude higher than that of its oxide counterpart (10^{-7} S cm $^{-1}$). The high ionic conductivity has been attributed due to the lower electronegativity and better polarization capability of sulfur compared to oxygen. Fig. 8 shows the typical doping method employed in LISICONs and thio-LISICONs.⁸⁸

In 2001, Kanno et al. prepared thio-LISICON type Li $_{3.25}$ Ge $_{0.25}$ P $_{0.75}$ S $_4$, which exhibited a room temperature ionic conductivity of 2.2×10^{-3} S cm $^{-1}$.⁸⁸ Thio-LISICON with a nominal composition Li $_{10}$ GeP $_2$ S $_{12}$ (LGPS) showed the highest Li $^{+}$ ionic conductivity of 1.2×10^{-2} S cm $^{-1}$ at 27 °C with an activation energy of 0.25 eV.²⁴ Fig. 9 shows the structure of Li $_{10.35}$ Ge $_{1.35}$ P $_{1.65}$ S $_{12}$ ($\delta = 0.35$) as determined by the Kanno group.⁸⁹ The crystal structure of LGPS consist of (Ge/P) $_4$ tetrahedra and Li $_2$ S $_6$ octahedra connected to one another by edge sharing.⁸⁹ The Li $_1$ S $_4$ and Li $_3$ S $_4$ tetrahedra, which are centered at the 16 h and 8f sites, form a one-dimensional tunnel along the c-axis. In this study, Kanno group is introducing a Li $_4$ site which is located at the 4c site with a fractional coordinate ($z \sim 0.2585$). The existence of Li $_4$ site was confirmed by detailed analysis of neutron diffraction data. Kuhn et al. reported the first single-crystal structure analysis of the tetragonal LGPS by X-ray diffraction and their study also revealed a fourth Li site.⁹⁰ The Li $_4$ is connected to six sulfide ions and forms Li $_4$ S $_6$ octahedra which is connected to PS $_4$ tetrahedra by edge sharing along the c direction. The Li $_4$ S $_6$ octahedra is also connected to four Li $_2$ S $_6$ octahedra and two Ge 1 S $_4$ tetrahedra by corner sharing.⁸⁹

Sulfide glasses have several advantages over the crystalline materials, including isotropic ionic conduction, negligible grain-boundary resistance, and ease of fabrication into thin films.^{91,92} The sulfide glasses show about one to two orders of magnitude higher conductivity compared to the crystalline phases.⁸⁸ The conductivity of glassy electrolytes can be further improved by the addition of LiCl, LiI, Li $_4$ SiO $_4$ and Li $_3$ PO $_4$.^{93,94} Sulfide glass-ceramics are prepared by the partial crystallization of glassy sulfides to reduce the grain-boundary resistance, and may exhibit ionic conductivities on the order of 10^{-3} S cm $^{-1}$, which is attributed to a simple room-temperature cold-press densification process.^{95,96} Table 4 lists the room temperature ionic conductivities and activation energies of different sulfide solid electrolytes.⁹⁷

Most of the work on glass-ceramic sulfide electrolytes has been carried out with Li $_2$ S–P $_2$ S $_5$ compositions. Li $_7$ P $_3$ S $_{11}$ exhibits an ionic conductivity of 2.2×10^{-3} S cm $^{-1}$ at room temperature.^{95,98} The boosted conductivity compared with that of glassy sulfides is attributed to the arrangements of the *pyro*-thiophosphate anion P $_2$ S $_7^{4-}$, which plays an important role in the fast Li $^{+}$ diffusion through a network of neighboring Li $^{+}$ cations composed of Li–Li chains. The conductivity can be further increased up to 1.7×10^{-2} S cm $^{-1}$ at room temperature by heat treatment. Fig. 10 shows the dependence of room-temperature ionic conductivity on Li concentration for sulfide glass and glass-ceramic solid electrolytes.⁹⁹

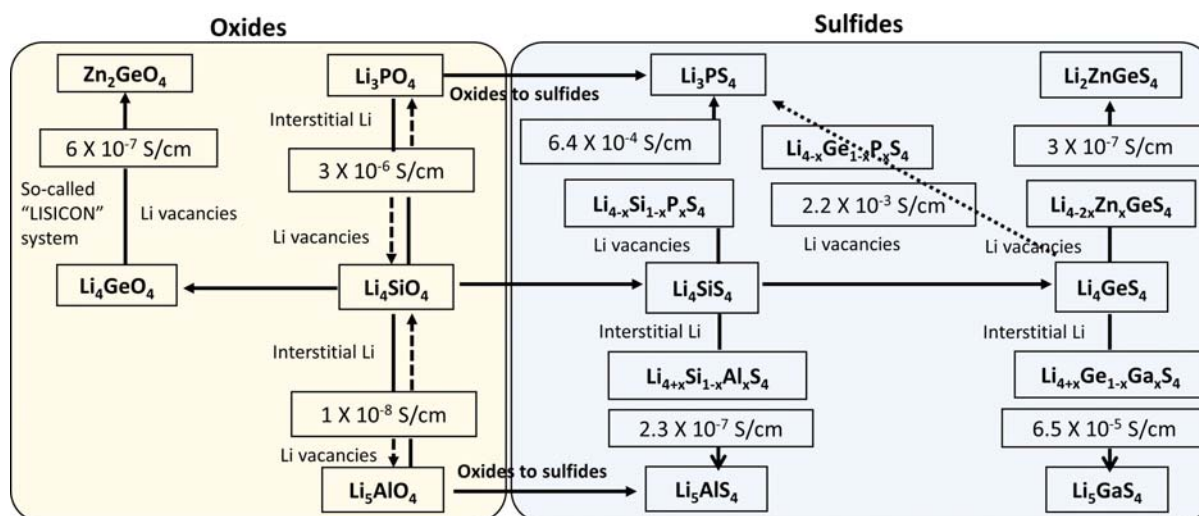


Fig. 8 The conduction mechanism and conductivity values of LISICONs and their S counter part thio-LISICONs.⁸⁸ Reproduced (adapted) with permission from Ref. Kanno, R.; Murayama, M. Lithium Ionic Conductor Thio-LISICON: The Li $_2$ S–GeS $_2$ –P $_2$ S $_5$ System. *J. Electrochem. Soc.* **2001**, *148* (7), A742–A746. <https://doi.org/10.1149/1.1379028>, Copyright (2001), IOP Publishing Ltd.

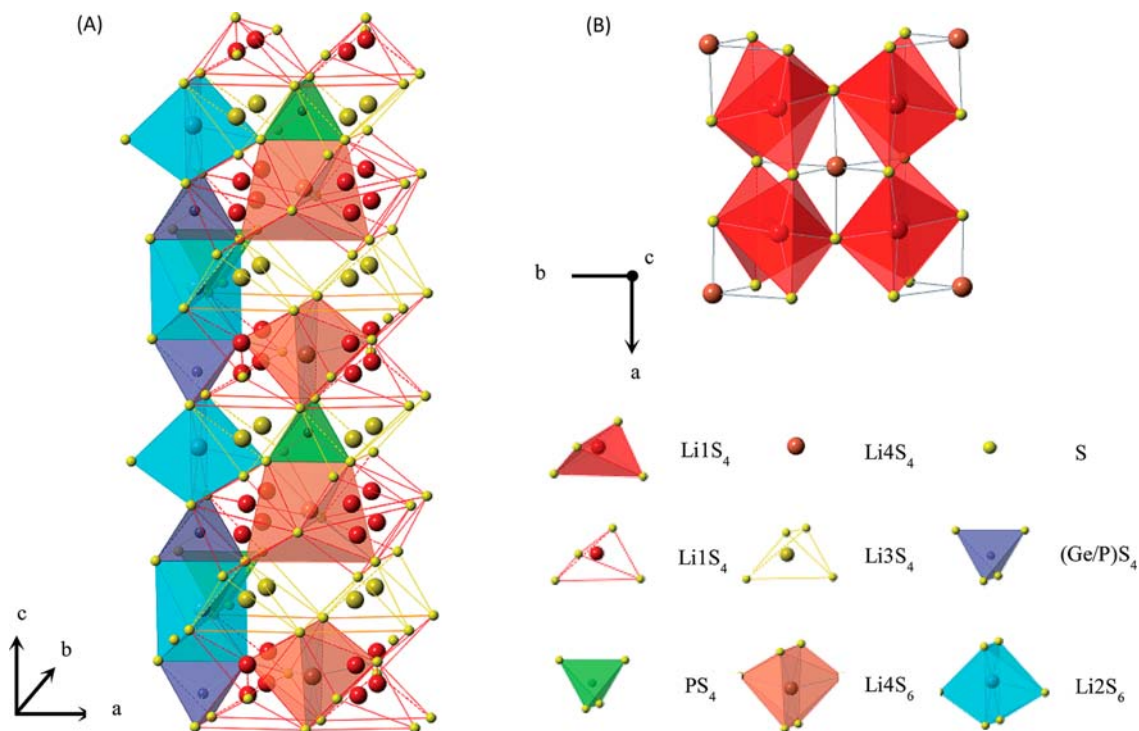


Fig. 9 (A) Crystal structure of $\text{Li}_{10+d}\text{Ge}_{1+d}\text{P}_{2-d}\text{S}_{12}$. Li_2S_6 octahedra and $(\text{Ge}/\text{P})\text{S}_4$ tetrahedra are connected by a common edge and form a one-dimensional framework with PS_4 tetrahedra situated between the Li_2S_6 octahedra by corner sharing to connect the one-dimensional chains, thus forming a three-dimensional framework structure. (B) Coordination of Li_4S_6 octahedra within the structure. Each Li_4S_6 octahedron shares its four edges with Li_1S_4 tetrahedral sites.⁹⁹ Reproduced from Ref. Kwon, O.; Hirayama, M.; Suzuki, K.; Kato, Y.; Saito, T.; Yonemura, M.; Kamiyama, T.; Kanno, R. Synthesis, Structure, and Conduction Mechanism of the Lithium Superionic Conductor $\text{Li}_{10+d}\text{Ge}_{1+d}\text{P}_{2-d}\text{S}_{12}$. *J. Mater. Chem. A* **2015**, 3 (1), 438–446. <https://doi.org/10.1039/C4TA05231E> with permission from the Royal Society of Chemistry.

Table 4 Comparison of the room-temperature ionic conductivities (σ) and activation energies (E_a) of sulfide solid electrolytes.⁹⁷

Sulfides	σ (S cm^{-1})	E_a (eV)
$50\text{Li}_2\text{S}-50\text{GeS}_2$	4×10^{-5}	0.51
$60\text{Li}_2\text{S}-40\text{SiS}_2$	5.3×10^{-4}	0.33
$67\text{Li}_2\text{S}-33\text{P}_2\text{S}_5$	10^{-4}	0.36
$\text{Li}_7\text{P}_3\text{S}_{11}$	1.7×10^{-2}	0.18
Li_3PS_4	2.8×10^{-4}	0.356
$78\text{Li}_2\text{S}-22\text{P}_2\text{S}_5$	1.78×10^{-3}	0.31
$\text{Li}_{3.25}\text{Ge}_{0.25}\text{P}_{0.75}\text{S}_4$	2.2×10^{-3}	0.207
$\text{Li}_{9.54}\text{Si}_{1.74}\text{P}_{1.44}\text{S}_{11.7}\text{Cl}_{0.3}$	2.5×10^{-2}	0.238
$\text{Li}_{10}\text{GeP}_2\text{S}_{12}$	1.2×10^{-2}	0.21
$\text{Li}_{10}\text{SnP}_2\text{S}_{12}$	4×10^{-3}	0.87
$\text{Li}_{10}\text{SiP}_2\text{S}_{12}$	2.3×10^{-3}	0.20
$\text{Li}_{11}\text{AlP}_2\text{S}_{12}$	8×10^{-4}	0.263
$\text{Li}_6\text{PS}_5\text{Cl}$	1.3×10^{-3}	0.33
$\text{Li}_6\text{PS}_5\text{Br}$	10^{-2}	0.20

Reproduced (adapted) from Ref. Lian, P.-J.; Zhao, B.-S.; Zhang, L.-Q.; Xu, N.; Wu, M.-T.; Gao, X.-P. Inorganic Sulfide Solid Electrolytes for all-Solid-State Lithium Secondary Batteries. *J. Mater. Chem. A* **2019**, 7 (36), 20540–20557. <https://doi.org/10.1039/C9TA04555D> with permission from the Royal Society of Chemistry.

4.19.3.3 Halide based solid electrolytes

4.19.3.3.1 Halide solid electrolytes with metal element

The chemical formula of Li halide solid electrolytes can be roughly categorized as $\text{Li}_a\text{A}_b\text{X}_c$, where X is a halogen and A is an electropositive element, which could be either a metal or a non-metal. Several recent review articles have provided in-depth and

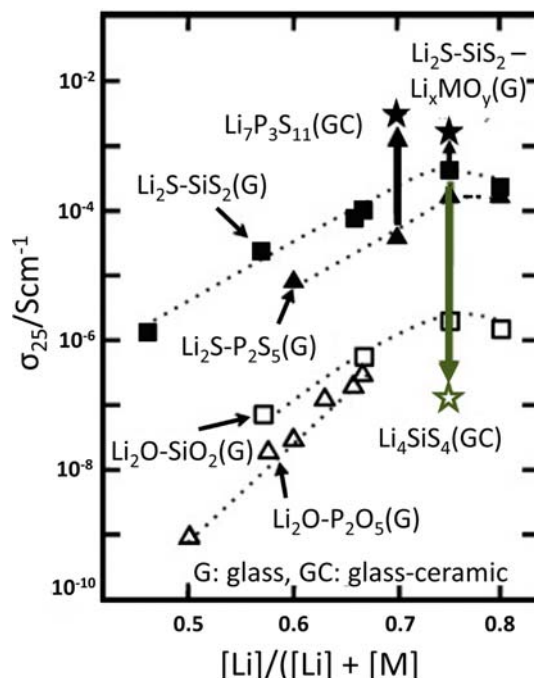


Fig. 10 Dependence of room-temperature ionic conductivity on lithium concentration for sulfide glass and glass-ceramic solid electrolytes.⁹⁹ Reprinted from Ref. Tatsumisago, M.; Hayashi, A. Superionic Glasses and Glass-Ceramics in the Li₂S–P₂S₅ System for All-Solid-State Lithium Secondary Batteries. *Solid State Ion.* **2012** 225, 342–345. <https://doi.org/10.1016/j.ssi.2012.03.013>, Copyright (2012), with permission from Elsevier.

comprehensive insights into the historical development and near-term advances of the field.^{18,20,28,100–102} It is considered that, compared to solid electrolytes containing a non-metallic element, the presence of a metallic element, such as Y, offers the benefit of a wider electrochemical window and a potentially higher operating voltage, but renders instability against metallic Li.²⁰ Some early-stage investigations of halide Li-conductors involve elements such as Al.^{103,104} The ionic conductivity of LiAlCl₄ was found to be 1.2×10^{-6} S cm⁻¹ at room temperature, with an activation enthalpy of 0.47 eV.¹⁰³ Predominant ionic conduction was confirmed by *dc* polarization experiment.¹⁰⁴

Spinel-type Li₂AX₄ halides, with divalent metal elements, including Mg, Zn and Cd, were studied, and it was postulated that its cubic close-packed anion framework helps to facilitate the transportation of Li ions.^{105–108} Furthermore, depending on the type of the divalent element and its subsequent occupation of the lattice site, the structure can be classified as either a normal spinel or an inverse spinel. In an inverse spinel structure, Li takes the position of the metal ion in the tetrahedral site while partially keeping its original octahedral site. The face-shared polyhedral arrangement in the structure lowers the diffusion barrier and improves the ionic conductivity. Li-deficient spinel compounds, such as Li_{1.9}Cd_{1.05}Cl₄ and Li_{1.52}Mn_{1.24}Cl₄, were reported to have the extra advantage of possessing an increased concentration of Li vacancies, which as long as it stays within the balanced range at one side of the “lattice vacancy—Li charger carrier” trade-off, is expected to exhibit a higher ionic conductivity.^{109,110} Li₃InBr₆ was investigated by Yasumasa et al. in 1998.¹¹¹ It was found that the superionic phase of Li₃InBr₆ (above 41 °C) possesses a distorted rock salt structure (monoclinic, C2/m),¹¹² and this phase exhibits a significantly higher conductivity ($\sim 10^{-3}$ S cm⁻¹) than its low-temperature phase.¹¹¹ However, the fast cation diffusion in the high temperature phase is intrinsic and can be suppressed by the distortion of the original lattice. For e.g., in the case of Mg-doped Li_{3-2x}Mg_xInBr₆, a decreasing trend in ionic conductivity was observed with increasing Mg content.¹¹³

Asano et al. prepared Li₃YCl₆ and Li₃YBr₆ via a mechano-chemical route, with $\sim 10^{-4}$ S cm⁻¹ conductivity at room temperature.²⁷ While the crystal structure and ionic motion of the same compositions have previously been studied in the past, the high conductivities found in this study were seen as an important breakthrough.^{114,20,27,115,116} Li et al. reported Li₃InCl₆ with a conductivity of 8.4×10^{-4} S cm⁻¹, which was further improved to 1.49×10^{-3} S cm⁻¹ by an annealing process.¹¹⁶ Recently, a water-mediated synthesis method was developed which has the advantages of being facile and scalable, rendering comparable room-temperature conductivity of 2.04×10^{-3} S cm⁻¹.¹¹⁷ Schlem et al. successfully synthesized the iodine-based Li₃ErI₆ with ionic conductivity in the order of 10^{-4} S cm⁻¹.¹¹⁸ Fig. 11 summarizes some of the representative room-temperature Li halide ionic conductivities.²⁰

4.19.3.3.2 Halide solid electrolytes with non-metallic element

Recently, a great amount of interest has been paid to the anti-perovskite system such as Li oxyhalides (Li₃OX), since the discovery of superionic conductivity in Li₃OCl and Li₃OCl_{0.5}Br_{0.5} by Zhao et al. in 2012.^{119,120} Fig. 12 shows the cubic anti-perovskite crystal structure of Li₃OCl. It was found that Li₃OCl demonstrated an impressive ionic conductivity of 8.5×10^{-4} S cm⁻¹ at room-

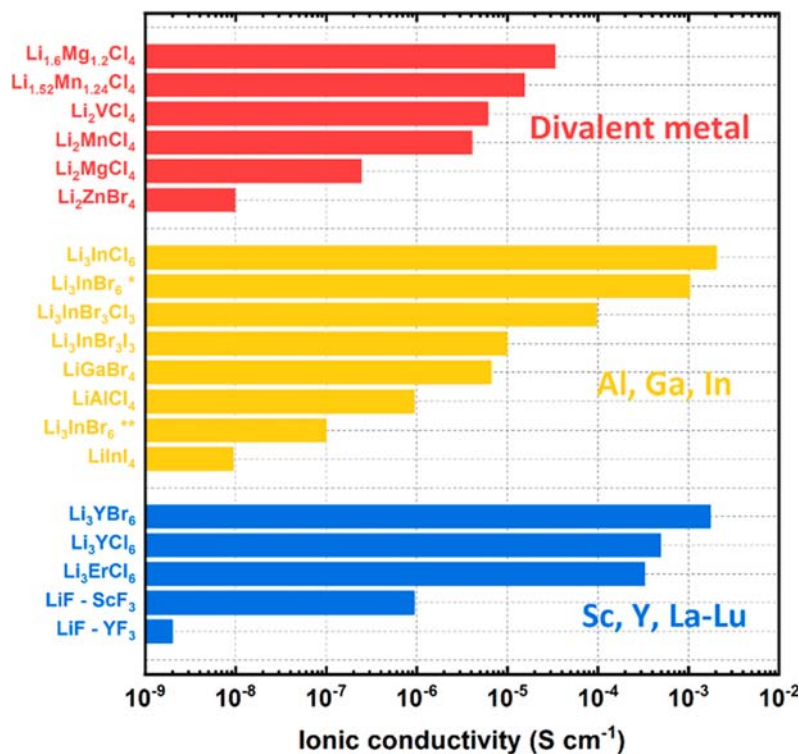


Fig. 11 Representative ionic conductivities of lithium halide solid electrolytes containing different types (divalent, group Al, Ga, In and group Sc, Y, La–Lu) of metal elements (Li₃InBr₆*—high temperature phase; Li₃InBr₆**—as prepared).²⁰

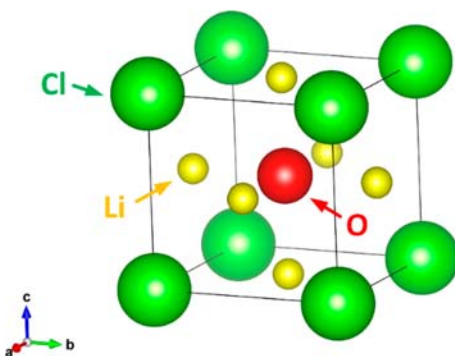


Fig. 12 Schematic crystal structure of the cubic anti-perovskite Li₃OCl.

temperature.¹¹⁹ The mixed-halogen compound Li₃OCl_{0.5}Br_{0.5} exhibited a further increased conductivity of $1.94 \times 10^{-3} \text{ S cm}^{-1}$ at room temperature.¹¹⁹ The comparably higher conductivity of the mixed-halogen phase was reasoned to be a balanced lattice distortion level at the dodecahedral halogen site.¹¹⁹ Deng et al. performed a theoretical study on the optimization of Cl/Br ratio and proposed that chemical compositions of $0.235 \leq x \leq 0.395$ in Li₃OCl_{1-x}Br_x would yield an even higher ionic conductivity if the materials were synthesized successfully.¹²¹

Glassy electrolytes of chemical formula Li_{3-2x}M_xOCl (M = Mg, Ca, Ba) was investigated by Braga et al.¹²² The materials were claimed to have benefits such as being chemically stable to metallic Li with the specific composition of Li_{2.99}Ba_{0.005}OCl achieving a high conductivity of $2.5 \times 10^{-2} \text{ S cm}^{-1}$ at 25 °C.¹²² Defect chemistry and charge carrier concentrations of Li₃OCl were studied computationally.^{123,124} Emly et al. investigated the ionic transport mechanisms and phase stability of Li₃OCl and Li₃OBr.¹²⁵ It is argued that extra carefulness must be paid in the synthesis procedures of these Li oxyhalides, given their strong nature of hygroscopicity.¹²⁶ A detailed research implementing a variety of characterization techniques was carried out by Hanghofer et al. on the structural difference between Li₃OCl and Li₂OHCl.¹²⁷ It was concluded that distinguishing the two phases merely by powder X-ray diffraction would be challenging due to the technique's weak response to Li and H.¹²⁷ In addition, immediate degradation of Li₃OCl to Li₂CO₃ and LiCl·xH₂O in air was confirmed.¹²⁷ The authors suggested that practically only Li₄(OH)₃Cl and Li₃(OH_x)Cl (x > 0) could be stable among the currently studied Li-rich anti-perovskites.¹²⁷

Table 5 Room-temperature conductivities (σ) of selected lithium halides containing non-metal elements ($\text{Li}_3\text{SBF}_4^*$ —calculated),^{20,119,137}

Lithium halide	σ (S cm^{-1})	Ref.
Li_3OCl	0.85×10^{-3}	119
$\text{Li}_3\text{OCl}_{0.5}\text{Br}_{0.5}$	1.94×10^{-3}	119
$\text{Li}_2(\text{OH})_{0.9}\text{F}_{0.1}\text{Cl}$	3.5×10^{-5}	136
$\text{Li}_{1.16}(\text{OH}_{1.84})\text{Cl}$	10^{-6}	20
$\text{Li}_{1.8}\text{N}_{0.6}\text{Cl}_{0.8}$	10^{-6}	20
$\text{Li}_3\text{SBF}_4^*$	10^{-2}	20

Halide hydroxide Li_2OHCl is known to undergo a phase transition between 30 °C and 50 °C, where its conductivity changes drastically—around two orders of magnitude.^{128–131} Hood et al. demonstrated that a stable solid electrolyte interphase can be formed between Li_2OHCl electrolyte and the metallic Li anode, making them compatible at elevated temperatures.¹²⁹ Compared to Li oxyhalide, the cubic phase of Li_2OHCl retains the structure of anti-perovskite but leaves two of the six Li-octahedral vertices unoccupied due to the presence of proton.¹³² The effect of proton was updated by Song et al. through a combination of experimental and computational studies ($\text{Li}_{3-x}(\text{OH}_x)\text{Cl}$, $0.7 < x \leq 1$ and Li_2OHBr).¹³² It was revealed that the motion of fast-rotating OH^- group in the cubic phase lattice can facilitate the formation of nearby Frenkel defect and which contributes to the enhanced mobility of Li ions.¹³² The same group reported a further investigation on the temperature-dependent proton dynamics in Li_2OHCl in a more recent study.¹³³ Optimization of different ratios of halogens in Li_2OHX ($X = \text{Cl}, \text{Br}$) was also explored by other researchers.¹³⁴ Unlike the high-temperature cubic phase, protonated orthorhombic Li_2OHCl tends to block Li transport pathway and hence the substitution of OH^- group with F^- was attempted to improve the ionic conductivity.^{120,135,136} Li et al. prepared the composition of $\text{Li}_2(\text{OH})_{0.9}\text{F}_{0.1}\text{Cl}$, whose ionic conductivity was measured to be $3.5 \times 10^{-5} \text{ S cm}^{-1}$ at 25 °C and $1.9 \times 10^{-3} \text{ S cm}^{-1}$ at 100 °C, with reported good electrochemical stability against metallic Li.¹³⁶ Effat et al. suggested a partial replacement of Cl, instead of OH^- group, by F to form the composition of $\text{Li}_2\text{OHF}_{0.1}\text{Cl}_{0.9}$ could further enhance the ionic conductivity.¹³⁵ Conductivities of selected Li halide solid-state electrolytes at room temperature are shown in Table 5.^{20,119,137}

4.19.4 All-solid-state Li batteries (ASSLBs)

Solid-state electrolytes are broadly classified as bulk solid-state electrolytes and thin film solid electrolytes, based on the degree of thickness of the electrolyte. Bulk solid-state electrolytes have thickness usually in the range of several hundred micrometers, whereas for thin film solid electrolytes it is in the range of hundreds of nanometers to several microns. Usually, bulk solid-state electrolytes are fabricated by processes, such as sintering and compaction, annealing and heat treatment, and mechanical milling,^{137,138} whereas

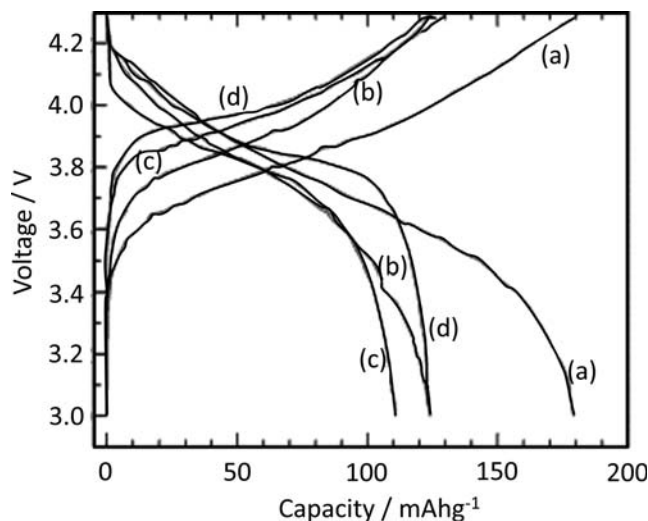


Fig. 13 Charge/discharge curves of $\text{Li}/\text{PEO}/\text{Li}_{1+x+y}\text{Al}_x\text{Ti}_{2-x}\text{Si}_y\text{P}_{3-y}\text{O}_{12}/\text{LiCoO}_2$ at 50 °C as a function of annealing temperature of $\text{Li}_{1+x+y}\text{Al}_x\text{Ti}_{2-x}\text{Si}_y\text{P}_{3-y}\text{O}_{12}/\text{LiCoO}_2$: (A) as-deposited, (B) 300 °C, (C) 400 °C, and (D) 500 °C.¹⁴¹ Reprinted from Ref. Xie, J.; Imanishi, N.; Zhang, T.; Hirano, A.; Takeda, Y.; Yamamoto, O. Li-Ion Transport in all-Solid-State Lithium Batteries with LiCoO_2 Using NASICON-Type Glass Ceramic Electrolytes. *J. Power Sources* **2009**, *189* (1), 365–370. <https://doi.org/10.1016/j.jpowsour.2008.08.015>, Copyright (2009), with permission from Elsevier.

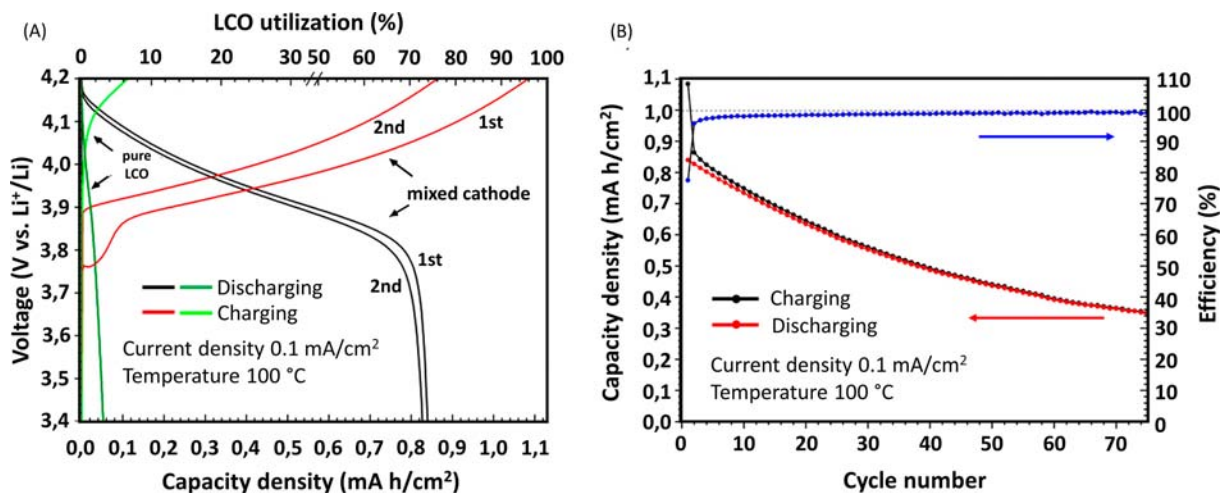


Fig. 14 (A) Charge/discharge curves of first cycle of a cell with $\text{Li}_{6,6}\text{La}_3\text{Zr}_{1,6}\text{Ta}_{0,4}\text{O}_{12}$ electrolyte and pure LiCoO_2 cathode and the first and second cycle of a cell with electrolyte mixed cathode, (B) capacity versus cycle number plot for 75 cycles of the cell with electrolyte mixed cathode.¹⁴³ Reprinted with permission from Ref. Finsterbusch, M.; Danner, T.; Tsai, C.-L.; Uhlenbruck, S.; Latz, A.; Guillon, O. High Capacity Garnet-Based all-Solid-State Lithium Batteries: Fabrication and 3D-Microstructure Resolved Modeling. *ACS Appl. Mater. Interfaces* **2018**, *10* (26), 22329–22339. <https://doi.org/10.1021/acsami.8b06705>, Copyright (2018) American Chemical Society.

methods like radio frequency magnetron sputtering, pulsed laser deposition, etc. are used to fabricate thin film solid-state electrolytes.^{139,140}

Solid-state batteries with Li metal anodes and non-flammable solid electrolytes are considered as the next generation rechargeable batteries due to their potential improvement in energy density and safety. Fig. 13 shows the charge and discharge curves of a $\text{Li}/\text{PEO}/\text{Li}_{1+x+y}\text{Al}_x\text{Ti}_2-x\text{Si}_y\text{P}_3-y\text{O}_{12}/\text{LiCoO}_2$ at 50 °C as a function of the annealing temperature of $\text{Li}_{1+x+y}\text{Al}_x\text{Ti}_2-x\text{Si}_y\text{P}_3-y\text{O}_{12}/\text{LiCoO}_2$.¹⁴¹ The cell fabricated with as-deposited LiCoO_2 showed a capacity of 180 mAh g^{-1} , which is a little higher than that of LiCoO_2 with liquid electrolytes.

It has been demonstrated that garnet electrolytes are chemically stable towards Li metal anodes and this distinctive characteristic of garnet electrolytes is promising for the development of ASSLBs. Abouli et al. recently reviewed a detailed summary of garnet-based ASSLBs.¹⁴² ASSLB composed of $\text{Li}_{6,6}\text{La}_3\text{Zr}_{1,6}\text{Ta}_{0,4}\text{O}_{12}$ electrolyte, Li anode and composite cathode (garnet + LiCoO_2) exhibited 81% utilization of theoretical capacity upon discharging at 100 °C (0.1 °C).¹⁴³ Solid-state cell with LiCoO_2 cathode was fabricated and the comparison of charge/discharge curves are given in Fig. 14A. The cell composed of composite cathode showed a fast degradation and lost half of its capacity within the first 50 cycles (Fig. 14B). Huo et al.¹⁴⁴ applied a rapid acid treatment (RAT) to remove Li_2CO_3 on the surface of LLZTO to decrease the interfacial resistance of Li and LLZTO. The $\text{Li}/\text{LLZTO-RAT}/\text{LCO}$ cell tested at 30 °C could deliver a discharge capacity of 101.2 mAh g^{-1} after 100 cycles at 0.1 °C with a Coulombic efficiency of over 99% (Fig. 15A). Also the charge-discharge profiles of the 1st, 50th and 100th cycles of the same cell (Fig. 15B) indicate a stable electrochemical behavior.¹⁴⁴

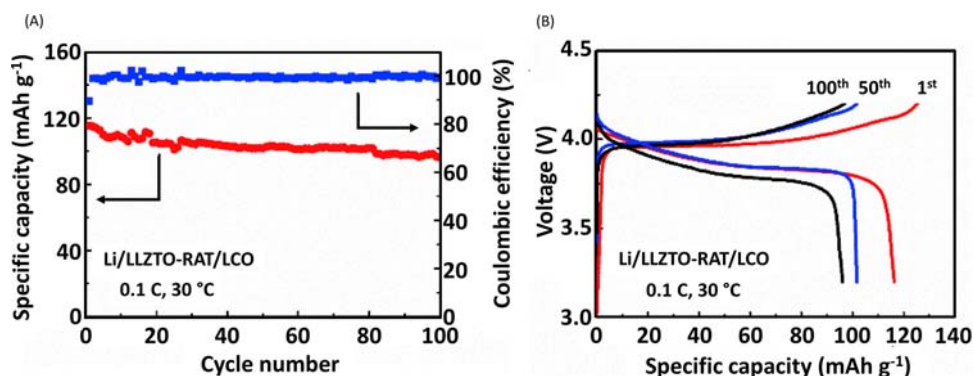


Fig. 15 (A) Cyclic performance and (B) charge/discharge profiles of $\text{Li}/\text{LLZTO-RAT}/\text{LCO}$ cell at 0.1 °C.¹⁴⁴ Reprinted from Ref. Huo, H.; Chen, Y.; Zhao, N.; Lin, X.; Luo, J.; Yang, X.; Liu, Y.; Guo, X.; Sun, X. In-Situ Formed Li_2CO_3 -Free Garnet/Li Interface by Rapid Acid Treatment for Dendrite-Free Solid-State Batteries. *Nano Energy* **2019**, *61*, 119–125. <https://doi.org/10.1016/j.nanoen.2019.04.058>, Copyright (2019), with permission from Elsevier.

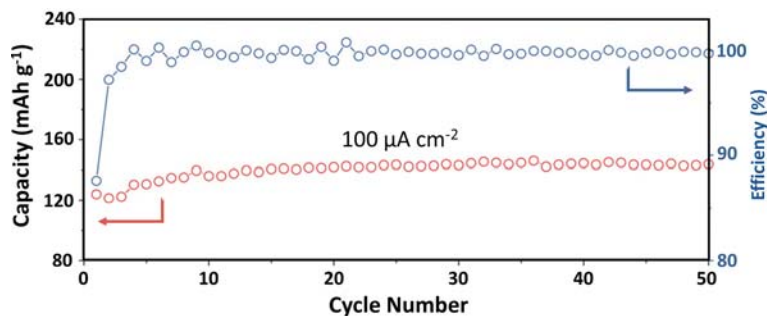


Fig. 16 Performance of a $\text{Li}/\text{Li}_{1.2}\text{Mg}_{0.1}\text{Zr}_{1.9}(\text{PO}_4)_3/\text{LiFePO}_4$ ASSLB at 60°C .¹⁴⁵ Reproduced with permission from Ref. Zhou, Q.; Xu, B.; Chien, P.-H.; Li, Y.; Huang, B.; Wu, N.; Xu, H.; Grundish, N. S.; Hu, Y.-Y.; Goodenough, J. B. NASICON $\text{Li}_{1.2}\text{Mg}_{0.1}\text{Zr}_{1.9}(\text{PO}_4)_3$ Solid Electrolyte for an all-Solid-State Li-Metal Battery. *Small Methods* **2020**, 4 (12), 2000764. <https://doi.org/10.1002/smt.202000764>, Copyright (2018), John Wiley and Sons.

NASICON-type solid electrolytes have also been used for ASSLBs. All-solid-state $\text{Li}/\text{Li}_{1.2}\text{Mg}_{0.1}\text{Zr}_{1.9}(\text{PO}_4)_3$ (LMZP) / LiFePO_4 cell showed specific capacities of 155 and 140 mAh g^{-1} at 0.05 and 0.1 mA cm^{-2} areal current rates, respectively, with a Coulombic efficiency as high as 99.5%. A capacity retention of 90% has been shown after 50 cycles in Fig. 16.¹⁴⁵ Fig. 17 illustrates electrochemical performances of the cells consisting LGPS as solid electrolyte together with conventional $\text{LiNi}_{0.8}\text{Co}_{0.15}\text{Al}_{0.05}\text{O}_2$ (NCA) and modified NCA cathodes (NCA-Ti), as the solid solution surface layer with 2 at.% Ti can improve the cycle stability of NCA at high cutoff voltages.¹⁴⁶ Both cells (NCA (Ti_2)/ $\text{Li}_{10}\text{GeP}_2\text{S}_{12}/\text{Li-In}$) show similar initial discharge specific capacities of 114 and

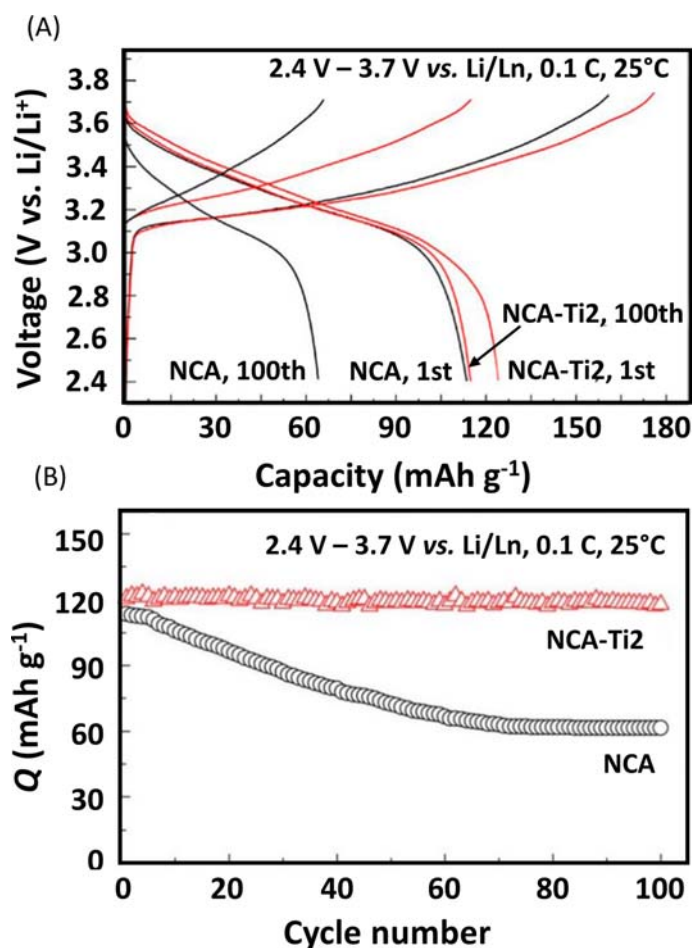


Fig. 17 (A) Charge/discharge profiles and (B) cyclic performances of NCA and NCA-Ti2 in cathode/ $\text{Li}_{10}\text{GeP}_2\text{S}_{12}/\text{Li-In}$ ASSLB at 25°C .¹⁴⁶ Reproduced with permission from Ref Yang, J.; Huang, B.; Yin, J.; Yao, X.; Peng, G.; Zhou, J.; Xu, X. Structure Integrity Endowed by a Ti-Containing Surface Layer towards Ultrastable $\text{LiNi}_{0.8}\text{Co}_{0.15}\text{Al}_{0.05}\text{O}_2$ for all-Solid-State Lithium Batteries. *J. Electrochem. Soc.* **2016**, 163 (8), A1530–A1534. <https://doi.org/10.1149/2.0331608jes>, Copyright (2016), IOP Publishing Ltd.

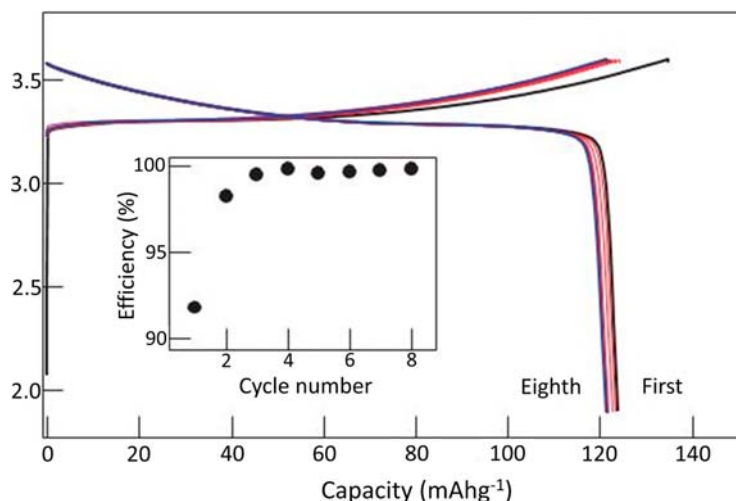


Fig. 18 Charge-discharge curves of an In/Li₁₀GeP₂S₁₂/LiCoO₂ ASSLB. Cyclic performance is given in the inset figure.²⁴ Reprinted by permission from Ref. Kamaya, N.; Homma, K.; Yamakawa, Y.; Hirayama, M.; Kanno, R.; Yonemura, M.; Kamiyama, T.; Kato, Y.; Hama, S.; Kawamoto, K.; Mitsui, A. A Lithium Superionic Conductor. *Nat. Mater.* **2011**, *10* (9), 682–686. <http://www.nature.com/nmat/journal/v10/n9/abs/nmat3066.html#supplementary-information>.

122 mAh g⁻¹, respectively. However, the modified NCA shows more stability than the un-treated NCA, delivering a reversible capacity of 115 mAh g⁻¹ with a capacity retention of 94% after 100 cycles.¹⁴⁶ Fig. 18 shows charge-discharge curves of an all-solid-state battery consisting of an indium metal anode, a Li₁₀GeP₂S₁₂ electrolyte, and a LiCoO₂ cathode.²⁴ The cell exhibited discharge capacity of over 120 mAh/g with an excellent discharge efficiency of 100% as shown in Fig. 18.

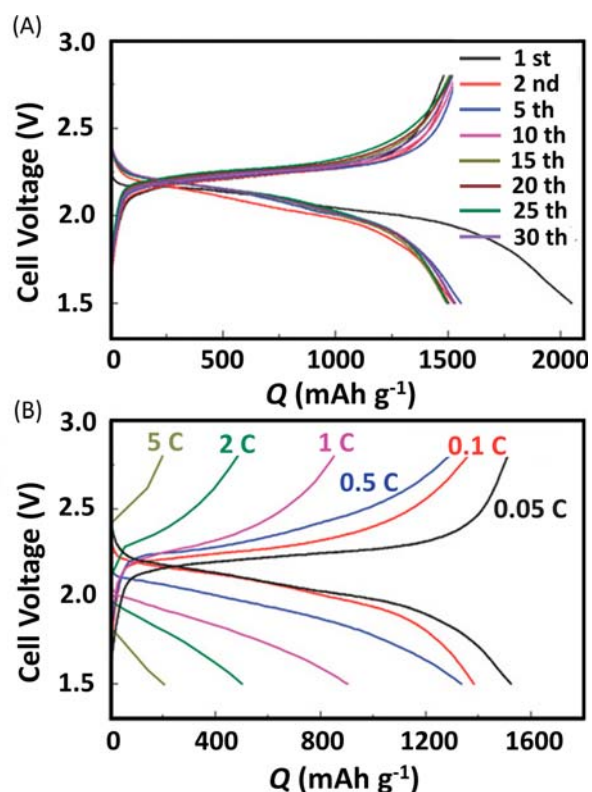


Fig. 19 Galvanostatic discharge/charge profiles of all-solid-state Li–S battery (A) under 0.05 C at 60 °C and (B) under different C rate at 60 °C.¹⁴⁷ Reproduced (adapted) with permission from Ref Yao, X.; Huang, N.; Han, F.; Zhang, Q.; Wan, H.; Mwisizerwa, J. P.; Wang, C.; Xu, X. High-Performance All-Solid-State Lithium–Sulfur Batteries Enabled by Amorphous Sulfur-Coated Reduced Graphene Oxide Cathodes. *Adv. Energy Mater.* **2017**, *7* (17): 1602923. <https://doi.org/10.1002/aenm.201602923>, Copyright 2017, John Wiley and Sons.

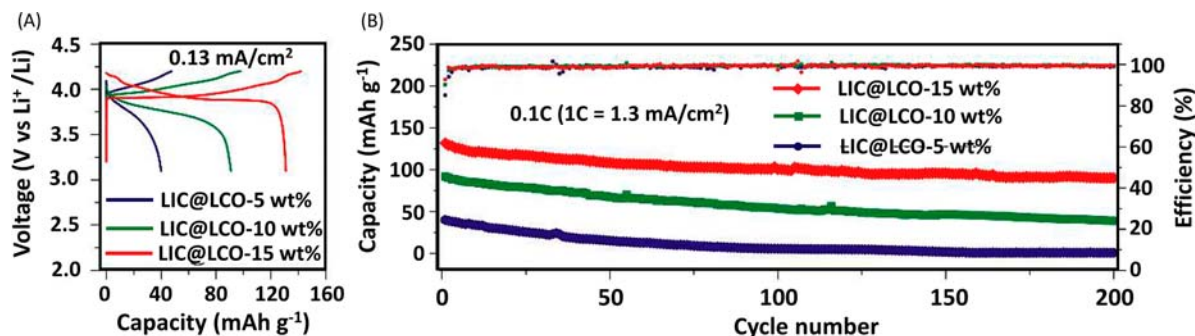


Fig. 20 (A) Charge/discharge profiles and (B) electrochemical performance of Li_3InCl_6 at LiCoO_2 electrodes.¹⁴⁸ Reprinted from Ref. Wang, C.; Liang, J.; Jiang, M.; Li, X.; Mukherjee, S.; Adair, K.; Zheng, M.; Zhao, Y.; Zhao, F.; Zhang, S.; Li, R.; Huang, H.; Zhao, S.; Zhang, L.; Lu, S.; Singh, C. V.; Sun, X. Interface-Assisted In-Situ Growth of Halide Electrolytes Eliminating Interfacial Challenges of all-Inorganic Solid-State Batteries. *Nano Energy* **2020**, *76*, 105015. <https://doi.org/10.1016/j.nanoen.2020.105015>, Copyright (2020), with permission from Elsevier.

Lithium-sulfur (Li-S) batteries are being considered as potential candidates for the next generation high energy density Li batteries because of the high theoretical specific capacity of S (1673 mAh/g). Most of the solid-state batteries with S cathode reported in literature have demonstrated a promising energy density larger than 300 Wh/kg. Yao et al. fabricated a Li-S solid-state battery with sulfide electrolyte ($\text{Li}_{10}\text{GeP}_2\text{S}_{12}$) in which S cathode is prepared by deposition of nanoamorphous sulfur on reduced graphene oxide.¹⁴⁷ The cell demonstrated a similar electrochemical performance as with a liquid organic electrolyte (60 °C) and it can maintain a high reversible capacity of 830 mAh/g at 1.0 °C for 750 cycles. Fig. 19A and B shows the charge/discharge profile of solid-state Li-S battery at different currents from 0.05 °C to 5 °C at 60 °C.¹⁴⁷

Wang et al. demonstrated an interfacial-assisted, in-situ synthesis of a highly Li ion conductive halide electrolyte (Li_3InCl_6) on LiCoO_2 cathode material.¹⁴⁸ A solid-state battery containing a Li_3InCl_6 electrolyte showed a high initial capacity of 131.7 mAh/g at 0.1 °C and can be operated up to 4 °C at room temperature. Fig. 20 shows the charge/discharge profiles and electrochemical performance for the same battery. The discharge capacity retains 90.3 mAh/g after 200 cycles.¹⁴⁸

4.19.5 Conclusions

All-solid-state Li batteries (ASSLBs) are considered as one of the most promising next-generation energy solutions with high level of safety and prominent energy storage features. To overcome the current limitations of the technology requires extensive research such as improving ionic conductivity and looking for materials of better chemical stability with elemental Li anode and cathodes. Garnet-type $\text{Li}_{6.75}\text{La}_3\text{Zr}_{1.75}\text{Ta}_{0.25}\text{O}_{12}$ electrolytes have demonstrated a Li^+ ionic conductivity of $1 \times 10^{-3} \text{ S cm}^{-1}$ at room temperature. The sulfide-based solid electrolytes, $\text{Li}_{10}\text{GeP}_2\text{S}_{12}$ exhibited a Li^+ ionic conductivity of $1.2 \times 10^{-2} \text{ S cm}^{-1}$ at room temperature, and halide-based Li_3ScCl_6 showed a room temperature conductivity of $3.02 \times 10^{-3} \text{ S cm}^{-1}$. Generally, the oxide-based perovskite structure Li solid electrolytes have better chemical stability in air than the garnet, LISICON, and NASICON structures, while garnets usually have a wider electrochemical stability window (up to 6 V vs. Li/Li^+) and are more compatible with metallic lithium.

Acknowledgments

The Natural Sciences and Engineering Research Council of Canada (NSERC) have supported this work through discovery grants to one of us (Venkataraman Thangadurai) (Award number: RGPIN-2021-02493).

References

- Armand, M.; Tarascon, J.-M. Building Better Batteries. *Nature* **2008**, *451* (7179), 652–657. <https://doi.org/10.1038/451652a>.
- Wakihara, M. Recent Developments in Lithium Ion Batteries. *Mater. Sci. Eng. R Reports* **2001**, *33* (4), 109–134. [https://doi.org/10.1016/S0927-796X\(01\)00030-4](https://doi.org/10.1016/S0927-796X(01)00030-4).
- World Scientific. Materials and Energy. In *Handbook of Solid State Batteries*, World Scientific, 2015; p 836.
- Wang, S.; Fang, R.; Li, Y.; Liu, Y.; Xin, C.; Richter, F. H.; Nan, C.-W. Interfacial Challenges for all-Solid-State Batteries Based on Sulfide Solid Electrolytes. *J. Mater.* **2021**, *7* (2), 209–218. <https://doi.org/10.1016/j.jmat.2020.09.003>.
- Xu, L.; Tang, S.; Cheng, Y.; Wang, K.; Liang, J.; Liu, C.; Cao, Y.-C.; Wei, F.; Mai, L. Interfaces in Solid-State Lithium Batteries. *Joule* **2018**, *2* (10), 1991–2015. <https://doi.org/10.1016/j.joule.2018.07.009>.
- Thangadurai, V.; Kaack, H.; Weppner, W. J. F. Novel Fast Lithium Ion Conduction in Garnet-Type $\text{Li}_5\text{La}_3\text{M}_2\text{O}_{12}$ (M = Nb, Ta). *J. Am. Ceram. Soc.* **2003**, *86* (3), 437–440. <https://doi.org/10.1111/j.1151-2916.2003.tb03318.x>.

7. Thangadurai, V.; Weppner, W. Recent Progress in Solid Oxide and Lithium Ion Conducting Electrolytes Research. *Ionics (Kiel)*. **2006**, *12* (1), 81–92. <https://doi.org/10.1007/s11581-006-0013-7>.
8. Wang, C.; Fu, K.; Palakkathodi Kammampata, S.; McOwen, W. D.; Junio Samson, A.; Zhang, L.; Hitz, G. T.; Nolan, A. M.; Wachsmann, E. D.; Mo, Y.; Thangadurai, V.; Hu, L. Garnet-Type Solid-State Electrolytes: Materials, Interfaces, and Batteries. *Chem. Rev.* **2020**, *120* (10), 4257–4300. <https://doi.org/10.1021/acs.chemrev.9b00427>.
9. Thangadurai, V.; Pinzaru, D.; Narayanan, S.; Baral, A. K. Fast Solid-State Li Ion Conducting Garnet-Type Structure Metal Oxides for Energy Storage. *J. Phys. Chem. Lett.* **2015**, *6* (2), 292–299. <https://doi.org/10.1021/jz501828v>.
10. Palakkathodi Kammampata, S.; Thangadurai, V. Cruising in Ceramics—Discovering New Structures for All-Solid-State Batteries—Fundamentals, Materials, and Performances. *Ionics (Kiel)*. **2018**, *24* (3), 639–660. <https://doi.org/10.1007/s11581-017-2372-7>.
11. Padma Kumar, P.; Yashonath, S. Ionic Conduction in the Solid State. *J. Chem. Sci.* **2006**, *118* (1), 135–154.
12. Huggins, R. A. Simple Method to Determine Electronic and Ionic Components of the Conductivity in Mixed Conductors A Review. *Ionics (Kiel)*. **2002**, *8* (3), 300–313. <https://doi.org/10.1007/bf02376083>.
13. Vink, H. A New Modified Hittorf Method for the Determination of Transport Numbers in Polyelectrolyte Solutions. *J. Chem. Soc. Faraday Trans.* **1984**, *80* (5), 1297–1304. <https://doi.org/10.1039/F19848001297>.
14. Tubandt, C.; Wein, F. W. H. *Handbuch Der Experimentalphysik, Vol. XII. Part I*; vol. 12; Akademie Verlag: Leipzig, 1932.
15. Hebb, M. H. Electrical Conductivity of Silver Sulfide. *J. Chem. Phys.* **1952**, *20*, 185–190.
16. Weppner, W.; and; Huggins, R. A. Electrochemical Methods for Determining Kinetic Properties of Solids. *Annu. Rev. Mater. Sci.* **1978**, *8* (1), 269–311. <https://doi.org/10.1146/annurev.ms.08.080178.001413>.
17. Lübke, S.; Wiernhöfer, H. D. Electronic Conductivity of Gd-Doped Ceria with Additional Pr-Doping. *Solid State Ion.* **1999**, *117*, 229–243. [https://doi.org/10.1016/S0167-2738\(98\)00408-1](https://doi.org/10.1016/S0167-2738(98)00408-1).
18. Bachman, J. C.; Mui, S.; Grimaud, A.; Chang, H. H.; Pour, N.; Lux, S. F.; Paschos, O.; Maglia, F.; Lupart, S.; Lamp, P.; Giordano, L.; Shao-Horn, Y. Inorganic Solid-State Electrolytes for Lithium Batteries: Mechanisms and Properties Governing Ion Conduction. *Chem. Rev.* **2016**, *116* (1), 140–162. <https://doi.org/10.1021/acs.chemrev.5b00563>.
19. Zhao, W.; Yi, J.; He, P.; Zhou, H. Solid-State Electrolytes for Lithium-Ion Batteries: Fundamentals, Challenges and Perspectives. *Electrochem. Energy Rev.* **2019**, *2* (4), 574–605. <https://doi.org/10.1007/s41918-019-00048-0>.
20. Li, X.; Liang, J.; Yang, X.; Adair, K. R.; Wang, C.; Zhao, F.; Sun, X. Progress and Perspectives on Halide Lithium Conductors for all-Solid-State Lithium Batteries. *Energ. Environ. Sci.* **2020**, *13* (5), 1429–1461. <https://doi.org/10.1039/C9EE03828K>.
21. Samson, A. J.; Hofstetter, K.; Bag, S.; Thangadurai, V. A Bird's-Eye View of Li-Stuffed Garnet-Type $\text{Li}_7\text{La}_3\text{Zr}_2\text{O}_{12}$ Ceramic Electrolytes for Advanced all-Solid-State Li Batteries. *Energ. Environ. Sci.* **2019**, *12* (10), 2957–2975. <https://doi.org/10.1039/C9EE01548E>.
22. Knauth, P. Inorganic Solid Li Ion Conductors: An Overview. *Solid State Ion.* **2009**, *180* (14–16), 911–916. <https://doi.org/10.1016/j.ssi.2009.03.022>.
23. Stramare, S.; Thangadurai, V.; Weppner, W. Lithium Lanthanum Titanates: A Review. *Chem. Mater.* **2003**, *15* (21), 3974–3990. <https://doi.org/10.1021/cm0300516>.
24. Kamaya, N.; Homma, K.; Yamakawa, Y.; Hirayama, M.; Kanno, R.; Yonemura, M.; Kamiyama, T.; Kato, Y.; Hama, S.; Kawamoto, K.; Mitsui, A. A Lithium Superionic Conductor. *Nat. Mater.* **2011**, *10* (9), 682–686. <http://www.nature.com/nmat/journal/v10/n9/abs/nmat3066.html#supplementary-information>.
25. Li, Y.; Han, J.-T.; Wang, C.-A.; Xie, H.; Goodenough, J. B. Optimizing Li^+ Conductivity in a Garnet Framework. *J. Mater. Chem.* **2012**, *22* (30), 15357–15361. <https://doi.org/10.1039/c2jm31413d>.
26. Liang, J.; Li, X.; Wang, S.; Adair, K. R.; Li, W.; Zhao, Y.; Wang, C.; Hu, Y.; Zhang, L.; Zhao, S.; Lu, S.; Huang, H.; Li, R.; Mo, Y.; Sun, X. Site-Occupation-Tuned Superionic $\text{Li}_x\text{ScCl}_{3-x}$ Halide Solid Electrolytes for all-Solid-State Batteries. *J. Am. Chem. Soc.* **2020**, *142* (15), 7012–7022. <https://doi.org/10.1021/jacs.0c00134>.
27. Asano, T.; Sakai, A.; Ouchi, S.; Sakaida, M.; Miyazaki, A.; Hasegawa, S. Solid Halide Electrolytes with High Lithium-Ion Conductivity for Application in 4 V Class Bulk-Type all-Solid-State Batteries. *Adv. Mater.* **2018**, *30* (44), 1803075. <https://doi.org/10.1002/adma.201803075>.
28. Manthiram, A.; Yu, X.; Wang, S. Lithium Battery Chemistries Enabled by Solid-State Electrolytes. *Nat. Rev. Mater.* **2017**, *2* (4), 16103. <https://doi.org/10.1038/natrevmats.2016.103>.
29. Aono, H.; Imanaka, N.; Adachi, G. Y. A. High Li^+ Conducting Ceramics. *Acc. Chem. Res.* **1994**, *27* (9), 265–270. <https://doi.org/10.1021/ar00045a002>.
30. West, A. R. *Crystalline Solid Electrolytes I: General Considerations and the Major Materials*, Cambridge University Press, 2009. <https://doi.org/10.1017/cbo9780511524790.003>.
31. Thangadurai, V.; Kaack, H.; Weppner, W. J. F. Novel Fast Lithium Ion Conduction in Garnet-Type $\text{Li}_5\text{La}_3\text{M}_2\text{O}_{12}$ (M: Nb, Ta). *ChemInform* **2003**, *34* (27), 437–440. <https://doi.org/10.1002/chin.200327009>.
32. Latie, L.; Villeneuve, G.; Conte, D.; Le Flem, G. Ionic Conductivity of Oxides with General Formula $\text{Li}_x\text{Ln}_{1-x}\text{Nb}_{1-x}\text{Ti}_x\text{O}_3$ (Ln = La, Nd). *J. Solid State Chem.* **1984**, *51* (3), 293–299. [https://doi.org/10.1016/0022-4596\(84\)90345-1](https://doi.org/10.1016/0022-4596(84)90345-1).
33. Belous, A. G.; Novitskaya, G. N.; Polyanskaya, S. V.; Gornikov, Y. I. Investigation into Complex Oxides of $\text{La}_{2/3-x}\text{Li}_x\text{Ti}_3\text{O}_3$ Composition. *Izv Akad Nauk SSSR, Neorg Mater* **1987**, *23* (3), 470–472.
34. Wu, Z.; Xie, Z.; Yoshida, A.; Wang, Z.; Hao, X.; Abudula, A.; Guan, G. Utmost Limits of Various Solid Electrolytes in all-Solid-State Lithium Batteries: A Critical Review. *Renew. Sustain. Energy Rev.* **2019**, *109* (April), 367–385. <https://doi.org/10.1016/j.rser.2019.04.035>.
35. Morata-Orrantia, A.; García-Martín, S.; Alario-Franco, M.Á. Optimization of Lithium Conductivity in La/Li Titanates. *Chem. Mater.* **2003**, *15* (21), 3991–3995. <https://doi.org/10.1021/cm0300563>.
36. Sun, C.; Alonso, J. A.; Bian, J. Recent Advances in Perovskite-Type Oxides for Energy Conversion and Storage Applications. *Adv. Energy Mater.* **2021**, *11* (2), 1–21. <https://doi.org/10.1002/aenm.202000459>.
37. Inaguma, Y.; Yu, J.; Shan, Y.; Itoh, M.; Nakamura, T. The Effect of the Hydrostatic Pressure on the Ionic Conductivity in a Perovskite Lanthanum Lithium Titanate. *J. Electrochem. Soc.* **1995**, *142* (1), L8–L11. <https://doi.org/10.1149/1.2043988>.
38. Yao, X.; Huang, B.; Yin, J.; Peng, G.; Huang, Z.; Gao, C.; Liu, D.; Xu, X. All-Solid-State Lithium Batteries with Inorganic Solid Electrolytes: Review of Fundamental Science. *Chinese Phys. B* **2016**, *25* (1), 18802. <https://doi.org/10.1088/1674-1056/25/1/018802>.
39. Meesala, Y.; Jena, A.; Chang, H.; Liu, R. S. Recent Advancements in Li-Ion Conductors for All-Solid-State Li-Ion Batteries. *ACS Energy Lett.* **2017**, *2*. <https://doi.org/10.1021/acseenergylett.7b00849>.
40. Chen, Y.; Wen, K.; Chen, T.; Zhang, X.; Armand, M.; Chen, S. Recent Progress in All-Solid-State Lithium Batteries: The Emerging Strategies for Advanced Electrolytes and their Interfaces. *Energy Storage Mater.* **2020**, *31*, 401–433. <https://doi.org/10.1016/j.ensm.2020.05.019>.
41. Huang, B.; Zhong, S.; Luo, J.; Huang, Z.; Wang, C. A Highly Dense Perovskite Electrolyte with a High Li^+ Conductivity for Li-Ion Batteries. *J. Power Sources* **2019**, *429*, 75–79. <https://doi.org/10.1016/j.jpowsour.2019.04.117>.
42. Zheng, Y.; Yao, Y.; Ou, J.; Li, M.; Luo, D.; Dou, H.; Li, Z.; Amine, K.; Yu, A.; Chen, Z. A Review of Composite Solid-State Electrolytes for Lithium Batteries: Fundamentals, Key Materials and Advanced Structures. *Chem. Soc. Rev.* **2020**. <https://doi.org/10.1039/d0cs00305k>.
43. Zheng, F.; Kotobuki, M.; Song, S.; Lai, M. O.; Lu, L. Review on Solid Electrolytes for all-Solid-State Lithium-Ion Batteries. *J. Power Sources* **2018**, *389*, 198–213. <https://doi.org/10.1016/j.jpowsour.2018.04.022>.
44. Chung, H. T.; Kim, J. G.; Kim, H. G. Dependence of the Lithium Ionic Conductivity on the B-Site Ion Substitution in $(\text{Li}_{0.5}\text{La}_{0.5})\text{Ti}_{1-x}\text{M}_x\text{O}_3$ (M = Sn, Zr, Mn, Ge). *Solid State Ion.* **1998**, *107* (1–2), 153–160. [https://doi.org/10.1016/s0167-2738\(97\)00525-0](https://doi.org/10.1016/s0167-2738(97)00525-0).
45. Hagman, L.-O.; Kierkegaard, P.; Karvonen, P.; Virtanen, A. I.; Paasivirta, J. The Crystal Structure of $\text{NaMe}_2^{\text{IV}}(\text{PO}_4)_3$; $\text{Me}^{\text{IV}} = \text{Ge}, \text{Ti}, \text{Zr}$. *Acta Chem. Scand.* **1968**, 1822–1832. <https://doi.org/10.3891/acta.chem.scand.22-1822>.

46. Goodenough, J. B.; Hong, H. Y.-P.; Kafalas, J. A. Fast Na^+ - Ion Transport in Skeleton Structures. *Mater. Res. Bull.* **1976**, *11*, 203–220.
47. Naqash, S.; Ma, Q.; Tietz, F.; Guillon, O. $\text{Na}_3\text{Zr}_2(\text{SiO}_4)_2(\text{PO}_4)$ Prepared by a Solution-Assisted Solid State Reaction. *Solid State Ion.* **2017**, *302*, 83–91. <https://doi.org/10.1016/j.ssi.2016.11.004>.
48. Reddy, M. V.; Julien, C. M.; Mauger, A.; Zaghib, K. Sulfide and Oxide Inorganic Solid Electrolytes for All-Solid-State Li Batteries: A Review. *Nanomaterials* **2020**, *10* (8), 1–80. <https://doi.org/10.3390/nano10081606>.
49. Hou, M.; Liang, F.; Chen, K.; Dai, Y.; Xue, D. Challenges and Perspectives of NASICON-Type Solid Electrolytes for All-Solid-State Lithium Batteries. *Nanotechnology* **2020**, *31* (13). <https://doi.org/10.1088/1361-6528/ab5be7>.
50. Thangadurai, V.; Shukla, K. A.; Gopalakrishnan, J. New Lithium-Ion Conductors Based on the NASICON Structure. *J. Mater. Chem.* **1999**, *9* (3), 739–741. <https://doi.org/10.1039/A807007E>.
51. Aatiq, A.; Ménétrier, M.; Croguennec, L.; Suard, E.; Delmas, C. On the Structure of $\text{Li}_3\text{Ti}_2(\text{PO}_4)_3$. *J. Mater. Chem.* **2002**, *12* (10), 2971–2978. <https://doi.org/10.1039/B203652P>.
52. Arbi, K.; Rojo, J. M.; Sanz, J. Lithium Mobility in Titanium Based Nasicon $\text{Li}_{1+x}\text{Ti}_{2-x}\text{Al}_x(\text{PO}_4)_3$ and $\text{LiTi}_{2-x}\text{Zr}_x(\text{PO}_4)_3$ Materials Followed by NMR and Impedance Spectroscopy. *J. Eur. Ceram. Soc.* **2007**, *27* (13–15), 4215–4218. <https://doi.org/10.1016/j.jeurceramsoc.2007.02.118>.
53. Pinus, I. Y.; Shaikhislamova, A. R.; Stenina, I. A.; Zhuravlev, N. A.; Yaroslavtsev, A. B. Phase Transitions of the NASICON-Type Mixed Phosphates $\text{LiM}_2(\text{PO}_4)_3$ (M = Ti, Zr) and $\text{LiInNb}(\text{PO}_4)_3$. *Inorg. Mater.* **2009**, *45* (12), 1370–1374. <https://doi.org/10.1134/s0020168509120127>.
54. Pinus, I. Y.; Khoroshilov, A. V.; Gavrichev, K. S.; Tarasov, V. P.; Yaroslavtsev, A. B. On Cationic Mobility in Nasicon Phosphates $\text{LiTi}_2(\text{PO}_4)_3$ and $\text{Li}_{0.9}\text{Ti}_{1.9}\text{Nb}_{0.1}(\text{PO}_4)_3$. *Solid State Ion.* **2012**, *212*, 112–116. <https://doi.org/10.1016/j.ssi.2012.01.035>.
55. Capsoni, D.; Bini, M.; Ferrari, S.; Mustarelli, P.; Massarotti, V.; Mozzati, M. C.; Spinella, A. Structural, Spectroscopic, and Electrical Features of Undoped and Mn-Doped $\text{LiTi}_2(\text{PO}_4)_3$. *J. Phys. Chem. C* **2010**, *114* (32), 13872–13878. <https://doi.org/10.1021/jp104571a>.
56. Liang, J.; Luo, J.; Sun, Q.; Yang, X.; Li, R.; Sun, X. Recent Progress on Solid-State Hybrid Electrolytes for Solid-State Lithium Batteries. *Energy Storage Mater.* **2019**, *21* (June), 308–334. <https://doi.org/10.1016/j.ensm.2019.06.021>.
57. DeWees, R.; Wang, H. Synthesis and Properties of NaSICON-Type LATP and LAGP Solid Electrolytes. *ChemSusChem* **2019**, *12* (16), 3713–3725. <https://doi.org/10.1002/cssc.201900725>.
58. Adachi, G. Y.; Imanaka, N.; Aono, H. Fast Li^+ Conducting Ceramic Electrolytes. *Adv. Mater.* **1996**, *8* (2), 127–135. <https://doi.org/10.1002/adma.19960080205>.
59. Xu, X.; Wen, Z.; Wu, X.; Yang, X.; Gu, Z. Lithium Ion-Conducting Glass-Ceramics of $\text{Li}_{1.5}\text{Al}_{0.5}\text{Ge}_{1.5}(\text{PO}_4)_3 \cdot x\text{Li}_2\text{O}$ ($x = 0.0\text{--}0.20$) with Good Electrical and Electrochemical Properties. *J. Am. Ceram. Soc.* **2007**, *90* (9), 2802–2806. <https://doi.org/10.1111/j.1551-2916.2007.01827.x>.
60. Leo, C. J.; Subba Rao, G. V.; Chowdari, B. V. R. Fast Ion Conduction in the Li-Analogues of Nasicon, $\text{Li}_{1+x}[(\text{Ta}_{1-x}\text{Ge}_x)\text{Al}](\text{PO}_4)_3$. *J. Mater. Chem.* **2002**, *12* (6), 1848–1853. <https://doi.org/10.1039/b110863h>.
61. Safanama, D.; Adams, S. High Efficiency Aqueous and Hybrid Lithium-Air Batteries Enabled by $\text{Li}_{1.5}\text{Al}_{0.5}\text{Ge}_{1.5}(\text{PO}_4)_3$ Ceramic Anode-Protecting Membranes. *J. Power Sources* **2017**, *340*, 294–301. <https://doi.org/10.1016/j.jpowsour.2016.11.076>.
62. Zhu, Y.; He, X.; Mo, Y. Origin of Outstanding Stability in the Lithium Solid Electrolyte Materials: Insights from Thermodynamic Analyses Based on First-Principles Calculations. *ACS Appl. Mater. Interfaces* **2015**, *7* (42), 23685–23693. <https://doi.org/10.1021/acsami.5b07517>.
63. West, A. R.; Glasser, F. P. Preparation and Crystal Chemistry of some Tetrahedral Li_3PO_4 -Type Compounds. *J. Solid State Chem.* **1972**, *4* (1), 20–28. [https://doi.org/10.1016/0022-4596\(72\)90127-2](https://doi.org/10.1016/0022-4596(72)90127-2).
64. West, A. R. Ionic Conductivity of Oxides Based on Li_4SiO_4 . *J. Appl. Electrochem.* **1973**, *3* (4), 327–335. <https://doi.org/10.1007/BF00613041>.
65. Hong, H. Y. P. Crystal Structure and Ionic Conductivity of $\text{Li}_{1.4}\text{Zn}(\text{GeO}_4)_4$ and Other New Li^+ Superionic Conductors. *Mater. Res. Bull.* **1978**, *13* (2), 117–124. [https://doi.org/10.1016/0025-5408\(78\)90075-2](https://doi.org/10.1016/0025-5408(78)90075-2).
66. Ivanov-Shits, A. K.; Kireev, V. V. Growth and Ionic Conductivity of $\text{Li}_{3+x}\text{P}_{1-x}\text{Ge}_x\text{O}_4$ ($x = 0.34$) Single Crystals. *Crystallogr. Reports* **2003**, *48* (1), 117–120.
67. Zhao, G.; Suzuki, K.; Yonemura, M.; Hirayama, M.; Kanno, R. Enhancing Fast Lithium Ion Conduction in Li_4GeO_4 - Li_3PO_4 Solid Electrolytes. *ACS Appl. Energy Mater.* **2019**, *2* (9), 6608–6615. <https://doi.org/10.1021/acsami.9b01152>.
68. Du, Y. A.; Holzwarth, N. A. W. Mechanisms of Li^+ Diffusion in Crystalline γ - and β - Li_3PO_4 Electrolytes from First Principles. *Phys. Rev. B - Condens. Matter Mater. Phys.* **2007**, *76* (17), 1–14. <https://doi.org/10.1103/PhysRevB.76.174302>.
69. Huggins, R. A. Recent Results on Lithium Ion Conductors. *Electrochim. Acta* **1977**, *22* (7), 773–781. [https://doi.org/10.1016/0013-4686\(77\)80034-0](https://doi.org/10.1016/0013-4686(77)80034-0).
70. Rodger, A. R.; Kuwano, J.; West, A. R. Li^+ Ion Conducting γ Solid Solutions in the Systems $\text{Li}_4\text{XO}_4 - \text{Li}_3\text{YO}_4$: X = Si, Ge, Ti; Y = P, As, V; $\text{Li}_4\text{XO}_x - \text{Li}_2\text{ZO}_2$: Z = Al, Ga, Cr and $\text{Li}_4\text{GeO}_4 - \text{Li}_2\text{CaGeO}_4$. *Solid State Ion.* **1985**, *15* (3), 185–198. [https://doi.org/10.1016/0167-2738\(85\)90002-5](https://doi.org/10.1016/0167-2738(85)90002-5).
71. Yamaki, J. I.; Ohtsuka, H.; Shodai, T. Rechargeable Lithium Thin Film Cells with Inorganic Electrolytes. *Solid State Ion.* **1996**, *86–88* (PART 2), 1279–1284. [https://doi.org/10.1016/0167-2738\(96\)00301-3](https://doi.org/10.1016/0167-2738(96)00301-3).
72. Binner, T.; Marcolongo, A.; Mottet, M.; Weber, V.; Laino, T. Comparison of Computational Methods for the Electrochemical Stability Window of Solid-State Electrolyte Materials. *J. Mater. Chem. A* **2020**, *8* (3), 1347–1359. <https://doi.org/10.1039/c9ta09401f>.
73. Kasper, H. M. A New Series of Rare Earth Garnets $\text{Ln}^{3+}_3\text{M}_2\text{Li}^{+}_3\text{O}_{12}$ (M = Te, W). *Inorg. Chem.* **1969**, *8* (4), 1000–1002. <https://doi.org/10.1021/ic50074a058>.
74. Thangadurai, V.; Weppner, W. $\text{Li}_6\text{Al}_2\text{Ta}_2\text{O}_{12}$ (A = Sr, Ba): Novel Garnet-like Oxides for Fast Lithium Ion Conduction. *Adv. Funct. Mater.* **2005**, *15* (1), 107–112. <https://doi.org/10.1002/adfm.200400044>.
75. Murugan, R.; Thangadurai, V.; Weppner, W. Fast Lithium Ion Conduction in Garnet-Type $\text{Li}_7\text{La}_3\text{Zr}_2\text{O}_{12}$. *Angew. Chem. Int. Ed.* **2007**, *46* (41), 7778–7781. <https://doi.org/10.1002/anie.200701144>.
76. Cussen, E. J. Structure and Ionic Conductivity in Lithium Garnets. *J. Mater. Chem.* **2010**, *20* (25), 5167–5173. <https://doi.org/10.1039/B925553B>.
77. Geiger, C. A.; Alekseev, E.; Lazić, B.; Fisch, M.; Armbruster, T.; Langner, R.; Fechteldord, M.; Kim, N.; Pettke, T.; Weppner, W. Crystal Chemistry and Stability of “ $\text{Li}_7\text{La}_3\text{Zr}_2\text{O}_{12}$ ” Garnet: A Fast Lithium-Ion Conductor. *Inorg. Chem.* **2011**, *50* (3), 1089–1097. <https://doi.org/10.1021/ic101914e>.
78. Awaka, J.; Takashima, A.; Kataoka, K.; Kijima, N.; Idemoto, Y.; Akimoto, J. Crystal Structure of Fast Lithium-Ion-Conducting Cubic $\text{Li}_7\text{La}_3\text{Zr}_2\text{O}_{12}$. *Chem. Lett.* **2011**, *40* (1), 60–62. <https://doi.org/10.1246/cl.2011.60>.
79. Jin, Y.; McGinn, P. J. Al-Doped $\text{Li}_7\text{La}_3\text{Zr}_2\text{O}_{12}$ Synthesized by a Polymerized Complex Method. *J. Power Sources* **2011**, *196* (20), 8683–8687. <https://doi.org/10.1016/j.jpowsour.2011.05.065>.
80. Wu, J.-F.; Chen, E.-Y.; Yu, Y.; Liu, L.; Wu, Y.; Pang, W. K.; Peterson, V. K.; Guo, X. Gallium-Doped $\text{Li}_7\text{La}_3\text{Zr}_2\text{O}_{12}$ Garnet-Type Electrolytes with High Lithium-Ion Conductivity. *ACS Appl. Mater. Interfaces* **2017**, *9* (2), 1542–1552. <https://doi.org/10.1021/acsami.6b13902>.
81. Zeier, W. G. Structural Limitations for Optimizing Garnet-Type Solid Electrolytes: A Perspective. *Dalton Trans.* **2014**, *43* (43), 16133–16138. <https://doi.org/10.1039/C4DT02162B>.
82. Ma, C.; Rangasamy, E.; Liang, C.; Sakamoto, J.; More, K. L.; Chi, M. Excellent Stability of a Lithium-Ion-Conducting Solid Electrolyte upon Exchange in Aqueous Solutions Reversible Li^+/H^+ . *Angew. Chem. Int. Ed.* **2015**, *54* (1), 131–135. <https://doi.org/10.1002/anie.201408124>. <https://doi.org/10.1002/ange.201408124>.
83. Liu, X.; Chen, Y.; Hood, Z. D.; Ma, C.; Yu, S.; Sharafi, A.; Wang, H.; An, K.; Sakamoto, J.; Siegel, D. J.; Cheng, Y.; Jalarvo, N. H.; Chi, M. Elucidating the Mobility of H^+ and Li^+ Ions in $(\text{Li}_{6.25-x}\text{H}_x\text{Al}_{0.25})\text{La}_3\text{Zr}_2\text{O}_{12}$ Via Correlative Neutron and Electron Spectroscopy. *Energy Environ. Sci.* **2019**, *12* (3), 945–951. <https://doi.org/10.1039/C8EE02981D>.
84. Hofstetter, K.; Samson, A. J.; Narayanan, S.; Thangadurai, V. Present Understanding of the Stability of Li-Stuffed Garnets with Moisture, Carbon Dioxide, and Metallic Lithium. *J. Power Sources* **2018**, *390*, 297–312. <https://doi.org/10.1016/j.jpowsour.2018.04.016>.
85. Zhao, N.; Khokhar, W.; Bi, Z.; Shi, C.; Guo, X.; Fan, L. Z.; Nan, C. W. Solid Garnet Batteries. *Aust. Dent. J.* **2019**, *3* (5), 1190–1199. <https://doi.org/10.1016/j.joule.2019.03.019>.

86. Wu, F.; Fitzhugh, W.; Ye, L.; Ning, J.; Li, X. Advanced Sulfide Solid Electrolyte by Core-Shell Structural Design. *Nat. Commun.* **2018**, *9* (1), 4037. <https://doi.org/10.1038/s41467-018-06123-2>.
87. Cao, C.; Li, Z.-B.; Wang, X.-L.; Zhao, X.-B.; Han, W.-Q. Recent Advances in Inorganic Solid Electrolytes for Lithium Batteries. *Front. Energy Res.* **2014**, *2*, 25. <https://doi.org/10.3389/fenrg.2014.00025>.
88. Kanno, R.; Murayama, M. Lithium Ionic Conductor Thio-LISICON: The $\text{Li}_2\text{S}-\text{GeS}_2-\text{P}_2\text{S}_5$ System. *J. Electrochem. Soc.* **2001**, *148* (7), A742–A746. <https://doi.org/10.1149/1.1379028>.
89. Kwon, O.; Hirayama, M.; Suzuki, K.; Kato, Y.; Saito, T.; Yonemura, M.; Kamiyama, T.; Kanno, R. Synthesis, Structure, and Conduction Mechanism of the Lithium Superionic Conductor $\text{Li}_{10+d}\text{Ge}_{1+d}\text{P}_{2-d}\text{S}_{12}$. *J. Mater. Chem. A* **2015**, *3* (1), 438–446. <https://doi.org/10.1039/C4TA05231E>.
90. Kuhn, A.; Köhler, J.; Lotsch, B. V. Single-Crystal X-Ray Structure Analysis of the Superionic Conductor $\text{Li}_{10}\text{GeP}_2\text{S}_{12}$. *Phys. Chem. Chem. Phys.* **2013**, *15* (28), 11620–11622. <https://doi.org/10.1039/C3CP51985F>.
91. Ravaine, D. Glasses as Solid Electrolytes. *J. Non Cryst. Solids* **1980**, *38–39*, 353–358. [https://doi.org/10.1016/0022-3093\(80\)90444-5](https://doi.org/10.1016/0022-3093(80)90444-5).
92. Minami, T. Recent Progress in Superionic Conducting Glasses. *J. Non Cryst. Solids* **1987**, *95–96*, 107–118. [https://doi.org/10.1016/S0022-3093\(87\)80103-5](https://doi.org/10.1016/S0022-3093(87)80103-5).
93. Kennedy, J. H.; Sahami, S.; Shea, S. W.; Zhang, Z. Preparation and Conductivity Measurements of $\text{SiS}_2-\text{Li}_2\text{S}$ Glasses Doped with LiBr and LiCl. *Solid State Ion.* **1986**, *18–19*, 368–371. [https://doi.org/10.1016/0167-2738\(86\)90142-6](https://doi.org/10.1016/0167-2738(86)90142-6).
94. Takada, K.; Aotani, N.; Iwamoto, K.; Kondo, S. Solid State Lithium Battery with Oxysulfide Glass. *Solid State Ion.* **1996**, *86–88*, 877–882. [https://doi.org/10.1016/0167-2738\(96\)00199-3](https://doi.org/10.1016/0167-2738(96)00199-3).
95. Mizuno, F.; Hayashi, A.; Tadanaga, K.; Tatsumisago, M. High Lithium Ion Conducting Glass-Ceramics in the System $\text{Li}_2\text{S}-\text{P}_2\text{S}_5$. *Solid State Ion.* **2006**, *177* (26), 2721–2725. <https://doi.org/10.1016/j.ssi.2006.04.017>.
96. Tatsumisago, M.; Mizuno, F.; Hayashi, A. All-Solid-State Lithium Secondary Batteries Using Sulfide-Based Glass-Ceramic Electrolytes. *J. Power Sources* **2006**, *159* (1), 193–199. <https://doi.org/10.1016/j.jpowsour.2006.04.037>.
97. Lian, P.-J.; Zhao, B.-S.; Zhang, L.-Q.; Xu, N.; Wu, M.-T.; Gao, X.-P. Inorganic Sulfide Solid Electrolytes for all-Solid-State Lithium Secondary Batteries. *J. Mater. Chem. A* **2019**, *7* (36), 20540–20557. <https://doi.org/10.1039/C9TA04555D>.
98. Minami, T.; Hayashi, A.; Tatsumisago, M. Recent Progress of Glass and Glass-Ceramics as Solid Electrolytes for Lithium Secondary Batteries. *Solid State Ion.* **2006**, *177* (26), 2715–2720. <https://doi.org/10.1016/j.ssi.2006.07.017>.
99. Tatsumisago, M.; Hayashi, A. Superionic Glasses and Glass-Ceramics in the $\text{Li}_2\text{S}-\text{P}_2\text{S}_5$ System for All-Solid-State Lithium Secondary Batteries. *Solid State Ion.* **2012**, *225*, 342–345. <https://doi.org/10.1016/j.ssi.2012.03.013>.
100. Karkera, G.; Reddy, M. A.; Fichtner, M. Recent Developments and Future Perspectives of Anionic Batteries. *J. Power Sources* **2021**, *481*, 228877. <https://doi.org/10.1016/j.jpowsour.2020.228877>.
101. Zhao, X.; Zhao-Karger, Z.; Fichtner, M.; Shen, X. Halide-Based Materials and Chemistry for Rechargeable Batteries. *Angew. Chem. Int. Ed.* **2020**, *59* (15), 5902–5949. <https://doi.org/10.1002/anie.201902842>.
102. El Kharbachi, A.; Zavorotynska, O.; Latroche, M.; Cuevas, F.; Yartys, V.; Fichtner, M. Exploits, Advances and Challenges Benefiting beyond Li-Ion Battery Technologies. *J. Alloys Compd.* **2020**, *817*, 153261. <https://doi.org/10.1016/j.jallcom.2019.153261>.
103. Weppner, W.; Huggins, R. A. Ionic Conductivity of Alkali Metal Chloroaluminates. *Phys. Lett. A* **1976**, *58* (4), 245–248. [https://doi.org/10.1016/0375-9601\(76\)90087-6](https://doi.org/10.1016/0375-9601(76)90087-6).
104. Weppner, W.; Huggins, R. A. Ionic Conductivity of Solid and Liquid LiAlCl_4 . *J. Electrochem. Soc.* **1977**, *124* (1), 35–38. <https://doi.org/10.1149/1.2133238>.
105. Maekawa, H.; Iwatani, T.; Shen, H.; Yamamura, T.; Kawamura, J. Enhanced Lithium Ion Conduction and the Size Effect on Interfacial Phase in Li_2ZnL_4 -Mesoporous Alumina Composite Electrolyte. *Solid State Ion.* **2008**, *178* (31–32), 1637–1641. <https://doi.org/10.1016/j.ssi.2007.10.018>.
106. Lutz, H.; Zhang, Z.; Pfitzner, A. Fast Ionic Conductivity of Ternary Iodides in the Systems $\text{LiI}-\text{M}^{\text{II}}\text{I}_2$ ($\text{M}^{\text{II}} = \text{Mn, Cd, Pb}$). *Solid State Ion.* **1993**, *62* (1–2), 1–3. [https://doi.org/10.1016/0167-2738\(93\)90245-X](https://doi.org/10.1016/0167-2738(93)90245-X).
107. Lutz, H. D.; Kuske, P.; Wussow, K. Ionic Motion of Tetrahedrally and Octahedrally Coordinated Lithium Ions in Ternary and Quaternary Halides. *Solid State Ion.* **1988**, *28–30* (5), 1282–1286. [https://doi.org/10.1016/0167-2738\(88\)90371-2](https://doi.org/10.1016/0167-2738(88)90371-2).
108. Lutz, H. D.; Schmidt, W.; Haeuselner, H. Chloride Spinel: A New Group of Solid Lithium Electrolytes. *J. Phys. Chem. Solid* **1981**, *42* (4), 287–289. [https://doi.org/10.1016/0022-3697\(81\)90142-6](https://doi.org/10.1016/0022-3697(81)90142-6).
109. Kanno, R.; Takeda, Y.; Yamamoto, O. Ionic Conductivity of Solid Lithium Ion Conductors with the Spinel Structure: Li_2MCl_4 ($\text{M} = \text{Mg, Mn, Fe, Cd}$). *Mater. Res. Bull.* **1981**, *16* (8), 999–1005. [https://doi.org/10.1016/0025-5408\(81\)90142-2](https://doi.org/10.1016/0025-5408(81)90142-2).
110. Kanno, R.; Takeda, Y.; Takada, K.; Yamamoto, O. Ionic Conductivity and Phase Transition of the Spinel System $\text{Li}_{2-2x}\text{M}_{1+x}\text{Cl}_4$ ($\text{M} = \text{Mg, Mn, Cd}$). *J. Electrochem. Soc.* **1984**, *131* (3), 469–474. <https://doi.org/10.1149/1.2115611>.
111. Tomita, Y.; Fuji-i, A.; Ohki, H.; Yamada, K.; Okuda, T. New Lithium Ion Conductor Li_3InBr_6 Studied by ^7Li NMR. *Chem. Lett.* **1998**, *27* (3), 223–224. <https://doi.org/10.1246/cl.1998.223>.
112. Yamada, K.; Kumano, K.; Okuda, T. Lithium Superionic Conductors Li_3InBr_6 and LiInBr_4 Studied by ^7Li , ^{115}In NMR. *Solid State Ion.* **2006**, *177* (19), 1691–1695. <https://doi.org/10.1016/j.ssi.2006.06.026>.
113. Tomita, Y.; Yonekura, H.; Yamauchi, Y.; Yamada, K.; Kobayashi, K. Substitution Effect in the Ion Conductor Li_3InBr_6 , Studied by Nuclear Magnetic Resonance. *Zeitschrift für Naturforsch. A* **2002**, *57* (6–7), 447–450. <https://doi.org/10.1515/zna-2002-6-728>.
114. Bohnsack, A.; Stenzel, F.; Zajonc, A.; Balzer, G.; Wickleder, M. S.; Meyer, G. Ternure Halogenide Vom Typ A_3MX_6 . VI [1]. Ternure Chloride Der Selten-Erd-Elemente Mit Lithium, Li_3MCl_6 ($\text{M} = \text{Tb-Lu, Y, Sc}$): Synthese, Kristallstrukturen Und Ionenbewegung. *Zeitschrift für Anorg. und Allg. Chemie* **1997**, *623* (7), 1067–1073. <https://doi.org/10.1002/zaac.19976230710>.
115. Steiner, H.-J.; Lutz, H. D. Neue Schnelle Ionenleiter Vom Typ $\text{M}_3\text{M}^{\text{III}}\text{Cl}_6$ ($\text{M}^{\text{I}} = \text{Li, Na, Ag}$; $\text{M}^{\text{III}} = \text{In, Y}$). *Zeitschrift für Anorg. und Allg. Chemie* **1992**, *613* (7), 26–30. <https://doi.org/10.1002/zaac.19926130104>.
116. Li, X.; Liang, J.; Luo, J.; Norouzi Banis, M.; Wang, C.; Li, W.; Deng, S.; Yu, C.; Zhao, F.; Hu, Y.; Sham, T.-K.; Zhang, L.; Zhao, S.; Lu, S.; Huang, H.; Li, R.; Adair, K. R.; Sun, X. Air-Stable Li_3InCl_6 Electrolyte with High Voltage Compatibility for all-Solid-State Batteries. *Energ. Environ. Sci.* **2019**, *12* (9), 2665–2671. <https://doi.org/10.1039/C9EE02311A>.
117. Li, X.; Liang, J.; Chen, N.; Luo, J.; Adair, K. R.; Wang, C.; Banis, M. N.; Sham, T.; Zhang, L.; Zhao, S.; Lu, S.; Huang, H.; Li, R.; Sun, X. Water-Mediated Synthesis of a Superionic Halide Solid Electrolyte. *Angew. Chem. Int. Ed.* **2019**, *58* (46), 16427–16432. <https://doi.org/10.1002/anie.201909805>.
118. Schlem, R.; Berges, T.; Li, C.; Kraft, M. A.; Minafra, N.; Zeier, W. G. Lattice Dynamical Approach for Finding the Lithium Superionic Conductor Li_3ErI_6 . *ACS Appl. Energy Mater.* **2020**, *3* (4), 3684–3691. <https://doi.org/10.1021/acsaem.0c00147>.
119. Zhao, Y.; Daemen, L. L. Superionic Conductivity in Lithium-Rich Anti-Perovskites. *J. Am. Chem. Soc.* **2012**, *134* (36), 15042–15047. <https://doi.org/10.1021/ja305709z>.
120. Li, M.; Wang, C.; Chen, Z.; Xu, K.; Lu, J. New Concepts in Electrolytes. *Chem. Rev.* **2020**. <https://doi.org/10.1021/acs.chemrev.9b00531>.
121. Deng, Z.; Radhakrishnan, B.; Ong, S. P. Rational Composition Optimization of the Lithium-Rich $\text{Li}_3\text{OCl}_{1-x}\text{Br}_x$ Anti-Perovskite Superionic Conductors. *Chem. Mater.* **2015**, *27* (10), 3749–3755. <https://doi.org/10.1021/acs.chemmater.5b00988>.
122. Braga, M. H.; Ferreira, J. A.; Stockhausen, V.; Oliveira, J. E.; El-Azab, A. Novel Li_3ClO Based Glasses with Superionic Properties for Lithium Batteries. *J. Mater. Chem. A* **2014**, *2* (15), 5470–5480. <https://doi.org/10.1039/C3TA15087A>.
123. Mouta, R.; Melo, M.Á. B.; Diniz, E. M.; Paschoal, C. W. A. Concentration of Charge Carriers, Migration, and Stability in Li_3OCl Solid Electrolytes. *Chem. Mater.* **2014**, *26* (24), 7137–7144. <https://doi.org/10.1021/cm503717e>.

124. Stegmaier, S.; Voss, J.; Reuter, K.; Luntz, A. C. Li⁺ Defects in a Solid-State Li Ion Battery: Theoretical Insights with a Li₃OCl Electrolyte. *Chem. Mater.* **2017**, *29* (10), 4330–4340. <https://doi.org/10.1021/acs.chemmater.7b00659>.
125. Emly, A.; Kioupakis, E.; Van der Ven, A. Phase Stability and Transport Mechanisms in Antiperovskite Li₃OCl and Li₃OBr Superionic Conductors. *Chem. Mater.* **2013**, *25* (23), 4663–4670. <https://doi.org/10.1021/cm4016222>.
126. Dawson, J. A.; Attari, T. S.; Chen, H.; Emge, S. P.; Johnston, K. E.; Islam, M. S. Elucidating Lithium-Ion and Proton Dynamics in Anti-Perovskite Solid Electrolytes. *Energ. Environ. Sci.* **2018**, *11* (10), 2993–3002. <https://doi.org/10.1039/C8EE00779A>.
127. Hanghofer, I.; Redhammer, G. J.; Rohde, S.; Hanzu, I.; Senyshyn, A.; Wilkening, H. M. R.; Rettenwander, D. Untangling the Structure and Dynamics of Lithium-Rich Anti-Perovskites Envisaged as Solid Electrolytes for Batteries. *Chem. Mater.* **2018**, *30* (22), 8134–8144. <https://doi.org/10.1021/acs.chemmater.8b02568>.
128. Wang, F.; Evans, H. A.; Kim, K.; Yin, L.; Li, Y.; Tsai, P.-C.; Liu, J.; Lapidus, S. H.; Brown, C. M.; Siegel, D. J.; Chiang, Y.-M. Dynamics of Hydroxyl Anions Promotes Lithium Ion Conduction in Antiperovskite Li₂OHCl. *Chem. Mater.* **2020**, *32* (19), 8481–8491. <https://doi.org/10.1021/acs.chemmater.0c02602>.
129. Hood, Z. D.; Wang, H.; Samuthira Pandian, A.; Keum, J. K.; Liang, C. Li₂OHCl Crystalline Electrolyte for Stable Metallic Lithium Anodes. *J. Am. Chem. Soc.* **2016**, *138* (6), 1768–1771. <https://doi.org/10.1021/jacs.5b11851>.
130. Yamamoto, T.; Shiba, H.; Mitsukuchi, N.; Sugumar, M. K.; Motoyama, M.; Iriyama, Y. Synthesis of the Metastable Cubic Phase of Li₂OHCl by a Mechanochemical Method. *Inorg. Chem.* **2020**, *59* (17), 11901–11904. <https://doi.org/10.1021/acs.inorgchem.0c01631>.
131. Koedtrud, A.; Patino, M. A.; Ichikawa, N.; Kan, D.; Shimakawa, Y. Crystal Structures and Ionic Conductivity in Li₂OHX (X = Cl, Br) Antiperovskites. *J. Solid State Chem.* **2020**, *286*, 121263. <https://doi.org/10.1016/j.jssc.2020.121263>.
132. Song, A.-Y.; Xiao, Y.; Turcheniuk, K.; Upadhy, P.; Ramanujapuram, A.; Benson, J.; Magasinski, A.; Olguin, M.; Meda, L.; Borodin, O.; Yushin, G. Protons Enhance Conductivities in Lithium Halide Hydroxide/Lithium Oxyhalide Solid Electrolytes by Forming Rotating Hydroxy Groups. *Adv. Energy Mater.* **2018**, *8* (3), 1700971. <https://doi.org/10.1002/aenm.201700971>.
133. Song, A.; Turcheniuk, K.; Leisen, J.; Xiao, Y.; Meda, L.; Borodin, O.; Yushin, G. Understanding Li-Ion Dynamics in Lithium Hydroxychloride (Li₂OHCl) Solid State Electrolyte Via Addressing the Role of Protons. *Adv. Energy Mater.* **2020**, *10* (8), 1903480. <https://doi.org/10.1002/aenm.201903480>.
134. Deng, Z.; Ou, M.; Wan, J.; Li, S.; Li, Y.; Zhang, Y.; Deng, Z.; Xu, J.; Qiu, Y.; Liu, Y.; Fang, C.; Li, Q.; Huang, L.; Zhu, J.; Han, S.; Han, J.; Zhao, Y. Local Structural Changes and Inductive Effects on Ion Conduction in Antiperovskite Solid Electrolytes. *Chem. Mater.* **2020**, *32* (20), 8827–8835. <https://doi.org/10.1021/acs.chemmater.0c02173>.
135. Effat, M. B.; Liu, J.; Lu, Z.; Wan, T. H.; Curcio, A.; Ciucci, F. Stability, Elastic Properties, and the Li Transport Mechanism of the Protonated and Fluorinated Antiperovskite Lithium Conductors. *ACS Appl. Mater. Interfaces* **2020**, *12* (49), 55011–55022. <https://doi.org/10.1021/acsami.0c17975>.
136. Li, Y.; Zhou, W.; Xin, S.; Li, S.; Zhu, J.; Lü, X.; Cui, Z.; Jia, Q.; Zhou, J.; Zhao, Y.; Goodenough, J. B. Fluorine-Doped Antiperovskite Electrolyte for all-Solid-State Lithium-Ion Batteries. *Angew. Chem. Int. Ed.* **2016**, *55* (34), 9965–9968. <https://doi.org/10.1002/anie.201604554>.
137. Kotobuki, M.; Munakata, H.; Kanamura, K.; Sato, Y.; Yoshida, T. Compatibility of Li₇La₃Zr₂O₁₂ Solid Electrolyte to All-Solid-State Battery Using Li Metal Anode. *J. Electrochem. Soc.* **2010**, *157* (10), A1076. <https://doi.org/10.1149/1.3474232>.
138. Rao, R. P.; Adams, S. Studies of Lithium Argyrodite Solid Electrolytes for all-Solid-State Batteries. *Phys. status solidi* **2011**, *208* (8), 1804–1807. <https://doi.org/10.1002/pssa.201001117>.
139. Kim, S.; Hirayama, M.; Taminato, S.; Kanno, R. Epitaxial Growth and Lithium Ion Conductivity of Lithium-Oxide Garnet for an all Solid-State Battery Electrolyte. *Dalton Trans.* **2013**, *42* (36), 13112–13117. <https://doi.org/10.1039/C3DT51795K>.
140. Kalita, D. J.; Lee, S. H.; Lee, K. S.; Ko, D. H.; Yoon, Y. S. Ionic Conductivity Properties of Amorphous Li–La–Zr–O Solid Electrolyte for Thin Film Batteries. *Solid State Ion.* **2012**, *229*, 14–19. <https://doi.org/10.1016/j.ssi.2012.09.011>.
141. Xie, J.; Imanishi, N.; Zhang, T.; Hirano, A.; Takeda, Y.; Yamamoto, O. Li-Ion Transport in all-Solid-State Lithium Batteries with LiCoO₂ Using NASICON-Type Glass Ceramic Electrolytes. *J. Power Sources* **2009**, *189* (1), 365–370. <https://doi.org/10.1016/j.jpowsour.2008.08.015>.
142. Abouali, S.; Yim, C.-H.; Merati, A.; Abu-Lebdeh, Y.; Thangadurai, V. Garnet-Based Solid-State Li Batteries: From Materials Design to Battery Architecture. *ACS Energy Lett.* **2021**, 1920–1941. <https://doi.org/10.1021/acsenenergylett.1c00401>.
143. Finsterbusch, M.; Danner, T.; Tsai, C.-L.; Uhlenbruck, S.; Latz, A.; Guillon, O. High Capacity Garnet-Based all-Solid-State Lithium Batteries: Fabrication and 3D-Microstructure Resolved Modeling. *ACS Appl. Mater. Interfaces* **2018**, *10* (26), 22329–22339. <https://doi.org/10.1021/acsami.8b06705>.
144. Huo, H.; Chen, Y.; Zhao, N.; Lin, X.; Luo, J.; Yang, X.; Liu, Y.; Guo, X.; Sun, X. In-Situ Formed Li₂CO₃-Free Garnet/Li Interface by Rapid Acid Treatment for Dendrite-Free Solid-State Batteries. *Nano Energy* **2019**, *61*, 119–125. <https://doi.org/10.1016/j.nanoen.2019.04.058>.
145. Zhou, Q.; Xu, B.; Chien, P.-H.; Li, Y.; Huang, B.; Wu, N.; Xu, H.; Grundish, N. S.; Hu, Y.-Y.; Goodenough, J. B. NASICON Li_{1.2}Mg_{0.1}Zr_{1.9}(PO₄)₃ Solid Electrolyte for an all-Solid-State Li-Metal Battery. *Small Methods* **2020**, *4* (12), 2000764. <https://doi.org/10.1002/smtid.202000764>.
146. Yang, J.; Huang, B.; Yin, J.; Yao, X.; Peng, G.; Zhou, J.; Xu, X. Structure Integrity Endowed by a Ti-Containing Surface Layer towards Ultrastable LiNi_{0.8}Co_{0.15}Al_{0.05}O₂ for all-Solid-State Lithium Batteries. *J. Electrochem. Soc.* **2016**, *163* (8), A1530–A1534. <https://doi.org/10.1149/2.0331608jes>.
147. Yao, X.; Huang, N.; Han, F.; Zhang, Q.; Wan, H.; Mwirerwa, J. P.; Wang, C.; Xu, X. High-Performance All-Solid-State Lithium–Sulfur Batteries Enabled by Amorphous Sulfur-Coated Reduced Graphene Oxide Cathodes. *Adv. Energy Mater.* **2017**, *7* (17), 1602923. <https://doi.org/10.1002/aenm.201602923>.
148. Wang, C.; Liang, J.; Jiang, M.; Li, X.; Mukherjee, S.; Adair, K.; Zheng, M.; Zhao, Y.; Zhao, F.; Zhang, S.; Li, R.; Huang, H.; Zhao, S.; Zhang, L.; Lu, S.; Singh, C. V.; Sun, X. Interface-Assisted In-Situ Growth of Halide Electrolytes Eliminating Interfacial Challenges of all-Inorganic Solid-State Batteries. *Nano Energy* **2020**, *76*, 105015. <https://doi.org/10.1016/j.nanoen.2020.105015>.

4.20 High pressure studies of transition metal oxides

Masaki Azuma^a, Ikuya Yamada^b, Kazunari Yamaura^c, Alexei A. Belik^c, Takafumi Yamamoto^a, and Masayuki Fukuda^c,

^aLaboratory for Materials and Structures, Tokyo Institute of Technology, Yokohama, Japan; ^bDepartment of Materials Science, Graduate School of Engineering, Osaka Metropolitan University, Sakai, Osaka, Japan; and ^cInternational Center for Materials Nanoarchitectonics (WPI-MANA), National Institute for Materials Science, Tsukuba, Ibaraki, Japan

© 2023 Elsevier Ltd. All rights reserved.

4.20.1	Introduction	681
4.20.2	HPHT synthesis of 3d-transition metal oxides and investigations at HT conditions	684
4.20.2.1	Sc oxides	684
4.20.2.2	Ti oxides	684
4.20.2.3	V oxides	685
4.20.2.4	Cr oxides	686
4.20.2.5	Mn oxides	687
4.20.2.6	Fe oxides	688
4.20.2.7	Co oxides	690
4.20.2.7.1	Co ⁴⁺ perovskites	690
4.20.2.7.2	Co ³⁺ perovskites	691
4.20.2.7.3	RP phases	691
4.20.2.7.4	Magnetoplumbite-related phases	691
4.20.2.8	Ni oxides	691
4.20.2.9	Cu oxides	693
4.20.3	HPHT synthesis of 4d, 5d transition metal oxides	695
4.20.4	Perovskite oxides with A-site ordering	698
4.20.4.1	A-site-ordered quadruple perovskite	698
4.20.4.1.1	Syntheses and crystal structures	698
4.20.4.1.2	Valence states	700
4.20.4.1.3	Physical properties and functions	701
4.20.4.1.4	Electrocatalytic properties	704
4.20.4.2	A-site columnar-ordered quadruple perovskites	705
4.20.5	Mixed-anion oxides	707
4.20.5.1	Overview	707
4.20.5.2	Oxyhalides	708
4.20.5.3	Oxyhydrides	709
4.20.5.4	Oxynitrides	710
References		710

Abstract

Transition metal oxides exhibit a wide variety of functions—such as metallic conductivity, superconductivity, magnetism, magnetoresistance, ferroelectricity, piezoelectricity and even catalytic activity—depending on the composition and structure. High pressure stabilizes dense structures with large coordination numbers such as perovskites, and also stabilizes cations with unusually high valences, such as Fe⁴⁺ and Ni³⁺. Because of these clear trends, high-pressure syntheses of functional transition metal oxides are intensively performed. Transition metal oxides prepared by high-pressure synthesis and investigations of structural and property changes under pressure will be reviewed.

4.20.1 Introduction

The Earth is a huge high pressure (HP) and high temperature (HT) vessel.¹ Geophysicists have long been driven to develop HP technology as a means to look into the interior. A silicate perovskite, Mg_{1-x}Fe_xSiO₃ ($x \geq 0.8$), is likely to be the most abundant single phase of the Earth.² The perovskite phase of MgSiO₃ does not form at atmospheric pressure because both Mg²⁺ and Si⁴⁺ ions are far too small to meet the qualifications for the perfect perovskite ABX₃: $r_A:r_B:r_X = 1:0.41:1$, where r_A , r_B and r_X respectively stand for the ionic radii of the A and B cations and the X anion.³

The tolerance factor t given by

$$t = \frac{r_A + r_X}{\sqrt{2}(r_B + r_X)}$$

measures the stability and distortion of perovskite structure. Polar tetragonal PbTiO_3 -type structure with a space group $P4mm$ is obtained for $t > 1$. Ideal cubic perovskite forms for $0.9 < t \leq 1$. GdFeO_3 -type orthorhombic distortion takes place for $t < 0.9$. The tilting of the BO_6 octahedron reducing the space at the A-site cation results in $\sqrt{2}a_p \times 2a_p \times \sqrt{2}a_p$ superstructure (a_p is the parameter of the cubic perovskite subcell) and space group $Pnma$ ($\sqrt{2}a_p \times \sqrt{2}a_p \times 2a_p$ for $Pbnm$). When t is smaller than 0.7–0.8, perovskite structure is no longer stable and transforms to ilmenite structure.

Pyroxene structure of MgSiO_3 where SiO_4 tetrahedra form corner-sharing chains transforms to ilmenite structure with octahedrally coordinated Mg and Si at 21 GPa and then to perovskite structure at 25 GPa.² MgSiO_3 quenched to ambient pressure (AP) and temperature exhibits a GdFeO_3 -type distorted perovskite structure in which the Mg ion is only 8-fold coordinated, not 12-fold coordinated as in the ideal perovskite structure. It is an accelerated contraction of the oxide ions that makes the Mg-Si-O combination tolerated under high pressure. In 2004 the “post-perovskite phase transition” that occurs at the conditions of the deepest part of the lower mantle was discovered by *in-situ* synchrotron X-ray diffraction study using diamond anvil cell and laser heating techniques.^{4,5} The post-perovskite phase has CaIrO_3 structure and is expected to explain the nature of the D'' layer that lies right above the core-mantle boundary.

HP techniques are utilized to develop new functional materials such as transition metal oxides. Kafalas and Longo determined the pressure necessary to obtain Ruddlesden-Popper (RP) phase $\text{Sr}_{n+1}\text{Ir}_n\text{O}_{3n+1}$.⁶ Only the $n = 1$ phase, Sr_2IrO_4 ($n = 1$, Fig. 1(b)), forms at AP. $\text{Sr}_3\text{Ir}_2\text{O}_7$ ($n = 2$, Fig. 1(c)) is obtained above 1 GPa. $\text{Sr}_4\text{Ir}_3\text{O}_{10}$, ($n = 3$, Fig. 1(d)) forms above 3.5 GPa and, finally, perovskite SrIrO_3 with $n = \infty$ (Fig. 1(a)) is stabilized above 4.5 GPa. Although the coordination number of Ir is constant at 6, that for Sr increases from 9 in Sr_2IrO_4 to 12 in SrIrO_3 .

Another remarkable tendency results from the electrostatic repulsion of cations of small sizes. Transition metal–oxygen octahedra are linked by face sharing in the 2H phase of BaMnO_3 , by corner sharing in the 3C phase of CaMnO_3 , and in a mixed way in 9R phases of BaRuO_3 and 4H phases of SrMnO_3 .^{7–9} As illustrated in Fig. 2, the sequential densification $2\text{H} \rightarrow 9\text{R} \rightarrow 4\text{H} \rightarrow 6\text{H} \rightarrow 3\text{C}$ (perovskite) results from a successive increase in the proportion of corner sharing. Because the distance between cations in a pair of corner-sharing octahedra is greater than the distance between those in face-sharing octahedra,

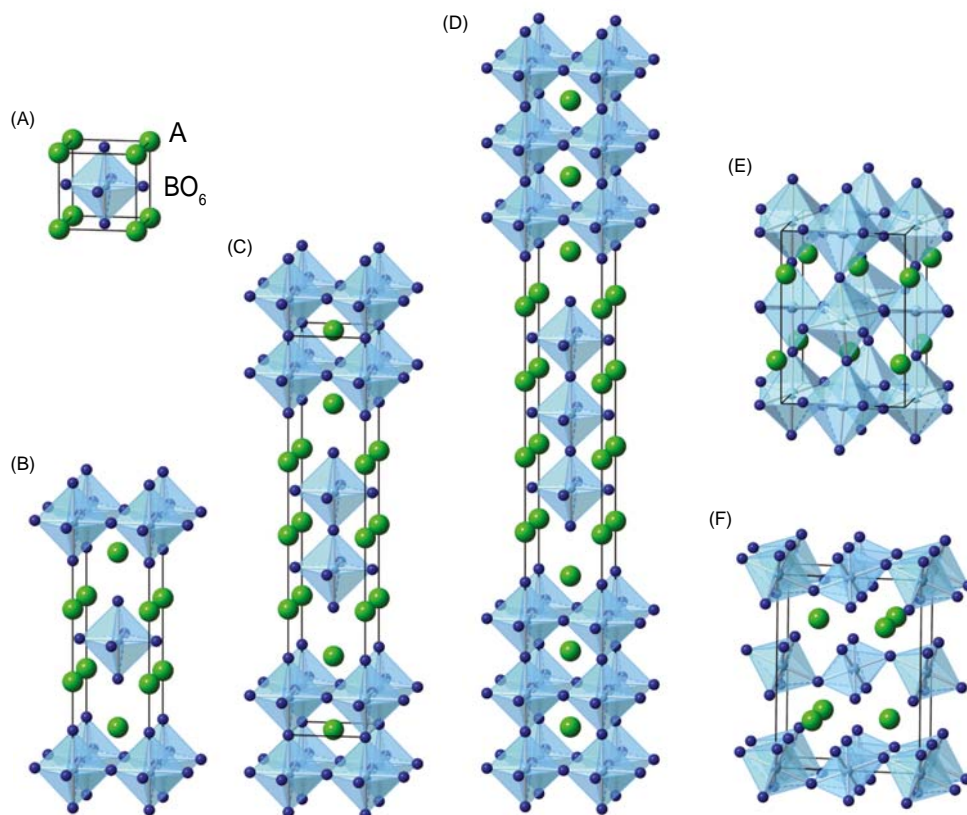


Fig. 1 Structures of Ruddlesden-Popper phases: (a) ABO_3 ($n = \infty$), (b) A_2BO_4 ($n = 1$), (c) $\text{A}_3\text{B}_2\text{O}_7$ ($n = 2$) and (d) $\text{A}_4\text{B}_3\text{O}_{10}$ ($n = 3$). (e) GdFeO_3 -type distorted perovskite and (f) Post perovskite structures.

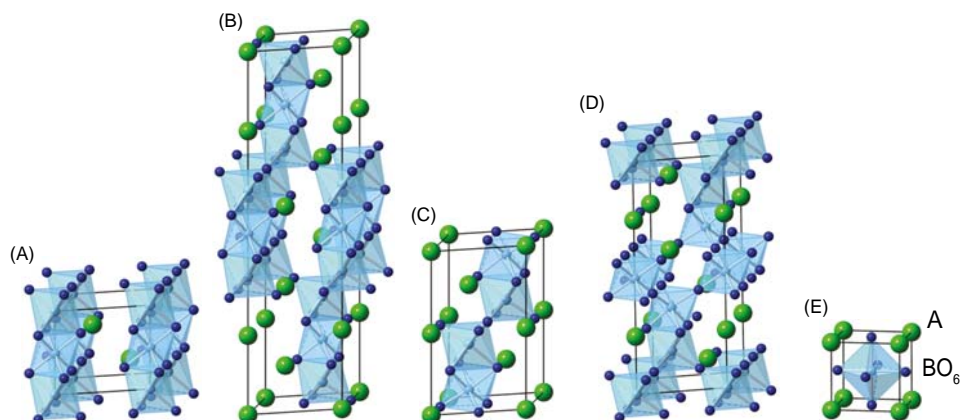


Fig. 2 Structures of hexagonal perovskites ABO_3 : (a) 2H, (b) 9R, (c) 4H, (d) 6H and (e) 3C phases.

the above transitions have been thought to imply that small cations are redistributed under pressure in order to reduce the electrostatic repulsion. No doubt this tendency is enhanced if the cations have high oxidation numbers.

The face-sharing octahedral dimer pair is found in ilmenite and $LiNbO_3$ structures as well. These are both derivatives of corundum structure, but the difference in the arrangement of two cations results in non-polar (ilmenite) and polar ($LiNbO_3$) structures. Pressure-induced transformation of ilmenite (Fig. 3a) to $LiNbO_3$ (Fig. 3b) structure is observed typically for $ZnSnO_3$.¹⁰ $LiNbO_3$ phase is recovered at AP as a result of the transformation from a perovskite phase stabilized at a high pressure as well.¹¹ The ordering of two cations in $LiNbO_3$ structure results in $A_2BB'O_6$ Ni_3TeO_6 phase shown in Fig. 3c, which attracts keen interest as a polar magnet.¹² Cation orderings in the perovskite structure are also intensively investigated. Ferromagnetism or ferrimagnetism are observed in many B-site ordered double perovskite oxides $A_2BB'O_6$ with NaCl-type ordering of magnetic cations. Most of these have either a $\sqrt{2}a_p \times \sqrt{2}a_p \times 2a_p$ unit cell with $P2_1/n$ space group as shown in Fig. 3d or a $2a_p \times 2a_p \times 2a_p$ unit cell with $Fm-3m$ space group, but other structures are also present.¹³ Layered ordering of B-site cations has been observed only for Cu^{2+}/Sn^{4+} , Cu^{2+}/Zr^{4+} and $Cu^{2+}/(Cu^{2+}_{0.5}Mo^{6+}_{0.5})$.¹⁴⁻¹⁶ The cation orderings in the A-site of perovskite structure result in A-site-ordered quadruple perovskite and A-site columnar ordered perovskite as discussed in Section 4.20.4.

Transition metal oxides exhibit a wide variety of functions—such as metallic conductivity, superconductivity, magnetism, magnetoresistance, ferroelectricity, piezoelectricity, and even catalytic activity—depending on their composition and structure. High pressure stabilizes dense structures with large coordination numbers, such as perovskites, as described above. In addition, unusually high valence cations, such as Fe^{4+} and Ni^{3+} , are also stabilized. Because of these clear trends, HP syntheses of functional transition metal oxides are intensively performed. Belt- and cubic anvil-type HP apparatuses are generally used for the syntheses at several gigapascals. A Kawai-type double-stage multi-anvil device is used for the syntheses at pressures higher than 10 GPa. Starting precursors are charged in capsules made of metals typically gold or platinum. Oxidizing agents such as $KClO_3$, $KClO_4$, $NaClO_3$ and Ag_2O which release O_2 at elevated temperatures are added when high-oxygen pressure is needed. The capsules are first compressed and then heated for several tens of minutes. This is followed by quenching to room temperature and releasing the pressure.

Diamond anvil cells (DACs) are used for measuring various physical properties (resistivity, dielectric constant, specific heat and so on) and for spectroscopies. The combination of DACs and synchrotron X-rays is a powerful tool for the observation of structural transitions at HP. Precise structural determination at HP is performed by neutron diffraction using a Paris-Edinburgh cell. The details of HP devices are found elsewhere.¹⁷

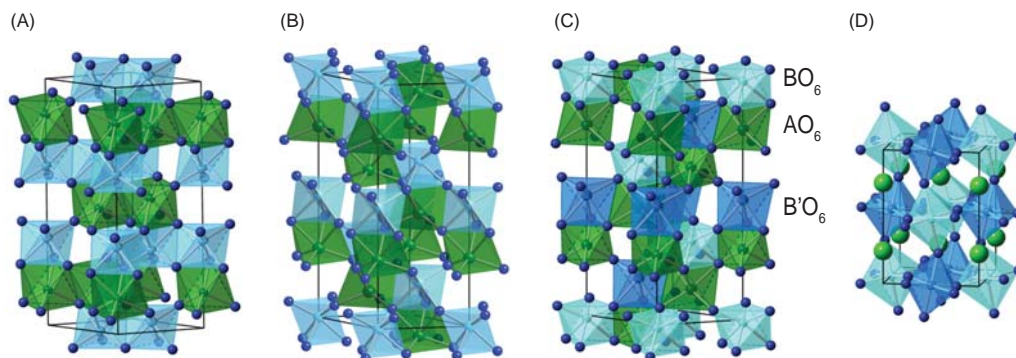


Fig. 3 Structures of (a) Ilmenite, (b) $LiNbO_3$, (c) Ni_3TeO_6 and (d) ordered double perovskite $A_2BB'O_6$.

In this review we survey transition metal oxides prepared by HP syntheses and investigations of structural and property changes under pressure. These are categorized by the transition elements (Sc, Ti, V, Cr, Mn, Fe, Co, Ni, Cu and 4d and 5d elements). A-site-ordered quadruple perovskites, A-site columnar ordered perovskites and mixed-anion compounds which attract keen interest because of their various functions are also summarized. Some compounds appear in multiple subsections.

4.20.2 HPHT synthesis of 3d-transition metal oxides and investigations at HT conditions

4.20.2.1 Sc oxides

Sc-containing compounds are summarized in **Table 1**. The Sc^{3+} cation ($r_{\text{VI}} = 0.745 \text{ \AA}$)³ is one of the largest of the 3d–5d transition-metal trivalent cations but is small enough for the majority of $R\text{ScO}_3$ perovskites (with the GdFeO_3 -type $Pnma$ structure) to form at AP for $R = \text{La-Ho}$.¹⁹ Its size becomes too large for smaller R^{3+} cations ($R = \text{Er-Lu}$), resulting in too small tolerance factors, which destabilize the perovskite structure at AP. The synthesis of $R\text{ScO}_3$ with $R = \text{Er-Lu}$ appeared to be challenging even at HP. For example, the synthesis of $R\text{ScO}_3$ with $R = \text{Er, Tm and Y}$ was reported at 2 GPa and 1270 K (and no perovskites formed at 3 GPa for $R = \text{Yb and Lu}$).¹⁸ On the other hand, no perovskite phases were formed in another work at 6 GPa and 1470 K for $R = \text{Tm, Yb and Lu}$, and only about 50% of perovskite phases were found for $R = \text{Er and Y}$.¹⁹ It was possible to synthesize YbScO_3 at 6.5 GPa and 1870 K, but LuScO_3 synthesized at these conditions still contained about 10% of monoclinic $\beta\text{-Lu}_2\text{O}_3$ -type impurity (unpublished results). BiScO_3 can be prepared only at HP (6 GPa).²⁰ It crystallizes in $C2/c$ space group with $a = a_p + 2b_p + c_p$, $b = -a_p + c_p$, $c = a_p - 2b_p + c_p$ unit cell, where a_p , b_p and c_p are the lattice constants of a simple perovskite structure (isostructural with BiMnO_3).^{21,22} Antiparallel displacement of Bi^{3+} ions in the b direction owing to the ordering of stereochemical $6s^2$ lone pairs suggests antiferroelectric nature, but it has not been experimentally confirmed. At about 3.5 GPa structural phase transition to a GdFeO_3 -type modification was observed at room temperature (RT).²³ A new modification of BiScO_3 can be obtained by heating the HP phase at AP above 750 K.^{21,24}

The Sc^{3+} cation ($r_{\text{VIII}} = 0.870 \text{ \AA}$)³ is the smallest of the R^{3+} cations, and tolerance factors of ScBO_3 are too small. Therefore, all ScBO_3 perovskites can be prepared only at HP. As the difference in sizes of Sc^{3+} and B^{n+} cations is small, ScBO_3 perovskites are prone to anti-site disorder and shifts in their stoichiometry to $(\text{Sc}_{1-x}\text{B}_x)\text{BO}_3$.^{35,38} $\text{Sc}_2\text{NiMnO}_6$ can be prepared with the ideal rock-salt B-site ordering³⁷ or with significant disordering, $(\text{Sc}_{0.94}\text{Mn}_{0.06}^{2+})(\text{Mn}_{0.41}\text{Mn}_{0.09}^{3+})(\text{Mn}_{0.15}\text{Ni}_{0.35}^{2+})\text{O}_3$.³⁸ The perovskite modification of ScFeO_3 is stable only at HPHT conditions³³; at AP and RT it recovers in the LiNbO_3 -type modification. ScTiO_3 and ScNiO_3 have not been prepared yet.

4.20.2.2 Ti oxides

Ti-containing compounds are summarized in **Table 2**. B-site Ti perovskite oxides, BaTiO_3 and PbTiO_3 , are of great use as constituents of ferroelectric and piezoelectric materials. The former was found by single crystal X-ray diffraction with a DAC to exhibit a transition from a polar tetragonal structure with space group $P4mm$ to the cubic one with $Pm-3m$ at 2.1 GPa.⁵⁵ Synchrotron X-

Table 1 Sc oxides obtained by HPHT synthesis.

Compounds	Structure type	$P(\text{GPa})$	References
$R\text{ScO}_3$, $R = \text{Er-Lu}$	Pv (GdFeO_3)	2–6.5	18,19
BiScO_3	Pv ($C2/c$; PbZrO_3 above 750 K)	6	20–24
ScAlO_3	Pv (GdFeO_3)	3.5–12	25,26
ScVO_3	Pv (GdFeO_3 , $P-1^a$ below 90 K)	8	27
ScCrO_3	Pv (GdFeO_3)	4.5–6	28–30
ScMnO_3	Pv ($P2_1/n$)	12.5	31,32
ScFeO_3	LN	15	33,34
$(\text{Sc}_{1-x}\text{Co}_x)\text{CoO}_3$	Pv (GdFeO_3)	6	35
ScRhO_3	Pv ($P2_1/n$, $Z = 8$)	6	36
$\text{Sc}_2\text{NiMnO}_6$	Pv ($P2_1/n$)	6	37
$(\text{Sc}_{0.94}\text{Mn}_{0.06})\text{Mn}_{0.65}\text{Ni}_{0.35}\text{O}_6$	Pv ($P-1^b$)	6–7	38
$(\text{Ti}_{1-x}\text{Sc}_x)\text{ScO}_3$	LN	6	39

Pv: perovskite. Symmetries are given for the perovskite-type modifications. $Pnma$ (GdFeO_3) and $P-1^a$ symmetries have $\sqrt{2}a_p \times 2a_p \times \sqrt{2}a_p$ superstructure (a_p is the parameter of the cubic perovskite subcell); $C2/c$ has $a_p + 2b_p + c_p$, $-a_p + c_p$, $a_p - 2b_p + c_p$ superstructure; $P2_1/n$ and $P-1^b$ have $\sqrt{2}a_p \times \sqrt{2}a_p \times 2a_p$ superstructure; $P2_1/n$ ($Z = 8$) has $2a_p \times 2a_p \times 2a_p$ superstructure. LN: lithium niobate.

Table 2 Ti oxides obtained by HPHT synthesis (>1 GPa).

Compounds	Structure type	P(GPa)	References
Eu _{0.2} Ba _{0.8} TiO ₃	Pv (PbTiO ₃)	4	40
Eu _{1-x} Ba _x TiO ₃ ($x \geq 0.3$)	Pv (cubic)	4	40
Eu _{1-x} K _x TiO ₃	Pv (cubic)	4	40
La _{0.7} Na _{0.3} TiO ₃	Pv (cubic)	4	40
La _{0.7} K _{0.3} TiO ₃	Pv (cubic)	4	40
LaTi _{0.75} Mg _{0.25} O ₃	Pv	4	41
LaTi _{0.5} Mg _{0.5} O ₃	Pv	4	41
Bi _{0.5} Ag _{0.5} TiO ₃	Pv (<i>lbam</i>)	14	42
Ca ₂ NdAgTi ₄ O ₁₂	Pv (GdFeO ₃)	14	43
Nd _{0.5} Ag _{0.5} TiO ₃	Pv (A-site order)	14	43
K _{2/3} Th _{1/3} TiO ₃	LN	7	44
CaFeTi ₂ O ₆	Pv	12–15	45
Ca ₂ TiSiO ₆	Pv	14	46
Bi ₂ ZnTiO ₆	Pv (PbTiO ₃)	6	47,48
CaFe ₃ Ti ₄ O ₁₂	A-QPv	15	49
MgTiSi ₂ O ₇	weberite	15	50
MnTiO ₃	LN	7	51
ZnTiO ₃	LN	7.5	52
FeTiO ₃	LN	18	53
HgTiO ₃	LN	6.5	54

Pv: perovskite. Symmetries are given for the perovskite-type modifications. *lbam* symmetry has $\sqrt{2}a_p \times \sqrt{2}a_p \times 2a_p$ superstructure; *Pnma* (GdFeO₃) has $\sqrt{2}a_p \times 2a_p \times \sqrt{2}a_p$ superstructure. A-QPv: A-site-ordered quadruple perovskite. LN: lithium niobate.

ray powder diffraction study revealed the presence of polar monoclinic phases between the AP tetragonal *P4mm* and HP non-polar *R-3c* phases of PbTiO₃.⁵⁶

Eu_{1-x}Ba_xTiO₃ ($0.6 \leq x \leq 0.8$), Eu_{1-x}K_xTiO₃ ($x = 0.2$ and 0.32), La_{0.7}Na_{0.3}TiO₃ and La_{0.7}K_{0.3}TiO₃ were stabilized by HP synthesis at 4.0 GPa and 1173 K. Mössbauer spectroscopy revealed that the fraction of Eu²⁺/Eu³⁺ changed depending on the amount of Ba and K substitution to preserve Ti⁴⁺. On the other hand, EPR measurements suggested the presence of Ti³⁺ as well as A-site cation vacancies in La_{0.7}Na_{0.3}TiO₃ and La_{0.7}K_{0.3}TiO₃. LaTi_{0.75}Mg_{0.25}O₃ and LaTi_{0.5}Mg_{0.5}O₃ were also prepared at 4 GPa and 1273 K and the presence of Ti³⁺ was confirmed by EPR.⁴¹

Bi_{0.5}Ag_{0.5}TiO₃ and Ca₂NdAgTi₄O₁₂ with random distributions of Bi³⁺/Ag⁺ and Ca²⁺/Nd³⁺/Ag⁺ were obtained by HP synthesis at 14 GPa and 1273 K. On the other hand, partial layered ordering of Nd³⁺ and Ag⁺ was observed in Nd_{0.5}Ag_{0.5}TiO₃ synthesized under those conditions.^{42,43} Bi₂ZnTiO₆ has a PbTiO₃-type polar tetragonal structure with a pronounced distortion of $c/a = 1.21$.^{47,48}

Partial layered ordering of K⁺ and Th⁴⁺ has also been observed in K_{2/3}Th_{1/3}TiO₃, while the ordering pattern of Ca²⁺/Fe²⁺ is columnar in CaFeTi₂O₆ as discussed in Section 4.20.4.2.^{44,45} 1:3 ordering of A-site cations leads to the formation of a quadruple perovskite CaFe₃Ti₄O₁₂.⁴⁹

Ilmenite-type MnTiO₃ and ZnTiO₃ were found to transform into LiNbO₃ type after HPHT treatments at 7 GPa and 973 K and 7.5 GPa and 1273 K, respectively.^{51,52} Coexistence of ferroelectricity and weak ferromagnetism was observed in LiNbO₃-type FeTiO₃ stabilized at 18 GPa.⁵³ HgTiO₃ was reported to adopt BiFeO₃-type polar rhombohedral structure.⁵⁴ A second-order transition to cubic structure was observed around 2 GPa.⁵⁷

4.20.2.3 V oxides

V-containing compounds are summarized in Table 3. Vanadium perovskite oxides *RVO*₃ (*R*: rare-earth elements) with trivalent vanadium ions attract much attention because of the orbital ordering (OO) and orbital-flipping transitions. Stabilization of C-type OO over G-type under pressure was observed for YVO₃ and TbVO₃ by synchrotron X-ray single crystal diffraction and the pressure-temperature phase diagrams were constructed.⁷⁸ On the other hand, G-type OO was found to be robust in DyVO₃.⁷⁹ ScVO₃ is stabilized by HP synthesis.²⁷

SrVO₃ and CaVO₃ with V⁴⁺ are also extensively studied. HP synthesis expands the variety of A²⁺V⁴⁺O₃ perovskites to BaVO₃ (cubic), PbVO₃ (tetragonal *P4mm*, isotypic with PbTiO₃) and CdVO₃ (GeFeO₃-type).^{58–61} Cd_{0.8}Na_{0.2}VO₃ as well as CdVO₃ was found to be metallic.⁶¹

PbVO₃ has a large tetragonal distortion ($c/a = 1.23$) compared with PbTiO₃ (1.064) owing to the d_{xy} orbital ordering. At 3 GPa it exhibits a transition to a paraelectric cubic structure accompanied by an insulator-to-metal transition and by 10.6% volume reduction.⁸⁰ Bi³⁺ substitution for Pb²⁺ introduces an additional electron in d_{yz} and d_{zx} orbitals (electron doping) leading to shrinkage of the *c*-axis and enables the transition to the cubic phase on heating at AP.⁸¹ The transition is of first order and the low-temperature

Table 3 V oxides obtained by HPHT synthesis (> 1 GPa).

Compounds	Structure type	P(GPa)	References
ScVO ₃	Pv (GdFeO ₃)	8	27
BaVO ₃	Pv (cubic)	12	58
PbVO ₃	Pv (PbTiO ₃)	6	59,60
CdVO ₃	Pv (GdFeO ₃)	6	61
Cd _{0.8} Na _{0.2} VO ₃	Pv (GdFeO ₃)	6	61
InVO ₃	LN	9	62
Na _{1/2} Bi _{1/2} VO ₃	Pv (PbTiO ₃)	6	63
K _{1/2} Bi _{1/2} VO ₃	Pv (PbTiO ₃)	6	63
PbFe _{1/2} V _{1/2} O ₃	Pv (PbTiO ₃)	7	64
CoVO ₃	Ilmenite	6.5	65
NiVO ₃	Ilmenite	6.5	66
CuVO ₃	Ilmenite	6–6.5	65
MnVO ₃	Ilmenite	–4.5	67
	Pv (GdFeO ₃)	4.5–	67
Bi ₂ ZnVO ₆	Pv (PbTiO ₃)	8	68
BiVO ₃	Pv (cubic)	25	69
La ₂ LivO ₆	B-DPv (<i>Fm-3m</i>)	6	70
Mn ₂ VSbO ₆	B-DPv (<i>P2₁/n</i>)	6	71
ACu ₃ V ₄ O ₁₂ (A = Na, Ca, Y)	A-QPv	9	72
CrVO ₄	Rutile	6	73
FeVO ₄	Wolframite	6	73
MV ₂ O ₆ (M = Ni, Mg, Co, Zn, Cd)	Columbite	5–8	74
Mn ₂ V ₂ O ₇	Pyrochlore	7	75
Cd ₂ V ₂ O ₇	Pyrochlore	8	76
Hg ₂ V ₂ O ₇	Pyrochlore	3–6.5	77

Pv: perovskite. Symmetries are given for the perovskite-type modifications. *Pnma* (GdFeO₃) symmetry has $\sqrt{2}a_p \times 2a_p \times \sqrt{2}a_p$ superstructure. B-DPv: B-site-ordered double perovskite. *Fm-3m* has $2a_p \times 2a_p \times 2a_p$ superstructure; *P2₁/n* has $\sqrt{2}a_p \times \sqrt{2}a_p \times 2a_p$ superstructure. A-QPv: A-site-ordered quadruple perovskite.

large-volume phase and the high-temperature small-volume phase coexist with the increase in the latter fraction on heating. Pb_{0.8}Bi_{0.2}VO₃ shows a negative thermal expansion (NTE) with a crystallographic volume contraction of 7.9%, the largest value reported so far for NTE materials. The electron doping can be achieved by F[−] substitution for O^{2−} and an NTE is observed in PbVO_{3−x}F_x as well.⁸² A half replacement of Pb²⁺ with Na⁺ (K⁺) reduces the *c/a* ratio of PbVO₃ to 1.085 (1.054) which is comparable to PbTiO₃. Bi₂ZnVO₆ also adopts PbTiO₃-type structure with a pronounced *c/a* ratio of 1.26.⁶⁸

Co²⁺V⁴⁺O₃, Ni²⁺V⁴⁺O₃ and Cu²⁺V⁴⁺O₃ adopt distorted ilmenite structures.^{65,66} Mn²⁺V⁴⁺O₃ prepared below 4.5 GPa also has the distorted ilmenite structure, while the sample prepared above 4.5 GPa has been found to be a GdFeO₃-type perovskite.⁶⁷

Fe³⁺ and V⁵⁺ are randomly arranged in PbFe_{1/2}V_{1/2}O₃ (Pb₂FeVO₆), while V³⁺ and Sb⁵⁺ in Mn₂VSbO₆ are ordered in a rock-salt manner.^{64,71} The most stable ambient-pressure form of CrVO₄ consists of octahedrally coordinated Cr³⁺ and tetrahedrally coordinated V⁵⁺. The crystal structure transforms to wolframite-type above 5 GPa, but the sample recovered to AP has been reported to have rutile-type structure.^{73,83} Wolframite-type FeVO₄ is obtained by HP synthesis.⁷³ HP syntheses of Mn²⁺V⁵⁺₂O₆ (M = Ni, Mg, Co, Zn, Mn and Cd) with columbite-type structure are reported.⁷⁴ Pyrochlore-type Mn₂V₂O₇, Cd₂V₂O₇ and Hg₂V₂O₇ are also reported^{75–77}.

4.20.2.4 Cr oxides

Cr-containing compounds are summarized in Table 4. Perovskite phases of SrCrO₃, CaCrO₃ and BiCrO₃ with M³⁺Cr³⁺O₃ charge distribution were reported to be obtained by HP synthesis in the 1960s.^{84,85,90} SrCrO₃ has a cubic perovskite structure, while CaCrO₃ has a GdFeO₃-type distortion. These are rare examples of antiferromagnetic (AFM) metal. BaCrO₃ synthesized at 3, 5, 9 and 22 GPa were respectively reported to be 5H, 4H, 6H and 3C perovskites.⁸⁶ BiCrO₃ has an antiferroelectric ordering of 6s² lone pair electrons of Bi³⁺ analogs to BiScO₃.⁹¹ PbCrO₃ was also reported in 1967, but it was recently found to be Pb²⁺_{0.5}Pb⁴⁺_{0.5}Cr³⁺O₃ with shortrange ordering of Pb²⁺ and Pb⁴⁺.^{88,89} A pressure-induced intermetallic charge transfer between Pb⁴⁺ and Cr³⁺ accompanied by a volume collapse of 9.8%¹⁰¹ leads to a metallic Pb²⁺Cr⁴⁺O₃ HP phase. The solid solution of these two compounds, Bi_{0.5}Pb_{0.5}CrO₃, has also been reported.⁹⁸

Sr₂CrO₄, Sr₃Cr₂O₇ and Sr₄Cr₃O₁₀ corresponding to *n* = 1, 2 and 3 of the RP phases, Sr_{*n*+1}Cr_{*n*}O_{3*n*+1}, as well as Ca₂CrO₄ have also been obtained by HP synthesis^{6,99,100}.

Table 4 Cr oxides obtained by HPHT synthesis (>1 GPa).

Compounds	Structure type	P(GPa)	References
SrCrO ₃	Pv (cubic)	12	84
CaCrO ₃	Pv (GdFeO ₃)	6.5	85
BaCrO ₃	5H	3	86,87
	4H	5	
	6H	9	
	3C	22	
PbCrO ₃	Pv	9	88,89
BiCrO ₃	Pv (C2/c)	6	90,91
TiCrO ₃	Pv (GdFeO ₃)	6	92
Bi ₂ FeCrO ₆	Pv (R3c)	6	93
Ba ₂ CrNbO ₆	B-DPv (<i>Fm-3m</i>)	3.5–5	94
Ba ₂ CrTaO ₆	B-DPv (<i>Fm-3m</i>)	8	95
Mn ₂ CrSbO ₆	B-DPv (<i>P2₁/n</i>)	8	96
Sr ₂ CrRuO ₆	Pv (cubic)	8	97
Bi _{0.5} Pb _{0.5} CrO ₃	Pv (GdFeO ₃)	7	98
Sr ₂ CrO ₄	K ₂ NiF ₄ (RP, <i>n</i> = 1)	6.5	6
Sr ₃ Cr ₂ O ₇	RP, <i>n</i> = 2	6.5	6
Sr ₄ Cr ₃ O ₁₀	RP, <i>n</i> = 3	4–6	99
Ca ₂ CrO ₄	K ₂ NiF ₄ (RP, <i>n</i> = 1)	5.5	100

Pv: perovskite. Symmetries are given for the perovskite-type modifications. *Pnma* (GdFeO₃) symmetry has $\sqrt{2}a_p \times 2a_p \times \sqrt{2}a_p$ superstructure (a_p is the parameter of the cubic perovskite subcell); *C2/c* has $a_p + 2b_p + c_p, -a_p + c_p, a_p - 2b_p + c_p$ superstructure; *R3c* has $\sqrt{2}a_p \times \sqrt{2}a_p \times 2\sqrt{3}a_p$ superstructure (hexagonal setting). 5H, 4H, 6H, 3C: Hexagonal perovskites. B-DPv: B-site-ordered double perovskite. *Fm-3m* has $2a_p \times 2a_p \times 2a_p$ superstructure; *P2₁/n* has $\sqrt{2}a_p \times \sqrt{2}a_p \times 2a_p$ superstructure.

4.20.25 Mn oxides

Mn-containing compounds are summarized in Table 5. B-site Mn³⁺ perovskite oxides have attracted much attention as multiferroic materials where electric polarization is induced by magnetic ordering and as parent compounds of colossal-magnetoresistance materials. The spin structure of RMnO₃ (*R* = rare earth) depends on the size of the *R* ion. TbMnO₃ and DyMnO₃ have a cycloidal magnetic ordering with a spin-induced electric polarization $\sim 0.1 \mu\text{C cm}^{-2}$ along the *c*-direction of GdFeO₃-type structure with space group *Pbnm*, while HoMnO₃ and YMnO₃ have E-type AFM ordering with an electric polarization along the *a*-direction. Change in the polar direction from *c*- to *a*-directions and enhancement of spin-induced electric polarization of TbMnO₃ owing to the spin structure change has been observed at 5.2 GPa.¹³¹ The spin structure change was confirmed by neutron diffraction study at HP on powder and single-crystalline samples.^{132,133} RMnO₃ with *R* = Ho-Lu and Y prepared at AP have a polar hexagonal structure, while a HPHT treatment changes the structure to an orthorhombic perovskite one.¹⁰² Bi_{0.5}Pb_{0.5}MnO₃ prepared at 6 GPa preserves the Mn³⁺ + Mn⁴⁺ charge order and dz² orbital order of Mn³⁺ up to 500 K as typically observed in colossal magnetoresistance materials La_{0.5}Ca_{0.5}MnO₃ and Nd_{0.5}Sr_{0.5}MnO₃ below 150 K.¹⁰⁸

Perovskite BiMnO₃ is a rare example of ferromagnetic (FM) insulator with *T_c* = 110 K owing to the ordering of the e_g orbital of Mn³⁺ ion.^{103,104} This compound attracted interest as a candidate FM ferroelectric, but convergent-beam electron diffraction (CBED) analysis revealed the presence of an inversion center indicating that the actual space group was non-polar C2/c.¹⁰⁴ The above-discussed ordering of the d_{z²} orbital was preserved in the C2/c structure refined based on the neutron powder diffraction. Bi₂NiMnO₆ also is a ferromagnet (with *T_c* = 140 K) owing to the NaCl-type ordering of Ni²⁺ with t_{2g}⁶e_g⁻² electronic configuration and Mn⁴⁺ without the e_g electron (t_{2g}³) as found in La₂NiMnO₆.¹⁰⁹ HP behavior of Lu₂NiMnO₆ was investigated by DC and AC magnetization and neutron diffraction measurements.¹³⁴ Disappearance of FM ordering owing to the change in superexchange magnetic interactions was observed. On the other hand, In₂NiMnO₆ and Sc₂NiMnO are antiferromagnets.^{37,110} 6H hexagonal PbMnO₃ synthesized at 8 GPa was converted to 3C perovskite phase by treatment at 15 GPa.¹¹² The charge distribution of this compound is still unclear.

Mn²⁺ is incorporated in the A-site of perovskite structures as found in the HP-synthesized MnVO₃ and (In_{1-y}Mn_y)MnO₃.^{67,113} This leads to the large number of B-site-ordered double perovskites such as Mn₂FeReO₆, which has a high ferrimagnetic ordering temperature of 520 K.^{95,96} Mn₂CrSbO₆ prepared at 8 GPa transforms to LiNbO₃ phase where Cr and Sb are randomly distributed after the heat treatment at AP. MgMnO₃ and ZnMnO₃ crystallize in ilmenite structure.¹²³ HgMnO₃ synthesized at 18 GPa also has a disordered ilmenite structure, but its synthesis at 20 GPa results in the formation of a perovskite-like structure.¹²⁴ Ordering of Mn, Sc and Sb in the corundum structure results in Ni₃TeO₆-type structure and the materials attract much attention as polar magnets. A-site-ordered quadruple perovskites such as MnCu₃V₄O₁₂ will be discussed in Section 4.20.4.1.^{118,119,129} A large magnetoresistance effect has been observed in a pyrochlore Ti₂Mn₂O₇ and has attracted much attention.¹³⁰

Table 5 Mn oxides obtained by HPHT synthesis (>1 GPa).

Compounds	Structure type	P(GPa)	References
$AMnO_3$ ($R = \text{Ho-Lu, Y}$)	Pv (GdFeO ₃)	5	102
BiMnO ₃	Pv (C2/c)	6	103,104
TiMnO ₃	Pv (GdFeO ₃)	6	105
SeMnO ₃	Pv (GdFeO ₃)	3.5	106
TeMnO ₃	Pv	5.8	107
Bi _{0.5} Pb _{0.5} MnO ₃	B-DPv ($P2_1/m$)	6	108
Bi ₂ NiMnO ₆	B-DPv	4	109
In ₂ NiMnO ₆	B-DPv	6	110
Sc ₂ NiMnO ₆	B-DPv ($P2_1/n$)	6	37
PbMnO ₃	6H	8	111
PbMnO ₃	Pv	12	112
MnVO ₃	Pv (GdFeO ₃)	4.5–6	67
(In _{1-x} Mn _x)MnO ₃ ($1/9 \leq x \leq 1/3$)	Pv ($P2_1/n$)	6	113
Mn ₂ ScSbO ₆	B-DPv ($P2_1/n$)	12	114
Mn ₂ VSbO ₆	B-DPv ($P2_1/n$)	6	71
Mn ₂ CrSbO ₆	B-DPv ($P2_1/n$)	8	96
Mn ₂ MnReO ₆	B-DPv ($P2_1/n$)	5, 8	115,116
Mn ₂ MnTeO ₆	B-DPv ($P2_1/n$)	8	117
Mn ₂ FeReO ₆	B-DPv ($P2_1/n$)	5, 8	118,119
Mn ₂ FeSbO ₆	B-DPv ($P2_1/n$)	6	120
Mn ₂ CoReO ₆	B-DPv ($P2_1/n$)	8	121
Mn ₂ NiReO ₆	B-DPv ($P2_1/n$)	8	122
MgMnO ₃	Ilmenite	6.5	123
ZnMnO ₃	Ilmenite	6.5	123
HgMnO ₃	Ilmenite	18	124
HgMnO ₃	Pv	20	124
Mn ₂ FeNbO ₆	LN	7	125
Mn ₂ FeTaO ₆	LN	7	125
Mn ₂ ScSbO ₆	Ni ₃ TeO ₆	5.5	114
Mn ₂ ScNbO ₆	Ni ₃ TeO ₆	6	126
Mn ₂ ScTaO ₆	Ni ₃ TeO ₆	6	126
Mn ₂ MnWO ₆	Ni ₃ TeO ₆	12	127
Mn ₂ FeWO ₆	Ni ₃ TeO ₆	8	12
Mn ₂ FeMoO ₆	Ni ₃ TeO ₆	8	128
MnCu ₃ V ₄ O ₁₂	A-QPv	12	129
Tl ₂ Mn ₂ O ₇	Pyrochlore	2.5	130

Pv: perovskite. Symmetries are given for the perovskite-type modifications. $Pnma$ (GdFeO₃) symmetry has $\sqrt{2}a_p \times 2a_p \times \sqrt{2}a_p$ superstructure (a_p is the parameter of the cubic perovskite subcell); $C2/c$ has $a_p + 2b_p + c_p, -a_p + c_p, a_p - 2b_p + c_p$ superstructure. 6H: Hexagonal perovskites. B-DPv: B-site-ordered double perovskite. $P2_1/m$ symmetry has $2\sqrt{2}a_p \times 2a_p \times \sqrt{2}a_p$ superstructure; $P2_1/n$ symmetries has $\sqrt{2}a_p \times \sqrt{2}a_p \times 2a_p$ superstructure. A-QPv: A-site-ordered quadruple perovskite. LN: lithium niobate.

4.20.2.6 Fe oxides

Fe-containing compounds are summarized in **Table 6**. Fe ions usually have divalent (e.g., FeO), trivalent (e.g., Fe₂O₃) and mixed-valence states (e.g., Fe₃O₄) in oxides. Fe²⁺ ions are found in LiNbO₃-type oxides such as FeTiO₃.⁵³ FeTiO₃ crystallizes in ilmenite structure because of smaller sizes of constituent ions. Extremely high pressures above 16 GPa stabilize the GdFeO₃-type perovskite structure for Fe oxides with small tolerance factors. However, the perovskite phase generated under HP cannot be quenched to AP, thus transforms to LiNbO₃-type phase upon decompression.¹⁶² The same phase relation is predominant in the Fe³⁺-based LiNbO₃-type oxides, ScFeO₃ and InFeO₃.^{33,155} The Fe⁴⁺-oxides are stabilized under highly oxidative conditions which can be generated by oxidizing agent (e.g., KClO₄) at a pressure of several gigapascals. CaFeO₃ and SrFeO₃ are typical Fe⁴⁺-containing perovskites synthesized from the brownmillerite Ca₂Fe₂O₅ and oxygen-deficient perovskite SrFeO_{3- δ} by using HPHT oxidation conditions.^{135,136} A double perovskite La₂LiFeO₆ contains Fe⁵⁺ species, where Li⁺ and Fe⁵⁺ are ordered at B sites in rock-salt manner.¹⁵⁶ Extremely HP conditions provide a rich variety of unconventional stoichiometry in Fe oxides (FeO₂, Fe₄O₅, Fe₅O₆, etc.).^{157–159,163} Fe₅O₆ undergoes a Verwey-type transition at 275 K, in which charge ordering and metal-insulator transitions simultaneously occur.¹⁵⁸

CaFeO₃ undergoes AFM and metal-insulator transitions associated with a charge disproportionation ($2\text{Fe}^{4+} \rightarrow \text{Fe}^{3+} + \text{Fe}^{5+}$) below 290 K,¹⁶⁴ together with rock-salt-type charge-ordering of Fe³⁺ and Fe⁵⁺.¹⁶⁵ The crystal structure changes from orthorhombic

Table 6 Fe oxides obtained by HPHT synthesis (> 1 GPa).

Compounds	Structure type	<i>P</i> (GPa)	References
CaFeO ₃	Pv (GdFeO ₃)	2	135
SrFeO ₃	Pv (cubic)	0.034	136
BaFeO ₃	Pv (cubic)	5	137,138
Ca _{1-x} Sr _x FeO ₃	Pv (GdFeO ₃ , cubic)	2	139
La _{1/3} Sr _{2/3} FeO ₃	Pv (<i>R</i> -3 <i>c</i>)	6	140,141
Ca _{0.5} Bi _{0.5} FeO ₃	Pv (GdFeO ₃)	5.3	142
CaFe _{1-x} Co _x O ₃	Pv (GdFeO ₃)	6	143
BiFe _{1-x} Co _x O ₃ (<i>x</i> ≤ 0.2)	Pv (<i>R</i> 3 <i>c</i>)	4–6	144,145
BiFe _{1-x} Co _x O ₃ (<i>x</i> ~ 0.3)	Pv (<i>Cm</i>)	4–6	144,146
BiFe _{1-x} Co _x O ₃ (<i>x</i> ≥ 0.4)	Pv (PbTiO ₃)	4–6	144
Bi ₂ FeAlO ₆	B-DPv (<i>R</i> 3)	6	147
Sr ₂ FeBiO ₆	B-DPv (<i>Fm</i> -3 <i>m</i>)	7.5	148
Ba ₂ FeBiO ₆	B-DPv (<i>Fm</i> -3 <i>m</i>)	4	148,149
Ca ₂ FeOsO ₆	B-DPv (<i>P</i> ₂ / <i>n</i>)	6	150
Sr ₂ FeOsO ₆	B-DPv (<i>P</i> ₂ / <i>n</i>)	6	151
PbFeO ₃	Pv	7	152
TlFeO ₃	Pv (GdFeO ₃)	7	153,154
FeTiO ₃	LN	18	53
ScFeO ₃	LN	15	33
InFeO ₃	LN	15	155
La ₂ LiFeO ₆	B-DPv (<i>R</i> -3)	6	156
Fe ₄ O ₅	CaFe ₃ O ₅	10	157
Fe ₅ O ₆		14–16	158
Fe ₅ O ₇		~70	159
Fe ₇ O ₉		24–26	160
Fe ₉ O ₁₁		12	161
Fe ₂₅ O ₃₂		~70	159

Pv: Perovskite. Symmetries are given for the perovskite-type modifications. *Pnma* (GdFeO₃) symmetry has $\sqrt{2}a_p \times 2a_p \times \sqrt{2}a_p$ superstructure (a_p is the parameter of the cubic perovskite subcell); *R*-3*c* and *R*3*c* have $\sqrt{2}a_p \times \sqrt{2}a_p \times 2\sqrt{3}a_p$ superstructure (hexagonal setting); *Cm* has $\sqrt{2}a_p \times \sqrt{2}a_p \times a_p$ superstructure. B-DPv: B-site-ordered double perovskite. *R*3 and *R*-3 have $\sqrt{2}a_p \times \sqrt{2}a_p \times 2\sqrt{3}a_p$ superstructure (hexagonal setting); *Fm*-3*m* has $2a_p \times 2a_p \times 2a_p$ superstructure; *P*₂/*n* has $\sqrt{2}a_p \times \sqrt{2}a_p \times 2a_p$ superstructure. LN: lithium niobate.

(*Pnma* space group) to monoclinic (*P*₂/*n*) in the charge disproportionation transition. The instability of the degenerate e_g orbitals for Fe⁴⁺ ($t_{2g}^3e_g^1$) is removed by the charge disproportionation into Fe³⁺ ($t_{2g}^3e_g^2$) and Fe⁵⁺ ($t_{2g}^3e_g^0$), which is in stark contrast to the Jahn-Teller instability in nominally isoelectronic Mn³⁺ perovskites (e.g., LaMnO₃). This is attributed to the ligand hole (\underline{L}) feature of Fe⁴⁺ ($d^5\underline{L}^1$ electron configuration rather than $t_{2g}^3e_g^1$),¹⁶⁶ in which an electron in an oxygen 2p orbital is transferred to an Fe 3d orbital because of the negative charge transfer energy Δ . A different type of charge ordering with Fe³⁺:Fe⁵⁺ = 2:1 is realized in the low-temperature phase of Sr_{2/3}La_{1/3}FeO₃.¹⁴⁰

SrFeO₃ retains a metallic conductivity with Fe⁴⁺ state at low temperatures down to several kelvins and has a helical magnetic structure, whose origin is explained by the double-exchange model with the strong Fe 3d and O 2p hybridization.¹⁶⁷ In addition to versatile magnetic structures in the *H*-*T* diagram of the pure SrFeO₃,^{168,169} A- or B-site substitutions in Fe⁴⁺-perovskites induce various magnetoelectronic properties. Partial substitution of Fe⁴⁺ with M⁴⁺ (*M* = Co, Ru, Rh) induces FM properties. As discussed in Section 4.20.4.1, ordered perovskite oxides containing nearly tetravalent Fe ions are achieved by 3/4-substitution at A-site with Cu ions, forming a quadruple perovskite series of ACu₃Fe₄O₁₂ (*A* = Ca, Sr, Cd, rare-earth metals).

BiFeO₃ is the most extensively investigated multiferroic compound with high ferroelectric (1103 K) and AFM (643 K) transition temperatures. HP synthesis enables the formation of BiFe_{1-x}Co_xO₃ in the entire composition range.¹⁴⁴ Change in the spin structure from a cycloidal one without the spontaneous magnetization to a collinear one with a spontaneous magnetization perpendicular to the electric polarization is observed for *x* ≤ 0.2.^{145,170} Reorientation of the magnetic easy plane in connection with 71° ferroelectric switching was observed by applying an electric field to a single crystal grown at 3 GPa.¹⁷¹ The crystal structure changes to tetragonal PbTiO₃-type for *x* > 0.4. Monoclinic phase with $\sqrt{2}a_p \times \sqrt{2}a_p \times a_p$ unit cell and *Cm* space group which enables the polarization rotation essentially the same as that of the morphotropic phase boundary phase of PbZr_xTi_{1-x}O₃ (PZT) is observed at the vicinity of *x* = 0.23.¹⁴⁶ A review of BiFe_{1-x}Co_xO₃ is available.¹⁷²

Unusual ordering of isovalent cations, Fe^{3+} and Al^{3+} , has been observed in polar $\text{Bi}_2\text{FeAlO}_6$.¹⁴⁷ Perovskite PbFeO_3 prepared at 6–7 GPa was reported to be $\text{Pb}^{2+}_{0.5}\text{Pb}^{4+}_{0.5}\text{Fe}^{3+}\text{O}_3$ based on the XPS results¹⁵² and the ordering of layer of Pb^{2+} ions and two layers made up of a mixture of Pb^{2+} and Pb^{4+} ions in a 1:3 ratio was determined.¹⁵⁴

Pressure-induced structure, spin-state, magnetic, and insulator-metal transitions are reported to occur in various Fe oxides. Perovskite AFeO_3 ($A = \text{Sr}, \text{Ca}$) with unusually high valence Fe^{4+} shows a rich phase diagram under high pressure: pressure-induced spin state and paramagnetic-to-AFM transitions were observed in both SrFeO_3 and CaFeO_3 .^{173,174} Furthermore, pressure-induced structural transition accompanied with suppression of charge disproportionation occurs in CaFeO_3 .¹⁷⁴ Charge disproportionation in $\text{Sr}_{2/3}\text{La}_{1/3}\text{FeO}_3$ is also suppressed under high pressure.¹⁷⁵ Intermetallic charge transfer is observed in FeTiO_3 ilmenite under high pressure.^{176,177} An electron transfer at 2 GPa ($\text{Fe}^{2+} + \text{Ti}^{4+} \rightarrow \text{Fe}^{3+} + \text{Ti}^{3+}$) is indicated by ^{57}Fe Mössbauer and X-ray absorption spectroscopies. Coexistence of weak ferromagnetism and ferroelectricity was observed in LiNbO_3 -type FeTiO_3 obtained by HPHT treatment at 18 GPa and 1200 °C.⁵³ A pressure-induced spin state transition is often observed in an octahedrally coordinated $3d$ transition metal center due to crossover between the crystal splitting energy and the Coulomb repulsion between the electrons, as commonly found in iron-containing minerals in earth crust.¹⁷⁸ In contrast, a spin transition in square planar and tetrahedrally coordinated metal center is quite rare: Square planar iron oxides SrFeO_2 and $\text{Sr}_3\text{Fe}_2\text{O}_5$ exhibit a pressure-induced spin transition from $S = 2$ to 1 accompanies with insulator-to-metal and antiferro-to-FM transitions.^{179,180} This transition can be explained by enhancement of a Fe-Fe interaction between adjacent face-to-face FeO_4 square-planar units¹⁶⁵.

4.20.2.7 Co oxides

4.20.2.7.1 Co^{4+} perovskites

Co-containing compounds are summarized in Table 7. High-valence Co^{4+} ions as well as high-valence Fe^{4+} ions can be stabilized by using strong oxidizing atmospheres under HP. CaCoO_3 and SrCoO_3 crystallize in cubic or orthorhombic perovskite structures,^{181–183} which are reported to be in an intermediate spin state ($t_{2g}^4e_g^1$). SrCoO_3 exhibits ferromagnetism at room temperature but CaCoO_3 is an antiferromagnet with Néel temperature (T_N) = 95 K. Both oxides retain metallic conductivity to a low temperature of several kelvins because of strong d-p hybridization with a partially filled π^* band.

The stoichiometric and lightly reduced $\text{BaCoO}_{3-\delta}$ ($\delta = 0-0.26$) crystallize in the structures consisting of face-sharing octahedra of 2H, 5H and 12H types due to the large tolerance factor ($t > 1$), although the heavily reduced $\text{BaCoO}_{2.22}$ has a cubic perovskite structure.¹⁹⁸ Single crystals of cubic perovskite $\text{Sr}_{1-x}\text{Ba}_x\text{CoO}_3$ ($x \leq 0.5$) are obtained by annealing the oxygen-deficient $\text{Sr}_{1-x}\text{Ba}_x\text{CoO}_{3-\delta}$ ($\delta \sim 0.5$) crystals grown by the traveling solvent floating zone method with strong oxidizing conditions (7.5 GPa, 480 °C) generated by decomposition of NaClO_3 .¹⁸⁵ The Ba substitution expands the lattice in simple cubic perovskite

Table 7 Co oxides obtained by HPHT synthesis (>1 GPa).

Compounds	Structure type	P(GPa)	References
Perovskites			
CaCoO_3	Pv (GdFeO ₃ , cubic)	8	181,182
SrCoO_3	Pv (cubic)	6	183
$\text{Sr}_{1-x}\text{Ca}_x\text{CoO}_3$ ($0 \leq x \leq 0.8$)	Pv (cubic)	6	184
$\text{Sr}_{1-x}\text{Ba}_x\text{CoO}_3$ ($0 \leq x \leq 0.5$)	Pv (cubic)	6	185
$\text{SrCo}_{1-x}\text{Fe}_x\text{O}_3$	Pv (cubic)	6	183
BiCoO_3	Pv (PbTiO ₃)	6	186
PbCoO_3	A-QPv	12	187
InCoO_3	Pv (GdFeO ₃)	15	188
SeCoO_3	Pv	3.5	189
TeCoO_3	Pv	5.8	107
RP phase			
Sr_2CoO_4	K_2NiF_4 (RP, $n = 1$)	6	190
$\text{Sr}_2\text{CoO}_3\text{F}$	K_2NiF_4 (RP, $n = 1$)	6	191
$\text{Sr}_{1.7}\text{Ca}_{0.3}\text{CoO}_3\text{F}$	K_2NiF_4 (RP, $n = 1$)	NA	192
Magnetoplumbite-related phase			
$\text{CaCo}_6\text{O}_{11}$	$\text{BaTi}_2\text{Fe}_4\text{O}_{11}$	8	193
$\text{SrCo}_6\text{O}_{11}$	$\text{BaTi}_2\text{Fe}_4\text{O}_{11}$	2	194
$\text{BaCo}_6\text{O}_{11}$	$\text{BaTi}_2\text{Fe}_4\text{O}_{11}$	8	193
$\text{LaCo}_6\text{O}_{11}$	$\text{BaTi}_2\text{Fe}_4\text{O}_{11}$	8	195
$\text{CaCo}_{12}\text{O}_{19}$	$\text{BaFe}_{12}\text{O}_{19}$	7	196
$\text{SrCo}_{12}\text{O}_{19}$	$\text{BaFe}_{12}\text{O}_{19}$	3	197
$\text{BaCo}_{12}\text{O}_{19}$	$\text{BaFe}_{12}\text{O}_{19}$	7	196

Pv: Perovskite. Symmetries are given for the perovskite-type modifications. *Pnma* (GdFeO₃) symmetry has $\sqrt{2}a_b \times 2a_b \times \sqrt{2}a_b$ superstructure (a_b is the parameter of the cubic perovskite subcell). A-QPv: A-site-ordered quadruple perovskite.

form, decreasing the Curie temperature down to 176 K ($x = 0.35$). The ferromagnetism disappears at $x = 0.4$ and helimagnetism emerges. The magnetic evolution is interpreted as the decrease in d-p hybridization by extension of Co–O bonds.

CaCoO₃ and SrCoO₃ also demonstrate highly active and stable electrocatalysis on oxygen evolution reaction (OER).¹⁹⁹ The origin of catalysis is proposed to be attributed to the unconventional reaction mechanisms including participation of surface lattice oxygen of the perovskites. The catalytic activity of high-valence transition metal ions on OER is investigated by systematic comparison on ABO₃ compounds ($A = \text{Ca, Sr, Y, La}$; $B = \text{Ti, V, Cr, Mn, Fe, Co, Ni, Cu}$), proposing that the charge-transfer energy, the difference between unoccupied 3d band center of B ions and occupied 2p band center of O, is the useful descriptor in perovskite OER catalysts.^{200,201}

4.20.2.7.2 Co³⁺ perovskites

Spin state transitions among low-, intermediate-, mixed- and high-spin configurations are a central topic in Co³⁺ oxides. The Co³⁺ ions in octahedral coordination like those at the B-site of perovskites undergo spin-state transition with external pressure and elevated temperature. LaCoO₃ demonstrates thermally induced spin transition from low-spin (LS) to mixed or intermediate state, whereas external pressures above 4 GPa drive the transition to LS.^{202,203} In contrast, the ground state of BiCoO₃ obtained at 6 GPa is high-spin (HS).¹⁸⁶ It has a largely distorted tetragonal PbTiO₃-type structure with the c/a ratio of 1.26 and a calculated P_S of 120 $\mu\text{C}/\text{cm}^2$. It has a C-type AFM ordering below the T_N of 460 K with the ordered moment of 3.24 μ_B , indicating that Co³⁺ is in the HS $t_{2g}^4 e_g^2$ state. A transition to the non-polar GdFeO₃ phase accompanied with a spin state transition and 13% volume contraction was observed at 3 GPa.²⁰⁴ PbCoO₃ has an A-site-ordered quadruple perovskite structure (see Section 4.20.4.1) with the $\text{Pb}^{2+}\text{Pb}^{4+}_3\text{Co}^{2+}_2\text{Co}^{3+}_2\text{O}_{12}$ valence distribution, a $2a_p \times 2a_p \times 2a_p$ superlattice, and the $Pn-3$ space group.¹⁸⁷ PbCoO₃ shows sequential HS-LS transition of Co²⁺ and charge transfer between Co²⁺ and Co³⁺ under pressure.²⁰⁵

4.20.2.7.3 RP phases

Sr₂CoO₄ crystallizes in K₂NiF₄ structure with Co⁴⁺.¹⁹⁰ This compound undergoes FM transition at $T_C = 255$ K. Electron doping into Co ions by substitution of Y for Sr decreases T_C down to 150 K ($x = 0.5$), and the FM property eventually vanishes ($x > 0.67$). The intermediate spin states are suggested, at least above the magnetic transition temperature.

Anion-substituted K₂NiF₄-type Co³⁺ oxyfluorides Sr₂CoO₃F and Sr_{1.7}Ca_{0.3}CoO₃F consist of Co₅F octahedra in which O and F anions are perfectly ordered.^{92,192} The octahedra can be regarded as CoO₅ square pyramids because of the Co–F bond much longer than five Co–O bonds. Magnetization and X-ray spectroscopic studies demonstrated that the Co³⁺ ions of these oxyfluorides were in the high-spin state as well as those in BiCoO₃ and that a spin crossover from high- to low-spin can be driven by high pressure.²⁰⁶ At 12 GPa the high-spin Co³⁺ ions in square pyramidal coordination are fully converted to low-spin ones in octahedral coordination.

4.20.2.7.4 Magnetoplumbite-related phases

SrCo₆O₁₁ single crystal is synthesized at 2 GPa and 700 °C by ion-exchange reaction: $6\text{Na}_x\text{CoO}_2 + 6x/2\text{SrCl}_2 \rightarrow \text{SrCo}_6\text{O}_{11} + 6x\text{NaCl} + \text{byproducts}$.¹⁹⁴ Single crystal structure analysis demonstrates that SrCo₆O₁₁ has a magnetoplumbite-derived layered structure in which three distinct crystallographic sites are occupied by Co ions. Two Co sites predominate electronic conductivity, whereas the other Co ions in bipyramidal coordination contribute to the frustrated Ising-like spin magnetism. SrCo₆O₁₁ exhibits field-induced magnetic-state transitions from intermediate 1/3-plateau to FM spin alignment. The spin-valve-like magnetoresistance in the interlayer direction is observed, which is attributed to the magnetic structure transition by magnetic field.²⁰⁷ The resonant soft X-ray scattering study illustrates a magnetic Devil's Staircase in the H - T phase diagram, where many types of magnetic ordering emerge depending on the temperature and applied field.²⁰⁸

CaCo₆O₁₁ and BaCo₆O₁₁ polycrystalline samples are synthesized from mixtures of metal oxides at higher pressure up to 8 GPa.¹⁹³ The magnetic state changes from the 1/3-plateau of SrCo₆O₁₁ to simple AFM-like (CaCo₆O₁₁) and FM-like ones. The magnetic evolution is interpreted as the structural change in CoO₅ trigonal bipyramids induced by A-site ions with different sizes.

4.20.2.8 Ni oxides

Ni-containing compounds are summarized in Table 8. Ruddlesden-Popper phases of Ni oxides and RNiO₂ ($R = \text{La, Nd}$) with the infinite-layer structure were intensively studied because of the structural and electronic configuration similarities to the copper oxide superconductors. Ni^{1.33+} ion in La₄Ni₃O₈ obtained by the reduction of La₄Ni₃O₁₀, $n = 3$ phase of RP phase, has d^{8.67} electronic configuration which is the same as that of Cu^{2.33+}. However, metallic conductivity was not observed even at HP. Structural transition associated with the shift of oxygen position was observed at 21 GPa.²¹⁹

Perovskite RNiO₃ ($R = \text{La-Lu}$ and Y) was first synthesized at the high oxygen pressure of 6.5 GPa.²⁰⁹ Those with $R = \text{La-Eu}$ can be obtained at the high oxygen pressure of 0.02 GPa as well. Ni³⁺ has seven 3d electrons, but because of the deep d level energetically lower than the O 2p band, the electronic configuration is $t_{2g}^6 \underline{\underline{L}}$ ($\underline{\underline{L}}$: ligand hole) rather than $t_{2g}^6 e_g^1$. RNiO₃ except for LaNiO₃ shows a charge disproportionation expressed as $2\text{Ni}^{3+} \rightarrow \text{Ni}^{2+} + \text{Ni}^{4+}$ ($2t_{2g}^6 \underline{\underline{L}} \rightarrow t_{2g}^6 + t_{2g}^6 \underline{\underline{L}}^2$) accompanied by a metal-to-insulator transition like that observed in CaFeO₃.^{220,221} The crystal structure changes from orthorhombic GdFeO₃-type to one with the same unit cell and $P2_1/n$ space group where Ni²⁺ and Ni⁴⁺ are arranged in the rock-salt manner. The transition temperature (T_{MI}) increases with decreasing radius of the R ion and those with $R = \text{Sm-Lu}$ and Y are insulating at room temperature. The T_{MI} was found to decrease under pressure.²²² Similarly, TlNi³⁺O₃ prepared at 7.5 GPa is an AFM insulator.

Table 8 Ni oxides obtained by HPHT synthesis (>1 GPa).

Compounds	Structure type	<i>P</i> (GPa)	Reference
$R\text{NiO}_3$ ($R = \text{Nd-Lu, Y}$)	Pv (GeFeO ₃)	6	209
LaNiO ₃	Pv (<i>R-3c</i>)	6	209
TiNiO ₃	Pv	7.5	210
BiNiO ₃	Pv (<i>P-1</i>)	6	211
SeNiO ₃	Pv (GeFeO ₃)	3.5	212
TeNiO ₃	Pv (GeFeO ₃)	3.5	213
PbNiO ₃	Pv (GeFeO ₃)	3	214
BiCr _{0.5} Ni _{0.5} O ₃	Pv (GeFeO ₃)	5.3	215
Mn ₂ NiReO ₆	B-DPv (<i>P2₁/n</i>)	8	122
Pb ₂ NiReO ₆	B-DPv (<i>I2/m</i>)	6	216
Lu ₂ NiIrO ₆	B-DPv (<i>P2₁/n</i>)	6	217
Sc ₂ NiMnO ₆	B-DPv (<i>P2₁/n</i>)	6	37
In ₂ NiMnO ₆	B-DPv (<i>P2₁/n</i>)	6	110
Bi ₂ NiMnO ₆	B-DPv (<i>C2</i>)	6	109
NiReO ₄	Rutile	5.8	218

Pv: Perovskite. Symmetries are given for the perovskite-type modifications. *Pnma* (GdFeO₃) symmetry has $\sqrt{2}a_p \times 2a_p \times \sqrt{2}a_p$ superstructure (a_p is the parameter of the cubic perovskite subcell); *R-3c* has $\sqrt{2}a_p \times \sqrt{2}a_p \times 2\sqrt{3}a_p$ superstructure (hexagonal setting); *P-1* has $\sqrt{2}a_p \times \sqrt{2}a_p \times 2a_p$ superstructure. B-DPv: B-site-ordered double perovskite. *P2₁/n* and *I2/m* have $\sqrt{2}a_p \times \sqrt{2}a_p \times 2a_p$ superstructure. *C2* has $a_p + 2b_p + c_p, -a_p + c_p, a_p - 2b_p + c_p$ superstructure.

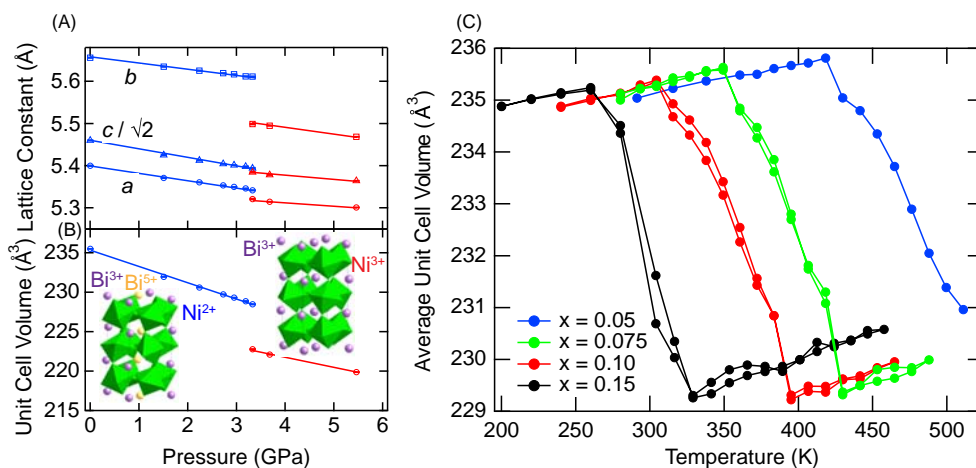


Fig. 4 Negative thermal expansion in $\text{BiNi}_{1-x}\text{Fe}_x\text{O}_3$. Pressure dependence of lattice parameters (a) and unit cell volume (b) of BiNiO_3 . (c) shows the temperature variation of average unit cell volume in $\text{BiNi}_{1-x}\text{Fe}_x\text{O}_3$ revealing negative thermal expansion. Adapted with permission from Azuma, M.; Chen, W. T.; Seki, H.; et al. *Nat. Commun.* **2011**, 2, 347; Nabetani, K.; Muramatsu, Y.; Oka, K.; et al. *Appl. Phys. Lett.* **2015**, 106 (6), 061912.

Charge disproportionation of Bi ion is found in the A-site of BiNiO_3 which crystallizes in a triclinically distorted structure (space group *P-1*) illustrated in the bottom left inset of Fig. 4(b).²¹¹ Bi^{3+} and Bi^{5+} occupy distinct crystallographic sites in BiNiO_3 , whose valence distribution is the unusual $\text{Bi}^{3+}_{0.5}\text{Bi}^{5+}_{0.5}\text{Ni}^{2+}\text{O}_3$. Results of neutron powder diffraction²²³ and X-ray absorption spectroscopy studies²²⁴ revealed a pressure-induced melting of the Bi charge disproportionation at 3–4 GPa and a simultaneous Ni-to-Bi charge transfer accompanied by an insulator-to-metal transition and a structural change to the orthorhombic GdFeO_3 -type perovskite superstructure with valence distribution $\text{Bi}^{3+}\text{Ni}^{3+}\text{O}_3$. The structural transition is accompanied by a discrete shrinkage of lattice parameters and a 2.5% unit cell volume drop (Fig. 4(b)).²²³ This large volume change results from the dominant contraction of the Ni-O perovskite framework as Ni^{2+} is oxidized to the smaller Ni^{3+} at the transition, which outweighs the lattice-expanding effects of reducing Bi^{5+} to Bi^{3+} and increases the Ni-O-Ni angles. Partial substitution of La^{3+} , Pb^{4+} , or Sb^{3+} for Bi or Fe^{3+} substitution for Ni^{2+} enables this charge transfer transition to occur on heating at AP, leading to technologically useful negative thermal expansion (NTE).^{225–230}

SeNiO_3 , TeNiO_3 and PbNiO_3 have been reported to be unusual $\text{A}^{4+}\text{B}^{2+}\text{O}_3$ perovskites with GeFeO_3 -type distortion.^{212–214} Later it turned out that the actual structure of PbNiO_3 was a polar one with space group *Pbn2₁*.²²⁷ Perovskite-type PbNiO_3 transforms to LiNbO_3 -type structure after heat treatment at AP.²¹⁴

PbMO₃ shows systematic charge distribution changes depending on the depth of the 3d level of the transition metal. PbVO₃ is Pb²⁺V⁴⁺O₃ as in Pb²⁺Ti⁴⁺O₃, as discussed in Section 4.20.2.3, but PbCrO₃ and PbFeO₃ have been found to be Pb²⁺_{0.5}Pb⁴⁺_{0.5}Cr³⁺O₃ with charge disproportionated Pb²⁺ and Pb⁴⁺.^{89,154} PbCoO₃ was found to be Pb²⁺Pb⁴⁺₃Co²⁺₂Co³⁺₂O₁₂.¹⁸⁷ PbNiO₃ has a valence distribution of Pb⁴⁺Ni²⁺O₃.²¹⁴ That is, PbMO₃ changes from Pb²⁺M⁴⁺O₃ to Pb²⁺_{0.5}Pb⁴⁺_{0.5}Cr³⁺O₃ (average valence state of Pb³⁺M³⁺O₃) to Pb²⁺_{0.25}Pb⁴⁺_{0.75}Co²⁺_{0.5}Co³⁺_{0.5}O₃ (Pb^{3.5+}Co^{2.5+}O₃) and finally to Pb⁴⁺M²⁺O₃ according to the order of M in the periodic table and the depth of the d level of M.

4.20.2.9 Cu oxides

Cu-containing compounds are summarized in Table 9. The quest for new Cu-oxide superconductors activated the HP research in 1990s. Most of the Cu-oxide superconductors comprise a common structural unit: the two-dimensional CuO₂ sheet (see Fig. 5(b)). La_{2-x}Ba_xCuO₄ ($x \approx 0.15$), the first Cu-oxide superconductor, crystallizes in the K₂NiF₄ structure. It is known that high-*T_c* superconductivity occurs if the CuO₂ sheets are properly oxidized or reduced, as first recognized from La_{2-x}Ba_xCuO₄ ($x \approx 0.15$) and Nd_{2-x}Ce_xCuO₄ ($x \approx 0.15$), respectively. It is clear that the Ba²⁺-for-La³⁺ substitution and the Ce⁴⁺-for-Nd³⁺ substitution work differently on the CuO₂ sheets, and from the sign of the carriers created in the CuO₂ sheets of these superconductors are classified into p-type and n-type, respectively. R₂CuO₄ crystallizes in the Nd₂CuO₄-type structure only for R = Pr, Nd, Sm, Eu and Gd when prepared at AP. HP synthesis expands the composition range to the smaller R ion side, R = Y, Dy, Ho, Er and Tm.²³¹

The hole doping to the parent compound of La_{2-x}Ba_xCuO₄, La₂CuO₄, was achieved by injection of excess oxygen to the interstitial sites by high-oxygen pressure treatment as well.²⁴⁷ High-oxygen pressure was utilized to stabilize YBa₂Cu₄O₈ which

Table 9 Cu oxides obtained by HPHT synthesis (> 1 GPa).

Compounds	P(GPa)	References
R ₂ CuO ₄ (R = Y, Dy-Tm)	6	231
(Cu,C)Ba ₂ Ca _{n-1} Cu _n O _{2n+3} (n = 3, 4)	5	232
(Cu,C)Sr ₂ Ca _{n-1} Cu _n O _{2n+3} (n = 2, 5)	6	232
(Cu,C) ₂ Ba ₃ Ca _{n-1} Cu _n O _{2n+5} (n = 3, 4, 5)	5	232
(Cu,S)Sr ₂ Ca _{n-1} Cu _n O _{2n+3} (n = 3-7)	6	232
(Cu,P)Sr ₂ (Ca,Y) _{n-1} Cu _n O _{2n+3} (n = 3-6)	5-6	232
(Cu,Ge)Sr ₂ (Ca,Y) _{n-1} Cu _n O _{2n+3} (n = 3, 4, 6)	6	232
(Cu,Cr)Sr ₂ Ca _{n-1} Cu _n O _{2n+3+δ} (n = 1-9)	6	232
(B,C)Sr ₂ Ca _{n-1} Cu _n O _{2n+3} (n = 1, 2, 3)	5	232
(B,C)Ba ₂ Ca _{n-1} Cu _n O _{2n+3} (n = 3)	5	232
BaSr ₂ Ca _{n-1} Cu _n O _{2n+3} (n = 3, 4, 5, 6)	6	232
AlSr ₂ Ca _{n-1} Cu _n O _{2n+3} (n = 3, 4, 5, 6)	5-6	232
GaSr ₂ Ca _{n-1} Cu _n O _{2n+3} (n = 2,3,4)	6	232
CCa ₂ CaCu ₂ O _{7+δ} (n = 2)	6	232
PbSr ₂ Ca _{n-1} Cu _n O _{2n+3} (n = 2,3,4)	6	232
HgBa ₂ Ca _{n-1} Cu _n O _{2n+2+δ} (n = 1-16)	1-4	232,233
Hg ₂ Ba ₂ YCu ₂ O _{8-y} (n = 2)	1.8	232
(Hg,Tl) ₂ Ba ₂ Ca _{n-1} Cu _n O _{2n+2+δ} (n = 2-5)	5	232
Ba ₂ Ca _{n-1} Cu _n O _{2n} (O, F) (n = 2-9)	3.5	234,235
Sr ₂ Ca _{n-1} Cu _n O _{2n+2} (n = 1-4)	5	232
Sr ₂ Ca _{n-1} Cu _n O _{2n} F _{2+δ} (n = 1-5)	5.5	232
Sr ₂ Ca _{n-1} Cu _n O _{2n+y} Cl _{2-y} (n = 2,3)	6	232
R ₂ CuSnO ₆ (R = Nd, Pr, Sm)	6-8	15
La ₂ CuZrO ₆	8	15
La ₄ Cu ₃ MoO ₁₂	6	16
Ba ₂ CuTeO ₆	5	236
Ba ₂ CuOsO ₆	6	237
ACuO ₂ (A = Ca-Sr _{2/3} Ba _{1/3})	6	238,239
Sr _{1-x} R _x CuO ₂ (R = La to Gd, x ≈ 0.1)	2.5	240
Ca _{2-x} Na _x CuO ₂ Cl ₂	2-8	241
SrCu ₂ O ₃	6	242
Sr ₂ Cu ₃ O ₅	6	242
LaCuO _{2.5}	6	243
Se _{1-x} Te _x CuO ₃ (0 ≤ x ≤ 1)	5.8	107,244
PrCuO ₃	7.5	245
CuNbO ₃	6.5	246
CuTaO ₃	6.5	246

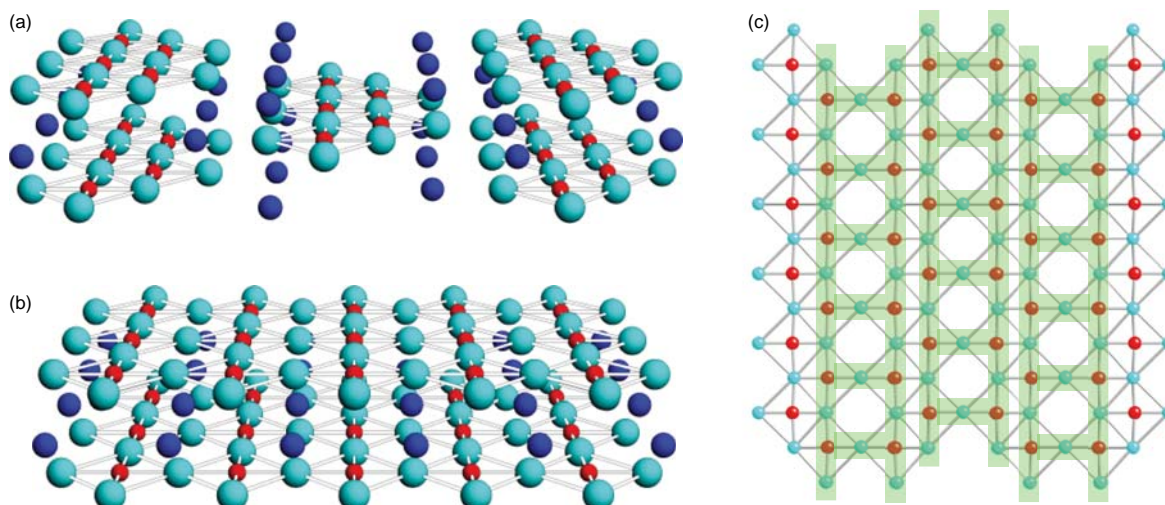


Fig. 5 Crystal structures of (a) AP phase and (b) HP-infinite-layer phase of SrCuO_2 and (c) Cu_2O_3 plane of SrCu_2O_3 . Blue, red and right blue spheres represent Sr, Cu and O, respectively.

has excess CuO chain compared with well-known $\text{YBa}_2\text{Cu}_3\text{O}_7$.²⁴⁸ Sintering in a HP atmosphere is adopted as a production method for commercially available $(\text{Bi,Pb})_2\text{Sr}_2\text{Ca}_2\text{Cu}_3\text{O}_{10-x}$ (Bi-2223) superconducting wire since 2004.²⁴⁹

$\text{La}_{2-x}\text{Ba}_x\text{CuO}_4$, $\text{YBa}_2\text{Cu}_3\text{O}_7$ and $(\text{Bi,Pb})_2\text{Sr}_2\text{Ca}_2\text{Cu}_3\text{O}_{10-x}$ respectively have one, two and three CuO_2 sheets separated by small Y^{3+} or Ca^{2+} ions. These are sandwiched by so-called “charge reservoir layers.” Bi-based cupric superconductors are generally expressed as $\text{Bi}_2\text{Sr}_2\text{Ca}_{n-1}\text{Cu}_n\text{O}_{2n+4}$ ($n = 1, 2$ and 3). Partial substitution of Pb for Bi stabilizes the $n = 3$ phase. A Hg-based superconductor with three CuO_2 layers, $\text{HgBa}_2\text{Ca}_2\text{Cu}_3\text{O}_{10-x}$, has the highest $T_C = 133$ K among the cupric oxide superconductors. The T_C increased up to 164 K under pressure²⁵⁰ and this value was the highest superconducting transition temperature for 20 years before the superconductivity at 203 K was discovered under a pressure of 155 GPa in H_2S generated by the pressure-induced decomposition of H_2S .^{251,252} Bi-based and Hg-based systems are so-called “homologous series.” HP synthesis has a significant effect on the stabilization of homologous series and more than 20 series were discovered as summarized in **Table 10**. Good review papers of homologous series are available.^{232,329} Many of the homologous series stabilized by HP synthesis have more than three CuO_2 layers. Among them, $\text{HgBa}_2\text{Ca}_{n-1}\text{Cu}_n\text{O}_{2n+2+\delta}$ and $\text{Ba}_2\text{Ca}_{n-1}\text{Cu}_n\text{O}_{2n}(\text{O}, \text{F})$ were intensively studied by NMR and carrier distributions in each CuO_2 plane were determined.³³⁰

$\text{La}_2\text{CuSnO}_6$ with alternating CuO_2 and SnO_2 planes is the only B-site layered ordered double perovskite obtained at AP. The composition can be expanded by HP synthesis to R_2CuSnO_6 ($\text{R} = \text{Pr}, \text{Nd}$ and Sm), $\text{La}_2\text{CuZrO}_6$ and $\text{La}_4\text{Cu}_3\text{MoO}_{12}$ ($\text{La}_2\text{Cu}(\text{Cu}, \text{Mo})\text{O}_{12}$).¹⁵ On the other hand, the arrangement of Cu and Te (Os) is NaCl-type in $\text{La}_2\text{CuTeO}_6$ and $\text{La}_2\text{CuOsO}_6$.^{236,250}

SrCuO_2 compressed at 6 GPa and 1200 K crystallizes in so-called “infinite layer” structure (**Fig. 5(b)**). This is the simplest structure containing the two-dimensional CuO_2 sheet. If the alkaline earth–copper–oxygen system is studied at atmospheric pressure, this structure is stabilized only for a narrow composition range of $\text{Ca}_{1-x}\text{Sr}_x\text{CuO}_2$ with $x \approx 0.1$ and only in a narrow temperature range near the melting point.³³¹ However, at 6 GPa and 1200 K the composition range can be extended from CaCuO_2 to $\text{Sr}_{2/3}\text{Ba}_{1/3}\text{CuO}_2$, passing SrCuO_2 .^{238,239} Because of the replacement of $\text{Ca}_{0.9}\text{Sr}_{0.1}$ with larger Sr, the CuO_2 plane in SrCuO_2 is subjected to a tensile stress. One way to relax the stress caused by the substitution of large alkaline-earth ions is to inject excess electrons into the CuO_2 sheets. The injection can be done by substituting trivalent rare-earth ions at the counter cation site so that $\text{A}_{1-x}\text{R}_x\text{CuO}_2$ ($\text{R} = \text{rare-earth elements, La to Gd}$) may form. $\text{Sr}_{1-x}\text{R}_x\text{CuO}_2$ ($\text{R} = \text{La to Gd}, x \approx 0.1$) is an n-type superconductor with a T_C of 43 K.²⁴⁰

In this context, $\text{Ca}_2\text{CuO}_2\text{Cl}_2$ was successfully doped with holes. $\text{A}_2\text{CuO}_2\text{Cl}_2$ ($\text{A} = \text{Sr}, \text{Ca}$) has the K_2NiF_4 structure but the apical oxygen is replaced with chlorine. While the Cu–O bond length of $\text{Sr}_2\text{CuO}_2\text{Cl}_2$, 1.99 Å, is too long for hole doping, even longer than that of SrCuO_2 , $\text{Ca}_2\text{CuO}_2\text{Cl}_2$ has the Cu–O bond length of 1.93 Å, close to that of $\text{YBa}_2\text{Cu}_3\text{O}_7$. $\text{Ca}_{2-x}\text{Na}_x\text{CuO}_2\text{Cl}_2$ prepared at 6 GPa shows superconductivity with the highest T_C of 28 K at $x \approx 0.2$.³³² Millimeter-sized single crystals with well-defined cleavage planes are grown as well.²⁴¹ The growth condition was determined through the observation of chemical reaction under pressure by synchrotron X-ray diffraction. Na content x is controlled by changing the Na-solubility limit through the applied pressure, without introducing appreciable compositional inhomogeneity.

SrCu_2O_3 and $\text{Sr}_2\text{Cu}_3\text{O}_5$ with layered structures similar to SrCuO_2 are also stabilized by HP synthesis.²⁴² As illustrated in **Fig. 5(c)**, the Cu_2O_3 plane and the Cu_3O_5 plane can be regarded as typical realizations of 2- and 3- leg spin ladders. The 2-leg ladder attracted much attention because of the presence of a large spin gap between the nonmagnetic singlet ground state and the triplet excited state and the theoretical prediction of high- T_C superconductivity. The spin gap of 420 K was confirmed for SrCu_2O_3 .³³³ Pressure-induced buckling of the Cu_2O_3 ladder plane was observed by synchrotron X-ray diffraction.³³⁴ The superconductivity with the highest T_C of 12 K was found under high-pressures of 3–4.5 GPa for $\text{Sr}_{0.4}\text{Ca}_{13.6}\text{Cu}_{24}\text{O}_{41.84}$ with essentially the same

Cu_2O_3 ladder plane prepared under high-oxygen pressure.³³⁵ Another 2-leg ladder cupric oxide, $\text{LaCuO}_{2.5}$, was also obtained by HP synthesis.²⁴³

Perovskites $\text{Se}^{4+}\text{Cu}^{2+}\text{O}_3$ and $\text{Te}^{4+}\text{Cu}^{2+}\text{O}_3$ have been obtained by HP synthesis.²⁴⁶ The change in Cu–O–Cu bond angle depending on the A-site ionic size in the solid solution $\text{Se}_{1-x}\text{Te}_x\text{CuO}_3$ results in FM to AFM crossover.²⁴⁴ LaCuO_3 with Cu^{3+} was stabilized by high-oxygen pressure, while Cu ion in PrCuO_3 was found to be closed to divalent.^{245,336} Formation of a one-dimensional chain of corner-sharing CuO_4 plaquettes was observed. Compared to Cu^{2+} ($r_{\text{VI}} = 0.73 \text{ \AA}$) and Cu^{3+} ($r_{\text{VI}} = 0.54 \text{ \AA}$), the ionic radius of Cu^+ ($r_{\text{VI}} = 0.77 \text{ \AA}$) is large enough to occupy the A site. Two A-site Cu^+ polar perovskite compounds, $\text{Cu}^+\text{Nb}^{5+}\text{O}_3$ and $\text{Cu}^+\text{Ta}^{5+}\text{O}_3$, have been synthesized at HP.^{246,253} 1:3 ordering of alkali, alkaline earth or rare earth elements and Cu^{2+} in the A-site of perovskite structure is observed in a large number of A-site-ordered quadruple perovskite as discussed in Section 4.20.4.1.

4.20.3 HPHT synthesis of 4d, 5d transition metal oxides

In this section, we introduce 4d and 5d oxides that were synthesized at high temperature and high pressure. Compounds containing 4d¹⁰ elements (e.g., Ag^+ , Cd^{2+}) or 5d¹⁰ elements (e.g., Hg^{2+}) were not considered because of space limitations.

During this survey, a common background of recent studies over the past two decades for 4d and 5d oxides emerges regardless of the synthesis method. In many studies, it has been stated that the 4d and 5d electronic states are significantly different from the 3d electronic state. This is because 4d and 5d electrons occupy a much more spatially extended orbital than the 3d orbital, and the spin–orbit coupling should be much stronger in nature. The 4d and 5d electronic states may be in a different competing situation, which cannot happen in the 3d system. Besides, the relativistic effect is often significant because findings such as Weyl semimetal and Rashba splitting were reported or predicted in this materials category.^{421–423} Therefore, it is often argued that the prospect for achieving new and potentially useful properties, which are hard to expect for the 3d system, is high. Characteristic properties such as extremely large coercive magnetic fields,⁴²⁴ bulk exchange bias,⁴²⁵ Slater transition and Lifshitz transition,^{426–429} Anderson and Blount-type transition,³⁸² and enhanced spin-phonon-electronic coupling⁴³⁰ have been reported in this category.

To illustrate how the electronic state changes over 3d to 5d, the electronic states of BaFeO_3 ,¹³⁷ BaRuO_3 ,²⁸⁸ and BaOsO_3 ,³⁹⁷ which share the cubic perovskite lattice (space group: $Pm\bar{3}m$), were theoretically calculated as shown in Fig. 6. Because the transition metals Fe, Ru and Os are of group 8 and tetravalent, the d electron count is fixed at d⁴ from 3d to 5d. Therefore, the calculation provides a better comparison of the d electronic states over 3d to 5d. The 3d oxide BaFeO_3 shows a relatively narrow d bandwidth with a larger density of states at the Fermi energy, whereas the bandwidth and density of states gradually become much broader and smaller, respectively, for the 4d and 5d oxides. Note that the contribution of spin–orbit coupling was considered in the non-

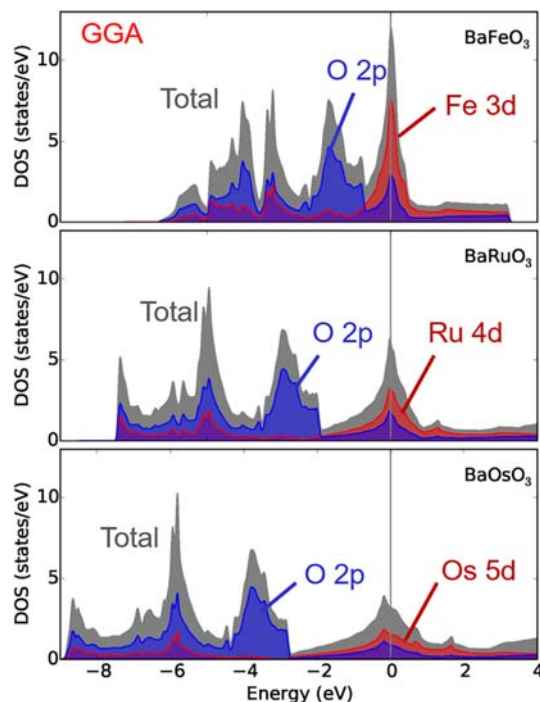


Fig. 6 The electronic state of the cubic perovskite ($Pm\bar{3}m$) of BaFeO_3 , BaRuO_3 and BaOsO_3 calculated by the density functional theory with generalized gradient approximation (GGA). The WIEN2K software package, which is based on the highly precise full-potential linearized augmented-plane-wave method, was used for the calculations.⁴³¹ The Spin-Orbit coupling (SOC) was considered in the non-magnetic calculations.

magnetic calculation but U (on-site repulsion) and t (hopping integral) were not.⁴³¹ Further consideration would be necessary to understand the observed correlated electron properties of those compounds.

An indispensable topic in the research field of this materials category is the post-perovskite structural transition (Fig. 7). Since a post-perovskite mineral, which is generally known as the CaIrO_3 -type, is believed to transform from the perovskite mineral of the upper mantle at a much deeper level,⁴ the isostructural oxide has been explored to assist in understanding the dynamics of the Earth's lower mantle. To date, a series of CaIrO_3 -type oxides have been synthesized mostly by the HP and HT method (see Tables 10 and 11). Meanwhile, the 4d and 5d properties of the CaIrO_3 -type oxides were studied and unusual characteristics were found.^{292,306,399} Note that 3d post-perovskite oxides are very few in number.⁴³²

Here we introduce a few selected 5d oxides that show remarkable properties; NaOsO_3 crystallizes in an GdFeO_3 -type structure.³⁸⁴ In the ternary system Na-Os-O, the perovskite can be synthesized only by a HT and HP method, while Na_5OsO_6 ⁴³³ and Na_3OsO_5 ⁴³⁴ have been reported instead when high pressure was not applied. The perovskite compounds may be difficult to be prepared without the compressed condition. The Os of the perovskite is pentavalent and thus the $5d^3$ configuration is responsible for the bulk electronic nature. A major feature of the HP-synthesized NaOsO_3 is the metal-to-insulator transition (MIT), which occurs at 410 K. It is very clear that the MIT is coupled with the AFM ordering, which is established at the same temperature.^{429,435} In general, magnetically driven MITs are quite rare in real materials; only a few 5d oxides such as $\text{A}_2\text{Ir}_2\text{O}_7$ ($A = \text{Y}$ or trivalent lanthanide; $T_{\text{MIT}} < 155 \text{ K}$)^{436,437} and $\text{Cd}_2\text{Os}_2\text{O}_7$ ($T_{\text{MIT}} = 227 \text{ K}$)⁴³⁸ show qualitatively similar MIT. The HP-synthesized perovskite NaOsO_3 has contributed substantially to the progress of research on the nature of the magnetically driven MIT, although the exact mechanism is still under debate. It should be noted that the perovskite NaOsO_3 transforms into a post-perovskite structure ($Cmcm$) when heated at 16 GPa.

A half-century has passed since Anderson and Blount proposed the concept of polar metal.⁴³⁹ A model substance of the polar metal LiOsO_3 was prepared under HP and HT conditions.³⁸² It has contributed to the progress on the research of polar metals.⁴⁴⁰ LiOsO_3 is isostructural to the ferroelectric oxide LiNbO_3 and undergoes a structurally equivalent transition at 140 K (Fig. 8), although LiOsO_3 is natively metallic. The transition is accompanied by the loss of the centrosymmetry. Because the polar metal is an electrical conductor, we have little expectation of using it as a replacement for practical ferroelectric oxides. However, when it is used as an internal electrode of a capacitor, it may overcome the critical-size problem, which is the technical bottleneck of ultra-thinning of the ferroelectric layer.⁴⁴¹ Although there is a leakage current problem due to ultra-thinning, it may be possible to develop a variety of nano-scaled capacitors (ferroelectric layer $< 1 \text{ nm}$), which contribute to the development of size-reduced devices. Other technical possibilities have also been proposed for polar metals.⁴⁴⁰

Other major progress in this materials category can be seen in the development of perovskite-related oxides with an atom order such as A-site-ordered perovskite and double perovskite. As shown in Tables 10 and 11, more than half of the HP-synthesized oxides are of this category. Ordered 3d and 5d elements in a perovskite lattice often result in unusual correlated properties; for

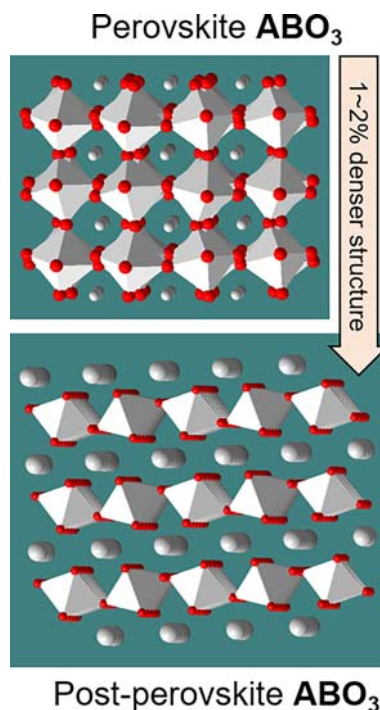


Fig. 7 General image of the structures of perovskite and post-perovskite oxides. The post-perovskite structure is usually 1–2% denser than the perovskite when the composition is not altered. The red and gray balls represent oxygen and A atoms, respectively. B atoms are at the centers of the octahedra.

Table 10 4d-transition metal oxides obtained by HPHT synthesis (>1 GPa).

Compounds	Structure type	P(GPa)	References
4d⁰ (Zr⁴⁺, Nb⁵⁺, Mo⁶⁺)			
La ₂ CuZrO ₆	Layered B-DPv	6	15
CuNbO ₃	Pv	6.5–12	246,253
Mn ₂ ScNbO ₆	Ni ₃ TeO ₆	6	126
Mn ₂ FeNbO ₆	LN	7	125
RbNbO ₃	Pv	6.5	254,255
Ba ₂ CrNbO ₆	Partial B-DPv	8	94
Pb ₂ RNbO ₆ (R = Y, Ho)	B-DPv	6	256
CaCu ₃ Fe ₂ Nb ₂ O ₁₂	A-QPv	9–9.5	257
CaCu ₃ Ga ₂ Nb ₂ O ₁₂	A-QPv	12.5	258
Sr ₂ CuMoO ₆	B-DPv	4	259
Pb ₂ CoMoO ₆	B-DPv	3.2	260
Mn ₂ FeMoO ₆	Ni ₃ TeO	8	128
R ₄ Cu ₃ MoO ₁₂ (R = La, Pr, Nd, Sm)	Layered B-DPv	6	16
A ₄ MoO ₃ (A = Na, K, Rb)	Tungsten bronze	6.5	261
A ₄ Nb ₂ O ₉ (A = Mn, Zn)	Ordered LN	9	262,263
AMoO ₄ (A = Mg, Mn, Fe, Co, Ni, Zn, Pd)	Wolframite	6–8	264,265
CuMoO ₄	CuWO ₄	6	266
AMoO ₄ (A = Ca, Sr, Ba)	Fergusonite	10, 12, 6	267–269
AMoO ₄ (A = Cd, Eu)	Fergusonite	12, 9	270,271
CeZrO ₄	La ₂ Ti ₂ O ₇	12	272
LaNbO ₄	BaZnF ₄	8–10	273
InNbO ₄	Wolframite-like	11	274
NaNb ₃ O ₈	NaNb ₃ O ₈ -II	2.5	275
AgNb ₃ O ₈	NaNb ₃ O ₈ -II	3.5	276
4d⁰⁻¹ (Mo⁵⁺, Mo⁶⁺)			
Na ₄ MoO ₃	Tungsten bronze	4	277
4d¹⁻² (Mo⁴⁺, Mo⁵⁺)			
Sr ₂ FeMoO ₆	B-DPv	2	278
Mn ₂ (Fe _{0.73} Mo _{0.27})MoO ₆	B-DPv	8	279
4d²⁻³ (Mo⁴⁺, Ru⁵⁺, Ru⁶⁺)			
PbMoO ₃	Pv	7	280
Ba ₃ NaRu ₂ O ₉	Ordered Pv	9	281
4d³ (Mo³⁺, Ru⁵⁺)			
Sr ₅ Ru _{4+d} O ₁₅	10H	4	282
Ba ₂ ScRuO ₆	B-DPv	6	283
Ba ₃ CaRu ₂ O ₉	Ordered Pv	8	284
Hg ₂ Ru ₂ O ₇	Pyrochlore	4	285
4d³⁻⁴ (Mo²⁺, Mo³⁺)			
KMo ₄ O ₆	Rutile-like	3	286
4d⁴ (Ru⁴⁺)			
BaRuO ₃	Pv, 6H, 4H	2.5, 18	287–291
CaRuO ₃	Post-Pv	23.5	292,293
PbRuO ₃	Pv	9	294,295
Ba ₂ RuO ₄	K ₂ NiF ₄ (RP, n = 1)	6.5	6
CaCu ₃ Ga ₂ Ru ₂ O ₁₂	A-QPv	12.5	296
Tl ₂ Ru ₂ O _{7-δ}	Pyrochlore	1–5	297
4d⁵ (Ru³⁺, Rh⁴⁺)			
PrRuO ₃	Pv	2	298,299
RRuO ₃ (R = Nd, Sm, Eu, Ho, Y)	Pv	10, 11	298
BaRhO ₃	4H, “18R”	6	300,301
SrRhO ₃	Pv, “6H”	6	302–304
CaRhO ₃	Pv, Intermediate phase, Post-Pv	6, 17	305–308
Sr ₃ Rh ₂ O ₇	RP phase (n = 2)	6	309
Sr ₄ Rh ₃ O ₁₀	RP phase (n = 3)	6	309
Ba ₂ RhO ₄	K ₂ NiF ₄ (RP, n = 1)	8	310
A ₂ Rh ₂ O ₇ (A = Lu, Tl)	Pyrochlore	6	311,312
4d⁵⁻⁶ (Rh³⁺, Rh⁴⁺)			

(Continued)

Table 10 4d-transition metal oxides obtained by HPHT synthesis (> 1 GPa).—cont'd

Compounds	Structure type	<i>P</i> (GPa)	References
CaCu ₃ Rh ₄ O ₁₂	A-QPv	15	313
Ba _{2-x} Rh ₄ O ₈	Hollandite	6–6.5	300
ARh ₂ O ₄ (A = Na, Ca, Cu, Cd)	CaFe ₂ O ₄	6	314–316
4d⁶ (Rh³⁺)			
LaMn ₃ Rh ₄ O ₁₂	A-QPv	8	317
ARhO ₃ (A = In, Sc)	Pv	6	36,318
Zn ₂ PdO ₄	Spinel	7	319
A ₂ Pd ₂ O ₇ (A = Sc, Y, In, Gd, Dy, Er, Yb)	Pyrochlore	6.5	320
A ₄ PdO ₆ (A = Ca, Sr)	K ₄ CdCl ₆	10	321
4d^{6, 8} (Pd²⁺, Pd⁴⁺)			
BiPd ₂ O ₄	PbPt ₂ O ₄	6	322
RPd ₂ O ₄ (R = Y, La, Pr, Nd, Gd)	UPd ₂ S ₄	2	323,324
4d⁷ (Pd³⁺)			
LaPdO ₃	Pv	5	325
4d⁸ (Pd²⁺, Ag³⁺)			
LaAgO ₃	Pv	6.5	
CaPd ₃ M ₄ O ₁₂ (M = Ti, V)	A-QPv	15	326
Lu ₂ PdO ₄	Nd ₂ CuO ₄	6	327
PbPd ₂ O ₄	UPd ₂ S ₄	6	322
4d^{8, 10} (Ag⁺, Ag³⁺)			
AgCu ₃ V ₄ O ₁₂	A-QPv	15	328

Pv: Perovskite. B-DPv: B-site NaCl ordered double perovskite. A-QPv: A-site-ordered quadruple perovskites. 4H, 6H, 10H, 18R: Hexagonal perovskites. " ": distorted polytypes. LN: lithium niobate.

example, Ba₂NiOsO₆ synthesized at a HP condition of 6 GPa and 1500 °C can be characterized as a FM Dirac-Mott insulator, which is a rare material.³⁷⁷ It crystallizes in a cubic lattice (*Fm-3m*) with fully ordered Ni and Os atoms, and its crystal density is 2.75% greater than that of hexagonal Ba₂NiOsO₆ (*P-3m1*) synthesized without high pressure.⁴⁴² Ca₂FeOsO₆ synthesized at 6 GPa shows magnetic ordering at a temperature higher than room temperature, whereas an isoelectronic Sr₂FeOsO₆ shows an entirely different magnetic order at temperatures below 140 K. The HP synthesis method seems to often be effective in enhancing the material properties of 4d and 5d perovskite oxides, which may be a clue to developing advanced technologies for quantum material devices.

4.20.4 Perovskite oxides with A-site ordering

4.20.4.1 A-site-ordered quadruple perovskite

4.20.4.1.1 Syntheses and crystal structures

A-site-ordered quadruple perovskite compounds are summarized in Table 12. The A-site-ordered quadruple perovskite structure (AA'₃B₄O₁₂) is a representative example of transition metal oxides which can be stabilized under high pressure. Fig. 9 illustrates the crystal structure of the cubic A-site-ordered quadruple perovskite AA'₃B₄O₁₂, whose unit cell can be derived from the 2a₀ × 2a₀ × 2a₀ multiple unit cells of simple cubic perovskite structure (a₀: lattice constant of ABO₃ perovskite, typically ~3.9 Å). The AA'₃B₄O₁₂ family crystallizes with a 1:3-type cation ordering at A-sites (= A- and A'-sites), where three quarters of original A-site are typically occupied by Jahn-Teller active ions (e.g., Cu²⁺, Mn³⁺) in pseudosquare planar coordination with 4 second nearest neighbor O ions (CN = 4 + 4), and the remaining quarter is occupied by conventional cations such as alkaline (Na⁺), alkaline-earth (Ca²⁺, Sr²⁺), rare-earth metals (Y³⁺, La³⁺, etc.), Cd²⁺, Pb²⁺, Bi³⁺, Th⁴⁺ and Ce⁴⁺ in icosahedral coordination (CN = 12). The corner-sharing BO₆ octahedra are involved as well as the simple ABO₃ perovskites, but the small unit cell (a₀ = a/2 = ~3.7 Å) caused by much smaller A'-site cations heavily bend the B–O–B bond angle down to ~140°. In most AA'₃B₄O₁₂ oxides, the cubic symmetry (*Im-3* space group) is retained by the a⁺a⁺a⁺ octahedral tilting, while several quadruple perovskite manganese oxides undergo symmetry lowering to rhombohedral (*R-3*), monoclinic (*I2/m, Im*) and triclinic (*I1*) structures due to the charge- and orbital-orderings.^{454,456,459,478–480} Another cubic symmetry (*Pn-3*) is realized by 1:1 cationic- or charge-ordering at the B-site in a rock-salt manner (AA'₃B₂B'₂O₁₂, see Fig. 9), as reported in CaCu₃Fe³⁺₂Fe⁵⁺₂O₁₂ and CaCu₃Ga₂Sb₂O₁₂.^{258,447}

Except for limited compounds (ACu₃Ti₄O₁₂, ACu₃Ru₄O₁₂ and CaMn₇O₁₂), the syntheses of quadruple perovskites need high pressures of gigapascal order. Early on, the compounds were synthesized in high pressures up to 8 GPa, then recent syntheses of new compounds were achieved at higher pressures up to 20 GPa using Kawai-type multi-anvil HP apparatus. Higher pressures above 10 GPa even enabled the incorporation of unusually smaller cations (Mn²⁺, Cu²⁺, Ag⁺) into icosahedral A-sites^{129,328,460} and also non Jahn-Teller ions (Fe²⁺, Co²⁺, Pd²⁺, Pb⁴⁺) into A'-sites.^{49,187,326,452} MnMn₃Mn₄O₁₂ is a striking example of pure Mn oxides with quadruple perovskite structure, emerging as ζ-Mn₂O₃ in the *P-T* phase diagram of manganese oxide.⁴⁵⁹ On the other

Table 11 5d-transition metal oxides obtained by HPHT synthesis (>1 GPa).

Compounds	Structure type	P(GPa)	References
5d⁰ (Ta⁵⁺, W⁶⁺, Re⁷⁺)			
CuTaO ₃	LN	6.5	246
LiTaO ₃	Pv	30	337
RbTaO ₃	Pv (GdFeO ₃)	9	254,255
Mn ₂ ScTaO ₆	Ni ₃ TeO ₆	6	126
Mn ₂ FeTaO ₆	LN	7	125
Zn ₂ FeTaO ₆	LN	9	338
CaCu ₃ Ga ₂ Ta ₂ O ₁₂	A-QPv	1212.5	258
Pb ₂ MWO ₆ (M = Mn, Fe, Zn)	Pv	2–3.5	260
Pb ₃ M ₂ WO ₉ (M = Cr, Mn)	Pv	3	260
NaRCoWO ₆ (R = Sm-Ho)	A-site-layer-ordered D-Pv	5	339
NaRCoWO ₆ (R = Er, Yb, Y)	A-site-layer-ordered D-Pv	5	339
NaNiWO ₆ (R = Dy, Ho, Yb, Y)	A-site-layer-ordered D-Pv	4.5	340
Sr ₈ CaRe ₃ Cu ₄ O ₂₄	B-site-ordered Pv	6	341
K ₃ NaRe ₂ O ₉	B-site ordered Pv	2	342
Mn ₄ Ta ₂ O ₉	Ordered LN-like	9	262
MnTa ₂ O ₆	Ordered α-PbO ₂ , post-α-PbO ₂	8, 9	262,343
LuCrWO ₆	Ordered Aeschynite-like	6	344
Sr ₃ W ₂ O ₉	Ba ₃ Re ₂ O ₉	6	345,346
Y ₃ ReO ₈	La ₃ ReO ₈	4	347
AWO ₄ (A = Ca, Sr, Eu)	Fergusonite	10, 8.5	268,348,349
AWO ₄ (A = Mn, Cd)	p-Wolframite	20, 22	350,351
AWO ₄ (A = Mg, Zn)	FeMoO ₄ -II	17	352
CuWO ₄	Wolframite	10	353
NdTaO ₄	LaTaO ₄	8	354
R ₂ WO ₆ (R = Dy, Ho)	Y ₂ WO ₆	6.5	355
NiTa ₂ O ₆	Ordered Flu	7	356
Mn ₃ WO ₆	Corundum	8	127
Na ₂ W ₂ O ₇	Sr ₂ Nb ₂ O ₇	3.2	357
Ba ₃ W ₂ O ₉	Ba ₂ RbFe ₂ F ₉	6	358
A ₂ W ₂ O ₇ (A = K, Rb)	K ₂ W ₂ O ₇	4	359
5d⁰⁻¹ (W⁵⁺, W⁶⁺)			
K ₄ WO ₃	Tungsten bronze	6.5	261
R ₄ WO ₃ (R = La, Nd)	Tungsten bronze	3	360
5d¹ (W⁵⁺, Re⁶⁺)			
AReO ₄ (A = Mg, Mn, Zn)	Wolframite	5.5–5.8	218,361
AReO ₄ (A = Ni, Co)	Ordered Rutile	5.8	218
Li _x WO ₃	LN	8	362
AWO ₃ (A = Na, K)	Pv	5–8	363,364
CaMn ₂ ReO ₆	A-site-column-ordered D-Pv	10	365
Mn ₃ ReO ₆	B-DPv	5, 8	115,116
Mn ₂ NiReO ₆	B-DPv	8	122
A ₂ CoReO ₆ (A = Mn, Pb)	B-DPv	8	121,366
In ₆ ReO ₁₂	Pr ₇ O ₁₂	5	367
5d¹⁻² (Re⁵⁺, Re⁶⁺)			
K _{0.3} ReO ₃	Tungsten bronze	6.5	368
5d² (Re⁵⁺, Os⁶⁺)			
AReO ₄ (A = Al, Ga, Fe)	Ordered Rutile	5.8	218
CrReO ₄ , Cr ₂ ReO ₆	Ordered Rutile	6	218,369
TlReO ₄	Wolframite	2	370
Pb ₂ CrReO ₆	Pv	8	366
Pb ₂ NiReO ₆	B-DPv	6	216
Mn ₂ FeReO ₆	B-DPv	11	118
CaMn ₂ ReO ₆	A-site columnar-ordered D-Pv	10	365
CaMnFeReO ₆	A-site columnar-ordered D-Pv	10	365
CaMn _{1/2} Cu _{1/2} FeReO ₆	A-site columnar-ordered D-Pv	10	365
Sr ₂ FeReO ₆	B-DPv	3.5	151
CaCu ₃ Fe ₂ Re ₂ O ₁₂	A-QPv	10	371
Na ₂ OsO ₄	Ca ₂ IrO ₄	6	372,373
A ₂ MgOsO ₆ (A = Ca, Sr)	B-DPv	6	374

(Continued)

Table 11 5d-transition metal oxides obtained by HPHT synthesis (> 1 GPa).—cont'd

Compounds	Structure type	P(GPa)	References
A_3OsO_6 ($A = Ca, Sr$)	B-DPv	6	375,376
Ba_2MOsO_6 ($M = Cu, Ni$)	B-DPv	6	237,377
$A_2Re_2O_7$ ($A = Ca, Cd, Pb$)	Pyrochlore	4	378
$5d^{2-3}$ (Os^{4+}, Os^{5+})			
$NaCu_3Fe_2Os_2O_{12}$	A-QPv	8–10	379
$K_{0.84}OsO_3$	KSbO ₃	6	380
$Bi_{2.93}Os_3O_{11}$	KSbO ₃	6	380
KOs_2O_6	Pyrochlore	3	381
$5d^3$ (Os^{5+}, Ir^{6+})			
$LiOsO_3$	LN	6	382
$NaOsO_3$	Pv, Post-Pv	6,16	383,384
Ca_2MOsO_6 ($M = Fe, In$)	B-DPv	6	237,385
Pb_2FeOsO_6	B-DPv	8	386
Sr_2YOsO_6	B-DPv	6	387
$Ba_3CuOs_2O_9$	Ordered 6H Pv	6	388
$CaCu_3Fe_2Os_2O_{12}$	A-QPv	8–10	389
Sr_2CuIrO_6	B-DPv	4	390
Ba_2ZnIrO_6	Pv	7	391–393
$BaLaLiIrO_6$	Pv	7.5	391–393
Sr_2AlrO_6 ($A = Ca, Mg$)	B-DPv	6	394
$CaCu_6Ir_2O_{12}$	A-Q Pv	8	395
$5d^{3-4}$ (Os^{4+}, Os^{5+})			
$CaCu_3Mn_2Os_2O_{12}$	A-QPv	5	396
$5d^4$ (Os^{4+}, Ir^{5+})			
$AOsO_3$ ($A = Ca, Sr, Ba$)	Pv	6,17	397
Sr_2FeOsO_6	B-DPv	6	398
$NaIrO_3$	Post-Pv	4.5	399
$Ba_3CaIr_2O_9$	Ordered 6H Pv	5	400
$IrSr_2TbCu_2O_8$	1212-type	9.2	401
$5d^{4-5}$ (Ir^{4+}, Ir^{5+})			
$Ba_3YIr_2O_9$	D-Pv	8	402
$5d^5$ (Ir^{4+})			
$BaIrO_3$	“6H,” “5H,” Pv	6,10,25	403–405
$SrIrO_3$	Pv	5	406–409
$Sr_3Ir_2O_7$	RP phase ($n = 2$)	1	6
$Sr_4Ir_3O_{10}$	RP phase ($n = 3$)	3.5	6
Ba_2IrO_4	K_2NiF_4 (RP, $n = 1$)	6	410
Lu_2NiIrO_6	B-DPv	6	217
$CaCu_3Ir_4O_{12}$	A-QPv	9	411
$5d^{5-6}$ (Ir^{3+}, Ir^{4+})			
$LaCu_3Ir_4O_{12}$	A-QPv	9	412
$5d^6$ (Pt^{4+})			
$CaPtO_3$	Post-Pv	4	413,414
$CaCu_3Pt_4O_{12}$	A-QPv	12	415
$LaCu_3Pt_{3.75}O_{12}$	A-QPv	15	416
$A_2Pt_2O_7$ ($A = Sc, Y, In, Pr, Nd, Sm-Lu, Tl$)	Pyrochlore	4	320,417,418
$5d^8$ (Au^{3+})			
$CaAu_2O_4$	UPd ₂ S ₄	12	419
$R_4Au_2O_9$ ($R = Nd, Gd$)	La ₄ Au ₂ O ₉	4	420

Pv: Perovskite. B-DPv: B-site NaCl ordered double perovskite. A-QPv: A-site-ordered quadruple perovskites. 5H, 6H: Hexagonal perovskites. “ ”: distorted polytypes. LN: lithium niobate.

hand, low-pressure and ambient-pressure syntheses are attempted by using wet-chemistry. $RCu_3Mn_4O_{12}$ are synthesized at relatively low pressure (~2 GPa) from mixtures prepared by the citric acid polymerization method.⁴⁸¹ And, furthermore, $CaCu_3Fe_2Sb_2O_{12}$ is synthesized at AP by using a wet-chemistry route.⁴⁸²

4.20.4.1.2 Valence states

Since most $AA'_3B_4O_{12}$ oxides include multiple valence-variable metals, the valence states are not unique. Typical valence states of quadruple perovskites are $Ca^{2+}Cu^{2+}_3M^{4+}_4O_{12}$ and $La^{3+}Mn^{3+}_3M^{3+}_4O_{12}$ as the Cu^{2+} and Mn^{3+} valences are usually stable in mixed

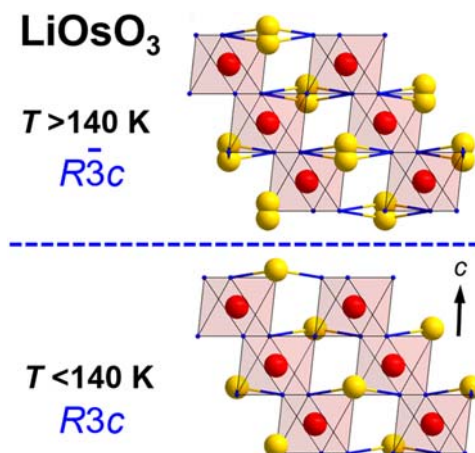


Fig. 8 Schematic views of the centrosymmetric (top, > 140 K) and non-centrosymmetric (bottom, < 140 K) structures of LiOsO_3 . With permission from Yamaura, K. *J. Solid State Chem.* **2016**, *236*, 45–54.

metal oxides. However, competing 3d band levels at A' - and B -site metals achieve unusual valence states including $\text{Cu}^{\sim 3+}$ and $\text{Mn}^{\sim 2+}$ as reported in $\text{Ca}^{2+}\text{Cu}^{3+}_3\text{Co}^{3.25+}_4\text{O}_{12}$ and $\text{La}^{3+}\text{Mn}^{2+}_3\text{V}^{3.75+}_4\text{O}_{12}$.^{448,471} Temperature-induced intersite charge transfers are observed in $\text{ACu}_3\text{Fe}_4\text{O}_{12}$ and $\text{ACu}_3\text{Cr}_4\text{O}_{12}$ series (see the following section),^{461,462,472} where electrons are transferred between A' - and B -sites at electronic phase transitions. The electrons doped by A -site-cation substitutions (e.g., $\text{Na}^+ \rightarrow \text{Ca}^{2+} \rightarrow \text{La}^{3+}$) are injected into either A' - or B -site metals, depending on their relative energy levels. Fig. 10 illustrates the electron doping sequences reported in the quadruple perovskites: (a) only B -site, (b) A' -site followed by B -site, and (c) B -site followed by A' -site (Fig. 10).

4.20.4.1.3 Physical properties and functions

Early $\text{AA}'_3\text{B}_4\text{O}_{12}$ oxides such as $\text{CaCu}_3\text{Ti}_4\text{O}_{12}$ and $\text{CaCu}_3\text{Mn}_4\text{O}_{12}$ were reported about five decades ago.^{443,446,450,454,483,484} Later, intriguing electronic properties were extensively investigated since 1990s. $\text{CaCu}_3\text{Ti}_4\text{O}_{12}$ and related compounds are widely investigated because of their large dielectric constants: $\sim 10^4$ – 10^5 ,^{485,486} which are attributed to extrinsic effects such as spatial inhomogeneity and local contact.^{487,488} $\text{CaCu}_3\text{Mn}_4\text{O}_{12}$ is a ferrimagnetic semiconductor involving a low-field magnetoresistance with tunneling-type extrinsic origin at room temperature.⁴⁸⁹ $\text{LaCu}_3\text{Mn}_4\text{O}_{12}$ also exhibits a similar magnetoresistance,⁴⁷⁴ whereas a half-metallic electronic character is obtained by first-principle calculation for $\text{LaCu}_3\text{Mn}_4\text{O}_{12}$ as well as $\text{Sr}_2\text{FeMoO}_6$ and $\text{Ti}_2\text{Mn}_2\text{O}_7$.^{130,490,491} A heavy-fermion-like behavior with a large electronic specific heat coefficient is reported in $\text{CaCu}_3\text{Ru}_4\text{O}_{12}$,⁴⁹² in which hybridization between localized Cu 3d and itinerant Ru 4d electrons is predominant.

Magnetic properties of Cu^{2+} and Mn^{3+} ions at pseudosquare-coordinated A' -sites are investigated in nonmagnetic B -site series. AFM ordering of Cu^{2+} spins is observed in $\text{CaCu}_3\text{Ti}_4\text{O}_{12}$ at $T_N = 24$ K,⁴⁹³ while FM ordering of Cu^{2+} spins is observed in $\text{CaCu}_3\text{Ge}_4\text{O}_{12}$ ($T_C = 13$ K) and $\text{CaCu}_3\text{Sn}_4\text{O}_{12}$ ($T_C = 10$ K).⁴⁵¹ The first-principle calculation for $\text{CaCu}_3\text{Ti}_4\text{O}_{12}$ indicates that the AFM superexchange interactions between Cu^{2+} ions are derived from the orbital overlapping between Ti 3d and O 2p orbitals, but it is not the case for $\text{CaCu}_3\text{Ge}_4\text{O}_{12}$ and $\text{CaCu}_3\text{Sn}_4\text{O}_{12}$. Similar interpretation is appropriate for $\text{CaCu}_3\text{Pt}_4\text{O}_{12}$ ($T_N = 40$ K) and $\text{LaCu}_3\text{Pt}_{3.75}\text{O}_{12}$ ($T_g = 3.7$ K).^{415,416} Theoretical study of the AFM ordering of Mn^{3+} ions at $\text{RMn}_3\text{Al}_4\text{O}_{12}$ ($R = \text{Y, Yb, Dy}$; $T_N = 29$ – 40 K)^{494,495} has demonstrated that the AFM Mn–O–Mn superexchange interaction is predominant.⁴⁹⁶

$\text{ACu}_3\text{Fe}_4\text{O}_{12}$ quadruple perovskites exhibit versatile structural, magnetic, and electric properties which are associated each other and depend on the valences and sizes of A -site ions. $\text{CaCu}_3\text{Fe}_4\text{O}_{12}$ was synthesized at very high pressures up to 15 GPa.⁴⁴⁷ The room-temperature valence state was firstly estimated to be $\text{Ca}^{2+}\text{Cu}^{2+}_3\text{Fe}^{4+}_4\text{O}_{12}$ at an early stage, but precise analysis using X-ray absorption spectroscopy revealed the mixed-valence state of $\text{Ca}^{2+}\text{Cu}^{2.4+}_3\text{Fe}^{3.65+}_4\text{O}_{12}$.⁴⁹⁷ The Fe ions undergo charge disproportionation transition ($2\text{Fe}^{4+} \rightarrow \text{Fe}^{3+} + \text{Fe}^{5+}$ in the simplified form) below 210 K simultaneously with metal-semiconductor and ferrimagnetic transitions. The Fe^{3+} and Fe^{5+} ions in the charge-disproportionated phase are ordered in the rock-salt manner, lowering the space group symmetry ($Im\bar{3} \rightarrow Pn\bar{3}$). The sudden drop of volume at the transition is derived from the Fe-to-Cu electron charge transfer ($3\text{Cu}^{2.4+} + 4\text{Fe}^{3.65+} \rightarrow 3\text{Cu}^{2.2+} + 4\text{Fe}^{3.8+}$), which differs from the Cu-to-Fe one in $\text{SrCu}_3\text{Fe}_4\text{O}_{12}$, as shown below (Fig. 11).

$\text{SrCu}_3\text{Fe}_4\text{O}_{12}$ demonstrates a negative thermal expansion (NTE) with a linear coefficient of thermal expansion, $\alpha_L = -2.26 \times 10^{-5} \text{ K}^{-1}$, below room temperature (Fig. 11).⁴⁶⁵ The NTE in $\text{SrCu}_3\text{Fe}_4\text{O}_{12}$ is driven by the intersite charge transfer between Cu and Fe on heating from ~ 200 K to ~ 270 K ($3\text{Cu}^{2.8+} + 4\text{Fe}^{3.4+} \rightarrow 3\text{Cu}^{2.4+} + 4\text{Fe}^{3.7+}$),⁴⁹⁸ resulting in shrinkage of Fe–O bonds. The lattice constant a is associated with the Fe–O bond length ($d_{\text{Fe-O}}$) and $\angle \text{Fe-O-Fe}$ bond angle (ψ); $a = 2d_{\text{Fe-O}} \times \sin(\psi/2)$. In the NTE temperature range, the contraction of the Fe–O bonds overcomes the opening of $\angle \text{Fe-O-Fe}$ angle. The chemical-substitution-free and second-order feature in NTE of $\text{SrCu}_3\text{Fe}_4\text{O}_{12}$ are in contrast to the first-order NTE observed in the $\text{Pb}_{1-x}\text{Bi}_x\text{VO}_3$ and BiNiO_3 derivatives (see Sections 4.20.2.3 and 4.20.2.8). The NTE in $\text{CaMn}_7\text{O}_{12}$

Table 12 A-site-ordered quadruple perovskites obtained by HPHT synthesis (> 1 GPa).

Compounds	Symmetry	P(GPa)	References
CaCu₃M₄O₁₂			
CaCu ₃ Ti ₄ O ₁₂	<i>I m-3</i>	AP	443
CaCu ₃ V ₄ O ₁₂	<i>I m-3</i>	8	444
CaCu ₃ Cr ₄ O ₁₂	<i>I m-3</i>	6	445
CaCu ₃ Mn ₄ O ₁₂	<i>I m-3</i>	5	446
CaCu ₃ Fe ₄ O ₁₂	<i>I m-3, P n-3</i>	15	447
CaCu ₃ Co ₄ O ₁₂	<i>I m-3</i>	9	448
CaCu ₃ Ge ₄ O ₁₂	<i>I m-3</i>	5–7	449
CaCu ₃ Ru ₄ O ₁₂	<i>I m-3</i>	AP	450
CaCu ₃ Rh ₄ O ₁₂	<i>I m-3</i>	15	313
CaCu ₃ Ir ₄ O ₁₂	<i>I m-3</i>	9	411
CaCu ₃ Pt ₄ O ₁₂	<i>I m-3</i>	12	415
CaCu ₃ Sn ₄ O ₁₂	<i>I m-3</i>	6	451
CaM₃(Ti/V)₄O₁₂			
CaFe ₃ Ti ₄ O ₁₂	<i>I m-3</i>	15	49
CaCo ₃ V ₄ O ₁₂	<i>I m-3</i>	15–16	452
CaPd ₃ Ti ₄ O ₁₂	<i>I m-3</i>	15	326
CaPd ₃ V ₄ O ₁₂	<i>I m-3</i>	15	326
AMn₇O₁₂			
NaMn ₇ O ₁₂	<i>I2/m, Im-3</i>	8	453
CaMn ₇ O ₁₂	<i>R-3, Im-3</i>	AP	454,455
LaMn ₇ O ₁₂	<i>I2/m, Im-3</i>	4	456
BiMn ₇ O ₁₂	<i>I1, Im, I2/m</i>	5	457
HgMn ₇ O ₁₂	<i>Pnn2, R-3, Im-3,</i>	8	457,458
ζ-Mn ₂ O ₃ (MnMn ₃ Mn ₄ O ₁₂)	<i>F-1</i>	18–20	459
MCu₃V₄O₁₂			
MnCu ₃ V ₄ O ₁₂	<i>Im-3</i>	12	129
CuCu ₃ V ₄ O ₁₂	<i>Im-3</i>	15	460
AgCu ₃ V ₄ O ₁₂	<i>Im-3</i>	15	328
ACu₃Fe₄O₁₂			
LaCu ₃ Fe ₄ O ₁₂	<i>Im-3</i>	9	461
R ³⁺ Cu ₃ Fe ₄ O ₁₂	<i>Im-3, Pn-3</i>	15	462,463
Ce ⁴⁺ Cu ₃ Fe ₄ O ₁₂	<i>Im-3</i>	15	464
SrCu ₃ Fe ₄ O ₁₂	<i>Im-3</i>	15	465
CdCu ₃ Fe ₄ O ₁₂	<i>Im-3</i>	20	466
CaCu₃M₂M'₂O₁₂			
CaCu ₃ Ga ₂ Sb ₂ O ₁₂	<i>Pn-3</i>	12–12.5	258
CaCu ₃ Ga ₂ Ta ₂ O ₁₂	<i>Pn-3</i>	12–12.5	258
CaCu ₃ Cr ₂ Sb ₂ O ₁₂	<i>Pn-3</i>	10	467
CaCu ₃ Fe ₂ Re ₂ O ₁₂	<i>Pn-3</i>	10	371
CaCu ₃ Fe ₂ Sb ₂ O ₁₂	<i>Pn-3</i>	10	468
CaCu ₃ Fe ₂ Nb ₂ O ₁₂	<i>Im-3, Pn-3</i>	9–9.5	257
Others			
BiMn ₃ (Fe _{0.25} Ti _{0.75}) ₄ O ₁₂	<i>Im-3</i>	6	469
LaMn ₃ Ti ₄ O ₁₂	<i>Im-3</i>	8–10	470
NaMn ₃ V ₄ O ₁₂	<i>Im-3</i>	7	471
CaMn ₃ V ₄ O ₁₂	<i>Im-3</i>	9	471
LaMn ₃ V ₄ O ₁₂	<i>Im-3</i>	9	471
YCu ₃ Cr ₄ O ₁₂	<i>Im-3</i>	9	472
LaCu ₃ Cr ₄ O ₁₂	<i>Im-3</i>	9	472
BiCu ₃ Cr ₄ O ₁₂	<i>Im-3</i>	7.7	473
LaCu ₃ Mn ₄ O ₁₂	<i>Im-3</i>	2	474
BiCu ₃ Mn ₄ O ₁₂	<i>Im-3</i>	6	475
PbCoO ₃ (Pb ²⁺ Pb ⁴⁺ ₃ Co ²⁺ ₂ Co ³⁺ ₂ O ₁₂)	<i>Pn-3</i>	12	187
PbHg ₃ Ti ₄ O ₁₂	<i>Im-3, Imm2</i>	6	476

M, M': transition metal.

Symmetry: *Im-3* is the parent structure of the A-site-ordered quadruple perovskites. *Pn-3*, *I2/m*, and *Pnn2* are with an additional rock-salt B-site ordering. *R-3* is with an additional 1:3-type B-site ordering. *I1* and *Im* are with distortions due to structural and orbital modulations. *F-1* is with complex distortion. *Imm2* is with a polar distortion.

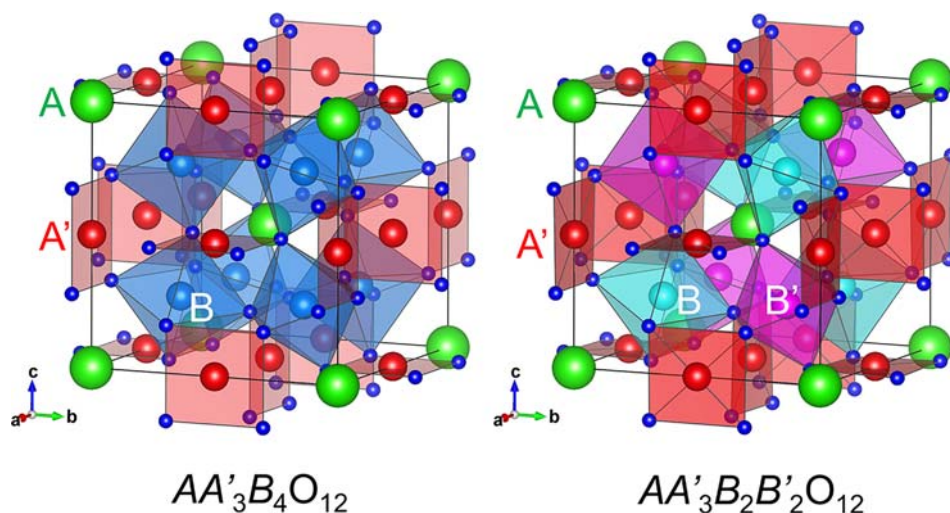


Fig. 9 Schematic crystal structures of cubic quadruple perovskites drawn using VESTA-3 software⁴⁷⁷: $AA'_3B_4O_{12}$ (left) and $AA'_3B_2B'_2O_{12}$ (right).

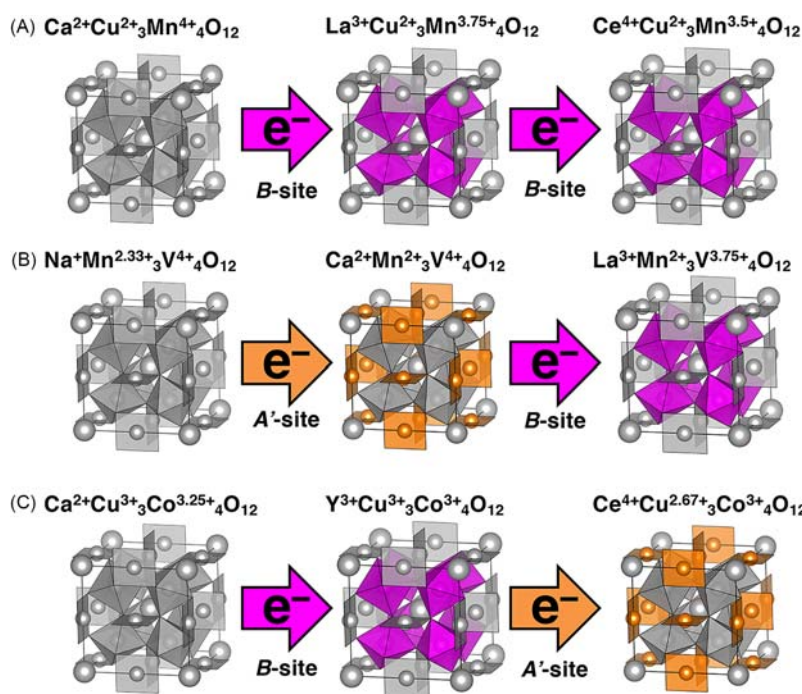


Fig. 10 Three different electron-doping sequences in quadruple perovskites. Adapted with permission from Yamada, I.; Otake, T.; Tanaka, A.; et al. *Inorg. Chem.* **2020**, *59* (13), 8699–8706.

($\alpha_L = -2.864 \times 10^{-5} \text{ K}^{-1}$),⁴⁵⁵ as well as that in Bi,Pb-based perovskites, is induced by the coexistence of high-temperature small-volume and low-temperature large-volume phases.

The $RCu_3Fe_4O_{12}$ series ($R =$ trivalent rare-earth metal) displays an intriguing structure-property relation associated with charge transfer and charge disproportionation. $LaCu_3Fe_4O_{12}$ possesses the valence state of $La^{3+}Cu^{2+}_3Fe^{3.75+}_4O_{12}$ at high temperature above ~ 400 K and undergoes an intersite-charge-transfer transition ($3Cu^{2+} + 4Fe^{3.75+} \rightarrow 3Cu^{3+} + 4Fe^{3+}$) below ~ 400 K.⁴⁶¹ This phase transition involves a large volume expansion of $\Delta V \sim 1\%$ (Fig. 11), AFM ordering of Fe^{3+} spins, and metal-insulator transition, although the $Im\bar{3}$ space group is retained. The intersite charge transfer is suppressed in $YCu_3Fe_4O_{12}$, although the valence state of the HT phase ($Y^{3+}Cu^{2+}_3Fe^{3.75+}_4O_{12}$) is formally isoelectronic to that of $LaCu_3Fe_4O_{12}$.⁴⁶³ A charge-disproportionation transition ($8Fe^{3.75+} \rightarrow 5Fe^{3+} + 3Fe^{5+}$) occurs below 250 K, simultaneously with the metal-semiconductor, ferrimagnetic and charge-ordering transitions. The A-site size effect on structure and electronic properties is systematically investigated on $R^{3+}Cu_3Fe_4O_{12}$ ($R =$ Pr, Nd, Sm, Eu, Gd, Tb, Dy, Ho, Er, Tm, Yb and Lu).⁴⁶² The crystal structure of a HT phase is evaluated by the bond valence method. The bond discrepancy factor (d_M), which can be calculated from the difference between the bond

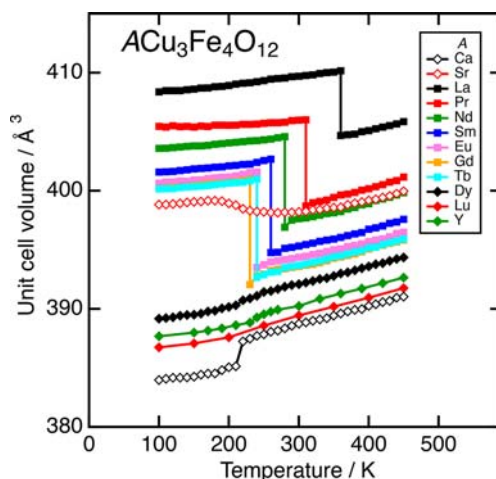


Fig. 11 Temperature dependence of unit cell volume for $ACu_3Fe_4O_{12}$. Adapted with permission from Yamada, I. J. *Cerma. Soc. Jpn.* **2014**, *122* (1430), 846–851.

valence sum (BVS) and nominal valence (V_M), i.e., $d_M = BVS - V_M$,⁴⁹⁹ demonstrates monotonic increase for R ions (overbonding in R–O bond) and decrease for Fe ions (underbonding in Fe–O bond). The most stable structure is realized in $DyCu_3Fe_4O_{12}$ because the global instability index (GII), which is an index of structure instability calculated from the root-mean square of d_M in the formula unit,⁴⁹⁹ becomes the minimum (GII = 0.04 valence unit (vu)), although both larger and smaller R ions tend to increase GII (0.19 vu for $LaCu_3Fe_4O_{12}$ and 0.10 vu for $LuCu_3Fe_4O_{12}$). The intersite charge-transfer occurs to remove the bond strain of the compressed Fe–O bond for $RCu_3Fe_4O_{12}$ with larger R ions ($R = La-Tb$) and the phase transition temperature monotonically decreases from 367 K ($R = La$) to 233 K ($R = Tb$) with GII decreases. In contrast, another type of phase transition, charge disproportionation and ferrimagnetism as $YCu_3Fe_4O_{12}$, occurs at almost the same temperature (~ 250 K) for $RCu_3Fe_4O_{12}$ with smaller R ions ($R = Dy-Lu$).

The intersite charge-transfer transition in $RCu_3Fe_4O_{12}$ can be utilized as robust thermal-energy storage with controllable operation temperature.⁵⁰⁰ The latent heat in the phase transition of $LaCu_3Fe_4O_{12}$ is evaluated by differential scanning calorimetry to be 25 J g^{-1} (154 J cm^{-3}), which is much larger than typical values in perovskite related compounds ($\sim 40 \text{ J cm}^{-3}$) and approaches that of the thermal-storage material VO_2 (234 J cm^{-3}).⁵⁰¹ The transition temperature decreases with R ion size decreases, whereas the transition entropy remains almost constant. The robustness of the latent-heat property in $RCu_3Fe_4O_{12}$ is in contrast to the significant depression in transition entropy in VO_2 -related materials with partial chemical substitutions.

The charge-transfer and charge-disproportionation transitions are also observed in the Cu-Cr system $ACu_3Cr_4O_{12}$ ($A = Y, La, Bi$).^{472,473} $YCu_3Cr_4O_{12}$ and $LaCu_3Cr_4O_{12}$ undergo charge transfer between Cu and Cr ions ($3Cu^{(2+\delta)+} + 4Cr^{(3.75-\delta')+) \rightarrow 3Cu^{(2+\delta+\epsilon)+} + 4Cr^{(3.75+\delta'-0.75\epsilon)+}$) at 220–250 K on cooling, exhibiting a positive volume change. In contrast, $BiCu_3Cr_4O_{12}$ demonstrates ferrimagnetic transition at 190 K associated with charge disproportionation of $Cr^{3.75+}$ into Cr^{3+} and Cr^{4+} .

A multiferroic property is reported in cubic quadruple perovskite $LaMn_3Cr_4O_{12}$.⁵⁰² Two distinct AFM sublattices of A'-site Mn^{3+} and B-site Cr^{3+} spins realize a noncentrosymmetric magnetic structure, leading to the spin-driven magnetoelectric property, although the cubic crystal symmetry is maintained. $BiMn_3Cr_4O_{12}$ demonstrates different types of multiferroic phases, which derives from stereochemical $6s^2$ lone pairs of Bi^{3+} ions.⁵⁰³ Spin-induced ferroelectricity was also observed in the AMn_7O_{12} series ($A = Mn$,⁵⁰⁴ Cd, Ca, Sr, Pb,⁵⁰⁵ and Hg⁵⁰⁶) and was due to complex spin structures coupled to structural and orbital modulations.⁵⁰⁶

Proper polar distortions were observed in $HgMn_7O_{12}$ ($Im-3 > R-3 > Pnn2$ at 470 and 260 K, respectively⁴⁵⁸), $Bi_{0.95}Mn_7O_{12}$ ($R3$ at RT⁵⁰⁷), and $BiCu_{0.1}Mn_{6.9}O_{12}$ ($Im-3 > I2/m > R-1(\alpha\beta\gamma)0 > R3(00\gamma)t$ at 546, 403, and 323 K, respectively⁵⁰⁸). The crystal structures of $BiCu_{0.1}Mn_{6.9}O_{12}$ are heavily modulated with the realization of an intermediate dipole density wave $R-1(\alpha\beta\gamma)0$ structure and a helicoidal texture of electric dipoles in the ground-state $R3(00\gamma)t$ structure.

$PbHg_3Ti_4O_{12}$ possesses a middle tolerance factor ($t \approx 0.88$) rather than smaller ones ($t < 0.8$) of any other quadruple perovskites because of larger ionic radius of Hg^{2+} at A'-site.⁴⁷⁶ $PbHg_3Ti_4O_{12}$ transforms from HT centrosymmetric phase ($Im-3$) to low-temperature noncentrosymmetric phase with ferroelectricity ($Imm2$) at 250 K.

4.20.4.1.4 Electrocatalytic properties

Quadruple perovskite oxides demonstrate catalytic activity for electrochemical oxygen reactions.^{509–511} The unusual high valence ions (e.g., Fe^{4+} and Co^{4+}) stabilized using the HP method are intrinsically active for electrochemical oxygen evolution reaction (OER).²⁰⁰ The OER activity of simple perovskite (e.g., $CaFeO_3$ and $SrFeO_3$) is further enhanced in the quadruple perovskite structure. $CaCu_3Fe_4O_{12}$ demonstrates highly active OER catalysis exceeding state-of-the-art catalyst materials such as $Ba_{0.5}Sr_{0.5}Co_{0.8}Fe_{0.2}O_{3-\delta}$ (BSCF) and RuO_2 (Fig. 12(a)). Similar enhancement in OER activity is commonly observed in $CaCu_3M_4O_{12}$ ($M = Ti, V, Cr, Mn, Fe$,

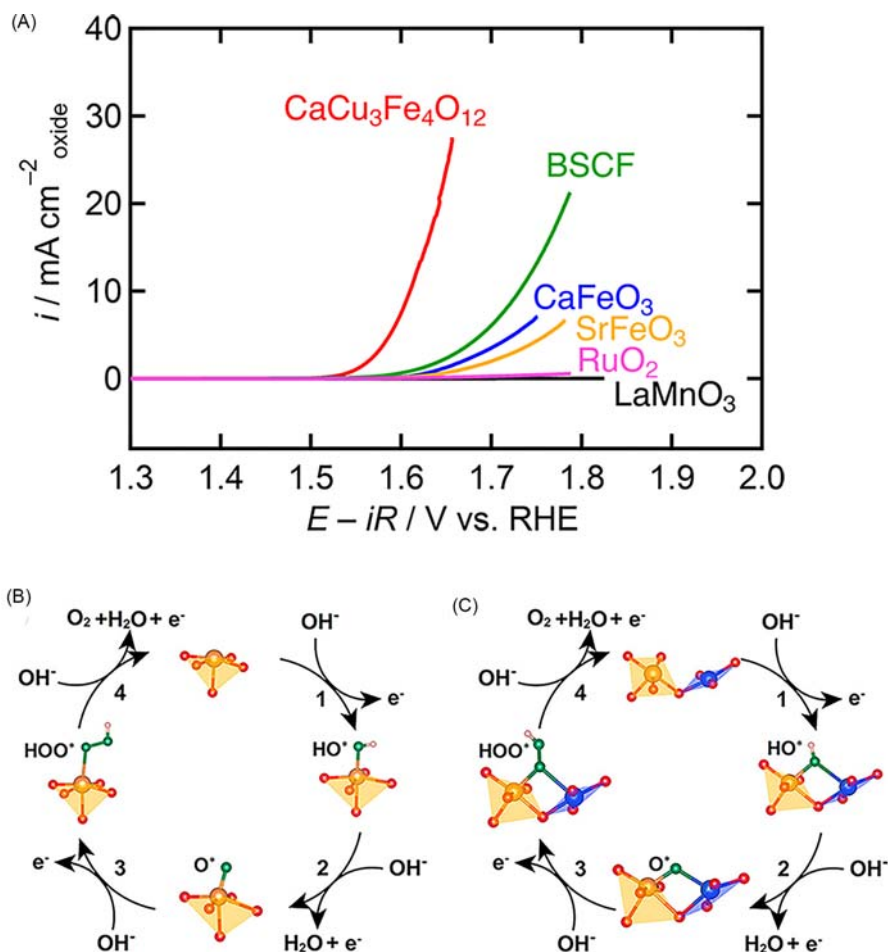


Fig. 12 (a) Linear sweep voltammograms for $\text{CaCu}_3\text{Fe}_4\text{O}_{12}$ and reference catalysts. (b) Conventional OER mechanism for simple perovskite structure. The coordinatively unsaturated B-site metal (orange on the (001) surface) serve as active site. (c) Proposed OER mechanism for quadruple perovskite oxides based on DFT calculation. A'-site metal (blue) in pseudosquare plane plays a role in secondary active site and the adsorbate bridges over B-site (orange) and A'-site metals. Adapted with permission from Yagi, S.; Yamada, I.; Tsukasaki, H.; et al. *Nat. Commun.* **2015**, *6*, 8249; Takamatsu, A.; Yamada, I.; Yagi, S.; Ikeno, H. *The Journal of Physical Chemistry C* **2017**, *121* (51), 28403–28411.

Co) compared to the simple perovskite counterparts.⁵¹¹ The monotonically increased OER catalytic activity for quadruple perovskites is driven by a structural feature of quadruple perovskite. DFT calculation reveals that the surface of a quadruple perovskite structure involves cationic arrangement to enable an unconventional OER mechanism in which A'-site transition metal ions play a role in OER as the secondary adsorption/reaction site together with the primary active site of B-site ions (Fig. 12(b) and (c)).⁵¹² This mechanism is in contrast to the conventional one in simple perovskite structure, where coordinatively unsaturated B-site ions solely contribute to OER as adsorption/reaction sites. Based on this mechanism, bifunctional oxygen reaction catalysis which serves to both oxidation and reduction of oxygen species is realized in Mn-based quadruple perovskites $\text{LaMn}_7\text{O}_{12}$ and $\text{CaMn}_7\text{O}_{12}$.⁵¹⁰

4.20.4.2 A-site columnar-ordered quadruple perovskites

When the ratio of A cations with quite different sizes is 1:1, a different tilt system can be realized under the right conditions, namely $a^+a^+c^-$. It produces $P4_2/nmc$ symmetry and three types of cavities for the A cations: 10-fold-coordinated (A), square-planar-coordinated (A'), and tetrahedrally coordinated (A'') cavities.⁵⁴¹ To form such A' and A'' sites, the BO_6 tilts should be quite large with B-O-B angles reaching 130–150°. A'-O and A''-O bond distances are similar (1.9–2.1 Å), but the coordination environments are fundamentally different. Therefore, the A' and A'' sites can, in principle, be occupied by different cations, and the general formula of such perovskites is better presented as $\text{A}_2\text{A}'\text{A}''\text{B}_4\text{O}_{12}$. They have intrinsic triple A-type ordering.⁵⁴¹ The AO_{10} polyhedra are connected through edges and form $-\text{AO}_{10}-\text{AO}_{10}-$ columns along the *c* axis (Fig. 13). The $\text{A}'\text{O}_4$ square units and $\text{A}''\text{O}_4$ tetrahedra are separated from each other but they are connected through edges if four longer A'-O bonds are considered, and the $-\text{A}'\text{O}_{4+4}-\text{A}''\text{O}_4-$ columns also

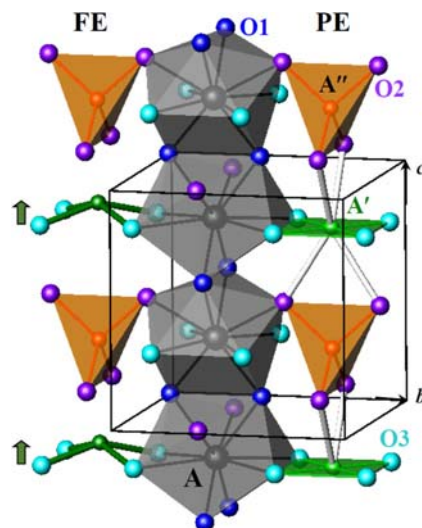


Fig. 13 A fragment of the parent structure of A-site columnar-ordered $A_2A'A''B_4O_{12}$ quadruple perovskites. Only the oxygen coordination of the A-, A'-, and A''-site ions are presented and the B-site ion is omitted. The AO_{10} polyhedra (gray) are connected through O1-O1 edges with each other along the c axis. The $A'O_4$ square-planar units are shown in green, and the $A''O_4$ tetrahedra are shown in orange. The A'-O2 white bonds show connections between $A'O_{4+4}$ and $A''O_4$ through longer distances along the c axis. The right-hand $A'O_4$ - $A''O_4$ column shows atomic arrangements in the paraelectric (PE) phase typically observed in $CaFeTi_2O_6$. The left-hand $A'O_4$ - $A''O_4$ column shows atomic arrangements in this column in the ferroelectric (FE) phase of $CaMnTi_2O_6$.

run along the c axis (Fig. 13). Considering these structural features and generic chemical formula $A_2A'A''B_4O_{12}$, such perovskites are called A-site columnar-ordered quadruple perovskites.⁵⁴¹

Table 13 lists the majority of known examples. All but $Ca_{2-x}Mn_xTi_2O_6$ ($0.3 \leq x \leq 0.6$)⁵⁴² require HPHT conditions for the synthesis. The A' and A'' cations are the same in many reported cases (Mn^{2+} and Fe^{2+}), and the formula can be further shortened to $AA'B_2O_6$. However, there are examples with different A' and A'' cations: $R_2MnGa(Mn_{4-x}Ga_x)O_{12}$ ($R = Ho$ and Y , $x = 0, 1, 2, 3$),^{519,520} $Ca(Mn_{0.5}Cu_{0.5})FeReO_6$,³⁶⁵ $R_2CuMnMn_4O_{12}$ ($R = Dy-Lu$),^{519,537} and $R_2MnZn(Mn_{4-x}Ti_x)O_{12}$ ($R = Sm$ and Dy) and $Y_2CuGaMn_4O_{12}$ (unpublished results). There are examples when $A' = Mn^{3+}$ and $A'' = Mn^{2+}$: RMn_3O_6 ($R = Gd-Tm, Y$)⁵³⁴⁻⁵³⁶

Table 13 A-site columnar-ordered quadruple perovskites obtained by HPHT synthesis (> 1 GPa).

Compound	Symmetry	P(GPa)	References
$CaFeTi_2O_6$	$P4_2/nmc$	12–15	45,49,513–517
$RMnGaTiO_6$ ($R = Sm, Gd$)	$P4_2/nmc$	6	518
$R_2MnGa(Mn_{4-x}Ga_x)O_{12}$, $R = Ho$ and Y , $x = 0, 1, 2, 3$	$P4_2/nmc$	6	519,520
$Sm_2MnMn(Mn_{4-x}Ti_x)O_{12}$, $x = 1, 2, 3$	$P4_2/nmc$	6	521,522
$NaRMn_2Ti_4O_{12}$, $R = Sm-Ho, Y$	$P4_2/nmc$	6	523
$R_2MnMn(MnTi_3)O_{12}$, $R = Nd, Eu, Gd$	$P4_2/nmc$	6	524
$CaMnTi_2O_6$	$P4_2mc$	7	517,525–529
$CaMn(Ti_{2-x}V_x)O_6$, $0 \leq x \leq 1.2$	$P4_2mc$	6	530
$MnRMnSbO_6$, $R = La-Sm$	$P4_2/n$	10	531,532
$CaMnFeReO_6$	$P4_2/n$	10	365
$CaMnMnReO_6$	$P4_2/n$	10	365
$Ca(Mn_{0.5}Cu_{0.5})FeReO_6$	$P4_2/n$	10	365
$CaMnCoReO_6$	$P4_2/n$	10	533
$CaMnNiReO_6$	$P4_2/n$	10	533
RMn_3O_6 , $R = Gd-Tm, Y$	$Pmnn$	6	521,534–536
$R_2CuMnMn_4O_{12}$, $R = Dy-Lu, Y$	$Pmnn$	6	519,537
$CaMnMnWO_6$	$P4_2/n$	10	538
$SmMnMnTaO_6$	$P4_2/n$	10	538
$CaMnFeTaO_6$	$P4_2/n$	10	539
$CaMnCrSbO_6$	$P4_2/n$	10	540
$CaMnFeSbO_6$	$P4_2/n$	10	540

Symmetry: $P4_2/nmc$ is the parent structure of the A-site columnar-ordered quadruple perovskites. $P4_2mc$ is with a polar distortion. $P4_2/n$ is with an additional rock-salt B-site ordering. $Pmnn$ is with an additional layered B-site ordering.

and $R_2\text{MnMn}(\text{Mn}_3\text{Ti})\text{O}_{12}$ ($R = \text{Nd}$ and Sm).^{521,522} So far, Mn^{2+} , Mn^{3+} , Fe^{2+} and Cu^{2+} cations were found at the A' site; and Mn^{2+} , Fe^{2+} , Ga^{3+} and Zn^{2+} cations were found at the A'' site (ignoring anti-site disorder with the A and B sites).

The parent structure of $A_2A'A''B_4\text{O}_{12}$ has $P4_2/nmc$ symmetry. Additional B-site orderings can reduce symmetry to $P4_2/n$ (producing rock-salt B-site ordering) and $Pmnm$ (producing layered B-site ordering). There are examples with a polar distortion ($P4_2mc$ symmetry).

$A_2A'A''B_4\text{O}_{12}$ perovskites have the following structural features. First, there are significant restraints on the bonding of the A site originating from the large $a^+a^+c^-$ tilts needed to form the A' and A'' sites. The A-O bonds are nearly constrained to 2.3–2.4 Å ($\times 4$), 2.4–2.5 Å ($\times 2$), and 2.7–2.9 Å ($\times 4$). Therefore, only Ca^{2+} , Na^+ , Y^{3+} , and all rare-earth (except Ce and Pm) cations have been found so far at the A site. Second, there are quite limited stability ranges when considering rare-earth series—this limitation is caused by the first feature. For example, MnRMnSbO_6 is stable for $R = \text{La-Sm}$,^{531,532} RMn_3O_6 for $R = \text{Gd-Tm}$ and Y ,⁵³⁴ $R_2\text{CuMnMn}_4\text{O}_{12}$ for $R = \text{Dy-Lu}$ and Y ,⁵¹⁹ and $R_2\text{MnMn}(\text{MnTi}_3)\text{O}_{12}$ for $R = \text{Nd-Gd}$.⁵²⁴ Rare-earth stability ranges (at certain synthesis conditions) strongly depend on the content of A' , A'' , and B sites. Third, cations at the A' square-planar site are often statistically disordered above and below the square-planar units. Fourth, there is a tendency in many cases for anti-site disorder among the A, A' , and A'' sites. Anti-site disorder is the general feature of all A-site and/or B-site ordered perovskites. As the sizes of cations located at the A' , A'' , and B sites are similar to each other, anti-site disorder among A' , A'' , and B is also possible.³⁶⁵ Fifth—and this feature is related to the fourth one—there is a tendency for compositional shifts due to “unequal anti-site disorder.” For example, the following real chemical compositions were found: $\text{CaMn}_{0.7}\text{Co}_{1.3}\text{ReO}_6$,⁵³³ $\text{CaMn}_{1.2}\text{Ni}_{0.8}\text{ReO}_6$,⁵³³ $\text{Gd}_{1.065}\text{Mn}_{2.935}\text{O}_6$,⁵³⁶ $\text{Er}_{0.89}\text{Mn}_{3.11}\text{O}_6$,⁵³⁶ $\text{Dy}_{2.22}\text{Cu}_{0.88}\text{Mn}_{4.9}\text{O}_{12}$,⁵³⁷ and $\text{Y}_{2.26}\text{Cu}_{0.79}\text{Mn}_{4.95}\text{O}_{12}$ ⁵³⁷ in comparison with the ideal compositions reported in Table 13.

Due to large BO_6 tilts, the strengths of B-B magnetic exchange should be significantly suppressed in $A_2A'A''B_4\text{O}_{12}$, as they are in $AA_3B_4\text{O}_{12}$ quadruple perovskites and ScBO_3 . Therefore, (A, A' , A'')-B exchange interactions should play the dominant role, and they can be selectively controlled by choice of A, A' , and A'' cations. Due to fundamentally different bonding geometries of $A_2A'A''B_4\text{O}_{12}$, they offer a new playground to study magnetism.⁵³⁷ In the majority of $A_2A'A''B_4\text{O}_{12}$ cases, ferrimagnetic (FiM) structures are observed with simultaneous ordering of magnetic cations at the A' , A'' , and B sites.^{521,522,531–533,535,537} But in CaMnFeReO_6 -based compounds,³⁶⁵ the B-sublattice orders first at a much higher temperature $T_B = 500$ – 560 K due to retained strong AFM interactions between Fe^{3+} and Re^{5+} ; the A'/A'' -sublattice orders at $T_A = 70$ – 160 K. Global FiM structures may be realized from different combinations of AFM and/or FM arrangements at the B site and at the A' - A'' sites depending on chemical compositions. In some cases, there exist spin-reorientation transitions at lower temperatures driven by rare-earth single-ion anisotropies and f - d exchange (and, therefore, magnetic ordering at the A site)^{531,532,535} or instability toward AFM spin canting.⁵³⁷ For example, from two to four magnetic transitions are realized in $R_2\text{CuMnMn}_4\text{O}_{12}$ ($R = \text{Dy-Lu, Y}$) (e.g., at 6, 18, 110, and 171 K for $R = \text{Er}$).^{519,537} $\text{CaMnTi}_2\text{O}_6$ -based compounds,^{525–530,542} including $\text{NaRMn}_2\text{Ti}_4\text{O}_{12}$ ($R = \text{Sm-Ho, Y}$),⁵²³ show pure C-type AFM transitions below $T_N \approx 12$ K, but with noticeably reduced ordered moments on Mn^{2+} cations and some effects of rare-earth magnetism. A purely FM transition was found in CaMnNiReO_6 below $T_C = 152$ K.⁵³³ No long-range magnetic ordering was found in $R_2\text{MnGa}(\text{Mn}_{4-x}\text{Ga}_x)\text{O}_{12}$ ($R = \text{Ho}$ and Y , $x = 0, 1, 2, 3$)^{519,520} despite large concentrations of Mn^{3+} cations at the B sites, in RMnGaTiO_6 ($R = \text{Sm, Gd}$)⁵¹⁸ probably due to noticeable A'' -B anti-site disorder, and in $\text{CaFeTi}_2\text{O}_6$.^{514,516}

$\text{CaMnTi}_2\text{O}_6$ is a ferroelectric (FE) material at RT with switchable ferroelectric polarization and a high FE Curie temperature of 630 K.⁵²⁵ Cooperative shifts of Mn^{2+} cations at the A' sites in one direction from the square-planar units (Fig. 13) and the off-center displacements of Ti^{4+} in TiO_6 octahedra are responsible for the polar structure. In the paraelectric centrosymmetric phase, Mn^{2+} cations at the A' sites are statistically disordered above and below the square-planar units.⁵²⁵ The polar structure is maintained in solid solutions $\text{CaMn}(\text{Ti}_{2-x}\text{V}_x)\text{O}_6$ ($0 \leq x \leq 1.2$) with the enhanced polarization for $x \leq 0.8$, but the FE Curie temperature decreases with increasing x .⁵³⁰ The synthesis of $\text{NaRMn}_2\text{Ti}_4\text{O}_{12}$ ($R = \text{Sm-Ho, Y}$) at 6 GPa and 1750 K stabilizes the centrosymmetric $P4_2/nmc$ structure,⁵²³ but we showed that at 6 GPa and 1550 K the polar $P4_2mc$ structure can be obtained (unpublished results). Relaxor ferroelectric properties were observed in $R_2\text{MnMn}(\text{MnTi}_3)\text{O}_{12}$ ($R = \text{Nd-Gd}$) at 250–295 K.^{521,524}

4.20.5 Mixed-anion oxides

4.20.5.1 Overview

Mixed-anion oxides are summarized in Table 14. Mixed-anion (or heteroanionic) compounds, solid-state materials containing multiple anionic species in a single phase, have recently attracted increasing attention due to their potential for having properties superior to those of a single-anion analog.^{561,562} For example, anion engineering in oxide-based compounds is a promising way to tune chemical and physical properties by incorporating additional anions of different size, electronegativity, and charge. However, it was not easy to synthesize a desired composition of a material by using conventional solid-state reaction since anionic species, such as nitrogen and fluorine, easily dissociate or evaporate under ambient conditions. A HP method is an effective approach to control an anionic composition since the HP reaction in sealed vessels prevent loss of volatile elements. One can expect that the compounds obtained by a HP method has a composition equal to its nominal one unless

Table 14 Mixed-anion oxides obtained by HPHT synthesis (>1 GPa).

Materials	Structure type	P(GPa)	References
<i>Oxyfluorides</i>			
BaTiO _{3-x} F _x	Pv	3	543
PbVO _{3-x} F _x	Pv	8	82
AgTiO ₂ F	Pv	4	544
AgFeOF ₂	Pv	7	545
Sr ₂ MO ₃ F (M = Mn, Co, Ni)	K ₂ NiF ₄ -type	6	191,546,547
MOF (M = Ti, V, Fe)	Rutile	6–6.5	548
<i>Oxychlorides</i>			
Sr ₂ NiO ₃ Cl	K ₂ NiF ₄ -type	3	547
Sr ₂ ZnO ₂ Cl ₂	K ₂ NiF ₄ -type	6	549
<i>Oxyhydrides</i>			
BaScO ₂ H	Pv	7	550
Ba ₂ ScO ₃ H	K ₂ NiF ₄ -type	3	551
Sr _{1-x} Na _x VO _{3-y} H _y	Pv	8	552
BaVO _{3-x} H _x	Pv, 6H	7, 3	553
Sr ₂ VO _{4-x} H _x	K ₂ NiF ₄ -type	5	554
SrCrO ₂ H	Pv	7	555
LaSrMnO _{3.3} H _{0.7}	K ₂ NiF ₄ -type	5	556
<i>Oxynitrides</i>			
RZrO ₂ N (R = Pr, Nd, Sm)	Pv	2–3	557
MnTaO ₂ N	LN	6	558
Mn(Mn _{1/6} Ta _{5/6})O _{2.5} N _{0.5}	LN	7.5	559
ZnTaO ₂ N	LN	6	560

Pv: Perovskite. 6H: Perovskite-polytypes. LN: lithium niobate.

secondary phases form. HP synthesis and properties of transition metal oxide based mixed-anion compounds are described in the following parts of this section.

4.20.5.2 Oxyhalides

Transition metal oxyhalides, such as oxyfluorides (oxide-fluoride) and oxychlorides (oxide-chloride), have been intensively studied in relevance to the high- T_c cuprates, such as Sr₂CuO₂F_{2+δ}⁵⁶³ and Ca_{2-x}Na_xCuO₂Cl₂ (see Section 4.20.2.9) with K₂NiF₄-type structure. Oxyfluorides are prepared by several synthetic approaches such as a conventional solid-state reaction between oxide and fluoride, a low-temperature reaction using fluorinating agents (F₂ gas, XeF₂, ZnF₂, PTFE, etc.), and hydrothermal reaction.⁵⁶⁴ A HP method is effective for obtaining the desired composition of an oxyfluoride.⁵⁶¹ K₂NiF₄-type Sr₂MO₃F

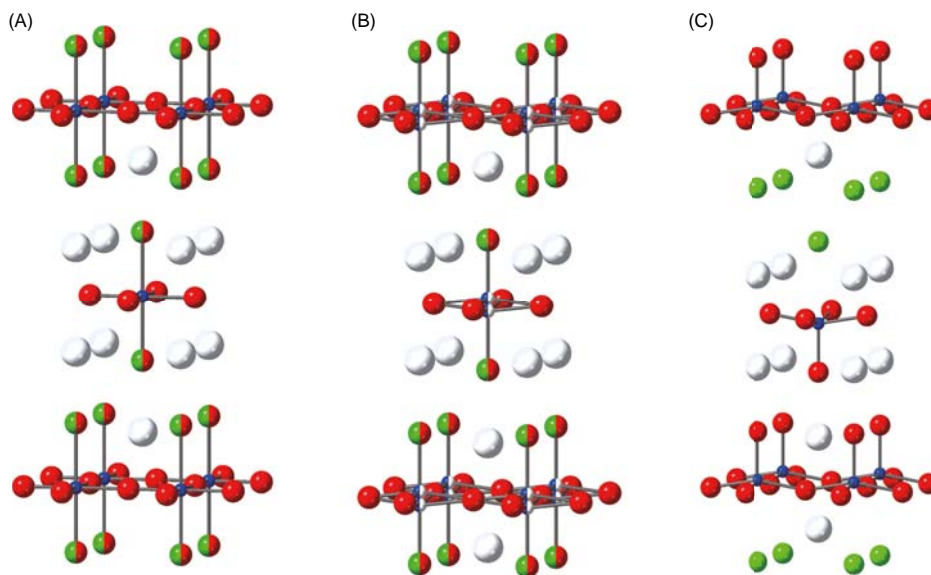


Fig. 14 Crystal structure of Sr₂MO₃X. (a) Sr₂MO₃F (M = Sc, Mn), (b) Sr₂MO₃F (M = Co, Ni), (c) Sr₂MO₃Cl (M = Mn, Co, Ni). White, blue, red, and green spheres respectively denote Sr, M, O, and X atoms.

(M = Mn, Co, Ni) are synthesized at 6 GPa and 1500–1800 °C.^{191,546,547} In these compounds, the fluoride ions favor the apical anion site with disordered manner. The transition metal cation is located at the center position of an octahedron for M = Mn, while it is disordered from the center to form a square-pyramidal MO₅ that is loosely linked by a fluoride ion for M = Co, Ni (Fig. 14(a) and (b)). While Sr₂NiO₃F shows spin glass behavior at low temperature,⁵⁴⁷ Sr₂MO₃F (M = Mn, Co) shows AFM transition at T_N = 133 K and 323 K for M = Mn and Co, respectively.^{546,565} Sr₂CoO₃F exhibits a pressure-induced transition from a high-spin state (S = 2) to a low-spin state (S = 0) between 0 GPa and 12 GPa.⁵⁶⁶ K₂NiF₄-type Sr₂NiO₃Cl is also prepared by HP synthesis at 3 GPa and 1300 °C,⁵⁴⁷ while Sr₂MO₃Cl (M = Mn, Co) can be prepared at AP.^{567,568} Chloride ions in Sr₂MO₃Cl also favor the apical anion site as in the case with the oxyfluorides, while O/Cl anions are fully ordered due to different ionic sizes between O and Cl (Fig. 14(c)). Sr₂NiO₃Cl shows AFM transition at T_N = 33 K in contrast to the spin-glass behavior seen in Sr₂NiO₃F.⁵⁴⁷ Perovskite-type oxyfluorides AB(O,F)₃ were also prepared by HP synthesis. Sr₂ZnO₂Cl₂ with square planar coordination, isostructural to A₂CuO₂Cl₂ (A = Sr, Ca, see Section 4.20.2.9), can be also prepared at 6 GPa and 1500 °C.⁵⁴⁹ Fluoride substitution of ferroelectric BaTiO₃ and PbVO₃ suppresses the tetragonal distortion leading to cubic structure (see Section 4.20.2.3).^{82,543} Silver-containing perovskites AgTiO₂F and AgFeOF₂ are prepared at 1000 °C under 4 GPa and 7 GPa, respectively.^{544,545} The O/F anions in these compounds are fully disordered.

4.20.5.3 Oxyhydrides

Oxyhydrides, where a transition metal center is coordinated to both oxide (O²⁻) and hydride (H⁻) ligands, have recently been developed as a new class of mixed-anion system, with a series of unprecedented chemical and physical properties that are not accessible in simple oxides.⁵⁶⁹ Examples are the lability of a hydride ion allowing topochemical anion exchange reactions and π blocking nature due to the lack of p orbitals in H⁻.^{561,569} However, the reports of transition oxyhydrides had been quite limited until a decade ago, since hydride itself is a strong reducing agent to reduce the transition metal to element. Thanks to recent development of synthesis methods, such as a topochemical hydride reduction method and a HP method, a growing number of transition metal oxyhydrides have been reported over the past decade.

HP synthesis of a transition metal (layered) perovskite oxyhydride was first reported by Bang *et al.*: Sr₂VO_{4-x}H_x (0 ≤ x ≤ 1.01) was synthesized from a mixture of SrO, VO, and SrH₂ with a hydrogen source (NaBH₄ + Ca(OH)₂) at 5 GPa and 1200 °C.⁵⁵⁴ The composition x can be adjusted by changing the composition of the starting mixture. Sr₂VO₃H (x = 1) is the n = 1 phase of layered perovskite oxyhydride Sr_{n+1}V_nO_{2n+1}H_n (n = 1, 2, ∞) with trans-VO₄H₂ octahedra (Fig. 15).⁵⁷⁰ Cubic perovskite Sr_{1-x}Na_xVO_{3-y}H_y (x ≤ 0.2) can be also synthesized at 8 GPa and 1000 °C.⁵⁵² The unique feature of this series is that the compounds are magnetically quasi-low-dimensional materials since V³⁺ has two electrons in t_{2g} orbitals and the t_{2g} orbitals are orthogonal to the H-1s orbital.⁵⁵⁴ HP experiments revealed that quasi-2D SrVO₂H (n = ∞) exhibits an unusual insulator-to-metal transition at ~50 GPa, with the quasi-2D nature persisting under high pressure.⁵⁷¹ In contrast to SrVO₂H, quasi-1D Sr₂VO₃H (x = 1) and Sr₃V₂O₅H₂ (x = 2) do not exhibit pressure-induced transition at pressures up to ~60 GPa.⁵⁷² Another unique feature of hydride ion is high compressibility. HP experiments for Sr_{n+1}V_nO_{2n+1}H_n (n = 1, 2, ∞) revealed that the compressibility of a hydride ion is twice than that of an oxide ion.^{571,572} This high compressibility induces unusual structural transitions in LnHO.^{573,574}

Cubic perovskite BaScO₂H and K₂NiF₄-type Ba₂ScO₃H are synthesized at 7 GPa and 1000 °C and at 3 GPa and 800 °C, respectively.^{550,551} Hydride ions are fully disordered in BaScO₂H, while in Ba₂ScO₃H they are located at apical sites and show hydride conduction (5.2 × 10⁻⁶ S cm⁻¹ at 300 °C). In BaVO_{3-x}H_x, hexagonal perovskite structure (6H-type) is obtained at 3 GPa, while cubic perovskite is obtained at 7 GPa,⁵⁵³ which can be also seen in oxide perovskites (see Section 4.20.1). In hexagonal BaVO_{2.7}H_{0.3}, hydride ions are located selectively at face-sharing sites, resulting in a quasi-two-dimensional metal with strong AFM fluctuations. Anion-disordered perovskite SrCrO₂H, synthesized at 7 GPa and 1000 °C, has the highest T_N (~380 K) among

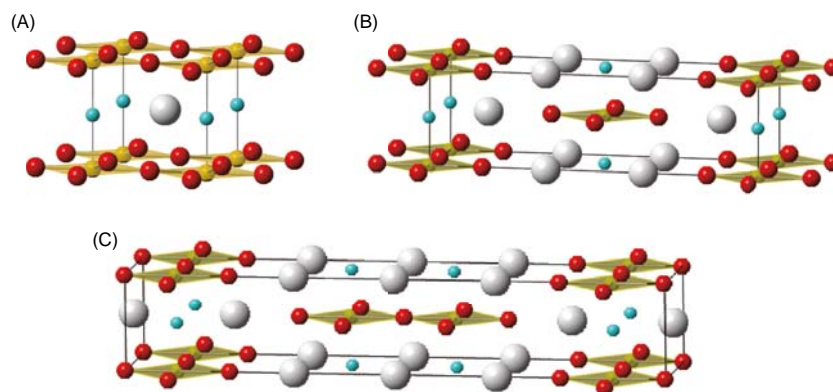


Fig. 15 Crystal structure of Sr_{n+1}V_nO_{2n+1}H_n (n = 1, 2, ∞). (a) SrVO₂H (n = ∞), (b) Sr₂VO₃H (n = 1), (c) Sr₃V₂O₅H₂ (n = 2). White, yellow, red, and sky blue spheres respectively denote Sr, V, O, and H atoms.

Cr³⁺-containing perovskites due to its ideal tolerance factor.⁵⁵⁵ Layered perovskite LaSrMnO_{3.3}H_{0.7}, prepared at 5 GPa and 1000 °C, shows spin-glass behavior at low temperatures due to competition of FM and AFM interactions.⁵⁵⁶ K₂NiF₄-type LaSrCoO₃H_{0.7} and LaSr₃NiRuO₄H₄ were also reported but they are prepared by using topochemical hydride reduction^{575,576} rather than a HP method. So far there is still no perovskite oxyhydride containing Fe and Cu.

4.20.5.4 Oxynitrides

Oxynitrides (oxide-nitrides) exhibit attractive properties, including visible-light responsive photocatalysis, but the highly reducing atmosphere of HT reaction with ammonia (ammonolysis) often makes it difficult to obtain the desired structures. Direct HP solid-state reactions should be suitable for obtaining desired oxynitrides because pressure suppresses decomposition to oxides and nitrogen. However, there are not many reports of direct solid-state syntheses of oxynitrides at high pressures. A novel ternary spinel Ga₃O₃N was synthesized from Ga₂O₃ and GaN at 5 GPa and 1500–1700 °C.⁵⁷⁷ Perovskite RZrO₂N (R = Pr, Nd, Sm) is synthesized at 2–3 GPa and 1200–1500 °C.⁵⁵⁷ Significant progress of HP synthesis of oxynitrides is synthesis of MnTaO₂N (obtained at 6 GPa and 1400 °C) containing magnetic Mn²⁺. This compound shows a nontrivial helical spin order at 25 K.⁵⁵⁸ Furthermore, the polar structure (LiNbO₃-type structure) indicates a candidate of new multiferroic material. Isostructural Mn(Mn_{1/6}Ta_{5/6})O_{2.5}N_{0.5} is also obtained at 7.5 GPa and 1300 °C.⁵⁵⁹ ZnTaO₂N, synthesized at 6 GPa and 1600 °C, crystallizes in a centrosymmetric HT LiNbO₃-type structure, revealing possible origin of ferroelectrics in the LiNbO₃-type structure.⁵⁶⁰

References

- Anderson, D. L. *New Theory of the Earth*, Cambridge University Press, 2007; pp 1–384.
- Navrotsky, A.; Weidner, D. J.; Liebermann, R. C.; Prewitt, C. T. *MRS Bull.* **1992**, *17* (5), 30–37.
- Shannon, R. D. *Acta Crystallogr. A* **1976**, *32* (Sep1), 751–767.
- Murakami, M.; Hirose, K.; Kawamura, K.; et al. *Science* **2004**, *304* (5672), 855–858.
- Oganov, A. R.; Ono, S. *Nature* **2004**, *430* (6998), 445–448.
- Kafalas, J. A.; Longo, J. M. *J. Solid State Chem.* **1972**, *4*, 55–59.
- Syono, Y.; Akimoto, S. I.; Kohn, K. *J. Physical Soc. Japan* **1969**, *26* (4), 993–999.
- Goodenough, J. B.; Graper, W.; Holtzberg, F.; et al. *Landolt-Börnstein, New Series, Group III*; vol. 4; Springer: Berlin, 1970. Part A.
- Muller, O.; Roy, R. *The Major Ternary Structural Families*, Springer: Berlin, 1974.
- Inaguma, Y.; Yoshida, M.; Katsumata, T. *J. Am. Chem. Soc.* **2008**, *130* (21), 6704–6705.
- Navrotsky, A. *Chem. Mater.* **1998**, *10* (10), 2787–2793.
- Li, M. R.; Croft, M.; Stephens, P. W.; et al. *Adv. Mater.* **2015**, *27* (13), 2177–2181.
- Howard, C. J.; Kennedy, B. J.; Woodward, P. M. *Acta Crystallogr. Sect. B: Struct. Sci.* **2003**, *59*, 463–471.
- Anderson, M. T.; Poeppelmeier, K. R. *Chem. Mater.* **1991**, *3* (3), 476–482.
- Azuma, M.; Kaimori, S.; Takano, M. *Chem. Mater.* **1998**, *10* (10), 3124–3130.
- Vander Griend, D. A.; Boudin, S.; Poeppelmeier, K. R.; et al. *J. Am. Chem. Soc.* **1998**, *120* (44), 11518–11519.
- Azuma, M.; Ohtaka, O.; Kumada, N. High-Pressure Synthesis of Solids. In *Encyclopedia of Inorganic and Bioinorganic Chemistry*, Wiley & Sons, Ltd., 2014; pp 1–17.
- Clark, J. B.; Richter, P. W.; Dutoit, L. *J. Solid State Chem.* **1978**, *23* (1–2), 129–134.
- Liferovich, R. P.; Mitchell, R. H. *J. Solid State Chem.* **2004**, *177* (6), 2188–2197.
- Belik, A. A.; Iikubo, S.; Kodama, K.; et al. *J. Am. Chem. Soc.* **2006**, *128* (3), 706–707.
- Belik, A. A. *J. Solid State Chem.* **2012**, *195*, 32–40.
- Yokosawa, T.; Belik, A. A.; Asaka, T.; et al. *Phys. Rev. B* **2008**, *77* (2), 024111.
- Belik, A. A.; Yusa, H.; Hirao, N.; et al. *Inorg. Chem.* **2009**, *48* (3), 1000–1004.
- Khalyavin, D. D.; Salak, A. N.; Fertman, E. L.; et al. *Chem. Commun.* **2019**, *55* (32), 4683–4686.
- Reid, A. F.; Ringwood, A. E. *J. Geophys. Res.* **1975**, *80* (23), 3363–3370.
- Sinclair, W.; Eggleton, R. A.; Ringwood, A. E. *Z. Kristallog.* **1979**, *149* (3–4), 307–314.
- Castillo-Martinez, E.; Bieringer, M.; Shafi, S. P.; et al. *J. Am. Chem. Soc.* **2011**, *133* (22), 8552–8563.
- Park, J. H.; Parise, J. B. *Mater. Res. Bull.* **1997**, *32* (12), 1617–1624.
- Belik, A. A.; Matsushita, Y.; Tanaka, M.; Takayama-Muromachi, E. *Chem. Mater.* **2012**, *24* (11), 2197–2203.
- Ding, L.; Manuel, P.; Khalyavin, D. D.; et al. *Phys. Rev. B* **2017**, *95* (5), 054432.
- Chen, H. Y.; Yu, T.; Gao, P.; et al. *Inorg. Chem.* **2013**, *52* (16), 9692–9697.
- Yu, T.; Tyson, T. A.; Chen, H. Y.; et al. *J. Phys. Condens. Matter* **2014**, *26* (49), 495402.
- Kawamoto, T.; Fujita, K.; Yamada, I.; et al. *J. Am. Chem. Soc.* **2014**, *136* (43), 15291–15299.
- Li, M. R.; Adem, U.; McMitchell, S. R. C.; et al. *J. Am. Chem. Soc.* **2012**, *134* (8), 3737–3747.
- Yi, W.; Presniakov, I. A.; Sobolev, A. V.; et al. *Sci. Technol. Adv. Mater.* **2015**, *16* (2), 024801.
- Belik, A. A.; Matsushita, Y.; Tanaka, M.; Takayama-Muromachi, E. *Inorg. Chem.* **2013**, *52* (20), 12005–12011.
- Yi, W.; Princep, A.; Guo, Y. F.; et al. *Inorg. Chem.* **2015**, *54* (16), 8012–8021.
- Thomas, C. I.; Suchomel, M. R.; Duong, G. V.; et al. *Philos. Trans. R. Soc. A Math. Phys. Eng. Sci.* **2014**, *372* (2013), 20130012.
- Belik, A. A.; Yi, W.; Kumaga, Y.; et al. *Inorg. Chem.* **2016**, *55* (4), 1940–1945.
- Li, L. P.; Li, G. S.; Miao, J. P.; et al. *J. Mater. Res.* **2001**, *16* (2), 417–424.
- Miao, J. P.; Li, L. P.; Song, Y. B.; et al. *Mater. Chem. Phys.* **2000**, *62* (3), 226–229.
- Park, J. H.; Woodward, P. M.; Parise, J. B.; et al. *Chem. Mater.* **1999**, *11* (1), 177–183.
- Park, J. H.; Woodward, P. M.; Parise, J. B. *Chem. Mater.* **1998**, *10* (10), 3092–3100.
- Chakhmouradian, A. R.; Mitchell, R. H. *Am. Mineral.* **2001**, *86* (9), 1076–1080.
- Leinenweber, K.; Parise, J. *J. Solid State Chem.* **1995**, *114* (1), 277–281.
- Leinenweber, K.; Parise, J. *Am. Mineral.* **1997**, *82* (5–6), 475–478.
- Suchomel, M. R.; Fogg, A. M.; Allix, M.; et al. *Chem. Mater.* **2006**, *18* (21), 4987–4989.

48. Suchomel, M. R.; Fogg, A. M.; Allix, M.; et al. *Chem. Mater.* **2006**, *18* (24), 5810.
49. Leinenweber, K.; Linton, J.; Navrotsky, A.; et al. *Phys. Chem. Miner.* **1995**, *22* (4), 251–258.
50. Bindi, L.; Sirotkina, E. A.; Bobrov, A. V.; et al. *Phys. Chem. Miner.* **2017**, *44* (6), 419–424.
51. Aimi, A.; Katsumata, T.; Mori, D.; et al. *Inorg. Chem.* **2011**, *50* (13), 6392–6398.
52. Inaguma, Y.; Aimi, A.; Shirako, Y.; et al. *J. Am. Chem. Soc.* **2014**, *136* (7), 2748–2756.
53. Varga, T.; Kumar, A.; Vlahos, E.; et al. *Phys. Rev. Lett.* **2009**, *103* (4), 047601.
54. Sleight, A. W.; Prewitt, C. T. *J. Solid State Chem.* **1973**, *6* (4), 509–512.
55. Malinowski, M.; Lukaszewicz, K.; Asbrink, S. *J. Appl. Cryst.* **1986**, *19*, 7–9.
56. Ahart, M.; Somayazulu, M.; Cohen, R. E.; et al. *Nature* **2008**, *451* (7178), 545–548.
57. Shan, Y. J.; Inaguma, Y.; Tetsuka, H.; et al. *Ferroelectrics* **2006**, *337*, 1243–1248.
58. Nishimura, K.; Yamada, I.; Oka, K.; et al. *J. Phys. Chem. Solid* **2014**, *75* (6), 710–712.
59. Shpanchenko, R. V.; Chernaya, V. V.; Tsirlin, A. A.; et al. *Chem. Mater.* **2004**, *16* (17), 3267–3273.
60. Belik, A.; Azuma, M.; Saito, T.; et al. *Chem. Mater.* **2005**, *17* (2), 269–273.
61. Belik, A. A.; Takayama-Muromachi, E. *J. Solid State Chem.* **2006**, *179* (6), 1650–1658.
62. Tan, Z.; Lussier, J. A.; Yamada, T.; et al. *Angew. Chem. Int. Ed. Engl.* **2022**, *61* (25), e202203669.
63. Yamamoto, H.; Ogata, T.; Patel, S.; et al. *Chem. Mater.* **2018**, *30* (19), 6728–6736.
64. Tsuchiya, T.; Katsumata, T.; Ohba, T.; Inaguma, Y. *J. Ceram. Soc. Jpn.* **2009**, *117* (1361), 102–105.
65. Chamberland, B. L. *J. Solid State Chem.* **1970**, *1* (2), 138–142.
66. Chamberland, B. L. *J. Solid State Chem.* **1970**, *2* (4), 521–524.
67. Syono, Y.; Akimoto, S. I.; Endoh, Y. *J. Phys. Chem. Solid* **1971**, *32* (1), 243–249.
68. Yu, R.; Hojo, H.; Oka, K.; et al. *Chem. Mater.* **2015**, *27* (6), 2012–2017.
69. Klein, R. A.; Altman, A. B.; Saballos, R. J.; et al. *Phys. Rev. Mater.* **2019**, *3* (6), 064411.
70. Demazeau, G.; Oh-Kim, E.; Choy, J.; Hagemuller, P. *Mater. Res. Bull.* **1987**, *22* (6), 735–740.
71. Bazuev, G. V.; Tyutyunnik, A. P.; Kuznetsov, M. V.; Zainulin, Y. G. *J. Supercond. Nov. Magn.* **2018**, *31* (9), 2907–2914.
72. Shiraki, H.; Saito, T.; Azuma, M.; Shimakawa, Y. *J. Physical Soc. Japan* **2008**, *77* (6), 064705.
73. Young, A. P.; Schwartz, C. M. *Acta Crystallogr.* **1962**, *15* (Dec), 1305.
74. Gondrand, M.; Collomb, A.; Joubert, J. C.; Shannon, R. D. *J. Solid State Chem.* **1974**, *11* (1), 1–9.
75. Subramanian, M. A. *Mater. Res. Bull.* **1992**, *27* (8), 939–943.
76. Sleight, A. W. *Mater. Res. Bull.* **1974**, *9* (9), 1185–1190.
77. Sleight, A. W. *Mater. Res. Bull.* **1972**, *7* (8), 827–830.
78. Bizen, D.; Nakatsuka, K.; Murata, T.; et al. *Phys. Rev. B* **2008**, *78* (22), 224104.
79. Zhou, J. S.; Goodenough, J. B.; Yan, J. Q.; et al. *Phys. Rev. B* **2009**, *80* (22), 224422.
80. Oka, K.; Yamauchi, T.; Kanungo, S.; et al. *J. Physical Soc. Japan* **2018**, *87* (2), 024801.
81. Yamamoto, H.; Imai, T.; Sakai, Y.; Azuma, M. *Angew. Chem. Int. Ed.* **2018**, *57* (27), 8170–8173.
82. Ogata, T.; Oka, K.; Azuma, M. *Appl. Phys. Express* **2019**, *12* (2), 023005.
83. Botella, P.; Lopez-Moreno, S.; Errandonea, D.; et al. *J. Phys. Condens. Matter* **2020**, *32* (38), 385403.
84. Chamberland, B. L. *Solid State Commun.* **1967**, *5* (8), 663–666.
85. Goodenough, J. B.; Longo, J. M.; Kafalas, J. A. *Mater. Res. Bull.* **1968**, *3* (6), 471–481.
86. Arevalo-Lopez, A. M.; Reeves, S. J.; Atfield, J. P. *Z. Anorg. Allg. Chem.* **2014**, *640* (14), 2727–2729.
87. Arévalo-López, A. M.; Paul Atfield, J. *J. Solid State Chem.* **2015**, *232*, 236–240.
88. Roth, W. L.; Devries, R. C. *J. Appl. Phys.* **1967**, *38* (3), 951–952.
89. Yu, R. Z.; Hojo, H.; Watanuki, T.; et al. *J. Am. Chem. Soc.* **2015**, *137* (39), 12719–12728.
90. Sugawara, F.; Iida, S.; Syono, Y.; Akimoto, S.-I. *J. Physical Soc. Japan* **1965**, *20*, 1529.
91. Belik, A. A.; Iikubo, S.; Kodama, K.; et al. *Chem. Mater.* **2008**, *20* (11), 3765–3769.
92. Yi, W.; Matsushita, Y.; Katsuya, Y.; et al. *Dalton Trans.* **2015**, *44* (23), 10785–10794.
93. Suchomel, M. R.; Thomas, C. I.; Allix, M.; et al. *Appl. Phys. Lett.* **2007**, *90* (11), 112909.
94. Choy, J. H.; Hong, S. T.; Choi, K. S. *J. Chem. Soc. Faraday Trans.* **1996**, *92* (6), 1051–1059.
95. Hong, S.-T.; Park, J.-H.; Choy, J.-H. *J. Phys. Chem.* **1995**, *99* (16), 6176–6181.
96. Dos santos-Garcia, A. J.; Solana-Madruga, E.; Ritter, C.; et al. *Dalton Trans.* **2015**, *44* (23), 10665–10672.
97. Williams, A. J.; Gillies, A.; Atfield, J. P.; et al. *Phys. Rev. B* **2006**, *73* (10), 104409.
98. Pirrotta, I.; Schmidt, R.; Dos Santos-Garcia, A. J.; et al. *J. Solid State Chem.* **2015**, *225*, 321–329.
99. Jeanneau, J.; Lepoittevin, C.; Sulpice, A.; et al. *J. Solid State Chem.* **2017**, *251*, 164–169.
100. Cao, L. P.; Jin, M. L.; Li, W. M.; et al. *AIP Adv.* **2016**, *6* (5), 055010.
101. Xiao, W.; Tan, D.; Xiong, X.; et al. *Proc. Natl. Acad. Sci. U. S. A.* **2010**, *107* (32), 14026–14029.
102. Uusi-Esko, K.; Malm, J.; Imamura, N.; et al. *Mater. Chem. Phys.* **2008**, *112* (3), 1029–1034.
103. Atou, T.; Chiba, H.; Ohoyama, K.; et al. *J. Solid State Chem.* **1999**, *145*, 639–642.
104. Belik, A.; Iikubo, S.; Yokosawa, T.; et al. *J. Am. Chem. Soc.* **2007**, *129* (4), 971–977.
105. Yi, W.; Kumagai, Y.; Spaldin, N. A.; et al. *Inorg. Chem.* **2014**, *53* (18), 9800–9808.
106. Alonso, J. A.; Martinez-Lope, M. J.; de la Calle, C.; et al. *Joint 21st Airapt and 45th Ehprg International Conference on High Pressure Science and Technology*; p 032004.
107. Kohn, K.; Inoue, K.; Horie, O.; Akimoto, S. *J. Solid State Chem.* **1976**, *18* (1), 27–37.
108. Wakazaki, S.; Nishikubo, T.; Sakai, Y.; et al. *Inorg. Chem.* **2020**, *59* (18), 13390–13397.
109. Azuma, M.; Takata, K.; Saito, T.; et al. *J. Am. Chem. Soc.* **2005**, *127* (24), 8889–8892.
110. Yi, W.; Liang, Q.; Matsushita, Y.; et al. *Inorg. Chem.* **2013**, *52* (24), 14108–14115.
111. Bougerol, C.; Gorius, M. F.; Bordet, P.; Grey, I. E. *Acta Crystallogr.* **2002**, *58*, C23.
112. Oka, K.; Azuma, M.; Hirai, S.; et al. *Inorg. Chem.* **2009**, *48* (5), 2285–2288.
113. Belik, A. A.; Matsushita, Y.; Tanaka, M.; Takayama-Muromachi, E. *Angew. Chem. Int. Ed.* **2010**, *49* (42), 7723–7727.
114. Solana-Madruga, E.; Dos Santos-Garcia, A. J.; Arevalo-Lopez, A. M.; et al. *Dalton Trans.* **2015**, *44* (47), 20441–20448.
115. Li, M. R.; Hodges, J. P.; Retuerto, M.; et al. *Chem. Mater.* **2016**, *28* (9), 3148–3158.
116. Arévalo-López, A. M.; Stegemann, F.; Atfield, J. P. *Chem. Commun.* **2016**, *52*, 5558–5560.
117. Arevalo-Lopez, A. M.; Solana-Madruga, E.; Aguilar-Maldonado, C.; et al. *Chem. Commun.* **2019**, *55* (96), 14470–14473.
118. Arevalo-Lopez, A. M.; McNally, G. M.; Atfield, J. P. *Angew. Chem. Int. Ed.* **2015**, *54* (41), 12074–12077.
119. Li, M. R.; Retuerto, M.; Deng, Z.; et al. *Angew. Chem. Int. Ed.* **2015**, *54* (41), 12069–12073.
120. Tyutyunnik, A. P.; Bazuev, G. V.; Kuznetsov, M. V.; Zainulin, Y. G. *Mater. Res. Bull.* **2011**, *46* (8), 1247–1251.

121. Frank, C. E.; McCabe, E. E.; Orlandi, F.; et al. *Chem. Commun.* **2019**, 55, 3331–3334.
122. Solana-Madruga, E.; Alharbi, K. N.; Herz, M.; et al. *Chem. Commun.* **2020**, 56 (83), 12574–12577.
123. Chamberland, B. L.; Sleight, A. W.; Weiher, J. F. *J. Solid State Chem.* **1970**, 1, 512–514.
124. Zhou, B.; Qin, S.; Ma, T.; et al. *Inorg. Chem.* **2020**, 59, 3887–3893.
125. Li, M.-R.; Walker, D.; Retuerto, M.; et al. *Angew. Chem. Int. Ed.* **2013**, 52, 8406–8410.
126. Feng, H. L.; Deng, Z.; Croft, M.; et al. *Inorg. Chem.* **2019**, 58 (23), 15953–15961.
127. Li, M. R.; McCabe, E. E.; Stephens, P. W.; et al. *Nat. Commun.* **2017**, 8 (1), 2037.
128. Li, M.-R.; Retuerto, M.; Walker, D.; et al. *Angew. Chem.* **2014**, 126 (40), 10950–10954.
129. Akizuki, Y.; Yamada, I.; Fujita, K.; et al. *Inorg. Chem.* **2013**, 52 (19), 11538–11543.
130. Shimakawa, Y.; Kubo, Y.; Manako, T. *Nature* **1996**, 379 (6560), 53–55.
131. Aoyama, T.; Yamauchi, K.; Iyama, A.; et al. *Nat. Commun.* **2014**, 5, 4927.
132. Makarova, O. L.; Mirebeau, I.; Kichanov, S. E.; et al. *Phys. Rev. B* **2011**, 84 (2), 020408.
133. Terada, N.; Khalyavin, D. D.; Manuel, P.; et al. *Phys. Rev. B* **2016**, 93 (8), 081104(R).
134. Terada, N.; Colin, C. V.; Qureshi, N.; et al. *Phys. Rev. B* **2020**, 102 (9), 094412.
135. Takeda, Y.; Naka, S.; Takano, M.; et al. *Mater. Res. Bull.* **1978**, 13 (1), 61–66.
136. Gallagher, P. K.; Buchanan, D. N.; Macchiesney, J. B. *J. Chem. Phys.* **1964**, 41 (8), 2429.
137. Hayashi, N.; Yamamoto, T.; Kageyama, H.; et al. *Angew. Chem. Int. Ed. Engl.* **2011**, 50 (52), 12547–12550.
138. Liu, Y. X.; Liu, Z. H.; Li, Z.; et al. *Phys. Rev. B* **2020**, 101 (14), 144421.
139. Takeda, T.; Kanno, R.; Kawamoto, Y.; et al. *Solid State Sci.* **2000**, 2 (7), 673–687.
140. Matsuno, J.; Mizokawa, T.; Fujimori, A.; et al. *Phys. Rev. B* **2002**, 66 (19), 193103.
141. Ghosh, S.; Kamaraju, N.; Seto, M.; et al. *Phys. Rev. B* **2005**, 71 (24), 245110.
142. Hosaka, Y.; Romero, F. D.; Ichikawa, N.; et al. *Angew. Chem. Int. Ed.* **2017**, 56 (15), 4243–4246.
143. Kawasaki, S.; Takano, M.; Kanno, R.; et al. *J. Physical Soc. Japan* **1998**, 67 (5), 1529–1532.
144. Azuma, M.; Niitaka, S.; Hayashi, N.; et al. *Jpn. J. Appl. Phys.* **2008**, 47 (9), 7579–7581.
145. Yamamoto, H.; Kihara, T.; Oka, K.; et al. *J. Phys. Soc. Japan* **2016**, 85 (6), 064704.
146. Oka, K.; Koyama, T.; Ozaaki, T.; et al. *Angew. Chem. Int. Ed.* **2012**, 51 (32), 7977–7980.
147. De, C.; Arevalo-Lopez, A. M.; Orlandi, F.; et al. *Angew. Chem. Int. Ed. Engl.* **2018**, 57 (49), 16099–16103.
148. Byeon, S. H.; Nakamura, T.; Itoh, M.; Matsuo, M. *Mater. Res. Bull.* **1992**, 27 (9), 1065–1072.
149. Byeon, S.-H.; Demazeau, G.; Jin-Ho, C.; Fournes, L. *Mater. Lett.* **1991**, 12 (3), 163–167.
150. Feng, H. L.; Arai, M.; Matsushita, Y.; et al. *J. Am. Chem. Soc.* **2014**, 136, 3326–3329.
151. Retuerto, M.; Martínez-Lope, M. J.; García-Hernández, M.; Alonso, J. A. *Mater. Res. Bull.* **2009**, 44, 1261–1264.
152. Tsuchiya, T.; Saito, H.; Yoshida, M.; et al. *Mater. Res. Soc. Symp. Proc.* **2007**, 988E, 0988.
153. Kim, S. J.; Demazeau, G.; Presniakov, I.; Choy, J. H. *J. Solid State Chem.* **2001**, 161 (2), 197–204.
154. Ye, X. B.; Zhao, J. F.; Das, H.; et al. *Nat. Commun.* **2021**, 12, 1917.
155. Fujita, K.; Kawamoto, T.; Yamada, I.; et al. *Chem. Mater.* **2016**, 28 (18), 6644–6655.
156. Demazeau, G.; Buffat, B.; Menil, F.; et al. *Mater. Res. Bull.* **1981**, 16 (11), 1465–1472.
157. Lavina, B.; Dera, P.; Kim, E.; et al. *Proc. Natl. Acad. Sci. U. S. A.* **2011**, 108 (42), 17281–17285.
158. Ovsyannikov, S. V.; Bykov, M.; Medvedev, S. A.; et al. *Angew. Chem. Int. Ed.* **2020**, 59 (14), 5632–5636.
159. Bykova, E.; Dubrovinsky, L.; Dubrovinskaja, N.; et al. *Nat. Commun.* **2016**, 7, 10661.
160. Sinmyo, R.; Bykova, E.; Ovsyannikov, S. V.; et al. *Sci. Rep.* **2016**, 6, 32852.
161. Ishii, T.; Uenver-Thiele, L.; Woodland, A. B.; et al. *Am. Mineral.* **2018**, 103 (11), 1873–1876.
162. Leinenweber, K.; Utsumi, W.; Tsuchida, Y.; et al. *Phys. Chem. Miner.* **1991**, 18 (4), 244–250.
163. Hu, Q. Y.; Kim, D. Y.; Yang, W. G.; et al. *Nature* **2016**, 534 (7606), 241–244.
164. Takano, M.; Nakanishi, N.; Takeda, Y.; et al. *Mater. Res. Bull.* **1977**, 12 (9), 923–928.
165. Woodward, P. M.; Cox, D. E.; Moshopoulou, E.; et al. *Phys. Rev. B* **2000**, 62 (2), 844–855.
166. Bocquet, A. E.; Fujimori, A.; Mizokawa, T.; et al. *Phys. Rev. B* **1992**, 45 (4), 1561–1570.
167. Mostovoy, M. *Phys. Rev. Lett.* **2005**, 94 (13), 137205.
168. Ishiwata, S.; Tokunaga, M.; Kaneko, Y.; et al. *Phys. Rev. B* **2011**, 84 (5), 054427.
169. Ishiwata, S.; Nakajima, T.; Kim, J. H.; et al. *Phys. Rev. B* **2020**, 101 (13), 134406.
170. Sosnowska, I.; Azuma, M.; Przenioslo, R.; et al. *Inorg. Chem.* **2013**, 52 (22), 13269–13277.
171. Yamamoto, H.; Sakai, Y.; Shigematsu, K.; et al. *Inorg. Chem.* **2017**, 56 (24), 15171–15177.
172. Hojo, H.; Oka, K.; Shimizu, K.; et al. *Adv. Mater.* **2018**, 30 (33), 1705665.
173. Kawakami, T.; Nasu, S.; Kuzushita, K.; et al. *J. Physical Soc. Japan* **2003**, 72 (1), 33–36.
174. Kawakami, T.; Nasu, S.; Sasaki, T.; et al. *J. Physical Soc. Japan* **2001**, 70 (6), 1491–1494.
175. Kawakami, T.; Nasu, S.; Sasaki, T.; et al. *Phys. Rev. Lett.* **2002**, 88 (3), 037602.
176. Seda, T.; Hearne, G. R. *J. Phys. Condens. Matter* **2004**, 16 (15), 2707–2718.
177. Wu, X.; Steinle-Neumann, G.; Narygina, O.; et al. *Phys. Rev. Lett.* **2009**, 103 (6), 065503.
178. Lin, J. F.; Speziale, S.; Mao, Z.; Marquardt, H. *Rev. Geophys.* **2013**, 51 (2), 244–275.
179. Kawakami, T.; Tsujimoto, Y.; Kageyama, H.; et al. *Nat. Chem.* **2009**, 1 (5), 371–376.
180. Yamamoto, T.; Tassel, C.; Kobayashi, Y.; et al. *J. Am. Chem. Soc.* **2011**, 133 (15), 6036–6043.
181. Osaka, T.; Takahashi, H.; Sagayama, H.; et al. *Phys. Rev. B* **2017**, 95 (22), 224440.
182. Xia, H. L.; Dai, J. H.; Xu, Y. J.; et al. *Phys. Rev. Mater.* **2017**, 1 (2), 024406.
183. Kawasaki, S.; Takano, M.; Takeda, Y. *J. Solid State Chem.* **1996**, 121 (1), 174–180.
184. Balamurugan, S.; Takayama-Muromachi, E. *J. Solid State Chem.* **2006**, 179 (7), 2231–2236.
185. Sakai, H.; Yokoyama, S.; Kuwabara, A.; et al. *Phys. Rev. Mater.* **2018**, 2 (10), 104412.
186. Belik, A.; Iikubo, S.; Kodama, K.; et al. *Chem. Mater.* **2006**, 18 (3), 798–803.
187. Sakai, Y.; Yang, J.; Yu, R.; et al. *J. Am. Chem. Soc.* **2017**, 139 (12), 4574–4581.
188. Fujita, K.; Kawamoto, T.; Yamada, I.; et al. *Inorg. Chem.* **2017**, 56 (18), 11113–11122.
189. Munoz, A.; Alonso, J. A.; Martínez-Lope, M. J.; et al. *Phys. Rev. B* **2006**, 73 (10), 104442.
190. Wang, X. L.; Takayama-Muromachi, E. *Phys. Rev. B* **2005**, 72 (6), 064401.
191. Tsujimoto, Y.; Li, J. J.; Yamaura, K.; et al. *Chem. Commun.* **2011**, 47 (11), 3263–3265.
192. Chin, Y. Y.; Hu, Z. W.; Su, Y.; et al. *Phys. Status Solidi Rapid Res. Lett.* **2018**, 12 (8), 1800147.
193. Yamada, I.; Toda, F.; Kawaguchi, S.; d'Astuto, M. *Mater. Chem. Front.* **2019**, 3 (12), 2696–2701.

194. Ishiwata, S.; Wang, D.; Saito, T.; Takano, M. *Chem. Mater.* **2005**, *17* (11), 2789–2791.
195. Toda, F.; Yamada, I.; Kawaguchi, S. *Int. J. Ceram. Eng. Sci.* **2022**, *4* (2), 123–129.
196. Toda, F.; Yamada, I.; Kawaguchi, S. *Inorg. Chem.* **2021**, *60* (11), 7680–7686.
197. Ishiwata, S.; Terasaki, I.; Azuma, M.; Takano, M. *J. Solid State Chem.* **2008**, *181* (5), 1273–1278.
198. Mentre, O.; Iorgulescu, M.; Huve, M.; et al. *Dalton Trans.* **2015**, *44* (23), 10728–10737.
199. Li, X.; Wang, H.; Cui, Z. M.; et al. *Sci. Adv.* **2019**, *5* (8), eaav6262.
200. Yamada, I.; Takamatsu, A.; Asai, K.; et al. *J. Phys. Chem. C* **2018**, *122* (49), 27885–27892.
201. Hong, W. T.; Stoerzinger, K. A.; Lee, Y. L.; et al. *Energ. Environ. Sci.* **2017**, *10* (10), 2190–2200.
202. Vogt, T.; Hriljac, J. A.; Hyatt, N. C.; Woodward, P. *Phys. Rev. B* **2003**, *67* (14), 140401(R).
203. Vankó, G.; Rueff, J.-P.; Mattila, A.; et al. *Phys. Rev. B* **2006**, *73* (2), 024424.
204. Oka, K.; Azuma, M.; Chen, W. T.; et al. *J. Am. Chem. Soc.* **2010**, *132* (27), 9438–9443.
205. Liu, Z.; Sakai, Y.; Yang, J.; et al. *J. Am. Chem. Soc.* **2020**, *142* (12), 5731–5741.
206. Tsujimoto, Y.; Matsushita, Y.; Hayashi, N.; et al. *Cryst. Growth Des.* **2014**, *14* (9), 4278–4284.
207. Ishiwata, S.; Terasaki, I.; Ishii, F.; et al. *Phys. Rev. Lett.* **2007**, *98* (21), 217201.
208. Matsuda, T.; Partzsch, S.; Tsuyama, T.; et al. *Phys. Rev. Lett.* **2015**, *114* (23), 236403.
209. Demazeau, G.; Marbeuf, A.; Pouchard, M.; Hagenmuller, P. *J. Solid State Chem.* **1971**, *3* (4), 582–589.
210. Kim, S.-J.; Demazeau, G.; Alonso, J. A.; Choy, J.-H. *J. Mater. Chem.* **2001**, *11* (2), 487–492.
211. Ishiwata, S.; Azuma, M.; Takano, M.; et al. *J. Mater. Chem.* **2002**, *12* (12), 3733–3737.
212. Munoz, A.; Alonso, J. A.; Martínez-Lope, M. J.; et al. *Dalton Trans.* **2006**, (41), 4936–4943.
213. Martínez-Lope, M. J.; Retuerto, M.; Alonso, J. A.; et al. *Dalton Trans.* **2011**, *40* (17), 4599–4604.
214. Inaguma, Y.; Tanaka, K.; Tsuchiya, T.; et al. *J. Am. Chem. Soc.* **2011**, *133* (42), 16920–16929.
215. Arevalo-Lopez, A. M.; Dos Santos-Garcia, A. J.; Levin, J. R.; et al. *Inorg. Chem.* **2015**, *54* (3), 832–836.
216. Stoyanova-Lyubenova, T.; Santos-García, A. J. D.; Urones-Garrote, E.; et al. *Dalton Trans.* **2014**, *43*, 1117–1124.
217. Feng, H. L.; Deng, Z.; Wu, M.; et al. *Inorg. Chem.* **2019**, *58*, 397–404.
218. Sleight, A. W. *Inorg. Chem.* **1975**, *14* (3), 597–599.
219. Cheng, J. G.; Zhou, J. S.; Goodenough, J. B.; et al. *Phys. Rev. Lett.* **2012**, *108* (23), 236403.
220. Alonso, J. A.; García-Muñoz, J. L.; Fernández-Díaz, M. T.; et al. *Phys. Rev. Lett.* **1999**, *82* (19), 3871–3874.
221. Alonso, J. A.; Martínez-Lope, M. J.; Casais, M. T.; et al. *J. Am. Chem. Soc.* **1999**, *121* (20), 4754–4762.
222. Cheng, J. G.; Zhou, J. S.; Goodenough, J. B.; et al. *Phys. Rev. B* **2010**, *82* (8), 085107.
223. Azuma, M.; Carlsson, S.; Rodgers, J.; et al. *J. Am. Chem. Soc.* **2007**, *129* (46), 14433–14436.
224. Mizumaki, M.; Ishimatsu, N.; Kawamura, N.; et al. *Phys. Rev. B* **2009**, *80* (23), 233104.
225. Azuma, M.; Chen, W. T.; Seki, H.; et al. *Nat. Commun.* **2011**, *2*, 347.
226. Nakano, K.; Oka, K.; Watanuki, T.; et al. *Chem. Mater.* **2016**, *28* (17), 6062–6067.
227. Sakai, Y.; Nishikubo, T.; Ogata, T.; et al. *Chem. Mater.* **2019**, *31* (13), 4748–4758.
228. Nishikubo, T.; Sakai, Y.; Oka, K.; et al. *Appl. Phys. Express* **2018**, *11* (6), 061102.
229. Nabetani, K.; Muramatsu, Y.; Oka, K.; et al. *Appl. Phys. Lett.* **2015**, *106* (6), 061912.
230. Nishikubo, T.; Sakai, Y.; Oka, K.; et al. *J. Am. Chem. Soc.* **2019**, *141* (49), 19397–19403.
231. Okada, H.; Takano, M.; Takeda, Y. *Phys. Rev. B* **1990**, *42* (10), 6813–6816.
232. Takayama-Muromachi, E. *Chem. Mater.* **1998**, *10* (10), 2686–2698.
233. Iyo, A.; Tanaka, Y.; Kito, H.; et al. *J. Physical Soc. Japan* **2007**, *76* (9), 094711.
234. Iyo, A.; Tanaka, Y.; Tokumoto, M.; Ihara, H. *Phys. C* **2001**, *366* (1), 43–50.
235. Iyo, A.; Tanaka, Y.; Kodama, Y.; et al. *Phys. C: Supercond. Appl.* **2006**, *445*, 17–22.
236. Iwanaga, D.; Inaguma, Y.; Itoh, M. *J. Solid State Chem.* **1999**, *147* (1), 291–295.
237. Feng, H. L.; Arai, M.; Matsushita, Y.; et al. *J. Solid State Chem.* **2014**, *217*, 9–15.
238. Takano, M.; Takeda, Y.; Okada, H.; et al. *Phys. C: Supercond. Appl.* **1989**, *159* (4), 375–378.
239. Kobayashi, N.; Hiroi, Z.; Takano, M. *J. Solid State Chem.* **1997**, *132* (2), 274–283.
240. Smith, M. G.; Manthiram, A.; Zhou, J.; et al. *Nature* **1991**, *351* (6327), 549–551.
241. Kohsaka, Y.; Azuma, M.; Yamada, I.; et al. *J. Am. Chem. Soc.* **2002**, *124* (41), 12275–12278.
242. Hiroi, Z.; Azuma, M.; Takano, M.; Bando, Y. *J. Solid State Chem.* **1991**, *95* (1), 230–238.
243. Hiroi, Z.; Takano, M. *Nature* **1995**, *377* (6544), 41–43.
244. Subramanian, M. A.; Ramirez, A. P.; Marshall, W. J. *Phys. Rev. Lett.* **1999**, *82* (7), 1558–1561.
245. Ito, M.; Takahashi, H.; Sakai, H.; et al. *Chem. Commun.* **2019**, *55* (61), 8931–8934.
246. Sleight, A. W.; Prewitt, C. T. *Mater. Res. Bull.* **1970**, *5*, 207–212.
247. Jorgensen, J. D.; Dabrowski, B.; Pei, S. Y.; et al. *Phys. Rev. B* **1988**, *38* (16), 11337–11345.
248. Karpinski, J.; Rusiecki, S.; Kaldis, E.; et al. *Physica C* **1989**, *160* (5–6), 449–457.
249. Sato, K.; Kobayashi, S.; Nakashima, T. *Jpn. J. Appl. Phys.* **2012**, *51* (1), 010006.
250. Gao, L.; Xue, Y. Y.; Chen, F.; et al. *Phys. Rev. B* **1994**, *50* (6), 4260–4263.
251. Drozdov, A. P.; Erements, M. I.; Troyan, I. A.; et al. *Nature* **2015**, *525* (7567), 73–76.
252. Einaga, M.; Sakata, M.; Ishikawa, T.; et al. *Nat. Phys.* **2016**, *12* (9), 835–838.
253. Fukuda, M.; Yamada, I.; Murata, H.; et al. *Chem. Mater.* **2020**, *32*, 5016–5027.
254. Goodenough, J. B.; Kafalas, J. A. *J. Solid State Chem.* **1973**, *6*, 493–501.
255. Kafalas, J. A. *Nat. Bur. Stand. (U. S.) Spec. Publ.* **1972**, *364*, 287–293.
256. Salak, A. N.; Vyshatko, N. P.; Ferreira, V. M.; et al. *Mater. Res. Bull.* **2003**, *38*, 453–460.
257. Senn, M. S.; Chen, W.-T.; Saito, T.; et al. *Chem. Mater.* **2014**, *26*, 4832–4837.
258. Byeon, S.-H.; Lufaso, M. W.; Parise, J. B.; et al. *Chem. Mater.* **2003**, *15*, 3798–3804.
259. Vasala, S.; Cheng, J.-G.; Yamauchi, H.; et al. *Chem. Mater.* **2012**, *24*, 2764–2774.
260. Fujita, T.; Fukunaga, O.; Nakagawa, T.; Nomura, S.-I. *Mater. Res. Bull.* **1970**, *5*, 759–764.
261. Bither, T. A.; Gillson, J. L.; Young, H. S. *Inorg. Chem.* **1966**, *5* (9), 1559–1562.
262. Tarakina, N. V.; Tyutyunnik, A. P.; D'yachkova, T. V.; et al. *J. Struct. Chem.* **2003**, *44* (2), 252–255.
263. Tarakina, N. V.; Tyutyunnik, A. P.; Zubkov, V. G.; et al. *Solid State Sci.* **2003**, *5*, 459–463.
264. Young, A. P.; Schwartz, C. M. *Science* **1963**, *141* (3578), 348–349.
265. Huang, S.; Lai, X.; Zhu, F.; et al. *Phys. Status Solidi B* **2015**, *252* (10), 2215–2221.
266. Sleight, A. W. *Mater. Res. Bull.* **1973**, *8* (7), 863–866.

267. Panchal, V.; Garg, N.; Sharma, S. M. *J. Phys. Condens. Matter* **2006**, *18*, 3917–3929.
268. Grzechnik, A.; Crichton, W. A.; Hanfland, M.; Smaalen, S. V. *J. Phys. Condens. Matter* **2003**, *15*, 7261–7270.
269. Errandonea, D.; Kumar, R. S.; Ma, X.; Tu, C. *J. Solid State Chem.* **2008**, *181*, 355–364.
270. Shieh, S. R.; Ming, L. C.; Jayaraman, A. *J. Phys. Chem. Solid* **1996**, *57* (2), 205–209.
271. Errandonea, D.; Santamaria-Perez, D.; Achary, S. N.; et al. *J. Appl. Phys.* **2011**, *109*, 043510-1043510-5.
272. Errandonea, D.; Kumar, R. S.; Achary, S. N.; et al. *J. Appl. Phys.* **2012**, *111*, 053519-1-053519-10.
273. Titov, Y. A.; Sych, A. M.; Sokolov, A. N.; et al. *High Press. Res.* **2001**, *21* (3–4), 175–181.
274. Garg, A. B.; Errandonea, D.; Popescu, C.; et al. *Inorg. Chem.* **2017**, *56*, 5420–5430.
275. Range, K.-J.; Wildenauer, M.; Heyns, A. M. *Angew. Chem.* **1988**, *100* (7), 973–975.
276. Range, K.-J.; Wildenauer, M. *Z. Naturforsch. B* **1989**, *44*, 499–501.
277. Li, X.; Liu, L.; Xu, L.; et al. *High Press. Res.* **2019**, *39*, 1–9.
278. Retuerto, M.; Martínez-Lope, M. J.; García-Hernández, M.; Alonso, J. A. *J. Phys. Condens. Matter* **2009**, *21* (18), 186003-1-186003-6.
279. Li, M.-R.; Stephens, P. W.; Croft, M.; et al. *Chem. Mater.* **2018**, *30*, 4508–4514.
280. Takatsu, H.; Hernandez, O.; Yoshimune, W.; et al. *Phys. Rev. B* **2017**, *95*, 155105-1-155105-5.
281. Arévalo-López, A. M.; Senn, M. S.; Skedd, L.; Atfield, J. P. Z. *Anorg. Allg. Chem.* **2014**, *640* (6), 1164–1167.
282. Yamamoto, A.; Hashizume, D.; Aruga-Katori, H.; et al. *Chem. Mater.* **2010**, *22*, 5712–5717.
283. Kayser, P.; Injac, S.; Ranjbar, B.; et al. *Inorg. Chem.* **2017**, *56*, 9009–9018.
284. Rijssenbeek, J. T.; Saito, T.; Malo, S.; et al. *J. Am. Chem. Soc.* **2005**, *127* (2), 675–681.
285. Miyazaki, M.; Kadono, R.; Satoh, K. H.; et al. *Phys. Rev. B* **2010**, *82*, 094413-1-0.4413-11.
286. Hoffmann, R.; Hoppe, R.; Bauer, K.; Range, K.-J. *J. Less-Common Met.* **1990**, *161*, 279–293.
287. Kayser, P.; Injac, S.; Kennedy, B. J.; et al. *Dalton Trans.* **2017**, *46*, 2974–2980.
288. Jin, C.-Q.; Zhou, J.-S.; Goodenough, J. B.; et al. *Proc. Natl. Acad. Sci.* **2008**, *105* (20), 7115–7119.
289. Zhao, J. G.; Yang, L. X.; Yu, Y.; et al. *J. Solid State Chem.* **2007**, *180*, 2816–2823.
290. Hong, S.-T.; Sleight, A. W. *J. Solid State Chem.* **1997**, *128*, 251–255.
291. Longo, J. M.; Kafalas, J. A. *Mater. Res. Bull.* **1968**, *3* (8), 687–692.
292. Shirako, Y.; Satsukawa, H.; Wang, X. X.; et al. *Phys. Rev. B* **2011**, *83*, 174411-1-174411-7.
293. Kojitani, H.; Shirako, Y.; Akaogi, M. *Phys. Earth Planet. In.* **2007**, *165* (3–4), 127–134.
294. Cheng, J.-G.; Zhou, J.-S.; Goodenough, J. B. *Phys. Rev. B* **2010**, *81*, 134412-1-134412-6.
295. Kafalas, J. A.; Longo, J. M. *Mater. Res. Bull.* **1970**, *5*, 193–198.
296. Byeon, S.-H.; Lee, S.-S.; Parise, J. B.; et al. *Chem. Mater.* **2004**, *16*, 3697–3701.
297. Takeda, T.; Nagata, M.; Kobayashi, H.; et al. *J. Solid State Chem.* **1998**, *140*, 182–193.
298. Sinclair, A.; Rodgers, J. A.; Topping, C. V.; et al. *Angew. Chem. Int. Ed.* **2014**, *53*, 8343–8347.
299. Greatrex, R.; Hu, G.; Munro, D. C. *Mater. Res. Bull.* **1986**, *21*, 797–802.
300. Siegrist, T.; Larson, E. M.; Chamberland, B. L. *J. Alloys Compd.* **1994**, *210*, 13–17.
301. Chamberland, B. L.; Anderson, J. B. *J. Solid State Chem.* **1981**, *39*, 114–119.
302. Li, Y.; Cheng, J.-G.; Alonso, J. A.; et al. *Inorg. Chem.* **2017**, *56*, 8187–8194.
303. Kennedy, B. J.; Yamaura, K.; Takayama-Muromachi, E. *J. Phys. Chem. Solid* **2004**, *65*, 1065–1069.
304. Yamaura, K.; Takayama-Muromachi, E. *Phys. Rev. B* **2001**, *64*, 224424-1-224424-5.
305. Shirako, Y.; Kojitani, H.; Oganov, A. R.; et al. *Am. Mineral.* **2012**, *97*, 159–163.
306. Yamaura, K.; Shirako, Y.; Kojitani, H.; et al. *J. Am. Chem. Soc.* **2009**, *131* (7), 2722–2726.
307. Shirako, Y.; Kojitani, H.; Akaogi, M.; et al. *Phys. Chem. Miner.* **2009**, *36*, 455–462.
308. Yamaura, K.; Takayama-Muromachi, E. *Phys. C* **2006**, *445–448*, 54–56.
309. Yamaura, K.; Huang, Q.-Z.; Young, D. P.; Takayama-Muromachi, E. *Chem. Mater.* **2004**, *16*, 3424–3430.
310. Kurata, I.; Flores-Livas, J. A.; Sugimoto, H.; et al. *Phys. Rev. Mater.* **2020**, *5* (8), 015001, 2010.06556 (8 pages).
311. Hallas, A. M.; Sharma, A. Z.; Mauws, C.; et al. *npj Quant. Mater.* **2019**, *4*, 9-1–9-6.
312. Sleight, A. W.; Gillson, J. L. *Mater. Res. Bull.* **1971**, *6*, 781–784.
313. Yamada, I.; Ochi, M.; Mizumaki, M.; et al. *Inorg. Chem.* **2014**, *53* (14), 7089–7091.
314. Yamaura, K.; Huang, Q.-Z.; Moldovan, M.; et al. *Chem. Mater.* **2005**, *17*, 359–365.
315. Wang, X.; Guo, Y.-F.; Shi, Y.-G.; et al. *Inorg. Chem.* **2012**, *51*, 6868–6875.
316. Ohgushi, K.; Gotou, H.; Yagi, T.; Ueda, Y. *J. Physical Soc. Japan* **2006**, *75*, 023707-1-023707-3.
317. Wu, M.; Frank, C. E.; Han, Y.; et al. *Inorg. Chem.* **2019**, *58*, 10280–10286.
318. Shannon, R. D. *Inorg. Chem.* **1967**, *6* (8), 1474–1478.
319. Demazeau, G.; Omeran, I.; Pouchard, M. *Mater. Res. Bull.* **1976**, *11*, 1449–1452.
320. Sleight, A. W. *Mater. Res. Bull.* **1968**, *3*, 699–704.
321. Wang, Y.; Walker, D.; Chen, B.-H.; Scott, B. A. *J. Alloys Compd.* **1999**, *285*, 98–104.
322. Yi, W.; Matsushita, Y.; Tanaka, M.; Belik, A. A. *Inorg. Chem.* **2012**, *51*, 7650–7656.
323. Krämer, G.; Jansen, M. *J. Solid State Chem.* **1995**, *114*, 206–210.
324. Krämer, G.; Hägele, E.; Wagner, N.; Jansen, M. *Z. Anorg. Allg. Chem.* **1996**, *622*, 1027–1034.
325. Kim, S.-J.; Lemaux, S.; Demazeau, G.; et al. *J. Am. Chem. Soc.* **2001**, *123*, 10413–10414.
326. Shiro, K.; Yamada, I.; Ikeda, N.; et al. *Inorg. Chem.* **2013**, *52* (3), 1604–1609.
327. Chen, B.-H.; Walker, D. *J. Solid State Chem.* **1997**, *131*, 185–188.
328. Akizuki, Y.; Yamada, I.; Fujita, K.; et al. *Inorg. Chem.* **2013**, *52*, 13824–13826.
329. Karppinen, M.; Yamauchi, H. *Mater. Sci. Eng. R. Rep.* **1999**, *26* (3), 51–96.
330. Mukuda, H.; Shimizu, S.; Iyo, A.; Kitaoka, Y. *J. Physical Soc. Japan* **2012**, *81* (1), 011008.
331. Siegrist, T.; Zahurak, S. M.; Murphy, D. W.; Roth, R. S. *Nature* **1988**, *334* (6179), 231–232.
332. Hiroi, Z.; Kobayashi, N.; Takano, M. *Nature* **1994**, *371* (6493), 139–141.
333. Azuma, M.; Hiroi, Z.; Takano, M.; et al. *Phys. Rev. Lett.* **1994**, *73* (25), 3463–3466.
334. Azuma, M.; Yoshida, H.; Saito, T.; et al. *J. Am. Chem. Soc.* **2004**, *126* (26), 8244–8246.
335. Uehara, M.; Nagata, T.; Akimitsu, J.; et al. *J. Physical Soc. Japan* **1996**, *65* (9), 2764–2767.
336. Demazeau, G.; Parent, C.; Pouchard, M.; Hagenmuller, P. *Mater. Res. Bull.* **1972**, *7* (9), 913–920.
337. Yamanaka, T.; Nakamoto, Y.; Takei, F.; et al. *J. Appl. Phys.* **2016**, *119*, 075902-1-075902-12.
338. Li, M.-R.; Stephens, P. W.; Retuerto, M.; et al. *J. Am. Chem. Soc.* **2014**, *136*, 8508–8511.
339. Zuo, P.; Colin, C. V.; Klein, H.; et al. *Inorg. Chem.* **2017**, *56*, 8478–8489.

340. Shankar PN, R.; Orlandi, F.; Manuel, P.; et al. *Chem. Mater.* **2020**, *32*, 5641–5649.
341. Takayama-Muromachi, E.; Drezen, T.; Isobe, M.; et al. *J. Solid State Chem.* **2003**, *175*, 366–371.
342. Range, K.-J.; Atzesdorfer, A. *Z. Naturforsch.* **1993**, *48b*, 237–239.
343. Tarakina, N. V.; Tyutyunnik, A. P.; Zubkov, V. G.; et al. *Solid State Sci.* **2003**, *5* (7), 983–994.
344. Kim, S. W.; Tan, X.; Frank, C. E.; et al. *Inorg. Chem.* **2020**, *59*, 3579–3584.
345. Urushihara, D.; Asaka, T.; Fukuda, K.; Sakurai, H. *Acta Crystallogr. C* **2018**, *74*, 120–124.
346. Urushihara, D.; Asaka, T.; Fukuda, K.; Sakurai, H. *Phys. Rev. B* **2019**, *99*, 094104-1-094104-9.
347. Baud, G.; Besse, J.-P.; Chevalier, R.; Gasperin, M. *J. Solid State Chem.* **1981**, *38*, 186–191.
348. Errandonea, D. *Phys. Stat. Sol.* **2005**, *242* (14), R125–R127.
349. Errandonea, D.; Pellicer-Porres, J.; Manjón, F. J.; et al. *Phys. Status Solidi B* **2005**, *72*, 174106-1-174106-14.
350. Ruiz-Fuertes, J.; Friedrich, A.; Errandonea, D.; et al. *Phys. Rev. B* **2017**, *95*, 174105-1-174105-9.
351. Ruiz-Fuertes, J.; Friedrich, A.; Gomis, O.; et al. *Phys. Rev. B* **2015**, *91*, 104109-1-104109-7.
352. Ruiz-Fuertes, J.; López-Moreno, S.; Errandonea, D.; et al. *J. Appl. Phys.* **2010**, *107*, 083506-1-083506-10.
353. Ruiz-Fuertes, J.; Errandonea, D.; Lacomba-Perales, R.; et al. *Phys. Rev. B* **2010**, *81*, 224115-1-224115-10.
354. Titov, Y. A.; Sych, A. M.; Sokolov, A. N.; et al. *J. Alloys Compd.* **2000**, *311* (2), 252–255.
355. Brixner, L. H.; Sleight, A. W.; Foris, C. M. *J. Solid State Chem.* **1973**, *7*, 418–421.
356. Ohshima, E.; Kusaba, K.; Onodera, S.; Kikuchi, M. *J. Phys. Chem. Solid* **2002**, *63* (3), 419–423.
357. Range, K.-J.; Haase, H. *Acta Crystallogr. C* **1990**, *46*, 317–318.
358. Urushihara, D.; Asaka, T.; Fukuda, K.; Sakurai, H. *Inorg. Chem.* **2017**, *56*, 13007–13013.
359. Range, K.-J.; Hegenbart, W.; Heyns, A. M.; et al. *Z. Naturforsch.* **1990**, *45b*, 107–110.
360. Grenthe, C.; Sundberg, M.; Filonenko, V. P.; Zibrov, I. P. *J. Solid State Chem.* **2000**, *154*, 466–475.
361. Bramnik, K. G.; Ehrenberg, H.; Buhre, S.; Fuess, H. *Acta Crystallogr. B* **2005**, *61*, 246–249.
362. Ishida, K.; Ikeuchi, Y.; Tassel, C.; et al. *Inorganics* **2019**, *7*, 63-1–63-7.
363. Ikeuchi, Y.; Takatsu, H.; Tassel, C.; et al. *Inorg. Chem.* **2019**, *58*, 6790–6795.
364. Ikeuchi, Y.; Takatsu, H.; Tassel, C.; et al. *Angew. Chem. Int. Ed.* **2017**, *56*, 5770–5773.
365. McNally, G. M.; Arévalo-López, Á. M.; Kearins, P.; et al. *Chem. Mater.* **2017**, *29*, 8870–8874.
366. Retuerto, M.; Li, M.-R.; Stephens, P. W.; et al. *Chem. Mater.* **2015**, *27*, 4450–4458.
367. Mikhailova, D.; Ehrenberg, H.; Fuess, H. *J. Solid State Chem.* **2006**, *179*, 3672–3680.
368. Sleight, A. W.; Bither, T. A.; Bierstedt, P. E. *Solid State Commun.* **1969**, *7*, 299–300.
369. Jiao, Y. Y.; Cui, Q.; Shahi, P.; et al. *Phys. Rev. B* **2018**, *97*, 014426-1-014426-11.
370. Ming, L. C.; Jayaraman, A.; Shieh, S. R.; Kim, Y. H. *Phys. Rev. B* **1995**, *51* (18), 12100–12106.
371. Chen, W. T.; Mizumaki, M.; Seki, H.; et al. *Nat. Commun.* **2014**, *5*, 3909.
372. Matar, S. F.; Demazeau, G.; Ouaini, N. *Solid State Sci.* **2011**, *13* (7), 1396–1400.
373. Shi, Y.-G.; Guo, Y.-F.; Yu, S.; et al. *J. Solid State Chem.* **2010**, *183*, 402–407.
374. Yuan, Y.; Feng, H. L.; Ghimire, M. P.; et al. *Inorg. Chem.* **2015**, *54*, 3422–3431.
375. Chen, J.; Feng, H. L.; Matsushita, Y.; et al. *Inorg. Chem.* **2020**, *59*, 4049–4057.
376. Feng, H. L.; Shi, Y.-G.; Guo, Y.-F.; et al. *J. Solid State Chem.* **2013**, *201*, 186–190.
377. Feng, H. L.; Calder, S.; Ghimire, M. P.; et al. *Phys. Rev. B* **2016**, *94* (23), 235158.
378. Ohgushi, K.; Yamaura, J.-I.; Ichihara, M.; et al. *Phys. Rev. B* **2011**, *83*, 125103-1-125103-6.
379. Wang, X.; Liu, M.; Shen, X.; et al. *Inorg. Chem.* **2019**, *58*, 320–326.
380. Yuan, Y.; Feng, H. L.; Shi, Y.-G.; et al. *Sci. Technol. Adv. Mater.* **2014**, *15*, 064901-1-064901-8.
381. Katrych, S.; Gu, Q. F.; Bukowski, Z.; et al. *J. Solid State Chem.* **2009**, *182*, 428–434.
382. Shi, Y.-G.; Guo, Y.-F.; Wang, X.; et al. *Nat. Mater.* **2013**, *12*, 1024–1027.
383. Crichton, W. A.; Yusenko, K. V.; Riva, S.; et al. *Inorg. Chem.* **2016**, *55* (12), 5738–5740.
384. Shi, Y.-G.; Guo, Y.-F.; Yu, S.; et al. *Phys. Rev. B* **2009**, *80*, 161104-1-161104-4.
385. Feng, H. L.; Sathish, C. I.; Li, J.; et al. *Phys. Procedia* **2013**, *45*, 117–120.
386. Zhao, Q.; Liu, M.; Dai, J.-H.; et al. *Inorg. Chem.* **2016**, *55*, 9816–9821.
387. Li, J.; Wang, X.; Wang, H.; et al. *J. Appl. Phys.* **2017**, *122*, 103905-1-103905-8.
388. Chen, J.; Feng, H. L.; Matsushita, Y.; et al. *J. Solid State Chem.* **2019**, *272*, 182–188.
389. Deng, H.-S.; Liu, M.; Dai, J.-H.; et al. *Phys. Rev. B* **2016**, *94*, 024414-1-024414-8.
390. Vasala, S.; Yamauchi, H.; Karpinen, M. *J. Solid State Chem.* **2014**, *220*, 28–31.
391. Demazeau, G.; Jung, D. Y.; Largeteau, A.; Choy, J. H. *Rev. High Press. Sci. Technol.* **1998**, *7*, 1025–1027.
392. Demazeau, G.; Jung, D. Y.; Largeteau, A.; et al. *J. Alloys Compd.* **1997**, *262–263*, 191–193.
393. Choy, J.-H.; Kim, D.-K.; Hwang, S.-H.; et al. *J. Am. Chem. Soc.* **1995**, *117*, 8557–8566.
394. Jung, D.-Y.; Demazeau, G. *J. Solid State Chem.* **1995**, *115*, 447–455.
395. Zhao, Q.; Yin, Y.-Y.; Dai, J.-H.; et al. *Chin. Phys. B* **2016**, *25* (2), 020701-1-020701-6.
396. Gao, L.; Wang, X.; Ye, X.; et al. *Inorg. Chem.* **2019**, *58*, 15529–15535.
397. Shi, Y.-G.; Guo, Y.-F.; Shirako, Y.; et al. *J. Am. Chem. Soc.* **2013**, *135* (44), 16507–16516.
398. Feng, H. L.; Tsujimoto, Y.; Guo, Y.-F.; et al. *High Press. Res.* **2013**, *33* (1), 221–228.
399. Bremholm, M.; Dutton, S. E.; Stephens, P. W.; Cava, R. J. *J. Solid State Chem.* **2011**, *184* (3), 601–607.
400. Zhao, J. G.; Yang, L. X.; Yu, Y.; et al. *J. Solid State Chem.* **2009**, *182*, 327–330.
401. Dos Santos-García, A. J.; van Duijn, J.; Saéz-Puche, R.; et al. *J. Solid State Chem.* **2008**, *181* (5), 1167–1175.
402. Dey, T.; Mahajan, A. V.; Kumar, R.; et al. *Phys. Rev. B* **2013**, *88*, 134425-1-134425-5.
403. Cheng, J.-G.; Ishii, T.; Kojitani, H.; et al. *Phys. Rev. B* **2013**, *88*, 205114-1-205114-7.
404. Cheng, J.-G.; Alonso, J. A.; Suard, E.; et al. *J. Am. Chem. Soc.* **2009**, *131* (21), 7461–7469.
405. Zhao, J.-G.; Yang, L.-X.; Yu, Y.; et al. *Inorg. Chem.* **2009**, *48* (10), 4290–4294.
406. Cui, Q.; Cheng, J.-G.; Fan, W.; et al. *Phys. Rev. Lett.* **2016**, *117*, 176603-1-176603-6.
407. Zhao, J.-G.; Yang, L.-X.; Yu, Y.; et al. *J. Appl. Phys.* **2008**, *103*, 103706-1-103706-5.
408. Chamberland, B. L.; Philpotts, A. R. *J. Alloys Compd.* **1992**, *182*, 355–364.
409. Longo, J. M.; Kafalas, J. A.; Arnott, R. J. *J. Solid State Chem.* **1971**, *3*, 174–179.
410. Okabe, H.; Isobe, M.; Takayama-Muromachi, E.; et al. *Phys. Rev. B* **2011**, *83*, 155118-1-155118-8.
411. Cheng, J. G.; Zhou, J. S.; Yang, Y. F.; et al. *Phys. Rev. Lett.* **2013**, *111* (17), 176403.
412. Li, M.-R.; Retuerto, M.; Deng, Z.; et al. *Chem. Mater.* **2015**, *27*, 211–217.

413. Ohgushi, K.; Matsushita, Y.; Miyajima, N.; et al. *Phys. Chem. Miner.* **2008**, *35*, 189–195.
414. Inaguma, Y.; Hasumi, K.-I.; Yoshida, M.; et al. *Inorg. Chem.* **2008**, *47* (6), 1868–1870.
415. Yamada, I.; Takahashi, Y.; Ohgushi, K.; et al. *Inorg. Chem.* **2010**, *49*, 6778–6780.
416. Ochi, M.; Yamada, I.; Ohgushi, K.; et al. *Inorg. Chem.* **2013**, *52*, 3985–3989.
417. Cui, Q.; Cai, Y.-Q.; Li, X.; et al. *Chin. Phys. B* **2020**, *29*, 047502-1-047502-5.
418. Hoekstra, H. R.; Gallagher, F. *Inorg. Chem.* **1968**, *7* (12), 2553–2557.
419. Park, J.-H.; Parise, J. B. *Chem. Mater.* **1995**, *7*, 1055–1056.
420. Steiner, C.; Andratschke, M.; Range, K.-J. *Z. Naturforsch.* **1996**, *51b*, 811–816.
421. Zhang, H.; Yan, X.; Zhang, X.; et al. *ACS Nano* **2019**, *13* (1), 609–615.
422. Du, Y.; Wan, X. *Comput. Mater. Sci.* **2016**, *112*, 416–427.
423. Kondo, T.; Nakayama, M.; Chen, R.; et al. *Nat. Commun.* **2015**, *6*, 10042.
424. Singleton, J.; Kim, J. W.; Topping, C. V.; et al. *Phys. Rev. B* **2016**, *94* (22), 224408.
425. Feng, H. L.; Adler, P.; Reehuis, M.; et al. *Chem. Mater.* **2017**, *29* (2), 886–895.
426. Kim, B.; Liu, P.; Ergönenc, Z.; et al. *Phys. Rev. B* **2016**, *94* (24), 241113.
427. Hiroi, Z.; Yamaura, J.; Hirose, T.; et al. *APL Mater.* **2015**, *3* (4), 041501.
428. Vecchio, I. L.; Perucchi, A.; Di Pietro, P.; et al. *Sci. Rep.* **2013**, *3* (1), 2990.
429. Calder, S.; Garlea, V. O.; McMorrow, D. F.; et al. *Phys. Rev. Lett.* **2012**, *108* (25), 257209.
430. Calder, S.; Lee, J. H.; Stone, M. B.; et al. *Nat. Commun.* **2015**, *6* (1), 8916.
431. Blaha, P.; Schwarz, K.; Tran, F.; et al. *J. Chem. Phys.* **2020**, *152* (7), 074101.
432. Shim, S.-H.; Bengtson, A.; Morgan, D.; et al. *Proc. Natl. Acad. Sci.* **2009**, *106* (14), 5508.
433. Betz, T.; Hoppe, R. *Z. Anorg. Allg. Chem.* **1985**, *524* (5), 17–25.
434. Mogare, K. M.; Klein, W.; Schilder, H.; et al. *Z. Anorg. Allg. Chem.* **2006**, *632* (15), 2389–2394.
435. Vale, J. G.; Calder, S.; Donnerer, C.; et al. *Phys. Rev. Lett.* **2018**, *120* (22), 227203.
436. Matsuhira, K.; Wakeshima, M.; Nakanishi, R.; et al. *J. Physical Soc. Japan* **2007**, *76* (4), 043706.
437. Dwivedi, V. K.; Mukhopadhyay, S. *AIP Conf. Proc.* **2018**, *1953* (1), 120002.
438. Yamaura, J.; Ohgushi, K.; Ohsumi, H.; et al. *Phys. Rev. Lett.* **2012**, *108* (24), 247205.
439. Anderson, P. W.; Blount, E. I. *Phys. Rev. Lett.* **1965**, *14* (7), 217–219.
440. Zhou, W. X.; Ariando, A. *Jpn. J. Appl. Phys.* **2020**, *59* (S1), S10802.
441. Puggioni, D.; Giovannetti, G.; Rondinelli, J. M. *J. Appl. Phys.* **2018**, *124* (17), 174102.
442. Treiber, U.; Kemmler-Sack, S. *ZAAC—J. Inorg. Gen. Chem.* **1980**, *470* (1), 95–102.
443. Deschanvres, A.; Raveau, B.; Tollemer, F. *Bull. Soc. Chim. Fr.* **1967**, (11), 4077–4078.
444. Volkov, V. L.; Kadyrova, N. I.; Zakharova, G. S.; et al. *Russ. J. Inorg. Chem.* **2007**, *52* (3), 329–333.
445. Subramanian, M. A.; Marshall, W. J.; Calvarese, T. G.; Sleight, A. W. *J. Phys. Chem. Solid* **2003**, *64* (9–10), 1569–1571.
446. Chenavas, J.; Joubert, J. C.; Marezio, M.; Bochu, B. *J. Solid State Chem.* **1975**, *14* (1), 25–32.
447. Yamada, I.; Takata, K.; Hayashi, N.; et al. *Angew. Chem. Int. Ed.* **2008**, *47* (37), 7032–7035.
448. Yamada, I.; Ishiwata, S.; Terasaki, I.; et al. *Chem. Mater.* **2010**, *22* (18), 5328–5332.
449. Ozaki, Y.; Ghedira, M.; Chenavas, J.; et al. *Acta Crystallogr. B Struct. Crystallogr. Cryst. Chem.* **1977**, *33* (11), 3615–3617.
450. Labeau, M.; Bochu, B.; Joubert, J. C.; Chenavas, J. *J. Solid State Chem.* **1980**, *33* (2), 257–261.
451. Shiraki, H.; Saito, T.; Yamada, T.; et al. *Phys. Rev. B* **2007**, *76* (14), 140403.
452. Ovsyannikov, S. V.; Zainulin, Y. G.; Kadyrova, N. I.; et al. *Inorg. Chem.* **2013**, *52* (20), 11703–11710.
453. Marezio, M.; Dernier, P. D.; Chenavas, J.; Joubert, J. C. *J. Solid State Chem.* **1973**, *6* (1), 16–20.
454. Bochu, B.; Buevoz, J. L.; Chenavas, J.; et al. *Solid State Commun.* **1980**, *36* (2), 133–138.
455. Gautam, K.; Shukla, D. K.; Francoual, S.; et al. *Phys. Rev. B* **2017**, *95* (14), 144112.
456. Bochu, B.; Chenavas, J.; Joubert, J. C.; Marezio, M. *J. Solid State Chem.* **1974**, *11* (2), 88–93.
457. Imamura, N.; Karpinen, M.; Motohashi, T.; et al. *J. Am. Chem. Soc.* **2008**, *130* (45), 14948–14949.
458. Chen, W.-T.; Wang, C.-W.; Wu, H.-C.; et al. *Phys. Rev. B* **2018**, *97* (14), 144102.
459. Ovsyannikov, S. V.; Abakumov, A. M.; Tsirlin, A. A.; et al. *Angew. Chem. Int. Ed. Engl.* **2013**, *52* (5), 1494–1498.
460. Akizuki, Y.; Yamada, I.; Fujita, K.; et al. *Angew. Chem. Int. Ed. Engl.* **2015**, *54* (37), 10870–10874.
461. Long, Y. W.; Hayashi, N.; Saito, T.; et al. *Nature* **2009**, *458* (7234), 60–63.
462. Yamada, I.; Etani, H.; Tsuchida, K.; et al. *Inorg. Chem.* **2013**, *52* (23), 13751–13761.
463. Etani, H.; Yamada, I.; Ohgushi, K.; et al. *J. Am. Chem. Soc.* **2013**, *135* (16), 6100–6106.
464. Yamada, I.; Etani, H.; Murakami, M.; et al. *Inorg. Chem.* **2014**, *53* (21), 11794–11801.
465. Yamada, I.; Tsuchida, K.; Ohgushi, K.; et al. *Angew. Chem. Int. Ed. Engl.* **2011**, *50* (29), 6579–6582.
466. Yamada, I.; Takamatsu, A.; Hayashi, N.; Ikeno, H. *Inorg. Chem.* **2017**, *56*, 9303–9310.
467. Byeon, S.-H.; Lee, S.-S.; Parise, J. B.; et al. *Chem. Mater.* **2005**, *17* (13), 3552–3557.
468. Chen, W. T.; Mizumaki, M.; Saito, T.; Shimakawa, Y. *Dalton Trans.* **2013**, *42* (28), 10116–10120.
469. Shimura, G.; Niwa, K.; Shirako, Y.; et al. *Solid State Commun.* **2016**, *234*, 40–44.
470. Long, Y.; Saito, T.; Mizumaki, M.; et al. *J. Am. Chem. Soc.* **2009**, *131* (44), 16244–16247.
471. Zhang, S.; Saito, T.; Mizumaki, M.; et al. *J. Am. Chem. Soc.* **2013**, *135* (16), 6056–6060.
472. Zhang, S.; Saito, T.; Mizumaki, M.; Shimakawa, Y. *Chem. A Eur. J.* **2014**, *20* (31), 9510–9513.
473. Etter, M.; Isobe, M.; Sakurai, H.; et al. *Phys. Rev. B* **2018**, *97* (19), 195111.
474. Alonso, J. A.; Sánchez-Benitez, J.; De Andrés, A.; et al. *Appl. Phys. Lett.* **2003**, *83* (13), 2623–2625.
475. Takata, K.; Yamada, I.; Azuma, M.; et al. *Phys. Rev. B* **2007**, *76* (2), 024429.
476. Zhao, J.; Gao, J.; Li, W.; et al. *Nat. Commun.* **2021**, *12* (1), 747.
477. Momma, K.; Izumi, F. *J. Appl. Cryst.* **2011**, *44* (6), 1272–1276.
478. Prodi, A.; Gilioli, E.; Gauzzi, A.; et al. *Nat. Mater.* **2004**, *3* (1), 48–52.
479. Belik, A. A.; Matsushita, Y.; Kumagai, Y.; et al. *Inorg. Chem.* **2017**, *56* (20), 12272–12281.
480. Prodi, A.; Gilioli, E.; Cabassi, R.; et al. *Phys. Rev. B* **2009**, *79* (8), 085105.
481. Sanchez-Benitez, J.; Alonso, J. A.; Martinez-Lope, M. J.; et al. *Inorg. Chem.* **2010**, *49* (12), 5679–5685.
482. Larregola, S. A.; Zhou, J.; Alonso, J. A.; et al. *Inorg. Chem.* **2014**, *53* (9), 4281–4283.
483. Collomb, A.; Samaras, D.; Bochu, B.; et al. *Physica B+ C* **1977**, *86–88*, 927–928.
484. Bochu, B.; Deschizeaux, M. N.; Joubert, J. C.; et al. *J. Solid State Chem.* **1979**, *29* (2), 291–298.
485. Ramirez, A. P.; Subramanian, M. A.; Gardel, M.; et al. *Solid State Commun.* **2000**, *115* (5), 217–220.

486. Homes, C. C.; Vogt, T.; Shapiro, S. M.; et al. *Science* **2001**, *293* (5530), 673–676.
487. Cohen, M. H.; Neaton, J. B.; He, L.; Vanderbilt, D. *J. Appl. Phys.* **2003**, *94* (5), 3299–3306.
488. Lunkenheimer, P.; Fichtl, R.; Ebbinghaus, S. G.; Loidl, A. *Phys. Rev. B* **2004**, *70* (17), 172102.
489. Zeng, Z.; Greenblatt, M.; Subramanian, M. A.; Croft, M. *Phys. Rev. Lett.* **1999**, *82* (15), 3164–3167.
490. Liu, X.-J.; Xiang, H.-P.; Cai, P.; et al. *J. Mater. Chem.* **2006**, *16* (43), 4243–4248.
491. Kobayashi, K. L.; Kimura, T.; Sawada, H.; et al. *Nature* **1998**, *395* (6703), 677–680.
492. Kobayashi, W.; Terasaki, I.; Takeya, J.-I.; et al. *J. Physical Soc. Japan* **2004**, *73* (9), 2373–2376.
493. Kim, Y. J.; Wakimoto, S.; Shapiro, S. M.; et al. *Solid State Commun.* **2002**, *121* (11), 625–629.
494. Tohyama, T.; Saito, T.; Mizumaki, M.; et al. *Inorg. Chem.* **2010**, *49* (5), 2492–2495.
495. Saito, T.; Tohyama, T.; Woodward, P. M.; Shimakawa, Y. *Bull. Chem. Soc. Jpn.* **2011**, *84* (7), 802–806.
496. Toyoda, M.; Saito, T.; Yamauchi, K.; et al. *Phys. Rev. B* **2015**, *92* (1), 014420.
497. Yamada, I.; Murakami, M.; Hayashi, N.; Mori, S. *Inorg. Chem.* **2016**, *55* (4), 1715–1719.
498. Yamada, I.; Shiro, K.; Etani, H.; et al. *Inorg. Chem.* **2014**, *53* (19), 10563–10569.
499. Brown, I. D. *Chem. Rev.* **2009**, *109* (12), 6858–6919.
500. Uchimura, T.; Yamada, I. *Chem. Commun. (Camb.)* **2020**, *56* (41), 5500–5503.
501. Chandrashekar, G. V.; Barros, H. L. C.; Honig, J. M. *Mater. Res. Bull.* **1973**, *8* (4), 369–374.
502. Wang, X.; Chai, Y.; Zhou, L.; et al. *Phys. Rev. Lett.* **2015**, *115* (8), 087601.
503. Zhou, L.; Dai, J.; Chai, Y.; et al. *Adv. Mater.* **2017**, *29* (44), 1703435.
504. Cong, J.; Zhai, K.; Chai, Y.; et al. *Nat. Commun.* **2018**, *9* (1), 2996.
505. Terada, N.; Glazkova, Y. S.; Belik, A. A. *Phys. Rev. B* **2016**, *93* (15), 155127.
506. Johnson, R. D.; Khalyavin, D. D.; Manuel, P.; et al. *Phys. Rev. B* **2016**, *93* (18), 180403(R).
507. Mezzadri, F.; Buzzi, M.; Pernechele, C.; et al. *Chem. Mater.* **2011**, *23* (16), 3628–3635.
508. Khalyavin, D. D.; Johnson, R. D.; Orlandi, F.; et al. *Science* **2020**, *369* (6504), 680–684.
509. Yagi, S.; Yamada, I.; Tsukasaki, H.; et al. *Nat. Commun.* **2015**, *6*, 8249.
510. Yamada, I.; Fujii, H.; Takamatsu, A.; et al. *Adv. Mater.* **2017**, *29* (4), 1603004.
511. Yamada, I.; Takamatsu, A.; Asai, K.; et al. *ACS Appl. Energy Mater.* **2018**, *1* (8), 3711–3721.
512. Takamatsu, A.; Yamada, I.; Yagi, S.; Ikeno, H. *J. Phys. Chem. C* **2017**, *121* (51), 28403–28411.
513. Yao, N.; Navrotsky, A.; Leinenweber, K. *J. Solid State Chem.* **1996**, *123* (1), 73–82.
514. Reiff, W. M.; Leinenweber, K.; Parise, J. *MRS Online Proceedings Library* **1996**, *453*, 387–392. <https://doi.org/10.1557/PROC-453-387>.
515. Li, H.; Liu, S.; Chen, L. et al. *Physica E* **2015**, *69*, 133–137.
516. Li, X.; Xu, W. M.; McGuire, M. A.; et al. *Phys. Rev. B* **2018**, *98* (6), 064201.
517. Andryushin, N. D.; Zinenko, V. I.; Pavlovskii, M. S.; Shinkorenko, A. S. *J. Exp. Theor. Phys.* **2020**, *129* (6), 1036–1044.
518. Shimura, G.; Niwa, K.; Shirako, Y.; Hasegawa, M. *Eur. J. Inorg. Chem.* **2017**, *2017* (4), 835–839.
519. Belik, A. A.; Khalyavin, D. D.; Zhang, L.; et al. *Chemphyschem* **2018**, *19* (19), 2449–2452.
520. Liu, R.; Khalyavin, D. D.; Tsunoda, N.; et al. *Inorg. Chem.* **2019**, *58* (21), 14830–14841.
521. Belik, A. A.; Zhang, L.; Liu, R.; et al. *Inorg. Chem.* **2019**, *58* (5), 3492–3501.
522. Vibhakar, A. M.; Khalyavin, D. D.; Manuel, P.; et al. *Phys. Rev. B* **2020**, *102* (21), 214428.
523. Liu, R.; Scatena, R.; Khalyavin, D. D.; et al. *Inorg. Chem.* **2020**, *59* (13), 9065–9076.
524. Liu, R.; Tanaka, M.; Mori, H.; et al. *J. Mater. Chem. C* **2021**, *9* (3), 947–956.
525. Aimi, A.; Mori, D.; Hiraki, K.-I.; et al. *Chem. Mater.* **2014**, *26* (8), 2601–2608.
526. Ruiz-Fuertes, J.; Bernert, T.; Zimmer, D.; et al. *Phys. Rev. B* **2017**, *96* (9), 094101.
527. Gou, G.; Charles, N.; Shi, J.; Rondinelli, J. M. *Inorg. Chem.* **2017**, *56* (19), 11854–11861.
528. Herrero-Martín, J.; Ruiz-Fuertes, J.; Bernert, T.; et al. *Phys. Rev. B* **2018**, *97* (23), 235129.
529. Antonov, V. N.; Kukusta, D. A.; Moklyak, S. V.; et al. *Phys. Rev. B* **2020**, *101* (5), 054441.
530. Fukuda, M.; Nishikubo, T.; Pan, Z.; et al. *Inorg. Chem.* **2020**, *59* (16), 11749–11756.
531. Solana-Madruga, E.; Arevalo-Lopez, A. M.; Dos Santos-Garcia, A. J.; et al. *Angew. Chem. Int. Ed. Engl.* **2016**, *55* (32), 9340–9344.
532. Solana-Madruga, E.; Arévalo-López, Á. M.; Dos Santos-García, A. J.; et al. *Phys. Rev. B* **2018**, *97* (13), 134408.
533. Solana-Madruga, E.; Sun, Y.; Arevalo-Lopez, A. M.; Attfield, J. P. *Chem. Commun. (Camb.)* **2019**, *55* (18), 2605–2608.
534. Zhang, L.; Matsushita, Y.; Yamaura, K.; Belik, A. A. *Inorg. Chem.* **2017**, *56* (9), 5210–5218.
535. Vibhakar, A. M.; Khalyavin, D. D.; Manuel, P.; et al. *Phys. Rev. B* **2019**, *99* (10), 104424.
536. Belik, A. A.; Zhang, L.; Matsushita, Y.; et al. *J. Solid State Chem.* **2019**, *275*, 43–48.
537. Vibhakar, A. M.; Khalyavin, D. D.; Manuel, P.; et al. *Phys. Rev. Lett.* **2020**, *124* (12), 127201.
538. Ji, K.; Alharbi, K. N.; Solana-Madruga, E.; et al. *Angew. Chem. Int. Ed. Engl.* **2021**, *60* (41), 22248–22252.
539. Kearns, P.; Solana-Madruga, E.; Ji, K.; et al. *J. Phys. Chem. C* **2021**, *125* (17), 9550–9555.
540. Solana-Madruga, E.; Kearns, P. S.; Alharbi, K. N.; et al. *Phys. Rev. Mater.* **2021**, *5* (5), 054412.
541. Belik, A. A. *Dalton Trans.* **2018**, *47* (10), 3209–3217.
542. Li, Z.; Cho, Y.; Li, X.; et al. *J. Am. Chem. Soc.* **2018**, *140* (6), 2214–2220.
543. Endo, T.; Kobayashi, T.; Sato, T.; Shimada, M. *J. Mater. Sci.* **1990**, *25* (1b), 619–623.
544. Inaguma, Y.; Sugimoto, K.; Ueda, K. *Dalton Trans.* **2020**, *49* (21), 6957–6963.
545. Takeiri, F.; Yamamoto, T.; Hayashi, N.; et al. *Inorg. Chem.* **2018**, *57* (11), 6686–6691.
546. Su, Y.; Tsujimoto, Y.; Matsushita, Y.; et al. *Inorg. Chem.* **2016**, *55* (5), 2627–2633.
547. Tsujimoto, Y.; Yamaura, K.; Uchikoshi, T. *Inorg. Chem.* **2013**, *52* (17), 10211–10216.
548. Chamberland, B. L.; Sleight, A. W. *Solid State Commun.* **1967**, *5* (9), 765–767.
549. Su, Y.; Tsujimoto, Y.; Miura, A.; et al. *Chem. Commun. (Camb.)* **2017**, *53* (27), 3826–3829.
550. Goto, Y.; Tassel, C.; Noda, Y.; et al. *Inorg. Chem.* **2017**, *56* (9), 4840–4845.
551. Takeiri, F.; Watanabe, A.; Kuwabara, A.; et al. *Inorg. Chem.* **2019**, *58* (7), 4431–4436.
552. Miyazaki, K.; Ochi, M.; Nishikubo, T.; et al. *Inorg. Chem.* **2021**, *60* (20), 15751–15758.
553. Yamamoto, T.; Shitara, K.; Kitagawa, S.; et al. *Chem. Mater.* **2018**, *30* (5), 1566–1574.
554. Bang, J.; Matsushita, S.; Hiraka, H.; et al. *J. Am. Chem. Soc.* **2014**, *136* (20), 7221–7224.
555. Tassel, C.; Goto, Y.; Kuno, Y.; et al. *Angew. Chem. Int. Ed. Engl.* **2014**, *53* (39), 10377–10380.
556. Tassel, C.; Goto, Y.; Watabe, D.; et al. *Angew. Chem. Int. Ed. Engl.* **2016**, *55* (33), 9667–9670.
557. Yang, M.; Rodgers, J. A.; Middler, L. C.; et al. *Inorg. Chem.* **2009**, *48* (24), 11498–11500.
558. Tassel, C.; Kuno, Y.; Goto, Y.; et al. *Angew. Chem. Int. Ed. Engl.* **2015**, *54* (2), 516–521.

559. Katsumata, T.; Ohba, C.; Tobe, A.; et al. *Chem. Lett.* **2018**, *47* (1), 37–39.
560. Kuno, Y.; Tassel, C.; Fujita, K.; et al. *J. Am. Chem. Soc.* **2016**, *138* (49), 15950–15955.
561. Kageyama, H.; Hayashi, K.; Maeda, K.; et al. *Nat. Commun.* **2018**, *9* (1), 772.
562. Harada, J. K.; Charles, N.; Poepelmeier, K. R.; Rondinelli, J. M. *Adv. Mater.* **2019**, *31* (19), e1805295.
563. Al-Mamouri, M.; Edwards, P. P.; Greaves, C.; Slaski, M. *Nature* **1994**, *369* (6479), 382–384.
564. Tsujimoto, Y.; Yamaura, K.; Takayama-Muromachi, E. *Appl. Sci.* **2012**, *2* (1), 206–219.
565. Tsujimoto, Y.; Sathish, C. I.; Hong, K. P.; et al. *Inorg. Chem.* **2012**, *51* (8), 4802–4809.
566. Tsujimoto, Y.; Nakano, S.; Ishimatsu, N.; et al. *Sci. Rep.* **2016**, *6*, 36253.
567. Knee, C. S.; Weller, M. T. *Chem. Commun.* **2002**, (3), 256–257.
568. McGlothlin, N.; Ho, D.; Cava, R. J. *Mater. Res. Bull.* **2000**, *35* (7), 1035–1043.
569. Kobayashi, Y.; Hernandez, O.; Tassel, C.; Kageyama, H. *Sci. Technol. Adv. Mater.* **2017**, *18* (1), 905–918.
570. Denis Romero, F.; Leach, A.; Moller, J. S.; et al. *Angew. Chem. Int. Ed. Engl.* **2014**, *53* (29), 7556–7559.
571. Yamamoto, T.; Zeng, D.; Kawakami, T.; et al. *Nat. Commun.* **2017**, *8* (1), 1217.
572. Yamamoto, T.; Morgan, H. W. T.; Zeng, D.; et al. *Inorg. Chem.* **2019**, *58* (22), 15393–15400.
573. Broux, T.; Ubukata, H.; Pickard, C. J.; et al. *J. Am. Chem. Soc.* **2019**, *141* (22), 8717–8720.
574. Yamashita, H.; Broux, T.; Kobayashi, Y.; et al. *J. Am. Chem. Soc.* **2018**, *140* (36), 11170–11173.
575. Hayward, M. A.; Cussen, E. J.; Claridge, J. B.; et al. *Science* **2002**, *295* (5561), 1882–1884.
576. Jin, L.; Lane, M.; Zeng, D.; et al. *Angew. Chem.* **2018**, *130* (18), 5119–5122.
577. Soignard, E.; Machon, D.; McMillan, P. F.; et al. *Chem. Mater.* **2005**, *17* (22), 5465–5472.